





TWENTY-FOURTH ANNUAL REPORT
OF THE
NATIONAL ADVISORY COMMITTEE
FOR AERONAUTICS

1938

INCLUDING TECHNICAL REPORTS
NOS. 612 TO 644



UNITED STATES
GOVERNMENT PRINTING OFFICE
WASHINGTON : 1939

TECHNICAL REPORTS

	Page		Page
No. 612. Heat-Transfer Processes in Air-Cooled Engine Cylinders. By Benjamin Pinkel, N. A. C. A.	49	No. 631. Airfoil Section Characteristics as Applied to the Prediction of Air Forces and Their Distribution on Wings. By Eastman N. Jacobs and R. V. Rhode, N. A. C. A.	357
No. 613. The Variation with Reynolds Number of Pressure Distribution over an Airfoil Section. By Robert M. Pinkerton, N. A. C. A.	65	No. 632. The Crinkling Strength and the Bending Strength of Round Aircraft Tubing. By William R. Osgood, National Bureau of Standards.	387
No. 614. Pressure Distribution over an N. A. C. A. 23012 Airfoil with an N. A. C. A. 23012 External-Airfoil Flap. By Carl J. Wenzinger, N. A. C. A.	85	No. 633. Pressure Distribution over an N. A. C. A. 23012 Airfoil with a Slotted and a Plain Flap. By Carl J. Wenzinger and James B. Delano, N. A. C. A.	403
No. 615. Column Strength of Tubes Elastically Restrained against Rotation at the Ends. By William R. Osgood, National Bureau of Standards.	101	No. 634. Calculation of the Chordwise Load Distribution over Airfoil Sections with Plain, Split, or Serially Hinged Trailing-Edge Flaps. By H. Julian Allen, N. A. C. A.	435
No. 616. Interrelation of Exhaust-Gas Constituents. By Harold C. Gerrish and Fred Voss, N. A. C. A.	139	No. 635. Theoretical Stability and Control Characteristics of Wings with Various Amounts of Taper and Twist. By Henry A. Pearson and Robert T. Jones, N. A. C. A.	451
No. 617. Auto-Ignition and Combustion of Diesel Fuel in a Constant-Volume Bomb. By Robert F. Selden, N. A. C. A.	147	No. 636. Approximate Stress Analysis of Multistringer Beams with Shear Deformation of the Flanges. By Paul Kuhn, N. A. C. A.	469
No. 618. Comparative Flight and Full-Scale Wind-Tunnel Measurements of the Maximum Lift of an Airplane. By Abe Silverstein, S. Katzoff, and James A. Hootman, N. A. C. A.	161	No. 637. Determination of Boundary-Layer Transition on Three Symmetrical Airfoils in the N. A. C. A. Full-Scale Wind Tunnel. By Abe Silverstein and John V. Becker, N. A. C. A.	491
No. 619. Drag of Cylinders of Simple Shapes. By W. F. Lindsey, N. A. C. A.	169	No. 638. The Influence of Lateral Stability on Disturbed Motions of an Airplane with Special Reference to the Motions Produced by Gusts. By Robert T. Jones, N. A. C. A.	507
No. 620. Pressure Distribution over Airfoils with Fowler Flaps. By Carl J. Wenzinger and Walter B. Anderson, N. A. C. A.	177	No. 639. The Effect of Compressibility on Eight Full-Scale Propellers Operating in the Take-Off and Climbing Range. By David Biermann and Edwin P. Hartman, N. A. C. A.	517
No. 621. Compressible Flow about Symmetrical Joukowski Profiles. By Carl Kaplan, N. A. C. A.	197	No. 640. The Aerodynamic Characteristics of Full-Scale Propellers Having 2, 3, and 4 Blades of Clark Y and R. A. F. 6 Airfoil Sections. By Edwin P. Hartman and David Biermann, N. A. C. A.	547
No. 622. A Photographic Study of Combustion and Knock in a Spark-Ignition Engine. By A. M. Rothrock and R. C. Spencer, N. A. C. A.	213	No. 641. The Negative Thrust and Torque of Several Full-Scale Propellers and Their Application to Various Flight Problems. By Edwin P. Hartman and David Biermann, N. A. C. A.	571
No. 623. A Study of the Torque Equilibrium of an Autogiro Rotor. By F. J. Bailey, Jr., N. A. C. A.	235	No. 642. Tests of Five Full-Scale Propellers in the Presence of a Radial and a Liquid-Cooled Engine Nacelle, Including Tests of Two Spinners. By David Biermann and Edwin P. Hartman, N. A. C. A.	589
No. 624. Two-Dimensional Subsonic Compressible Flow past Elliptic Cylinders. By Carl Kaplan, N. A. C. A.	245	No. 643. The Aerodynamic Characteristics of Four Full-Scale Propellers Having Different Plan Forms. By Edwin P. Hartman and David Biermann, N. A. C. A.	617
No. 625. A Discussion of Certain Problems Connected with the Design of Hulls of Flying Boats and the Use of General Test Data. By Walter S. Diehl, Bureau of Aeronautics, Navy Department.	253	No. 644. The Torsional and Bending Deflection of Full-Scale Aluminum-Alloy Propeller Blades under Normal Operating Conditions. By Edwin P. Hartman and David Biermann, N. A. C. A.	627
No. 626. The Transition Phase in the Take-Off of an Airplane. By J. W. Wetmore, N. A. C. A.	261		
No. 627. The experimental and Calculated Characteristics of 22 Tapered Wings. By Raymond F. Anderson, N. A. C. A.	273		
No. 628. Aerodynamic Characteristics of a Large Number of Airfoils Tested in the Variable-Density Wind Tunnel. By Robert M. Pinkerton and Harry Greenberg, N. A. C. A.	297		
No. 629. On Some Reciprocal Relations in the Theory of Nonstationary Flows. By I. E. Garrick, N. A. C. A.	347		
No. 630. A Flight Comparison of Conventional Ailerons on a Rectangular Wing and of Conventional and Floating Wing-Tip Ailerons on a Tapered Wing. By H. A. Soulé and W. Gracey, N. A. C. A.	351		

LETTER OF TRANSMITTAL

TO THE CONGRESS OF THE UNITED STATES:

In compliance with the provisions of the act of March 3, 1915, establishing the National Advisory Committee for Aeronautics, I transmit herewith the Twenty-fourth Annual Report of the Committee covering the fiscal year ended June 30, 1938.

FRANKLIN D. ROOSEVELT.

THE WHITE HOUSE,
January 9, 1939.

LETTER OF SUBMITTAL

NATIONAL ADVISORY COMMITTEE, FOR AERONAUTICS,
Washington, D. C., December 17, 1938.

MR. PRESIDENT:

In compliance with the provisions of the act of Congress approved March 3, 1915 (U. S. C., title 50, sec. 153), I have the honor to submit herewith the Twenty-fourth Annual Report of the National Advisory Committee for Aeronautics covering the fiscal year 1938.

The past year has been one of continued progress in the technical development of both military and commercial aircraft. In the light of world events, it has become increasingly important that American aircraft, both military and commercial, have the highest possible efficiency. In the development of air strength for national defense, and in the extension of commercial trade routes in the air, a definite advantage will lie with that nation that has the most efficient aircraft.

Up to the present, the United States has led in the technical development of aircraft. The major reason for that leadership has been the farsighted support of organized scientific research in the Committee's laboratories at Langley Field, Va. American leadership is now threatened by the great expansion of research facilities in other nations. The Committee is making an earnest study of the problem presented by this condition, and is determined to make every effort to provide the scientific data necessary to keep America first in the technical development of aircraft. This will undoubtedly require material expansion in research facilities to keep pace with the accelerated research progress abroad. Upon the completion of studies now in progress, a special report on this subject will be submitted.

Respectfully submitted.

JOSEPH S. AMES, *Chairman.*

THE PRESIDENT,
The White House, Washington, D. C.

NATIONAL ADVISORY COMMITTEE FOR AERONAUTICS

HEADQUARTERS, NAVY BUILDING, WASHINGTON, D. C.
LABORATORIES, LANGLEY FIELD, VA.

Created by act of Congress approved March 3, 1915, for the supervision and direction of the scientific study of the problems of flight (U. S. Code, Title 50, Sec. 151). Its membership was increased to 15 by act approved March 2, 1929. The members are appointed by the President, and serve as such without compensation.

- JOSEPH S. AMES, Ph. D., *Chairman*,
Baltimore, Md.

VANNEVAR BUSH, Sc. D., *Vice Chairman*,
Washington, D. C.

CHARLES G. ABBOT, Sc. D.,
Secretary, Smithsonian Institution.

HENRY H. ARNOLD, Major General, United States Army,
Chief of Air Corps, War Department.

GEORGE H. BRETT, Brigadier General, United States Army,
Chief Matériel Division, Air Corps, Wright Field, Dayton,
Ohio.

LYMAN J. BRIGGS, Ph. D.,
Director, National Bureau of Standards.

ARTHUR B. COOK, Rear Admiral, United States Navy,
Chief, Bureau of Aeronautics, Navy Department.
- CLINTON M. HESTER, A. B., LL. B.,
Administrator, Civil Aeronautics Authority.

JEROME C. HUNSAKER, Sc. D.,
Cambridge, Massachusetts.

SYDNEY M. KRAUS, Captain, United States Navy,
Bureau of Aeronautics, Navy Department.

CHARLES A. LINDBERGH, LL. D.,
New York City.

EDWARD J. NOBLE, A. B.,
Chairman, Civil Aeronautics Authority.

FRANCIS W. REICHELDERFER, A. B.,
Chief, United States Weather Bureau.

EDWARD P. WARNER, Sc. D.,
Greenwich, Conn.

ORVILLE WRIGHT, Sc. D.,
Dayton, Ohio.

GEORGE W. LEWIS, *Director of Aeronautical Research*
JOHN F. VICTORY, *Secretary*

HENRY J. E. REID, *Engineer-in-Charge, Langley Memorial Aeronautical Laboratory, Langley Field, Va.*
JOHN J. IDE, *Technical Assistant in Europe, Paris, France*

TECHNICAL COMMITTEES

- AERODYNAMICS

POWER PLANTS FOR AIRCRAFT

AIRCRAFT MATERIALS
- AIRCRAFT STRUCTURES

AIRCRAFT ACCIDENTS

INVENTIONS AND DESIGNS

Coordination of Research Needs of Military and Civil Aviation
Preparation of Research Programs
Allocation of Problems
Prevention of Duplication
Consideration of Inventions

LANGLEY MEMORIAL AERONAUTICAL LABORATORY

LANGLEY FIELD, VA.

OFFICE OF AERONAUTICAL INTELLIGENCE

WASHINGTON, D. C.

Unified conduct, for all agencies, of scientific research on the
fundamental problems of flight.

Collection, classification, compilation, and dissemination of
scientific and technical information on aeronautics.



NATIONAL ADVISORY COMMITTEE FOR AERONAUTICS.

MEETING, OCTOBER 20, 1938.

Left to right: Hon. C. M. Hester; Capt. S. M. Kraus, U. S. N.; Brig. Gen. A. W. Robins, U. S. A.; Dr. L. J. Briggs; Dr. E. P. Warner; Dr. Orville Wright; Dr. Joseph S. Ames, Chairman; Dr. C. G. Abbot; J. F. Victory, Secretary; Rear Adm. A. B. Cook, U. S. N.; Hon. E. J. Noble; Dr. Vannevar Bush; Dr. J. C. Hunsaker; Dr. G. W. Lewis, Director of Aeronautical Research; Capt. C. A. Lindbergh and Maj. Gen. H. H. Arnold, U. S. A. (One vacancy; U. S. Weather Bureau.)

TWENTY-FOURTH ANNUAL REPORT

OF THE

NATIONAL ADVISORY COMMITTEE FOR

AERONAUTICS

WASHINGTON, D. C., *November 15, 1938.*

TO THE CONGRESS OF THE UNITED STATES:

In accordance with the act of Congress approved March 3, 1915 (U. S. C., title 50, section 151), which established the National Advisory Committee for Aeronautics, the Committee submits herewith its Twenty-fourth Annual Report for the fiscal year 1938.

Overshadowing influence of air power.—The crisis in Europe in the fall of 1938 brought forcibly to world-wide attention the overshadowing influence of air power in international affairs. The realization that aircraft had been built in great numbers and developed to a point where they are capable of operating at high speeds over long distances with large bombing loads thrust upon the world a new concept of national defense. The imminent prospect of noncombatants being subject to indiscriminate attack by aircraft stirred the imaginations and fears of all peoples. The sudden and rather general appreciation of the potentialities of modern air power is the most significant event that has occurred in modern times in connection with strengthening the desires of peoples to avoid war.

The Committee in its annual report for 1924 discussed the increasing importance of aircraft in warfare in the light of the failure of the Limitations of Armaments Conference, held in Washington in 1921–22, to place any limitations upon the use of aircraft in warfare. The Committee at that time pointed out some of the appalling possibilities in the indiscriminate use of aircraft. These included not merely air attacks on recognized military objectives, but also attacks on civilian populations. Subsequent attempts by international conference to minimize the consequences to noncombatants have been without avail.

The Committee, therefore, in the interests of peace and security, recommends the development by the Army and Navy of adequate and effective air arms, and the early adoption of a sound program for expanding the productive capacity of the aircraft industry and for training the necessary active and reserve personnel.

Relation of aeronautical research to national defense.—

The history of 1938 bears witness as to how a nation in the space of a few years, by concentrating much of its scientific research and industrial resources, on the development of air power, could gain, for the time being, a dominating position. The continued effectiveness of an air arm, however large, is dependent on constant progress in the new engineering science of aeronautics. The efficiency of an air force is in approximately direct proportion to the emphasis that is placed on scientific research in aeronautics, combined of course with engineering development, production, and training.

What has happened during the past few years that has so greatly increased the relative importance of air power in the national defense programs of nations? Of first importance are the contributions of research laboratories which have so greatly extended the speed, range, and carrying capacity of aircraft. Methods of construction also have been improved. These have included a trend toward designs of aircraft that would permit of duplicating many of the parts by the use of machinery, and thus has an approach to mass production been made. Although the designs of military aircraft of the different categories and the manufacturing methods employed in the United States have not differed widely from those in Europe, nevertheless in Europe the larger quantities manufactured have accelerated progress toward mass production methods.

Once a nation has embarked upon a program intended to develop its air strength to maximum effectiveness, the provision of adequate laboratory research facilities and the training of skilled research personnel become of fundamental importance. The major European powers at the present time are engaged on relatively large aircraft building programs which are being prosecuted under feverish pressure. Mere numbers of aircraft, however, are not in themselves sufficient for an adequate modern air force. It is of even greater importance that the aircraft be of the most effective design. The advances in aeronautical science are so rapid that assiduous attention to the subject can-

not with safety be suspended for even a brief period. Where a few years ago we were pleased with speeds of around 200 miles per hour, we now seek to attain with fully loaded service airplanes speeds of 300 and 400 miles per hour. It is not only good policy from a financial consideration, but also vital from the standpoint of national defense, that American aircraft have a performance equal or superior to that of a potential enemy. This principle necessitates serious consideration of American aeronautical research and experimental facilities.

The President and the Congress of the United States have wisely supported what has heretofore been considered a liberal program of scientific research in aeronautics. This program for years was in advance of that of other nations, and the result was that American aircraft, civil and military, have for years had superior performance, efficiency, and safety. In the commercial field, where direct evidence is available, this is proved by the large number of American-built commercial airplanes used by foreign air lines.

During the past 4 years, however, there has been increasing emphasis on aeronautical research on the part of European powers. They have greatly developed and extended their research facilities. In the rapidly advancing science of aeronautics, research problems increase in number and in difficulty with every material advance in speed, and the importance of prompt solution becomes relatively greater. The Committee's laboratories at Langley Field, Va., are working under high pressure. The requirements of the Army, the Navy, and the Civil Aeronautics Authority for the immediate solution of pressing problems are being met. But they are met at the expense of interfering with or neglecting the more fundamental scientific long-range investigations that in the end mean much to the advancement of American aeronautics. The Committee, therefore, in October 1938, created a Special Committee on Future Research Facilities. It is expected that its recommendations will be made the subject of a special report to the Congress. In the meantime, the addition to the Committee's research facilities at Langley Field of a structures research laboratory is urgently needed, as herein-after set forth.

Relation of aeronautical research to commercial air transportation and to private flying.—Remarkable advances continue to be made in the field of commercial air transportation, and in this field the United States has for years held a recognized leadership. Although in private flying the progress has not been so rapid, the United States nevertheless has definitely excelled other nations in this field also. These gratifying conditions have been due to a combination of causes. The Civil Aeronautics Authority has provided indispensable assistance in the encouragement and regulation

of civil and commercial aviation. The American aircraft industry, with its highly trained technical personnel and excellent manufacturing facilities, has been keenly alert to improve the design and quality of aircraft. The air transport lines have shown commendable initiative and efficiency in operation and have done their utmost to eliminate accidents and the causes of accidents. The high efficiency and safety of American civil and commercial aircraft are in no small measure due to the fact that the results of the scientific investigations of the Committee are generally applicable to the design of civil and commercial aircraft as well as to military aircraft.

Although popular attention during the past year has been largely focused on the significance of military aircraft developments, farsighted and determined efforts are also being made by European nations to extend their commercial and political influence by establishing and extending world trade routes of the air. Service by air lines operating under the American flag to South America and across the Pacific will soon be augmented by regular trans-Atlantic service, and it is expected that there will be inaugurated during the coming year trans-Atlantic service to the Mediterranean area. The British have established a through service by air from England to the Straits Settlements, India, and Australia, with connection to Hong Kong. One significant development in Great Britain is the policy of carrying all first-class mail by airplane throughout the Empire wherever there is air service. This practice is gradually becoming general in European nations. The British, French, and Germans have made test flights preparatory to inaugurating North Atlantic air transport services. In addition, the French are preparing to establish a service across the South Atlantic. The Dutch air transport lines now extend from Holland to Australia. Japan is rapidly expanding its air lines in eastern Asia.

In the highly competitive field of international air transportation a definite advantage will lie with that nation that has the most efficient aircraft. Continued active support of scientific laboratory research will not only pay large dividends in this field, but is absolutely essential to success.

The use of private aircraft on a much larger scale in the United States would, of course, be desirable in that it would enlarge the productive capacity of the aircraft industry, create a reservoir of pilots constituting a distinct national asset in the event of war, and provide in effect a new industry in the United States with large opportunities for employment. The technical improvement of the instruments of air transportation will be reflected in lower operating costs and in increasing availability for public service. The Committee believes that civil aeronautics will in time prove

as revolutionary in the lives of the people as the automobile. To achieve such a contribution to the progress of civilization will require not merely sound economic promotional impetus, such as the good-roads movement gave to the development of the automobile, but it will definitely require the earnest and serious support of scientific research and encouragement of experimental engineering development that will put into useful form the results of laboratory research.

The Civil Aeronautics Act of 1938.—The Civil Aeronautics Act of 1938 superseded and largely repealed the Air Commerce Act of 1926. Briefly, it established a Civil Aeronautics Authority of five members and an Administrator, for the encouragement and regulation of civil and commercial aviation, and transferred to that organization the Bureau of Air Commerce of the Department of Commerce and the Bureau of Air Mail of the Interstate Commerce Commission. The act also established an Air Safety Board for the impartial and constructive investigation of aircraft accidents. The Civil Aeronautics Authority was by that act given representation on the National Advisory Committee for Aeronautics equal to that accorded by law to the Army and the Navy. In addition, therefore, to having two members on the main Committee, the Authority also has representation on the various technical subcommittees of the National Advisory Committee for Aeronautics on the same basis as the Army and the Navy.

In connection with the broad powers given the Authority by the act to encourage the development of civil and commercial aviation, the Authority, the Administrator, and the Air Safety Board are authorized to "avail themselves of the assistance of the National Advisory Committee for Aeronautics and any research or technical agency" of the Government. Those agencies are "authorized to conduct such scientific and technical researches, investigations, and tests as may be necessary to aid the Authority, the Administrator, and the Air Safety Board in the exercise and performance of their powers and duties." To assure continuance of the proven policy of coordination of the research needs of military and civil aviation and to prevent overlapping or duplication in this field, the Civil Aeronautics Act of 1938 further provided that "Nothing contained in this act shall be construed to authorize the duplication of the laboratory research activities of any existing governmental agency."

Responsibilities of the Committee.—The functions of the Committee as prescribed by its organic act are "to supervise and direct the scientific study of the problems of flight, with a view to their practical solution" and "to direct and conduct research and experiment in aeronautics."

To determine the present and future research needs

of aviation, civil and military, the Committee has established standing technical subcommittees on aerodynamics, power plants for aircraft, aircraft materials, and aircraft structures. The subcommittees are composed primarily of specially qualified representatives of the governmental agencies concerned. The members of the subcommittees, like the members of the main Committee, serve as such without compensation.

The subcommittees recommend research programs. Most of the problems recommended for investigation are assigned to the Committee's laboratory at Langley Field, Va. Some problems are assigned to the National Bureau of Standards, when it is to the advantage of the Government to do so in order effectively to utilize existing facilities and to avoid duplication. Problems are also assigned to universities and technical schools. This policy, the Committee believes, stimulates and coordinates aeronautical research, and also has the advantage of training research personnel.

The Committee regards it as its duty to recognize in advance the trend of aeronautical development, civil and military; to anticipate the research problems that will arise; to design and provide research equipment as needed to solve the problems; to conduct the more fundamental scientific investigations in its own laboratories; and then to transmit the results directly to the governmental agencies and to those units of the aircraft industry that are most concerned.

Research facilities.—With the consistent support of the President and of the Congress, the Committee has developed at Langley Field, Va., a large and well-equipped aeronautical research laboratory, known as the Langley Memorial Aeronautical Laboratory. The rapid advance in the relatively new engineering science of aeronautics has been made possible chiefly by the design and construction of novel research equipment as needed.

At the present time the laboratories of this Committee comprise the following units: The 8-foot 500-mile-per-hour wind tunnel; the full-scale wind tunnel with a throat 60 by 30 feet; the 20-foot propeller-research-tunnel; the 5-foot variable-density wind tunnel; a 7- by 10-foot wind tunnel; a 4- by 6-foot vertical wind tunnel; a 15-foot free-spinning wind tunnel; two high-velocity jet-type wind tunnels of 11- and 24-inch throat diameters, respectively; the 2,900-foot N. A. C. A. tank; an engine-research laboratory; a flight-research laboratory; and an instrument laboratory.

In a serious effort to be prepared to solve the fundamental problems as they arise, the Committee has recently constructed three new pieces of research equipment: A 19-foot pressure wind tunnel that will permit the investigation of the characteristics of large models under conditions much more nearly paralleling those of

free flight than can be obtained in any existing wind tunnel; a refrigerated wind tunnel with a throat $7\frac{1}{2}$ by 3 feet, for the investigation of problems of ice formation on aircraft; and a free-flight wind tunnel 12 feet in diameter, for studying stability and control characteristics of airplanes. The Committee has also constructed an additional shop building in which to prepare models for test in the full-scale wind tunnel and in the 19-foot pressure tunnel.

The Committee has under construction a two-dimensional flow wind tunnel, the purpose of which is to conduct investigations at higher values of Reynolds Number. The Committee has submitted estimates to modernize its 20-foot propeller-research tunnel constructed in 1927. At that time it was the largest wind tunnel in the world. It has been an exceedingly valuable piece of equipment, but the science has progressed to a point where much greater accuracy in research equipment is required. Hence the necessity for modernization. The Committee has also just completed modernizing its 7- by 10-foot wind tunnel and its 5-foot vertical wind tunnel.

Need for research on aircraft structures.—The Committee on Aircraft Structures urgently recommends that the main Committee provide at the earliest possible date a laboratory for research on aircraft structures. With the advance in size and speed of aircraft and the increasing complexity and efficiency of metal construction, the problems involved require the conduct of laboratory research on structures on an increasing scale. The main Committee, in approving the subcommittee's recommendation, came to the conclusion that this is the greatest single need for additional research equipment and that, in the interests of safety and of further progress in aeronautics, it should be provided at the earliest possible date.

Airships.—It is noted with satisfaction that approval has been given to the building of a rigid airship for naval uses as authorized by the Congress in June 1938.

Although the dimensions of this airship are to be small in comparison with the largest airships heretofore built, its construction will serve to keep alive the older of the two branches of aeronautical science. From a technical standpoint it is inadvisable that airships, which have contributed so much in the past and which those familiar with the status of their development believe can contribute much more of value in the future to aeronautics, should be allowed to stand idle while other branches of aeronautics are intensively developed.

There is reason to believe that the application of recent aerodynamic knowledge, improved materials, and modern engines can be combined to produce more efficient airships. It would be a mistake to regard the airship as a craft which has reached the zenith of its development.

Building even a small airship at this time is a favorable augury that the airship branch of aeronautics, neglected in this country during the past few years, may soon resume its appropriate place in the progress of aeronautical science.

Status of Committee in time of war.—The late Maj. Gen. Oscar Westover, Chief of the Army Air Corps, shortly before his death on September 21, 1938, had, as Chairman of a Special Committee on the Relation of the National Advisory Committee for Aeronautics to National Defense in Time of War, submitted a report on this subject. The report covered the need for maintaining the efficient functioning of the Committee's organization in time of war and recommended a plan, to go into effect upon the declaration of an emergency, whereby the Committee's organization will be stabilized and may be increased as necessary to meet the needs of the Army and the Navy. The recommendations in the Westover report were approved by the main Committee. Upon their approval by the Secretaries of War and of the Navy, the plan will become effective under the provisions of the National Defense Act of 1920 as amended.

PART I

REPORTS OF TECHNICAL COMMITTEES

In order to carry out effectively its principal function of the supervision, conduct, and coordination of the scientific study of the problems of aeronautics, the National Advisory Committee for Aeronautics has established a group of technical committees and subcommittees. These technical committees prepare and recommend to the main Committee programs of research to be conducted in their respective fields, and as a result of the nature of their organization, which includes representation of the various agencies concerned with aeronautics, they act as coordinating agencies, providing effectively for the interchange of information and ideas and the prevention of duplication.

In addition to its standing committees and subcommittees, it is the policy of the National Advisory Committee for Aeronautics to establish from time to time special technical subcommittees for the study of particular problems as they arise.

The Committee has four principal technical committees—the Committee on Aerodynamics, the Committee on Power Plants for Aircraft, the Committee on Aircraft Materials, and the Committee on Aircraft Structures. Under these committees there are six standing subcommittees. The membership of these technical committees and subcommittees is listed in Part II.

The Committees on Aerodynamics and Power Plants for Aircraft have direct control of the aerodynamic and aircraft-engine research, respectively, conducted at the Committee's laboratory at Langley Field, and of special investigations conducted at the National Bureau of Standards. Most of the research under the supervision of the Committee on Aircraft Materials is conducted by the National Bureau of Standards. A large part of the research under the cognizance of the Committee on Aircraft Structures is carried on by the National Bureau of Standards. In addition, a number of structural investigations, including in particular investigations of a theoretical nature, are conducted at the Committee's laboratory at Langley Field and at educational institutions.

The four technical committees recommend to the main Committee the investigations in their respective fields to be undertaken by educational institutions under contract with the National Advisory Committee for Aeronautics, and keep in touch with the progress of the work and the results obtained. The experimen-

tal investigations in aerodynamics, aircraft power plants, aircraft materials, and aircraft structures undertaken by the Army Air Corps, the Bureau of Aeronautics of the Navy, the National Bureau of Standards, and other Government agencies are reported to these four committees.

REPORT OF COMMITTEE ON AERODYNAMICS

LANGLEY MEMORIAL AERONAUTICAL LABORATORY

LANDING SPEED AND SPEED RANGE

Wing flaps are now universally used on high-performance airplanes. Although previous research conducted by the Committee has established the relative merits of the usual types of flap employed, it has become apparent that more specific design data for flap application are essential. This is particularly true of flaps that are used over only part of the span. In addition, it has seemed advisable to carry further the development of the flaps that show greatest promise of improvement in airplane performance, in particular the slotted-flap and the multiple-flap arrangements. The work of the Committee on high-lift devices during the past year has been directed towards these objectives.

In the 7- by 10-foot wind tunnel, an investigation for the further development of the slotted flap mentioned in the last annual report has been carried out. By careful attention to the shape of the slot and the flap position, it has been possible to develop a maximum lift coefficient of 2.8. With reasonably high lift coefficients, it was possible to obtain drag coefficients lower than those obtained with any other type of flap tested to date. The latter flap characteristics should result in improved take-off and climb characteristics. With the flap in the retracted position, the drag of the wing at high speed is not increased by the flap installation when a small auxiliary flap is used to close the gap formed by the slot on the lower surface. The results are being prepared for publication.

An investigation has been made in the 7- by 10-foot wind tunnel of a multiple-flap arrangement in which a slotted flap was combined with a smaller plain flap, a split flap, and a second slotted flap. The results indicate that the double slotted flap is the most promising. Further work is planned with flaps of larger chord and with airfoil sections other than the

N. A. C. A. 23012, which is the only airfoil thus far used in the investigation.

Tests have also been made in the 7- by 10-foot wind tunnel of a Clark Y wing having split flaps with a gap between the flap and the lower surface of the wing. The results, given in Technical Note No. 650, show that any gap between the flap and the wing reduced the lift, the drag, and the pitching moments, but that the center-of-pressure movement and the ratio of lift to drag were little affected.

The effects of partial-span plain flaps have been investigated on both rectangular and tapered wings. The Clark Y airfoils tested were equipped with center-section and with tip-section flaps. The results (Technical Note No. 663) showed that the aerodynamic characteristics of partial-span plain flaps were, in general, similar to those of split flaps of the same span but that the lift and the drag were less for the wing with plain flaps than for the wing with split flaps of comparable size.

The "venetian-blind" type of flap has recently been receiving some attention in Europe, and tests of several different arrangements of this device have been completed in the 7- by 10-foot tunnel. The results thus far obtained indicate that the venetian-blind flap functioned similarly to a split flap when its axis was located forward of the trailing edge of the wing a distance equal to the flap chord. When the flap axis was moved back to the wing trailing edge and the flap was deflected, it acted like a multiple slotted flap and high lifts were obtained, together with low drag. The maximum lift, for the same size of flap, exceeded that of the Fowler flap, which has given the highest lifts up to the present time. Further investigation of this type of flap is contemplated.

The investigation of airfoils with flaps in the variable-density tunnel has been continued for the purpose of providing more reliable design data on the airfoil section characteristics of wing-flap combinations at the usual full-scale values of the Reynolds Number. The results of tests of ordinary and split flaps are being prepared for publication. The characteristics of the high-lift low-drag slotted flap arrangement developed in the 7- by 10-foot wind tunnel are being determined at high Reynolds Number. Preliminary results indicate a large maximum lift increment that is substantially constant over the entire scale range.

In order to provide further design data for flap application, and in particular to furnish information for structural design of the wing and the flap, pressure-distribution tests have been made in the 7- by 10-foot wind tunnel of several different wing-flap combinations. The results of such an investigation of an N. A. C. A. 23012 airfoil with an N. A. C. A. 23012 external-airfoil flap are presented in Technical Report

No. 614, and a similar investigation of Clark Y and N. A. C. A. 23012 airfoils equipped with Fowler flaps is described in Technical Report No. 620. The results of pressure-distribution measurements made with a slotted flap and with a plain flap on N. A. C. A. 23012 airfoils have been published in Technical Report No. 633. Similar results from a split flap on a Clark Y-H airfoil were published in Technical Note No. 627.

The results of the investigation mentioned in the last annual report on the variation in the maximum lift coefficient obtainable with a given airplane in flight, depending upon differences in wing loading, altitude, wing-surface roughness, and the rate of change of angle of attack have been published as Technical Note No. 622. Data were obtained on the same airplane in the full-scale tunnel, and a comparison between lift coefficients measured in flight and in the full-scale tunnel is presented in Technical Report No. 618. These results show a rather close agreement between flight and tunnel measurements provided the influence of the propeller, the tail load for trim, and the effect of rate of change of angle of attack with time are taken into account.

CONTROL AND CONTROLLABILITY

As was stated in the last annual report, a critical analysis of the Committee's research on lateral-control devices which has been carried out in the past several years indicated that, for normal-flight conditions, ordinary ailerons with the gap between the aileron and the wing sealed are the most generally satisfactory. The flight investigation to verify this conclusion has since been completed and the results published in Technical Note No. 632. Additional data obtained on the same subject in conjunction with other tests on a pursuit-type airplane further substantiate the conclusion that any gap, even a very small one, is detrimental. In the case of the pursuit airplane, the maximum rate of roll obtainable was increased about 20 percent by sealing the gap of the ailerons, although the gap was only slightly more than one-eighth inch.

A method of reducing aileron operating forces suggested and analyzed in Technical Note No. 586 has been investigated in flight and the results presented in Technical Note No. 653. The method involves the use of a differential movement of the ailerons in conjunction with up-floating angle of the ailerons to obtain some degree of balance. The use of narrow-chord full-span tabs deflected downward on both ailerons was found effective in adjusting the up-floating angle to a desired value, and this in conjunction with the proper differential linkage is very effective in reducing aileron operating forces.

The results of the flight investigation of conventional and floating wing-tip ailerons on a tapered wing have been published in Technical Report No. 630.

The angular accelerations of an airplane in roll due to the application of ailerons is one of the factors representative of the control effectiveness. In order to determine what relation exists between airplane size and the angular accelerations in roll, a study is being made of data obtained over a period of several years on airplanes of various sizes. An analysis based on consideration of the time required to deflect the ailerons with a given effort by the pilot shows that the inertia of the control system is a factor of major importance as regards the accelerations obtainable.

The results of an experimental study of the forces that a pilot can exert on the control wheel of an airplane have been published in Technical Note No. 623. These data are supplementary to those previously published on the forces that can be exerted on the control stick and rudder pedal.

Lateral controls for use with full-span flaps.—Since it appears desirable to maintain as high lift coefficients as possible both for landing and taking off, the use of full-span flaps is indicated as being desirable. In this connection, the problem of satisfactory lateral control is of primary importance, and several devices for obtaining lateral control with full-span flaps have been investigated in the 7- by 10-foot wind tunnel during the past year.

A wing with a full-span slotted flap was tested with ailerons of three different types: retractable ailerons, slot-lip ailerons with the lip of the slot acting as aileron, and plain ailerons on the trailing edge of the slotted flap. The results are published in Technical Note No. 659 and indicate that, from considerations of rolling and yawing moments produced and of stick forces desired, the retractable aileron is the most satisfactory means of lateral control for use with a full-span slotted flap.

Another investigation was made to determine the control characteristics of a rectangular and a tapered N. A. C. A. 23012 wing with plain trailing-edge ailerons and full-span split flaps, the flaps retracting ahead of the ailerons. The results, published in Technical Note No. 661, show that satisfactory control could be obtained with the plain ailerons and the full-span split flap arranged to extend and retract with a hinge axis fixed ahead of the ailerons, or with the flap axis moved back to the aileron axis when the flap was deflected.

Flight with unsymmetrical power.—The failure or the intentional stopping of one engine on a multi-engine airplane results in peculiarities of control and has important effects on the performance of the airplane. In order to determine the magnitude of these effects, a large model simulating a modern twin-engine transport airplane, was investigated in the 20-foot wind tunnel. Various changes in the angle of the engines to the wing (toe-out) were tried, as well as several tail-

surface arrangements. The results indicated that toeing-out of the engines or toeing-in of the rudders appear impracticable as methods of reducing the yawing moment after engine stoppage. From considerations of performance the yawed mode of flight on one engine increased the drag somewhat more than the banked mode of flight. With the particular model tested, the yaw angle required for balanced flight averaged about 5° and the bank angle required was about 2° . The results of the tests have been published in Technical Note No. 646.

MANEUVERABILITY

The investigation of the maneuverability of several Navy airplanes for the purpose of determining principally the maximum acceleration in roll and pitch to which the airplanes may be subjected has been continued. The results obtained on two airplanes have been reported to the Navy. A third airplane is now undergoing test.

An investigation has also been made of the maneuverability of a low-wing monoplane with a wing loading of 20 pounds per square foot. Previous tests of this nature, the results of which have been published, have been on airplanes with much lighter wing loadings. In general, the radii of the paths followed in recent maneuvers were considerably greater than for the machines previously tested. A report on this investigation is in preparation.

STABILITY

The extensive program of systematic research on stability problems that was formulated after a review of all the available data on the subject has continued to serve as the basis for the investigations of stability being conducted with the various facilities available to the Committee.

Research to determine the most desirable degree of stability for airplanes has been continued. One phase of the work, a mathematical study of the lateral motion induced by different types of asymmetric gusts, has been completed and the results have been published in Technical Report No. 638. The report deals with the effect of various amounts of dihedral and fin area on the motion resulting from encounters with unsymmetrical gusts of various types. The importance of proper coordination between fin area and dihedral, and in particular an unfavorable effect of relatively excessive dihedral with small fin area, is indicated.

As stability research progresses, it becomes increasingly evident that the effect of the various factors on the control and maneuverability of an airplane is of more importance than their effect on the stability itself. The requirements for stability and control generally conflict—that is, conditions that lead to greater stability also lead to greater control stiffness

and less maneuverability—and compromises must be made in design. With the increase in airplane size, the nicety of adjustment needed to produce both good stability and good control characteristics is considerably increased. Several analyses are in progress with a view to obtaining detailed information on the effect of varying the stability on the control characteristics.

The study of the relationship between the longitudinal-stability characteristics and the elevator control effectiveness is well advanced. Although no definite conclusions can be drawn as yet, it appears that the effect on the elevator control force of varying the degree of longitudinal stability through a wide range may be considerably smaller than generally supposed. A similar investigation with regard to lateral stability has revealed the fact that very little information exists on the normal flying requirements for rudder control. Most design parameters are based on the amount of control needed to prevent ground looping and to recover from spins and do not apply satisfactorily to airplanes with wheel brakes or stable landing gears, nor to the spinning categories. The investigation has therefore been extended to include a study of the functions of the rudder control.

Allied to these investigations, which primarily deal with improvement of the airplane for operation by the human pilot, is a study being made of the stability of the airplane when operated by an automatic pilot. The operation of an ideal pilot, one in which the response to a disturbance is instantaneous, has been investigated and the results prepared for publication. The effect of practical factors, such as the amount the airplane may deviate from the desired conditions before the pilot starts to respond and the time taken for the pilot to deflect the control surface, are now being considered.

With the continued study of stability problems, a better understanding of the subject is being obtained and more application of the findings is being made in actual design. As a result, there is a need for more information on the influence of the different variables in design on the stability derivatives upon which stability depends. During the past year, study was made of all available data on the derivative N_v , the change of yawing moment with change of sideslip, and the need for a systematic series of experiments on different fuselage shapes and fin arrangements is clearly indicated. A compilation of the data reviewed has been published in Technical Note No. 636.

Technical Report No. 635 has been published giving the results of an analytical investigation of the effect of the wing on the stability derivatives. The effects of taper, twist, dihedral, and aspect ratio are treated, and the data given in the report make possible the ready computation of the stability derivatives of a wing with any combination of these variables.

The stability problem is further complicated by the effect on the tail of the downwash from the wings and the wake of the wings. In the full-scale wind tunnel, downwash angles and wake characteristics have been measured in the tailplane region behind wings of various taper and aspect ratios and for flaps of various spans. From an analysis of these data, it was possible to derive a satisfactory theoretical basis for predicting downwash and wake phenomena. A report is being prepared presenting the results obtained. Also under preparation is a report containing a large number of charts covering plain and flapped wings of various types, by means of which the designer may readily compute downwash angles, wake velocities, and wake thickness in the region of the tailplane. The work is being extended to include the effects of slipstream and fuselage interference.

The investigation of wing-fuselage interference in the variable-density wind tunnel, which was extended to include the effect of adding tail surfaces to typical combinations, has been completed. A report dealing, among other things, with the wake effect and downwash angles at the tail is being prepared.

Stalling.—During the past year the considerable attention that has been given to the study of the stall has been necessitated by the undesirable stalling characteristics that exist in some airplanes of modern design.

In Technical Note No. 645 the stalling problem as related to modern low-wing monoplanes is discussed, and it is noted that basically the solution of the stalling problem consists of the elimination of rolling instability of wings. In view of the merit of low-wing monoplanes in other respects there is great need for research on this subject. For the present it seems desirable to provide means to forewarn the pilot of the approaching loss of stability when the angle of attack is being increased. The various aerodynamic effects that give warning of the stall are considered in detail.

The special wing of 5:1 taper equipped with stall-control flaps mentioned in the last annual report has been tested in flight and in the full-scale wind tunnel. The stall-control flaps are of large chord, being hinged at the 40 percent point of the wing chord. They have the effect of shifting the lift curve to the left and therefore of causing the stall to occur at a lower angle of attack. By means of these flaps it was possible to vary the span loading in any desired manner and to cause the stall to start either at the wing root or at the tip. The shape of the peak of the lift curve could be varied without materially altering the value of the maximum lift coefficient. With what appeared to be about the optimum flap setting as regards maximum lift and development of the stall, the lift curve for the complete wing was shifted about 6° to the left. The effect of this shift of the lift curve on the proper attitude of the airplane during an approach glide and landing was some-

what confusing to the pilot accustomed to the characteristics of the plain wing. Confusion would be eliminated, of course, if all landings were made with the flaps in the same position. The results of this investigation are now being prepared for publication.

The stalling characteristics of a number of airplanes ranging in size from small single-engine machines to the largest four-engine types have been studied in flight during the past year. These studies have been made by visual and photographic observations of silk tufts attached to the upper surface of the wing. Such tufts appear to be a reliable means of indicating the manner in which the stall spreads along the span, after some experience is acquired in the proper interpretation of their behavior. It has been found that the loss of lift corresponding to the stall is indicated when the tufts reverse direction or become entirely limp, whereas a fluttering or unsteadiness of the tufts is simply an indication that the stall is impending.

From observations made in these tests it appears that the type of stall which starts at the center and progresses towards the tip is the only one that produces sufficient change in the behavior of the airplane as the stall is approached to serve as a pronounced warning before rolling instability actually develops. A violent rolling motion, however, is not necessarily associated with a stall that starts at the tip. In fact, on one machine the stall started at the tip and progressed inboard so gradually and symmetrically that a gentle stall was obtained. When the stall spreads suddenly over a large portion of the wing, large rolling moments and a violent action are likely to occur, for in such cases the spread of the stall on the two wings is not likely to be symmetrical. An early stall at the wing root provides a warning of the impending loss of control but in certain cases the tail buffeting accompanying root stalling has been regarded as objectionable.

The conflicting requirements therefore leave many questions yet to be answered regarding the attainment of desirable stalling characteristics. One point not to be overlooked is that strong static longitudinal stability at high angles of attack makes it difficult to stall a machine completely; in such a case the likelihood of an inadvertent stall is much reduced.

An investigation in the variable-density wind tunnel is now in progress to determine the relative efficiency of various methods, such as twist, change of section, and change of camber, for the prevention of tip stalling. In the same wind tunnel, another investigation is in progress on wings with sweepback and sweep-forward and different amounts of taper to investigate the effect of these factors on the spanwise location of the stall.

One promising method of maintaining lateral control and quasi-stability until the stall is well developed

over the inner portions of the wing is the use of leading-edge slots over the outer part of the wings in front of the ailerons. In order to establish data on the best type of fixed slot for use with the N. A. C. A. 23012 airfoil, fixed slots of several forms and at several chord locations with and without slotted flaps have been investigated in the 7- by 10-foot wind tunnel. The results are being prepared for publication.

A mechanical device has been developed to provide a warning of the impending stall on airplanes in cases where the warning is not an inherent feature caused by the nature of the airflow around the wing and the tail. This N. A. C. A. stall-warning indicator operates when the angle of attack reaches the maximum safe value regardless of the air speed, so that it gives a warning independent of the wing loading. The warning indicator thus functions in proper relation to the critical airflow conditions over the wing regardless of variations in the weight carried by the machine or of variation in acceleration as in turns. Experimental installations of this device have thus far given very promising results.

SPINNING

During the past year the 15-foot free-spinning wind tunnel has been chiefly occupied in determining the spinning characteristics of scale models of ten specific airplanes. Tests for the purpose of making a direct comparison between model and full-scale spin behavior on a low-wing monoplane have been made and the results analyzed. Progress has also been made in the systematic investigation mentioned in the last annual report to determine the effects of changes in wing arrangement, in tail arrangement, and in mass distribution.

Observations made in the course of routine tests of specific designs have been definitely useful in extending the general knowledge of spinning. It has been pointed out in a published report that the effect of aileron setting on spin characteristics may be appreciable. This conclusion is substantiated by more recent results both with models and in flight. For models of modern low-wing monoplanes it has been found that recovery is frequently expedited by leaving the ailerons deflected with the spin (right aileron up in a right spin), and a study is being made of the possibility of utilizing aileron deflections to improve recovery.

General conclusions previously presented with regard to satisfactory tail design have been verified during the past year by observations made in the course of routine tests. It is of interest to note that three models having dual fin and rudder construction have been tested and all have shown very satisfactory recovery characteristics.

Experience gained in the testing of four models in the trainer and the observation-scout categories indicates that spin characteristics for the landplane type

will be less satisfactory than for the single-float seaplane.

In order to increase the available information as to the degree of reliability of the free-spinning tunnel in the prediction of full-scale characteristics for specific designs, a comparison has been made of the spinning and recovery characteristics of a low-wing monoplane tested in this tunnel and in flight. This comparison, together with the additional information obtained as a result of flight service trials, indicates that model tests give a useful, but not infallible, indication of full-scale spin behavior.

Discrepancies that have appeared between model and full-scale results indicate the need for further research on scale effect, effect of power, and effect of manner of control operation.

The investigation of the relative importance of wing arrangement, tail arrangement, and mass distribution that was mentioned in the last annual report is now about half completed. Results published thus far (Technical Notes Nos. 608, 630, and 664) have indicated that the choice of wing design may be affected by the mass distribution. Unpublished results of additional tests indicate that a forward location of the center of gravity is preferable to a rearward location regardless of wing or tail arrangement. An analysis has been started with the object of evolving a suitable airplane-spin criterion to aid designers in securing satisfactory recovery.

The results of the investigation with the spinning balance in the 5-foot vertical tunnel of the effect of stagger of rectangular biplane cellules, mentioned last year, have been published as Technical Note No. 625. An investigation of the effects of airfoil section on the spinning characteristics of rectangular monoplane wings with rounded tips has been described in Technical Note No. 633. The airfoil sections investigated were the N. A. C. A. 0009, 23018, and 6718, and the data for the Clark Y wing presented in Technical Note No. 612 were included for comparison. These data can be used in studying the steady-spinning characteristics of particular airplanes, and the results of the analysis given in these papers can be used to predict whether changing the wing loading or the weight distribution of an airplane will be beneficial or detrimental to its steady-spinning characteristics. For comparable cases, these results and the results obtained on models in the free-spinning wind tunnel have shown the same general tendencies.

In connection with the determination of spinning characteristics of various models in the spin tunnel, there has been a continued demand for the Committee to determine experimentally the moments of inertia of full-size airplanes. These measurements are carried out by means of the swinging gear, which has been in use for several years.

TAKE-OFF

The investigation discussed in the last annual report of the transition period in take-off between the end of the ground run and the beginning of the climb has since been described in Technical Report No. 626. Additional data concerning the ground run and the transition to climbing flight in take-off have been obtained in conjunction with an investigation of the effect of two types of full-span flap on take-off, one being a high-drag type represented by the Zap flap and the other being a low-drag type represented by the external-airfoil flap. These tests are an extension of an earlier investigation made with a machine of such low power that the results were not representative of conditions ordinarily encountered in transport or military operation. The data obtained in these tests are now being analyzed.

As has been pointed out, the characteristics of the propeller have a pronounced influence on the take-off. An extensive investigation of full-scale propellers has been conducted in the 20-foot wind tunnel to provide information on modern propellers. This constitutes a considerable extension of the Committee's early investigations to provide propeller design data and covers principally the changes in design necessitated by higher engine power and airplane speed. These trends call for propellers of higher pitch, more blades, and changes in blade form. The investigation has now been completed, and is discussed more completely in a later part of this report. Of six reports published during the year on the results of the investigation, three (Technical Reports Nos. 639, 640, and 643) contain data directly applicable to the take-off problem.

LANDING

In connection with the general study of landing characteristics of airplanes, an investigation of ground effect has been carried out with a glider of aspect ratio 7.5 towed by an automobile at various heights above the ground up to about 50 feet. The data obtained in this investigation, which was made both with a plain wing and with a wing fitted with a split flap, are now being analyzed. For the plain wing the slope of the lift curve was increased about 30 percent with the glider 5 feet above the ground, as compared with the slope when it is 50 feet above the ground. The drag at a lift coefficient of 1.0 was about 15 percent less when the glider was close to the ground. The maximum lift coefficient of the plain wing was much higher (about 25 percent) in actual landings than in simulated landings made at considerable altitude.

Landing loads.—As stated in the last annual report, the Committee is undertaking the accumulation of statistical information on the loads experienced by the landing gear. This investigation has been continued during the past year and tests have been made with seven additional airplanes covering the complete range

of sizes of airplanes now in operation. A tricycle type of landing gear as well as conventional types was included. The attitude and the vertical velocities of the airplanes immediately prior to contact, in addition to the linear and angular accelerations, were determined.

Tricycle-type landing gear.—There has been a very definite growth of interest among American manufacturers in the use of tricycle-type landing gears during the past year, and the indications are that many new models of transport and private-owner machines, in particular, will be equipped with this type of gear. During the past year the Committee has continued the investigation of the shimmy of castering wheels and also its study of the landing loads experienced with the tricycle-type landing gear.

The analytical study of the shimmy of castering wheels that was mentioned in the last annual report has been completed and the results are being prepared for publication. The report will give methods for estimating the spindle damping that is necessary to avoid shimmy.

An airplane fitted with a nose wheel was used in tests of the effect of caster length on the tendency of the wheel to shimmy for comparison with tests made on a small-size model. A conclusion based on model tests that the provision of lateral freedom of the wheel would eliminate shimmy was not confirmed by the tests of the full-size machine.

Apparatus has been constructed for conducting tests with various types of airplane wheels in order to determine the friction required to prevent shimmy. By means of this apparatus the weight, the caster length, and the spindle angle can be varied as desired in order to cover a wide range of conditions. Tires ranging in characteristics from those of the extra-low-pressure type to those of a solid tire are being investigated.

As noted previously, landing-load tests have been made with one airplane having a tricycle type of landing-gear arrangement. Plans are also under way for tests of another machine having this type of landing gear. In both of these cases, particular attention is being paid to the determination of the loads on the nose wheel.

It has been found advantageous to employ actual airplanes or relatively large models of large airplanes in the Committee's full-scale tunnel in order to study various changes that may be made to improve service airplanes. Difficulties may sometimes be located and changes studied by means of wake surveys. From the test results, it was found that, for the high-speed condition, the drag of retracted landing gears accounted for from 2 to 9 percent of the drag of the airplanes. It was shown that this drag could be greatly reduced by improving the fairing of the landing gear in the retracted condition. In one case it was found possible to

reduce the drag of an airplane by 14 percent by modifying the engine cowling. Other reductions in drag were found to be possible by redesigning exhaust stacks. The profile drag of service wings was measured by momentum surveys in the wakes of the respective wings, and by a comparison of this information with data obtained on smooth wings of the same sections it was found that the surface roughness, consisting of protruding rivet heads, lap joints, etc., accounted for from 10 to 35 percent of the wing profile drag. These investigations indicated the possibility of increasing the speeds of several airplanes by varying amounts of from 15 to 23 miles per hour and they demonstrate the advantage of being able to put the actual airplane in the tunnel as compared with the use of models.

AIRFOILS

Section characteristics.—Comparisons of airfoil data from the variable-density wind tunnel with results of other large-scale tests, including data now becoming available from the N. A. C. A. full-scale wind tunnel, other large wind tunnels, and the British compressed-air tunnel, have been of decided assistance to the program of airfoil investigation. These comparative data have aided in formulating turbulence corrections for wind-tunnel test data, such as those employing the concept of an "effective Reynolds Number," but such corrections cannot be considered ultimately satisfactory. The basic program of airfoil investigation has therefore been primarily concerned during the year with the development of better methods of conducting tests, and of methods for the derivation of new airfoil forms in the light of modern boundary-layer theory.

Investigations of airfoil section in the variable-density wind tunnel of the type that led to the development of the commonly used sections of the N. A. C. A. 230 series have been continued. Profile-drag coefficients determined from tests in the variable-density wind tunnel have, however, tended to appear high as compared with results from the N. A. C. A. full-scale tunnel and from foreign sources. The results from the variable-density wind tunnel have also indicated larger rates of increase of drag with airfoil thickness than have those from other sources. These discrepancies have been considered and corrections for turbulence and tip effects have been applied which tended to reduce them.

Further investigations of this subject have been made, including tests of three symmetrical airfoils in the full-scale wind tunnel (Technical Report No. 637). The results of these tests confirmed the existence of discrepancies in addition to those arising from differences in turbulence between airfoil data from the full-scale and variable-density wind tunnels. The results from the full-scale tunnel indicated the presence of support-

strut-interference effects in the variable-density tunnel causing the measured drag to be too large, the drag increments due to support interference being greater for thick airfoils than for thin ones.

A subsequent investigation in the variable-density wind tunnel confirmed the presence of marked drag increments due to support-strut interference, the increment increasing with airfoil thickness. The application of corrections for this factor to the data obtained from the variable-density wind tunnel substantially removes the above-mentioned discrepancies. The most important result is that the smaller increase of drag with thickness affects the choice of optimum airfoil sections for airplane wings. Reports are being prepared presenting the results of these investigations.

A preliminary investigation has been made in the variable-density wind tunnel to study the stalling processes for four typical airfoil sections over the critical range of Reynolds Number. The flow was studied by means of tufts and a mixture of lampblack and oil spread on the surface and the observations were correlated with force measurements. The results tend to substantiate the analysis of stalling in Technical Report No. 586.

Transition on airfoils.—Because the aerodynamic characteristics of airfoils in relation both to maximum lift and minimum drag depend markedly on the transition from laminar to turbulent flow in the boundary layer, knowledge of the region in which transition occurs is a matter of considerable practical importance. The maximum possible extent of the laminar boundary layer is therefore of particular interest. In one respect, this extent is limited by the position of the laminar separation point. Of the various methods available for calculating this position, the method presented in Technical Report No. 504 seems to be the most reliable. This method, however, has the disadvantage that the computations are usually cumbersome and lengthy.

A method of rapidly estimating the position of the laminar separation point from the given pressure distribution along a body has been found; the method is applicable to a fairly wide variety of cases. The laminar separation point was found by the method of Technical Report No. 504 for a particular series of velocity distributions along a flat plate. They consisted of a region of uniform velocity followed by a region of uniformly decreasing velocity. It was found that such a velocity distribution can frequently be assumed equivalent to the actual velocity distribution along a body in so far as the effects on laminar separation are concerned. The agreement between the position of the separation point calculated according to the present method and that found from more elaborate calculations is very good. This rapid method of estimating the position of the laminar separation point is

soon to be presented in a Technical Note and should find frequent use in connection with estimates of possible position of the transition point and the attendant effects in various practical cases.

As another part of the Committee's general program for studying transition, measurements have been made on the N. A. C. A. 0009, 0012, and 0018 airfoils in the full-scale wind tunnel. The smoothly polished airfoils were of 6-foot chord and were tested over a range of Reynolds Number from approximately 1,500,000 to 5,000,000. Measurements were made both by means of total-head tubes in the boundary layer, so as to obtain the boundary-layer profiles, and by means of a hot wire at the airfoil surface. The results of this investigation, which show a variation of the transition point as a function of airfoil thickness, Reynolds Number, and lift coefficient, are published in Technical Report No. 637.

Another investigation of boundary-layer conditions, especially dealing with the location of the transition from laminar to turbulent flow, is in progress in the 8-foot high-speed tunnel. Here, by the use of two airfoils of different size and with the possible speed range and the low-turbulence air stream of this tunnel, the combined effects of scale and compressibility in relation to transition may be investigated.

A determination of the profile drag and the transition point in the boundary layer on a very smooth wing section in flight has been carried out at a Reynolds Number of about 4,500,000 with one airplane. These data are of value for comparison with data from the full-scale tunnel to evaluate any residual effects of the relatively small turbulence of the full-scale wind tunnel on the characteristics of aerodynamically smooth bodies.

In order to extend the range of profile-drag measurements at low turbulence to high Reynolds Numbers, flight tests were also made on an airplane of such size and speed that a Reynolds Number of 15,000,000, based on the chord length, was obtained. A portion of the wing of this airplane was made very smooth by the application of a combination of rubber and metal coatings. A paper on the results of these measurements is in preparation.

Roughness.—A continuation of the investigation of wing-surface conditions is being carried out in the 8-foot high-speed tunnel. The effect on wing drag of various construction conditions occurring in practice, such as butt joints with gaps, butt joints that are not flush, faired lap joints, spot welds, rib stitching, etc., have been determined. The investigation concludes with a systematic study of irregularities in wing profile.

Compressibility effects.—The analysis of a large amount of data obtained from investigations of the nature of the compressibility burble has been com-

pleted and prepared for publication as a Technical Report. An investigation of the variation of the drag coefficients of cylinders of simple shape for a wide range of Reynolds Number and speed that has been conducted as time permitted has been completed and the results published in Technical Report No. 619.

Work now in progress in the 24-inch high-speed wind tunnel consists of an extension of the earlier wing development carried out in the 11-inch high-speed wind tunnel. The energy loss involved in the compressibility burble tends to act as a limiting condition for the speeds of airplanes of current and typical design either through propeller restrictions or ultimately through restrictions on other parts of the airplanes. Although knowledge of the phenomenon has increased markedly through experimental work over the last four years, the phenomenon is still one of the most important flow problems in current aerodynamics. Further study of the mechanics of this flow phenomenon is being made.

Wing characteristics.—The calculation of the characteristics of 22 tapered wings of varying aspect ratios and taper ratios has been completed and shows reasonably good agreement with experimentally determined values of pitching moment, aerodynamic-center position, lift-curve slope, and drag variation. The results have been published as Technical Report No. 627.

The same aerodynamic characteristics have also been calculated for a few wings with partial-span flaps. Fair agreement with test results was obtained in most cases. The results are to be published, together with information on the theoretical factors involved in the determination of characteristics of tapered wings with partial-span flaps.

As a part of a recent study of the stalling of wings, a series of tests is in progress in which photographs are obtained of the action of tufts on wings with sweepback and sweepforward and different amounts of taper, to investigate the effect of sweep on the spanwise location of stalling. Another investigation using wings of different taper is being made to find the relative efficiency of various methods of preventing tip stalling.

AERODYNAMIC INTERFERENCE

The investigations conducted in the variable-density wind tunnel of the effects of split flaps and special junctures on the aerodynamic interference between wing and fuselage have been published as Technical Notes Nos. 640, 641, and 642. The investigation of the effects of adding tail surfaces has been completed and a report presenting the results is being prepared. Of interest are the small size of the increments to the drag caused by the tail surfaces, as well as the agreement between theoretical considerations and experimental determination of the wake effects and the down-

wash angle at the tail. The induced interference of the fuselage on the downwash angle, moreover, was negligible at low angles of attack and small at high angles. Asymmetrical combinations, however, showed initial deviations in the flow direction at the tail at low lift coefficients.

An experimental investigation of the mutual effects of interference and compressibility phenomena is in progress in the 8-foot high-speed wind tunnel. Results have been obtained for several arrangements of radial-engine nacelles on a wing to determine the effect of present-day nacelle arrangements at high speeds, but conclusions cannot as yet be drawn.

DRAG AND COOLING

Engine location.—One of the most obvious possibilities for substantial improvement in aerodynamic efficiency lies in the reduction of the drag of the engine installation and the cooling system. Tests were conducted in the full-scale wind tunnel on a representative 4-engine model to evaluate the drag of a typical liquid-cooled power plant. These tests showed that the engine nacelles increased the drag of the airplane about 8 percent and the cooling system (prestone and oil radiators) accounted for over 15 percent more. Further tests were made simulating the arrangement of engines placed within the wing with extension shafts to either tractor or pusher propellers. The extension-shaft drive practically eliminated the nacelle drag.

For the development of an efficient cooling system for engines or radiators located in the wing, investigations have been conducted in the 7- by 10-foot atmospheric wind tunnel and in the full-scale wind tunnel. The general principle of the arrangements investigated is that of low-velocity cooling with the cooling element placed at the largest section of a duct. Arrangements already tested have shown large reductions in drag under all flight conditions.

In the 7- by 10-foot wind tunnel the tests were made to simulate a radiator or engines enclosed entirely within the wing and cooled by air led through ducts from the wing surface. The results obtained on a wing model with full-span ducts and radiators have been reported in preliminary form. For certain locations of the duct inlet and outlet the total power required to cool such an installation is only the power required to force the air through the radiator. Thus the cooling power may be of the order of 2 or 3 percent of the engine power as compared with the 10 to 15 percent now required on radiator installations. The results of these tests will be published as a Technical Report.

Radiator study.—A comprehensive study of aircraft-radiator design and installation has been made. The choice of radiator dimensions is made on the basis of cooling efficiency, which is the ratio of heat dissipated to power required for cooling. The power required for

cooling is made up of three factors: (1) power to force the cooling air through the radiator; (2) power to carry the weight of the radiator; (3) power to overcome form drag. The importance of these three power expenditures varies with installation, airplane performance, pressure drop, coolant, and altitude. The heat dissipation varies with mass flow of air through the radiator, the length-diameter ratio of the radiator tubes, and the temperature difference between air and coolant.

This study on radiators comprises one phase of the heat-transfer problem. The problem of intercooler design and installation is also under investigation at the present time. The radiator problem is concerned with the case where nearly all the thermal resistance is at one surface, while the intercooler problem is concerned with a case of two surfaces having relatively the same thermal resistance.

Cowling research.—The information from tests on the propeller-cowling-nacelle combinations presented in Reports Nos. 592, 593, and 596 and Technical Note No. 620 has been summarized for design purposes in a report entitled "Design of N. A. C. A. Cowlings for Radial Air-Cooled Engines." The main emphasis of this report is placed on the method of obtaining the dimensions of the cowling. A practical method of designing cowlings and some examples are presented.

A study of the factors affecting the pressure available for ground cooling in front of air-cooled engine cowlings has been made. Most of the work was conducted on a model of about one-third full scale. A number of isolated tests on four full-scale airplanes were made as a basis of comparison of model and full-scale results. The available pressure in front of the cowling increases rapidly with the diameter of the opening of the cowling up to 30 or 40 percent of the propeller radius. The cowling should be located as close to the propeller as practicable. Disks located in the front of the nose of the cowling greatly increased the average pressure in front of the engine. It is important that the plane of the disk be even with the nose of the cowling. The size of the disk should be such that the area of the front opening is optimum for the total conductivity used. A report is being prepared on this investigation.

Investigation of the nose-slot cowling has been continued on a full-size airplane. The ground cooling of the engine was improved by proper cowling design and a $\Delta P/q$ of 1.6 was obtained in full-throttle climb. In order to expedite the study of the problem, it was decided to continue the work in the 20-foot wind tunnel. These tests are now in progress and should supply sufficient information to determine the best design of nose-slot cowling for any given design condition. In connection with the wind-tunnel investigation the cost in drag of the bluntness of the radial-engine cowling is being investigated and means to reduce this drag are being studied.

Scoops and vents.—An investigation of air-inlet and outlet openings suitable for cooling and ventilating systems, carburetor intake, and engine exhaust has been undertaken. A momentum theory of the generalized induced-flow system was derived to serve as a basis for the explanation and the correlation of experimental results, particularly the results of wind-tunnel tests of separate openings. This theory provides a simple method of determining roughly the effects of the internal induced-flow system. It suggests the optimum locations for inlet openings, the optimum angle and velocity of the jet for outlet openings, and the cost of departures from those optimums; and it illustrates the close relationship of the several types of induced-flow system. An extensive experimental investigation was made in the N. A. C. A. 5-foot vertical wind tunnel of a large number of openings in a flat plate and of a few in an airfoil, all tests covering the complete range of self-induced flow and the practically useful range of blower-induced flow. The experimental results verified the trends indicated by the theory wherever comparisons were practicable, and the quantitative agreement between theory and experiment is considered satisfactory for the most efficient opening shapes and locations. The test conditions and the models were systematically varied so that the results indicate the effects of wind velocity; size, shape, and location of openings; length and angle of ducts; and some of the interference between an opening and a body, and between inlet and outlet openings in the same body.

The location of the carburetor intake has been separately investigated in the propeller-research wind tunnel. A ramming effect due to the dynamic pressure of the air stream may be desirable. Tests of several intakes were made with the radial engine cowling used in the propeller investigation. The best results were obtained with a well-rounded entrance located near the leading edge of the cowling on the outside. The propeller also contributed to the ramming effect when the scoop was so located. The results of the tests are published in Technical Note No. 631.

PROPELLERS

An extensive investigation of full-scale propellers started last year has been completed. A number of propellers with various airfoil sections, different numbers of blades, and several plan forms and pitch distributions were tested in conjunction with two bodies representing radial-engine and liquid-cooled-engine nacelles. A range of positive blade-angle settings up to 45° at the 75-percent radius was covered, as well as some negative settings.

Many of the conclusions were presented in the last annual report and these have not been altered by the tests made this year. Because of the large amount of data, it was found advisable to prepare a series of re-

ports each devoted to a particular phase of the study. Eight reports have been prepared, six of which have been published as Technical Reports Nos. 639 to 644.

With regard to compressibility, Technical Report No. 639 indicates that at normal pitch settings losses in efficiency become evident at tip speeds of from 0.5 to 0.7, the velocity of sound for the take-off and climbing conditions of flight. The loss increases rapidly with speed and amounts to more than 20 percent of the thrust power in some instances for tip speeds of 0.8 the velocity of sound.

The loss for the take-off condition increased with blade-angle setting up to about 20° , diminishing at higher values. For the climbing condition the loss increased up to a 25° setting. The loss in efficiency for controllable propellers is partly regained by the lower blade angles necessitated by the higher power coefficients developed at the higher tip speeds. On the other hand, the loss for fixed-pitch propellers is increased by the loss in speed and power caused by the higher power coefficient. The complex effects of compressibility were subject to detailed study and an appendix to the report develops methods for making corrections in practical problems.

Technical Report No. 640 discusses the effect of the number of blades, indicating that, for the same solidity (total blade width), the efficiency is increased by increasing the number of blades. Even when the solidity was doubled by changing a 2-blade to a 4-blade propeller, the loss in efficiency was only 2 percent. At the same time the take-off efficiency was improved.

The negative thrust condition occurs in diving at high speeds and idling at low speeds. Technical Report No. 641 gives data and examples for calculating the magnitude of the thrust developed under these conditions of operation.

When a spinner is added to the propeller of a radial air-cooled engine, the principal effect is an improvement in the flow through the engine cowl. With some installations of liquid-cooled engines, however, the spinner covers up the propeller hub and the round blade shanks. The propulsive efficiency was increased 6 percent in one case. Blade shanks of good airfoil shape were found superior to the round shanks with both types of nacelles. (See Technical Report No. 642.)

Technical Report No. 643, relating to plan forms, indicates that some improvement may be expected by having the blade width in the inner half of the blade greater than is the usual practice. The take-off efficiency, however, is reduced.

A more accurate method of measuring propeller deflections was developed and is described in Technical Report No. 644. Measurements gave much smaller deflections than the methods formerly used. Torsional

deflections of only $\frac{1}{10}^\circ$ at the 0.70 radius were noted. The bending deflection was also small.

The results of the study of airfoil sections indicate that no section thus far tried is the best for all conditions of operation. Highest maximum efficiencies were obtained with airfoils of low camber such as the N. A. C. A. 2400-34 and the Clark Y. For both controllable and fixed-pitch propellers of the same diameter, the R. A. F. 6 was best in the take-off range. Blade sections for controllable propellers, not limited in diameter, should be selected mainly on a basis of drag.

There has been a feeling that propellers designed with low basic pitches and then set to high angles suffered because of the large change in pitch with radius. Tests in which a propeller was twisted to give a uniform pitch when set at 35° gave a lower maximum efficiency than a normal propeller set to this angle. A gain in take-off efficiency at low angle settings was noted.

Tests in wind tunnels do not yield data on the static thrust of propellers because the propeller creates an appreciable velocity through the tunnel. The static thrust is useful in certain aspects of performance computation and, in order to obtain this information for direct comparison with values obtained in the tunnel, the wind-tunnel set-up has been installed on an outdoor rig. A series of tests on propellers previously tested in the tunnel has been completed and the data are now being analyzed.

THEORETICAL AERODYNAMICS

Normal force and pressure distribution over airfoils.—For the calculation of air loads along the wing chord in airplane design it has been customary for the designer to employ an arbitrary normal-force distribution that agrees only very roughly in form to the distribution which would result from experimental observations. This method, while admittedly crude, is rapidly and easily employed. Consequently, it is frequently used in preference to the theoretical method of Technical Report No. 411. Moreover, the theoretical method itself predicts a distribution which is in none too good agreement with experiment. A modification of this theoretical method (Technical Report No. 563) that yields results in good agreement with experiment has been advanced but this modified theory is even more laborious to employ.

A method for the prediction of the chordwise normal-force distribution in which attempt is made to retain the simplicity of the arbitrary method and the exactness of the modified theoretical method has recently been developed by the Committee. This method is applicable to ordinary airfoils (Technical Report No. 631) and to airfoils with plain, split, and serially hinged trailing-edge flaps (Technical Report No. 634) but

does not give separately the pressure acting on the upper and lower surfaces of the airfoils. At present the Committee is continuing work on a method of determining these pressures. This method as evolved is easily and rapidly applied and to date appears to be accurate enough for design purposes.

Theory of unsteady flow.—A theoretical study has been made of transient, or nonstationary flows, about airfoils and the results presented in Technical Report No. 629. It has been shown that the two-dimensional problem can be made to depend on two significant functions: one introduced by Wagner and the other introduced by Theodorsen. These functions are Laplacian transforms of each other. The growth of lift on an airfoil in two dimensions becomes analogous to the growth of electric current in a circuit. The function of Wagner then corresponds to the indicial current admittance and the function of Theodorsen to the alternating current complex admittance. As in electric-circuit theory the current due to any applied voltage can be built up by superposition, so in the case of the airfoil the lift due to any "applied vertical velocity" can be obtained by superposition. Thus, many practical general problems concerning the transient behavior of lift under changing flow conditions can be handled.

In the analysis of some of the results recently obtained in the wind tunnels, more particularly in the gust tunnel, application has been made of the fundamental theory of unsteady flow. The existing theory, however, considers only the case of a wing of infinite span and consequently does not entirely fit the conditions of the tunnel tests. A study has therefore been started to extend the theory to cover the three-dimensional case of the wing with finite span. Although a rigorous treatment has not yet been evolved, a practical extension to the two-dimensional theory has been worked out. A Technical Note presenting the present development is in preparation. A second note presenting an operational mathematical method of applying the unsteady-lift theory to specific dynamical problems is also being prepared.

Compressible flow.—A theoretical investigation of the effects of compressibility on the flow past an obstacle was made and the results applied to the cases of symmetrical Joukowski profiles and elliptical profiles. The results were obtained in a closed form and are exact in so far as the second approximation to the compressible flow is concerned, the first approximation being the result for the corresponding incompressible potential flow. For the case of the symmetrical Joukowski profile (Technical Report No. 621) the angle of attack was taken to be arbitrary and the circulation chosen according to the Kutta condition. Formulas were developed for the velocity increments at the surface of the airfoil due to compressibility. In addition, formulas for the lift and the moment were given for thin pro-

files at small angles of attack. For the case of the elliptical profile, since the angle of attack was taken to be zero, expressions for the velocity distribution at the surface only were obtained (Technical Report No. 624). At the present time an investigation is in progress concerning the moment on an elliptic cylinder immersed in a two-dimensional subsonic compressible flow.

WIND-TUNNEL CORRECTIONS

Reasonably satisfactory theoretical methods have been available for years for correcting the results from open and closed wind tunnels of different commonly used sections, such as circular and square, in which the span of the airfoil or airplane model does not exceed about 75 percent of the tunnel width or diameter. It is still necessary to determine experimentally the corrections to allow for individual shapes of throat, as in the case of the oval throat of the full-scale wind tunnel, or for the cases in which the airfoil spans the jet completely, as in the cases of the Committee's high-speed wind tunnels.

The full-scale wind tunnel.—Comparisons between test data obtained in flight and in the full-scale wind tunnel have shown that the results obtained in the tunnel closely approximate free-flight conditions. The results of a comparison of the maximum lift coefficients obtained with a Fairchild 22 airplane in flight and in the tunnel, mentioned in the last annual report, have now been published as Technical Report No. 618.

As a part of a general research program which has as its objective the improvement of the correlation of data obtained in the various wind tunnels of the Committee, the aerodynamic characteristics of three 6- by 36-foot airfoils of symmetrical section have been determined in the full-scale wind tunnel. The thickness ratios of these airfoils ranged from 9 to 18 percent to cover a normal range of wing thickness. A comparison of these data with results obtained with the same airfoil sections in other wind tunnels will result in improving the precision with which wind-tunnel data may be applied to flight conditions. The results of this investigation are presented in Technical Report No. 647.

The 7- by 10-foot and the 4- by 6-foot wind tunnels.—An investigation has been started in the 7- by 10-foot wind tunnel, in which the airfoils span the rectangular throat, to determine the correction necessary to reduce airfoil data obtained in that tunnel to true airfoil section characteristics. Thus far, the investigation has yielded a satisfactory correction to the lift that is in good agreement with the theory. The corrections for the drag and the pitching moment are not yet considered entirely satisfactory, and further tests are contemplated.

Until recently the 5-foot diameter vertical tunnel has been used principally for investigations relating to the

spinning problem. This tunnel has now been changed to have a rectangular 4- by 6-foot closed throat and is to be used chiefly for studies involving two-dimensional flow. The modification of this tunnel now makes available a piece of equipment that should be fairly well adapted to this type of work and also well adapted to general aerodynamic research at moderate values of the Reynolds Number.

The 11-inch, the 24-inch, and the 8-foot high-speed wind tunnels.—Preparatory to an investigation of special airfoils suitable for high-speed applications, an extensive investigation of tunnel-wall effects has been made for the 11-inch, the 24-inch, and the 8-foot high-speed wind tunnels. Inasmuch as these tunnels are all of circular throat and the airfoils are mounted similarly in all, it was possible by a comparison of the results from airfoils of corresponding chord from the three tunnels to determine the correction for each. Preliminary work was conducted in the 11-inch and the 24-inch wind tunnels. Later, tests identical in nature were made in the 24-inch and the 8-foot wind tunnels to check the preliminary work and finally to evaluate the wall effect and the end-leakage corrections for the drag and the lift-curve slope.

EFFECTS OF ICE FORMATION AND ITS PREVENTION

The icing of aircraft is still one of the most serious problems confronting airplane operators. An investigation was made during the past year in the full-scale wind tunnel to determine what effect ice formation has on the aerodynamic characteristics of a wing. A formation simulating one depicted in photographs forwarded by one of the air-line companies was built up on an N. A. C. A. 23012 airfoil and tested. It was found that the maximum lift coefficient was reduced from 1.32 to 0.80 by the formation and the profile-drag coefficient was increased by 90 percent. It can be seen that the increased stalling speed resulting from such a formation could be very dangerous, particularly if the pilot had to rely upon his air-speed indicator to warn him of the approaching stall.

In order to obtain a clear statement of the various aspects of the icing problem, a questionnaire was submitted to air-line operators during the past year requesting them to outline the difficulties experienced in flight and to suggest a line of research. The replies obtained from this questionnaire have served as the basis for the preparation of a comprehensive program of research. The carrying out of this program will be facilitated by the new refrigerated tunnel, which has been recently added to the Committee's equipment. This tunnel makes possible the testing of models having a chord up to 6 feet.

Preliminary tests have been carried out in this tunnel to study the use of exhaust heat as a means of

preventing ice formation on the leading edge of a wing. The possibility of using steam generated by the exhaust heat to prevent ice formation is being investigated on an airplane in flight. In these tests, the exhaust from one cylinder of a 9-cylinder engine is used to generate steam that is conducted to a condenser covering a portion of the leading edge of the wing. From the results of the tests both in the wind tunnel and in flight, it appears that, although there is plenty of heat available in the exhaust, merely heating the leading edge of the wing is insufficient. It is now planned to extend the study to investigate means of distributing heat over the entire wing chord.

Additional flight tests have been made to test the usefulness of preparations that decrease the adhesion of ice to the wing. Preparations containing soluble materials have thus far been found to be practically worthless. Other tests conducted with a mercury-amalgamated surface showed that, even though the adhesion of ice to the wing was reduced to a very small amount, the ice would continue to form in practically the same manner as on the untreated surface.

ROTATING-WING AIRCRAFT

In the hope of developing an improved method of direct control for rotating-wing aircraft, research during the past year has been restricted to a theoretical study of rotor control systems. The effect of periodically feathering the blades of an articulated rotor has been analyzed in detail and the aerodynamic identity of the Hafner and Cierva control systems has been mathematically demonstrated. As yet the study has not been extended to cover feathering control of rigid rotors but it is hoped that this can be done in the near future.

A study of the torque equilibrium in the autogiro rotor has been completed and the results published in Technical Report No. 623. This study simplifies and improves the previous method of calculating the inflow velocity required to maintain autorotation in a given rotor. Correct estimation of the inflow is particularly important because all rotor characteristics depend directly on inflow velocity.

MISCELLANEOUS TESTS OF MODELS AND AIRPLANES

In accordance with requests of the Army and Navy and in keeping with the policy of the Committee, a large number of complete airplane models have been investigated in the full-scale, the 20-foot, and the 7-by 10-foot wind tunnels. Most of the models have been tested for the military services but some have been tested for manufacturers at their expense.

In order to determine means for eliminating errors due to variations of wind velocity with height, a series of flight performance tests has been made with airplanes under conditions such that the effect of the

gradients could be determined. The results of these tests, which are now being analyzed, indicate that such gradients as are experienced in ordinary weather may influence the rate of climb by as much as 10 percent.

NATIONAL BUREAU OF STANDARDS

WIND-TUNNEL INVESTIGATIONS

The aerodynamic activities of the National Bureau of Standards have been conducted in cooperation with the National Advisory Committee for Aeronautics.

Wind-tunnel turbulence.—The most useful method of describing the statistical properties of wind-tunnel turbulence appears to be that in terms of intensity and scale, corresponding to the description of the molecular motion of a gas by average molecular velocity and mean free path. Extensive measurements of scale and intensity and of their aerodynamic effects on the drag of spheres were published last year in Technical Report No. 581.

It is also possible to give a somewhat more detailed picture by considering the fact that eddies of different size are present and investigating the distribution of intensity with size. The procedure is analogous to the classical treatment of light waves. By inserting electrical filters in the amplifier circuit of the usual hot-wire equipment, it is possible to determine the "spectrum" of turbulence. The spectral distribution curve gives the fraction of the total energy of the turbulence arising from frequencies in a narrow region as a function of the mean frequency of the region.

Some studies of this type have been made during the past year. In the interim G. I. Taylor has shown that the spectrum curve is the Fourier transform of the correlation curve used in determining the longitudinal scale of the turbulence, and one may readily be computed from the other. Our measurements confirm this result, and the forms of the curves suggest that wind-tunnel turbulence is a generalized chance phenomena.

The study of the change in the spectrum as the turbulence decays shows that the energy in various frequency bands does not decay independently or according to any simple law but that there is a continual transfer from low frequencies to high frequencies.

The results of these studies were presented at the Fifth International Congress for Applied Mechanics and will be published in the proceedings of the Congress.

Effect of turbulence on boundary layers.—In the annual report last year a rather extensive account was given of the work then in progress on the study of the speed distribution in the boundary layer of an elliptic cylinder at tunnel speeds high enough to produce transition from laminar to eddying flow and for intensities of turbulence of 0.85 and 4.0 percent. A description was given

of a simple device consisting of a hot wire on a sliding band, for quickly locating the transition. With this device a survey was made of the effect of intensity and scale of turbulence on the location of the transition zone. It was found that the distance of the transition zone from the nose was a function of the product of the intensity of the turbulence by the fifth root of the ratio of a characteristic dimension of the cylinder to the scale of the turbulence, corresponding to the theoretical relation suggested by G. I. Taylor. A report on the work is in process of publication as a Technical Report.

Investigation of boundary layer by diffusion of heat.—Studies of turbulence within a thick boundary layer in which the flow is eddying have been continued. The layer is formed on the surface of a flat plate 10 feet wide and 24 feet long installed in the 10-foot wind tunnel. At a distance of 18 feet from the leading edge, the boundary layer is about 3 inches thick. The distribution of the fluctuations of the component in the direction of mean flow has been measured by the usual hot-wire equipment. The component of the fluctuations normal to the plate has been measured by the method of thermal diffusion and some work has been done by the same method on the component parallel to the plate but normal to the direction of mean flow.

Dr. H. K. Skramstad has devised a relatively simple method of measuring the eddy shearing stress, or more specifically, the mean value of the product of the component of the velocity fluctuation in the direction of the mean flow and the component at right angles to the plate. The exploring head is a hot wire at 45° to the direction of the mean flow and measurements are made with the wire in various planes with respect to the direction of the velocity gradient, the wire holder being rotated about an axis parallel to the direction of mean flow. The head is used with the usual compensated amplifier and thermal milliammeter. It can be shown that the eddy shearing stress is proportional to the difference between the maximum and minimum readings which are found at opposite inclinations of the wire in the plane of the velocity gradient. Measurements are in progress with this apparatus.

Modernization of wind tunnel.—It has been obvious for some time that further progress could be expedited with a wind tunnel of low turbulence. The 4½-foot wind tunnel has been rebuilt as a return-circuit wind tunnel, the same 75-horsepower motor being used and the 4½-foot octagonal working section being retained. A contraction ratio of 7.1 was found feasible in the present building. A series of wire screens of no. 18 mesh is used in place of a honeycomb, although provision is made for a honeycomb if its installation proves desirable. There is every indication that the turbulence in this modernized tunnel is less than one-tenth percent of the mean speed.

AERONAUTIC-INSTRUMENT INVESTIGATIONS

The work on aeronautic instruments has been conducted in cooperation with the National Advisory Committee for Aeronautics and the Bureau of Aeronautics of the Navy Department.

Investigations.—A report on the results on experiments to determine the performance characteristics of venturi tubes used in aircraft for operating air-driven gyroscopic instruments has been issued as Technical Note No. 624.

The gyroscopic instruments now used in navigating aircraft have been described, and data on their performance given, in a report which is to be submitted for publication as a Technical Note. The report includes a discussion of the new gyromagnetic compass.

A report on the theory and performance of rate-of-climb indicators as now designed is in preparation. The latest instruments indicate rate of climb in the standard atmosphere and are compensated for temperature.

An investigation of corrugated diaphragms has been started during the fiscal year. A satisfactory procedure of manufacturing the diaphragms hydraulically has been evolved. Performance data are being obtained on single, geometrically similar diaphragms of various diameters and thicknesses of beryllium copper and phosphor bronze. The manufacturers of aircraft instruments have cooperated, particularly by furnishing information on methods of manufacture and in suggesting problems for investigation.

Considerable progress has been made in the development of a synthetic lubricant for use in instruments. The lubricant does not spread on brass, steel, or jewels, has a low vapor pressure, and may be usable at temperatures down to about -30°C . Life tests are in progress.

Tests and test methods.—A turntable used to test accelerometers has been modified so that single-component instruments may be subjected to a continuous sinusoidal acceleration and to a part cycle of such an acceleration. The frequency and the amplitude of the acceleration are controllable to an adequate degree. The modification consists of the addition of a fixed pulley concentric with the turntable, and a pulley free to turn at the rim of turntable. When the pulleys are connected by a belt and the turntable rotates, the rim pulley rotates with respect to the turntable. A single-component accelerometer properly mounted on the rim pulley is thus subjected to a sinusoidal acceleration. Varying the diameter of the rim pulley gives an independent control of the frequency of the sinusoidal acceleration. Part cycles are obtained by the use of a friction clutch and stops to control the rim pulley.

An apparatus for subjecting aircraft instruments to a drop test has been designed and constructed.

Extensive tests were made on experimental resistance thermometers for use in measuring oil and intake-air temperatures. As a result, manufacturers greatly improved the reliability of the instruments under adverse service conditions.

A test apparatus for measuring oxygen delivered by oxygen regulators at various altitudes was designed, orifices being utilized for making the flow measurement.

New instruments.—Development is being continued on an air speed-acceleration recorder and a fuel flow-meter of the orifice type. A stick-force indicator was constructed. A number of pressure gauges were modified to indicate either suction or pressure when applied to the inside of the diaphragm capsule.

SUBCOMMITTEE ON AIRSHIPS

The Subcommittee on Airships formulates and recommends programs of airship research to be undertaken at the Langley Memorial Aeronautical Laboratory, and maintains contact with the work in progress.

The present program provides for an investigation in the Committee's 20-foot wind tunnel of boundary-layer control on airship forms. The investigation is to be conducted on a model approximately 20 feet in length, having a fineness ratio of 6. An arrangement with blower in the nose and an arrangement with stern propeller, with control of the boundary layer by both suction and discharge jets, will be included.

The information being obtained by the Committee's laboratory on the subject of gust intensities and gradients, in connection with the problem of structural loads on airplanes in flight, is of interest also in connection with airship design and operation. This work is described briefly in the report of the Committee on Aircraft Structures.

The subcommittee has kept informed of the latest developments in connection with airship design, construction, and operation, particularly the activities in Germany, where interest in the airship remains active, in spite of the unfortunate disaster to the *Hindenburg*. A technical Note (No. 637) has been issued by the Committee giving the results of an investigation by the Goodyear-Zeppelin Corporation of the fatigue strength of aluminum-alloy airship girders of several different types. A number of translations of German papers dealing with airship problems have been issued by the Committee as Technical Memorandums.

SUBCOMMITTEE ON METEOROLOGICAL PROBLEMS

The Subcommittee on Meteorological Problems keeps in contact with the progress of investigations being conducted by the various agencies on problems relating to atmospheric conditions which are of particular

importance in connection with aircraft design and operation.

Atmospheric disturbances and their effect on airplane accelerations.—The study by the Langley Memorial Aeronautical Laboratory of gust intensities and gradients and their effect on the accelerations on airplanes in flight has been continued. Additional data have been obtained in flight investigations with light airplanes. Measurements have also been made on two very large airplanes, and the more recent results indicate that there is no correlation between gust intensity and gradient. One particularly interesting acceleration record obtained on a very large airplane indicated a true gust velocity of approximately 57 feet per second, and the gust was found to reach maximum intensity in a distance of about 150 feet. This gust was downward in direction, and was experienced within a cumulo-nimbus cloud associated with a warm front.

Through the cooperation of a number of air-transport operators, the accumulation of data on accelerations on transport airplanes due to atmospheric disturbances has been continued. The total flying time represented by the records obtained is 57,000 hours. Records have been obtained in air-line operation over practically every part of the United States, on the routes from the East Coast to Bermuda, and to the northern part of South America, over the Andes Mountains, and across the Pacific.

A number of acceleration-altitude recorders recently completed are now being adjusted and calibrated for distribution to various Weather Bureau stations to obtain information as to the relation between gust intensity and altitude. A special instrument has been developed to indicate to the pilot when an acceleration of 2 g is reached, in order that he may observe particularly the atmospheric conditions involved.

Lightning hazards to aircraft.—The possible hazards to aircraft in flight due to lightning has been given special attention by the Subcommittee on Meteorological Problems during the past year. A special meeting of the subcommittee, to which representatives of the airline operators were invited, was held on November 30, 1937, for the discussion of this problem. A number of experiences of pilots in connection with electrical phenomena were described. It was noted that, while there had been a number of instances of airplanes being struck, the resulting damage to the aircraft was of a very minor nature, and in most cases passengers, and occasionally even the pilots, were not aware of the incident. As a result of the discussion, it was agreed that, although the lightning hazards to aircraft did not appear serious at the present time, it was desirable that the problem be given further study. A Special Subcommittee on Lightning Hazards to Aircraft was therefore appointed, particularly to prepare two programs of investigation—one a short-range program,

for the study of problems of immediate importance; and the other a long-range program, to provide for the extension of the present rather meager scientific knowledge of the nature of these electrical disturbances and the ways in which they may affect aircraft in flight.

Under the cognizance of this special subcommittee, investigations are being conducted in electrical research laboratories, of the effect of electric discharges simulating lightning strokes on sheet metal of the type used in aircraft construction. As the first step in the long-range program, information is being collected by means of questionnaires distributed among air-line pilots, as to incidents of electrical phenomena and the accompanying atmospheric conditions.

Ice formation on aircraft.—The study by the Langley Memorial Aeronautical Laboratory of the problem of ice formation on aircraft has been continued. The Committee has recently completed the N. A. C. A. ice tunnel for model tests in connection with this program, and a program of investigation of the aerodynamic effects of ice formation on airplanes and means of prevention or elimination is being initiated. In addition, the feasibility of ice prevention on airplanes by the utilization of heat from the exhaust is being investigated on an airplane in flight.

SUBCOMMITTEE ON SEAPLANES

The world-wide interest in seaplanes of large size has been intensified by the serious discussion of the possibility of replacing the very large and very fast luxury liners by fleets of large flying boats as proposed in the report of the United States Maritime Commission on "Aircraft and the Merchant Marine." The full effects of this proposal, together with those of the announced intention to build machines of practically double the size of existing machines for this country's own transoceanic services, have not yet appeared, but that they will have an important bearing on both domestic and foreign developments cannot be doubted.

In the case of such large craft, with the high wing loadings proposed, the aerodynamic drag of the hull becomes an important part of the total drag, even though the size of the hull may be reduced somewhat by putting accommodations in the wings. The air speed and the fuel required for a given voyage may be quite seriously affected if the requirements for taking off from the water are considered without reference to the more important requirement of low drag in flight. Work on the improvement of the forms of hulls suitable for flying boats of large size is being conducted with these facts in mind.

A large part of the hydrodynamic research in the past year has been devoted to investigations of a specific nature at the N. A. C. A. tank in connection with the development of projected seaplanes. These in-

vestigations were chiefly concerned with the effect of changes in hull form on water resistance and spray and required the use of larger models than may be towed in other tanks in the United States. The N. A. C. A. tank therefore has an important relation to the present development of large military and commercial flying boats.

In the specific investigations as well as the general research program, the projects of immediate interest to the military services have been given first priority. Tests of models of fifteen flying-boat hulls have been completed in the past year. Tank tests of a special nature, not applying to aeronautics but requiring high towing speeds, have also been conducted for the Bureau of Construction and Repair, the Bureau of Ordnance, and the Bureau of Engineering of the Navy Department. The magnitude of the work on these projects caused a reduction in the time devoted to fundamental hydrodynamic problems but gave an opportunity for a more detailed study of some accumulated data and the preparation of the data for publication.

Plant and equipment.—The enlargement and improvement of the N. A. C. A. tank, begun last year, have been completed and a very definite improvement in the operation of the tank has been observed. The basin now has a length of 2880 feet and the towing carriage is powered to travel at speeds up to 80 miles per hour. As anticipated, these features have increased the speed and efficiency of routine testing. In addition, a reserve capacity has been created for hydrodynamic research at speeds greater than are obtainable elsewhere.

The enlargement of the tank has required parallel improvement of the associated equipment. The great length of the basin has necessitated the development of new methods of aligning and leveling the rails, and the suppression of waves and surges. Various refinements and additions have been made to the carriage and the towing gear for the purpose of improving the ease and accuracy of recording the results of tests. A number of auxiliary devices have been constructed for use in the special tests that have been made and the range of adaptability of the equipment has been greatly increased.

Tests of models of representative flying-boat hulls.—In the investigation of the effect of form of hull on hydrodynamic resistance, tests have been made of large models of the hulls representing a variety of methods used to obtain satisfactory take-off performance.

N. A. C. A. model 36 was originally designed to be used in tests of stub-wing stabilizers and, in order to facilitate fitting different types of stubs, was given a rather long parallel middle-body. This form has proved to be of considerable interest to seaplane de-

signers, not only because the parallel body gives a form of hull that makes it possible to use a convenient arrangement of the interior, but also because the aerodynamic drag as measured in the Committee's twenty-foot wind tunnel over a wide range of angle of attack is quite low. The general tank tests indicate that the hydrodynamic characteristics are favorable and that the water resistance at the hump speed is exceptionally low. The results of these tests are presented in Technical Note No. 638.

Effect of rivet heads on frictional resistance.—The increasing use of flush riveting in the construction of all-metal aircraft has led to a need for information as to the effect of rivet heads on hydrodynamic resistance during take-off. The increase in frictional resistance caused by typical rivet heads was determined at the N. A. C. A. tank by tests of planing surfaces fitted with full-size rivets. The surfaces were towed at the high water speeds encountered by seaplanes during take-off and the relative resistance of the various shapes of head were measured. An analysis of the data, published in Technical Note No. 648, shows that for the rivet heads investigated the increase in frictional resistance is directly proportional to the height of the head. The order of merit of commonly used heads for seaplane hulls is therefore flush countersunk, oval countersunk, brazier, and round. The magnitude of the increase in hydrodynamic resistance depends, of course, on the number of rivets required in the structure.

Uses of tank data.—Investigations of resistance in the N. A. C. A. tank are made general in application by the fact that the models are tested over a wide range of speed, load, and trim. The results are intended to be used as a basis for design calculations to determine take-off resistance and to compare the advantages and disadvantages of various forms of hull. A discussion of possible uses of the "general" test data is presented in Technical Report No. 625. Among the subjects treated in this report are selection of best beam, importance of maximum trim, location of the center of gravity, and comparison of hull lines. It is concluded that the ranges of load and speed employed in the general tests are ample to cover future increases in the size of seaplanes.

In Technical Note No. 643 it is shown that in the solution of some design problems the normal resistance curve for a flying boat may be approximated by two straight lines. By the use of this approximation, charts are developed to aid in the rapid solution of certain problems involving the effect of the shape of the resistance curve on take-off time and distance or the determination of the accelerating forces required to meet specified take-off performance.

The N. A. C. A. trim indicator.—Further experience with the N. A. C. A. trim indicator has emphasized the importance of holding a seaplane at the trims that give least resistance during take-off.

The Committee has constructed and made available for loan to operators and manufacturers a form of trim indicator based on the principle described in Technical Note No. 486. The instruments have proved to be of great assistance in the test flying of large flying boats of new design, particularly those designed for commercial transoceanic service. It is in these types of service and on long-range military seaplanes, which, heavily loaded, must take off with comparatively little reserve power, that a "precision" take-off is essential. A relatively small increase in the total load with which a seaplane may safely take off represents a large increase in payload. Accordingly, it appears that a trim indicator of some form is essential to economical operation of seaplanes in transoceanic service.

In seaplanes that have a large excess power that may be used for take-off, the use of a trim indicator is of much less importance for routine service.

For test flying and in the training of pilots to fly a particular design the optical type of instrument is very useful and is simple and easily adapted to almost any arrangement of instrument board and windshield. An interesting application of the N. A. C. A. trim indicator in this manner was its installation and use for 100 hours of testing in an experimental flying model of a large flying boat.

SPECIAL SUBCOMMITTEE ON VIBRATION AND FLUTTER

As a result of the trend toward larger and relatively more elastic structures in airplane design, the problem of flutter has become increasingly important. The study of this problem at the Langley Memorial Aeronautical Laboratory and by other organizations has been continued during the past year.

The Special Subcommittee on Vibration and Flutter has held two meetings during the past year particularly for the consideration of the subject of flutter. Because of the activities of a special subcommittee recently appointed by the Committee on Aircraft Structures in the study of stresses due to resonant vibration and of the proof testing of aircraft structures in flight, the discussion at these meetings was chiefly limited to the subject of flutter. Reports of progress in the investigation of the subject were presented by the representatives of the various Government organizations. At the second meeting the report recently completed by the Committee's laboratory for issuance in advance confidential form to American manufacturers was presented and discussed.

The flutter problem.—The theoretical investigation of flutter started more than four years ago by the Langley Memorial Aeronautical Laboratory has been extended and generalized. In particular, the scheme of calculation of the critical flutter speed has been simplified to a routine method of calculation that includes the effect of structural damping. A large number of charts have been prepared to facilitate judgment of the effects of the various wing parameters affecting the flutter speed. The effects of the essential parameters in the cases of flexure-torsion, flexure-aileron, torsion-aileron, and flexure-torsion-aileron flutter have been listed and discussed. A series of nearly one hundred experiments in the high-speed tunnel recently completed has shown that the flutter speed can be calculated on the basis of the theory with good accuracy if the parameters are correctly specified or measured. Experiments made on cantilever wings indicate that, by slight modifications, the two-dimensional flutter theory can be used to predict the flutter speed, even for wings of fairly small aspect ratio. A study has been made of the actual mode of vibration involved in flutter and of the respects in which this mode differs from the vibration modes at zero air speed. A number of interesting conclusions have been reached; in particular, that the bending frequency involved in a flutter problem is greater than the frequency involved in a vibration mode at zero air speed, the difference depending mainly on the structural damping. The three-dimensional flutter problem is essentially understood as a problem of minimum boundary value, which fortunately can be handled by slight semi-empirical modifications of the two-dimensional flutter theory.

The problems of identifying the parameters and possible types of flutter on an airplane have been discussed. In the case of the airplane tail assemblage this may be particularly difficult and ground or flight tests may be necessary or desirable. The effects on the flutter speed of large bodies, such as nacelles or floats, on the wing or attached to it have also been investigated, as well as the effect of wing bracing and restraining wires. A report has been prepared presenting the results of this work. This report will include also a theoretical study of forced vibrations and air damping of the wing system, supplying a clearer perspective of the nature of flutter.

Vibration of tapered beams.—An exact solution has been developed for the equation of torsional vibration of a large class of tapered beams. Experimental measurements on five model beams give frequencies in agreement with the theory.

Air damping of vibration.—Fundamental data have been obtained on air damping by vibrating a flat plate in a chamber in which the pressure and the nature of the gas could be changed. The results have been ex-

pressed in terms of two new nondimensional coefficients which play a role in vibration similar to that of drag coefficient and Reynolds Number in steady flow.

Damping of propeller vibration.—A technique and method of analysis of the separate components of damping of the vibration of a freely suspended propeller have been developed. Air damping of the blades and friction in the hub were found to be predominant, in comparison with internal damping in the material of the blade.

Airplane vibration.—A systematic method of measurement and analysis of airplane vibration is being planned in order to be able to predict flutter velocities in actual airplanes. Measurements have been made on the tail assembly of one airplane to determine the frequencies and modes of vibration that determine the flutter characteristics.

REPORT OF COMMITTEE ON POWER PLANTS FOR AIRCRAFT

LANGLEY MEMORIAL AERONAUTICAL LABORATORY

INCREASE IN ENGINE POWER

The power output of air-cooled engines has been limited by the quantity of waste heat that could be dissipated efficiently by the fins to the cooling air. The dimensions of the fins used on the cast-aluminum cylinder heads of present engines are dictated by the casting technique of the foundry. As the final step in the Committee's research on the effect of fin dimensions on heat transfer a method has been developed for attaching preformed metal fins to air-cooled cylinders so that advantage can be taken of the improvement in cooling resulting from large increases in the fin surface. This method removes all restriction in regard to dimensions of the cooling fins that can be used and opens the way to more efficient cooling and to a further large increase in the power of air-cooled engines.

High octane number fuels.—The continued increase in the power output of aircraft engines is principally obtained by the use of premium fuels having high antiknock values. The investigation to determine the maximum permissible engine performance with these fuels has been continued at the Committee's laboratory. The work is being carried out on fuels having octane numbers of 87 to 100 to which various amounts of tetraethyl lead have been added. This investigation is under the cognizance of the Subcommittee on Aircraft Fuels and Lubricants and is described in the report of that subcommittee.

Flow through poppet valves.—The intermittent air flow through poppet valves in engines is calculated by the use of coefficients determined under conditions of steady air flow. The Committee is determining the coefficients of flow for large-diameter poppet valves when operated

in the same manner as in the engine. Measurements of the flow coefficients have been made at camshaft speeds from 130 to 1,200 revolutions per minute, at pressure differences up to 7.5 pounds per square inch and at valve lifts from 0.1 to 0.6 inch. The flow coefficients measured with steady flow can be applied to intermittent conditions without correction for valve opening speed or camshaft speed. The results of this investigation are being prepared for publication.

Piston temperatures.—With increase in the power of aircraft engines the aluminum-alloy piston and the cast-iron piston rings are required to transmit proportionally larger quantities of heat to the cylinder wall. An investigation is in progress to determine the important factors controlling piston cooling and to study the effect of engine and cooling conditions on piston temperatures. A method has been developed for attaching thermocouples to the piston and measuring piston temperatures under engine operating conditions. The thermocouple and potentiometer circuit is completed at bottom center for 20° of crank angle through contacts mounted on pneumatically operated plungers. Piston temperatures are being surveyed on a high-output single-cylinder Diesel engine and a modern air-cooled engine.

The 2-stroke-cycle engine.—The use of the 2-stroke instead of the 4-stroke cycle is an attractive method for increasing engine power per unit of displacement. The 2-stroke-cycle engine requires a pump to force the combustion and scavenging air into the engine cylinder. The Committee's research on the liquid-cooled spark-ignition fuel-injection engine has included a study of the effect on performance of variable exhaust-valve and inlet-port timing, scavenging pressure, and engine speed.

The sleeve-valve engine.—The two outstanding advantages of the single sleeve-valve engine over the poppet-valve engine are increased breathing capacity and higher allowable rotative speeds. These characteristics are fundamental requirements of future aircraft engines. The Committee's analysis indicates a decided superiority of the sleeve-valve over the two-poppet-valve type and a somewhat lesser superiority of the sleeve-valve over the four-poppet-valve type, equal flow coefficients being assumed for the sleeve and poppet valves. Since the flow coefficients may differ enough in the two cases to modify these conclusions appreciably, an investigation is in progress to determine the relative coefficients of flow through inlet and exhaust valves and sleeve ports under conditions of steady and intermittent flow.

COMBUSTION RESEARCH

The study of combustion in spark-ignition engines has been continued. New knowledge has been obtained of the combustion under knocking conditions with fuels of high octane number. Particular attention has been

given to the determination of the effect of air flow within the cylinder on the distribution of fuel sprays, the rate of combustion, and the reproducibility of successive engine cycles. Several methods have been investigated for the recovery of waste heat from the engine exhaust gases.

Ignition lag in compression-ignition engines.—The variations in ignition lag and combustion associated with changes in air temperature and density have been studied for a Diesel fuel in a constant-volume bomb. The highest temperature of the bomb approximated that attained in a compression-ignition engine in the usual range of injection advance angles. The ignition lag was found to be essentially independent of the quantity of injected fuel. In order to obtain the best combustion and thermal efficiency, it was desirable to use the largest ignition lag consistent with a permissible rate of pressure rise. Technical Report No. 617 has been published giving the results of this investigation.

Knock in aircraft engines, if continued, may cause preignition, with consequent loss in engine power. The N. A. C. A. combustion apparatus is being used for a series of tests in which conditions causing knock are compared to conditions causing preignition. The preignition is caused by an electrically heated hot spot that can be maintained at a maximum temperature of 1,900° F. It is possible to adjust the hot-spot temperature so that flame proceeding from the spark plug at the opposite side of the combustion chamber causes auto-ignition of the charge at the hot spot. The results of this investigation are being prepared for publication.

Detonation research.—A photographic study of the combustion in a spark-ignition engine has been made, including both schlieren and flame photographs taken at high rates of speed. The results of this investigation have been published in Technical Report No. 622.

Exhaust-gas analysis.—In order to determine the lower heating value of a fuel from its calorimetric heat of combustion it is necessary to know the hydrogen-carbon ratio of the fuel. The methods described in the literature have not given satisfactory results with gasoline. An investigation is being made to develop a satisfactory method of analysis for these volatile hydrocarbons.

An investigation has been made to determine the interrelationship of the constituents of the exhaust gases of internal-combustion engines and the effect of engine performance on these relations. The work has included a study of single-cylinder and multi-cylinder spark-ignition engines and single-cylinder compression-ignition engines. Definite relations independent of engine design and operating conditions were found between the constituents of exhaust gases, air-fuel ratio, water of combustion, and combustion efficiency.

Technical Report No. 616 gives the results of this investigation.

Air flow in cylinders.—With fuel injection into the engine cylinder, increased air turbulence assists in atomizing and distributing the fuel spray. The air flow within the cylinder of an engine has been investigated by the use of an engine with a glass cylinder. The data are recorded by motion pictures taken at rates of 2,500 frames per second of the motion of goose down inducted with the inlet air. The shrouded inlet valves considerably increased the distribution of the fuel within the cylinder. The air flow reduced the penetration of fuel sprayed from an annular orifice more than from round-hole orifices. The tangential swirl set up during the inlet stroke was found to continue throughout the compression and expansion strokes. A report is in preparation describing the investigation.

An investigation of the effect of air flow within the combustion chamber of a spark-ignition engine has been conducted on the N. A. C. A. combustion apparatus. By means of spark-schlieren photography and time-pressure records, a study has been made of the effects of air swirl on the combustion propagation. The air flow was produced by shrouds on the inlet valves, and was comparable with that obtained in the glass-cylinder engine. Directing the air in an orderly swirl resulted in great improvement in the reproducibility of successive engine cycles. When the velocity of the intake air was changed by blocking one of the inlet valves without changing the engine speed, there was a considerable increase in the rate of combustion. This same increase was obtained when two inlet valves were used by doubling the engine speed. The results of this investigation are being prepared for publication as a Technical Report.

FUEL CONSUMPTION

For modern long-range aircraft, the fuel load is approximately one-half the useful load, and means must be found for reducing the fuel consumption of the engines under cruising conditions. Research has been conducted on the design and development of an N. A. C. A. indicating fuel flowmeter and a mixture-ratio indicator for use in flight. The effect of operation at various percentages of full-load torque and of rated speed on the minimum specific fuel consumption of an air-cooled engine has been determined.

Fuel distribution.—The use of a fuel-injection system instead of the conventional carburetor should result in more uniform fuel distribution, more rapid engine acceleration, and satisfactory engine operation irrespective of the attitude of the aircraft. An investigation has been completed to obtain a comparison of the performance of an engine with a carburetor, with fuel injection into the inlet manifold, and with fuel injection

into the cylinder. The results of this investigation, which are being prepared for publication as a Technical Note, show that slightly more power was obtained when the fuel was injected into the cylinder because of the increased volumetric efficiency due to the cooling action of the fuel spray. Fuel injection into the cylinder also permitted the use of manifolding that offered less restriction to the air flow. The minimum specific fuel consumption and the cylinder-head temperatures were the same regardless of the method used for distributing the fuel to the air.

The N. A. C. A. fuel flowmeter.—The use of a fuel flowmeter, which indicates instantaneous rates of fuel flow, makes it possible to operate aircraft engines at mixture ratios which will result in low specific fuel consumptions. In multiengine aircraft the fuel flowmeter makes it possible for all engines to be operated at the required rates of fuel flow. The N. A. C. A. flowmeter, which indicates mass rate of fuel flow, has been modified as a result of flight tests of the Army Air Corps and is now considered a satisfactory instrument for use in flight.

Mixture-ratio indicator.—The need in aircraft for a mixture-ratio indicator capable of indicating mixtures both leaner and richer than the theoretically correct mixture has led to the development by the Committee of an instrument capable of indicating any practical fuel-air ratio. A laboratory design has been used successfully and a design suitable for flight testing has been built. A report on the flight performance of this instrument is being prepared for publication.

ENGINE COOLING

The power output and the specific fuel consumption at which air-cooled engines can be operated are dependent upon satisfactory engine cooling. The use of radial air-cooled engines having two and three banks of cylinders for the obtaining of increased power requires a large increase in the effectiveness of the cooling fins placed on the cylinder head and barrel. Particular attention must be given to the cooling of the cylinder barrel to insure satisfactory operation of the piston and piston rings with engines of higher power.

Fin dimensions.—The quantity of heat dissipated from a finned surface is a function of the dimensions of the fins. The analysis being made to determine the best proportions for metal fins for given rates of heat flow has been continued. Thin, closely spaced aluminum fins of optimum proportions were found to give approximately 25 percent more cooling for the same fin weight and pressure drop (4 inches of water) than thicker, correctly proportioned fins having a spacing of 0.14 inch. As the heat dissipation from the cylinder walls of air-cooled engines is proportional to the 0.65 power of the indicated horsepower developed, it follows that a 25-percent improvement in cooling

should permit a 42-percent increase in the engine power.

The power required to cool the widely spaced finned cylinders was slightly more than for the closely spaced finned cylinders at a pressure drop of 4 inches of water. For a pressure drop of 12 inches of water, however, the power required to cool the widely spaced fins was found to be approximately 25 percent more than for the fins of optimum design. Although thin, closely spaced fins are difficult to construct by present methods they have been found to be desirable, especially when constructed of metals of high thermal conductivity.

Heat-transfer coefficients.—The investigation to determine the surface heat-transfer coefficients of finned cylinders has been continued. Heat-transfer tests have been conducted on fin surfaces spaced 0.010 inch and on widely spaced, thick-finned surfaces. The object of these tests was to determine the trend of curves correlating the surface heat-transfer coefficients. A report is being prepared presenting the results of this investigation.

Flow around finned cylinders.—In order to obtain a better understanding of the phenomena attending the cooling of air-cooled engines, photographs were taken, by the use of titanium tetrachloride, of the air flow between the fins of a large-scale cylinder model. The double spiral, which has been shown to occur in the flow through bent pipes, was observed. The flow has an outward radial component, away from the cylinder axis, in the region near the center of the fin space, and an inward radial component along the fin surfaces. The radial components of the velocity tend to disappear as the fin spacing is reduced. At a fin space corresponding to $\frac{5}{32}$ inch for a cylinder diameter of 4.66 inches, the radial components were very clearly evident, whereas, at a fin spacing corresponding to $\frac{1}{8}$ inch, no indication of a radial velocity component could be detected. The radial components also disappeared at low velocity.

The problem was studied further by tests on model finned cylinders both in ducts and in the front of an engine cowl. Two Technical Notes, Nos. 649 and 655, show the effect of streamlining the cylinder and the effect of baffle length on optimum fin spacing. Also, it is shown by analysis and from experimental results that cooling on a finned cylinder obeys the same physical laws known to apply to heat transfer for pipes. The solution of a practical case is made comparatively easy by the use of these laws and knowledge of the cooling performance of actual engines.

An investigation has been undertaken to determine the characteristics of the cooling in the front of a cowed engine. The irregular flow existing in this region results in a cooling dependent on air speed in a little-understood manner. The tests show the effect on the cooling of variations of position, fin orientation, fin

spacing, and fin width, with the propeller operated to simulate the cruising condition and the ground condition, and with a spinner to increase cooling pressure in take-off. The results from these tests will show both the nature of the phenomenon and how to make the best use of it for cooling.

Cylinder temperature correction factors.—Technical Report No. 645 has been prepared presenting the results of the investigation made to determine the correction factor for correcting cylinder temperatures of air-cooled engines to a standard atmospheric temperature. The correction factors include flight-test conditions such as level flight, climb, and take-off, the condition with the airplane stationary on the ground, and the conditions of a constant mass flow of cooling air, and of a constant velocity of the cooling air.

Heat-transfer process.—A study has been made of the transfer of heat from the gases of combustion to the cylinder wall, and from the cylinder wall to the cooling fins on air-cooled cylinders. Necessary empirical constants in the heat-transfer equations have been determined from engine tests of a Wright Cyclone cylinder. The effects on cylinder temperature of the following engine conditions were determined: Exhaust back pressure, air fuel ratio, spark timing, carburetor air temperature, engine speed, brake mean effective pressure, cooling-air temperature, and pressure drop across baffled cylinder. Equations were obtained for the cylinder head and barrel temperatures as functions of the engine and cooling conditions. A simple method of comparing the cooling of different air-cooled engines has been developed. A report on this investigation is being prepared.

Blower cooling of engines.—Preliminary studies have been made to determine the relative merits of cooling air-cooled engines by induced flow and by a blower. The necessity for blower cooling at high altitudes with present engines and at sea level with future engines requiring higher pressure drop has been reviewed. Blowers and blower arrangements of several types have been examined with the object of determining their suitability for various conditions with special reference to large airplanes and to flying at high altitudes.

The N. A. C. A. air-cooled cylinder.—The cylinders of air-cooled engines are formed of a cast aluminum head screwed and shrunk onto a steel liner. The dimensions of the fins that can be cast on the head are limited by the casting technique of the foundry. The dimensions of the fins on the barrel are limited by difficulties in machining. The Committee has discovered a method of attaching preformed fins to the cylinder head so that all restrictions as to fin dimensions that can be used are removed and advantage can be taken of the improvement in cooling resulting from large increases in the fin surface. The internal drag horsepower required to cool the N. A. C. A. cylinder is a negligible

amount of the engine power developed. This method of construction should make possible large increases in the power output of air-cooled engines without sacrifice of satisfactory engine cooling.

SUPERCHARGER RESEARCH

The altitude selected for flight with transport aircraft is dependent to a large extent upon weather conditions. The requirement of flight at high altitudes has greatly increased the interest in highly supercharged engines.

Performance of superchargers.—Computations have been made to determine the power required and the heat that must be dissipated to maintain discharge-air temperatures of from 60° to 240° F. when an airplane is operating at altitudes from sea level to 80,000 feet with superchargers having a range of compression exponents from 1.0 to 2.0. The boost pressures covered a range from zero to 100 pounds per square inch. The results of this analysis will be applied to an engine to determine the net power and the fuel consumption under these supercharged conditions with gear-driven and turbine-driven superchargers.

Air intercoolers.—The reduction in the antiknock quality of a fuel with increase in inlet-air temperature necessitates the use of an efficient intercooler to reduce the air temperature on supercharged and boosted engines. The present core-type intercoolers have been found to crack and leak at boost pressures of the order of 15 pounds per square inch. A new type of finned intercooler has been tested to determine its heat transfer.

Supercharging of aircraft cabins.—An analysis has been made of the requirements of superchargers for maintaining cabin pressures at high altitude. The results indicate that the Roots-type blower should be very satisfactory for this service because the volume of air required can be controlled by the quantity of by-passed air. The power expended on the by-passed air is small.

COMPRESSION-IGNITION ENGINES

The use of compression-ignition engines in aircraft offers advantages because of the inherent low fuel consumption and the reduction in fire hazard. These two characteristics are of particular importance for transoceanic aircraft. The Committee's research on the compression-ignition engine for aircraft includes a study of the factors influencing the injection and combustion of fuel sprays suitable for this type of engine and the development of a combustion-chamber form that gives good mixing of the fuel and the air. The problems involved in the application of this combustion chamber to the radial air-cooled engine are being investigated.

Combustion research.—The ignition lag and the rate of combustion of the fuel oil in compression-ignition engines can be varied by the addition of small quantities of certain chemicals to the fuel oil. The Com-

mittee has investigated a range of fuel oils, mixtures of fuel oil and alcohol, and fuel-oil dopes to determine their effect on power output and fuel consumption. The engine power has been shown to be practically unaffected by fuel quality; fuels with long ignition lag may be expected to result in rough running. Combustion inhibitors in the form of small percentages of isoamyl nitrate, ethyl nitrate, and tetranitromethane have been shown to lower the rate of pressure rise and to have a negligible effect in increasing power outputs. Alcohol mixed with fuel oil may give a maximum power increase of 4 percent at, however, a prohibitive increase in fuel consumption. In general, it has been found that special fuels are unnecessary in obtaining best performance with a compression-ignition engine; that no gain in power or economy results from their use. A Technical Report presenting the results of this investigation is being prepared.

A study of combustion rates as influenced by the type of fuel, the rate of injection, and the injection advance angle has been started to cover a range of engine speeds from 1,500 to 2,500 r. p. m. The combustion rates are being determined from an analysis of indicator diagrams.

The investigation of ignition lag with the constant-volume bomb has been extended to include several Diesel fuels of different cetane number and different concentrations of Diesel fuel dopes. The results indicate that, at the lower air temperatures in the bomb, the variation in fuel rating order for a series of fuels is somewhat greater than it is in the C. F. R. engine or the N. A. C. A. test engines. The variation in ignition lag over a range in cetane number decreases markedly with increase in air temperature and density. A summary of these results is being prepared for publication.

The 4-stroke-cycle engine.—The problems connected with the adaptation of the N. A. C. A. displacer type of combustion chamber to an air-cooled cylinder having a 5-inch bore and a stroke of $5\frac{1}{2}$ inches are being investigated. Indicated mean effective pressures of 250 pounds per square inch have been obtained at 2,200 r. p. m. with a boost pressure of 10 pounds per square inch. The dimensions and arrangement of the finning on the aluminum cylinder head and the steel cylinder barrel are being studied to insure adequate cooling.

A report describing tests under simulated altitude conditions has been prepared and published as Technical Note No. 619.

A liquid-cooled cylinder has been designed for a single-cylinder engine having a bore of $6\frac{1}{8}$ inches and a stroke of 7 inches to investigate problems peculiar to obtaining a high output from a cylinder of a size comparable with the largest air-cooled engine cylinder now in use. The N. A. C. A. displacer-piston combustion

chamber will be used with a conventional air-cooled engine and a pushrod-operated valve gear.

As a means of obtaining better utilization of the combustion air, a cylinder head has been constructed embodying a modification of the vertical-disk displacer combustion chamber to allow the use of two inlet and two exhaust valves, and two advantageously located injection valves. With this arrangement all the combustion air will be forced to flow past the fuel-injection valves. Preliminary performance tests of the cylinder head have been made with a single fuel-injection valve mounted in the top of the cylinder for comparison with the performance obtained with the two fuel-injection valves.

The 2-stroke-cycle engine.—An investigation of the effect of variation of the exhaust function has been completed over a wide range of exhaust timings and exhaust-valve cam dwells for several engine speeds and scavenging pressures. Tests have been made to compare the engine performance with the 62 inlet ports in the cylinder liner arranged to direct the air into the cylinder at a common angle or in several bands at different angles to the radial. The best performance was obtained with the single-entry angle of 56° common to all ports. Design alterations to the connecting rod, exhaust valve cams, and inlet ports have been made to make it possible to increase the maximum engine speed from 1,900 to 2,400 r. p. m.

NATIONAL BUREAU OF STANDARDS

Phenomena of combustion.—A spherical bomb with central ignition and auxiliary equipment which yields simultaneous photographic records of the travel of flame and the development of pressure during gaseous explosions has been in use throughout the year. In such a bomb the samples of fuel required are very small, initial conditions may be accurately controlled, and combustion progresses under idealized circumstances, since the spreading flame is undisturbed by turbulence, by contact with restraining walls, or by heat losses other than the unavoidable loss due to radiation. It is therefore possible to study the rate of energy liberation and the speed of flame relative to the remaining unburned charge throughout the succeeding stages of the burning. Although these factors are of fundamental importance in the engine cylinder, they cannot be accurately measured there because of the complicated geometrical configuration of the combustion chamber.

Early experiments with the spherical bomb indicated clearly that high accuracy in the measurement of pressure and flame radius was essential to satisfactory results. The difficulties of attaining such high accuracy in following the extremely rapid course of an explosion necessitated careful development of both the experimen-

tal apparatus and the technique of securing and analyzing the observations.

During this development period, mixtures of carbon monoxide and oxygen were used. The results of these test experiments show not only that the apparatus is capable of serving the purpose for which it was designed, but also indicate some interesting characteristics of this particular explosion process.

In general, the inflammation of a unit mass of this mixture produces an increase in pressure which does not vary greatly with the temperature and pressure prevailing in the unburned charge. However, the energy liberation per unit mass of charge is, without exception, less than would be expected if the burning were completed in the front surface of the flame.

Very early in the explosion, while the rise in pressure is too small to measure, the flame records all show that the spatial velocity increases for a short time. These low initial velocities cannot be accounted for solely by low speeds of advance of the flame into the unburned mixture, but indicate that the amount of expansion or energy liberation per unit mass of charge is much lower in the very early part of the explosion than later on.

The observed behavior of the flame can be explained by assuming that the burning is not complete in the flame front, but continues throughout a zone of considerable thickness behind the front. Other possible ways to study this hypothesis in the light of more direct evidence are being considered.

Records have been made of explosions of the hydrocarbon fuels benzene, N-heptane and iso-octane with air, but these results are not yet sufficiently complete for presentation.

Explosions in tubes.—At the request of the Bureau of Air Commerce, now the Civil Aeronautics Authority, the possible hazards of explosions of maximum-power mixtures of gasoline vapor and air in tubes simulating gasoline-dump ducts were studied. The results indicated that destructive peak pressures are not to be expected in any open-end tubes of dimensions appropriate for dump ducts on aircraft. The ducts should be free from constrictions and from weak, flat areas which might be caused to vibrate violently during an explosion.

Ignition cable.—The energy which must be furnished by the spark coil to cause the spark plug to fire is proportional to the capacitance of the secondary circuit. In many ignition systems the greatest portion of the capacitance is due to the high-tension ignition cable. By decreasing the capacitance of the ignition cable with respect to the engine, less energy is required from the spark coil and consequently less energy from the battery. The capacitance of the cable is decreased by decreasing the size of the conductor.

Measurements have shown current discharges of 30 to 80 amperes across the spark electrodes. These discharges last about one millionth part of a second and consist of 10 to 14 oscillations. After the initial discharge it is desirable to damp out all other oscillations as quickly as possible so as to reduce electrode wear. This is done by the use of a high-resistance conductor.

Decrease in heat transfer from the spark plug to the rubber insulation may be accomplished by using a conductor in the cable which is a poor conductor of heat.

With the decreased cross-sectional area the conductor must be sufficiently strong to make it possible to draw the cable through conduit.

A material which has been found to satisfy these requirements is stainless steel.

Spark plugs.—The present methods of testing spark plugs have failed to supply the necessary information for selecting a suitable plug for a particular engine operating under service conditions. New methods of testing are now under investigation.

Electrical equipment.—Studies have been made of low-tension cable, and tests of auxiliary electrical equipment. Facilities have been provided for testing electric motors which operate at speeds in excess of 24,000 r. p. m.

Temperature surveys.—Temperature surveys have been made on all new types of Navy airplanes, both on the ground and in flight. The measurements have been extended to include oil temperature and intake-mixture temperature.

Flow characteristics of fuel lines.—In connection with the aviation vapor-lock project of the Cooperative Fuels Research Committee, the Bureau is investigating the resistance to fuel flow in component parts of aircraft fuel systems as a function of rate of flow and relative amounts of liquid and vapor flowing. The object of this work is to provide the designers of fuel-feed systems with reliable data on gasoline flow under vaporizing conditions.

Engine testing.—For the information of the military services, two small experimental engines were subjected to approximate altitude tests. These engines were submitted in connection with the development of auxiliary power plants for use in large aircraft. At the request of the Matériel Division of the Army Air Corps, a series of 50-hour endurance tests were conducted on the torque stand on a 9-cylinder radial aircraft engine, for the purpose of comparing different oils and two types of oil tank.

Measurement of surface wear.—A new method of evaluating surface wear, by successive measurement of minute indentations made in the surface with a diamond point, has been developed. This method seems particularly promising for the measurement of piston and

cylinder wear in engines, where measured clearances, including as they do the effects of piston growth and cylinder distortion, frequently give highly misleading indications as to wear.

SUBCOMMITTEE ON AIRCRAFT FUELS AND LUBRICANTS

Engine performance with iso-octane fuels.—As mentioned above in the report of the Langley Memorial Aeronautical Laboratory, the Committee has continued the investigation to determine the maximum permissible engine performance with fuels having octane numbers of 87 to 100 to which tetraethyl lead has been added. Data have been obtained on a pent-roof combustion chamber and on a flat-disk combustion chamber. The results have indicated that the knocking characteristics of any one fuel in a given engine can be expressed as a curve showing the critical relationship between the inlet-air temperature and the density of the combustion gases at top center. From this curve it can be determined whether or not various combinations of inlet-air pressure, inlet-air temperature, and compression ratio will result in knock. This method (described in Technical Note No. 647) of expressing the knocking characteristics of a fuel has been suggested as a means of rating fuels.

The effect of irregular spark timing on the knocking properties of fuels has been discussed in Technical Note No. 651. It was found that on the Committee's high-speed engine a change of one crankshaft degree in spark timing was equivalent to a change of 0.4 pound per square inch in allowable inlet pressure.

The investigation of the correlation of the effects of the engine variables on the knocking limits of the fuel is being conducted on a high-speed C. F. R. engine. Tests are being made to determine the effect of mixture density and temperature on knock at various engine speeds. Tests are also being conducted on four fuels each having an octane number of 100 by the C. F. R. method. The fuels differ, however, in the amount of tetraethyl lead added to the base fuel to bring the octane number to 100.

Stability of aviation oils.—The original program has been completed on the investigation of the stability of aircraft engine lubricating oil, conducted by the National Bureau of Standards in cooperation with the Bureau of Aeronautics of the Navy. From extensive laboratory data obtained on a large number of aviation oils by the use of several variations of each of three general methods, a laboratory method has been found which gives a satisfactory correlation with data on the same oils obtained in a Pratt and Whitney Hornet engine. This correlation has been verified by service tests, and makes possible the prediction of the service stability of an aviation oil from the results of comparatively simple laboratory tests.

Additional information has been obtained on the evaporation losses which occur at temperatures approximately those on the cylinder wall near the combustion chamber and around the upper piston ring. These data throw considerable light on the effect of refining processes on oil consumption.

Work on the stability of compounded oils has been continued and information on this characteristic has been obtained for many of the compounding materials found effective commercially for reducing engine wear.

Ring-sticking with aviation oils.—Preliminary work at the National Bureau of Standards with a single-cylinder engine has indicated the possibility of evaluating the ring-sticking characteristics of aviation oils by tests of this type, and of investigating the effect of compounding agents in reducing the tendency to cause ring-sticking.

Extensive information has been obtained on the thickening of oils at the high temperatures encountered around the upper rings and a considerable amount of useful data obtained relating the extent of thickening to the processes used in manufacturing the oil.

Wear, oiliness, and corrosion characteristics of aviation oils.—In cooperation with the Bureau of Aeronautics and the Air Corps, work has been continued at the National Bureau of Standards on the investigations of the relations between oil characteristics and bearing corrosion, with special reference to master rod bearings, and wear reduction of cylinder-wall and piston-ring materials. Most of the necessary equipment has been constructed and assembled, and some preliminary information has been obtained, but the work has not progressed sufficiently far to permit any conclusions to be drawn as yet. Emphasis is being placed on the effects of compounding agents in reducing bearing corrosion, wear of cylinder walls and piston rings, and frictional losses in master-rod bearings.

The first run of an R-1535 engine to study the problem of wear with various oils was terminated after 35 hours by a mechanical failure. Further running under different conditions and with a smaller engine is being considered. In spite of the fact that no other data which are exactly comparable will thus be obtained, very valuable information has been collected regarding the relative merits of wear determination by the indentation method as well as by conventional gauge measurements. The former is a new method and consists of making almost microscopic indentations in the wearing surfaces, and the surface wear is then accurately indicated by optically measuring the changes in the lengths of these marks. By this method excellent data are obtained on the actual thickness of the material worn off the surface, and the results so far indicate that on engine cylinders and pistons even the most accurate conventional gauge measurements may be deceptive in the region of small total wear, or

where the differences in wear are small. Since in the case of the R-1535 engine test both methods were used, some very interesting data on distortion as well as on wear are being obtained. The report on the tests with this engine is in preparation.

REPORT OF COMMITTEE ON AIRCRAFT MATERIALS

SUBCOMMITTEE ON METALS USED IN AIRCRAFT

Effect of weathering on light-metal alloys.—A report on this investigation has been prepared for publication summarizing the effect of continuous exposure to the weather on aluminum and magnesium alloys in sheet form as used in aircraft. The tests included the various alloys and protective surface treatments commercially available when the investigation was started. The results of the five-year program have definitely established the relative merits of most of the commonly used alloys and protective treatments with respect to atmospheric corrosion resistance, as follows:

(a) **Aluminum alloys.**—Aluminum alloys containing magnesium as the essentially alloying constituent are very resistant to attack even under the very severe exposure conditions prevailing in many of the tests. They head the list of all the alloys tested. Next in order are the alloys containing magnesium and silicon. The third group of alloys, those containing copper, are susceptible to intercrystalline corrosive attack and, when in thin-sheet form, often lose much of their initial tensile strength and ductility as a result of a corrosive attack of this character.

(b) **Surface treatment.**—For prolonged exposure of aluminum alloys, a surface layer of pure aluminum is overwhelmingly superior to any other protective method available. Of the other protective measures, the most satisfactory ones depend upon surface oxidation. This forms an excellent basis for the adherence of coatings applied thereon. The surface film produced by anodic oxidation is by far superior to any other of this type of treatment, although it too should be followed by another coating for most satisfactory service. All oxide surface films can be greatly improved by "sealing." The use of the chromic acid solution in one type of anodizing treatment is excellent for this purpose, according to the test results.

(c) **Applied organic coatings.**—All the various kinds of vehicle of the varnish type used in the applied coatings yielded excellent results when pigmented with aluminum. Other pigments were decidedly less satisfactory.

(d) **Magnesium alloys.**—Magnesium-alloy sheet properly protected by (1) suitable surface treatment to obtain adherence of the coating, (2) a primer, and (3) surface coating of the kind mentioned above, withstood very satisfactorily five years' continuous exposure

to the weather in a tropical marine location (Coco Solo, Canal Zone).

New series of exposure tests of aircraft metals.—During the year a comprehensive series of exposure panels was installed, with the cooperation of the Bureau of Aeronautics of the Navy Department, at the Naval Air Station at Hampton Roads, Virginia. The materials used are representative of commercial aluminum and magnesium alloy and of stainless-steel sheet of various kinds. The light-metal alloy sheets are exposed (a) in the bare condition, (b) after being coated in accordance with the principles established in the previous work, (c) joined together in couples, the components of which are of different compositions, by spot welding and by rivets of various compositions. This last phase of the test is considered to be of major importance in this series of exposure tests. The stainless-steel panels are exposed in the same manner, except that no coatings have been applied. To provide information on conditions such as those involved in the use of sea aircraft, two types of exposures have been used. In one series, the panels are exposed continuously to the marine atmosphere; in the second, the racks are located at mean tide level so as to provide total immersion at high tide followed by free exposure to the air at periods of low tide. Samples are removed at intervals for testing in the laboratory to determine the changes in surface conditions resulting from corrosion and the attendant changes in mechanical properties. Yearly reports summarizing the results are planned.

Structural changes in aircraft metals occurring as a result of service stressing.—A report has been prepared for publication by the Committee entitled "Effect of Working Stress on the Impact Resistance, X-ray Diffraction Patterns and Microstructure of 25S Aluminum Alloy." The aluminum alloy 25S, because of its importance as a propeller material, was the material tested. In general, the results were negative in their nature. No evidence was obtained to indicate a decrease in impact resistance, either at normal or sub-zero temperature, as a result of continued fatigue stressing below the endurance limit; nor was any indication obtained by X-ray diffraction examination of impending fatigue failure of material severely fatigue-stressed but without actual crack formation. Certain suspected microstructural features first observed to occur in used propeller blades, but later noted in unused blades, were found not to be indicative of inferior mechanical properties. Work on this subject on the possible deleterious effect of continued fatigue-stressing has been extended to chromium-molybdenum steel (SAE X4130) of the type used extensively in aircraft construction.

Effect of sub-zero temperatures on aircraft metals.—Study has been continued to determine the factors responsible for the decrease in impact resistance of

ferritic steels with decreasing temperature and to endeavor to improve this condition. The results of tests of welded steels at low temperature, -80°C ., indicate that this question is one of real importance in welded structures.

Elastic properties of high-strength aircraft metals.—An extensive report has been prepared for publication summarizing the work done in this investigation. It is entitled "Elastic Properties of 18-8 Chromium-Nickel Steel as Affected by Plastic Deformation." A new approach is offered for the determination of the elastic properties, yielding results of a more practical and useful nature than those by more conventional testing procedure. Despite the fact that the austenitic steels, of which this is a representative, possess only pseudo-elastic properties, their other characteristics make them very desirable for many structural applications.

Durability of magnesium.—The durability of magnesium alloys, especially in sheet form, is largely determined by the surface protective measures used in connection with such materials. This is most marked in a marine atmosphere but, as mentioned above, properly protected magnesium alloy in sheet form has withstood continuous exposure under tropical marine conditions for five years without serious impairment of its properties. Study has been continued with the hope of simplifying and improving current methods of surface treatment of magnesium. It has not yet been deemed advisable, however, to substitute a new process for the widely used anodic treatment in the dichromate-phosphate solution, despite the encouraging results obtained.

SUBCOMMITTEE ON MISCELLANEOUS MATERIALS AND ACCESSORIES

The problems investigated by this subcommittee at the National Bureau of Standards during the past year included the development of a flexible substitute for glass, of a substitute for silk for parachute shroud lines, and of a plastic material for aircraft structures.

Two items mentioned in the 1937 report are omitted from this. The problem of finding a substitute for linen webbing is considered completed. Materials for acoustical and thermal insulation are now in general use and are considered satisfactory when first installed. The subcommittee is watching their performance to see whether or not they deteriorate with age under service conditions.

Development of flexible substitute for glass.—During the current year efforts in connection with the development of a flexible substitute for glass for windshields have been largely concentrated on the development of improved compositions of the cellulose acetate and methyl methacrylate types, particularly with regard to shrink-

age and weathering characteristics. This work has been carried on with the active cooperation of the manufacturers' laboratories and it is believed that the marked improvement which has been noted in the commercial sheets in recent months can be attributed at least in part to the stimulus which this investigation has provided to the development of better formulations and methods of processing.

It has been found that the tendency of the early methyl methacrylate resin to craze in service was due either to the presence of a small amount of monomer or solvent in the sheet or to strains left in the finished sheet or produced during forming operations. Seasoning the sheet at a high temperature and careful control of the temperature during shaping have eliminated the crazing, at least for the two-year period during which such sheets have been exposed. Accordingly, heat seasoning of the methacrylate sheets has been adopted by the manufacturers, with the result that today these products have improved surface hardness and freedom from crazing and undergo practically no shrinkage when exposed to the weather.

For the cellulose acetate sheets, the primary problem has been one of increasing the resistance to sunlight or weathering in general. In order to study the effect of various plasticizers on this property, approximately 60 experimental sheets were made by cooperating manufacturers during the course of the year. These are now being examined for weathering stability by means of both accelerated and roof exposure tests, and some of these have been found to be remarkably resistant to deterioration by ultraviolet light. The tests have also indicated that by suitable heat seasoning of the cellulose acetate sheet during manufacture shrinkage as observed in laboratory heating tests can be reduced to a small percentage of that now obtained with the commercial products. Specimens of the original and of the heated materials have been placed on the roof to observe their further shrinkage upon aging.

A reliable accelerated aging test for transparent plastics would be very helpful in evaluating proposed new windshield materials and in experimental work on improvement in formulation of existing types. Accordingly, considerable emphasis has been placed recently on the determination of the effect of ultraviolet light from various sources on the deterioration of plastics. Mercury arc, carbon arc, and so-called sunshine bulbs have been used as the light source, and both temperature and humidity conditions have been varied. Specimens of the transparent plastics used in these tests are at present being exposed at Coco Solo, Miami, and Washington. It is expected that as a result of this experimental work a laboratory test can be developed which will enable the suitability of new products for use as windshields on aircraft to be speedily determined.

Substitute for silk shroud lines for parachutes.—Cotton shroud lines have been made which, though of lower strength-weight ratio than is obtainable from silk, appear to have equal or greater ability to absorb shock. These cords are to be given a practical service test.

New types of synthetic fibers which are being produced on a semicommercial scale have great promise for shroud lines. Arrangements have been made for the production of some experimental lines from these fibers.

Development of plastic material for aircraft structures.—An investigation was initiated to develop a reinforced plastic which will be satisfactory for airplane construction with respect to strength, stiffness, bending endurance, resistance to flow under load, and related properties. The major problem of devising a molding process adaptable to the fabrication of large sections is being given special consideration. The preparation of specimens with various types of resins and reinforcing agents and the determination of the stress-strain curves of these experimental materials both in tension and in compression is in progress.

REPORT OF COMMITTEE ON AIRCRAFT STRUCTURES

During the past year there was organized under the Committee on Aircraft Structures a Special Subcommittee to Make Survey of Technique and Equipment for Elastic Examination of Large Aircraft Structures in Lieu of Destruction Tests. This subcommittee was appointed for the purpose of maintaining active contact with developments in strain gauges and other equipment necessary to determine strains and other elastic phenomena in complete airplane structures. In addition, the subcommittee recommends financial support, when considered desirable, for those developments that show promise of producing useful instruments for work of this nature. As a result of recommendation of the subcommittee, research at the Massachusetts Institute of Technology to develop electrically strain-sensitive materials and technique for their application has been sponsored.

There has also been organized under the Committee on Aircraft Structures a Special Subcommittee to Direct Research in Applied Structures, for the purpose of making recommendations as to special facilities which should be made available for aircraft structural research, and as to the program of investigations to be conducted. This subcommittee is maintaining close contact with investigations of aircraft structural problems, and in particular with the research programs of the Langley Memorial Aeronautical Laboratory and the National Bureau of Standards.

LANGLEY MEMORIAL AERONAUTICAL LABORATORY

STRESSED-SKIN DESIGN

When the National Advisory Committee for Aeronautics was established in 1915, relatively little was known regarding aerodynamics and aircraft engines as compared with the knowledge of structures. As a consequence the Committee directed its first researches mainly in the less well known fields. With the introduction of the stressed-skin, or monocoque, type of structure in recent years, there has developed a need for research in airplane structures. Accordingly, the Committee has for some time been conducting theoretical research in structures at Langley Field. In order to supplement this theoretical research, facilities are now being provided where a limited amount of structural testing can be done to check the theories developed.

Stress analysis of monocoque structures.—It has been known for some time that the stress distribution in box beams is affected materially by the shear deformation of the flanges, a phenomenon sometimes referred to as "shear lag." The subject has been investigated theoretically and experimentally.

The investigation of simple structures, which was mentioned last year, has been extended to cover more complicated structures. Technical Report No. 636 presents a method of stress analysis applicable to structures, such as wings or fuselages, and describes strain-gauge tests made to verify the theory.

General stability of monocoque structures.—One of the important problems that confronts the designer of monocoque structures is that of the stiffness required of the transverse members to hold the stiffened shell in shape. As these members are not required to carry loads of any appreciable magnitude, the problem is mainly one of elastic instability. The problem has been studied theoretically with the result that solutions have been obtained for certain cases. Tests are now being planned to check the design formulas derived.

Fixity coefficients for panel columns.—In the design of the compression panels in stressed-skin wings and monocoque fuselages, one of the problems is to determine the end fixity of these parts. As a preparation for this study, the end fixity of compression members in continuous beams and rigid-joint trusses have been studied. In this connection two papers have been published: Technical Note No. 617, which is concerned with the basic theory, and Technical Note No. 652, which contains a set of tables that are necessary for the solution of practical problems.

Extensions have recently been made to the theory presented in Technical Note No. 617 to render it more

useful in the solution of practical problems. For example, when the equation for neutral stability is tested for three assumed loads, each of which is less than the true critical load, it is possible to estimate the true critical load. A paper on this method of estimating the critical load is now in preparation.

The essential principles of the foregoing theory are now being applied to determine the critical buckling strength of parallel columns in stressed-skin structures, with the result that practical formulas have been derived for some cases.

Skin-stiffener panels.—Theoretical studies of the compressive strength of skin stiffener panels have been continued. Most of the work on this problem, however, has been experimental. Preparations are being made to check the theory for the strength of skin-stiffener panels in compression presented in Technical Report No. 582. When these tests are completed, it will be possible to plan more satisfactorily the program for future studies of this problem.

Analysis of experimental observations in problems of elastic stability.—In 1932 Southwell presented a method for the analysis of experimental observations in problems of elastic stability. Briefly, the method is concerned with the interpretation of simultaneous readings of load and deflection. As therein presented, the method requires that the initial deflection reading be taken at zero load. In the vicinity of zero load, deflection readings are usually somewhat questionable. The deflection readings are reliable only after enough load has been applied thoroughly to seat the specimen and the loading fixtures. Furthermore, it is not always convenient to take the initial deflection reading at zero load. Also, something may happen to render the first few readings valueless and it may not be practicable to repeat them. For use under such circumstances, a more general method has been devised wherein the initial readings may be taken at any load less than the critical load. This general method has been presented in Technical Note No. 658.

Buckling above the elastic limit.—In nearly all practical structures the designer tries to proportion the parts so that the material is efficiently used. This objective requires that the cross-sectional area of each part be as small as possible. The result is that much of the material is subjected to stresses above the elastic range. The problem of buckling above the elastic range is therefore a very important one.

A number of theoretical studies have been undertaken in the investigation of this problem. One part of the theoretical study has been to determine what parts of the problem should be experimentally studied.

Local failure of compression members.—Several extensive studies have been made of local failure in compres-

sion members of thin metal. The greater importance attached to other problems has delayed completion of these investigations. It is hoped, however, that during the coming year at least one paper on this subject will be published.

STRUCTURAL LOADS ON AIRPLANES IN FLIGHT

Applied loads on airplane structures—gust loads.—Coordinated measurements of acceleration and air speed on transport airplanes have been continued, and the total flying time represented on the records has been extended to 57,000 hours. In several cases high accelerations were recorded on the largest airplanes coming within the scope of the program, the most outstanding being an acceleration of -2.2 g, measured from the $+1$ g level-flight datum, on a four-engine airplane of 52,000 pounds gross weight. The effective gust velocity of -38 feet per second in this case occurred within a cumulo-nimbus cloud associated with a warm front.

Gust research.—Measurements of gust intensities and gradients on light airplanes have been continued and the data extended. Meanwhile tests in the gust tunnel on models of these airplanes have indicated minimum and maximum limits of gust gradient beyond which the airplane is incapable of indicating accurately the true gust characteristics. The tests have therefore been extended to include measurements on two very large airplanes in order to obtain data beyond the limitations of the smaller airplanes. The more recent results of this research indicate that there is no correlation between gust intensity and gradient, so that the problem is reduced to the question of finding the steepest gradient likely to occur coincident with the stronger gusts. In one outstanding case measured on a very large airplane, a true gust velocity of approximately 57 feet per second was found to reach maximum intensity in a distance of about 150 feet.

Gust tunnel.—During the past year the gust tunnel has been provided with means for controlling the velocity distribution so that gusts ranging from those having substantially a sharp edge (viz, gusts reaching maximum velocity in a distance from one-quarter to one-half the chord length of the models) to those having mild linear gradients, can be represented. The equipment has been developed so as to function very satisfactorily and a number of tests have been made.

In sharp-edge gusts, Küssner's original theoretical results have been verified and his assumptions applicable to finite rectangular wings have been found to apply for aspect ratios as low as 2.0. The experimental accelerations in general are very slightly below the theoretical ones. It has also been found that the theoretical results are valid for tapered wings when the mean geometrical chord is used as the basis of the calculations.

In gusts with moderate gradients, the effect of pitching has been determined on a number of models, and relations between gust gradient, airplane size, and acceleration have been evolved, with pitching taken into account. In a few cases anomalous results indicate the existence of influences the nature of which is not yet understood; it has been concluded, for this reason, that, in general, calculations based on the usual assumptions or data on stability are likely to be in error, and that close approximations to the true motion must be determined by experiment.

Tests of a model equipped with a dynamically overbalanced flap indicated that such a gust-alleviating device is ineffective in sharp-edge gusts but causes appreciable reduction in acceleration in gusts with moderate gradient. In the particular case investigated, the acceleration was reduced about 40 percent in a gust reaching maximum intensity in 14 chord lengths with a flap having a chord 10 percent of that of the wing.

Load distribution.—A study of the variation of the net wing loads under combined angular and normal accelerations has been undertaken. The study includes consideration of the loading conditions produced by unsymmetrical landings, aileron deflection, and unsymmetrical gusts, as well as conditions produced by angular accelerations in yaw. The results are to be applied to the analysis of several types of airplane for the purpose of determining those conditions, in addition to the usual symmetrical loading conditions, that should be included in a complete rational analysis of the structural strength for each respective type.

Tail loads.—The problem of tail loads in maneuvers has been reviewed in the light of present available information on the controlling physical factors. Flight tests have been planned for the purpose of verifying computed results.

The problem of tail loads in gusts is receiving attention experimentally. A bomber-type airplane has been equipped with a special vertical tail unit permitting the measurement of gust loads during normal flight in rough air. A number of records have been obtained.

Hull pressures and stresses.—In addition to several routine tests to determine hull pressures and accelerations during rough-water landings of new seaplanes and flying boats, an extensive installation of recording instruments has been made on a large flying boat. These instruments include bottom-pressure gauges, strain gauges, and several instruments for measuring the motion of the airplane in landing and take-off. A large number of tests have been made but the data have not yet been fully analyzed.

Dynamic overstress.—Measurements of acceleration and wing stress have been made on an M-130 flying boat (*Hawaii Clipper*) of Pan American Airways during a round-trip flight between Alameda, California, and Hong Kong. As this airplane is large, with a wing

frequency in bending of only 4.33 cycles per second, the results supply significant practical evidence of the existence or absence of overstress in gusts resulting from rapid application of load. Although several strong, abrupt gusts were encountered at air speeds as high as 200 miles per hour, no evidence of overstress was observed, the measured stresses showing excellent agreement with the datum stresses at unit load factor multiplied by the measured gust load factors determined by an accelerometer.

Stress history.—A fairly complete stress history obtained during the flight on the M-130 flying boat provided data applicable to the problem of fatigue of airplane structures. Although the fatigue resistance of the structure under flight conditions is not definitely known, it can be stated on the basis of existing data on this subject that fatigue failure resulting solely from stress variations in rough air (viz, in the absence of serious vibration) does not appear to be a possibility within the probable life of any airplane.

NATIONAL BUREAU OF STANDARDS

Aircraft tubing.—Two reports on tubing used in aircraft have been published within the last year, one on column strength, as Technical Report No. 615 of the National Advisory Committee for Aeronautics, and the other on crinkling strength and bending strength, as Technical Report No. 632. The report on column strength covers round and streamline tubing of four different materials, namely, chromium-molybdenum steel, 17ST aluminum alloy, stainless steel, and heat-treated chromium-molybdenum steel. The report on crinkling strength and bending strength is the result of tests completed during the year on round chromium-molybdenum steel and 17ST aluminum-alloy tubing.

Both reports give an account of the tests, including the laboratory work and the subsequent analysis of the laboratory data; they consider the theoretical aspects of the problem; and finally, empirical formulas are given for the column strength, in the first report, and for the crinkling strength and the bending strength in the second report, in terms of the dimensions of the tubes and the yield strengths of the materials. These formulas have also been written for materials just complying with applicable Navy Department Specifications.

Considerable attention has been given to the testing of round aircraft tubing under combined axial, compressive, transverse, and torsional loading. Apparatus has been designed and constructed for such tests.

Round heat-treated chromium-molybdenum steel tubing has been donated by the Summerhill Tubing Company for the purpose of making crinkling tests, bending tests, torsional tests, and tests under combined loading.

Flat plates under normal pressure.—Seven circular plates of 17ST aluminum alloy 5 inches in diameter

and ranging in thickness from 0.021 to 0.072 inch have been tested under normal pressure with their edges clamped, and the measured deformations have been compared with those predicted from Way's theory of such plates. Way's curves were extended to ratios of center deflection to plate thickness equal to 1.5. Satisfactory agreement was obtained up to center deflections of this order between the observed and calculated center deflections. Comparison of the measured and the calculated distribution of radial stresses for one of the plates also showed close agreement for all portions of the plate except those near the edge, where the measurements are most difficult to make and where errors due to deviations from the ideal clamping conditions have a maximum effect.

A plot of the "Navy yield pressure" (an arbitrary measure of appreciable yielding obtained from the pressure-set curve) for these plates, led to a simple empirical relation which described this quantity as a function of the tensile strength of the plate material and the dimensions of the plate within ± 20 percent.

With the existence of such a relation for circular plates it appears probable that a similar relation could be derived from tests of rectangular plates in the presence of nearly ideal clamping conditions. The tests of square plates made to date gave values for yield pressure scattering within ± 70 percent about the same curve as that derived from the tests of circular plates.

Beams and stressed-skin research.—A report of the study of strain distribution and buckle shape, and stringer deformation in the two sheet stringer panels has been submitted to the National Advisory Committee for Aeronautics for publication as a Technical Note. The report includes a comparison of the measured buckle shape and measured strain distribution in these panels with those given by theories of S. Timoshenko, J. M. Frankland, and K. Marguerre. The measured effective width was compared with that given by nine different formulas for effective width that have been presented in the literature. Southwell's method of plotting was applied to the measurements of stringer deformation and stringer strain. In many cases the points on the plots of twisting and bending rotation of the stringers and of bending strain were scattered about a straight line throughout their entire range, and in all these cases the slope of the straight line was in agreement with the observed measured buckling load of the panel. It should be mentioned in this connection that the failure of these particular panels occurred at stresses considerably below the yield strength of the material.

An experimental study of the effect of rivet spacing and of spot spacing on the strength of sheet-stringer panels has been started with tests to failure of four 24ST aluminum alloy panels. The rivet spacing in these particular panels was unusually large, ranging from 2 to 6 inches, and consequently the first pronounced de-

formation of the sheet was a buckling between rivets. This occurred in every case at a stress close to that predicted from Howland's assumption that the sheet between rivets should buckle like an Euler column with clamped ends.

Fourteen more panels remain to be tested. The whole series includes rivet spacings from 0.5 to 6 inches, spot spacings from 0.75 to 4 inches, sheet thicknesses from 0.024 to 0.107 inch, and stringer spacings from 1.5 to 4 inches.

Generalization of Southwell's method.—Analysis of the observed deformations of the stringers in the sheet-stringer panels tested at this Bureau had indicated that the elastic buckling loads of many structures may be predicted from deflection or strain readings below the buckling load by making use of a method of plotting which was developed by Southwell for the particular case of the instability of an initially bent column. An explanation for the wide applicability of this method of plotting has been derived by L. B. Tuckerman from Westergaard's general theory of the buckling of elastic structures. This generalization of Southwell's method also indicates more clearly the limitations of the method. It shows, also, how the method may theoretically be used to derive not only the lowest buckling load but buckling loads of higher order as well. This was checked experimentally by obtaining the first, second, and third Euler loads from strain readings on bent columns and the first and second Euler loads from strain readings on an eccentrically loaded column. It seems doubtful, however, whether the experimental accuracy on complicated structures will be sufficient to make this possibility practical. A paper describing this work has been prepared for publication in the *Journal of Research of the National Bureau of Standards*.

Monocoque boxes.—Experimental work on this project during the past year has been limited to column tests of extruded 24ST aluminum-alloy H-sections with freely supported ends and with elastically restrained ends. Similar sections are used as stiffeners in monocoque constructions. The tests were desired in connection with Lundquist's analysis of sheet-stringer panels under compression.

The results of the tests were embodied in a detailed report which has been submitted for publication as a Technical Report of the National Advisory Committee for Aeronautics. The report gives an account of the tests and the subsequent analysis of the laboratory data, and also an empirical nondimensional column formula (straight-line) for the plastic range and the resulting formula for E/E . These formulas are also presented in the conventional form to apply to material just complying with Navy Department Specification 46A9a.

The experimental work on the monocoque boxes themselves has been delayed by the difficulty of obtaining

suitable specimens. Because of the cost of the specimens, it was found that for the present only one box could be procured, and it was decided to make this of more or less typical construction, 10 by 24 by 95 inches, of 24ST material, with approximately five bays spaced by bulkheads of typical stiffness.

The tests which are to be made with this specimen during the coming year are to include strain explorations under axial load, under pure bending about the lift axis, under bending about the lift axis combined with bending about the drag axis, and under bending about the lift axis combined with shear. The load is to be kept below the ultimate in each test so that the specimen will still be intact after each loading. After the completion of all the tests within the elastic range the specimen is to be tested to failure in end compression.

Strength of riveted joints in aluminum alloy.—In view of the interest of airplane manufacturers in riveted joints of the flush type the work done on this investigation during the past year has been limited chiefly to determining the mechanical properties of flush riveted joints and preparing a report of the results.

Shearing and tensile tests have been completed on joints fabricated by eight manufacturers in accordance with their own practice. Among the types represented are two types of 78-degree rivets, two types of 100-degree rivets and the "flush brazier" rivet, all used with various combinations of counterpressed and countersunk sheets. Joints employing brazier-head and special-oval-countersunk-head rivets were fabricated at the National Bureau of Standards and were included for comparison.

The shearing strength of joints having counterpressed sheets was considerably greater at some values of the ratio of rivet diameter to sheet thickness than the strength of joints made with brazier-head rivets. There was a marked decrease in the shearing strength with increase of this ratio. In several joints the sheet was found to contain injurious cracks which originated during the counterpressing operations.

A report showing the mechanical properties in graphical form, together with photomicrographs and drawings, is being prepared.

Airplane vibration.—Close cooperation was maintained throughout the year with the Bureau of Aeronautics in its program for the development of suitable equipment for picking up and recording vibration amplitudes and strains on airplanes in flight. A number of schemes for accomplishing this were discussed at conferences between the Bureau of Aeronautics, representatives of various commercial organizations, and representatives of the National Bureau of Standards.

As part of this program calibration tests were carried out on strain gauges of the electromagnetic type and of the variable-inductance type, both constructed by the Sperry Gyroscope Company, as well as tests of

the carbon-resistance strain gauges known as "Ess strips" which have been developed by Professor de Forest.

In connection with the calibration tests a device was constructed for subjecting dynamic strain gauges to uniform sinusoidal strains up to 0.001 over a range of frequencies from 0.05 to 200 cycles per second. The device has been subjected to preliminary trials and a number of changes in design have been made to give a more nearly uniform axial strain on the strip of sheet metal to which the gauges are attached.

Investigation of fatigue resistance of fabricated structural elements of aircraft.—The method and test equipment developed for testing the fatigue strength of aluminum-alloy wing beams were described in detail in Technical Note No. 660. This paper also gives the results of tests on two wing beams that had been removed from an airplane. Further tests are in progress.

The magnitude of the alternating axial load applied to the two beams tested was computed from the amplitude of strain as indicated by 2-inch Tuckerman optical strain gauges, and also, on the assumption that the motion was sinusoidal, from the mass, amplitude, and frequency of one of the terminal weights. The results of the two methods of computation differed by 8 percent and 10 percent in the two cases. The results of the second method were the smaller in both cases. The overall strain could not be used because of uncertainties in the effective length due to reinforced portions along the beams and to unknown deformations at the terminals. A fourth method, contemplated in future tests, consists in determining the mass and acceleration of one of the weights directly. This would require an accelerometer of very short relaxation time. A tentative design for such an instrument has been made.

The test program is somewhat complicated by the fact that some of the specimens contain asymmetric reinforcements near the center. As a consequence, the centroidal axes of these beams are not straight, and centering the load requires a large displacement of the centers of gravity of the terminal weights from the line connecting the centroids of the end sections. It is desirable to include these asymmetric reinforcements in the test length of the specimens in order to investigate the possibly serious stress concentrations due to their presence in the airplane structure. Terminal attachments have been designed to permit ample adjustment of the transverse displacement of the terminal weights.

Tensile and compressive properties of duralumin, magnesium and alloy steels.—A paper entitled "The 'Pack' Method for Compressive Tests of Thin Specimens of Materials Used in Thin-walled Structures" is in process of publication as a Technical Report of the National Advisory Committee for Aeronautics. This

paper includes a detailed description of the procedure for making "pack" compressive tests. It also includes the results of tests to give a comparison of the stress-strain graphs of packs and compact solid specimens taken from the same bar of metal, and to determine the reproducibility of the test where two or more packs were taken longitudinally or transversely from sheets of 17ST aluminum alloy, No. 1025 carbon steel, and annealed chromium-molybdenum steel. An abstract of a résumé of this paper, which was presented at the Fifth International Congress for Applied Mechanics, was published in the Journal of Applied Mechanics of

the American Society for Mechanical Engineers, for September 1938.

The "pack" compressive test has been found useful during the past year in determining the compressive stress-strain graphs of materials taken from thin-walled structural sections, as well as from sheet. Tests made on packs assembled from specimens taken from channels of high-strength aluminum alloy showed no evidence that the packs failed by primary instability, despite deviations from flatness in the formed material which led to the presence of small voids between the specimens of the pack.

PART II

ORGANIZATION AND GENERAL ACTIVITIES

ORGANIZATION

The National Advisory Committee for Aeronautics was established by act of Congress approved March 3, 1915 (U. S. Code, title 50, sec. 151). The Committee is composed of fifteen members appointed by the President and serving as such without compensation. The duties of the Committee are to "supervise and direct the scientific study of the problems of flight, with a view to their practical solution," and to "direct and conduct research and experiment in aeronautics" in such laboratories as may be placed under its direction.

Prior to the enactment of the Civil Aeronautics Act of 1938, the membership of the Committee as provided by law included two representatives each from the War and Navy Departments; one each from the Smithsonian Institution, the United States Weather Bureau, and the National Bureau of Standards; and eight other persons "acquainted with the needs of aeronautical science, either civil or military, or skilled in aeronautical engineering or its allied sciences." In recent years one of these eight positions has been filled by a representative of the Bureau of Air Commerce. The Civil Aeronautics Act of 1938 provided that the Civil Aeronautics Authority therein created for the encouragement and regulation of civil and commercial aviation should have two representatives on the Committee, the same as the Army and the Navy. As the total membership remains at fifteen, the result is that the governmental members now number nine and the nongovernmental members six.

The Civil Aeronautics Act of 1938 also provided that, upon the effective date of the act (August 22, 1938) the terms of office of the nongovernmental members of the Committee should expire, and that the President should appoint successors to six, two each for periods of one, three, and five years, respectively, and thereafter for terms of five years. The provision of law referred to is Section 1107 (e) of the Civil Aeronautics Act of 1938, which reads as follows:

"The ninth paragraph of the Act approved March 3, 1915 (38 Stat. 930), as amended by the Act of March 2, 1929 (45 Stat. 1451; U. S. C., 1934 ed., title 50, sec. 151), is further amended by inserting after the words 'naval aeronautics'; in that paragraph the following: 'two members from the Civil Aeronautics Authority'; by striking out the word 'eight' in that paragraph and

inserting in lieu thereof the word 'six', and by striking out the colon after the words 'allied sciences' and inserting in lieu thereof a period and the following: 'The members of the National Advisory Committee for Aeronautics, not representing governmental agencies, in office on the date of enactment of the Civil Aeronautics Act of 1938, shall continue to serve as members of the Committee until the effective date of section 1107 of the Civil Aeronautics Act of 1938. Upon the expiration of their terms of office the President is authorized to appoint successors to six of such members for terms of office to expire, as designated by the President at the time of appointment, two at the end of one year, two at the end of three years, and two at the end of five years from December 1, 1938. Successors to those first appointed shall be appointed by the President for terms of five years from the date of the expiration of the terms of the members whom they succeed, except that any such successor, appointed to fill a vacancy occurring prior to the expiration of a term, shall be appointed only for the unexpired term of the member whom he succeeds:'"

In accordance with the above provision of law, the President, under date of August 23, 1938, made the following appointments as members of the Committee:

To represent the Civil Aeronautics Authority (without definite tenure):

Honorable Edward J. Noble, Chairman, Civil Aeronautics Authority.

Honorable Clinton M. Hester, Administrator, Civil Aeronautics Authority.

For the terms expiring December 1, 1943:

Dr. Joseph S. Ames.

Dr. Orville Wright.

For the terms expiring December 1, 1941:

Dr. Edward P. Warner.

Dr. Vannevar Bush.

For the terms expiring December 1, 1939:

Colonel Charles A. Lindbergh.

Dr. Jerome C. Hunsaker.

Of the eight appointments thus made by the President, four were reappointments and four were new appointments. The four members reappointed are:

Dr. Joseph S. Ames (Chairman), President Emeritus of Johns Hopkins University, the last of the original members of the Committee appointed by the President

in 1915, who served as Chairman of the Executive Committee from 1919 to 1937, and as Chairman of the main Committee from 1927 to the present time.

Dr. Orville Wright, of Dayton, Ohio, the world's first aviator, who has served continuously since his appointment by the President in 1920.

Dr. Edward P. Warner, of Greenwich, Connecticut, former Assistant Secretary of the Navy for Aeronautics, who has served continuously since his appointment by the President in 1929, and has also served as Chairman of the Committee on Aerodynamics since 1935.

Colonel Charles A. Lindbergh, who has served continuously as a member since his appointment by the President in 1931.

The four new appointments are:

Honorable Edward J. Noble, Chairman, Civil Aeronautics Authority.

Honorable Clinton M. Hester, Administrator, Civil Aeronautics Authority.

Dr. Vannevar Bush, President, Carnegie Institution of Washington, D. C.

Dr. Jerome C. Hunsaker, Professor in Charge, The Daniel Guggenheim Aeronautical Laboratory, Massachusetts Institute of Technology.

The four members whose terms expired August 22, 1938, and who were not reappointed, are:

Honorable Harry F. Guggenheim.

Dr. William P. MacCracken.

Dr. Denis Mulligan.

Dr. David W. Taylor.

Dr. Taylor was first appointed a naval member of the Committee February 16, 1917, while serving as Chief Constructor, United States Navy, with the rank of Rear Admiral. When he retired from the Navy, he was immediately reappointed on October 16, 1922, as a member of the Committee from private life, in recognition of his outstanding ability. He was a great source of strength to the organization. His twenty-one years as a member included four years as Secretary of the Committee, eleven years as Vice Chairman of the Committee, and eight years as Chairman of the Committee on Aerodynamics.

Dr. MacCracken was Assistant Secretary of Commerce for Aeronautics when he was appointed a member of the Committee April 5, 1929, and throughout the entire period of his service he was an active and interested member. He rendered faithful and valuable service on various committees, and for six years was Chairman of the Committee on Power Plants for Aircraft. He had also served as Vice Chairman of the Executive Committee since October 21, 1937.

Mr. Guggenheim was President of the Daniel Guggenheim Fund for the Promotion of Aeronautics, Incorporated, when he was appointed a member of the Committee April 5, 1929. He brought to the Committee a well-informed and independent viewpoint on the

problems of flight, which made him especially valuable as a constructive critic.

Dr. Mulligan had succeeded Dr. Fred D. Fagg, Jr., who had resigned, as Director of the Bureau of Air Commerce, and Dr. Mulligan accordingly succeeded Dr. Fagg as a member of the Committee April 16, 1938. Both Dr. Fagg and Dr. Mulligan, as successive heads of the Bureau of Air Commerce, had been thoroughly cooperative with the Committee in seeking to advance the science of aeronautics through unified control and conduct by the Committee of scientific laboratory research.

During the past year the Committee lost through death two other members, namely, Dr. Willis Ray Gregg, Chief of the United States Weather Bureau, on September 14, 1938, and Major General Oscar Westover, Chief of the Army Air Corps, on September 21, 1938.

Dr. Gregg had served as the Weather Bureau representative on the Committee since October 10, 1934, and had served as Chairman of the Executive Committee since April 22, 1937. He had given unsparingly of his time and talents to promote the effective organization and prosecution of the Committee's work.

General Westover had served as a War Department representative on the Committee since January 25, 1936. Prior to that he had become very familiar with the organization and work of the Committee, having had three previous tours of duty in the office of the Chief of the Army Air Corps since 1919 and one as Commanding Officer of Langley Field, where the Committee's laboratories are located. During this entire period he was deeply interested in the Committee's work and did much to assist this organization by promoting cooperation between the Army Air Corps and the Committee.

Major General Henry H. Arnold, who had succeeded General Westover as Chief of the Army Air Corps, was appointed a member of the Committee on October 10, 1938.

The present membership of the Committee is shown on page vi of this report. There is one vacancy on the Committee, the filling of which will await the appointment of a new Chief of the United States Weather Bureau.

Under the rules and regulations governing the work of the Committee as approved by the President, the Chairman and Vice Chairman of the Committee are elected annually. At the meeting held on October 20, 1938, Dr. Joseph S. Ames was reelected Chairman for the ensuing year, and Dr. Vannevar Bush was elected Vice Chairman to succeed Dr. David W. Taylor. At the meeting held on December 16, 1938, Dr. Vannevar Bush was elected Chairman of the Executive Committee and Dr. Charles G. Abbot Vice Chairman of the Executive Committee for the ensuing year.

The Committee's headquarters, including its offices of aeronautical intelligence and aeronautical inventions, are located in the Navy Building, Washington, D. C., in close proximity to the air organizations of the Army and Navy.

The office of aeronautical intelligence was established in the early part of 1918 as an integral branch of the Committee's activities. Scientific and technical data on aeronautics secured from all parts of the world are classified, catalogued, and disseminated by this office.

To assist in the collection of current scientific and technical information and data, the Committee maintains a technical assistant in Europe (Mr. John J. Ide), with headquarters at the American Embassy in Paris.

CONSIDERATION OF AERONAUTICAL INVENTIONS

By act of Congress approved July 2, 1926, an Aeronautical Patents and Design Board was established consisting of Assistant Secretaries of the Departments of War, Navy, and Commerce. In accordance with that act as amended by the act approved March 3, 1927, the National Advisory Committee for Aeronautics passes upon the merits of aeronautical inventions and designs submitted to any aeronautical division of the Government, and submits reports thereon to the Aeronautical Patents and Design Board. That board is authorized, upon the favorable recommendation of the Committee, to "determine whether the use of the design by the Government is desirable or necessary and evaluate the design and fix its worth to the United States in an amount not to exceed \$75,000."

During the past year the inventions section received for consideration 1,100 new submissions. It conducted the necessary correspondence and granted interviews as requested by the inventors. Approximately three percent of the new submissions were received through the Aeronautical Patents and Design Board. In those cases reports on the merits of the submissions were made to that board, and in all other cases replies were submitted directly to the inventors.

AERONAUTICAL RESEARCH IN EDUCATIONAL INSTITUTIONS

The Committee has continued to follow the policy initiated as a result of recommendation of the Federal Aviation Commission, of making available a special allotment of \$25,000 from each year's funds for aeronautical research in educational institutions. Under this allotment during the fiscal year 1938, contracts were made with five universities and technical schools for ten special investigations and reports, on the basis of the probable usefulness and value of the information to aeronautics.

Several of the papers prepared under contracts have been published by the Committee, and in other cases the results obtained in the investigations have supplied

a basis for further research. During the past year two contract reports have been issued as Technical Notes, and four others are now being revised and edited for publication by the Committee.

COOPERATION WITH THE AVIATION INDUSTRY

In the formulation of its research programs, the Committee includes provision for the problems of aeronautical research which are of particular importance to the aviation industry, in connection with both the design and operation of aircraft. The representatives of the industry refer their problems of this nature to the Committee as they arise, either by correspondence or through personal contact. The Committee avails itself of every opportunity to obtain suggestions and recommendations from representatives of the aircraft manufacturers and operators as to investigations which are of special importance to them.

Although it was found necessary this year to postpone for one year the Aircraft Engineering Research Conference usually held each May at the Committee's laboratory at Langley Field, the Committee has continued to maintain close contact with the research needs of the industry. The conference was postponed because of the extensive program of construction of new research facilities being carried out at the laboratory, which had been undertaken by the Committee to meet the challenge offered by the great emphasis being placed by the principal foreign nations on scientific research in aeronautics, and their greatly increased research activities. As has been the long-standing policy of the Committee, when the need arises in connection with any particular problem of the industry a special conference is called, or, as previously stated, a special subcommittee is established, including in either case representation from the industry.

One of the important problems of the industry at the present time is the problem of flutter, and the Special Subcommittee on Vibration and Flutter, established under the Committee on Aerodynamics, is giving this subject special attention. It is believed that the recent results obtained by the Committee's laboratory on this subject, which are being made available in advance confidential form to American manufacturers, will be of great importance in connection with this problem. The investigation is described briefly in the report of the special subcommittee in part I.

Another problem of great importance in connection with airplane design is the aerodynamic loads imposed on the structure in flight as a result of atmospheric disturbances. As previously stated, the Committee has accumulated, with the cooperation of air-transport operators over a period of a number of years, a large amount of statistical data on these loads. These data have been obtained by means of the N. A. C. A. V-G recorder, which gives a record of accelerations and air

speeds. At the present time about 25 of these instruments are in use on American air lines, and the records obtained to date represent a total of approximately 57,000 flying hours. Further information regarding this study is presented in the report of the Committee on Aircraft Structures.

The problem of lightning hazards to aircraft has been brought to the Committee's attention by the air-transport operators, and to assist in the study of this problem a Special Subcommittee on Lightning Hazards to Aircraft has been established under the Subcommittee on Meteorological Problems, as was mentioned in the report of that subcommittee. Under the cognizance of this special subcommittee investigation is being made of the effect of electrical discharges simulating lightning strokes on sheet metal of the type used in aircraft construction. In addition, in order to obtain information as to the meteorological aspects of the problem, the air lines are supplying data from their pilots as to incidents of lightning strokes and the atmospheric conditions observed in connection with these incidents.

Realizing that frequently the value of information is greatly enhanced by its prompt availability, every effort is made to place in the hands of the industry at the earliest possible date the results of researches that are of particular interest to commercial aviation. It sometimes appears, in the course of an extensive investigation being conducted by the Committee, that the results so far obtained will be of special interest and value to the aircraft industry if made available immediately. In such cases the Committee issues the information in advance confidential form to American manufacturers and the Government services.

SUBCOMMITTEES

The Advisory Committee has organized four main standing technical committees, with subcommittees, for the purpose of supervising its work in their respective fields. The four main technical Committees on Aerodynamics, Power Plants for Aircraft, Aircraft Materials, and Aircraft Structures and their subcommittees supervise and direct the aeronautical research conducted by the Advisory Committee and coordinate the investigations conducted by other agencies.

As previously stated, it is the policy of the Committee to establish from time to time special technical subcommittees for the study of particular problems as they arise. In accordance with this policy a Special Subcommittee on Vibration and Flutter has been organized under the Committee on Aerodynamics. During the past year three such special subcommittees have been formed: a Special Subcommittee on Lightning Hazards to Aircraft, under the Subcommittee on Meteorological Problems; and, under the Committee on Aircraft Structures, a Special Subcommittee to Make Survey of Technique and Equipment for Elastic Examination of Large

Aircraft Structures in Lieu of Destruction Tests, and a Special Subcommittee to Direct Research in Applied Structures.

The work of the standing technical committees and subcommittees has been described in part I.

The organization of the committees and of the subcommittees is as follows:

COMMITTEE ON AERODYNAMICS

Dr. Edward P. Warner, Chairman.
 Dr. George W. Lewis, National Advisory Committee for Aeronautics, Vice Chairman.
 Dr. L. J. Briggs, National Bureau of Standards.
 Comdr. W. S. Diehl, United States Navy.
 Dr. H. L. Dryden, National Bureau of Standards.
 John Easton, Civil Aeronautics Authority.
 Lt. Comdr. L. M. Grant, United States Navy.
 J. T. Gray, Civil Aeronautics Authority.
 Maj. Carl F. Greene, Air Corps, United States Army, Matériel Division, Wright Field.
 Delbert M. Little, United States Weather Bureau.
 Maj. Alfred J. Lyon, Air Corps, United States Army, Matériel Division, Wright Field.
 Elton W. Miller, National Advisory Committee for Aeronautics.
 Comdr. F. W. Pennoyer, Jr., United States Navy.
 H. J. E. Reid, National Advisory Committee for Aeronautics.
 Maj. John P. Richter, Air Corps, United States Army, Matériel Division, Wright Field.
 Dr. A. F. Zahm, Division of Aeronautics, Library of Congress.

SUBCOMMITTEE ON AIRSHIPS

Dr. J. C. Hunsaker, Chairman.
 Starr Truscott, National Advisory Committee for Aeronautics, Vice Chairman.
 John Easton, Civil Aeronautics Authority.
 Commander Garland Fulton, United States Navy.
 Maj. C. F. Greene, Air Corps, United States Army, Matériel Division, Wright Field.
 Dr. George W. Lewis, National Advisory Committee for Aeronautics (ex officio member).

SUBCOMMITTEE ON METEOROLOGICAL PROBLEMS

Francis W. Reichelderfer, United States Weather Bureau, Chairman.
 Col. E. S. Gorrell, Air Transport Association of America.
 Dr. W. J. Humphreys, United States Weather Bureau.
 Dr. J. C. Hunsaker, Massachusetts Institute of Technology.
 R. W. Knight, Civil Aeronautics Authority.
 Dr. George W. Lewis, National Advisory Committee for Aeronautics (ex officio member).
 Delbert M. Little, United States Weather Bureau.
 Comdr. Wilber M. Lockhart, United States Navy.
 Dr. Charles F. Marvin.
 Dr. C. G. Rossby, Massachusetts Institute of Technology.
 Maj. B. J. Sherry, United States Army, Signal Corps, War Department.

SPECIAL SUBCOMMITTEE ON LIGHTNING HAZARDS TO AIRCRAFT

Delbert M. Little, United States Weather Bureau, Chairman.
 J. C. Franklin, Transcontinental & Western Air, Inc.
 Lt. Comdr. L. M. Grant, United States Navy.
 Charles H. Helms, National Advisory Committee for Aeronautics.

Dr. George W. Lewis, National Advisory Committee for Aeronautics (ex officio member).

K. B. McEachron, General Electric Company.

Irving R. Metcalf, Civil Aeronautics Authority.

Lt. C. K. Moore, Air Corps, United States Army, Matériel Division, Wright Field.

Dr. F. B. Silsbee, National Bureau of Standards.

Dr. John B. Whitehead, Johns Hopkins University.

SUBCOMMITTEE ON SEAPLANES

Dr. J. C. Hunsaker, Chairman.

Theophile dePort, Matériel Division, Army Air Corps, Wright Field.

Comdr. W. S. Diehl, United States Navy.

J. T. Gray, Civil Aeronautics Authority.

Dr. George W. Lewis, National Advisory Committee for Aeronautics (ex officio member).

Lt. C. K. Moore, Air Corps, United States Army, Matériel Division, Wright Field.

A. L. Morse, Civil Aeronautics Authority.

Capt. H. C. Richardson, United States Navy.

Lt. Comdr. A. O. Rule, United States Navy.

Starr Truscott, National Advisory Committee for Aeronautics.

SPECIAL SUBCOMMITTEE ON VIBRATION AND FLUTTER

H. J. E. Reid, National Advisory Committee for Aeronautics, Chairman.

Lt. Frederick R. Dent, Jr., Air Corps, United States Army, Matériel Division, Wright Field.

Comdr. W. S. Diehl, United States Navy.

Charles H. Helms, National Advisory Committee for Aeronautics.

Dr. George W. Lewis, National Advisory Committee for Aeronautics (ex officio member).

Comdr. R. D. MacCart, United States Navy.

Irving R. Metcalf, Civil Aeronautics Authority.

Ford L. Prescott, Matériel Division, Army Air Corps, Wright Field.

Dr. Walter Ramberg, National Bureau of Standards.

Edward I. Ryder, Civil Aeronautics Authority.

Dr. Theodore Theodorsen, National Advisory Committee for Aeronautics.

COMMITTEE ON POWER PLANTS FOR AIRCRAFT

Dr. Vannevar Bush, Chairman.

Dr. George W. Lewis, National Advisory Committee for Aeronautics, Vice Chairman.

Comdr. Rico Botta, United States Navy.

Dr. H. C. Dickinson, National Bureau of Standards.

John H. Geisse, Civil Aeronautics Authority.

Carlton Kemper, National Advisory Committee for Aeronautics.

Gaylord W. Newton, Civil Aeronautics Authority.

Maj. E. R. Page, Air Corps, United States Army, Matériel Division, Wright Field.

SUBCOMMITTEE ON AIRCRAFT FUELS AND LUBRICANTS

Dr. H. C. Dickinson, National Bureau of Standards, Chairman.

Comdr. Rico Botta, United States Navy.

Lt. J. W. C. Brand, United States Navy.

Dr. O. C. Bridgeman, National Bureau of Standards.

H. K. Cummings, National Bureau of Standards.

L. S. Hobbs, The Pratt and Whitney Aircraft Company.

Robert V. Kerley, Matériel Division, Army Air Corps, Wright Field.

Dr. George W. Lewis, National Advisory Committee for Aeronautics (ex officio member).

Gaylord W. Newton, Civil Aeronautics Authority.

Arthur Nutt, Wright Aeronautical Corporation.

Maj. E. R. Page, Air Corps, United States Army, Matériel Division, Wright Field.

Addison M. Rothrock, National Advisory Committee for Aeronautics.

COMMITTEE ON AIRCRAFT MATERIALS

Dr. L. J. Briggs, National Bureau of Standards, Chairman.

Prof. H. L. Whittemore, National Bureau of Standards, Vice Chairman.

S. K. Colby, Aluminum Co. of America.

Lt. Comdr. C. F. Cotton, United States Navy.

Edgar H. Dix, Jr., American Magnesium Corporation.

John Easton, Civil Aeronautics Authority.

Warren E. Emley, National Bureau of Standards.

Comdr. Garland Fulton, United States Navy.

J. T. Gray, Civil Aeronautics Authority.

C. H. Helms, National Advisory Committee for Aeronautics.

J. B. Johnson, Matériel Division, Army Air Corps, Wright Field.

Capt. Paul H. Kemmer, Air Corps, United States Army, Matériel Division, Wright Field.

Dr. George W. Lewis, National Advisory Committee for Aeronautics (ex officio member).

H. S. Rawdon, National Bureau of Standards.

E. C. Smith, Republic Steel Corporation.

Paul F. Voigt, Jr., Carnegie-Illinois Steel Corporation.

Dr. Edward P. Warner.

SUBCOMMITTEE ON METALS USED IN AIRCRAFT

H. S. Rawdon, National Bureau of Standards, Chairman.

A. W. Dallas, Civil Aeronautics Authority.

E. H. Dix, Jr., American Magnesium Corporation.

Comdr. Garland Fulton, United States Navy.

J. B. Johnson, Matériel Division, Army Air Corps, Wright Field.

Dr. George W. Lewis, National Advisory Committee for Aeronautics (ex officio member).

E. C. Smith, Republic Steel Corporation.

Prof. H. L. Whittemore, National Bureau of Standards.

SUBCOMMITTEE ON MISCELLANEOUS MATERIALS AND ACCESSORIES

Warren E. Emley, National Bureau of Standards, Chairman.

C. J. Cleary, Matériel Division, Army Air Corps, Wright Field.

A. W. Dallas, Civil Aeronautics Authority.

C. H. Helms, National Advisory Committee for Aeronautics.

E. F. Hickson, National Bureau of Standards.

Dr. George W. Lewis, National Advisory Committee for Aeronautics (ex officio member).

J. E. Sullivan, Bureau of Aeronautics, Navy Department.

G. W. Trayer, Forest Service, Department of Agriculture.

COMMITTEE ON AIRCRAFT STRUCTURES

Dr. L. J. Briggs, National Bureau of Standards, Chairman.

John Easton, Civil Aeronautics Authority.

Lt. Comdr. L. M. Grant, United States Navy.

Capt. Paul H. Kemmer, Air Corps, United States Army, Matériel Division, Wright Field.

Dr. George W. Lewis, National Advisory Committee for Aeronautics (ex officio member).

Eugene E. Lundquist, National Advisory Committee for Aeronautics.

Comdr. R. D. MacCart, United States Navy.

Lt. C. K. Moore, Air Corps, United States Army, Matériel Division, Wright Field.

Dr. Walter Ramberg, National Bureau of Standards.

Richard V. Rhode, National Advisory Committee for Aeronautics.

Edward I. Ryder, Civil Aeronautics Authority.

Dr. L. B. Tuckerman, National Bureau of Standards.

Dr. Edward P. Warner.

SPECIAL SUBCOMMITTEE TO MAKE SURVEY OF TECHNIQUE AND EQUIPMENT FOR ELASTIC EXAMINATION OF LARGE AIRCRAFT STRUCTURES IN LIEU OF DESTRUCTION TESTS

Richard V. Rhode, National Advisory Committee for Aeronautics, Chairman.

Lt. Comdr. L. M. Grant, United States Navy.

Capt. Paul H. Kemmer, Air Corps, United States Army, Matériel Division, Wright Field.

Dr. George W. Lewis, National Advisory Committee for Aeronautics (ex officio member).

Comdr. R. D. MacCart, United States Navy.

Irving R. Metcalf, Civil Aeronautics Authority.

R. L. Templin, Aluminum Company of America.

Dr. L. B. Tuckerman, National Bureau of Standards.

SPECIAL SUBCOMMITTEE TO DIRECT RESEARCH IN APPLIED STRUCTURES

Lt. Comdr. L. M. Grant, United States Navy, Chairman.

Capt. Paul H. Kemmer, Air Corps, United States Army, Matériel Division, Wright Field.

Dr. George W. Lewis, National Advisory Committee for Aeronautics (ex officio member).

Eugene E. Lundquist, National Advisory Committee for Aeronautics.

Edward I. Ryder, Civil Aeronautics Authority.

Dr. L. B. Tuckerman, National Bureau of Standards.

COMMITTEE ON AIRCRAFT ACCIDENTS

Dr. Edward P. Warner, Chairman.

Lt. W. A. Evans, United States Navy.

Maj. E. V. Harbeck, Jr., Air Corps, United States Army.

J. W. Lankford, Civil Aeronautics Authority.

Dr. George W. Lewis, National Advisory Committee for Aeronautics.

Lt. Comdr. A. O. Rule, United States Navy.

Maj. Lowell H. Smith, Air Corps, United States Army.

Grove Webster, Civil Aeronautics Authority.

COMMITTEE ON AERONAUTICAL INVENTIONS AND DESIGNS

Dr. L. J. Briggs, National Bureau of Standards, Chairman.

Hon. Clinton M. Hester, Civil Aeronautics Authority.

Dr. J. C. Hunsaker.

Capt. S. M. Kraus, United States Navy.

Brig. Gen. A. W. Robins, Air Corps, United States Army, Matériel Division, Wright Field.

John F. Victory, Secretary.

COMMITTEE ON PUBLICATIONS AND INTELLIGENCE

Dr. Joseph S. Ames, Chairman.

Dr. Charles G. Abbot.

Miss M. M. Muller, Secretary.

COMMITTEE ON PERSONNEL, BUILDINGS, AND EQUIPMENT

Dr. Joseph S. Ames, Chairman.

Dr. Vannevar Bush.

John F. Victory, Secretary.

TECHNICAL PUBLICATIONS OF THE COMMITTEE

The Committee has four series of publications, namely, technical reports, technical notes, technical memorandums, and aircraft circulars.

The technical reports present the results of fundamental research in aeronautics. The technical notes are mimeographed and present the results of short research investigations and the results of studies of specific detail problems which form parts of long investigations. The technical memorandums are mimeographed and contain translations and reproductions of important foreign aeronautical articles. The aircraft circulars are mimeographed and contain descriptions of new types of foreign aircraft.

The following are lists of the publications issued:

LIST OF TECHNICAL REPORTS ISSUED DURING THE PAST YEAR

- | | |
|------|---|
| No. | |
| 612. | Heat-Transfer Processes in Air-Cooled Engine Cylinders. By Benjamin Pinkel, N. A. C. A. |
| 613. | The Variation with Reynolds Number of Pressure Distribution over an Airfoil Section. By Robert M. Pinkerton, N. A. C. A. |
| 614. | Pressure Distribution over an N. A. C. A. 23012 Airfoil with an N. A. C. A. 23012 External-Airfoil Flap. By Carl J. Wenzinger, N. A. C. A. |
| 615. | Column Strength of Tubes Elastically Restrained against Rotation at the Ends. By William R. Osgood, National Bureau of Standards. |
| 616. | Interrelation of Exhaust-Gas Constituents. By Harold C. Gerrish and Fred Voss, N. A. C. A. |
| 617. | Auto-Ignition and Combustion of Diesel Fuel in a Constant-Volume Bomb. By Robert F. Selden, N. A. C. A. |
| 618. | Comparative Flight and Full-Scale Wind-Tunnel Measurements of the Maximum Lift of an Airplane. By Abe Silverstein, S. Katzoff, and James A. Hootman, N. A. C. A. |
| 619. | Drag of Cylinders of Simple Shapes. By W. F. Lindsey, N. A. C. A. |
| 620. | Pressure Distribution over Airfoils with Fowler Flaps. By Carl J. Wenzinger and Walter B. Anderson, N. A. C. A. |
| 621. | Compressible Flow about Symmetrical Joukowski Profiles. By Carl Kaplan, N. A. C. A. |
| 622. | A Photographic Study of Combustion and Knock in a Spark-Ignition Engine. By A. M. Rothrock and R. C. Spencer, N. A. C. A. |
| 623. | A Study of the Torque Equilibrium of an Autogiro Rotor. By F. J. Bailey, Jr., N. A. C. A. |
| 624. | Two-Dimensional Subsonic Compressible Flow past Elliptic Cylinders. By Carl Kaplan, N. A. C. A. |
| 625. | A Discussion of Certain Problems Connected with the Design of Hulls of Flying Boats and the Use of General Test Data. By Walter S. Diehl, Bureau of Aeronautics, Navy Department. |
| 626. | The Transition Phase in the Take-Off of an Airplane. By J. W. Wetmore, N. A. C. A. |
| 627. | The Experimental and Calculated Characteristics of 22 Tapered Wings. By Raymond F. Anderson, N. A. C. A. |
| 628. | Aerodynamic Characteristics of a Large Number of Airfoils Tested in the Variable-Density Wind Tunnel. By Robert M. Pinkerton and Harry Greenberg, N. A. C. A. |

629. On Some Reciprocal Relations in the Theory of Nonstationary Flows. By I. E. Garrick, N. A. C. A.
630. A Flight Comparison of Conventional Ailerons on a Rectangular Wing and of Conventional and Floating Wing-Tip Ailerons on a Tapered Wing. By H. A. Soulé and W. Gracey, N. A. C. A.
631. Airfoil Section Characteristics as Applied to the Prediction of Air Forces and Their Distribution on Wings. By Eastman N. Jacobs and R. V. Rhode, N. A. C. A.
632. The Crinkling Strength and the Bending Strength of Round Aircraft Tubing. By William R. Osgood, National Bureau of Standards.
633. Pressure Distribution over an N. A. C. A. 23012 Airfoil with a Slotted and a Plain Flap. By Carl J. Wenzinger and James B. Delano, N. A. C. A.
634. Calculation of the Chordwise Load Distribution over Airfoil Sections with Plain, Split, or Serially Hinged Trailing-Edge Flaps. By H. Julian Allen, N. A. C. A.
635. Theoretical Stability and Control Characteristics of Wings with Various Amounts of Taper and Twist. By Henry A. Pearson and Robert T. Jones, N. A. C. A.
636. Approximate Stress Analysis of Multistringer Beams with Shear Deformation of the Flanges. By Paul Kuhn, N. A. C. A.
637. Determination of Boundary-Layer Transition on Three Symmetrical Airfoils in the N. A. C. A. Full-Scale Wind Tunnel. By Abe Silverstein and John V. Becker, N. A. C. A.
638. The Influence of Lateral Stability on Disturbed Motions of an Airplane with Special Reference to the Motions Produced by Gusts. By Robert T. Jones, N. A. C. A.
639. The Effect of Compressibility on Eight Full-Scale Propellers Operating in the Take-Off and Climbing Range. By David Biermann and Edwin P. Hartman, N. A. C. A.
640. The Aerodynamic Characteristics of Full-Scale Propellers Having 2, 3, and 4 Blades of Clark Y and R. A. F. 6 Airfoil Sections. By Edwin P. Hartman and David Biermann, N. A. C. A.
641. The Negative Thrust and Torque of Several Full-Scale Propellers and Their Application to Various Flight Problems. By Edwin P. Hartman and David Biermann, N. A. C. A.
642. Tests of Five Full-Scale Propellers in the Presence of a Radial and a Liquid-Cooled Engine Nacelle, Including Tests of Two Spinners. By David Biermann and Edwin P. Hartman.
643. The Aerodynamic Characteristics of Four Full-Scale Propellers Having Different Plan Forms. By Edwin P. Hartman and David Biermann, N. A. C. A.
644. The Torsional and Bending Deflection of Full-Scale Aluminum-Alloy Propeller Blades under Normal Operating Conditions. By Edwin P. Hartman and David Biermann.
620. Energy Loss, Velocity Distribution, and Temperature Distribution for a Baffled Cylinder Model. By Maurice J. Brevoort, N. A. C. A.
621. Pressure Drop across Finned Cylinders Enclosed in a Jacket. By Vern G. Rollin and Herman H. Ellerbrock, Jr., N. A. C. A.
622. Flight Tests of an Airplane Showing Dependence of the Maximum Lift Coefficient on the Test Conditions. By H. A. Soulé and James A. Hootman, N. A. C. A.
623. Maximum Forces Applied by Pilots to Wheel-Type Controls. By William H. McAvoy, N. A. C. A.
624. Performance Characteristics of Venturi Tubes Used in Aircraft for Operating Air-Driven Gyroscopic Instruments. By Harcourt Sontag and Daniel P. Johnson, National Bureau of Standards.
625. Spinning Characteristics of Wings. IV—Changes in Stagger of Rectangular Clark Y Biplane Cellules. By M. J. Bamber and R. O. House, N. A. C. A.
626. Static Thrust Analysis of the Lifting Airscrew. By Montgomery Knight and Ralph A. Hefner, Georgia School of Technology.
627. Pressure Distribution over a Clark Y-H Airfoil Section with a Split Flap. By Carl J. Wenzinger, N. A. C. A.
628. Plastics as Structural Materials for Aircraft. By G. M. Kline, National Bureau of Standards.
629. A Sound Pressure-Level Meter without Amplification. By E. Z. Stowell, N. A. C. A.
630. Free-Spinning Wind-Tunnel Tests of a Low-Wing Monoplane with Systematic Changes in Wings and Tails. II—Mass Distributed along the Fuselage. By Oscar Seidman and A. I. Neihouse, N. A. C. A.
631. Wind-Tunnel Tests of Carburetor-Intake Rams. By Frank H. Highley, N. A. C. A.
632. Improvement of Aileron Effectiveness by the Prevention of Air Leakage through the Hinge Gap as Determined in Flight. By H. A. Soulé and W. Gracey, N. A. C. A.
633. Spinning Characteristics of Wings. V—N. A. C. A. 0009, 23018, and 6718 Monoplane Wings. By M. J. Bamber and R. O. House, N. A. C. A.
634. The N. A. C. A. Optical Engine Indicator. By Robert E. Tozier, N. A. C. A.
635. Tank Tests of a Model of One Hull of the Savoia S-55-X Flying Boat—N. A. C. A. Model 46. By John M. Allison, N. A. C. A.
636. The Estimation of the Rate of Change of Yawing Moment with Sideslip. By Frederick H. Imlay, N. A. C. A.
637. Preliminary Fatigue Studies on Aluminum Alloy Aircraft Girders. By Goodyear-Zeppelin Corporation.
638. Tank Tests of Model 36 Flying-Boat Hull. By John M. Allison, N. A. C. A.
639. A Preliminary Investigation of Boundary-Layer Transition along a Flat Plate with Adverse Pressure Gradient. By Albert E. von Doenhoff, N. A. C. A.
640. Interference of Wing and Fuselage from Tests of 18 Combinations in the N. A. C. A. Variable-Density Tunnel—Combinations with Split Flaps. By Albert Sherman, N. A. C. A.
641. Interference of Wing and Fuselage from Tests of 17 Combinations in the N. A. C. A. Variable-Density Tunnel—Combinations with Special Junctions. By Albert Sherman, N. A. C. A.
642. Interference of Wing and Fuselage from Tests of Eight Combinations in the N. A. C. A. Variable-Density Tunnel—Combinations with Tapered Fillets and Straight-Side Junctions. By Albert Sherman, N. A. C. A.
643. A Study of Flying-Boat Take-Off. By Walter S. Diehl, Bureau of Aeronautics, Navy Department.

LIST OF TECHNICAL NOTES ISSUED DURING THE PAST YEAR

- No.
616. The Measurement of Air Speed of Airplanes. By F. L. Thompson, N. A. C. A.
617. Stability of Structural Members under Axial Load. By Eugene E. Lundquist, N. A. C. A.
618. Increasing the Strength of Aluminum-Alloy Columns by Prestressing. By M. Holt and E. C. Hartmann, Aluminum Research Laboratories.
619. Compression-Ignition Engine Performance at Altitudes and at Various Air Pressures and Temperatures. By Charles S. Moore and John H. Collins, N. A. C. A.

644. Flight and Wind-Tunnel Tests of an XBM-1 Dive Bomber. By Philip Donely and Henry A. Pearson, N. A. C. A.
645. Some Aspects of the Stalling of Modern Low-Wing Monoplanes. By Hartley A. Soulé and Melvin N. Gough, N. A. C. A.
646. Wind-Tunnel Tests of a 2-Engine Airplane Model as a Preliminary Study of Flight Conditions Arising on the Failure of One Engine. By Edwin P. Hartman, N. A. C. A.
647. Engine Performance and Knock Rating of Fuels for High-Output Aircraft Engines. By A. M. Rothrock and Arnold E. Biermann, N. A. C. A.
648. The Increase in Frictional Resistance Caused by Various Types of Rivet Heads as Determined by Tests of Planing Surfaces. By Starr Truscott and J. B. Parkinson, N. A. C. A.
649. The Effect of Air-Passage Length on the Optimum Fin Spacing for Maximum Cooling. By Maurice J. Brevoort, N. A. C. A.
650. Wind-Tunnel Tests of a Clark Y Wing Having Split Flaps with Gaps. By Carl J. Wenzinger, N. A. C. A.
651. Effect of Spark-Timing Regularity on the Knock Limitations of Engine Performance. By Arnold E. Biermann, N. A. C. A.
652. Tables of Stiffness and Carry-Over Factor for Structural Members under Axial Load. By Eugene E. Lindquist and W. D. Kroll, N. A. C. A.
653. A Flight Investigation of the Reduction of Aileron Operating Force by Means of Fixed Tabs and Differential Linkage, with Notes on Linkage Design. By H. A. Soulé and James A. Hootman, N. A. C. A.
654. Fuel Consumption of a Carburetor Engine at Various Speeds and Torques. By Oscar W. Schey and J. Denny Clark, N. A. C. A.
655. Principles Involved in the Cooling of a Finned and Baffled Cylinder. By M. J. Brevoort, N. A. C. A.
656. Hydrodynamic and Aerodynamic Tests of Models of Floats for Single-Float Seaplanes—N. A. C. A. Models 41-D, 41-E, 61-A, 73, and 73-A. By J. B. Parkinson and R. O. House, N. A. C. A.
657. Tank Tests to Show the Effect of Rivet Heads on the Water Performance of a Seaplane Float. By J. B. Parkinson, N. A. C. A.
658. Generalized Analysis of Experimental Observations in Problems of Elastic Stability. By Eugene E. Lundquist, N. A. C. A.
659. Wind-Tunnel Tests of Three Lateral-Control Devices in Combination with a Full-Span Slotted Flap on an N. A. C. A. 23012 Airfoil. By Carl J. Wenzinger and Millard J. Bamber, N. A. C. A.
660. Fatigue Testing of Wing Beams by the Resonance Method. By William M. Bleakney, National Bureau of Standards.
661. Wind-Tunnel Investigation of Rectangular and Tapered N. A. C. A. 23012 Wings with Plain Ailerons and Full-Span Split Flaps. By Carl J. Wenzinger and Milton B. Ames, Jr., N. A. C. A.
662. Gyroscopic Instruments for Instrument Flying. By W. G. Brombacher and W. C. Trent, National Bureau of Standards.
663. The Effects of Partial-Span Plain Flaps on the Aerodynamic Characteristics of a Rectangular and a Tapered Clark Y Wing. By R. O. House, N. A. C. A.
664. Free-Spinning Wind-Tunnel Tests of a Low-Wing Monoplane with Systematic Changes in Wings and Tails. III—Mass Distributed along the Wings. By Oscar Seidman and A. I. Neihouse, N. A. C. A.

665. Tests of N-85, N-86, and N-87 Airfoil Sections in the 11-Inch High-Speed Wind Tunnel. By John Stack and W. F. Lindsey, N. A. C. A.
666. Longitudinal Stability in Relation to the Use of an Automatic Pilot. By Alexander Klemin, Perry A. Pepper, and Howard A. Wittner, New York University.

LIST OF TECHNICAL MEMORANDUMS ISSUED DURING THE PAST YEAR

No.

839. The Design of Airplane Engine Superchargers. By Werner von der Nüll. From *Luftfahrtforschung*, April 20, 1937.
840. Research and Design Problems Introduced by Increased Power Output. By Oskar Kurtz. From *Luftwissen*, April 1937.
841. Synthetic Resins in Aircraft Construction—Their Composition, Properties, Present State of Development and Application to Light Structures. By K. Riechers. From *Luftwissen*, August 1937.
842. Universal Logarithmic Law of Velocity Distribution as Applied to the Investigation of Boundary Layer and Drag of Streamline Bodies at Large Reynolds Number. By G. Gurjienko. From Report No. 257 of the Central Aero-Hydrodynamical Institute, Moscow, 1936.
843. Detonation and Autoignition. Some Considerations on Methods of Determination. By G. D. Boerlage. From *Journées Techniques Internationales de L'Aeronautique*, November 23-27, 1936.
844. Flow in Smooth Straight Pipes at Velocities above and below Sound Velocity. By W. Frössel. From *Forschung auf dem Gebiete des Ingenieurwesens*, March-April 1936.
845. On the Theory of Hydrofoils and Planing Surfaces. By F. Weinig. From *Luftfahrtforschung*, June 20, 1937.
846. The Buckling of Curved Tension-Field Girders. By G. Limpert. From *Luftfahrtforschung*, July 20, 1937.
847. Stresses in Reinforcing Rings Due to Axial Forces in Cylindrical and Conical Stressed Skins. By K. Drescher and H. Gropler. From *Luftfahrtforschung*, February 20, 1937.
848. Planing-Surface Tests at Large Froude Numbers—Airfoil Comparison. By A. Sambraus. From *Luftfahrtforschung*, August 20, 1936.
849. Rate-of-Climb Recorder. By Helmut Danielzig. From *Luftwissen*, May 1937.
850. Engines and Propellers for Powered Gliders and Light Airplanes. By H. Gropp. From *Flugsport*, November 24, 1937.
851. Twisting Failure of Centrally Loaded Open-Section Columns in the Elastic Range. By Robert Kappus. From *Luftfahrtforschung*, September 20, 1937.
852. Systematic Airfoil Tests in the Large Wind Tunnel of the DVL. By H. Doetsch and M. Kramer. From *Luftfahrtforschung*, October 12, 1937.
853. Effect of Air-Fuel Ratio on Detonation in Gasoline Engines. By L. A. Peletier. From Second World Petroleum Congress, Paris, June 1937.
854. Twisting of Thin-Walled Columns Perfectly Restrained at One End. By Lucio Lazzarino. From *L'Aerotecnica*, October 1937.
855. Model Experiments on the Forces and Moments on an End Plate Fitted to a Wing. By O. Schrenk. From *Luftfahrtforschung*, November 20, 1937.
856. The Lift Distribution of Wings with End Plates. By W. Mangler. From *Luftfahrtforschung*, November 20, 1937.

FINANCIAL REPORT

The general appropriation for the National Advisory Committee for Aeronautics for the fiscal year 1938, as contained in the Independent Offices Appropriation Act approved June 28, 1937, was \$1,259,850. A supplemental appropriation of \$453,000 was made available in the Second Deficiency Appropriation Act, fiscal year 1937, approved May 28, 1937, for the same purposes specified in the Committee's regular appropriation act for 1937, to continue available until June 30, 1938, and providing that \$353,000 should be available only for the construction and equipment of facilities and for the purchase of an airplane of the light metal private type; and providing further, that the unexpended balance of the supplemental appropriation of \$1,367,000 for 1937 be continued available until June 30, 1938. That unexpended balance was \$206,071. The total amount available for expenditure during the fiscal year 1938, therefore, was \$1,918,921. The amount expended and obligated was \$1,918,868, itemized as follows:

Personal services	\$987,571
Supplies and materials	118,162
Communication service	3,037
Travel expenses	13,454
Transportation of things	3,509
Furnishing of electricity	39,828
Repairs and alterations	28,625
Special investigations and reports	92,671
Equipment	255,049
Structures	376,962
Expended and obligated	1,918,868
Unobligated balance	53

Total, general appropriation 1,918,921

The appropriation for printing and binding for 1938 was \$21,000, of which \$20,987 was expended.

The sum of \$7,786 was received during the fiscal year 1938 as special deposits to cover the estimated cost of scientific services to be furnished private parties. The total cost of investigations completed for private parties during the fiscal year, amounting to \$4,940, was deposited in the Treasury to the credit of Miscellaneous Receipts. The sum of \$7,184 remained in special deposits on account of tests started during the fiscal year 1937 and unfinished as at June 30, 1937. The cost of these investigations, which were completed during fiscal year 1938, amounting to \$6,178, was also deposited in the Treasury to the credit of Miscellaneous Receipts, making a total of \$11,118 so deposited during the fiscal year 1938.

An allotment of \$250 was received from the State Department for payments during the fiscal year 1938 to employees stationed abroad, on account of exchange losses due to appreciation of foreign currencies. Of this amount \$144 was paid during the fiscal year 1938 to employees of the Committee stationed in the Paris

857. Investigation of Ignition and Combustion Processes of Diesel Engines Operating with Turbulence and Air-Storage Chambers. By Hans Petersen. From *Forschung auf dem Gebiete des Ingenieurwesens*, November-December 1937.
858. The Focke Helicopter. By H. Focke. From *Luftwissen*, February 1938.
859. A New Spinning-Test Method. By M. Kramer and K. B. Krüger. From *Luftfahrtforschung*, October 12, 1937.
860. The Design of Floats. By W. Sottorf. From *Luftfahrtforschung*, April 20, 1937.
861. Compression Struts with Nonprogressively Variable Moment of Inertia. By B. Radomski. From *Luftfahrtforschung*, September 20, 1937.
862. The Influence of Notches under Static Stress. By K. Matthaes. From *Luftfahrtforschung*, January 20, 1938.
863. On the Determination of the Take-Off Characteristics of a Seaplane. By A. Perelmutter. From Report No. 255, Central Aero-Hydrodynamical Institute, Moscow, 1936.
864. Load Tests on a Stiffened Circular Cylindrical Shell. By E. Schapitz and G. Krümling. From *Luftfahrtforschung*, December 20, 1937.
865. Behavior of Static Pressure Heads at High Speeds. By Helmut Danielzig. From *Luftfahrtforschung*, June 20, 1937.
866. Calculation of Load Distribution in Stiffened Cylindrical Shells. By H. Ebner and H. Köller. From *Luftfahrtforschung*, December 20, 1937.
867. Theoretical Study of Various Airplane Motions after Initial Disturbance. By Fr. Haus. From *Bulletin du Service Technique de L'Aeronautique*, No. 17, June 1937.
868. The Dornier Wind Tunnel. By H. Schlichting. From *Luftfahrtforschung*, March 20, 1938.
869. The Conversion of Energy in a Radiator. By A. Weise. From *Gesammelte Vorträge der Hauptversammlung 1937 der Lilienthal-Gesellschaft für Luftfahrtforschung* vorgelesen in München vom 12-14, October 1937.
870. Behavior of a Plate Strip under Shear and Compressive Stresses beyond the Buckling Limit. By A. Kromm and K. Marguerre. From *Luftfahrtforschung*, December 20, 1937.
871. Performance of Rotating-Wing Aircraft. By K. Hohenemser. From *Ingenieur-Archiv*, December 1937.
872. The Present Status of Airship Construction, Especially of Airship-Framing Construction. By Hans Ebner. From *Zeitschrift für Flugtechnik und Motorluftschiffahrt*, June 6 and June 28, 1933.
873. Experimental Study of Ignition by Hot Spot in Internal Combustion Engines. By Max Serruys. From *Publications Scientifiques et Techniques du Ministère de L'Air*, No. 115, 1937.
874. Effect of Propeller Slipstream on Wing and Tail. By J. Stüper. From *Luftfahrtforschung*, April 6, 1938.
875. Heat-Stressed Structural Components in Combustion-Engine Design. By Otto Kraemer. From *Zeitschrift des Vereins deutscher Ingenieure*, March 12, 1938.
876. Investigations on the Downwash behind a Tapered Wing with Fuselage and Propeller. By H. Muttray. From *Luftfahrtforschung*, March 20, 1938.
877. Wind-Tunnel Investigations on Flexural-Torsional Wing Flutter. By H. Voigt. From *Luftfahrtforschung*, September 20, 1937.

AIRCRAFT CIRCULAR ISSUED DURING THE PAST YEAR

- No.
209. Fairey "Battle" Medium Bomber Airplane (British). An All-Metal Low-Wing Cantilever Monoplane. From *The Aeroplane*, June 16 and August 18, 1937.

Office, leaving a balance of \$106 which was turned back into the Treasury.

Of the allotment of \$2,000 for participation in the Greater Texas and Pan American Exposition at Dallas, which closed October 31, 1937, the amount of \$1,995 was expended and the unobligated balance of \$5 was returned to the original appropriation.

CONCLUDING STATEMENT

Air power at the present time is a dominant factor in the strength of a nation and in enabling it to maintain its independent existence and territorial integrity. Accepted theories of warfare give a steadily increasing place to air power.

Air power is primarily dependent not only upon numbers of airplanes, but the airplanes themselves must have performance at least equal to that of an enemy. The fact that modern military aircraft require frequent replacement by improved types brings forcibly to our attention the necessity of basing their design upon the best and most reliable data from research laboratories. New information is being obtained in the aeronautical laboratories of many nations, and unless our own laboratories keep pace, the United States cannot hope to compete with foreign nations in the development of either military or commercial aircraft.

The relation of laboratory research to the development of efficient aircraft is being increasingly appreciated by the world powers. The United States for a number of years has held undisputed leadership in the field of aeronautical research. At the present time that leadership is being challenged. Unless, therefore, we fully recognize the challenge and make provision for extending the Committee's research facilities and for increasing the number of its trained research personnel, the United States will definitely fall behind.

The struggle of nations to extend their influence to other countries, is resulting in determined efforts to establish air trade routes. A few years ago, great distances were an insuperable barrier to transoceanic air transportation, but the rapid improvement of aircraft has shrunk the map of the world.

Looking to the future, the progressive nations are making sacrifices and expending their national energies and resources for the purpose of advancing their air commerce. The United States, in extending and developing its domestic and international air commerce, is confronted with serious competition in the operation of air lines over the Atlantic and Pacific Oceans and to South America. In this connection the importance of scientific research cannot be overemphasized, as the long distances of flight over water demand a maximum

of efficiency in aircraft. The United States leads at the present time in domestic and international air commerce. It should cherish this position and bend every effort to extend further its commercial air transportation.

The establishment of the Civil Aeronautics Authority has improved governmental aeronautical organization. The governmental agencies concerned with aeronautics are now organized on a sound and logical basis and function in cooperation. The aircraft manufacturing and operating industries have shown a commendable spirit of cooperation with the Government and with each other, and are alert to apply the results of the Committee's researches in a constant effort to improve the performance, efficiency, and safety of both military and civil aircraft. The Committee believes that the continuous and systematic conduct of scientific laboratory research on the basic problems of flight is the most fundamental activity of the Government in connection with the development of aeronautics. The Army, Navy, and Civil Aeronautics Authority are equally represented on the Committee. With their hearty cooperation the Committee coordinates the research needs of military, naval, and commercial aviation, and conducts the more fundamental scientific investigations in one central Government laboratory at Langley Field, Va. In this way a maximum of progress is obtained at minimum expense without overlapping or duplication.

In the rapidly advancing science of aeronautics the technical development of aircraft is directly dependent upon scientific laboratory research. The recent great expansion of research facilities by other nations will bring to an end the period of American leadership in the technical development of aircraft unless the United States also constructs additional research facilities. This subject is being studied by a special committee which includes in its membership the heads of the Army Air Corps, the Navy Bureau of Aeronautics, and the Civil Aeronautics Authority. The recommendations of that special committee will probably become the subject of a special report to the President and the Congress.

The Committee is grateful to the President and the Congress for the support accorded its work in the fields of basic and applied research in aeronautics. The Committee is determined to make every effort to meet its responsibilities by providing the scientific foundation for keeping America first in the technical development of both military and commercial aircraft.

Respectfully submitted.

NATIONAL ADVISORY COMMITTEE

FOR AERONAUTICS,

JOSEPH S. AMES, *Chairman*.

REPORT No. 612

HEAT-TRANSFER PROCESSES IN AIR-COOLED ENGINE CYLINDERS

By BENJAMIN PINKEL

SUMMARY

From a consideration of heat-transfer theory, semi-empirical expressions are set up for the transfer of heat from the combustion gases to the cylinder of an air-cooled engine and from the cylinder to the cooling air. Simple equations for the average head and barrel temperatures as functions of the important engine and cooling variables are obtained from these expressions. The expressions involve a few empirical constants, which may be readily determined from engine tests. Numerical values for these constants were obtained from single-cylinder engine tests for cylinders of the Pratt & Whitney 1535 and 1340-H engines. The equations provide a means of calculating the effect of the various engine and cooling variables on the cylinder temperatures and also of correlating the results of engine-cooling tests. An example is given of the application of the equations to the correlation of cooling-test data obtained in flight.

INTRODUCTION

Researches on the effect of the engine and cooling variables on the cylinder temperatures of air-cooled engines in wind tunnels and in flight and on blower-cooled single-cylinder test units, supplemented by studies of the cooling of electrically heated finned cylinders, have been made by various investigators. The results are characterized by an apparent lack of correlation. The effects of the engine and cooling variables on cylinder temperature have been found to differ for different engines and for the same engines operating at different conditions.

In the present report an analysis will be made of the heat-transfer processes of an air-cooled engine for the purpose of determining the manner in which the various engine and cooling conditions combine to determine the cylinder temperature. Besides providing a means by which the test results may be correlated, the analysis will give a better insight into the relation between the effects of the various important operating conditions and will indicate a method for reducing the testing to a minimum. The average head and barrel temperatures will each be given as a simple function of the important conditions making it possible to correct cylinder tem-

peratures of a given engine for variation in engine power, air-fuel ratio, mass flow of cooling air, and atmospheric temperature.

In the study of the cylinder temperatures of air-cooled engines there are two processes to be considered: First, the transfer of heat from the combustion gases to the cylinder and, second, the transfer of heat from the cylinder through the fins to the cooling air. From a consideration of heat-transfer theory, semiempirical expressions for the heat transferred by these two processes will be set up. These expressions will contain constants, the values of which will be determined from tests of engine cylinders. From these expressions equations will be obtained for the average head and barrel temperatures as functions of the fundamental engine and cooling variables.

Tests were made of two modern air-cooled engine cylinders to check the analysis and to provide the necessary experimental constants.

HEAT TRANSFER FROM THE COMBUSTION GASES TO THE CYLINDER

HEAT-TRANSFER COEFFICIENT

The transfer of heat from the combustion gases to the cylinder takes place by radiation and convection. Radiation contributes to the heat transfer mainly during and immediately following the short period when the gases are burning. From tests of low-speed engines, Nusselt (reference 1) has shown that radiation accounts for less than 10 percent of the heat transferred. For high-speed engines it is reasonable to expect that radiation, as compared with convection, is of even less importance. In the present analysis the heat transfer will be assumed to take place entirely by convection.

It is now well established from theoretical considerations and tests of bodies of various shapes that, in general, the surface heat-transfer coefficients q for cooling by forced convection may be set up as functions of the Reynolds Number $\rho VD/\mu$, of the Prandtl number $\mu c_p/k$, and of nondimensional ratios of the various important dimensions of the body. Thus

$$q_o = \frac{\mu c_p}{D} f\left(\frac{\rho VD}{\mu}, \frac{\mu c_p}{k}, \frac{S}{D}, r\right) \quad (1)$$

where q_g is the rate of heat transfer per unit area per unit temperature difference between the gases of combustion and the cylinder. (The term "cylinder" is used to refer, in general, to both the head and the barrel.)

ρ , density of gas.

V , velocity of gas.

S , stroke.

D , bore.

r , compression ratio.

μ , coefficient of viscosity of gas.

c_p , specific heat of gas at constant pressure.

k , thermal conductivity of gas.

The usefulness of equation (1) is evident since, by grouping the many variables into factors such as the Reynolds Number and the Prandtl number, the testing required to establish the equation for q is reduced to a minimum.

The convection of heat from a surface by a moving gas is brought about by the same mechanism that gives rise to surface friction. It may be recalled that the friction between two adjacent fluid layers moving at different velocities is caused by an interchange of fluid particles between the layers resulting from the random molecular movement associated with fluid temperature for laminar flow and, in addition, from small swirls for turbulent flow. These same interlayer movements interchange particles in the warmer layers with particles in the colder layers and result in a diffusion of heat in the direction of the colder layers. With transition from laminar to turbulent flow, a large increase in heat transfer naturally occurs.

The values of the viscosity, conductivity, and specific heat in equation (1) vary with temperature; however, the Prandtl number for gases remains practically constant.

Heat-transfer tests have shown that, in general, q is proportional to $(\rho V)^n$ where the value of n depends on the body cooled and on the range of Reynolds Number involved. For example, in the cooling of a flat plate, $n=0.5$ for a laminar boundary layer and 0.8 for a turbulent boundary layer. It is clear that, for q_g to be proportional to $(\rho V)^n$, the function of the Reynolds Number must be $(\rho VD/\mu)^n$. The equation for q_g for a gas may then be written

$$q_g = \frac{\mu c_p}{D} \left(\frac{\rho VD}{\mu} \right)^n f\left(\frac{S}{D}, r\right) \quad (2)$$

Several attempts have been made to obtain the variation of the instantaneous heat-transfer coefficient during the engine cycle (references 1 and 2). The difficulty of the problem is seen from the fact that, in addition to the continual variation in V , ρ , μ , c_p , and k during the cycle, account must also be taken of the varying gas turbulence. The present paper deals with the simpler problem of obtaining the average rate of heat transfer over the entire cycle.

Gas velocity.—The various gas movements that take part in the transfer of heat are the flow of the gases through the intake and exhaust ports, the sweeping of the gases over the cylinder barrel and head surfaces produced by the piston movement, and the turbulence that may be set up in the gases. A source of turbulence is the high gas velocity through the intake port, which reduces to a swirl when the gas enters the cylinder. During combustion there is evidence of the existence within the charge of a field of small swirls. As an explanation of the fact that the rate of flame propagation increased with engine speed, Marvin and his associates (reference 3) suggested that these swirls are the mechanism whereby the flame is propagated in the cylinder. It is evident that this mechanism would also transfer heat and, although little is known about it, that it may be one of the most important contributing factors. Possible sources of this small-grain turbulence may be the breaking down of the swirl introduced during the suction stroke or of an unstable flow condition set up by the rapid compression of the engine gases. Finally, additional gas turbulence may result from the friction of the gases in flowing over the cylinder surfaces and from the combustion of the charge.

In all the components of this complicated gas movement, the characteristic is evident that the linear and rotational velocities are proportional, or nearly proportional, to the engine speed. The assumption will therefore be made that the velocity V in equation (2) can be replaced by a product of the engine speed and a function of the crank angle. It will also be assumed that for a given engine the function of crank angle is independent of the engine-operating conditions.

Engine and gas parameters.—The quantities S , D , and r are constants for a given engine. Other ratios of the engine dimensions may be of importance but they also are either constants or known functions of the crank angle. The density ρ is obviously equal to the product of the weight of gases in the cylinder and a function of crank angle.

It will later be shown that the value of c_p/μ^{n-1} corresponding to an average effective gas temperature for the gas cycle does not appreciably vary for the range encountered in ordinary operation. Although c_p/μ^{n-1} varies during any given cycle, it will be assumed that its effect is the same for all cycles.

When the foregoing assumptions are introduced into equation (2), the instantaneous heat-transfer coefficient of the gas is

$$q_g = W_i^n f(\theta) \quad (3)$$

where W_i is the product of the weight of gases in the cylinder and the number of cycles per minute, and $f(\theta)$ combines the variation with crank angle of all the factors in equation (2) and also the constants of the equation. In accordance with the preceding discus-

sion, $f(\theta)$ is independent of the engine-operating conditions. The quantity W_t may be looked upon as the weight of gas flowing through the engine per minute adjusted to include the weight of the residuals.

Heat transfer to head.—Over the entire cycle the average of the rate of heat transfer to the cylinder head is obviously given by

$$H = \frac{a_1}{4\pi} \int_0^{4\pi} q_g (T - T_h) d\theta$$

or

$$H = \frac{a_1 W_t^n}{4\pi} \int_0^{4\pi} f(\theta) (T - T_h) d\theta \quad (4)$$

where H is the heat transferred per unit time.

a_1 , the internal area of the head.

T_h , the average temperature of the head surface.

T , the instantaneous gas temperature.

It should be noted that q_g and T are average values over the cylinder head.

If B is defined as

$$B = \frac{1}{4\pi} \int_0^{4\pi} f(\theta) d\theta$$

it may be seen from equation (3) that BW_t^n is the mean heat-transfer coefficient over the complete cycle. The temperature obtained by averaging the product of the instantaneous gas temperature and the ratio of the instantaneous to the mean heat-transfer coefficient over the complete cycle will be referred to as the "effective gas temperature."

The effective gas temperature by definition is given by the following expression

$$T_g = \frac{1}{4\pi B} \int_0^{4\pi} T f(\theta) d\theta \quad (5)$$

Equation (4) may now be written

$$H = B a_1 W_t^n (T_g - T_h) \quad (6)$$

Equation (6) thus gives a simple expression for the rate of heat transfer to the head.

The indicated horsepower I of an engine is proportional to the weight of mixture inducted into the engine per unit time for a constant air-fuel ratio. In the range to the rich side of the theoretically correct mixture, I varies only slightly with air-fuel ratio. The weight of mixture differs from the total weight in the engine by the weight of residuals. The difference, however, is sufficiently small so that an equation similar to equation (6) but involving I instead of W_t may be written

$$H = \bar{B} a_1 I^{n'} (T_g - T_h) \quad (7)$$

This equation is applicable in the range of air-fuel ratios to the rich side of the theoretically correct mixture. In the lean-mixture range, I depends not only on the weight of charge inducted into the engine but also on the air-fuel ratio. For a small range to the lean side of the theoretically correct mixture, however, the effect of air-fuel ratio may approximately be taken care of by including it in the curve of T_g against

air-fuel ratio. Equation (7) does not predict the small variation in heating that occurs when a constant indicated horsepower is maintained and when the weight of residuals is varied by varying the exhaust pressure.

Heat transfer to barrel.—The equations for the barrel will be assumed to take the same form as equations (5), (6), and (7). The values of the constants and of T_g will, however, be different. In order to avoid complicating the notation, the same set of symbols will be used for the barrel with the exception that T_h will be replaced by T_b , the average cylinder-barrel temperature. Part of the heat is transmitted to the barrel by the piston. The heating of the piston by the engine gases is similar in process to the heating of the cylinder head. In the conduction of heat from the piston to the barrel, however, additional factors, such as the resistance to the flow of heat through the piston, piston rings, and oil films, appear. The cooling produced by the flow of oil and the heating due to friction also affect the barrel temperatures. Some of these factors are taken care of by the empirical constants in the equations. The final justification for the foregoing assumption is, however, that good results are obtained by the use of the equations. Some variation in the constants B and \bar{B} for the barrel may be expected as the condition of the piston, piston rings, and cylinder changes and also as the quantity of circulating oil changes.

Temperature of combustion gases.—The important factors upon which T_g depends can be determined from a consideration of the engine cycle. It will be shown that T_g may be taken as being independent of the weight of the charge inducted into the engine and the engine speed but depending on the air-fuel ratio, the carburetor-air temperature, the spark timing, and the compression ratio. As only first-order effects will be considered, a constant specific heat will be assumed.

Equating the heat added by combustion to the sum of the increase in internal energy and the increment of work, the familiar equation is obtained

$$dq = w_i c_v dT + \frac{P dv}{J}$$

From the gas law

$$Pv = w_i R T$$

there is obtained $P dv + v dP = w_i R dT$

The expression for dq then becomes

$$dq = \frac{c_v}{R} (\gamma P dv + v dP)$$

From which

$$v^{\gamma-1} dq = \frac{c_v}{R} d(Pv^{\gamma}) \quad (8)$$

Integrating from the start of compression where $q=0$, $P=P_1$, and $v=v_1$ to the point up to which the quantity of heat q is liberated, there is obtained for the pressure at that point

$$P = P_1 \left(\frac{v_1}{v} \right)^{\gamma} + (\gamma - 1) \frac{J}{v^{\gamma}} \int_0^q v^{\gamma-1} dq$$

An expression for the average gas temperature at any instant in the cycle may be obtained from the preceding equation by making use of the gas law

$$T = \frac{P_1 v_1 \left(\frac{v_1}{v}\right)^{\gamma-1}}{w_i R} + (\gamma-1) \frac{J h w_f}{w_i v^{\gamma-1} R} \int_0^L v^{\gamma-1} dL \quad (9)$$

where P_1 is the initial pressure of the charge when the volume is v_1 .

v_1 , the total volume of the cylinder with the piston at bottom center.

v , the variable volume.

γ , the ratio of the specific heat at constant pressure to the specific heat at constant volume.

J , the mechanical equivalent of heat.

q , the quantity of heat added up to any point in the cycle.

c_v , specific heat at constant volume.

L , the ratio of weight of mixture burned up to any point in the cycle to the weight inducted.

h , the heat content per pound of fuel $\times A/15.1$.

R , the gas constant.

$w_i = w + w_r$, the total weight of gas in cylinder after combustion is complete.

w_r , the weight of residuals.

$w = w_a + w_f$, the weight of fresh charge.

w_a , the weight of air.

$w_f = \frac{w}{A+1}$, the weight of fuel.

A , the air-fuel ratio.

Since the gas constant R for the residual gas is close to that for the fresh charge

$$P_1 v_1 = R(w T_m + w_r T_r)$$

where T_m is the temperature of the inlet charge.

T_r , the temperature of the residual gas.

$$T = \frac{(w T_m + w_r T_r) \left(\frac{v_1}{v}\right)^{\gamma-1}}{w_i} + \frac{(\gamma-1) h w J \left(\frac{v_1}{v}\right)^{\gamma-1}}{R(A+1) w_i} \int_0^L \left(\frac{v}{v_1}\right)^{\gamma-1} dL$$

The number of variables in this equation may be reduced by eliminating the ones having only a small effect on T . The quantity $w_r T_r$ is equal to $P_a v_c / R$, where P_a is the pressure at the end of the exhaust stroke and v_c is the clearance volume of the cylinder. The quantity P_a would be expected to increase slightly with weight of charge. The term $w_r T_r$, however, is only a small factor in determining the value of T and, in seeking a first approximation, the effect of variation in the quantity $w_r T_r / w_i$ will be neglected. When w is large compared with w_r , w_i is practically proportional to w , and the variation of w/w_i with weight of charge is small. For the purpose at hand it will be assumed that w/w_i is constant. This assumption applies fairly well at full open throttle and its accuracy decreases as the

load is decreased. The quantity L is a function of crank angle and, for a given air-fuel ratio, spark timing, and cylinder, has been found to vary only slightly with weight of charge and engine speed. Curves illustrating this point will be shown later.

The expression for T may then be written

$$T = T_m \left(\frac{v_1}{v}\right)^{\gamma-1} + f_1(\theta, r, s, A)$$

where r is the compression ratio.

s , the spark timing.

θ , the crank angle at which T is the gas temperature.

This equation applies during the compression and expansion strokes.

During exhaust

$$T = T_m + f_1(2\pi, r, s, A)$$

and, during intake, neglecting the residuals,

$$T = T_m \text{ (approximately)}$$

It is evident that an expression of the form

$$T = T_m f_2(r, \theta) + f_3(\theta, r, s, A) \quad (10)$$

covers the variation of T over the entire cycle. It is noted that, based on the foregoing assumptions, T is independent of the quantity of charge, the weight of residuals, and the engine speed in the practical range of operation.

When equation (10) is substituted into equation (5), there results

$$T_g = T_m f_4(r) + f_5(r, s, A) \quad (11)$$

The value of T_g is also independent of the charge inducted, the weight of residuals, and the engine speed, since $f(\theta)$ in equation (5) is independent of the engine conditions. The variation of T_g for both the head and barrel with A , s , and T_m will be obtained from engine tests. The values of the constants B , \bar{B} , n , and n' for the head and the barrel will also be obtained from engine tests.

HEAT TRANSFER FROM CYLINDER TO COOLING AIR

Over-all heat-transfer coefficient.—The transfer of heat from the cylinder wall through the fins to the cooling air will now be considered. It is possible to obtain theoretical solutions for the rate of flow of heat through fins as a function of the fin dimensions and the surface heat-transfer coefficient of the fins. Harper and Brown (reference 4) have made a detailed analysis of the heat flow through fins of rectangular, tapered, and parabolic section mounted on flat plates and cylinders. The following convenient approximate expression given in reference 5 has been found to predict with a good degree of accuracy the heat transfer for circular fins of both rectangular and tapered section:

$$U = \frac{q}{p} \left[\frac{2}{a} \left(1 + \frac{w}{2R_b} \right) \tanh(aw') + s_b \right] \quad (12)$$

where

$$a = \sqrt{\frac{2q}{kt}}$$

U is the rate of heat dissipation per unit cylinder-wall area per degree difference in temperature between the cylinder wall and the air.

q , the average surface heat-transfer coefficient of fins is the rate of heat dissipation per unit surface area of the fins per degree difference in temperature between the fin surface and the air.

w , width of fin.

p , fin pitch ($s+t$).

s , average air space between fins.

t , average fin thickness.

w' , width of fin plus $\frac{1}{2}$ tip thickness.

s_b , length of cylinder wall exposed between two adjacent fins.

R_b , radius to base of fins.

k , thermal conductivity of fin material.

Equation (12) may be written

$$U = bq^x$$

where b and x are functions of the fin dimensions and of the value of q . For a given engine the fin dimensions are fixed and the variation of q is limited to the range corresponding to adequate cooling. Within this range b and x are found to be constants for a given engine.

The surface of the fin is cooled by convection and an equation similar to equation (1) can be written for the heat-transfer coefficient q where D is replaced by s , and r , by s/R_b . As indicated in the previous discussion, q is proportional to $(\rho V)^n$. In this case also the variation of the viscosity μ with cooling-air temperature introduces only a small variation in q , which will be neglected.

Since the pressure drop $\Delta P \rho / \rho_0$ across a finned cylinder mounted in a jacket or in a cowling varies as a power of the mass flow, the following expression may be written for U :

$$U = K(\Delta P \rho / \rho_0)^m \quad (13)$$

where K and m are constants for a given engine and ρ_0 is a standard density (taken as corresponding to 70° F. at 29.92 inches of Hg). The quantity ρ is the average density of the air entering and leaving the fins. The values of K and m will differ for the head and barrel.

Heat transfer to cooling air.—The heat transferred from the head to the cooling air is given by

$$H = a_0 K (\Delta P \rho / \rho_0)^m (T_h - T_a) \quad (14)$$

where a_0 is the outside head area.

T_h , the average head temperature.

T_a , the inlet temperature of the cooling air.

A similar expression may be obtained for the barrel.

Average temperatures.—If H in equation (14) is equated to the value given in equation (7), an expression can be set up for the average head temperature:

$$T_h - T_a = \frac{T_g - T_a}{\frac{a_0 K (\Delta P \rho / \rho_0)^m}{a_1 B I^{n'}} + 1} \quad (15)$$

An expression similar to (15) but involving a different set of constants may be written for the barrel. The

average head and barrel temperatures, by means of these expressions, can be calculated from the engine and cooling conditions.

An equation similar to (15), but involving the weight of gas in the engine cylinder, may be obtained from equations (14) and (6):

$$T_h - T_a = \frac{T_g - T_a}{\frac{a_0 K (\Delta P \rho / \rho_0)^m}{a_1 B W_t^n} + 1} \quad (16)$$

Maximum cylinder temperature.—The rear spark-plug temperature and the temperature between the rear spark plug and the exhaust port are the highest external temperatures on the head. The practice at present is to set a temperature of about 475° F. as the maximum that a point on the cylinder head may attain. A maximum of 300° F. is also usually imposed on barrel temperatures.

No attempt will be made here to obtain an equation for the temperature at individual points on the cylinder as a function of the cooling and engine variables. The variation of the average head and barrel temperatures may, however, be taken as a close indication of the variation of the maximum cylinder temperatures when engine and cooling conditions are changed. The maximum temperatures have been found to exceed the average temperatures by from 120° F. to 150° F. on the head and 30° F. on the barrel for the Pratt & Whitney 1340-H cylinder in the single-cylinder tests. Different values depending on the fin and baffle design will be obtained for other cylinders.

The rate of heat transfer from the hot gases to the cylinder wall varies from point to point on the cylinder. In the case of the barrel it may be assumed that the heat-transfer coefficient from the gases to the wall is the same for any point at a given height on the barrel but that it varies as the point moves axially. The problem is even more complicated for the head, as the position of the point relative to the spark plugs results in a difference in heating during combustion. In addition, various parts of the head are subject to different degrees of gas movement. The region near the intake port is cooled by the flow of the fresh charge into the cylinder, and the region near the exhaust port is heated by the movement of hot gases at high velocity through the exhaust port.

The rate of heat transfer from the cylinder wall to the cooling air also varies with position on the cylinder. The cooling of the front of the cylinder depends on the degree of turbulence of the air. Inferior cooling of the rear of the cylinder results from the heating of the air as it flows around the cylinder and from the poor flow conditions directly at the rear.

In the treatment of the cooling of individual points on the cylinder, consideration must also be given to the conduction through the metal from the hot regions to the cold, and particularly in the case of the cylinder head because of the high conductivity of aluminum and the thickness of the walls.

It is evident that, even if it could be obtained, an equation taking all these factors into consideration would be complicated and of little practical value.

APPARATUS

The cylinders on which the tests were made were a Pratt & Whitney 1535 and a Pratt & Whitney 1340-H.

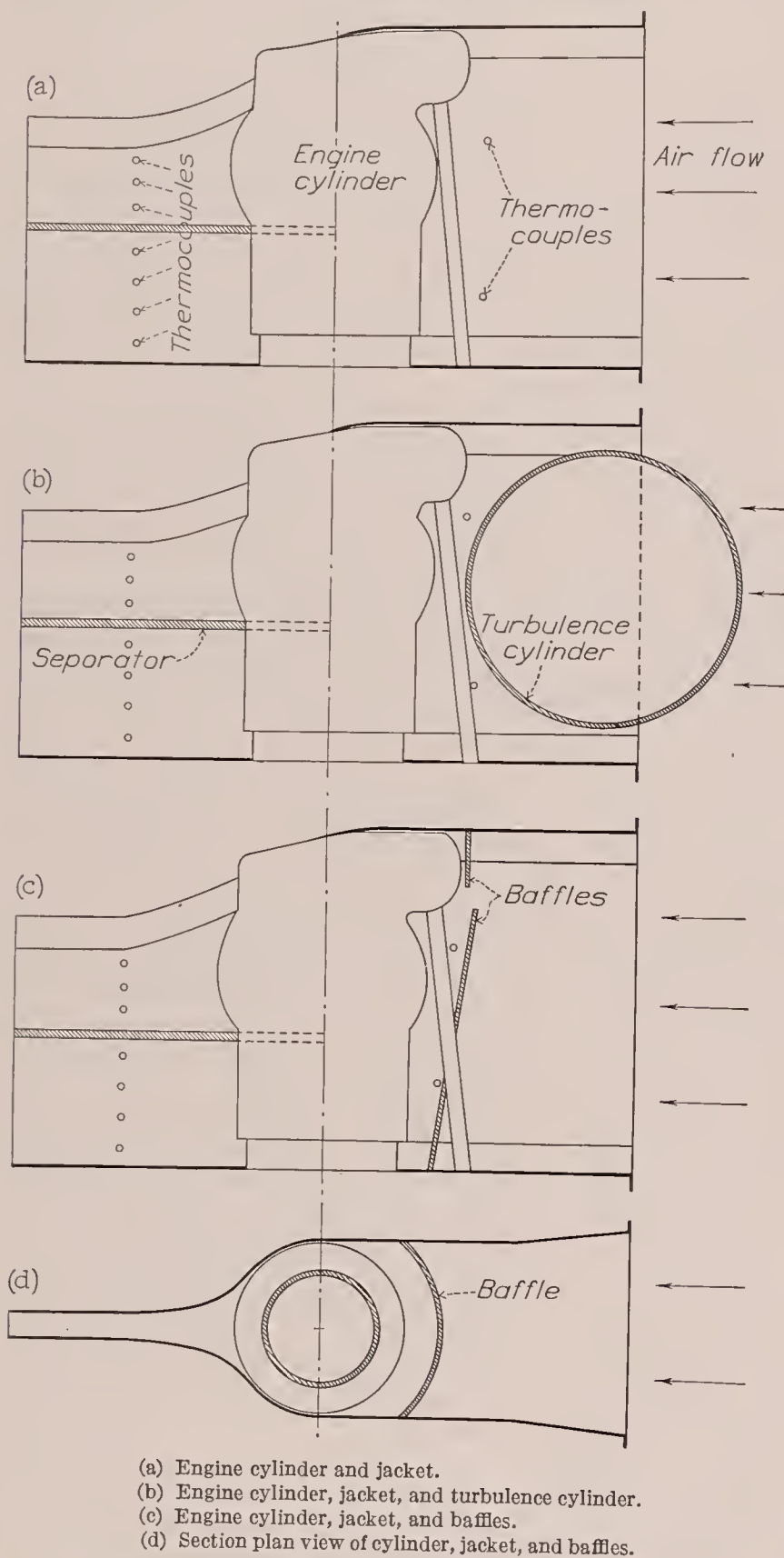


FIGURE 1.—Diagram of engine cylinder, jacket, and turbulence devices.

The bore, stroke, and compression ratio for the 1535 cylinder were $5\frac{3}{16}$ inches, $5\frac{1}{2}$ inches, and 6.73, respectively, and for the 1340-H were $5\frac{1}{4}$ inches, 6 inches, and 5.6. Each cylinder was mounted on a single-cylinder test stand enclosed in a jacket (see fig. 1 (a)) through which cooling air was forced by a centrifugal blower. The jacket had a wide entrance section to provide a low air velocity over the front half of the cylinder;

over the rear half the jacket fitted closely against the fins to provide a high air velocity.

The 1535 cylinder was provided with two devices for disturbing the air flow over the front of the cylinder to determine the additional cooling due to the disturbed motion of the air in front of the cylinders of a cowled engine in flight. One of the devices was a cylinder 9 inches in diameter mounted about 4 inches ahead of the fin tips with its axis at right angles to the cylinder axis, as shown in figure 1(b). The other device consisted of baffles for directing the cooling air downward over the front of the head and barrel, as shown in figures 1(c) and (d). The lower baffle, a semicircular sheet placed about $1\frac{1}{2}$ inches from the fin tips, provided a fairly high vertical velocity of the air.

A partition was located in the exit duct for separating the air that flowed over the head from the air that flowed over the barrel. Thermocouples were located in the jacket ahead of the cylinder and in the exit passages from the head and barrel for measuring the increase in temperature of the cooling air. The jacket of the 1340-H cylinder was covered with felt insulation to reduce heat losses from the cooling-air stream.

The temperatures of the two cylinders were measured in each case by 22 thermocouples on the cylinder head, 10 on the barrel, and 2 on the flange, located in similar positions for both cylinders.

A static tube was located in the space ahead of the cylinder, where the velocity head was negligible, for measuring the pressure difference between the front of the cylinder and the room. Impact tubes were located between the fins on the head and barrel at 45° from the front of the cylinder. The space between the fins and the jacket was still large in the region of the impact tubes. As the velocity head was only a small part of the total head in this region, there was little loss in energy and the readings of the impact tubes were the same as that of the static tube. In the tests with the turbulence devices the pressure drop was obtained from the readings of the impact tubes.

The quantity of cooling air supplied to the jacket was determined from the readings of a thin-plate orifice tank connected to the inlet of the blower. Electrical heaters located in the air duct between the blower and the jacket were provided to vary the cooling-air temperature. Electrical heaters were also located in the intake system of the engine for varying the carburetor-air temperature.

The standard test-engine equipment was used for measuring brake mean effective pressure, engine speed, fuel consumption, and air temperature at the inlet to the carburetor. The mixture strength was determined by means of a Cambridge air-fuel ratio meter and was used for calculating the weight of carburetor air supplied to the engine. A gasometer was connected to the intake manifold for determining the air quantity supplied to the engine during the tests in which the

air-fuel ratio was varied. These measurements were used for calibrating the Cambridge meter. A Farnboro indicator was used in the tests of the 1340-H cylinder to obtain indicator cards.

METHODS AND TESTS

The following tests were made of both cylinders:

1. Calibration tests were made to determine the weight of air flowing over the head and the barrel as functions of the pressure drop across the cylinder.

2. The engine conditions and weight velocity of the cooling air were maintained constant and the cooling-air temperature was varied to determine the value of T_g at an air-fuel ratio of 12.5.

3. The cooling conditions and air-fuel ratio were held constant (the latter at a value of about 12.5) and the indicated horsepower was varied by varying the brake mean effective pressure and engine speed to determine the constants B , \bar{B} , n , and n' in equations (6) and (7).

The tests covered the following range of conditions:

	Pratt & Whitney 1535	Pratt & Whitney 1340-H
Engine speed, r. p. m.	1,300-2,100	1,500-2,100
Brake mean effective pressure, lb./sq. in.	72-126	75-117
Air-fuel ratio	11.3-14.7	10.6-14.1
Cooling-air temperature, °F	100-216	80-215
Pressure drop across cylinder, in. water	5-15	7.8-25
Carburetor-air temperature, °F	180	88-215
Spark timing, deg. B. T. C.	120	17-32

¹ Approximately.

More tests than were necessary to establish the values of the constants were made to check the validity of the equations over a range of engine and cooling conditions. Only two accurate tests are required to establish the value of the constants for the normal operating range of an engine: The pressure drop across the cylinder is varied in one and the indicated horsepower is varied in the other. From the first test, the constants of equation

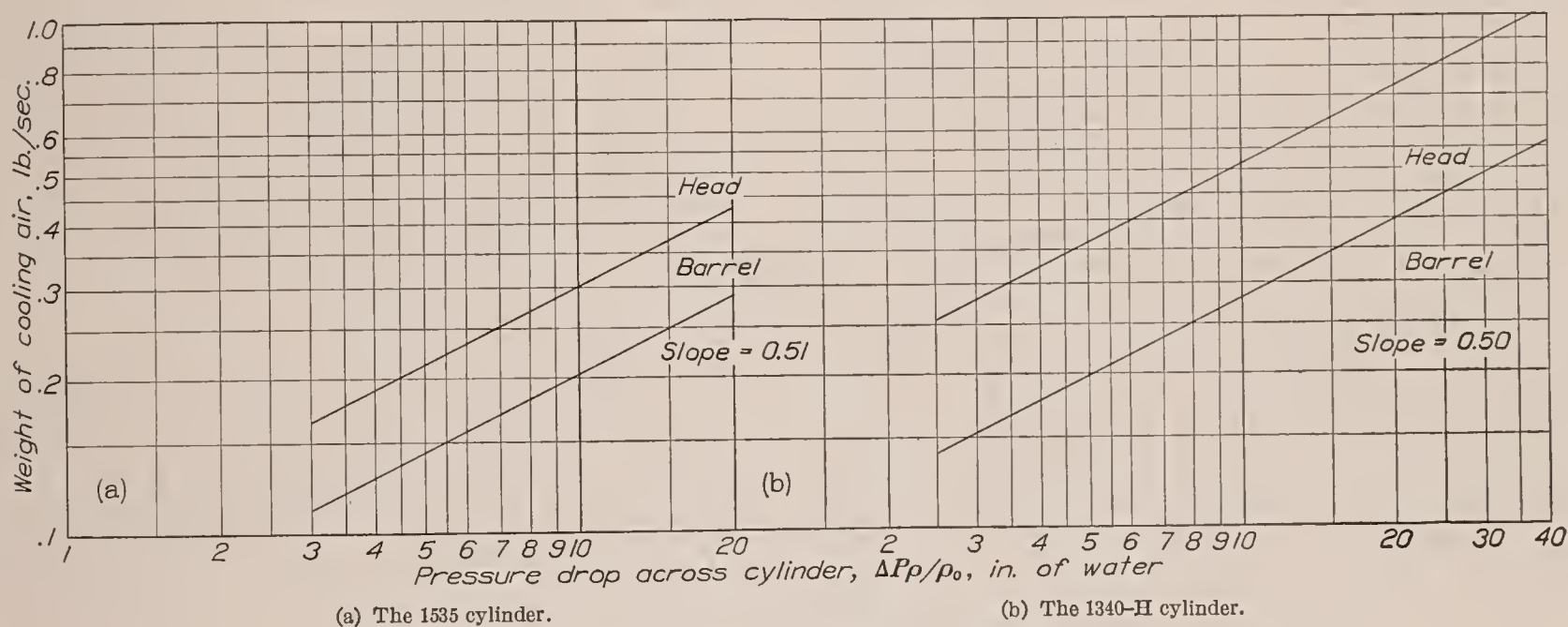


FIGURE 2.—Calibration of the jacket as an air duct.

4. The engine conditions were held constant and the mass flow of the cooling air was varied to determine the constants m and K in equation (14). These tests provided additional data for determining T_g .

5. The cooling conditions and the weight of air delivered to the engine per cycle were held constant and the air-fuel ratio was varied to determine the variation of T_g with air-fuel ratio.

In addition, the following tests were made of the 1340-H cylinder:

6. The weight of the charge and the air-fuel ratio were held constant and the spark setting was varied to obtain the variation of T_g with spark timing.

7. The weight of the charge and the air-fuel ratio were held constant and the temperature of the carburetor air was varied to obtain the variation of T_g with carburetor-air temperature.

8. Indicator cards were obtained in runs during which the brake mean effective pressure and engine speed were varied to determine their effect on L .

(14) may be obtained; and, from the second, the constants of equations (6) and (7).

The calibration tests (item 1) were made by blocking, in turn, the exits for the head and the barrel and by measuring with the thin-plate orifice tank the quantity of air flowing through the jacket for various pressure drops across the cylinder. A correction, which was obtained by blocking both passages, was applied for the leakage from the jacket. The calibration curves are shown in figure 2.

The heat dissipated from the head and barrel was calculated by the formula

$$H = W_c c_p \Delta T$$

where W_c is the weight of air flowing over the head or barrel per unit time as obtained from figure 2, and ΔT is the increase in cooling-air temperature.

The values of T_g for the head and barrel, corresponding to an air-fuel ratio of 12.5, were obtained from the tests described in item 2 by plotting the heat output

from the head and the barrel against the average head and barrel temperatures, respectively. The curves were extrapolated to zero heat output, at which points the average head and barrel temperatures are equal to their respective effective gas temperatures T_g . (See

items 5, 6, and 7, and the results were plotted against air-fuel ratio, spark setting, and carburetor-air temperature, respectively.

By the use of the data obtained in the tests described in item 4, the heat-transfer coefficients U were calcu-

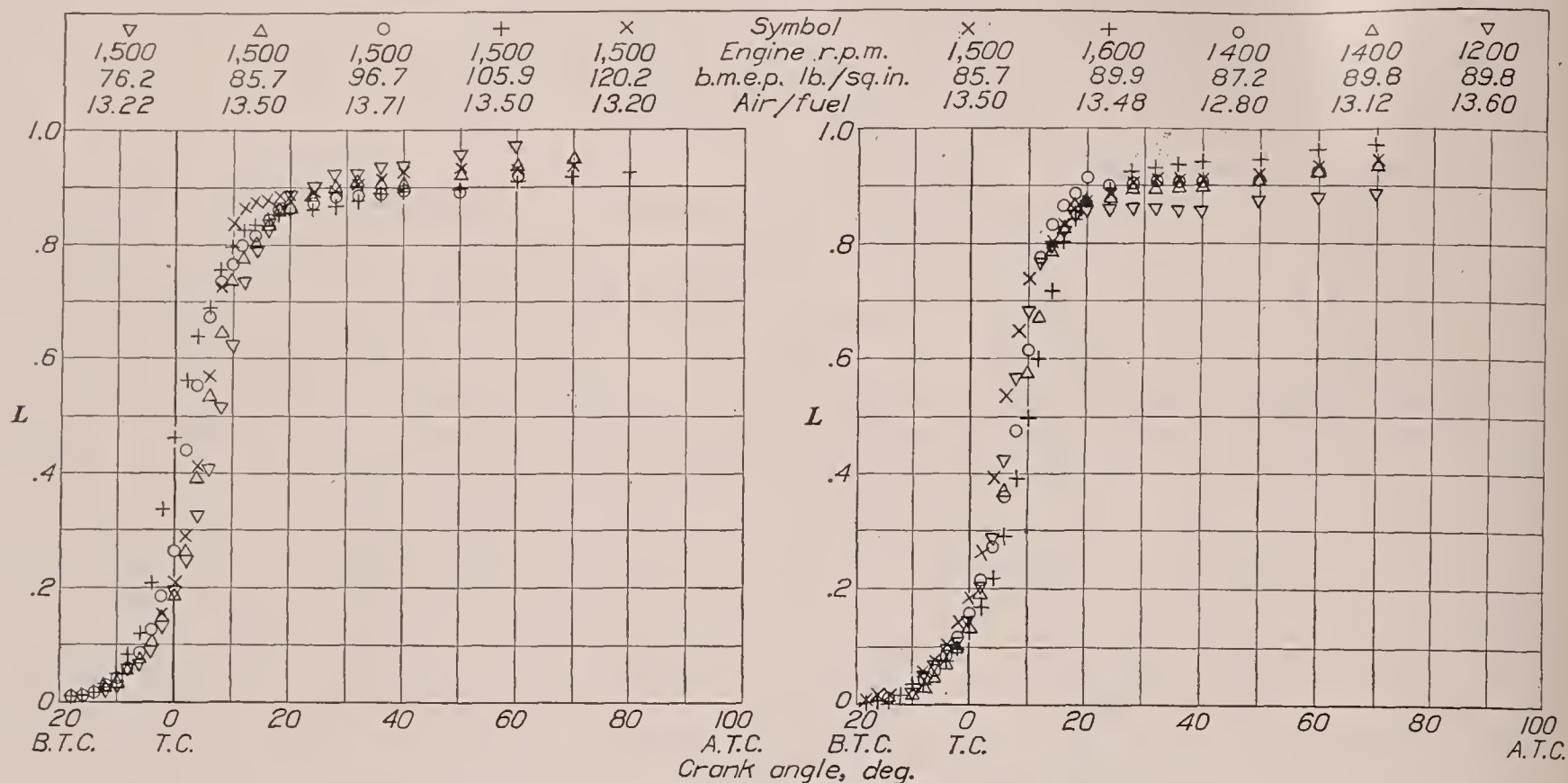


FIGURE 3.—Values of L for Pratt & Whitney 1340-H cylinder for different engine conditions.

equation (7).) The average head and barrel temperatures are an average of the 22 thermocouple readings for the head and of the 10 for the barrel, respectively.

The values of $H/(T_g - T_h)$ and $H/(T_g - T_b)$ were plotted against I and W_i on logarithmic coordinates

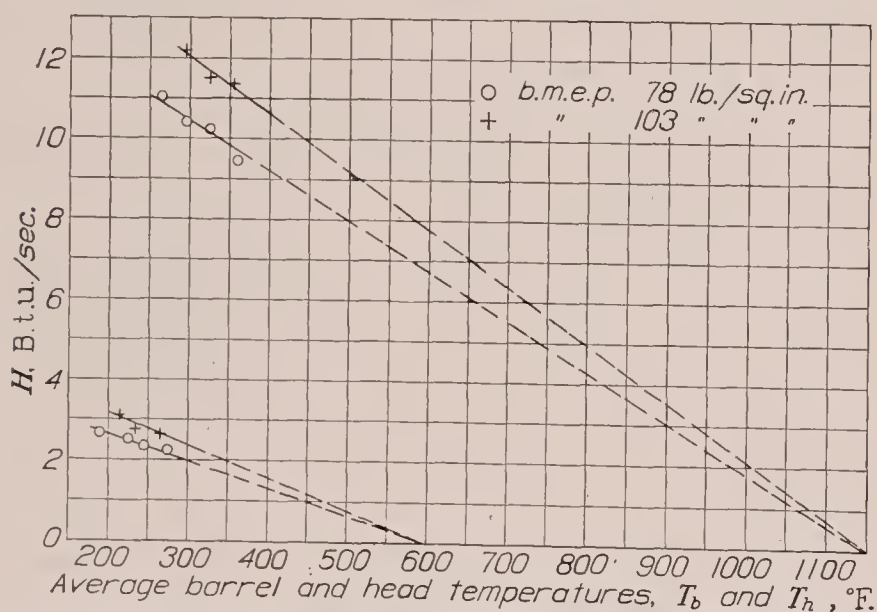


FIGURE 4.—Variation of heat transfer from combustion gases to head and barrel with average head and barrel temperatures. Carburetor-air temperature, 85°F.; spark timing, 26° B. T. C.; air-fuel ratio, 12.3; engine speed, 1,500 r. p. m.

for the tests described in item 3 to obtain the constants B , \bar{B} , n , and n' in equations (6) and (7). The values of T_g found in the manner described in the preceding paragraphs were used in calculating $H/(T_g - T_h)$ and $H/(T_g - T_b)$, inasmuch as the air-fuel ratios were approximately 12.5.

These constants and equations (6) and (7) were used to calculate the values of T_g from the tests described in

lated for the head from $H/[a_0 (T_h - T_a)]$ (see equation (14)) and for the barrel from a similar equation. The values of K and m were obtained from a plot on logarithmic coordinates of U against $\Delta P \rho / \rho_0$.

The curves for L were calculated from the indicator cards, making use of a convenient equation derived from equation (8).

RESULTS AND DISCUSSION

Gas temperature T_g .—The values of L are shown plotted in figure 3 against crank angle for various engine brake mean effective pressures and engine speeds. As pointed out in the development of the expression for T_g , there is only a small spread between the values of L for these different conditions.

Some scattering was found in the values of the gas temperature T_g , obtained as described in the section on methods, by extrapolating the curves of heat output from the head and the barrel plotted against the average head and barrel temperatures. Part of the scattering was due to the large distance through which the extrapolation had to be made as compared with the range covered by test data and part was due to small experimental errors in the data. Consideration of a large number of these curves led to a choice of 1,150° F. and of 600° F. for the values of T_g for the head and the barrel, respectively, for both the 1535 and 1340-H cylinders. Figure 4 shows two typical sets of data for determining T_g for the Pratt & Whitney 1340-H cylinder. The lines are drawn through the points to pass through the temperatures of 1,150° F. and 600° F. at $H=0$ for the head and

barrel, respectively. The curves illustrate that a single determination cannot, in general, be relied on to determine T_g .

Heat transfer from combustion gas to cylinder.—The values of $H/(T_g - T_h)$ and $H/(T_g - T_b)$ were calculated using the preceding values of T_g ; they are plotted in figure 5 on logarithmic coordinates against I , W_a , and W_t for both cylinders. The points for the head of the 1535 cylinder fall on the same curve whether the

by the individual runs. The parallel shifting from one run to the next does not indicate a trend with brake mean effective pressure or engine speed because the results of the tests in which the brake mean effective pressure was varied and the engine speed was held constant are parallel to those for which the reverse was true. Check runs taken on different days also show about the same order of magnitude of shift. The scattering is attributed to the poor condition of the

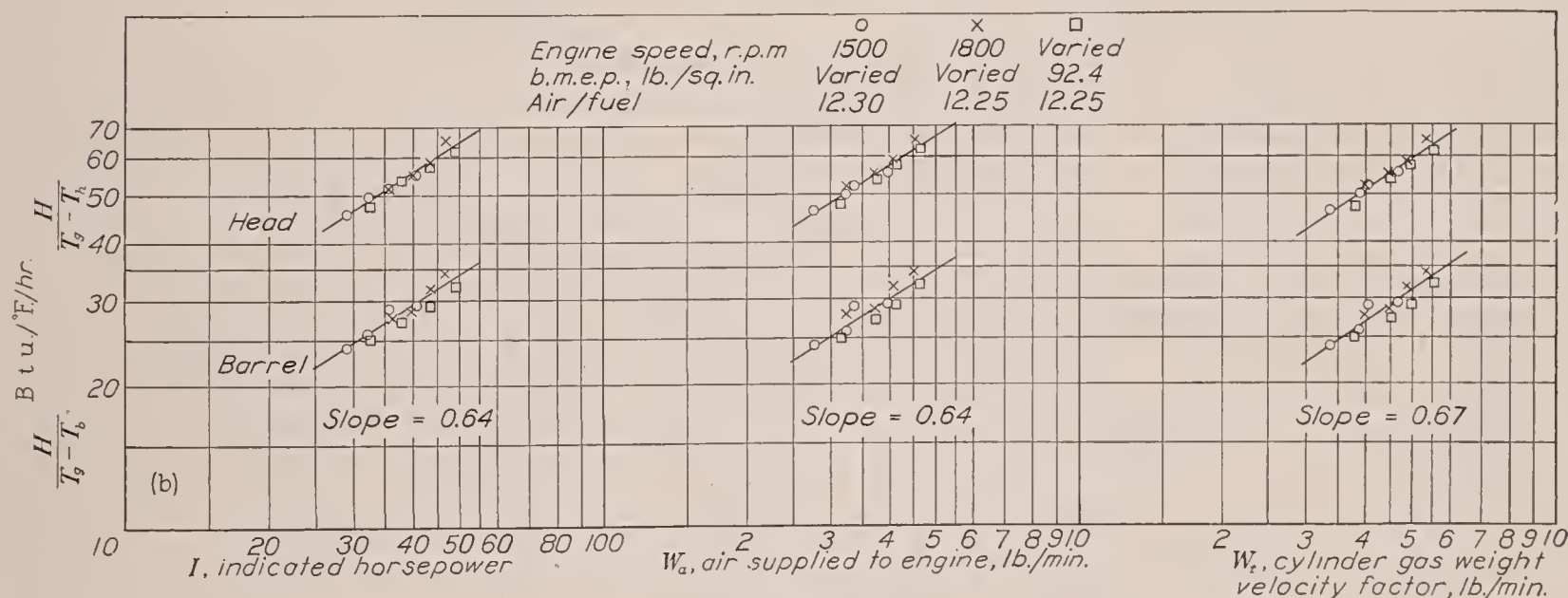
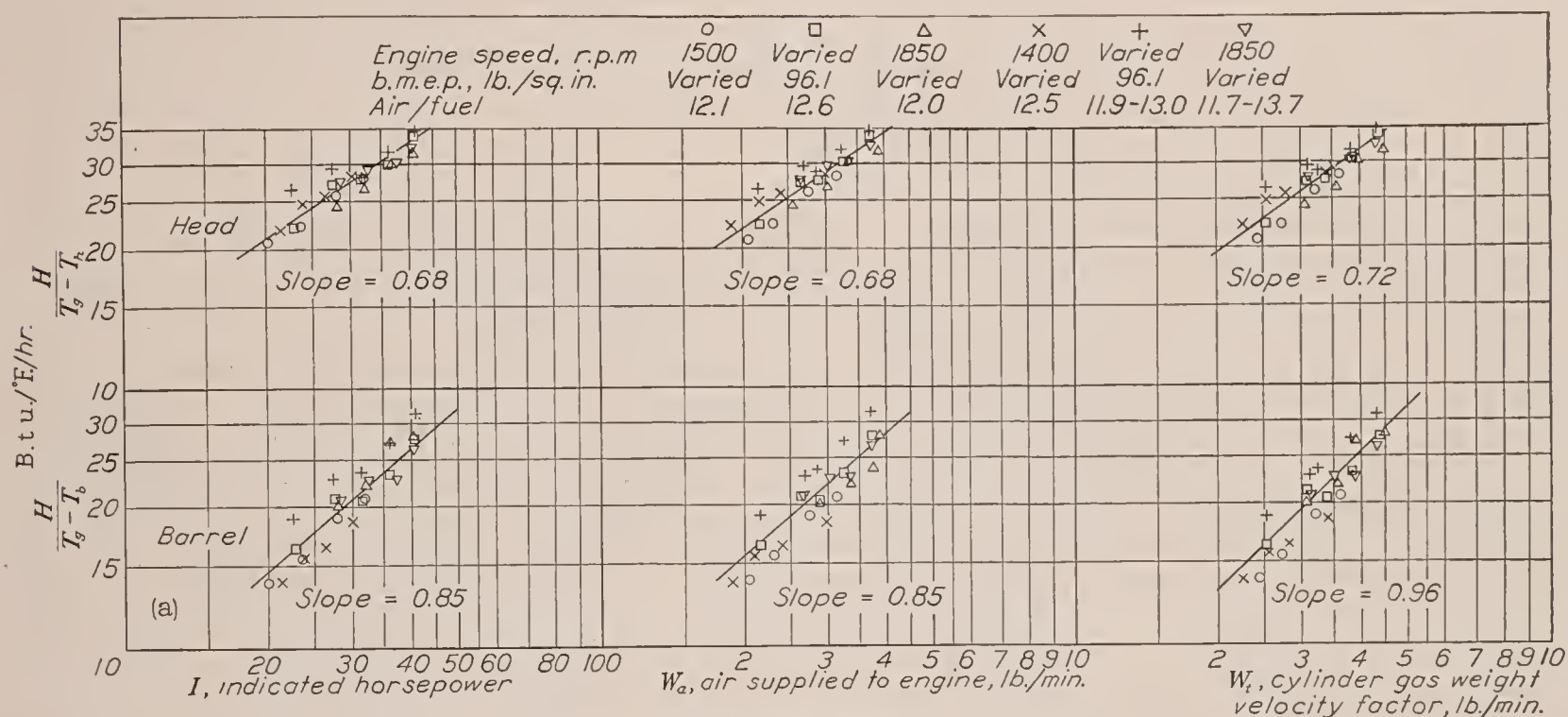


FIGURE 5.—Variation of $H/(T_g - T_h)$ and $H/(T_g - T_b)$ with I , W_a , and W_t .

change in indicated horsepower was obtained by varying the brake mean effective pressure or the engine speed, as was expected from a consideration of equations (6) and (7). The same general result was found for the head and barrel of the 1340-H cylinder. The points for the barrel of the 1535 cylinder show more scattering, although the points for the various runs form straight lines having a common slope. A line was drawn through the average of the points and in the direction indicated

piston rings of the 1535 cylinder and the results are considered as not very reliable. Other tests of a Pratt & Whitney 1535 engine indicate that the value of n' for the barrel is the same as the value for the head.

In two of the runs plotted in figure 5 the air-fuel ratio varied over a small region in the rich range. The points for these two runs agree with the rest of the data. It will later be seen that, for the range covered, the variation of T_g with air-fuel ratio is small.

The curves of $H/(T_g - T_h)$ and $H/(T_g - T_b)$ plotted against I and W_a are parallel, having a slope of 0.68 for the head and of 0.85 for the barrel for the 1535 cylinder and of 0.64 for both the head and the barrel for the 1340-H. This parallelism is to be expected, as the indicated horsepower is directly proportional to the air weight per second. The slopes of the curves of $H/(T_g - T_h)$ and $H/(T_g - T_b)$ plotted against W_t are 0.72 for the head and 0.96 for the barrel of the 1535

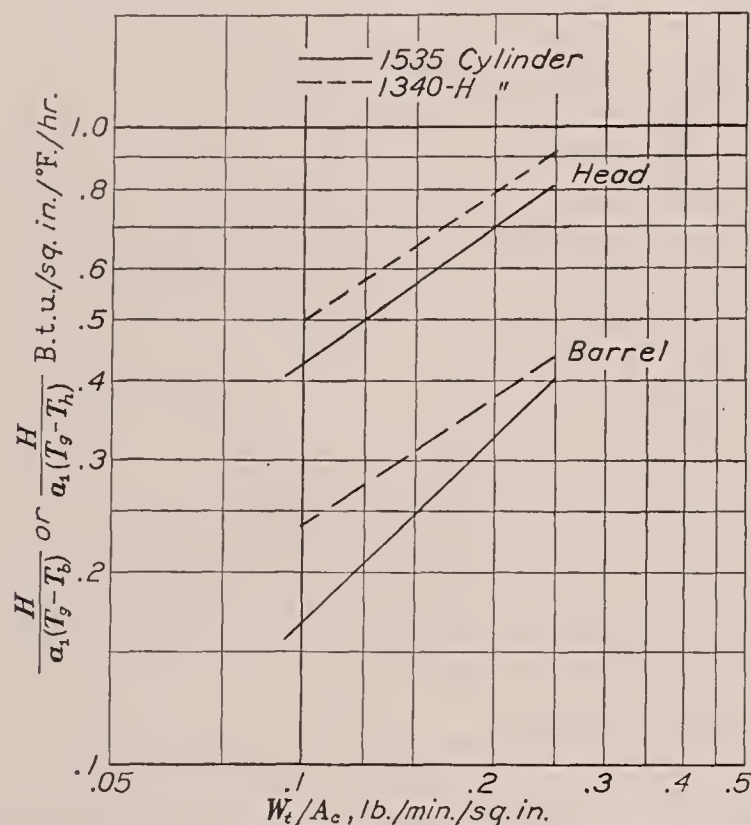


FIGURE 6.—Variation of heat-transfer coefficient from combustion gases to head and barrel with W_t/A_c .

cylinder and 0.67 for both the head and the barrel of the 1340-H.

The constants for equations (6) and (7) were obtained from figure 5; the equations are tabulated as follows:

	Head	Barrel
1535	$H = 2.71 I^{0.68} (T_g - T_h)$ $H = 13.5 W_a^{0.68} (T_g - T_h)$ $H = 11.6 W_t^{0.72} (T_g - T_h)$	$H = 1.135 I^{0.85} (T_g - T_b)$ $H = 8.46 W_a^{0.85} (T_g - T_b)$ $H = 6.68 W_t^{0.96} (T_g - T_b)$
1340-H	$H = 5.22 I^{0.64} (T_g - T_h)$ $H = 23.8 W_a^{0.64} (T_g - T_h)$ $H = 20.0 W_t^{0.67} (T_g - T_h)$	$H = 2.77 I^{0.64} (T_g - T_b)$ $H = 12.4 W_a^{0.64} (T_g - T_b)$ $H = 10.3 W_t^{0.67} (T_g - T_b)$

Units of H are B. t. u. per hour; units of W_a and W_t are pounds per minute.

A comparison will be made between the two cylinders of the rate of heat transfer from the gas to the cylinder walls. Dividing $H/(T_g - T_h)$ by the internal area of the head and doing the same for the barrel gives the heat-transfer coefficient of the gas to the head and the barrel. The internal area of the head included the exposed internal surface of the head with the valves closed and the surface of the liner down to the end of the head. The area of the valve faces was included but the area of the exhaust passage above the valve was not. Although the exhaust-passage area should be considered, it is difficult to state its importance in comparison with the internal area of the head. The coefficients, as previously calculated, may be considered as

approximate values for purposes of comparison. The internal area of the barrel was taken from the end of the head to the position of the bottom compression ring when the piston was at bottom center.

In order to compare the heat-transfer coefficients of the two cylinders, the ratio of W_t to the cross-sectional area of the piston was taken as a measure of the weight velocity of the gas moving by the cylinder surfaces.

Curves of $H/[a_1(T_g - T_h)]$ and $H/[a_1(T_g - T_b)]$ are shown in figure 6 plotted against W_t/A_c , where A_c is the internal cross-sectional area of the cylinder. The values of a_1 and A_c are given in the following table:

	a_1 , sq. in.		A_c , sq. in.
	Head	Barrel	
Pratt & Whitney 1535.....	47.1	82.6	21.1
Pratt & Whitney 1340-H.....	76.8	84.2	25.9

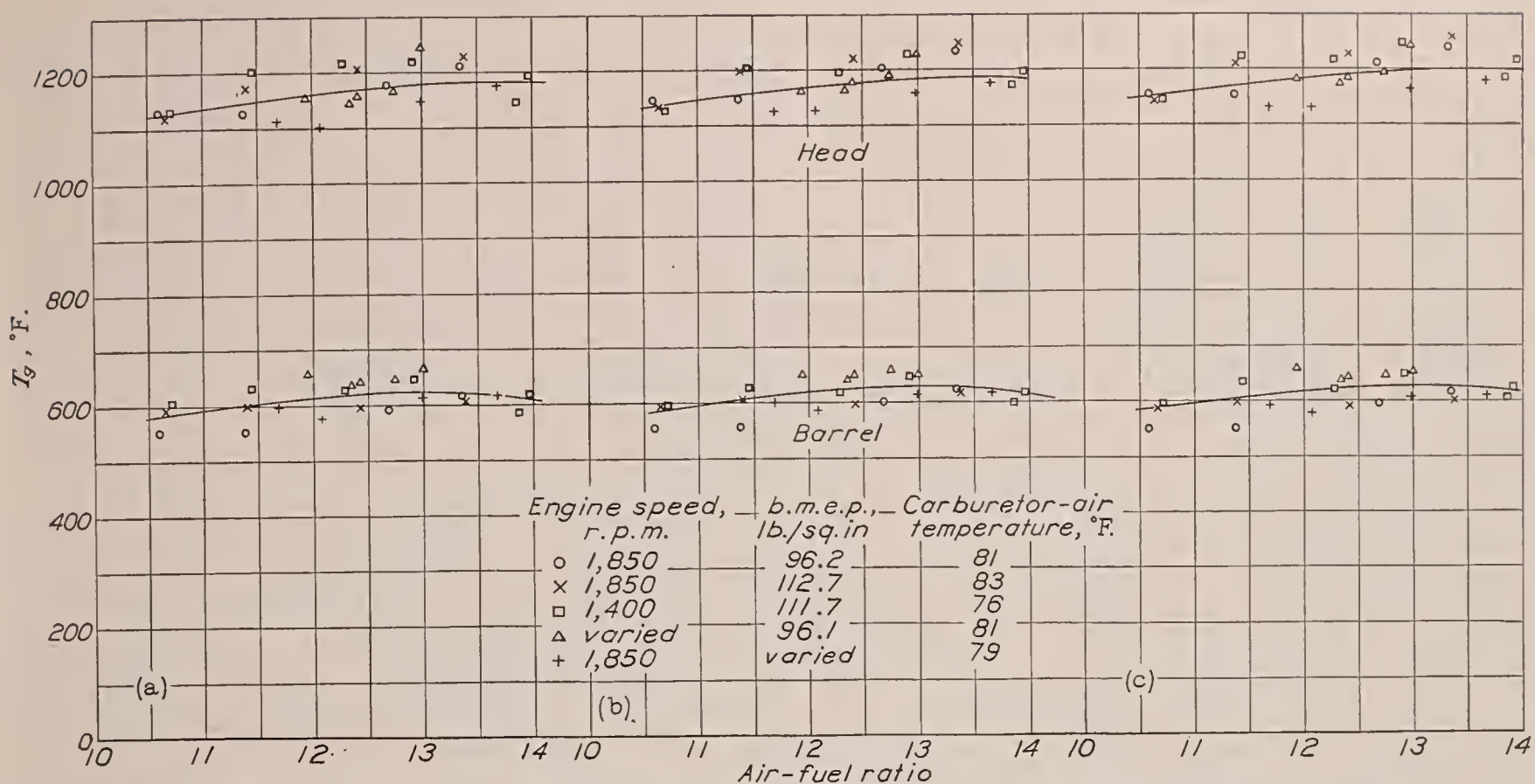
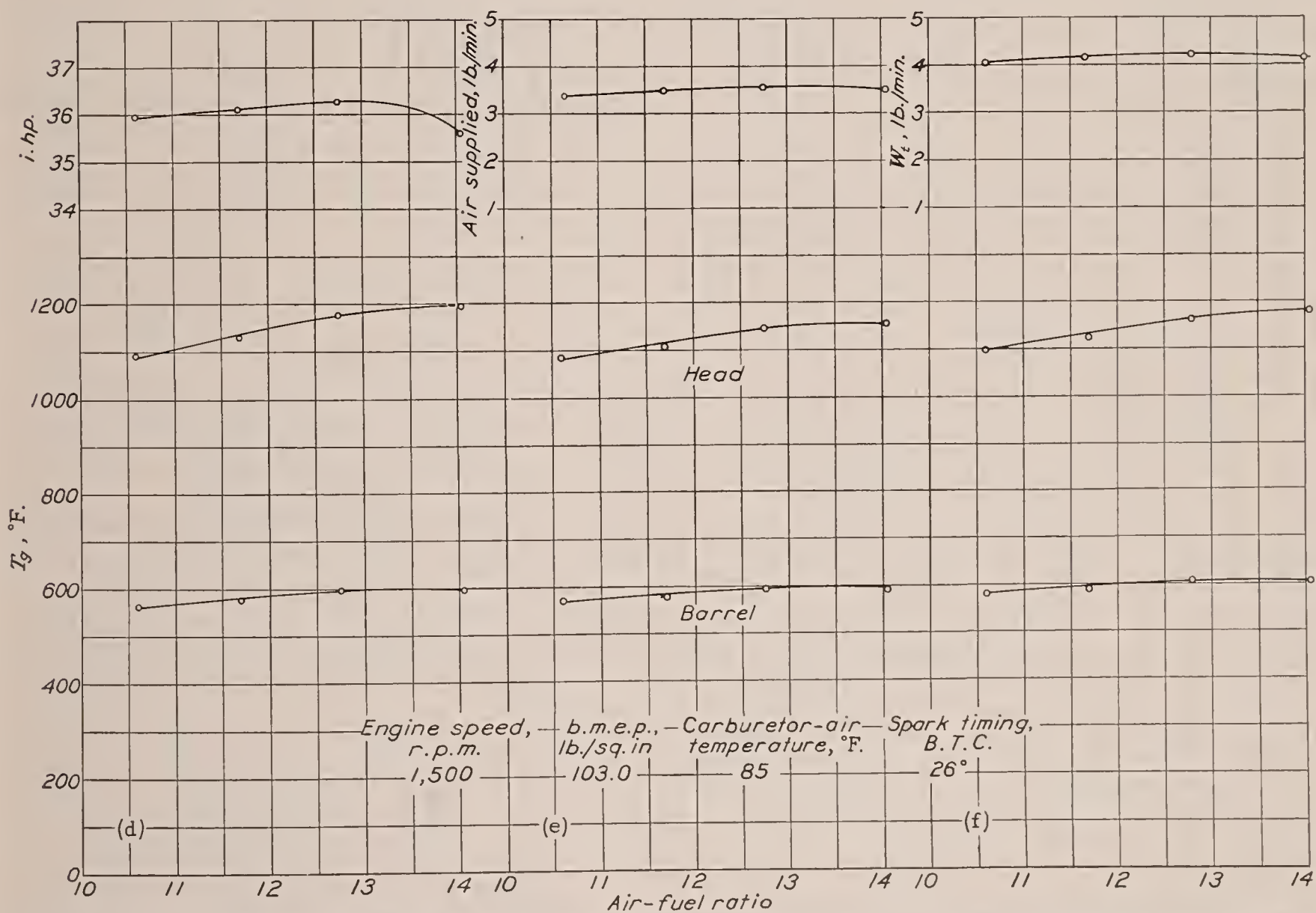
The curves for the 1340-H cylinder are somewhat higher than those for the 1535. It was expected that the results for the two cylinders would be fairly close together as there is no great difference in their general design. A large difference would be expected if means were provided in one of the cylinders for obtaining additional swirl of the charge. Much closer agreement between the two cylinders is obtained when $H/[a_1(T_g - T_h)]$ and $H/[a_1(T_g - T_b)]$ are plotted against W_t .

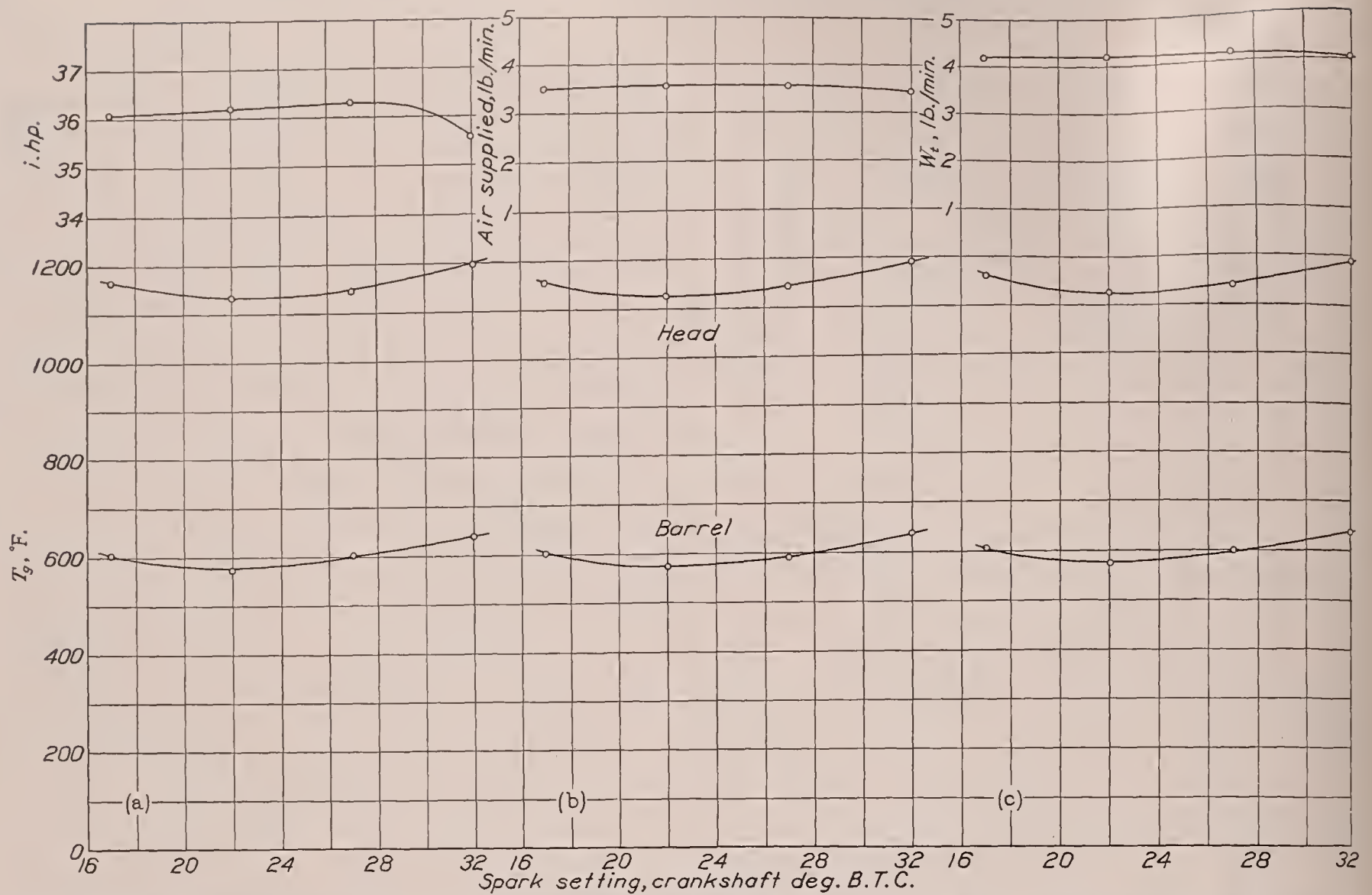
Variation of T_g with engine conditions.—Equations (17) were used to calculate T_g from the test results in which air-fuel ratio and spark timing were varied. Three curves were obtained for the head and barrel by using in turn the equations involving I , W_a , and W_t . Figure 7 shows the value of T_g plotted against air-fuel ratio. The three curves for T_g for each cylinder are practically the same and indicate that T_g increases only slightly in going from an air-fuel ratio of 12 to 14.

Figure 8 shows the values of T_g plotted against spark setting for the 1340-H cylinder. The value of T_g remains practically constant over a wide range of spark setting covering usual operating conditions; it increases, however, for both greatly advanced and retarded spark timings. Although W_a was held practically constant, the indicated horsepower decreases at both extremes of the spark-timing range.

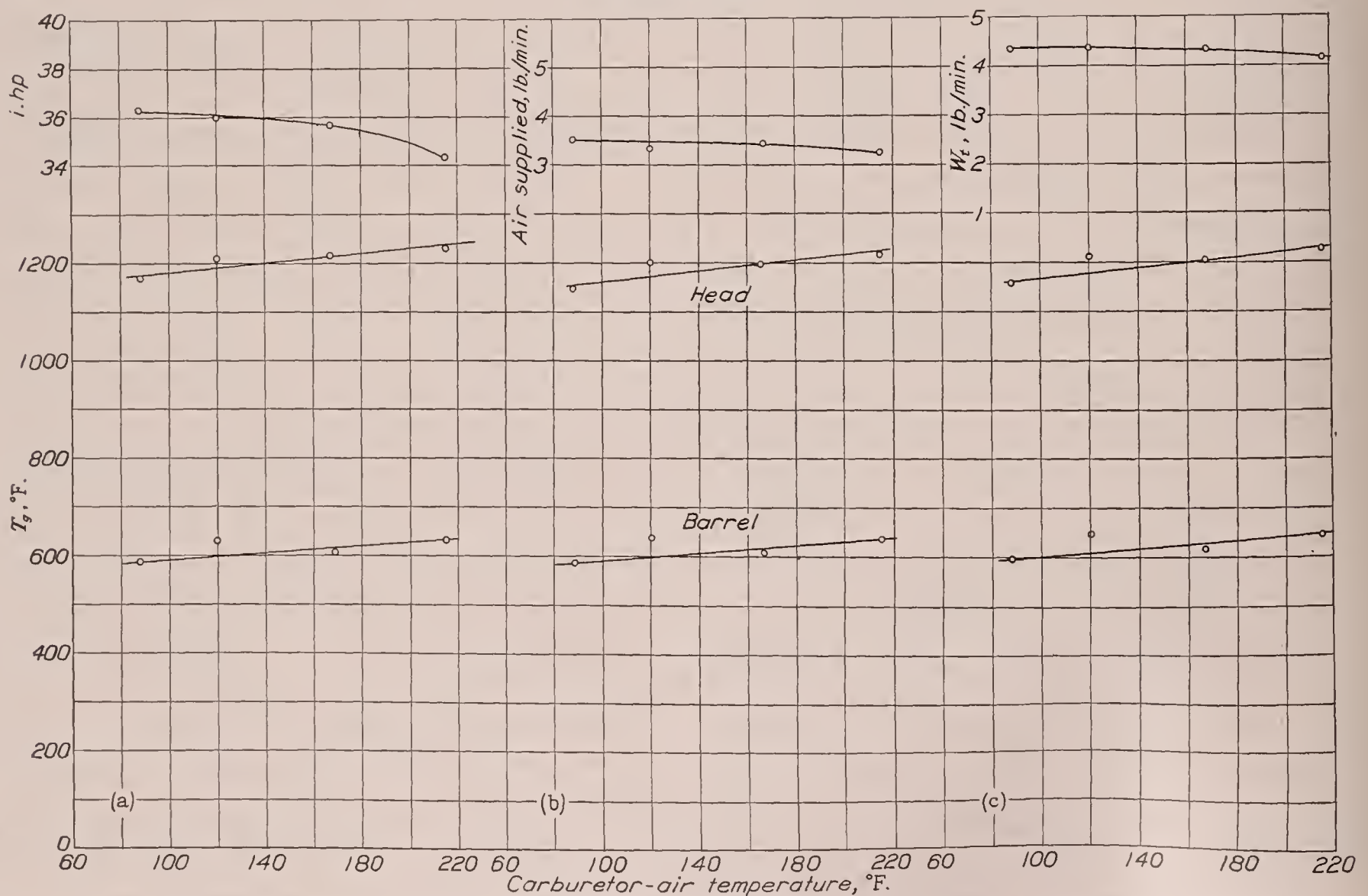
In figure 9 T_g is shown plotted against the temperature of the carburetor air for the 1340-H cylinder. It was found, in general, to be difficult to obtain consistent runs in the tests of the effect of carburetor-air temperature on cylinder temperature. The curves in figure 9 indicate that a 100° F. rise in carburetor-air temperature results in approximately a 58° F. rise in T_g for the head and barrel.

If reference is had to equations (2) and (3), an estimate may be made of the error introduced by assuming that the value of $\mu^{1-n}c_p$ corresponding to T_g does not vary appreciably with change in engine conditions. The value of n for the head is about 0.7.

(a) T_g based on indicated horsepower, I ; 1535 cylinder.(b) T_g based on air supplied to engine, W_a ; 1535 cylinder.(c) T_g based on cylinder gas weight flow factor, W_t ; 1535 cylinder.(d) T_g based on indicated horsepower, I ; 1340-H cylinder.(e) T_g based on air supplied to engine, W_a ; 1340-H cylinder.(f) T_g based on cylinder gas weight flow factor, W_t ; 1340-H cylinder.FIGURE 7.—Variation of T_g with air-fuel ratio.



(a) T_g based on indicated horsepower, I . (b) T_g based on air supplied to engine, W_a . (c) T_g based on cylinder gas weight flow factor, W_t .
 FIGURE 8.—Variation of T_g with spark setting. The 1340-H cylinder; engine speed, 1,500 r. p. m.; b. m. e. p., 102.0 pounds per square inch; air-fuel ratio, 12.34; carburetor air temperature, 93° F.



(a) T_g based on indicated horsepower, I . (b) T_g based on air supplied to engine, W_a . (c) T_g based on cylinder gas weight flow factor, W_t .
 FIGURE 9.—Variation of T_g with carburetor-air temperature. The 1340-H cylinder; engine speed, 1,500 r. p. m.; b. m. e. p., 101.5 pounds per square inch; air-fuel ratio, 12.25; spark timing, 26° B. T. C.

The heat-transfer coefficient q must, therefore, vary as $\mu^{0.3}c_p$. Assuming that the effective gas temperature T_g is $1,150^\circ\text{F}$., a change in gas temperature of 100°F . will produce a change in μ of 4.8 percent and a negligible change in c_p resulting in a change in the value of q of 1.6 percent. As the variation of T_g is less than 100°F . for the usual range of variation of air-fuel ratio, carburetor-air temperature, and spark timing, it is evident that the variation in q resulting from the change in μ and c_p may be neglected.

Heat transfer from cylinder to cooling air.—The heat-transfer coefficients U for the 1535 cylinder are shown in figure 10(a) plotted against $\Delta P\rho/\rho_0$ for three conditions: Without a turbulence device, with the 9-inch cylinder, and with the vertical baffles. The 9-inch cylinder and the baffles illustrate the effect of providing turbulence over the front of the cylinder, a condition which is present in the cooling of an engine in flight. To reproduce flight conditions on a single-cylinder blower-cooled engine involves several natural difficulties. The nature of the turbulence produced by any device of the type described is different from that obtained in flight and, in addition, part of the air that cools the front of the cylinder in flight spills out of the cowling, resulting in a lower temperature of the air that enters the baffles and cools the rear of the cylinder. With regard to turbulence, it may be sufficient, without exactly reproducing the flow, to provide a large-scale turbulence in which is dissipated the same percentage of the available dynamic head as in flight. The present results may be considered to indicate the effect of providing turbulence over the front of the cylinder.

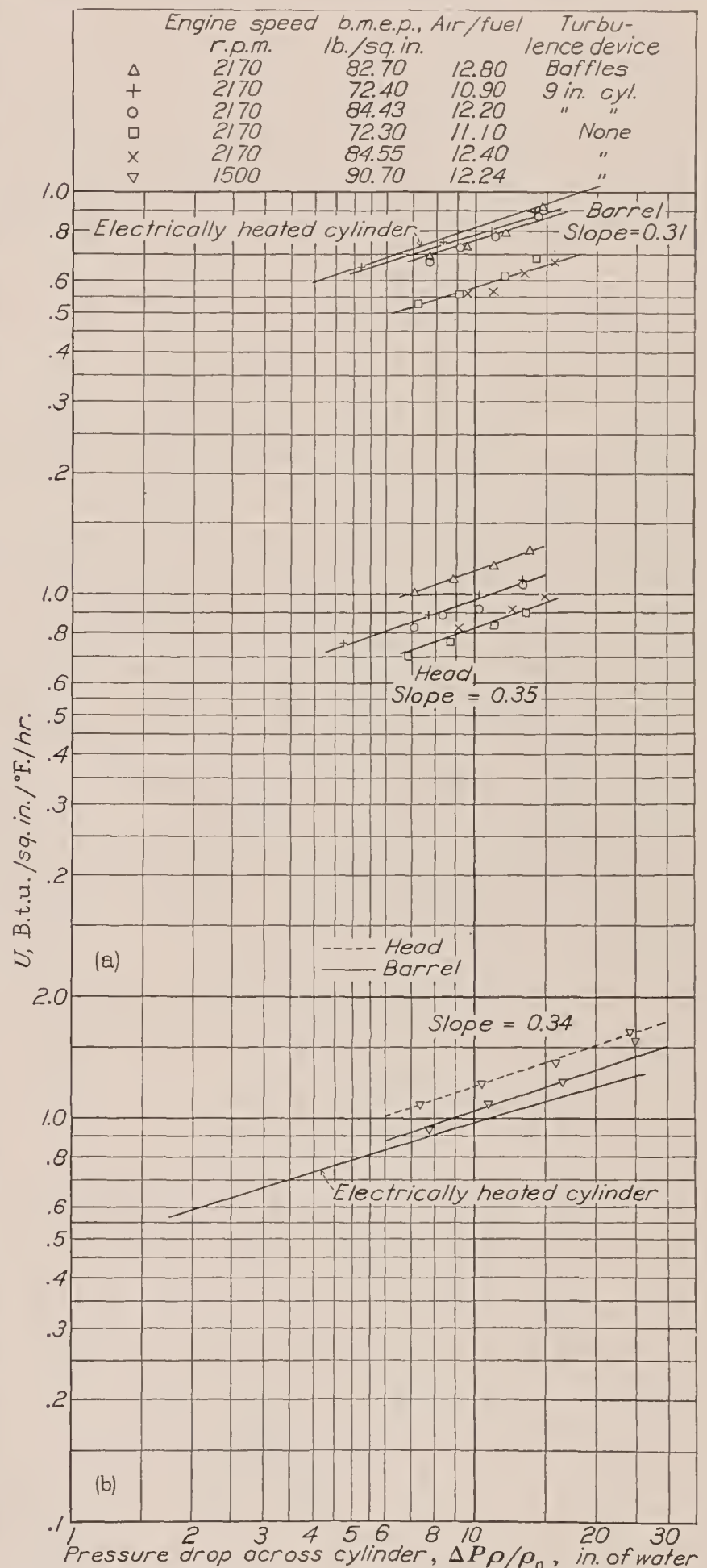
The curves for the three conditions are parallel and have a slope of 0.35 for the head and 0.31 for the barrel. Similar curves for the 1340-H cylinder without any turbulence device are shown in figure 10(b). The slopes of these curves are 0.34 for the head and barrel. Plotted in figure 10 for comparison with the over-all heat-transfer coefficient U of the barrel fins are curves calculated by means of equation (12) using the fin dimensions of the barrel and values of q obtained from blower cooling tests on electrically heated, finned cylinders (reference 6).

The equations for the heat transferred to the cooling air obtained from figure 10 are tabulated as follows:

Cylinder	Turbulence device	Head	Barrel
1535	None.....	$H=34.5 (\Delta P\rho/\rho_0)^{0.35}$ (T_h-T_a)	$H=17.1 (\Delta P\rho/\rho_0)^{0.31}$ (T_b-T_a)
1535	9-inch cylinder.	$H=40.5 (\Delta P\rho/\rho_0)^{0.35}$ (T_h-T_a)	$H=22.9 (\Delta P\rho/\rho_0)^{0.31}$ (T_b-T_a)
1535	Baffles.....	$H=47.6 (\Delta P\rho/\rho_0)^{0.35}$ (T_h-T_a)	$H=22.3 (\Delta P\rho/\rho_0)^{0.31}$ (T_b-T_a)
1340-H	None.....	$H=78.1 (\Delta P\rho/\rho_0)^{0.34}$ (T_h-T_a)	$H=33.0 (\Delta P\rho/\rho_0)^{0.34}$ (T_b-T_a)

Units of H are B. t. u./hr.; units of ΔP are inches of water.

For the 1535 cylinder the area a_0 for the outside barrel surface covered by fins is 61.5 square inches and for the head is 94.5 square inches. The areas are 68.5



(a) The 1535 cylinder.

(b) The 1340-H cylinder.

FIGURE 10.—Variation of heat-transfer coefficient of fins on head and barrel with pressure drop across cylinder.

and 142 square inches, respectively, for the barrel and head of the 1340-H cylinder.

The heat-transfer coefficients obtained when the 9-inch cylinder and the baffles were used are, respec-

tively, 17 and 38 percent higher on the head and 34 and 30 percent higher on the barrel than for the condition of no turbulence.

Average head and barrel temperatures.—If H is eliminated between equations (17) and (18), expressions may be obtained for T_h and T_b in the form given by equations (15) and (16). For example, if the expression for the heat transfer as a function of the indicated horsepower is selected from equations (17) and the expression for the heat transfer corresponding to the case of no turbulence device from equations (18),

Figure 11 shows the values of T_h and T_b for the 1340-H cylinder, calculated by means of equation (19) using the foregoing values of T_g , compared with values obtained from tests in which the indicated horsepower, ΔP , and T_a were varied independently. A fair agreement will be noted.

Expressions similar to (19) for the average head and barrel temperatures of the 1535 cylinder, but applying more closely to flight conditions, may be obtained by using an equation in set (18) corresponding to one of the turbulence devices. For instance, by the use of the

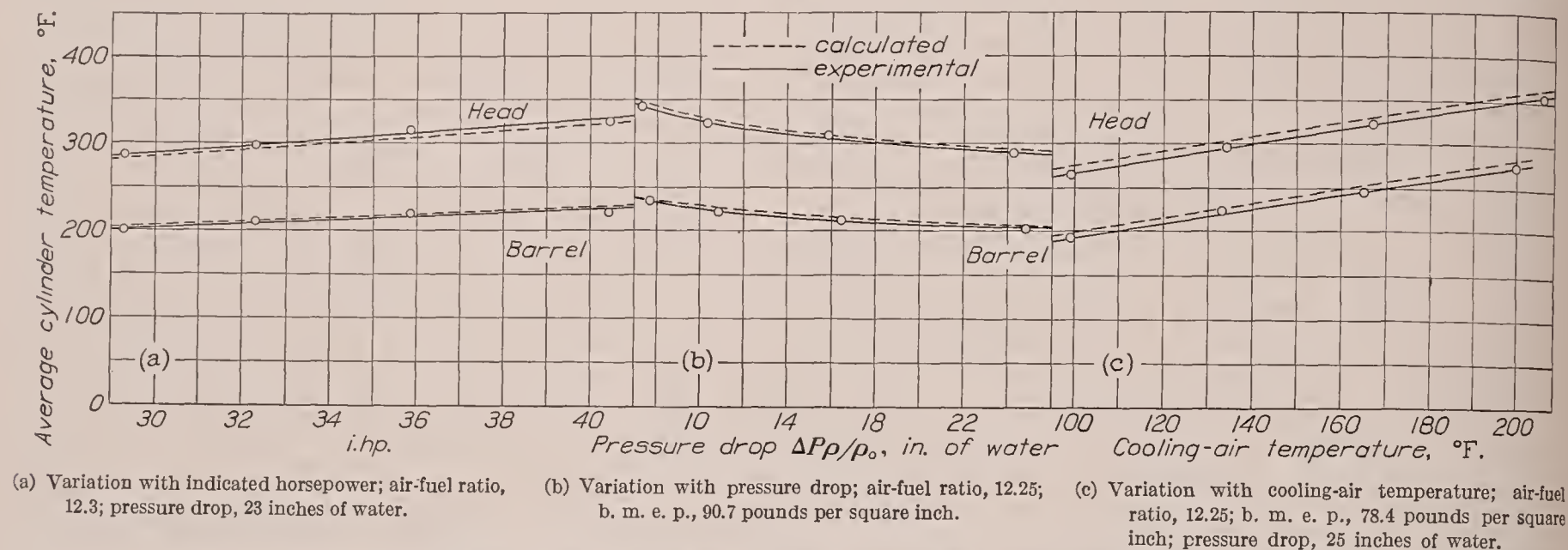


FIGURE 11.—Comparison of calculated and experimental values of average head and barrel temperatures at various test conditions. The 1340-H cylinder; engine speed, 1,500 r. p. m.

the following expressions give the average temperature of the head and barrel, respectively, for the 1535 and 1340-H cylinders.

Pratt & Whitney 1535 cylinder:

$$\text{Head} \\ T_h - T_a = \frac{T_g - T_a}{12.7 \frac{(\Delta P \rho / \rho_0)^{0.35}}{I^{0.68}} + 1}$$

$$\text{Barrel} \\ T_b - T_a = \frac{T_g - T_a}{15.1 \frac{(\Delta P \rho / \rho_0)^{0.31}}{I^{0.85}} + 1}$$

Pratt & Whitney 1340-H cylinder:

$$\text{Head} \\ T_h - T_a = \frac{T_g - T_a}{15.0 \frac{(\Delta P \rho / \rho_0)^{0.34}}{I^{0.64}} + 1}$$

$$\text{Barrel} \\ T_b - T_a = \frac{T_g - T_a}{11.9 \frac{(\Delta P \rho / \rho_0)^{0.34}}{I^{0.64}} + 1}$$

An examination of figures 8 and 9 indicates that a value for T_g of 1,150° F. for the head and of 600° F. for the barrel holds fairly well for the range of air-fuel ratios and spark settings used in practical operation.

equations for the baffles, the following expressions will be obtained:

$$\left. \begin{aligned} T_h - T_a &= \frac{T_g - T_a}{17.55 \frac{(\Delta P \rho / \rho_0)^{0.35}}{I^{0.68}} + 1} \\ T_b - T_a &= \frac{T_g - T_a}{19.55 \frac{(\Delta P \rho / \rho_0)^{0.31}}{I^{0.85}} + 1} \end{aligned} \right\} \quad (20)$$

The effect of providing turbulence was to increase the value of the coefficient of $(\Delta P \rho / \rho_0)^m / I^{n'}$. Where considerable change in the weight of residuals is experienced as in flight at various altitudes, an expression involving W , instead of I is more accurate (i. e., as given by equation (16)).

Equations (19) and (20) indicate that, to maintain a constant average head temperature, the pressure drop $\Delta P \rho / \rho_0$ must vary approximately as the square of the indicated horsepower or, since the mass flow varies almost as the square root of the pressure drop, the mass flow must be increased approximately in direct proportion to the indicated horsepower.

The heat-transfer coefficient U for the head is proportional to $(\Delta P \rho / \rho_0)^m$ and it is evident from equations (19) and (20) that, as U is increased (by improving the fin design or the air flow), the indicated horsepower may be increased approximately according to the relation

$$\frac{I_2}{I_1} = \left(\frac{U_2}{U_1} \right)^{1.5}$$

APPLICATIONS

1. Equations (15) and (16) provide a means for plotting the results of all cooling tests for a given engine on a single curve. For example, equation (15) may be written

$$\frac{T_g - T_h}{T_h - T_a} I^{n'} = \left(\Delta P \frac{\rho}{\rho_0} \right)^m \times \text{constant}$$

or

$$\frac{T_g - T_h}{T_h - T_a} I^{n'} = K \left(V \frac{\rho}{\rho_0} \right)^\gamma$$

where γ is approximately equal to $2m$ as $\Delta P \rho / \rho_0$ varies as a power of the mass flow in the neighborhood of 2.

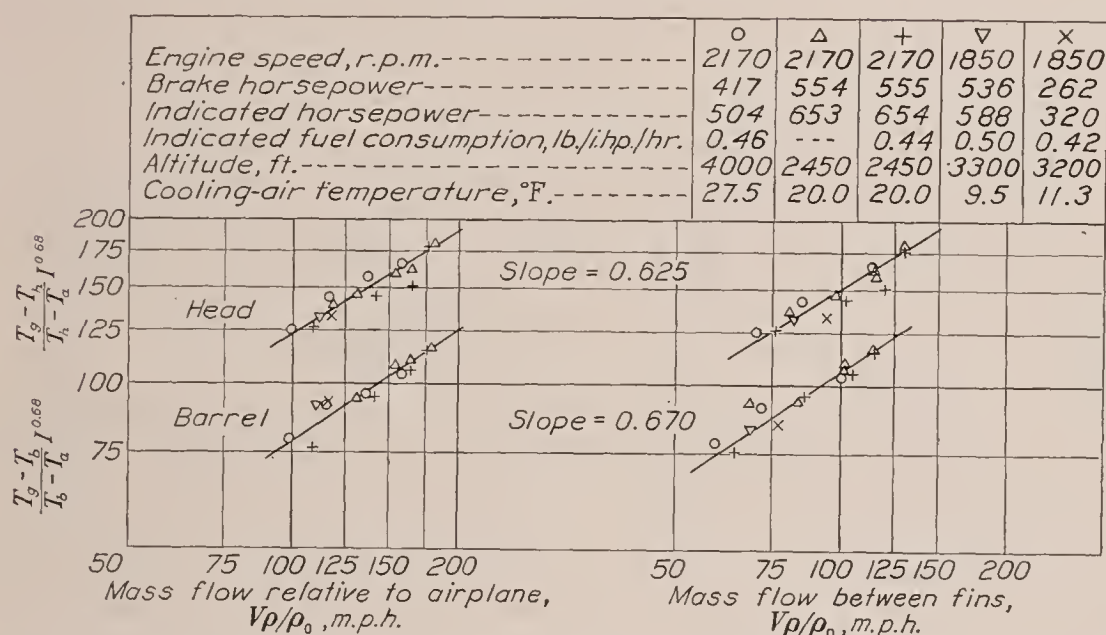


FIGURE 12.—Variation of $(T_g - T_h)/(T_h - T_a) I^{0.68}$ and $(T_g - T_b)/(T_b - T_a) I^{0.68}$ with mass flow from flight tests of a cylinder of a Pratt & Whitney 1535 engine in a Grumman Scout airplane.

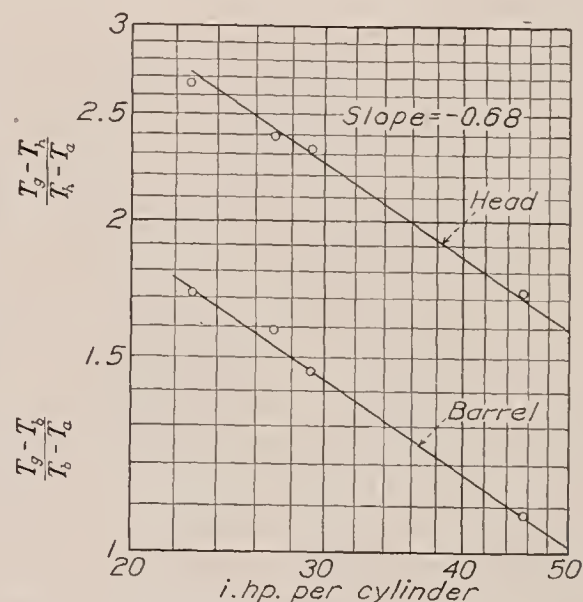


FIGURE 13.—Variation of $T_g - T_h/T_h - T_a$ and $T_g - T_b/T_b - T_a$ with indicated horsepower for a constant mass flow of cooling air from flight tests of a cylinder of a Pratt & Whitney 1535 engine in a Grumman Scout airplane. $V\rho/\rho_0 = 134$ m. p. h. (relative to airplane).

Figure 12 shows $(T_g - T_h)/(T_h - T_a) I^{n'}$ obtained in flight plotted against $V\rho/\rho_0$ for a cylinder of a Pratt & Whitney 1535 two-row radial engine mounted in a Grumman Scout airplane. The details of the tests are given in reference 7. The cooling-air velocity between the fins was found to be proportional to the airplane velocity for the range covered in the tests. The values of T_g corresponding to the air-fuel ratios obtained in the tests were taken from figure 6. A value for n' of 0.68 for the head and for the barrel was obtained in the flight tests. (See fig. 13.) This value confirms that obtained for the head in the laboratory tests of the Pratt & Whitney 1535 cylinder and was used in plotting figure 12. It will be noted that the test points in figure 12 fall on a single curve, irrespective of engine conditions. The slopes of the curves differ slightly from the slopes that might be expected from the laboratory tests of the 1535 cylinder.

2. Assume that the Grumman airplane is equipped with a supercharger capable of maintaining an indicated horsepower of 550 up to an altitude of 30,000 feet. A comparison is desired of the cylinder-head temperatures in climb at sea level and at 30,000 feet in a standard atmosphere at the same indicated air speed and engine

power. Take 115 miles per hour as the velocity of climb at sea level. For a constant indicated air speed the velocity in climb at 30,000 feet is

$$V_{alt} = V_{SL} \sqrt{\frac{\rho_{SL}}{\rho_{alt}}} = 115 \sqrt{\frac{1}{0.374}} = 188 \text{ m. p. h.}$$

$$\text{At sea level, } T_a = 59^\circ \text{F., } \frac{\rho_{SL}}{\rho_0} = \frac{530}{519} = 1.02$$

since ρ_0 is taken in this report as the density at a temperature of 70°F. and standard sea-level pressure.

$$V \frac{\rho}{\rho_0} = 1.02 \times 115 = 117 \text{ m. p. h.}$$

$$\text{At 30,000 feet } \frac{\rho_{alt}}{\rho_0} = 0.374 \times \frac{530}{519} = 0.381$$

$$V \frac{\rho}{\rho_0} = 188 \times 0.381 = 71.6 \text{ m. p. h.}$$

$$I = 550 \text{ hp. } I^{0.68} = 73$$

The carburetor-air temperature and air-fuel ratio are assumed constant and T_g is taken as $1,150^\circ \text{F.}$

From figure 12

$$\text{at sea level } T_a = 59^\circ \text{F. } \frac{T_g - T_h}{T_h - T_a} I^{0.68} = 135$$

$$\frac{1150 - T_h}{T_h - 59} = \frac{135}{73} = 1.85$$

$$T_h = 441^\circ \text{F.}$$

$$\text{at 30,000 feet } T_a = -48^\circ \text{F. } \frac{T_g - T_h}{T_h - T_a} I^{0.68} = 99$$

$$\frac{1150 - T_h}{T_h + 48} = \frac{99}{73} = 1.355$$

$$T_h = 460^\circ \text{F.}$$

An increase in average head temperature of only 19°F. is indicated. The preceding calculation neglects the

reduction in the weight of residual gas in the cylinder with increase in altitude. If the variation in the weight of the residual gas were considered, the temperature increase would be even less than 19°F .

The cylinder temperatures were assumed to have attained equilibrium in both cases. Because of the heat capacity of the cylinder materials, the cylinder temperatures do not respond instantly to a change in engine or cooling conditions. This fact tends to complicate the comparison of cylinder temperatures obtained in climb tests. Where large changes in conditions occur, as when going from level flight into a climb, a fast-climbing airplane may climb to considerable height before the cylinder temperatures are within 10°F . of equilibrium.

CONCLUSIONS

1. The heat-transfer coefficient for the transfer of heat from the combustion gases to the cylinder head varied as the 0.68 power of the indicated horsepower for the Pratt & Whitney 1535 cylinder and as the 0.64 power of the indicated horsepower for the Pratt & Whitney 1340-H cylinder.

2. The heat-transfer coefficient for the transfer of heat from the combustion gases to the cylinder barrel varied as the 0.68 power of the indicated horsepower for the Pratt & Whitney 1340-H cylinder.

3. The values of the effective gas temperatures were practically independent of the engine speed and brake mean effective pressure and for the normal range of operation were equal to $1,150^{\circ}\text{F}$. for the head and 600°F . for the barrel for both the Pratt & Whitney 1535 and the 1340-H cylinders.

4. The values of the effective gas temperature (a) decreased slightly as the air-fuel ratio decreased on the rich side of the theoretically correct mixture, (b) remained constant for a range of spark timing to either side of normal operation and increased for both extremely retarded and advanced spark timing, and (c) increased 58°F . for 100°F . increase in the inlet-air temperature for the Pratt & Whitney 1340-H cylinder.

5. The rate of heat transfer from the head and the barrel to the cooling air varied, respectively, as the 0.35 and 0.31 powers of the pressure drop across the cylinder for the Pratt & Whitney 1535 cylinder and as the 0.34

power for both the head and the barrel of the 1340-H cylinder.

6. The turbulence devices in front of the cylinder provided an increase in the heat-transfer coefficient of the order of 30 percent for the same pressure drop.

7. For the cylinders tested, in order to maintain a constant cylinder-head temperature for a given cylinder, it was necessary to increase the pressure drop across the cylinder directly as the square of the indicated horsepower.

8. The equations indicate that to improve the heat transfer from the fins by improving the fin design or by using higher air speeds allows the indicated horsepower to be increased as the 1.5 power of the heat-transfer coefficient U with practically no increase in cylinder-head temperature.

LANGLEY MEMORIAL AERONAUTICAL LABORATORY,
NATIONAL ADVISORY COMMITTEE FOR AERONAUTICS,
LANGLEY FIELD, VA., *June 11, 1937.*

REFERENCES

1. Nusselt, Wilhelm: Transfer of Heat in the Internal Combustion Engine. *Dieselmashinen*, V. D. I. (Berlin), 1923, pp. 48-55.
2. Herzfeld, August: Der Wärmeübergang und die thermodynamische Berechnung der Leistung bei Verpuffungsmaschinen insbesondere bei Kraftfahrzeug-Motoren. Julius Springer (Berlin), 1925.
3. Marvin, Charles F., Jr., Wharton, Armistead, and Roeder, Carl H.: Further Studies of Flame Movement and Pressure Development in an Engine Cylinder. T. R. No. 556, N. A. C. A., 1936.
4. Harper, D. R., 3d, and Brown, W. B.: Mathematical Equations for Heat Conduction in the Fins of Air-Cooled Engines. T. R. No. 158, N. A. C. A., 1923.
5. Biermann, Arnold E., and Pinkel, Benjamin: Heat Transfer from Finned Metal Cylinders in an Air Stream. T. R. No. 488, N. A. C. A., 1934.
6. Schey, Oscar W., and Ellerbrock, Herman H., Jr.: Blower Cooling of Finned Cylinders. T. R. No. 587, N. A. C. A., 1937.
7. Schey, Oscar W., and Pinkel, Benjamin: Effect of Several Factors on the Cooling of a Radial Engine in Flight. T. N. No. 584, N. A. C. A., 1936.

REPORT No. 613

THE VARIATION WITH REYNOLDS NUMBER OF PRESSURE DISTRIBUTION OVER AN AIRFOIL SECTION

By ROBERT M. PINKERTON

SUMMARY

Pressures were simultaneously measured at 54 orifices distributed over the midspan section of a 5- by 30-inch rectangular model of the N. A. C. A. 4412 airfoil in the variable-density tunnel. These measurements were made at 17 angles of attack from -20° to 30° for eight values of the effective Reynolds Number from approximately 100,000 to 8,200,000. Accurate data were thus obtained for studying the variation of pressure distribution with Reynolds Number.

These results on the N. A. C. A. 4412 section indicate that the pressure distribution is practically unaffected by changes in Reynolds Number except where separation is involved.

INTRODUCTION

The need for pressure-distribution data over an airfoil section and the methods of obtaining those data are discussed in detail in reference 1. Briefly, such data provide directly the load distributions required for design purposes and, in addition, the comparison of measured pressures with those computed from potential-flow (nonviscous fluid) theory provides a means of studying the effects of viscous forces on the flow about the airfoil section. Moreover, with the wide range of Reynolds Numbers in use, it is desirable to know how the pressure distribution varies with Reynolds Number. Indications of changes in the character of the flow with Reynolds Number may also be deduced from the measured pressure distributions.

An extensive investigation of the pressure distribution over one section of the N. A. C. A. 4412 airfoil has been carried out in the variable-density wind tunnel. The purpose was twofold: First, to provide adequate experimental data to compare with theoretical results; and second, to study the variations with Reynolds Number. Reference 1 presents the most important phase of the investigation and is divided into two parts. The first part gives a detailed discussion of the experimental technique and a presentation of the results at the highest Reynolds Number. In the second part a comparison is made of experimental with calculated pressure distributions, and a modified method of calcu-

lation, giving more accurate results than those obtained by the usual potential-flow method, is developed.

The present report presents the complete experimental data for the same airfoil at eight values of the Reynolds Number and an analysis of the variations with Reynolds Number.

APPARATUS AND TESTS

The model used in this pressure-distribution investigation was a standard duralumin airfoil of N. A. C. A. 4412 section with a span of 30 inches and a chord of 5 inches. Pressure orifices, placed in two rows one-quarter inch apart, were located at 54 stations around the midspan section as given in table I. In order to evaluate the pressure force parallel to the chord, a relatively large number of orifices were located at the nose of the airfoil (fig. 1); well-defined distributions of pressure along a normal to the chord were thus assured.

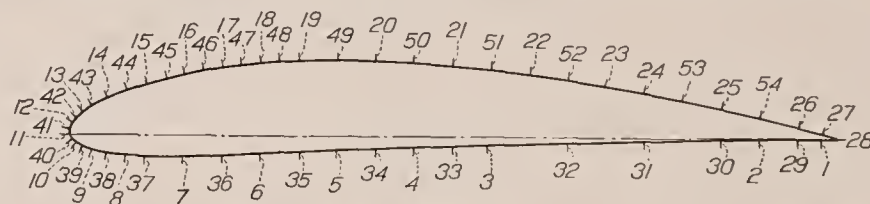


FIGURE 1.—Distribution of pressure orifices about the N. A. C. A. 4412 profile.

Pressures were measured at 17 angles of attack from -20° to 30° to obtain data throughout the range including the stall at both positive and negative angles of attack. These measurements were made at eight values of the Reynolds Number obtained by varying the density of the air in the tank that houses the tunnel (reference 2). Values of the effective Reynolds Number, obtained by multiplying the test Reynolds Number by the turbulence factor 2.64 (reference 3), and the corresponding tank pressures are given below.

Tank pressure (atmospheres):	Effective Reynolds Number
$\frac{1}{4}$ -----	0.10×10^6
$\frac{1}{2}$ -----	.24
1-----	.45
2-----	.90
4-----	1.80
8-----	3.40
15-----	6.30
21-----	8.20

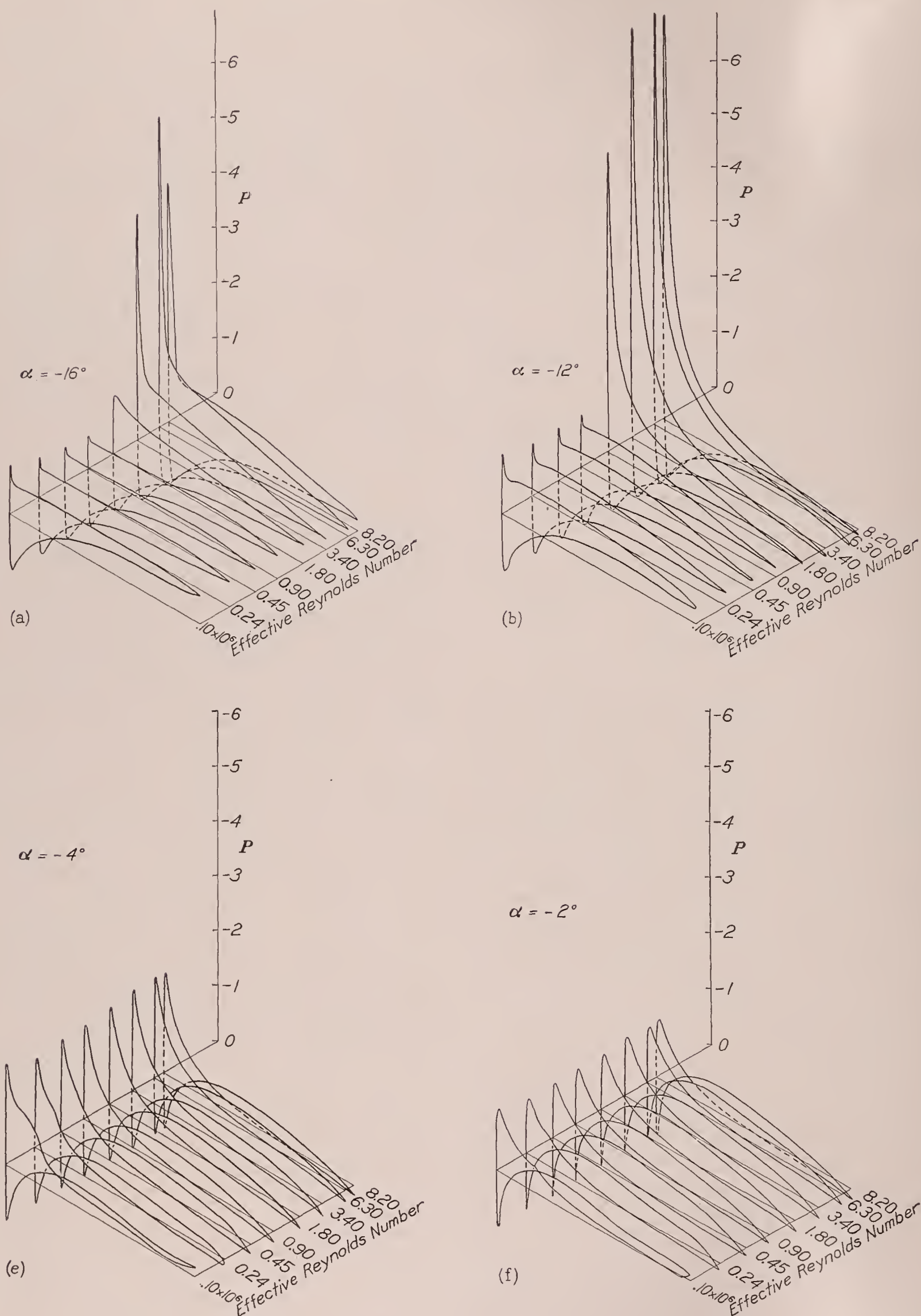


FIGURE 2(a) to 2(p).—Pressure-distribution diagrams for the N. A. C. A. 4412 airfoil.

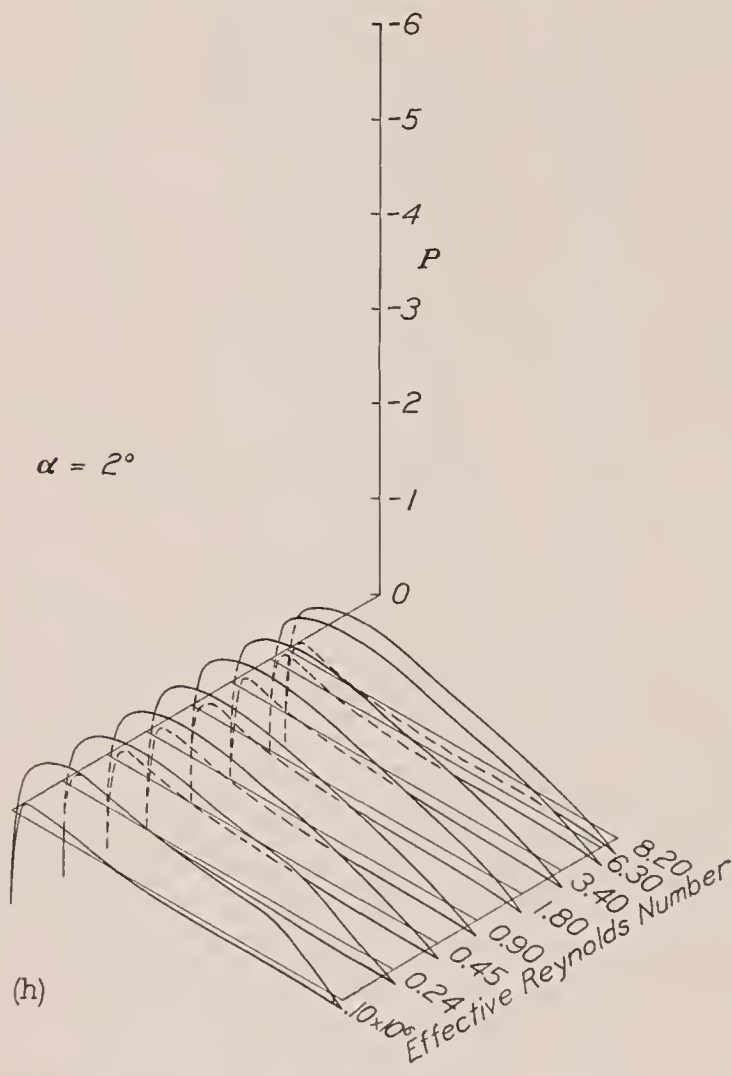
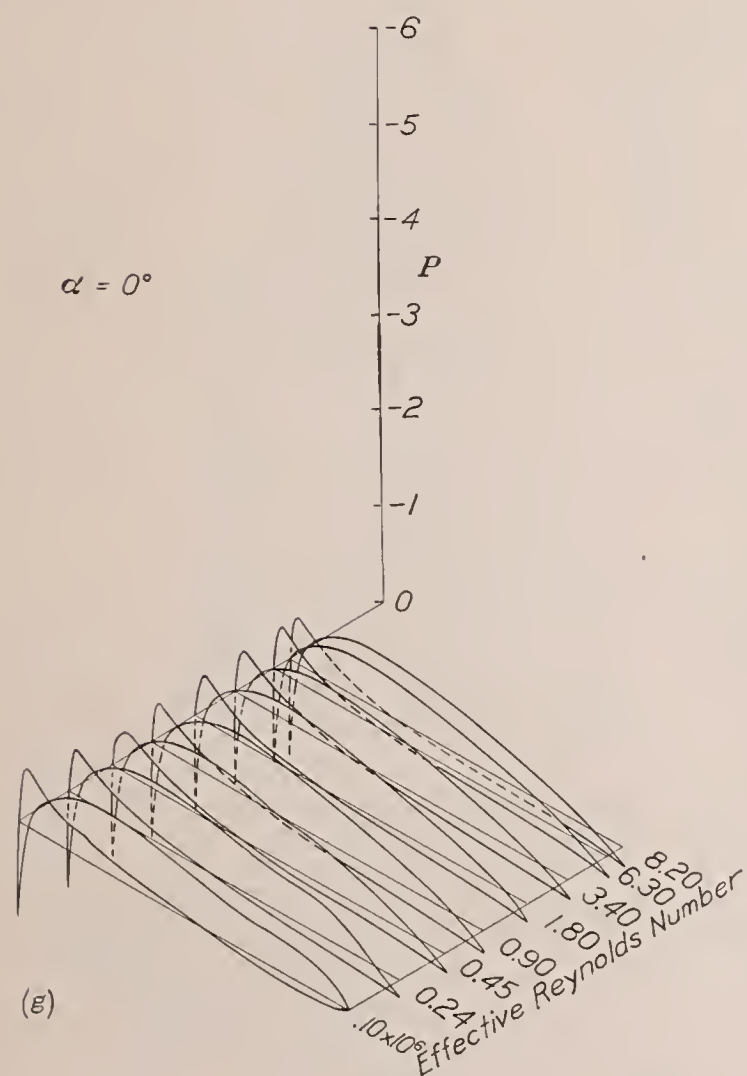
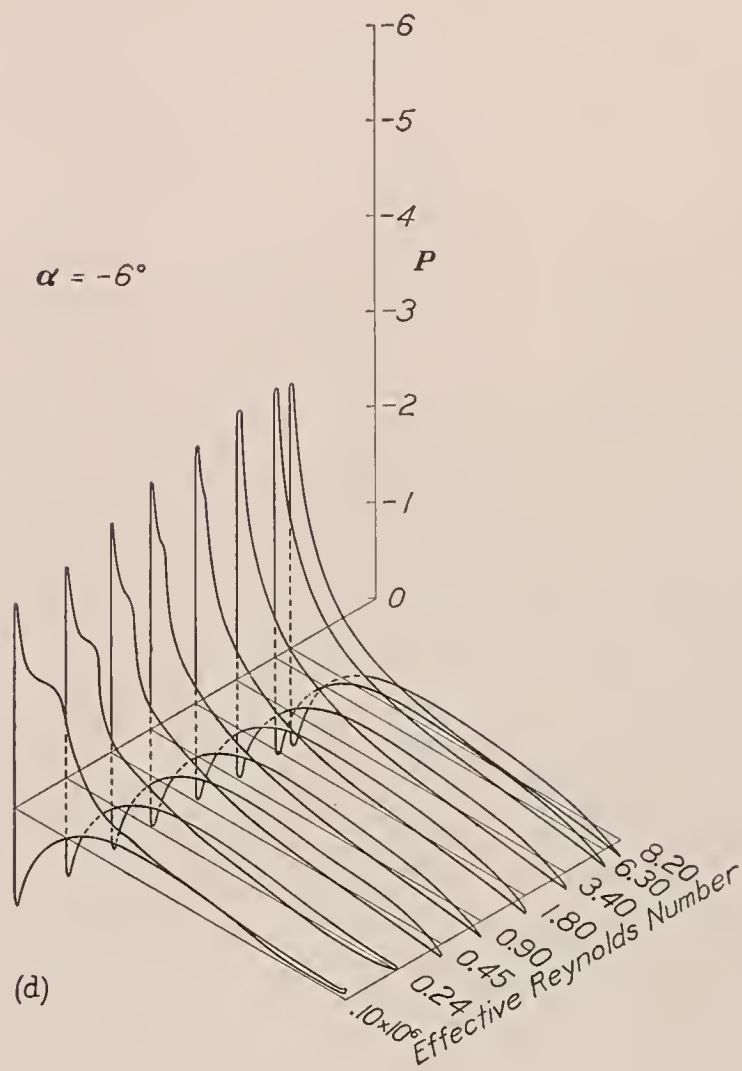
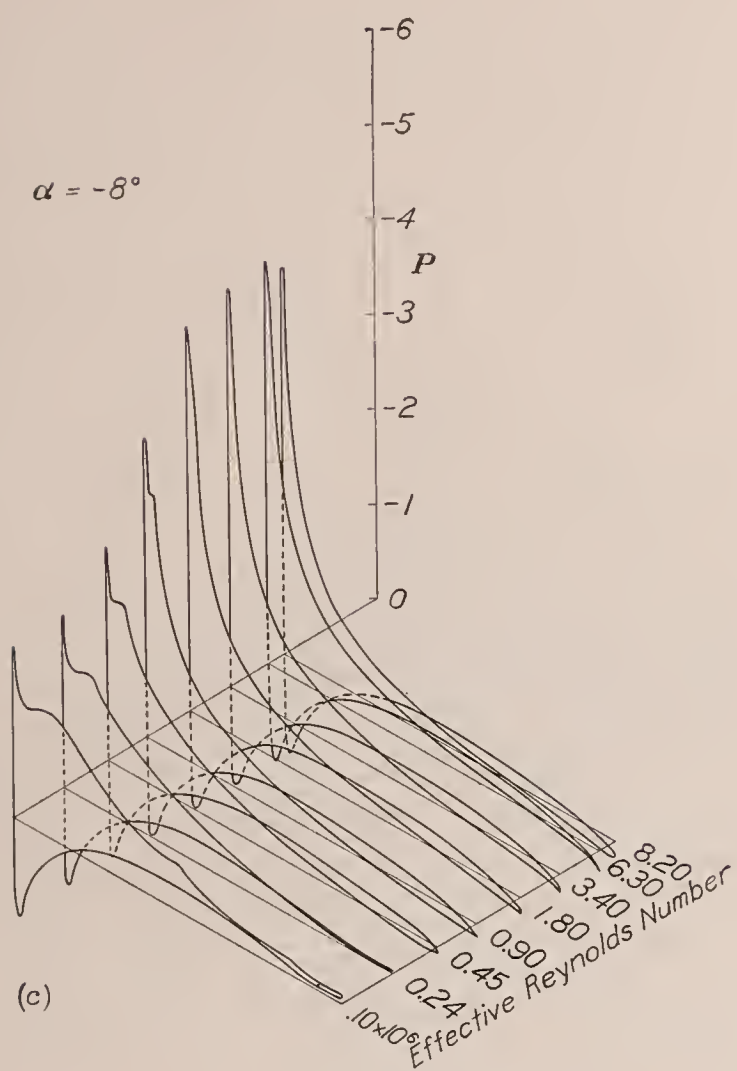


FIGURE 2.—Continued. Pressure-distribution diagrams for the N. A. C. A. 4412 airfoil.

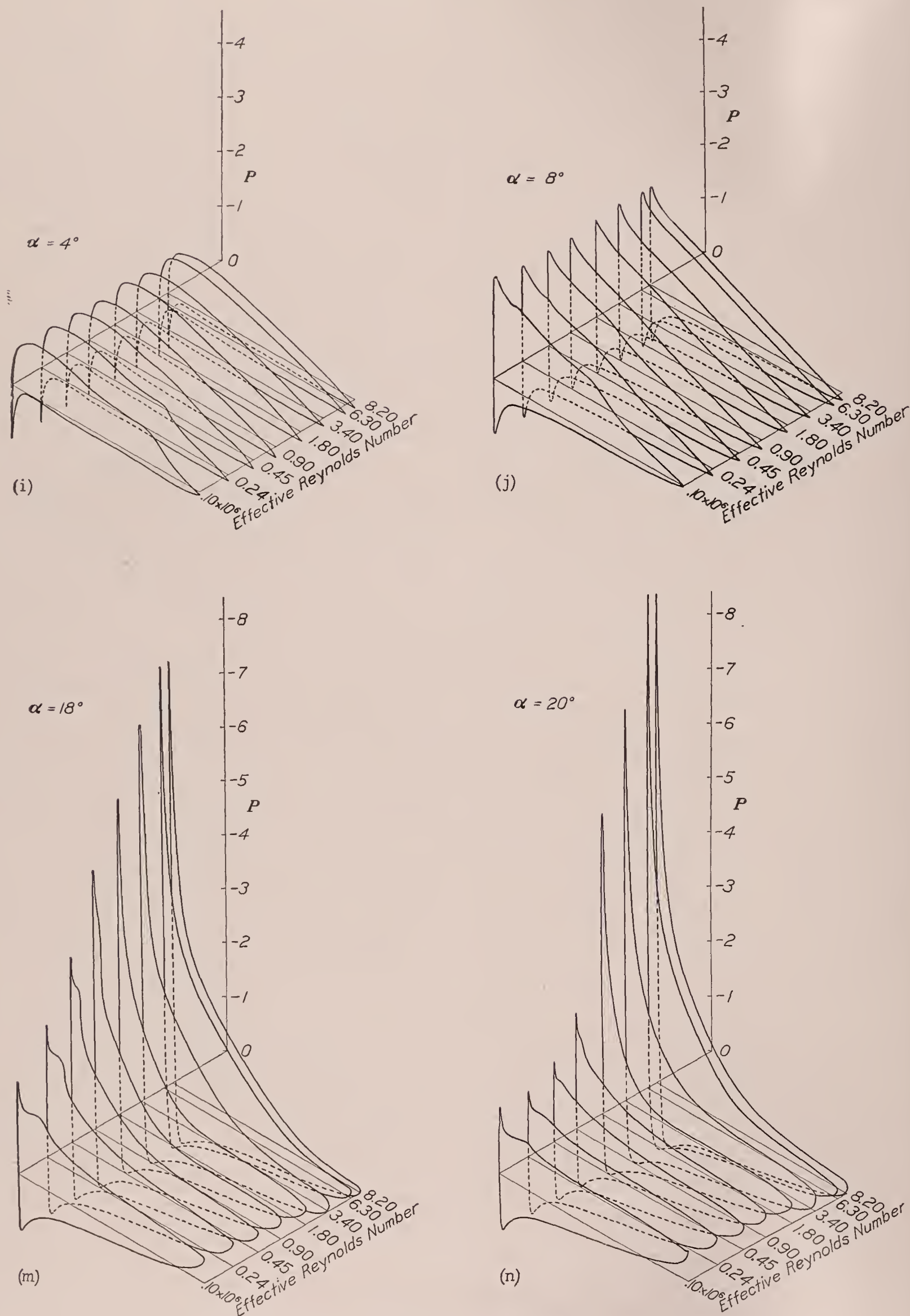


FIGURE 2.—Continued. Pressure-distribution diagrams for the N. A. C. A. 4412 airfoil.

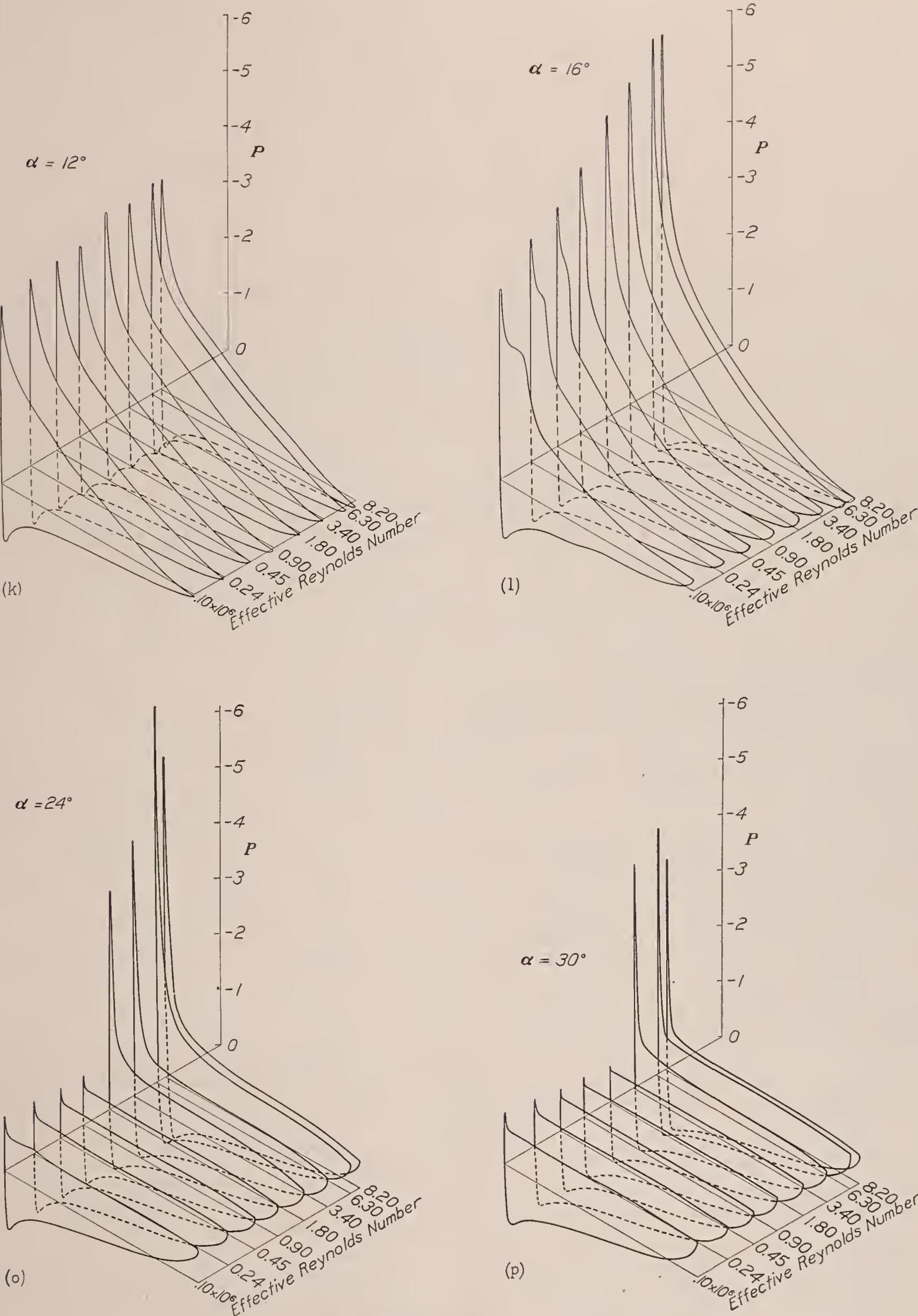


FIGURE 2.—Continued. Pressure-distribution diagrams for the N. A. C. A. 4412 airfoil.

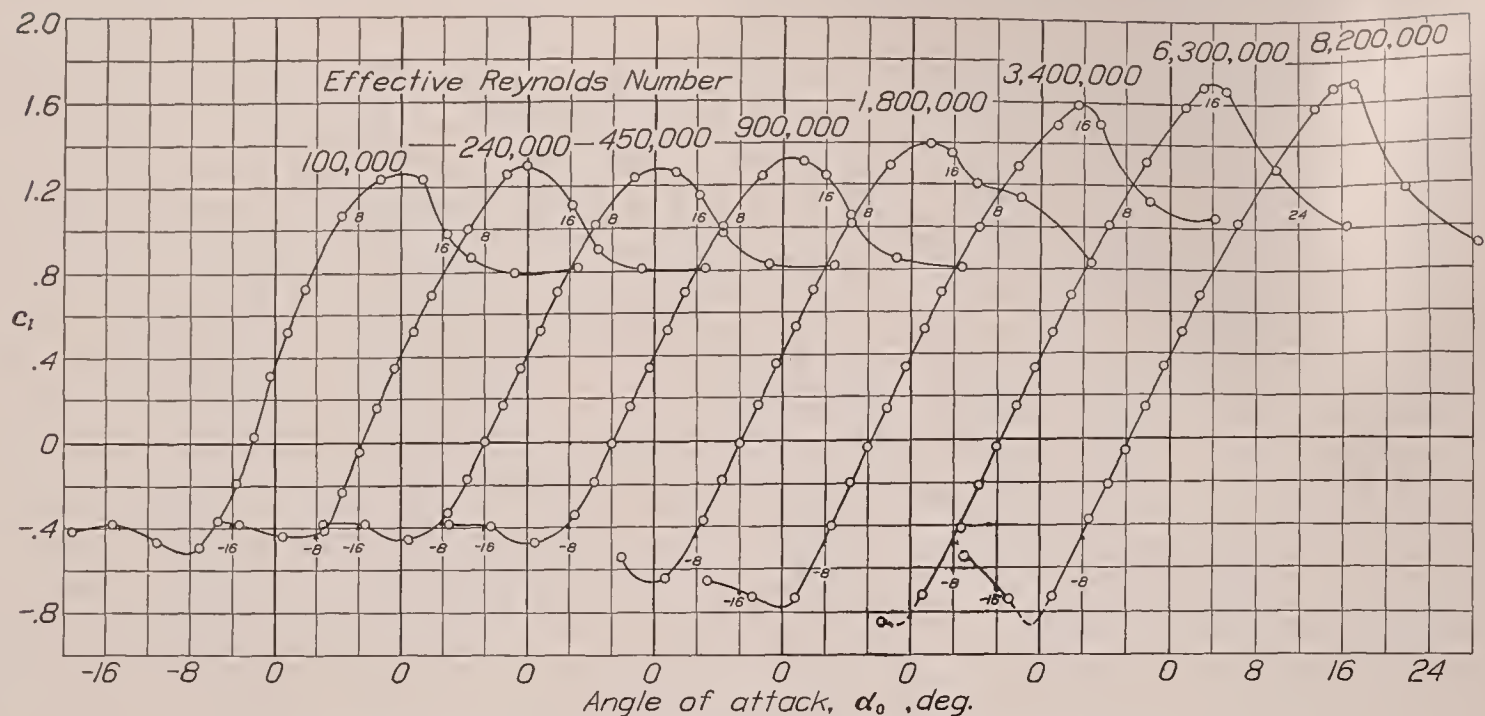


FIGURE 3.—Lift curves for the N. A. C. A. 4412 airfoil at several values of the Reynolds Number.

In order to keep the pressure measurements as accurate as possible, it was necessary to obtain large deflections of the manometer liquids, which was accomplished by using three liquids of widely different specific gravities.

Liquid:	Specific gravity
Mercury.....	13.6
Tetrabromoethane.....	3.0
Alcohol.....	.9

The proper choice of the angle of attack and Reynolds Number groups and of the liquid enabled the use of large and comparable deflections throughout all conditions of the investigation. Repeat tests using the same and different manometer liquids provided data on the precision of the tests.

The values of the pressure coefficient $P = (p - p_\infty)/q$ at each orifice on the airfoil and for all angles of attack are tabulated in table I; the table is divided into sections (a) to (h), each section comprising the data for one value of the Reynolds Number. The pressures p and p_∞ are, respectively, the pressures at the orifice and in the undisturbed stream.

As in reference 1, the data were reduced to the following section coefficients for the midspan section of the airfoil.

$$c_n = \frac{1}{c} \int P dx$$

$$c_c = \frac{1}{c} \int P dy$$

$$c_{m_{c/4}} = \frac{1}{c^2} \left[\int P (c/4 - x) dx + \int P y dy \right]$$

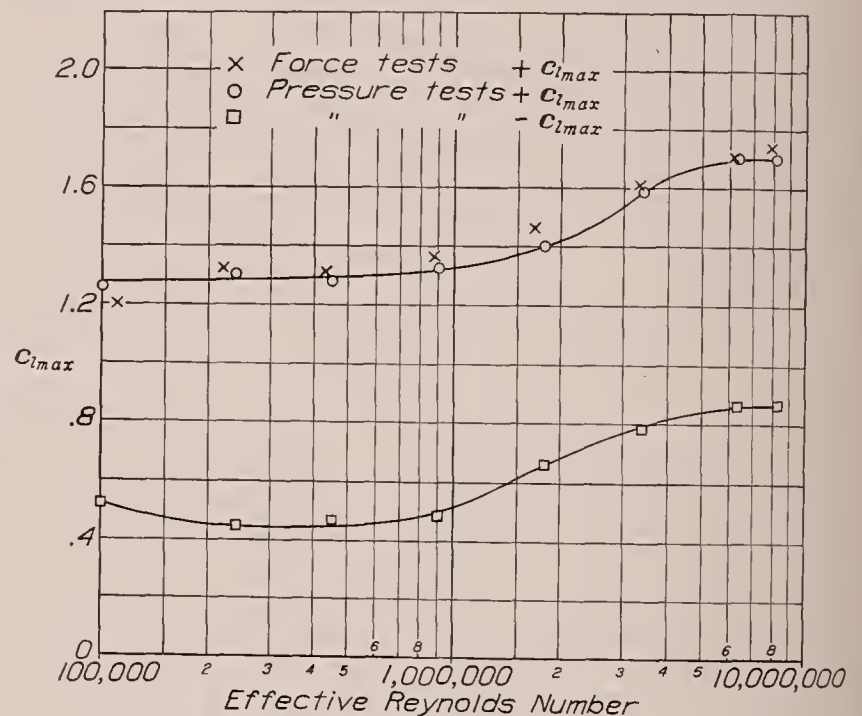
where c_n is the section normal-force coefficient.

c_c , section chord-force coefficient.

$c_{m_{c/4}}$, section pitching-moment coefficient.

Lift coefficients were obtained from the pressure measurements by the following equation:

$$c_l = c_n \cos \alpha - c_c \sin \alpha$$

FIGURE 4.—Variation of C_{lmax} with Reynolds Number.

The effective angle of attack is given by

$$\alpha_0 = \alpha - \alpha_i$$

and the induced angle of attack of the midspan section by

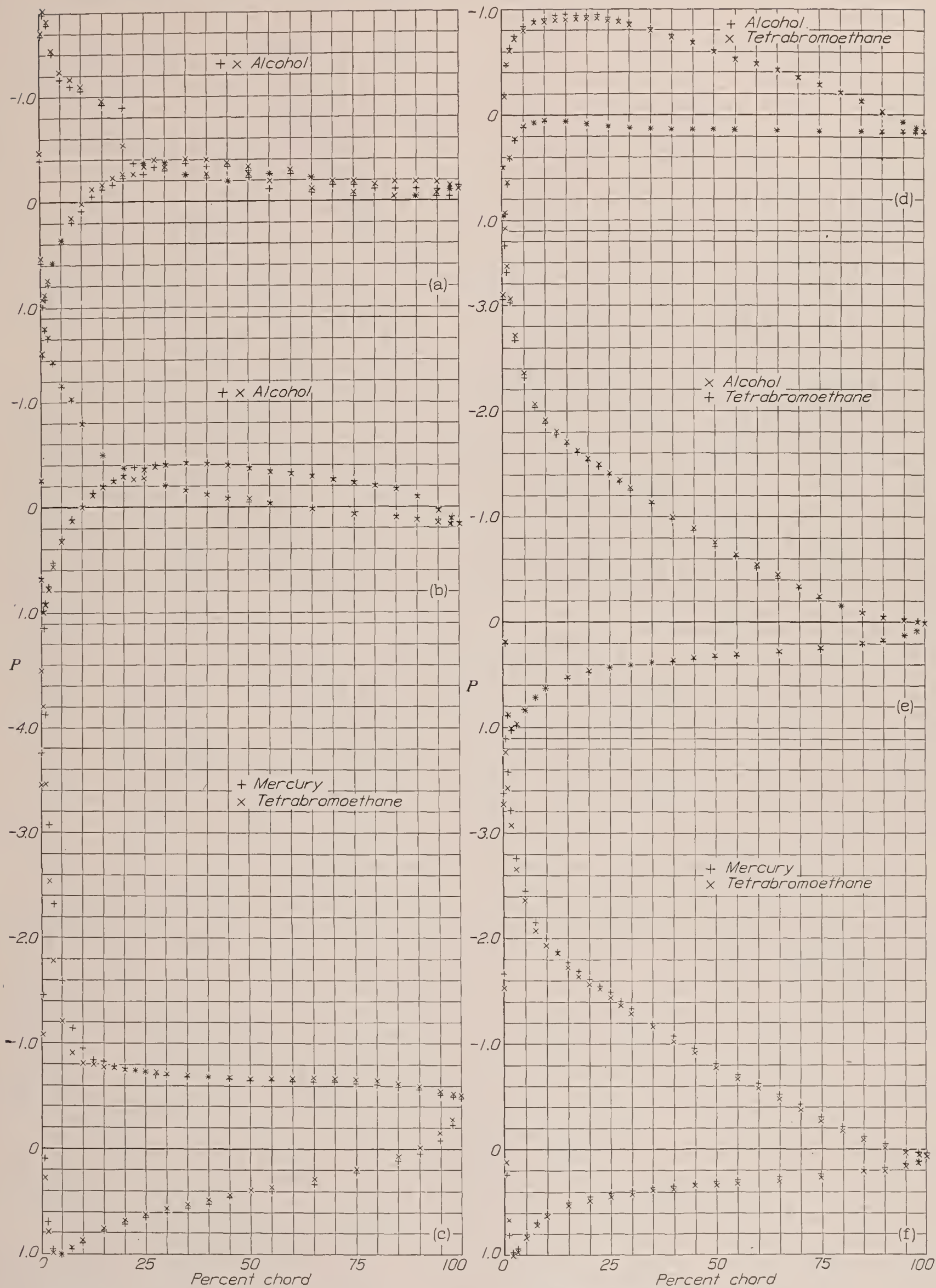
$$\alpha_i = 1.584 c_l$$

where α is the geometric angle of attack measured from the mean direction of flow in the tunnel.

α_i , the angle that the flow in the region of the airfoil section makes with the direction of the undisturbed flow.

Values of c_n , c_c , $c_{m_{c/4}}$, c_l , α_i , and α_0 for the 17 values of α are given in table II; the sections (a) to (h) correspond to the respective Reynolds Numbers of table I(a) to (h).

Isometric plots of normal pressure against position along the chord are presented in figure 2, one set of plots containing the pressures for the eight Reynolds Numbers at each angle of attack. The effect of Reynolds Number on the lift characteristics is shown in figures 3 and 4.


 (a) Effective Reynolds Number, 100,000; $\alpha = -4^\circ$.

 (b) Effective Reynolds Number, 450,000; $\alpha = -4^\circ$.

 (c) Effective Reynolds Number, 3,400,000; $\alpha = 24^\circ$.

 (d) Effective Reynolds Number, 3,400,000; $\alpha = 4^\circ$.

 (e) Effective Reynolds Number, 1,800,000; $\alpha = 12^\circ$.

 (f) Effective Reynolds Number, 6,300,000; $\alpha = 12^\circ$.

FIGURE 5.—Pressure-distribution diagrams from repeat tests at various angles of attack and values of the Reynolds Number. Values indicated by X are also given in table I.

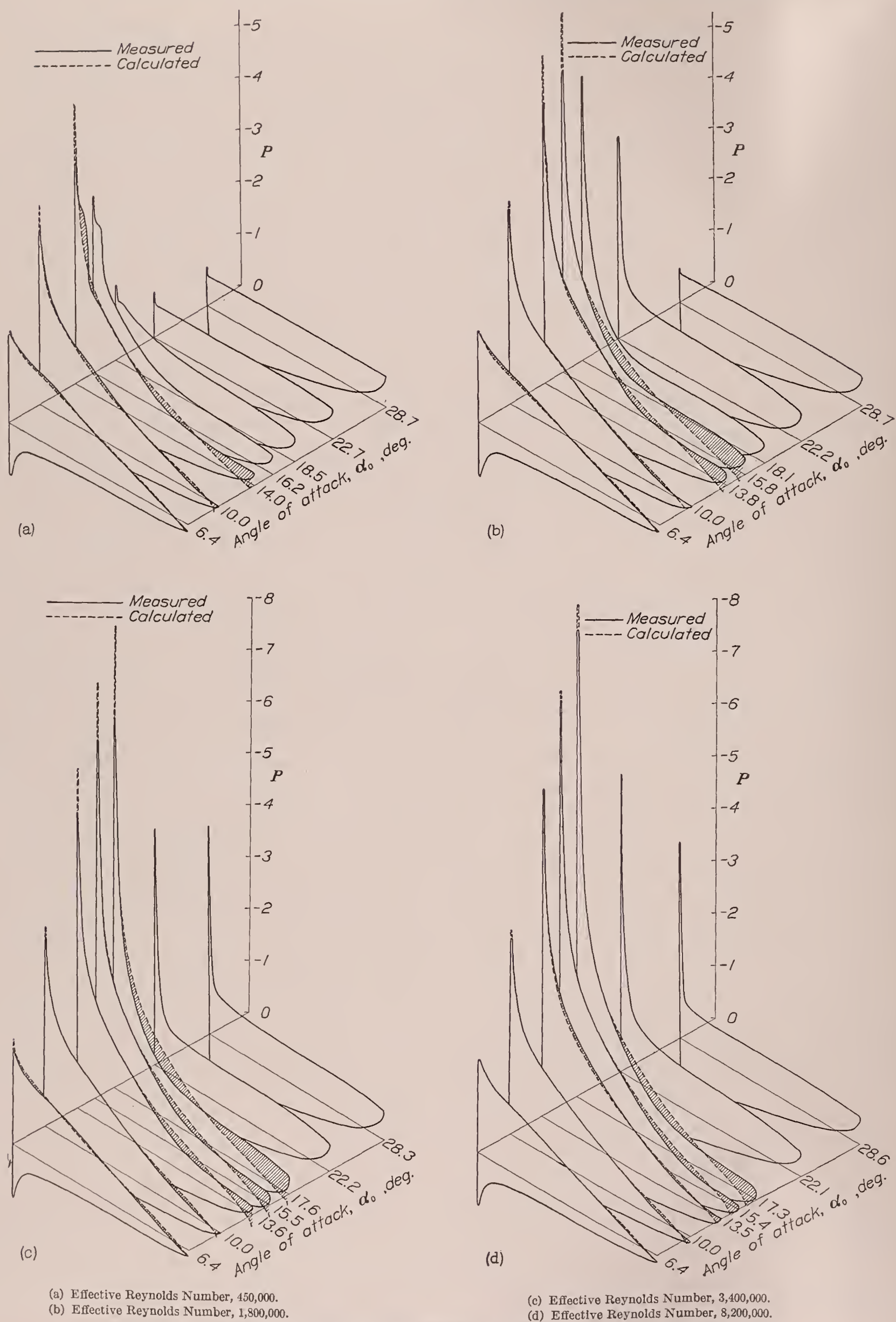


FIGURE 6.—Pressure-distribution diagrams showing the spread of separation at four values of the Reynolds Number.

PRECISION

The precision of the pressure measurements at Reynolds Numbers other than that for the data published in reference 1 is indicated by the diagrams given in figure 5. At the lowest Reynolds Number (fig. 5 (a)) the capacity to repeat measured pressures is markedly less than for higher Reynolds Numbers. It should be noted, however, that the precision was good enough to establish the occurrence of the supposedly laminar separation near the leading edge. The precision at Reynolds Numbers corresponding to the atmospheric runs and at higher values is consistently good even when the section has stalled, as in the diagram for 24° .

DISCUSSION

The general nature of the variation of the pressure distribution with Reynolds Number may be observed by means of the isometric plots in figure 2. At normal angles of attack, where stalling is not involved, the distributions are practically unaffected and hence the modified method of calculation presented in reference 1 is applicable at those attitudes for any Reynolds Number. Differences that do occur in the pressure diagrams are entirely of a local nature; they are probably associated with separation and the changes in the character of the boundary layer as the Reynolds Number is varied.

Boundary layer and the pressure distribution.—The formation of the boundary layer due to the viscous forces and the resulting effect on the pressure distribution is discussed in reference 1. A comparison of actual pressures with those computed for a potential, or non-viscous, fluid led to the development of the previously mentioned modified method of calculation, which gives good results at attitudes where separation is not involved.

Separation of the flow from the surface would be expected to be indicated on the pressure diagrams by a region of approximately constant pressures. The start and growth of separation are best observed in figure 6, which presents isometrically the pressure diagrams for an increasing angle-of-attack range. Calculated diagrams obtained by the method of reference 1 for a non-separated viscous flow are superposed for comparison. The differences between the measured and calculated distributions are attributed to separation and hence the shaded area may be considered as a measure of the effect of separation. The inclusion of four groups of diagrams, one for each of four values of the Reynolds Number, provides a means of studying the scale effect on separation phenomena.

The occurrence of separation is markedly affected by changes in the Reynolds Number, as may be seen in figure 6. Moreover, the only observable scale effects on pressure distributions (fig. 2) are probably due to the nature of the separation and the changes in the separa-

tion phenomena experienced with changing Reynolds Number. Most of these changes, of course, appear near either the positive or negative stall but at low Reynolds Numbers (below $R_e=900,000$ approximately) some effects of separation, even in the low-drag range, are apparent from a careful analysis of the distributions. The presence of some such effects is indicated especially by pressure-drag integrations which, in this range, show a definite increase of drag with decreasing Reynolds Number. These results, however, are not presented as such since pressure-drag determinations are subject to some uncertainty owing to the inherent difficulty in obtaining them. The following analysis is based on changes in pressure distribution occurring near the stall.

A detailed discussion of these phenomena based on analyses of force tests of a large number of airfoils of widely different shapes is given in reference 3. The pressure-distribution data presented herein provide confirmatory and supplementary information for one particular type of airfoil section represented by the N. A. C. A. 4412 airfoil. This airfoil is one of medium thickness and camber producing a fairly gradual stall (type D lift-curve peak, reference 3). The stalling process of this section is a complicated one involving both trailing- and leading-edge types of separation.

At the low Reynolds Number (fig. 6 (a)) separation occurs prior to the stall as indicated in two distinct regions on the N. A. C. A. 4412 airfoil: One in the turbulent boundary layer near the rear of the airfoil, and the other in what is probably the laminar boundary layer near the nose. Instability of the laminar flow after separation results in a breakdown of the smooth laminae into an eddying flow. The scouring action of the eddying flow may then sweep the dead air from the surface and cause the reestablishment of unseparated flow with a turbulent boundary layer instead of the laminar layer. This laminar separation and the subsequent establishment of eddying flow account for the so-called "bubble" of dead air occurring in the flow at the low Reynolds Numbers. The turbulent layer, unable to maintain itself at high angles of attack, starts separating near the trailing edge and spreads forward as the angle is increased until the stall, resulting from the combined laminar and turbulent separations, is reached.

At the highest Reynolds Numbers (fig. 6) marked local laminar separation near the nose of the airfoil is apparently prevented. This prevention is accounted for by a transition from laminar to turbulent flow nearly at the laminar separation point or before the laminar flow has reached separation conditions. A movement forward of this transition region with increasing Reynolds Number has been observed in smoke-flow studies. Moreover, figure 6 indicates that, for the N. A. C. A. 4412 airfoil in the Reynolds Number range included, the separation in the turbulent bound-

ary layer is slightly delayed with increasing Reynolds Number. Hence, at the high Reynolds Number, with possibly a delayed turbulent separation and no marked local laminar separation, the airfoil section increased its lift to a higher angle before stalling than was possible at the low Reynolds Number.

This analysis of the separation phenomena and the changes with Reynolds Number has been confirmed in some respects by measurements in the boundary layer of the N. A. C. A. 4412 airfoil at several values of the Reynolds Number. These data are a part of an N. A. C. A. investigation of boundary-layer phenomena.

Concluding remarks.—The results of this investigation indicate that the pressure distribution except near maximum lift is practically unaffected by changes in the Reynolds Number above a certain critical value, which is below the usual full-scale range. This critical

value is probably the value at which there is no definite local separation.

LANGLEY MEMORIAL AERONAUTICAL LABORATORY,
NATIONAL ADVISORY COMMITTEE FOR AERONAUTICS,
LANGLEY FIELD, VA., *July 14, 1937.*

REFERENCES

1. Pinkerton, Robert M.: Calculated and Measured Pressure Distributions Over the Midspan Section of the N. A. C. A. 4412 Airfoil. T. R. No. 563, N. A. C. A., 1936.
2. Jacobs, Eastman N., and Abbott, Ira H.: The N. A. C. A. Variable-Density Wind Tunnel. T. R. No. 416, N. A. C. A., 1932.
3. Jacobs, Eastman N., and Sherman, Albert: Airfoil Section Characteristics as Affected by Variations of the Reynolds Number. T. R. No. 586, N. A. C. A., 1937.

TABLE Ia.—EXPERIMENTAL DATA

[N. A. C. A. 4412 airfoil; effective Reynolds Number, 100,000; test, variable-density tunnel 1097-4; manometer liquid, alcohol]

Orifices			Values of pressure coefficient, $P = \frac{p - p_{\infty}}{q}$, for different angles of attack																
Designation	Station (percent c from L. E. of chord)	Ordinate (percent c above chord)	-20°	-16°	-12°	-8°	-6°	-4°	-2°	0°	2°	4°	8°	12°	16°	18°	20°	24°	30°
28-----	100.00	0	-0.533	-0.498	-0.289	-0.080	-0.115	-0.150	-0.115	-0.045	0.094	0.059	0.018	0.030	-0.204	-0.438	-0.568	-0.603	-0.603
1-----	97.92	-.16	-.568	-.498	-.324	-.080	-.045	-.115	-.045	.025	.094	.094	.055	.064	-.104	-.304	-.394	-.429	-.428
29-----	94.86	-.16	-.603	-.533	-.359	-.080	-.045	-.080	-.010	.059	.094	.094	.055	.097	-.003	-.204	-.254	-.289	-.254
2-----	89.90	-.22	-.603	-.568	-.394	-.080	-.045	-.045	-.010	.059	.094	.129	.091	.164	.064	-.070	-.150	-.150	-.115
30-----	84.94	-.28	-.638	-.568	-.463	-.150	-.045	-.045	-.010	.059	.059	.129	.091	.164	.130	-.003	-.080	-.080	-.010
31-----	74.92	-.52	-.603	-.568	-.533	-.185	-.080	-.080	-.010	.059	.059	.129	.127	.231	.231	.097	.060	.060	.129
32-----	64.94	-.84	-.603	-.603	-.603	-.254	-.150	-.115	-.045	.024	.059	.094	.127	.231	.231	.164	.094	.129	.199
3-----	54.48	-1.24	-.603	-.603	-.638	-.359	-.220	-.185	-.080	-.010	.059	.094	.127	.264	.264	.197	.199	.199	.303
33-----	49.98	-1.44	-.707	-.672	-.672	-.498	-.324	-.254	-.115	-.080	-.045	.024	.055	.197	.231	.197	.199	.164	.233
4-----	44.90	-1.64	-.603	-.603	-.672	-.498	-.254	-.185	-.115	-.045	.024	.094	.127	.331	.365	.264	.233	.303	.408
34-----	39.98	-1.86	-.603	-.603	-.672	-.568	-.289	-.254	-.150	-.080	.024	.094	.164	.331	.365	.298	.303	.338	.443
5-----	34.90	-2.10	-.603	-.603	-.742	-.672	-.359	-.254	-.185	-.115	.024	.094	.164	.331	.431	.331	.338	.373	.477
35-----	29.96	-2.30	-.603	-.603	-.742	-.777	-.394	-.324	-.254	-.150	-.010	.059	.164	.365	.431	.365	.373	.408	.512
6-----	24.90	-2.54	-.603	-.603	-.742	-.916	-.533	-.359	-.324	-.185	-.045	.059	.200	.398	.465	.398	.408	.477	.582
36-----	19.98	-2.76	-.568	-.603	-.742	-1.091	-.742	-.533	-.463	-.254	-.080	.024	.200	.431	.498	.431	.443	.512	.652
7-----	14.94	-2.90	-.533	-.533	-.742	-1.265	-1.300	-.951	-.498	-.289	-.115	.024	.273	.498	.599	.532	.547	.582	.721
37-----	9.96	-2.86	-.568	-.568	-.742	-1.300	-1.474	-1.091	-.638	-.394	-.150	.024	.309	.599	.699	.632	.617	.686	.826
8-----	7.38	-2.72	-.568	-.568	-.742	-1.265	-1.474	-1.160	-.742	-.463	-.185	.024	.345	.666	.799	.699	.686	.756	.861
38-----	4.94	-2.46	-.533	-.533	-.672	-1.230	-1.474	-1.230	-.847	-.533	-.150	.094	.491	.799	.900	.833	.791	.861	1.000
9-----	2.92	-2.06	-.533	-.568	-.672	-1.265	-1.578	-1.439	-1.021	-.603	-.115	.199	.709	.933	1.000	.933	.895	1.000	1.000
39-----	1.66	-1.60	-.568	-.568	-.742	-1.369	-1.787	-1.718	-1.125	-.533	.059	.373	.855	1.000	.933	1.000	1.000	1.000	.895
10-----	.92	-1.20	-.568	-.603	-.812	-1.578	-2.066	-1.822	-1.056	-.324	.304	.617	1.000	.900	.666	.866	.930	.895	.721
40-----	.36	-.70	-.742	-.847	-1.056	-1.787	-2.136	-1.613	-.707	.094	.652	.895	.891	.264	-.204	.365	.547	.443	.129
11-----	0	0	-.707	-.568	-.568	-.951	-.986	-.463	.268	.756	1.000	.930	.164	-1.140	-1.876	-.672	-.324	-.359	-.638
41-----	0	.68	-.045	.164	.268	.164	.233	.547	.861	.965	.861	-.478	-.927	-2.612	-3.281	-1.609	-1.091	-.951	-.881
12-----	.44	1.56	.721	.826	.895	.861	.895	.930	.930	.686	.373	-.184	-1.727	-3.181	-3.381	-1.709	-1.195	-.812	-.678
42-----	.94	2.16	.895	.930	.965	.930	.965	.895	.791	.443	.059	-.462	-1.872	-3.013	-3.013	-1.475	-.986	-.707	-.638
13-----	1.70	2.78	1.000	.965	.965	.930	.895	.756	.582	.233	-.150	-.602	-1.872	-2.779	-2.746	-1.308	-.847	-.638	-.603
43-----	2.94	3.64	.930	.861	.826	.791	.721	.582	.373	.024	-.324	-.741	-1.800	-2.478	-2.579	-1.274	-.812	-.638	-.603
14-----	4.90	4.68	.826	.721	.652	.582	.512	.373	.164	-.185	-.498	-.845	-1.691	-2.244	-2.511	-1.241	-.812	-.638	-.603
44-----	7.50	5.74	.721	.582	.477	.408	.338	.164	-.010	-.289	-.603	-.881	-1.618	-2.043	-2.478	-1.241	-.812	-.638	-.603
15-----	9.96	6.56	.547	.443	.338	.304	.233	.024	-.115	-.394	-.672	-.950	-1.545	-1.943	-2.478	-1.274	-.812	-.638	-.603
45-----	12.58	7.34	.443	.303	.233	.129	.094	-.115	-.254	-.498	-.742	-.985	-1.545	-1.843	-2.344	-1.241	-.847	-.672	-.638
16-----	14.92	7.88	.373	.233	.164	.094	.024	-.150	-.289	-.533	-.777	-.985	-1.509	-1.742	-1.910	-1.174	-.847	-.672	-.638
46-----	17.44	8.40	.303	.164	.094	.024	-.045	-.220	-.324	-.568	-.777	-.950	-1.436	-1.642	-1.508	-1.040	-.812	-.638	-.603
17-----	19.96	8.80	.199	.094	.024	-.045	-.115	-.254	-.394	-.603	-.811	-.985	-1.400	-1.575	-1.308	-1.007	-.777	-.638	-.603
47-----	22.44	9.16	.129	-.115	-.185	-.254	-.289	-.254	-.463	-.533	-.707	-.845	-1.182	-1.241	-1.074	-.873	-.742	-.638	-.638
18-----	24.92	9.52	.094	-.010	-.080	-.115	-.150	-.324	-.394	-.603	-.742	-.916	-1.255	-1.408	-1.107	-.839	-.707	-.603	-.568
48-----	27.44	9.62	.024	-.080	-.185	-.185	-.185	-.394	-.429	-.638	-.742	-.951	-1.253	-1.341	-1.074	-.839	-.742	-.638	-.603
19-----	29.88	9.76	-.045	-.115	-.185	-.185	-.220	-.359	-.463	-.638	-.742	-.881	-1.218	-1.274	-1.007	-.806	-.707	-.503	-.603
49-----	34.98	9.90	-.115	-.185	-.254	-.254	-.254	-.394	-.463	-.638	-.707	-.847	-1.145	-1.107	-.906	-.773	-.672	-.603	-.638
20-----	39.90	9.84	-.150	-.254	-.254	-.254	-.254	-.394	-.429	-.568	-.638	-.742	-1.073	-.973	-.773	-.706	-.672	-.603	-.603
50-----	44.80	9.64	-.220	-.289	-.289	-.254	-.254	-.359	-.394	-.533	-.603	-.707	-1.036	-.873	-.672	-.672	-.672	-.603	-.638
21-----	49.92	9.22	-.254	-.324	-.324	-.254	-.254	-.324	-.359	-.498	-.568	-.672	-1.000	-.739	-.605	-.672	-.672	-.603	-.638
51-----	54.92	8.76	-.254	-.324	-.289	-.220	-.185	-.254	-.324	-.463	-.498	-.638	-.891	-.605	-.505	-.605	-.638	-.603	-.603
22-----	59.94	8.16	-.359	-.394	-.324	-.220	-.185	-.289	-.289	-.429	-.498	-.638	-.745	-.538	-.438	-.639	-.672	-.638	-.638
52-----	64.90	7.54	-.394	-.394	-.359	-.220	-.185	-.220	-.254	-.394	-.498	-.638	-.600	-.438	-.405	-.605	-.672	-.638	-.638
23-----	69.86	6.76	-.394	-.394	-.324	-.185	-.150	-.185	-.220	-.359	-.463	-.603	-.455	-.338	-.338	-.572	-.672	-.638	-.638
53-----	74.90	5.88	-.429	-.429	-.324	-.150	-.115	-.185	-.220	-.394	-.463	-.533	-.382	-.271	-.338	-.605	-.672	-.638	-.638
24-----	79.92	4.92	-.429	-.429	-.289	-.115	-.115	-.150	-.220	-.359	-.429	-.359	-.309	-.171	-.271	-.572	-.638	-.638	-.603
25-----	84.88	3.88	-.463	-.429	-.254	-.080	-.080	-.115	-.185	-.324	-.324	-.185	-.200	-.104	-.237	-.538	-.603	-.603	-.603
54-----	89.88	2.74	-.463	-.429	-.254	-.045	-.080	-.115	-.185	-.289	-.150	-.080	-.127	-.037	-.237	-.505	-.603	-.603	-.603
26-----	94.90	1.48	-.498	-.463	-.289	-.045	-.080	-.150	-.185	-.185	-.045	-.010	-.055	-.003	-.237	-.472	-.568	-.603	-.603
27-----	98.00	.68	-.498	-.463	-.254	-.045	-.080	-.150	-.150	-.080	.024	.024	-.018	.030	-.204	-.438	-.533	-.568	-.603
28-----	100.00	0																	

TABLE Ib.—EXPERIMENTAL DATA

[N. A. C. A. 4412 airfoil; effective Reynolds Number, 240,000; test, variable-density tunnel 1097-3; manometer liquid, alcohol]

Orifices			Values of pressure coefficient, $P = \frac{p-p_\infty}{q}$, for different angles of attack																
Designation	Station (percent c from L. E. of chord)	Ordinate (percent c above chord)	-20°	-16°	-12°	-8°	-6°	-4°	-2°	0°	2°	4°	8°	12°	16°	18°	20°	24°	30°
28	100.00	0	-0.491	-0.443	-0.238	-0.029	0.003	0.068	0.131	0.148	0.148	0.131	0.115	0.033	-0.230	-0.443	-0.495	-0.574	-0.574
1	97.92	-16	-509	-460	-254	-013	052	116	131	148	148	131	131	066	-098	-279	-334	-377	-377
29	94.86	-16	-509	-492	-286	-013	052	100	115	148	131	131	148	098	-016	-164	-206	-262	-246
2	89.90	-22	-525	-525	-318	-013	052	100	098	131	131	131	164	148	082	-049	-093	-131	-115
30	84.94	-28	-541	-557	-366	-045	035	068	082	115	115	131	164	180	115	016	-029	-049	-016
31	74.92	-52	-541	-574	-431	-093	003	051	066	098	115	131	180	213	197	098	084	082	131
32	64.94	-84	-541	-557	-511	-158	-045	003	033	082	098	115	197	246	246	180	164	164	230
3	54.48	-1.24	-525	-574	-575	-254	-093	-029	-016	049	066	098	197	279	295	230	228	230	312
33	49.98	-1.44	-557	-574	-608	-286	-141	-061	-016	016	033	082	180	262	312	262	244	246	328
4	44.90	-1.64	-525	-557	-624	-350	-158	-077	-049	016	049	115	230	312	344	295	293	312	410
34	39.98	-1.86	-525	-557	-640	-447	-190	-109	-065	-016	049	098	230	328	377	312	325	344	443
5	34.90	-2.10	-509	-557	-672	-527	-238	-158	-098	-033	033	098	230	344	410	361	357	377	492
35	29.96	-2.30	-509	-541	-672	-624	-302	-206	-148	-065	016	098	246	377	443	394	405	426	525
6	24.90	-2.54	-509	-541	-672	-752	-383	-270	-213	-115	-016	082	246	410	476	426	437	459	574
36	19.98	-2.76	-509	-541	-672	-881	-479	-350	-311	-164	-049	049	262	426	525	476	470	508	639
7	14.94	-2.90	-491	-525	-656	-1.042	-608	-527	-426	-230	-082	049	295	508	607	557	550	590	721
37	9.96	-2.86	-509	-525	-656	-1.283	-1.379	-913	-557	-311	-148	049	344	590	705	656	646	689	803
8	7.38	-2.72	-509	-525	-656	-1.331	-1.556	-994	-639	-377	-164	066	410	672	803	754	727	754	885
38	4.94	-2.46	-491	-525	-640	-1.283	-1.122	-787	-443	-164	115	525	803	918	853	823	869	951	
9	2.92	-2.06	-491	-525	-624	-1.283	-1.653	-1.331	-918	-475	-098	230	705	934	1.000	951	936	967	1.000
39	1.66	-1.60	-509	-509	-640	-1.331	-1.894	-1.556	-1.000	-410	033	410	869	984	918	951	1.000	984	918
10	.92	-1.20	-509	-525	-672	-1.508	-2.183	-1.621	-902	-229	279	656	984	869	623	771	920	885	721
40	.36	-.70	-624	-721	-929	-1.797	-2.199	-1.395	-541	180	656	902	885	246	-426	066	486	459	148
11	0	0	-640	-525	-511	-929	-977	-254	394	836	967	934	213	-1.230	-2.328	-1.279	-431	-361	-639
41	0	.68	.000	.213	.325	.212	.276	.678	.934	1.000	.852	.492	-.869	-2.787	-3.951	-2.426	-1.186	-.918	-.820
12	.44	1.56	.738	.869	.920	.920	.936	1.000	.934	.705	.344	-.180	-1.623	-3.328	-4.000	-2.410	-1.154	-.738	-.606
42	.94	2.16	.918	1.000	1.000	1.000	1.000	.936	.738	.459	.066	-.459	-1.738	-3.164	-3.574	-2.115	-.977	-.656	-.590
13	1.70	2.78	.967	1.000	1.000	.968	.920	.791	.541	.246	-.148	-.606	-1.721	-2.902	-3.311	-2.000	-.913	-.639	-.590
43	2.94	3.64	.951	.918	.871	.823	.759	.566	.312	.016	-.328	-.738	-1.656	-2.590	-3.164	-1.984	-.881	-.623	-.574
14	4.90	4.68	.836	.770	.695	.630	.534	.357	.082	-.180	-.492	-.836	-1.590	-2.344	-3.115	-1.984	-.913	-.639	-.574
44	7.50	5.74	.688	.606	.518	.453	.357	.164	-.082	-.311	-.590	-.885	-1.492	-2.131	-3.016	-1.951	-.913	-.639	-.574
15	9.96	6.56	.557	.476	.389	.325	.228	.035	-.196	-.410	-.656	-.918	-1.443	-1.984	-2.197	-1.639	-.897	-.639	-.574
45	12.58	7.34	.442	.344	.260	.196	.084	-.077	-.311	-.508	-.721	-.951	-1.410	-1.852	-1.738	-1.361	-.849	-.639	-.590
16	14.92	7.88	.361	.278	.196	.116	.019	-.141	-.360	-.541	-.738	-.951	-1.361	-1.738	-1.639	-1.229	-.817	-.639	-.590
46	17.44	8.40	.295	.180	.116	.051	-.045	-.206	-.393	-.574	-.754	-.951	-1.295	-1.623	-1.557	-1.147	-.784	-.623	-.574
17	19.96	8.80	.213	.114	.051	-.013	-.109	-.270	-.442	-.606	-.770	-.951	-1.262	-1.541	-1.459	-1.082	-.768	-.623	-.590
47	22.44	9.16	.082	.000	-.061	-.093	-.158	-.366	-.525	-.574	-.705	-.836	-1.082	-1.459	-1.410	-1.098	-.833	-.639	-.606
18	24.92	9.52	.098	.000	-.029	-.093	-.174	-.302	-.475	-.623	-.770	-.902	-1.180	-1.377	-1.295	-.967	-.704	-.606	-.574
48	27.44	9.62	.016	-.065	-.093	-.158	-.222	-.350	-.508	-.639	-.787	-.902	-1.148	-1.328	-1.213	-.934	-.704	-.623	-.590
19	29.88	9.76	-.016	-.098	-.125	-.174	-.238	-.350	-.508	-.623	-.770	-.869	-1.115	-1.262	-1.131	-.902	-.704	-.623	-.590
49	34.98	9.90	-.098	-.164	-.190	-.206	-.254	-.366	-.508	-.606	-.721	-.820	-1.033	-1.131	-.967	-.820	-.688	-.606	-.590
20	39.90	9.84	-.147	-.213	-.206	-.222	-.270	-.350	-.475	-.574	-.672	-.770	-.967	-.984	-.803	-.754	-.672	-.606	-.606
50	44.80	9.64	-.213	-.262	-.238	-.222	-.270	-.334	-.459	-.541	-.623	-.721	-.902	-.885	-.688	-.705	-.672	-.623	-.606
21	49.92	9.22	-.246	-.279	-.238	-.222	-.254	-.318	-.426	-.492	-.574	-.672	-.786	-.754	-.574	-.672	-.672	-.623	-.606
51	54.92	8.76	-.262	-.279	-.238	-.190	-.222	-.286	-.377	-.442	-.525	-.623	-.639	-.639	-.459	-.639	-.656	-.623	-.606
22	59.94	8.16	-.295	-.311	-.254	-.190	-.206	-.270	-.360	-.410	-.508	-.606	-.541	-.557	-.410	-.623	-.656	-.639	-.606
52	64.90	7.54	-.345	-.344	-.270	-.174	-.190	-.238	-.311	-.393	-.475	-.557	-.459	-.459	-.361	-.606	-.656	-.639	-.623
23	69.86	6.76	-.361	-.344	-.254	-.141	-.158	-.206	-.278	-.360	-.459	-.442	-.393	-.361	-.311	-.590	-.640	-.639	-.606
24	74.90	5.88	-.393	-.360	-.254	-.109	-.125	-.174	-.262	-.344	-.410	-.311	-.311	-.279	-.295	-.574	-.640	-.639	-.623
53	79.92	4.92	-.393	-.377	-.254	-.077	-.093	-.158	-.245	-.311	-.278	-.213	-.229	-.197	-.279	-.541	-.624	-.639	-.606
25	84.88	3.88	-.426	-.393	-.238	-.061	-.077	-.125	-.229	-.229	-.148	-.131	-.148	-.115	-.246	-.525	-.592	-.623	-.590
54	89.88	2.74	-.443	-.410	-.222	-.029	-.077	-.125	-.180	-.082	-.049	-.065	-.049	-.049	-.246	-.508	-.559	-.606	-.590
26	94.90	1.48	-.475	-.426	-.222	-.045	-.077	-.077	-.032	049	033	016	033	016	033	-.475	-.543	-.590	-.574
27	98.00	.68	-.475	-.426	-.222	-.029	-.029	019	082	115	098	082	082	016	033	-.443	-.511	-.557	-.574
28	100.00	0																	

TABLE 1c.—EXPERIMENTAL DATA

[N. A. C. A. 4412 airfoil; effective Reynolds Number, 450,000; test, variable-density tunnel 1097-1; manometer liquid, alcohol]

Orifices			Values of pressure coefficient, $P = \frac{p-p_\infty}{q}$, for different angles of attack																
Designation	Station (percent <i>c</i> from L. E. of chord)	Ordinate (percent <i>c</i> above chord)	−20°	−16°	−12°	−8°	−6°	−4°	−2°	0°	2°	4°	8°	12°	16°	18°	20°	24°	30°
28-----	100.00	0	−0.477	−0.396	−0.201	0.067	0.148	0.164	0.172	0.172	0.172	0.156	0.131	0.002	−0.234	−0.364	−0.461	−0.558	−0.558
1-----	97.92	−.16	−.485	−.420	−.209	.083	.148	.164	.156	.156	.172	.172	.148	.058	−.104	−.218	−.274	−.380	−.356
29-----	94.86	−.16	−.502	−.453	−.242	.075	.131	.148	.140	.148	.172	.172	.164	.117	−.015	−.103	−.161	−.250	−.209
2-----	89.90	−.22	−.518	−.485	−.282	.058	.115	.123	.123	.131	.169	.172	.180	.156	.085	.002	−.047	−.120	−.071
30-----	84.94	−.28	−.526	−.518	−.323	.034	.083	.099	.107	.123	.148	.169	.198	.172	.123	.058	.026	−.047	.010
31-----	74.92	−.52	−.526	−.534	−.404	−.015	.042	.067	.075	.108	.145	.169	.213	.221	.205	.156	.131	.075	.148
32-----	64.94	−.84	−.526	−.542	−.485	−.071	−.006	.018	.050	.083	.123	.169	.221	.253	.261	.221	.213	.164	.246
3-----	54.48	−1.24	−.518	−.542	−.575	−.153	−.063	−.031	.001	.058	.117	.148	.229	.278	.310	.278	.269	.237	.335
33-----	49.98	−1.44	−.502	−.534	−.615	−.193	−.096	−.080	−.006	.034	.091	.148	.221	.296	.334	.318	.310	.278	.383
4-----	44.90	−1.64	−.502	−.526	−.656	−.242	−.128	−.080	−.031	.026	.091	.145	.245	.310	.367	.343	.343	.318	.424
34-----	39.98	−1.86	−.502	−.526	−.689	−.307	−.169	−.112	−.055	.010	.075	.131	.253	.334	.383	.375	.367	.351	.464
5-----	34.90	−2.10	−.502	−.518	−.713	−.388	−.209	−.153	−.080	−.015	.067	.131	.261	.351	.415	.407	.407	.391	.505
35-----	29.96	−2.30	−.494	−.518	−.729	−.494	−.274	−.201	−.120	−.055	.042	.115	.269	.375	.464	.448	.440	.432	.545
6-----	24.90	−2.54	−.485	−.510	−.729	−.615	−.364	−.274	−.177	−.104	.010	.117	.278	.417	.497	.489	.481	.472	.594
36-----	19.98	−2.76	−.485	−.502	−.729	−.769	−.477	−.372	−.266	−.161	−.023	.091	.294	.432	.537	.537	.521	.513	.651
7-----	14.94	−2.90	−.477	−.494	−.721	−.940	−.623	−.494	−.404	−.218	−.055	.075	.328	.497	.610	.610	.494	.594	.732
37-----	9.96	−2.86	−.485	−.494	−.713	−1.200	−.818	−.794	−.558	−.315	−.120	.058	.375	.586	.716	.707	.692	.692	.821
8-----	7.38	−2.72	−.477	−.485	−.696	−1.476	−1.403	−1.029	−.648	−.372	−.128	.075	.440	.675	.813	.797	.773	.765	.886
38-----	4.94	−2.46	−.477	−.485	−.688	−1.735	−1.727	−1.159	−.786	−.445	−.136	.125	.554	.797	.919	.903	.878	.862	.959
9-----	2.92	−2.06	−.469	−.477	−.680	−1.719	−1.841	−1.386	−.932	−.477	−.088	.237	.716	.927	.992	.976	.976	.959	1.000
39-----	1.66	−1.60	−.469	−.477	−.672	−1.687	−2.101	−1.622	−1.013	−.445	−.034	.416	.894	.992	.919	.919	1.000	.984	.927
10-----	.92	−1.20	−.469	−.485	−.696	−1.906	−2.393	−1.703	−.940	−.250	.278	.651	1.000	.870	.595	.635	.984	.886	.724
40-----	.36	−.70	−.526	−.623	−.932	−2.239	−2.377	−1.468	−.574	.156	.659	.919	.903	.221	−.502	−.315	.383	.456	.156
11-----	0	0	−.615	−.494	−.542	−1.224	−1.037	−.258	.383	.813	.984	.944	.198	−1.265	−2.506	−2.019	−.648	−.355	−.599
41-----	0	.68	.026	.237	.302	.067	.351	.683	.935	.984	.854	.411	−.891	−2.815	−4.203	−3.407	−1.451	−.891	−.745
12-----	.44	1.56	.756	.878	.919	.886	.959	1.000	.935	.708	.351	−.185	−1.654	−3.383	−4.275	−3.261	−1.330	−.680	−.567
42-----	.94	2.16	.951	.992	1.000	1.000	1.000	.927	.748	.448	.042	−.453	−1.744	−3.180	−3.846	−3.010	−1.192	−.648	−.567
13-----	1.70	2.78	1.000	1.000	.984	.968	.927	.781	.554	.237	−.136	−.599	−1.719	−2.912	−3.578	−2.912	−1.195	−.640	−.558
43-----	2.94	3.64	.976	.919	.870	.830	.740	.562	.318	.010	−.323	−.721	−1.646	−2.620	−3.464	−2.896	−1.183	−.640	−.591
14-----	4.90	4.68	.870	.773	.700	.635	.529	.326	.099	−.185	−.485	−.826	−1.573	−2.369	−3.326	−2.612	−1.167	−.648	−.591
44-----	7.50	5.74	.724	.619	.521	.448	.326	.131	−.080	−.323	−.583	−.867	−1.484	−2.125	−2.068	−1.800	−1.062	−.656	−.591
15-----	9.96	6.56	.610	.489	.399	.310	.188	.002	−.185	−.420	−.648	−.899	−1.427	−1.930	−1.922	−1.672	−.997	−.648	−.575
45-----	12.58	7.34	.489	.367	.269	.172	.067	−.112	−.291	−.502	−.705	−.932	−1.394	−1.800	−1.833	−1.500	−.956	−.648	−.575
16-----	14.92	7.88	.599	.286	.188	.091	−.015	−.185	−.347	−.542	−.729	−.932	−1.346	−1.703	−1.711	−1.394	−.916	−.640	−.575
46-----	17.44	8.40	.318	.205	.115	.026	−.080	−.242	−.396	−.567	−.737	−.932	−1.305	−1.597	−1.589	−1.281	−.883	−.640	−.591
17-----	19.96	8.80	.245	.123	.042	−.039	−.136	−.291	−.437	−.599	−.761	−.932	−1.273	−1.532	−1.484	−1.192	−.859	−.640	−.575
47-----	22.44	9.16	.140	.042	−.031	−.104	−.242	−.266	−.477	−.623	−.737	−.859	−1.192	−1.386	−1.338	−1.110	−.859	−.688	−.631
18-----	24.92	9.52	.115	.010	−.055	−.128	−.218	−.356	−.485	−.623	−.761	−.907	−1.192	−1.386	−1.289	−1.013	−.810	−.631	−.575
48-----	27.44	9.62	.058	−.038	−.104	−.168	−.258	−.380	−.510	−.640	−.761	−.899	−1.159	−1.321	−1.200	−.940	−.786	−.631	−.575
19-----	29.88	9.76	.018	−.080	−.128	−.193	−.274	−.396	−.510	−.631	−.745	−.867	−1.127	−1.256	−1.094	−.867	−.769	−.631	−.583
49-----	34.98	9.90	−.063	−.144	−.185	−.226	−.299	−.412	−.502	−.615	−.705	−.810	−1.029	−1.127	−.916	−.745	−.721	−.631	−.583
20-----	39.90	9.84	−.120	−.185	−.201	−.242	−.299	−.404	−.485	−.575	−.664	−.761	−.932	−.981	−.745	−.648	−.696	−.631	−.591
50-----	44.80	9.64	−.185	−.234	−.234	−.258	−.315	−.396	−.469	−.542	−.623	−.705	−.834	−.883	−.615	−.583	−.680	−.640	−.591
21-----	49.92	9.22	−.209	−.250	−.242	−.242	−.291	−.364	−.437	−.494	−.567	−.663	−.705	−.745	−.494	−.542	−.664	−.640	−.591
51-----	54.92	8.76	−.234	−.258	−.234	−.226	−.258	−.331	−.396	−.453	−.518	−.607	−.599	−.640	−.404	−.502	−.640	−.640	−.591
22-----	59.94	8.16	−.274	−.291	−.250	−.218	−.250	−.315	−.364	−.420	−.485	−.534	−.534	−.542	−.347	−.494	−.631	−.648	−.591
52-----	64.90	7.54	−.315	−.315	−.258	−.209	−.234	−.291	−.339	−.388	−.445	−.437	−.469	−.445	−.323	−.477	−.623	−.656	−.607
23-----	69.86	6.76	−.339	−.323	−.250	−.185	−.209	−.258	−.307	−.347	−.364	−.347	−.388	−.347	−.299	−.461	−.615	−.656	−.599
24-----	74.90	5.88	−.364	−.339	−.250	−.161	−.177	−.226	−.274	−.299	−.291	−.282	−.299	−.266	−.282	−.461	−.607	−.656	−.599
53-----	79.92	4.92	−.389	−.347	−.242	−.136	−.144	−.201	−.234	−.209	−.193	−.217	−.218	−.185	−.266	−.445	−.591	−.648	−.599
25-----	84.88	3.88	−.412	−.364	−.226	−.104	−.120	−.169	−.161	−.112	−.128	−.144	−.128	−.104	−.266	−.429	−.567	−.631	−.591
54-----	89.88	2.74	−.429	−.364	−.209	−.071	−.088	−.096	−.047	−.039	−.039	−.055	−.039	−.055	−.258	−.420	−.550	−.615	−.575
26-----	94.90	1.48	−.461	−.380	−.193	−.047	−.006	.034	.050	.050	.050	.042	.050	−.023	−.250	−.404	−.501	−.591	−.591
27-----	98.00	.68	−.477	−.388	−.185	.010	.091	.115	.115	.123	.123	.125	.118	.002	−.242	−.380	−.477	−.567	−.558
28-----	100.00	0																	

77

TABLE 1e.—EXPERIMENTAL DATA

[N. A. C. A. 4412 airfoil; effective Reynolds Number 1,800,000; test numbers and manometer liquids given in footnotes]

Orifices			Values of pressure coefficient, $P=\frac{p-p_{\infty}}{q}$, for different angles of attack																
Designation	Station (percent <i>c</i> from L. E. of chord)	Ordinate (percent <i>c</i> above chord)	−20°	α−16°	α−12°	β−8°	β−6°	β−4°	β−2°	β 0°	β 2°	β 4°	β 8°	β 12°	α 16°	α 18°	α 20°	α 24°	α 30°
28	100.00	0		−0.309	0.043	0.181	0.193	0.199	0.201	0.193	0.191	0.178	0.134	0.016	−0.194	−0.324	−0.381	−0.547	−0.540
1	97.92	−.16		−.331	.043	.156	.170	.176	.178	.170	.176	.172	.154	.085	−.058	−.137	−.209	−.317	−.323
29	94.86	−.16		−.352	.000	.130	.146	.154	.156	.154	.166	.168	.170	.130	−.029	−.036	−.094	−.187	−.187
2	89.90	−.22		−.388	−.029	.097	.116	.128	.136	.138	.158	.168	.191	.178	.115	.065	.029	−.050	−.050
30	84.94	−.28		−.410	−.072	.067	.099	.103	.128	.126	.150	.166	.201	.205	.173	.137	.108	.043	.036
31	74.92	−.52		−.467	−.144	.012	.043	.067	.089	.105	.140	.165	.219	.249	.245	.230	.216	.165	.165
32	64.94	−.84		−.525	−.223	−.047	−.010	.024	.055	.083	.126	.158	.231	.280	.302	.302	.295	.259	.266
3	54.48	−1.24		−.576	−.295	−.120	−.071	−.028	.014	.053	.106	.148	.239	.306	.344	.353	.360	.331	.353
33	49.98	−1.44		−.597	−.410	−.158	−.101	−.053	−.004	.034	.093	.140	.243	.320	.374	.388	.396	.381	.396
4	44.90	−1.64		−.626	−.388	−.199	−.136	−.079	−.024	.028	.093	.142	.256	.341	.403	.417	.432	.410	.432
34	39.98	−.86		−.640	−.460	−.247	−.174	−.110	−.047	.014	.085	.140	.266	.363	.439	.453	.468	.453	.475
5	34.90	−2.10		−.676	−.496	−.306	−.223	−.150	−.075	−.006	.073	.134	.276	.385	.468	.489	.511	.496	.525
35	29.96	−2.30		−.691	−.590	−.379	−.284	−.199	−.112	−.030	.053	.128	.284	.410	.504	.525	.547	.532	.568
6	24.90	−2.54		−.727	−.669	−.491	−.377	−.274	−.170	−.075	.018	.108	.290	.434	.547	.566	.604	.590	.619
36	19.98	−2.76		−.755	−.791	−.637	−.497	−.371	−.247	−.136	−.020	.091	.300	.469	.597	.626	.655	.640	.669
7	14.94	−2.90		−.784	−1.007	−.848	−.671	−.507	−.349	−.217	−.061	.075	.327	.523	.662	.698	.727	.712	.741
37	9.96	−2.86		−.892	−1.331	−1.189	−.937	−.712	−.525	−.312	−.110	.069	.385	.621	.777	.820	.849	.820	.834
8	7.38	−2.72		−.942	−1.676	−1.450	−1.130	−.882	−.643	−.369	−.128	.083	.454	.708	.863	.899	.928	.906	.899
38	4.94	−2.46		−.971	−2.151	−1.842	−1.503	−1.191	−.789	−.436	−.134	.130	.556	.826	.957	.978	1.014	.964	.971
9	2.92	−2.06		−1.007	−2.921	−2.785	−2.079	−1.456	−.941	−.473	−.081	.249	.730	.963	1.007	1.000	1.022	1.000	1.007
39	1.66	−1.60		−.978	−4.072	−3.331	−2.406	−1.693	−1.024	−.428	.049	.436	.901	1.006	.878	.806	.820	.856	.935
10	.92	−1.20		−1.036	−4.928	−3.761	−2.696	−1.955	−.955	−.243	.288	.667	1.006	.870	.432	.266	.288	.410	.727
40	.36	−.70		−1.007	−5.360	−4.018	−2.651	−1.547	−.584	.176	.669	.933	.905	.185	−.921	−1.259	−1.201	−.619	.144
11	0	0		−1.022	−3.906	−2.363	−1.181	−.281	.400	.830	.939	.937	.178	−1.438	−3.302	−3.799	−3.604	−2.691	−.583
41	0	.68		−.187	−1.655	−.497	.223	.688	.947	.984	.844	.458	−.974	−3.097	−5.295	−5.820	−5.468	−3.676	−.640
12	.44	1.56		.748	.317	.769	.955	1.004	.933	.686	.312	−.231	−1.765	−3.722	−5.403	−5.755	−5.302	−3.878	−.568
42	.94	2.16		.957	.806	.976	1.000	.933	.747	.424	.028	−.487	−1.808	−3.367	−4.820	−5.151	−4.763	−3.259	−.576
13	1.70	2.78		1.014	.996	.994	.923	.781	.546	.207	−.176	−.645	−1.769	−3.065	−4.288	−4.360	−3.849	−2.554	−.568
43	2.94	3.64		.971	.996	.884	.744	.562	.310	−.014	−.357	−.765	−1.669	−2.718	−3.338	−3.345	−2.935	−1.410	−.561
14	4.90	4.68		.835	.871	.694	.523	.328	.083	−.217	−.517	−.862	−1.592	−2.363	−2.892	−2.856	−2.388	−1.273	−.561
44	7.50	5.74		.683	.705	.497	.325	.138	−.087	−.353	−.611	−.901	−1.495	−2.065	−2.475	−2.374	−1.892	−1.029	−.554
15	9.96	6.56		.554	.568	.353	.185	.006	−.201	−.444	−.673	−.929	−1.438	−1.909	−2.230	−2.079	−1.532	−.964	−.554
45	12.58	7.34		.432	.446	.225	.061	−.108	−.300	−.523	−.730	−.959	−1.398	−1.805	−2.043	−1.849	−1.281	−.892	−.554
16	14.92	7.88		.345	.360	.140	−.016	−.174	−.355	−.560	−.748	−.957	−1.347	−1.706	−1.892	−1.647	−1.065	−.870	−.561
46	17.44	8.40		.259	.266	.061	−.085	−.235	−.406	−.594	−.769	−.957	−1.302	−1.623	−1.763	−1.489	−.935	−.849	−.561
17	19.96	8.80		.187	.201	−.006	−.146	−.285	−.444	−.623	−.783	−.955	−1.264	−1.548	−1.640	−1.317	−.784	−.842	−.561
47	22.44	9.16		.123	.129	−.063	−.197	−.329	−.479	−.645	−.793	−.951	−1.235	−1.493	−1.547	−1.187	−.719	−.827	−.561
18	24.92	9.52		.072	.086	−.108	−.231	−.359	−.497	−.653	−.791	−.937	−1.189	−1.414	−1.430	−1.029	−.640	−.827	−.561
48	27.44	9.62		.022	.036	−.146	−.266	−.383	−.513	−.657	−.785	−.921	−1.146	−1.347	−1.324	−.914	−.612	−.820	−.568
19	29.88	9.76		−.007	.000	−.172	−.284	−.394	−.517	−.653	−.771	−.897	−1.093	−1.274	−1.216	−.791	−.568	−.827	−.568
49	34.98	9.90		−.079	−.058	−.211	−.310	−.408	−.515	−.633	−.732	−.842	−1.002	−1.140	−1.029	−.662	−.554	−.813	−.576
20	39.90	9.84		−.122	−.086	−.215	−.312	−.398	−.491	−.594	−.680	−.771	−.892	−.998	−.827	−.568	−.532	−.813	−.583
50	44.80	9.64		−.165	−.122	−.241	−.320	−.394	−.477	−.566	−.641	−.712	−.819	−.890	−.676	−.532	−.532	−.806	−.583
21	49.92	9.22		−.172	−.115	−.227	−.294	−.357	−.428	−.507	−.566	−.619	−.708	−.753	−.518	−.504	−.525	−.777	−.583
51	54.92	8.76		−.194	−.129	−.213	−.270	−.325	−.385	−.450	−.493	−.542	−.617	−.639	−.439	−.511	−.532	−.791	−.590
22	59.94	8.16		−.209	−.137	−.211	−.258	−.304	−.359	−.412	−.448	−.495	−.548	−.542	−.367	−.489	−.525	−.748	−.583
52	64.90	7.54		−.237	−.144	−.201	−.241	−.280	−.325	−.367	−.400	−.438	−.471	−.444	−.345	−.496	−.532	−.770	−.590
23	69.86	6.76		−.252	−.137	−.178	−.213	−.243	−.278	−.314	−.341	−.371	−.385	−.339	−.317	−.482	−.525	−.755	−.590
24	74.90	5.88		−.259	−.129	−.150	−.174	−.199	−.227	−.260	−.278	−.298	−.298	−.241	−.302	−.475	−.518	−.735	−.590
53	79.92	4.92		−.280	−.122	−.122	−.140	−.158	−.178	−.203	−.215	−.229	−.213	−.156	−.288	−.468	−.511	−.712	−.590
25	84.88	3.88		−.280	−.108	−.083	−.095	−.105	−.120	−.138	−.142	−.150	−.120	−.087	−.273	−.453	−.504	−.691	−.576
54	89.88	2.74		−.287	−.079	−.026	−.030	−.035	−.041	−.051	−.053	−.020	−.039	−.020	−.260	−.432	−.482	−.647	−.568
26	94.90	1.48		−.295	−.029	.043	.049	.053	.051	.047	.055	.055	.067	−.012	−.252	−.396	−.439	−.612	−.554
27	98.00	.68		−.324	−.007	.105	.118	.126	.128	.124	.130	.128	.114	.004	−.230	−.360	−.410	−.583	−.547
28	100.00	0																	

^a Test, variable-density tunnel 1099-1; manometer liquid, tetrabromoethane.
^b Test, variable-density tunnel 1097-5; manometer liquid, alcohol.

TABLE II.—EXPERIMENTAL DATA

[N. A. C. A. 4412 airfoil; effective Reynolds Number, 3,400,000; test numbers and manometer liquids given in footnotes]

Orifices			Values of pressure coefficient, $P = \frac{p - p_{\infty}}{q}$, for different angles of attack																
Designation	Station (percent c from L. E. of chord)	Ordinate (percent c above chord)	$\alpha=20^\circ$	$\alpha=16^\circ$	$\alpha=12^\circ$	$\alpha=8^\circ$	$\alpha=6^\circ$	$\alpha=4^\circ$	$\alpha=2^\circ$	$\alpha=0^\circ$	$\alpha=2^\circ$	$\alpha=4^\circ$	$\alpha=8^\circ$	$\alpha=12^\circ$	$\alpha=16^\circ$	$\alpha=18^\circ$	$\alpha=20^\circ$	$\alpha=24^\circ$	$\alpha=30^\circ$
28.....	100.00	0	-.378	-.170	0.178	0.193	0.196	0.200	0.200	0.186	0.175	0.150	0.110	0.013	-0.134	-0.178	-0.338	-0.511	-0.568
1.....	97.92	-.16	-.406	-.177	.157	.168	.182	.168	.182	.171	.173	.150	.132	.082	.006	.061	-.019	-.285	-.324
29.....	94.86	-.16	-.432	-.209	.128	.139	.157	.146	.160	.157	.164	.153	.156	.128	.085	.134	.077	-.152	-.177
2.....	89.90	-.22	-.468	-.249	.092	.103	.125	.121	.142	.146	.164	.157	.178	.175	.164	.220	.188	-.019	-.033
30.....	84.94	-.28	-.493	-.292	.056	.074	.099	.103	.128	.139	.160	.160	.196	.203	.214	.268	.236	.067	.067
31.....	74.92	-.52	-.539	-.385	-.015	.020	.053	.067	.099	.121	.149	.160	.214	.246	.282	.348	.331	.192	.207
32.....	64.94	-.84	-.582	-.471	-.091	-.044	-.001	.024	.064	.099	.135	.153	.225	.278	.340	.395	.395	.282	.308
3.....	54.48	-1.24	-.633	-.586	-.184	-.112	-.062	-.030	.020	.067	.117	.146	.236	.308	.383	.443	.459	.365	.397
33.....	49.98	-1.44	-.658	-.636	-.238	-.155	-.094	-.055	-.005	.046	.106	.139	.239	.318	.404			.390	.433
4.....	44.90	-1.64	-.668	-.694	-.295	-.195	-.127	-.080	-.019	.042	.106	.142	.254	.343	.437	.522	.522	.440	.487
34.....	39.98	-1.86	-.676	-.740	-.360	-.241	-.163	-.105	-.037	.031	.103	.142	.268	.368	.469	.554	.570	.483	.534
5.....	34.90	-2.10	-.701	-.805	-.453	-.313	-.227	-.163	-.084	-.012	.089	.135	.272	.382	.498	.586	.602	.523	.580
35.....	29.96	-2.30	-.704	-.841	-.550	-.374	-.277	-.195	-.109	-.015	.074	.132	.286	.408	.534	.618	.650	.569	.630
6.....	24.90	-2.54	-.722	-.898	-.694	-.485	-.367	-.274	-.170	-.058	.046	.110	.290	.436	.573	.650	.682	.620	.677
36.....	19.98	-2.76	-.772	-.959	-.891	-.633	-.493	-.374	-.245	-.116	.006	.089	.300	.469	.627	.714	.745	.677	.742
7.....	14.94	-2.90	-.808	-1.002	-1.185	-.851	-.672	-.518	-.356	-.195	-.044	.067	.325	.526	.697	.809	.809	.756	.817
37.....	9.96	-2.86	-.887	-1.049	-1.662	-1.196	-.948	-.726	-.507	-.299	-.091	.056	.383	.623	.813	.904	.920	.867	.921
8.....	7.38	-2.72	-.916	-1.063	-2.071	-1.469	-1.156	-.877	-.622	-.363	-.112	.074	.448	.709	.896	.984	1.000	.935	.978
38.....	4.94	-2.46	-.973	-1.140	-2.739	-1.913	-1.490	-1.142	-.805	-.439	-.119	.107	.552	.828	.986	1.064	1.032	1.000	.978
9.....	2.92	-2.06	-1.056	-1.361	-3.776	-2.552	-1.989	-1.480	-.977	-.478	-.062	.221	.731	.968	1.025	1.000	.968	.989	.975
39.....	1.66	-1.60	-1.551	-2.089	-4.985	-3.360	-2.495	-1.734	-1.070	-.435	.067	.401	.907	1.004	.857	.745	.650	.781	.709
10.....	.92	-1.20	-1.601	-2.577	-6.334	-3.923	-2.821	-1.840	-1.020	-.267	.300	.638	1.014	.864	.354	.061	-.115	.275	-.186
40.....	.36	-.70	-2.947	-4.077	-7.407	-4.167	-2.778	-1.605	-.658	.157	.688	.925	.918	.150	-1.153	-1.819	-2.089	-1.088	-1.174
11.....	0	0	-1.978	-2.617	-5.265	-2.383	-1.232	-.299	.368	.842	1.021	.957	.121	-1.670	-4.034	-4.755	-5.035	-3.456	-3.151
41.....	0	.68	-1.232	-1.472	-2.635	-.572	.164	.666	.946	1.007	.871	.501	-.923	-3.108	-5.717	-6.930	-7.153	-4.544	-3.977
12.....	.44	1.56	.390	.369	-.023	.756	.960	1.011	.957	.716	.340	-.170	-1.673	-3.650	-5.728	-6.750	-6.834	-4.206	-3.324
42.....	.94	2.16	.760	.767	.641	.978	1.022	.943	.774	.440	.038	-.478	-1.824	-3.474	-5.225	-5.920	-5.911	-3.467	-2.333
13.....	1.70	2.78	.968	.986	.935	1.000	.950	.792	.577	.232	-.148	-.604	-1.752	-3.058	-4.274	-4.750	-4.669	-2.545	-1.598
43.....	2.94	3.64	1.014	1.022	1.007	.896	.774	.580	.343	.010	-.335	-.715	-1.652	-2.642	-3.578	-3.890	-3.775	-1.784	-1.138
14.....	4.90	4.68	.950	.943	.928	.702	.552	.347	.125	-.180	-.478	-.798	-1.544	-2.337	-3.065	-3.268	-3.045	-1.217	-.873
44.....	7.50	5.74	.831	.806	.778	.512	.354	.153	-.055	-.328	-.597	-.877	-1.454	-2.075	-2.613	-2.725	-2.471	-.920	-.859
15.....	9.96	6.56	.713	.684	.645	.368	.214	.024	-.166	-.410	-.640	-.877	-1.397	-1.931	-2.358	-2.438	-2.137	-.819	-.808
45.....	12.58	7.34	.602	.566	.519	.239	.092	-.084	-.263	-.489	-.686	-.898	-1.350	-1.809	-2.154	-2.200	-1.834	-.808	-.826
16.....	14.92	7.88	.512	.476	.426	.153	.017	-.155	-.317	-.525	-.704	-.898	-1.311	-1.716	-1.996	-2.024	-1.643	-.780	-.765
46.....	17.44	8.40	.426	.390	.340	.074	-.058	-.216	-.371	-.561	-.722	-.902	-1.275	-1.634	-1.863	-1.865	-1.452	-.780	-.769
17.....	19.96	8.80	.351	.318	.264	.010	-.116	-.270	-.406	-.586	-.733	-.902	-1.235	-1.555	-1.741	-1.722	-1.293	-.758	-.729
47.....	22.44	9.16	.282	.247	.196	-.051	-.170	-.313	-.442	-.618	-.758	-.912	-1.221	-1.504	-1.648	-1.611	-1.166	-.747	-.729
18.....	24.92	9.52	.218	.193	.142	-.091	-.202	-.338	-.453	-.615	-.740	-.884	-1.164	-1.418	-1.526	-1.500	-1.038	-.740	-.704
48.....	27.44	9.62	.164	.142	.096	-.127	-.234	-.360	-.471	-.618	-.737	-.873	-1.128	-1.350	-1.429	-1.372	-.911	-.733	-.704
19.....	29.88	9.76	.117	.103	.064	-.152	-.252	-.371	-.471	-.611	-.719	-.841	-1.074	-1.275	-1.325	-1.261	-.847	-.715	-.683
49.....	34.98	9.90	.035	.028	.003	-.195	-.281	-.385	-.475	-.597	-.686	-.794	-.984	-1.146	-1.135	-1.038	-.704	-.704	-.676
20.....	39.90	9.84	-.015	-.012	-.033	-.202	-.281	-.371	-.446	-.554	-.633	-.726	-.877	-1.006	-.948	-.846	-.656	-.686	-.661
50.....	44.80	9.64	-.073	-.062	-.066	-.220	-.292	-.371	-.439	-.532	-.597	-.676	-.801	-.895	-.787	-.687	-.608	-.683	-.661
21.....	49.92	9.22	-.098	-.076	-.066	-.202	-.263	-.328	-.389	-.468	-.521	-.586	-.686	-.755	-.615	-.560	-.592	-.668	-.658
51.....	54.92	8.76	-.130	-.094	-.069	-.191	-.245	-.302	-.353	-.417	-.464	-.514	-.597	-.636	-.485	-.496	-.576	-.676	-.661
22.....	59.94	8.16	-.170	-.127	-.087	-.191	-.241	-.292	-.335	-.396	-.420	-.471	-.525	-.543	-.396	-.432	-.545	-.672	-.661
52.....	64.90	7.54	-.206	-.148	-.087	-.184	-.224	-.267	-.299	-.351	-.374	-.414	-.446	-.446	-.328	-.401	-.529	-.679	-.665
23.....	69.86	6.76	-.227	-.155	-.080	-.163	-.195	-.231	-.256	-.299	-.313	-.346	-.363	-.342	-.281	-.337	-.496	-.668	-.661
24.....	74.90	5.88	-.249	-.159	-.066	-.130	-.159	-.188	-.206	-.238	-.249	-.274	-.274	-.238	-.249	-.305	-.496	-.661	-.654
53.....	79.92	4.92	-.277	-.173	-.055	-.109	-.130	-.148	-.159	-.184	-.191	-.206	-.191	-.155	-.231	-.273	-.464	-.651	-.651
25.....	84.88	3.88	-.303	-.180	-.033	-.069	-.084	-.098	-.102	-.116	-.116	-.123	-.098	-.087	-.206	-.273	-.464	-.625	-.636
54.....	89.88	2.74	-.317	-.177	.010	-.015	-.023	-.026	-.026	-.033	-.026	-.030	-.008	-.041	-.191	-.258	-.449	-.597	-.622
26.....	94.90	1.48	-.385	-.177	.060	.056	.060	.060	.071	.067	.084	.064	.067	-.012	-.173	-.242	-.401	-.550	-.586
27.....	98.00	.68	-.396	-.195	.103	.117	.124	.128	.135	.132	.135	.121	.096	.003	-.163	-.226	-.353	-.529	-.572
28.....	100.00	0																	

* Test, variable-density tunnel 1099-2; manometer liquid, tetrabromoethane.

† Test, variable-density tunnel 1096-1; manometer liquid, mercury.

TABLE Ig.—EXPERIMENTAL DATA

[N. A. C. A. 4412 airfoil; effective Reynolds Number, 6,300,000; test numbers and manometer liquids given in footnotes]

Orifices			Values of pressure coefficient, $P = \frac{p-p_\infty}{q}$, for different angles of attack																
Designation	Station (percent c from L. E. of chord)	Ordinate (percent c above chord)	-20°	a-16°	a-12°	a-8°	b-6°	b-4°	b-2°	b 0°	b 2°	b 4°	b 8°	b 12°	a 16°	a 18°	a 20°	a 24°	a 30°
28	100.00	0		-0.106	0.207	0.234	0.208	0.208	0.205	0.196	0.186	0.167	0.131	0.063	-0.011	-0.124	-0.194	-0.533	-0.620
1	97.92	-.16		-.185	.155	.146	.177	.177	.186	.181	.177	.167	.162	.128	.085	.016	-.045	-.306	-.315
29	94.86	-.16		-.236	.129	.112	.145	.150	.167	.168	.171	.165	.179	.162	.155	.103	.051	-.167	-.167
2	89.90	-.22		-.272	.059	.077	.118	.128	.148	.156	.168	.169	.200	.204	.216	.181	.146	-.028	-.028
30	84.94	-.28		-.333	.042	.042	.078	.092	.118	.129	.143	.154	.194	.209	.251	.225	.208	.042	.059
31	74.92	-.52		-.411	-.019	-.011	.044	.068	.104	.126	.150	.169	.230	.268	.312	.295	.294	.172	.198
32	64.94	-.84		-.506	-.115	-.063	-.006	.027	.072	.122	.137	.164	.244	.297	.356	.355	.373	.268	.303
3	54.48	-1.24		-.620	-.202	-.141	-.071	-.025	.030	.072	.114	.152	.251	.322	.390	.408	.425	.355	.399
33	49.98	-1.44		-.628	-.254	-.176	-.105	-.056	.003	.048	.100	.150	.253	.333	.416	.425	.451	.416	.452
4	44.90	-1.64		-.725	-.306	-.228	-.134	-.076	-.008	.046	.100	.152	.271	.341	.452	.468	.504	.425	.468
34	39.98	-1.86		-.776	-.359	-.272	-.177	-.113	-.035	.027	.087	.142	.276	.375	.495	.521	.530	.477	.512
5	34.90	-2.10		-.829	-.455	-.333	-.225	-.149	-.064	.010	.078	.142	.289	.390	.512	.538	.564	.521	.564
35	29.96	-2.30		-.890	-.559	-.403	-.282	-.194	-.096	-.014	.066	.138	.304	.426	.547	.582	.617	.564	.608
6	24.90	-2.54		-.934	-.690	-.515	-.377	-.273	-.155	-.057	.037	.124	.311	.452	.599	.625	.669	.617	.660
36	19.98	-2.76		-.985	-.899	-.664	-.499	-.372	-.231	-.113	.002	.102	.320	.484	.652	.686	.721	.669	.721
7	14.94	-2.90		-1.055	-1.186	-.881	-.676	-.511	-.334	-.184	-.048	.077	.343	.537	.713	.756	.800	.739	.782
37	9.96	-2.86		-1.117	-1.700	-1.221	-.975	-.722	-.482	-.282	-.113	.059	.394	.630	.826	.852	.896	.843	.869
8	7.38	-2.72		-1.256	-2.110	-1.482	-1.159	-.869	-.585	-.347	-.126	.081	.467	.722	.913	.930	.965	.913	.930
38	4.94	-2.46		-1.379	-2.790	-1.951	-1.503	-1.122	-.765	-.432	-.143	.116	.569	.838	.991	.991	1.000	.930	.965
9	2.92	-2.06		-1.935	-3.825	-2.589	-1.992	-1.466	-.935	-.475	-.096	.234	.745	.973	1.000	.922	.852	.861	.904
39	1.66	-1.60		-3.000	-5.070	-3.400	-2.493	-1.731	-1.029	-.430	.037	.413	.916	1.008	.800	.582	.390	.521	.634
10	.92	-1.20		-4.520	-6.510	-3.965	-2.825	-1.840	-.966	-.259	.264	.649	1.015	.665	.225	-.202	-.611	-.236	.050
40	.36	-.70		-5.600	-7.460	-4.210	-2.770	-1.599	-.603	.154	.653	.935	.918	.120	-1.379	-2.222	-3.016	-2.100	-1.342
11	0	0		-4.410	-5.460	-2.485	-1.286	-.341	.392	.830	1.004	.971	.185	-1.530	-4.035	-5.380	-4.855	-3.225	-1.342
41	0	.68		-2.310	-2.660	-.603	.164	.667	.958	1.010	.868	.499	-.989	-3.278	-6.257	-7.755	-9.030	-6.680	-4.363
12	.44	1.56		-.036	-.071	.730	.949	1.008	.950	.726	.362	-.159	-1.700	-3.762	-6.261	-7.475	-8.430	-5.890	-3.730
42	.94	2.16		.582	.617	.922	1.006	.943	.771	.459	.072	-.436	-1.793	-3.423	-5.420	-6.255	-6.820	-4.770	-2.482
13	1.70	2.78		.896	.913	.965	.935	.794	.567	.245	-.128	-.593	-1.744	-3.072	-4.590	-5.270	-5.725	-3.790	-1.671
43	2.94	3.64		1.000	1.000	.887	.758	.573	.327	.017	-.319	-.711	-1.630	-2.658	-3.818	-4.340	-4.655	-2.850	-1.001
14	4.90	4.68		.956	.913	.695	.539	.341	.101	-.189	-.486	-.830	-1.544	-2.360	-3.250	-3.642	-3.820	-2.030	-.760
44	7.50	5.74		.826	.765	.486	.344	.156	-.063	-.316	-.559	-.824	-1.424	-2.070	-2.763	-3.050	-3.148	-1.535	-.723
15	9.96	6.56		.721	.626	.347	.204	.023	-.181	-.406	-.616	-.874	-1.391	-1.933	-2.492	-2.720	-2.763	-1.264	-.705
45	12.58	7.34		.608	.495	.216	.084	-.086	-.273	-.480	-.668	-.905	-1.369	-1.860	-2.284	-2.476	-2.460	-1.125	-.705
16	14.92	7.88		.529	.416	.138	.005	-.155	-.326	-.515	-.690	-.896	-1.311	-1.728	-2.128	-2.285	-2.240	-1.064	-.705
46	17.44	8.40		.443	.312	.051	-.061	-.208	-.368	-.543	-.710	-.902	-1.272	-1.644	-1.989	-2.129	-2.050	-.985	-.699
17	19.96	8.80		.373	.234	-.010	-.120	-.261	-.410	-.574	-.726	-.902	-1.237	-1.571	-1.874	-1.989	-1.875	-.925	-.688
47	22.44	9.16		.312	.164	-.072	-.181	-.314	-.460	-.612	-.759	-.919	-1.230	-1.528	-1.770	-1.875	-1.752	-.908	-.680
18	24.92	9.52		.251	.112	-.106	-.206	-.324	-.462	-.606	-.736	-.886	-1.170	-1.441	-1.665	-1.752	-1.570	-.865	-.680
48	27.44	9.62		.207	.077	-.132	-.222	-.353	-.475	-.610	-.734	-.871	-1.128	-1.369	-1.560	-1.640	-1.422	-.846	-.688
19	29.88	9.76		.164	.051	-.158	-.250	-.360	-.475	-.599	-.713	-.840	-1.075	-1.293	-1.466	-1.526	-1.282	-.829	-.680
49	34.98	9.90		.103	-.002	-.176	-.280	-.377	-.476	-.587	-.681	-.794	-.988	-1.164	-1.281	-1.309	-1.021	-.795	-.671
20	39.90	9.84		.042	-.045	-.211	-.280	-.366	-.452	-.546	-.627	-.723	-.882	-1.027	-1.125	-1.126	-.820	-.777	-.688
50	44.80	9.64		-.002	-.088	-.219	-.295	-.368	-.442	-.526	-.593	-.677	-.806	-.920	-.969	-.951	-.673	-.760	-.688
21	49.92	9.22		-.011	-.088	-.219	-.263	-.328	-.391	-.461	-.515	-.585	-.694	-.779	-.811	-.777	-.585	-.750	-.688
51	54.92	8.76		-.028	-.097	-.202	-.244	-.299	-.350	-.414	-.458	-.519	-.602	-.666	-.672	-.629	-.515	-.750	-.688
22	59.94	8.16		-.063	-.124	-.211	-.244	-.294	-.335	-.391	-.425	-.471	-.536	-.582	-.568	-.524	-.472	-.750	-.688
52	64.90	7.54		-.080	-.115	-.185	-.219	-.261	-.296	-.339	-.368	-.410	-.458	-.480	-.437	-.411	-.429	-.734	-.688
23	69.86	6.76		-.088	-.106	-.158	-.190	-.223	-.250	-.288	-.307	-.340	-.372	-.377	-.332	-.333	-.376	-.707	-.680
24	74.90	5.88		-.097	-.080	-.115	-.155	-.181	-.200	-.228	-.245	-.267	-.282	-.272	-.228	-.272	-.359	-.707	-.688
53	79.92	4.92		-.097	-.080	-.098	-.122	-.141	-.152	-.174	-.181	-.198	-.198	-.179	-.158	-.246	-.333	-.690	-.680
25	84.88	3.88		-.106	-.036	-.054	-.076	-.088	-.094	-.106	-.107	-.116	-.105	-.090	-.106	-.202	-.306	-.664	-.671
54	89.88	2.74		-.097	.007	-.002	-.012	-.015	-.016	-.021	-.016	-.022	-.010	-.017	-.071	-.176	-.259	-.629	-.653
26	94.90	1.48		-.106	.077	.077	.068	.072	.078	.076	.084	.080	.076	.030	-.036	-.159	-.254	-.576	-.628
27	98.00	.68		-.132	.112	.155	.135	.141	.148	.146	.148	.137	.116	.055	-.028	-.150	-.219	-.542	-.610
28	100.00	0																	

^a Test, variable-density tunnel 1096-2; manometer liquid, mercury.^b Test, variable-density tunnel 1099-3; manometer liquid, tetrabromoethane.

TABLE 1h.—EXPERIMENTAL DATA

[N. A. C. A. 4412 airfoil; effective Reynolds Number, 8,200,000; test numbers and manometer liquids given in footnotes]

Designation	Orifices		Values of pressure coefficient, $P = \frac{p-p_{\infty}}{q}$, for different angles of attack																
	Station (percent c from L. E. of chord)	Ordinate (percent c above chord)	$\alpha=20^\circ$	$\alpha=16^\circ$	$\alpha=12^\circ$	$\alpha=8^\circ$	$\beta=6^\circ$	$\beta=4^\circ$	$\beta=2^\circ$	$\beta=0^\circ$	$\beta=2^\circ$	$\beta=4^\circ$	$\beta=8^\circ$	$\alpha=12^\circ$	$\alpha=16^\circ$	$\alpha=18^\circ$	$\alpha=20^\circ$	$\alpha=24^\circ$	$\alpha=30^\circ$
28.....	100.00	0	-0.421	-0.199	0.114	0.198	0.217	0.204	0.207	0.200	0.181	0.158	0.134	0.101	0.010	-0.062	-0.173	-0.466	-0.513
1.....	97.92	-16	-.454	-.251	.159	.224	.181	.178	.180	.183	.164	.157	.167	.140	.121	.094	.049	-.291	-.304
29.....	94.86	-16	-.466	-.291	.107	.185	.152	.151	.158	.166	.154	.156	.180	.166	.179	.166	.127	-.160	-.167
2.....	89.90	-.22	-.505	-.330	.074	.153	.122	.128	.140	.156	.152	.160	.203	.199	.231	.237	.224	-.030	-.036
30.....	84.94	-.28	-.538	-.382	.035	.107	.072	.082	.098	.118	.118	.158	.211	.212	.257	.270	.263	.049	.042
31.....	74.92	-.52	-.558	-.454	-.043	.055	.049	.068	.095	.126	.136	.158	.231	.251	.322	.348	.374	.179	.179
32.....	64.94	-.84	-.564	-.539	-.101	.002	.000	.028	.062	.104	.120	.154	.244	.283	.374	.407	.453	.270	.289
3.....	54.48	-1.24	-.571	-.643	-.199	-.082	-.063	-.024	.021	.072	.100	.157	.250	.309	.414	.452	.492	.348	.368
33.....	49.98	-1.44	-.571	-.695	-.252	-.115	-.099	-.053	-.005	.050	.091	.134	.252	.316	.426	.472	.531	.381	.407
4.....	44.90	-1.64	-.571	-.721	-.304	-.160	-.128	-.075	-.017	.048	.088	.140	.268	.342	.459	.505	.570	.413	.446
34.....	39.98	-1.86	-.558	-.754	-.368	-.206	-.169	-.105	-.041	.031	.071	.136	.265	.362	.485	.544	.609	.466	.498
5.....	34.90	-2.10	-.551	-.773	-.447	-.258	-.217	-.146	-.073	.010	.066	.133	.290	.387	.516	.576	.642	.504	.544
35.....	29.96	-2.30	-.545	-.786	-.545	-.330	-.274	-.190	-.105	-.011	.048	.116	.293	.414	.551	.609	.687	.557	.596
6.....	24.90	-2.54	-.545	-.806	-.688	-.427	-.367	-.266	-.165	-.054	.025	.115	.313	.433	.589	.661	.726	.609	.648
36.....	19.98	-2.76	-.551	-.819	-.896	-.591	-.490	-.365	-.244	-.111	-.011	.093	.321	.472	.627	.687	.752	.642	.700
7.....	14.94	-2.90	-.558	-.825	-1.178	-.799	-.663	-.502	-.348	-.180	-.053	.076	.345	.518	.713	.785	.857	.733	.778
37.....	9.96	-2.86	-.551	-.832	-1.660	-1.143	-.946	-.716	-.501	-.279	-.111	.059	.402	.616	.818	.883	.948	.824	.876
8.....	7.38	-2.72	-.577	-.916	-2.070	-1.407	-1.153	-.867	-.596	-.333	-.131	.071	.462	.713	.896	.961	1.019	.902	.941
38.....	4.94	-2.46	-.571	-.897	-2.807	-1.861	-1.490	-1.106	-.777	-.428	-.150	.109	.568	.818	.980	1.013	1.046	.948	.980
9.....	2.92	-2.06	-.702	-1.242	-3.745	-2.468	-1.931	-1.380	-.932	-.467	-.098	.231	.748	.948	.993	.948	.909	.883	.941
39.....	1.66	-1.60	-1.053	-1.947	-4.940	-3.198	-2.478	-1.709	-1.059	-.436	.028	.409	.916	.974	.791	.596	.433	.602	.713
10.....	.92	-1.20	-2.082	-3.212	-6.177	-3.770	-2.765	-1.812	-.995	-.266	.254	.643	1.013	.831	.264	-.173	-.518	.003	.244
40.....	.36	-.70	-3.204	-4.300	-7.337	-4.052	-2.732	-1.559	-.631	-.156	.639	.924	.905	.094	-1.379	-2.285	-3.012	-1.671	-1.059
11.....	0	0	-2.623	-3.433	-5.480	-2.397	-1.232	-.296	.356	.834	.989	.952	.157	-1.555	-3.648	-5.060	-6.073	-3.695	-2.382
41.....	0	.68	-1.178	-1.549	-2.625	-.538	.184	.681	.945	1.010	.854	.473	-1.000	-3.250	-6.230	-7.775	-8.941	-5.660	-3.730
12.....	.44	1.56	.322	.231	-.043	.765	.955	.994	.948	.720	.336	-.202	-1.740	-3.738	-5.961	-7.125	-7.954	-4.698	-2.552
42.....	.94	2.16	.739	.720	.596	.974	1.009	.939	.770	.468	.055	-.456	-1.793	-3.399	-5.210	-6.110	-6.681	-3.881	-2.006
13.....	1.70	2.78	.928	.935	.883	1.000	.939	.782	.569	.246	-.148	-.611	-1.743	-3.053	-4.478	-5.190	-5.620	-3.010	-1.249
43.....	2.94	3.64	.987	1.000	.974	.896	.761	.559	.332	.018	-.336	-.728	-1.647	-2.637	-3.765	-4.285	-4.562	-2.200	-.786
14.....	4.90	4.68	.922	.935	.896	.713	.542	.333	.110	-.179	-.485	-.813	-1.547	-2.343	-3.190	-3.570	-3.731	-1.529	-.695
44.....	7.50	5.74	.804	.798	.752	.498	.344	.139	-.066	-.312	-.568	-.831	-1.432	-2.057	-2.709	-2.981	-3.060	-1.235	-.644
15.....	9.96	6.56	.687	.687	.622	.374	.208	.017	-.168	-.388	-.623	-.872	-1.391	-1.912	-2.440	-2.662	-2.681	-1.059	-.630
45.....	12.58	7.34	.583	.576	.498	.263	.089	-.091	-.271	-.468	-.676	-.899	-1.350	-1.802	-2.240	-2.415	-2.382	-1.007	-.611
16.....	14.92	7.88	.498	.485	.407	.178	.014	-.152	-.309	-.500	-.700	-.912	-1.308	-1.769	-2.149	-2.285	-2.180	-.955	-.604
46.....	17.44	8.40	.414	.407	.329	.100	-.052	-.210	-.360	-.537	-.721	-.910	-1.272	-1.620	-1.952	-2.062	-1.984	-.910	-.604
17.....	19.96	8.80	.335	.335	.257	.036	-.111	-.262	-.402	-.568	-.740	-.914	-1.239	-1.548	-1.841	-1.927	-1.815	-.870	-.598
47.....	22.44	9.16	.263	.257	.172	-.024	-.176	-.322	-.452	-.609	-.769	-.930	-1.224	-1.502	-1.758	-1.822	-1.685	-.851	-.591
18.....	24.92	9.52	.212	.211	.140	-.063	-.196	-.332	-.454	-.599	-.746	-.895	-1.163	-1.418	-1.640	-1.692	-1.592	-.825	-.591
48.....	27.44	9.62	.166	.165	.100	-.096	-.228	-.355	-.471	-.606	-.742	-.881	-1.122	-1.347	-1.535	-1.573	-1.391	-.812	-.591
19.....	29.88	9.76	.114	.133	.068	-.114	-.241	-.364	-.469	-.594	-.722	-.851	-1.071	-1.280	-1.438	-1.463	-1.254	-.786	-.591
49.....	34.98	9.90	.036	.055	.009	-.154	-.275	-.381	-.473	-.596	-.693	-.804	-.982	-1.144	-1.269	-1.255	-1.005	-.760	-.591
20.....	39.90	9.84	-.017	.009	-.030	-.173	-.272	-.370	-.447	-.542	-.635	-.732	-.880	-1.007	-1.099	-1.059	-.798	-.727	-.584
50.....	44.80	9.64	-.095	-.044	-.069	-.194	-.291	-.371	-.439	-.519	-.609	-.691	-.809	-.902	-.961	-.910	-.655	-.720	-.591
21.....	49.92	9.22	-.121	-.056	-.075	-.173	-.256	-.329	-.389	-.455	-.525	-.595	-.690	-.759	-.786	-.734	-.538	-.715	-.591
51.....	54.92	8.76	-.147	-.069	-.075	-.161	-.238	-.303	-.351	-.406	-.471	-.527	-.601	-.649	-.649	-.584	-.473	-.700	-.591
22.....	59.94	8.16	-.199	-.101	-.095	-.161	-.244	-.298	-.342	-.391	-.438	-.487	-.541	-.576	-.551	-.460	-.414	-.695	-.591
52.....	64.90	7.54	-.225	-.108	-.082	-.128	-.214	-.264	-.296	-.334	-.378	-.421	-.456	-.460	-.414	-.343	-.369	-.688	-.591
23.....	69.86	6.76	-.252	-.121	-.082	-.115	-.181	-.225	-.250	-.282	-.319	-.351	-.371	-.375	-.316	-.264	-.337	-.682	-.584
53.....	74.90	5.88	-.277	-.128	-.056	-.082	-.148	-.183	-.200	-.222	-.252	-.279	-.285	-.264	-.212	-.212	-.310	-.655	-.584
24.....	79.92	4.92	-.297	-.147	-.069	-.076	-.115	-.144	-.155	-.169	-.191	-.210	-.199	-.180	-.147	-.173	-.291	-.642	-.578
25.....	84.88	3.88	-.330	-.154	-.024	-.024	-.068	-.091	-.094	-.101	-.116	-.113	-.106	-.082	-.082	-.140	-.271	-.604	-.565
54.....	89.88	2.74	-.356	-.161	.022	.028	-.006	-.019	-.016	-.017	-.026	-.032	-.009	-.004	-.043	-.114	-.246	-.565	-.552
26.....	94.90	1.48	-.388	-.174	.075	.100	.073	.069	.078	.082	.076	.070	.079	.062	.016	-.095	-.226	-.519	-.519
27.....	98.00	.68	-.434	-.200	.127	.165	.141	.139	.147	.150	.143	.127	.120	.088	-.004	-.075	-.200	-.479	-.506
28.....	100.00	0																	

* Test, variable-density tunnel 1098; manometer liquid, mercury.

* Test, variable-density tunnel 1099-4; manometer liquid, tetrabromoethane.

TABLE IIa.—INTEGRATED AND DERIVED CHARACTERISTICS

[N. A. C. A. 4412 airfoil; effective Reynolds Number, 100,000]

α (deg.)	c_n	c_e	$c_{m_c/4}$	c_l	α_i (deg.)	α_0 (deg.)
-20	-0.479	0.0916	0.023	-0.418	-0.7	-19.3
-16	-.425	.0864	.016	-.384	-.6	-15.4
-12	-.491	.0671	.025	-.466	-.7	-11.3
-8	-.504	.0238	-.028	-.496	-.8	-7.2
-6	-.370	.0050	-.061	-.367	-.6	-5.4
-4	-.191	.0118	-.067	-.191	-.3	-3.7
-2	.025	.0227	-.080	.026	0	-2.0
0	.317	.0240	-.114	.317	.5	-.5
2	.522	.0093	-.106	.521	.8	1.2
4	.722	-.0166	-.108	.721	1.1	2.9
8	1.061	-.0954	-.089	1.064	1.7	6.3
12	1.224	-.1855	-.063	1.238	2.0	10.0
16	1.229	-.2060	-.058	1.238	2.0	14.0
18	1.011	-.0600	-.114	.980	1.6	16.4
20	.916	-.0093	-.127	.864	1.4	18.6
24	.874	.0070	-.127	.795	1.3	22.7
30	.948	.0062	-.143	.818	1.3	28.7

TABLE IIb.—INTEGRATED AND DERIVED CHARACTERISTICS

[N. A. C. A. 4412 airfoil; effective Reynolds Number, 900,000]

α (deg.)	c_n	c_e	$c_{m_c/4}$	c_l	α_i (deg.)	α_0 (deg.)
-20	-0.442	0.0900	0.018	-0.384	-0.6	-19.4
-16	-.437	.0856	.025	-.396	-.6	-15.4
-12	-.494	.0634	.011	-.470	-.7	-11.3
-8	-.342	-.0199	-.096	-.341	-.5	-7.5
-6	-.190	-.0098	-.096	-.190	-.3	-5.7
-4	-.008	.0051	-.100	-.008	0	-4.0
-2	.162	.0122	-.096	.162	.3	-2.3
0	.344	.0108	-.097	.344	.5	-.5
2	.521	-.0033	-.093	.520	.8	1.2
4	.696	-.0248	-.092	.696	1.1	2.9
8	1.000	-.0990	-.082	1.004	1.6	6.4
12	1.231	-.1948	-.063	1.244	2.0	10.0
16	1.290	-.2587	-.059	1.311	2.1	13.9
18	1.231	-.2360	-.076	1.244	2.0	16.0
20	1.093	-.0747	-.131	1.054	1.7	18.3
24	.938	.0077	-.143	.853	1.4	22.6
30	.934	.0074	-.142	.806	1.3	28.7

TABLE IIb.—INTEGRATED AND DERIVED CHARACTERISTICS

[N. A. C. A. 4412 airfoil; effective Reynolds Number, 240,000]

α (deg.)	c_n	c_e	$c_{m_c/4}$	c_l	α_i (deg.)	α_0 (deg.)
-20	-0.428	0.0896	0.013	-0.371	-0.6	-19.4
-16	-.425	.0852	.020	-.384	-.6	-15.4
-12	-.464	.0670	.019	-.440	-.7	-11.3
-8	-.422	.0215	-.049	-.415	-.7	-7.3
-6	-.236	.0000	-.085	-.234	-.4	-5.6
-4	-.045	.0112	-.095	-.046	-.1	-3.9
-2	.161	.0186	-.104	.162	.3	-2.3
0	.350	.0151	-.104	.350	.6	-.6
2	.522	.0032	-.100	.521	.8	1.2
4	.690	-.0210	-.093	.690	1.1	2.9
8	.999	-.0968	-.082	1.000	1.6	6.4
12	1.242	-.1921	-.064	1.256	2.0	10.0
16	1.281	-.2410	-.052	1.299	2.1	13.9
18	1.129	-.1134	-.106	1.108	1.8	16.2
20	.953	-.0162	-.134	.901	1.4	18.6
24	.891	.0086	-.137	.810	1.3	22.7
30	.938	.0061	-.143	.809	1.3	28.7

TABLE IIc.—INTEGRATED AND DERIVED CHARACTERISTICS

[N. A. C. A. 4412 airfoil; effective Reynolds Number, 1,800,000]

α (deg.)	c_n	c_e	$c_{m_c/4}$	c_l	α_i (deg.)	α_0 (deg.)
-20	-0.582	0.0646	0.016	-0.542	-0.9	-15.1
-16	-.640	-.0659	-.069	-.640	-1.0	-11.0
-12	-.368	-.0407	-.101	-.370	-.6	-7.4
-8	-.182	-.0124	-.099	-.182	-.3	-5.7
-4	-.009	.0045	-.100	-.009	0	-4.0
-2	.170	.0117	-.098	.170	.3	-2.3
0	.360	.0085	-.097	.360	.6	-.6
2	.531	-.0047	-.094	.530	.8	1.2
4	.705	-.0288	-.092	.705	1.1	2.9
8	1.015	-.1026	-.081	1.019	1.6	6.4
12	1.277	-.2014	-.066	1.291	2.0	10.0
16	1.374	-.2672	-.058	1.396	2.2	13.8
18	1.335	-.2768	-.084	1.356	2.2	15.8
20	1.199	-.2284	-.099	1.204	1.9	18.1
24	1.198	-.1138	-.167	1.140	1.8	22.2
30	.950	.0080	-.149	.826	1.3	28.7

TABLE IIc.—INTEGRATED AND DERIVED CHARACTERISTICS

[N. A. C. A. 4412 airfoil; effective Reynolds Number, 450,000]

α (deg.)	c_n	c_e	$c_{m_c/4}$	c_l	α_i (deg.)	α_0 (deg.)
-20	-0.440	0.0912	0.014	-0.383	-0.6	-19.4
-16	-.425	.0844	.023	-.385	-.6	-15.4
-12	-.483	.0655	.013	-.458	-.7	-11.3
-8	-.335	.0051	-.086	-.331	-.5	-7.5
-6	-.172	-.0044	-.102	-.172	-.3	-5.7
-4	.001	.0079	-.103	.002	0	-4.0
-2	.170	.0148	-.099	.171	.3	-2.3
0	.349	.0113	-.096	.349	.6	-.6
2	.520	-.0008	-.093	.520	.8	1.2
4	.704	-.0244	-.092	.704	1.1	2.9
8	1.014	-.0978	-.080	1.018	1.6	6.4
12	1.225	-.1922	-.062	1.239	2.0	10.0
16	1.243	-.2432	-.048	1.261	2.0	14.0
18	1.155	-.1677	-.086	1.152	1.8	16.2
20	1.023	-.0378	-.135	.975	1.5	18.5
24	.906	.0091	-.139	.824	1.3	22.7
30	.948	.0073	-.149	.817	1.3	28.7

TABLE IIe.—INTEGRATED AND DERIVED CHARACTERISTICS

[N. A. C. A. 4412 airfoil; effective Reynolds Number, 3,400,000]

α (deg.)	c_n	c_e	$c_{m_c/4}$	c_l	α_i (deg.)	α_0 (deg.)
-20	-0.713	0.0411	0.028	-0.656	-1.0	-19.0
-16	-.761	.0058	.009	-.730	-1.2	-14.8
-12	-.725	-.1204	-.105	-.734	-1.2	-10.8
-8	-.395	-.0405	-.098	-.397	-.6	-7.4
-6	-.197	-.0128	-.096	-.194	-.3	-5.7
-4	-.031	.0030	-.095	-.031	0	-4.0
-2	.148	.0104	-.094	.148	.2	-2.2
0	.341	.0086	-.094	.341	.5	-.5
2	.521	-.0040	-.089	.520	.8	1.2
4	.691	-.0253	-.090	.692	1.1	2.9
8	.994	-.0933	-.078	.997	1.6	6.4
12	1.275	-.2034	-.060	1.290	2.0	10.0
16	1.456	-.3171	-.059	1.488	2.4	13.6
18	1.547	-.3585	-.079	1.581	2.5	15.5
20	1.470	-.3292	-.119	1.495	2.4	17.6
24	1.165	-.1408	-.150	1.121	1.8	22.2
30	1.150	-.1015	-.160	1.046	1.7	28.3

TABLE IIg.—INTEGRATED AND DERIVED CHARACTERISTICS

[N. A. C. A. 4412 airfoil; effective Reynolds Number, 6,300,000]

α (deg.)	c_n	c_c	$c_{m_c/4}$	c_l	α_i (deg.)	α_0 (deg.)
-20	-0.869	-0.0497	0.026	-0.849	-1.3	-14.7
-16	-0.712	-0.1245	-0.103	-0.722	-1.1	-10.9
-12	-0.410	-0.0417	-0.089	-0.412	-0.7	-7.3
-8	-0.209	-0.0155	-0.094	-0.210	-0.3	-5.7
-4	-0.036	0.0029	-0.093	-0.036	0	-4.0
-2	0.157	0.0118	-0.092	0.157	0.2	-2.2
0	0.333	0.0079	-0.091	0.333	0.5	-0.5
2	0.501	-0.0034	-0.087	0.500	0.8	1.2
4	0.674	-0.0256	-0.086	0.674	1.1	2.9
8	1.002	-0.0998	-0.080	1.006	1.6	6.4
12	1.300	-0.2126	-0.073	1.315	2.1	9.9
16	1.550	-0.3410	-0.064	1.584	2.5	13.5
18	1.633	-0.4020	-0.067	1.678	2.7	15.3
20	1.605	-0.4425	-0.061	1.661	2.6	17.4
24	1.300	-0.2329	-0.143	1.283	2.0	22.0
30	1.111	-0.1019	-0.171	1.014	1.6	28.4

TABLE IIh.—INTEGRATED AND DERIVED CHARACTERISTICS

[N. A. C. A. 4412 airfoil; effective Reynolds Number, 8,200,000]

α (deg.)	c_n	c_c	$c_{m_c/4}$	c_l	α_i (deg.)	α_0 (deg.)
-20	-0.592	0.0318	0.030	-0.545	-0.9	-19.1
-16	-0.767	-0.0170	0.035	-0.742	-1.2	-14.8
-12	-0.722	-0.1264	-0.092	-0.732	-1.2	-10.8
-8	-0.372	-0.0445	-0.096	-0.374	-0.6	-7.4
-6	-0.210	-0.0151	-0.096	-0.211	-0.3	-5.7
-4	-0.026	0.0043	-0.095	-0.026	0	-4.0
-2	0.146	0.0107	-0.092	0.146	0.2	-2.2
0	0.338	0.0098	-0.091	0.338	0.5	-0.5
2	0.501	-0.0034	-0.087	0.501	0.8	1.2
4	0.677	-0.0258	-0.087	0.677	1.1	2.9
8	1.020	-0.1003	-0.084	1.024	1.6	6.4
12	1.275	-0.2043	-0.074	1.289	2.0	10.0
16	1.548	-0.3357	-0.068	1.579	2.5	13.5
18	1.626	-0.4040	-0.063	1.671	2.6	15.4
20	1.640	-0.4374	-0.080	1.690	2.7	17.3
24	1.212	-0.1838	-0.141	1.182	1.9	22.1
30	1.009	-0.0776	-0.146	0.913	1.4	28.6

REPORT No. 614

PRESSURE DISTRIBUTION OVER AN N. A. C. A. 23012 AIRFOIL WITH AN N. A. C. A. 23012 EXTERNAL-AIRFOIL FLAP

By CARL J. WENZINGER

SUMMARY

Pressure-distribution tests of an N. A. C. A. 23012 airfoil with an N. A. C. A. 23012 external-airfoil flap were made in the 7- by 10-foot wind tunnel. The pressures were measured on the upper and lower surfaces at one chord section on both the main airfoil and on the flap for several different flap deflections and at several angles of attack. A test installation was used in which the airfoil was mounted horizontally in the wind tunnel between vertical end planes so that two-dimensional flow was approximated.

The data are presented in the form of pressure-distribution diagrams and as graphs of calculated coefficients for the airfoil-and-flap combination and for the flap alone. The pressure-distribution tests showed that, as with other types of flap, the greater part of the increment of total maximum lift due to deflecting the external-airfoil flap downward arises from the increased load carried by the main airfoil. The maximum normal-force coefficient of the external-airfoil flap was about the same as that of a split flap. The hinge moments, however, were much lower because of the axis location used with the external-airfoil flap. The pressure diagrams showed that, when the plain airfoil and the flapped airfoil are compared at the same total lift, the flap reduces the adverse pressure gradients and the tendency of the main airfoil to stall. When the plain and flapped airfoils are compared at the same angle of attack, it is apparent that the flap influences the air flow around the main airfoil so that the airfoil carries a much greater load without stalling than is possible without the flap.

INTRODUCTION

The external-airfoil flap in combination with a main airfoil appears to be one of the most generally satisfactory high-lift devices investigated up to the present time. Previous investigations of this arrangement (references 1, 2, and 3) have shown that it is capable of developing high lift coefficients and that it gives lower drag at these high lift coefficients than do plain or split flaps.

Several different combinations of airfoil section for

both the main airfoil and the flap have been investigated; the most promising arrangement thus far obtained has the N. A. C. A. 23012 section for both main airfoil and flap. In addition, a survey of the flap hinge-axis location has been made (reference 2) to obtain one that would give low flap-operating moments and good aerodynamic characteristics.

In order to complete the information required for structural-design purposes, pressure-distribution tests were made to obtain the air-load distribution over the main airfoil and flap. The combination tested has the N. A. C. A. 23012 section for both main airfoil and flap and uses the hinge axis previously developed for this flap.

APPARATUS AND TESTS

MODEL

The main airfoil was built of laminated mahogany to the N. A. C. A. 23012 profile and has a span and chord each of 20 inches. The external-airfoil flap was built of brass, also to the N. A. C. A. 23012 profile, and has a span of 20 inches and a chord of 4 inches (20 percent of the main airfoil chord). The flap was supported on the main airfoil by metal fittings at each end and by two intermediate fittings spaced equally along the span. The flap hinge axis (see fig. 1) was that previously developed as described in reference 2, the flap being arranged for locking at any desired deflection between -10° and 60° .

A main row of pressure orifices was built into the upper and lower surfaces of both the main airfoil and the external-airfoil flap at the midspan section. These orifices were located on the model as tabulated in figure 1, the tubes from the orifices being brought through the model and out at one end. The pressures were photographically recorded by a multiple-tube manometer.

Two auxiliary rows of pressure orifices were also built into the upper and lower surfaces of only the main airfoil, one row being located 2 inches and the other row $\frac{1}{2}$ inch from the end. These orifices, together with those at the midspan location, were used incidentally to measure the distribution of pressures along the span of the model between end planes for a few conditions.

TEST INSTALLATION

The model was mounted in the N. A. C. A. 7- by 10-foot open-jet wind tunnel (reference 4) as shown by figure 2. The main airfoil was rigidly attached to two large circular end plates to which the flap was also fastened but arranged to rotate so that its setting might be changed. The two end plates were supported in

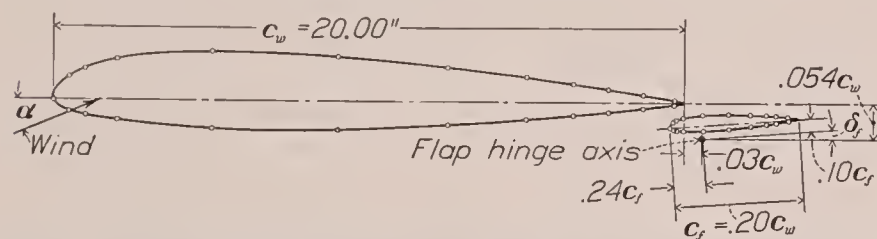


FIGURE 1.—Cross section of model showing orifice locations used in pressure-distribution tests. N. A. C. A. 23012 airfoil with 0.20 c_w 23012 external-airfoil flap.

Orifice	Location from leading edge—	
	Of wing (fractions c_w)	Of flap (fractions c_f)
0	0.000	0.000
1	.024	.025
2	.050	.050
3	.100	.100
4	.250	.250
5	.450	.450
6	.625	.625
7	.750	.750
8	.825	.825
9	.881	.925
10	.936	
11	.986	

circular cut-outs in two large vertical end planes that extended from top to bottom of the air stream and some distance ahead of and behind the model. The angle of attack of the model was set by rotating the large circular plates and locking them at the desired angle. Approximately two-dimensional flow is obtained with this type of installation and the section characteristics of the model under test may be determined.

TESTS

The tests were all carried out at a dynamic pressure of 16.37 pounds per square foot, corresponding to an air speed of 80 miles per hour at standard sea-level conditions. The average test Reynolds Number, based on the sum of the main airfoil and flap chords, was 1,460,000. This test Reynolds Number, when converted to an effective Reynolds Number (reference 5) that takes account of the turbulence in the air stream, is 2,040,000. (Effective Reynolds Number = test Reynolds Number \times turbulence factor; turbulence factor for the tunnel is 1.4.)

The model was tested with the external-airfoil flap set at angles of -3° , 0° , 10° , 20° , 30° , and 40° . The main airfoil was also tested by itself without the flap for purposes of comparison. The angles of attack ranged from -16° to 16° and the lift coefficients included those from approximately maximum negative to maximum positive. With the model at a given angle of attack and with a given flap setting, a few minutes were allowed for all test conditions to become steady; a

record was then taken of the pressures at the orifices by means of the photographic manometer.

PRESENTATION OF DATA

PRESSURE DIAGRAMS

Diagrams of the pressures over the upper and lower surfaces of the main airfoil without flap (fig. 3) are given as ratios of orifice pressure p to dynamic pressure of the air stream q for the angles of attack investigated.

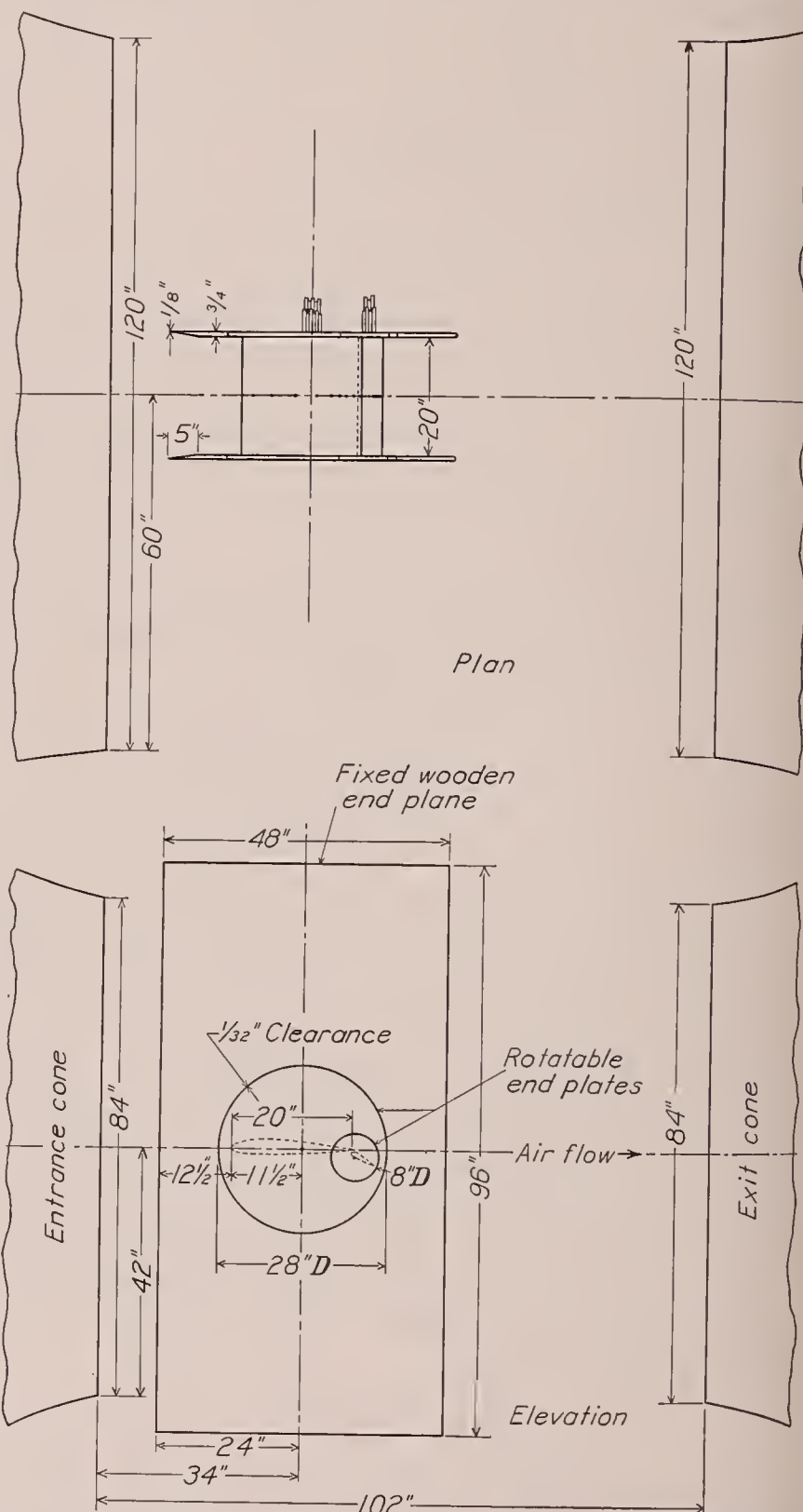


FIGURE 2.—Diagram of model with external-airfoil flap installed between end planes in the 7- by 10-foot wind tunnel.

Pressure diagrams for the combination of main airfoil with external-airfoil flap are given in figures 4 to 11 for the various flap deflections and angles of attack tested. On the diagrams the pressures are plotted normal to the main-airfoil chord and to the flap chord, the pressure values being measured from the main chord for the main-airfoil pressures and from the flap chord for the flap pressures.

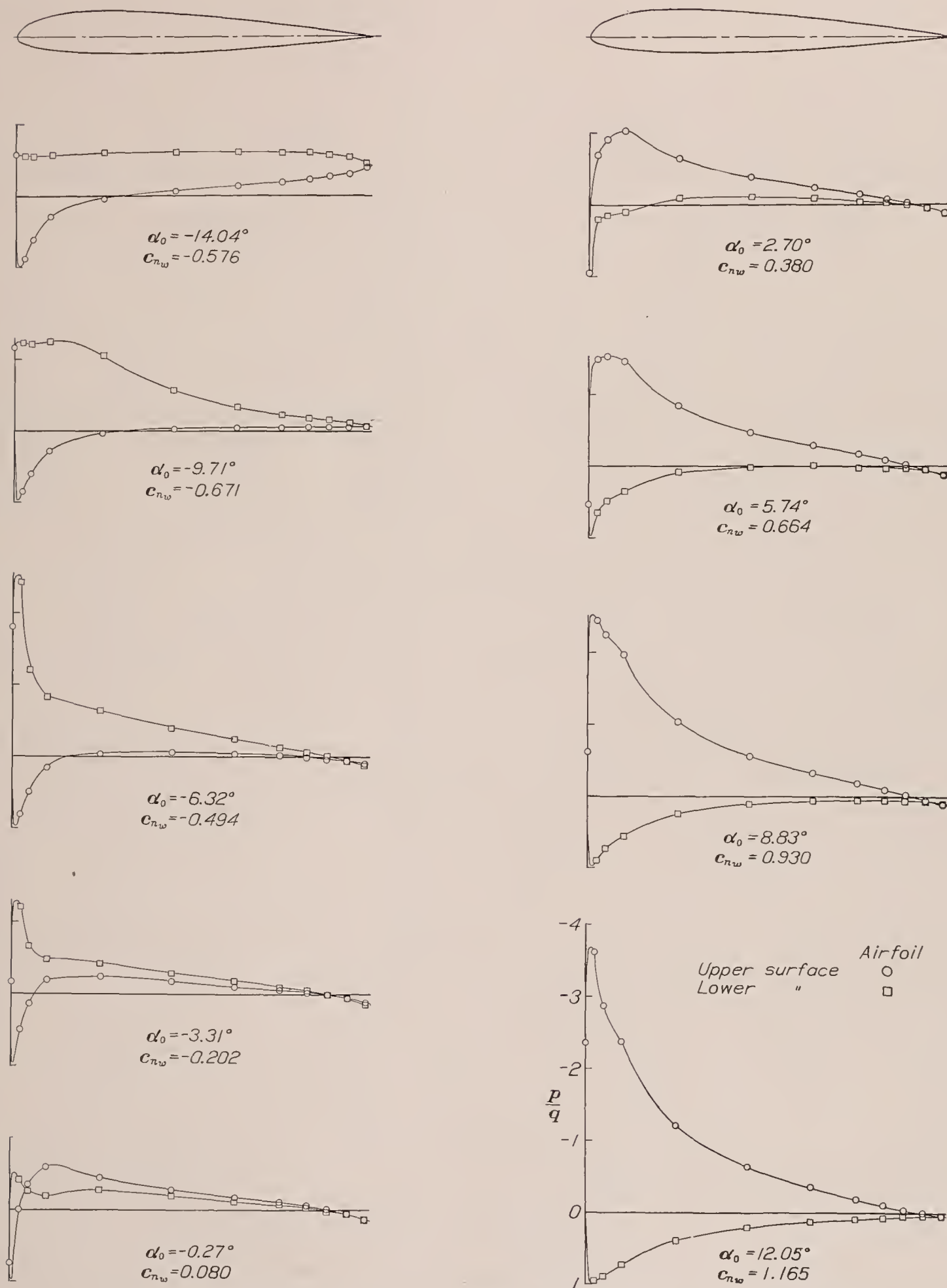


FIGURE 3.—Pressure distribution on the N. A. C. A. 23012 main airfoil without flaps at various angles of attack.

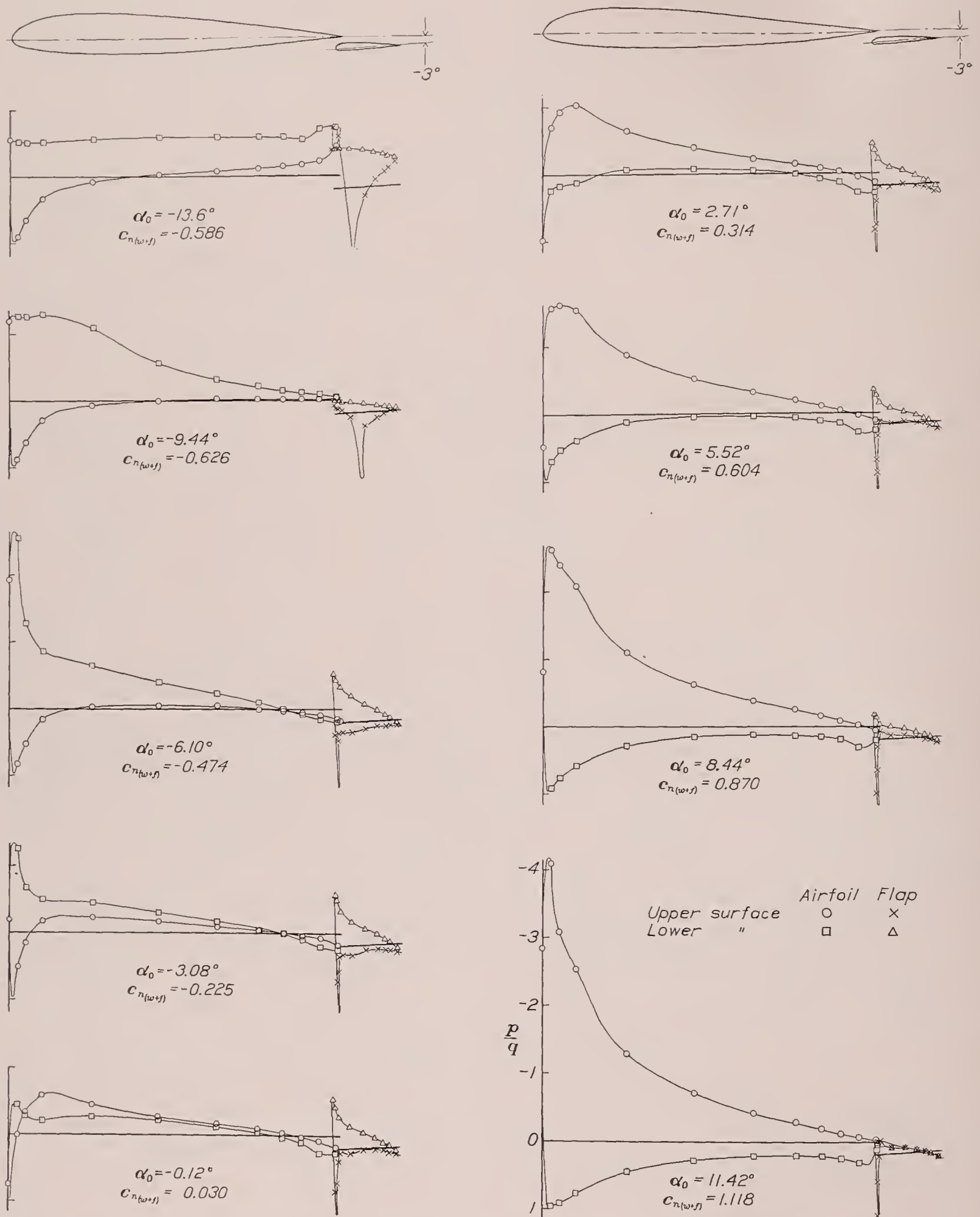


FIGURE 4.—Pressure distribution on the N. A. C. A. 23012 airfoil with N. A. C. A. 23012 external-airfoil flap at various angles of attack. Flap deflected -3° .

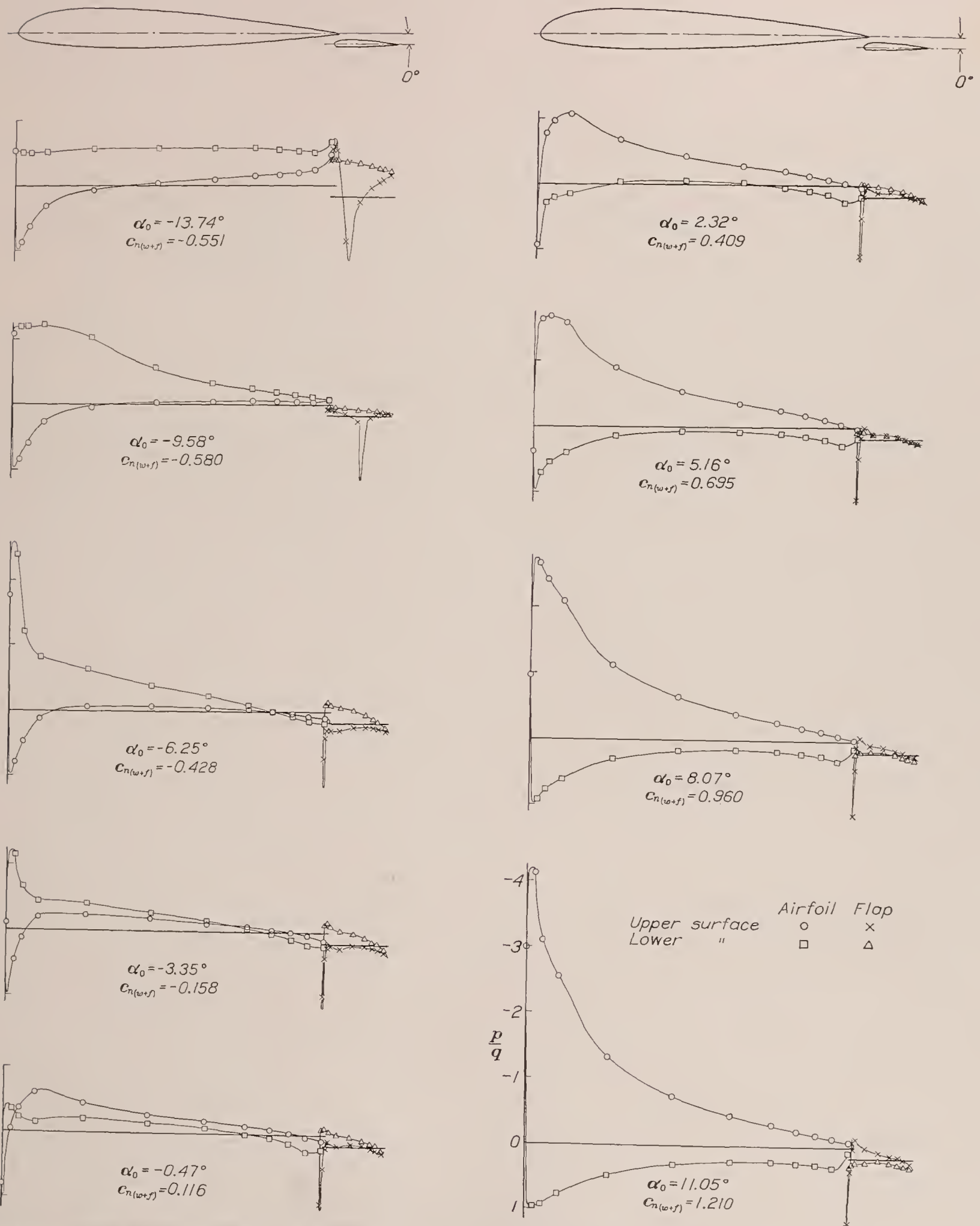


FIGURE 5.—Pressure distribution on the N. A. C. A. 23012 airfoil with N. A. C. A. 23012 external-airfoil flap at various angles of attack. Flap deflected 6°.

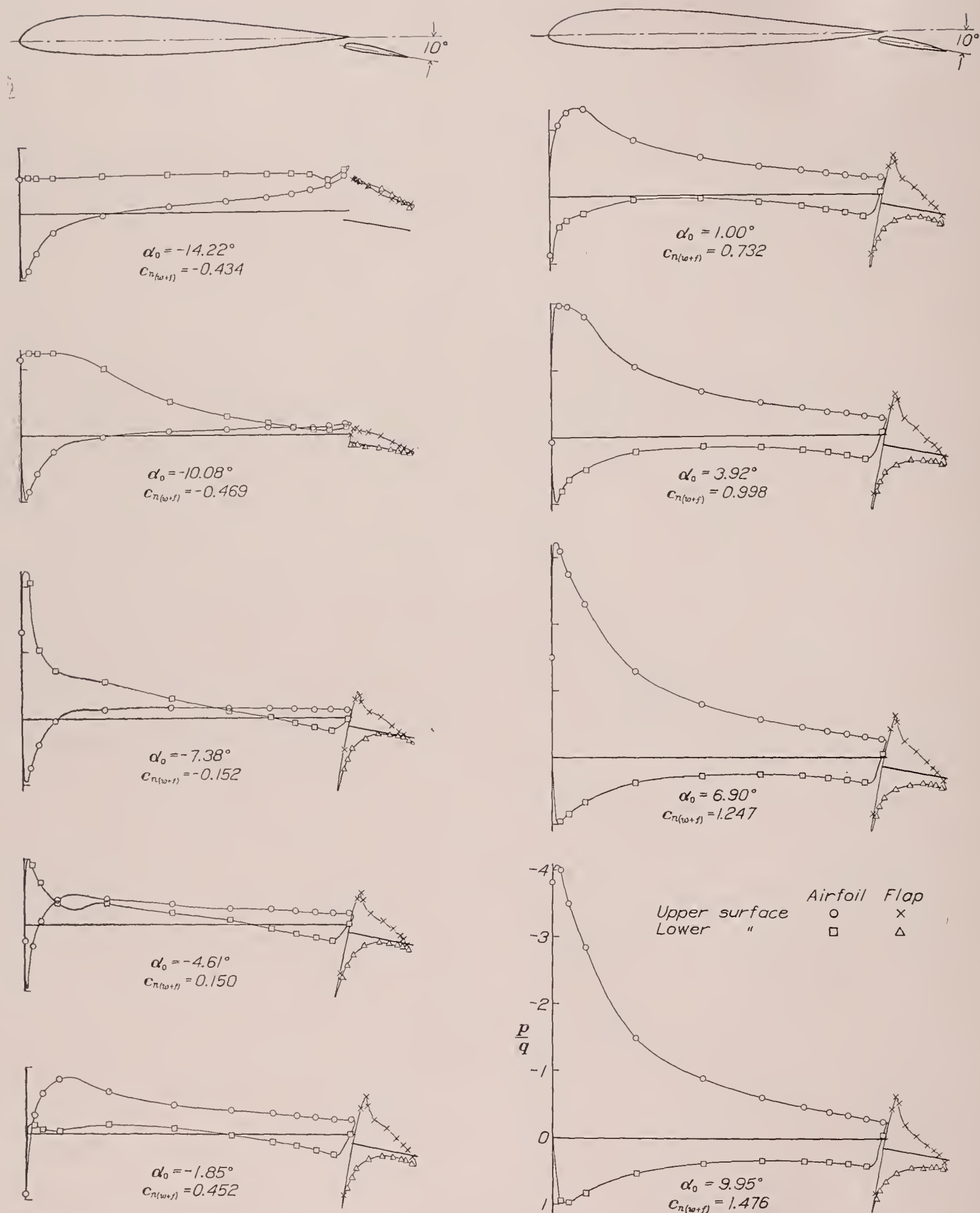
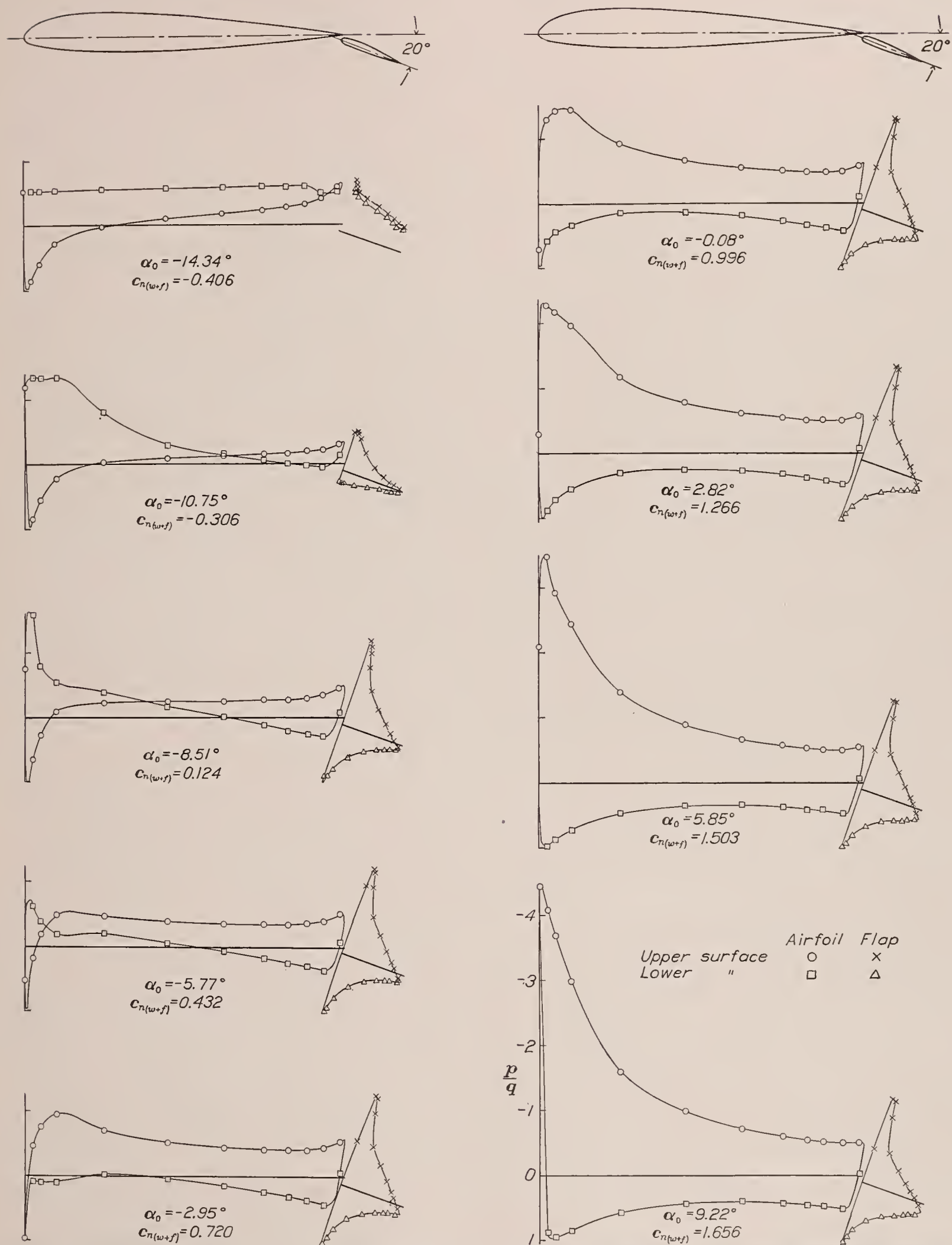


FIGURE 6.—Pressure distribution on the N. A. C. A. 23012 airfoil with N. A. C. A. 23012 external-airfoil flap at various angles of attack. Flap deflected 10°.

FIGURE 7.—Pressure distribution on the N. A. C. A. 23012 airfoil with N. A. C. A. 23012 external-airfoil flap at various angles of attack. Flap deflected 20° .

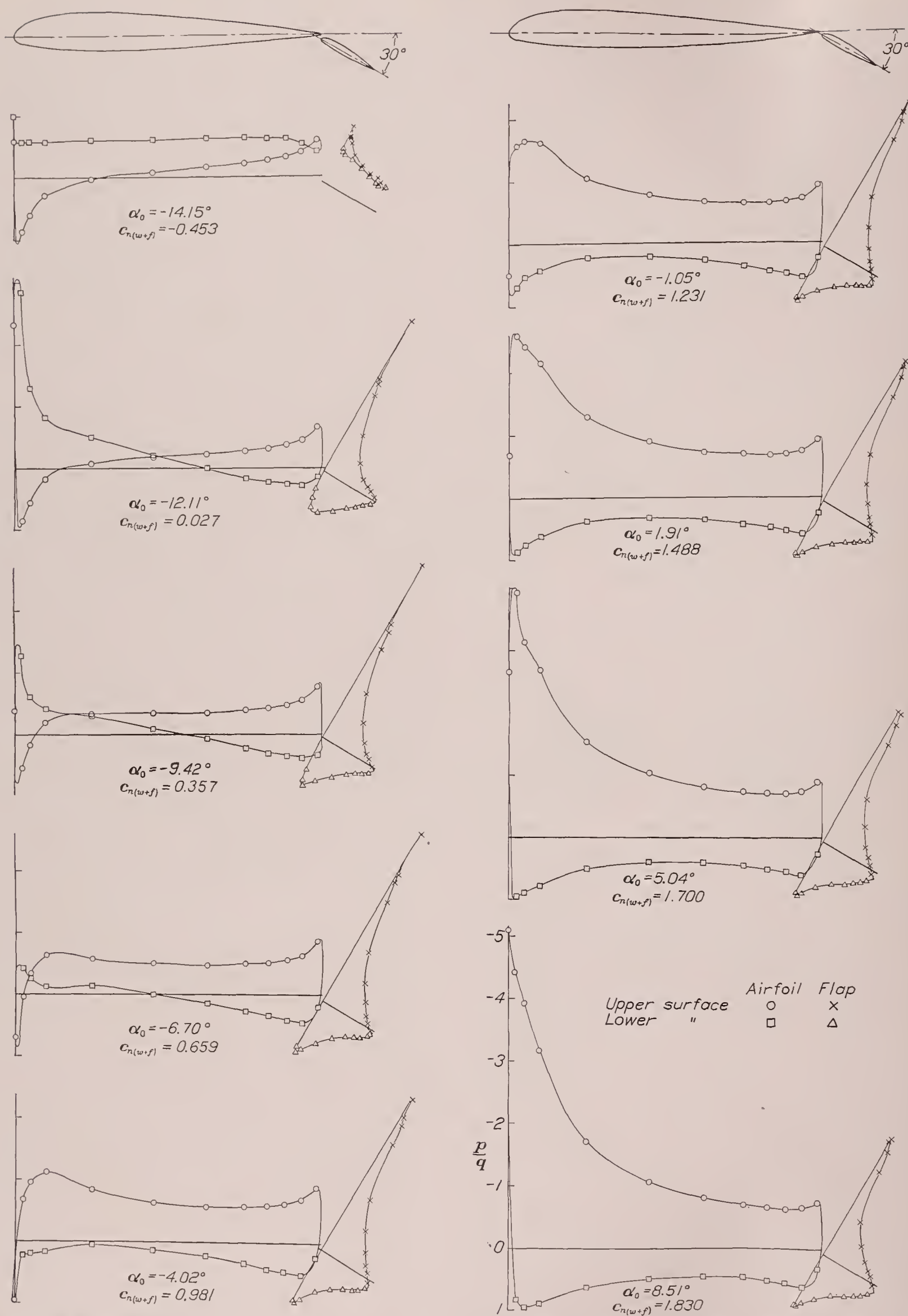


FIGURE 8.—Pressure distribution on the N. A. C. A. 23012 airfoil with N. A. C. A. 23012 external-airfoil flap at various angles of attack. Flap deflected 30° .

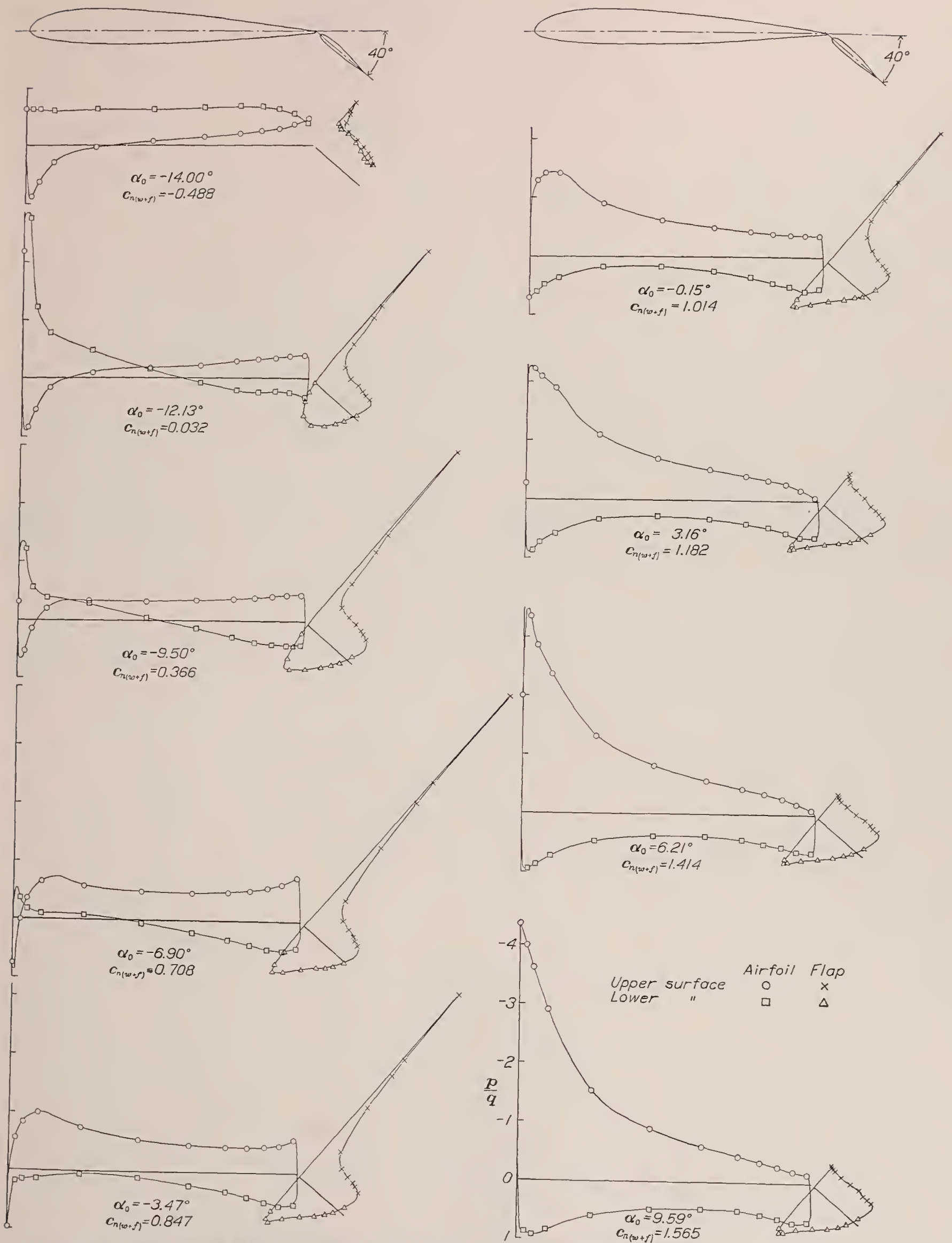


FIGURE 9.—Pressure distribution on the N. A. C. A. 23012 airfoil with N. A. C. A. 23012 external-airfoil flap at various angles of attack. Flap deflected 40°.

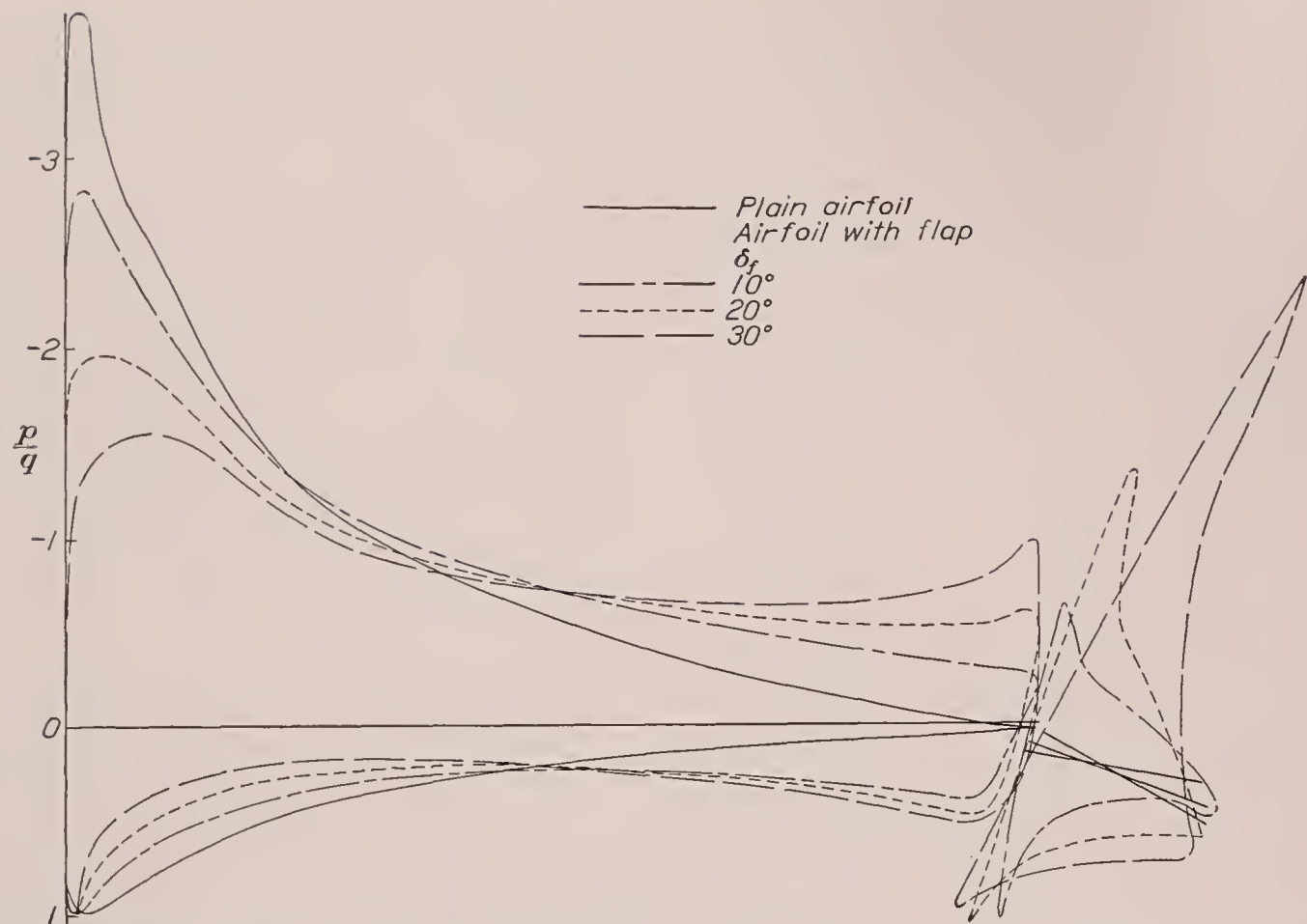


FIGURE 10.—Comparison of the pressure distribution on an N. A. C. A. 23012 airfoil with a $0.20c_w$ external-airfoil flap with that on the plain airfoil at the same lift, $c_n=1.165$.

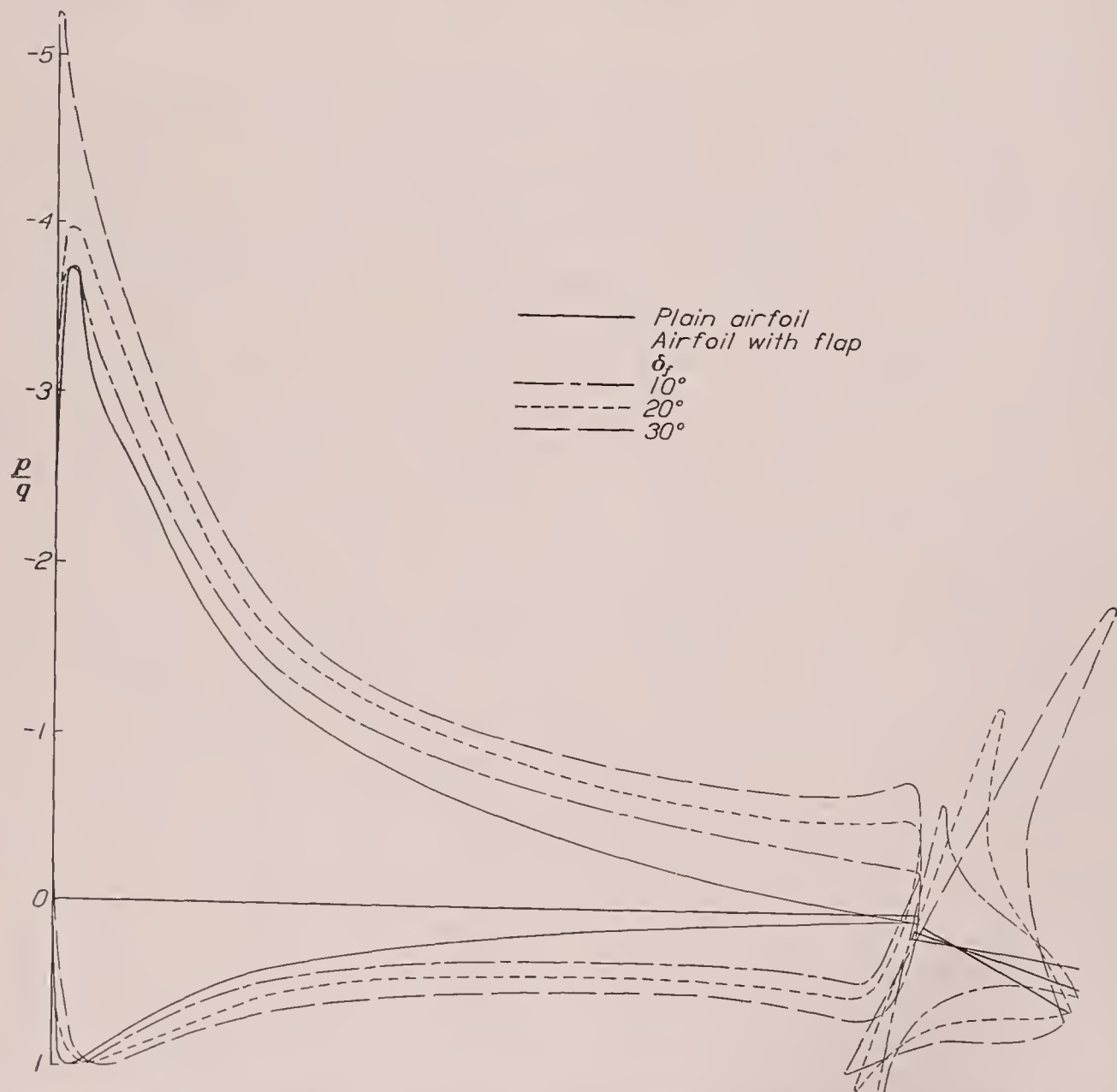


FIGURE 11.—Comparison of the pressure distribution on an N. A. C. A. 23012 airfoil with a $0.20c_w$ external-airfoil flap with that on the plain airfoil at the same angle of attack, $\alpha_0=8.5^\circ$.

COEFFICIENTS

The pressure diagrams were mechanically integrated to obtain data from which section coefficients could be computed. The section coefficients are defined as follows:

$$c_{n_w} = \frac{n_w}{qc_w}, \text{ normal-force coefficient of main airfoil alone.}$$

$$c_{n_{(w+f)}} = \frac{n_{(w+f)}}{qc_{(w+f)}}, \text{ normal-force coefficient of main airfoil with flap.}$$

$$c_{m_w} = \frac{m_w}{qc_w^2}, \text{ pitching-moment coefficient of main airfoil alone about quarter-chord point.}$$

$$c_{m_{(w+f)}} = \frac{m_{(w+f)}}{qc_{(w+f)}^2}, \text{ pitching-moment coefficient of main airfoil with flap about quarter-chord point of combination.}$$

$$c_{n_f} = \frac{n_f}{qc_f}, \text{ normal-force coefficient of flap.}$$

$$c_{h_f} = \frac{h_f}{qc_f^2}, \text{ hinge-moment coefficient of flap about hinge axis.}$$

$$(c.p.)_w = \left(0.25 - \frac{c_{m_w}}{c_{n_w}}\right) \times 100, \text{ center of pressure of main airfoil alone in percentage of chord from leading edge.}$$

$$(c.p.)_{(w+f)} = \left(0.25 - \frac{c_{m_{(w+f)}}}{c_{n_{(w+f)}}}\right) \times 100, \text{ center of pressure of main airfoil with flap in percentage of chord of combination from leading edge.}$$

$$(c.p.)_f = \left(0.25 - \frac{c_{h_f}}{c_{n_f}}\right) \times 100, \text{ center of pressure of flap in percentage of flap chord from leading edge.}$$

where the forces and moments per unit span are

n_w , normal force of main airfoil.

$n_{(w+f)}$, normal force of main airfoil with flap.

m_w , pitching moment of main airfoil about quarter-chord point.

$m_{(w+f)}$, pitching moment of main airfoil with flap about quarter-chord point of combination.

n_f , normal force of flap.

h_f , hinge moment of flap about hinge axis.

and

q , dynamic pressure.

c_w , main-airfoil chord.

c_f , flap chord.

$c_{(w+f)}$ chord of combination ($c_w + c_f$).

The center-of-pressure positions and the pitching-moment coefficients were derived from the normal forces, the chord forces being neglected except for the effect of the flap, in which case the flap deflection was taken into account.

The calculated results from the present tests were all corrected to infinite aspect ratio characteristics in accordance with methods given by Glauert (reference 6) that have been found satisfactory from other tests of a similar arrangement in the 7- by 10-foot wind tunnel (reference 7). Another check on the theoretical cor-

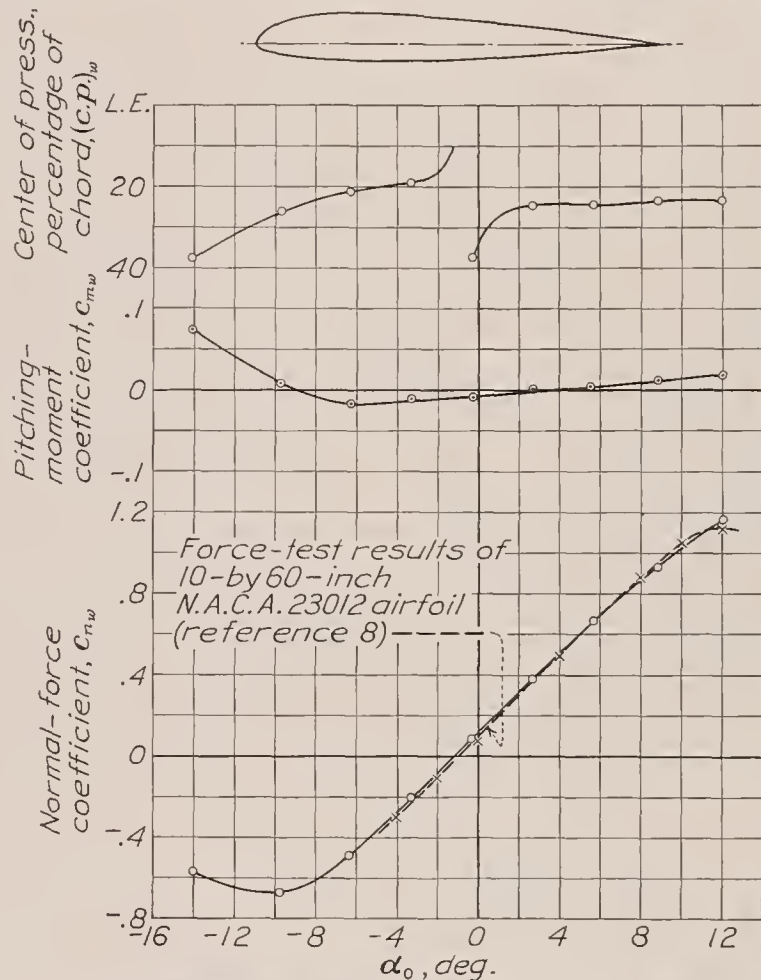


FIGURE 12.—Section characteristics of the plain N. A. C. A. 23012 airfoil.

rection is shown in figure 12, where the corrected results of the pressure-distribution tests are compared with force-test results (reference 8) for a 10- by 60-inch N. A. C. A. 23012 plain wing corrected to infinite aspect ratio by the usual methods.

For the case of the pressure-distribution tests

$$\alpha_0 = \alpha + \Delta\alpha$$

where

$$\Delta\alpha(\text{deg.}) = -\left(0.25 \frac{c}{h} c_n\right) \times 57.3$$

c is the total chord.

h , the height of the jet.

(The quantity c_n is substituted for C_L in the present correction and the substitution results in only a slight error because of the small difference in value between the two quantities.) Curves of the various calculated coefficients are given in figures 12 to 18.

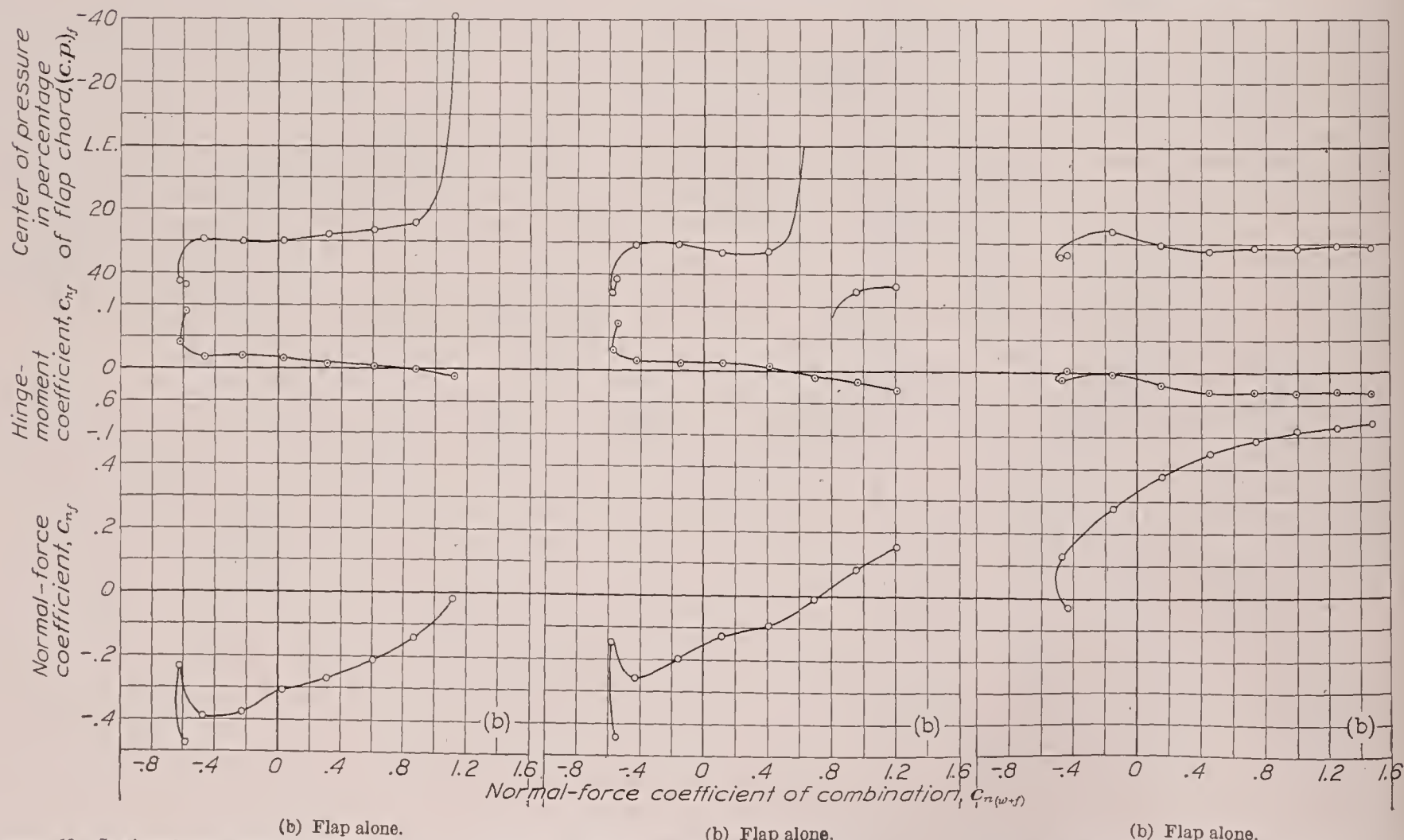
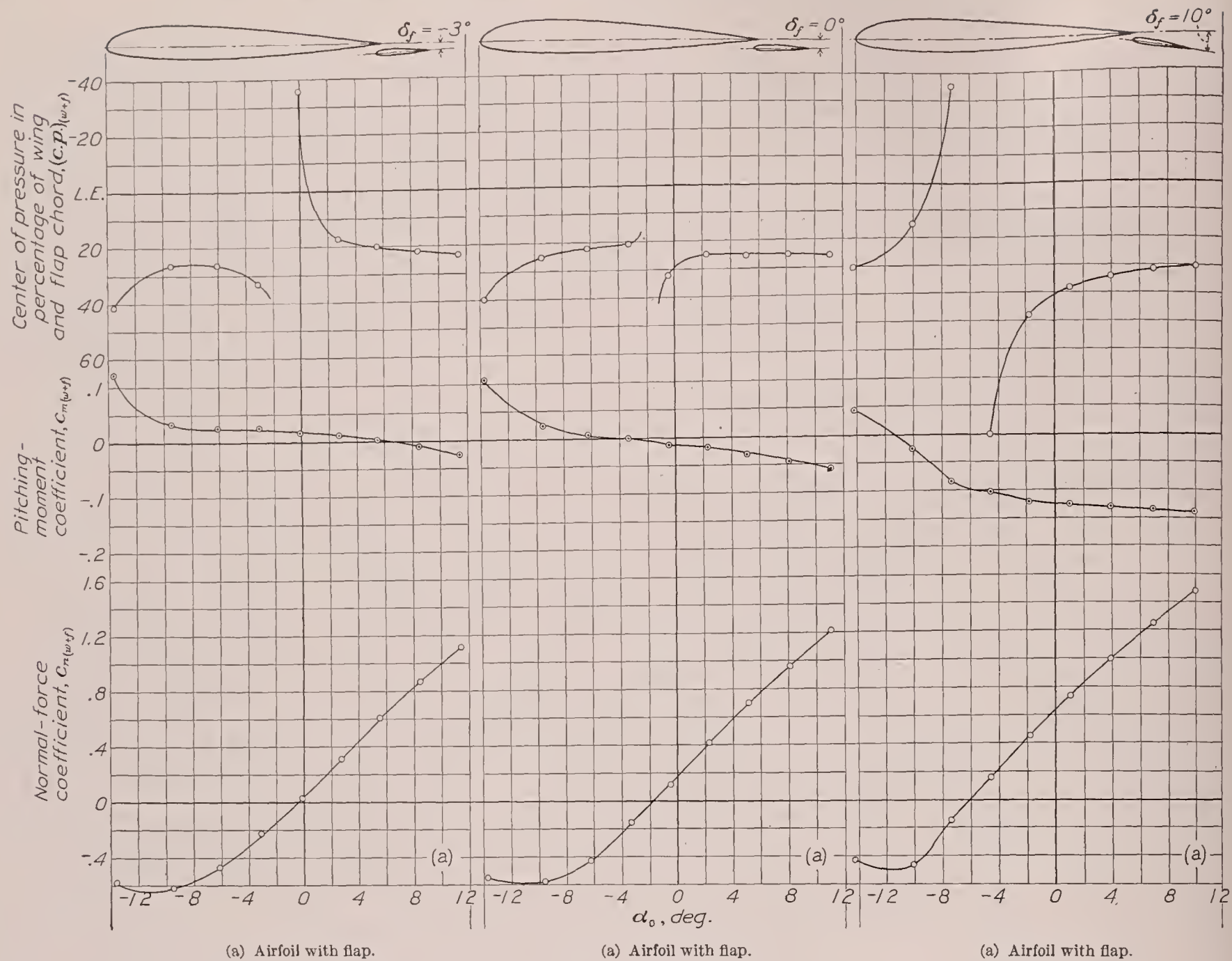
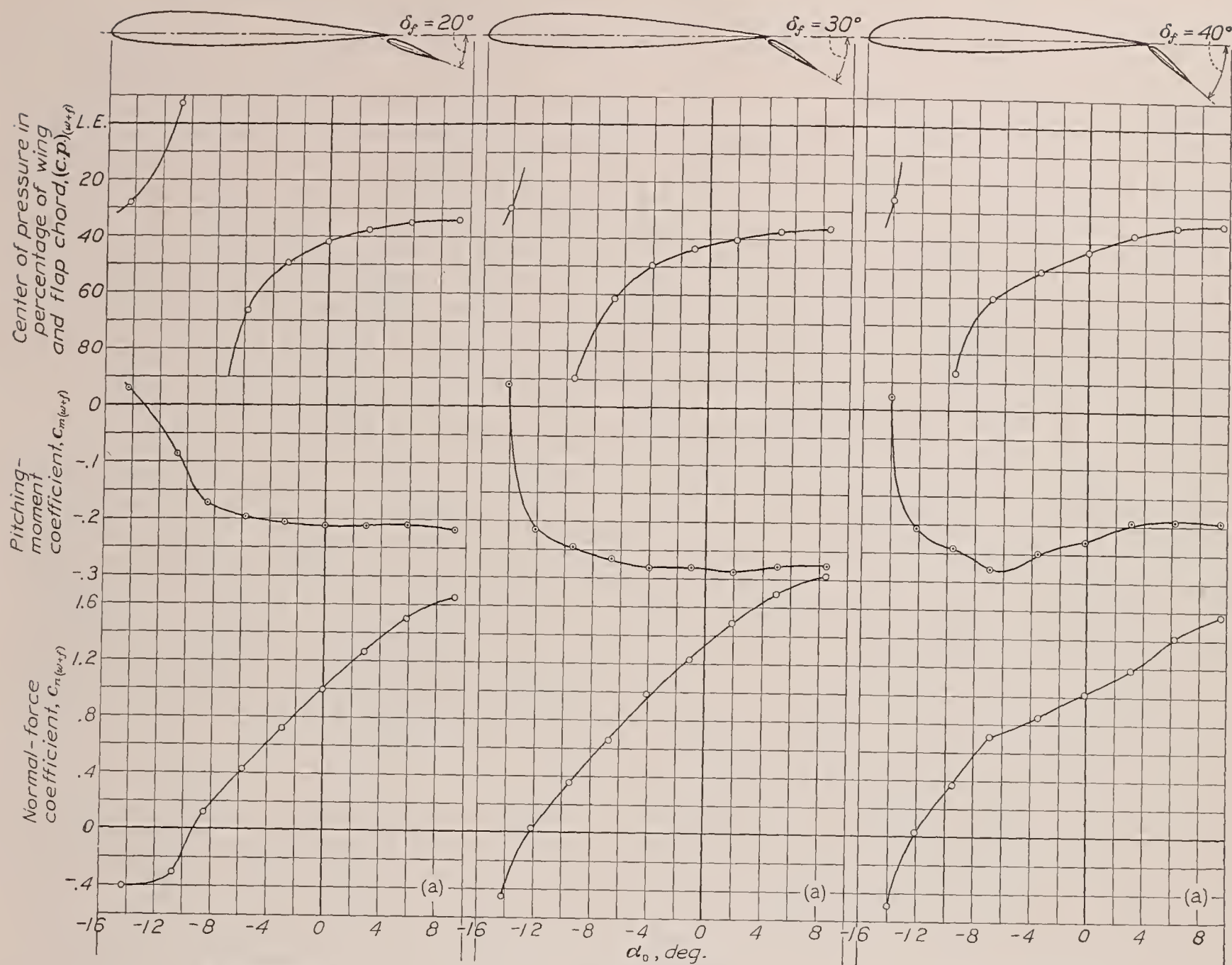


FIGURE 13.—Section characteristics of the N. A. C. A. 23012 airfoil with a 0.20c_w N. A. C. A. 23012 external-airfoil flap set at -3°.

FIGURE 14.—Section characteristics of the N. A. C. A. 23012 airfoil with a 0.20c_w N. A. C. A. 23012 external-airfoil flap set at 0°.

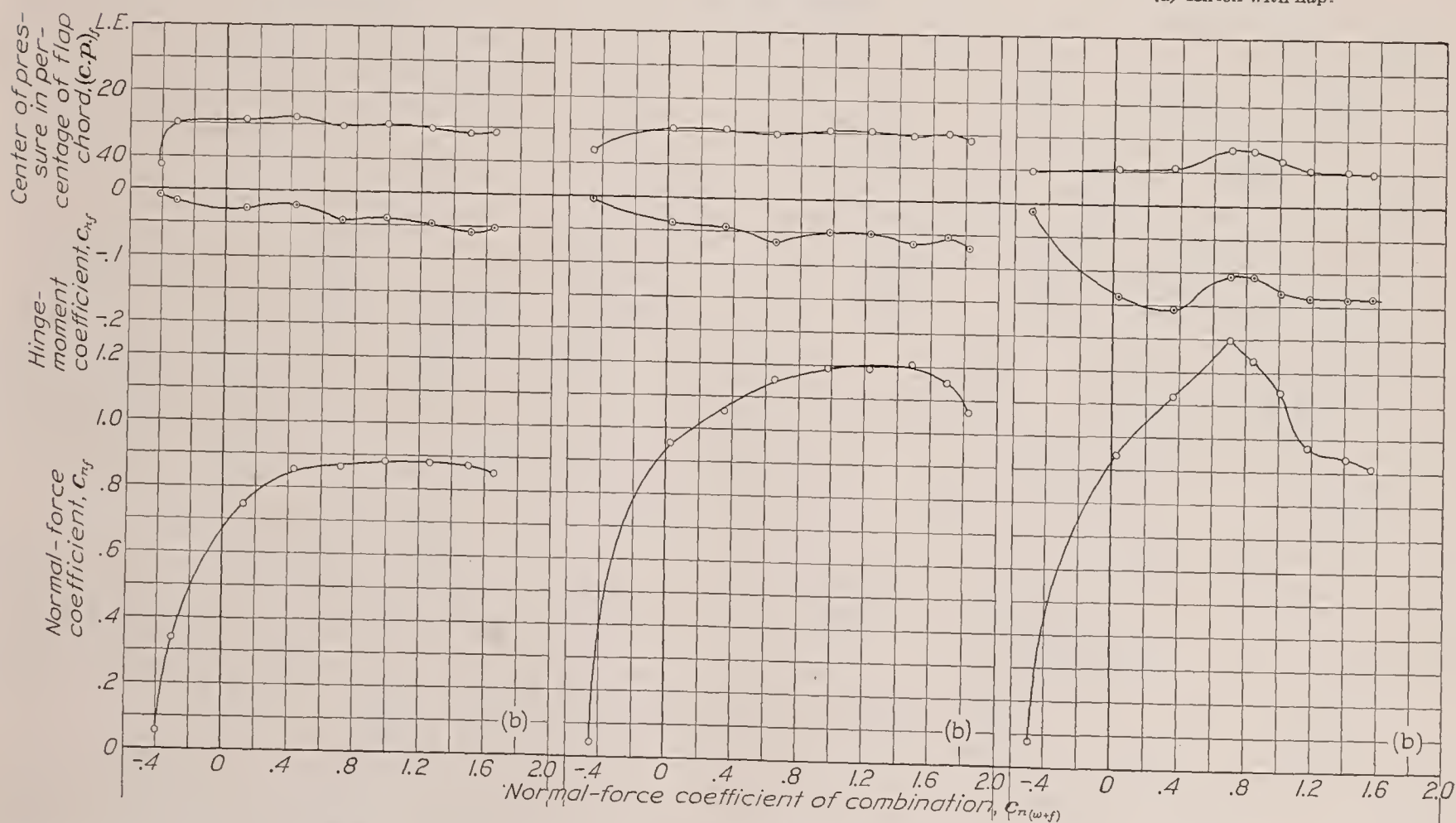
FIGURE 15.—Section characteristics of the N. A. C. A. 23012 airfoil with a 0.20c_w N. A. C. A. 23012 external-airfoil flap set at 10°.



(a) Airfoil with flap.

(a) Airfoil with flap.

(a) Airfoil with flap.



(b) Flap alone.

(b) Flap alone.

(b) Flap alone.

FIGURE 16.—Section characteristics of the N. A. C. A. 23012 airfoil with a 0.20c_w N. A. C. A. 23012 external-airfoil flap set at 20°.FIGURE 17.—Section characteristics of the N. A. C. A. 23012 airfoil with a 0.20c_w N. A. C. A. 23012 external-airfoil flap set at 30°.FIGURE 18.—Section characteristics of the N. A. C. A. 23012 airfoil with a 0.20c_w N. A. C. A. 23012 external-airfoil flap set at 40°.

PRECISION

No air-flow alinement tests were made in the wind tunnel with the test arrangement used in the investigation, so the absolute setting of the angle of attack may be slightly in error; the relative angles are, however, accurate to $\pm 0.1^\circ$. The flap deflections were set to the specified angles to within $\pm 0.1^\circ$. The orifice pressures based on check tests in which both the angle of attack and the flap settings were independently changed showed that they agreed to within ± 2 percent, with the exception of upper-surface pressures near the leading edges, which, at high angles of attack, checked to within ± 5 percent. The dynamic pressure recorded on each diagram was accurate to within ± 0.25 percent for all tests.

The distribution of pressures along the span of the model indicated that two-dimensional flow was obtained with the installation used. The pressures, for a given location along the chord of the airfoil, were the same from midspan to within at least $\frac{1}{2}$ inch of the ends (the row of orifices nearest the end of the model).

RESULTS AND DISCUSSION

SECTION PRESSURE DISTRIBUTION

The pressure-distribution diagrams (figs. 3 to 9) are useful to show the chordwise distribution of the air loads on the main airfoil and on the flap and may be regarded as satisfactory for application to rib and flap design. The diagrams also illustrate certain special features of the action of external-airfoil flaps.

Comparison of pressure diagrams for the plain airfoil and for the airfoil-flap combination at the *same lift* (fig. 10) shows the effect of the flap. Increasing the flap angle and decreasing the angle of attack to maintain constant lift had the following effects: (1) The magnitudes of the peak pressures at the leading edge of the main airfoil were progressively reduced, and (2) the magnitudes of both positive and negative pressures at the trailing edge of the main airfoil and at the leading edge of the flap were progressively increased.

The flap, in addition, obstructed the flow of air below the airfoil and caused the pressures to build up on the lower surface. The air flowing through the slot over the upper surface of the flap produced a higher average velocity and increased the negative pressure on the flap upper surface. Thus, the influence of the flap was to reduce the adverse pressure gradients and the tendency of the main airfoil to stall.

The external-airfoil flap itself had a pressure distribution similar to that of a plain airfoil, so that the flap would have a small wake as long as it remained unstalled. The wake of the combination would therefore be small, particularly near the stall; this small wake permitted the development of high lift together with low profile drag. In this respect slotted flaps, in general, appear better than plain or split flaps.

Comparison of pressure diagrams for the plain airfoil and for the airfoil-flap combination at the *same angle of attack* (fig. 11) shows that the flap increased the negative pressure over the entire upper surface of the main airfoil and increased the positive pressure on the lower surface near the trailing edge. The pressure gradients remained about the same except at the trailing edge of the main airfoil, where they were reduced. The pressures on the upper and the lower surfaces of the flap both increased with flap deflection. The important effect of the flap in this case was its ability to influence the air flow around the main airfoil so that the airfoil carried a much greater load without stalling than was possible without the flap.

One other interesting item is suggested by the progressive increase in flow velocity over the main-airfoil upper surface relative to free-stream velocity as the flap is deflected. This characteristic suggested that the use of this type of flap would increase the rolling effectiveness of ailerons located on the trailing edge of the main airfoil. An investigation of such an arrangement (reference 3) recently completed in the N. A. C. A. 7-by 10-foot wind tunnel indicated that such an improvement could be realized.

SECTION LOADS AND MOMENTS

The section coefficients are plotted in figures 12 to 18. It will be noted that the flap loads build up rapidly at relatively low lifts of the combination and that they also increase rapidly with flap deflection (figs. 13 to 18). The maximum flap loads appear, in general, to reach somewhat higher values than are obtained with an airfoil of the same size tested alone at the appropriate Reynolds Number. (Test Reynolds Number for flap alone based on flap chord and free-stream velocity = 244,000.) The greater part of the increment of total $c_{n_{max}}$ due to deflecting the flap downward, however, arises from the increased load carried by the main airfoil.

It is interesting to note that the maximum normal-force coefficient of the external-airfoil flap tested has about the same value as that attained by split flaps in a previous investigation (reference 9). Owing to the use of the hinge axis chosen, however, the hinge moments of the external-airfoil flap are much smaller than those of corresponding sizes of split flap.

CONCLUSIONS

1. Pressure-distribution tests show that, as with other types of flap, the greater part of the increment of total maximum lift due to deflecting the external-airfoil flap downward arises from the increased load carried by the main airfoil.

2. The maximum normal-force coefficient of the external-airfoil flap investigated had about the same value as that attained by split flaps. The hinge mo-

ments, however, were much lower because of the axis location used with the external-airfoil flap.

3. The pressure diagrams showed that, when the plain airfoil and the airfoil with the external-airfoil flap were compared at the *same total lift*, the flap reduced the adverse pressure gradients and the tendency of the main airfoil to stall. When these plain and flapped airfoils were compared at the *same angle of attack*, it was apparent that the flap influenced the air flow around the main airfoil so that the airfoil carried a much greater load without stalling than was possible without the flap.

LANGLEY MEMORIAL AERONAUTICAL LABORATORY,
NATIONAL ADVISORY COMMITTEE FOR AERONAUTICS,
LANGLEY FIELD, VA., *July 29, 1937.*

REFERENCES

1. Platt, Robert C.: Aerodynamic Characteristics of Wings with Cambered External-Airfoil Flaps, Including Lateral Control with a Full-Span Flap. T. R. No. 541, N. A. C. A., 1935.
2. Platt, Robert C., and Abbott, Ira H.: Aerodynamic Characteristics of N. A. C. A. 23012 and 23021 Airfoils with 20-Percent-Chord External-Airfoil Flaps of N. A. C. A. 23012 Section. T. R. No. 573, N. A. C. A., 1936.
3. Platt, Robert C., and Shortal, Joseph A.: Wind-Tunnel Investigation of Wings with Ordinary Ailerons and Full-Span External-Airfoil Flaps. T. R. No. 603, N. A. C. A., 1937.
4. Harris, Thomas A.: The 7 by 10 Foot Wind Tunnel of the National Advisory Committee for Aeronautics. T. R. No. 412, N. A. C. A., 1931.
5. Platt, Robert C.: Turbulence Factors of N. A. C. A. Wind Tunnels as Determined by Sphere Tests. T. R. No. 558, N. A. C. A., 1936.
6. Glauert, H.: Wind Tunnel Interference on Wings, Bodies, and Airscrews. R. & M. No. 1566, British A. R. C., 1933.
7. Wenzinger, Carl J.: Wind-Tunnel Investigation of the Aerodynamic Balancing of Upper-Surface Ailerons and Split Flaps. T. R. No. 549, N. A. C. A., 1935.
8. Wenzinger, Carl J.: Wind-Tunnel Investigation of Ordinary and Split Flaps on Airfoils of Different Profile. T. R. No. 554, N. A. C. A., 1936.
9. Wenzinger, Carl J.: Wind-Tunnel Measurements of Air Loads on Split Flaps. T. N. No. 498, N. A. C. A., 1934.

REPORT No. 615

COLUMN STRENGTH OF TUBES ELASTICALLY RESTRAINED AGAINST ROTATION AT THE ENDS

By WILLIAM R. OSGOOD

SUMMARY

A study was made of the effects of known end restraint on commercially available round and streamline tubing of chromium-molybdenum steel, duralumin, stainless steel, and heat-treated chromium-molybdenum steel; and a more accurate method than any previously available, but still a practical method, was developed for designing compression members in riveted or welded structures, particularly aircraft.

Two hundred specimens were tested as short, medium-length, and long columns with freely supported ends or elastically restrained ends. The test specimens were centered under load on knife edges held in carriers, and the free lengths were computed by a rational method not heretofore used. Tensile and compressive tests were made on each piece of original tubing from which column specimens were cut. The column data were reduced with the aid of these tests, and formulas were constructed to represent the column strengths in terms of specified tensile yield strengths of the four materials used.

It was found possible to extend work done by Bleich on the design of elastically restrained compression members in bridges and to present a method that should be suitable for designing such members in aircraft. The design is facilitated greatly by the use of tables and a nomographic chart, both included in this paper. A numerical example is also given.

INTRODUCTION

Compression members, particularly in riveted or welded structures like bridges and fuselages of airplanes are columns elastically restrained against rotation at the ends, and the strengths of such members lie between the strengths they would have if perfectly free to rotate at the ends, on the one hand, and if perfectly fixed at the ends, on the other hand. The interest of the Bureau of Aeronautics, Navy Department, and of the National Advisory Committee for Aeronautics in the strengths of compression members of the kind mentioned led to the transfer of funds to the National Bureau of Standards in July 1928 and thereafter for an investigation of the subject.

The column strengths of round and of streamline tubular specimens of chromium-molybdenum steel, of duralumin, of stainless steel, and of heat-treated

chromium-molybdenum steel have been studied. The diameters of the round tubes ranged from 1 inch to 2 inches and the basic diameters of the streamline tubes from $1\frac{1}{8}$ to $2\frac{1}{2}$ inches. The thicknesses of both sets of tubes ranged from 0.035 to 0.083 inch. Tests were made which included comprehensive tensile and compressive tests of the material used, 186 tests of specimens as initially centrally loaded columns with freely supported ends and with various known equal elastic restraints at both ends, and 14 such tests with one end freely supported and the other end restrained elastically in a known manner. In this paper these tests are described, and the column tests, further, are interpreted in the light of the double-modulus theory of column action and are related to the mechanical properties of the materials of the tubes. The question of designing elastically restrained compression members is also considered.

The author is particularly indebted to Dr. L. B. Tuckerman for advice and suggestions during the progress of the investigation, and to several other members of the Engineering Mechanics Section of the National Bureau of Standards for ideas and helpful suggestions in smoothing difficulties encountered from time to time in the laboratory work. It is a pleasure to acknowledge the assistance received in this way. Mr. E. E. Lundquist of the National Advisory Committee for Aeronautics was much interested in the problem of designing compression members elastically restrained against rotation at the ends and offered valuable criticism of the section on the design of such members. His comments resulted in a great improvement in this section.

The author wishes also to express appreciation for the tubing donated by the Aluminum Co. of America, by the Summerill Tubing Co., and by the Navy Department, and for the heat treatment of the heat-treated chromium-molybdenum-steel tubing by Metallurgical Laboratories, Inc.

A considerable part of this paper was submitted as a thesis in partial fulfillment of the requirements for the degree of Doctor of Philosophy in engineering in the graduate school of the University of Illinois, 1933. Acknowledgment is here made for permission granted by the graduate school of the University of Illinois to use this material.

MATERIAL AND MATERIAL TESTS

THE MATERIAL AND ITS PREPARATION FOR TEST

The round chromium-molybdenum-steel tubing had been bought under U. S. Army Specification No. 57-180-2A now covered by U. S. Army Specification No. 57-180-2C, the equivalent of Navy Department Specification 44T18c, Feb. 1, 1937: Tubing, Steel (Chrome-molybdenum) Round, Seamless (Aircraft Use). In the latter specification:

The specified minimum yield strength was raised from 60,000 to 75,000 lb. per sq. in. for the sizes of tubing that were used, and a more precise method of determining the yield strength was specified.

The specified minimum elongation in 2 in. was raised from 10 to 12 percent for sizes 0.036 to 0.188 in. thick.

The round duralumin tubing, donated by the Aluminum Co. of America, Pittsburgh, Pa., was supplied to conform with Navy Department Specification 44A2, now covered by Navy Department Specification 44T21b, May 1, 1937: Tubing, Aluminum-alloy (Aluminum-copper-magnesium-manganese), Round, Seamless, Condition "T", heat treated. In the latter specification:

The specified minimum yield strength was raised from 30,000 to 40,000 lb. per sq. in., and a more precise method of determining the yield strength was specified.

The specified percentage elongation in 2 in. was lowered by 2 for all sizes covered in the earlier specification ($\frac{1}{4}$ to $3\frac{1}{2}$ in., inclusive, nominal outside diameter).

The round stainless-steel tubing was bought under Proposed Navy Department Specification M-55b, temper C tubing, now covered by Bureau of Aeronautics Specification 44T27 (INT) 22 April 1937 for Tubing, Steel, Corrosion-resisting (18 percent Chromium and 8 percent Nickel) Seamless, Drawn, Round, Structural $\frac{3}{4}$ H-Cold-Drawn, Pickled. In the latter specification:

The specified yield strength was lowered from 150,000 lb. per sq. in. to a minimum of 135,000 lb. per sq. in. and at the same time the method of determining the yield strength was changed to conform in effect to the definition given in Navy Department Specification 44T27, "The yield strength is the load per square inch of original cross section at which the material exhibits an extension under load of 0.002 inch per inch in excess of that which would be computed from Young's modulus of elasticity of 25,000,000 pounds per square inch and the usual formula: Unit stress = Young's modulus \times unit deformation."

The specified elongation in 2 in. was lowered from 8 percent for a full-tube specimen to a minimum of 5 percent for material over 0.02 in. thick and not over 0.049 in. thick and to a minimum of 6 percent for material over 0.049 in. thick.

Flattening requirements were added.

All the chromium-molybdenum-steel tubing that was heat treated was donated by the Summerill Tubing Co., Bridgeport, Pa., and was heat treated free of charge by Metallurgical Laboratories, Inc., Philadelphia, Pa., to a requested tensile strength of 175,000 lb. per sq. in., no specification applying.

The streamline chromium-molybdenum-steel tubing donated by the Summerill Tubing Co., Bridgeport, Pa., was supplied to conform with Navy Department Specification 44T17a, now covered by Navy Depart-

ment Specification 44T17b, Dec. 1, 1936: Tubing, Steel (Chrome Molybdenum), Structural, Streamline Cross Section, Seamless (Aircraft Use). In the latter specification:

The specified minimum yield strength was raised 10,000 lb. per sq. in., but the method of determining the yield strength was changed so that most material passing the old specification would probably also pass the new one.

The streamline duralumin tubing, donated by the Aluminum Co. of America, Pittsburgh, Pa., was supplied to conform with Navy Department Specification 44T22, now covered by Navy Department Specification 44T22a, Feb. 1, 1937: Tubing, Aluminum-alloy (Aluminum-copper-magnesium-manganese), Streamline (Aircraft Use). In the latter specification:

Maximum chemical contents of iron, silicon, chromium, and other elements (including zinc) were specified.

The specified minimum yield strength was raised from 30,000 to 32,000 lb. per sq. in.

The streamline stainless-steel tubing was supplied by the Navy Department, which bought it under Navy Department Tentative Specification M-55C, either Grade 1 or 2 tubing with physical properties specified for temper "B" and with cross-sectional dimensions to conform to those shown in table 2 of Navy Department Specification 44T22, now covered by Navy Department Specification 49T11, May 1, 1937: Tubing, Steel, Corrosion-Resisting (18 percent Chromium and 8 percent Nickel), Seamless-Drawn, Streamline-Cross-Section (Aircraft Use), $\frac{1}{2}$ H-Cold-drawn, Pickled. In the latter specification:

The specified yield strength was lowered from 125,000 to 110,000 lb. per sq. in., and the method of determining the yield strength was changed to conform in effect to the definition noted under the description of the round stainless-steel tubing.

This specified percentage elongation in 2 in. was lowered from 15 for a strip specimen to 13 for material over 0.049 in. thick and to 8 for material not over 0.049 in. thick.

Since for the purpose of the present investigation the latest specifications are, with the exceptions noted, essentially the same as those under which the tubing was supplied, reference to specifications hereinafter will be confined to the latest specifications.

The nominal dimensions of the tubes used are given in table I. One tensile specimen and one compressive specimen were taken from each tube, usually from opposite ends, most of the remainder of the tube being available as column specimens. All these specimens were weighed, their lengths and the outside diameters of the round specimens were measured, and representative determinations of density were made by the Division of Weights and Measures of the Bureau. The cross-sectional area of each specimen was computed from the weight, the length, and the density. The least radii of gyration of the cross-sectional areas of the round specimens were determined from the actual dimensions and of the streamline specimens by subjecting representative specimens to pure bending,

measuring deflections, and computing the radii of gyration from the results so obtained and the values of the moduli of elasticity found for the compressive specimens.

The initial deflections of all the column specimens except a few short ones were measured.

TENSILE AND COMPRESSIVE TESTS

The tensile tests were made in a 100,000-lb. (50,000-kg) Amsler machine having scale ranges from 0 to 10,000, 20,000, 50,000 and 100,000 lb. Most of the compressive tests were made in a 50,000-lb. compound-lever machine, having scale ranges from 0 to 5,000 and 50,000 lb., in which the movable head could be maintained very rigid. Most of the compressive specimens were tested with the lower end against a flat block and the upper end against a hemispherical bearing.

Strains were measured with a Ewing extensometer, when possible, on a 2-inch gage length; otherwise Tuckerman strain gages were used for determinations of moduli of elasticity, and Huggenberger extensometers for determinations of yield strengths. The moduli of elasticity were obtained from stress-strain data by means of difference curves (reference 1) drawn for each of the tensile and compressive specimens. The stress-strain data for determining the modulus of elasticity were usually taken after the specimen had been strained to about 0.002 and the strain released. This procedure "ironed out" some of the initial stresses in the material and in many cases, particularly that of the stainless steel, made the determination of the modulus of elasticity much more definite than it would have been if determined from readings taken during the first loading. In these cases, owing to the immediate curvature of the stress-strain diagram at low stresses, the modulus of elasticity would have had to have been determined as the tangent modulus at zero stress, a very unsatisfactory determination.

In most cases the tensile yield strengths were obtained from stress-strain diagrams, according to the definitions in the latest Navy Department specifications applying to the type of tubing tested.¹ The compressive yield strength was obtained from a stress-strain diagram as the stress corresponding to the intersection with the stress-strain curve of a line drawn through the origin with a slope βE , where $0 < \beta < 1$ and E is the modulus of elasticity. This method is discussed later. The values of β used were: for the chromium-molybdenum steel, 5/9; for duralumin, 2/3; for stainless steel, 5/8; and for heat-treated chromium-molybdenum steel, 5/7.

Typical stress-strain diagrams are shown in figures 1, 2, 3, and 4.

¹ In the case of the heat-treated chromium-molybdenum-steel the tensile yield strength was taken as the stress at the intersection with the stress-strain curve of a line with a slope equal to that of the modulus line and at a strain 0.002 from it.

COLUMN TESTS

The primary series of column tests were tests with freely supported ends. As can readily be shown theoretically, the buckling strength of an ideal column having known elastic restraints at the ends is the same as the buckling strength of a column with freely supported ends having a length equal to the distance between the successive points of inflection of the center line of the column with restrained ends. Local, crinkling failures are not considered here. The length of the equivalent freely supported column is called the "free length" of the column. Although the double-modulus theory of column action (reference 2)² furnishes a method of determining the free length of an ideal column, as will be shown later, the imperfections of real columns made an experimental check seem advisable, and at Dr. L. B. Tuckerman's suggestion a considerable number of specimens were tested with known elastic restraints. The restrained ends also simulate more nearly the practical condition under which actual columns are used.

APPARATUS FOR PROCURING RESTRAINTS AT ENDS

The diagrammatic sketch (fig. 5), shows the lower fixture used for procuring an elastic restraint at the lower end of a column. Except for unimportant details, the upper fixture is the same as the lower. Each fixture consists essentially of a carrier with a knife edge which bears on a seat on a stationary support clamped to the weighing table of the testing machine. Means are provided for holding the end of the test specimen in position on the carrier and moving it horizontally under low loads in a direction perpendicular to the knife edge. Rotation of the carrier about the knife edge is restrained by the helical springs shown. The degree of restraint may be varied by changing the active lengths of the springs, provision for which is furnished. By means of a dial gage, not shown in the figure, it is possible to measure the rotation of the carrier about the knife edge. Wing nuts on the ends of the rods through the springs make it possible to compress the latter so that rotation of the carrier will not cause one spring to go out of action (the springs cannot be used in tension).

PROCEDURE FOR MAKING A TEST

The same vertical testing machine was used for the column tests as for most of the compressive tests previously mentioned. Before a series of columns with elastically restrained ends was tested, it was necessary to adjust the active lengths of the springs to procure the degree of restraint against rotation desired and then, after compressing the springs by means of the wing nuts, to determine the restraint accurately. This determination was made by hanging a series of known

² As indicated in this paper, the theory was developed by contributions of several men. It cannot justly be named after any one of them, nor even two, without denying credit due elsewhere. Dr. L. B. Tuckerman suggested the name "double-modulus theory."

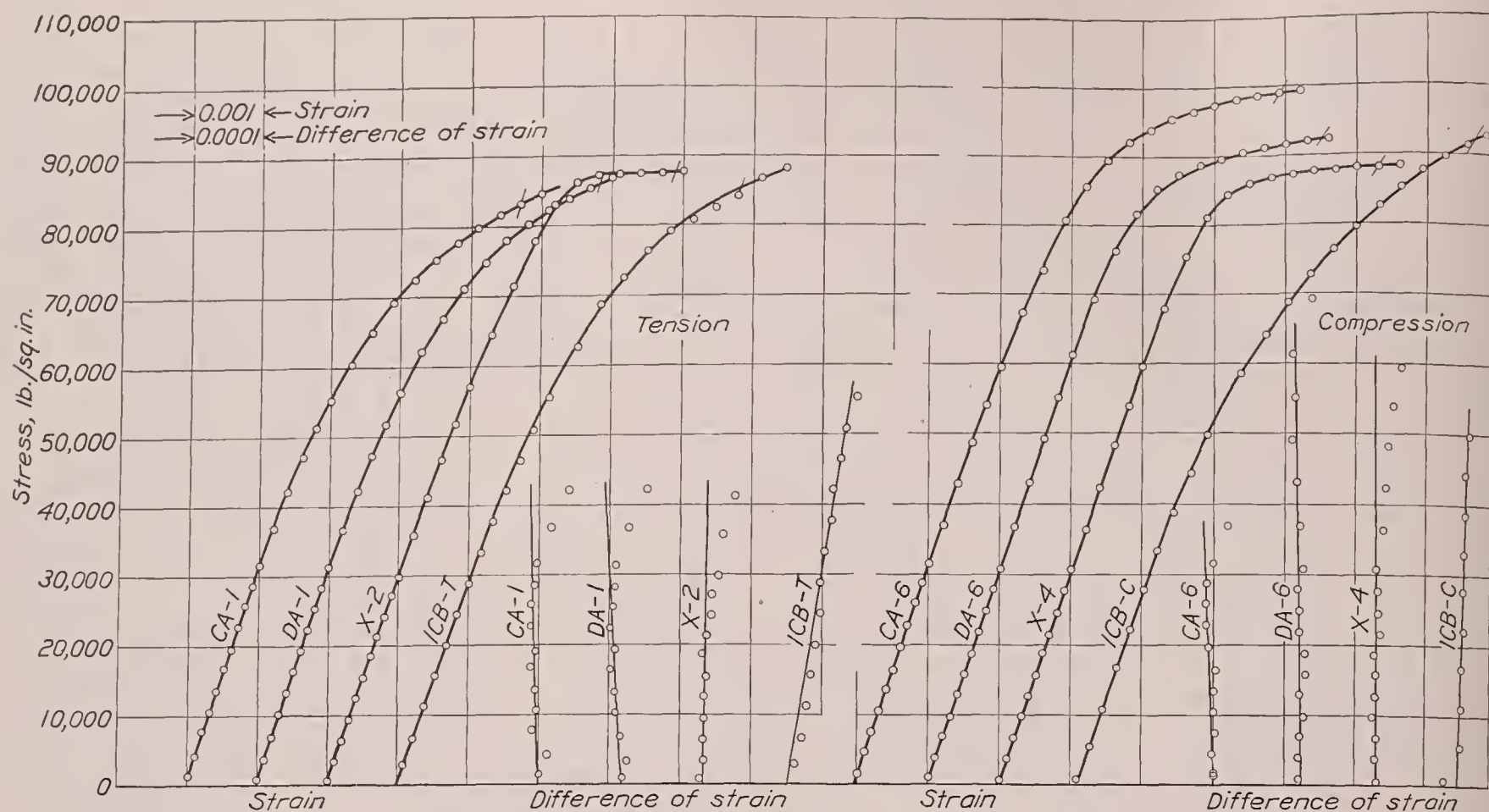


FIGURE 1.—Typical stress-strain diagrams of chromium-molybdenum steel.

$$\text{Difference of strain} = \text{Strain} - \frac{\text{Stress}}{\text{Trial modulus}}$$

Trial modulus = 30,000,000 lb. per sq. in.

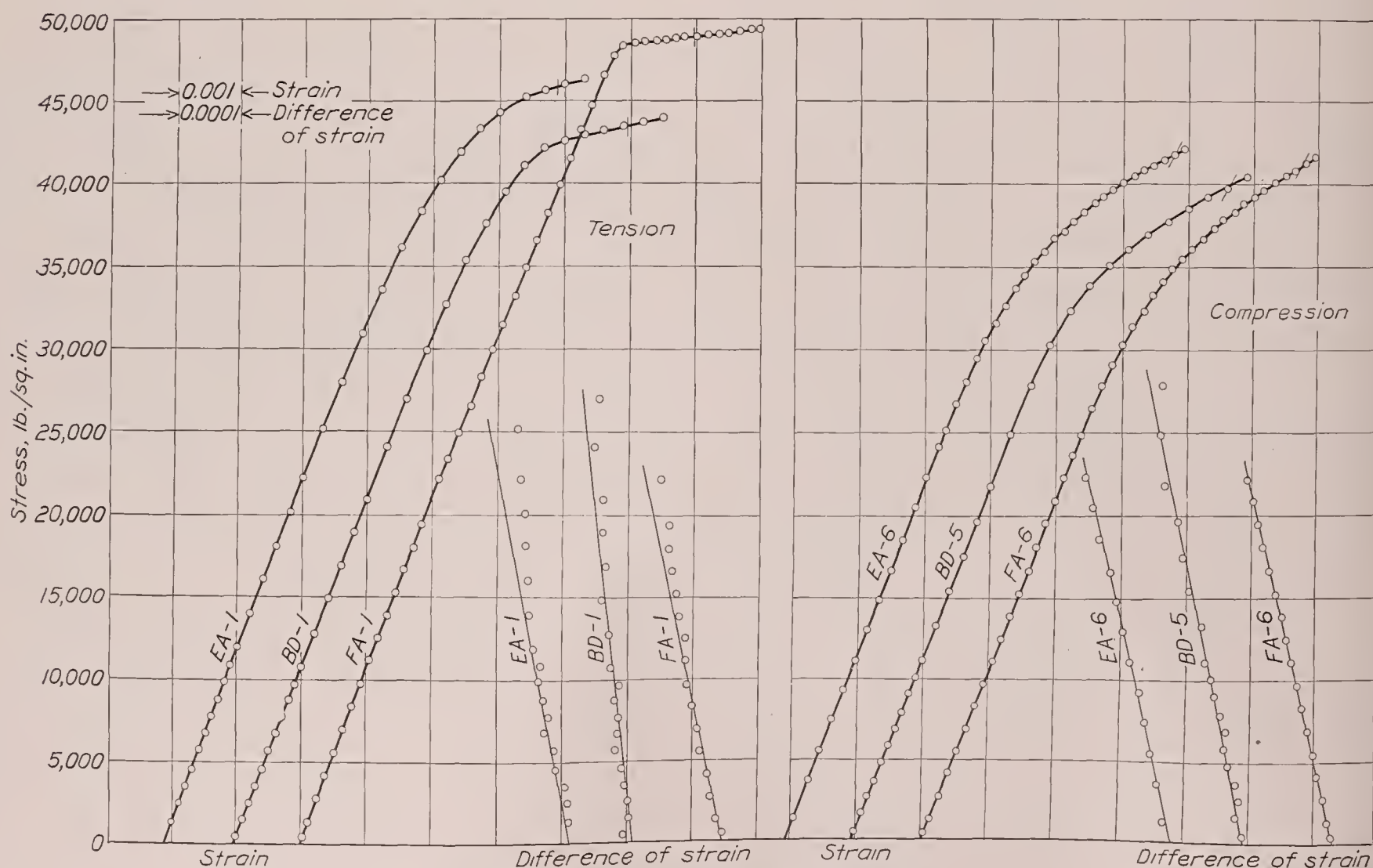


FIGURE 2.—Typical stress-strain diagrams of duralumin.

$$\text{Difference of strain} = \text{Strain} - \frac{\text{Stress}}{\text{Trial modulus}}$$

Trial modulus = 10,000,000 lb. per sq. in.

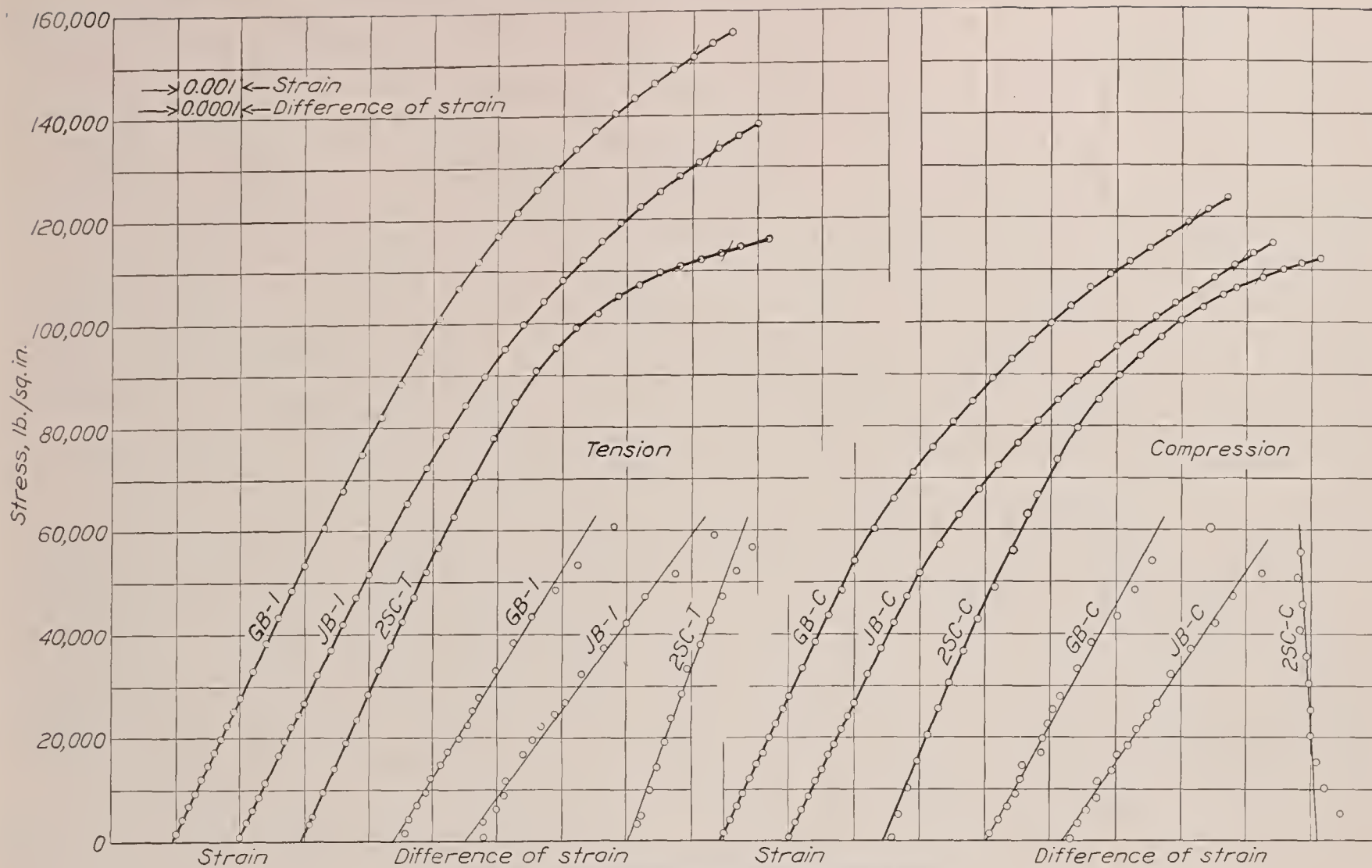


FIGURE 3.—Typical stress-strain diagrams of stainless steel.

$$\text{Difference of strain} = \text{Strain} - \frac{\text{Stress}}{\text{Trial modulus}}$$

Trial modulus = 30,000,000 lb. per sq. in.

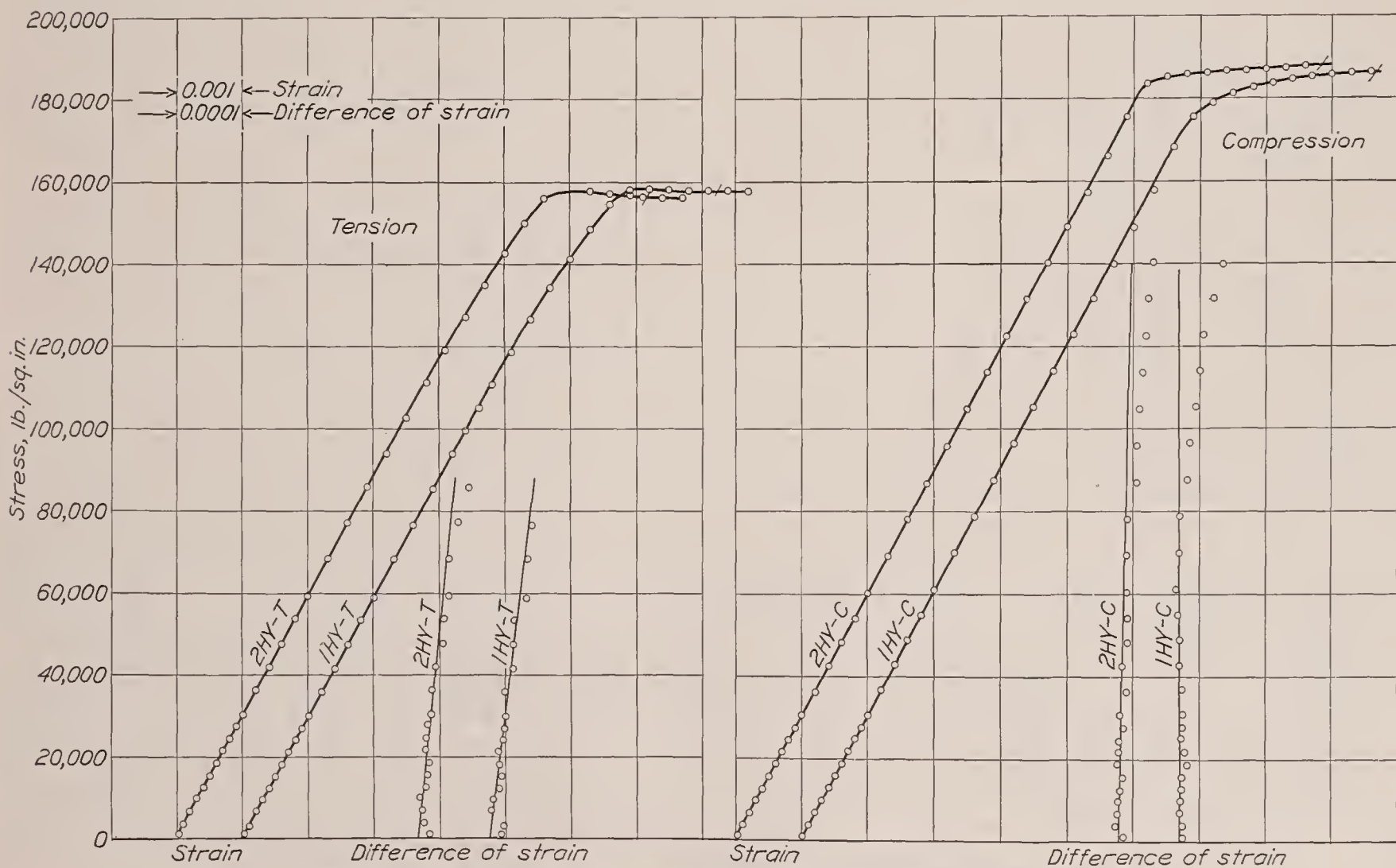


FIGURE 4.—Typical stress-strain diagrams of heat-treated chromium-molybdenum steel.

$$\text{Difference of strain} = \text{Strain} - \frac{\text{Stress}}{\text{Trial modulus}}$$

Trial modulus = 30,000,000 lb. per sq. in.

weights on one of the hangers at the ends of the carrier (fig. 5), thus causing the carrier to rotate about the knife edge, and noting the corresponding readings of the dial gage indicating rotation (not shown in the figure). From data obtained in this way the moment on the carrier could be plotted against the rotation of the carrier, and the moment per unit angular rotation, which will be called the "restraint", m , could be determined as the slope of the resulting diagram. The restraints used are given in table I.

The procedure proper, for making a column test consisted in placing the specimen between the upper and lower carriers, centering under load³ with the springs out of action, and then bringing the springs

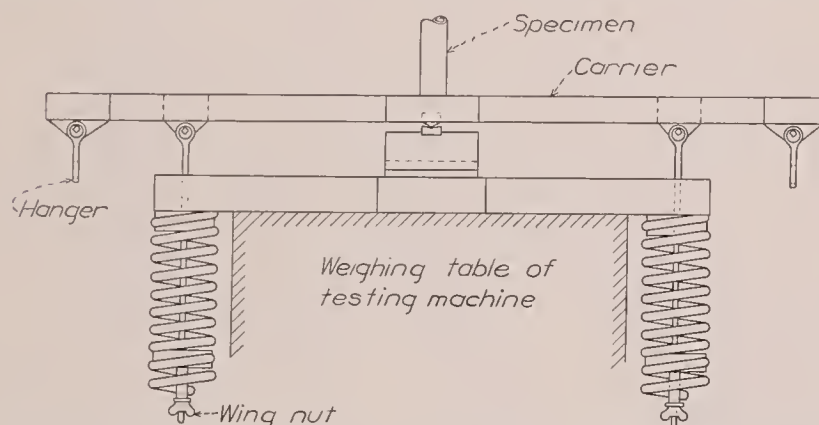


FIGURE 5.—Diagrammatic sketch showing apparatus for procuring elastic restraint at end of column.

into action if the test was to be made with restrained ends, and loading to failure.

RESULTS

DETERMINATION OF THE FREE LENGTH

The results of the column tests were plotted in terms of the ratio of slenderness, based on the free length, and the average stress at failure, and also in terms of nondimensional variables that took into account the properties of the material. The first question that presented itself in preparing such a graphical representation was the determination of the free length. The rigid carriers at the ends of the columns complicated the situation somewhat. Engesser (reference 5) had shown in the case of straight elastic columns how such rigid portions of equal lengths at freely supported ends could be treated rationally. The problem of the straight elastic column of uniform cross section elastically restrained against rotation at the ends had been treated by Nater and others (references 6, 7, and 8), and Bleich (reference 9) considered the case of the straight inelastic column so restrained. In the present investigation there were many slightly curved, inelastic columns with rigid portions and both with and without elastic restraints at the ends. All these columns were centered under load with the expectation that such

centering would idealize the elastically restrained columns as well as the freely supported columns.⁴ A rational method of determining the lengths, and thus the ratios of slenderness, of equally strong columns freely supported at the ends was then sought. The strength of the different columns could then be studied as a function of the ratio of slenderness based on the free lengths so found.

If the double-modulus theory (reference 2) of column action is adequate to describe the behavior of columns under load, as is being questioned less and less today, and if the departures from straightness of the columns are not too great, then it should be possible to determine the free length of any test column on the basis of this theory.⁵ If, when the free lengths of the test columns have been computed, plots of average stress at failure against ratio of slenderness based on the computed free length, or modifications of these quantities that take into account the variations in the properties of the material, lie on a reasonably smooth curve, this fact may be regarded as proof that small initial curvatures under conditions of proper centering do not affect the strengths of even inelastic columns freely supported or elastically restrained at the ends.

The equations determining the free length of an axially loaded straight column of uniform cross section with rigid portions and elastic restraints at the ends may be obtained as outlined in the following sections. The procedure is to write down the differential equation for the deflection of the center line, to integrate it, to introduce the boundary conditions, and to determine under what conditions the displacement of the center line becomes indeterminate. It will be found that this displacement becomes indeterminate at a definite load, the buckling load.

The notation that will be used is:

- A , the cross-sectional area of the column
- i , the least radius of inertia or radius of gyration of the cross section of the column measured parallel to the plane of bending.
- $I = Ai^2$
- l , the length of the column specimen.
- s_0 , the length of the rigid portion between the upper end of the specimen and the upper knife edge.
- s_1 , the length of the rigid portion between the lower end of the specimen and the lower knife edge.

⁴ Well-known tests by von Kármán (reference 10) show that slight imperfections such as small initial curvatures do not affect the strengths of freely supported columns when centered under load. Zimmermann (reference 11) has shown theoretically that the strength of elastic columns is not affected by slight initial curvature when the columns are centered properly, and Rein (reference 12), in a careful series of tests, has included some definitely bent columns of structural steel, confirming Zimmermann's results.

³ Christie (reference 3) was probably the first to compensate for imperfections in an actual column by shifting the ends of the column relative to the supports. Considère (reference 4) seems to have been the first to employ centering under load systematically in a series of column tests.

⁵ In this theory it is assumed that the columns are straight, that the material is homogeneous, that the load is applied in line with the axis of the column, and that deformations due to shear are negligible. Since the behavior of a material stressed beyond the proportional limit in a column depends upon its previous strain history, the strength of columns in which the material is so stressed depends on the loading history. A standard loading history must therefore also be assumed in the theory. It is assumed that the compression is uniform over all the cross section until the buckling load is reached, and not until then does bending take place.

and

$$\nu' = \frac{\mu - \frac{s}{l}}{1 + \frac{2s}{l}} = \frac{\frac{m}{Pl} - \frac{s}{l} \left(1 + \frac{2s}{l}\right)}{\left(1 + \frac{2s}{l}\right)^2} \quad (6)$$

and by factoring the left-hand side obtain

$$\left(\frac{1 + \cos \phi}{\sin \phi} + \nu\phi\right)[(1 + 2\nu')(1 - \cos \phi) - \nu'\phi \sin \phi] = 0 \quad (7)$$

It may be noted that if $\phi = 2n\pi$, where n is an integer, the left-hand side of this equation becomes indeterminate. Substitution of this value of ϕ into the original equation, (2), shows that $\phi = 2n\pi$ is not a solution. If the first of the factors on the left-hand side of equation (7) is equated to zero, the solution obtained corresponds to the case $\psi_0 = -\psi_1$ (fig. 6) and, if the second factor is equated to zero, the solution obtained corresponds to the case $\psi_0 = \psi_1$. The first solution yields the smallest value of ϕ and is the only one of practical interest. There is obtained then in a convenient form

$$\cot \frac{\phi}{2} + \nu\phi = 0 \quad (8)$$

Equation (8) may also be written in terms of the trigonometric functions

$$s = \frac{\phi}{\sin \phi} - 1 \text{ and } t = 1 - \frac{\phi}{\tan \phi} \quad (9)$$

$$t + s = -\frac{1}{\nu} \quad (8a)$$

Where tables of $t+s$ (reference 13) are available, equation (8a) will be the most convenient form for use.

If, when $s_0 = s_1 = s$ and $\mu_0 = 0$, there is introduced the nondimensional variable

$$\nu'' = \frac{\mu_1 - \frac{2s}{l}}{1 + \frac{2s}{l}} = \frac{\frac{m_1}{Pl} - \frac{2s}{l} \left(1 + \frac{2s}{l}\right)}{\left(1 + \frac{2s}{l}\right)^2} \quad (10)$$

equation (2) for the determination of ϕ reduces to

$$t = -\phi^2 \frac{s}{l} \left(1 + \frac{s}{l} + \frac{1}{\nu''} \frac{s}{l}\right) - \frac{1}{\nu''} \quad (11)$$

which may be solved by trial with the aid of table VII.

Finally, if $s_0 = s_1 = 0$, equation (2) may be written in the form

$$\mu_0 \mu_1 (t^2 - s^2) + (\mu_0 + \mu_1)t + 1 = 0 \quad (12)$$

Zimmermann (reference 13) gives this equation and Prager (reference 14) gives it in a modified form, but they assume it to apply for elastic buckling only. It has also been presented in a paper by the author (reference 15). The equation may be solved by trial with the aid of table VII, or it may be solved directly

by means of the nomogram (fig. 7) the idea for which is due to L. B. Tuckerman.⁷

In order to use the nomogram, a straight line is run through the points of the circle determined by the values of μ_0 and μ_1 read on the circular scale. This line will intersect the spiral curve in at least one point. The value of ϕ/π corresponding to this point, or the lower value if there are two intersections,⁸ read on the scale of the spiral curve will be the lowest value for which buckling can occur.

The necessary constants for the column specimens with equal (or no) restraints at opposite ends and for the column specimens freely supported at the top and restrained at the bottom being computed, equations (8), or (8a), and (11) could be solved for ϕ and the free lengths determined from equation (4). The ratios of slenderness, l_0/i could now be found; and the corresponding average stresses at failure, P/A , were obtained from the maximum loads and the cross-sectional areas. The values of m and m_1 that were used ranged from 0 to about 450,000 lb.-in. per radian. (See table I.)

COLUMN DATA

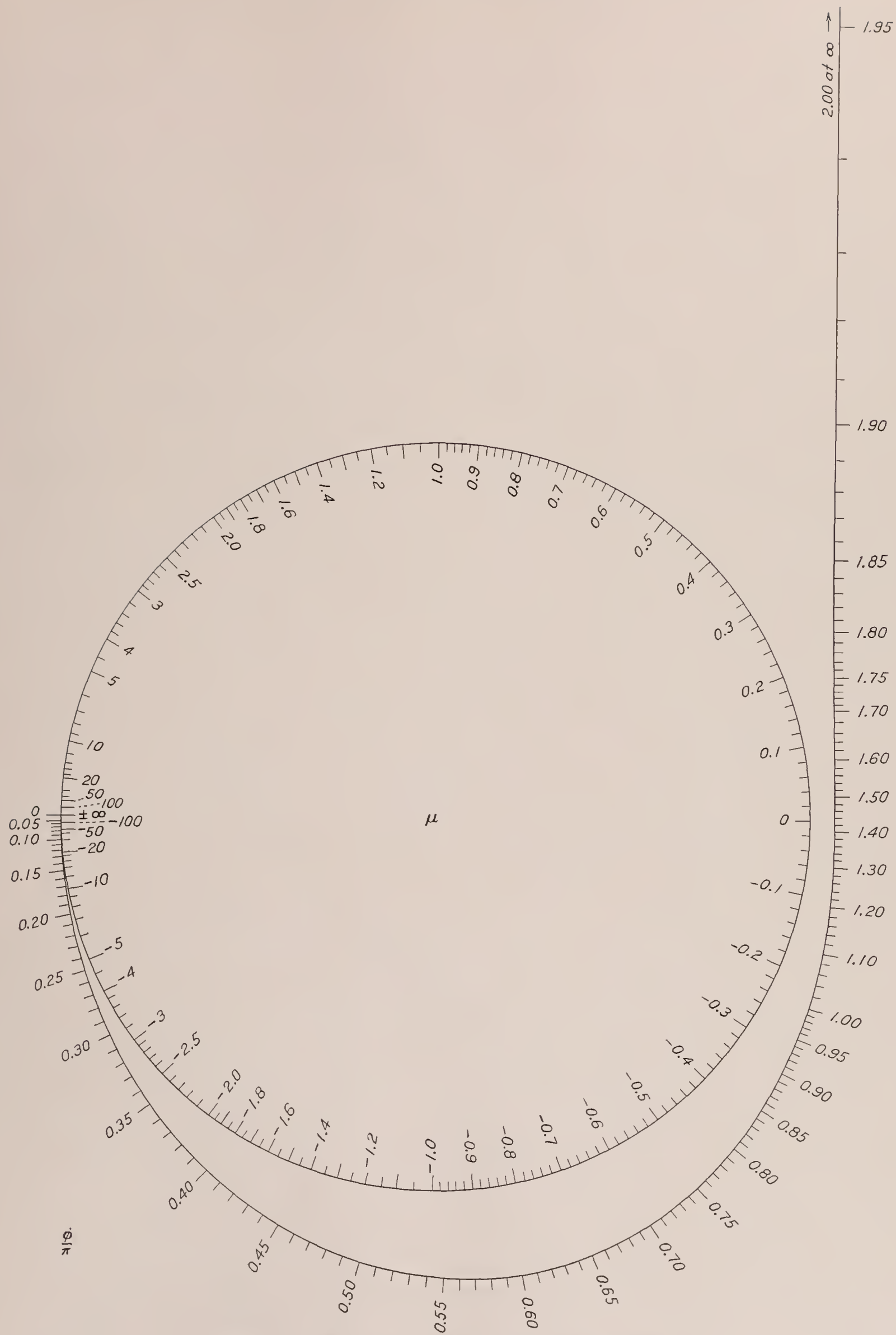
The values of ratio of slenderness, l_0/i , and corresponding average stress, P/A , are given in table II and are plotted for the chromium-molybdenum-steel specimens in figure 8, for the duralumin specimens in figure 9, for the round stainless-steel specimens in figure 10, and for the heat-treated chromium-molybdenum-steel specimens in figure 11. One of the main causes, probably the main cause, of the scatter in the points in these diagrams is the unavoidable variation in the properties of the material from tube to tube and along the length of any one tube from which specimens were cut. This variability can be corrected for to the extent to which the compressive stress-strain relations remain invariable along the length of any one given specimen and are affinely related from specimen to specimen.

Suppose, for example, that there is determined from the compressive stress-strain diagram of the material in each specimen a certain stress, S , as the intersection with the stress-strain curve of a line through the origin having a slope βE , where β is a constant for a given material and $0 < \beta < 1$, and E is the modulus of elasticity of the material. Let there now be constructed in each case a reduced compressive stress-strain diagram in which there is plotted, instead of stress against strain, stress divided by S against strain divided by S/E .⁹

⁷ Equation (12) is in one of Clark's canonical forms of equations of nomographic order 4. (See reference 16.)

⁸ In the case of two points of intersection the higher value of ϕ/π corresponds to an unstable condition of equilibrium.

⁹ The reduced stress-strain diagram has been used by Hohenemser (reference 17), who does not, however, determine S specifically by the method here used.



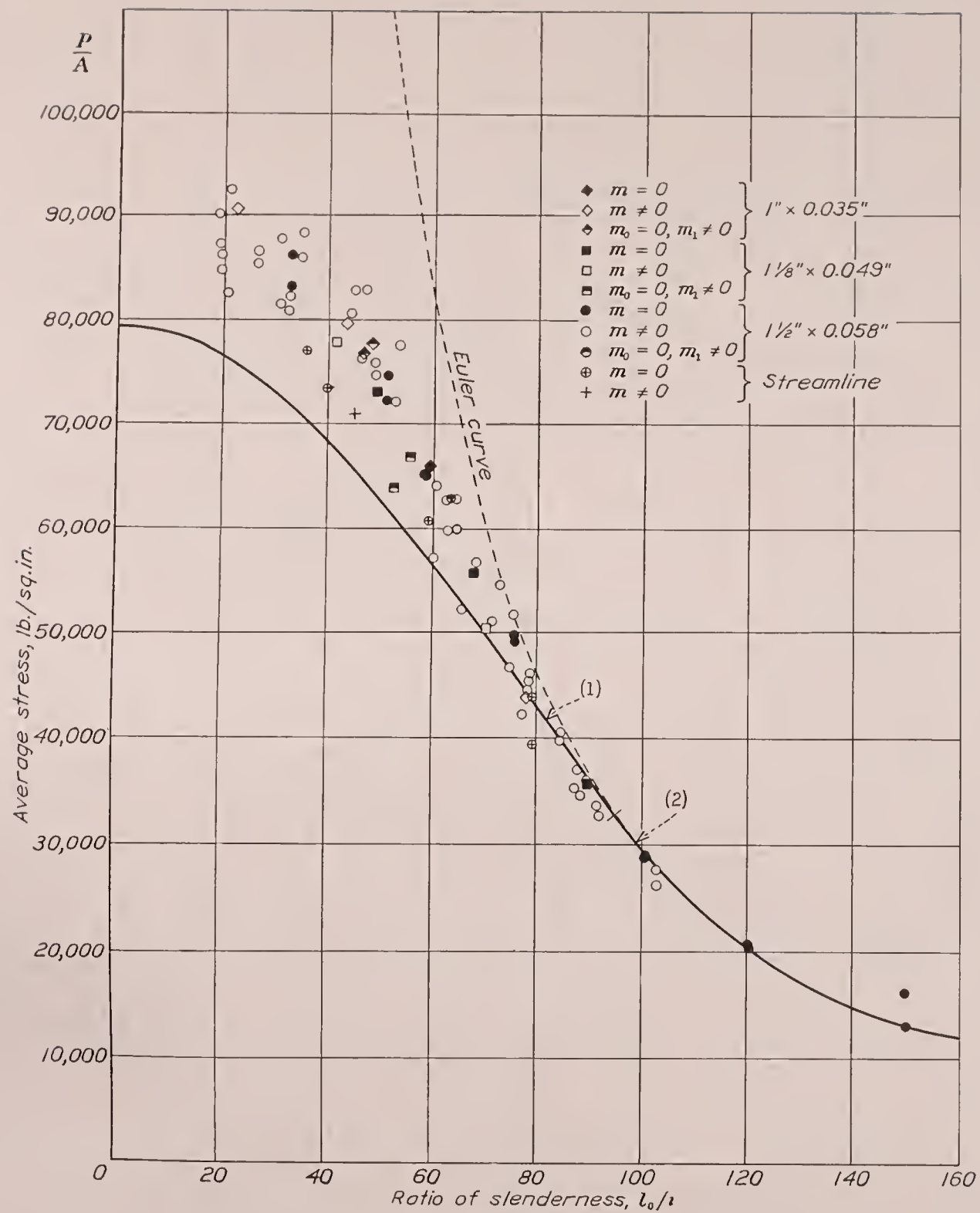


FIGURE 8.—The $\frac{l_0}{i}, \frac{P}{A}$ —diagram for chromium-molybdenum-steel tubes.

$$(1) \frac{P}{A} = \frac{22,000 - \left(\frac{l_0}{i}\right)^2}{20,700 + \left(\frac{l_0}{i}\right)^2}$$

$$(2) \frac{P}{A} = \frac{294,000,000}{\left(\frac{l_0}{i}\right)^2}$$

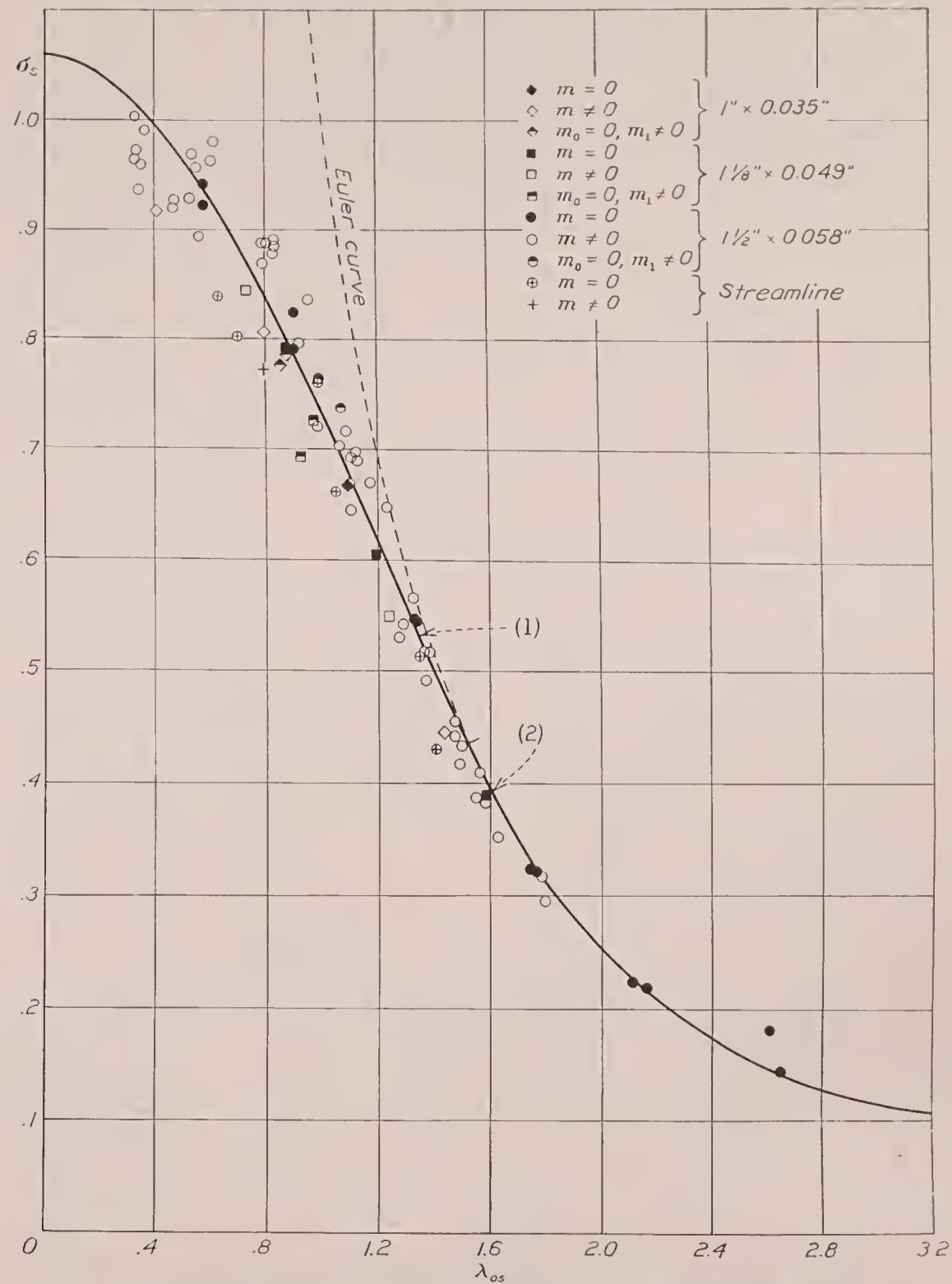


FIGURE 12.—The λ_{os}, σ_s —diagram for chromium-molybdenum-steel tubes.

$$(1) \sigma_s = \frac{5.6 - \lambda_{os}^2}{5.29 + \lambda_{os}^2}$$

$$(2) \sigma_s = \frac{1}{\lambda_{os}^2}$$

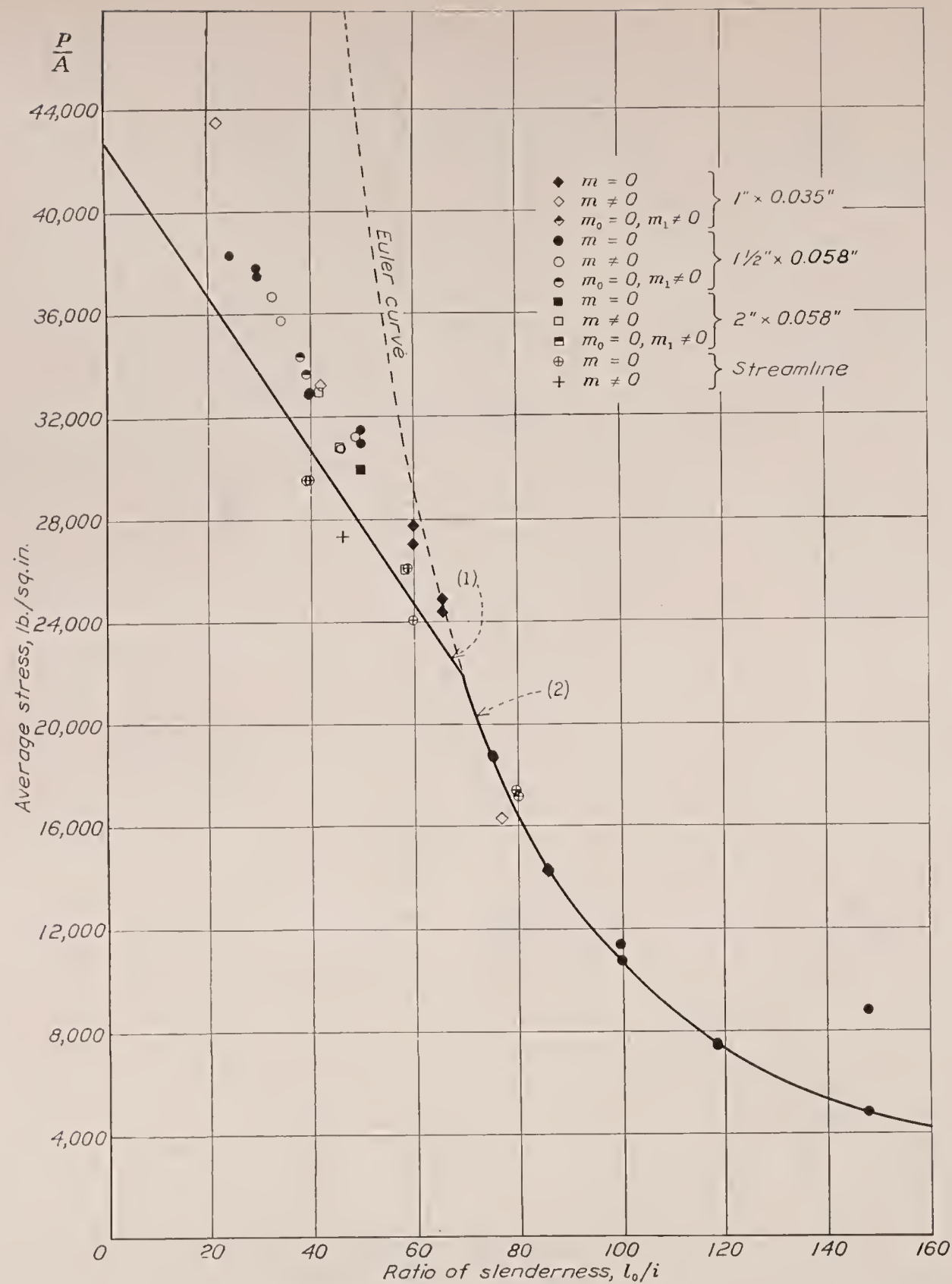


FIGURE 9.—The $\frac{l_0}{i}, \frac{P}{A}$ —diagram for duralumin tubes.
 (1) $\frac{P}{A} = 42,700 \left(1 - 0.00707 \frac{l_0}{i} \right)$ (2) $\frac{P}{A} = \frac{104,500,000}{\left(\frac{l_0}{i} \right)^2}$

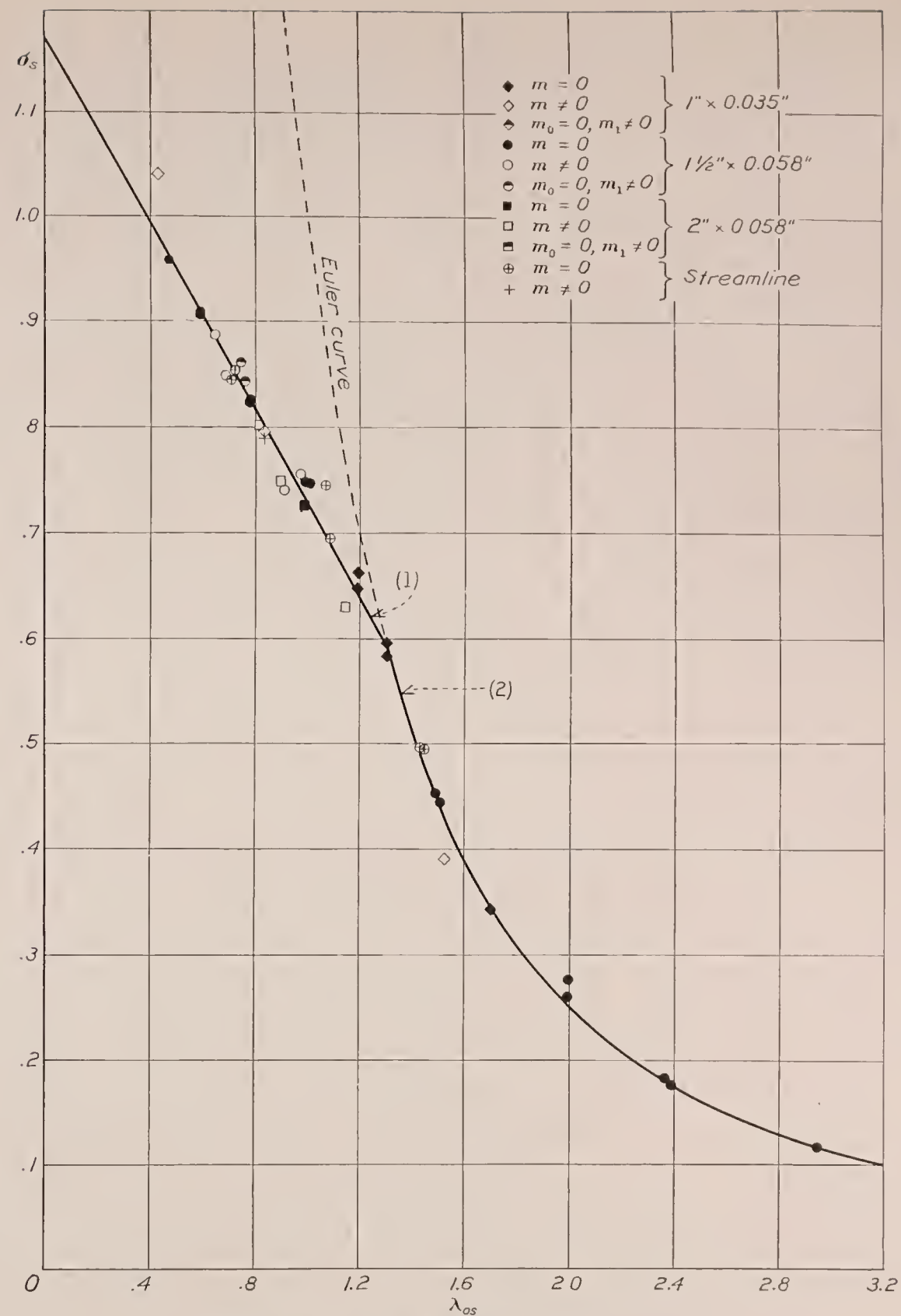
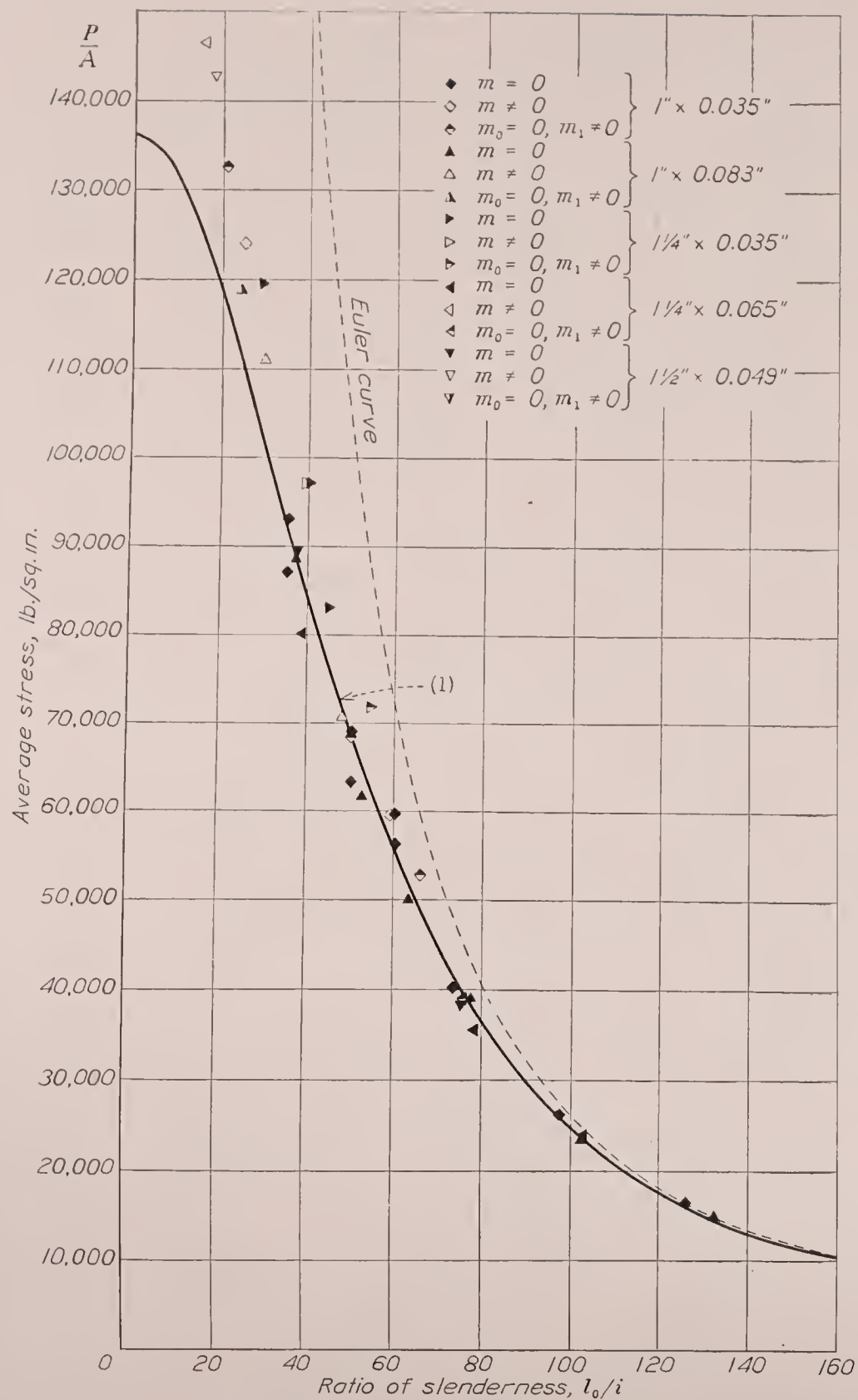
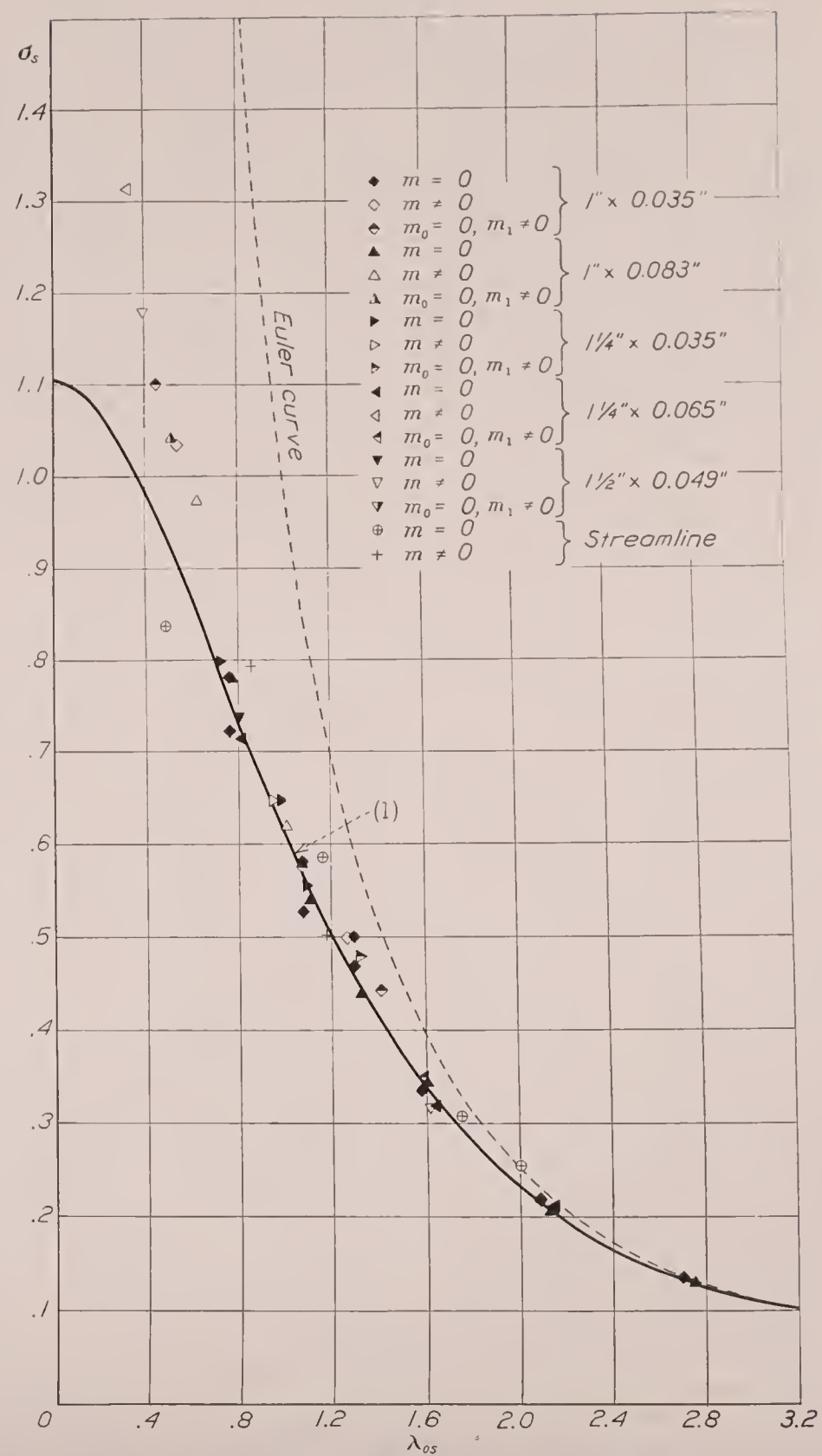


FIGURE 13.—The λ_{as}, σ_a —diagram for duralumin tubes.
 (1) $\sigma_a = 1.175 - 0.445 \lambda_{as}$
 (2) $\sigma_a = \frac{1}{\lambda_{as}^2}$

FIGURE 10.—The $\frac{l_0}{i}, \frac{P}{A}$ —diagram for stainless-steel tubes.

$$(1) \frac{P}{A} = \frac{123,400}{0.000223 \left(\frac{l_0}{i}\right)^2 + 0.32 \sqrt{0.000000226 \left(\frac{l_0}{i}\right)^4 + 8}}$$

FIGURE 14.—The λ_{os}, σ_s —diagram for stainless-steel tubes.

$$(1) \sigma_s = \frac{1}{0.68 \lambda_{os}^2 + 0.32 \sqrt{\lambda_{os}^4 + 8}}$$

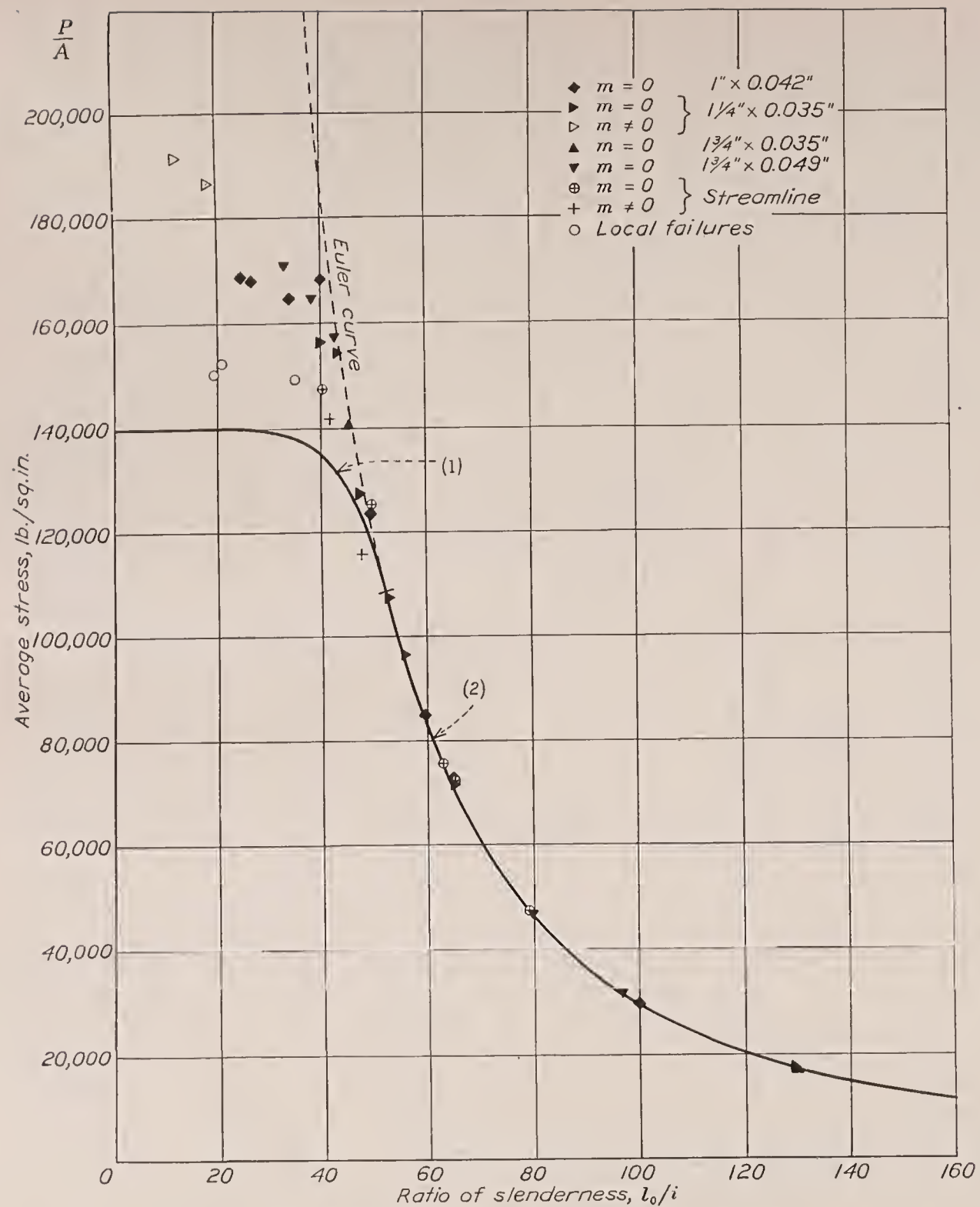


FIGURE 11.—The $\frac{l_0}{i}, \frac{P}{A}$ —diagram for heat-treated chromium-molybdenum-steel tubes.

$$(1) \frac{P}{A} = 140,000 \left[1 - \left(0.0155 \frac{l_0}{i} \right)^7 \right]$$

$$(2) \frac{P}{A} = \frac{296,100,000}{\left(\frac{l_0}{i} \right)^2}$$

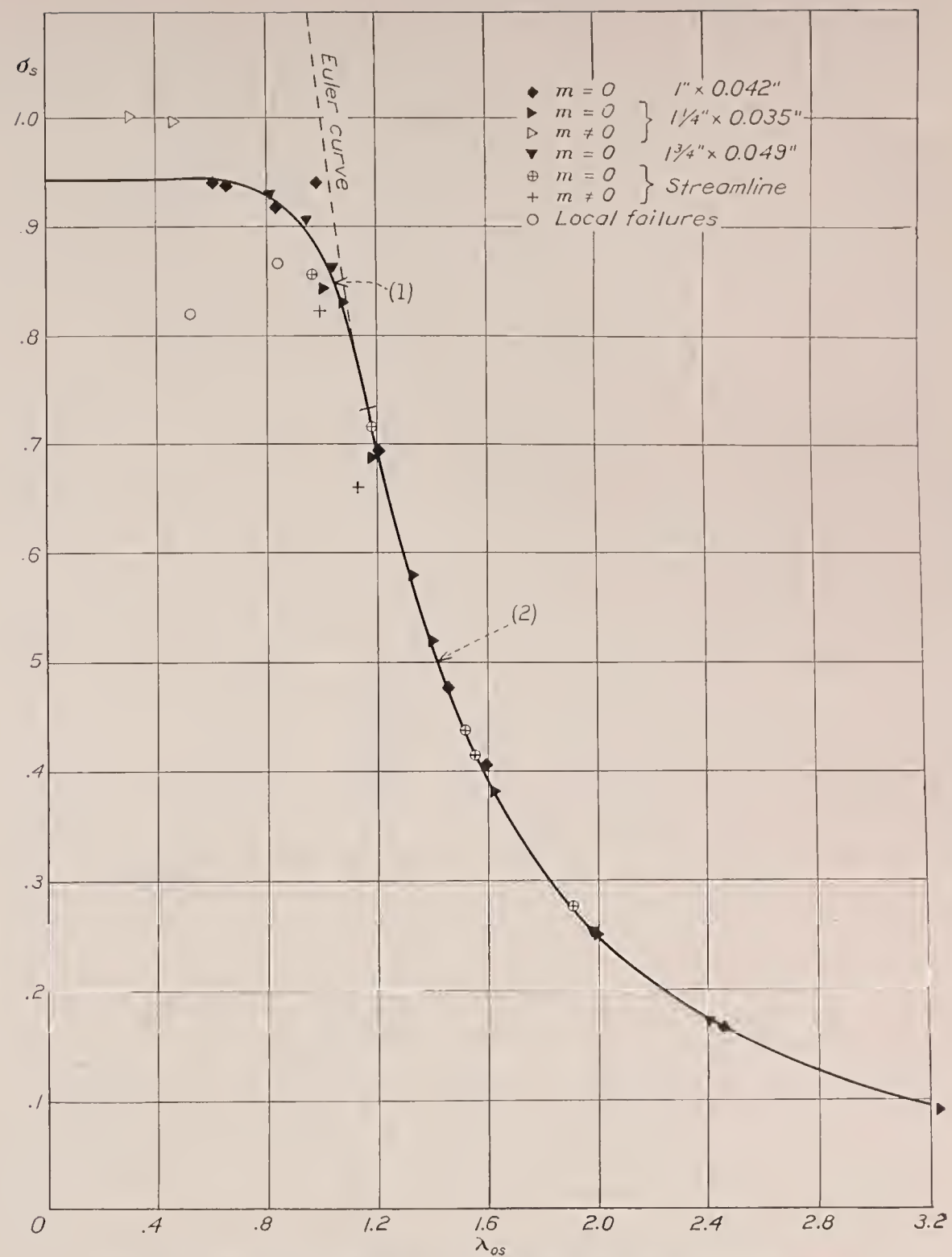


FIGURE 15.—The λ_{os}, σ_s —diagram for heat-treated chromium-molybdenum-steel tubes.

$$(1) \sigma_s = 0.943(1 - 0.07509\lambda_{os}^7)$$

$$(2) \sigma_s = \frac{1}{\lambda_{os}^2}$$

If the various original stress-strain curves are affinely related,¹⁰ then they all reduce to one and the same curve, in particular, that part of the reduced diagram within the elastic range is identical for all materials. Just as there is corresponding to any given stress-strain curve, a definite double-modulus column curve, $P/A = \pi^2 \bar{E} / (l_0/i)^2$, so there is corresponding to our reduced stress-strain curve, a definite reduced double-modulus column curve in which P/A and \bar{E} in the double-modulus formula are replaced by $P/(AS)$ and \bar{E}/E , respectively, and in which l_0 must be replaced by $l_0 \sqrt{S/E}$.¹¹

If now there are introduced the nondimensional variables¹²

$$\lambda_{os} = \frac{1}{\pi} \frac{l_0}{i} \sqrt{\frac{S}{E}} \quad \sigma_s = \frac{P}{AS} \quad (13)$$

the reduced column curve

$$\sigma_s = \frac{\bar{E}}{\lambda_{os}^2 E} \quad (14)$$

is identically the same for all columns having geometrically similar cross sections (\bar{E} depends among other things on the shape of the cross section) and made of materials having compressive stress-strain diagrams that are affinely related.

Although it is too much to expect all the compressive stress-strain curves of a material to be affinely related, nevertheless they are to some degree of approximation so related; and experience has shown that, where the properties of the material differ widely, the correction proposed is a real correction (reference 18). Accordingly, the values of λ_{os} and σ_s , equations (13), were computed for each column specimen. For E in each case was used the modulus of elasticity of the compressive specimen for the tube from which the column specimen was cut. For the determination of S , which may be called the "compressive yield strength", in the case of the chromium-molybdenum steel and the duralumin tubes, β was so chosen that were the tensile yield strength to be determined for a material just passing specifications, then by the βE method exactly the same yield strength would be obtained as by the method specified for round tubing. This consideration gave $\beta = \frac{5}{9}$ for the chromium-molybdenum steel and $\beta = \frac{2}{3}$ for the duralumin. The value of β determined in the same way for the $\frac{3}{4}$ -H stainless steel gave $\beta = \frac{27}{37}$; this value was arbitrarily reduced to $\frac{5}{8}$, which was the value used for all the stainless-steel specimens. For the heat-treated chromium-molybdenum steel $\beta = \frac{5}{7}$ was used. This value would correspond to a specified yield strength of 150,000 lb. per sq. in., determined as indi-

cated in footnote 1. For curves that are strictly affinely related the value of β is immaterial, within the limits $0 < \beta < 1$ within which it has any meaning. For curves that are approximately affinely related the best value of β is that value which most nearly brings them all to the same reduced stress-strain curve, but practically the best value may be regarded as the value which is most effective in reducing the scatter in the l_0/i , P/A -diagrams. In order to make sure that the values of β adopted were reasonably good, other values were tried: $\frac{1}{2}$ for chromium-molybdenum steel and duralumin, and $\frac{27}{37}$ and $\frac{5}{9}$ for stainless steel. There was little difference in the results, which were not made significantly better nor worse. This result was to be expected, for in order that the method have any value at all, the stress-strain curves must show some semblance of affine relationship, and if they do, the value of β most convenient to use will be practically as good as any other.

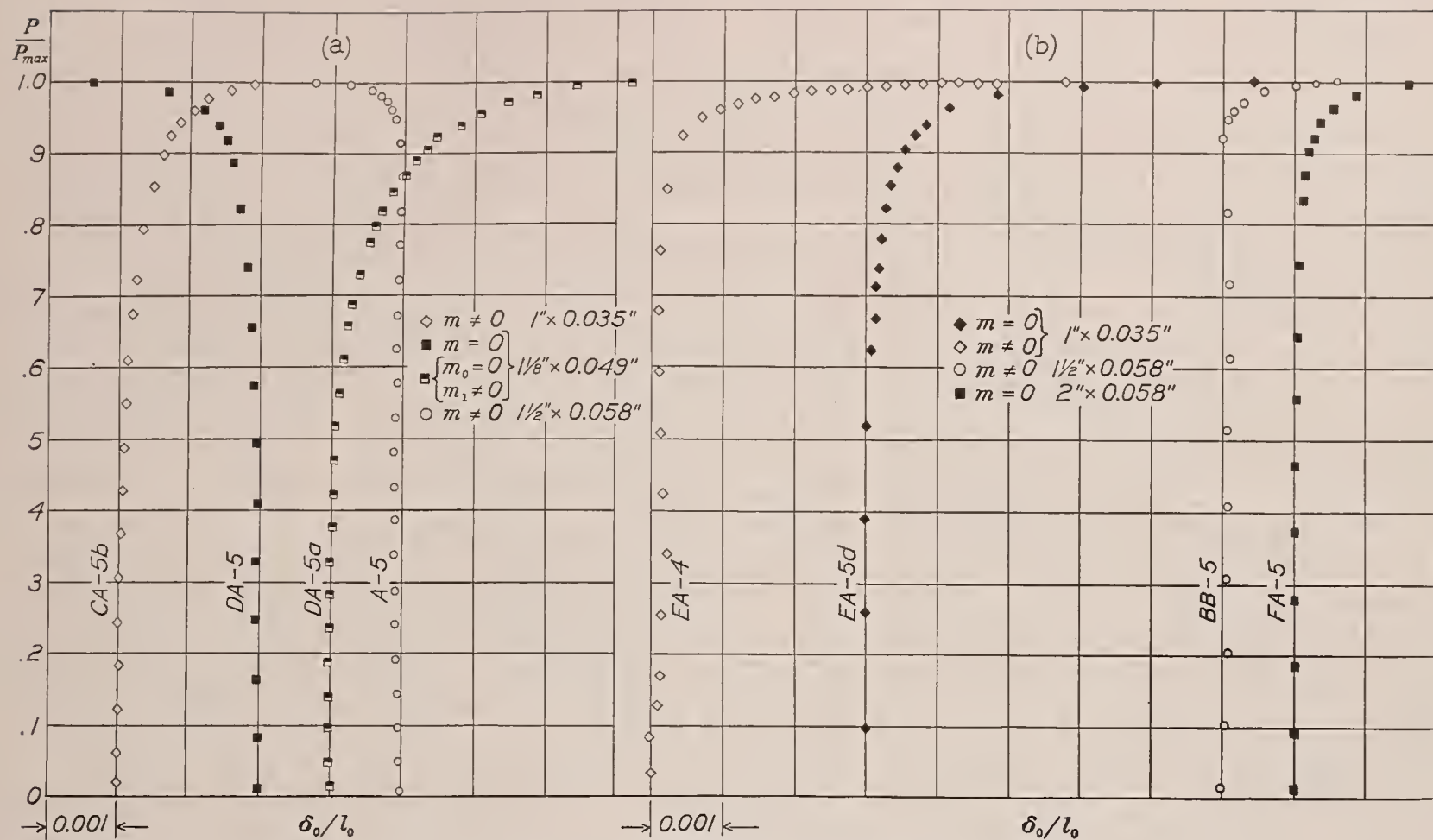
The λ_{os}, σ_s -diagrams that result from the procedure just outlined are shown in figures 12, 13, 14, and 15. Comparisons of the chromium-molybdenum-steel diagrams (figs. 8 and 12) and the duralumin diagrams (figs. 9 and 13) show some improvement; but the improvement is most marked in the stainless steel and the heat-treated chromium-molybdenum-steel diagrams (figs. 10 and 14 and figs. 11 and 15). That the improvement is not greater in the chromium-molybdenum-steel results may be explained by the fact that the mechanical properties of the material vary considerably along the length of a given tube. The value of the compressive yield strength for a column specimen may differ appreciably from the value of the compressive yield strength as actually determined on the compressive specimen. Moreover, the compressive stress-strain curves of the chromium-molybdenum-steel showed comparatively poor affine relationship. No great improvement in the duralumin results would be expected because of the general uniformity of all the material used.

The next most probable cause of scatter in the l_0/i , P/A - and λ_{os}, σ_s -diagrams after variations in the properties of the materials, is the uncertainty of the conditions at the ends of the test columns. The best measure of the success with which a column has been centered is the subsequent load-deflection curve obtained on testing the column; or better, for comparative purposes, a plot of load, P , divided by maximum load, P_{max} , against deflection within the free length divided by the free length (reference 19). The sharper the "knee" of such a diagram, that is, the smaller the smallest radius of curvature of the reduced load deflection curve, the better centered or the better adjusted the ends of the column may be assumed to have been. Representative diagrams of this kind are shown in figures 16 and 17. The deflection, δ_0 , in the free length was obtained from the observed deflections on the assumption that equation (1) represented the deflected center line.

¹⁰ By affine relation is meant the relation that exists between the curves $F(e, f) = 0$ and $F(pe, qf) = 0$, where p and q are constants.

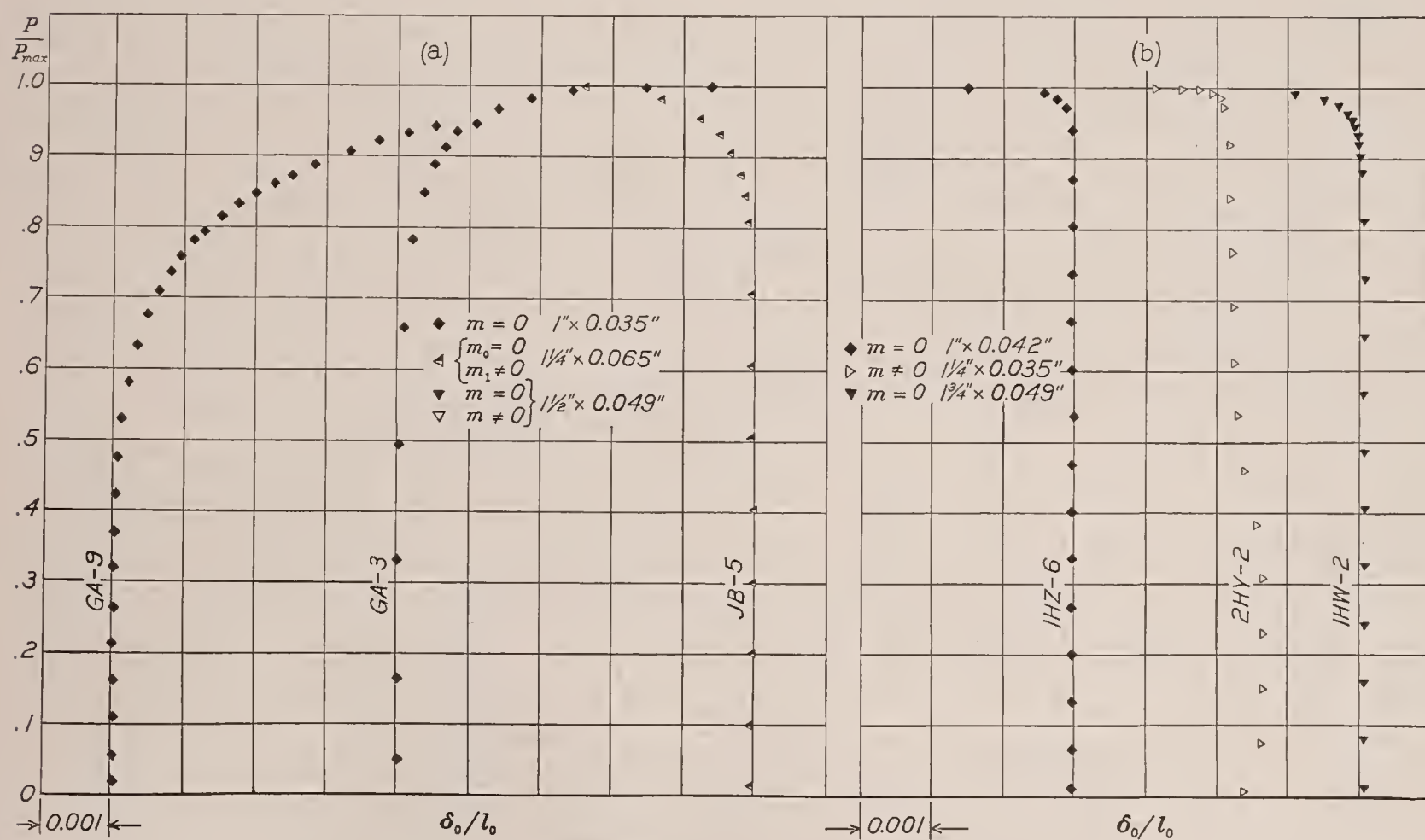
¹¹ The quantity $l_0 \sqrt{S/E}$ is the length of an elastic column which would buckle at the average stress S .

¹² Similar variables were used by Tuckerman, Petrenko, and Johnson (reference 18).



(a) Chromium-molybdenum steel. (b) Duralumin.

FIGURE 16.—Representative reduced load-deflection curves for chromium-molybdenum-steel and for duralumin tubes.



(a) Stainless steel.

(b) Heat-treated chromium-molybdenum steel.

FIGURE 17.—Representative reduced load-deflection curves for stainless-steel and heat-treated chromium-molybdenum-steel tubes.

Comparison of the low points on the λ_{os}, σ_s -diagrams with the reduced load-deflection diagrams for the corresponding specimens indicated that one chromium-molybdenum-steel, three duralumin, four stainless-steel, and two heat-treated chromium-molybdenum-steel columns were probably tested with unsatisfactory end conditions, since the reduced load-deflection curves showed large radii of curvature at the knees.

The error in the free length, l_0 , due to an error in the restraint, m , was estimated to be not greater than 1 percent in any case.

The tests on freely supported round columns are regarded as the primary data, the tests with restrained ends and the tests of the streamline sections being regarded as check data. The degree to which the check data agree with the primary data is an indication of the accuracy of the method of computing free length by means of equations (4) and (8) or (11). It will be noted that, in general, in figures 12, 13, 14, and 15 the points representing the check data fall in approximately equal numbers above and below the point representing the primary data.

FORMULAS AND CURVES FOR DESIGNING

The data were adapted for use in designing by the following procedure. Empirical formulas were developed to give a good approximation to the λ_{os}, σ_s -values for each of the materials, curves representing these formulas being shown in figures 12, 13, 14, and 15. Use of these formulas or curves requires a knowledge of the compressive yield strength of the material, and this information is not usually available to the designer. The specified property most nearly related to it is the tensile yield strength. Therefore, the average ratios of compressive yield strength to tensile yield strength were determined for the several materials, and the values of the specified tensile yield strength in the several current specifications were introduced into the empirical equations to give the column strength as a function of ratio of slenderness for material just passing the specification. Curves representing these results are shown in figures 8, 9, 10, and 11. The details of this procedure will now be taken up.

The results of the tests on the freely supported round chromium-molybdenum-steel columns can be represented in the λ_{os}, σ_s -diagram by a curve of the form ^{12a}

$$\sigma_s = \frac{K_0 - \lambda_{os}^2}{\frac{1}{4}(K_0 - K_1)^2 + K_1 \lambda_{os}^2} \text{ for } \frac{4K_0}{(K_0 - K_1)^2} \geq \sigma_s \geq \frac{2}{K_0 - K_1} \quad (15a)$$

and the reduced Euler curve

$$\sigma_s = \frac{1}{\lambda_{os}^2} \text{ for } \frac{2}{K_0 - K_1} \geq \sigma_s > 0 \quad (15b)$$

^{12a} This type of curve, in terms of the ratio of slenderness and the average stress, was proposed by Kreüger (reference 20).

where K_0 and K_1 are empirical constants. These curves are shown in figure 12 for $K_0=5.6$ and $K_1=1$:

$$\sigma_s = \frac{5.6 - \lambda_{os}^2}{5.29 + \lambda_{os}^2} \text{ for } \frac{560}{529} \geq \sigma_s \geq \frac{10}{23} \quad (16a)$$

$$\sigma_s = \frac{1}{\lambda_{os}^2} \text{ for } \frac{10}{23} \geq \sigma_s > 0. \quad (16b)$$

It may be noted that for $K_1=0$, equation (15a) reduces to the Johnson parabolic formula.

The results of the tests on the freely supported round duralumin columns can be represented in the λ_{os}, σ_s -diagram by the straight line and the reduced Euler curve

$$\sigma_s = 1.175 - 0.575\sqrt{0.6\lambda_{os}} \text{ for } 1.175 \geq \sigma_s \geq 0.6$$

$$\text{or } \sigma_s = 1.175 - 0.445\lambda_{os} \text{ for } 1.175 \geq \sigma_s \geq 0.6 \quad (17a)$$

$$\text{and } \sigma_s = \frac{1}{\lambda_{os}^2} \text{ for } 0.6 \geq \sigma_s > 0 \quad (17b)$$

which are shown in figure 13.

The results of the tests on the freely supported round stainless-steel columns can be represented in the λ_{os}, σ_s -diagram by a modification of a curve proposed by Aarflot ¹³

$$\sigma_s = \frac{1}{K_2 \lambda_{os}^2 + (1 - K_2) \sqrt{\lambda_{os}^4 + K_3}}, K_2 \leq 1, K_3 \geq 0 \quad (18)$$

for all values of λ_{os} , K_2 and K_3 being empirical constants. The curve is shown in figure 14 for $K_2=0.68$, $K_3=8$:

$$\sigma_s = \frac{1}{0.68 \lambda_{os}^2 + 0.32 \sqrt{\lambda_{os}^4 + 8}} \quad (19)$$

It may be noted that for $K_2=1$ or $K_3=0$ equation (18) reduces to the Euler formula.

The results of the tests on the freely supported round heat-treated chromium-molybdenum-steel columns can be represented in the λ_{os}, σ_s -diagram by the seventh-degree parabola and the Euler curve,

$$\sigma_s = 0.943(1 - 0.0751\lambda_{os}^7) \text{ for } 0.943 \geq \sigma_s \geq 0.733 \quad (20a)$$

$$\sigma_s = \frac{1}{\lambda_{os}^2} \text{ for } 0.733 \geq \sigma_s > 0 \quad (20b)$$

which are shown in figure 15.

The relations between l_0/i and P/A , usually desired, may be obtained by substituting the values of λ_{os} and σ_s from (13) in (16a) to (20b), solving for P/A , and introducing the numerical values of the quantities S and E ; but this procedure would result in equations applicable only to the particular material tested. What is wanted are equations in l_0/i and P/A which give safe results when applied to any material passing specifications. The specified property most closely related to the compressive yield strength of a material is the tensile yield strength, and if the ratio of these two strengths is known for a particular material, a

¹³ Aarflot (reference 21) proposes

$$\sigma = \frac{1}{\frac{1}{2}\lambda_0^2 + \frac{1}{2}\sqrt{\lambda_0^4 + 4}}$$

column formula written in terms of the compressive yield strength may be given in terms of the specified yield strength. The average ratios of the compressive yield strength to the tensile yield strength for the round tubes of the four materials used in this investigation were found to be 1.000, 0.908, 0.827, and 1.120 for chromium-molybdenum steel, duralumin, stainless steel, and heat-treated chromium-molybdenum steel, respectively.

Navy Department Specification 44T18c for chromium-molybdenum-steel tubing requires a tensile yield strength not less than 75,000 lb. per sq. in. for tubing up to 0.188 inch thick. The compressive yield strength of tubing just passing this specification may be expected to be $S=1.000 \times 75000=75,000$ lb. per sq. in. The average value found for E for the round tubes was 29,800,000 lb. per sq. in. Consequently, the column strength in pounds per square inch of tubing up to 0.188 inch thick which passes the specification just mentioned and for which the ratio of diameter d to thickness t does not exceed about 50 (value obtained from unpublished tests on short specimens) may be represented by the formulas

$$\frac{P}{A}=75000 \frac{22000 - \left(\frac{l_0}{i}\right)^2}{20700 + \left(\frac{l_0}{i}\right)^2} \text{ for } 79400 \geq \frac{P}{A} \geq 32600, \quad (21a)$$

$$\frac{P}{A} = \frac{294\,000\,000}{\left(\frac{l_0}{i}\right)^2} \text{ for } 32600 \geq \frac{P}{A} > 0. \quad (21b)$$

Curves corresponding to these formulas are shown in figure 8. They represent the strength that may be expected from tubes which just pass the specification.

Navy Department Specification 44T21b for heat-treated duralumin tubing requires a tensile yield strength not less than 40,000 lb. per sq. in. The compressive yield strength of tubing just passing this specification may be expected to be $S=0.908 \times 40000=36,320$ lb. per sq. in. The average value found for E for the round tubes was 10,590,000 lb. per sq. in. Consequently, the column strength in pounds per square inch of tubing which passes the specification just mentioned and for which the ratio of diameter d to thickness t does not exceed 55 (value obtained from unpublished tests on short specimens) may be represented by the formulas.

$$\frac{P}{A}=42700 \left(1 - 0.00707 \frac{l_0}{i}\right) \text{ for } 42700 \geq \frac{P}{A} \geq 21800 \quad (22a)$$

$$\frac{P}{A} = \frac{104\,500\,000}{\left(\frac{l_0}{i}\right)^2} \text{ for } 21800 \geq \frac{P}{A} \geq 0. \quad (22b)$$

Curves corresponding to these formulas are shown in figure 9. They represent the strength that may be expected from tubes which just pass the specification.

Navy Department Specification 44T27 (INT) for stainless-steel tubing, 3/4 H—Cold drawn, requires a tensile yield strength not less than 135,000 lb. per sq. in. The compressive yield strength of tubing just passing

this specification may be expected to be $S=0.827 \times 135000=111,600$ lb. per sq. in. The average value found for E for the round tubes was 26,300,000 lb. per sq. in. Consequently, the column strength in pounds per square inch of tubing which passes the specification just mentioned and for which the ratio of diameter d to thickness t does not exceed about 35 (see table I) may be represented by the formula

$$\frac{P}{A} = \frac{123\,400}{\left(0.01798 \frac{l_0}{i}\right)^2 + \sqrt{1 + \left(0.01233 \frac{l_0}{i}\right)^4}} \quad (23)$$

The curve represented by this formula is shown in figure 10. It represents the strength that may be expected from tubes which just pass the specification.

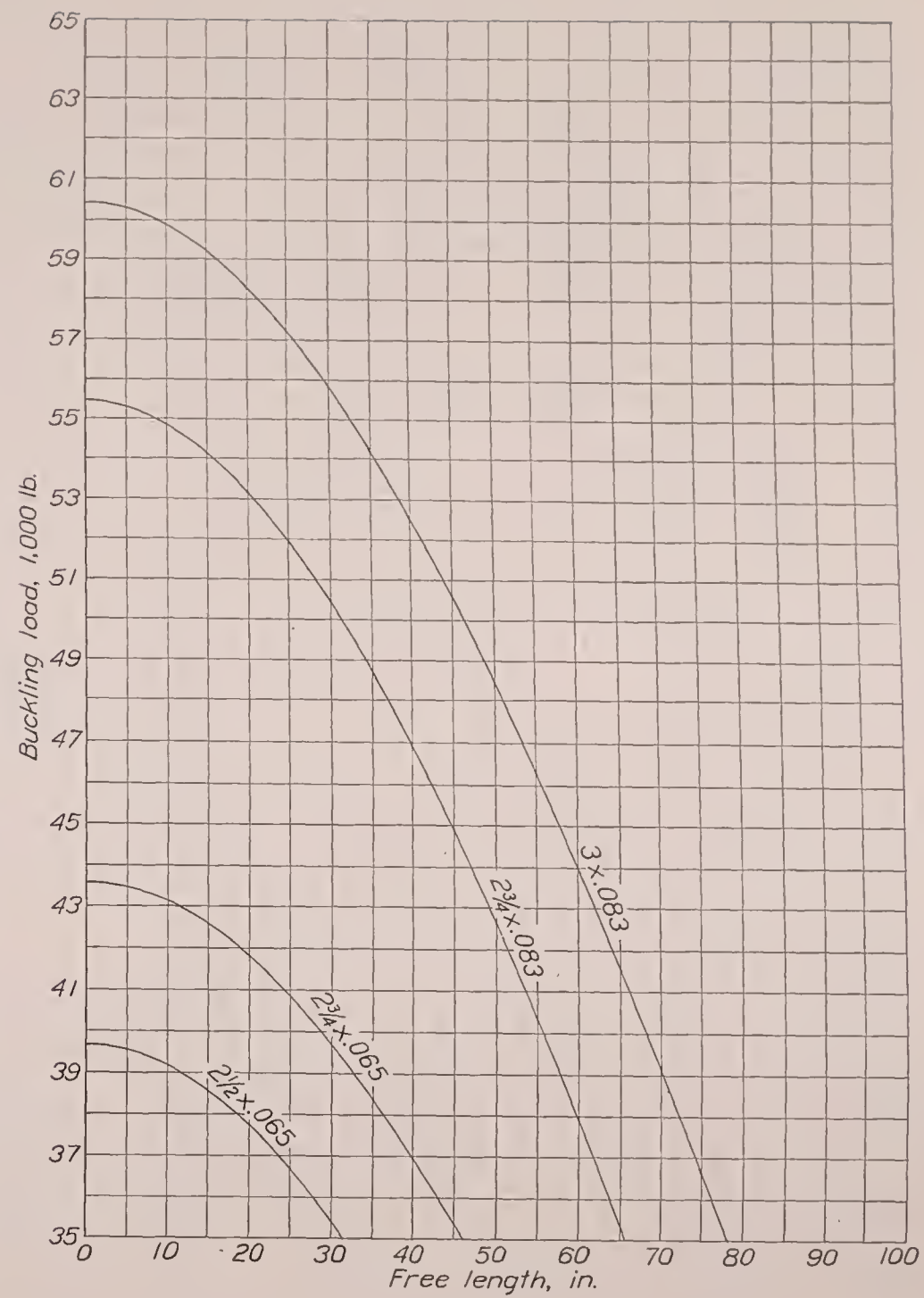
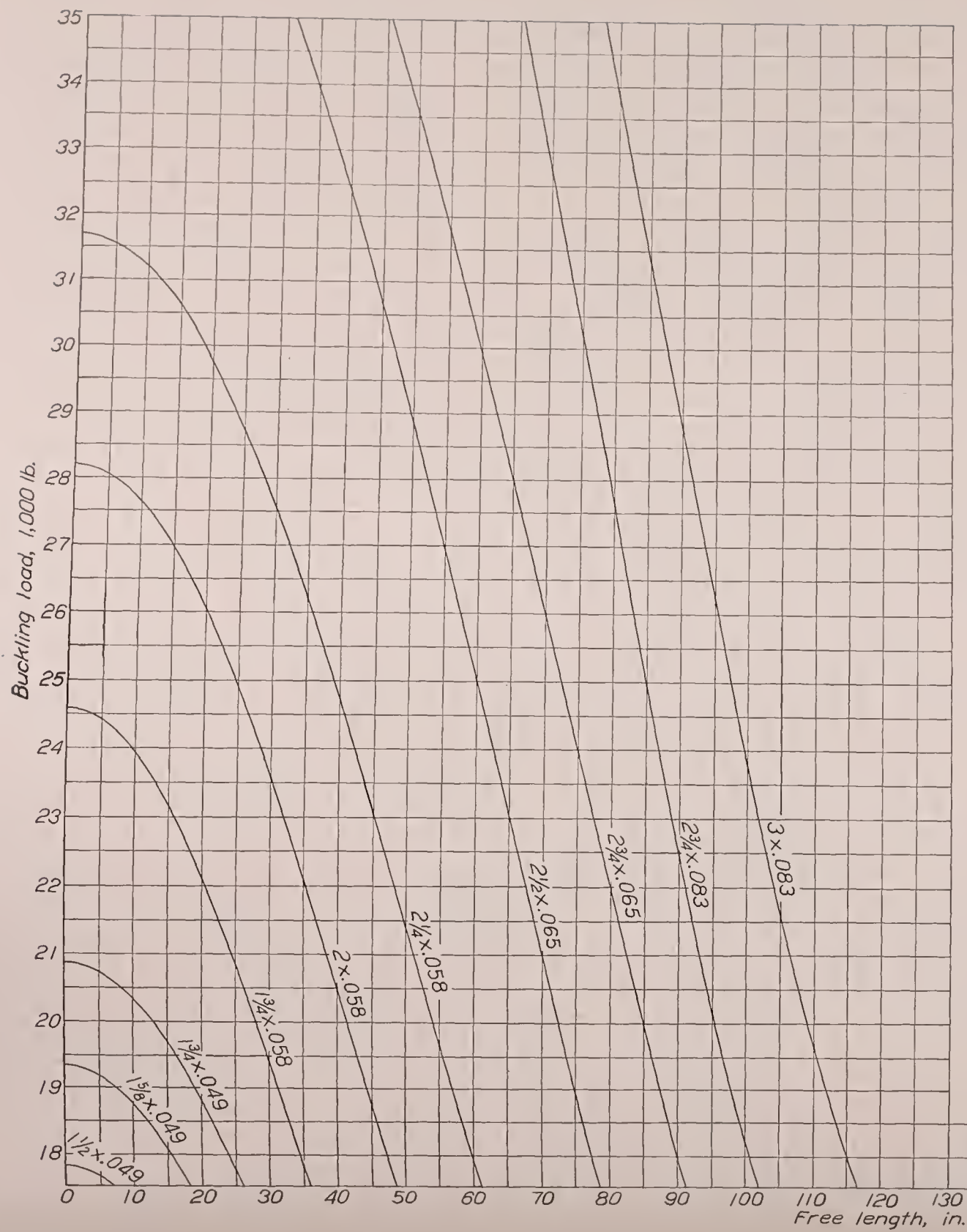
As stated previously, no specifications apply to the heat-treated chromium-molybdenum-steel tubing, but all the tensile specimens showed a yield strength above 150,000 lb. per sq. in. determined as indicated in footnote 1. The variation in the ratios of compressive yield strength to tensile yield strength was so great, more than 20 percent, and the number of tubes, five, from which specimens were cut was so small that instead of using the average ratio for this material, it seems desirable from considerations of safety to use the least ratio found of compressive yield strength to tensile yield strength, namely, 0.99, in obtaining a relation between P/A and l_0/i based on a specified tensile yield strength. If a specified minimum tensile yield strength of 150,000 lb. per sq. in. is assumed, the compressive yield strength of tubing just passing the specification may be expected to be $S=0.99 \times 150000=148,500$ lb. per sq. in. The average value found for E for the round tubes was 30,000,000 lb. per sq. in. Consequently, the column strength in pounds per square inch of heat-treated chromium-molybdenum-steel tubing similar to that tested, having a specified minimum tensile yield strength of 150,000 lb. per sq. in., for which the ratio of diameter d to thickness t does not exceed about 35¹⁴ (see table I) may be represented by the formulas

$$\frac{P}{A}=140000[1 - (0.01547 l_0/i)^7] \text{ for } 140000 \leq \frac{P}{A} \leq 108900 \quad (24a)$$

$$\frac{P}{A} = \frac{296\,100\,000}{\left(l_0/i\right)^2} \text{ for } 108900 \geq \frac{P}{A} > 0 \quad (24b)$$

Curves represented by these formulas are shown in figure 11. They represent the strength that may be expected from tubes which just pass a specification requiring a minimum tensile yield strength of 150,000 lb. per sq. in.

¹⁴ It is true that one column specimen with $d/t=35.7$ failed by crinkling at one end but this specimen was the shortest one tested with so high a value of d/t . Five other longer specimens with the same value of d/t , two of them cut from the same tube as the specimen in question, failed by primary buckling at higher average stresses. It is extremely difficult to center a short specimen because the deflections under the centering load are so small. This condition is not of great importance for such specimens when failure occurs by primary buckling, but it is likely to affect appreciably the average stress at failure when the failure is by crinkling. It seems probable, therefore, that the specimen mentioned was loaded eccentrically, and that the strength does not represent the strength which would have been obtained under a centrally applied load.



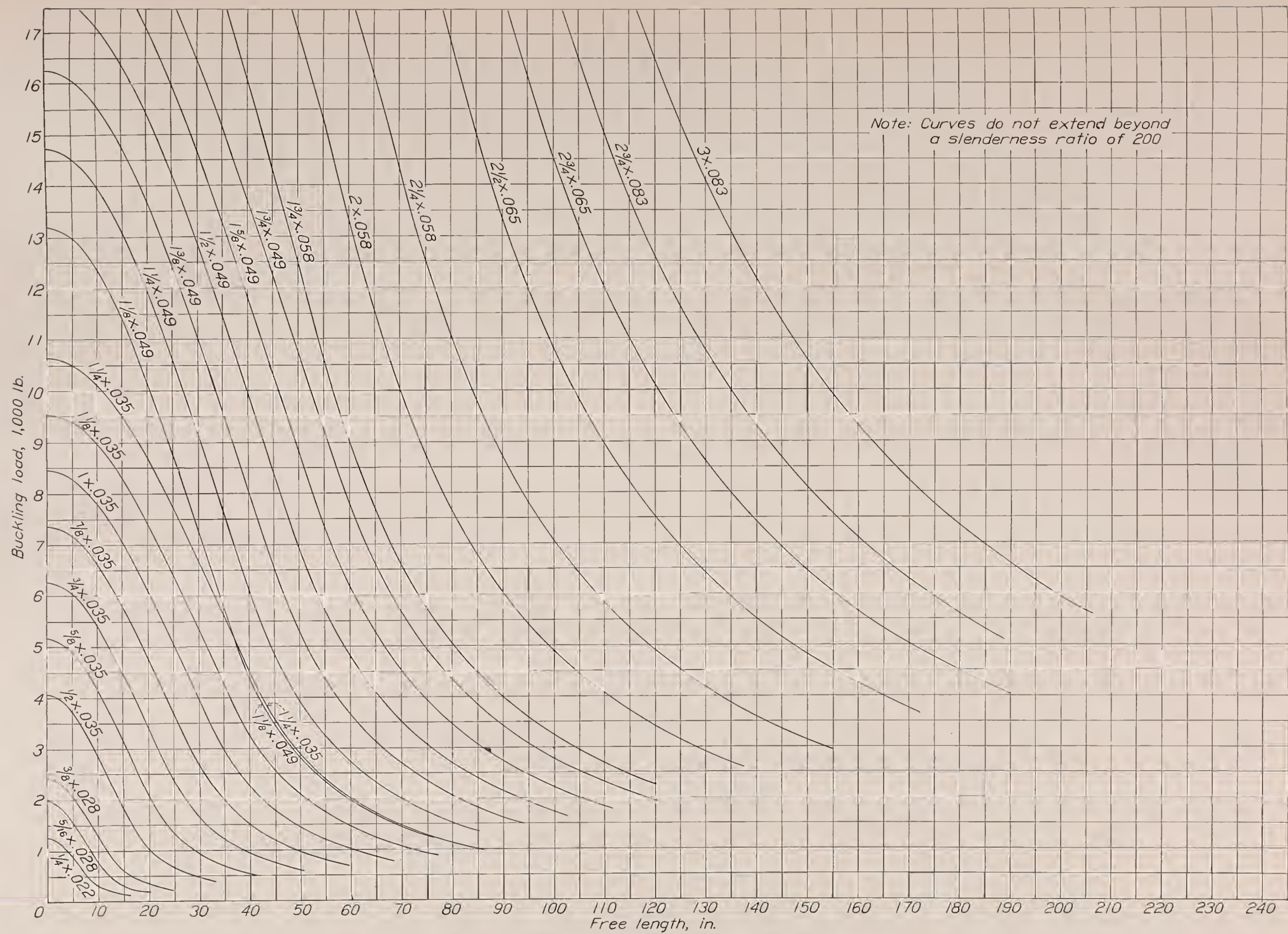
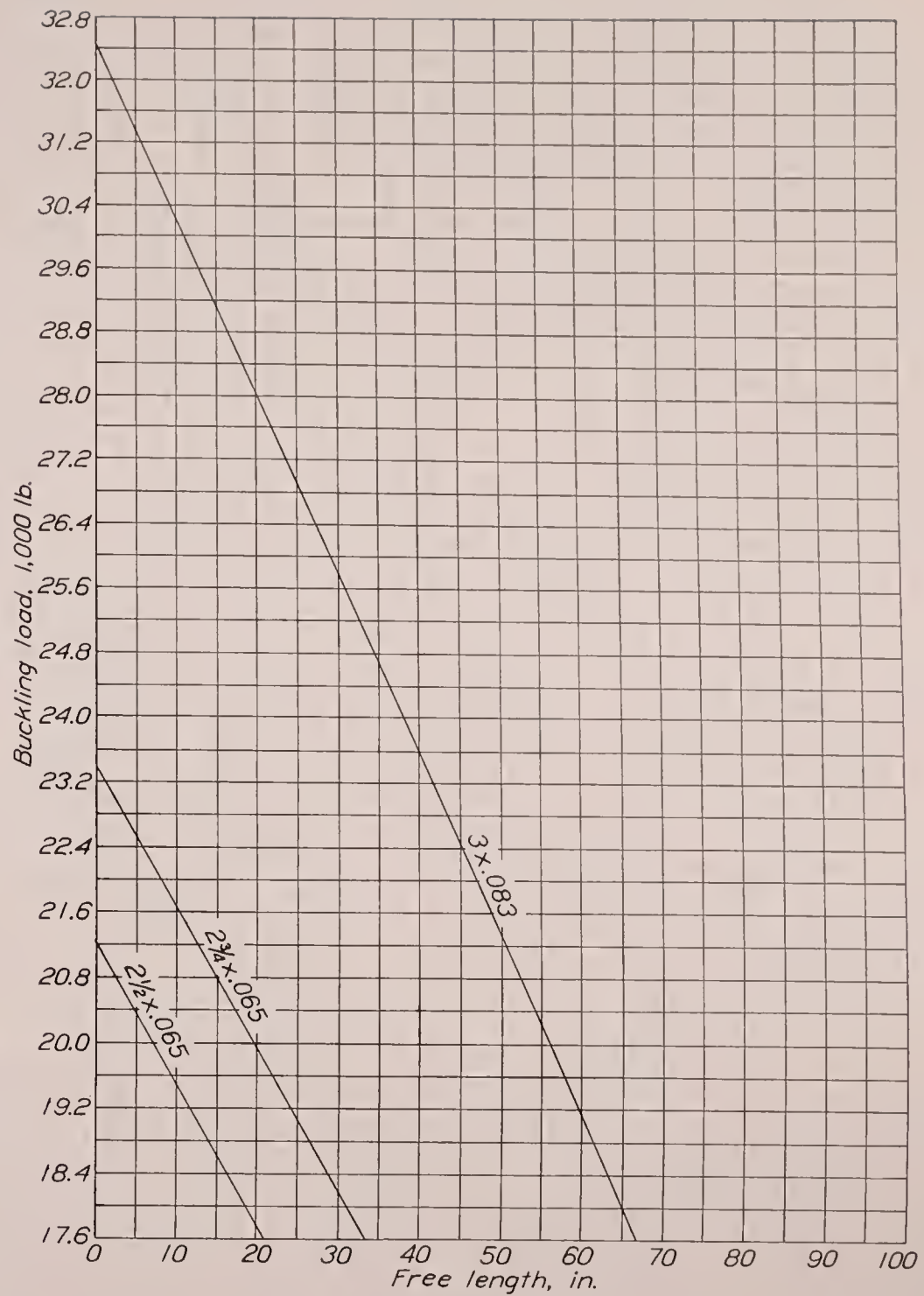
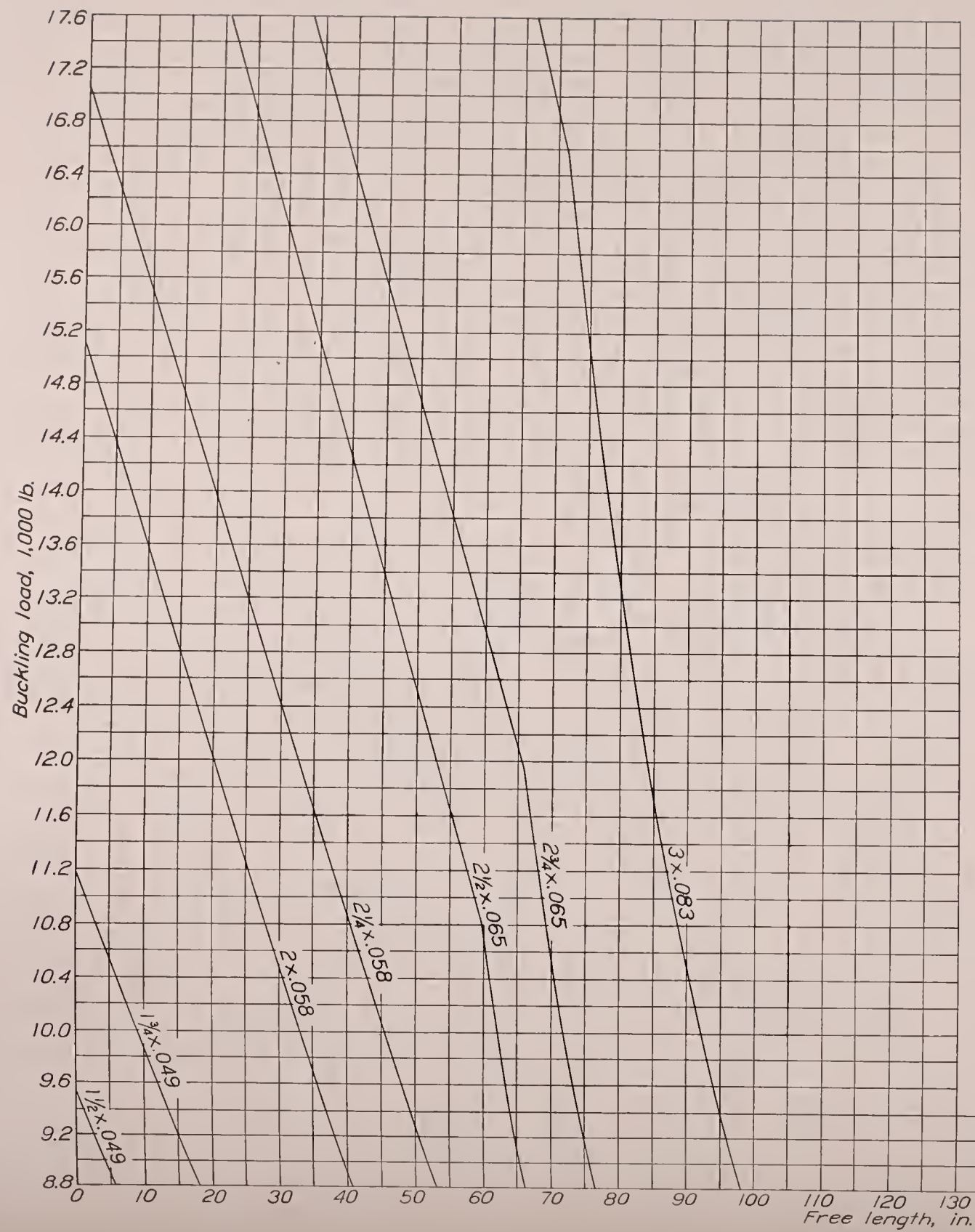


FIGURE 18.—The σ , P —diagram for Navy standard chromium-molybdenum-steel tubes.
 $Y. S. = 75,000$ lb. per sq. in.
 $E = 29,800,000$ lb. per sq. in.



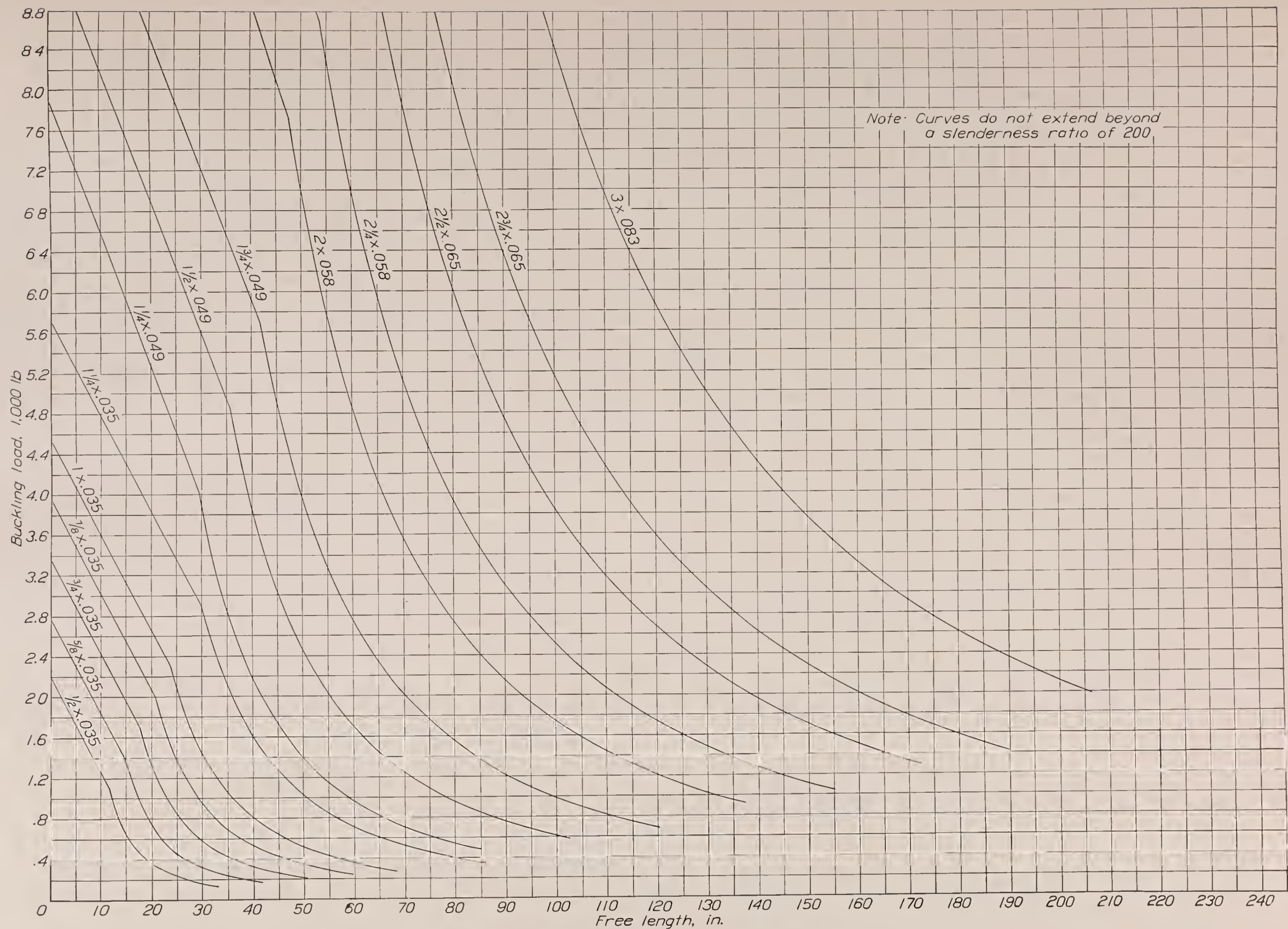
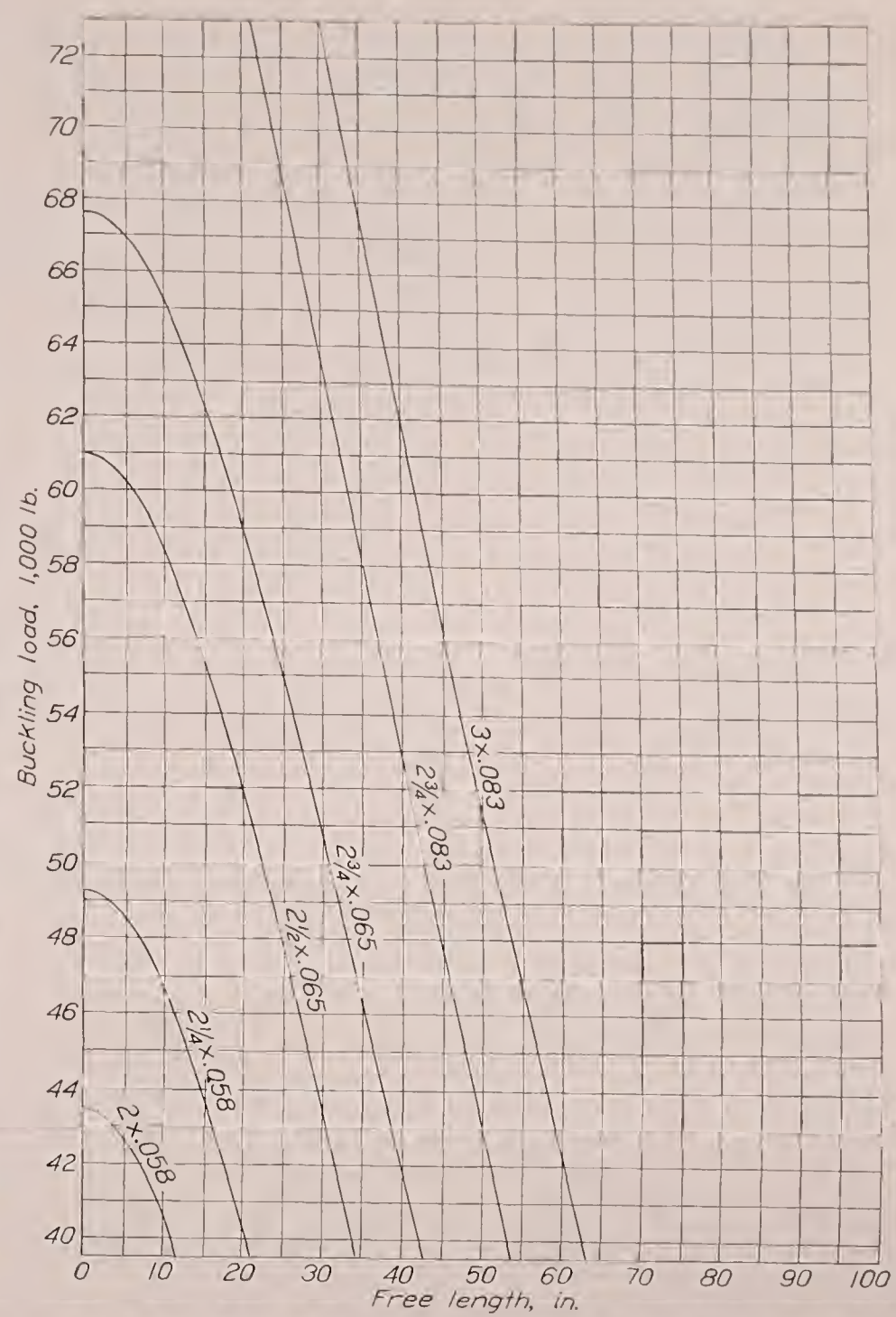
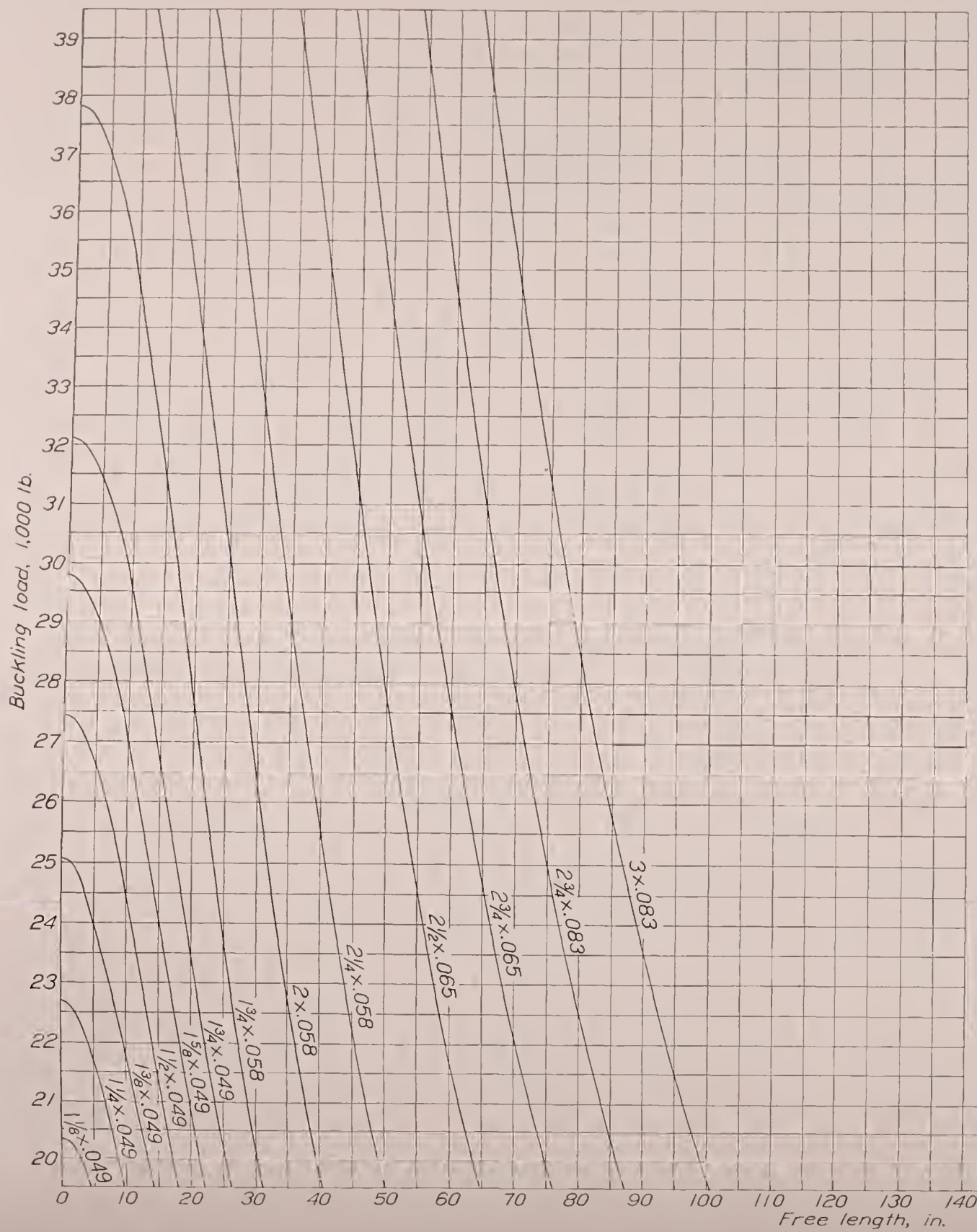


FIGURE 19.—The l_0, P —diagram for Navy standard duralumin tubes.
 $Y. S. = 40,000$ lb. per sq. in.
 $E = 10,590,000$ lb. per sq. in.



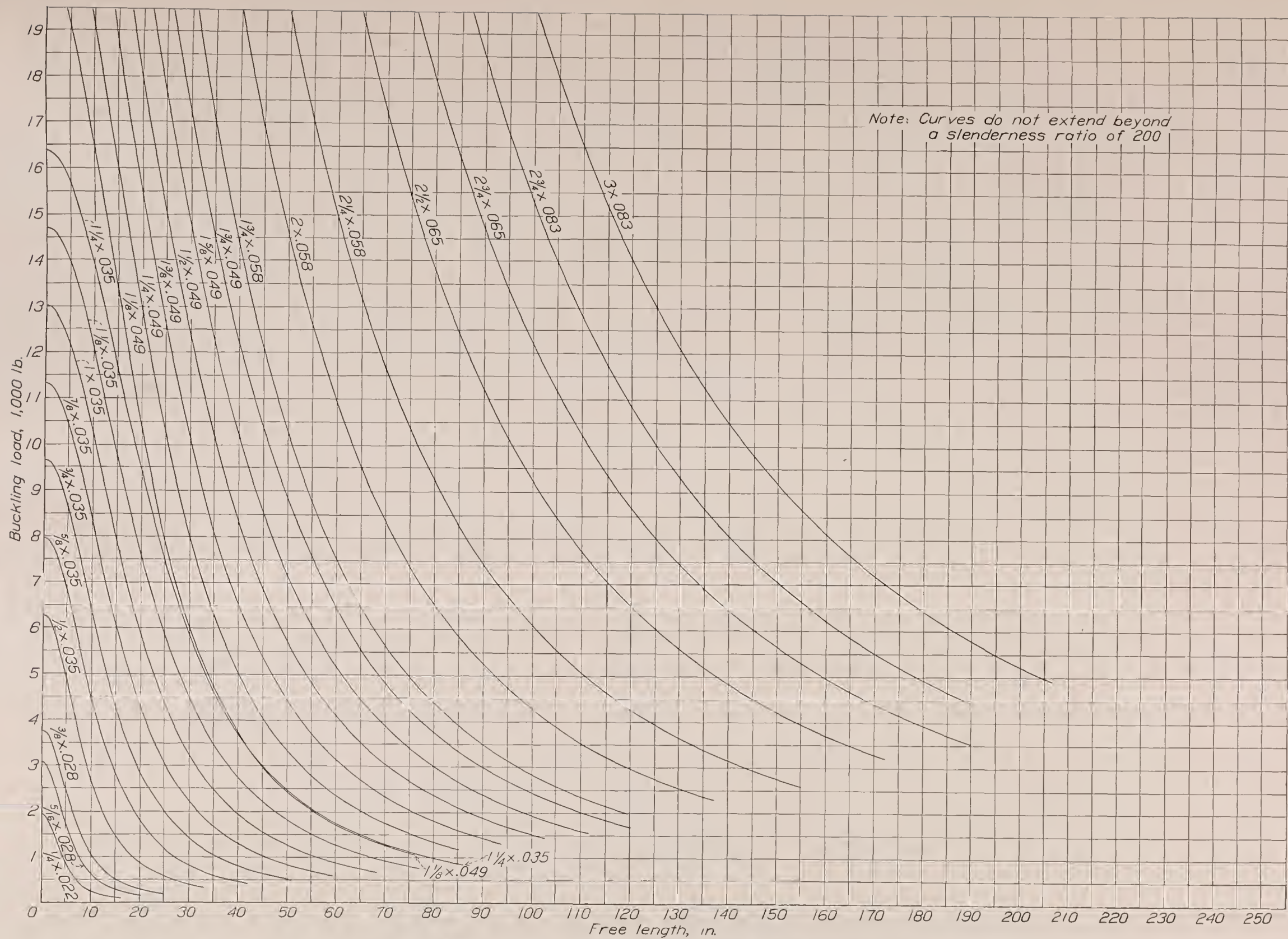
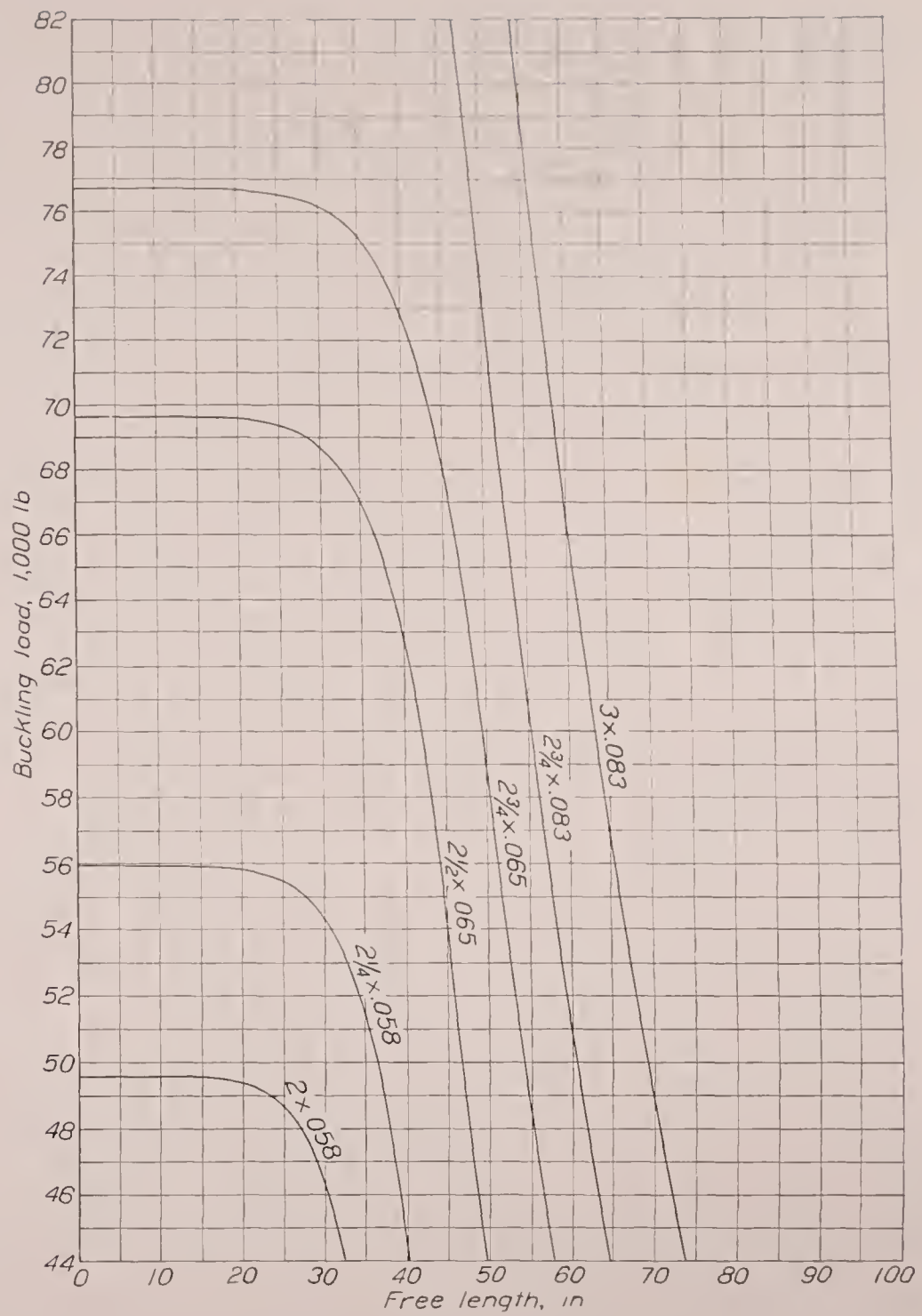
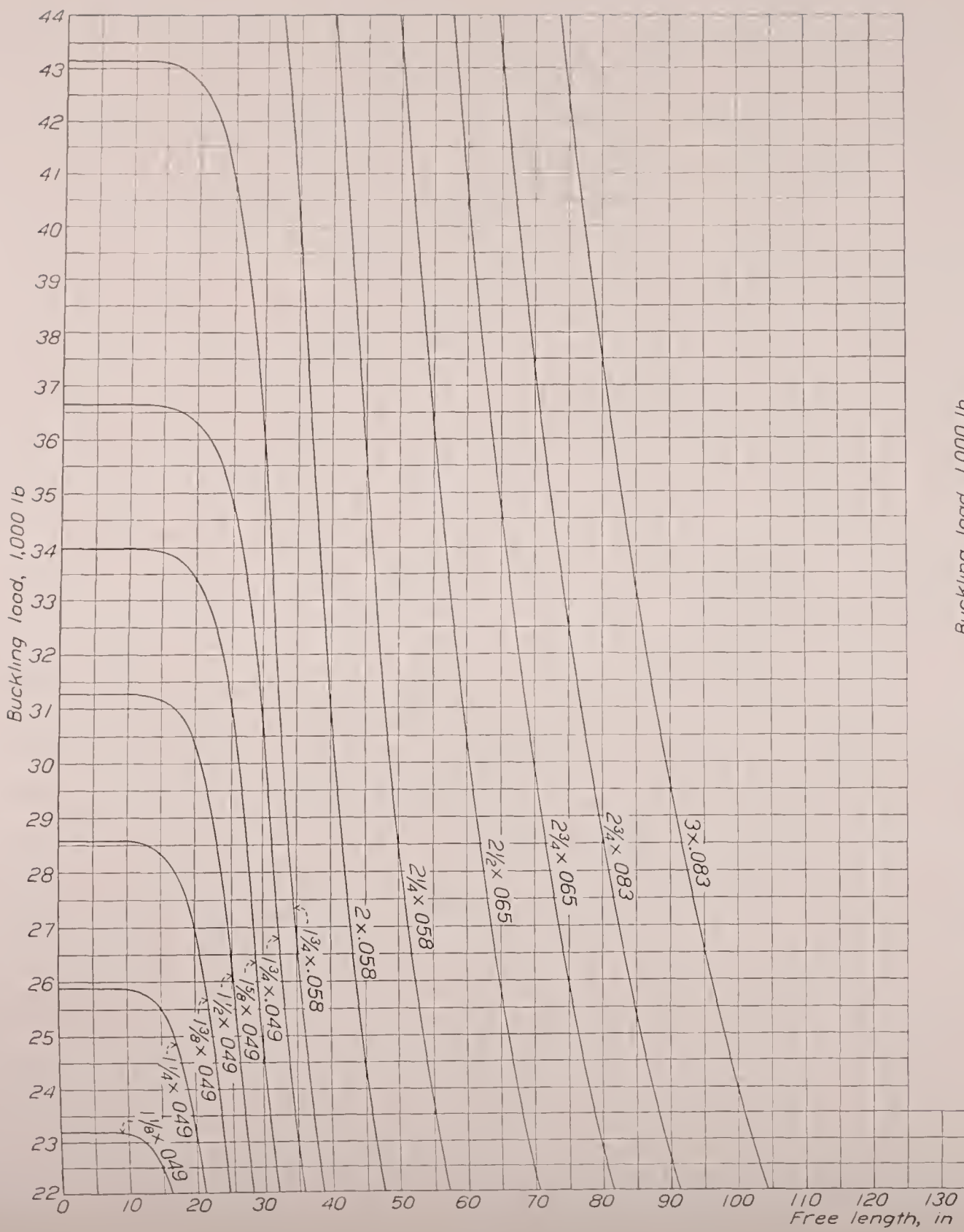


FIGURE 20.—The l , P —diagram for Navy standard stainless-steel tubes

$Y. S. = 135,000$ lb. per sq. in.
 $E = 26,300,000$ lb. per sq. in.



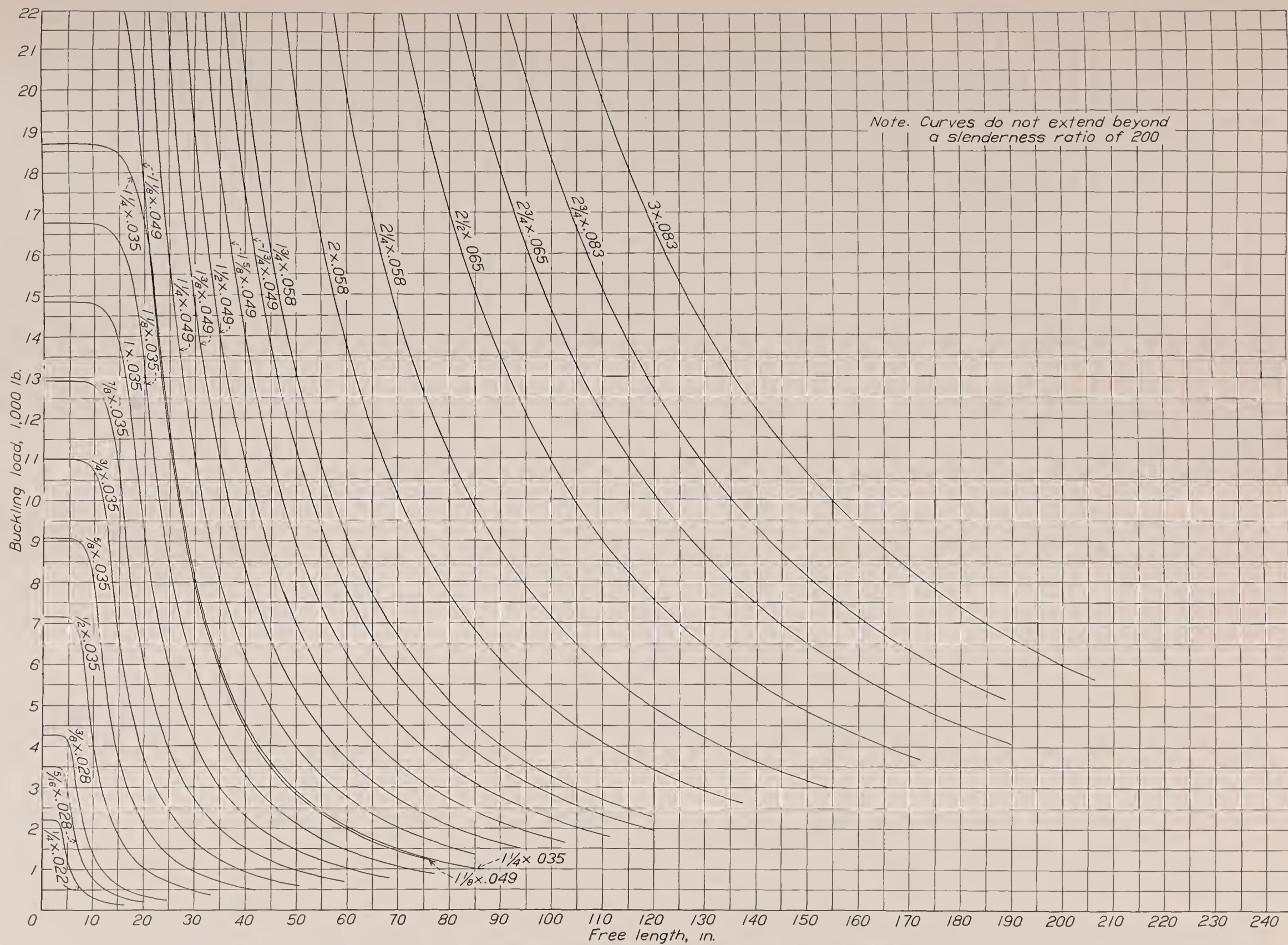


FIGURE 21.—The σ_c , P —diagram for heat-treated Navy standard chromium-molybdenum-steel tubes.

$Y. S. = 150,000$ lb. per sq. in.
 $E = 30,000,000$ lb. per sq. in.

Figures 18, 19, 20, and 21 represent curves of buckling load P , plotted against free length, l_0 , for Navy Department standard sizes of tubing up to and including 3 inches in diameter. These curves were obtained from equations (21a) and (24b) by inserting the appropriate values of A and i and solving for P in terms of l_0 .

In the analysis of trusses continuous at the joints it is necessary to use the ratio $\tau = \bar{E}/E$, which is a function of the average stress on the cross section of a column at the instant of buckling, since \bar{E} is a function of this stress. The relation between τ and the average stress may be obtained by eliminating λ_{os} from equation (14) and the empirical equation applying for the particular material being used, and then substituting for σ_s its value in terms of P/A . Thus, for chromium-molybdenum steel, by eliminating λ_{os} from equations (16a) and (14) and substituting

$$\sigma_s = \frac{P}{1.000 \cdot 75000A} \left(\frac{P}{A} \text{ in lb. per sq. in.} \right)$$

$$\tau = 0.00007467 \frac{P}{A} \frac{1 - 0.00001260 \frac{P}{A}}{1 + 0.00001333 \frac{P}{A}} \text{ for } 79400 \geq \frac{P}{A} \geq 32600 \quad (25a)$$

$$\text{and from (16b) } \tau = 1, \text{ for } 32600 \geq \frac{P}{A} > 0. \quad (25b)$$

Similarly for duralumin, equations (17a) and (14) give on substituting $\sigma_s = \frac{P}{0.908 \cdot 40000A} \left(\frac{P}{A} \text{ in lb. per sq. in.} \right)$

$$\tau = 0.0001920 \frac{P}{A} \left(1 - 0.00002343 \frac{P}{A} \right)^2 \text{ for } 42700 \geq \frac{P}{A} \geq 21800, \quad (26a)$$

$$\text{and from (17b) } \tau = 1, \text{ for } 21800 \geq \frac{P}{A} > 0 \quad (26b)$$

And for stainless steel, equations (19) and (14) give on substituting $\sigma_s = \frac{P}{0.827 \cdot 135000A} \left(\frac{P}{A} \text{ in lb. per sq. in.} \right)$

$$\tau = \frac{17}{9} - \frac{8}{9} \sqrt{1 + \left(0.00001520 \frac{P}{A} \right)^2} \quad (27)$$

Finally, for heat-treated chromium-molybdenum steel, equations (20a) and (14) give, on substituting

$$\sigma_s = \frac{P}{0.99 \cdot 150000A} \left(\frac{P}{A} \text{ in lb. per sq. in.} \right)$$

$$\tau = 0.00001411 \frac{P}{A} \left(1 - \frac{P}{140000A} \right)^2 \text{ for } 140000 \geq \frac{P}{A} \geq 108900 \quad (28a)$$

$$\text{and from (20b)} \quad \tau = 1 \text{ for } 108900 \geq \frac{P}{A} > 0. \quad (28b)$$

Tables III, IV, V, and VI give values of τ for different values of P/A in equations (25a) to (28b). The quantity $\frac{1}{\pi} \sqrt{\frac{1}{E\tau}}$ is also listed in these tables as it will be found convenient to have it.

DISCUSSION

Some of the material used for test did not pass specifications in all particulars, and in the evaluation of the results of the tests, this matter should be considered. One failure to meet specifications which might be considered significant in the present investigation is the failure to reach the specified tensile yield strength, but this failure can be adequately corrected for by using the λ_{os} , σ_s -method of plotting, provided that enough specimens which do pass the specification for yield strength are also tested as checks. Two round column specimens did not pass the specification for straightness (maximum allowable departure from straightness: ratio of initial deflection to length 1 to 600), but these specimens showed no lower strength than other comparable specimens; nor was the effect of initial deflection on the strength apparent in any other case.

Occasional high points in the l_0/i , P/A - and λ_{os} , σ_s -diagrams, as in figures 8 and 9, and figures 12 and 13, were due to friction at the knife edges and have no practical significance. This friction was minimized in the later tests by vibrating the specimen slightly by means of a light buzzer attached to the middle of the specimen during test. Three conspicuously low points in figures 11 and 15 were due to failure by local buckling at the ends of the specimens where they bore on the plates of the carriers. Two of these specimens were from round tubes with ratios of diameter to thickness of 35.7 and 50.0, respectively, and the third was from a streamline tube with ratio of basic round diameter to thickness of 32.1.

It seems safe now to conclude that round tubes having ratios of diameter to thickness not greater than was mentioned previously and conforming to Navy Department Specifications 44T18c, 44T21b for heat-treated tubing or 44T27 (INT) for $\frac{3}{4}$ H-cold drawn tubing, in particular tubes having departures from straightness not much greater than allowed by the specifications, may be designed as columns with elastically restrained ends on the basis of the double modulus and equations (21a), (21b) for chromium-molybdenum steel; (22a), (22b) for duralumin; and (23) for stainless steel. Similarly, round heat-treated chromium-molybdenum-steel tubes with ratios of diameter to thickness not much greater than 35 and with tensile yield strengths not less than 150,000 lb. per sq. in. may be designed with the aid of equations (24a) and (24b).

As far as the shape of the cross section is concerned, theoretically the streamline tubes should be slightly weaker than the round tubes; but this difference would be so small as to be masked by other considerations in a series of tests made under necessarily practical conditions. If the difference did show itself, it should do so independently of the material; but no such consistent difference appears in the test results.

The points representing the chromium-molybdenum-steel streamline tubing in the λ_{os}, σ_s -diagram (fig. 12) are all low except one, but these low values are believed to be due to the appreciably flatter knee of the compressive stress-strain diagram (reference 22) of the material of the streamline tubes. (See 1CB-C in fig. 1.) If this particularly flat knee may also be expected in round chromium-molybdenum-steel tubing, further tests with round tubing having this characteristic would be desirable. The results available indicate that for streamline chromium-molybdenum-steel tubing not over 0.186 inch thick, passing Navy Department Specification 44T17b, for which the ratio of basic round diameter d to thickness t does not appreciably exceed 35 (see table I), formula (21a) may be replaced by

$$\frac{P}{A} = 82400 \frac{20000 - \left(\frac{l_o}{i}\right)^2}{18900 + \left(\frac{l_o}{i}\right)^2} \text{ for } 87200 \geq \frac{P}{A} \geq 35800$$

For values of P/A less than 35,800 lb. per sq. in., equation (21b) applies.

The points representing the duralumin streamline tubing in the λ_{os}, σ_s -diagram (fig. 13) all except one high one closely follow the points for the round tubing.

The points representing the stainless-steel streamline tubing in the λ_{os}, σ_s -diagram (fig. 14) are the most erratic of any for the four materials tested, but this fact is not altogether surprising since the material was not the same as that of the round stainless-steel tubes. The trend of the points for the streamline tubing relative to those for the round tubing is consistent with the differences shown by the compressive stress-strain diagrams. The stress-strain curves of the material of the streamline tubing had sharper knees than those of the material of the round tubes (see 2SC-C in fig. 3) and the streamline-column specimens show high values of σ_s for high values of λ_{os} and low values of σ_s for low values of λ_{os} , which would be expected (reference 22).

The points representing the heat-treated chromium-molybdenum-steel tubing (fig. 15) closely follow the points for the round tubing, except two which are the results of tests on specimens with restrained ends. The restraint was heavy, 440,000 lb.-in. per radian and the reduced load-deflection curves for these specimens were not smooth at low loads and showed very blunt "knees." It is probable that, as load was applied, the movable head of the testing machine did not move parallel to itself, thus producing a rotation of the top end of the specimen and bending, which resulted in a very nonuniform distribution of stress. Since the knee of the stress-strain curve of this material is so sharp, premature bending of the specimen would lower the column strength more pronouncedly than would be the case with a material with a blunt knee.

NOTE ON THE DESIGN OF COMPRESSION MEMBERS ELASTICALLY RESTRAINED AT THE ENDS

In a truss or a framework (*Stabnetz*) continuous at the joints the members are interdependent, and in particular the buckling strength of a member depends on the restraining moments (positive or negative) produced at its ends by the other members meeting there. These moments, moreover, depend on the geometrical and material properties of all the members of the truss or framework. It is not possible, therefore, to consider the buckling of a compression member by itself but only as part of the structure as a whole. Theoretically, it is possible to determine with given conditions of loading the maximum load to produce failure of any truss, but practically, the solution of the transcendental equations involved is out of the question except for the simplest cases. Approximate solutions based on simplifying assumptions at present seem to offer the only way out.

Only planar trusses with the joints assumed to be immovable will be considered here. The case of movable joints has been treated by Bleich (reference 9), Prager (reference 23), and others; the case of space structures has been treated notably by Friedrich and Hans Bleich (reference 24).

In order to get anywhere it is necessary to assume that the truss can be broken up into sufficiently simple groups of members to enable the stability of each group to be investigated separately. Two such groups are (a) an individual compression member and the members meeting it at its ends, the far ends of the latter members being considered as freely supported (fig. 22); and (b) three members forming a triangle (fig. 23). As will be shown presently by examples, the first group can be treated by means of equation (12), and the stability of the second group can be investigated by means of the condition of buckling of a triangle.

$$\begin{vmatrix} t'_{ij} + t'_{jk} & s'_{jk} & s'_{ij} \\ s'_{jk} & t'_{jk} + t'_{ki} & s'_{ki} \\ s'_{ij} & s'_{ki} & t'_{ki} + t'_{ij} \end{vmatrix} = 0 \quad (25)$$

where

$$s' = \frac{E}{Pl} s \text{ and } t' = \frac{E}{Pl} t$$

and the subscripts refer to the members as shown in figure 23. This equation is given as applying to the elastic case by Borkmann (reference 25) and may be derived by applying the equation of four moments, Bleich (reference 9), successively to the members ij , jk ; jk , ki ; and ki , ij .

In the groups of members the stability of which is to be considered, P for each member represents the load in the member, positive for compression and negative for tension. The quantity ϕ , which occurs in the expressions for s and t , is always given by

$$\phi = l \sqrt{\frac{P}{EI}} \quad (26)$$

but when P is negative (tension), s and t become

$$s = \frac{\phi}{\sinh \phi} - 1 \text{ and } t = 1 - \frac{\phi}{\tanh \phi} \quad (9a)$$

If a member carries no load, or is assumed to carry no load, an assumption which may be made for sim-

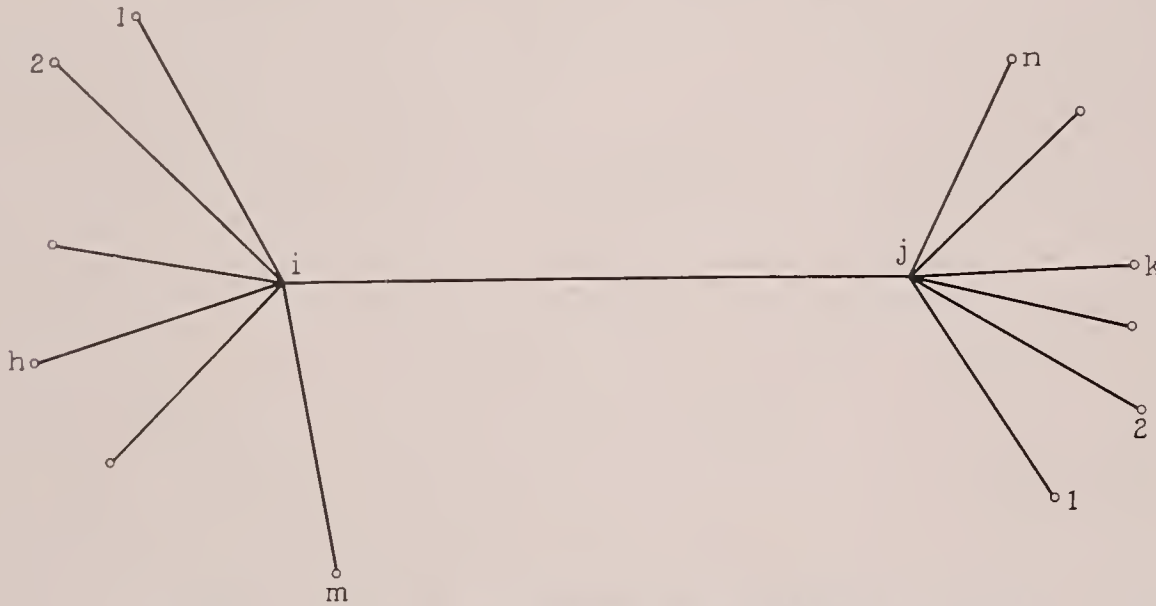


FIGURE 22.—A member of a truss, together with the members meeting it at its ends.



FIGURE 23.—Three members of a truss forming a triangle.

plicity and with safety for most practical tension members (see the appendix) then s' and t' or $s/(Pl)$ and $t/(Pl)$ become indeterminate. These quantities may be evaluated by the usual methods, and one finds

$$\frac{s}{Pl} = \frac{l}{6EI} \text{ and } \frac{t}{Pl} = \frac{l}{3EI} \quad (9b)$$

Equation (12) applied to the group of members shown in figure 22 may be written

$$\mu_i \mu_j (t_{ij}^2 - s_{ij}^2) + (\mu_i + \mu_j) t_{ij} + 1 = 0 \quad (27)$$

and

$$m_j + m_{j1} + m_{j2} + \dots + m_{jk} + \dots + m_{jn} = 0,$$

there can be obtained by simple substitution¹⁵

$$\left. \begin{aligned} \mu_i &= \frac{1}{P_{ij} l_{ij}} \left(\frac{P_{i1} l_{i1}}{t_{i1}} + \frac{P_{i2} l_{i2}}{t_{i2}} + \dots + \frac{P_{im} l_{im}}{t_{im}} \right) \\ \mu_j &= \frac{1}{P_{ij} l_{ij}} \left(\frac{P_{j1} l_{j1}}{t_{j1}} + \frac{P_{j2} l_{j2}}{t_{j2}} + \dots + \frac{P_{jn} l_{jn}}{t_{jn}} \right) \end{aligned} \right\} \quad (28)$$

The method of treating such groups of members as those designated (a) and (b) depends on whether it is

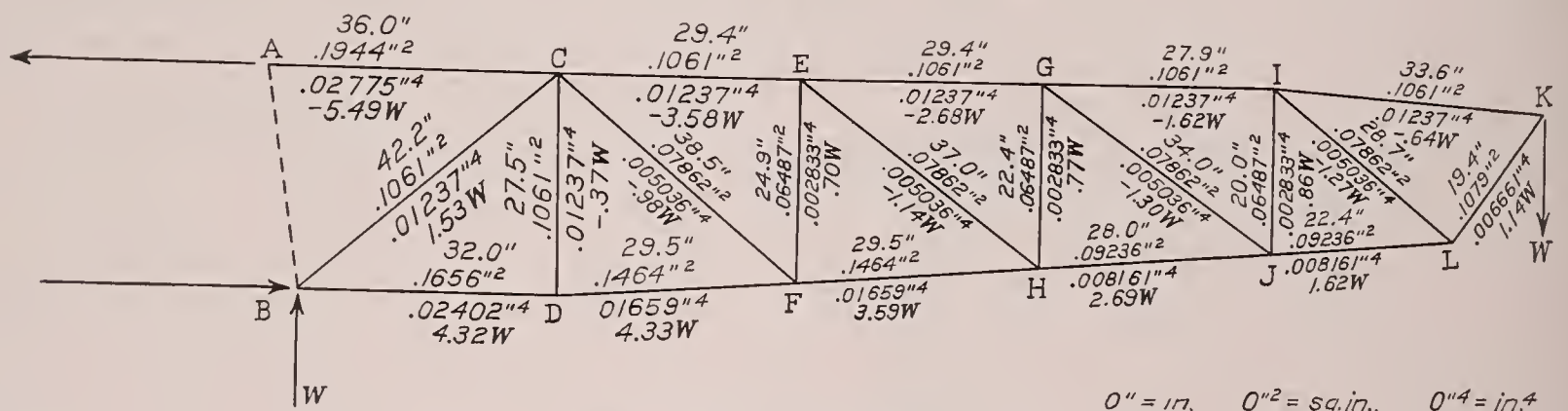


FIGURE 24.—Portion of a fuselage.

where μ_i and μ_j are the values of μ at i and j , respectively, and it is necessary to determine μ_i and μ_j in terms of the loads and the dimensions of the members of the group. The quantities μ_i and μ_j depend on the restraints offered by the members meeting ij at i and at j and may be found easily by applying equation (12) to these members. Thus if the member hi is considered and the value of μ at h is put equal to $\mu_{hi} = 0$, since the member is supposed freely supported at h , there is obtained on solving for the value of μ at i for this member

$$\mu_{ih} = \frac{m_{ih}}{P_{ih} l_{ih}} = -\frac{1}{t_{ih}}$$

desired merely to check the stability of existing groups under given loads or whether the groups are to be designed to carry specific loads. The actual procedure may be much the same in the two cases. In the first case the left-hand side of equation (27) or (25) is computed, whichever one applies, and is compared with the right-hand side, 0. No simple criteria can be given for assuring stability by means of such a comparison, however, and it is recommended that for a group like that shown in figure 22 the nomogram, figure 7, be used in conjunction with equation (27) to

¹⁵ The expressions for μ_i and μ_j were differently determined in reference 15 and were there called T_i and T_j .

determine whether a member is stable. It should be noted that no value of $\phi/\pi > 1.4303$ must be allowed to occur in any member *ih* or *jk*, because $\phi/\pi = 1.4303$ represents the condition of one end freely supported and the other end fixed. For a triangular group (fig. 23), care must be exercised in using equation (25) that no values of ϕ/π occur larger than those which correspond to the lowest critical loading. In the second case, that of designing members for specific loads, equation (27) or (25) must be solved for one unknown, ϕ , if the other members are assumed to be known, or if more than one member is unknown, the equation that applies must be solved by trial for such a combination of ϕ 's as will satisfy it. A numerical example will help to clarify the procedure.

Example: Figure 24 shows in outline a portion of a loaded chromium-molybdenum-steel truss. Posted on each member is its length l , cross-sectional area A , cross-sectional moment of inertia I , and load P . By a consideration of the group of members *FE*, *FC*, *FD*, *FH*, *HJ*, *HG*, and *HE*, it has been found that this group just reaches a neutral state of equilibrium when $W = 1,450$ pounds. It is desired to check the other compression members in order to determine whether they are in stable equilibrium and possibly to redesign some of them. Only two groups will be considered here, the group (a) *JL*, *JG*, *JL*, *LK*, *LI* and the group (b) *BC*, *CD*, and *DB*. It is convenient to arrange at least part of the computation in some such tabular form as the following:

1 Member	2 (in.)	3 A (sq. in.)	4 I (in. ⁴)	5 P (lb.)	6 $\frac{P}{A}$ (lb. per sq. in.)	7 $\frac{10^3}{\pi} \sqrt{\frac{1}{E\tau}}$ (in./lb. ^{1/2})	8 $\sqrt{\frac{P}{I}}$ (lb. ^{1/2} /in. ²)	9 $\frac{\phi}{\pi}$	10 s	11 t	12 $t^2 - s^2$	13 $\frac{10^3}{Pl}$ (1/lb.-in.)	14 $\frac{10^3 s}{Pl}$ (1/lb.-in.)	15 $\frac{Pl}{10^3 t}$ (lb.-in.)
JL	20.0	0.06487	0.002833	1,247	19,220	0.0583	663.5	0.774	-----	3.831	-----	0.4010	-----	6.510
JG	34.0	.07862	.005036	0	0	.0583	0	0	-----	0	-----	∞	-----	13.24
JL	22.4	.09236	.008161	2,349	25,430	.0583	536.5	.701	-----	2.611	3.829	.01900	-----	20.16
LK	19.4	.1079	.006661	1,653	15,320	.0583	498.2	.533	-----	1.355	-----	.03118	-----	23.67
LI	28.7	.07862	.005036	0	0	.0583	0	0	-----	0	-----	∞	-----	15.69
BC	42.2	.1061	.01237	2,218	20,910	.0583	423.4	1.042	-26.07	-23.86	-110.6	.01068	-0.2784	-3.925
CD	27.5	.1061	.01237	-536	-5,052	.0583	208.2	.334	-1.623	-3.424	.0909	-.06784	.01101	43.05
DB	32.0	.1656	.02402	6,264	37,830	.0589	510.7	.963	25.56	27.38	96.73	.00499	.1275	7.321

The values of P in the table are obtained from figure 24 with $W = 1,450$ pounds; the values in column 7 are obtained from table III; those in column 9 are 1 one-thousandth of the product of those in Columns 2, 7, and 8; those in columns 10, 11, and 12 are obtained from table VII except for member *CD*; and the source of the other entries is obvious. It was assumed for simplicity, and to be on the safe side, that members *JG* and *LI* carried no stress.

If equation (27) is now applied to the group (a), there is first obtained from equation (2)

$$\mu_J = 0.01900 (6.510 + 13.24) = 0.3752$$

$$\mu_L = 0.01900 (23.67 + 15.69) = 0.7478$$

Now substitute into equation (27) and find $0.3752 \times 0.7477 \times 3.829 + (0.3752 + 0.7478) \times 2.611 + 1 > 0$. The group is safe. The design, however, may be uneconomical and the possibility of redesigning the member *JL* is investigated. Any of the other members or any two or more members might have been considered. Substitute μ_J and μ_L as just found into equation (27) and solve it for ϕ_{JL} by trial with the aid of table VII or, more simply, determine ϕ_{JL} directly from the nomogram of figure 7:

$$\frac{\phi_{JL}}{\pi} = 1.784$$

This is the value of ϕ/π required for the member *JL* in order to bring the group (a) into neutral equilibrium. The value of ϕ/π in the original design is only 0.701, so that a considerably smaller member *JL* would be adequate. Assuming tubular construction, such a

member may be picked from the chart of figure 18 by entering it at the load $P_{JL} = 2,349$ lb. and the free length, computed from equation (4)

$$l_0 = \frac{l_{JL}}{\frac{\phi_{JL}}{\pi}} = \frac{22.4}{1.784} = 12.56 \text{ in.}$$

It is found that a 1/2-in. by 0.035-in. tube would be satisfactory. Whether this tube would represent a practical possibility is, of course, another matter.

If some member of the group other than the member *JL* were to be redesigned, equation (27) with the expressions for μ from equation (28) could be solved directly for the value of t required for the member. The required value of ϕ/π could then be looked up in table VII in the case of a compression member, or computed from equation (9a) in the case of a tension member. A new compression member could then be picked from figure 18 as just explained. A new tension member would have to be chosen by satisfying equation (26) by trial. If more than one member of the group were to be redesigned, a relation connecting the various ϕ/π 's could be obtained from equations (27) and (28) and this relation satisfied by trial. It would probably be at least as expeditious, however, to modify one member at a time rather than two or more simultaneously.

Let the second group of members now be considered—the triangle composed of the members *BC*, *CD*, *DB*. Proceed in the same general way as with the first group, that is, compare the left-hand side of equation (25) with zero. If the determinant is expanded, the values of s' and t' in terms of E , P , l , s , and t are substituted,

and the result is divided through by E^3 , there may be written

$$\begin{aligned} & \left(\frac{t_{BC}}{P_{BC}l_{BC}} + \frac{t_{CD}}{P_{CD}l_{CD}} \right) \left(\frac{t_{CD}}{P_{CD}l_{CD}} + \frac{t_{DB}}{P_{DB}l_{DB}} \right) \left(\frac{t_{DB}}{P_{DB}l_{DB}} + \frac{t_{BC}}{P_{BC}l_{BC}} \right) \\ & + 2 \frac{s_{BC}s_{CD}s_{DB}}{P_{BC}l_{BC}P_{CD}l_{CD}P_{DB}l_{DB}} - \frac{s_{BC}^2}{P_{BC}^2l_{BC}^2} \left(\frac{t_{CD}}{P_{CD}l_{CD}} + \frac{t_{DB}}{P_{DB}l_{DB}} \right) \\ & - \frac{s_{CD}^2}{P_{CD}^2l_{CD}^2} \left(\frac{t_{DB}}{P_{DB}l_{DB}} + \frac{t_{BC}}{P_{BC}l_{BC}} \right) \\ & - \frac{s_{DB}^2}{P_{DB}^2l_{DB}^2} \left(\frac{t_{BC}}{P_{BC}l_{BC}} + \frac{t_{CD}}{P_{CD}l_{CD}} \right) = 0 \end{aligned} \quad (29)$$

Substitution from the table gives

$$0.004375 - 0.0007816 - 0.01239 + 0.00001433 + 0.003766 = -0.005017 < 0.$$

The group is safe. The design may be uneconomical, however, and the possibility of redesigning the member BC is investigated. Any of the other members or any two of them might have been considered. For the present purpose it is more convenient to write equation (29) in the form

$$\begin{aligned} & \frac{1}{P_{BC}^2l_{BC}^2} \left(\frac{t_{CD}}{P_{CD}l_{CD}} + \frac{t_{DB}}{P_{DB}l_{DB}} \right) (t_{BC}^2 - s_{BC}^2) \\ & + \frac{1}{P_{BC}l_{BC}} \left[\left(\frac{t_{CD}}{P_{CD}l_{CD}} + \frac{t_{DB}}{P_{DB}l_{DB}} \right)^2 - \left(\frac{s_{CD}^2}{P_{CD}^2l_{CD}^2} + \frac{s_{DB}^2}{P_{DB}^2l_{DB}^2} \right) \right] t_{BC} \\ & + 2 \frac{s_{CD}s_{DB}s_{BC}}{P_{CD}l_{CD}P_{DB}l_{DB}P_{BC}l_{BC}} + \frac{(t_{DB}^2 - s_{DB}^2)t_{CD}}{P_{DB}^2l_{DB}^2P_{CD}l_{CD}} \\ & + \frac{(t_{CD}^2 - s_{CD}^2)t_{DB}}{P_{CD}^2l_{CD}^2P_{DB}l_{DB}} = 0 \end{aligned}$$

Substitution from the table of all values except s_{BC} and t_{BC} gives after simplification

$$t_{BC}^2 - s_{BC}^2 + 5.366t_{BC} + 1.645s_{BC} + 6.194 = 0$$

Solution of this equation by trial with the aid of table VII gives for the value of ϕ/π required to cause buckling,

$$\frac{\phi_{BC}}{\pi} = 1.799$$

Since this value is greater than the actual value, 1.043, a smaller member may be picked from figure 18. If, as before, the free length is determined

$$l_0 = \frac{l_{BC}}{\frac{\phi_{BC}}{\pi}} = 23.46 \text{ in.}$$

and the chart (fig. 18) entered with this length and the load $P_{BC} = 2,218 \text{ lb.}$, a $\frac{3}{4}$ -in. by 0.035-in. tube is found to be adequate.

It may be noted that when for any member ϕ/π is less than unity, the member has reserve strength considered as a freely supported column and can act to restrain the members meeting at its ends. In the previous example, the values of ϕ/π for all the members were less than unity except for the member BC. No value of ϕ/π greater than 2 is possible if the structure is to remain stable.

It may happen that the most severe condition of loading for a given member is not the one that produces the greatest average compressive stress in the member. Strictly, then, every member should be investigated for each condition of loading which produces compression in it. Practically, however, this procedure will not be necessary, and if a member in compression is satisfactory for the condition of loading producing the greatest average compressive stress in it, it will usually be possible to tell by inspection whether other conditions of loading should also be considered.

NATIONAL BUREAU OF STANDARDS,
Washington, D. C., September 9, 1937.

APPENDIX

The simplifying assumption that tension members in a group carry no load is safe so long as the quantities $\frac{Pl}{s}$ and $\frac{Pl}{t}$ which occur for these members satisfy the conditions

$$\frac{Pl}{s} = \frac{-|P|l}{\frac{\phi}{\sinh \phi} - 1} \geq \frac{6EI}{l} \quad (a)$$

and

$$\frac{Pl}{t} = \frac{-|P|l}{1 - \frac{\phi}{\tanh \phi}} \geq \frac{3EI}{l} \quad (b)$$

respectively. In order to investigate whether these conditions are satisfied in any given case, it is necessary to know the value of τ for computing ϕ . Since no information concerning τ will usually be available for tension members, it is suggested that the values given for the same stress in compression be used. It is not to be expected that the discrepancy will be large. For $\tau = 1$ conditions (a) and (b) will always be satisfied, and for any practical member it is almost certain that

they will be. In case of doubt, for example, extremely high values of $|P|/A$, the simplifying assumption should not be made.

REFERENCES

1. Tuckerman, L. B.: Discussion of paper by R. L. Templin, The Determination and Significance of the Proportional Limit in the Testing of Metals. Proc. Am. Soc. Testing Mats., vol. 29, pt. II, 1929, pp. 538-546.
2. Osgood, William R.: The Double-Modulus Theory of Column Action. Civil Engineering, vol. 5, no. 3, March 1935, pp. 173-175.
3. Christie, James: Experiments on the Strength of Wrought-Iron Struts. Trans. Am. Soc. Civ. Eng., vol. 13, April 1884, p. 85.
4. Considère, A.: Résistance des Pièces Comprimées. Congrès International des Procédés de Construction, 1891, p. 371.
5. Engesser, Fr.: Über die Knickfestigkeit von Stäben veränderlichen Trägheitsmomentes. Zeit. d. Österreich. Ing.-u. Arch.-Vereines, vol. 61, 1909, p. 544.
6. Nater, H.: Knickung elastisch eingespannter Stäbe. Schweizerische Bauzeitung, Bd. 71, 18. Mai 1918, S. 215.
7. Usinger, P.: Beiträge zur Knicktheorie. Der Eisenbau, Bd. 9, Aug. 1918, S. 169.

8. Leduc, R.: Contribution à l'Étude des Poutres Prismatiques. Services Techniques de l'Aéronautique, Bulletin Technique No. 60, Juin 1929, p. 43.

9. Bleich, Fr.: Theorie und Berechnung der eisernen Brücken. Julius Springer (Berlin), 1924; also Die Knickfestigkeit elastischer Stabverbindungen. Der Eisenbau, Bd. 10, Feb. 1919, S. 27.

10. von Kármán, Th.: Untersuchungen über Knickfestigkeit, Mitteilungen über Forschungsarbeiten. Ver. deutsch. Ing., Heft 81, 1910.

11. Zimmermann, H.: Die Knickfestigkeit von Stäben mit nicht gerader Achse. Sitzungsberichte der Preussischen Akademie der Wissenschaften, 18. Oktober 1923, S. 262; also Lehre vom Knicken auf neuer Grundlage, Wilhelm Ernst und Sohn (Berlin), 1930.

12. Rein, W.: Versuche zur Ermittlung der Knickspannungen für verschiedene Baustähle. Julius Springer (Berlin), 1930.

13. Zimmermann, H.: Knickfestigkeit der Stabverbindungen. Wilhelm Ernst und Sohn (Berlin), 1925.

14. Prager, W.: The Buckling of an Elastically Encastred Strut. Jour. R. A. S., vol. 49, no. 311, Nov. 1936, pp. 833-834.

15. Osgood, Wm. R.: Contribution to the Design of Compression Members in Aircraft. Bur. Standards Jour. Res., vol. 13, no. 1, July 1934, pp. 157-160.

16. Soreau, Rodolphe: Nomographie ou Traité des Abaques. Tome I, Etienne Chiron (Paris), 1921, p. 172.

17. Hohenemser, K.: Fließversuche an Rohren aus Stahl bei kombinierter Zug- und Torsionbeanspruchung. Z. A. M. M., Bd. 11, Feb. 1931, S. 15.

18. Tuckerman, L. B., Petrenko, S. N., and Johnson, C. D.: Strength of Tubing under Combined Axial and Transverse Loading. T. N. No. 307, N. A. C. A., 1929.

19. Domke, O.: Die Ausbiegung eines Druckstabes bei Überschreitung der Knicklast. Die Bautechnik, Bd. 4, 26. Nov. 1926, S. 747.

20. Kreüger, H.: Bidrag till frågen om sträfvors knäckning. Teknisk Tidskrift (Sweden), Väg- och Vattenbyggnadskonst., vol. 45, Sept. 15, 1915, p. 101.

21. Aarflot, M. G.: A New Column Formula. Bul. Am. Soc. Swedish Eng., vol. 26, Feb. 1931, p. 7.

22. Osgood, William R.: Column Curves and Stress-Strain Diagrams. Research Paper No. 492, Bur. Standards Jour. Res., vol. 9, no. 4, Oct. 1932, pp. 571-582.

23. Prager, W.: Elastic Stability of Plane Frameworks. Jour. Aero. Sci., vol. 3, no. 11, Sept. 1936, p. 388.

24. Bleich, Friedrich, und Bleich, Hans: Die Stabilität räumlicher Stabverbindungen. Zeit. d. Österreich. Ing.- u. Arch.-Vereines, Bd. 80, 1928, S. 345.

25. Borkmann, K.: Charts for Checking the Stability of Compression Members in Trusses. T. M. No. 800, N. A. C. A., 1936.

TABLE I.—NOMINAL DIMENSIONS OF TUBES AND RESTRAINTS USED

Nominal diameter or basic round diameter d (in.)	Nominal thickness t (in.)	Nominal d/t	Nominal area A (sq. in.)	Radius of gyration i (in.)	Restraints ¹
ROUND TUBES					
Chromium-molybdenum steel					
1-----	0.035	28.6	0.1061	0.3414	<i>A CHab</i>
1½-----	.049	23.0	.1656	.3808	<i>A CHab</i>
1¾-----	.058	25.9	.2628	.5102	<i>ABDEGgb</i>
Duralumin					
1-----	0.035	28.6	0.1061	0.3414	<i>A CH</i>
1½-----	.058	25.9	.2628	.5102	<i>A CHab</i>
2-----	.058	34.5	.3539	.6869	<i>A CH</i>
Stainless steel					
1-----	0.035	28.6	0.1061	0.3414	<i>A Gab</i>
1-----	.083	12.0	.2391	.3255	<i>ACGa</i>
1¼-----	.035	35.7	.1336	.4297	<i>ACb</i>
1¼-----	.065	19.2	.2420	.4196	<i>AGa</i>
1½-----	.049	30.6	.2234	.5133	<i>AC</i>
Heat-treated chromium-molybdenum steel					
1-----	0.042	23.8	0.1264	0.3390	<i>A</i>
1¼-----	.035	35.7	.1336	.4297	<i>AF</i>
1¾-----	.035	50.0	.1886	.6065	<i>A</i>
1¾-----	.049	35.7	.2618	.6016	<i>A</i>
STREAMLINE TUBES					
Chromium-molybdenum steel					
1¼-----	0.035	35.7	0.1336	0.2509	<i>AF</i>
2½-----	.083	30.1	.6302	.4993	<i>A</i>
Duralumin					
1¼-----	0.035	35.7	0.1336	0.2509	<i>AF</i>
2½-----	.065	38.5	.4972	.5167	<i>A</i>
Stainless steel					
1¼-----	0.035	35.7	0.1336	0.2509	<i>AF</i>
1½-----	.049	30.6	.2234	.2997	<i>AF</i>
2-----	.058	34.5	.3539	.4122	<i>A</i>
2½-----	.065	38.5	.4972	.5167	<i>A</i>
Heat-treated chromium-molybdenum steel					
1⅝-----	0.035	32.1	0.1198	0.2251	<i>AF</i>
2¼-----	.058	38.8	.3994	.4527	<i>AF</i>

¹ Restraints are designated in lb.-in. per radian as follows: equal restraints at both ends, *A*=0; *B*=132,000; *C*=233,000; *D*=250,000; *E*=330,000; *F*=440,000; *G*=451,000; *H*=452,000; restraint at lower end only, *a*=233,000; *b*=450,000.

TABLE II.—RESULTS OF TESTS ON COLUMNS
ROUND TUBING

BOTH ENDS FREELY SUPPORTED OR RESTRAINED

Specimen	End re- straint $10^{-3}m$ (lb.-in. per radian)	Ratio of slender- ness l_0/i	Average stress P/A (lb. per sq. in.)	$\lambda_{os} = \frac{1}{\pi} \frac{l_0}{i} \sqrt{\frac{S}{E}}$	$\sigma_s = \frac{P}{AS}$	Specimen	End re- straint $10^{-3}m$ (lb.-in. per radian)	Ratio of slender- ness l_0/i	Average stress P/A (lb. per sq. in.)	$\lambda_{os} = \frac{1}{\pi} \frac{l_0}{i} \sqrt{\frac{S}{E}}$	$\sigma_s = \frac{P}{AS}$
CHROMIUM-MOLYBDENUM STEEL											
1 in. diameter by 0.035 in. thick. Nominal $d/t=28.6$											
CA-4.....	233	22.27	90,910	0.406	0.917	CA-5.....	0	59.85	66,080	1.092	0.667
CA-5b.....	233	43.65	79,730	.797	.805	CA-2.....	452	78.08	44,080	1.425	.445
1 1/8 in. diameter by 0.049 in. thick. Nominal $d/t=23.0$											
DA-3.....	233	41.34	77,960	0.728	0.845	DA-2.....	452	70.29	50,580	1.237	0.548
DA-5.....	0	49.78	73,190	.876	.793	DA-4.....	0	89.85	35,830	1.582	.388
DA-5c.....	0	67.79	55,780	1.193	.604						
1 1/2 in. diameter by 0.058 in. thick. Nominal $d/t=25.9$											
D-6.....	451	19.07	87,420	0.334	0.964	AD-2.....	250	65.52	52,200	1.100	0.644
O-3.....	330	19.77	86,470	.338	1.004	N-3.....	330	64.30	59,980	1.106	.693
A-6.....	451	19.06	90,250	.339	.972	AC-2.....	451	71.08	51,120	1.120	.696
D-3.....	330	19.61	84,880	.343	.936	Q-3.....	330	64.12	62,960	1.127	.688
O-6.....	250	20.57	82,690	.352	.959	X-3.....	250	68.05	56,800	1.174	.644
AK-2.....	250	21.08	92,650	.375	.991	AF-2.....	451	72.90	54,650	1.234	.646
A-3.....	132	26.42	85,380	.469	.920	AB-2.....	250	76.99	42,400	1.271	.529
B-3.....	132	26.45	86,610	.472	.926	N-2.....	330	74.70	46,780	1.285	.541
T-2.....	451	30.57	81,540	.529	.928	Q-2.....	330	75.29	51,700	1.324	.565
AJ-2.....	451	30.75	87,890	.538	.969	P-3.....	0	75.59	49,870	1.329	.545
O-2.....	330	32.45	82,280	.555	.956	I-3.....	0	75.66	49,300	1.335	.544
D-2.....	330	32.16	80,950	.563	.893	F-3.....	132	78.28	45,510	1.363	.517
L-5.....	0	32.82	83,430	.579	.920	S-2.....	250	77.99	44,560	1.367	.491
P-5.....	0	32.96	86,240	.579	.942	I-3.....	132	78.69	46,210	1.379	.515
V-3.....	250	34.84	86,020	.607	.961	V-2.....	451	84.65	40,640	1.474	.454
Z-3.....	250	34.99	88,470	.613	.980	Z-2.....	451	84.32	39,920	1.477	.442
A-2.....	132	44.38	80,620	.788	.869	R-2.....	330	87.25	35,390	1.488	.416
O-5.....	451	46.19	76,340	.790	.887	J-2.....	330	87.77	37,130	1.499	.433
B-2.....	132	44.93	82,870	.801	.886	I-2.....	132	88.37	34,670	1.548	.387
U-3.....	451	47.00	82,980	.833	.891	F-2.....	132	89.55	35,970	1.560	.409
R-3.....	330	48.91	74,730	.834	.879	T-5.....	250	91.23	33,680	1.580	.383
J-3.....	330	48.89	75,910	.835	.885	U-2.....	250	91.70	32,700	1.626	.351
P-4.....	0	51.21	72,300	.900	.790	E-3.....	0	100.3	28,830	1.741	.323
L-4.....	0	51.27	74,750	.905	.824	M-3.....	0	100.4	29,040	1.766	.321
D-5.....	250	52.55	72,190	.920	.796	H-2.....	132	102.5	27,780	1.781	.317
A-5.....	250	53.49	77,600	.950	.836	G-2.....	132	102.7	26,390	1.795	.295
AI-2.....	451	60.13	57,300	.986	.720	P-2.....	0	120.3	20,360	2.114	.223
AII-2.....	451	60.39	64,060	1.061	.703	K-2.....	0	120.2	20,720	2.160	.219
H-3.....	132	62.60	62,750	1.088	.716	E-4.....	0	150.0	16,330	2.604	.183
G-3.....	132	62.85	59,820	1.098	.668	M-2.....	0	150.2	13,110	2.643	.145
DURALUMIN											
1 in. diameter by 0.035 in. thick. Nominal $d/t=28.6$											
EA-4.....	233	21.84	43,500	0.436	1.041	EA-5b.....	0	65.34	24,350	1.304	0.582
EA-3.....	233	41.95	33,220	.837	.795	EA-2.....	452	76.44	16,330	1.525	.391
EA-5a.....	0	59.74	27,050	1.192	.647	EA-5d.....	0	85.29	14,310	1.702	.342
EA-5.....	0	59.84	27,690	1.194	.662	EA-5e.....	0	85.32	14,280	1.702	.342
EA-5c.....	0	65.23	24,930	1.301	.596						
1 1/2 in. diameter by 0.058 in. thick. Nominal $d/t=25.9$											
BD-2b.....	0	24.46	38,240	0.478	0.958	BC-6.....	0	49.94	31,410	1.006	0.746
BA-6.....	0	29.94	37,670	.597	.908	BA-5.....	0	74.82	18,780	1.492	.453
BB-7.....	0	29.97	37,410	.598	.906	BC-4.....	0	74.97	18,700	1.510	.444
BB-5.....	452	32.75	36,620	.653	.887	BA-3.....	0	99.88	10,740	1.991	.259
BC-5.....	233	34.27	35,730	.690	.849	BB-3.....	0	99.88	11,370	1.992	.275
BD-2.....	0	39.87	32,840	.780	.823	BB-2.....	0	118.4	7,520	2.361	.182
BD-2a.....	0	39.89	32,910	.780	.825	BC-3.....	0	118.6	7,400	2.389	.176
BA-4.....	452	45.97	30,720	.916	.740	BA-2.....	0	147.7	4,840	2.945	.117
BB-4.....	233	48.76	31,180	.973	.755	BC-2.....	0	147.9	8,800	2.980	.209
BB-6.....	0	49.90	30,850	.995	.747						
2 in. diameter by 0.058 in. thick. Nominal $d/t=34.5$											
FA-3.....	452	41.38	32,990	0.819	0.801	FA-5.....	0	49.93	29,920	0.988	0.726
FA-4.....	233	45.36	30,840	.898	.749	FA-2.....	452	58.02	25,960	1.148	.630
STAINLESS STEEL											
1 in. diameter by 0.035 in. thick. Nominal $d/t=28.6$											
GA-7.....	451	25.23	124,400	0.541	1.034	GB-6.....	0	60.43	59,870	1.292	0.501
GA-9.....	0	35.52	87,180	.762	.724	GA-6.....	0	60.31	56,400	1.294	.468
GB-10.....	0	35.64	93,250	.762	.780	GA-5.....	0	73.76	40,350	1.582	.335
GB-8.....	0	50.35	69,130	1.077	.578	GA-3.....	0	97.60	26,260	2.094	.218
GA-8.....	0	50.22	63,410	1.077	.527	GA-2.....	0	126.0	16,470	2.702	.137
GB-2.....	451	59.12	59,510	1.264	.498						

TABLE II.—RESULTS OF TESTS ON COLUMNS—Continued

Specimen	End re- straint 10 ⁻³ <i>m</i> (lb.-in. per radian)	Ratio of slender- ness <i>l</i> ₀ / <i>i</i>	Average stress <i>P</i> / <i>A</i> (lb. per sq. in.)	$\lambda_{os} =$ $\frac{1}{\pi} \frac{l_o}{i} \sqrt{\frac{S}{E}}$	$\sigma_s =$ $\frac{P}{A}$	Specimen	End re- straint 10 ⁻³ <i>m</i> (lb.-in. per radian)	Ratio of slender- ness <i>l</i> ₀ / <i>i</i>	Average stress <i>P</i> / <i>A</i> (lb. per sq. in.)	$\lambda_{os} =$ $\frac{1}{\pi} \frac{l_o}{i} \sqrt{\frac{S}{E}}$	$\sigma_s =$ $\frac{P}{AS}$
STAINLESS STEEL—Continued											
1 in. diameter by 0.083 in. thick. Nominal <i>d/t</i> =12.0											
HB-7-----	233	30.02	111,200	0.626	0.974	HB-6-----	0	63.38	50,080	1.322	0.439
HB-9-----	0	37.37	88,680	.779	.777	HB-5-----	0	77.46	39,150	1.615	.343
HB-4-----	451	48.34	70,660	1.008	.619	HB-3-----	0	102.4	23,530	2.136	.206
HB-8-----	0	52.82	61,520	1.102	.539	HB-2-----	0	132.2	14,890	2.756	.130
1¼ in. diameter by 0.035 in. thick. Nominal <i>d/t</i> =35.7											
IG-10-----	0	29.61	119,800	0.720	0.798	IG-9-----	0	40.33	97,300	0.981	0.649
IG-5-----	233	39.25	97,180	.955	.648	IG-8-----	0	45.02	83,080	1.095	.554
1¼ in. diameter by 0.065 in. thick. Nominal <i>d/t</i> =19.2											
JB-9-----	451	15.89	146,800	0.333	1.311	JB-8-----	0	78.18	35,650	1.640	0.318
JB-10-----	0	38.71	80,120	.812	.715	JB-6-----	0	102.6	23,760	2.153	.212
1½ in. diameter by 0.049 in. thick. Nominal <i>d/t</i> =30.6											
KB-8-----	233	18.12	143,100	0.389	1.178	KB-7-----	0	75.52	38,310	1.622	0.315
KB-9-----	0	37.92	89,710	.814	.738						
HEAT-TREATED CHROMIUM-MOLYBDENUM STEEL											
1 in. diameter by 0.042 in. thick. Nominal <i>d/t</i> =23.8											
1HZ-2-----	0	24.50	168,800	0.604	0.939	1HZ-6-----	0	49.10	123,900	1.207	0.692
1HZ-38-----	0	26.51	168,100	.653	.936	1HZ-7-----	0	59.16	85,320	1.455	.477
1HZ-1-----	0	34.00	164,900	.838	.917	1HZ-4-----	0	64.74	72,790	1.592	.407
1HZ-5-----	0	39.95	168,300	.982	.940	1HZ-3-----	0	99.76	29,860	2.455	.167
1¼ in. diameter by 0.035 in. thick. Nominal <i>d/t</i> =35.7											
2HY-1-----	440	12.07	191,300	0.304	1.020	1HY-7-----	0	52.95	107,800	1.326	0.580
2HY-2-----	440	18.44	186,900	.465	.996	1HY-8-----	0	55.92	96,760	1.400	.521
1HY-9-----	0	20.93	^a 152,200	.524	.819	1HY-3-----	0	64.75	71,230	1.621	.383
1HY-6-----	0	40.08	156,600	1.004	.843	1HY-4-----	0	79.82	47,250	1.999	.254
1HY-59-----	0	43.15	154,300	1.081	.830	1HY-5-----	0	129.6	17,740	3.245	.095
1HY-2-----	0	47.37	127,500	1.186	.686						
1¾ in. diameter by 0.035 in. thick. Nominal <i>d/t</i> =50.0											
1HX-1-----	0	19.37	^a 150,200	-----	-----	1HX-2-----	0	129.8	17,530	-----	-----
1HX-23-----	0	45.25	140,800	-----	-----	Values of <i>S</i> could not be obtained.					
1¼ in. diameter by 0.049 in. thick. Nominal <i>d/t</i> =35.7											
1HW-1-----	0	33.02	170,700	0.818	0.930	1HW-2-----	0	79.78	46,810	1.977	0.256
1HW-35-----	0	38.09	164,700	.946	.907	1HW-3-----	0	96.77	31,860	2.402	.175
1HW-34-----	0	42.18	157,100	1.046	.863						
LOWER END RESTRAINED											
CHROMIUM-MOLYBDENUM STEEL											
1 in. diameter by 0.035 in. thick. Nominal <i>d/t</i> =28.6											
CA-5c-----	450	46.90	76,880	0.856	0.776	CA-5d-----	233	48.06	77,920	0.877	0.786
1½ in. diameter by 0.049 in. thick. Nominal <i>d/t</i> =23.0											
DA-5a-----	450	52.68	63,900	0.927	0.692	DA-5b-----	233	55.60	66,910	0.979	0.725
1½ in. diameter by 0.058 in. thick. Nominal <i>d/t</i> =25.9											
AA-2-----	450	58.56	65,180	0.994	0.763	AA-2a-----	233	63.07	62,950	1.071	0.737
DURALUMIN											
1½ in. diameter by 0.058 in. thick. Nominal <i>d/t</i> =25.9											
BD-3-----	450	38.07	34,330	0.745	0.861	BD-4-----	233	39.24	33,610	0.767	0.842

TABLE II.—RESULTS OF TESTS ON COLUMNS—Continued

STAINLESS STEEL

Specimen	End re- straint $10^{-3}m$ (lb.-in. per radian)	Ratio of slender- ness t_0/i	Average stress P/A (lb. per sq. in.)	$\lambda_{os} =$ $\frac{1}{\pi} \frac{t_0}{i} \sqrt{\frac{S}{E}}$	$\sigma_e =$ $\frac{P}{AS}$	Specimen	End re- straint $10^{-3}m$ (lb.-in. per radian)	Ratio of slender- ness t_0/i	Average stress P/A (lb. per sq. in.)	$\lambda_{os} =$ $\frac{1}{\pi} \frac{t_0}{i} \sqrt{\frac{S}{E}}$	$\sigma_e =$ $\frac{P}{AS}$
1 in. diameter by 0.035 in. thick. Nominal $d/t=28.6$											
GA-10.....	450	21.17	132,800	0.454	1.103	GB-4.....	450	65.92	52,930	1.410	0.443
GB-5.....	233	50.13	68,820	1.072	.575						
1 in. diameter by 0.083 in. thick. Nominal $d/t=12.0$											
HB-10.....	233	24.67	119,000	0.515	1.042						
$1\frac{1}{4}$ in. diameter by 0.035 in. thick. Nominal $d/t=35.7$											
IG-6.....	450	54.26	71,850	1.320	0.479						
$1\frac{1}{4}$ in. diameter by 0.065 in. thick. Nominal $d/t=19.2$											
JB-5.....	233	75.84	39,040	1.591	0.349						

STREAMLINE TUBING ^b

BOTH ENDS FREELY SUPPORTED OR RESTRAINED

CHROMIUM-MOLYBDENUM STEEL

1.685 by 0.714 by 0.035 in. Nominal $d/t=35.7$

ICB-4a.....	0	35.65	77040	0.630	0.839	ICB-2.....	0	59.37	60690	1.049	0.661
ICB-1.....	0	39.61	73530	.700	.801	ICB-3.....	0	79.51	39500	1.405	.430
ICB-4b.....	440	44.91	70990	.794	.773						

3.372 by 1.429 by 0.083 in. Nominal $d/t=30.1$

ICA-1.....	0	58.80	65070	0.993	0.760	ICA-3.....	0	79.74	43870	1.346	0.512
------------	---	-------	-------	-------	-------	------------	---	-------	-------	-------	-------

DURALUMIN

1.685 by 0.714 by 0.035 in. Nominal $d/t=35.7$

IDB-1.....	0	39.97	29560	0.722	0.854	IDB-2.....	0	59.80	24030	1.080	0.695
IDB-4a.....	440	46.25	27320	.836	.790	IDB-3.....	0	79.98	17130	1.445	.495

3.372 by 1.429 by 0.065 in. Nominal $d/t=38.5$

IDC-2.....	0	39.24	29550	0.706	0.844	IDC-3.....	0	79.70	17380	1.434	0.497
IDC-1.....	0	59.14	26040	1.064	.744						

STAINLESS STEEL

1.685 by 0.714 by 0.035 in. Nominal $d/t=35.7$

ISB-2a.....	440	42.48	86100	0.860	0.793	ISB-1.....	0	99.05	27510	2.006	0.253
-------------	-----	-------	-------	-------	-------	------------	---	-------	-------	-------	-------

2.023 by 0.857 by 0.049 in. Nominal $d/t=30.6$

ISD-2.....	440	53.90	67910	1.181	0.502	ISD-1.....	0	80.16	41360	1.757	0.306
------------	-----	-------	-------	-------	-------	------------	---	-------	-------	-------	-------

2.697 by 1.143 by 0.058 in. Nominal $d/t=34.5$

ISF-2a.....	0	22.65	110300	0.493	0.837						
-------------	---	-------	--------	-------	-------	--	--	--	--	--	--

3.372 by 1.429 by 0.065 in. Nominal $d/t=38.5$

2SC-1.....	0	59.32	64460	1.168	0.585						
------------	---	-------	-------	-------	-------	--	--	--	--	--	--

HEAT-TREATED CHROMIUM-MOLYBDENUM STEEL

1.517 by 0.643 by 0.035 in. Nominal $d/t=32.1$

1HG-3c.....	440	35.00	^a 149200	0.841	0.865	1HG-1.....	0	63.09	75780	1.516	0.439
1HG-3a.....	0	40.43	147400	.971	.855	1HG-2.....	0	79.34	47790	1.906	.277
1HG-5.....	440	41.43	141800	.995	.822						

3.035 by 1.286 by 0.058 in. Nominal $d/t=38.8$

1HE-3.....	440	47.55	115900	1.131	0.662	1HE-2.....	0	65.43	72550	1.557	0.415
1HE-1.....	0	49.77	125100	1.184	.715						

^a Local failure.^b Sizes are given by major diameter, minor diameter, and thickness. Nominal d/t is given for basic round diameter.

TABLE III.—VALUES OF τ AND $\frac{1}{\pi}\sqrt{\frac{1}{E\tau}}$ FOR CHROMIUM-MOLYBDENUM STEEL

 $E = 29,800,000 \text{ lb. per sq. in.}$ [illegible]

TABLE IV.—VALUES OF τ AND $\frac{1}{\pi}\sqrt{\frac{1}{E\tau}}$ FOR DURALUMIN

$$E=10,590.000 \text{ lb. per sq. in.}$$

P/A (lb. per sq. in.)	τ	Δ	$\frac{10^3}{\pi} \sqrt{\frac{1}{E\tau}}$ (in./lb. ^{1/2})	Δ	P/A (lb. per sq. in.)	τ	Δ	$\frac{10^3}{\pi} \sqrt{\frac{1}{E\tau}}$ (in./lb. ^{1/2})	Δ	P/A (lb. per sq. in.)	τ	Δ	$\frac{10^3}{\pi} \sqrt{\frac{1}{E\tau}}$ (in./lb. ^{1/2})	Δ
0 to														
21,800	1		0.0978		29,000	0.572		0.1294		36,000	0.169		0.238	
22,000	.991	9	.0982	4	29,500	.540	32	.1331	37	36,500	.147	22	.255	17
22,500	.965	26	.0996	14	30,000	.508	32	.1372	41	37,000	.126	21	.276	21
23,000	.939	26	.1010	14	30,500	.477	31	.1417	45	37,500	.106	20	.301	25
23,500	.911	28	.1025	15	31,000	.445	32	.1466	49	38,000	.088	18	.331	30
24,000	.882	29	.1041	16	31,500	.415	30	.1519	53	38,500	.071	17	.368	37
24,500	.853	29	.1059	18	32,000	.384	31	.1578	59	39,000	.056	15	.415	47
25,000	.823	30	.1078	19	32,500	.355	29	.164	6	39,500	.042	14	.477	62
25,500	.793	30	.1098	20	33,000	.326	29	.171	7	40,000	.030	12	.563	86
26,000	.762	31	.1120	22	33,500	.297	29	.179	8	40,500	.020	10	.688	125
26,500	.731	31	.1144	24	34,000	.270	27	.188	9	41,000	.012	8	.888	200
27,000	.699	32	.1170	26	34,500	.243	27	.198	10	41,500	.006	6	1.258	370
27,500	.668	31	.1197	27	35,000	.217	26	.210	12	42,000	.002	4	2.175	917
28,000	.636	32	.1227	30	35,500	.193	24	.223	13	42,500	.000	2	8.304	6129
28,500	.604	32	.1259	32			24		15			0	∞	∞
		32		35						42,700	0		∞	

TABLE V.—VALUES OF τ AND $\frac{1}{\pi}\sqrt{\frac{1}{E\tau}}$ FOR STAINLESS STEEL $E=26,300,000$ lb. per sq. in.

P/A (lb. per sq. in.)	τ	Δ	$\frac{10^3}{\pi}\sqrt{\frac{1}{E\tau}}$ (in./lb. ^{1/2})	Δ	P/A (lb. per sq. in.)	τ	Δ	$\frac{10^3}{\pi}\sqrt{\frac{1}{E\tau}}$ (in./lb. ^{1/2})	Δ	P/A (lb. per sq. in.)	τ	Δ	$\frac{10^3}{\pi}\sqrt{\frac{1}{E\tau}}$ (in./lb. ^{1/2})	Δ
0	1		0.0621		42,000	0.834		0.0680		84,000	0.447		0.0928	
2,000	1.000	0	.0621	0	44,000	.819	15	.0686	6	86,000	.426	21	.0951	23
4,000	.998	2	.0621	0	46,000	.804	15	.0692	6	88,000	.405	21	.0976	25
6,000	.996	2	.0622	1	48,000	.789	15	.0699	7	90,000	.383	22	.1003	27
8,000	.993	3	.0623	1	50,000	.773	16	.0706	7	92,000	.361	22	.1033	30
10,000	.990	3	.0624	1	52,000	.756	17	.0714	8	94,000	.339	22	.1066	33
12,000	.985	5	.0625	1	54,000	.739	17	.0722	8	96,000	.317	22	.1103	37
14,000	.980	5	.0627	2	56,000	.722	17	.0731	9	98,000	.295	22	.1144	41
16,000	.974	6	.0629	2	58,000	.704	18	.0740	9	100,000	.272	23	.1191	47
18,000	.967	7	.0631	2	60,000	.686	18	.0750	10	102,000	.249	23	.1244	53
20,000	.960	7	.0633	2	62,000	.668	18	.0760	10	104,000	.226	23	.1305	61
22,000	.952	8	.0636	3	64,000	.649	19	.0771	11	106,000	.203	23	.1377	72
24,000	.943	9	.0639	3	66,000	.630	19	.0782	11	108,000	.180	23	.1462	85
26,000	.933	10	.0642	3	68,000	.611	19	.0794	12	110,000	.157	23	.1566	104
28,000	.923	10	.0646	4	70,000	.591	20	.0807	13	112,000	.134	23	.1696	130
30,000	.912	11	.0650	4	72,000	.571	20	.0821	14	114,000	.111	23	.1867	171
32,000	.900	12	.0654	4	74,000	.551	20	.0836	15	116,000	.088	23	.2104	237
34,000	.888	12	.0658	4	76,000	.531	20	.0852	16	118,000	.064	24	.2464	360
36,000	.876	12	.0663	5	78,000	.510	21	.0869	17	120,000	.040	24	.3110	646
38,000	.863	13	.0668	5	80,000	.489	21	.0887	18	122,000	.016	24	.4893	1783
40,000	.849	14	.0674	6	82,000	.468	21	.0907	20	123,400	0	16	∞	∞
		15		6			21		21					

TABLE VI.—VALUES OF τ AND $\frac{1}{\pi}\sqrt{\frac{1}{E\tau}}$ FOR HEAT-TREATED CHROMIUM-MOLYBDENUM STEEL $E=30,000,000$ lb. per sq. in.

P/A (lb. per sq. in.)	τ	Δ	$\frac{10^3}{\pi}\sqrt{\frac{1}{E\tau}}$ (in./lb. ^{1/2})	Δ	P/A (lb. per sq. in.)	τ	Δ	$\frac{10^3}{\pi}\sqrt{\frac{1}{E\tau}}$ (in./lb. ^{1/2})	Δ	P/A (lb. per sq. in.)	τ	Δ	$\frac{10^3}{\pi}\sqrt{\frac{1}{E\tau}}$ (in./lb. ^{1/2})	Δ
0 to														
108,900	1		0.0581		118,000	.982		.0586		129,000	.880		.0619	
109,000	1.000	0	.0581	0	119,000	.977	5	.0588	2	130,000	.863	17	.0625	6
110,000	1.000	0	.0581	0	120,000	.971	6	.0590	2	131,000	.844	19	.0632	7
111,000	.999	1	.0581	0	121,000	.965	6	.0592	2	132,000	.822	22	.0641	9
112,000	.998	1	.0582	1	122,000	.958	7	.0594	2	133,000	.797	25	.0651	10
113,000	.996	2	.0582	0	123,000	.950	8	.0596	2	134,000	.769	28	.0663	12
114,000	.994	2	.0583	1	124,000	.941	9	.0599	3	135,000	.735	34	.0678	15
115,000	.992	2	.0583	0	125,000	.932	9	.0602	3	136,000	.695	40	.0697	19
116,000	.989	3	.0584	1	126,000	.921	11	.0606	4	137,000	.645	50	.0724	27
117,000	.986	3	.0585	1	127,000	.909	12	.0610	4	138,000	.579	66	.0764	40
		4		1	128,000	.895	14	.0614	4	139,000	.478	101	.0840	76
							15		5	140,000	0	478	∞	∞

TABLE VII.—VALUES OF s, t, AND t²—s²

$s = \frac{\phi}{\sin \phi} - 1$ $t = 1 - \frac{\phi}{\tan \phi}$

Interpolation for s, t, and t²—s² when $0.99 < \frac{\phi}{\pi} < 1.01$ is not possible, and it will be sufficiently accurate to take $s = \frac{2\frac{\phi}{\pi}-1}{1-\frac{\phi}{\pi}}$, $t = \frac{1}{1-\frac{\phi}{\pi}}$, and $t^2-s^2 = \frac{4\frac{\phi}{\pi}}{1-\frac{\phi}{\pi}}$. Similarly, interpolation for s and t when $1.99 < \frac{\phi}{\pi} < 2.00$ is not possible, and then with sufficient accuracy $s = \frac{2}{\frac{\phi}{\pi}-2}$ and $t = \frac{2}{2-\frac{\phi}{\pi}}$.

ϕ/π	ϕ	s	t	t²—s²	ϕ/π	ϕ	s	t	t²—s²
0	0	0	0	0	.87	2.73319	5.8820	7.3160	18.926
.01	.03142	.00016	.00033	.00000	.88	2.76460	6.5100	7.9326	21.342
.02	.06283	.00066	.00132	.00000	.89	2.79602	7.2542	8.7662	24.223
.03	.09425	.00148	.00296	.00001	.90	2.82743	8.1498	9.7019	27.709
.04	.12566	.00264	.00527	.00002	.91	2.85885	9.2471	10.840	32.002
.05	.15708	.00412	.00824	.00005	.92	2.89027	10.622	12.257	37.404
.06	.18850	.00595	.01187	.00011	.93	2.92168	12.393	14.071	44.392
.07	.21991	.00811	.01617	.00020	.94	2.95310	14.760	16.481	53.760
.08	.25133	.01061	.02114	.00033	.95	2.98451	18.078	19.843	66.936
.09	.28274	.01345	.02679	.00054	.96	3.01593	23.063	24.874	86.778
.10	.31416	.01664	.03312	.00082	.97	3.04734	31.381	33.238	119.95
.11	.34558	.02018	.04013	.00120	.98	3.07876	48.032	49.935	186.46
.12	.37699	.02409	.04783	.00171	.99	3.11018	98.016	99.967	386.29
.13	.40841	.02835	.05623	.00236	1.00	3.14159	±∞	±∞	±∞
.14	.43982	.03298	.06533	.00318	1.01	3.17301	-102.02	-99.967	-414.04
.15	.47124	.03799	.07514	.00420	1.02	3.20442	-52.034	-49.933	-214.20
.16	.50265	.04339	.08567	.00546	1.03	3.23584	-35.384	-33.232	-147.70
.17	.53407	.04917	.09694	.00698	1.04	3.26726	-27.069	-24.863	-114.54
.18	.56549	.05535	.10894	.00880	1.05	3.29867	-22.087	-19.827	-94.708
.19	.59690	.06195	.12168	.01097	1.06	3.33009	-18.772	-16.457	-81.547
.20	.62832	.06896	.13519	.01352	1.07	3.36150	-16.410	-14.039	-72.196
.21	.65973	.07640	.14948	.01651	1.08	3.39292	-14.643	-12.215	-65.227
.22	.69115	.08429	.16454	.01997	1.09	3.42434	-13.274	-10.787	-59.847
.23	.72257	.09263	.18041	.02397	1.10	3.45575	-12.183	-9.6357	-55.580
.24	.75398	.10143	.19709	.02856	1.11	3.48717	-11.295	-8.6860	-52.121
.25	.78540	.11072	.21460	.03379	1.12	3.51858	-10.558	-7.8869	-49.271
.26	.81681	.12051	.23296	.03975	1.13	3.55000	-9.9387	-7.2036	-46.887
.27	.84823	.13081	.25218	.04649	1.14	3.58142	-9.4114	-6.6109	-44.871
.28	.87965	.14164	.27229	.05408	1.15	3.61283	-8.9579	-6.0906	-43.150
.29	.91106	.15302	.29331	.06262	1.16	3.64425	-8.5645	-5.6289	-41.667
.30	.94248	.16497	.31525	.07217	1.17	3.67566	-8.2208	-5.2152	-40.382
.31	.97389	.17751	.33814	.08283	1.18	3.70708	-7.9184	-4.8414	-39.262
.32	1.00531	.19066	.36201	.09470	1.19	3.73850	-7.6511	-4.5010	-38.281
.33	1.03673	.20446	.38688	.10788	1.20	3.76991	-7.4138	-4.1888	-37.417
.34	1.06814	.21891	.41278	.12247	1.21	3.80133	-7.2021	-3.9006	-36.656
.35	1.09956	.23406	.43975	.13859	1.22	3.83274	-7.0129	-3.6330	-35.982
.36	1.13097	.24993	.46780	.15637	1.23	3.86416	-6.8432	-3.3830	-35.384
.37	1.16239	.26656	.49699	.17595	1.24	3.89557	-6.6907	-3.1484	-34.854
.38	1.19381	.28397	.52734	.19745	1.25	3.92699	-6.5536	-2.9270	-34.382
.39	1.22522	.30221	.55889	.22103	1.26	3.95841	-6.4301	-2.7172	-33.964
.40	1.25664	.32131	.59169	.24686	1.27	3.98982	-6.3190	-2.5175	-33.592
.41	1.28805	.34131	.62579	.27511	1.28	4.02124	-6.2189	-2.3267	-33.261
.42	1.31947	.36227	.66122	.30597	1.29	4.05265	-6.1289	-2.1436	-32.969
.43	1.35088	.38422	.69804	.33964	1.30	4.08407	-6.0482	-1.9673	-32.711
.44	1.38230	.40723	.73631	.37632	1.31	4.11549	-5.9759	-1.7969	-32.483
.45	1.41372	.43134	.77609	.41626	1.32	4.14690	-5.9115	-1.6317	-32.283
.46	1.44513	.45662	.81744	.45970	1.33	4.17832	-5.8543	-1.4711	-32.109
.47	1.47655	.48313	.86043	.50692	1.34	4.20973	-5.8040	-1.3143	-31.958
.48	1.50796	.51095	.90513	.55819	1.35	4.24115	-5.7600	-1.1610	-31.829
.49	1.53938	.54014	.95162	.61384	1.36	4.27257	-5.7220	-1.0105	-31.720
.50	1.57080	.57080	1	.67419	1.37	4.30398	-5.6897	-0.8625	-31.629
.51	1.60221	.60300	1.0504	.7396	1.38	4.33540	-5.6628	-0.7165	-31.554
.52	1.63363	.63686	1.1028	.8105	1.39	4.36681	-5.6412	-0.5721	-31.496
.53	1.66504	.67247	1.1574	.8873	1.40	4.39823	-5.6246	-0.4291	-31.452
.54	1.69646	.70994	1.2143	.9705	1.41	4.42965	-5.6128	-0.2869	-31.421
.55	1.72788	.74941	1.2737	1.0606	1.42	4.46106	-5.6058	-0.1454	-31.403
.56	1.75929	.79102	1.3356	1.1581	1.43	4.49248	-5.6033	-0.0042	-31.397
.57	1.79071	.83490	1.4003	1.2637	1.44	4.52389	-5.6055	0.1370	-31.403
.58	1.82212	.88123	1.4678	1.3780	1.45	4.55531	-5.6121	0.2785	-31.418
.59	1.85354	.93018	1.5385	1.5018	1.46	4.58673	-5.6232	0.4206	-31.443
.60	1.88496	.98196	1.6125	1.6358	1.47	4.61814	-5.6387	0.5635	-31.478
.61	1.91637	1.03678	1.6899	1.7810	1.48	4.64956	-5.6588	0.7075	-31.521
.62	1.94779	1.09490	1.7712	1.9383	1.49	4.68097	-5.6833	0.8529	-31.572
.63	1.97920	1.15657	1.8565	2.1089	1.50	4.71239	-5.7124	1	-31.631
.64	2.01062	1.22210	1.9461	2.2939	1.51	4.74380	-5.7461	1.1491	-31.698
.65	2.04204	1.29183	2.0405	2.4947	1.52	4.77522	-5.7847	1.3004	-31.771
.66	2.07345	1.36613	2.1399	2.7128	1.53	4.80664	-5.8281	1.4544	-31.851
.67	2.10487	1.44541	2.2448	2.9500	1.54	4.83805	-5.8765	1.6112	-31.937
.68	2.13628	1.53016	2.3557	3.2081	1.55	4.86947	-5.9302	1.7712	-32.030
.69	2.16770	1.62090	2.4732	3.4892	1.56	4.90088	-5.9893	1.9349	-32.127
.70	2.19911	1.71826	2.5978	3.7959	1.57	4.93230	-6.0540	2.1025	-32.231
.71	2.23053	1.82290	2.7302	4.1309	1.58	4.96372	-6.1247	2.2745	-32.339
.72	2.26195	1.93564	2.8712	4.4974	1.59	4.99513	-6.2017	2.4512	-32.452
.73	2.29336	2.05736	3.0219	4.8990	1.60	5.02655	-6.2852	2.6332	-32.570
.74	2.32478	2.18913	3.1831	5.3399	1.61	5.05796	-6.3758	2.8210	-32.693
.75	2.35619	2.33216	3.3562	5.8251	1.62	5.08938	-6.4738	3.0150	-32.819
.76	2.38761	2.4879	3.5425	6.3601	1.63	5.12080	-6.5797	3.2160	-32.950
.77	2.41903	2.6579	3.7438	6.9518	1.64	5.15221	-6.6941	3.4244	-33.085
.78	2.45044	2.8443	3.9621	7.6081	1.65	5.18363	-6.8177	3.6412	-33.223
.79	2.48186	3.0493	4.1996	8.3382	1.66	5.21504	-6.9512	3.8670	-33.365
.80	2.51327	3.2758	4.4592	9.1536	1.67	5.24646	-7.0953	4.1027	-33.510
.81	2.54469	3.5272	4.7444	10.068	1.68	5.27788	-7.2510	4.3494	-33.659
.82	2.57611	3.8077	5.0593	11.098	1.69	5.30929	-7.4193	4.6082	-33.811
.83	2.60752	4.1224	5.4091	12.264	1.70	5.34071	-7.6015	4.8803	-33.966
.84	2.63894	4.4778	5.8002	13.592	1.71	5.37212	-7.7988	5.1670	-34.123
.85	2.67035	4.8820	6.2409	15.115	1.72	5.40354	-8.0129	5.4702	-34.284
.86	2.70177	5.3455	6.7416	16.874					

TABLE VII.—VALUES OF s , t , AND t^2-s^2 —Continued

ϕ/π	ϕ	s	t	t^2-s^2	ϕ/π	ϕ	s	t	t^2-s^2
1.73	5.43496	-8.2455	5.7916	-34.447	1.87	5.87478	-15.792	14.576	-36.946
1.74	5.46637	-8.4988	6.1333	-34.612	1.88	5.90619	-17.044	15.917	-37.136
1.75	5.49779	-8.7750	6.4978	-34.780	1.89	5.93761	-18.529	17.492	-37.328
1.76	5.52920	-9.0772	6.8880	-34.950	1.90	5.96903	-20.316	19.371	-37.520
1.77	5.56062	-9.4085	7.3073	-35.123	1.91	6.00044	-22.508	21.654	-37.713
1.78	5.59203	-9.7729	7.7596	-35.297	1.92	6.03186	-25.255	24.493	-37.907
1.79	5.62345	-10.175	8.2497	-35.474	1.93	6.06327	-28.795	28.126	-38.102
1.80	5.65487	-10.621	8.7833	-35.652	1.94	6.09469	-33.526	32.949	-38.297
1.81	5.68628	-11.116	9.3671	-35.832	1.95	6.12611	-40.161	39.679	-38.494
1.82	5.71770	-11.671	10.010	-36.014	1.96	6.15752	-50.129	49.742	-38.690
1.83	5.74911	-12.294	10.721	-36.198	1.97	6.18894	-66.764	66.472	-38.887
1.84	5.78053	-12.999	11.515	-36.383	1.98	6.22035	-100.07	99.870	-39.085
1.85	5.81195	-13.802	12.407	-36.569	1.99	6.25177	-200.03	199.93	-39.281
1.86	5.84336	-14.724	13.418	-36.757	2.00	6.28319	$-\infty$	∞	-39.478

REPORT No. 616

INTERRELATION OF EXHAUST-GAS CONSTITUENTS

By HAROLD C. GERRISH and FRED VOSS

SUMMARY

An investigation was made to determine the interrelation of the constituents of the exhaust gases of internal-combustion engines and the effect of engine performance on these relations. Six single-cylinder, liquid-cooled test engines and one 9-cylinder radial air-cooled engine were tested. Various types of combustion chambers were used and the engines were operated at compression ratios from 5.1 to 7.0 using spark ignition and from 13.5 to 15.6 using compression ignition. The investigation covered a range of engine speeds from 1,500 to 2,100 r. p. m. The fuels used were two grades of aviation gasoline, Auto Diesel fuel, and Laboratory Diesel fuel. Power, friction, and fuel-consumption data were obtained from the single-cylinder engines at the same time that the exhaust-gas samples were collected.

Definite relations, which were independent of engine design and operating conditions, were found among the constituents of exhaust gases, air-fuel ratio, water of combustion, and combustion efficiency. Combustion efficiency and amount of water of combustion increased approximately linearly with air-fuel ratio for rich mixtures and were independent of mixture strength for lean mixtures. These relations make it possible to obtain a complete exhaust-gas analysis simply by determining the air-fuel ratio or the CO_2 and O_2 content. The results also showed that compression-ignition engines may be operated at the same air-fuel ratio as spark-ignition engines without loss in combustion efficiency.

INTRODUCTION

The mixture strength, or ratio of air to fuel, of internal-combustion engines is of paramount importance, not only because it is a fundamental factor for the correlation of all engine-performance data but because of its effect on the specific fuel consumption and the temperature of the engine cylinder.

The direct method of determining the mixture strength of conventional engines is to measure the air and fuel entering the engine cylinder. The inconvenience of such a procedure necessitates the substitution of some indirect method, such as noting the decrease of

engine speed with a constant-pitch propeller when the mixture is leaned, noting the temperature of the cylinder head, or analyzing the exhaust gases.

Various instruments are commercially available for indicating the mixture strength. As the operation of the more promising types of instruments for aircraft depends upon one or more constituents or on some property of the constituents of the exhaust gases, it is essential to know the correlation of these constituents with mixture strength. If the relation of all the products of combustion to one particular component could be established, especially to one that could readily be determined, the measurement and control of the mixture strength of aircraft engines, especially for cruising conditions, would come into more general use.

This investigation was made to establish the relationship among the constituents of the exhaust gases of internal-combustion aircraft engines and to determine the influence of engine design and operating conditions upon these relationships.

APPARATUS AND METHOD

A modified Bureau of Mines gas-analysis apparatus with Bureau of Standards type pipettes was used for the analysis of the exhaust-gas samples. (See reference 1.) Caustic potash was used for absorbing CO_2 and alkaline pyrogallol for absorbing O_2 . By means of simple stoichiometric equations and "oxygen and nitrogen balances," the air-fuel ratio, H-C ratio of the fuel, and water of combustion were computed.

Combustion efficiency was computed from the heat liberated, which is the heat evolved by the formation of CO_2 , H_2O , and CO , and from the potential heat, which is the sum of the amount of heat liberated and the amount that could be evolved by the combustion of the unburned combustibles, CO , H_2 , and CH_4 . Values of the molecular heats of combustion given in reference 2 were used in the calculations.

Six single-cylinder, liquid-cooled test engines and one commercial 9-cylinder radial air-cooled engine were used in this investigation. Table I shows the engine test conditions and the fuels used. The fighting grade

TABLE I.—ENGINE TEST CONDITIONS

En- gine	Num- ber of cyl- inders	Dis- place- ment (cubic inches)	Type of combustion chamber	Type of ignition	Type of cooling	Fuel system	Fuel	Com- pres- sion ratio	Engine speed (r.p.m.)	Valve timing
1	1	137	Pent roof.....	Spark.....	Liquid.....	Carburetor and injection.	Standard grade aviation gaso- line.	5.5	1,500	Standard.
2	1	137	Bulb prechamber.....	Compression.....	do.....	Injection.....	Auto Diesel and Laboratory Diesel.	13.5	1,500	Do.
3	1	137	Vertical disk.....	do.....	do.....	do.....	Auto Diesel.....	15.6	1,500	19° overlap.
4	1	137	Vertical disk with displacer piston.	do.....	do.....	do.....	do.....	15.3	1,500	60° overlap.
5	1	143	Pent roof.....	Spark.....	do.....	Carburetor and injection.	Standard grade aviation gaso- line.	5.8	1,500	Standard.
6	1	143	do.....	do.....	do.....	do.....	do.....	7.0	1,500 to 2,100	130° overlap.
7	9	1,750	Spherical.....	do.....	Air.....	Carburetor.....	Fighting grade aviation gasoline.	5.1	1,475 to 1,550	Standard.

aviation gasoline complied with Army Specification No. Y-3557-G and the standard grade aviation gasoline with Aeronautical Specification No. 7G3. The distillation curves of these fuels are given in figure 1. In spite

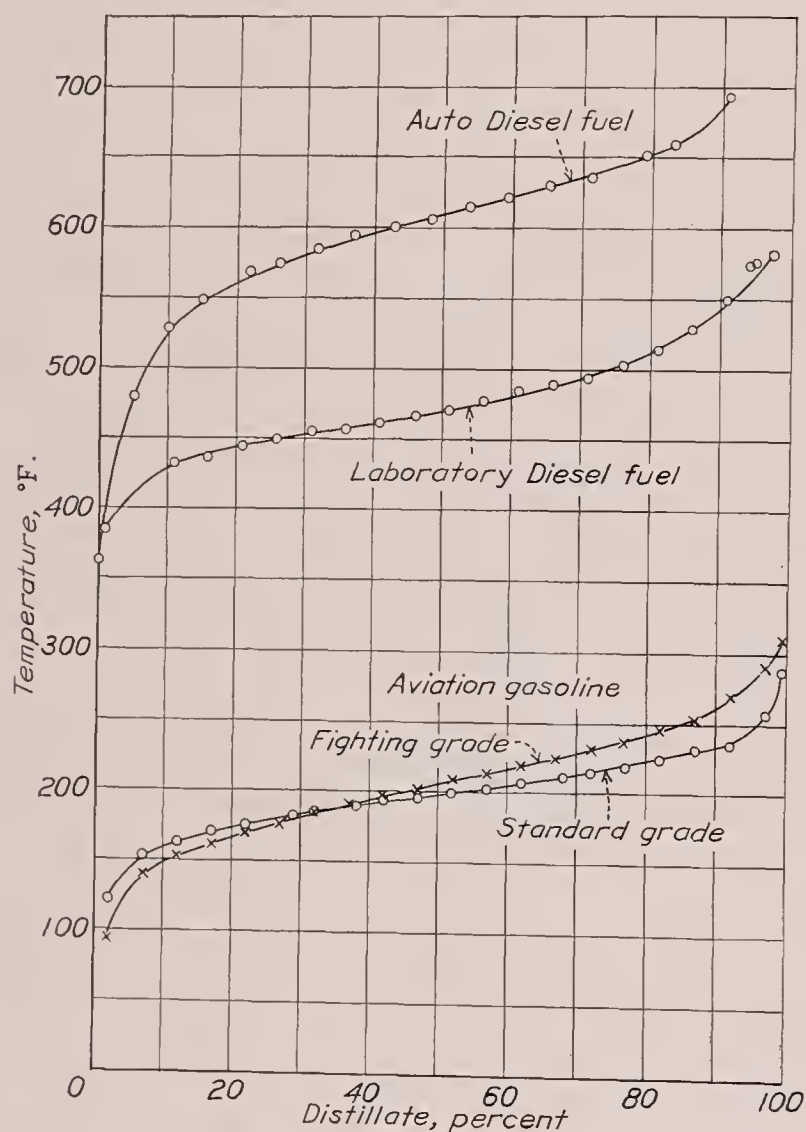


FIGURE 1.—Distillation curves (A. S. T. M.).

of the differences in distillation characteristics, all the fuels had practically the same H-C ratio, 0.175, as determined from exhaust-gas analyses. (See reference 1.)

Power, friction, and fuel-consumption data were obtained from the test engines at the same time that the exhaust-gas samples were collected. The i. m. e. p. was obtained by the addition of the f. m. e. p. and the b. m. e. p.

COMBUSTION CHARACTERISTICS OF AVIATION GASOLINES AND DIESEL FUELS

Exhaust-gas composition.—The combustion of a hydrocarbon with excess air in an internal-combustion

engine results in the formation of H_2O and CO_2 with N_2 and O_2 left from the air. The combustion of a hydrocarbon with a deficiency of air produces H_2O , CO_2 , N_2 , only a trace of O_2 , and also CO , H_2 , and CH_4 . Some investigators have shown the presence of unsaturated hydrocarbons but tests at this laboratory with fuming sulphuric acid gave no indication of their presence.

Figure 2 shows the composition (by volume) of the exhaust gases from spark- and compression-ignition engines using fuels with an H-C ratio of 0.175. As the composition is given on the usual dry basis, the in-

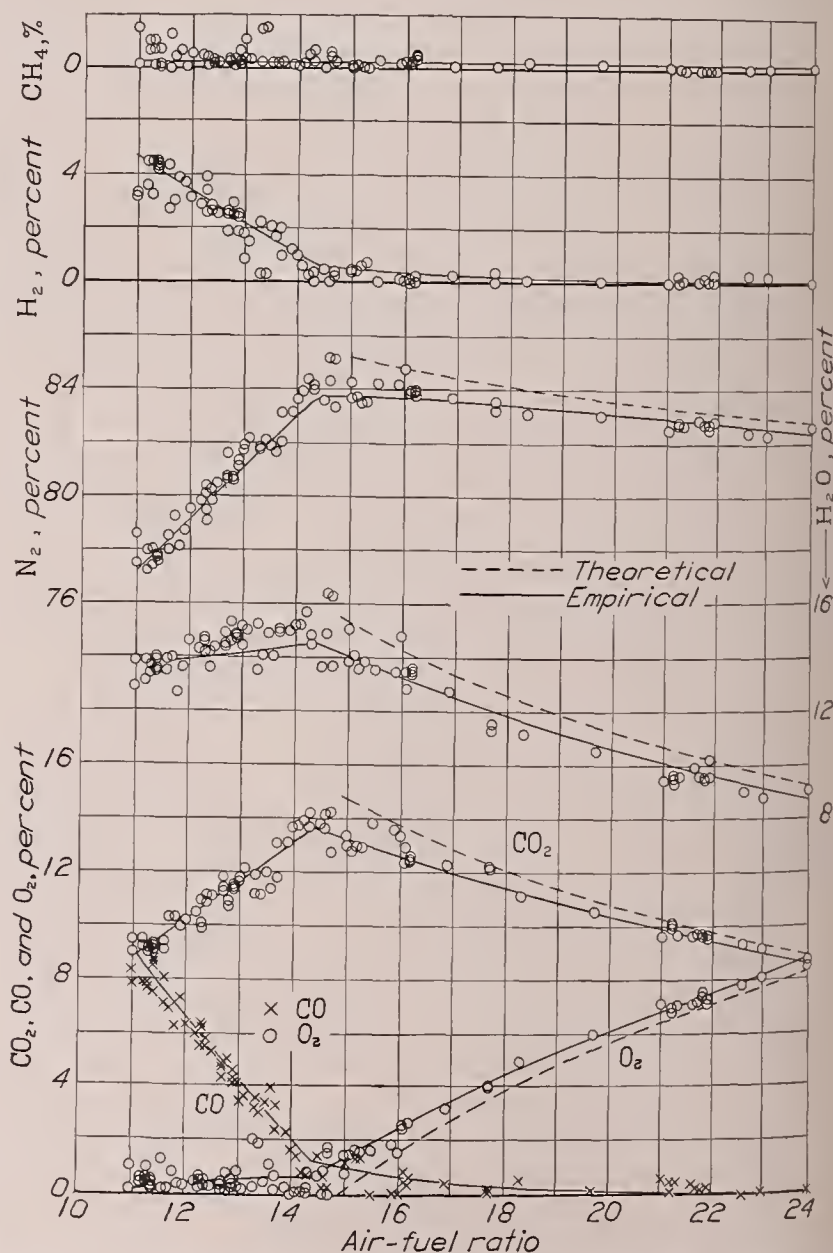


FIGURE 2.—Composition of exhaust gases from spark- and compression-ignition engines using fuels with H-C ratio of 0.175.

clusion of H_2O gives a total percentage greater than 100. The largest constituent is N_2 , varying from 77 to 85 percent of the exhaust gases; CO_2 varies from 9 to approximately 14 percent; and H_2O varies from 9 to about 16 percent. The maximum values of N_2 , CO_2 , and H_2O occur at approximately the chemically correct mixture. The amount of CO and O_2 varied from 0 to 9 percent, O_2 being small in the rich region and CO small in the lean region. The amount of H_2 is approximately half the quantity of CO . The amount of CH_4 is small and approximately constant for all mixtures.

The presence of O_2 in rich mixtures and of CO in lean mixtures has been questioned by different investi-

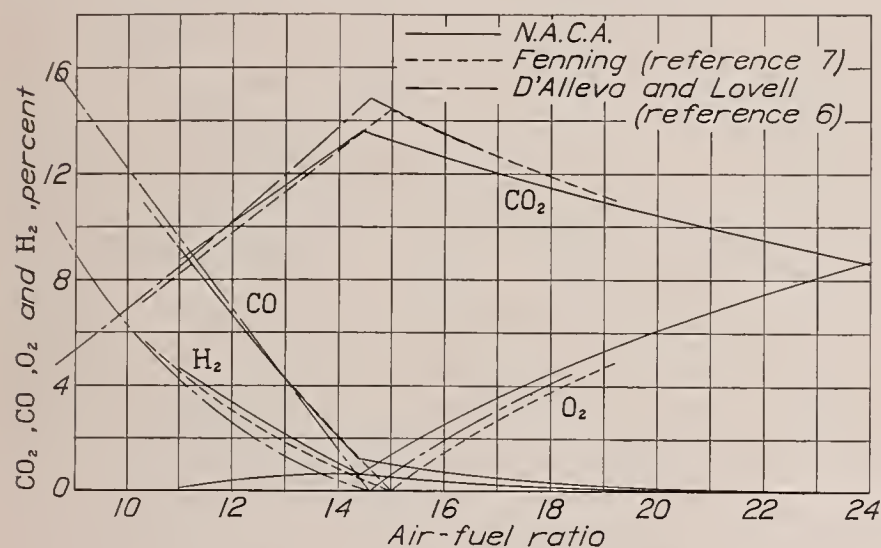


FIGURE 3.—Comparison of exhaust-gas analyses.

gators. Dicksee (reference 3) found neither constituent, but Best (reference 4) gives analyses that contain both CO and O_2 . Minter (reference 5) states that O_2 is always present in the exhaust even when rich mixtures are used and concludes that the presence of O_2 is due to unequal distribution of the fuel. D'Alleva and Lovell (reference 6) also found O_2 present in the exhaust gas of rich mixtures, the O_2 content averaging 0.2 percent.

For rich mixtures the solid line (fig. 2) drawn through the test points for CO_2 was assumed to be straight and was located by the method of least squares. For lean mixtures a curve similar to the theoretical one was drawn. The point of intersection of the two solid curves corresponds to an air-fuel ratio of 14.4. The O_2 curve was calculated from the relation of air-fuel ratio to CO_2 and O_2 (equation (12)) and the CH_4 curve, from equation (2). All of the other curves were calculated by substituting the determined values of CO_2 and O_2 in equations (6), (7), (8), and (10). The equations are presented in the appendix and were developed from the empirical relations established in reference 1. Note that these equations are applicable only to fuels having H-C ratios of 0.175.

The dashed lines of figure 2 for lean mixtures (air-fuel ratios greater than 15) show the amounts of O_2 , CO_2 , H_2O , and N_2 that would result from complete

combustion of the fuel. The theoretical values of CO_2 and H_2O are larger than the empirical values, which indicates incomplete combustion of the C and H_2 . The empirical value of O_2 is larger than the theoretical on account of the O_2 that was not used to burn the C to CO_2 and the H_2 to H_2O .

The results obtained at this laboratory are compared in figure 3 with those obtained by Fenning (reference 7) and D'Alleva and Lovell (reference 6). Fenning's exhaust-gas samples were obtained from a single-cylinder sleeve-valve engine of $4\frac{1}{16}$ -inch bore and $5\frac{5}{16}$ -inch stroke, operating at 800 r. p. m. He used a high-grade commercial gasoline designated as "Bowley's Special petrol." D'Alleva and Lovell used commercial gasoline in one 8-cylinder and two 6-cylinder automobile engines. Exhaust-gas samples were taken from an exhaust pipe common to all the cylinders. The three investigations show approximately the same relationship. This agreement is especially interesting in view of the fact that over 20 years elapsed between Fenning's and the other two investigations.

Water of combustion.—The weight ratio of the water formed by combustion of the fuel to the amount of fuel used is of importance when water recovery is considered as a means of maintaining the equilibrium of an airship. Under normal operating conditions the amount of water recovered is from 90 to 100 percent of the fuel used (reference 8). This percentage depends upon the water of combustion, the efficiency of the condenser, and the humidity of the air.

Figure 4 shows the effect of air-fuel ratio on the ratio of the water of combustion to the amount of fuel used.

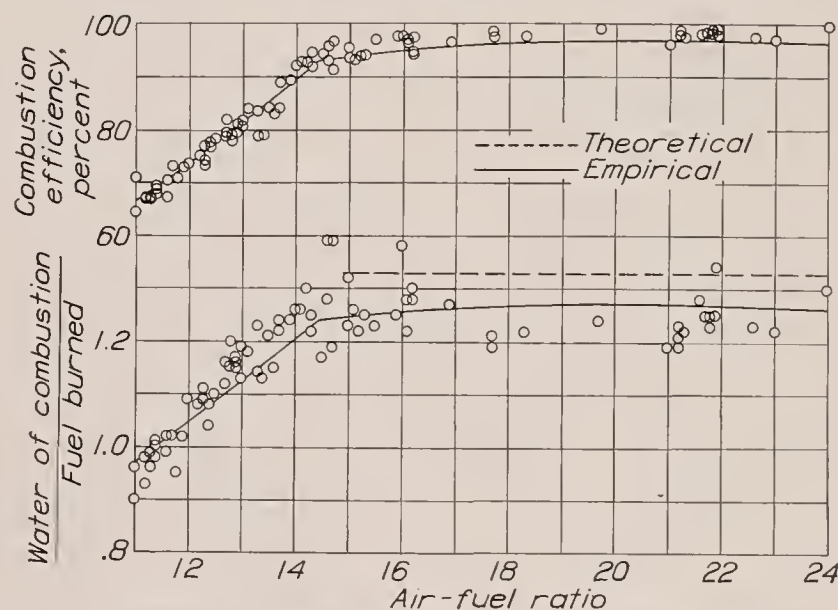


FIGURE 4.—Combustion efficiency and water of combustion.

The water of combustion increases approximately linearly with the air-fuel ratio for rich mixtures and is independent of mixture strength for lean mixtures. The curve drawn through the points was obtained from a solution of equation (14), proper values of CO_2 and O_2 being used. The dashed line is the ratio that would result from complete combustion of the hydrogen in the fuel.

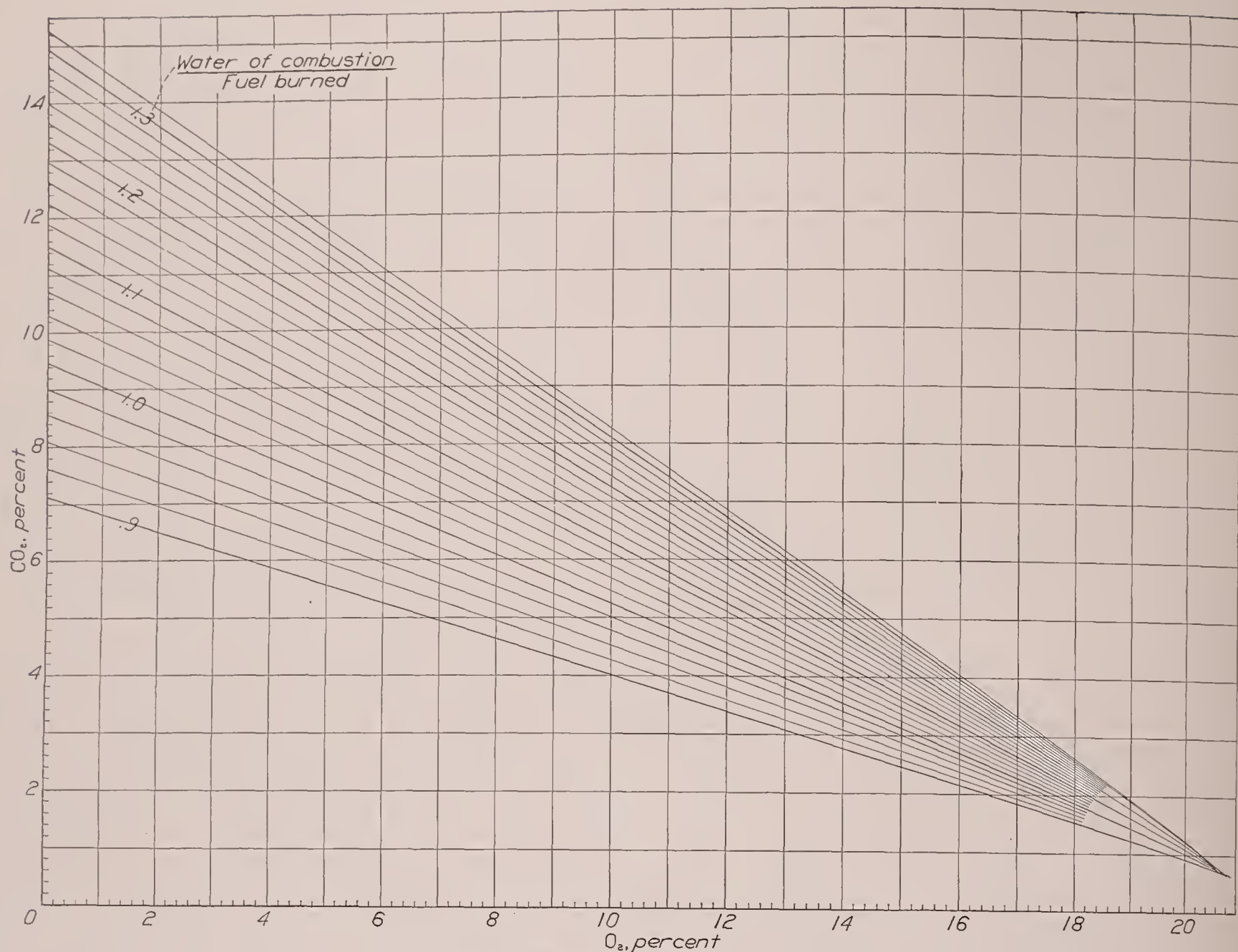


FIGURE 5.—Water-of-combustion chart (empirical).

Figure 5 is a chart constructed from equation (14) correlating the ratio of water of combustion to fuel burned with CO_2 and O_2 . The water of combustion in the exhaust may be rapidly determined for any period of time from the weight of the fuel used during this interval and the percentages of CO_2 and O_2 present. Figure 6 has been prepared to show the agreement between the values of the ratio of water of combustion to fuel burned obtained from figure 5 and from the experimental values. The agreement is not particularly good, there being a deviation of approximately ± 10 percent. The discrepancy may be due to inaccurate determinations of the experimental values of water of combustion (see fig. 4) inasmuch as any error in the determination of N_2 , CO_2 , O_2 , and CO enters into the experimental determination of these values.

Combustion efficiency.—Figure 4 also shows the influence of air-fuel ratio on combustion efficiency. Note that combustion efficiency increases approximately linearly with air-fuel ratio for rich mixtures and is approximately constant at a value of about 97 percent for lean mixtures. The increase in combustion efficiency with air-fuel ratio indicates the large im-

provement possible in thermal efficiency and, therefore, the economy of present-day aircraft engines.

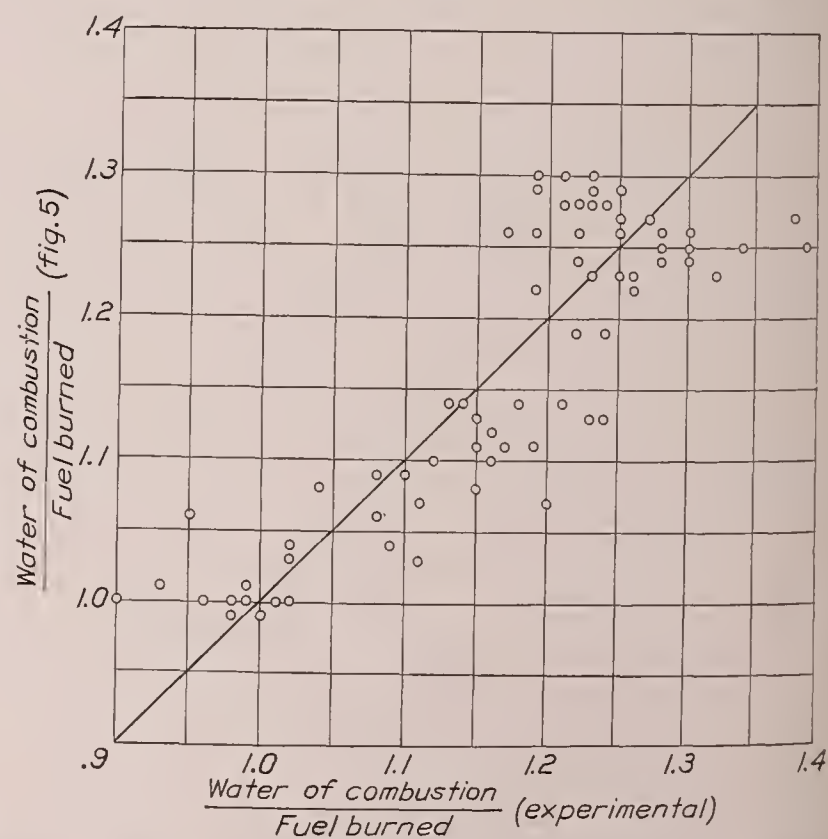


FIGURE 6.—Agreement of empirical and experimental values of water of combustion.

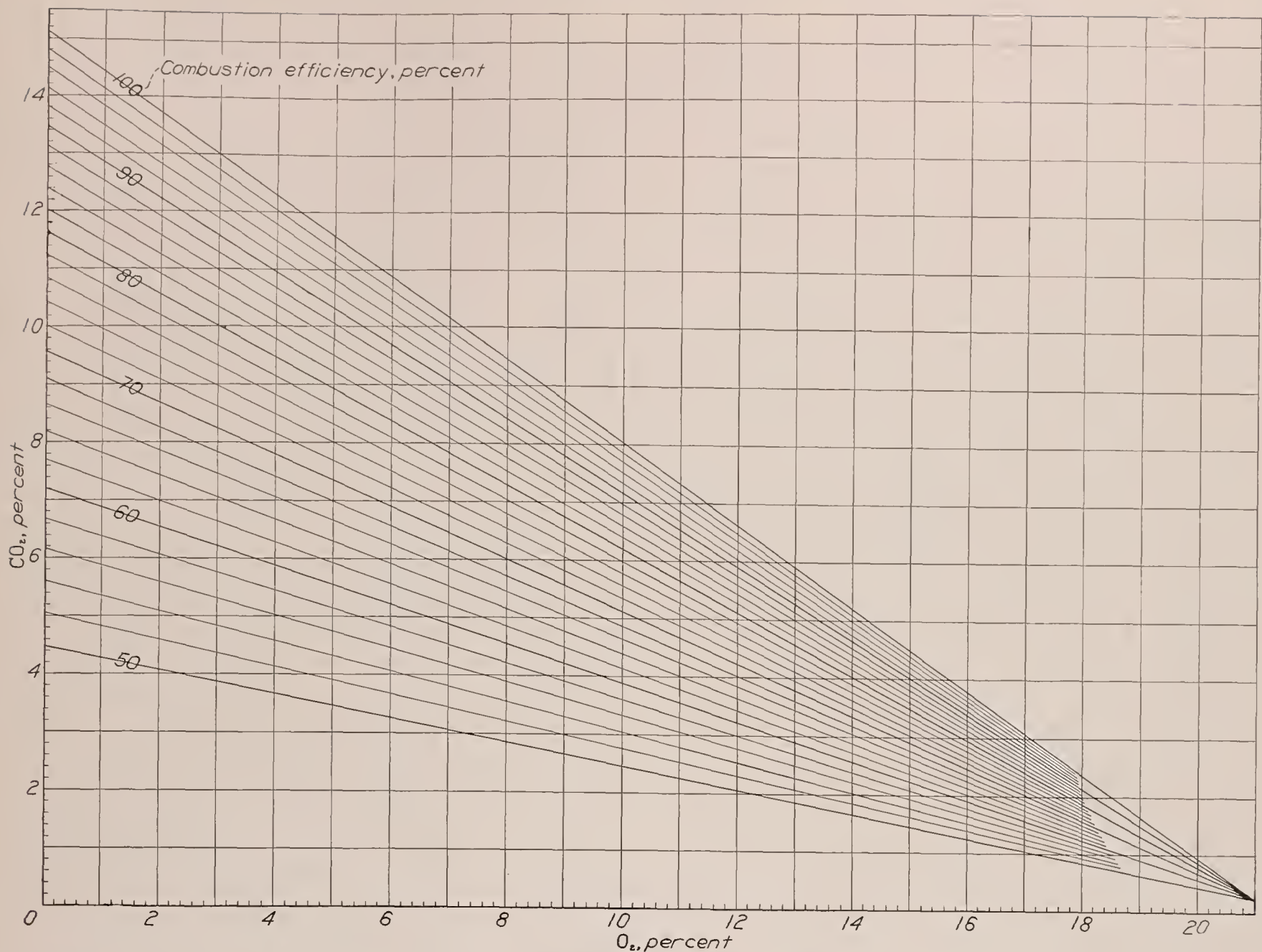


FIGURE 7.—Combustion-efficiency chart (empirical).

The data also show that combustion in the compression-ignition engine and in the spark-ignition engine is equally good for all mixtures. The curve (fig. 4)

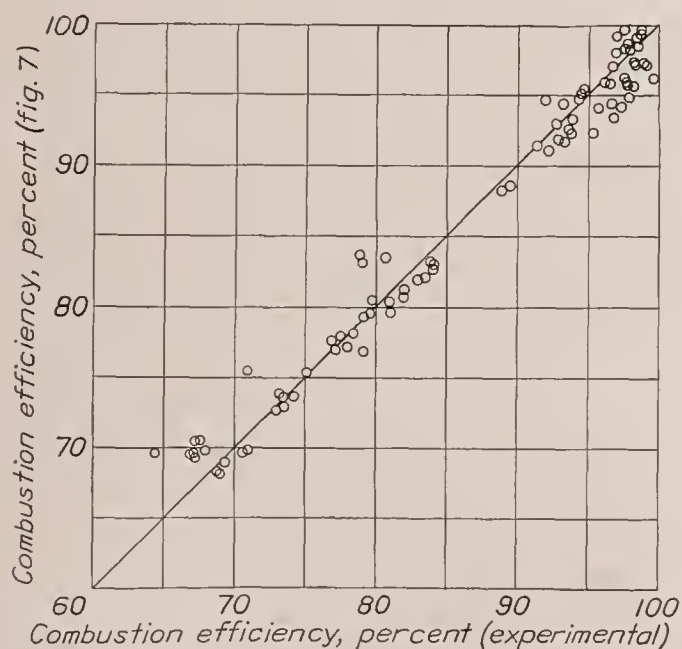


FIGURE 8.—Agreement of empirical and experimental values of combustion efficiency.

was determined by the method used for figure 2 except that equation (16) was used. This equation, correlating combustion efficiency with CO_2 and O_2 , is shown

graphically in figure 7. By means of this figure and a simple Orsat apparatus the combustion efficiency may readily be determined. Figure 8 shows the agreement between values of combustion efficiency determined from figure 7 and those determined by experiment.

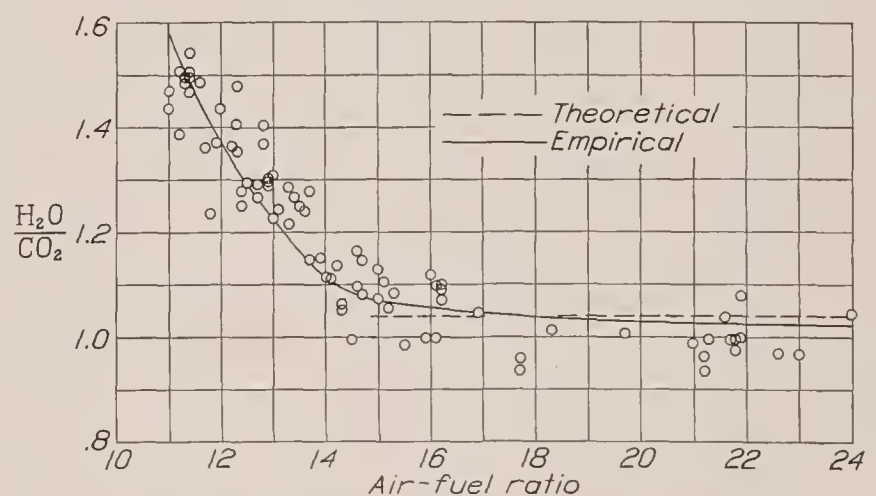


FIGURE 9.—Relative combustion of hydrogen and carbon.

Combustion of hydrogen and carbon.—The effect of mixture strength on the ratio of the products of complete combustion ($\text{H}_2\text{O}/\text{CO}_2$) is plotted in figure 9. The solid curve through the points was obtained from the empirical values of CO_2 and H_2O . The data show

that, for lean mixtures, there is sufficient O_2 to burn both H_2 and C and the ratio of the products of complete combustion is constant. Theoretically this ratio for complete combustion is 1.04 but, owing to the incompleteness of combustion in this region, the ratio is slightly less. For rich mixtures the H_2 burns more readily than the C in the fuel. The fuel does not burn as free H_2 and free C but, probably, as various hydrocarbons in such a manner that relatively more H_2 is

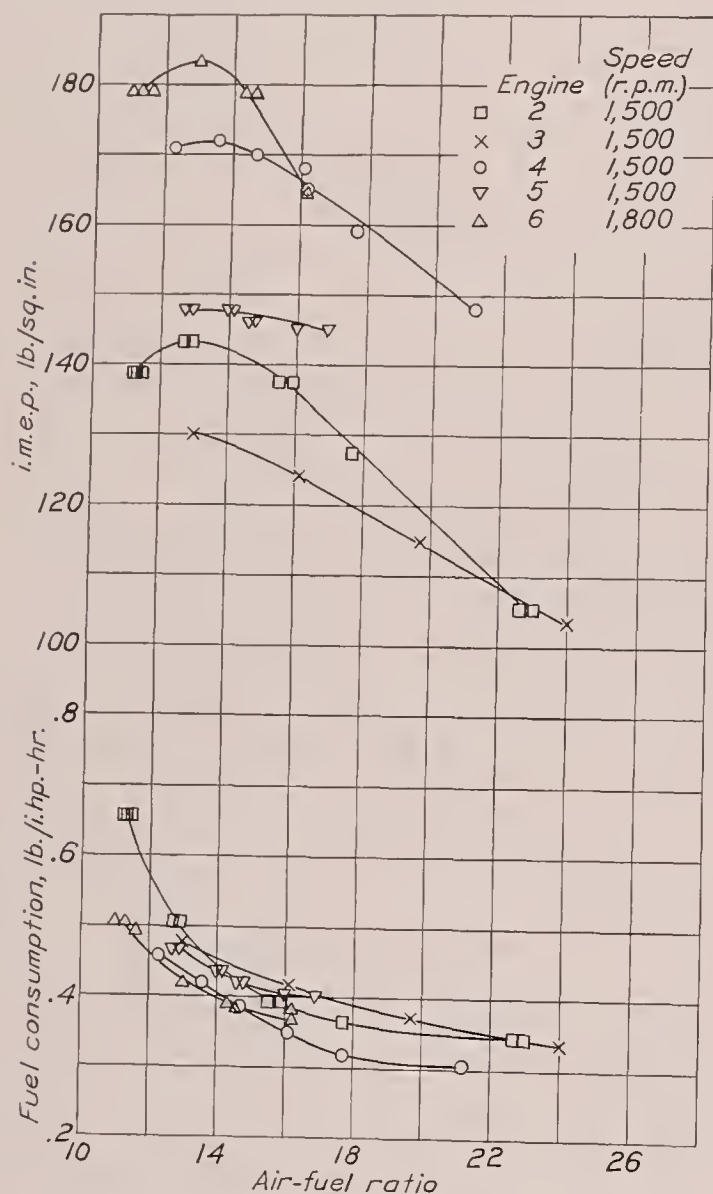


FIGURE 10.—Effect of air-fuel ratio on engine performance.

consumed than C. Gerrish and Foster (reference 9) have shown that, when sufficient Diesel fuel is present in the engine cylinder to utilize all the O_2 , the addition of H_2 increases the quantity of H_2O formed and decreases the amount of CO_2 .

Engine performance.—In figure 10 the engine performance has been shown as a factor of the air-fuel ratio for the compression-ignition engines 2, 3, and 4 and the spark-ignition engines 5 and 6 operating with a carburetor under the conditions shown in table I. The positions of maximum power for the different

engines and conditions on this basis are identical and occur at a definite air-fuel ratio, approximately 13. All engines investigated are on an equivalent basis as regards air-fuel ratio and combustion efficiency; the differences in their performance are due to the amount of charge present and the efficiency of the cycle.

It was thought that some of the differences in the performance of the engines might be the cause of the scatter of the experimental data presented in figures 2, 4, and 9. It was impossible, however, to obtain closer agreement by grouping the data according to engines or engine conditions and it is therefore concluded that the exhaust-gas constituents, air-fuel ratio, water of combustion, combustion efficiency, and their relationships are independent of engine design and manner of operation.

CONCLUSIONS

The following conclusions have been drawn from the results presented.

1. The constituents of the exhaust gases from internal-combustion engines bore a definite interrelation.
2. Factors computed from exhaust-gas analyses, such as air-fuel ratio, water of combustion, and combustion efficiency, bore a definite relation to one another and to the constituents of the exhaust gas.
3. Engine performance and operating conditions, such as compression ratio, engine speed, injection advance angle, and method of ignition, did not affect the relations between the exhaust-gas constituents and the factors computed from them.
4. The relations of the constituents and factors make it possible to obtain a complete exhaust-gas analysis simply by determining the air-fuel ratio or the amount of CO_2 and O_2 .
5. For rich mixtures the H_2 of hydrocarbon fuels burned more readily than the C.
6. Compression-ignition engines were operated at the same air-fuel ratio as spark-ignition engines without loss in combustion efficiency.
7. Combustion efficiency and water of combustion increased approximately linearly with air-fuel ratio for rich mixtures and were independent of mixture strength for lean mixtures.

LANGLEY MEMORIAL AERONAUTICAL LABORATORY,
NATIONAL ADVISORY COMMITTEE FOR AERONAUTICS,
LANGLEY FIELD, VA., September 7, 1937.

APPENDIX

DEVELOPMENT OF EMPIRICAL RELATIONSHIPS AMONG THE CONSTITUENTS OF THE EXHAUST GASES FROM INTERNAL-COMBUSTION ENGINES

According to reference 1 for standard and fighting grades of aviation gasolines, Auto Diesel fuel, and Laboratory Diesel fuel

$$H_2 = 0.51 \text{ CO} \quad (1)$$

$$CH_4 = 0.22 \quad (2)$$

$$K = \frac{H}{C} = 0.175 \quad (3)$$

$$H_2O = 5.955 K (CO_2 + CO + CH_4) - H_2 - 2CH_4 \quad (4)$$

and

$$O_2 + CO_2(1 + 2.355 K) + CO(0.604 + 2.355 K) - 0.186 H_2 - CH_4(0.582 - 2.355 K) = 20.9 \quad (5)$$

Inserting the values of H_2 , CH_4 , and K in equation (5) and then solving for CO ,

$$CO = 22.733 - 1.086 O_2 - 1.533 CO_2 \quad (6)$$

Inserting this value of CO in equation (1),

$$H_2 = 11.594 - 0.554 O_2 - 0.782 CO_2 \quad (7)$$

Inserting the values of H_2 , CH_4 , K , and CO in equation (4),

$$H_2O = 11.885 - 0.578 O_2 + 0.226 CO_2 \quad (8)$$

By differences there is obtained

$$N_2 = 100 - CO_2 - O_2 - CO - H_2 - CH_4 \quad (9)$$

Substituting the values of H_2 , CH_4 , and CO in equation (9),

$$N_2 = 65.453 + 0.6395 O_2 + 1.3148 CO_2 \quad (10)$$

The air-fuel ratio (A/F) is

$$\frac{A}{F} = \frac{28.84 \left(\frac{N_2}{0.791} \right)}{12(CO_2 + CO + CH_4) + 2.015(H_2 + H_2O + 2CH_4)} \quad (11)$$

where the values outside the parentheses are the molecular weights of air, carbon, and hydrogen and 0.791 is the volumetric ratio of N_2 to air.

Substituting in equation (11) the values previously found for N_2 , CH_4 , H_2 , CO , and H_2O ,

$$\frac{A}{F} = 1.523 \left(\frac{102.350 + O_2 + 2.056 CO_2}{21.139 - O_2 - 0.491 CO_2} \right) \quad (12)$$

The ratio of the water of combustion to the fuel present (W/F) is

$$\frac{W}{F} = \frac{18.015 H_2O}{12(CO_2 + CO + CH_4) + 2.015(H_2 + H_2O + 2CH_4)} \quad (13)$$

Substituting the values previously found for H_2O , CO , CH_4 , and H_2 ,

$$\frac{W}{F} = 0.680 \left(\frac{20.562 - O_2 + 0.391 CO_2}{21.139 - O_2 - 0.491 CO_2} \right) \quad (14)$$

In the determination of the combustion efficiency, the heat of vaporization of H_2O is not included because the cylinder gases are exhausted at a temperature considerably above the boiling point of water. The heats of combustion of the fuels have been computed from the heats of combustion of the elementary constituents. This method is in error by the heat of formation of the fuel. The error is small, however, amounting to about 1 percent in combustion efficiency for air-fuel ratios giving maximum power. The heats of combustion utilized in the calculations are given in kilojoules (absolute) at 18°C . and 1 atmosphere (reference 2).

The heat liberated by the formation of CO_2 , H_2O , and CO is

$$395 CO_2 + 110.6 CO + 242 H_2O$$

The heat that could be evolved by the combustion of the unburned combustibles is

$$242 H_2 + 284.4 CO + 799 CH_4$$

The combustion efficiency may be expressed as the ratio of the heat liberated to the sum of the heat liberated and the heat that still could be evolved.

Combustion efficiency

$$= \frac{CO_2 + 0.280 CO + 0.613 H_2O}{CO_2 + CO + 0.613 H_2O + 0.613 H_2 + 2.023 CH_4} \quad (15)$$

Substituting the values previously found for H_2O , CO , CH_4 , and H_2 ,

Combustion efficiency

$$= 0.370 \left(\frac{20.74 - O_2 + 1.079 CO_2}{21.11 - O_2 - 0.491 CO_2} \right) \quad (16)$$

A summary of the solution of the equations is given in table II.

REFERENCES

1. Gerrish, Harold C., and Tessmann, Arthur M.: Relation of Hydrogen and Methane to Carbon Monoxide in Exhaust Gases from Internal-Combustion Engines. T. R. No. 476, N. A. C. A., 1933.
2. National Research Council: International Critical Tables, vol. V, McGraw-Hill Book Company, Inc., 1929, pp. 176 and 181.

3. Dicksee, C. B.: Exhaust Gas Analysis. Auto. Eng., vol. XXI, no. 285, Oct. 1931, pp. 401-406.
4. Best, H. W.: Report on Air-Fuel-Ratio Tests. S. A. E. Jour., vol. XXV, no. 5, Nov. 1929, pp. 532-534.
5. Minter, Clarke C.: Interpretation of Exhaust Gas. S. A. E. Jour., vol. XXI, no. 5, Nov. 1927, pp. 573-575.
6. D'Alleva, B. A., and Lovell, W. G.: Relation of Exhaust Gas Composition to Air-Fuel Ratio. S. A. E. Jour., vol. 38, no. 3, March 1936, pp. 90-98, p. 116.
7. Fenning, Robert W.: The Composition of the Exhaust from Liquid-Fuel Engines. Jour. Inst. Mech. Eng., March 1916, pp. 185-236.
8. Fulton, Garland: Improving Airship Performance. A. S. M. E. Trans., AER-56-8, vol. 56, no. 5, May 1934, pp. 301-303.
9. Gerrish, Harold C., and Foster, Hampton H.: Hydrogen as an Auxiliary Fuel in Compression-Ignition Engines. T. R. No. 535, N. A. C. A., 1935.

TABLE II.—SUMMARY OF VALUES COMPUTED FROM EMPIRICAL EQUATIONS

Air Fuel	CO ₂ (per- cent)	O ₂ (per- cent)	CO (per- cent)	H ₂ (per- cent)	N ₂ (per- cent)	H ₂ O (per- cent)	H ₂ O CO ₂	Water Fuel	Com- bus- tion effi- ciency (per- cent)
11	8.76	0.15	9.14	4.66	77.08	13.78	1.57	0.972	66.7
12	10.18	.44	6.65	3.39	79.13	13.93	1.37	1.043	73.8
13	11.60	.59	4.31	2.20	81.09	14.16	1.22	1.122	81.5
14	13.02	.63	2.09	1.07	82.99	14.46	1.11	1.205	89.6
15	13.23	1.35	.99	.50	83.72	14.09	1.06	1.247	93.8
16	12.62	2.49	.68	.35	83.65	13.30	1.05	1.256	94.8
17	12.00	3.55	.48	.25	83.51	12.54	1.05	1.261	95.5
18	11.45	4.49	.30	.16	83.39	11.88	1.04	1.267	96.2
19	10.90	5.36	.20	.10	83.23	11.25	1.03	1.269	96.5
20	10.40	6.15	.11	.06	83.07	10.68	1.03	1.272	96.9
21	9.92	6.86	.08	.04	82.90	10.16	1.03	1.271	96.9
22	9.44	7.55	.06	.03	82.71	9.65	1.02	1.268	96.8
23	9.00	8.18	.05	.03	82.53	9.19	1.02	1.266	96.7
24	8.60	8.74	.06	.03	82.37	8.78	1.02	1.264	96.6

REPORT No. 617

AUTO-IGNITION AND COMBUSTION OF DIESEL FUEL IN A CONSTANT-VOLUME BOMB

By ROBERT F. SELDEN

SUMMARY

The variations in ignition lag and combustion associated with changes in air temperature and density have been studied for a Diesel fuel in a constant-volume bomb. The test results have been discussed in terms of engine performance wherever comparisons could be drawn. The highest test temperature approximated that attained in a compression-ignition engine in the usual range of injection advance angles. The test air densities ranged from something less than the compression density with normal aspiration to a value corresponding to considerable boost.

The most important conclusions drawn from this investigation are: The ignition lag was essentially independent of the injected fuel quantity. Extrapolation of the curves for the fuel used shows that the lag could not be greatly decreased by exceeding the compression temperatures and densities attained in modern high-speed compression-ignition engines. In order to obtain the best combustion and thermal efficiency, it was desirable to use the longest ignition lag consistent with a permissible rate of pressure rise.

INTRODUCTION

The development of the high-speed compression-ignition engine in recent years has necessitated a more critical attitude toward the nature of the fuel employed than was required for its precursor, the low-speed oil engine. The primary reasons for this change in attitude are the necessity of a light engine structure, together with a high specific output, and the usual fuel economy requirement that the crank-angle combustion period shall not become excessively large at high engine speeds. These requirements are, in a sense, contradictory in that the attainment of a high specific output necessitates a high rate of combustion that may result in severe structural loadings, which ordinarily do not occur in the more massive low-speed engine.

In order to secure a high specific output, the fuel must be partly mixed with available air, ignited, and burned in an extremely short time. The extent to which the mixing process is completed before ignition is obviously determined, in part, by the ignition lag. It is for this reason that the ignition quality of a fuel has such an important bearing on the satisfactory utilization of a

given fuel in a given engine. If the lag is too short, thorough mixing is not accomplished early enough to permit effective combustion; whereas, if the lag is too long, the rate of combustion may be objectionable. This contention is supported by results obtained with the N. A. C. A. combustion apparatus (reference 1) and with engines (references 2 and 3).

Numerous attempts have been made to investigate, with relatively simple apparatus, the influence of air density and temperature upon the ignition quality of fuels; but the test conditions, in general, differed so greatly from those in an engine that the results have little practical value (references 4 and 5). Attempts to simulate engine conditions by injecting the fuel into heated bombs have also been reported (references 6 to 11) but the ignition lags in every case were considerably greater than those permissible in high-speed engines. The results reported by Michailova and Neumann (reference 11) indicate that such an apparatus should prove satisfactory for rating Diesel fuels on the basis of their ignition quality. The employment of engines for this purpose has been reviewed in references 12 and 13.

It is the purpose of this report to present experimental results obtained with a constant-volume bomb, showing the effects of air temperature, air density, and concentration of residual gases upon the ignition lag of a fuel, together with some of the accompanying variations in combustion. Such data permit a clearer understanding of the extent and manner in which engine combustion is affected by operating conditions. Most of the tests were carried out at densities ranging from 0.59 to 1.48 pounds per cubic foot. The lower value approximates the air density in an engine (compression ratio=14) at 15° B. T. C., and the higher value that at T. C. with considerable boost. The temperature range corresponds roughly to that in the same engine between 35° and 15° B. T. C. The air-fuel ratios were, in general, above 20.

The ignition-lag data correspond to the period from the start of injection to the first evidence of a pressure increase. Some flame may exist before any appreciable change in pressure occurs (references 1 and 14); nevertheless, the lag as herein defined should be the best measure of the interval available for the mixing of fuel and air prior to the general inflammation. Hetzel

(reference 12) has employed a similarly defined lag in his investigation of methods of rating fuels in a modified C. F. R. engine.

APPARATUS AND PROCEDURE

The apparatus consisted essentially of an electrically heated stainless-steel bomb, provided with an injection system capable of delivering a single charge of fuel and with an optical-type indicator for recording pressures photographically. Figure 1 is a diagrammatic sketch

with guides to fix the position of the bomb with respect to the optical system. The furnace (C—C, fig. 1) is divided into two parts with the top half hinged to the lower rigid section. The inlet valve J and the exhaust valve E' are so designed that they can be quickly opened or closed. The thermocouple P', inserted through a lug in the side of the bomb to within $\frac{1}{4}$ inch of the inner wall, served to indicate the bomb temperature. The thermocouple F in the top, or hottest part, of the furnace and the pyrometer U' served to control

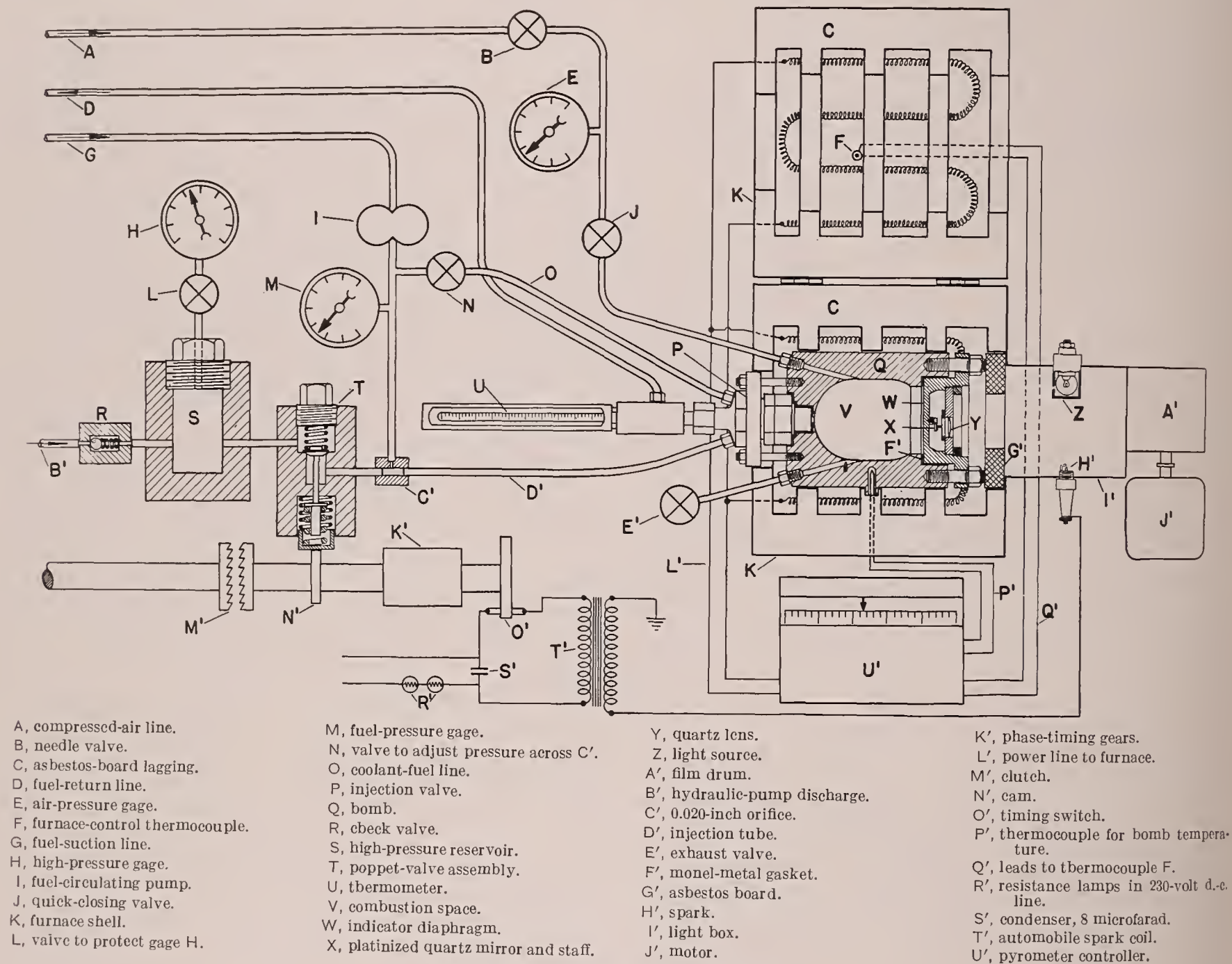


FIGURE 1.—Diagrammatic sketch of apparatus.

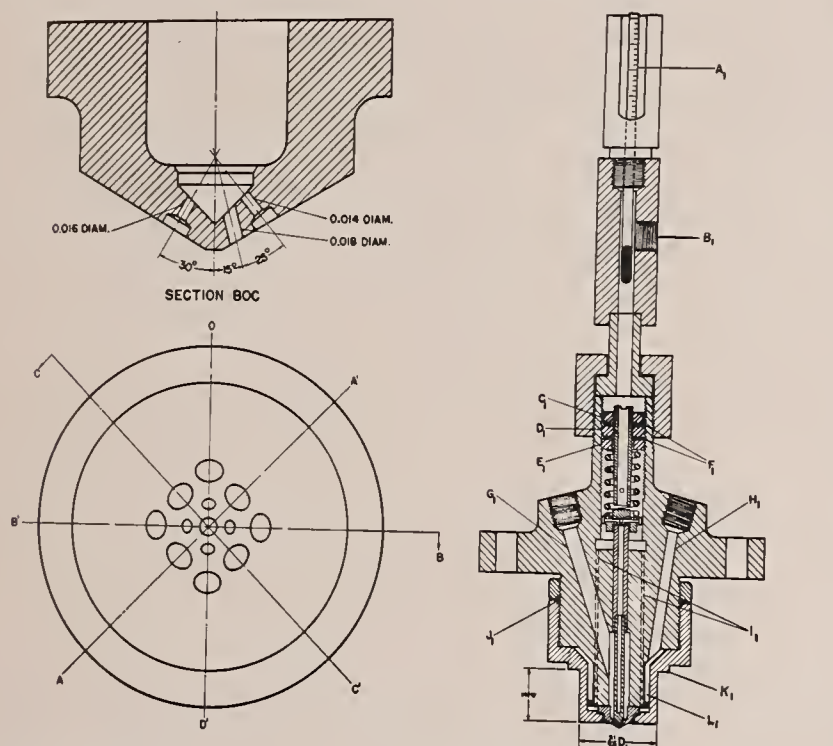
of the assembled apparatus. A manually operated hydraulic pump (not shown) was employed to force the fuel through tube B' into reservoir S. The fuel tank contained heating and cooling units that maintained the desired temperature of the circulating fuel (130° F.) at thermometer U for all save a few tests at the highest bomb temperature. The increase in temperature as the fuel passed through the injection valve was approximately 15° F.

The bomb has a maximum inside diameter of 3 inches, a length from nozzle to indicator diaphragm of about $3\frac{7}{8}$ inches, and a measured volume of 21.7 cubic inches (356 cm³). The bomb support was arranged

the furnace temperature and, indirectly, the bomb temperature. The large thermal lag of the bomb relative to that of the heating elements necessitated this arrangement to avoid destruction of these elements.

A sketch of the injection valve and of an enlarged section of the nozzle is shown in figure 2. The heat flow in the neighborhood of the nozzle was minimized by placing the narrow seal (K₁, fig. 2) between the valve body and the bomb some distance back from the nozzle. Thermocouples spot-welded to the interior surface of the bomb wall showed that the cooled region was confined to the curved surface at the valve end of the bomb and that the total temperature difference

never exceeded 270° F. The valve was cooled by two fuel streams (see figs. 1 and 2): The main stream passed through tube O, then passage H₁, jacket L₁, and the four passages (two of which are indicated as l₁) to the return line B₁; the smaller stream passed through orifice C', injection tube D', passage G₁, and the two small holes in the valve stem to be mixed with the main stream in the return line B₁ (or D). The area of these stem holes and of orifice C' is so much smaller than that of the nozzle orifices that a relatively small portion of the hydraulic injection impulse was dissipated at these points. The pressure in the line between pump 1 and orifice C' was adjusted to 150 pounds per square inch



Twelve-orifice nozzle.

Plane DD' is identical with BB'.

Plane CC' is identical with AA'.

A₁, thermometer for fuel temperature.

B₁, connection between valve and fuel return line.

C₁, upper lock nut for stem stop.

D₁, lock-nut and stem-stop support.

E₁, nut for adjusting spring load.

F₁, lock washers.

G₁, injection passage.

H₁, passage for main coolant stream.

I₁, return passages from jacket K.

J₁, oil seal around valve body.

K₁, sealing surface.

L₁, coolant jacket around end of valve.

Injection-valve assembly.

FIGURE 2.—Injection-valve assembly and nozzle.

by means of the bypass valve N. Small readjustments of this valve were necessary for each bomb temperature. Seal J₁, which prevents fuel leakage into the furnace, consists of a number of turns of soft electric fuse wire forced tightly against the threads on the valve body by the clamping nut shown. The fact that this wire is satisfactory in spite of its low melting point is a good indication of the effectiveness of the cooling system.

The optical indicator is an adaptation of the one described in reference 15. All parts were constructed of a high-tungsten steel for which the manufacturer claims a yield point of 120,000 pounds per square inch at 1,100° F. The platinized quartz mirror proved fairly satisfactory although it gradually lost its mirror finish and reflectivity at the higher temperatures. It was necessary, therefore, to retouch certain of the prints of the original records in order to get satisfactory half-tone reproduction.

The indicator was calibrated by recording photographically the deflections corresponding to several static gas pressures over the range of interest with the indicator bolted to the hot bomb as for an explosion test. The calibration pressures were determined by a Bourdon gage, which had been checked against a dead-weight gage tester. The error involved in measuring the records is believed to be larger than any involved in the calibration procedure and, since most deflections were relatively small, the derived data may involve appreciable errors. These errors are not particularly important, however, as trends, rather than exact magnitudes, are of primary interest. Except, perhaps, for extremely high rates of pressure rise, it is believed that this indicator, in view of its high natural frequency, satisfactorily recorded the instantaneous explosion pressures. Very great rates of pressure rise, such as accompanied the larger fuel weights under conditions giving long ignition lags, invariably led to severe vibration, which loosened the mirror staff in its bearings.

The fuel employed in these tests was found by the U. S. Naval Engineering Experiment Station, Annapolis, Md., to have the following characteristics:

Diesel index.....	70.1
Aniline point.....	183.7
Specific gravity, 60/60° F.....	0.834
A. P. I. gravity.....	38.2
Flash point, closed cup.....° F.....	242
Cloud point.....° F.....	28
Pour point.....° F.....	25
Color N. P. A.....	1.0
Saybolt Universal viscosity:	
At 32° F.....seconds.....	87
At 100° F.....do.....	43
Carbon residue.....percent.....	0.01
Sulphur.....do.....	0.04
Heat value, calorimeter gross.....B. t. u. per pound.....	19,996

Distillation characteristics:

	° F.
First drop.....	526
5 cm ³	531
10 cm ³	532
20 cm ³	538
30 cm ³	546
40 cm ³	553
50 cm ³	562
60 cm ³	572
70 cm ³	584
80 cm ³	599
90 cm ³	627
End point.....	681
Recovered.....percent.....	98.3

The cetane number was found to be 64 on the Diesel conversion of the C. F. R. engine in conjunction with the modified magnetic pick-up method recommended in reference 16. This ignition quality compares favorably with the better commercial fuels (reference 17).

During tests the pyrometer controller was set to give a furnace temperature corresponding to the desired bomb temperature, the circulating pump 1 (see fig. 1)

was started, and the flow of cooling water through the coils in the fuel tank was adjusted to give the requisite fuel temperature. The bomb was filled with air to the desired pressure, needle valve B being used for close control of the air flow. Fuel was then forced into reservoir S to a predetermined pressure such that the desired weight of fuel could be injected. Finally, the motor J' was started, valve J closed to protect gage E, and the injection made by means of a "trip-hammer" mechanism

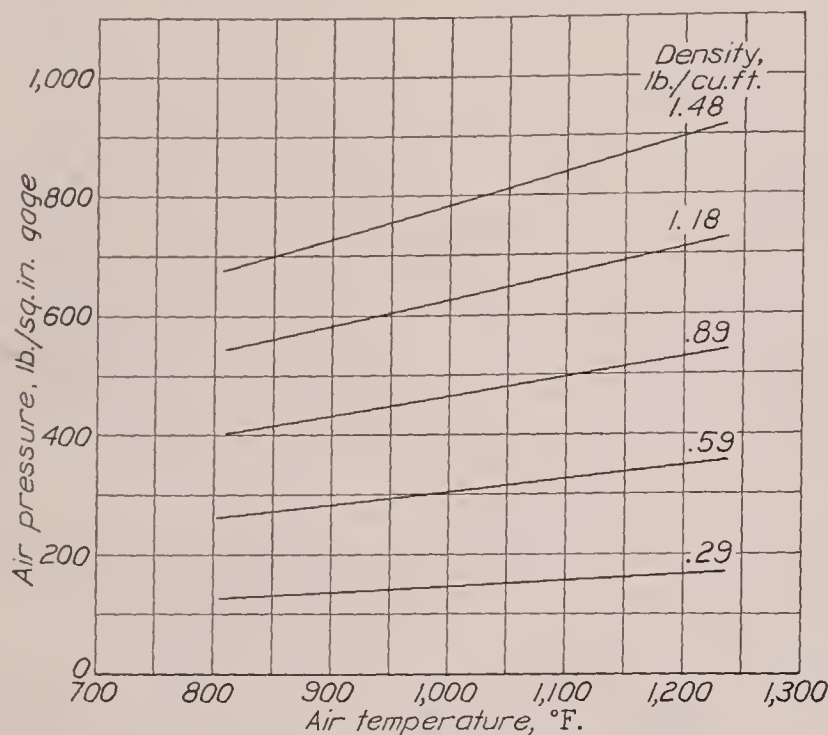


FIGURE 3.—Relations of temperature, pressure, and density.

that permitted the engagement of clutch M' for a single revolution of the driving shaft. The motion of the trip-mechanism handle automatically closed the circuit for lamp Z for a period beginning before injection and extending beyond the combustion period. The resulting film trace shows both the initial pressure and the pressure changes resulting from combustion. This film, together with the reference trace (zero gage pressure) taken before admitting air to the bomb, constitutes the pressure record.

The engagement of the clutch M' lifted a poppet valve T by means of cam N', thus admitting the full pressure from reservoir S to the injection line D'. This operation also closed switch O', producing a spark at gap H' and a corresponding trace on the film at right angles to the constant-pressure traces. This spark served to denote the start of injection on the film record, the two having been properly phased by means of the gears K' as described in reference 18, before the tests were begun.

The air pressures used were arbitrarily selected to give densities corresponding to 5, 10, 15, 20, 25, and 30 atmospheres absolute at 212° F. For convenience in the examination of the experimental results, the relations of temperature, density, and gage pressure are shown graphically in figure 3. Air density rather than air pressure was used as one of the primary variables because of the better correlation with spray development (reference 19) and of the better control of what-

ever mass-action effects there may have been in the ignition and combustion of the fuel. The air-fuel ratios were based upon the weight of air in the bomb prior to injection without considering the small amount of air compressed, as a result of combustion, into the small inlet and exhaust passages and into the space about the end of the injection valve. In any case, these ratios are not indicative of the wide range of actual air-fuel ratios from point to point in the fuel spray. The desired fuel quantities were obtained by varying the pressure in the reservoir S between 4,600 and 7,600 pounds per square inch.

RESULTS

Typical records for an air-fuel ratio of 30, reproduced in figure 4, show the effect of air temperature on the ignition lag at a density of 0.59 pound per cubic foot. Ignition-lag data taken from these and similar records for air-fuel ratios ranging from 20 to 80 are plotted in figure 5, together with data obtained at twice this density, 1.18 pounds per cubic foot.

A similar set of records (fig. 6) for an air-fuel ratio of 20 shows the effect of air density on the ignition

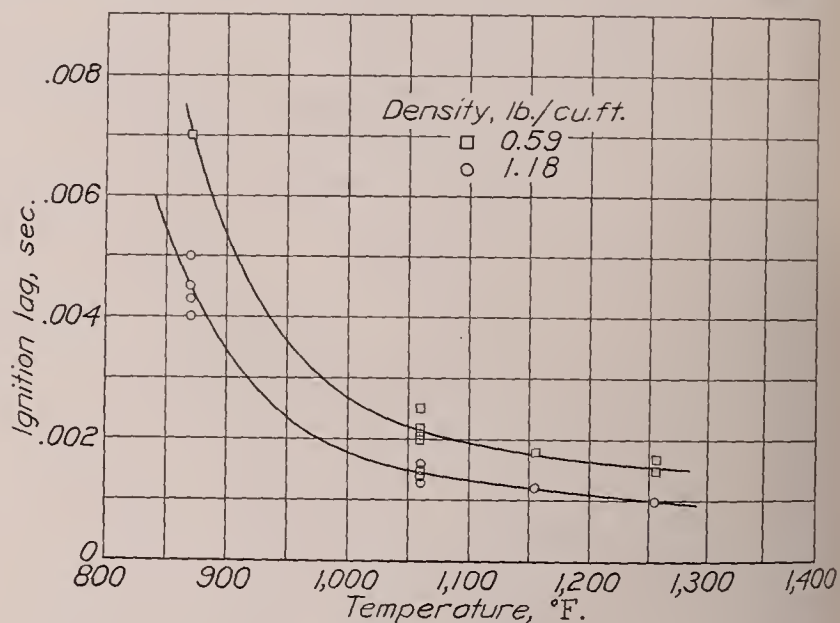


FIGURE 5.—Effect of temperature on ignition lag. Variable air-fuel ratio.

lag at the highest temperature (1,155° F.) for which the indicator was suitable for continuous service. Ignition-lag data obtained with various air-fuel ratios at this and several other gas temperatures are shown in figure 7. A summary of the data for figures 5 and 7 is given in table I.

The effectiveness of combustion (insofar as it is defined by the ratio of the pressure 0.004 second after ignition to the initial pressure) is shown as a function of the ignition lag by the solid curves of figure 8. These curves correspond to data obtained at two air densities and at several air temperatures (870°, 1,060°, 1,155°, and 1,255° F.). The 0.004-second period was arbitrarily taken as the longest in which combustion of the fuel would efficiently produce power in a moderately high-speed engine. For this reason the highest pressure indicated on the records reproduced in the

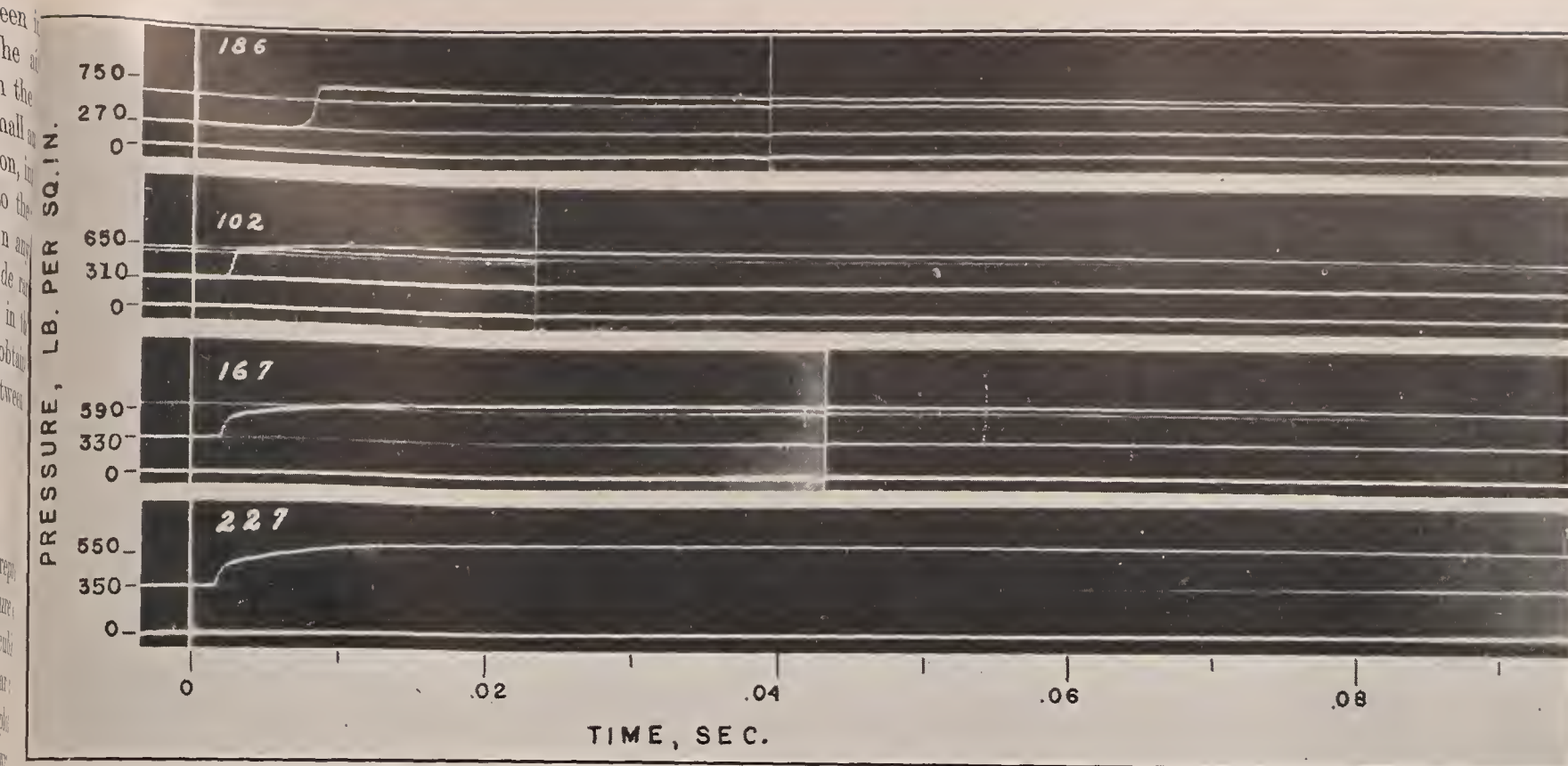


FIGURE 4.—Effect of temperature on ignition lag. Air density, 0.59 pound per cubic foot; air-fuel ratio, 30.

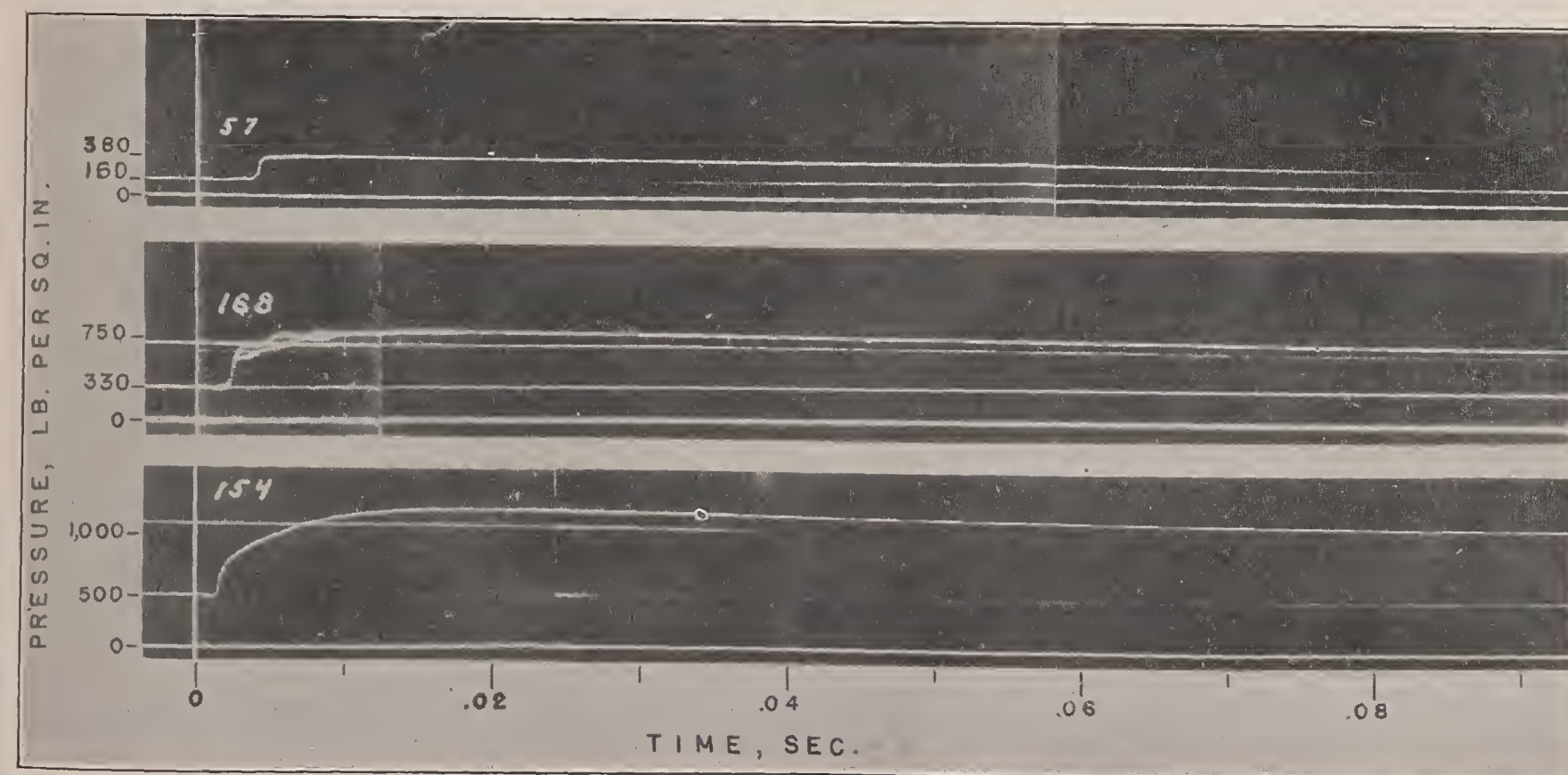


FIGURE 6.—Effect of air density on ignition lag. Air temperature, 1,155° F.; air-fuel ratio, 20.

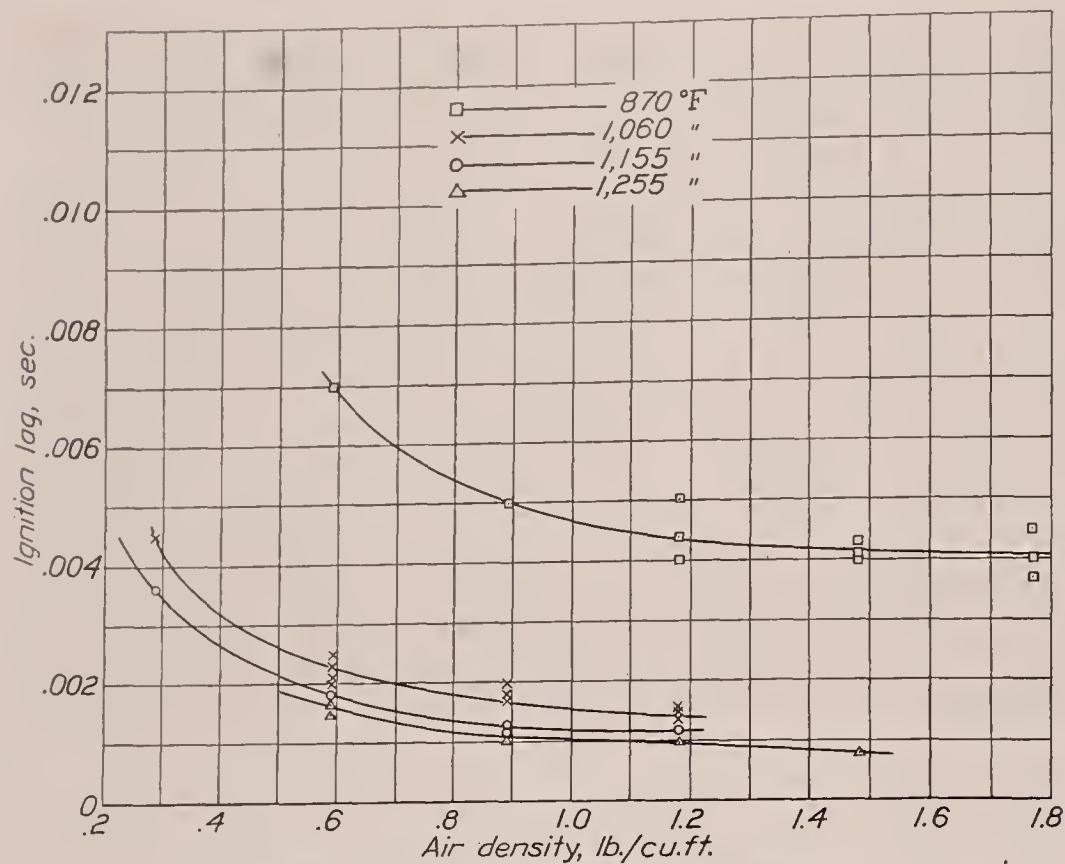


FIGURE 7.—Effect of air density on ignition lag. Variable air-fuel ratio.

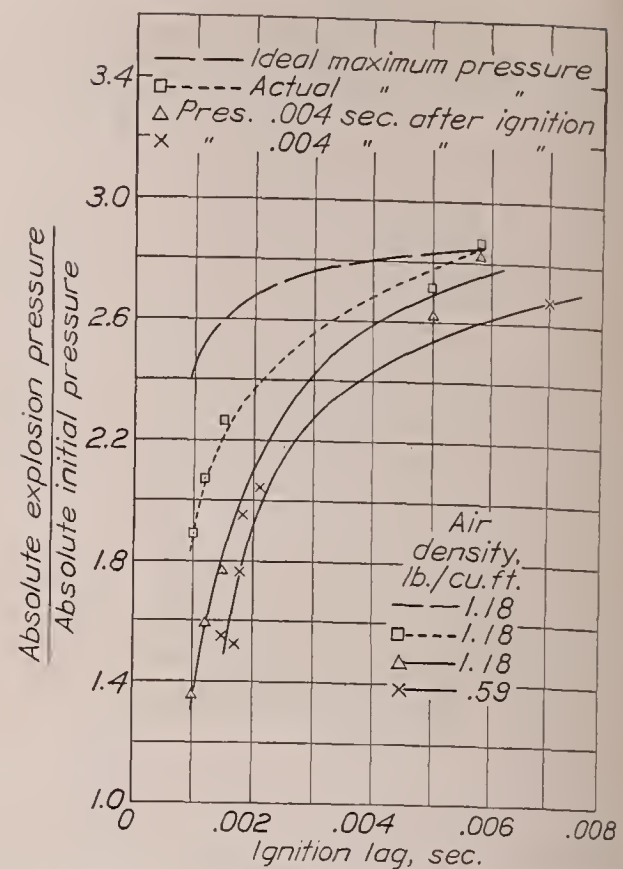
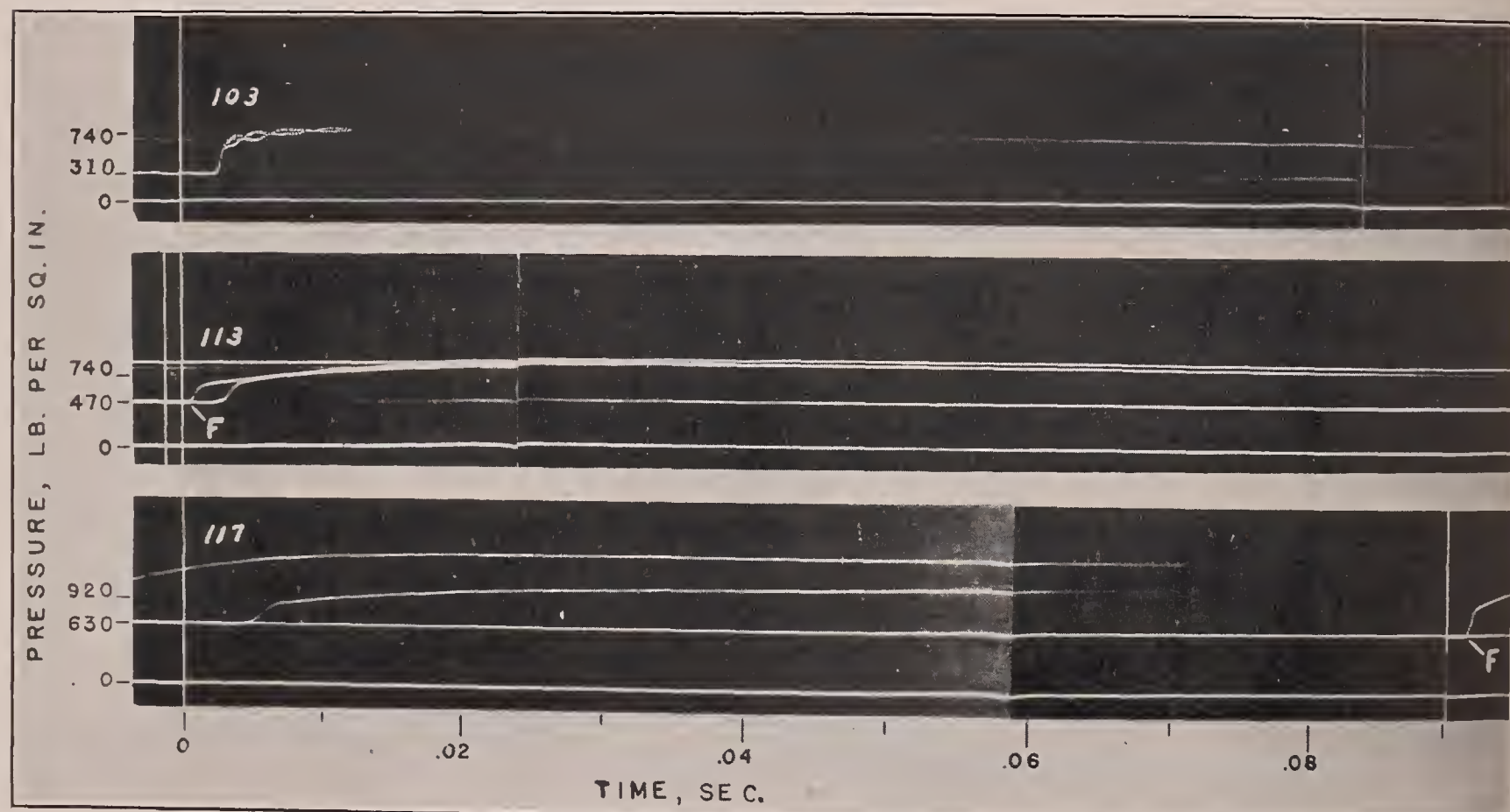


FIGURE 8.—Effect of ignition lag on combustion. Air-fuel ratio, 30.



Record	Air-fuel ratio	Density (lb./cu. ft.)	Ignition lag (sec.)	Maximum explosion pressure (lb./sq. in.)
103	25	0.59 (air)-----	0.0023	800
113F	45	0.89 (air)-----	.0018	880
113	25	0.59 (air)-----	.0027	900
117F	30	0.32 (products)-----		
117	25	1.18 (air)-----	.0017	1,440
		0.59 (air)-----	.0047	1,140
		0.63 (products)-----		

FIGURE 9.—Effect of combustion products on ignition lag and combustion with a gas temperature of 1,060° F.

several figures corresponds to the pressure prevailing at the end of this period.

The dotted curve of figure 8 corresponds to similar ratios of the observed maximum explosion pressure to the initial pressure for the same ignition lags at the higher air density. The dashed "ideal" curve was derived from the dotted curve and indicates what the ratios of maximum to initial pressure should be for complete combustion and no appreciable heat losses. The ideal curve was obtained on the basis of two approximations: first, that the observed ratio of maximum to initial pressure of 2.84 at an ignition lag of 0.0058 second corresponded to complete combustion under the prevailing conditions with negligible heat losses; and, second, that the same temperature rise should occur at all initial temperatures. The second approximation can be valid only for a constant specific heat and an invariant chemical equilibrium. The 2.84 ratio corresponds to the lowest experimental temperature and the longest lag; hence the approximate increase in temperature resulting from this explosion was $(2.84-1) \times (870+460)$. The other values used in plotting the dashed curve were obtained by dividing the sums of this temperature increment and the individual absolute initial temperatures (corresponding to the particular ignition lags plotted in fig. 8) by the respective absolute initial temperatures. The difference between the dotted and the dashed curves at the shorter ignition lags resulted from a combination of heat losses and incomplete combustion.

Three records are reproduced in figure 9 to show the effect of the concentration of combustion products on the ignition lag and on the rate of combustion at 1,060° F., and at an air-fuel ratio of approximately 25. The gas density was different for each case. Records 113 and 117 show traces for two separate explosions, the first of which (marked F in this and later figures) served to reduce the initial oxygen concentration to a value calculated to be equivalent to that for record 103. The total gas densities were slightly greater after the preliminary explosions, owing to the weight of fuel injected to provide the combustion products. The concentration of these products before the second injection was twice as great for record 117 as for record 113. The zero of the time scale for each of the second explosions corresponds to that for record 103.

In order to show the relative influence of the specific action of the combustion products and of an inert gas on the ignition and combustion for an air-fuel ratio of 20 at 1,155° F., two groups of three records each, at effective air concentrations of 0.59 and 0.89 pound per cubic foot, respectively, are reproduced in figure 10. The uppermost record in each group (168 and 154) corresponds to a normal explosion in pure air. The center records (161 and 147) correspond to mixtures of air and nitrogen such that the air concentration was the same as in records 168 and 154, respectively, but with a

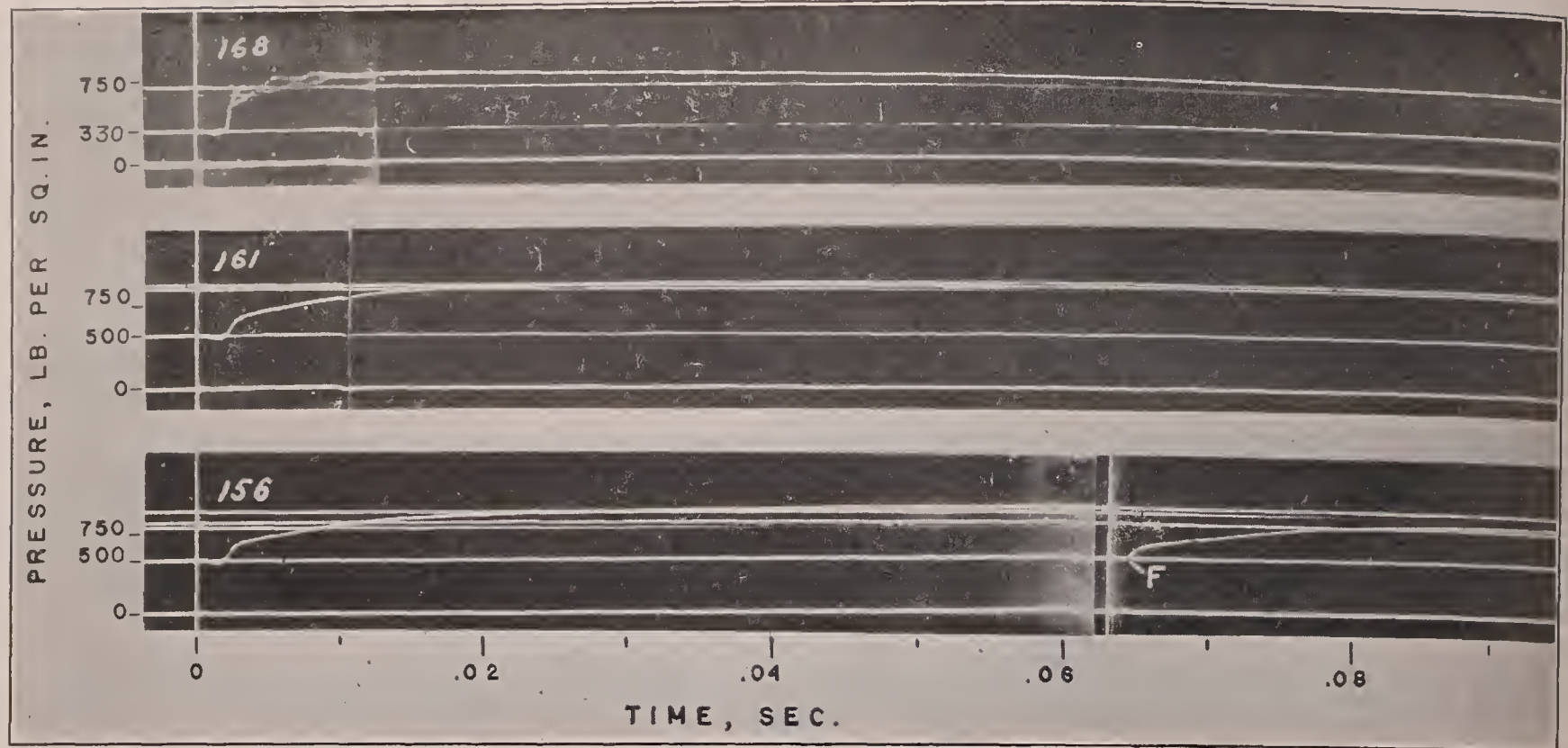
total gas density roughly equivalent to the corresponding lowest record in each group. These records (156 and 142), for air plus combustion products, were obtained as outlined for figure 9. The total densities of the nitrogen-air and combustion products-air mixtures were not quite equal, owing to their method of preparation, but both were higher than for the corresponding pure-air explosions. The nitrogen mixtures were made up by admitting air to the bomb to the same respective pressures as for records 168 and 154 and then admitting enough nitrogen to bring the total pressure to the value corresponding to the next highest experimental density as computed for air, i. e., 0.89 and 1.18 pounds per square inch, respectively. This procedure neglects, of course, the small density differences between air and nitrogen. Aside from this limitation, the initial air densities for the double-injection records (156 and 142) were the same as for the nitrogen-air records.

The fact that the presence of combustion products or of excess nitrogen reduced the initial rate of pressure rise made it possible to inject a larger amount of fuel into such a mixture without damaging the indicator than was possible with an equivalent amount of pure air. The records in figure 11 are indicative of the permissible decrease in air-fuel ratio at a temperature of 1,155° F. Record 168, obtained with pure air, shows a rate of pressure rise considerably greater than either the nitrogen-air record (165) or the double-injection record (159) even though the air-fuel ratio for it was 20, whereas that for the two latter records was about 13.5. The effective air concentration, 0.59 pound per cubic foot, was the same for each record.

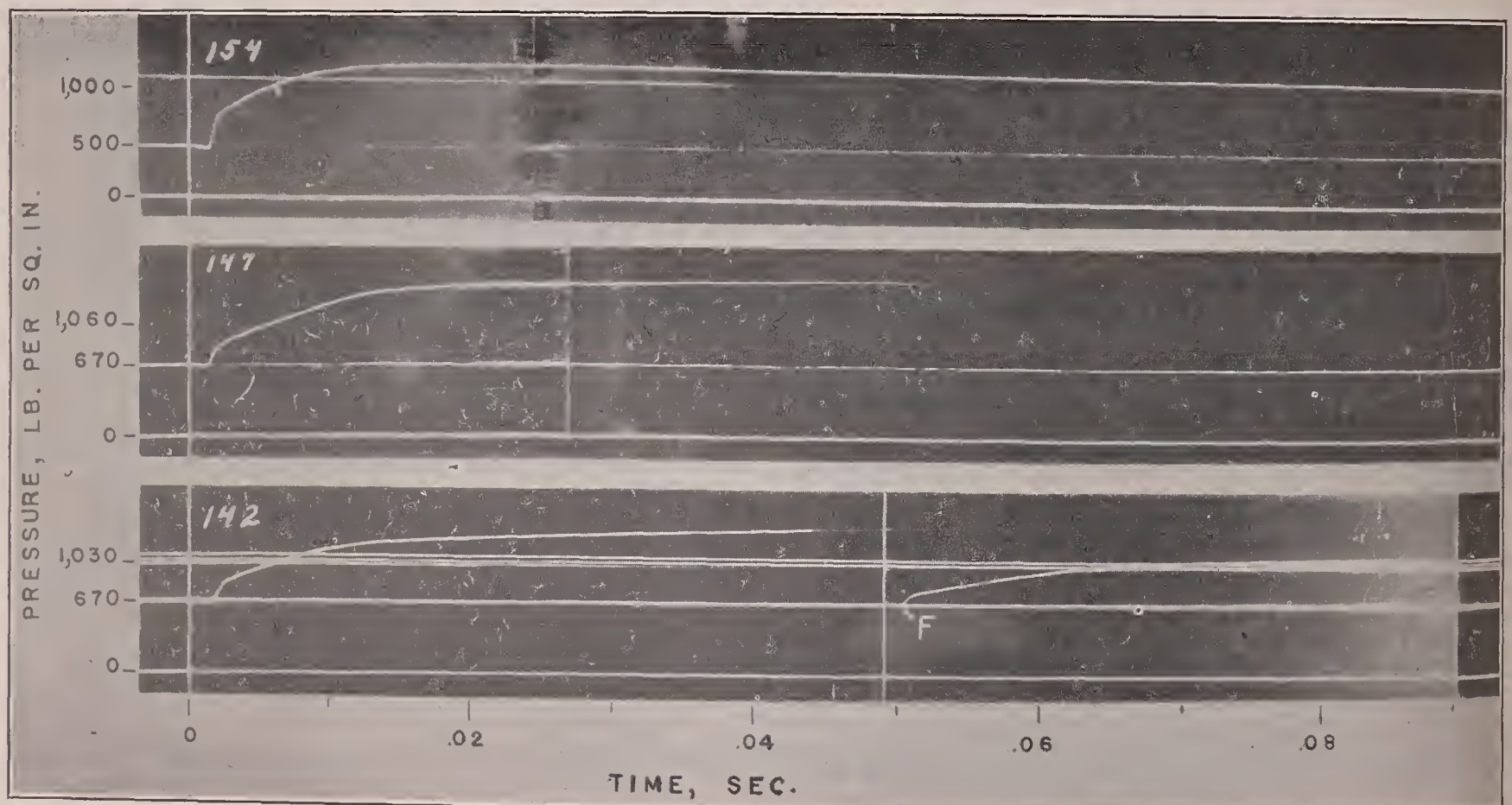
DISCUSSION

The present test conditions differed from conditions in a compression-ignition engine in that there was no turbulence in the air charge prior to injection and the wall temperatures were perhaps higher than in an engine. The effect of these factors upon the lag data presented herein is evidently very small in view of the fact that an extrapolation of the curves in figure 5 to the air temperatures that are probably attained before ignition in an engine indicates ignition lags of the same magnitude as those observed in an engine using the same fuel. Other investigations have led to conflicting conclusions as to the effect of turbulence on ignition lag (references 9, 20, and 21). In the case of engines this uncertainty may be caused by the difficulty of appreciably altering the degree of turbulence without simultaneously effecting changes in other influential variables.

Engine tests, as well as the present results, indicate that ignition lag is an important criterion in determining the rate and, to some extent, the effectiveness of combustion; hence the trends shown by the present results must have their counterpart in the compression-ignition engine as the intake-air pressure or temperature and

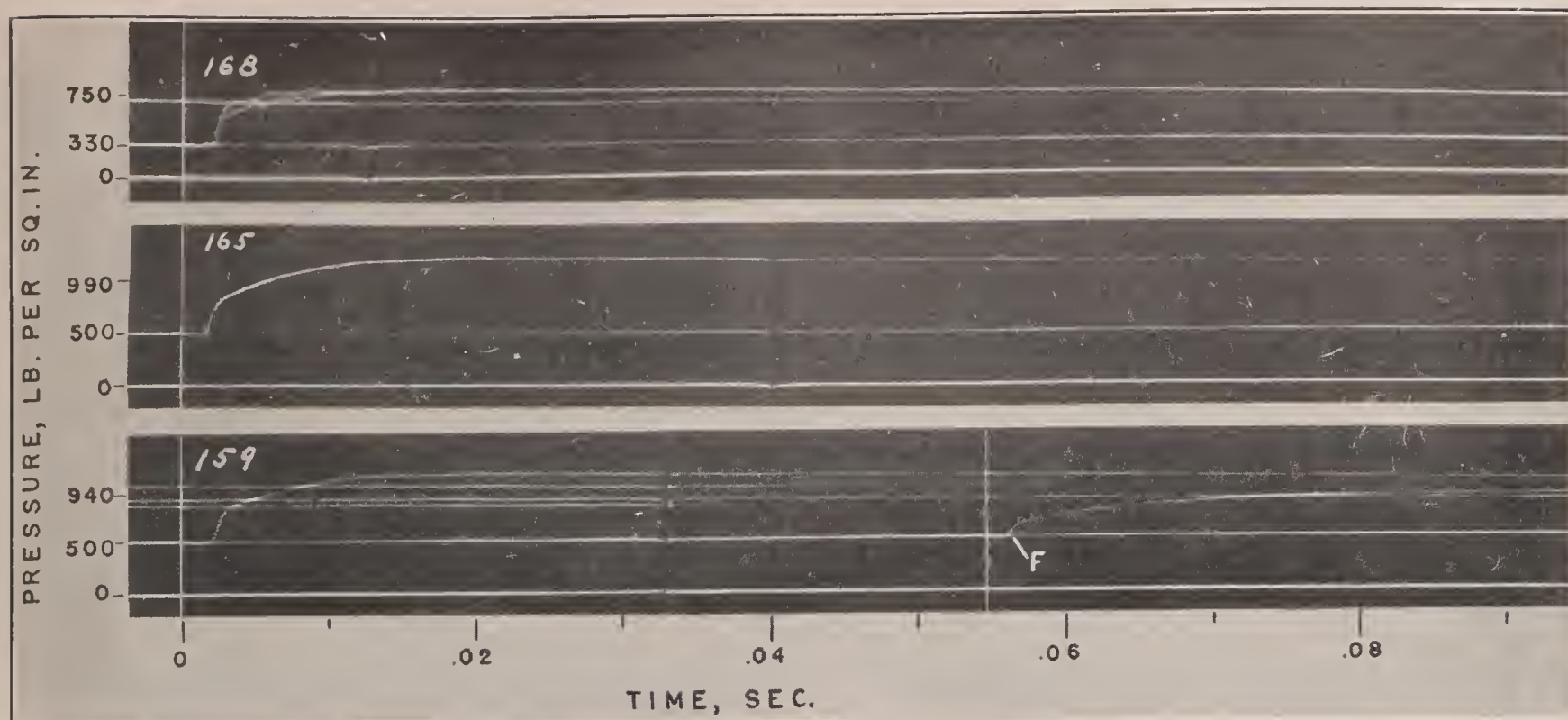


Record	Air-fuel ratio	Density (lb./cu. ft.)	Ignition lag (sec.)	Maximum explosion pressure (lb./sq. in.)
168	20	0.59 (air)-----	0.0018	800
161	20	0.59 (air)-----	.0020	960
		0.29 (nitrogen)-----		
156 F	45	0.89 (air)-----	.0013	860
156	20	0.59 (air)-----	.0018	970
		0.32 (products)-----		



Record	Air-fuel ratio	Density (lb./cu. ft.)	Ignition lag (sec.)	Maximum explosion pressure (lb./sq. in.)
154	20	0.89 (air)-----	0.0013	1,260
147	20	0.89 (air)-----	.0014	1,480
		0.28 (nitrogen)-----		
142 F	60	1.18 (air)-----	.0012	1,150
142	20	0.89 (air)-----	.0018	1,420
		0.31 (products)-----		

FIGURE 10.—Effect of inert gases on ignition and combustion with a gas temperature of 1,155° F.



Record	Air-fuel ratio	Density (lb./cu. ft.)	Ignition lag (sec.)	Maximum explosion pressure (lb./sq. in.)
168	20	0.59 (air)-----	0.0018	800
165	13.3	{0.59 (air)-----	.0017	1,220
		{0.29 (nitrogen)-----		
159 F	45	0.89 (air)-----	.0015	880
159	13.5	{0.59 (air)-----	.0020	1,100
		{0.32 (products)-----		

FIGURE 11.—Effect of added inert gases on permissible air-fuel ratio. Air temperature, 1,155° F.; air density, 0.59 pound per cubic foot.

the compression ratio are varied. The manner and extent in which these trends are altered as the ignition quality of the fuel is changed must await further tests.

FACTORS AFFECTING THE IGNITION LAG

The ignition lag, as shown in figures 4 to 7, decreased as either the density or temperature of the gas was increased. The fact that the lags were considerably shorter for supposedly equivalent conditions than those obtained by Michailova and Neumann (reference 11) with a fuel of superior ignition quality (cetene) indicates that the range of temperatures in their bomb must have been rather wide. The air-fuel ratio appeared to have little or no influence upon the ignition lag, presumably because the optimum conditions for ignition always exist somewhere in the spray envelope. A consideration of the data in table I or a comparison of record 154 (fig. 6) with the first explosion on record 156 (fig. 10) or 159 (fig. 11) and of record 167 (fig. 4) with 168 (fig. 6) shows that the spread of the points in figure 5 must have been due to slight variations in temperature; certainly there is no correlation with air-fuel ratio. It follows from the results shown in figure 5 that the decrease in ignition lag, accompanying an increase in the compression ratio of a compression-ignition engine, is due partly to the increase in temperature and partly to the increase in air density. This

conclusion confirms the results of previous engine tests, in which the intake-air temperature and pressure were independently varied (references 2, 22, and 23). The fact that some methods of rating fuels, which certainly do not simulate actual engine conditions (references 12, 13, and 16), correlate other rating methods and engine requirements reasonably well indicates that the curves in these figures would be merely shifted with very little change in shape if the ignition quality were varied. This contention is partly substantiated by the curves shown in reference 24.

The results of the present tests verify, in principal, the conclusion drawn by Michailova and Neumann (reference 11) that the ignition lag shows little tendency to decrease further at the higher temperatures and densities. (See figs. 5 and 7.) Engine tests indicated the same tendency (reference 24) but the necessary conditions varied somewhat with the fuel used. A determination in this laboratory of the air consumption and compression pressure of a motored engine having a known clearance volume indicated a gas temperature of 1,290° F. and a density of 0.87 pound per cubic foot at top center for a compression ratio of 14.6. Under operating conditions the temperature should exceed this value, owing to the heating of the air charge and to the presence of residual combustion products. Figure 7 indicates that this compression temperature might

be considerably reduced by decreasing the intake-air temperature, provided that the same air density is maintained, without exceeding an ignition lag of 0.0015 second. This indication is in agreement with engine results (reference 22). Such a lag and its associated rate of pressure rise have been found in this laboratory to be permissible in test engines.

INFLUENCE OF IGNITION LAG ON COMBUSTION

The solid curves in figure 8 show qualitatively, for two air densities, the influence of the ignition lag on the effectiveness of the combustion within a reasonable period after ignition. Rothrock and Waldron (reference 1) have observed a corresponding decrease in engine efficiency as the ignition lag was decreased below the value giving the greatest permissible rate of pressure rise. The same trend may be seen in figures 4 and 6; the shorter the lag, the greater the ensuing combustion period or the time necessary to attain maximum pressure. This tendency accounts for the approach of the upper solid curve to the dashed curve in figure 8 at long ignition lags since the heat losses were a minimum for this condition. The lower solid curve corresponds to a density approximating that in a normally aspirated compression-ignition engine during injection.

The trends in this combustion effectiveness should be indicative of similar trends in engine mean effective pressure, provided that all but a negligible portion of the combustion occurs soon after top center. Under these conditions the mean effective pressure is a function of, but not directly proportional to, the ratio of explosion to compression pressure. The fact that this ratio becomes a maximum in an engine only when appreciable combustion occurs before top center necessarily tends to nullify the advantage, in terms of mean effective pressure, accruing from a high value of this ratio; hence an intermediate ratio gives the best results in actual practice. Moreover, the expansion of the gases in an engine prevents the attainment of as high a value of maximum explosion pressure to maximum compression pressure as would occur if the same degree of combustion could be realized at top center or in a bomb. Actual engine ratios appear to be in the neighborhood of 1.5 to 1.8 (references 23 and 25) when the maximum cylinder pressures are limited to moderate values. The ratio can be increased to some extent, of course, by permitting higher cylinder pressures. The present values of the pressure ratio after 0.004 second are of this order even for the shortest ignition lags but are not strictly comparable with the engine ratios because of different conditions and air-fuel ratios. Within limits, however, these trends should be apparent in either an engine or a bomb.

To what extent the curves in figure 8 are representative of an engine possessing considerable turbulence is unknown. A qualitative comparison can be made, however, with available combustion efficiency data for

a quiescent combustion-chamber engine. Thus, the ratio of a point on the upper solid curve to a corresponding point (same ignition lag) on the dashed curve is approximately proportional to the ratio of the energy derived from burned fuel in the 0.004-second interval to the total available energy, that is, to the combustion efficiency for the particular conditions. If attention is confined to lags of 0.001 and 0.0015 second, the respective ratios for the bomb are 0.55 and 0.72, which compare favorably with efficiencies ranging from 59 to 69 percent for the total combustion in a quiescent combustion-chamber engine (reference 26). The heat losses are necessarily indicated as unburned fuel in both instances. This agreement indicates that the combustion in the bomb, even for the short lags, was comparable with that in this particular engine.

The solid curves of figure 8 show that the 0.004-second pressure ratio increased as the density was increased, particularly for ignition lags acceptable in an engine. Since this ratio should be independent of density for a given air-fuel ratio, negligible heat losses, and the same percentage of fuel burned, it follows that a greater percentage of fuel burned in the designated period at the higher density. Compression-ignition engines in this laboratory have not shown a similar trend as evidenced by a constant indicated specific fuel consumption for a given air-fuel ratio and all boost pressures. (See fig. 7, reference 22.) It is possible that, in the bomb, the combination of the higher air density and larger fuel quantity merely resulted in better mixing without any chemical effect; whereas, in the engine, this effect would be minimized by air movement. On the other hand, the data presented in reference 27 for hydrogen, carbon monoxide, and methane-air mixtures indicate that the gas density does affect the burning of these homogeneous mixtures but what the effect should be for the higher hydrocarbons is unknown. Furthermore, some reduction in indicated specific fuel consumption with increasing boost has been reported for spark-ignition engines of low compression ratio (reference 28). Whether all of this reduction can be attributed to a decrease in the percentage of residuals is not known. At higher compression ratios, for which the necessary range of ignition advance angle was greater, there was first a reduction in fuel consumption and then a continuous increase with increasing intake-air density. This fact indicates that, for the high compression ratios, other factors more than offset the improvement in burning that might have been expected on the basis of the low-compression-ratio results.

EFFECT OF COMBUSTION PRODUCTS ON COMBUSTION

It has been customary in most discussions of combustion in compression-ignition engines to attribute the slow burning in the latter part of the power stroke to poor mixing of the fuel and air. This assumption is

undoubtedly true to some extent; otherwise increasing the air turbulence would not result in an improvement in engine performance such as has been obtained (reference 29). On the other hand, there is abundant evidence that the rates of some reactions are altered by their products, either by some specific action or by altering some physical factor such as the flame temperature. Slow burning in a compression-ignition engine could conceivably be attributed to the fact that portions of the unburned fuel are encompassed by mixtures of combustion products and air. It was to investigate this point that tests were conducted in which nitrogen or combustion products (of which a large fraction was also nitrogen) were mixed with air of a fixed concentration before the fuel in question was injected. The most pronounced effect of increasing the percentage of combustion products was an increase in the ignition lag together with some decrease in the maximum rate of pressure rise (fig. 9). Bird (reference 7) has reported similar results for repeated injections into the same air charge, but the comparisons were between different air concentrations for each injection. The effect of the combustion products on the ratio of the explosion to initial pressure after 0.004 second was less real than is apparent from a casual inspection of the records. Thus, even if the fuel burned in this period remained constant, a decrease in the pressure ratio was to be expected because of the necessity of heating a respectively greater mass of gas for records 113 and 117 than for record 103. For example, the ratio of the absolute pressure after 0.004 second to the absolute initial pressure for record 103 multiplied by the ratio of the initial absolute pressure for record 103 to that for record 113 gives an approximate value of the pressure ratio that should be observed for record 113. This calculated ratio happened to be identical with the observed ratio for this case, thus proving that the extent of the combustion within this interval was about the same for records 103 and 113. The observed pressure ratio for record 117 was slightly greater than the calculated ratio, which might have been due to the better mixing permitted by the much longer ignition lag.

Figure 10 shows that the addition of nitrogen or of combustion products to an air charge of fixed concentration definitely decreased the maximum rate of pressure rise. For the lower effective air density, at least, the addition of nitrogen or combustion products had less influence on the ignition lag at the higher temperature corresponding to figure 10 than is evident from figure 9. This difference may be seen by comparing records 168 and 156 with records 103 and 113, the initial concentration of combustion products being the same for records 156 and 113. At a higher effective air density (0.89 pound per cubic foot), however, a definite change in ignition lag for the air-combustion products mixture is evident. Incidentally, the presence of water vapor in Wentzel's tests (reference 10) prob-

ably accounted in part for the long lags he observed but, as the ignition quality of his fuel is unknown, no direct comparisons are possible. MacGregor (reference 30) has shown that variations in humidity affect the knocking characteristics of a fuel in spark-ignition engines.

Figure 11 illustrates the fact that, in spite of the tendency of diluent gases to reduce the maximum rate of pressure rise, very high rates could be obtained by sufficiently decreasing the air-fuel ratio. The maximum rates of pressure rise for records 168, 165, and 159 were by no means equal; nevertheless, the permissible decrease in the air-fuel ratio made possible by the addition of inert gases to air of the same effective concentration was very definite.

CONCLUSIONS

1. For fuel injection into a constant-volume bomb containing stagnant air at a temperature and a pressure approximating those in a compression-ignition engine, the ignition lag was essentially independent of the injected fuel quantity and was of the same magnitude as in the engine.

2. For the fuel used, the possible decrease in the ignition lag for a given increase in air temperature or density became quite small at temperatures and densities in excess of those generally occurring in compression-ignition engines.

3. The combustion efficiency improved as the ignition lag was lengthened; hence it should be worth while to use those fuels in an engine whose ignition lags correspond to the higher permissible rates of pressure rise. The useless "afterburning" decreased as the ignition lag was lengthened.

4. The ignition lag tended to increase and the maximum rate of pressure rise definitely decreased upon the addition of inert gases to an air charge of fixed concentration.

LANGLEY MEMORIAL AERONAUTICAL LABORATORY,
NATIONAL ADVISORY COMMITTEE FOR AERONAUTICS,
LANGLEY FIELD, VA., *October 5, 1937.*

REFERENCES

1. Rothrock, A. M., and Waldron, C. D.: Some Effects of Injection Advance Angle, Engine-Jacket Temperature, and Speed on Combustion in a Compression-Ignition Engine. T. R. No. 525, N. A. C. A., 1935.
2. Boerlage, G. D., and Broeze, J. J.: Ignition Quality of Diesel Fuels as Expressed in Cetene Numbers. S. A. E. Jour., vol. 31, no. 1, July 1932, pp. 283-293.
3. Good, R. F.: Cetane Numbers—Life Size. S. A. E. Jour., vol. 40, no. 6, June 1937, pp. 232-241.
4. Tausz, J., and Schulte, F.: Ignition Points and Combustion Reactions in Diesel Engines. Part I. T. M. No. 483, and Part II, T. M. No. 484, N. A. C. A., 1928.

5. Schäfer, D.: Neuere Anschauungen über motorische Entzündungs- und Verbrennungsvorgänge. Jahrbuch der Schiffbautechnischen Gesellschaft, Bd. 33, 1932, S. 181-211.
6. Bird, A. L.: Experiments on Oil Jets and Their Ignition. Proc. Inst. Mech. Engrs., 1926, vol. II (Nov.) pp. 955-995.
7. Bird, A. L.: Some Characteristics of Nozzles and Sprays for Oil Engines. Trans. Second World Power Conference, Bd. VIII, sec. 29, VDI-Verlag G. M. B. H. (Berlin), 1930, pp. 260-270.
8. Hartner-Seberich: Der Zündverzug bei flüssigen Brennstoffen. Forschungsarbeiten auf dem Gebiete des Ingenieurwesens, Heft 299, VDI-Verlag G. M. B. H. (Berlin), 1928.
9. Neumann, Kurt: Experiments on Self-Ignition of Liquid Fuels. T. M. No. 391, N. A. C. A., 1926.
10. Wentzel, Wolfram: Der Zünd- und Verbrennungsvorgang im kompressorlosen Dieselmotor. VDI-Forschungsheft 366, VDI-Verlag (Berlin), 1934, S. 14-26.
11. Michailova, M. N., and Neumann, M. B.: The Cetene Scale and the Induction Period Preceding the Spontaneous Ignition of Diesel Fuels in Bombs. T. M. No. 813, N. A. C. A., 1936.
12. Hetzel, T. B.: The Development of Diesel Fuel Testing. Eng. Exp. Sta. Bull. No. 45, Penn. State Coll., 1936.
13. MacGregor, J. R.: Diesel Fuels—Significance of Ignition Characteristics. S. A. E. Jour., vol. 38, no. 6, June 1936, pp. 217-223.
14. Rose, R. A., Wilson, G. C., and Benedict, R. R.: Photo-Electric Combustion Analysis. S. A. E. Jour., vol. 39, no. 5, Nov. 1936, pp. 459-468.
15. Tozier, Robert E.: The N. A. C. A. Optical Engine Indicator. T. N. No. 634, N. A. C. A., 1938.
16. Baxley, C. H., and Rendel, T. B.: Report of the Volunteer Group for Compression-Ignition Fuel Research. Paper presented at the May 4-9, 1937, meeting of the S. A. E., White Sulphur Springs, W. Va.
17. Geschelin, Joseph: Fuels for Diesels. Auto Ind., vol. 75, no. 4, July 25, 1936, pp. 114-116.
18. Selden, Robert F., and Spencer, Robert C.: Heat Transfer to Fuel Sprays Injected into Heated Gases. T. R. No. 580, N. A. C. A., 1937.
19. Joachim, W. F., and Beardsley, Edward G.: The Effects of Fuel and Cylinder Gas Densities on the Characteristics of Fuel Sprays for Oil Engines. T. R. No. 281, N. A. C. A., 1927.
20. LeMesurier, L. J., and Stansfield, R.: Combustion in Heavy Oil Engines. Trans. North-East Coast Institution of Engineers and Shipbuilders, England, vol. XLVIII, 1932, pp. 195-220.
21. Judge, Arthur W.: High Speed Diesel Engines. Chapman and Hall, Ltd. (London), 1935, pp. 75-77.
22. Moore, Charles S., and Collins, John H., Jr.: Compression-Ignition Engine Performance at Altitude. S. A. E. Jour., vol. 40, no. 6, June 1937, pp. 263-272.
23. Moore, Charles S., and Collins, John H., Jr.: Compression-Ignition Engine Performance at Altitudes and at Various Air Pressures and Temperatures. T. N. No. 619, N. A. C. A., 1937.
24. Wilson, G. C., and Rose, R. A.: Behavior of High- and Low-Cetane Diesel Fuels. S. A. E. Jour., vol. 41, no. 2, Aug. 1937, pp. 343-348.
25. Moore, Charles S., and Foster, Hampton H.: Boosted Performance of a Compression-Ignition Engine with a Displacer Piston. T. N. No. 569, N. A. C. A., 1936.
26. Rothrock, A. M.: Combustion in a High-Speed Compression-Ignition Engine. T. R. No. 401, N. A. C. A., 1931.
27. Bone, William A., Newitt, Dudley M., and Townend, Donald T. A.: Gaseous Combustion at High Pressures. Longmans, Green & Co. Ltd. (London), 1929 p. 337.
28. Mucklow, G. F.: Experiments with a Supercharged Single-Cylinder Unit. R. & M. No. 1460, British A. R. C., 1932.
29. Moore, C. S., and Foster, H. H.: Performance Tests of a Single-Cylinder Compression-Ignition Engine with a Displacer Piston. T. N. No. 518, N. A. C. A., 1935.
30. MacGregor, J. R.: Influence of Humidity on Knock Ratings. S. A. E. Jour., vol. 40, no. 6, June 1937, pp. 243-249.

TABLE I
IGNITION LAGS ($\times 10^3$) CORRESPONDING TO FIGURES 5 AND 7

[Record numbers given in parentheses]

<div>Air-fuel ratio Density (lb /cu. ft.)</div>	15	20	23	25	27	30	33	35	37	40	45	50	60	75	80	90	100	120
Bomb temperature, 870° F.																		
0.59						7.0(186)				7.0(185)								
.89		5.0(59)							5.0(184)		5.0(183)		5.0(182)					
1.18							5.0(181)			4.3(190)		4.0(189)	4.0(188)		4.0(187)			
1.48								4.1(199)	4.3(198)	4.0(197)		4.1(196)	4.1(195)	4.3(194)			4.0(193)	
1.77										4.0(206)	3.7(205)	3.7(204)	4.0(203)	3.7(202)		3.7(201)		4.0(200)
1.77										4.5(207)								
Bomb temperature, 1,060° F.																		
0.59		2.5(53)		2.3(103)		2.1(102)				2.0(101)								
.89			1.7(91)	2.0(77)		2.0(76)					2.0(75)		1.8(74)					
.89						1.7(90)					1.7(89)		1.7(88)					
1.18					1.4(70)	1.5(68)	1.5(67)			1.6(66)			1.3(65)		1.4(64)			
1.18					1.5(69)													
Bomb temperature, 1,155° F.																		
0.59	1.8(41)	1.8(40)		1.8(173)		1.8(39)				1.8(166)								
.59		1.8(43)				1.8(167)												
.59		1.8(168)																
.89		1.3(38)	1.2(37)	1.3(151)		1.3(36)					1.3(35)		1.3(148)					
.89		1.3(154)	1.3(152)	1.3(153)		1.3(150)					1.3(149)							
1.18					1.2(134)	1.2(133)				1.2(132)			1.2(131)		1.2(130)			
Bomb temperature, 1,255° F.																		
0.59						1.7(219)				1.7(226)								
.59						1.5(227)												
.89			1.0(232)			1.2(220)					1.3(230)		1.0(229)					
.89						1.2(231)												
1.18			1.0(232)			1.0(221)					1.3(230)				1.0(222)			
1.48												0.8(223)						

REPORT No. 618

COMPARATIVE FLIGHT AND FULL-SCALE WIND-TUNNEL MEASUREMENTS OF THE MAXIMUM LIFT OF AN AIRPLANE

By ABE SILVERSTEIN, S. KATZOFF, and JAMES A. HOOTMAN

SUMMARY

Determinations of the power-off maximum lift of a Fairchild 22 airplane were made in the N. A. C. A. full-scale wind tunnel and in flight. The results from the two types of test were in satisfactory agreement. It was found that, when the airplane was rotated positively in pitch through the angle of stall at rates of the order of 0.1° per second, the maximum lift coefficient was considerably higher than that obtained in the standard tests, in which the forces are measured with the angles of attack fixed. Scale effect on the maximum lift coefficient was also investigated.

INTRODUCTION

The purpose of the present investigation was to obtain a direct comparison between flight and full-scale wind-tunnel measurements of the maximum lift coefficient of a Fairchild 22 airplane. The comparison was desirable in order to indicate the extent to which the various wind-tunnel effects and both wind-tunnel and flight techniques might influence maximum-lift determinations. The turbulence in the full-scale tunnel (reference 1) was of particular concern.

Obviously, a high order of accuracy must exist in both flight and wind-tunnel measurements if the comparison is to be significant. The many possibilities for experimental error in both series of tests required that great care be exercised in obtaining the test data. Previous comparisons between flight and full-scale wind-tunnel results (references 2 and 3) were incidental to other studies and unsuited for the accuracy here desired.

Inasmuch as, in the flight determinations of maximum lift, the airplane was rotated through the angle of stall, some wind-tunnel tests were made with the airplane rotating at corresponding angular velocities in order to investigate the effect of this technique on the results.

Wind-tunnel tests to determine the Reynolds Number effects on the maximum lift coefficient and on the minimum drag coefficient were also made.

FULL-SCALE WIND-TUNNEL INVESTIGATION

APPARATUS AND TESTS

The N. A. C. A. full-scale wind tunnel and its equipment are described in reference 2. Figure 1 is a 3-view

drawing of the Fairchild 22 parasol monoplane. Two positions of the center of gravity are indicated, corresponding to two airplane loadings used in the flight tests. The airplane was equipped for these tests with a specially surfaced wing of N. A. C. A. 2R₁₂ section. A paint filler was applied over the forward 15 percent

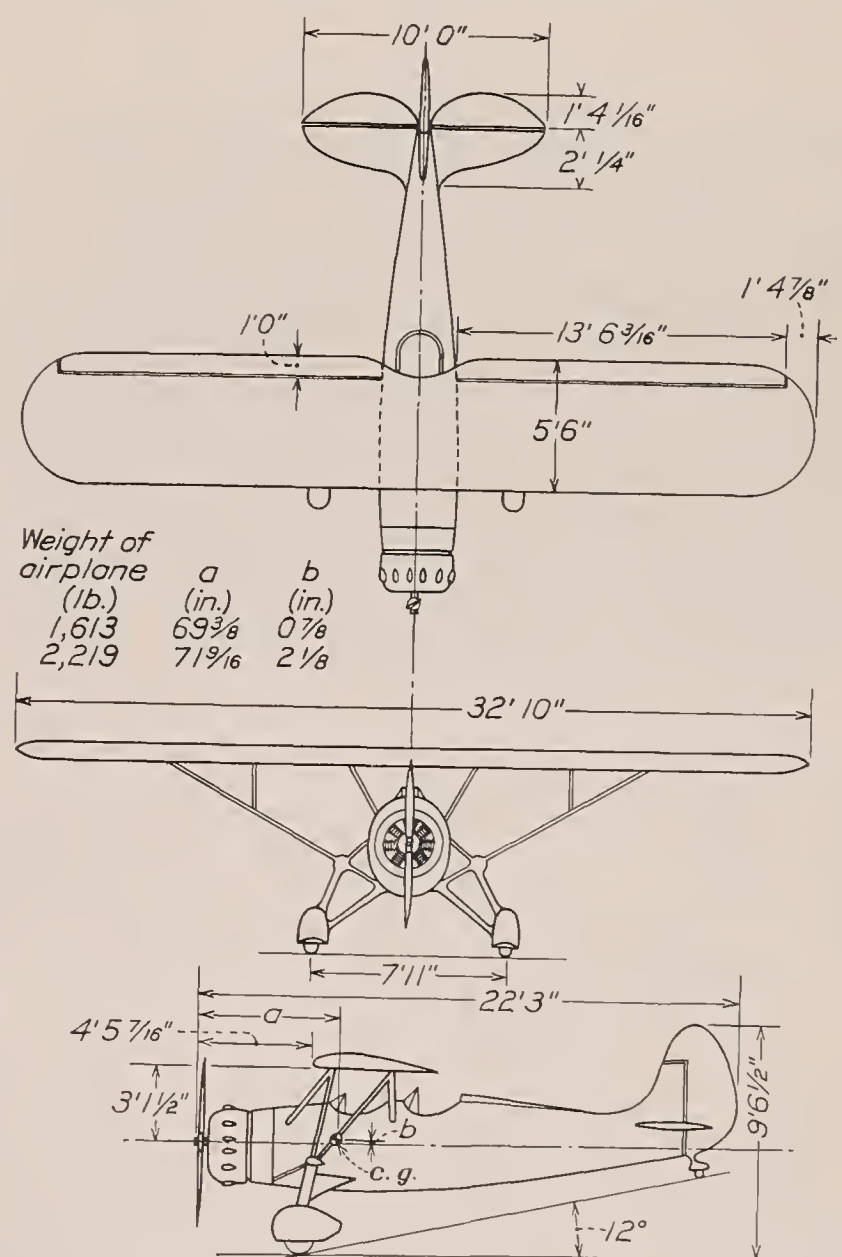


FIGURE 1.—Fairchild 22 airplane with wing of N. A. C. A. 2R₁₂ section.

of the wing surface and waxed to a reflecting finish, the polish being maintained throughout both wind-tunnel and flight tests. The purpose of the polish was not only to provide a reproducible surface but also to increase any differences between the wind-tunnel and flight results due to turbulence in the wind tunnel. All the tests were made with the airplane at 0° yaw and

roll and with the ailerons locked in the neutral position. The propeller was locked in the vertical position except where otherwise noted. Figure 2 shows the airplane mounted on the wind-tunnel balance supports.

The tests were of two types. The tests designated "standard" were similar to those normally made in the wind tunnel, in which the force readings are not taken until a number of seconds after the airplane has been brought to rest at the desired attitude. In the other type of test, force readings were taken at regular intervals while the angle of attack was being changed at a constant rate. The rates of change of angle of attack in these runs were varied between 0.025° and 0.2° per second, this range including that used in the flight tests.

Except in the tests to determine minimum drag, all measurements were made in the region of maximum lift, the angle-of-attack range being usually from 12° to 20° .

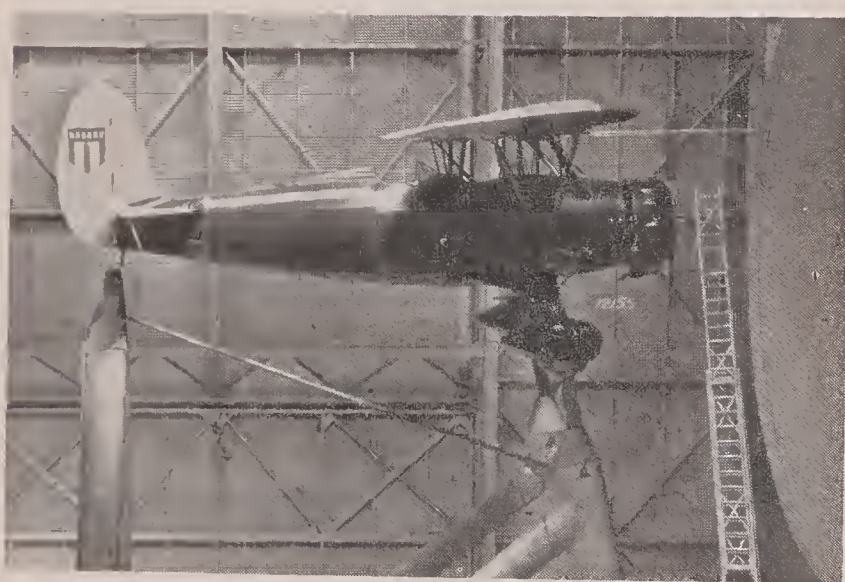


FIGURE 2—Fairchild 22 airplane in full-scale wind tunnel.

Air speeds ranged from 29 to 63 miles per hour, except for the minimum-drag tests, in which air speeds up to 119 miles per hour were used. Much of the work was done at an air speed of 56 miles per hour, which is approximately flight speed at maximum lift.

RESULTS AND DISCUSSION

The results of the wind-tunnel tests are summarized in figures 3 to 19. Except where otherwise noted, the figures refer to tests of the standard type. All measurements were corrected for jet-boundary effect at the wing, balance-support tare values, and blocking, as described in reference 4.

In figure 3 the lift, the drag, and the pitching-moment coefficients, and the lift-drag ratio are plotted against the angle of attack of the thrust axis, α_T , for the airplane with the horizontal tail removed. The test data were obtained at an air speed of 56 miles per hour. The pitching-moment coefficient was based on a center-of-gravity position as determined for a gross weight of 1,613 pounds. (See fig. 1.)

Scale effect.—Figure 4 shows the lift curves obtained at five different air speeds for the airplane with the horizontal tail removed. It will be observed that, with increasing air speed, the maximum lift coefficient reaches higher values and the entire lift curve is slightly raised, even over the linear range. The break in the lift curve at the peak becomes sharper with increasing air speed, indicating a variation in the mechanism of stalling. It may be noted that beyond the stall the lift curve represents only a rough average, for there is wide scatter of the points in this region.

The variation of the maximum lift coefficient with air speed is shown in figure 5 for three different test

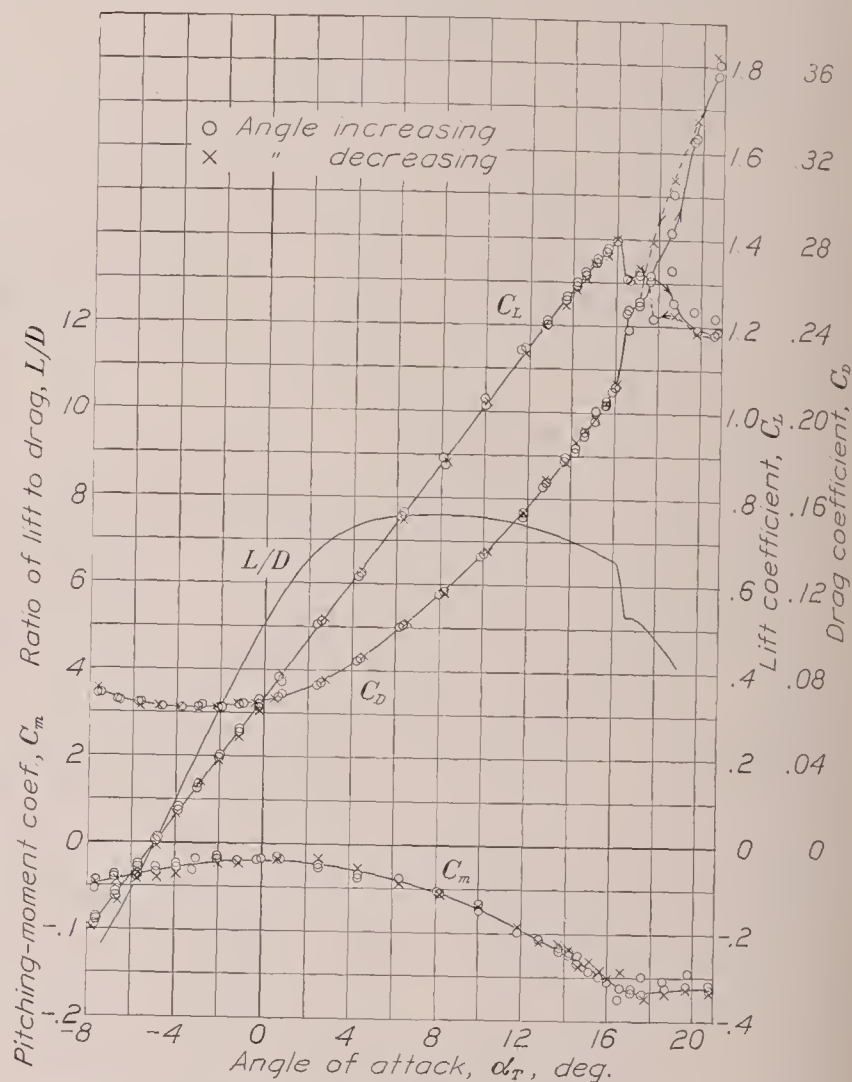


FIGURE 3.—Characteristics of Fairchild 22 airplane with the horizontal tail removed. C_m for airplane based on weight of 1,613 pounds. Air speed, 56 m. p. h.

conditions, namely, tail removed, tail on, and tail on with the angle changing at the rate of 0.1° per second. The indicated stabilizer angle (δ_s) and elevator angle (δ_e) correspond approximately to trim at maximum lift. All the tests show essentially the same variation of maximum lift coefficient with air speed. Results from the tests in the variable-density tunnel of the plain airfoil are also shown in the figure, and it will be seen that, except for a vertical displacement due to difference in plan form and to the effect of the fuselage, the agreement is very good.

Experiments to determine whether the presence of the propeller fixed in the vertical or the horizontal position materially influenced the maximum lift showed that the propeller in either position had a negligible effect (fig. 6).

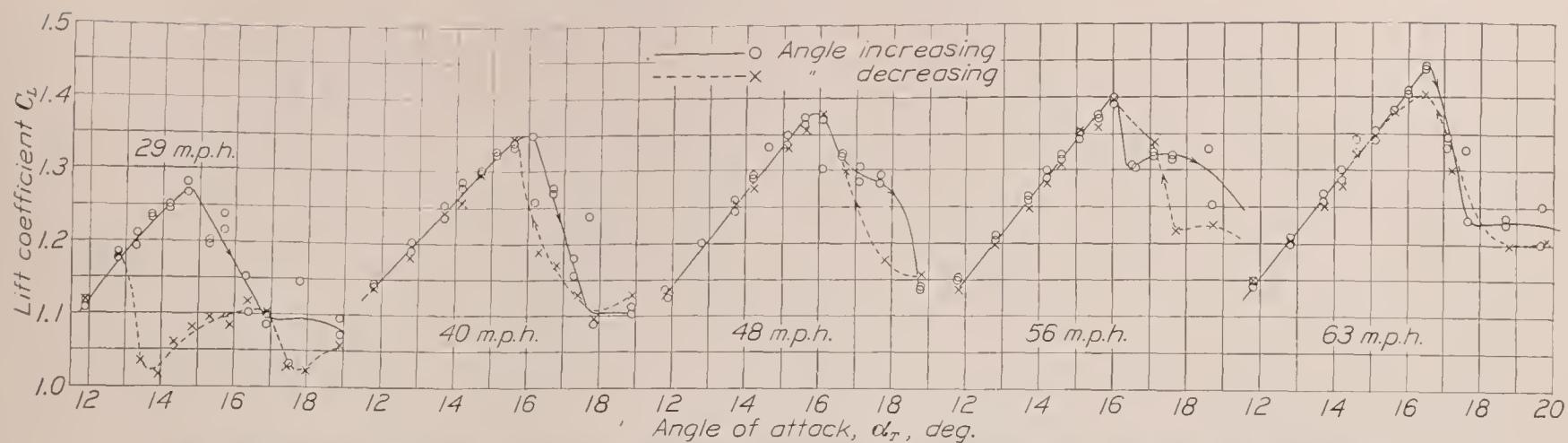


FIGURE 4.—Scale effect, Fairchild 22 airplane. Variation of maximum lift coefficient with air speed. Horizontal tail removed.

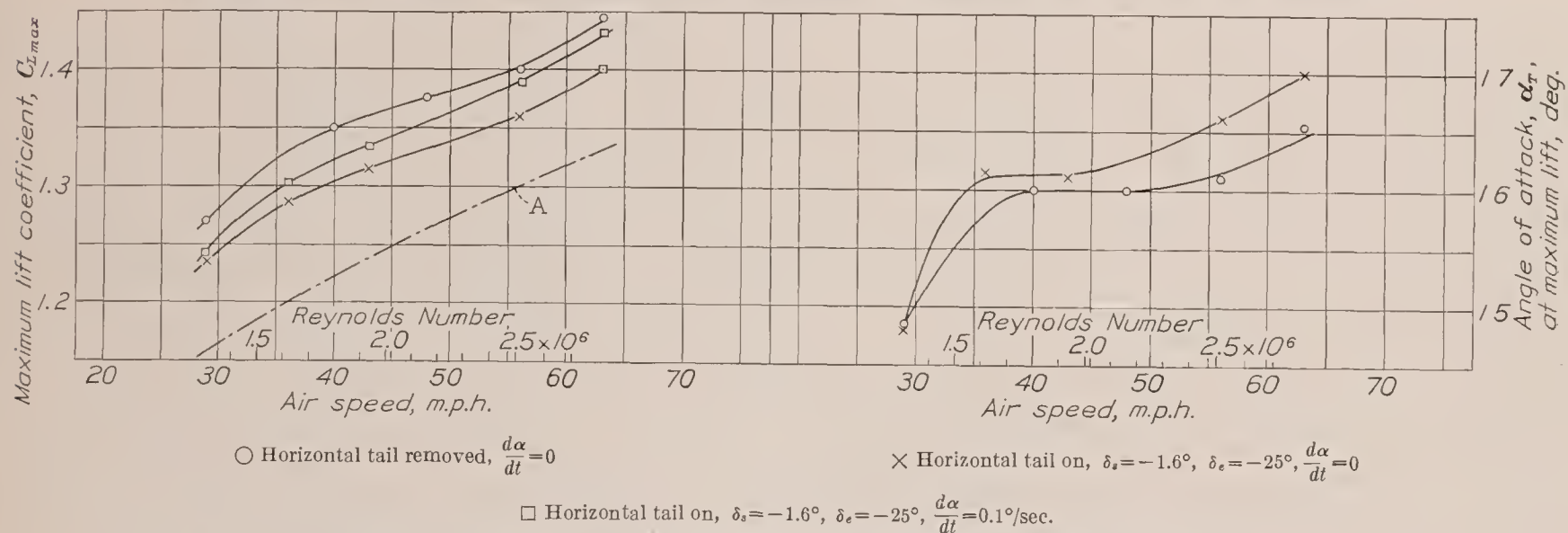


FIGURE 5.—Scale effect, Fairchild 22 airplane. Variation with air speed of α_T at maximum lift and of the maximum lift coefficient, for three test conditions.

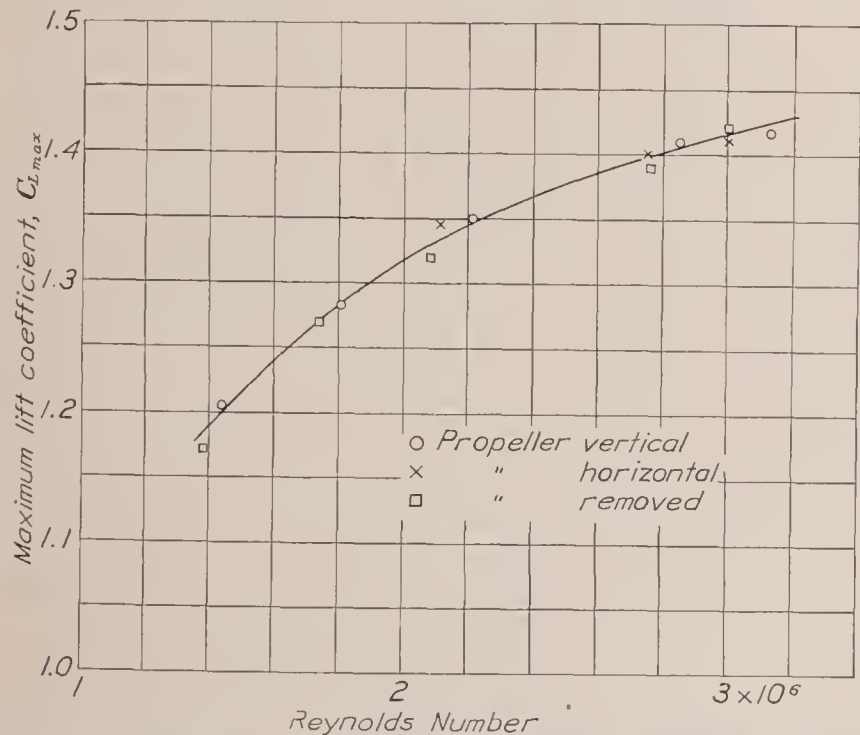


FIGURE 6.—Propeller effect on maximum lift. Fairchild 22 airplane; $\delta_s, -1.6^\circ$; $\delta_e, -25^\circ$.

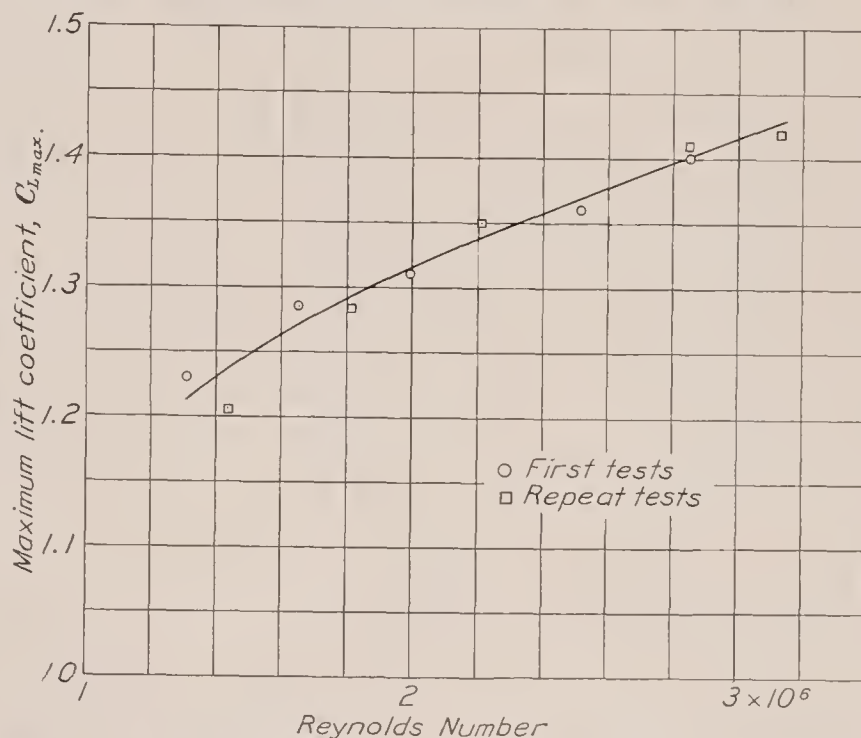


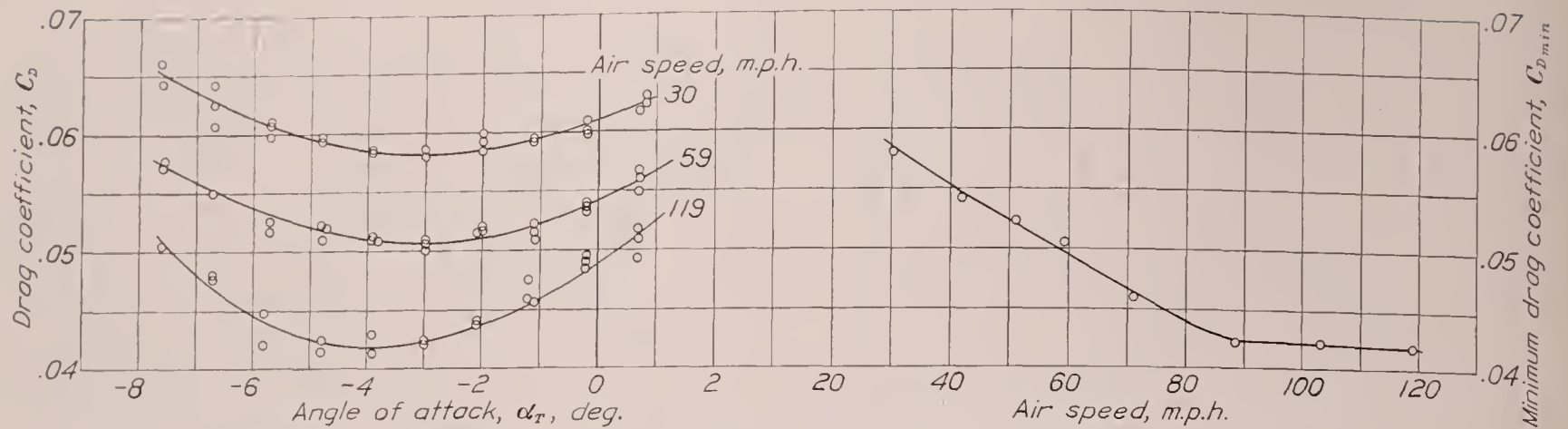
FIGURE 7.—Comparison of maximum-lift determinations made 6 months apart. Fairchild 22 airplane; $\delta_s, -1.6^\circ$; $\delta_e, -25^\circ$.

Six months after the completion of the wind-tunnel tests, some of the measurements were repeated in order to test for a suspected deterioration of the wing. The repeat tests failed to show any appreciable effect of deterioration, the results being in satisfactory agreement with the earlier measurements (fig. 7).

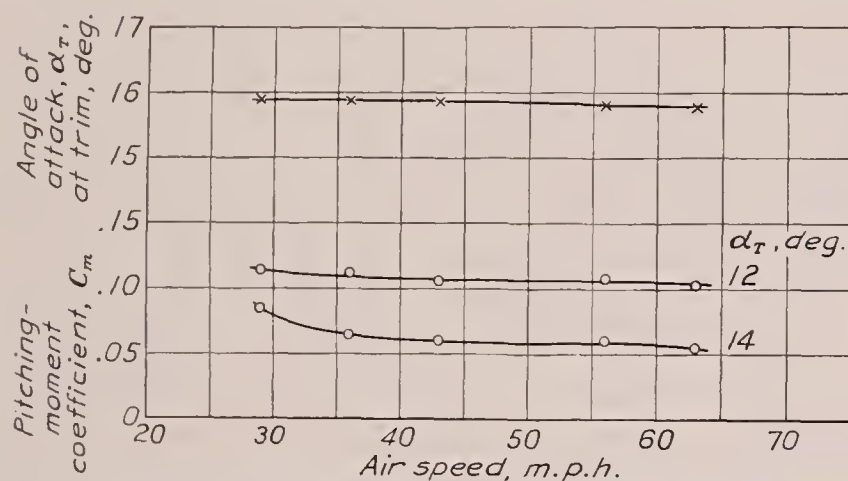
The scale effect on minimum drag is shown in figure 8. The minimum drag coefficient decreases from 0.058 to 0.042 as the speed increases from 30 to 119 miles per hour. This decrease in the drag coefficient is many

times greater than that to be expected from the wing alone and may be attributed to a large scale effect on the junctures, struts, and smaller parts of the airplane.

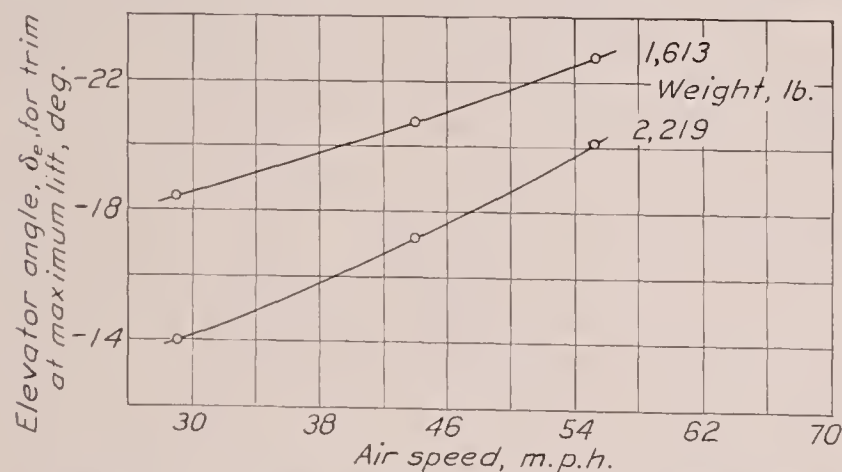
The effects of scale on the pitching-moment coefficient and on the angle of attack for trim are shown in figure 9 to be negligible, except where reduction in air speed causes stalling, as at the first point on the 14° curve. The elevator angle for trim at maximum lift is plotted against air speed in figure 10; the variation is due to the scale effect on maximum lift.

FIGURE 8.—Scale effect, Fairchild 22 airplane. Variation of C_D and C_{Dmin} with air speed. Horizontal tail removed.

Trim lift curves.—In order to obtain lift curves corresponding to flight, the wind-tunnel results were adjusted to the trim condition at all angles of attack. Trim lift curves were determined from the wind-tunnel data for two positions of the center of gravity, corre-

FIGURE 9.—Scale effect, Fairchild 22 airplane. Variation with air speed of angle of attack for trim and of pitching-moment coefficient at two angles of attack. Weight, 1,613 pounds; δ_a , -1.6° ; δ_e , -25° .

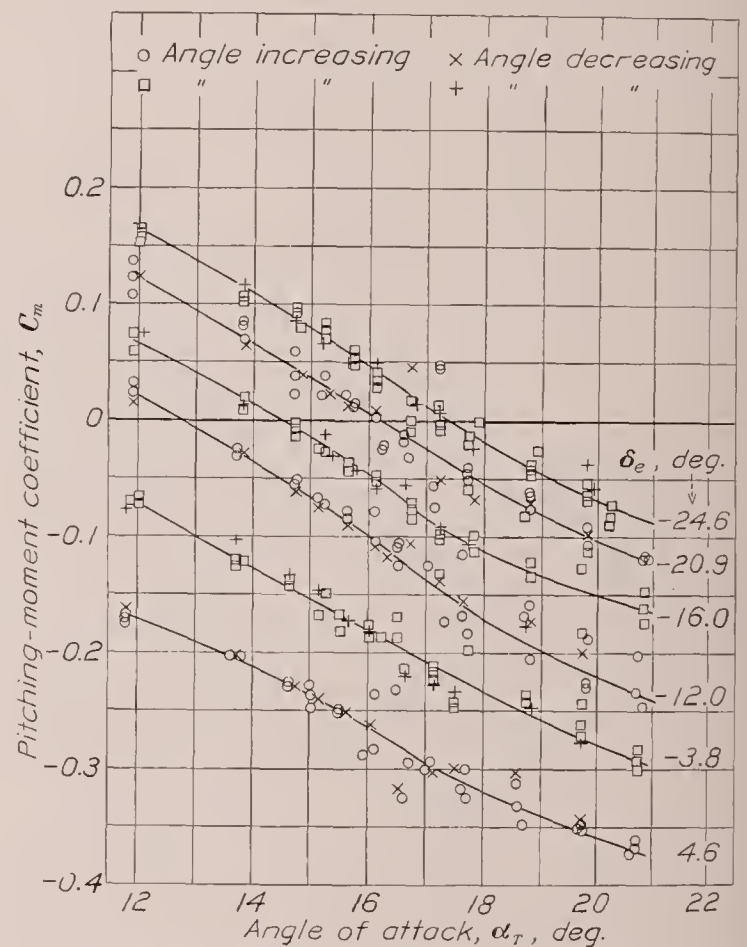
sponding to the two airplane loadings used in the flight tests. The plots used in deriving the trim lift curves are shown in figures 11, 12, and 13. In figure 11 the effect of elevator deflection on the pitching-moment coefficient is shown. At each elevator setting, the angle of

FIGURE 10.—Scale effect, Fairchild 22 airplane. Variation with air speed of elevator setting for trim at maximum lift. δ_a , -3.6° .

attack for trim is found where the curve crosses the axis. Cross plots of these data are shown in figure 12 where the elevator angle for trim is plotted against angle of attack for both airplane weights and for two stabilizer settings. In figure 13 the variation of lift coefficient with elevator angle is shown for several

angles of attack. From figures 12 and 13 the trim lift curves are constructed (fig. 14) for a constant speed of 56 miles per hour.

These trim lift curves, however, do not actually represent the conditions that would be found in flight tests, for in flight (1) the air speed varies with the lift coefficient, thus giving rise to a small scale effect, and (2) the changing of the angle of attack has an effect,

FIGURE 11.—Pitching-moment curves at different elevator angles. Fairchild 22 airplane; weight, 1,613 pounds; δ_a , -3.6° ; air speed, 56 m. p. h.

apparent mainly as increased maximum lift. Both of these corrections were applied in the construction of the "flight-speed" curves of figure 14. The variation with Reynolds Number of the maximum lift coefficient, determined at $d\alpha/dt=0.1^\circ$ per second and corrected to the trim condition, is compared with flight results in figure 15.

The effect of angular velocity on maximum lift.—During the course of the investigation it was observed, as previously mentioned, that the maximum lift coefficients obtained in the tests with changing angle of

attack were considerably higher than those obtained in the standard tests. In figure 16 are given lift curves showing the manner in which the peak of the lift curve rises with increasing rate of change of angle. For the standard tests the maximum value is 1.405, whereas, with the angle changing at the rate of 0.2° per second, it is 1.480. In figure 17 the maximum lift coefficients

in the figure; the variation parallels that of the lift coefficient.

In order to establish the validity of these results, particularly as regards the possibility of error due to balance characteristics, it was ascertained that, on the one hand, the damping was too low and, on the other hand, the natural frequency of the balance was too

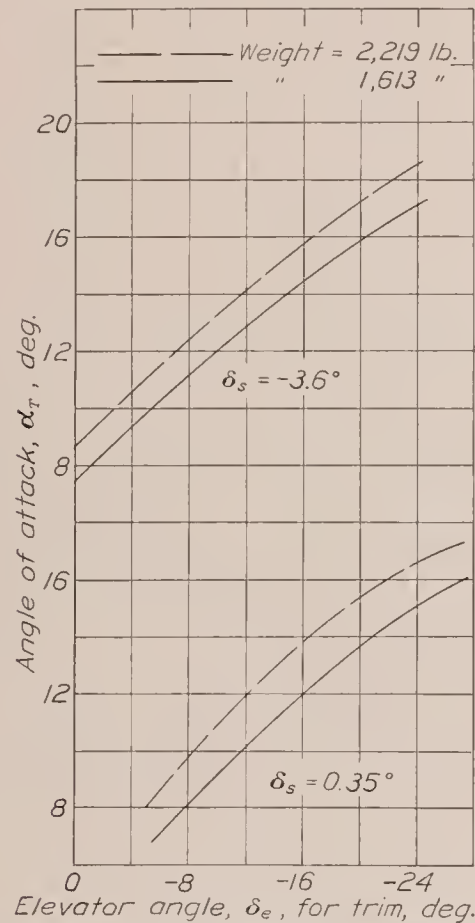


FIGURE 12.—Elevator settings for trim. Fairchild 22 airplane; air speed, 56 m. p. h.

for two different airplane conditions are plotted against the nondimensional parameter $\frac{c}{V} \frac{d\alpha}{dt}$, in which c and V are the chord and the velocity, respectively. The upper curve is for the tail-removed condition, while the lower curve represents a tail-on condition with the elevator set approximately for trim at maximum lift. The angle of attack at maximum lift is also plotted

high to cause any appreciable discrepancy between the indicated and the actual forces. As a further check on the work, a small airfoil of N. A. C. A. 2R₁₂ section was tested at corresponding rates of change of angle of attack in the N. A. C. A. variable-density tunnel. The results of these tests were in very good agreement with the results just discussed.

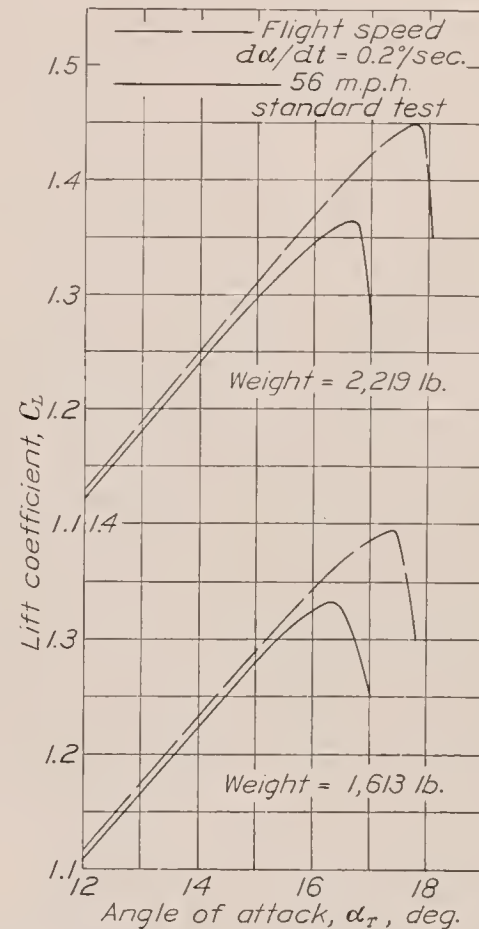


FIGURE 14.—Trim lift curves. Fairchild 22 airplane.

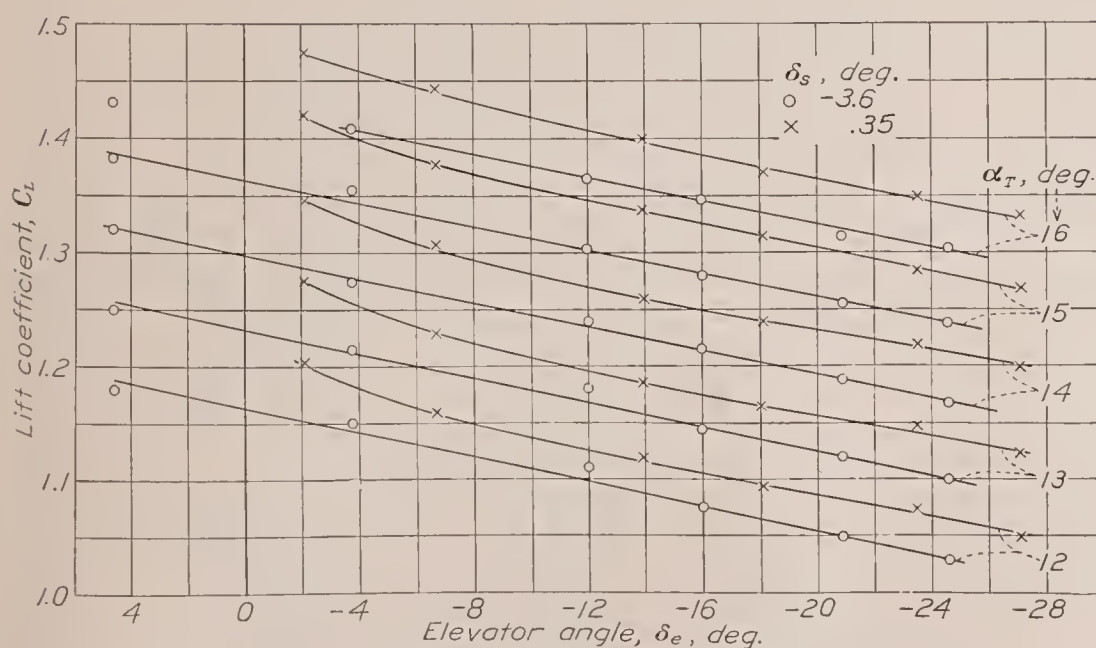


FIGURE 13.—Effect of tail setting on lift. Fairchild 22 airplane; air speed, 56 m. p. h.

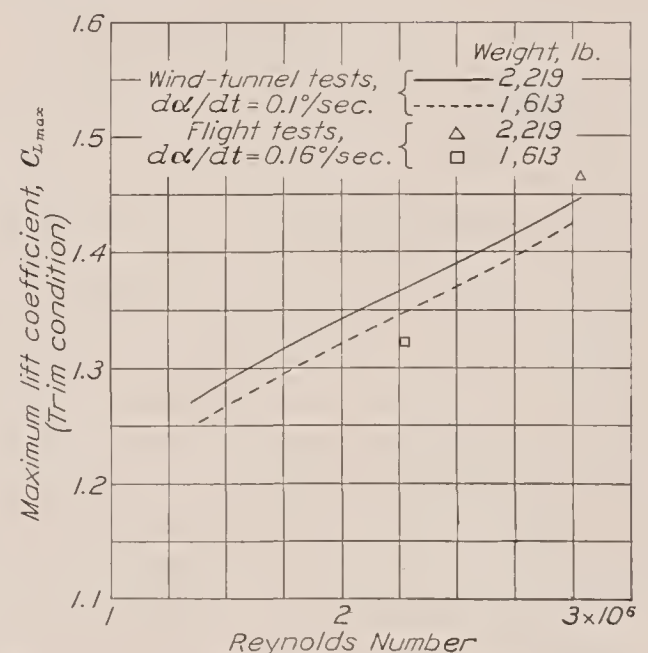


FIGURE 15.—Comparison of wind-tunnel with flight determination of the maximum lift coefficient. Variation with air speed of the maximum lift coefficient at trim. Fairchild 22 airplane.

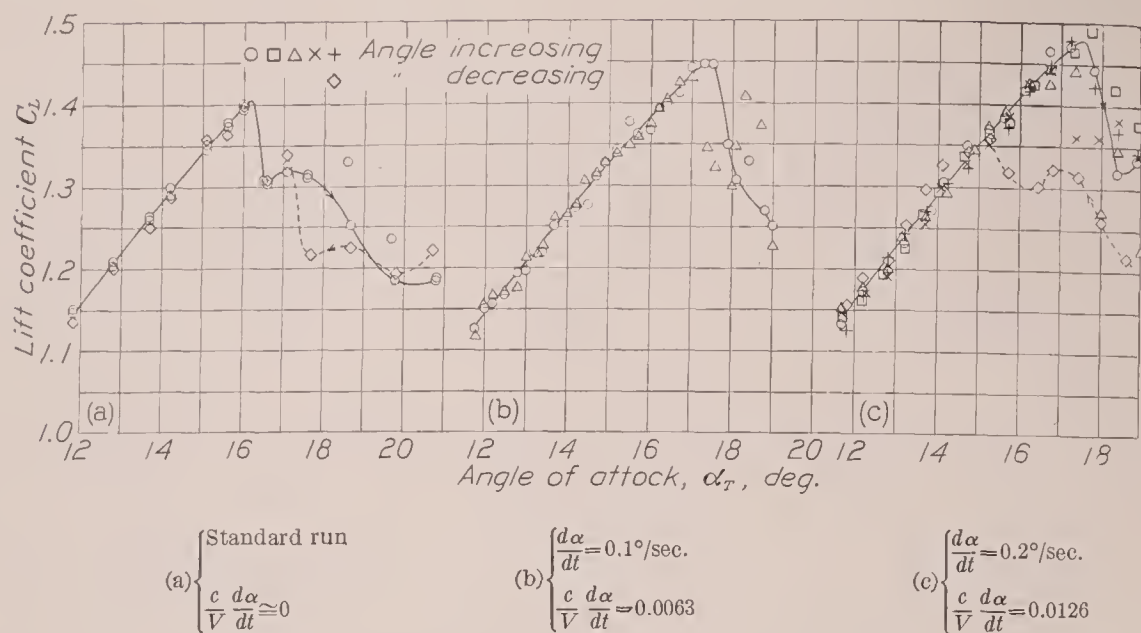


FIGURE 16.—Lift curves for different angular velocities. Fairchild 22 airplane; horizontal tail removed; air speed, 56 m. p. h.

The effect upon the maximum lift of the rate of change of angle of attack is well known, but the magnitude observed here was much higher than had been anticipated on the basis of previous investigations. Thus, Kramer's formula (reference 5), which has been approximately confirmed both at low Reynolds Numbers (reference 6) and in flight (reference 7), predicts only 1/20 of the observed increase. The failure of Kramer's formula in this case may be due to the fact

to investigate the general character of the time variation of the lift at fixed angles of attack in this range, a few tests were made in which the angle was increased at a rate of 0.1° per second up to a certain value and then held constant while observations of lift force were made. The results are shown in figure 18. The highest angle of attack at which the lift is maintained indefinitely is about 16.6° . When the angle of attack is increased above this value and then fixed, the flow breaks down within a few seconds and wide fluctuations occur in the lift.

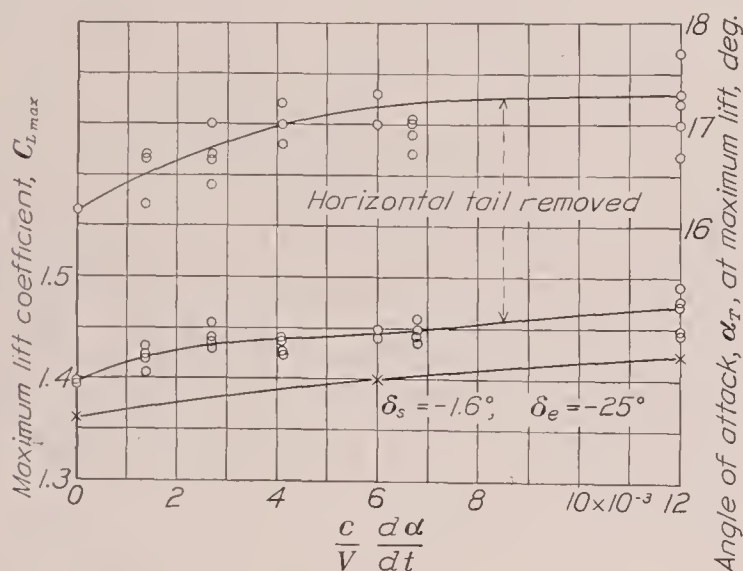


FIGURE 17.—Variation with $\frac{c}{V} \frac{d\alpha}{dt}$ of α_T at maximum lift and of the maximum lift coefficient. Fairchild 22 airplane; air speed, 56 m. p. h.

that the formula was based on experimental results obtained at very high values of $\frac{c}{V} \frac{d\alpha}{dt}$. It is also possible that the phenomenon is not so independent of the wing section characteristics as has been heretofore supposed.

The influence of air speed on the phenomenon is shown in figure 5, where a set of standard runs at different air speeds is compared with a corresponding set in which the angle of attack was changed at the rate of 0.1° per second.

It is clear that the value of the lift coefficient in the neighborhood of and beyond the maximum is not uniquely determined by the angle of attack. In order

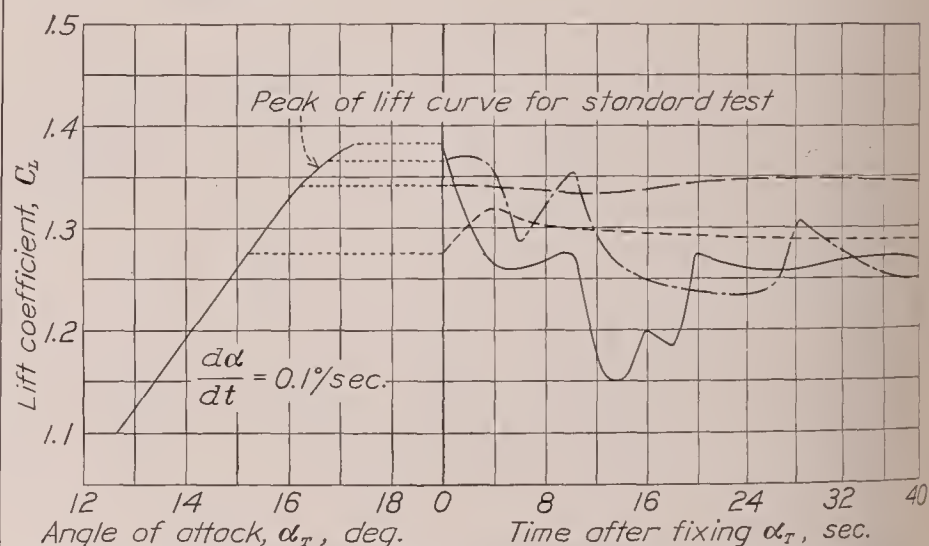


FIGURE 18.—Decay with time of added lift due to angular velocity, and fluctuations in lift beyond the stall. Angle of attack increased at 0.1° per second up to the values shown, and then fixed. Fairchild 22 airplane; $\delta_s = -1.6^\circ$; $\delta_e = -25^\circ$; air speed, 56 m. p. h.

Figure 19 further illustrates the vagaries in the behavior of the lift coefficient near and beyond the angle of maximum lift. Three separate lift curves are shown, obtained under apparently identical conditions. Each is fairly smooth, yet different from the other two.

FLIGHT TESTS

The flight tests consisted in recording in flight sufficient data to obtain the acceleration normal to the flight path, the angle of attack, and the dynamic pressure while the angle of attack was being slowly increased over a range of several degrees below and

including the angle of stall. The recording instruments consisted of an air-speed meter, an angle-of-attack meter, a two-component accelerometer, and a timer. The air-speed recorder was connected to a swiveling pitot-static head mounted on a light boom about one chord length forward of the leading edge at the semi-span and slightly below the plane of the chord. This head was calibrated against a suspended static head down to the minimum stalling speed of the airplane. The angle-of-attack recorder, which was calibrated in steady glides, consisted of a differential-pressure type of yaw head mounted on a boom similar to that employed for the air-speed head, but on the opposite side of the airplane.

The lift was computed from the normal acceleration and the gross weight at the time of the test. After the

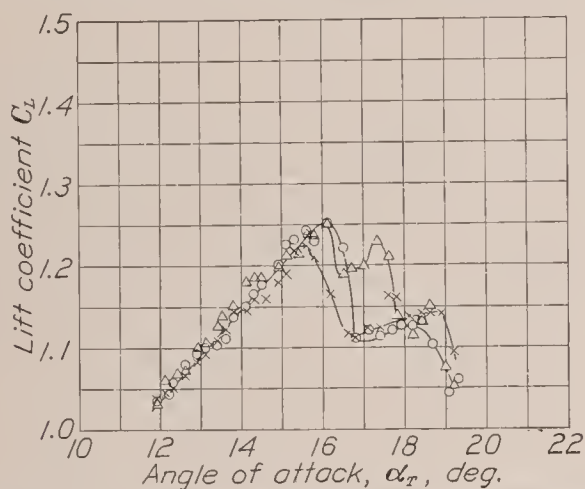


FIGURE 19.—Three different lift curves obtained under apparently identical conditions. Fairchild 22 airplane; δ_s , -1.6° ; δ_e , -25° ; $\frac{c}{V} \frac{d\alpha}{dt} = 0.0124$; air speed, 29 m. p. h.; $\frac{d\alpha}{dt}$, $0.1^\circ/\text{sec}$.

approximate time of stall was determined by inspection of the records, calculations of C_L were made for different instants during the maneuver until the maximum value was obtained.

The tests were made with the propeller stopped in the vertical position and with an average rate of change of angle of attack of 0.16° per second for 3° to 4° preceding the stalling angle.

The variation of the Reynolds Number was obtained by flying the airplane first heavily loaded at the lowest possible safe altitude and then with the least possible load at high altitude (approximately 10,000 feet). A number of flights were made, several tests being made in each flight. The corresponding average Reynolds Numbers for the 14 individual tests made at low altitude and the 16 tests at high altitude were 3.04×10^6 and 2.28×10^6 , respectively. For the various flights, the average deviation of the individual results from the mean was about 1 percent.

COMPARISON OF FLIGHT AND WIND-TUNNEL RESULTS

Points representing the average maximum lift coefficients for the two flight Reynolds Numbers are

plotted in figure 15 for comparison with the wind-tunnel results. It will be noted that the values are not directly comparable, since the rates of change of angle of attack are slightly different. Correcting the wind-tunnel results to the angular velocity used in flight would, however, increase the wind-tunnel values by only one-half percent. The agreement, accordingly, is satisfactory and indicates that, within the experimental accuracy, there is no important systematic discrepancy, such as might be due to turbulence, between the two types of measurement.

CONCLUSIONS

1. Satisfactory agreement exists between the maximum lift coefficients measured in flight and those measured in the full-scale wind tunnel.

2. It is necessary, in the comparison of flight and wind-tunnel measurements of the maximum lift coefficient, that the comparison be made at corresponding rates of change of angle of attack. Values of $\frac{c}{V} \frac{d\alpha}{dt}$ of the order of 0.01 may appreciably increase the maximum lift coefficient of an airplane over the values obtained in the standard test, in which the forces are measured with the angles of attack fixed.

LANGLEY MEMORIAL AERONAUTICAL LABORATORY,
NATIONAL ADVISORY COMMITTEE FOR AERONAUTICS,
LANGLEY FIELD, VA., October 26, 1937.

REFERENCES

1. Platt, Robert C.: Turbulence Factors of N. A. C. A. Wind Tunnels as Determined by Sphere Tests. T. R. No. 558, N. A. C. A., 1936.
2. DeFrance, Smith J.: The N. A. C. A. Full-Scale Wind Tunnel. T. R. No. 459, N. A. C. A., 1933.
3. Theodorsen, Theodore, and Silverstein, Abe: Experimental Verification of the Theory of Wind-Tunnel Boundary Interference. T. R. No. 478, N. A. C. A., 1934.
4. Silverstein, Abe: Scale Effect on Clark Y Airfoil Characteristics from N. A. C. A. Full-Scale Wind-Tunnel Tests. T. R. No. 502, N. A. C. A., 1934.
5. Kramer, Max: Increase in the Maximum Lift of an Airplane Wing due to a Sudden Increase in its Effective Angle of Attack Resulting from a Gust. T. M. No. 678, N. A. C. A., 1932.
6. Farren, W. S.: The Reaction on a Wing Whose Angle of Incidence is Changing Rapidly. Wind Tunnel Experiments with a Short Period Recording Balance. R. & M. No. 1648, British A. R. C., 1935.
7. Rhode, Richard V.: The Pressure Distribution over the Wings and Tail Surfaces of a PW-9 Pursuit Airplane in Flight. T. R. No. 364, N. A. C. A., 1930.

REPORT No. 619

DRAG OF CYLINDERS OF SIMPLE SHAPES

By W. F. LINDSEY

SUMMARY

In order to determine the effect of shape, compressibility, and Reynolds Number on the drag and critical speed for simple forms, the drag forces on models of various simple geometric cross sections were measured in the N. A. C. A. 11-inch high-speed wind tunnel.

The models were circular, semitubular, elliptical, square, and triangular (isosceles) cylinders. They were tested over a speed range from 5 percent of the speed of sound to a value in excess of the critical speed, corresponding, for each model, approximately to a tenfold Reynolds Number range, which extended from a minimum of 840 for the smallest model to a maximum of 310,000 for the largest model.

INTRODUCTION

The aerodynamic drag of simple forms was one of the earliest subjects of aerodynamic research. Although numerous investigations have been conducted, drag data for many forms, especially as affected by Reynolds Number and compressibility, are incomplete or have never been obtained. In accordance with a suggestion made at one of the annual engineering conferences, tests to investigate the variation of drag for various simple forms with Reynolds Number were considered for the variable-density wind tunnel. There was available, however, a large amount of data on the drag of fundamental shapes that had been obtained under conditions involving rather large and uncertain turbulence effects. It was therefore considered preferable to transfer the investigation to the 11-inch high-speed tunnel, where disturbing turbulence effects were much smaller and where new information could be obtained concerning compressibility effects.

Previous investigations of the drag of simple forms have included the effects of Reynolds Number on the drag of circular cylinders (references 1 and 2), the effect of compressibility on the drag of circular cylinders (reference 3), the variation of drag with angle of attack for square cylinders (reference 4), the drag of flat plates normal to the wind (reference 4), and tests of elliptical cylinders of various fineness ratios. Test results, however, were not available for either triangular or semitubular cylinders, nor were any previous in-

vestigations available that included the effects of compressibility on the drag characteristics of any of these forms, except the circular cylinder (reference 3).

The present investigation, comprising measurements of the drag of cylinders having various cross sections, was conducted over a range extending from 5 percent of the speed of sound to a speed above the value at which the compressibility burble occurred. This speed range corresponded, for each model, approximately to a tenfold Reynolds Number range, which extended from 840 to 8,400 for the smallest model and from 31,000 to 310,000 for the largest model.

The experiments were conducted from 1933 to 1936 in the N. A. C. A. 11-inch high-speed wind tunnel.

APPARATUS AND METHODS

The N. A. C. A. 11-inch high-speed wind tunnel, in which the tests were made, is an induction-type closed-throat tunnel having a circular air passage. The tunnel is equipped with a balance, which is of the three-component, photorecording, spring type. The balance was designed for testing airfoils at speeds from approximately 35 percent of the velocity of sound to a speed approaching the velocity of sound. A detailed description of the tunnel and of the photorecording balance is given in reference 5.

For some of the tests reported herein, the photorecording balance was not sufficiently sensitive to measure the drag, and an auxiliary drag balance was therefore used. This balance was of the pendulum type and was designed to measure very small drag forces on small models at low speeds. The forces were measured by visual observation of the movement of a beam. Three balance sensitivities were used; a 1-inch deflection equaled 0.01 pound, 0.10 pound, or 1.0 pound. By the variation of the sensitivity and by the addition of counterweights, forces were measured from a minimum of 0.001 pound to a maximum of 10 pounds. One of the features incorporated in the construction of the balance was a means for applying tension to the model in order to overcome vibration difficulties encountered with some of the models in portions of the speed range.

The models tested were (a) circular, (b) semitubular, (c) elliptical, (d) square, and (e) triangular (isosceles) cylinders. The shapes and the dimensions of the cross sections are shown in figure 1. Because of the small size of the models and the relatively large forces involved, the models were constructed of steel. The surfaces were highly polished, and the edges of the semitubular, the square, and the triangular cylinders were sharp.

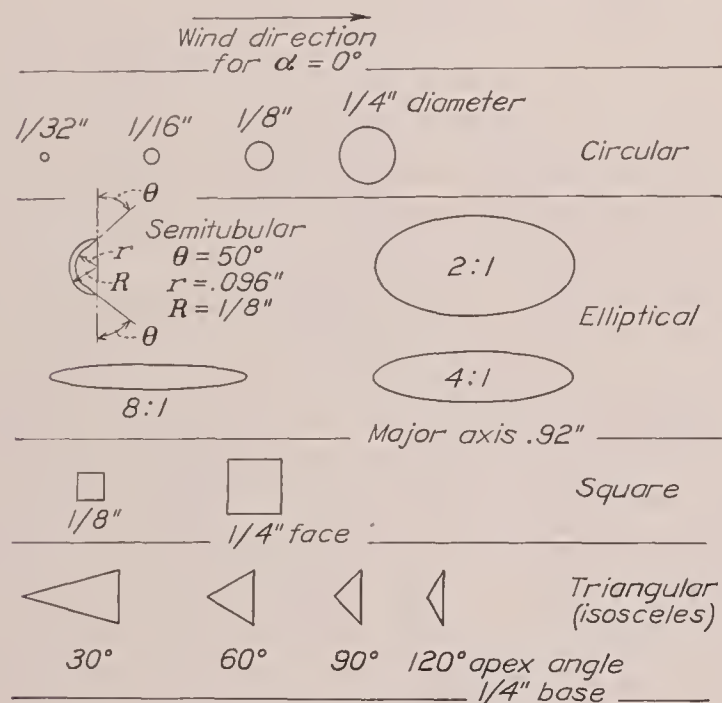


FIGURE 1.—Cross sections of cylinders.

The models were so mounted that they extended across the tunnel and passed through holes in the tunnel wall. These holes were covered with circular end plates of thin brass, which fitted into recesses in the tunnel wall and maintained the contour of the walls. Holes of the same shape but slightly larger than the model were cut in the end plates and provided a small clearance so that the end plates and the model did not touch. Previous investigations indicated that the results so obtained approximate infinite-aspect-ratio data.

The tests were conducted over a speed range from 5 percent of the speed of sound to a value above the speed at which the compressibility burble occurred.

The dynamic pressure, $\frac{1}{2} \rho V^2$, and the ratio of the velocity at the test section to the speed of sound at the test section, V/V_c , were determined from pressures measured at calibrated static-pressure orifices.

The areas used in computing the coefficients were taken as the product of a transverse dimension and the "effective span." The effective span, 10.93 inches, was determined from an impact-pressure survey across the tunnel. The computed coefficients are based on frontal area unless otherwise specified on the figures.

The angles of attack were measured from an arbitrarily chosen initial reference position ($\alpha=0^\circ$), shown in figure 1 for each of the models.

PRECISION

The various factors affecting the accuracy of these data may, in general, be divided into two classes: (a) accidental errors, and (b) systematic errors.

The accidental errors, indicated by the scatter of the test points on the curves, arose from slight changes in the calibrations of the balances and of the static-pressure orifices, from very small variations in the direction of the air flow, and from similar sources. The magnitude of these errors was estimated to be ± 2 percent from an examination of the point scatter.

The systematic errors, arising from tunnel-wall effects and end interference, were impossible to evaluate without a special series of tests but, because the models were small in relation to the tunnel and tests of several sizes of circular cylinders indicated that the correction for the data presented is small, a correction was considered unnecessary.

PRESENTATION OF DATA

The results are presented in the standard nondimensional coefficient form; that is, the force divided by the product of $\frac{1}{2} \rho V^2$ and the area. The area used in computing the coefficients is the frontal area, except as shown on the figures. The coefficients are plotted against the speed ratio V/V_c and against Reynolds Number. Cross plots and summary plots of the data are included to facilitate analysis and for purposes of comparison.

The Reynolds Numbers for the data presented are based on the length of the model parallel to the wind direction, except for the semitubular cylinder for which the characteristic length, like that for the circular cylinder, is taken as the outside diameter.

DISCUSSION

The resistance, or drag, coefficients of the various bodies depend on both Reynolds Number and compressibility. Because the turbulence of the tunnel air stream is small, the Reynolds Number almost entirely determines the flow pattern around the model at low speeds; whereas, at high speeds the compressibility effects become important and, ultimately, as the speed increases, become relatively so large that the Reynolds Number effects may, to a first approximation, be disregarded. Accordingly, throughout the discussion, Reynolds Number effects are considered as those changes in the coefficient that occur at low speeds and compressibility effects as those that occur at high speeds. Furthermore, the speed at which the flow breakdown occurs due to compressibility phenomenon is referred to as the "critical speed." Previous tests (reference 6) have demonstrated the critical speed to be that value of the translational velocity for which the

sum of the maximum induced velocity near the surface of the body and the translational velocity equals the local speed of sound. The flow change at the critical speed is called, in accordance with earlier terminology, the "compressibility burble."

The values of the critical speed indicated by the drag curves for the bodies investigated are less definite than the values indicated by drag curves for finely shaped bodies, such as airfoils, because the rise in drag at high speeds is not very sharp. For the circular cylinder, however, visual observations of the flow by means of the schlieren method were made, and these observations served as a guide in the selection of the value of the critical speed from the drag curves for the circular cylinders.

Circular cylinder.—The results from the tests of the drag of circular cylinders are presented in figures 2 and 3; the results as affected by Reynolds Number

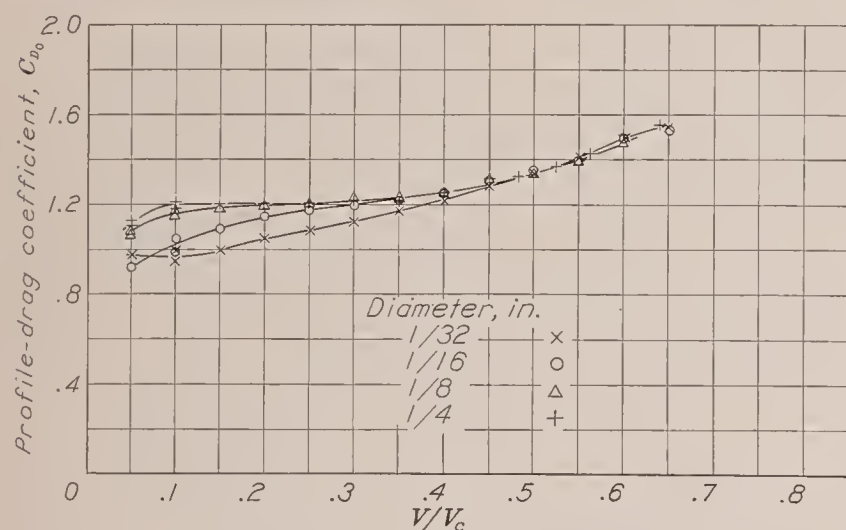


FIGURE 2.—Variation in C_{D0} with V/V_c for the circular cylinders.

(fig. 3) are in good agreement with Relf's results (reference 2).

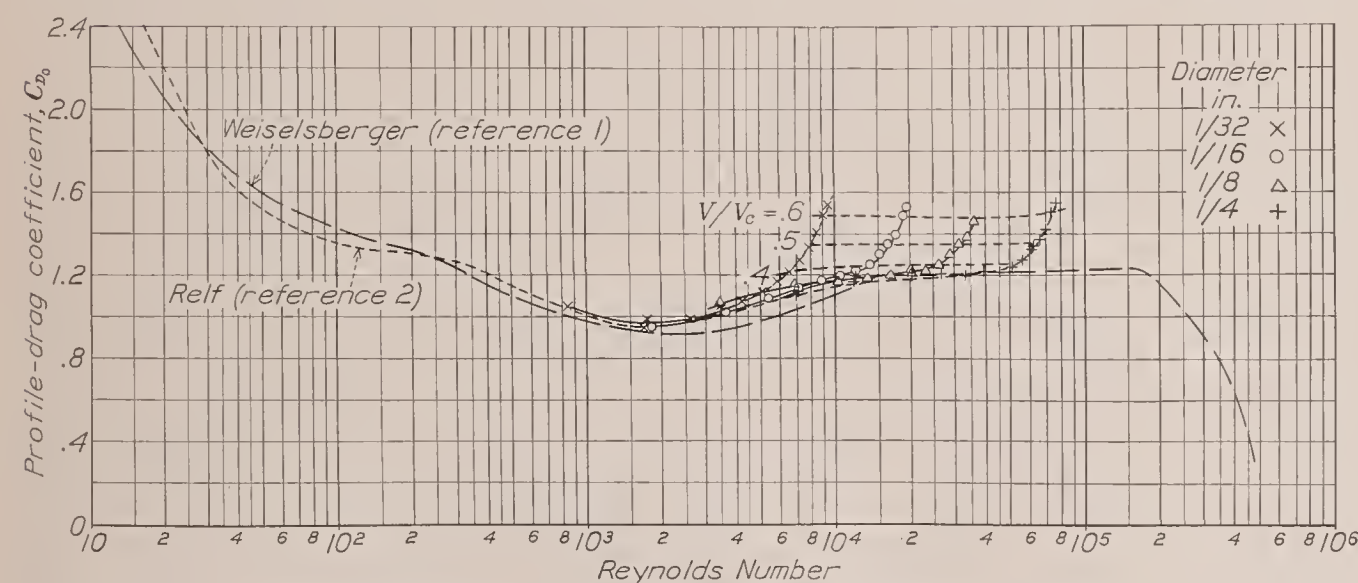


FIGURE 3.—Variation in C_{D0} with Reynolds Number for the circular cylinders.

Further, these tests indicate that the critical speed is independent of Reynolds Number within the range investigated. The critical speed for the circular cylinder at values of the Reynolds Numbers above the critical probably differs somewhat from that given herein because of the change in the pressure distribu-

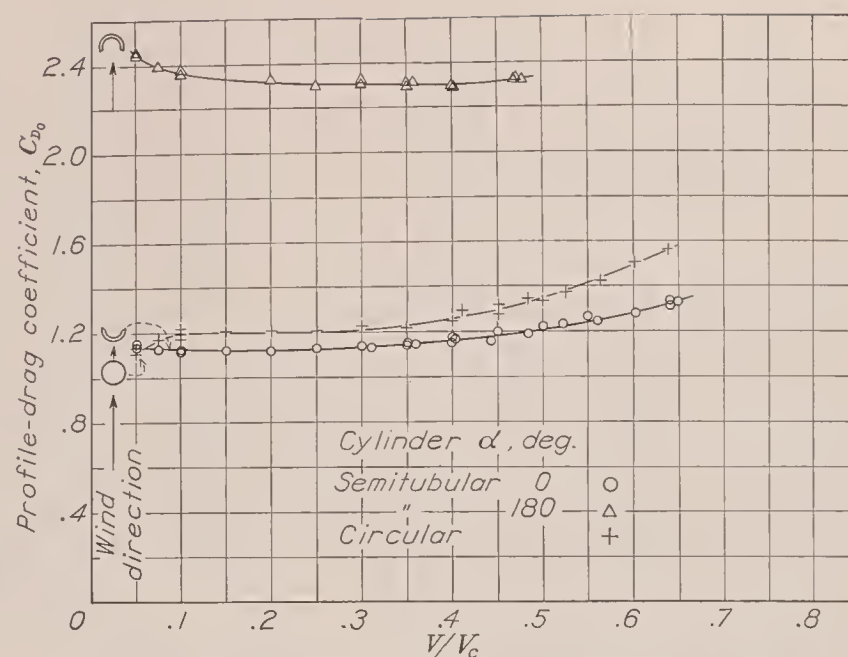


FIGURE 4.—Variation in C_{D0} with V/V_c for the semitubular cylinder.

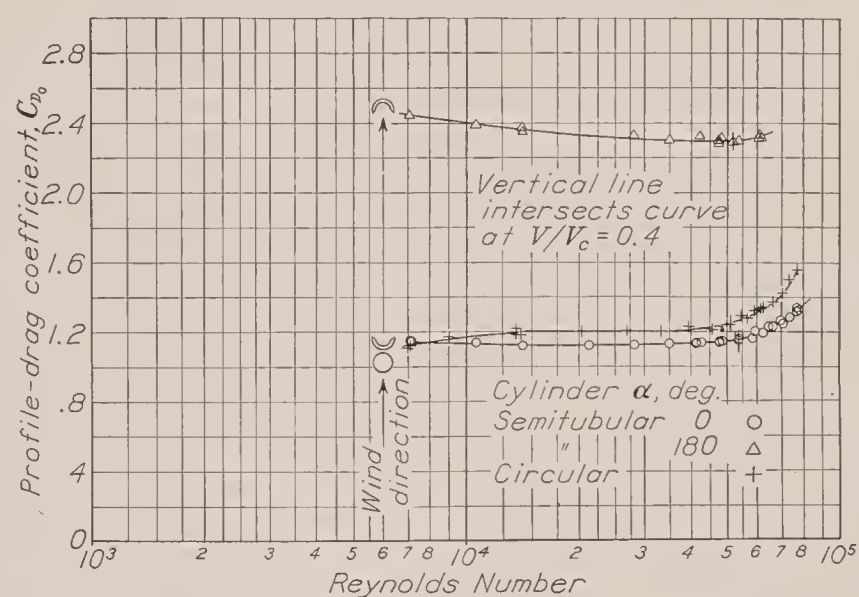


FIGURE 5.—Variation in C_{D0} with Reynolds Number for the semitubular cylinder.

tion for the circular cylinder that occurs after the critical Reynolds Number is exceeded. The present results, however, indicate that the critical speed is unaffected by Reynolds Number for ranges wherein no marked changes in the flow pattern occur. Unfortunately, these tests could not be extended to higher values of the Reynolds Number because tests of larger cylinders indicated serious tunnel-wall effects that could not readily be evaluated.

For speeds higher than the critical, the test results (figs. 2 and 3) indicate the drag coefficient to be a function of the speed ratio, or compressibility index, V/V_c . This statement is not a general conclusion inasmuch as figure 3 shows that the Reynolds Number range corresponding to this speed range occurs within

the region where the drag coefficient is approximately constant.

Semitubular cylinder.—The data from the tests of the semitubular cylinder (figs. 4 and 5) indicate that the drag coefficient, when the concave surface is to the wind ($\alpha=180^\circ$), is approximately twice as large as when the convex surface is to the wind ($\alpha=0^\circ$). A large increase in drag would be expected from elementary considerations.

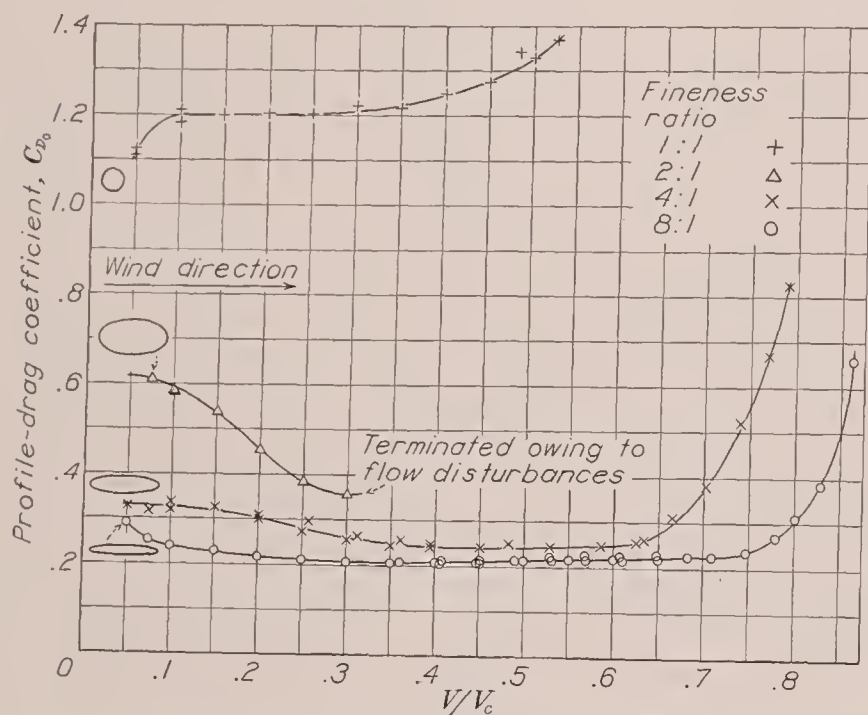


FIGURE 6.—Variation in C_{D_0} with V/V_c for the elliptical cylinders.

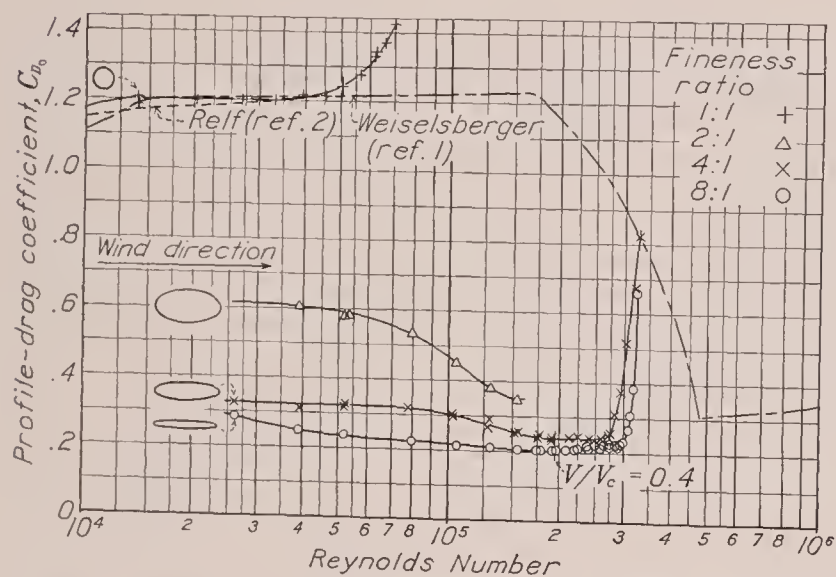


FIGURE 7.—Variation in C_{D_0} with Reynolds Number for the elliptical cylinders.

Elliptical cylinder.—A study of the compressibility effects on elliptical cylinders (figs. 6 and 7) shows a marked decrease in critical speed with decrease in fineness ratio. This result is to be expected from previous investigations since experiments have indicated (reference 6) that the compressibility burble occurs when the velocity at any point in the field of flow around the model exceeds a value corresponding to the local speed of sound, and investigations of the pressure distribution around elliptical cylinders (reference 7) show that the induced velocities decrease with increasing fineness ratio.

Relations between the fineness ratio and the critical speed can be obtained quantitatively from theoretical considerations. From the potential-flow theory, the induced pressure over the elliptical cylinder can be obtained from the equation

$$\frac{\Delta p}{q} = 1 - \frac{(a+b)^2 y^2}{b^4 + (a^2 - b^2)y^2} \quad (\text{reference 8, equation (14)})$$

where a is the semimajor axis.

b , the semiminor axis.

Δp , the difference between the undisturbed stream pressure and p , the pressure at the surface of the model.

y , the ordinate from the major axis to the point of pressure, p .

For the maximum negative value of $\Delta p/q$, y is equal to b .

The equation easily reduces to the form $\left(\frac{\Delta p}{q}\right)_{\max} = -t(2+t)$ where t is the thickness-chord ratio. The

relation between the maximum induced pressure $\left(\frac{\Delta p}{q}\right)_{\max}$ (from low-speed tests or as calculated from the potential-flow theory for incompressible fluids) and the critical speed is developed and presented graphically in reference 9. The results from references 8 and 9 may be combined to give the relation between the critical speed and the thickness-chord ratio presented in figure 8. A comparison of the theoretical with the experimental results, also shown in figure 8, indicates

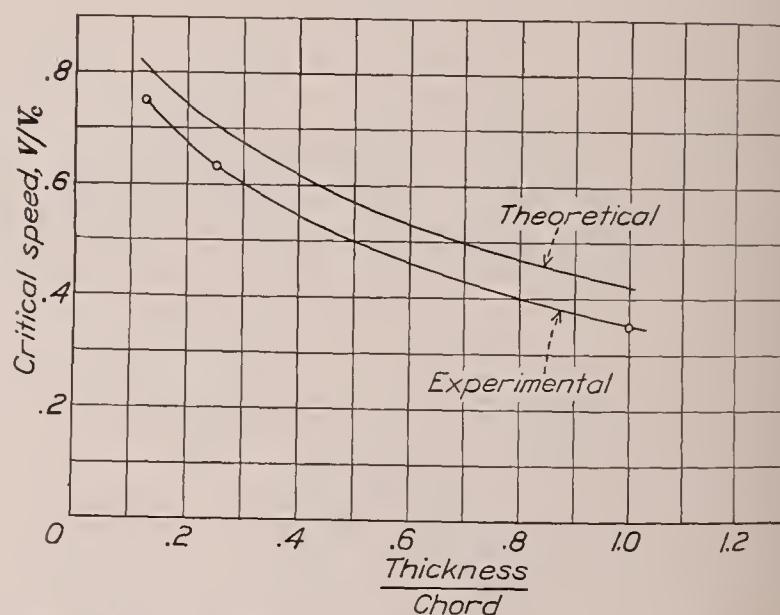


FIGURE 8.—Variation in critical speed with thickness-chord ratio for the elliptical cylinders.

that the theory gives a fair approximation of the critical speed for elliptical cylinders. The predicted values are somewhat high. Even higher values are obtained if, instead of the theoretically derived values, low-speed measurements of $\left(\frac{\Delta p}{q}\right)_{\max}$ are used in computing the critical speeds.

As regards Reynolds Number effects, the results of tests of the model (fig. 7) having the highest fineness ratio (8:1) indicate no pronounced change in drag coefficient with Reynolds Number. With decrease in

fineness ratio to the 2:1 ellipse, however, the change becomes pronounced.

The results of Wieselberger's tests of circular cylinders of infinite aspect ratio (reference 1) are included in figure 7. A comparison of these results (considered as data for an elliptical cross section having a fineness ratio of 1:1 and obtained under conditions of turbulence either equal to or greater than the low turbulence of the 11-inch high-speed tunnel) and the results of the present investigation of the elliptical cross section having a fineness ratio of 2:1 indicates a decrease in critical Reynolds Number with increase in fineness ratio.

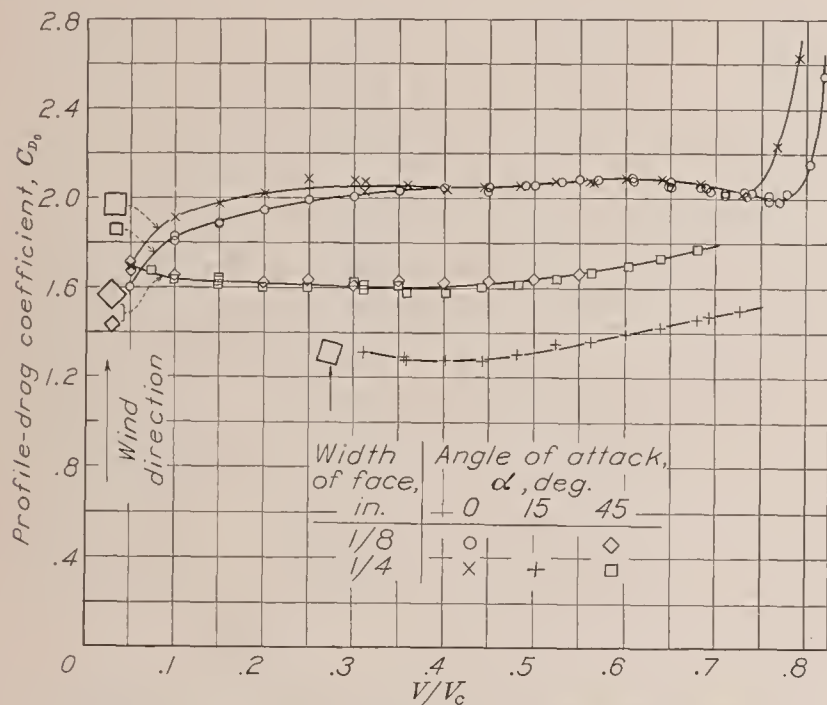


FIGURE 9.—Variation in C_{D0} with V/V_c for the square cylinders.

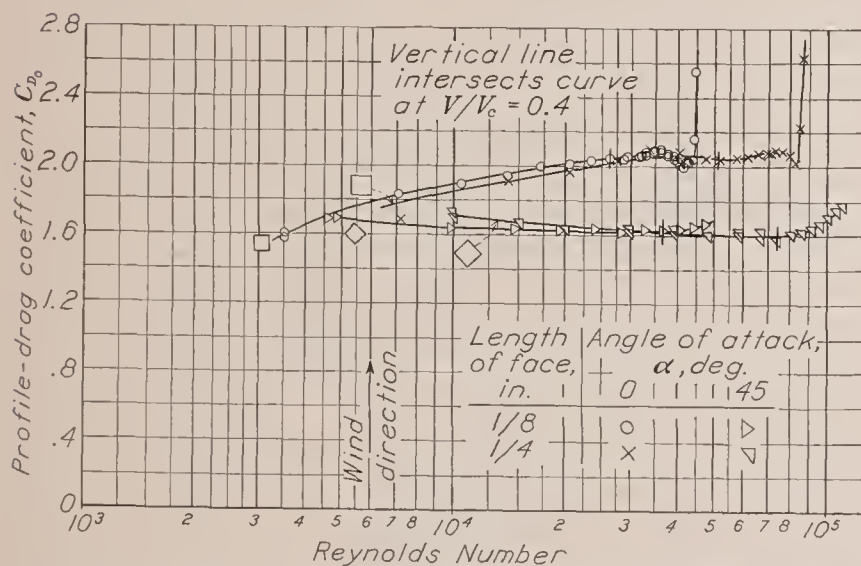


FIGURE 10.—Variation in C_{D0} with Reynolds Number for the square cylinders.

Square cylinder.—The results of the drag tests at the various angles of attack for the square cylinders are presented in figures 9 and 10. These results indicate that the drag coefficient is smaller when a diagonal is parallel to the wind ($\alpha=45^\circ$) than when the face of the model is normal to the wind ($\alpha=0^\circ$). The total drag of models of the same size, however, is smaller at $\alpha=0^\circ$ than at $\alpha=45^\circ$.

Figure 10 indicates that there is but little Reynolds Number effect on the drag coefficient of the models

with a diagonal parallel to the wind. Inasmuch as the flow probably separates at the sharp edges for all values of the Reynolds Number, the pressure drag coefficient tends to remain constant and is such a large part of the total drag coefficient that the effect of Reynolds Number is relatively small.

For the square cylinders, face normal to the wind ($\alpha=0^\circ$ in fig. 10), at the higher values of Reynolds Number, the drag coefficient is practically constant and approximates that of a flat plate set normal to the wind. At the lower values of the Reynolds Number, however, the drag coefficient appears to decrease with decreasing Reynolds Number; incomplete separation at the forward edges possibly causes this change.

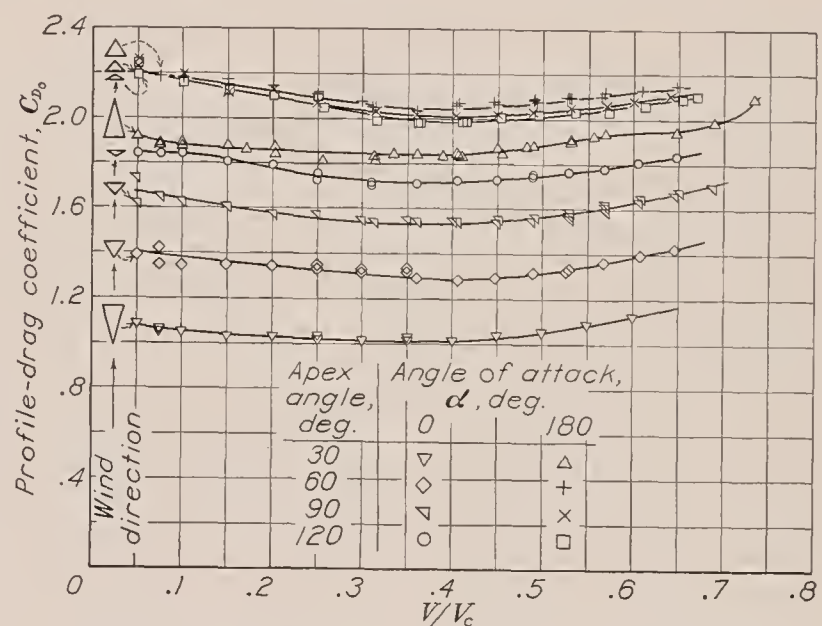


FIGURE 11.—Variation in C_{D0} with V/V_c for the triangular cylinders.

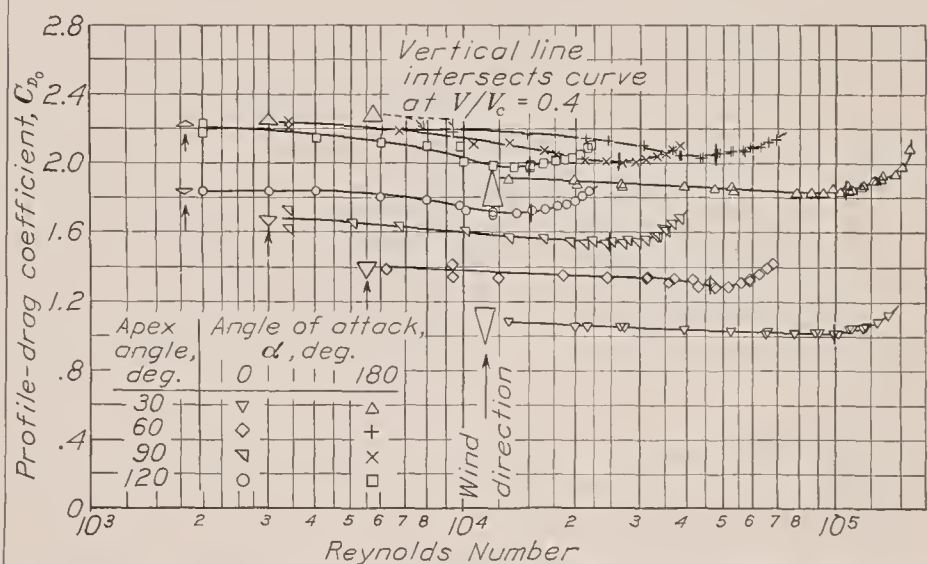


FIGURE 12.—Variation in C_{D0} with Reynolds Number for the triangular cylinders.

Within the Reynolds Number range investigated, no sudden changes in flow were indicated by the results of the tests at any of the angles of attack.

The compressibility effects for models with a diagonal parallel to the wind ($\alpha=45^\circ$ in figs. 9 and 10) appear to be independent of Reynolds Number within the range investigated. This result is in general agreement with the results of the tests of circular cylinders.

Triangular cylinder.—The effect of the apex angle on the drag coefficient of triangular (isosceles) cylinders is

shown in figure 11. As the apex angle is increased and with either apex or base to the wind, the drag coefficient increases and approaches that of a flat plate normal to the wind, as is to be expected since the model tends to become a flat plate as the apex angle approaches 180° . With the base of the triangular cylinder to the wind, there is no appreciable effect on the drag coefficient from increasing the apex angle above a value of 60° . With the apex to the wind, however, there is a continuous increase in drag coefficient with increase in apex angle above 30° .

Reynolds Number has but little effect on the drag coefficient of models having triangular cross sections (fig. 12). The same characteristic is shown by the results from tests of models having square cross section with the diagonal parallel to the wind (fig. 10).

The compressibility effects (figs. 11 and 12) appear to be independent of apex angle and are the same for angles of attack of 0° (apex to the wind) and of 180° (base normal to the wind). The compressibility effects for both triangular (isosceles) cylinders and for square cylinders with a diagonal parallel to the wind direction ($\alpha=45^\circ$) are approximately the same.

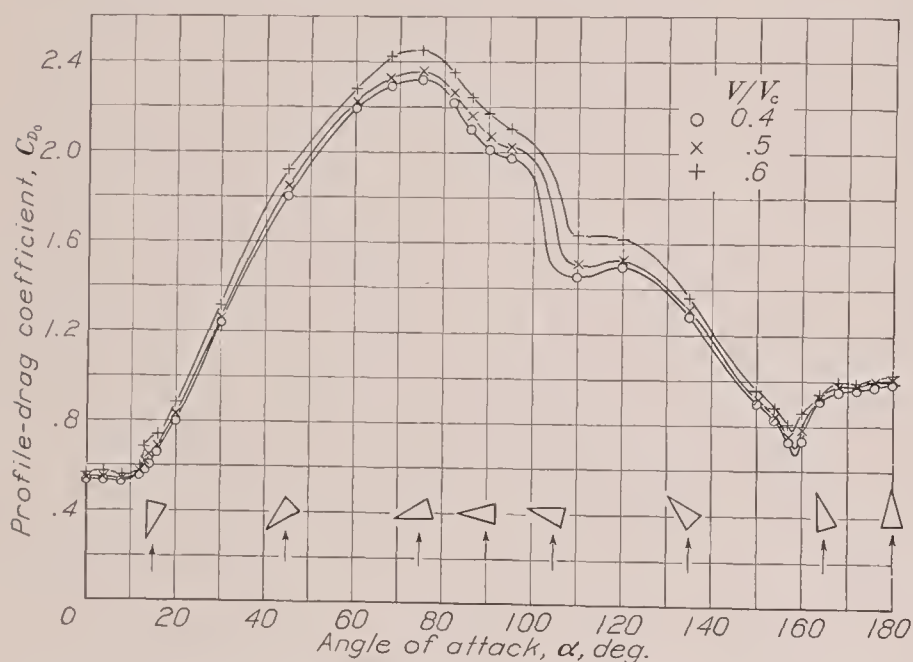


FIGURE 13.—Variation in C_{D_0} with α for the triangular cylinder having an apex angle of 30° . Area=altitude \times span.

The test results of figure 13 show the variation in drag coefficient, based on a constant area (product of altitude and effective span), with angle of attack for each of several values of the speed ratio V/V_c . Each curve indicates, for a particular value of the speed ratio V/V_c , the variation in total drag for a triangular cross section having an apex angle of 30° . The maximum drag occurs when one of the long sides is normal to the wind, the condition corresponding to an angle of attack of 75° .

The results indicate abrupt changes in the flow pattern within certain ranges of angle of attack, as evidenced by the sudden changes in drag coefficient. It is of interest to note that, at or near these critical

angles of attack, one of the long sides of the model becomes either parallel or perpendicular to the direction of the wind, as illustrated by figure 13.

The variation in drag coefficient with the speed ratio for several representative angles of attack is presented in figure 14 to show the compressibility effects. Apparently the compressibility effects are greater at or near the critical angle-of-attack ranges, as indicated by steeper slopes of the curves in figure 14 and by the vertical displacement of the curves in figure 13.

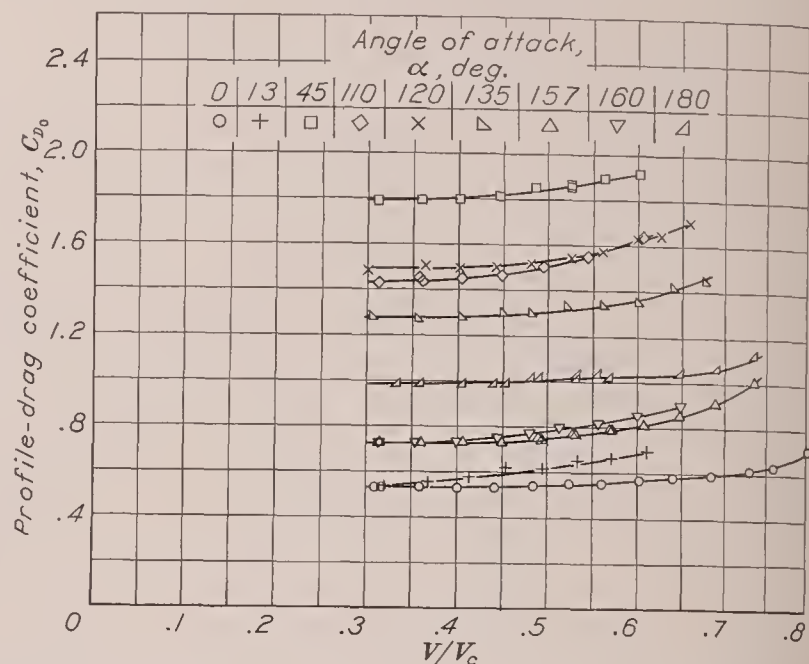


FIGURE 14.—Variation in C_{D_0} with V/V_c for the triangular cylinder having an apex angle of 30° . Area=altitude \times span.

The variation in lift coefficient with angle of attack is shown in figure 15 for three values of the speed ratio, V/V_c . The results show that sudden variations in the lift coefficient occur in the same critical angle-of-attack ranges in which the drag coefficient changes, a further indication that there are abrupt changes in the flow pattern. The variation in lift coefficient with V/V_c for angles of attack within the critical angle-of-attack range is presented in figure 16.

An extrapolation of the drag coefficient of triangular cylinders having various apex angles with the base to the wind is presented in figure 17, in which the drag coefficient is plotted against the ratio of altitude to base h/b for each of several values of the speed ratio, V/V_c . As h/b approaches zero, the triangular section approaches an infinitely thin flat plate set normal to the wind. Thus, the extrapolation of the results of tests of models having triangular cross sections to a value of $h/b=0$ should give a good estimate of the drag coefficient for flat plates of infinite aspect ratio set normal to the wind. The drag coefficient, obtained from this extrapolation, decreases slightly with increase in Reynolds Number. At equal Reynolds Numbers based on width normal to the stream, the extrapolated results are in good agreement with values from German tests conducted over limited Reynolds Number and speed ranges (reference 4).

Effect of shape on drag.—Figure 18 illustrates the relative drag of all the models and shows the general effect of shape on the drag coefficient. The drag coefficient, based on frontal area for all the models, is plotted against the speed ratio, V/V_c . The sizes of

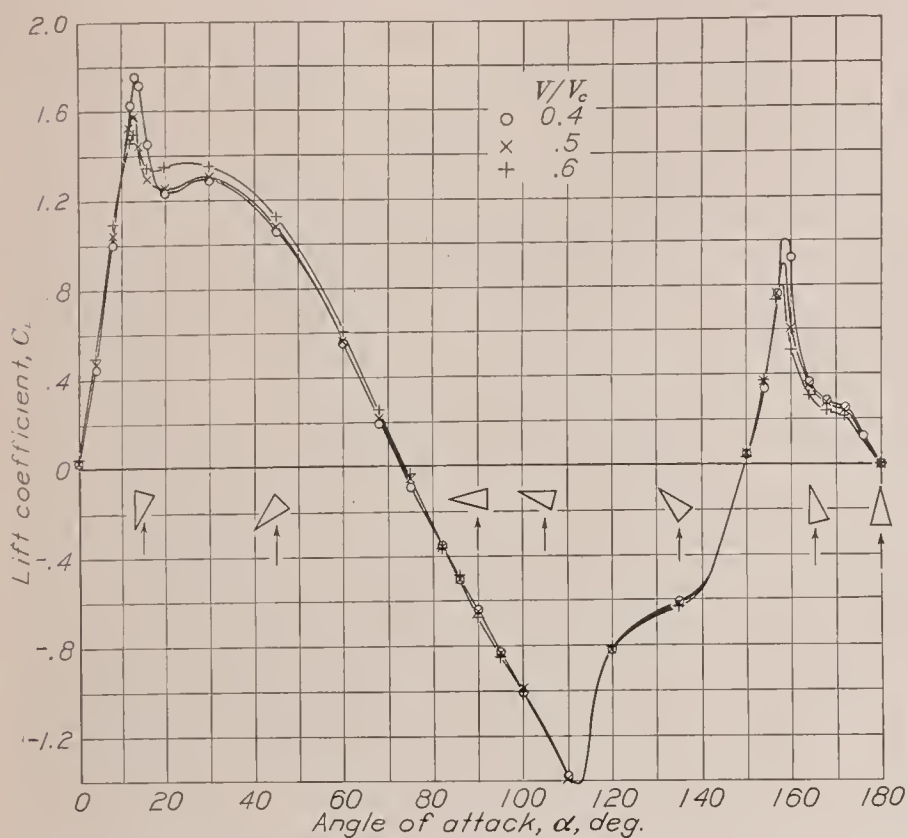


FIGURE 15.—Variation in C_L with α for the triangular cylinder having an apex angle of 30° . Area=altitude \times span.

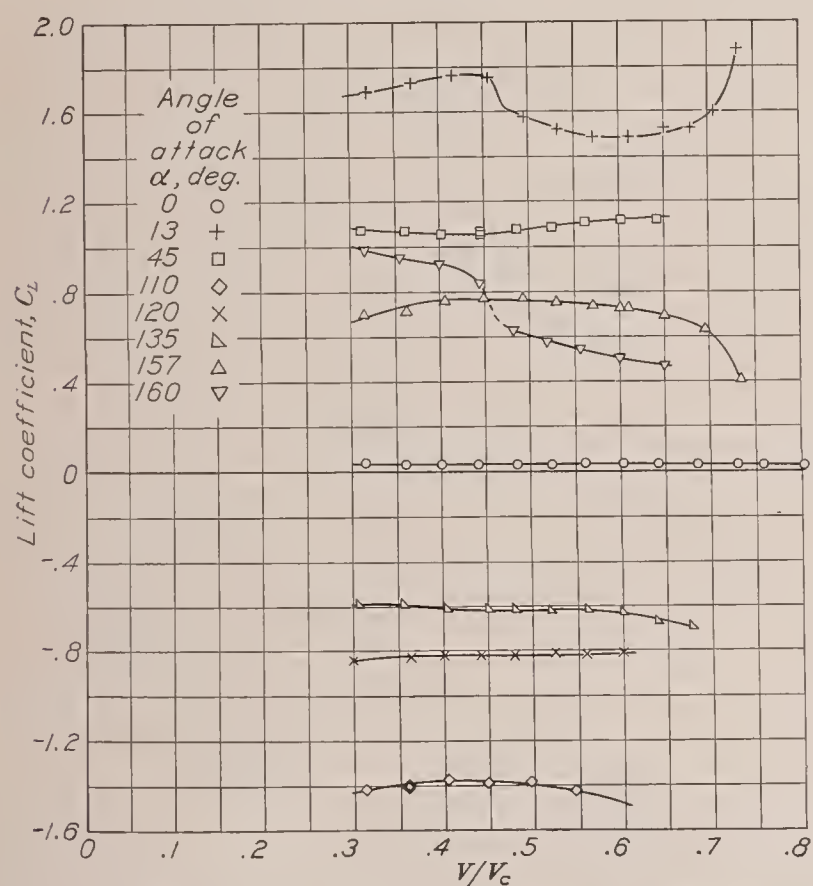


FIGURE 16.—Variation in C_L with V/V_c for the triangular cylinder having an apex angle of 30° . Area=altitude \times span.

the models were consistent in that the frontal areas were approximately equal. The drag coefficient of the N. A. C. A. 0012-63 airfoil (reference 10) is included for comparison.

The agreement in drag coefficient between the semitubular cylinder with convex surface to the wind ($\alpha=0^\circ$) and the circular cylinder is reasonably close and is to be expected in this Reynolds Number range because separation occurs in front of the central plane. At values of the Reynolds Number above the critical value, however, a greater difference in drag coefficient for the two forms is to be expected because the separation occurs back of the central plane for the circular

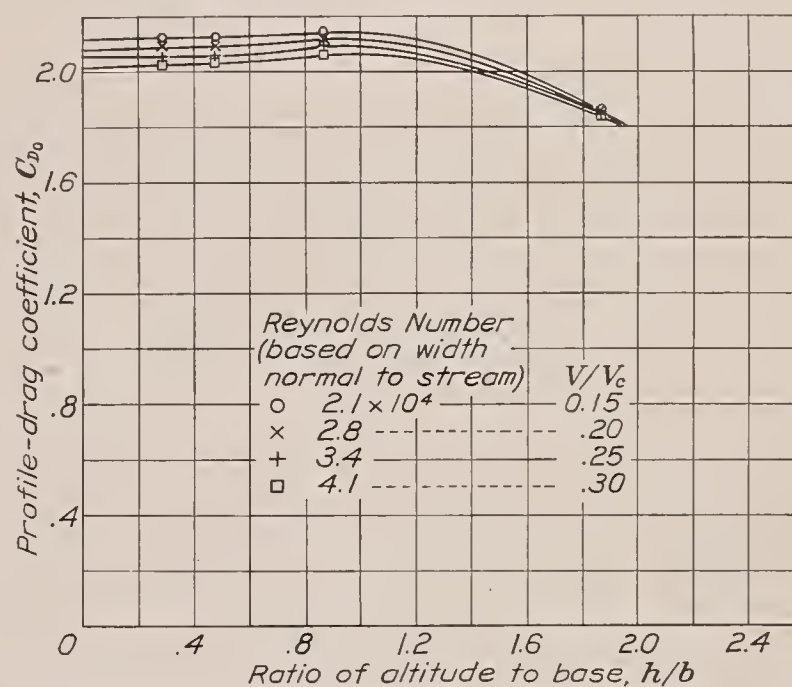


FIGURE 17.—Extrapolation for C_{D_0} of flat plates normal to the wind.

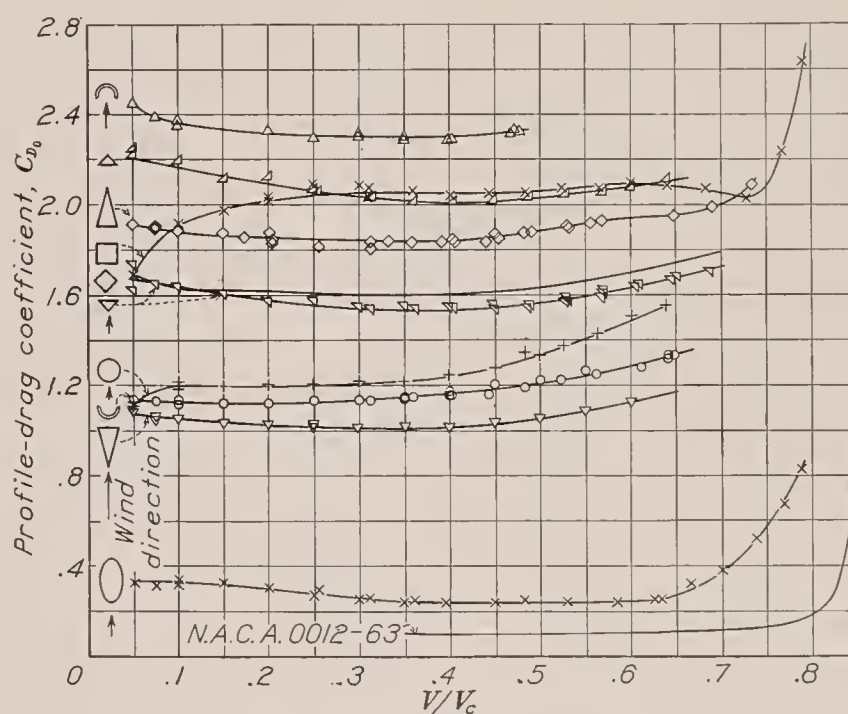


FIGURE 18.—Effect of shape on C_{D_0} .

cylinder and at the central plane for the semitubular cylinder.

Similarly, the drag coefficient of the triangular cylinder having a 90° apex angle with the apex to the wind is only slightly less than the drag coefficient of the square cylinder with a diagonal parallel to the wind. This condition of approximately equal drag coefficients is to be expected because the point of separation is fixed for both forms at the sharp edges.

In general, the data show that, except for the square cylinder with a face normal to the wind, the higher-drag bodies have, in general, less rapid rise in drag coefficient at the higher speeds.

CONCLUSIONS

1. The compressibility effects appear to be independent of Reynolds Number for ranges wherein there are no marked changes in the flow pattern caused by Reynolds Number effects.

2. The critical speed of elliptical cylinders decreases with decrease in fineness ratio.

3. For bodies having sharp edges that may be expected to define the separation point, the Reynolds Number effects are small. This result substantiates earlier investigations.

LANGLEY MEMORIAL AERONAUTICAL LABORATORY,
NATIONAL ADVISORY COMMITTEE FOR AERONAUTICS,
LANGLEY FIELD, VA., *October 27, 1937.*

REFERENCES

1. Wieselsberger, C.: New Data on the Laws of Fluid Resistance. T. N. No. 84, N. A. C. A., 1922.
2. Relf, E. F.: Discussion of the Results of Measurements of the Resistance of Wires, with Some Additional Tests on the Resistance of Wires of Small Diameter. R. & M. No. 102, British A. C. A., 1914.
3. Stanton, T. E.: On the Effect of Air Compression on Drag and Pressure Distribution in Cylinders of Infinite Aspect Ratio. R. & M. No. 1210, British A. R. C., 1929.
4. Wieselsberger, C.: Der Widerstand verschiedener Körper. Ergebnisse der Aerodynamischen Versuchsanstalt zu Göttingen. II. Lieferung, 1923, S. 33-34.
5. Stack, John: The N. A. C. A. High-Speed Wind Tunnel and Tests of Six Propeller Sections. T. R. No. 463, N. A. C. A., 1933.
6. Stack, John: The Compressibility Burble. T. N. No. 543, N. A. C. A., 1935.
7. Parsons, John F., and Wallen, Jarvis A.: An Investigation of the Phenomenon of Separation in the Air Flow around Simple Quadric Cylinders. T. N. No. 354, N. A. C. A., 1930.
8. Zahm, A. F.: Flow and Drag Formulas for Simple Quadrics. T. R. No. 253, N. A. C. A., 1927.
9. Jacobs, Eastman N.: Methods Employed in America for the Experimental Investigation of Aerodynamic Phenomena at High Speeds. Misc. Paper No. 42, N. A. C. A., 1936.
10. Stack, John, and von Doenhoff, Albert E.: Tests of 16 Related Airfoils at High Speeds. T. R. No. 492, N. A. C. A., 1934.

REPORT No. 620

PRESSURE DISTRIBUTION OVER AIRFOILS WITH FOWLER FLAPS

By CARL J. WENZINGER and WALTER B. ANDERSON

SUMMARY

Pressure-distribution tests were made of a Clark Y airfoil with a 0.20c_w Clark Y Fowler flap and of an N. A. C. A. 23012 airfoil with 0.20c_w, 0.30c_w, and 0.40c_w N. A. C. A. 23012 Fowler flaps. Some of the tests were made in the 7- by 10-foot wind tunnel and others in the 5-foot vertical wind tunnel. The pressures were measured on the upper and lower surfaces at one chord section both on the main airfoils and on the flaps for several angles of attack with the flaps located at the maximum-lift settings. A test installation was used in which the model was mounted in the wind tunnel between large end planes so that two-dimensional flow was approximated.

The data are given in the form of pressure-distribution diagrams and as plots of calculated coefficients for the airfoil-and-flap combinations and for the flaps alone. The pressure-distribution tests show that the effect of increasing the chord of the Fowler flap, for a given lift of combined airfoil and flap, is to increase the portion of the total load carried by the flap and to decrease the adverse pressure gradients of the main airfoil and thereby its tendency to stall. The maximum values of the normal-force coefficient of the Fowler flap were found to be much smaller than previously indicated and approximately the same as those of the external-airfoil flap and of the simple split flap. The flap-load data given in this report supersede those given in Report No. 534.

INTRODUCTION

The Fowler flap in combination with a main airfoil appears to be one of the most effective high-lift devices investigated up to the present time. Previous investigations of this device (references 1, 2, and 3) have shown that it is capable of developing high lift coefficients and that it gives lower drags at the high lift coefficients than do plain or split flaps. The Fowler flap, in addition, differs from the external-airfoil flap in that it is fully retractable for the high-speed-flight condition.

Several sizes of flap combined with a given main airfoil have been investigated, the flap ranging in chord up to 40 percent of the main airfoil chord. (See reference 1.) In addition, tests have been made with these sizes of flap to determine the required locations for each to give its best aerodynamic characteristics.

In order to supply the information requested by designers for structural-design purposes, the present pres-

sure-distribution tests were made to obtain the air-load distribution over the main airfoil and flap. The combinations tested have either the Clark Y or the N. A. C. A. 23012 sections for both the main airfoil and the flap, the flap positions being those giving approximately the highest maximum lift for each arrangement.

APPARATUS AND TESTS

MODELS

Two models, built of laminated mahogany and having a span and chord each of 20 inches, were used for the main airfoils; one was of Clark Y section and the other of N. A. C. A. 23012 section. The upper surfaces of these airfoils from midchord to the trailing edge were formed by a thin steel plate suitably supported by metal ribs at each end and by two intermediate ribs. The space between the plate and the lower surface was filled by wooden blocks cut to the proper contour and arranged for easy removal to form retracting wells for flaps having chords 20, 30, or 40 percent of the main airfoil chord.

Four models (fig. 1) were used for the Fowler flaps, one of Clark Y section and three of N. A. C. A. 23012 section. The Clark Y flap was of brass and had a span of 20 inches and a chord of 4 inches (20 percent of the main airfoil chord). The N. A. C. A. 23012 flaps were of duralumin, each having a span of 20 inches and chords of 4, 6, and 8 inches (20, 30, and 40 percent of the main airfoil chord, respectively). The flaps were supported on the main airfoils by metal fittings at each end and by two intermediate fittings, spaced equally along the span.

A single row of pressure orifices was built into the upper and lower surfaces of each main airfoil and flap at only the midspan section, the tests of reference 4 having shown that other orifices were unnecessary. These orifices were located on the models as listed in table I, the tubes from the orifices being brought through the model and out at one end. The pressures were photographically recorded by a multiple-tube manometer.

TEST INSTALLATION

The entire investigation was originally intended to be made in a single wind tunnel but, because the necessity arose for making changes to that tunnel during the course of the investigation, it was found desirable to

complete the tests in a different tunnel so that the results would not be unnecessarily delayed. Some of the models were tested in the N. A. C. A. 7- by 10-foot open-jet wind tunnel (reference 5) and were mounted as shown by figure 2. The main airfoil was rigidly attached to two circular end plates with the flap set at the position and deflection (30°) giving about the highest $C_{L_{max}}$ of the combination. The end plates were supported in circular cut-outs in two large vertical end planes that extended from top to bottom of the air stream and also some distance ahead of and behind the model. The angle of attack of the model was set by

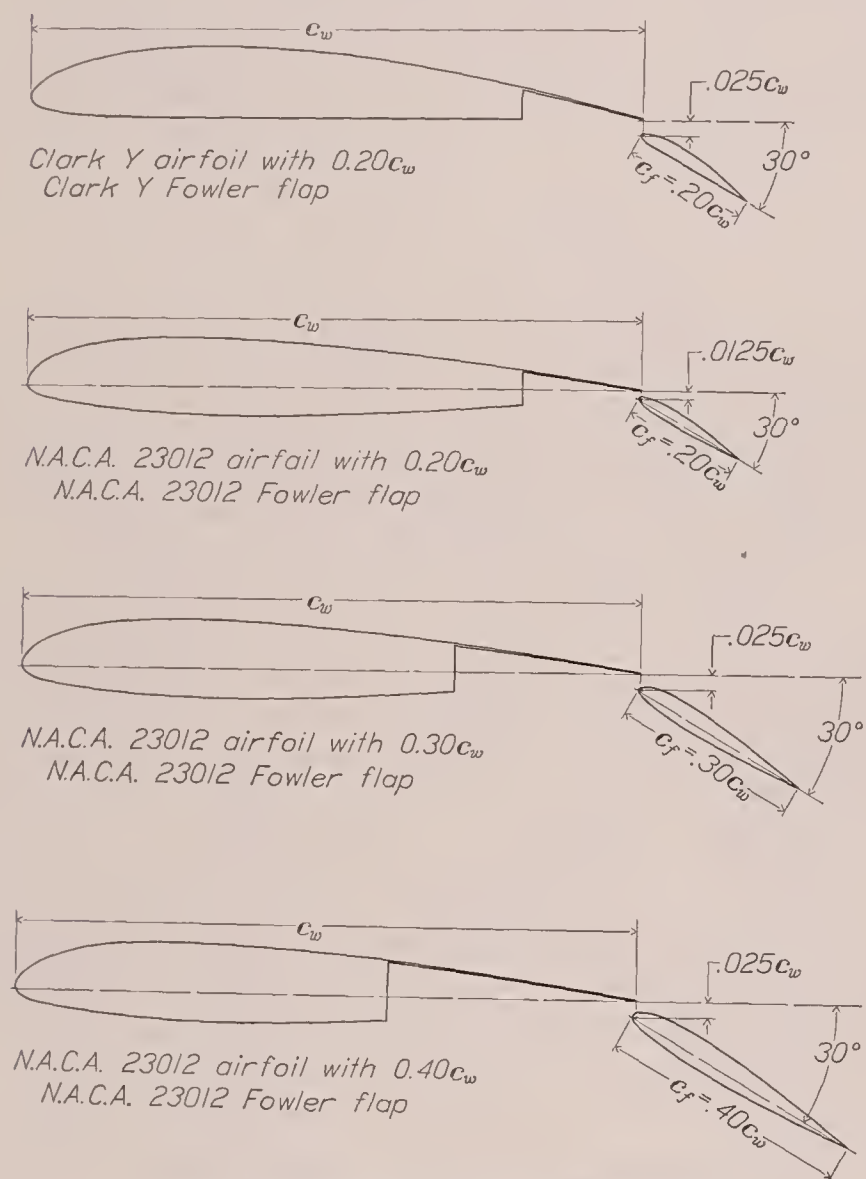


FIGURE 1.—Sections of airfoil and flap combinations tested.

rotating the circular plates and locking them at the desired angle. Approximately two-dimensional flow is obtained with this type of installation and the section characteristics of the model under test may be determined. (See reference 4.)

The remaining models were tested in the N. A. C. A. 5-foot open-jet vertical wind tunnel (reference 6) and were mounted as shown in figure 3. This installation was very similar to that used in the 7- by 10-foot tunnel; the model set-up for testing and the multiple-tube manometer are shown in figure 4.

TESTS

The tests were carried out at a dynamic pressure of 16.37 pounds per square foot, corresponding to an air

speed of 80 miles per hour at standard sea-level conditions. The average test Reynolds Numbers, based on the sum of main airfoil and flap chords, varied from 1,220,000 for the plain airfoil to 1,700,000 for the airfoil with the $0.40c_w$ Fowler flap. The turbulence factor for the 7- by 10-foot open-jet wind tunnel is 1.4 and for the 5-foot vertical tunnel, 1.7, from which the effective Reynolds Numbers may be computed. (Effec-

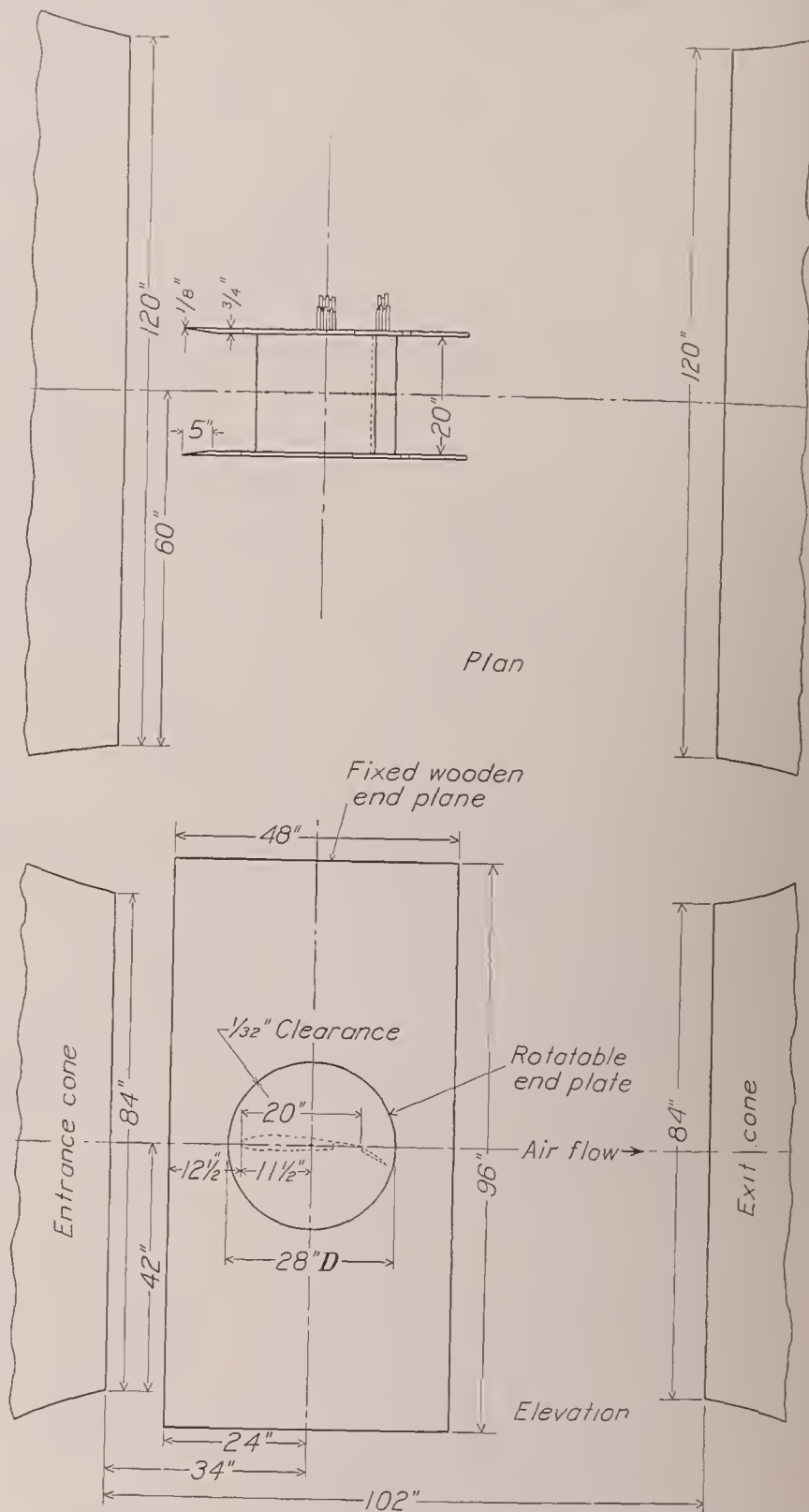


FIGURE 2.—Diagram of model with Fowler flap installed between end planes in the 7- by 10-foot wind tunnel.

tive Reynolds Number = test Reynolds Number \times turbulence factor (reference 7).)

The Clark Y and the N. A. C. A. 23012 plain airfoils, and the same airfoils with $0.20c_w$ Clark Y and N. A. C. A. 23012 Fowler flaps, respectively, were tested in the 7- by 10-foot wind tunnel. The N. A. C. A. 23012 main airfoil with $0.20c_w$, $0.30c_w$, and $0.40c_w$ N. A. C. A. 23012 Fowler flaps was tested in the 5-foot vertical wind tunnel. All flaps were set at the position and angle

(30°) that gave nearly maximum lift for all the combinations tested. The angles of attack ranged from -20° to 24° and the lift coefficients included those from approximately maximum negative through maximum positive lift. With the model at a given angle of attack, a few minutes were allowed for all test condi-

6) are given as ratios of orifice pressure p to dynamic pressure of the air stream q for the angles of attack investigated. Pressure diagrams for the combinations of main airfoils with Fowler flaps are given in figures 7 to 10 for the various angles of attack tested. On these diagrams the pressures are plotted normal to the main-

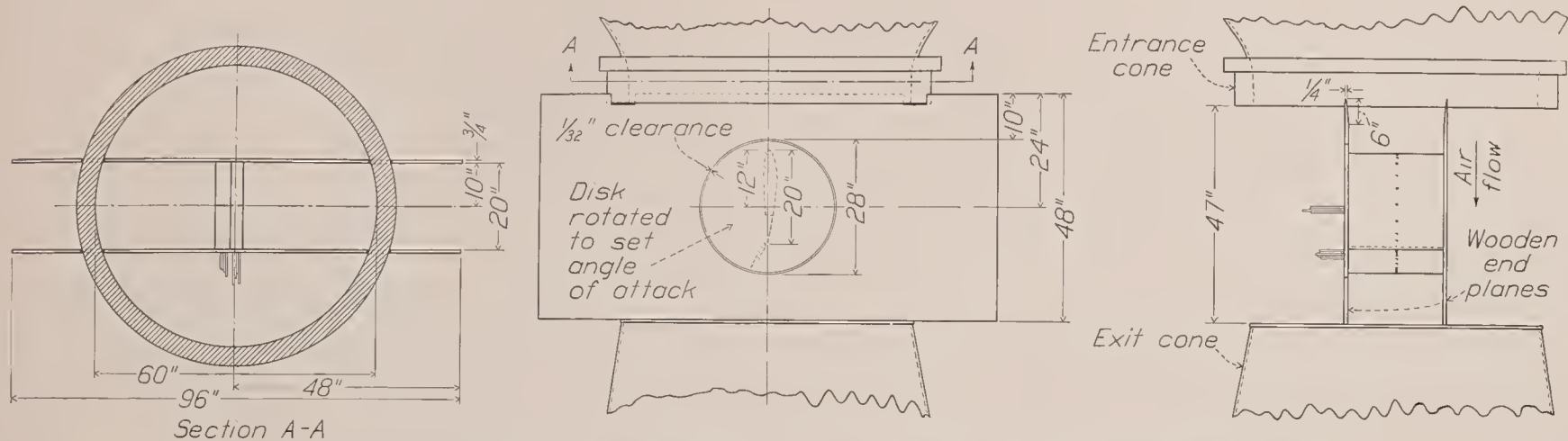


FIGURE 3.—Diagram of model with Fowler flap installed between end planes in the 5-foot vertical wind tunnel.

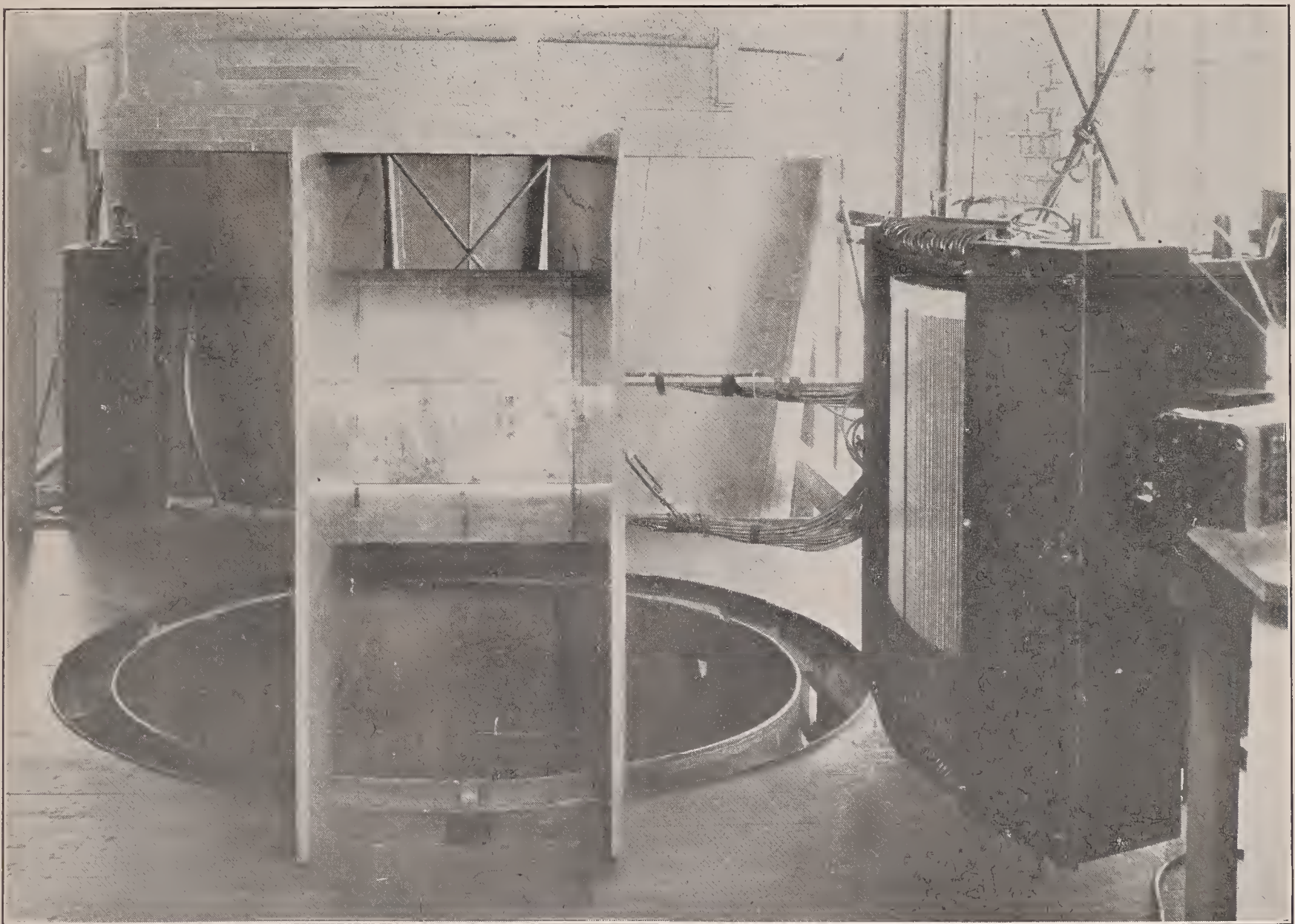


FIGURE 4.—Model and manometer set-up for tests in the 5-foot vertical wind tunnel.

tions to become steady; a record was then taken of the pressures at the orifices by means of the manometer.

PRESENTATION OF DATA PRESSURE DIAGRAMS

Diagrams of the pressures over the upper and lower surfaces of the main airfoils without flaps (figs. 5 and

airfoil chord and to the flap chord, the pressure values being measured from the main chord for the main-airfoil pressures and from the flap chord for the flap pressures. Figures 11 and 12 give comparisons, at the same total lift, of the pressure distribution over the various airfoil-flap arrangements tested.

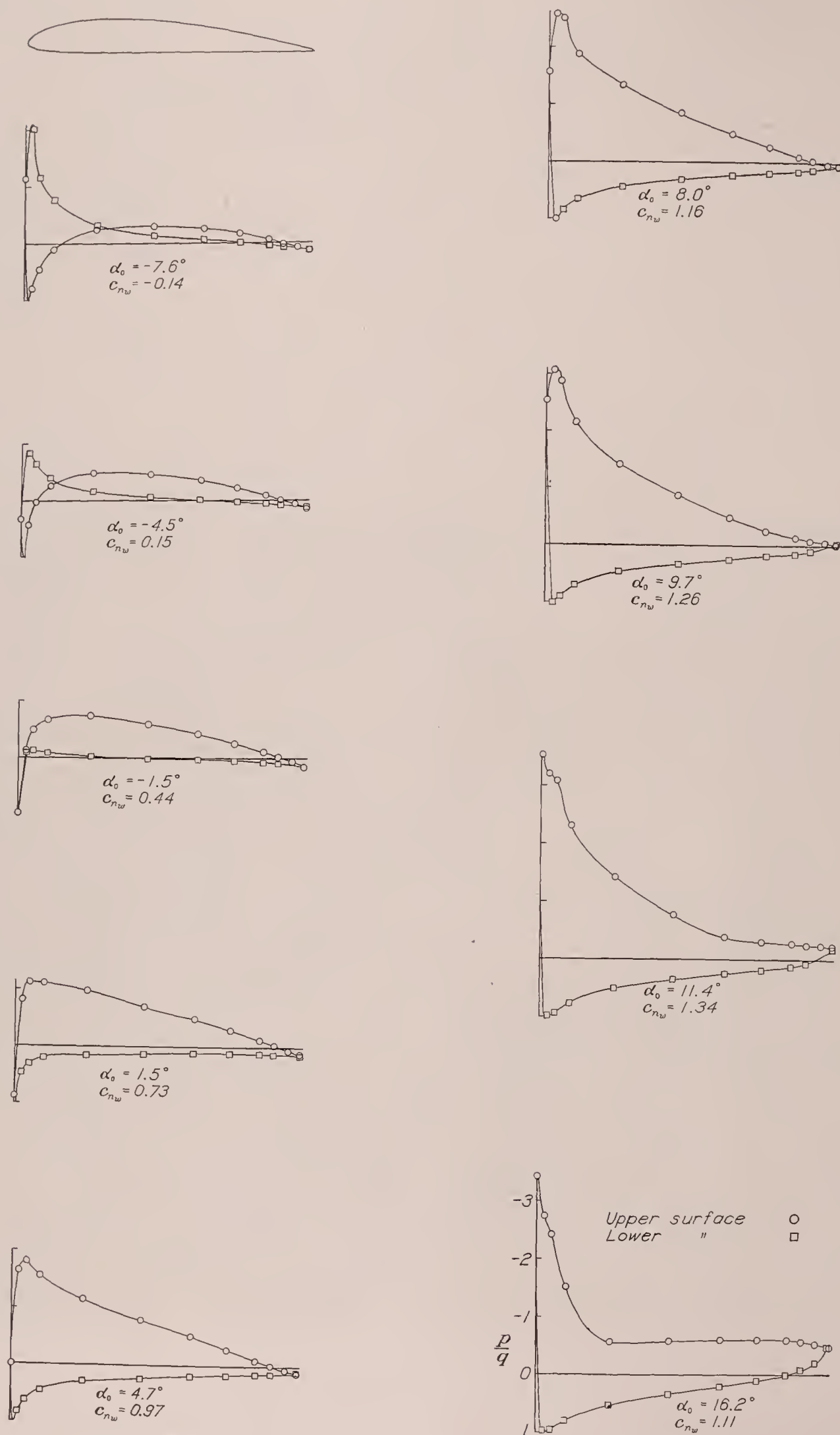


FIGURE 5.—Pressure distribution on the plain Clark Y airfoil, without flap, at various angles of attack.

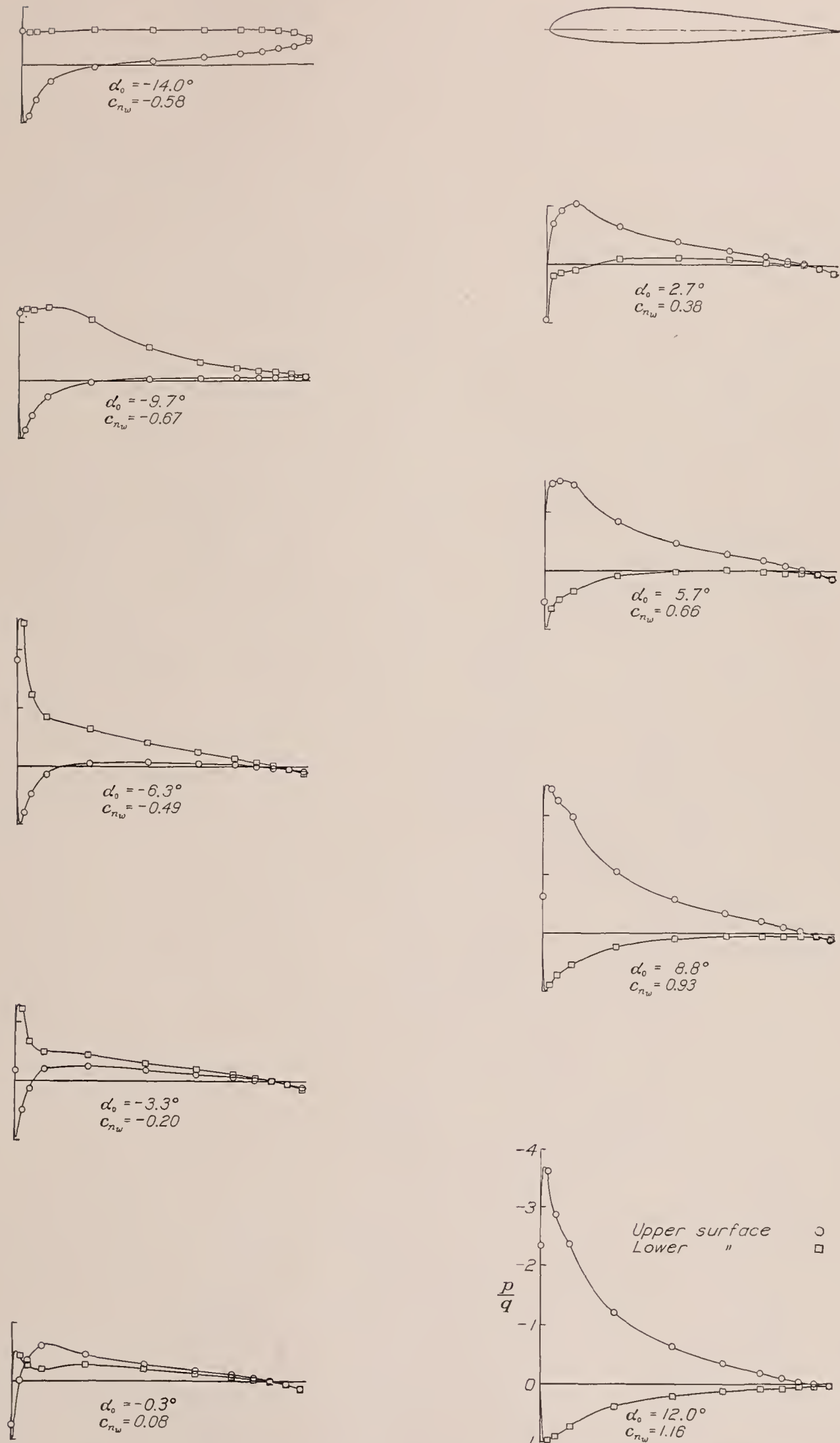


FIGURE 6.—Pressure distribution on the plain N. A. C. A. 23012 airfoil, without flap, at various angles of attack.

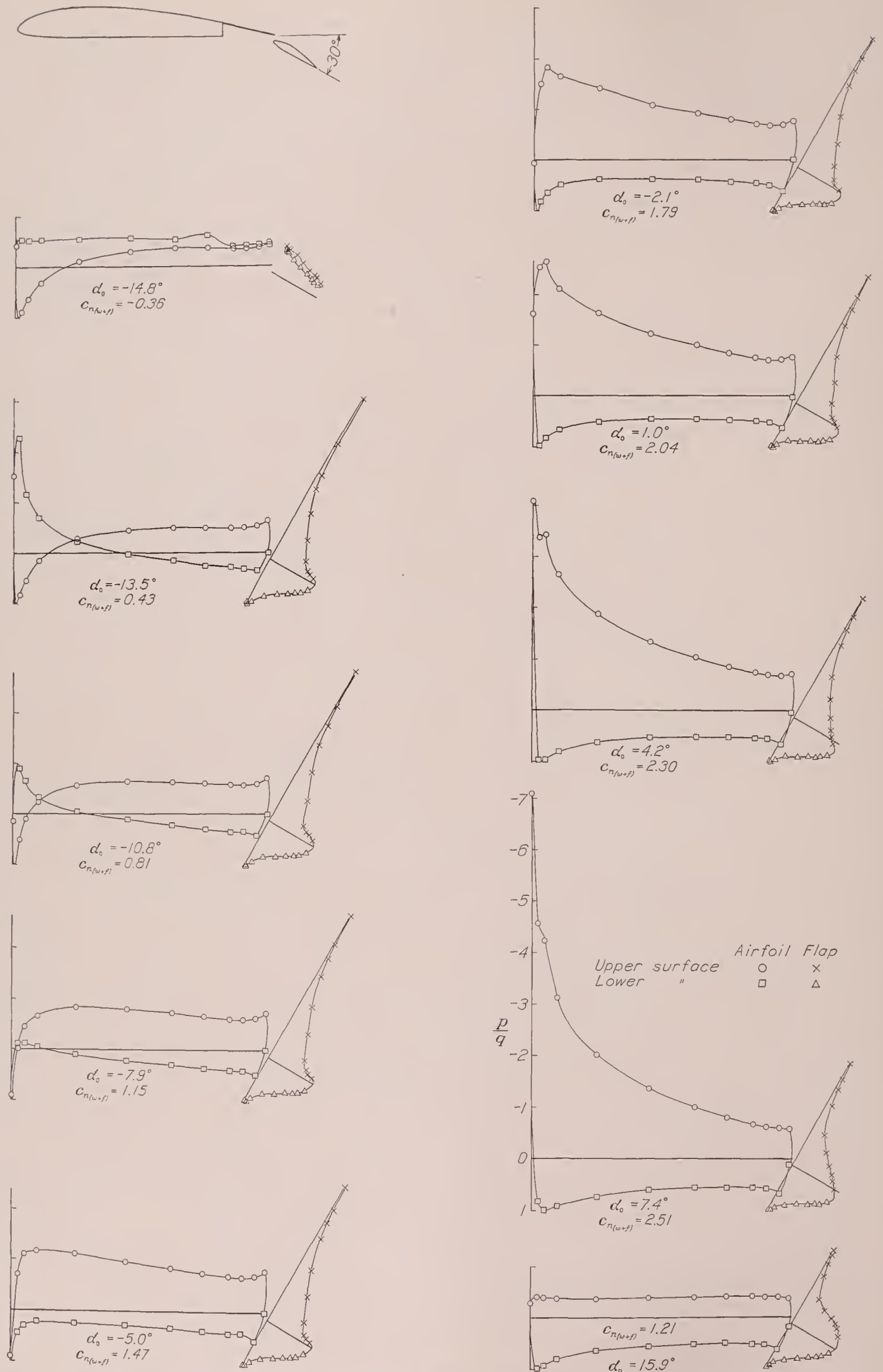


FIGURE 7.—Pressure distribution on the Clark Y airfoil, with the 0.20 c_w Clark Y Fowler flap, at various angles of attack. Flap deflected 30°.

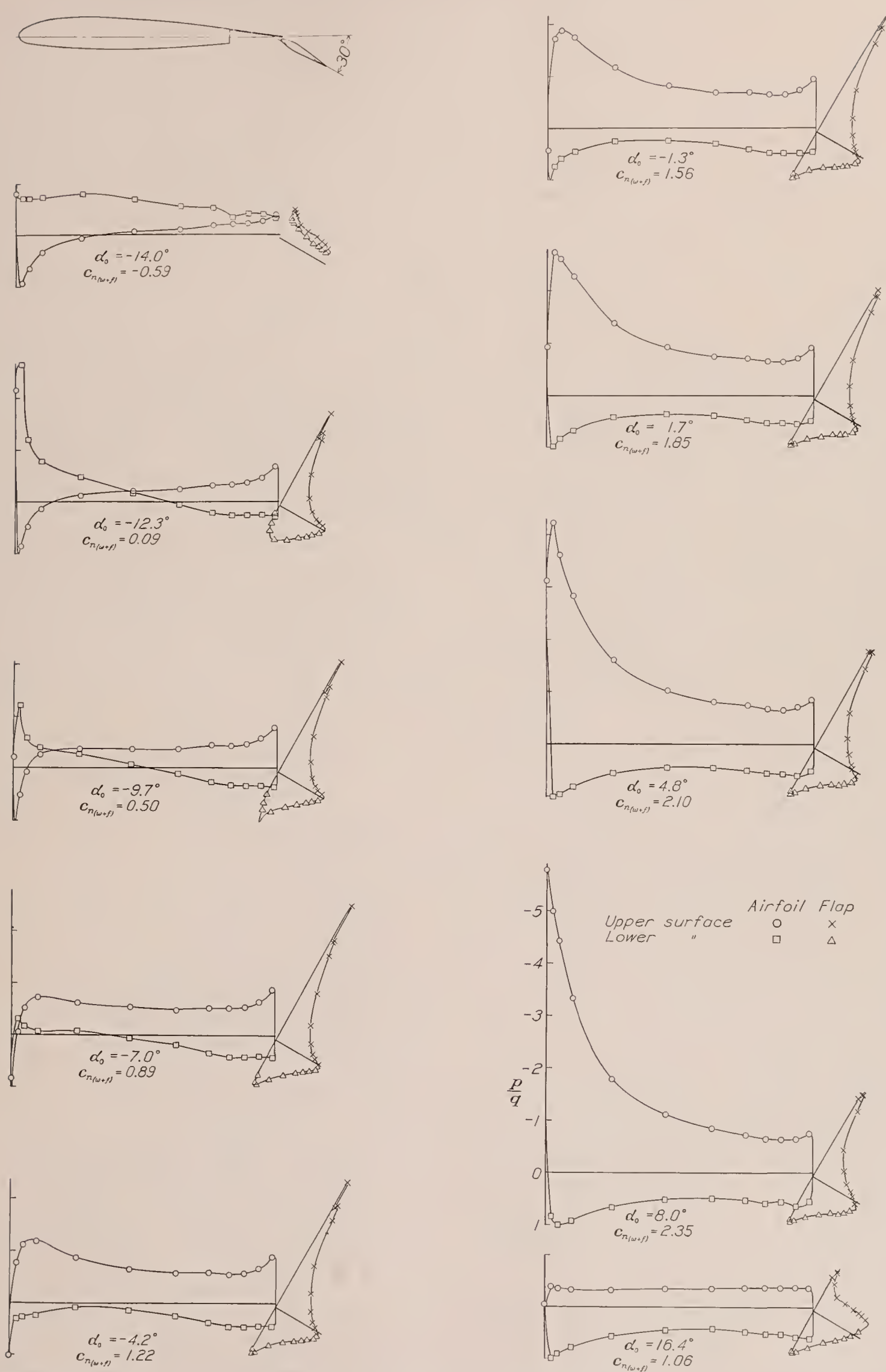


FIGURE 8.—Pressure distribution on the N. A. C. A. 23012 airfoil, with the 0.20 c_w N. A. C. A. 23012 Fowler flap, at various angles of attack. Flap deflected 30°

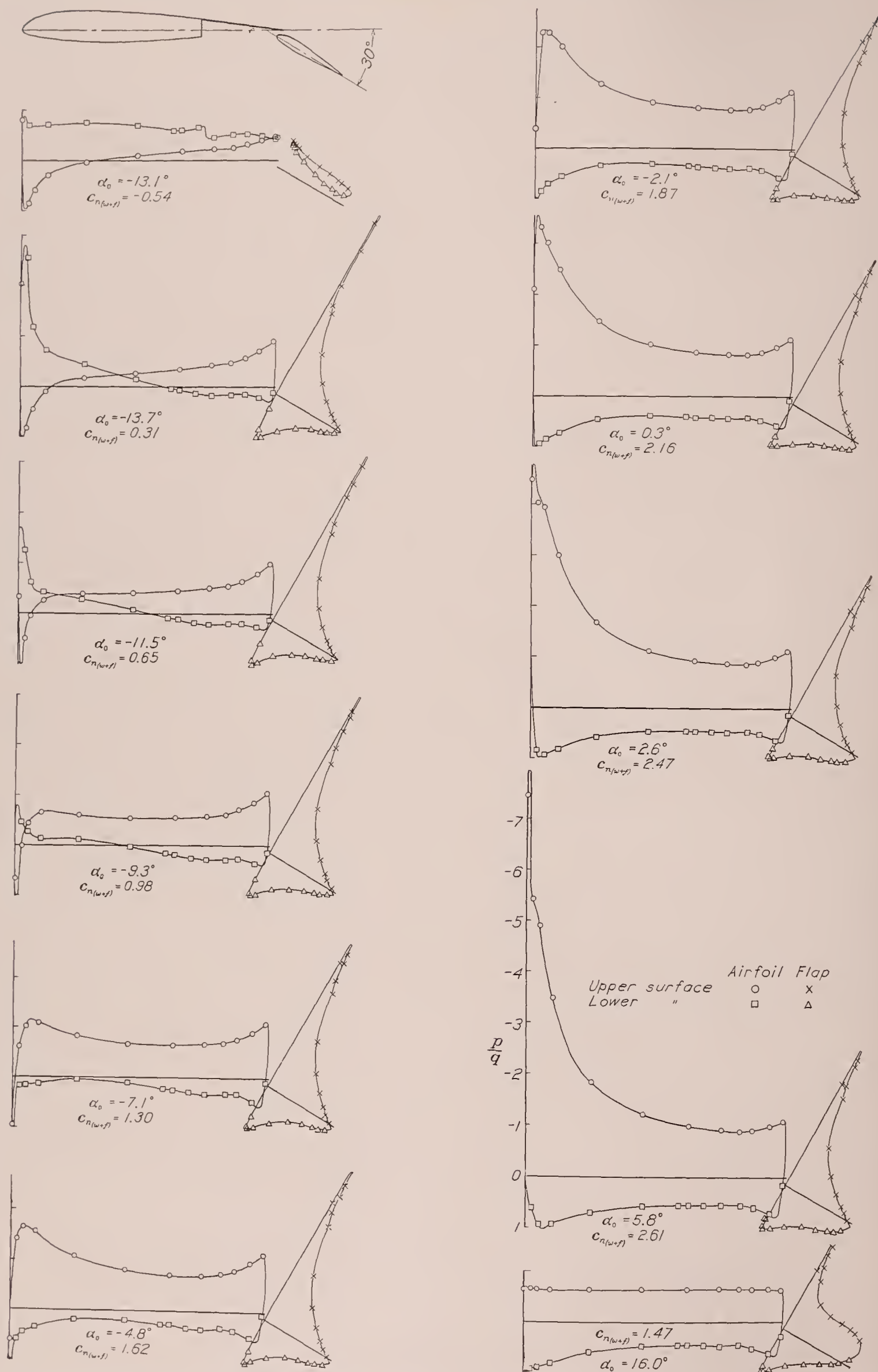


FIGURE 9.—Pressure distribution on the N. A. C. A. 23012 airfoil, with the 0.30c_u N. A. C. A. 23012 Fowler flap, at various angles of attack. Flap deflected 30°.

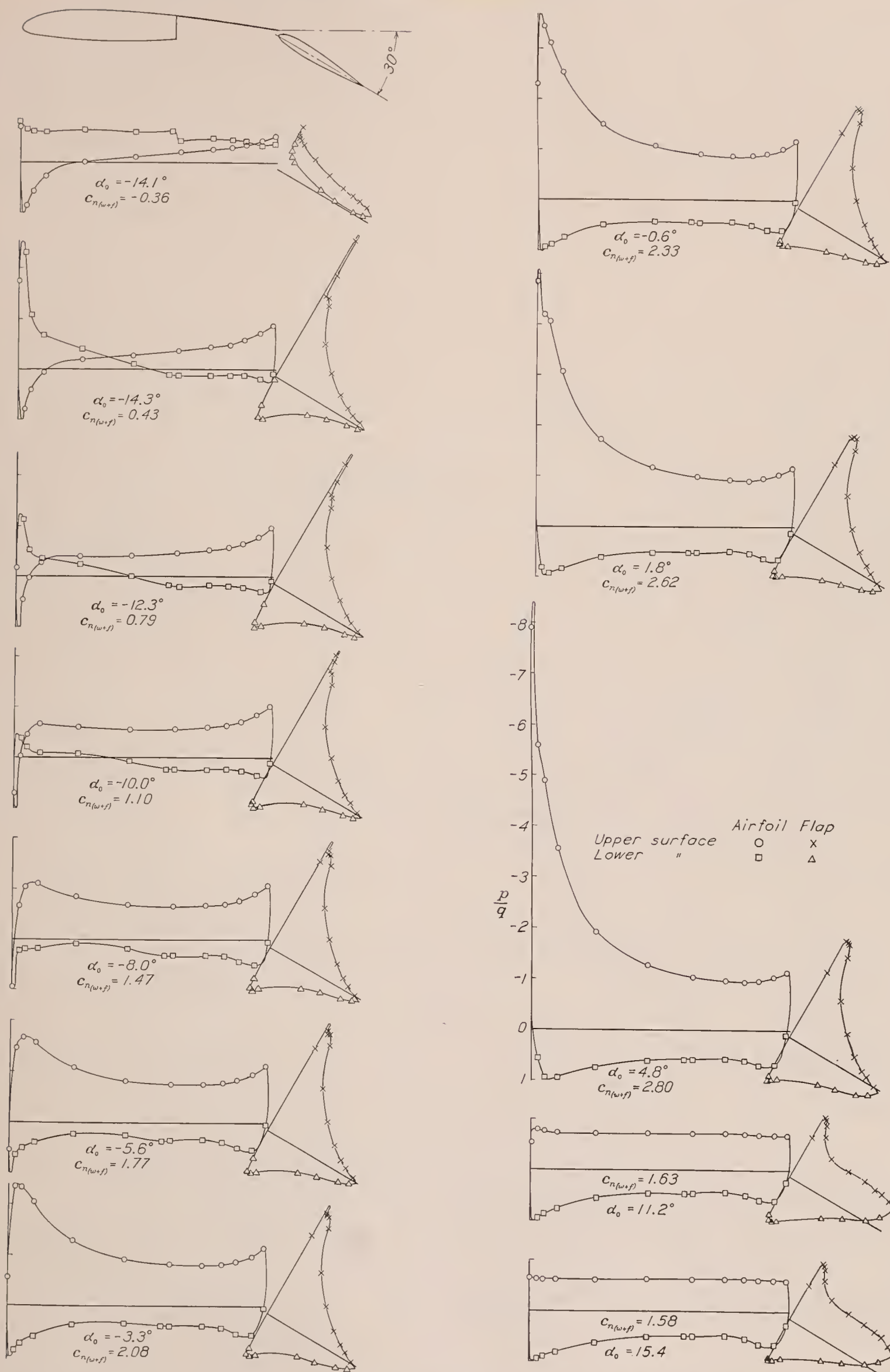


FIGURE 10.—Pressure distribution on the N. A. C. A. 23012 airfoil, with the $0.40c_w$ N. A. C. A. 23012 Fowler flap, at various angles of attack. Flap deflected 30° .

In addition to these normal-pressure diagrams, figures 13 and 14 are included to show the pressures parallel to the chords of the $0.30c_w$ and $0.40c_w$ N. A. C. A. 23012 Fowler flaps. These pressures are also given as ratios of orifice pressure to the dynamic pressure of the air stream; however, the pressure values are plotted parallel to, instead of normal to, the flap chord and are measured from the maximum thickness line of the flap, instead of from the chord line.

$$c_{n(w+f)} = \frac{n_{(w+f)}}{qc_w}, \text{ normal-force coefficient of main airfoil with flap.}$$

$$c_{m_w} = \frac{m_w}{qc_w^2}, \text{ pitching-moment coefficient of main airfoil alone about quarter-chord point.}$$

$$c_{m(w+f)} = \frac{m_{(w+f)}}{qc_w^2}, \text{ pitching-moment coefficient of main airfoil with flap, about quarter-chord point of main airfoil.}$$

$$c_{n_f} = \frac{n_f}{qc_f}, \text{ normal-force coefficient of flap.}$$

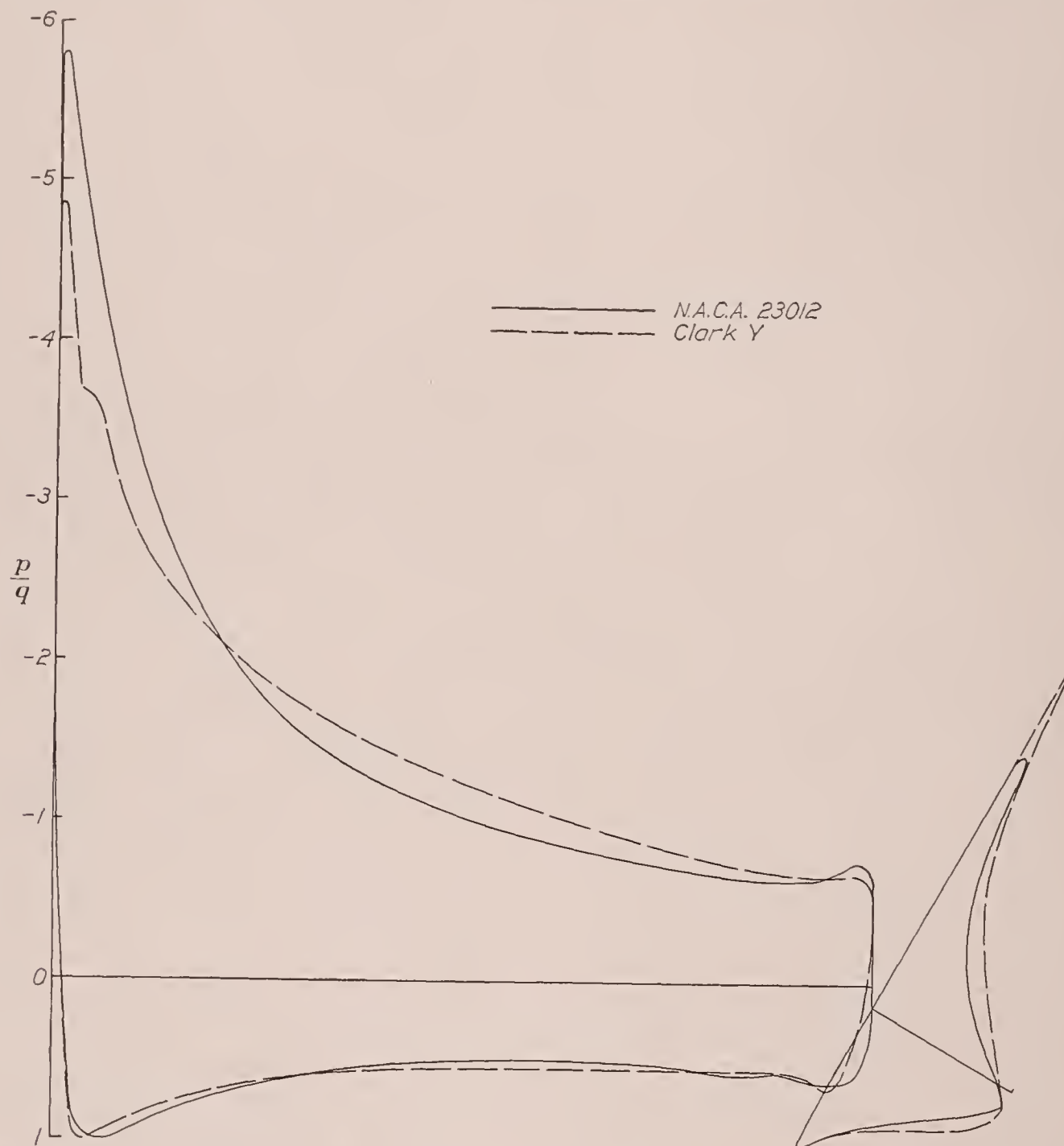


FIGURE 11.—Comparison of the pressure distribution, at the same lift, on the Clark Y airfoil and the $0.20c_w$ Clark Y Fowler flap with that on the N. A. C. A. 23012 airfoil and the $0.20c_w$ N. A. C. A. 23012 Fowler flap. $c_{n(w+f)} = 2.35$.

COEFFICIENTS

The pressure diagrams were mechanically integrated to obtain data from which section coefficients could be computed. The section coefficients are defined as follows:

$$c_{n_w} = \frac{n_w}{qc_w}, \text{ normal-force coefficient of main airfoil alone.}$$

$$c_{m_f} = \frac{m_f}{qc_f^2}, \text{ pitching-moment coefficient of flap about quarter-chord point of flap.}$$

$$(c.p.)_w = \left(0.25 - \frac{c_{m_w}}{c_{n_w}}\right) \times 100, \text{ center of pressure of main airfoil alone, in percentage of chord from leading edge.}$$

$(c.p.)_{(w+f)} = \left(0.25 - \frac{c_{m(w+f)}}{c_{n(w+f)}}\right) \times 100$, center of pressure of main airfoil with flap, in percentage of main-airfoil chord from leading edge.

m_w , pitching moment of main airfoil about quarter-chord point.
 $m_{(w+f)}$, pitching moment of main airfoil with flap about quarter-chord point of main airfoil.
 n_f , normal force of flap.
 m_f , pitching moment of flap about quarter-chord point of flap.

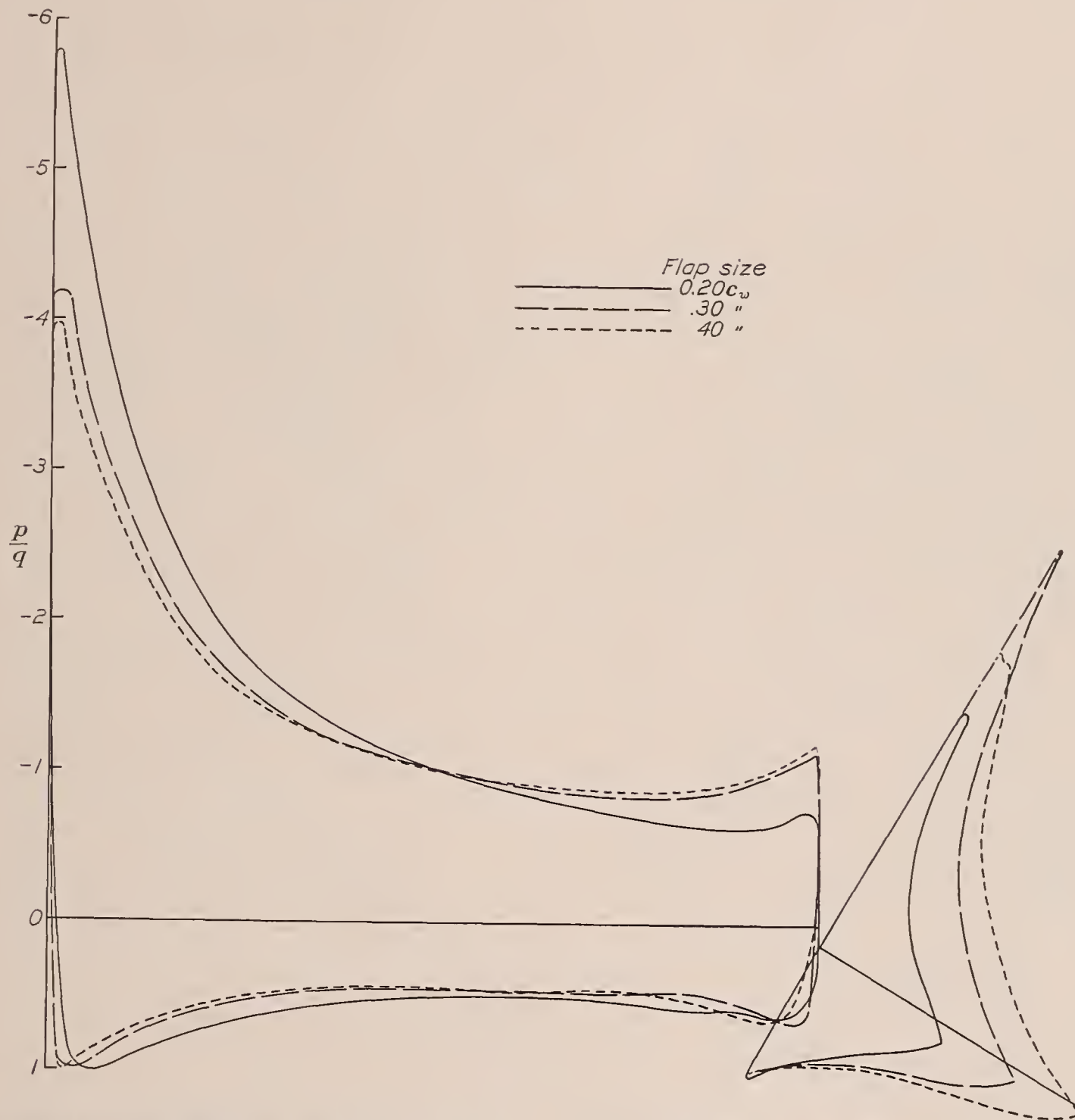


FIGURE 12.—Comparison of the pressure distribution, at the same lift, on the N. A. C. A. 23012 airfoil with the $0.20c_w$, the $0.30c_w$, and the $0.40c_w$ N. A. C. A. 23012 Fowler flaps. $c_{n(w+f)} = 2.35$.

$(c.p.)_f = \left(0.25 - \frac{c_{m_f}}{c_{n_f}}\right) \times 100$, center of pressure of flap in percentage of flap chord from leading edge of flap.

$c_{c_f} = \frac{x_f}{qc_f}$, chord-force coefficient of flap.

where the forces per unit span are:

n_w , normal force of main airfoil.
 $n_{(w+f)}$, normal force of main airfoil with flap.

x_f , chord force of flap.
 and

q , dynamic pressure.
 c_w , main-airfoil chord.
 c_f , flap chord.

The center-of-pressure positions and the pitching-moment coefficients were derived from the normal forces, the chord forces being neglected except for the effect of the flap, in which case the flap deflection was taken into account.

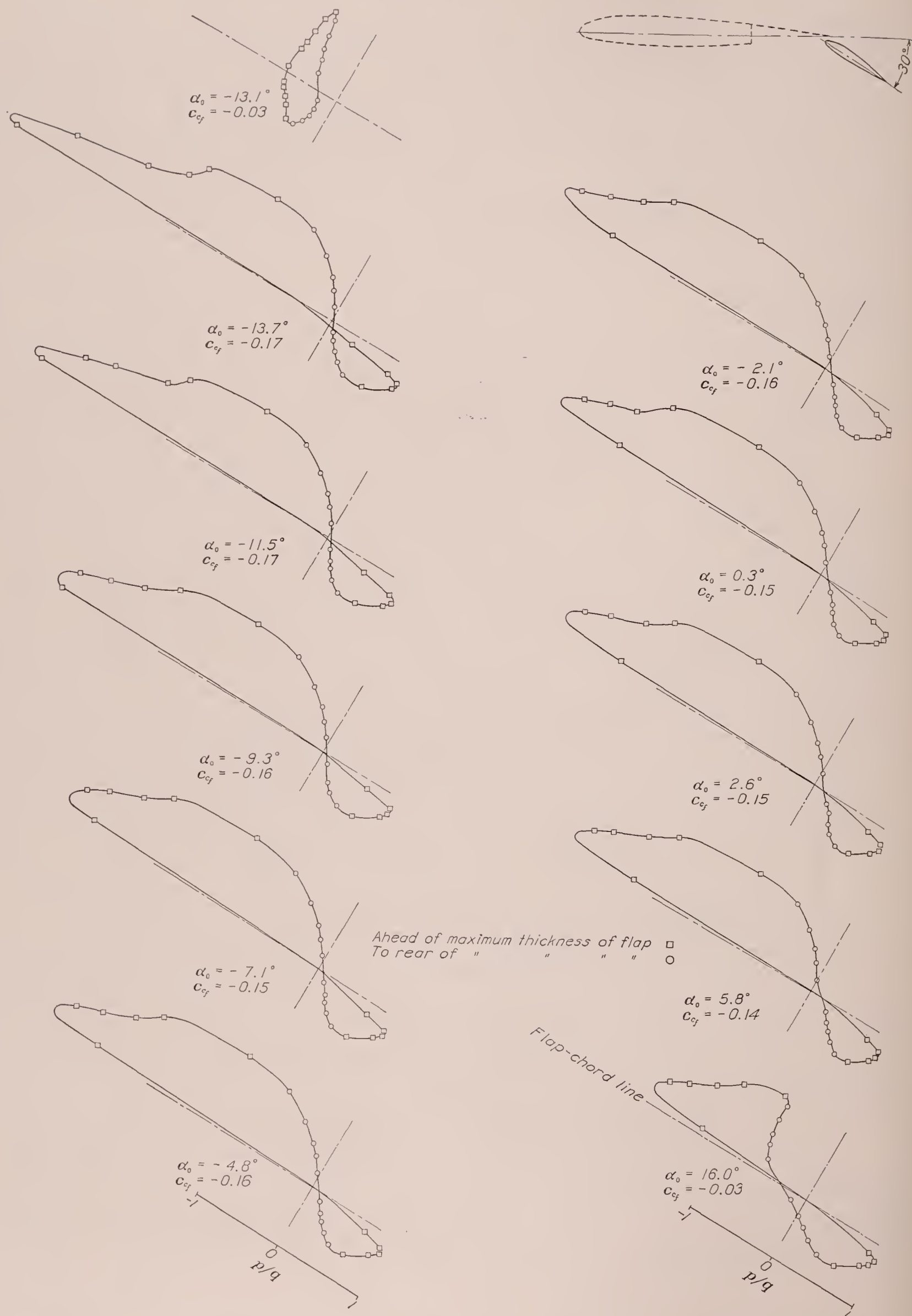
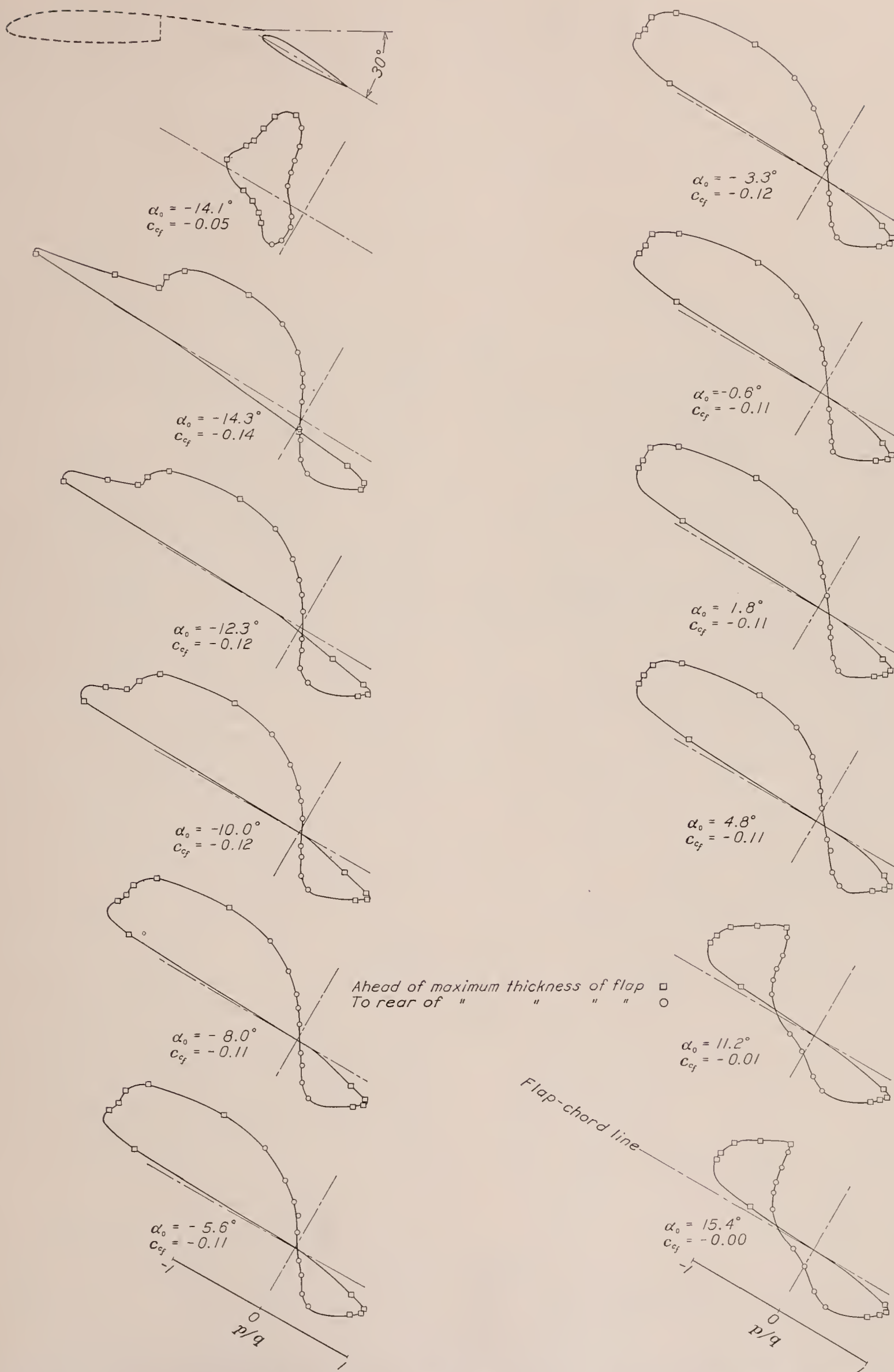


FIGURE 13.—Chord pressure distribution on the 0.30 c_w N. A. C. A. 23012 Fowler flap mounted on the N. A. C. A. 23012 airfoil. Flap deflected 30°.



The calculated results from the present tests were all corrected to infinite aspect ratio in accordance with methods given by Glauert (reference 8). A check on the theoretical correction is shown in figure 15, where the corrected results of the pressure-distribution tests are compared with force-test results (reference 9) for a 10- by 60-inch N. A. C. A. 23012 plain wing corrected to infinite aspect ratio by the usual methods.

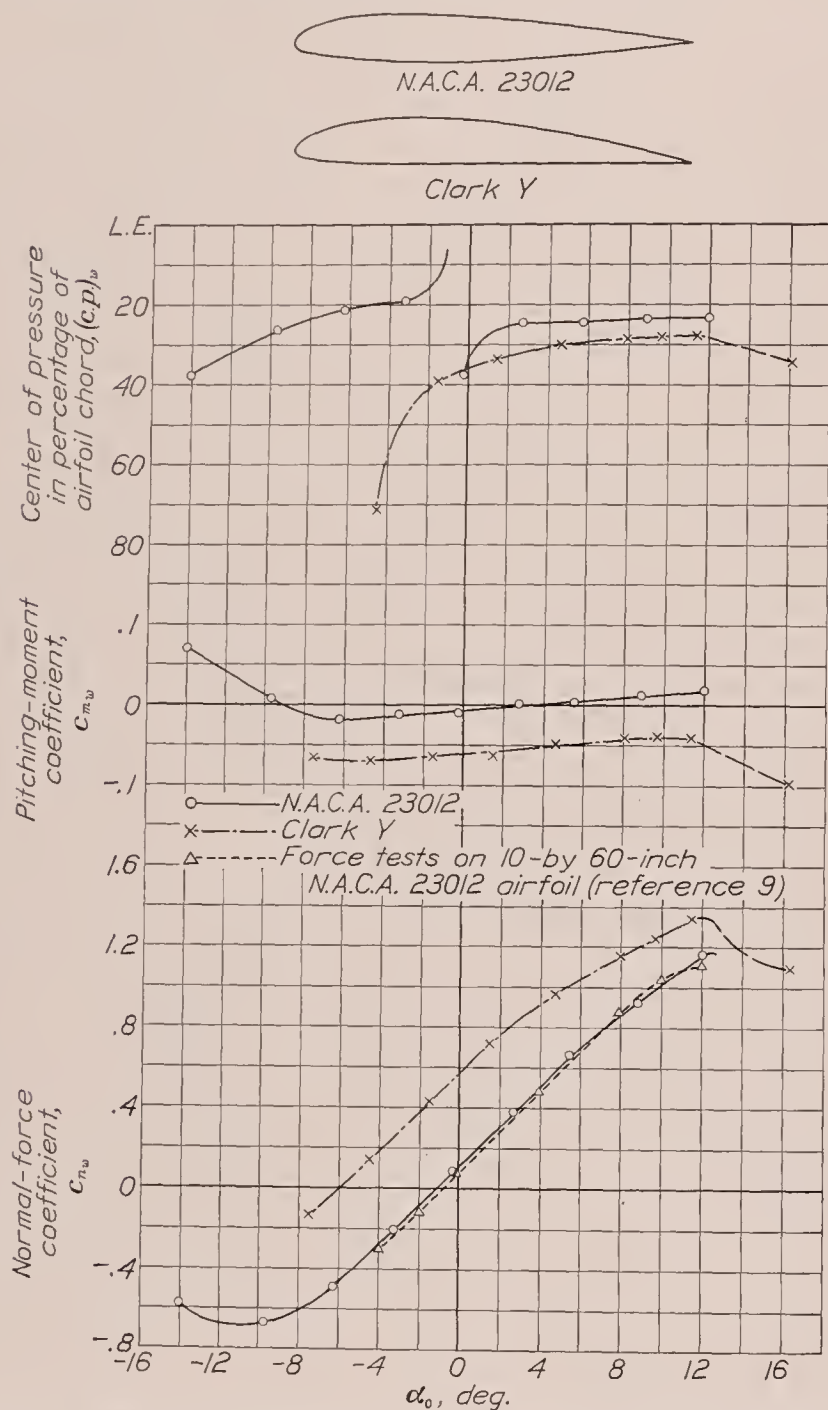


FIGURE 15.—Section characteristics of the N. A. C. A. 23012 and the Clark Y airfoils.

For the case of the pressure-distribution tests—

$$\alpha_0 = \alpha + \Delta\alpha$$

where

$$\Delta\alpha \text{ (deg.)} = -\left(0.25 \frac{c}{h} c_n\right) \times 57.3$$

c is the total chord.

h , height of the jet.

(The quantity c_n is substituted for C_L in the present correction and the substitution results in only a slight error because of the small difference in value between the two quantities.) Curves of the various calculated coefficients are given in figures 15 to 18.

PRECISION

As no air-flow alinement tests were made in either wind tunnel with the test arrangements used in the investigation, the absolute setting of the angle of attack may be slightly in error; the relative angles are, however, accurate to within $\pm 0.1^\circ$. The flaps were set to the specified angle to within $\pm 0.1^\circ$. The orifice pressures based on check tests in which the angles of attack were changed showed that they agreed to within ± 2 percent, with the exception of upper-surface pressures near the leading edges, which, at high angles of attack, checked within ± 5 percent. The dynamic pressure recorded on each diagram was accurate to within ± 0.25 percent for all tests. Pressure orifices were not sufficiently numerous to determine the peak pressures accurately at the airfoil nose, but this fact should not appreciably affect the results.

RESULTS AND DISCUSSION

SECTION PRESSURE DISTRIBUTION

The pressure-distribution diagrams (figs. 5 to 14) show the distribution of the air loads on the main airfoils and on the flaps and may be considered satisfactory for application to rib and flap design. The diagrams of forces normal to the chord shown in figures 7 to 10 are very similar to those for an airfoil with an external-airfoil flap (reference 4), indicating that the effects produced by the Fowler flap and by the external-airfoil flap are very much alike.

Comparison of the normal-pressure diagram for the N. A. C. A. 23012 airfoil and N. A. C. A. 23012 Fowler flap with that for the Clark Y airfoil and Clark Y Fowler flap at the same total lift (fig. 11) shows the effect of changes in airfoil section. Changing from a Clark Y to an N. A. C. A. 23012 section for both main airfoil and flap had the following effects: (1) The loads on the flap were reduced and (2) the adverse pressure gradients of the main airfoil, and thereby its tendency to stall, were increased.

Comparison of normal-pressure diagrams for the N. A. C. A. 23012 airfoil with various sizes of N. A. C. A. 23012 Fowler flap (fig. 12) shows the effect of changing the flap chord for a given lift of the combination. Increasing the flap chord had the following effects: (1) The portion of the load carried by the flap was increased; and (2) the adverse pressure gradients of the main airfoil were decreased so that higher lifts could be obtained before stalling.

The chord pressure diagrams for the 0.30 c_w and 0.40 c_w Fowler flaps (figs. 13 and 14) were included because it was thought that relatively large forces existed which acted in a direction to retract the flap from its maximum-lift setting. As indicated by these diagrams, the negative component overbalances the positive for practically all of the arrangements tested, so that the total chord pressure force is directed forward. This force, however,

does not include the skin-friction forces, which also act nearly parallel to the chord and in such a way as to increase the magnitude of the total chord force if positive or to decrease it if negative.

Fowler flap gives a higher maximum lift than the N. A. C. A. 23012 airfoil with N. A. C. A. 23012 Fowler flap (fig. 16). This fact is partly accounted for, however, by the higher maximum lift of the plain Clark Y

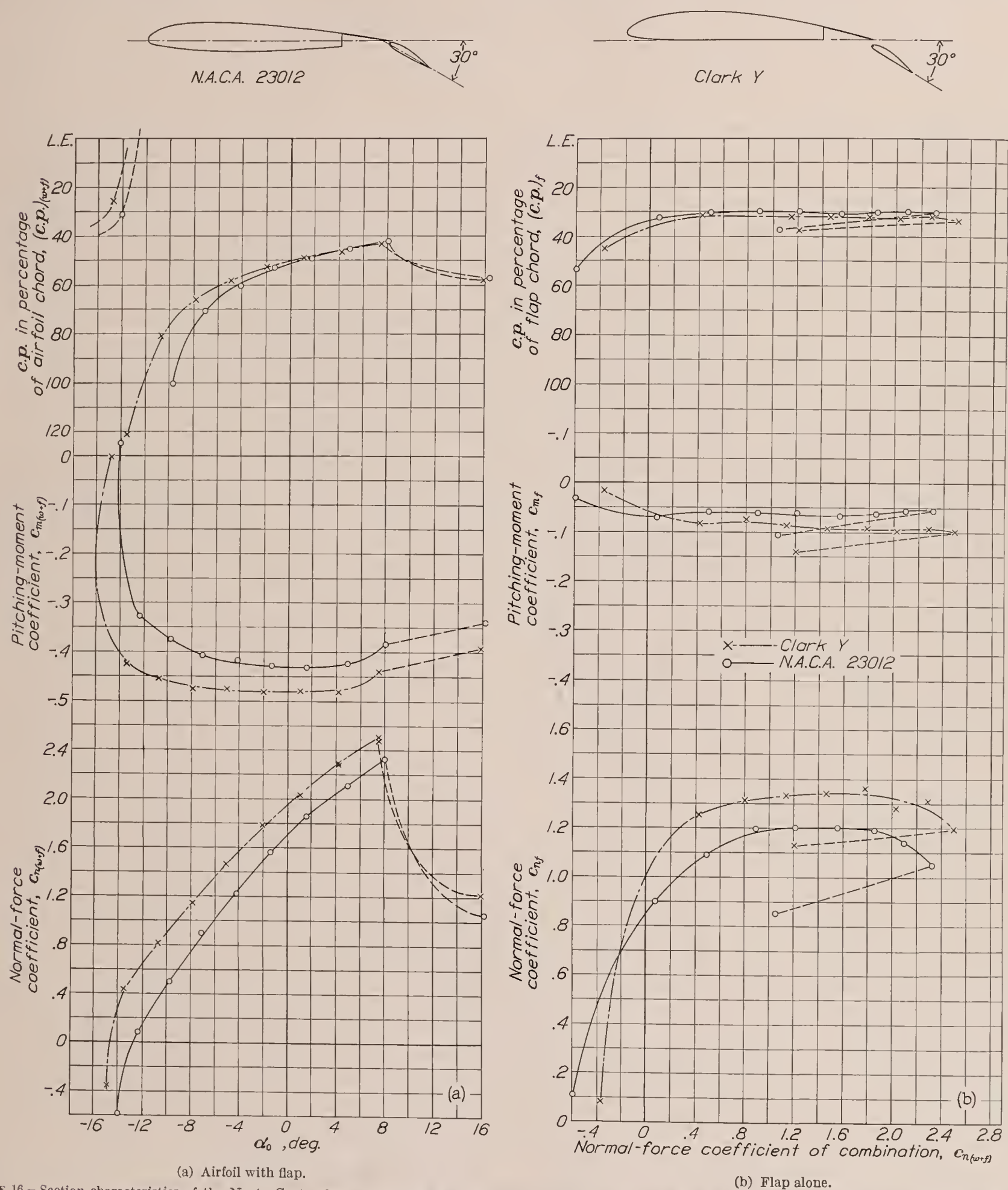


FIGURE 16.—Section characteristics of the N. A. C. A. 23012 airfoil with the $0.20c_w$ N. A. C. A. 23012 Fowler flap and of the Clark Y airfoil with the $0.20c_w$ Clark Y Fowler flap. Flaps deflected 30° .

SECTION LOADS AND MOMENTS

Pressure-distribution results.—The airfoil and flap section coefficients are given in figures 15 to 18. It will be noted that the Clark Y airfoil with Clark Y

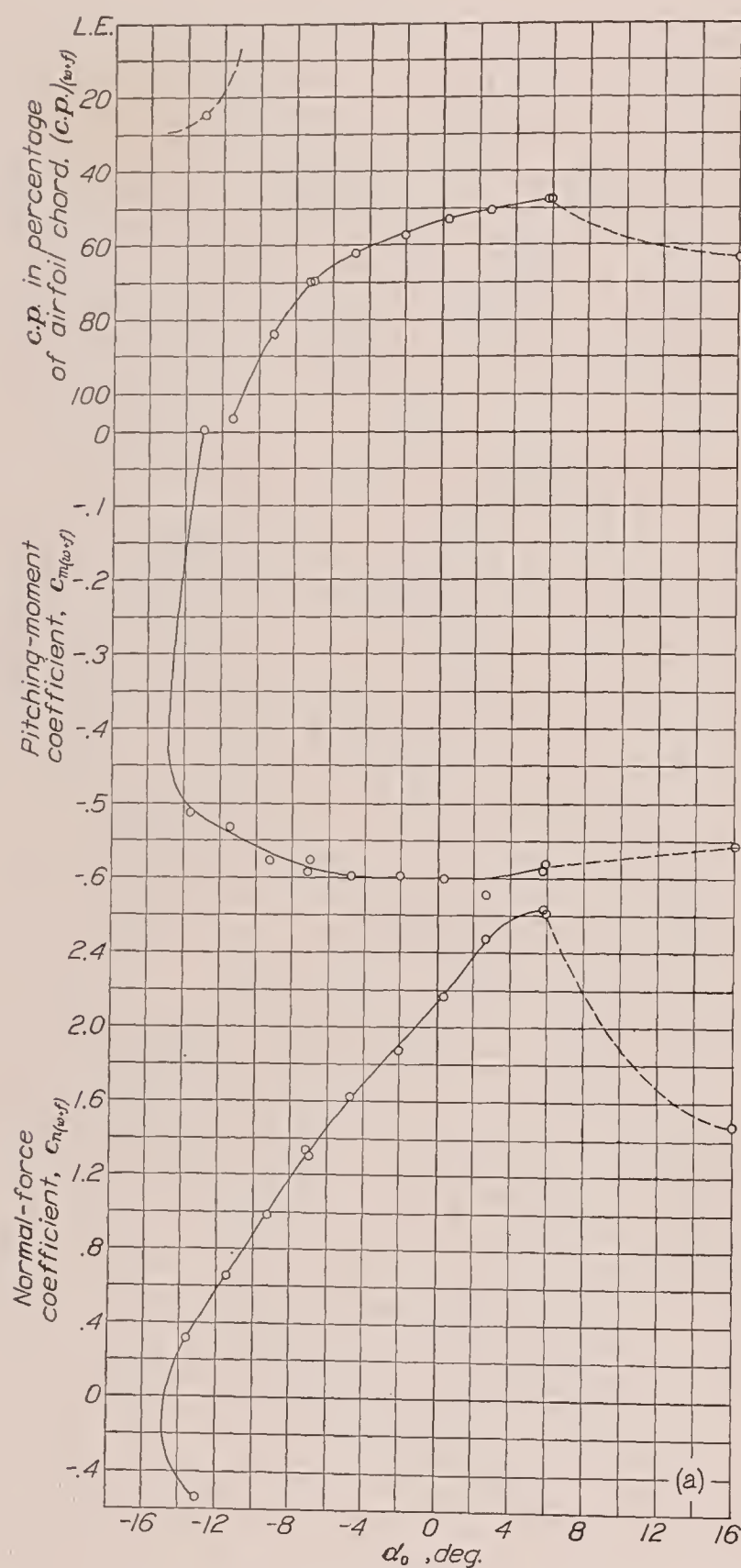
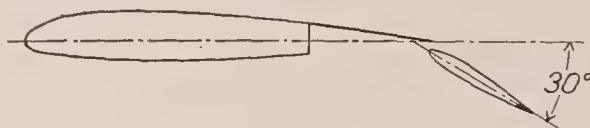
airfoil at the Reynolds Numbers of the tests, the increment in maximum lift due to the flap being approximately the same with either airfoil combination. In addition, the normal-force coefficients of the Clark

Y Fowler flap are somewhat higher than those of the N. A. C. A. 23012 flap.

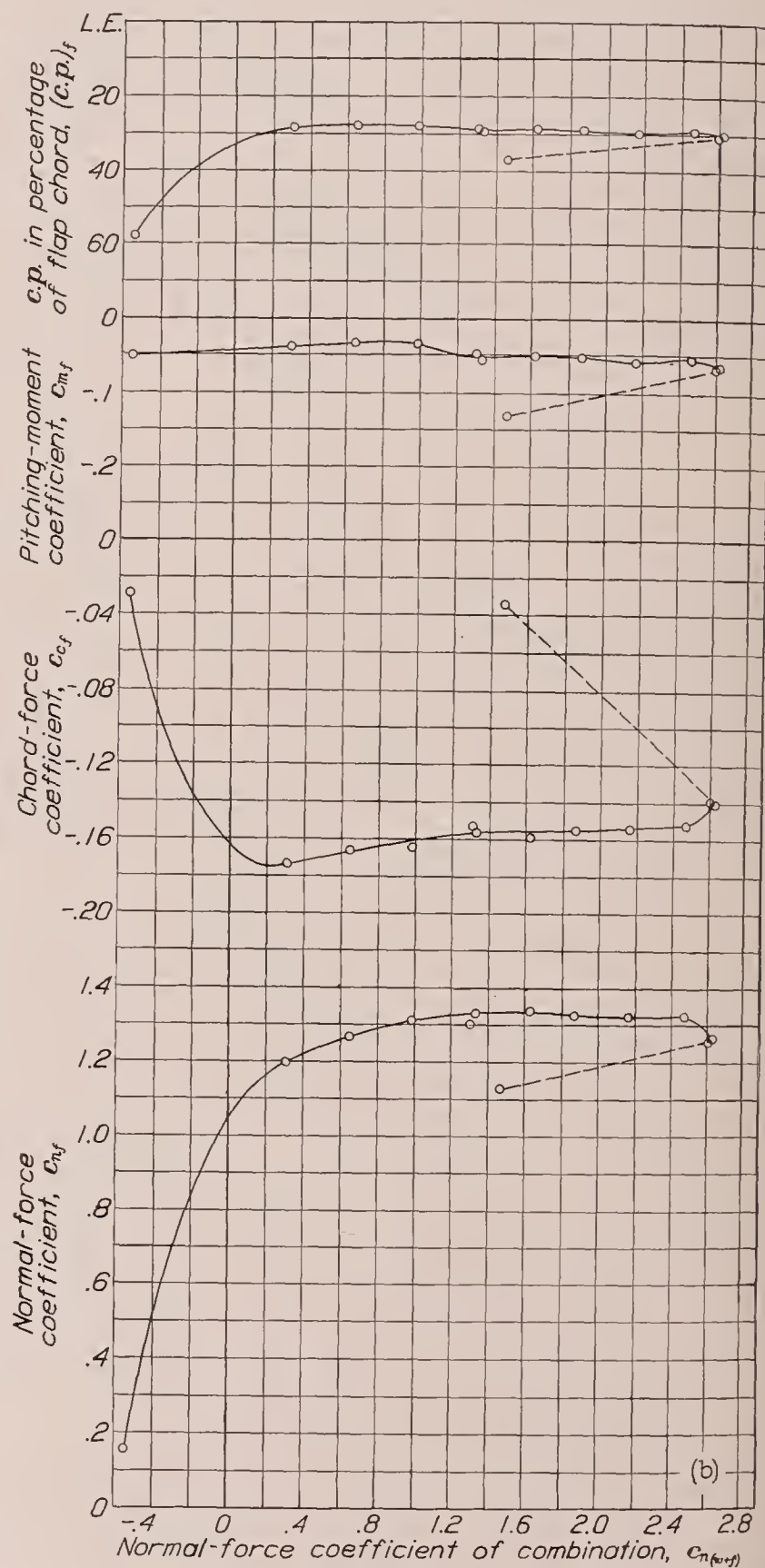
In all the arrangements investigated, the flap loads build up rapidly at relatively low lifts of the combina-

airfoil flap (reference 4) and also for simple split flaps (references 10 and 11).

The chord-force coefficients of the Fowler flaps (figs. 17 and 18) are all negative in sign; that is, the



(a) Airfoil with flap.



(b) Flap alone.

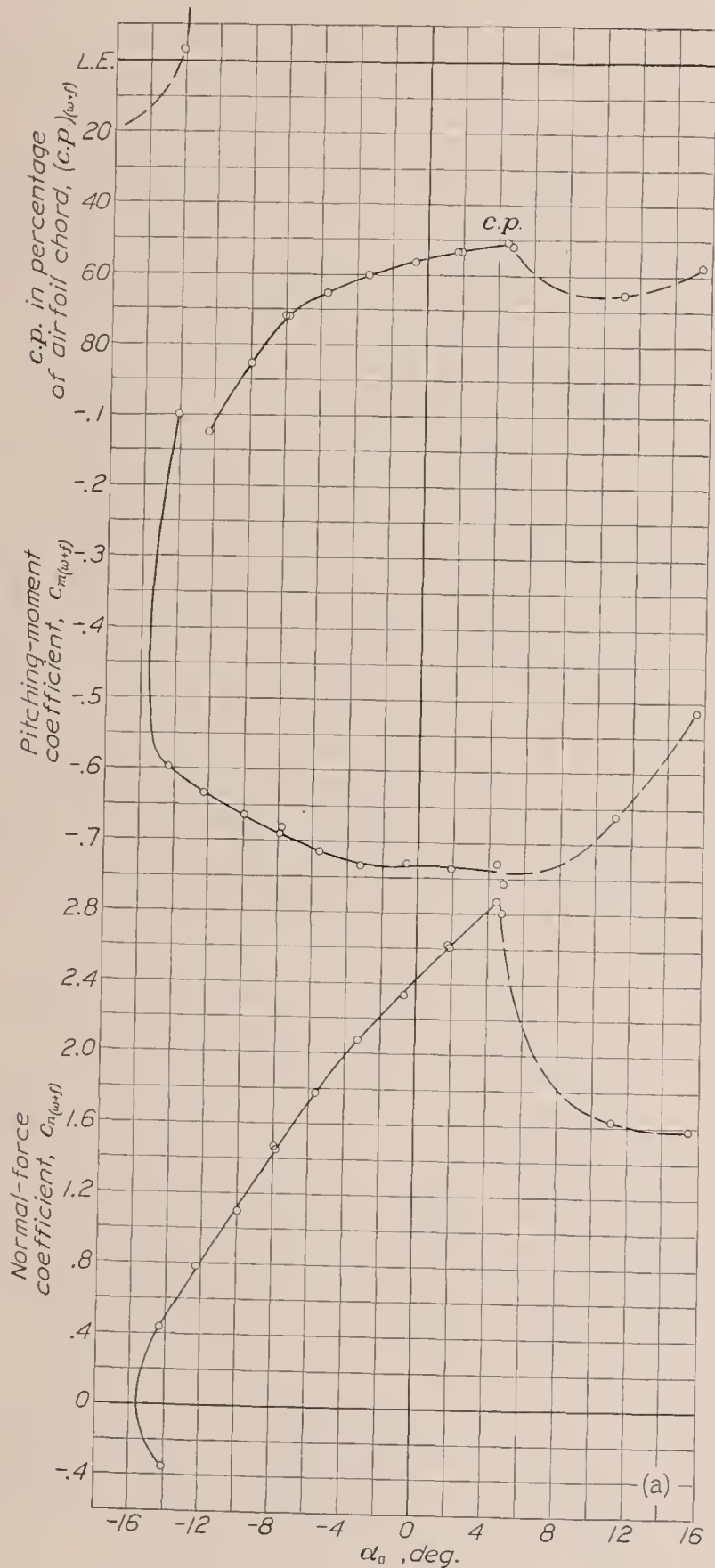
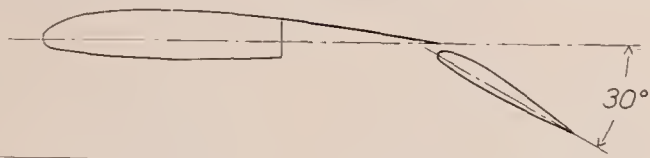
FIGURE 17.—Section characteristics of the N. A. C. A. 23012 airfoil with the 0.30c_w N. A. C. A. 23012 Fowler flap. Flap deflected 30°.

tion, but the normal-force coefficients do not differ greatly for the three sizes of N. A. C. A. 23012 Fowler flap. The range of the maximum values of the Fowler flap normal-force coefficient is from 1.20 to 1.33, which approximates the maximum values for the external-

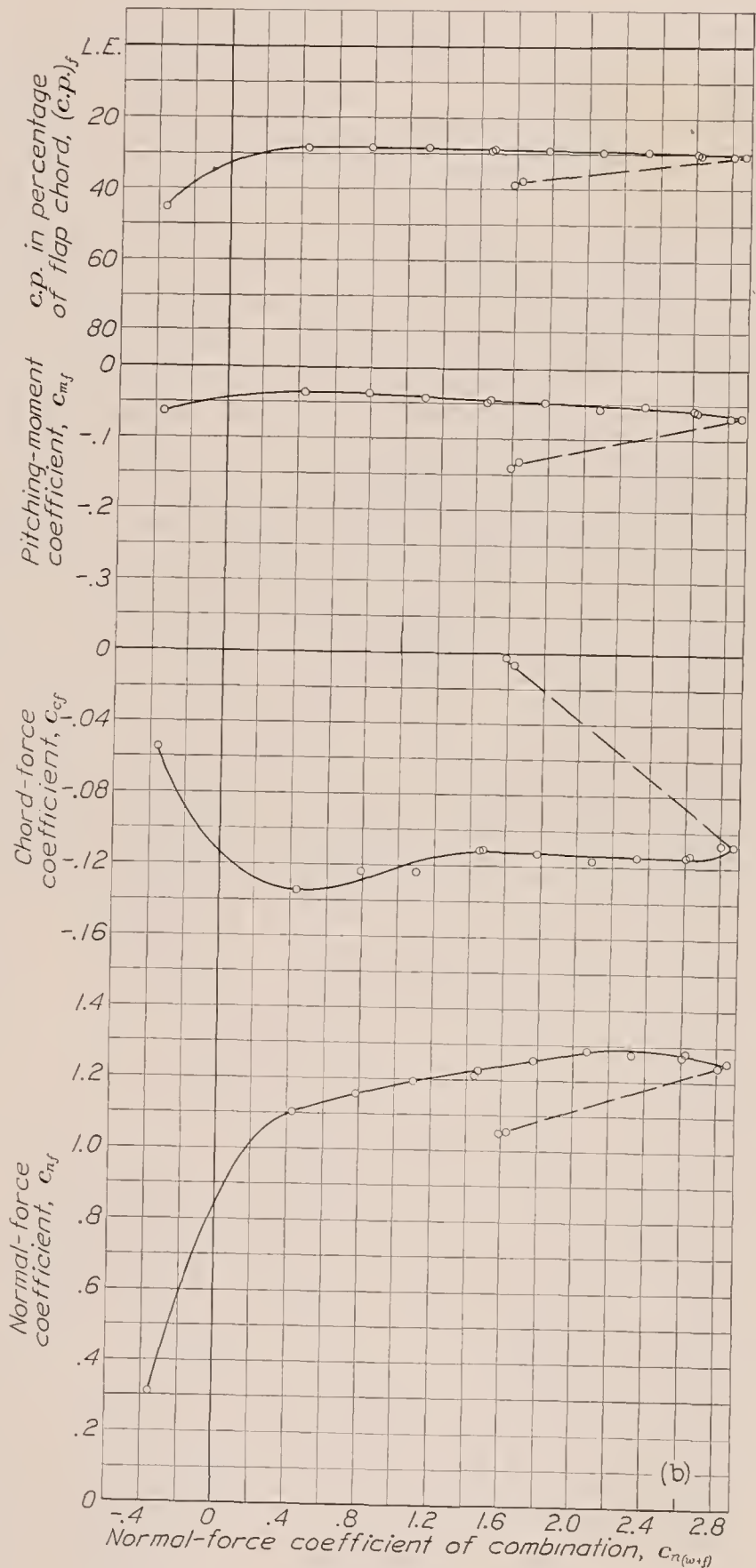
pressure forces parallel to the chord are directed forward along the chord. The magnitudes of these forces are relatively small and, as previously mentioned, they would be decreased by the skin-friction forces that have not been included.

Comparison with force-test measurements of flap loads.—A comparison of some loads on Fowler flaps obtained from force-test measurements in an earlier investigation (reference 1) with those from the present

pendently of the main airfoil at the position and angle for maximum lift and then measuring the forces on the airfoil alone mounted on the balance in the presence of the flap. The flap loads were then computed by



(a) Airfoil with flap.



(b) Flap alone.

FIGURE 18.—Section characteristics of the N. A. C. A. 23012 airfoil with the 0.40c_w N. A. C. A. 23012 Fowler flap. Flap deflected 30°.

pressure-distribution measurements indicates that a serious disagreement exists between the two. In the case of the force tests, air loads acting on the Fowler flaps were determined by supporting the flaps inde-

pendently of the main airfoil at the position and angle for maximum lift and then measuring the forces on the airfoil alone mounted on the balance in the presence of the flap. The flap loads were then computed by

deducting the forces on the main airfoil in the presence of the flap from those on the main airfoil with the flap attached.

The disagreement between the results from the two

types of test has been found traceable to deflections of the model in the force tests (reference 1) resulting in displacement of the flap with respect to the main airfoil. The combination thus failed to develop the full lift coefficient available when set up for the flap-load tests, thereby resulting in the observation of small forces on the main airfoil with the flap separately supported. The resulting flap loads, calculated as previously described, were consequently considerably exaggerated. The present pressure-distribution results, however, are believed reliable in view of the test methods and the rigid models used in the investigation and should therefore be considered as superseding the flap-load data given in reference 1.

CONCLUSIONS

1. The pressure-distribution tests show that the effect of increasing the chord of the Fowler flap, for a given lift of combined main airfoil and flap, was to increase the portion of the total load carried by the flap and to decrease the adverse pressure gradients of the main airfoil and thereby its tendency to stall.

2. The maximum values of normal-force coefficient of the Fowler flap are much smaller than previously indicated and are approximately the same as those of the external-airfoil flap and of the simple split flap.

LANGLEY MEMORIAL AERONAUTICAL LABORATORY,
NATIONAL ADVISORY COMMITTEE FOR AERONAUTICS,
LANGLEY FIELD, VA., *November 24, 1937.*

REFERENCES

1. Platt, Robert C.: Aerodynamic Characteristics of a Wing with Fowler Flaps Including Flap Loads, Downwash, and Calculated Effect on Take-Off. T. R. No. 534, N. A. C. A., 1935.
2. Weick, Fred E., and Platt, Robert C.: Wind-Tunnel Tests of the Fowler Variable-Area Wing. T. N. No. 419, N. A. C. A., 1932.
3. Weick, Fred E., and Platt, Robert C.: Wind-Tunnel Tests on Model Wing with Fowler Flap and Specially Developed Leading-Edge Slot. T. N. No. 459, N. A. C. A., 1933.
4. Wenzinger, Carl J.: Pressure Distribution over an N. A. C. A. 23012 Airfoil with an N. A. C. A. 23012 External-Airfoil Flap. T. R. No. 614, N. A. C. A., 1938.
5. Harris, Thomas A.: The 7 by 10 Foot Wind Tunnel of the National Advisory Committee for Aeronautics. T. R. No. 412, N. A. C. A., 1931.
6. Wenzinger, Carl J., and Harris, Thomas A.: The Vertical Wind Tunnel of the National Advisory Committee for Aeronautics. T. R. No. 387, N. A. C. A., 1931.
7. Platt, Robert C.: Turbulence Factors of N. A. C. A. Wind Tunnels as Determined by Sphere Tests. T. R. No. 558, N. A. C. A., 1936.
8. Glauert, H.: Wind Tunnel Interference on Wings, Bodies, and Airscrews. R. & M. No. 1566, British A. R. C., 1933.
9. Wenzinger, Carl J.: Wind-Tunnel Investigation of Ordinary and Split Flaps on Airfoils of Different Profile. T. R. No. 554, N. A. C. A., 1936.
10. Wenzinger, Carl J.: Wind-Tunnel Measurements of Air Loads on Split Flaps. T. N. No. 498, N. A. C. A., 1934.
11. Wenzinger, Carl J., and Harris, Thomas A.: Pressure Distribution over a Rectangular Airfoil with a Partial-Span Split Flap. T. R. No. 571, N. A. C. A., 1936.

TABLE I

ORDINATES AND ORIFICE LOCATIONS OF AIRFOIL AND FOWLER FLAP COMBINATIONS TESTED

<p>(a)</p> <p>Clark Y airfoil: Section ordinates in percent of chord</p> <table> <tr> <th>Station</th><th>Upper</th><th>Lower</th></tr> <tr><td>0</td><td>3.60</td><td>3.60</td></tr> <tr><td>1.25</td><td>5.38</td><td>1.86</td></tr> <tr><td>2.5</td><td>6.43</td><td>1.42</td></tr> <tr><td>5</td><td>7.83</td><td>.91</td></tr> <tr><td>7.5</td><td>8.79</td><td>.59</td></tr> <tr><td>10</td><td>9.56</td><td>.39</td></tr> <tr><td>15</td><td>10.63</td><td>.12</td></tr> <tr><td>20</td><td>11.32</td><td>.01</td></tr> <tr><td>30</td><td>11.68</td><td>.00</td></tr> <tr><td>40</td><td>11.37</td><td>.00</td></tr> <tr><td>50</td><td>10.49</td><td>.00</td></tr> <tr><td>60</td><td>9.13</td><td>.00</td></tr> <tr><td>70</td><td>7.34</td><td>.00</td></tr> <tr><td>80</td><td>5.21</td><td>.00</td></tr> <tr><td>90</td><td>2.79</td><td>.00</td></tr> <tr><td>95</td><td>1.50</td><td>.00</td></tr> <tr><td>100</td><td>.12</td><td>.00</td></tr> </table>	Station	Upper	Lower	0	3.60	3.60	1.25	5.38	1.86	2.5	6.43	1.42	5	7.83	.91	7.5	8.79	.59	10	9.56	.39	15	10.63	.12	20	11.32	.01	30	11.68	.00	40	11.37	.00	50	10.49	.00	60	9.13	.00	70	7.34	.00	80	5.21	.00	90	2.79	.00	95	1.50	.00	100	.12	.00	<p>(b)</p> <p>Clark Y 20-inch airfoil, plain and with 0.20c_w flap: Orifice locations on surfaces in percent of chord from leading edge</p> <table> <tr> <th>Orifice</th><th>Upper</th><th>Lower</th></tr> <tr><td>0</td><td>0.00</td><td>0.00</td></tr> <tr><td>1</td><td>2.50</td><td>2.50</td></tr> <tr><td>2</td><td>5.00</td><td>5.00</td></tr> <tr><td>3</td><td>10.00</td><td>10.00</td></tr> <tr><td>4</td><td>25.00</td><td>25.00</td></tr> <tr><td>5</td><td>45.00</td><td>45.00</td></tr> <tr><td>6</td><td>62.50</td><td>62.50</td></tr> <tr><td>7</td><td>75.00</td><td>75.00</td></tr> <tr><td>8</td><td>85.00</td><td>85.00</td></tr> <tr><td>9</td><td>90.00</td><td>90.00</td></tr> <tr><td>10</td><td>95.00</td><td>95.00</td></tr> <tr><td>11</td><td>99.00</td><td>99.00</td></tr> </table>	Orifice	Upper	Lower	0	0.00	0.00	1	2.50	2.50	2	5.00	5.00	3	10.00	10.00	4	25.00	25.00	5	45.00	45.00	6	62.50	62.50	7	75.00	75.00	8	85.00	85.00	9	90.00	90.00	10	95.00	95.00	11	99.00	99.00	<p>(c)</p> <p>Clark Y 0.20c_w flap: Orifice locations on surfaces in percent of flap chord from leading edge</p> <table> <tr> <th>Orifice</th><th>Upper</th><th>Lower</th></tr> <tr><td>0</td><td>0.00</td><td>0.00</td></tr> <tr><td>1</td><td>2.50</td><td>2.50</td></tr> <tr><td>2</td><td>5.00</td><td>5.00</td></tr> <tr><td>3</td><td>10.00</td><td>10.00</td></tr> <tr><td>4</td><td>25.00</td><td>25.00</td></tr> <tr><td>5</td><td>45.00</td><td>45.00</td></tr> <tr><td>6</td><td>62.50</td><td>62.50</td></tr> <tr><td>7</td><td>75.00</td><td>75.00</td></tr> <tr><td>8</td><td>82.50</td><td>82.50</td></tr> <tr><td>9</td><td>92.50</td><td>92.50</td></tr> </table>	Orifice	Upper	Lower	0	0.00	0.00	1	2.50	2.50	2	5.00	5.00	3	10.00	10.00	4	25.00	25.00	5	45.00	45.00	6	62.50	62.50	7	75.00	75.00	8	82.50	82.50	9	92.50	92.50			
Station	Upper	Lower																																																																																																																																	
0	3.60	3.60																																																																																																																																	
1.25	5.38	1.86																																																																																																																																	
2.5	6.43	1.42																																																																																																																																	
5	7.83	.91																																																																																																																																	
7.5	8.79	.59																																																																																																																																	
10	9.56	.39																																																																																																																																	
15	10.63	.12																																																																																																																																	
20	11.32	.01																																																																																																																																	
30	11.68	.00																																																																																																																																	
40	11.37	.00																																																																																																																																	
50	10.49	.00																																																																																																																																	
60	9.13	.00																																																																																																																																	
70	7.34	.00																																																																																																																																	
80	5.21	.00																																																																																																																																	
90	2.79	.00																																																																																																																																	
95	1.50	.00																																																																																																																																	
100	.12	.00																																																																																																																																	
Orifice	Upper	Lower																																																																																																																																	
0	0.00	0.00																																																																																																																																	
1	2.50	2.50																																																																																																																																	
2	5.00	5.00																																																																																																																																	
3	10.00	10.00																																																																																																																																	
4	25.00	25.00																																																																																																																																	
5	45.00	45.00																																																																																																																																	
6	62.50	62.50																																																																																																																																	
7	75.00	75.00																																																																																																																																	
8	85.00	85.00																																																																																																																																	
9	90.00	90.00																																																																																																																																	
10	95.00	95.00																																																																																																																																	
11	99.00	99.00																																																																																																																																	
Orifice	Upper	Lower																																																																																																																																	
0	0.00	0.00																																																																																																																																	
1	2.50	2.50																																																																																																																																	
2	5.00	5.00																																																																																																																																	
3	10.00	10.00																																																																																																																																	
4	25.00	25.00																																																																																																																																	
5	45.00	45.00																																																																																																																																	
6	62.50	62.50																																																																																																																																	
7	75.00	75.00																																																																																																																																	
8	82.50	82.50																																																																																																																																	
9	92.50	92.50																																																																																																																																	
<p>(d)</p> <p>N. A. C. A. 23012 airfoil: Section ordinates in percent of chord</p> <table> <tr> <th>Station</th><th>Upper</th><th>Lower</th></tr> <tr><td>0</td><td></td><td></td></tr> <tr><td>1.25</td><td>2.67</td><td>-1.23</td></tr> <tr><td>2.5</td><td>3.61</td><td>-1.71</td></tr> <tr><td>5</td><td>4.91</td><td>-2.26</td></tr> <tr><td>7.5</td><td>5.80</td><td>-2.61</td></tr> <tr><td>10</td><td>6.43</td><td>-2.92</td></tr> <tr><td>15</td><td>7.19</td><td>-3.50</td></tr> <tr><td>20</td><td>7.50</td><td>-3.97</td></tr> <tr><td>25</td><td>7.60</td><td>-4.28</td></tr> <tr><td>30</td><td>7.55</td><td>-4.46</td></tr> <tr><td>40</td><td>7.14</td><td>-4.48</td></tr> <tr><td>50</td><td>6.41</td><td>-4.17</td></tr> <tr><td>60</td><td>5.47</td><td>-3.67</td></tr> <tr><td>70</td><td>4.36</td><td>-3.00</td></tr> <tr><td>80</td><td>3.08</td><td>-2.16</td></tr> <tr><td>90</td><td>1.68</td><td>-1.23</td></tr> <tr><td>95</td><td>.92</td><td>-.70</td></tr> <tr><td>100</td><td>.13</td><td>-.13</td></tr> </table> <p>L. E. radius=1.58 Slope through zero=0.305</p>	Station	Upper	Lower	0			1.25	2.67	-1.23	2.5	3.61	-1.71	5	4.91	-2.26	7.5	5.80	-2.61	10	6.43	-2.92	15	7.19	-3.50	20	7.50	-3.97	25	7.60	-4.28	30	7.55	-4.46	40	7.14	-4.48	50	6.41	-4.17	60	5.47	-3.67	70	4.36	-3.00	80	3.08	-2.16	90	1.68	-1.23	95	.92	-.70	100	.13	-.13	<p>(e)</p> <p>N. A. C. A. 23012 20-inch plain airfoil: Orifice locations on surfaces in percent of chord from leading edge</p> <table> <tr> <th>Orifice</th><th>Upper</th><th>Lower</th></tr> <tr><td>0</td><td>0.00</td><td>0.00</td></tr> <tr><td>1</td><td>2.40</td><td>2.40</td></tr> <tr><td>2</td><td>5.00</td><td>5.00</td></tr> <tr><td>3</td><td>10.00</td><td>10.00</td></tr> <tr><td>4</td><td>25.00</td><td>25.00</td></tr> <tr><td>5</td><td>45.00</td><td>45.00</td></tr> <tr><td>6</td><td>62.50</td><td>62.50</td></tr> <tr><td>7</td><td>75.00</td><td>75.00</td></tr> <tr><td>8</td><td>82.50</td><td>82.50</td></tr> <tr><td>9</td><td>88.10</td><td>88.10</td></tr> <tr><td>10</td><td>93.60</td><td>93.60</td></tr> <tr><td>11</td><td>98.60</td><td>98.60</td></tr> </table>	Orifice	Upper	Lower	0	0.00	0.00	1	2.40	2.40	2	5.00	5.00	3	10.00	10.00	4	25.00	25.00	5	45.00	45.00	6	62.50	62.50	7	75.00	75.00	8	82.50	82.50	9	88.10	88.10	10	93.60	93.60	11	98.60	98.60	<p>(f)</p> <p>N. A. C. A. 23012 0.20c_w flap: Orifice locations on surfaces in percent of flap chord from leading edge</p> <table> <tr> <th>Orifice</th><th>Upper</th><th>Lower</th></tr> <tr><td>0</td><td>0.00</td><td>0.00</td></tr> <tr><td>1</td><td>2.50</td><td>2.50</td></tr> <tr><td>2</td><td>5.00</td><td>5.00</td></tr> <tr><td>3</td><td>10.00</td><td>10.00</td></tr> <tr><td>4</td><td>25.00</td><td>25.00</td></tr> <tr><td>5</td><td>45.00</td><td>45.00</td></tr> <tr><td>6</td><td>62.50</td><td>62.50</td></tr> <tr><td>7</td><td>75.00</td><td>75.00</td></tr> <tr><td>8</td><td>82.50</td><td>82.50</td></tr> <tr><td>9</td><td>92.50</td><td>92.50</td></tr> </table>	Orifice	Upper	Lower	0	0.00	0.00	1	2.50	2.50	2	5.00	5.00	3	10.00	10.00	4	25.00	25.00	5	45.00	45.00	6	62.50	62.50	7	75.00	75.00	8	82.50	82.50	9	92.50	92.50
Station	Upper	Lower																																																																																																																																	
0																																																																																																																																			
1.25	2.67	-1.23																																																																																																																																	
2.5	3.61	-1.71																																																																																																																																	
5	4.91	-2.26																																																																																																																																	
7.5	5.80	-2.61																																																																																																																																	
10	6.43	-2.92																																																																																																																																	
15	7.19	-3.50																																																																																																																																	
20	7.50	-3.97																																																																																																																																	
25	7.60	-4.28																																																																																																																																	
30	7.55	-4.46																																																																																																																																	
40	7.14	-4.48																																																																																																																																	
50	6.41	-4.17																																																																																																																																	
60	5.47	-3.67																																																																																																																																	
70	4.36	-3.00																																																																																																																																	
80	3.08	-2.16																																																																																																																																	
90	1.68	-1.23																																																																																																																																	
95	.92	-.70																																																																																																																																	
100	.13	-.13																																																																																																																																	
Orifice	Upper	Lower																																																																																																																																	
0	0.00	0.00																																																																																																																																	
1	2.40	2.40																																																																																																																																	
2	5.00	5.00																																																																																																																																	
3	10.00	10.00																																																																																																																																	
4	25.00	25.00																																																																																																																																	
5	45.00	45.00																																																																																																																																	
6	62.50	62.50																																																																																																																																	
7	75.00	75.00																																																																																																																																	
8	82.50	82.50																																																																																																																																	
9	88.10	88.10																																																																																																																																	
10	93.60	93.60																																																																																																																																	
11	98.60	98.60																																																																																																																																	
Orifice	Upper	Lower																																																																																																																																	
0	0.00	0.00																																																																																																																																	
1	2.50	2.50																																																																																																																																	
2	5.00	5.00																																																																																																																																	
3	10.00	10.00																																																																																																																																	
4	25.00	25.00																																																																																																																																	
5	45.00	45.00																																																																																																																																	
6	62.50	62.50																																																																																																																																	
7	75.00	75.00																																																																																																																																	
8	82.50	82.50																																																																																																																																	
9	92.50	92.50																																																																																																																																	
<p>(g)</p> <p>N. A. C. A. 23012 20-inch airfoil with 0.20c_w and 0.30c_w flaps: Orifice locations on surfaces in percent of chord from leading edge</p> <table> <tr> <th>Orifice</th><th>Upper</th><th>Lower</th></tr> <tr><td>0</td><td>0.00</td><td>0.00</td></tr> <tr><td>1</td><td>2.40</td><td>2.40</td></tr> <tr><td>2</td><td>5.00</td><td>5.00</td></tr> <tr><td>3</td><td>10.00</td><td>10.00</td></tr> <tr><td>4</td><td>25.00</td><td>25.00</td></tr> <tr><td>5</td><td>45.00</td><td>45.00</td></tr> <tr><td>5a</td><td>none</td><td>58.80</td></tr> <tr><td>6</td><td>62.50</td><td>62.50</td></tr> <tr><td>6a</td><td>none</td><td>68.80</td></tr> <tr><td>7</td><td>75.00</td><td>75.00</td></tr> <tr><td>8</td><td>82.50</td><td>82.50</td></tr> <tr><td>9</td><td>88.10</td><td>88.10</td></tr> <tr><td>10</td><td>93.60</td><td>93.60</td></tr> <tr><td>11</td><td>98.60</td><td>98.60</td></tr> </table>	Orifice	Upper	Lower	0	0.00	0.00	1	2.40	2.40	2	5.00	5.00	3	10.00	10.00	4	25.00	25.00	5	45.00	45.00	5a	none	58.80	6	62.50	62.50	6a	none	68.80	7	75.00	75.00	8	82.50	82.50	9	88.10	88.10	10	93.60	93.60	11	98.60	98.60	<p>(h)</p> <p>N. A. C. A. 23012 20-inch airfoil with 0.40c_w flap: Orifice locations on surfaces in percent of chord from leading edge</p> <table> <tr> <th>Orifice</th><th>Upper</th><th>Lower</th></tr> <tr><td>0</td><td>0.00</td><td>0.00</td></tr> <tr><td>1</td><td>2.40</td><td>2.40</td></tr> <tr><td>2</td><td>5.00</td><td>5.00</td></tr> <tr><td>3</td><td>10.00</td><td>10.00</td></tr> <tr><td>4</td><td>25.00</td><td>25.00</td></tr> <tr><td>5</td><td>45.00</td><td>45.00</td></tr> <tr><td>5a</td><td>none</td><td>58.80</td></tr> <tr><td>6</td><td>62.50</td><td>62.50</td></tr> <tr><td>7</td><td>75.00</td><td>75.00</td></tr> <tr><td>8</td><td>82.50</td><td>82.50</td></tr> <tr><td>9</td><td>88.10</td><td>88.10</td></tr> <tr><td>10</td><td>93.60</td><td>93.60</td></tr> <tr><td>11</td><td>98.60</td><td>98.60</td></tr> </table>	Orifice	Upper	Lower	0	0.00	0.00	1	2.40	2.40	2	5.00	5.00	3	10.00	10.00	4	25.00	25.00	5	45.00	45.00	5a	none	58.80	6	62.50	62.50	7	75.00	75.00	8	82.50	82.50	9	88.10	88.10	10	93.60	93.60	11	98.60	98.60	<p>(i)</p> <p>N. A. C. A. 23012 0.30c_w and 0.40c_w flaps: Orifice locations on surfaces in percent of flap chord from leading edge</p> <table> <tr> <th>Orifice</th><th>Upper</th><th>Lower</th></tr> <tr><td>0</td><td>0.00</td><td>0.00</td></tr> <tr><td>1</td><td>1.20</td><td>1.20</td></tr> <tr><td>2</td><td>2.50</td><td>2.50</td></tr> <tr><td>3</td><td>5.00</td><td>5.00</td></tr> <tr><td>4</td><td>10.00</td><td>10.00</td></tr> <tr><td>5</td><td>25.00</td><td>25.00</td></tr> <tr><td>6</td><td>45.00</td><td>45.00</td></tr> <tr><td>7</td><td>62.50</td><td>62.50</td></tr> <tr><td>8</td><td>75.00</td><td>75.00</td></tr> <tr><td>9</td><td>82.50</td><td>82.50</td></tr> <tr><td>10</td><td>92.50</td><td>92.50</td></tr> </table>	Orifice	Upper	Lower	0	0.00	0.00	1	1.20	1.20	2	2.50	2.50	3	5.00	5.00	4	10.00	10.00	5	25.00	25.00	6	45.00	45.00	7	62.50	62.50	8	75.00	75.00	9	82.50	82.50	10	92.50	92.50						
Orifice	Upper	Lower																																																																																																																																	
0	0.00	0.00																																																																																																																																	
1	2.40	2.40																																																																																																																																	
2	5.00	5.00																																																																																																																																	
3	10.00	10.00																																																																																																																																	
4	25.00	25.00																																																																																																																																	
5	45.00	45.00																																																																																																																																	
5a	none	58.80																																																																																																																																	
6	62.50	62.50																																																																																																																																	
6a	none	68.80																																																																																																																																	
7	75.00	75.00																																																																																																																																	
8	82.50	82.50																																																																																																																																	
9	88.10	88.10																																																																																																																																	
10	93.60	93.60																																																																																																																																	
11	98.60	98.60																																																																																																																																	
Orifice	Upper	Lower																																																																																																																																	
0	0.00	0.00																																																																																																																																	
1	2.40	2.40																																																																																																																																	
2	5.00	5.00																																																																																																																																	
3	10.00	10.00																																																																																																																																	
4	25.00	25.00																																																																																																																																	
5	45.00	45.00																																																																																																																																	
5a	none	58.80																																																																																																																																	
6	62.50	62.50																																																																																																																																	
7	75.00	75.00																																																																																																																																	
8	82.50	82.50																																																																																																																																	
9	88.10	88.10																																																																																																																																	
10	93.60	93.60																																																																																																																																	
11	98.60	98.60																																																																																																																																	
Orifice	Upper	Lower																																																																																																																																	
0	0.00	0.00																																																																																																																																	
1	1.20	1.20																																																																																																																																	
2	2.50	2.50																																																																																																																																	
3	5.00	5.00																																																																																																																																	
4	10.00	10.00																																																																																																																																	
5	25.00	25.00																																																																																																																																	
6	45.00	45.00																																																																																																																																	
7	62.50	62.50																																																																																																																																	
8	75.00	75.00																																																																																																																																	
9	82.50	82.50																																																																																																																																	
10	92.50	92.50																																																																																																																																	

REPORT No. 621

COMPRESSIBLE FLOW ABOUT SYMMETRICAL JOUKOWSKI PROFILES

By CARL KAPLAN

SUMMARY

The method of Poggi is employed for the determination of the effects of compressibility upon the flow past an obstacle. A general expression for the velocity increment due to compressibility is obtained. This general result holds whatever the shape of the obstacle; but, in order to obtain the complete solution, it is necessary to know a certain Fourier expansion of the square of the velocity of flow past the obstacle. An application is made to the case of a symmetrical Joukowski profile with a sharp trailing edge, fixed in a stream of velocity v_0 at an arbitrary angle of attack and with the circulation determined by the Kutta condition. The results are obtained in a closed form and are exact insofar as the second approximation to the compressible flow is concerned, the first approximation being the result for the corresponding incompressible flow. Formulas for the lift and moment analogous to the Blasius formulas in incompressible flow are developed and are applied to thin symmetrical Joukowski profiles for small angles of attack.

Since actual experimental data for Joukowski profiles are lacking, the theoretical results are applied to a thin and a thick profile at zero angle of attack, and the velocity and pressure distributions are calculated and compared with those for the corresponding incompressible cases. The critical values for the ratio of the stream velocity v_0 to the velocity of sound in the stream c_0 , corresponding to the attainment of the local velocity of sound c by the fluid on the surface of the airfoils, are also obtained.

INTRODUCTION

When a compressible fluid streams past a fixed body with a velocity small enough so that nowhere in the fluid is the local velocity of sound exceeded, the flow may be represented by a velocity potential. The effect of compressibility is to distort the streamline picture associated with the corresponding incompressible flow. This distortion has been calculated by Janzen (reference 1) and Rayleigh (reference 2) for circular cylinders and spheres and recently for elliptical cylinders by Hooker (reference 3). The methods used by these authors, however, are not feasible for the determination of the flow about obstacles other than the simple ones mentioned. On the other hand, a method introduced

by Poggi (reference 4) may be used in determining the flow about shapes resembling airfoil profiles.

The method due to Poggi is as follows: When the fluid is compressible, the equation of continuity may be written as

$$\frac{\partial v_x}{\partial x} + \frac{\partial v_y}{\partial y} = -\frac{1}{\rho} \frac{D\rho}{Dt} \quad (1)$$

where the symbol D/Dt denotes, as usual, the operator $\frac{\partial}{\partial t} + v_x \frac{\partial}{\partial x} + v_y \frac{\partial}{\partial y}$; v_x , v_y , the fluid velocity components; and ρ , the variable density of the fluid.

This divergence will introduce extra terms in the expressions for the velocity components, the divergence at an element $dxdy$ being equivalent to a simple source

of strength $-\frac{1}{2\pi} \frac{D\rho}{\rho Dt} dxdy$. Poggi thus replaces the compressible flow by an incompressible flow due to a suitable distribution of sources throughout the region of flow.

If the motion of the fluid is steady, then the equation of continuity and Euler's differential equations of motion become:

$$\left. \begin{aligned} \frac{\partial v_x}{\partial x} + \frac{\partial v_y}{\partial y} &= -\frac{v_x}{\rho} \frac{\partial \rho}{\partial x} - \frac{v_y}{\rho} \frac{\partial \rho}{\partial y} \\ v_x \frac{\partial v_x}{\partial x} + v_y \frac{\partial v_x}{\partial y} &= -\frac{1}{\rho} \frac{\partial p}{\partial x} \\ v_x \frac{\partial v_y}{\partial x} + v_y \frac{\partial v_y}{\partial y} &= -\frac{1}{\rho} \frac{\partial p}{\partial y} \end{aligned} \right\} \quad (2)$$

Assuming the pressure p to be a function of the density ρ only and introducing the local velocity of sound $c \left(= \sqrt{\frac{dp}{d\rho}} \right)$, equations (2) yield the following:

$$\frac{\partial v_x}{\partial x} + \frac{\partial v_y}{\partial y} = \frac{1}{c^2} \left[v_x^2 \frac{\partial v_x}{\partial x} + v_x v_y \left(\frac{\partial v_x}{\partial y} + \frac{\partial v_y}{\partial x} \right) + v_y^2 \frac{\partial v_y}{\partial y} \right]$$

or if

$$v^2 = v_x^2 + v_y^2$$

then

$$\frac{\partial v_x}{\partial x} + \frac{\partial v_y}{\partial y} = \frac{1}{2c^2} \left(v_x \frac{\partial v^2}{\partial x} + v_y \frac{\partial v^2}{\partial y} \right) \quad (3)$$

If it is further assumed that the motion of the fluid is irrotational, then

$$\frac{\partial v_y}{\partial x} - \frac{\partial v_x}{\partial y} = 0$$

and a velocity potential ϕ may be introduced, where

$$v_x = -\frac{\partial \phi}{\partial x}, \quad v_y = -\frac{\partial \phi}{\partial y}$$

The strength of the source at a point (x, y) , given by the expression on the right-hand side of equation (3), then becomes

$$-\frac{1}{4\pi c^2} \left(\frac{\partial \phi}{\partial x} \frac{\partial v^2}{\partial x} + \frac{\partial \phi}{\partial y} \frac{\partial v^2}{\partial y} \right)$$

Suppose now that (ξ, η) and (x, y) are the rectangular coordinates of points in the ζ and z planes, respectively, and furthermore that these two planes are conformally related, that is

$$\zeta = f(z)$$

where $\zeta = \xi + i\eta$, $z = x + iy$. Let the ζ plane be the plane of the profile and the z plane, the plane of the circle into which the profile is mapped by the foregoing conformal transformation. It is well known that, at a pair of corresponding points at which ζ and z possess no singularities, a source at one such point corresponds to

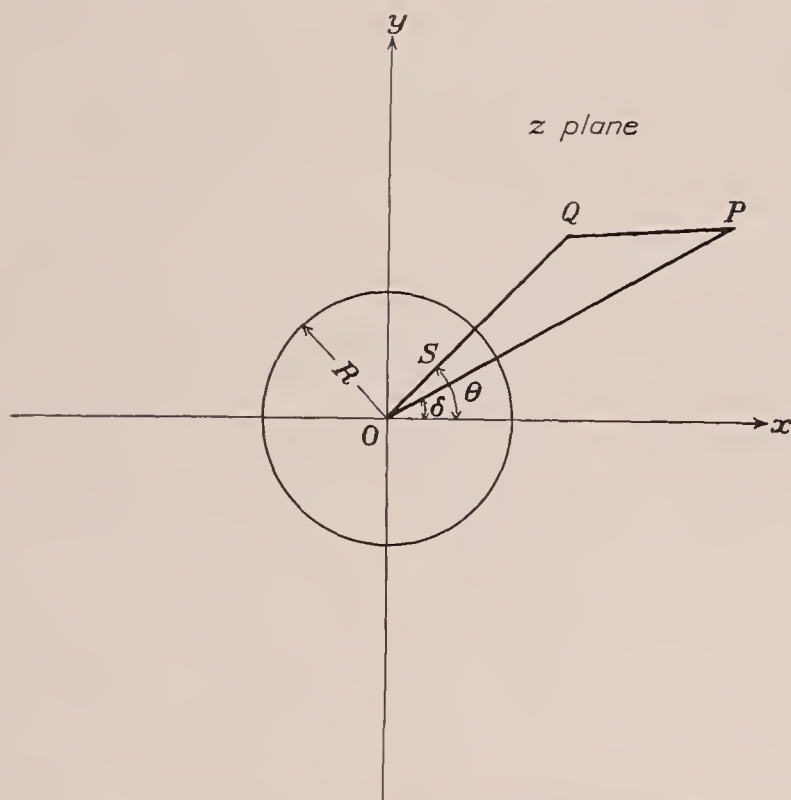


FIGURE 1.—Image of a simple source with regard to a circle.

a source of equal strength at the other. It follows then that at corresponding elements

$$\begin{aligned} & -\frac{1}{4\pi c^2} \left(\frac{\partial \phi}{\partial \xi} \frac{\partial v^2}{\partial \xi} + \frac{\partial \phi}{\partial \eta} \frac{\partial v^2}{\partial \eta} \right) d\xi d\eta \\ & = -\frac{1}{4\pi c^2} \left(\frac{\partial \phi}{\partial x} \frac{\partial v^2}{\partial x} + \frac{\partial \phi}{\partial y} \frac{\partial v^2}{\partial y} \right) dx dy \end{aligned} \quad (4)$$

where, in the expression on the right-hand side, ϕ is the velocity potential in the z plane while v is the magnitude of the velocity in the ζ plane.

In polar coordinates (r, θ) the strength of a source at an element $dx dy$ of the z plane is

$$-\frac{1}{4\pi c^2} \left(\frac{\partial \phi}{\partial r} \frac{\partial v^2}{\partial r} + \frac{1}{r^2} \frac{\partial \phi}{\partial \theta} \frac{\partial v^2}{\partial \theta} \right) r dr d\theta$$

or, introducing a new variable $\lambda = \frac{R}{r}$ (where R is the radius of the circle into which the profile is mapped), and

$$v_r = -\frac{\partial \phi}{\partial r}, \quad v_\theta = -\frac{1}{r} \frac{\partial \phi}{\partial \theta}, \quad \text{this expression becomes}$$

$$\frac{1}{4\pi c^2} \left(v_r \frac{\partial v^2}{\partial \lambda} - \frac{v_\theta}{\lambda} \frac{\partial v^2}{\partial \theta} \right) \frac{R}{\lambda} d\lambda d\theta \quad (5)$$

With the source distribution known in the plane of the circle and given by equation (5), the induced tangential velocity at the circular boundary may be calculated.

Thus consider a unit source located at a point Q of the z plane. In the presence of a circular boundary of radius R , the velocity induced at any point P external to or on the boundary is given by

$$\frac{dw}{dz} = -\left(\frac{1}{z - z_Q} + \frac{1}{z - z_S} - \frac{1}{z} \right)$$

where S is the point inverse to Q in the circle. (See fig. 1.) Since the normal velocity at the boundary is zero, the velocity there is wholly tangential and is given by

$$\left(\frac{dw}{dz} \right)_{tan} = -\frac{2\lambda \sin(\theta - \delta)}{R[1 - 2\lambda \cos(\theta - \delta) + \lambda^2]} \quad (6)$$

where $z = Re^{i\delta}$; $z_Q = re^{i\theta}$; and $z_S = \frac{R^2}{r} e^{i\theta}$

Hence, the total velocity induced at any point of the circular boundary by the system of sources given by equation (5) is

$$\Delta v = \frac{1}{2\pi c_0^2} \int_0^1 \int_0^{2\pi} \frac{v_r \frac{\partial v^2}{\partial \lambda} - \frac{v_\theta}{\lambda} \frac{\partial v^2}{\partial \theta}}{1 - 2\lambda \cos(\theta - \delta) + \lambda^2} \sin(\theta - \delta) d\lambda d\theta \quad (7)$$

The justification for replacing c by c_0 in equation (7) may be shown in the following way. From the Euler equations of motion (2) and the condition for irrotational motion, it follows that

$$\frac{1}{2} dv^2 + \frac{1}{\rho} dp = 0$$

Then when adiabatic conditions prevail so that the relation between p and ρ is

$$p = p_0 \left(\frac{\rho}{\rho_0} \right)^\gamma$$

it follows by integration that

$$c^2 = c_0^2 \left[1 + \frac{\gamma - 1}{2} \left(1 - \frac{v^2}{v_0^2} \right) \frac{v_0^2}{c_0^2} \right] \quad (8)$$

where the zero subscripts denote the corresponding magnitudes in the undisturbed stream. From the foregoing equation it is seen that c has a maximum value at the stagnation point where $v = 0$, that is

$$c_{max}^2 = c_0^2 \left(1 + \frac{\gamma - 1}{2} \frac{v_0^2}{c_0^2} \right)$$

Furthermore, as the streamline corresponding to the boundary of the obstacle is traversed, a point is reached where, for a definite value of the ratio v_0/c_0 , the velocity of the fluid equals that of the local velocity of sound. This critical velocity is obtained from equation (8) by putting $c=v$ and solving for v . Thus

$$v_{crit}^2 = \frac{2}{\gamma+1} c_0^2 \left(1 + \frac{\gamma-1}{2} \frac{v_0^2}{c_0^2} \right) \quad (9)$$

For example, let $v_0/c_0 = 0.75$. Then with $\gamma = 1.408$ (for air)

$$c_{max} = 1.056 c_0$$

and

$$c_{min} = v_{crit} = 0.962 c_0$$

Away from the obstacle, v approaches v_0 and c approaches c_0 . Thus it is seen that the variation of the local velocity of sound from c_0 is, in general, small enough to permit replacing c by c_0 , at least to a first approximation.

Equation (7) is a functional equation for the fluid velocity v and may be solved by a method of successive substitutions. The procedure, due to Poggi, is to substitute for v_r , v_θ , and v^2 values pertaining to the corresponding incompressible flow and thus obtain a first approximation to the sink-source distribution in the plane of the circle. The method thus considers the incompressible flow to be the first approximation to the compressible flow. The second approximation is then obtained by superposing on the incompressible flow the effect of the sink-source distribution as given by equation (7); that is

$$v_{comp} = v_{incomp} + \Delta v \quad (10)$$

GENERAL DEVELOPMENTS

Before equation (7) is applied to any particular case, it is expedient to consider it first in a general way. Thus, suppose that v^2 can be developed in a Fourier series so that

$$\frac{v^2}{v_0^2} = \frac{1}{2} a_0 + \sum_{n=1}^{\infty} (a_n \cos n\theta + b_n \sin n\theta) \quad (11)$$

where the a_n , b_n are functions of λ and also contain the parameters of the shape.

Then

$$\frac{\partial v^2}{\partial \lambda} = v_0^2 \left[\frac{1}{2} a_0' + \sum_{n=1}^{\infty} (a_n' \cos n\theta + b_n' \sin n\theta) \right]$$

$$\frac{\partial v^2}{\partial \theta} = v_0^2 \sum_{n=1}^{\infty} n [b_n \cos n\theta - a_n \sin n\theta]$$

where the primes denote differentiation with regard to λ . Expressions for v_r and v_θ are obtained from the complex potential of the flow past a circular cylinder of radius R , with the circulation determined by the Kutta condition. Let the stream of velocity v_0 make an angle α with the negative direction of the x axis.

Then the potential is

$$w = v_0 \left(z e^{i\alpha} + \frac{R^2}{z e^{i\alpha}} \right) + v_0 R (e^{i\alpha} - e^{-i\alpha}) \log \frac{z}{R}$$

and

$$\frac{dw}{dz} = v_0 \frac{(z+R)(ze^{i\alpha} - Re^{-i\alpha})}{z^2} \quad (12)$$

Then

$$v_r = -v_0(1-\lambda^2) \cos(\theta+\alpha) = v_0(c_1 \cos \theta + c_2 \sin \theta)$$

and

$$\begin{aligned} v_\theta &= v_0(1+\lambda^2) \sin(\theta+\alpha) + 2v_0\lambda \sin \alpha \\ &= v_0 \left(\frac{d_0}{2} + d_1 \cos \theta + d_2 \sin \theta \right) \end{aligned}$$

where

$$\begin{aligned} c_1 &= -(1-\lambda^2) \cos \alpha \\ c_2 &= (1-\lambda^2) \sin \alpha \\ \frac{d_0}{2} &= 2\lambda \sin \alpha \\ d_1 &= (1+\lambda^2) \sin \alpha \\ d_2 &= (1+\lambda^2) \cos \alpha \end{aligned}$$

Therefore

$$\begin{aligned} v_r \frac{\partial v^2}{\partial \lambda} &= \frac{1}{2} v_0^3 a_0' (c_1 \cos \theta + c_2 \sin \theta) \\ &\quad + \frac{1}{2} v_0^3 \sum_{n=1}^{\infty} \{ a_n' c_1 [\cos(n-1)\theta + \cos(n+1)\theta] \\ &\quad + b_n' c_1 [\sin(n+1)\theta + \sin(n-1)\theta] \\ &\quad + a_n' c_2 [\sin(n+1)\theta - \sin(n-1)\theta] \\ &\quad + b_n' c_2 [\cos(n-1)\theta - \cos(n+1)\theta] \} \end{aligned}$$

and

$$\begin{aligned} \frac{v_\theta}{\lambda} \frac{\partial v^2}{\partial \theta} &= -\frac{v_0^3}{2\lambda} \sum_{n=1}^{\infty} n \{ a_n d_1 [\sin(n+1)\theta + \sin(n-1)\theta] \\ &\quad - b_n d_1 [\cos(n-1)\theta + \cos(n+1)\theta] \\ &\quad + a_n d_2 [\cos(n-1)\theta - \cos(n+1)\theta] \\ &\quad - b_n d_2 [\sin(n+1)\theta - \sin(n-1)\theta] \\ &\quad + a_n d_0 \sin n\theta - b_n d_0 \cos n\theta \} \end{aligned}$$

The following definite integrals will be found useful in evaluating equation (7):

$$\begin{aligned} \int_0^{2\pi} \frac{\sin(\theta-\delta)}{1-2\lambda \cos(\theta-\delta) + \lambda^2} \sin n\theta d\theta &= \begin{cases} 0 & \text{if } n=0 \\ \pi \lambda^{n-1} \cos n\delta & \text{if } n \geq 1 \end{cases} \\ \int_0^{2\pi} \frac{\sin(\theta-\delta)}{1-2\lambda \cos(\theta-\delta) + \lambda^2} \cos n\theta d\theta &= \begin{cases} 0 & \text{if } n=0 \\ -\pi \lambda^{n-1} \sin n\delta & \text{if } n \geq 1 \end{cases} \end{aligned}$$

Then substituting the foregoing expressions for $v_r \frac{\partial v^2}{\partial \lambda}$ and $\frac{v_\theta}{\lambda} \frac{\partial v^2}{\partial \theta}$ into equation (7) and integrating with regard to θ , it follows, after replacing the derivatives a_n' , b_n' by a_n , b_n by means of partial integrations, that

$$\begin{aligned}
\Delta v = \frac{v_0^3}{4c_0^2} & \left[-(a_0)_{\lambda=0} \sin(\delta + \alpha) - (a_2)_{\lambda=0} \sin(\delta - \alpha) \right. \\
& + (b_2)_{\lambda=0} \cos(\delta - \alpha) - \sum_{n=2}^{\infty} 2n \cos(n\delta + \alpha) \int_0^1 \lambda^n b_{n-1} d\lambda \\
& + \sum_{n=1}^{\infty} 2n \cos(n\delta - \alpha) \int_0^1 \lambda^{n-2} b_{n+1} d\lambda \\
& + \sum_{n=1}^{\infty} 2n \sin(n\delta + \alpha) \int_0^1 \lambda^n a_{n-1} d\lambda \\
& - \sum_{n=1}^{\infty} 2n \sin(n\delta - \alpha) \int_0^1 \lambda^{n-2} a_{n+1} d\lambda \\
& + \sin \alpha \sum_{n=1}^{\infty} 4n \sin n\delta \int_0^1 \lambda^{n-1} b_n d\lambda \\
& \left. + \sin \alpha \sum_{n=1}^{\infty} 4n \cos n\delta \int_0^1 \lambda^{n-1} a_n d\lambda \right] \quad (13)
\end{aligned}$$

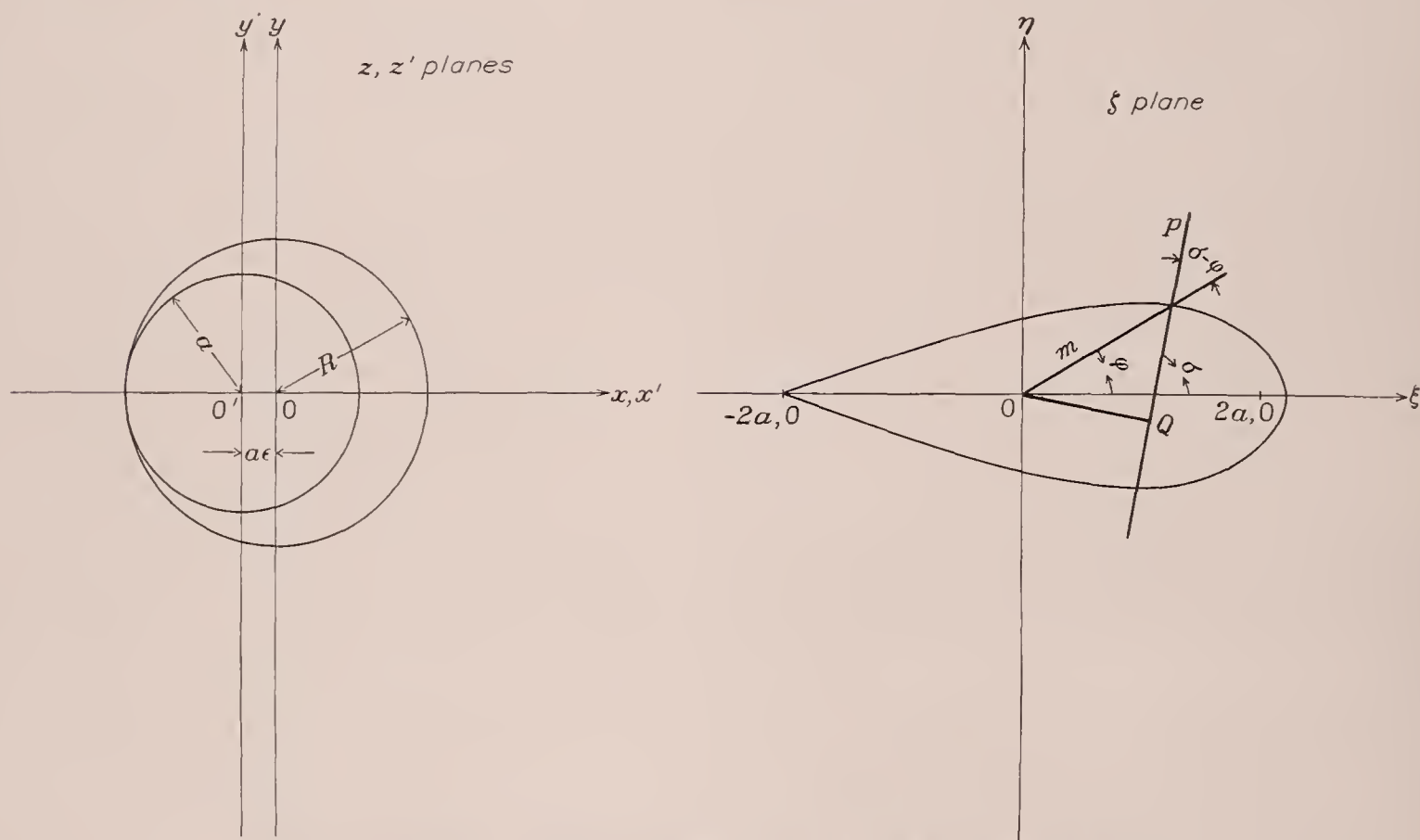


FIGURE 2.—Transformation of a symmetrical Joukowski profile into a circular contour.

It is to be especially noted that this expression for Δv is perfectly general and independent of the type of profile considered. All that is required for a complete solution of equation (13) is a knowledge of the Fourier development for v^2/v_0^2 .

APPLICATION TO SYMMETRICAL JOUKOWSKI PROFILES

Suppose now that the boundary in the ζ plane is a symmetrical Joukowski profile with a sharp trailing edge. The Joukowski transformation given by

$$\zeta = z' + \frac{a^2}{z'} \quad (14)$$

maps the circle of radius a with center at the origin O' of the z' plane into the line segment $(-2a, 0; 2a, 0)$ in the

ζ plane, and the circle of radius R with center at the origin O of the z plane into a Joukowski profile with a sharp trailing edge in the ζ plane. (See fig. 2.) The distance OO' is denoted by $a\epsilon$ and ϵ is therefore a measure of the thickness of the profile. Since the profile has a sharp trailing edge, the two circles touch at the corresponding point $(-a, 0)$. The relation between the z, z' planes is

$$z' = \epsilon a + z$$

If w denotes the complex potential of the incompressible flow in the ζ plane, then the complex velocity is given by

$$\frac{dw}{d\zeta} = \frac{dw}{dz} \frac{dz}{dz'} \frac{dz'}{d\zeta}$$

where

$$\frac{dz}{dz'} = 1 \text{ and } \frac{dz'}{d\zeta} = \frac{z'^2}{(z' + a)(z' - a)}$$

According to equation (12)

$$\frac{dw}{dz} = v_0 \frac{(z + R)(ze^{i\alpha} - Re^{-i\alpha})}{z^2}$$

Hence

$$\frac{dw}{d\zeta} = v_0 \frac{(z + R)(ze^{i\alpha} - Re^{-i\alpha})z'^2}{z^2(z' + a)(z' - a)}$$

But

$$z' + a = z + a(1 + \epsilon) = z + R$$

$$z' - a = z - a(1 - \epsilon)$$

Therefore

$$\frac{dw}{d\zeta} = v_0 \frac{(z + \epsilon a)^2 (ze^{i\alpha} - Re^{-i\alpha})}{z^2 [z - a(1 - \epsilon)]}$$

Introducing

$$\lambda = \frac{R}{r}, \quad \frac{\epsilon a}{R} = h, \quad \text{and} \quad \frac{a(1-\epsilon)}{R} = k$$

it follows that

$$v^2 = \left| \frac{dw}{dz} \right|^2 = v_0^2 \frac{(1 + 2h\lambda \cos \theta + h^2\lambda^2)^2 [1 - 2\lambda \cos (\theta + 2\alpha) + \lambda^2]}{1 - 2k\lambda \cos \theta + k^2\lambda^2}$$

It is now required to obtain the Fourier series for v^2/v_0^2 . Thus, making use of the following developments:

$$\begin{aligned} \frac{\sin \theta}{1 - 2k\lambda \cos \theta + k^2\lambda^2} &= \sum_{n=1}^{\infty} (k\lambda)^{n-1} \sin n\theta \\ \frac{\cos \theta - k\lambda}{1 - 2k\lambda \cos \theta + k^2\lambda^2} &= \sum_{n=1}^{\infty} (k\lambda)^{n-1} \cos n\theta \\ \frac{1}{1 - 2k\lambda \cos \theta + k^2\lambda^2} &= \frac{1}{1 - k^2\lambda^2} \left[1 + 2 \sum_{n=1}^{\infty} (k\lambda)^n \cos n\theta \right] \end{aligned}$$

it follows that

$$\begin{aligned} \frac{v^2}{v_0^2} &= (1 + 2h\lambda \cos \theta + h^2\lambda^2)^2 \left[\frac{1 + \lambda^2 - 2k\lambda^2 \cos 2\alpha}{1 - k^2\lambda^2} \right. \\ &\quad + 2\lambda \sin 2\alpha \sum_{n=1}^{\infty} (k\lambda)^{n-1} \sin n\theta \\ &\quad \left. + 2 \frac{k(1 + \lambda^2) - (1 + k^2\lambda^2) \cos 2\alpha}{k(1 - k^2\lambda^2)} \sum_{n=1}^{\infty} (k\lambda)^n \cos n\theta \right] \end{aligned}$$

Reducing this expression to the form of a Fourier series, it turns out that, for $n > 2$

$$\left. \begin{aligned} a_n &= 2k^{n-3}(h+k)^2(1+hk\lambda^2)^2\lambda^n \\ &\quad \left[\cos 2\alpha + \frac{k(1+\lambda^2) - 2\cos 2\alpha}{1 - k^2\lambda^2} \right] \\ b_n &= 2k^{n-3}(h+k)^2(1+hk\lambda^2)^2\lambda^n \sin 2\alpha \end{aligned} \right\} \quad (15)$$

For later use it will be convenient to introduce the following notation for $n \geq 0$:

$$\left. \begin{aligned} a_n^1 &= 2k^{n-3}(h+k)^2(1+hk\lambda^2)^2\lambda^n \cos 2\alpha \\ a_n^2 &= 2k^{n-3}(h+k)^2(1+hk\lambda^2)^2\lambda^n \frac{k(1+\lambda^2) - 2\cos 2\alpha}{1 - k^2\lambda^2} \\ \bar{b}_n &= 2k^{n-3}(h+k)^2(1+hk\lambda^2)^2\lambda^n \sin 2\alpha \\ \bar{a}_n &= a_n^1 + a_n^2 \end{aligned} \right\} \quad (16)$$

Also

$$\left. \begin{aligned} \frac{1}{2}a_0 &= AD + (B + Ck\lambda)Fk\lambda \\ a_1 &= 2BD + (A + Bk\lambda + Ck^2\lambda^2)Fk\lambda \\ a_2 &= 2CD + (B + Ak\lambda + Bk^2\lambda^2 + Ck^3\lambda^3)Fk\lambda \\ b_1 &= E(A + Bk\lambda + Ck^2\lambda^2) \\ b_2 &= E(B + Ak\lambda + Bk^2\lambda^2 + Ck^3\lambda^3) \end{aligned} \right\} \quad (17)$$

where

$$\begin{aligned} A &= 1 + 4h^2\lambda^2 + h^4\lambda^4 \\ B &= 2h\lambda(1 + h^2\lambda^2) \\ C &= h^2\lambda^2 \end{aligned}$$

$$D = \frac{1 + (1 - 2k \cos 2\alpha)\lambda^2}{1 - k^2\lambda^2}$$

$$E = 2\lambda \sin 2\alpha$$

$$F = \frac{2(k - \cos 2\alpha) + 2k(1 - k \cos 2\alpha)\lambda^2}{k(1 - k^2\lambda^2)}$$

It is seen that

$$(a_0)_{\lambda=0} = 2 \quad \text{and} \quad (a_2)_{\lambda=0} = (b_2)_{\lambda=0} = 0$$

Equation (13) then becomes

$$\begin{aligned} \Delta v &= \frac{v_0^3}{4c_0^2} \left[-2 \sin(\delta + \alpha) + 2 \cos(\delta - \alpha) \int_0^1 (b_1 - \bar{b}_1) d\lambda \right. \\ &\quad + 4 \cos(2\delta - \alpha) \int_0^1 \lambda(b_2 - \bar{b}_2) d\lambda \\ &\quad - 2 \cos(\delta + \alpha) \int_0^1 (b_1 - \bar{b}_1) d\lambda \\ &\quad - 4 \cos(2\delta + \alpha) \int_0^1 \lambda(b_2 - \bar{b}_2) d\lambda \\ &\quad - 4 \cos(2\delta + \alpha) \int_0^1 \lambda^2(b_1 - \bar{b}_1) d\lambda \\ &\quad - 6 \cos(3\delta + \alpha) \int_0^1 \lambda^3(b_2 - \bar{b}_2) d\lambda \\ &\quad + 2 \cos(\delta + \alpha) \int_0^1 \lambda \bar{b}_0 d\lambda \\ &\quad + 2 \sin(\delta + \alpha) \int_0^1 (a_1 - \bar{a}_1) d\lambda \\ &\quad + 4 \sin(2\delta + \alpha) \int_0^1 \lambda(a_2 - \bar{a}_2) d\lambda \\ &\quad - 2 \sin(\delta - \alpha) \int_0^1 (a_1 - \bar{a}_1) d\lambda \\ &\quad - 4 \sin(2\delta - \alpha) \int_0^1 \lambda(a_2 - \bar{a}_2) d\lambda \\ &\quad + 2 \sin(\delta + \alpha) \int_0^1 \lambda(a_0 - \bar{a}_0) d\lambda \\ &\quad + 4 \sin(2\delta + \alpha) \int_0^1 \lambda^2(a_1 - \bar{a}_1) d\lambda \\ &\quad + 6 \sin(3\delta + \alpha) \int_0^1 \lambda^3(a_2 - \bar{a}_2) d\lambda \\ &\quad + 2 \cos(\delta - \alpha) \int_0^1 \frac{1}{\lambda} (b_2 - \bar{b}_2) d\lambda \\ &\quad - 2 \sin(\delta - \alpha) \int_0^1 \frac{1}{\lambda} (a_2 - \bar{a}_2) d\lambda \\ &\quad - \sum_{n=1}^{\infty} 2n \cos(n\delta + \alpha) \int_0^1 (\lambda^n \bar{b}_{n-1} + \lambda^{n-1} \bar{b}_n) d\lambda \\ &\quad + \sum_{n=1}^{\infty} 2n \cos(n\delta - \alpha) \int_0^1 (\lambda^{n-2} \bar{b}_{n+1} + \lambda^{n-1} \bar{b}_n) d\lambda \\ &\quad + \sum_{n=1}^{\infty} 2n \sin(n\delta + \alpha) \int_0^1 (\lambda^n \bar{a}_{n-1} + \lambda^{n-1} \bar{a}_n) d\lambda \\ &\quad \left. - \sum_{n=1}^{\infty} 2n \sin(n\delta - \alpha) \int_0^1 (\lambda^{n-2} \bar{a}_{n+1} + \lambda^{n-1} \bar{a}_n) d\lambda \right] \quad (18) \end{aligned}$$

where

$$\left. \begin{aligned} a_0 - \bar{a}_0 &= \frac{2}{k^3} \{ (h+k)^2 (\cos 2\alpha - k) + k^3 + [k(h^4 + k^2) \\ &\quad - k(1+h^2)(h+k)^2 + 2hk(h+k)^2 \cos 2\alpha \\ &\quad + 2h^2k^2 \cos 2\alpha] \lambda^2 + [-h^2k(h+k)^2 \\ &\quad + h^4k + h^2k^2(h+k)^2 \cos 2\alpha] \lambda^4 \} \\ a_1 - \bar{a}_1 &= \frac{2\lambda \cos 2\alpha}{k^2} [h(h+2k) + 2h^3k\lambda^2] \\ &\quad - \frac{2h^2\lambda}{k} \frac{1 + \lambda^2(1 - 2k \cos 2\alpha)}{1 - k^2\lambda^2} \\ a_2 - \bar{a}_2 &= \frac{2h^2}{k} \lambda^2 \cos 2\alpha \\ b_1 - \bar{b}_1 &= -\frac{2\lambda \sin 2\alpha}{k^2} [h(h+2k) + 2h^3k\lambda^2] \\ b_2 - \bar{b}_2 &= -\frac{2h^2}{k} \lambda^2 \sin 2\alpha \\ b_0 &= \frac{2}{k^3} (h+k)^2 (1 + hk\lambda^2)^2 \sin 2\alpha \end{aligned} \right\} \quad (19)$$

It is a great simplification to replace \bar{a}_n by $a_n^1 + a_n^2$ in the last two integrals of equation (18) before performing the integrations. Then

$$\left. \begin{aligned} & -\sum_{n=1}^{\infty} 2n \cos (n\delta + \alpha) \int_0^1 (\lambda^n \bar{b}_{n-1} + \lambda^{n-1} \bar{b}_n) d\lambda \\ & + \sum_{n=1}^{\infty} 2n \sin (n\delta + \alpha) \int_0^1 (\lambda^n a_{n+1}^1 + \lambda^{n-1} a_n^1) d\lambda \\ & = (1+k)(h+k)^2 \sum_{n=1}^{\infty} 4nk^{n-4} \sin (n\delta - \alpha) \\ & \quad \int_0^1 (1 + hk\lambda^2)^2 \lambda^{2n-1} d\lambda \\ \text{and} \quad & \sum_{n=1}^{\infty} 2n \cos (n\delta - \alpha) \int_0^1 (\lambda^{n-2} \bar{b}_{n+1} + \lambda^{n-1} \bar{b}_n) d\lambda \\ & - \sum_{n=1}^{\infty} 2n \sin (n\delta - \alpha) \int_0^1 (\lambda^{n-2} a_{n+1}^1 + \lambda^{n-1} a_n^1) d\lambda \\ & = -(1+k)(h+k)^2 \sum_{n=1}^{\infty} 4nk^{n-3} \sin (n\delta - 3\alpha) \\ & \quad \int_0^1 (1 + hk\lambda^2)^2 \lambda^{2n-1} d\lambda \end{aligned} \right\} \quad (20)$$

Also

$$\left. \begin{aligned} & \sum_{n=1}^{\infty} 2n \sin (n\delta + \alpha) \int_0^1 (\lambda^n a_{n-1}^2 + \lambda^{n-1} a_n^2) d\lambda \\ & = -(1+k)(h+k)^2 \sum_{n=1}^{\infty} 4nk^{n-5} \sin (n\delta + \alpha) \\ & \quad \int_0^1 (1 + hk\lambda^2)^2 \lambda^{2n-1} d\lambda \\ & \quad + (1 - 2k \cos 2\alpha + k^2) (1+k)(h+k)^2 \\ & \quad \sum_{n=1}^{\infty} 4nk^{n-5} \sin (n\delta + \alpha) \int_0^1 \frac{(1 + hk\lambda^2)^2 \lambda^{2n+1}}{1 - k^2\lambda^2} d\lambda \end{aligned} \right\} \quad (21a)$$

and

$$\left. \begin{aligned} & \sum_{n=1}^{\infty} 2n \sin (n\delta - \alpha) \int_0^1 (\lambda^{n-2} a_{n+1}^2 + \lambda^{n-1} a_n^2) d\lambda \\ & = -(1+k)(h+k)^2 \sum_{n=1}^{\infty} 4nk^{n-4} \sin (n\delta - \alpha) \\ & \quad \int_0^1 (1 + hk\lambda^2)^2 \lambda^{2n-1} d\lambda \\ & \quad + (1 - 2k \cos 2\alpha + k^2) (1+k)(h+k)^2 \\ & \quad \sum_{n=1}^{\infty} 4nk^{n-4} \sin (n\delta - \alpha) \int_0^1 \frac{(1 + hk\lambda^2)^2 \lambda^{2n-1}}{1 - k^2\lambda^2} d\lambda \end{aligned} \right\} \quad (21b)$$

Consider now the integrals

$$J_2 = \sum_{n=1}^{\infty} nk^n \sin (n\delta + \beta) \int_0^1 (1 + hk\lambda^2)^2 \lambda^{2n-1} d\lambda$$

and

$$J_1 = \sum_{n=1}^{\infty} nk^n \cos (n\delta + \beta) \int_0^1 (1 + hk\lambda^2)^2 \lambda^{2n-1} d\lambda$$

Then

$$J_1 + iJ_2 = e^{i\beta} \sum_{n=1}^{\infty} \int_0^1 (1 + hk\lambda^2)^2 nk^n \lambda^{2n-1} e^{in\delta} d\lambda$$

Let $s = k\lambda^2$. Then

$$J_1 + iJ_2 = \frac{e^{i\beta}}{2} \int_0^k \frac{e^{i\delta}(1+hs)^2}{(1-se^{i\delta})^2} ds = \frac{e^{-i(\delta-\beta)}}{2} \left[h^2k + \frac{(1+he^{-i\delta})^2}{e^{-i\delta}-k} \right. \\ \left. - e^{i\delta}(1+he^{-i\delta})^2 + 2h(1+he^{-i\delta}) \log (1-ke^{i\delta}) \right]$$

Hence

$$J_2 = \frac{k(1+hk)^2}{2} \frac{\sin (\delta + \beta) - k \sin \beta}{1 - 2k \cos \delta + k^2} \\ - h \left[\cos (\delta - \beta) \tan^{-1} \frac{k \sin \delta}{1 - k \cos \delta} \right. \\ \left. + \frac{1}{2} \sin (\delta - \beta) \log (1 - 2k \cos \delta + k^2) - k \sin \beta \right] \\ - h^2 \left[k \sin (\delta - \beta) + \cos (2\delta - \beta) \tan^{-1} \frac{k \sin \delta}{1 - k \cos \delta} \right. \\ \left. + \frac{1}{2} \sin (2\delta - \beta) \log (1 - 2k \cos \delta + k^2) - \frac{1}{2} k^2 \sin \beta \right]$$

Replacing β by α , $-\alpha$, or -3α , the corresponding integrals in equations (20) and (21) are obtained.

Consider finally the integrals

$$I_1 = \sum_{n=1}^{\infty} nk^n \cos n\delta \int_0^1 \frac{(1 + hk\lambda^2)^2 \lambda^{2n-1}}{1 - k^2\lambda^2} d\lambda$$

and

$$I_2 = \sum_{n=1}^{\infty} nk^n \sin n\delta \int_0^1 \frac{(1 + hk\lambda^2)^2 \lambda^{2n-1}}{1 - k^2\lambda^2} d\lambda$$

Then

$$I_1 + iI_2 = \int_0^1 \frac{(1 + hk\lambda^2)^2}{\lambda(1 - k^2\lambda^2)} \sum_{n=1}^{\infty} n(k\lambda^2)^n e^{in\delta} d\lambda$$

Again let $s=k\lambda^2$. Then

$$I_1 + iI_2 = \frac{e^{i\delta}}{2} \int_0^k \frac{(1+hs)^2}{(1-ks)(1-se^{i\delta})^2} ds =$$

$$-\frac{(h+k)^2 e^{i\delta}}{2k(k-e^{i\delta})^2} \log(1-k^2)$$

$$-\frac{h(h+e^{i\delta})}{2e^{i\delta}(k-e^{i\delta})} \log(1-ke^{i\delta})$$

$$+\frac{(h+k)(h+e^{i\delta})}{2(k-e^{i\delta})^2} \log(1-ke^{i\delta})$$

$$-\frac{k(h+e^{i\delta})^2}{2(1-ke^{i\delta})(k-e^{i\delta})}$$

Therefore

$$I_1 = \frac{(h+k)^2}{2k} \frac{2k - (1+k^2) \cos \delta}{(1-2k \cos \delta + k^2)^2} \log(1-k^2)$$

$$-\frac{h}{4} \frac{(hk-1) \cos \delta + k - h \cos 2\delta}{1-2k \cos \delta + k^2} \log(1-2k \cos \delta + k^2)$$

$$+\frac{h}{2} \frac{(hk-1) \sin \delta - h \sin 2\delta}{1-2k \cos \delta + k^2} \tan^{-1} \frac{k \sin \delta}{1-k \cos \delta}$$

$$+\frac{h+k}{4} \frac{[hk^2 - 2k + (1-2kh+k^2) \cos \delta + h \cos 2\delta]}{(1-2k \cos \delta + k^2)^2}$$

$$\log(1-2k \cos \delta + k^2)$$

$$-\frac{h+k}{2} \frac{(1-2kh-k^2) \sin \delta + h \sin 2\delta}{(1-2k \cos \delta + k^2)^2} \tan^{-1} \frac{k \sin \delta}{1-k \cos \delta}$$

$$+\frac{k}{2} \frac{(1+h^2) \cos \delta + 2h}{1-2k \cos \delta + k^2}$$

and

$$I_2 = \frac{(h+k)^2}{2k} \frac{(1-k^2) \sin \delta}{(1-2k \cos \delta + k^2)^2} \log(1-k^2)$$

$$+\frac{h}{4} \frac{(hk-1) \sin \delta - h \sin 2\delta}{1-2k \cos \delta + k^2} \log(1-2k \cos \delta + k^2)$$

$$+\frac{h}{2} \frac{(hk-1) \cos \delta + k - h \cos 2\delta}{1-2k \cos \delta + k^2} \tan^{-1} \frac{k \sin \delta}{1-k \cos \delta}$$

$$-\frac{h+k}{2} \frac{hk^2 - 2k + (1-2hk+k^2) \cos \delta + h \cos 2\delta}{(1-2k \cos \delta + k^2)^2}$$

$$\tan^{-1} \frac{k \sin \delta}{1-k \cos \delta}$$

$$-\frac{h+k}{4} \frac{(1-2hk-k^2) \sin \delta + h \sin 2\delta}{(1-2k \cos \delta + k^2)^2}$$

$$\log(1-2k \cos \delta + k^2)$$

$$+\frac{k}{2} \frac{(1-h^2) \sin \delta}{1-2k \cos \delta + k^2}$$

From equations (18), (19), and (20) and the integrals J_2 , I_1 , and I_2 , it follows that

$$\frac{\Delta v}{v_0} = \frac{\mu}{4} \left\{ \left[1 - \frac{(9+5h^2)(h+k)^2}{3k^2} - \frac{3h^2}{k} + \frac{5h^4}{3k^2} - \frac{2h(h+2k)}{k^2} \right] \right.$$

$$\sin(\delta+\alpha) + \left[\frac{2(3+3hk+h^2k^2)(h+k)^2}{3k^3} + \frac{2h^2}{k} \right.$$

$$+ \left. \frac{2h(h+2k)}{k^2} \right] \sin(\delta+3\alpha) - \frac{16h^2}{3k} \sin(2\delta+\alpha)$$

$$+ \left[\frac{10h^2}{3k} + \frac{2h(h+2k)}{k^2} \right] \sin(2\delta+3\alpha) + \frac{2h^2}{k} \sin(3\delta+3\alpha)$$

$$+ \frac{4h^2}{k} \sin(\delta-\alpha) + \frac{8(1+k)(h+k)^2}{k^4} J_2(-\alpha)$$

$$- \frac{4(1+k)(h+k)^2}{k^3} J_2(-3\alpha) - \frac{4(1+k)(h+k)^2}{k^5} J_2(\alpha)$$

$$+ \frac{4(1+k)^2(h+k)^2}{k^5} (1-2k \cos 2\alpha + k^2) I_1 \sin \alpha$$

$$+ \left. \frac{4(1-k^2)(h+k)^2}{k^5} (1-2k \cos 2\alpha + k^2) I_2 \cos \alpha \right\} \quad (22)$$

where $J_2(-\alpha)$, for example, means that in the expression for $J_2(\beta)$, $-\alpha$ has been substituted for β ; and $\mu = \left(\frac{v_0}{c_0}\right)^2$. There is no difficulty in evaluating $\Delta v/v_0$ for any value of h except $h=0$. For $h=0$, $k=1$, however, the Joukowski profile degenerates into a line segment and

$$\frac{\Delta v}{v_0} = \mu \sin \alpha \left[\cos(\delta+2\alpha) + 2 \sin \alpha \frac{\sin(\delta+\alpha) + \sin \alpha}{1-\cos \delta} \right.$$

$$\left. - \frac{2 \sin^2 \alpha}{1-\cos \delta} \log 2(1-\cos \delta) - \frac{4 \sin^2 \alpha}{1-\cos \delta} \sum_{n=1}^{\infty} \frac{1}{n} \right] \quad (23)$$

The last term in this expression contains the divergent series $\sum_{n=1}^{\infty} \frac{1}{n}$, which approaches infinity like $\lim_{n \rightarrow \infty} \log n$.

This infinite term shows that streamline flow cannot be maintained about a straight-line profile except for the trivial case of zero angle of attack.

CORRECTION FOR THE CIRCULATION

It is noted that the expression for the complex velocity about the circular profile given by equation (12) was obtained with the circulation fixed by the Kutta condition. When Δv , representing the effect of compressibility, is added to the incompressible velocity obtained from equation (12) to yield the compressible velocity, the Kutta condition no longer holds. In order to restore the Kutta condition, an additional circulation $\Delta \Gamma$ is added to the incompressible one. Thus, the

velocity at the boundary of the circular profile is given by

$$\frac{v_c}{v_0} = 2 \sin(\delta + \alpha) + \frac{\Gamma_0 + \Delta\Gamma}{2\pi R v_0} + \frac{\Delta v}{v_0} \quad (24)$$

where $\Gamma_0 + \Delta\Gamma = \Gamma$ and $\Gamma_0 = 4\pi R v_0 \sin \alpha$, the circulation in the incompressible flow. The Kutta condition, i. e., $\left(\frac{v_c}{v_0}\right)_{\delta=\pi} = 0$, thus serves to evaluate $\Delta\Gamma$. For $\delta = \pi$ the expressions for $J_2(\beta)$, I_1 , and I_2 simplify considerably. Thus

$$(J_2(\beta))_{\delta=\pi} = -\left\{ \frac{k(1+hk)^2}{2(1+k)} + h[\log(1+k) - k] + h^2\left[k - \frac{1}{2}k^2 - \log(1+k)\right] \right\} \sin \beta$$

$$(I_1)_{\delta=\pi} = \frac{h^2}{2k} \log(1+k) + \frac{1}{8k} \log(1-k) - \frac{k}{8}$$

$$(I_2)_{\delta=\pi} = 0$$

The relation between the velocities in the plane of the circle and the plane of the profile is given by

$$\frac{dw}{d\zeta} = \frac{dw}{dz} \frac{dz}{dz'} \frac{dz'}{d\zeta}$$

where $z' = z + a\epsilon$ and $\zeta = z' + \frac{a^2}{z'}$.

Then

$$\left| \frac{dz}{dz'} \right| = 1 \text{ and}$$

$$\left| \frac{dz'}{d\zeta} \right| = \frac{1 + 2h\lambda \cos \delta + h^2\lambda^2}{\sqrt{1 + 2\lambda \cos \delta + \lambda^2} \sqrt{1 - 2k\lambda \cos \delta + k^2\lambda^2}}$$

It follows that on the profile where $\lambda = 1$

$$\frac{v_P}{v_0} = \frac{1 + 2h \cos \delta + h^2}{\sqrt{2(1 + \cos \delta)} \sqrt{1 - 2k \cos \delta + k^2}} \frac{v_c}{v_0} \quad (25)$$

where v_P is the velocity on the profile corresponding to v_c on the circle.

When the profile is assumed to be thin so that only the first power of h is retained and the angle of attack is small so that $\cos \alpha \cong 1$ and $\sin \alpha \cong \alpha$, then the Kutta condition leads to the following expression for $\frac{\Delta\Gamma}{2\pi R v_0}$

$$\frac{\Delta\Gamma}{2\pi R v_0} = \mu(1+h)\alpha \quad (26)$$

It then follows that

$$\frac{\Gamma}{\Gamma_0} = 1 + \frac{1+h}{2}\mu \quad (27)$$

This value for the ratio Γ/Γ_0 corroborates Glauert's result (reference 5)

$$\frac{\Gamma}{\Gamma_0} = \frac{1}{\sqrt{1-\mu}} = 1 + \frac{1}{2}\mu + \dots$$

when the profile is very thin, i. e., when h is negligible in comparison with unity.

Since the rigorous expressions are available, it may be interesting to compare the approximate result

given by equation (26) with the exact result obtained from equation (22). Thus, for a very thin profile defined by $\epsilon = 0.01$ ($h = \frac{1}{101}$, $k = \frac{99}{101}$) and for the more conventional profiles defined by $\epsilon = 0.05$ ($h = \frac{1}{21}$, $k = \frac{19}{21}$) and $\epsilon = 0.10$ ($h = \frac{1}{11}$, $k = \frac{9}{11}$), at angles of attack $\alpha = 10^\circ$ and $\alpha = 5^\circ$, the following table presents the results:

α (deg.)	$\epsilon = 0.01$		$\epsilon = 0.05$		$\epsilon = 0.10$	
	$\frac{\Delta\Gamma}{2\pi R v_0}$ (approximate)	$\frac{\Delta\Gamma}{2\pi R v_0}$ (exact)	$\frac{\Delta\Gamma}{2\pi R v_0}$ (approximate)	$\frac{\Delta\Gamma}{2\pi R v_0}$ (exact)	$\frac{\Delta\Gamma}{2\pi R v_0}$ (approximate)	$\frac{\Delta\Gamma}{2\pi R v_0}$ (exact)
10	0.17625 μ	0.20796 μ	0.18281 μ	0.20281 μ	0.19036 μ	0.26850 μ
5	.08816 μ	.09218 μ	.09146 μ	.09446 μ	.09524 μ	.09897 μ

It is to be noticed that for $\alpha = 10^\circ$ the exact evaluation of $\Delta\Gamma/2\pi R v_0$ yields a greater value for $\epsilon = 0.01$ than for $\epsilon = 0.05$, a fact not given by the approximate equation (26). This reversal appears, in general, for larger values of ϵ as the angle of attack increases; e. g., for $\epsilon = 0.05$ at $\alpha = 20^\circ$. This feature of the exact expression for the additional lift has no practical significance, however, insofar as the lift is concerned, since the appropriate combination of ϵ and α showing this reversal is outside the practical range.

In the calculation of the local velocities and pressures on the surface of the airfoil, the rigorous expressions for $\Delta v/v_0$ are to be used. The rigorous derivation, however, of the total integrated lift and moment on the airfoil involves great mathematical difficulties. A simplified form for $\Delta v/v_0$ may, however, be obtained for a thin Joukowski profile at small angles of attack. Its use in integrating for the lift yields, as will be shown later, the expected result that

$$\text{Lift} = \rho_0 v_0 \Gamma$$

$$\text{where } \Gamma = \Gamma_0 \left(1 + \frac{1+h}{2}\mu \right)$$

This result justifies the use of the simplified form of $\Delta v/v_0$ in calculating the lift, but its use in integrating for the moment, although reasonable, is somewhat uncertain.

If, then, only the first power of h is retained and the angle of attack taken small enough so that $\cos \alpha \cong 1$ and $\sin \alpha \cong \alpha$, it follows from equation (22) that

$$\frac{\Delta v}{v_0} = \mu \{ [\cos \delta + h(4 + 8 \cos \delta + 3 \cos 2\delta)]\alpha + h(\sin \delta + \sin 2\delta) \}$$

The expression for v_c/v_0 , replacing $\Delta\Gamma/2\pi R v_0$ by the value given by equation (26), then becomes:

$$\begin{aligned} \frac{v_c}{v_0} = & 2 \sin \delta + 2\alpha(1 + \cos \delta) \\ & + \mu[(1 + \cos \delta)\alpha + h(5 + 8 \cos \delta + 3 \cos 2\delta)\alpha \\ & + h(\sin \delta + \sin 2\delta)] \end{aligned} \quad (28)$$

CALCULATION OF THE PRESSURE AND LIFT ON THE AIRFOIL

According to equation (8)

$$c^2 = c_0^2 \left[1 + \frac{\gamma-1}{2} \left(1 - \frac{v^2}{v_0^2} \right) \frac{v_0^2}{c_0^2} \right]$$

Then from the adiabatic equation of state

$$p = p_0 \left(\frac{\rho}{\rho_0} \right)^\gamma$$

and the definition of the local velocity of sound c

$$c = \sqrt{\frac{dp}{d\rho}}$$

it follows that

$$\frac{c^2}{c_0^2} = \left(\frac{\rho}{\rho_0} \right)^{\gamma-1} = \left(\frac{p}{p_0} \right)^{\frac{\gamma-1}{\gamma}}$$

Therefore

$$\frac{p}{p_0} = \left[1 + \frac{\gamma-1}{2} \left(1 - \frac{v^2}{v_0^2} \right) \frac{v_0^2}{c_0^2} \right]^{\frac{\gamma}{\gamma-1}} \quad (29)$$

Expanding the right-hand side of the foregoing equation according to powers of $\frac{v_0^2}{c_0^2} (= \mu)$ it follows that

$$p = p_0 + \frac{1}{2} \rho_0 v_0^2 \left(1 - \frac{v^2}{v_0^2} \right) + \frac{1}{8} \rho_0 v_0^2 \mu \left(1 - \frac{v^2}{v_0^2} \right)^2 + \dots \quad (30)$$

The pressure distribution may be calculated by means of equation (29) together with the values for v/v_0 obtained from equations (22), (24), and (25). Equation (30) will be used in obtaining the total lift and moment on the airfoil.

Since the profile is a streamline, the normal velocity $-\partial\phi/\partial n = 0$ and, accordingly, if s denotes the length along it, then Bernoulli's equation may be written

$$p = \text{constant} - \frac{1}{2} \rho_0 \left(1 + \frac{1}{2} \mu \right) \left(\frac{\partial\phi}{\partial s} \right)^2 + \frac{1}{8} \frac{\rho_0 \mu}{v_0^2} \left(\frac{\partial\phi}{\partial s} \right)^4 + \dots$$

Let n denote the inward-drawn normal to the contour. Then from figure 2, it is seen that $p \cos (\xi, n)$ and $p \cos (\eta, n)$ are the components of the pressure along the ξ and η axes, respectively. Accordingly, the force on the airfoil is given by

$$\begin{aligned} \bar{P} = P_\xi - iP_\eta = & -\frac{\rho_0}{2} \left(1 + \frac{1}{2} \mu \right) \oint_C \left(\frac{\partial\phi}{\partial s} \right)^2 [\cos (\xi, n) \\ & - i \cos (\eta, n)] ds + \frac{\rho_0 \mu}{8 v_0^2} \oint_C \left(\frac{\partial\phi}{\partial s} \right)^4 [\cos (\xi, n) \\ & - i \cos (\eta, n)] ds \end{aligned}$$

where the profile C is traversed in the counterclockwise positive sense. On the other hand

$$d\xi = ds \cos (\eta, n), \quad d\eta = ds \cos [\pi - (\xi, n)] = -ds \cos (\xi, n)$$

and therefore

$$\begin{aligned} \bar{P} = & \frac{i\rho_0}{2} \left(1 + \frac{1}{2} \mu \right) \oint_C \left(\frac{\partial\phi}{\partial s} \right)^2 (d\xi - id\eta) \\ & - \frac{i\rho_0 \mu}{8 v_0^2} \oint_C \left(\frac{\partial\phi}{\partial s} \right)^4 (d\xi - id\eta) \end{aligned}$$

Now, by definition,

$$\frac{dw}{d\zeta} = -v_\xi + iv_\eta = \frac{\partial\phi}{\partial\xi} - i\frac{\partial\phi}{\partial\eta}$$

and, since the velocity normal to the profile equals zero, it follows that

$$\frac{\partial\phi}{\partial\xi} = \frac{\partial\phi}{\partial s} \sin (\xi, n), \quad \frac{\partial\phi}{\partial\eta} = \frac{\partial\phi}{\partial s} \sin (\eta, n)$$

Therefore

$$\frac{dw}{d\zeta} = \frac{\partial\phi}{\partial s} \frac{d\xi - id\eta}{ds}$$

But

$$ds^2 = d\xi^2 + d\eta^2 = (d\xi + id\eta)(d\xi - id\eta)$$

or

$$d\xi - id\eta = \frac{ds^2}{d\zeta}$$

Hence

$$\frac{\partial\phi}{\partial s} = \frac{dw}{d\zeta} \frac{\partial\zeta}{\partial s}$$

and

$$\bar{P} = \frac{i\rho_0}{2} \left(1 + \frac{1}{2} \mu \right) \oint_C \left(\frac{dw}{d\zeta} \right)^2 d\zeta - \frac{i\rho_0 \mu}{8 v_0^2} \oint_C \left(\frac{dw}{d\zeta} \right)^4 \left(\frac{\partial\zeta}{\partial s} \right)^2 d\zeta$$

Now

$$\left(\frac{\partial\zeta}{\partial s} \right)^2 = \frac{d\bar{\zeta}}{d\zeta} \text{ where } \bar{\zeta} \text{ is the conjugate of } \zeta$$

Therefore

$$\bar{P} = \frac{i\rho_0}{2} \left(1 + \frac{1}{2} \mu \right) \oint_C \left(\frac{dw}{d\zeta} \right)^2 d\zeta - \frac{i\rho_0 \mu}{8 v_0^2} \oint_C \left(\frac{dw}{d\zeta} \right)^4 \frac{d\bar{\zeta}}{d\zeta} d\zeta \quad (31)$$

Referring to the plane of the circle of radius R

$$\begin{aligned} \bar{P} = & \frac{i\rho_0}{2} \left(1 + \frac{1}{2} \mu \right) \oint_{\text{circle}} \left(\frac{dw}{dz} \right)^2 \frac{dz}{d\zeta} d\zeta \\ & - \frac{i\rho_0 \mu}{8 v_0^2} \oint_{\text{circle}} \left(\frac{dw}{dz} \right)^4 \left(\frac{dz}{d\zeta} \right)^2 \frac{d\bar{z}}{d\zeta} d\zeta \end{aligned} \quad (32)$$

where $z = e^{i\delta}$ and δ is the polar angle of the circle of radius R .

Since by definition

$$\frac{dw}{dz} = R(-v_x + iv_y)$$

it follows from equation (28) that

$$\frac{dw}{dz} = iRv_e e^{-i\delta} = Rv_e \left(a_1 z + a_0 + \frac{a_{-1}}{z} + \frac{a_{-2}}{z^2} + \frac{a_{-3}}{z^3} \right) \quad (33)$$

where

$$a_0 = \left(1 + \frac{h\mu}{2} \right) + i\alpha \left(1 + \frac{\mu}{2} + 4h\mu \right)$$

$$a_1 = \frac{h\mu}{2} + \frac{3}{2} i h \mu \alpha$$

$$a_{-1} = i\alpha(2 + \mu + 5h\mu)$$

$$a_{-2} = -\left(1 + \frac{h\mu}{2} \right) + i\alpha \left(1 + \frac{\mu}{2} + 4h\mu \right)$$

$$a_{-3} = -\frac{h\mu}{2} + \frac{3}{2} i h \mu \alpha$$

Also from the Joukowski transformation

$$\zeta = z' + \frac{a^2}{z'}$$

and the relation

$$z' = R(z + h)$$

it follows that

$$\frac{dz}{d\zeta} = \frac{1}{R \left[1 - \frac{(1-h)^2}{(z+h)^2} \right]}$$

$$= \frac{1}{R} \left(1 + \frac{1-2h}{z^2} - \frac{2h}{z^3} + \frac{1-4h}{z^4} - \frac{4h}{z^5} + \dots \right)$$

$$\frac{d\bar{z}}{d\bar{\zeta}} = \frac{1}{R \left[1 - \frac{(1-h)^2 z^2}{(1+h\bar{z})^2} \right]}$$

$$\frac{dz}{d\bar{z}} = -z^2$$

Then making use of the well-known relations

$$\oint z^m dz = 0; \text{ if } m \neq -1$$

and

$$\oint_C \frac{dz}{z} = 2\pi i; \text{ if } m = -1$$

it turns out, neglecting as usual terms containing powers of μ , h , and α higher than the first, that

$$\bar{P} = P_\xi - iP_\eta = -i\rho_0 v_0 \Gamma_0 \left[1 + \left(1 + \frac{7}{2}h \right) \mu \right] + i\rho_0 v_0 \Gamma_0 \frac{\mu}{2} (1 + 6h)$$

$$= -i\rho_0 v_0 \Gamma_0 \left(1 + \frac{1+h}{2} \mu \right)$$

or

$$P_\eta = \rho_0 v_0 \Gamma_0 \left(1 + \frac{1+h}{2} \mu \right)$$

This last expression shows that, when the angle of attack is assumed small enough so that only the first power of α is retained, the component P_ξ of the lift vanishes in comparison with the component P_η .

Thus

$$\text{Lift} = P_\eta = \rho_0 v_0 \Gamma \quad (34)$$

This expression agrees in form with the corresponding one in incompressible flow with the auxiliary definition $\Gamma = \Gamma_0 \left(1 + \frac{1+h}{2} \mu \right)$, e. g., equation (27).

CALCULATION OF THE MOMENT

The moment arm $OQ = m \sin(\sigma - \varphi)$ and the force per unit length along the airfoil is pds (fig. 2). Hence the total moment about the origin 0 is given by

$$M = \oint_C p m \sin(\sigma - \varphi) ds = \oint_C p (m \sin \sigma \cos \varphi - m \cos \sigma \sin \varphi) ds$$

But

$$d\xi = ds \cos \sigma \text{ and } d\eta = -ds \sin \sigma$$

Hence

$$M = \oint_C p (m \cos \varphi d\xi + m \sin \varphi d\eta)$$

$$= \oint_C p (\xi d\xi + \eta d\eta) = \frac{1}{2} \oint_C p dm^2$$

Now

$$\xi d\xi + \eta d\eta = R.P. \zeta d\bar{\zeta}$$

and since $d\bar{\zeta} = \frac{ds^2}{d\zeta}$

$$\xi d\xi + \eta d\eta = R.P. \zeta \frac{ds^2}{d\zeta}$$

Substituting for the pressure p the expression

$$\text{Const.} - \frac{1}{2} \rho_0 \left(1 + \frac{1}{2} \mu \right) \left(\frac{\partial \phi}{\partial s} \right)^2 + \frac{1}{8} \frac{\rho_0 \mu}{v_0^2} \left(\frac{\partial \phi}{\partial s} \right)^4 + \dots$$

it follows that

$$M = -\frac{1}{2} \rho_0 \left(1 + \frac{1}{2} \mu \right) R.P. \oint_C \left(\frac{dw}{d\zeta} \right)^2 \zeta d\zeta$$

$$+ \frac{1}{8} \frac{\rho_0 \mu}{v_0^2} R.P. \oint_C \left(\frac{dw}{d\zeta} \right)^4 \frac{d\zeta}{d\bar{\zeta}} \zeta d\zeta \quad (35)$$

Referring to the plane of the circle of radius R

$$M = -\frac{1}{2} \rho_0 \left(1 + \frac{1}{2} \mu \right) R.P. \oint_{\text{circle}} \left(\frac{dw}{dz} \right)^2 \zeta \frac{dz}{d\bar{\zeta}} dz$$

$$+ \frac{1}{8} \frac{\rho_0 \mu}{v_0^2} R.P. \oint_{\text{circle}} \left(\frac{dw}{dz} \right)^4 \left(\frac{dz}{d\bar{\zeta}} \right)^2 \frac{dz}{d\bar{\zeta}} \zeta d\bar{\zeta} \quad (36)$$

Performing the integrations in a manner analogous to that for the lift, it turns out that

$$M = 4\pi \rho_0 R^2 v_0^2 \alpha \left[1 - h + \left(1 + \frac{9}{2}h \right) \mu \right] - \pi \rho_0 R^2 v_0^2 \mu \alpha (2 + 6h)$$

or

$$M = 4\pi \rho_0 R^2 v_0^2 \alpha \left(1 - h + \frac{1+6h}{2} \mu \right) \quad (37)$$

This expression represents the moment about the origin of coordinates, and the moment about the center of the circle of radius R (into which the profile is mapped) can be obtained at once as

$$M_c = M - La\epsilon = 4\pi \rho_0 v_0^2 a^2 \alpha + 4\pi \rho_0 v_0^2 a^2 \alpha \frac{1+7h}{2} \mu$$

or

$$M_c = M_0 \left(1 + \frac{1+7h}{2} \mu \right) \quad (38)$$

where $M_0 = 4\pi \rho_0 v_0^2 a^2 \alpha$ is the moment about the center of the circle of radius R for the corresponding incompressible flow.

If now d represents the distance of the center of pressure from the origin of coordinates, then

$$M = Ld$$

or

$$d = \frac{4\pi \rho_0 R^2 v_0^2 \alpha \left(1 - h + \frac{1+6h}{2} \mu \right)}{4\pi \rho_0 R v_0^2 \alpha \left(1 + \frac{1+h}{2} \mu \right)} \cong a(1 + 3h\mu) \quad (39)$$

This expression shows that the airfoil has a constant center of pressure at a distance equal to $1/4 (1-3h\mu)$ of the chord from the leading edge. For a thin airfoil, say $\epsilon=0.05$ and for a stream velocity $v_0=0.835 c_0$, the center of pressure, as compared with the corresponding

incompressible case, is nearer to the leading edge by about 2.5 percent of the chord.

LANGLEY MEMORIAL AERONAUTICAL LABORATORY,
NATIONAL ADVISORY COMMITTEE FOR AERONAUTICS,
LANGLEY FIELD, VA., *November 19, 1937.*

APPENDIX A

APPLICATION OF THE THEORETICAL RESULTS

As an example of the application of the theory to any particular case, the flows past a thin and a fairly thick symmetrical Joukowski profile for zero angle of attack will be calculated. Since no experimental results are available for purposes of comparison, it was considered hardly worth while to perform the rather lengthy and tedious calculations associated with angle of attack or circulation.

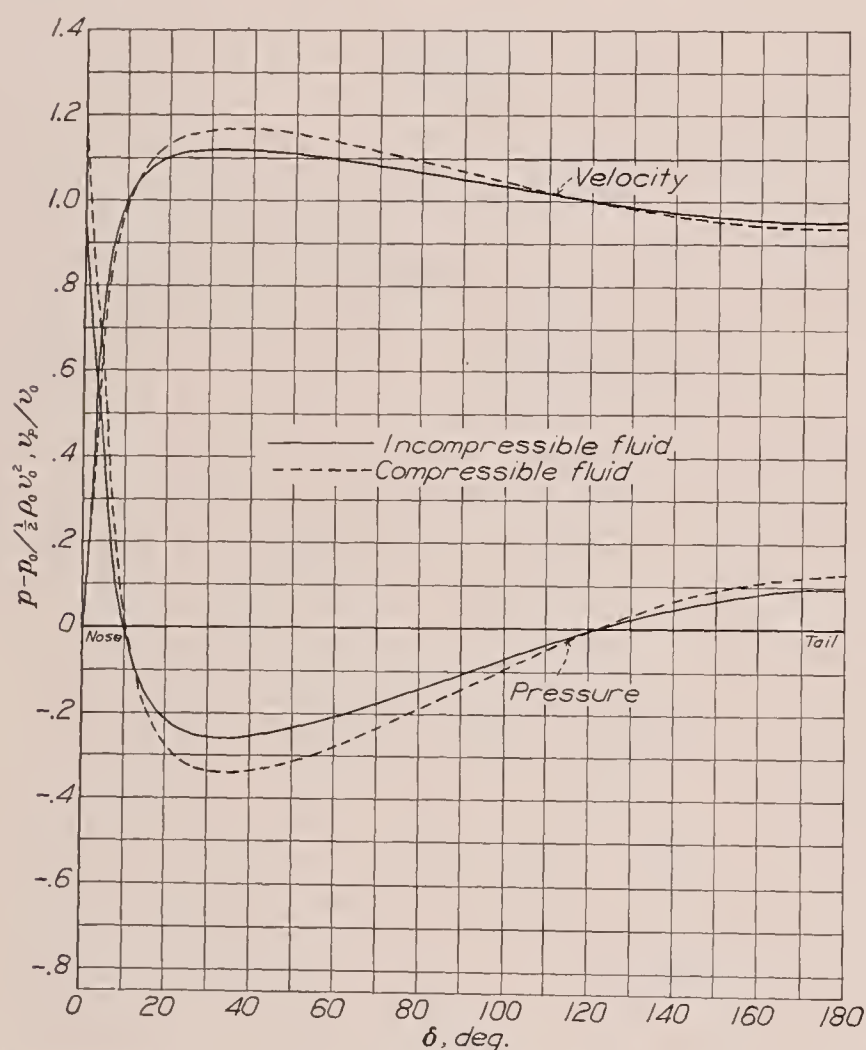


FIGURE 3.—Pressure and velocity distribution for the symmetrical Joukowski airfoil section $\epsilon=0.05$. $\mu=0.70$, $\alpha=0^\circ$.

where

$$J_2(0) = \frac{(1+2h)(1-4h^2)(1-h)^2}{2} \frac{\sin \delta}{1-2k \cos \delta + k^2} - h^2 k \sin \delta - h(\cos \delta + h \cos 2\delta) \tan^{-1} \frac{k \sin \delta}{1-k \cos \delta} - \frac{h}{2} (\sin \delta + h \sin 2\delta) \log (1-2k \cos \delta + k^2)$$

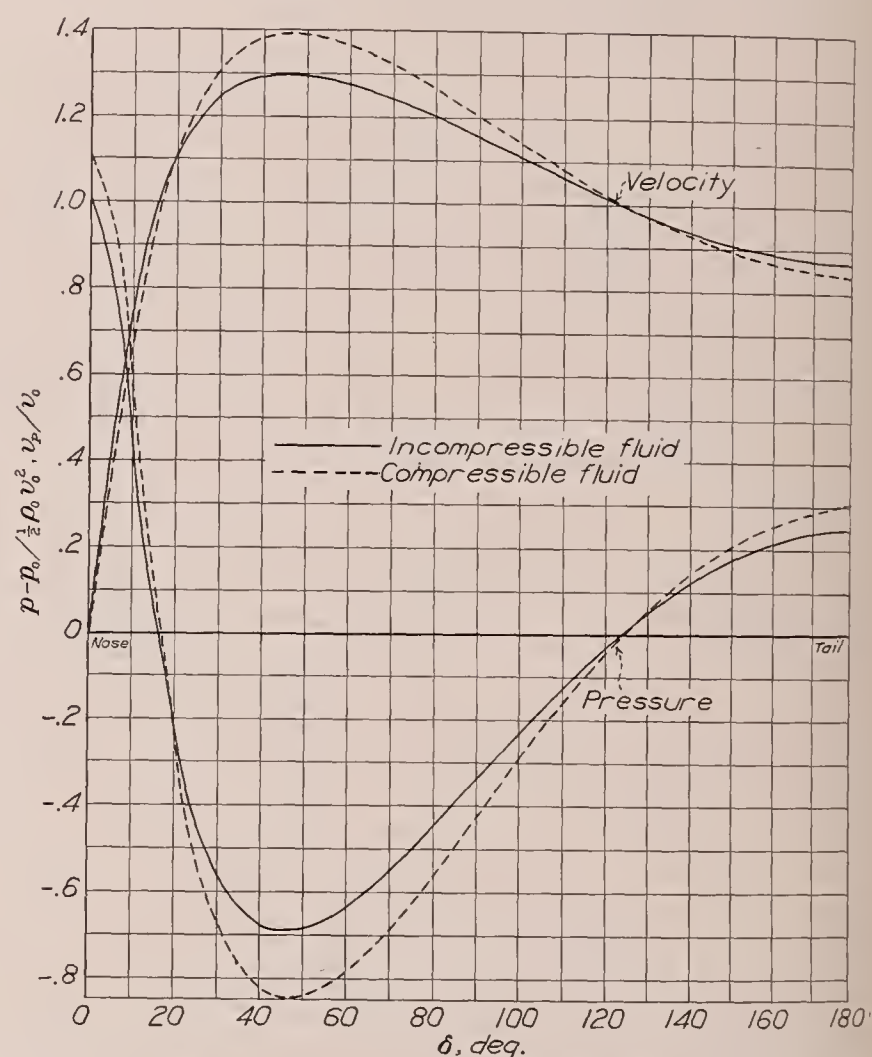


FIGURE 4.—Pressure and velocity distributions for the symmetrical Joukowski airfoil section $\epsilon=0.15$. $\mu=0.47$, $\alpha=0^\circ$.

Equation (23) for $\Delta v/v_0$ simplifies considerably when the angle of attack α is taken to be zero. Thus

$$\frac{\Delta v}{v_0} = \frac{\mu}{4} \left[\frac{h(12-21h-4h^2+30h^3-24h^4-8h^5)}{3k^3} \sin \delta + \frac{4h(1-h)^2}{k^2} \sin 2\delta + \frac{2h^2}{k} \sin 3\delta - \frac{32h^2(1-h)^3}{k^5} J_2(0) + \frac{64h^3(1-h)^3}{k^5} I_2 \right] \quad (40)$$

The profiles chosen are defined by $\epsilon=0.05$ and $\epsilon=0.15$ or $h=1/21$, $k=19/21$; and $h=3/23$, $k=17/23$, respectively. Tables I and II present the calculations and figures 3 and 4 show the velocity and pressure distributions for both incompressible and compressible flow. The values of μ chosen were the critical values obtained by plotting $(v_P/v_0)_{max}$ against v_0/c_0 and then noting the intersection of this graph with that of $(v/v_0)_{crit}$ against v_0/c_0 as given by equation (9). Table III

presents the data and figure 5 shows the corresponding graphs.

The expressions for $\Delta v/v_0$ are given by:

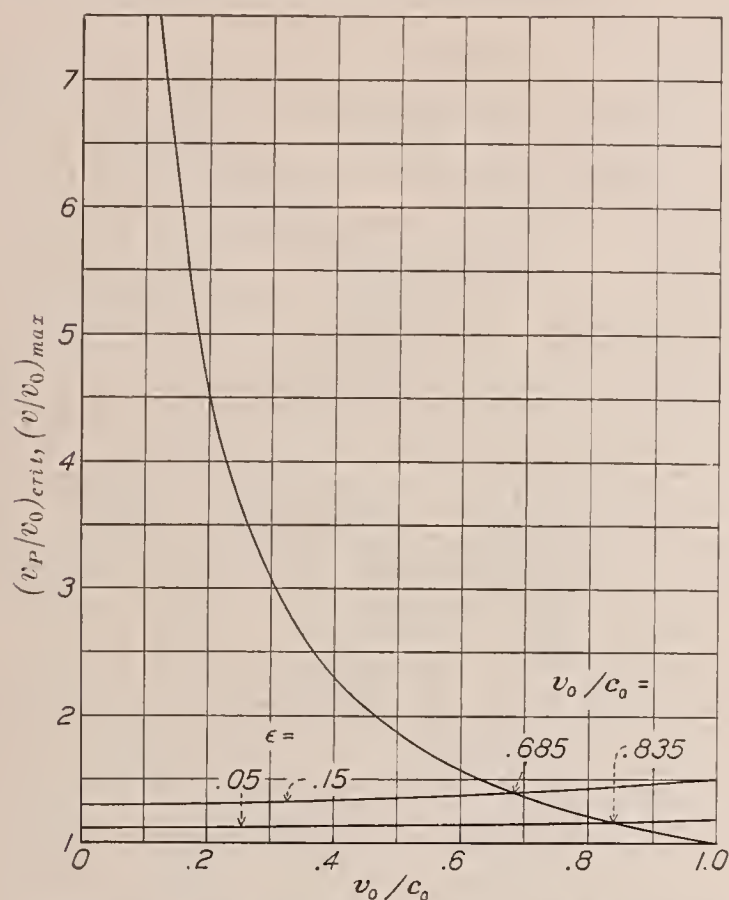


FIGURE 5.—Limiting values of v_0/c_0 at zero angle of attack for $\epsilon=0.05$ and $\epsilon=0.15$

for $\epsilon=0.05$

$$\frac{\Delta v}{v_0} = \mu[0.05890 \sin \delta + 0.05276 \sin 2\delta + 0.00125 \sin 3\delta - 0.02585 J_2(0) + 0.00246 I_2]$$

and

for $\epsilon=0.15$

$$\frac{\Delta v}{v_0} = \mu[0.24905 \sin \delta + 0.18053 \sin 2\delta + 0.01151 \sin 3\delta - 0.40568 J_2(0) + 0.10583 I_2]$$

It is to be noted in tables I, II, and III that the maximum velocity v_P/v_0 for the incompressible flow occurs at about $\delta=35^\circ$ and $\delta=45^\circ$ for $\epsilon=0.05$ and $\epsilon=0.15$,

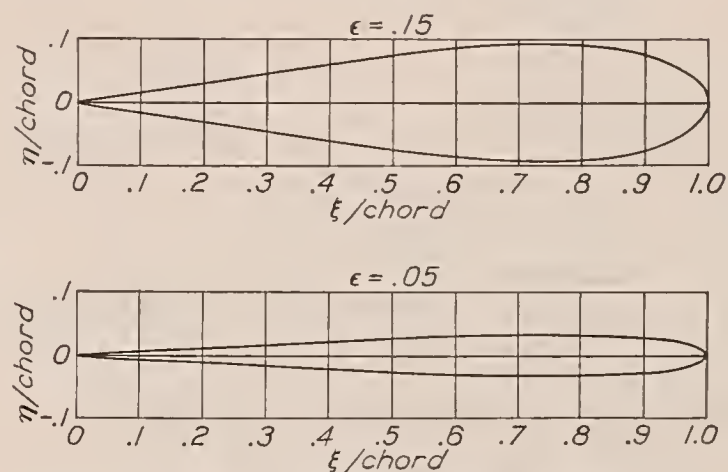


FIGURE 6.—Symmetrical Joukowski profiles $\epsilon=0.05$ and $\epsilon=0.15$.

respectively. It is then assumed that the position of maximum velocity is independent of μ and maximum values for v_P/v_0 are calculated for various values of μ . These values of $(v_P/v_0)_{max}$ are given in table III and are used in obtaining the critical values of μ as shown in figure 5. The coordinates of the airfoils $\epsilon=0.05$, $\epsilon=0.15$ are given in table IV and the corresponding contours in figure 6.

APPENDIX B

NOTATION

$x, y,$	rectangular coordinates in the plane of the circle.
$\xi, \eta,$	rectangular coordinates in the plane of the profile.
$z = x + iy, \zeta = \xi + i\eta$	
$r, \theta,$	plane polar coordinates in the z plane.
$v_x, v_y,$	fluid velocity components along the x and y axes, respectively.
$v_c,$	tangential velocity on the circle.
$v_P,$	tangential velocity on the profile corresponding to v_c .
$v = \sqrt{v_x^2 + v_y^2},$	magnitude of the fluid velocity.
$c,$	local velocity of sound in the fluid.
$\rho,$	density of the fluid.
$p,$	static pressure in the fluid.
$v_0, c_0, \rho_0, p_0,$	corresponding magnitudes in the undisturbed stream.
$\mu = \left(\frac{v_0}{c_0}\right)^2$	
$\Delta v,$	correction term to the velocity in incompressible flow due to compressibility.
$\phi,$	velocity potential of the incompressible flow.
$v_r = -\frac{\partial \phi}{\partial r},$	component of velocity along the radius vector.
$v_\theta = -\frac{1}{r} \frac{\partial \phi}{\partial \theta},$	component of velocity perpendicular to the radius vector in the sense of θ increasing.
$\lambda = \frac{R}{r}$	
$R,$	radius of circle into which the profile is mapped.
$\gamma,$	ratio of specific heats.
$w,$	complex potential of the incompressible flow in the ζ plane.
$\alpha,$	angle of attack.

$\epsilon,$	thickness coefficient of Joukowski profile (see fig. 2).
$h = \frac{\epsilon}{1 + \epsilon}$	
$k = \frac{1 - \epsilon}{1 + \epsilon} = 1 - 2h$	
$\Gamma,$	circulation about profile in the compressible fluid.
$\Gamma_0,$	circulation about profile in the incompressible fluid.
$\Delta \Gamma = \Gamma - \Gamma_0,$	contribution to the circulation due to compressibility.
$\bar{P},$	force vector on the airfoil.
$P_\xi, P_\eta,$	components of \bar{P} along the ξ and η axes, respectively.
$M,$	moment about origin of coordinates in the plane of compressible flow.
$M_c,$	moment about center of circle of radius R in the plane of compressible flow.
$M_0,$	moment corresponding to M_c in the plane of incompressible flow.

REFERENCES

1. Janzen, O.: Beitrag zu einer Theorie der stationären Strömung kompressibler Flüssigkeiten. *Phys. Zeitschr.*, 14 Jahr., S. 639-643, 1913.
2. Lord Rayleigh: On the Flow of Compressible Fluid Past an Obstacle. *Phil. Mag.*, ser. 6, vol. 32, no. 187, July 1916, pp. 1-6.
3. Hooker, S. G.: The Two-Dimensional Flow of Compressible Fluids at Sub-Sonic Speeds Past Elliptic Cylinders. *R. & M. No. 1684*, British A. R. C., 1936.
4. Poggi, Lorenzo: Campo di velocità in una corrente piana di fluido compressibile. Parte II.—Caso dei profili ottenuti con rappresentazione conforme dal cerchio ed in particolare dei profili Joukowski. *L'Aerotecnica*, vol. XIV, fasc. 5, 1934, pp. 532-549.
5. Glauert, H.: The Effect of Compressibility on the Lift of an Aerofoil. *Proc. Roy. Soc., A*, vol. 118, p. 113, 1928 (also, *R. & M. No. 1135*, British A. R. C., 1928).

TABLE I

Case 1: $\epsilon=0.05$, $h=\frac{1}{21}$, $k=\frac{19}{21}$, $\alpha=0$

δ (deg.)	$J_2(0)$	I_2	$\frac{1}{\mu} \frac{\Delta v}{v_0}$	Jaco- bian ¹	$\frac{v_P}{v_0}$ (in- com- pres- sible)	$\frac{v_P}{v_0}$ ($\mu=0.70$)	$\frac{p-p_0}{\frac{1}{2}\rho_0 v_0^2}$	
							Com- pres- sible	Incom- pressible
0	0.0000	0.0000	0.0000	5.7619	0.0000	0.0000	1.1743	1.0000
5	2.6629	10.8700	-.0275	4.3458	.7576	.6743	.5971	.4261
10	2.3054	8.2345	-.0104	2.8772	.9993	.9784	.0431	.0015
15	1.7670	5.5612	.0105	2.0752	1.0742	1.0894	-.1808	-.1539
20	1.3904	3.9260	.0289	1.6122	1.1028	1.1353	-.2744	-.2162
30	.9477	2.2576	.0575	1.1197	1.1197	1.1645	-.3340	-.2537
40	.7041	1.4804	.0764	.8700	1.1185	1.1648	-.3346	-.2510
50	.5508	1.0536	.0861	.7247	1.1103	1.1538	-.3120	-.2327
60	.4448	.7907	.0872	.6341	1.0983	1.1368	-.2774	-.2062
70	.3665	.6148	.0807	.5767	1.0838	1.1163	-.2355	-.1747
80	.3055	.4893	.0683	.5422	1.0679	1.0937	-.1894	-.1404
90	.2560	.3951	.0520	.5255	1.0511	1.0701	-.1415	-.1047
100	.2146	.3214	.0341	.5250	1.0341	1.0466	-.0938	-.0694
110	.1789	.2593	.0168	.5414	1.0176	1.0239	-.0480	-.0354
120	.1474	.2112	.0020	.5785	1.0020	1.0028	-.0055	-.0039
130	.1190	.1779	-.0089	.6448	.9878	.9839	.0322	.0242
140	.0929	.1294	-.0151	.7588	.9755	.9675	.0647	.0485
150	.0683	.0944	-.0165	.9657	.9657	.9546	.0902	.0674
160	.0540	.0617	-.0139	1.4010	.9584	.9448	.1094	.0876
170	.0223	.0305	-.0077	2.7465	.9539	.9391	.1205	.0002
180	.0600	.0000	.0000	.0000	.9524	.9358	.1270	.0930

¹Jacobian = $\frac{221+21 \cos \delta}{21 \cos (\delta / 2) \sqrt{862-798 \cos \delta}}$

TABLE II

Case 2: $\epsilon=0.15$, $h=\frac{3}{23}$, $k=\frac{17}{23}$, $\alpha=0$

δ (deg.)	$J_2(0)$	I_2	$\frac{1}{\mu} \frac{\Delta v}{v_0}$	Jaco- bian ¹	$\frac{v_P}{v_0}$ (in- com- pres- sible)	$\frac{v_P}{v_0}$ ($\mu=0.47$)	$\frac{p-p_0}{\frac{1}{2}\rho_0 v_0^2}$	
							Com- pres- sible	Incom- pressible
0	0.0000	0.0000	0.0000	2.4493	0.0000	0.0000	1.1175	1.0000
5	.5079	.9412	-.0504	2.3542	.4104	.3546	.9640	.8316
10	.8207	1.4940	-.0641	2.1253	.7381	.6741	.5805	.4559
15	.9299	1.6509	-.0397	1.8598	.9627	.9280	.1410	.0732
20	.9199	1.5876	.0060	1.6162	1.1055	1.1101	-.2260	-.2222
30	.7844	1.2790	.1095	1.2473	1.2473	1.3115	-.6590	-.5556
40	.6468	.9927	.1930	1.0064	1.2938	1.3851	-.8193	-.6739
50	.5249	.7786	.2438	.8465	1.2970	1.3940	-.8386	-.6821
60	.4345	.6215	.2615	.7376	1.2775	1.3681	-.7825	-.6320
70	.3630	.5038	.2504	.6619	1.2439	1.3218	-.6816	-.5474
80	.3052	.4130	.2170	.6106	1.2026	1.2649	-.5576	-.4463
90	.2571	.3409	.1693	.5783	1.1566	1.2026	-.4229	-.3378
100	.2163	.2818	.1156	.5629	1.1087	1.1393	-.2876	-.2293
110	.1807	.2321	.0635	.5646	1.0611	1.0780	-.1589	-.1260
120	.1491	.1893	.0189	.5865	1.0158	1.0210	-.0422	-.0318
130	.1205	.1516	-.0141	.6360	.9743	.9701	.0592	.0507
140	.0940	.1175	-.0335	.7299	.9384	.9269	.1432	.1195
150	.0692	.0860	-.0393	.9090	.9090	.8922	.2088	.1737
160	.0456	.0564	-.0334	1.2972	.8873	.8670	.2556	.2126
170	.0226	.0279	-.0190	2.5166	.8740	.8516	.2837	.2361
180	.0000	.0000	.0000	.0000	.8696	.8389	.3067	.2439

¹Jacobian = $\frac{269+69 \cos \delta}{23 \cos (\delta / 2) \sqrt{818-782 \cos \delta}}$

TABLE III

$\frac{v_0}{c_0}$	$\left(\frac{v_P}{v_0}\right)_{max}$		$^1\left(\frac{v}{v_0}\right)_{crit}$
	$\epsilon=0.05$	$\epsilon=0.15$	
0.0	1.120	1.300	0.000
.2	1.122	1.307	4.575
.4	1.130	1.333	2.315
.5	1.136	1.350	1.870
.6	1.143	1.372	1.574
.7	1.151	1.400	1.366
.8	1.161	1.430	1.211
1.0	1.185	1.503	1.000

$^1\left(\frac{v}{v_0}\right)_{crit}^2 = \frac{2}{\gamma+1} \frac{1}{\mu} + \frac{\gamma-1}{\gamma+1}$, with $\gamma=1.408$

or $\left(\frac{v}{v_0}\right)_{crit}^2 = \frac{0.83056}{\mu} + 0.16944$

TABLE IV

COORDINATES OF THE AIRFOILS

δ (deg.)	$\epsilon=0.05$		$\epsilon=0.15$	
	$\frac{\xi}{\text{chord}}$	$\frac{\eta}{\text{chord}}$	$\frac{\xi}{\text{chord}}$	$\frac{\eta}{\text{chord}}$
0	¹ 1.0000	0.0000	1.0000	0.0000
10	.9930	.0080	.9938	.0213
20	.9723	.0155	.9751	.0414
30	.9474	.0220	.9444	.0592
40	.8917	.0270	.9023	.0739
50	.8339	.0304	.8495	.0845
60	.7662	.0318	.7871	.0907
70	.6904	.0315	.7163	.0922
80	.6084	.0295	.6386	.0891
90	.5226	.0261	.5558	.0820
100	.4355	.0218	.4695	.0715
110	.3496	.0171	.3830	.0589
120	.2678	.0124	.2980	.0454
130	.1928	.0082	.2178	.0324
140	.1271	.0049	.1457	.0211
150	.0732	.0025	.0849	.0123
160	.0331	.0010	.0388	.0062
170	.0084	.0003	.0098	.0025
180	² .0000	.0000	.0000	.0000

¹ Nose.

² Tail.

REPORT No. 622

A PHOTOGRAPHIC STUDY OF COMBUSTION AND KNOCK IN A SPARK-IGNITION ENGINE

By A. M. ROTHROCK and R. C. SPENCER

SUMMARY

A photographic study of the combustion in a spark-ignition engine has been made, using both schlieren and flame photographs taken at high rates of speed. Although shock waves are present after knock occurs, there was no evidence of any type of sonic or supersonic compression waves existing in the combustion gases prior to the occurrence of knock. Artificially induced shock waves in the engine did not in themselves cause knock. The photographs also indicate that, although auto-ignition ahead of the flame front may occur in conjunction with knock, it is not necessary for the occurrence of knock. There is also evidence that the reaction is not completed in the flame front but continues for some time after the flame front has passed through the charge.

INTRODUCTION

Speculation and controversy concerning the nature and causes of combustion knock have existed from the very earliest recognition of knock as a problem associated with the spark-ignition engine. Various investigators have gradually added to the general fund of knowledge and, at the present time, it is generally accepted that combustion knock is associated with the last part of the charge to burn (references 1 and 2).

Early in 1936, the N. A. C. A. started a program of research on combustion in a spark-ignition engine, using the altered N. A. C. A. combustion apparatus. The preliminary results obtained from these tests are given in reference 3. A later investigation, reported herein, was carried out during the summer and fall of 1936. In the later study the physical phenomena accompanying knocking combustion were investigated by schlieren photography, high-speed motion pictures, and indicator cards.

APPARATUS AND METHOD

In the present tests, the N. A. C. A. combustion apparatus was used in conjunction with a high-speed motion-picture camera, an optical-type pressure indicator, and the N. A. C. A. spark-photography apparatus. The combustion apparatus (references 3 and 4) is a

5- by 7-inch single-cylinder test engine with a glass window in the cylinder head, so that the combustion may be studied photographically. The engine is motored at the test speed by an electric motor and is then fired once by injecting and igniting a single charge of fuel. The engine temperature is maintained constant by circulating hot glycerin through the engine. A diagrammatic sketch of the combustion apparatus is shown in figure 1. The cylinder head is of the pent-roof type, similar in shape to the one used by Schey and Young in the tests reported in reference 5. In the present design the space normally occupied by two valves on one side of the head is taken by the opening for the glass window. As the engine fires only once, the two remaining valves operate simultaneously and act both for exhaust and intake. The valves are timed to open 55° before bottom center on the power stroke and to close 35° after bottom center on the following compression stroke. Six spark-plug locations are provided in the cylinder head, affording alternate positions for the injection valve, the spark plugs, and the auxiliary fittings.

The ignition system employs a condenser discharge through an induction coil with the discharge occurring on "make" instead of "break" as in the conventional system. Maximum variation in timing with this system is about $\pm 1^\circ$ of crankshaft rotation.

The observation window, roughly $2\frac{1}{2}$ by 5 inches (fig. 1), consists of two heavy glass plates with an air space between them. Compressed air is admitted to the space between the plates.

The injection system, a cross section of which is included in figure 1, is spring-operated. The spring is held compressed by a rocker arm, holding the lapped plunger retracted and leaving a port uncovered in the side of the sleeve. Fuel is circulated under pressure by a primary pump through the sleeve and thence to the injection valve, which is arranged to permit continuous circulation of the fuel (reference 4). For the injection of the fuel, the rocker arm is released by a drop cam. The fuel is delivered to the injection valve at a pressure of about 2,500 pounds per square inch.

The fuel quantity is regulated by changing the length of the plunger travel. During most of the tests, a seven-orifice injection nozzle (fig. 2) was used. This nozzle is similar to the one used by Schey and Young in the work reported in reference 5. The injection valve was mounted opposite the intake valves so that the fuel was injected counter to the intake air flow. Injection was timed to start 20° after top center on the intake stroke and the injection period was about 120° .

The engine-jacket temperature was maintained at 250° F. throughout the tests. The compression ratio was 7.0. The injection started at 20° A. T. C. on the intake stroke and, for the full-load fuel quantity, lasted

straight-line relationship for the mixtures having been assumed.

The pressure indicator has been described in reference 6. A steel blank, which fits into the window opening, is used for mounting the indicator directly in the combustion-chamber wall.

Three different types of photograph were taken: (1) High-speed 16 mm motion pictures; (2) streak schlieren photographs using a continuous light source and moving film, recording the combustion travel along a narrow slit across the chamber; and (3) spark schlieren motion pictures. The last method uses the same film-drum camera as the second, but the light for the schlieren photo-

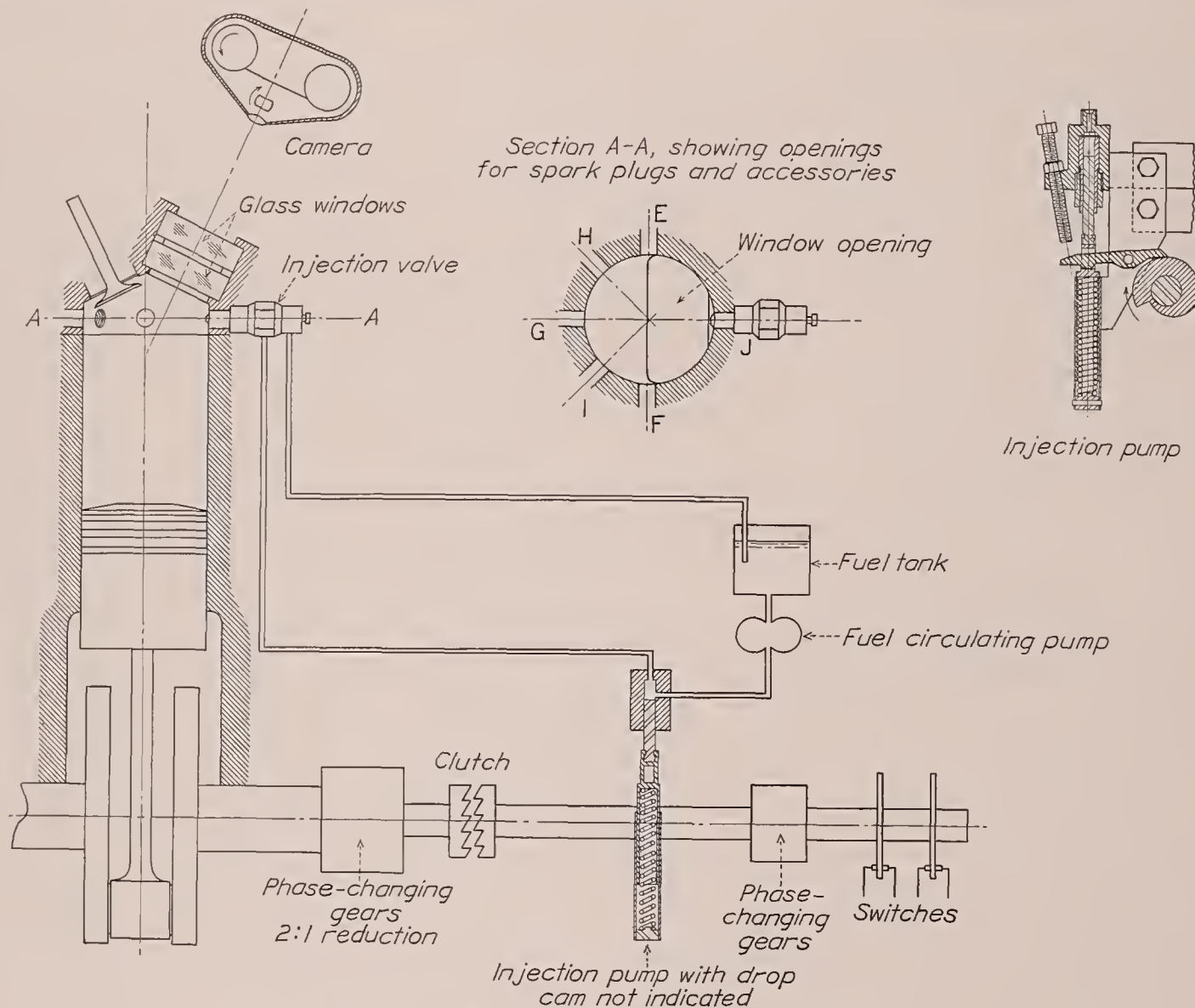


FIGURE 1.—Diagrammatic sketch of combustion apparatus.

for about 0.015 second. For the tests at an engine speed of 500 r. p. m., the spark advance was 30° B. T. C. and, at 1,500 r. p. m., it was 20° B. T. C. The earlier spark was used at the lower speed to increase the tendency to knock.

Four fuels having different octane ratings were used in the tests: A commercial iso-octane with an octane number of 100, containing approximately 90 percent 2, 2, 4 trimethyl pentane; aviation gasoline to Army Specification Y-3557-6, having an octane number of 87; ordinary automobile gasoline having an octane number of about 65; and a special fuel having an octane number of 18. In addition, blends of the 18-octane fuel with the 65-octane gasoline were used, having estimated octane ratings of approximately 30, 40, and 50, a

graphs is furnished by a series of spark discharges and the entire window is photographed.

The high-speed motion-picture camera (reference 7) was mounted above the combustion apparatus with the camera lens on the center line of the window and parallel to the plane of the window. The N. A. C. A. spark-photography apparatus has been described in reference 8. For these tests, the apparatus was used in conjunction with the schlieren optical arrangement (reference 9), by which slight differences in index of refraction of a gaseous medium may be made visible or photographed. The differences may be caused by air flow, by waves traveling through the medium, or by temperature differences.

During most of the tests in which the schlieren method was used, the film-drum camera of the spark-photography apparatus was used in conjunction with a high-

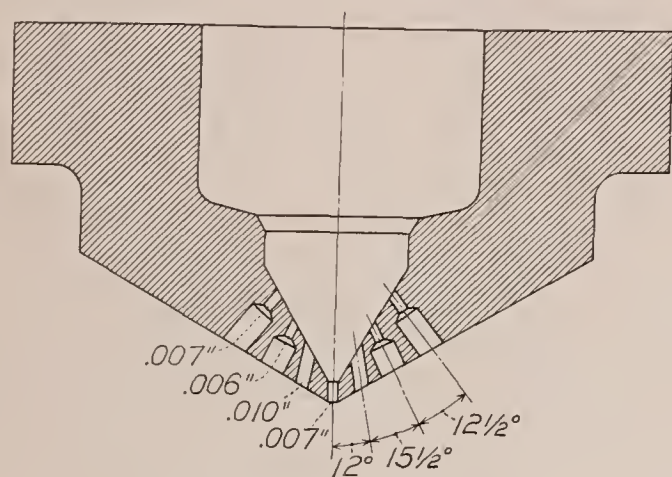


FIGURE 2.—The seven-orifice nozzle.

intensity arc light. The optical arrangement is shown diagrammatically in figure 3. In this set-up, light from the arc is brought to a focus on the round hole in the metal plate by the first lens. This round hole, placed at

of only a $\frac{1}{8}$ -inch strip across the combustion chamber is photographed. An electromagnetic shutter is synchronized with the engine, so as to expose the film for only the part of the cycle that is of interest.

When sparks are used as the light source for the schlieren pictures, the round-hole light source is replaced by a horizontal spark gap enclosed in a glass tube to confine the spark to a straight path, and the stop to obtain the schlieren effect consists of a slit in a plate. The condensers and distributor of the spark-photography apparatus give 13 sparks at a rate of about 1,000 per second.

With the schlieren set-up, most of the light from the combustion flame is eliminated in the optical train and does not register on the film. The combustion front is

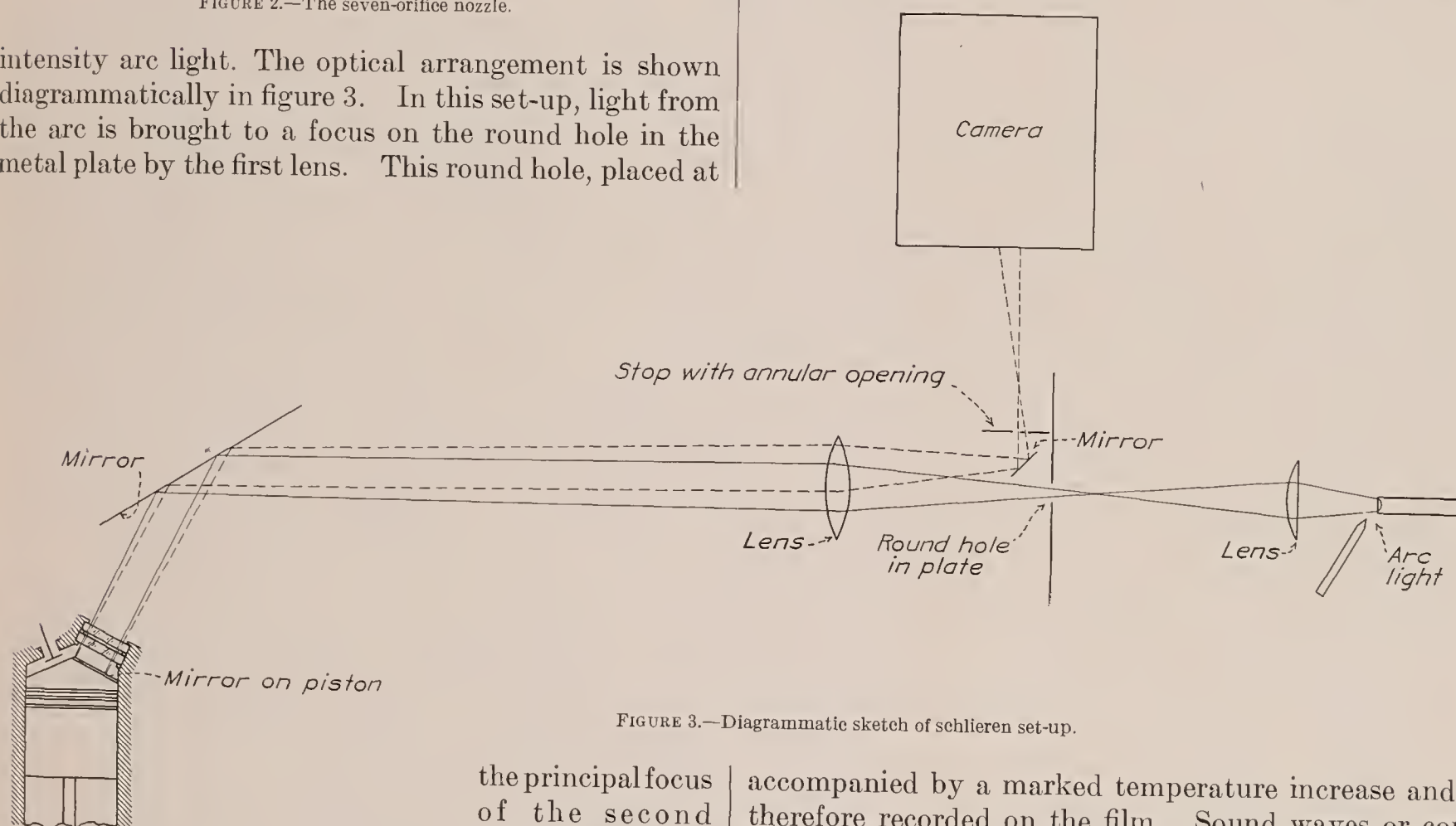


FIGURE 3.—Diagrammatic sketch of schlieren set-up.

the principal focus of the second lens, serves as the source of light. Light passing through the second lens is rendered parallel and is directed into the combustion chamber by the mirror and reflected back slightly offset from its original path by the mirror on the piston. The settings of the mirrors are such that the light is brought back through the second lens and to a focus slightly to one side of the original source. Thus it is possible to insert a small mirror in the optical path just before the light comes to a focus and to reflect the entire beam at a right angle. The round stop to obtain the schlieren effect is placed in the plane of the image, allowing only an annular ring of light to pass. The film drum of the camera is placed at the image of the combustion chamber formed by the second lens. A stop with a $\frac{1}{8}$ -inch slit is placed in front of the film drum, so that the image

accompanied by a marked temperature increase and is therefore recorded on the film. Sound waves or compression waves, which are accompanied by local changes in density, also are shown by the schlieren method. A $\frac{1}{2}$ -inch space on the side of the chamber nearest the usual position of the spark plug was not covered by the mirror on the piston.

RESULTS

The high-speed motion pictures reproduced in figure 4 show the effect of air-fuel ratio on nonknocking flame propagation with spark plugs at E and F (fig. 1). These tests were made at an engine speed of 1,500 r. p. m. The irregular flame fronts are characteristic of all the flame photographs that have been taken. The rate of flame propagation was somewhat slower for the lean mixtures, and two distinctly different types of afterburning were present in the rich and lean mixtures.

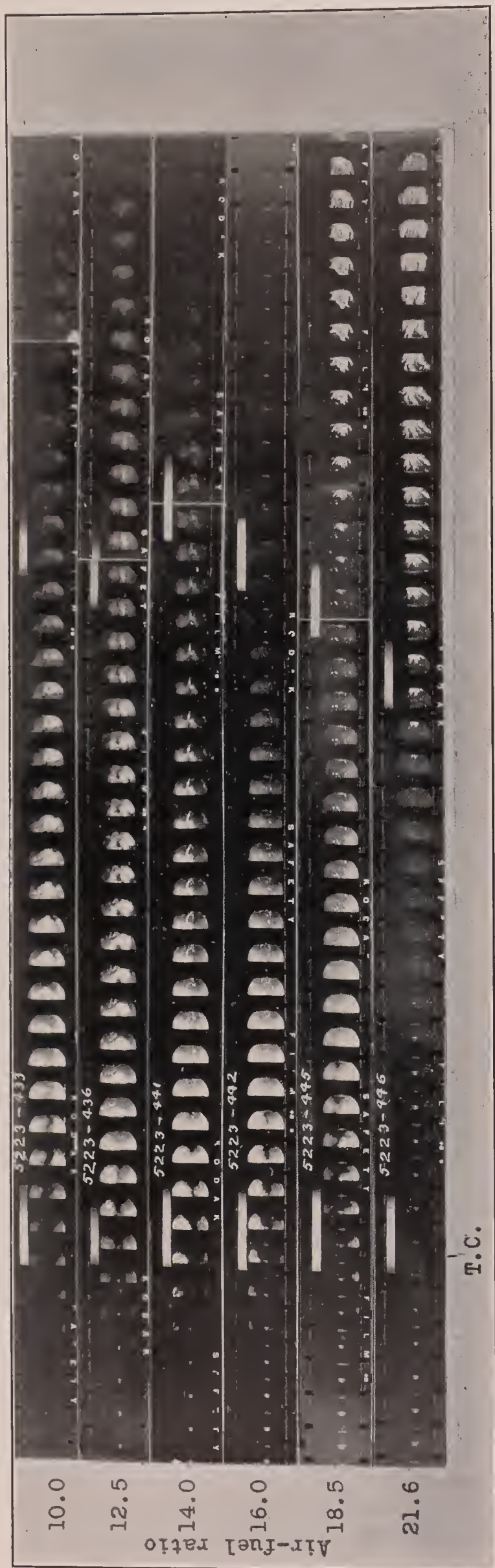


FIGURE 4.—Effect of air-fuel ratio on flame propagation. White marks on upper edge of each film correspond to T. C. and 90° A. T. C. Engine speed, 1,500 r. p. m.; two spark plugs; 87-octane fuel.

Details of the photographs are shown to better advantage in the enlargements in figures 5 and 6. In figure 5, at air-fuel ratios of 10 and 12.5, after the flame apparently passed through part of the chamber, an area of very bright illumination appeared behind the flame front as in the frames marked C, and in the succeeding frames this area spread rapidly across the window. In the last frames of the enlargements this bright area is the most prominent feature of the photograph. These areas, which appear suddenly and spread rapidly, do not behave like other regions of brightness, such as the region in the lower part of the window at an air-fuel ratio of 10 and the other bright spots that appear in many of the pictures. Withrow and Rassweiler observed a somewhat similar effect in their tests (reference 2) and attributed it to burning lubricating oil. This explanation appeared reasonable in their case because the brightness appeared as soon as the flame reached the edge of the cylinder. The piston and cylinder of the N. A. C. A. combustion apparatus, however, are lubricated by graphite and the apparatus has no oil in the crankcase. Hence, some other explanation must be sought. The effect appeared only at the richer mixtures and is probably associated with incomplete combustion. For the ratios of 18.5 and 21.6 the flame completely crossed the chamber; then, after the charge had apparently been burned, "afterburning" began and continued until long after the exhaust valves opened. To the eye the exhaust appeared a brilliant violet color.

Enlargements of the burning at the air-fuel ratio of 18.5 are shown in figure 6, and it can be seen that the flame had traversed the chamber by 30° after top center. The afterburning, as shown in the figure, always originates near the spray nozzle and is probably caused by the sudden addition of a small amount of fuel to the hot combustion gases, which still contain oxygen. Records of the pressure in the injection system indicated that a secondary injection of fuel might occur more than one crankshaft revolution after the start of the main spray. One other possible source of fuel is the well between the nozzle seat and the spray orifices. Approximately 0.003 gram of fuel is trapped in this well. It is not known whether such a small quantity of fuel vaporizing into the combustion gases could cause the intense illumination shown in the figures. Further tests are being conducted on the effects of air-fuel ratio.

In most of the photographs, small local areas of brighter illumination appear throughout the flame. These areas are not believed to be caused by uneven distribution of the fuel inasmuch as 100-octane fuel, differing little in volatility from the other fuels, burned with very uniform illumination.



FIGURE 5.—Effect of air-fuel ratio on flame propagation. Enlargements of high-speed motion pictures of figure 4 for air-fuel ratios of 10, 12.5, 14, and 16. Engine speed, 1,500 r. p. m.; two spark plugs; 87-octane fuel.

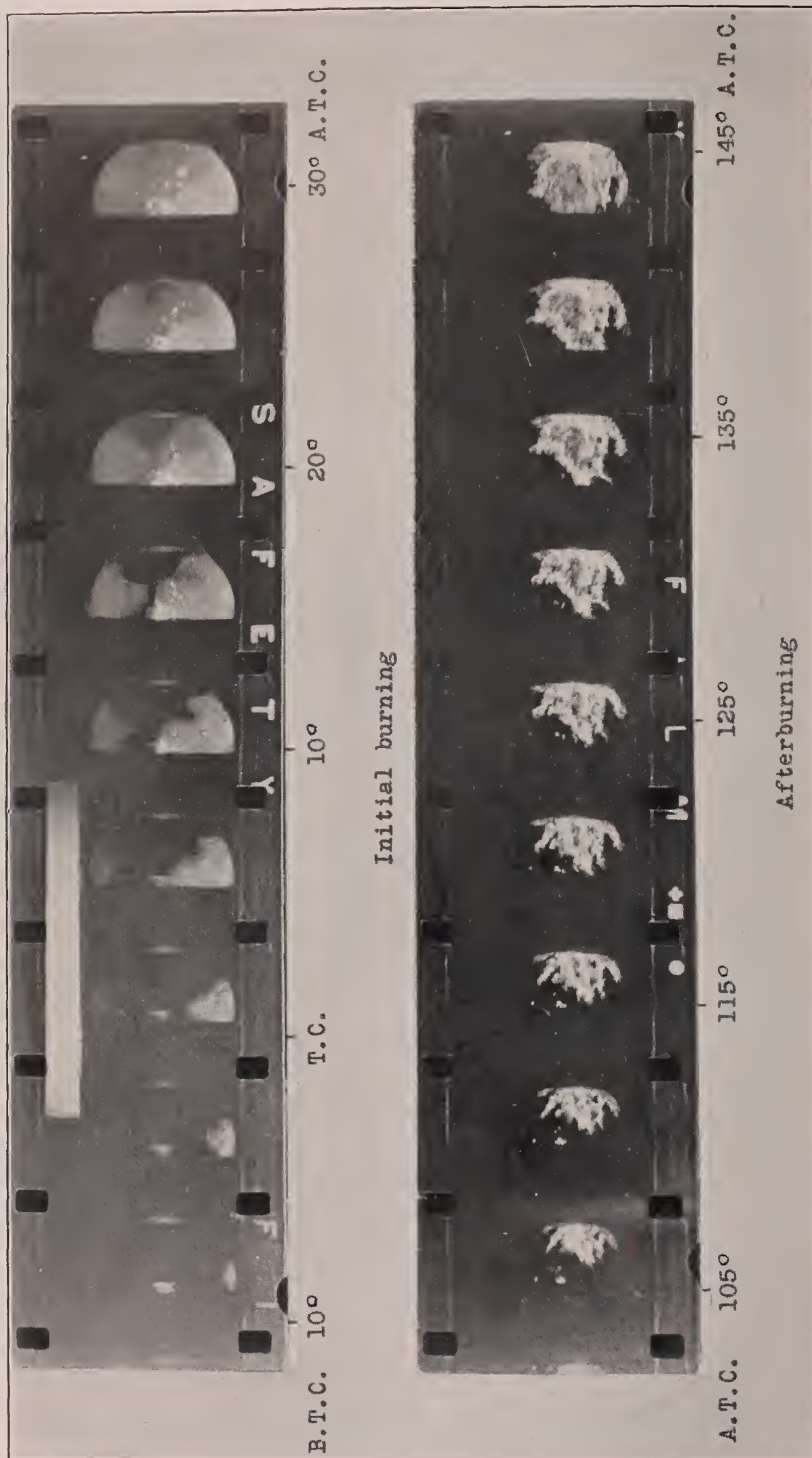


FIGURE 6.—Afterburning of lean mixture, after flame has traversed charge. Air fuel ratio, 18.5; exhaust valves open 125° A. T. C.; engine speed, 1,500 r. p. m.; two spark plugs; 87-octane fuel.

The high-speed motion pictures in figure 7 show the flames for fuels of different octane ratings with one spark plug at E. The outlines of the flames, for the first several frames, have been marked by a series of white dots for purposes of reproduction. Details of the photographs are more easily seen in the enlargements of figures 8 and 9. The photographs show an even illumination and a uniform rate of flame propagation for the nonknocking burning with the 100-octane fuel. For the knocking explosions, there was a sudden and definite increase in the intensity of illumination at the time in the cycle that knock occurred. This sudden increase in brightness at the time of occurrence of knock is characteristic of all the knocking explosions and increases in intensity with increasing violence of knock. It is not to be confused with the bright light given off by the 100-octane fuel, which has a very high actinic value, the inflamed area being very bright and uniform throughout the entire explosion. The first appearance of the bright illumination is indicated by the frame marked A. It will later be shown that the time of appearance of the bright light coincides exactly with the appearance of pressure waves, hence may be used to indicate the first appearance of knock.

The records for octane ratings of 18 and 30 show a sudden inflammation of the end gas just prior to the appearance of the bright illumination. The photographs for the 40- and 50-octane fuels also indicate that a sudden inflammation of the end gas took place but, in this case, the sudden increase in flame travel and the sudden increase in illumination are shown in the same frame. The record for 65-octane fuel shows that the flame proceeded at a uniform rate across the chamber; then, after the chamber was filled with flame, the characteristic bright light associated with knock appeared. As nearly as can be determined, the violent vibrations that appear on indicator cards of knocking explosions correspond in point of time to the appearance of this bright light. The vibrations shown on the indicator cards for the 65-octane fuel were more violent than those for explosions of some of the fuels of lower octane ratings.

Figure 10 is a composite of indicator cards and streak schlieren photographs, taken with fuels of different octane ratings. The spark plug (at E, fig. 1) was located at the bottom of the strip as it is shown in the figure. For 100-octane fuel, the rate of combustion-front travel was somewhat slower than the rate for the other fuels. This result may or may not be significant. There is no indication of any vibration in the gas. The maximum pressure shown by the indicator card for the 100-octane fuel is about 800 pounds per square inch.

Each of the other three records shows knocking explosions with the characteristic gas vibrations, the frequency of which corresponds approximately to the frequency recorded on the indicator cards. The slit through which the photographs were taken did not

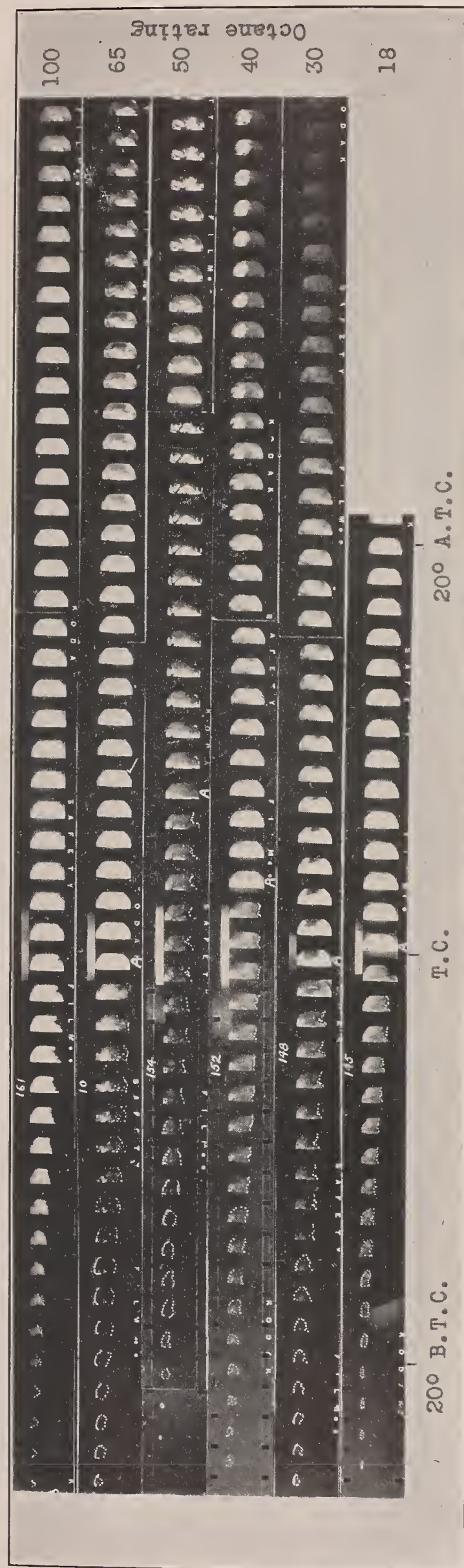


FIGURE 7.—High-speed motion pictures showing effect of fuels of different octane ratings on combustion knock. Air-fuel ratio, 14; A, first evidence of knock; engine speed, 500 r. p. m.; one spark plug.

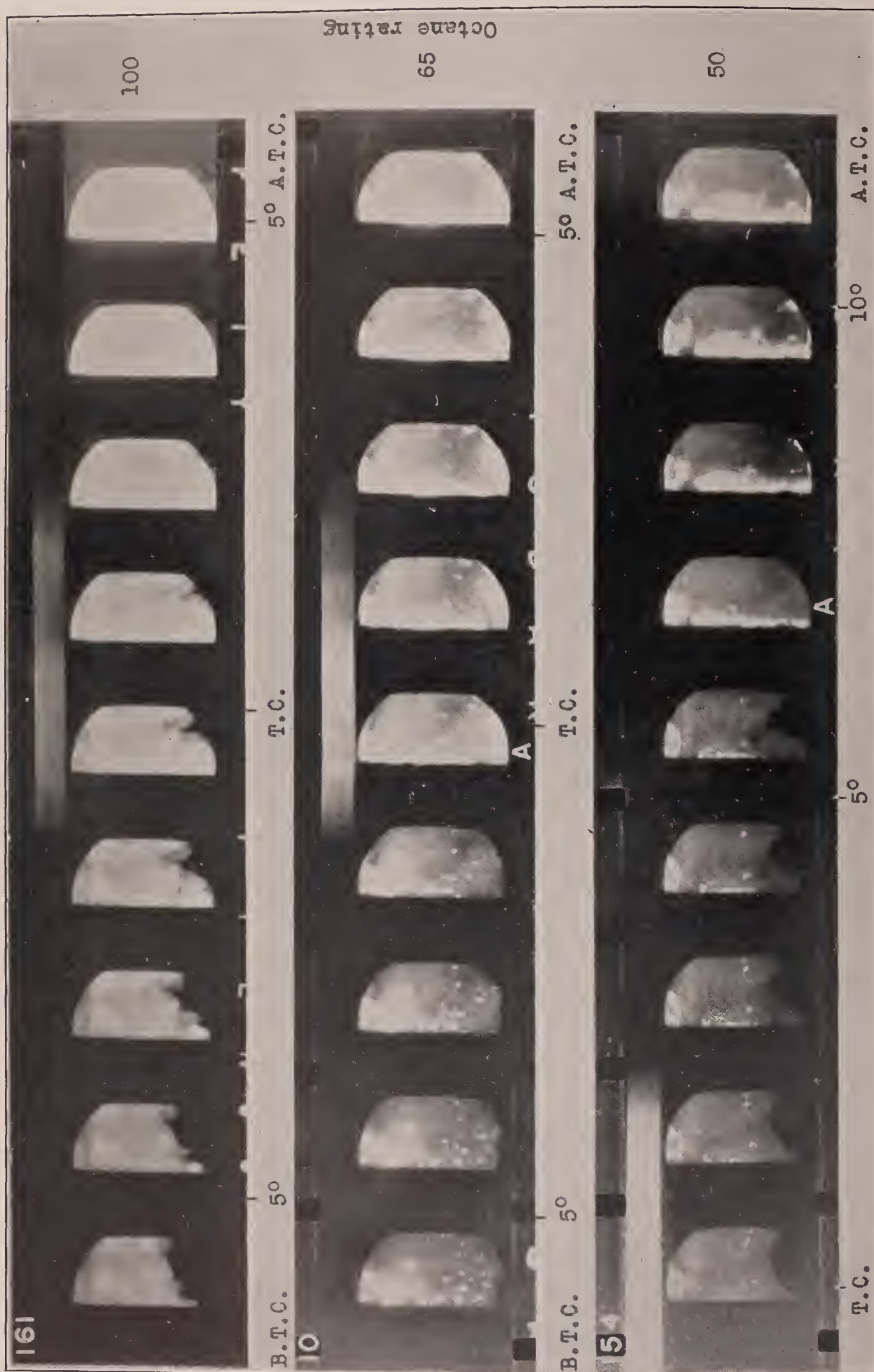


FIGURE 8.—Enlargements of high-speed motion pictures showing effect of different octane ratings on combustion knock. Air-fuel ratio, 14; A, first evidence of knock; engine speed, 500 r. p. m.; one spark plug. Octane ratings, 100, 65, and 50.

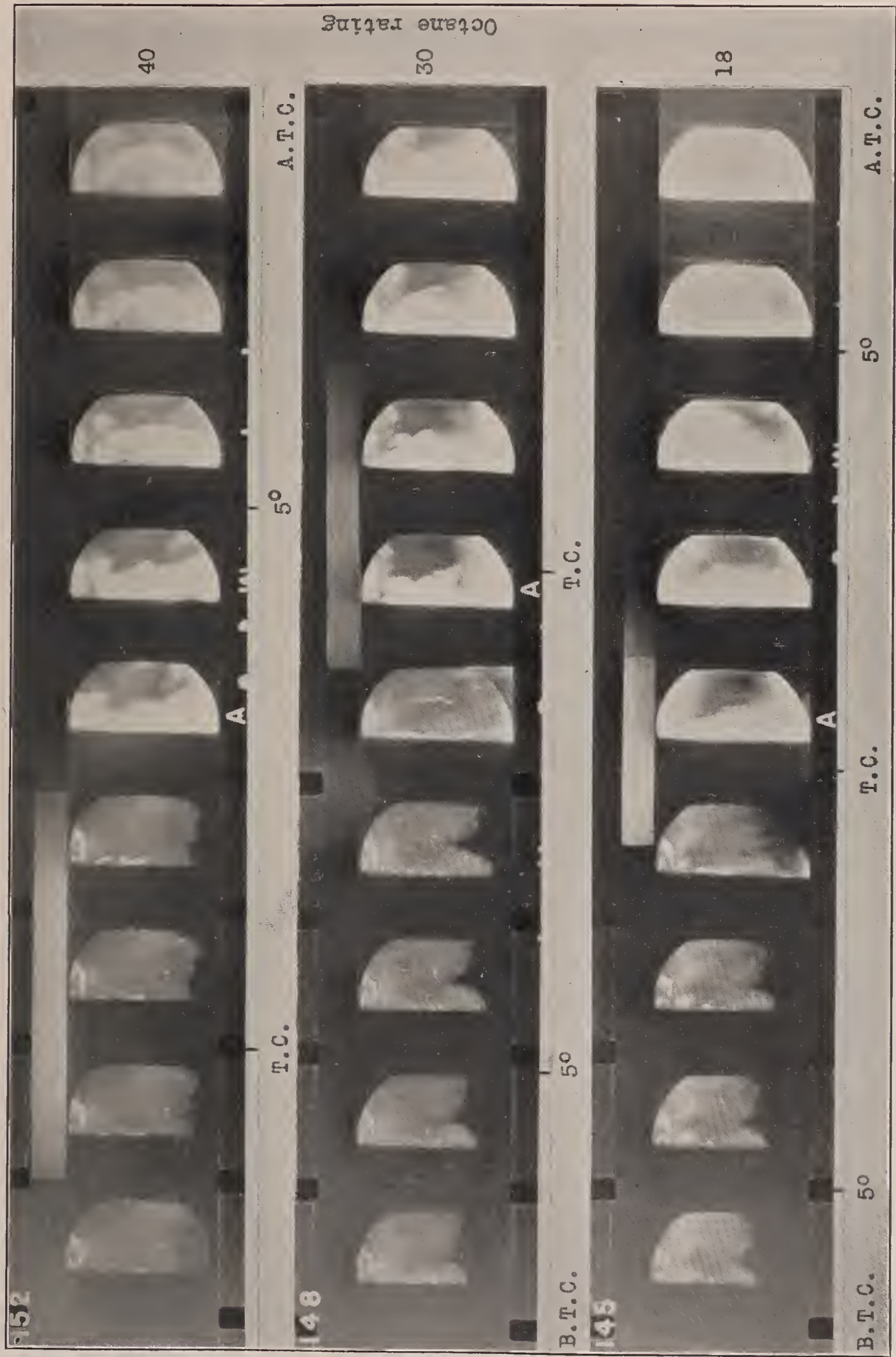


FIGURE 9.—Enlargements of high-speed motion pictures showing effect of different octane ratings on combustion knock. Air-fuel ratio, 14; A, first evidence of knock; engine speed, 500 r. p. m.; one spark plug. Octane ratings, 40, 30, and 18.

necessarily include the knocking zone. With the two fuels of lowest octane number, there is a marked reverse movement in the combustion front before the appearance of the gas vibrations. The indicator cards for these two fuels show a sudden slight rise in pressure just prior to the violent vibrations in the pressure record. Evidently there is a sudden release of energy during this latter part of the burning, and it appears probable that the slight rise in pressure prior to knock

bands is the same as the frequency of the waves in the schlieren record, visible in the right-hand portion of the record; they begin simultaneously with the pressure waves and are believed to be caused by successive reillumination of the charge as the pressure waves passed through it. Therefore either a sudden appearance of a brighter light, as at A in figure 7, or the appearance of pressure waves may be used to indicate the start and occurrence of knocking.

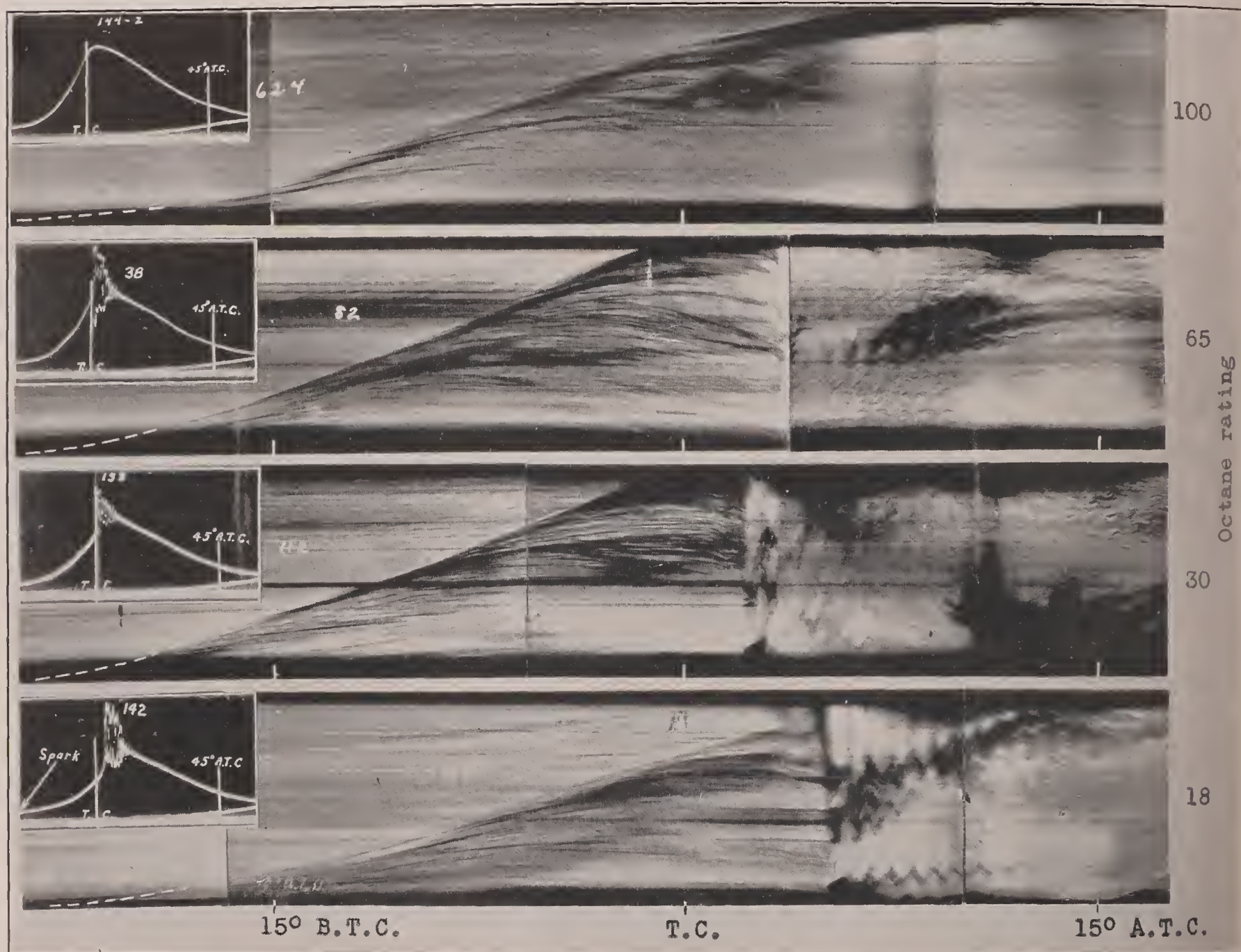


FIGURE 10.—Indicator cards and schlieren photographs showing effect of different octane ratings on combustion knock. Air-fuel ratio, 14; engine speed, 500 r. p. m.; one spark plug.

and the reverse movement in the combustion gases are caused by the auto-ignition of the end gas. It is important to note that only the records for explosions in which auto-ignition is indicated show this slight rise.

For the record presented in figure 11, adjustments were made to the optical system to permit more of the intensely brilliant light from the knocking combustion to record on the film. In this case, some of the light from the combustion prior to knock also recorded in the $\frac{1}{2}$ -inch space nearest the spark plug, where the mirror did not cover the piston. The series of vertical bright bands across the record are evidently successive images of the $\frac{1}{8}$ -inch slit. The "frequency" of these

Motion pictures of the flame and spark schlieren motion pictures taken simultaneously but from slightly different angles are reproduced in figure 12 for a single spark plug at position G. When the refractive index of the charge is uniform throughout, the spark schlieren field appears uniformly illuminated except for spots, lines, and shaded areas caused, respectively, by dirty spots, strain lines, and irregularities in the mirror or window surfaces. When combustion appears in the field, it is visible because of the temperature change and, with the type of schlieren arrangement used, the combustion front appears darker than the field. The region back of the combustion front also appears dark

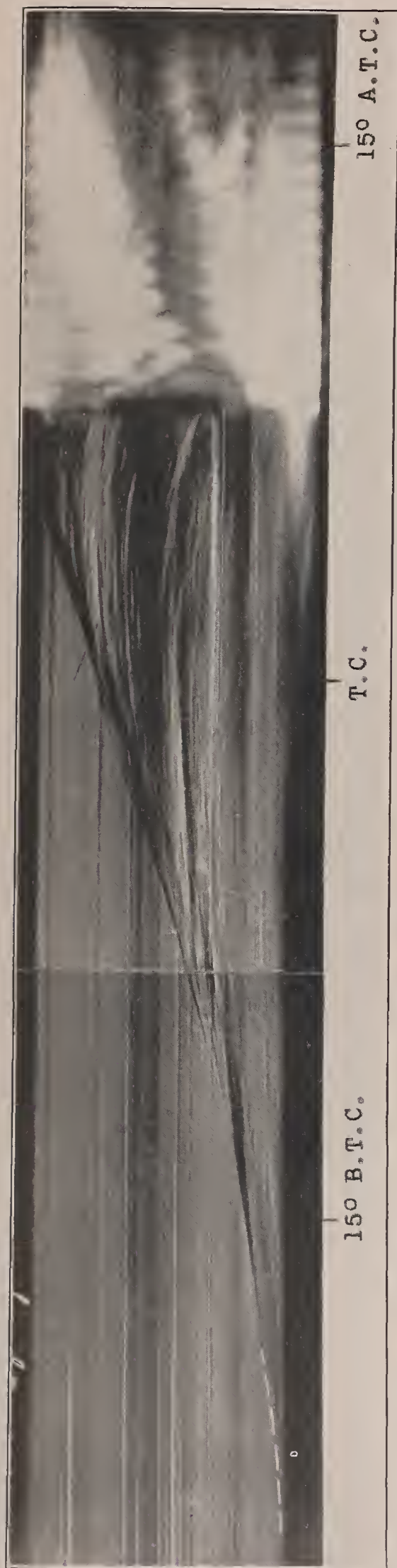


FIGURE 11.—Schlieren photograph of knocking combustion, with light from knock recording on film. Air-fuel ratio, 14; engine speed, 500 r. p. m.; one spark plug; 50-octane fuel.

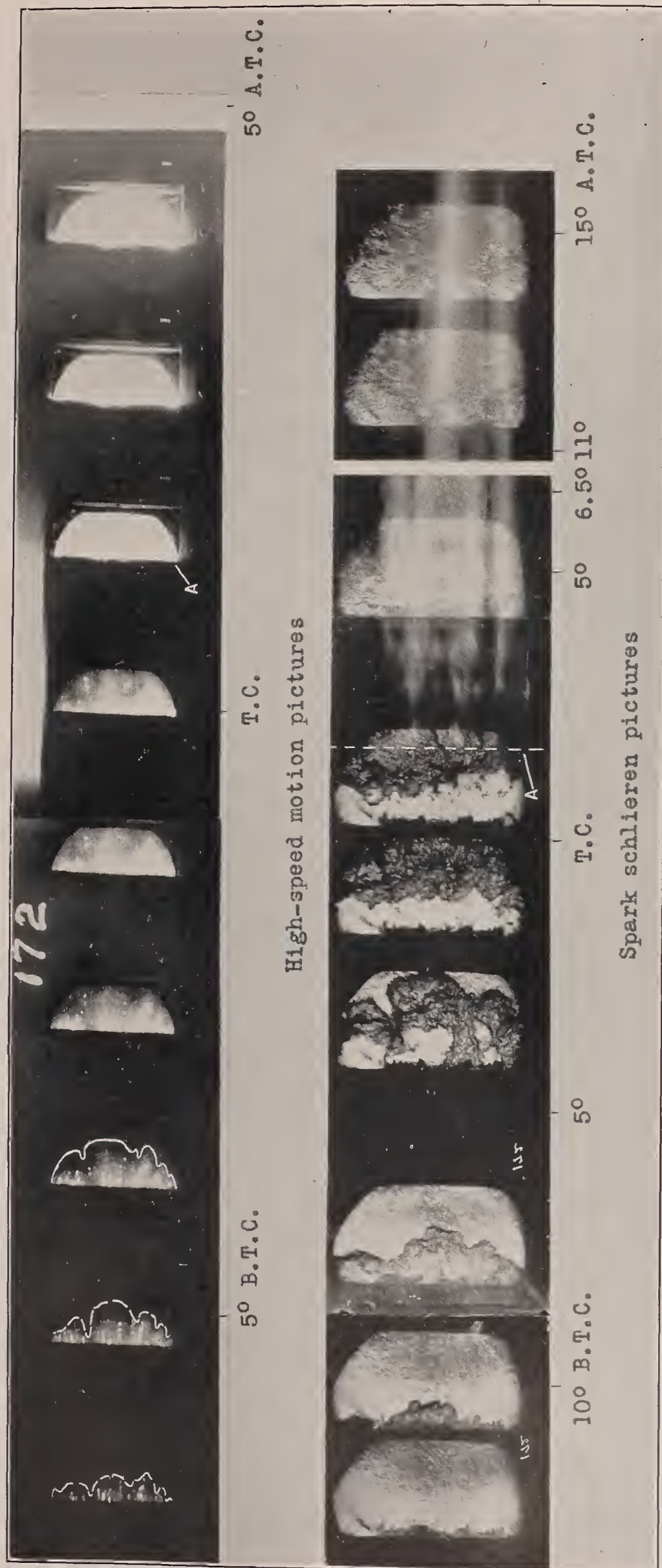


FIGURE 12.—High-speed motion pictures and spark schlieren photographs taken simultaneously, showing flame propagation and knock. Air-fuel ratio, 14; A, first evidence of knock; engine speed, 500 r. p. m.; one spark plug at back of chamber; 55-octane fuel.

for a distance of from 1 to 2 inches, then a sharp line of demarcation appears between this dark region and the area that has been burned. This dark region will hereinafter be referred to as the "reaction zone." One of the most striking features of the spark schlieren pictures is the sharp distinction between the reaction zone and the burned gases behind it, which appear fully as uniform in refractive index as the unburned charge ahead of the flame.

In the photographs of figure 12, since the spark plug was located at the back of the chamber, the combustion was halfway across the chamber before it was visible. The first frame on the left of the schlieren series shows the field as it appeared before the flame reached the window. The irregular dark region along the left-hand edge of the window, which might at first be taken for the combustion front just appearing in the field, was caused by the fuel spray that struck the upper edge of the mirror and evaporated, leaving a slight deposit of dust and carbon particles. The combustion front appears first in the second frame. The third frame shows the front still farther across the window and, in the fourth frame, the combustion front had almost crossed the window, with some areas of unburned charge still remaining. In this frame, the clear spaces back of the reaction zone (on the left in the figure) first appeared. The reaction zone in this case appeared to cover somewhat more than half of the $2\frac{1}{2}$ -inch width of the window. In the next frame (fifth from the left), the combustion front had crossed the window and the rear edge of the reaction zone had become more even, leaving a clear space between the edge of the window and the rear of the reaction zone. The reaction zone advanced very little between the fifth and sixth frames and, immediately after the sixth frame, knock occurred. The time of occurrence of knock was determined by the fogging of the film by the sudden bright light accompanying knock. Line A indicates the beginning of the fogged streaks. The point where the streaks start, of course, is the point at which the light from the knocking combustion at the left-hand edge of the window first struck the film.

After the reaction zone has passed through the chamber, the spark schlieren pictures again show a relatively clear field. There are no longer any large regions of different refractive index but the entire field has a rippled or corrugated appearance. These ripples may indicate air flow, local areas of smoke or soot, or some system of heterogeneous waves in the combustion gases. Referring to the high-speed motion pictures of figure 12, note that the frame just to the left of top center corresponds most nearly in time to the fifth schlieren picture. The direct flame photograph makes no distinction between the reaction zone and the burned region. Furthermore, the most intense light, as shown by the flame photograph, came from the region back of the reaction zone where the schlieren photograph shows no marked temperature gradients.

It should be noted particularly, when the spark schlieren pictures are compared with the flame pictures, that the outlines of the combustion front as shown by the schlieren pictures appear to correspond very closely to the outlines of the visible flame in the flame pictures. The third frame from the left of the flame photographs and the fourth frame of the schlieren photographs correspond fairly closely in point of time.

In the first three frames of the motion picture, the flame front has been outlined in white for purposes of reproduction. By the fourth frame, the flame had covered most of the chamber and, in the next two frames, it covered the chamber and the intensity of illumination increased. Knock then occurred, and the brilliant illumination was first evident in the frame marked A, just after top center.

Investigations of combustion in bombs have indicated that shock waves, originating at or behind the flame front, may traverse the charge at a velocity greatly in excess of the flame velocity and gain such intensity as to cause auto-ignition of the charge at the opposite end of the chamber (reference 10). Although the streak schlieren photographs of knocking combustion (figs. 10 and 11) showed no evidence of such waves, a further investigation was undertaken to determine the effect of artificially induced waves on the knocking tendency.

Figure 13 is a composite of indicator cards and streak schlieren photographs and shows the effects of artificially induced shock waves on the combustion. The waves were induced by discharging a 2-microfarad condenser charged to 30,000 volts through a 0.004-inch diameter copper wire stretched inside the engine at E. When the condenser was discharged, the wire exploded with considerable violence. At these conditions, knock was intermittent when no shock waves were induced. Figure 13 (a) shows the wire exploding behind the combustion front that was started by a spark plug at E, when the combustion was about halfway across the chamber, as indicated by the point B. The shock waves traversing the chamber caused pronounced ripples in the trace of the combustion front as it was alternately accelerated and decelerated. There is no indication that knock occurred. Figure 13 (b) is a similar photograph, with the wire exploding slightly earlier. Knock occurred in this case, but there is no indication that it was influenced by the shock waves from the exploding wire. When the combustion was started from the spark plug at E, the wire could not be exploded at any later time than shown because the wire melted from the combustion heat.

Figures 13 (c) and 13 (d) show the effect when the combustion started from the opposite side of the chamber (spark plug at F); the wire exploded when the combustion was about halfway across the chamber. The charge knocked both times. Figure 13 (e) shows the wire exploding at a later stage of the burning; in this case there was no knock.

Records (not shown) taken with the wire exploding after the combustion crossed the chamber always showed knock occurring at the same time the wire exploded. Apparently if the charge was about ready to knock of its own accord, the shock from the exploding wire acted as a "trigger" to set off the knock.

The indicator cards (fig. 13) were taken at conditions similar to those represented by the schlieren records

spark plugs on opposite sides of the chamber (E and F). In both photographs of figure 14 the two combustion fronts apparently meet and continue through each other, covering about half of the remaining distance across the chamber before merging with the general pattern of the burning. The combustion space is about 1 inch deep at this time, so there is little possibility that the two fronts passed each other at different

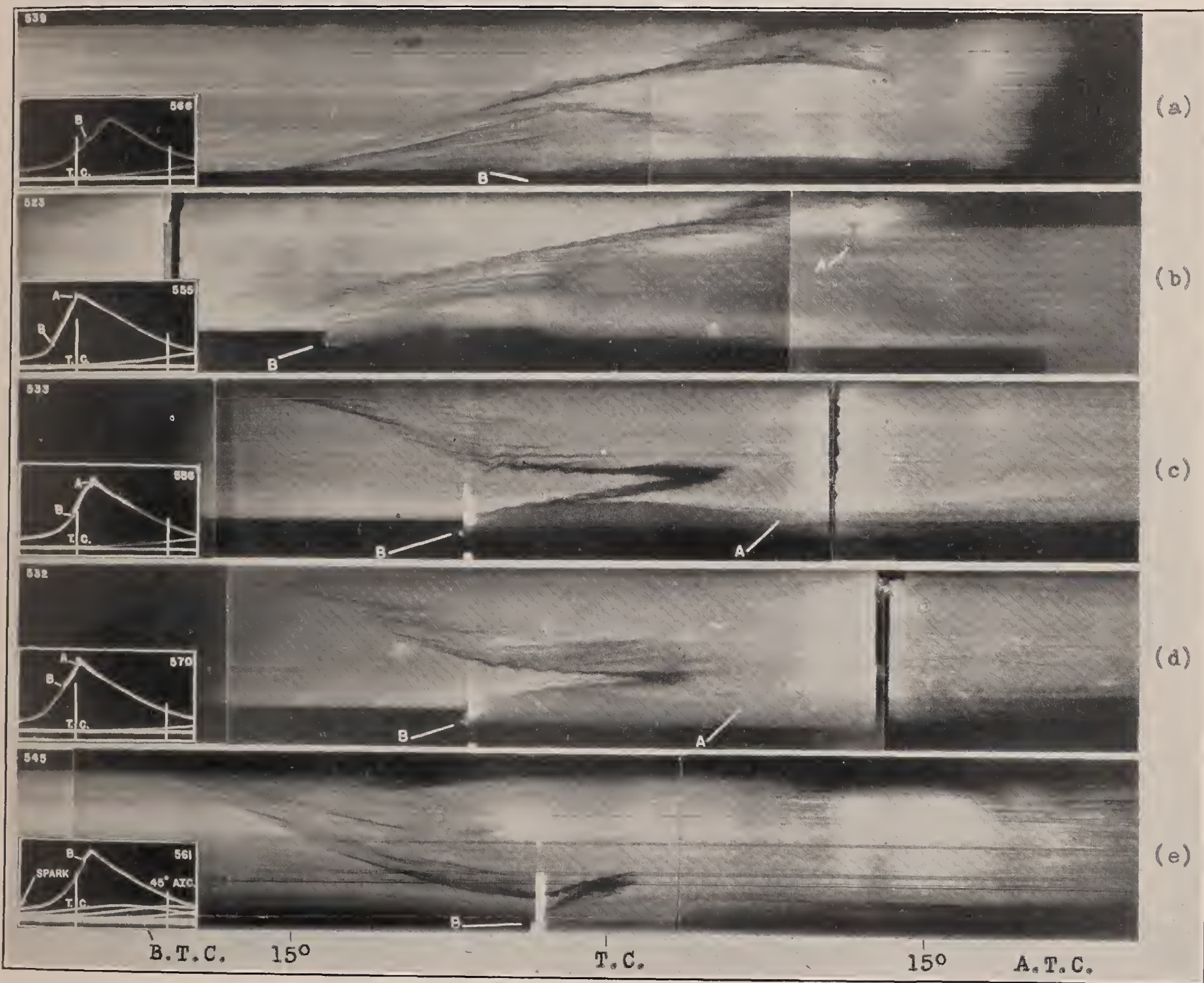


FIGURE 13.—Indicator cards and schlieren photographs showing effect of exploding wires on combustion knock. Air-fuel ratio, 14; A, first evidence of knock; B, wire explodes; engine speed, 500 r. p. m.; one spark plug; 87-octane fuel.

and show the gas vibrations caused by the exploding wire. Records 566 and 561 show no knock, whereas each of the other cards shows that knock occurred at or near the end of the combustion period.

The amplitude of the shock waves shown in figure 13 is comparable with the amplitude of the waves set up by moderate knock. There is no indication, however, that waves of this intensity will in themselves cause knock.

Figures 14 and 15 are schlieren photographs showing combustion, with and without knock, started from two

levels in the chamber. In the knocking explosion, the two flame fronts had met before knock occurred.

Figure 15 also shows that the two combustion fronts in the knocking explosion met each other before knock occurred, so that no region of noninflamed charge remained in the visible field to auto-ignite. A region of noninflamed charge may have existed in the half of the combustion chamber not covered by the window. The photographs of the nonknocking explosion show the reaction zones meeting at the fifth frame from the left. A small, roughly triangular region still remained on

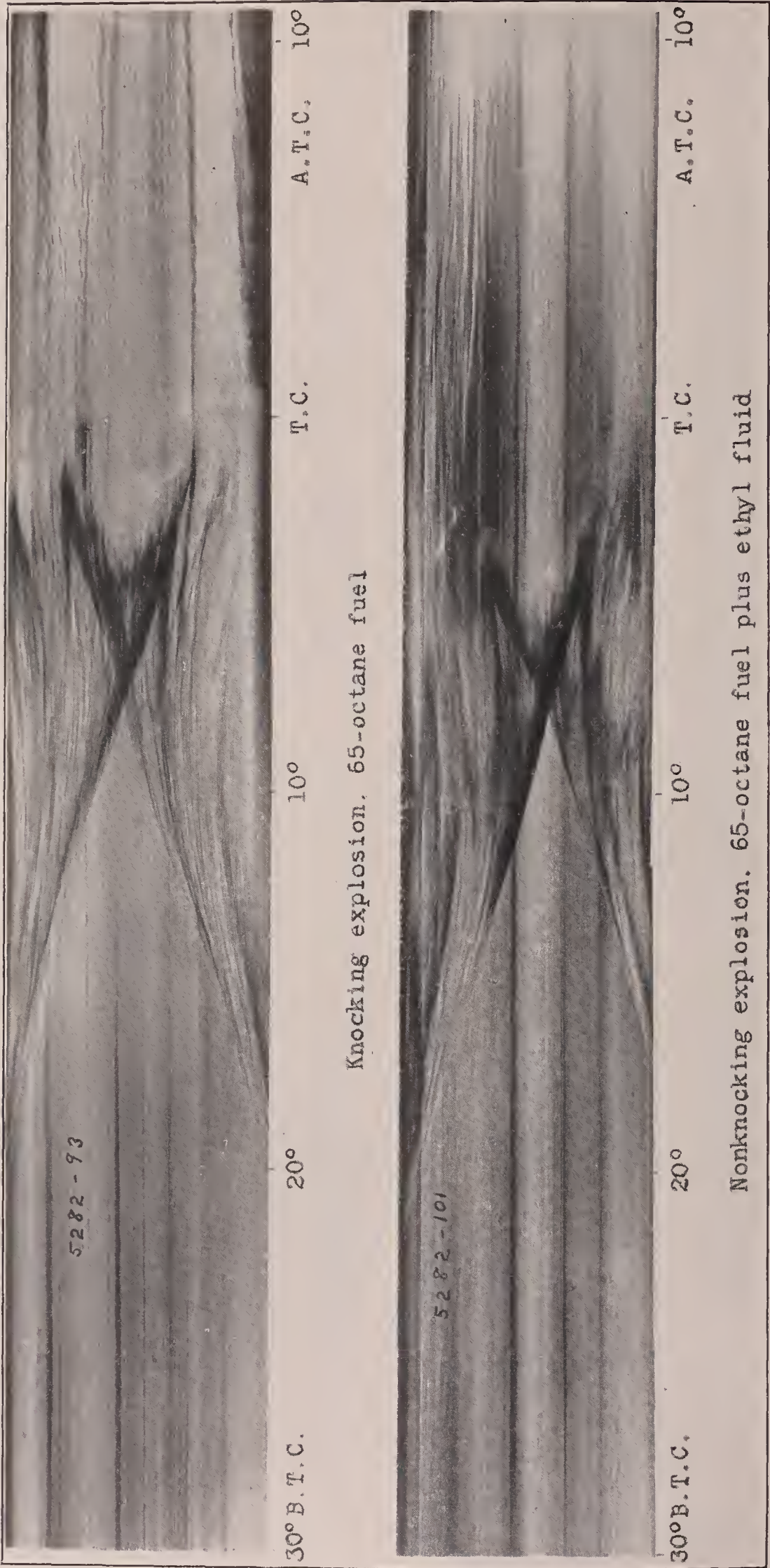


FIGURE 14.—Schlieren photographs showing two flame fronts passing through each other. Air-fuel ratio, 14; engine speed, 500 r. p. m.; two spark plugs.

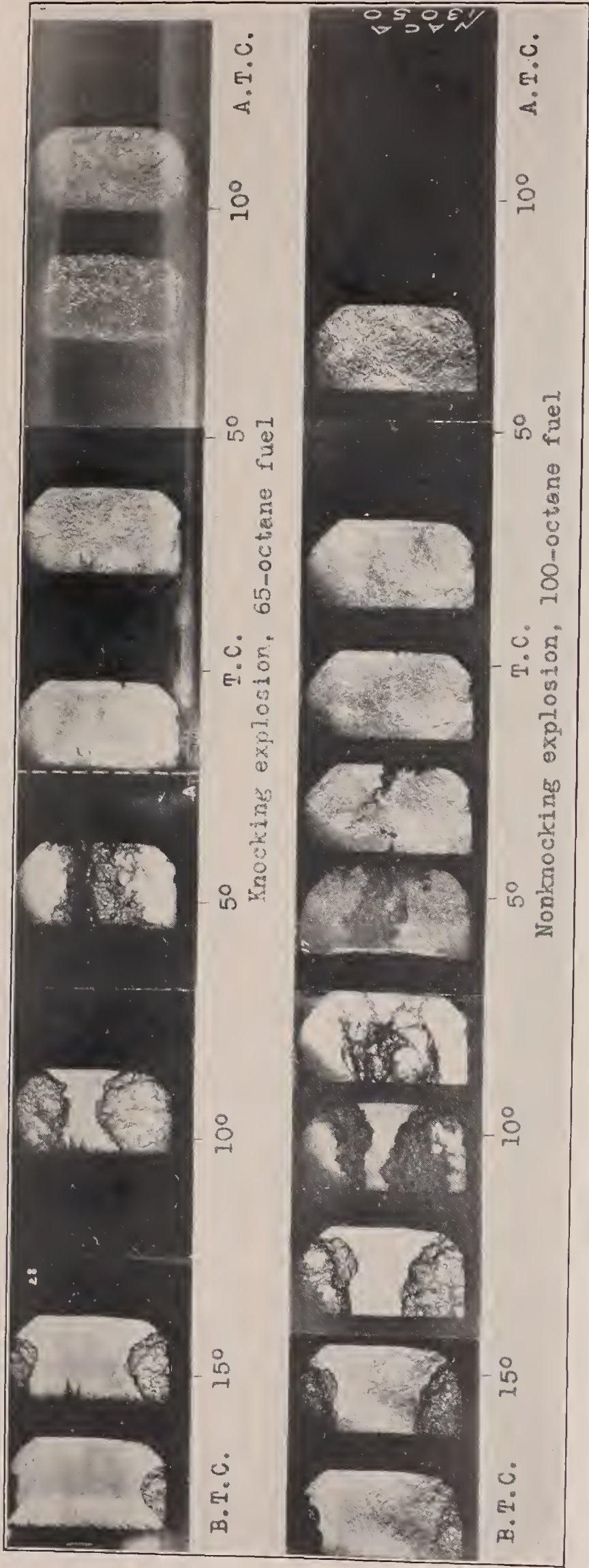


FIGURE 15.—Spark schlieren photographs of knocking and nonknocking explosions. Air-fuel ratio, 14; A, first evidence of knock; engine speed, 500 r. p. m.; two spark plugs.

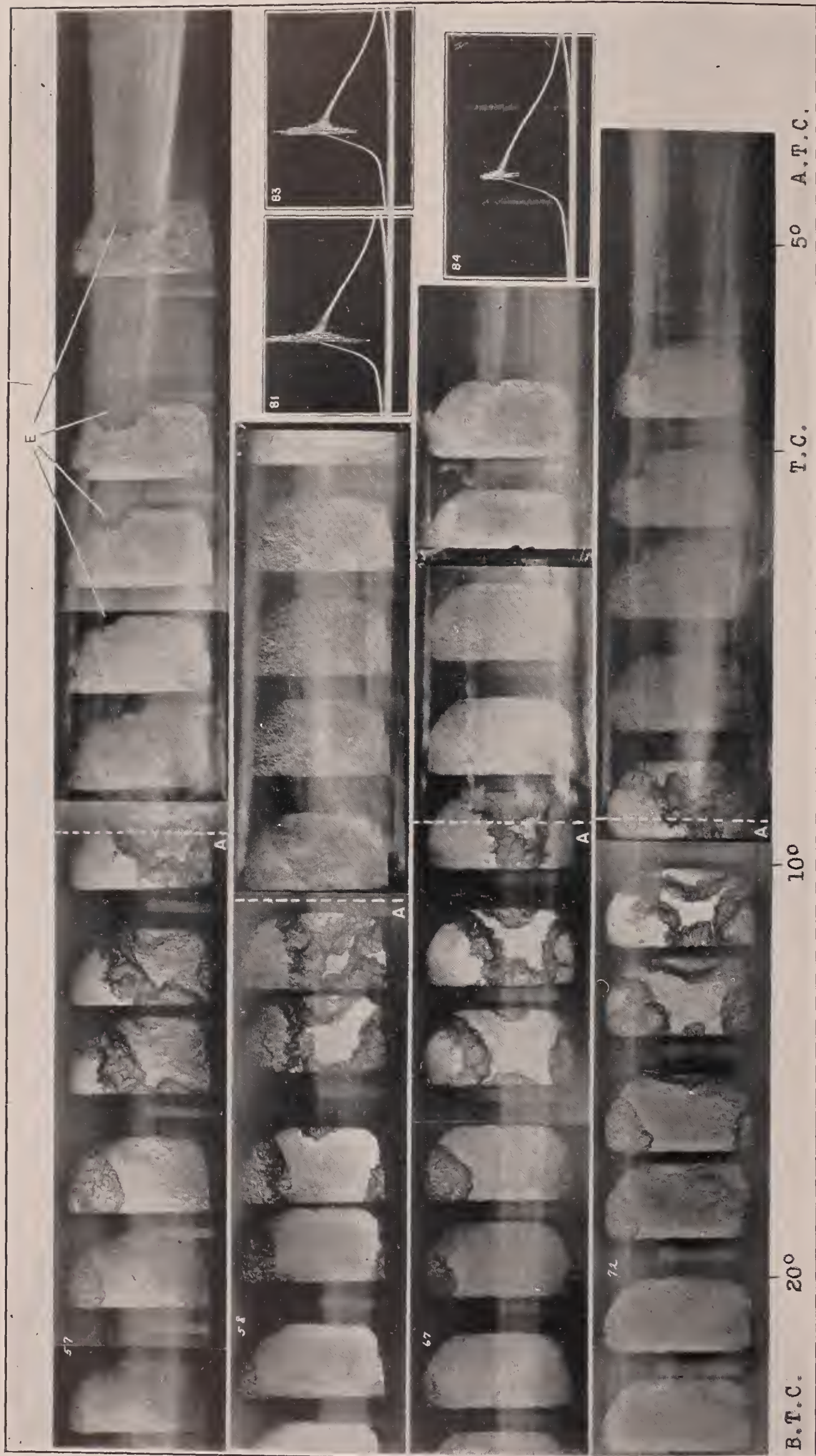


FIGURE 16.—Schlieren photographs and indicator cards of knocking explosions with last part of charge to burn localized beneath window. Air-fuel ratio, 14; A, first evidence of knock; E, indications of smoke; octane rating, between 50 and 60; engine speed, 500 r. p. m.; four spark plugs; spark advance, left-hand plug 30°, other three plugs 27°.

the right-hand side of the frame, as yet not reached by the reaction. The sixth frame shows the reaction zone still persisting, though somewhat narrower than in the previous frame. Apparently the entire chamber had been reached by the reaction. In the seventh frame, most of the reaction zone had disappeared but a small spot, corresponding roughly in shape and location to the noninflamed spot in the fifth frame, still persisted. The appearance of the succeeding frames is very similar to that of the corresponding frames for the knocking explosion, showing only the rippled or corrugated appearance characteristic of the combustion gases when the reaction is apparently completed.

In order to insure that the last part of the charge to burn was in the field of view, photographs (fig. 16) were taken showing the combustion when four spark plugs were so arranged that the last point reached by combustion was directly beneath the window. The four spark plugs were located at E, F, G, and J, and the injection valve was located at H. The spark plug at G was timed to fire 3° ahead of the other three plugs, so that the combustion front from the back of the chamber reached the window with the other three combustion fronts. In each of the four strips of photographs, the combustion fronts approached each other from the four sides of the window, localizing a small portion of the charge directly beneath the window. The bottom strip in figure 16 (record 72) shows that the four combustion fronts had merged before knock occurred, and other photographs that have been taken with this arrangement indicate the same merging preceding knock. Generally, the last frame before knock occurred showed a small region not yet reached by the combustion, as shown in the other three strips in figure 16. There is no reason to believe, however, that this small region had not been reached by the combustion before knock occurred because in each case sufficient time for the combustion fronts to merge had apparently elapsed between the time the last frame before knock was taken and the time of occurrence of knock. The white dashed lines, marked A on the figure, correspond to the position of the left-hand edge of the image of the window when knock occurred. Inasmuch as the film was wrapped on a rapidly rotating drum and the light from the knock continued for as long a period as one revolution of the drum, the fogged streaks usually continued around the film and show on the left-hand part of the pictures.

In no case, in the more than 50 photographs taken at these same conditions, was there any indication of any auto-ignition ahead of the combustion fronts, or of any sudden increase or decrease in the speed of combustion propagation.

The indicator cards shown in figure 16 are representative cards taken at the same conditions as the photo-

graphs. It is seen that the intensity of knock varied greatly from cycle to cycle. The extreme violence of the vibrations in record 81 is probably caused by the location of the indicator diaphragm immediately above the last portion of the charge to burn. It was noted during the work that fine cracks appeared in the surfaces of the glass mirror and the window in the general region of the last part of the charge to burn. These cracks were probably caused by the intense heat of the knocking combustion.

Another feature of interest appears in the upper strip of figure 16. In the eighth frame from the left, a small dark area appears in the image, where no light was transmitted. This area (marked E) grows rapidly larger in the succeeding frames. Simultaneously, with the appearance of the opaque area, a very bright fogged streak begins in exactly the same region and grows larger in unison with the opaque area. Evidently this area, although opaque to the light from the sparks for the schlieren pictures, is at the same time emitting light of extreme intensity. It is believed that the opaqueness of the area is caused by smoke. The appearance of black smoke in connection with knock is often observed. This black smoke is frequently encountered with the combustion apparatus, which is kept free from carbon and is run without oil. Evidence of the same effect appears to a lesser extent in the other pictures of figure 16, and to a greater or a lesser degree in a great many of the photographs of knocking explosions. Record 117 (fig. 10) shows the same effect in a streak schlieren picture.

Schlieren photographs of four explosions are shown in figure 17, in which the spark plug was located at position H so that the flame traveled diagonally across the window. With this arrangement, the half of the chamber not covered by the window was crossed by the combustion before combustion was completed under the window, and the last portion of the charge to burn was located in a part of the chamber most of which was in the field of view of the camera. The outline of the cylinder is shown in white around the frame photographed just prior to knock. In each case, the combustion is shown to be either across the chamber or almost across, before knock occurred.

DISCUSSION

Any study of combustion in internal-combustion engines is necessarily handicapped by the fact that the individual investigator works with relatively few types of engines; whereas the results must be correlated with a great variety of engines and operating conditions. This handicap is particularly true in a photographic study of combustion, where the combustion-chamber shape and engine operating conditions are necessarily limited.



FIGURE 17.—Schlieren photographs and indicator card of knocking explosions with one spark plug at H (fig. 1). Air-fuel ratio, 14; A, first evidence of knock; C, outline of cylinder; engine speed, 500 r. p. m.; spark advance, 30°; 75-octane fuel.

The combustion apparatus in its present form is very similar to some types of engine, with the exception that, inasmuch as the combustion apparatus fires only once, there can be no exhaust gases present in the charge. The cylinder walls are also cooler than would be the case in an engine running continuously. The preliminary tests reported in reference 3 have shown that the apparatus behaves in a manner similar to that of a conventional engine, and it is believed that data obtained with this engine are as generally applicable as are the results obtained on any one engine.

Shock waves.—Payman and Titman (reference 10) have published a series of flame and schlieren photographs of explosions and detonations in a tubular bomb. These photographs show very clearly the formation of a shock wave preceding the combustion front and causing auto-ignition at the end of the bomb. It has been believed that possibly a similar wave may occur in engines under knocking conditions. The data presented in this report show no evidence of any such high-velocity wave and show, in addition, that if such waves are artificially induced in the engine cylinder they do not cause knocking. The flame photographs shown by Boerlage (reference 11), however, are very similar to the flame photographs shown by Payman and Titman, which show auto-ignition at the end of the combustion chamber. The schlieren photographs of Payman and Titman show the auto-ignition to be caused by a shock wave. Although the auto-ignition of the charge at the end of the combustion chamber away from the spark plug in Boerlage's tests may be caused by the hot wall of the chamber, the possibility of a detonation wave must not be overlooked.

The brilliant light given off by knocking explosions is evidently caused by the shock waves that follow knocking, further compressing the hot gases in the combustion chamber. The record in figure 11 shows this phenomenon to best advantage. The recompressed gases may be so highly heated by the shock waves that dissociation occurs, giving free carbon in the exhaust and resulting in smoke, as indicated in figure 16. The light areas shown in figures 10 and 13 at about 15° A. T. C. are due to the change in the direction of the light beam caused by the piston slap and are not to be confused with the sharply defined phenomenon shown in figure 11 or the light streaks shown in figures 12, 15, 16, and 17.

Relation of auto-ignition to knock.—Some of the photographs shown herein indicate that auto-ignition of the last part of the charge to burn occurred during some of the more severe knocking explosions. (See figs. 9 and 10.) This result is in accordance with the findings of Withrow and Rassweiler reported in reference 2. In a number of other instances, however, the combustion front appeared to be across the chamber before the occurrence of knock, as is shown in figures 8 and 10 (record 82) to 17. The explosions shown in figures 16

and 17 knocked with extreme violence, yet the reaction fronts had crossed the chamber before knock occurred. Results similar to these have been obtained in a bomb by Maxwell and Wheeler (reference 12). Their photographs of explosions of hydrocarbon vapors and air show, in a number of instances, the flame traversing the chamber before knock occurred. They also obtained ignition of the unburned charge ahead of the advancing flame, although the explosions in those cases were no louder than usual and the pressure records showed no unusual features. Some investigators have suggested the probability that more than one kind of knock can occur. Stansfield and Thole (reference 13) mention three types as being possible; namely, "true pinking"; auto-ignition of the unburned portion of the charge when compressed adiabatically by the advancing flame front; and preignition. They define preignition as auto-ignition of unburned mixture either before the spark passes or, more usually, before more than a small part of the charge has burned. Boerlage and his coworkers (references 14 and 15) mention "pink" and "knock" as being distinct phenomena.

It is probable that the distinction should be limited to that between "knocking" (detonation) and "post-ignition." Postignition is a secondary combustion front originated by a hot surface ahead of the primary combustion front, whereas knocking is a gaseous reaction taking place with sufficient violence to set up sonic or supersonic waves in the combustion gases. Postignition may result in rough running from excessive flame velocities as found by Souders and Brown (reference 16), which may in turn develop into knocking. A distinction becomes particularly important in the matter of rating fuels. The fact that Withrow and Rassweiler's results (see reference 2) show a time interval of about 0.0013 second for the knocking explosion to fill the unburned portion of the chamber indicates that the phenomena they recorded may have been postignition from the combustion chamber wall rather than knocking. The same fact may be true in regard to the results presented by Boerlage in reference 11.

Duration of the reaction.—The afterburning (as distinct from postignition) shown in figure 5 for rich mixtures indicates that a reaction causing a reillumination of parts of the charge may occur after the flame front has passed through the charge. The two streak schlieren photographs of figure 14 and all the spark schlieren photographs indicate that some reaction which changes the density of the charge or, more precisely, the refractive index, continues for some time after the combustion front has passed through the charge. This interpretation of the schlieren photographs presupposes that no extreme curvature or tilting of the combustion front occurs. If the combustion advanced across the chamber as a narrow tongue, with a region of unburned charge between the inflamed region and the window, then the upper surface would appear as a dark area in

the schlieren field. Undoubtedly, some curvature of the combustion front does exist but the extreme distortion necessary to produce the large dark areas shown seems improbable, particularly when it is considered that no such curvature can be seen about the edges of the flame as seen from above. Rassweiler and Withrow (reference 17) mention the possibility of error caused by observation of a curved flame front. They say, however, that observations in an engine used for studying absorption spectra indicated that throughout most of the flame propagation the curvature of the flames in the vertical plane is not very marked.

Some disagreement exists in the literature concerning the probability of burning in the mixture after the flame front has passed. In the combustion of gaseous mixtures, Lewis and von Elbe (reference 18) hold that no cogent arguments have been advanced in favor of afterburning and that the evidence available supports the theory that the reaction is completed very quickly. Among others, Ellis and Morgan (reference 19) and Souders and Brown (reference 16) have conducted tests that they believe indicated the presence of afterburning. The illumination in the region back of the reaction zone before maximum pressure is reached can, of course, be caused by the adiabatic compression of these gases (reference 18).

The researches of Maxwell and Wheeler on the combustion of hydrocarbon vapors (reference 12) led them to conclude that combustion is not completed in the flame front, in either knocking or nonknocking explosions, but that in a knocking explosion the reaction is not continuous, being completed very suddenly following a certain delay period after the flame front has passed through.

In the combustion of gasoline-air mixtures, Withrow, Rassweiler, and coworkers have conducted tests which indicated that the reaction was completed in a very narrow zone. Tests with the sampling valve (reference 20) indicated that the free oxygen at a point in the combustion chamber disappeared almost as soon as the flame arrived. Experiments with the spectrograph (references 21 and 22) showed that the spectrum of the flame fronts was characteristic of burning hydrocarbons and that the spectrum of the afterglow was characteristic of carbon dioxide. In the sampling-valve experiments, however, it appears possible that the reaction may have completed itself after entering the sampling valve. The analysis presented in reference 17 is based on the assumption that the reaction is completed in the flame front. The final curves of "percent mass burned" agree remarkably well with the curves of "percent pressure rise"; hence, it may be that the portion of the charge left unburned after the flame front passes is small.

In general, the photographs presented herein indicate that reaction continues for an appreciable time after the combustion front passes through. If the photo-

graphs are accepted as showing that the combustion was across the chamber before knock occurred, then again it must be believed that the reaction is not completed in the combustion front and that knocking combustion probably consists of a sudden and very violent completion of a reaction already started.

CONCLUSIONS

1. No evidence was found that shock waves or any type of violent compression waves are associated with knock until after the actual occurrence of knock. Artificially induced shock waves in the engine did not in themselves cause knock.
2. Although auto-ignition ahead of the flame front may occur in conjunction with severe knock, probably it is not necessary nor does it always occur with knock.
3. The photographs indicate that the reaction is not completed in the combustion or flame front but continues for some time after these fronts have passed through the charge.

LANGLEY MEMORIAL AERONAUTICAL LABORATORY,
NATIONAL ADVISORY COMMITTEE FOR AERONAUTICS,
LANGLEY FIELD, VA., *December 6, 1937.*

REFERENCES

1. Marek, L. F., and Hahn, Dorothy A.: The Catalytic Oxidation of Organic Compounds in the Vapor Phase. The Chemical Catalog Co., Inc., 1932, chap. XI.
2. Withrow, Lloyd, and Rassweiler, Gerald M.: Slow Motion Shows Knocking and Non-Knocking Explosions. *S. A. E. Jour.*, vol. 39, no. 2, Aug. 1936, pp. 297-303 and p. 312.
3. Rothrock, A. M., and Spencer, R. C.: A Preliminary Study of Flame Propagation in a Spark-Ignition Engine. *T. N. No. 603, N. A. C. A.*, 1937.
4. Rothrock, A. M., and Waldron, C. D.: Some Effects of Injection Advance Angle, Engine-Jacket Temperature, and Speed on Combustion in a Compression-Ignition Engine. *T. R. No. 525, N. A. C. A.*, 1935.
5. Schey, Oscar W., and Young, Alfred W.: Performance of a Fuel-Injection Spark-Ignition Engine Using a Hydrogenated Safety Fuel. *T. R. No. 471, N. A. C. A.*, 1933.
6. Rothrock, A. M., and Cohn, Mildred: Some Factors Affecting Combustion in an Internal-Combustion Engine. *T. R. No. 512, N. A. C. A.*, 1934.
7. Tuttle, F. E.: A Non-Intermittent High-Speed 16 mm Camera. *Soc. Motion Picture Eng. Jour.*, vol. XXI, no. 6, Dec. 1933, pp. 474-477.
8. Beardsley, Edward G.: The N. A. C. A. Photographic Apparatus for Studying Fuel Sprays from Oil Engine Injection Valves and Test Results from Several Researches. *T. R. No. 274, N. A. C. A.*, 1927.
9. Taylor, H. G., and Waldram, J. M.: Improvements in the Schlieren Method. *Jour. Sci. Inst.*, vol. 10, no. 12, Dec. 1933, pp. 378-389.
10. Payman, W., and Titman, H.: Explosion Waves and Shock Waves. III. The Initiation of Detonation in Mixtures of Ethylene and Oxygen and of Carbon Monoxide and Oxygen. *Proc. Roy. Soc. (London)*, series A, vol. 152, no. 876, Nov. 1, 1935, pp. 418-445.

11. Boerlage, G. D.: Detonation and Autoignition. Some Considerations on Methods of Determination. T. M. No. 843, N. A. C. A., 1937.
12. Maxwell, G. B., and Wheeler, R. V.: Some Flame Characteristics of Motor Fuels. Ind. and Eng. Chem., vol. 20, no. 10, Oct. 1928, pp. 1041-1044.
13. Stansfield, R., and Thole, F. B.: The Influence of Engine Conditions on the Anti-Knock Rating of Motor Fuels. Engineering, vol. 130, no. 3378, Oct. 10, 1930, pp. 468-470, and vol. 130, no. 3380, Oct. 24, 1930, pp. 512-514.
14. Boerlage, G. D., and van Dyck, W. J. D.: Causes of Detonation in Petrol and Diesel Engines. R. A. S. Jour., vol. XXXVIII, no. 288, Dec. 1934, pp. 953-986.
15. Boerlage, G. D., Broeze, J. J., van Driel, H., and Peletier, L. A.: Detonation and Stationary Gas Waves in Petrol Engines. Engineering, vol. CXLIII, no. 3712, March 5, 1937, pp. 254-255.
16. Souders, Mott, Jr., and Brown, Geo. Granger: Gaseous Explosions. VIII—Effect of Tetraethyl Lead, Hot Surfaces, and Spark Ignition on Flame and Pressure Propagation. Ind. and Eng. Chem., vol. 21, no. 12, Dec. 1929, pp. 1261-1268.
17. Rassweiler, Gerald M., and Withrow, Lloyd: High Speed Motion Pictures of Engine Flames Correlated with Pressure Cards. Paper presented at annual S. A. E. meeting, Detroit, Mich., Jan. 10-14, 1938.
18. Lewis, Bernard, and von Elbe, Guenther: On the Question of "Afterburning" in Gaseous Explosions. Jour. Chem. Phys., vol. 2, Oct. 1934, pp. 659-664.
19. Ellis, Oliver C. de C., and Morgan, E.: The Temperature Gradient in Flames. Trans. Faraday Soc., vol. 30, part 1, 1934, pp. 287-298.
20. Withrow, Lloyd, Lovell, W. G., and Boyd, T. A.: Following Combustion in the Gasoline Engine by Chemical Means. Ind. and Eng. Chem., vol. 22, no. 9, Sept. 1930, pp. 945-951.
21. Withrow, Lloyd, and Rassweiler, Gerald M.: Spectroscopic Studies of Engine Combustion. Ind. and Eng. Chem., vol. 23, no. 7, July 1931, pp. 769-776.
22. Rassweiler, Gerald M., and Withrow, Lloyd: Emission Spectra of Engine Flames. Ind. and Eng. Chem., vol. 24, no. 5, May 1932, pp. 528-538.

REPORT No. 623

A STUDY OF THE TORQUE EQUILIBRIUM OF AN AUTOGIRO ROTOR

By F. J. BAILEY, Jr.

SUMMARY

Two improvements have been made in the method developed in N. A. C. A. Reports Nos. 487 and 591 for the estimation of the inflow velocity required to overcome a given decelerating torque in an autogiro rotor. At low tip-speed ratios, where the assumptions necessary for the analytical integrations of the earlier papers are valid, the expressions therein derived are greatly simplified by combining and eliminating terms with a view to minimizing the numerical computations required. At high tip-speed ratios, by means of charts based on graphical integrations, errors inherent in the assumptions associated with the analytical method are largely eliminated.

The suggested method of estimating the inflow velocity presupposes a knowledge of the decelerating torque acting on the rotor; all available full-scale experimental information on this subject is therefore included.

INTRODUCTION

The results reported in reference 1 showed the agreement between the calculated and the experimental values of the forces and moments on an autogiro rotor to be unsatisfactory at tip-speed ratios greater than 0.3. An attempt to isolate the sources of the disagreement was made by comparing values of the analytically integrated expressions for thrust and accelerating torque from reference 1 with values obtained by graphical integration of the elemental forces. This comparison indicated that the simplifications introduced in reference 1 to make possible the analytical integration of the basic expression for accelerating torque are not valid at high tip-speed ratios. Consequently, the relation therein given between accelerating torque and inflow velocity results in an erroneous estimation of the inflow velocity required to overcome a given decelerating torque at high tip-speed ratios. Because the value of the inflow velocity so estimated must be used in calculating all the rotor forces and moments from the other expressions of reference 1, this error introduces corresponding errors into the predicted values for all the various items constituting the rotor performance.

In the present paper an attempt is made to establish a more satisfactory method of expressing the relation between the accelerating torque and the inflow velocity, so that the inflow velocity required to overcome a given

decelerating torque at high tip-speed ratios may be readily estimated with an accuracy comparable with that previously attainable only at low tip-speed ratios. At the same time, the original method of estimating the inflow velocity at low tip-speed ratios is simplified by regrouping the terms in the torque equation in a manner designed to eliminate most of the tedious numerical computations previously required.

The method given presupposes a knowledge of the decelerating torque arising from the drag of the blade elements. Consequently all available full-scale experimental information on this subject is included as a guide to the designer until such time as a satisfactory method is devised for predicting decelerating torque from blade airfoil characteristics.

ANALYSIS

GENERAL

The values of the expressions for the forces and moments on an autogiro rotor, as derived in references 1 and 2, are all critically dependent on the mean value of the inflow velocity through the rotor disk. Any attempt to predict the performance of a particular rotor therefore requires, first, an accurate determination of the inflow velocity necessary to maintain steady autorotation of the rotor under the given conditions. If use is made of the physical requirement that the net torque on the rotor must be zero in steady autorotation, the estimation of the inflow velocity may be accomplished in two steps: first, the estimation of the decelerating torque on the rotor due to the profile drag of the blade elements; and, second, the estimation of the inflow velocity required to generate in the rotor an accelerating torque just equal to the estimated decelerating torque. The present paper being primarily concerned with the prediction of the inflow velocity when the decelerating torque is known, the second of these steps will first be considered.

Throughout the following analysis it will be assumed, as in reference 1, that the inflow velocity is uniform over the disk area and that the contribution of the radial-velocity components to the elemental forces is negligible. The notation used is identical with that of reference 2; for convenience, however, a list of symbols and their definitions has been included.

SYMBOLS AND DEFINITIONS

- Ω , rotor angular velocity, radians per second.
 R , blade radius.
 V , forward speed.
 α , rotor angle of attack, radians.
 $\lambda\Omega R$, speed of axial flow through rotor.
 $\mu\Omega R$, component of forward speed in plane of disk.
 b , number of blades.
 ψ , blade azimuth angle measured from down wind in direction of rotation, radians.
 c , blade chord.
 B , tip-loss factor.
 xR , radius of blade element.
 $u_T\Omega R$, velocity component at blade element perpendicular to blade span and parallel to rotor disk.
 $u_P\Omega R$, velocity component at blade element perpendicular both to blade span and to $u_T\Omega R$.

$$\phi = \tan^{-1} \frac{u_P}{u_T}$$

a , slope of lift coefficient against angle of attack of blade airfoil section (radian measure).

Q , rotor torque.

Q_a , accelerating rotor torque.

Q_d , decelerating rotor torque.

$$C_Q = \frac{Q}{\rho\Omega^2\pi R^5}$$

T , rotor thrust.

$$C_T = \frac{T}{\rho\Omega^2\pi R^4}$$

σ , solidity, ratio of total blade area to swept-disk area, $bc/\pi R$.

θ_0 , blade pitch angle at hub, radians.

θ_1 , difference between hub and tip pitch angles, radians.

θ_e , equivalent constant pitch angle, radians.

a_n , coefficient of $\cos n\psi$ in Fourier series expressing blade flapping angle, radians.

b_n , coefficient of $\sin n\psi$ in Fourier series expressing blade flapping angle, radians.

ϵ_n , coefficient of $\cos n\psi$ in Fourier series expressing periodic blade twist angle, radians.

η_n , coefficient of $\sin n\psi$ in Fourier series expressing periodic blade twist angle, radians.

I_1 , mass moment of inertia of rotor blade about horizontal hinge.

$$\gamma = \frac{c\rho a R^4}{I_1}, \text{ mass constant of rotor blade.}$$

M_W , weight moment of blade about horizontal hinge.

ACCELERATING TORQUE

The basic expression for the accelerating torque on an autogiro rotor is

$$Q_a = \frac{b}{2\pi} \frac{1}{2} \rho c \Omega^2 R^4 \sum_0^{2\pi} \Delta\psi \sum_0^B u_T^2 C_L \frac{\sin \phi}{\cos^2 \phi} x \Delta x \quad (1)$$

By definition

$$Q_a = C_{Q_a} \rho \Omega^2 \pi R^5$$

and

$$\sigma = \frac{bc}{\pi R}$$

Then

$$\frac{C_{Q_a}}{\sigma} = \frac{1}{2} \left(\frac{1}{2\pi} \sum_0^{2\pi} \Delta\psi \sum_0^B u_T^2 C_L \frac{\sin \phi}{\cos^2 \phi} x \Delta x \right) \quad (2)$$

The indicated summation may be performed analytically on the assumptions that C_L varies linearly with angle of attack of the element, regardless of the magnitude of this angle, and that the angle ϕ is always so small that the sine, tangent, and angle are interchangeable. This integration has been covered in reference 1 for blades having a constant twist and has been extended in reference 2 to cover the more general case in which the blade twist varies periodically with the azimuth position of the blade. The final expression is:

$$\begin{aligned} \frac{C_{Q_a}}{\sigma} = & \frac{a}{2} \left\{ \lambda^2 \left(\frac{1}{2} B^2 - \frac{1}{4} \mu^2 \right) + \lambda \left(\frac{1}{3} \theta_0 B^3 + \frac{2}{9\pi} \mu^3 \theta_0 + \frac{1}{4} \theta_1 B^4 \right. \right. \\ & + \left. \frac{1}{32} \mu^4 \theta_1 \right) + \mu \lambda a_1 \left(\frac{1}{2} B^2 - \frac{3}{8} \mu^2 \right) + a_0^2 \left(\frac{1}{4} \mu^2 B^2 - \frac{1}{16} \mu^4 \right) \\ & - \frac{1}{3} \mu a_0 b_1 B^3 + a_1^2 \left(\frac{1}{8} B^4 + \frac{3}{16} \mu^2 B^2 \right) + b_1^2 \left(\frac{1}{8} B^4 + \frac{1}{16} \mu^2 B^2 \right) \\ & - a_2 \left(\frac{1}{4} \mu^2 a_0 B^2 + \frac{1}{6} \mu b_1 B^3 \right) + \frac{1}{2} a_2^2 B^4 \\ & + b_2 \left(\frac{1}{8} \mu^2 \theta_0 B^2 + \frac{1}{12} \mu^2 \theta_1 B^3 + \frac{1}{6} \mu a_1 B^3 \right) + \frac{1}{2} b_2^2 B^4 \\ & + \epsilon_0 \left(\frac{1}{4} \lambda B^4 + \frac{1}{12} \mu^2 b_2 B^3 + \frac{1}{32} \mu^4 \lambda \right) \\ & + \frac{1}{2} \epsilon_1 \left(-\frac{1}{4} \mu a_0 B^4 + b_1 \left[\frac{1}{5} B^5 + \frac{1}{12} \mu^2 B^3 \right] - \frac{1}{8} \mu a_2 B^4 \right) \\ & + \frac{1}{2} \eta_1 \left(\frac{1}{3} \mu \lambda B^3 - a_1 \left[\frac{1}{5} B^5 - \frac{1}{12} \mu^2 B^3 \right] - \frac{1}{8} \mu b_2 B^4 \right) \\ & + \frac{1}{2} \epsilon_2 \left(\frac{1}{4} \mu a_1 B^4 + \frac{2}{5} b_2 B^5 \right) \\ & \left. + \frac{1}{2} \eta_2 \left(-\frac{1}{6} \mu^2 a_0 B^3 + \frac{1}{4} \mu b_1 B^4 - \frac{2}{5} a_2 B^5 \right) \right\} \quad (3) \end{aligned}$$

When this expression is compared with equation (35) of reference 2, it must be remembered that the term $\frac{\delta}{4a} \left(1 + \mu^2 - \frac{1}{8} \mu^4 \right)$ in equation (35) of reference 2 is in reality $2C_{Q_a}/\sigma a$. This quantity will equal $2C_{Q_a}/\sigma a$ in steady autorotation. Consequently, C_{Q_a}/σ will be $a/2$ times the sum of the remaining terms in equation (35) of reference 2.

Expressions for the Fourier coefficients of blade flapping, also derived in reference 2 (equations (22), (23), (24), (27), and (28)), are:

$$\begin{aligned} a_0 = & \frac{1}{2} \gamma \left\{ \frac{1}{3} \lambda B^3 + 0.080 \mu^3 \lambda + \frac{1}{4} \theta_0 \left(B^4 + \mu^2 B^2 - \frac{1}{8} \mu^4 \right) \right. \\ & + \frac{1}{5} (\theta_1 + \epsilon_0) \left(B^5 + \frac{5}{6} \mu^2 B^3 \right) + \frac{1}{8} \mu^2 b_2 B^2 + \frac{1}{4} \mu \eta_1 B^4 \\ & \left. - \frac{1}{12} \mu^2 \epsilon_2 B^3 \right\} - \frac{M_W}{I_1 \Omega^2} \quad (4) \end{aligned}$$

$$a_1 = \frac{2\mu}{B^4 - \frac{1}{2}\mu^2 B^2} \left\{ \lambda \left(B^2 - \frac{1}{4}\mu^2 \right) + \theta_0 \left(\frac{4}{3}B^3 + 0.106\mu^3 \right) + (\theta_1 + \epsilon_0)B^4 - \frac{1}{3}b_2 B^3 + \frac{\eta_1}{\mu} \left(\frac{2}{5}B^5 + \frac{1}{2}\mu^2 B^3 \right) - \frac{1}{2}\epsilon_2 B^4 \right\} \quad (5)$$

$$b_1 = \frac{4\mu}{B^4 + \frac{1}{2}\mu^2 B^2} \left\{ a_0 \left(\frac{1}{3}B^3 + 0.035\mu^3 \right) + \frac{1}{6}a_2 B^3 - \frac{\epsilon_1}{\mu} \left(\frac{1}{5}B^5 + \frac{1}{12}\mu^2 B^3 \right) - \frac{1}{4}\eta_2 B^4 \right\} \quad (6)$$

$$a_2 = \frac{\mu^2 \gamma}{\gamma^2 B^8 + 144} \left\{ \lambda B \left(16 + \frac{7}{108}\gamma^2 B^8 \right) + \theta_0 B^2 \left(\frac{46}{3} + \frac{7}{144}\gamma^2 B^8 \right) + (\theta_1 + \epsilon_0)B^3 \left(12 + \frac{7}{180}\gamma^2 B^8 \right) - \frac{1}{30} \frac{\epsilon_1}{\mu} \gamma B^8 + \frac{2}{5} \frac{\eta_1}{\mu} B^4 + \frac{24}{5} \frac{\epsilon_2}{\mu^2} B^5 + \frac{2}{5} \frac{\eta_2}{\mu^2} \gamma B^9 \right\} \quad (7)$$

$$b_2 = \frac{-\mu^2 \gamma^2}{\gamma^2 B^8 + 144} \left\{ \frac{5}{9} \lambda B^5 + \frac{25}{36} \theta_0 B^6 + \frac{8}{15} (\theta_1 + \epsilon_0) B^7 + \frac{2}{5} \frac{\epsilon_1}{\gamma \mu} B^8 + \frac{1}{30} \frac{\eta_1}{\mu} B^8 + \frac{2}{5} \frac{\epsilon_2}{\mu^2} B^9 - \frac{24}{5} \frac{\eta_2}{\gamma \mu^2} B^5 \right\} \quad (8)$$

Substituting from equations (4), (5), (6), (7), and (8) into equation (3), retaining only terms of the order of μ^4 or lower, and regrouping

$$\frac{C_{Qa}}{\sigma} = \frac{a}{2} \left\{ K_1 \lambda^2 + \left[K_2 \theta_0 + K_3 (\theta_1 + \epsilon_0) + K_7 \eta_1 + K_{10} \epsilon_1 + K_{11} \epsilon_2 + K_{12} \eta_2 + K_{24} \frac{M_w}{I_1 \Omega^2} \right] \lambda + K_4 \theta_0^2 + K_5 \theta_0 (\theta_1 + \epsilon_0) + K_6 (\theta_1 + \epsilon_0)^2 + K_8 \theta_0 \eta_1 + K_9 (\theta_1 + \epsilon_0) \eta_1 + K_{13} \theta_0 \epsilon_1 + K_{14} \theta_0 \epsilon_2 + K_{15} \theta_0 \eta_2 + K_{16} (\theta_1 + \epsilon_0) \epsilon_1 + K_{17} (\theta_1 + \epsilon_0) \epsilon_2 + K_{18} (\theta_1 + \epsilon_0) \eta_2 + K_{19} \epsilon_1^2 + K_{20} \epsilon_1 \eta_1 + K_{21} \eta_1^2 + K_{22} (\epsilon_1 \epsilon_2 + \eta_1 \eta_2) + K_{23} (\epsilon_1 \eta_2 - \eta_1 \epsilon_2) + \frac{M_w}{I_1 \Omega^2} \left[K_{25} \theta_0 + K_{26} (\theta_1 + \epsilon_0) + K_{27} \epsilon_1 + K_{28} \eta_1 + K_{29} \epsilon_2 + K_{30} \eta_2 + K_{31} \frac{M_w}{I_1 \Omega^2} \right] \right\} \quad (9)$$

where the coefficients K_1 to K_{31} , for which complete expressions are given in the appendix, are functions of μ , B , and γ only.

The magnitudes of the coefficients K_{24} to K_{31} are such that, when a value less than 0.01 is assigned to $M_w/I_1 \Omega^2$, the resulting contribution of the terms involving these coefficients to C_{Qa}/σ is negligible over the entire range of tip-speed ratios. The influence of γ on C_{Qa}/σ is also of a secondary nature; comparison of values of the coefficients K_1 to K_{23} for $\gamma=0$ with those for $\gamma=15$ indicates that no appreciable error will arise from the use of a value of $\gamma=15$ for any conventional rotor at any attainable altitude. Inasmuch as the chord-span

ratio of the blades used in present-day rotors varies only within small limits, it is possible to assign arbitrarily a value of 0.970 to the tip-loss factor B with the assurance that only minor departures from the recommended value of $1 - \frac{1}{2} \frac{c}{R}$ (reference 1) will result.

By the use of the foregoing values for γ and B with extreme values of tip-speed ratio, pitch, twist, and inflow velocity, it can be shown that the terms involving K_{10} , K_{13} , K_{16} , K_{19} , K_{20} , K_{22} , and K_{23} are negligible. Of the remaining coefficients, K_{11} , K_{12} , K_{14} , K_{15} , K_{17} , K_{18} , and K_{21} are merely constants multiplied by μ^2 ; whereas, K_1 to K_9 involve two or more powers of μ .

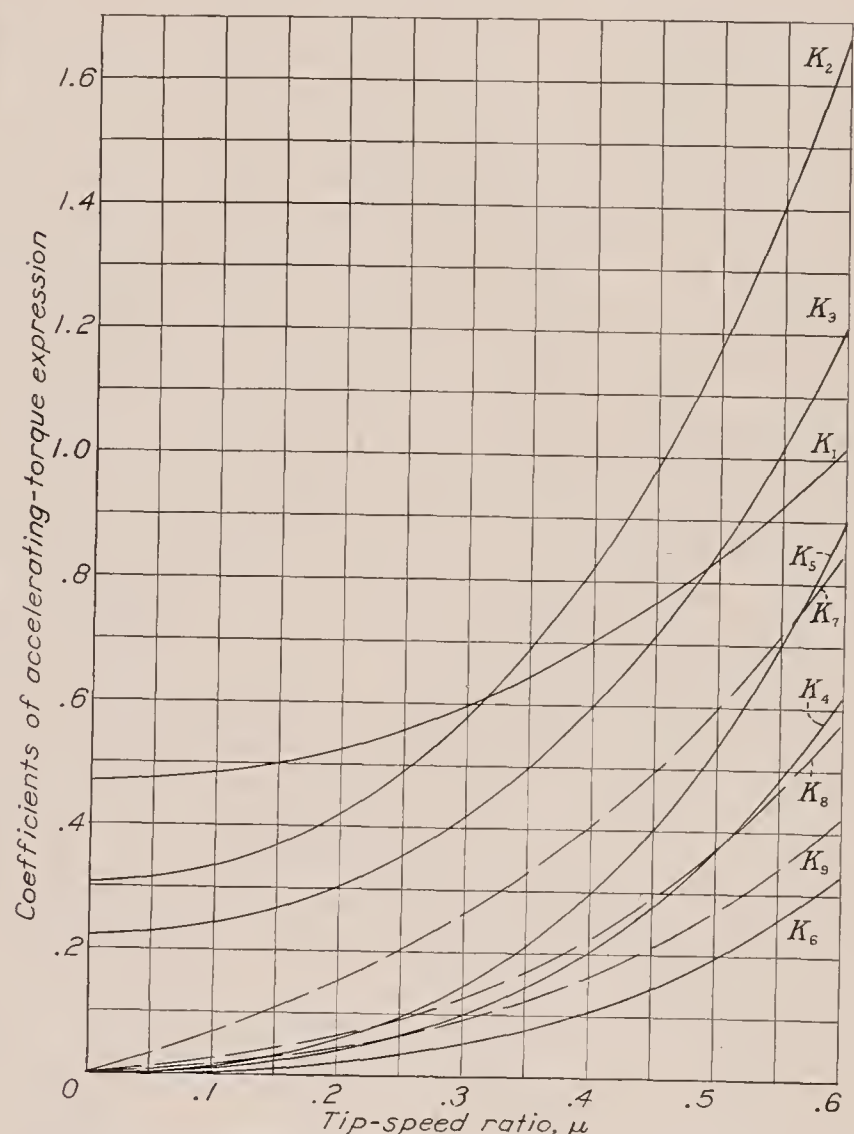
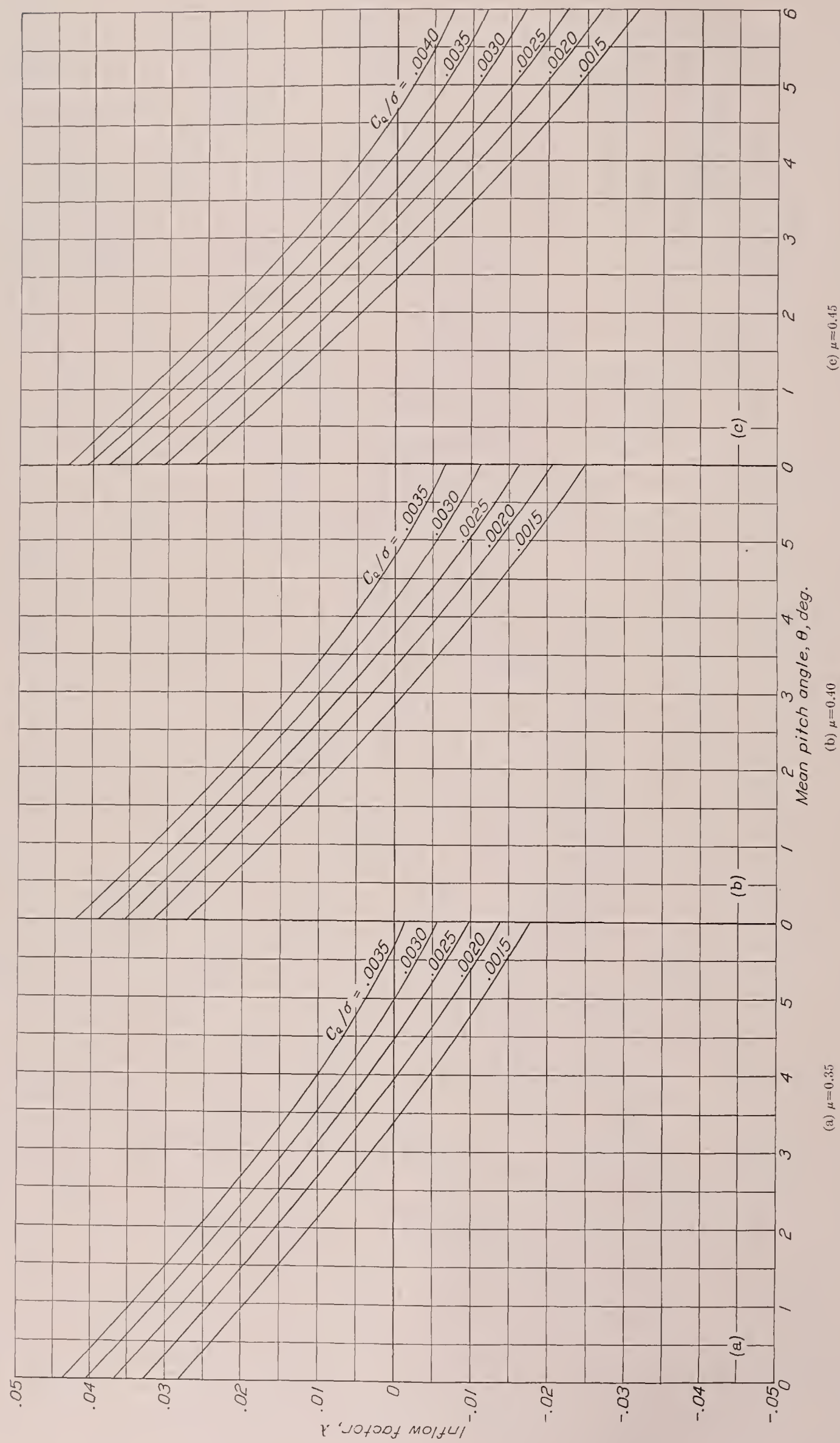


FIGURE 1.—Coefficients K_1 to K_9 of accelerating-torque expression.

Expression (9) may then be reduced to

$$\frac{C_{Qa}}{\sigma} = \frac{a}{2} \left\{ K_1 \lambda^2 + [K_2 \theta_0 + K_3 (\theta_1 + \epsilon_0) + K_7 \eta_1 - (0.614 \epsilon_2 + 0.141 \eta_2) \mu^2] \lambda + K_4 \theta_0^2 + K_5 \theta_0 (\theta_1 + \epsilon_0) + K_6 (\theta_1 + \epsilon_0)^2 + K_8 \theta_0 \eta_1 + K_9 (\theta_1 + \epsilon_0) \eta_1 - [(0.284 \epsilon_2 + 0.059 \eta_2) \theta_0 + (0.205 \epsilon_2 + 0.047 \eta_2) (\theta_1 + \epsilon_0) - 0.260 \eta_1^2] \mu^2 \right\} \quad (10)$$

Values of coefficients K_1 to K_9 may be found directly from figure 1 or for specified tip-speed ratios from table I.



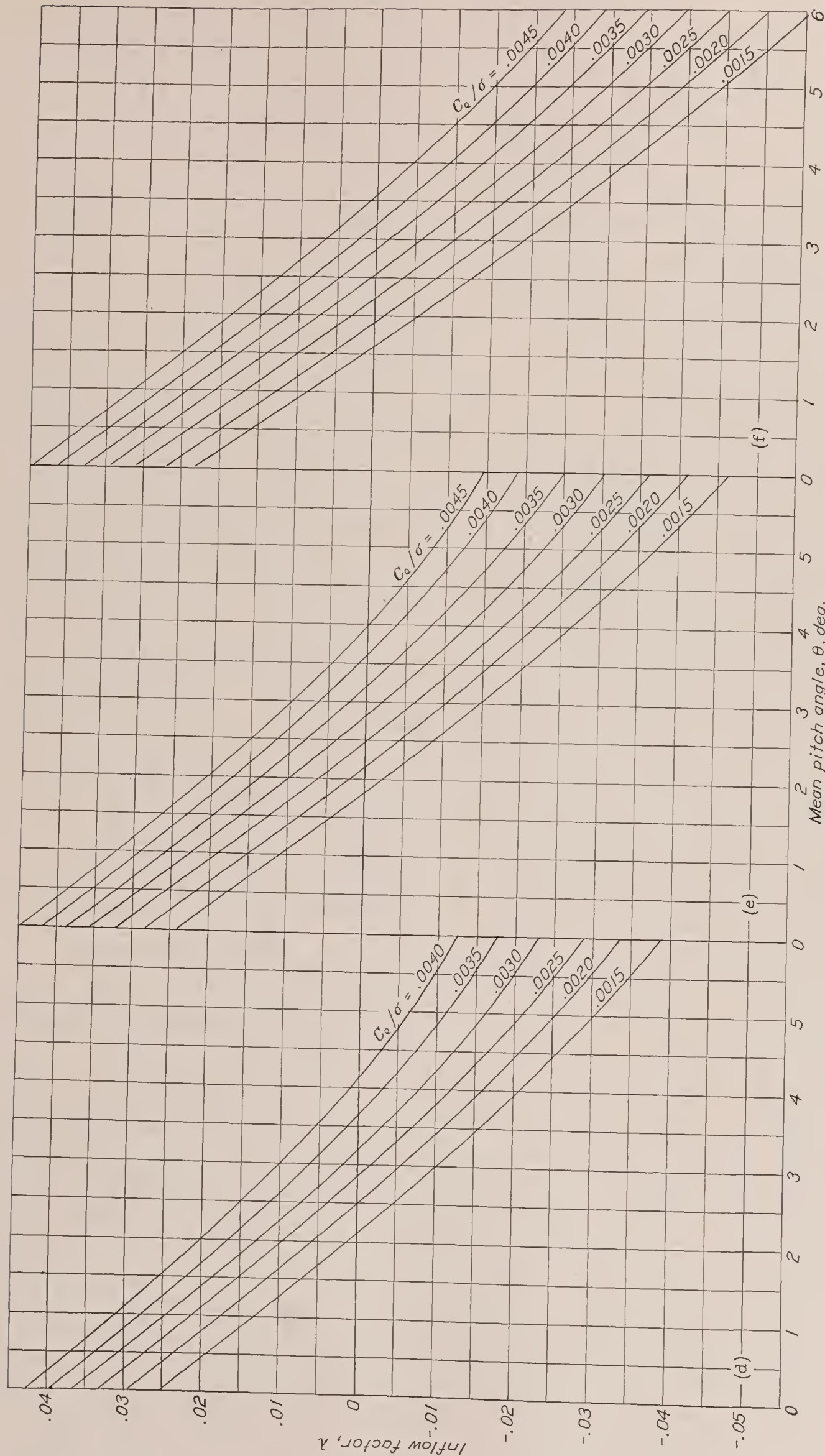


FIGURE 2.—Charts for determination of the inflow factor, λ .

Substitution of numerical values for the pitch setting and twist coefficients in equation (10) results in a quadratic in λ that may be solved for λ at any given value of C_{Qa}/σ .

For rotors in which the pitch is constant along the radius of the blade and does not vary with azimuth position of the blade, equation (10) reduces to the form

$$\frac{C_{Qa}}{\sigma} = \frac{a}{2} \{K_1 \lambda^2 + K_2 \theta \lambda + K_4 \theta^2\} \quad (11)$$

At tip-speed ratios above 0.4 with low pitch settings or above 0.3 with very high pitch settings, equations (9), (10), and (11) are inaccurate. The omission of terms of higher order than μ^4 becomes questionable and the overestimation of the lift coefficients of the stalled elements introduces a very serious error. Errors arising from the assumption that the angle ϕ is small are also too large to ignore. Consequently, some other method of integrating the basic expression must be found to extend the relation between torque and inflow to higher tip-speed ratios.

Reference to equation (2) shows that the indicated summation may also be made by evaluating the torque for a series of elements throughout the disk and integrating graphically over the disk area. This summation is accomplished for any combination of tip-speed ratio, pitch setting, and inflow velocity by first calculating u_P and u_T , the perpendicular and tangential components, respectively, of the velocity relative to each chosen element. The angle ϕ of the resultant velocity at each element to the plane of the disk is then $\tan^{-1} u_P/u_T$. Adding to ϕ the angle θ of the chord of the element to the plane of the disk, as defined by $\theta_0, \theta_1, \epsilon_0, \epsilon_1, \eta_1, \epsilon_2$, and η_2 , gives the angle of attack of each element. From a lift curve of the airfoil section, the corresponding lift coefficient of the element is determined. Where u_T is negative, the use of $-\phi - \theta$ in place of $\phi + \theta$ allows for the effect of the reversed flow over the blade in the same manner in which this problem was handled in the analytical expressions of references 1 and 2.

For rotors without blade twist, a sufficient number of graphical integrations of this type have been carried out to permit the construction of the charts of figure 2 from which the value of λ corresponding to a given C_{Qa}/σ may be directly determined. Because accelerating and decelerating torques are equal in steady autorotation, the subscript has been omitted from the torque coefficient in figure 2. Comparison of the values of λ given by the charts with those obtained from the analytical expression (11) at the same C_{Qa}/σ will demonstrate the error in expression (11). As in the analytical expression, values of $\gamma=15$ and $B=0.97$ have been used throughout the graphical integrations in the belief that the generality of the results is not appreciably impaired by these substitutions. A further limitation of the generality of the charts, imposed by the use throughout the graphical integrations of the lift characteristics of the N. A. C. A. 0012 airfoil section, is not considered

serious because only small departures from these characteristics are to be expected in blade sections commonly used for rotors at the present time.

Obviously, it is impossible to supply charts covering all possible combinations of fixed and varying twist. It is reasonable to believe, however, that equations (10) and (11), although quantitatively in error as to the total accelerating torque produced by a given inflow velocity, correctly express the relative merit of rotors with and without twist as torque-generating devices. This belief amounts merely to the assumption that the percentage error inherent in the analytical method is the same for rotors with twist as for those without twist. Hence, it should be satisfactory at high tip-speed ratios to use equations (10) and (11) solely as a means of determining, for any rotor with twist, the pitch of what may be termed an "equivalent" constant-pitch rotor, that is, a rotor with no twist capable of generating the same accelerating torque at the same inflow velocity. The charts (fig. 2) for constant-pitch rotors may then be used to find the true value of the inflow velocity for the equivalent constant-pitch rotor, and the value so found may be considered to apply also to the original twisted rotor. In detail the procedure is as follows:

1. Substitute values for C_{Qa}/σ , a , μ , K_1 to K_9 , θ_0 , θ_1 , ϵ_0 , η_1 , ϵ_2 , η_2 , and solve equation (10) for λ .
2. Using this value of λ in equation (11), together with the original value of C_{Qa}/σ , solve equation (11) for θ . The value of θ obtained is then the pitch of a constant-pitch rotor capable of generating the required torque at the same inflow velocity as the original rotor.
3. From the charts for constant-pitch rotors (fig. 2), determine the true inflow factor λ for a constant-pitch rotor of pitch θ generating torque C_{Qa}/σ . The value of λ for the original rotor is, by hypothesis, identical with that of the equivalent constant-pitch rotor as found in step 3.

DECELERATING TORQUE

It will be noted that, in order to estimate the inflow velocity by the method of the preceding section, it is necessary to know the value of the accelerating torque C_{Qa}/σ . On the strength of the physical requirement that accelerating and decelerating torques must be equal in steady autorotation, this quantity is normally determined by estimating the decelerating torque on the rotor from an integration over the disk area of the decelerating torque arising from the profile drag of a blade element. Hence

$$\frac{C_{Qa}}{\sigma} = \frac{C_{Qd}}{\sigma} = \frac{1}{2} \left(\frac{1}{2\pi} \int_0^{2\pi} d\psi \int_0^1 u_T^2 C_D \sec \phi x dx \right) \quad (12)$$

The rigorous evaluation of the integral of expression (12) is possible only by graphical means because the elemental profile-drag coefficient C_D is a nonlinear function of both the angle of attack and the Reynolds Number at the element. Even then, uncertainty concerning the value of C_D in the presence of high radial velocities or in the stalled portion of the disk makes the validity

of the results extremely doubtful. Nor does there appear to be any merit in the idea of replacing $C_D \sec \phi$ by a mean value δ , as was done in reference 1, so that

$$\frac{1}{2\pi} \int_0^{2\pi} d\psi \int_0^1 u_T^2 C_D \sec \phi dx = \delta \frac{1}{2\pi} \int_0^{2\pi} d\psi \int_0^1 u_T^2 dx$$

$$= \delta \left(\frac{1}{4} + \frac{1}{4} \mu^2 \right)$$

or, when the effect of the reversed-velocity region is included as in reference 1,

$$= \delta \left(\frac{1}{4} + \frac{1}{4} \mu^2 - \frac{1}{32} \mu^4 \right) \quad (13)$$

because both graphical integration and experiment indicate that the magnitude of δ will vary with both pitch

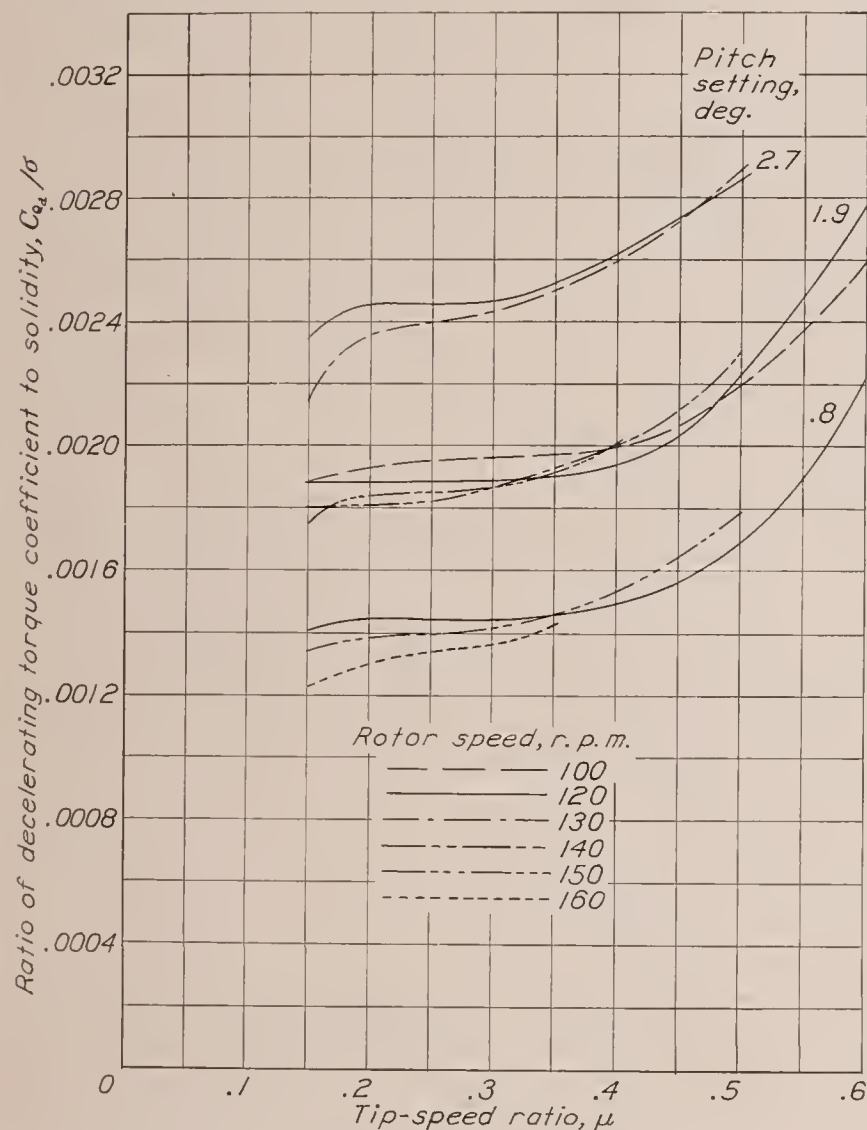


FIGURE 3.—Experimental decelerating torque of the PCA-2 rotor.

setting and tip-speed ratio and hence will require empirical information for its estimation. It seems fully as desirable and much simpler to formulate the empirical rules for the direct estimation of C_{Qd}/σ . Unfortunately, the only reliable full-scale experimental information available for this purpose is confined to a single rotor, the PCA-2; and it is obviously impossible to establish such rules with any degree of finality at the present time. It does seem desirable, however, to study these data rather thoroughly in an effort to develop a tentative method of estimating C_{Qd}/σ that may be expected to be subject to only minor alterations as additional data are accumulated.

Experimental data on C_{Qd}/σ , from full-scale wind-tunnel tests of the PCA-2 rotor, are shown in figure 3. The values given were obtained by substituting experimental values of thrust and blade-motion coefficients in the thrust-coefficient expression of reference 2 and solving for λ . The value of C_{Qd}/σ , and hence of C_{Qd}/σ , corresponding to this value of λ was then obtained by a process the reverse of the one described in the preceding section of this paper.

A comparison of the values of C_{Qd}/σ given in figure 3 with the experimental values of the ratio C_T/σ shown in figure 4 reveals that, at any given tip-speed ratio, C_{Qd}/σ at all the pitch settings tested is almost directly proportional to C_T/σ . The closeness of this relationship is indicated in figure 5 where experimental values of the

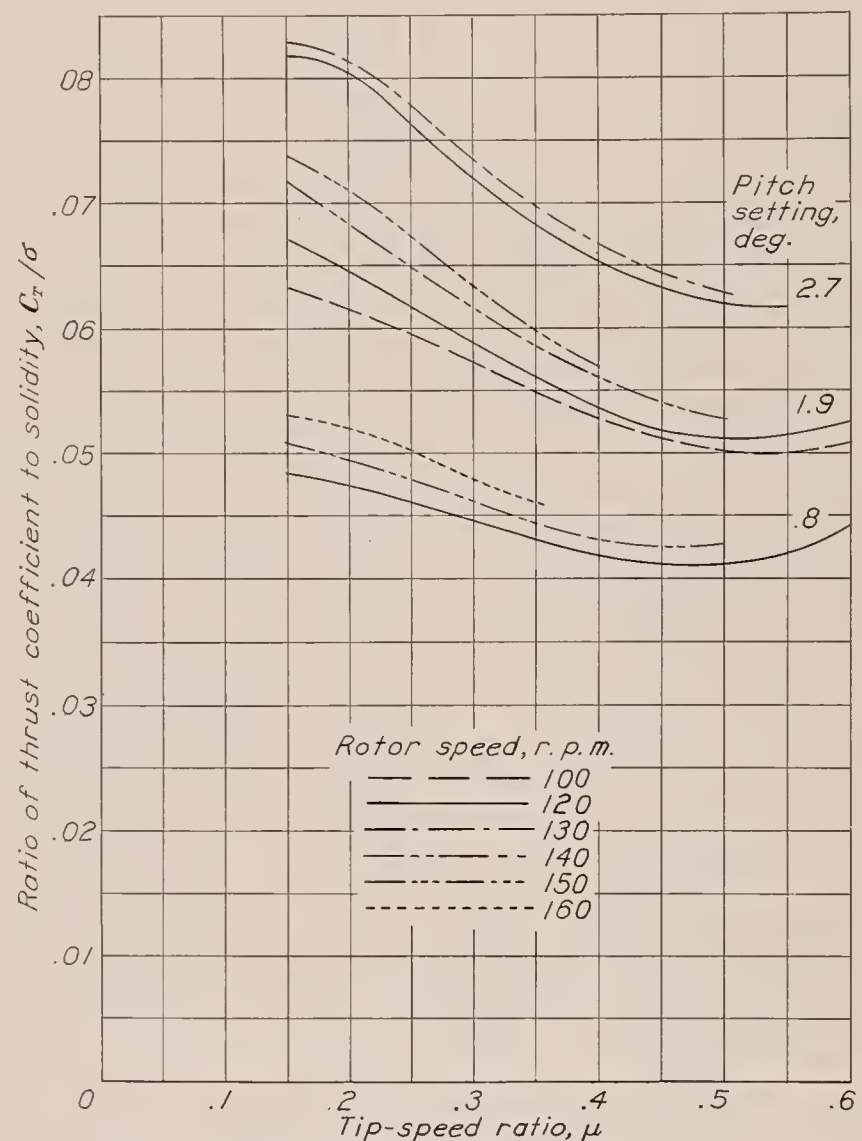


FIGURE 4.—Experimental thrust coefficient of the PCA-2 rotor.

quotient C_Q/C_T are plotted as functions of μ for the pitch settings given in figures 3 and 4.

From the designer's viewpoint, the curve shown in figure 5 provides a possible, although tedious, method of estimating the performance of a new design. As the various steps involved may not be instantly apparent, it seems desirable to outline briefly the recommended procedure.

Normally, from considerations of rotor efficiency, it is mandatory that the designer secure some definite value of C_T/σ at a particular tip-speed ratio. From this point, the problem becomes one of determining, first,

the pitch angle required to satisfy this condition; and second, the performance of a rotor of this pitch as a function of the tip-speed ratio. On the assumption that the geometric and aerodynamic characteristics of the blades are known, the steps required in the solution are as follows:

1. Compute $(\theta_1 + \epsilon_0)$, η_1 , ϵ_2 , and η_2 from the expressions of reference 3, neglecting the influence of the λ , θ_0 , and $(\theta_1 + \epsilon_0)$ terms.
2. From C_T/σ and μ find C_{Q_d}/σ from figure 5.
3. Assume a series of values of θ_0 and, using C_{Q_d}/σ from step 2, find the corresponding values of λ by the method described in the preceding section of this paper.
4. By substituting values of λ and θ_0 from step 3 into the thrust expression of reference 2, ignoring the terms

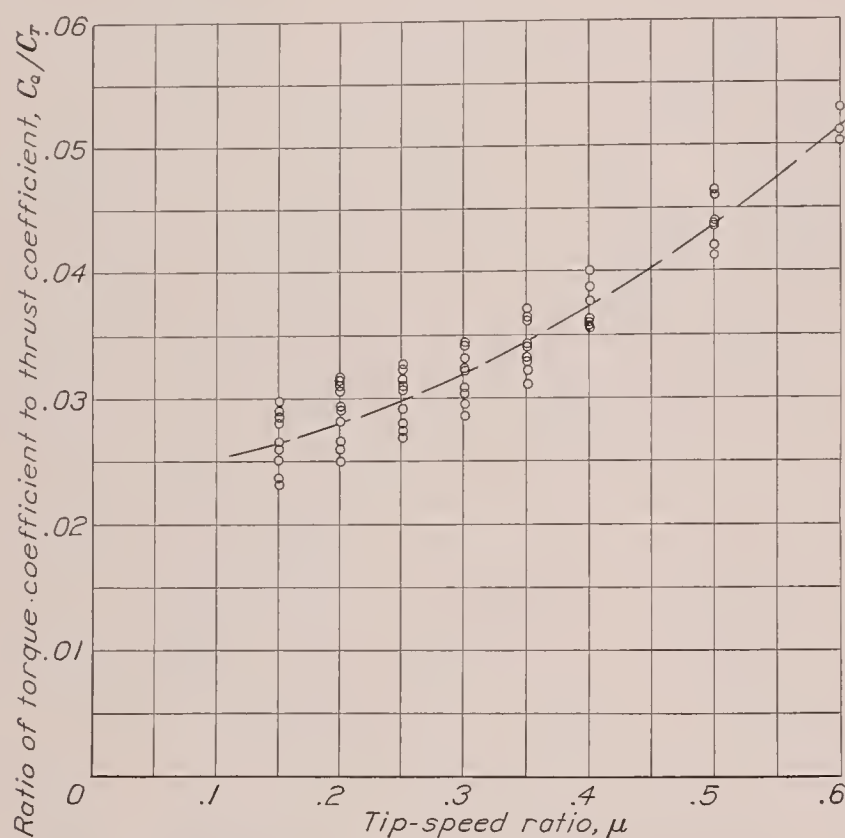


FIGURE 5.—Experimental torque-thrust ratio, C_Q/C_T , for the PCA-2 rotor.

involving a_1 and b_2 , which almost cancel one another, obtain C_T/σ as a function of θ_0 .

5. Fix θ_0 at the value corresponding to the required C_T/σ .

The twist coefficients may now be recalculated without neglecting the λ , θ_0 , and θ_1 terms and the entire process repeated to determine more accurately the required θ_0 . The change in θ_0 resulting from this second approximation may be expected to be very small since the twist coefficients are only slightly affected by inflow velocity and pitch. The small change can probably be safely neglected except in unusual designs.

It will be noted, of course, that at low tip-speed ratios, where equations (10) and (11) are valid, λ may be obtained in step 3 as an analytical function of θ_0 ; this function may then be substituted into the expression for C_T/σ in step 4. The result will be a quadratic in θ_0 that can be solved directly for θ_0 at the design value of C_T/σ . Although this approach appears, at first glance, to be the more direct, in actual practice it will be found simpler to proceed as originally outlined, even at low tip-speed ratios.

The performance of the rotor of pitch θ_0 at other tip-speed ratios can be determined as follows:

1. Assume a value of C_T/σ at the new tip-speed ratio. Figure 4 may be used as a guide to a reasonable choice.
2. Obtain the corresponding C_{Q_d}/σ from figure 5.
3. Calculate ϵ_0 , η_1 , ϵ_2 , and η_2 for the new tip-speed ratio by the method of reference 3, neglecting terms involving λ .
4. Determine λ by the method described in the first part of this paper.
5. Calculate C_T/σ from the thrust-coefficient expression given in reference 2 and check against the value assumed in step 1.
6. Repeat, modifying the assumed value until agreement is obtained.

LANGLEY MEMORIAL AERONAUTICAL LABORATORY,
NATIONAL ADVISORY COMMITTEE FOR AERONAUTICS,
LANGLEY FIELD, VA., January 10, 1938.

APPENDIX

Complete expressions follow for the coefficients K_1 to K_{31} appearing in equation (9). For convenience of reference, the term to which each coefficient is attached is given in parentheses immediately preceding the expression for the coefficient.

$$\begin{aligned}
 (\lambda^2), K_1 &= \frac{1}{2}B^2 + \left(\frac{5}{4} + \frac{1}{1296}\gamma^2B^8\right)\mu^2 + \left[\frac{1}{2B^2} + \frac{\gamma^2B^6}{(144+\gamma^2B^8)^2}\left(\frac{4}{3} - \frac{37}{162}\gamma^2B^8 - \frac{77}{46656}\gamma^4B^{16}\right)\right]\mu^4 \\
 (\lambda\theta_0), K_2 &= \frac{1}{3}B^3 + \left(\frac{8}{3}B + \frac{1}{864}\gamma^2B^9\right)\mu^2 + \frac{2}{9\pi}\mu^3 + \left[\frac{8}{3B} + \frac{\gamma^2B^7}{(144+\gamma^2B^8)^2}\left(\frac{224}{9} - \frac{11}{648}\gamma^2B^8 - \frac{41}{31104}\gamma^4B^{16}\right)\right]\mu^4 \\
 (\lambda[\theta_1 + \epsilon_0]), K_3 &= \frac{1}{4}B^4 + \left(2B^2 + \frac{1}{1080}\gamma^2B^{10}\right)\mu^2 + \left[\frac{65}{32} + \frac{\gamma^2B^8}{(144+\gamma^2B^8)^2}\left(\frac{236}{15} - \frac{7}{108}\gamma^2B^8 - \frac{47}{38880}\gamma^4B^{16}\right)\right]\mu^4 \\
 (\theta_0^2), K_4 &= \left(\frac{8}{9}B^2 + \frac{1}{2304}\gamma^2B^{10}\right)\mu^2 + \left[\frac{20}{9} + \frac{\gamma^2B^8}{(144+\gamma^2B^8)^2}\left(\frac{305}{36} + \frac{65}{1296}\gamma^2B^8 - \frac{5}{82944}\gamma^4B^{16}\right)\right]\mu^4 \\
 (\theta_0[\theta_1 + \epsilon_0]), K_5 &= \left(\frac{4}{3}B^3 + \frac{1}{1440}\gamma^2B^{11}\right)\mu^2 + \left[\frac{10}{3}B + \frac{\gamma^2B^9}{(144+\gamma^2B^8)^2}\left(\frac{57}{5} + \frac{7}{144}\gamma^2B^8 - \frac{11}{51840}\gamma^4B^{16}\right)\right]\mu^4 \\
 ([\theta_1 + \epsilon_0]^2), K_6 &= \left(\frac{1}{2}B^4 + \frac{1}{3600}\gamma^2B^{12}\right)\mu^2 + \left[\frac{5}{4}B^2 + \frac{\gamma^2B^{10}}{(144+\gamma^2B^8)^2}\left(\frac{92}{25} + \frac{1}{150}\gamma^2B^8 - \frac{17}{129600}\gamma^4B^{16}\right)\right]\mu^4 \\
 (\lambda\eta_1), K_7 &= \frac{23}{30}B^3\mu + \left[\frac{11}{6}B + \frac{1}{864}\gamma^2B^9 - \frac{1}{144+\gamma^2B^8}\frac{49}{2160}\gamma^2B^9 + \frac{1}{(144+\gamma^2B^8)^2}\left(\frac{32}{5}\gamma^2B^9 + \frac{2}{45}\gamma^4B^{17}\right)\right]\mu^3 \\
 (\theta_0\eta_1), K_8 &= \frac{4}{15}B^4\mu + \left[\frac{89}{45}B^2 + \frac{1}{1152}\gamma^2B^{10} - \frac{1}{144+\gamma^2B^8}\frac{53}{1728}\gamma^2B^{10} + \frac{1}{(144+\gamma^2B^8)^2}\left(\frac{92}{15}\gamma^2B^{10} + \frac{23}{540}\gamma^4B^{18}\right)\right]\mu^3
 \end{aligned}$$

$$\begin{aligned}
 ([\theta_1 + \epsilon_0]\eta_1), K_9 &= \frac{1}{5}B^5\mu + \left[\frac{89}{60}B^3 + \frac{1}{1440}\gamma^2B^{11} - \frac{1}{144+\gamma^2B^8}\frac{43}{1800}\gamma^2B^{11} + \frac{1}{(144+\gamma^2B^8)^2}\left(\frac{24}{5}\gamma^2B^{11} + \frac{1}{30}\gamma^4B^{19}\right)\right]\mu^3 \\
 (\lambda\epsilon_1), K_{10} &= \frac{1}{720}\gamma B^7\mu + \left[-\frac{1}{540}\gamma B^5 + \frac{1}{144+\gamma^2B^8}\left(\frac{1}{5}\gamma B^5 + \frac{5}{1728}\gamma^3B^{13}\right) - \frac{1}{(144+\gamma^2B^8)^2}\left(\frac{14}{45}\gamma^3B^{13} + \frac{7}{3240}\gamma^5B^{21}\right)\right]\mu^3 \\
 (\lambda\epsilon_2), K_{11} &= \left[-\frac{3}{4}B^2 - \frac{1}{144+\gamma^2B^8}\frac{16}{45}\gamma^2B^{10} + \frac{1}{(144+\gamma^2B^8)^2}\left(\frac{384}{5}\gamma^2B^{10} + \frac{8}{15}\gamma^4B^{18}\right)\right]\mu^2 \\
 (\lambda\eta_2), K_{12} &= \left[\frac{1}{72}\gamma B^6 - \frac{1}{144+\gamma^2B^8}\left(\frac{24}{5}\gamma B^6 + \frac{2}{45}\gamma^3B^{14}\right) + \frac{1}{(144+\gamma^2B^8)^2}\left(\frac{56}{15}\gamma^3B^{14} + \frac{7}{270}\gamma^5B^{22}\right)\right]\mu^2 \\
 (\theta_0\epsilon_1), K_{13} &= \frac{1}{960}\gamma B^8\mu + \left[-\frac{1}{2880}\gamma B^6 + \frac{1}{144+\gamma^2B^8}\left(\frac{1}{72}\gamma B^6 + \frac{5}{2304}\gamma^3B^{14}\right) - \frac{1}{(144+\gamma^2B^8)^2}\left(\frac{7}{30}\gamma^3B^{14} + \frac{7}{4320}\gamma^5B^{22}\right)\right]\mu^3 \\
 (\theta_0\epsilon_2), K_{14} &= \left[-\frac{1}{3}B^3 - \frac{1}{144+\gamma^2B^8}\frac{17}{36}\gamma^2B^{11} + \frac{1}{(144+\gamma^2B^8)^2}\left(\frac{368}{5}\gamma^2B^{11} + \frac{23}{45}\gamma^4B^{19}\right)\right]\mu^2 \\
 (\theta_0\eta_2), K_{15} &= \left[\frac{1}{96}\gamma B^7 - \frac{1}{144+\gamma^2B^8}\left(\frac{37}{15}\gamma B^7 + \frac{1}{30}\gamma^3B^{15}\right) + \frac{1}{(144+\gamma^2B^8)^2}\left(\frac{42}{15}\gamma^3B^{15} + \frac{7}{360}\gamma^5B^{23}\right)\right]\mu^2 \\
 ([\theta_1 + \epsilon_0]\epsilon_1), K_{16} &= \frac{1}{1200}\gamma B^9\mu + \left[-\frac{1}{2400}\gamma B^7 + \frac{1}{144+\gamma^2B^8}\left(\frac{1}{60}\gamma B^7 + \frac{1}{576}\gamma^3B^{15}\right) - \frac{1}{(144+\gamma^2B^8)^2}\left(\frac{14}{75}\gamma^3B^{15} + \frac{7}{5400}\gamma^5B^{23}\right)\right]\mu^3 \\
 ([\theta_1 + \epsilon_0]\epsilon_2), K_{17} &= \left[-\frac{1}{4}B^4 - \frac{1}{144+\gamma^2B^8}\frac{11}{30}\gamma^2B^{12} + \frac{1}{(144+\gamma^2B^8)^2}\left(\frac{288}{5}\gamma^2B^{12} + \frac{2}{5}\gamma^4B^{20}\right)\right]\mu^2
 \end{aligned}$$

$$\begin{aligned}
([\theta_1 + \epsilon_0]\eta_2), K_{18} &= \left[\frac{1}{120} \gamma B^8 - \frac{1}{144 + \gamma^2 B^8} \left(2\gamma B^8 + \frac{2}{75} \gamma^3 B^{16} \right) \right. \\
&\quad \left. + \frac{1}{(144 + \gamma^2 B^8)^2} \left(\frac{56}{25} \gamma^3 B^{16} + \frac{7}{450} \gamma^5 B^{24} \right) \right] \mu^2 \\
(\epsilon_1^2), K_{19} &= \left[-\frac{1}{144 + \gamma^2 B^8} \frac{1}{7200} \gamma^2 B^{12} \right. \\
&\quad \left. + \frac{1}{(144 + \gamma^2 B^8)^2} \left(\frac{2}{25} \gamma^2 B^{12} + \frac{1}{1800} \gamma^4 B^{20} \right) \right] \mu^2 \\
\epsilon_1 \eta_1, K_{20} &= \frac{1}{960} \gamma B^8 \mu^2 \\
(\eta_1^2), K_{21} &= \left[\frac{22}{75} B^4 - \frac{1}{144 + \gamma^2 B^8} \frac{1}{7200} \gamma^2 B^{12} \right. \\
&\quad \left. + \frac{1}{(144 + \gamma^2 B^8)^2} \left(\frac{2}{25} \gamma^2 B^{12} + \frac{1}{1800} \gamma^4 B^{20} \right) \right] \mu^2 \\
(\epsilon_1 \epsilon_2 + \eta_1 \eta_2), K_{22} &= -\frac{1}{144 + \gamma^2 B^8} \frac{3}{50} \gamma B^9 \mu \\
(\epsilon_1 \eta_2 - \eta_1 \epsilon_2), K_{23} &= \left[\frac{1}{144 + \gamma^2 B^8} \frac{1}{120} \gamma^2 B^{13} \right. \\
&\quad \left. - \frac{1}{(144 + \gamma^2 B^8)^2} \left(\frac{48}{25} \gamma^2 B^{13} + \frac{1}{75} \gamma^4 B^{21} \right) \right] \mu \\
\left(\lambda \frac{M_w}{I_1 \Omega^2} \right), K_{24} &= -\frac{1}{108} \gamma B^5 \mu^2 \\
&\quad + \frac{1}{144 + \gamma^2 B^8} \left(\frac{47}{9} \gamma B^3 + \frac{7}{486} \gamma^3 B^{11} \right) \mu^4 \\
\left(\theta_0 \frac{M_w}{I_1 \Omega^2} \right), K_{25} &= -\frac{1}{144} \gamma B^6 \mu^2 \\
&\quad + \frac{1}{144 + \gamma^2 B^8} \left(\frac{485}{108} \gamma B^4 + \frac{5}{1296} \gamma^3 B^{12} \right) \mu^4 \\
([\theta_1 + \epsilon_0] \frac{M_w}{I_1 \Omega^2}), K_{26} &= -\frac{1}{180} \gamma B^7 \mu^2 \\
&\quad + \frac{1}{144 + \gamma^2 B^8} \left(\frac{18}{5} \gamma B^5 + \frac{13}{3240} \gamma^3 B^{13} \right) \mu^4
\end{aligned}$$

$$\begin{aligned}
\left(\epsilon_1 \frac{M_w}{I_1 \Omega^2} \right), K_{27} &= -\frac{1}{120} B^4 \mu \\
&\quad + \left(\frac{1}{90} B^2 - \frac{1}{144 + \gamma^2 B^8} \frac{17}{1080} \gamma^2 B^{10} \right) \mu^3 \\
\left(\eta_1 \frac{M_w}{I_1 \Omega^2} \right), K_{28} &= \left(-\frac{1}{144} \gamma B^6 + \frac{1}{144 + \gamma^2 B^8} \frac{17}{90} \gamma B^6 \right) \mu^3 \\
\left(\epsilon_2 \frac{M_w}{I_1 \Omega^2} \right), K_{29} &= \frac{1}{144 + \gamma^2 B^8} \frac{34}{15} \gamma B^7 \mu^2 \\
\left(\eta_2 \frac{M_w}{I_1 \Omega^2} \right), K_{30} &= \left(-\frac{1}{12} B^3 + \frac{1}{144 + \gamma^2 B^8} \frac{17}{90} \gamma^2 B^{11} \right) \mu^2 \\
\left(\left[\frac{M_w}{I_1 \Omega^2} \right]^2 \right), K_{31} &= \frac{1}{36} B^2 \mu^2 + \frac{7}{144} \mu^4
\end{aligned}$$

REFERENCES

1. Wheatley, John B.: An Aerodynamic Analysis of the Autogiro Rotor with a Comparison between Calculated and Experimental Results. T. R. No. 487, N. A. C. A., 1934.
2. Wheatley, John B.: An Analytical and Experimental Study of the Effect of Periodic Blade Twist on the Thrust, Torque, and Flapping Motion of an Autogiro Rotor. T. R. No. 591, N. A. C. A., 1937.
3. Wheatley, John B.: An Analysis of the Factors That Determine the Periodic Twist of an Autogiro Rotor Blade, with a Comparison of Predicted and Measured Results. T. R. No. 600, N. A. C. A., 1937.

TABLE I.—COEFFICIENTS K_1 TO K_9 OF ACCELERATING-TORQUE EXPRESSION FOR DIFFERENT TIP-SPEED RATIOS

Coefficient	Tip-speed ratio, μ									
	0.15	0.20	0.25	0.30	0.35	0.40	0.45	0.50	0.55	0.60
K_1	0.502	0.526	0.558	0.598	0.646	0.702	0.766	0.840	0.923	1.017
K_2	.369	.421	.490	.579	.689	.824	.986	1.179	1.407	1.675
K_3	.268	.306	.356	.420	.500	.598	.714	.854	1.018	1.210
K_4	.022	.040	.066	.100	.145	.203	.276	.368	.481	.618
K_5	.032	.058	.096	.146	.212	.296	.403	.536	.700	.900
K_6	.012	.021	.035	.053	.077	.108	.147	.195	.255	.328
K_7	.112	.156	.206	.264	.330	.407	.496	.598	.716	.850
K_8	.042	.063	.090	.125	.169	.223	.290	.369	.465	.576
K_9	.031	.046	.066	.091	.123	.163	.212	.270	.339	.421

REPORT No. 624

TWO-DIMENSIONAL SUBSONIC COMPRESSIBLE FLOW PAST ELLIPTIC CYLINDERS

By CARL KAPLAN

SUMMARY

The method of Poggi is used to calculate, for perfect fluids, the effect of compressibility upon the flow on the surface of an elliptic cylinder at zero angle of attack and with no circulation. The result is expressed in a closed form and represents a rigorous determination of the velocity of the fluid at the surface of the obstacle insofar as the second approximation is concerned.

Comparison is made with Hooker's treatment of the same problem according to the method of Janzen and Rayleigh and it is found that, for thick elliptic cylinders, the two methods agree very well. The labor of computation is, moreover, considerably reduced by the present solution.

The third approximation to the compressible flow about circular cylinders, including the terms involving the factor $(v_0/c_0)^4$, is also obtained and compared with the result given by Poggi. It is found that the expression given by Poggi is incomplete with regard to the terms containing the factor $(v_0/c_0)^4$.

INTRODUCTION

The purpose of this paper is to employ the method of Poggi (reference 1) to determine the effect of compressibility on the flow about elliptic cylinders. This problem has already been considered by Hooker (reference 2) who made use of the method of Janzen and Rayleigh but, owing to the necessity for expanding a certain function in the analysis, the "thickness ratio" of the ellipse to which his result applies is limited. The thickness ratio of an ellipse is defined as the ratio b/a , where a and b are the semimajor and semiminor axes, respectively. The method of Poggi, on the other hand, not only permits an unrestricted thickness ratio but also reduces the labor of computation.

Briefly, it may be said that Poggi considers compressible flow to be replaced by an incompressible flow due to a distribution of sinks and sources throughout the region of flow. The strength of the distribution in the plane of the profile is given by

$$-\frac{1}{4\pi c^2} \left(\frac{\partial \phi}{\partial \xi} \frac{\partial v^2}{\partial \xi} + \frac{\partial \phi}{\partial \eta} \frac{\partial v^2}{\partial \eta} \right) d\xi d\eta$$

and in the plane of the circle, into which the profile is mapped by a suitable conformal transformation, by

$$\frac{1}{4\pi c^2} \left(v_r \frac{\partial v^2}{\partial \lambda} - \frac{v_\theta}{\lambda} \frac{\partial v^2}{\partial \theta} \right) \frac{R}{\lambda} d\lambda d\theta$$

where

r, θ are the polar coordinates of a point in the plane $z(=x+iy)$ of the circle.

R, δ the radius of the circle into which the profile is mapped and the angular coordinate on this circle, respectively.

$\lambda = \frac{R}{r}$; $v_r = -\frac{\partial \phi}{\partial r}$; $v_\theta = -\frac{1}{r} \frac{\partial \phi}{\partial \theta}$; ϕ is the velocity

potential of the flow.

v , the magnitude of the velocity of the fluid in the plane of the profile.

c , the magnitude of the local velocity of sound.

Poggi then finds that the total velocity induced, at any point $P(R, \delta)$ of the circular boundary by the foregoing system of sinks and sources, is:

$$\Delta v = \frac{1}{2\pi} \int_0^1 \int_0^{2\pi} \frac{v_r \frac{\partial v^2}{\partial \lambda} - \frac{v_\theta}{\lambda} \frac{\partial v^2}{\partial \theta}}{c^2 \{ 1 - 2\lambda \cos(\theta - \delta) + \lambda^2 \}} \sin(\theta - \delta) d\lambda d\theta \quad (1)$$

Poggi's method of approximating the compressible flow of a perfect fluid is based on the assumption that the incompressible flow is a suitable first approximation and that therefore the values pertaining to that flow may be substituted for v_r , v_θ , and v^2 in equation (1). The value of Δv thus obtained then represents the effect due to compressibility and is to be added to the already known value for the velocity of the incompressible flow. That is,

$$v_{comp} = v_{incomp} + \Delta v \quad (2)$$

It is to be noted that, in equation (1), the local velocity of sound c is not a constant but is related to the velocity v of the fluid in the plane of the profile by means of Bernoulli's equation and the equation of state of the fluid. Thus, if the adiabatic equation of state is adopted,

$$c^2 = c_0^2 \left[1 + \frac{\gamma - 1}{2} \frac{v_0^2}{c_0^2} \left(1 - \frac{v^2}{v_0^2} \right) \right] \quad (3)$$

where c_0, v_0 are the corresponding magnitudes in the undisturbed stream and $\gamma = 1.408$ for air.

In order to facilitate the solution of equation (1), it has been the custom to replace c by c_0 . This simpli-

fication of the problem may be justified by the following argument. It has been tacitly understood that nowhere in the fluid must the velocity of the fluid exceed that of the local velocity of sound since the incompressible flow has already been assumed to be a good first approximation and the effect of compressibility is merely to distort the streamlines associated with the incompressible flow. As the maximum fluid velocity occurs at the surface of the obstacle, there exists a value of v_0^2/c_0^2 for which the maximum fluid velocity equals that of the local velocity of sound. This critical velocity of the fluid is obtained from equation (3) by replacing v by c . Thus

$$c_{least}^2 = v_{crit}^2 = \frac{2c_0^2}{\gamma+1} \left(1 + \frac{\gamma-1}{2} \frac{v_0^2}{c_0^2} \right) \quad (4)$$

This value for c is a lower limit under the condition that nowhere in the fluid is the local velocity of sound exceeded. The maximum value of c occurs at the stagnation point $v=0$ and is given by

$$c_{max}^2 = c_0^2 \left(1 + \frac{\gamma-1}{2} \frac{v_0^2}{c_0^2} \right) \quad (5)$$

Thus both the maximum and the least values of c occur on the obstacle and everywhere else $c_{max} > c > c_{least}$. It follows from equations (4) and (5) that

$$\frac{c_{max} - c_{least}}{c_0} = 0.0887 \left(1 + 0.204 \frac{v_0^2}{c_0^2} \right)^{1/2}$$

which increases very slowly as v_0/c_0 approaches unity.

In fact, it is seen that the upper limit for $\frac{c_{max} - c_{least}}{c_0}$ is 0.0973. The foregoing discussion thus shows that c/c_0 may, as a first approximation, be taken to be unity. Equation (1) then becomes

$$\Delta v = \frac{1}{2\pi c_0^2} \int_0^1 \int_0^{2\pi} \frac{v_r \frac{\partial v^2}{\partial \lambda} - \frac{v_\theta}{\lambda} \frac{\partial v^2}{\partial \theta}}{1 - 2\lambda \cos(\theta - \delta) + \lambda^2} \sin(\theta - \delta) d\lambda d\theta \quad (6)$$

THE FLOW OF A PERFECT COMPRESSIBLE FLUID PAST AN ELLIPTIC CYLINDER

Let the ζ plane be the plane of the ellipse and the z plane be the plane of the corresponding circle. Then it is well known that the Joukowski transformation

$$\zeta = z + \frac{a^2}{z} \quad (7)$$

maps the circle of radius a with its center at the origin of the z plane into the line segment $(-2a, 0; 2a, 0)$ in the ζ plane. Also, the circles concentric with the circle of radius a are transformed into a family of confocal ellipses with common foci at $(-2a, 0)$ and $(2a, 0)$. If $R(>a)$ denotes the radius of one of these circles, then the semimajor and semiminor axes of the ellipse into

which it is transformed are, respectively, $R + \frac{a^2}{R}$ and $R - \frac{a^2}{R}$. The thickness ratio t then becomes:

$$t = \frac{R - \frac{a^2}{R}}{R + \frac{a^2}{R}} = \frac{1 - \sigma^2}{1 + \sigma^2}$$

or

$$\sigma^2 = \frac{1-t}{1+t}$$

where

$$\sigma = \frac{a}{R}$$

If w denotes the complex potential of the incompressible flow in the z plane when a stream of velocity v_0 impinges on a circle of radius R in the direction of the negative x axis, then

$$w = v_0 \left(z + \frac{R^2}{z} \right) \quad (8)$$

The complex velocity in the ζ plane is then given by

$$\frac{dw}{d\zeta} = \frac{dw}{dz} \frac{dz}{d\zeta}$$

or

$$\frac{dw}{d\zeta} = v_0 \frac{z^2 - R^2}{z^2 - a^2} \quad (9)$$

When $\lambda = \frac{R}{r}$ and $\sigma = \frac{a}{R}$ are introduced, it follows that

$$v^2 = \left| \frac{dw}{d\zeta} \right|^2 = v_0^2 \frac{1 - 2\lambda^2 \cos 2\theta + \lambda^4}{1 - 2\sigma^2 \lambda^2 \cos 2\theta + \sigma^4 \lambda^4} \quad (10)$$

Following Poggi's procedure, the Fourier development of v^2/v_0^2 will be obtained. Thus, by the use of the expansion

$$\frac{1}{1 - 2\sigma^2 \lambda^2 \cos 2\theta + \sigma^4 \lambda^4} = \frac{1}{1 - \sigma^4 \lambda^4} \left[1 + 2 \sum_{n=1}^{\infty} (\sigma \lambda)^{2n} \cos 2n\theta \right]$$

(see appendix, sec. I),

it follows that

$$\frac{v^2}{v_0^2} = \frac{1}{2} a_0 + \sum_{n=1}^{\infty} a_{2n} \cos 2n\theta \quad (11)$$

where

$$a_0 = 2 \frac{1 + (1 - 2\sigma^2) \lambda^4}{1 - \sigma^4 \lambda^4}$$

and for $n=1, 2, \dots$

$$a_{2n} = 2 \frac{(1 - \sigma^2)(\sigma^2 \lambda^4 - 1)}{\sigma^2(1 - \sigma^4 \lambda^4)} (\sigma \lambda)^{2n}$$

Also from equation (8)

$$\begin{cases} v_r = -v_0(1 - \lambda^2) \cos \theta \\ v_\theta = v_0(1 + \lambda^2) \sin \theta \end{cases} \quad (12)$$

Then, inserting the expressions for v^2 , v_r , and v_θ given by equations (11) and (12) into equation (6) and making use of the integrals

$$\int_0^{2\pi} \frac{\sin(\theta-\delta)}{1-2\lambda \cos(\theta-\delta)+\lambda^2} \sin n\theta d\theta = \begin{cases} 0 & \text{if } n=0 \\ \pi \lambda^{n-1} \cos n\delta & \text{if } n \geq 1 \end{cases}$$

(see appendix, sec. II)

$$\int_0^{2\pi} \frac{\sin(\theta-\delta)}{1-2\lambda \cos(\theta-\delta)+\lambda^2} \cos n\theta d\theta = \begin{cases} 0 & \text{if } n=0 \\ -\pi \lambda^{n-1} \sin n\delta & \text{if } n \geq 1 \end{cases}$$

it follows without difficulty that

$$\frac{\Delta v}{v_0} = \frac{\mu}{2} \left[-\sin \delta + \sum_{n=0}^{\infty} (2n+1) \sin(2n+1)\delta \int_0^1 (\lambda^{2n+1} a_{2n} - \lambda^{2n-1} a_{2n+2}) d\lambda \right] \quad (13)$$

where

$$\mu = \frac{v_0^2}{c_0^2}$$

Substituting for the a_{2n} 's from equation (11), equation (13) takes the form

$$\frac{\Delta v}{v_0} = \frac{\mu}{2} \frac{1-\sigma^2}{\sigma^2} \left[\sin \delta - (1-\sigma^2) \sum_{n=0}^{\infty} (2n+1) \sin(2n+1)\delta \int_0^1 \frac{1-\sigma^2 \lambda^4}{1-\sigma^4 \lambda^4} (\sigma^2 \lambda^4)^n d\lambda^2 \right]$$

Replacing λ^2 by τ , for purposes of integration only, it follows that

$$I = \sum_{n=0}^{\infty} (2n+1) \sin(2n+1)\delta \int_0^1 \frac{1-\sigma^2 \lambda^4}{1-\sigma^4 \lambda^4} (\sigma^2 \lambda^4)^n d\lambda^2 \\ = -R.P. \text{ of } i \sum_{n=0}^{\infty} (2n+1) e^{i(2n+1)\delta} \int_0^1 \frac{1-\sigma^2 \tau^2}{1-\sigma^4 \tau^2} (\sigma \tau)^{2n} d\tau$$

or

$$I = R.P. \text{ of } i e^{i\delta} \int_0^1 \frac{1+\sigma^2 \tau^2 e^{2i\delta}}{(1-\sigma^2 \tau^2 e^{2i\delta})^2} \frac{1-\sigma^2 \tau^2}{1-\sigma^4 \tau^2} d\tau \\ = \frac{1}{(1-2\sigma^2 \cos 2\delta + \sigma^4)^2} \left\{ \frac{(1-\sigma^2)^2}{2\sigma^2} [(1+3\sigma^2+\sigma^4) \sin \delta + \sigma^2 \sin 3\delta] \log \frac{1+\sigma^2}{1-\sigma^2} \right. \\ \left. + \frac{1-\sigma^2}{\sigma} [(1+\sigma^4) \cos 2\delta - 2\sigma^2] \tan^{-1} \frac{2\sigma \sin \delta}{1-\sigma^2} - \frac{(1+\sigma^2)(1-\sigma^2)^2}{2\sigma} \sin 2\delta \log \frac{1+2\sigma \cos \delta + \sigma^2}{1-2\sigma \cos \delta + \sigma^2} \right. \\ \left. + 2[(1+\sigma^2+\sigma^4) \sin \delta - \sigma^2 \sin 3\delta] \right\}$$

Therefore

$$\frac{\Delta v}{v_0} = \frac{\mu}{2} \frac{1-\sigma^2}{\sigma^2} \left(\sin \delta - \frac{1-\sigma^2}{(1-2\sigma^2 \cos 2\delta + \sigma^4)^2} \left\{ \frac{(1-\sigma^2)^2}{2\sigma^2} [(1+3\sigma^2+\sigma^4) \sin \delta + \sigma^2 \sin 3\delta] \log \frac{1+\sigma^2}{1-\sigma^2} \right. \right.$$

$$\left. - \frac{(1+\sigma^2)(1-\sigma^2)^2}{2\sigma} \sin 2\delta \log \frac{1+2\sigma \cos \delta + \sigma^2}{1-2\sigma \cos \delta + \sigma^2} + \frac{1-\sigma^2}{\sigma} [(1+\sigma^4) \cos 2\delta - 2\sigma^2] \tan^{-1} \frac{2\sigma \sin \delta}{1-\sigma^2} \right. \\ \left. + 2[(1+\sigma^2+\sigma^4) \sin \delta - \sigma^2 \sin 3\delta] \right\} \quad (14)$$

For $\delta = \frac{\pi}{2}$, the position of maximum velocity on the surface of the elliptic cylinder,

$$\left(\frac{\Delta v}{v_0} \right)_{\delta=\frac{\pi}{2}} = \frac{\mu}{2} \frac{1-\sigma^2}{\sigma^2} \left\{ 1 - \frac{1-\sigma^2}{(1+\sigma^2)^2} \left[\frac{(1-\sigma^2)^2}{2\sigma^2} \log \frac{1+\sigma^2}{1-\sigma^2} - 2 \frac{1-\sigma^2}{\sigma} \tan^{-1} \sigma + 2 \right] \right\} \quad (15)$$

It is interesting to note that the expression for $\Delta v/v_0$ at the surface of a circular cylinder fixed in a stream of velocity v_0 impinging on it in the direction of the negative x axis may be obtained from equation (14) by allowing $\sigma (= \frac{a}{R})$ to approach zero. Thus, making use of the expansions

$$\frac{1}{(1-2\sigma^2 \cos 2\delta + \sigma^4)^2} = \frac{1}{(1-\sigma^4)^3} \left\{ (1+\sigma^4) + 2 \sum_{n=1}^{\infty} [(n+1) - (n-1)\sigma^4] \sigma^{2n} \cos 2n\delta \right\} \quad (\text{see appendix, sec. III})$$

$$\log \frac{1+2\sigma \cos \delta + \sigma^2}{1-2\sigma \cos \delta + \sigma^2} = 4 \sum_{n=0}^{\infty} \frac{\sigma^{2n+1}}{2n+1} \cos(2n+1)\delta$$

$$\tan^{-1} \frac{2\sigma \sin \delta}{1-\sigma^2} = 2 \sum_{n=0}^{\infty} \frac{\sigma^{2n+1}}{2n+1} \sin(2n+1)\delta$$

$$\log \frac{1+\sigma^2}{1-\sigma^2} = 2 \sum_{n=0}^{\infty} \frac{\sigma^{2(2n+1)}}{2n+1}$$

it follows, neglecting terms containing powers of σ higher than the second, that

$$\frac{\Delta v}{v_0} = \frac{\mu}{2} (1-\sigma^2) \left(\frac{4}{3} \sin \delta - \sin 3\delta \right)$$

or

$$\lim_{\sigma \rightarrow 0} \frac{\Delta v}{v_0} = \mu \left(\frac{2}{3} \sin \delta - \frac{1}{2} \sin 3\delta \right) \quad (16)$$

This expression for $\Delta v/v_0$ agrees with that obtained by the methods of Janzen, Rayleigh, and Poggi (reference 3).

The effect of compressibility, i. e., $\Delta v/v_0$, having been found, it follows according to equation (2) that the total velocity at the circular boundary in the z plane is given by

$$\left(\frac{v}{v_0} \right)_{\text{circle}} = 2 \sin \delta + \frac{\Delta v}{v_0} \quad (17)$$

and on the elliptic profile in the ζ plane by

$$\left(\frac{v}{v_0} \right)_{\text{ellipse}} = \frac{1}{(1-2\sigma^2 \cos 2\delta + \sigma^4)^{1/2}} \left(\frac{v}{v_0} \right)_{\text{circle}} \quad (18)$$

Table I shows the comparison between the values of $(v/v_0)_{ellipse}$ calculated according to equation (18) and those obtained by Hooker for an ellipse of thickness ratio $t=1/2$ or $\sigma^2=1/2$. The values for the corresponding incompressible flow are included. It is seen that the results of the two methods agree very well. This agreement is not unexpected since Hooker's method is particularly applicable to thick ellipses. Consider, however, a slender ellipse, say $t=1/10$ or $\sigma^2=1/10$. Table II shows the comparison between the exact calculations of the present method and the results obtained according to Hooker's method. The disagreement is more evident than that shown in table I for the thicker ellipse.

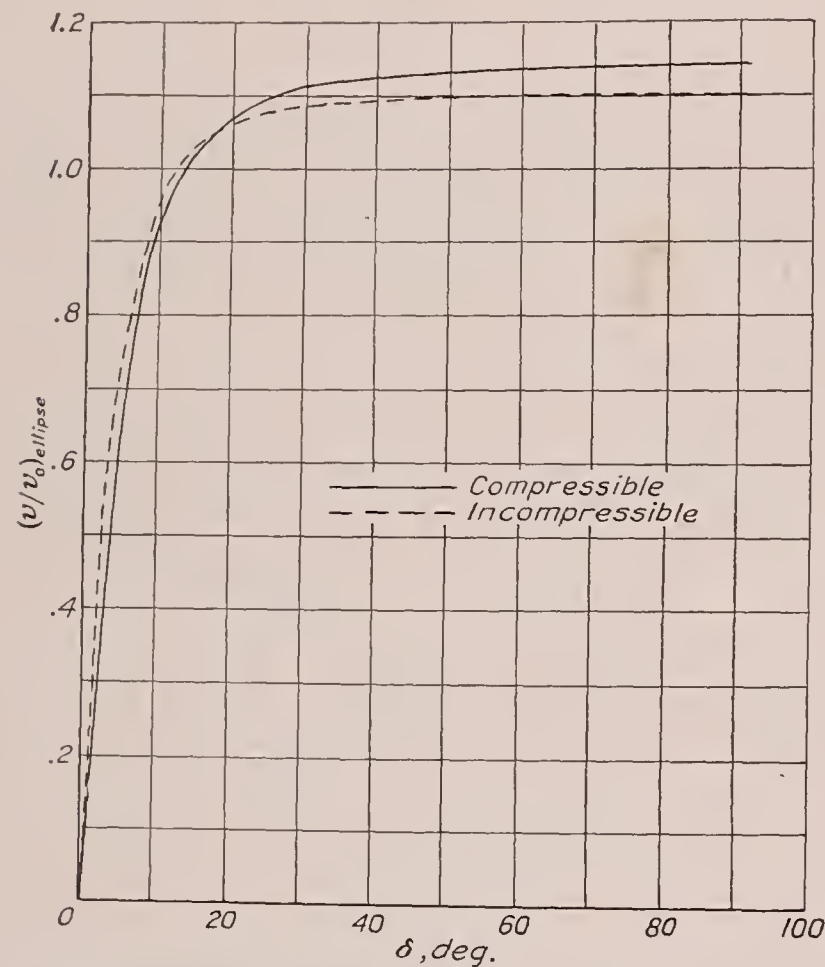


FIGURE 1.—The velocity of the fluid on the surface of an elliptic cylinder of thickness ratio 1/10 for compressible and incompressible flows with $v_0/c_0=0.857$.

Figure 1 shows the graph $(v/v_0)_{ellipse}$ calculated according to Poggi's method for both the compressible and the incompressible flows past the ellipse of thickness ratio $1/10$ with $v_0/c_0=0.857$.

TABLE I

$v_0/c_0=0.5$; thickness ratio= $1/2$

δ (deg.)	$(\frac{v}{v_0})_{ellipse}$		
	Hooker's method	Poggi's method	Incompressible
0	0	0	0
15	.667	.6683	.7085
30	1.130	1.1310	1.1339
45	1.380	1.3869	1.3417
60	1.513	1.5184	1.4412
75	1.575	1.5809	1.4867
90	1.607	1.5994	1.5000

TABLE II

$v_0/c_0=0.857$; thickness ratio= $1/10$

δ (deg.)	$(\frac{v}{v_0})_{ellipse}$		
	Hooker's method	Poggi's method	Incompressible
0	0	0	0
5	.6793	.6342	.7244
10	.9005	.9395	.9569
15	.9904	1.0056	1.0307
20	1.0433	1.0749	1.0608
30	1.1080	1.1146	1.0839
40	1.1332	1.1271	1.0924
50	1.1320	1.1338	1.0962
60	1.1273	1.1374	1.0983
70	1.1346	1.1394	1.0994
80	1.1501	1.1403	1.0999
90	1.1582	1.1406	1.1000

THE PRESSURE DISTRIBUTION

According to Bernoulli's theorem and the adiabatic equation of state, if p and ρ are the pressure and density of the fluid, then

$$\frac{p}{p_0} = \left(\frac{\rho}{\rho_0}\right)^\gamma = \left[1 + \frac{\gamma-1}{2} \mu \left(1 - \frac{v^2}{v_0^2}\right)\right]^{\frac{\gamma}{\gamma-1}}$$

where p_0 and ρ_0 are the pressure and density, respectively, in the undisturbed stream. Expanding the right-hand side of the foregoing equation and neglecting

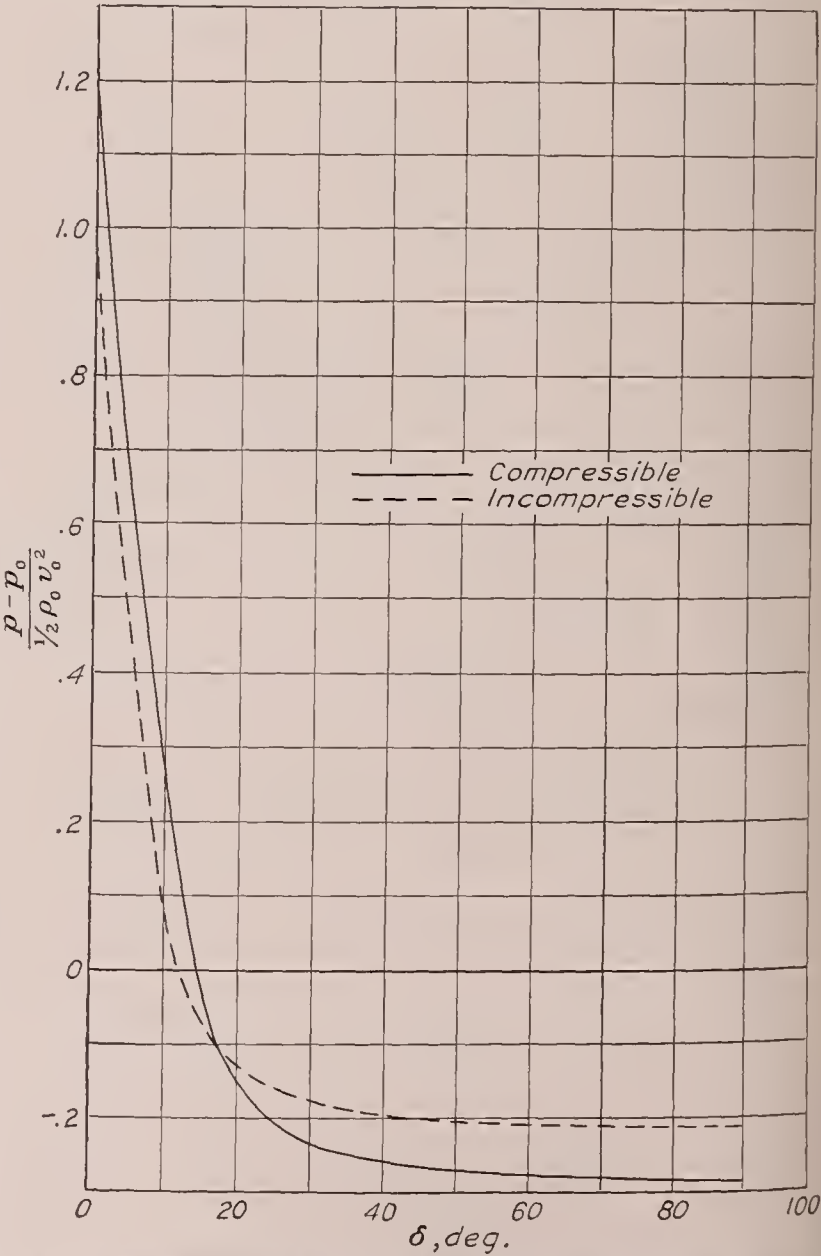


FIGURE 2.—The pressure of the fluid on the surface of an elliptic cylinder of thickness ratio 1/10 for compressible and incompressible flows with $v_0/c_0=0.857$.

terms involving powers of μ higher than the first yields

$$\frac{p-p_0}{\frac{1}{2}\rho_0 v_0^2} = \left(1 - \frac{v^2}{v_0^2}\right) + \frac{\mu}{4} \left(1 - \frac{v^2}{v_0^2}\right)^2 + \dots \quad (19)$$

The pressure distribution is then obtained by substituting for v/v_0 from equation (18). Table III shows the pressure distribution over the surface of an ellipse of thickness ratio 1/10 with $v_0/c_0=0.857$, and figure 2 shows the graph of this distribution together with the one due to the corresponding incompressible flow.

TABLE III

$v_0/c_0=0.857$; thickness ratio = 1/10

δ (deg.)	$\frac{p-p_0}{\frac{1}{2}\rho_0 v_0^2}$	
	Compressible	Incompressible
0	1.1836	1.0000
5	.6635	.4753
10	.1198	.0843
15	-.0113	-.0623
20	-.1511	-.1253
30	-.2315	-.1748
40	-.2570	-.1933
50	-.2706	-.2017
60	-.2779	-.2063
70	-.2818	-.2087
80	-.2838	-.2098
90	-.2843	-.2100

THE ATTAINMENT OF THE LOCAL VELOCITY OF SOUND AT THE SURFACE OF AN ELLIPTIC CYLINDER

According to equation (4) the critical velocity of the fluid is given by

$$\left(\frac{v_{crit}}{v_0}\right)^2 = \frac{2}{\gamma+1} \frac{1}{\mu} + \frac{\gamma-1}{\gamma+1} \quad (20)$$

For an elliptic cylinder, at zero angle of attack, the critical velocity occurs at $\delta=\frac{\pi}{2}$, the position of maximum velocity on the cylinder and also in the region of flow. Hence substituting from equation (18) for $(v/v_0)_{ellipse}$ at $\delta=\frac{\pi}{2}$ yields a cubic equation in the variable μ .

Thus, from equation (15), if

$$f(\sigma) = \frac{1-\sigma^2}{2\sigma^2} \left\{ 1 - \frac{1-\sigma^2}{(1+\sigma^2)^2} \left[\frac{(1-\sigma^2)^2}{2\sigma^2} \log \frac{1+\sigma^2}{1-\sigma^2} - 2 \frac{1-\sigma^2}{\sigma} \tan^{-1} \sigma + 2 \right] \right\}$$

then

$$[f(\sigma)]^2 \mu^3 + 4f(\sigma) \mu^2 + \left[4 - \frac{\gamma-1}{\gamma+1} (1+\sigma^2)^2 \right] \mu - \frac{2(1+\sigma^2)^2}{\gamma+1} = 0 \quad (21)$$

where $\gamma=1.408$ for air.

Table IV gives the critical values of v_0/c_0 for the entire range of thickness ratios including the limiting cases of the straight-line segment and the circular

profile. Figure 3 shows the critical values of $v_0/c_0 (= \sqrt{\mu})$ plotted against the thickness ratio.

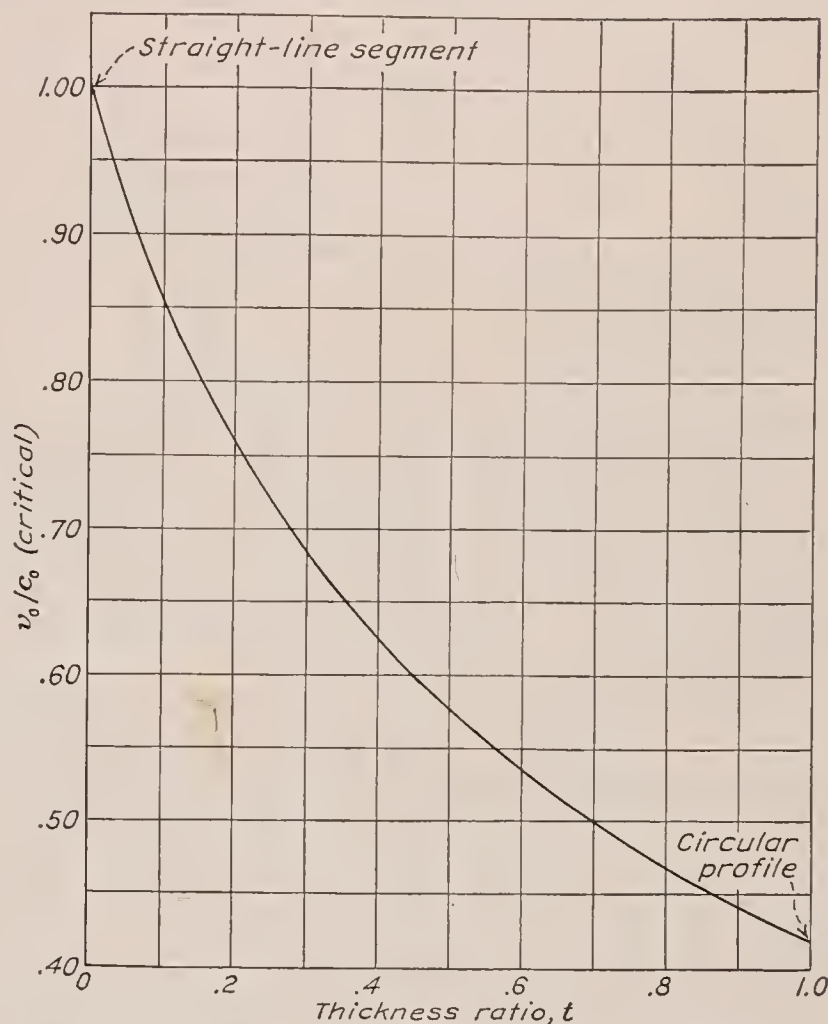
FIGURE 3.—The critical ratio v_0/c_0 as a function of the thickness ratio t .

TABLE IV

σ^2	Thickness ratio	$\frac{v_0}{c_0}$ (critical)
1	0	1.000
19/21	1/20	.919
9/11	1/10	.857
4/5	1/9	.845
7/9	1/8	.830
3/4	1/7	.811
5/7	1/6	.788
2/3	1/5	.759
3/5	1/4	.719
1/2	1/3	.663
1/3	1/2	.577
1/5	2/3	.512
1/7	3/4	.485
1/19	9/10	.444
0	1	.420

THE THIRD APPROXIMATION TO THE COMPRESSIBLE FLOW ABOUT CIRCULAR CYLINDERS

In reference 2, the opinion is expressed by Hooker that the terms involving $(v_0/c_0)^4$, thus far neglected, may become of considerable importance as the local velocity of sound is approached on the ellipse. Hooker, however, did not investigate the matter any further. In reference 4, Poggi calculated these terms for the compressible flow about a circular cylinder, but a close examination of his work shows that not all such terms were taken into account. In what follows the terms neglected by Poggi will be obtained and compared with the already existing ones.

The fundamental integral equation (1) may be written as follows:

$$\frac{\Delta v}{v_0} = \frac{\mu}{2\pi} \int_0^1 \int_0^{2\pi} \frac{\frac{v_r}{v_0} \frac{\partial \frac{v^2}{v_0^2}}{\partial \lambda} - \frac{1}{\lambda} \frac{v_\theta}{v_0} \frac{\partial \frac{v^2}{v_0^2}}{\partial \theta}}{1 - 2\lambda \cos(\theta - \delta) + \lambda^2} \left[1 - \frac{\gamma-1}{2} \mu \left(1 - \frac{v^2}{v_0^2} \right) + \dots \right] \sin(\theta - \delta) d\lambda d\theta \quad (22)$$

where $1/c^2$ has been replaced by a power series in $\mu (= v_0^2/c_0^2)$ obtained from equation (3); i. e.:

$$\frac{1}{c^2} = \frac{1}{c_0^2} \left[1 - \frac{\gamma-1}{2} \mu \left(1 - \frac{v^2}{v_0^2} \right) + \dots \right]$$

The method followed by Poggi was to substitute for v_r , v_θ , and v^2 expressions pertaining to the incompressible flow and thus obtain the following result:¹

$$\frac{\Delta v}{v_0} = \left(\frac{2}{3} \sin \delta - \frac{1}{2} \sin 3\delta \right) \mu + (\gamma-1) \left(\frac{23}{120} \sin \delta - \frac{11}{40} \sin 3\delta + \frac{1}{8} \sin 5\delta \right) \mu^2 + \dots \quad (23)$$

The velocity for the compressible flow at the surface of the circular cylinder then becomes:

$$\frac{v_{comp}}{v_0} = \frac{v_{incomp}}{v_0} + \frac{\Delta v}{v_0} \quad (24)$$

where $\Delta v/v_0$ is given by equation (23).

Equation (24) thus represents the second approximation to the compressible flow, the first approximation being the purely incompressible flow given by v_{incomp}/v_0 .

The third approximation may be obtained, at least in principle, by substituting for v_r , v_θ , and v^2 in equation (22) expressions based on the second approximation. Such expressions, as far as the terms involving μ are concerned, are given in reference 3 and are as follows:

$$\frac{v_r}{v_0} = -(1 - \lambda^2) \cos \theta - \mu \left[\left(-\frac{13}{12} \lambda^2 + \frac{3}{2} \lambda^4 - \frac{5}{12} \lambda^6 \right) \cos \theta + \left(\frac{1}{4} \lambda^2 - \frac{1}{4} \lambda^4 \right) \cos 3\theta \right] + \dots$$

$$\frac{v_\theta}{v_0} = (1 + \lambda^2) \sin \theta + \mu \left[\left(\frac{13}{12} \lambda^2 - \frac{1}{2} \lambda^4 + \frac{1}{12} \lambda^6 \right) \sin \theta + \left(-\frac{3}{4} \lambda^2 + \frac{1}{4} \lambda^4 \right) \sin 3\theta \right] + \dots$$

$$\frac{v^2}{v_0^2} = (1 + \lambda^4) - \lambda^4 \cos 2\theta + \mu \left[\left(\frac{19}{6} \lambda^4 - \frac{7}{3} \lambda^6 + \frac{1}{2} \lambda^8 \right) + \left(-\frac{8}{3} \lambda^2 + \lambda^4 - \lambda^6 + \frac{1}{3} \lambda^8 \right) \cos 2\theta + \lambda^2 \cos 4\theta \right] + \dots$$

¹ The corresponding terms involving $(\gamma-1) \mu^2$ were obtained for elliptic cylinders and it was found that they reduce to those given in equation (23) for the circle. However, in reference 4 the coefficients of $\sin \delta$ and $\sin 5\delta$ are given, respectively, as $13/120$ and $1/8$ owing to a slight error in the calculations. Pistolesi (reference 3) gives for the coefficient of $\sin \delta$ the value $43/120$ which, in view of the independent check of Poggi's results by the author, is believed to be a misprint.

where it is recalled that $\lambda = \frac{R}{r}$.

When the foregoing expressions are substituted into equation (22) and only the terms involving μ and μ^2 are evaluated, it is found that, besides the terms given by equation (23), the following ones involving μ^2 must be included:

$$\mu^2 \left(\frac{37}{40} \sin \delta - \frac{25}{24} \sin 3\delta + \frac{3}{8} \sin 5\delta \right) \quad (25)$$

These terms seem to have been overlooked by both Poggi and Pistolesi (reference 3).

The third approximation to the compressible flow at the surface of the circular cylinder then becomes:

$$\begin{aligned} \frac{v_{comp}}{v_0} = & 2 \sin \delta + \left(\frac{2}{3} \sin \delta - \frac{1}{2} \sin 3\delta \right) \mu \\ & + \left[\left(\frac{37}{40} \sin \delta - \frac{25}{24} \sin 3\delta + \frac{3}{8} \sin 5\delta \right) \right. \\ & + (\gamma-1) \left(\frac{23}{120} \sin \delta - \frac{11}{40} \sin 3\delta \right. \\ & \left. \left. + \frac{1}{8} \sin 5\delta \right) \right] \mu^2 + \dots \quad (26) \end{aligned}$$

It is interesting to compare the magnitudes of the various terms in equation (26) at the position of maximum velocity $\delta = \pi/2$ and for the critical value $\mu = 0.1670$ (obtained by means of equations (20) and (26)). Thus

$$(2 \sin \delta)_{\delta=\pi/2} = 2$$

$$\mu \left(\frac{2}{3} \sin \delta - \frac{1}{2} \sin 3\delta \right)_{\delta=\pi/2} = 0.1948$$

$$\mu^2 \left(\frac{37}{40} \sin \delta - \frac{25}{24} \sin 3\delta + \frac{3}{8} \sin 5\delta \right)_{\delta=\pi/2} = 0.0653$$

$$\mu^2 (\gamma-1) \left(\frac{23}{120} \sin \delta - \frac{11}{40} \sin 3\delta + \frac{1}{8} \sin 5\delta \right)_{\delta=\pi/2} = 0.0067$$

Thus, it is seen that the terms involving μ^2 do become of importance with regard to the μ terms as the local velocity of sound is approached on the circle and that the main contribution is made by expression (25).

LANGLEY MEMORIAL AERONAUTICAL LABORATORY,
NATIONAL ADVISORY COMMITTEE FOR AERONAUTICS,
LANGLEY FIELD, VA., February 11, 1938.

APPENDIX

I. The Fourier Expansion of $\frac{1}{1-2\sigma^2\lambda^2\cos 2\theta+\sigma^4\lambda^4}$

If $2\cos 2\theta$ is replaced by $e^{2i\theta}+e^{-2i\theta}$, then

$$H = \frac{1}{1-2\sigma^2\lambda^2\cos 2\theta+\sigma^4\lambda^4} = \frac{1}{(1-\sigma^2\lambda^2e^{2i\theta})(1-\sigma^2\lambda^2e^{-2i\theta})}$$

Since, by the binomial theorem,

$$(1-\sigma^2\lambda^2e^{2i\theta})^{-1} = \sum_{j=0}^{\infty} (\sigma^2\lambda^2)^j e^{2ij\theta}$$

and

$$(1-\sigma^2\lambda^2e^{-2i\theta})^{-1} = \sum_{k=0}^{\infty} (\sigma^2\lambda^2)^k e^{-2ik\theta}$$

it follows that

$$H = \sum_{j=0}^{\infty} \sum_{k=0}^{\infty} (\sigma^2\lambda^2)^{j+k} e^{2i(j-k)\theta}$$

Let

$$j+k=n$$

and therefore

$$j-k=n-2k, \quad j=n-k$$

The double series then becomes

$$H = \sum_{n=0}^{\infty} \sum_{k=0}^n (\sigma^2\lambda^2)^n e^{2i(n-2k)\theta}$$

The terms of this series can be grouped in pairs such that

$$H = 2 \sum_{n=0}^{\infty} \sum_{k=0}^{\frac{n}{2}, \frac{n-1}{2}} (\sigma^2\lambda^2)^n \cos(n-2k)2\theta \quad (1)$$

where $\frac{n}{2}$ or $\frac{n-1}{2}$ is the upper limit according as n is even or odd and where the factor 2 is omitted from the term for which n is even and $k=\frac{n}{2}$. This term is independent of θ and there is only one such term, not two.

The series (1) may be written as

$$H = \sum_{n=0}^{\infty} \sum_{k=0}^{\frac{n}{2}, \frac{n-1}{2}} A_n \cos(n-2k)2\theta$$

where

$$A_n = 2(\sigma^2\lambda^2)^n$$

Expanding this series and rearranging the terms in the form of a Fourier series,

$$H = \frac{1}{2} \sum_{n=0}^{\infty} A_{2n} + \sum_{n=1}^{\infty} \cos 2n\theta \sum_{k=0}^{\infty} A_{n+2k}$$

But

$$\frac{1}{2} \sum_{n=0}^{\infty} A_{2n} = \sum_{n=0}^{\infty} (\sigma^4\lambda^4)^n = \frac{1}{1-\sigma^4\lambda^4}$$

and

$$\sum_{k=0}^{\infty} A_{n+2k} = 2(\sigma^2\lambda^2)^n \sum_{k=0}^{\infty} (\sigma^4\lambda^4)^k = \frac{2(\sigma^2\lambda^2)^n}{1-\sigma^4\lambda^4}$$

Therefore

$$H = \frac{1}{1-\sigma^4\lambda^4} \left[1 + 2 \sum_{n=1}^{\infty} (\sigma\lambda)^{2n} \cos 2n\theta \right] \quad (2)$$

II. The Integrals

$$J_1 = \int_0^{2\pi} \frac{\sin(\theta-\delta)}{1-2\lambda\cos(\theta-\delta)+\lambda^2} \cos n\theta d\theta$$

and

$$J_2 = \int_0^{2\pi} \frac{\sin(\theta-\delta)}{1-2\lambda\cos(\theta-\delta)+\lambda^2} \sin n\theta d\theta$$

If $2\cos(\theta-\delta)$ is replaced by $e^{i(\theta-\delta)}+e^{-i(\theta-\delta)}$,

then

$$\begin{aligned} \frac{1}{1-2\lambda\cos(\theta-\delta)+\lambda^2} &= \frac{1}{\{1-\lambda e^{i(\theta-\delta)}\}\{1-\lambda e^{-i(\theta-\delta)}\}} \\ &= \frac{1}{e^{i(\theta-\delta)}-e^{-i(\theta-\delta)}} \left\{ \frac{e^{i(\theta-\delta)}}{1-\lambda e^{i(\theta-\delta)}} - \frac{e^{-i(\theta-\delta)}}{1-\lambda e^{-i(\theta-\delta)}} \right\} \\ &= \frac{1}{2i\sin(\theta-\delta)} \left[\sum_{m=0}^{\infty} \lambda^m e^{i(m+1)(\theta-\delta)} - \sum_{m=0}^{\infty} \lambda^m e^{-i(m+1)(\theta-\delta)} \right] \end{aligned}$$

Therefore

$$J_1 + iJ_2 = \frac{1}{2i} \int_0^{2\pi} \left\{ \sum_{m=0}^{\infty} \lambda^m e^{i(m+1)(\theta-\delta)} - \sum_{m=0}^{\infty} \lambda^m e^{-i(m+1)(\theta-\delta)} \right\} e^{in\theta} d\theta$$

Replacing $e^{i\theta}$ by z ,

$$\begin{aligned} J_1 + iJ_2 &= -\frac{1}{2} \oint \left\{ \sum_{m=0}^{\infty} \lambda^m e^{-i(m+1)\delta} z^{m+n} \right. \\ &\quad \left. - \sum_{m=0}^{\infty} \lambda^m e^{i(m+1)\delta} z^{-(m-n+2)} \right\} dz \end{aligned}$$

Since

$$\oint z^p dz = \begin{cases} 0, & \text{in general} \\ 2\pi i, & \text{when } p = -1 \end{cases}$$

it follows that $m=n-1$ and therefore

$$J_1 + iJ_2 = \pi i \lambda^{n-1} e^{in\delta}$$

Hence, for $n \geq 1$,

$$J_1 = -\pi \lambda^{n-1} \sin n\delta \text{ and } J_2 = \pi \lambda^{n-1} \cos n\delta \quad (3)$$

III. The Fourier Expansion of

$$\frac{1}{(1-2\sigma^2\lambda^2\cos 2\theta+\sigma^4\lambda^4)^2}$$

In analogy to section I, replace $2\cos 2\theta$ by $e^{2i\theta}+e^{-2i\theta}$.

Then

$$\begin{aligned} H^2 &= \frac{1}{(1-2\sigma^2\lambda^2\cos 2\theta+\sigma^4\lambda^4)^2} \\ &= \frac{1}{(1-\sigma^2\lambda^2e^{2i\theta})^2(1-\sigma^2\lambda^2e^{-2i\theta})^2} \end{aligned}$$

According to the binomial theorem

$$(1-\sigma^2\lambda^2e^{2i\theta})^{-2} = \sum_{j=0}^{\infty} (j+1)(\sigma^2\lambda^2)^j e^{2ij\theta}$$

and

$$(1-\sigma^2\lambda^2e^{-2i\theta})^{-2} = \sum_{k=0}^{\infty} (k+1)(\sigma^2\lambda^2)^k e^{-2ik\theta}$$

Therefore

$$H^2 = \sum_{j=0}^{\infty} \sum_{k=0}^{\infty} (j+1)(k+1)(\sigma^2 \lambda^2)^{j+k} e^{2i(j-k)\theta}$$

Let

$$j+k=n$$

and therefore

$$j-k=n-2k, j=n-k$$

Then

$$H^2 = \sum_{n=0}^{\infty} \sum_{k=0}^n (n-k+1)(k+1)(\sigma^2 \lambda^2)^n e^{2i(n-2k)\theta}$$

The exponent of e is $2i[(n-k)-k]\theta$. If k and $n-k$ are interchanged, the exponent of e changes sign but the coefficient of e remains unaltered. The terms can therefore be grouped in pairs so that:

$$H^2 = 2 \sum_{n=0}^{\infty} \sum_{k=0}^{\frac{n}{2}, \frac{n-1}{2}} (n-k+1)(k+1)(\sigma^2 \lambda^2)^n \cos(n-2k)2\theta \quad (4)$$

where the factor 2 is omitted from the term for which

n is even and $k = \frac{n}{2}$.

The series (4) may be written as

$$H^2 = \sum_{n=0}^{\infty} \sum_{k=0}^{\frac{n}{2}, \frac{n-1}{2}} A_{n,k} \cos(n-2k)2\theta$$

where

$$A_{n,k} = 2(n-k+1)(k+1)(\sigma^2 \lambda^2)^n$$

Expanding this series and rearranging the terms in the form of a Fourier series,

$$H^2 = \frac{1}{2} \sum_{2k=0}^{\infty} A_{2k,k} + \sum_{n=1}^{\infty} \cos 2n\theta \sum_{k=0}^{\infty} A_{n+2k,k}$$

But

$$\frac{1}{2} \sum_{k=0}^{\infty} A_{2k,k} = \sum_{k=0}^{\infty} (k+1)^2 (\sigma^4 \lambda^4)^k = \frac{1 + \sigma^4 \lambda^4}{(1 - \sigma^4 \lambda^4)^3}$$

and

$$\begin{aligned} \sum_{k=0}^{\infty} A_{n+2k,k} &= 2(\sigma^2 \lambda^2)^n \sum_{k=0}^{\infty} (n+k+1)(k+1)(\sigma^4 \lambda^4)^k \\ &= 2(\sigma^2 \lambda^2)^n \frac{(n+1) - (n-1)\sigma^4 \lambda^4}{(1 - \sigma^4 \lambda^4)^3} \end{aligned}$$

Therefore

$$\begin{aligned} H^2 &= \frac{1}{(1 - \sigma^4 \lambda^4)^3} \left\{ (1 + \sigma^4 \lambda^4) + 2 \sum_{n=1}^{\infty} [(n+1) \right. \\ &\quad \left. - (n-1)\sigma^4 \lambda^4] (\sigma^2 \lambda^2)^n \cos 2n\theta \right\} \quad (5) \end{aligned}$$

REFERENCES

1. Poggi, Lorenzo: Campo di velocità in una corrente piana di fluido compressibile. Parte II.—Caso dei profili ottenuti con rappresentazione conforme dal cerchio ed in particolare dei profili Joukowski. *L'Aerotecnica*, vol. XIV, fasc. 5, May 1934, pp. 532-550.
2. Hooker, S. G.: The Two-Dimensional Flow of Compressible Fluids at Sub-Sonic Speeds Past Elliptic Cylinders. R. & M. No. 1684, British A. R. C., 1936.
3. Pistolesi, Enrico: La portanza alle alte velocità inferiori a quella del suono. *Reale Accademia d'Italia, Classe delle Scienze Fisiche, Matematiche e Naturali*, vol. XIII, 1935.
4. Poggi, Lorenzo: Campo di velocità in una corrente piana di fluido compressibile. *L'Aerotecnica*, vol. XII, fasc. 12, Dec. 1932, pp. 1579-1593.

REPORT No. 625

A DISCUSSION OF CERTAIN PROBLEMS CONNECTED WITH THE DESIGN OF HULLS OF FLYING BOATS AND THE USE OF GENERAL TEST DATA

By WALTER S. DIEHL

SUMMARY

A survey of the problems encountered in applying general test data to the design of flying-boat hulls. It is shown how basic design features may be readily determined from special plots of test data. A study of the effect of the size of a flying boat on the probable limits to be covered by the general test data is included and recommendations for special tests and new methods of presenting test data for direct use in design are given.

INTRODUCTION

The National Advisory Committee for Aeronautics has published a number of Technical Reports, Technical Notes, and Technical Memorandums (references 1 to 23, inclusive) giving data obtained from general tests on flying-boat hulls. A full description of the general method of testing a flying-boat hull may be found in references 3 and 23.

The term "general test" implies that the full range of useful loadings, trim angles, and speeds are investigated rather than one particular or specific condition corresponding to a normal unloading during a take-off. The general test requires determination, for a series of constant loads and at each of a series of fixed trim angles, of the curves of resistance and moment against speed. These data may be cross-plotted to obtain the best trim for each load and speed. The final data are usually given in coefficient form for the best trim condition.

Model test data on hull lines are used primarily and, in order of importance, for (1) comparison of relative advantages and disadvantages of various lines, (2) determination of best beam for a given load and get-away speed, and (3) calculation of take-off resistance. Extended use of the available general test data has brought out a number of modifications that appear desirable from the viewpoint of the designer. These modifications are concerned less with methods of testing than with presentation and possible interpretations of the data. It is believed that a general discussion of the problems of interpreting hull data may serve a useful purpose in clarifying some of the points involved.

SELECTION OF BEST BEAM

In reference 3, Shoemaker and Parkinson give a method of selecting the best beam from the data obtained in a complete tank test, as follows:

"The first step in determining the water resistance is the selection of the proper beam. A number of formulas are in common use for determining the beam but, since the best compromise depends upon the characteristics of the hull used, they are only rough guides. The curves of figure 1 [same as fig. 10, reference 3] offer a somewhat better means for making a first approximation, which can be corrected after the final resistance curve is constructed. The smallest beam which does not make the hump resistance seriously high should be chosen, because a small beam is favorable to low resistance in the high-speed range. Considerations of structural weight also favor a small beam. It should be noted, however, that excessive reduction in beam may cause objectionable spray characteristics.

"The hump of the total resistance curve will occur at approximately the same speed coefficient as the hump of the best-angle curves * * *. For model No. 11 the value of C_V at the hump is about 2.3. Referring to figure 1, the value of Δ/R for this speed is 4.5 at

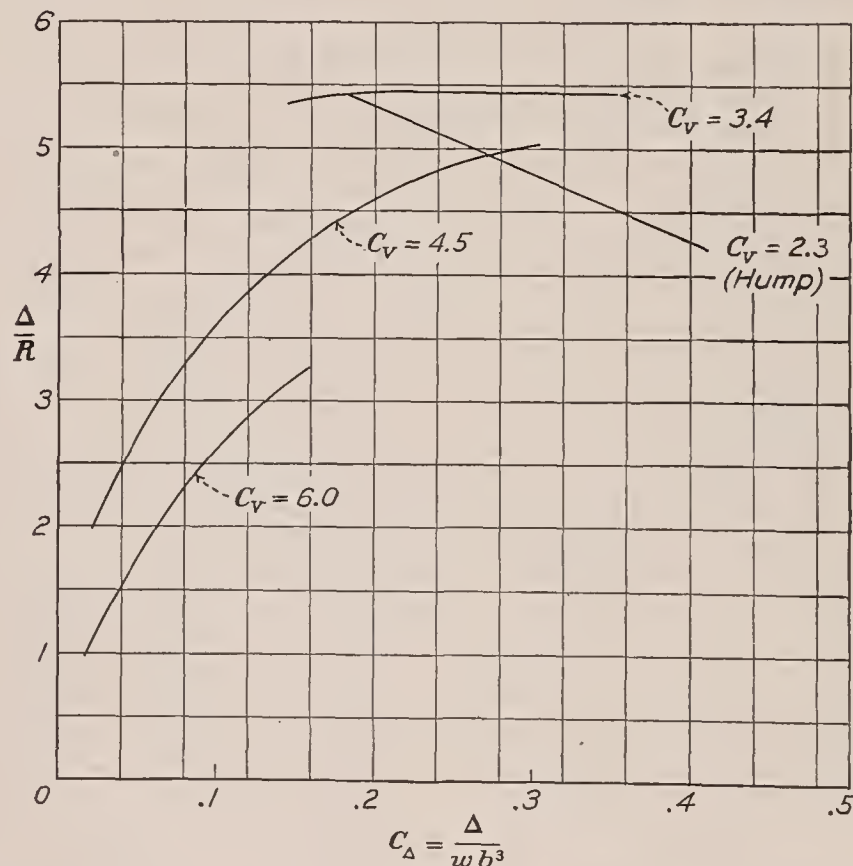


FIGURE 1.—Variation of Δ/R with C_Δ for model 11 (same as fig. 10 of reference 3).

$C_\Delta = 0.35$. This value of Δ/R is about the lowest that will give satisfactory performance at the hump; hence the beam should not be decreased beyond this point,

at least for the first trial. It may be assumed that the load Δ at the hump is roughly nine-tenths of the gross load."

This method has the desirable advantages of being direct and easy to use. Experience shows, however, that the indiscriminate use of data based on the best angle of trim may lead to erroneous conclusions. Unfortunately, the tests in reference 3 do not cover enough range in trim angles and loadings to illustrate the marked difference between free-to-trim and best-trim data. Later tests in reference 10 cover a greater range and may be used for the purpose of illustrating the point involved. Figure 2 gives the Δ/R at hump speed for best trim as taken from figure 11 of reference 10 and for free-to-trim condition as calculated from the test data. If a value of $\Delta/R \geq 5.0$ is required, the best trim-angle data indicates $C_\Delta = 0.42$ whereas the free-to-trim data indicates $C_\Delta = 0.22$. These values represent a difference of about 25 percent in the beam required. There is ample evidence to show that the free-to-trim hump resistance may be 20 to 30 percent greater than the resistance at best trim. There is also sufficient evidence to show that in most cases the actual operating conditions approximate very closely the free-to-trim condition at the hump. It seems highly desirable to base the actual design calculations on the free-to-trim condition only. A discussion of the free-to-trim data will be given later.

There is reason to believe that the superior planing action of a narrow beam hull has been overemphasized. The test data on hull lines show that although it is sometimes possible to obtain improved lines, enabling the use of heavier load coefficients, there is normally very little gain in planing action with a narrow beam in a geometrically similar series. The general effect of variation in beam may be clearly shown on a plot of Δ/R contours with C_Δ as ordinates and C_V^2 as abscissas. Constant angle unloading is shown on this plot by a straight line drawn from the initial load coefficient C_{Δ_0} to the get-away value of C_V^2 . An example of this type of plotting is given on figure 3 taken from an unpublished N. A. C. A. test. The solid diagonal line sloping downward from left to right represents a constant angle take-off with $C_{\Delta_0} = 0.62$ and $C_{VG^2} = 38.0$. The value of C_{Δ_0} varies inversely as the cube of the beam and the value of C_{VG^2} varies inversely as the beam. The effect of a 10-percent change in beam is shown by the two broken lines, the upper line being for the smaller beam. Points representing 80 percent V_G are indicated by circles. The approximate values of Δ/R at the hump and at 80 percent V_G are:

Beam ratio b/b_0 -----	0.90	1.00	1.10
Δ/R at hump-----	4.48	4.72	4.95
Δ/R at $0.80 V_G$ -----	4.70	4.55	4.45

A 10-percent reduction in beam therefore gives about 3 percent reduction in resistance at $0.80 V_G$ but this reduction appears to be more than offset by about 5 percent increase in hump resistance.

Data plotted in figure 3 are based on best trim. This figure would be more useful in the determination of best beam if free-to-trim data were used for values of C_V^2 less than about 10. An abridged form may be employed for this purpose. A curve drawn through the lowest points on each contour in the upper left-hand side of figure 3 locates the values of C_Δ , C_V^2 , and Δ/R at the hump. This curve can be drawn alone on a separate chart as on figure 4, which is simply an approximation based on the free-to-trim curve of figure 2. The

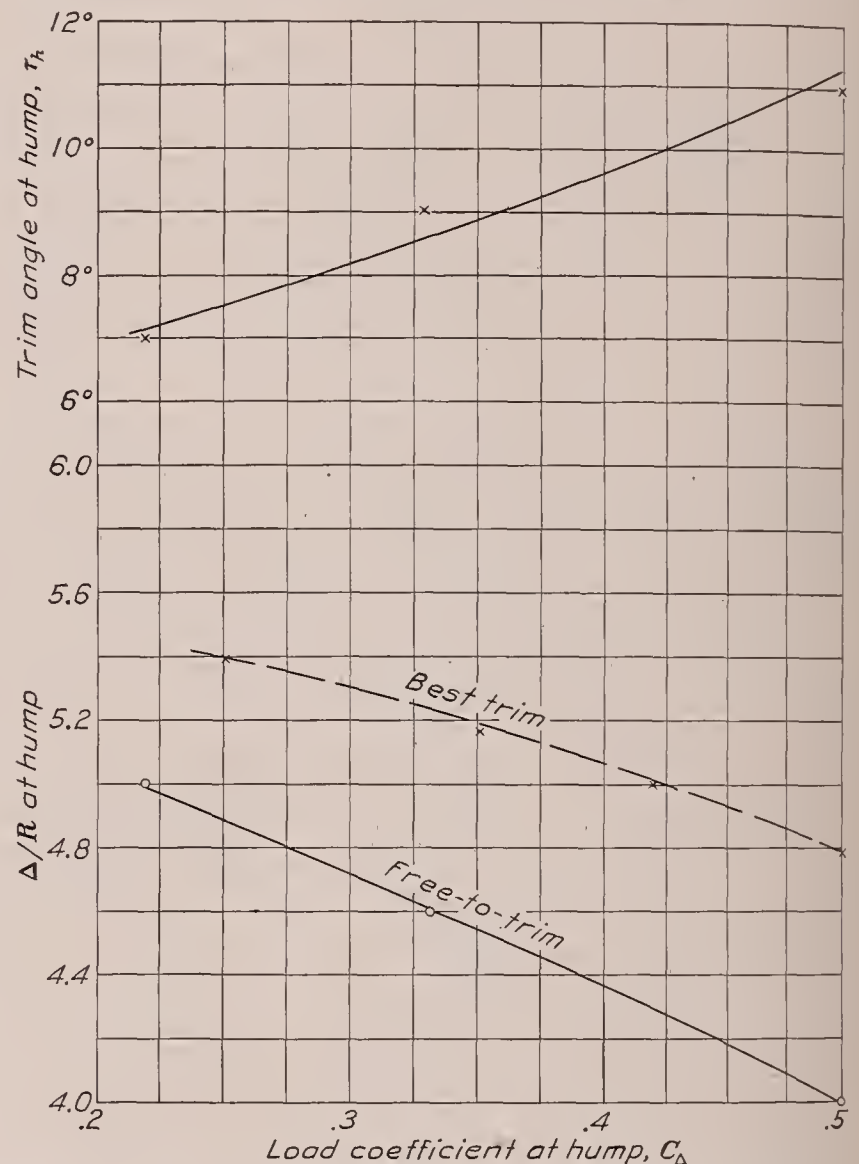


FIGURE 2.—Variation of Δ/R and maximum trim angle at hump for model 11G (based on data from reference 10).

value of C_V at the hump would normally increase slightly as the load coefficient is increased so that the graduated line on figure 4 should incline very slightly to the right. The main value of figure 3 is to emphasize the importance of hump resistance in determining the beam. If a minimum value of Δ/R is specified or required at the hump there is not very much allowable range in beam. The value of C_V^2 at the get-away normally lies between 30 and 50 but extreme values of 20 and 100 may be assumed to illustrate the restricted variation in beam. Light broken lines are drawn on figure 4 to pass through the $\Delta/R = 4.5$ point and intersect the C_V^2 axis at 20 and at 100. These two lines intersect the C_Δ axis at 0.47 and 0.37. Since C_Δ varies inversely as the cube of the beam

$$\frac{b_1}{b_2} = \sqrt[3]{\frac{0.47}{0.37}} = 1.08$$

or the total variation in beam will be less than 10 percent. A plotting in the form shown on figure 2 will ordinarily be sufficiently accurate. Its value can be increased slightly by inclusion of the curve of C_V against C_Δ so that the initial value of C_Δ may be obtained. When C_V is known for hump speed, it is unnecessary to assume

$$C_{\Delta h} = 0.9 C_{\Delta 0}$$

Since

$$C_{\Delta h} = C_{\Delta 0} \left[1 - \left(\frac{C_{Vh}}{C_{VG}} \right)^2 \right]$$

or

$$C_{\Delta 0} = \frac{C_{\Delta h}}{\left[1 - \left(\frac{C_{Vh}}{C_{VG}} \right)^2 \right]} \quad (1)$$

the subscript h denoting hump values.

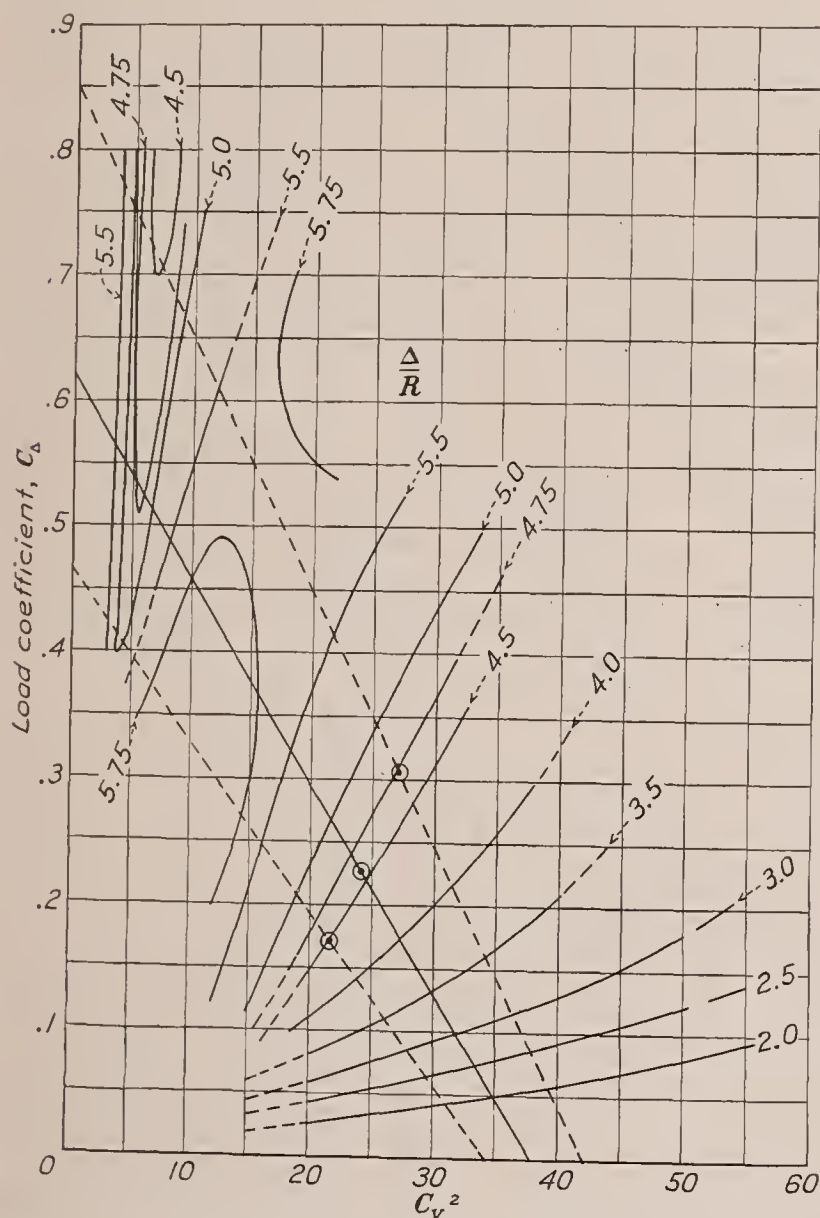


FIGURE 3.—Linear unloading chart for constant angle take-off. Δ/R contours against C_Δ and C_V^2 .

It is important to note that in these approximations C_{VG} must be based on the get-away speed corresponding to the wing angle of attack at hump speed. The hull angle τ_{\max} is given in figure 2 and from it the wing angle may be obtained. The get-away speed is usually assumed to be about 5 percent greater than the stalling speed.

MAXIMUM ANGLE OF TRIM

In free-to-trim tests the maximum angle of trim assumed in passing through the hump increases as the initial load is increased. This characteristic serves to limit the load that can be carried on a given beam since large angles of trim mean high resistance, objectionable spray, etc. The maximum desirable trim angle at the hump decreases slightly as the size of the hull is increased. For a small flying boat it is probably of the order of 12° ; for a very large flying boat it probably should be of the order of 10° , or even 8° if practicable.

The maximum angle free-to-trim can be obtained by cross-plotting the usual general test data, but it would be highly desirable for the designer to have this angle given as a part of the general test data. A very satisfactory form appears to be a plot of τ_h against C_Δ as shown in figure 2.

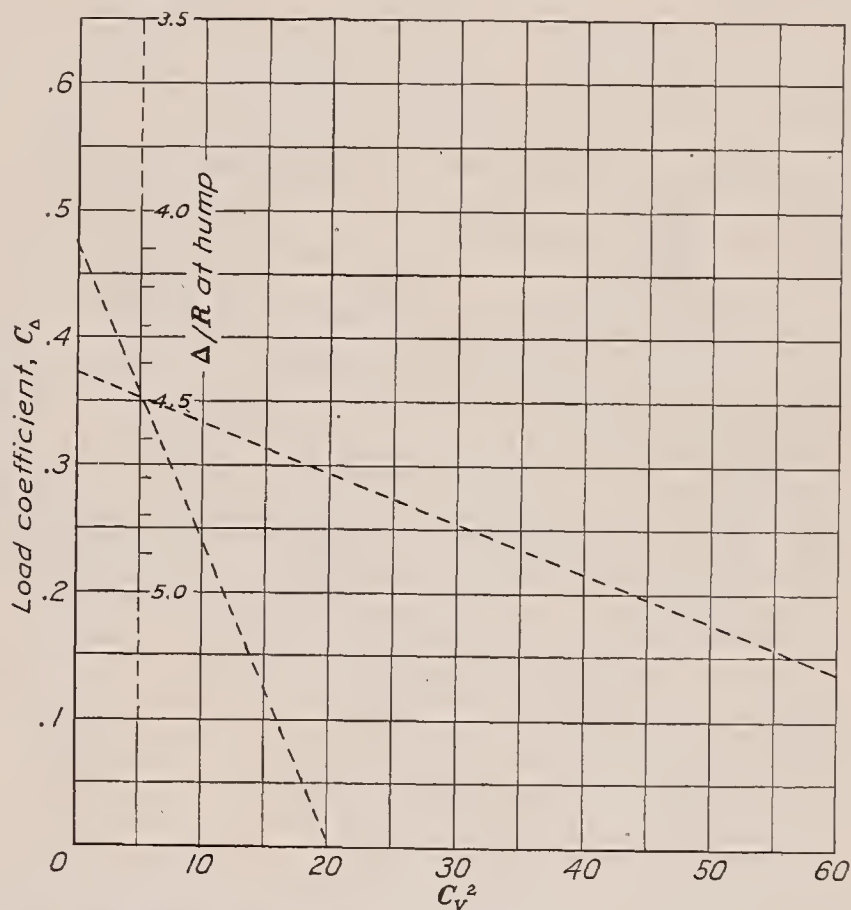


FIGURE 4.—Simplified chart for selection of minimum beam. Δ/R at hump speed against C_Δ and C_V^2 .

The maximum trim at the hump can be controlled only within narrow limits. Moving the center of gravity forward may result in porpoising at planing speeds. This condition will be discussed later. Some diving moment is obtained from the thrust moment and from full-down elevators. An analysis of a number of wind-tunnel model tests shows that the maximum elevator moment corresponds to a lift coefficient of $C_{LT} = 1.00$ for horizontal tail surface or

$$M = q_e S_t l \quad (2)$$

where q_e is the effective dynamic pressure over the tail surfaces. As a first approximation the slipstream ve-

locity may be assumed at 100 miles per hour. For preliminary design purposes it is desirable to have the available moments in terms of the initial displacement. These values can be obtained by using

$$M = K\Delta_0^{4/3} \quad (3)$$

The variation in K is less than might be expected, extreme values being approximately $K=0.040$ and $K=0.080$ with most of the designs grouped around 0.060.

The effect of elevator moment could be simulated by including curves with diving moments $M = -0.060\Delta_0^{4/3}$ and $M = -0.120\Delta_0^{4/3}$. These values are intended to apply only in the region of the hump but, where slipstream velocity is a determining factor, they will also apply at planing speeds.

MOMENTS—VECTOR DIAGRAMS

It has been customary to give moments in coefficient form defined by

$$C_M = \frac{M}{wb^4} \quad (4)$$

This form is consistent with the load and resistance coefficients, $C_\Delta = \frac{\Delta}{wb^3}$ and $C_R = \frac{R}{wb^3}$. It is of interest to note the relation

$$M = \Delta \left(\frac{C_M b}{C_\Delta} \right) \quad (5)$$

where $\left(\frac{C_M b}{C_\Delta} \right)$ is the arm upon which the displacement Δ must act to produce the moment M . A coefficient in this form has considerable merit and may eventually be found the best available. However, a moment coefficient defined by

$$C_M = \frac{M}{\Delta^{4/3}} \quad (6)$$

has obvious advantages in preliminary studies where the beam is unknown. This form has shown considerable promise in analyses of data from the Washington Navy Yard towing basin.

Moments about the reference *c. g.* may be converted to any desired actual *c. g.* by either analytical or graphical methods similar to those used in converting wind-tunnel test data. The graphical method is usually employed. In this method the resultant force $F = \sqrt{\Delta^2 + R^2}$ is divided into the moment M to obtain the moment arm a . A circle of radius a is then drawn with the reference *c. g.* as its center. The lift acts normal to the water surface and the drag acts parallel to the water surface. The resultant vector will be tangent to the moment circle and incline aft from the vertical by the angle

$$\Phi = \tan^{-1} (R/\Delta) \quad (7)$$

If the calculations are made in coefficient form the radius of the moment circle will be in terms of the beam.

The vector diagram is very helpful when properly used. All presentations of test data should contain at least one diagram of the resultant force vectors for the benefit of those who are familiar with its use. Several types may be considered. One type would be the vectors at a series of values of C_Δ for a best trim-angle take-off starting with an initial displacement giving a standard minimum Δ/R at the hump, as previously outlined in the discussion of free-to-trim data. A plot of the vectors at hump speeds for a series of load coefficients would also be of value. It is unnecessary to give a great number of vectors spaced at brief intervals—the diagram is probably clearer and more useful when a limited number of selected vectors are shown.

LOCATION OF CENTER OF GRAVITY

The location of the center of gravity with respect to the step must be selected to give the best compromise at rest, at hump speed, and at high speed. The basic condition may be taken as the initial trim τ_0 . Operation reports covering values of τ_0 from about 0° to 5° indicate that best results are probably obtained with the main planing bottom between 1° and 2° to the horizontal for flying-boat hulls and between 2° and 3° for seaplane floats. The second condition in importance is to avoid high moments and inefficient trim at planing speeds. The third condition is to avoid excessive trim by the stern at hump speed. Unstable longitudinal oscillations, or porpoising, are highly undesirable at any speed. In general, these conditions are most likely to be met, but not necessarily so, when the initial trim is within the limits given. Some compromise will often be necessary in order to obtain zero or low moments in the high-speed planing condition.

Moving the center of gravity forward to reduce excessive trim at the hump is equivalent to reducing trim at rest and at planing speed also. An appreciable improvement can sometimes be obtained, but porpoising may be expected if the initial trim is too low. Satisfactory designs employing hulls of the type represented by the N. A. C. A. model 11 (reference 3) may be expected to give optimum performance with the center of gravity so located that a plane passed through the center of gravity and the step edge at a point midway between the keel and chines makes an angle of about 20° with the transverse plane defined by the step. Extreme limits of satisfactory operation have been between 15° and 25° for this dihedral angle for hulls of the "Model 11" type. The actual angle giving best results is apparently some function of the relative length of the forebody and afterbody measured on the static water line. The published N. A. C. A. data have not included representative water lines at rest, so that accurate tabulation on this basis is impracticable. On the basis of over-all lengths, the center of gravity locations used in the tests are:

Model	Reference	Ratio forebody (total length)	Center of gravity angle (deg.)
11-----	3	0.63	18
11-----	10	.63	32
26-----	9	.61	18
44-----	17	.62	29
40 Ac-----	2	.56	15
47-----	21	.51	7
16-----	5	.48	0

The variation of the angle with the relative forebody length is approximately linear. This fact simply means that the center of gravity location is a function of the distribution of displacement rather than of the actual step location. There is no assurance, however, that the performance of the models listed could not be improved by relocating the step to give some reasonably constant relation between the center of gravity and the step. This point is one that should be covered in a general test, preferably as a preliminary investigation, so that the general test is confined to the best step location for the lines in question. The general test data should certainly include curves of static trim, hump trim, and planing trim angles as a function of the fore-and-aft location of the center of gravity and an effort should be made to define the safe limits.

The vertical location of the center of gravity is of less concern than the horizontal location. There is some evidence indicating that the present average height of the center of gravity above the keel line of about 80 per cent of the beam will be maintained. For a single-float type seaplane the average height of the center of gravity above the keel line is about 160 percent of the beam.

CALCULATION OF WATER RESISTANCE

A complete method of calculating take-off resistance and best wing setting is given in reference 3. This method is entirely satisfactory if free-to-trim data are used up to the speed at which sufficient control is available to attain best trim. This speed varies with the type of hull and the load coefficient. It also varies with the characteristics of the flying boat such as center of gravity location, height of thrust line, and amount of control available. One reasonable solution is to fair in connecting links between the free-to-trim curves at the hump and the fixed-trim curves at a speed about 25 percent greater. A suitable alternative is to use free-to-trim data up to a speed 20 percent greater than the hump speed and best trim data from this point to the get-away.

During take-off the wings are close to the water in terms of the span, and it is necessary to make allowance for the increased effective aspect ratio. The increase in lift and reduction in drag at a given angle of attack have an appreciable effect on best wing setting and on take-off.

STICKING

"Sticking" is a term used to designate a rapid increase in resistance just prior to take-off with either increase in speed free to trim or increase in a fixed-angle trim. When the sticking characteristic is pronounced, it may limit possible take-off to a low angle-of-attack fly-off or it may entirely prevent take-off. The trouble is often due to suction near the stern when large curved or chineless areas make contact with the sides or bottom of the trough created by the step. This characteristic is essentially a high speed, light-load phenomenon that should be investigated as a part of the routine preliminary work leading up to a general test. In other words, a set of lines should not be given a complete test until sticking is eliminated or found absent within the useful range in C_{Δ} .

THE COMPARISON OF HULL LINES

A complete comparison of hull lines requires consideration of many factors: hump resistance, planing resistance, air resistance, moments, spray characteristics, etc. This discussion will be concerned only with the water resistance.

It is important to note that the usual comparison of hull performance in the form of curves of Δ/R against C_{Δ} using C_V as the parameter may be misleading. The basic design condition is normally a limiting minimum Δ/R at the hump. This characteristic determines the beam of the hull just as a specified stalling speed determines the area required with a given wing section. Comparisons of hulls on the basis of Δ/R at the same speed coefficient is exactly analogous to comparison of wing characteristics at the same lift coefficient. The differences sought are obtained by comparison at the same speed, or at the same percentage of get-away speed, and not at the same value of C_V (unless the beams happen to be the same).

Experience indicates that a comparison of Δ/R curves plotted against V/V_G is a simple and very effective means of evaluating the merits of hull lines. This method requires that free-to-trim data be used through the hump and that best-trim data be used from the hump to get-away. Such curves can be obtained from the usual presentation of general test data but the effort and time required are greater than most engineers are willing or able to expend. It is highly desirable that all reports contain data of this type for use in preliminary design studies. One of the difficulties encountered in any attempt to include this data is the necessity for adopting some particular condition to be represented. If a true comparison is desired, it is not satisfactory to adopt standard values of $C_{\Delta 0}$ and $C_{V G}$. A standard method should allow for the adoption of the best beam to meet a given set of conditions. One very simple solution would be to adopt a standard weight and

standard get-away speed and then to determine the value of C_{Δ_0} and C_{V_G} required to give a standard minimum value of free-to-trim Δ/R at the hump. The minimum value of $\Delta/R=4.5$ used in reference 3 is as good as any. In order to simplify the calculations the standard value of Δ_0 might be taken as 1,000 w so that

$$\text{Standard } b = 10 \sqrt[3]{\frac{1}{C_{\Delta_0}}} \quad (8)$$

Likewise the standard value of V_g might be taken as $20\sqrt{g}$ so that

$$\text{Standard } C_{V_G} = \frac{20}{\sqrt{b}} \quad (9)$$

If these, or some similar standard values, are adopted all reports on general tests could include comparative curves of Δ/R against V/V_G .

RANGE OF TESTS

It is exceedingly annoying to find that the range of a test has been insufficient to cover new design conditions. The determination of test limits to avoid this defect is not simple, but it is possible to make certain approximations that serve as a guide.

The conditions at hump speeds are highly important from the standpoint of the designer. Many of the general tests have not covered sufficient range in load coefficient and trim angle at the hump. The tests should be carried far enough to construct complete diagrams of the types shown in figure 2 and figure 4. These diagrams are probably incomplete unless they extend to the load coefficient giving $\Delta/R=4.0$ at best trim.

The range to be covered by the tests will depend to an appreciable extent on the anticipated variation in C_{Δ_0} and C_{V_G} with gross weight. The variation of C_{Δ_0} with gross weight appears to be determined by simple requirements. Physically, C_{Δ} is the ratio of the weight carried to the weight of a cube of water having b as the length of one side. For a geometrically similar series of flying boats Δ will vary as b^3 , and hence C_{Δ} will remain constant. If the weight increases more rapidly than b^3 , then C_{Δ} and the relative draft must increase; but this increase would mean an increase in hump resistance and an increase in maximum trim angle. In a normal design C_{Δ_0} is determined by the restrictions imposed on hump resistance and maximum trim. These restrictions tend to be more severe as the size is increased. Unless a pronounced favorable scale effect is obtained, the value of C_{Δ_0} required for a given value of Δ/R at the hump is independent of the size of the airplane. It therefore appears unlikely that the values of C_{Δ_0} can be increased as the size of the airplane is increased—unless such increase is obtained by basic improvement in hull lines. In other words, for a given set of lines the range in loading is determined by the limiting conditions at the hump.

The range in speeds to be covered by a general test depends on the extreme values of C_{V_G} , the value of C_V at get-away speed. Since $C_{V_G}=V_g/\sqrt{gb}$, the answer must be found in the variation of V_G with Δ .

It is a generally accepted design axiom that the wing loading must be increased as the design load is increased. The nature and extent of this increase may have an appreciable effect on the range to be covered in hull model tests. It is therefore desirable to investigate the relation between wing loading and gross weight.

If a design series is made geometrically similar in every detail, the gross weight will vary as the cube and the wing area will vary as the square of any given linear dimension. Hence, $W \propto S^{3/2}$ and $S \propto W^{2/3}$ or

$$\frac{W}{S} \propto W^{1/3} \quad (10)$$

This increase in wing loading is sometimes referred to as the "law of the squares and cubes" since it is related to the problems involving the ratio of surface area to volume.

If equation (10) could not be avoided, it would serve as a definite restriction on the size of airplane that could be built and flown. Actually, an exact geometrical similarity in the assumed hypothetical series is not likely to be attained. As the size of the airplane is increased, it is possible to use more efficient structures and more efficient materials with an appreciable saving in structural weight. The general form of equation (10) would therefore be

$$\frac{W}{S} \propto W^n \quad (11)$$

and the exponent should be less than one-third.

Reference 24 contains a chapter entitled "Notes on Giant Aeroplanes," prepared by José Weiss and Alexander Keith in 1916. In this chapter it is claimed that the observations of José Weiss on insect flight, bird flight, and gliding experiments show that for satisfactory performance the gross load must vary as the 4/3 power of the wing area. The relation given by Weiss is

$$P = 8.5S^{1.33} \quad (12)$$

where P is in kilograms and S is in square meters. Weiss states on pages 152-153 of reference 24 that the load can be increased well above that represented by equation (12) if sufficient power is available but that the natural gliding characteristics may be adversely affected.

Equation (12) is equivalent to

$$\frac{W}{S} \propto W^{1/4} \quad (13)$$

Design practice in the past has shown a marked tendency to approximate the Weiss equation, although there is naturally an appreciable spread due to differences in construction and purpose of the airplanes considered. It is interesting to compare the wing

loadings corresponding to equations (10) and (13) as follows:

Gross weight W	Equation (10) $\frac{W}{S} \propto W^{1/3}$	Equation (13) $\frac{W}{S} \propto W^{1/4}$
1,000	10	10
8,000	20	16.8
27,000	30	22.8
64,000	40	28.3
125,000	50	33.4
216,000	60	38.3
343,000	70	43.0
512,000	80	47.6

The initial value of 10 pounds per square foot was selected arbitrarily to facilitate comparison but it approximates an average value. Equation (13) appears to give a reasonable variation in wing loading, while equation (10) certainly demands too great an increase in large sizes.

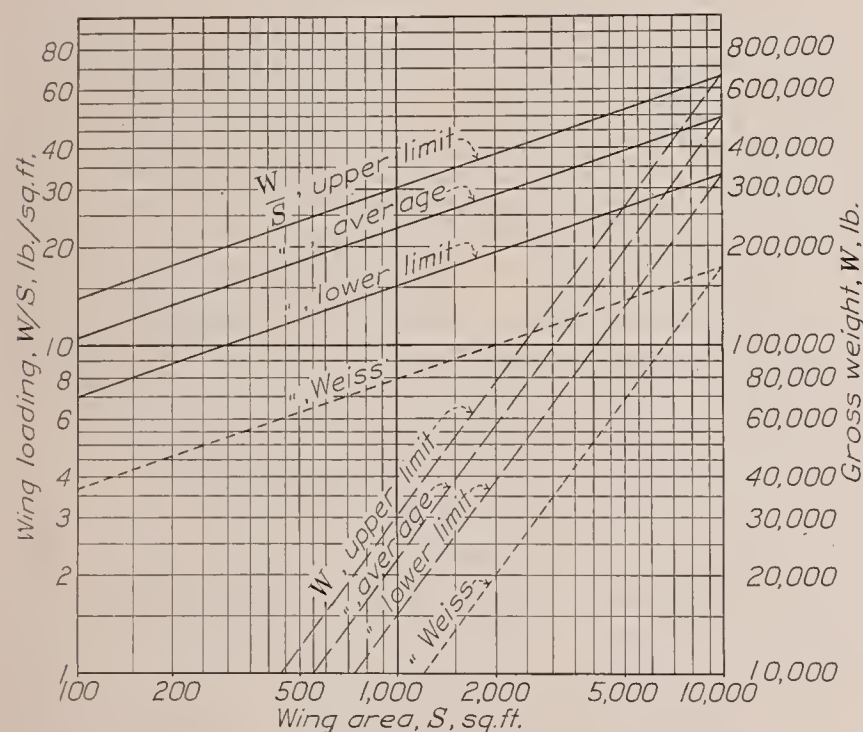


FIGURE 5.—Variation of wing loading with gross weight.

Figure 5 contains a plot of wing loading and gross weight against wing area, based on a tabulation of normal designs. Values from the original Weiss equation are also given. It should be emphasized that the upper limit and lower limit indicated on figure 5 are simply arbitrary values obtained from a tabulation representing normal designs.

Since the value of V_G may be taken directly proportional to the wing loading or, from equation (13),

$$V_G \propto \left(\frac{W}{S}\right)^{1/2} \propto W^{1/8} \quad (14)$$

With constant C_{Δ} , the beam varies as the cube root of the weight. Hence

$$C_{VG} \propto \frac{V_G}{b^{1/2}} \propto \frac{W^{1/8}}{W^{1/6}} \propto W^{-1/24} \quad (15)$$

This equation indicates a very slow decrease in the value of C_{VG} as the weight is increased. A hundredfold increase in W would reduce C_{VG} less than 18 percent. It therefore appears unnecessary to make any special provision for testing at extreme speeds insofar as the effect of future increase in size is concerned.

CONCLUSIONS

The main conclusions indicated by this study are:

1. The complete general test should not be made on a set of lines until preliminary tests have shown no objectionable characteristics.

2. A standard weight and a standard get-away speed should be adopted to facilitate comparison of lines. The adoption of a standard minimum value of Δ/R free-to-trim at hump speed is also desirable.

3. The value of general hull test data can be greatly increased for design purposes by the inclusion of the following additional data:

(a) A plot of C_{Δ} against C_V^2 with Δ/R as the parameter using free-to-trim up to a speed about 25 percent above hump speed and best trim data at all higher speeds. (See fig. 3.)

(b) A curve of C_{Δ} at hump against C_V^2 with Δ/R divisions or graduations along the curve (as in fig. 4).

(c) Curve of maximum trim at the hump as a function of C_{Δ} for the free-to-trim condition. The form used in figure 2 has some advantages.

(d) Vector diagram at hump speed for a series of values of C_{Δ} using best trim data.

(e) A vector diagram for a series of values of C_v in a constant lift coefficient take-off for a standard weight and get-away speed.

(f) Curves of static angle of trim as a function of $C_{\Delta 0}$ and $c.g.$ location. Such curves can be constructed from the static data now supplied, but both forms of presentation are desirable.

4. The range of loads and speeds necessary to supply data for a normal size flying boat appear to be ample to cover future increases in size.

5. There appears to be need for investigation of the following:

(a) Fore-and-aft location of step and best location of $c.g.$ relative to step.

(b) Best initial trim.

(c) Effect of thrust moment and elevator moment on trim angles. This will probably require measurement of pitching moments in the full-scale wind tunnel.

REFERENCES

1. Truscott, Starr: The N. A. C. A. Tank—A High-Speed Towing Basin for Testing Models of Seaplane Floats. T. R. No. 470, N. A. C. A., 1933.
2. Parkinson, John B., and Dawson, John R.: Tank Tests of N. A. C. A. Model 40 Series of Hulls for Small Flying Boats and Amphibians. T. R. No. 543, N. A. C. A., 1936.
3. Shoemaker, James M., and Parkinson, John B.: A Complete Tank Test of a Model of a Flying-Boat Hull—N. A. C. A. Model No. 11. T. N. No. 464, N. A. C. A., 1933.
4. Parkinson, John B.: A Complete Tank Test of a Model of a Flying-Boat Hull—N. A. C. A. Model No. 11-A. T. N. No. 470, N. A. C. A., 1933.
5. Shoemaker, James M.: A Complete Tank Test of a Model of a Flying-Boat Hull—N. A. C. A. Model 16. T. N. No. 471, N. A. C. A., 1933.
6. Shoemaker, James M.: A Complete Tank Test of a Flying-Boat Hull with a Pointed Step—N. A. C. A. Model No. 22. T. N. No. 488, N. A. C. A., 1934.
7. Shoemaker, James M., and Parkinson, John B.: Tank Tests of a Family of Flying-Boats Hulls. T. N. No. 491, N. A. C. A., 1934.
8. Shoemaker, James M., and Bell, Joe W.: Complete Tank Tests of Two Flying-Boat Hulls with Pointed Steps—N. A. C. A. Models 22-A and 35. T. N. No. 504, N. A. C. A., 1934.
9. Dawson, John R.: A Complete Tank Test of the Hull of the Sikorsky S-40 Flying Boat—American Clipper Class. T. N. No. 512, N. A. C. A., 1934.
10. Parkinson, J. B.: Tank Tests of Model 11-G Flying-Boat Hull. T. N. No. 531, N. A. C. A., 1935.
11. Bell, Joe W.: The Effect of Depth of Step on the Water Performance of a Flying-Boat Hull—N. A. C. A. Model 11-C. T. N. No. 535, N. A. C. A., 1935.
12. Dawson, John R.: A General Tank Test of N. A. C. A. Model 11-C Flying-Boat Hull, Including the Effect of Changing the Plan Form of the Step. T. N. No. 538, N. A. C. A., 1935.
13. Allison, John M.: The Effect of the Angle of Afterbody Keel on the Water Performance of a Flying-Boat Hull Model. T. N. No. 541, N. A. C. A., 1935.
14. Parkinson, J. B.: Tank Tests of a Model of a Flying-Boat Hull Having a Longitudinally Concave Planing Bottom. T. N. No. 545, N. A. C. A., 1935.
15. Dawson, John R.: Tank Tests of Three Models of Flying-Boat Hulls of the Pointed-Step Type with Different Angles of Dead Rise—N. A. C. A. Model 35 Series. T. N. No. 551, N. A. C. A., 1936.
16. Parkinson, J. B.: Tank Tests of Models of Floats for Single-Float Seaplanes—First Series. T. N. No. 563, N. A. C. A., 1936.
17. Bell, Joe W.: Tank Tests of a Model of the NC Flying-Boat Hull—N. A. C. A. Model No. 44. T. N. No. 566, N. A. C. A., 1936.
18. Allison, John M., and Ward, Kenneth E.: Tank Tests of Models of Flying-Boat Hulls Having Longitudinal Steps. T. N. No. 574, N. A. C. A., 1936.
19. Allison, John M.: Tank Tests of a Model of the Hull of the Navy PB-1 Flying Boat—N. A. C. A. Model 52. T. N. No. 576, N. A. C. A., 1936.
20. Dawson, John R., and Truscott, Starr: A General Tank Test of a Model of the Hull of the British Singapore IIC Flying Boat. T. N. No. 580, N. A. C. A., 1936.
21. Ward, Kenneth E.: Hydrodynamic Tests in the N. A. C. A. Tank of a Model of the Hull of the Short Calcutta Flying Boat. T. N. No. 590, N. A. C. A., 1937.
22. Seewald, Friedrich: On Floats and Float Tests. T. M. No. 639, N. A. C. A., 1931.
23. Schröder, P.: Towing Tests of Models as an Aid in the Design of Seaplanes. T. M. No. 676, N. A. C. A., 1932.
24. Weiss, J. Bernard: Gliding and Soaring Flight, A Survey of Man's Endeavour to Fly by Natural Methods. Sampson Low, Marston & Co., Ltd., London.

REPORT No. 626

THE TRANSITION PHASE IN THE TAKE-OFF OF AN AIRPLANE

By J. W. WETMORE

SUMMARY

An investigation was undertaken to determine the character and importance of the transition phase between the ground run and steady climb in the take-off of an airplane and the effects of various factors on this phase and on the air-borne part of the take-off as a whole. The information was obtained from a series of step-by-step integrations, which defined the motion of the airplane during the transition and which were based on data derived from actual take-off tests of a Verville AT airplane. Both normal and zoom take-offs under several loading and take-off speed conditions were considered. The effects of a moderate wind with a corresponding wind gradient and the effect of proximity of the ground were also investigated.

The results show that, for normal take-offs, the best transition was realized at the lowest possible take-off speed. Moreover, this speed gave the shortest over-all take-off distance for normal take-offs. Zoom take-offs required a shorter over-all take-off run than normal take-offs, particularly with a heavy loading, if the obstacle to be cleared was sufficiently high, e. g., greater than 50 feet; no advantage was indicated for the airplane with a light loading if the height to be cleared was less. The error that would result from the neglect of the transition in the calculation of the air-borne distance of take-off was found to vary from 4 percent with the heaviest loading considered to -4 percent with the lightest loading for normal take-offs over a 100-foot obstacle; the percentage error was twice as great for a 50-foot obstacle. For zoom take-offs the error attained much greater values. The average wind gradient corresponding to a 5-mile-per-hour surface wind reduced the air-borne distance required to clear a 50-foot obstacle by about 9 percent with the lightest loading and 16 percent with the heaviest loading; for a 100-foot obstacle, the reduction was about 10 percent in both cases. The over-all reduction due to this wind was approximately twice that resulting from the wind gradient alone. A simple expression for the reduction of observed take-off performance to no-wind conditions is presented. Ground effect is shown to reduce the air-borne distance to attain a height of 50 feet by 10 percent with the lightest loading and 16 percent with the heaviest loading; for a 100-foot obstacle, the percentage reduction was about one-half as great.

INTRODUCTION

In the process of taking off, the course of an airplane consists of three phases: a run along the ground to attain flying speed, a transition curve in which the flight path changes from the horizontal direction of the ground run to an inclination suitable for climbing, and a more or less steady climb to a height at which any obstacles at the edge of the airport will be surmounted. The motion of an airplane in the ground-run and steady-climb stages is relatively simple and therefore can be predicted for prescribed conditions with reasonable accuracy, presupposing an adequate knowledge of the airplane characteristics. The transition, on the other hand, can be accurately defined only by very complex relations; hence, common practice in calculating take-off performance has been to regard this phase as negligible or to account for it with approximations of uncertain validity.

The investigation described herein was undertaken to provide an indication of the character and relative importance of the transition and of the effects of various factors on the transition itself and on the air-borne portion of the take-off as a whole. For this purpose a series of take-off tests was conducted with a conventional biplane. The tests included both normal take-offs, wherein the air speed was maintained as nearly constant as possible from the instant of leaving the ground, and zoom take-offs, in which the speed was reduced after leaving the ground. The test conditions for each type of take-off covered two loadings and several take-off speeds. The motion of the airplane in the take-offs was measured with a recording photodolite.

The results of these tests were not used directly, as originally intended, inasmuch as they were found to be confused by rather wide variations in piloting procedure and wind condition. Instead, the force relations pertaining to the airplane under take-off conditions were derived from data provided by the tests and served as the basis for a series of step-by-step integrations whereby the motion of the airplane during take-off was determined for various conditions without the effects of piloting and wind. The calculations covered the range of loading and speed conditions included by the actual

tests, and an additional loading condition was also considered.

A measure of the effect of ground proximity on the airplane characteristics was obtained from the test data and, with this information, the influence of ground effect on the take-off was investigated for each of two loading conditions. For the same conditions the effects of a wind increasing in velocity with altitude were also evaluated.

APPARATUS

A Verville AT airplane (fig. 1) was used for the take-off tests. The pertinent characteristics of this airplane are given in table I. The following standard N. A. C. A. recording instruments were mounted in the airplane: an air-speed recorder; an accelerometer located near the center of gravity and recording accelerations along the normal, or Z , axis of the airplane; an inclinometer recording the direction of the resultant of the external forces imposed on the airplane; a recording engine tachometer; and a control-position recorder connected



FIGURE 1.—The Verville AT airplane.

to the elevators. Half-second intervals of time were recorded by all the instruments from impulses produced by a standard timer.

An N. A. C. A. recording phototheodolite, essentially a combination of a motion-picture camera and a recording theodolite, provided records from which the horizontal and vertical displacements of the airplane relative to the ground and its attitude angle could be determined at intervals of $\frac{1}{16}$ second. A timer was also used in conjunction with this instrument.

Synchronization of the phototheodolite records with those of the airplane instruments was accomplished by means of an electrically operated device mounted on the landing gear of the airplane and connected through the instrument switch so that, at the instant the pilot threw the switch to start the instruments, a quantity of white powder was discharged and formed a cloud that was readily discernible in the photographs.

The wind speed at the ground was measured with an indicating vane anemometer.

TEST PROCEDURE

A series of eight take-offs was made with each of two loading conditions: 2,060 pounds and 2,378 pounds gross weight. For four of the take-offs of each series,

which will be designated "normal" take-offs, the pilot was requested to leave the ground at speeds ranging from 3 to 15 miles per hour in excess of the minimum level-flight speed and to climb at the same speeds, attaining steady climbing conditions as quickly as possible. For the four remaining runs, given the designation of "zoom" take-offs, the speeds at the instant of take-off were in the same range but were reduced after the airplane left the ground, the climbs in all cases being made at a speed slightly in excess of the minimum. In all the take-offs the airplane was headed directly into the wind. The engine was operated at full throttle throughout each run.

The phototheodolite was set up on the ground at a suitable distance from the course of the airplane and recorded its motion during the latter third of the ground run and throughout the transition and climb to a height of about 100 feet. The procedure followed in the operation of the phototheodolite and in the evaluation of the data obtained therefrom was substantially the same as that described for the landing tests of reference 1, although the instrument used for the present tests is of a later and improved design.

COMPUTATIONS

The results of the foregoing tests gave evidence of sufficiently great irregularities in the wind conditions and piloting to obscure completely the effects that the tests were expected to disclose; hence, the purpose of the investigation was not directly accomplished by the tests alone. The data obtained from the take-off tests, however, made possible the derivation of the force relations required as the basis for a series of step-by-step integrations defining the motion of the airplane during take-off for various conditions. In this way the troublesome factors of wind and piloting were eliminated.

Derivation of force relations.—Synchronized readings of the data recorded by the airplane instruments and the phototheodolite during the take-offs were made at frequent intervals throughout the records, thus covering a considerable range of flight conditions. Values of lift and excess thrust were obtained for each set of readings according to the following procedure. The normal and longitudinal components of the aerodynamic forces acting on the airplane F_z and F_x , respectively, were determined from the relations

$$F_z = \frac{W}{g} a_z$$

and

$$F_x = \frac{W}{g} a_z \tan \theta$$

where W is the gross weight of the airplane.

g , the acceleration of gravity.

a_z , the normal acceleration as recorded by the accelerometer.

θ , the angle of the inclinometer pendulum relative to the normal axis of the airplane.

The flight-path angle γ , referred to wind axes, was given by

$$\gamma = \sin^{-1} \frac{V_v}{V}$$

where V_v is the vertical velocity, determined by differentiation of the time-distance curves derived from the phototheodolite records.

V , the air speed along the flight path.

It was necessary, of course, to assume here that the wind had no vertical component, apparently a reasonable assumption for average conditions according to the information of reference 1.

The angle of attack α was then obtained from

$$\alpha = \lambda - \gamma$$

where λ is the attitude angle of the airplane, provided

of two variables, angle of attack and air speed. It would consequently be difficult to plot these data directly. For this reason the effective propeller thrust T , shown in figure 3, was calculated by means of the information provided in references 2 and 3. The drag D could then be determined from the equation

$$D = T - T_{ex}$$

and thence the drag coefficient

$$C_D = \frac{D}{\frac{1}{2} \rho S V^2}$$

which could, of course, also be plotted as a function of angle of attack to establish a suitably faired curve. With the data in this form, the relation of excess thrust

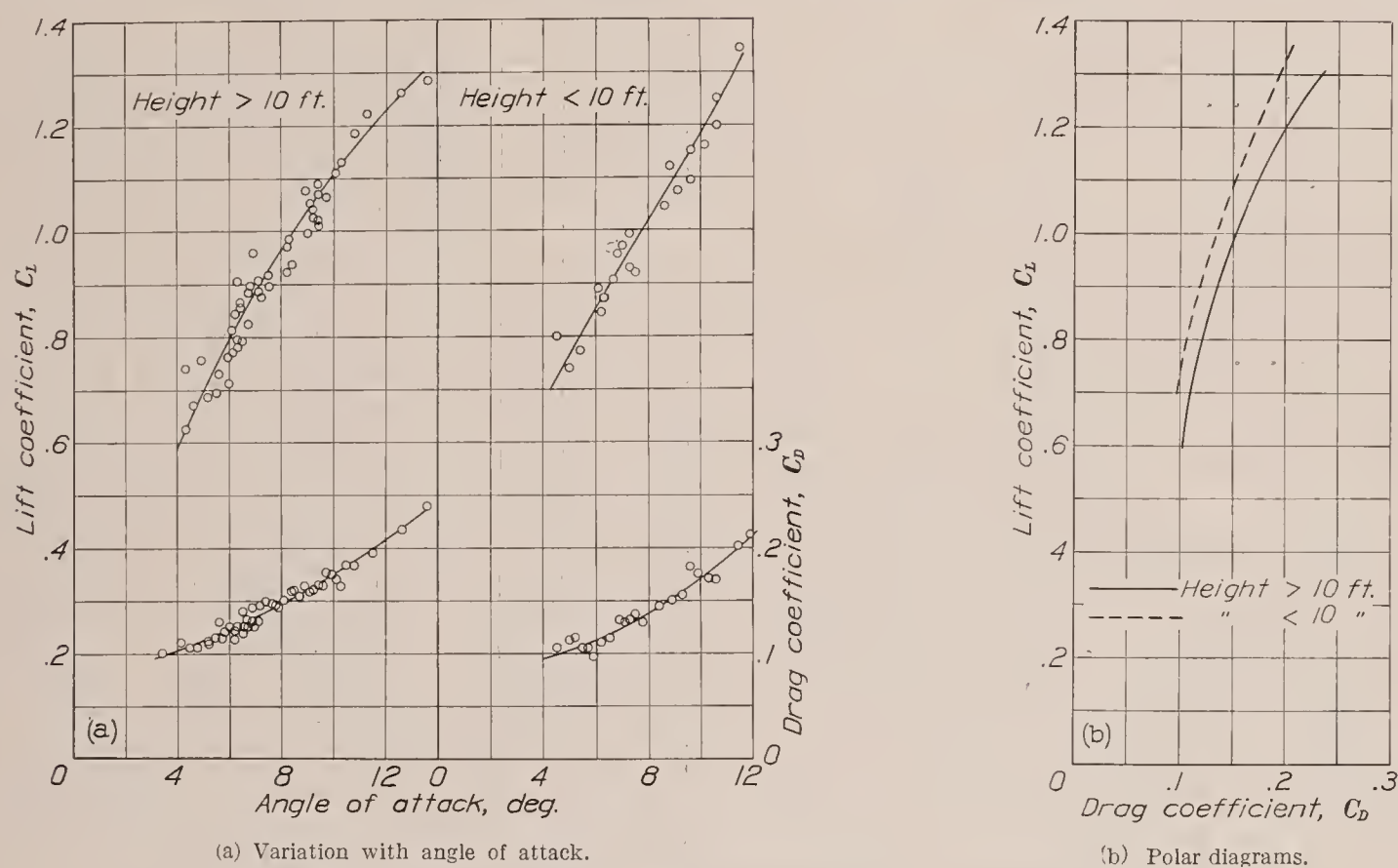


FIGURE 2.—Lift and drag characteristics of the Verville AT airplane as determined from take-off tests.

by the phototheodolite records. With the foregoing information it was possible to determine values for the lift L and the excess thrust T_{ex} by resolving the forces F_x and F_z along the flight-path axes or

$$L = F_z \cos \alpha + F_x \sin \alpha = \frac{W}{g} a_z (\cos \alpha + \tan \theta \sin \alpha)$$

$$T_{ex} = F_x \cos \alpha - F_z \sin \alpha = \frac{W}{g} a_z (\tan \theta \cos \alpha - \sin \alpha)$$

The values of lift were converted to the coefficient form C_L with the relation

$$C_L = \frac{L}{\frac{1}{2} \rho S V^2}$$

Thus the data could be readily plotted and faired as a function of angle of attack. (See fig. 2 (a).)

The full-throttle excess thrust is, in effect, a function

to air speed and lift coefficient was determined by using the faired results in a reversal of the procedure.

In order to take into account the effect of ground proximity on the lift and drag characteristics, hence on the excess thrust, the data were divided into two groups and were plotted separately, according to whether they were obtained when the wheels of the airplane were above or below a height of 10 feet from the ground. This height was arbitrarily chosen as the line of demarcation between the region of strongest ground effect and the region in which, for the purposes of the present investigation, the ground effect could be considered as negligible. The data available were insufficient to warrant further division.

The lift and drag coefficients evaluated by the foregoing methods are plotted against angle of attack in figure 2 (a) and as polars in figure 2 (b). In figure 3

the excess thrust within and outside of the region of principal ground effect is shown as a function of lift coefficient and air speed.

Step-by-step integrations.—At quarter-second intervals throughout the transition phase of the take-off, the vertical acceleration a_v and the horizontal acceleration a_h of the airplane were calculated by successive approximations according to the relations

$$a_v = \frac{g(L \cos \gamma + T_{ex} \sin \gamma - W)}{W}$$

and

$$a_h = \frac{g(T_{ex} \cos \gamma - L \sin \gamma)}{W}$$

Corresponding velocities were determined from

$$V_v = V_{v0} + \frac{0.25(a_{v0} + a_{v1})}{2} + \frac{0.25(a_{v1} + a_{v2})}{2} + \dots + \frac{0.25(a_{vn-1} + a_{vn})}{2}$$

and

$$V_h = V_{h0} + \frac{0.25(a_{h0} + a_{h1})}{2} + \frac{0.25(a_{h1} + a_{h2})}{2} + \dots + \frac{0.25(a_{hn-1} + a_{hn})}{2}$$

Vertical and horizontal displacements were similarly determined; the flight-path angle was obtained from

$$\gamma = \tan^{-1} \frac{V_v}{V_h}$$

The initial values of a_v and V_v , i. e., at the instant of leaving the ground, were, of course,

$$a_{v0} = 0$$

and

$$V_{v0} = 0$$

The horizontal speed V_{h0} at the same instant was the assumed take-off speed and, since at this instant $L = W$, the value of the excess thrust T_{ex} and thence the value of a_{h0} could be determined. For subsequent intervals the quantities involved in the calculations were determined by the usual methods of successive approximation.

The course of the lift coefficient in the early part of the transition was prescribed by the assumption that the transition should be of as short duration as possible. This limitation, of course, required that the airplane be pulled up quickly to the angle of attack for maximum lift coefficient, as soon as the desired speed for taking off was attained, and held at this angle as long as possible. The lift coefficient was then reduced in time to prevent the flight-path velocity from decreasing, by reason of the increasing climb angle, below the value designated for the steady climb and to permit the adjustment of the lift coefficient necessary to provide a smooth approach to the steady-climb conditions without

exceeding reasonable values for the corresponding rate of change of the angle of attack. Examples of the variation in lift coefficient followed in performing the calculations are shown in figure 4.

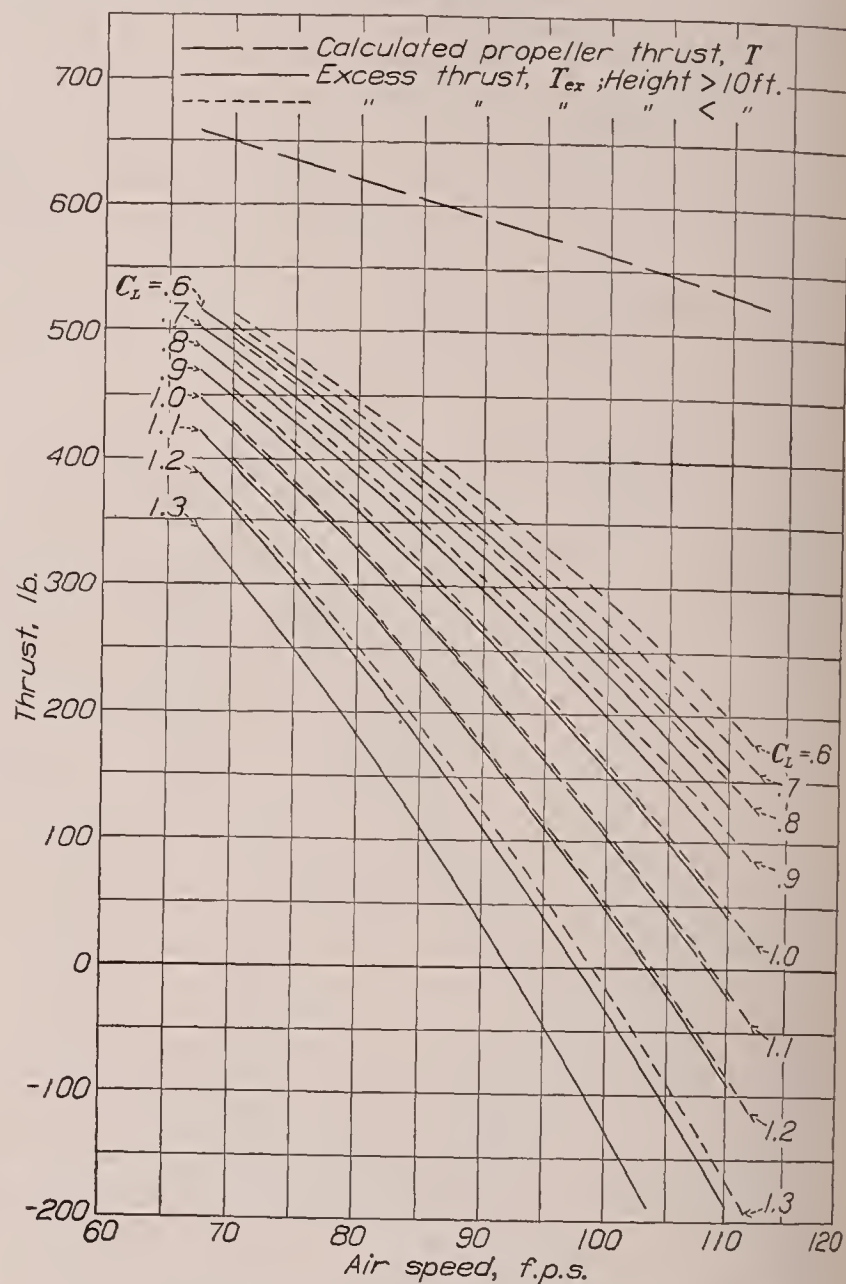


FIGURE 3.—Excess-thrust characteristics of the Verville AT airplane.

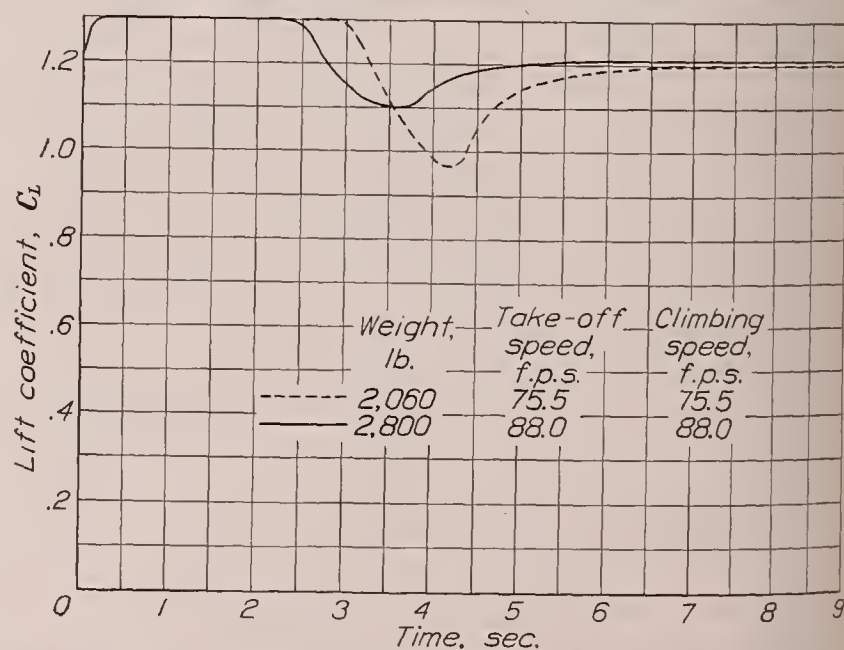


FIGURE 4.—Examples of assumed variation in lift coefficient during transition. The Verville AT airplane.

The excess thrust corresponding to the lift coefficient and speed occurring at a particular instant was taken from the curves of figure 3, according to whether the height at that instant was greater or less than 10 feet. In this way allowance was made for the ground effect.

The computations covered three loading conditions: gross weights of 2,060 pounds, 2,378 pounds, and 2,800 pounds. For each load the calculations were carried through for three normal take-offs at different speeds ranging from an assumed minimum allowable speed to 20 percent in excess of this value. Similarly, two zoom take-offs were calculated for take-off speeds 10 percent and 20 percent greater than the minimum allowable speed at which the final steady climb was assumed to be made in both cases. The minimum allowable speed was arbitrarily taken as 4 percent in excess of the speed corresponding to the maximum lift coefficient, 1.3. For all the foregoing conditions there was assumed to be no wind.

The effects of wind were determined for two cases: one with the heaviest loading and the other with the lightest loading. For these cases there was introduced into the calculations a wind velocity of 5-miles-per-hour magnitude at the ground, increasing with height according to the relationship given by reference 1 as representing an average wind gradient, which is

$$\frac{V_w}{V_{w0}} = \left(\frac{H_e}{H_0} \right)^{1/7}$$

where V_{w0} , which was assigned a value of 5 miles per hour, is the wind speed corresponding to H_0 , the effective height of the airplane while in contact with the ground, assumed to be 5 feet; and V_w is the wind speed at any other effective height H_e , i. e., the height of the wheels above the ground plus 5 feet.

For the same two loading conditions, the effect of ground proximity on the air-borne phase of take-off was investigated by using the excess-thrust data obtained above the 10-foot level, hence sensibly outside the influence of ground effect, throughout the integrations and comparing the results with those obtained for similar cases in which the ground effect was included.

The ground-run phase of the take-off was considered only insofar as was necessary to show the effects of variations in take-off speeds and methods on the complete take-off. In all cases only the distance required to accelerate from a common speed of 75 feet per second up to the take-off speed was calculated. In the determination of these distances, the rolling-friction coefficient was assumed to be 0.05, corresponding to an average turf surface. The air forces were taken from the data obtained within the region of ground effect.

RESULTS

A summary of the results obtained from the calculations is given in table II. Figures 5 through 7 show the calculated flight paths of the airplane during the transition and steady climb for all the conditions investigated. In figure 8 the distance on the ground required to accelerate from a speed of 75 feet per second

to the take-off speed is plotted against take-off speed for the three loading conditions. Figures 9 through 11 show the variation due to take-off speed in the air-borne distances required to clear heights of 50 and 100 feet for both normal and zoom take-offs. These figures also show the effect of take-off speed on the over-all take-off distance, i. e., including the ground run after a velocity of 75 feet per second is attained.

Figure 12 shows the percentage difference for various take-off speeds between the air-borne distance as calculated by the methods previously described, where due consideration was given to the transition, and the distance that would be obtained were the transition to be neglected. For the normal take-offs, the value for the distance with the transition neglected was taken as

$$D = \frac{H}{\tan \gamma}$$

where H is the obstacle height to be cleared and γ is the flight-path angle corresponding to a given speed. This relation was based on the assumption that steady-climbing conditions obtained from the instant of leaving the ground. For the zoom take-offs the most obvious approximate relation for the air-borne distance appeared to be

$$D = \frac{H - \frac{V_1^2 - V_2^2}{2g}}{\tan \gamma}$$

where V_1 and V_2 are the initial and final flight-path velocities, respectively, and γ is the flight-path angle corresponding to V_2 . This equation was based on the assumptions that constant excess power was available throughout the climb and that steady conditions were realized before the height H was attained. Figure 12 is intended to indicate the extent to which the take-off is affected by the transition and the magnitude of the error that might be introduced by the neglect of the transition in the calculation of take-off distances.

The effect on the air-borne distance of an average wind gradient corresponding to a surface wind velocity of 5 miles per hour is shown in figure 13 for normal take-offs with the heaviest and lightest loads. In figure 14 the influence of ground effect is shown for the same loading conditions.

DISCUSSION

The nature of the flight path during the transition phase of the take-off is shown in figures 5, 6, and 7. The initially increasing slope of the path followed later by a decrease is apparently characteristic, at least for the airplane and conditions considered herein. In the case of normal take-off, the reason for this reversal of curvature lies in the fact that the airplane continues to accelerate immediately after leaving the ground and, in being slowed to its original speed, assumes a climbing angle too steep to be maintained. The flight-path angle

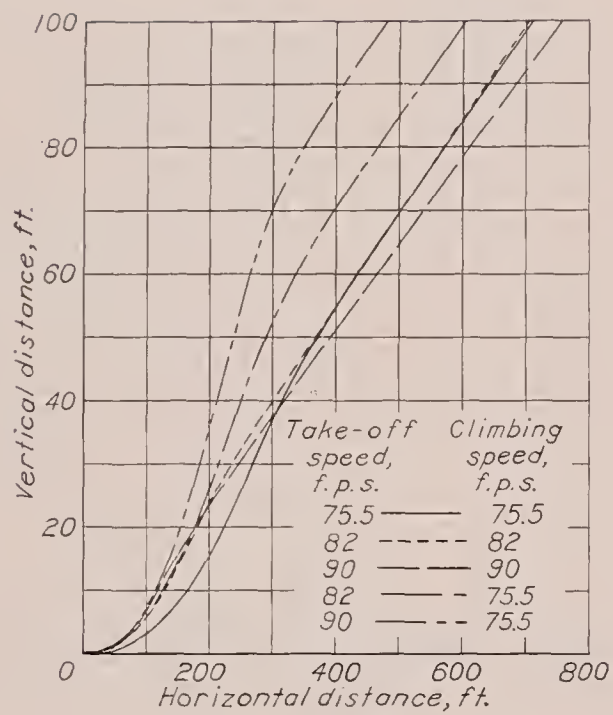


FIGURE 5.—Weight, 2,060 pounds.

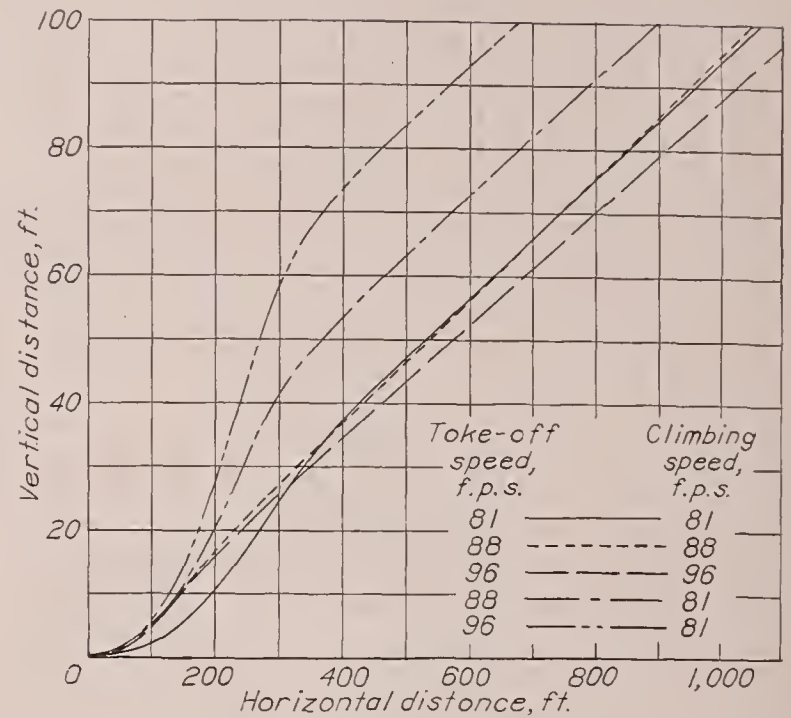


FIGURE 6.—Weight, 2,378 pounds.

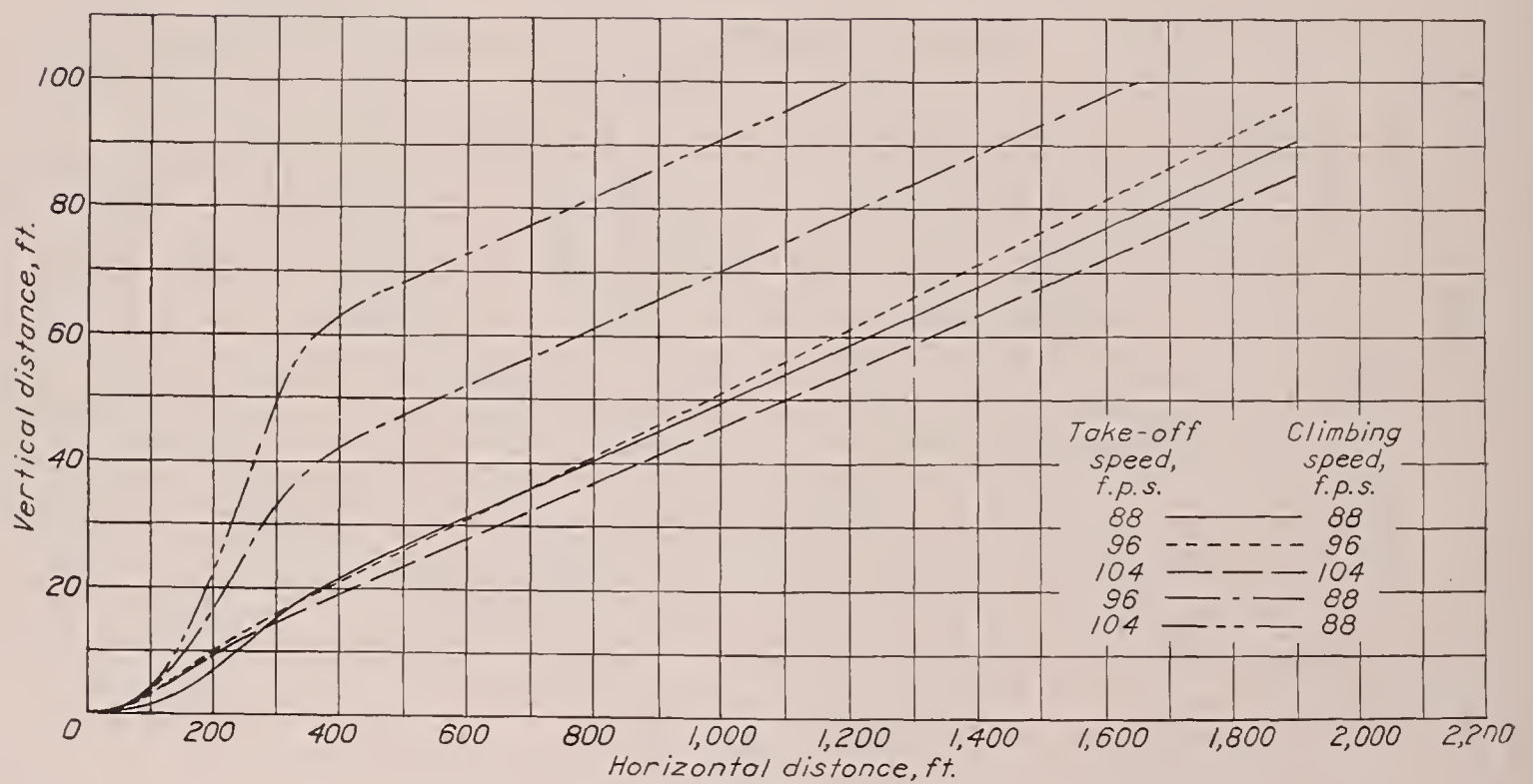


FIGURE 7.—Weight, 2,800 pounds.

FIGURES 5 TO 7.—Flight paths followed in transition and steady climb for normal and zoom take-offs for the Verville AT airplane at various speeds.

must therefore be reduced to a value at which the airplane can climb steadily. The flight paths for the zoom take-offs have a generally similar shape, but variations in the slope are more pronounced owing to the greater changes in speed.

Inasmuch as most airplanes probably have, in part by virtue of the ground effect, an excess of thrust in the initial stage of the transition and hence will accelerate, it is likely that the form of the transition curve shown is representative of the form that would generally be experienced.

The procedure that would be required in controlling an airplane along a path such as that described is indicated in figure 4. The control column would first be pulled back to put the airplane in an attitude of high lift and held until the angle of climb was sufficient to cause a deceleration. It would then be pushed forward to reduce the angle of attack to a value considerably below that corresponding to the steady climb in time to prevent the speed from dropping below that prescribed for the climb. Finally, it would again be pulled back as the angle of climb decreased so that the correct flight-path angle and the angle of attack for steady climbing might be simultaneously realized. In practice, it would probably not be possible to synchronize, exactly, the attainment of the proper flight-path angle and angle of attack; consequently, an oscillatory rather than a steady flight path would result. If sufficient effort were made to maintain constant speed, however, the amplitude of the oscillation would not be great and the mean flight path would probably correspond closely to the one that would be obtained under steady conditions.

For normal take-offs, it is apparent from the curves of figures 5, 6, and 7 that, insofar as the transition alone is concerned, the optimum take-off speed, in the range considered, is the lowest value shown. Higher speeds provide an initially greater excess of lift and, consequently, a higher vertical acceleration, so that the transition is completed more quickly and with less variation in forward velocity. At the slower speed, however, there is a greater excess thrust available which, although partly converted to kinetic energy at first, eventually goes toward increasing the height or potential energy of the airplane; thus, when the transition is completed, the height attained is greater in proportion to the horizontal distance covered than that for the higher-speed take-offs.

The maximum angle of climb occurs at approximately the intermediate speed shown so that, in the range of speeds between the minimum and that for best angle of climb, the effects of variations in take-off speed on the transition and on the steady climb are opposed. For an obstacle height of 50 feet a considerable portion of the air-borne distance is occupied by the transition so that the opposing effects are nearly balanced. Hence there is little change in the air-borne distance with

increasing take-off speed up to the speed for best angle of climb (figs. 9, 10, and 11); beyond this speed the distance, of course, increases. Obviously then, since the ground-run distance (fig. 8) increases with the take-off speed, the shortest over-all take-off distance required to gain a height of 50 feet, in a normal take-off, would be realized with the lowest possible take-off speed.

With an obstacle height of 100 feet the transition is a relatively small part of the air-borne distance. The effect of take-off speed on the steady climb is therefore predominant and consequently the shortest air-borne distance occurs at or near the speed for best angle of climb. The reduction in air-borne distance, however, is more than offset by the increased ground run so that, in this case also, the lowest take-off speed gives the shortest over-all distance.

In zoom take-offs the airplane is held in contact with the ground until the speed reaches a value considerably

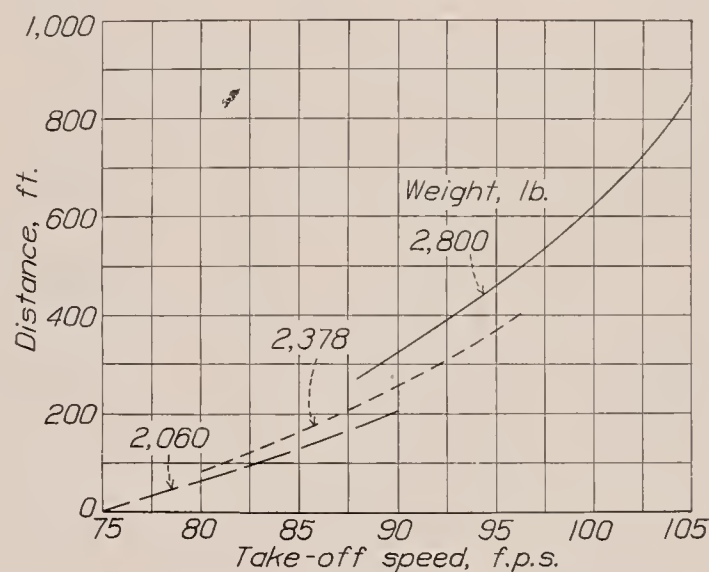


FIGURE 8.—Ground distance required for the Verville AT airplane to accelerate from 75 feet per second to take-off speed for all loading conditions.

above the minimum flying speed. It is then pulled off abruptly into a steep climb during which the speed is reduced. It may be shown that an airplane running along the ground at its most efficient attitude, i. e., the attitude corresponding to the minimum value of $C_D - \mu C_L$, will ordinarily have, in the range of speeds between the minimum flying speed and a speed considerably in excess of the minimum, appreciably less resistance, hence greater excess thrust, than if it were completely air-borne at similar speeds. The excess kinetic energy gained in running a given distance along the ground would be greater, therefore, than the potential energy that might be gained in flight in the same distance. Thus, if the excess kinetic energy could be converted to potential energy without too great loss, it should be possible to attain a greater height in a given distance from a zoom take-off than from the shortest normal take-off. This argument is borne out in figures 9, 10, and 11 for an obstacle height of 100 feet where, with the lightest load, the total horizontal distance required to gain this height from a ground speed of 75 feet per second is about 5 percent less for the shortest zoom

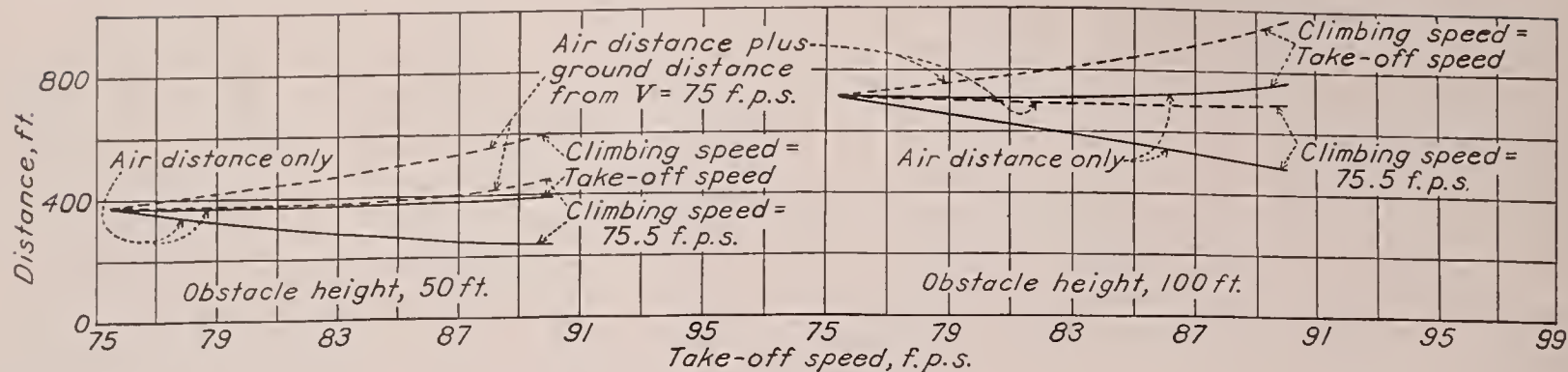


FIGURE 9.—Weight, 2,060 pounds.

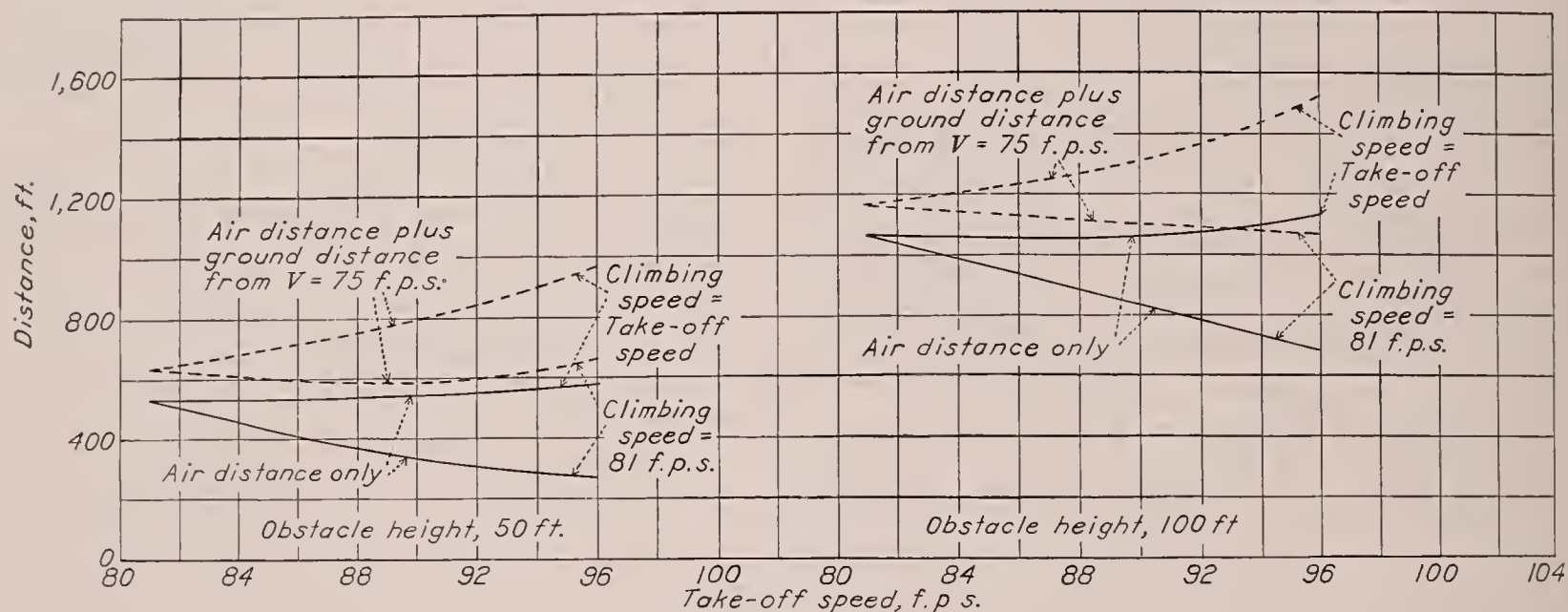


FIGURE 10.—Weight, 2,378 pounds.

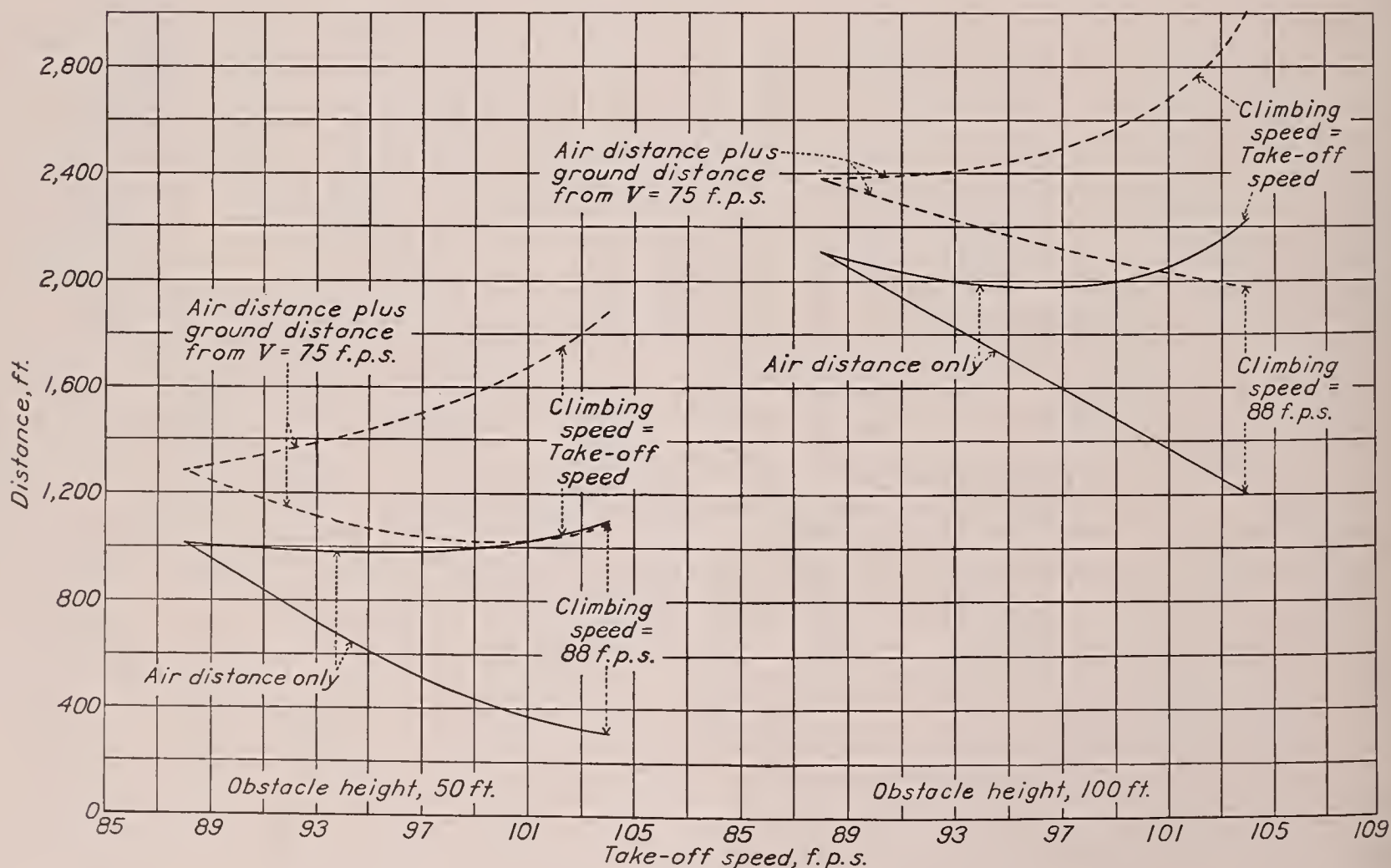


FIGURE 11.—Weight, 2,800 pounds.

FIGURES 9 TO 11.—Variation of take-off distances with take-off speed for the Verville AT airplane.

take-off than for the shortest normal take-off; with the heaviest load there is a larger difference, about 17 percent, owing to the fact that, with other conditions remaining equal, the difference between the excess thrust on the ground and that in flight increases with increasing weight.

In figures 5, 6, and 7 it will be noted that in some cases, particularly with the lighter loads and higher take-off speeds, the height attained before the conversion of energy is completed is greater than 50 feet. In these cases, at an obstacle height of 50 feet, there is still an excess of kinetic energy remaining, which is equivalent to a loss. Therefore the zoom take-off provides little or no advantage over the normal take-off, as may be seen in figures 9, 10, and 11.

An indication of the extent of the error that might be introduced into the calculation of take-off performance by the neglect of the transition is provided in figure 12. This figure shows the percentage difference between

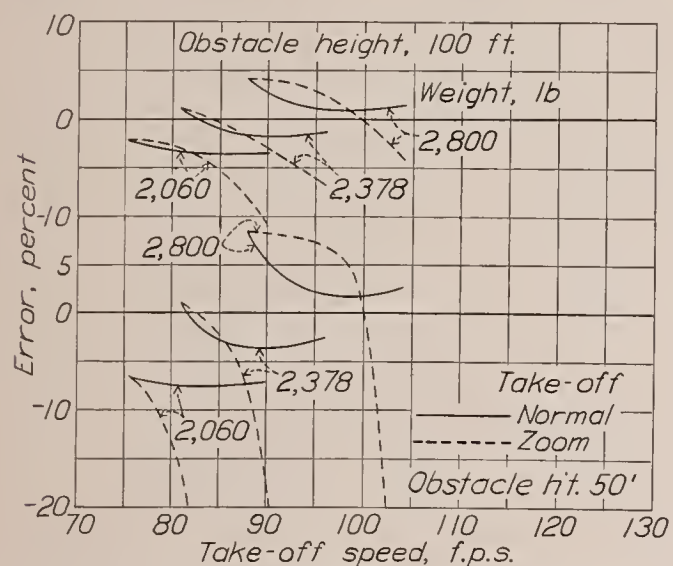


FIGURE 12.—Error in air-borne distance due to neglect of transition for the Verville AT airplane.

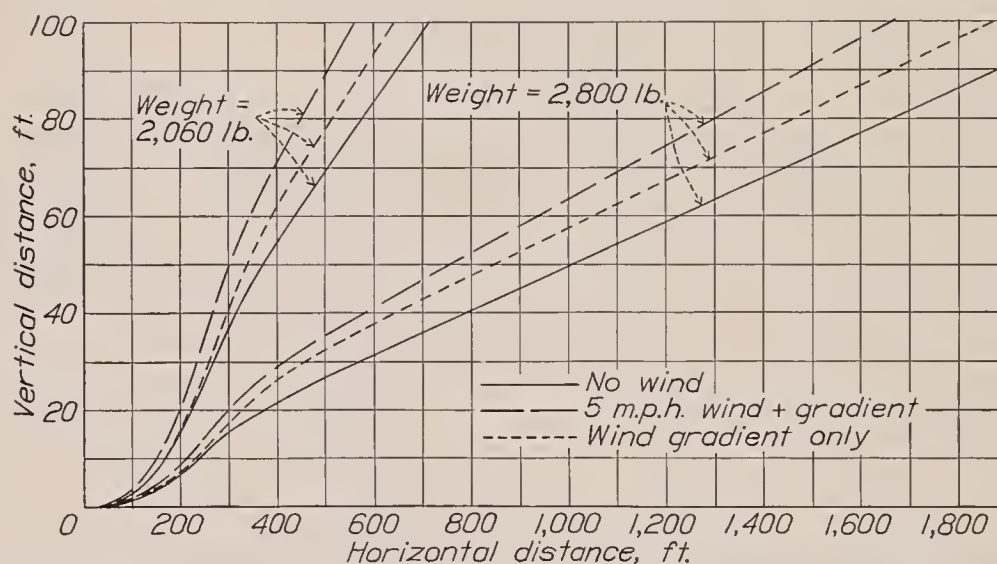


FIGURE 13.—Effect of wind and wind gradient on the flight path of the Verville AT airplane during transition and steady climb. Surface wind velocity, 5 miles per hour.

the air-borne distance as calculated by the rigorous method and the distance resulting from the assumption that the change from the conditions of the ground run to those of the steady climb occurs instantaneously and without effective loss of energy. For normal take-offs over a 100-foot obstacle the error ranges from a maximum positive value of about 4 percent with the heaviest load, i. e., the approximate distance is too great, to a maximum negative value of the same magnitude. The fact of a positive error is undoubtedly attributable to the influence of ground effect. With a 50-foot obstacle height the error is about twice as great in the same sense for corresponding conditions, since the error in actual distance is about the same.

For the zoom take-offs over a 100-foot obstacle, the error is comparable at the lower take-off speeds with that for the normal take-offs but becomes increasingly negative as the take-off speed departs more from the minimum value. The largest error in this case, in the range of conditions covered, occurs with the lightest load and has a negative value of about 10 percent. For

the 50-foot obstacle height, the error increases rapidly with take-off speed to very large values, particularly with the lighter loads. The large errors are due to the fact that the conversion from kinetic to potential energy is not completed until after the 50-foot height has been reached, in which case the assumption of an instantaneous change from ground-run to steady-climb conditions is not justified.

The scope of this investigation is not sufficiently wide for a definite determination of the relationship that might exist between this error and the airplane characteristics, but it is believed that this relationship could be established with the aid of similar data for other types of airplanes. It would then be possible to obtain a measure of the inherent take-off capabilities of a given airplane, exclusive of the troublesome factor of piloting procedure, by means of a rather simple method. The relation between ground-run distance and speed would be determined in one series of tests;

other tests, made at some safe altitude providing steady-air conditions, would establish the relationship between angle of climb and speed. These quantities, which should be largely independent of piloting effects, could then be combined, with a suitable correction for a standard type of transition, to give the total distance required to take off over obstacles of any desired height.

The effects on the air-borne portion of the take-off of a wind increasing in velocity with height are: a reduction in the speed of the airplane relative to the ground, consequently a reduction in the horizontal distance covered in a given time; and an increased vertical velocity due to the velocity gradient. These effects in combination and the effect of the wind gradient alone are shown in figure 13 for normal take-offs with the heaviest and the lightest loads. For the heavy-load condition, the over-all reduction in the distance required to clear a 50-foot obstacle is 25 percent; the reduction due to the wind gradient alone is 16 percent. For an obstacle height of 100 feet, the reductions are 21 percent and 11 percent, respectively. With the light

load the distance to clear the 50-foot obstacle is reduced 19 percent by the over-all effect of wind and 9 percent by reason of the wind gradient alone. For a 100-foot obstacle the reductions are 21 percent and 10 percent, respectively.

The method used in this report, i. e., step-by-step integration, would be too laborious for general use in evaluating the corrections for wind; but it has been found that these corrections can be determined with sufficient accuracy through the aid of rather simple relations: Still regarding the effects of wind velocity and velocity gradient as separate, the correction to the air-borne distance for the effect of wind velocity is

$$\Delta D_1 = \int_0^T V_w dt$$

where V_w is the wind velocity at any time t and T is the time required, from the instant of leaving the ground, to attain the height H .

For the average wind gradient, previously defined, the correction becomes, for $H=50$ feet,

$$\Delta D_1 = 1.27 V_{w0} T$$

where V_{w0} is the wind velocity at the ground.
For $H=100$ feet

$$\Delta D_1 = 1.38 V_{w0} T$$

The effect of a wind-velocity gradient on the height attained in a given time T is found from the energy relations to be

$$\Delta H = \frac{V \cos \gamma \Delta V_w}{g}$$

where ΔH is the difference between the heights attained with and without the benefit of a wind gradient, in the same period of time, which is very nearly equivalent

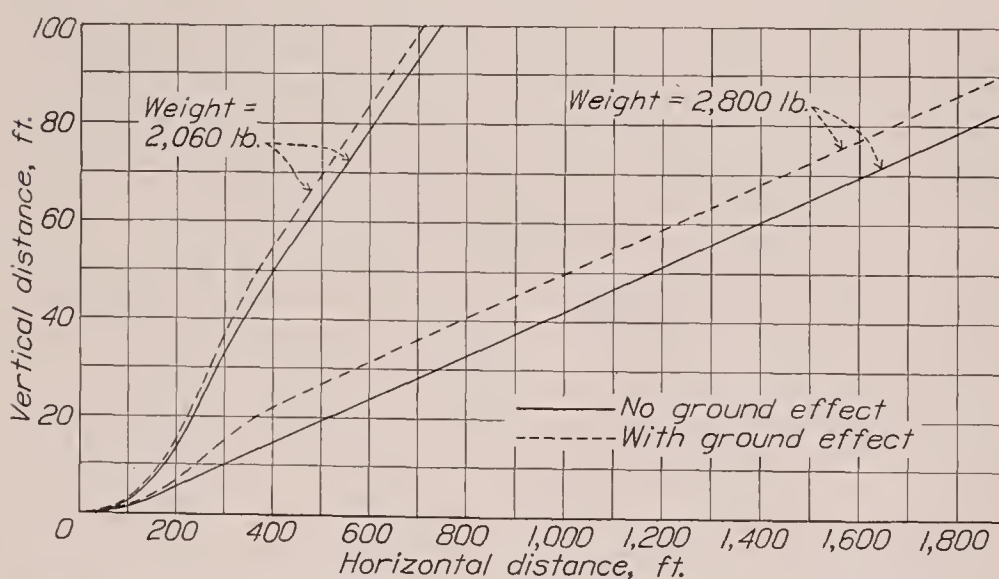


FIGURE 14.—Effect of ground proximity on the flight path of the Verville AT airplane during transition and steady climb.

to the same horizontal distance; V is the air speed at the height H ; γ is the flight-path angle relative to the air at the height H ; ΔV_w is the difference between the wind speed at 5 feet from the ground and at the effective

height H_e . The correction to the observed air-borne distance for the wind gradient is then

$$\Delta D_2 = \frac{\Delta H}{\tan \gamma_1}$$

where γ_1 is the angle of climb that would obtain were there no wind gradient; it is given closely enough by

$$\gamma_1 = \gamma - \tan^{-1} \frac{dV_w}{dH} \times \frac{V \sin \gamma}{g}$$

For the average wind gradient

$$\Delta V_w = 0.41 V_{w0}, \text{ at a height of 50 feet.}$$

and

$$\Delta V_w = 0.55 V_{w0}, \text{ at a height of 100 feet.}$$

The angle of climb for no wind is given, for an obstacle height of 50 feet, by

$$\gamma_1 = \gamma - \tan^{-1} 0.0037 V_{w0} \times \frac{V \sin \gamma}{g}$$

and, for an obstacle height of 100 feet, by

$$\gamma_1 = \gamma - \tan^{-1} 0.0021 V_{w0} \times \frac{V \sin \gamma}{g}$$

The over-all correction to no-wind conditions is then, for an obstacle height of 50 feet,

$$\Delta D = 1.27 V_{w0} T + \frac{V \cos \gamma \times 0.41 V_{w0}}{g \tan \left(\gamma - \tan^{-1} 0.0037 \frac{V_{w0} V \sin \gamma}{g} \right)}$$

and, for an obstacle height of 100 feet,

$$\Delta D = 1.38 V_{w0} T + \frac{V \cos \gamma \times 0.55 V_{w0}}{g \tan \left(\gamma - \tan^{-1} 0.0021 \frac{V_{w0} V \sin \gamma}{g} \right)}$$

The corrections as computed from the foregoing equations agreed closely with those determined by the step-by-step integrations, the difference being less than 2 percent of the air-borne distance in all the cases considered. In the absence of specific data on the variation of the wind velocity with altitude, it is believed that the assumption of an average wind gradient will provide a good approximation.

The effect of proximity of the ground on the distance required for the air-borne stages of the take-off is shown in figure 14. The ground effect reduces the distance required to attain an altitude of 50 feet by 10 percent with the lightest load and by 16 percent with the heaviest load. For an obstacle height of 100 feet, the percentage reductions are about one-half of those for the 50-foot obstacle. The greater difference for the heavier load is probably due to the fact that the airplane climbs more slowly than with the light load; hence it is in the region of strongest ground effect for a longer period.

CONCLUSIONS

1. For normal take-offs the horizontal distances covered in the transition in proportion to the heights attained were least at the slowest possible take-off speed. Likewise, the shortest over-all distance required in taking off over an obstacle was obtained with the slowest speed.

2. For normal ground conditions, zoom take-offs required shorter over-all distances than normal take-offs, particularly with heavy loads if the obstacle to be surmounted was sufficiently high. With light loadings and low obstacle heights, the zoom take-offs provided no advantage.

3. The error resulting from neglect of the transition in calculating the air-borne distance in take-off varied from 8 percent with the heaviest load considered to -8 percent with the lightest load for normal take-offs over a 50-foot obstacle. For a 100-foot obstacle the percentage error was about one-half of that for the 50-foot obstacle. For zoom take-offs the error arising from neglect of the transition was much greater.

4. The effect of the average wind gradient corresponding to a 5-mile-per-hour surface wind was a reduction in the air-borne distance to clear a 50-foot obstacle of about 9 percent with the lightest load and about 16 percent with the heaviest load. For the 100-foot obstacle height the reduction was about 10 percent for both loads. The over-all reduction due to this wind was approximately twice that due to the wind gradient alone. The correction of observed take-off performance to no-wind conditions can be accomplished through the use of relatively simple expressions.

5. The ground effect reduced the air-borne distance required to attain a height of 50 feet by about 10 percent with the lightest loading and by about 16 percent with the heaviest loading. For an obstacle height of 100 feet the percentage reduction was about one-half as great.

LANGLEY MEMORIAL AERONAUTICAL LABORATORY,
NATIONAL ADVISORY COMMITTEE FOR AERONAUTICS,
LANGLEY FIELD, VA., *October 26, 1937.*

REFERENCES

1. Thompson, F. L., Peck, W. C., and Beard, A. P.: Air Conditions Close to the Ground and the Effect on Airplane Landings. T. R. No. 489, N. A. C. A., 1934.
2. Hartman, Edwin P.: Working Charts for the Determination of Propeller Thrust at Various Air Speeds. T. R. No. 481, N. A. C. A., 1934.
3. Freeman, Hugh B.: Comparison of Full-Scale Propellers Having R. A. F.-6 and Clark Y Airfoil Sections. T. R. No. 378, N. A. C. A., 1931.

TABLE I.—CHARACTERISTICS OF THE VERVILLE AT AIRPLANE

Engine—Continental A-70.....	165 hp. at 2,000 r. p. m.
Propeller—Metal, fixed pitch:	
Blade section.....	Clark Y
Diameter.....	8 ft. 5 in.
Blade-angle setting at 0.75 R.....	12.8°
Wing dimensions—Clark Y-15:	
Total area.....	262.5 sq. ft.
Span, upper wing.....	31 ft.
Span, lower wing.....	31 ft.
Chord, upper wing.....	50 in.
Chord, lower wing.....	50 in.
Test loadings:	
Gross weight.....	2,060 lb.
Wing loading.....	7.8 lb. per sq. ft.
Power loading.....	12.5 lb. per hp.
Gross weight.....	2,378 lb.
Wing loading.....	9.1 lb. per sq. ft.
Power loading.....	14.4 lb. per hp.

TABLE II.—TAKE-OFF DISTANCES FOR THE VERVILLE AT AIRPLANE FROM STEP-BY-STEP INTEGRATIONS

Weight (lb.)	Power loading (lb./hp.)	Wing loading (lb./sq. ft.)	Take-off speed (air) (f. p. s.)	Climb-speed (air) (f. p. s.)	Ground-run distance from V=75 f. p. s. (Feet)	Height attained in transition (Feet)	Horizontal distance for transition (Feet)	Tangent of angle of steady climb, γ	Obstacle height=50 ft.			Obstacle height=100 ft.			Remarks
									Horizontal distance for steady climb (Feet)	Total air-borne distance (Feet)	Total distance from V=75 f. p. s. (Feet)	Horizontal distance for steady climb (Feet)	Total air-borne distance (Feet)	Total distance from V=75 f. p. s. (Feet)	
2,060	12.5	7.8	75.5	75.5	7	74.5	534	0.1441	-----	370	377	176	710	717	Normal... Zoom... Normal... Zoom... Normal... Zoom... No wind.
			82.0	82.0	89	47.2	348	.1464	20	368	457	359	707	796	
			90.0	90.0	208	39.2	314	.1366	78	392	600	444	758	966	
			82.0	75.5	89	82.5	483	.1441	-----	287	374	121	604	693	
			90.0	75.5	208	101.0	490	.1441	-----	237	445	-----	482	690	
2,378	14.4	9.1	81.0	81.0	98	46.2	491	.0930	40	531	629	572	1,063	1,161	Normal... Zoom... Normal... Zoom... Normal... Zoom... No wind.
			88.0	88.0	217	36.5	396	.0969	139	535	752	654	1,050	1,267	
			96.0	96.0	392	28.6	335	.0894	238	573	965	799	1,134	1,526	
			88.0	81.0	217	65.0	519	.0930	-----	367	584	376	895	1,112	
			96.0	81.0	392	88.3	550	.0930	-----	269	661	125	675	1,067	
2,800	17.0	10.7	88.0	88.0	274	28.0	526	.0455	482	1,008	1,282	1,581	2,107	2,381	Normal... Zoom... Normal... Zoom... Normal... Zoom... No wind.
			96.0	96.0	490	22.7	432	.0503	543	975	1,465	1,540	1,972	2,462	
			104.0	104.0	782	15.0	312	.0443	786	1,098	1,880	1,917	2,229	3,011	
			96.0	88.0	490	49.5	542	.0455	-----	555	1,045	1,108	1,650	2,140	
			104.0	88.0	782	68.7	509	.0455	-----	302	1,084	686	1,195	1,977	
2,060	12.5	7.8	75.5	75.5	-----	-----	-----	-----	-----	300	-----	-----	561	-----	5 m. p. h. wind+gradient.
2,800	17.0	10.7	88.0	88.0	-----	-----	-----	-----	-----	337	-----	-----	642	-----	Wind gradient only.
2,060	12.5	7.8	88.0	88.0	-----	63.3	495	-----	-----	756	-----	-----	1,665	-----	5 m. p. h. wind+gradient.
2,800	17.0	10.7	75.5	75.5	-----	-----	-----	-----	-----	844	-----	-----	1,878	-----	Wind gradient only.
2,800	17.0	10.7	88.0	88.0	-----	10.6	308	-----	865	404	-----	254	749	-----	No ground effect.
										1,173	-----	1,962	2,270	-----	No ground effect.

REPORT No. 627

THE EXPERIMENTAL AND CALCULATED CHARACTERISTICS OF 22 TAPERED WINGS

By RAYMOND F. ANDERSON

SUMMARY

The experimental and calculated aerodynamic characteristics of 22 tapered wings are compared, using tests made in the variable-density wind tunnel. The wings had aspect ratios from 6 to 12 and taper ratios from 1.6:1 to 5:1. The compared characteristics are the pitching moment, the aerodynamic-center position, the lift-curve slope, the maximum lift coefficient, and the curves of drag. The method of obtaining the calculated values is based on the use of wing theory and experimentally determined airfoil section data. In general, the experimental and calculated characteristics are in sufficiently good agreement that the method may be applied to many problems of airplane design.

INTRODUCTION

Considerable work has been done on the calculation of the aerodynamic characteristics of tapered wings. A method of calculating the important characteristics of tapered wings was given in reference 1 together with comparisons of experimental and calculated characteristics. It is the purpose of this report to extend reference 1 to include the calculation of the drag of all the wings contained in that report and to include the characteristics of additional wings tested in the variable-density tunnel. The additional wings comprise the 3 described in reference 2 and 10 other wings, including 7 with sections of the N. A. C. A. 230 series. Experimental lift, drag, and pitching-moment data are given and, for comparison, calculated values of pitching moment, aerodynamic-center position, lift-curve slope, maximum lift coefficient, and curves of drag.

SYMBOLS

The symbols used are as follows:

- S , wing area.
- b , span.
- A , aspect ratio, b^2/S .
- c , chord at any section along the span.
- c_t , tip chord (for rounded tips, c_t is the fictitious chord obtained by extending the leading and trailing edges to the extreme tip).
- c_s , chord at root of wing or plane of symmetry.

- Λ , angle of sweepback, measured between the lateral axis and a line through the aerodynamic centers of the wing sections. (The symbol β was used in reference 1 but Λ has since been adopted as standard.)
- ϵ , aerodynamic twist, in degrees, from root to tip, measured between the zero-lift directions of the center and the tip sections, positive for washin.
- $x_{a.c.}$, longitudinal coordinate of wing aerodynamic center measured from the quarter-chord point of the root section.
- a , wing lift-curve slope, per degree.
- a_0 , section lift-curve slope, per degree.
- α_{l_0} , angle of zero lift of the root section.
- $\alpha_{s(L=0)}$, wing angle of attack for zero lift, measured from root chord.
- c_l , section lift coefficient; $c_l = c_{l_a} + c_{l_b}$
- c_{l_b} , part of lift coefficient due to aerodynamic twist (computed for $C_L = 0$).
- c_{l_a} , part of lift coefficient due to angle of attack at any C_L ; $c_{l_a} = C_L c_{l_{a1}}$
- $c_{l_{a1}}$, part of lift coefficient due to angle of attack for $C_L = 1.0$; $c_{l_{a1}} = \frac{S}{cb} L_a$
- L_a , additional load distribution parameter.
- $c_{m_{a.c.}}$, section pitching-moment coefficient about section aerodynamic center.
- C_{m_s} , wing pitching-moment coefficient due to the pitching moments of the wing sections.
- $C_{m_{a.c.}}$, wing pitching-moment coefficient about its aerodynamic center.
- C_L , wing lift coefficient.
- C_{D_v} , wing induced-drag coefficient.
- $C_{D_e} = C_D - C_L^2/\pi A$, effective profile-drag coefficient.
- E, H, J, f , factors given in reference 1.
- R , Reynolds Number.
- R_e , effective Reynolds Number; the Reynolds Number of variable-density-tunnel tests multiplied by the turbulence factor 2.64.
- std , a subscript designating standard airfoil test results from the variable-density wind tunnel at an effective Reynolds Number of about 8,000,000.

APPARATUS AND TESTS

Standard aluminum-alloy models having an area of 150 square inches were used in the tests. In the construction of the wings, straight-line elements were used between corresponding points of the root section and the construction tip sections, except for the N. A. C. A. 23013-43010 and the elliptical N. A. C. A. 4412 wings. These wings were made by cutting several sections along the span and then fairing between the sections. The general characteristics of the models are given in table I and the principal dimensions of the plan forms, in terms of the mean chord S/b , are given

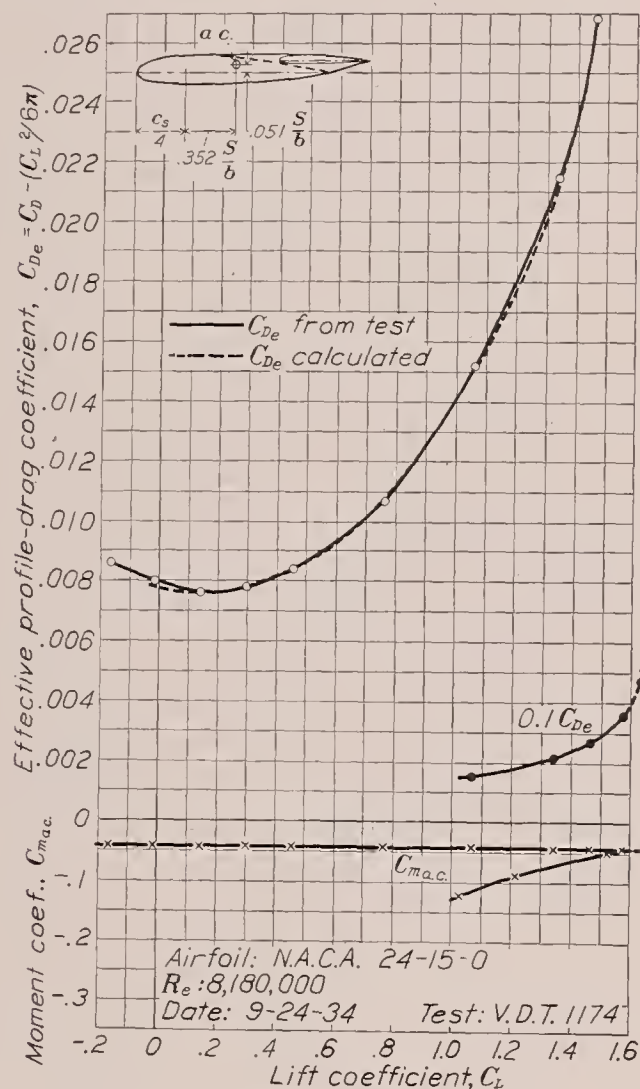


FIGURE 1.—Tapered N. A. C. A. 24-15-0 airfoil.

on the plots. The ordinates of the airfoil sections not already published in references 1, 2, and 3 are given in tables II and III.

The designating numbers of the first nine wings listed in table I are formed from numbers representing the airfoil section mean line, the sweepback, and the washout, respectively. (See reference 1.) The wings with sections of the 230 series and high aspect ratio all have a tip thickness of 9 percent of the chord and differ only in taper ratio, aspect ratio, and root thickness. Numbers representing these three quantities are therefore used to designate the wings; i. e., N. A. C. A. 3-10-18 represents a wing of 3:1 taper, aspect ratio 10, and root thickness of 18 percent.

The tests were made in the variable-density wind tunnel, which is described in reference 4. The lift, the

drag, and the pitching moment of the wings were measured for positive angles of attack at a tunnel pressure of 20 atmospheres, which corresponds to a test Reynolds Number of 3,100,000 based on a 5-inch chord (effective Reynolds Number 8,200,000). The lift-curve peak was also determined for most of the wings at a lower Reynolds Number.

EXPERIMENTAL RESULTS

The results of the tests are given in figures 1 to 20 in the form of the usual dimensionless coefficients. The corrections that were applied to the tunnel data, including the method of correcting for tunnel-wall effect, are described in reference 4.

In figures 11 to 20 for the plots against angle of attack, the lift-curve peaks are given for two values of effective Reynolds Number in order to show the scale effect on $C_{L_{max}}$. The Reynolds Number is based on the mean chord S/b . In the plots against lift coefficient (figs. 1 to 20) the drag has been plotted with the minimum induced drag deducted (reference 1); thus, $C_{D_e} = C_D - \frac{C_L^2}{\pi A}$. The drag values differ from those on the plots against angle of attack in that the C_{D_e} values have been corrected to effective Reynolds Number. This correction allows for the reduction in skin friction when converting from the test to the effective Reynolds Number and amounts to a C_D increment of 0.0011 (reference 5).

The pitching-moment coefficients are given about an axis for which they are practically constant for lift coefficients up to $C_{L_{max}}$ (aerodynamic center). The aerodynamic centers were found by the method given in the appendix. The coefficients are based on the mean chord S/b in the form $C_m = \frac{M}{qS(S/b)} = \frac{Mb}{qS^2}$. The choice of a chord length for use in calculating C_m is arbitrary in any case. It is considered best, however, to use a chord length that may be conveniently found from given quantities, such as the area and the span. Coefficients so determined do not tend to be equal for wings of the same section and different taper ratios, as they would if based on the so-called "mean aerodynamic chord," but indicate directly the relative magnitude of the pitching moments of wings having equal areas and spans.

As a reference chord for the center of pressure it might appear logical to use the chord upon which the pitching-moment coefficients are based (mean chord); however, for the general case of a wing with taper and twist, if the mean chord were used, it would not be easy to decide how its location along the span and its angular attitude should be specified. The position of the root chord is known; and, as the center-of-pressure chord is simply a reference line, it was decided to base the center of pressure on the root chord.

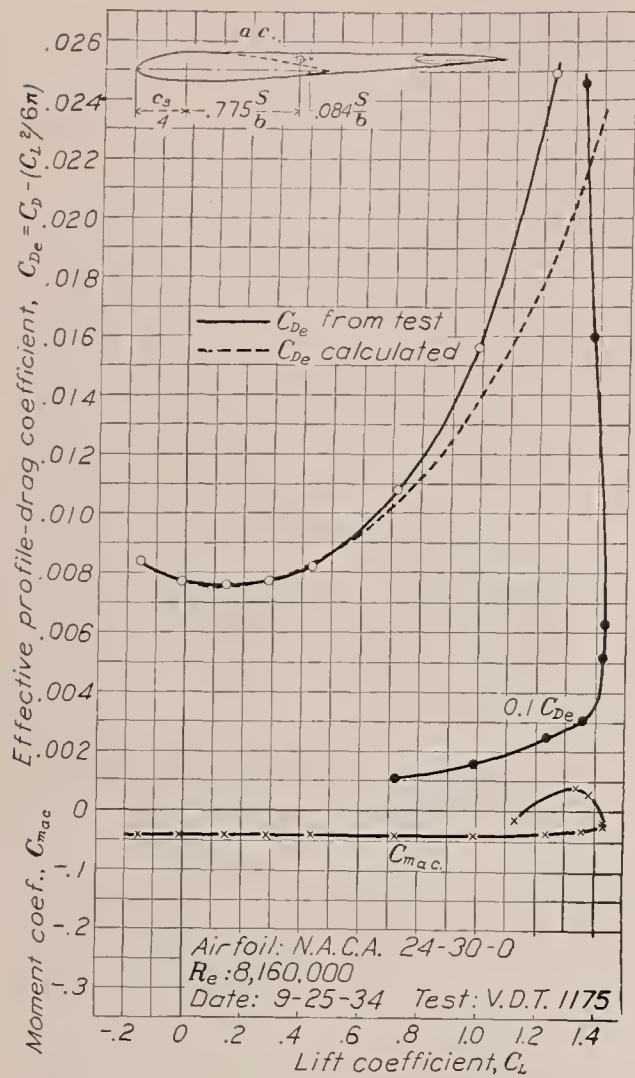


FIGURE 2.—Tapered N. A. C. A. 24-30-0 airfoil.

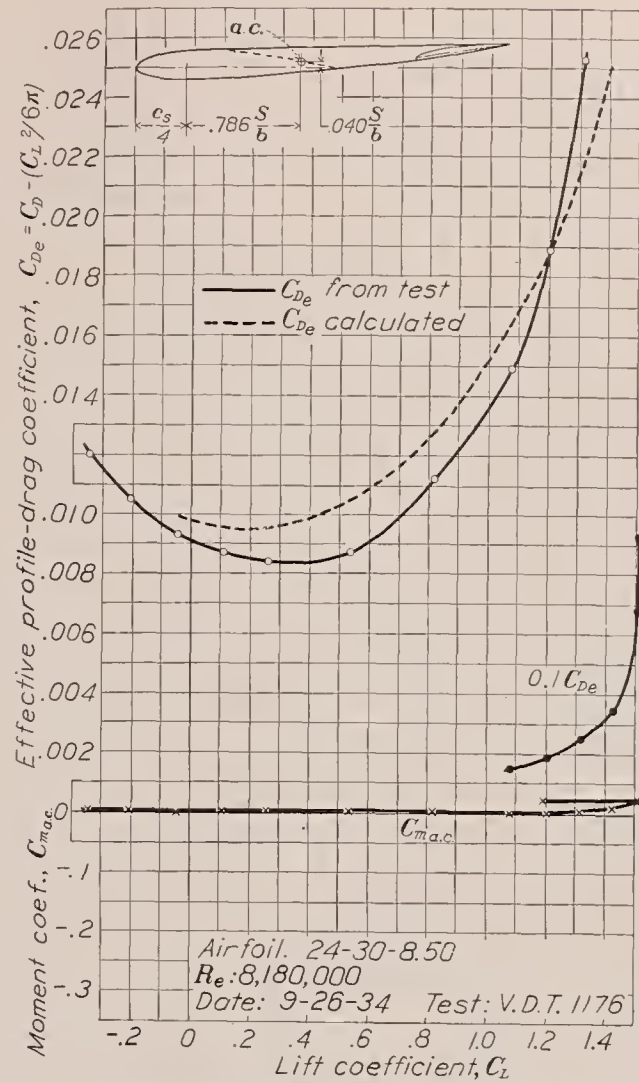
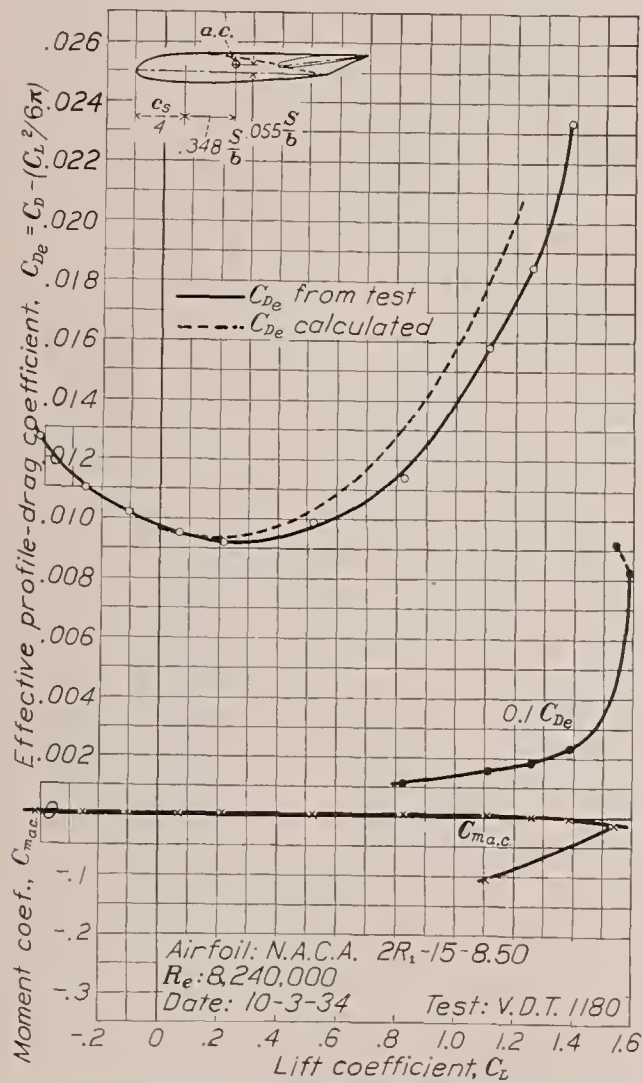
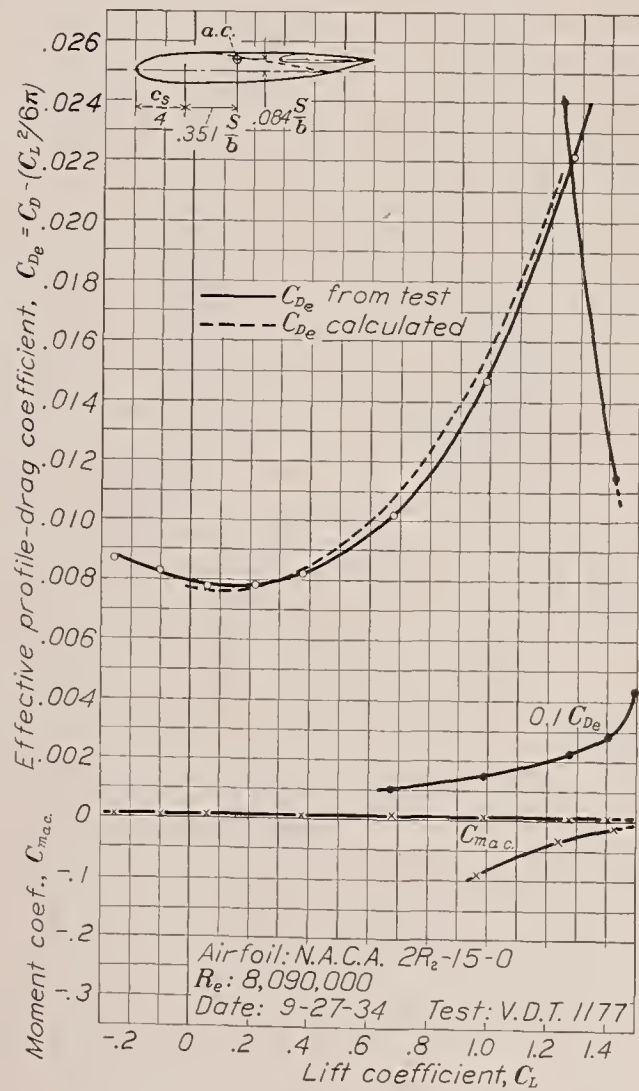


FIGURE 3.—Tapered N. A. C. A. 24-30-8.50 airfoil.

FIGURE 4.—Tapered N. A. C. A. 2R₁-15-8.50 airfoilFIGURE 5.—Tapered N. A. C. A. 2R₂-15-0 airfoil.

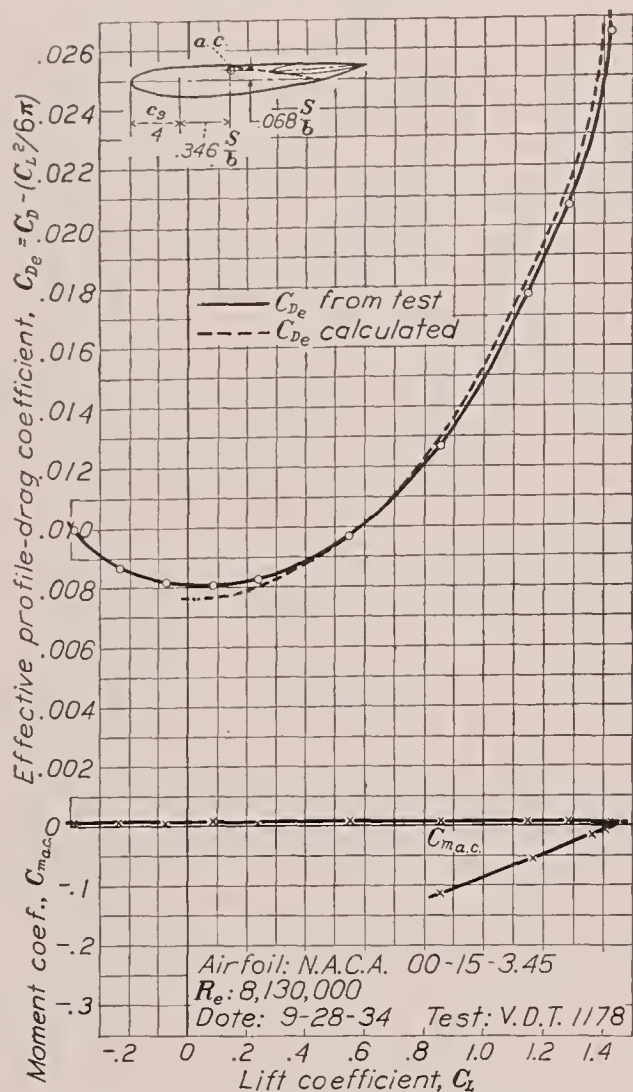


FIGURE 6.—Tapered N. A. C. A. 00-15-3.45 airfoil.

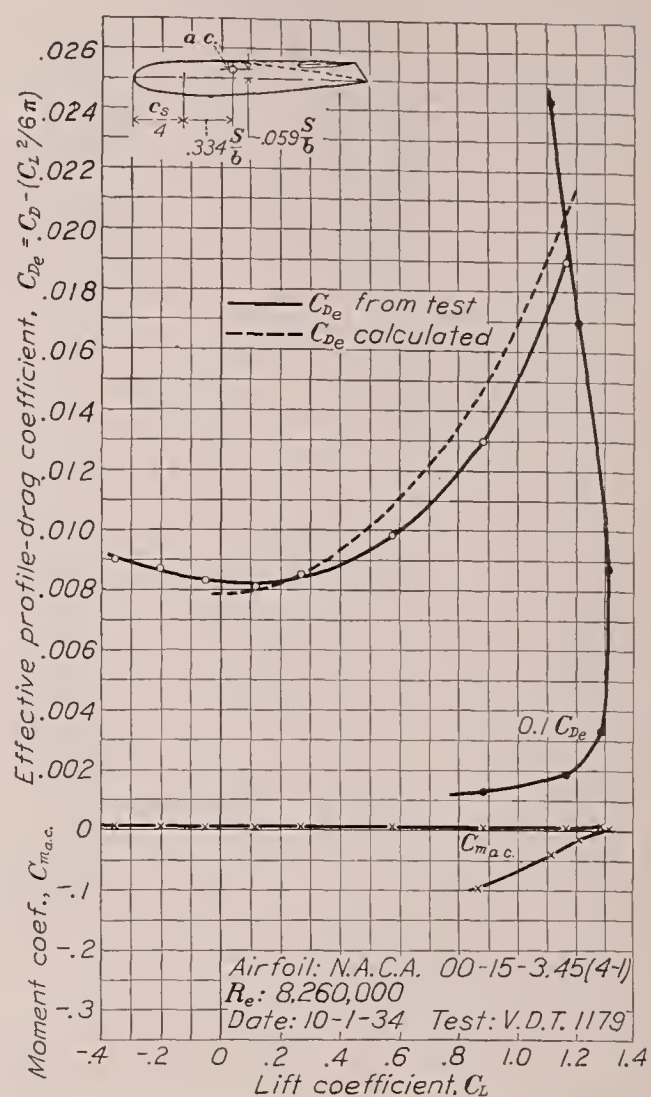


FIGURE 7.—Tapered N. A. C. A. 00-15-3.45 (4:1) airfoil.

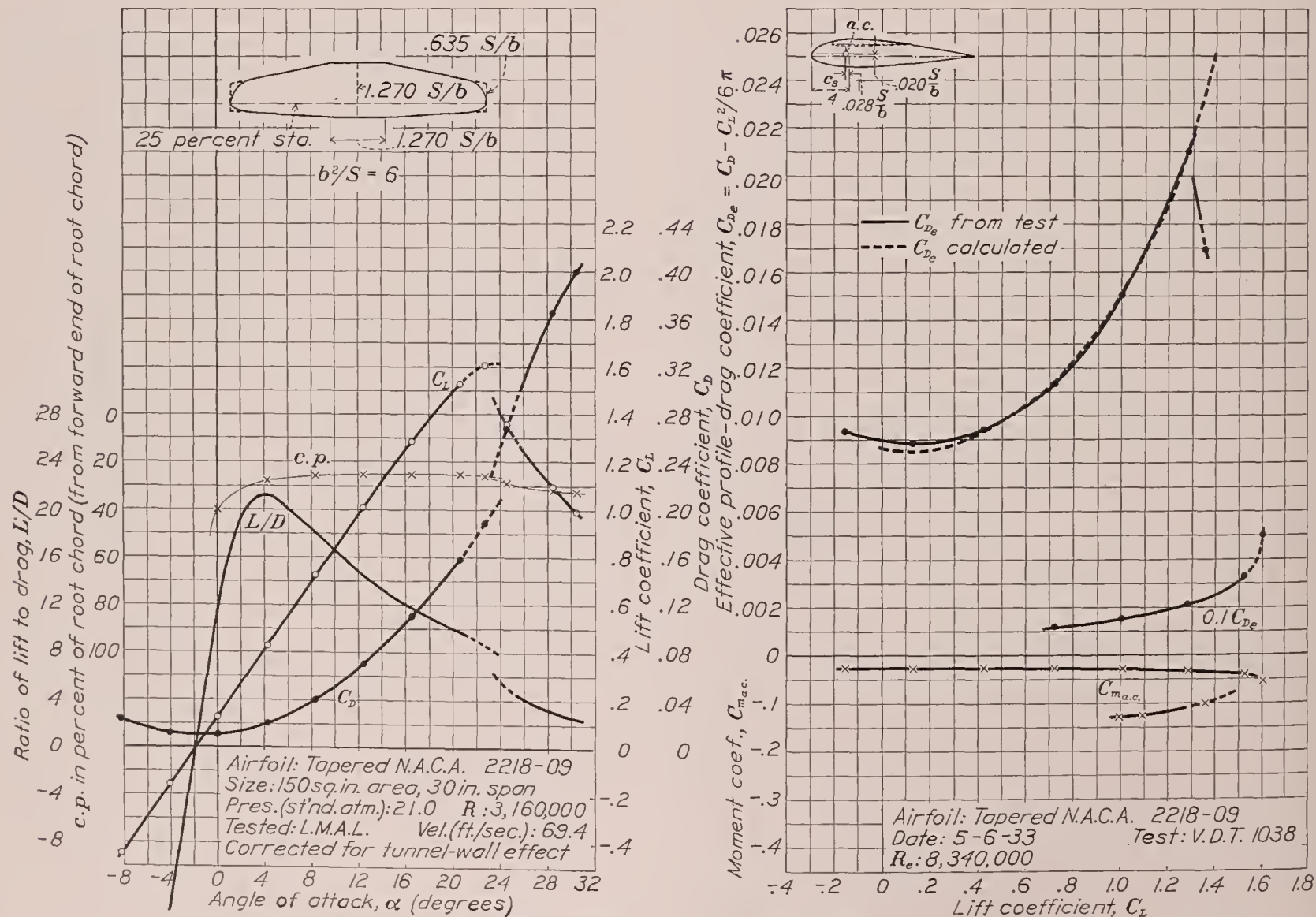


FIGURE 8.—Tapered N. A. C. A. 2218-09 airfoil.

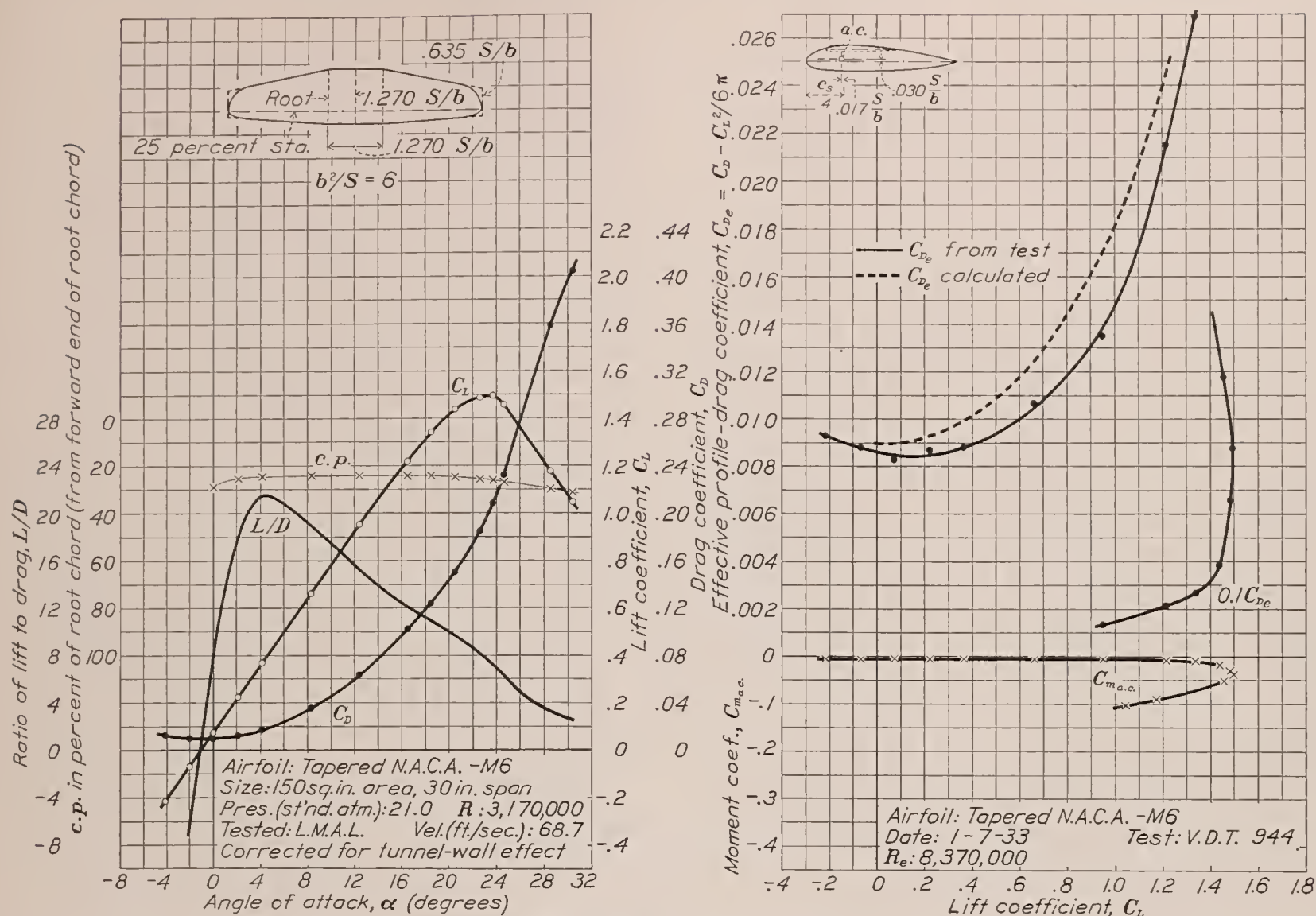


FIGURE 9.—Tapered N. A. C. A.-M6 airfoil.

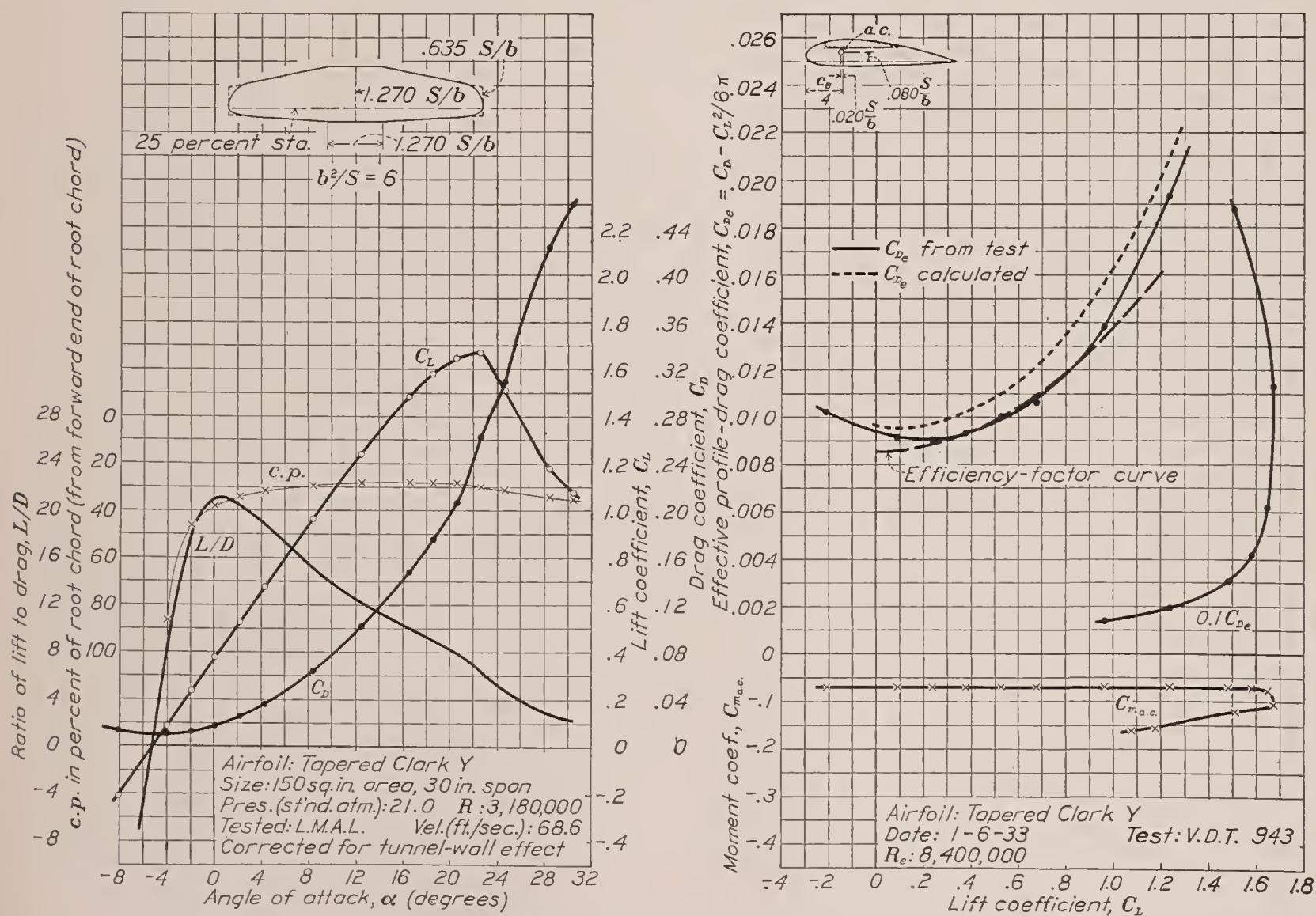


FIGURE 10.—Tapered Clark Y airfoil.

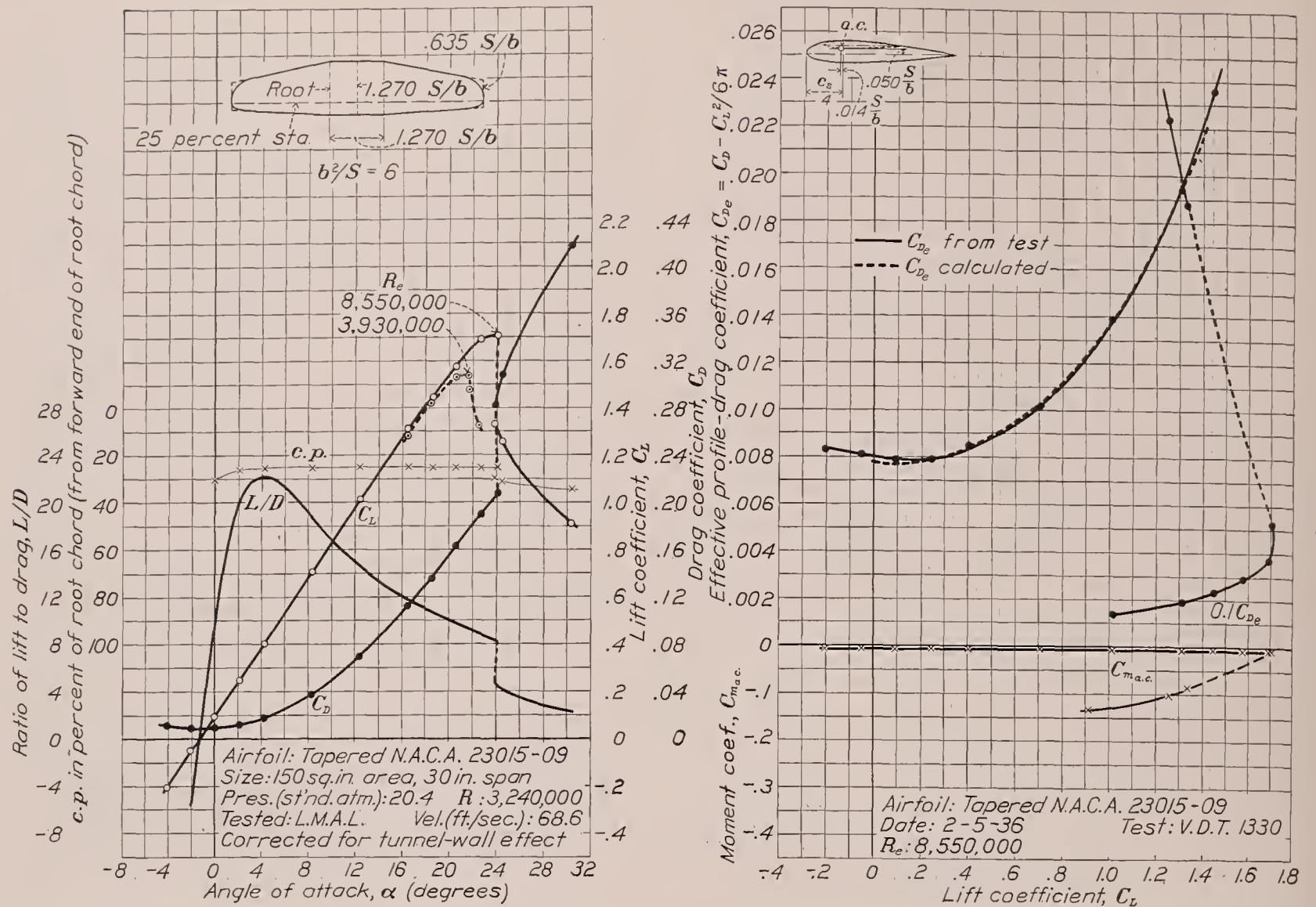


FIGURE 11.—Tapered N. A. C. A. 23015-09 airfoil.

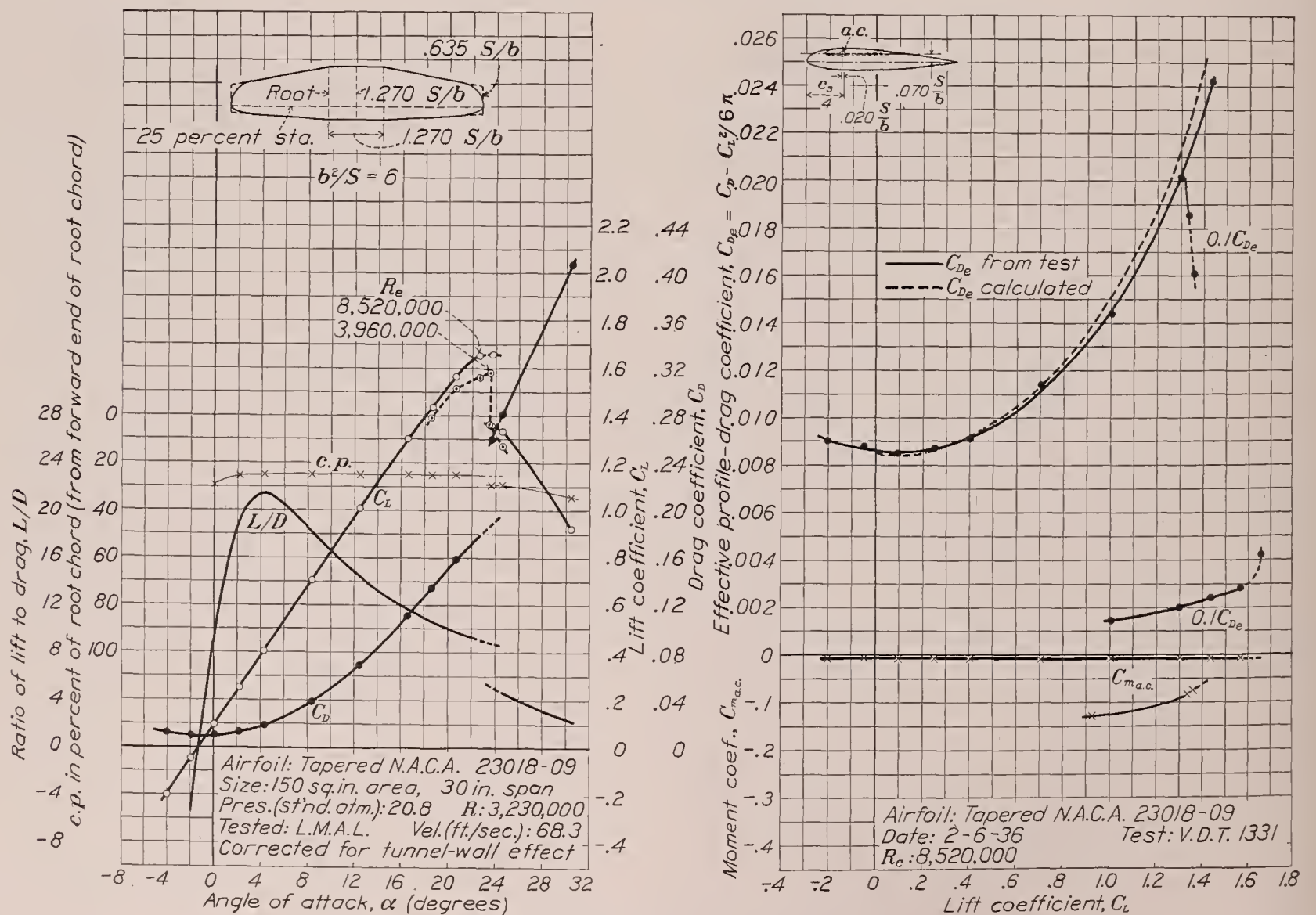


FIGURE 12.—Tapered N. A. C. A. 23018-09 airfoil.

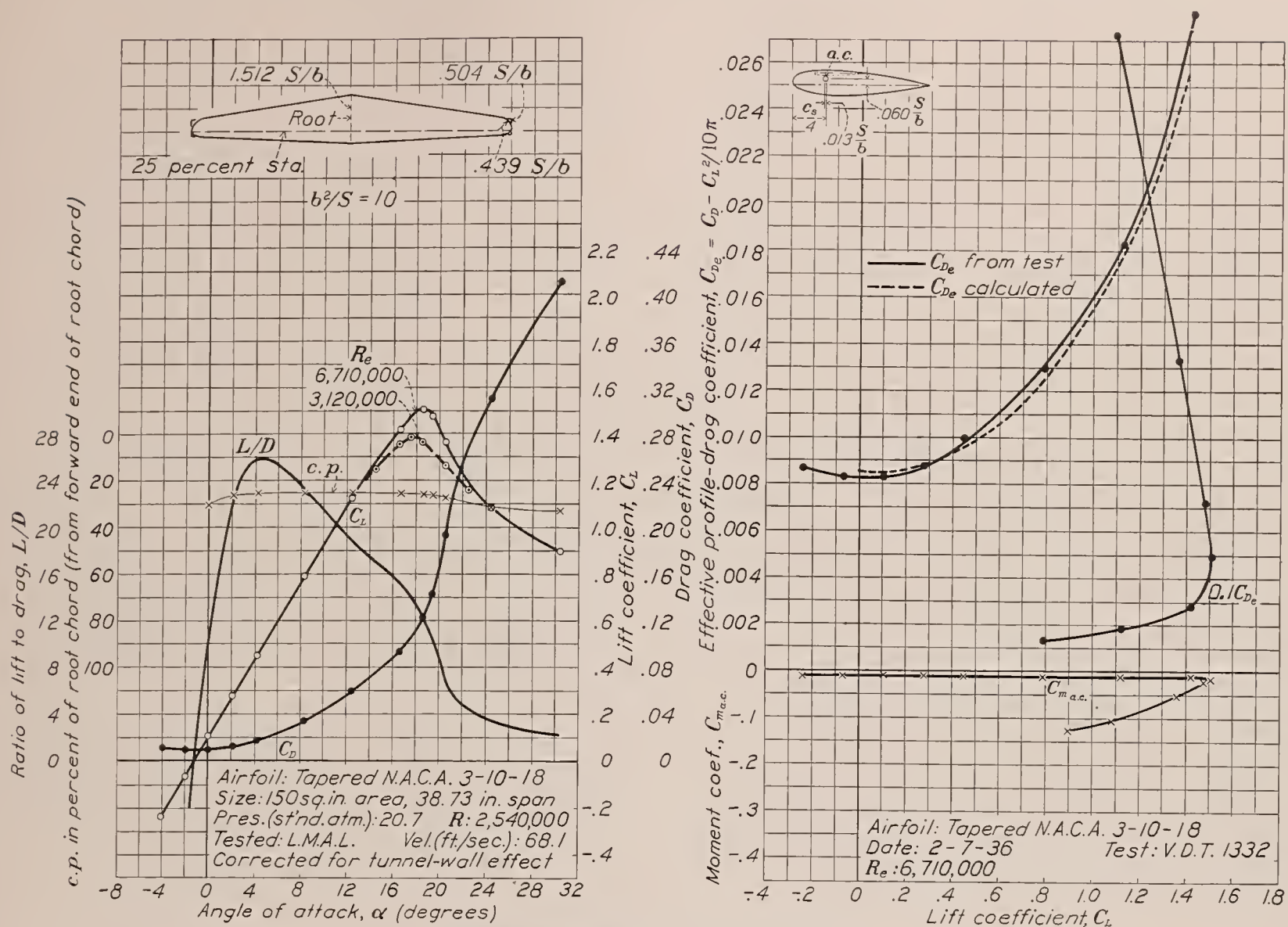


FIGURE 13.—Tapered N. A. C. A. 3-10-18 airfoil.

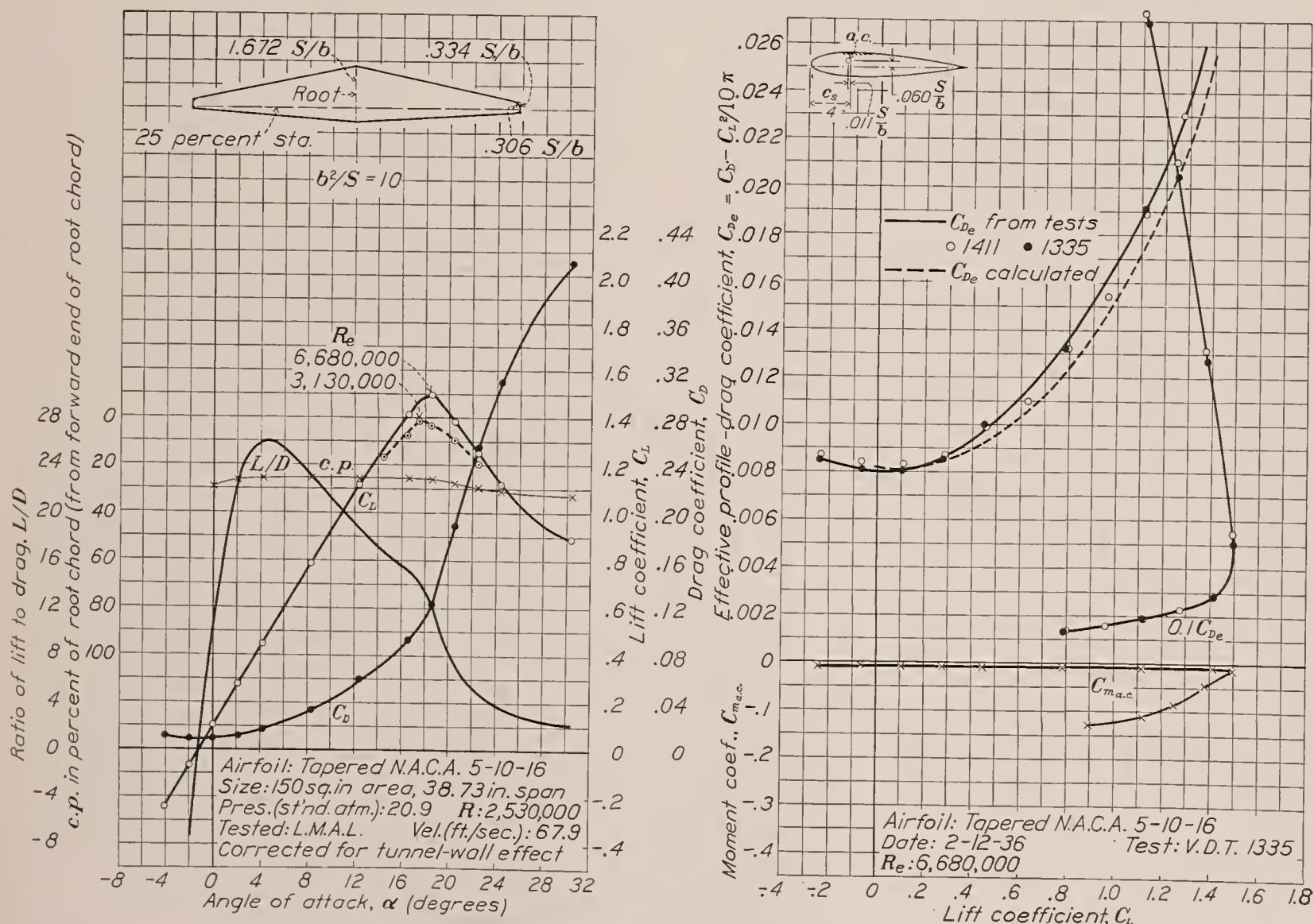


FIGURE 14.—Tapered N. A. C. A. 5-10-16 airfoil.

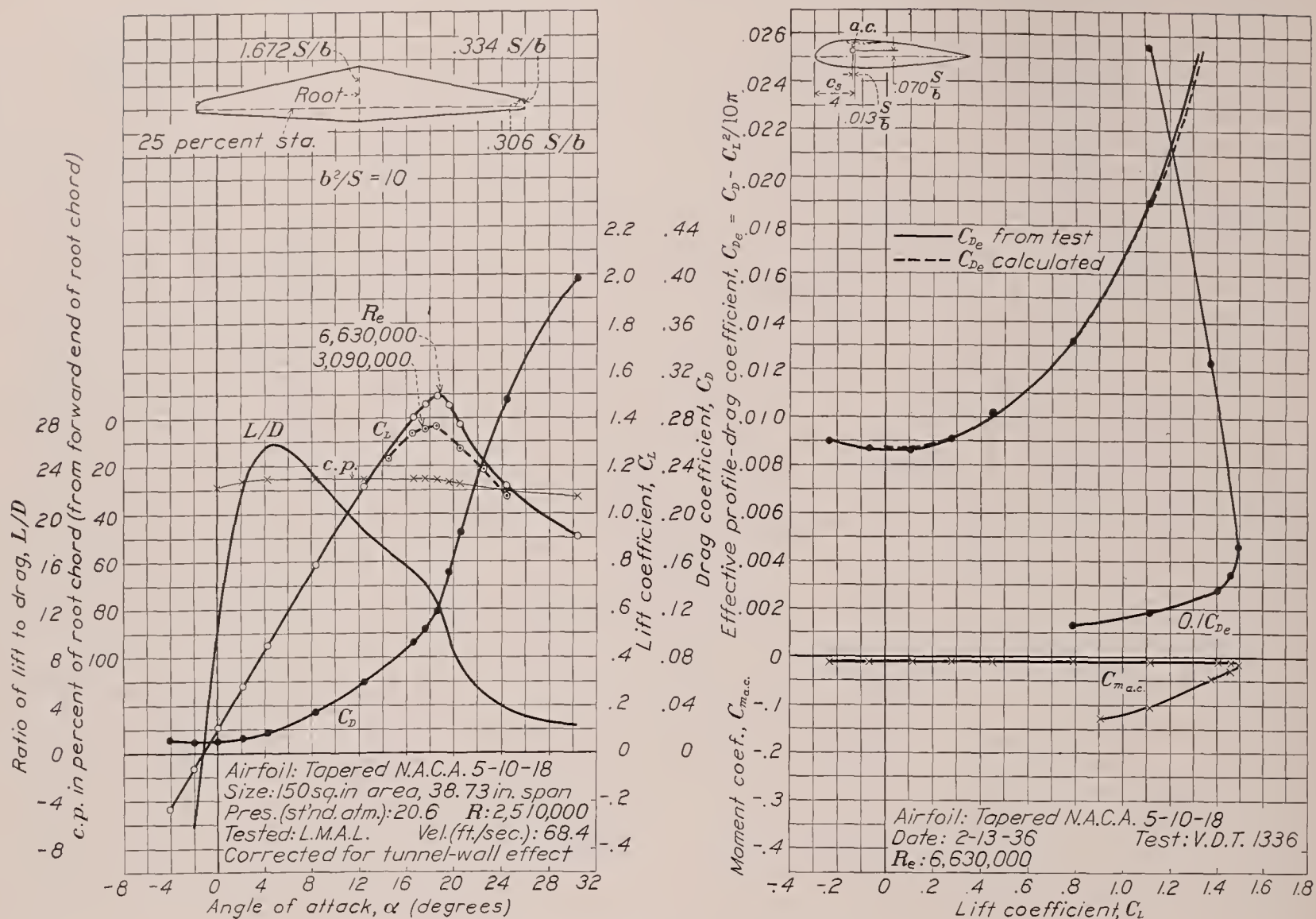


FIGURE 15.—Tapered N. A. C. A. 5-10-18 airfoil.

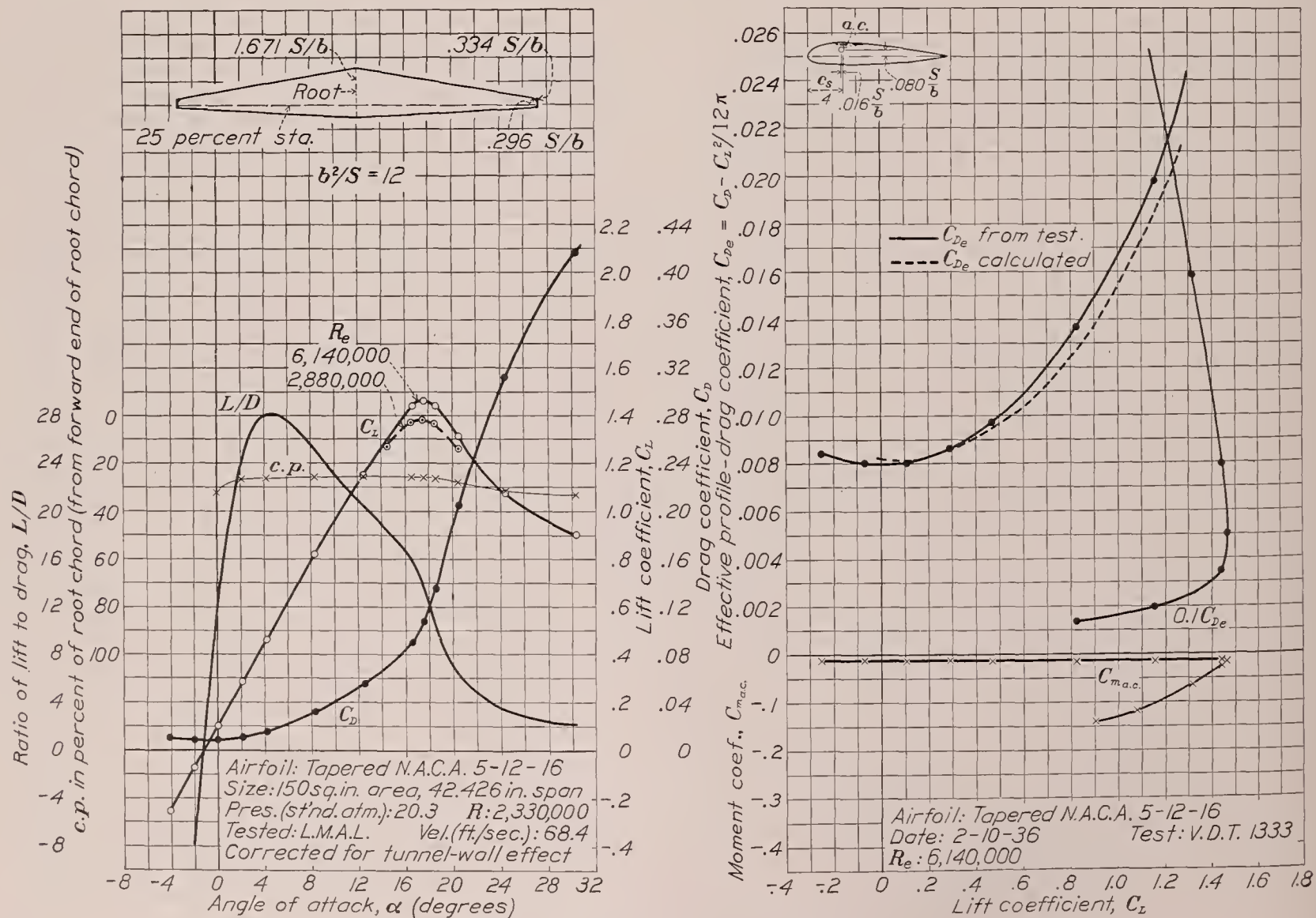


FIGURE 16.—Tapered N. A. C. A. 5-12-16 airfoil.

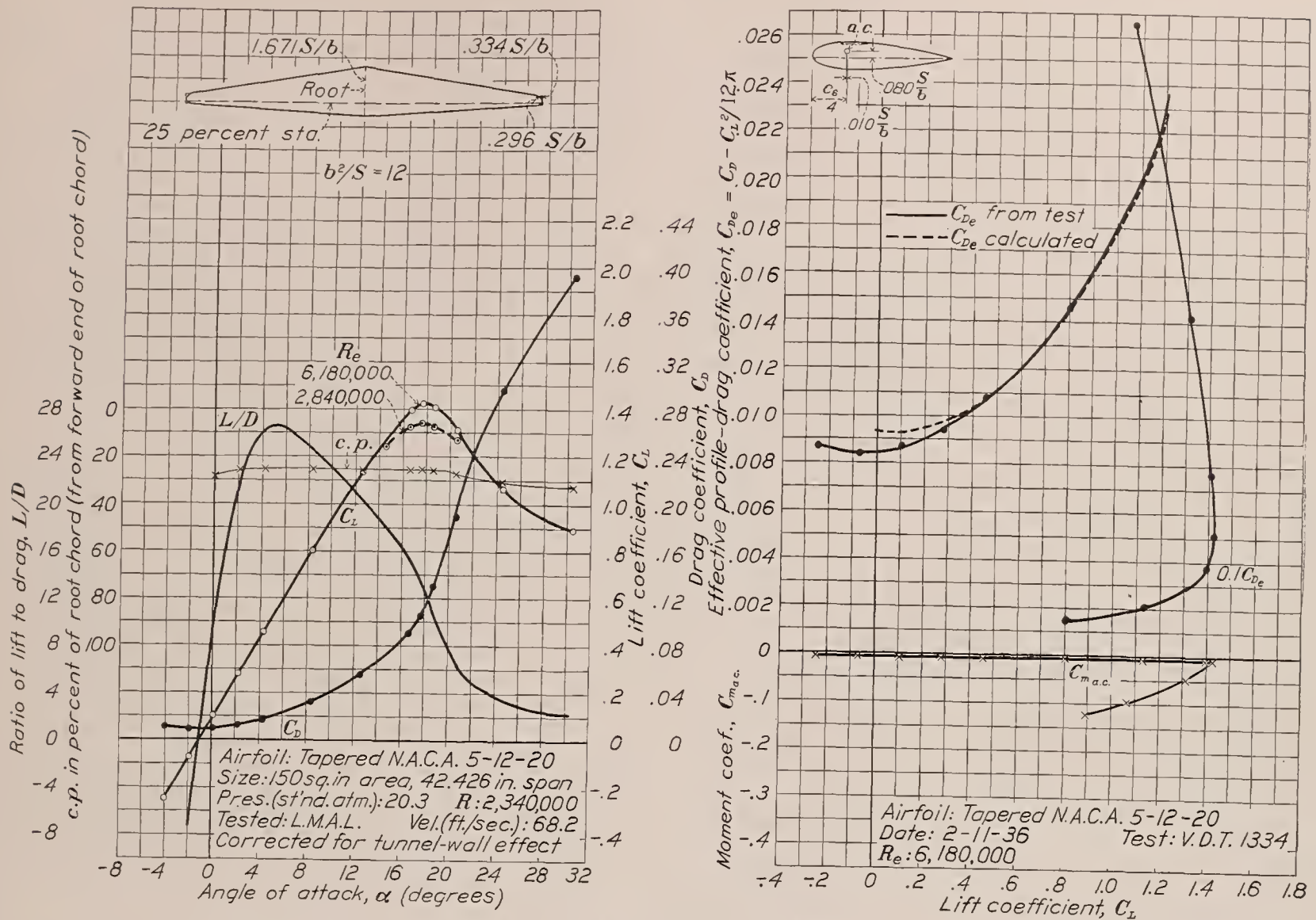


FIGURE 17.—Tapered N. A. C. A. 5-12-20 airfoil.

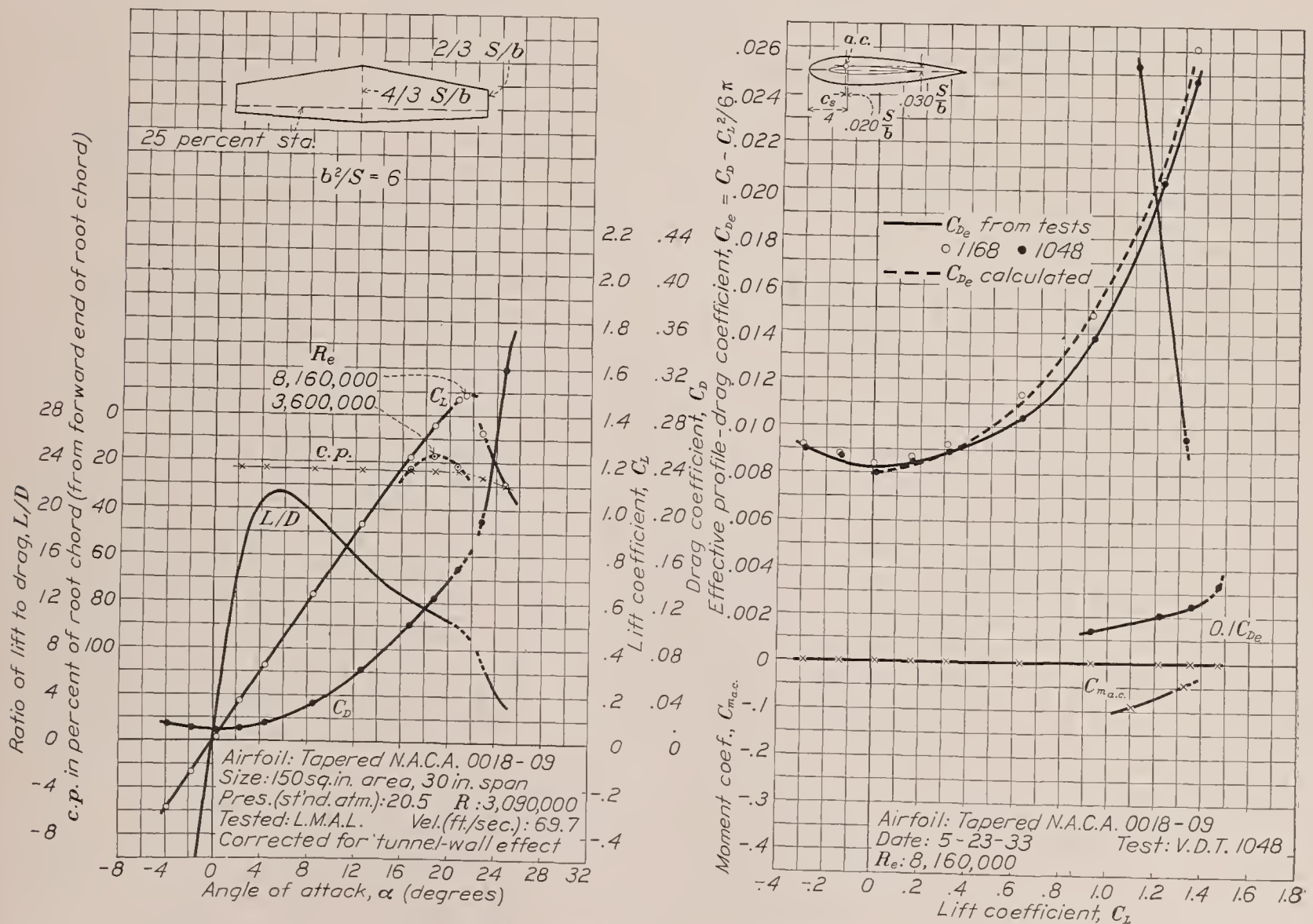


FIGURE 18.—Tapered N. A. C. A. 0018-09 airfoil.

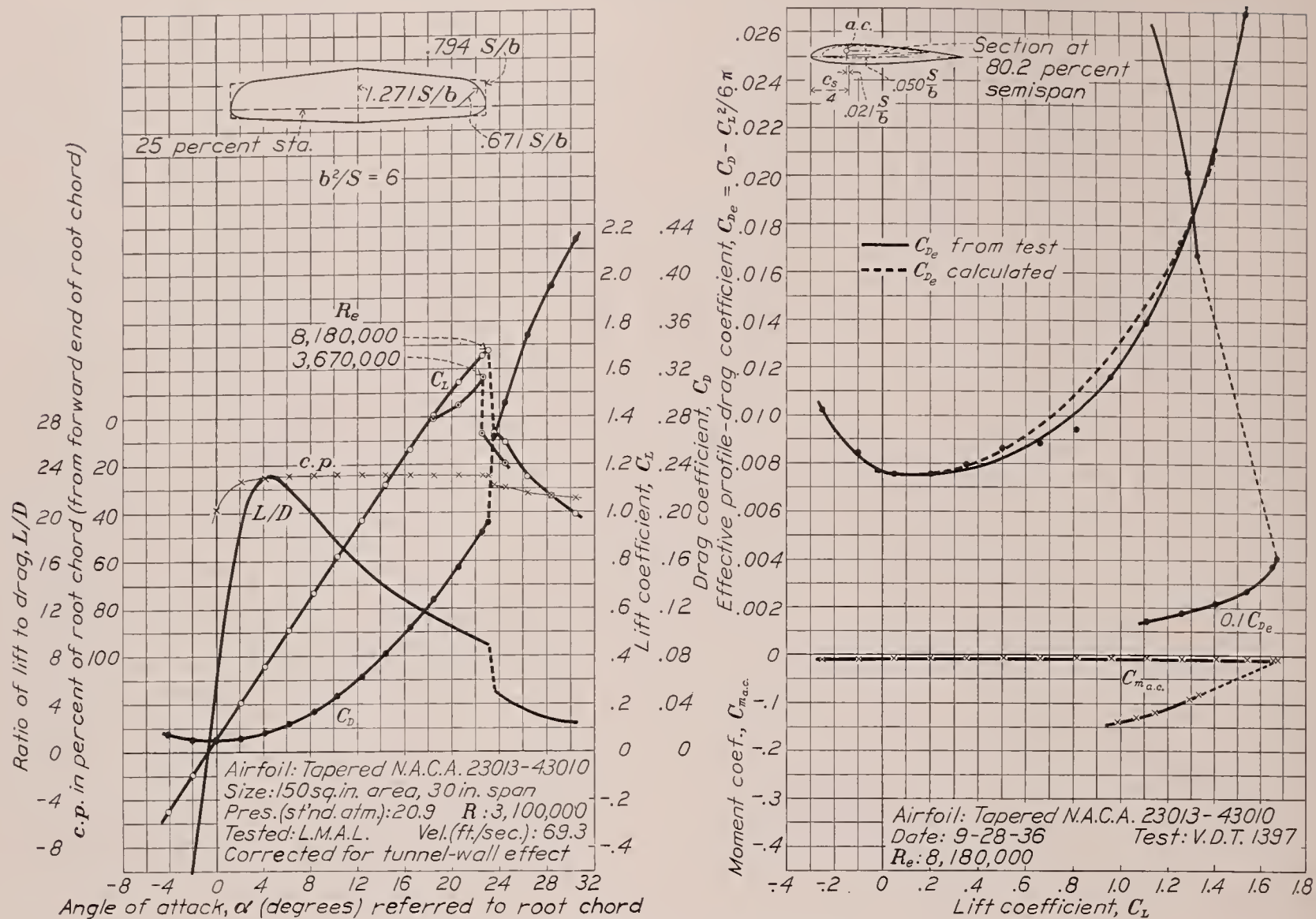


FIGURE 19.—Tapered N. A. C. A. 23013-43010 airfoil.

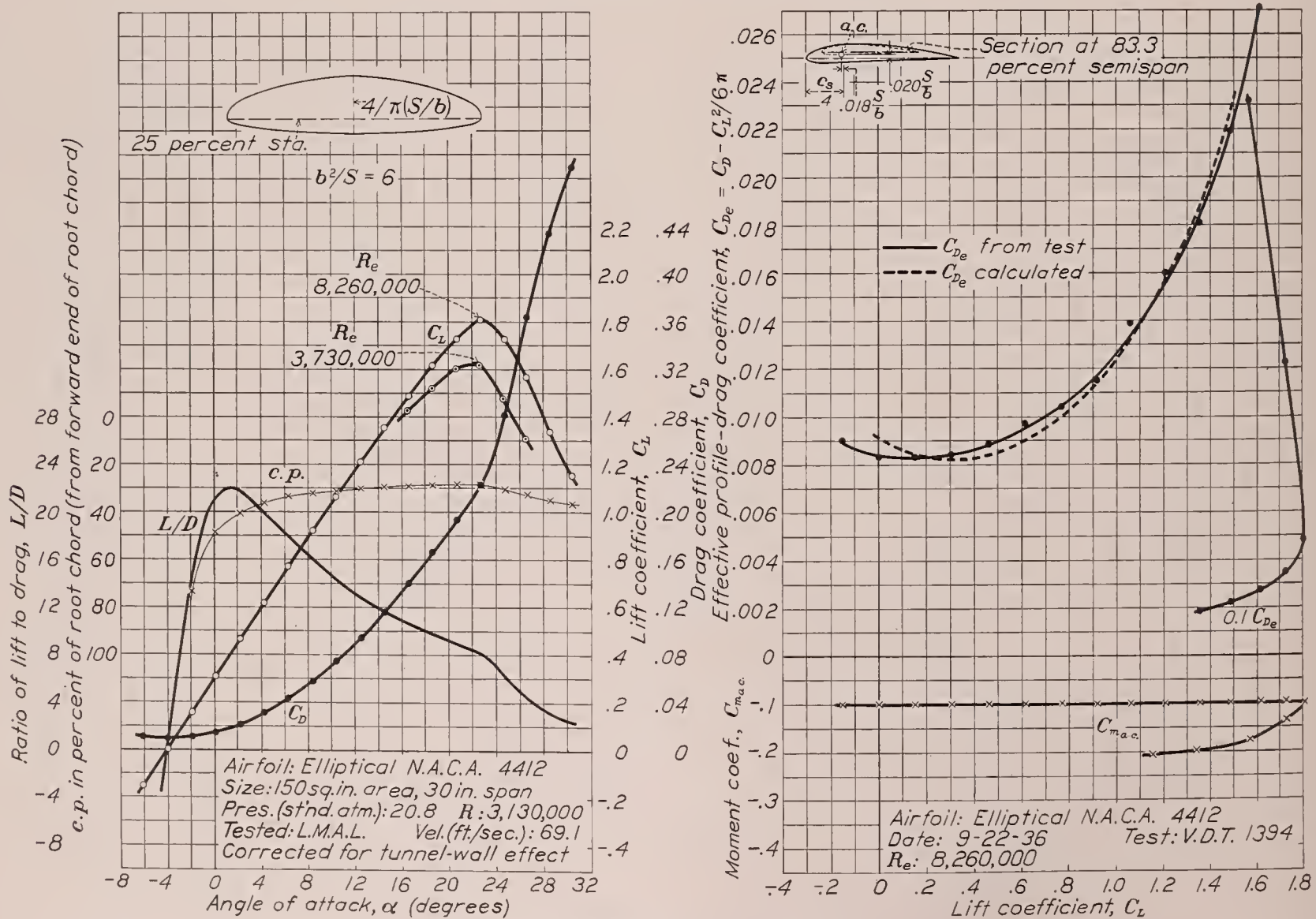


FIGURE 20.—Elliptical N. A. C. A. 4412 airfoil.

Inasmuch as the plots of lift, drag, and center of pressure against angle of attack for the first nine wings listed in table I and the plots of calculated C_{D_e} against C_L of the first two wings listed are given in reference 1, these data have been omitted from this report.

CALCULATED RESULTS

The general method of obtaining the calculated results is fully outlined in reference 1. The formulas are summarized here for convenience:

$$C_{m_{a.c.}} = C_{m_S} + C_{m_{i_b}} \quad (1)$$

$$C_{m_S} = E c_{m_{a.c.}} \quad (c_{m_{a.c.}} \text{ constant across the span}) \quad (2)$$

$$C_{m_S} = \frac{2b}{S^2} \int_0^{b/2} c_{m_{a.c.}} c^2 dy \quad (c_{m_{a.c.}} \text{ variable across span or nonlinear chord distribution}) \quad (3)$$

$$\frac{x_{a.c.}}{S/b} = HA \tan \Lambda \quad (4)$$

$$\alpha_{s(L=0)} = \alpha_{i_{0s}} + J\epsilon \quad (5)$$

$$a = f \frac{a_0}{1 + \frac{57.3a_0}{\pi A}} \quad (6)$$

The calculation of $C_{m_{a.c.}}$ for the first nine wings of table I has already been described (reference 1). For the remaining wings, $C_{m_{i_b}} = 0$ and, for those of straight taper, C_{m_S} was then calculated from the average of the root and tip section values of $c_{m_{a.c.}}$ and the factor E . For the wings with standard Army plan form for which E was not given in reference 1 and for the tapered N. A. C. A. 23013-43010 wing, where $c_{m_{a.c.}}$ varied appreciably across the span, C_{m_S} was calculated from equation (3). The results are given in table I.

The aerodynamic-center positions of the wings as calculated in reference 1 were based on a wing axis through the quarter-chord points of the airfoil sections, which is the section aerodynamic center according to thin-airfoil theory. A refinement consists in using as the wing axis a line through the experimental aerodynamic-center positions of the root and tip sections. The angle of sweepback is thereby slightly changed but the same value of H in equation (4) may still be used. Calculations using both angles of sweepback have been made (table I). Both aerodynamic-center positions have been referred to the quarter-chord point of the root chord for comparison.

In the computation of values of the lift-curve slope a , from equation (6), values of a_0 corrected to section data were used. For the 230 series of wings, the average value of a_0 was 0.098 per degree.

The effective profile-drag coefficient was calculated from the sum of the profile and induced-drag coefficients with the minimum induced-drag coefficient deducted:

$$C_{D_e} = C_{D_0} + C_{D_i} - \frac{C_L^2}{\pi A} \quad (7)$$

where

$$C_{D_0} = \frac{2}{S} \int_0^{b/2} c_{d_0} c dy$$

In order to show how C_{D_0} was calculated and to aid in making similar calculations, the method has been illustrated for the N. A. C. A. 5-10-18 wing. The calculations are listed in table IV and were obtained as follows:

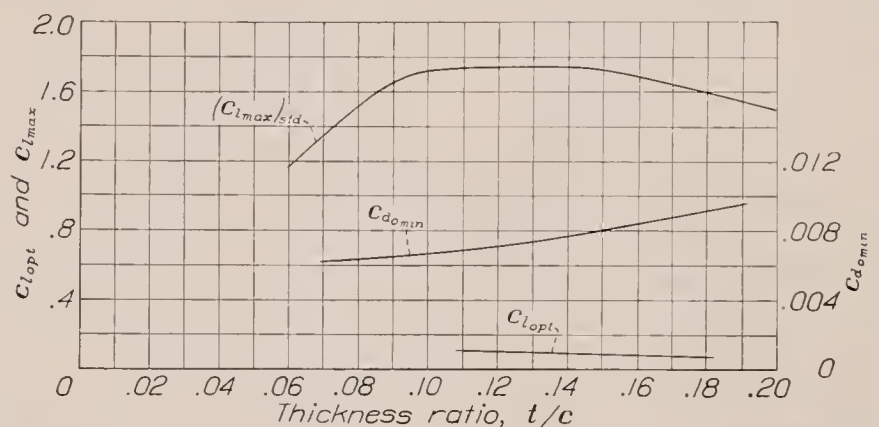


FIGURE 21.—Variation of section data with thickness. The N. A. C. A. 230 series airfoils; effective Reynolds Number, 8,200,000.

Column 1. Convenient intervals of the semispan.

Column 2. Maximum thickness of the airfoil sections at these intervals.

Column 3. Chord length.

Column 4. Effective Reynolds Number of each section along the semispan $\left(R_e = \frac{c}{S/b} 6,630,000\right)$. In the case

of an airplane wing the Reynolds Numbers should correspond to the particular value of C_L .

Column 5. Airfoil section maximum lift coefficient for an effective Reynolds Number of 8,200,000 as given in N. A. C. A. reports of airfoil section data. (For the method of deriving section data see reference 5, p. 17.) The value of $(c_{l_{max}})_{std}$ for the various sections along the span may be conveniently determined from a plot such as figure 21.

Column 6. Correction increment to correct the section maximum lift coefficient to the actual Reynolds Number of each section along the semispan (fig. 22). Figure 22 is figure 44 of reference 5 reproduced here for convenience.

Column 7. The maximum lift coefficient of each section along the semispan, $c_{l_{max}} = (c_{l_{max}})_{std} + \Delta c_{l_{max}}$.

Column 8. Values of minimum profile-drag coefficient for an effective Reynolds Number of 8,200,000, corrected to section data. (See reference 5.) The value of $(c_{d_0_{min}})_{std}$ may be conveniently obtained by making a plot against thickness ratio, such as figure 21.

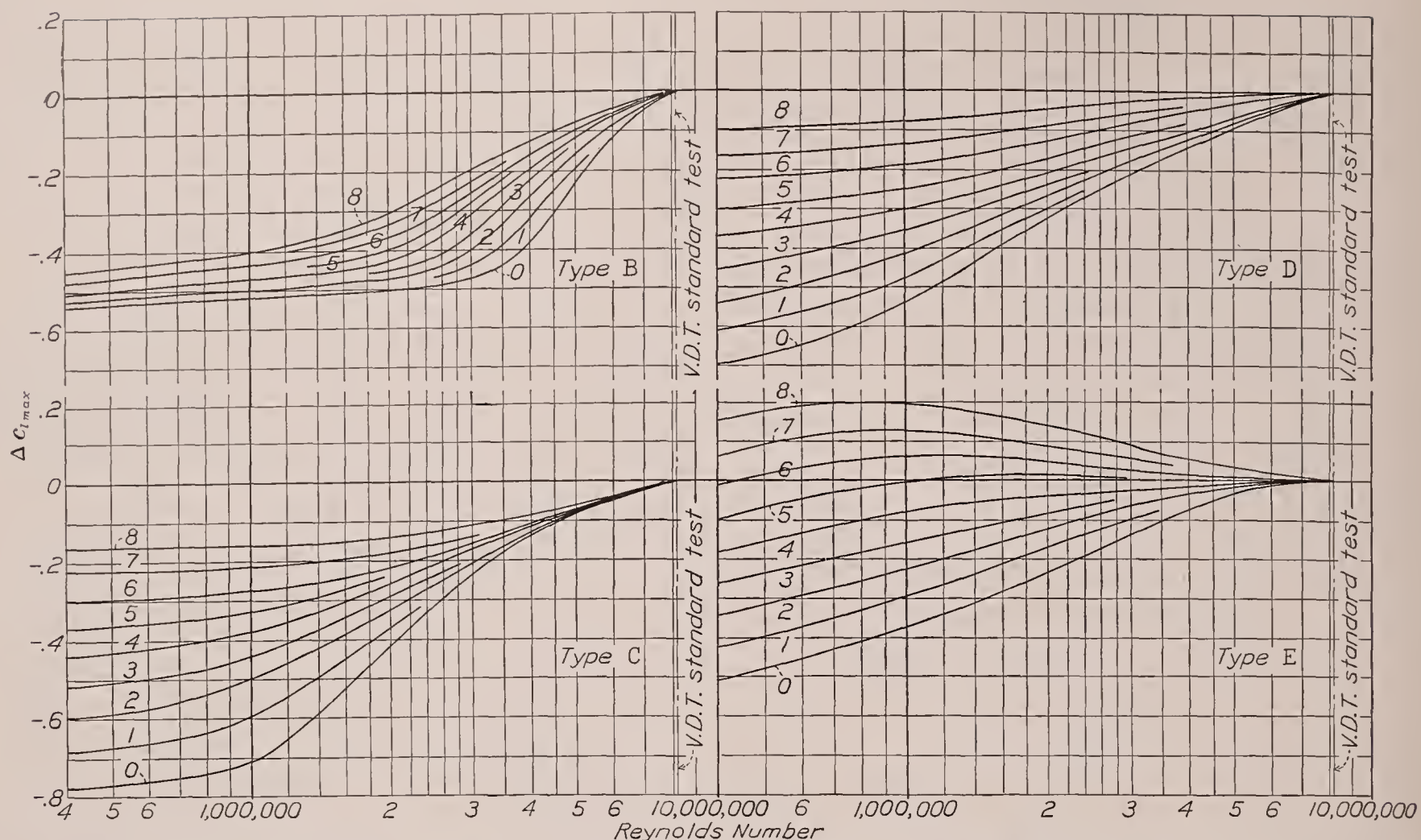


FIGURE 22.—Scale-effect corrections for $c_{l_{max}}$. In order to obtain the section maximum lift coefficient at the desired Reynolds Number, apply to the standard-test value the increment indicated by the curve that corresponds to the scale-effect designation (types B, C, D, or E) of the airfoil. (See reference 5, p. 32, and table II.)

Column 9. Values of the minimum profile-drag coefficient corrected to the Reynolds Number of each section along the semispan by use of figure 23. The basis of the correction formula is explained in reference 5. The line is plotted to provide a convenient graphi-

the Reynolds Number in question to read the corresponding $c_{d_{0_{min}}}$. Although extrapolation by this method to Reynolds Numbers below 6,000,000 is not strictly accurate, the extrapolation has been made to 2,600,000

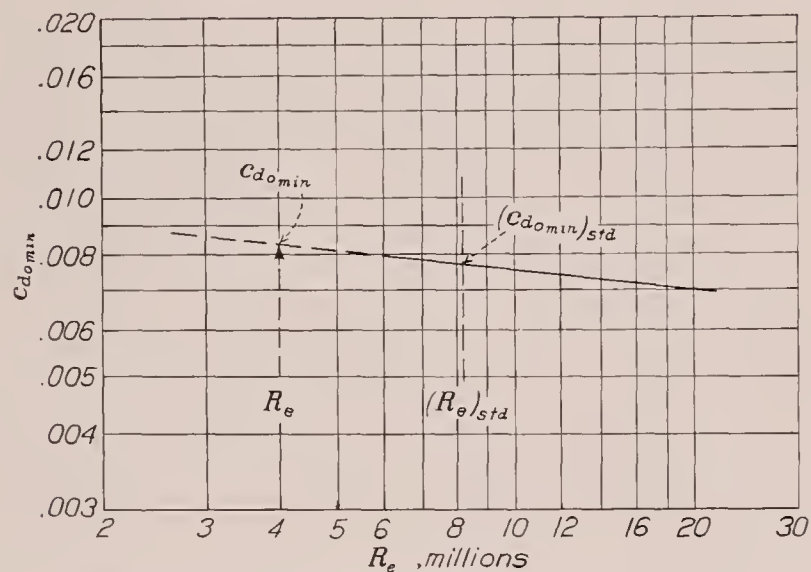


FIGURE 23.—Graph for estimating variation of $c_{d_{0_{min}}}$ with R_e .

$$c_{d_{0_{min}}} = (c_{d_{0_{min}}})_{std} \left(\frac{(R_e)_{std}}{R_e} \right)^{0.11}$$

cal solution of the formula. The standard effective Reynolds Number of variable-density-tunnel tests is $(R_e)_{std}$. To find $c_{d_{0_{min}}}$ for any other Reynolds Number, locate the point for $(c_{d_{0_{min}}})_{std}$ from tests in the variable-density tunnel and travel parallel to the line to

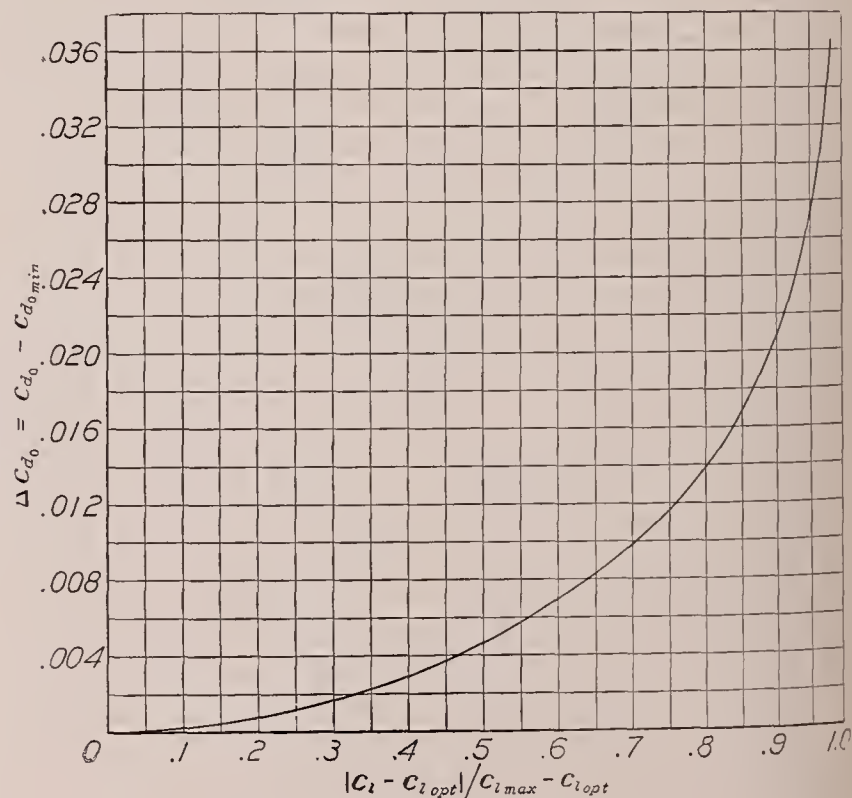


FIGURE 24.—Generalized variation of Δc_{d_0} .

for the tip sections of some of the 230 wings, as the tips contribute only a small part of the drag. The agreement of the calculated and experimental results indicates that no appreciable error was introduced.

Column 10. $c_{l_{opt}}$ is given in the tables of basic airfoil section data of N. A. C. A. reports and may be determined from a plot against thickness ratio, as in figure 21.

Column 11. $c_{l_{max}} - c_{l_{opt}}$.

Column 12. L_a is the additional load distribution parameter obtained from the tables in reference 1 for the appropriate aspect ratio and taper ratio.

Column 13. Section additional lift coefficient for a wing C_L of 1; $c_{l_{a1}} = \frac{S}{c_b} L_a$.

From the foregoing basic data, the profile drag of each section along the span may now be calculated for a given wing lift coefficient. For an airplane, this lift coefficient would be the one corresponding to the speed and Reynolds Number originally assumed. The cal-

The value of C_{D_0} for the wing is obtained from the area under the curve, as indicated.

The value of C_{D_i} for formula (7) was calculated from reference 1, except for the wings with standard Army plan form. For these wings the C_{D_i} and also the c_i distribution were calculated by the Lotz method. (See reference 6.)

The data given in table IV were also used for the calculation of $C_{L_{max}}$ by the method given in reference 1. The calculation is repeated here to complete the example and to give a quick method of estimating the wing maximum lift coefficient.

The maximum lift coefficients of the sections and the c_i distribution for $C_L = 1.0$ are plotted as in figure 26. Stalling is considered to begin at the C_L at which c_i reaches $c_{l_{max}}$ at any point along the span. The tangent

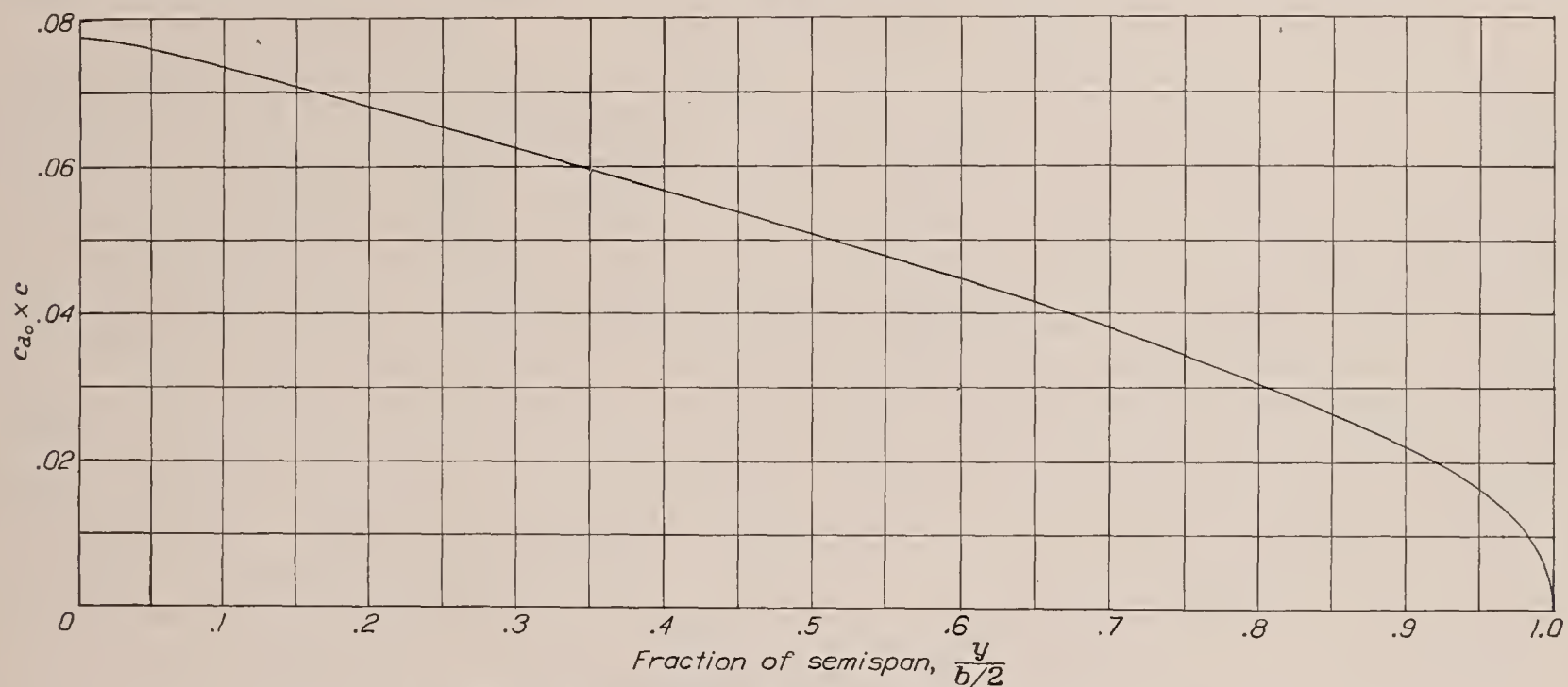


FIGURE 25.—Calculation of C_{D_0} of the N. A. C. A. 5-10-18 wing; $C_L = 0.8$.

$$C_{D_0} = \frac{2}{S} \int_0^{b/2} c_{d_0} c dy = \frac{b}{S} \int_0^1 c_{d_0} c d\left(\frac{y}{b/2}\right) = \frac{38.73}{150} [(\text{area}) (0.02) (0.1)] = 0.0127$$

culations are given in columns 14 to 19 for a C_L of 0.8 as follows:

Column 14. $c_i = C_L \times c_{l_{a1}} = 0.8 c_{l_{a1}}$. (See reference 1 for method for a twisted wing.)

Column 15. $c_i - c_{l_{opt}}$.

Column 16. $|c_i - c_{l_{opt}}| / (c_{l_{max}} - c_{l_{opt}})$.

Column 17. The increment Δc_{d_0} by which c_{d_0} is increased as the lift coefficient departs from the optimum. The generalized increase for any airfoil section is obtained from figure 24. This curve was obtained from tests of airfoils of moderate camber and thickness at an effective Reynolds Number of 8,000,000 and may be applied with reasonable accuracy down to an effective Reynolds Number of 2,000,000. (See reference 5 for discussion.)

Column 18. c_{d_0} corresponding to each value of c_i along the span is $c_{d_{0_{min}}} + \Delta c_{d_0}$.

Column 19. Values of $c_{d_0} \times c$ are plotted in figure 25.

curve of c_i and the corresponding C_L are most conveniently found from the minimum value of $c_{l_{max}}/c_{l_{a1}}$ along the span, as shown. Thus, the minimum value is 1.50, which is considered to be $C_{L_{max}}$ for the wing. The measured value is 1.49. Part of the c_i curve for $C_L = 1.50$ has been drawn in to show more clearly the location of the predicted stalling point. For a wing with twist, the ratio method may be used by finding the minimum value of $(c_{l_{max}} - c_{l_b})/c_{l_{a1}}$.

The calculated and experimental values of $C_{L_{max}}$ are not always in good agreement. In the case of the elliptical N. A. C. A. 4412 wing the values of $c_{l_{max}}$ of the sections decrease at the tips due to the decrease in Reynolds Number and, as c_i is constant across the span, stalling would be predicted practically at the tips at a low value of $C_{L_{max}}$. The flow near the tips is modified by the tip vortex, however, so that it is no longer two-dimensional and the method does not apply. If it were assumed that stalling begins at an arbitrary

distance in from the tip equal to the chord, the predicted $C_{L_{max}}$ would be 1.74. The $C_{L_{max}}$ actually measured was 1.81, which is surprisingly high, especially as the root section $c_{l_{max}}$ is only 1.77.

For a conventional airplane in flight it is not likely that the computed $C_{L_{max}}$ would be exceeded if stalling began near the tips because of a loss of lateral control. The tapered N. A. C. A. 23013-43010 wing (fig. 19) is an example of a wing designed to avoid tip stalling. In order to cause stalling at the center, a combination of moderate taper, washout, and progression to sections

M6, and the Clark Y wings and best for the wings of high aspect ratio and taper ratio and for the elliptical wing. The experimental and calculated values of $C_{L_{max}}$ are also in good agreement except for the wings with large sweepback or large twist.

Reference to the experimental and calculated C_{D_e} curves of figures 2 to 4 shows that the agreement of the C_{D_e} curves is not so good for the wings with large sweepback and large twist as for the wings with moderate or no sweepback and twist. This result would be expected, however, as the similarity of the flow conditions

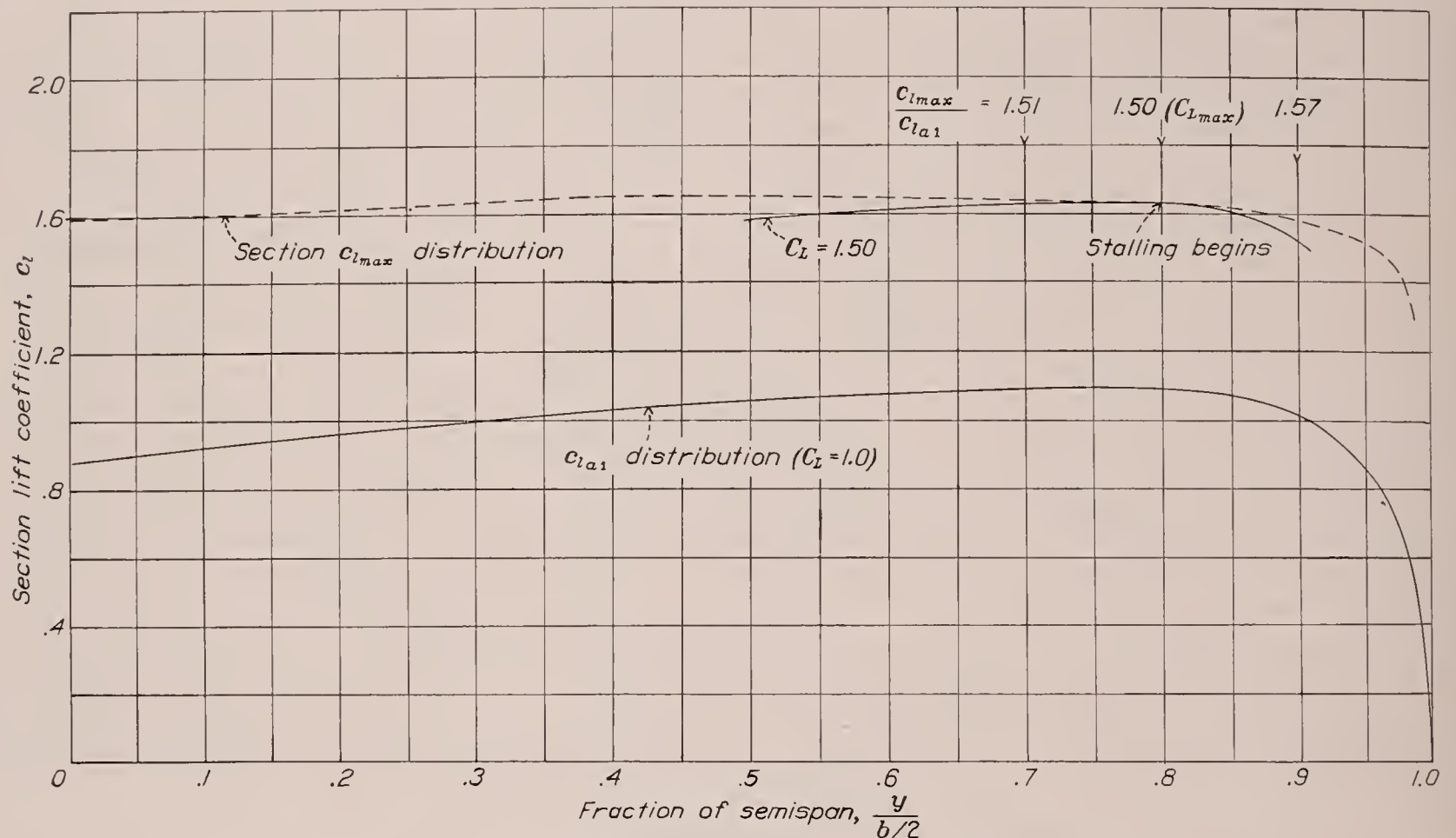


FIGURE 26.—Calculation of the C_L at which the N. A. C. A. 5-10-18 wing begins to stall.

having increasing $c_{l_{max}}$ (increased camber) toward the tips was used.

DISCUSSION

COMPARISON OF EXPERIMENTAL AND CALCULATED VALUES

The experimental and calculated values compared in table I are, in general, in satisfactory agreement. The values of $C_{m_{a.c.}}$ are usually in agreement within the experimental error of the tests. Of the two computed values of aerodynamic-center position, better agreement is obtained by considering the lift to act at the experimental aerodynamic-center position of the sections, except for the wings with sweepback and twist. It may be concluded that for most airplane wings, which usually have little or no sweepback, it is best to calculate the wing aerodynamic-center position on the basis of the experimental section aerodynamic centers.

The angle of zero lift and the lift-curve slope need little comment except to note that for the lift-curve slope the agreement of calculated and experimental values is poorest for the N. A. C. A. 2218-09, the N. A. C. A.—

assumed in the calculation to the actual flow becomes less as the sweepback and twist are increased.

When the C_{D_e} curves are compared, the large scale to which they are plotted should be considered, as this factor accentuates the differences. Most of the differences do not exceed the experimental error of drag measurements, which may be as much as $C_D=0.0006$ for $C_L=0$ and may increase to 0.0015 for $C_L=1.0$.

Of the wings with standard Army plan form (figs. 8 to 12) only the N. A. C. A.—M6 and the Clark Y fail to show excellent agreement of the C_{D_e} curves. For these curves the greatest difference is equal to the maximum experimental error. This difference is probably due to the lack of data for sections of various thicknesses for these wings. The agreement of the C_{D_e} curves for wings with the standard Army plan form where adequate section data are available (N. A. C. A. 2218-09, 23015-09, and 23018-09 wings) is of interest because a belief has been expressed that the abrupt change in plan form at the ends of the straight center section might cause an increase in drag.

For the five wings of high aspect ratio and taper ratio (figs. 13 to 17) the C_{D_e} curves agree, in general, within the experimental error of the tests. The C_{D_e} curves for the N. A. C. A. 0018-0009, the tapered N. A. C. A. 23013-43010, and the elliptical N. A. C. A. 4412 wings (figs. 18 to 20) also show reasonably good agreement, except for a difference in the $C_{L_{opt}}$ values for the elliptical N. A. C. A. 4412 wing. It is interesting to note that for the elliptical N. A. C. A. 4412 wing there is no residual induced drag and therefore C_{D_e} is C_{D_0} for the wing.

From the C_{D_e} curves, the minimum values of C_{D_e} and the corresponding values of C_L , i. e., $C_{L_{opt}}$, are listed in table I. These values are useful for comparing the drag and lift coefficients in the high-speed region.

EFFICIENCY FACTOR

The C_{D_e} curves were analyzed with a view to finding an efficiency factor corresponding to the airplane efficiency factor used in reference 7. Incorporation of this factor in the induced-drag term permits the determination of a nearly constant drag residual over the working range of lift coefficients amounting to $C_D - \frac{C_L^2}{\pi A e}$,

which in terms of C_{D_e} is $C_{D_e} - \frac{C_L^2}{\pi A} \left(\frac{1}{e} - 1 \right)$.

Values of e were determined from the plots of C_{D_e} against C_L by using curves of $\frac{C_L^2}{\pi A} \left(\frac{1}{e} - 1 \right)$ against C_L for various values of e . The value of e was then found from the superimposed curve of $\frac{C_L^2}{\pi A} \left(\frac{1}{e} - 1 \right)$ that best fitted the C_{D_e} curve. The curves were made to fit as well as possible for a C_L range of 0.2 to 1.0. The values of e are given in table I. As an example of how the

efficiency-factor curves fit the test or calculated curves, an efficiency-factor curve has been plotted in figure 10 for comparison with the test curve. This curve is typical for the wings and shows how the efficiency-factor curve departs from the C_{D_e} curves below $C_L=0.2$ to 0.4 and above $C_L=1.0$. Reference to table I shows that the N. A. C. A. 24-30-8.50 and 2R₁-15-8.50 wings, which have the largest $C_{L_{opt}}$, have values of e equal to and larger than e , respectively, for the elliptical N. A. C. A. 4412 wing. This result is obtained because shifting the C_{D_e} curve to the right makes it fit a flatter e curve, and hence one with a higher value of e . If $C_{L_{opt}}$ had been zero for all the wings and they had differed only in plan form, the values of e would indicate the departure of the drag of the wings from that of the ideal elliptical wing. The wings, in fact, are sufficiently similar and the variations of the C_{D_0} values with lift are near enough alike so that there is a general reduction of e as the wings depart from the elliptical plan form toward the wings of high taper.

CONCLUSION

From the foregoing comparison of calculated and test results it may be concluded that the usual characteristics of conventional tapered wings, as determined by wind-tunnel tests, may be calculated with accuracy sufficient for use in many airplane design problems. The method of calculation should be of value for reducing wind-tunnel testing and for selecting the best wing for a given airplane design.

LANGLEY MEMORIAL AERONAUTICAL LABORATORY,
NATIONAL ADVISORY COMMITTEE FOR AERONAUTICS,
LANGLEY FIELD, VA., November 17, 1937.

APPENDIX

CALCULATION OF THE AERODYNAMIC-CENTER POSITION FROM EXPERIMENTAL DATA

The aerodynamic-center position of the wings and the value of $C_{m_{a.c.}}$ were determined from the test data by the following method. The forces acting at the axis about which the pitching moment is measured may be considered to be the normal and the chord forces and the pitching moment. The forces are represented as coefficients in figure 27.

For most airfoils there is some axis about which the pitching-moment coefficient may be considered constant for lift coefficients practically to $C_{L_{max}}$ (aerodynamic

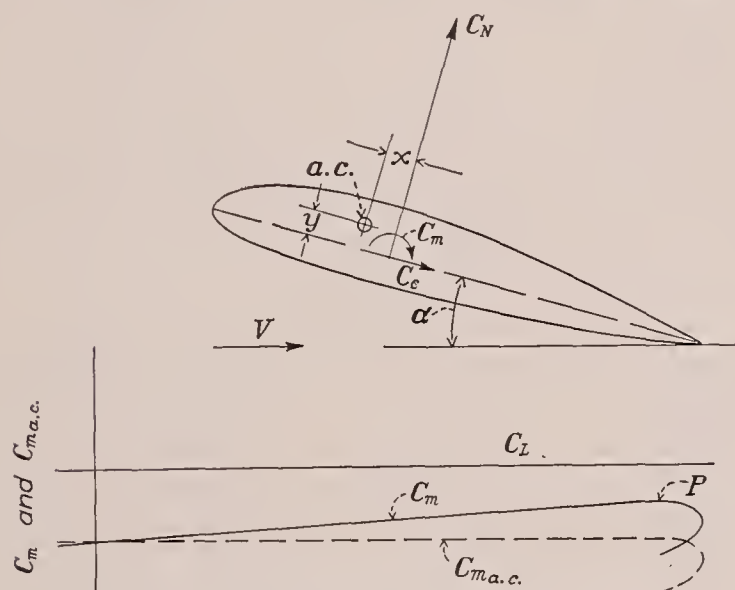


FIGURE 27.—Aerodynamic center and pitching moment.

center). The aerodynamic center is located by x and y , which are distances in terms of the mean chord S/b ,

i. e., $x = \frac{x_{a.c.}}{S/b}$. Then, if C_m is the pitching-moment coefficient about the support point, the pitching-moment coefficient about the aerodynamic center may be written:

$$C_{m_{a.c.}} = C_m - xC_N - yC_C \quad (1)$$

so that

$$C_m = C_{m_{a.c.}} + xC_N + yC_C \quad (2)$$

also

$$C_N = C_L \cos \alpha + C_D \sin \alpha \quad (3)$$

$$C_C = C_D \cos \alpha - C_L \sin \alpha \quad (4)$$

In order to find the three unknowns, $C_{m_{a.c.}}$, x , and y , the basic equation (2) may be used to write three equations corresponding to three conditions of the pitching-moment curve of the airfoil.

For the first condition, values of C_m , C_N , and C_C are taken for a point P on the pitching-moment curve before it curves greatly (fig. 27):

$$C_{m_P} = C_{m_{a.c.}} + xC_{N_P} + yC_{C_P} \quad (5)$$

The second condition is taken at $C_L = 0$:

$$C_{m_0} = C_{m_{a.c.}} + xC_{D_{L_0}} \sin \alpha_{s(L=0)} + yC_{D_{L_0}} \cos \alpha_{s(L=0)} \quad (6)$$

The third condition is taken as the slope of the pitching-moment curve at $C_L = 0$:

$$\frac{dC_m}{dC_L} = n_0 = x \left[\left(\frac{dC_D}{dC_L} \right)_0 \sin \alpha_{s(L=0)} + \left(1 + C_{D_{L_0}} \frac{d\alpha'}{dC_L} \right) \cos \alpha_{s(L=0)} \right] - y \left[\left(1 + C_{D_{L_0}} \frac{d\alpha'}{dC_L} \right) \sin \alpha_{s(L=0)} - \left(\frac{dC_D}{dC_L} \right)_0 \cos \alpha_{s(L=0)} \right] \quad (7)$$

where

α' , is angle of attack in radians.

n , slope of pitching-moment curve, $\frac{dC_m}{dC_L}$.

P , a subscript indicating values for a point near $C_{L_{max}}$.

0 and L_0 , subscripts indicating values for $C_L = 0$.

The other symbols have their usual significance.

For normal airfoils, negligible error is introduced by making the approximations

$$\sin \alpha_{s(L=0)} = \alpha_{s(L=0)}', \quad \cos \alpha_{s(L=0)} = 1, \quad 1 + C_{D_{L_0}} \frac{d\alpha'}{dC_L} = 1,$$

$$\left(\frac{dC_D}{dC_L} \right)_0 \sin \alpha_{s(L=0)} = 0, \quad \left(\frac{dC_D}{dC_L} \right)_0 \cos \alpha_{s(L=0)} = 0$$

in equations (5), (6), and (7), and the approximations

$$C_{D_{L_0}} \alpha_{s(L=0)}' = 0, \quad C_{D_{L_0}} (\alpha_{s(L=0)}')^2 = 0$$

when they are solved simultaneously. The solution gives x and y in the form.

$$x = \frac{(C_{m_0} - C_{m_P}) \alpha_{s(L=0)}' + n_0 (C_{D_{L_0}} - C_{C_P})}{C_{D_{L_0}} - C_{C_P} - C_{N_P} \alpha_{s(L=0)}'}$$

$$y = \frac{C_{m_0} - C_{m_P} + xC_{N_P}}{C_{D_{L_0}} - C_{C_P}}$$

When x and y have been found by substituting the appropriate test data, the $C_{m_{a.c.}}$ curve may be computed from

$$C_{m_{a.c.}} = C_m - xC_N - yC_C$$

The value of $C_{m_{a.c.}}$ is practically equal to C_{m_0} so that the $C_{m_{a.c.}}$ curve is as shown in figure 27.

REFERENCES

1. Anderson, Raymond F.: Determination of the Characteristics of Tapered Wings. T. R. No. 572, N. A. C. A., 1936.
2. Anderson, Raymond F.: Tests of Three Tapered Airfoils Based on the N. A. C. A. 2200, the N. A. C. A.-M6, and the Clark Y Sections. T. N. No. 487, N. A. C. A., 1934.
3. Jacobs, Eastman N., Ward, Kenneth E., and Pinkerton, Robert M.: The Characteristics of 78 Related Airfoil Sections from Tests in the Variable-Density Wind Tunnel. T. R. No. 460, N. A. C. A., 1933.
4. Jacobs, Eastman N., and Abbott, Ira H.: The N. A. C. A. Variable-Density Wind Tunnel. T. R. No. 416, N. A. C. A., 1932.
5. Jacobs, Eastman N., and Sherman, Albert: Airfoil Section Characteristics as Affected by Variations of the Reynolds Number. T. R. No. 586, N. A. C. A., 1937.
6. Pearson, H. A.: Span Load Distribution for Tapered Wings with Partial-Span Flaps. T. R. No. 585, N. A. C. A., 1937.
7. Oswald, W. Bailey: General Formulas and Charts for the Calculation of Airplane Performance. T. R. No. 408, N. A. C. A., 1932.

TABLE I
COMPARISON OF EXPERIMENTAL AND CALCULATED CHARACTERISTICS

Wing ¹	Plan form	Taper ratio	$\frac{c_t}{c_r}$	Aspect ratio	Root section ¹	Tip section ¹	Sweepback (degrees)	Aerodynamic twist (degrees)	$C_{m_{a.e.}}$		$\frac{L_{a.c.}}{S/b}$			$\alpha_z(L=0)$		a		$C_{L_{max}}$		$C_{D_{e_{min}}}$ at R_e		$C_{L_{opt}}$		e	
									Experimental	Calculated	Experimental	Calculated		Experimental	Calculated	Experimental	Calculated	Experimental	Calculated	Experimental	Calculated	Experimental	Calculated	Experimental	Calculated
												a. c. data	c/4 points												
00-0-0-----		2:1	0.50	6	0015-----	0009-----	0	0	0	0	-0.014	-0.011	0	0	0	0.075	0.074	1.53	1.54	0.0076	0.0072	0.04	0	0.89	0.88
24-0-0-----		2:1	.50	6	2415-----	2409-----	0	0	-.040	-.043	-.022	-.012	0	-1.7	-1.7	.074	.074	1.68	1.61	.0077	.0075	.14	.13	.90	.90
24-15-0-----		2:1	.50	6	2415-----	2409-----	15	0	-.043	-.043	.352	.330	.345	-1.9	-1.7	.075	.074	1.63	1.61	.0076	.0075	.19	.15	.90	.90
24-30-0-----		2:1	.50	6	2415-----	2409-----	30	0	-.042	-.043	.775	.726	.744	-1.9	-1.7	.072	.074	1.43	1.61	.0076	.0075	.16	.12	.88	.90
24-30-8.50-----		2:1	.50	6	2415-----	2409-----	30	-8.50	.002	.010	.786	.725	.744	.7	.9	.076	.074	1.51	1.56	.0084	.0095	.36	.20	.92	.91
2R ₁ -15-8.50-----		2:1	.50	6	2R ₁ 15-----	2R ₁ 09-----	15	-8.50	.003	.006	.348	.330	.345	1.2	1.1	.076	.074	1.59	1.46	.0092	.0094	.26	.19	.93	.90
2R ₂ -15-0-----		2:1	.50	6	2R ₂ 15-----	2R ₂ 09-----	15	0	.004	.004	.351	.330	.345	-.7	-.6	.078	.074	1.50	1.48	.0078	.0076	.16	.10	.89	.87
00-15-3.45-----		2:1	.50	6	0015-----	0009-----	15	-3.45	.007	.010	.346	.331	.345	1.0	1.1	.076	.074	1.48	1.55	.0081	.0076	.06	0	.90	.88
00-15-3.45 (4:1)-----		4:1	.25	6	0015-----	0009-----	15	-3.45	.005	-----	.334	.330	.327	.7	.5	.076	.075	1.32	1.38	.0082	.0078	.10	0	.90	.86
2218-09-----		2:1	.50	6	2218-----	2209-----	0	0	-.029	-.029	-.028	-.015	0	-1.8	-1.8	.071	.075	1.60	1.61	.0088	.0085	.15	.13	.91	.90
M6-----		2:1	.50	6	M6 (M-18)---	M6 (M-9)---	0	0	-.006	.002	-.017	-.015	0	-1.1	-.7	.070	.074	1.49	1.45	.0084	.0090	.18	.05	.90	.86
Clark Y-----		2:1	.50	6	Clark Y M-18.	Clark Y M-9--	0	0	-.071	-.071	-.020	-.016	0	-5.2	-5.1	.071	.074	1.67	1.61	.0091	.0095	.22	.11	.91	.89
23015-09-----		2:1	.50	6	23015-----	23009-----	0	0	-.007	-.007	-.014	-.012	0	-1.3	-1.1	.074	.076	1.71	1.70	.0079	.0076	.17	.11	.91	.91
23018-09-----		2:1	.50	6	23018-----	23009-----	0	0	-.007	-.005	-.020	-.015	0	-1.3	-1.1	.073	.075	1.66	1.63	.0085	.0084	.11	.11	.90	.89
3-10-18-----		3:1	.33	10	23018-----	23009-----	0	0	-.011	-.006	-.013	-.017	0	-1.2	-1.1	.083	.083	1.51	1.59	.0083	.0085	.04	.08	.80	.82
5-10-16-----		5:1	.20	10	23016-----	23009-----	0	0	-.009	-.007	-.011	-.016	0	-1.2	-1.1	.083	.083	1.50	1.49	.0080	.0081	.03	.10	.78	.82
5-10-18-----		5:1	.20	10	23018-----	23009-----	0	0	-.011	-.006	-.013	-.018	0	-1.2	-1.1	.083	.083	1.49	1.50	.0086	.0087	.05	.08	.81	.81
5-12-16-----		5:1	.20	12	23016-----	23009-----	0	0	-.014	-.007	-.016	-.016	0	-1.2	-1.1	.086	.085	1.46	1.49	.0079	.0081	.02	.10	.76	.79
5-12-20-----		5:1	.20	12	23020-----	23009-----	0	0	-.007	-.005	-.010	-.022	0	-1.2	-1.1	.084	.084	1.42	1.48	.0084	.0093	0	.08	.74	.76
0018-09-----		2:1	.50	6	0018-----	0009-----	0	0	0	0	-.020	-.016	0	-----	-----	.074	.074	1.48	1.52	.0082	.0080	0	0	.90	.87
23013-43010-----		1.6:1	.625	6	23013-----	43010-----	0	-2	-.009	-.011	-----	-.011	0	-.7	-.5	.074	.076	1.67	1.67	.0074	.0074	-----	-----	-----	-----
Elliptical 4412-----		-----	-----	6	4412-----	4412-----	0	0	-.100	-.095	-.018	-.010	0	-4.0	-4.0	.074	.075	1.81	-----	.0083	.0082	.15	.33	.92	.93

¹ All N. A. C. A. sections except the Clark Y.

ORDINATES OF N. A. C. A. 23015-09 TAPERED AIRFOIL IN PERCENT OF CHORD

ORDINATES OF N. A. C. A. 23018-09 TAPERED AIRFOIL IN PERCENT OF CHORD

ORDINATES OF N. A. C. A. 23018-09 TAPERED AIRFOIL IN PERCENT OF CHORD

Slope of radius through end of chord 0.305

TABLE II—Continued

[illegible]

ORDINATES OF N. A. C. A. 5-10-16 TAPERED AIRFOIL IN PERCENT OF CHORD

[illegible]

ORDINATES OF N. A. C. A. 5-10-18 TAPERED AIRFOIL IN PERCENT OF CHORD

ORDINATES OF N. A. C. A. 5-12-16 TAPERED AIRFOIL IN PERCENT OF CHORD[illegible]

ORDINATES OF N. A. C. A. 5-12-20 TAPERED AIRFOIL IN PERCENT OF CHORD

[illegible]

TABLE III

ORDINATES OF N. A. C. A. CENTER-STALLING WING

DATA ON SECTIONS										ORDINATES—Continued							
[Total geometric washout, 3.2°; total aerodynamic washout, 2° at construction tip]										Section 4				Section 5			
Section	Root	1	2	3	4	5	6	7	8	Upper surface		Lower surface		Upper surface		Lower surface	
Position, fraction semispan--	0	0.200	0.400	0.600	0.802	0.853	0.900	0.940	0.973	Station	Ordinate	Station	Ordinate	Station	Ordinate	Station	Ordinate
Geometric washout, degrees----	0	.37	.89	1.47	2.24	2.47	2.70	2.91	3.02	0	0	0	0	0	0	0	0
										.54	2.17	1.96	-.95	.53	2.15	1.97	-.88
										1.63	3.34	3.37	-1.06	1.62	3.33	3.38	-.96
										4.13	5.08	5.87	-1.11	4.12	5.09	5.88	-.97
										6.81	6.30	8.19	-1.17	6.80	6.32	8.20	-1.00
										9.55	7.13	10.45	-1.29	9.54	7.16	10.46	-1.10
										15.00	7.99	15.00	-1.67	15.00	8.02	15.00	-1.46
										20.20	8.22	19.80	-2.15	20.20	8.24	19.80	-1.94
										25.20	8.21	24.80	-2.52	25.21	8.22	24.79	-2.31
										30.21	8.08	29.79	-2.77	30.21	8.08	29.79	-2.57
										40.20	7.52	39.80	-2.97	40.20	7.51	39.80	-2.78
										50.18	6.68	49.82	-2.89	50.18	6.66	49.82	-2.72
										60.16	5.64	59.84	-2.60	60.16	5.62	59.84	-2.47
										70.13	4.45	69.87	-2.17	70.13	4.43	69.87	-2.07
										80.09	3.13	79.91	-1.61	80.09	3.11	79.91	-1.54
										90.05	1.69	89.95	-.93	90.05	1.68	89.95	-.89
										95.03	.92	94.97	-.54	95.03	.91	94.97	-.52
										100.00	.11	100.00	-.11	100.00	.11	100.00	-.11
L. E. radius----- 1.295 on 0.524 slope										L. E. radius----- 1.248 on 0.544 slope							
ORDINATES																	
[Percent of chord]																	
Root section				Section 1													
Upper surface		Lower surface		Upper surface		Lower surface											
Station	Ordinate	Station	Ordinate	Station	Ordinate	Station	Ordinate	Station	Ordinate	Station	Ordinate	Station	Ordinate	Station	Ordinate	Station	Ordinate
0	0	0	0	0	0	0	0	0	0	0	0	0	0	0	0	0	0
.72	2.34	1.78	-1.63	.68	2.31	1.82	-1.50										
1.87	3.43	3.13	-2.10	1.81	3.41	3.19	-1.90										
4.38	4.96	5.62	-2.64	4.32	4.98	5.68	-2.35										
7.01	6.02	7.99	-3.03	6.96	6.07	8.04	-2.68										
9.69	6.76	10.31	-3.36	9.66	6.83	10.34	-2.97										
15.00	7.63	15.00	-3.95	15.00	7.70	15.00	-3.52										
20.14	7.98	19.86	-4.45	20.15	8.02	19.85	-4.01										
25.14	8.09	24.86	-4.78	25.16	8.11	24.84	-4.35										
30.14	8.05	29.86	-4.95	30.16	8.05	29.84	-4.54										
40.14	7.61	39.86	-4.96	40.15	7.59	39.85	-4.58										
50.13	6.84	49.87	-4.63	50.14	6.81	49.86	-4.30										
60.11	5.83	59.89	-4.06	60.12	5.79	59.88	-3.78										
70.09	4.63	69.91	-3.30	70.10	4.60	69.90	-3.09										
80.06	3.28	79.94	-2.40	80.07	3.25	79.93	-2.25										
90.04	1.79	89.96	-1.35	90.04	1.77	89.96	-1.27										
95.02	.98	94.98	-.76	95.02	.97	94.98	-.72										
100.00	.14	100.00	-.14	100.00	.13	100.00	-.13										
L. E. radius----- 1.859 on 0.305 slope				L. E. radius-----1.744 on 0.346 slope													
Section 2				Section 3													
Upper surface		Lower surface		Upper surface		Lower surface											
Station	Ordinate	Station	Ordinate	Station	Ordinate	Station	Ordinate	Station	Ordinate	Station	Ordinate	Station	Ordinate	Station	Ordinate	Station	Ordinate
0	0	0	0	0	0	0	0	0	0	0	0	0	0	0	0	0	0
.63	2.27	1.87	-1.35	.58	2.22	1.92	-1.17										
1.75	3.39	3.25	-1.67	1.69	3.37	3.31	-1.40										
4.26	5.01	5.74	-2.01	4.19	5.04	5.81	-1.61										
6.92	6.13	8.08	-2.27	6.86	6.21	8.14	-1.78										
9.62	6.91	10.38	-2.51	9.59	7.02	10.41	-1.97										
15.00	7.77	15.00	-3.01	15.00	7.88	15.00	-2.42										
20.16	8.07	19.84	-3.50	20.18	8.15	19.82	-2.90										
25.17	8.14	24.83	-3.85	25.19	8.18	24.81	-3.26										
30.17	8.06	29.83	-4.06	30.19	8.07	29.81	-3.48										
40.17	7.57	39.83	-4.14	40.18	7.55	39.82	-3.62										
50.15	6.77	49.85	-3.91	50.17	6.74	49.83	-3.46										
60.13	5.75	59.87	-3.46	60.14	5.71	59.86	-3.08										
70.11	4.55	69.89	-2.84	70.12	4.51	69.88	-2.54										
80.08	3.22	79.92	-2.07	80.08	3.18	79.92	-1.87										
90.04	1.75	89.96	-1.17	90.05	1.72	89.95	-1.07										
95.02	.96	94.98	-.67	95.02	.94	94.98	-.61										
100.00	.13	100.00	-.13	100.00	.12	100.00	-.12										
L. E. radius----- 1.613 on 0.395 slope				L. E. radius----- 1.470 on 0.453 slope													
Section 4								Section 5									
Upper surface				Lower surface				Upper surface				Lower surface					
Station	Ordinate	Station	Ordinate	Station	Ordinate	Station	Ordinate	Station	Ordinate	Station	Ordinate	Station	Ordinate	Station	Ordinate	Station	Ordinate
0	0	0	0	0	0	0	0	0	0	0	0	0	0	0	0	0	0
.51	2.12	1.99	-.73	.51	2.12	1.99	-.73										
1.59	3.32	3.41	-.72	1.59	3.32	3.41	-.72										
4.08	5.13	5.92	-.60	4.08	5.13	5.92	-.60										
6.77	6.40	8.23	-.56	6.77	6.40	8.23	-.56										
9.52	7.26	10.48	-.61	9.52	7.26	10.48	-.61										
15.00	8.13	15.00	-.93	15.00	8.13	15.00	-.93										
20.21	8.31	19.79	-1.40	20.21	8.31	19.79	-1.40										
25.22	8.27	24.78	-1.78	25.22	8.27	24.78	-1.78										
30.22	8.10	29.78	-2.05	30.22	8.10	29.78	-2.05										
40.21	7.50	39.79	-2.32	40.21	7.50	39.79	-2.32										
50.19	6.64	49.81	-2.32	50.19	6.64	49.81	-2.32										
60.17	5.59	59.83	-2.13	60.17	5.59	59.83	-2.13										
70.13	4.40	69.87	-1.80	70.13	4.40	69.87	-1.80										
80.10	3.08	79.90	-1.35	80.10	3.08	79.90	-1.35										
90.05	1.66	89.95	-.79	90.05	1.66	89.95	-.79										
95.03	.90	94.97	-.47	95.03	.90	94.97	-.47										
100.00	.11	100.00	-.11	100.00	.11	100.00	-.11										
L. E. radius----- 1.135 on 0.597 slope																	

TABLE IV
CALCULATION OF C_{D_0}

[N. A. C. A. 5-10-18 wing. R_e (based on $\frac{S}{b}$) = 6,630,000]

1	2	3	4	5	6	7	8	9	10	11
Fraction semispan, $\frac{y}{b/2}$	Thickness $\frac{t}{c}$ Chord	Chord length, c (inches)	R_e (millions)	$(c_{l_{max}})_{std}$ ($R_e=8,200,000$)	$\Delta c_{l_{max}}$	$c_{l_{max}}$	$(c_{d_0_{min}})_{std}$ ($R_e=8,200,000$)	$c_{d_0_{min}}$	$c_{l_{apt}}$	$c_{l_{max}}-c_{l_{apt}}$
0	0.180	6.48	11.10	1.59	0	1.59	0.0091	0.0088	0.08	1.51
.2	.176	5.44	9.30	1.61	0	1.61	.0089	.0088	.08	1.53
.4	.170	4.40	7.53	1.65	0	1.65	.0087	.0088	.08	1.57
.6	.160	3.37	5.76	1.69	-.05	1.64	.0084	.0087	.09	1.55
.8	.140	2.33	3.98	1.75	-.12	1.63	.0077	.0083	.10	1.53
.9	.122	1.82	3.11	1.75	-.17	1.58	.0071	.0079	.10	1.48
.95	.109	1.56	2.66	1.74	-.22	1.52	.0068	.0077	.11	1.41

1	12	13	14	15	16	17	18	19
Fraction semispan, $\frac{y}{b/2}$	L_a	$\frac{S}{cb} L_a = c_{l_{a1}}$	$0.8 \times c_{l_{a1}} = c_l$	$c_l - c_{l_{apt}}$	$\frac{ c_l - c_{l_{apt}} }{c_{l_{max}} - c_{l_{apt}}}$	Δc_{d_0}	$c_{d_0_{min}} + \Delta c_{d_0} = c_{d_0}$	$c_{d_0} \times c$
0	1.473	0.881	0.705	0.625	0.414	0.0032	0.0120	0.0777
.2	1.347	.959	.767	.687	.449	.0037	.0125	.0680
.4	1.167	1.026	.821	.741	.472	.0041	.0129	.0568
.6	.929	1.069	.855	.765	.494	.0046	.0133	.0448
.8	.653	1.086	.869	.769	.503	.0047	.0130	.0303
.9	.472	1.007	.806	.706	.477	.0042	.0121	.0220
.95	.346	.862	.690	.580	.411	.0031	.0108	.0168

REPORT No. 628

AERODYNAMIC CHARACTERISTICS OF A LARGE NUMBER OF AIRFOILS TESTED IN THE VARIABLE-DENSITY WIND TUNNEL

By ROBERT M. PINKERTON and HARRY GREENBERG

SUMMARY

The aerodynamic characteristics of a large number of miscellaneous airfoils tested in the variable-density tunnel have been reduced to a comparable form and are published in this report for convenient reference. Plots of the standard characteristics are given for each airfoil and, in addition, the important characteristics are given in tabular form. Included also is a tabulation of important characteristics for the related airfoils reported in N. A. C. A. Report No. 460.

This report, in conjunction with N. A. C. A. Report No. 610, makes available in comparable and convenient form the aerodynamic data for airfoils tested in the variable-density tunnel since January 1, 1931.

INTRODUCTION

A large number of miscellaneous airfoils not included in the systematic investigations reported in references 1 and 2 have been tested in the variable-density tunnel. The larger part of these airfoils consists of unrelated sections, tests of which were requested by various agencies; and the results, except those published in reference 3, have not heretofore been available in published form. The rest of the airfoils consist of small groups of related sections tested to study the effects of certain local variations in shape.

One of these local shape variations involved changes of the nose shape, consisting primarily of changes of the leading-edge radius. The effects of these changes were determined by tests of modifications of the Göttingen 398 (reference 4), of the Clark Y (reference 5), and of the N. A. C. A. 2412 (unpublished). References 4 and 5 present data on the effect of sharp leading edges. The modifications to the N. A. C. A. 2412 consisted in varying the leading-edge radius from normal to zero (N. A. C. A. 2412, N. A. C. A. 15, 16, 19, and 20) and in dropping the leading edge from the normal position (N. A. C. A. 17 and 18). A second local shape variation involved the rear portion of the airfoil and consisted in reflexing the mean line. Such modifications were made on the Göttingen 398, the Boeing 106, and the N-60 sections, and the results of the tests were published in reference 6. A series of related forward-

camber airfoils having reflexed mean lines was tested, and the results were published in reference 7. Another series of reflexed airfoils, for which the results have not been published, includes the N. A. C. A. 21, 23, 24, 25, 26, and 27 airfoils.

The results of these tests, including both published and unpublished data, have not heretofore been available in comparable form nor convenient for ready reference by the user. It has therefore been deemed desirable to collect these data into one report.

This report, in conjunction with reference 2, makes available, in convenient form, comparable data for sections tested in the variable-density tunnel since January 1, 1931. The important fully corrected characteristics for the miscellaneous sections described earlier and also for the sections reported in reference 1 are tabulated for easy reference. In addition to the tabulated data, plots of standard aerodynamic characteristics are presented for the miscellaneous airfoils.

TESTS AND APPARATUS

Routine airfoil tests were made in the variable-density tunnel at an effective Reynolds Number of approximately 8,000,000. Tests of some of the models were extended through the range of negative angles of attack. Airfoils for which these results were obtained are designated "inverted" sections. The duralumin models were of rectangular plan form with a 5-inch chord and a 30-inch span. A description of the tunnel, the test procedure, and the method of constructing the models is given in reference 8.

The precision of the tests and of the results is discussed in references 1 and 9.

RESULTS

The method chosen to present these results is intended to be convenient for designers. The important characteristics, fully corrected as described in references 9 and 10, are presented in tables I and II and are comparable with those given in reference 2. These important characteristics are:

$c_{l_{max}}$, the section maximum lift coefficient.

α_{l_0} , the angle of zero lift.

a_0 , the section lift-curve slope.

$c_{l_{opt}}$, the optimum lift coefficient, or the section lift coefficient corresponding to $c_{d_{0min}}$.

$c_{d_{0min}}$, the minimum profile-drag coefficient.

$c_{m_{a.c.}}$, the pitching-moment coefficient about the section aerodynamic center.

$a.c.$, the aerodynamic center, or the point, with respect to the airfoil section, about which the pitching-moment coefficient tends to remain constant over the range of lift coefficients between zero and maximum lift.

$c.p.$, the position of the center of pressure in percentage of the chord behind the leading edge.

m_6 , the lift-curve slope for aspect ratio 6.

A more complete description of these characteristics is presented in references 9 and 10.

Tables I and II contain these data for available sections tested in the variable-density tunnel, except those given in reference 2. Reference is made to the original publication for the airfoil results that have been previously reported.

Plots of the standard characteristics (figs. 1 to 88) are given for the miscellaneous sections (exclusive of those for the N. A. C. A. 22112, 23112, 24112, and 25112 sections, which are published in reference 7) because they are not available elsewhere. Plots for the sections in table I are given in reference 1.

LANGLEY MEMORIAL AERONAUTICAL LABORATORY,
NATIONAL ADVISORY COMMITTEE FOR AERONAUTICS,
LANGLEY FIELD, VA., *October 1, 1937.*

REFERENCES

1. Jacobs, Eastman N., Ward, Kenneth E., and Pinkerton, Robert M.: The Characteristics of 78 Related Airfoil Sections from Tests in the Variable-Density Wind Tunnel. T. R. No. 460, N. A. C. A., 1933.
2. Jacobs, Eastman N., Pinkerton, Robert M., and Greenberg, Harry: Tests of Related Forward-Camber Airfoils in the Variable-Density Wind Tunnel. T. R. No. 610, N. A. C. A., 1937.
3. Anderson, Raymond F.: The Aerodynamic Characteristics of Airfoils at Negative Angles of Attack. T. N. No. 412, N. A. C. A., 1932.
4. Jacobs, Eastman N.: Characteristics of Two Sharp-Nosed Airfoils Having Reduced Spinning Tendencies. T. N. No. 416, N. A. C. A., 1932.
5. Weick, Fred E., and Scudder, Nathan F.: The Effect on Lift, Drag, and Spinning Characteristics of Sharp Leading Edges on Airplane Wings. T. N. No. 447, N. A. C. A., 1933.
6. DeFoe, George L.: A Comparison of the Aerodynamic Characteristics of Three Normal and Three Reflexed Airfoils in the Variable-Density Wind Tunnel. T. N. No. 388, N. A. C. A., 1931.
7. Jacobs, Eastman N., and Pinkerton, Robert M.: Tests in the Variable-Density Wind Tunnel of Related Airfoils Having the Maximum Camber Unusually Far Forward. T. R. No. 537, N. A. C. A., 1935.
8. Jacobs, Eastman N., and Abbott, Ira H.: The N. A. C. A. Variable-Density Wind Tunnel. T. R. No. 416, N. A. C. A., 1932.
9. Jacobs, Eastman N., and Sherman, Albert: Airfoil Section Characteristics as Affected by Variations of the Reynolds Number. T. R. No. 586, N. A. C. A., 1937.
10. Jacobs, Eastman N., and Rhode, R. V.: Airfoil Section Characteristics as Applied to the Prediction of Air Forces and Their Distribution on Wings. T. R. No. 631, N. A. C. A., 1938.

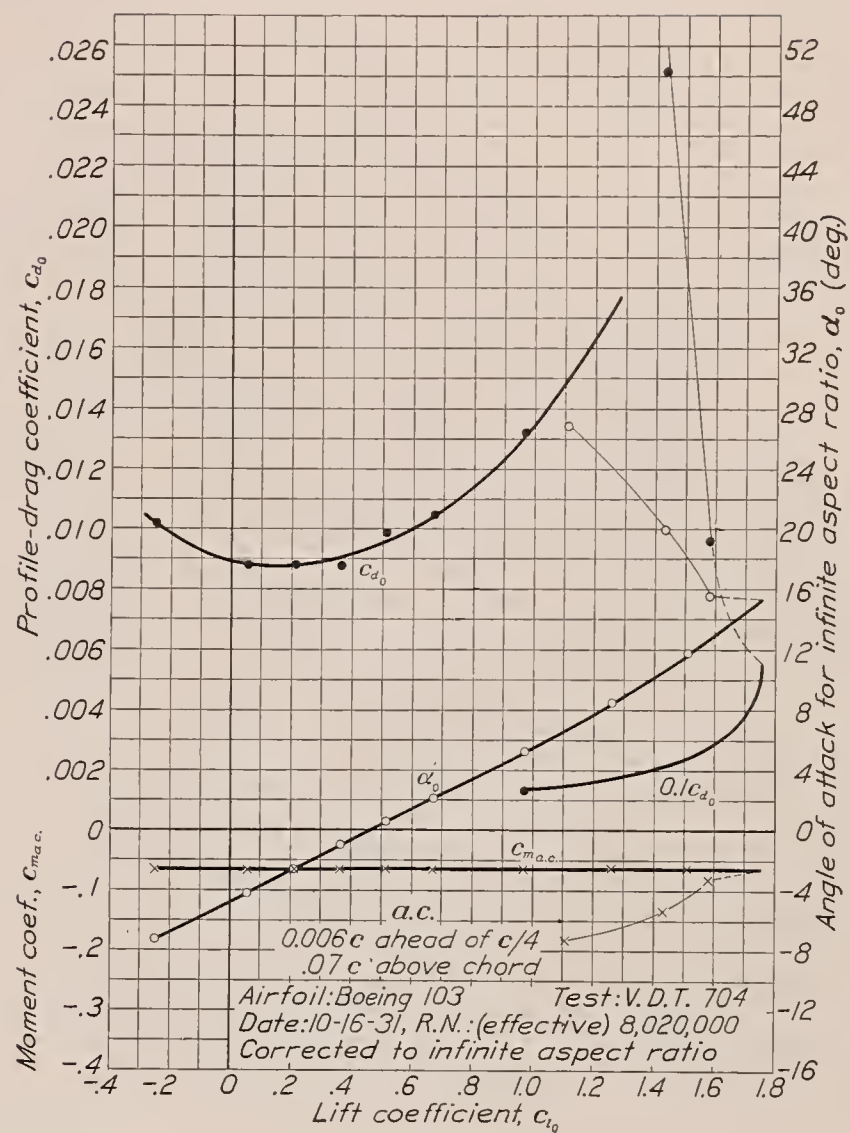
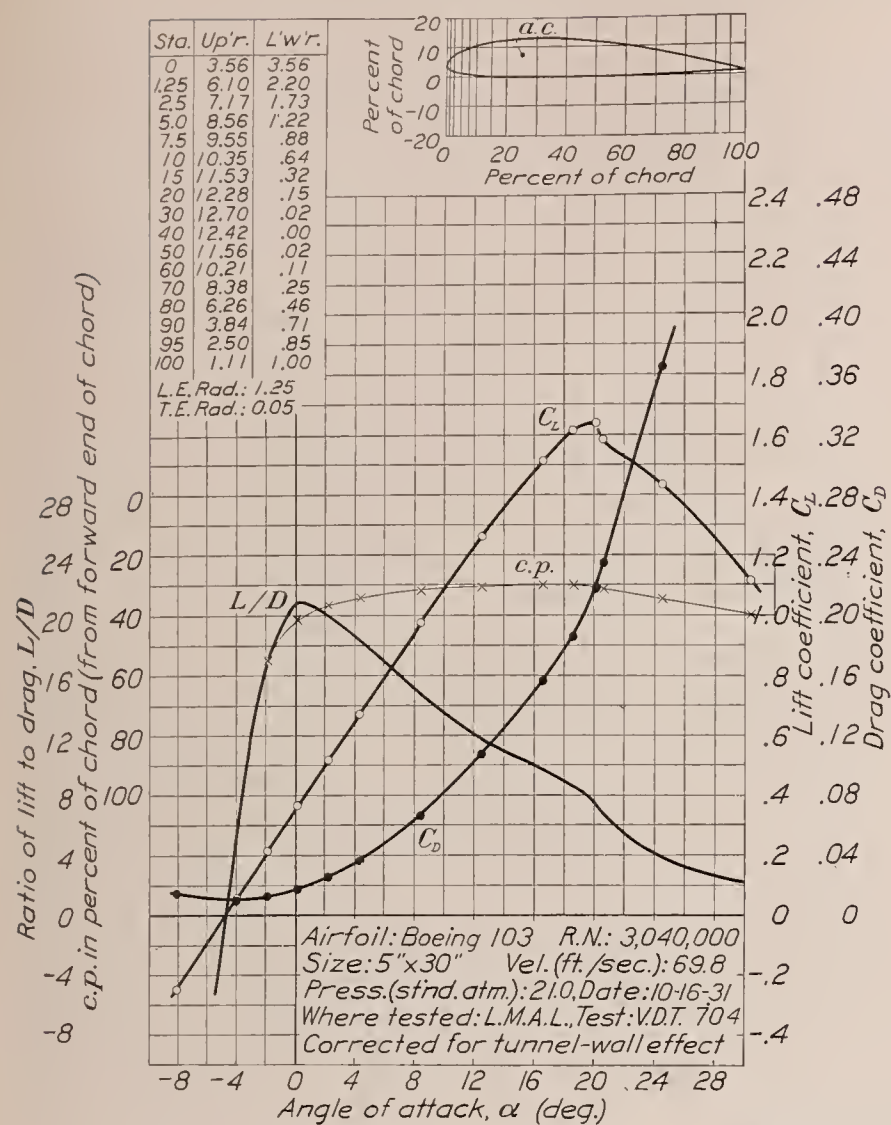


FIGURE 1.—Boeing 103 airfoil.

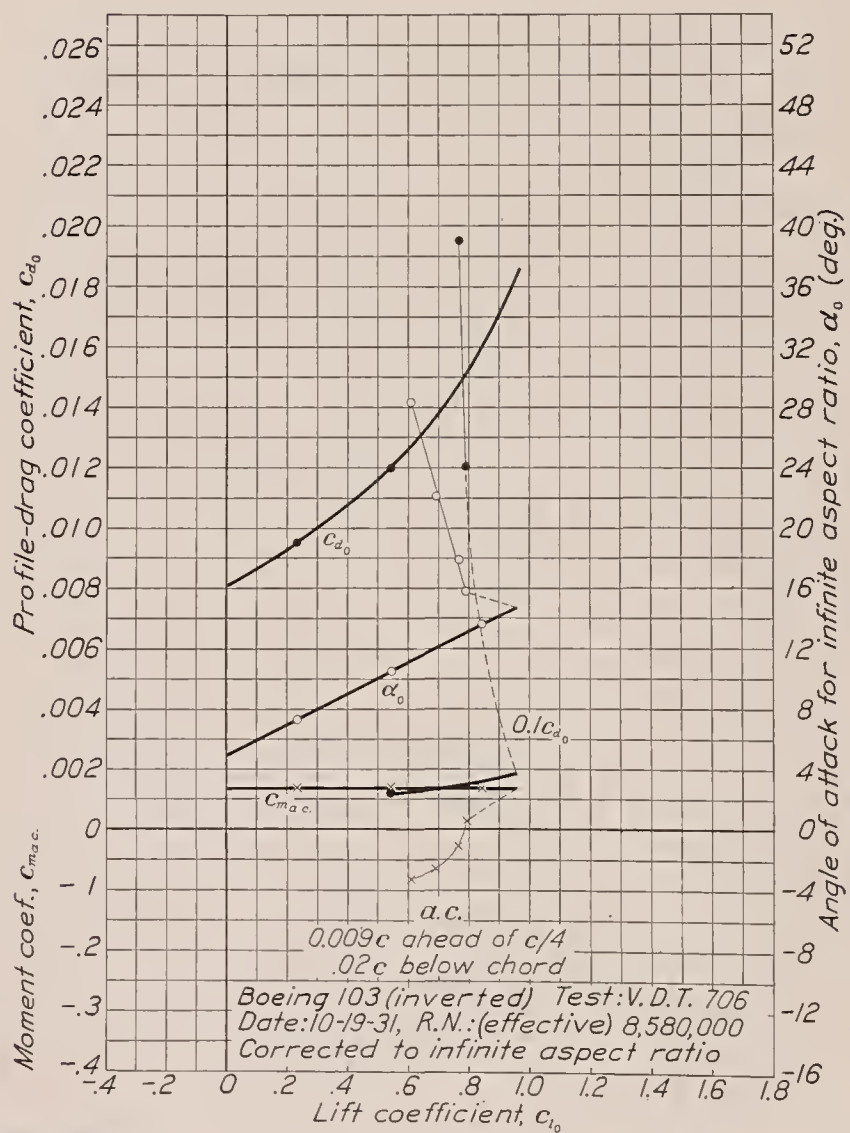
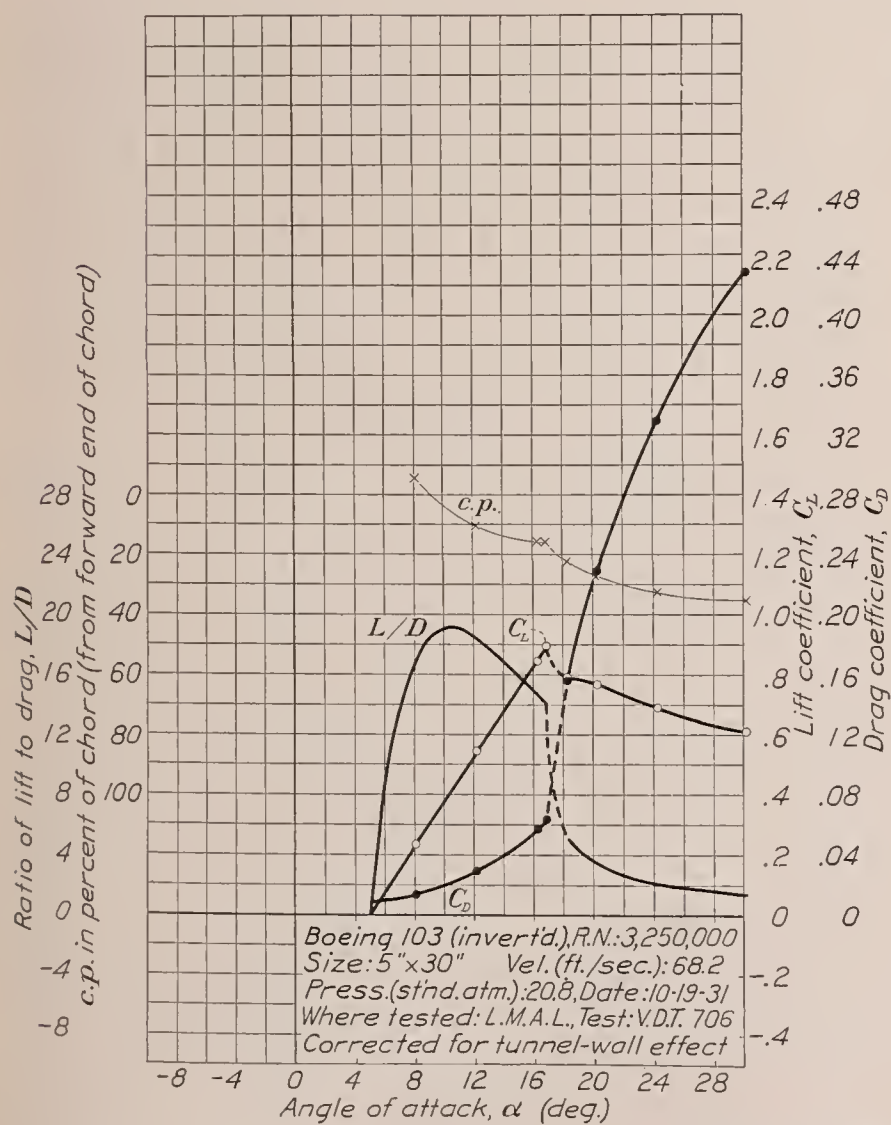


FIGURE 2.—Boeing 103 airfoil (inverted).

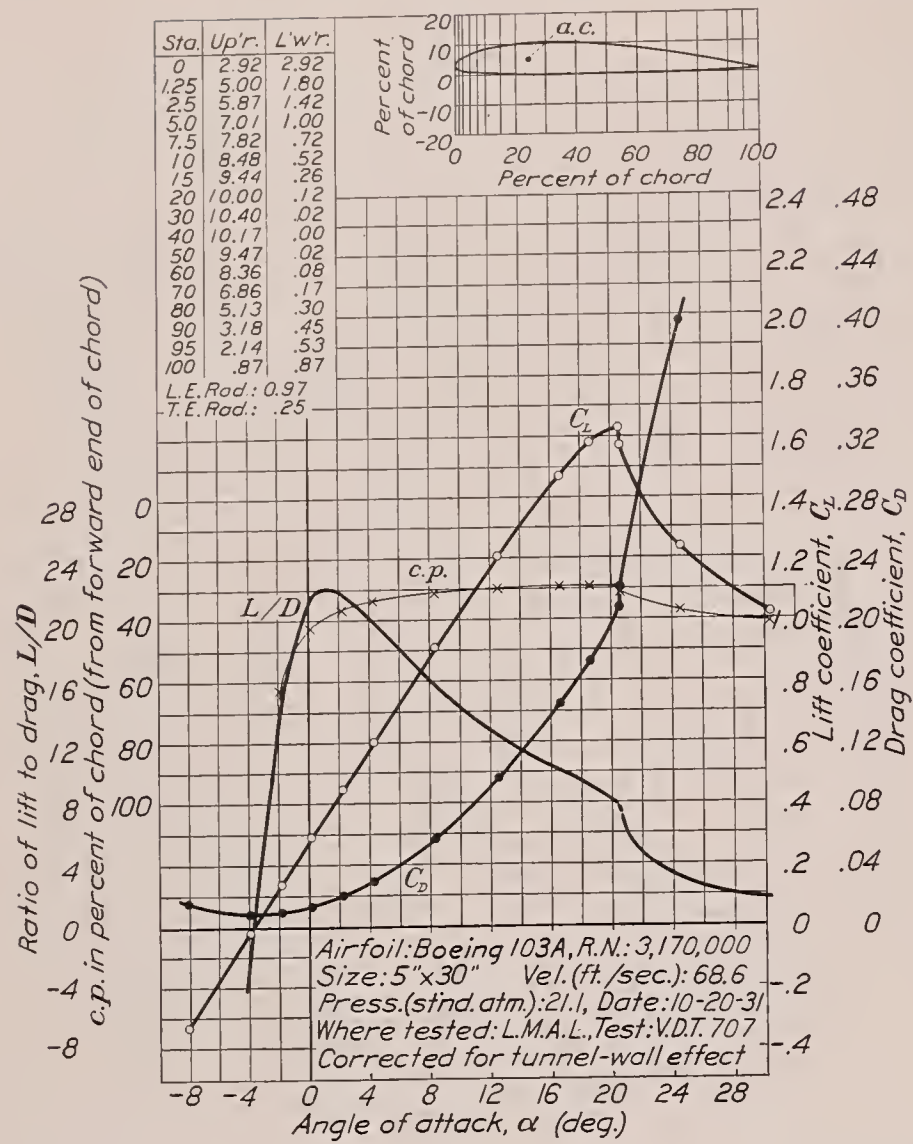


FIGURE 3.—Boeing 103 A airfoil.

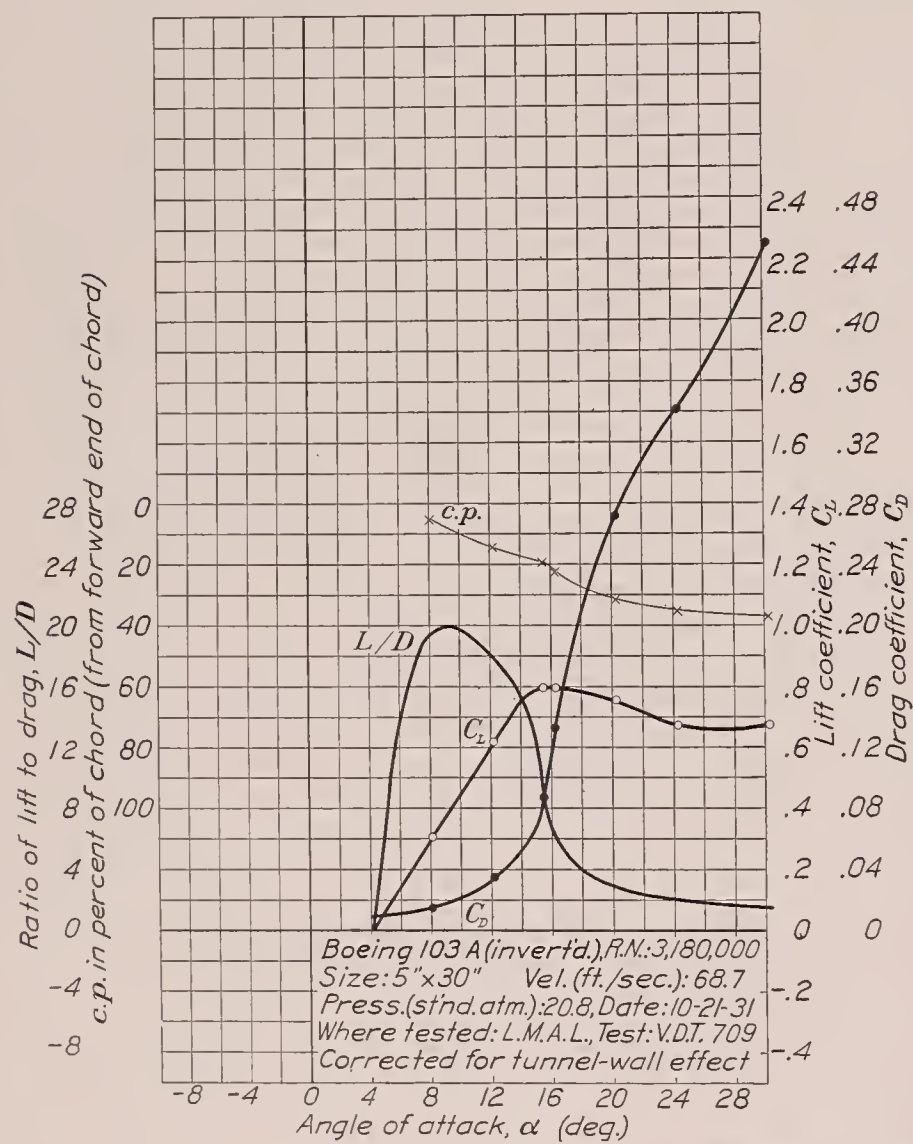


FIGURE 4.—Boeing 103 A airfoil (inverted).

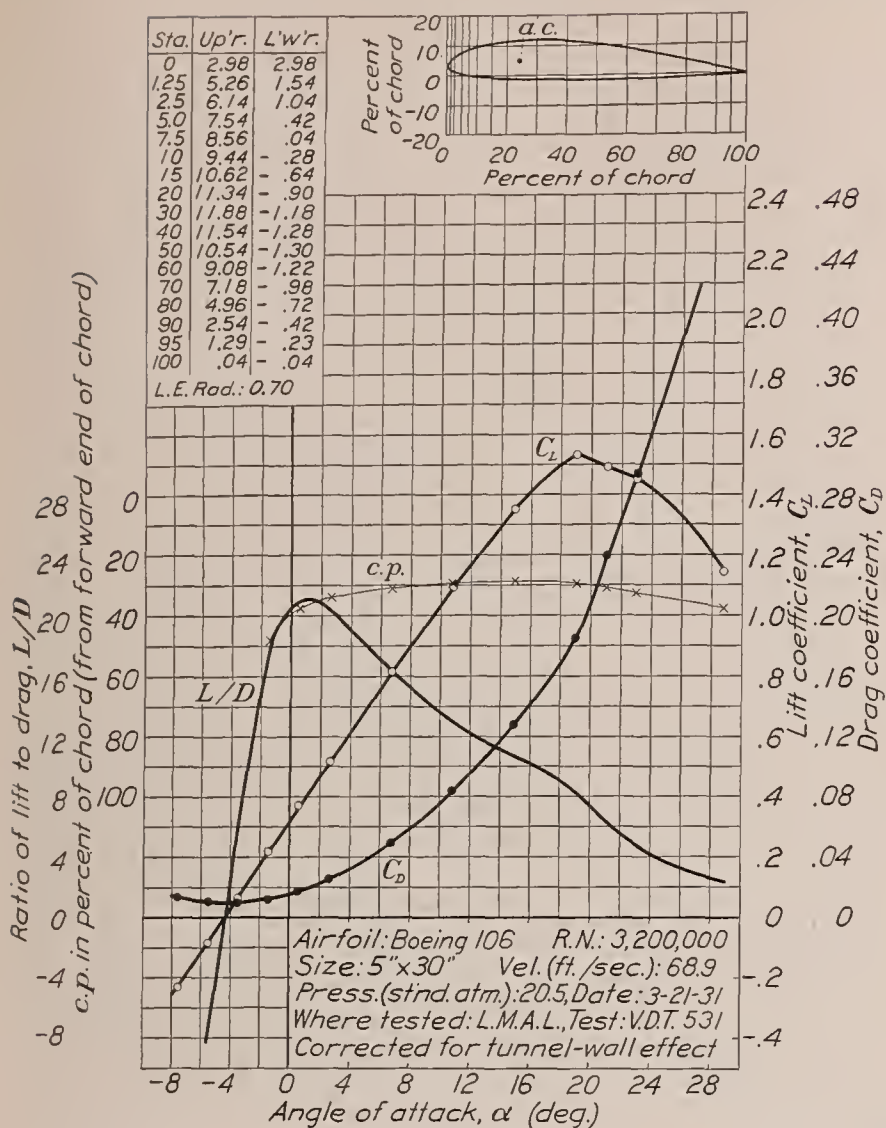


FIGURE 5.—Boeing 106 airfoil.

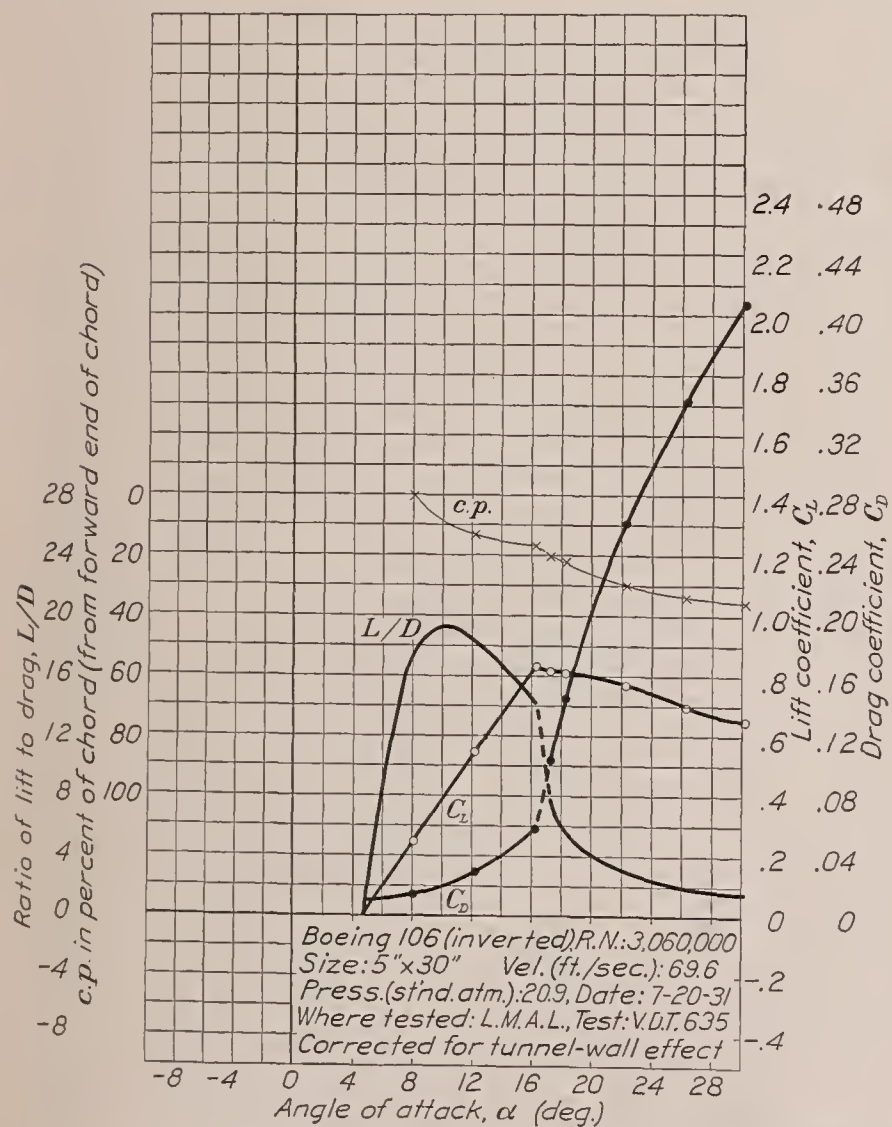
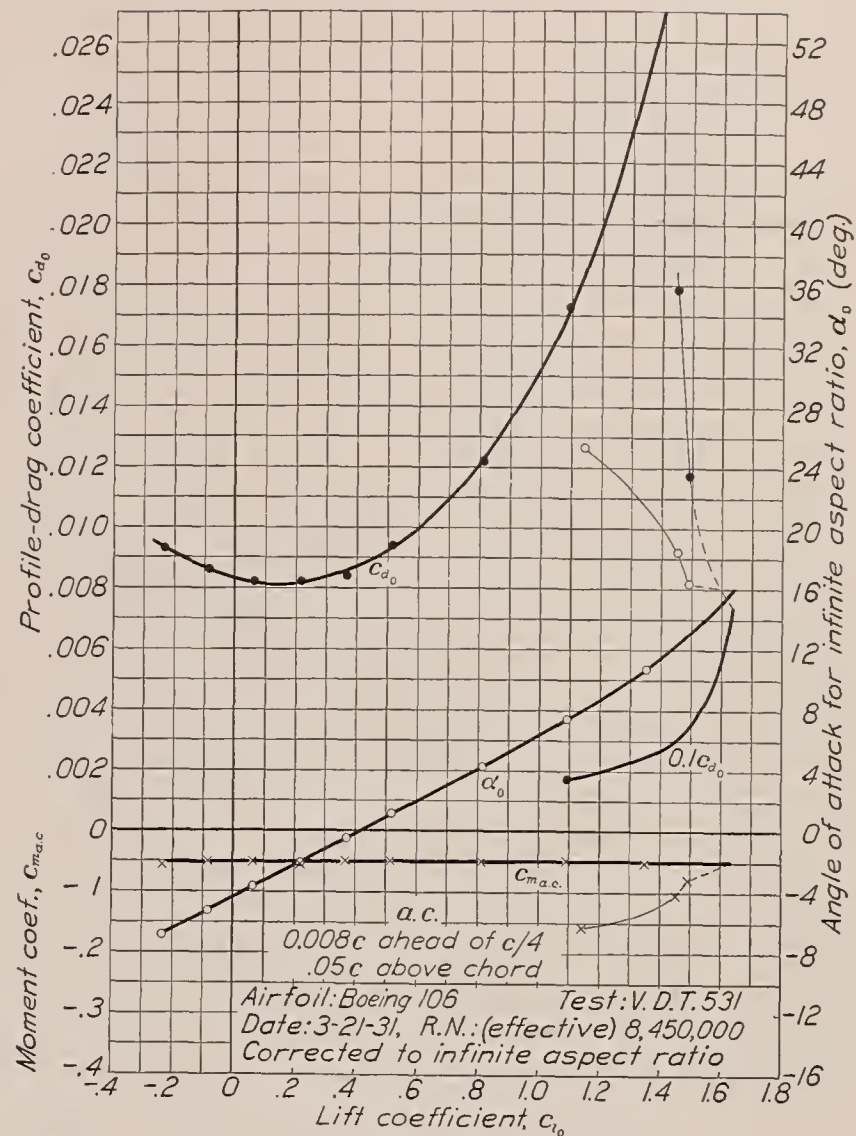
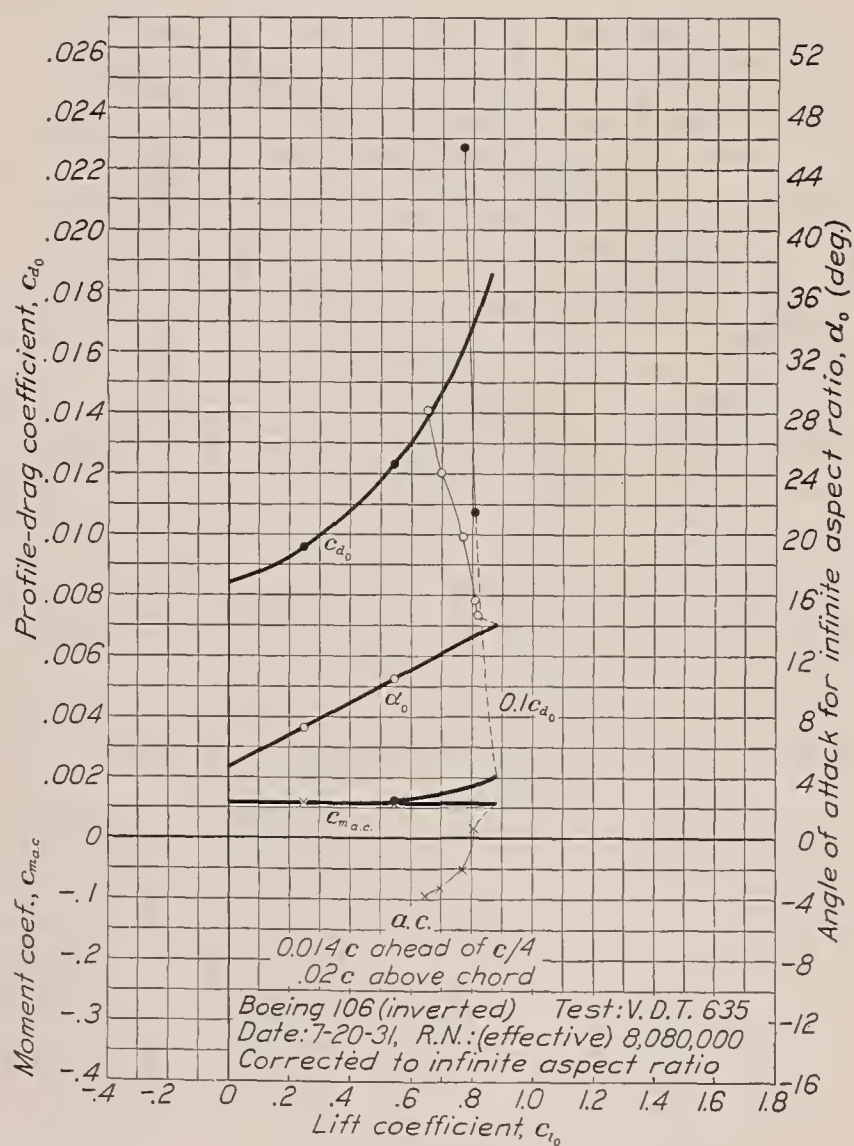


FIGURE 6.—Boeing 106 airfoil (inverted).



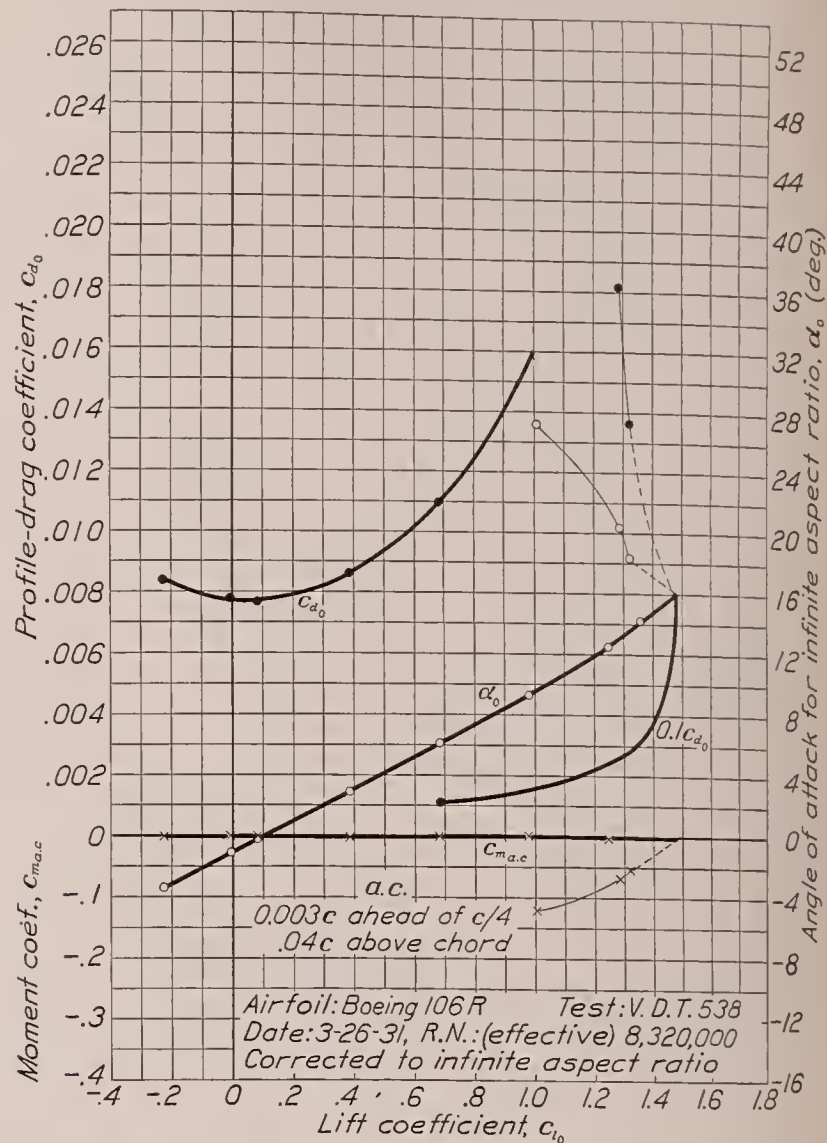
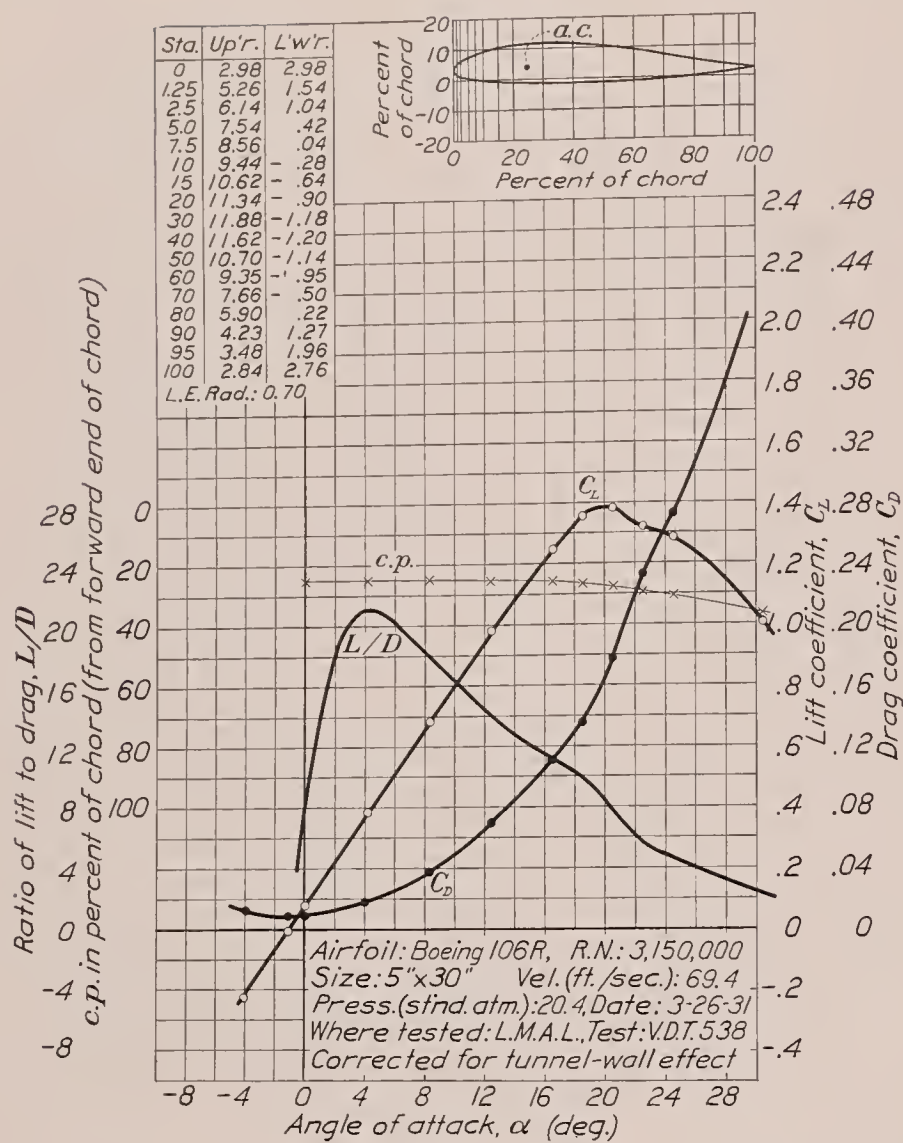


FIGURE 7.—Boeing 106 R airfoil.

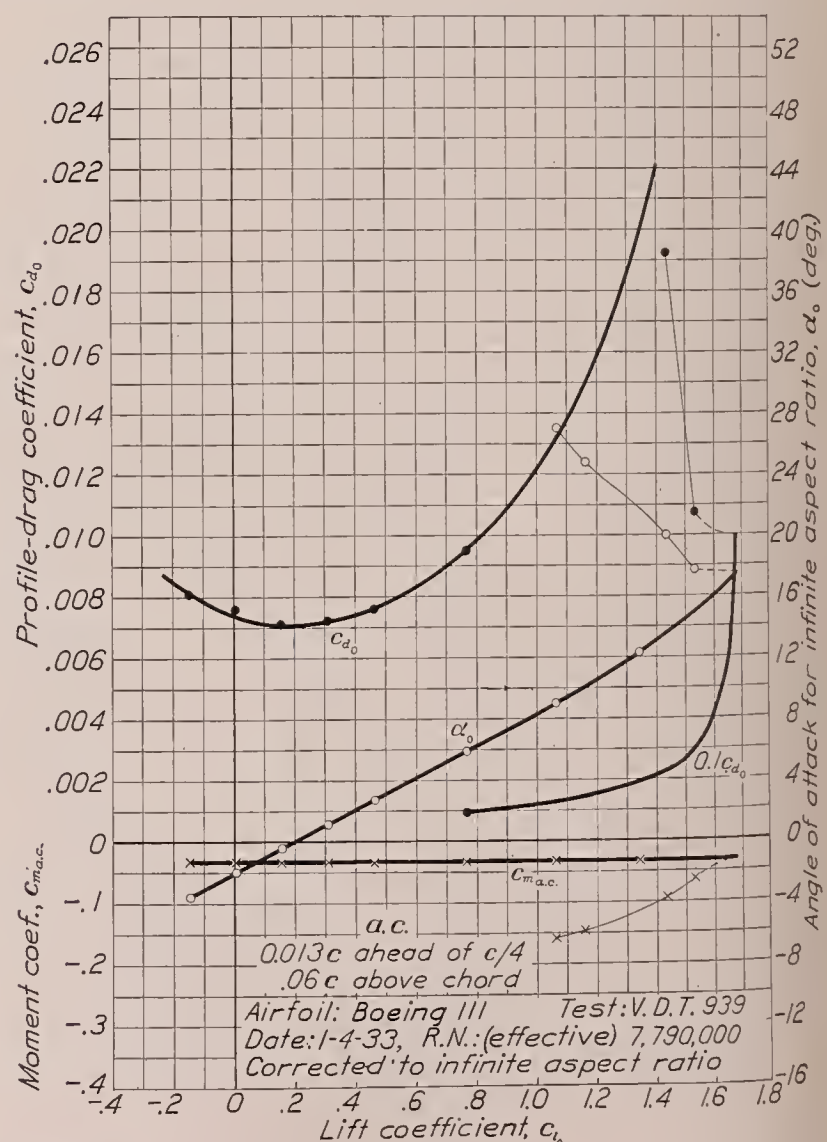
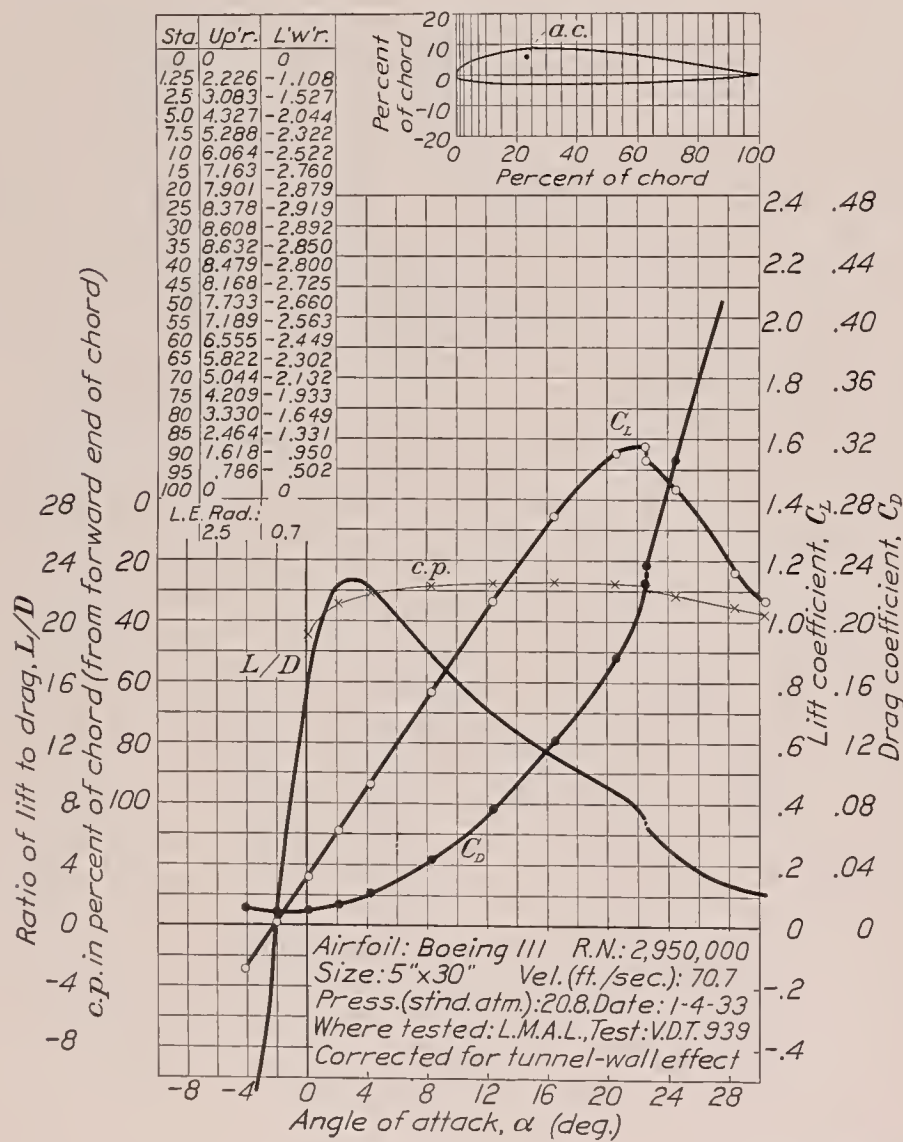


FIGURE 8.—Boeing 111 airfoil.

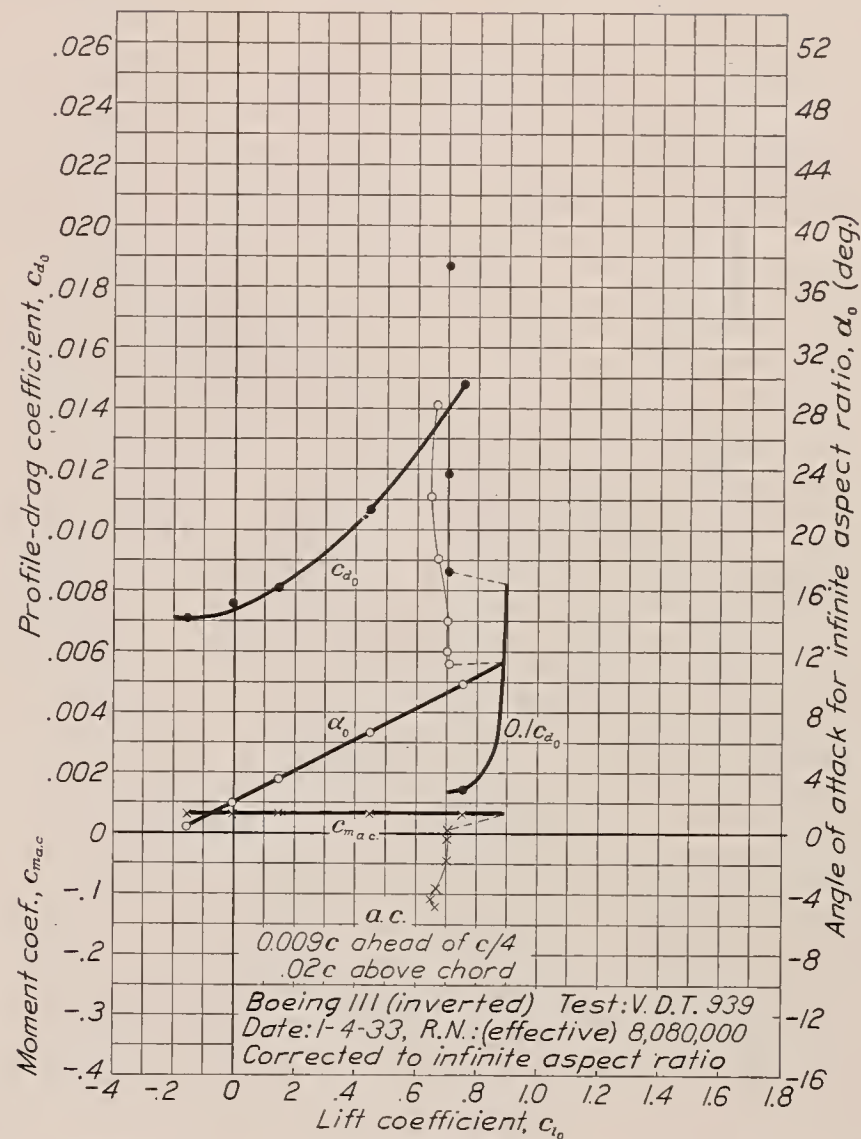
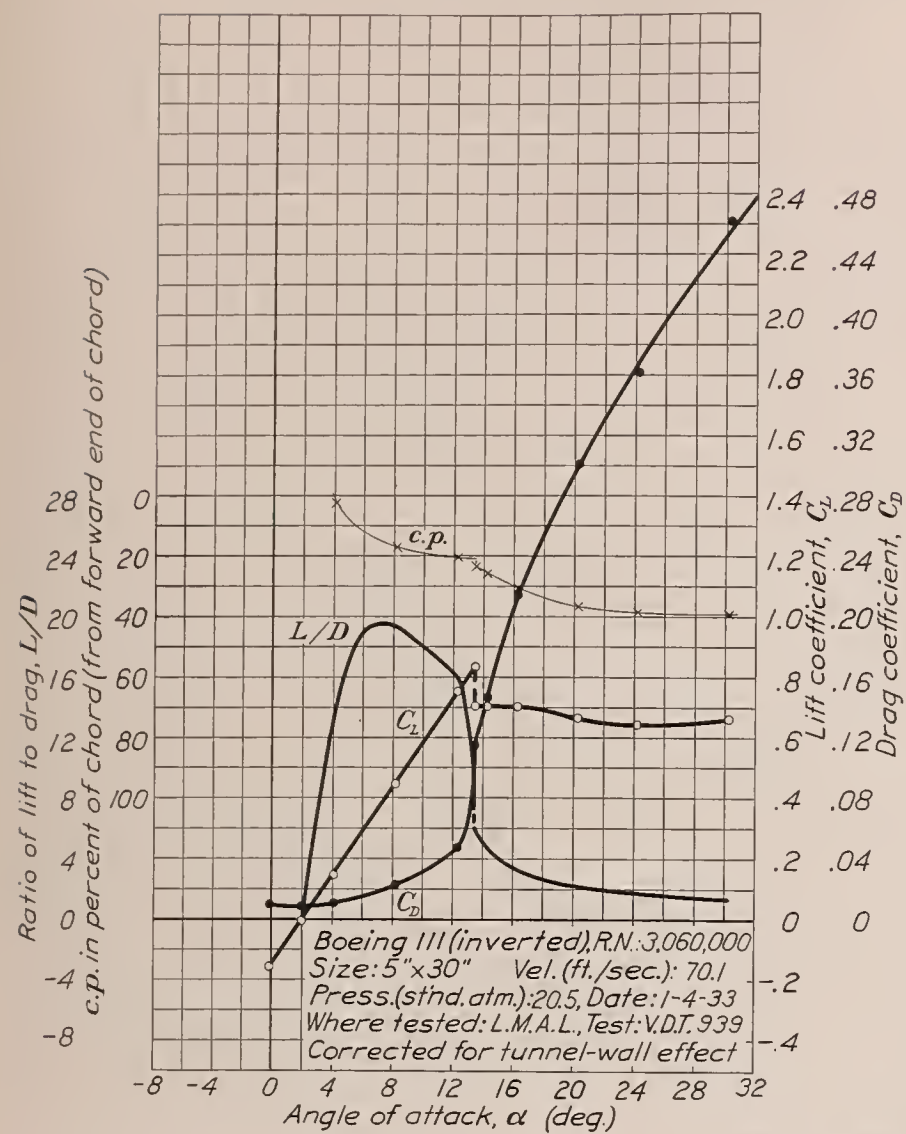


FIGURE 9.—Boeing 111 airfoil (inverted).

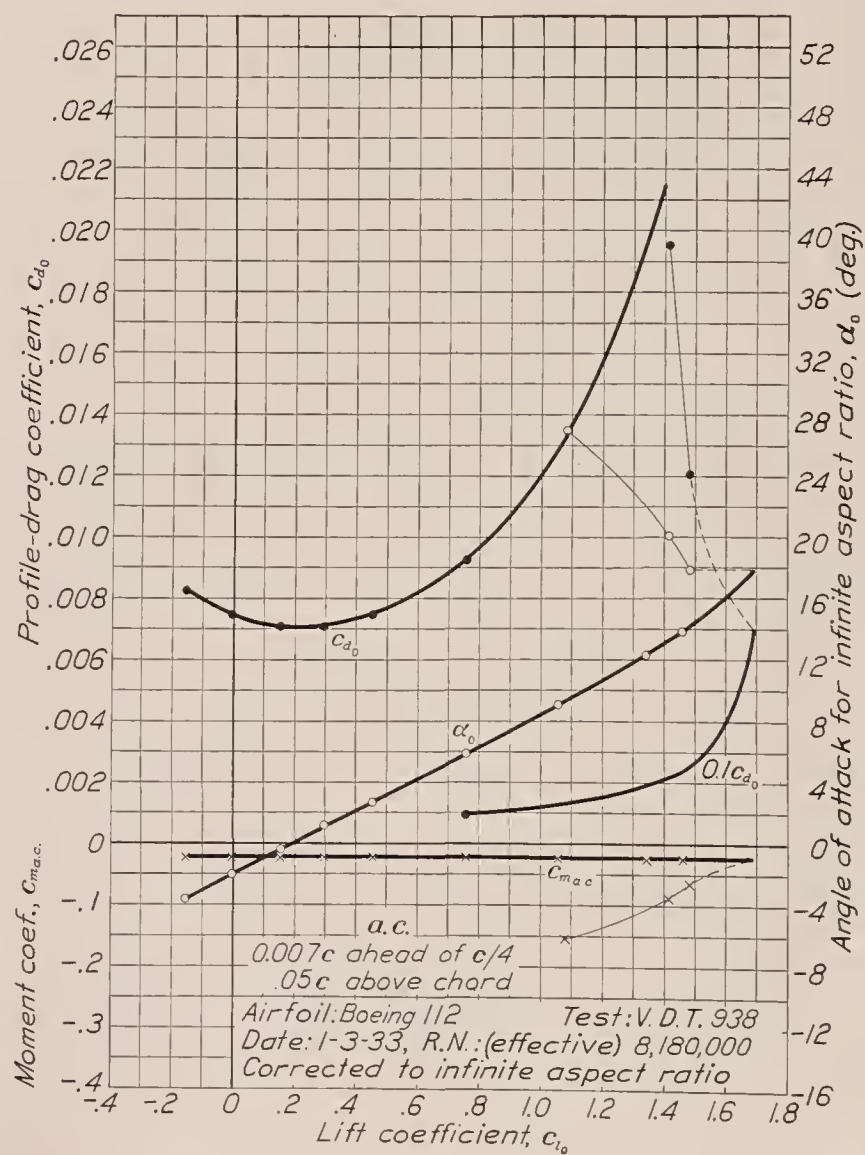
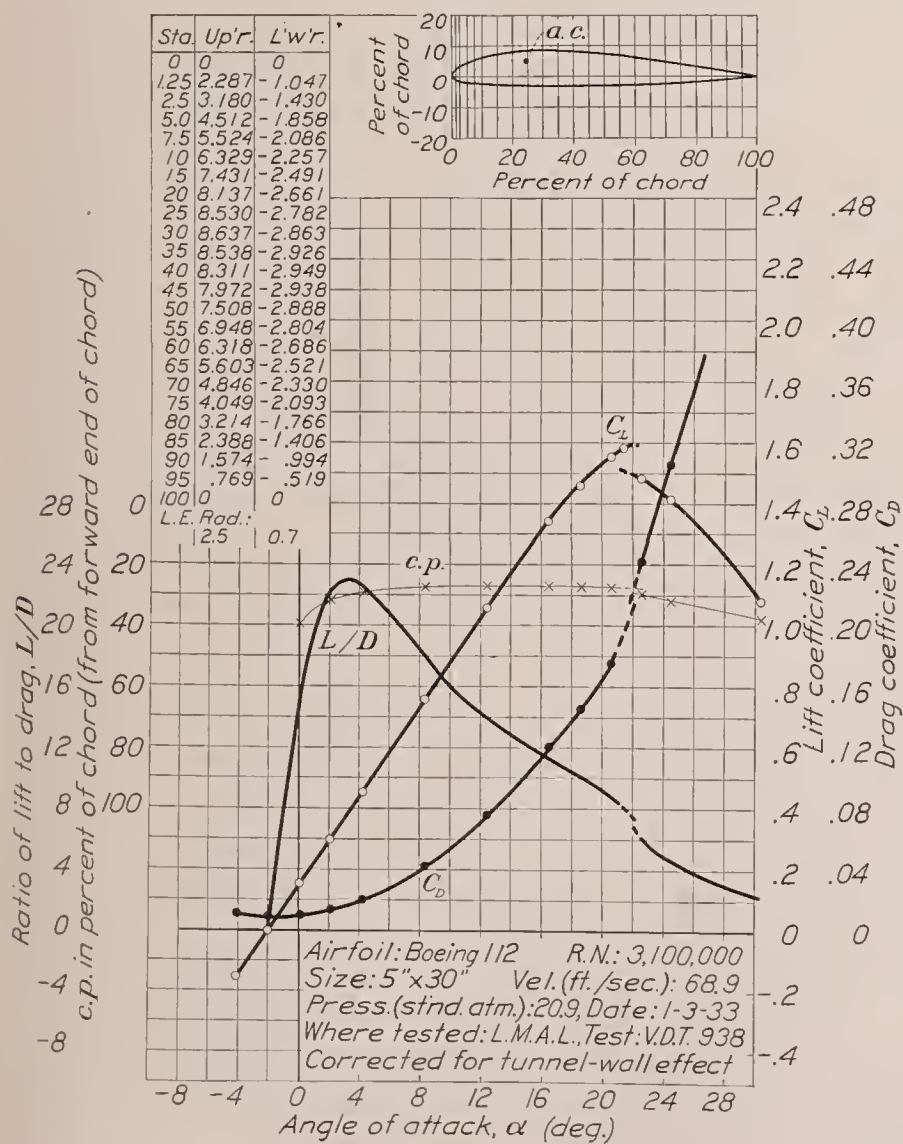


FIGURE 10.—Boeing 112 airfoil.

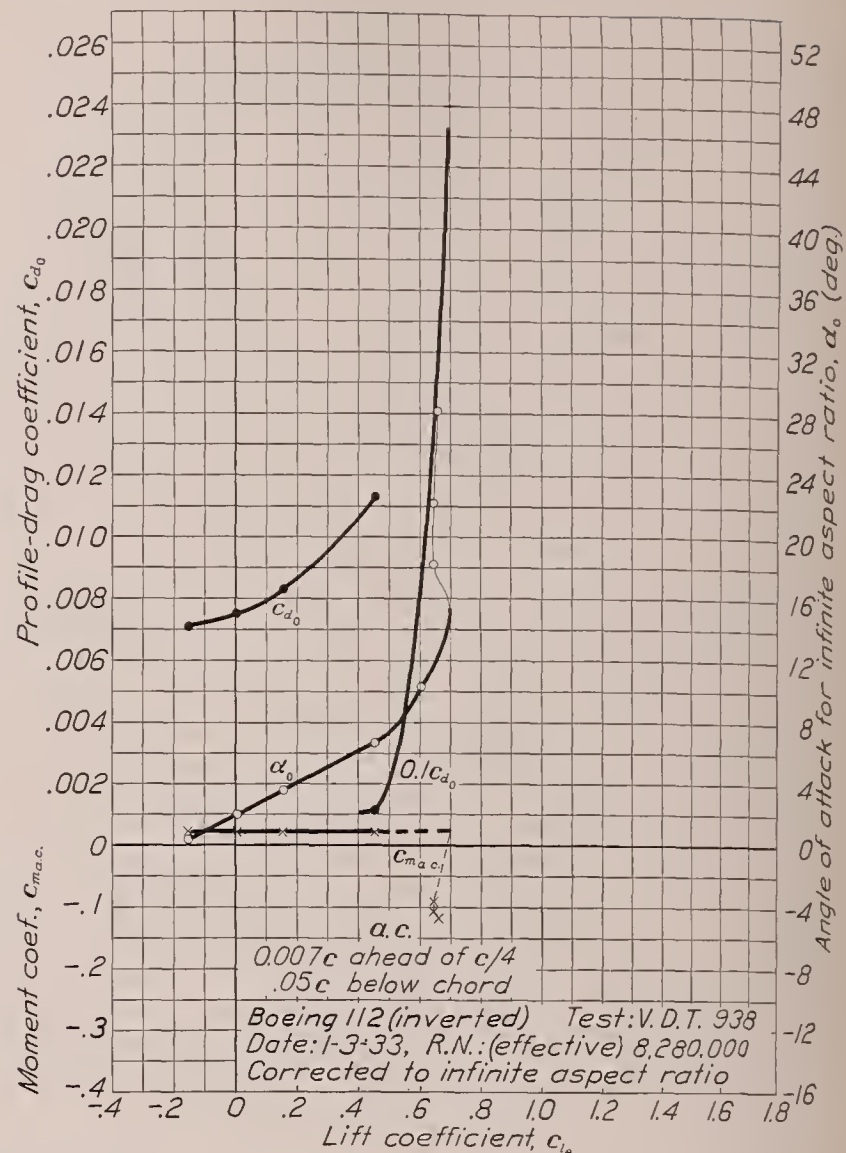
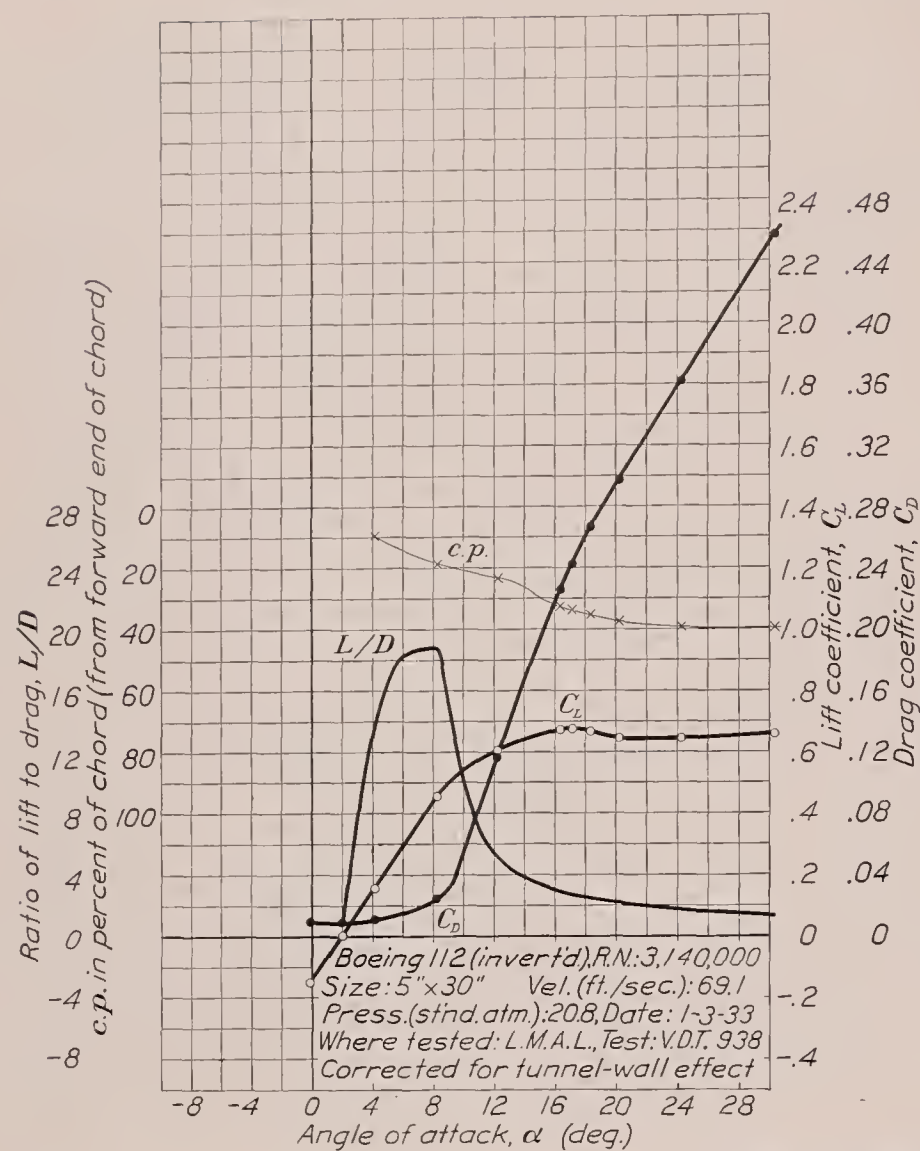


FIGURE 11.—Boeing 112 airfoil (inverted).

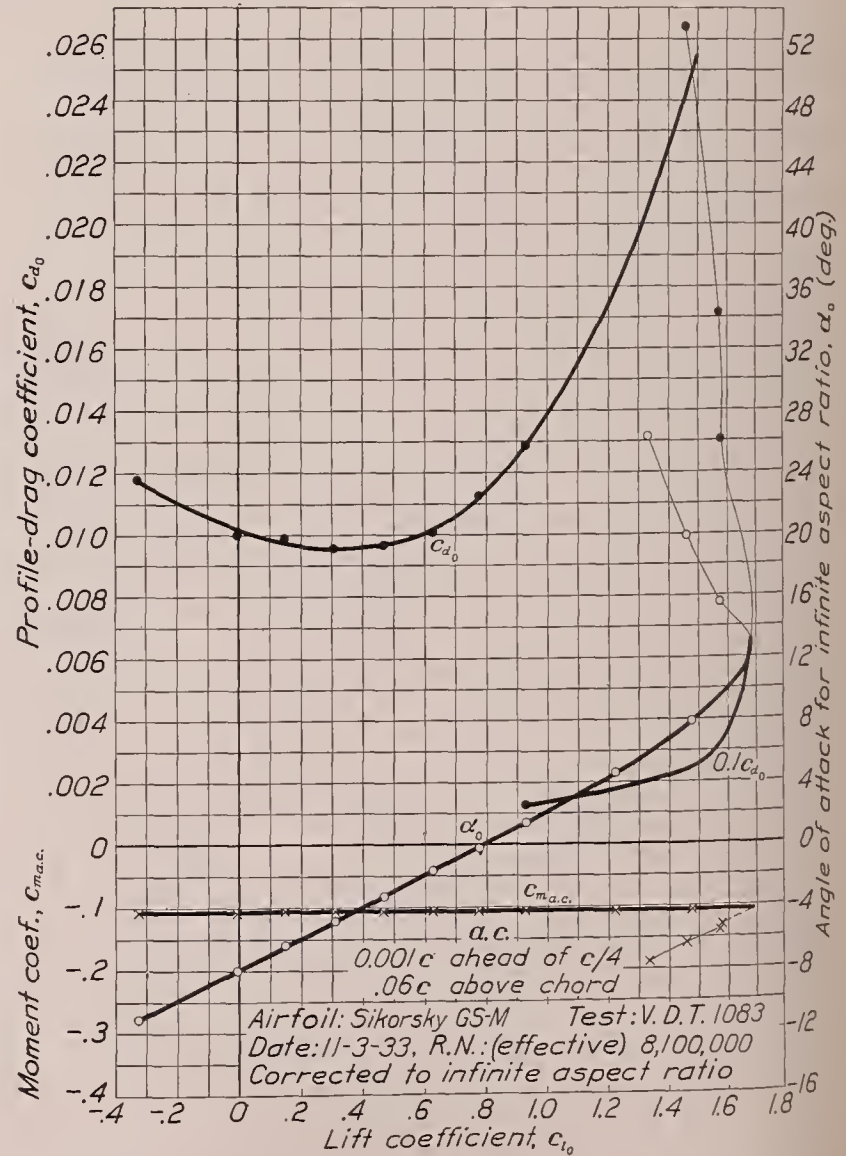
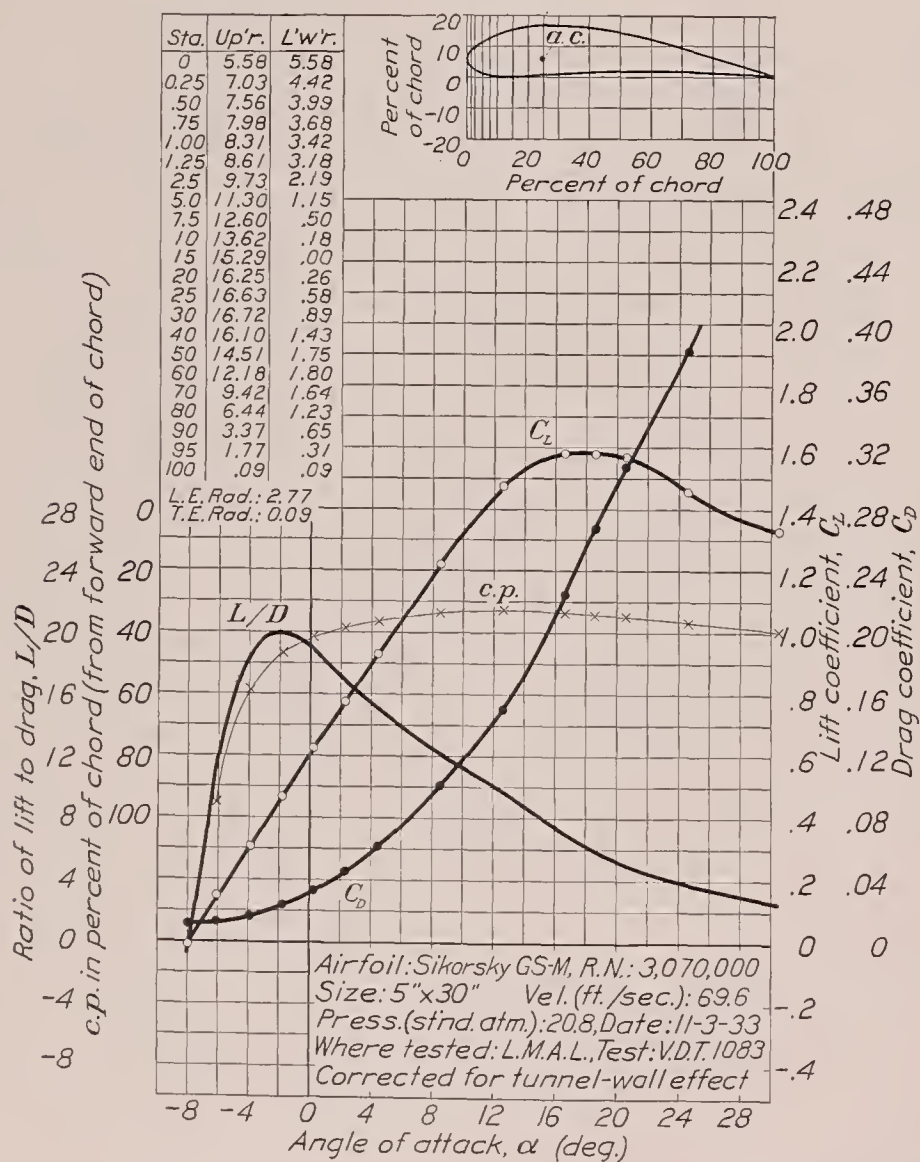


FIGURE 12.—Sikorsky GS-M airfoil.

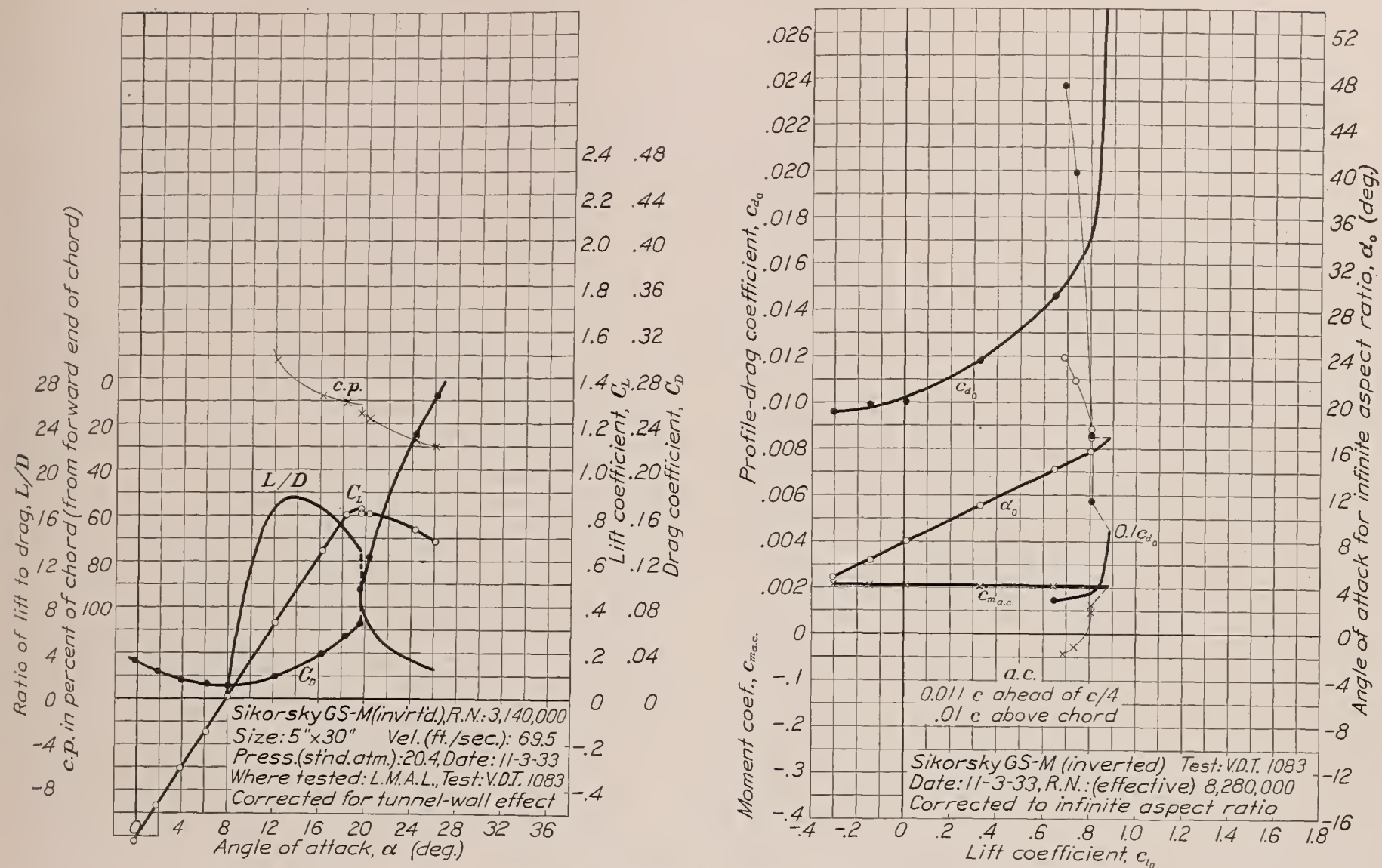


FIGURE 13.—Sikorsky GS-M airfoil (inverted).

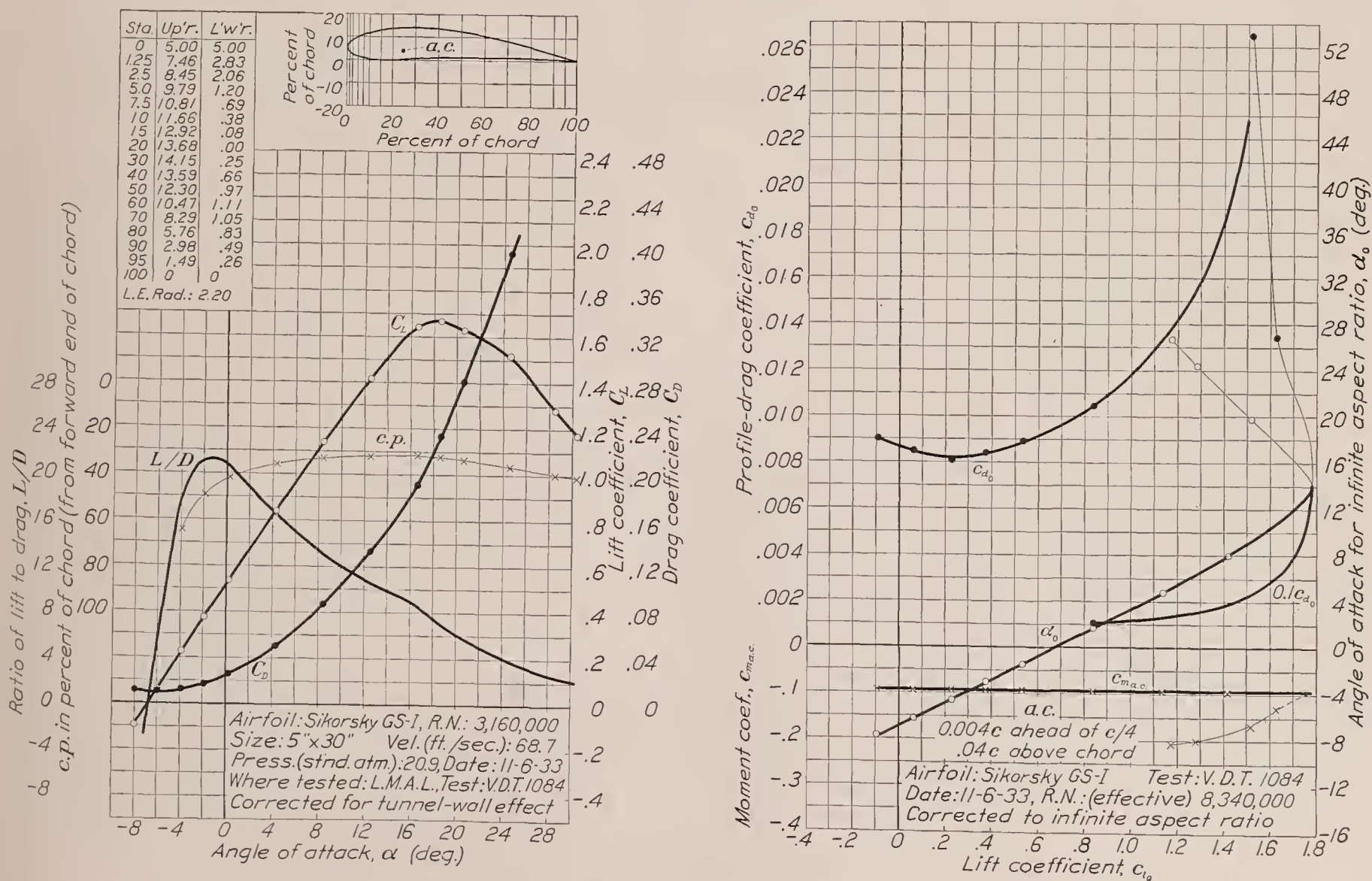


FIGURE 14.—Sikorsky GS-I airfoil.

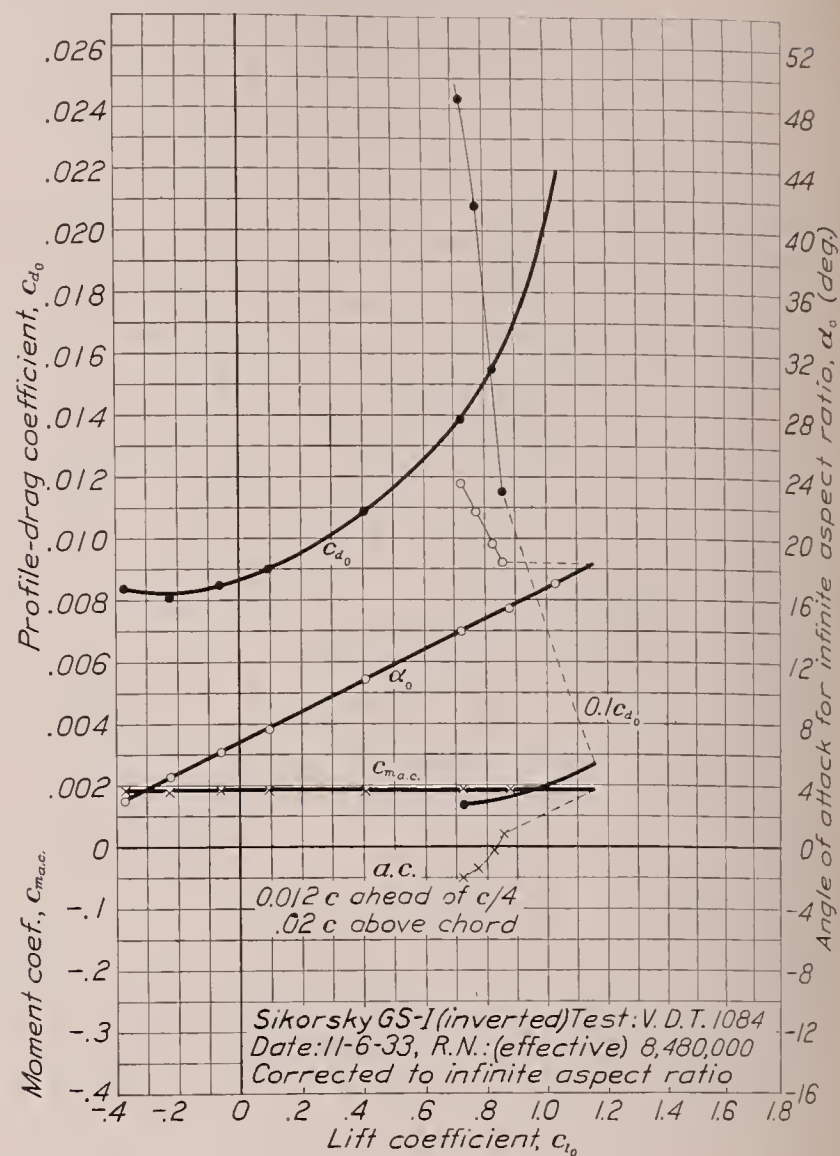
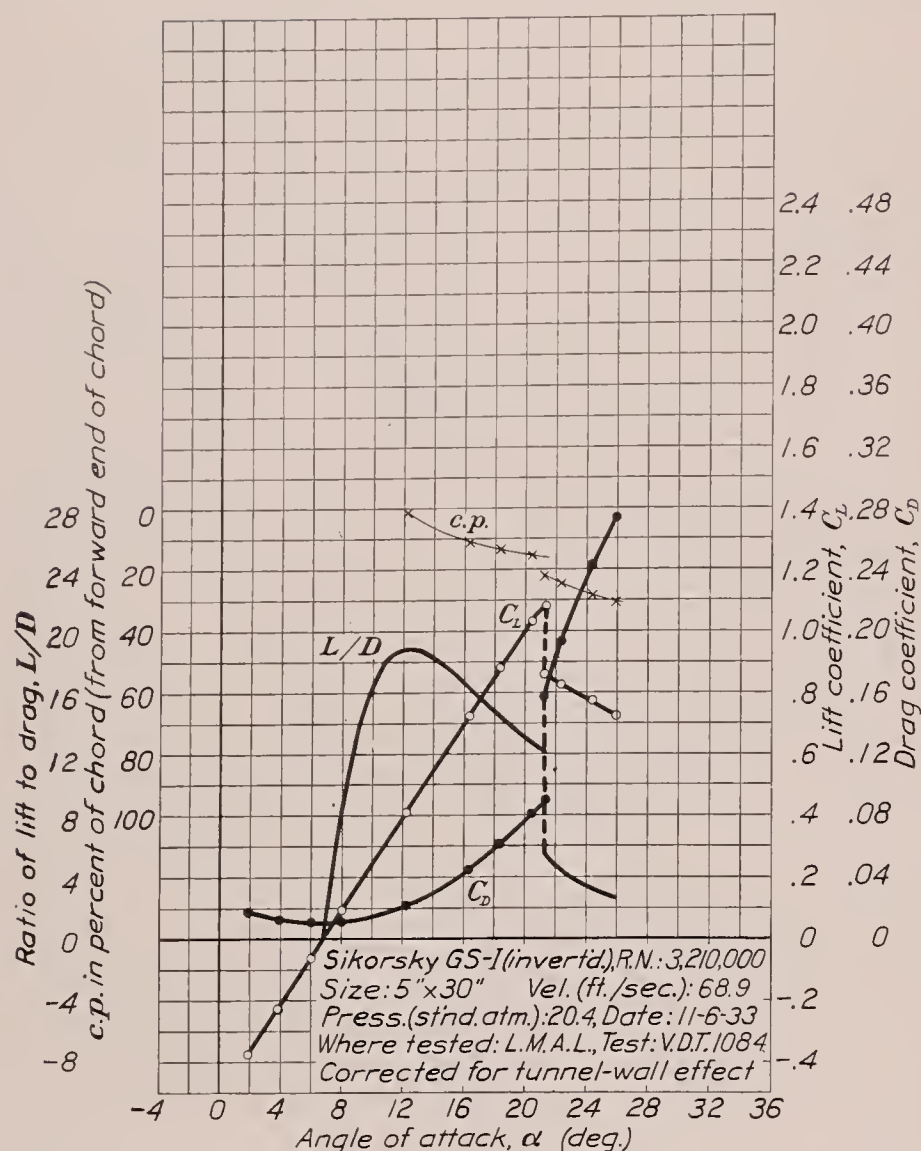


FIGURE 15.—Sikorsky GS-I airfoil (inverted).

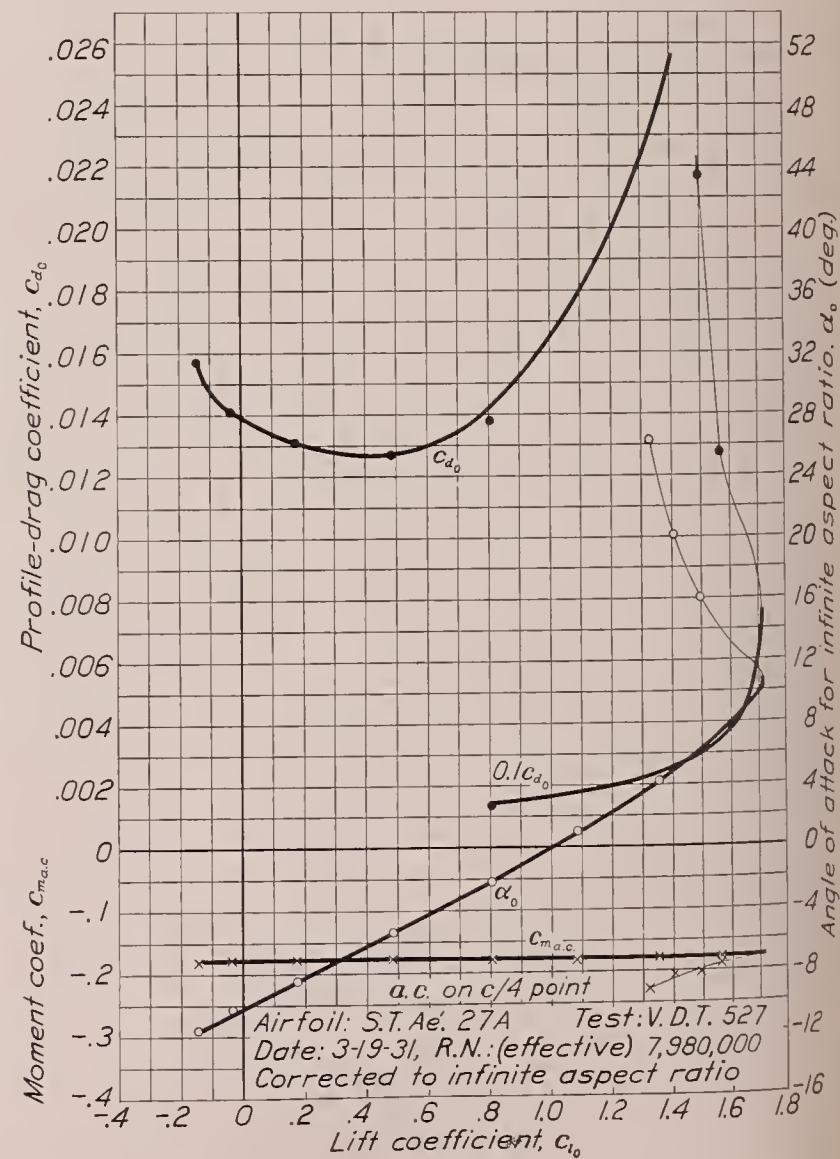
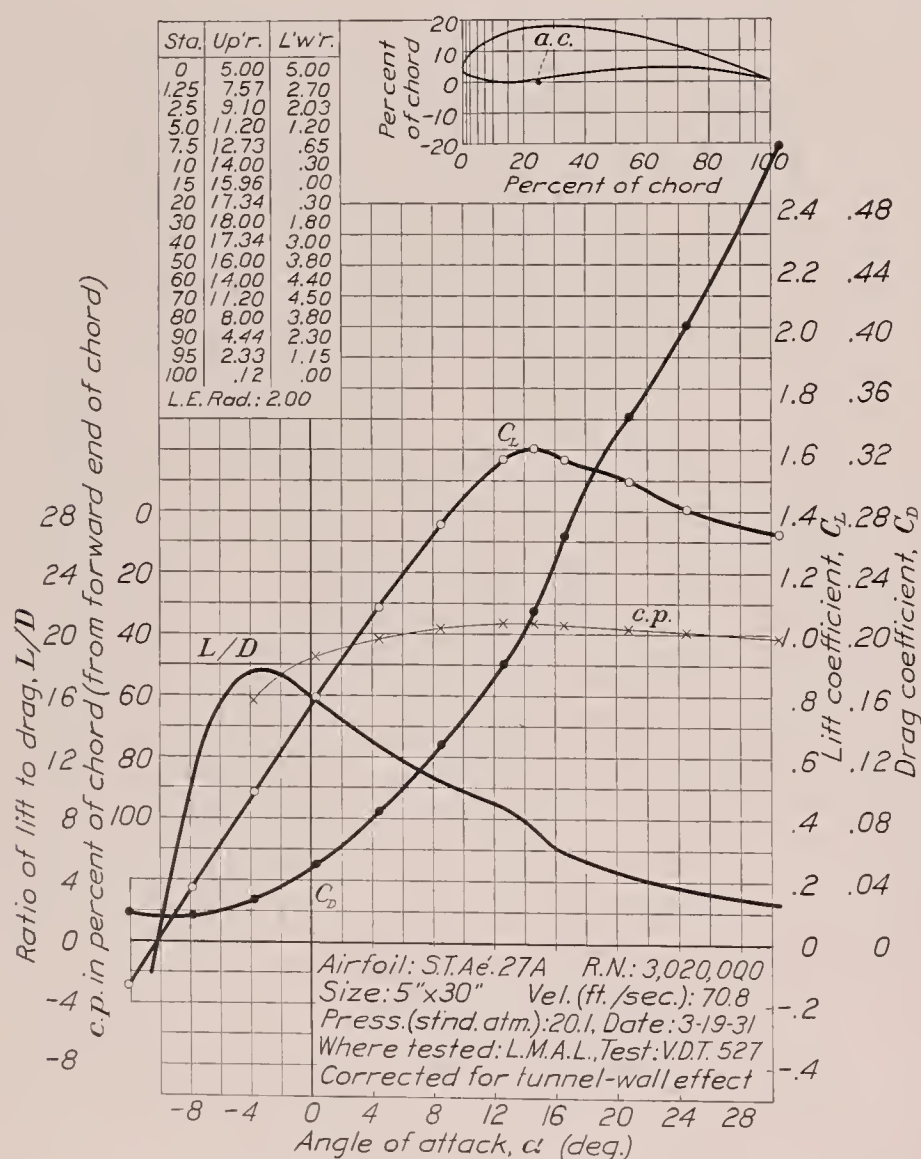


FIGURE 16.—S. T. A6. 27A airfoil.

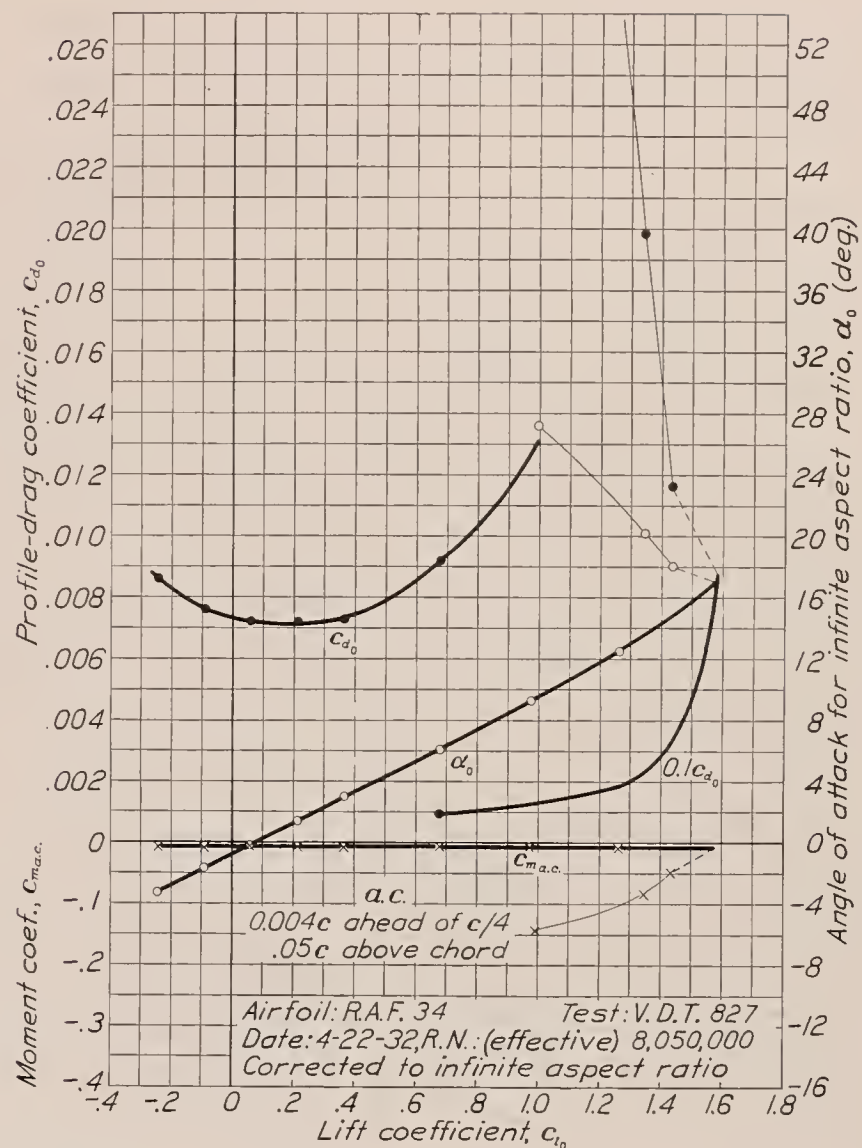
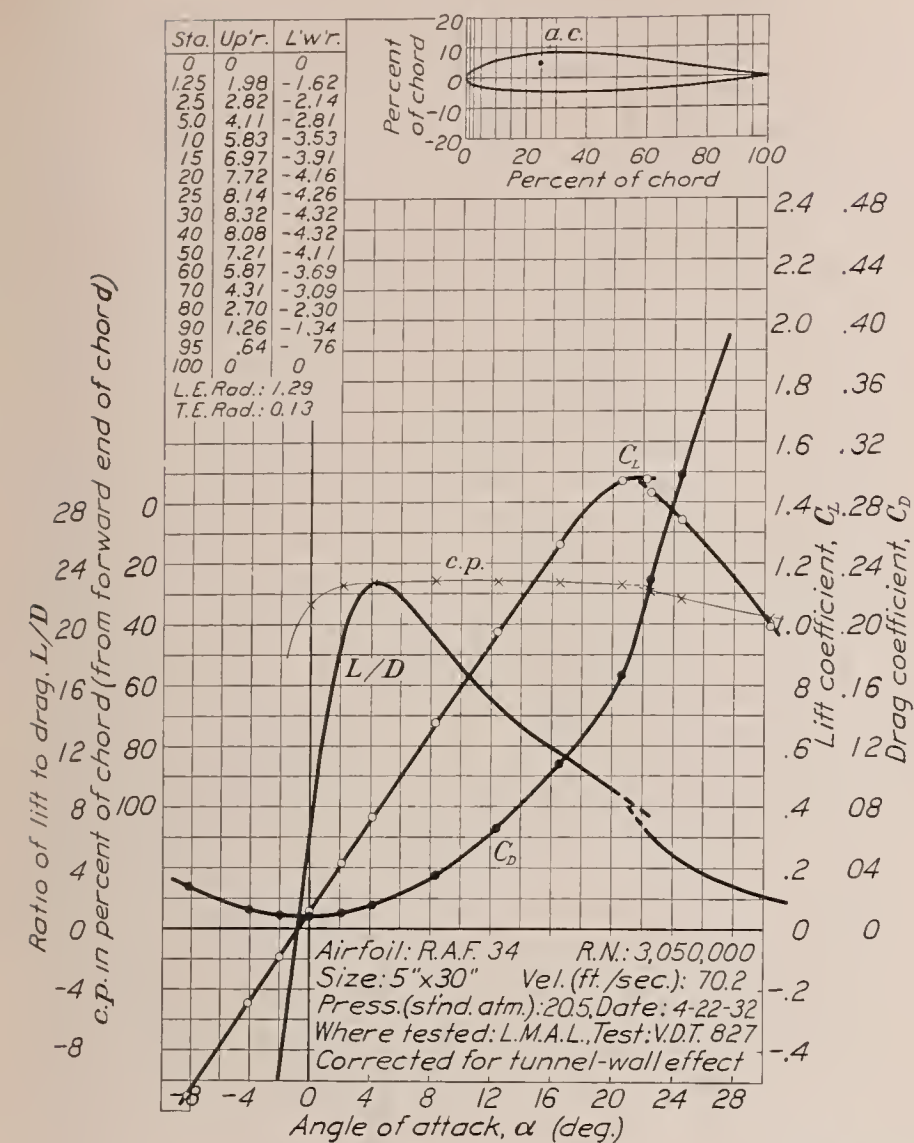


FIGURE 17.—R. A. F. 34 airfoil.

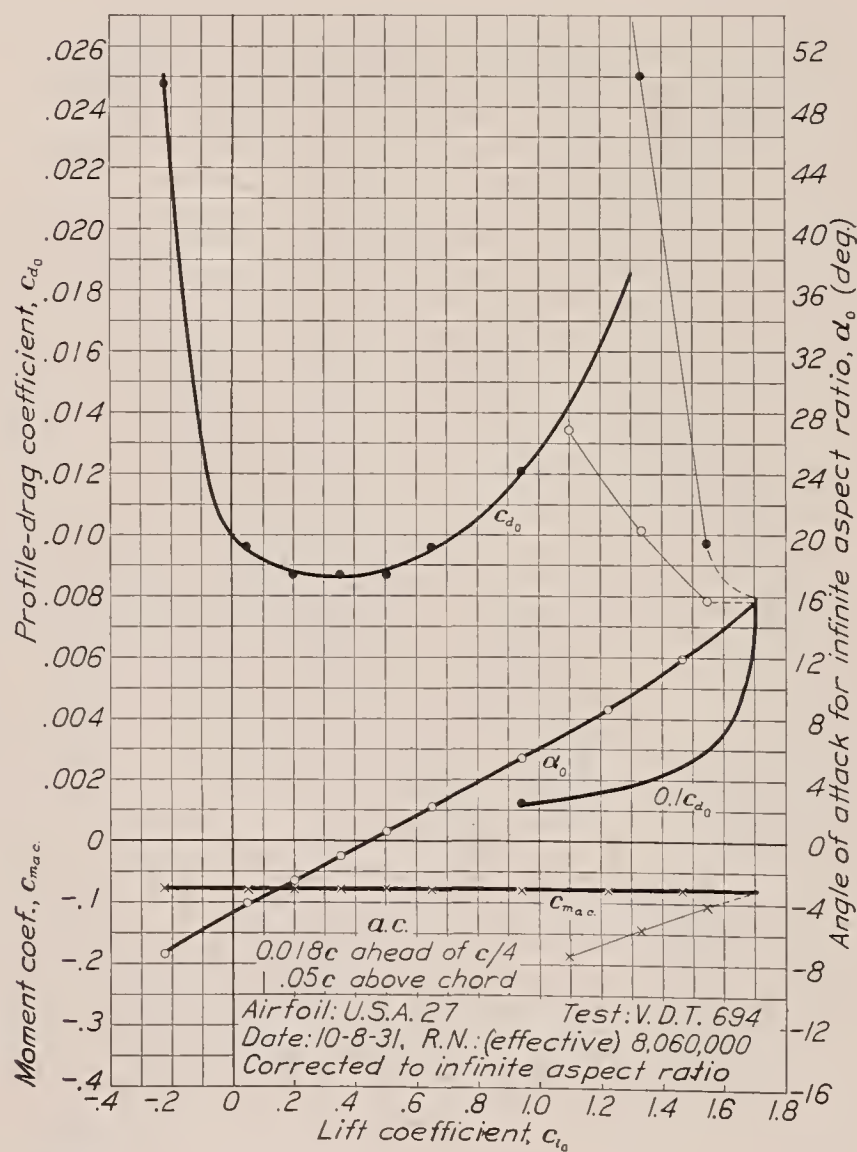
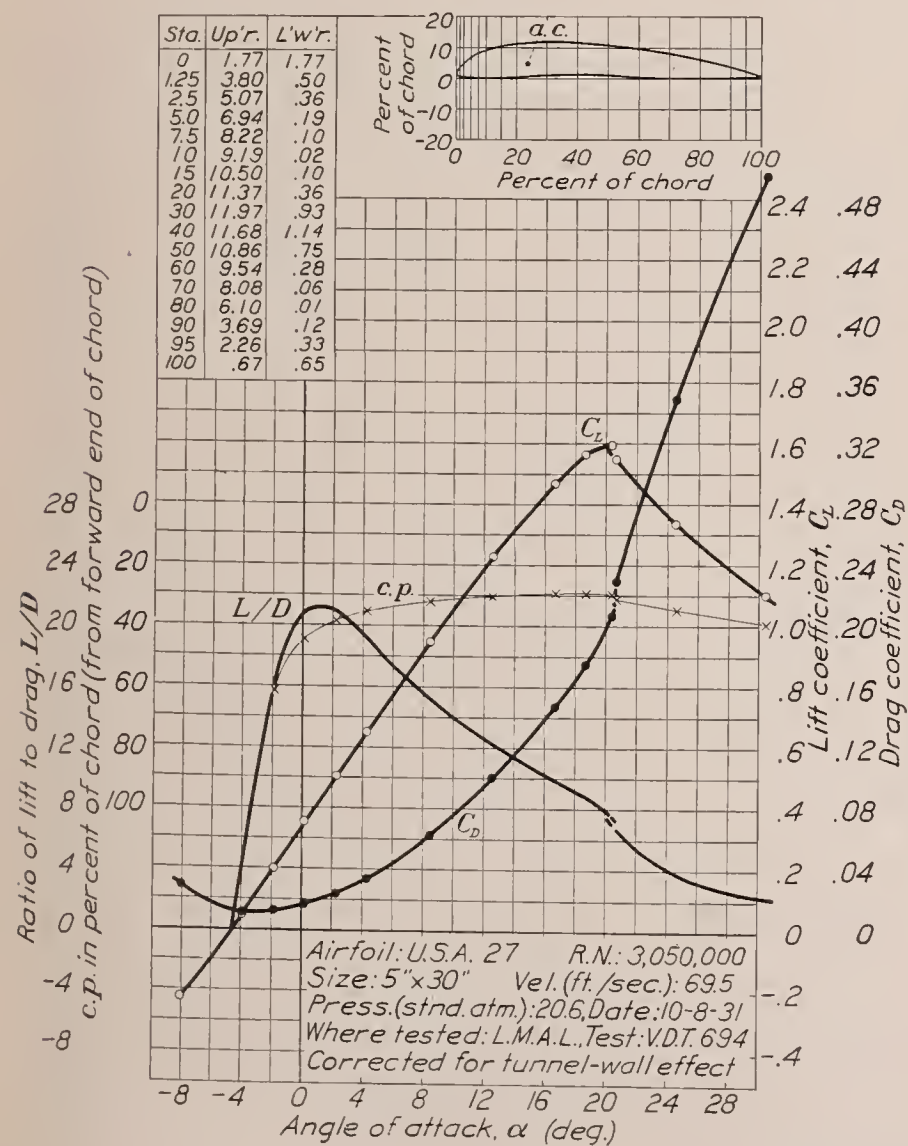


FIGURE 18.—U. S. A. 27 airfoil.

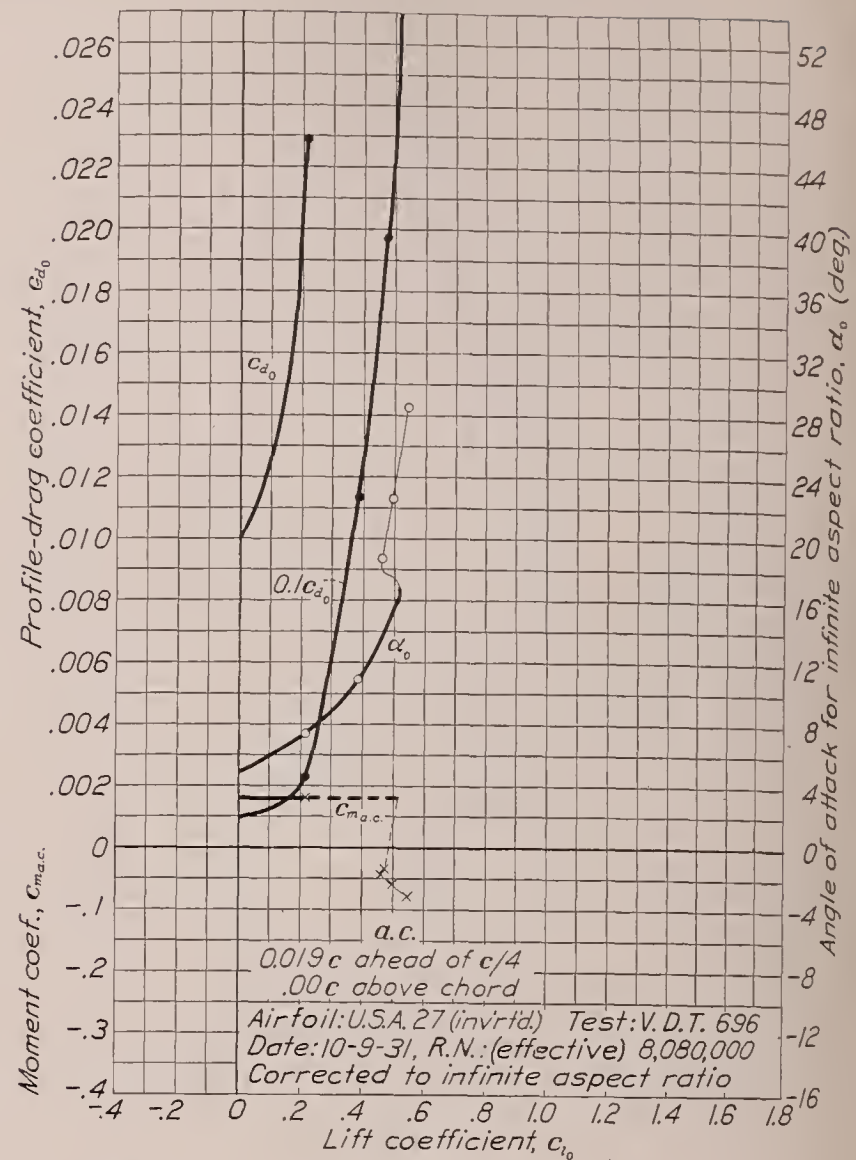
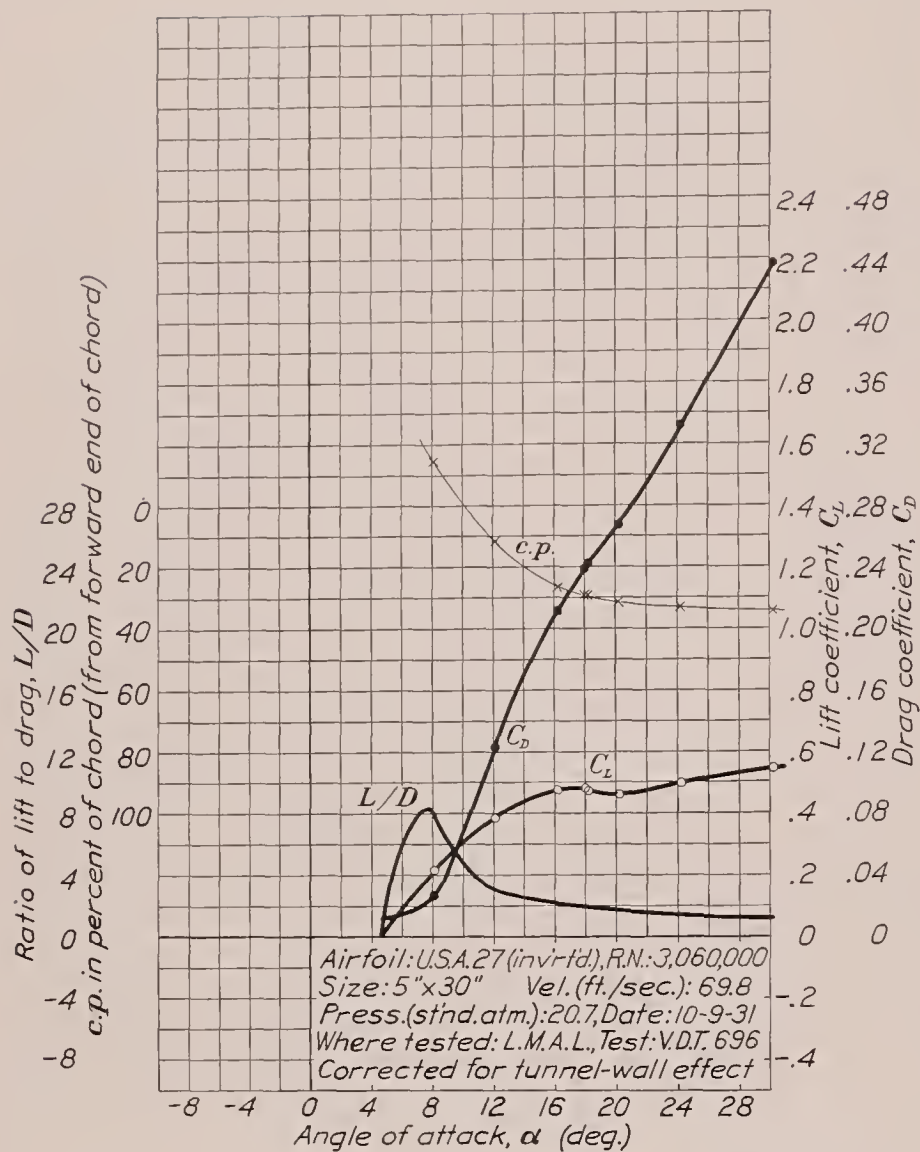


FIGURE 19.—U. S. A. 27 airfoil (inverted).

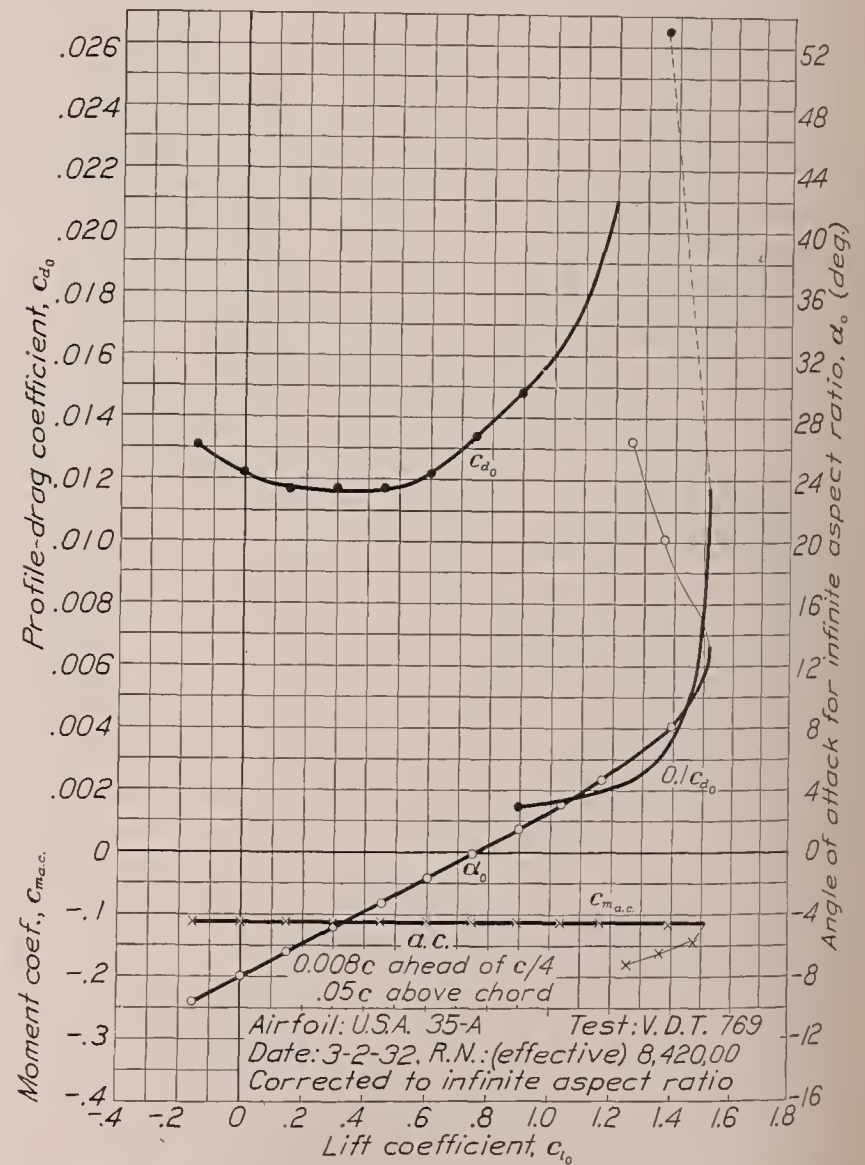
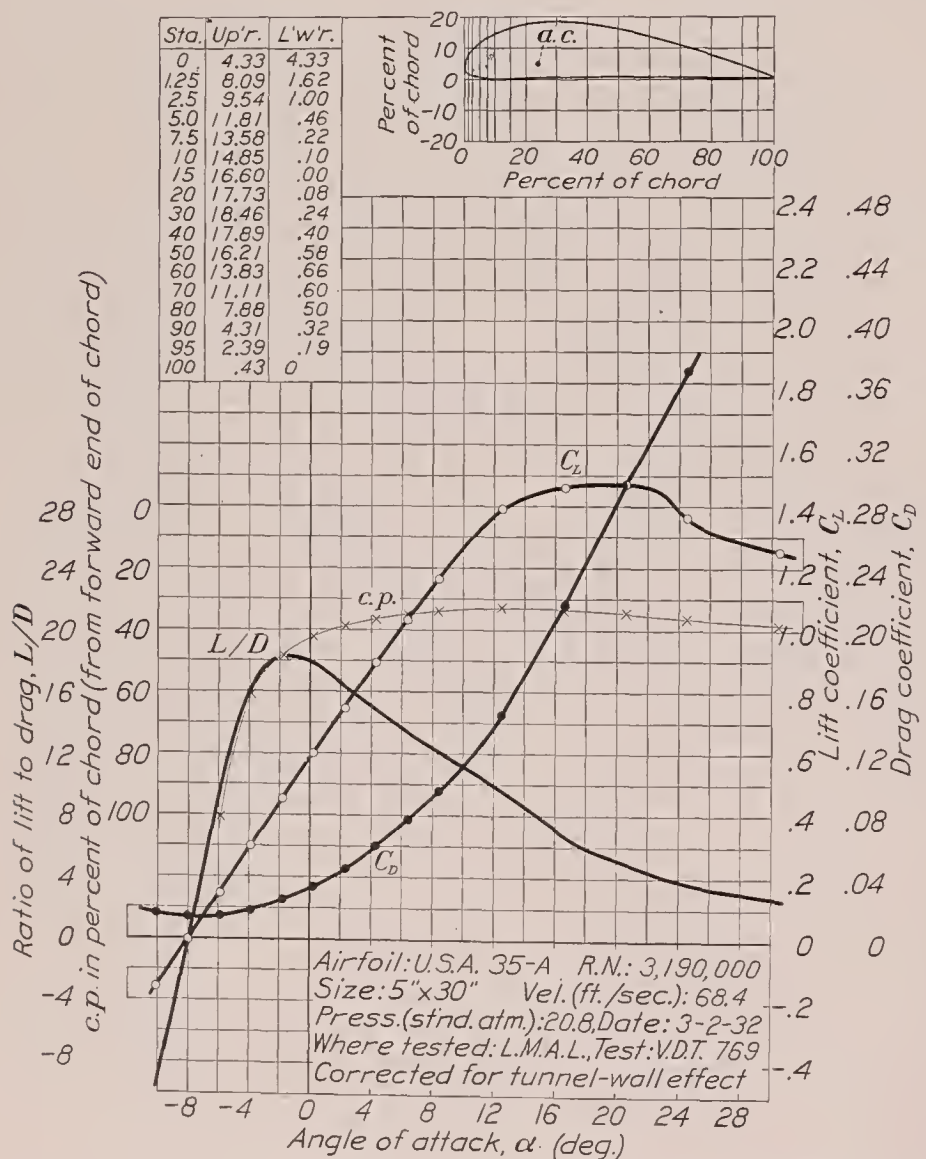


FIGURE 20.—U. S. A. 35-A airfoil.

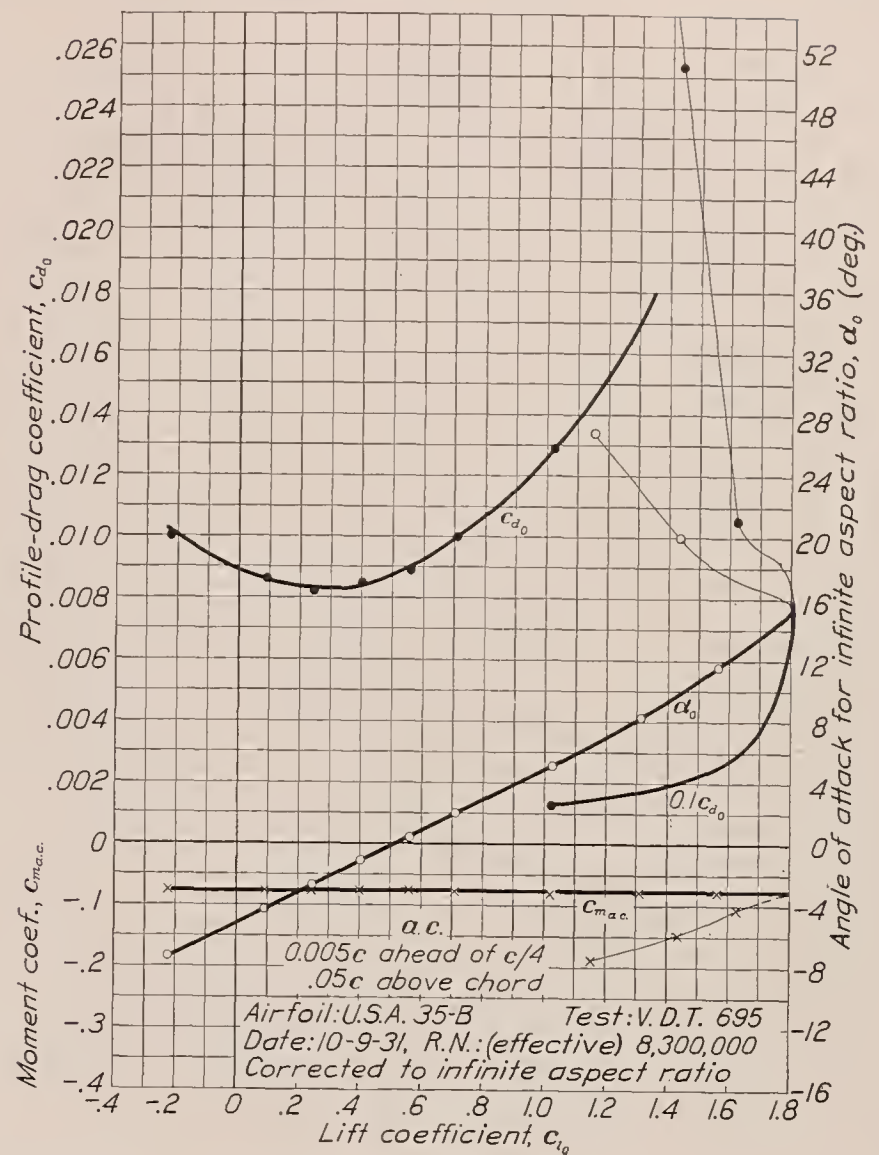
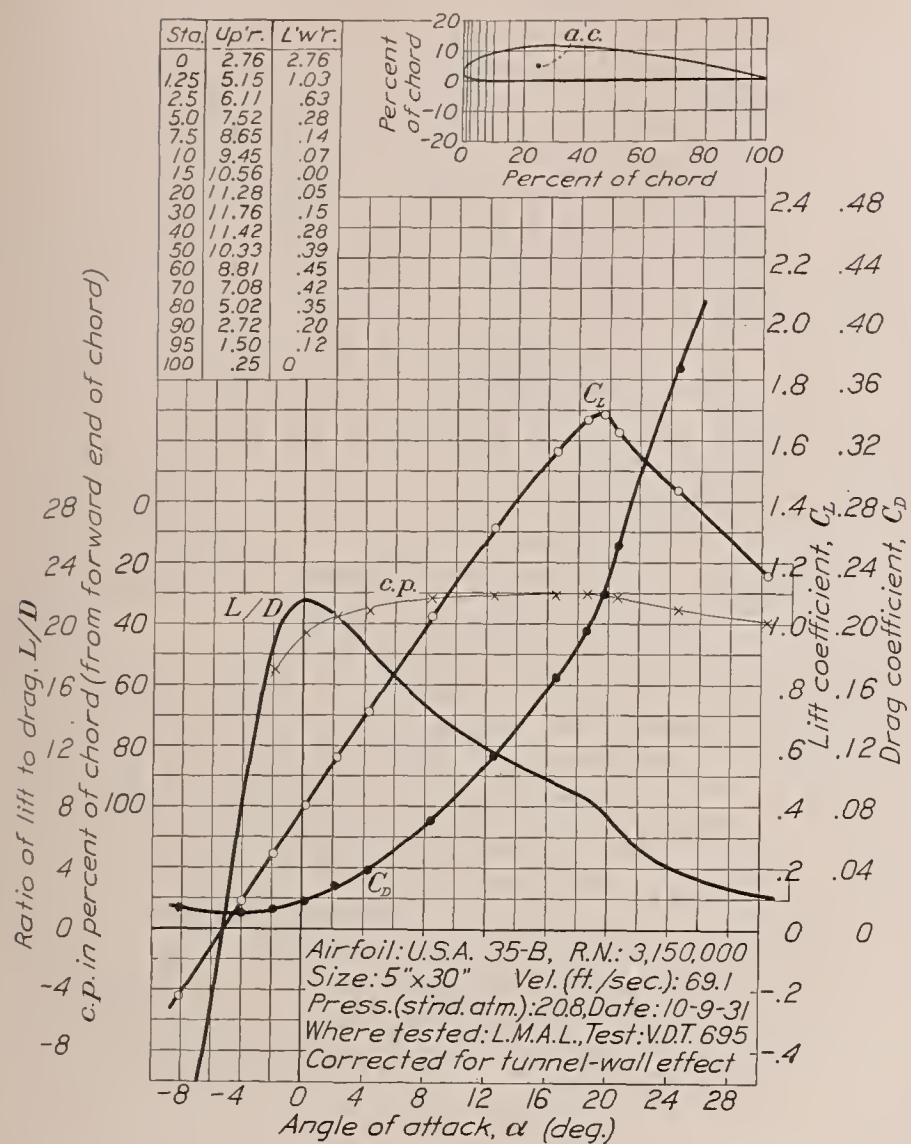


FIGURE 21.—U. S. A. 35-B airfoil.

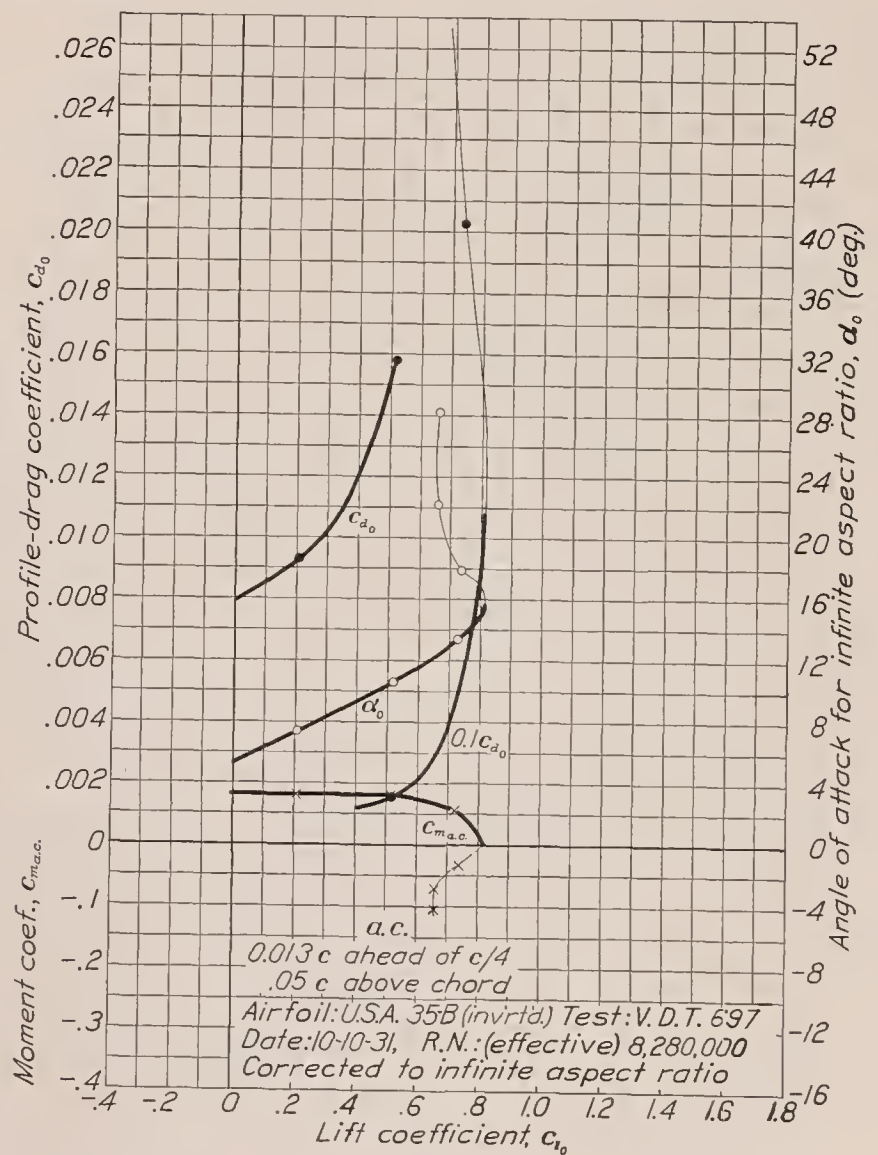
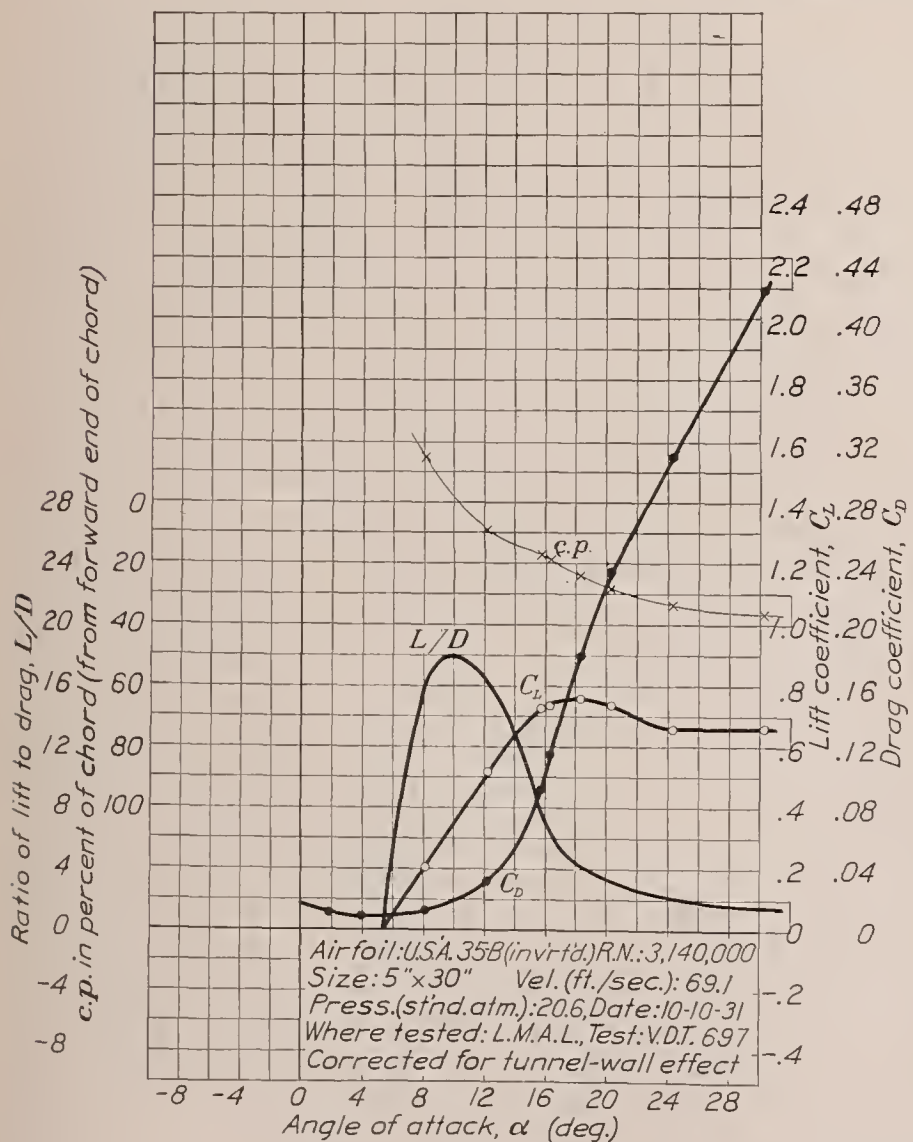


FIGURE 22.—U. S. A. 35-B airfoil (inverted).

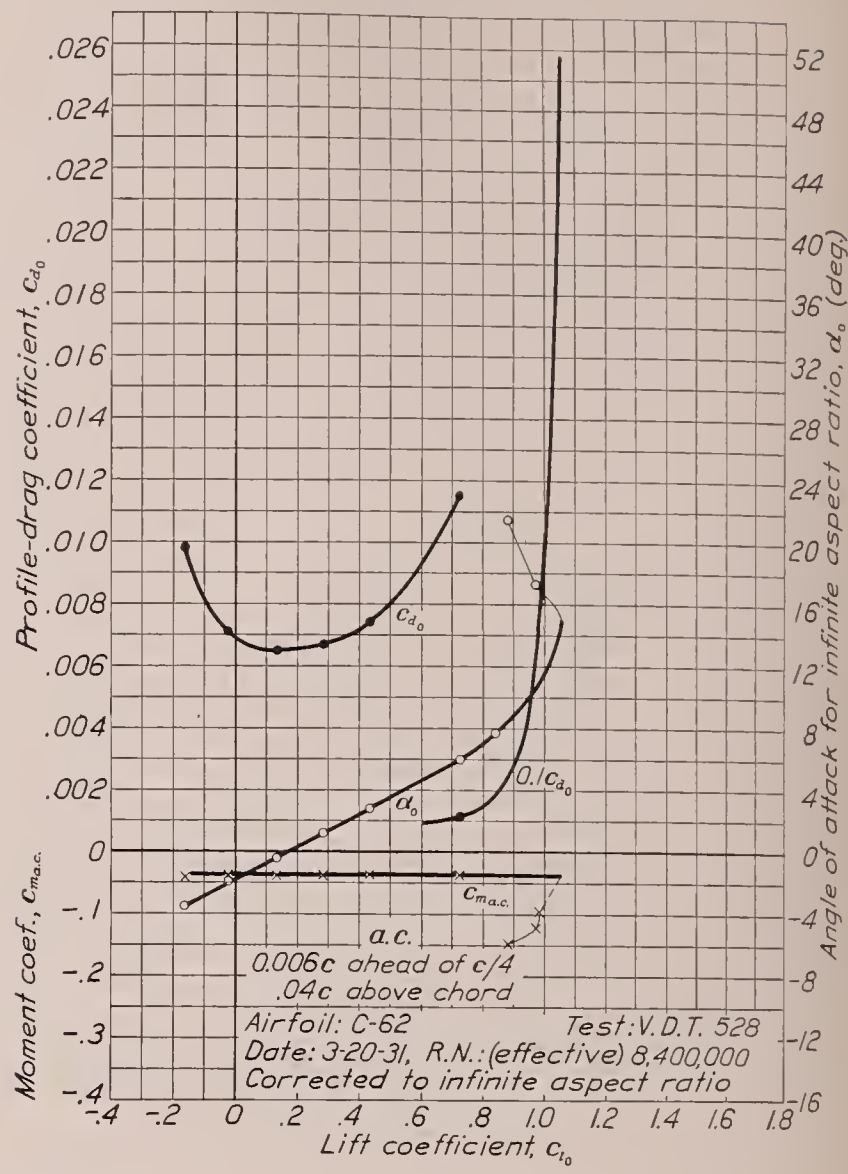
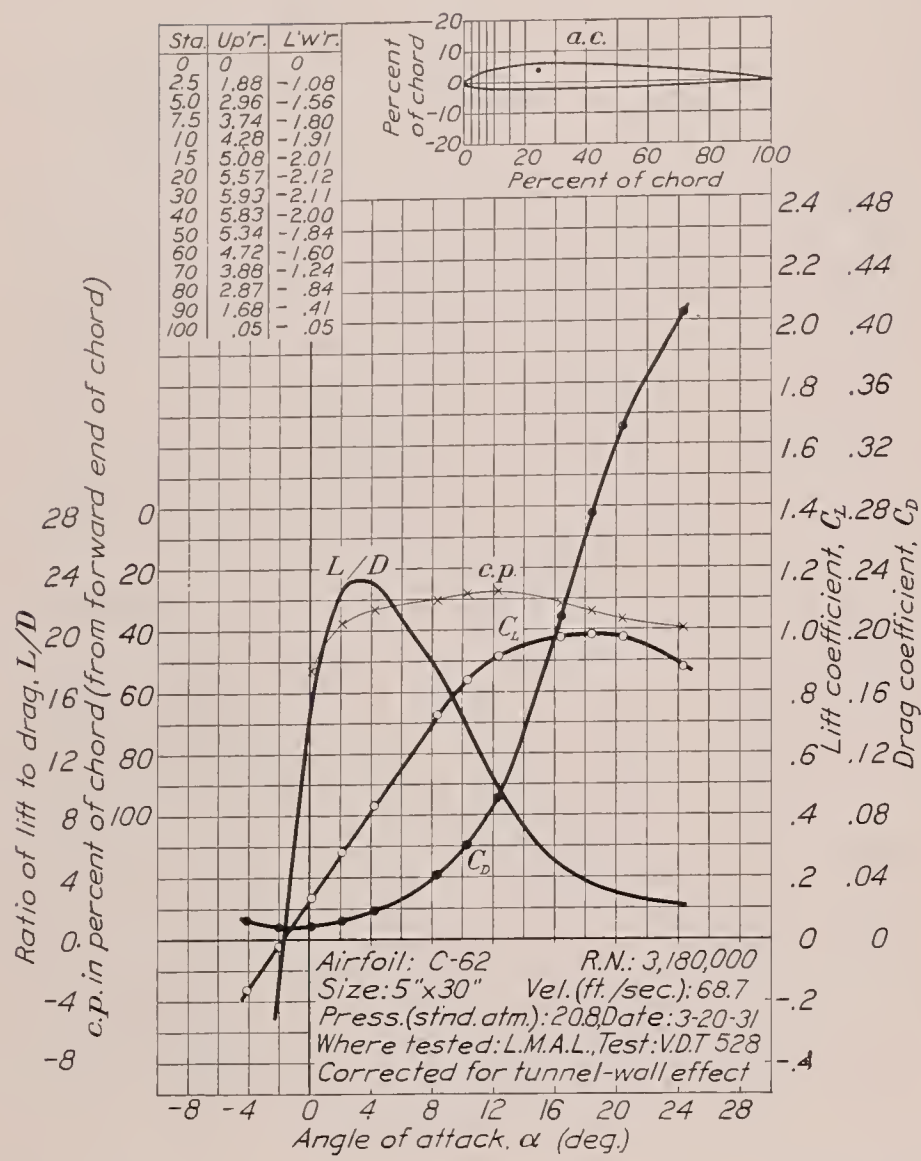


FIGURE 23.—C-62 airfoil.

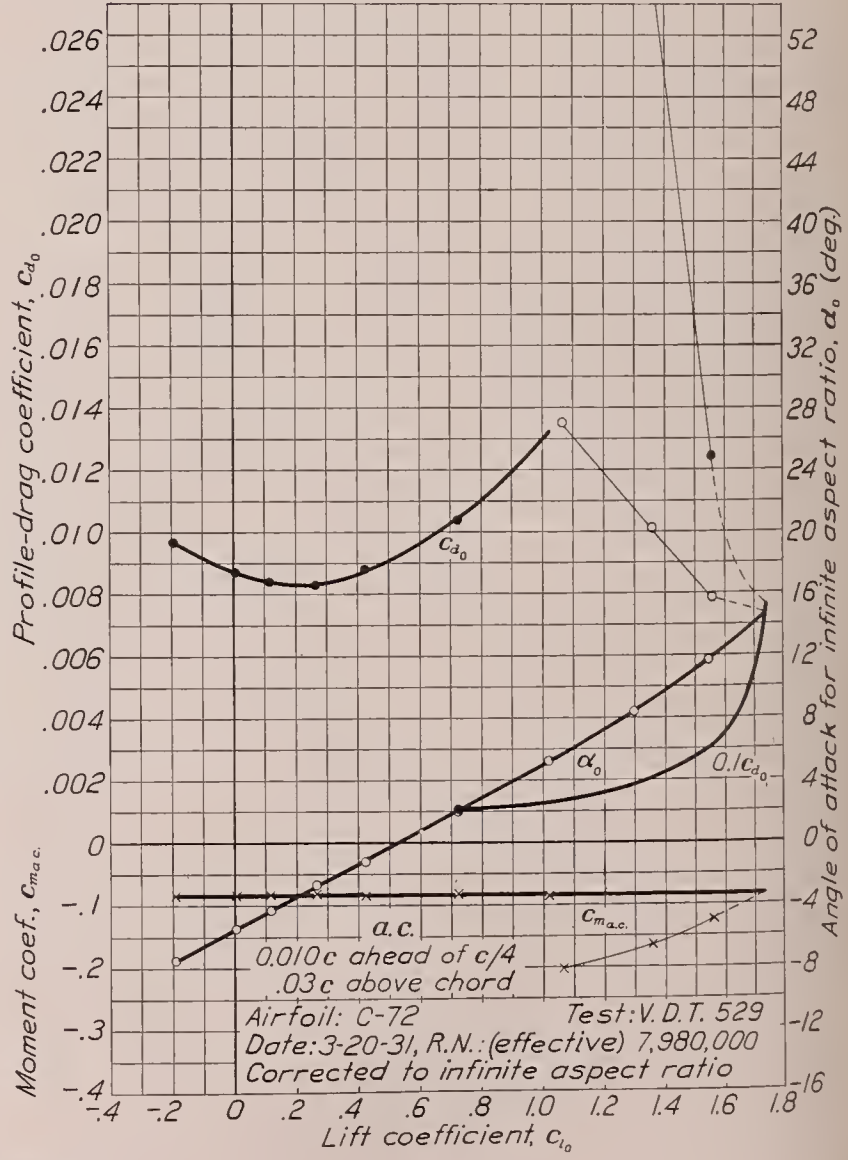
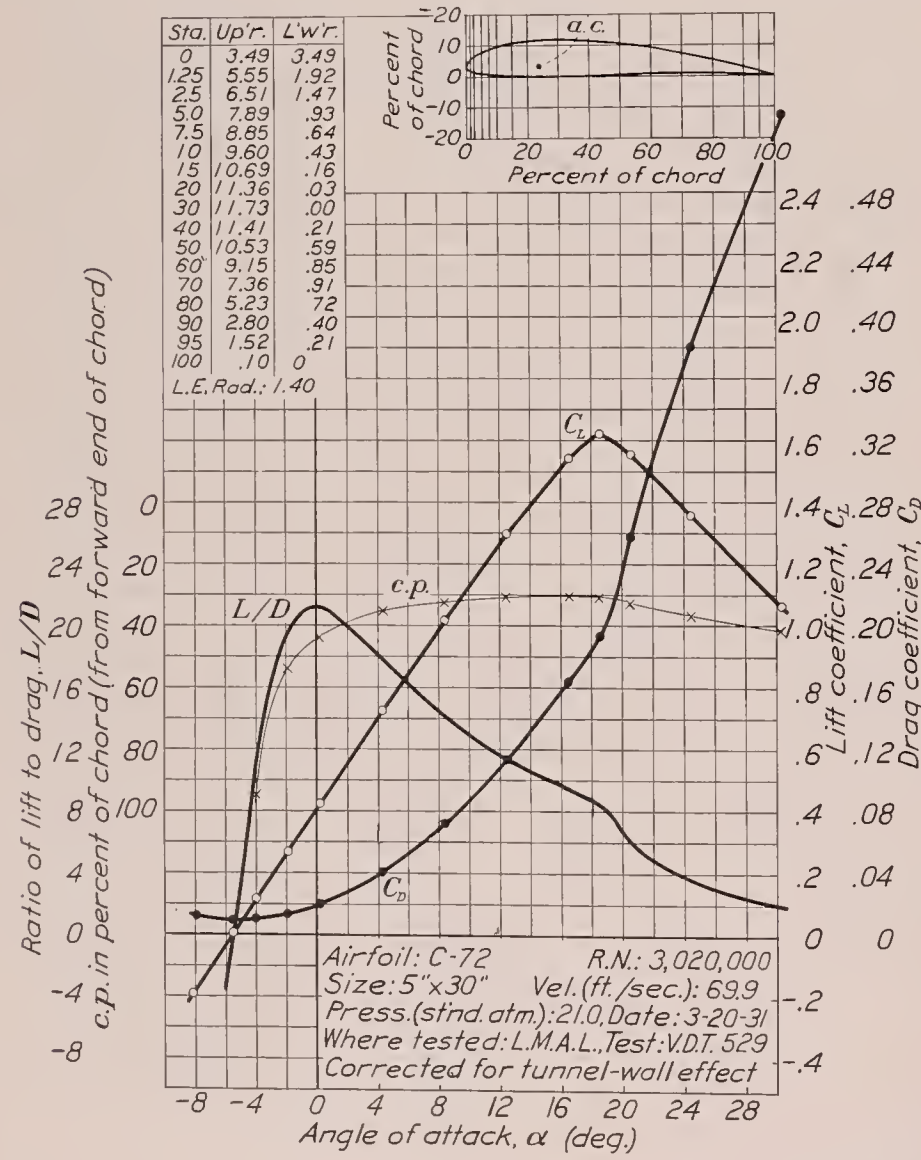


FIGURE 24.—C-72 airfoil.

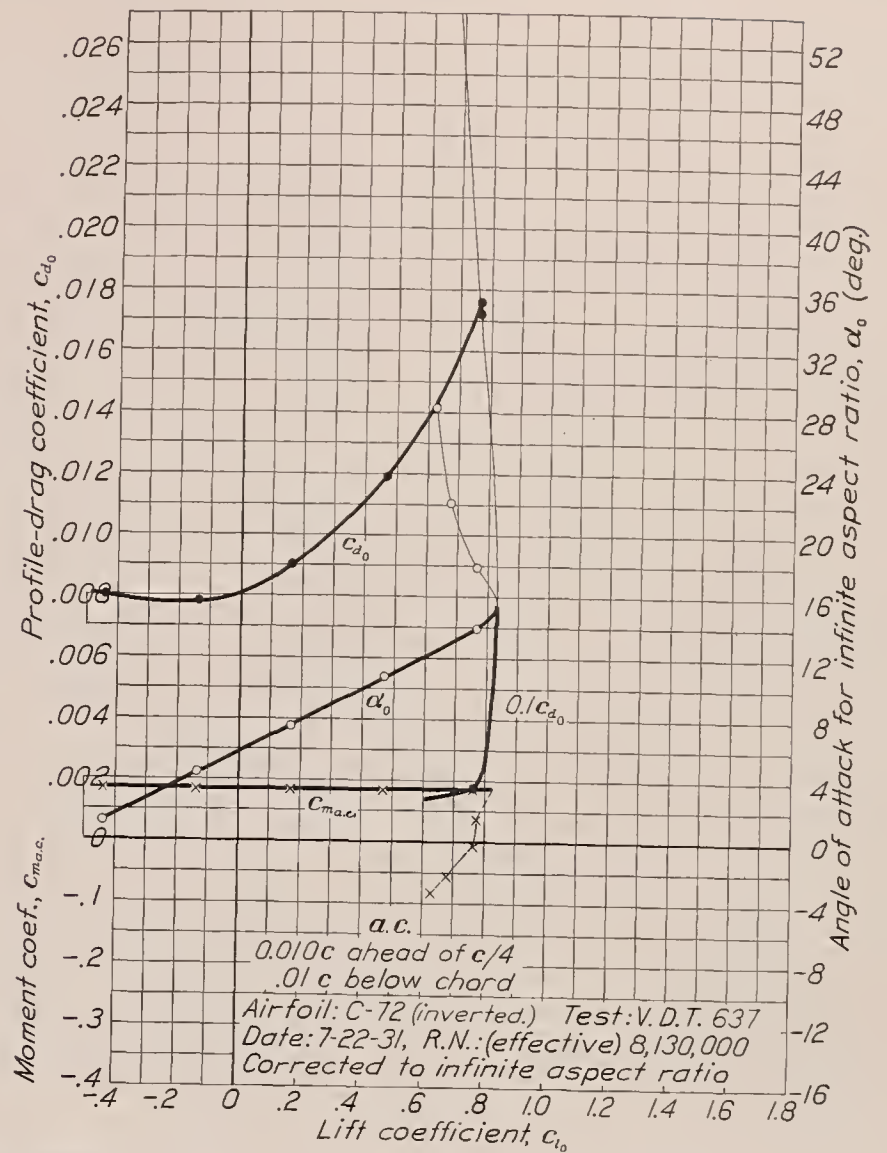
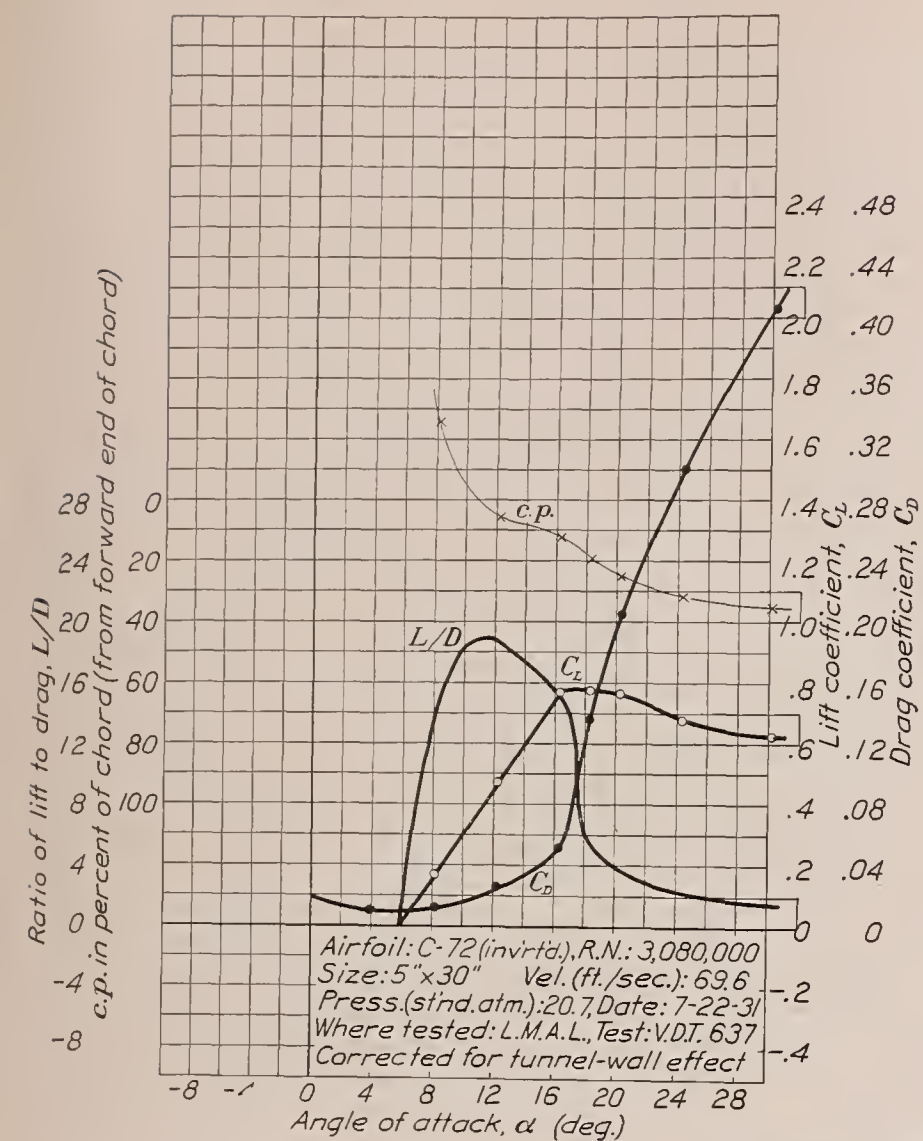


FIGURE 25.—C-72 airfoil (inverted).

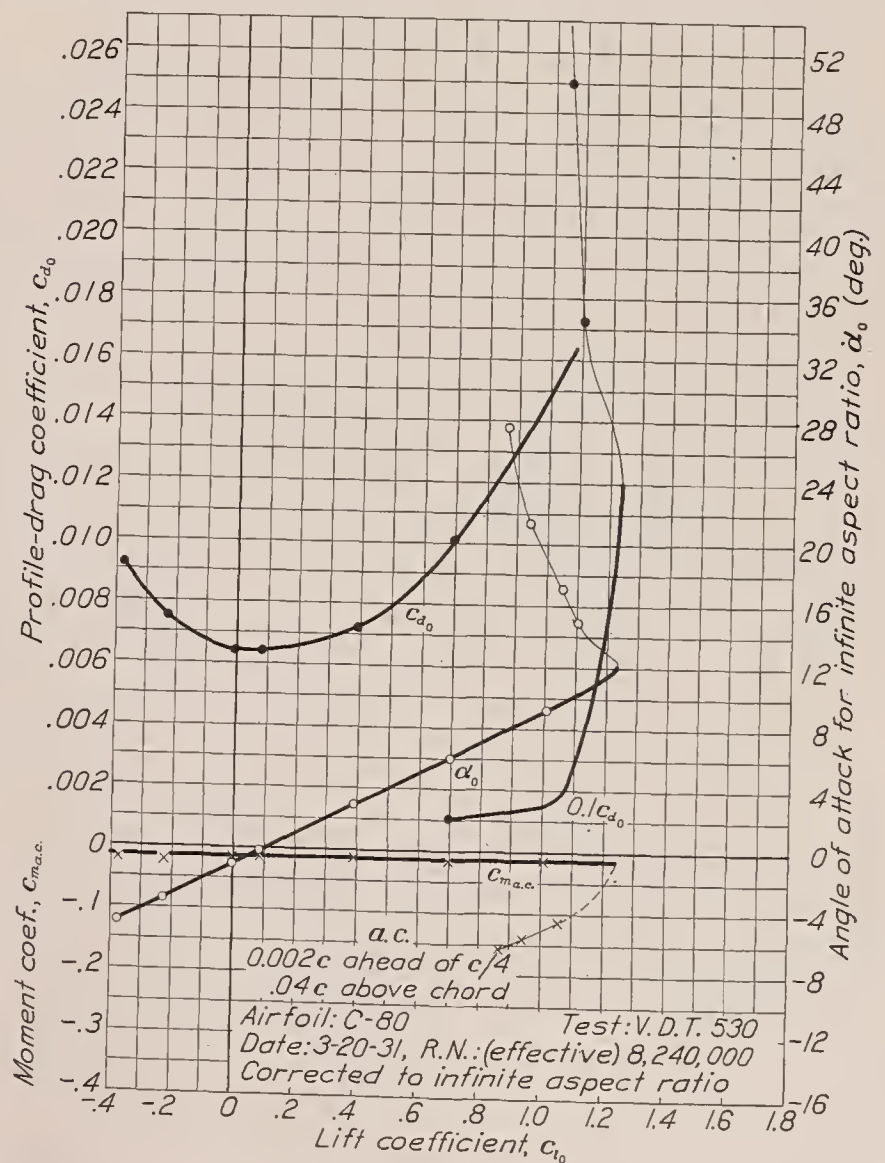
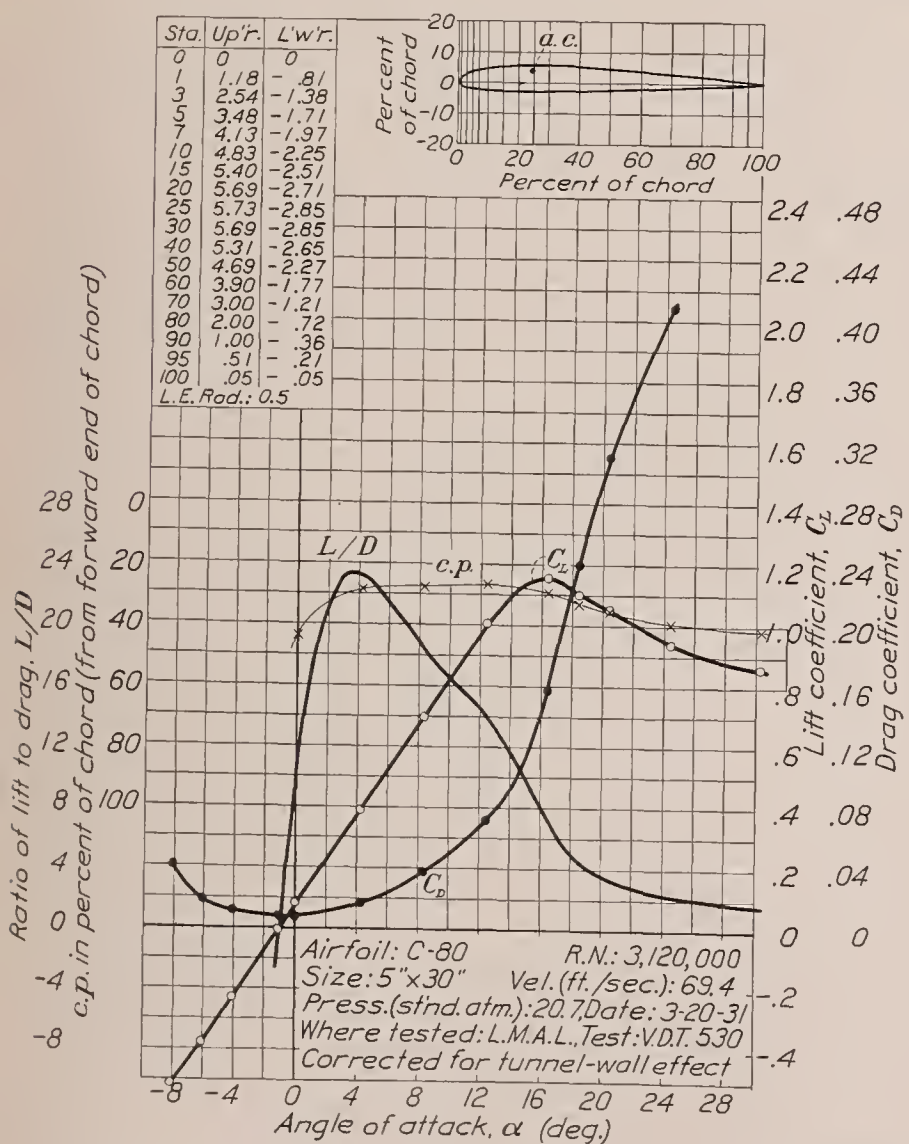


FIGURE 26.—C-80 airfoil.

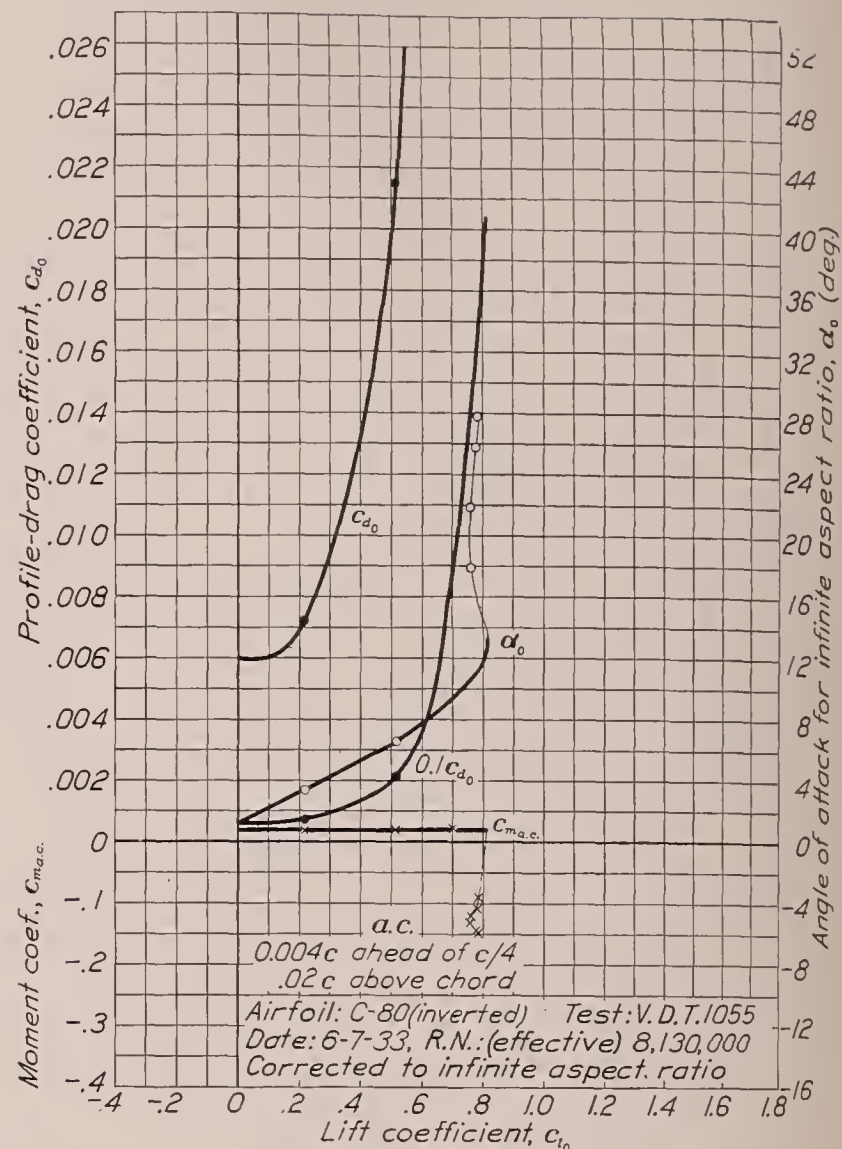
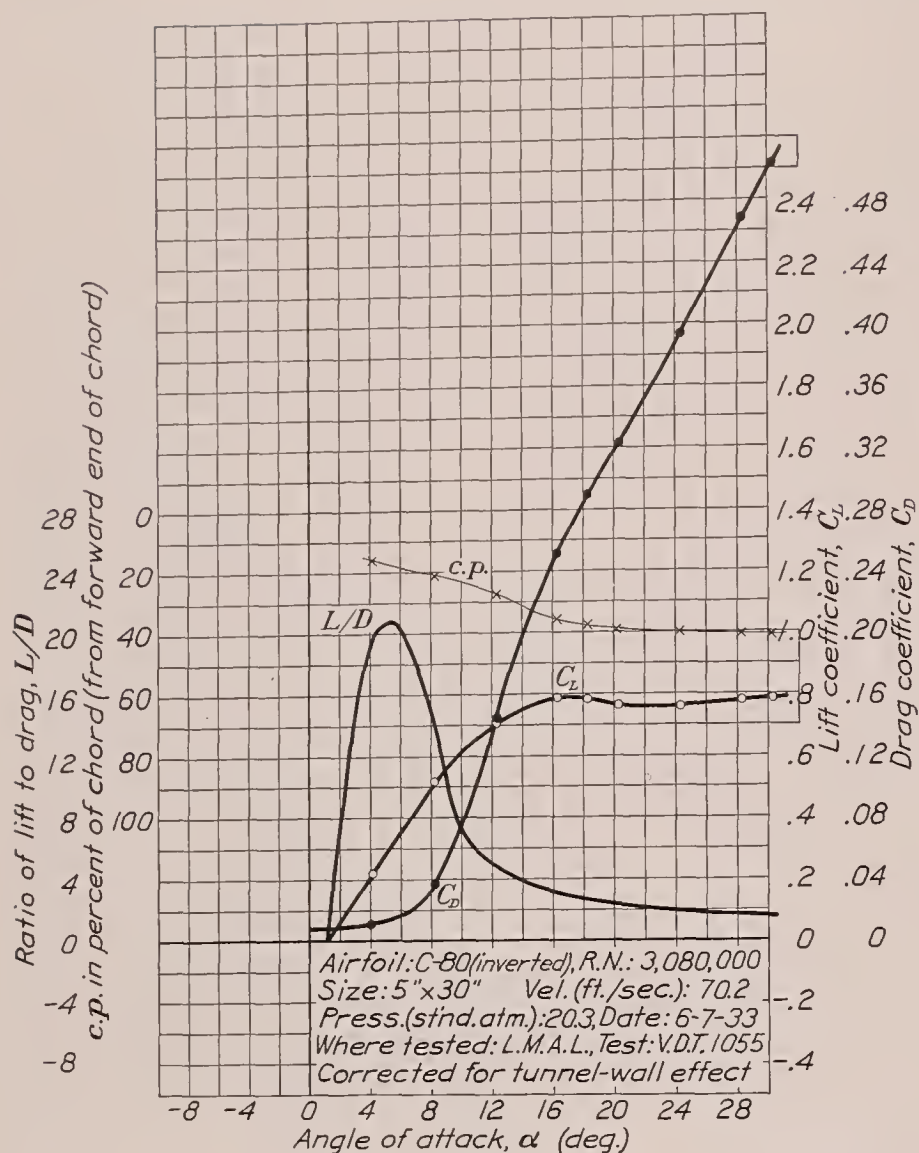


FIGURE 27.—C-80 airfoil (inverted).

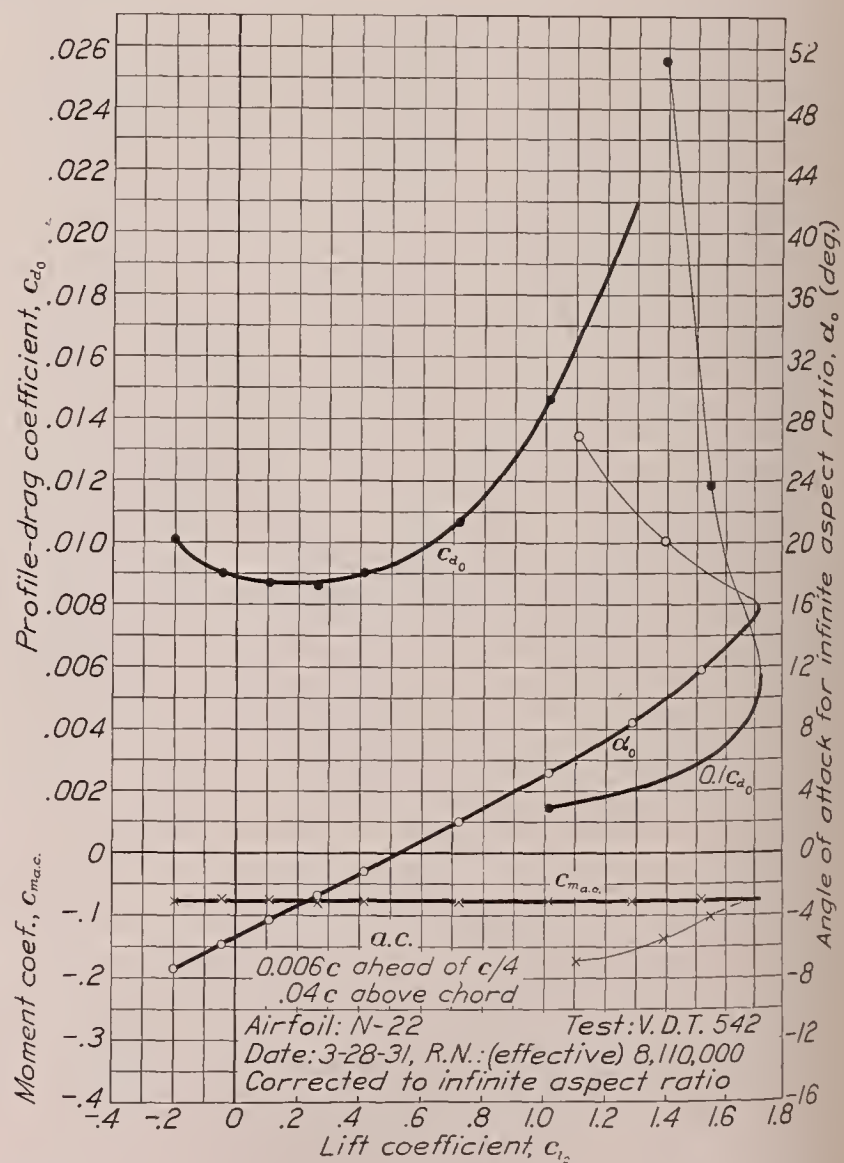
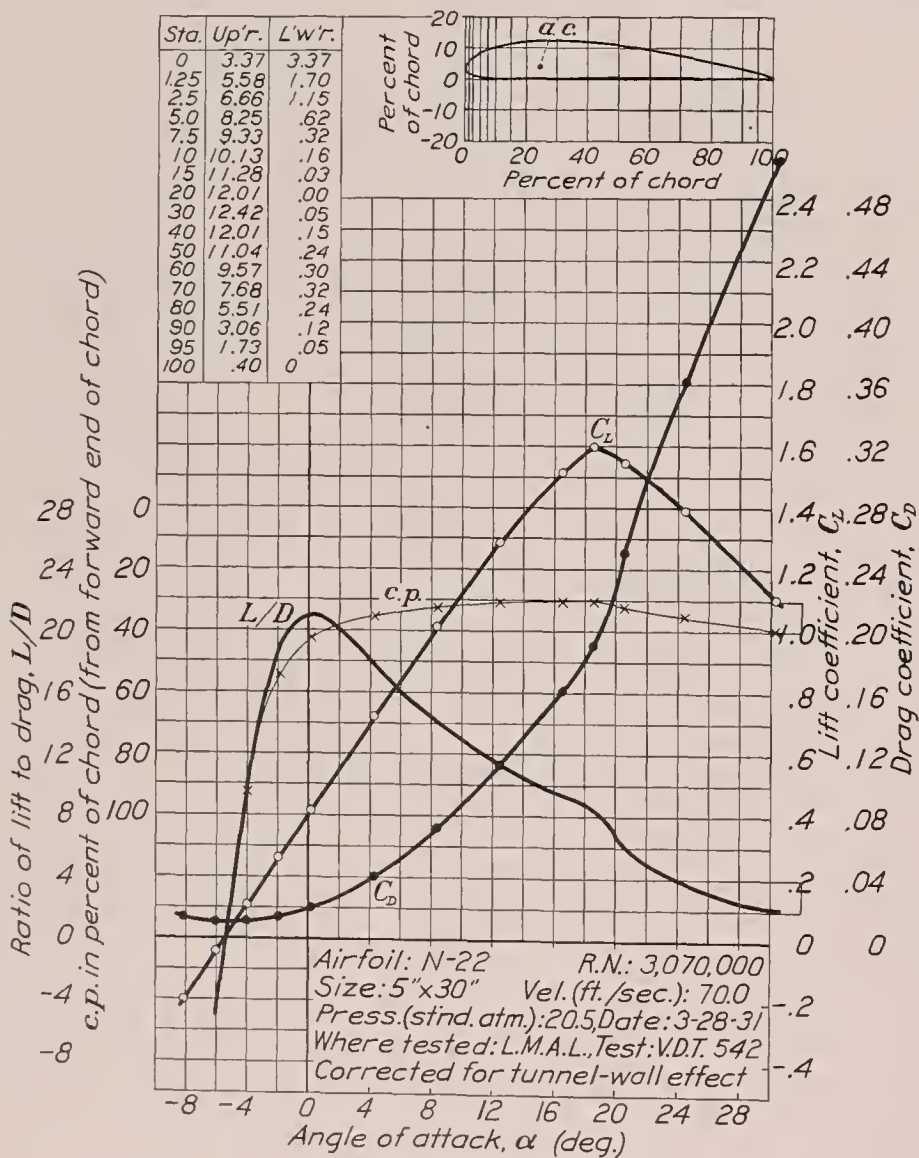


FIGURE 28.—N-22 airfoil.

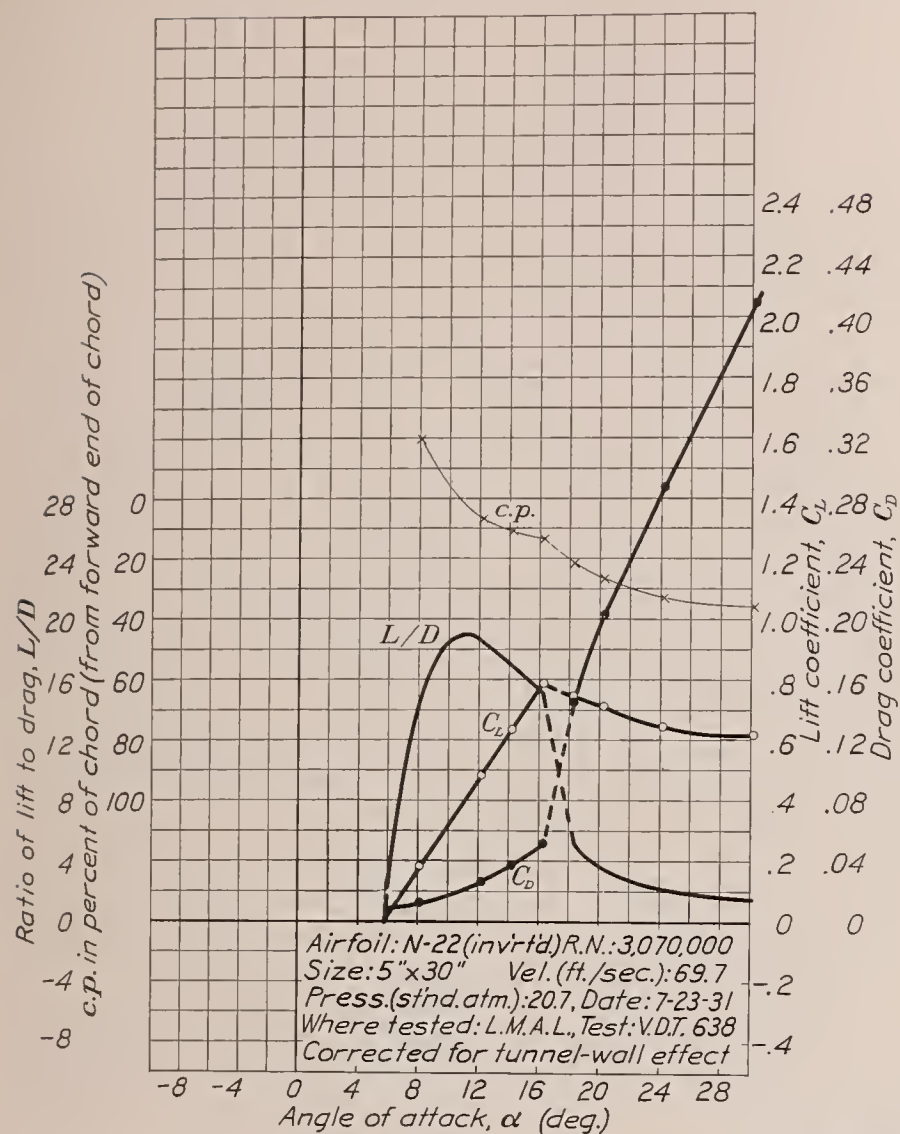


FIGURE 29.—N-22 airfoil (inverted).

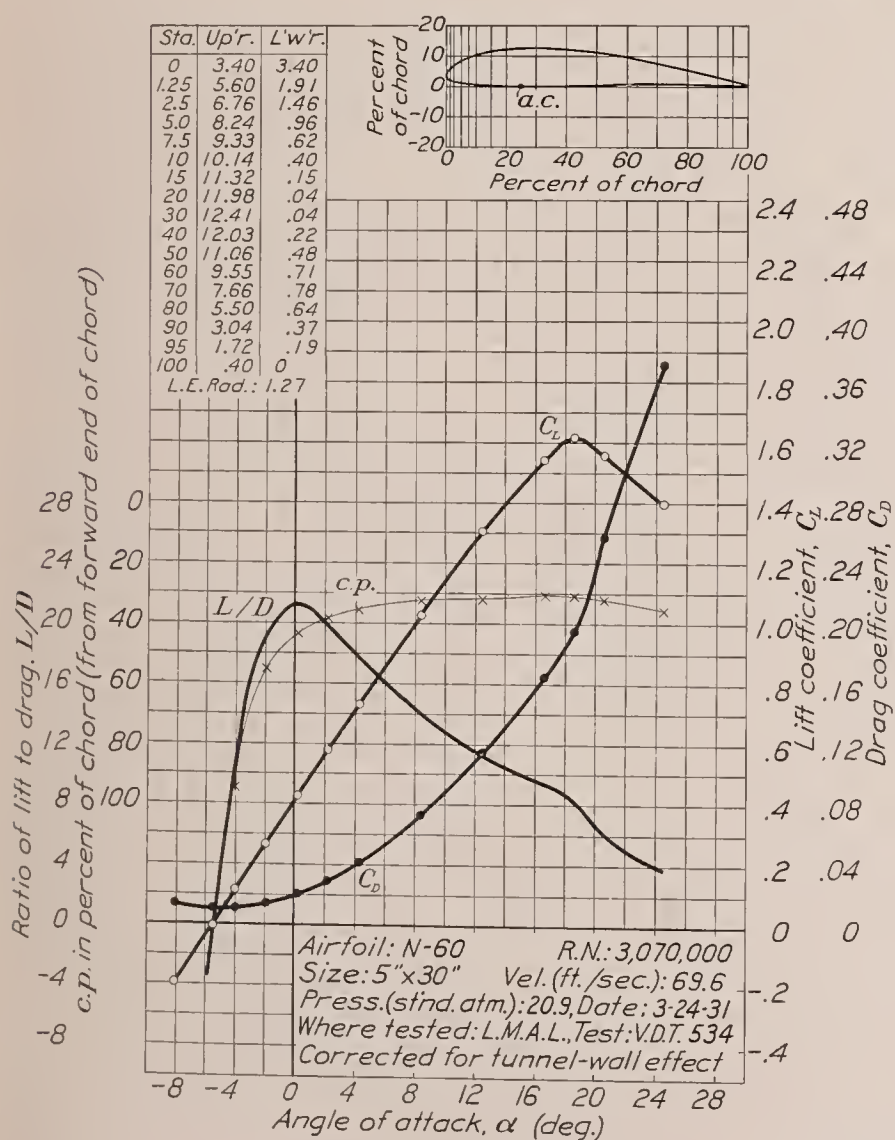
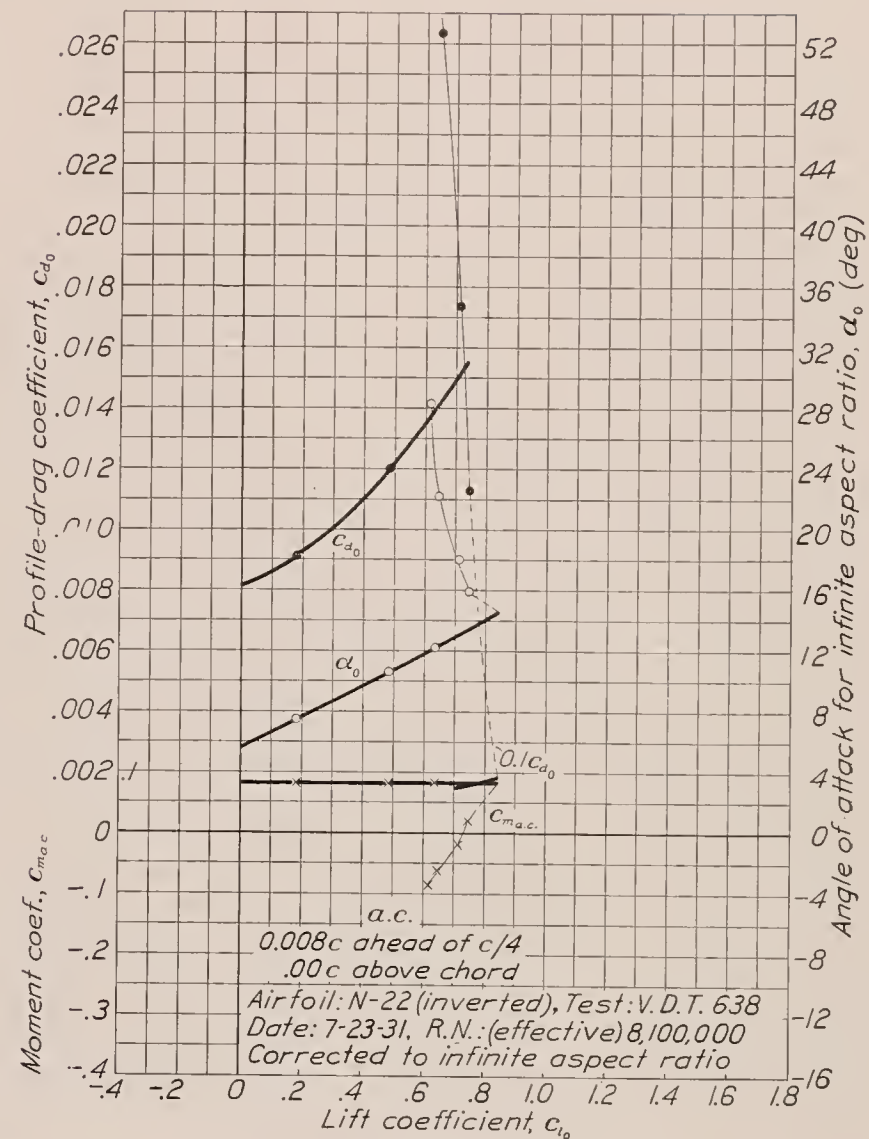
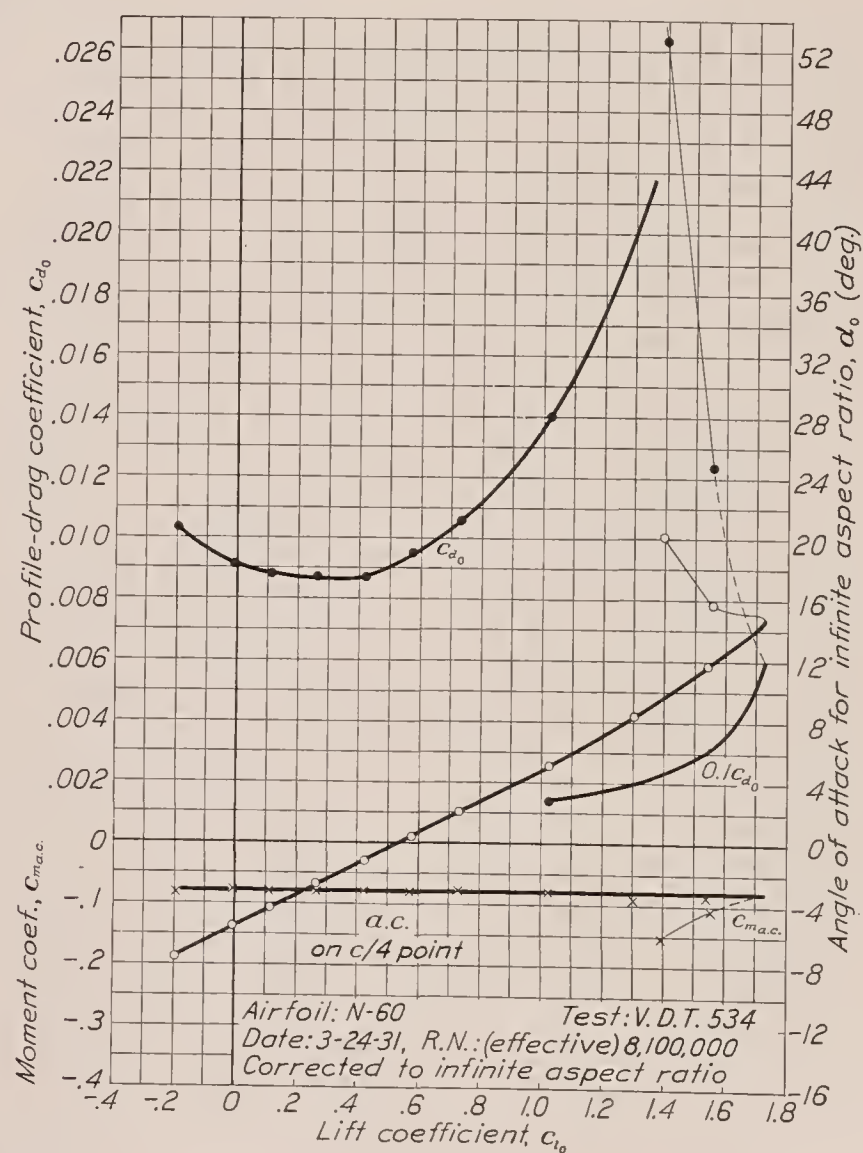


FIGURE 30.—N-60 airfoil.



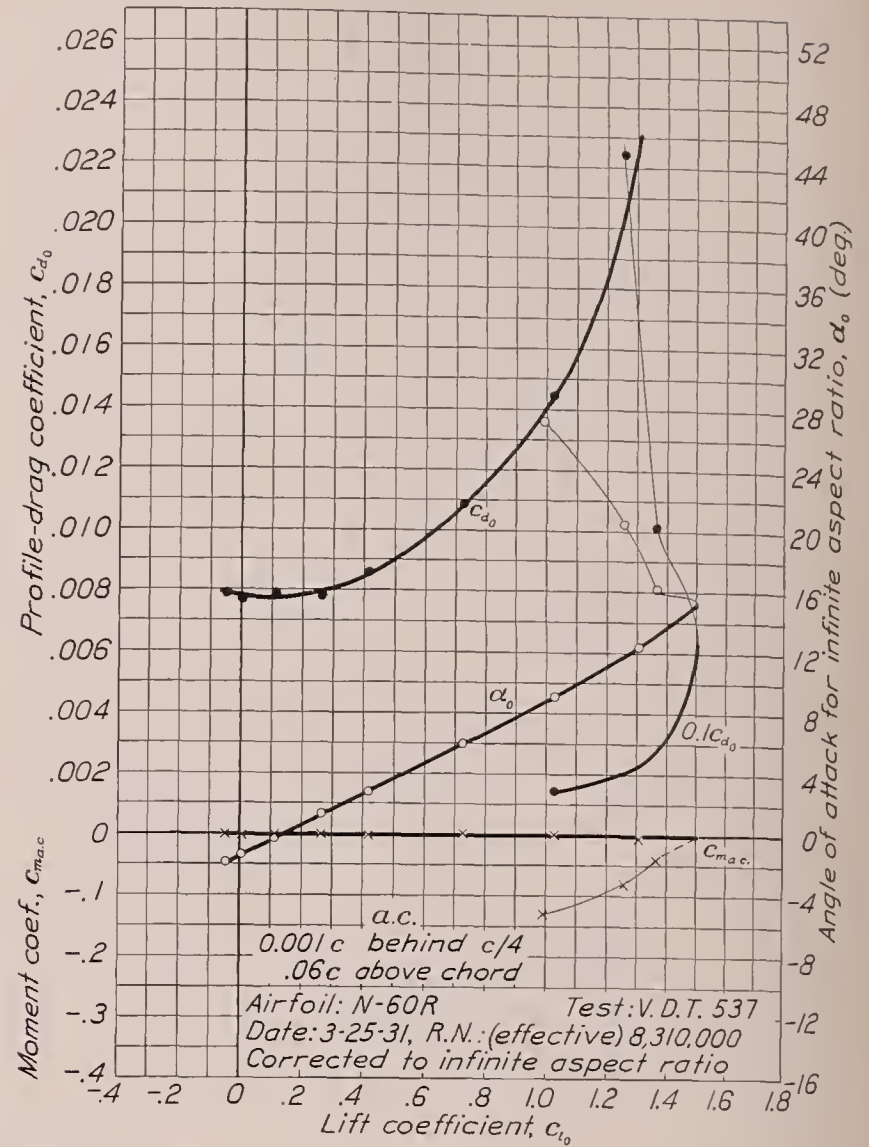
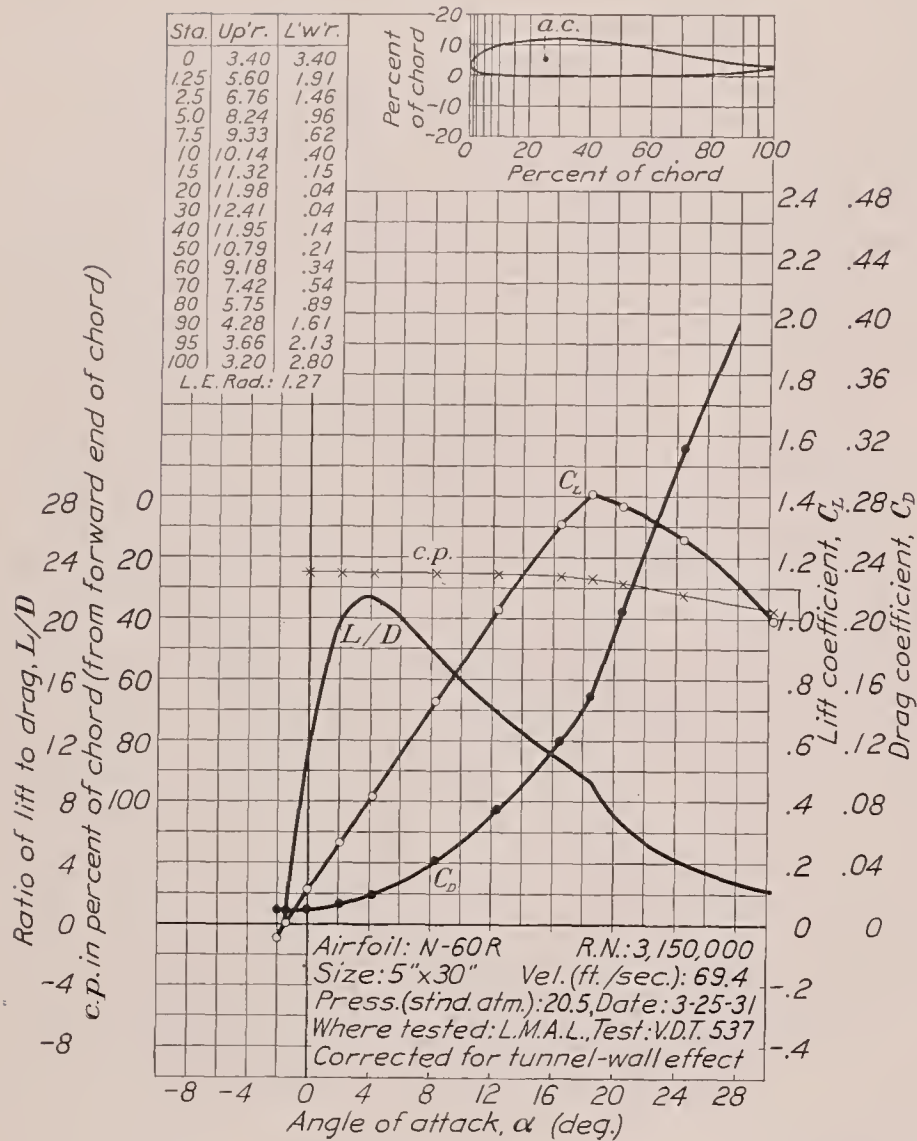


FIGURE 31.—N-60 R airfoil.

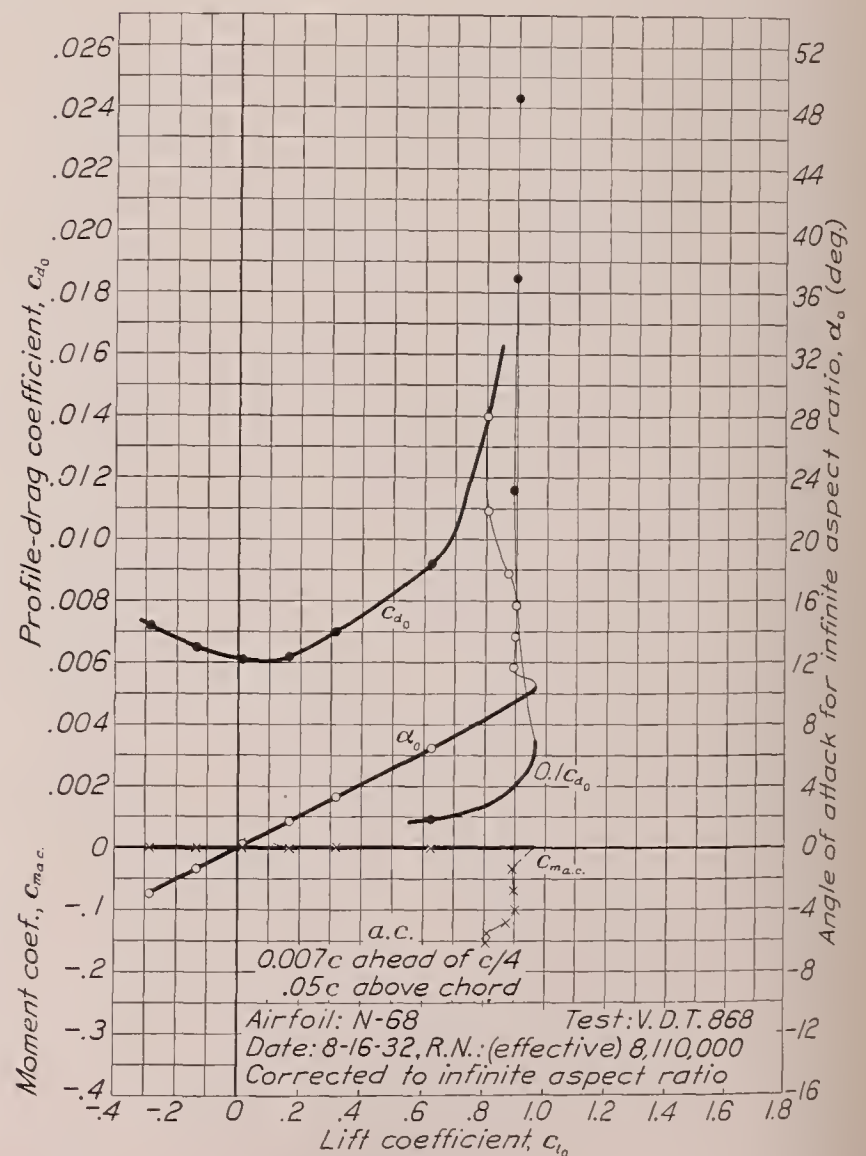
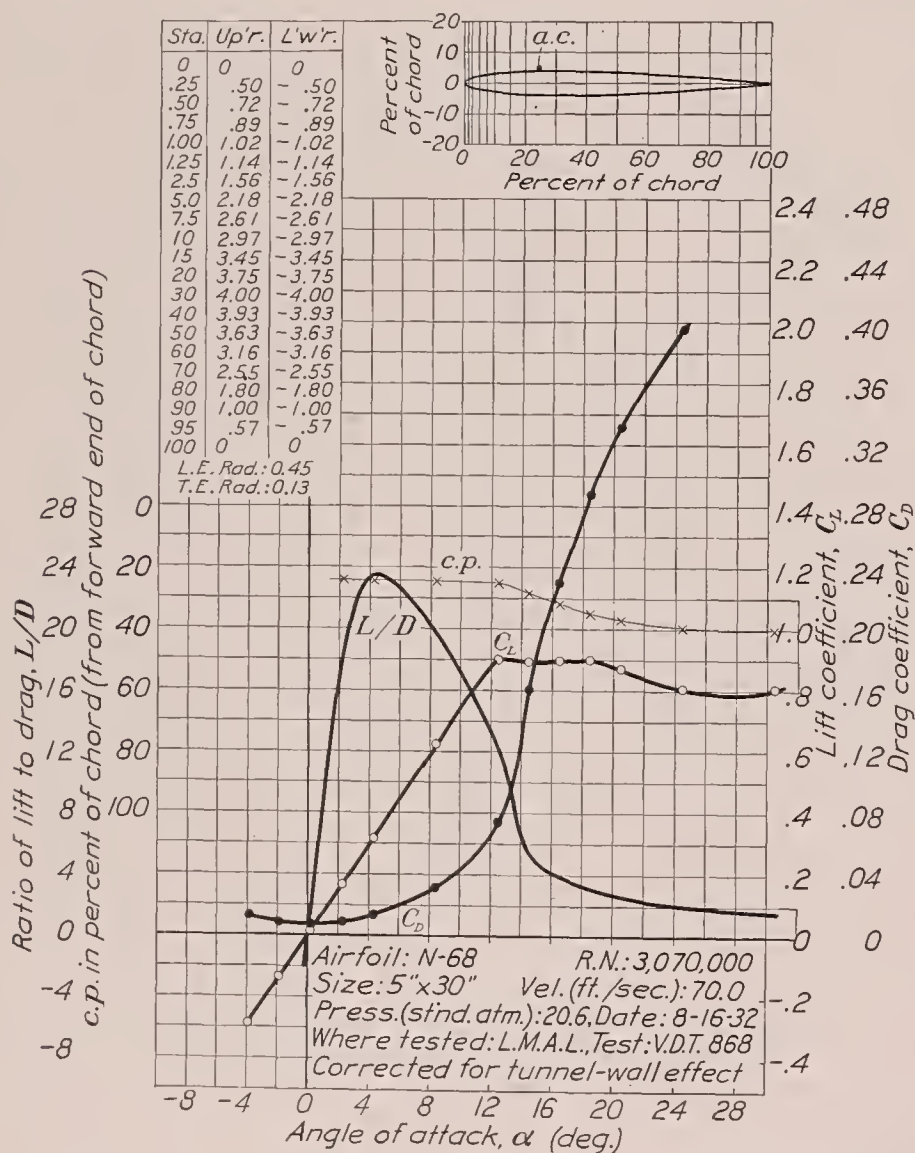


FIGURE 32.—N-68 airfoil.

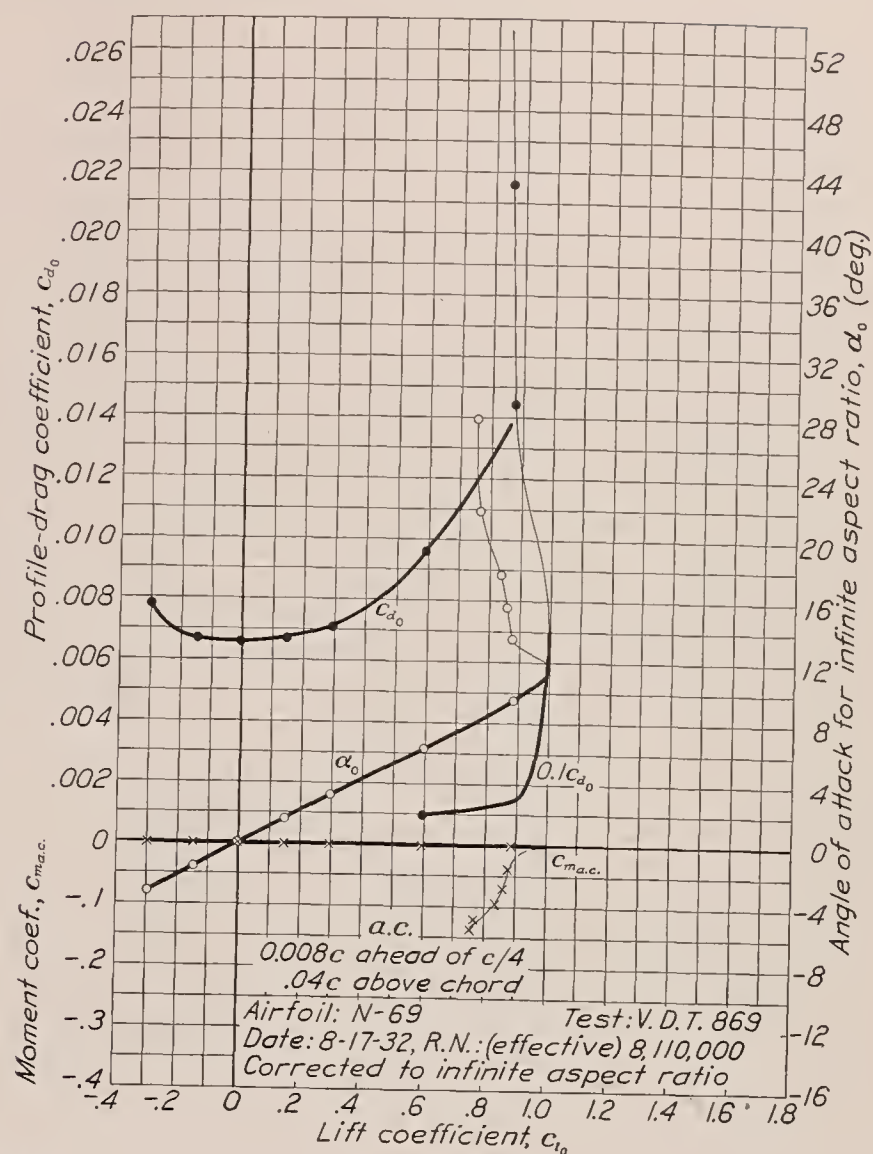
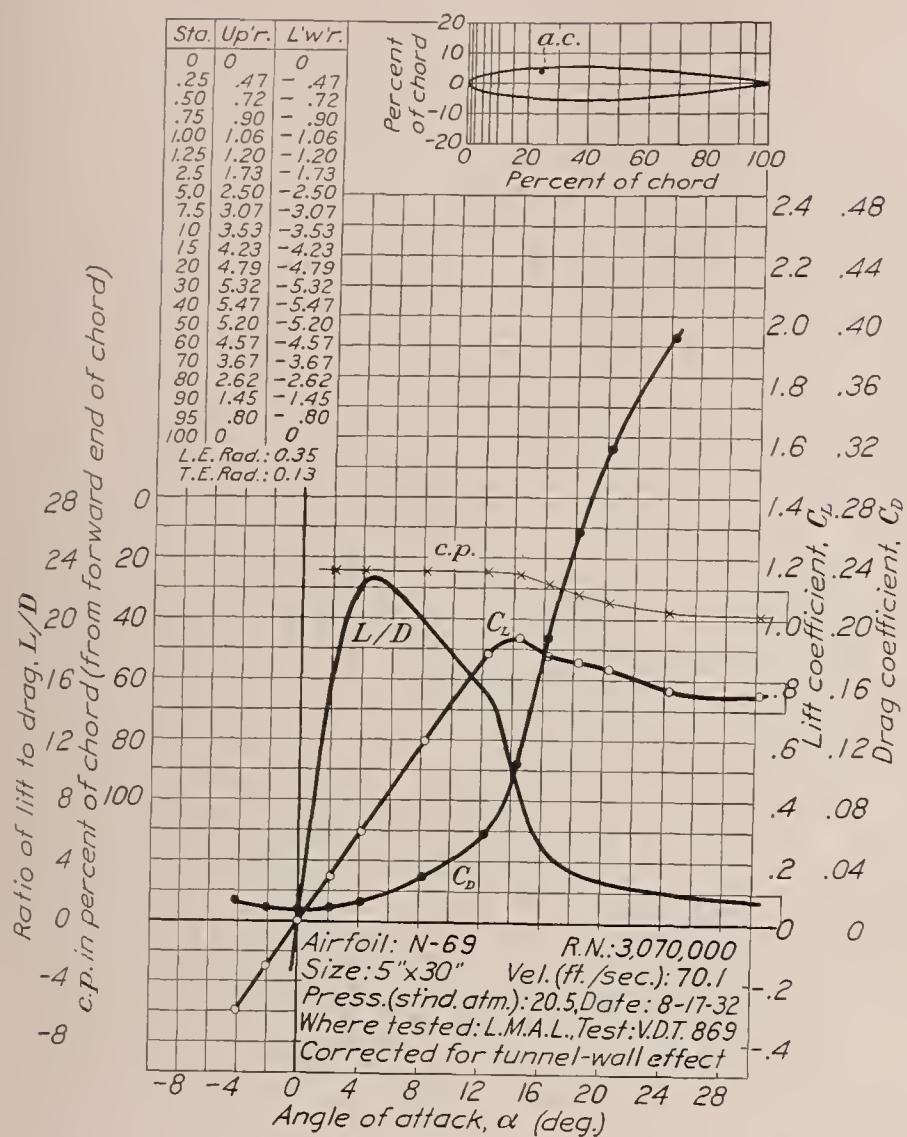


FIGURE 33.—N-69 airfoil.

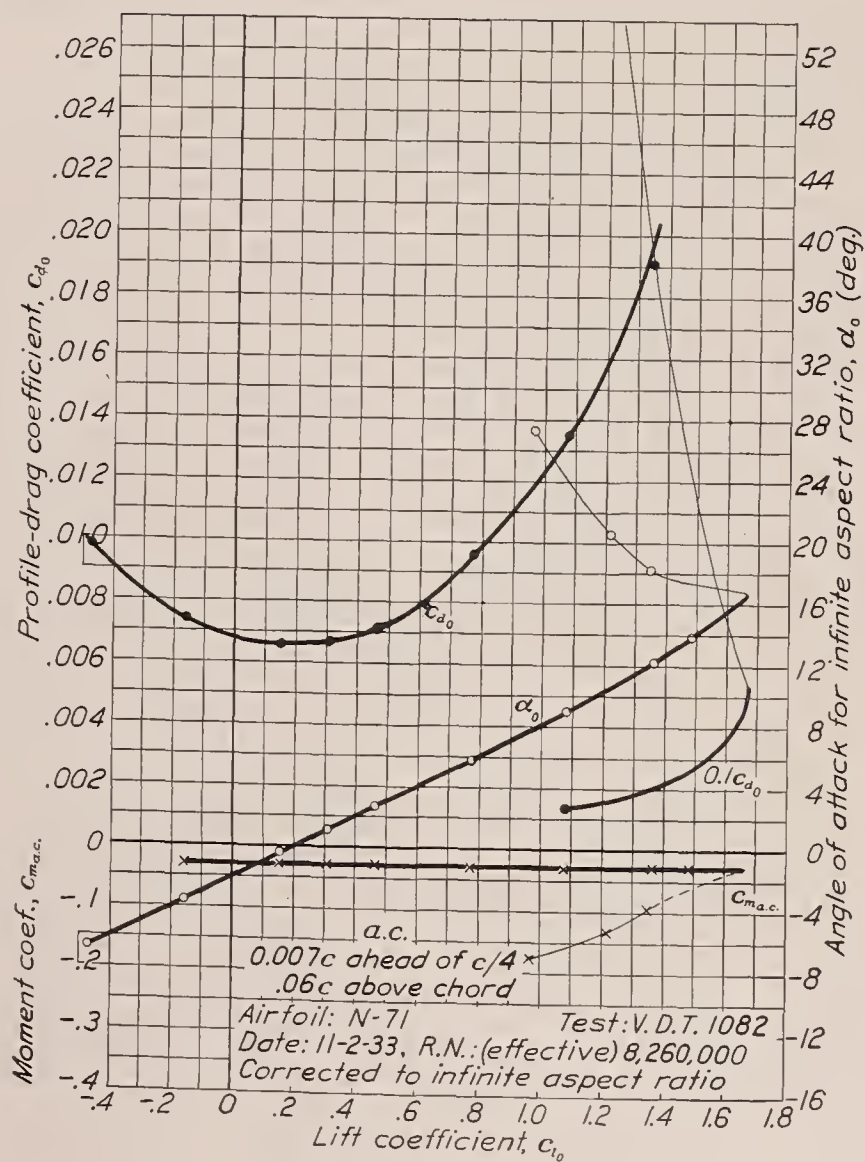
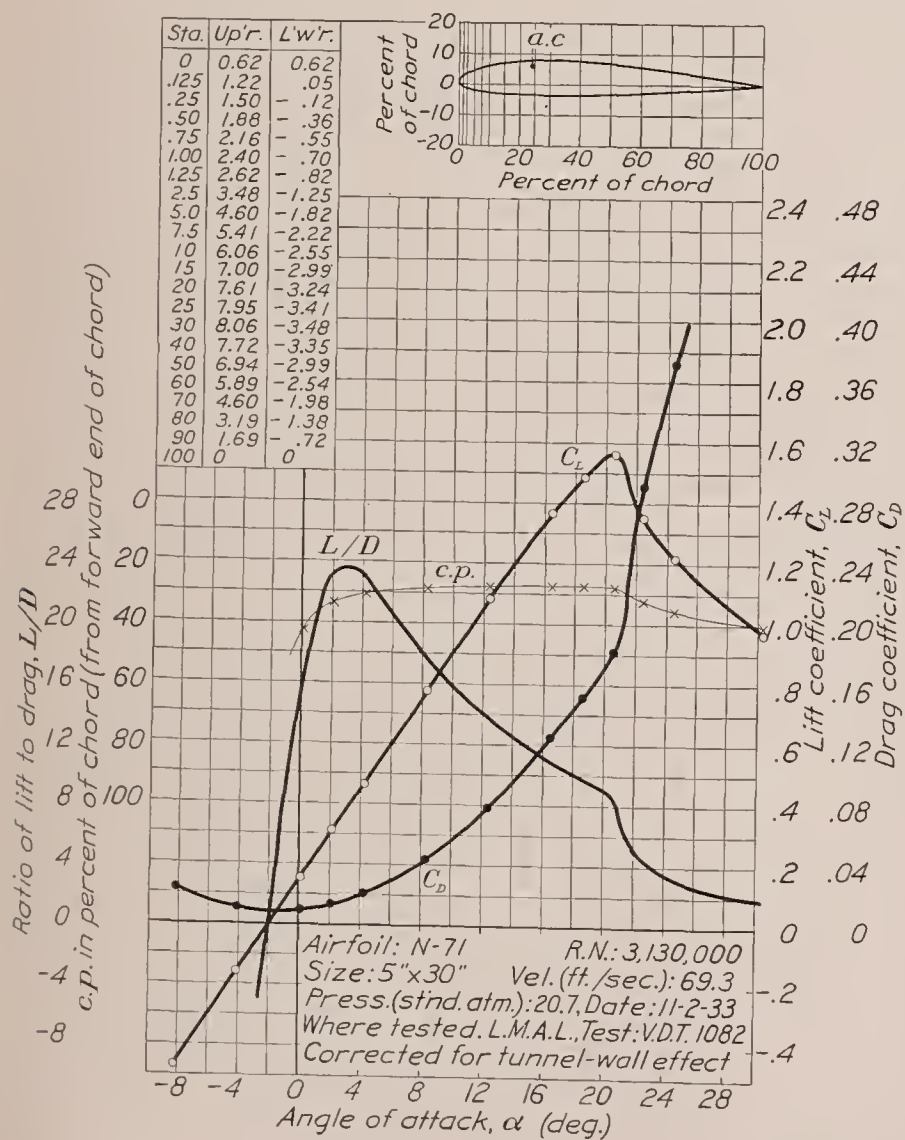


FIGURE 34.—N-71 airfoil.

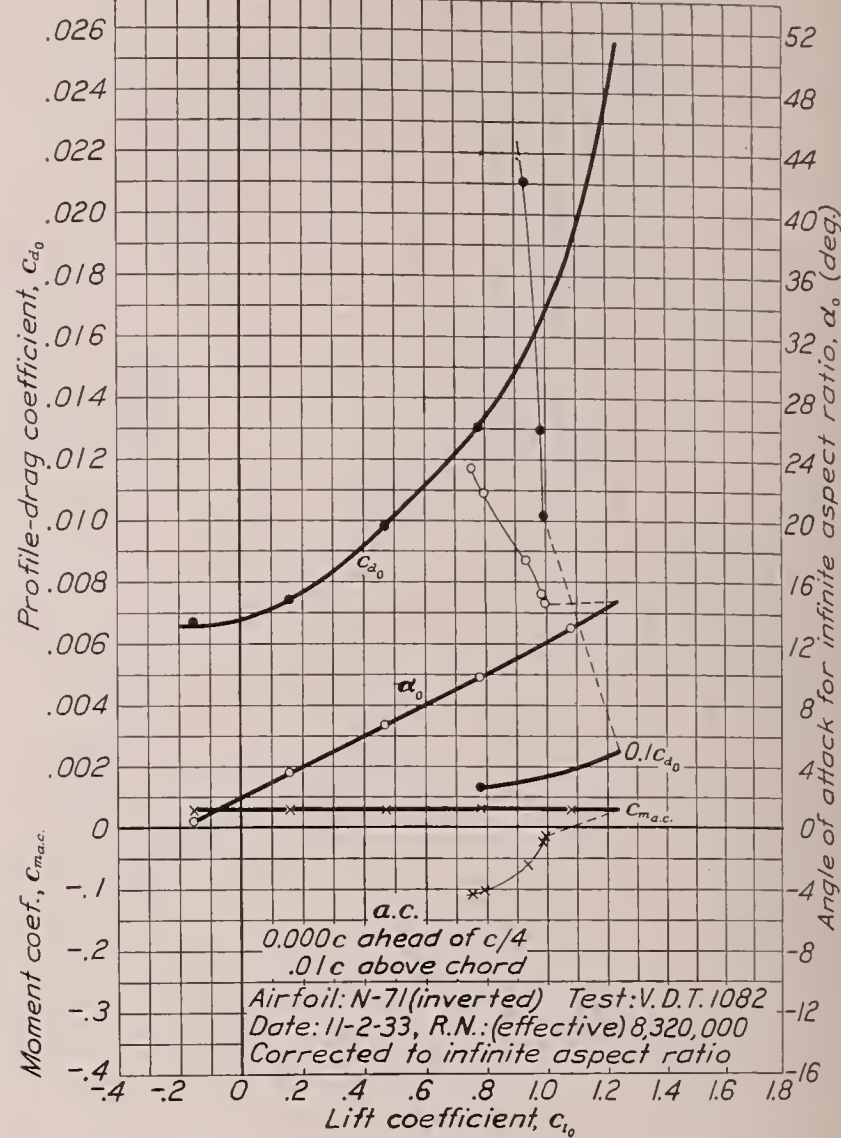
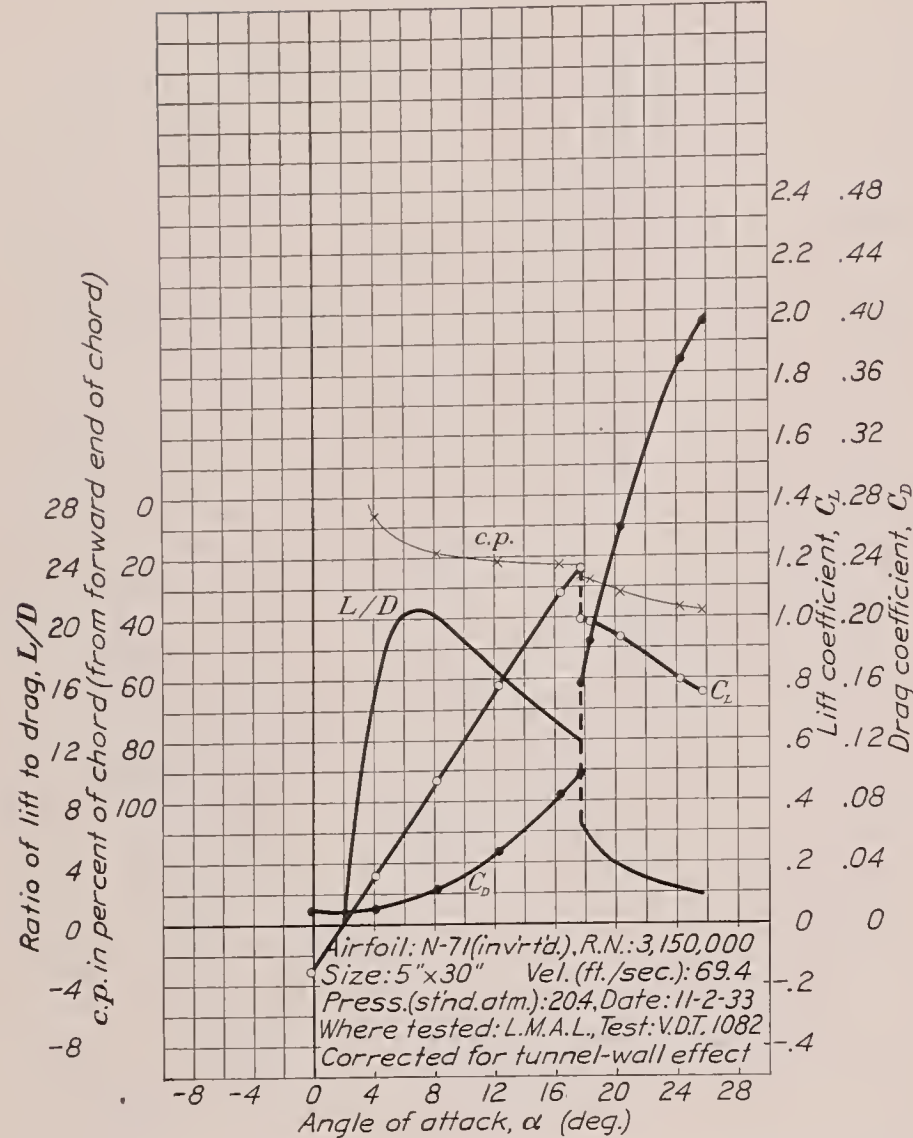


FIGURE 35.—N-71 airfoil (inverted).

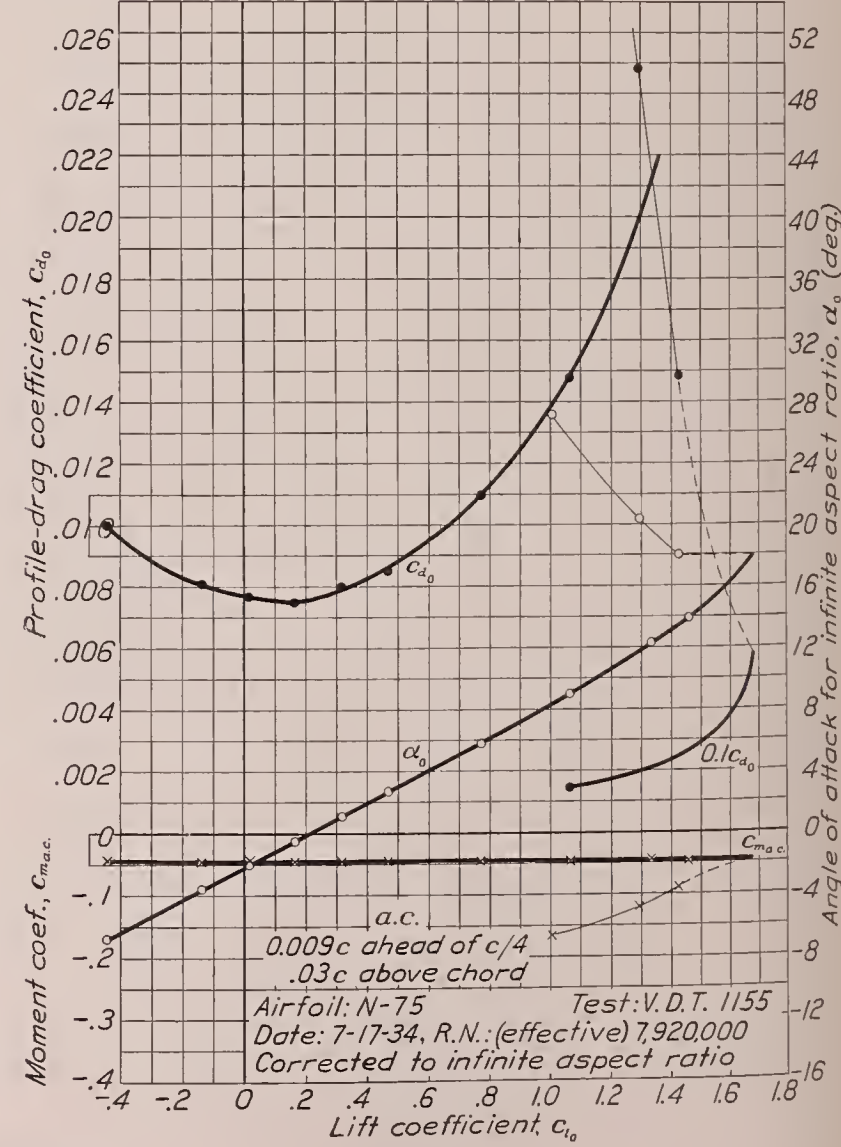
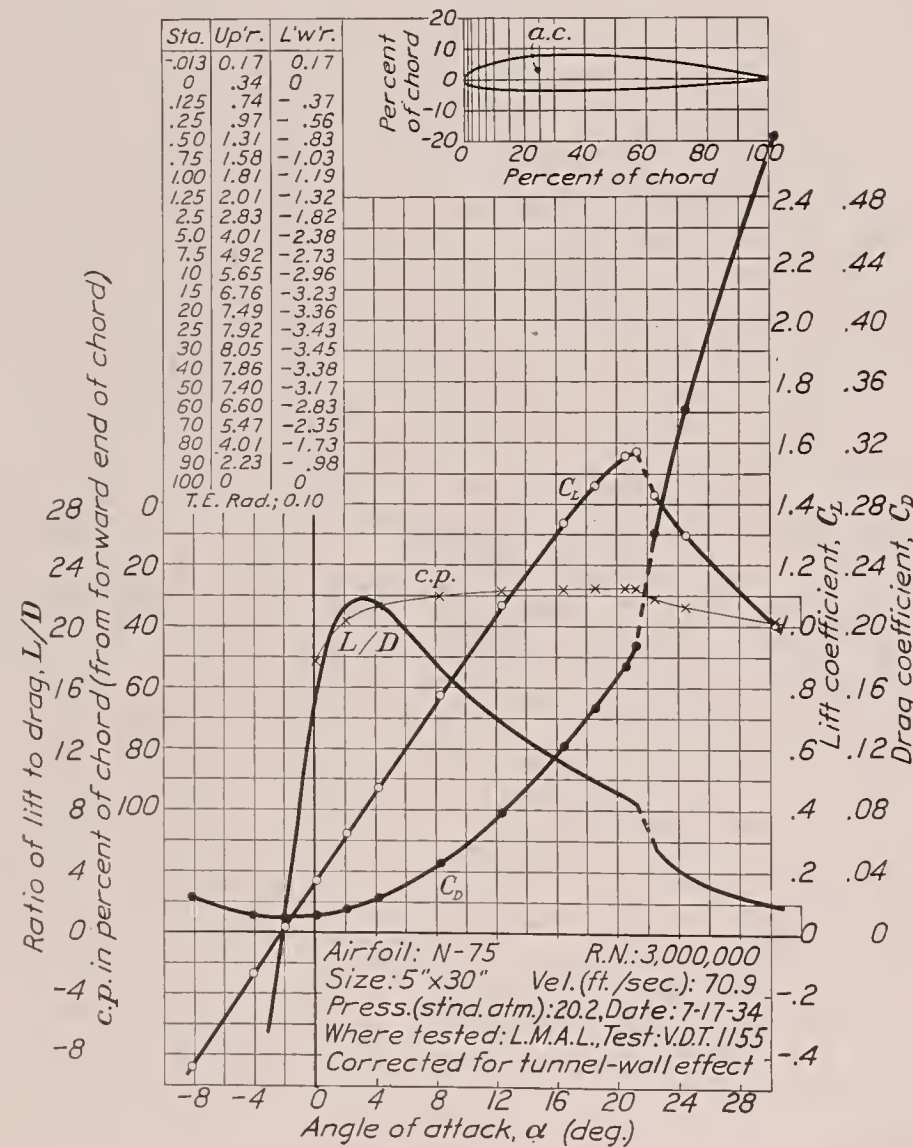


FIGURE 36.—N-75 airfoil.

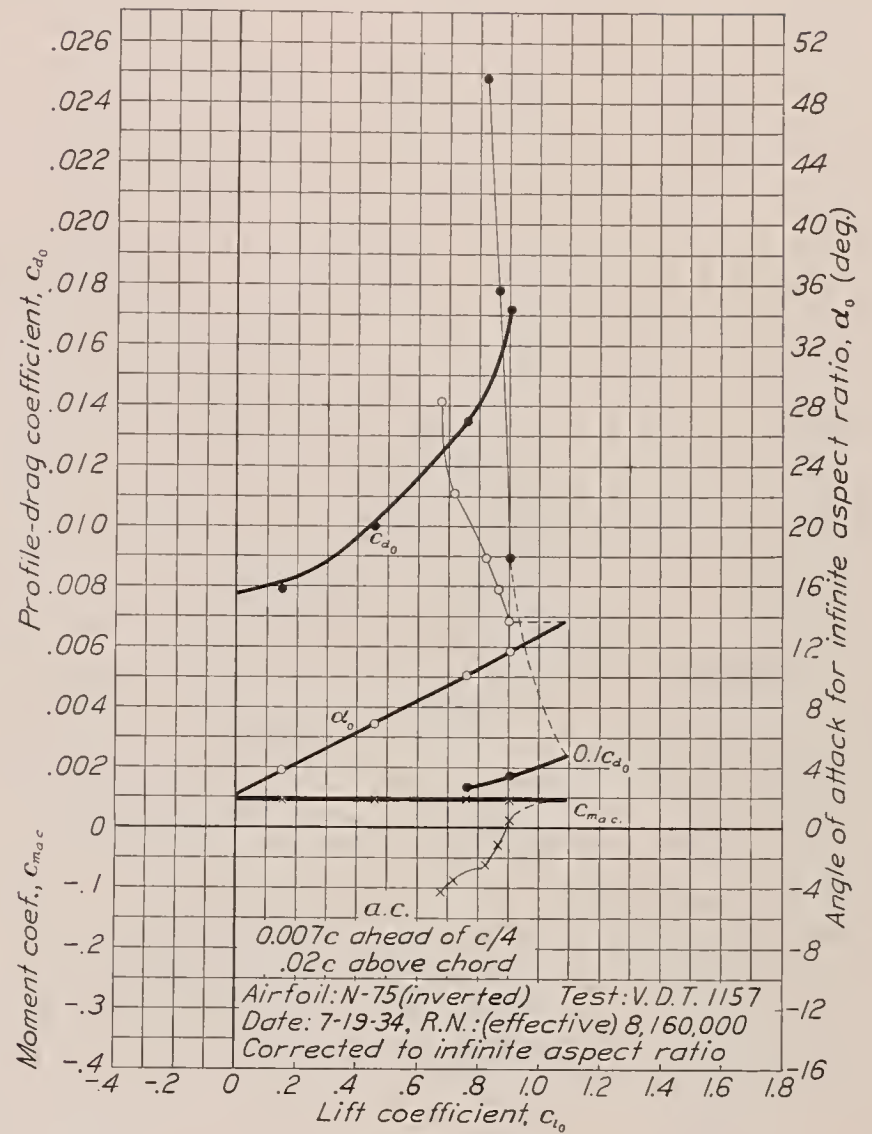
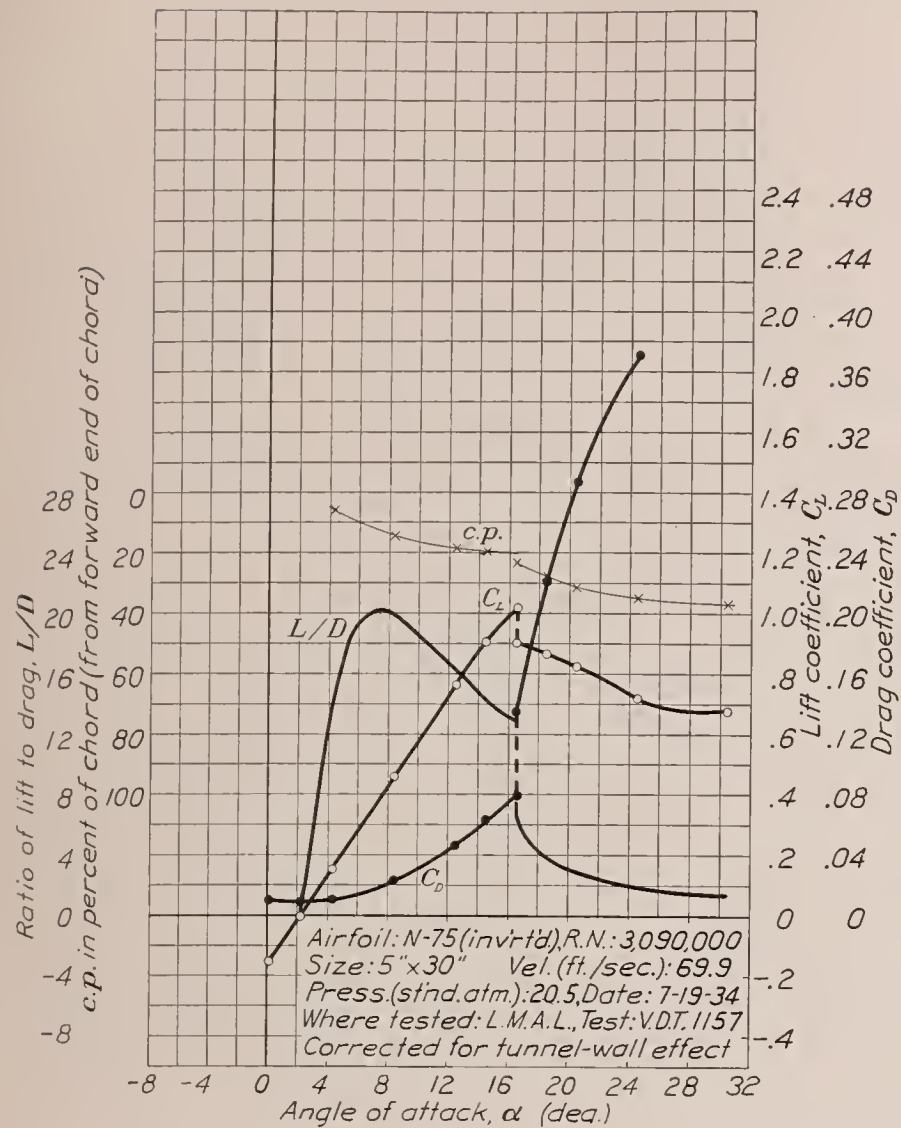


FIGURE 37.—N-75 airfoil (inverted).

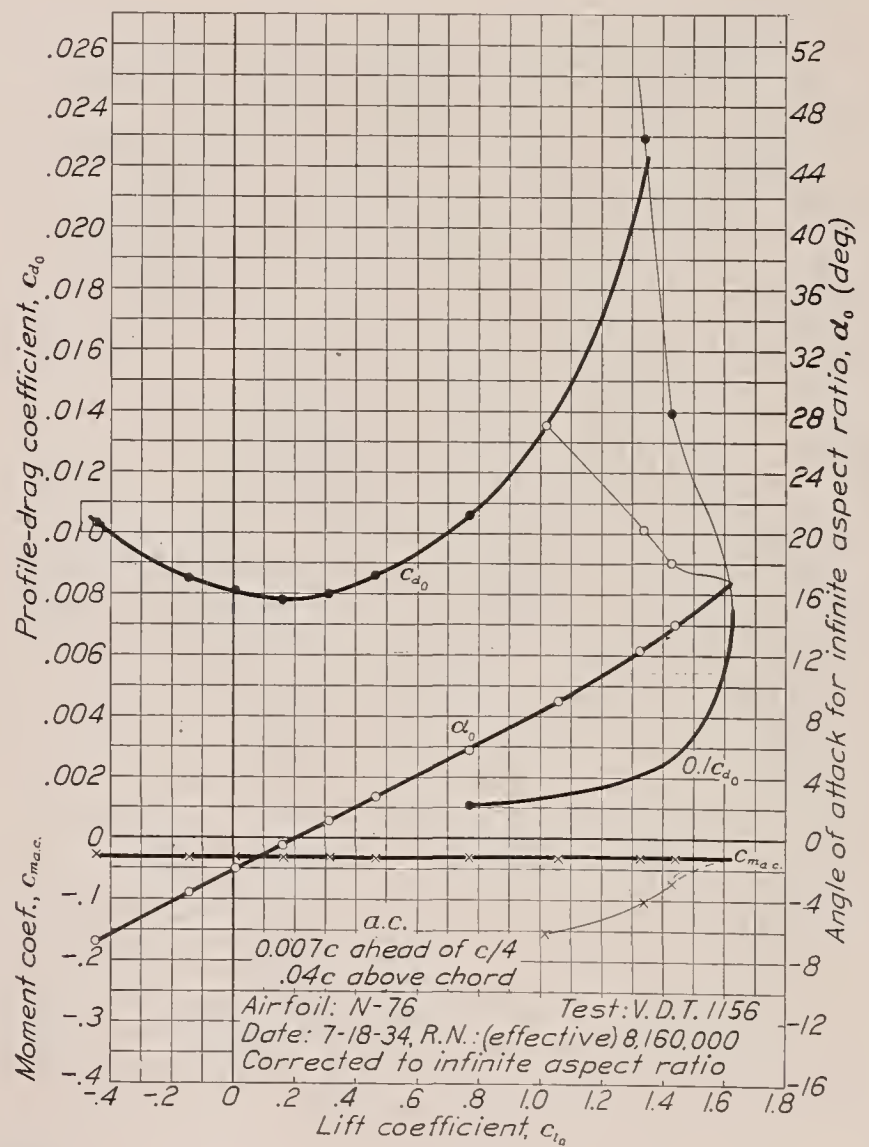
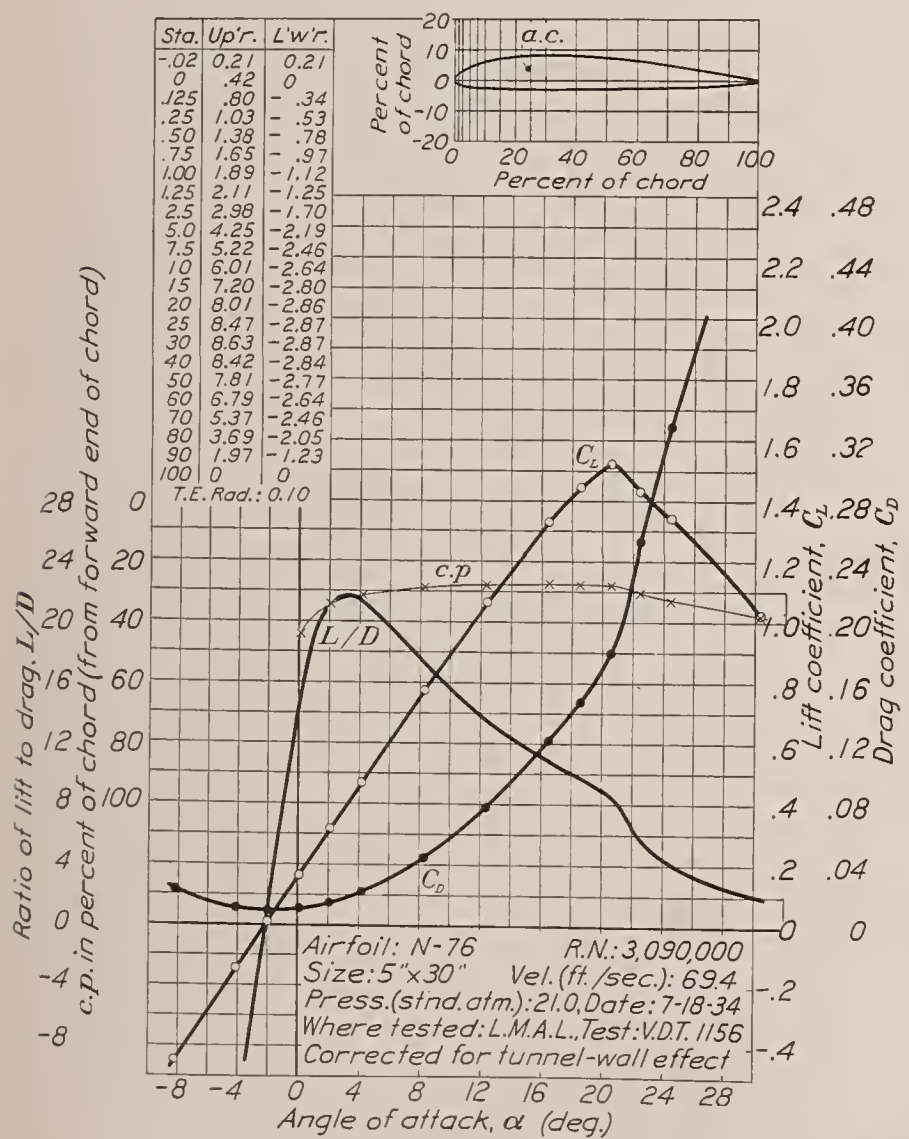


FIGURE 38.—N-76 airfoil.

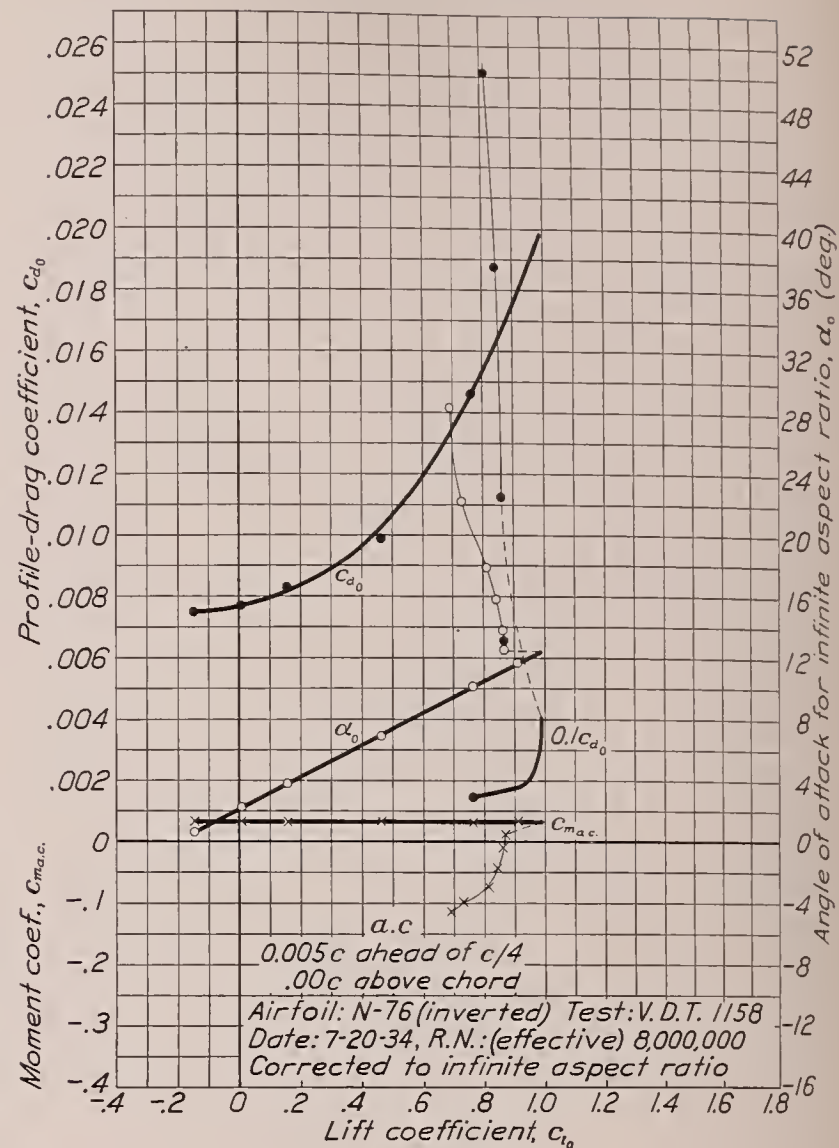
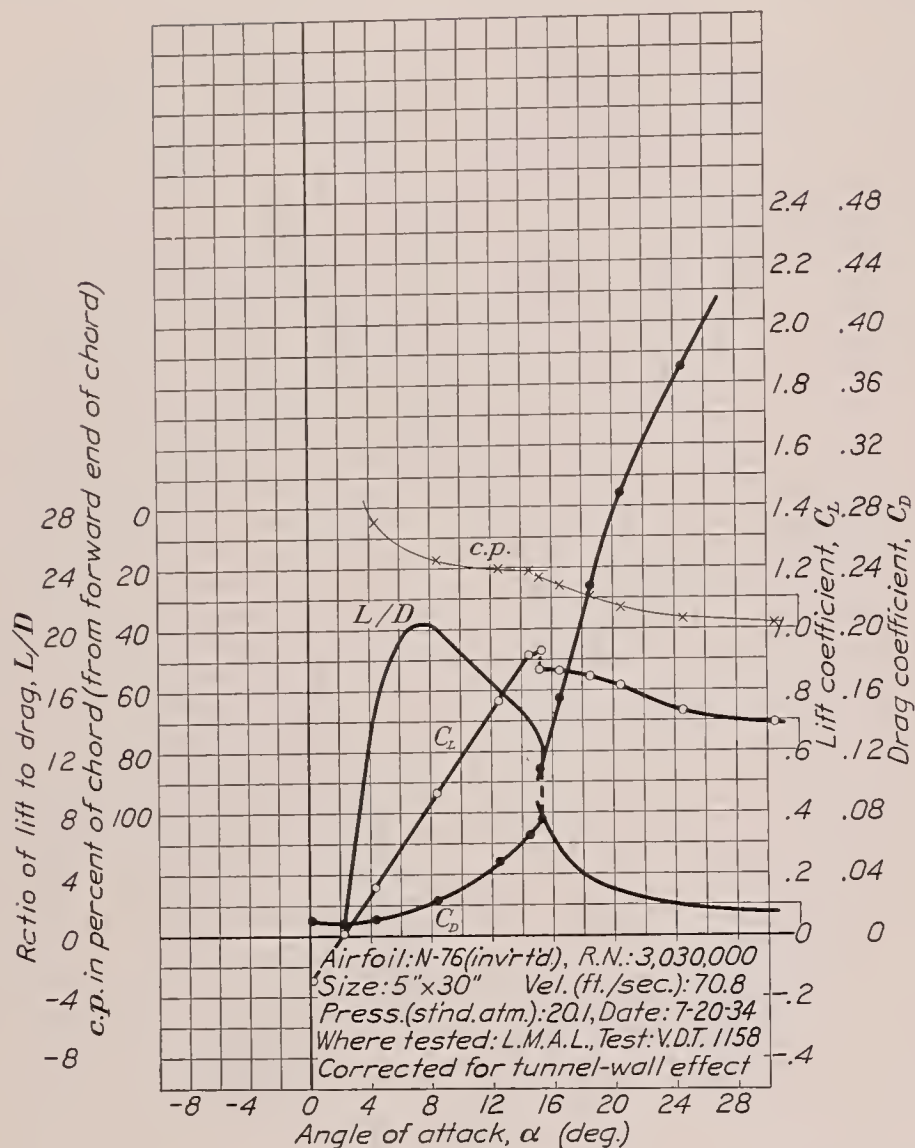


FIGURE 39.—N-76 airfoil (inverted).

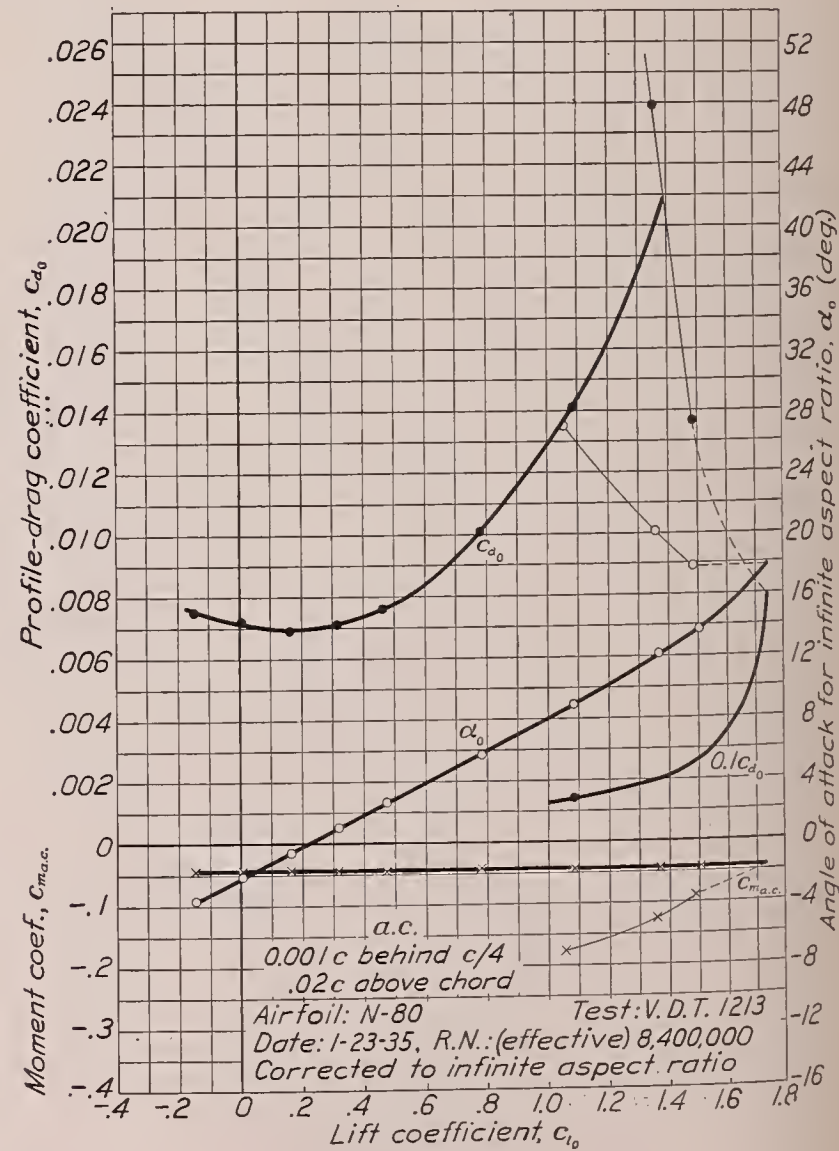
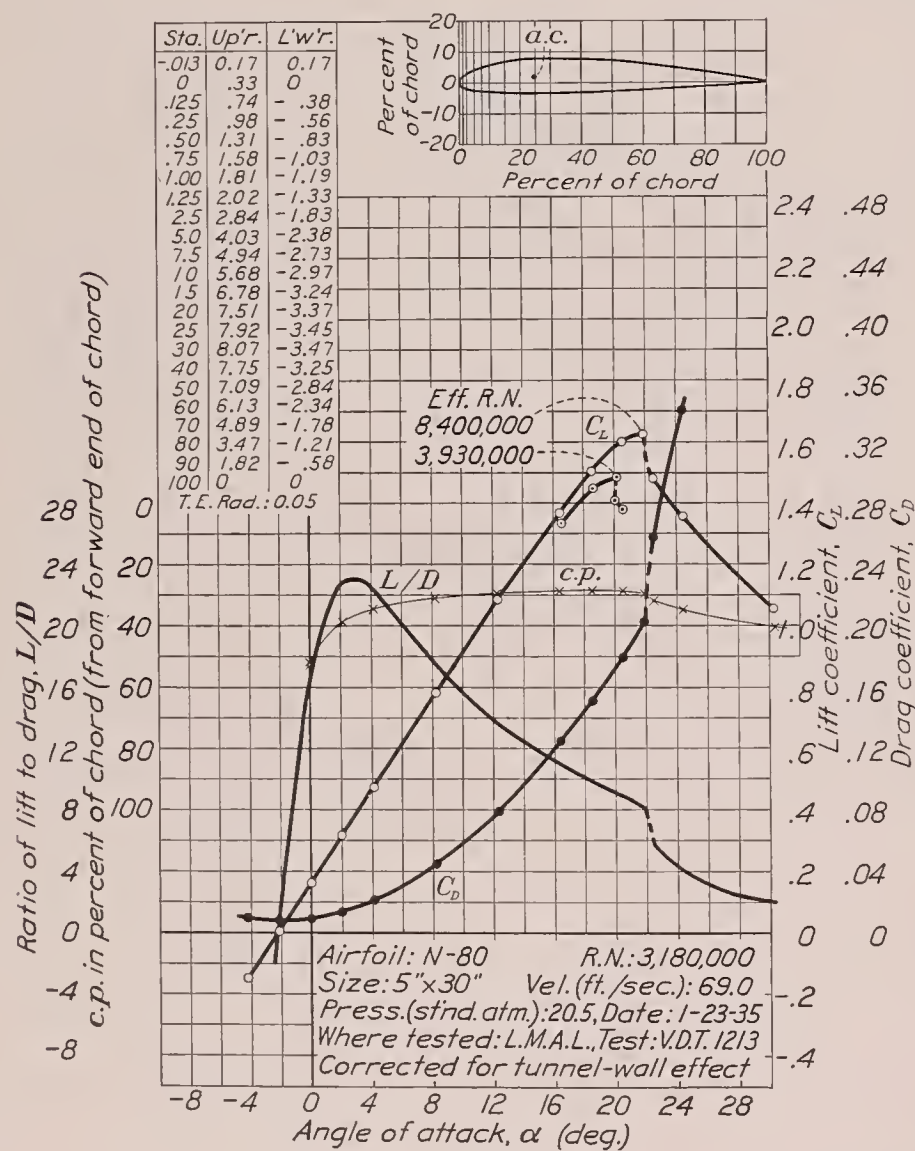


FIGURE 40.—N-80 airfoil.

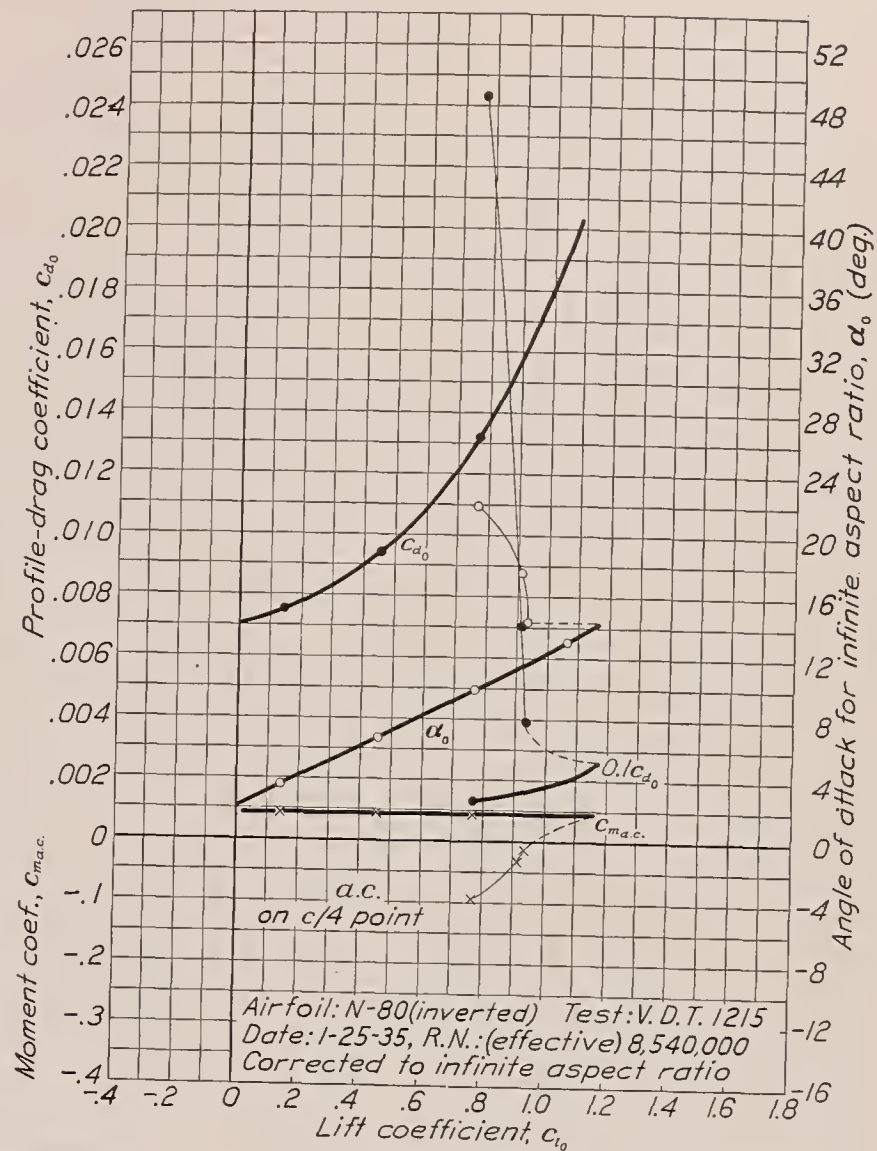
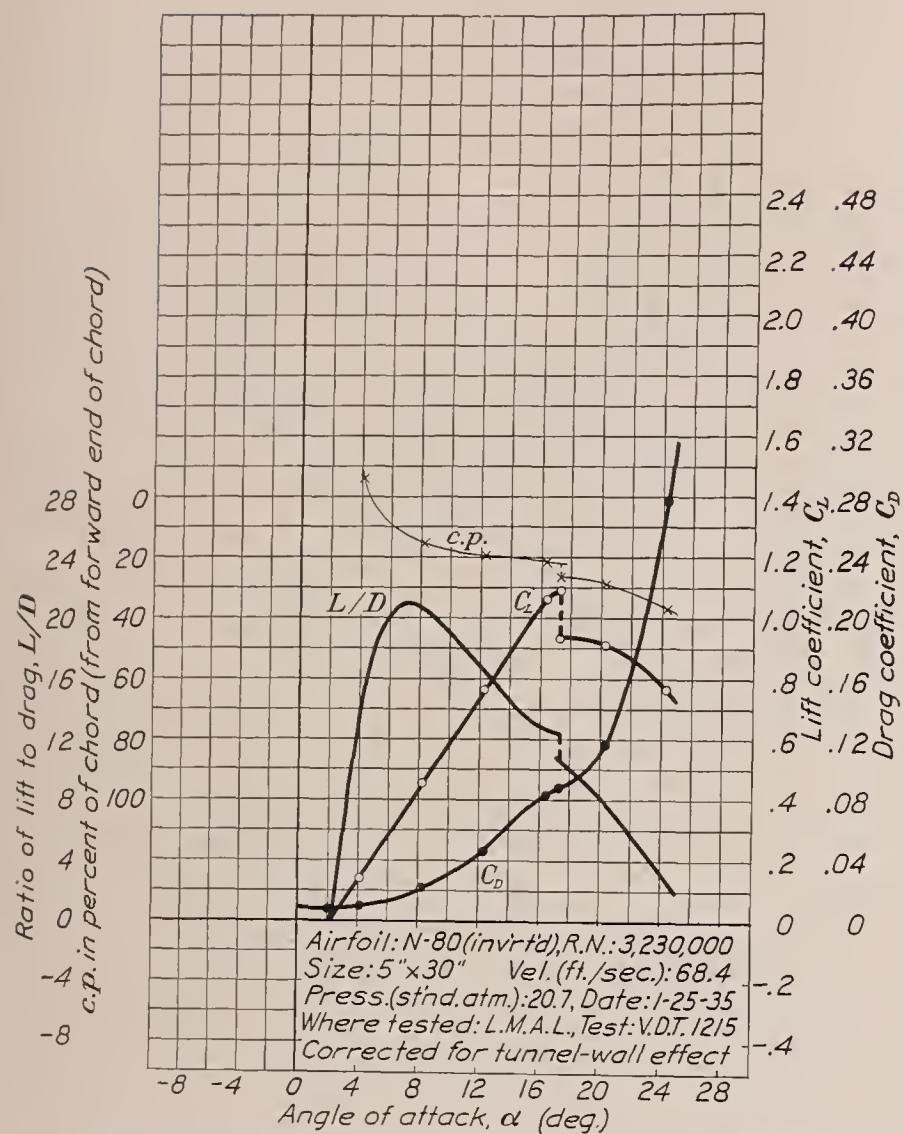


FIGURE 41.—N-80 airfoil (inverted)

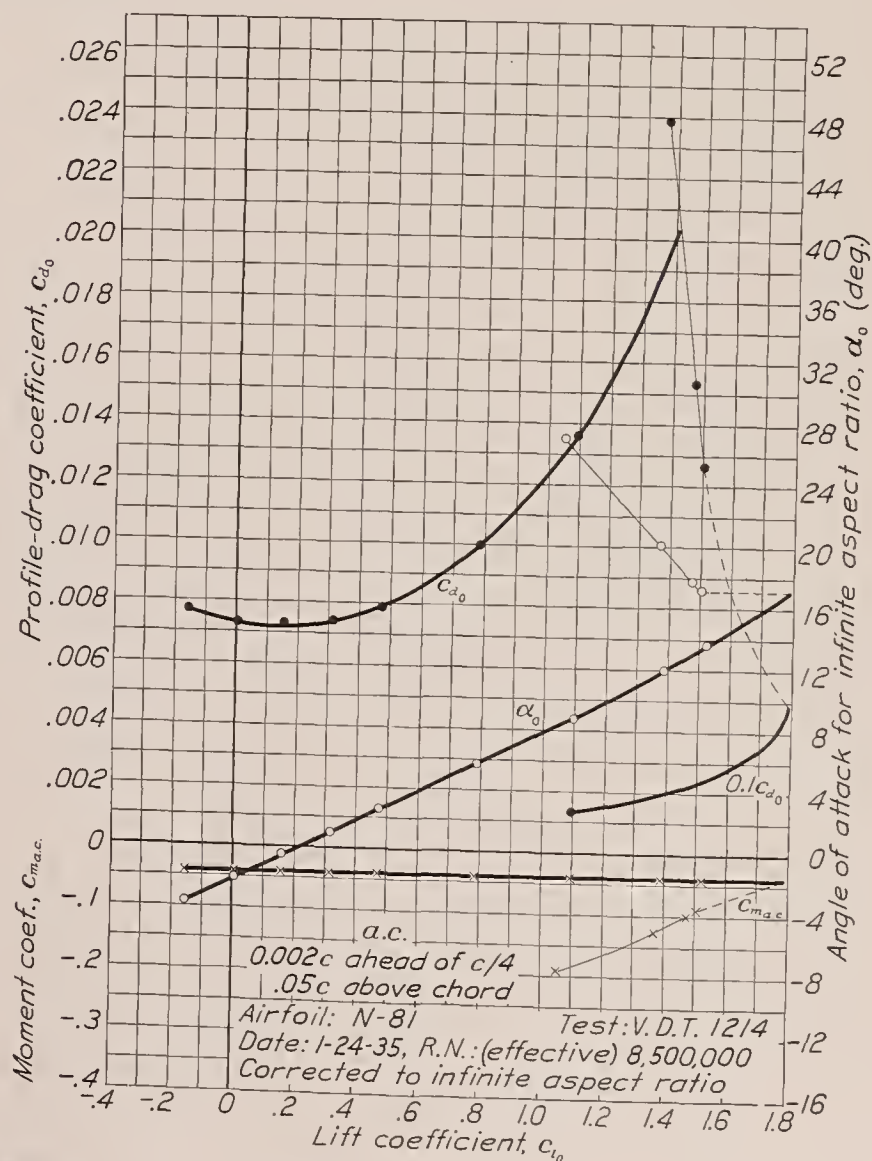
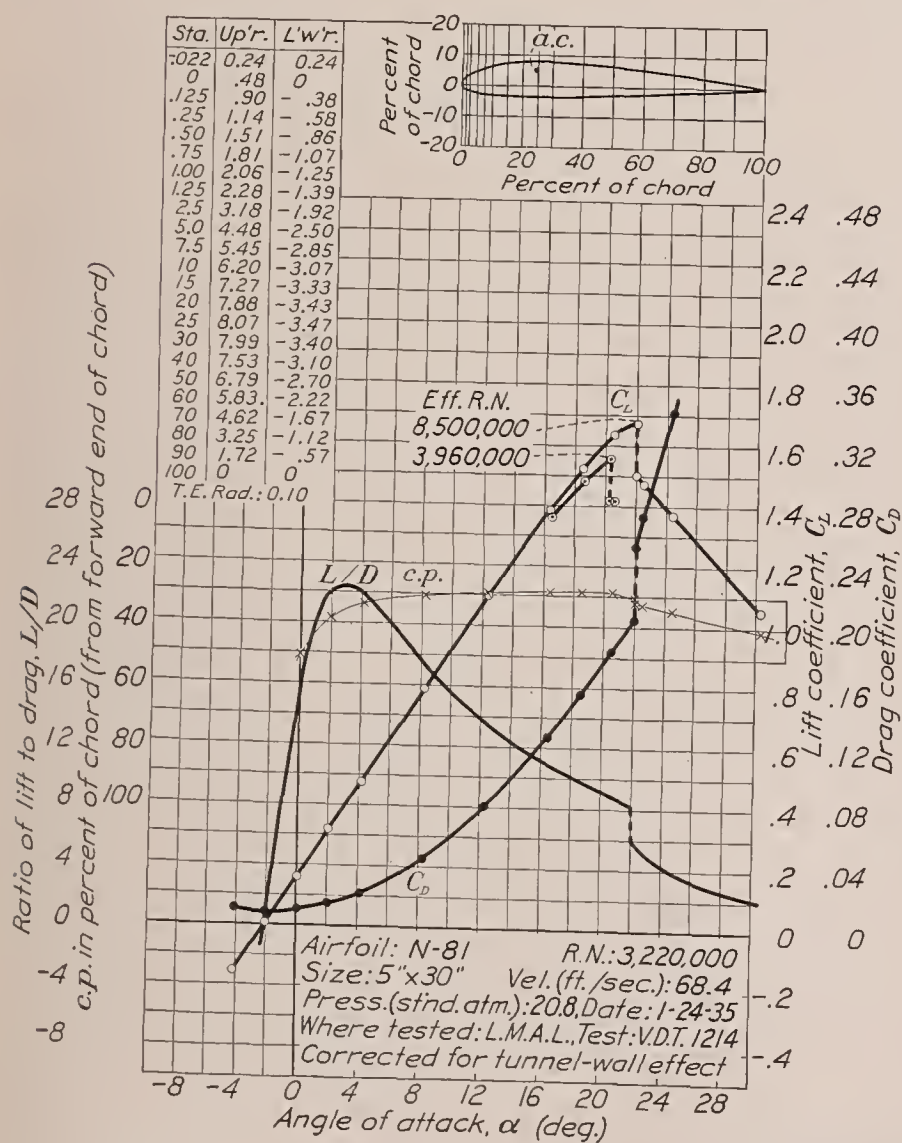


FIGURE 42.—N-81 airfoil.

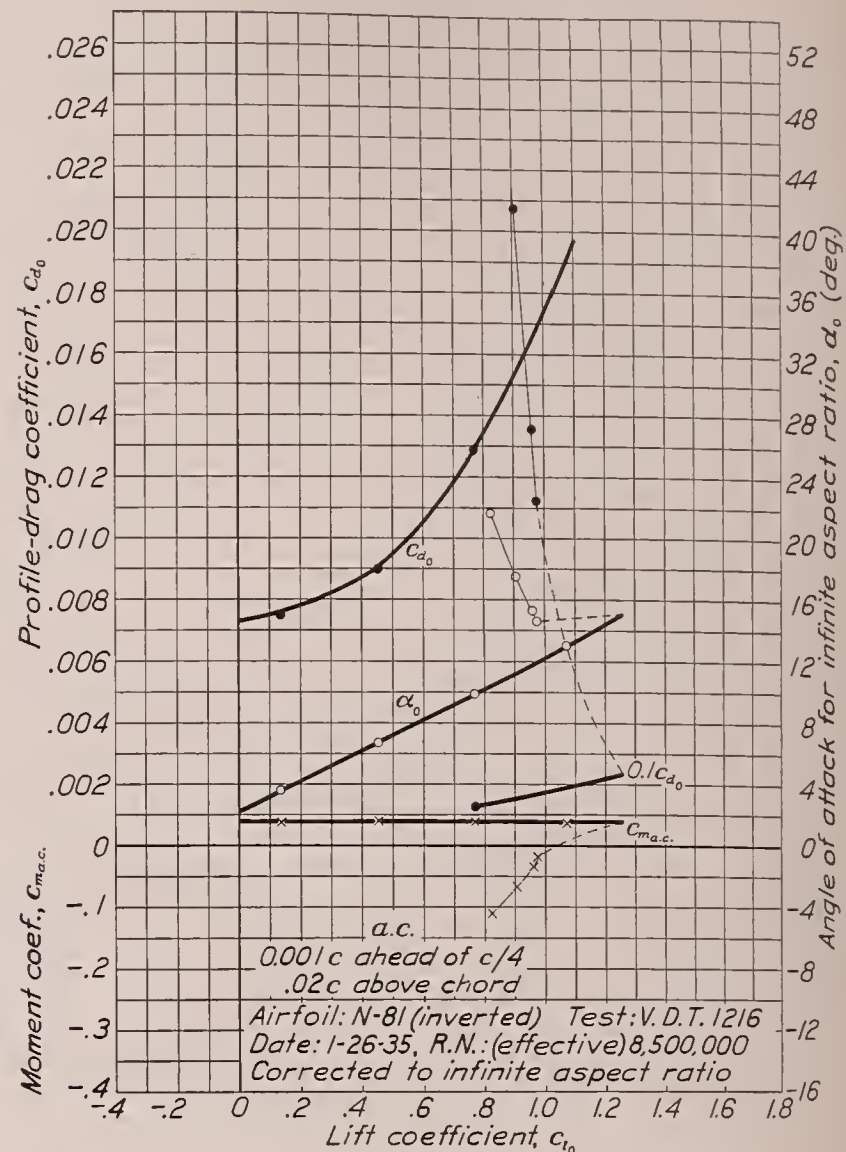
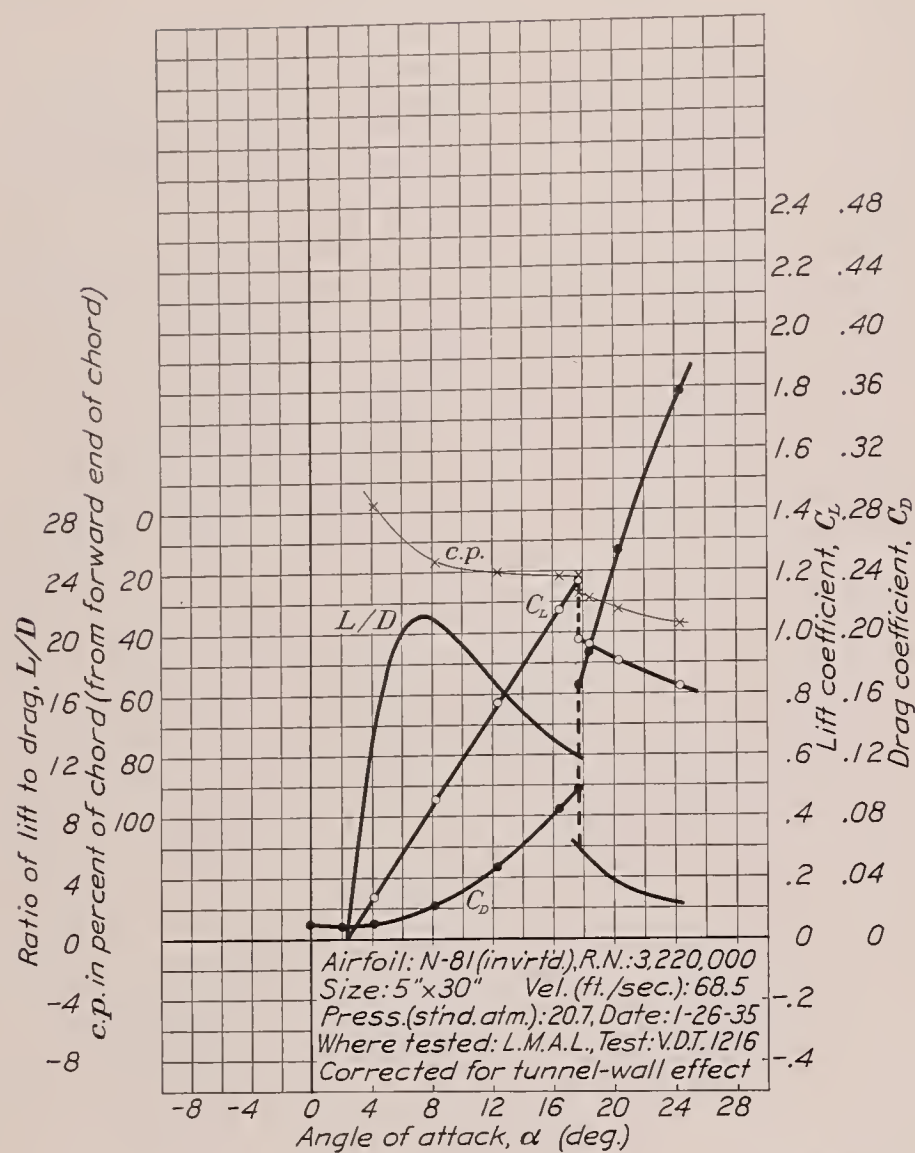


FIGURE 43.—N-81 airfoil (inverted).

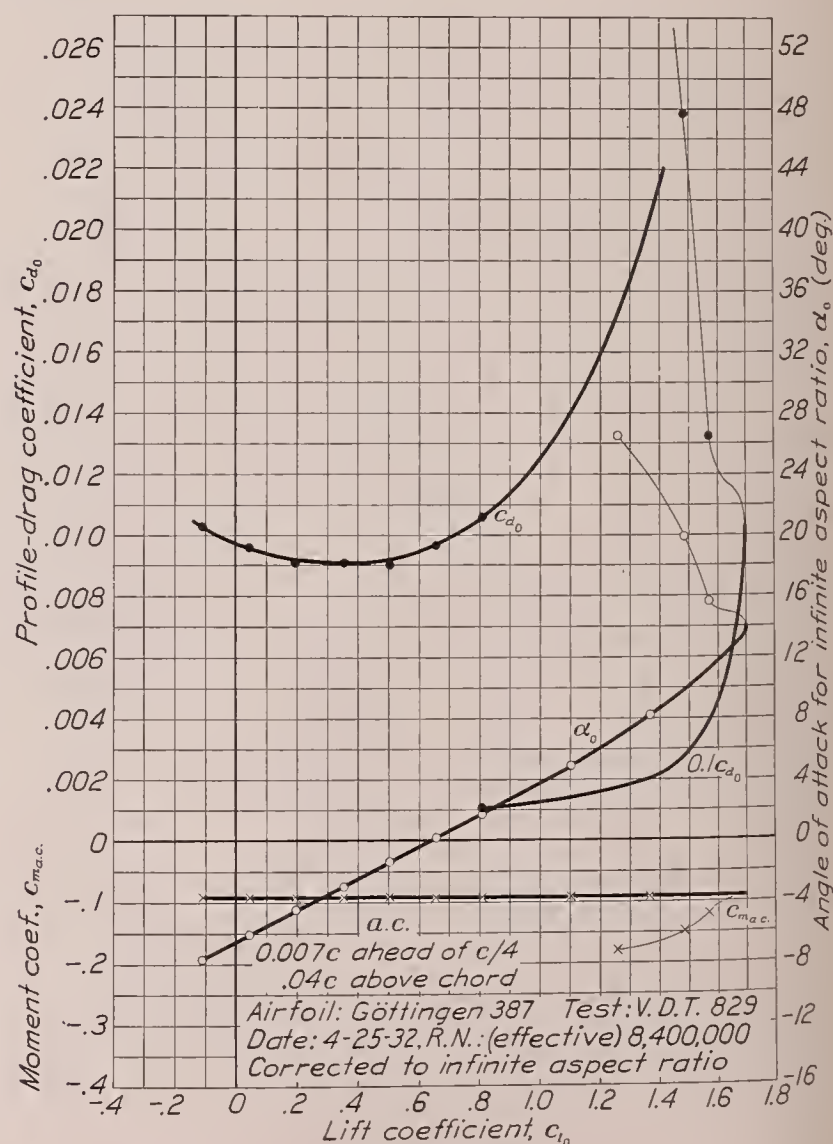
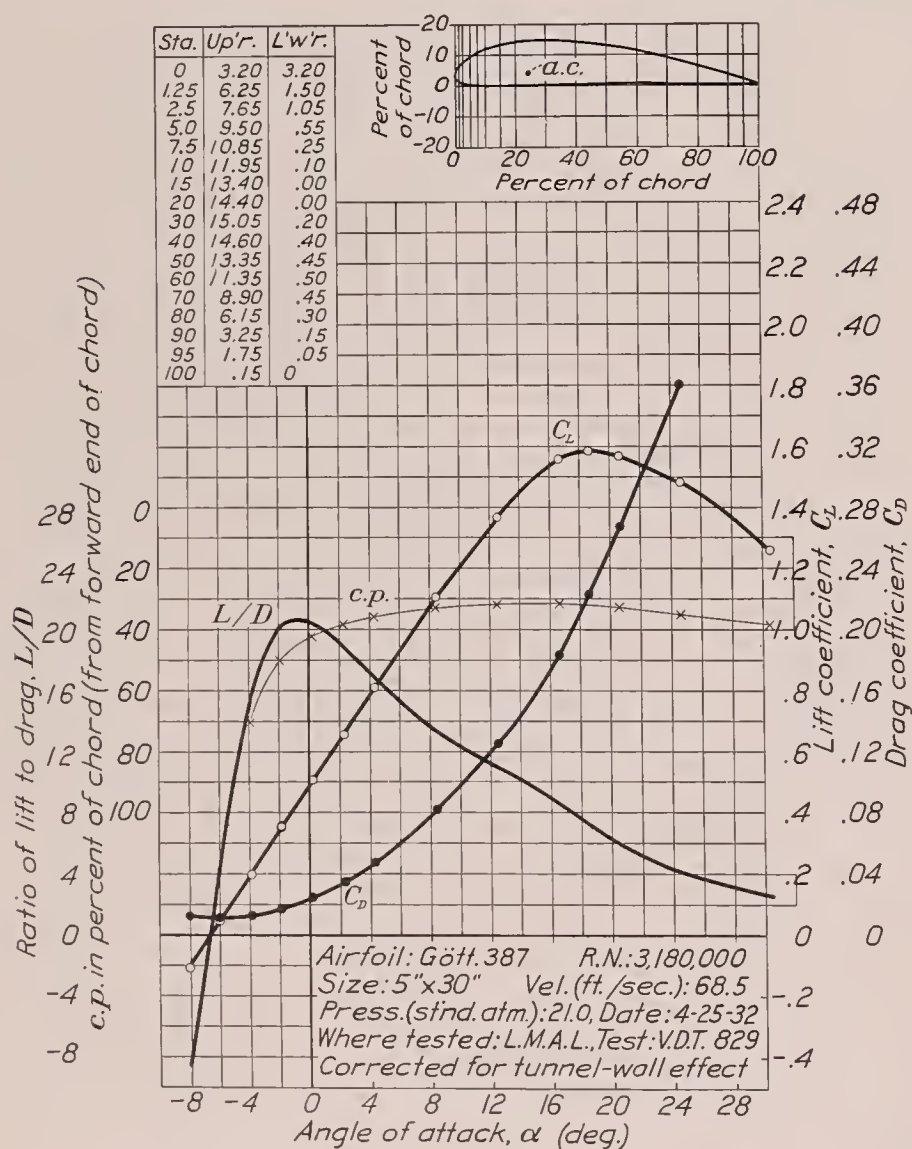


FIGURE 44.—Göttingen 387 airfoil.

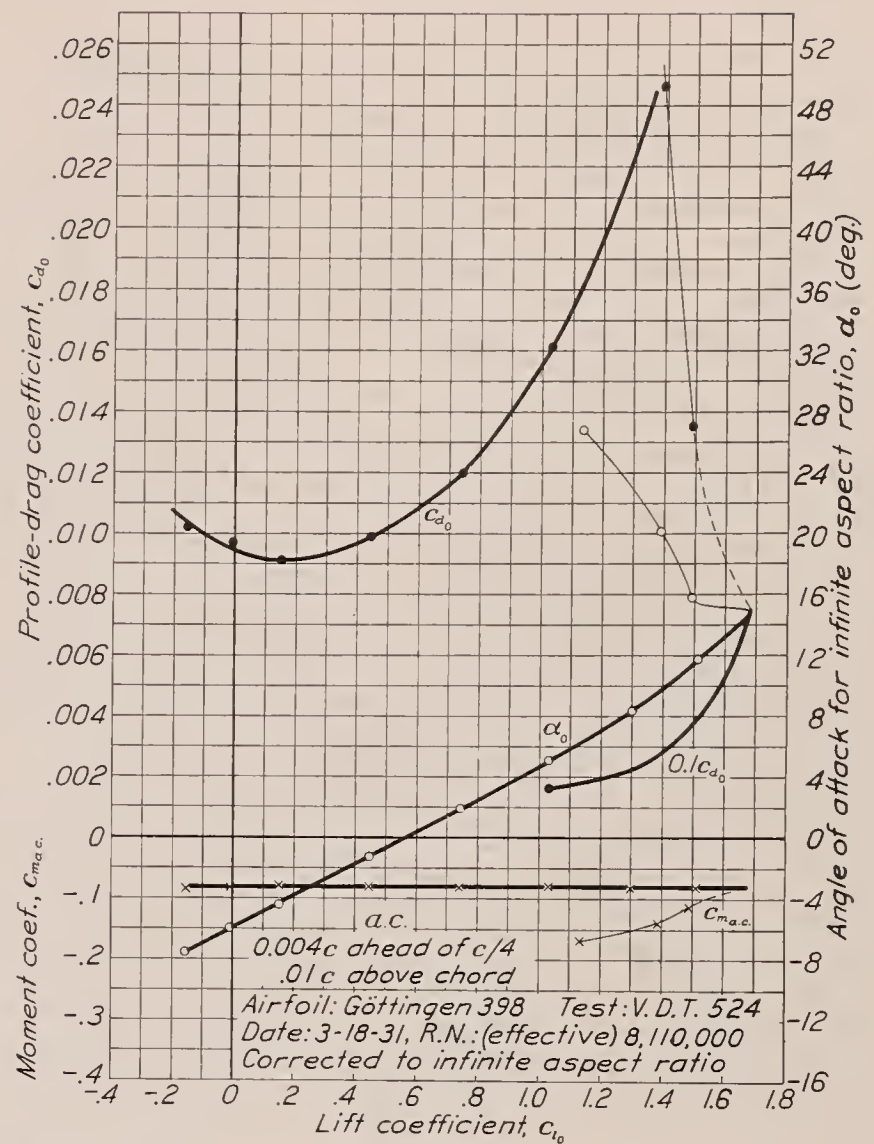
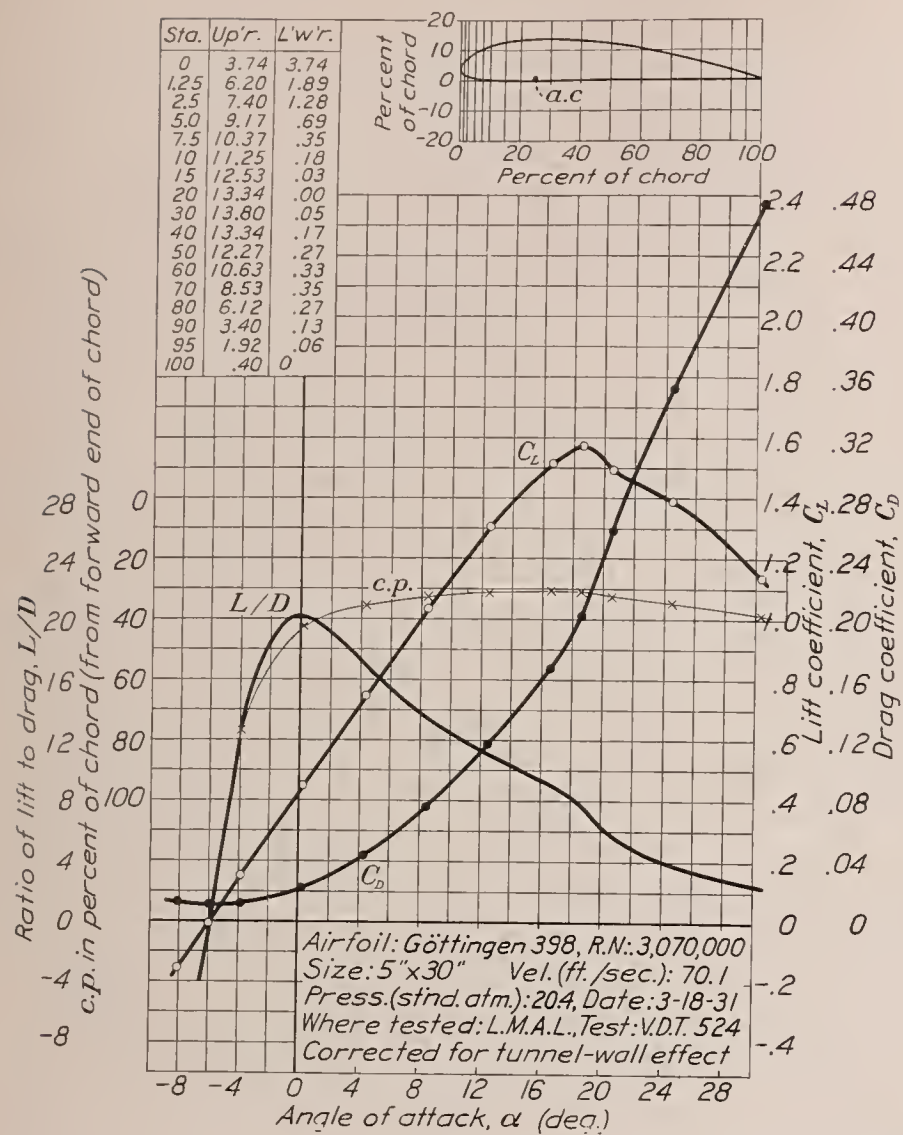


FIGURE 45.—Göttingen 398 airfoil.

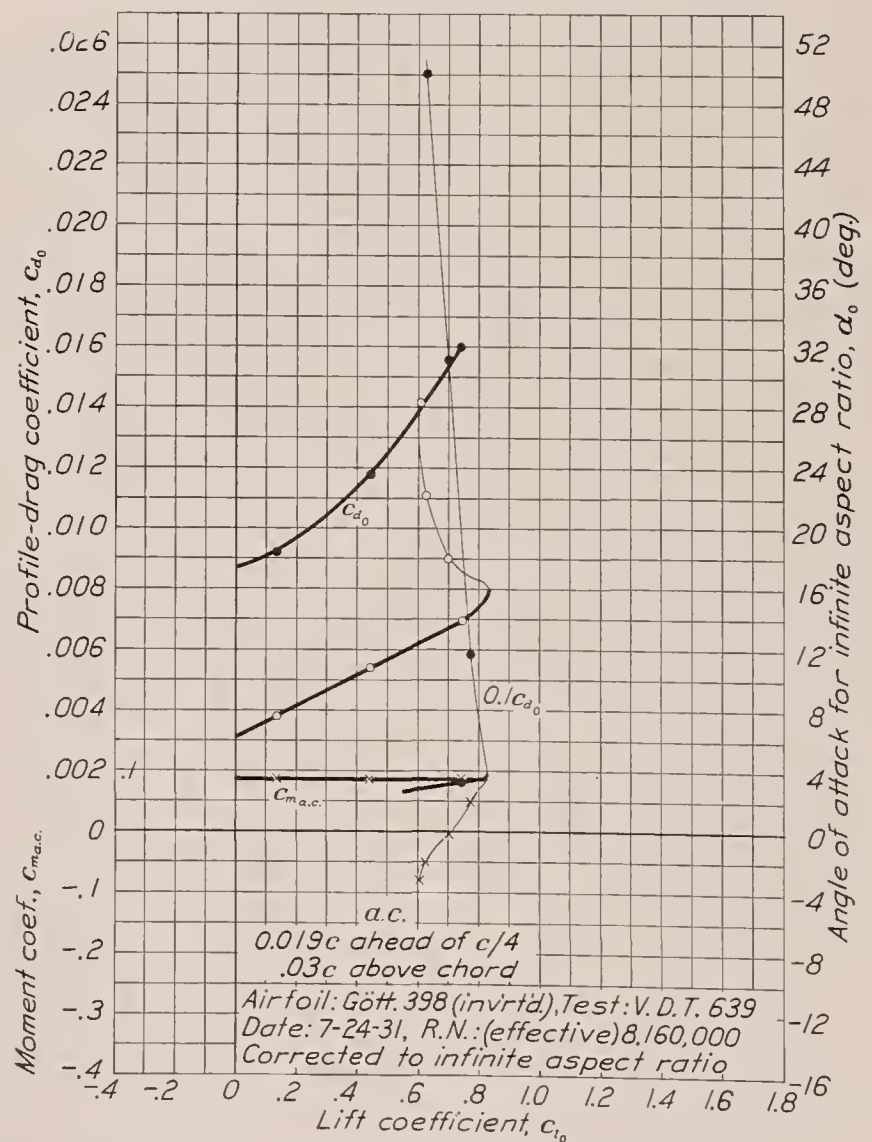
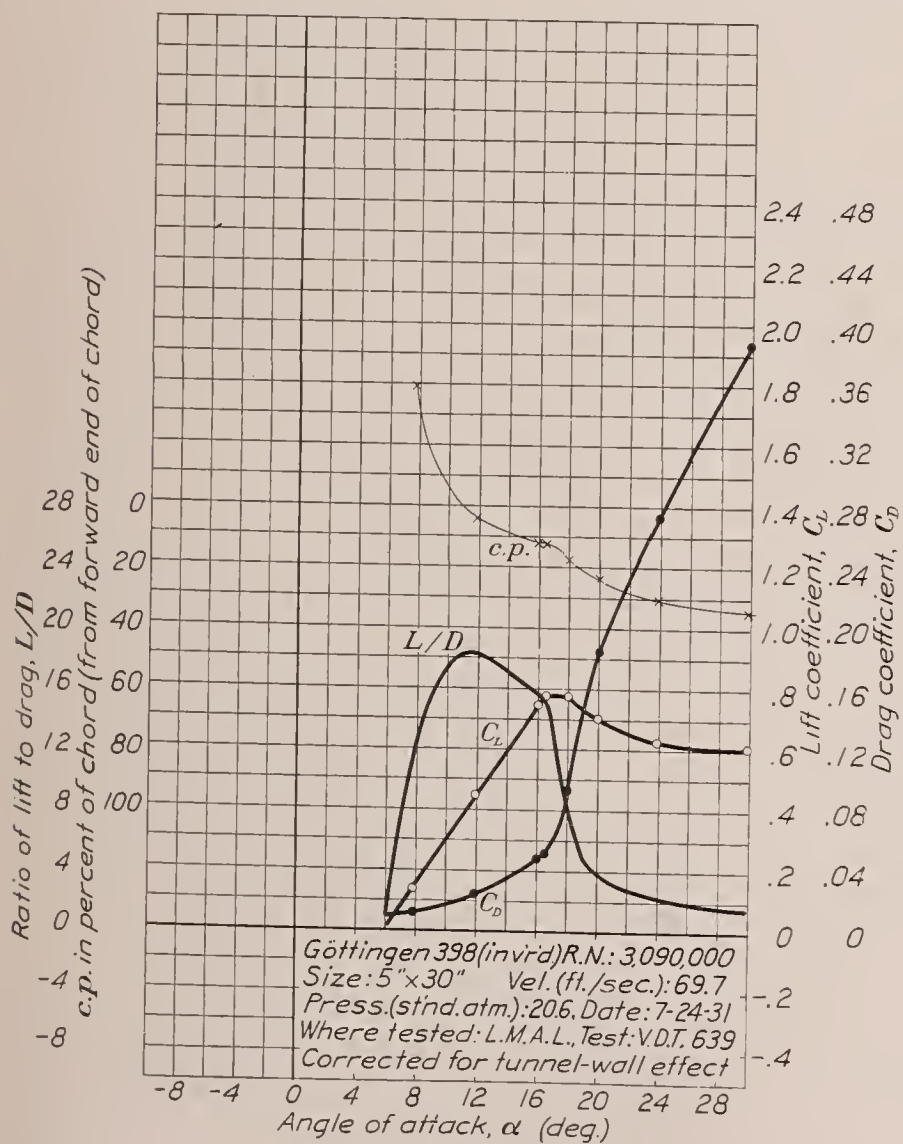


FIGURE 46.—Göttingen 398 airfoil (inverted).

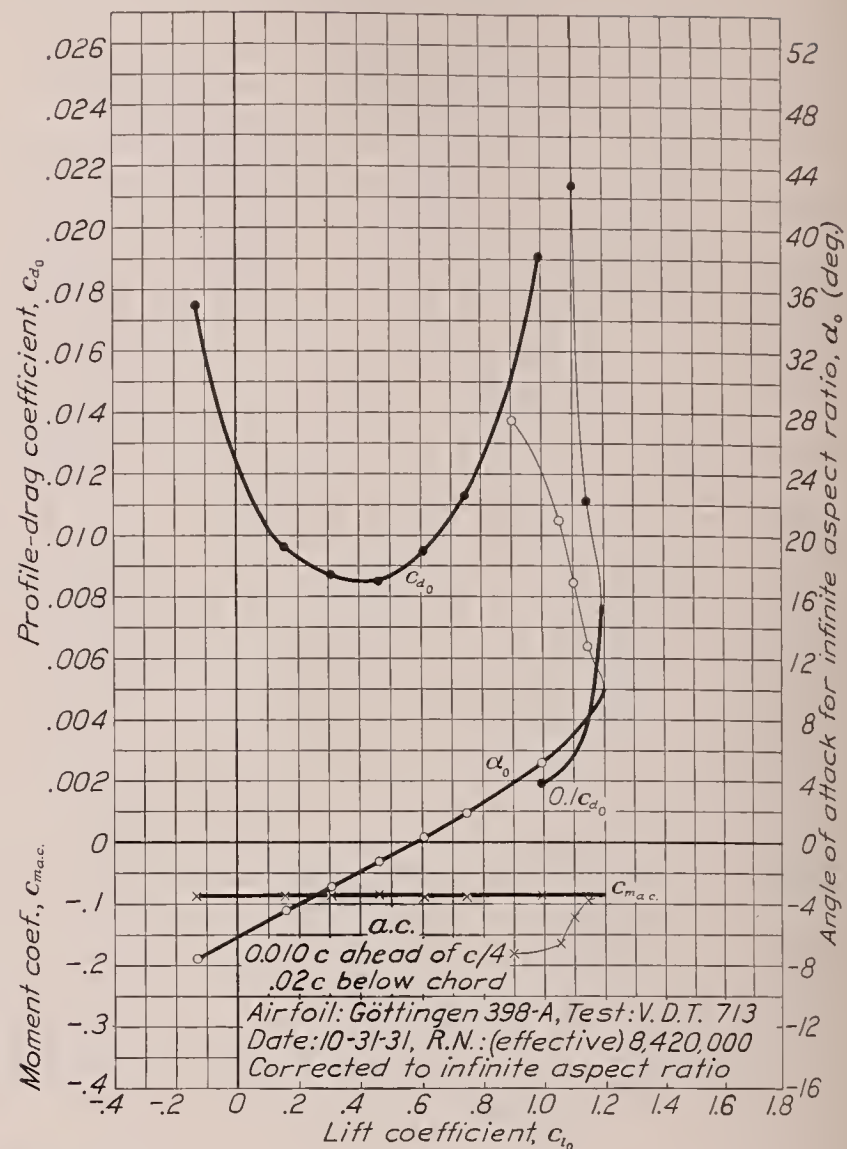
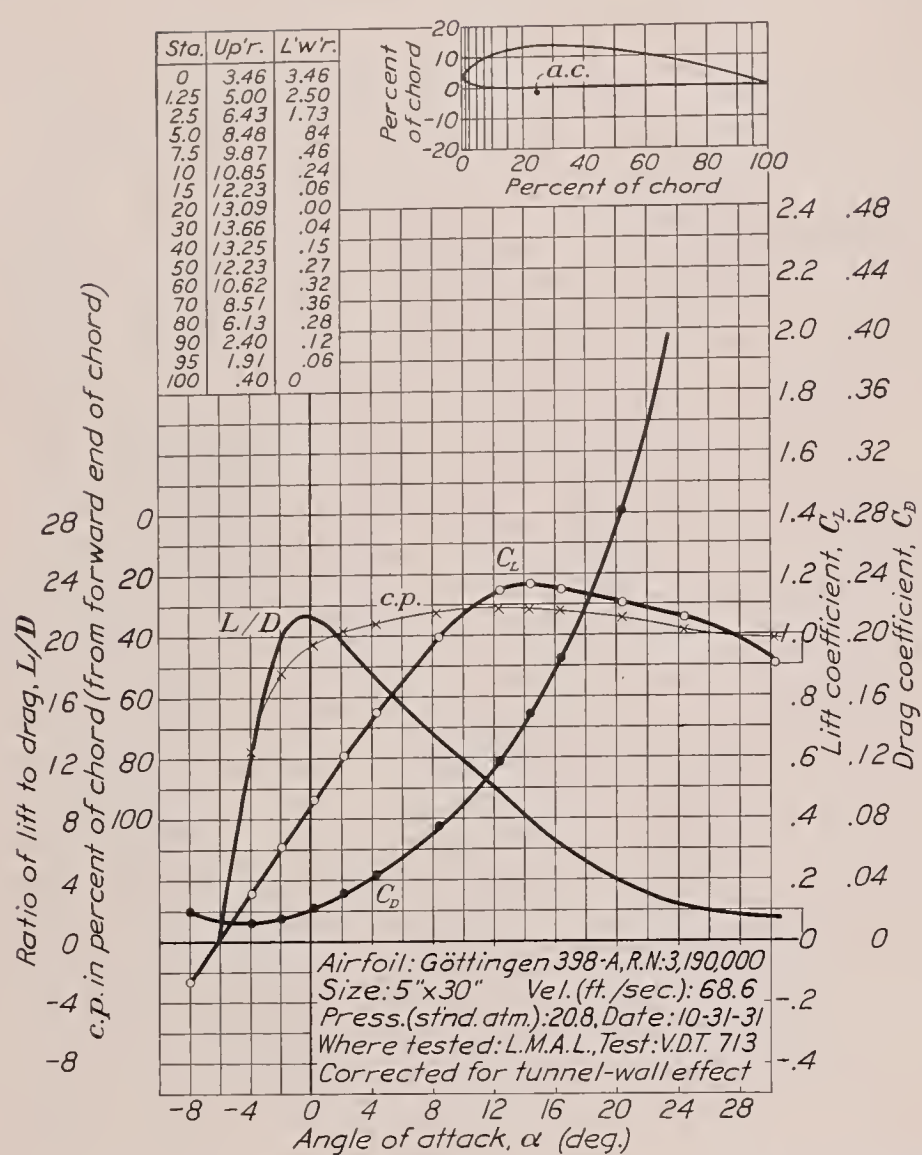


FIGURE 47.—Göttingen 398-A airfoil.

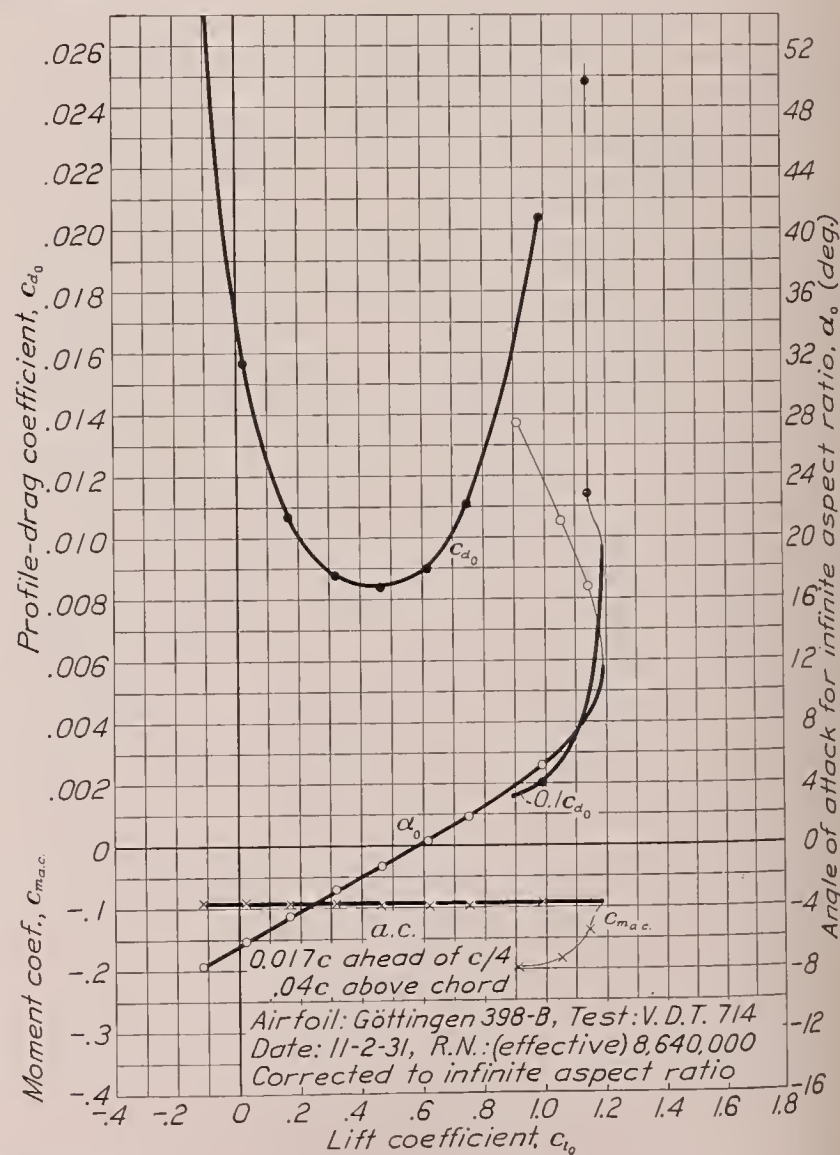
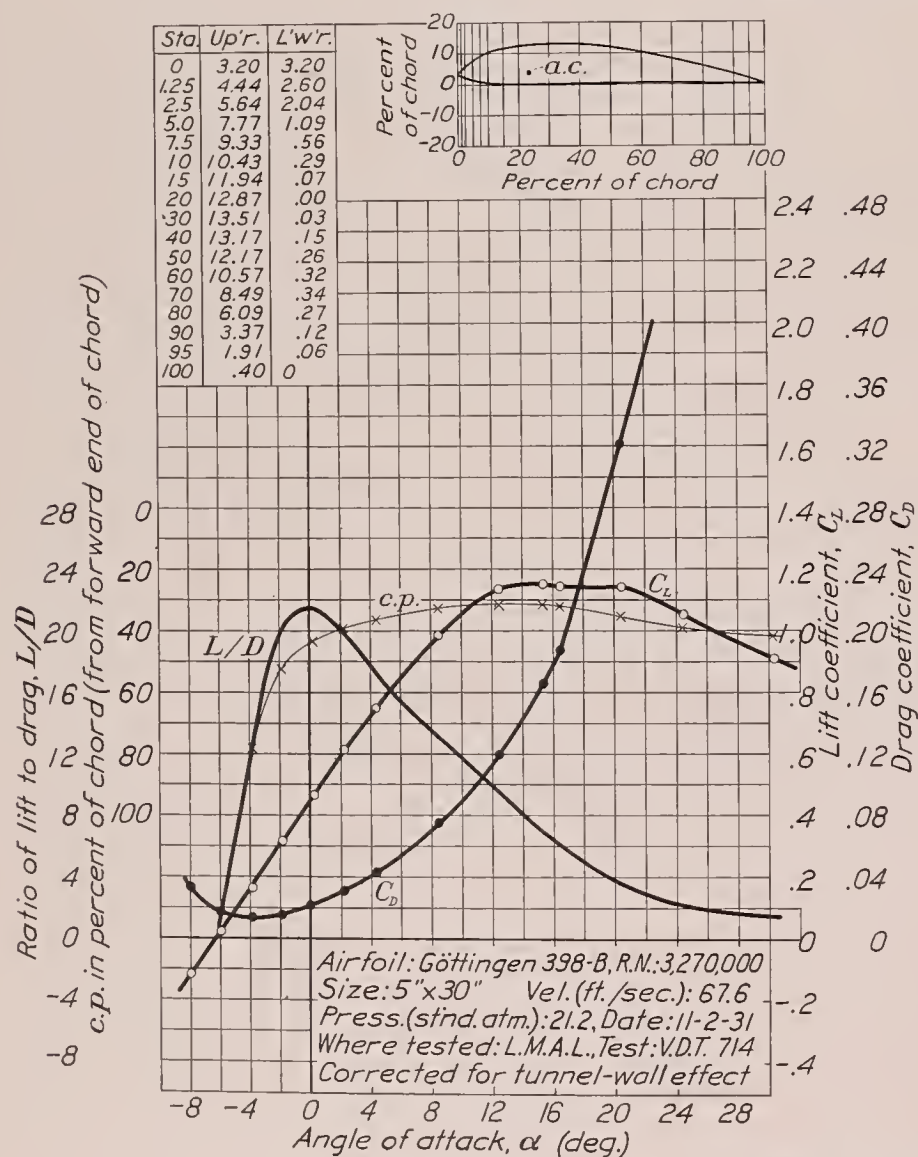


FIGURE 48.—Göttingen 398-B airfoil.

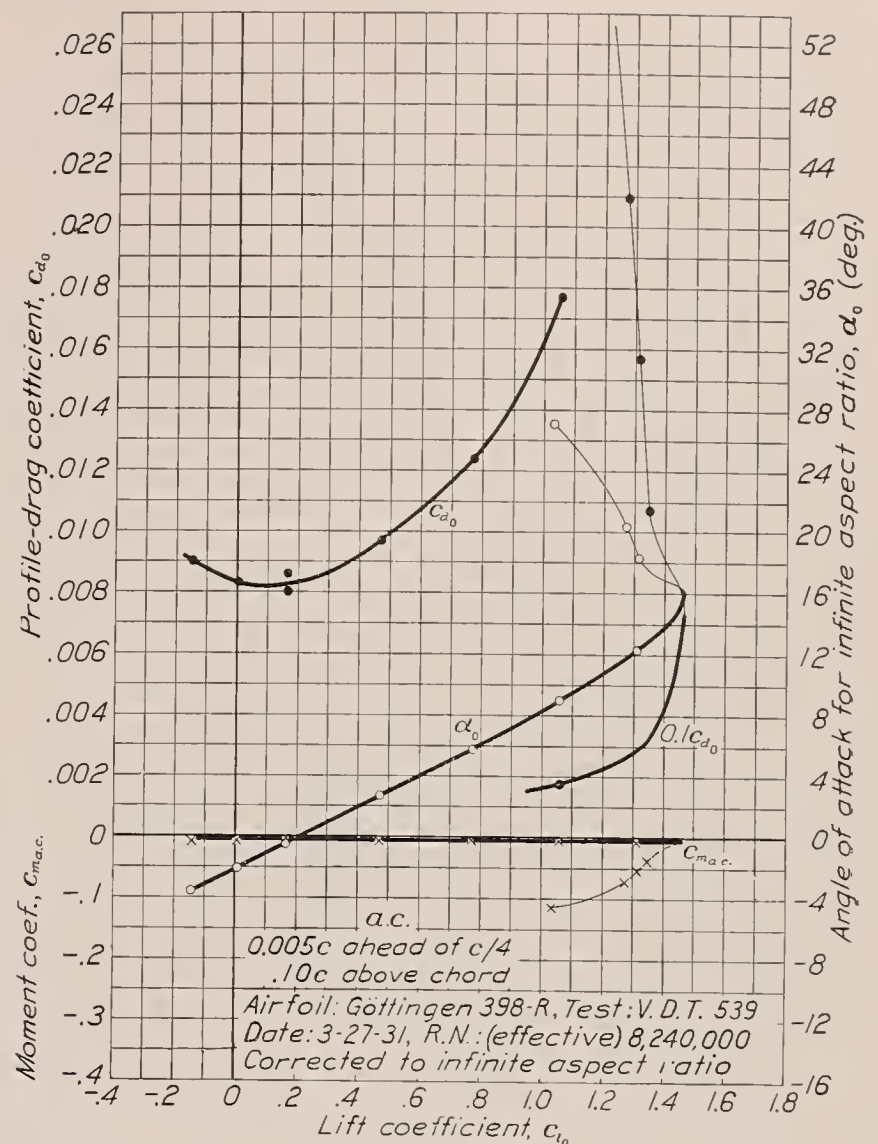
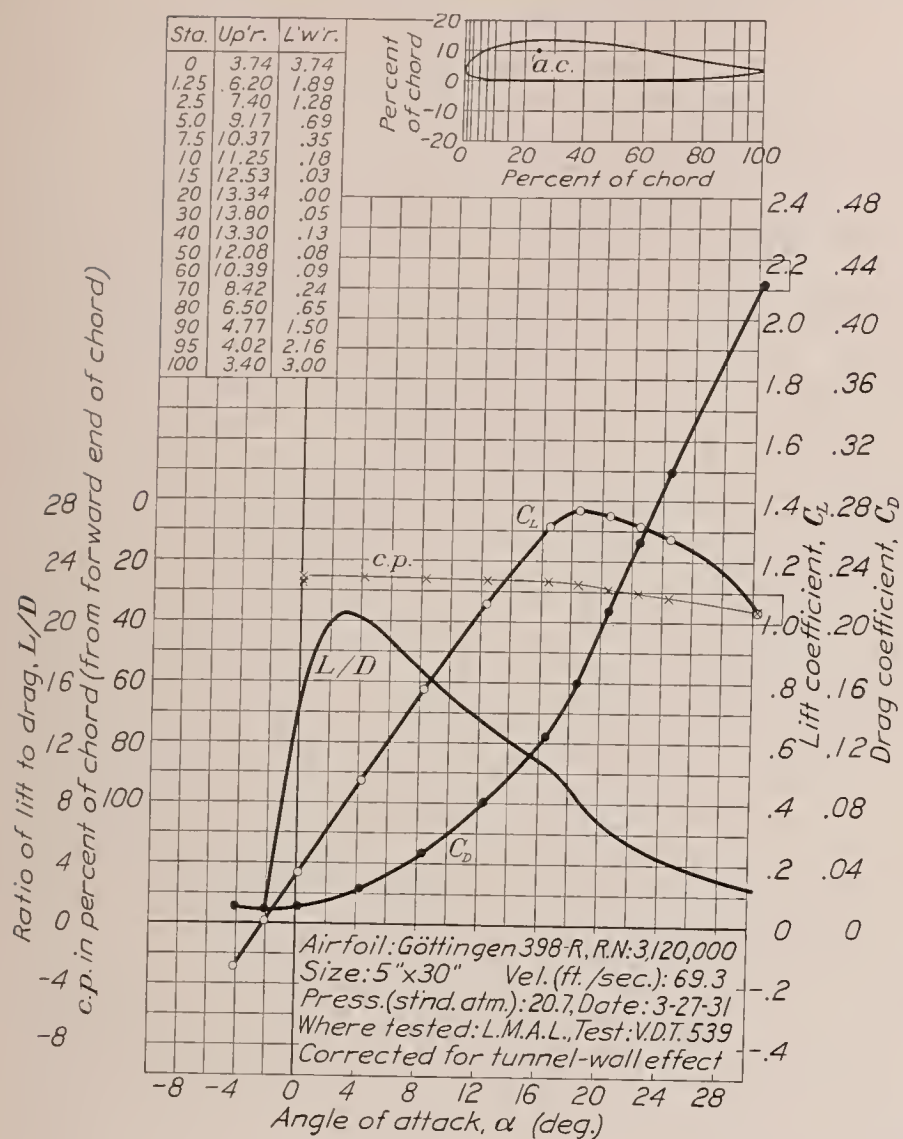


FIGURE 49.—Göttingen 398-R airfoil.

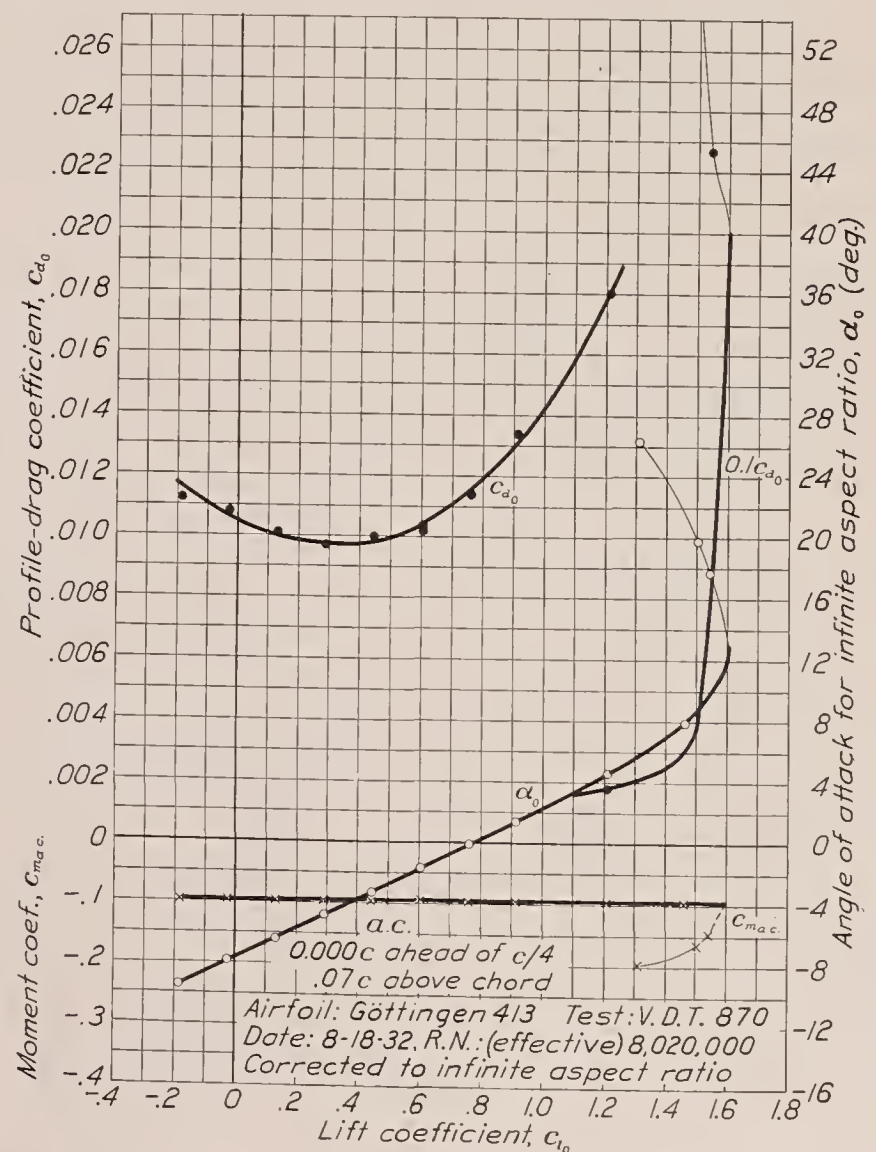
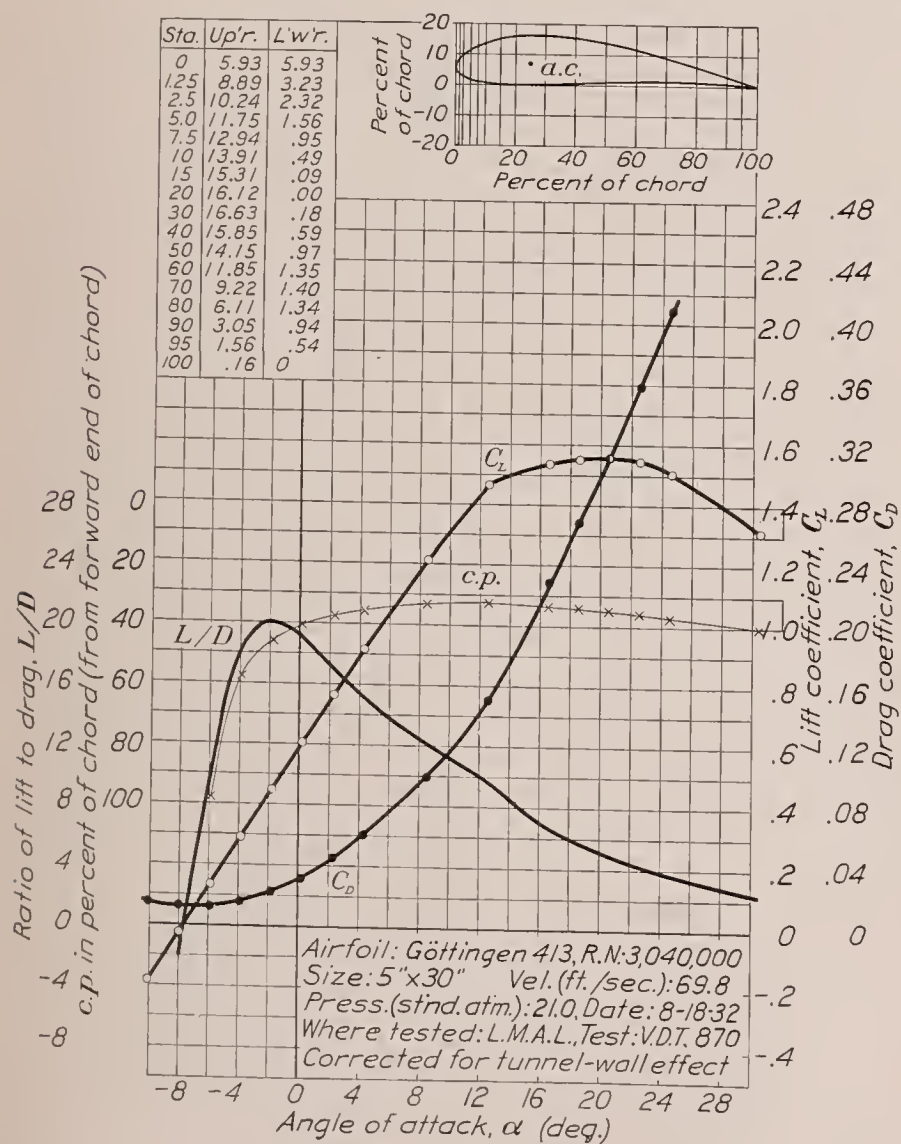


FIGURE 50.—Göttingen 413 airfoil.

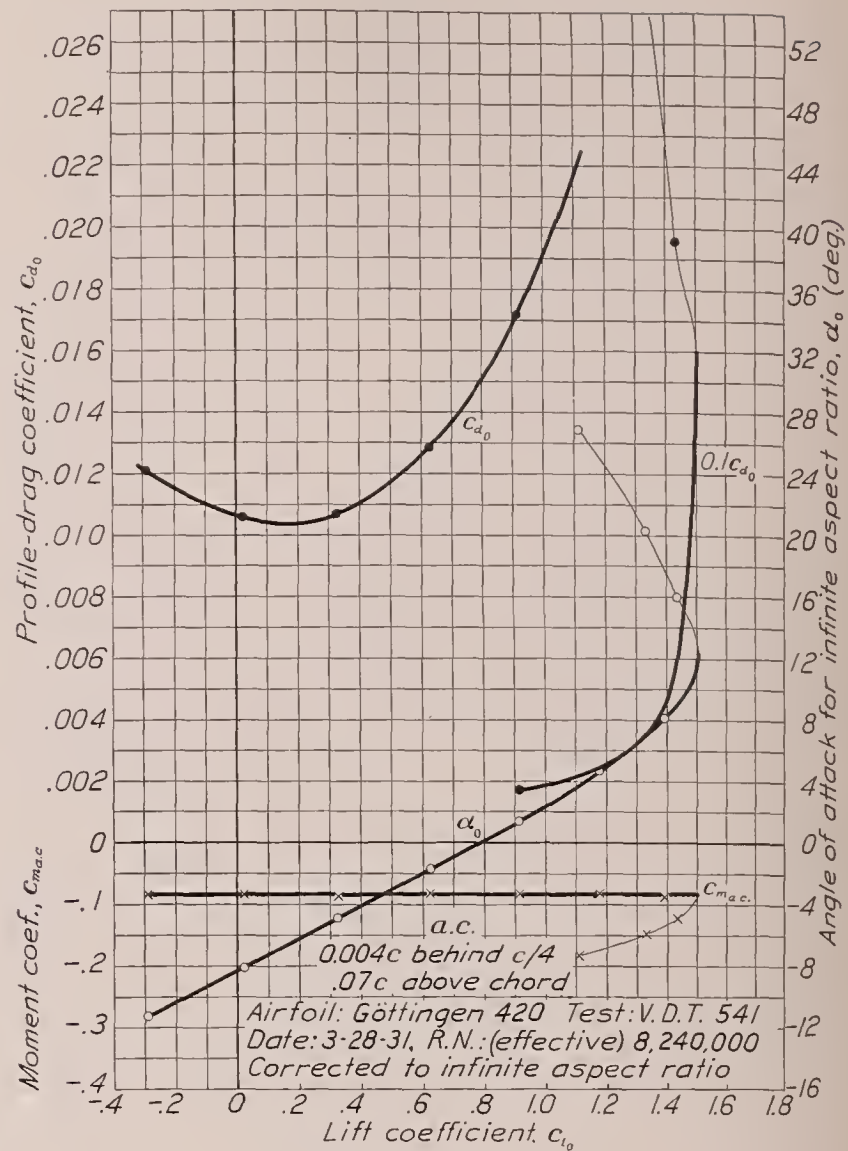
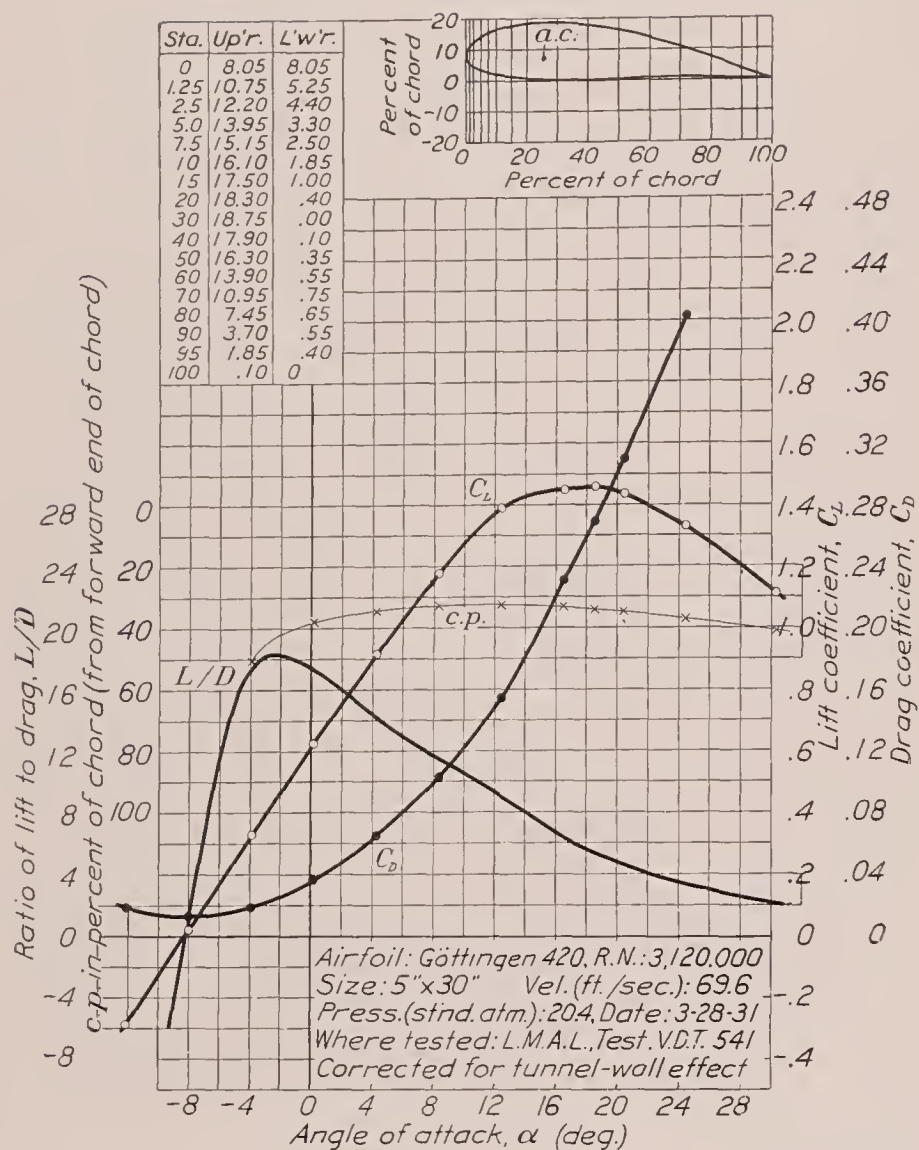


FIGURE 51.—Göttingen 420 airfoil.

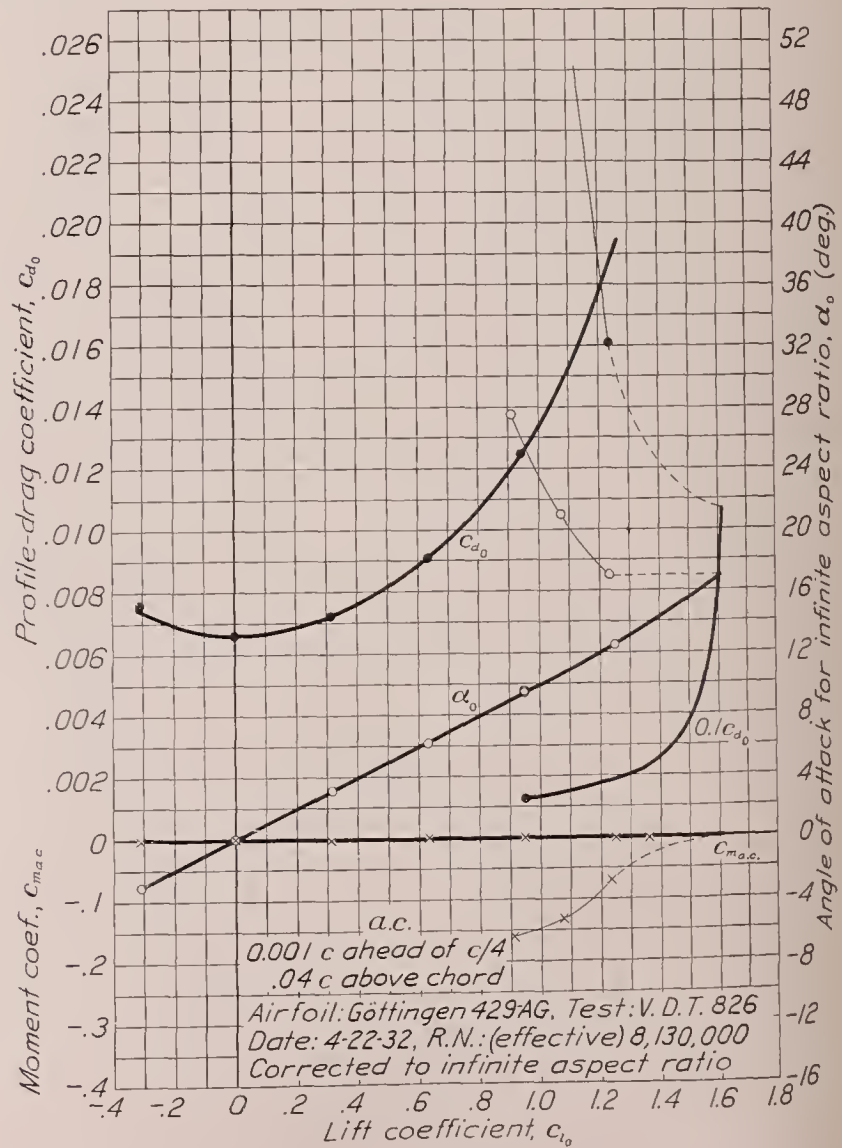
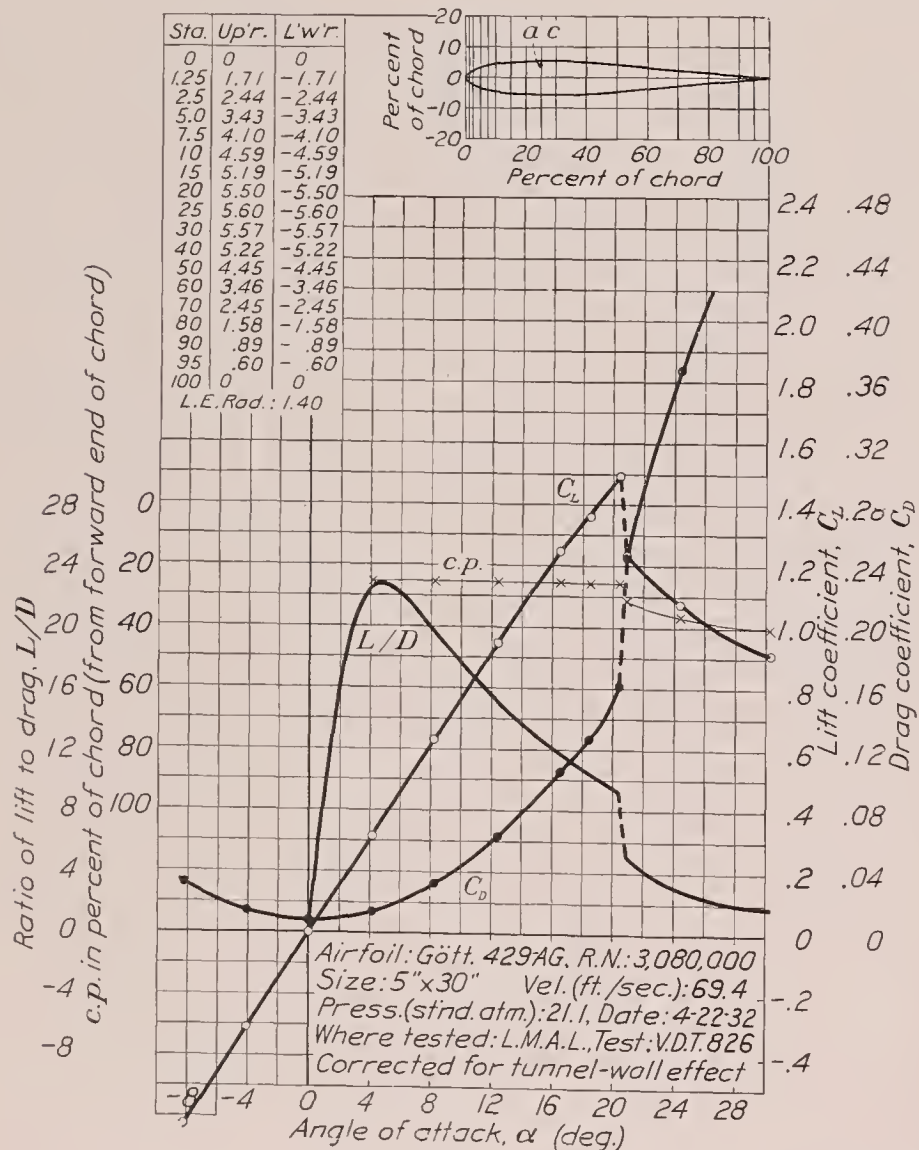


FIGURE 52.—Göttingen 429-AG airfoil.

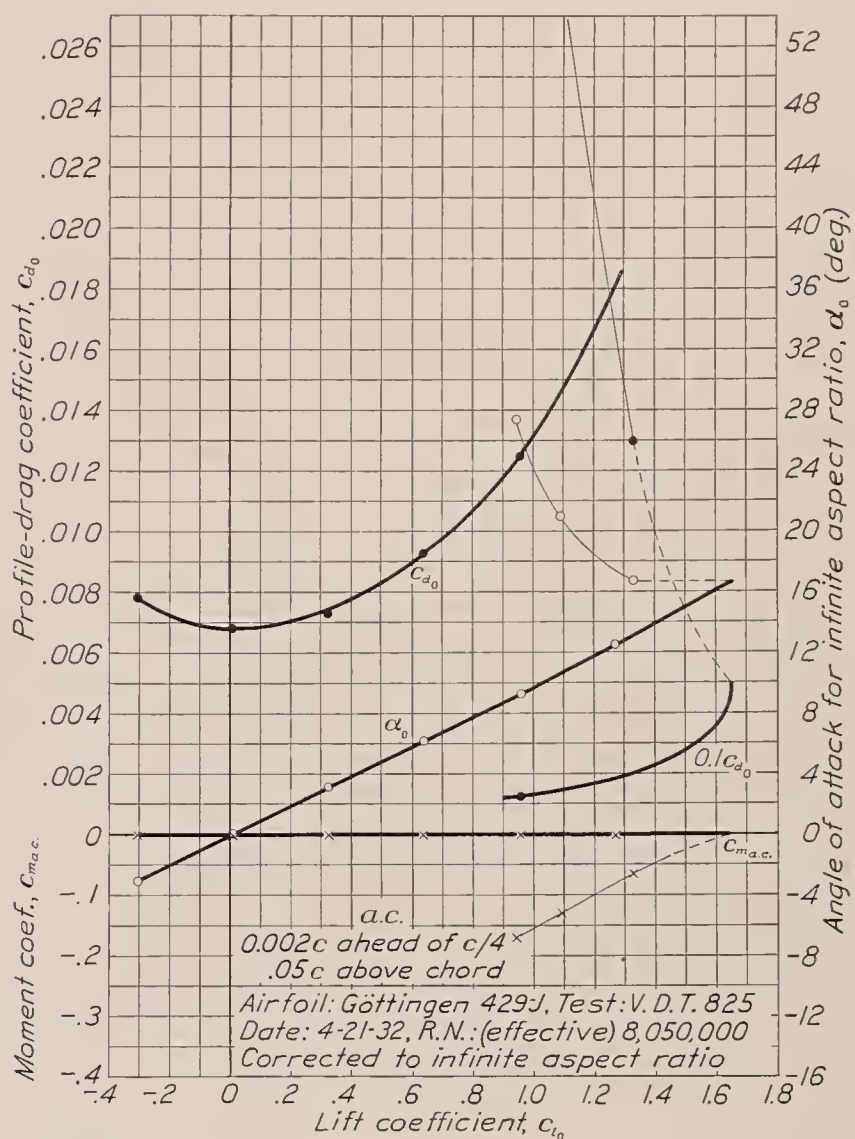
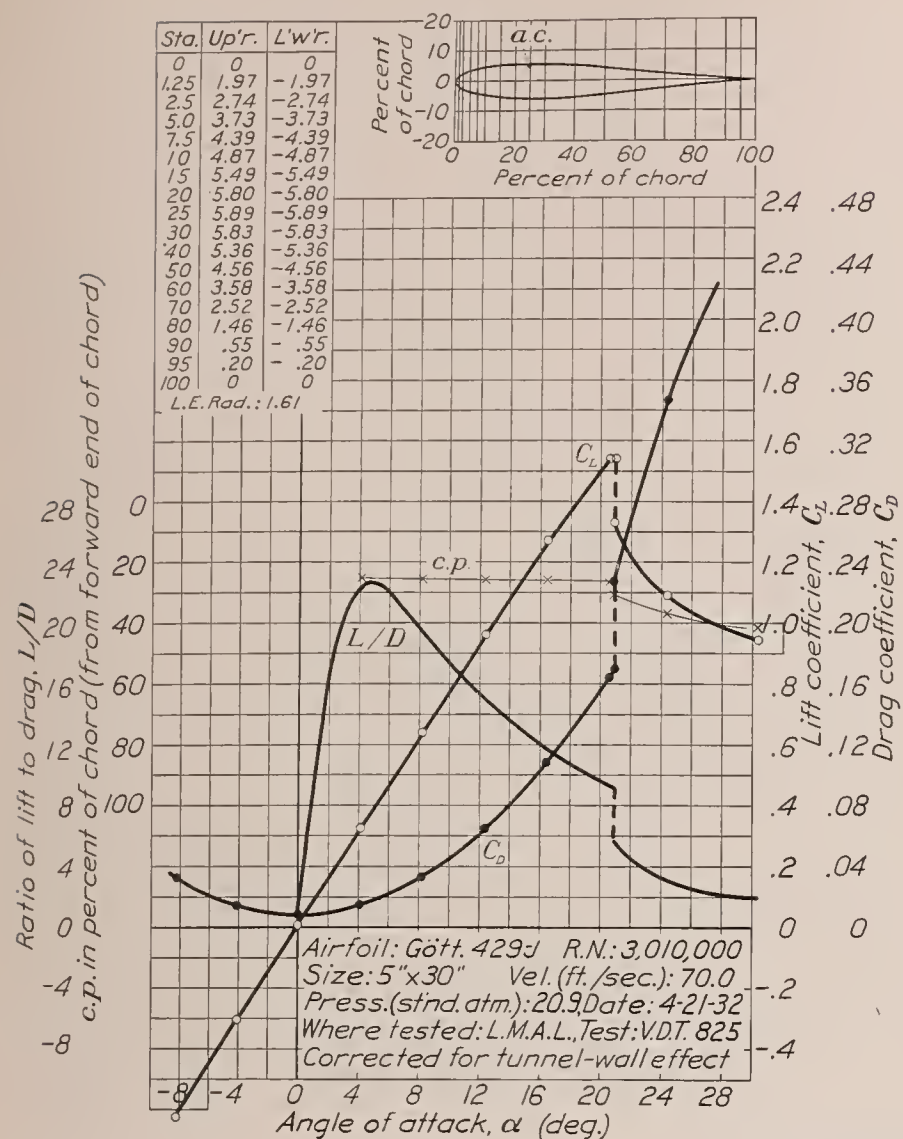


FIGURE 53.—Göttingen 429-J airfoil.

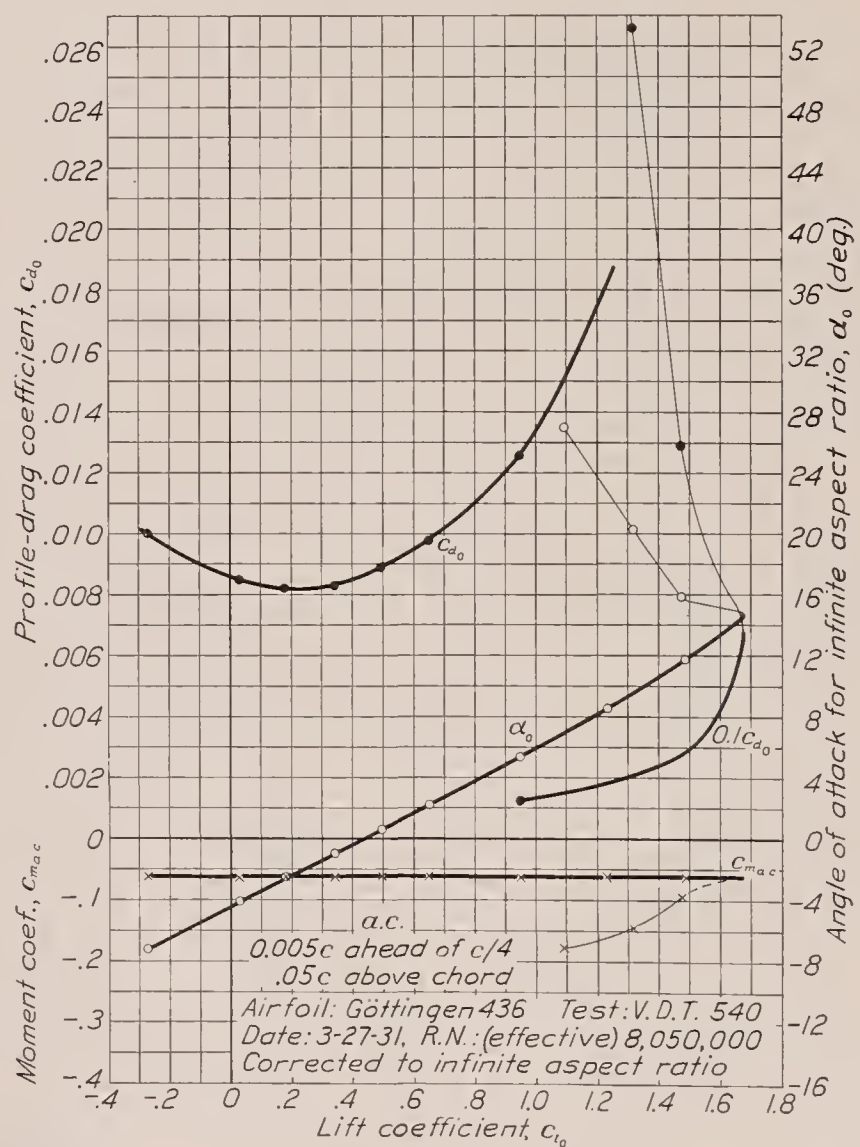
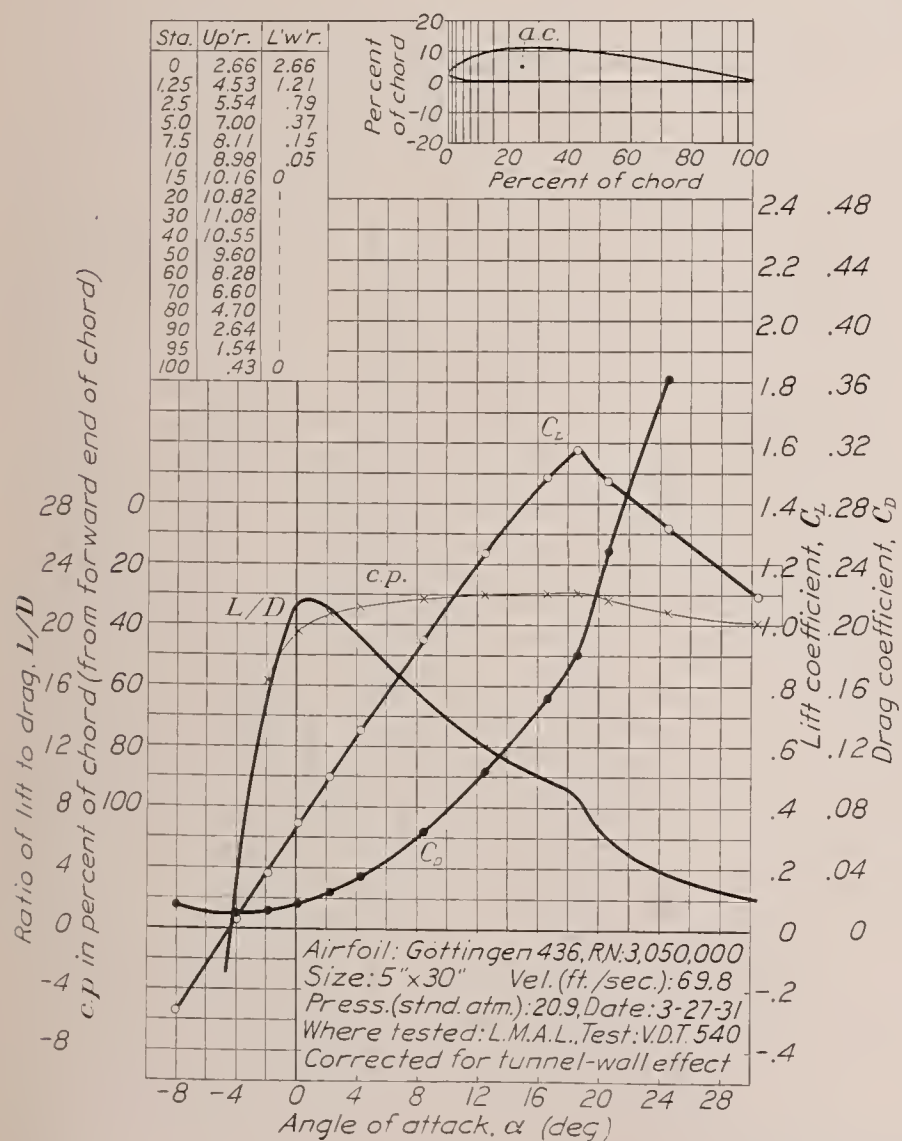


FIGURE 54.—Göttingen 436 airfoil.

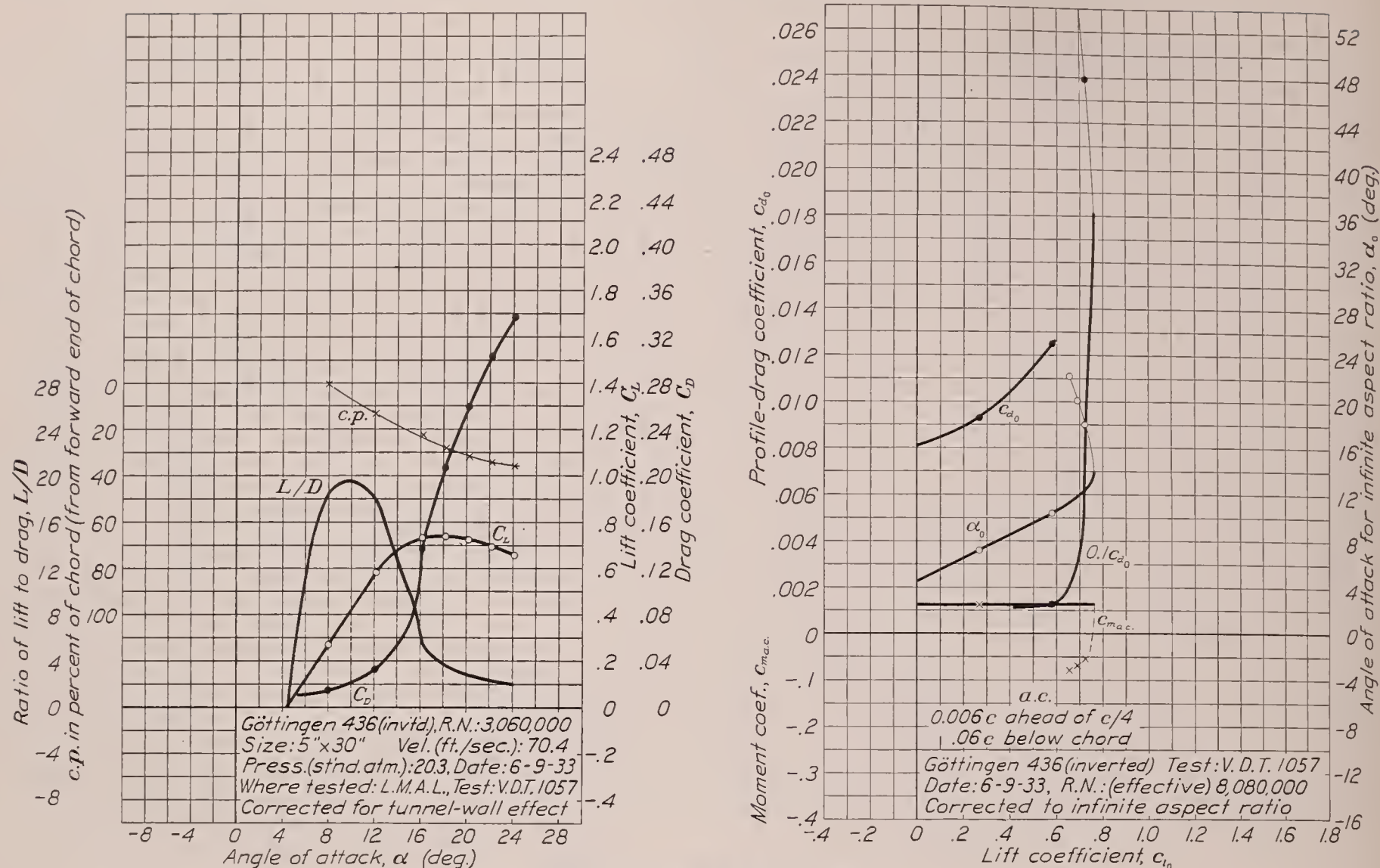


FIGURE 55.—Göttingen 436 airfoil (inverted).

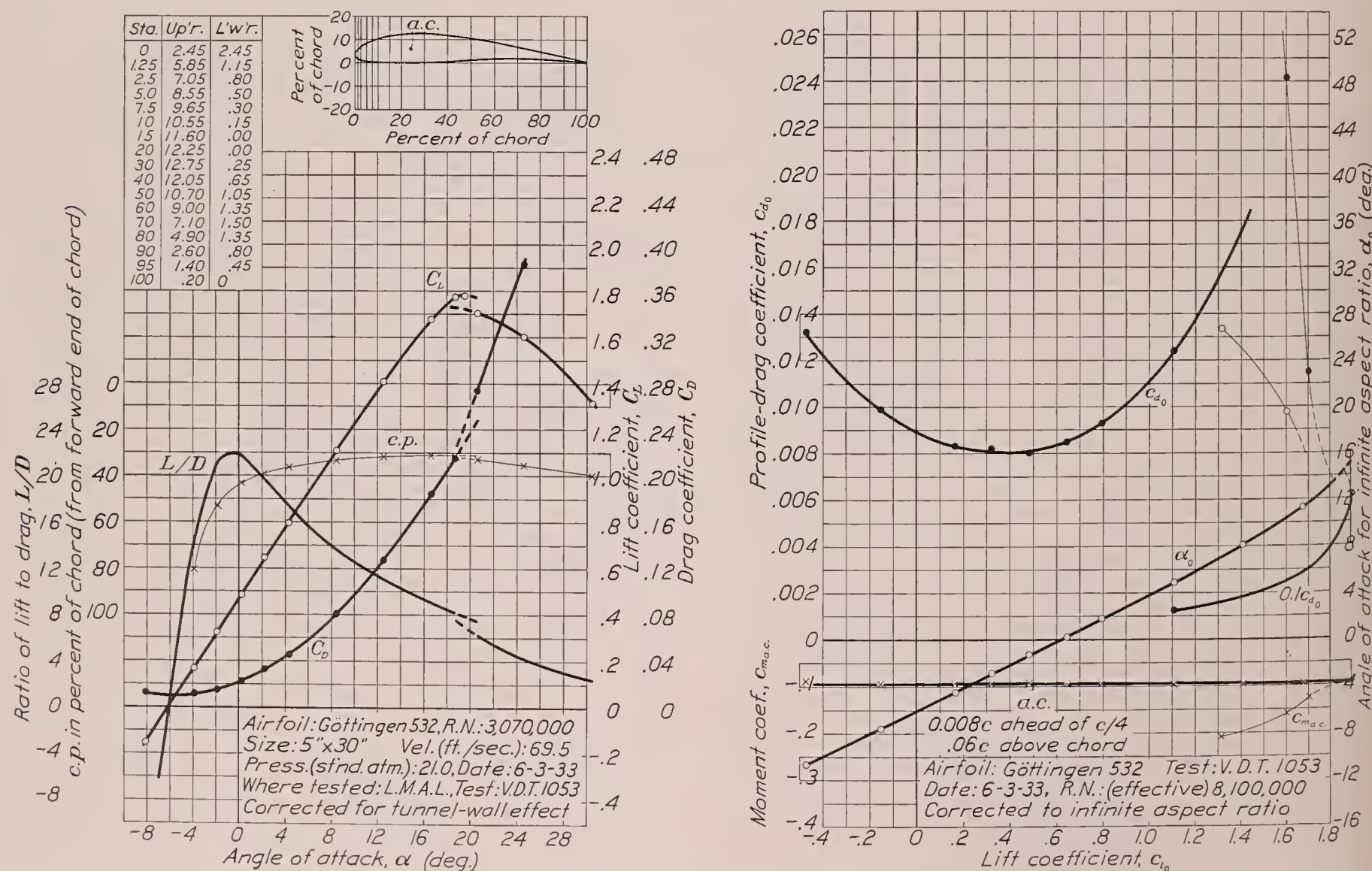


FIGURE 56.—Göttingen 532 airfoil.

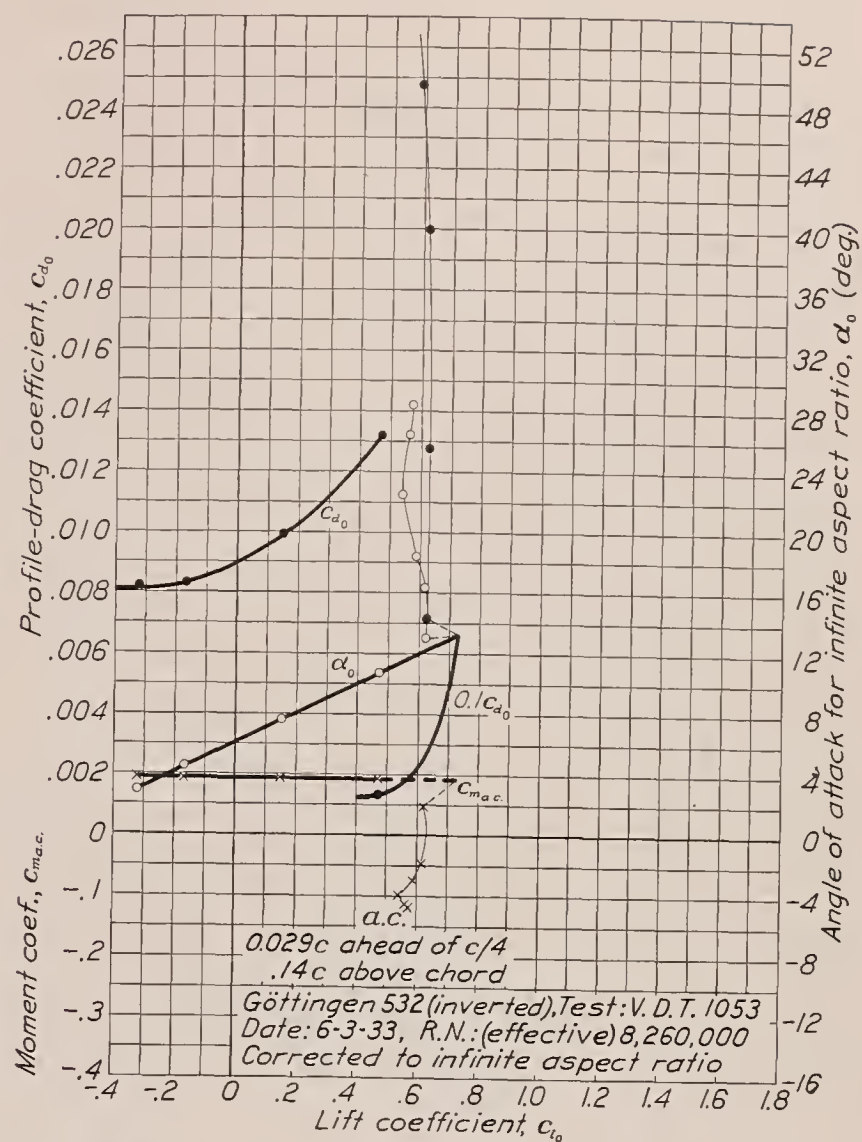
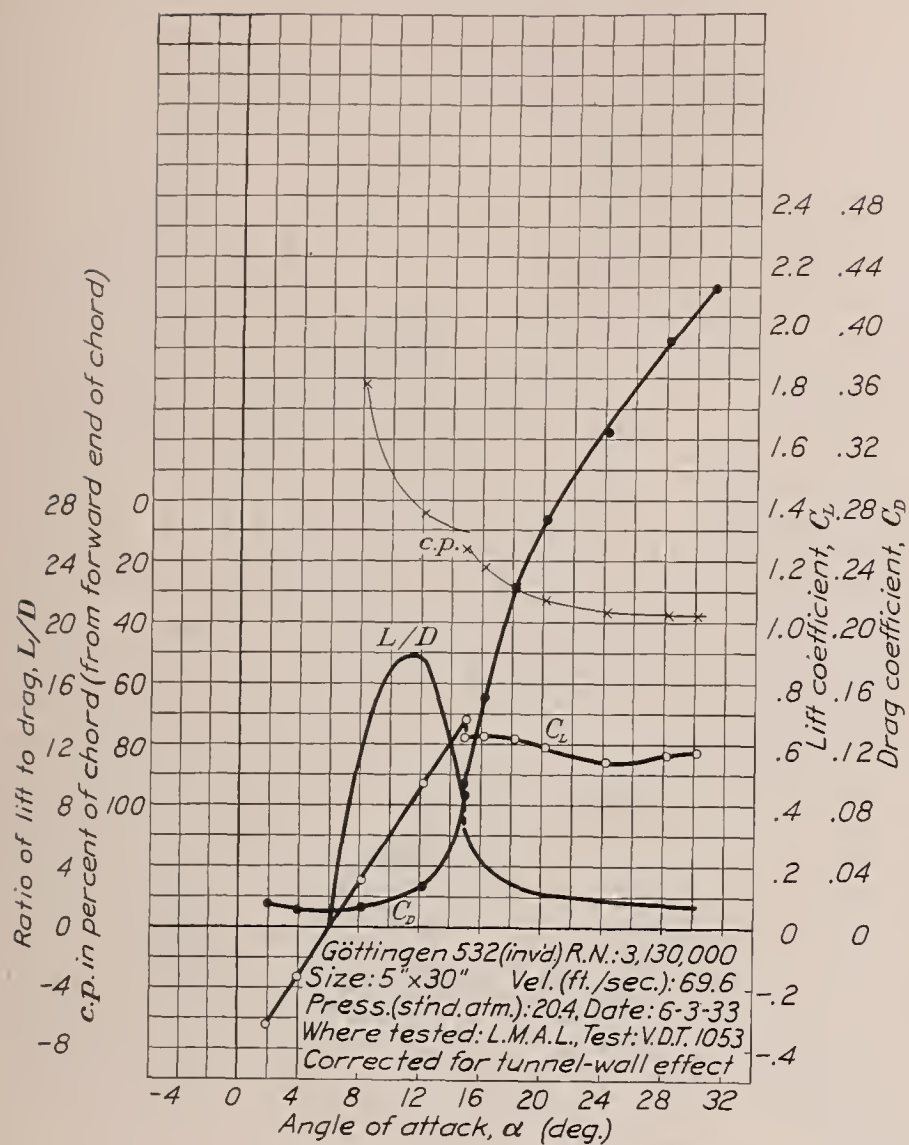


FIGURE 57.—Göttingen 532 airfoil (inverted).

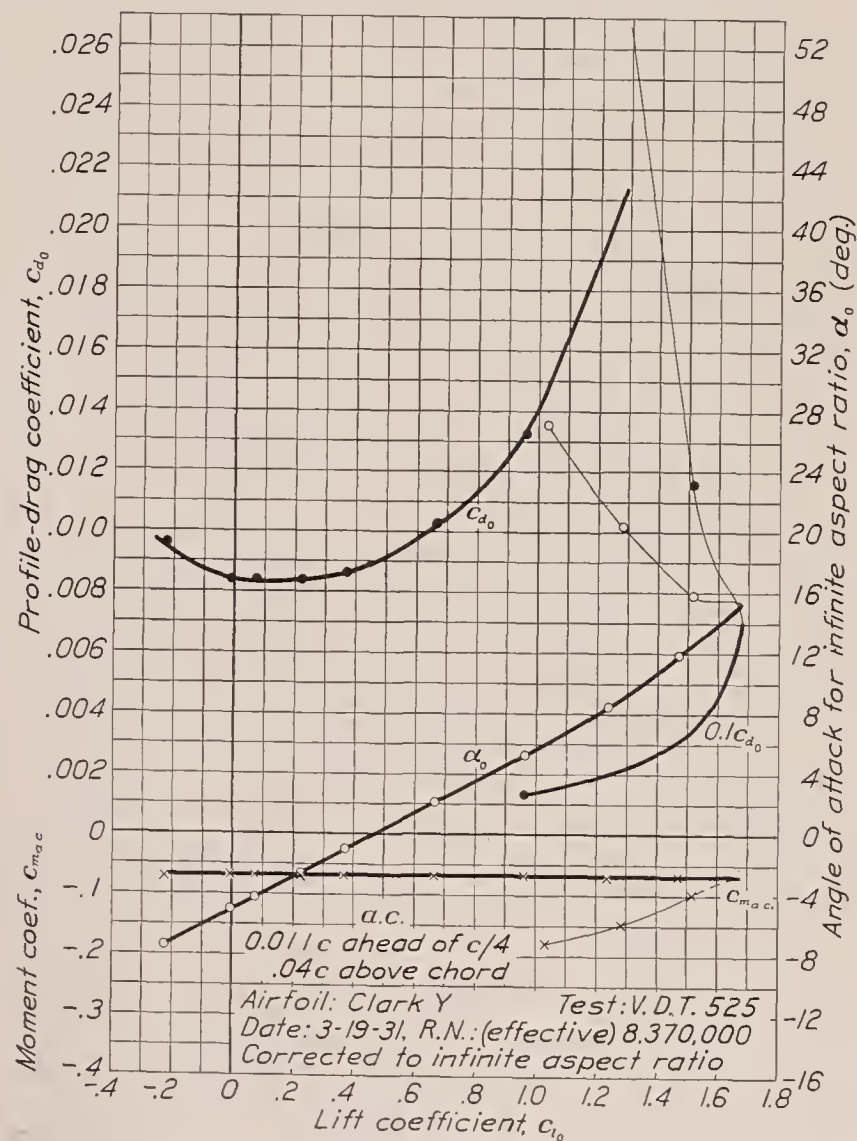
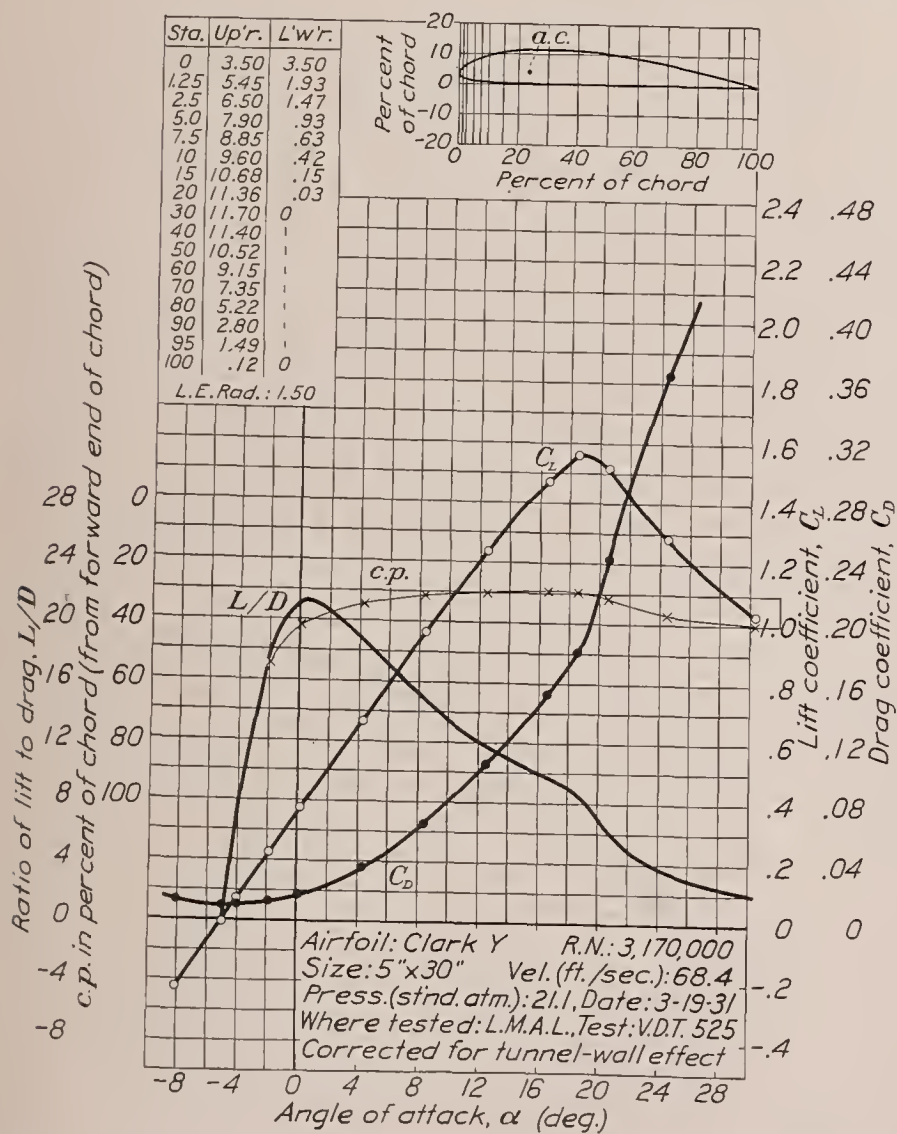


FIGURE 58.—Clark Y airfoil.

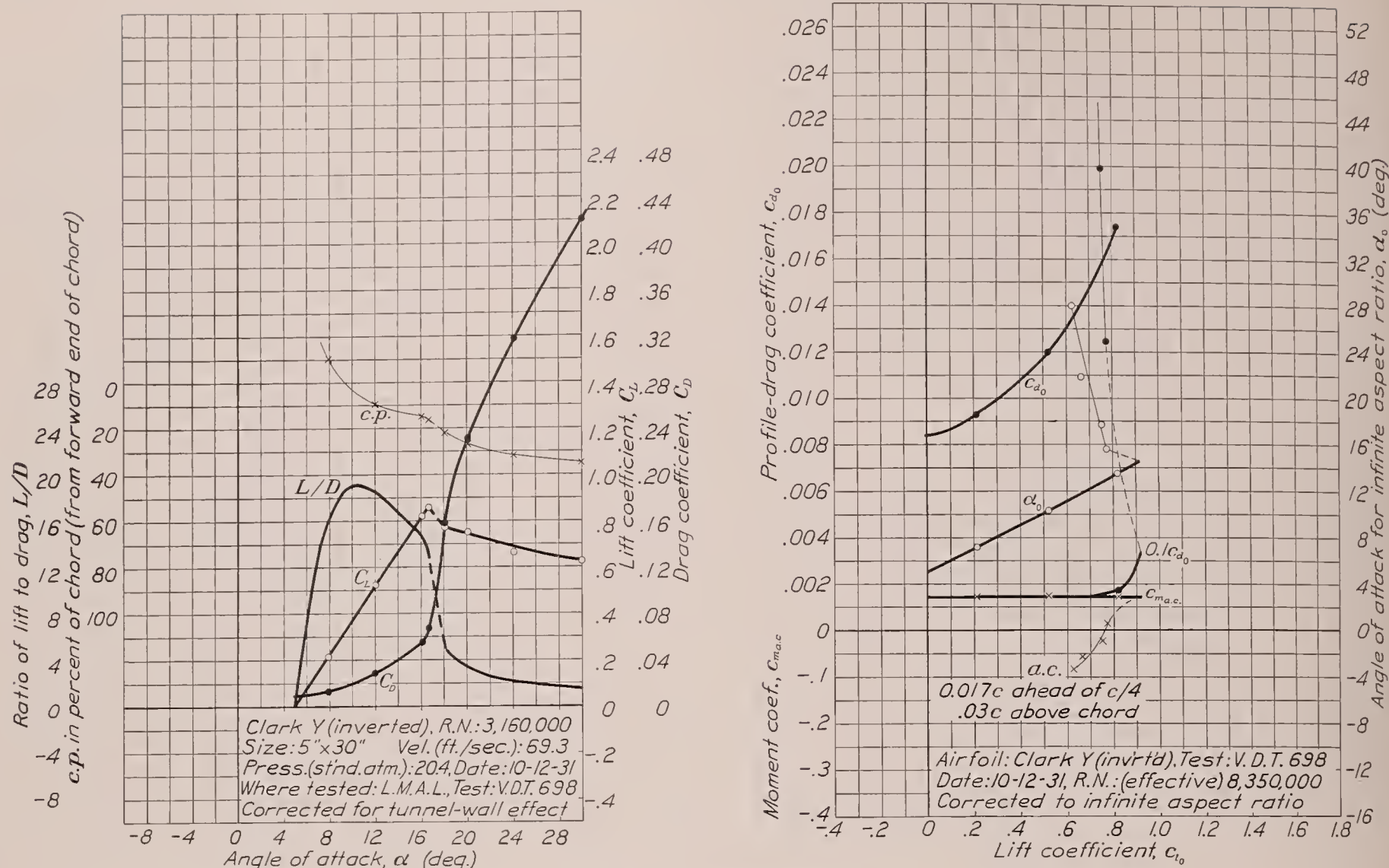


FIGURE 59.—Clark Y airfoil (inverted).

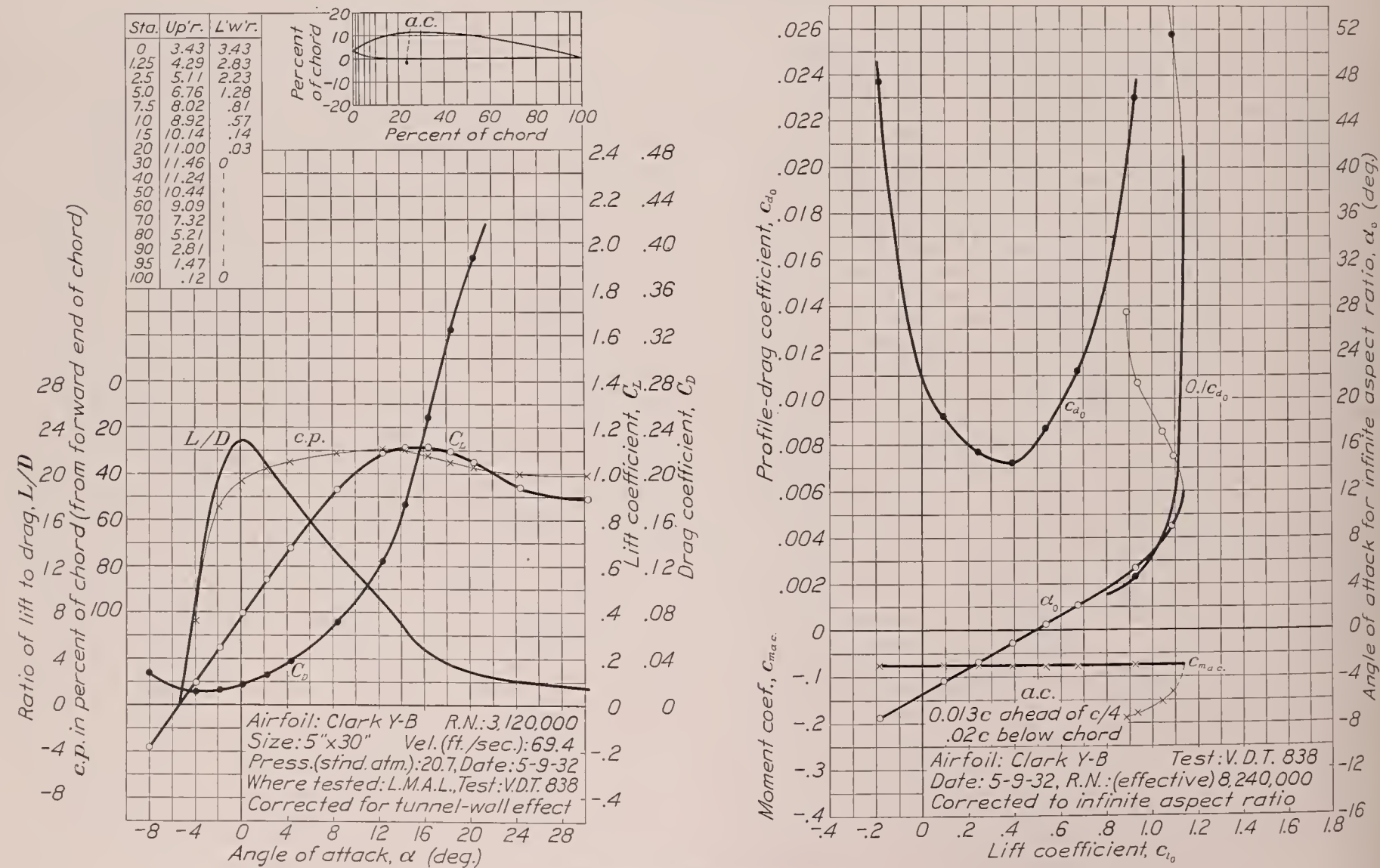


FIGURE 60.—Clark Y-B airfoil.

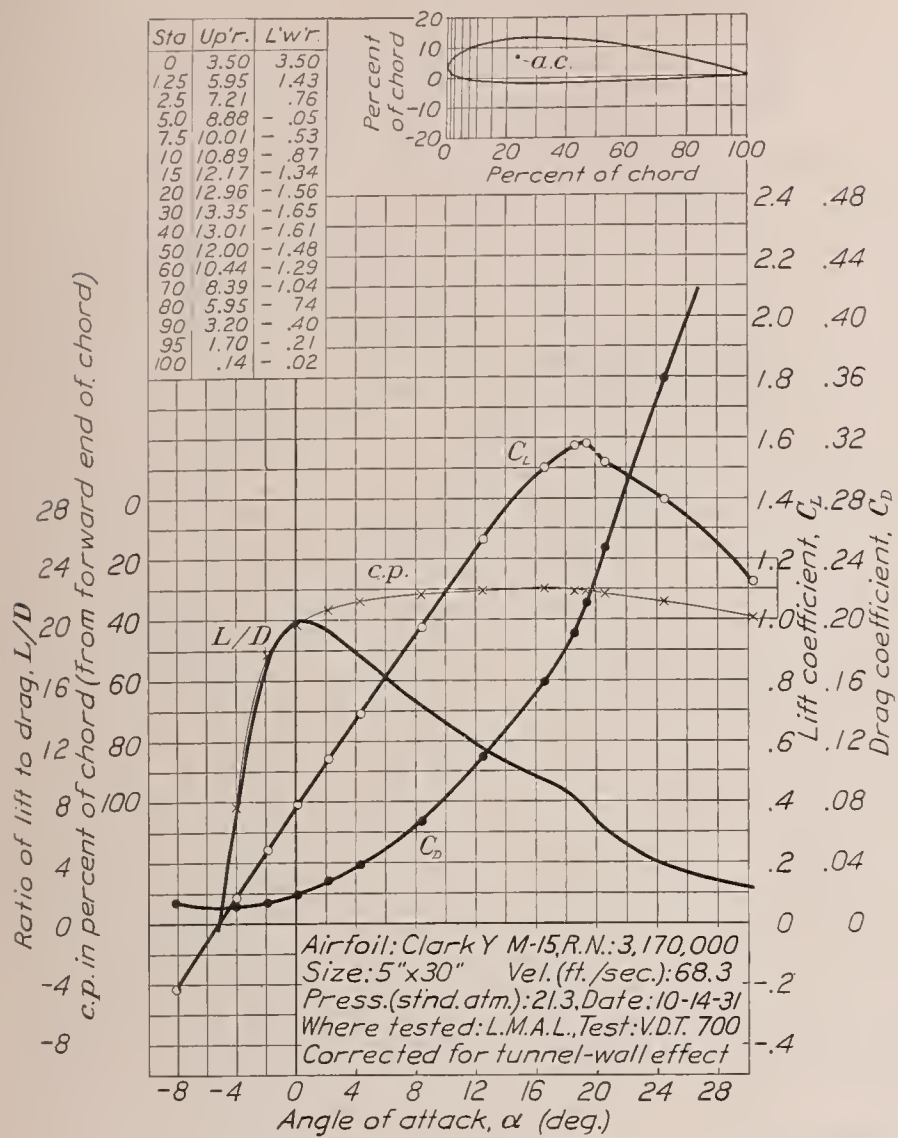


FIGURE 61.—Clark Y M-15 airfoil.

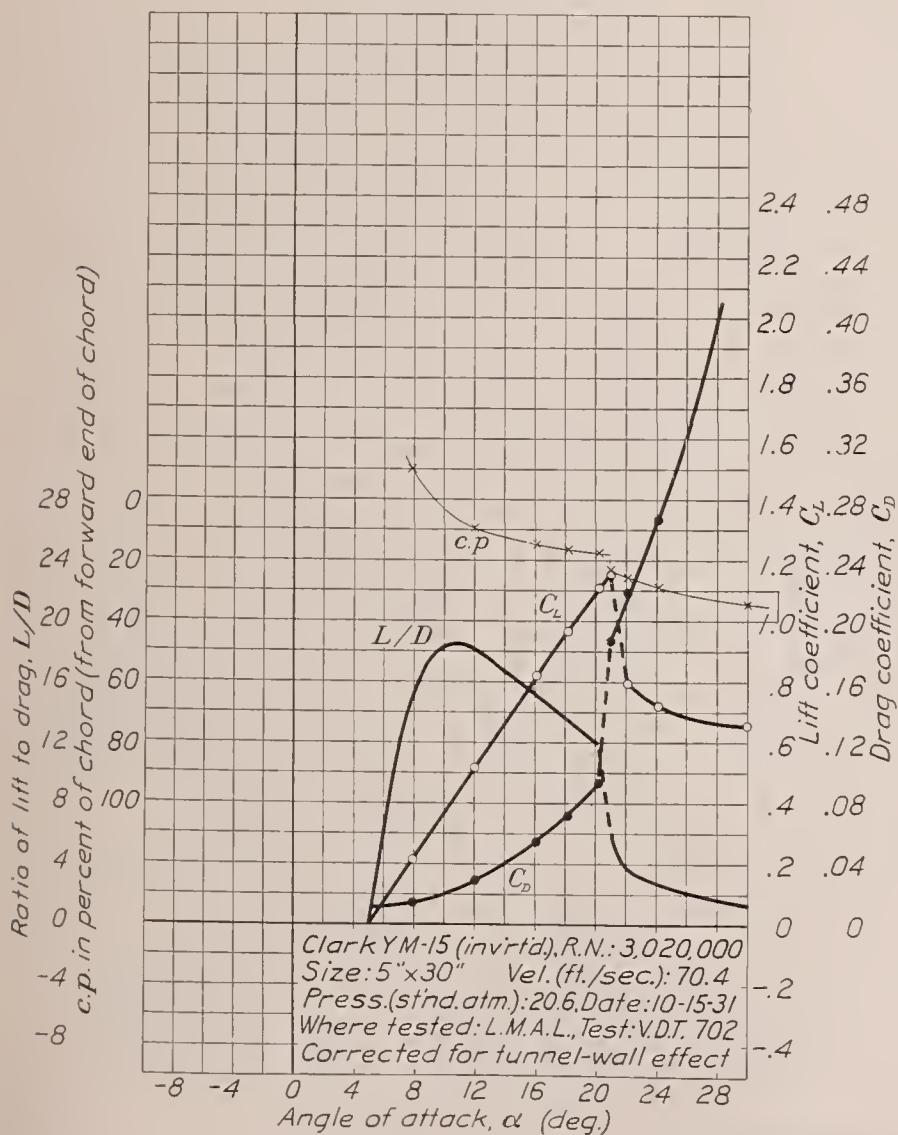
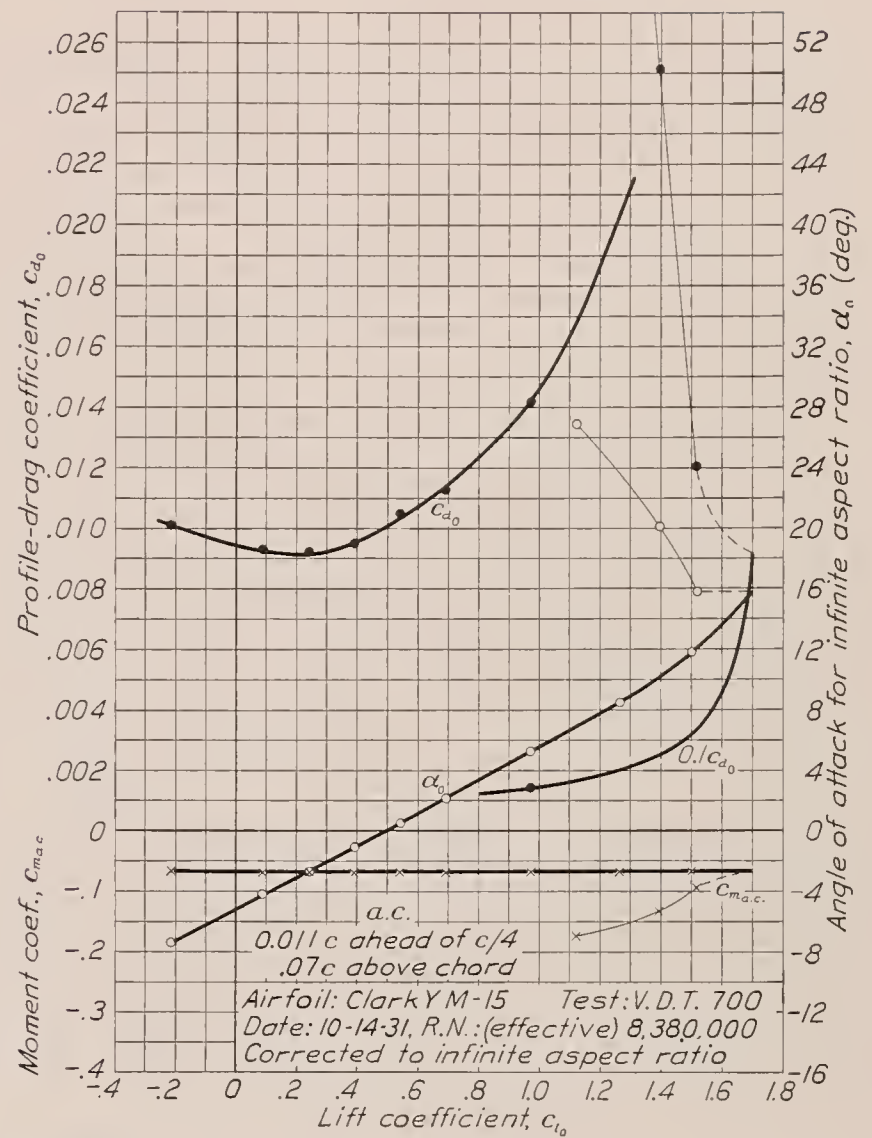
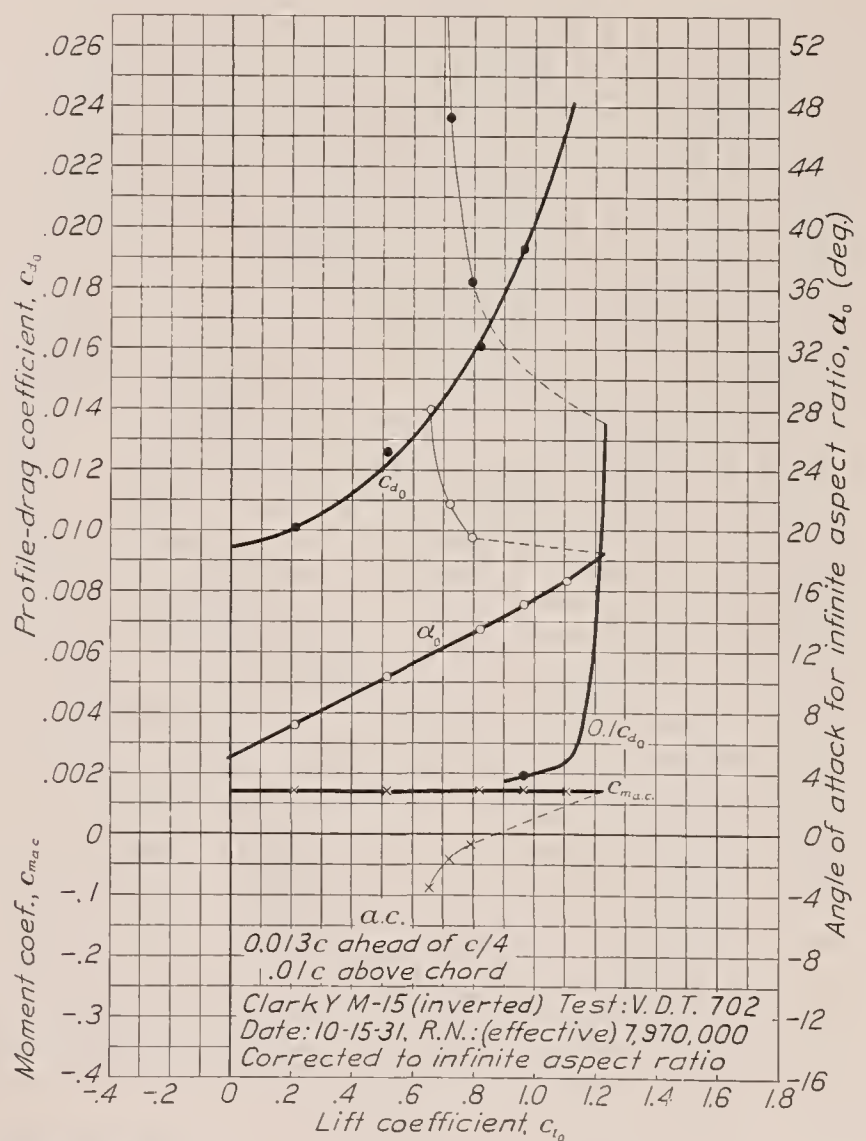


FIGURE 62.—Clark Y M-15 airfoil (inverted).



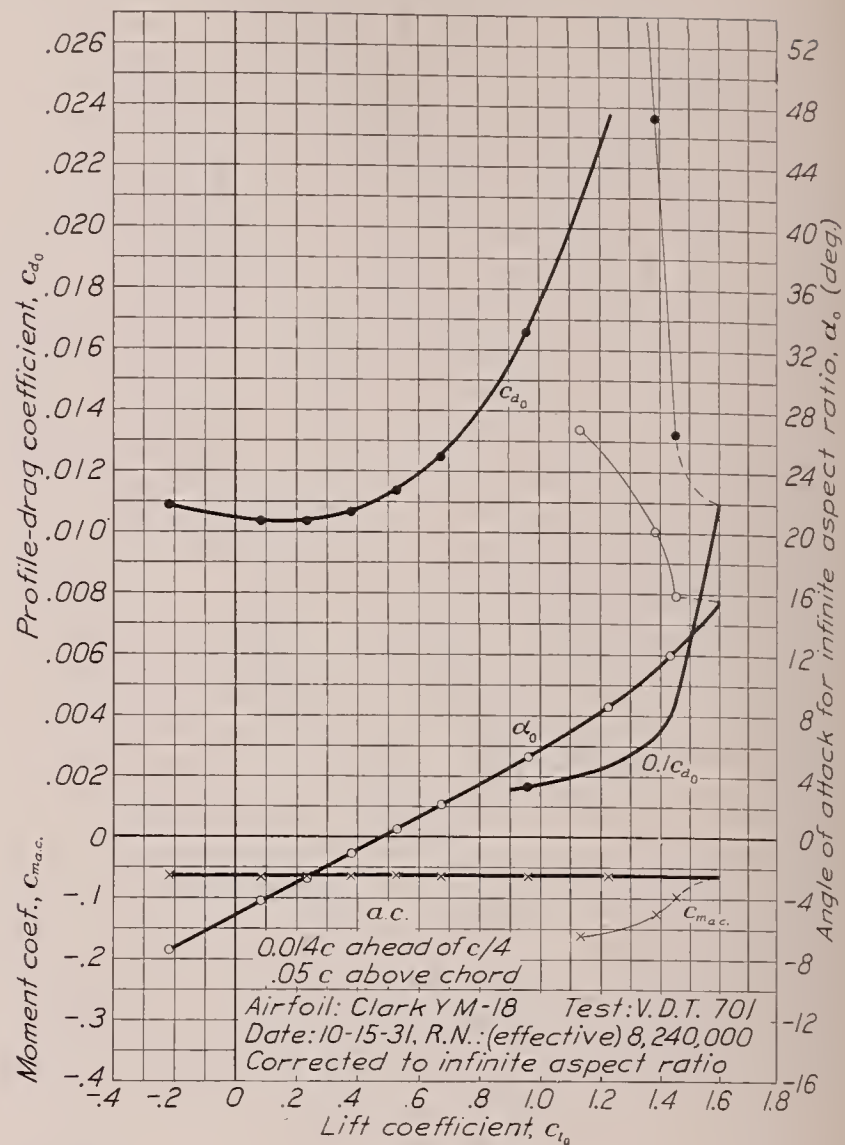
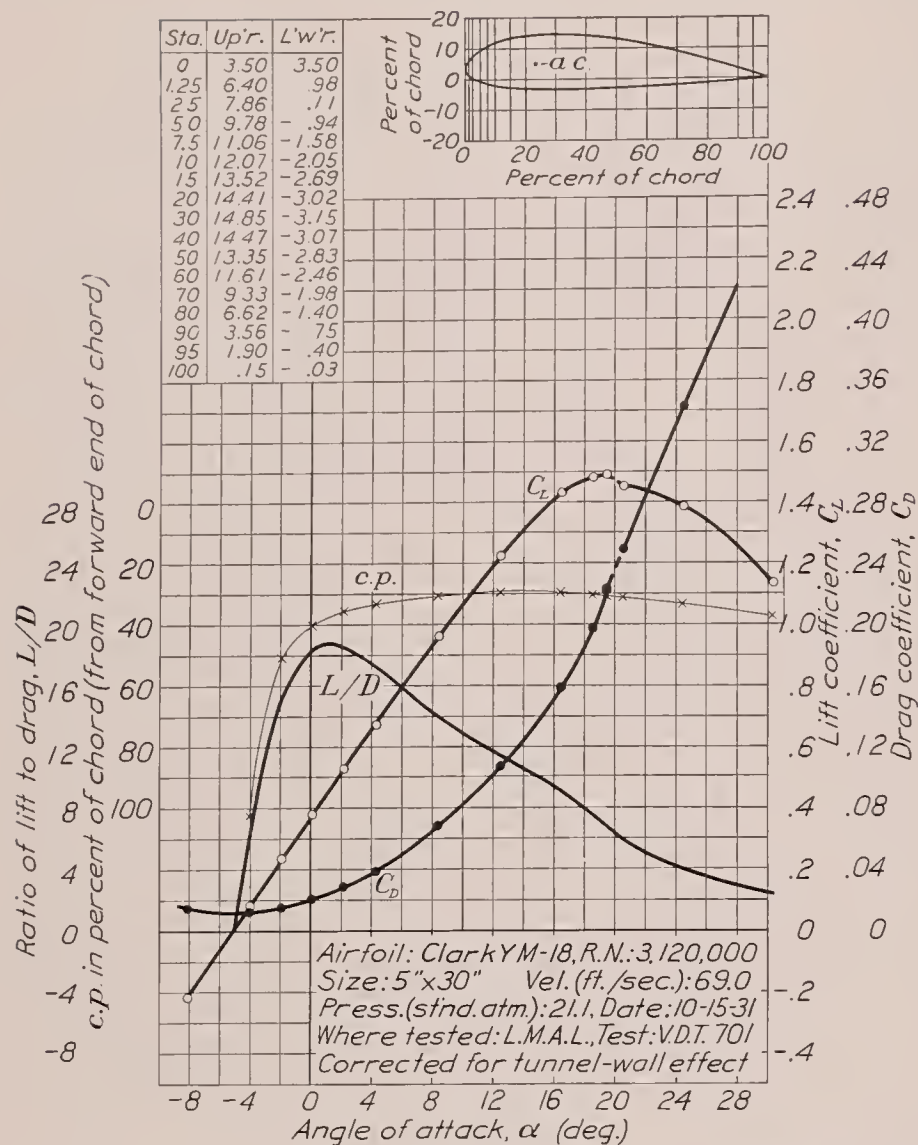


FIGURE 63.—Clark Y M-18 airfoil.

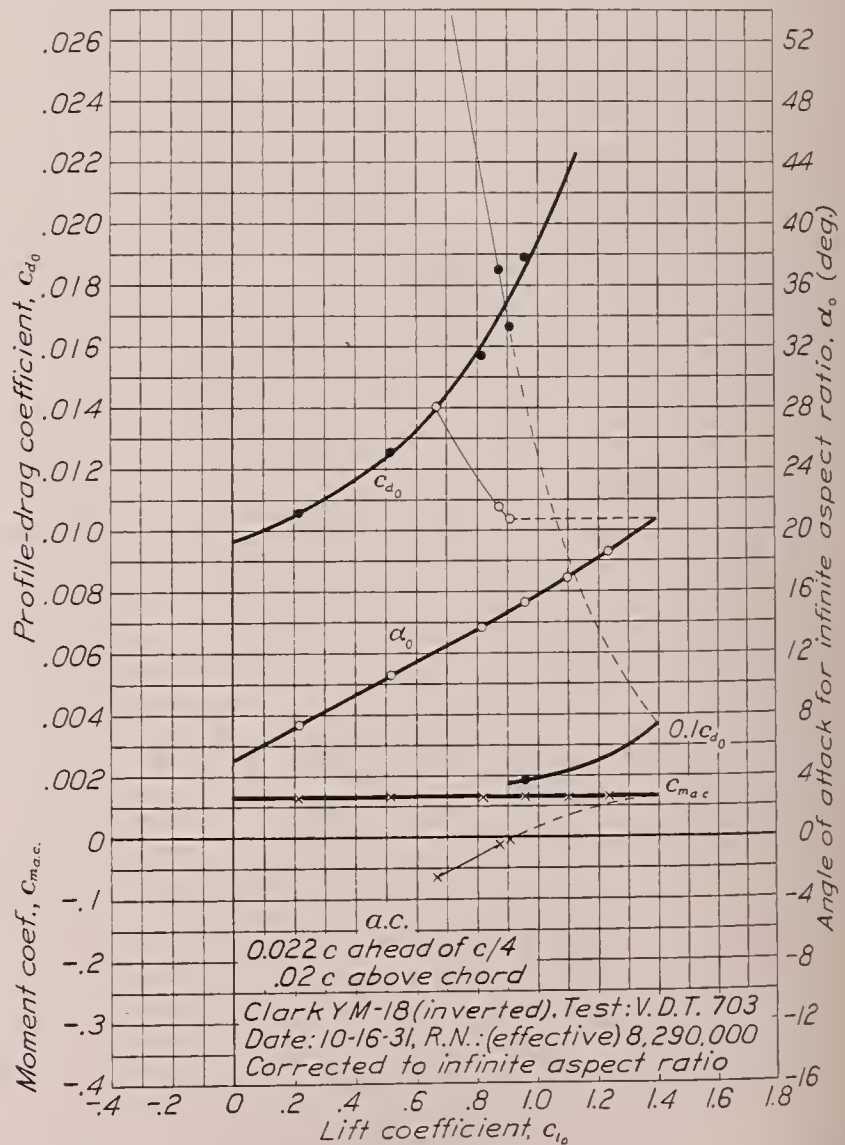
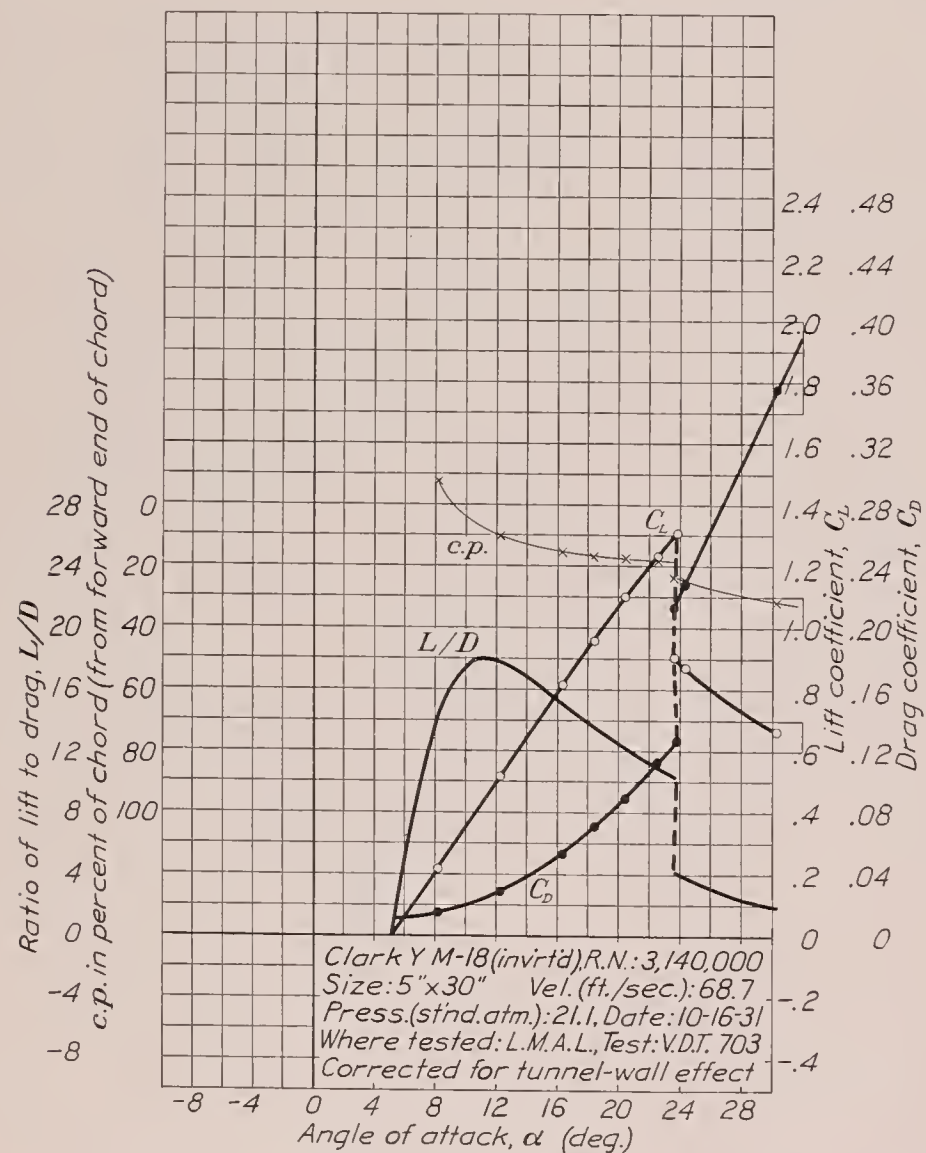


FIGURE 64.—Clark Y M-18 airfoil (inverted).

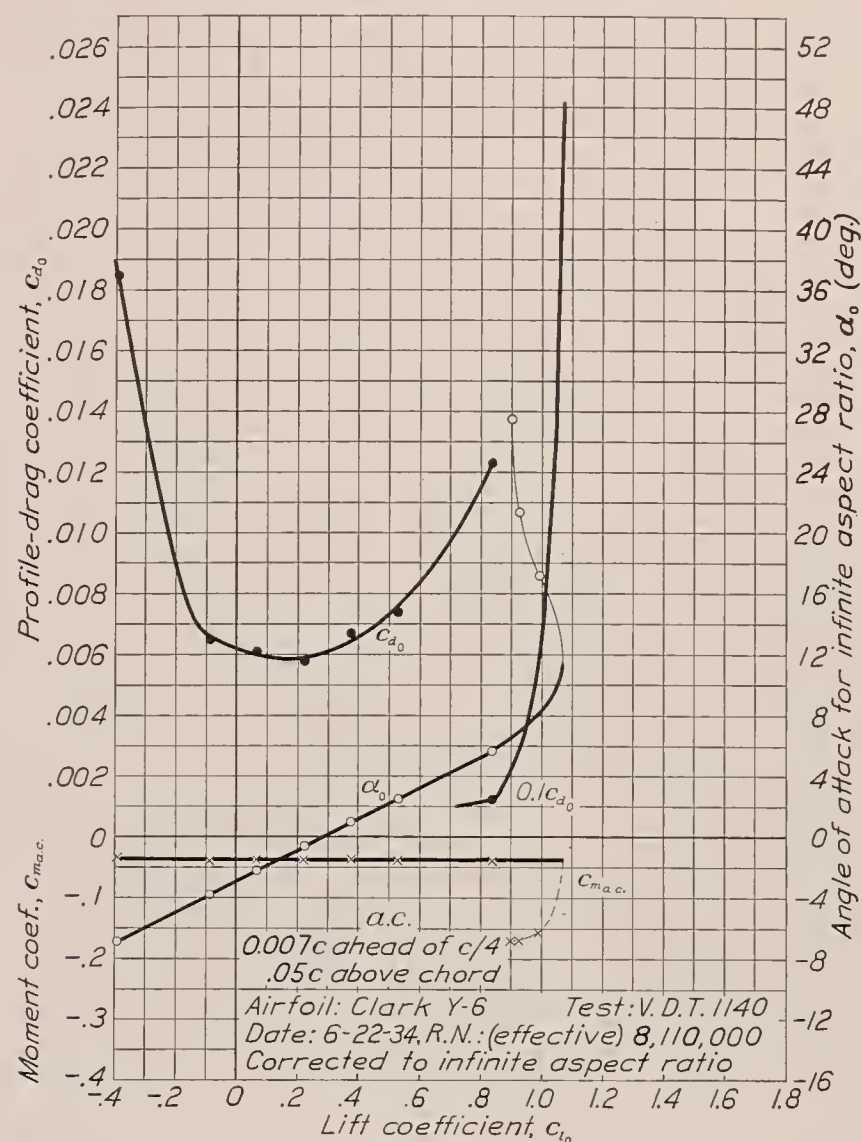
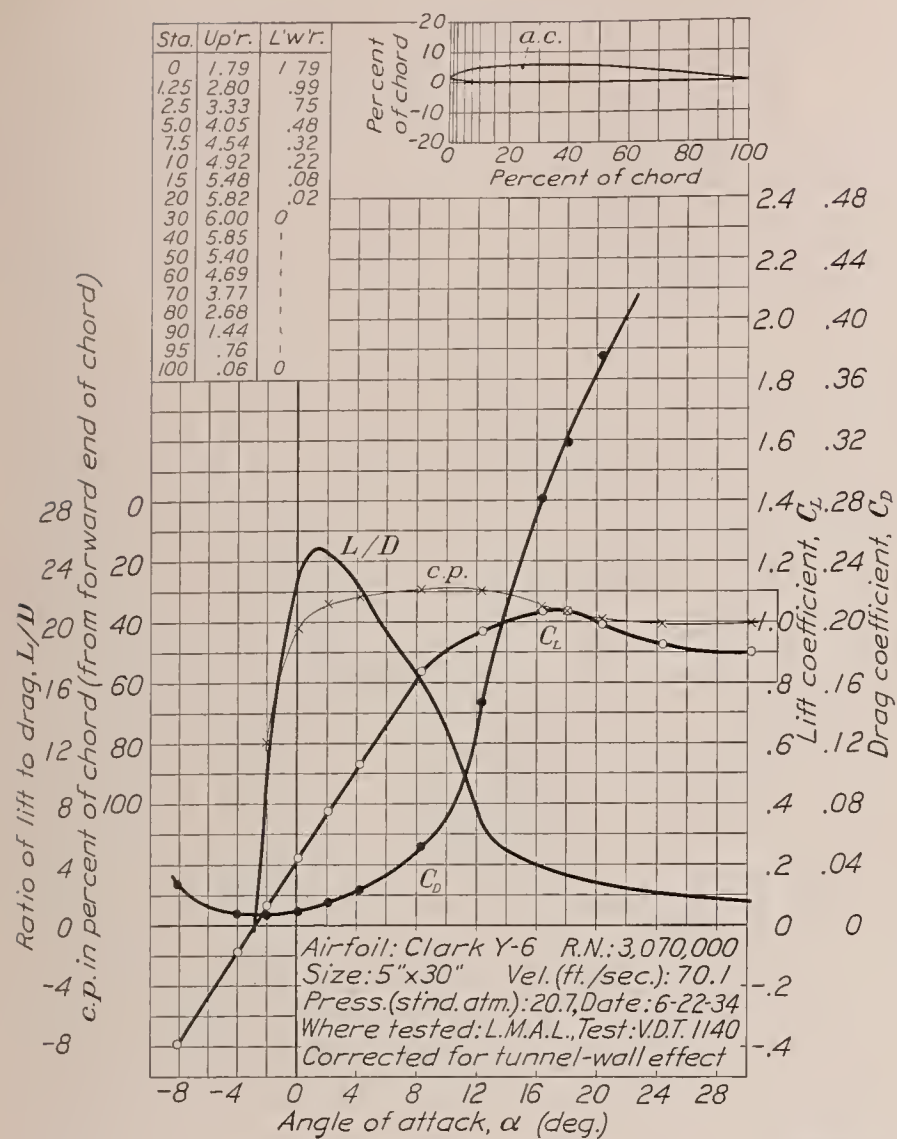


FIGURE 65.—Clark Y-6 airfoil.

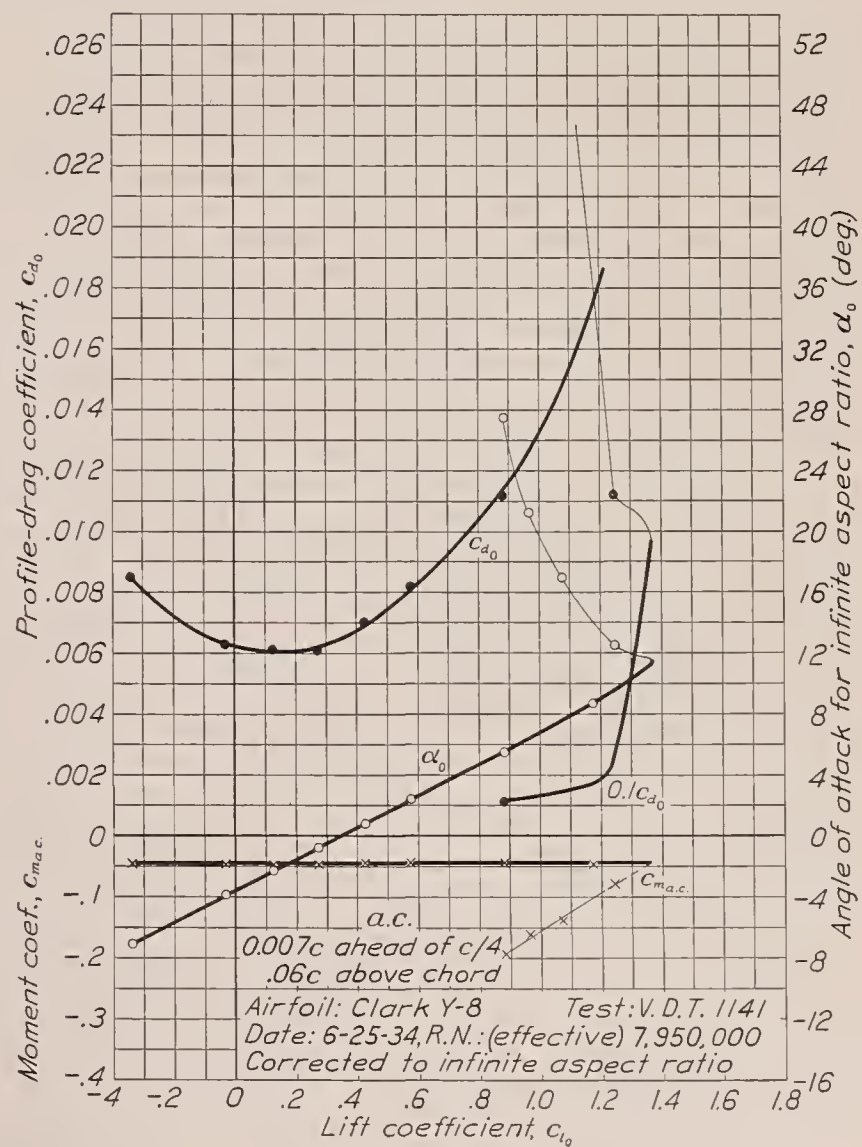
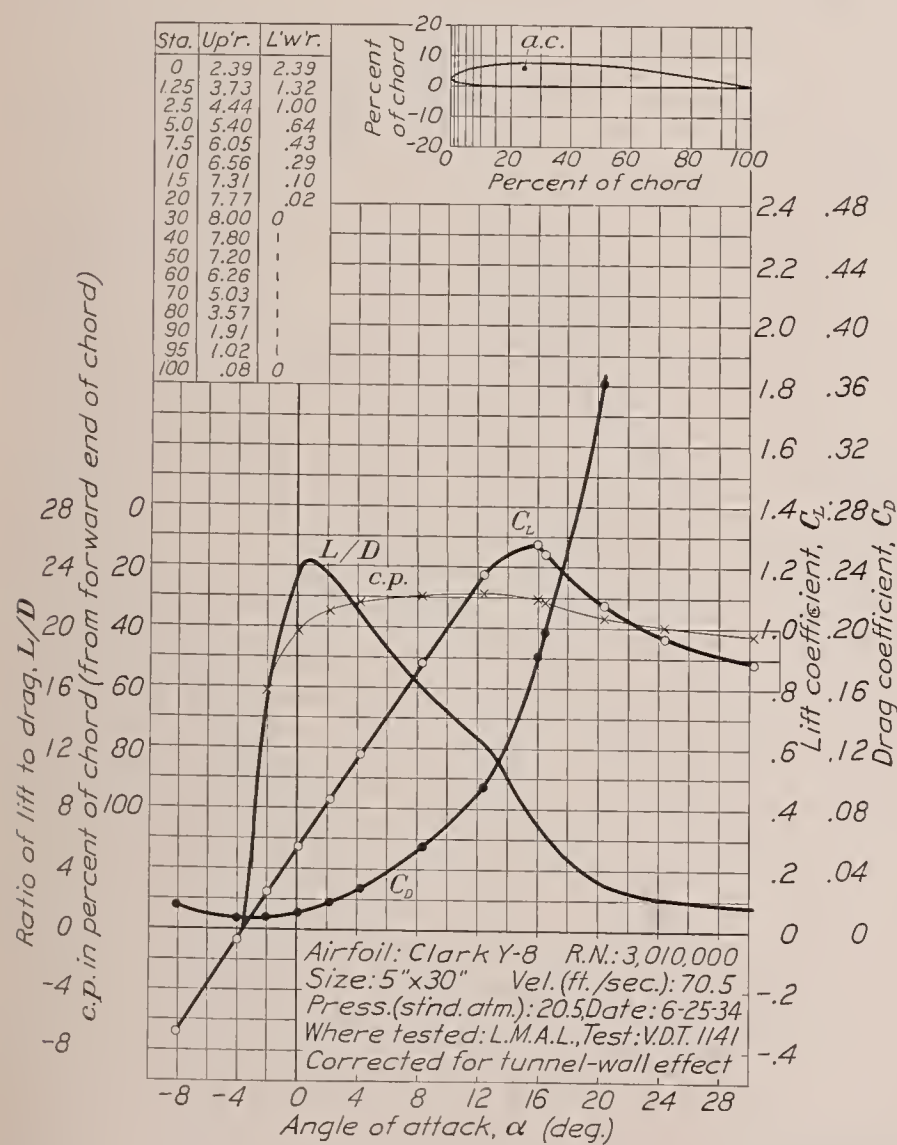


FIGURE 66.—Clark Y-8 airfoil.

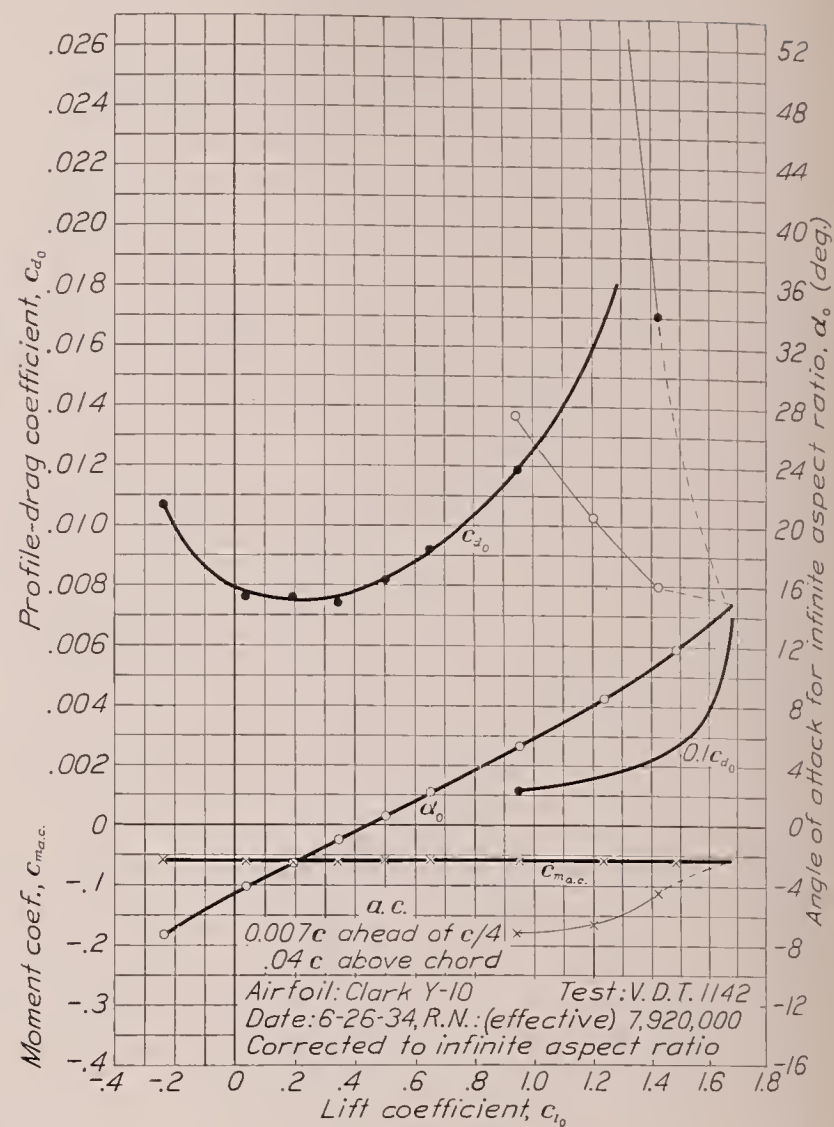
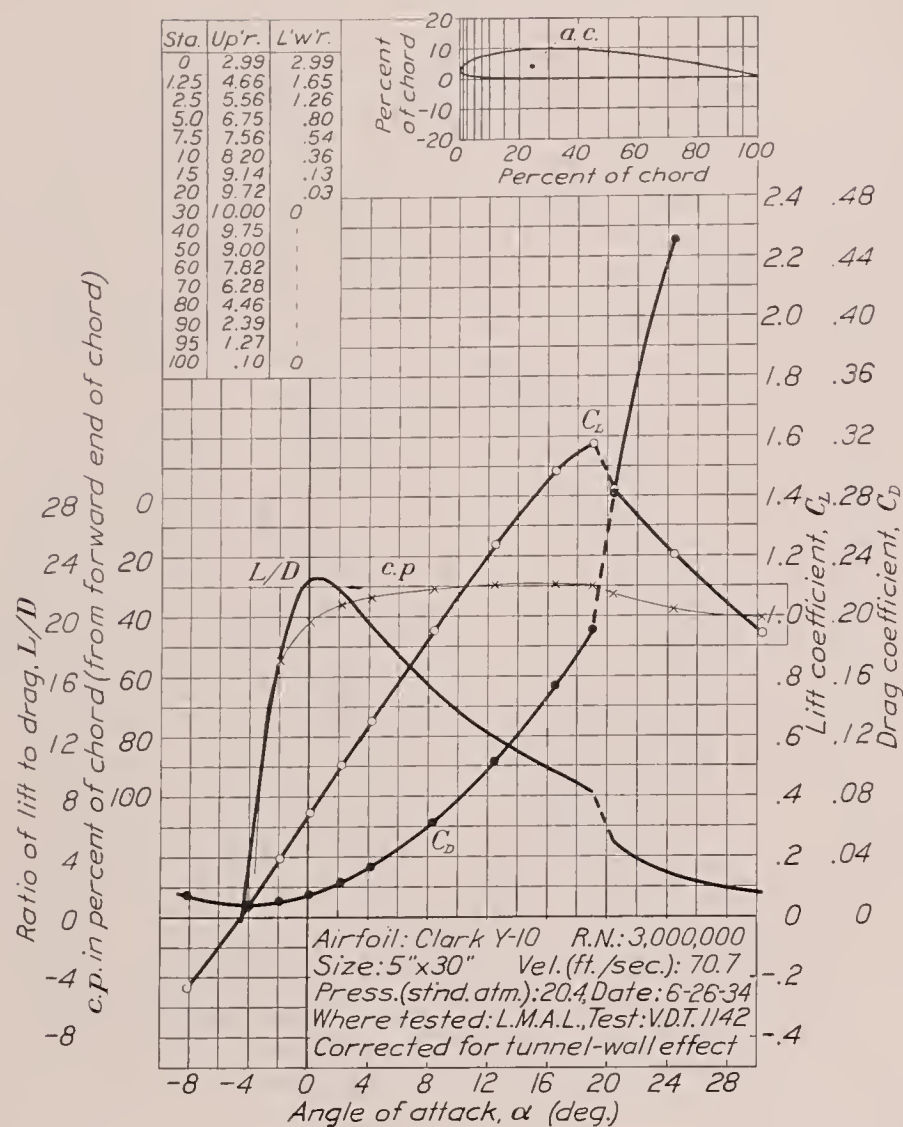


FIGURE 67.—Clark Y-10 airfoil.

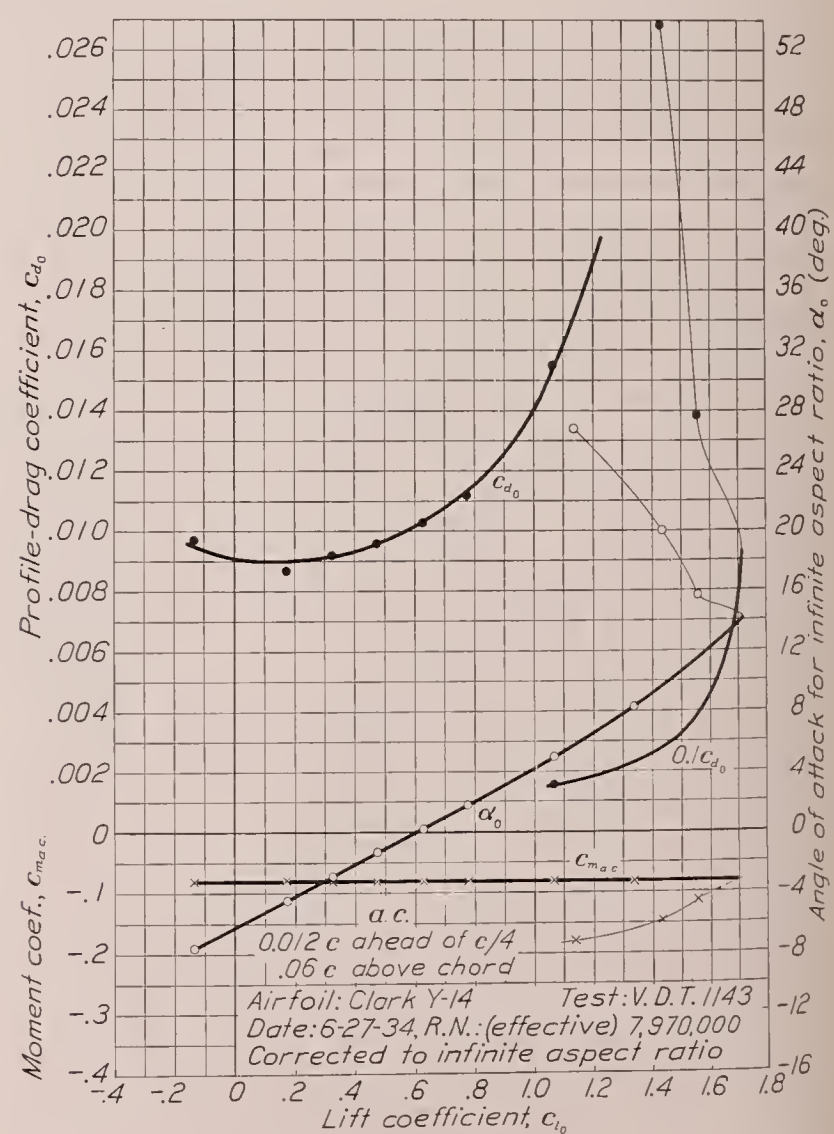
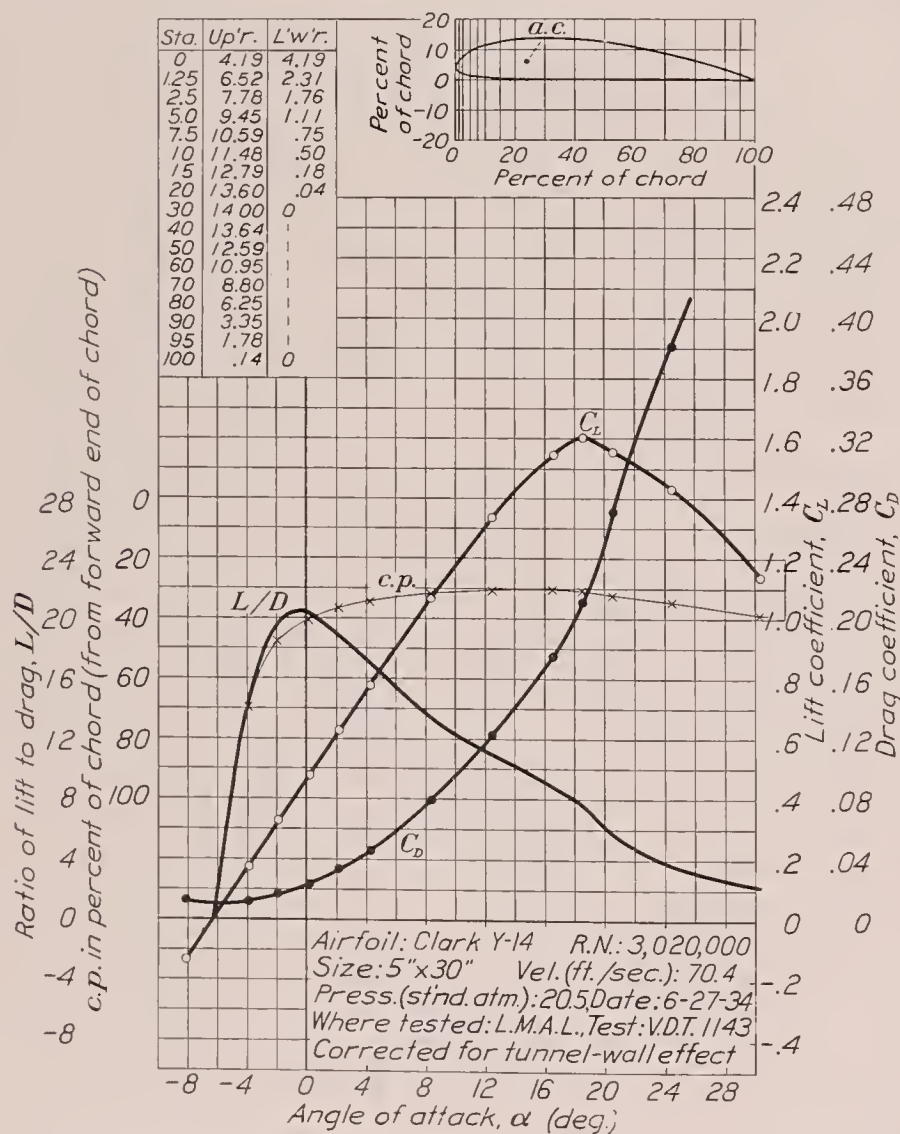


FIGURE 68.—Clark Y-14 airfoil.

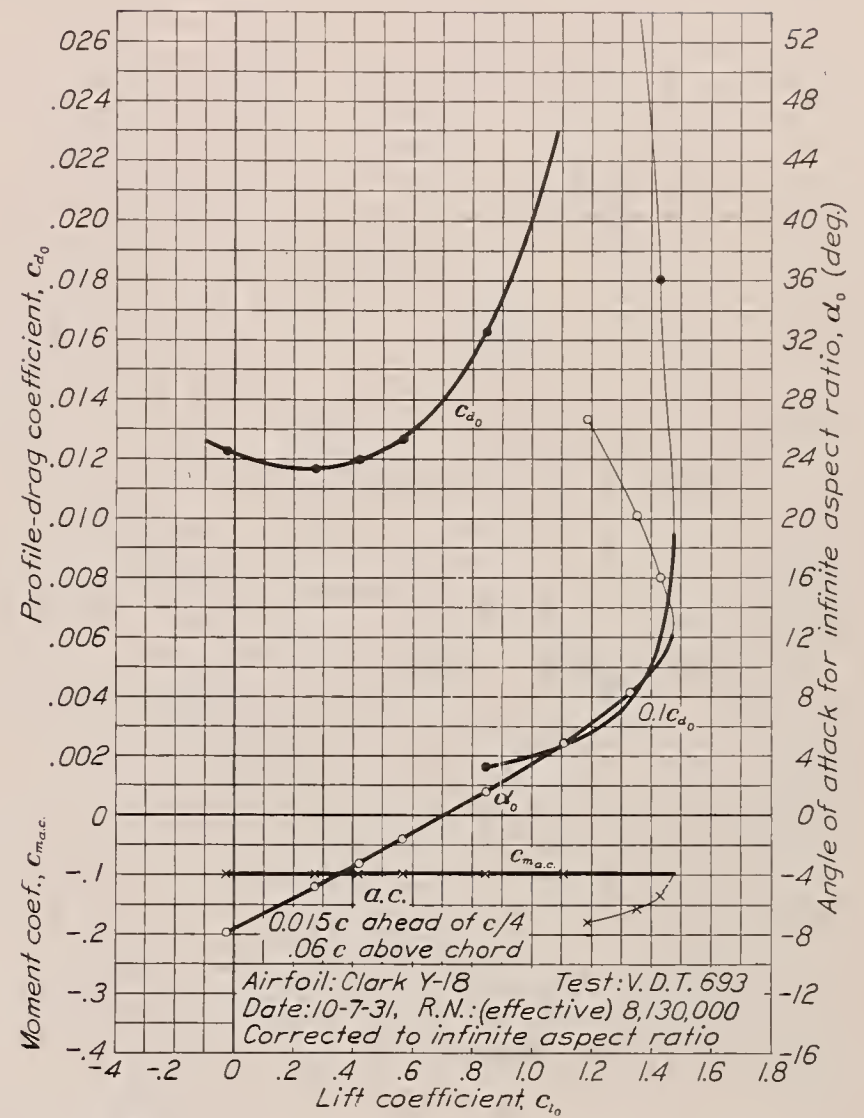
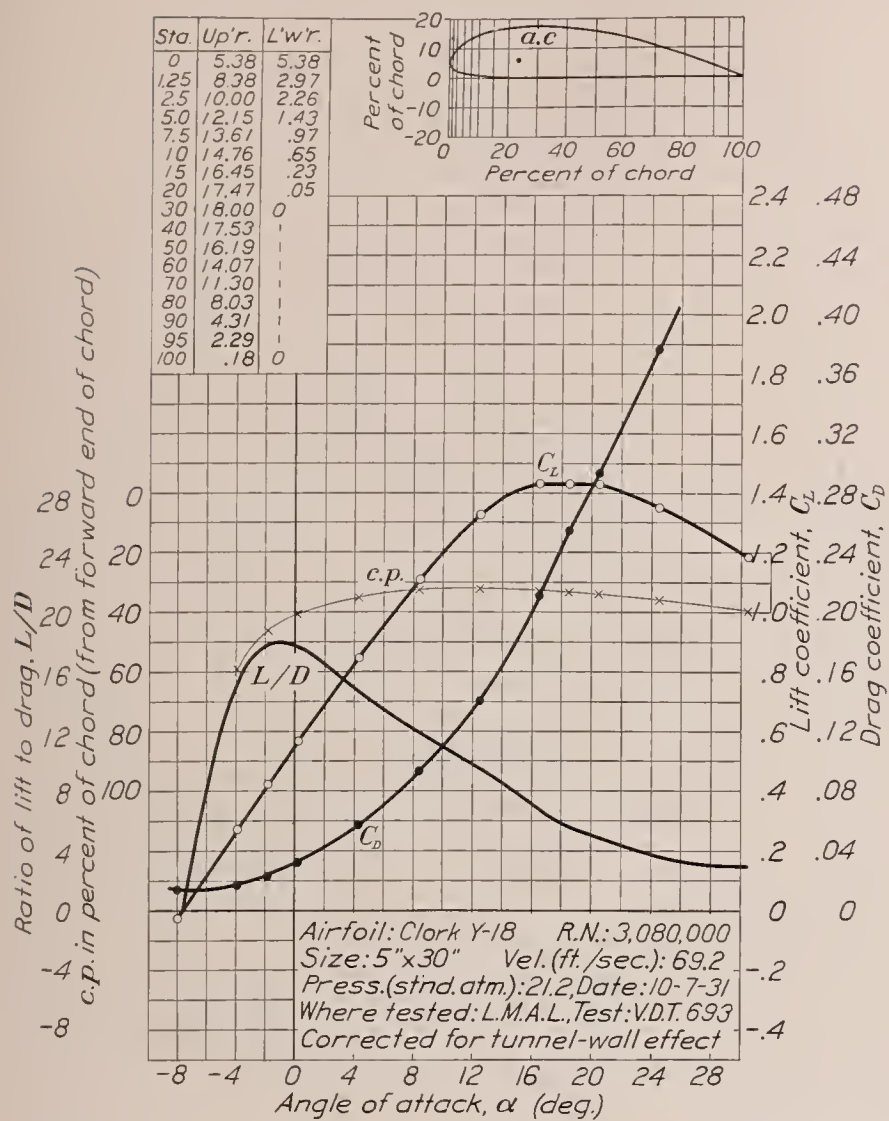


FIGURE 69.—Clark Y-18 airfoil.

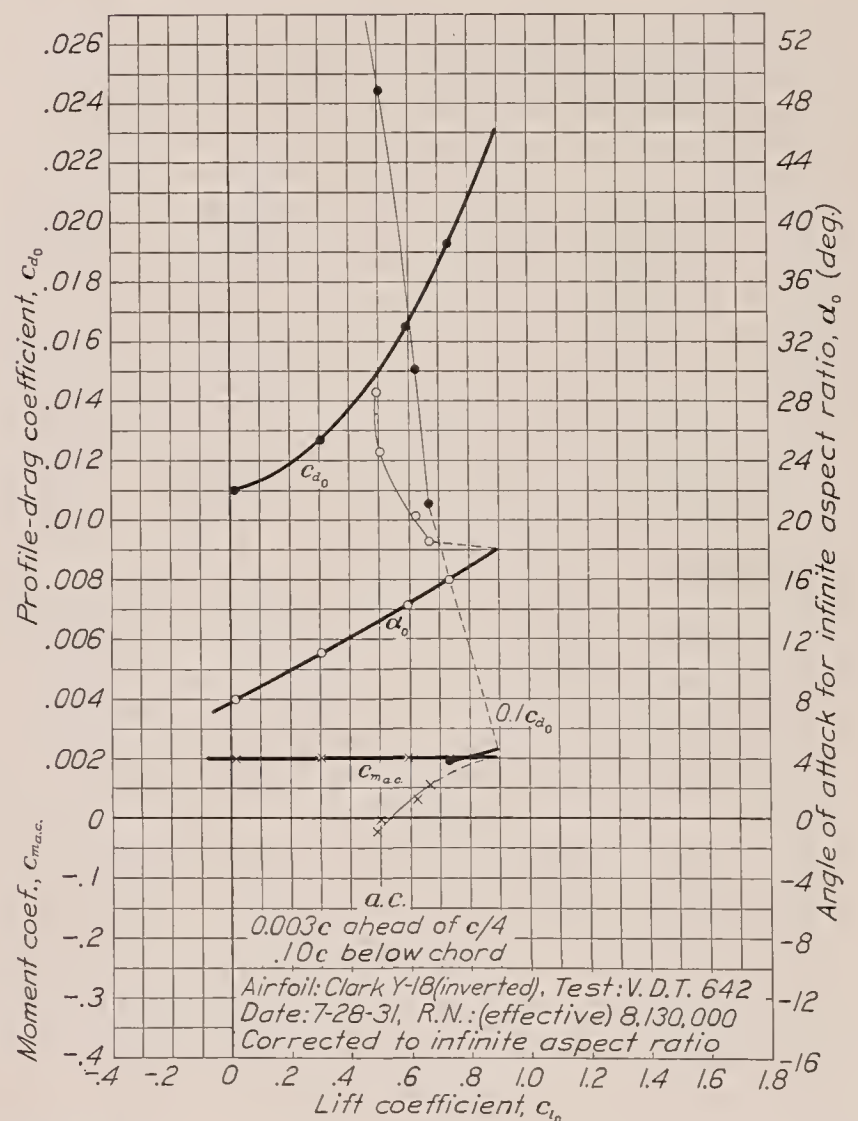
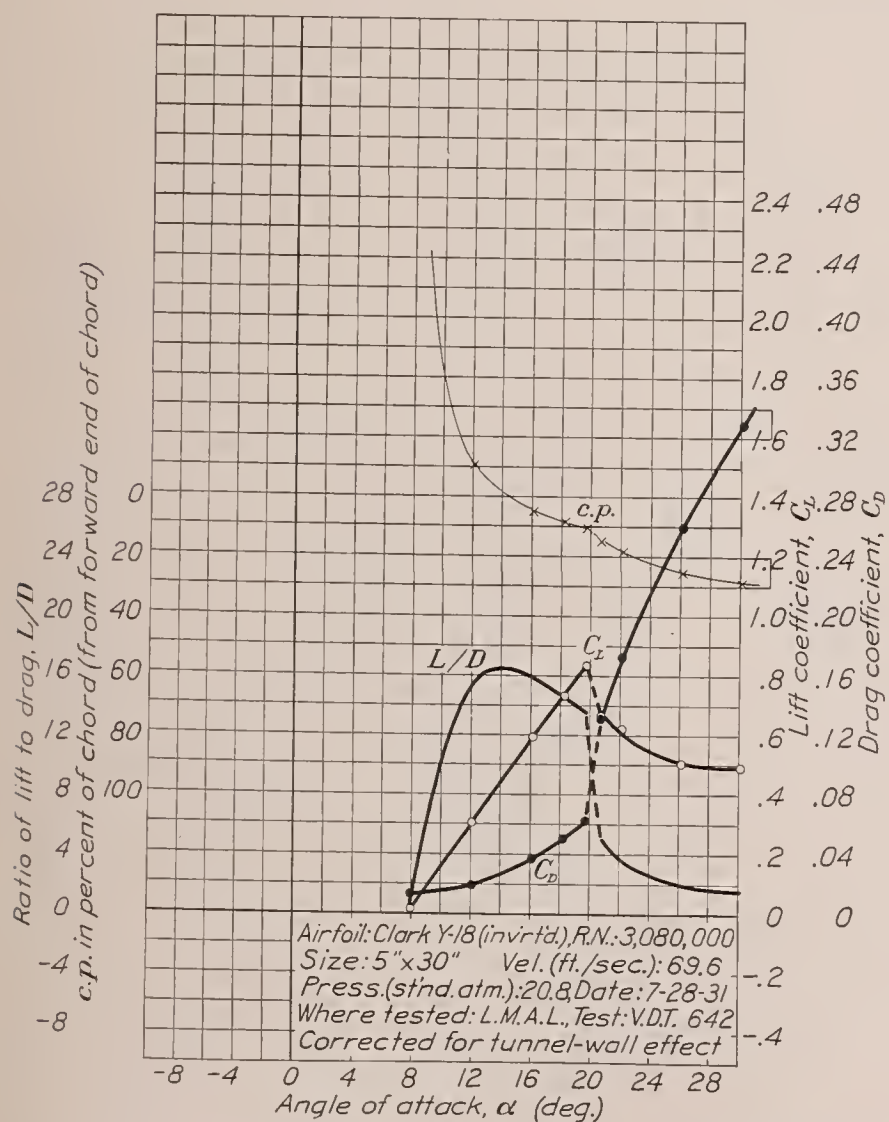


FIGURE 70.—Clark Y-18 airfoil (inverted).

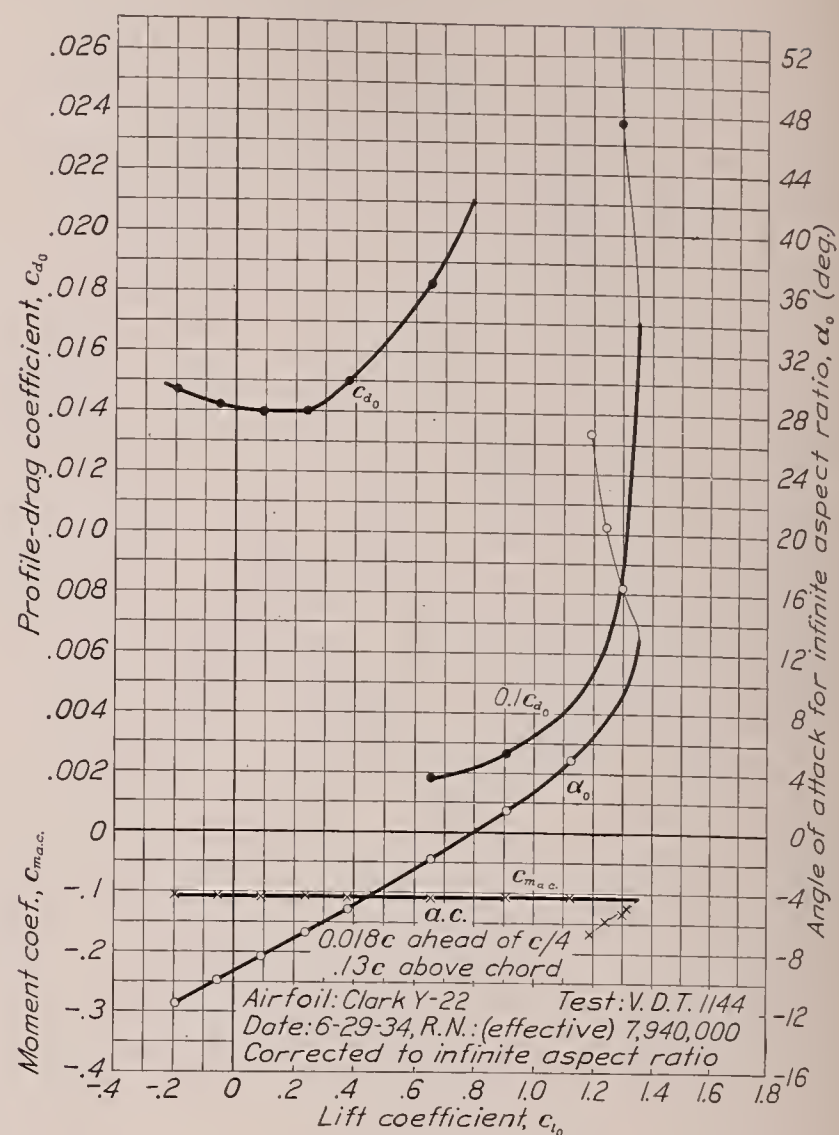
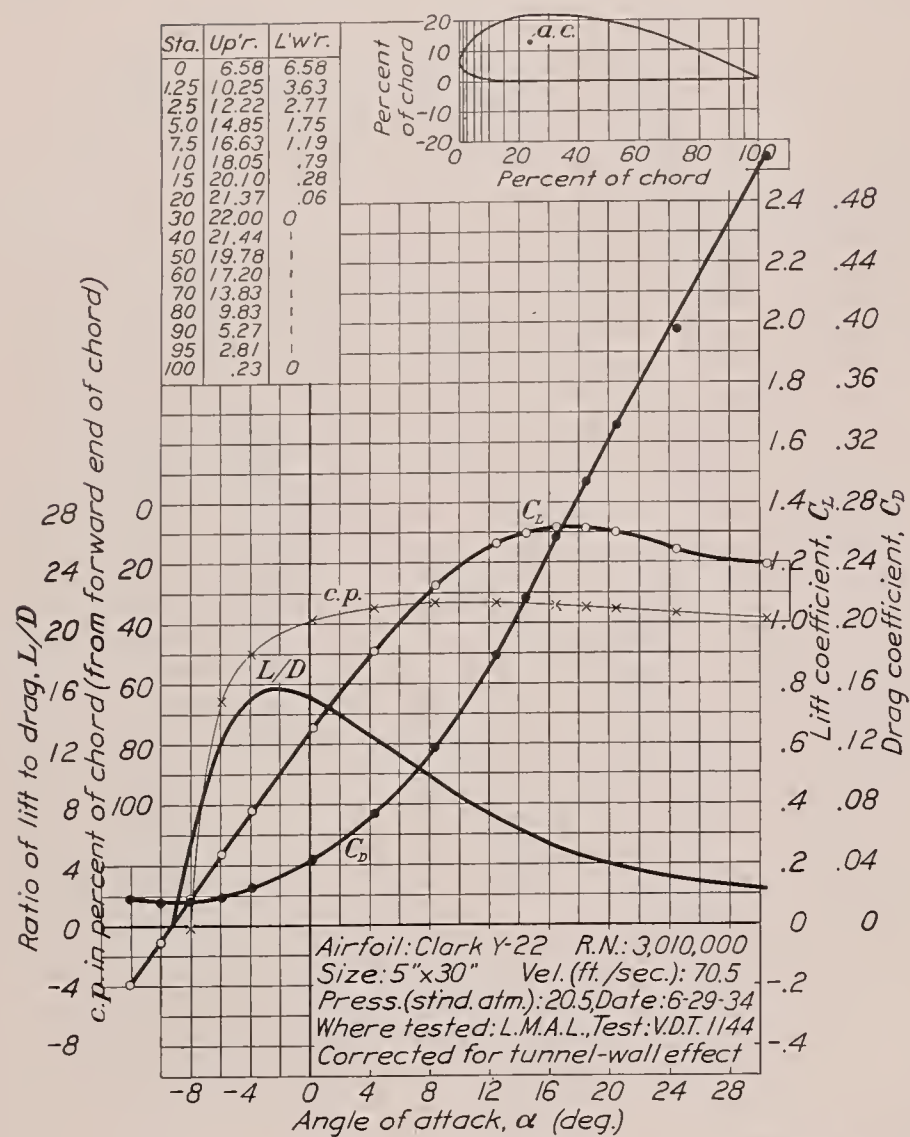


FIGURE 71.—Clark Y-22 airfoil.

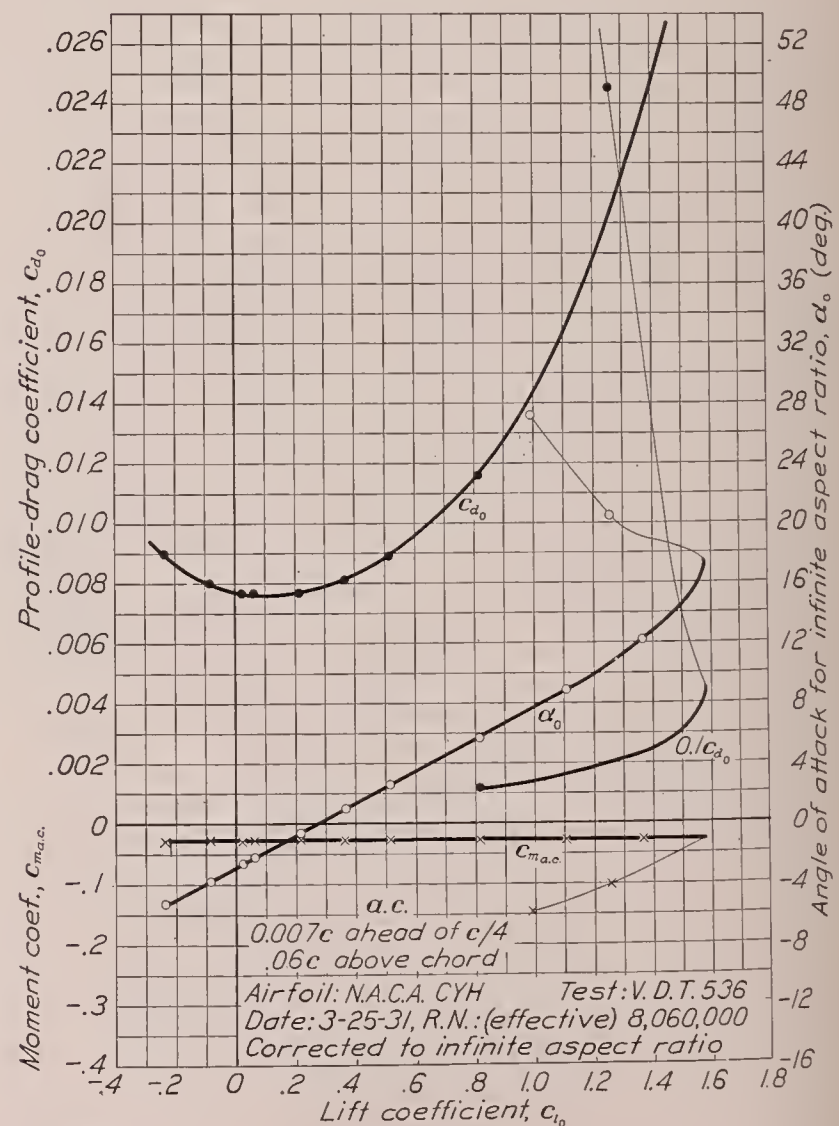
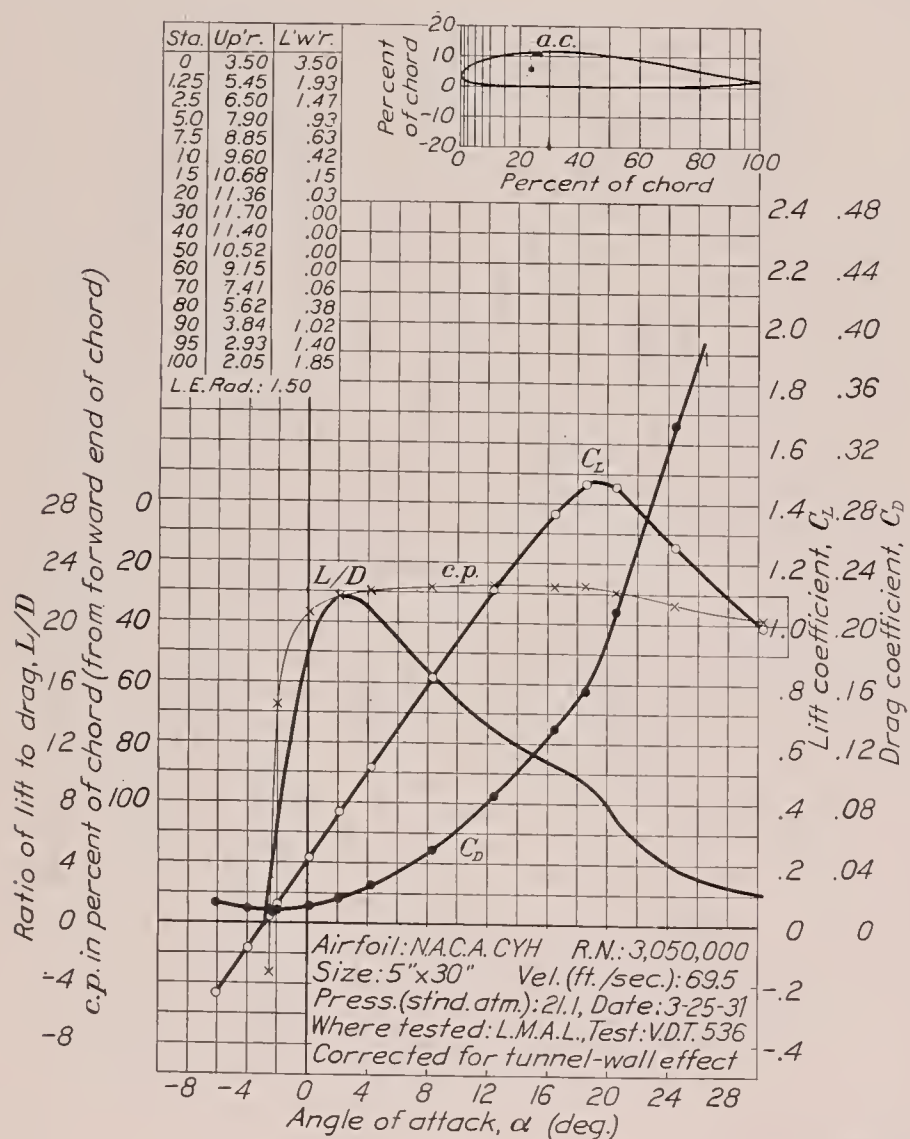


FIGURE 72.—N. A. C. A. CYH airfoil.

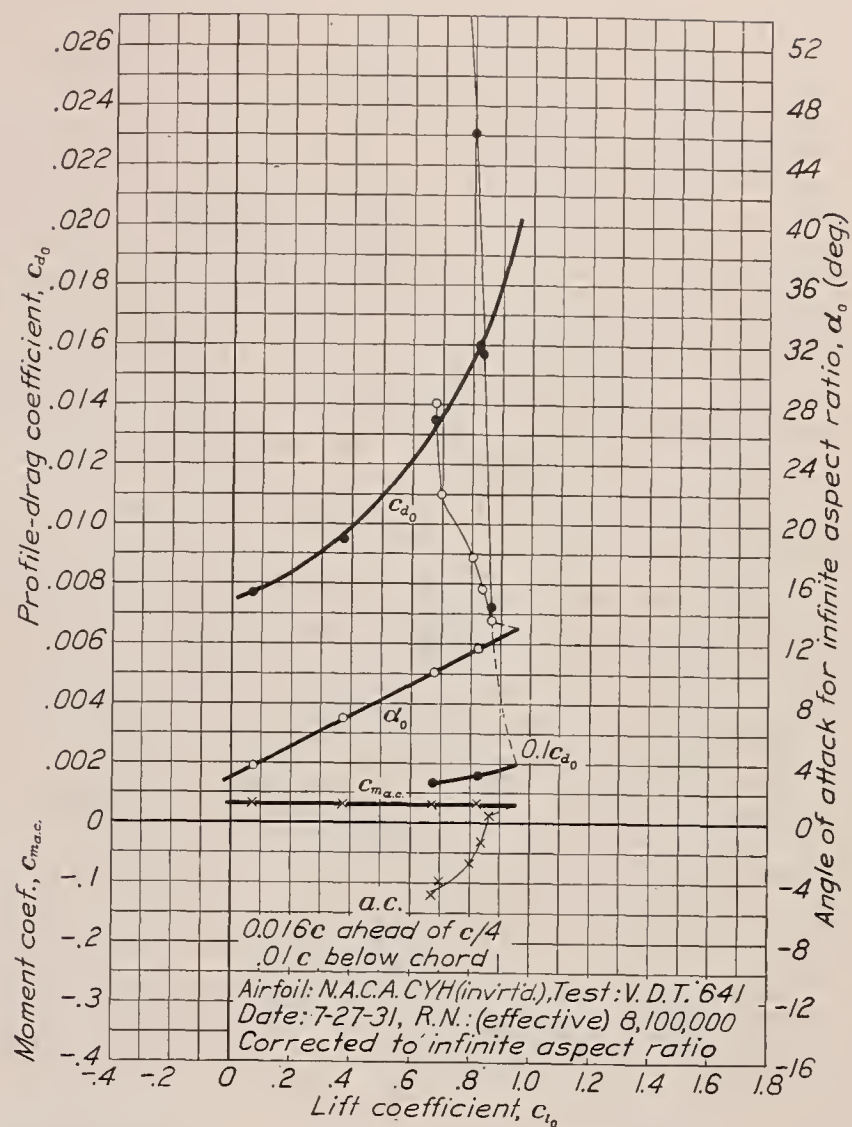
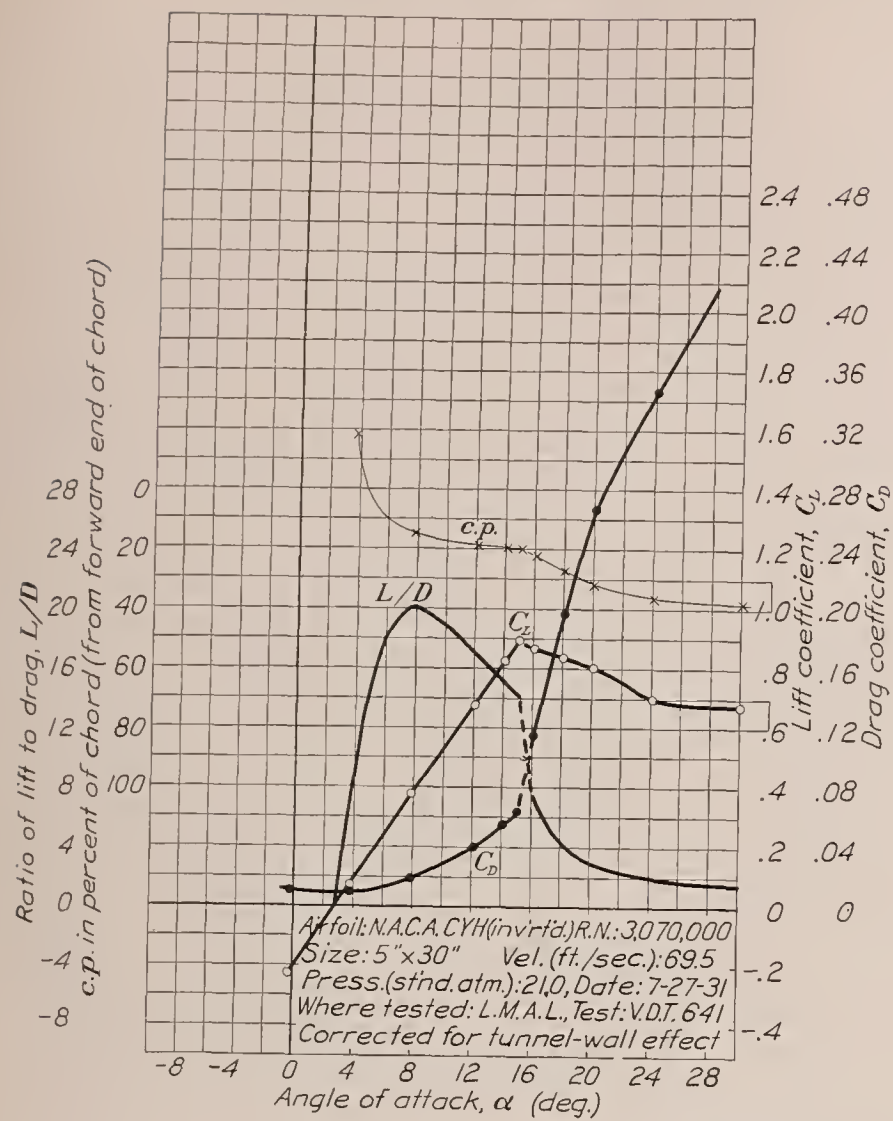


FIGURE 73.—N. A. C. A. CYH airfoil (inverted).

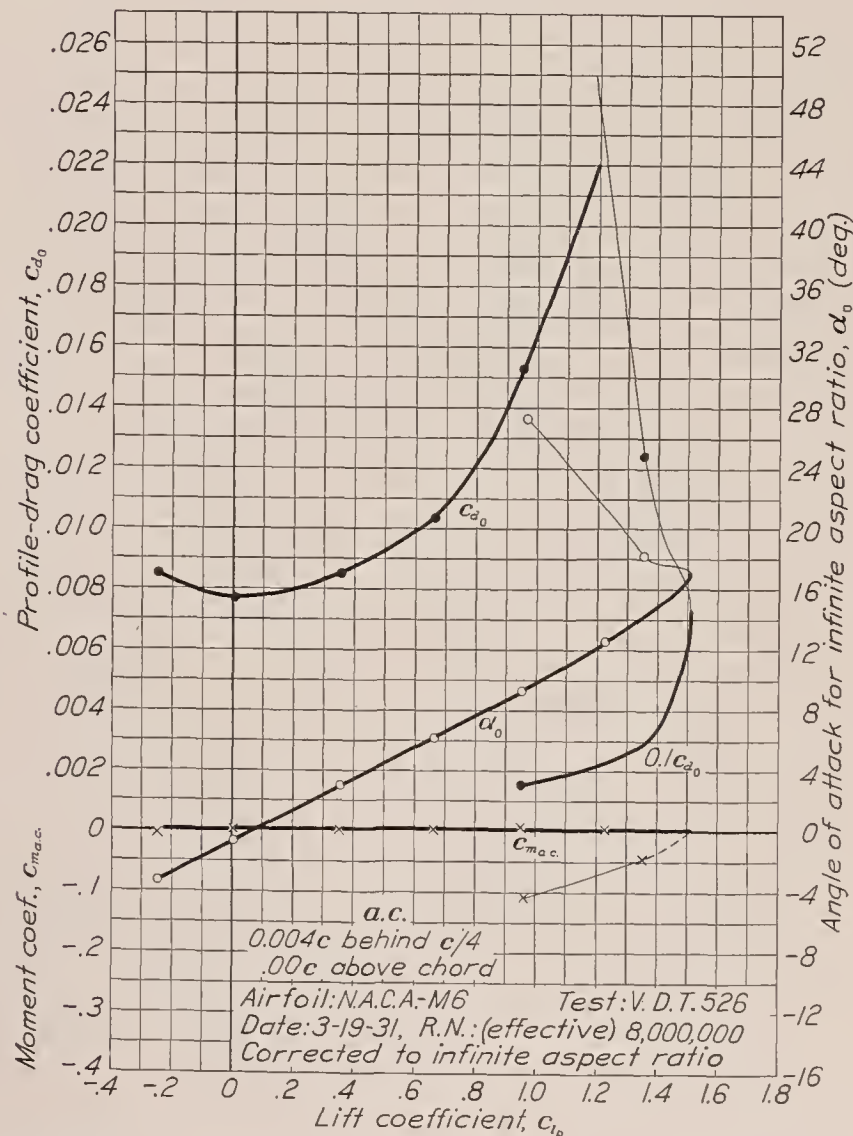
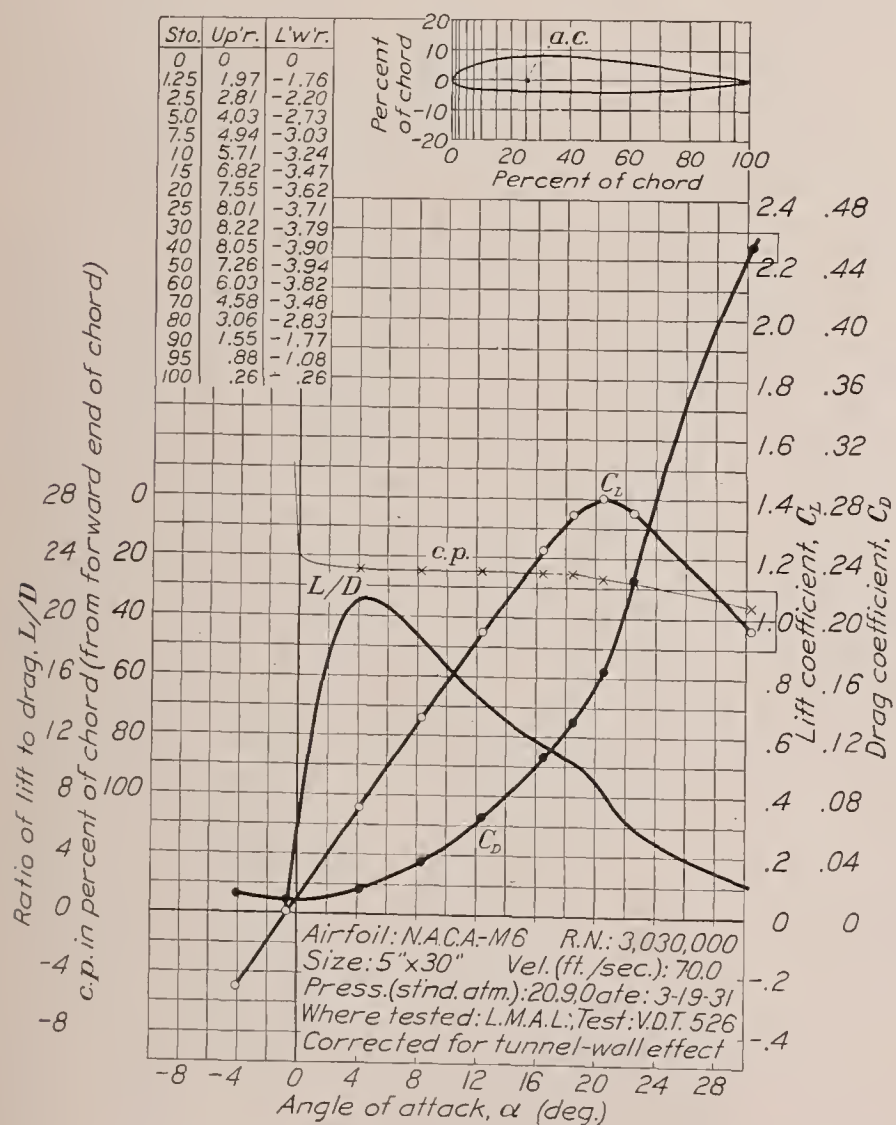


FIGURE 74.—N. A. C. A. —M6 airfoil.

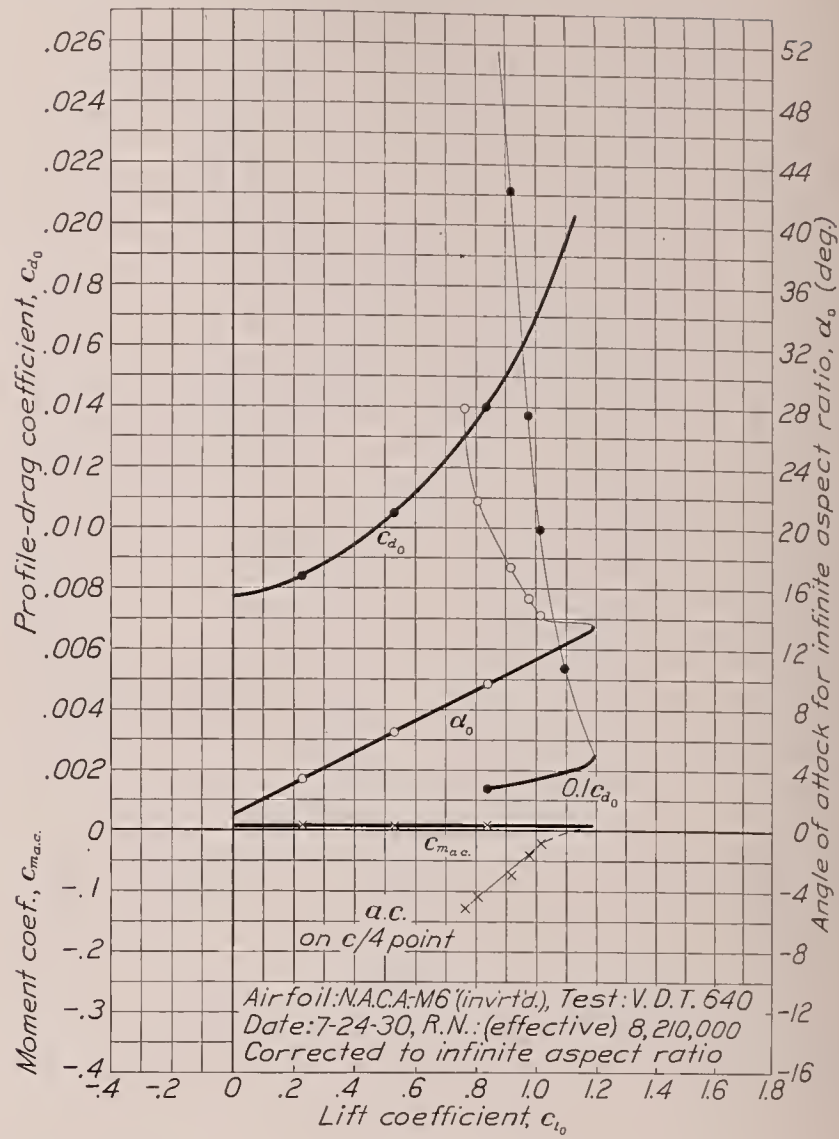
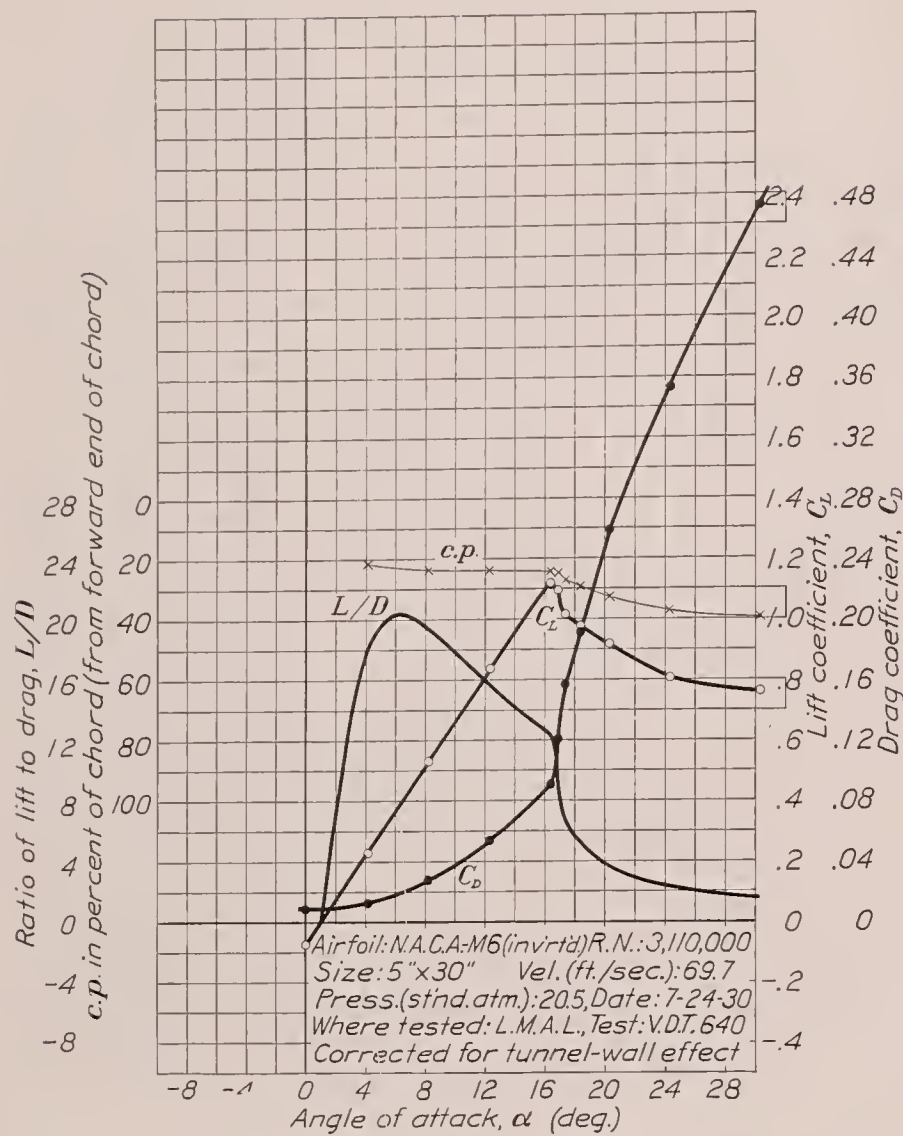


FIGURE 75.—N. A. C. A. —M6 airfoil (inverted).

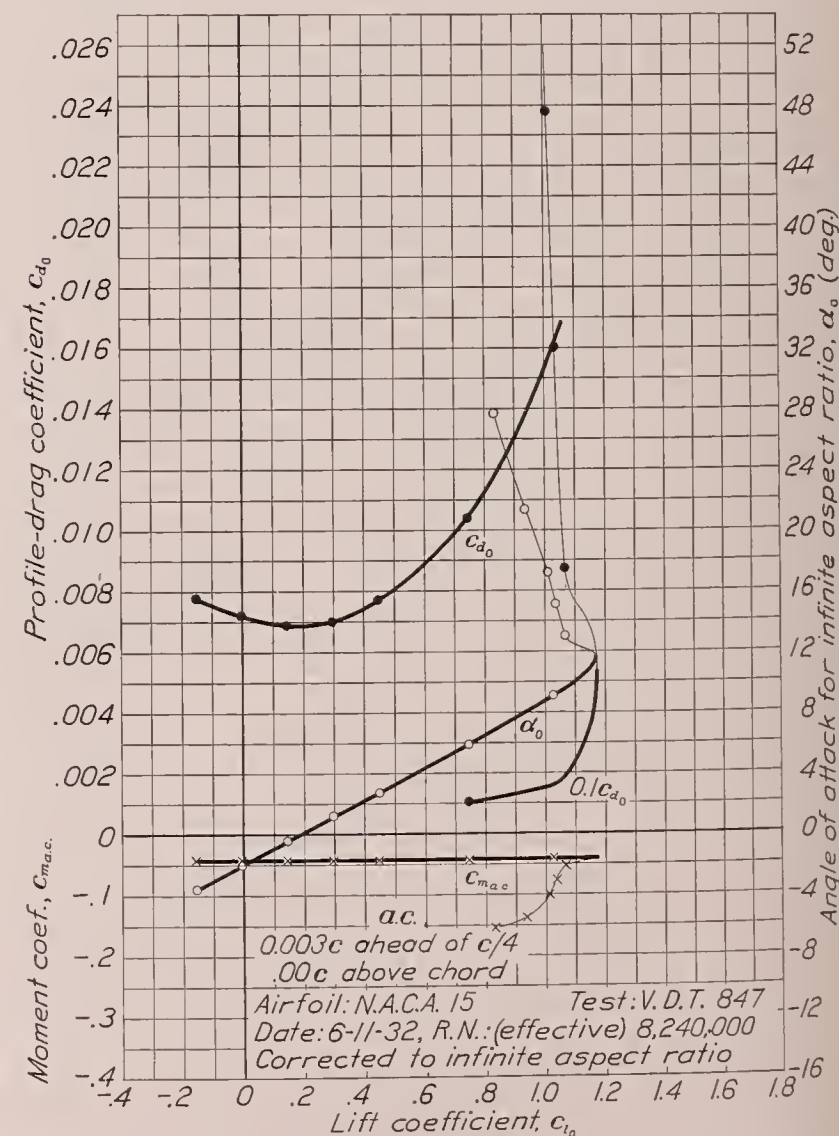
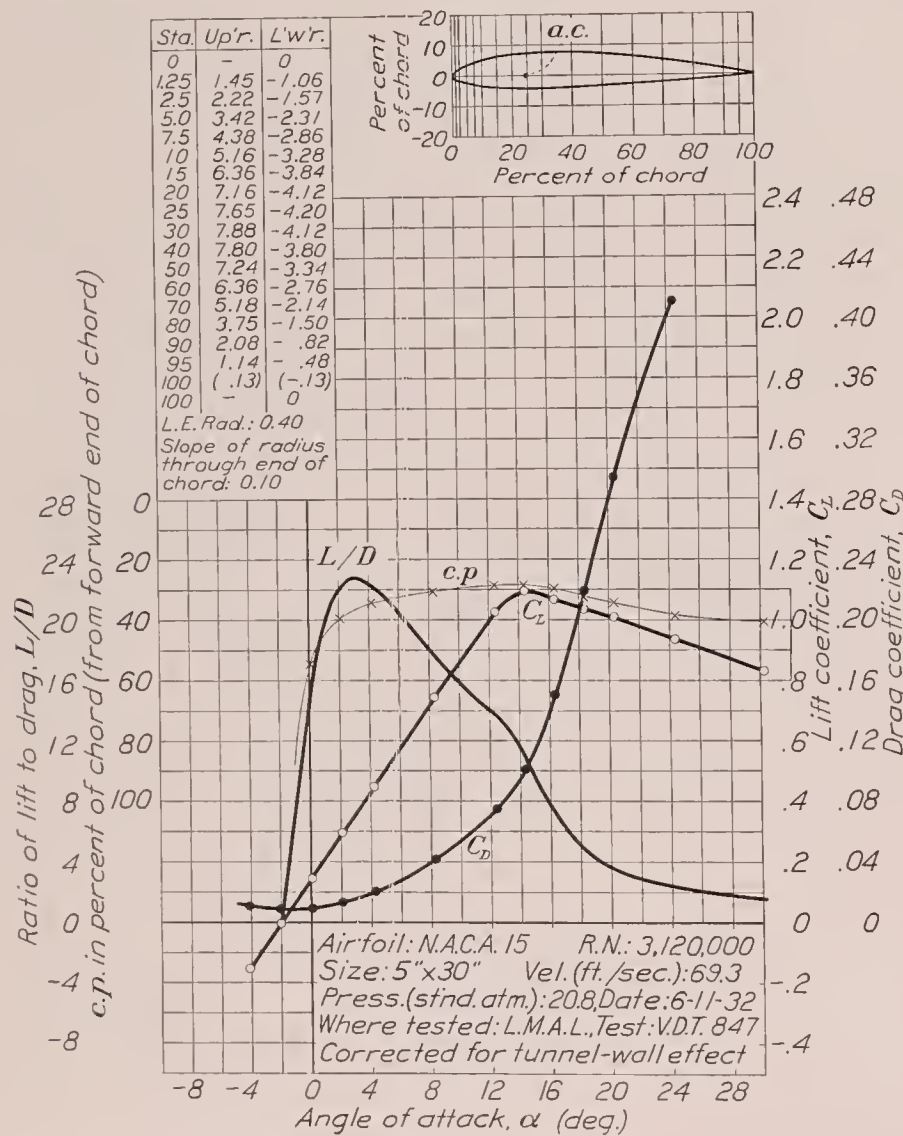


FIGURE 76.—N. A. C. A. 15 airfoil.

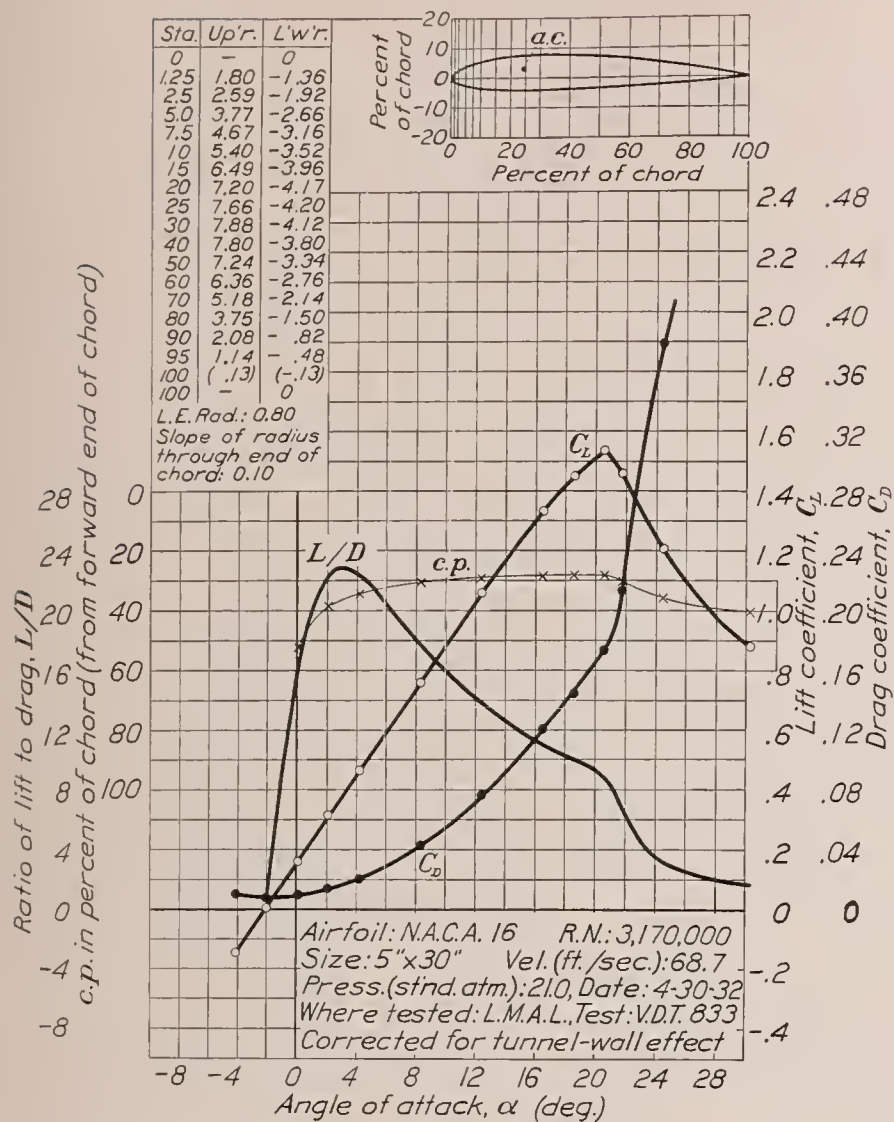


FIGURE 77.—N. A. C. A. 16 airfoil.

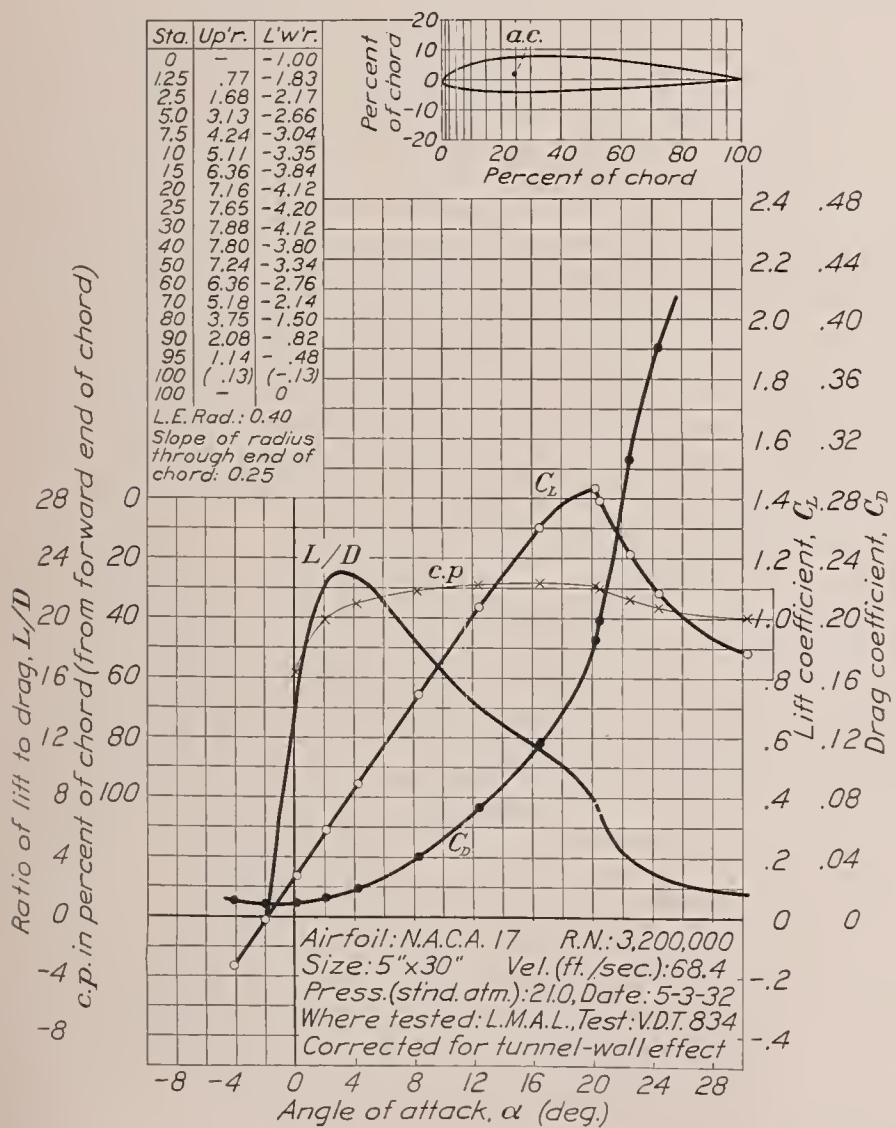
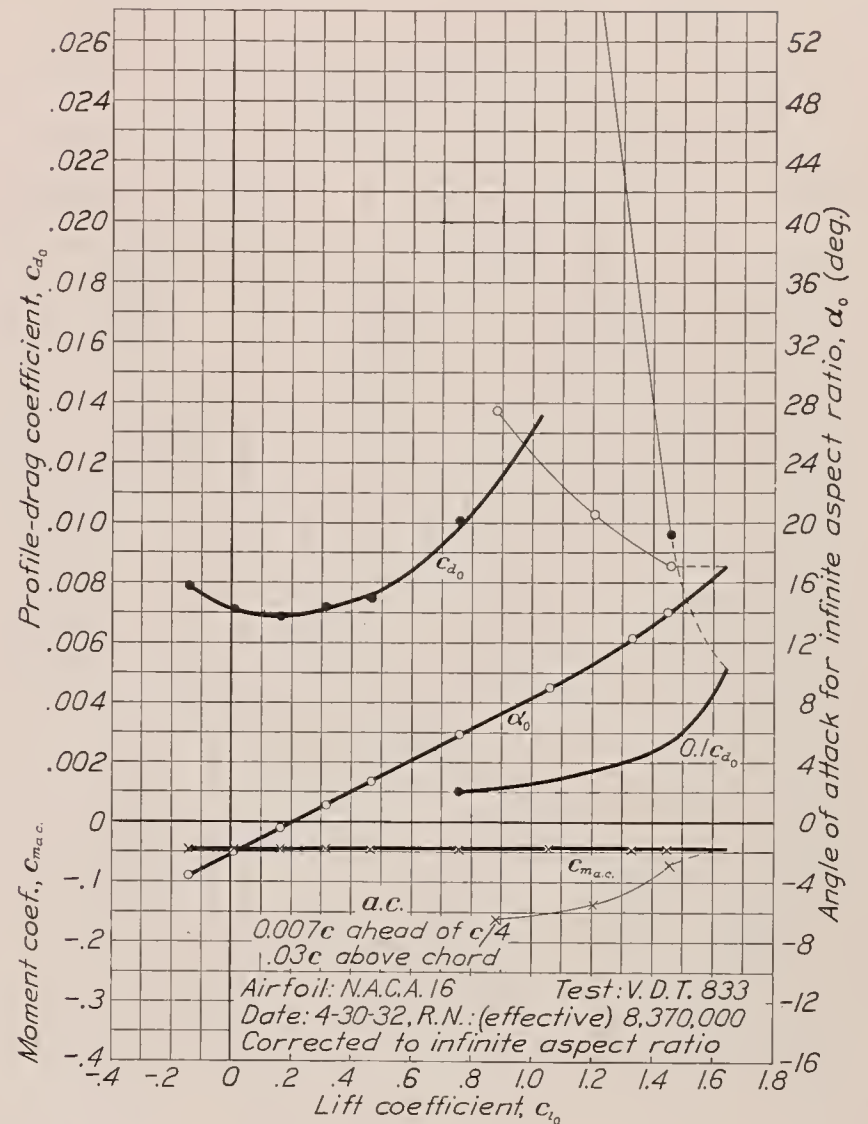
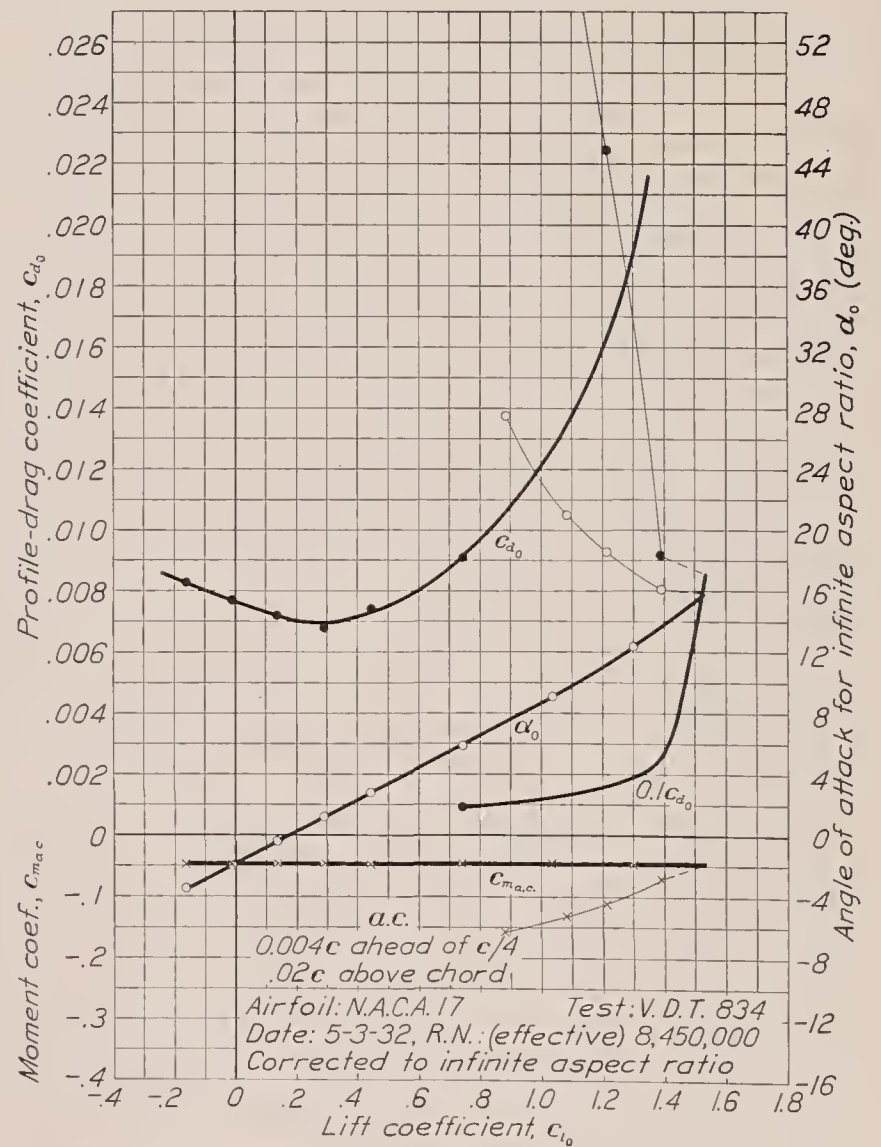


FIGURE 78.—N. A. C. A. 17 airfoil.



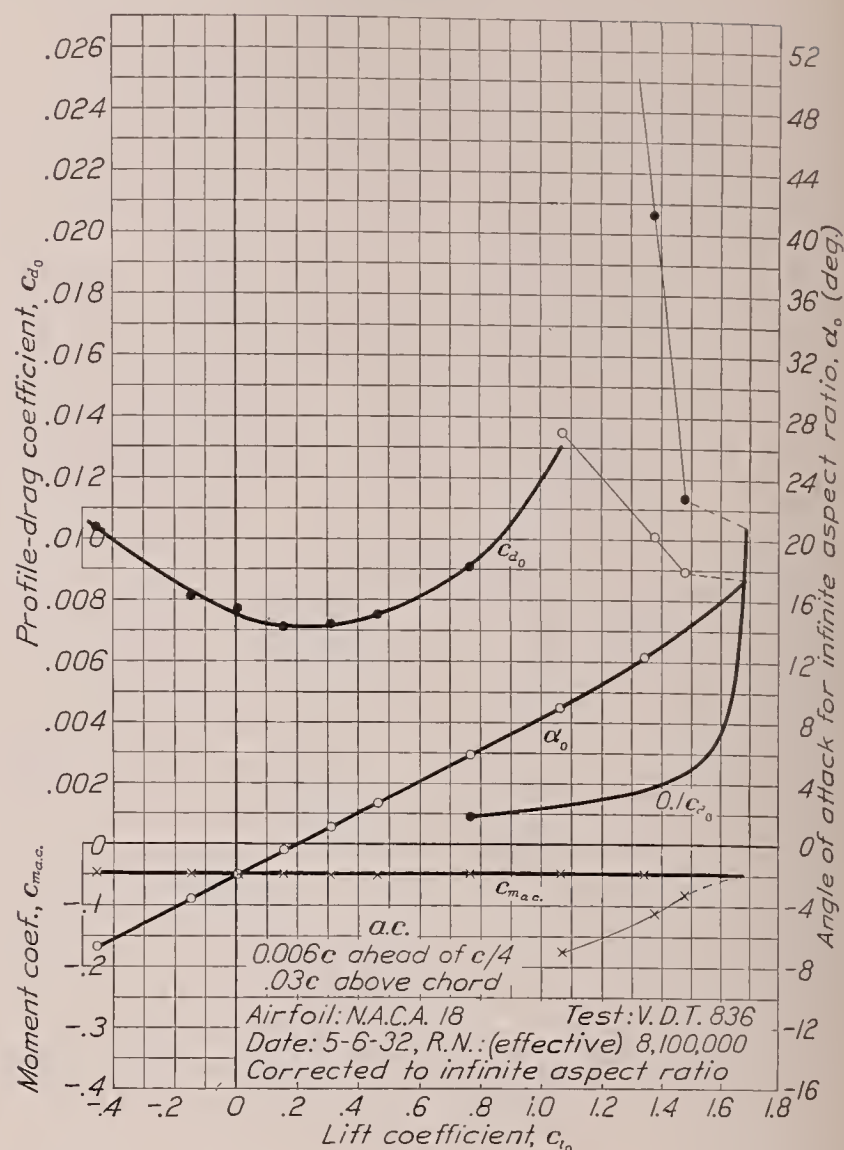
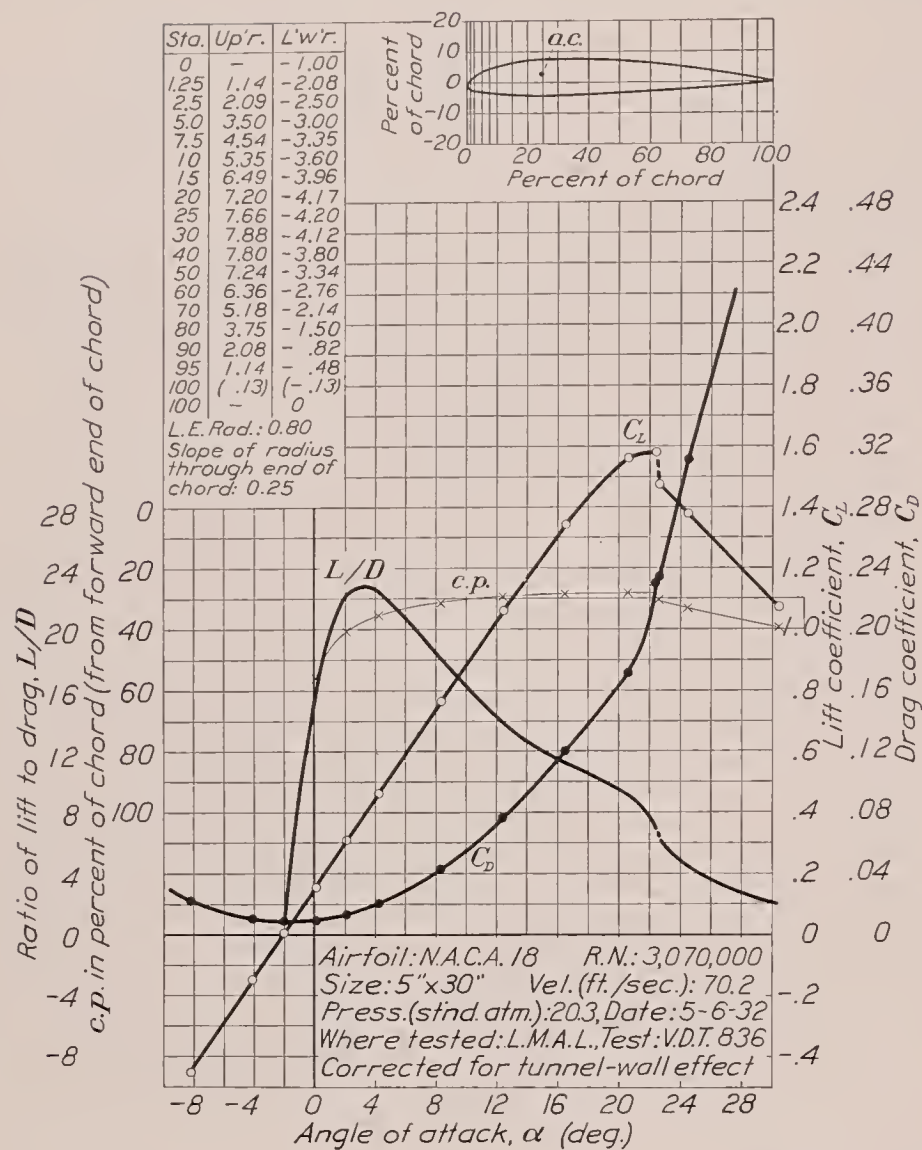


FIGURE 79.—N. A. C. A. 18 airfoil.

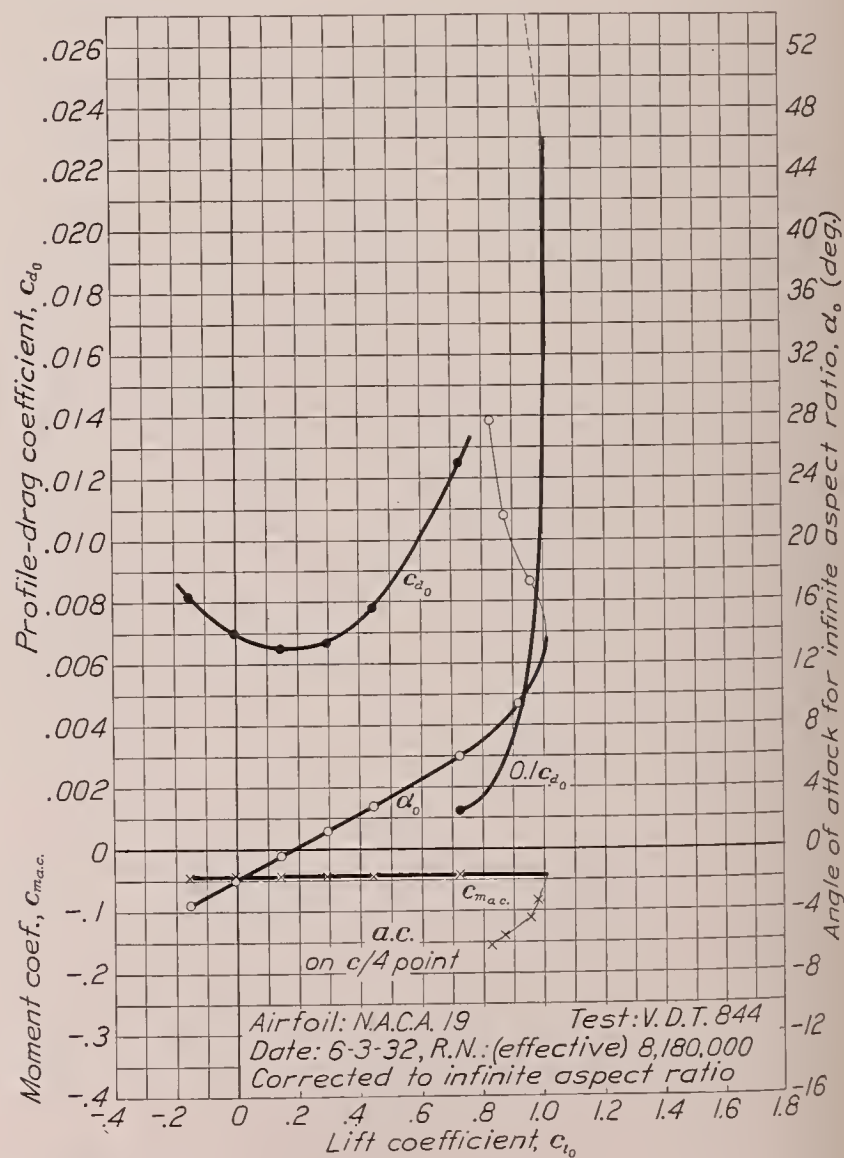
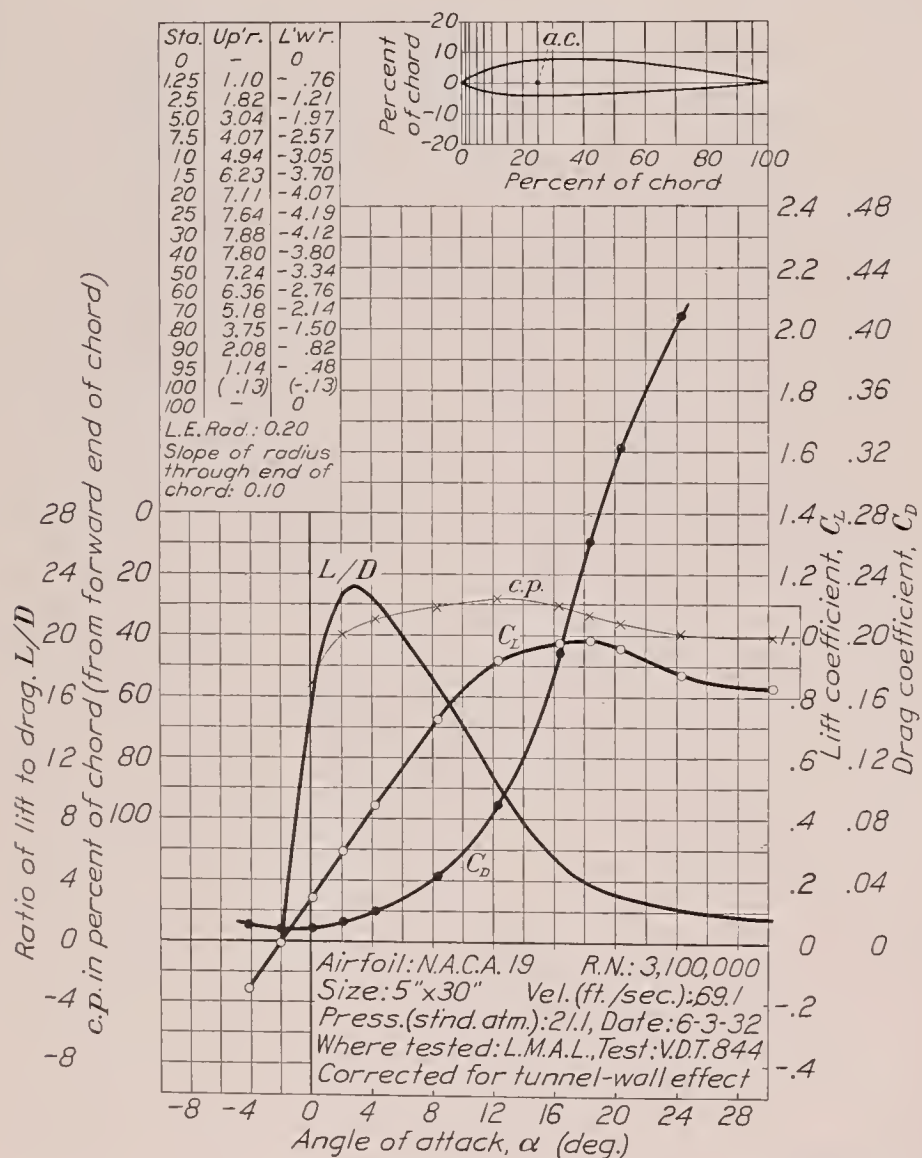


FIGURE 80.—N. A. C. A. 19 airfoil.

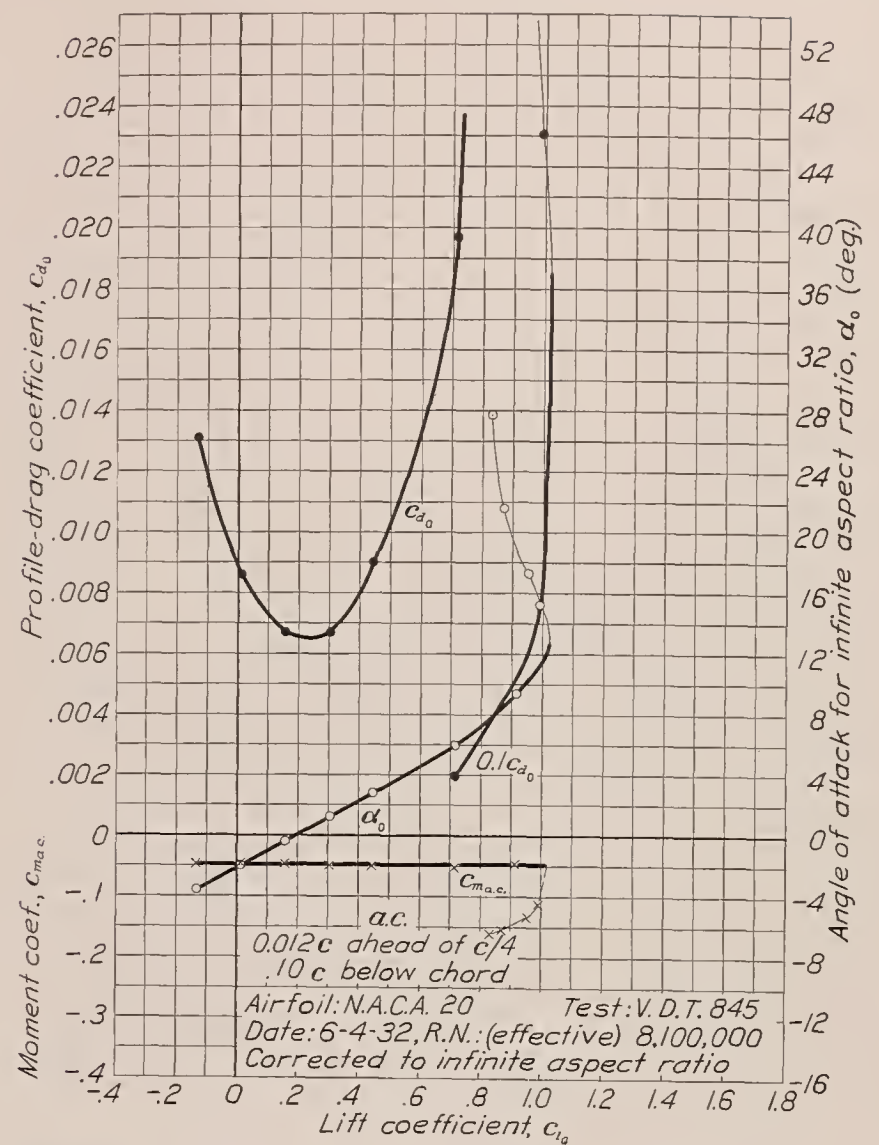
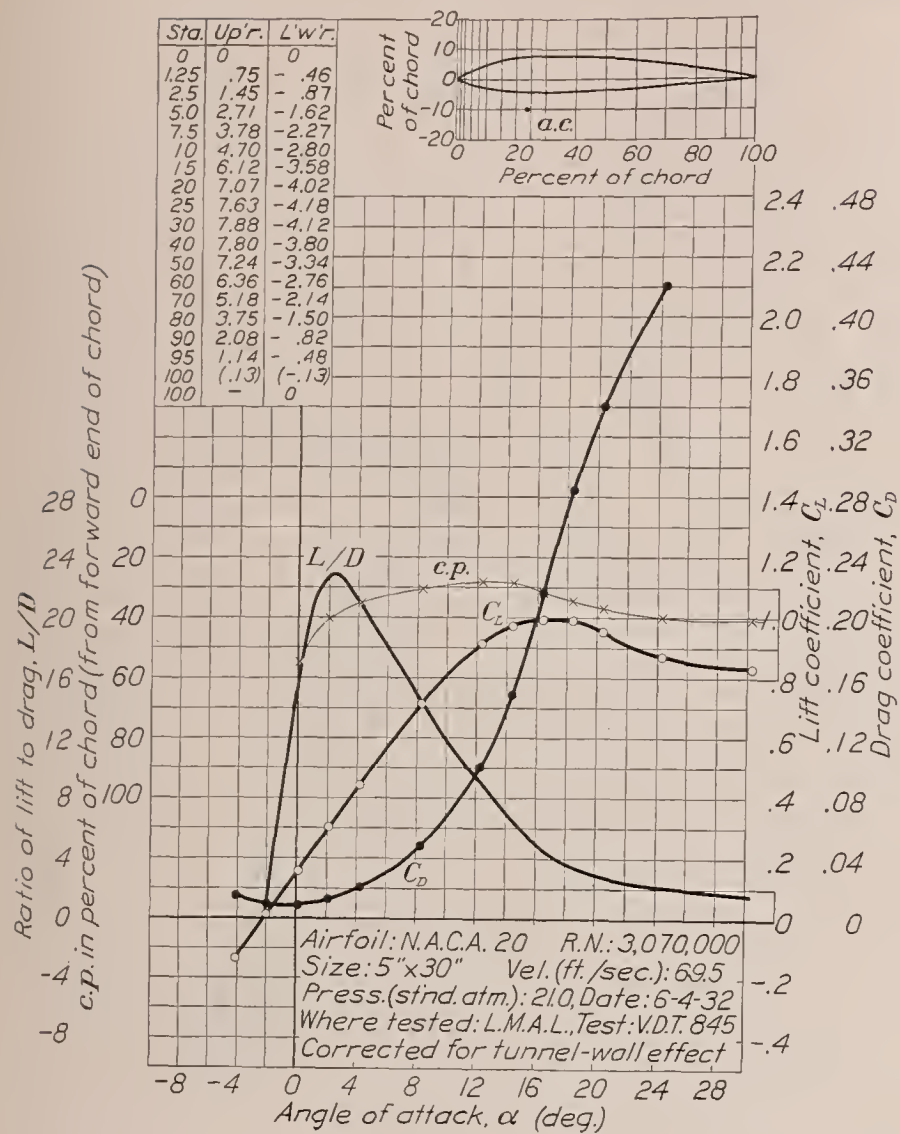


FIGURE 81.—N. A. C. A. 20 airfoil.

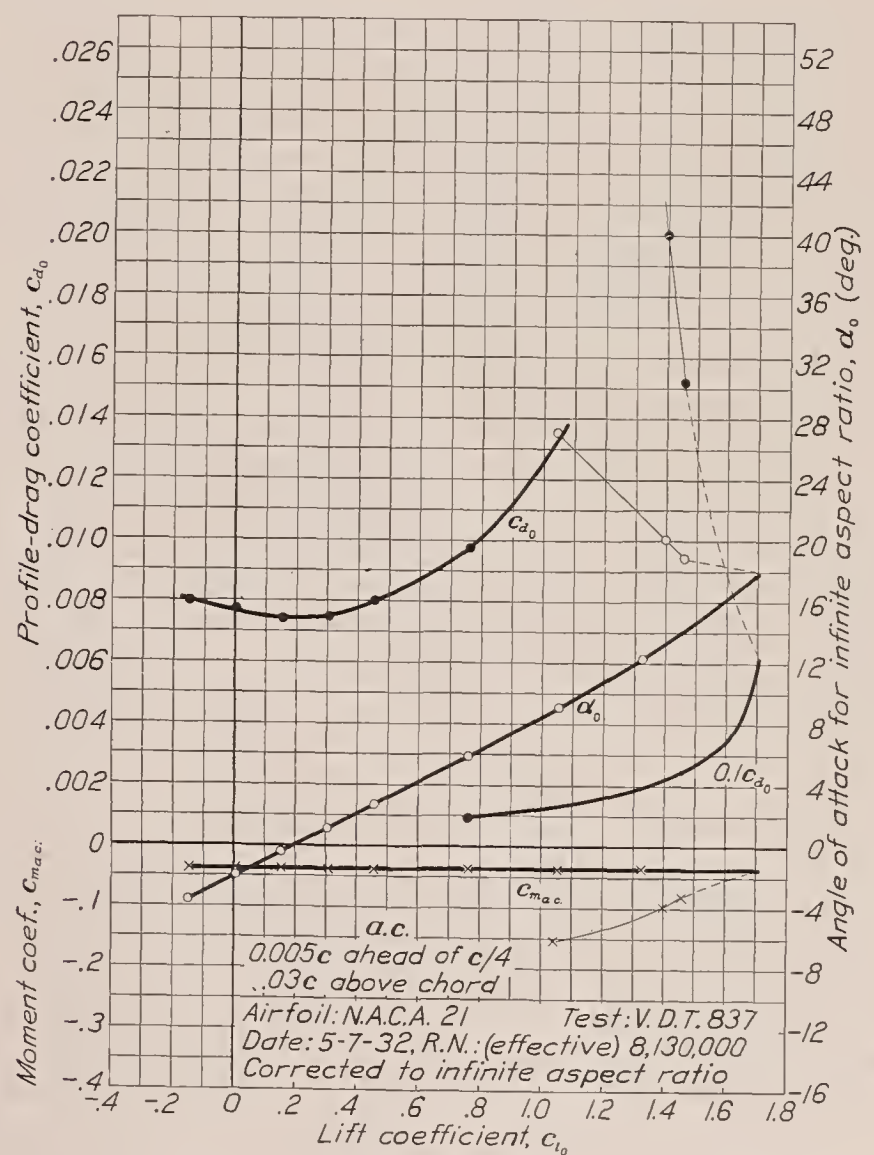
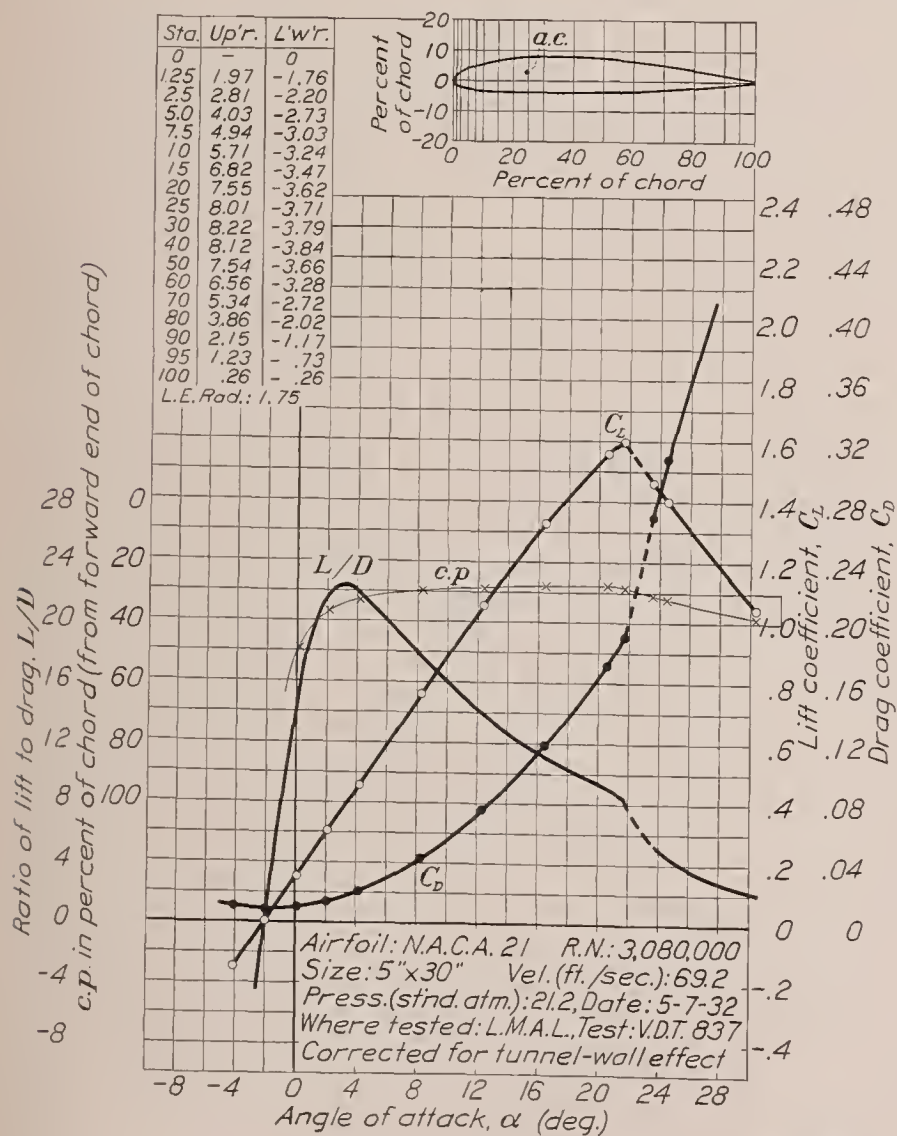


FIGURE 82.—N. A. C. A. 21 airfoil.

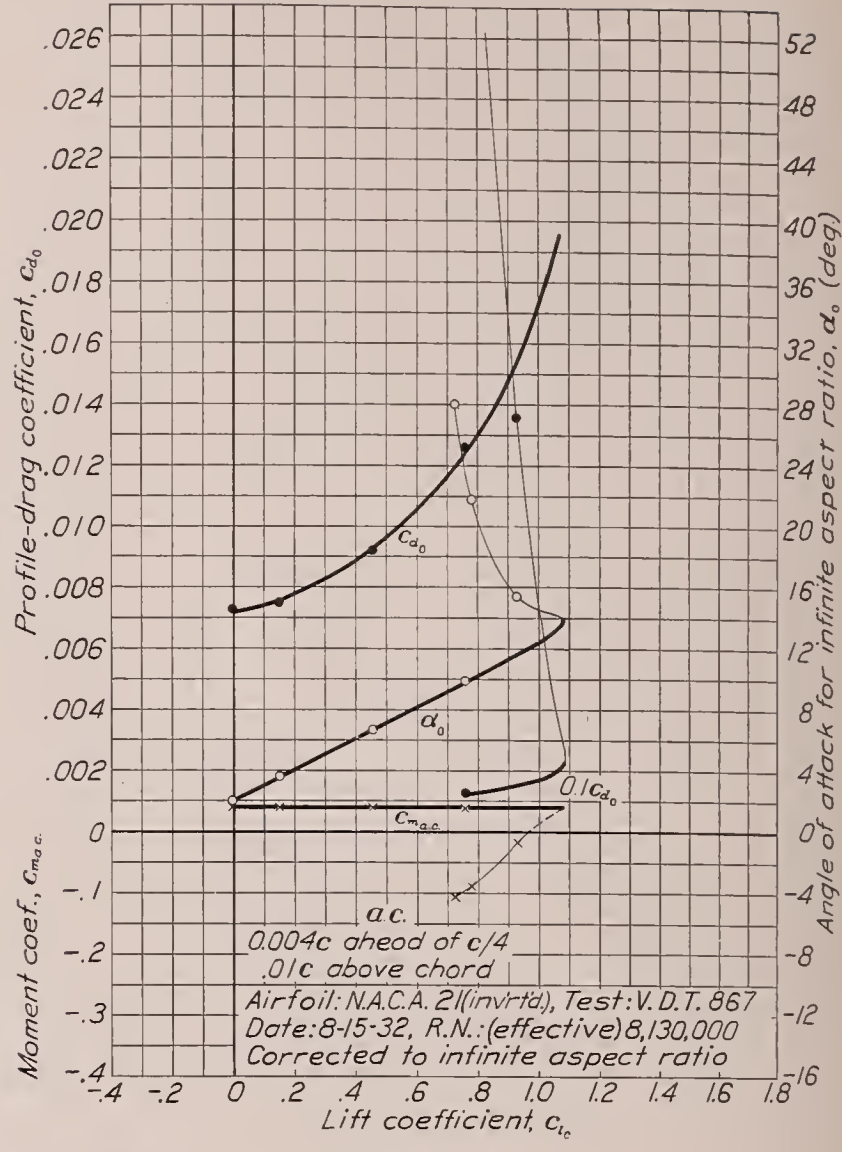
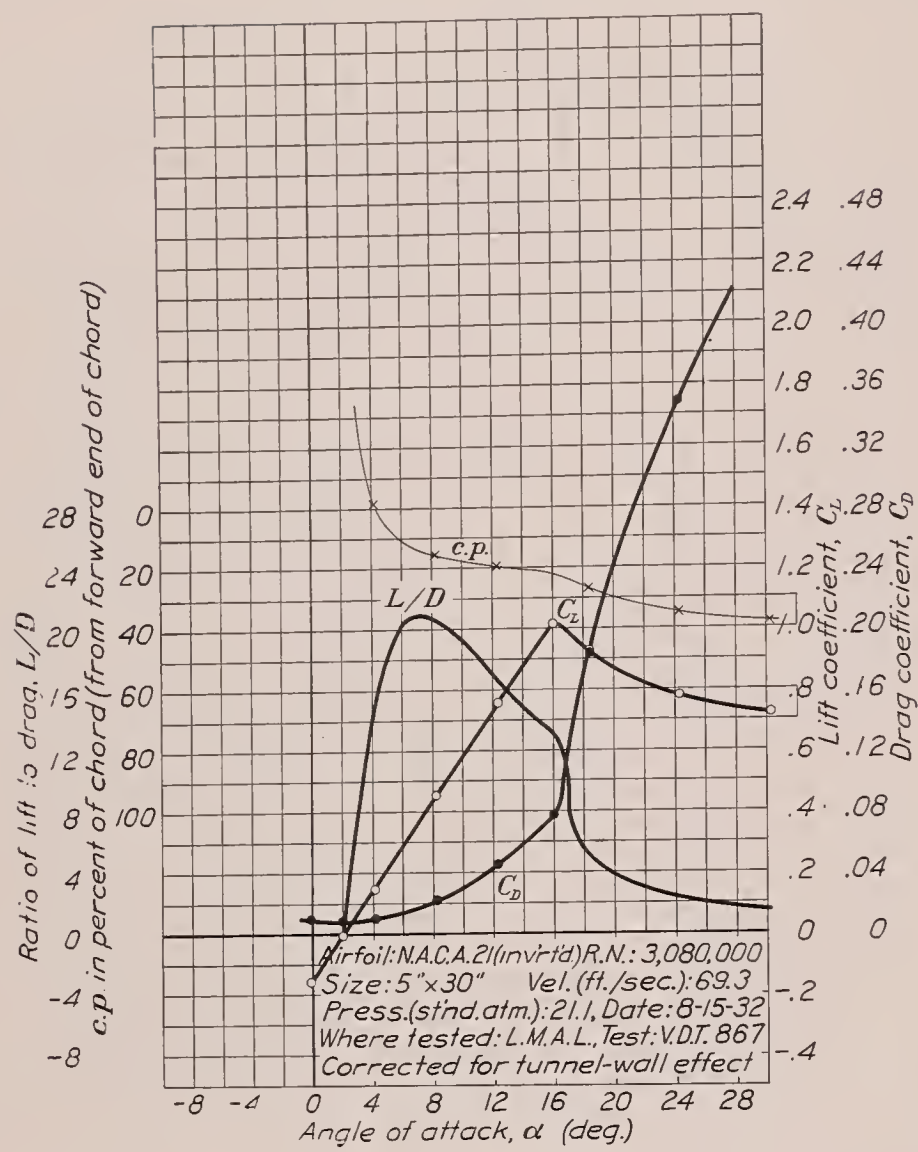


FIGURE 83.—N. A. C. A. 21 airfoil (inverted).

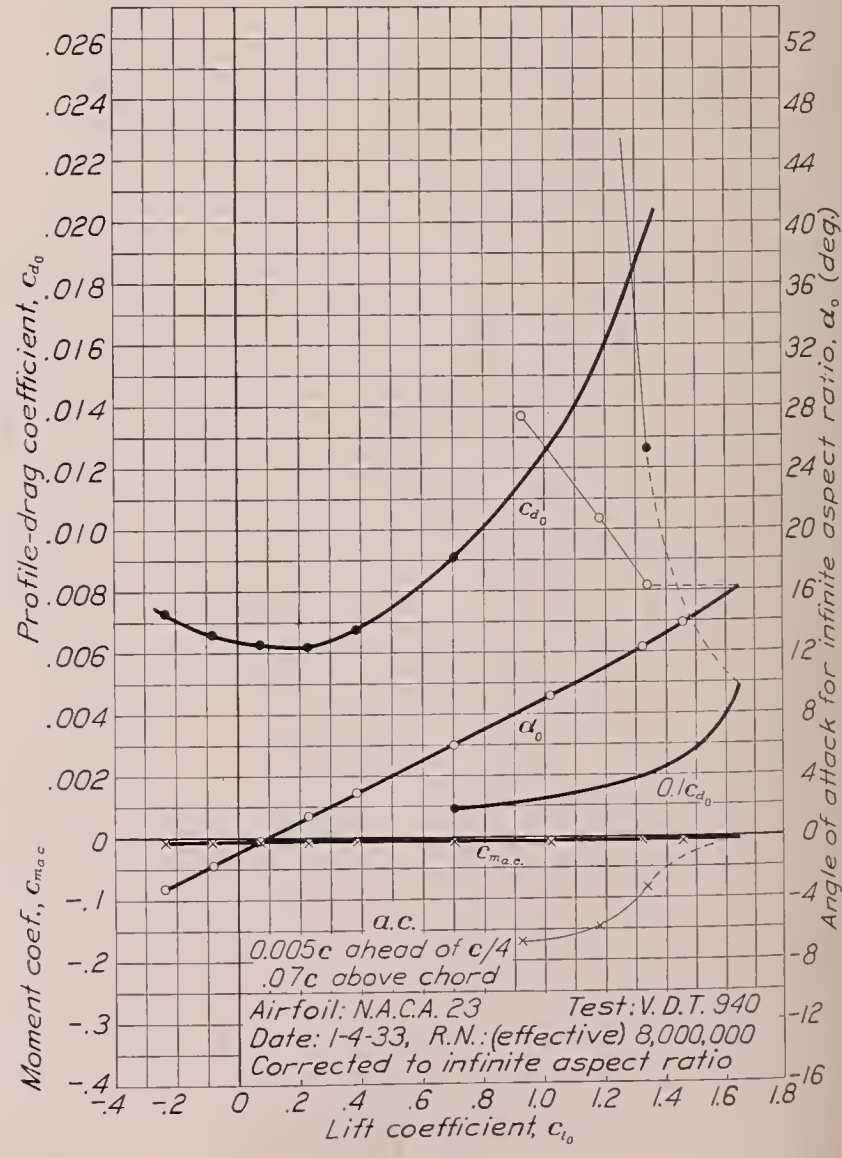
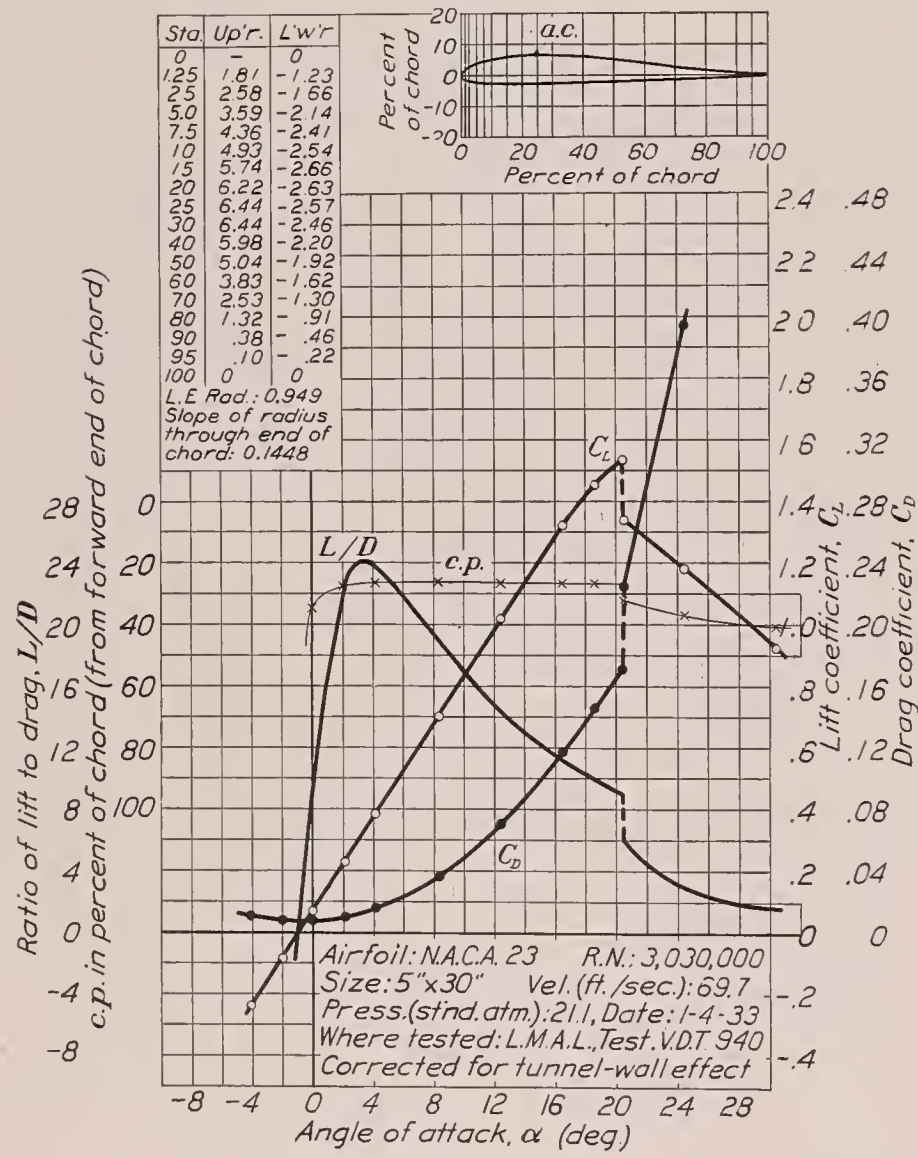


FIGURE 84.—N. A. C. A. 23 airfoil.

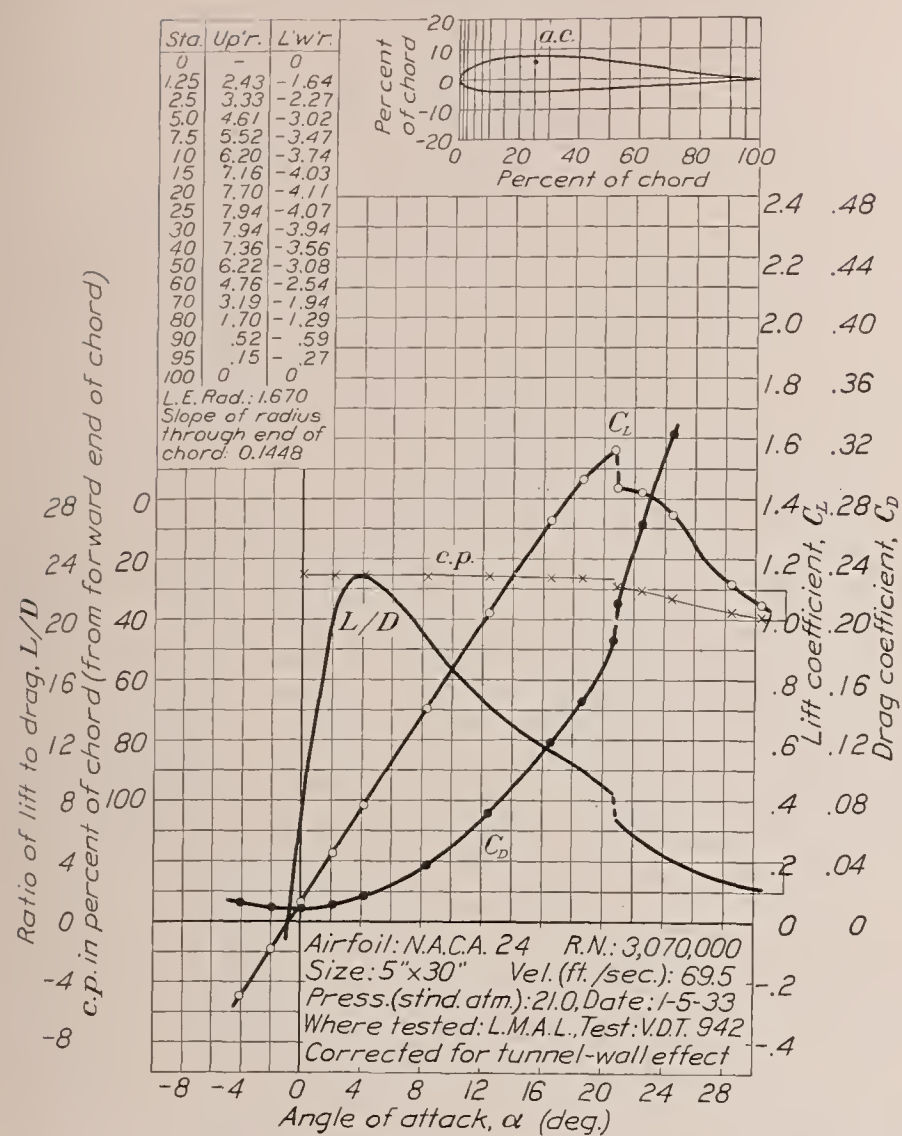


FIGURE 85.—N. A. C. A. 24 airfoil.

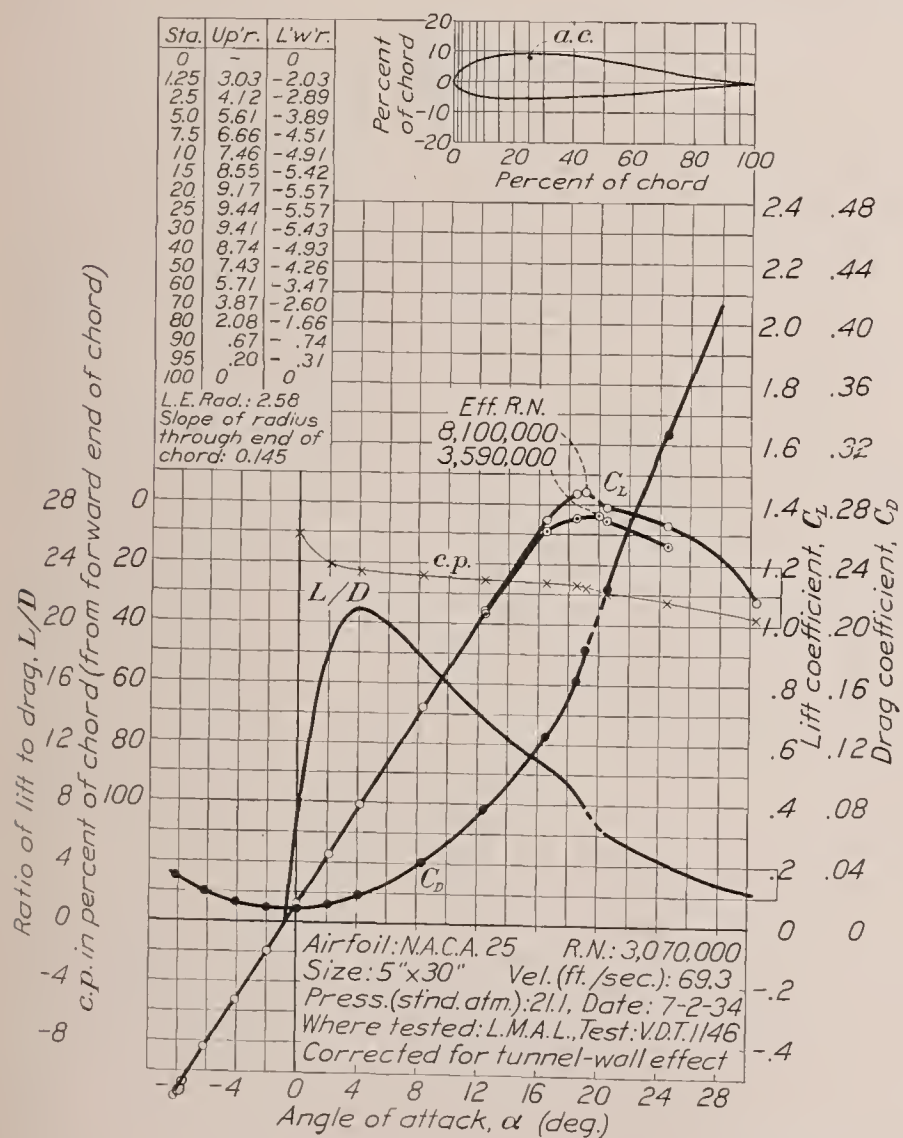
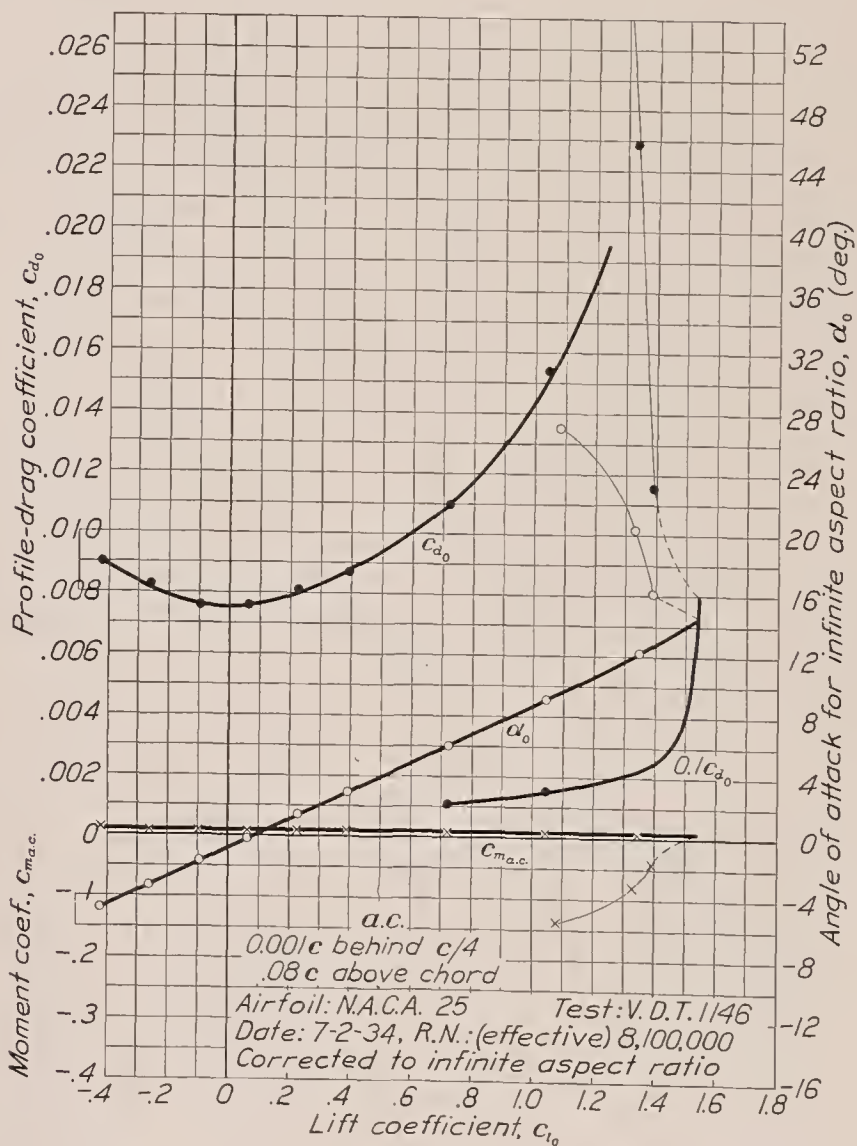
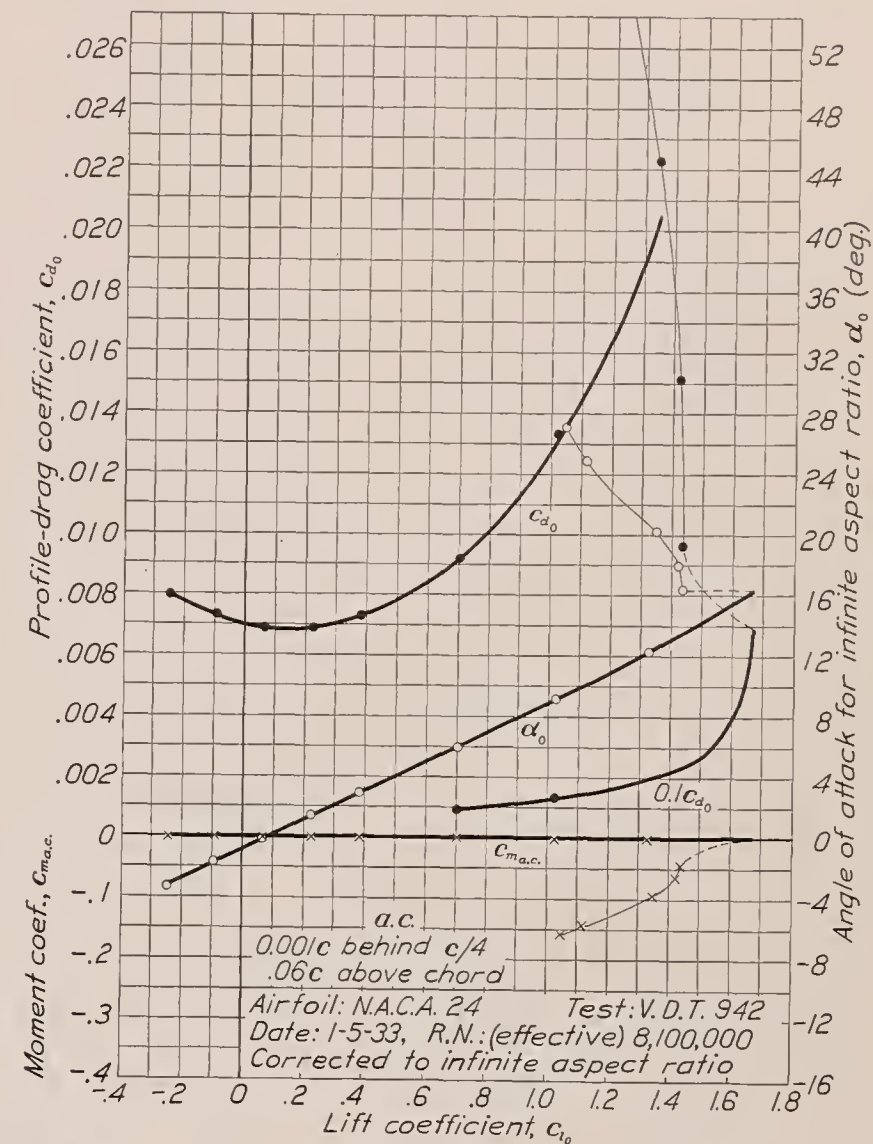


FIGURE 86.—N. A. C. A. 25 airfoil.



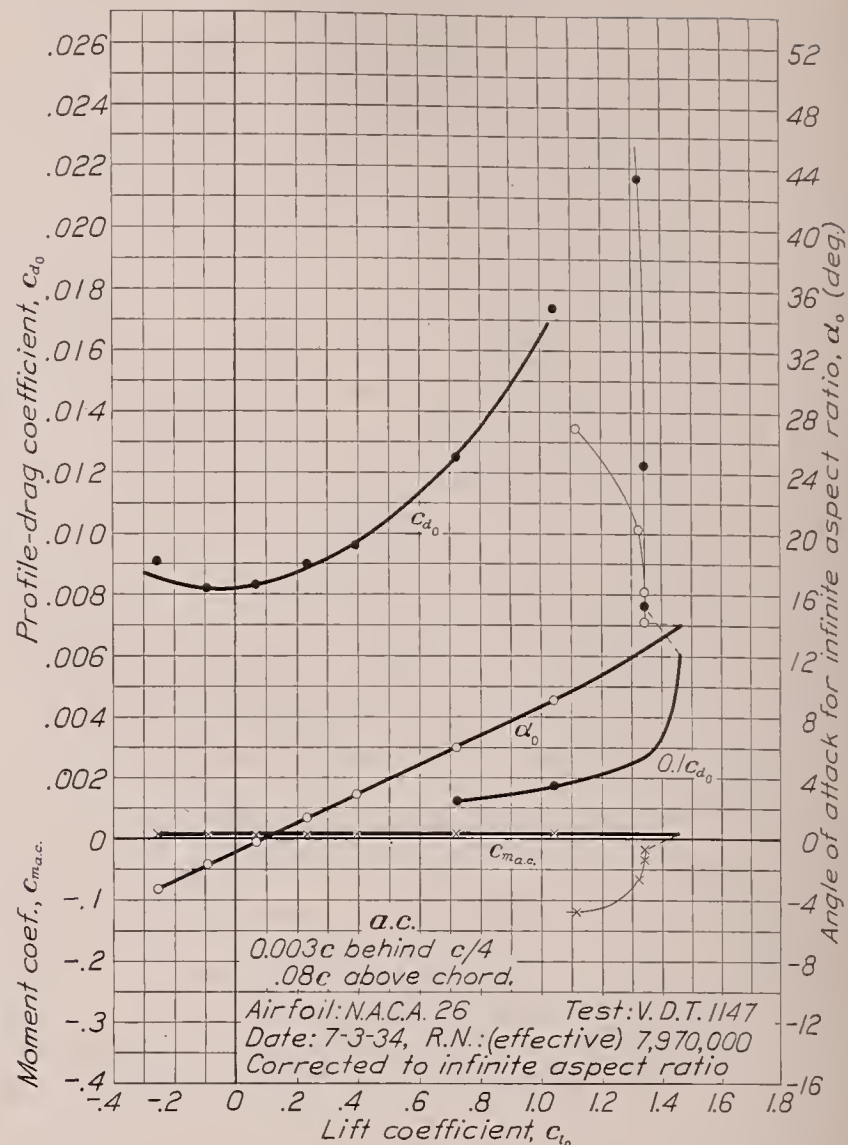
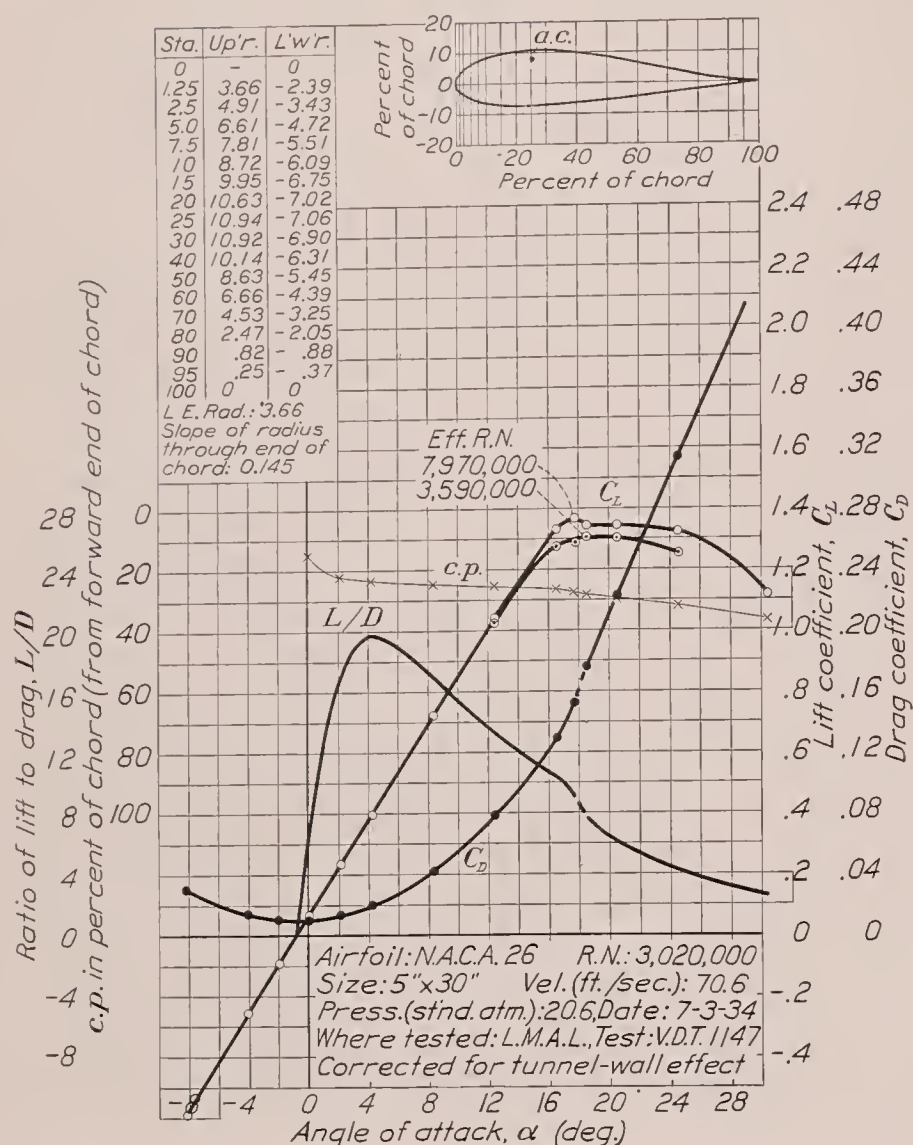


FIGURE 87.—N. A. C. A. 26 airfoil.

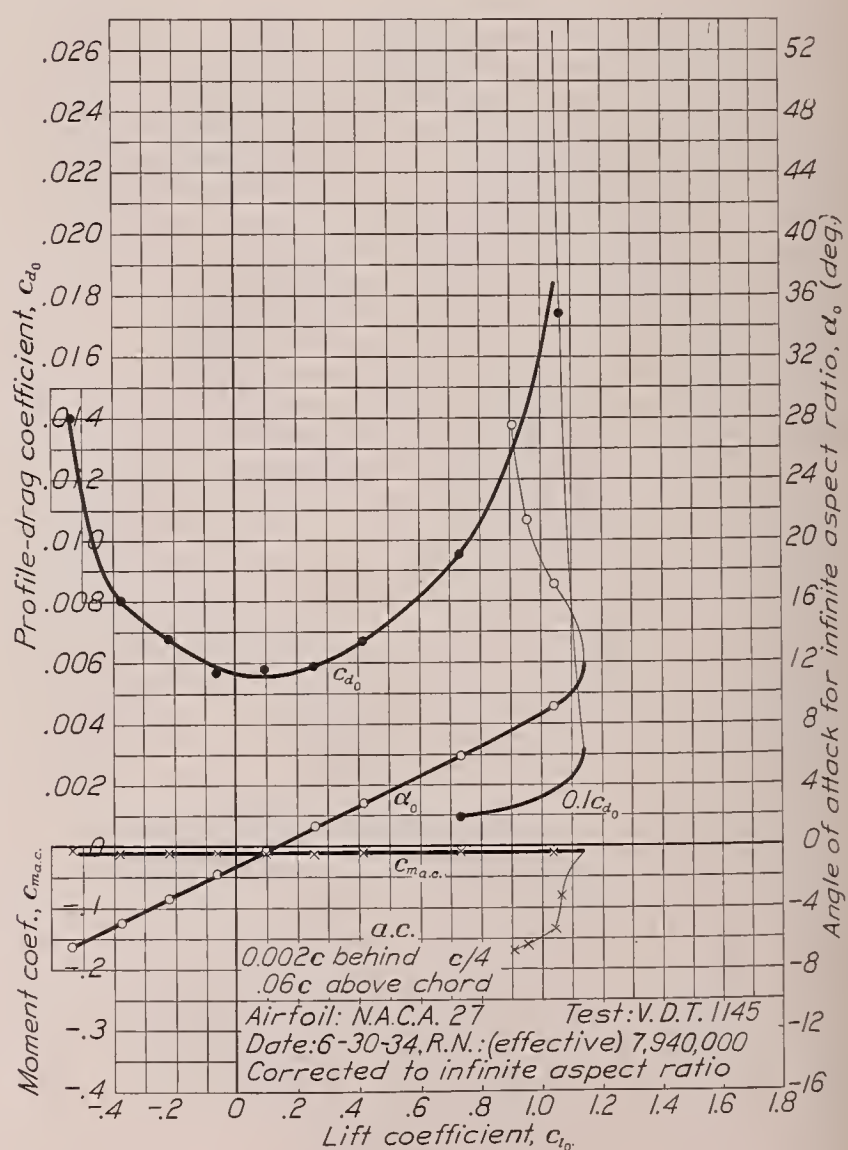
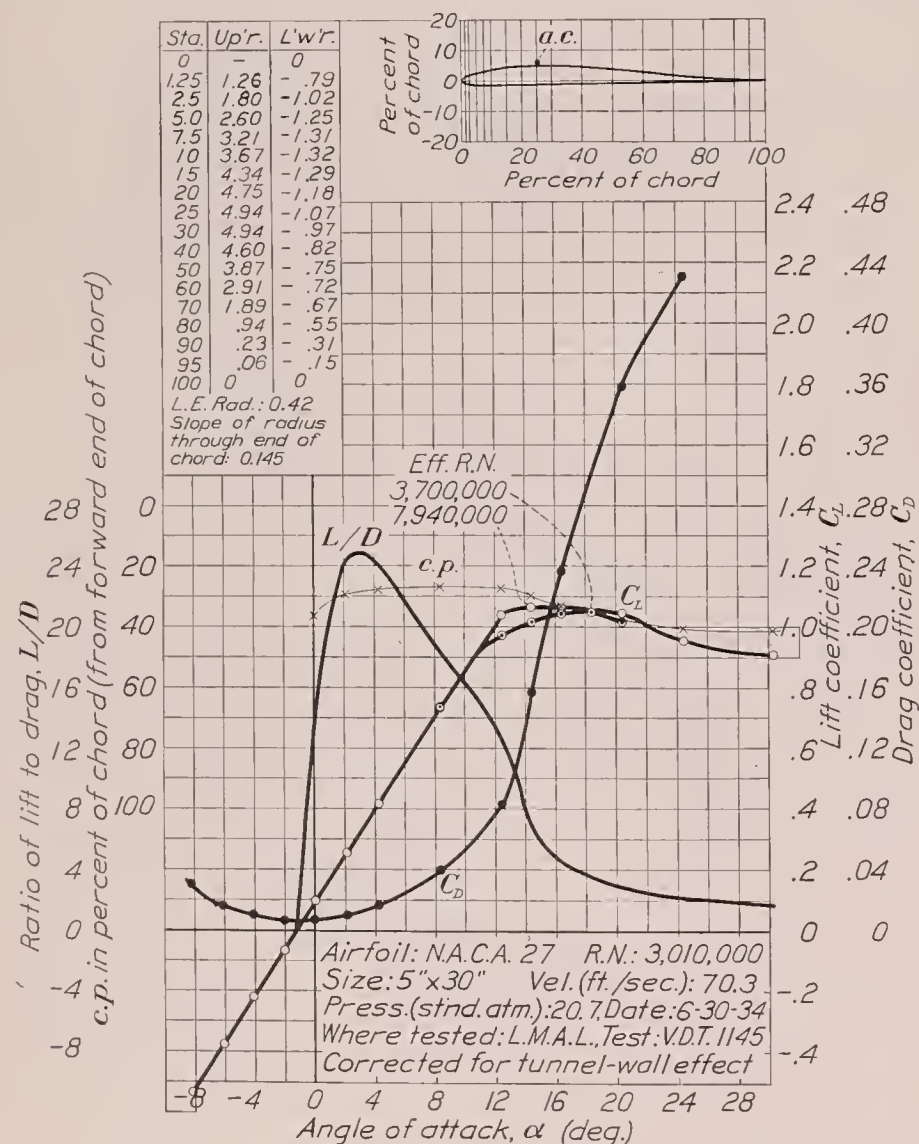


FIGURE 88.—N. A. C. A. 27 airfoil.

TABLE I.—CHARACTERISTICS OF RELATED N. A. C. A. AIRFOILS REPORTED IN REFERENCE 1

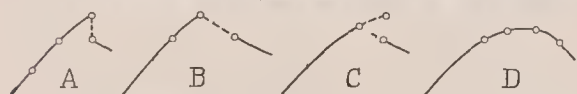
Airfoil	Classification				Effective Reynolds Number (millions)	Fundamental section characteristics								Derived and additional characteristics that may be used for structural design									
	Chord	PD	SE	$C_{L_{max}}$		$c_{l_{max}}$	α_0 (deg.)	a_0 (per deg.)	$c_{l_{opt}}$	$c_{d_{0min}}$	$c_{m_{a-c}}$	a. c. (percent c from c/4)		$\frac{c_{l_{max}}}{c_{d_{0min}}}$	c. p. at $C_{L_{max}}$ (percent c)	Wing characteristics $A=6$; round tips		Thickness at—			Camber (percent c)		
												Ahead	Above			m_0 (per radian)	$C_{D_{min}}$	0.15c (percent c)	0.65c (percent c)	Maximum (percent c)			
N. A. C. A.:	(1)	(2)	(3)	(4)	(5)	(6)	(6)	(6)	(6)	(6)													
0006	A	A10	A	D	8.5	0.91	0	0.098	0	0.0054	0	0.7	2	169	35	4.28	0.0054	5.35	4.13	6	0		
0009	A	B10	B0	A	8.3	1.39	0	0.098	0	0.0064	0	1.0	5	217	26	4.28	0.0064	8.02	6.20	9	0		
0012	A	C10	C0	A	8.4	1.66	0	0.099	0	0.0069	0	.6	3	241	26	4.32	0.0069	10.69	8.27	12	0		
0015	A	D10	D0	A	8.6	1.66	0	0.097	0	0.0077	0	1.2	4	216	25	4.24	0.0077	13.36	10.33	15	0		
0018	A	E10	E0	A	7.8	1.53	0	0.096	0	0.0088	0	1.7	4	174	25	4.20	0.0088	16.04	12.40	18	0		
0021	A	F10	E1	A	8.3	1.48	0	0.093	0	0.0100	0	3.0	6	148	24	4.11	0.0100	18.71	14.46	21	0		
0025	A		E2	B	8.5	1.28	0	0.085	0	0.0119	0	2.7	5	108	25	3.82	0.0119	22.27	17.22	25	0		
2212	A	C12	C3	B	8.4	1.72	-1.8	0.099	.12	0.0072	-.029	.9	5	238	27	4.31	0.0073	10.69	8.25	12	2		
2306	A	A10	A	D	8.1	1.11	-1.8	0.100	.14	0.0063	-.036	.4	4	176	29	4.34	0.0064	5.36	4.14	6	2		
2309	A	B10	B2	A	7.8	1.62	-2.0	0.099	.14	0.0070	-.037	.8	5	239	29	4.31	0.0072	8.04	6.21	9	2		
2312	A	C10	C2	B	8.2	1.72	-1.9	0.097	.12	0.0074	-.039	1.2	4	232	27	4.24	0.0075	10.71	8.27	12	2		
2315	A	D10	D2	B	8.0	1.65	-1.7	0.098	.08	0.0083	-.034	.9	3	199	28	4.28	0.0084	13.38	10.36	15	2		
2406	A	A10	A	D	8.2	1.04	-1.7	0.099	.18	0.0060	-.039	.4	4	173	34	4.31	0.0063	5.34	4.14	6	2		
2409	A	B10	B2	B	8.1	1.62	-1.7	0.099	.08	0.0067	-.044	.7	4	242	28	4.31	0.0069	8.02	6.20	9	2		
2412	A	C10	C2	B	8.2	1.72	-2.0	0.098	.14	0.0071	-.043	.5	3	242	28	4.28	0.0072	10.71	8.27	12	2		
2415	A	D10	D2	C	8.0	1.66	-1.7	0.097	.10	0.0082	-.040	1.4	5	201	28	4.24	0.0083	13.39	10.34	15	2		
2418	A	E10	E2	C	8.0	1.53	-1.9	0.094	.06	0.0093	-.038	1.1	2	165	27	4.14	0.0094	16.08	12.39	18	2		
2421	A	F10	E3	D	7.9	1.44	-1.7	0.093	.06	0.0106	-.035	1.4	2	136	28	4.11	0.0106	18.75	14.46	21	2		
2506	A	A10	A	D	8.1	1.06	-2.0	0.099	.14	0.0062	-.048	0	0	171	37	4.31	0.0064	5.36	4.13	6	2		
2509	A	B10	B2	D	8.0	1.48	-2.0	0.098	.13	0.0068	-.051	.3	2	218	29	4.28	0.0069	8.04	6.21	9	2		
2512	A	C10	C2	B	8.1	1.73	-2.1	0.098	.18	0.0074	-.054	1.0	2	234	28	4.28	0.0076	10.70	8.27	12	2		
2515	A	D10	D2	B	8.1	1.64	-2.0	0.095	.09	0.0085	-.050	.9	2	193	28	4.18	0.0087	13.38	10.33	15	2		
2518	A	E10	E2	D	8.1	1.58	-2.0	0.092	.06	0.0093	-.047	1.1	2	170	28	4.07	0.0093	16.07	12.41	18	2		
2521	A	F10	E3	B	8.2	1.48	-1.8	0.091	.02	0.0105	-.044	2.3	4	141	28	4.04	0.0105	18.72	14.47	21	2		
2612	A	C10	C1	B	8.4	1.78	-2.3	0.096	.16	0.0075	-.062	1.4	2	237	28	4.20	0.0076	10.70	8.26	12	2		
2712	A	C10	C0	B	8.0	1.80	-2.6	0.096	.16	0.0076	-.075	1.0	1	237	29	4.20	0.0079	10.69	8.25	12	2		
4212	A	C10	C5	A	8.5	1.83	-3.4	0.098	.28	0.0078	-.060	.6	2	235	29	4.28	0.0084	10.70	8.27	12	2		
4306	A	A10	A	D	8.1	1.28	-3.8	0.099	.28	0.0071	-.075	.5	2	180	31	4.31	0.0079	5.40	4.14	6	4		
4309	A	B10	B5	B	8.1	1.71	-3.6	0.099	.24	0.0077	-.073	.7	3	222	29	4.31	0.0080	8.09	6.21	9	4		
4312	A	C10	C5	B	8.3	1.74	-3.9	0.096	.27	0.0080	-.076	.9	3	218	30	4.20	0.0085	10.77	8.27	12	4		
4315	A	D10	D4	B	8.2	1.67	-3.6	0.099	.10	0.0090	-.069	1.2	4	186	29	4.31	0.0091	13.47	10.34	15	4		
4318	A	E10	E4	B	8.1	1.56	-3.5	0.095	.16	0.0101	-.065	1.3	3	154	29	4.18	0.0103	16.14	12.41	18	4		
4321	A	F10	E5	D	8.2	1.38	-3.6	0.091	.04	0.0113	-.058	1.8	3	122	31	4.04	0.0113	18.81	14.46	21	4		
4406	A	A10	A	D	8.1	1.32	-3.9	0.100	.32	0.0067	-.087	.4	0	197	32	4.34	0.0077	5.40	4.16	6	4		
4409	A	B10	B4	A	8.1	1.77	-3.9	0.096	.26	0.0073	-.088	.6	2	242	31	4.20	0.0077	8.07	6.21	9	4		
4412	A	C10	C4	D	7.9	1.74	-4.0	0.098	.32	0.0082	-.088	.8	2	212	31	4.28	0.0084	10.77	8.28	12	4		
4415	A	D10	D4	C	7.9	1.72	-4.0	0.097	.22	0.0090	-.085	1.0	1	191	31	4.24	0.0092	13.45	10.34	15	4		
4418	A	E10	E4	D	8.1	1.57	-3.7	0.092	.13	0.0097	-.078	1.4	1	162	31	4.07	0.0100	16.15	12.40	18	4		
4421	A	F10	E5	D	8.2	1.41	-3.4	0.089	.08	0.0111	-.071	1.9	2	127	32	3.96	0.0112	18.79	14.48	21	4		
4506	A	A10	A	D	8.0	1.18	-4.3	0.100	.34	0.0078	-.110	.5	-1	151	36	4.34	0.0088	5.38	4.14	6	4		
4509	A	B10	B3	D	8.2	1.67	-4.1	0.099	.27	0.0081	-.106	.3	0	206	31	4.31	0.0086	8.08	6.21	9	4		
4512	A	C10	C3	B	8.4	1.81	-4.2	0.093	.21	0.0081	-.106	1.1	0	223	31	4.11	0.0085	10.74	8.28	12	4		
4515	A	D10	D3	D	8.0	1.73	-4.1	0.097	.17	0.0097	-.097	.9	0	178	31	4.24	0.0099	13.44	10.35	15	4		
4518	A	E10	E3	D	8.2	1.65	-3.9	0.092	.13	0.0106	-.093	1.4	2	156	31	4.07	0.0107	16.14	12.41	18	4		
4521	A	F10	E4	D	8.2	1.50	-3.4	0.091	.06	0.0117	-.082	1.6	2	128	32	4.04	0.0117	18.80	14.47	21	4		
4612	A	C10	C2	B	8.3	1.88	-4.6	0.094	.24	0.0086	-.124	1.0	0	219	31	4.14	0.0090	10.73	8.27	12	4		

TABLE II.—CHARACTERISTICS OF MISCELLANEOUS AIRFOILS

[An inverted airfoil is considered as another distinct section]

Airfoil	Figure No.	N. A. C. A. reference, R= report, N= note	Classification				Effective Reynolds Number (millions)	Fundamental section characteristics										Derived and additional characteristics that may be used for structural design									
			Chord	PD	SE	$C_{L_{max}}$		$c_{l_{max}}$	α_{l_0} (deg.)	a_0 (per deg.)	$c_{l_{opt}}$	$c_{d_{0min}}$	$c_{m_{a.c.}}$	$a. c.$ (percent c from $c/4$)		$\frac{c_{l_{max}}}{c_{d_{0min}}}$	$c. p.$ at $c_{l_{max}}$ (percent c)	Wing characteristics $A=6$; round tips		Thickness at			Camber (percent c)				
														Ahead	Above			m_0 (per radian)	$C_{D_{min}}$	0.15c (percent c)	0.65c (percent c)	Maximum (percent c)					
Boeing 103	1	N 412	(1) B	(2) C10	(3) C4	(4) B	(5) 8.0	(6) 1.76	—4.8	(6) 0.097	(6) 0.15	(6) 0.0088	—0.065	0.6	7	200	30	4.24	0.0089	11.21	9.14	12.68	4.2				
Boeing 103 (inv.)	2	N 412				B	8.6	.96		.098			.069	.9	—2	16	16	4.28									
Boeing 103A	3	N 412	B	B10	C3	A	8.4	1.74	—3.8	.098	.17	.0075	—0.053	.5	5	232	29	4.28	.0077	9.18	7.52	10.38	3.2				
Boeing 103A (inv.)	4	N 412				D	8.4	.85		.100			.058	.8	0	20	20	4.34									
Boeing 106	5	N 412	C	C10	B4	D	8.4	1.64	—4.4	.094	.14	.0081	—0.052	.8	5	202	29	4.14	.0082	11.26	9.26	13.06	3.5				
Boeing 106 (inv.)	6	N 412				B	8.1	.88		.093			.057	1.4	2	17	17	4.11									
Boeing 106R	7	N 388	C	C11	B3	D	8.3	1.48	—1.1	.095	.05	.0077	—0.001	.3	4	192	27	4.18	.0077	11.26	9.29	13.06	2.0				
Boeing 111	8		A	C10	D3	A	7.8	1.68	—2.1	.096	.17	.0071	—0.033	1.3	6	137	28	4.20	.0073	9.92	8.14	11.50	3.0				
Boeing 111 (inv.)	9					A	8.1	.89		.096			.033	.9	2	21	21	4.20									
Boeing 112	10		A	C10	D2	C	8.2	1.69	—2.0	.096	.20	.0071	—0.023	.7	5	238	28	4.20	.0074	9.92	8.12	11.50	2.8				
Boeing 112 (inv.)	11					D	8.3	.70		.096			.023	.7	—5	34	34	4.20									
Sikorsky GS-M	12		B	D10	D6	D	8.1	1.69	—7.9	.099	.30	.0096	—0.105	.1	6	176	34	4.31	.0101	15.29	9.11	16.05	5.5				
Sikorsky GS-M (inv.)	13					A	8.3	.89		.101			.105	1.1	1	12	12	4.37									
Sikorsky GS-I	14		B	D10	D4	D	8.3	1.78	—6.8	.097	.25	.0082	—0.094	.4	4	217	32	4.24	.0086	12.84	8.31	13.98	4.5				
Sikorsky GS-I (inv.)	15					A	8.5	1.16		.100			.093	1.2	2	16	16	4.34									
S. T. A6. 27A	16		B	F10	E8	D	8.0	1.72	—10.2	.100	.40	.0127	—0.177	0	0	135	36	4.34	.0137	15.96	8.20	19.80	8.0				
R. A. F. 34	17		A	C11	C1	C	8.0	1.58	—8	.098	.20	.0071	—0.006	.4	5	222	27	4.28	.0072	10.88	8.55	12.64	1.8				
U. S. A. 27	18	N 412	B	C10	C6	B	8.1	1.71	—4.7	.094	.30	.0086	—0.078	1.8	5	199	30	4.14	.0098	10.40	8.70	11.12	5.6				
U. S. A. 27 (inv.)	19	N 412				D	8.1	.52		.094			.080	1.9	0	29	29	4.14									
U. S. A. 35-A	20		B	E10	E6	D	8.4	1.52	—8.0	.095	.38	.0116	—0.111	.8	5	131	34	4.18	.0121	16.60	11.90	18.18	7.3				
U. S. A. 35-B	21	N 412	B	C10	C5	B	8.3	1.81	—5.2	.099	.35	.0083	—0.076	.5	5	218	30	4.31	.0087	10.56	7.54	11.61	4.6				
U. S. A. 35-B (inv.)	22	N 412				D	8.3	.81		.102			.081	1.3	5	24	24	4.41									
C-62	23		A	D10	A	D	8.4	1.06	—1.8	.095	.15	.0065	—0.038	.6	4	163	34	4.18	.0067	7.09	5.72	8.04	1.9				
C-72	24	N 412	B	C10	C4	D	8.0	1.74	—5.6	.095	.23	.0083	—0.084	1.0	3	210	30	4.18	.0087	10.53	7.39	11.73	4.0				
C-72 (inv.)	25	N 412				D	8.1	.83		.096			.085	1.0	—1	19	19	4.20									
C-80	26		A	B10	A	D	8.2	1.24	—1.0	.098	.05	.0064	—0.015	.2	4	194	29	4.28	.0064	7.91	5.77	8.58	1.3				
C-80 (inv.)	27					D	8.1	.81		.100			.018	.4	2	36	36	4.34									
N-22	28	N 412	B	C10	C4	D	8.1	1.72	—5.4	.096	.17	.0087	—0.075	.6	4	198	30	4.20	.0089	11.25	8.36	12.37	4.3				
N-22 (inv.)	29	N 412				B	8.1	.84		.098			.082	.8	0	14	14	4.28									
N-60	30	N 388	B	C10	C4	D	8.1	1.73	—5.5	.097	.30	.0086	—0.078	0	0	201	31	4.24	.0090	11.17	7.88	12.37	4.0				
N-60 R	31	N 388	B	C11	C3	D	8.3	1.50	—1.5	.098	.09	.0077	—0.001	—0.1	6	195	27	4.28	.0078	11.17	7.88	12.37	2.8				
N-68	32		A	B10	A	D	8.1	.96	0	.097	0	.0060	0	.7	5	160	25	4.24	.0061	6.90	5.76	8.00	0				
N-69	33		A	B10	A	D	8.1	1.00	0	.093	0	.0066	0	.8	4	152	25	4.11	.0066	8.46	8.22	10.94	0				
N-71	34		C	C10	C2	D	8.3	1.67	—2.0	.099	.18	.0066	—0.029	.7	6	253	28	4.31	.0068	9.99	7.52	11.54	2.0				
N-71 (inv.)	35					A	8.3	1.24		.099			.030	0	1	23	23	4.31									
N-75	36		C	C10	C2	B	7.9	1.68	—2.2	.097	.15	.0075	—0.045	.9	3	224	28	4.24	.0077	9.99	8.69	11.50	2.0				
N-75 (inv.)	37					A	8.2	1.09		.096			.046	.7	2	20	20	4.20									
N-76	38		C	C10	C3	D	8.2	1.63	—2.1	.096	.19	.0078	—0.032	.7	4	209	28	4.20	.0081	10.00	8.69	11.50	2.7				
N-76 (inv.)	39					A	8.0	.99		.095			.032	.5	0	21	21	4.18									
N-80	40		C	C10	C2	B	8.4	1.74	—2.2	.098	.16	.0069	—0.044	—0.1	2	252	29	4.28	.0071	10.02	7.59	11.54	2.0				
N-80 (inv.)	41					A	8.5	1.17		.100			.043	0	0	22	22	4.34									
N-81	42		C	C10	C2	A	8.5	1.79	—2.2	.100	.14	.0072	—0.041	.2	5	249	29	4.34	.0073	10.60	7.18	11.54	2.0				
N-81 (inv.)	43					A	8.5	1.26		.101			.038	.1	2	22	22	4.37									
Gött. 387	44	N 428	B	D10	D6	D	8.4	1.70	—6.6	.097	.30	.0091	—0.093	.7	4	187	32	4.24	.0097	13.40	9.69	14.85	5.9				
Gött. 398	45	N 412	B	D10	D5	D	8.1	1.68	—6.0	.094	.15	.0091	—0.081	.4	1	185	31	4.14	.0094	12.50	9.27	13.75	4.9				
Gött. 398 (inv.)	46	N 412				D	8.2	.83		.097			.086	1.9	3	12	12	4.24									
Gött. 398-A	47	N 416	B	C10	A	D	8.4	1.20	—6.1	.095	.40	.0085	—0.086	1.0	—2	141	31	4.18	.0108	12.17	9.25	13.62	4.5				
Gött. 398-B	48	N 416	B	C10	A	D	8.6	1.19	—6.4	.090	.45	.0084	—0.093	1.7	4	142	31	4.00	.0122	11.87	9.24	13.48	4.5				
Gött. 398-R	49	N 388	B	D11	D4	D	8.2	1.46	—2.2	.098	.10	.0082	—0.005	.5	10	178	28	4.28	.0083	12.50	9.27	13.75	3.5				
Gött. 413	50		B	D10	D5	D	8.0	1.61	—7.7	.101	.35	.0097	—0.096	0	7	166	35	4.37	.0104	15.22	9.21	16.45	5.0				

Gött. 420	51		B	E10	E4	D	8.2	1.51	-8.3	.095	.18	.0104	-.084	-.4	7	145	34	4.18	.0107	16.50	11.84	18.75	4.5
Gött. 429-AG	52		A	C10	C0	A	8.1	1.61	0	.100	0	.0066	0	.1	4	244	26	4.34	.0066	10.38	5.90	11.20	0
Gött. 429-J	53		A	C10	C0	A	8.0	1.65	0	.102	0	.0068	0	.2	5	243	27	4.41	.0068	10.98	6.10	11.78	0
Gött. 436	54		B	C10	C4	D	8.0	1.68	-4.4	.098	.22	.0082	-.061	.5	5	205	30	4.28	.0085	10.16	7.47	11.10	3.9
Gött. 436 (inv.)	55					D	8.1	.76		.099			.062	.6	-6		28	4.31					
Gött. 532	56		B	C10	C5	C	8.1	1.91	-6.1	.101	.37	.0080	-.095	.8	6	239	31	4.37	.0088	11.60	6.63	13.00	4.8
Gött. 532 (inv.)	57					A	8.3	.73		.101			.095	2.9	14		10	4.37					
Clark Y	58	N 412	B	C10	C4	D	8.4	1.68	-5.0	.092	.12	.0083	-.069	1.1	4	202	29	4.07	.0085	10.53	8.30	11.70	3.9
Clark Y (inv.)	59	N 412				B	8.4	.92		.098			.072	1.7	3		16	4.28					
Clark Y-B	60	N 447	B	C10	A	D	8.2	1.14	-5.4	.089	.35	.0072	-.075	1.3	-2	158	30	3.96	.0096	10.00	8.26	11.46	3.3
Clark Y M-15	61	N 412	C	D10	D4	C	8.4	1.70	-5.2	.094	.10	.0091	-.068	1.1	7	187	30	4.14	.0093	13.51	10.63	15.00	4.0
Clark Y M-15 (inv.)	62	N 412				B	8.0	1.23		.097			.071	1.3	1		18	4.24					
Clark Y M-18	63	N 412	C	E10	E4	C	8.2	1.60	-5.1	.091	.07	.0104	-.064	1.4	5	154	30	4.04	.0104	16.21	12.72	18.00	4.0
Clark Y M-18 (inv.)	64	N 412				A	8.3	1.39		.094			.065	2.2	2		18	4.14					
Clark Y-6	65		B	A10	A	D	8.1	1.07	-2.9	.098	.15	.0059	-.038	.7	5	181	37	4.28	.0062	5.40	4.24	6.00	1.9
Clark Y-8	66		B	B10	B3	D	8.0	1.37	-3.6	.096	.14	.0060	-.045	.7	6	228	30	4.20	.0062	7.21	5.68	8.00	2.6
Clark Y-10	67		B	B10	C3	B	7.9	1.68	-4.5	.098	.23	.0075	-.059	.7	4	224	30	4.28	.0078	9.01	7.08	10.00	3.2
Clark Y-14	68		B	D10	D4	D	8.0	1.72	-6.2	.096	.15	.0090	-.080	1.2	6	191	31	4.20	.0091	12.61	9.93	14.00	4.6
Clark Y-18	69	N 412	B	E10	E6	D	8.1	1.48	-7.6	.092	.23	.0117	-.098	1.5	6	126	33	4.07	.0121	16.22	12.74	18.00	6.3
Clark Y-18 (inv.)	70	N 412				B	8.1	.89		.089			.101	.3	-10		10	3.96					
Clark Y-22	71		B	F10	E8	D	7.9	1.36	-9.3	.088	.15	.0140	-.107	1.8	13	97	34	3.93	.0141	19.82	15.53	22.00	8.0
N. A. C. A.:																							
CYH	72	N 412	B	C11	C3	D	8.1	1.58	-2.9	.095	.08	.0076	-.027	.7	6	208	28	4.18	.0077	10.53	8.30	11.70	3.1
CYH (inv.)	73	N 412				B	8.1	.96		.095			.032	1.6	-1		20	4.18					
-M6	74	N 412	A	C11	C3	D	8.0	1.51	-.8	.095	.03	.0077	.002	-.4	0	196	26	4.18	.0077	10.29	9.00	12.01	2.4
-M6 (inv.)	75	N 412				D	8.2	1.19		.097			.007	0	0		24	4.24					
15	76		A	C10	A	D	8.2	1.17	-2.0	.094	.15	.0069	-.043	.3	0	170	29	4.14	.0071	10.20	8.27	12.00	2.0
16	77		A	C10	B4	D	8.4	1.64	-2.1	.095	.17	.0069	-.045	.7	3	238	28	4.18	.0071	10.45	8.27	12.00	2.0
17	78		C	C10	B4	B	8.4	1.53	-1.9	.095	.25	.0069	-.047	.4	2	222	29	4.18	.0076	10.20	8.27	12.00	2.6
18	79		C	C10	C2	A	8.1	1.69	-2.0	.096	.25	.0071	-.049	.6	3	238	28	4.20	.0074	10.45	8.27	12.00	2.6
19	80		A	B10	A	D	8.2	1.01	-1.9	.093	.17	.0065	-.044	0	0	155	33	4.11	.0068	9.93	8.27	12.00	2.0
20	81		A	B10	A	D	8.1	1.02	-2.2	.090	.24	.0065	-.048	1.2	-10	157	31	4.00	.0078	9.70	8.27	12.00	2.0
21	82		A	C11	C2	B	8.1	1.71	-2.1	.096	.20	.0074	-.038	.5	3	231	28	4.20	.0077	10.29	8.96	12.00	2.4
21 (inv.)	83					D	8.1	1.08		.097			.040	.4	1		22	4.24					
23	84		A	B11	B2	A	8.0	1.65	-1.0	.100	.18	.0062	-.007	.5	7	266	27	4.34	.0064	8.40	4.67	9.00	2.0
24	85		A	C11	C2	A	8.1	1.67	-.8	.103	.15	.0068	0	-.1	6	246	27	4.44	.0070	11.19	6.21	12.00	2.0
25	86		A	D11	D2	B	8.1	1.54	-.8	.105	0	.0075	.008	-.1	8	205	27	4.51	.0075	13.97	7.79	15.00	2.0
26	87		A	E11	E2	D	8.0	1.46	-.9	.104	-.05	.0082	.008	-.3	8	178	27	4.47	.0082	16.70	9.38	18.00	2.0
27	88		A	A11	A	D	7.9	1.14	-1.3	.102	.10	.0056	-.010	-.2	6	204	30	4.41	.0057	5.63	3.10	6.00	2.0
22112		R 537	A	C11	D2	B	8.5	1.64	-.8	.100	.06	.0072	.001	1.0	5	228	25	4.34	.0073	10.69	8.27	12.00	1.6
23112		R 537	A	C11	D2	A	8.2	1.73	-.8	.100	.08	.0074	.002	1.5	8	234	25	4.34	.0075	10.69	8.28	12.00	2.1
24112		R 537	A	C11	C3	A	8.0	1.67	-.9	.100	.10	.0074	0	1.4	8	226	26	4.34	.0074	10.71	8.26	12.00	2.4
25112		R 537	A	C11	C3	B	8.2	1.62	-1.2	.100	.08	.0074	-.002	1.3	7	219	25	4.34	.0075	10.73	8.28	12.00	2.7

¹ Type of chord. See reference 10.² Type of pressure distribution. See reference 10.³ Type of scale effect on maximum lift. A signifies practically no scale effect. For other designations see reference 9, fig. 44.⁴ Type of lift-curve peak as shown in the sketches:⁵ Turbulence factor is 2.64.⁶ These data have been corrected for tip effect.

REPORT No. 629

ON SOME RECIPROCAL RELATIONS IN THE THEORY OF NONSTATIONARY FLOWS

By I. E. GARRICK

SUMMARY

In the theory of nonstationary flows about airfoils, the "indicial lift" function $k_1(s)$ of Wagner and the "alternating lift" function $C(k)$ of Theodorsen have fundamental significance. This paper reports on some interesting relations of the nature of Fourier transforms that exist between these functions. General problems in transient flows about airfoils may be given a unified broad treatment when these functions are employed. Certain approximate results also are reported which are of notable simplicity, and an analogy with transient electrical flows is drawn.

INTRODUCTION

There exist at the present time two significant functions that have been introduced into the two-dimensional potential theory of nonuniform motion of airfoils, one by Wagner (reference 1) and the other by Theodorsen (reference 2). Wagner's function concerns the growth of circulation or lift about an airfoil at a small fixed angle of attack starting impulsively from rest to a uniform velocity v . Theodorsen's function describes the lift due to circulation about an airfoil oscillating sinusoidally and moving with uniform velocity v . It is the object of this paper to note the usefulness of these functions in handling a wide class of problems in transient flows about airfoils and to point out certain interesting relations existing between them. These relations are of the nature of Fourier transforms, which occur with remarkable abundance in numerous fields of physics and which are one of the main studies of the recently popular operational-calculus methods. A noteworthy analogy between transient hydrodynamic flows and transient electrical flows is also mentioned.

A third interesting function, which concerns the behavior of an airfoil upon entering a gust, has been introduced by Küssner in reference 3, which is an excellent survey of the status of the problem of nonstationary flows about airfoils. This function and its relation to Wagner's function will also be discussed.

THEORY OF NONSTATIONARY FLOWS

Wagner's function, $k_1(s)$.—Let the chord of the airfoil be $2b$ and let the angle of attack (assumed small) be α . Also let the impulsive motion from rest to uniform velocity v take place at the origin, $s=0$ (fig. 1). The vertical velocity at the airfoil surface is $w=v \sin \alpha$.

Then, based on the physical assumption that the velocity at the trailing edge is finite for all time, Wagner derives for the lift, as a function of $s=vt/b$,

$$L=2\pi b\rho vw k_1(s) \quad (1)$$

The function $k_1(s)$ is illustrated in figure 2. Wagner does not derive an explicit analytic expression for $k_1(s)$ but gives only numerical values. Küssner (reference 3) derives a slowly convergent expression in series form for $k_1(s)$ that checks Wagner's values. The expression is rather long and will not be reproduced

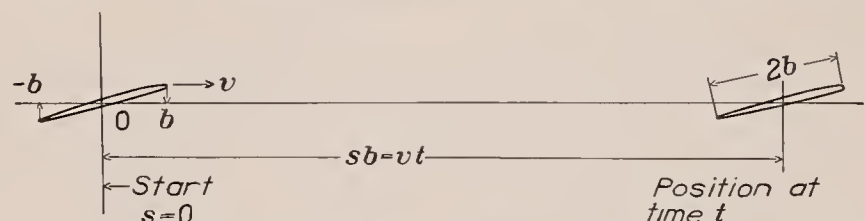


FIGURE 1.—Illustration of nondimensional parameter s , distance traversed in terms of half chord b .

here. It is of great interest to note that the following simple expression

$$k_1(s) \cong 1 - \frac{2}{4+s} \quad (1a)$$

agrees within 2 percent in the entire range $0 < s < \infty$. (Cf. table I.) This expression, which may be regarded as a fortunate choice of the author, is especially good

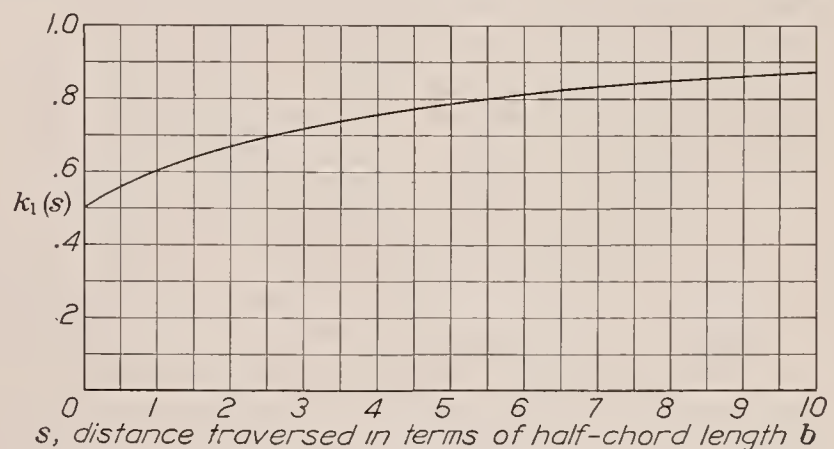


FIGURE 2.—The function $k_1(s)$ of Wagner.

in the range s small; it may be reasoned that it represents the actual physical state more closely than the theoretical solution, since it approaches the steady condition ($s=\infty$) somewhat more slowly.

It is observed that half the final lift is assumed at once and that the lift gradually approaches its asymptote, $2\pi b\rho vw$, in agreement with the results for stationary flows.

The function $k_1(s)$ is analogous to what is termed in electrical-circuit theory the "indicial-admittance function" $A(t)$, which is the current response of a linear network to a suddenly applied unit voltage; substitute lift for current and unit vertical velocity for unit voltage to complete the analogy.

Theodorsen's function, $C(k)$.—The lift on an airfoil oscillating sinusoidally through a small angle of attack and moving with uniform velocity v is given by the sum of two parts: (a) A classical noncirculatory part and (b) a part due to circulation. This paper is not concerned with the classical part, which consists of the virtual inertia terms, the general concepts of which go back to the time of Kirchhoff and Kelvin.

The steady-state part of the lift due to circulation about an oscillating airfoil moving with velocity v has been given by Theodorsen as

$$L = 2\pi b \rho v C(k) Q \quad (2)$$

where

$Q = we^{i\omega t}$ is the vertical velocity at the three-quarter chord point¹ in complex form,

and where

$k = \frac{\omega b}{v}$, where ω is the angular frequency.

The parameter k permits the substitution of distance s in place of time t since $\omega t = \frac{\omega b}{v} \frac{vt}{b} = ks$. The function $C(k)$ is defined as

$$C(k) = \frac{H_1^{(2)}}{H_1^{(2)} + iH_0^{(2)}} \quad (3)$$

where $H_0^{(2)}$ and $H_1^{(2)}$ are Hankel functions (Bessel functions of the third kind), or, separated into real and imaginary parts and expressed in terms of Bessel functions of the first and second kinds,

$$C(k) = F(k) + iG(k) \quad (4)$$

where

$$F(k) = \frac{J_1(J_1 + Y_0) + Y_1(Y_1 - J_0)}{(J_1 + Y_0)^2 + (Y_1 - J_0)^2}$$

$$G(k) = -\frac{Y_1 Y_0 + J_1 J_0}{(J_1 + Y_0)^2 + (Y_1 - J_0)^2}$$

These functions are illustrated in two ways in figure 3.

It is important to note that, in the interpretation of equation (2), $C(k)$ is considered to operate on the function Q . Thus, suppose the actual vertical velocity is $w_0 \sin ks$. This quantity must be expressed as *I. P.* $w_0 e^{iks}$. Then the lift is

$$\text{I. P. } 2\pi b \rho v w_0 C(k) e^{iks}$$

or

$$2\pi b \rho v w_0 (F^2 + G^2)^{\frac{1}{2}} \sin \left(ks + \tan^{-1} \frac{G}{F} \right)$$

¹ It is a remarkable fact that the vertical velocity at the three-quarter chord point determines the circulation force on the airfoil in oscillatory motions. The lift due to circulation acts at the one-quarter chord point. The terms "forward neutral point" and "rear neutral point" have been introduced by Küssner to designate these characteristic points.

The lift thus has the same frequency as the vertical velocity and both its magnitude and phase are functions of k .

The analogy with alternating currents in electrical networks can be mentioned. The function $C(k)$ corresponds to the complex admittance function for alternating currents (reciprocal of the complex impedance function $Z(\omega)$). The real and imaginary components F and G are analogous, respectively, to the alternating-current power and quadrature components; the lift due to complex vertical velocity Q corresponds to current due to complex voltage E .

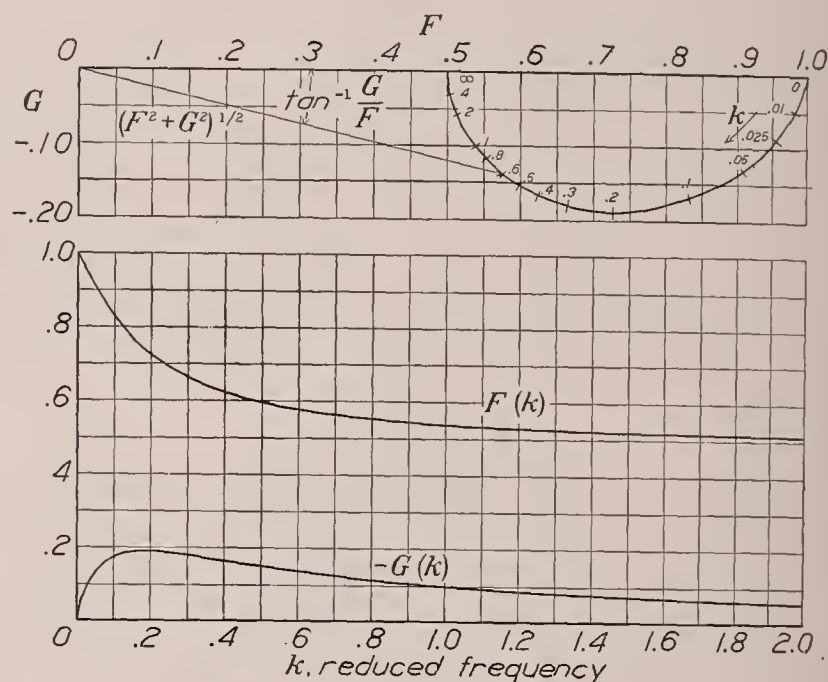


FIGURE 3.—The function $C(k) = F + iG$ of Theodorsen.

Superposition principle.—Linearity of the equations of Wagner permits one to write, in general, for the lift due to a vertical-velocity function $w(s)$ (at the three-quarter chord point) suddenly applied at the instant when $s=0$,

$$\frac{L}{2\pi b \rho v} = w(0)k_1(s) + \int_0^s k_1(s-s_1) \frac{dw}{ds_1} ds_1 \quad (5)$$

where $w(0)$ is the value of w at $s=0$. This result can be derived by replacing the function $w(s)$ by a step function the envelope of which is $w(s)$ and by going to the limit. The equation is a well-known mathematical result and is often employed in electrical-circuit theory (reference 4, p. 68).

Several useful forms of this equation exist, of which one is

$$\frac{L}{2\pi b \rho v} = w(0)k_1(s) + \int_0^s k_1(s_1) \frac{d}{ds_1} w(s-s_1) ds_1 \quad (5a)$$

Equation (5) expresses a noteworthy result, since it permits the handling (at least formally or graphically) of many problems in transient flows that would otherwise be quite laborious. As an example of its application, and as a means of obtaining an interesting result, let equation (5a) be applied to the vertical-velocity function of the form $w(s) = w_0 e^{iks}$.

There results for the lift, when the vertical velocity $w_0 e^{iks}$ is suddenly applied at $s=0$,

$$\frac{L}{2\pi b \rho v} = w_0 k_1(s) + w_0 i k e^{iks} \int_0^s k_1(s_1) e^{-iks_1} ds_1 \quad (5b)$$

In order to isolate the transient and steady-state parts, the familiar device of separating the interval 0 to s into an interval 0 to ∞ minus an interval s to ∞ is used.

Then, for the steady-state part only (writing s in place of s_1 in the definite integral),

$$L = 2\pi b \rho v w_0 i k e^{iks} \int_0^\infty k_1(s) e^{-iks} ds$$

This equation must agree with Theodorsen's result (equation (2)), which may be written in this case

$$L = 2\pi b \rho v w_0 C(k) e^{iks}$$

Hence it must follow that

$$C(k) = i k \int_0^\infty k_1(s) e^{-iks} ds \quad (6)$$

or, in better mathematical form,

$$C(k) - 1 = i k \int_0^\infty [k_1(s) - 1] e^{-iks} ds \quad (6a)$$

It follows, for the components of $C(k) = F + iG$, that

$$\frac{F(k)}{k} = \int_0^\infty k_1(s) \sin ks ds \quad (7)$$

$$\frac{G(k)}{k} = \int_0^\infty [k_1(s) - 1] \cos ks ds \quad (8)$$

These equations can be inverted by the properties of Fourier transforms (reference 4, p. 183). Then

$$k_1(s) = \frac{2}{\pi} \int_0^\infty \frac{F(k)}{k} \sin ks dk \quad (9)$$

$$= 1 + \frac{2}{\pi} \int_0^\infty \frac{G(k)}{k} \cos ks dk \quad (10)$$

Some approximate results.—The integration expressed in equation (6) can be performed directly when

the approximate expression $k_1(s) \cong 1 - \frac{2}{4+s}$ is employed.

Then the following simpler expressions for $C(k)$, F , and G , which hold within a few percent, are obtained (cf. Jahnke-Emde, "Tables of Functions," p. 80):²

$$C(k) - 1 \cong 2 i k e^{4ik} \text{Ei}(-4ik) \quad (6b)$$

$$\frac{F-1}{2k} \cong \cos 4k \text{si} 4k - \sin 4k \text{Ci} 4k$$

$$\frac{G}{2k} \cong \cos 4k \text{Ci} 4k + \sin 4k \text{si} 4k$$

The following approximate result is also of interest. Let the vertical-velocity function be of the form $w(s) = w_0(1 - e^{-\gamma s})$ where γ determines the rate at which $w(s)$ approaches w_0 . Then from (5), using the approximate expression for $k_1(s)$,

² The expression (6b) may be considered the limit, as $s \rightarrow \infty$, of the function (cf. equation (5b)):

$$C(k, s) - 1 \cong 2 i k e^{4ik} \{\text{Ei}(-4ik) - \text{Ei}[-(4+s)ik]\}$$

The transient term containing s approaches 0 as $s \rightarrow \infty$.

$$\frac{L}{2\pi b \rho v w_0} = 1 - e^{-\gamma s} - 2\gamma e^{-(4+s)\gamma} [\text{Ei}(4+s)\gamma - \text{Ei}(4\gamma)]$$

Second derivation of equation (6).—The result expressed in equation (6) can be demonstrated in still another way, which, essentially, is Küssner's treatment. (Cf. reference 3, p. 420.) A common artifice in the treatment of unit discontinuities is to represent the unit "jump" function

$$1(s) = 1 \text{ for } s > 0$$

$$1(s) = 0 \text{ for } s < 0$$

by the following integral in the complex k plane, which can be evaluated by residue theory:

$$1(s) = \frac{1}{2\pi i} \int_{-\infty}^{\infty} \frac{e^{iks}}{k} dk$$

Here the hook integral means integrate from $-\infty$ to $+\infty$, bypassing the singular point at the origin by a small semicircle from below. In effect, a spectrum analysis

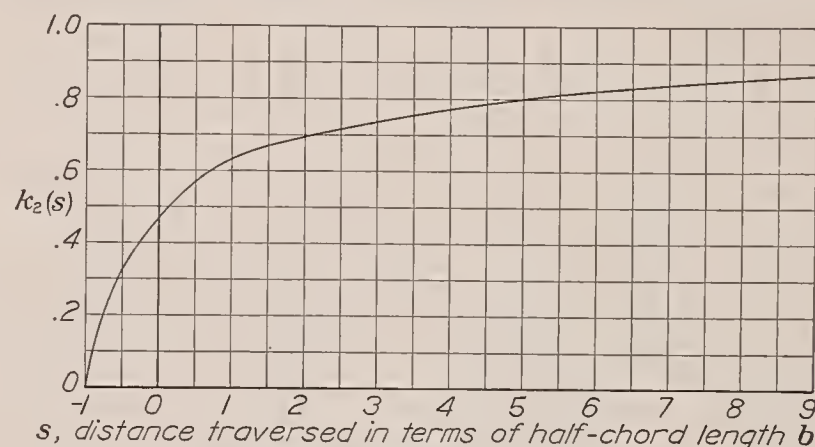


FIGURE 4.—The function $k_2(s)$ of Küssner.

of the unit jump function has been made as a limit of a sum of exponential terms. To each exponential term of vertical velocity there corresponds the lift given by multiplication with Theodorsen's function $C(k)$. Then,³ by addition

$$\begin{aligned} k_1(s) &= \frac{1}{2\pi i} \int_{-\infty}^{\infty} \frac{C(k)}{k} e^{iks} dk \\ &= 1 + \frac{1}{2\pi i} \int_{-\infty}^{\infty} \frac{C(k) - 1}{k} e^{iks} dk \quad [s > 0] \\ &= 0 \quad [s < 0] \end{aligned}$$

Separating $C(k)$ into $F(k) + iG(k)$ and noting that $C(-k) = F(k) - iG(k)$, there results

$$\begin{aligned} k_1(s) &= 1 + \frac{2}{\pi} \int_0^\infty \frac{G(k)}{k} \cos ks dk \\ &= \frac{2}{\pi} \int_0^\infty \frac{F(k)}{k} \sin ks dk \end{aligned}$$

which check equations (9) and (10) and hence also equations (7) and (8).

Küssner's function, $k_2(s)$.—Küssner has derived a function $k_2(s)$ (fig. 4), which gives the lift on an airfoil as it penetrates into a sudden vertical-gust region without change in direction. If the change in vertical

³ The relation between $C(k)$ and $k_1(s)$ is expressed in the operational calculus as $C(k)1(s) = k_1(s)$, where ik is the operator d/ds and the expression is interpreted "the function $C(k)$ operating on the unit jump function $1(s)$."

velocity in the gust region is w (assumed constant), the change in lift as the airfoil leading edge penetrates the gust region is

$$L = 2\pi b \rho v w k_2(s) \quad (11)$$

Note that the function $k_2(s)$ is defined for $s > -1$, and is 0 for $s < -1$, i. e., before the leading edge has penetrated the gust region.

In order to obtain the relation of $k_2(s)$ to $k_1(s)$, note that the operational equivalent of $k_2(s)$ (in the same sense⁴ that $C(k)1(s) = k_1(s)$) is $C(k) [J_0(k) + iJ_1(k)]$ (reference 3, p. 420). This latter function describes the steady-state lift due to circulation on an airfoil moving with uniform velocity v and whose vertical velocity is oscillating sinusoidally but progressing in the form of waves from point to point, i. e., the vertical velocity is of the form

$$w_0 e^{i(\omega t + kx)} = w_0 e^{ik(s+x)}$$

where x defines any point of the airfoil measured from the center.

Then, the following relations hold, writing σ for $s+1$,

$$\begin{aligned} C(k) 1(\sigma) &= k_1(\sigma) \\ [J_0(k) + iJ_1(k)] 1(\sigma) &= S(\sigma) = \frac{1}{2} + \frac{1}{\pi} \arcsin(\sigma - 1) \\ &\quad + \frac{1}{\pi} \sqrt{1 - (\sigma - 1)^2} \quad [0 < \sigma < 2] \\ &= 1 \quad [\sigma > 2] \end{aligned}$$

The second relation is given by Nielsen in "Handbuch der Cylinderfunctionen," page 197. By superposition, there results for the combined operator

$$C(k) [J_0(k) + iJ_1(k)] 1(\sigma),$$

$$k_2(s) = \int_0^\sigma k_1(\sigma - \lambda) S'(\lambda) d\lambda$$

where

$$\begin{aligned} S'(\lambda) &= \frac{1}{\pi} \sqrt{\frac{2-\lambda}{\lambda}} \quad [0 < \lambda < 2] \\ &= 0 \quad [\lambda > 2] \end{aligned}$$

Hence,

$$\begin{aligned} k_2(s) &= \frac{1}{\pi} \int_0^\sigma k_1(\sigma - \lambda) \sqrt{\frac{2-\lambda}{\lambda}} d\lambda \quad [0 < \sigma < 2] \quad (12) \\ &= \frac{1}{\pi} \int_0^2 k_1(\sigma - \lambda) \sqrt{\frac{2-\lambda}{\lambda}} d\lambda \quad [\sigma > 2] \end{aligned}$$

or, expressed in terms of s ,

$$\begin{aligned} k_2(s) &= \frac{1}{\pi} \int_{-1}^s k_1(s - s_1) \sqrt{\frac{1-s_1}{1+s_1}} ds_1 \quad [-1 < s < 1] \\ &= \frac{1}{\pi} \int_{-1}^1 k_1(s - s_1) \sqrt{\frac{1-s_1}{1+s_1}} ds_1 \quad [s > 1] \end{aligned} \quad (12a)$$

The effect of an arbitrary gust function $w(\sigma)$ can be written directly by superposition ($\sigma = s+1$)

$$\frac{L}{2\pi b \rho v} = w(0)k_2(\sigma) + \int_0^\sigma k_2(\sigma_1) \frac{d}{d\sigma_1} w(\sigma - \sigma_1) d\sigma_1 \quad (13)$$

⁴ For a correction to an error in sign that exists in reference 3, p. 420, consult reference 5. The values of $k_2(s)$ here given therefore need to be modified; the corrected values, including the apparent-mass effect due to change of shape, are presented in reference 5.

The approximate expression $k_1(s) \cong 1 - \frac{2}{4+s}$ may be put into equation (12). Then (cf. table I),

$$\begin{aligned} k_2(\sigma) &\cong 2 \sqrt{\frac{2+\sigma}{4+\sigma}} - 1 \quad [\sigma > 2] \\ &\cong \frac{1}{\pi} \left[\sqrt{\sigma(2-\sigma)} - \cos^{-1}(1-\sigma) \right. \\ &\quad \left. + 4 \sqrt{\frac{2+\sigma}{4+\sigma}} \sin^{-1} \sqrt{\frac{\sigma(2+\sigma)}{8}} \right] \quad [\sigma < 2] \end{aligned} \quad (12b)$$

CONCLUDING REMARKS

It has been shown that the functions $C(k)$ and $k_1(s)$ are of considerable significance in the theory of non-stationary flows. To a certain extent, the results are formal since many of the analytic properties of these functions lie hidden in their complicated structures. Further mathematical studies of the function $C(k)$ when k is a complex variable would appear to be desirable, since this function is associated with the lift due to a general damped sinusoidal motion of the airfoil. In many problems in transient flows, it is therefore of value to employ the approximate expressions for $C(k)$, $k_1(s)$, and $k_2(s)$ given and thus to obtain quickly a simpler perspective of the problem.

LANGLEY MEMORIAL AERONAUTICAL LABORATORY,
NATIONAL ADVISORY COMMITTEE FOR AERONAUTICS,
LANGLEY FIELD, VA., March 28, 1938.

REFERENCES

1. Wagner, Herbert: Über die Entstehung des dynamischen Auftriebes von Tragflügeln. Z. f. a. M. M., Bd. 5, Heft 1, Feb. 1925, S. 17-35.
2. Theodorsen, Theodore: General Theory of Aerodynamic Instability and the Mechanism of Flutter. T. R. No. 496, N. A. C. A., 1935.
3. Küssner, H. G.: Zusammenfassender Bericht über den instationären Auftrieb von Flügeln. Luftfahrtforschung, Bd. 13, Nr. 12, 20. Dez. 1936, S. 410-424.
4. Bush, V.: Operational Circuit Analysis. John Wiley & Sons, Inc., 1929.
5. Garrick, I. E.: On Some Fourier Transforms in the Theory of Nonstationary Flows. Proc. Fifth International Congress of Applied Mechanics, Cambridge, Mass., John Wiley and Sons, 1939.

TABLE I.—VALUES OF $k_1(s)$ AND $k_2(s)$

s	$^1 k_1(s)$	$^2 k_1(s)_{\text{approx.}}$	$^3 k_2(s)$	$^4 k_2(s)_{\text{approx.}}$
≤ -1	0	0	0	0
$-.5$	0	0	.328	.328
0	.5000	.5000	.468	.468
.5	.5557	.5556	.568	.568
1	.6006	.6000	.634	.633
2	.6693	.6667	.693	.690
3	.7195	.7143	.737	.732
4	.7582	.7500	.772	.764
5	.7880	.7778	.799	.789
6	.8125	.8000	.822	.809
7	.8325	.8182	.840	.826
8	.8485	.8333	.855	.840
9	.8625	.8461	.868	.852
10	.8745	.8572	.877	.860
20	.9321	.9167	.934	.918
∞	1.0000	1.0000	1.000	1.000

¹ Values of $k_1(s)$ taken from references 1 and 3.

² From equation (1a).

³ Values of $k_2(s)$ calculated from equation (12).

⁴ From equation (12b).

REPORT No. 630

A FLIGHT COMPARISON OF CONVENTIONAL AILERONS ON A RECTANGULAR WING AND OF CONVENTIONAL AND FLOATING WING-TIP AILERONS ON A TAPERED WING

By H. A. SOULÉ and W. GRACEY

SUMMARY

Flight tests comparing the relative effectiveness of conventional ailerons of the same size on wings of rectangular and tapered plan forms were made with a Fairchild 22 airplane. Information is included comparing conventional and floating wing-tip ailerons on a tapered wing. The results showed that the conventional ailerons were somewhat more effective on the tapered than on the rectangular wing. The difference, however, was so small as to be imperceptible to the pilots. The floating wing-tip ailerons were only half as effective as the conventional ailerons and, for this reason, were considered unsatisfactory.

INTRODUCTION

At the request of the Matériel Division of the Army Air Corps, the N. A. C. A. has conducted a series of flight tests to compare the relative effectiveness of conventional ailerons of a given size on wings having rectangular and tapered plan forms. Earlier wind-tunnel tests are reported in references 1, 2, and 3. The flight tests were made with two Fairchild 22 airplanes. The two wings used in the investigation were of the same area and span. One had a rectangular plan form with semicircular tips and the other a taper ratio of 2:1. The conventional ailerons with which these wings were fitted had the same plan-form dimensions and were arranged during the flight tests to have approximately the same deflections.

The tests consisted of the determination of the effectiveness of the ailerons (1) for different degrees of deflection at two air speeds, and (2) for full deflection at various air speeds throughout the speed range of the airplane. The comparisons are based on the maximum measured rolling accelerations and velocities, the observed yawing action, and the computed rolling-moment coefficients.

In addition to being fitted with the conventional ailerons, the tapered wing was equipped with detachable wing tips that could be replaced by floating wing-tip ailerons. The floating wing-tip ailerons were also tested during the investigation and were compared with the conventional ailerons on the same wing.

AIRPLANES AND WINGS

The Fairchild 22 airplanes used in the investigation are shown in figures 1 and 2. The rectangular wing, which had the same plan form as the standard wing for the Fairchild 22 airplanes, had a span of 32 feet 10 inches, a chord of 5 feet 6 inches, an area of 171 square feet, and an N. A. C. A. 2R₁₂ airfoil section. The conventional ailerons with which this wing was fitted had a span of 13 feet 3 $\frac{3}{16}$ inches (81 percent $b/2$) and a chord of 12 inches (18 percent c). They were

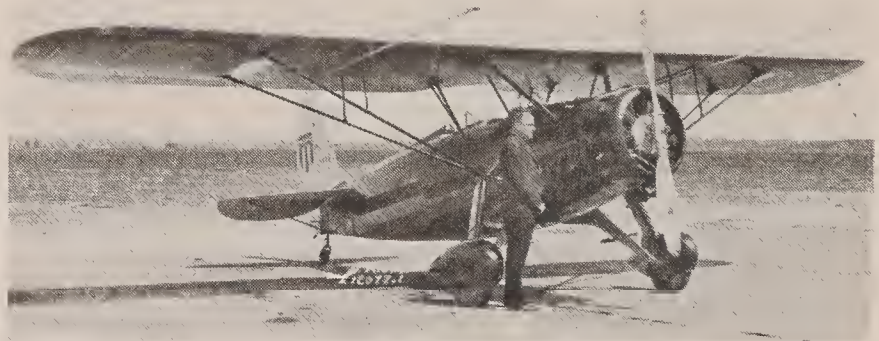


FIGURE 1.—Fairchild 22 airplane used for tests of conventional ailerons on a rectangular wing.

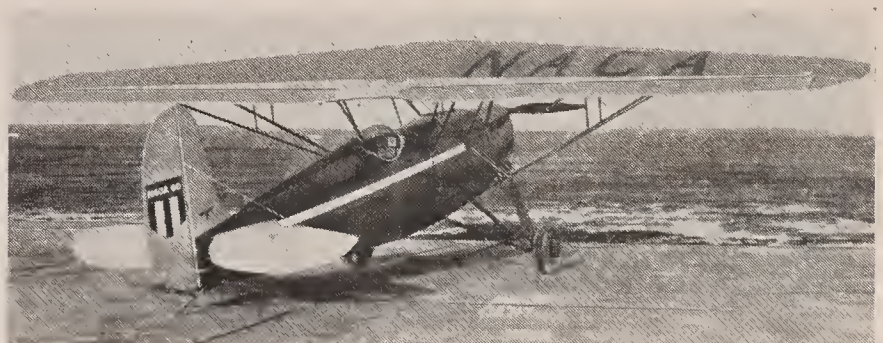


FIGURE 2.—Fairchild 22 airplane used for tests of conventional ailerons on a tapered wing.

operated differentially, having a maximum upward deflection of 17° and a downward deflection of 9°.

The tapered wing (figs. 2 to 5) had the same span and area as the rectangular wing. It had a 2:1 taper ratio with a straight trailing edge. The trailing edge was made straight so that the aerodynamic centers of the tapered and rectangular wings could be located at the same point relative to the fuselage while still permitting access to the rear cockpit. In external dimensions the tapered wing was comparable with an in-

ternally braced wing although it was supported externally for the tests. The airfoil section varied from an N. A. C. A. 2218 section at the root to an N. A. C. A. 2209 section at 15 feet from the axis of symmetry. The

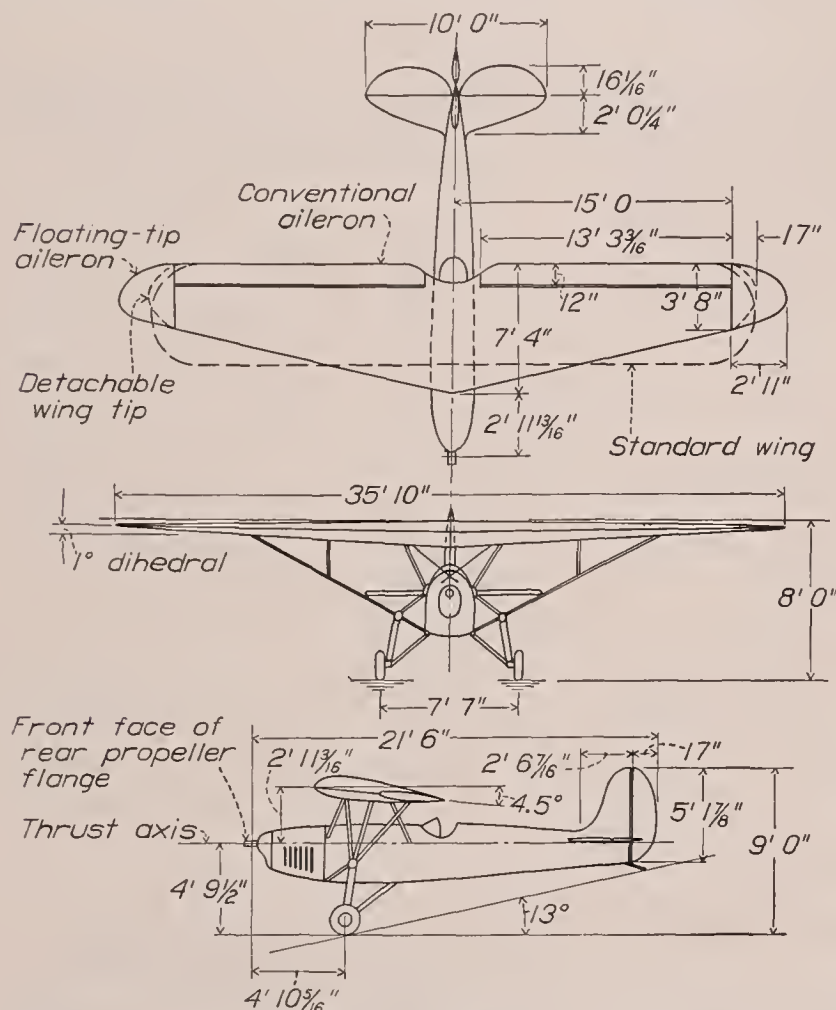


FIGURE 3.—Three-view drawing showing the installation of the tapered wing on a Fairchild 22 airplane.

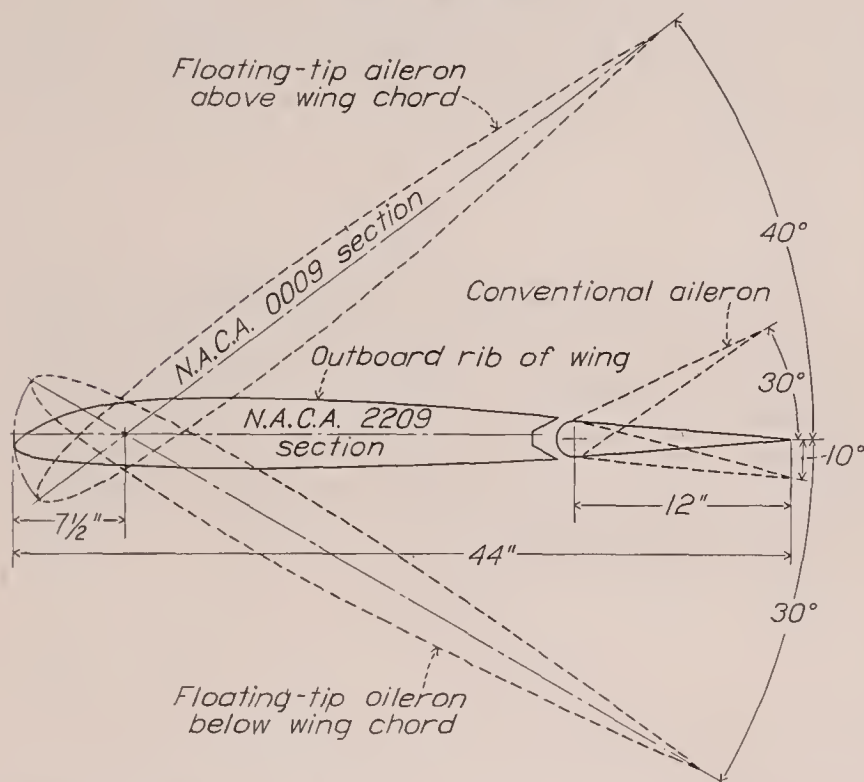


FIGURE 4.—Section through tapered wing at outboard end of conventional aileron.

wing tips were rounded. The chord varied from 7 feet 4 inches at the root to 3 feet 8 inches at the 15-foot station.

The conventional ailerons on this wing had the same span and chord and were located in the same position relative to the wing span as were the conventional

aileron on the rectangular wing. They were operated differentially and, for the tests, were limited so that the maximum upward deflection was 18° and the downward deflection 9° . Owing to differences in the aileron-operating mechanism, the maximum aileron deflections on the tapered wing were obtained with a stick deflection of 14° ; whereas, with the rectangular wing, the maximum deflections were obtained with a stick deflection of 20° . The plan view in figure 3, on which the rectangular wing has been drawn in outline, gives a direct comparison of the wings and the conventional-aileron installation.



(a) Installation of fixed wing tip.



(b) Installation of floating wing-tip aileron.

FIGURE 5.—View of right wing.

For the installation of the floating wing-tip ailerons, the fixed tips of the tapered wing outboard of the 15-foot station were removed and the conventional ailerons were locked in their neutral position. The floating wing-tip ailerons had a symmetrical N. A. C. A. 0009 airfoil section at the root. Each aileron had an area of 7.9 square feet and a span of 35 inches; the wing area and the span with these ailerons were 177 square feet and 35 feet 10 inches, respectively. These ailerons were statically balanced about a hinge axis 17 percent back of their leading edges and were permitted to float freely between limiting positions of 40° up and 30° down. The ailerons could be deflected relative to one another to obtain a maximum angular difference of 30° with a stick movement of 24° .

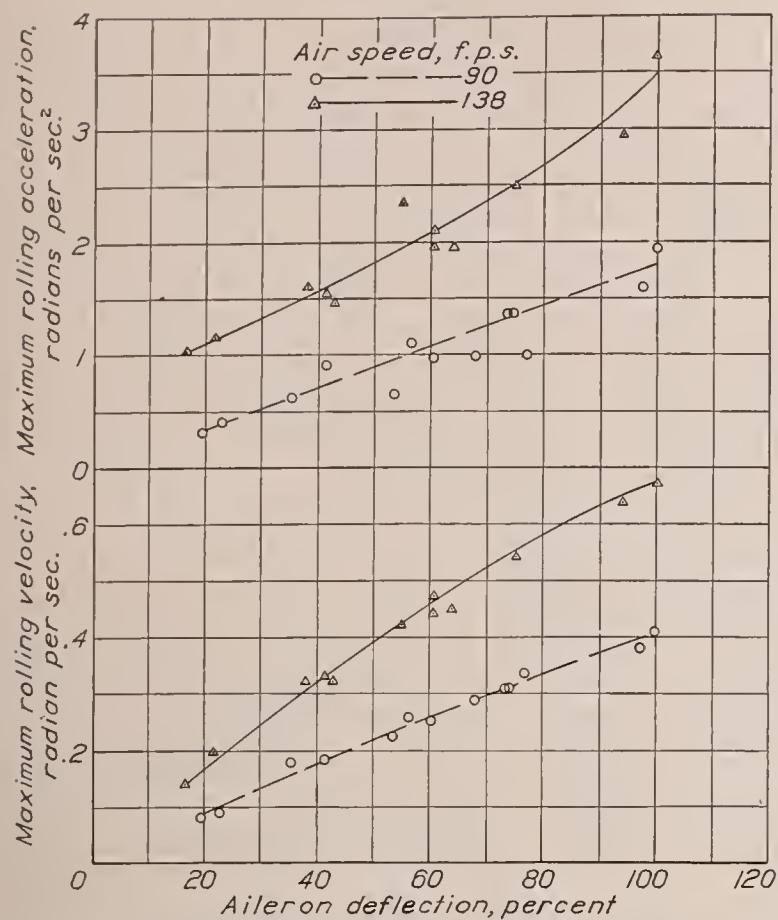


FIGURE 6.—Variation of the maximum rolling velocities and accelerations with deflection of conventional ailerons on the rectangular wing.

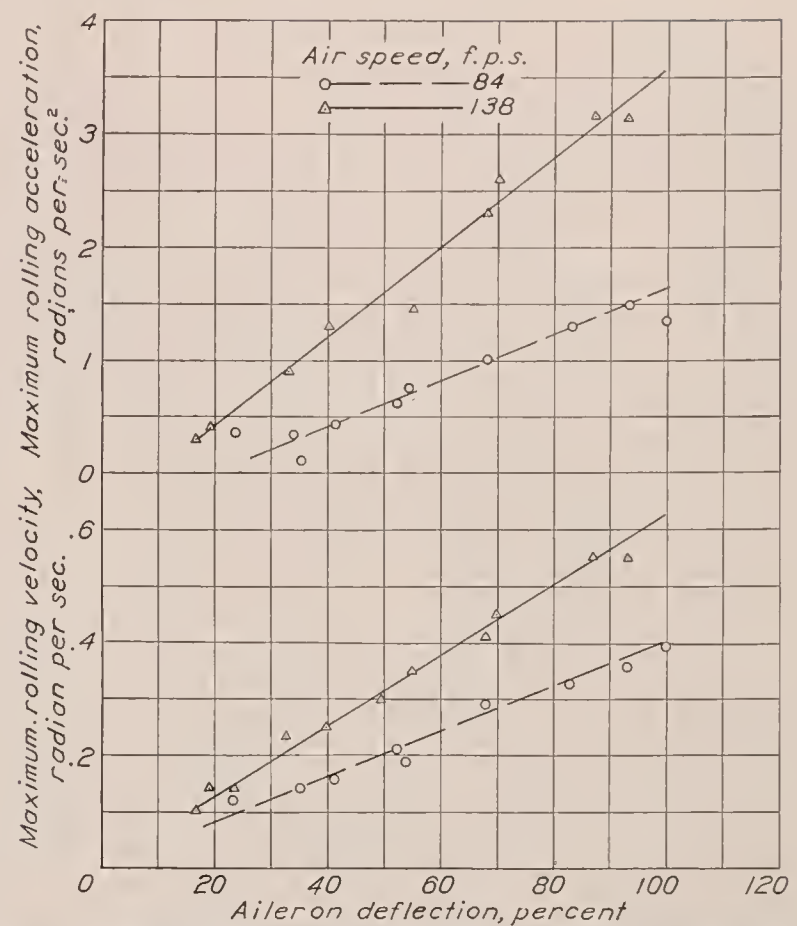


FIGURE 7.—Variation of the maximum rolling velocities and accelerations with deflection of conventional ailerons on the tapered wing.

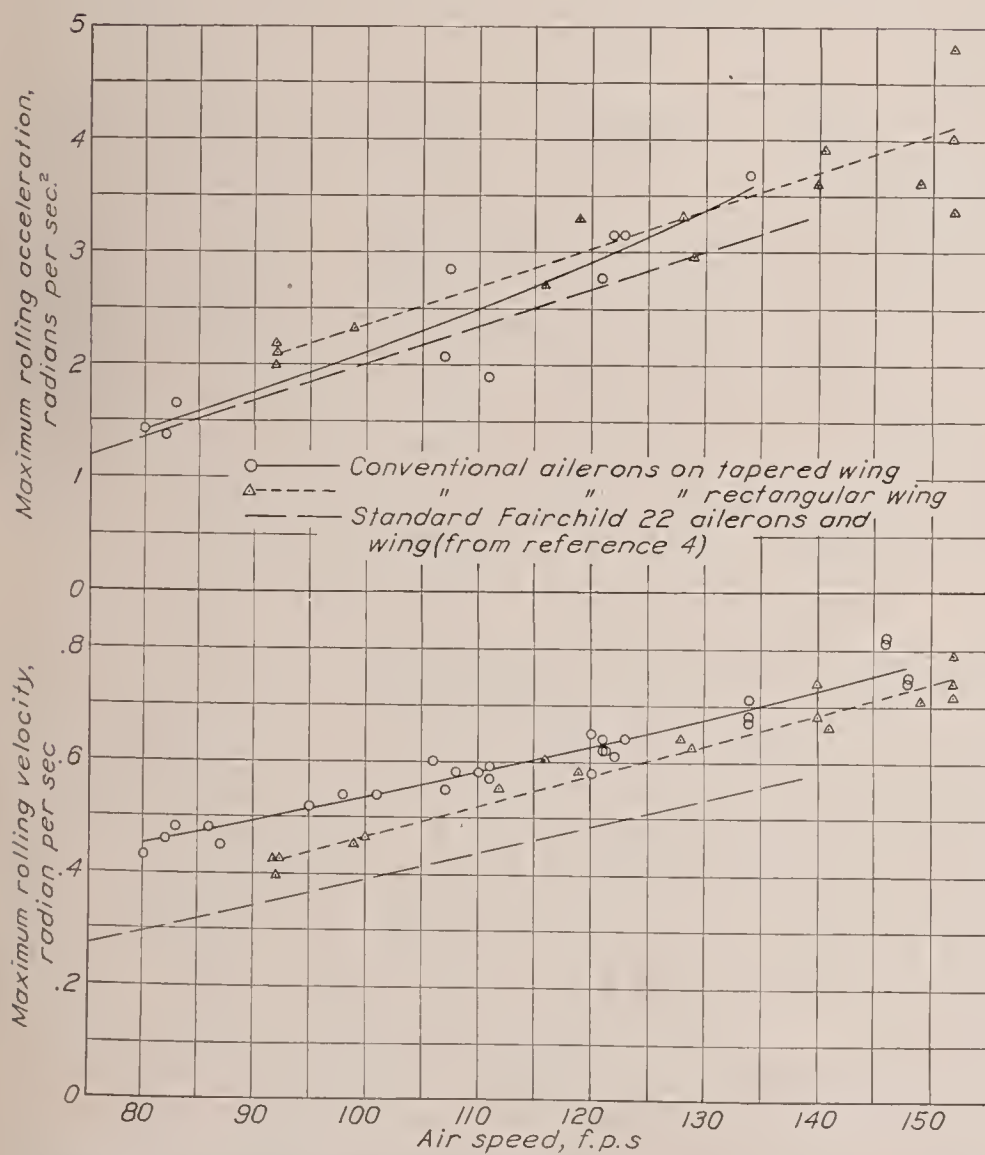


FIGURE 8.—Comparison of the maximum rolling velocities and accelerations with full deflection of conventional ailerons on the rectangular and the tapered wings.

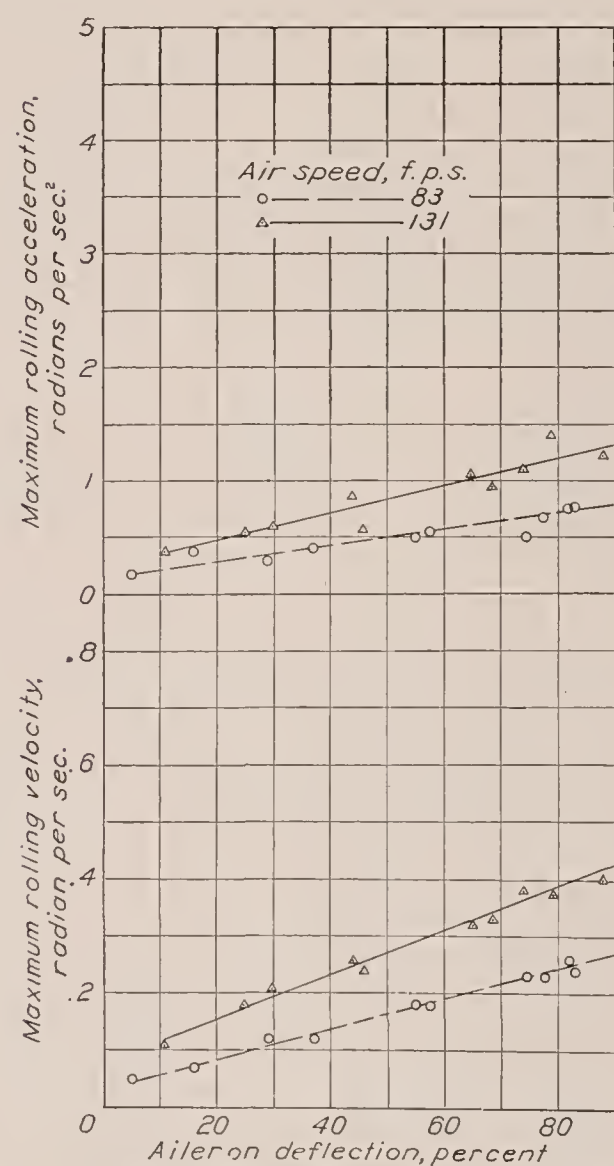


FIGURE 9.—Variation of the maximum rolling velocities and accelerations with deflection of floating wing-tip ailerons on the tapered wing.

TESTS AND RESULTS

With each of the lateral-control systems, two series of tests were made. In one series, the ailerons were abruptly moved to their maximum deflections during steady flight at various speeds throughout the flight range. In the other series, the amount the ailerons were moved was varied at each of two air speeds, one in the high-speed and the other in the low-speed range. Each series of tests was made in gliding flight for only right deflections of the stick. Records were made of

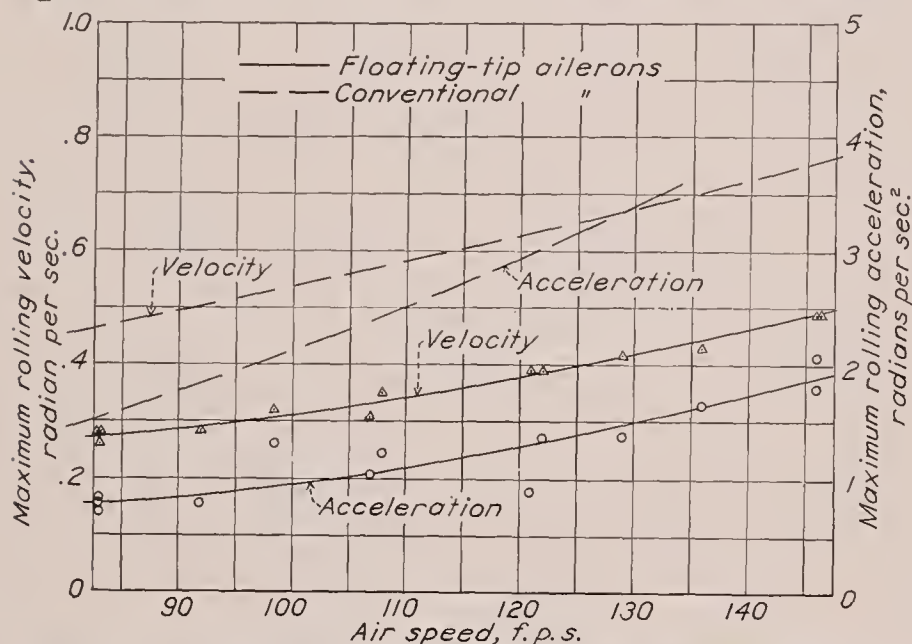


FIGURE 10.—Comparison of the maximum rolling velocities and accelerations with full deflection of the conventional and floating wing-tip ailerons on the tapered wing.

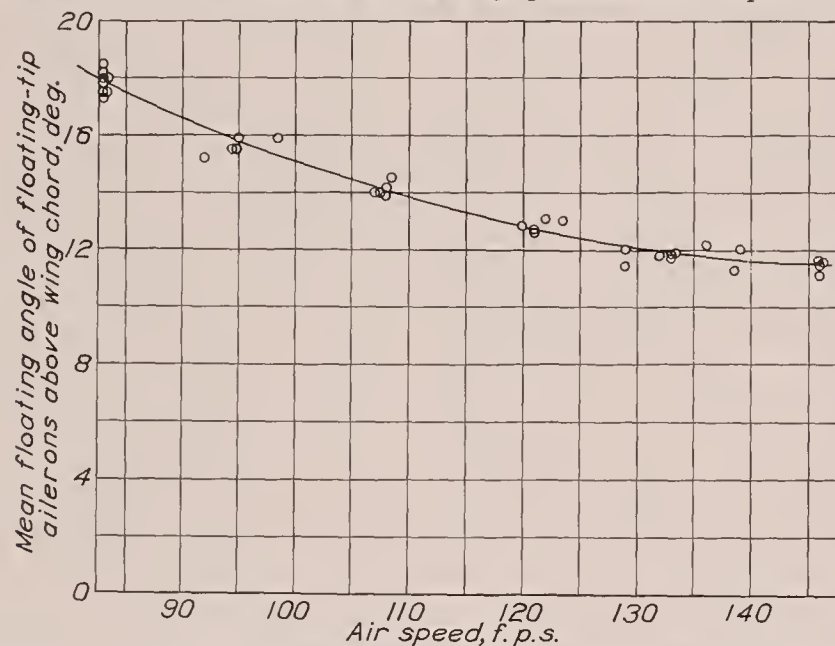


FIGURE 11.—Variation of the mean floating angle of the wing-tip ailerons with speed.

the initial air speed, the amount the ailerons were moved, and the angular velocities of the airplane in rolling and yawing. These measurements were supplemented by pilots' observations of the control action and control force.

The records were inspected for any lag or sluggishness in the response of the airplane to the aileron movement and for the direction of the initial yawing velocity. From the records of the rolling velocity, the maximum rate of roll resulting from a given aileron movement was directly obtained. The maximum angular accelerations in roll were obtained by differentiation of the rolling-velocity records.

The results of the measurements are presented in figures 6 to 12. Figures 6 and 7 show the results of the partial-deflection tests of the conventional ailerons on the rectangular and tapered wings. The aileron-deflection scales of these figures are based on the differences between the angles of the up and down ailerons. For the three aileron systems tested in the investigation, the aileron deflections were approximately proportional to the deflections of the control stick. Figure 8 compares the rolling effectiveness for full deflection

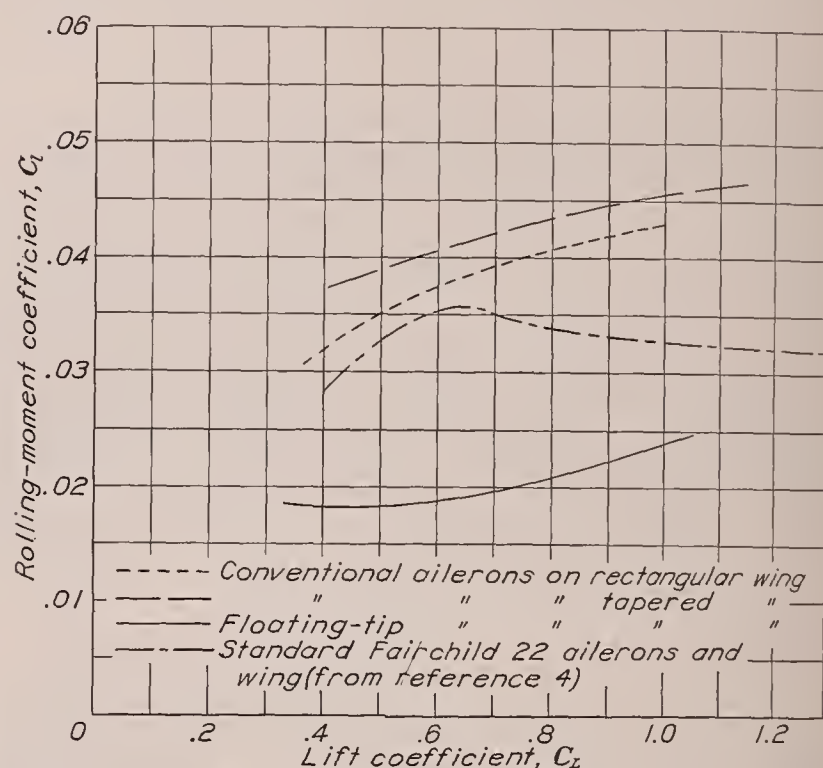


FIGURE 12.—Comparison of the rolling-moment coefficients of the lateral-control systems tested.

of the ailerons on the two wings. Also shown in this figure are the results of tests of the standard wing for the Fairchild 22 airplane. These results were used as a basis for comparison of the different types of lateral controls treated in reference 4. Data similar to those given in figures 6 and 8 for the conventional ailerons are given in figures 9 and 10 for the floating wing-tip ailerons. The mean floating angles of the wing-tip ailerons at various speeds in steady flight are shown in figure 11.

Figure 12 has been prepared to compare the lateral-control systems on the basis of the rolling-moment coefficients. The method of computation used in the preparation of this figure involves a correction of the measured acceleration to zero rate of roll so that the computed coefficients are comparable with those obtained from wind-tunnel tests. (See reference 4 for details of method.) The moments of inertia of the airplanes about the X body axes were required for the computations. The moment of inertia of the airplane with the rectangular wing was 707 slug-feet²; that for the airplane with the tapered wing was 766 slug-feet² as flown for tests of the conventional ailerons and 1,018 slug-feet² as flown for the tests of the floating wing-tip ailerons.

DISCUSSION

COMPARISON OF CONVENTIONAL AILERONS ON RECTANGULAR AND TAPERED WINGS

The rolling effectiveness of the conventional ailerons on the rectangular and the tapered wings may be compared on the basis of the information given in figures 8 and 12. Figure 8 shows that the maximum rolling accelerations given by the ailerons on the two wings were approximately the same. The maximum rolling velocities attained were slightly greater with the tapered than with the rectangular wing. The difference in the rolling velocities was of a magnitude sufficient to make a difference of 2° to 3° out of approximately 25° in the angle of bank attained in 1 second after the control movement. This difference was not discernible to the pilots making the tests, who reported that the rolling effectiveness was equally good with either wing.

The rolling-moment coefficients given in figure 12 also showed that the conventional ailerons, when installed on the tapered wing, are somewhat superior to the same ailerons when installed on the rectangular wing. The improvement varied slightly with lift coefficient and was of the order of 5 percent at the higher lift coefficients, where normally the greatest difficulty is met in obtaining adequate control. This result is in agreement with the wind-tunnel tests of reference 1 and was indicated by an analysis of the two aileron installations made in accordance with the procedure given in reference 3.

With both wings, the ailerons showed a normal variation of effectiveness with control deflection (figs. 6 and 7). No lag or sluggishness was noted in the response of the airplanes to control movements. The yawing action with both wings was small and adverse and was slightly greater with the tapered than with the rectangular wing. This result is at variance with the wind-tunnel tests of reference 1 and with the theoretical treatment of reference 3, both of which indicate that the tapered wing should have the smaller yawing action. No analysis was made regarding this discrepancy because the yawing action was relatively small with either wing. No comparison was made of the control forces with the two different wings because of the difference in the mechanical advantage for the two control systems. From the fact that the stick travel for the tapered wing was only two-thirds that for the rectangular wing, it was expected that the control force for the tapered wing would be of the order of one and one-half times that for the rectangular wing. The pilots' reports were in agreement with this rough analysis.

COMPARISON OF CONVENTIONAL AND FLOATING WING-TIP AILERONS ON THE TAPERED WING

A comparison of the rolling effectiveness of the conventional and the floating wing-tip ailerons on the tapered wing is given by figures 10 and 12. These results show the floating wing-tip ailerons to be only about one-half as effective as the conventional ailerons. Observations

made of the control effectiveness at and beyond the stall showed that, although the airplane could not be controlled laterally at the stall with either of the ailerons, some control effectiveness was retained beyond the stall with the floating wing-tip ailerons but not with the conventional ailerons.

Aside from the low rolling effectiveness of the wing-tip ailerons, their behavior was normal. The results of the partial-deflection tests given in figure 9 show that the variation of control effectiveness with aileron deflection is nearly linear. No lag or sluggishness was recorded or observed by the pilots. A small positive yawing action was noted. The pilots estimated that the stick forces with the wing-tip ailerons were about one-quarter of those for the conventional ailerons on the rectangular wing.

It is appreciated that the area of the wing-tip ailerons could be considerably increased in size with an accompanying increase in effectiveness before the stick forces approach those of conventional ailerons. (See reference 5.) This increase in aileron area could not be accomplished, however, without unduly increasing the span and weight of the wing. It is believed that the wing-tip ailerons tested are the largest size practicable for the wing.

CONCLUSIONS

1. The effectiveness of the conventional ailerons was slightly greater on the tapered than on the rectangular wing but the difference was not sufficient to be appreciated by the pilots.
2. The floating wing-tip ailerons were considered unsatisfactory because their rolling action was approximately half that for the conventional ailerons.

LANGLEY MEMORIAL AERONAUTICAL LABORATORY,
NATIONAL ADVISORY COMMITTEE FOR AERONAUTICS,
LANGLEY FIELD, VA., *October 27, 1937.*

REFERENCES

1. Weick, Fred E., and Wenzinger, Carl J.: Wind-Tunnel Research Comparing Lateral Control Devices, Particularly at High Angles of Attack. IX. Tapered Wings with Ordinary Ailerons. T. N. No. 449, N. A. C. A., 1933.
2. Wenzinger, Carl J.: Wind-Tunnel Investigation of Tapered Wings with Ordinary Ailerons and Partial-Span Split Flaps. T. R. No. 611, N. A. C. A., 1937.
3. Weick, Fred E., and Jones, Robert T.: Résumé and Analysis of N. A. C. A. Lateral Control Research. T. R. No. 605, N. A. C. A., 1937.
4. Soulé, H. A., and McAvoy, W. H.: Flight Investigation of Lateral Control Devices for Use with Full-Span Flaps. T. R. No. 517, N. A. C. A., 1935.
5. Weick, Fred E., and Harris, Thomas A.: Wind-Tunnel Research Comparing Lateral Control Devices, Particularly at High Angles of Attack. XI. Various Floating Tip Ailerons on Both Rectangular and Tapered Wings. T. N. No. 458, N. A. C. A., 1933.

REPORT No. 631

AIRFOIL SECTION CHARACTERISTICS AS APPLIED TO THE PREDICTION OF AIR FORCES AND THEIR DISTRIBUTION ON WINGS

By EASTMAN N. JACOBS and R. V. RHODE

SUMMARY

The results of previous reports dealing with airfoil section characteristics and span load distribution data are coordinated into a method for determining the air forces and their distribution on airplane wings. Formulas are given from which the resultant force distribution may be combined to find the wing aerodynamic center and pitching moment. The force distribution may also be resolved to determine the distribution of chord and beam components. The forces are resolved in such a manner that it is unnecessary to take the induced drag into account.

An illustration of the method is given for a monoplane and a biplane for the conditions of steady flight and a sharp-edge gust. The force determination is completed by outlining a procedure for finding the distribution of load along the chord of airfoil sections.

INTRODUCTION

This report originated in a request of the Bureau of Air Commerce, Department of Commerce, for a coordinated system of applying airfoil section data to the determination of wing forces and their distribution.

The system presented herein yields, within the limitations of our present knowledge of aerodynamics, a general solution of the resultant wing forces and moments and their distribution. For the sake of completeness and facility in use, the report contains a table of the important section parameters for many commonly used sections and all other necessary data required to solve the most practical design problems coming within the scope of the system.

Although the usefulness of the system extends into several phases of airplane design, its application to structural design is illustrated by following through a wing loading condition corresponding to that specified in reference 1.

Two basic principles underlie the system employed. First, a force coefficient is treated as the independent variable, thus eliminating, as far as possible, the angle of attack; and second, the forces are derived throughout in terms of certain basic parameters of the airfoil section, which are tabulated for each airfoil section. The method followed then builds up the forces progressively from simple combinations of certain basic forces and simple formulas involving the basic airfoil section pa-

rameters. As the forces are thus built up, they are resolved into any convenient components. This method also has another important advantage in that the induced drag, which is really only a component of the local lift at each section, may be entirely eliminated from the analysis.

In some problems it is desirable to know the location of the aerodynamic center of the wing and the pitching-moment coefficient about this center in order to construct the balance diagram of the complete airplane. Methods are therefore given for determining these two properties. For problems in which the aerodynamic center and the pitching moment are not required, a direct solution of the forces and force distribution can be made.

BASIC CONSIDERATIONS

The forces on a wing may be considered to be functions of the characteristics of the airfoil sections and of the spanwise distribution of lift. At a given section lift coefficient, the resultant air force and moment on the section are, according to wing theory, assumed to be independent of all geometric properties of the wing except the section shape; moreover, the forces and moments acting on any individual section may be considered to be independent of adjacent sections or of other characteristics of the wing, except as they affect the lift distribution and thus the local lift coefficient at that section.

The problem is thus divided into two parts: First, the determination of the spanwise lift distribution; and, second, the determination of the corresponding forces and moments at each section and the summation of these quantities to obtain the corresponding forces and moments for the entire wing. The spanwise lift distribution is obtained in terms of values of the local section lift coefficient c_{l_0} for a number of sections distributed along the span. The subscript zero is used to distinguish this section lift coefficient, perpendicular to the local relative wind at the section, from the lift coefficient c_l perpendicular to the relative wind at a great distance from the wing. The lower-case letters used for these coefficients have been chosen to distinguish the lift coefficient for a section ($c_l = dL/qcdy$) from the usual lift coefficient for the wing, C_L .

In order to permit easy reference, the symbols used in the text, the figures, and the tables are grouped in appendix C.

For many purposes, it is convenient to express the air forces in terms of components along two axes fixed with respect to the airplane rather than as the usual components, lift and drag. This resolution is conveniently accomplished from the c_{l_0} values, when the profile drag and other fundamental characteristics of the airfoil section are taken into account, by means of simple formulas involving parameters given for each airfoil section in a table of airfoil characteristics. This method has an important advantage in that the induced drag, which is really only a component of the c_{l_0} at each section, is entirely eliminated from the analysis.

For the purpose of determining the lift distribution corresponding to the c_{l_0} values along the span, the lift load along the span is considered as being made up of two independent parts that will be referred to as the "basic lift distribution" and the "additional lift distribution." The basic lift distribution is represented by the c_{l_0} distribution along the span when the total wing lift is zero. This basic lift distribution, which is the distribution arising by virtue of aerodynamic twist, may be considered to exist unaltered as the lift and angle of attack are changed. The additional lift distribution, as the name implies, represents the distribution of additional lift associated with changing the angle of attack. Wing theory indicates that, as long as the airfoil sections of the wing are working within a range of normal lift-curve slope, the form of the additional lift distribution is the same at all lift coefficients and is independent of wing twist, of aileron or flap displacements, and of other characteristics that affect only the basic lift distribution. Experiment shows that this deduction is approximately correct for wings with well-rounded tips. For such wings, the additional lift distribution is given as a function of the plan form and aspect ratio in terms of the additional lift coefficients $c_{l_{a1}}$, that is, the section additional lift coefficients for a wing lift coefficient of 1. The lift distribution for any wing is then found in terms of the wing lift coefficient C_L , the basic lift coefficient c_{l_b} , and the additional lift coefficient $c_{l_{a1}}$

$$c_{l_0} = c_{l_b} + C_L c_{l_{a1}} \quad (1)$$

GENERAL PROCEDURE

MONOPLANE

It is advisable first to choose a backward fore-and-aft reference axis x usually parallel to the reference axis, or thrust line, of the airplane and an upward z axis perpendicular to it. (See fig. 1.) Upward and backward air forces and distances are thus considered positive. Air-force components along these axes are then expressed at each section of the wing by

$$dX = c_x q c dy \quad (2)$$

and

$$dZ = c_z q c dy \quad (3)$$

where X and Z are the components of air load along the axes, and c_x and c_z are determined from c_{l_0} and the known characteristics and attitude of each airfoil section. The pitching moment about the origin contributed by each section is

$$dM = c_{m_{a.c.}} q c^2 dy + c_x q c z dy - c_z q c x dy \quad (4)$$

where x and z are distances measured from the origin to the aerodynamic center of the airfoil section (see table I and appendix B) and the signs of the terms are so taken that stalling moments are positive.

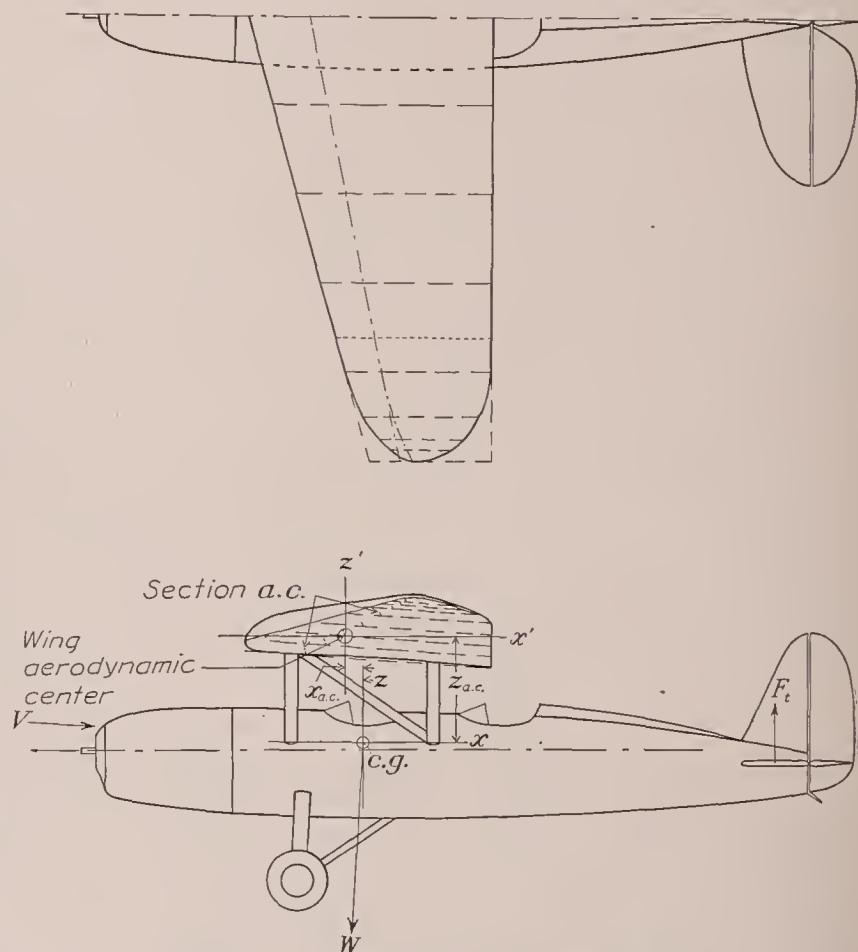


FIGURE 1.—Airplane drawing and balance diagram.

Thus far the origin has been arbitrarily chosen. If, with this arbitrarily chosen origin, the coordinates $x_{a.c.}$ and $z_{a.c.}$ of the aerodynamic center of the entire wing (fig. 1) are found, the origin of coordinates may then be moved to this point and from equation (4) there may be determined a value of $M_{a.c.}/q$ that has sensibly the same value for all flight conditions.

Aerodynamic center and additional lift distribution.—For the purpose of finding the aerodynamic center of the wing, it is necessary to consider only the additional distribution. In fact, the aerodynamic center of the wing may be considered as the centroid of all the additional loads. For wings with linear taper and rounded tips, values of L_a , giving the load distribution for $C_L=1$, may be found from table II for various sections along the span. The values of L_a were derived as outlined in reference 2. The corresponding values of $c_{l_{a1}}$ for various sections along the span are found from the relation $c_{l_{a1}} = \frac{L_a S}{cb}$. The corresponding values of c_{d_0} at each

section are calculated using the method indicated in figure 2 or, if the profile-drag polar curve for the section is available, they may be read from it. Then

$$c_{xa1} = c_{d0} \cos \theta_{za} - c_{la1} \sin \theta_{za} \quad (5)$$

and

$$c_{za1} = c_{la1} \cos \theta_{za} + c_{d0} \sin \theta_{za} \quad (6)$$

in which $\theta_{za} = \frac{c_{la1}}{a_0} + \alpha_{l_0} - i$; a_0 , the section lift-curve

slope, and α_{l_0} , the angle of attack of zero lift, are given in table I; and i is the incidence of the chord at each section with respect to the x axis.

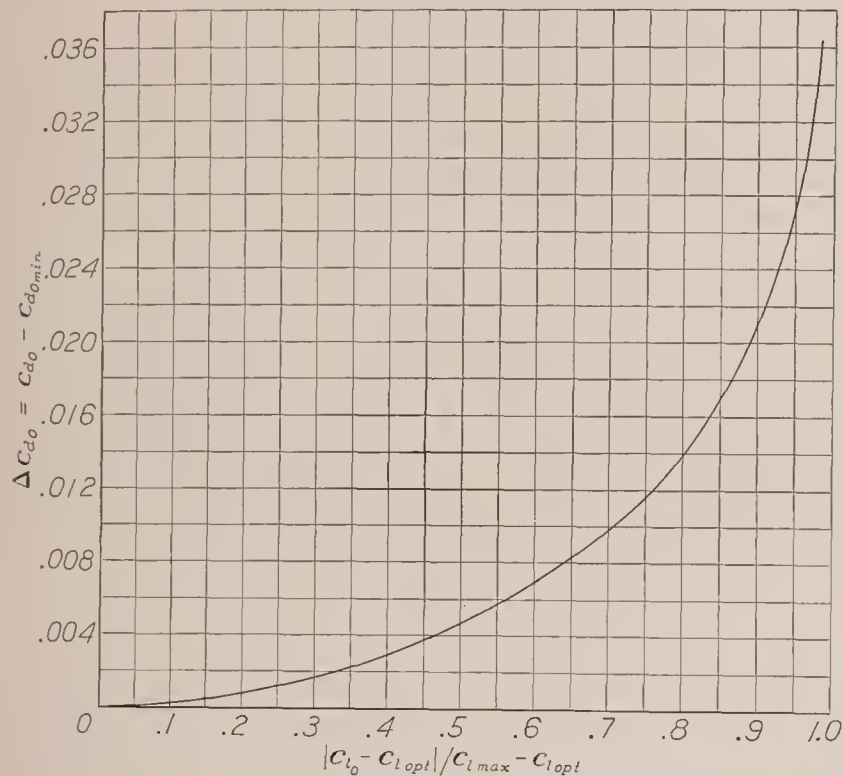


FIGURE 2.—Chart for the determination of the profile-drag coefficient c_{d0} at any lift coefficient c_{l_0} .

The next step is to plot $c_{xa1}c$, $c_{za1}c$, $c_{xa1}cz$, and $-c_{za1}cx$ against y and to fair curves through the plotted points. Twice the area under each curve from $y=0$ to $y=b/2$ is then, respectively: X_{a1}/q , Z_{a1}/q , M_{xa1}/q , M_{za1}/q . The coordinates of the aerodynamic center of the wing are then found

$$x_{a.c.} = \frac{-M_{za1}}{Z_{a1}} \quad (7)$$

$$z_{a.c.} = \frac{M_{xa1}}{X_{a1}} \quad (8)$$

Pitching moment about the wing aerodynamic center.—The additional load distribution for $C_L=1$ and the position of the aerodynamic center are now known. The next step is the determination of the basic load distribution (that corresponding to $C_L=0$) and from it the basic pitching moment or the aerodynamic pitching moment of the wing about the aerodynamic center. The basic distribution for wings with linear twist may be obtained from table III in terms of the load parameter L_b for a number of sections along the span. The method of deriving the L_b values is given in reference 2. When the wing has partial-span flaps, the basic distribution may be obtained from reference 3.

Following the system that was previously used, c_{l_b} values corresponding to the basic lift distribution are found for each section from $c_{l_b} = L_b \frac{ea_0 S}{cb}$, corresponding c_{d0} values determined, and c_{xb} and c_{zb} calculated from the formulas

$$c_{xb} = c_{d0} \cos \theta_{zb} - c_{l_b} \sin \theta_{zb} \quad (9)$$

$$c_{zb} = c_{l_b} \cos \theta_{zb} + c_{d0} \sin \theta_{zb} \quad (10)$$

where $\theta_{zb} = \frac{c_{l_b}}{a_0} + \alpha_{l_0} - i$.

Likewise are plotted curves of $c_{xb}cz'$ and $-c_{zb}cx'$, where z' and x' are the new coordinates of the section aerodynamic center from the aerodynamic center of the wing. The areas are then determined. In addition, another curve formed by plotting $c_{m_{a.c.}}c^2$ is drawn and the area determined. Twice these areas then give, respectively, $(M_{xb}/q)_{a.c.}$, $(M_{zb}/q)_{a.c.}$, and M_s/q . The desired wing pitching moment about the aerodynamic center is found from

$$\frac{M_{a.c.}}{q} = \left(\frac{M_{xb}}{q} \right)_{a.c.} + \left(\frac{M_{zb}}{q} \right)_{a.c.} + \frac{M_s}{q} \quad (11)$$

Lift distribution and total lift.—When the total wing lift or normal-force coefficients are known or specified by design conditions, the force distribution may be found immediately in terms of c_{l_0} values along the span from

$$c_{l_0} = c_{l_b} + C_L c_{l_{a1}}$$

For wings having well-rounded tips, the lift distribution may thus be found in terms of the c_{l_b} and $c_{l_{a1}}$ values previously determined. This method will give a good approximation of the actual lift distribution in such cases. When, for any reason, the tip loads are of critical importance, that is, if the wing is tapered less than 2:1 and has a tip blunter than semicircular, the lift distribution should be determined according to the method given in appendix A or reference 4. If the wing plan form departs from a straight taper, the lift distribution should be determined from suitable theoretical methods (references 2 and 3). In any event, the loads are represented by the c_{l_0} distribution and may then be resolved to give chord and beam components and moments.

In general, the wing lift coefficient C_L' for the steady-flight condition preceding an accelerated-flight condition will be first determined. After the tail load and, finally, the wing lift L are determined from the balance diagram for the steady-flight condition, the corresponding wing lift coefficient is found

$$C_L' = \frac{L}{qS} \quad (12)$$

The wing lift coefficient C_L for an accelerated-flight condition may then be determined. For example, it may be that the acceleration is produced by a sharp-edge gust, and the wing lift coefficient is determined by the simplified formula

$$C_L = C_L' + m \frac{U}{V} \quad (13)$$

where C_L' has just been found, U/V is the ratio of the gust velocity to the flight velocity, and m is the slope of the wing lift curve, which may be determined from the values of a_0 or m_0 , tabulated for the airfoil sections, by employing the method indicated later in figure 12.

The required lift distribution is then found in terms of the value of c_{l_0} at each section from

$$c_{l_0} = c_{l_b} + C_L c_{l_{a1}} \quad (14)$$

From these values of the lift coefficient at each section, the required coefficients representing the components of the air load may be computed and the total load components then determined as before by measuring the areas under curves representing $c_x q c$ and $c_z q c$. Some question exists, however, in regard to the values of c_{a_0} that should be used in the computation of c_x and c_z for the accelerated-flight condition.

Conditions and forces encountered instantaneously in accelerated-flight conditions after a suddenly changed angle of attack.—In an accelerated-flight condition the C_L value calculated from (13) and the c_{l_0} values from (14) may exceed the maximum lift coefficients. Such conditions are possible on entering a sharp-edge gust or in abrupt maneuvers owing to the considerable time required to accumulate the increased volume of reduced-energy air associated with the increased boundary-layer thickness or separated flow that will finally prevail at the increased angle of attack. Lift values should be based on the lift-curve slope extended without regard to the usual burbling. Such lift values are obtained simply by following the outlined procedure. The c_{a_0} values, however, deserve special consideration. The increasing profile-drag coefficients at the higher lift coefficients are likewise associated with a thickening boundary layer or a separating flow that will not occur at once when the angle of attack is suddenly increased.

The profile-drag coefficient for these transient conditions for a given lift, whether or not the lift exceeds the value given by wind-tunnel tests as the maximum, is undoubtedly less than the profile drag determined in the wind tunnel under steady conditions. The true value, however, is unknown and, in fact, a series of values increasing with time will exist. It may therefore be expedient in some cases to determine the force components on the wing by assuming that c_{a_0} retain its initial steady-flight value throughout the subsequent relative pitching motion of the wing. On the other hand, if it is desired to investigate the higher values that

the profile drag will later assume, c_{a_0} may be found in the usual way from the wind-tunnel data unless c_{l_0} is greater than $c_{l_{max}}$, in which case some value of c_{a_0} may be assumed. The value $c_{a_0} = 0.1$ is suggested.

The distribution of the resolved components and moments and the total wing components.—Values of c_{a_0} and c_{l_0} for the sections along the span having now been established, the distribution of the air-force components, given by values of c_x and c_z , may be found from

$$c_x = c_{a_0} \cos \theta_z - c_{l_0} \sin \theta_z \quad (15)$$

$$c_z = c_{l_0} \cos \theta_z + c_{a_0} \sin \theta_z \quad (16)$$

where

$$\theta_z = \frac{c_{l_0}}{a_0} + \alpha_{l_0} - i$$

The torsional moment contributed by each section about its aerodynamic center is simply

$$dM_{s.a.c.} = c_{m.a.c.} q c^2 dy \quad (17)$$

For some problems, components and moments with respect to axes in the wing may be desired rather than the components given by c_x and c_z with respect to the airplane. For example, "chord-truss" and "beam" components may be desired at each section. These components represented by c_c and c_b may be obtained from a slight modification of (15) and (16).

$$c_c = c_{a_0}(1 + \tan \theta_c \tan \phi) \cos \theta_c - c_{l_0}(1 - \cot \theta_c \tan \phi) \sin \theta_c \quad (18)$$

$$c_b = c_{l_0}(1 - \tan \theta_b \tan \phi) \cos \theta_b + c_{a_0}(1 + \cot \theta_b \tan \phi) \sin \theta_b \quad (19)$$

where

$$\theta_c = \frac{c_{l_0}}{a_0} + \alpha_{l_0} - i_c$$

$$\theta_b = \frac{c_{l_0}}{a_0} + \alpha_{l_0} - i_b$$

$$\phi = i_b - i_c$$

and i_c is the incidence of the section chord with respect to the chord-truss direction (plane of the drag truss) and i_b is the incidence of the section chord with respect to the perpendicular to the beam direction (the perpendicular to the spar web). The distribution of the chord and beam components C and B may then be calculated from

$$dC = c_c q c dy \quad (20)$$

$$dB = c_b q c dy \quad (21)$$

Torsional moments contributed by the sections about some axes in the wing other than the axes of the aerodynamic centers of the sections as, for example, the wing torsional axis, may be desired in some instances. The moment about the torsional axis M_T is found from

$$dM_T = c_{m.a.c.} q c^2 dy + c_c q c z_T dy + c_b q c x_T dy \quad (22)$$

where z_T is the distance of the torsional axis below the chord plane through the aerodynamic center and x_T is the distance of the torsional axis behind the beam plane through the aerodynamic center of the airfoil section.

The total forces and moments may then be found from the components or, more conveniently for Z and $M_{a.c.}$, from the summations previously made:

$$\frac{Z}{q} = \frac{Z_b}{q} + C_L \frac{Z_a}{q}$$

and $M_{a.c.}/q$ is a value obtained from (11). In order to find X/q , however, the c_x components should be summed.

Permissible approximations.—For the practical application of this method, certain approximations will often be justifiable. The approximations that will be found convenient and usually justifiable are made by assuming that

$$\cos \theta_z = 1$$

and

$$c_{d0} \sin \theta_z = 0$$

The magnitude, but not the direction, of C_L and C_N may then be taken as the same; the following quantities are also equal in magnitude but not in direction:

$$c_{l_0}, c_n, c_z$$

BIPLANE

The present unsatisfactory status of biplane theory and the large number of variables in the biplane shape or arrangement combine to prevent a completely rational solution of biplane problems by either theoretical or empirical methods. It is possible, however, to compute the forces and moments on "conventional" biplane wings by semiempirical methods that give fairly satisfactory results.

In general, the biplane calculations follow the principles and procedure previously outlined for the monoplane, the main extensions therefrom lying in the determination of the lift distribution between the wings and the determination of the biplane effect on the moments of the individual wings. The lift distribution between the wings is found according to the method developed by Diehl in references 5 and 6; the biplane effect on the moments of the individual wings is found according to a procedure outlined later in this report. Although a biplane has no aerodynamic center, a locus of points about which the pitching-moment coefficient of the cellule remains constant can be found. This locus is analogous to the aerodynamic center of the monoplane but lacks its practical utility. Nevertheless, since it leads to a better understanding of biplane phenomena, the locus of points of constant pitching moment will first be discussed.

Locus of points of constant pitching moment.—According to Diehl's solution of the lift distribution between the wings, the lift coefficients of the individual

wings plotted as functions of the biplane coefficient are straight lines that intersect at some value of the biplane lift which is, in general, not equal to zero. A typical

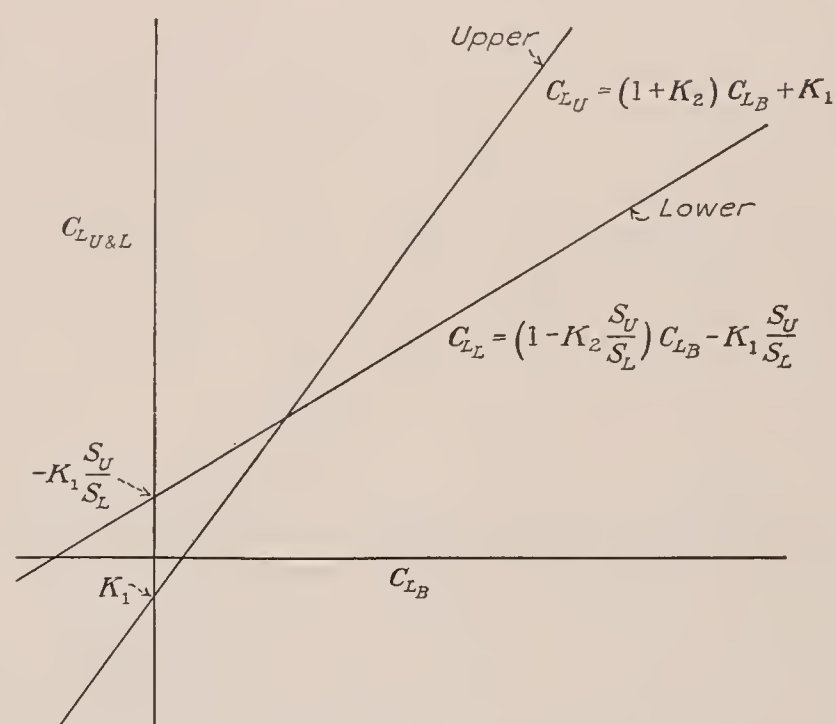


FIGURE 3.—Typical biplane wing lift curves.

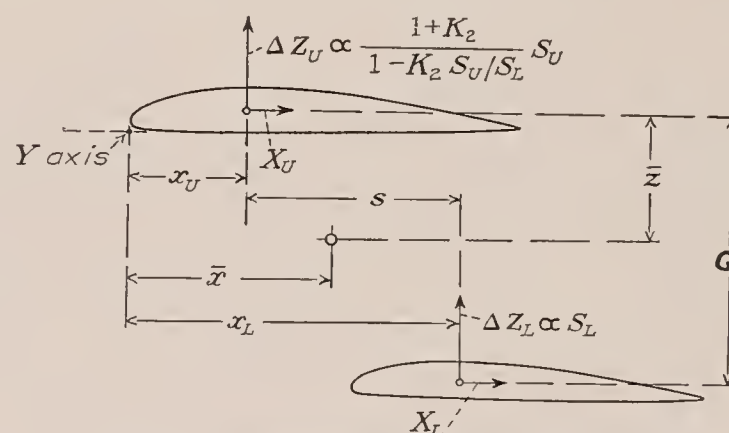


FIGURE 4.—Force diagram for determination of \bar{x} and \bar{z} .

case is shown in figure 3. These individual wing lifts may be considered to have their points of application at the aerodynamic centers of the individual wings, because, as will be indicated later, the monoplane value of the aerodynamic center of either wing is not affected by the opposite wing; only the basic moment is affected.

Now, if it be assumed that the biplane lift relations are equally applicable to the Z components,¹ it is clear that the location of the center of the Z components may be considered fixed in the direction of x , the ratio of the change in Z force on the upper wing to the change on the lower wing being constant. Reference to figure 4 shows that the x location of the locus of constant moment can be found from the relation

$$\bar{x} = \frac{\left(\frac{1 + K_2}{1 - K_2 \frac{S_U}{S_L}} \right) S_U x_U + S_L x_L}{S_L + \left(\frac{1 + K_2}{1 - K_2 \frac{S_U}{S_L}} \right) S_U}$$

¹ This assumption is perfectly valid in this case, since the slight error involved is within the error of the semiempirical method of determining the lift distribution.

in which K_2 is Diehl's biplane lift function, as indicated in figure 3.

Unlike the ratio of the Z forces, the ratio of the X components is not independent of the biplane lift because of the nonlinear relation between profile drag and lift in combination with the inequality in lift on the upper and lower wings and because of the trigonometric relation between the lift and its X component. The point about which the pitching moment remains constant therefore moves in the z direction with changes in lift or in X force ratio. Thus, according to figure 4, at any value of the biplane lift for which the X components may be determined

$$\bar{z} = \frac{X_L G}{X_U + X_L}$$

A graphic illustration of the behavior of \bar{z} is given in figure 5, which shows values calculated for the bi-

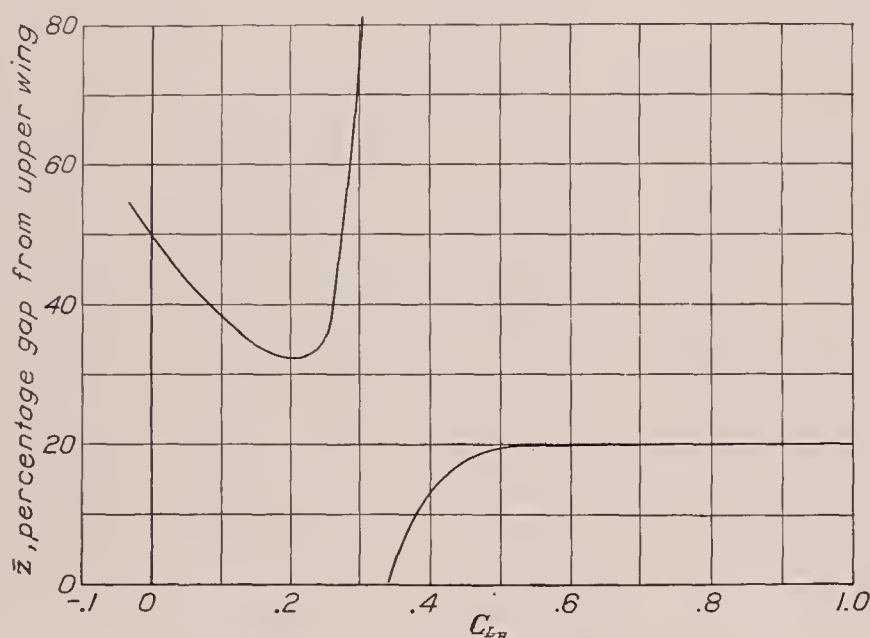


FIGURE 5.—Variation of \bar{z} with biplane lift coefficient.

plane selected for the illustrative example given later in the report. At the higher values of the lift coefficient, the points of constant moment are close to the upper wing. In this condition both upper and lower X components act forward, the upper component being the larger. At a lift coefficient of about 0.33, \bar{z} is indeterminate because the upper and lower X components are equal in magnitude but opposite in direction. In this condition the resultant force is in the z direction and the X components form a pure couple. At the lower lift coefficients both X components act rearward and are of nearly equal magnitude so that \bar{z} is approximately half the gap.

It can be seen from the foregoing discussion that the biplane has no useful counterpart of the monoplane aerodynamic center. For this reason, biplane problems are best solved by proceeding directly to a solution of the forces and moments.

Lift coefficients of individual wings.—The first step in the biplane solution is to determine the lift coefficients of the individual wings as functions of the lift coefficient of the cellule. As previously indicated, this step may

be performed according to the method developed by Diehl in references 5 and 6. When this method is used, however, it is recommended that, in cases involving large negative stagger, values of K_{20} be determined from a curve faired through the experimental points of figure 13 of reference 5, rather than from the linear relation between K_{20} and s/c (equation (15a), reference 5).

Distribution of force components.—The wing lifts corresponding to any biplane lift having been found, the force distribution on the individual wings is determined in the same manner as for monoplanes. This procedure neglects the effect of interaction of the individual wings and leads to some error, which is probably small in practical cases.

Pitching moment of biplane cellule.—The pitching moment of the whole cellule about any arbitrarily selected Y axis is found in the same manner as for the monoplane from a summation of the moments due to the Z and X components of force and to the section characteristics. To this total moment a correction, constant throughout the lift range, may be applied to staggered arrangements to obtain a more accurate result.

The correction is based on the fact, indicated by available test data, that the couple created by the lift forces on the individual wings of a staggered biplane with no decalage at zero cellule lift is exactly balanced by predominating increments of moment on the individual wings plus a secondary couple due to the biplane effect on the drags of the individual wings. The moment correction, therefore, constitutes simply a subtraction of the couple created by the K_1 forces due to thickness-gap ratio, stagger, and overhang from the total moment M previously found. Thus

$$M_{YY} = \Sigma M - (K_{10} + K_{11} + K_{13}) S_U s q$$

where K_{10} , K_{11} , and K_{13} are Diehl's lift functions for thickness-gap ratio, stagger, and overhang and s is the stagger measured between the aerodynamic centers of the individual wings.

The function K_{12} , which is due to decalage, is not included in the correction.

Pitching moments of individual wings.—As previously mentioned, the couple due to the K_1 forces, if decalage is neglected, is exactly balanced by predominating opposite moments on the individual wings and a less important couple due to biplane effect on the drags. This drag moment is small compared with the K_1 couple and therefore negligible, since the K_1 couple itself is small. The K_1 couple may therefore be considered to be entirely balanced by increments of moment on the individual wings. No information exists, however, as to the distribution of these moment increments between the upper and lower wings; a consideration of this problem led to the conclusion that a reasonable assumption would be to divide the balancing couple equally between

the wings. This assumption leads to very low increments of pitching-moment coefficient on the individual wings; in several cases that have been examined the values were well below 0.01. In view of such low values and the uncertainties in regard to the distribution, it is believed advisable to neglect these increments in computing the pitching moments of the individual wings.

Another biplane effect on the individual wing moments, however, should be taken into account. Its physical cause is not known at present, but it is probably due to the profile drag of the wings, which results in a pressure gradient from the leading to the trailing edge between the wings and to the curvature in the streamlines at each wing induced by the opposite wing. An examination of test data obtained both in flight and in wind tunnels showed that this biplane effect on the wing moments is, for all practical purposes, a linear function of the thickness-gap ratio given by the relation

$$\Delta c_{m_0} \left(\frac{t}{G} \right) = 0.1 \frac{t}{G}$$

These increments, for the data available, do not noticeably contribute to the resultant biplane moment; the total increment of moment on the upper wing must therefore be approximately equal and opposite to that on the lower wing.

In order to effect the practical application of these increments to the wings, it is assumed: (1) That the increment is distributed along the entire span of the shorter wing but only along that portion of the span of the longer wing that lies within the projected span of the shorter wing; and (2) that the increment of pitching-moment coefficient is distributed uniformly along the span of each wing between the limits of the pitching-moment distribution. On the basis of assumption (1), the value of $\Delta c_{m_0} \left(\frac{t}{G} \right)$ is found for the upper wing from the foregoing relation using the average value of t/G based on the lower wing for the portion of the span affected. Then

$$\Delta c_{m_0} \left(\frac{t}{G} \right)_L = -\Delta c_{m_0} \left(\frac{t}{G} \right)_U \times \frac{S_U'}{S_L'} \times \frac{c_U'}{c_L'}$$

where S_U' is the area of the portion of the upper wing involved.

S_L' , the area of the portion of the lower wing involved.

c_U' , average chord of the portion of the upper wing involved.

c_L' , average chord of the portion of the lower wing involved.

LOAD DISTRIBUTION OVER AIRFOIL SECTION

The solution of the general problem has been completed except that the distribution of the air forces along the chord at each section has not been determined,

the net section lift, drag, and pitching-moment coefficients having been employed heretofore rather than the distributed air loads at each section. Although the distribution of the air load around the airfoil section may not always be required, this distribution will be considered in order to make the analysis complete.

General procedure.—The previous analysis gives the section lift coefficient c_{l_0} , the method of finding the normal- and chord-force coefficients c_n and c_c , and the pitching-moment coefficient $c_{m_{a.c.}}$ at each section corresponding to any given loading condition of the complete airplane with which the designer is concerned. The corresponding distribution of the air load over the section will be given in terms of the normal-force coefficient by giving the distribution of the normal-pressure coefficient P along the chord of the section. Of course, this distribution gives no chord force but the chord force is known and may be considered as applied at the aerodynamic center. Its distribution will not be considered, the chord force being small and distributed over only a small distance equal to the wing thickness. Although the moment contributed by this distribution cannot be entirely neglected, the normal-force distribution will be slightly modified, more or less arbitrarily, so that it will give exactly the correct pitching moment about the aerodynamic center.

Determination of normal-pressure coefficients.—As previously stated, the distribution of the air load along the chord is found by determining the normal-pressure coefficient P , that is, the ratio of the pressure difference that may be considered as acting at any point along the chord to the dynamic pressure q . The distribution is defined by the values of P at a number of points along the chord. As with the span load distributions, it is convenient to consider the distribution as made up of two independent parts, one the distribution for zero normal force P_0 and the other an additional distribution giving all the normal force. The total normal-pressure coefficient at each point is then

$$P = P_0 + c_n P_a \quad (23)$$

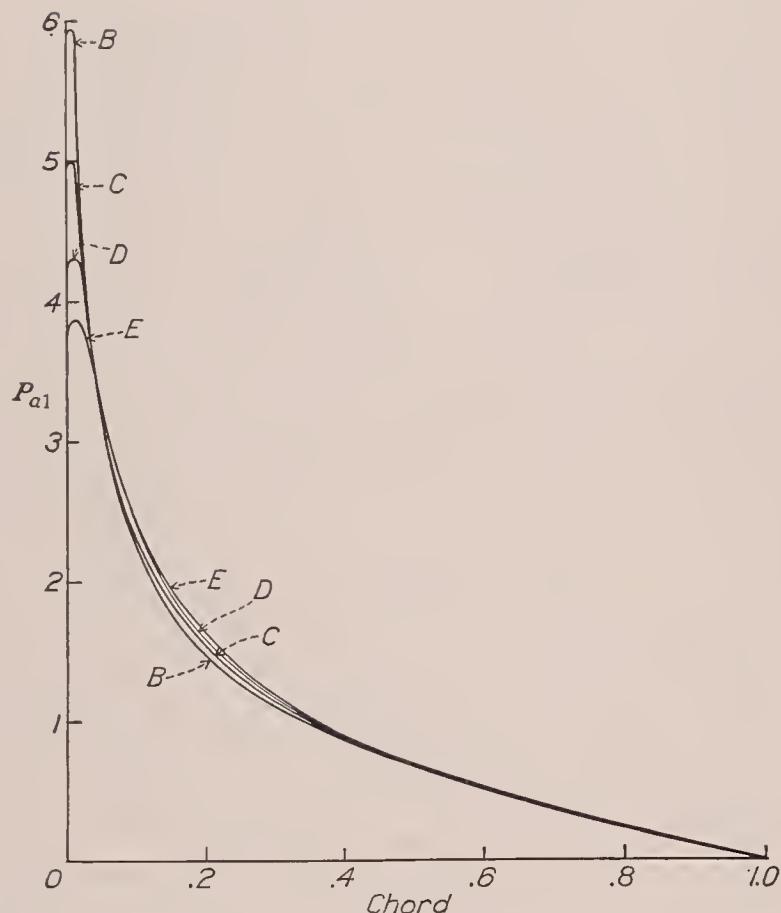
The value of P_a is found from

$$P_a = P_{a1} + \frac{x_{a.c.}}{c} P_{a.c.} \quad (24)$$

where values of P_{a1} and $P_{a.c.}$ are given by curves and tables for typical airfoils in figure 6. The designation of the airfoil class in this respect corresponds to a letter given for each section in the PD column of table I. Values of $x_{a.c.}/c$ are also found from table I by dividing by 100 the x coordinate of the aerodynamic center. A single table of the $P_{a.c.}$ distribution, which is taken as the same for all airfoils, is given in figure 6.

The value of P_0 is found from the so-called "basic distribution," thus

$$P_0 = P_b - c_{nb} P_a \quad (25)$$



Station	$P_{a.c.}$	P_{a1}			
		Class B	Class C	Class D	Class E
0	0	0	0	0	0
1.25	3.2	5.93	4.98	4.32	3.87
2.5	4.5	4.37	4.23	4.02	3.81
5	5.5	3.20	3.22	3.25	3.27
7.5	5.9	2.63	2.68	2.76	2.81
10	5.7	2.26	2.32	2.39	2.44
15	5.0	1.77	1.85	1.90	1.95
20	4.3	1.47	1.54	1.58	1.62
30	2.9	1.10	1.14	1.16	1.18
40	1.4	.86	.87	.88	.89
50	0	.67	.68	.68	.69
60	-1.4	.51	.51	.51	.51
70	-2.9	.38	.37	.37	.36
80	-4.3	.25	.24	.24	.23
90	-5.7	.13	.12	.12	.11
95	-5.5	.06	.06	.06	.06
100	0	0	0	0	0

NOTE.—Type A distributions have not yet been determined.

FIGURE 6.—Pressure distribution—additional.

The basic distribution P_b and the basic normal-force coefficient c_{nb} are, in turn, found as the sum of two parts due respectively to moment and camber, thus

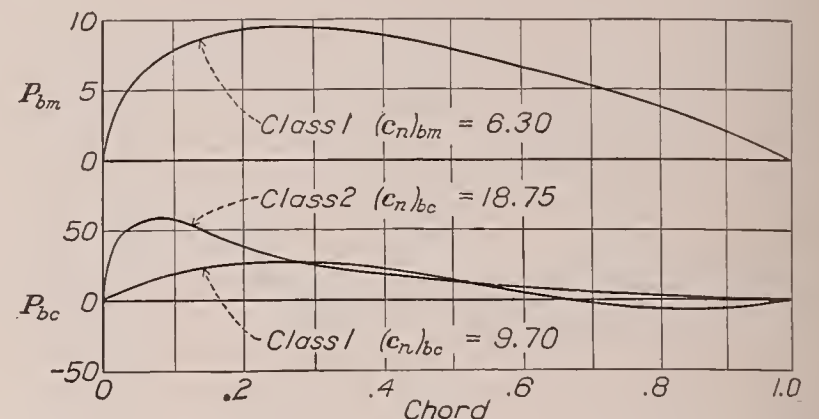
$$P_b = -c_{m_{a.c.}} P_{bm} + \frac{z_c}{c} P_{bc} \quad (26)$$

and

$$c_{nb} = -c_{m_{a.c.}} (c_n)_{bm} + \frac{z_c}{c} (c_n)_{bc} \quad (27)$$

Values of P_{bm} and the corresponding values of $(c_n)_{bm}$ are given in figure 7, as well as values of P_{bc} and $(c_n)_{bc}$ for airfoils of classes as indicated in the airfoil table by the number following the letter in the PD column. For example, the number 10 indicates that P_{bm} is class 1 and P_{bc} is class 0. The zero signifies that P_{bc} and $(c_n)_{bc}$ are both zero. The values of $c_{m_{a.c.}}$ and the section camber z_c/c are both found from table I, z_c/c being found by dividing the mean camber as given, in percent of the chord, by 100.

When the actual calculation for any given airfoil section is made, values of P_0 and P_a should be calculated and tabulated for the standard stations along the chord. For any section normal-force coefficient c_n , the corresponding values of P are then found simply from (23) by multiplying the values of P_a by c_n and adding to P_0 . The actual pressure difference acting at each point in pounds per square foot is, of course, obtained by multiplying by the dynamic pressure in consistent units.



Station	P_{bm}	P_{bc}		
	Class 1	Class 0	Class 1	Class 2
0	0	0	0	0
1.25	2.85		2.5	32.5
2.5	4.25		5.5	47.0
5	6.05		10.0	56.5
7.5	7.10		14.5	59.0
10	7.80		18.0	57.5
15	8.80		23.0	47.5
20	9.30		25.0	37.0
30	9.50		25.0	24.5
40	8.80		20.5	18.0
50	7.75		14.0	13.0
60	6.60		6.0	9.0
70	5.30		-2.5	5.5
80	3.75		-5.5	3.5
90	2.05		-4.5	1.5
95	1.10		-2.5	1.0
100	0		0	0
$(c_n)_{bm} = 6.30$		0	9.70	18.75
				$= (c_n)_{bc}$

$$P_b = -c_{m_{a.c.}} P_{bm} + \frac{z_c}{c} P_{bc}$$

$$c_{nb} = -c_{m_{a.c.}} (c_n)_{bm} + \frac{z_c}{c} (c_n)_{bc}$$

FIGURE 7.—Pressure distribution—basic.

Finally, consider briefly how the air pressures are divided between the upper and the lower surfaces. Pressure-distribution diagrams, given elsewhere, indicate the pressure on the upper and on the lower surface as measured from the static pressure as a reference. The designer, however, is not primarily concerned with these pressures but with the pressure differences across the wing covering which, of course, produce the air load on it. These pressure differences are a function of the internal pressure, that is, the pressure within the wing. If the wing is well vented, the internal pressure and the upper and lower covering loads may be estimated. For this purpose the lower-surface pressure distribution is estimated, remembering that the positive pressure cannot exceed by $1q$ the static pressure, and the upper-surface distribution determined from the known values of the differential-pressure coefficient P . If greater

accuracy is required, the method of reference 7 or the results of reference 8 may be employed to calculate the pressure distribution on the lower surface.

SAMPLE CALCULATION

MONOPLANE

In order to make this example as general as possible, a case is chosen for which the design condition representing a 30-foot-per-second gust encountered at high speed causes the lift coefficient to exceed the usual maximum lift coefficient for the airfoil. The example does not, however, deal specifically with the procedure to be followed in cases for which portions of the wing are replaced by the fuselage or nacelles. The treatment, nevertheless, is exactly the same in such cases if the standard N. A. C. A. wing area, including those portions of the wing imagined as inside the fuselage or nacelles, is used for S . The solution is thus found by considering those portions of the wing to be actually present and undisturbed, the wing being imagined as extending continuously over those portions of the span. The calculated loads for these imaginary portions of the wings may later be applied to the fuselage and nacelles. In extreme cases a special treatment may be required. A wing of the U. S. A. 35 type is chosen so that some aerodynamic twist will be present in spite of the fact that the wing is not twisted with reference to the airfoil chords. The drag truss, for generality, is taken at an angle to the plane of the airfoil chords. The analysis is begun from the airplane drawing in figure 1 and from the following data on the airplane and wing:

Weight.....	1,000 lb.
Power.....	35 hp.
Propeller efficiency.....	75 percent.
High speed.....	95.3 f. p. s.
Wing incidence.....	4°.

Wing: U. S. A. 35 type, aspect ratio 5, rounded tips, area 180 sq. ft., root chord 8.268 ft., taper ratio 0.5, no geometric twist, beam direction perpendicular to chord, drag truss (chord direction) inclined upward at the leading edge with respect to the chord 4° at root to 2° at tip, airfoil section at root U. S. A. 35-A, at tip U. S. A. 35-B.

Calculation of wing aerodynamic center.—The first step in the procedure is to choose the reference axes. The axes are chosen, for generality, originating at the center of gravity with one axis parallel to the thrust line although, in this instance, some simplification might have resulted from choosing an axis in the direction of an airfoil chord because this direction is the same along the wing (no geometric twist) and perpendicular to the beam direction. Table IV is then filled in to give the necessary data for computing the aerodynamic center of the wing. The various columns leading first to the calculation of the additional-load curves for $C_L=1$ and finally to the position of the wing aerodynamic center are filled in as follows:

Column 1.—Stations along the span chosen arbitrarily or to agree with those in table II. These stations are indicated on the airplane drawing (fig. 1).

Column 2.—Values of L_a from additional-load table (table II) for aspect ratio 5, taper ratio 0.5.

Column 3.—Values of c from the airplane drawing.

Column 4.—Values of $c_{l_{a1}}$ from the multiplication of (2) by S/cb .

Column 5.—Values of a_0 from airfoil characteristics (table I) interpolating between U. S. A. 35-A and U. S. A. 35-B sections for intermediate sections of wing.

Column 6.—Values of $c_{l_{a1}}/a_0$ from (4) and (5).

Column 7.—Values of α_{l_0} by the same method as (5).

Column 8.—Values of $-i$, the incidence of the wing chords with respect to the x axis with reversed sign, from airplane drawing.

Column 9.—Values of c_{d_0} . The profile-drag coefficients are calculated for each section as indicated in table IV-A. The thickness ratio of each section t/c is obtained from the airplane drawing. Minimum profile-drag coefficients $c_{d_{0min}}$ are obtained from a curve of profile-drag coefficient against section thickness, paralleling the typical curve given in reference 9 (fig. 91) but passing through the values indicated in table I for the U. S. A. 35-A and U. S. A. 35-B sections. Values of $c_{l_{opt}}$ and $c_{l_{max}}$ are obtained from table I. From the values in the preceding columns, the ratio $\frac{c_{l_{a1}} - c_{l_{opt}}}{c_{l_{max}} - c_{l_{opt}}}$ is computed.

From this ratio and the curve of figure 2, the Δc_{d_0} values are obtained, which are added to the values of $c_{d_{0min}}$ to give the desired c_{d_0} .

Column 10.—Values of θ_{za} . From the addition of (6), (7), and (8), where θ_{za} is $\left(\frac{c_{l_{a1}}}{a_0} + \alpha_{l_0} - i\right)$. (See equations (5) and (6).)

Columns 11 to 16.—From preceding columns.

Column 17.—Values of $c_{x_{a1}}$ from (13) + (14) following equation (5).

Column 18.—Values of $c_{z_{a1}}$ from (15) + (16) following equation (6).

Column 19.—Values of z from the airplane drawing, upward coordinate of aerodynamic center of section. May be obtained from airplane drawing after locating the aerodynamic center of the tip and the center sections from table I. The corresponding aerodynamic-center positions for the intermediate sections may be taken along the straight line joining these points except for the rounded-tip sections.

Column 20.—Values of x , backward coordinate of aerodynamic center of section, obtained from the airplane drawing as with (19).

Columns 21 to 24.—Products from previous columns. These pitching-moment and loading results are plotted as in figures 8 and 9, and the areas measured to find $M_{z_{a1}}/q$, $M_{x_{a1}}/q$, Z_{a1}/q , and X_{a1}/q . From these values

the coordinates of the wing aerodynamic center are found from equations (7) and (8).

$$x_{a.c.} = \frac{-110.08}{180.0} = -0.612 \text{ ft.}$$

$$z_{a.c.} = \frac{15.08}{4.18} = 3.6 \text{ ft.}$$

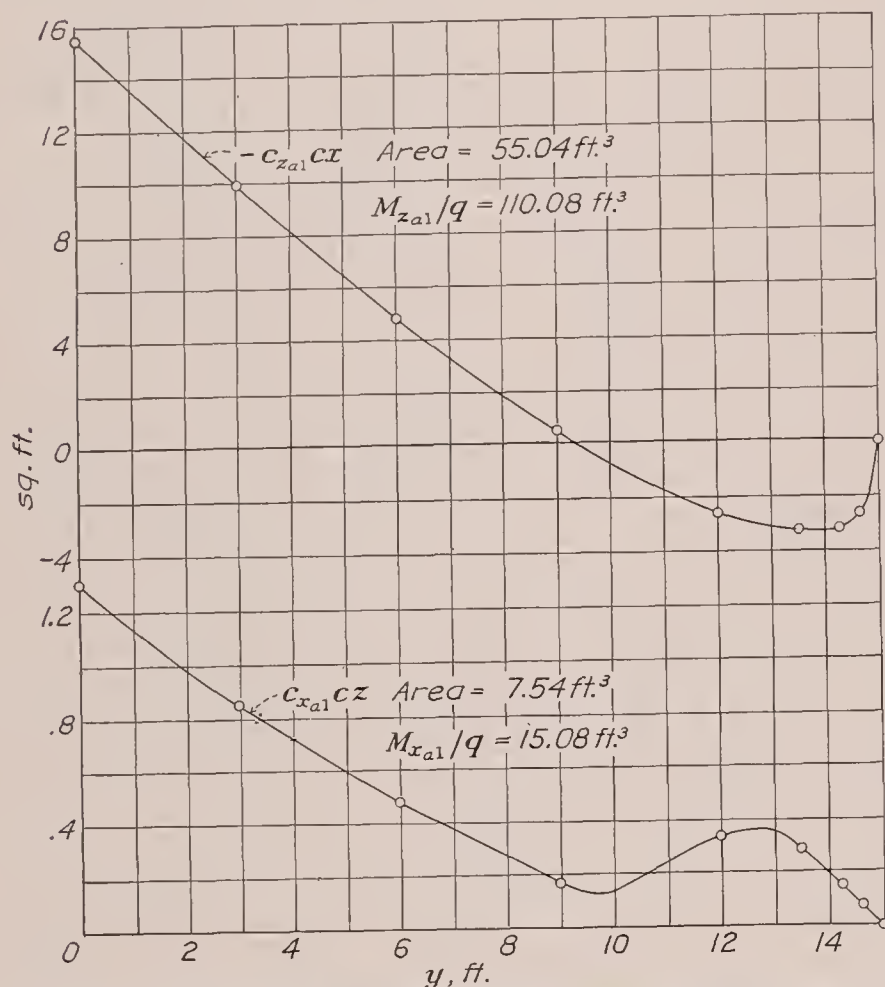


FIGURE 8.—Plots for the determination of the components of the additional wing pitching moments and the wing aerodynamic center.

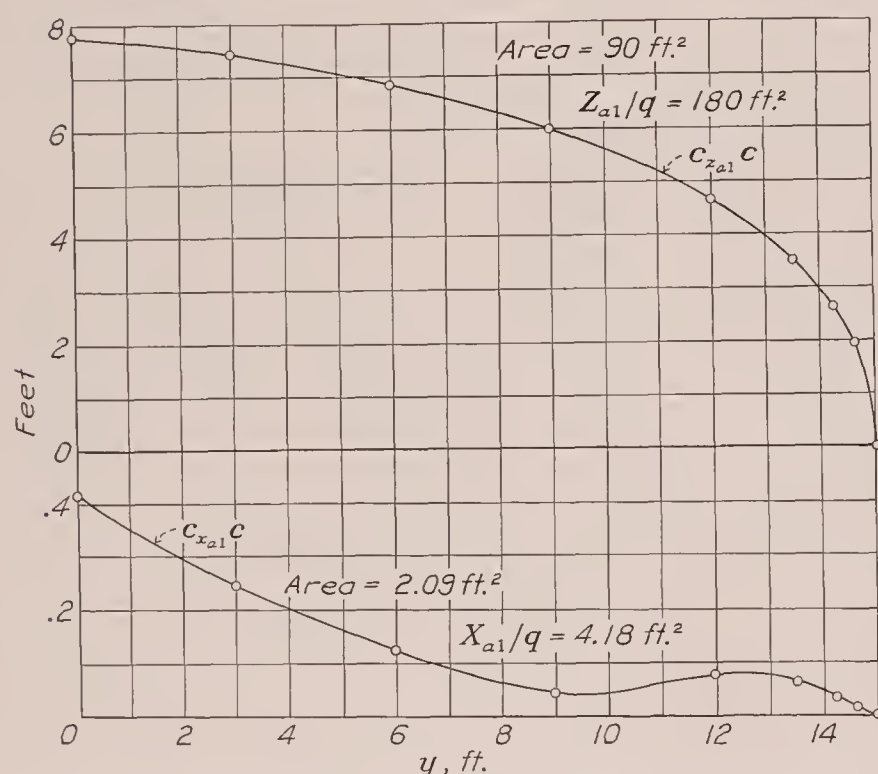


FIGURE 9.—Distribution of additional z and x components and determination of additional wing components.

Calculation of wing pitching moment about aerodynamic center.—The next step is to carry out practically the same procedure for the basic load distribution in order to find the wing pitching moment about the aerodynamic center. The origin of coordinates is moved to

the aerodynamic center and another set of calculations is made for the basic load distribution as indicated in table V. The only differences worth noting are the different values taken from the tables, values for the basic load distribution L_b from table III, and the method of obtaining from these the c_{l_b} values in table V. The c_{l_b} values follow from those in the second column taken from table III, by multiplying by $\epsilon a_0 S/cb$.

The term ϵa_0 takes into account the aerodynamic twist of the wing, which is assumed to vary linearly along the span. The twist ϵ is measured with respect to the zero lift directions for the center and tip sections, being positive when the effective incidence is washed in from the center toward the tip. It is evident that the term ϵa_0 is a c_l difference between airfoil sections corresponding to the center and tip sections when the section angles of attack have the same relation as in the wing. In other words, ϵa_0 may be calculated as follows:

$$\epsilon a_0 = [a_0(\alpha - \alpha_{l_0})]_{tip} - [a_0(\alpha - \alpha_{l_0})]_{center}$$

This procedure is strictly correct theoretically only when a_0 does not vary along the span. When a_0 varies, the best practical result is probably obtained by calculating ϵa_0 as a Δc_l for an α near the value at which the load distribution is desired.

The value of α may be taken as zero for the center section and, because no geometrical twist is present, the value of α at the tip is then also zero in this instance.

$$\begin{aligned} \epsilon a_0 &= (-a_0 \alpha_{l_0})_{tip} - (-a_0 \alpha_{l_0})_{center} \\ &= [-(0.099)(-5.2)] - [-(0.095)(-8.0)] \\ &= 0.515 - 0.760 = -0.245 \end{aligned}$$

Values of the factor $\epsilon a_0 S/cb$ are then obtained at each station along the span by which the values taken from table III are multiplied to obtain the c_{l_b} values. From the c_{l_b} values, the calculations proceed to the final results, which are given in the last columns of table V. These results are plotted and the areas determined to find $(M_{x_b}/q)_{a.c.}$, $(M_{z_b}/q)_{a.c.}$, and $(M_s/q)_{a.c.}$ as in figure 10. These values are added to obtain $M_{a.c.}/q$.

$$\frac{M_{a.c.}}{q} = 0 + 4.84 - 113.36 = -108.5$$

which, multiplied by q , gives $M_{a.c.}$, the required pitching moment of the wing about its aerodynamic center.

Calculation of forces and moments in accelerated-flight condition.—The exact procedure to be followed from this point on is dependent on the result desired. If a result meeting arbitrary design requirements is desired, the particular specified procedure will be followed. If, on the other hand, the most reliable actual air loads for a given design condition are desired, another procedure may be advisable.

From the method of references 1 and 10, for example, the applied load factor n_1 is determined and the wing normal-force coefficient C_{N_1} is taken as $n_1 s/q_L$ where s is the effective wing loading and q_L is the dynamic

pressure for the design speed. Corresponding values of the chord-force coefficient c_c are obtained as more or less arbitrarily specified, and the pitching characteristics of the wing are rather arbitrarily given by specifying that the center-of-pressure position be taken as the most forward position for the wing between $C_L = C_{N_1}$ and $C_L = C_{L_{max}}$, unless C_{N_1} exceeds $C_{L_{max}}$, in which case a value taken from the extended center-of-pressure curve is specified. After C_L is calculated from the specified C_{N_1} , the lift-coefficient distribution may be found by adding the basic and additional lift coefficients in accordance with the relation

$$c_{l_0} = c_{l_b} + C_L c_{l_{a1}}$$

and including, when necessary, the tip corrections given in appendix A. The corresponding specified values of the center of pressure and of c_c may then be applied at each section and the forces and moments resolved as desired for structural analysis.

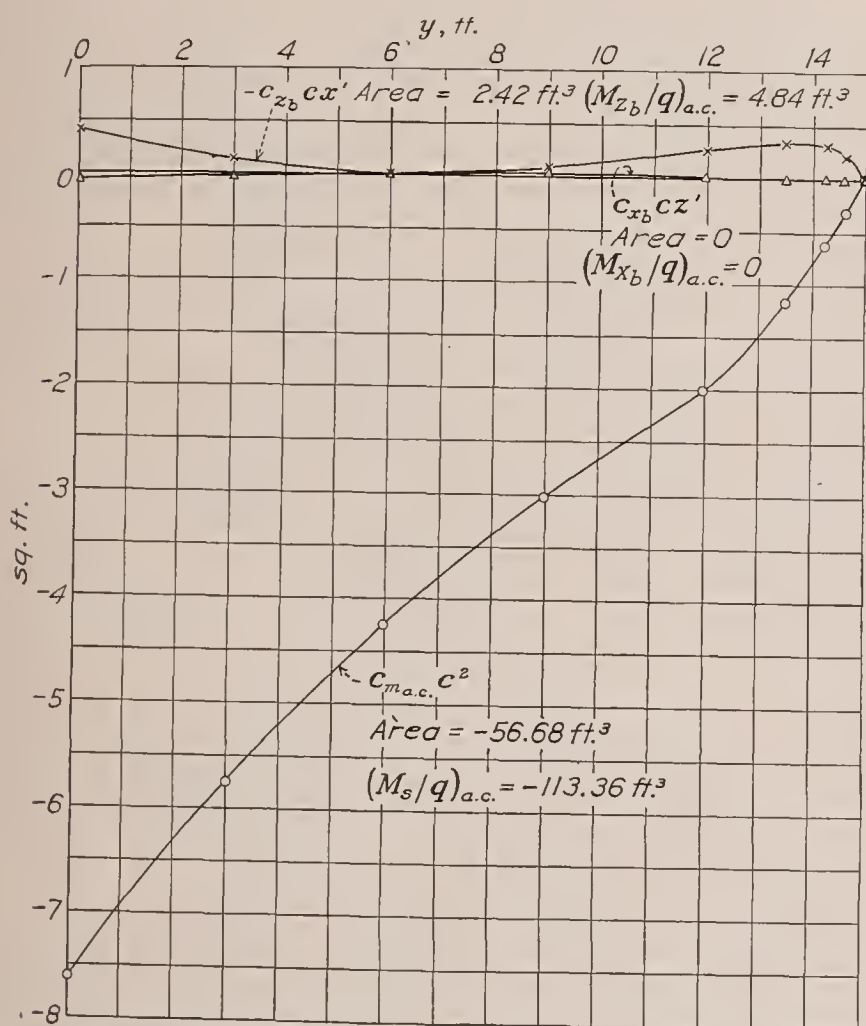


FIGURE 10.—Plots for the determination of the components of the basic wing pitching moment.

The foregoing procedure, however, will not be followed in this example. Specified design conditions and methods vary and, in many instances, it is believed that designers will wish to investigate loadings under conditions other than those specified. The example will therefore be carried through using the procedure

that may be expected to give the best approximation to the actual air forces.

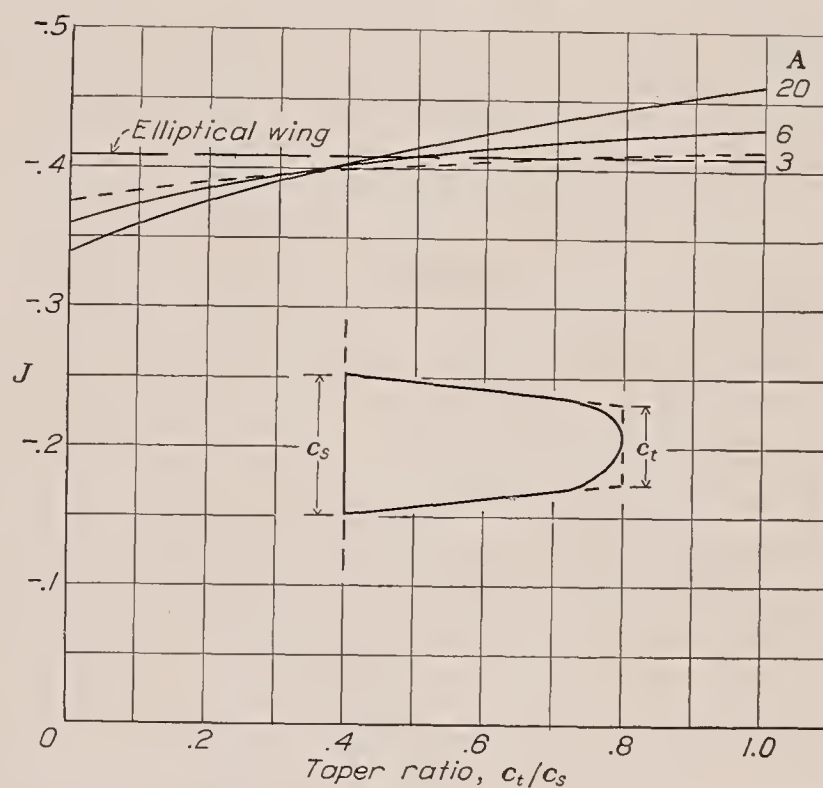
The first step is to obtain the lift coefficient C_L' corresponding to the steady-flight condition before entry into the gust. For the present example, this condition is represented by high-speed level flight. The corresponding C_L' value is obtained from the balance diagram for the airplane for this condition.

For the construction of the balance diagram, it is necessary to know the angle of the flight path so that the direction of the weight vector may be determined. A trial value of C_L' is first taken, assuming a down tail

load of 30 pounds, $\frac{W + F_t}{qS} = 0.530$. The wing angle of

attack as measured by α_s , the angle of attack referred to the chord of the center section, may then be determined by the method indicated in figure 11:

$$\alpha_s = \frac{C_L}{a} + (\alpha_{l_0})_s + J\epsilon$$



Determine the angle of attack from:

$$\alpha_s = C_L/a + (\alpha_{l_0})_s + J\epsilon$$

where α_s , angle of attack referred to the chord of the central section of the wing.

C_L , wing lift coefficient.

a , wing lift-curve slope per degree.

$(\alpha_{l_0})_s$, angle of zero lift of the central section.

ϵ , angle of aerodynamic twist.

A , aspect ratio.

$C_L = a[\alpha_s - (\alpha_{l_0})_s - J\epsilon]$ or, angle of zero lift for the wing referred to the chord of the center section $= (\alpha_{l_0})_s + J\epsilon$.

FIGURE 11.—Lift in terms of angle of attack for tapered wings with twist.

From figure 12

$$a = f \frac{a_0}{1 + \frac{57.3a_0}{\pi A}}$$

Taking $a_0=0.096$ as a mean value for the sections of the wing

$$a = 0.999 \frac{0.096}{1 + \frac{57.3 \times 0.096}{\pi 5}} = 0.0711$$

The angle of zero lift for the root section $(\alpha_{l_0})_s$ is taken from table I. The twist ϵ is $\epsilon a_0/a_0$ or $-0.245/0.096 = -2.55^\circ$. The factor J from figure 11 is -0.408 . Then

$$\begin{aligned} \alpha_s &= \frac{C_L}{a} + (\alpha_{l_0})_s + J\epsilon \\ &= \frac{0.530}{0.0711} - 8 + (-0.408)(-2.55) \\ &= 0.5^\circ \end{aligned}$$

As the incidence of the center section is 4° , the angle of the thrust line with the horizontal is $0.5^\circ - 4.0^\circ = -3.5^\circ$. The weight vector may therefore be drawn as indicated in figure 1 and the pitching moments may be taken about the wing aerodynamic center to determine the tail load F_t . The dynamic pressure is

$$\begin{aligned} q &= \frac{1}{2} (0.002378) (95.3)^2 \\ &= 10.79 \text{ lb./sq. ft.} \end{aligned}$$

$$\begin{aligned} M_{a.c.} &= \left(\frac{M_{a.c.}}{q} \right) q \\ &= -108.52 \times 10.79 \\ &= -1,171 \text{ lb.-ft.} \end{aligned}$$

Although for other purposes, such as balance calculations, a better moment analysis may be necessary, the thrust moment in this case may be determined with sufficient accuracy on the assumption that three-quarters of the thrust is used in overcoming parasite drag, which may be assumed to act approximately along the thrust axis and therefore to contribute no moment about the wing aerodynamic center. The thrust is

$$\frac{35 \times 550 \times 0.75}{95.3} = 151.5 \text{ lb.}$$

Then writing the moment equation

$$(0.25 \times 151.5 \times 3.82) + (1,000 \times 0.82) - 1,171 - F_t 14.62 = 0$$

$$F_t = -14.3 \text{ lb.}$$

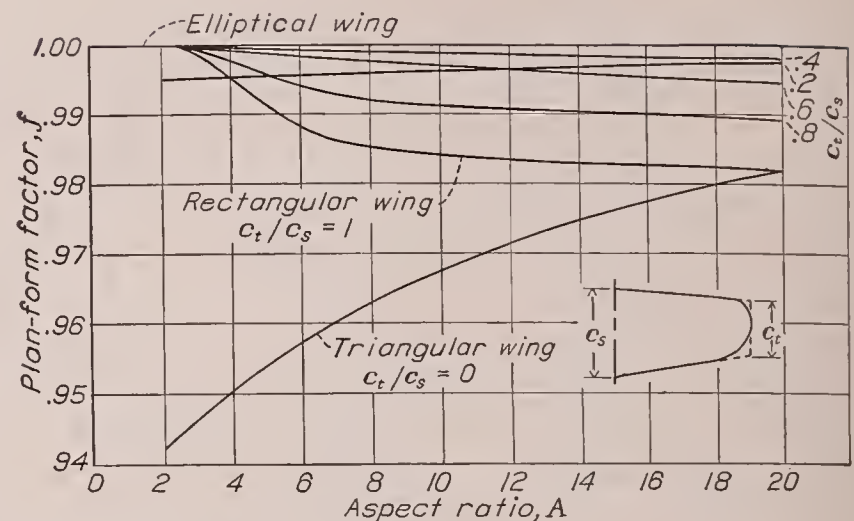
The final value of the lift coefficient for steady flight C_L' may then be computed

$$\begin{aligned} C_L' &= \frac{1,000 + 14.3}{10.79 \times 180} \\ &= 0.522 \end{aligned}$$

The new wing lift coefficient C_L after entry into the gust is now determined from the slope m of the wing lift curve and the gust velocity U

$$C_L = C_L' + m \frac{U}{V}$$

$$C_L = 0.522 + 4.07 \frac{30}{95.3} = 1.803$$



Compute the lift-curve slope from the equation:

$$m = f \frac{57.3 a_0}{1 + 57.3 a_0 / \pi A} \text{ or } a = f \frac{a_0}{1 + 57.3 a_0 / \pi A} \text{ (per degree)}$$

where m , lift-curve slope (per radian).
 a_0 , section lift-curve slope (per degree).
 a , wing lift-curve slope (per degree).
 A , aspect ratio (b^2/S).
 f , plan-form factor.

When the lift-curve slope is normal, the following approximate equations may be used:

$$m = f \frac{57.3 a_0}{1 + 1.843/A} \text{ or } m = f \frac{m_a}{0.761 + 1.403/A}$$

where m_a , lift-curve slope (per radian) for wing of aspect ratio 6 with rounded tips.

$$\text{Taper ratio} = \frac{c_t}{c_s} = \frac{\text{tip chord}}{\text{center chord}}$$

FIGURE 12.—Values of f for computing the lift-curve slope.

where the value of m is found from figure 12 and table I.

The lift distribution is now determined by calculating the c_{l_0} values in table VI from

$$c_{l_0} = c_{l_b} + C_L c_{l_{a1}}$$

where c_{l_b} is taken from table V and $c_{l_{a1}}$, from table VI. The calculations indicated in table VI proceed then to the determination of chord and beam components from equations (18) and (19).

It will be noted that the steady-flight value of the profile-drag coefficient c_{d_0}' has been used in the accelerated-flight condition. This procedure should be followed when a large forward-acting chord force is critical for the structure.

The last three columns of table VI give the required data on the air-force distribution as chord and beam forces and pitching moments per running foot of span. In order to complete the balance diagram, however, the total air forces and moments on the wing are required. The pitching moment of the entire wing in this case is the same as that previously found for the steady-flight condition, because $M_{a.c.}/q$ has not changed.

$$\begin{aligned} M_{a.c.} &= \left(\frac{M_{a.c.}}{q} \right) q \\ &= -108.5 \times 10.79 = -1,171 \text{ lb.-ft.} \end{aligned}$$

The total wing air-force component Z perpendicular to the thrust line may be found with sufficient accuracy from the Z_{a1}/q value previously determined without the necessity of resolving and summing the section forces

$$\begin{aligned} Z &= \left(C_L \frac{Z_{a1}}{q} \right) q \\ &= 1.803 \times 180.0 \times 10.79 \\ &= 3,510 \text{ lb.} \end{aligned}$$

The total component X for the wing, however, should be found by resolving the section forces along the x direction and summing to find the total force component X . The values of c_{d0} and c_{l0} are taken from table VI and resolved by equation (15) to find the c_x values at the various sections along the span. In this example a large forward-acting chord component is assumed to be conservative so that the profile-drag coefficient c_{d0} for the accelerated-flight condition is taken as equal to that in the preceding steady-flight condition for the determination of c_x . These values are then multiplied by c , plotted as in figure 13, and the area determined to give X . The result is

$$X = -42.2 \times 10.79 = -455 \text{ lb.}$$

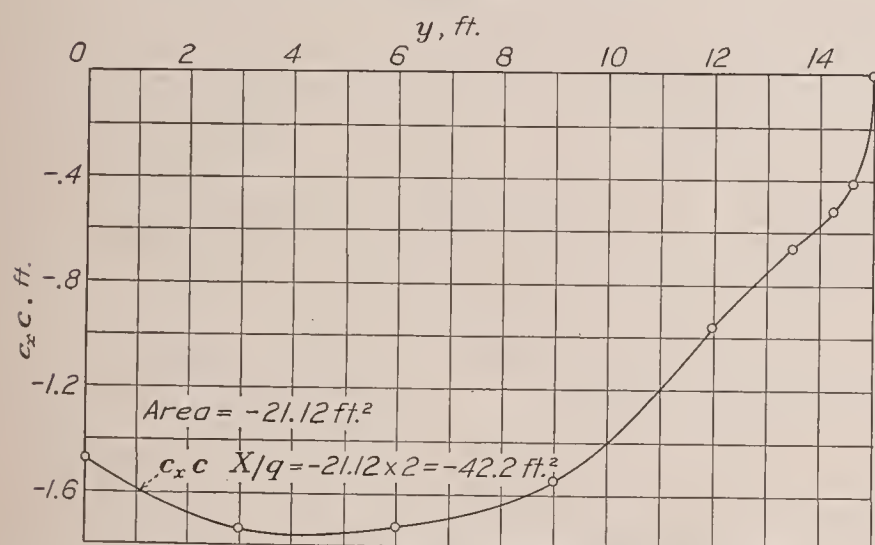


FIGURE 13.—Distribution of X component in the accelerated-flight condition.

It will be noted that the preceding calculations of the forces in the accelerated-flight condition have been made on the basis that the dynamic pressure q remains unaltered after encountering the gust. This condition is possible when the gust has a small angle with the vertical, and the procedure is further justified by the fact that the gust velocities specified have been largely determined on the basis of their effects on airplanes as indicated by the simple gust formula without taking into account such changes of velocity. In some instances, however, it may be desired to take into account the dynamic-pressure increase due to a gust, in which case the gust velocity should not be taken as nearly vertical but may be taken at an angle with the horizontal and the angle determined to give the maximum load.

The total air forces and moments are now known and may be applied at the aerodynamic center of the wing so that the balance diagram may be completed for the accelerated-flight condition, thus completing the solution with the exception of the determination of the air-force distributions over the ribs.

Calculation of the air-force distribution over a rib.—In order to complete the example, the rib distribution will be determined for the central section of the wing. Reference to table I will show the pressure-distribution classification of the U. S. A. 35-A section to be E10. The additional pressure distribution is therefore found from the class E P_{a1} distribution. Values of P_{a1} and $P_{a.c.}$ are taken from figure 6, and the additional pressure distribution is then calculated from equation (24)

$$P_a = P_{a1} + \frac{x_{a.c.}}{c} P_{a.c.}$$

where $x_{a.c.}$ is the distance of the section aerodynamic center forward of the quarter-chord point, from table I. The calculation may be carried out in tabular form as shown in table VII.

The basic pressure distribution as given by values of P_b is then found. From equation (26)

$$P_b = -c_{m_{a.c.}} P_{bm} + \frac{z_c}{c} P_{bc}$$

The designation in table I of the basic pressure distribution for this airfoil section is indicated by the number 10 following the E. The designation 10 indicates that P_{bm} is class 1 and P_{bc} is class zero, that is, $P_{bc} = 0$. The basic pressures may then be computed as indicated in table VIII, taking values of P_{bm} from figure 7 and the value of the pitching-moment coefficient $c_{m_{a.c.}}$ from table I.

The zero lift distribution given by values of P_0 is then obtained by deducting a part of the P_a distribution corresponding to c_{nb} according to equation (25)

$$P_0 = P_b - c_{nb} P_a$$

The value of c_{nb} is obtained from equation (27)

$$c_{nb} = -c_{m_{a.c.}} (c_n)_{bm} + \frac{z_c}{c} (c_n)_{bc}$$

where the values of $(c_n)_{bm}$ and $(c_n)_{bc}$ are given in figure 7, for the various distributions. In this case $(c_n)_{bm} = 6.30$ and $(c_n)_{bc} = 0$, hence

$$\begin{aligned} c_{nb} &= 0.111 \times 6.30 + 0 \\ &= 0.699 \end{aligned}$$

and

$$P_0 = P_b - 0.699 P_a$$

For the accelerated-flight condition, the pressure distribution as given by values of P is then found from

$$P = P_0 + c_n P_a$$

where c_n in this case is the same as the beam-component

coefficient c_b and is taken from table VI for the center section,

$$P = P_0 + 1.695 P_a$$

Finally, the actual pressure differences p are obtained by multiplying by the dynamic pressure, $q = 10.79$ pounds per square foot. These pressures, calculated as indicated in table VIII and giving the final result, are plotted in figure 14.

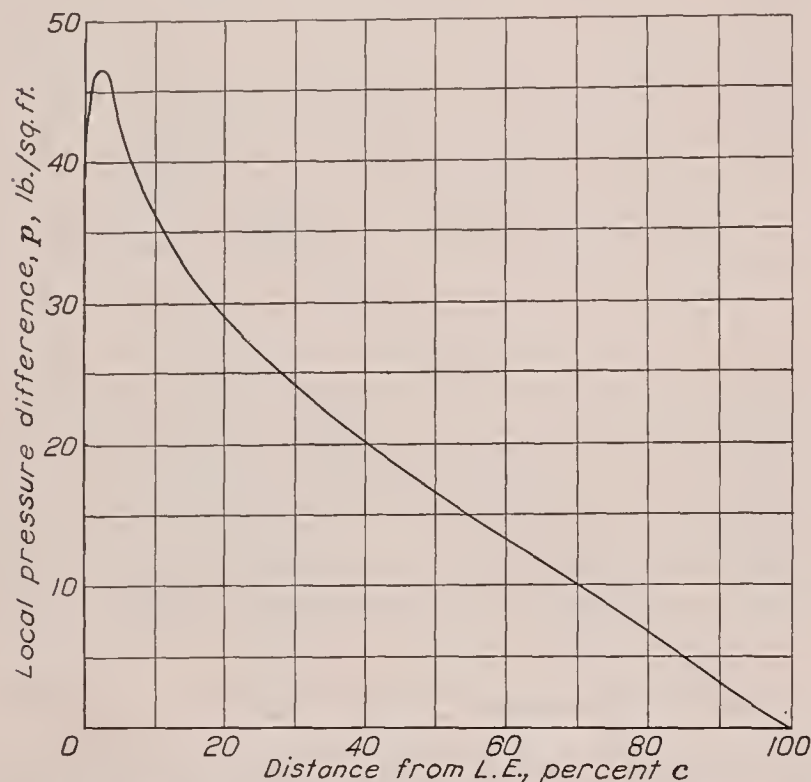


FIGURE 14.—Pressure distribution over center section in the accelerated-flight condition.

BIPLANE

The following example is given to illustrate the application of the method to biplane problems and also to illustrate the alternative method of finding the force distribution in a case where the empirical tip corrections may be important. A simple biplane (fig. 15)

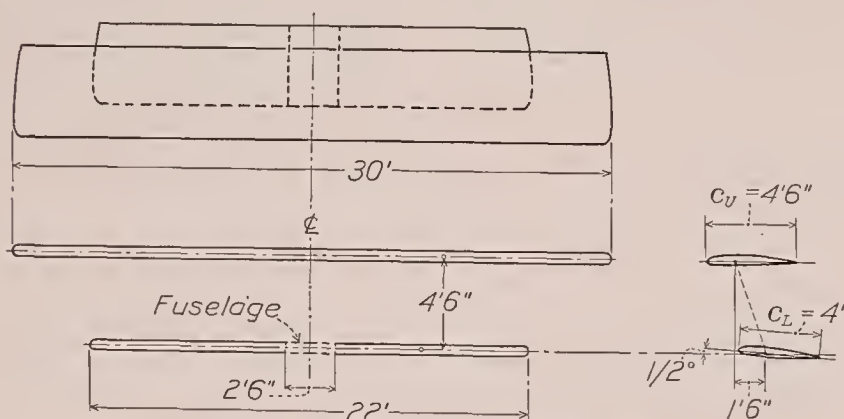


FIGURE 15.—Biplane cellule for illustrative example.

has been chosen in order to avoid, as far as possible, steps that have already been illustrated in the example for the general monoplane. The calculations are made for an airplane having the following characteristics:

Weight 1,636 lb.
High speed 100 m. p. h. ($q = 25.6$ lb./sq. ft.).
Wing cellule:

Upper: N. A. C. A. 2412 section, span 30 ft., chord $4\frac{1}{2}$ ft., area 135 sq. ft., no taper, no twist, no dihedral, incidence 0° .

Lower: N. A. C. A. 2412 section, span 22 ft., chord 4 ft., area (including projection through fuselage) 88 sq. ft.

Distance from leading edge of upper wing to c. p. of tail plane (l), 15 ft.
Distance from leading edge of upper wing to c. g. ($x_{c.g.}$), 1.75 ft.

The objective of the calculations in this example is the solution of the force and moment distribution along the upper wing in the 30-foot-per-second gust, corresponding to design Condition I of reference 1. In order to make the example more illustrative, the wing lift coefficient for the initial condition of steady flight is found from a balance computation, as in the monoplane example, but only the tail load is considered as an extraneous force. Because the biplane has no aerodynamic center, an exact balance can be obtained only through a process of trial and error; in the example the calculations are not repeated to obtain the exact solution.

Lift coefficients of individual wings.—The following data are pertinent to the solution of the lift distribution between the wings:

Effective stagger s_0 between one-third-chord points at zero lift, 1.67 ft.

$$\text{Overhang, } \frac{30-22}{30} = 0.267.$$

$$\frac{s_0}{c_L} = \frac{1.67}{4} = 0.42.$$

$$\frac{c_L}{c_U} = \frac{4}{4.5} = 0.889.$$

$$\frac{G}{c_L} = \frac{4.5}{4} = 1.125.$$

$$\frac{t}{G} = \frac{0.12}{1.125} = 0.1065.$$

$$\frac{t}{c} = 0.12.$$

With the foregoing data, the method of reference 6 yields—

$$K_{10} = -0.0178$$

$$K_{11} = 0.0123$$

$$K_{12} = -0.0274$$

$$K_{13} = -0.0178$$

$$K_1 = K_{10} + K_{11} + K_{12} + K_{13} = -0.0507$$

$$F_2 K_{20} = 0.0951$$

$$K_{21} = 0.0083$$

$$K_{22} = 0.0650$$

$$K_2 = F_2 K_{20} + K_{21} + K_{22} = 0.1684$$

$$C_{LU} = C_{LB} + (K_1 + K_2 C_{LB}) \quad (28)$$

$$= 1.168 C_{LB} - 0.0507$$

$$C_{LL} = C_{LB} - (K_1 + K_2 C_{LB}) \frac{S_U}{S_L} \quad (29)$$

$$= 0.742 C_{LB} + 0.0778$$

Wing lift coefficient in steady flight (first trial).—Neglecting tail load,

$$C_{LB}' = \frac{W}{(S_U + S_L)q} = \frac{1,636}{(135 + 88)25.6} = 0.286$$

With this value of C_{LB}' the general method can be applied to each wing for the lift coefficients derived from equations (28) and (29) to find the moment about some arbitrary Y axis and, from this result, the tail load. The simplicity of the biplane cellule chosen permits, however, a relatively simple solution of the moment. Since the wings are rectangular and of constant section, the aerodynamic centers of each wing lie on the locus of the aerodynamic centers of the sections; the resultant wing forces may therefore be considered to apply at

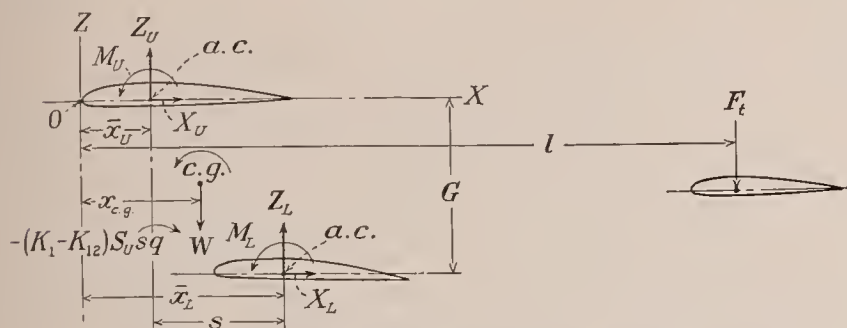


FIGURE 16.—Skeleton diagram of airplane for biplane example.

these centers. Reference to figure 16 indicates that the moment about the axis 0 may be expressed as

$$Z_U \bar{x}_U + Z_L \bar{x}_L + M_U + M_L + X_L G \\ = F_t l + W x_{c.g.} + (K_1 - K_{12}) S_U s q$$

in which s is now the stagger between the aerodynamic centers of the individual wings, and $(K_1 - K_{12}) S_U s q$ is the moment correction to allow for the increments of moment, which are not taken into account on the individual wings.

For the steady-flight condition the resultant forces at the aerodynamic centers of the individual wings are

$$\begin{aligned} Z_U' &= C_{LU}' q S_U \\ &= (1.168 C_{LB} - 0.0507) \times 25.6 \times 135 \\ &= 1,035 \text{ lb.} \\ Z_L' &= C_{LL}' q S_L \\ &= (0.742 C_{LB} + 0.0778) \times 25.6 \times 88 \\ &= 654 \text{ lb.} \end{aligned}$$

The forces X_U' and X_L' are found by summation of the force components along the span in accordance with the general procedure described in the report. For this purpose the span distribution of c_{l_0}' (or $c_{z'}'$) has been found according to the alternative method given in appendix A, neglecting the tip corrections, which at low lift coefficients are very small.

$$X_U' = 1.78 \text{ lb.}$$

$$X_L' = 6.14 \text{ lb.}$$

$$M_U = C_{m_0} S_U c_{Uq} = -684 \text{ lb.-ft.}$$

$$M_L = C_{m_0} S_L c_{Lq} = -397 \text{ lb.-ft.}$$

$$K_1 - K_{12} = -0.0234$$

With the foregoing data, and from the airplane

characteristics, $F_t = 69$ lb., acting downward. The corrected value of C_{LB}' is

$$C_{LB}' = \frac{1,636 + 69}{25.6 (135 + 88)} = 0.30$$

which is the value taken for the initial steady-flight condition prior to entry into the gust.

Wing lift coefficient in accelerated flight.—The increment in lift coefficient due to the gust is determined from the slope m of the cellule lift curve and the gust velocity U . The slope of the lift curve may be deter-

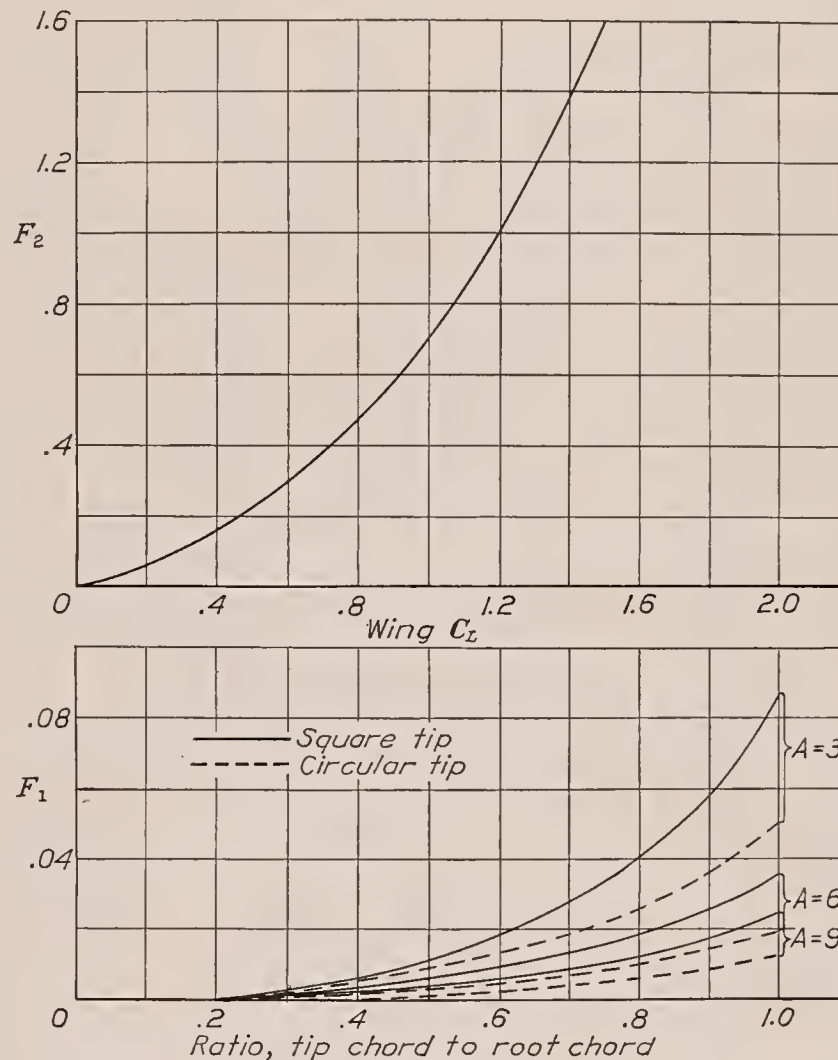


FIGURE 17.—Correction factors for wing C_L .

mined, as in the case of the monoplane, from the expression

$$m = f \frac{57.3 a_0}{1 + \frac{57.3 a_0}{\pi A}}$$

For the biplane, f may be taken as unity and $A = \frac{(kb)^2}{S_U + S_L}$ in which Munk's span factor k may be determined from reference 11. In the present example,

$$m = \frac{57.3 \times 0.097}{1 + \frac{57.3 \times 0.097}{\pi \frac{(1.02 \times 30)^2}{135 + 88}}} = 3.91$$

$$\begin{aligned} C_{LB} &= C_{LB}' + m \frac{U}{V} \\ &= 0.30 + 3.91 \frac{30}{146.6} = 1.10 \end{aligned}$$

From this point, the distribution of forces and moments on the upper wing are to be determined by using the method for finding the span load distribution given in appendix A. The first step is to find the lift coefficient of the upper wing.

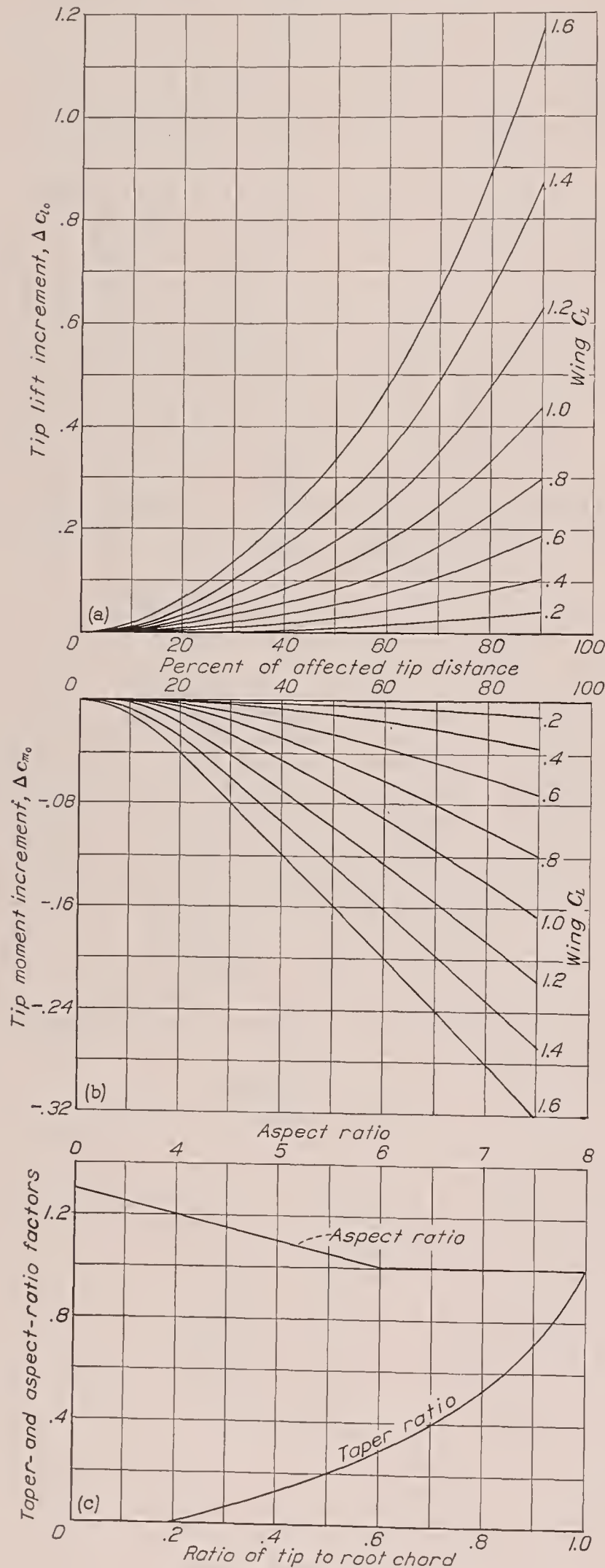


FIGURE 18.—Tip corrections.

1. From C_{LB} and equation (28)

$$C_{LU} = 1.168 \times 1.10 - 0.0507 = 1.233$$

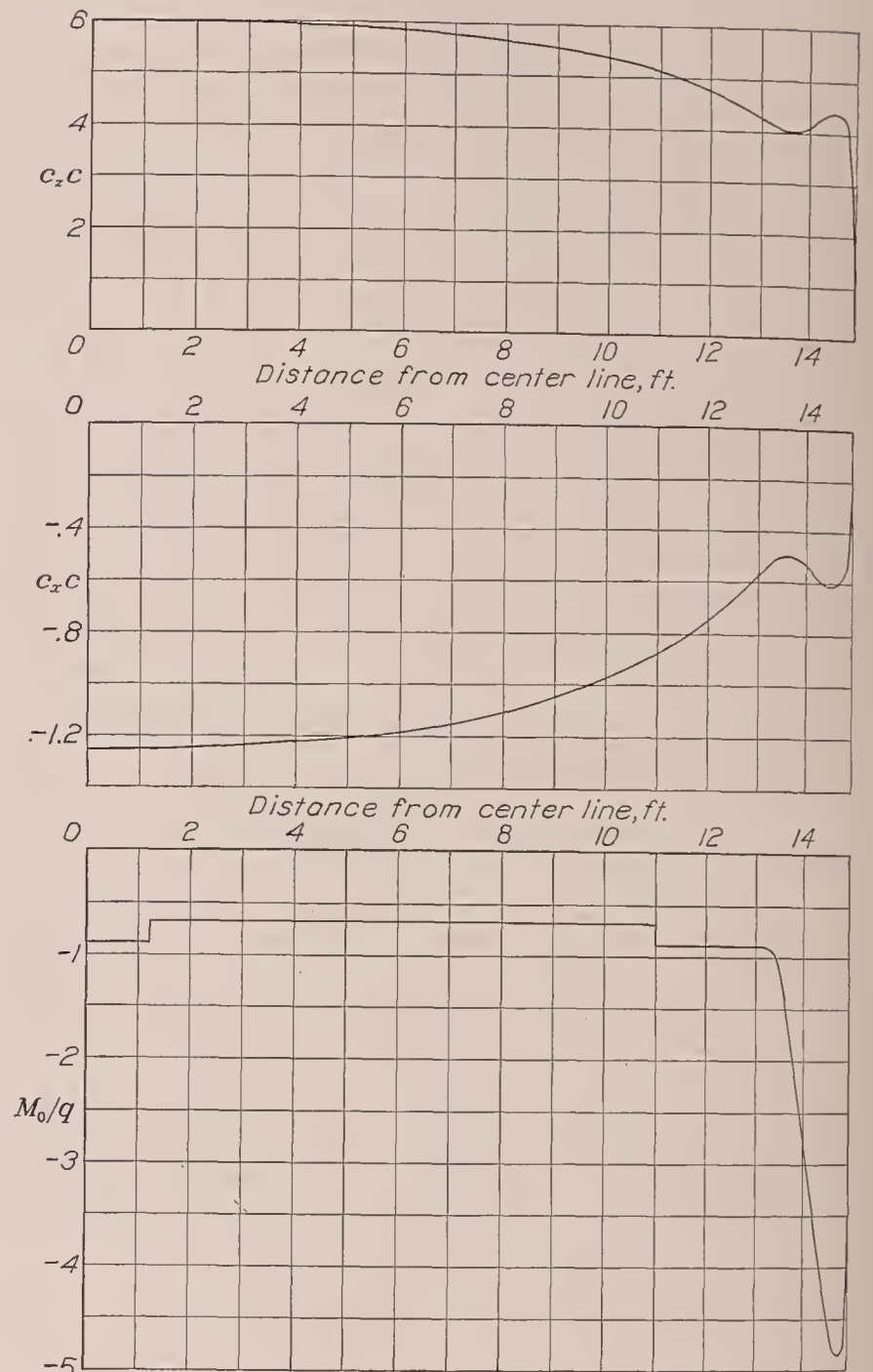


FIGURE 19.—Distribution of forces and moments on upper wing of biplane.

2. In order to reduce C_{LU} to allow for the tip correction, F_1 and F_2 are found from figure 17

$$F_1 = 0.038$$

$$F_2 = 1.06$$

$$F_1 \times F_2 = 0.040$$

The value of C_{LU} used to enter the charts is (tables IX and X)

$$C_{LU}'' = 1.233 - 0.040 = 1.193$$

3. The aspect ratio of the upper wing is

$$\frac{(30)^2}{135} = 6.67$$

4. The distribution of $c_{l_{a1}}$ is found from table IX, which gives the distribution for aspect ratio 6. The aspect ratio of the upper wing will be considered herein as sufficiently close to 6 to require no interpolation.

Values of $c_{l_{a1}}$ are tabulated in column 2 and values of $C_{LU}'' \times c_{l_{a1}}$ are tabulated in column 3 of table XI.

5. Since there is no twist, the values of c_{l_b} are zero.

6. The tip increments are determined from figure 18 and are tabulated in column 4 of table XI.

7. The tip corrections are added to the values of c_{l_0}'' to obtain the final c_{l_0} values tabulated in column 5 of table XI.

From this point the procedure follows the general method of this report to find the values of $c_z c$ of column 14 and $c_x c$ of column 17. The values of Δc_{d_0} given in table XI have been computed for the initial steady-flight condition in accordance with the principle of the delay in the growth of the boundary layer in accelerated flight. These values give the distribution required; they are plotted in figure 19.

In order to find the moment distribution, the basic section moment coefficients are tabulated in column 18, and to these are added the increments due to t/G and the tip effect. The value of $\Delta c_{m_0}(\frac{t}{G})$ is found from the

expression

$$\Delta c_{m_0}(\frac{t}{G}) = 0.1 \left(\frac{t}{G} \right)_{a_0} \\ = 0.1 \times 0.1065 = 0.011$$

These values are applied only along that portion of the span of the wing which lies between the projected tips of the lower wing, as indicated in column 19.

The tip-moment increments are found from figure 18 and are tabulated in column 20. The resultant distribution of c_{m_0} is given in column 21, and the final values of moment are tabulated in column 22 and plotted in figure 19.

LANGLEY MEMORIAL AERONAUTICAL LABORATORY,
NATIONAL ADVISORY COMMITTEE FOR AERONAUTICS,
LANGLEY FIELD, VA., *March 25, 1938.*

APPENDIX A

DETERMINATION OF SPAN LOAD DISTRIBUTION FOR SPECIAL CASES

The tables of span load ordinates (tables II and III) referred to in the development of the method and used in the monoplane example are, in general, suitable for the determination of resultant wing forces and for the determination of force distribution for structural applications except in cases, such as some externally braced wings, in which the tip loading has an important influence. For such excepted cases empirical tip corrections should be applied, in accordance with the following procedure. Also, in cases in which the plan form departs widely from the straight tapered shape or in which there are discontinuities in twist such as occur with partial-span flaps, the span load distribution should be determined from the basic wing theory. For such cases, the method discussed in reference 3 is recommended.

The results from reference 4 are to be used. The following procedure should be utilized for obtaining the span load distribution with special tip corrections:

1. From the conditions of the problem determine

C_L , based on the actual wing area, for which the distribution is to be determined.

2. Find $\Delta C_L(F_1 \times F_2)$ from figure 17, interpolating when necessary. Subtract ΔC_L from the value of C_L found from step (1).

3. Determine the geometric aspect ratio of the actual wing.

4. From table IX find the $c_{l_{a1}}$ distribution and multiply by the value from step (2).

5. Add to the distribution found in step (4) the c_{l_b} distribution from table X, reduced or increased in proportion to the actual twist.

6. Find the tip corrections (Δc_{l_0}) from figure 18(a). The affected distance is 40 percent of S/b . The tip increments of figure 18(a) are multiplied by both the aspect-ratio and taper-ratio factors given in figure 18(c).

7. Add the Δc_{l_0} increments, corrected for aspect ratio and taper, to the distribution of step (5).

8. Add to the section c_{m_0} values the tip Δc_{m_0} increments from figure 18(b) corrected for aspect ratio and taper ratio by the factors given in 18(c).

APPENDIX B

TABLE OF AIRFOIL CHARACTERISTICS (TABLE I)

A form of presentation of the airfoil characteristics has been adopted that permits all the characteristics necessary for the solution of problems such as those considered in this paper to be compactly presented. All such characteristics for a given airfoil section are presented by entries across a single line of a table. Characteristics are given in this form for certain well-known and commonly used airfoil sections in table I. The information presented for each section is discussed in the following paragraphs under subheadings corresponding to the column headings in the table.

Airfoil: The first column of the table gives the commonly used designations of the airfoil sections.

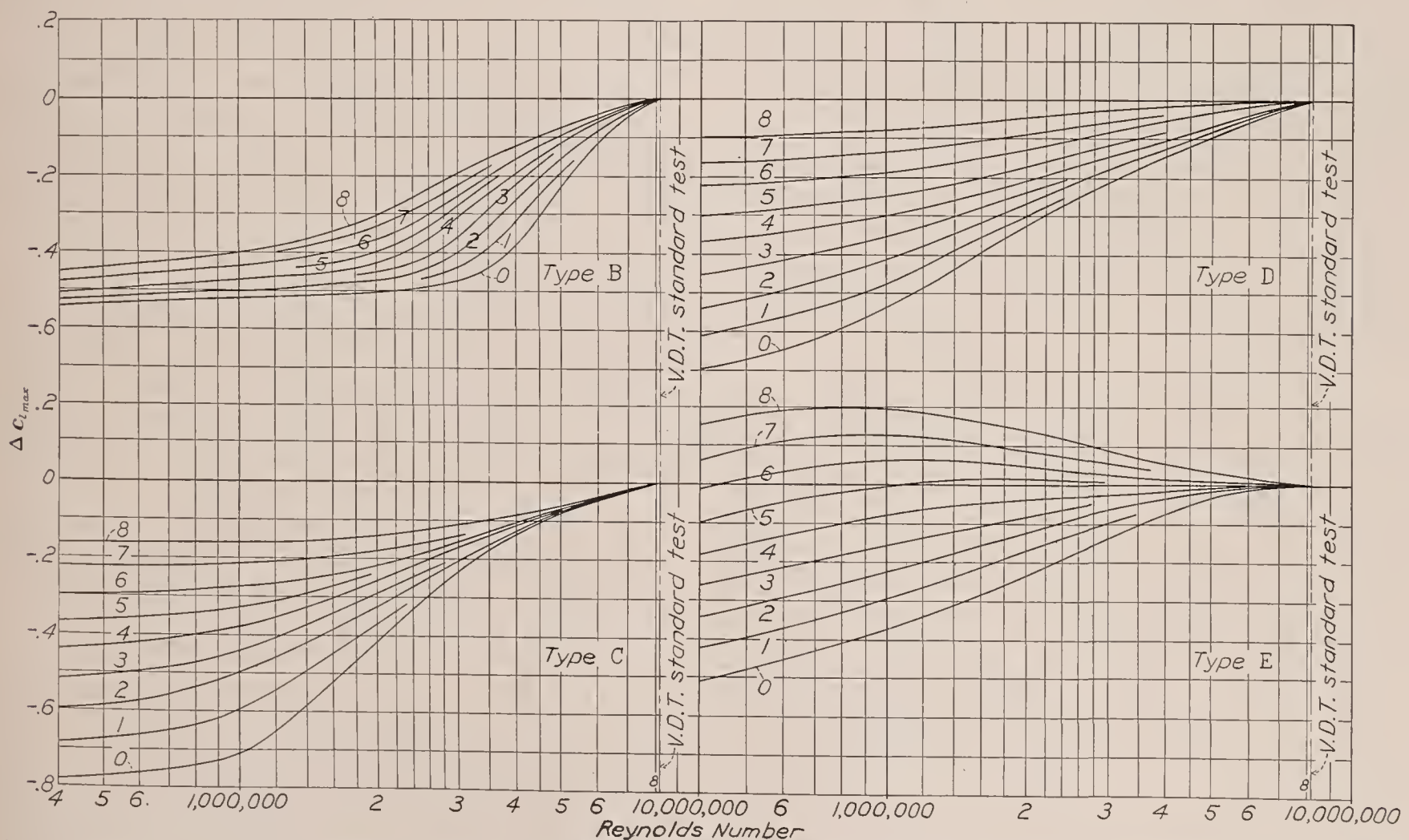
Reference: The second column gives the reference to an N. A. C. A. report or technical note (R or N), in which additional data for the section, including the official table of ordinates, may be found.

CLASSIFICATION

Chord: The letters in this column classify the airfoil sections with respect to the type of their chord. The letter A designates a chord joining the extremities of the mean line, the N. A. C. A. 2412, for example; B designates the chord as being tangent to the lower surface; and C designates an arbitrary chord from which the section ordinates are specified.

PD: The letters and numbers in column PD classify the airfoil section with respect to the character of the pressure distribution about the section. The letter refers to the character of the additional and the accompanying numbers to the character of the basic pressure distribution. The section of the present paper that discusses load distribution over an airfoil section, figures 6 and 7 that give the various distributions for the airfoil classes indicated, and the sample calculation of the pressure distribution about the U. S. A. 35-A section should be referred to for further details. The typical pressure distributions employed are based on Theodorsen's method (reference 7) modified to improve the agreement with experiment. The modified method and some experimental results may be found in reference 12. No data are available for class A airfoils.

SE: The character of the scale effect as affecting the maximum lift coefficient is indicated by the classification in column SE. The numbers and letters correspond to the designations of the typical scale-effect curves presented in figure 20 except that no data are available for class A airfoils. This information is necessary for determinations of stalling speeds. The Reynolds Number corresponding approximately to the stalling speed is first determined. Then from the curve of figure 20 corresponding to the designation in the SE column, the increment $\Delta C_{L_{max}}$ corresponding to this Reynolds Num-



To obtain the section maximum lift coefficient at the desired Reynolds Number, apply to the standard-test value the increment indicated by the curve that corresponds to the scale-effect designation of the airfoil. For type A, $\Delta C_{l_{max}} = 0$.

FIGURE 20.—Scale-effect corrections for $c_{l_{max}}$.

ber is obtained. This increment is added to the standard test value of the maximum lift coefficient given in table I to obtain the maximum lift coefficient to be expected for the particular airfoil section in flight at the Reynolds Number corresponding to the stalling speed. Application of the section data to the prediction of the $C_{L_{max}}$ of tapered wings may be found in reference 2.

This method for the prediction of maximum lift coefficients in flight is based on scale-effect tests of a number of related airfoils. The experimental data and a more complete discussion of the subject may be found in reference 13.

$C_{L_{max}}$: Under the heading $C_{L_{max}}$ the airfoil sections are classified according to the character of the lift-curve peak. The airfoils are classified A, B, C, and D in accordance with behavior in the neighborhood of maximum lift.

In type A the lift is more or less steady until it breaks suddenly to a lower value without an appreciable change of angle of attack.

In type B the lift becomes so unsteady and erratic as to preclude the taking of measurements for a range of angles of attack beyond an angle referred to as that of maximum lift.

In type C, before reaching the lift referred to as the "maximum," the lift breaks intermittently from a rather definite value to another rather definite but lower value, and then returns to the higher value. As the angle of attack is increased, the breaks become more frequent and of longer duration. The maximum lift is taken as the higher value occurring at an angle of attack at which it is a maximum or beyond which the higher value can no longer be determined with confidence.

In type D the lift is reasonably steady in the neighborhood of the maximum or any breaks occurring are small so that average values of the lift are measured throughout the range and the lift coefficients are represented by a continuous curve in the neighborhood of the maximum.

FUNDAMENTAL SECTION CHARACTERISTICS

Effective Reynolds Number: The values in this column represent the values of the Reynolds Number at which the section characteristics should be considered as applying to flight. The effective Reynolds Number is obtained from the actual test Reynolds Number by the application of a factor to allow for the effects of turbulence present in the tunnel. The turbulence factor 2.64 has been used for the variable-density tunnel. Comparative tests (reference 14) indicate that, at the effective Reynolds Number, maximum lift results from the tunnel tend to agree with those in flight.

$c_{l_{max}}$: This column gives the maximum lift coefficients corrected to represent values for the airfoil sections.

α_0 : In this column are tabulated the angles of zero lift in degrees.

a_0 : This column gives the slope (per degree) of the curve of lift coefficient against section angle of attack, that is, the lift-curve slope for a section of a wing of infinite span. The corresponding slopes for wings of finite span are found from the a_0 values by the method indicated in figure 12.

$c_{l_{opt}}$: The optimum lift coefficient, that is, the lift coefficient corresponding to the minimum profile-drag coefficient for the section, appears in this column. The profile-drag coefficient for the section at any lift coefficient may be inferred approximately from $c_{l_{opt}}$, $c_{d_{0_{min}}}$, and $c_{l_{max}}$ by the method indicated in figure 2.

$c_{d_{0_{min}}}$: The values in this column give the minimum profile-drag coefficients. The values given, however, are not the ones read from the usual plots of profile-drag coefficient made directly from the test data. They are corrected for the different skin-friction coefficients to be expected at the effective rather than at the test Reynolds Number (see footnote on p. 21 of reference 13) and for support interference. The support-interference correction, which gives an important reduction of drag for the thicker airfoils, was evaluated only recently and results published heretofore do not include the correction. Furthermore, another small correction is applied to these data to allow for a tip effect present in the tests of rectangular-tip airfoils. A corresponding correction has been applied to certain other characteristics including a_0 and the maximum lift coefficient; other characteristics are indirectly affected. A discussion of this subject may be found in reference 13.

$c_{m_{a.c.}}$: The values in this column give the pitching-moment coefficients referred to the aerodynamic center of the section rather than to the usual quarter-chord point. The aerodynamic center, by definition, is the point about which the pitching-moment coefficient is constant. Experimental results indicate that, by the use of an empirically derived aerodynamic-center position as suggested by Diehl, a constant pitching-moment coefficient $c_{m_{a.c.}}$ may be specified for each section that does not depart from the measured pitching-moment coefficients by more than the experimental error, over the range of lift coefficients between zero lift and slightly below maximum lift.

$a. c.$: In these two columns the coordinates of the aerodynamic center ahead of and above the quarter-chord point are given in percentage of the chord.

DERIVED AND ADDITIONAL CHARACTERISTICS

$c_{l_{max}}/c_{d_{0_{min}}}$: The values of this ratio are given because the ratio has been employed as a speed-range index. Strictly speaking, for this purpose, values of $c_{l_{max}}$ and $c_{d_{0_{min}}}$ should not be taken at the same value of the Reynolds Number; but the method has the advantage of simplicity and is of some value in comparing airfoil sections.

c. p. at $c_{l_{max}}$: Values are given in this column representing the center-of-pressure position in percentage of the chord behind the leading edge, or the forward end of the chord. The values are the measured values.

Wing characteristics $A=6$: Wing characteristics are given for a wing of aspect ratio 6 having the given airfoil section and for a modified rectangular plan form with rounded tips. (Tip length approximately one chord.) The values of m_6 represent the slope of the curve of lift coefficient against angle of attack expressed as changes

in lift coefficient per radian. The values of $C_{D_{min}}$ represent the minimum drag coefficients for the wings.

Thickness.—Data are given in three columns that refer to the airfoil section thickness at the indicated representative stations. The thicknesses are measured along perpendiculars to the chord and are expressed in percentages of the chord.

Camber.—The camber expressed in percentage of the chord is represented by giving the maximum displacement of the mean line from the straight line joining its extremities.

APPENDIX C

SYMBOLS

BASIC CONSIDERATIONS

- S , wing area.
 L , lift.
 q , dynamic pressure ($1/2\rho V^2$).
 c , chord.
 b , span.
 $C_L = \frac{L}{qS}$, wing lift coefficient.
 $c_l = \frac{dL}{qcdy}$, section lift coefficient.
 c_{l_0} , section lift coefficient acting perpendicular to local relative wind.

Subscripts:

- a_1 , refers to additional part of load distribution for $C_L=1$.
 a , refers to additional part of load distribution for any C_L .
 b , refers to basic part of load distribution for $C_L=0$.
 y , distance along lateral airplane axis.

GENERAL PROCEDURE

MONOPLANES

- x , distance along longitudinal airplane axis.
 z , distance along normal airplane axis.
 $x_{a.c.}, z_{a.c.}$, x and z coordinates of wing aerodynamic center.
 L_a , additional load parameter, $c_{l_{a1}} \frac{b}{S}$.
 x', z' , x and z coordinates with respect to a system of axes originating at the wing aerodynamic center.
 L_b , basic load parameter, $c_{l_b} \frac{c}{\epsilon a_0} \frac{b}{S}$.
 X, Z , components of air force in the x and z directions.
 c_x, c_z , section force coefficients.
 M , wing pitching moment.
 $M_{a.c.}$, wing pitching moment about wing aerodynamic center.
 M_s , part of wing moment due to section pitching moments about their aerodynamic centers.
 M_X, M_Z , parts of wing moment due to X force and Z force.
 M_T , wing pitching moment about torsional axis.
 z_T, x_T , distances of the torsional axis below the chord plane through the section aerodynamic

center and behind the beam plane through the section aerodynamic center.

- $c_{m_{a.c.}}$, section pitching-moment coefficient about section aerodynamic center.
 c_{d_0} , section profile-drag coefficient acting parallel to local relative wind.
 a_0 , section lift-curve slope (per degree).
 α_{i_0} , section angle of attack for zero lift.
 i , incidence of section chord with respect to x axis.
 c_t , tip chord (for rounded tips, c_t is the fictitious chord obtained by extending leading and trailing edges to the extreme tip).
 c_s , chord at center of wing or plane of symmetry.
 A , aspect ratio, b^2/S .
 ϵ , aerodynamic twist, assumed linear, and measured as the angle between the zero lift directions of the center and tip sections, positive for washin.
 C_L' , wing lift coefficient for steady-flight condition preceding accelerated-flight condition.
 m , slope of wing lift curve (per radian).
 m_6 , slope of lift curve for nontapered wing with rounded tips and aspect ratio 6 (per radian).
 $c_{d_{0min}}$, minimum section profile-drag coefficient.
 $c_{l_{opt}}$, optimum section lift coefficient, lift coefficient corresponding to $c_{d_{0min}}$.
 V , flight velocity or air speed.
 U , velocity of gust.
 a , slope of wing lift curve (per degree).
 f , plan-form factor.
 B , beam component of force.
 C , chord component of force.
 c_b, c_c , section coefficients of beam and chord components.
 $\theta_z = \frac{c_{i_0}}{a_0} + \alpha_{i_0} - i$
 $\theta_b = \frac{c_{i_0}}{a_0} + \alpha_{i_0} - i_b$
 $\theta_c = \frac{c_{i_0}}{a_0} + \alpha_{i_0} - i_c$
 $\phi = i_b - i_c$
 i_b , incidence of section chord with respect to the perpendicular to the beam direction.
 i_c , incidence of section chord with respect to the chord-truss direction.
 C_N , wing normal-force coefficient.
 c_n , section normal-force coefficient.

BIPLANES

- \bar{x}, \bar{z} , distances defining the locus of the aerodynamic centers of the biplane cellule.
- K_1, K_2 , etc., Diehl's biplane lift functions (references 5 and 6).
- G , gap.
- t , thickness of wing.
- s , stagger, distance between aerodynamic centers of upper and lower wings measured parallel to x axis.
- s_0 , stagger, distance between $\frac{1}{3}$ -chord points of upper and lower wings measured parallel to the zero-lift direction.
- M_{YR} , net biplane pitching moment about arbitrary y axis.
- $\Delta c_{m0}(\frac{t}{G})$, increment in section moment coefficient due to biplane parameter t/G .
- S_U' , portion of upper wing area to which the t/G moment correction applies.
- S_L' , portion of lower wing area to which the t/G moment correction applies.
- c_U' , average chord of the portion of the upper wing corresponding to S_U' .
- c_L' , average chord of the portion of the lower wing corresponding to S_L' .

Subscripts:

- U , refers to upper wing.
- L , refers to lower wing.
- B , refers to biplane.

LOAD DISTRIBUTION OVER AIRFOIL SECTION

- P , normal-pressure coefficient, p/q .
- p , the pressure difference across the wing section at any station along the chord.
- P_0 , value of P for the pressure distribution at zero lift.
- P_a , value of P for the additional part of the pressure distribution when the additional section lift coefficient is 1.
- $P_{a1}, \frac{x_{a.c.}}{c} P_{a.c.}$, components of P_a . (See fig. 6 and equation (24).)
- $\frac{x_{a.c.}}{c}$, distance in terms of chord of section aerodynamic center forward of quarter-chord point. (See table I.)
- P_b , value of P for the basic part of the pressure distribution.
- $-c_{m_{a.c.}} P_{bm}, \frac{z_c}{c} P_{bc}$, components of P_b . (See fig. 7.)
- $\frac{z_c}{c}$, camber ratio; distance, in terms of chord, of the minimum height of the section mean line above the straight line joining its extremities. (See table I.)
- c_{nb} , section normal-force coefficient corresponding to basic pressure distribution.
- $-c_{m_{a.c.}} (c_n)_{bm}, \frac{z_c}{c} (c_n)_{bc}$, components of c_{nb} . (See fig. 7.)

SAMPLE CALCULATION

- W , weight of airplane.
- F_t , force on horizontal tail surfaces.
- n_1 , applied wing load factor, basic design Condition I (a), reference 1.
- s , effective wing loading, reference 1.
- q_L , dynamic pressure corresponding to design high speed.
- C_{N1} , wing normal-force coefficient corresponding to n_1 .
- α_s , wing angle of attack based on chord of central section.
- $(\alpha_{l_0})_s$, angle of zero lift of the central section.
- J , parameter for determining angle of zero lift of twisted wing. (See fig. 11.)
- c_{d_0}' , section profile-drag coefficient for steady-flight condition.
- q' , dynamic pressure for steady-flight condition.

BIPLANE

- l , distance from y axis to $c.p.$ of horizontal surfaces.
- F_1, F_2 , factors for reducing wing lift coefficient to allow for tip increment. (See fig. 17.)
- k , Munk's span factor.

REFERENCES

1. Bureau of Air Commerce, Dept. Commerce: Airworthiness Requirements for Aircraft. Aero. Bull. No. 7-A, U. S. Dept. Commerce, 1934.
2. Anderson, Raymond F.: Determination of the Characteristics of Tapered Wings. T. R. No. 572, N. A. C. A., 1936.
3. Pearson, H. A.: Span Load Distribution for Tapered Wings with Partial-Span Flaps. T. R. No. 585, N. A. C. A., 1937.
4. Pearson, H. A.: Empirical Corrections to the Span Load Distribution at the Tip. T. N. No. 606, N. A. C. A., 1937.
5. Diehl, Walter S.: Relative Loading on Biplane Wings. T. R. No. 458, N. A. C. A., 1933.
6. Diehl, Walter S.: Relative Loading on Biplane Wings of Unequal Chords. T. R. No. 501, N. A. C. A., 1934.
7. Theodorsen, Theodore: Theory of Wing Sections of Arbitrary Shape. T. R. No. 411, N. A. C. A., 1931.
8. Garrick, I. E.: Determination of the Theoretical Pressure Distribution for Twenty Airfoils. T. R. No. 465, N. A. C. A., 1933.
9. Jacobs, Eastman N., Ward, Kenneth E., and Pinkerton, Robert M.: The Characteristics of 78 Related Airfoil Sections from Tests in the Variable-Density Wind Tunnel. T. R. No. 460, N. A. C. A., 1933.
10. Bureau of Air Commerce, Dept. Commerce: Design Information for Aircraft. Aero. Bull. No. 26, sec. 7 (D), U. S. Dept. Commerce, 1934.
11. Diehl, Walter Stuart: Engineering Aerodynamics. The Ronald Press Co., 1936, p. 34.
12. Pinkerton, Robert M.: Calculated and Measured Pressure Distributions over the Midspan Section of the N. A. C. A. 4412 Airfoil. T. R. No. 563, N. A. C. A., 1936.
13. Jacobs, Eastman N., and Sherman, Albert: Airfoil Section Characteristics as Affected by Variations of the Reynolds Number. T. R. No. 586, N. A. C. A., 1937.
14. Jacobs, Eastman N., and Clay, William C.: Characteristics of the N. A. C. A. 23012 Airfoil from Tests in the Full-Scale and Variable-Density Tunnels. T. R. No. 530, N. A. C. A., 1935.

TABLE I.—AIRFOIL SECTION CHARACTERISTICS ¹

Airfoil	N. A. C. A. reference (R=report; N=technical note)	Classification				Fundamental section characteristics									Derived and additional characteristics that may be used for structural design							
		Chord	PD	SE	$C_{L_{max}}$	Effective Reynolds Number (mil-lions)	$c_{l_{max}}$	α_{l_0} (deg.)	a_0 (per deg.)	$c_{l_{opt}}$	$c_{d_{0min}}$ (1)	$c_{m_{a. c.}}$	$a. c.$ (percent c from $c/4$)		$\frac{c_{l_{max}}}{c_{d_{0min}}}$	$c. p.$ at $c_{l_{max}}$ (per-cent c)	Wing characteris-tics $A=6$; round tips		Thickness (percent c) at—			Cam-ber 100 $\frac{z_c}{c}$ (per-cent c)
													Ahead	Above			m_0 (per radian)	$C_{D_{min}}$	0.15c	0.65c	Maxi-mum	
Clark Y.....	R416	B	C10	C4	D	8.37	1.68	−5.0	0.092	0.12	0.0071	−0.069	1.1	4	237	29	4.07	0.0072	10.53	8.30	11.70	3.9
Clark YM-15.....	N412	C	D10	D4	C	8.38	1.70	−5.2	.094	.10	.0076	−.068	1.1	7	224	30	4.14	.0079	13.51	10.63	15.00	4.0
Clark YM-18.....	N412	C	E10	E4	C	8.24	1.60	−5.1	.091	.07	.0085	−.064	1.4	5	188	30	4.04	.0086	16.21	12.72	18.00	4.0
Curtiss C-72.....	N412	B	C10	C4	D	7.98	1.74	−5.6	.095	.23	.0071	−.084	1.0	3	245	30	4.18	.0075	10.53	7.39	11.73	4.0
Göttingen 387.....	N428	B	D10	D6	D	8.40	1.70	−6.6	.097	.30	.0076	−.093	.7	4	224	32	4.24	.0081	13.40	9.69	14.85	5.9
Göttingen 398.....	N412	B	D10	D5	D	8.11	1.68	−6.0	.094	.15	.0076	−.081	.4	1	221	31	4.14	.0079	12.50	9.27	13.75	4.9
N-22.....	N412	B	C10	C4	D	8.11	1.72	−5.4	.096	.17	.0075	−.075	.6	4	229	30	4.20	.0076	11.25	8.36	12.37	4.3
N. A. C. A. CYH.....	N412	B	C11	C3	D	8.06	1.58	−2.9	.095	.08	.0065	−.027	.7	6	243	28	4.18	.0066	10.53	8.30	11.70	3.1
N. A. C. A. -M6.....	N412	A	C11	C3	D	8.00	1.51	−.8	.095	.03	.0066	.002	−.4	0	229	26	4.18	.0066	10.29	9.00	12.01	2.4
R. A. F. 15.....	R352	C	A10	A2	D	8.51	1.30	−2.2	.096	.25	.0060	−.053	1.7	10	217	29	4.20	.0063	6.38	5.04	6.38	2.6
U. S. A. 27.....	N412	B	C10	C6	B	8.06	1.71	−4.7	.094	.30	.0075	−.078	1.8	5	228	30	4.14	.0084	10.40	8.70	11.12	5.6
U. S. A. 35-A.....	R628	B	E10	E6	D	8.42	1.52	−8.0	.095	.38	.0094	−.111	.8	5	162	34	4.18	.0099	16.60	11.90	18.18	7.3
U. S. A. 35-B.....	N412	B	C10	C5	B	8.30	1.81	−5.2	.099	.35	.0071	−.076	.5	5	255	30	4.31	.0076	10.56	7.54	11.61	4.6
N. A. C. A. 0006.....	R628	A	A10	A	D	8.47	.91	0	.098	0	.0051	0	.7	2	178	35	4.28	.0051	5.35	4.13	6.00	0
N. A. C. A. 0012.....	R628	A	C10	C0	A	8.37	1.66	0	.099	0	.0060	0	.6	3	277	26	4.32	.0060	10.69	8.27	12.00	0
N. A. C. A. 2212.....	R460	A	C12	C3	B	8.42	1.72	−1.8	.099	.12	.0062	−.029	.9	5	277	27	4.31	.0062	10.69	8.25	12.00	2.0
N. A. C. A. 2409.....	R460	A	B10	B2	B	8.14	1.62	−1.7	.099	.08	.0060	−.044	.7	4	270	28	4.31	.0062	8.02	6.20	9.00	2.0
N. A. C. A. 2412.....	R628	A	C10	C2	B	8.24	1.72	−2.0	.098	.14	.0061	−.043	.5	3	282	28	4.28	.0062	10.71	8.27	12.00	2.0
N. A. C. A. 2415.....	R460	A	D10	D2	C	8.00	1.66	−1.7	.097	.10	.0068	−.040	1.4	5	244	28	4.24	.0068	13.39	10.34	15.00	2.0
N. A. C. A. 2418.....	R460	A	E10	E2	C	7.98	1.53	−1.9	.094	.06	.0076	−.038	1.1	2	201	27	4.14	.0076	16.08	12.39	18.00	2.0
N. A. C. A. 4412.....	R628	A	C10	C4	D	7.92	1.74	−4.0	.098	.32	.0071	−.088	.8	2	245	31	4.28	.0073	10.77	8.28	12.00	4.0
N. A. C. A. 23006.....	R610	A	A12	A	D	8.29	1.17	−1.2	.100	.15	.0057	−.012	1.0	8	205	26	4.34	.0058	5.34	4.13	6.00	1.8
N. A. C. A. 23009.....	R610	A	B12	C2	A	8.26	1.66	−1.1	.099	.08	.0059	−.009	.9	7	281	25	4.32	.0060	8.02	6.21	9.00	1.8
N. A. C. A. 23012.....	R610	A	C12	D2	A	8.37	1.74	−1.2	.100	.08	.0060	−.008	1.2	7	290	25	4.34	.0061	10.69	8.25	12.00	1.8
N. A. C. A. 23015.....	R610	A	D12	D2	A	8.37	1.73	−1.1	.098	.10	.0067	−.008	1.1	6	258	24	4.28	.0068	13.36	10.35	15.00	1.8
N. A. C. A. 23018.....	R610	A	E12	E2	B	8.16	1.58	−1.2	.097	.08	.0074	−.006	1.7	6	214	24	4.24	.0074	16.04	12.39	18.00	1.8
N. A. C. A. 23021.....	R610	A	F12	E2	B	8.21	1.50	−1.2	.092	.07	.0080	−.005	2.3	7	188	24	4.07	.0080	18.70	14.44	21.00	1.8

¹ Recently airfoil data from the variable-density tunnel have been found to be subject to a correction for support interference. These corrections have been applied to the data in table I, hence the discrepancy between the drag coefficients in the table and those appearing in previous publications and in the calculations of the example of this report.

TABLE II.—ADDITIONAL SPAN LIFT DISTRIBUTION DATA
VALUES OF L_a FOR ROUNDED-TIP WINGS

$A \backslash \frac{c_l}{c_s}$	0	0.1	0.2	0.3	0.4	0.5	0.6	0.7	0.8	0.9	1.0	0	0.1	0.2	0.3	0.4	0.5	0.6	0.7	0.8	0.9	1.0
Spanwise station $\frac{y}{b/2}=0$												Spanwise station $\frac{y}{b/2}=0.8$										
2-----	1.439	1.400	1.367	1.339	1.316	1.301	1.298	1.292	1.290	1.287	1.282	0.615	0.678	0.712	0.731	0.740	0.745	0.746	0.746	0.747	0.747	0.748
3-----	1.489	1.430	1.385	1.350	1.322	1.302	1.288	1.275	1.263	1.253	1.246	.589	.659	.700	.726	.743	.754	.764	.772	.782	.790	.799
4-----	1.527	1.452	1.400	1.360	1.329	1.302	1.279	1.260	1.242	1.226	1.211	.568	.644	.691	.723	.746	.764	.781	.795	.806	.816	.824
5-----	1.559	1.473	1.414	1.369	1.333	1.301	1.272	1.248	1.225	1.204	1.186	.548	.632	.685	.720	.748	.769	.790	.808	.822	.834	.844
6-----	1.585	1.492	1.428	1.378	1.338	1.300	1.267	1.237	1.211	1.187	1.163	.531	.619	.675	.717	.748	.775	.800	.820	.838	.851	.862
7-----	1.609	1.510	1.440	1.386	1.340	1.300	1.264	1.232	1.203	1.176	1.149	.517	.609	.670	.713	.748	.778	.802	.827	.845	.861	.875
8-----	1.629	1.534	1.456	1.392	1.344	1.300	1.264	1.229	1.198	1.165	1.135	.504	.600	.663	.710	.748	.779	.808	.834	.854	.872	.886
10-----	1.661	1.558	1.473	1.409	1.355	1.306	1.264	1.222	1.187	1.152	1.120	.486	.585	.653	.704	.748	.783	.815	.842	.868	.887	.905
12-----	1.686	1.578	1.490	1.420	1.361	1.308	1.261	1.219	1.180	1.143	1.109	.472	.576	.648	.702	.748	.788	.850	.850	.877	.899	.919
14-----	1.708	1.592	1.502	1.429	1.366	1.309	1.260	1.214	1.172	1.136	1.100	.462	.569	.641	.699	.748	.789	.825	.858	.887	.911	.933
16-----	1.726	1.610	1.513	1.433	1.368	1.309	1.255	1.208	1.165	1.127	1.090	.456	.564	.638	.698	.748	.791	.830	.862	.894	.921	.944
18-----	1.741	1.623	1.525	1.441	1.370	1.308	1.252	1.203	1.160	1.118	1.080	.450	.559	.636	.698	.750	.796	.835	.870	.901	.930	.953
20-----	1.755	1.632	1.531	1.446	1.372	1.307	1.250	1.199	1.152	1.109	1.070	.444	.545	.629	.698	.753	.801	.842	.878	.909	.937	.962
Spanwise station $\frac{y}{b/2}=0.2$												Spanwise station $\frac{y}{b/2}=0.9$										
2-----	1.369	1.329	1.300	1.279	1.267	1.260	1.258	1.256	1.253	1.250	1.248	0.378	0.465	0.508	0.525	0.531	0.534	0.535	0.536	0.537	0.538	0.539
3-----	1.405	1.346	1.308	1.279	1.260	1.248	1.241	1.234	1.228	1.221	1.214	.352	.447	.500	.528	.543	.552	.559	.564	.568	.571	.575
4-----	1.434	1.363	1.318	1.284	1.260	1.243	1.232	1.220	1.209	1.198	1.186	.331	.435	.495	.532	.554	.569	.581	.590	.598	.603	.609
5-----	1.459	1.377	1.324	1.288	1.260	1.240	1.223	1.208	1.194	1.181	1.168	.314	.424	.490	.531	.560	.583	.600	.613	.622	.630	.636
6-----	1.477	1.388	1.329	1.290	1.259	1.236	1.218	1.200	1.184	1.169	1.151	.300	.416	.487	.531	.565	.595	.615	.631	.643	.652	.659
7-----	1.491	1.393	1.332	1.291	1.259	1.236	1.214	1.193	1.174	1.157	1.138	.290	.410	.484	.535	.572	.603	.628	.646	.660	.671	.678
8-----	1.502	1.401	1.338	1.294	1.261	1.236	1.212	1.189	1.168	1.148	1.129	.282	.403	.481	.536	.579	.612	.638	.658	.673	.686	.696
10-----	1.513	1.411	1.347	1.299	1.265	1.236	1.209	1.182	1.158	1.137	1.114	.266	.383	.472	.541	.590	.628	.656	.679	.698	.712	.723
12-----	1.520	1.417	1.349	1.302	1.265	1.233	1.202	1.172	1.148	1.126	1.102	.253	.376	.469	.542	.597	.639	.669	.698	.718	.736	.751
14-----	1.527	1.423	1.354	1.307	1.268	1.232	1.201	1.170	1.144	1.119	1.094	.245	.370	.468	.545	.602	.648	.684	.715	.739	.759	.776
16-----	1.532	1.428	1.358	1.308	1.269	1.232	1.199	1.164	1.135	1.110	1.087	.239	.366	.468	.547	.609	.659	.698	.729	.756	.780	.801
18-----	1.539	1.429	1.359	1.309	1.270	1.231	1.195	1.160	1.130	1.103	1.078	.234	.367	.470	.552	.618	.669	.710	.743	.773	.800	.822
20-----	1.547	1.431	1.360	1.311	1.271	1.230	1.190	1.155	1.123	1.098	1.069	.231	.368	.473	.560	.625	.679	.722	.759	.791	.819	.846
Spanwise station $\frac{y}{b/2}=0.4$												Spanwise station $\frac{y}{b/2}=0.95$										
2-----	1.217	1.190	1.178	1.172	1.172	1.171	1.170	1.169	1.169	1.168	1.168	0.231	0.296	0.334	0.358	0.370	0.379	0.381	0.383	0.386	0.388	0.390
3-----	1.220	1.191	1.176	1.166	1.161	1.160	1.159	1.158	1.157	1.156	1.155	.209	.290	.339	.369	.389	.401	.407	.412	.416	.418	.420
4-----	1.223	1.192	1.173	1.162	1.156	1.151	1.149	1.148	1.147	1.146	1.145	.191	.286	.342	.378	.402	.420	.428	.434	.440	.444	.446
5-----	1.226	1.193	1.172	1.159	1.149	1.142	1.140	1.138	1.136	1.134	1.133	.176	.281	.344	.384	.415	.436	.449	.458	.463	.469	.471
6-----	1.229	1.193	1.171	1.155	1.145	1.138	1.132	1.128	1.127	1.126	1.125	.166	.278	.346	.392	.428	.451	.466	.475	.482	.490	.496
7-----	1.229	1.193	1.170	1.152	1.140	1.131	1.124	1.121	1.120	1.119	1.118	.155	.272	.346	.398	.438	.464	.481	.494	.502	.510	.515
8-----	1.229	1.192	1.168	1.150	1.138	1.128	1.120	1.116	1.113	1.111	1.110	.148	.261	.346	.403	.446	.475	.495	.510	.521	.529	.534
10-----	1.228	1.192	1.167	1.148	1.132	1.121	1.113	1.108	1.104	1.102	1.100	.138	.255	.346	.410	.460	.495	.520	.538	.553	.566	.575
12-----	1.228	1.192	1.166	1.145	1.125	1.111	1.107	1.102	1.099	1.094	1.090	.132	.254	.348	.419	.473	.511	.542	.566	.583	.598	.608
14-----	1.228	1.191	1.161	1.136	1.116	1.104	1.100	1.096	1.090	1.087	1.082	.129	.252	.349	.423	.482	.529	.562	.588	.609	.628	.640
16-----	1.228	1.189	1.158	1.131	1.112	1.101	1.097	1.091	1.086	1.081	1.075	.126	.252	.351	.432	.495	.546	.581	.610	.635	.655	.671
18-----	1.228	1.186	1.152	1.129	1.111	1.100	1.092	1.087	1.080	1.076	1.070	.122	.254	.357	.439	.503	.558	.598	.629	.658	.682	.702
20-----	1.228	1.182	1.149	1.127	1.110	1.098	1.089	1.083	1.078	1.071	1.065	.121	.258	.364	.449	.516	.569	.613	.648	.680	.707	.730
Spanwise station $\frac{y}{b/2}=0.6$												Spanwise station $\frac{y}{b/2}=0.975$										
2-----	0.970	0.976	0.984	0.992	1.003	1.010	1.012	1.014	1.016	1.018	1.019	0.132	0.172	0.207	0.239	0.263	0.272	0.274	0.277	0.279	0.281	0.282
3-----	.950	.962	.975	.985	.996	1.004	1.011	1.018	1.023	1.030	1.038	.119	.166	.210	.250	.278	.289	.291	.294	.298	.300	.301
4-----	.932	.948	.962	.978	.992	1.002	1.008	1.014	1.023	1.035	1.050	.107	.163	.214	.258	.288	.					

TABLE III.—BASIC SPAN LIFT DISTRIBUTION DATA
VALUES OF L_b FOR ROUNDED-TIP WINGS

$A \backslash \frac{c_t}{c_s}$	0	0.1	0.2	0.3	0.4	0.5	0.6	0.7	0.8	0.9	1.0	0	0.1	0.2	0.3	0.4	0.5	0.6	0.7	0.8	0.9	1.0	
Spanwise station $\frac{y}{b/2}=0$												Spanwise station $\frac{y}{b/2}=0.8$											
2-----	-0.118	-0.121	-0.122	-0.122	-0.122	-0.121	-0.121	-0.121	-0.120	-0.120	-0.120	0.072	0.079	0.080	0.082	0.083	0.085	0.085	0.086	0.086	0.084	0.081	
3-----	-.153	-.160	-.162	-.163	-.165	-.164	-.164	-.163	-.162	-.161	-.160	.088	.098	.101	.102	.104	.108	.109	.110	.110	.108	.106	
4-----	-.183	-.192	-.197	-.199	-.199	-.199	-.198	-.197	-.196	-.194	-.192	.100	.113	.120	.123	.126	.128	.128	.130	.130	.130	.129	
5-----	-.211	-.221	-.224	-.226	-.225	-.225	-.224	-.224	-.221	-.219	-.218	.109	.125	.135	.138	.140	.143	.147	.148	.148	.148	.149	
6-----	-.235	-.248	-.253	-.253	-.252	-.252	-.250	-.247	-.244	-.243	-.242	.115	.135	.148	.152	.156	.160	.160	.162	.163	.164	.165	
7-----	-.256	-.269	-.275	-.276	-.274	-.272	-.270	-.268	-.264	-.261	-.258	.121	.142	.158	.163	.169	.172	.173	.173	.174	.174	.175	
8-----	-.274	-.288	-.293	-.293	-.291	-.290	-.288	-.285	-.282	-.279	-.276	.126	.149	.164	.174	.180	.182	.182	.183	.183	.184	.184	
10-----	-.304	-.318	-.322	-.323	-.321	-.320	-.318	-.315	-.311	-.305	-.299	.136	.160	.178	.188	.195	.200	.201	.202	.203	.201	.198	
12-----	-.329	-.342	-.350	-.349	-.348	-.346	-.341	-.337	-.331	-.323	-.317	.145	.170	.188	.200	.208	.212	.214	.216	.216	.214	.210	
14-----	-.350	-.364	-.370	-.370	-.368	-.365	-.360	-.355	-.350	-.342	-.334	.152	.182	.200	.210	.216	.221	.223	.227	.228	.225	.220	
16-----	-.367	-.380	-.386	-.385	-.382	-.379	-.375	-.370	-.362	-.358	-.348	.159	.186	.205	.216	.222	.229	.232	.233	.236	.232	.229	
18-----	-.384	-.399	-.405	-.403	-.400	-.393	-.387	-.380	-.376	-.368	-.360	.161	.197	.215	.224	.230	.235	.239	.242	.243	.242	.238	
20-----	-.398	-.411	-.417	-.415	-.410	-.404	-.399	-.392	-.386	-.378	-.369	.166	.201	.220	.232	.237	.241	.243	.248	.248	.248	.247	
Spanwise station $\frac{y}{b/2}=0.2$												Spanwise station $\frac{y}{b/2}=0.9$											
2-----	-0.076	-0.080	-0.082	-0.085	-0.086	-0.086	-0.086	-0.085	-0.085	-0.084	-0.083	0.059	0.068	0.072	0.073	0.075	0.076	0.075	0.075	0.075	0.075	0.075	
3-----	-.098	-.108	-.111	-.112	-.113	-.113	-.113	-.113	-.112	-.110	-.108	.068	.083	.092	.098	.099	.100	.100	.100	.100	.100	.100	
4-----	-.117	-.130	-.135	-.138	-.137	-.137	-.137	-.137	-.137	-.135	-.132	.074	.098	.111	.118	.121	.122	.123	.123	.123	.123	.123	
5-----	-.131	-.148	-.156	-.159	-.159	-.158	-.158	-.158	-.157	-.156	-.152	.081	.107	.122	.131	.138	.140	.141	.141	.142	.142	.142	
6-----	-.145	-.162	-.173	-.176	-.176	-.176	-.176	-.176	-.175	-.172	-.170	.087	.117	.136	.148	.154	.159	.160	.160	.160	.160	.160	
7-----	-.156	-.178	-.189	-.192	-.192	-.192	-.191	-.191	-.190	-.190	-.189	.090	.123	.146	.160	.167	.171	.171	.172	.172	.172	.172	
8-----	-.168	-.189	-.200	-.204	-.204	-.205	-.205	-.206	-.205	-.204	-.204	.092	.131	.153	.170	.179	.182	.183	.184	.185	.186	.187	
10-----	-.182	-.207	-.220	-.224	-.225	-.225	-.226	-.226	-.225	-.225	-.225	.098	.139	.166	.184	.197	.201	.203	.205	.207	.209	.210	
12-----	-.197	-.226	-.239	-.240	-.239	-.238	-.238	-.238	-.237	-.237	-.237	.100	.147	.178	.198	.210	.218	.221	.225	.228	.229	.230	
14-----	-.206	-.234	-.248	-.249	-.248	-.248	-.248	-.248	-.248	-.248	-.248	.102	.156	.188	.208	.220	.231	.238	.241	.243	.245	.246	
16-----	-.212	-.242	-.256	-.258	-.257	-.256	-.256	-.256	-.256	-.256	-.255	.103	.161	.197	.219	.231	.241	.249	.253	.258	.259	.260	
18-----	-.219	-.247	-.260	-.264	-.265	-.265	-.265	-.265	-.265	-.264	-.262	.105	.166	.202	.228	.243	.252	.260	.263	.269	.271	.275	
20-----	-.222	-.255	-.269	-.271	-.271	-.271	-.272	-.272	-.272	-.272	-.270	.107	.172	.211	.233	.248	.260	.268	.273	.279	.282	.285	
Spanwise station $\frac{y}{b/2}=0.4$												Spanwise station $\frac{y}{b/2}=0.95$											
2-----	-0.006	-0.011	-0.013	-0.015	-0.016	-0.016	-0.016	-0.016	-0.016	-0.016	-0.015	0.038	0.051	0.058	0.059	0.060	0.060	0.060	0.060	0.059	0.059	0.058	
3-----	-.002	-.010	-.012	-.015	-.016	-.016	-.016	-.016	-.016	-.017	-.018	.044	.063	.073	.078	.079	.080	.080	.080	.080	.079	.078	
4-----	0	-.006	-.011	-.012	-.016	-.016	-.016	-.018	-.019	-.020	-.021	.050	.072	.076	.092	.095	.097	.099	.100	.100	.100	.099	
5-----	.004	-.004	-.010	-.012	-.016	-.018	-.020	-.021	-.021	-.022	-.023	.052	.083	.100	.107	.110	.112	.113	.114	.116	.117	.116	
6-----	.009	-.002	-.008	-.012	-.016	-.018	-.020	-.021	-.022	-.022	-.024	.054	.088	.109	.119	.122	.128	.130	.132	.132	.131	.130	
7-----	.012	-.001	-.010	-.013	-.017	-.018	-.020	-.022	-.025	-.027	-.029	.056	.093	.116	.130	.135	.140	.144	.148	.150	.149	.145	
8-----	.014	0	-.008	-.012	-.017	-.019	-.021	-.025	-.029	-.030	-.030	.057	.100	.125	.140	.146	.152	.158	.160	.161	.160	.159	
10-----	.021	.007	-.002	-.010	-.017	-.020	-.022	-.027	-.030	-.032	-.032	.058	.107	.138	.152	.162	.171	.178	.182	.186	.187	.183	
12-----	.028	.009	-.001	-.010	-.017	-.021	-.025	-.029	-.032	-.036	-.038	.059	.112	.143	.165	.179	.189	.198	.200	.202	.205	.204	
14-----	.036	.013	0	-.010	-.017	-.021	-.028	-.031	-.035	-.040	-.042	.060	.116	.151	.174	.190	.202	.211	.215	.218	.221	.222	
16-----	.043	.019	.002	-.008	-.016	-.022	-.029	-.034	-.038	-.041	-.045	.061	.121	.159	.184	.203	.218	.222	.229	.233	.236	.238	
18-----	.049	.022	.004	-.008	-.015	-.022	-.031	-.038	-.041	-.043	-.046	.061	.126	.166	.194	.213	.229	.236	.241	.248	.251	.255	
20-----	.050	.023	.006	-.006	-.014	-.022	-.031	-.038	-.041	-.046	-.049	.061	.128	.173	.203	.225	.239	.245	.251	.259	.265	.271	
Spanwise station $\frac{y}{b/2}=0.6$												Spanwise station $\frac{y}{b/2}=0.975$											
2-----	0.052	0.052	0.051	0.050	0.050	0.050	0.050	0.050	0.049	0.049	0.048	0.019	0.030	0.035	0.037	0.037	0.037	0.037	0.036	0.036	0.035	0.034	
3-----	.070	.069	.068	.068	.068	.068	.068	.068	.068	.068	.068	.022	.039	.045	.049	.050	.051	.052	.054	.053	.052	.051	
4-----	.085	.082	.081	.080	.080	.080	.080	.080	.080	.080	.080	.026	.043	.054	.060	.062	.064	.068	.069	.069	.068	.067	
5-----	.099	.095	.092	.091	.091	.091	.091	.091	.090	.090	.090	.029	.051	.065	.070	.071	.075	.078	.081	.082	.083	.083	
6-----	.109	.107	.104	.102	.101	.101	.100	.100	.100	.100	.100	.030	.055	.071	.079	.082	.088	.091	.094	.097	.097	.097	
7-----	.119	.117	.114	.112	.111	.110	.110	.110	.110	.109	.108	.030	.060	.078	.087	.091	.098	.101	.107	.110	.110	.110	
8-----	.128	.122	.121	.120	.119	.119	.119	.118	.118	.117	.116	.030	.062	.081	.091	.100	.107	.112	.120	.121	.121	.121	
10-----	.139	.138	.135	.132	.131	.130	.130	.129	.128	.126	.124	.031	.067	.090	.105	.115	.124						

TABLE IV.—CALCULATION OF THE ADDITIONAL FORCES AND MOMENTS LEADING TO THE DETERMINATION OF THE WING AERODYNAMIC CENTER

1	2	3	4	5	6	7	8	9	10	11	12
Station from center line $\frac{y}{b/2}$	L_a	c (ft.)	$c_{l_{a1}}$	a_0 (per deg.)	$\frac{c_{l_{a1}}}{a_0}$ (deg.)	α_{l_0} (deg.)	$-i$ (deg.)	c_{d_0}	θ_{z_a} (deg.)	$\cos \theta_{z_a}$	$\sin \theta_{z_a}$
0	1.301	8.27	0.944	0.095	9.9	-8.0	-4	0.0157	-2.1	0.999	-0.0366
.2	1.240	7.44	1.000	.096	10.4	-7.4	-4	.0159	-1.0	1.000	-.0175
.4	1.142	6.62	1.035	.097	10.7	-6.9	-4	.0157	-.2	1.000	-.0035
.6	1.000	5.79	1.036	.097	10.7	-6.3	-4	.0147	.4	1.000	.0070
.8	.775	4.92	.945	.098	9.6	-5.8	-4	.0124	-.2	1.000	-.0035
.9	.583	3.84	.911	.099	9.2	-5.5	-4	.0117	-.3	1.000	-.0052
.95	.436	2.83	.924	.099	9.3	-5.3	-4	.0115	0	1.000	0
.975	.320	2.04	.942	.099	9.5	-5.3	-4	.0115	.2	1.000	.0035
1.0	0	0	-----	.099	-----	-5.2	-----	-----	-----	-----	-----

1	13	14	15	16	17	18	19	20	21	22	23	24
Station from center line $\frac{y}{b/2}$	$c_{d_0} \cos \theta_{z_a}$	$-c_{l_{a1}} \sin \theta_{z_a}$	$c_{l_{a1}} \cos \theta_{z_a}$	$c_{d_0} \sin \theta_{z_a}$	$c_{x_{a1}}$	$c_{z_{a1}}$	z (ft.)	x (ft.)	$c_{x_{a1}} c$ (ft.)	$c_{z_{a1}} c$ (ft.)	$c_{x_{a1}} c_z$ (ft. ²)	$-c_{z_{a1}} c_x$ (ft. ²)
0	0.0157	0.0346	0.943	-0.0006	0.0503	0.942	3.14	-1.98	0.416	7.79	1.31	15.42
.2	.0159	.0175	1.000	-.0003	.0334	1.000	3.43	-1.34	.248	7.44	.85	9.97
.4	.0157	.0036	1.035	-.0001	.0193	1.035	3.76	-.70	.128	6.85	.48	4.80
.6	.0147	-.0073	1.036	.0001	.0074	1.036	4.04	-.08	.043	6.00	.17	.48
.8	.0124	.0033	.945	0	.0157	.945	4.34	.56	.077	4.65	.34	-2.60
.9	.0117	.0047	.911	-.0001	.0164	.911	4.54	.94	.063	3.50	.29	-3.29
.95	.0115	0	.924	0	.0115	.924	4.68	1.24	.033	2.61	.15	-3.24
.975	.0115	-.0033	.942	0	.0082	.942	4.78	1.40	.017	1.92	.08	-2.69

TABLE IV-A.—CALCULATION OF c_{d_0} VALUES FOR
TABLE IV

Station	t/c	$c_{d_{0min}}$	$c_{l_{opt}}$	$c_{l_{max}}$	$\frac{ c_{l_{a1}} - c_{l_{opt}} }{c_{l_{max}} - c_{l_{opt}}}$	Δc_{d_0}	c_{d_0}
0	0.1818	0.0116	0.38	1.57	0.47	0.0041	0.0157
.2	.1745	.0112	.37	1.62	.50	.0047	.0159
.4	.1653	.0106	.37	1.66	.52	.0051	.0157
.6	.1536	.0100	.36	1.72	.50	.0047	.0147
.8	.1380	.0092	.36	1.76	.42	.0032	.0124
.9	.1280	.0089	.35	1.79	.39	.0028	.0117
.95	.1224	.0086	.35	1.80	.40	.0029	.0115
.975	.1194	.0084	.35	1.80	.41	.0031	.0115
1	.1161	.0083	.35	1.81	-----	-----	-----

TABLE V.—CALCULATION OF THE BASIC FORCES AND MOMENTS LEADING TO THE DETERMINATION OF THE WING PITCHING MOMENT

1	2	3	4	5	6	7	8	9	10	11	12	13	14
Station from center line $\frac{y}{b/2}$	L_b	c (ft.)	c_{l_b}	a_0 (per deg.)	$\frac{c_{l_b}}{a_0}$ (deg.)	α_{l_0} (deg.)	$-i$ (deg.)	c_{d_0}	θ_{z_b} (deg.)	$\cos \theta_{z_b}$	$\sin \theta_{z_b}$	$c_{d_0} \times \cos \theta_{z_b}$	$-c_{l_b} \times \sin \theta_{z_b}$
0	−0.225	8.27	0.0400	0.095	0.42	−8.0	−4	0.0132	−11.6	0.980	−0.2011	0.0129	0.0080
.2	−.158	7.44	.0312	.096	.32	−7.4	−4	.0126	−11.1	.981	−.1925	.0124	.0060
.4	−.018	6.62	.0040	.097	.04	−6.9	−4	.0122	−10.9	.982	−.1891	.0120	.0008
.6	.091	5.79	−.0231	.097	−.24	−6.3	−4	.0115	−10.5	.983	−.1822	.0113	−.0042
.8	.143	4.92	−.0427	.098	−.44	−5.8	−4	.0108	−10.2	.984	−.1771	.0106	−.0076
.9	.140	3.84	−.0536	.099	−.54	−5.5	−4	.0104	−10.0	.985	−.1754	.0102	−.0094
.95	.112	2.83	−.0582	.099	−.59	−5.3	−4	.0101	−9.9	.985	−.1719	.0099	−.0100
.975	.075	2.04	−.0540	.099	−.55	−5.3	−4	.0099	−9.9	.985	−.1719	.0098	−.0093

1	15	16	17	18	19	20	21	22	23	24	25	26
Station from center line $\frac{y}{b/2}$	$c_{l_b} \times \cos \theta_{z_b}$	$c_{d_0} \times \sin \theta_{z_0}$	c_{x_b}	c_{z_b}	$c_{x_b}c$ (ft.)	$c_{z_b}c$ (ft.)	x' (ft.)	z' (ft.)	$c_{x_b}c_{z'}$ (ft. ²)	$-c_{z_b}c_{x'}$ (ft. ²)	$c_{m_{a.c.}}$	$c_{m_{a.c.}}c^2$ (ft. ²)
0	0.0392	−0.0027	0.0209	0.0365	0.173	0.302	−1.37	−0.47	−0.08	0.41	−0.111	−7.59
.2	.0306	−.0024	.0184	.0282	.137	.210	−.73	−.18	−.02	.15	−.104	−5.76
.4	.0039	−.0023	.0128	.0016	.085	.011	−.09	.15	.02	.00	−.097	−4.25
.6	−.0227	−.0021	.0071	−.0248	.041	−.144	.53	.43	.02	.08	−.090	−3.02
.8	−.0420	−.0019	.0030	−.0439	.015	−.216	1.17	.73	.01	.25	−.083	−2.01
.9	−.0528	−.0018	.0008	−.0546	.003	−.210	1.55	.93	.00	.33	−.079	−1.16
.95	−.0573	−.0017	−.0001	−.0590	.000	−.167	1.85	1.07	.00	.31	−.078	−.62
.975	−.0532	−.0017	.0005	−.0549	.001	−.112	2.01	1.17	.00	.23	−.077	−.32

TABLE VI.—CALCULATION OF THE CHORD AND BEAM COMPONENTS
[Numbers in parentheses are columns]

1	2	3	4	5	6	7	8	9	10	11	12	13	14	15	16	17	18
Station from center line $\frac{y}{b/2}$	c_{l_b}	$CLC_{l_{a1}}$	c_{l_0}	$c_{m_{a.c.}}$	c_{d_0}'	c_{d_0}	$\frac{c_{l_0}}{a_0}$ (deg.)	α_{l_0} (deg.)	$-i_b$ (deg.)	$-i_c$ (deg.)	θ_b (deg.)	θ_c (deg.)	ϕ (deg.)	$\cos \theta_c$	$\sin \theta_c$	$\cos \theta_b$	$\sin \theta_b$
0	0.040	1.702	1.742	−0.111	0.0120	0.0120	18.3	−8.0	0	4.0	10.3	14.3	4.0	0.969	0.2470	0.984	0.1788
.2	.031	1.803	1.834	−.104	.0116	.0116	19.1	−7.4	0	3.6	11.7	15.3	3.6	.965	.2639	.979	.2028
.4	.004	1.865	1.869	−.097	.0110	.0110	19.3	−6.9	0	3.2	12.4	15.6	3.2	.963	.2689	.977	.2147
.6	−.023	1.866	1.843	−.090	.0104	.0104	19.0	−6.3	0	2.8	12.7	15.5	2.8	.964	.2672	.976	.2199
.8	−.043	1.703	1.660	−.083	.0093	.0093	16.9	−5.8	0	2.4	11.1	13.5	2.4	.972	.2335	.981	.1925
.9	−.054	1.642	1.588	−.079	.0090	.0090	16.0	−5.5	0	2.2	10.5	12.7	2.2	.976	.2199	.983	.1822
.95	−.058	1.666	1.608	−.078	.0087	.0087	16.2	−5.3	0	2.1	10.9	13.0	2.1	.974	.2250	.982	.1891
.975	−.054	1.698	1.644	−.077	.0085	.0085	16.6	−5.3	0	2.0	11.3	13.3	2.0	.973	.2301	.981	.1960

1	19	20	21	22	23	24	25	26	27	28	29	30	31	32	33	34	35	36
Station from center line $\frac{y}{b/2}$	$\tan \phi$	$\tan \theta_c$	$\cot \theta_c$	$\tan \theta_b$	$\cot \theta_b$	$\tan \theta_c$	$\cot \theta_c$	$\tan \theta_b$	$\cot \theta_b$	$c_{l_0}(1 - \tan \theta_b \tan \phi) \cos \theta_b$	$c_{d_0}(1 + \cot \theta_b \tan \phi) \sin \theta_b$	$c_{d_0}(1 + \tan \theta_c \tan \phi) \cos \theta_c$	$-c_{l_0}(1 - \cot \theta_c \tan \phi) \sin \theta_c$	$c_b = (28) + (29)$	$c_c = (30) + (31)$	dB/dy (lb./ft.)	dC/dy (lb./ft.)	$dM_{a.c.}/dy$ (ft.-lb./ft.)
0	0.0699	0.2549	3.923	0.1817	5.500	0.0178	0.2741	0.0127	0.3842	1.692	0.0029	0.0118	−0.3124	1.695	−0.3006	151.3	−26.8	−81.9
.2	.0629	.2717	3.681	.2071	4.829	.0171	.2315	.0130	.3037	1.772	.0031	.0114	−.3720	1.775	−.3606	142.5	−28.9	−62.1
.4	.0559	.2811	3.558	.2199	4.548	.0157	.1989	.0123	.2542	1.804	.0030	.0108	−.4026	1.807	−.3918	129.1	−28.0	−45.9
.6	.0489	.2811	3.558	.2254	4.437	.0137	.1740	.0110	.2170	1.779	.0028	.0101	−.4067	1.782	−.3966	111.3	−24.8	−32.6
.8	.0419	.2419	3.971	.1962	5.097	.0101	.1664	.0082	.2136	1.615	.0022	.0091	−.3231	1.617	−.3140	85.8	−16.7	−21.7
.9	.0384	.2272	4.401	.1853	5.396	.0087	.1690	.0071	.2072	1.550	.0019	.0089	−.2902	1.552	−.2813	64.3	−11.7	−12.6
.95	.0367	.2309	4.333	.1926	5.193	.0085	.1590	.0071	.1906	1.568	.0019	.0086	−.3043	1.570	−.2957	47.9	−9.0	−6.7
.975	.0349	.2364	4.230	.1998	5.005	.0083	.1476	.0070	.1747	1.602	.0020	.0084	−.3223	1.604	−.3139	35.3	−6.9	−3.5

TABLE VII.—CALCULATION OF P_a

Station $100\frac{x}{c}$	P_{a1}	$P_{a.c.}$	$\frac{P_{a.c.} \frac{x_{a.c.}}{c}}{P_{a.c.} \times 0.008}$	P_a
0	0	0	0	0
1.25	3.87	3.2	.03	3.90
2.50	3.81	4.5	.04	3.85
5	3.27	5.5	.04	3.31
7.5	2.81	5.9	.05	2.86
10	2.44	5.7	.05	2.49
15	1.95	5.0	.04	1.99
20	1.62	4.3	.03	1.65
30	1.18	2.9	.02	1.20
40	.89	1.4	.01	.90
50	.69	.0	.00	.69
60	.51	-1.4	-.01	.50
70	.36	-2.9	-.02	.34
80	.23	-4.3	-.03	.20
90	.11	-5.7	-.04	.07
95	.06	-5.5	-.05	.01
100	0	0	0	0

TABLE VIII.—CALCULATION OF PRESSURE DISTRIBUTION

Station $100\frac{x}{c}$	P_{bm} class 1	$-P_{bm}c_{ma.c.}$	P_{bc}	$\frac{z_c}{c}P_{bc}$	P_b	$-c_{nb}P_a$	P_θ	c_nP_a	P	p (lb./sq.ft.)
0	0	0	0	0	0	0	0	0	0	0
1.25	2.85	.32	0	0	.32	-2.73	-2.41	6.61	4.20	45.3
2.5	4.25	.47	0	0	.47	-2.69	-2.22	6.52	4.30	46.4
5	6.05	.67	0	0	.67	-2.31	-1.64	5.61	3.97	42.8
7.5	7.10	.79	0	0	.79	-2.00	-1.21	4.85	3.64	39.3
10	7.80	.87	0	0	.87	-1.74	-.87	4.22	3.35	36.2
15	8.80	.98	0	0	.98	-1.39	-.41	3.37	2.96	31.9
20	9.30	1.03	0	0	1.03	-1.15	-.12	2.80	2.68	28.9
30	9.50	1.05	0	0	1.05	-.84	.21	2.03	2.24	24.2
40	8.80	.98	0	0	.98	-.63	.35	1.52	1.87	20.2
50	7.75	.86	0	0	.86	-.48	.38	1.17	1.55	16.7
60	6.60	.73	0	0	.73	-.35	.38	.85	1.23	13.3
70	5.30	.59	0	0	.59	-.24	.35	.58	.93	10.0
80	3.75	.42	0	0	.42	-.14	.28	.34	.62	6.7
90	2.05	.23	0	0	.23	-.05	.18	.12	.30	3.2
95	1.10	.12	0	0	.12	-.01	.11	.02	.13	1.4
100	0	0	0	0	0	0	0	0	0	-----

TABLE IX.—THEORETICAL DISTRIBUTION OF c_{la1}
[Straight tips, $C_L=1.0$]

Taper ratio	Rib location in percent semispan							
	0	20	40	60	80	90	95	97.5
Aspect ratio 4								
0.0	0.754	0.890	1.025	1.185	1.444	1.650	-----	-----
.1	.790	.917	1.030	1.140	1.304	1.342	1.326	1.173
.2	.828	.945	1.036	1.109	1.175	1.125	.976	.783
.3	.870	.972	1.043	1.088	1.090	.995	.818	.645
.4	.911	1.000	1.053	1.073	1.030	.910	.734	.567
.5	.954	1.027	1.066	1.064	.986	.844	.674	.513
.6	.997	1.058	1.081	1.056	.953	.794	.632	.476
.7	1.039	1.086	1.093	1.050	.927	.756	.596	.446
.8	1.082	1.112	1.104	1.045	.906	.727	.566	.422
.9	1.124	1.136	1.112	1.041	.889	.703	.541	.402
1.0	1.166	1.158	1.117	1.039	.873	.684	.519	.385
Aspect ratio 6								
0.0	0.783	0.920	1.030	1.154	1.340	1.470	1.618	1.800
.1	.807	.937	1.030	1.113	1.225	1.267	1.180	1.028
.2	.838	.954	1.034	1.088	1.141	1.110	.965	.777
.3	.874	.975	1.044	1.073	1.079	1.002	.847	.660
.4	.914	1.000	1.056	1.065	1.028	.927	.763	.588
.5	.953	1.026	1.064	1.060	.994	.876	.705	.539
.6	.992	1.051	1.070	1.055	.970	.840	.663	.506
.7	1.030	1.075	1.078	1.050	.950	.810	.632	.480
.8	1.067	1.097	1.086	1.046	.932	.782	.609	.458
.9	1.103	1.114	1.094	1.042	.914	.757	.589	.437
1.0	1.137	1.129	1.104	1.038	.898	.734	.571	.417
Aspect ratio 8								
0.0	0.797	0.930	1.030	1.136	1.294	1.375	1.448	1.620
.1	.820	.945	1.037	1.099	1.194	1.228	1.160	.964
.2	.849	.964	1.042	1.072	1.118	1.106	.973	.768
.3	.884	.983	1.046	1.058	1.065	1.013	.852	.660
.4	.919	1.004	1.051	1.050	1.028	.942	.773	.600
.5	.952	1.027	1.060	1.048	1.000	.896	.725	.564
.6	.987	1.050	1.068	1.049	.979	.860	.694	.538
.7	1.021	1.071	1.077	1.049	.960	.832	.669	.515
.8	1.055	1.090	1.083	1.047	.944	.808	.646	.494
.9	1.086	1.103	1.090	1.043	.930	.788	.624	.474
1.0	1.114	1.113	1.094	1.038	.917	.770	.605	.454

TABLE X.—THEORETICAL DISTRIBUTION OF c_{l_b} [Straight tips, $C_L=0$; $\epsilon=10^\circ$; $A=6$]

Taper ratio	Rib location in percent semispan									
	0	20	40	50	60	70	80	90	95	97.5
0	0.218	0.165	0.043	-0.023	-0.082	-0.128	-0.166	-0.174	-0.154	-0.122
.1	.208	.158	.040	-.025	-.086	-.133	-.170	-.179	-.160	-.127
.2	.200	.154	.037	-.028	-.089	-.137	-.175	-.190	-.168	-.134
.3	.191	.149	.034	-.030	-.093	-.142	-.182	-.202	-.178	-.146
.4	.184	.145	.030	-.033	-.096	-.148	-.189	-.216	-.194	-.160
.5	.175	.140	.026	-.037	-.100	-.154	-.198	-.233	-.214	-.176
.6	.165	.134	.023	-.039	-.104	-.160	-.210	-.250	-.239	-.192
.7	.153	.126	.019	-.041	-.107	-.167	-.223	-.275	-.270	-.214
.8	.137	.117	.016	-.044	-.112	-.175	-.240	-.307	-.313	-.264
.9	.115	.103	.012	-.046	-.115	-.185	-.260	-.354	-.396	-.370
1.0	.078	.083	.008	-.048	-.116	-.197	-.287	-.421	-.581	-.800

TABLE XI.—COMPUTATION OF THE FORCE DISTRIBUTION ON THE UPPER WING OF BIPLANE

[Numbers in parentheses are columns]

1	2	3	4	5	6	7	8	9	10	11	12
Distance from center line (ft.)	$c_{l_{a1}}$	$c_{l_0}'' = C_{L_U}'' c_{l_{a1}}$	Δc_{l_0}	$c_{l_0} = (3) + (4)$	c_{l_0}/a_0 (deg.)	$\theta_s = \alpha_{l_0} - i + (6)$ (deg.)	$\cos \theta_s$	$\sin \theta_s$	$c_{l_0} c \cos \theta_s$	Δc_{d_0}	$c_{d_0} = c_{d_{0min}} + (11)$
0	1.137	1.357	0	1.357	14.0	12.2	0.978	0.2111	5.965	0.0004	0.0075
3	1.130	1.349	0	1.349	13.9	12.1	.978	.2097	5.935	.0004	.0075
6	1.105	1.319	0	1.319	13.6	11.8	.979	.2045	5.810	.0004	.0075
9	1.039	1.240	0	1.240	12.8	11.0	.982	.1906	5.475	.0003	.0074
12	.897	1.070	0	1.070	11.0	9.2	.987	.1605	4.750	.0002	.0073
13	.798	.952	0	.952	9.8	8.0	.990	.1395	4.240	.0002	.0073
13.5	.735	.877	.022	.899	9.3	7.5	.992	.1300	4.013	.0002	.0073
14	.638	.761	.160	.921	9.5	7.7	.991	.1340	4.107	.0001	.0072
14.5	.480	.573	.410	.983	10.1	8.3	.989	.1449	4.375	-----	.0071

1	13	14	15	16	17	18	19	20	21	22
Distance from center line (ft.)	$c_{d_0} c \sin \theta_s$	$c_s c = (10) + (13)$	$c_{l_0} c \sin \theta_s$	$c_{d_0} c \cos \theta_s$	$c_s = (15) + (16)$	c_{m_0}	$\Delta c_{m_0} \left(\frac{t}{a} \right)$	Δc_{m_0}	$(18) + (19) + (20)$	$c^2 (21)$
0	0.007	5.972	-1.291	0.033	-1.258	-0.044	0	0	-0.044	-0.891
3	.007	5.942	-1.273	.033	-1.240	-.044	.011	0	-.033	-.669
6	.007	5.817	-1.214	.033	-1.181	-.044	.011	0	-.033	-.669
9	.006	5.481	-1.064	.033	-1.031	-.044	.011	0	-.033	-.669
12	.005	4.760	-.773	.033	-.740	-.044	0	0	-.044	-.891
13	.005	4.245	-.598	.033	-.565	-.044	0	0	-.044	-.891
13.5	.004	4.017	-.526	.033	-.493	-.044	0	-.010	-.054	-1.093
14	.004	4.111	-.556	.032	-.523	-.044	0	-.090	-.134	-2.716
14.5	.005	4.380	-.641	.032	-.609	-.044	0	-.170	-.214	-4.340

REPORT No. 632

THE CRINKLING STRENGTH AND THE BENDING STRENGTH OF ROUND AIRCRAFT TUBING

By WILLIAM R. OSGOOD

SUMMARY

The upper limit of the column strength of structural members composed of thin material is the maximum axial stress such members can carry when short enough to fail locally, by crinkling. This stress is a function of the mechanical properties of the material and of the geometrical shape of the cross section. The bending strength, as measured by the modulus of rupture, of structural members is also a function of these same variables. Tests were made of round tubes of chromium-molybdenum steel and of duralumin to determine the crinkling strengths and the bending strengths in terms of the specified yield strength and the ratio of diameter to thickness. Empirical formulas are given relating these quantities.

INTRODUCTION

The column strength of structural members of closed sections, such as tubes, composed of thin material is found to increase with decreasing ratio of slenderness up to a limiting stress at which crinkling occurs. This stress may be called the crinkling strength. The crinkling strength is the upper limit of the column strength and is practically independent of the length of the member below the length at which it is first reached. The crinkling strength must be known for each geometric shape of cross section used in a compression member of a given material if the column strength is to be completely known.

The bending strength, measured by the modulus of rupture, is also a function of the shape of the cross section, as is well known, and for a given material must be determined for those shapes of cross section used in designing.

The interest of the Bureau of Aeronautics, Navy Department, and of the National Advisory Committee for Aeronautics in the strength of aircraft tubing led to the allotment of funds to the National Bureau of Standards for an investigation of the subject.

Almost all of the carefully made tests in the past to determine the crinkling strength or the bending strength of round tubing have been made on specimens with far higher ratios of diameter to thickness than are commonly used in aircraft. Timoshenko (reference 1) refers to many of these tests, and an excellent piece of work has been done recently by Hansen (reference 2).

In the present investigation the crinkling strength

and the bending strength of round tubular specimens of chromium-molybdenum steel and of duralumin were studied. The diameters of the tubes ranged from 1 inch to 2 inches, and the thicknesses from 0.025 inch to 0.109 inch. The ratios of diameter to thickness ranged approximately from 15 to 100. The experimental work included comprehensive tests to determine the tensile properties of the chromium-molybdenum-steel tubing, the tensile and compressive properties of the duralumin tubing, 60 crinkling tests, and 38 bending tests. In this paper these tests are described, and the results are interpreted for practical use in design.

The author is indebted to the Aluminum Company of America for donation of all of the duralumin tubing, and to the Summerill Tubing Company for donation of three thin sizes of the chromium-molybdenum-steel tubing.

MATERIAL AND MATERIAL TESTS

THE MATERIAL AND ITS PREPARATION FOR TEST

Most of the chromium-molybdenum-steel tubing was manufactured to comply with Navy Department Specification 44T18c, Feb. 1, 1937: Tubing, Steel (Chromium-molybdenum) Round, Seamless (Aircraft Use).

The duralumin tubing was of the type commonly known as 17ST aluminum-alloy tubing. It complied with Navy Department Specification 44T21b, May 1, 1937: Tubing, Aluminum-alloy (Aluminum-copper-magnesium-manganese), Round, Seamless, Condition "T", heat treated.

The nominal cross-sectional properties of the tubes are given in table I.

One tensile specimen and one compressive specimen were taken from each tube, the remainder of the tube being available for crinkling-test and transverse-test specimens. In order to determine the actual cross-sectional properties of the specimens, more than half of the specimens were weighed and their lengths, outside diameters at the middle, and maximum and minimum thicknesses at the ends were measured. The densities of representative samples were determined by the Division of Weights and Measures of the National Bureau of Standards. The cross-sectional areas of the specimens were computed from the weights, the lengths, and the densities; and the average thicknesses and the section moduli were computed from the cross-sectional areas and the outside diameters.

TENSILE AND COMPRESSIVE TESTS

A tensile test was made of each tube, and a compressive test was made of each duralumin tube. Compressive tests were made of as many of the chromium-molybdenum-steel tubes as possible. The results were not used, however, since it was not possible to determine the yield strengths of the thin specimens; these specimens failed by crinkling before the yield strengths were reached.

The tensile tests were made in a pendulum, hydraulic machine having a capacity of 100,000 pounds and scale

head. This condition, causing a slight eccentricity of loading, is especially undesirable in compression testing, but with the short specimens and comparatively low loads of the present investigation, the effect was not considered to be serious. Another possible source of error in making compressive tests in this type of machine arises from the possibility of rotation of the platen about a horizontal axis. The platen is rigidly connected to the piston of the hydraulic jack, which is packed, and the clearance between the cylinder and the piston permits rotation of the platen under eccentric

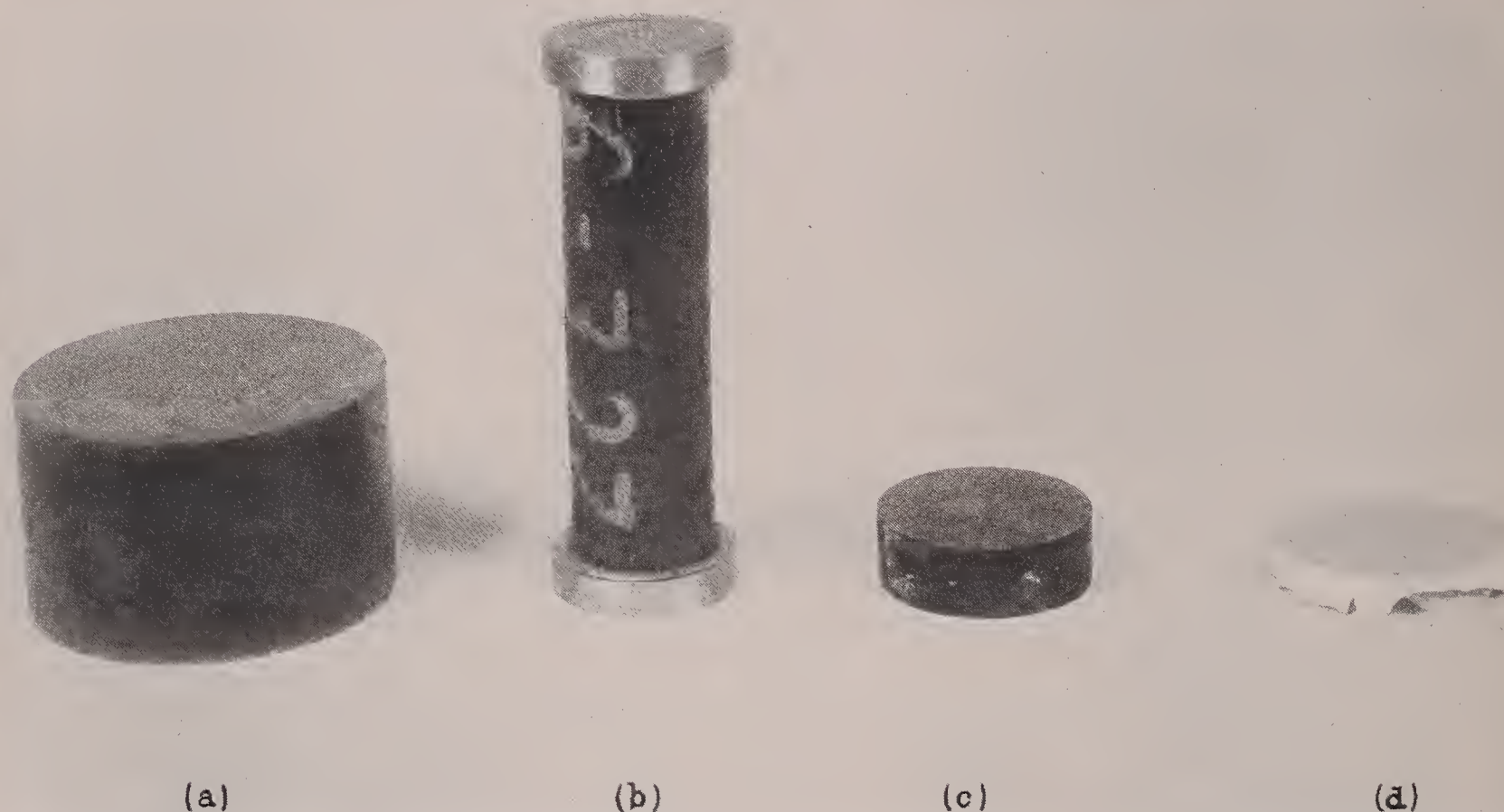


FIGURE 1.—Specimen (b), bearing blocks (a and c), and plaster cap (d).

ranges of 0 to 10,000, 0 to 20,000, 0 to 50,000 and 0 to 100,000 pounds. Most of the compressive tests were made in a fluid-support, Bourdon-tube, hydraulic machine having a capacity of 100,000 pounds and scale ranges of 0 to 10,000, 0 to 50,000, and 0 to 100,000 pounds. Auxiliary nuts on the screws of this machine were tightened against the lower surface of the adjustable head to bring it into contact with the lower surface of the threads on the screws, so that rotation of the head relative to the platen of the machine due to clearance between the nuts of the head and the screws was obviated. The unsymmetrical position of the motor, the hand-wheel, and the other mechanism for raising and lowering the adjustable head causes it to exert on the portion of the two screws below it a constant moment of roughly 1,000 pound-inches in a plane normal to that of the screws. As a consequence the screws are slightly bent elastically and, as they tend to straighten out under load, produce rotation of the

load. This effect can be minimized by keeping as much of the piston in the cylinder as possible.

Tensile tests were made of "full-tube" specimens as required in the specifications for the material. Compressive tests were made on specimens 4 or 5 (preferably 4 when possible) diameters long with ends machined plane and normal to the axis of the tubes. Each end of a specimen was embedded in Wood's metal to a depth of one-quarter of the diameter of the specimen, as shown in figure 1 (b). It is believed that somewhat more nearly uniform conditions are obtained at the ends by this procedure than by simply leaving the ends unsupported laterally. The specimen was then placed centrally on a ground, hardened-steel bearing block located centrally in the testing machine, figures 1 (a) and 2, and a similar, smaller block (fig. 1 (c)) was placed centrally on the upper end of the specimen. In order to secure as nearly uniform bearing as practically possible, the upper bearing block was capped

with plaster of paris (fig. 1 (d)). A stiff "mix" was found most satisfactory. It was placed between two sheets of relatively nonabsorbent oiled tracing paper and transferred to the bearing block. Load was applied immediately, arbitrarily 500 pounds per inch of diameter of specimen. The plaster was allowed to set for at least 15 minutes before testing.

Strains were measured with a Ewing extensometer when possible, on a 2-inch gage length; otherwise Tuckerman strain gages were used for determinations of moduli of elasticity, and Huggenberger extensometers for determinations of yield strengths. The moduli of elasticity were obtained from stress-strain data by means of difference curves (reference 3) drawn for each of the tensile and compressive specimens. The stress-strain data used for determining the modulus of elasticity were taken after first loading the specimen to produce a strain of about 0.002 and then removing the load. This procedure made the determination of the modulus of elasticity more definite than a determination from readings taken during the first loading, particularly in the case of some of the chromium-molybdenum-steel specimens the initial stress-strain diagrams of which were apparently curved at all stresses, however low.

The tensile yield strengths were obtained from stress-strain diagrams according to the definitions in the Navy Department specifications applying; that is, the yield strength of the chromium-molybdenum steel was taken as the stress at a strain 0.002 in excess of the elastic strain corresponding to this stress, and that of the

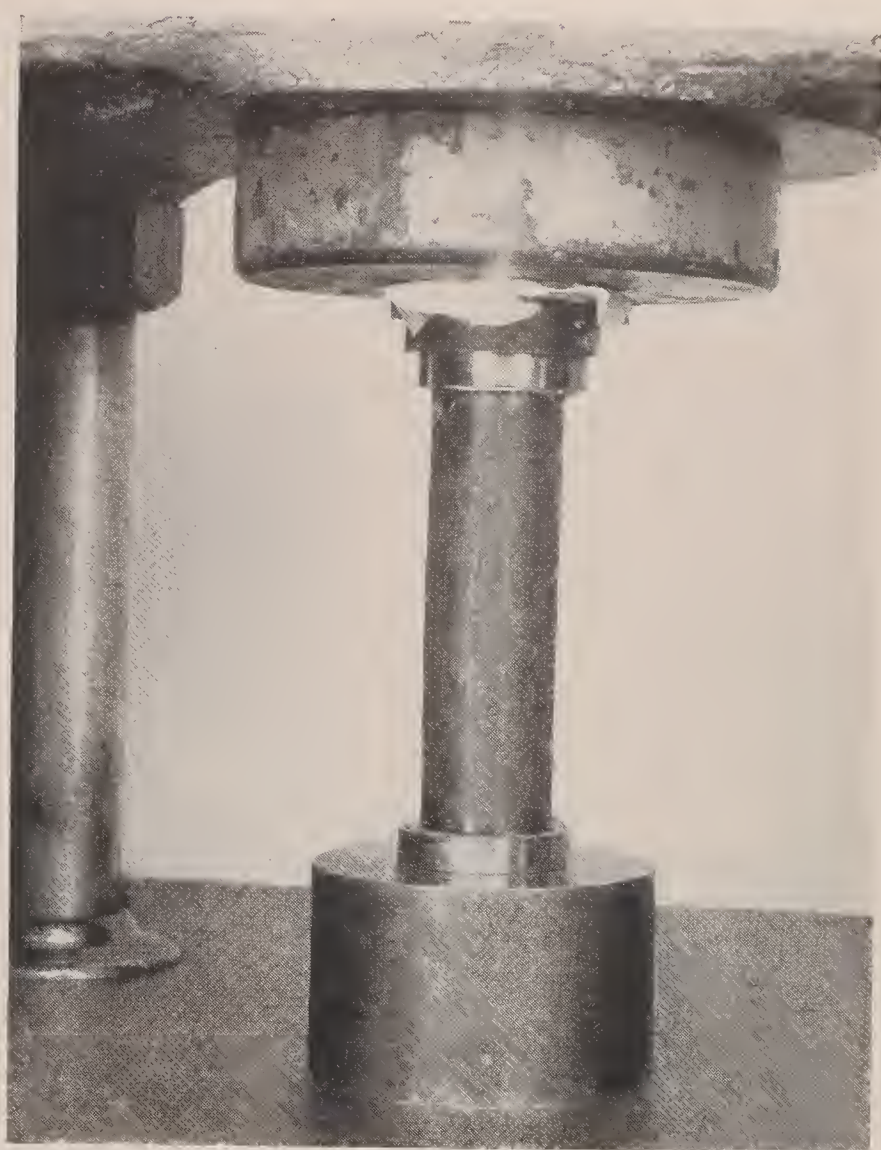


FIGURE 2.—Specimen in machine after test.

duralumin as the stress at a strain of 0.006. The compressive yield strength of the duralumin was

obtained as the stress corresponding to the intersection with the stress-strain curve of a line drawn through the origin with a slope $\frac{2}{3}E$, where E is the modulus of elasticity (reference 4). Figures 3 and 4 show typical stress-strain diagrams.

CRINKLING TESTS

The procedure for making crinkling tests was exactly the same as that for making compressive tests, except that only the maximum loads were measured. Inasmuch as the compressive specimens failed by crinkling, these specimens also furnished values of the crinkling strength. Figure 5 shows some typical crinkling-test specimens after testing.

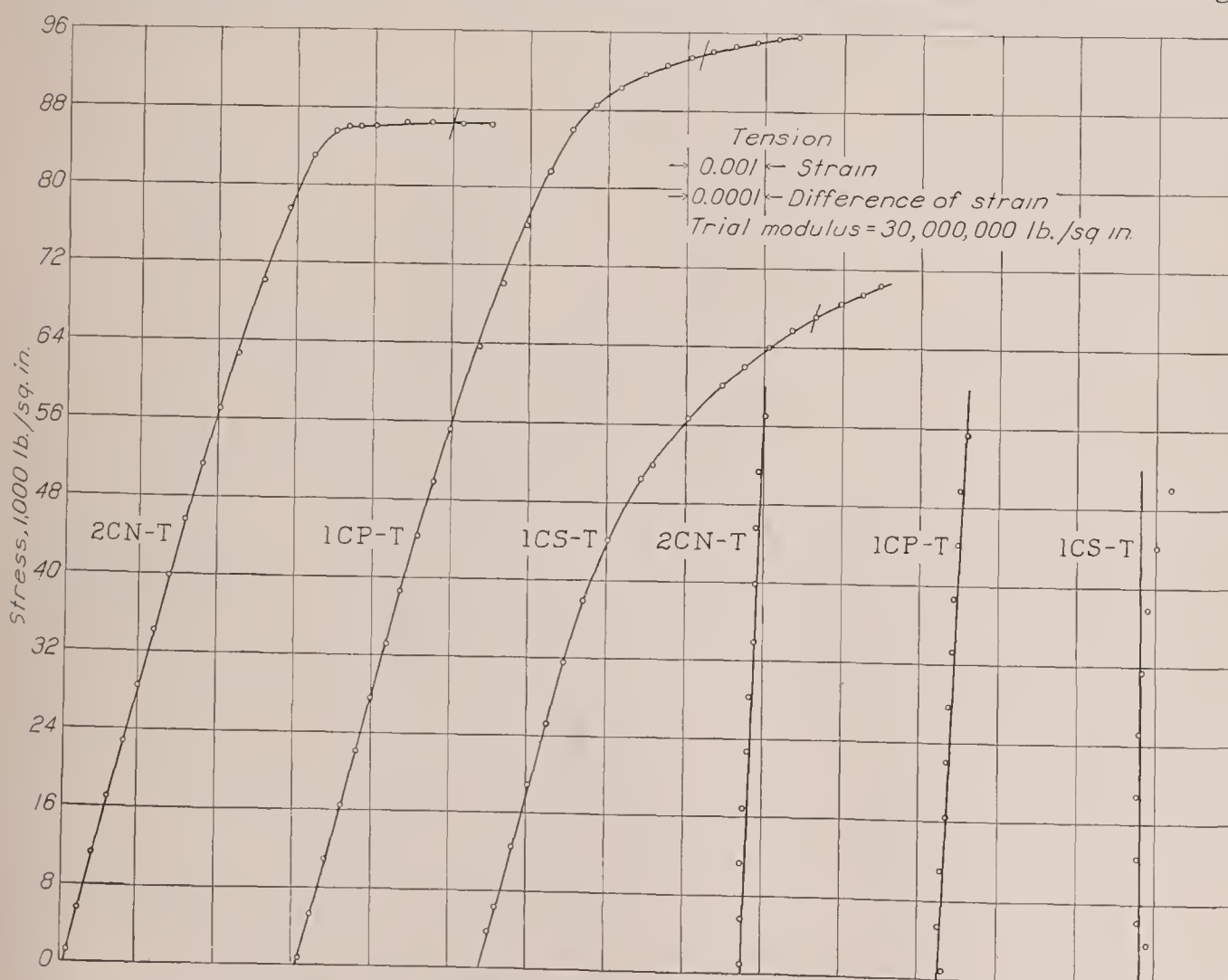


FIGURE 3.—Typical stress-strain diagrams of chromium-molybdenum steel.

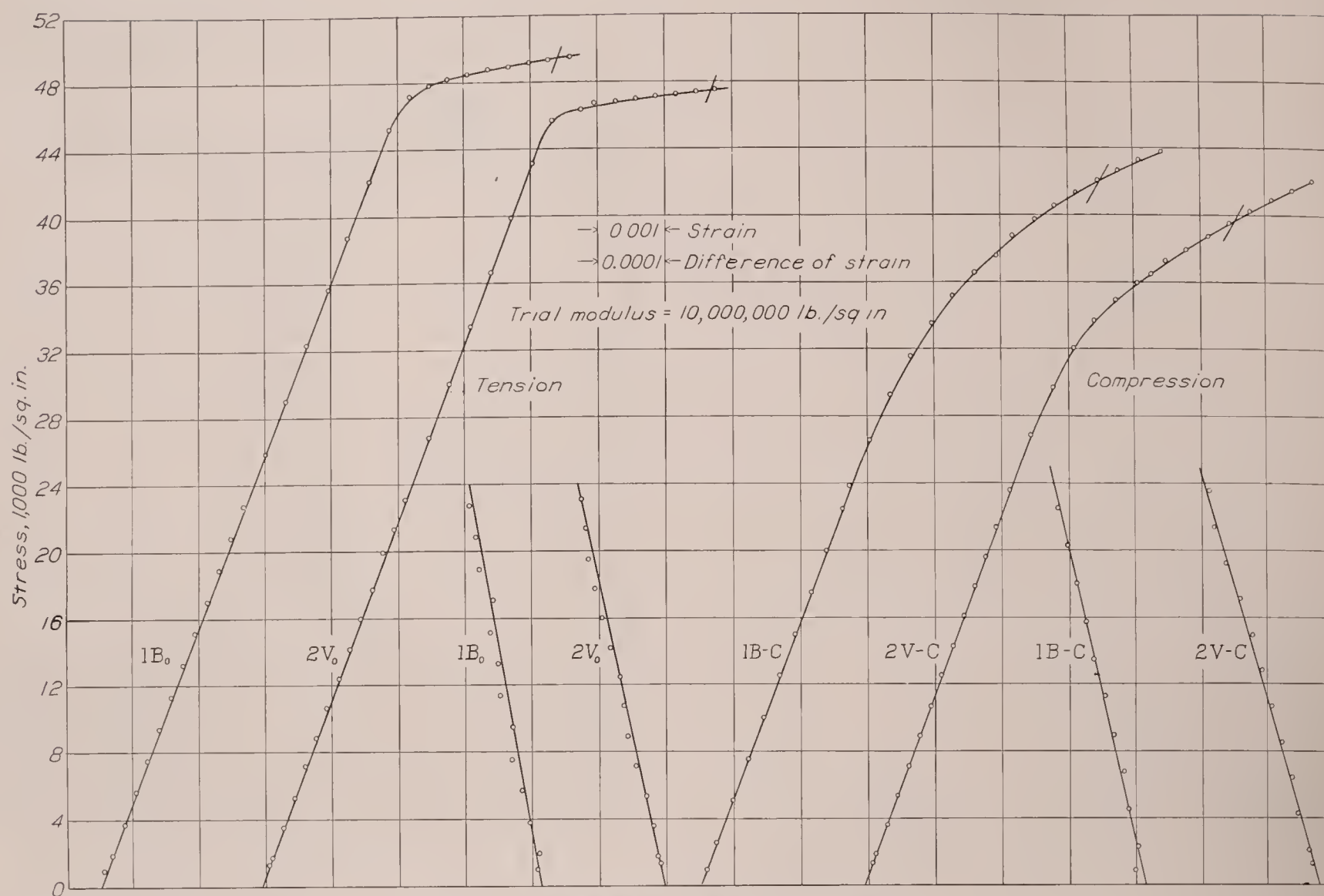


FIGURE 4.—Typical stress-strain diagrams of 17ST duralumin.

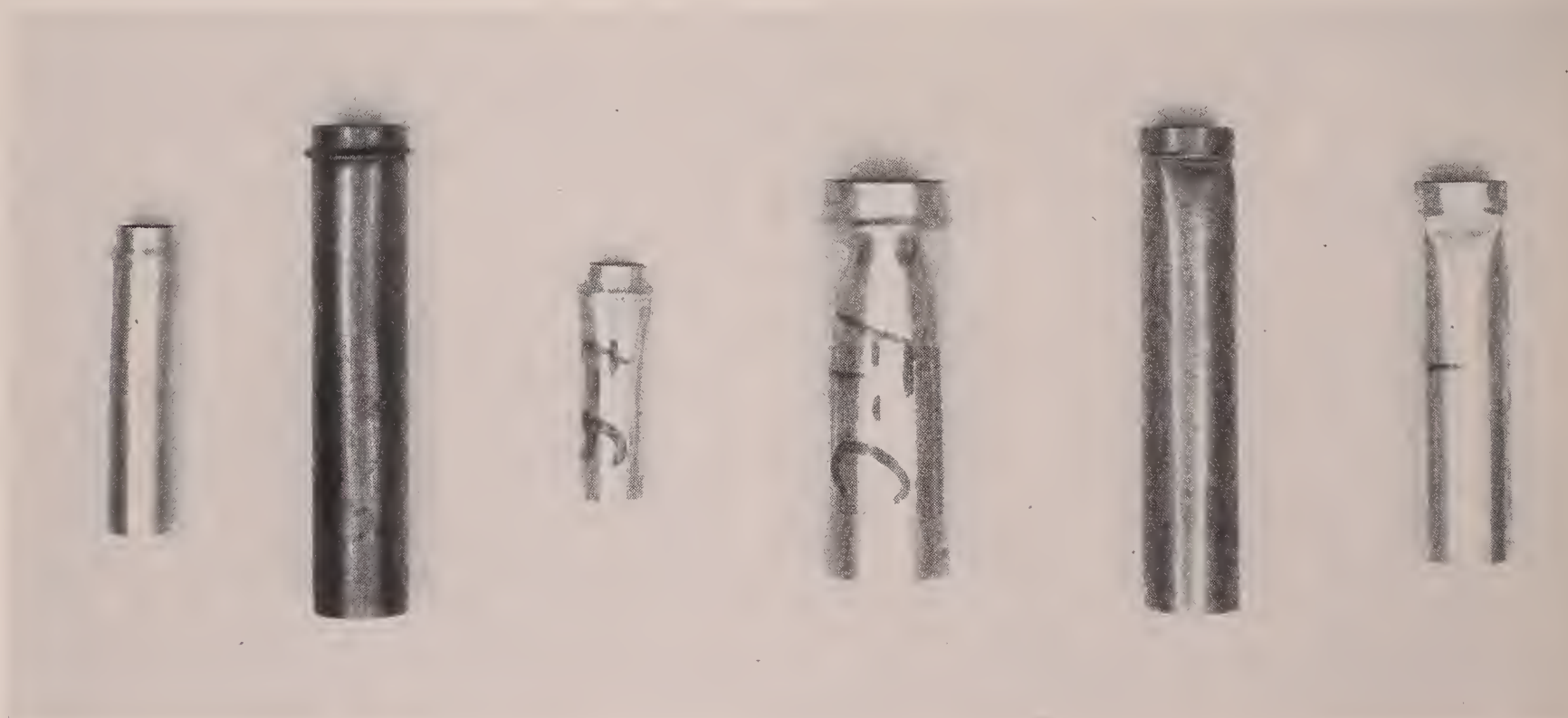


FIGURE 5.—Crinkling-test specimens.

BENDING TESTS

Figure 6 shows the method of making the bending tests. The test specimen A was supported at the ends and was loaded symmetrically at the third-points until the bending moment in the middle portion became a maximum. It was desired to obtain failure in a part of the specimen that was free to assume its "natural" shape at failure, unaffected by local restraints or con-

of at least six diameters between loading points. The loads were applied through knife edges on the clamps by means of hangers C, which extended down to an equalizer. The equalizer bore on knife edges on the lower ends of the hangers and was itself loaded through a knife edge at the center by the movable head of a beam-and-poise testing machine having a capacity of 20,000 pounds. The scale ranges of the machine were

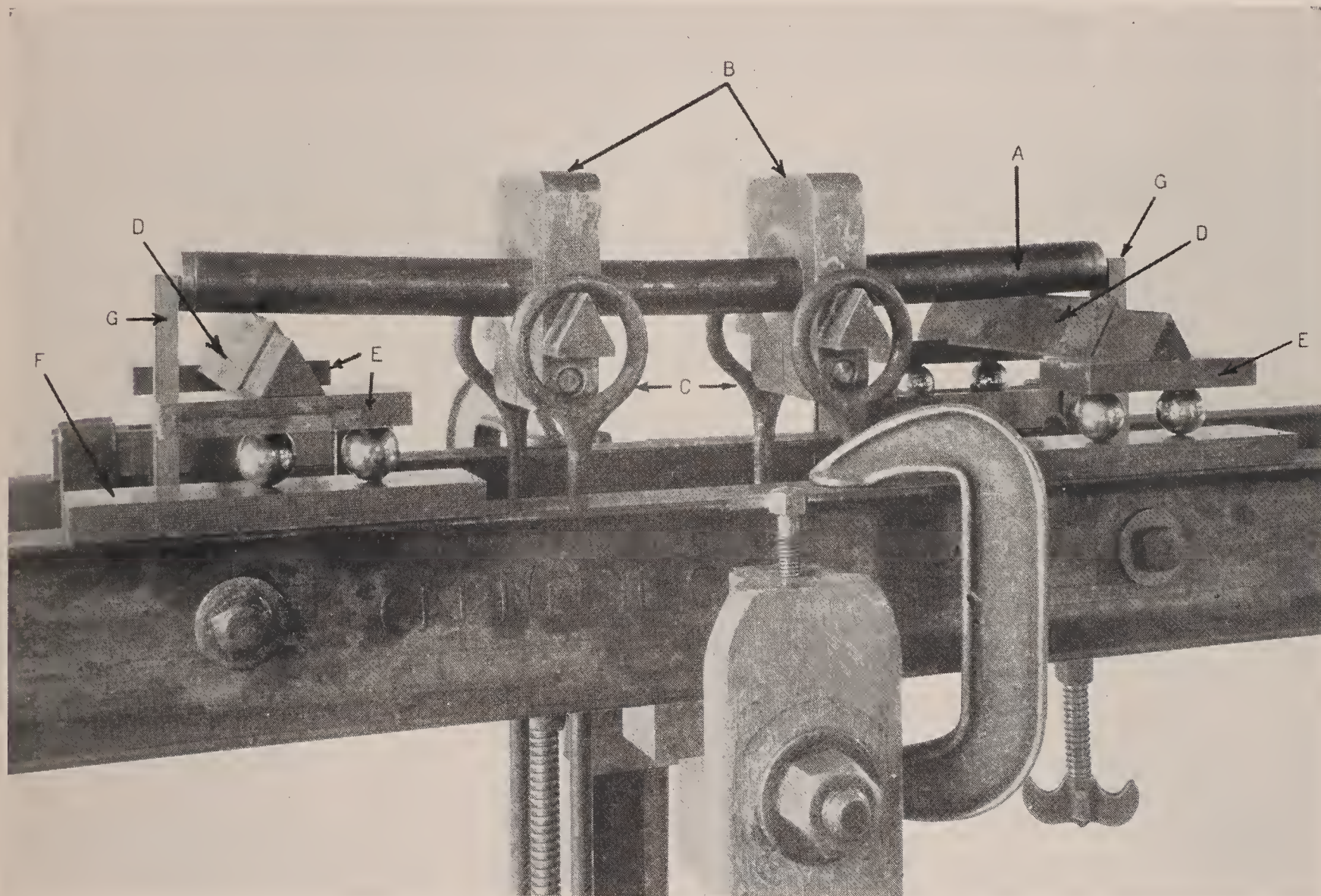


FIGURE 6.—Test to determine bending strength.

centrated loads. In order to effect this condition, the loads were applied through stiff clamps B, which fit the tube snugly at the third-points. One of the clamps was always tightened to a sliding fit only, so that no excessive torsional stresses might be introduced in the specimen by any possible rotation of the clamps relative to each other about the axis of the specimen. The clamps held the tube circular at the loaded sections at all times and thus prevented flattening at these sections. The middle of the tube, on the other hand, subjected to the same bending moment, was free to deform at will and of course took a characteristic flattened shape at failure. All failures occurred at or near the middle. Preliminary tests showed that a distance of five diameters between loading points was sufficient to permit the middle section to assume its natural shape. All but three specimens, however, were tested with a distance

0 to 2,000 and 0 to 20,000 pounds. The specimen was usually cut 19 diameters long, the ends were plugged, and it was supported on knife edges D with the thinnest part of the specimen up (in compression). The supporting knife edges were spaced accurately by means of spacer bars (not shown in the figure) and rested on hard steel plates E which bore on hard steel balls. The balls were free to roll on other hard steel plates F thus practically eliminating axial stresses in the specimen. The whole assembly was carried on structural steel channels at the top of the testing machine. The hangers were long enough so that the error due to their not being parallel when the specimen failed was negligible. Stops G were provided at the ends of the specimen to prevent "the whole thing from rolling on the floor," which it did once or twice anyway. The stops did not make contact during a test.

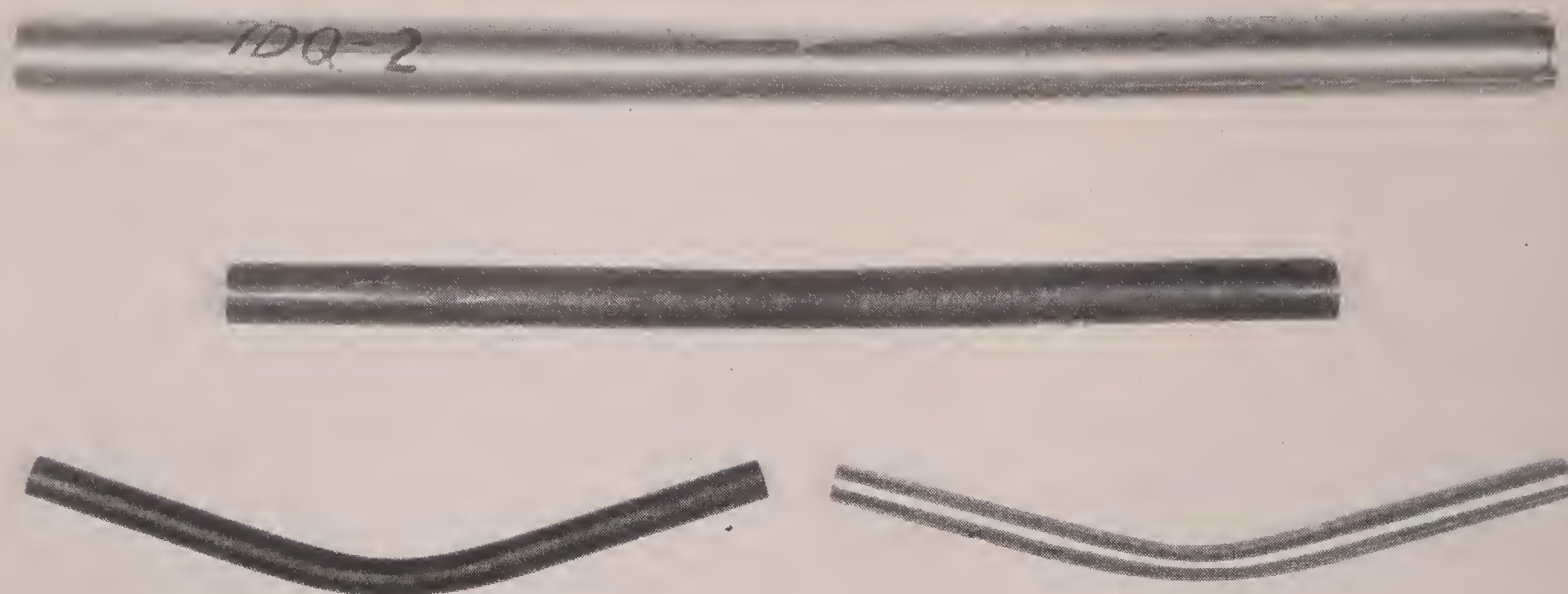


FIGURE 7.—Bending-test specimens.

Some of the specimens (the thick ones) deflected so much that the horizontal distance from a supporting knife edge to the knife edge on the nearer clamp was appreciably reduced. This distance and the corresponding load were consequently read simultaneously as the test proceeded. It was found in some cases that a maximum moment was reached for a load less than the maximum. Figure 7 shows some typical bending-test specimens after testing.

THEORY

The theory of elastic failure by buckling of thin circular cylinders has been presented by numerous authors (see reference 1) but no complete theory of plastic failure exists. Geckeler (reference 5) has presented a theory for the case of axially symmetrical buckling (single lobes reaching around the circumference of the tube). It is probable, by analogy with the elastic case, that the critical stress he obtains would not differ greatly from the theoretical critical stress for the most general (multilobed) type of buckling. Probably largely on account of the impossibility of satisfying the theoretical end conditions and ideal requirements of shape, homogeneity of material, etc., it has not been possible to obtain even an approximate check of any theory in the laboratory. For practical purposes the most valuable contribution of theory has been to give an indication of how the buckling or crinkling strength probably depends on the geometry and the mechanical properties of the material of the specimen or structural element.

Geckeler finds for the crinkling strength for axially symmetrical failure

$$f_{cr} = \frac{2tE}{d_m} \sqrt{\frac{\tau}{3(1-\mu^2)}} \quad (1)$$

where f_{cr} is the crinkling strength,

t , the thickness of the tube,

$d_m = d - t$, the mean diameter of the tube,

E , the modulus of elasticity of the material,

$$\tau = \frac{\bar{E}}{E} = \frac{4E'/E}{(1 + \sqrt{E'/E})^2}, \quad \bar{E} \text{ being the double-modu-}$$

lus and E' the tangent modulus at the stress f_{cr} ,

μ , Poisson's ratio.

By introducing the nondimensional variables

$$\delta_s = \frac{S}{E} \frac{d_m}{t} \text{ and } \sigma_{crs} = \frac{f_{cr}}{S} \quad (2)$$

where S is the compressive yield strength, and by dividing equation (1) by S , the crinkling strength for axially symmetrical failure may be expressed in nondimensional form as

$$\sigma_{crs} = \frac{2}{\delta_s} \sqrt{\frac{\tau}{3(1-\mu^2)}} \quad (3)$$

If S is determined as the intersection with the stress-strain curve of a line through the origin having a slope βE ($0 < \beta < 1$), equation (3) will represent one and the same curve for all materials having affinely related stress-strain curves¹ (reference 4). It is probable that

¹ Strictly, curves for which the quantity $\tau/(1-\mu^2)$ is the same for corresponding equal values of σ_{crs} , but the effect of variations in μ would, in any case, almost certainly be small.

the case of multilobed crinkling failure, just like that of single-lobed failure, is governed by some relation analogous to (3) between δ_s and σ_{crs} . It is to be expected then that any empirical relation found between δ_s and σ_{crs} as the result of tests in the laboratory will show less scatter than a relation for example between $\frac{d}{t}$ and f_{cr} .

The theoretical situation as regards the bending strength of thin circular cylinders is in a less satisfactory state than the theory that applies to the crinkling strength. Even the elastic case (reference 6) becomes so involved as to be quite intractable in any practical way. So far as is known, no one has attempted a solution of the plastic case. Nevertheless, because of

the similarity in type between bending failures of thin tubes and crinkling failures, it seems reasonable to expect a closer relation to exist between

$$\delta_s = \frac{S}{E} \frac{d_m}{t} \text{ and } \sigma_{rs} = \frac{f_r}{S} \quad (4)$$

where f_r is the modulus of rupture, for materials having affinely related stress-strain curves, than between $\frac{d}{t}$ and f_r .

RESULTS

The results of the crinkling tests are given in table II and are shown for the chromium-molybdenum-steel specimens in figures 8 and 9 and for the duralumin specimens in figures 10 and 11. The results of the

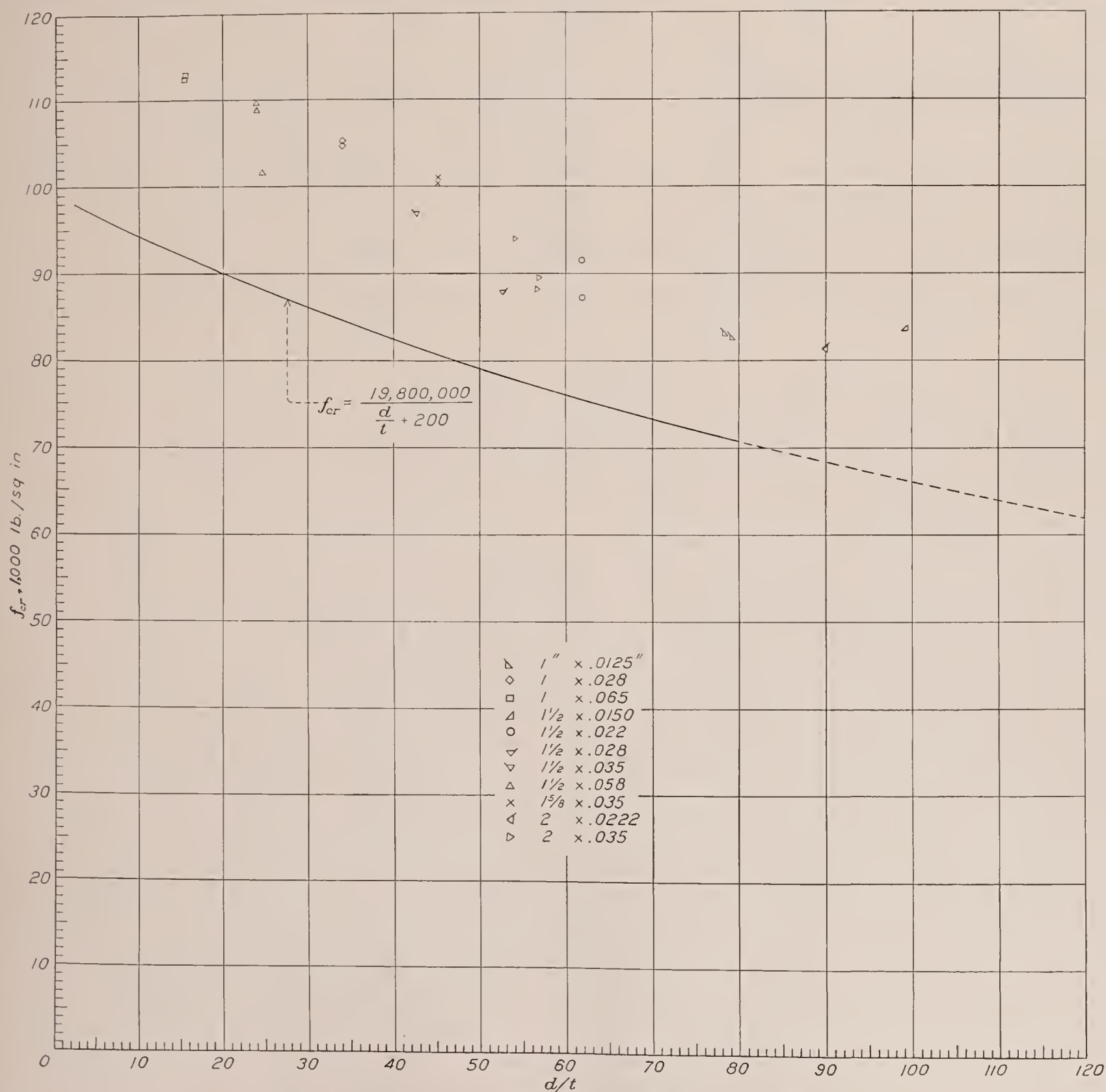
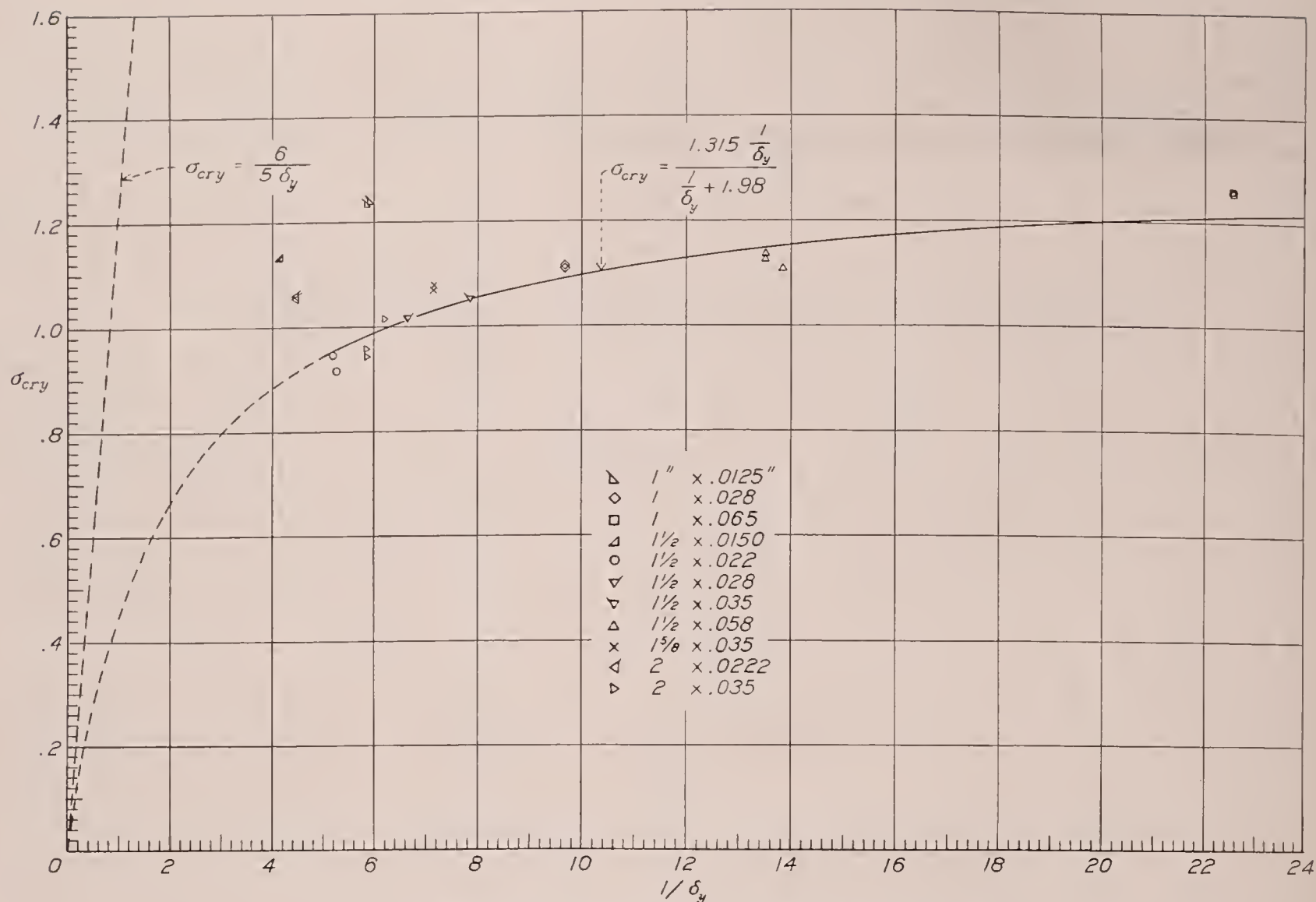
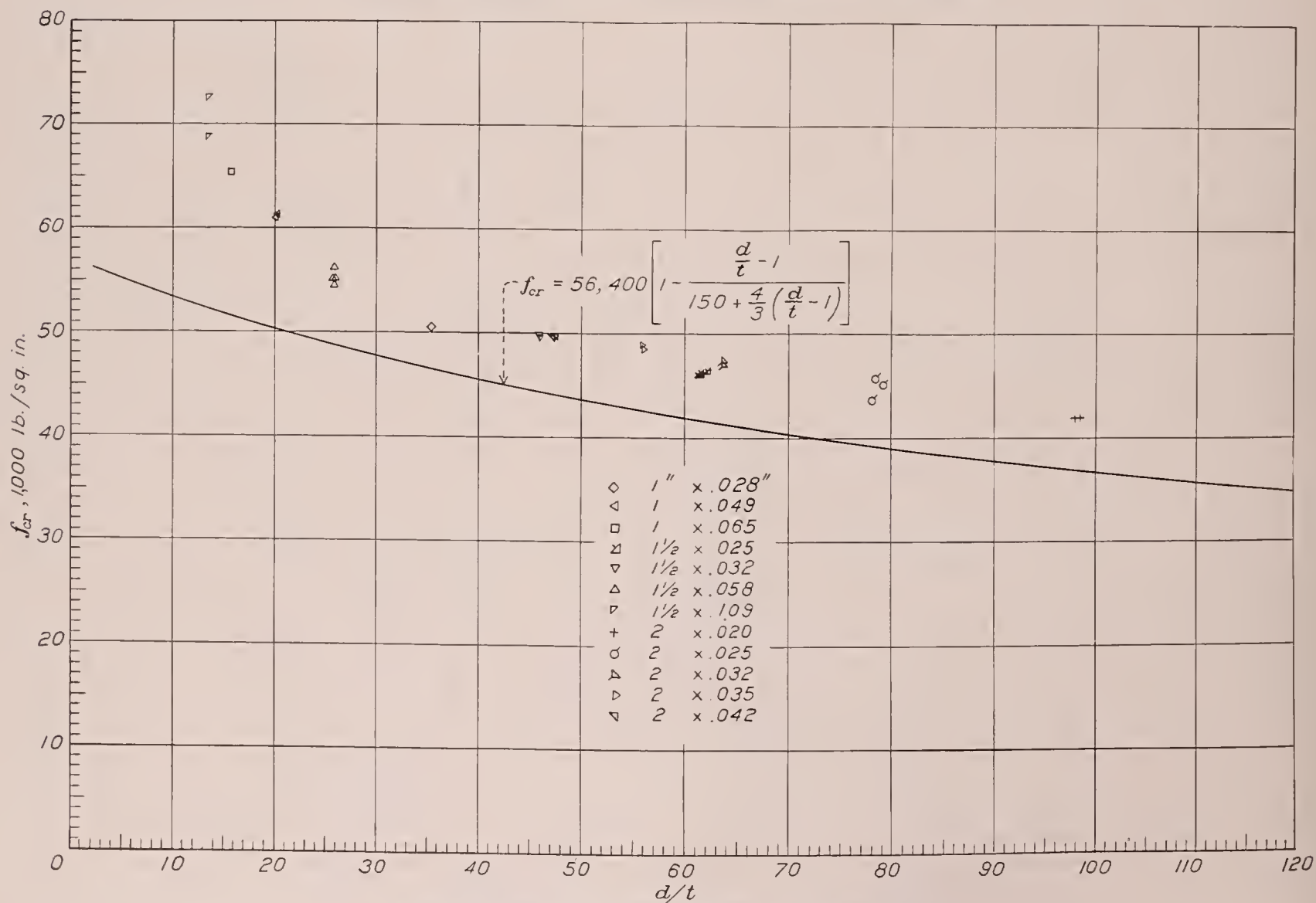


FIGURE 8.—Diagram of f_{cr} , d/t for chromium-molybdenum steel (axial loading).

FIGURE 9.—Diagram of σ_{cry} , $1/\delta_y$ for chromium-molybdenum steel (axial loading).FIGURE 10.—Diagram of f_{cr} , d/t for duralumin (axial loading).

bending tests are given in table III and are shown for the chromium-molybdenum-steel specimens in figures 12 and 13 and for the duralumin specimens in figures 14 and 15. The measured diameters and the computed average thicknesses have been used in determining the values of d/t in tables II and III and in the figures. The crinkling strength, f_{cr} , is the maximum axial load carried by the specimen divided by its cross-sectional

$$\delta_v = \frac{Y}{E} \frac{d_m}{t} \text{ and } \sigma_{cry} = \frac{f_{cr}}{Y}, \sigma_{rv} = \frac{f_r}{Y} \quad (5)$$

were used in figures 9 and 13 instead of δ_s and σ_{crs} , σ_{rs} as defined in equations (2) and (4). It is seen that the scatter of the points for the chromium-molybdenum-steel specimens in the $\sigma_v, 1/\delta_v$ -diagrams of figures 9 and 13 is materially less than in the $f, d/t$ -diagrams of figures 8 and 12 except for the three sets of points representing

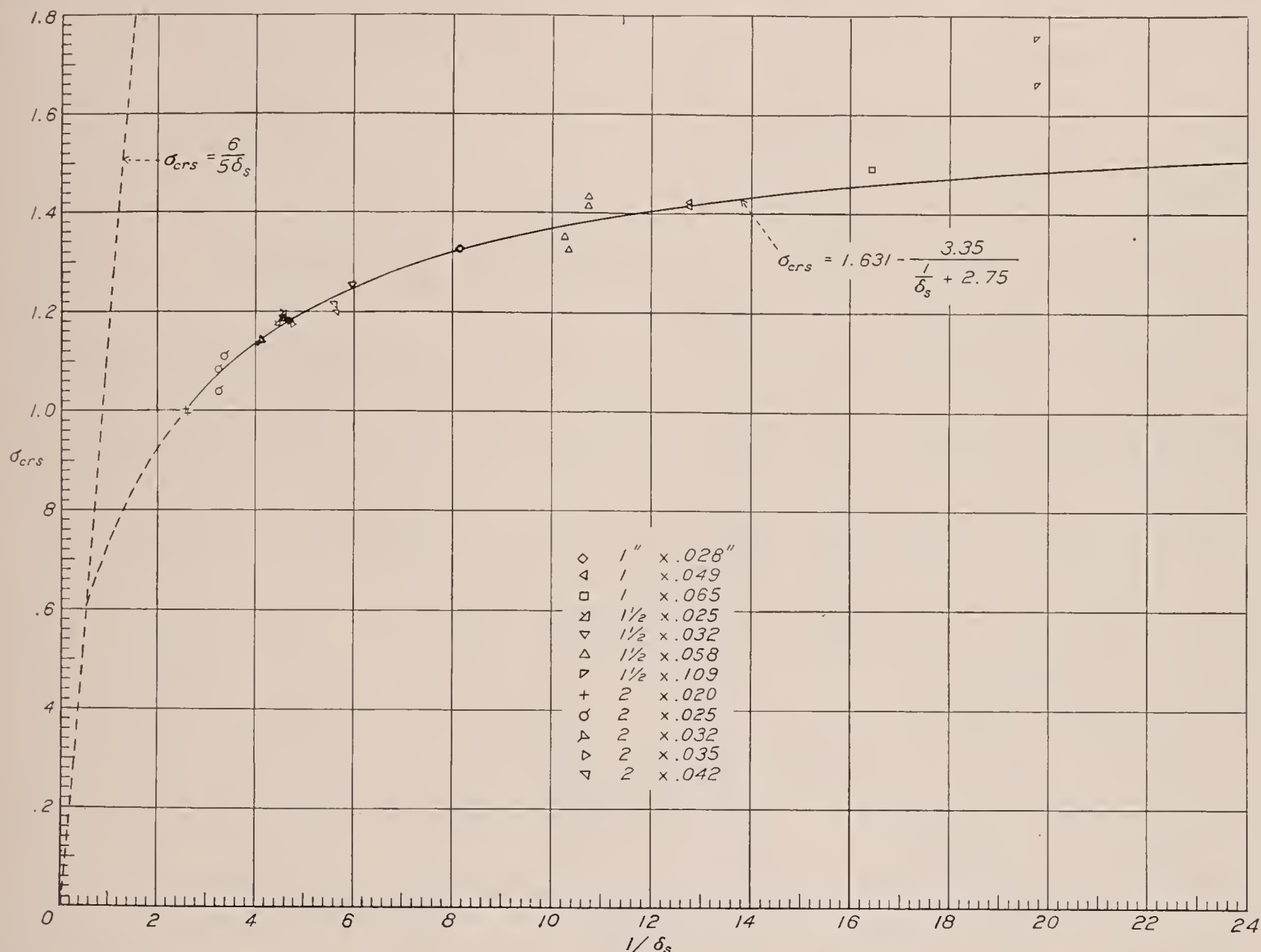


FIGURE 11.—Diagram of $\sigma_{crs}, 1/\delta_s$ for duralumin (axial loading).

area. The modulus of rupture, f_r , has been computed from the common flexure formula

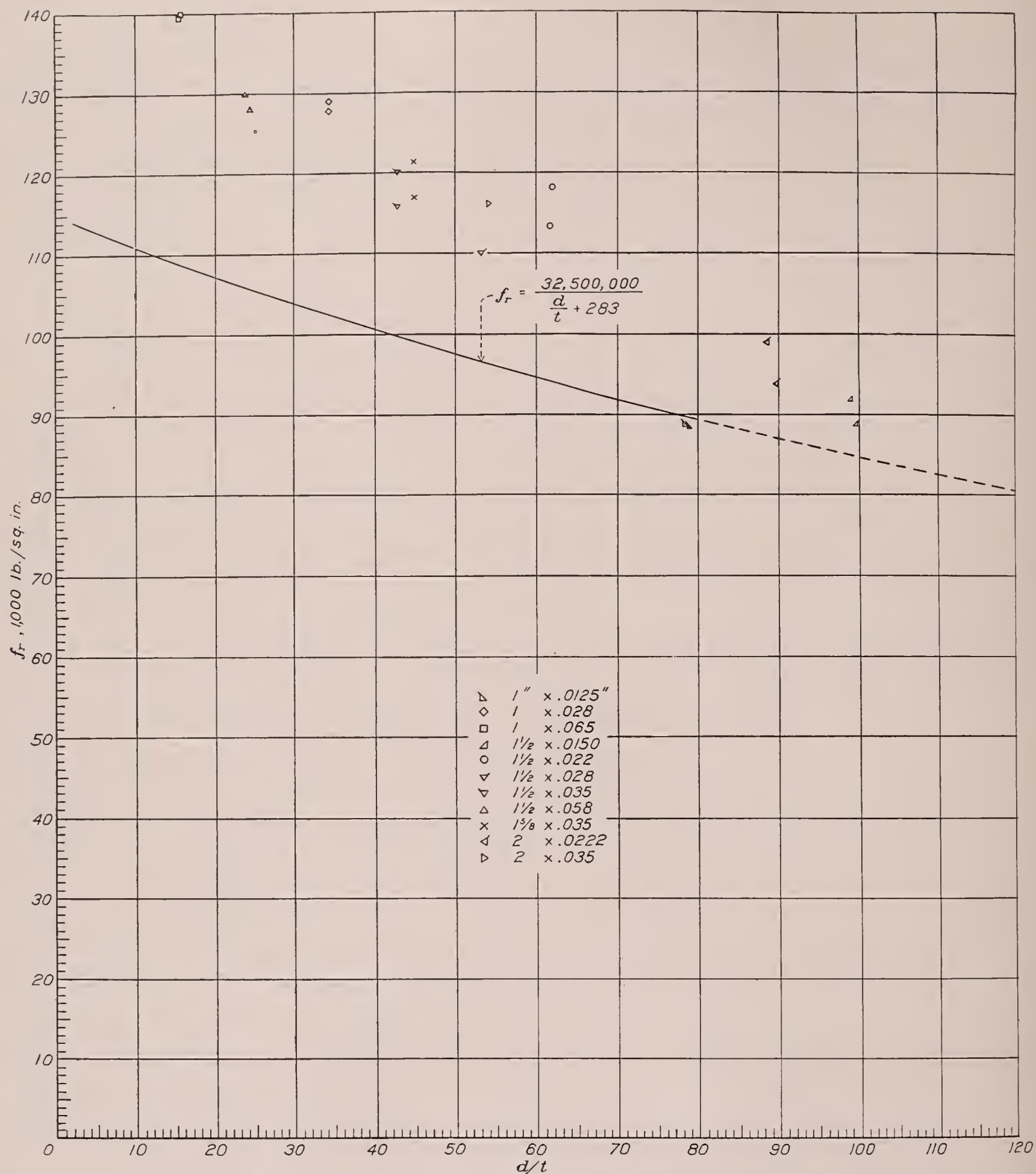
$$f_r = \frac{Mc}{I}$$

where M is the maximum moment resisted by the specimen, and I/c is its section modulus. The data in figures 8, 10, 12, and 14 have been plotted in the conventional way and in figures 9, 11, 13, and 15 in terms of the nondimensional variables δ and σ . Because compressive yield strengths of the thin chromium-molybdenum-steel tubes could not be obtained, the tensile yield strengths, Y , were used in the expressions for δ and σ ; that is,

the three sizes of tubes, 1 by 0.0125 inch, 1½ by 0.0150 inch, and 2 by 0.0222 inch. For the duralumin specimens, the points in the $\sigma_s, 1/\delta_s$ -diagrams of figures 11 and 15 lie on somewhat smoother curves than the points in the $f, d/t$ -diagrams of figures 10 and 14. Greater improvement in the nondimensional representation would be expected for the chromium-molybdenum-steel data than for the duralumin data because the former material was somewhat more variable in its mechanical properties than the latter.

It is not difficult to find an explanation for the apparently anomalous behavior of the three chromium-molybdenum-steel tubes mentioned. The tensile stress strain curves for these tubes were gradually curved from low stresses on (1CS-T, fig. 3), whereas all the other tubes had stress-strain curves with relatively sharp knees. Since the material is supposed to be

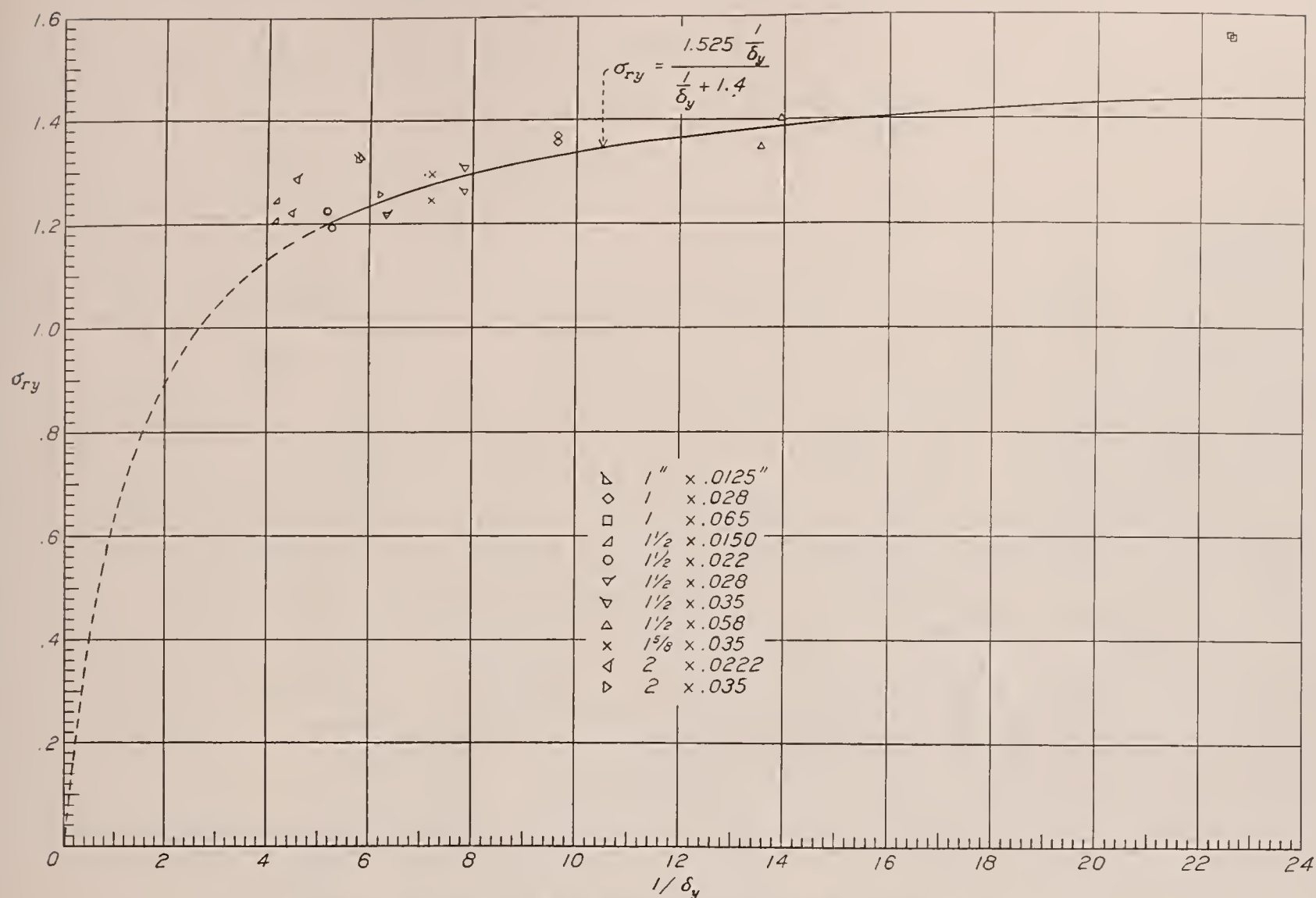
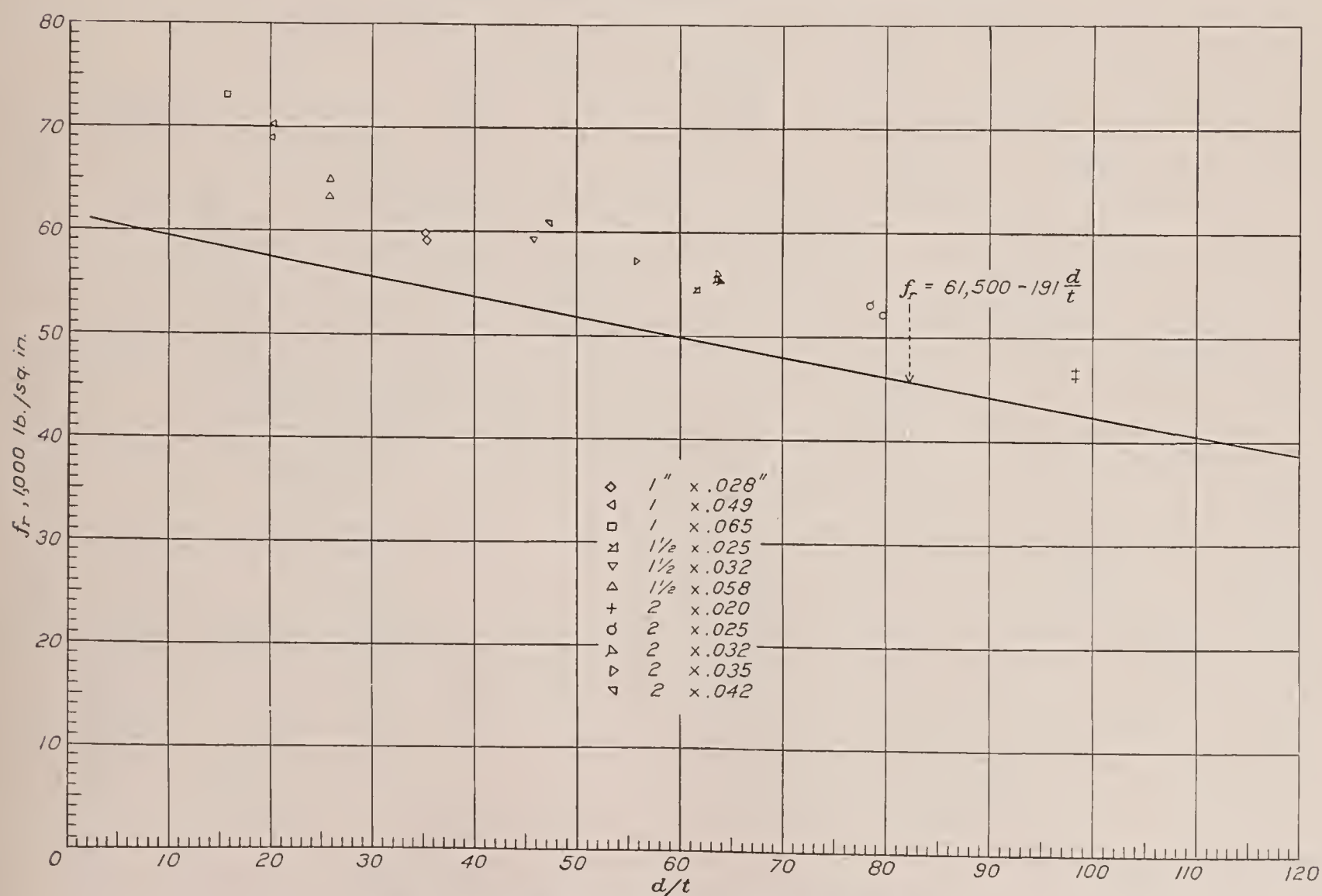
² Where δ , σ_{cr} , σ_y , σ_s , σ , and f are used, the context will indicate whether δ_s or δ_v ; σ_{crs} , σ_{cry} , σ_{rs} , or σ_{rv} ; and f_{cr} or f_r is meant.

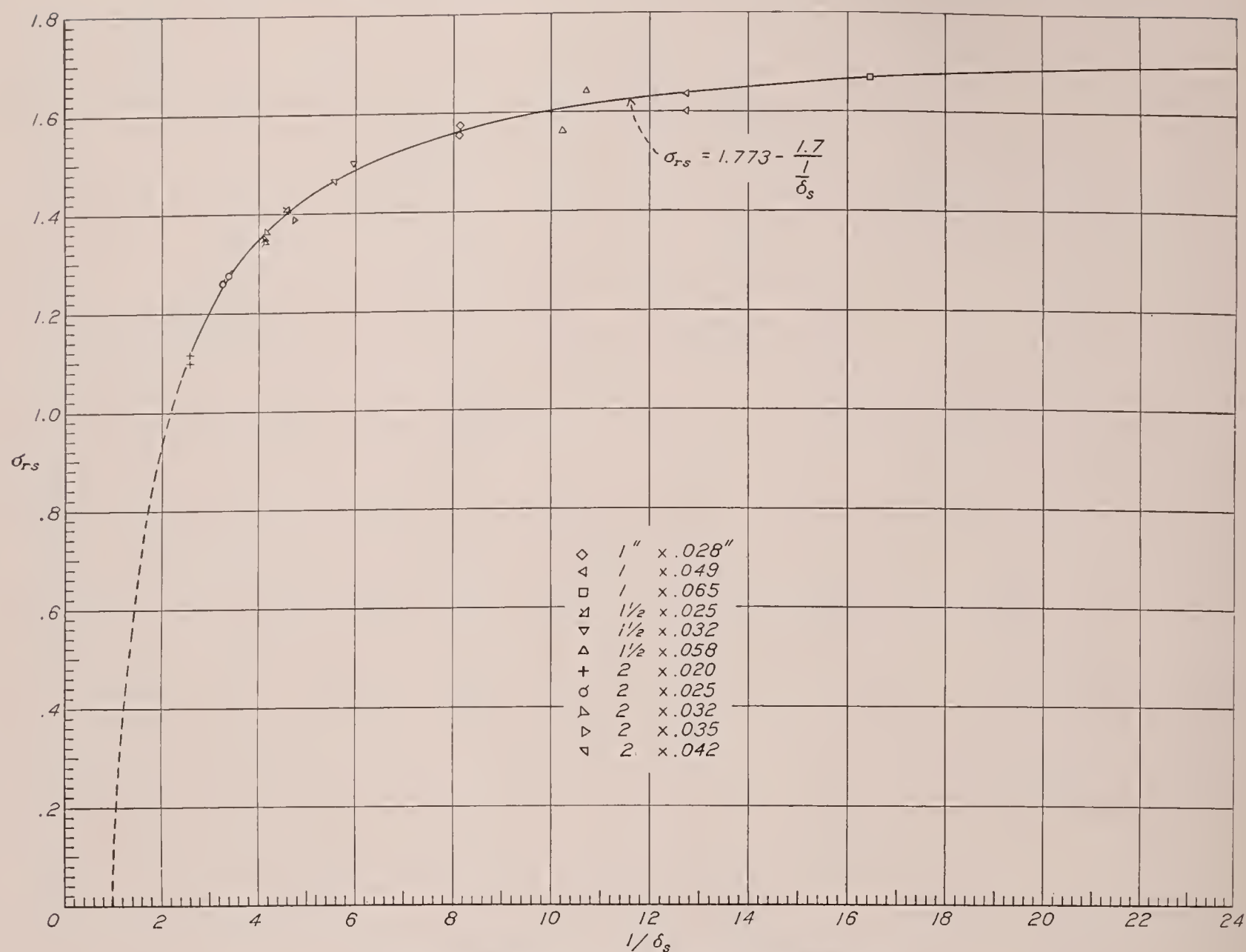
FIGURE 12.—Diagram of f_r , d/t for chromium-molybdenum steel (transverse loading).

normalized, it is not unreasonable to expect similar stress-strain curves in compression. If this is the case, then for a given yield strength S for the two types of material and at a given stress $f > S$ at failure,³ the value of τ , which depends on the tangent modulus, will be greater for the material with the blunt-knee stress-strain curve than for the material with the sharp-knee

³ The statement that follows is true not only for $f > S$ but for f greater than the stress at which the slopes of the two stress-strain curves become equal. The values of E are assumed to be equal.

stress-strain curve. Now, unquestionably, the strength increases with τ and decreases with d/t (whether equation (1) is right or not) and, consequently, for a given strength, represented by f , a high value of τ will be associated with a high value of d/t and a low value of τ with a low value of d/t . It is to be expected, then, that the three sets of points representing the tests on the thin tubes in figures 7 and 11 would be shifted to the left. They are "off the beaten track" of the other

FIGURE 13.—Diagram of σ_{ry} , $1/\delta_y$ for chromium-molybdenum steel (transverse loading).FIGURE 14.—Diagram of f_r , d/t for duralumin (transverse loading).

FIGURE 15.—Diagram of σ_{rs} , $1/\delta_s$ for duralumin (transverse loading).

points because the stress-strain curves of the material they represent are not even approximately affinely related to the stress-strain curves of the other material.

It will be noted that smooth curves drawn to represent the σ , $1/\delta$ -data would rise concave upward to meet the points for which $1/\delta$ is greater than 19. These points represent the strengths of relatively thick specimens, and it is to be expected that the strengths of such specimens would increase rapidly with decrease in ratio of diameter to thickness. If $d/t=2$, the tube becomes a solid bar, the crinkling strength becomes infinite, and the bending strength becomes very high, depending now on the tensile strength of the material. These high values of crinkling strength and bending strength, however, have no practical significance since the deformations required to obtain them are so great as to be quite intolerable in a structure. The more or less abrupt rise in strength at low values of the ratio of diameter to thickness is analogous to that which occurs in columns at low values of the ratio of slenderness.

Empirical curves have been fitted to the σ , $1/\delta$ -data of figures 9, 11, 13, and 15. In doing so, the points for

which $1/\delta$ was greater than 19 have not been used, in accordance with the preceding discussion, nor have the three sets of points for the chromium-molybdenum-steel specimens previously discussed been taken into account, since they represent essentially a different material. The omission from consideration of all these points is on the safe side. All four curves are hyperbolas. They are shown solid in the figures for the range covered by the tests, and they are extended as dotted curves. The crinkling strength, in nondimensional form, of the chromium-molybdenum-steel tubes was found to be given by

$$\sigma_{cry} = \frac{1.315 \frac{1}{\delta_y}}{\frac{1}{\delta_y} + 1.98}, \quad \frac{1}{\delta_y} > 5 \quad (6)$$

The crinkling strength, in nondimensional form, of the duralumin tubes was found to be given by

$$\sigma_{crs} = 1.631 - \frac{3.35}{\frac{1}{\delta_s} + 2.75}, \quad \frac{1}{\delta_s} > 2.5 \quad (7)$$

The modulus of rupture, in nondimensional form, of the chromium-molybdenum-steel tubes was found to be given by

$$\sigma_{ry} = \frac{1.525 \frac{1}{\delta_y}}{\frac{1}{\delta_y} + 1.4}, \quad \frac{1}{\delta_y} > 5 \quad (8)$$

The modulus of rupture, in nondimensional form, of the duralumin tubes was found to be given by

$$\sigma_{rs} = 1.773 - \frac{1.7}{\frac{1}{\delta_s}}, \quad \frac{1}{\delta_s} > 2.5 \quad (9)$$

Figures 9 and 11 show also the theoretical curve (straight line) for axially symmetrical elastic failure.

If one assumes, for convenience, $\mu = \frac{1}{3} \sqrt{\frac{2}{3}} = 0.2722$, one obtains from equation (3)

$$\sigma_{cr} = \frac{6\sqrt{\tau}}{5\delta} \quad (10)$$

and, since for elastic failure, $\tau = 1$

$$\sigma_{cr} = \frac{6}{5\delta} \quad (11)$$

When σ_{cr} is plotted against $1/\delta$, equation (11) may be represented by the straight line shown in the figures.

It immediately appears that, by substituting for τ in equation (10) the expression found from column tests, or otherwise, a theoretical relation between δ and σ_{cr} might be obtained in the plastic range. This substitution might be done for the range of values of σ for which an expression for τ was reliable; but no agreement with the results of crinkling tests would be expected because crinkling failures obtained in the laboratory in the plastic range are not stability failures but bending failures. This condition is necessarily true because of the impossibility of satisfying the end and other conditions required by theory for a stability failure.

It remains to obtain expressions for the crinkling strength and the bending strength of tubing that just complies with specifications. Such expressions may be obtained immediately from equations (2) and equations (4) to (9), inclusive. The specified minimum yield strength of chromium-molybdenum-steel tubing such as used in this investigation is, according to Navy Department Specification 44T18c for tubing not over 0.188 inch thick, 75,000 pounds per square inch, and the modulus of elasticity may be taken as 29,800,000 pounds per square inch (reference 4). Substituting these values in equations (5) and then replacing δ_y and σ_{cry} in equation (6) by the expressions obtained from equations (5), and solving for the crinkling strength, f_{cr} , gives after rounding off,

$$f_{cr} = \frac{19\,800\,000}{\frac{d}{t} + 200}, \quad \frac{d}{t} < 80 \quad (12)$$

in lb per sq in.

The specified minimum tensile yield strength of duralumin tubing such as used in this investigation is, according to Navy Department Specification 44T21b for Condition "T" heat-treated tubing, 40,000 pounds per square inch. The average ratio of compressive yield strength to tensile yield strength of the tubes used in this investigation was found to be 0.864. The average value of the modulus of elasticity was 10,610,000 pounds per square inch. Substituting $S = 0.864 \times 40,000 = 34,560$ pounds per square inch and $E = 10,610,000$ pounds per square inch in equations (2) and then replacing δ_s and σ_{crs} in equation (7) by the expressions obtained from equations (2), and solving for the crinkling strength, f_{cr} , gives, after rounding off,

$$f_{cr} = 56\,400 \left[1 - \frac{\frac{d}{t} - 1}{150 + \frac{4}{3} \left(\frac{d}{t} - 1 \right)} \right], \quad \frac{d}{t} < 125 \quad (13)$$

in lb per sq in.

An expression for the modulus of rupture of chromium-molybdenum-steel tubing that just complies with Navy Department Specification 44T18c for tubing not over 0.188 inch thick may be found, as just outlined, from equations (5) and (8):

$$f_r = \frac{32\,500\,000}{\frac{d}{t} + 283}, \quad \frac{d}{t} > 80 \quad (14)$$

in lb per sq in.

An expression for the modulus of rupture of duralumin tubing that just complies with Navy Department Specification 44T21b for Condition "T" heat-treated tubing may be found, as outlined, from equations (4) and (9):

$$f_r = 61\,500 - 191 \frac{d}{t}, \quad \frac{d}{t} < 125 \quad (15)$$

in lb per sq in.

The curves representing equations (12), (13), (14), and (15) are shown⁴ in figures 8, 10, 12, and 14, respectively. They indicate, for the range of values of ratio of diameter to thickness covered, the crinkling strengths and the moduli of rupture that may be expected from tubing which just complies with the applicable specifications noted.

DISCUSSION

As explained in the introduction, the crinkling strength is the upper limit of column strength. With the determination of the crinkling strength, it now becomes possible to indicate where the column curves for the two materials of this investigation must be "cut off" at their upper ends for tubing of a given ratio of diameter to thickness, namely, at the stresses given by equations (12) and (13).

⁴ The two points in figure 12 that are below the curve represent the results of tests on specimens the material of which did not comply with the requirement of the specification for chemical composition nor yield strength (ICS-T, fig. 3).

If the stresses from equations (12) and (13) are equated to the highest average column stresses (ratio of slenderness equal to zero), the highest values of d/t may be found for which the column curves for the two materials apply over their entire range without cutting off at the top.⁵ For chromium-molybdenum-steel tubes, the limiting column stress was found in reference 4 to be 79,400 lb. per sq. in., and, if one equates this quantity to the right-hand side of equation (12),

$$79\,400 = \frac{19\,800\,000}{\frac{d}{t} + 200}$$

and solves for d/t , one obtains $d/t=50$. Similarly, for duralumin tubes the limiting column stress was found in reference 4 to be 42,700 lb. per sq. in., and if one equates this quantity to the right-hand side of equation (13),

$$42\,700 = 56\,400 \left[1 - \frac{\frac{d}{t} - 1}{150 + \frac{4}{3} \left(\frac{d}{t} - 1 \right)} \right]$$

and solves for d/t , one obtains $d/t=55$. The column formulas given in reference 4 may therefore be used over their entire respective ranges for tubing for which d/t does not exceed 50 in the case of chromium-molybdenum steel and d/t does not exceed 55 in the case of duralumin.

The question may arise as to whether clamps used in practice for transferring transverse loads to tubing are sufficiently effective in holding the tube round to prevent failure at the clamp. Preliminary bending tests made with several types of clamps, both with clamps furnished by manufacturers and more flexible clamps made for the purpose, indicated that, so long as the transverse load was applied through a tension member, the clamp would not weaken the tube. The type of connection most likely to weaken a tube locally is a

⁵ The use of equations (12) and (13) assumes that the column curves are based on the same compressive yield strength as the crinkling curves. If the compressive yield strength of the column material is higher, as it was for the duralumin tubes of reference 4, the values of d/t obtained will be on the conservative side.

weld. A relatively small compression member transferring its load to the tube in question through a weld might easily promote a dent and cause local failure at lower stresses than those given by equation (14).

It may not be out of place here to call attention to possible failure by transverse shear. The transverse shearing strength of tubing has not been studied in the present investigation. All that can be said is that no evidence of failure due to transverse shear was observed in any specimen. Hansen (reference 2) found, for much thinner tubes, that the modulus of rupture was unaffected by shear when the cantilevered end of the tube was as short as three diameters.

NATIONAL BUREAU OF STANDARDS,
WASHINGTON, D. C., *March 28, 1938.*

TABLE I
NOMINAL CROSS-SECTIONAL PROPERTIES OF TUBES

Diameter d (in.)	Thick- ness t (in.)	Ratio $\frac{d}{t}$	Area A (sq. in.)	Section modulus I/c (in. ³)
CHROMIUM-MOLYBDENUM STEEL				
1	0.0125	80.0	0.0388	0.00887
1	.028	35.7	.0855	.02021
1	.065	15.4	.1909	.04193
1½	.0150	100.0	.0700	.02572
1½	.022	68.2	.1022	.03720
1½	.028	53.6	.1295	.04678
1½	.035	42.9	.1611	.05765
1½	.058	25.9	.2628	.09121
1¾	.035	46.4	.1748	.06803
2	.0222	90.0	.1379	.06746
2	.035	57.1	.2161	.10432
DURALUMIN				
1	0.028	35.7	0.0855	0.02021
1	.049	20.4	.1464	.03319
1	.065	15.4	.1909	.04193
1½	.025	60.0	.1158	.04202
1½	.032	46.9	.1476	.05303
1½	.058	25.9	.2628	.09121
1½	.109	13.8	.4763	(a)
2	.020	100.0	.1244	.06097
2	.025	80.0	.1551	.07564
2	.032	62.5	.1978	.09581
2	.035	57.1	.2161	.10432
2	.042	47.6	.2584	.12386

^a No bending tests were made of this size.

TABLE II
RESULTS OF CRINKLING TESTS
CHROMIUM-MOLYBDENUM STEEL

Specimen	$\frac{d}{t}$	Crinkling strength f_{cr} (lb./sq.in.)	$\frac{1}{\delta_y} = \frac{E}{Y} \frac{t}{d_m}$	$\sigma_{cr y} = \frac{f_{cr}}{Y}$	Specimen	$\frac{d}{t}$	Crinkling strength f_{cr} (lb./sq.in.)	$\frac{1}{\delta_y} = \frac{E}{Y} \frac{t}{d_m}$	$\sigma_{cr y} = \frac{f_{cr}}{Y}$
1CL-Cr	15.5	112500	22.58	1.253	1CO-C	54.1	94000	6.19	1.018
1CL-9	15.6	112900	22.55	1.257	2CO-C	56.7	88200	5.85	.945
2CE-9	24.0	109600	13.51	1.135	2CO-Cr	56.9	89500	5.84	.959
2CE-C	24.0	108900	13.51	1.127	1CM-C	61.8	91500	5.16	.946
1CE-1a	24.6	101500	13.87	1.108	2CM-C	61.8	87200	5.22	.917
1CK-9	34.0	105300	9.68	1.115	1CS-3	78.4	82900	5.80	1.239
1CK-C	34.0	104800	9.68	1.110	1CS-C	79.1	82600	5.74	1.234
1CT-C	42.7	96900	7.86	1.052	1CU-C	89.8	81200	4.47	1.056
1CP-3C	45.2	100900	7.12	1.076	1CU-3	89.8	81100	4.47	1.054
1CP-C	45.2	100300	7.12	1.069	1CC-3	99.3	83600	4.16	1.132
2CN-C	52.7	87900	6.64	1.019	1CC-C	99.4	83700	4.16	1.132
DURALUMIN									
Specimen	$\frac{d}{t}$	Crinkling strength f_{cr} (lb./sq.in.)	$\frac{1}{\delta_s} = \frac{E}{S} \frac{t}{d_m}$	$\sigma_{cr s} = \frac{f_{cr}}{S}$	Specimen	$\frac{d}{t}$	Crinkling strength f_{cr} (lb./sq.in.)	$\frac{1}{\delta_s} = \frac{E}{S} \frac{t}{d_m}$	$\sigma_{cr s} = \frac{f_{cr}}{S}$
1DR-1	13.5	72500	19.74	1.756	F-C	47.4	49900	5.59	1.211
1DR-C	13.5	68700	19.74	1.663	E-4	55.8	48800	4.73	1.178
v-6C	15.7	65400	16.43	1.494	E-C	55.9	48400	4.73	1.175
t-C	20.1	61000	12.77	1.416	1V-C	61.4	46000	4.56	1.185
t-6	20.2	61300	12.74	1.423	V-C	61.5	46200	4.57	1.195
b-C	25.6	55100	10.34	1.324	V-7	61.5	46000	4.57	1.185
1b-4C	25.8	55100	10.73	1.431	2V-C	62.2	46300	4.44	1.172
b-7	25.9	56100	10.25	1.350	DH-4	63.7	47400	4.14	1.145
1b-C	25.9	54400	10.71	1.413	DH-C	63.7	47000	4.14	1.141
1p-C	35.3	50500	8.14	1.328	1B-C	78.1	43600	3.26	1.038
1p-9	35.3	50500	8.13	1.328	1B-5	78.4	45600	3.24	1.081
X-4	45.9	49700	5.98	1.254	B-4C	79.2	45200	3.37	1.109
X-C	45.9	49600	5.98	1.253	1DQ-1	97.9	41900	2.62	.994
1F-3C	47.3	49700	5.61	1.198	1DQ-C	98.4	41800	2.60	.995

TABLE III
RESULTS OF BENDING TESTS
CHROMIUM-MOLYBDENUM STEEL

Specimen	$\frac{d}{t}$	Modulus of Rupture f_r (lb./sq. in.)	$\frac{1}{\delta_y} = \frac{E}{Y} \frac{t}{d_m}$	$\sigma_{r y} = \frac{f_r}{Y}$	Specimen	$\frac{d}{t}$	Modulus of Rupture f_r (lb./sq. in.)	$\frac{1}{\delta_y} = \frac{E}{Y} \frac{t}{d_m}$	$\sigma_{r y} = \frac{f_r}{Y}$
1CL-1a	15.5	139500	22.60	1.553	1CN-3	53.1	110000	6.31	1.215
1CL-3	15.6	140000	22.52	1.559	1CO-3	54.4	116100	6.16	1.258
2CE-3	24.0	129900	13.51	1.345	2CM-2	61.9	113300	5.22	1.191
1CE-3a	24.5	128200	13.92	1.400	1CM-3	62.1	118200	5.13	1.222
1CK-7	34.3	128900	9.61	1.365	1CS-2	78.4	88800	5.80	1.327
1CK-3	34.3	127800	9.61	1.354	1CS-1	79.0	88500	5.75	1.322
1CT-2	42.8	120100	7.84	1.304	1CU-1	88.6	99000	4.54	1.288
1CT-1	42.8	116000	7.84	1.260	1CU-2	89.8	93800	4.47	1.220
1CP-2	44.9	121400	7.16	1.294	1CC-2	99.3	91800	4.16	1.243
1CP-1	44.9	116900	7.16	1.246	1CC-1	100.0	89000	4.13	1.204
DURALUMIN									
Specimen	$\frac{d}{t}$	Modulus of Rupture f_r (lb./sq. in.)	$\frac{1}{\delta_s} = \frac{E}{S} \frac{t}{d_m}$	$\sigma_{r s} = \frac{f_r}{S}$	Specimen	$\frac{d}{t}$	Modulus of Rupture f_r (lb./sq. in.)	$\frac{1}{\delta_s} = \frac{E}{S} \frac{t}{d_m}$	$\sigma_{r s} = \frac{f_r}{S}$
v-3	15.7	73100	16.49	1.669	E-3	55.8	57200	4.73	1.389
t-4	20.2	70300	12.73	1.632	V-4	61.6	54400	4.56	1.408
t-5	20.2	69000	12.73	1.600	DH-2	63.7	56100	4.15	1.361
b-5	25.9	65000	10.24	1.561	DH-3	63.7	55600	4.14	1.350
1b-5	25.9	63200	10.71	1.642	DH-1	63.9	55300	4.13	1.342
1p-6	35.3	59100	8.14	1.556	1B-4	78.4	52900	3.24	1.259
1p-8	35.3	59900	8.13	1.576	B-5	79.6	52100	3.36	1.277
X-3	45.9	59400	5.98	1.501	1DQ-2	98.4	46200	2.60	1.099
1F-4	47.4	60900	5.59	1.467	1DQ-4	98.4	46800	2.60	1.115

REFERENCES

1. Timoshenko, S.: Theory of Elastic Stability. McGraw-Hill Book Co., Inc., 1936.

2. Hansen, Knud E.: Bending Strength of Thin-Walled Cylindrical Tubes. Bygningsstatistiske Meddelelser, vol. 9, no. 1 (Copenhagen), 1937.

3. Tuckerman, L. B.: Discussion of paper "The Determination and Significance of the Proportional Limit in the Testing of Metals," by R. L. Templin. A. S. T. M. Proc., vol. 29, pt. II, 1929, pp. 538-546.

4. Osgood, William R.: Column Strength of Tubes Elastically Restrained against Rotation at the Ends. T. R. No. 615, N. A. C. A., 1938.

5. Geckeler, J. W.: Plastisches Knicken der Wandung von Hohlzylindern und einige andere Faltungserscheinungen an Schalen und Blechen. Z. f. a. M. M., Bd. 8, Heft 5, Oktober 1928, S. 341-352.

6. Flügge, W.: Die Stabilität der Kreiszylinderschale. Ingenieur-Archiv, Bd. III, Heft 5, Dez. 1932, S. 463-506.

REPORT No. 633

PRESSURE DISTRIBUTION OVER AN N. A. C. A. 23012 AIRFOIL WITH A SLOTTED AND A PLAIN FLAP

By CARL J. WENZINGER and JAMES B. DELANO

SUMMARY

Pressure-distribution tests of an N. A. C. A. 23012 airfoil equipped with a slotted flap and with a plain flap were made in the 7- by 10-foot wind tunnel. A test installation was used in which the 7-foot-span airfoil was mounted vertically between the upper and lower sides of the closed test section so that two-dimensional flow was approximated. The pressures were measured on the upper and lower surfaces at one chord section both on the main airfoil and on the flaps for several different flap deflections and at several angles of attack.

The data are presented in the form of pressure-distribution diagrams and as graphs of calculated section coefficients for the airfoil-and-flap combinations and also for the flaps alone. The results are useful for application to rib and flap structural design; in addition, the plain-flap data furnish considerable information applicable to the structural design of plain ailerons.

INTRODUCTION

Up to the present time, many high-lift devices have been developed and investigated, but each appears to have some disadvantages. One of the most promising high-lift devices thus far developed is the combination of a slotted flap with a main airfoil. Investigations of this arrangement (reference 1) have shown that it is capable of developing high lifts and that it gives lower drags at these high lifts than do external-airfoil, plain, or split flaps.

The force tests of reference 1, in which several combinations of an N. A. C. A. 23012 airfoil with flaps of different sections and with slots of several different shapes were investigated, indicated that the best arrangement thus far obtained is a combination of an airfoil and a slotted flap, the flap having an airfoil shape and the slot an easy entrance; this combination is designated flap 2-h in reference 1. A survey of flap location with respect to the main airfoil was made to obtain the best aerodynamic characteristics. It was also found that some particular flap path would give optimum aerodynamic characteristics; the flap path developed is reported in reference 1.

Very few data are available for application to the structural design of slotted flaps. Some recent data

(references 2 and 3) are available but, as the reported tests were not very comprehensive, the present investigation was undertaken to supply information applicable to the structural design of slotted flaps. Similar data are already available for the design of split, external-airfoil, and Fowler flaps (references 4, 5, and 6).

Pressure-distribution tests were made in the 7- by 10-foot wind tunnel of an N. A. C. A. 23012 airfoil in combination with a slotted flap. The optimum flap path previously developed for this flap (reference 1) was used in these tests. Pressure-distribution tests were also made over the same airfoil in combination with a plain flap for purposes of comparison and also to obtain additional information for the detailed structural design of both flaps and ailerons.

APPARATUS AND TESTS

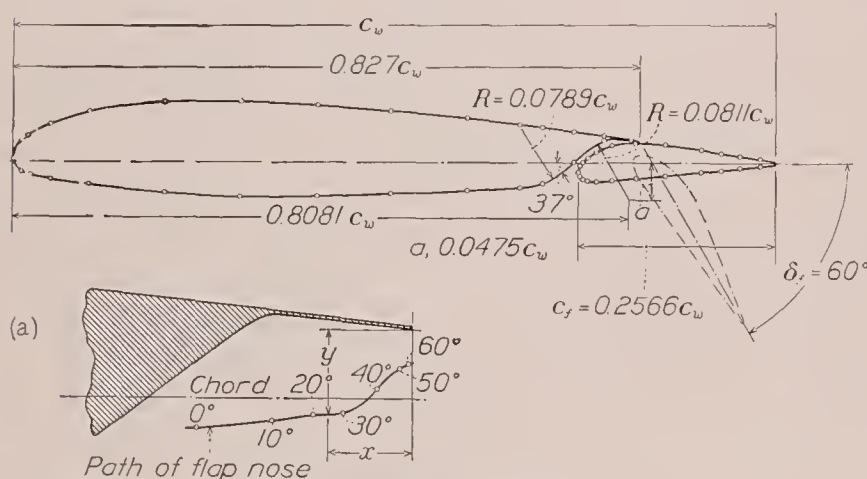
MODELS

The models used in the present tests are the ones previously used in the force tests reported in reference 1. The main airfoil, made of laminated pine to the N. A. C. A. 23012 profile, has a uniform chord of 3 feet and a span of 7 feet. A removable full-span trailing-edge section permits the testing of different full-span flaps in combination with the same main airfoil. Both a slotted flap and a plain flap made of laminated pine were tested; each was supported on the main airfoil by three metal fittings, one located at mid-span and one inboard of each flap tip.

The slotted flap tested (fig. 1) is the one previously developed by the N. A. C. A. and designated 2-h in reference 1; it has a chord of 9.238 inches (25.66 percent of the over-all airfoil chord). A full-span fixed lip made of strip brass is located on the upper surface of the main airfoil over the flap-slot exit to seal the slot when the flap is neutral and to direct the passage of air downward over the flap when the flap is deflected. The path of the nose point of the flap chosen (fig. 1) is the optimum one reported in the tests described in reference 1. The nose point of the flap is defined as the point of tangency of a line drawn normal to the airfoil chord and tangent to the leading-edge arc of the flap when neutral. The flap is arranged for locking at downward flap deflections between 0° and 60° in increments of 10° .

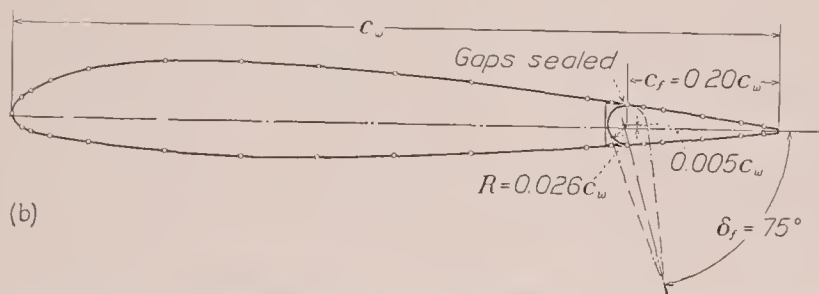
The plain flap (fig. 1) has a chord of 7.20 inches (20.0 percent of the over-all airfoil chord). The flap gap was sealed for all flap deflections by interchangeable full-span brass lips on the upper and lower surfaces of the airfoil to prevent a flow of air through the gap. The flap is arranged for locking at flap deflections between 45° up and 75° down in increments of 15° .

A single row of pressure orifices was built into the upper and lower surfaces of both the main airfoil and the flaps at a chord section 21 inches from one end of the models (fig. 2). The orifices were located on the models as listed in table I, the tubes from the orifices being brought through the models and out at one end. The pressures were photographically recorded by a multiple-tube liquid manometer.



(a) N. A. C. A. 23012 airfoil with a $0.2566c_w$ slotted flap.

δ_f (deg.)	Path of flap nose for various flap deflections. Distances measured from lower edge of lip in percent airfoil chord c_w	
	x	y
0	8.36	3.91
10	5.41	3.63
20	3.83	3.45
30	2.63	3.37
40	1.35	2.43
50	.50	1.63
60	.12	1.48



(b) N. A. C. A. 23012 airfoil with a $0.20c_w$ plain flap.

FIGURE 1.—Cross sections of model showing airfoil-flap combinations used in pressure-distribution tests.

TEST INSTALLATION

The model was mounted in the N. A. C. A. 7- by 10-foot closed-jet wind tunnel (references 1 and 7) as indicated in figure 2. The main airfoil was rigidly attached to the balance frame by torque tubes, which extended through the upper and lower sides of the tunnel. The angle of attack of the model was set from

outside the tunnel by rotating the torque tubes with a calibrated electric drive. Approximately two-dimensional flow is obtained with this type of installation, and the section characteristics of the model under test may be determined.

TESTS

All the tests were made at a dynamic pressure of 16.37 pounds per square foot, corresponding to an air

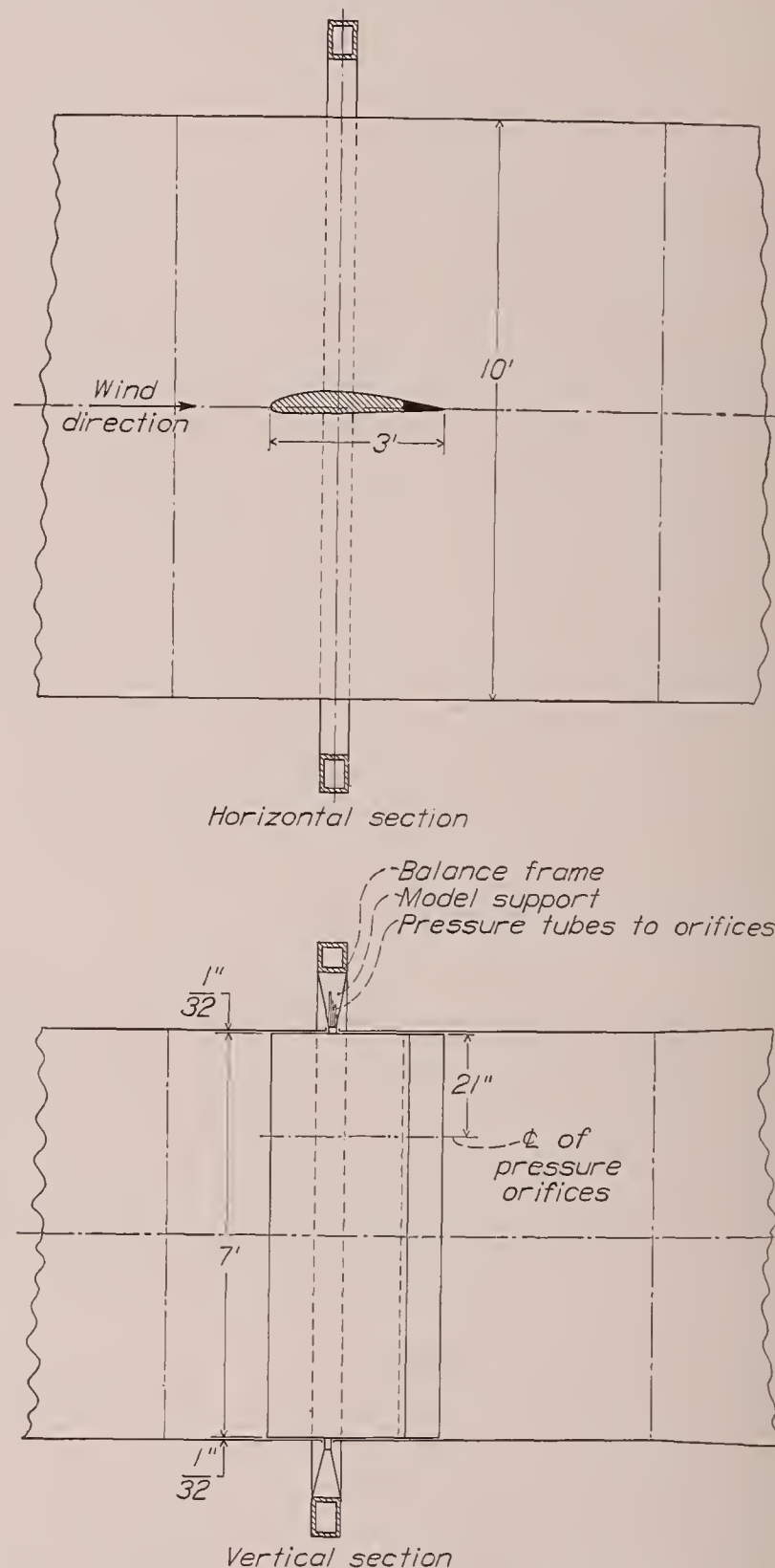


FIGURE 2.—Model installation for two-dimensional flow tests in the 7- by 10-foot wind tunnel.

speed of about 80 miles per hour at standard sea-level conditions. The average test Reynolds Number, based on the plain airfoil chord, was 2,190,000. This test Reynolds Number, when converted to an effective Reynolds Number (reference 8) that takes account of the turbulence in the air stream, is 3,500,000. (Effective Reynolds Number=average test Reynolds Number \times turbulence factor; turbulence factor for the tunnel is 1.6.)

The model was tested with the slotted flap set at angles of 0° , 10° , 20° , 30° , 40° , 50° , and 60° down; and with the plain flap set at angles of 45° , 30° , and 15° up, 0° , and 15° , 30° , 45° , 60° , and 75° down. The angles of attack ranged from -14° to 20° , and the lift coefficients included those from approximately maximum negative to maximum positive. With the model at a given angle of attack and with a given flap setting, tunnel conditions were allowed to become steady before a record of the pressures at the orifices was taken.

PRESENTATION OF DATA

PRESSURE DIAGRAMS

All diagrams of pressures over the upper and lower surfaces of the airfoil-flap combinations are given as ratios of the orifice pressure p to the dynamic pressure q of the free air stream for the flap deflections and for the angles of attack investigated. Pressure diagrams for the airfoil with the slotted flap are shown in figures 3 to 15 and, for the airfoil with the plain flap, in figures 16 to 24. The effect of the flaps on the pressure distribution over the main airfoil is shown by a comparison of the pressures over the plain airfoil with the pressures over both the slotted-flap and the plain-flap combinations at the same total normal-force coefficient and also at the same angle of attack (figs. 25 and 26). In figures 3 to 9 and 16 to 26, the pressures over the main airfoil are plotted normal to the airfoil chord and the pressures over the flaps are plotted normal to a reference line which is parallel to the main airfoil chord when the flap is neutral but which deflects with the flap.

Figures 10 to 15 are included to show the pressures parallel to the chord of the slotted flap. These pressures are also given as ratios of orifice pressure to the dynamic pressure of the air stream; however, the pressure values are plotted parallel to, instead of normal to, the flap reference line and are measured from the maximum ordinates of the flap instead of from its reference line.

COEFFICIENTS

The pressure diagrams were mechanically integrated to obtain data from which section coefficients were computed. Where the term "flap alone" is used, reference is made to the characteristics of the flap in the presence of the main airfoil. The section coefficients are defined as follows:

$c_{n_w} = \frac{n_w}{qc_w}$, normal-force coefficient of main airfoil with flap.

$c_{n_f} = \frac{n_f}{qc_f}$, normal-force coefficient of flap alone.

$c_{m_w} = \frac{m_w}{qc_w^2}$, pitching-moment coefficient of main airfoil with flap about quarter-chord point of airfoil.

$c_{m_f} = \frac{m_f}{qc_f^2}$, pitching-moment coefficient of slotted flap alone about quarter-chord point of flap.

$c_{h_f} = \frac{h_f}{qc_f^2}$, hinge-moment coefficient of plain flap about flap hinge axis.

$c_{c_f} = \frac{x_f}{qc_f}$, chord-force coefficient of slotted flap alone.

$(c.p.)_w = \left(0.25 - \frac{c_{m_w}}{c_{n_w}}\right) \times 100$, center-of-pressure location of main airfoil with flap in percent airfoil chord from leading edge.

$(c.p.)_f = \left(0.25 - \frac{c_{m_f}}{c_{n_f}}\right) \times 100$, center-of-pressure location of flap alone in percent flap chord from leading edge of flap.

where the forces and moments per unit span are:

n_w , normal force on main airfoil with flap (this force is normal to chord of main airfoil and is equal to $n_m + n_f \cos \delta_f$, neglecting the normal component of the flap chord force).

n_m , normal force on main portion of the airfoil without flap (this force is normal to chord of main airfoil and is equal to $n_w - n_f \cos \delta_f$).

n_f , normal force on flap alone normal to chord of flap.

m_w , pitching moment of main airfoil with flap about quarter-chord point of airfoil.

m_f , pitching moment of slotted flap about quarter-chord point of flap.

h_f , hinge moment of plain flap.

x_f , chord force on slotted flap alone.

and

q , dynamic pressure of free air stream.

c_w , chord of main airfoil.

c_f , chord of flap.

The coefficients for the combination were derived from the normal forces alone, the chord forces of the flaps being neglected. In the case of the slotted flap, however, neglecting the flap chord-force component in the computation of the total normal-force coefficient of the combination reduces these coefficients by a maximum of about 0.08.

Because the model completely spanned the jet, the integrated results, which are given in coefficient form in figures 27 to 42, may be taken to be section characteristics. The normal-force coefficients of the airfoil-flap combinations include an experimentally determined correction for tunnel-wall effects, which was made as in reference 1.

PRECISION

No air-flow alinement tests were made in the wind tunnel with the test arrangement used in this investigation, so the absolute angle of attack may be slightly in error; the relative angles are correct to within $\pm 0.1^\circ$. The flaps were set to specified angles to within $\pm 0.1^\circ$. The orifice pressures, based on check tests in which both the angle of attack and the flap setting were independently changed, show that they agreed to within ± 2 percent, with the exception of upper-surface

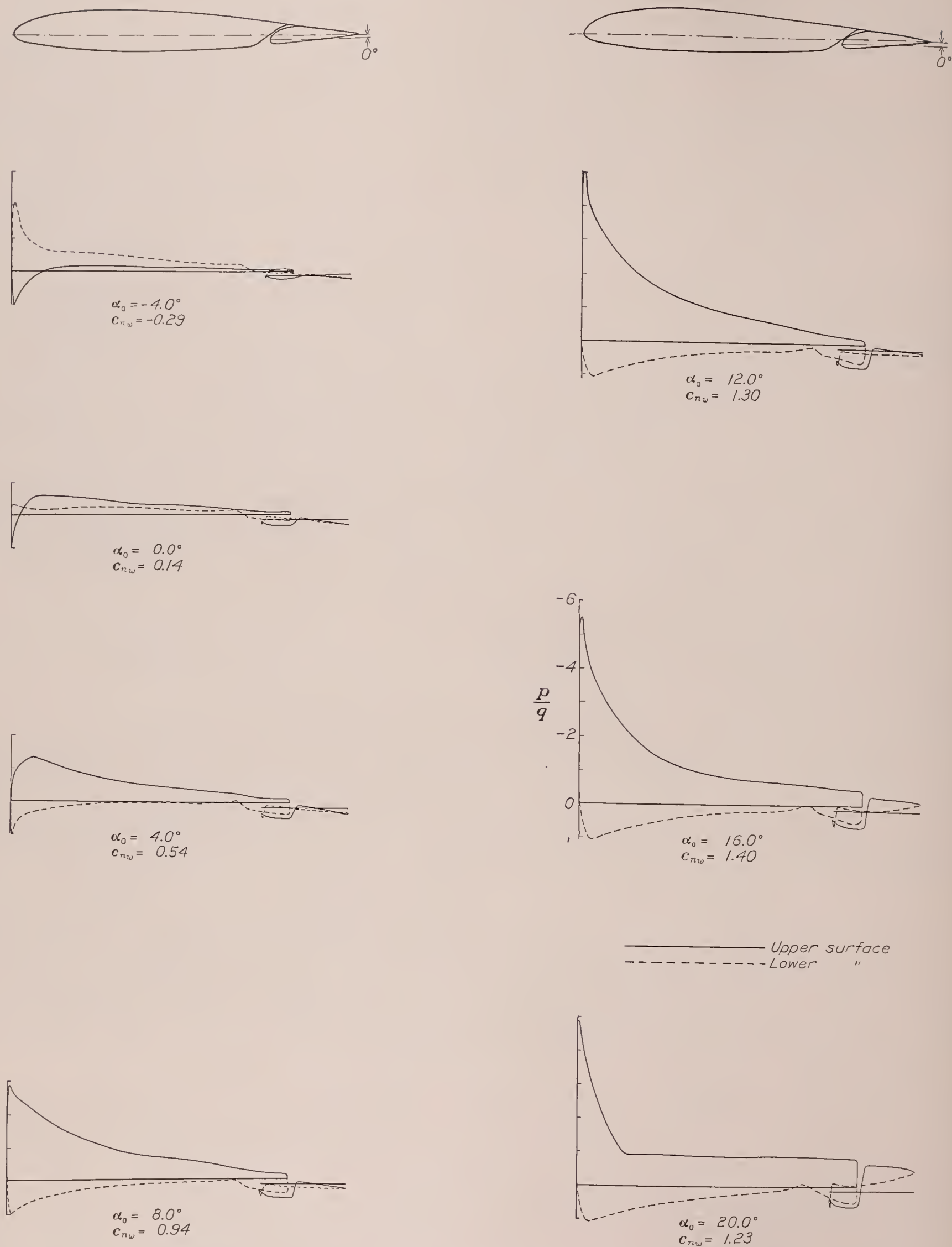


FIGURE 3.—Pressure distribution on the N. A. C. A. 23012 airfoil with a 0.2566 c_w slotted flap, at various angles of attack. Flap set at 0°.

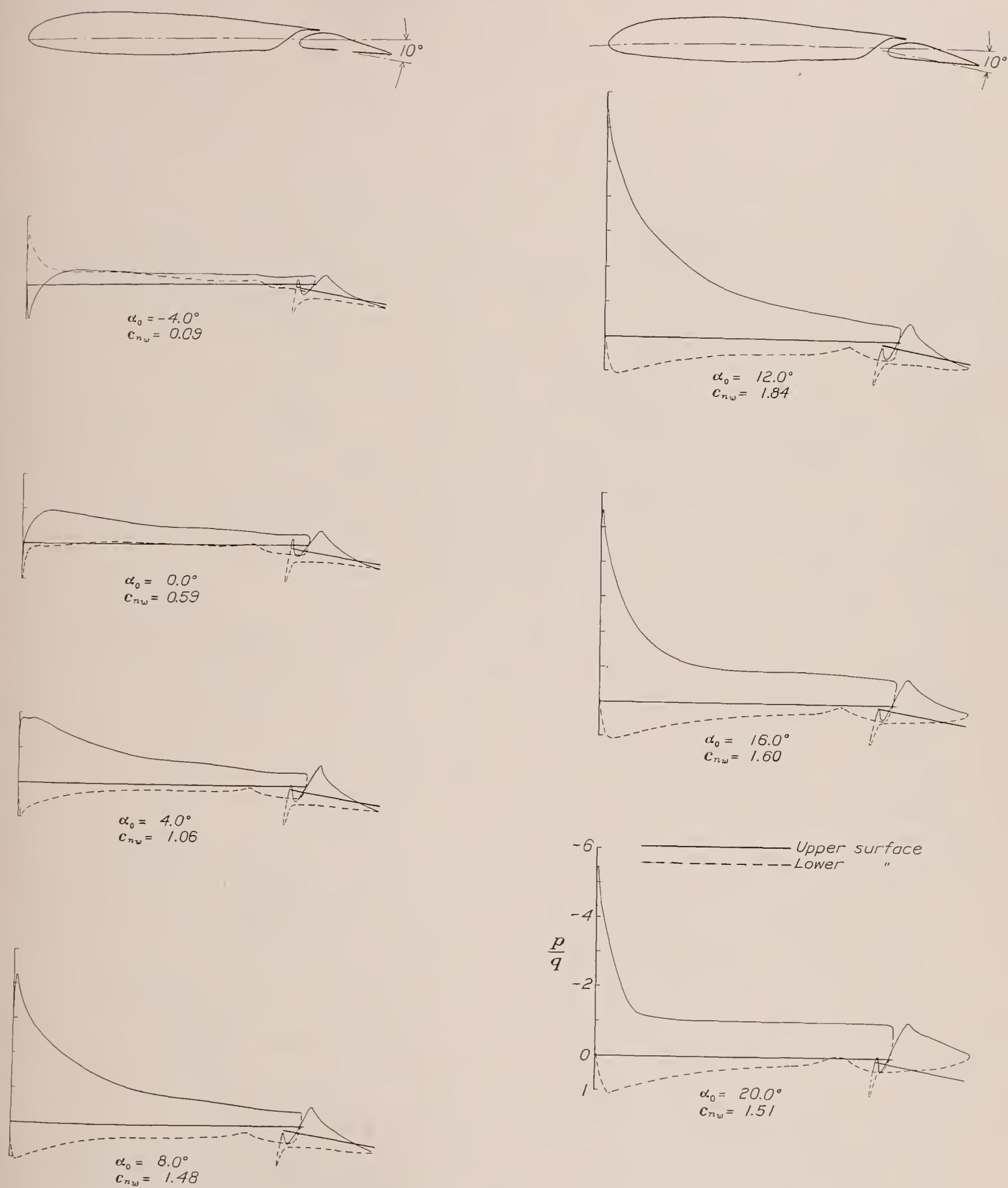


FIGURE 4.—Pressure distribution on the N. A. C. A. 23012 airfoil with a 0.2566 c_w slotted flap, at various angles of attack. Flap set at 10°.

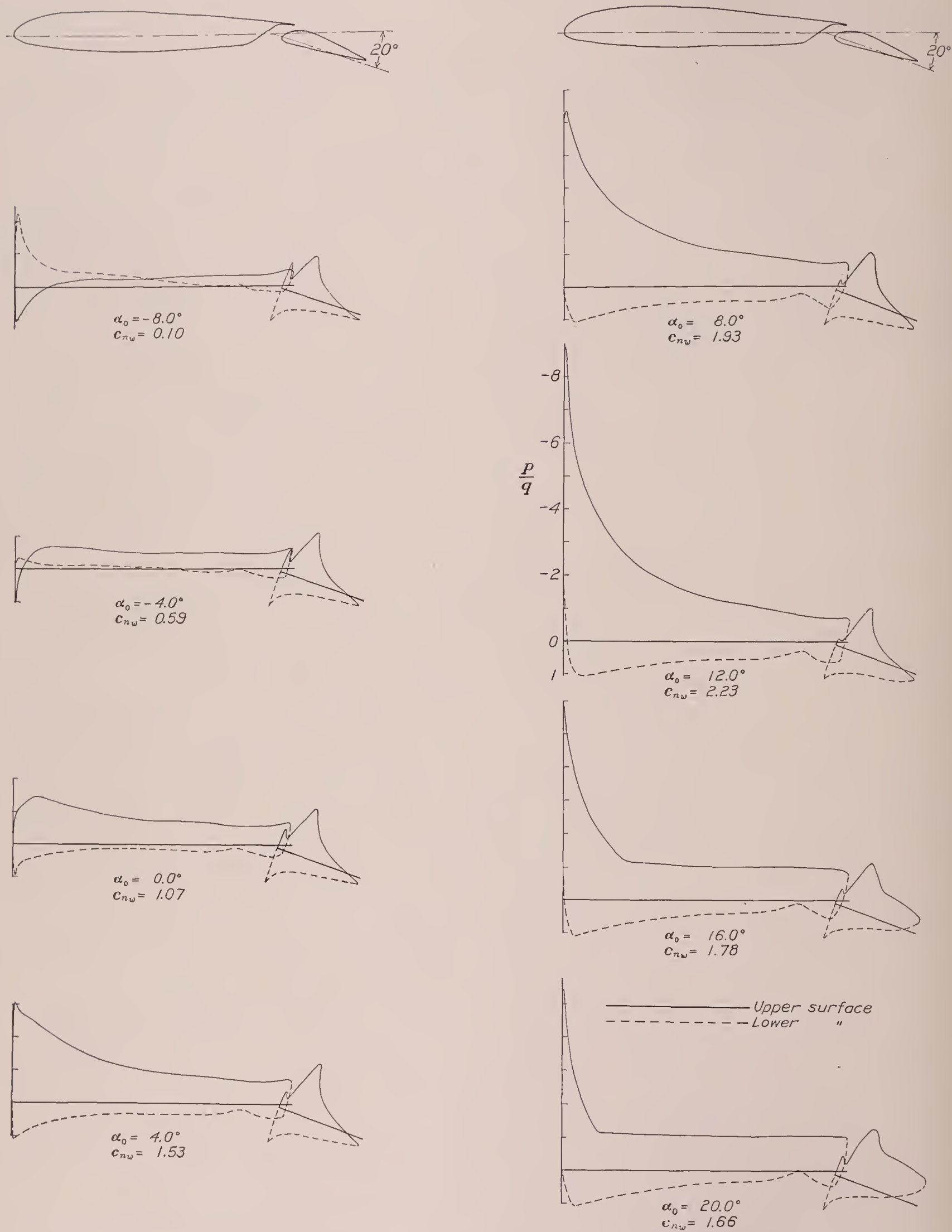
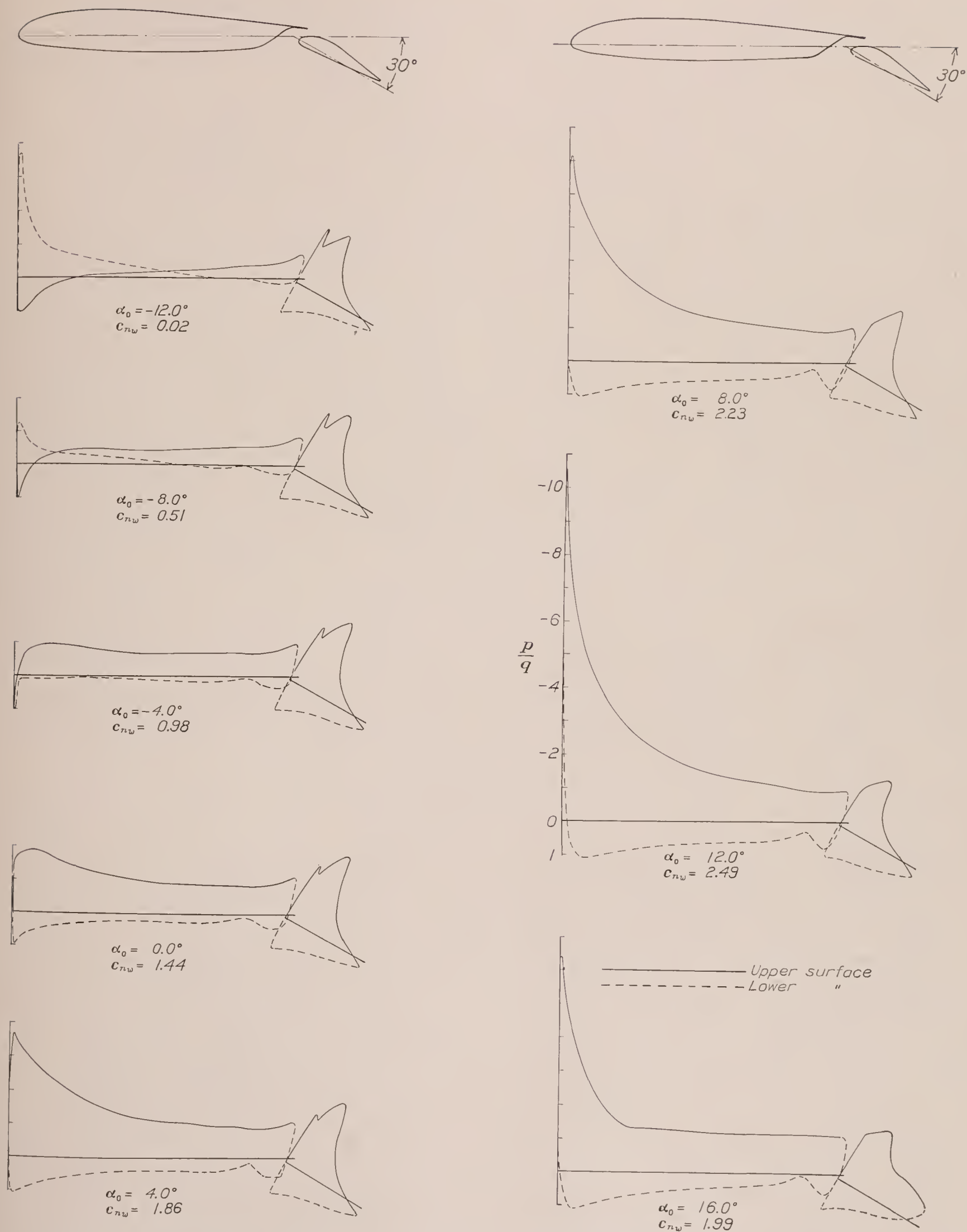


FIGURE 5.—Pressure distribution on the N. A. C. A. 23012 airfoil with a 0.2566 c_w slotted flap, at various angles of attack. Flap set at 20°.

FIGURE 6.—Pressure distribution on the N. A. C. A. 23012 airfoil with a 0.2566 c_w slotted flap, at various angles of attack. Flap set at 30°.

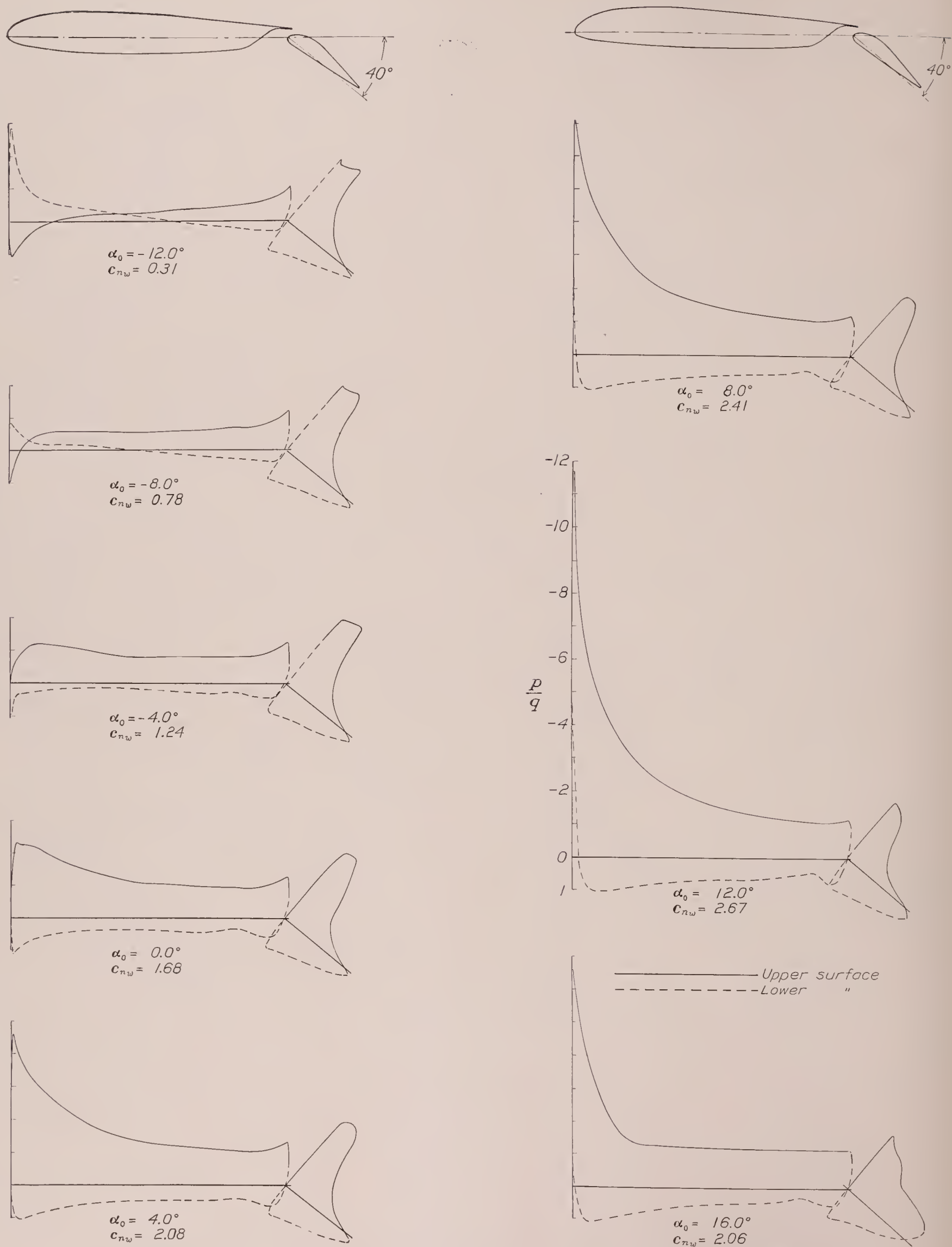


FIGURE 7.—Pressure distribution on the N. A. C. A. 23012 airfoil with a 0.2566 c_w slotted flap, at various angles of attack. Flap set at 40°.

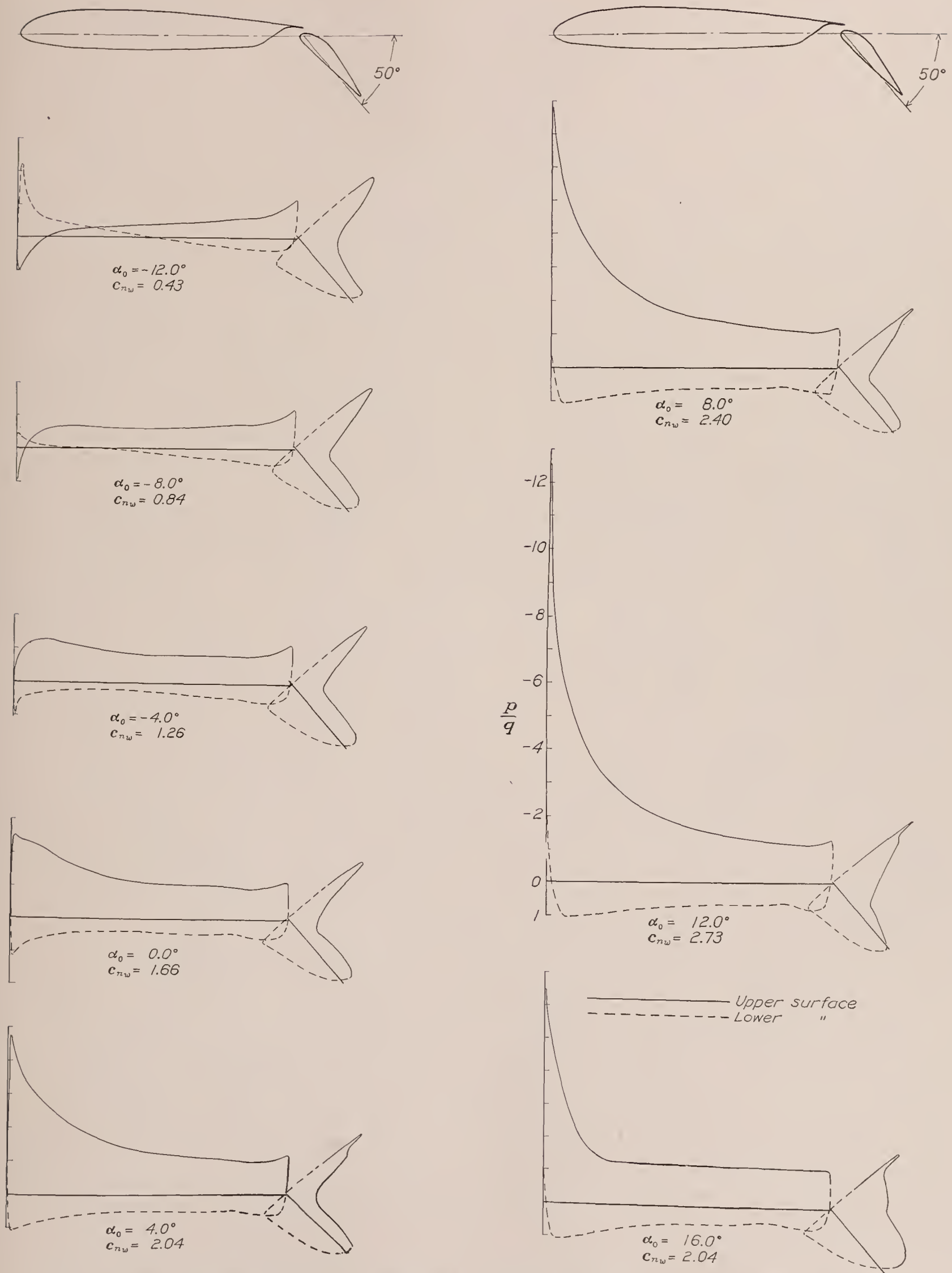


FIGURE 8.—Pressure distribution on the N. A. C. A. 23012 airfoil with a 0.2566 c_w slotted flap, at various angles of attack. Flap set at 50°.

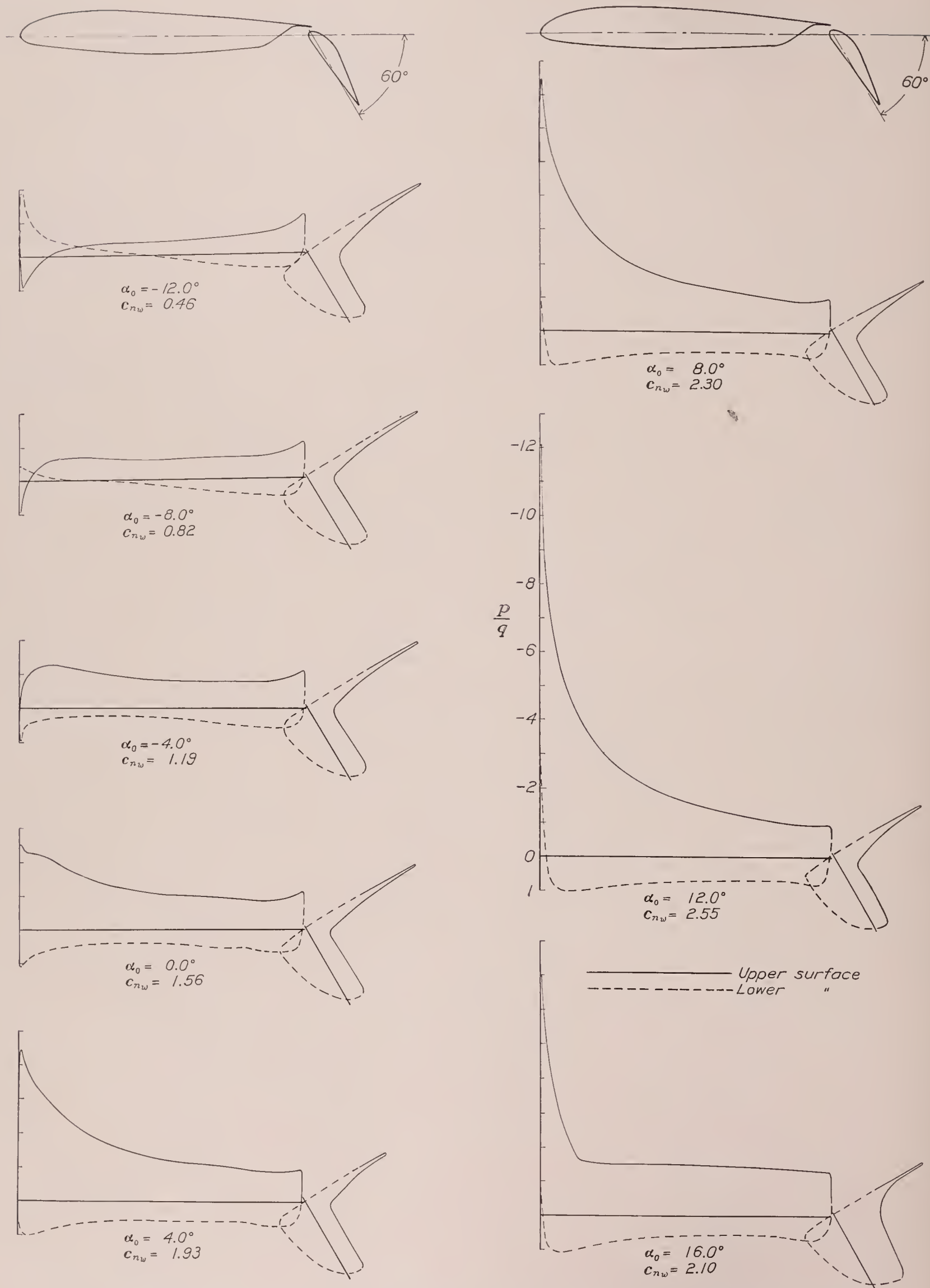


FIGURE 9.—Pressure distribution on the N. A. C. A. 23012 airfoil with a 0.2566 c_x slotted flap, at various angles of attack. Flap set at 60°.

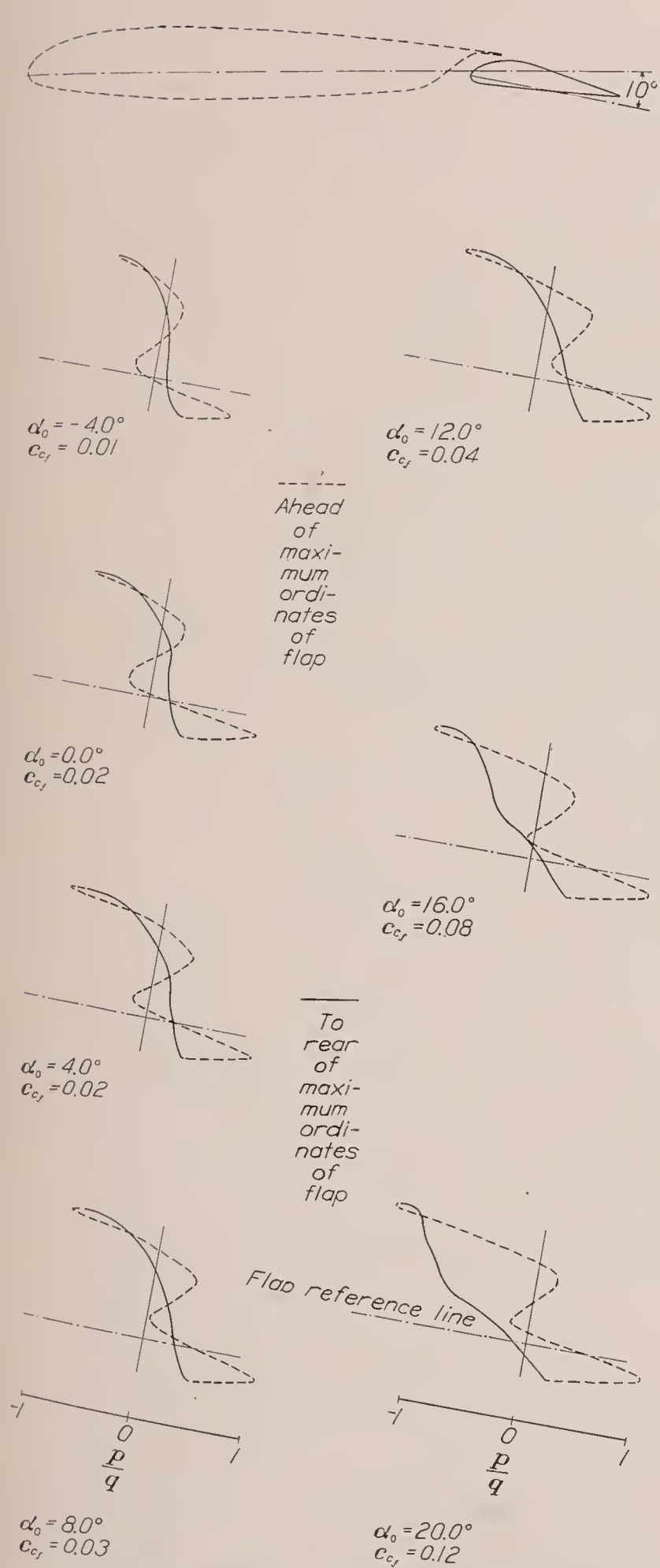


FIGURE 10.—Chord pressure distribution on a 0.2566 c_w slotted flap mounted on the N. A. C. A. 23012 airfoil. Flap set at 10°.

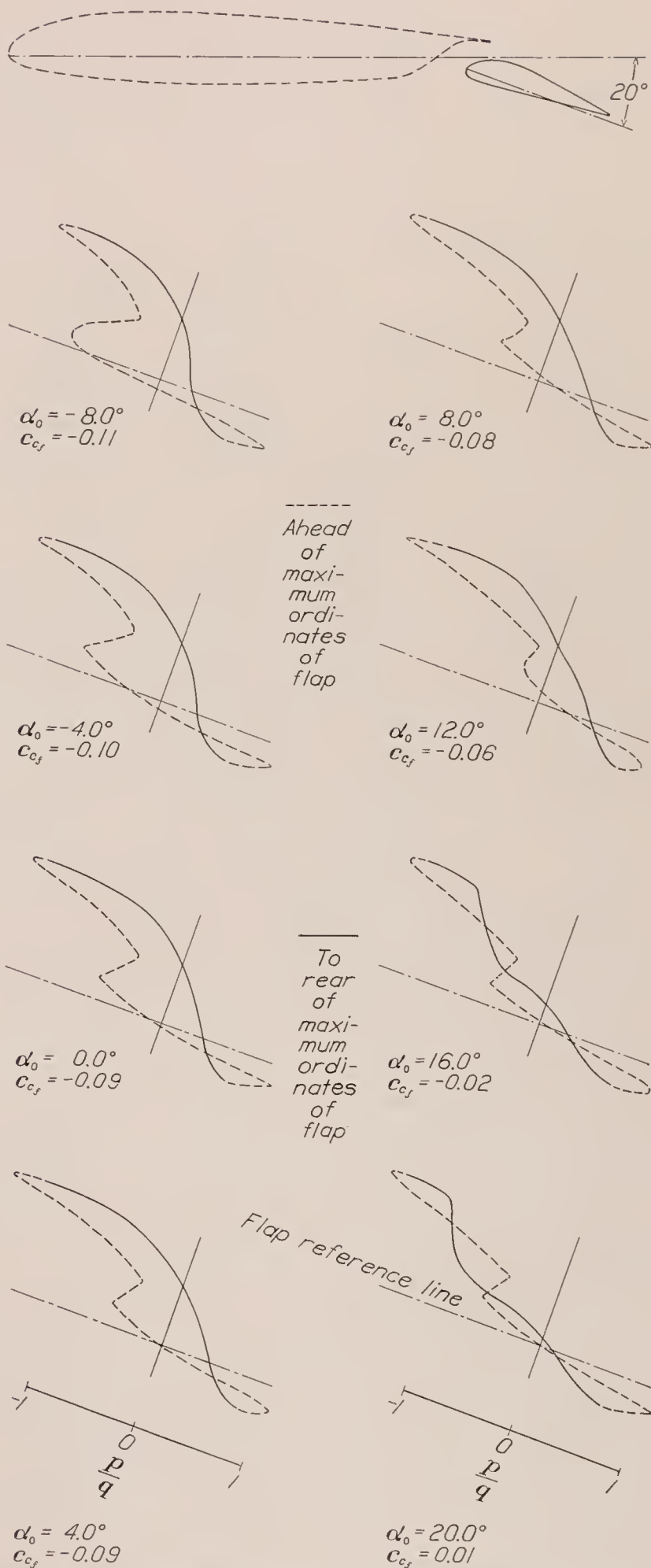


FIGURE 11.—Chord pressure distribution on a 0.2566 c_w slotted flap mounted on the N. A. C. A. 23012 airfoil. Flap set at 20°.

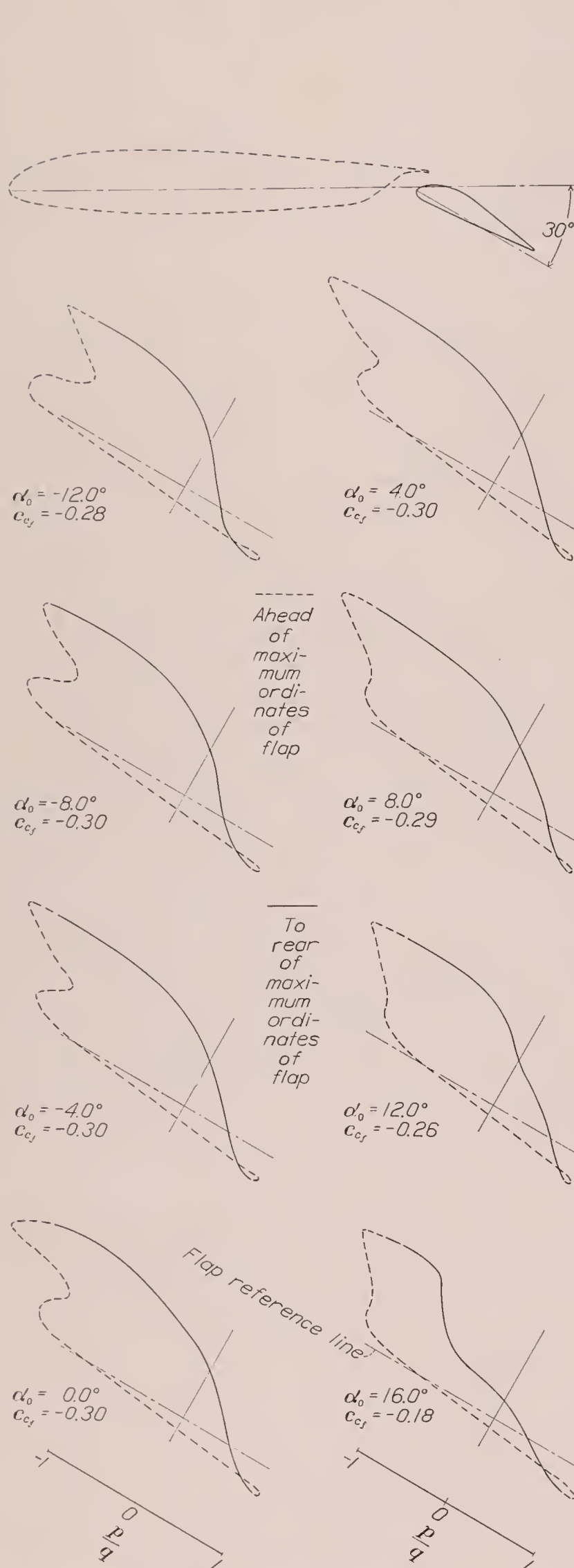


FIGURE 12.—Chord pressure distribution on a $0.2566c_w$ slotted flap mounted on the N. A. C. A. 23012 airfoil. Flap set at 30° .

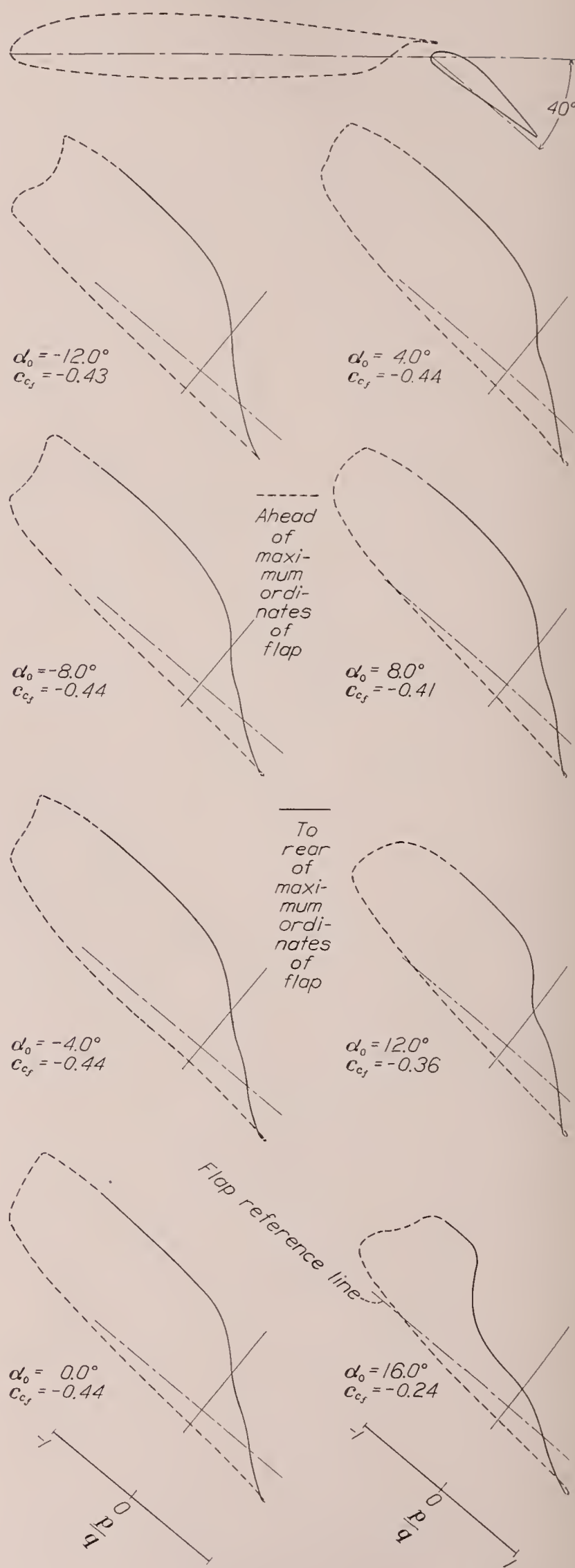


FIGURE 13.—Chord pressure distribution on a $0.2566c_w$ slotted flap mounted on the N. A. C. A. 23012 airfoil. Flap set at 40° .

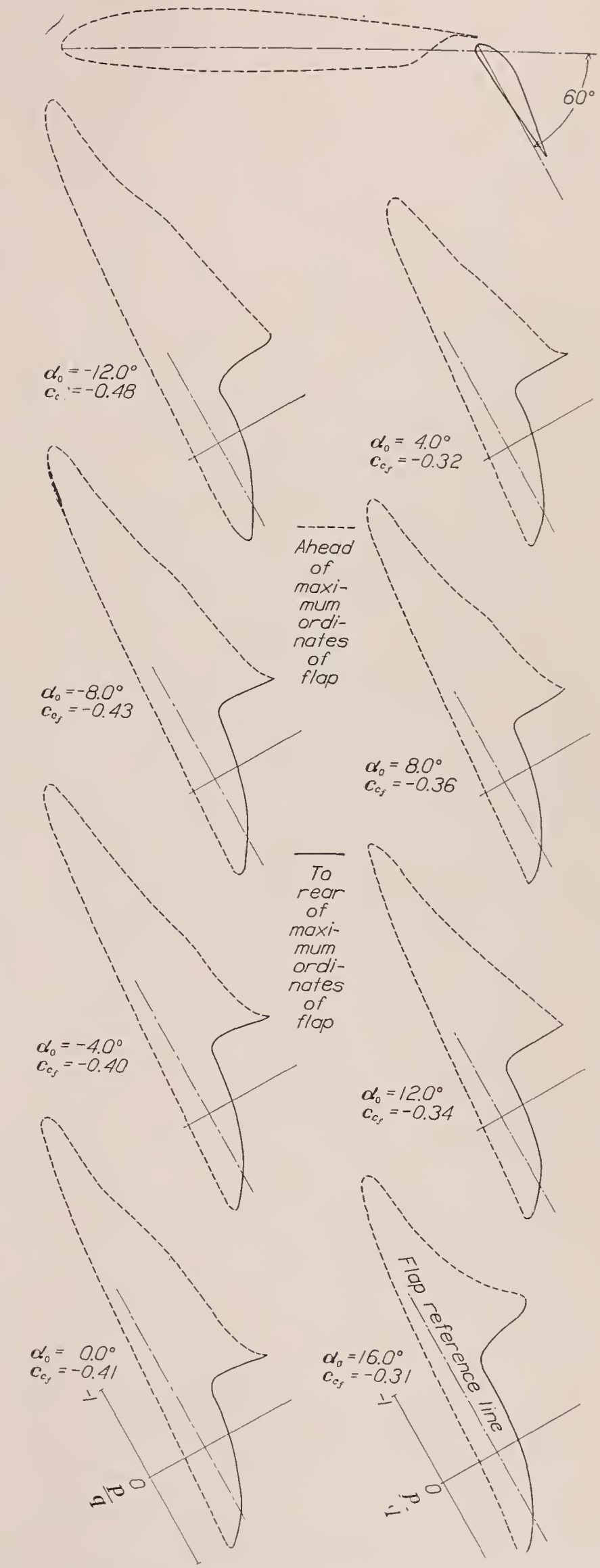
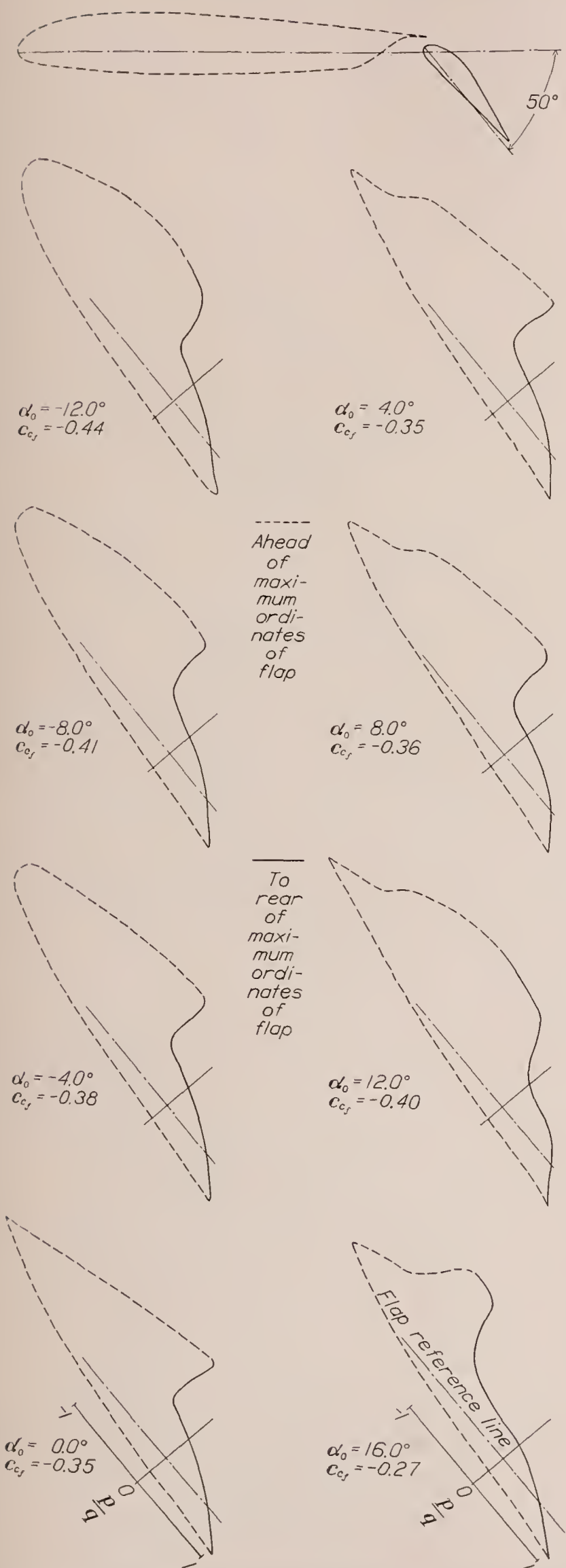


FIGURE 14.—Chord pressure distribution on a 0.2566 c_w slotted flap mounted on the N. A. C. A. 23012 airfoil. Flap set at 50°.

FIGURE 15.—Chord pressure distribution on a 0.2566 c_w slotted flap mounted on the N. A. C. A. 23012 airfoil. Flap set at 60°.

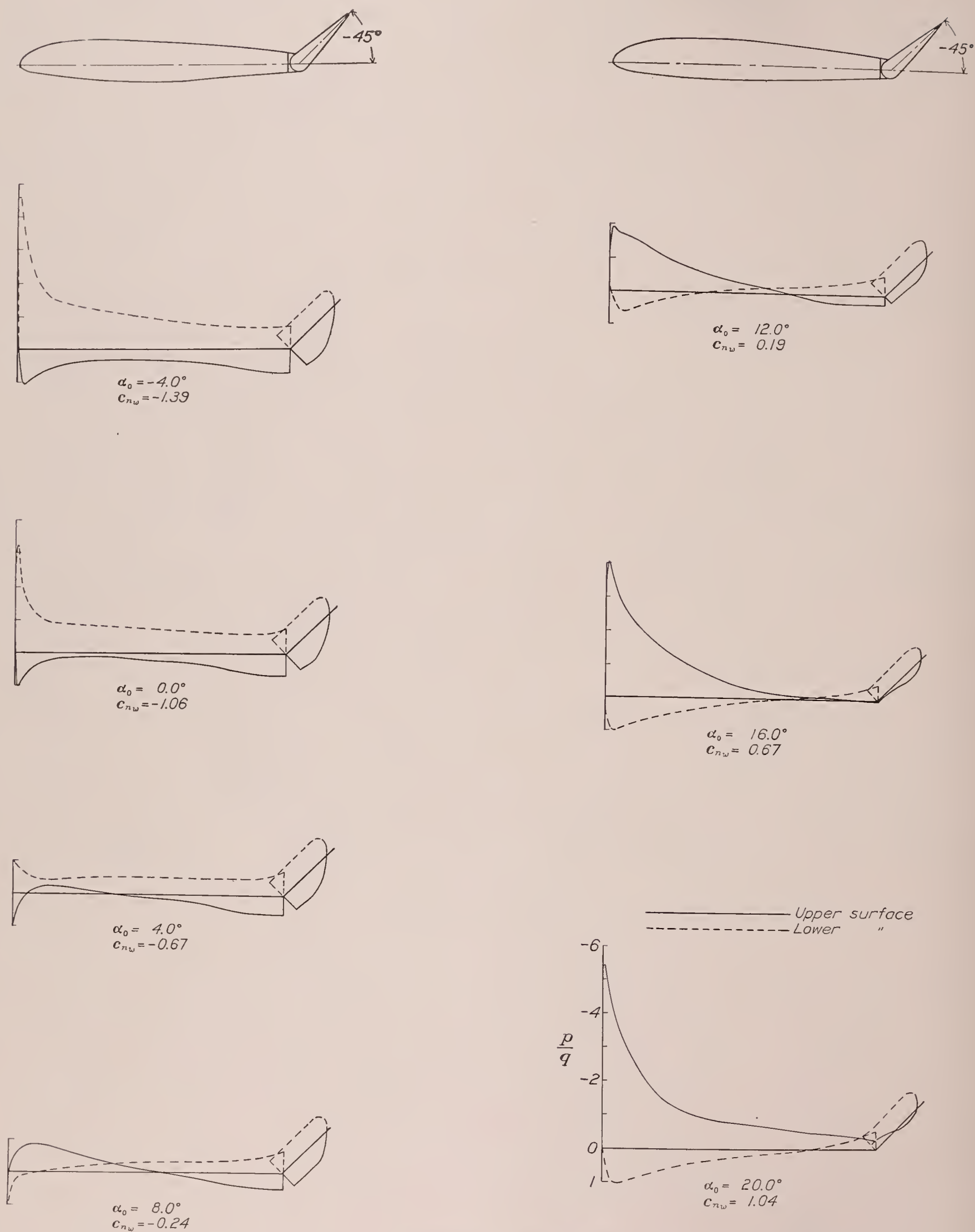


FIGURE 16.—Pressure distribution on the N. A. C. A. 23012 airfoil with a $0.20c_w$ plain flap, at various angles of attack. Flap set at -45° .

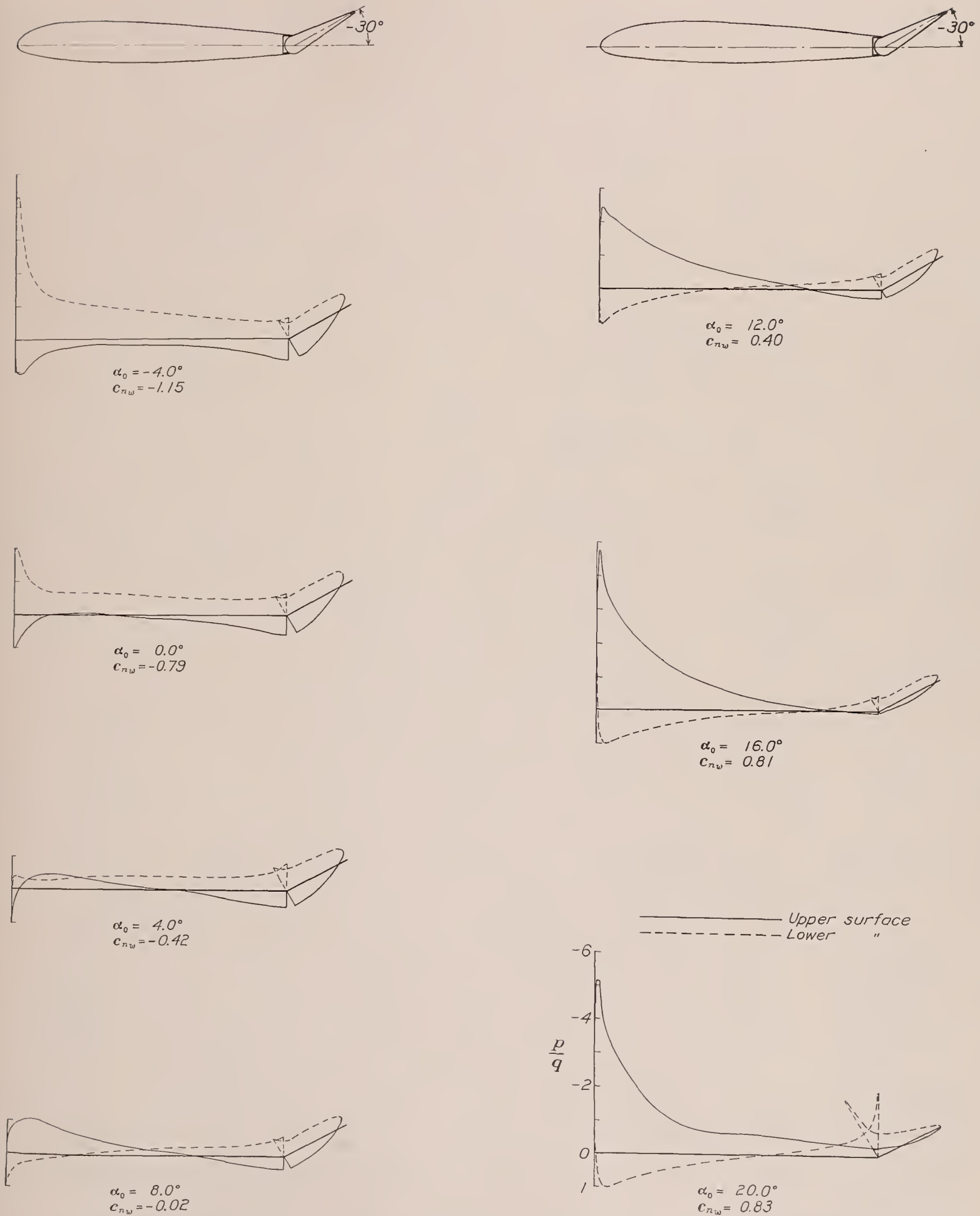


FIGURE 17.—Pressure distribution on the N. A. C. A. 23012 airfoil with a 0.20 c_w plain flap, at various angles of attack. Flap set at -30° .

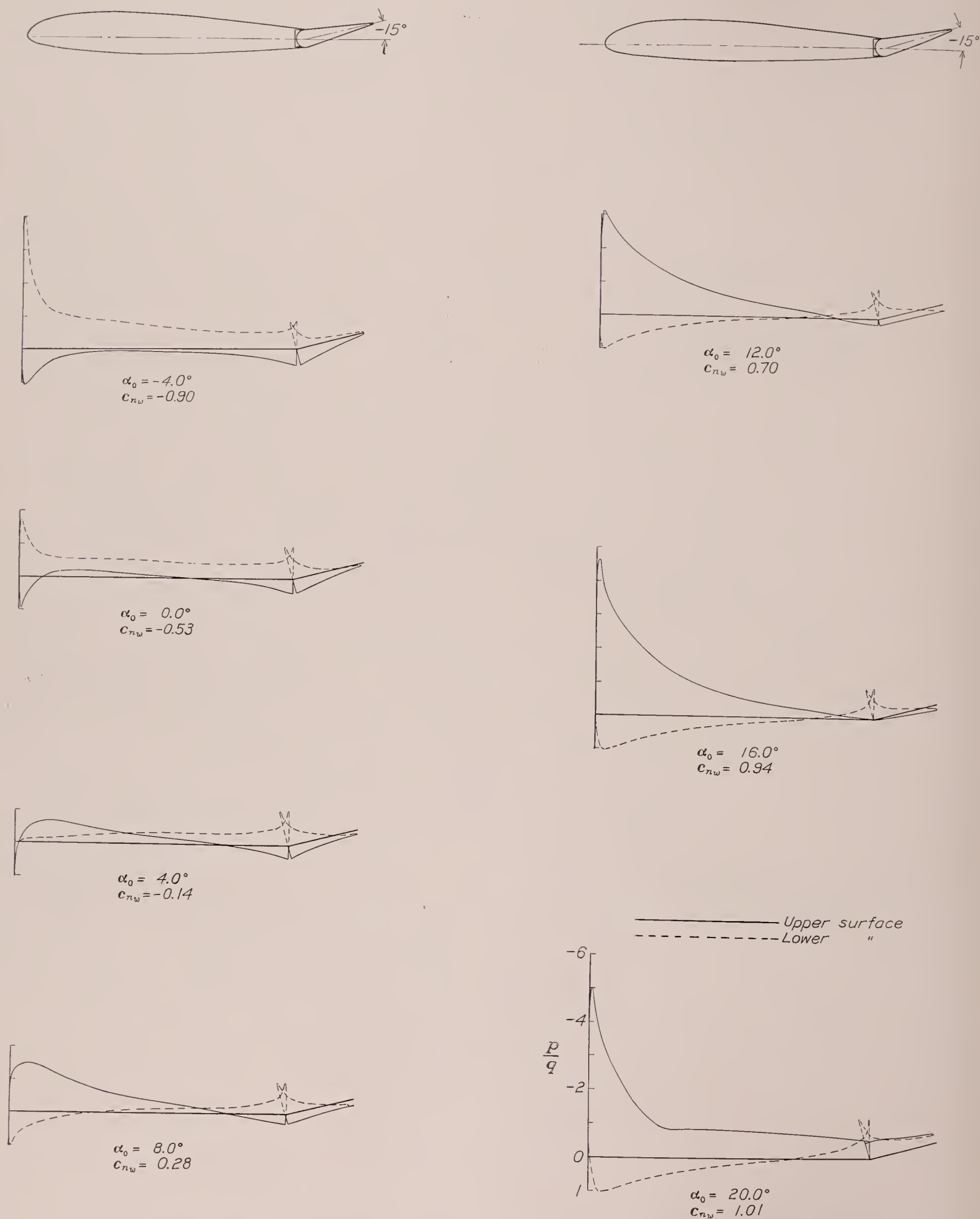


FIGURE 18.—Pressure distribution on the N. A. C. A. 23012 airfoil with a $0.20c_w$ plain flap, at various angles of attack. Flap set at -15° .

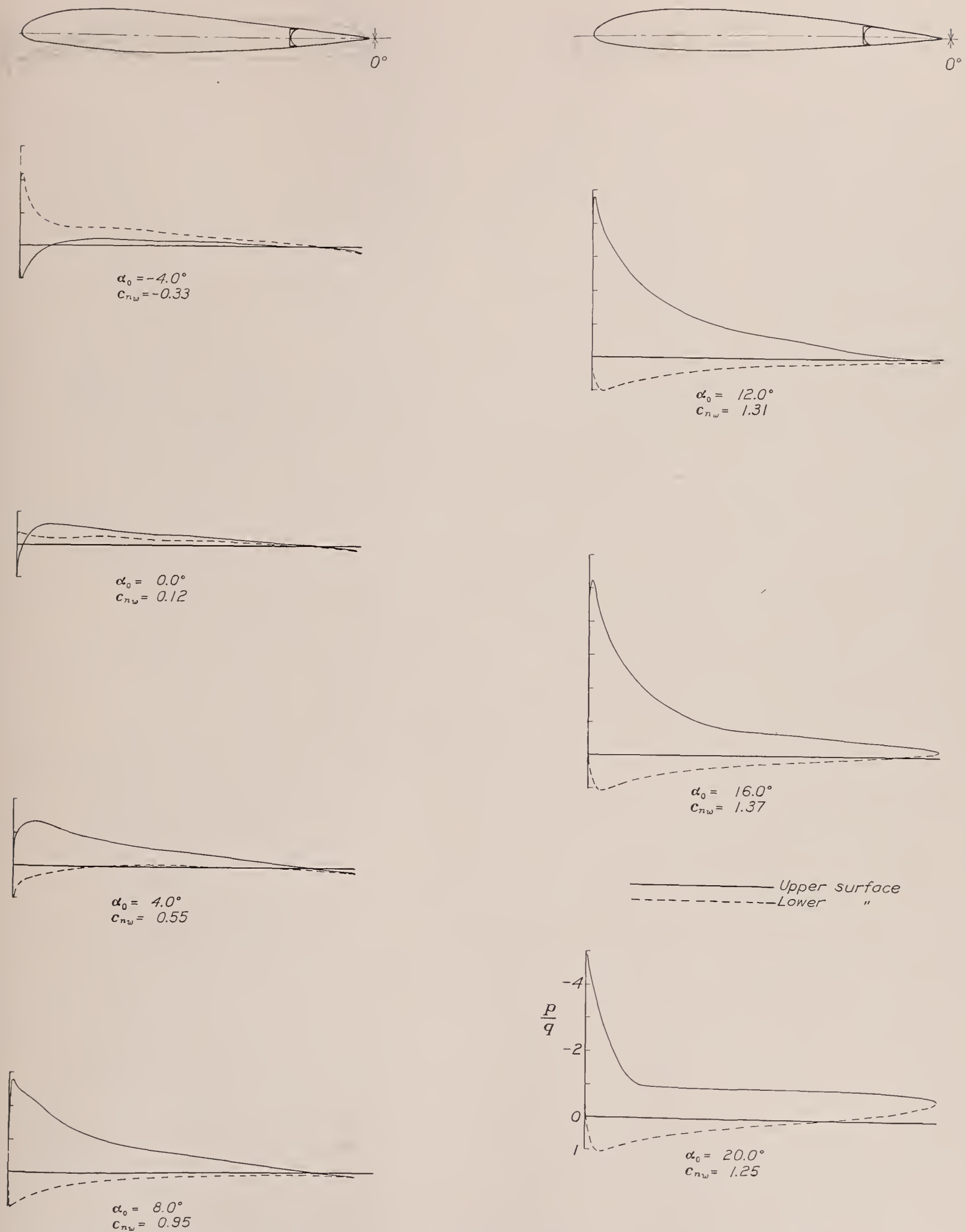


FIGURE 19.—Pressure distribution on the N. A. C. A. 23012 airfoil with a $0.20c_w$ plain flap, at various angles of attack. Flap set at 0° .

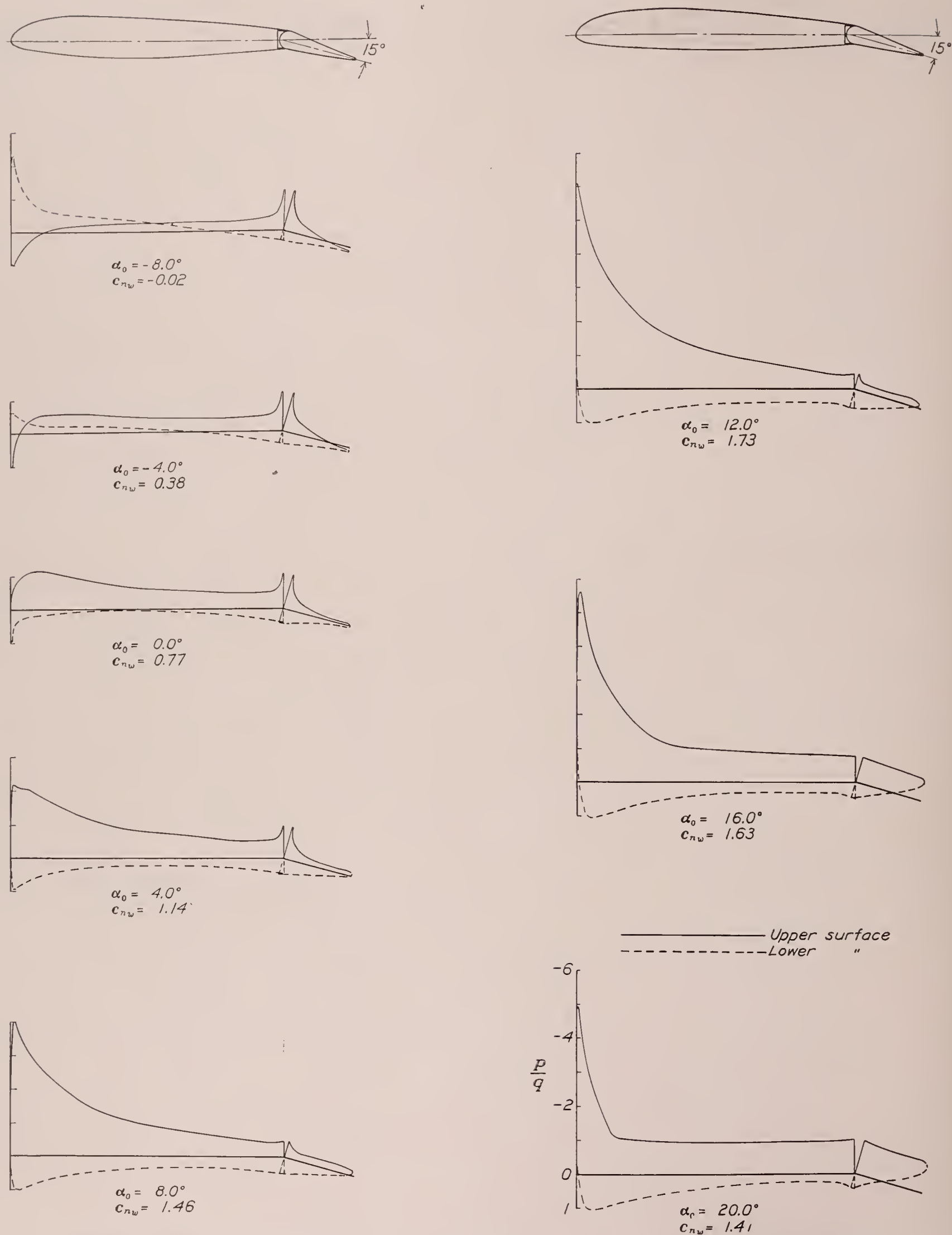
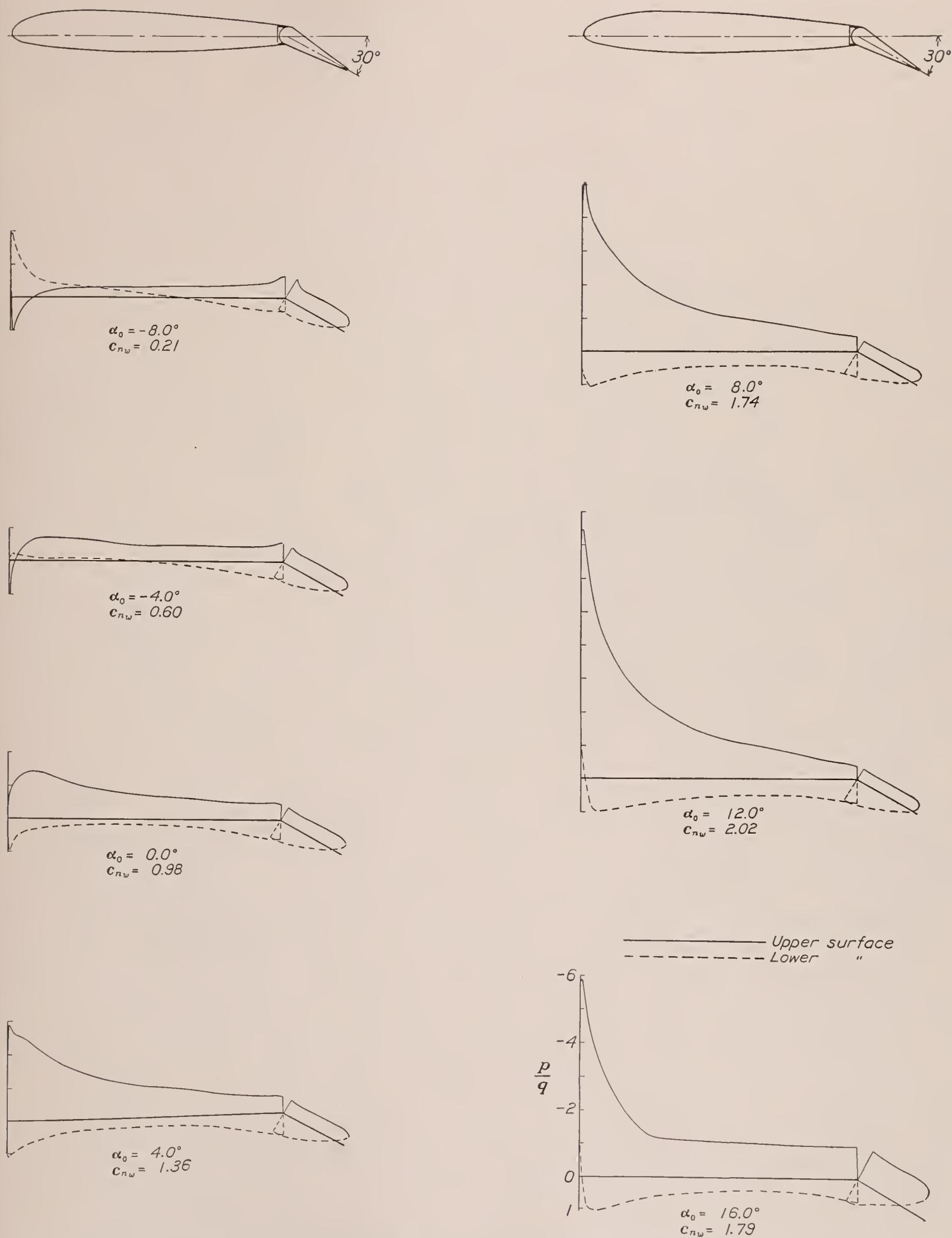


FIGURE 20.—Pressure distribution on the N. A. C. A. 23012 airfoil with a 0.20 c_w plain flap, at various angles of attack. Flap set at 15°.

FIGURE 21.—Pressure distribution on the N. A. C. A. 23012 airfoil with a 0.20 c_w plain flap, at various angles of attack. Flap set at 30°.

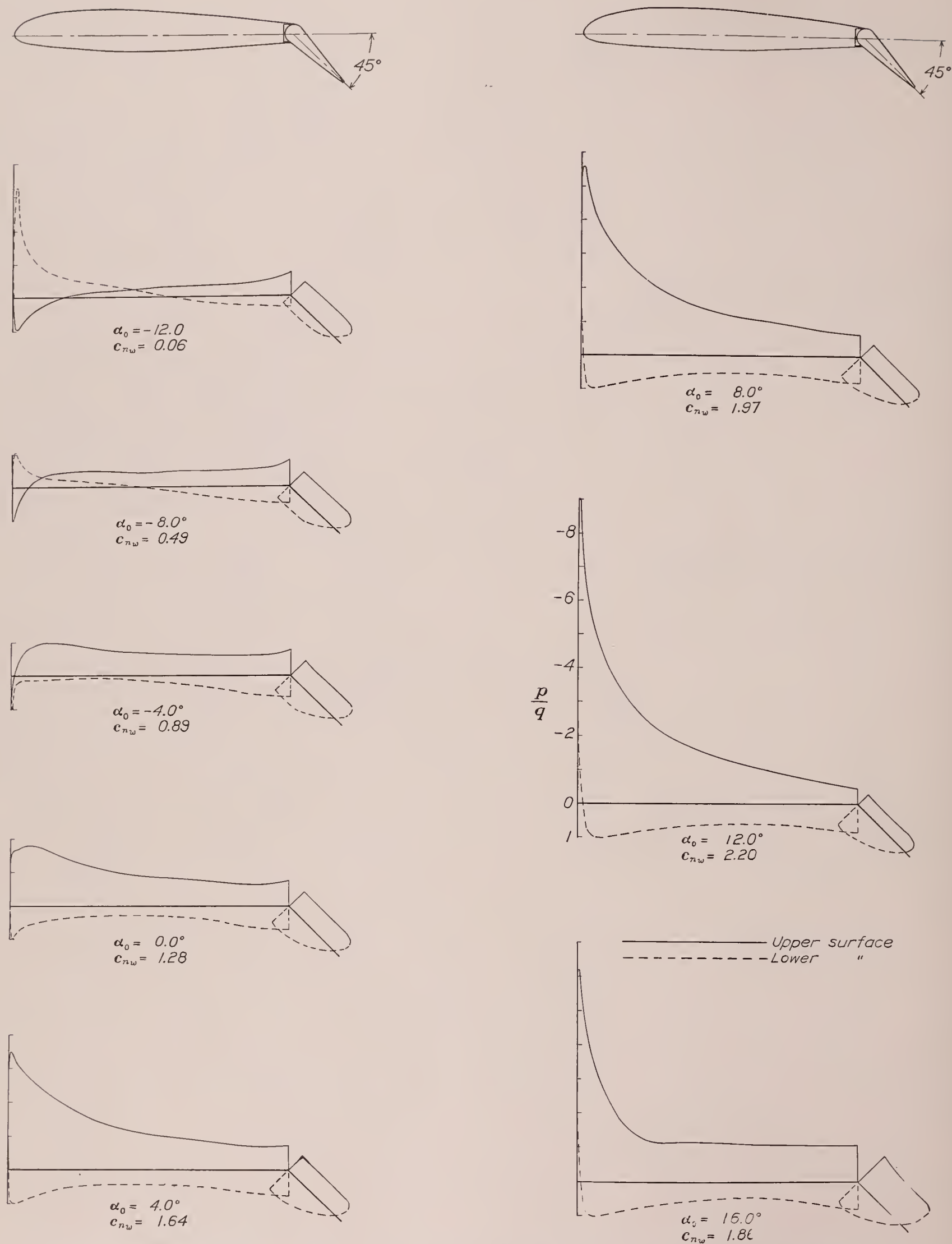


FIGURE 22.—Pressure distribution on the N. A. C. A. 23012 airfoil with a $0.20c_w$ plain flap, at various angles of attack. Flap set at 45° .

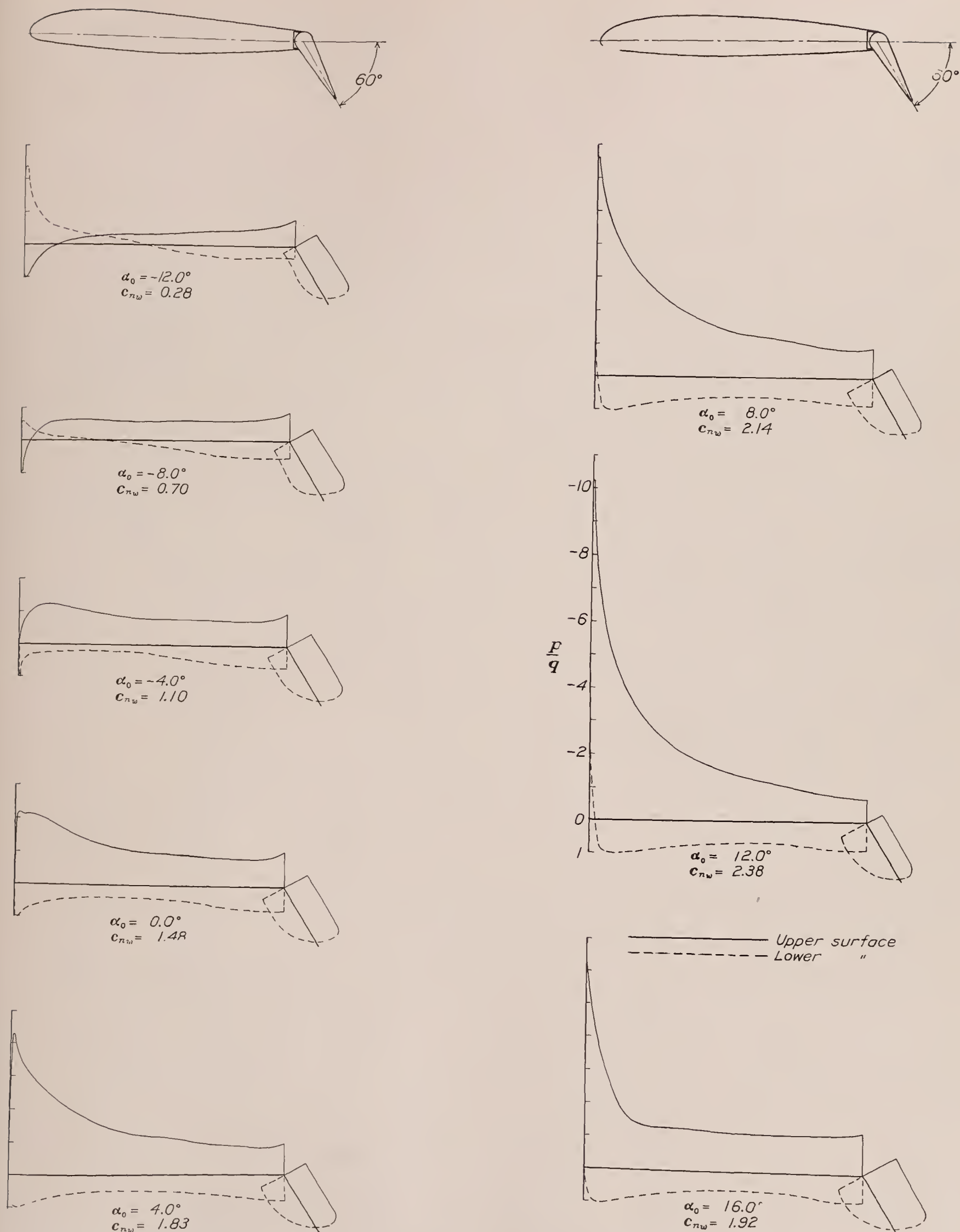


FIGURE 23.—Pressure distribution on the N. A. C. A. 23012 airfoil with a 0.20 c_w plain flap, at various angles of attack. Flap set at 60°.

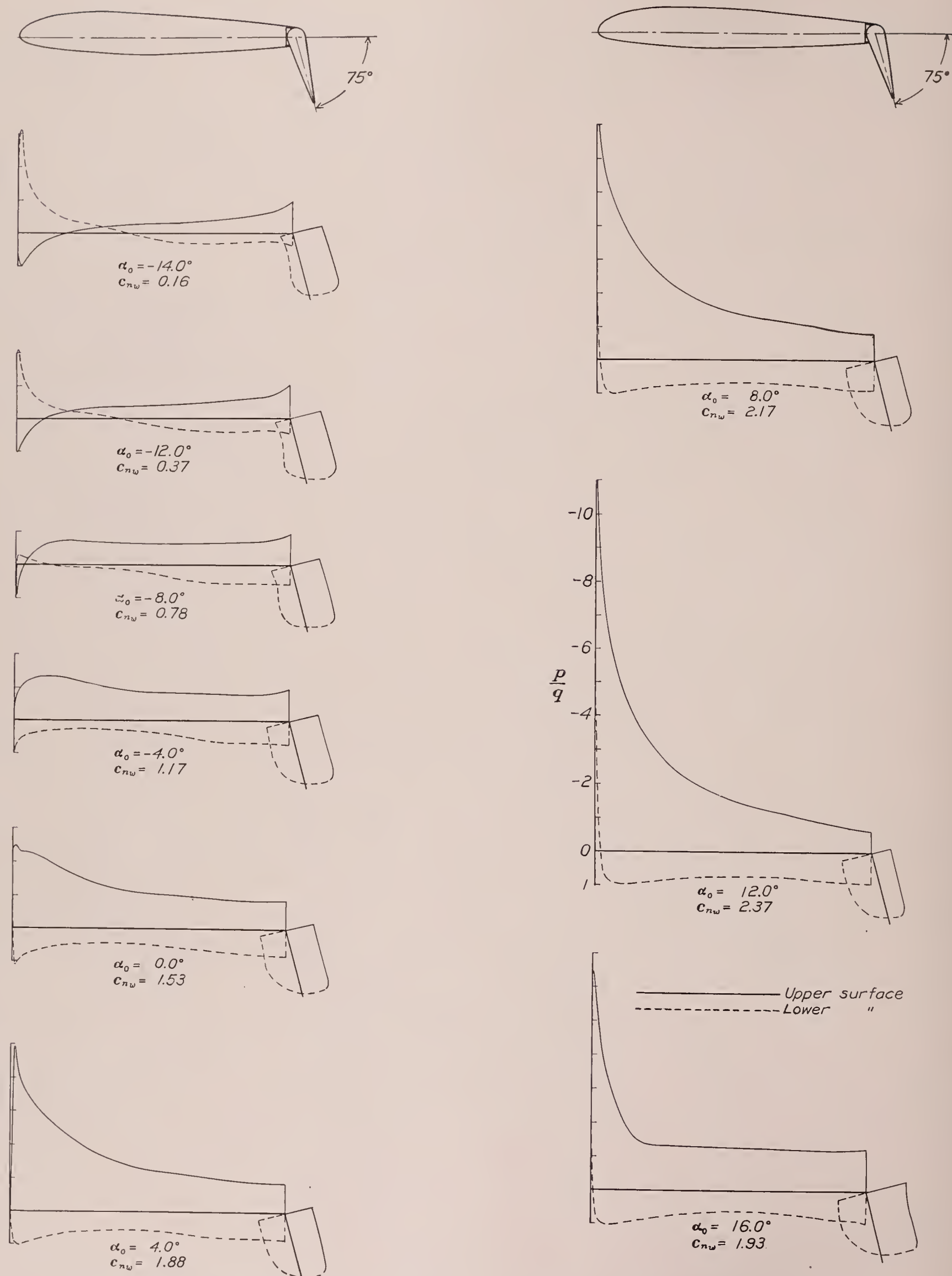
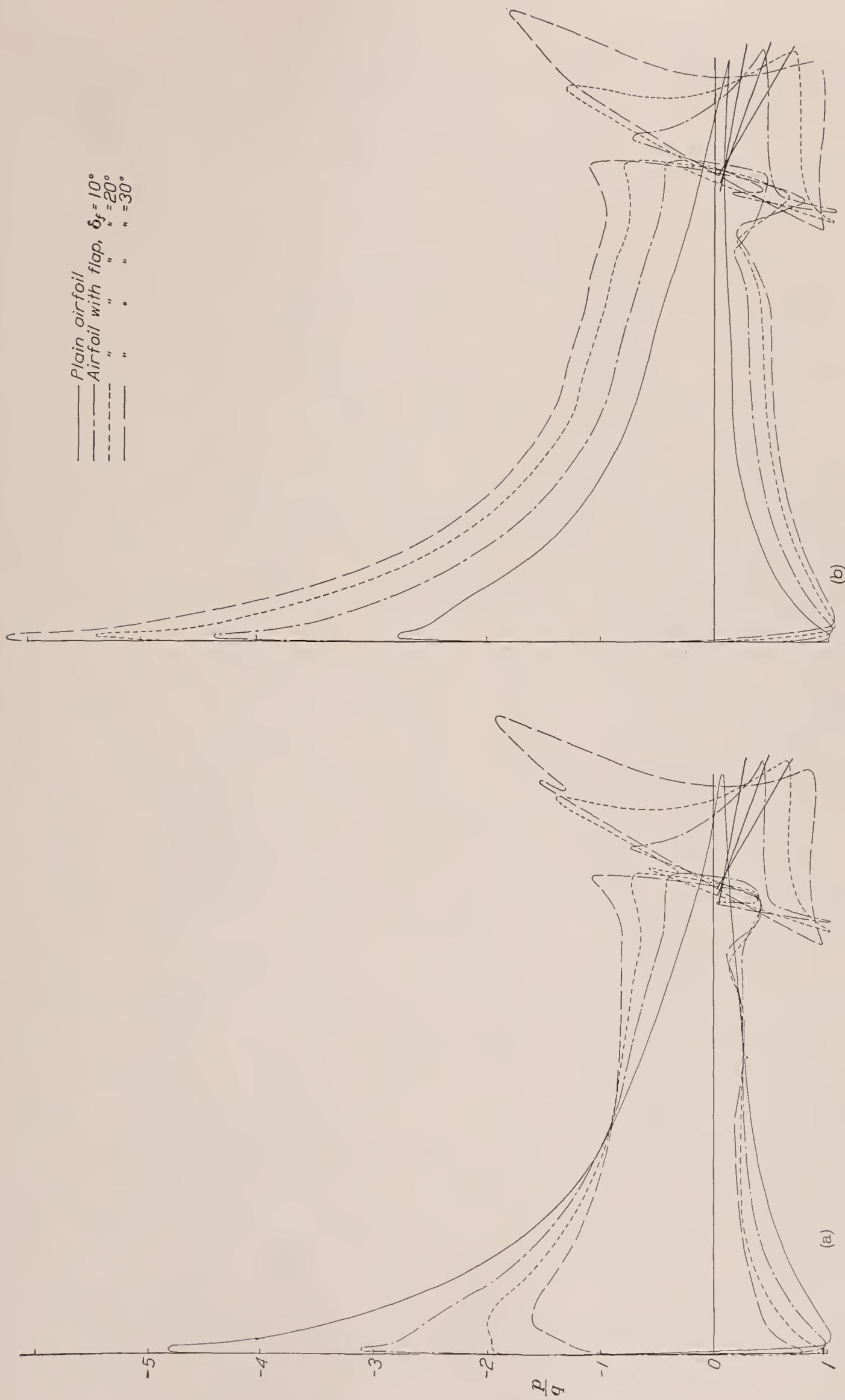


FIGURE 24.—Pressure distribution on the N. A. C. A. 23012 airfoil with a 0.20 c_w plain flap, at various angles of attack. Flap set at 75°.



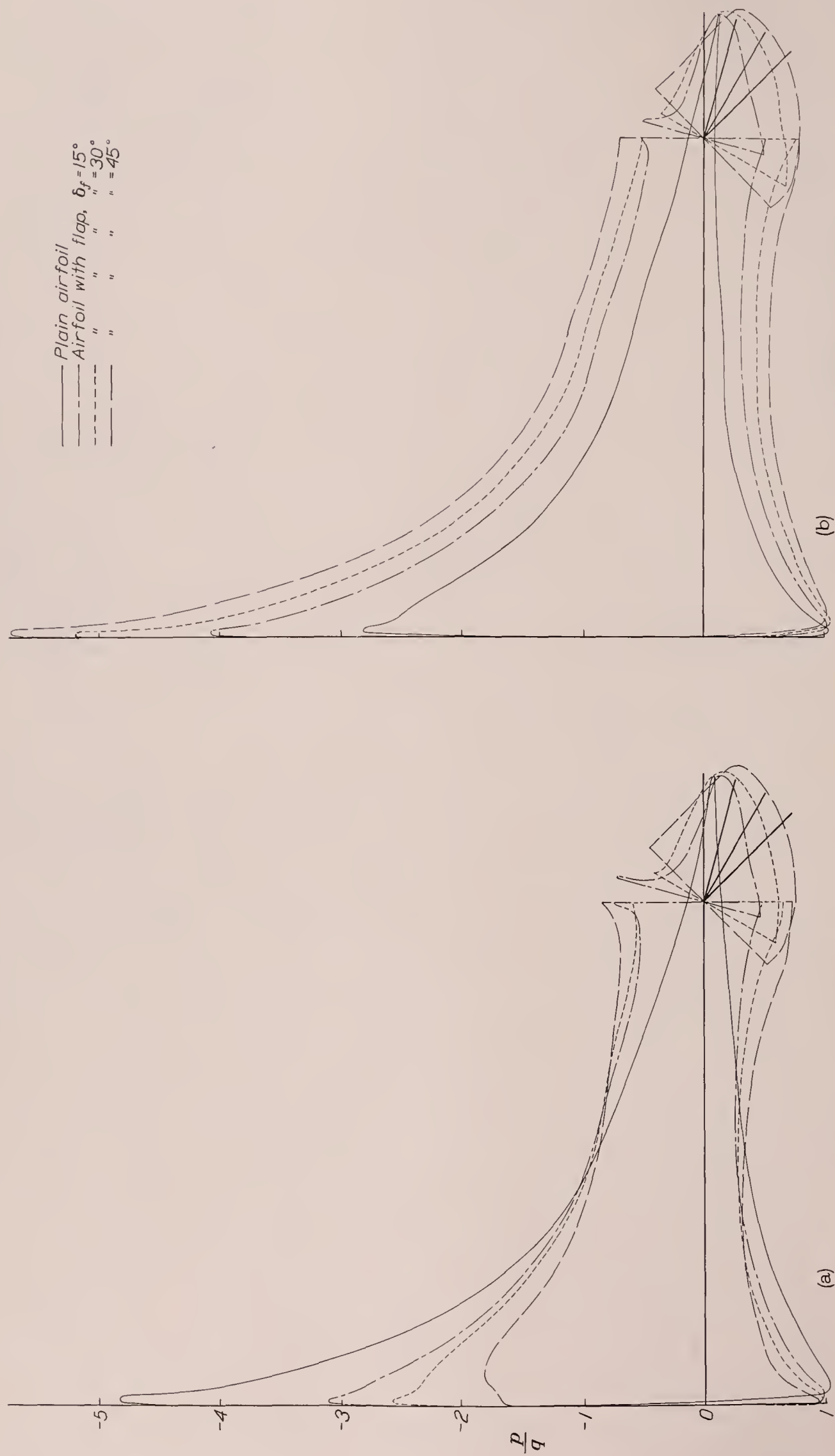


FIGURE 26.—Comparison of the pressure distribution on an N. A. C. A. 23012 airfoil and a 0.20 c_w plain flap with that on the plain airfoil.

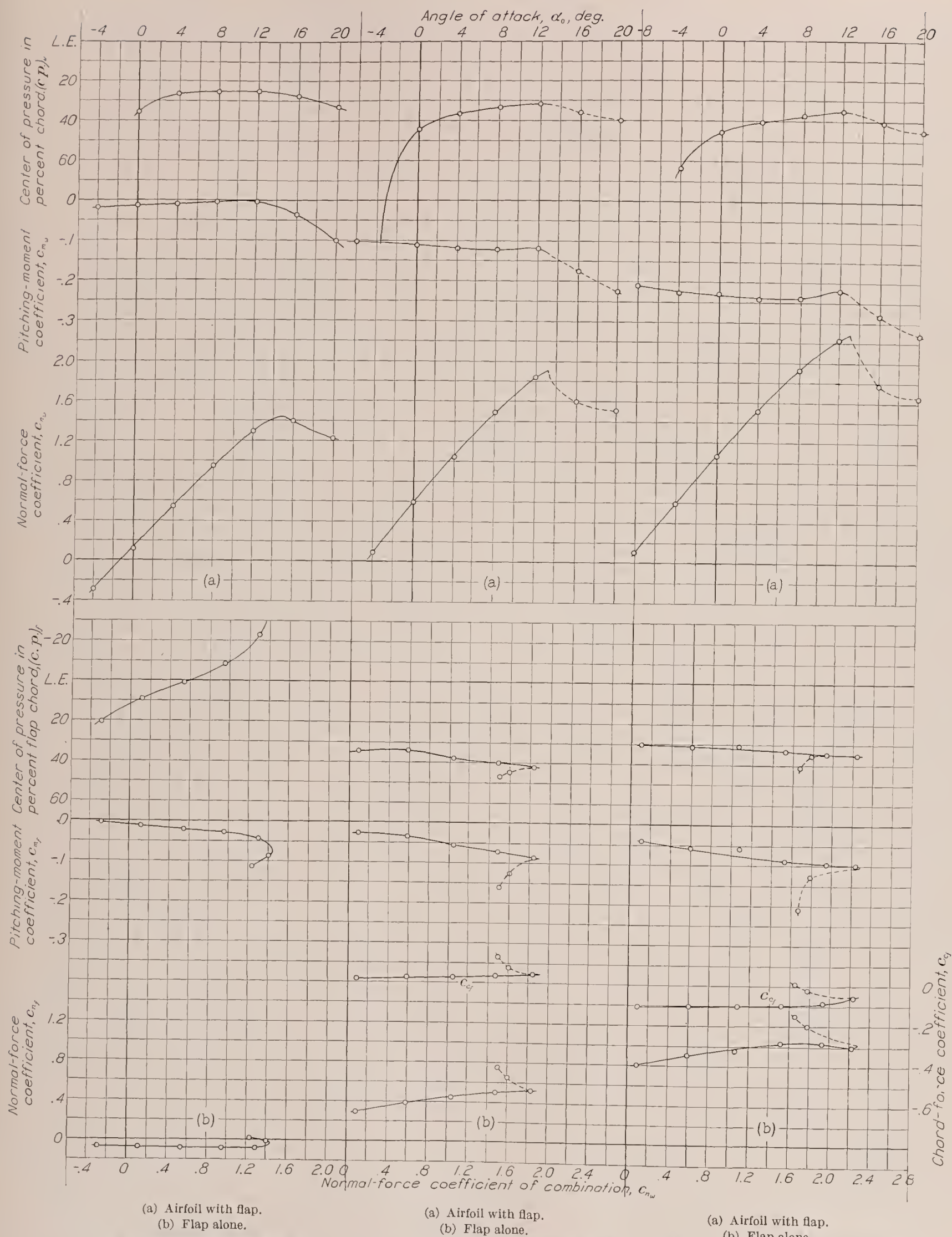


FIGURE 27.—Section characteristics of the N. A. C. A. 23012 airfoil with a $0.2566c_w$ slotted flap set at 0° .

FIGURE 28.—Section characteristics of the N. A. C. A. 23012 airfoil with a $0.2566c_w$ slotted flap set at 10° .

FIGURE 29.—Section characteristics of the N. A. C. A. 23012 airfoil with a $0.2566c_w$ slotted flap set at 20° .

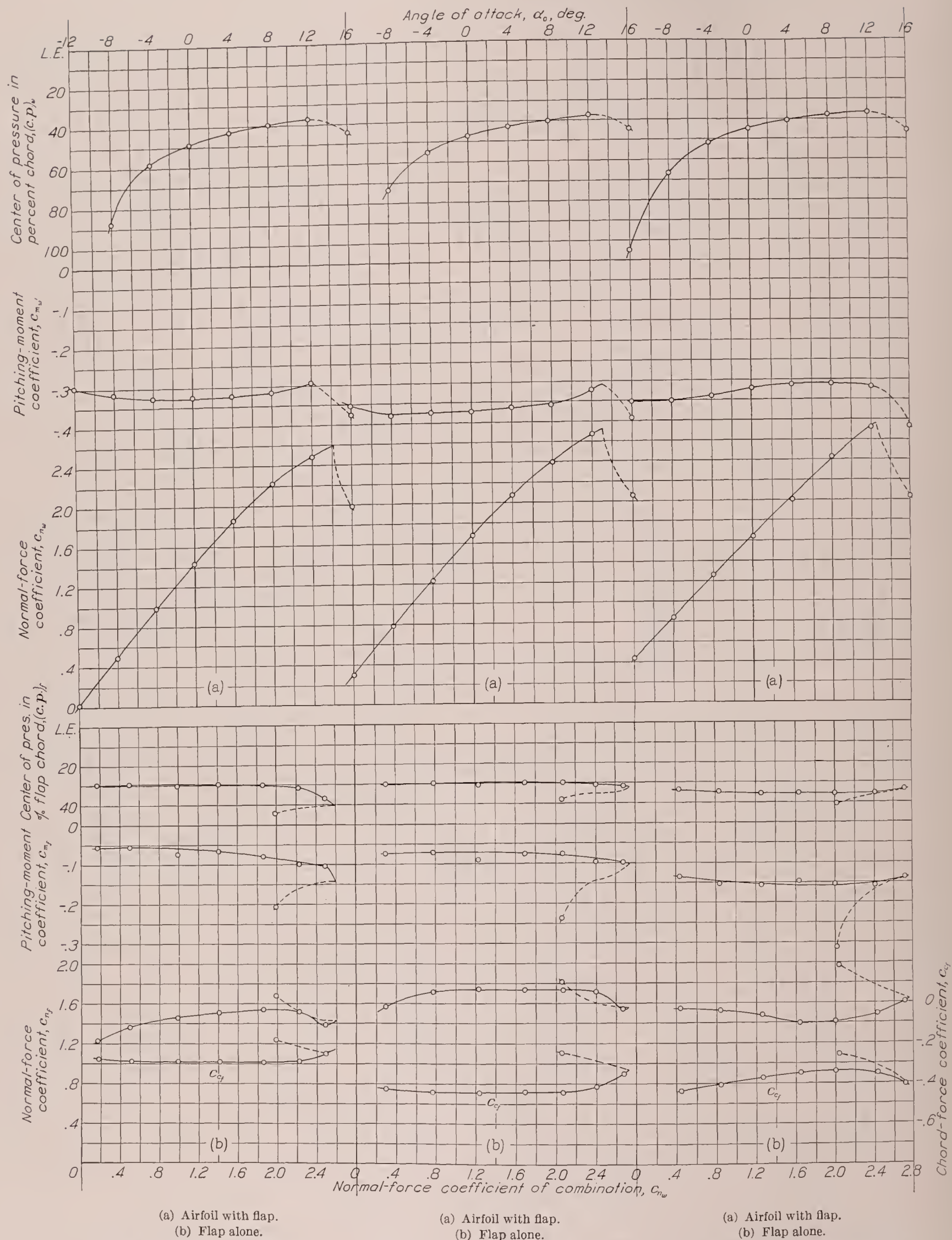


FIGURE 30.—Section characteristics of the N. A. C. A. 23012 airfoil with a $0.2566c_w$ slotted flap set at 30° .

FIGURE 31.—Section characteristics of the N. A. C. A. 23012 airfoil with a $0.2566c_w$ slotted flap set at 40° .

FIGURE 32.—Section characteristics of the N. A. C. A. 23012 airfoil with a $0.2566c_w$ slotted flap set at 50° .

pressures near the leading edges, which, at high angles of attack, checked to within ± 5 percent. The dynamic pressure recorded was accurate to within ± 0.25 percent for all tests. Pressure orifices were not sufficiently numerous to determine accurately the peaks of pressures on the airfoil nose, but this deficiency should not materially affect the results.

RESULTS AND DISCUSSION

SECTION PRESSURE DISTRIBUTION

The distributions of air loads on the main airfoil and on the two types of flap are shown in figures 3 to 26. These pressure diagrams may be applied to the structural design of ribs and flaps and, in addition, figures 16 to 24 are useful in that they supply considerable detailed information for the structural design of plain ailerons. The pressure diagrams also serve to illustrate some important effects of the action of flaps on the distribution of pressures over the airfoil.

A comparison of the pressures over the upper surface of the slotted flap (figs. 3 to 9) with those of the plain flap (figs. 16 to 24), or with those of either the external-airfoil flap (reference 5) or some Fowler flaps (reference 6), indicates certain differences, the most obvious of which is a double-peak negative pressure region near the nose. These peaks may be interpreted as indicating the existence of relatively high-velocity regions with a low-velocity region between them.

An analysis of figures 4 to 7 shows that this region of decreased velocity, or increased pressure, moved forward on the flap as the flap deflection was increased. For flap deflections of 10° , 20° , 30° , and 40° this region was located at approximately 2, $1\frac{1}{2}$, 1, and $\frac{1}{2}$ percent of the main airfoil chord, respectively, behind the leading edge of the flap. Because of its path, the nose of the flap moved back correspondingly greater increments when the flap was deflected; therefore the resultant movement of the region of decreased velocity was backward toward the edge of the lip as the flap deflection was increased. The double-peak pressures finally disappeared at high angles of attack for a flap deflection of 30° (fig. 6) and at low angles of attack for a flap deflection of 40° (fig. 7). As the angle of attack was increased for a given flap deflection (figs. 4 to 7), the double-peak pressure distribution slowly approached a single-peak pressure distribution. It is interesting to note that these peak negative pressures on the slotted flap extended over a greater portion of the flap chord than did corresponding peak pressures over other flaps (references 5 and 6).

The peak pressures over the upper surface of the slotted flap are not so high as the corresponding peak pressures over an external-airfoil flap, but they are much higher than those over the plain flap (figs. 16 to 24). No data are available, however, for the external-airfoil flap for flap deflections above 40° , but it is believed that the slotted flap would develop higher

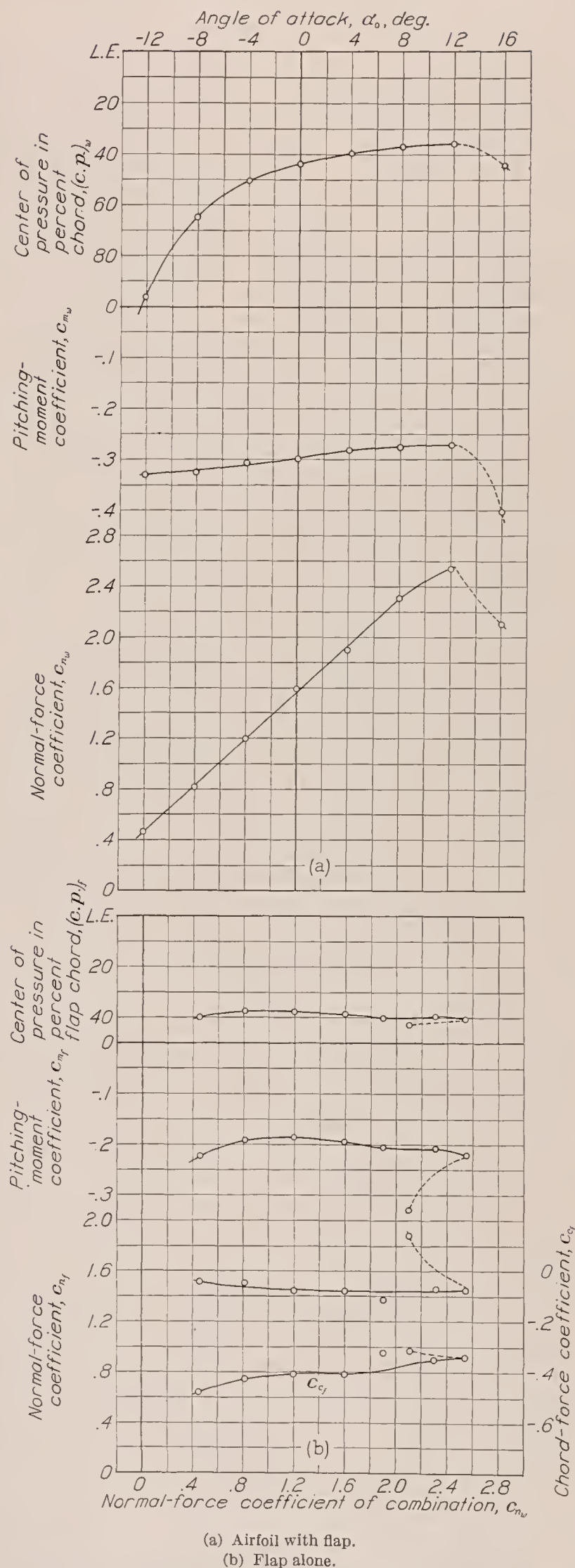


FIGURE 33.—Section characteristics of the N. A. C. A. 23012 airfoil with a $0.2566c_w$ slotted flap set at 60° .

peak pressures because it can be set at higher flap deflections before completely stalling. The upper surface of

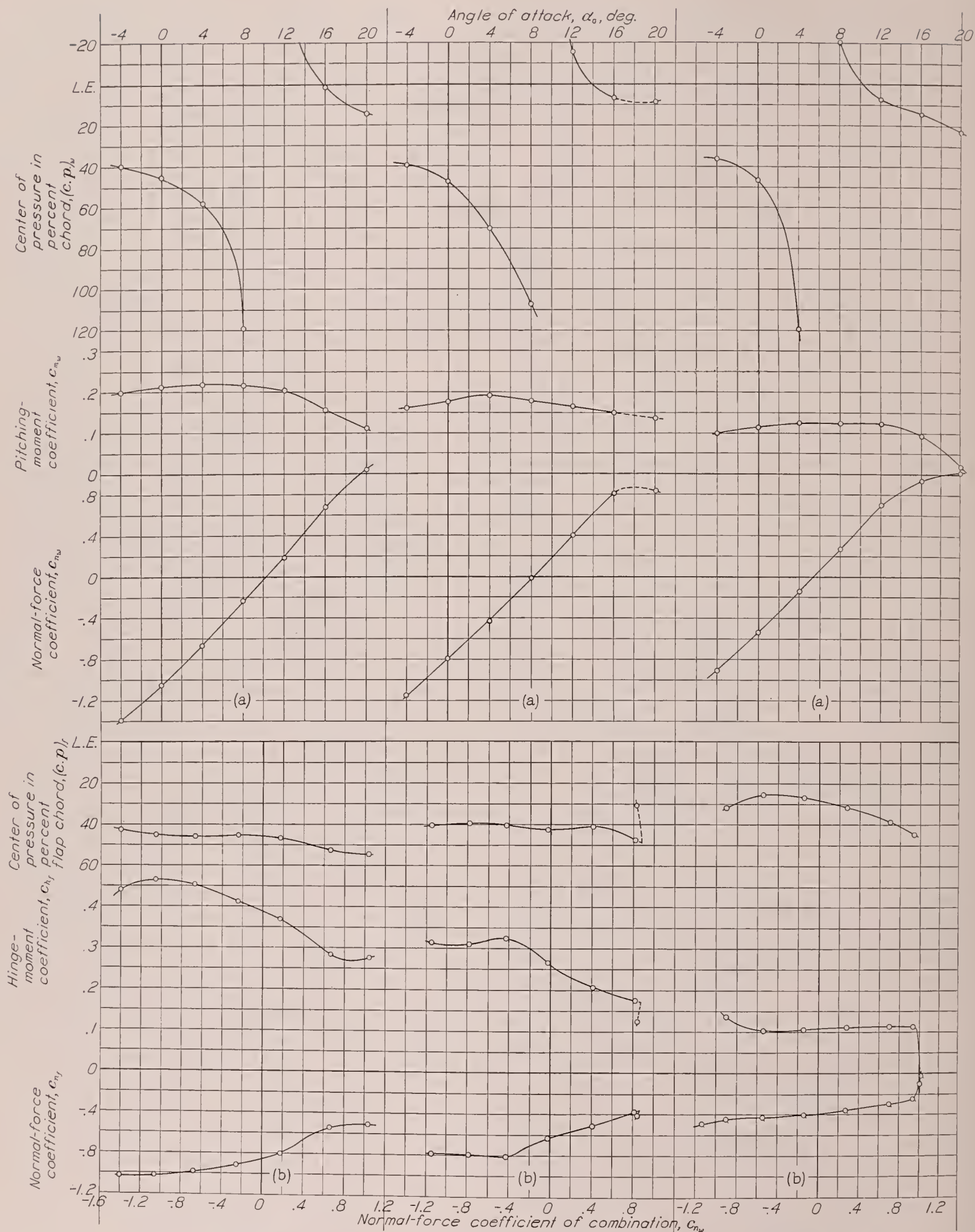


FIGURE 34.—Section characteristics of the N. A. C. A. 23012 airfoil with a $0.20c_w$ plain flap set at -45° .

FIGURE 35.—Section characteristics of the N. A. C. A. 23012 airfoil with a $0.20c_w$ plain flap set at -30° .

FIGURE 36.—Section characteristics of the N. A. C. A. 23012 airfoil with a $0.20c_w$ plain flap set at -15° .

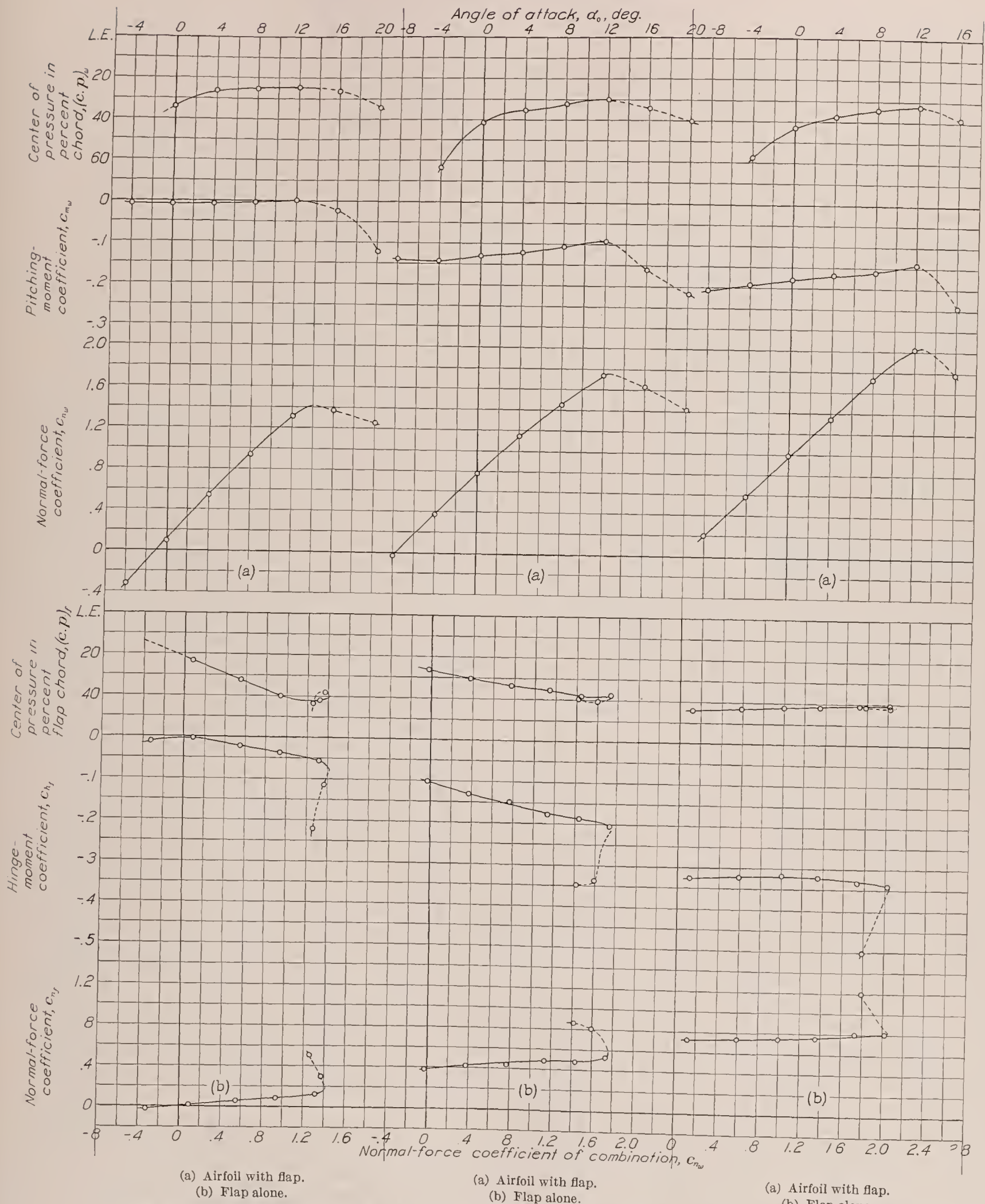


FIGURE 37.—Section characteristics of the N. A. C. A. 23012 airfoil with a $0.20c_w$ plain flap set at 0° .

FIGURE 38.—Section characteristics of the N. A. C. A. 23012 airfoil with a $0.20c_w$ plain flap set at 15° .

FIGURE 39.—Section characteristics of the N. A. C. A. 23012 airfoil with a $0.20c_w$ plain flap set at 30° .

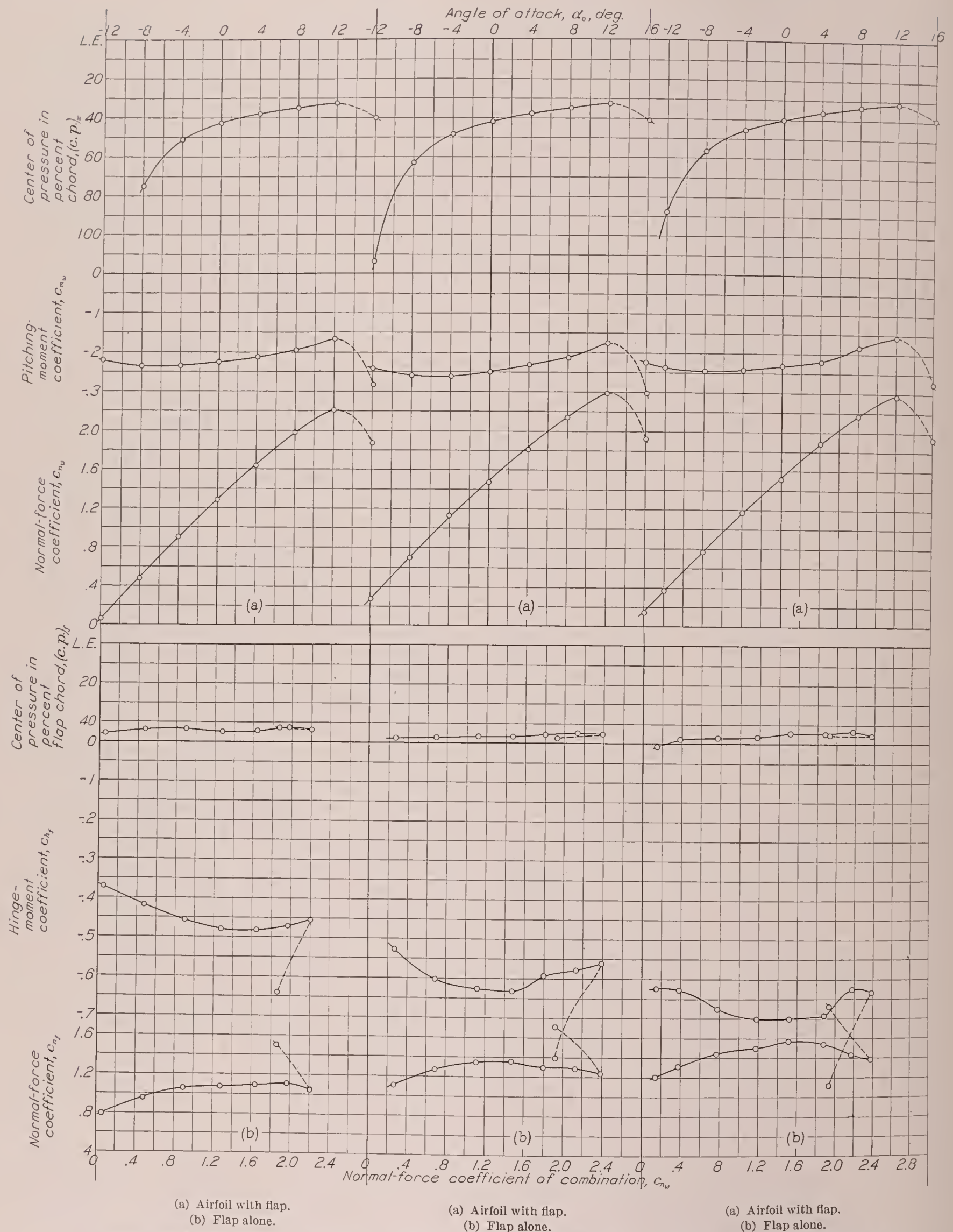


FIGURE 40.—Section characteristics of the N. A. C. A. 23012 airfoil with a 0.20 c_w plain flap set at 45°.

FIGURE 41.—Section characteristics of the N. A. C. A. 23012 airfoil with a 0.20 c_w plain flap set at 60°.

FIGURE 42.—Section characteristics of the N. A. C. A. 23012 airfoil with a 0.20 c_w plain flap set at 75°.

the slotted flap (figs. 3 to 9) was only partly stalled for high angles of attack at high flap deflections; whereas the upper surface of an external-airfoil flap (reference 5) was completely stalled for angles of attack above 3° at a flap deflection of 40° . The slotted flap taken as a whole was completely stalled (no increase in flap load with flap deflection) for a flap deflection between 40° and 50° (figs. 8 and 9), and the external-airfoil flap previously tested (reference 5) was completely stalled for a flap deflection between 30° and 40° .

The chord pressure diagrams for the slotted flap (figs. 10 to 15) are included because it is believed that relatively large forces probably existed that acted in a direction to retract this flap from its maximum-lift setting. As shown by these diagrams, the negative and positive components act in the same direction for nearly all of the arrangements tested except the 10° setting, so that the total chord pressure force is directed forward in practically all cases. These diagrams are considerably different from those of some Fowler flaps previously tested (reference 6), in which the negative and positive components acted in opposite directions and tended to counteract each other. It should be noted that the chord pressure forces do not include the skin-friction forces, which act nearly parallel to the chord and in such a way as to decrease the magnitude of the total chord force if negative or to increase it if positive.

No pressure-distribution tests were made to determine the effect of slight deviations of the flap from its optimum path. An analysis of the data presented in reference 1 and in this report, however, indicates that slight deviations from the optimum flap path would not be expected materially to affect the magnitudes and the distribution of the pressures over the flap. Any appreciable deviation from this optimum path would affect the total lift and the total drag of the airfoil-flap combination as noted in reference 1.

The distribution of pressures over the plain flap (figs. 16 to 24) is similar to that of a symmetrical plain flap reported in reference 9. High negative pressures for practically all angles of attack were found on the lower surface at the flap nose for flap deflections of -30° and -15° and on the upper surface for a flap deflection of 15° . For flap deflections above 15° , high negative pressures appeared on the upper surface at the flap nose. For flap deflections of 30° to 75° (figs. 21 to 24), the upper surface of the flap was stalled.

Comparison of pressure diagrams for the plain airfoil and for the airfoil-flap combinations at the *same lift* (figs. 25 and 26) shows the effect of the flaps. Increasing the flap angle and decreasing the angle of attack to maintain constant lift had the following effects: At the leading edge of the main airfoil, for both combinations, the magnitudes of the peak pressures were progressively reduced. At the trailing edge of the main airfoil, for the slotted-flap combination, the magnitudes of negative pressures were increased and the magnitudes

of positive pressure were practically constant; whereas, for the plain-flap combination, the magnitudes of both positive and negative pressures were increased as the flap deflection was increased.

The flaps also obstructed the flow of air below the airfoil and caused the pressures to build up on the lower surfaces. The air flowing through the slot produced a high average velocity and increased the negative pressure on the upper surface of the slotted flap; the negative pressures on the upper surface of the plain flap changed very little.

The slotted flap had a pressure distribution similar to that of the plain airfoil, except for the double-peak pressures, indicating that, as long as the flap remains unstalled, it would have a small wake, as would the plain airfoil. Near the stall, however, the wake of the combination would still be small because of the slot effect, which permitted the attainment of high lifts with relatively low drag. This effect is absent for the plain flap on account of the large wake, especially near the stall.

Comparison of pressure diagrams for the plain airfoil and for the airfoil-flap combinations at the *same angle of attack* (figs. 25 and 26) shows that the flaps increased the negative pressure over the entire upper surface of the main airfoil and increased the positive pressure on the lower surface of the main airfoil except near the leading edge. The pressure gradients remained about the same except at the trailing edge of the main portion of the airfoil for the slotted-flap combination, where the adverse pressure gradients were decreased on the upper surface and increased on the lower surface. The pressures on the upper and lower surfaces of the flaps increased with flap deflection but more so for the slotted flap. The important effect of the flap, as shown by these diagrams, was its ability to influence the air flow around the main airfoil so that the airfoil carried a much greater load without stalling than was possible without the flap. The slotted flap was superior to the plain flap in this respect.

SECTION LOADS AND MOMENTS

The section coefficients are plotted in figures 27 to 42. Flap loads build up slowly for most lifts of the combination. The loads on the slotted flap increase more rapidly with flap deflection (figs. 27 to 33) than do the loads both on the plain flap (figs. 34 to 42) and on the external-airfoil flap (reference 5). The highest flap loads seem to be obtained with the slotted flap, the maximum normal-force coefficient being about 30 percent higher than for the external-airfoil flap. It is believed that slight deviations of the flap from its optimum path would not materially affect the flap loads. The greater part of the increment of normal-force coefficient of the combination due to deflecting the flaps downward, however, arises from the increased load carried by the main airfoil.

The chord-force coefficients of the slotted flap (figs. 28 to 33) are nearly all negative in sign; that is, the pressure forces parallel to the flap reference line are directed forward. The magnitudes of these forces are relatively high and considerably greater than those of some Fowler flaps of N. A. C. A. 23012 section that were recently tested (reference 6). The chord forces should be taken into account in design when consideration is being given to the resultant air loads acting on the slotted flap. As mentioned previously, the magnitudes of these forces would be somewhat decreased by the skin-friction forces that have not been included.

The pitching-moment coefficients of the slotted flap alone about its quarter-chord point were slightly higher than the pitching-moment coefficients of the external-airfoil flap (reference 5) for flap deflections up to about 30° (figs. 27 to 30). The pitching-moment center for both flaps was at about the same location. For a flap deflection of 40° (fig. 31), the pitching-moment coefficients for the slotted flap were much smaller than they were for the external-airfoil flap. For higher flap deflections, the pitching-moment coefficients increased quite rapidly (figs. 32 and 33). The hinge moments for the plain flap were high and increased rapidly with an increase in flap deflection (figs. 34 to 42).

CONCLUSIONS

1. These pressure-distribution tests show that, as with other types of flap, the greater part of the increment of total maximum lift due to deflecting the slotted flap downward arises from the increased load carried by the main airfoil.

2. The maximum normal-force coefficient for the slotted flap investigated had a higher value than that attained by other types of flap, and the magnitudes of the pressure chord-force coefficient were relatively large.

3. The pitching-moment coefficients for the slotted flap alone were slightly higher than the pitching-moment coefficients for an external-airfoil flap alone (moment centers had approximately the same location) for flap deflections up to 30° .

4. The pressure diagrams showed that, when the plain airfoil and airfoil-flap combinations were compared at the same total normal-force coefficient, the flap reduced the adverse pressure gradients and the tendency of the main airfoil to stall. The slotted flap was more effective in this respect than the plain flap or an external-airfoil flap.

5. The pressure diagrams showed that, when the plain airfoil and the airfoil-flap combinations were compared at the same angle of attack, the flap influenced the flow of air around the main airfoil so that the airfoil carried a much greater load without stalling than was possible without the flap. The slotted flap was more

effective in this respect than the plain flap or an external-airfoil flap.

LANGLEY MEMORIAL AERONAUTICAL LABORATORY,
NATIONAL ADVISORY COMMITTEE FOR AERONAUTICS,
LANGLEY FIELD, VA., March 17, 1938.

REFERENCES

1. Wenzinger, Carl J., and Harris, Thomas A.: Tests of an N. A. C. A. 23012 Airfoil with Various Arrangements of Slotted Flaps in the Closed-Throat 7- by 10-Foot Wind Tunnel, to be published at a later date.
2. Kiel, Georg: Pressure Distribution on a Wing Section with Slotted Flap in Free Flight Tests. T. M. No. 835, N. A. C. A., 1937.
3. Ruden, P.: Versuche an einem Düsenflügel. Jahrbuch 1937 der Deutschen Luftfahrtforschung. S. I 75-I 86.
4. Wenzinger, Carl J., and Harris, Thomas A.: Pressure Distribution over a Rectangular Airfoil with a Partial-Span Split Flap. T. R. No. 571, N. A. C. A., 1936.
5. Wenzinger, Carl J.: Pressure Distribution over an N. A. C. A. 23012 Airfoil with an N. A. C. A. 23012 External-Airfoil Flap. T. R. No. 614, N. A. C. A., 1938.
6. Wenzinger, Carl J., and Anderson, Walter B.: Pressure Distribution over Airfoils with Fowler Flaps. T. R. No. 620, N. A. C. A., 1938.
7. Harris, Thomas A.: The 7 by 10 Foot Wind Tunnel of the National Advisory Committee for Aeronautics. T. R. No. 412, N. A. C. A. 1931.
8. Platt, Robert C.: Turbulence Factors of N. A. C. A. Wind Tunnels as Determined by Sphere Tests. T. R. No. 558, N. A. C. A., 1936.
9. Jacobs, Eastman N., and Pinkerton, Robert M.: Pressure Distribution over a Symmetrical Airfoil Section with Trailing Edge Flap. T. R. No. 360, N. A. C. A., 1930.

TABLE I.—ORIFICE LOCATIONS ON AIRFOIL-FLAP COMBINATIONS TESTED

N. A. C. A. 23012 36-inch airfoil with a 0.20c _w plain flap		N. A. C. A. 23012 36-inch airfoil with a 0.2566c _w slotted flap			
Orifice locations on upper and lower surfaces in percent chord from leading edge		Orifice locations on upper and lower surfaces of main portion of airfoil in percent chord from leading edge		Orifice locations on upper and lower surfaces of flap in percent flap chord from leading edge	
Orifice	Location	Orifice	Location	Orifice	Location
0	0.00	0	0.00	0	0.00
1	1.25	1	1.25	1	1.25
2	2.50	2	2.50	2	2.50
3	5.00	3	5.00	3	5.00
4	10.00	4	10.00	4	10.00
5	20.00	5	20.00	5	18.00
6	30.00	6	30.00	6	30.00
7	40.00	7	40.00	7	45.00
8	50.00	8	50.00	8	62.50
9	60.00	9	60.00	9	72.50
10	70.00	10	67.00	10	82.50
11	75.00	11	70.00	11	92.50
12	78.00	12	74.00		
13	80.00	13	78.00		
14	82.50	14	81.50		
15	85.00				
16	90.00				
17	95.00				
18	98.00				

REPORT No. 634

CALCULATION OF THE CHORDWISE LOAD DISTRIBUTION OVER AIRFOIL SECTIONS WITH PLAIN, SPLIT, OR SERIALY HINGED TRAILING-EDGE FLAPS

By H. JULIAN ALLEN

SUMMARY

A method is presented for the rapid calculation of the incremental chordwise normal-force distribution over an airfoil section due to the deflection of a plain flap or tab, a split flap, or a serially hinged flap. This report is intended as a supplement to N. A. C. A. Report No. 631, wherein a method is presented for the calculation of the chordwise normal-force distribution over an airfoil without a flap or, as it may be considered, an airfoil with flap (or flaps) neutral.

The calculations are made possible through the correlation, by means of thin-airfoil theory, of numerous experimental normal-force distributions. The method enables the determination of the form and magnitude of the incremental normal-force distribution to be made for an airfoil-flap combination for which the section characteristics have been determined.

A method is included for the calculation of the flap normal-force and hinge-moment coefficients without necessitating a determination of the normal-force distribution.

INTRODUCTION

The general importance of airfoils equipped with trailing-edge flaps has promoted both experimental and theoretical determinations of the chordwise distribution of normal force over such surfaces in an effort to increase the structural efficiency of their design.

The theoretical investigations have been made under the assumption that the fluid viscosity is negligibly small. This assumption must be made, for the present at least, in order that the problem may be analytically handled. Unfortunately, as experiments have shown, viscosity clearly is not a negligible factor in this problem and, consequently, the theory is not able to predict adequately either the magnitude of the incremental normal force brought about by the deflection of the flaps or the nature of the chordwise distribution of this incremental normal force.

On the other hand, the large number of variables involved in the problem makes it too difficult to develop an adequate method, applicable in the general case, for the calculation of the incremental normal force and the incremental normal-force distribution from the experimental pressure-distribution measurements that have been made.

In this report a method is developed for the calculation of the incremental normal-force distribution due to the deflection of the flap based upon the results of experimental investigations; the theoretical relationships are used as a basis for the coordination of the experimental observations. Employment of experimentally determined airfoil section characteristics makes it possible, moreover, to obtain a distribution consistent in magnitude with that obtained by experiment. The method has been made applicable to an airfoil section equipped with a plain flap or tab, a split flap, or a serially hinged flap. This report is intended as a supplement to reference 1, wherein a method, similar in its details of development, is presented for the calculation of the chordwise normal-force distribution over an airfoil section without a flap or, as it may be considered, an airfoil section with flap (or flaps) neutral.

In order to facilitate the employment of this method, the report has been divided into two sections:

I. The Derivation of the Method.

II. The Application of the Method.

In the derivation, Glauert's theoretical chordwise lift distribution is discussed and the empirical alteration of the theory is treated. In addition, the development of the requisite equations for the determination of the magnitude of the distribution from force-test results is given. In the application, the general procedure to be followed in using this method either for airfoil sections with plain or split flaps or for airfoil sections with serially hinged flaps is given in concise form along with an illustrative example. The mathematical derivation of the theory is given in the appendix.

I. THE DERIVATION OF THE METHOD

Glauert (references 2 and 3) has treated analytically the problem of the symmetrical airfoil with a plain flap, assuming the airfoil to be of infinitesimal thickness. The thin-airfoil theory is treated in the appendix of this paper. It is shown that the incremental lift distribution or, as it will be regarded, the incremental normal-force distribution due to the deflection of a flap may be considered, for convenience, to be composed of two component distributions: (a) the incre-

mental additional distribution $P_{a\delta}$, and (b) the incremental basic distribution $P_{b\delta}$. The incremental additional distribution is, in form, independent of the flap-chord ratio and does not contribute to the quarter-chord pitching moment, whereas the incremental basic distribution is, in form, dependent upon the flap-chord ratio and is responsible for the entire incremental quarter-chord pitching moment due to the deflection of the flap.

The theoretical additional distribution, as given by the thin-airfoil theory (appendix, equation (A-17)), is shown by the dotted curve in figure 1. Since the incre-

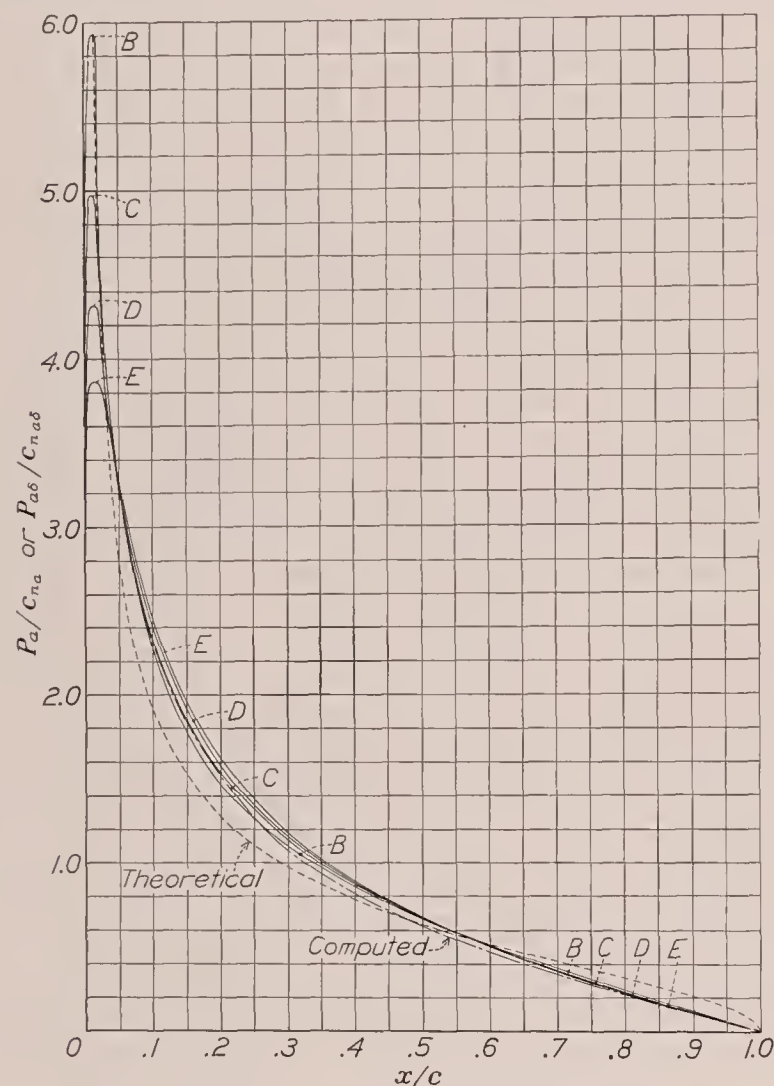


FIGURE 1.—Additional normal-force distributions.

mental additional distribution due to the deflection of the flap is identical in form with the additional distribution for the airfoil with flaps neutral, the experimentally determined additional distributions given in reference 1 will be used for this method. The four classes of additional distribution presented in reference 1 are given in table I and figure 1 (solid lines) of the present report. A key to the class of distribution to be employed for 22 airfoils is given in table II of the present report. (The letters A, B, C, D, and E in column "Classification PD" designate the class of distribution.) The remaining airfoil characteristics for these airfoils are given in table I of reference 1.

The shape of the theoretical incremental basic lift distribution (appendix, equation (A-19)) or, of what is considered to be its equivalent, the incremental basic

normal-force distribution is shown by the dotted lines of figures 2 to 6. Proceeding rearward from the leading edge of the airfoil, the pressure difference, which is zero at the leading edge, increases rapidly at first, then more slowly and, as the hinge is approached, it increases more and more rapidly until the pressure difference becomes unlimited at the hinge point, where the airfoil radius of curvature is zero. Rearward from the hinge, the pressure difference drops rapidly at first, then more slowly, and finally more rapidly again to zero pressure difference at the trailing edge. With a hinge radius of curvature other than zero, the basic pressure difference at the hinge becomes finite.

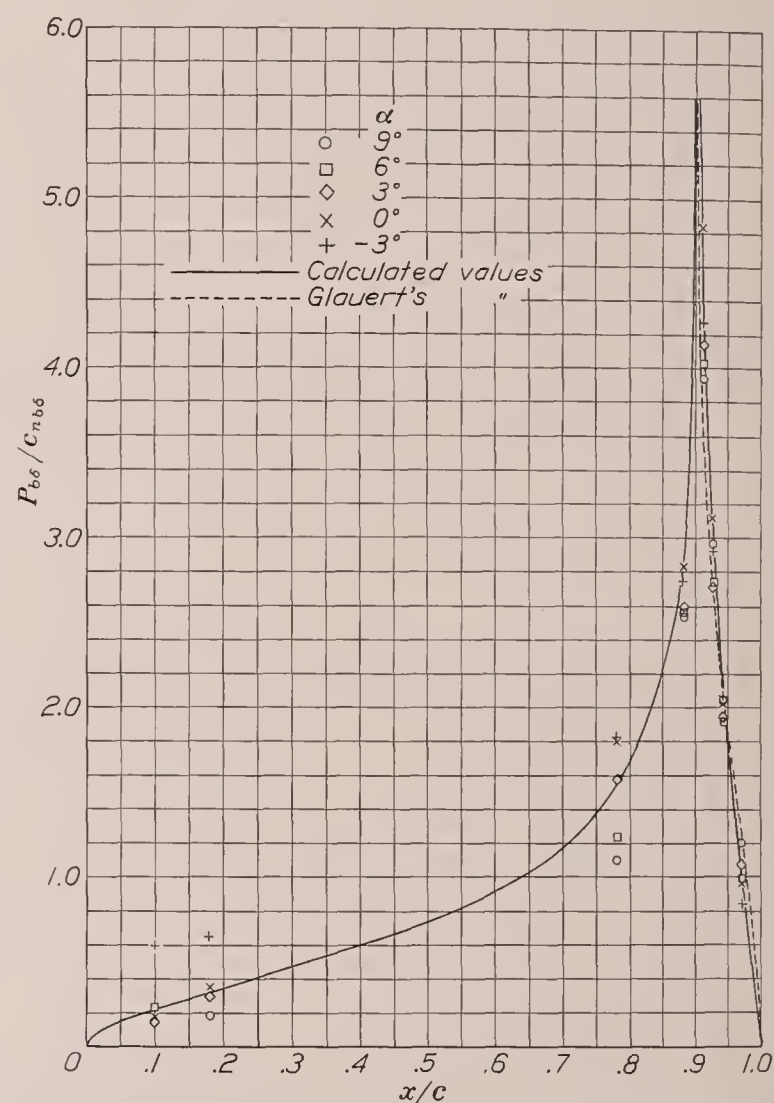


FIGURE 2.—Basic incremental normal-force distribution. R. A. F. 30 section; 0.10c plain flap at $\delta=10^\circ$.

Numerous comparisons between experimental (made with 0.10c, 0.20c, and 0.30c plain-flap airfoils with flap deflections ranging from 10° to 60°) and theoretical incremental basic normal-force distributions ($P_{b\delta}/c_{n_{b\delta}}$) for plain-flap airfoils generally showed good agreement ahead of the hinge but poor agreement behind the hinge, particularly for large flap angles. This result is to be anticipated for ahead of the hinge favorable pressure gradients retard the growth of the boundary layer and, conversely, back of the hinge adverse gradients accelerate the growth of the boundary layer. An examination of these comparisons, however, disclosed that, for all three flap-chord ratios at any one given flap deflection, the ratio of the experimental basic normal

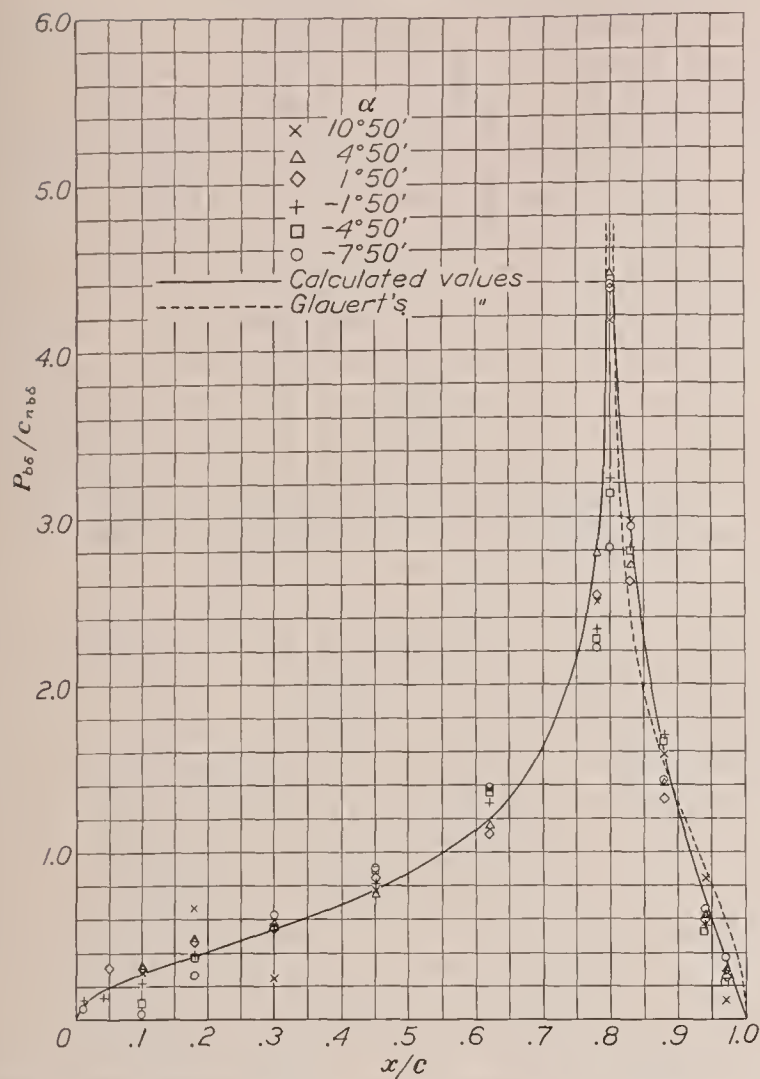


FIGURE 3.—Basic incremental normal-force distribution. R. A. F. 30 section; 0.20c plain flap at $\delta=10^\circ$.

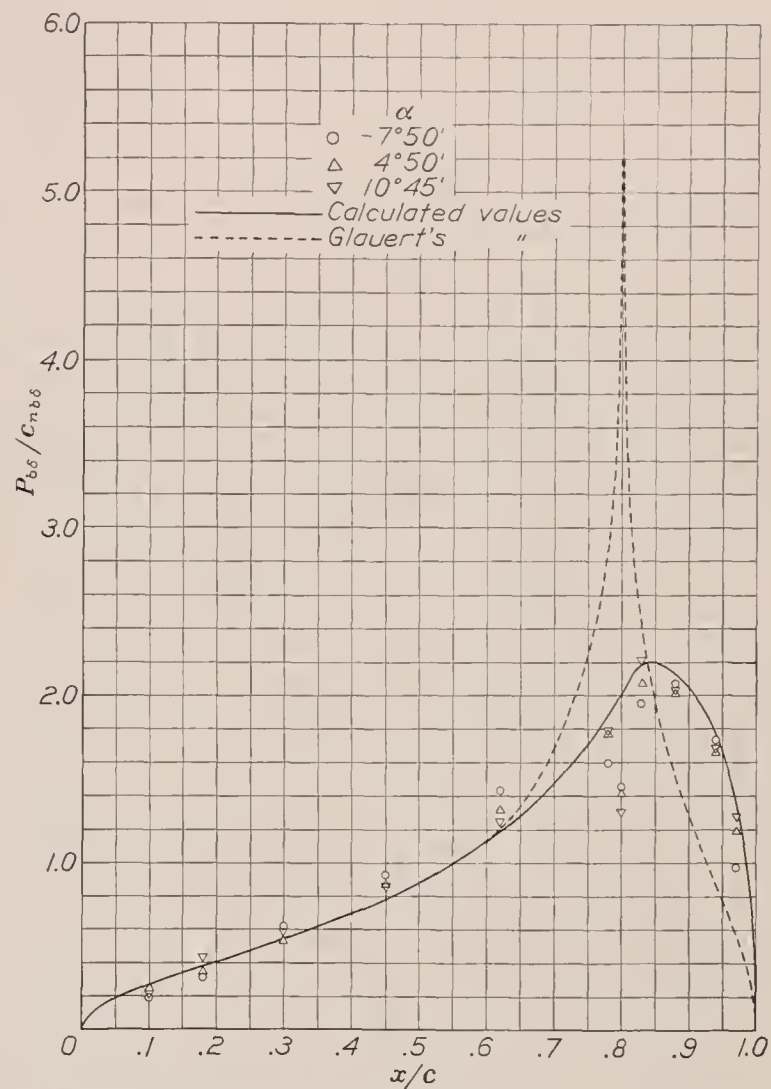


FIGURE 5.—Basic incremental normal-force distribution. R. A. F. 30 section; 0.20c plain flap at $\delta=50^\circ$.

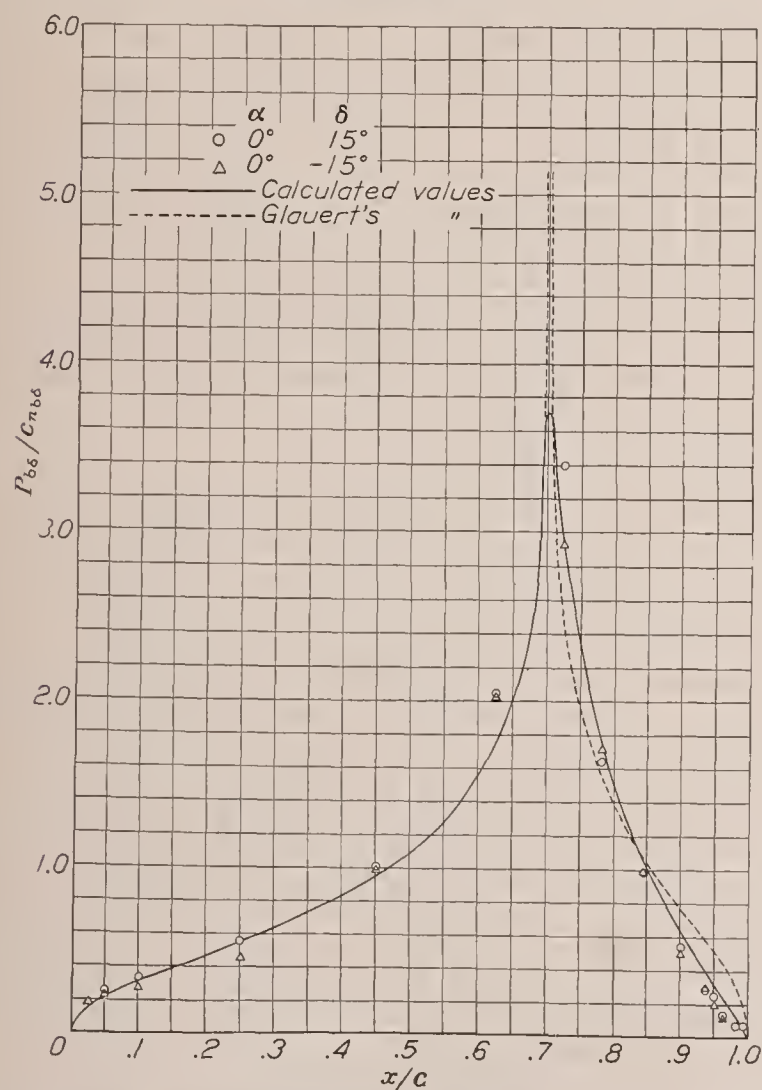


FIGURE 4.—Basic incremental normal-force distribution. Clark Y section; 0.30c plain flap at $\delta=\pm 15^\circ$.

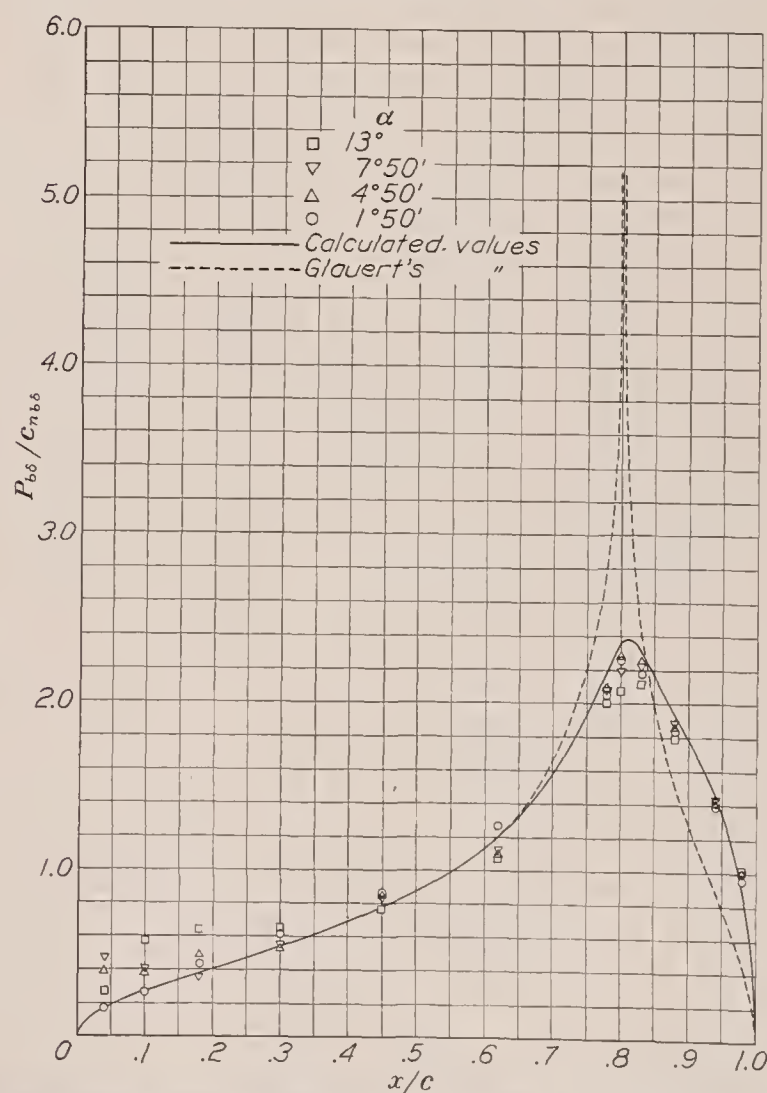


FIGURE 6.—Basic incremental normal-force distribution. R. A. F. 30 section; 0.20c plain flap at $\delta=30^\circ$.

force to the theoretical was practically constant for corresponding points along the airfoil. That is, if β is defined as

$$\beta = \frac{\left(\frac{P_{b\delta}}{c_{n_{b\delta}}}\right)_{exp.}}{\left(\frac{P_{b\delta}}{c_{n_{b\delta}}}\right)_{theor.}} \quad (1)$$

it has been found that values of β computed from experimental pressure-distribution measurements made over 0.10c, 0.20c, and 0.30c plain-flap airfoils with the same flap deflection (references 4 and 5), when plotted in the form of curves of β against both $\frac{x/c}{1-E}$ (points ahead of the hinge) and $\frac{1-(x/c)}{E}$ (points back of the hinge), lie very nearly on the same curve. In these expressions, E is the flap-chord ratio.

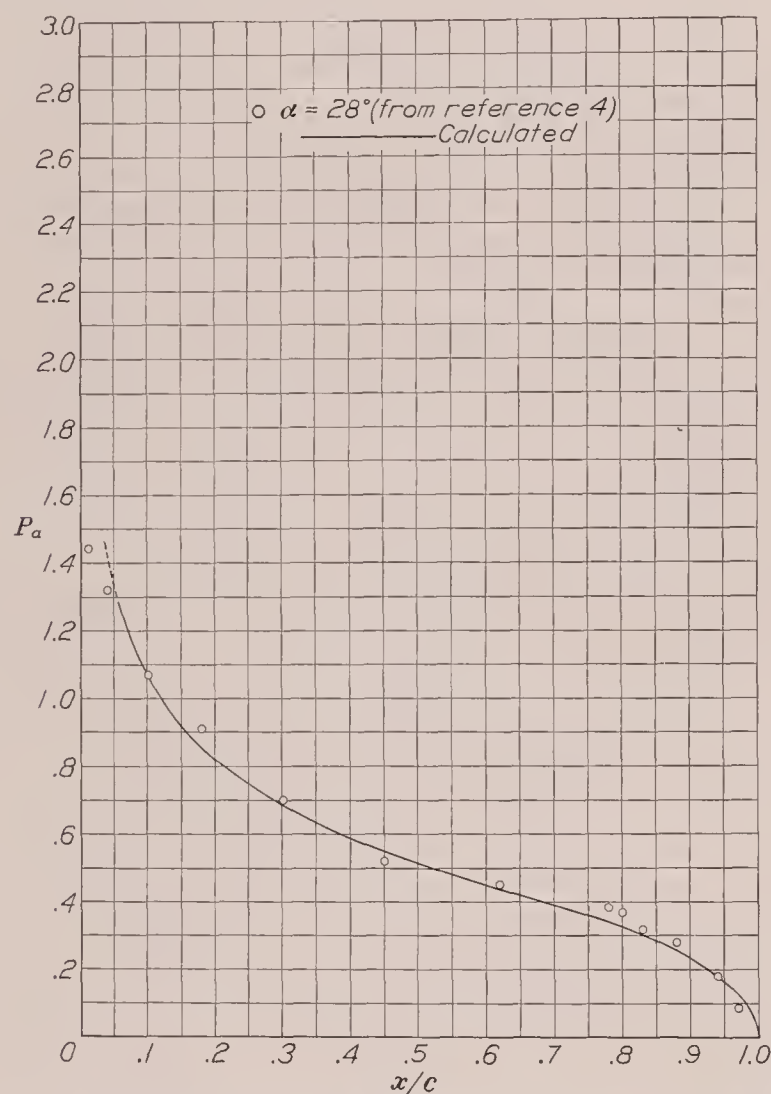


FIGURE 7.—Additional normal-force distribution for a stalled symmetrical airfoil. R. A. F. 30 section.

This result is used as a basis for extending the analysis to cases where no experimental data are available. Curves of the mean values of β for flap deflections of 10° to 60° were determined. It was found that, for flap deflections of 15° or less, a single β curve applied. At these small angles the departure between theory and experiment is slight, which shows that the boundary layer is still thin and the flow pattern is still reasonably like that predicted by theory. As the flap deflection is increased, the adverse pressure gradients back of the hinge are increased and separation finally takes place;

the incremental basic normal-force distribution then becomes markedly different from that predicted by theory. This abrupt change in the nature of the flow takes place at or near 20° flap deflection. The exact angle at which this stalling occurs is a function of a number of variables (angle of attack, Reynolds Number, surface irregularities, hinge leakage) and no single β curve can apply very near this flap angle.

Values of $P_{b\delta}/c_{n_{b\delta}}$ have been computed from numerous pressure-distribution measurements (references 4 and 5) and are plotted in figures 2 to 6 along with the theoretical distributions and the computed distributions obtained by use of the computed curves of mean β values.

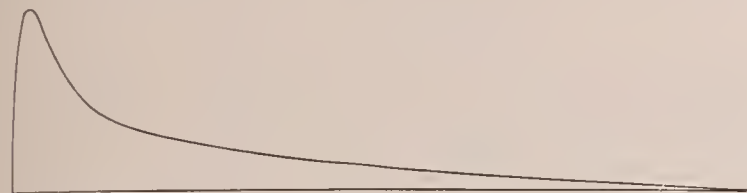
In table III (a) to (f), the computed distributions of $P_{b\delta}/c_{n_{b\delta}}$ (equation (1)) are given for various flap-chord ratios and flap deflections.

The expansion of the experimental results, taken with plain flaps where the flap-chord ratio never exceeded 0.30, to the much higher values given in table III is justified as follows. When the flap-chord ratio is 1.0 for a symmetrical airfoil, the incremental normal-force distribution becomes the incremental additional normal-force distribution and, when corrected by the mean β values, the incremental additional distribution should be expected to agree with the experimentally determined additional distribution if the β values are truly independent of the flap-chord ratio. In figure 1, the computed distribution obtained by use of the β values for the unstalled flow (i. e., $\delta=5^\circ$, 10° , and 15°) is shown along with the additional distributions of reference 1. In figure 7, the computed and experimental distributions for a stalled symmetrical airfoil ($\alpha=\delta=28^\circ$) are shown. From the close agreement between the experimental and the computed distributions shown in figures 1 to 4 for the unstalled flap and in figures 5 to 7 for the stalled airfoil, it is concluded that, for design purposes, the β values may be considered independent of the flap-chord ratio.

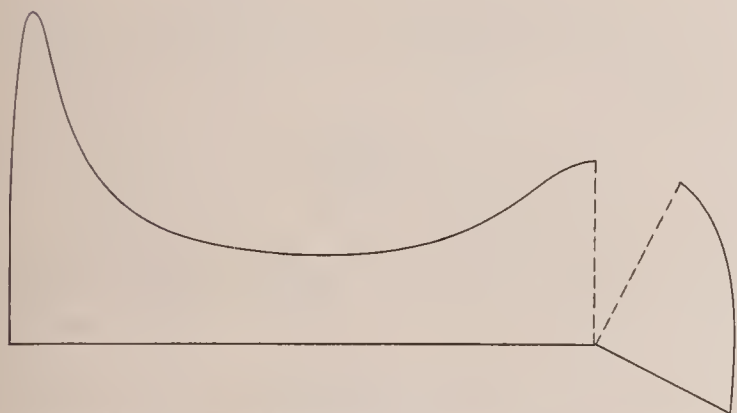
The method of correlating experimental pressure distributions for airfoils with plain flaps may be employed for airfoils with split flaps. Consider the airfoils with split flaps to be analogous to the airfoils with plain flaps, the boundary-layer displacement thickness at any point back of the hinge for the airfoils with split flaps being as great as the distance from the lower surface of the flap to the upper surface of the undeflected portion of the airfoil back of the hinge. Analysis of the problem in this manner permits the values of β to be determined from experimental data, provided that some assumption is made regarding the lift distribution on the undeflected portion of the airfoil back of the hinge. Assume that over this portion at all points back of the hinge the pressure differences are negligibly small compared with the corresponding pressure differences over the split flap itself. This assumption is consistent with the analogy (pressures are propagated undiminished

through a boundary layer) and is supported fairly well by experiment (references 6 and 7), particularly for positive angles of attack and the larger flap deflections.

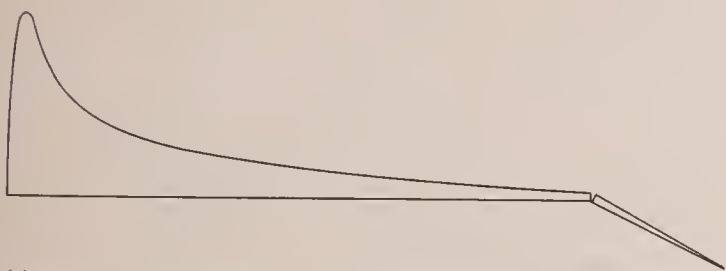
Values of β were obtained for split flaps using the incremental pressure distributions of reference 6. It was found that, for flap deflections of 40° or more, the



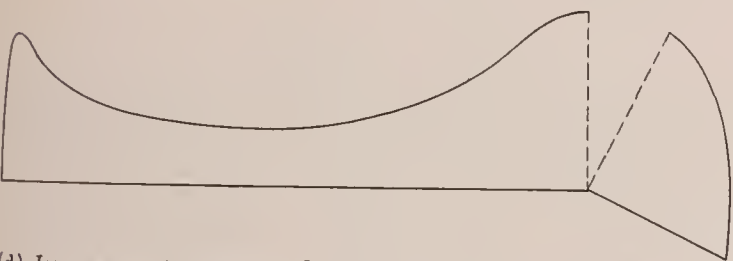
(a) Normal-force distribution for airfoil with flap neutral.



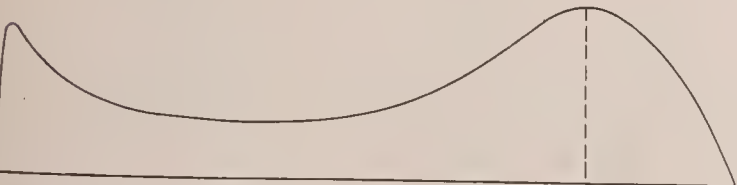
(b) Normal-force distribution for airfoil with flap deflected.



(c) Distribution shown in (a) plotted normal to flap-deflected chord.



(d) Increment normal-force distribution due to deflection of flap.



(e) Distribution shown in (d) plotted normal to flap-neutral chord.

FIGURE 8.—Normal-force distribution and incremental normal-force distribution for flaps neutral and deflected.

β values for plain- and split-flap airfoils were the same. In table III (d) to (h), the computed distributions of $P_{\delta\delta}/c_{n\delta\delta}$ are given for various flap-chord ratios and flap

deflections. Again the assumption is made that a single β curve applies for all flap-chord ratios for any given flap deflection.

The development of the requisite equations to determine the magnitude of the incremental additional and incremental basic distribution from wind-tunnel force tests will now be considered. From force tests of the airfoil with flap neutral, c_{m_1} (quarter-chord pitching-moment coefficient) and c_{n_1} (normal-force coefficient) corresponding to the normal-force distribution shown in figure 8 (a) are obtained. Again, from force tests of the airfoil at the same attitude with the flap deflected, c_{m_2} and c_{n_2} corresponding to the normal-force distribution shown in figure 8 (b) are obtained.

Let

$$\left. \begin{aligned} \Delta c_m &= c_{m_2} - c_{m_1}' \\ \Delta c_n &= c_{n_2} - c_{n_1}' \end{aligned} \right\} \quad (2)$$

where c_{m_1}' and c_{n_1}' are the pitching-moment and normal-force coefficients corresponding to the normal-force distribution for the airfoil with flap neutral when plotted normal to the chord of the airfoil with flap deflected, as shown in figure 8 (c). Then Δc_m and Δc_n are the pitching-moment and normal-force coefficients of the incremental normal-force distribution when the incremental distribution is plotted normal to the chord of airfoil with flap deflected, as shown in figure 8 (d).

For the commonly used airfoils, the approximation

$$\left. \begin{aligned} c_{n_1} &= c_{n_1}' \\ c_{m_1} &= c_{m_1}' \end{aligned} \right\} \quad (3)$$

is sufficiently exact except in the rare case when the flap-chord ratio E and the flap deflection δ are simultaneously large. (See figs. 8 (a) and (c).)

Let $\Delta c_m'$ and $\Delta c_n'$ be the pitching-moment and the normal-force coefficients of the incremental normal-force distribution plotted normal to the flap-neutral chord, as shown in figure 8 (e). Since the incremental basic normal-force distribution is responsible for the entire quarter-chord pitching moment, then, if G is the moment arm in terms of the chord of the basic normal force about the quarter-chord point,

$$\Delta c_m' = G c_{n_{b\delta}}$$

$$\Delta c_n' = c_{n_{a\delta}} + c_{n_{b\delta}}$$

or

$$\left. \begin{aligned} c_{n_{b\delta}} &= \frac{\Delta c_m'}{G} \\ c_{n_{a\delta}} &= \Delta c_n' - \frac{\Delta c_m'}{G} \end{aligned} \right\} \quad (4)$$

The value of G is a function of E and δ . Values of G are given in table IV.

The correlation between the fictitious values of $\Delta c_m'$ and $\Delta c_n'$ and the measured values of Δc_m and Δc_n must be established in order to determine $c_{n_{b\delta}}$ and

$c_{n_{a\delta}}$ from force tests. Let the incremental flap normal-force coefficient for unit span be given by

$$c_{n_{f\delta}} = \frac{n_{f\delta}}{qEc} \quad (5)$$

where $n_{f\delta}$ is the incremental flap normal force per unit span and q is the dynamic pressure in the air stream.

Then

$$\left. \begin{aligned} \Delta c_n' &= \Delta c_n + E c_{n_{f\delta}} (1 - \cos \delta) \\ \Delta c_m' &= \Delta c_m - E c_{n_{f\delta}} (1 - \cos \delta) \left(\frac{3}{4} - E \right) \end{aligned} \right\} \quad (6)$$

The incremental flap normal force may be considered as a combination of two components due to the incremental additional and the incremental basic normal-force distributions. Let $\gamma_{a\delta}$ and $\gamma_{b\delta}$ be the ratio of the flap normal force to the airfoil normal force for the incremental additional and the incremental basic normal forces, respectively; then

$$c_{n_{f\delta}} = \gamma_{a\delta} c_{n_{a\delta}} + \gamma_{b\delta} c_{n_{b\delta}} \quad (7)$$

or

$$c_{n_{f\delta}} = \gamma_{a\delta} \left(\Delta c_n' - \frac{\Delta c_m'}{G} \right) + \gamma_{b\delta} \frac{\Delta c_m'}{G} \quad (8)$$

The contribution of the additional normal-force distribution is small compared with the basic contribution so that, for the purpose of determining $\Delta c_m'$ and $\Delta c_n'$, the following approximation may be employed:

$$c_{n_{f\delta}} = \gamma_{b\delta} \frac{\Delta c_m'}{G}$$

and equations (6) become

$$\begin{aligned} \Delta c_n' &= \Delta c_n + E \gamma_{b\delta} \frac{\Delta c_m'}{G} (1 - \cos \delta) \\ \Delta c_m' &= \Delta c_m - E \gamma_{b\delta} \frac{\Delta c_m'}{G} (1 - \cos \delta) \left(\frac{3}{4} - E \right) \end{aligned}$$

so that

$$\left. \begin{aligned} \Delta c_m' &= \tau_m \Delta c_m \\ \Delta c_n' &= \Delta c_n + \tau_n \Delta c_m \end{aligned} \right\} \quad (9)$$

where

$$\begin{aligned} \tau_n &= \frac{E(1 - \cos \delta) \frac{\gamma_{b\delta}}{G}}{1 + \left[E(1 - \cos \delta) \left(\frac{3}{4} - E \right) \frac{\gamma_{b\delta}}{G} \right]} \\ \tau_m &= \frac{1}{1 + \left[E(1 - \cos \delta) \left(\frac{3}{4} - E \right) \frac{\gamma_{b\delta}}{G} \right]} \end{aligned}$$

The values of τ_n and τ_m have been determined and are given in tables V and VI.

Then, given c_{n_2} , c_{n_1} , c_{m_2} , and c_{m_1} (c_l may be considered as c_n ; c_m may be calculated if $c_{m_{a.c.}}$, the pitching-moment coefficient about the aerodynamic center, and $x_{a.c.}/c$, the chordwise distance of the aerodynamic center from the quarter-chord point of the section in terms of the chord, are given instead of c_m)

$$\left. \begin{aligned} \Delta c_m &= c_{m_2} - c_{m_1} \\ \Delta c_n &= c_{n_2} - c_{n_1} \end{aligned} \right\} \quad (10)$$

and using the values of τ_n and τ_m from tables V and VI depending on the type of flap, then (equation (9))

$$\begin{aligned} \Delta c_m' &= \tau_m \Delta c_m \\ \Delta c_n' &= \Delta c_n + \tau_n \Delta c_m \end{aligned}$$

The incremental basic and additional normal-force coefficients may be obtained from equations (4), which are

$$\begin{aligned} c_{n_{b\delta}} &= \frac{\Delta c_m'}{G} \\ c_{n_{a\delta}} &= \Delta c_n' - \frac{\Delta c_m'}{G} \end{aligned}$$

When the appropriate values of the incremental basic normal-force distribution, $P_{b\delta}/c_{n_{b\delta}}$, from table III are used, then

$$P_{b\delta} = \left(\frac{P_{b\delta}}{c_{n_{b\delta}}} \right) c_{n_{b\delta}} \quad (11)$$

By the use of the proper class of incremental additional normal-force distribution, $P_{a\delta}/c_{n_{a\delta}}$, from table I

$$P_{a\delta} = \left(\frac{P_{a\delta}}{c_{n_{a\delta}}} \right) c_{n_{a\delta}} \quad (12)$$

The incremental basic and additional distributions may be added to give the entire incremental normal-force distribution,

$$P_\delta = P_{a\delta} + P_{b\delta} \quad (13)$$

and this incremental normal-force distribution may be added to the distribution for the airfoil section with undeflected flap, P_1 (which distribution may be obtained by the method of reference 1), to give the normal-force distribution for the airfoil with the deflected flap

$$P_2 = P_1 + P_\delta \quad (14)$$

The incremental flap normal-force coefficient is given by equation (7) and the corresponding flap hinge-moment coefficient can be written by analogy.

$$\left. \begin{aligned} c_{n_{f\delta}} &= \frac{n_{f\delta}}{qEc} = \gamma_{a\delta} c_{n_{a\delta}} + \gamma_{b\delta} c_{n_{b\delta}} \\ c_{h_{f\delta}} &= \frac{h_{f\delta}}{qE^2c^2} = \eta_{a\delta} c_{n_{a\delta}} + \eta_{b\delta} c_{n_{b\delta}} \end{aligned} \right\} \quad (15)$$

Values of $\gamma_{b\delta}$ and $\eta_{b\delta}$ are given in tables VII and VIII. As the incremental additional and additional distributions are identical in form

$$\begin{aligned} \gamma_{a\delta} &= \gamma_a \\ \eta_{a\delta} &= \eta_a \end{aligned}$$

Values of γ_a and η_a are given in tables IX and X, respectively.

The flap normal-force and hinge-moment coefficients for the airfoil with flap neutral may be determined by considering the contributions of each of the component distributions that make up the flap-neutral normal-force distribution. In reference 1 the flap-neutral normal-force distribution is considered to be composed of four component distributions: (a) the moment basic (class 1), (b) the camber basic (class 0, 1, or 2), (c) the aerodynamic center, and (d) the additional (classes A, B, C, D, and E). The class of each distribution to be employed for a number of airfoils is given in table II (or tables I and II of reference 8) in the column "Classification PD." The letter (A, B, C, D, or E) designates the class of the additional distribution; the first number (1) designates the class of the moment basic distribution; the second number (0, 1, or 2) designates the class of the camber basic distribution.

The moment basic normal-force coefficient may be obtained from

$$c_{n_{bm}} = -6.30c_{m_{a.c.1}} \text{ for class 1} \quad (16)$$

The camber basic normal-force coefficient may be obtained from

$$\left. \begin{aligned} c_{n_{bc}} &= 0 && \text{for class 0} \\ c_{n_{bc}} &= 9.70 \frac{z_c}{c} && \text{for class 1} \\ c_{n_{bc}} &= 18.75 \frac{z_c}{c} && \text{for class 2} \end{aligned} \right\} \quad (17)$$

where z_c/c is the camber in terms of the chord. Values of z_c/c are given for a small number of airfoils in table II and for a large number of airfoils in tables I and II of reference 8. The additional normal-force coefficient may be obtained from

$$c_{n_a} = c_{n_1} - c_{n_{bc}} - c_{n_{bm}} \quad (18)$$

The aerodynamic-center distribution coefficient is given by

$$c_{a.c.} = \frac{x_{a.c.}}{c} c_{n_a} \quad (19)$$

Values of $x_{a.c.}/c$ are given for a small number of airfoils in table II (column 3) and for a large number in tables I and II of reference 8.

Finally, the flap normal-force coefficient is given by

$$c_{n_{f1}} = \gamma_a c_{n_a} + \gamma_{bc} c_{n_{bc}} + \gamma_{bm} c_{n_{bm}} + \gamma_{a.c.} c_{a.c.} \quad (20)$$

and the flap hinge-moment coefficient is given by

$$c_{h_{f1}} = \eta_a c_{n_a} + \eta_{bc} c_{n_{bc}} + \eta_{bm} c_{n_{bm}} + \eta_{a.c.} c_{a.c.} \quad (21)$$

The various γ and η values are given in tables IX and X.

The flap normal-force and hinge-moment coefficients for the airfoil section with flap deflected are

$$\left. \begin{aligned} c_{n_{f2}} &= c_{n_{f1}} + c_{n_{f\delta}} \\ c_{h_{f2}} &= c_{h_{f1}} + c_{h_{f\delta}} \end{aligned} \right\} \quad (22)$$

This method for the determination of incremental chordwise normal-force distribution for airfoils with flaps was developed for airfoils of normal profile and camber, and therefore it cannot be presupposed that this method might be applied to airfoil sections of abnormal form.

The values of $P_{b\delta}/c_{n_{b\delta}}$ for airfoils with both plain and split flaps were determined from tests of airfoils having very small gaps between the wing and the leading edge of the flap. It has been found (reference 9) that any gap between the wing and the leading edge of a plain flap has a detrimental effect upon the aerodynamic characteristics. It is probable that this gap effect will also be true for split-flap airfoils. In the absence of evidence to the contrary, the method presented cannot be considered applicable to plain-flap or split-flap airfoils with large gaps.

The flap hinges of all plain-flap airfoils, from the tests of which the $P_{b\delta}/c_{n_{b\delta}}$ values for the plain flap were determined, were midway between the upper and lower surfaces of the airfoils; that is, the radius of curvature of the upper surface above the hinge for each airfoil was half the depth of the airfoil at the hinge. Tests have been conducted to determine the effect of changing the radius of curvature at this point from zero to the full depth of the airfoil at the hinge. (The results of these tests have not been published.) The airfoil employed in the test was equipped with a $0.60c$ plain flap deflected 12° and with a $0.20c$ plain flap deflected 15° ; the effect of changing the radius of curvature at the $0.60c$ -flap hinge alone was determined. The results of these tests show only a negligible change in the aerodynamic characteristics (and presumably in the normal-force distribution) with a change in the radius of curvature. Because of the limited nature of the tests, these results cannot be considered conclusive for plain-flap airfoils in general, and the method presented must be considered strictly applicable to plain-flap airfoils with upper-surface curvatures not less than half the airfoil depth at the hinge.

The $P_{b\delta}/c_{n_{b\delta}}$ values for plain-flap airfoils were determined from airfoil tests made at an effective Reynolds Number of about 1,000,000. Comparison of these tests with tests made at an effective Reynolds Number of about 17,000,000 indicates that the effect of scale is unimportant although, it may be mentioned, in the critical region of flap deflections (i. e., for δ near 20°) there is a tendency at higher scales to maintain the unstalled incremental basic distribution (i. e., the $\delta = 5^\circ$, 10° , and 15° type of distribution) up to slightly greater flap deflections. Pressure-distribution measurements on split-flap airfoils made at effective Reynolds Numbers of 1,700,000 and 3,200,000 showed apparently no effect from this small change of scale.

It is difficult to make any general statement regarding the accuracy of this method for the determination of the

incremental chordwise normal-force distribution. The dispersion of experimental pressure-measurement results shown in figures 2 to 6 may be considered typical.

II. THE APPLICATION OF THE METHOD

THE GENERAL PROCEDURE FOR AN AIRFOIL WITH A PLAIN OR A SPLIT FLAP

In order to determine at a given lift coefficient the incremental normal-force distribution over a given airfoil section due to the deflection of a plain or a split flap, it is necessary to have the following experimentally determined characteristics for the airfoil section:

(a) With flap deflected:

c_{l_2} , the section lift coefficient (given).

$c_{m_{a.c.2}}$, the section pitching-moment coefficient about the aerodynamic center.

$\left(\frac{x_{a.c.}}{c}\right)_2$, the chordwise coordinate of the aerodynamic-center position in terms of the chord.

(b) With flap neutral (with the airfoil section at the same angle of attack):

c_{l_1} , the section lift coefficient.

$c_{m_{a.c.1}}$, the section pitching-moment coefficient about the aerodynamic center.

$\left(\frac{x_{a.c.}}{c}\right)_1$, the chordwise coordinate of the aerodynamic-center position in terms of the chord.

(c) The class of additional normal-force distribution to be employed.

For illustrative purposes, given: an N. A. C. A. 23012 airfoil section with a 0.20c split flap ($E=0.20$) set at 45° ($\delta=45^\circ$). To determine: the incremental normal-force distribution for this airfoil, when, with the flap deflected, the lift coefficient c_{l_2} is 1.40. From reference 10, when

$$c_{l_2}=1.40$$

then

$$c_{m_{a.c.2}}=-0.229$$

$$\left(\frac{x_{a.c.}}{c}\right)_2=0.012$$

$$\alpha=2.0^\circ$$

For the airfoil with flap retracted, when $\alpha=2.0^\circ$, from reference 11,

$$c_{l_1}=0.34$$

$$c_{m_{a.c.1}}=-0.005$$

and from table II of the present report

$$\left(\frac{x_{a.c.}}{c}\right)_1=0.012$$

and the C class of additional distribution is to be employed.

The quarter-chord pitching-moment coefficient is obtained from

$$c_m=c_{m_{a.c.}}+c_l\left(\frac{x_{a.c.}}{c}\right)$$

and the approximation is made

$$c_n=c_l$$

so that, for the example cited,

$$c_{m_2}=-0.229+1.40(0.012)=-0.212$$

$$c_{n_2}=1.40$$

and

$$c_{m_1}=-0.005+0.34(0.012)=-0.001$$

$$c_{n_1}=0.34$$

The quarter-chord pitching-moment and normal-force coefficients for the incremental normal-force distribution considered normal to the airfoil chord with flap deflected are given by

$$\left. \begin{aligned} \Delta c_m &= c_{m_2} - c_{m_1} \\ \Delta c_n &= c_{n_2} - c_{n_1} \end{aligned} \right\} \quad (10)$$

(equations are numbered as in part I of the report) so that, for the example cited,

$$\Delta c_m = -0.212 + 0.001 = -0.211$$

$$\Delta c_n = 1.40 - 0.34 = 1.06$$

The pitching-moment and normal-force coefficients for the incremental normal-force distribution, considered normal to the airfoil chord with flap neutral, are given by

$$\left. \begin{aligned} \Delta c_m' &= \tau_m \Delta c_m \\ \Delta c_n' &= \Delta c_n + \tau_n \Delta c_m \end{aligned} \right\} \quad (9)$$

Values of τ_n and τ_m are given in tables V and VI. For the example cited, by interpolation from the tables,

$$\tau_m = 1.16$$

$$\tau_n = -0.30$$

so that

$$\Delta c_m' = 1.16 (-0.211) = -0.245$$

$$\Delta c_n' = 1.06 + (-0.30) (-0.211) = 1.12$$

The incremental normal-force distribution is considered to be composed of two component distributions: (a) the incremental additional distribution, and (b) the incremental basic distribution. The magnitude of the incremental basic normal-force coefficient is given by

$$c_{n_{b\delta}} = \frac{\Delta c_m'}{G} \quad (4)$$

Values of G are given in table IV for airfoils with plain and split flaps.

For the example cited by interpolation from the table

$$G = -0.412$$

and so

$$c_{n_{b\delta}} = \frac{-0.245}{-0.412} = 0.60$$

The incremental additional normal force is obtained from

$$c_{n_{a\delta}} = \Delta c_n' - c_{n_{b\delta}} \quad (4)$$

For the example cited

$$c_{na\delta} = 1.12 - 0.60 = 0.52$$

The incremental additional distribution may then be obtained from

$$P_{a\delta} = \left(\frac{P_{a\delta}}{c_{na\delta}} \right) c_{na\delta} \quad (12)$$

Values of $P_{a\delta}/c_{na\delta}$ at a number of stations along the chord are given for the various classes of distributions in table I and figure 1. The quantity $P_{a\delta}$ is the pressure difference in terms of q , the stream dynamic pressure.

For the example cited

$$P_{a\delta} = \left(\frac{P_{a\delta}}{c_{na\delta}} \right) 0.52$$

so that for the class C distribution (table I) the values of $P_{a\delta}$ in the following table are obtained.

COMPUTATION OF INCREMENTAL ADDITIONAL DISTRIBUTION

x/c	$P_{a\delta}/c_{na\delta}$	$P_{a\delta}$
0	0	0
.0125	4.98	2.59
.025	4.23	2.20
.050	3.22	1.67
.075	2.68	1.39
.100	2.32	1.21
.150	1.85	.96
.200	1.54	.80
.300	1.14	.59
.400	.87	.45
.500	.68	.35
.600	.51	.27
.700	.37	.20
.800	.24	.13
.900	.12	.06
.950	.06	.03
1.000	0	0

The incremental basic distribution is found from

$$P_{b\delta} = \left(\frac{P_{b\delta}}{c_{nb\delta}} \right) c_{nb\delta} \quad (11)$$

Values of $P_{b\delta}/c_{nb\delta}$ at a number of stations along the chord are given in table III for plain and split flaps.

For the example cited,

$$P_{b\delta} = \left(\frac{P_{b\delta}}{c_{nb\delta}} \right) 0.60$$

Values of $P_{b\delta}/c_{nb\delta}$ are obtained by interpolation from table III and computed values of $P_{b\delta}$ are given in the following table. Again, $P_{b\delta}$ is the pressure difference in terms of q .

COMPUTATION OF INCREMENTAL BASIC DISTRIBUTION

$\frac{x/c}{1-E}$	$\frac{x}{c}$	$\frac{P_{b\delta}}{c_{nb\delta}}$	$P_{b\delta}$	$\frac{1-x/c}{E}$	$\frac{x}{c}$	$\frac{P_{b\delta}}{c_{nb\delta}}$	$P_{b\delta}$
0	0	0	0	1.00	0.80	2.06	1.23
.05	.04	.16	.10	.90	.82	2.19	1.31
.10	.08	.24	.14	.80	.84	2.21	1.32
.20	.16	.35	.21	.70	.86	2.18	1.31
.30	.24	.46	.28	.60	.88	2.12	1.27
.40	.32	.57	.34	.50	.90	2.02	1.21
.50	.40	.69	.41	.40	.92	1.89	1.13
.60	.48	.83	.50	.30	.94	1.70	1.02
.70	.56	1.02	.61	.20	.96	1.47	.88
.80	.64	1.26	.75	.10	.98	1.10	.66
.90	.72	1.59	.95	.05	.99	.82	.49
1.00	.80	2.06	1.23	0	1.00	0	0

Finally the incremental normal-force distribution is found by addition:

$$P_{\delta} = P_{a\delta} + P_{b\delta} \quad (13)$$

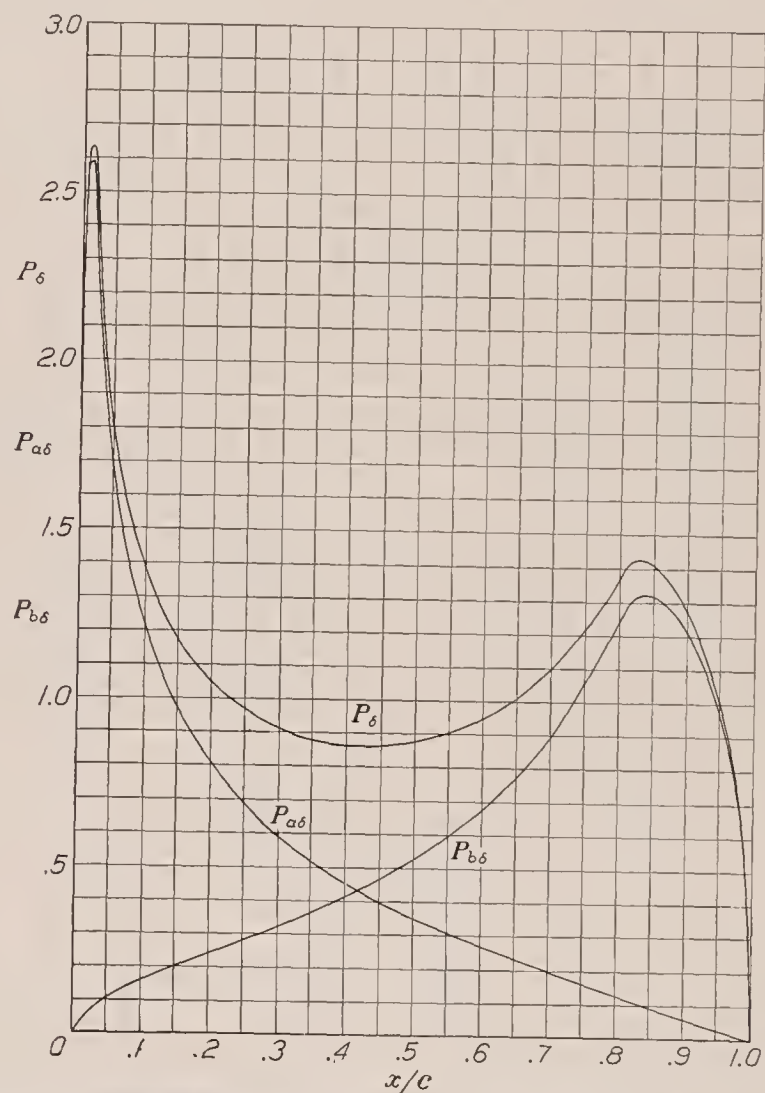


FIGURE 9.—Calculated incremental normal-force distribution. N. A. C. A. 23012 airfoil section at $\alpha = 2^\circ$ with a $0.20c$ split flap at $\delta = 45^\circ$.

This addition has been made for the example cited. In figure 9 the distributions of $P_{a\delta}$, $P_{b\delta}$, and P_{δ} are given.

The incremental normal-force distribution may be added to the normal-force distribution for the airfoil

with flap neutral (as may be obtained from an experimental pressure-distribution investigation or by the method of reference 1) to give the normal-force distribution for the airfoil with flap deflected

$$P_2 = P_1 + P_\delta \quad (14)$$

The incremental flap section normal-force and flap section hinge-moment coefficients are found as the sum of the contributions from the incremental additional and the incremental basic distributions:

$$\left. \begin{aligned} c_{nf\delta} &= \frac{n_{f\delta}}{qEc} = \gamma_{a\delta}c_{na\delta} + \gamma_{b\delta}c_{nb\delta} \\ c_{hf\delta} &= \frac{h_{f\delta}}{qE^2c^2} = \eta_{a\delta}c_{na\delta} + \eta_{b\delta}c_{nb\delta} \end{aligned} \right\} \quad (15)$$

where $n_{f\delta}$ and $h_{f\delta}$ are the incremental flap normal force and hinge moment per unit span, respectively. The values of $\gamma_{a\delta}$ and $\eta_{a\delta}$ are given in tables IX and X. Values of $\gamma_{b\delta}$ and $\eta_{b\delta}$ are given in tables VII and VIII.

For the example cited, from tables IX and X

$$\gamma_{a\delta} = 0.12; \quad \eta_{a\delta} = -0.04$$

and by interpolation from tables VII and VIII

$$\gamma_{b\delta} = 1.79; \quad \eta_{b\delta} = -0.77$$

so that, using the values of $c_{na\delta}$ and $c_{nb\delta}$ already determined,

$$\begin{aligned} c_{nf\delta} &= 0.12 (0.52) + 1.79 (0.60) = 1.13 \\ c_{hf\delta} &= -0.04 (0.52) - 0.77 (0.60) = -0.48 \end{aligned}$$

By a similar method, the flap normal-force and hinge-moment coefficients for the airfoil with flap neutral may be determined from

$$c_{nf_1} = \gamma_a c_{na} + \gamma_{bc} c_{nbc} + \gamma_{bm} c_{nbm} + \gamma_{a.c.} c_{a.c.} \quad (20)$$

$$c_{hf_1} = \eta_a c_{na} + \eta_{bc} c_{nbc} + \eta_{bm} c_{nbm} + \eta_{a.c.} c_{a.c.} \quad (21)$$

where c_{na} , c_{nbc} , and c_{nbm} are the normal-force coefficients of the additional, camber basic, and moment basic distributions given in reference 1, and $c_{a.c.}$ is a measure of the magnitude of the aerodynamic-center distribution given in reference 1. These coefficients may be found from equations (16) to (19) in part I. Values of γ and η are given in tables IX and X.

For the example cited, the pressure-distribution classification is given in table II as C12 and

$$\frac{z_c}{c} = 0.018$$

Hence, from equations (16) to (19),

$$\begin{aligned} c_{nbm} &= -6.30(-0.005) = 0.03 \\ c_{nbc} &= 18.75(0.018) = 0.34 \\ c_{na} &= 0.34 - 0.34 - 0.03 = -0.03 \\ c_{a.c.} &= -0.03(0.012) = 0.000 \end{aligned}$$

From tables IX and X

$$\begin{aligned} \gamma_a &= 0.12 & \eta_a &= -0.04 \\ \gamma_{bc} &= 0.09 & \eta_{bc} &= -0.03 \\ \gamma_{bm} &= 0.32 & \eta_{bm} &= -0.11 \end{aligned}$$

so that

$$\begin{aligned} c_{nf_1} &= (0.12)(-0.03) + (0.09)(0.34) + (0.32)(0.03) = 0.04 \\ c_{hf_1} &= (-0.04)(-0.03) + (-0.03)(0.34) + (-0.11)(0.03) \\ &= -0.01 \end{aligned}$$

The flap normal-force and flap hinge-moment coefficients are, by addition,

$$\left. \begin{aligned} c_{nf_2} &= c_{nf_1} + c_{nf\delta} \\ c_{hf_2} &= c_{hf_1} + c_{hf\delta} \end{aligned} \right\} \quad (22)$$

For the example cited,

$$\begin{aligned} c_{nf_2} &= 0.04 + 1.13 = 1.17 \\ c_{hf_2} &= -0.01 - 0.48 = -0.49 \end{aligned}$$

THE GENERAL PROCEDURE FOR AN AIRFOIL WITH A SERIALLY HINGED FLAP

The incremental distribution for an airfoil with a serially hinged plain flap is obtained by determining the incremental distribution for the airfoil with each of the several flaps deflected and then by adding the various distributions.

This superposition method will always be applicable provided that all flaps of the system are unstalled (i. e., no flap is deflected more than 15°) with the exception of the final (smallest) flap, which may be stalled or unstalled. If, in a combination of a large flap and a small flap (e. g., a tab), the small flap is deflected oppositely to the large flap, experiment has shown that the method is applicable whether either flap is stalled or not.

It is necessary to integrate the normal-force distribution curve to determine the several flap normal-force and hinge-moment coefficients for the airfoil with serially hinged flaps.

LANGLEY MEMORIAL AERONAUTICAL LABORATORY,
NATIONAL ADVISORY COMMITTEE FOR AERONAUTICS,
LANGLEY FIELD, VA., April 12, 1938.

APPENDIX

THEORETICAL RELATIONSHIPS FOR THE THIN AIRFOIL WITH PLAIN FLAP

The application of thin-airfoil theory to the problem of the airfoil with a plain flap is detailed in the following section.

Designate $\left(\frac{d\Gamma}{dx}\right)dx$ as the value of the elemental spanwise circulation at any point x back of the leading edge of the airfoil of chord c subjected to the stream velocity V . Glauert has shown that, if a distribution of vorticity along the chord of the airfoil with a plain flap is assumed in the form

$$\left(\frac{d\Gamma}{dx}\right)dx = cV[A_0(1 + \cos \theta) + \sum_1^{\infty} A_n \sin n\theta \sin \theta]d\theta \quad (A-1)$$

where

$$\theta = \cos^{-1}\left(1 - \frac{2x}{c}\right)$$

or

$$x = \frac{c}{2}(1 - \cos \theta) \quad (A-2)$$

then, in order that Kutta's criterion may be satisfied and that the flow across the chord shall be everywhere tangential to the camber line of the airfoil, the coefficients of equation (A-1) must be given by

$$\left. \begin{aligned} A_0 &= \alpha' + \left(\frac{\pi - \theta_0}{\pi}\right)\delta \\ A_1 &= \left(\frac{2 \sin \theta_0}{\pi}\right)\delta \\ \dots \dots \dots \\ A_n &= \left(\frac{2 \sin n\theta_0}{n\pi}\right)\delta \end{aligned} \right\} \quad (A-3)$$

where α' is the angle between the direction of stream flow and the unflapped portion of the airfoil, δ is the flap angle measured from the unflapped section, and θ_0 is the value of θ at the flap hinge, i. e.,

$$\left. \begin{aligned} \cos \theta_0 &= -(1 - 2E) \\ \sin \theta_0 &= 2\sqrt{E(1 - E)} \end{aligned} \right\} \quad (A-4)$$

where E is the flap-chord ratio

$$E = \frac{c_f}{c}$$

The pressure difference P (in terms of the stream dynamic head q) at any point x along the airfoil section is the lift per unit span experienced by the airfoil at that point in terms of q , or

$$P = \frac{p}{q} = \frac{dL}{dx} \quad (A-5)$$

but, from wing theory, the lift of an element of chord per unit span is

$$dL = \rho V \frac{d\Gamma}{dx} dx \quad (A-6)$$

(ρ is the fluid density) and, since by differentiation of equation (A-2)

$$dx = \frac{1}{2}c \sin \theta d\theta$$

then

$$\begin{aligned} P &= \frac{\rho V^2 c}{q} [A_0(1 + \cos \theta) + \sum_1^{\infty} A_n \sin n\theta \sin \theta] \frac{d\theta}{dx} \\ &= 4[A_0\left(\frac{1 + \cos \theta}{\sin \theta}\right) + \sum_1^{\infty} A_n \sin n\theta] \end{aligned} \quad (A-7)$$

Substituting the value of the coefficients (equation (A-3))

$$P = \left[\frac{4(1 + \cos \theta)}{\sin \theta} \right] \left[\alpha' + \left(\frac{\pi - \theta_0}{\pi}\right)\delta \right] + \sum_1^{\infty} \frac{8\delta \sin n\theta_0 \sin n\theta}{n\pi}$$

When the flap is neutral ($\delta = 0$), the lift distribution is (using the subscript ₁ for the flap-neutral case)

$$P_1 = \left[\frac{4(1 + \cos \theta)}{\sin \theta} \right] \alpha' \quad (A-8)$$

The incremental lift distribution due to flap deflection is

$$P_\delta = \left[\frac{4(1 + \cos \theta)(\pi - \theta_0)}{\pi \sin \theta} + \sum_1^{\infty} \frac{8 \sin n\theta_0 \sin n\theta}{n\pi} \right] \delta \quad (A-9)$$

Perring (reference 12) has shown that, for airfoils with serially hinged flaps, the elemental chordwise distribution of circulation may be expressed by equation (A-1), provided that the coefficients be given by

$$\left. \begin{aligned} A_0 &= \alpha + \frac{\pi - \theta_{01}}{\pi}\delta_1 + \frac{\pi - \theta_{02}}{\pi}\delta_2 + \dots + \frac{\pi - \theta_{0r}}{\pi}\delta_r \\ A_1 &= \frac{2 \sin \theta_{01}}{\pi}\delta_1 + \frac{2 \sin \theta_{02}}{\pi}\delta_2 + \dots + \frac{2 \sin \theta_{0r}}{\pi}\delta_r \\ \dots \dots \dots \\ A_n &= \frac{2 \sin n\theta_{01}}{n\pi}\delta_1 + \frac{2 \sin n\theta_{02}}{n\pi}\delta_2 + \dots + \frac{2 \sin n\theta_{0r}}{n\pi}\delta_r \end{aligned} \right\} \quad (A-10)$$

where $\theta_{01}, \theta_{02}, \dots, \theta_{0r}$ and $\delta_1, \delta_2, \dots, \delta_r$ are the values of θ_0 and δ for each of the r number of flaps.

Hence, the lift distribution over an airfoil with serially hinged flaps may be expressed by

$$P_2 = P_1 + P_{\delta_1} + P_{\delta_2} + P_{\delta_3} + \dots + P_{\delta_r} \quad (A-11)$$

where P_1 denotes the distribution with all flaps neutral (given by equation (A-8)) and $P_{\delta_1}, P_{\delta_2}, \dots, P_{\delta_r}$ are the incremental distributions due to the individual deflection of flaps 1, 2, \dots, r , respectively.

A characteristic feature of the thin-airfoil theory is that the incremental distribution due to the deflection of one or more flaps is independent of the original shape of the mean camber line of an airfoil. An airfoil with a curved mean camber line may be considered essentially

as a symmetrical airfoil with an infinite system of serially hinged flaps deflected so as to produce that curvature. It has already been seen that the incremental distribution due to the deflection of any one of a number of serially hinged flaps is independent of the deflections of any of the other flaps.

Thus the incremental lift distribution as given by equation (A-9) is equally applicable to every flapped airfoil of infinitesimal thickness.

Now consider the incremental lift distribution given by equation (A-9) to be the sum of (1) the incremental additional distribution

$$P_{a\delta} = \left[\frac{4(\pi - \theta_0)(1 + \cos \theta)}{\pi \sin \theta} \right] \delta \quad (\text{A-12})$$

and (2) the incremental basic distribution

$$P_{b\delta} = \left[\sum_1^{\infty} \frac{8 \sin n \theta_0 \sin n \theta}{n \pi} \right] \delta \quad (\text{A-13})$$

The general form of the incremental additional distribution, unlike the incremental basic distribution, is not a function of the flap-chord ratio, E .

Glauert (reference 3) has shown that the incremental lift coefficient (i. e., for $\alpha' = 0$) is given by

$$c_{l\delta} = 2[(\pi - \theta_0) + \sin \theta_0] \delta \quad (\text{A-14})$$

The incremental additional lift coefficient is given by

$$\begin{aligned} c_{l_{a\delta}} &= \frac{L_{a\delta}}{qc} = \frac{1}{qc} \int_0^c P_{a\delta} q dx \\ &= \frac{2(\pi - \theta_0)\delta}{\pi} \int_0^\pi (1 + \cos \theta) d\theta \\ &= 2(\pi - \theta_0)\delta \end{aligned} \quad (\text{A-15})$$

and, from equations (A-14) and (A-15)

$$c_{l_{b\delta}} = 2 \sin \theta_0 \delta \quad (\text{A-16})$$

Substitution of the values of $c_{l_{a\delta}}$ and $c_{l_{b\delta}}$ in equations (A-12) and (A-13), gives

$$\frac{P_{a\delta}}{c_{l_{a\delta}}} = \frac{2(1 + \cos \theta)}{\pi \sin \theta} \quad (\text{A-17})$$

$$\frac{P_{b\delta}}{c_{l_{b\delta}}} = \frac{4}{\pi \sin \theta_0} \sum_1^{\infty} \frac{\sin n \theta_0 \sin n \theta}{n} \quad (\text{A-18})$$

Equation (A-18) may be rewritten as the sum of two series

$$\frac{P_{b\delta}}{c_{l_{b\delta}}} = \frac{2}{\pi \sin \theta_0} \left[\sum_1^{\infty} \frac{\cos n(\theta_0 - \theta)}{n} - \sum_1^{\infty} \frac{\cos n(\theta_0 + \theta)}{n} \right]$$

But

$$\sum_1^{\infty} \frac{\cos nr}{n} = -\log_e 2 - \log_e \sin \frac{r}{2}$$

Hence

$$\frac{P_{b\delta}}{c_{l_{b\delta}}} = \frac{2}{\pi \sin \theta_0} \log_e \left[\frac{\sin \frac{1}{2}(\theta_0 + \theta)}{\sin \frac{1}{2}(\theta_0 - \theta)} \right] \quad (\text{A-19})$$

The moment of the incremental additional lift about the quarter-chord point of the airfoil may be shown to be zero, hence the incremental basic lift is responsible for the entire incremental quarter-chord moment.

REFERENCES

1. Jacobs, Eastman N., and Rhode, R. V.: Airfoil Section Characteristics as Applied to the Prediction of Air Forces and Their Distribution on Wings. T. R. No. 631, N. A. C. A., 1938.
2. Glauert, H.: Theoretical Relationships for an Aerofoil with Hinged Flap. R. & M. No. 1095, British A. R. C., 1927.
3. Glauert, H.: The Elements of Aerofoil and Airscrew Theory. Cambridge University Press, 1930.
4. Jacobs, Eastman N., and Pinkerton, Robert M.: Pressure Distribution over a Symmetrical Airfoil Section with Trailing Edge Flap. T. R. No. 360, N. A. C. A., 1930.
5. Wenzinger, Carl J.: Pressure Distribution over an Airfoil Section with a Flap and Tab. T. R. No. 574, N. A. C. A., 1936.
6. Wallace, Rudolf: Investigation of Full-Scale Split Trailing-Edge Wing Flaps with Various Chord and Hinge Locations. T. R. No. 539, N. A. C. A., 1935.
7. Wenzinger, Carl J., and Harris, Thomas A.: Pressure Distribution over a Rectangular Airfoil with a Partial-Span Split Flap. T. R. No. 571, N. A. C. A., 1936.
8. Pinkerton, Robert M., and Greenberg, Harry: Aerodynamic Characteristics of a Large Number of Airfoils tested in the Variable-Density Tunnel. T. R. No. 628, N. A. C. A., 1938.
9. Wenzinger, Carl J.: Wind-Tunnel Investigation of Ordinary and Split Flaps on Airfoils of Different Profile. T. R. No. 554, N. A. C. A., 1936.
10. Abbott, Ira H., and Greenberg, Harry: Tests in the Variable-Density Wind Tunnel of the N. A. C. A. 23012 Airfoil with Plain and Split Flaps. T. R. (to be published).
11. Jacobs, Eastman N., and Pinkerton, Robert M.: Tests in the Variable-Density Wind Tunnel of Related Airfoils Having the Maximum Camber Unusually Far Forward. T. R. No. 537, N. A. C. A., 1935.
12. Perring, W. G. A.: The Theoretical Relationships for an Aerofoil with a Multiply Hinged Flap System. R. & M. No. 1171, British A. R. C., 1928.

TABLE I

ADDITIONAL NORMAL-FORCE DISTRIBUTION

P_a/c_{n_a} or $P_{a\delta}/c_{n_{a\delta}}$

[Class A distribution has not yet been determined]

Station x/c	Class B	Class C	Class D	Class E
0	0	0	0	0
.0125	5.93	4.98	4.32	3.87
.025	4.37	4.23	4.02	3.81
.050	3.20	3.22	3.25	3.27
.075	2.63	2.68	2.76	2.81
.100	2.26	2.32	2.39	2.44
.150	1.77	1.85	1.90	1.95
.200	1.47	1.54	1.58	1.62
.300	1.10	1.14	1.16	1.18
.400	.86	.87	.88	.89
.500	.67	.68	.68	.69
.600	.51	.51	.51	.51
.700	.38	.37	.37	.36
.800	.25	.24	.24	.23
.900	.13	.12	.12	.11
.950	.06	.06	.06	.06
1.000	0	0	0	0

TABLE II

CHARACTERISTICS FOR 22 AIRFOILS

Airfoil	Classification PD	a. c. (percent c ahead of $c/4$)	Camber (percent c) 100 z_c/c
Clark Y	C10	1.1	3.9
Clark YM-15	D10	1.1	4.0
Clark YM-18	E10	1.4	4.0
Curtiss C-72	C10	1.0	4.0
Göttingen 387	D10	.7	5.9
Göttingen 398	D10	.4	4.9
N-22	C10	.6	4.3
N. A. C. A. 0006	A10	.7	0
N. A. C. A. 0012	C10	1.3	0
N. A. C. A. 2212	C12	.9	2.0
N. A. C. A. 2409	B10	.7	2.0
N. A. C. A. 2412	C10	1.2	2.0
N. A. C. A. 2415	D10	1.4	2.0
N. A. C. A. 2418	E10	1.1	2.0
N. A. C. A. 4412	C10	.7	4.0
N. A. C. A. 23012	C12	1.2	1.8
N. A. C. A. CYH	C11	.7	3.1
N. A. C. A. -M6	C11	.4	2.4
R. A. F. 15	A10	1.7	2.6
U. S. A. 27	C10	1.8	5.6
U. S. A. 35-A	E10	.8	7.3
U. S. A. 35-B	C10	.5	4.6

TABLE III

$P_{b\delta}/c_{n_{b\delta}}$ DISTRIBUTION

(a) PLAIN FLAP AT $\delta=5^\circ, 10^\circ$, AND 15°																(b) PLAIN FLAP AT $\delta=20^\circ$															
$E \longrightarrow$		0.05	0.10	0.15	0.20	0.25	0.30	0.35	0.40	0.45	0.50	0.55	0.60	0.65	0.70	0.05	0.10	0.15	0.20	0.25	0.30	0.35	0.40	0.45	0.50	0.55	0.60				
\uparrow x/c (ahead of hinge) \downarrow	0	0	0	0	0	0	0	0	0	0	0	0	0	0	0	0	0	0	0	0	0	0	0	0	0	0	0				
	.05	.15	.15	.16	.16	.17	.17	.18	.19	.20	.21	.22	.23	.25	.27	.15	.15	.16	.16	.17	.17	.18	.19	.20	.21	.22	.23				
	.10	.22	.23	.23	.24	.25	.25	.26	.27	.29	.30	.32	.34	.36	.39	.22	.23	.23	.24	.25	.25	.26	.27	.29	.30	.32	.34				
	.20	.33	.34	.34	.35	.36	.38	.39	.40	.42	.44	.46	.49	.52	.56	.33	.34	.34	.35	.36	.38	.39	.40	.42	.44	.46	.49				
	.30	.43	.44	.45	.46	.47	.49	.50	.52	.54	.57	.60	.63	.67	.72	.43	.44	.45	.46	.47	.49	.50	.52	.54	.57	.60	.63				
	.40	.54	.55	.56	.57	.58	.60	.62	.64	.67	.70	.73	.77	.82	.88	.54	.55	.56	.57	.58	.60	.62	.64	.67	.70	.73	.77				
	.50	.66	.66	.67	.69	.71	.73	.75	.77	.80	.84	.88	.92	.98	1.05	.66	.66	.67	.69	.71	.73	.75	.77	.80	.84	.88	.92				
	.60	.79	.80	.82	.83	.85	.88	.90	.93	.96	1.00	1.05	1.10	1.17	1.25	.79	.80	.82	.83	.85	.88	.90	.93	.96	1.00	1.05	1.10				
	.70	.97	.98	1.00	1.01	1.03	1.05	1.08	1.11	1.15	1.19	1.24	1.30	1.39	1.48	.97	.98	1.00	1.01	1.03	1.05	1.08	1.11	1.15	1.19	1.24	1.30				
	.80	1.23	1.24	1.26	1.27	1.29	1.31	1.34	1.38	1.42	1.46	1.52	1.59	1.67	1.78	1.23	1.24	1.26	1.27	1.29	1.31	1.34	1.38	1.42	1.46	1.52	1.59				
\uparrow $1-x/c$ (back of hinge) \downarrow	.90	1.73	1.74	1.75	1.76	1.77	1.79	1.81	1.84	1.88	1.92	1.98	2.06	2.16	2.29	1.73	1.74	1.75	1.76	1.77	1.79	1.81	1.84	1.88	1.92	1.98	2.06				
	1.00	8.74	6.04	4.89	4.40	4.01	3.71	3.50	3.35	3.23	3.15	3.11	3.06	3.04	3.02	5.83	4.05	3.38	3.02	2.83	2.70	2.63	2.58	2.56	2.56	2.58	2.62				
	.90	6.45	4.48	3.78	3.32	2.99	2.77	2.60	2.48	2.39	2.32	2.26	2.22	2.19	2.16	5.08	3.53	2.98	2.61	2.36	2.18	2.05	1.96	1.88	1.83	1.78	1.75				
	.80	4.96	3.51	2.92	2.57	2.31	2.12	2.00	1.90	1.81	1.74	1.69	1.64	1.60	1.57	4.23	2.99	2.50	2.19	1.97	1.81	1.70	1.62	1.55	1.49	1.44	1.40				
	.70	3.85	2.72	2.23	1.97	1.77	1.64	1.53	1.44	1.37	1.32	1.27	1.22	1.19	1.16	3.71	2.63	2.16	1.90	1.71	1.58	1.48	1.39	1.32	1.27	1.22	1.18				
	.60	3.09	2.18	1.78	1.57	1.41	1.30	1.21	1.14	1.08	1.04	1.00	.96	.93	.91	3.33	2.35	1.92	1.69	1.52	1.40	1.30	1.22	1.17	1.12	1.08	1.04				
	.50	2.46	1.72	1.42	1.24	1.11	1.02	.95	.89	.85	.81	.77	.75	.72	.70	2.98	2.09	1.73	1.50	1.35	1.24	1.15	1.08	1.03	.98	.94	.91				
	.40	1.90	1.34	1.10	.96	.86	.78	.73	.69	.65	.62	.59	.57	.55	.53	2.65	1.87	1.54	1.34	1.19	1.09	1.02	.96	.91	.86	.83	.80				
	.30	1.40	.99	.81	.70	.63	.57	.53	.50	.47	.45	.43	.42	.40	.39	2.32	1.63	1.34	1.16	1.04	.95	.88	.82	.78	.75	.72	.69				
	.20	.92	.65	.53	.46	.41	.38	.35	.33	.31	.29	.28	.27	.26	.25	1.93	1.35	1.11	.96	.86	.79	.73	.68	.65	.62	.59	.56				
0	.05	.32	.19	.16	.14	.12	.11	.10	.10	.09	.08	.08	.08	.07	1.16	.70	.58	.50	.45	.40	.38	.35	.33	.31	.30	.28					

(c) PLAIN FLAP AT $\delta=30^\circ$											(d) PLAIN OR SPLIT FLAP AT $\delta=40^\circ$								
$E \longrightarrow$		0.05	0.10	0.15	0.20	0.25	0.30	0.35	0.40	0.45	0.50	0.05	0.10	0.15	0.20	0.25	0.30	0.35	0.40
\uparrow x/c (ahead of hinge) \downarrow	0	0	0	0	0	0	0	0	0	0	0	0	0	0	0	0	0	0	0
	.05	.15	.15	.16	.16	.17	.17	.18	.19	.20	.21	.15	.15	.16	.16	.17	.17	.18	.19
	.10	.22	.23	.23	.24	.25	.25	.26	.27	.29	.30	.22	.23	.23	.24	.25	.25	.26	.27
	.20	.33	.34	.34	.35	.36	.38	.39	.40	.42	.44	.33	.34	.35	.36	.38	.39	.40	.42
	.30	.43	.44	.45	.46	.47	.49	.50	.52	.54	.57	.43	.44	.45	.46	.47	.49	.51	.52
	.40	.54	.55	.56	.57	.58	.60	.62	.64	.67	.70	.54	.55	.56	.57	.58	.60	.62	.64
	.50	.66	.66	.67	.69	.71	.73	.75	.77	.80	.84	.66	.66	.66	.68	.69	.71	.73	.75
	.60	.79	.80	.82	.83	.85	.88	.90	.93	.96	1.00	.79	.80	.82	.83	.85	.88	.90	.93
	.70	.97	.98	1.00	1.01	1.03	1.05	1.08	1.11	1.15	1.19	.97	.98	1.00	1.01	1.03	1.05	1.08	1.11
	.80	1.23	1.24	1.26	1.27	1.29	1.31	1.34	1.38	1.42	1.46	1.22	1.23	1.25	1.26	1.28	1.30	1.33	1.36
\uparrow $1-x/c$ (back of hinge) \downarrow	.90	1.67	1.68	1.69	1.70	1.71	1.72	1.73	1.74	1.77	1.80	1.58	1.59	1.60	1.61	1.61	1.62	1.62	1.63
	1.00	4.50	3.12	2.66	2.36	2.22	2.13	2.08	2.05	2.01	1.99	4.10	2.90	2.42	2.12	1.99	1.88	1.81	1.76
	.90	4.61	3.20	2.70	2.37	2.15	2.01	1.90	1.83	1.77	1.73	4.24	3.01	2.52	2.23	2.02	1.88	1.78	1.72
	.80	4.34	3.07	2.56	2.24	2.02	1.86	1.75	1.66	1.59	1.52	4.29	3.04	2.53	2.22	2.00	1.84	1.73	1.66
	.70	4.08	2.89	2.37	2.09	1.88	1.73	1.62	1.52	1.45	1.40	4.27	3.02	2.48	2.18	1.96	1.81	1.70	1.59
	.60	3.82	2.69	2.20	1.94	1.74	1.60	1.49	1.40	1.34	1.28	4.14	2.91	2.39	2.10	1.89	1.74	1.62	1.52
	.50	3.55	2.49	2.05	1.79	1.61	1.47	1.37	1.29	1.22	1.17	3.92	2.75	2.27	1.98	1.77	1.62	1.51	1.42
	.40	3.25	2.29	1.88	1.64	1.46	1.34	1.25	1.17	1.11	1.06	3.64	2.56	2.11	1.83	1.64	1.50	1.40	1.31
	.30	2.89	2.04	1.68	1.45	1.29	1.18	1.10	1.03	.98	.93	3.28	2.31	1.90	1.64	1.47	1.34	1.24	1.17
	.20	2.44	1.72	1.41	1.22	1.09	1.00	.93	.87	.82	.78	2.82	1.98	1.62	1.40	1.26	1.15	1.07	1.00
0	.05	1.53	.92	.76	.66	.59	.53	.49	.46	.44	1.79	1.08	.89	.77	.69	.63	.58	.54	

$P_{b\delta}/c_{n_{b\delta}}$ DISTRIBUTION

(e) PLAIN OR SPLIT FLAP AT $\delta=50^\circ$										(f) PLAIN OR SPLIT FLAP AT $\delta=60^\circ$							
$E \rightarrow$		0.05	0.10	0.15	0.20	0.25	0.30	0.35	0.40	0.05	0.10	0.15	0.20	0.25	0.30	0.35	0.40
\uparrow $\frac{x/c}{1-E}$ (ahead of hinge) \downarrow	0	0	0	0	0	0	0	0	0	0	0	0	0	0	0	0	0
	.05	.15	.15	.16	.16	.17	.17	.18	.19	.15	.15	.16	.16	.17	.17	.18	.19
	.10	.22	.23	.23	.24	.25	.25	.26	.27	.22	.23	.23	.24	.25	.25	.26	.27
	.20	.33	.34	.35	.35	.36	.38	.39	.40	.33	.34	.35	.35	.36	.38	.39	.40
	.30	.43	.44	.45	.46	.47	.49	.51	.52	.43	.44	.45	.46	.47	.49	.51	.52
	.40	.54	.55	.56	.57	.58	.60	.62	.64	.54	.55	.56	.57	.58	.60	.62	.64
	.50	.66	.66	.68	.69	.71	.73	.75	.77	.66	.67	.68	.69	.71	.73	.75	.77
	.60	.79	.80	.82	.83	.85	.88	.90	.93	.79	.80	.82	.83	.85	.88	.90	.93
	.70	.97	.98	1.00	1.03	1.05	1.08	1.11	1.14	.97	.98	.99	1.01	1.02	1.05	1.07	1.10
	.80	1.21	1.22	1.23	1.25	1.26	1.29	1.32	1.35	1.20	1.21	1.22	1.24	1.25	1.28	1.29	1.32
	.90	1.54	1.55	1.56	1.57	1.57	1.57	1.57	1.57	1.52	1.53	1.54	1.55	1.54	1.53	1.51	1.50
\uparrow $\frac{1-x/c}{E}$ (back of hinge) \downarrow	1.00	3.81	2.68	2.27	2.00	1.86	1.77	1.71	1.67	3.84	2.59	2.22	1.97	1.81	1.71	1.63	1.59
	.90	4.18	2.90	2.45	2.15	1.95	1.81	1.72	1.66	4.04	2.80	2.36	2.08	1.88	1.76	1.68	1.62
	.80	4.25	3.00	2.50	2.20	1.98	1.82	1.72	1.64	4.16	2.94	2.45	2.15	1.94	1.78	1.68	1.59
	.70	4.27	3.02	2.48	2.18	1.96	1.81	1.70	1.59	4.27	3.02	2.48	2.18	1.96	1.81	1.70	1.59
	.60	4.21	2.97	2.43	2.14	1.92	1.77	1.65	1.55	4.27	3.01	2.46	2.17	1.95	1.79	1.67	1.57
	.50	4.07	2.86	2.36	2.06	1.84	1.69	1.57	1.48	4.18	2.93	2.42	2.11	1.89	1.73	1.62	1.52
	.40	3.86	2.71	2.24	1.95	1.73	1.59	1.48	1.39	4.01	2.82	2.33	2.02	1.80	1.65	1.54	1.45
	.30	3.52	2.49	2.04	1.76	1.58	1.44	1.34	1.25	3.71	2.62	2.15	1.86	1.66	1.52	1.41	1.32
	.20	3.06	2.15	1.76	1.53	1.37	1.25	1.16	1.09	3.27	2.29	1.88	1.63	1.46	1.33	1.24	1.16
	.10	2.34	1.64	1.33	1.16	1.05	.96	.90	.84	2.51	1.76	1.43	1.25	1.13	1.03	.96	.90
	.05	2.02	1.22	1.00	.87	.78	.70	.65	.61	2.18	1.31	1.08	.93	.84	.76	.71	.66
0	0	0	0	0	0	0	0	0	0	0	0	0	0	0	0	0	

(g) SPLIT FLAP AT $\delta=20^\circ$											(h) SPLIT FLAP AT $\delta=30^\circ$										
$E \rightarrow$		0.05	0.10	0.15	0.20	0.25	0.30	0.35	0.40	0.45	0.50	0.05	0.10	0.15	0.20	0.25	0.30	0.35	0.40	0.45	0.50
\uparrow $\frac{x/c}{1-E}$ (ahead of hinge) \downarrow	0	0	0	0	0	0	0	0	0	0	0	0	0	0	0	0	0	0	0	0	0
	.05	.15	.15	.16	.16	.17	.17	.18	.19	.20	.21	.15	.15	.16	.16	.17	.17	.18	.19	.20	.21
	.10	.22	.23	.23	.24	.25	.25	.26	.27	.29	.30	.22	.23	.23	.24	.25	.25	.26	.27	.29	.30
	.20	.33	.34	.35	.35	.36	.38	.39	.40	.42	.44	.33	.34	.35	.35	.36	.38	.39	.40	.42	.44
	.30	.43	.44	.45	.46	.47	.49	.51	.52	.55	.57	.43	.44	.45	.46	.47	.49	.51	.52	.55	.57
	.40	.54	.55	.56	.57	.58	.60	.62	.64	.67	.70	.54	.55	.56	.57	.58	.60	.62	.64	.67	.70
	.50	.66	.66	.68	.69	.71	.73	.75	.77	.80	.84	.66	.66	.68	.69	.71	.73	.75	.77	.80	.84
	.60	.79	.80	.82	.83	.85	.88	.90	.93	.96	1.00	.79	.80	.82	.83	.85	.88	.90	.93	.96	1.00
	.70	.97	.98	1.00	1.01	1.03	1.05	1.08	1.11	1.15	1.19	.97	.98	1.00	1.01	1.03	1.05	1.08	1.11	1.15	1.19
	.80	1.23	1.24	1.26	1.27	1.29	1.31	1.34	1.38	1.42	1.46	1.23	1.24	1.26	1.27	1.29	1.31	1.34	1.38	1.42	1.46
	.90	1.69	1.70	1.71	1.72	1.73	1.73	1.73	1.73	1.74	1.74	1.64	1.65	1.66	1.67	1.68	1.68	1.68	1.69	1.70	1.70
\uparrow $\frac{1-x/c}{E}$ (back of hinge) \downarrow	1.00	4.79	3.33	2.79	2.44	2.22	2.08	1.97	1.90	1.86	1.84	4.55	3.15	2.63	2.32	2.14	1.98	1.89	1.83	1.78	1.73
	.90	4.84	3.36	2.83	2.49	2.26	2.09	1.98	1.90	1.83	1.79	4.60	3.19	2.69	2.36	2.14	1.99	1.88	1.80	1.73	1.68
	.80	4.65	3.29	2.74	2.40	2.16	1.99	1.87	1.78	1.70	1.63	4.49	3.18	2.65	2.32	2.09	1.92	1.81	1.72	1.64	1.58
	.70	4.32	3.06	2.51	2.21	1.99	1.84	1.72	1.61	1.54	1.48	4.27	3.02	2.48	2.19	1.97	1.82	1.70	1.59	1.52	1.46
	.60	3.94	2.77	2.27	2.00	1.80	1.65	1.54	1.45	1.38	1.32	4.02	2.83	2.32	2.04	1.83	1.69	1.57	1.48	1.41	1.35
	.50	3.51	2.46	2.03	1.77	1.59	1.46	1.36	1.28	1.21	1.16	3.71	2.60	2.14	1.87	1.68	1.54	1.43	1.35	1.28	1.22
	.40	3.05	2.15	1.77	1.54	1.37	1.26	1.17	1.10	1.04	.99	3.35	2.36	1.94	1.69	1.51	1.38	1.29	1.21	1.15	1.09
	.30	2.60	1.83	1.51	1.30	1.16	1.06	.98	.92	.88	.84	2.95	2.08	1.71	1.48	1.32	1.21	1.12	1.05	1.00	.95
	.20	2.13	1.50	1.23	1.06	.95	.87	.81	.76	.72	.68	2.68	1.88	1.54	1.33	1.19	1.09	1.01	.95	.90	.85
	.10	1.54	1.08	.88	.77	.69	.63	.59	.55	.52	.49	1.91	1.34	1.08	.95	.86	.79	.73	.68	.64	.61
	.05	1.29	.78	.64	.55	.50	.45	.42	.39	.37	.35	1.63	.98	.81	.70	.63	.57	.53	.49	.47	.44
0	0	0	0	0	0	0	0	0	0	0	0	0	0	0	0	0	0	0	0	0	

TABLE IV
VALUES OF G

$E \backslash \delta$ (deg.)	5, 10, 15	20	30	40	50	60
(a) PLAIN FLAPS						
0.05	-0.474	-0.476	-0.477	-0.478	-0.479	-0.479
.10	-.448	-.451	-.453	-.455	-.456	-.456
.15	-.423	-.428	-.431	-.434	-.435	-.436
.20	-.397	-.404	-.408	-.411	-.414	-.415
.25	-.372	-.380	-.387	-.392	-.395	-.396
.30	-.347	-.357	-.366	-.372	-.375	-.377
.35	-.320	-.334	-.346	-.352	-.357	-.360
.40	-.294	-.311	-.325	-.332	-.339	-.342
.45	-.268	-.288	-.304			
.50	-.242	-.265	-.283			
.55	-.215	-.242				
.60	-.189	-.220				
.65	-.163					
.70	-.136					
(b) SPLIT FLAPS						
0.05		-0.476	-0.477	-0.478	-0.479	-0.479
.10		-.452	-.454	-.455	-.456	-.456
.15		-.430	-.432	-.434	-.435	-.436
.20		-.407	-.409	-.411	-.414	-.415
.25		-.385	-.388	-.392	-.395	-.396
.30		-.363	-.367	-.372	-.375	-.377
.35		-.342	-.347	-.352	-.357	-.360
.40		-.320	-.327	-.333	-.339	-.342
.45		-.299	-.307			
.50		-.278	-.287			

TABLE V
VALUES OF τ_n

$E \backslash \delta$ (deg.)	10	20	30	40	50	60
(a) PLAIN FLAPS						
0	0	0	0	0	0	0
.05	.00	-.02	-.05	-.09	-.14	-.21
.10	-.01	-.03	-.07	-.14	-.23	-.34
.15	-.01	-.04	-.09	-.18	-.30	-.47
.20	-.01	-.05	-.11	-.23	-.38	-.59
.25	-.01	-.06	-.14	-.27	-.46	-.72
.30	-.02	-.07	-.16	-.32	-.54	-.85
.35	-.02	-.08	-.19	-.37	-.63	-.98
.40	-.02	-.09	-.21	-.42	-.71	-1.11
.45	-.03	-.11	-.25			
.50	-.03	-.12	-.28			
.55	-.04	-.14				
.60	-.05	-.17				
.65	-.06					
.70	-.07					
(b) SPLIT FLAPS						
0		0	0	0	0	0
.05		-.02	-.05	-.09	-.14	-.21
.10		-.03	-.07	-.14	-.23	-.34
.15		-.04	-.10	-.18	-.30	-.47
.20		-.05	-.12	-.23	-.38	-.59
.25		-.06	-.15	-.27	-.46	-.72
.30		-.07	-.17	-.32	-.54	-.85
.35		-.08	-.20	-.37	-.63	-.98
.40		-.10	-.23	-.42	-.71	-1.11
.45		-.11	-.26			
.50		-.13	-.29			

TABLE VI
VALUES OF τ_m

$E \backslash \delta$ (deg.)	10	20	30	40	50	60
(a) PLAIN FLAPS						
0	1.00	1.00	1.00	1.00	1.00	1.00
.05	1.00	1.01	1.03	1.06	1.10	1.15
.10	1.00	1.02	1.05	1.09	1.15	1.22
.15	1.01	1.02	1.06	1.11	1.18	1.28
.20	1.01	1.03	1.06	1.12	1.21	1.32
.25	1.01	1.03	1.07	1.14	1.23	1.36
.30	1.01	1.03	1.07	1.14	1.24	1.38
.35	1.01	1.03	1.07	1.15	1.25	1.39
.40	1.01	1.03	1.08	1.15	1.25	1.39
.45	1.01	1.03	1.07			
.50	1.01	1.03	1.07			
.55	1.01	1.03				
.60	1.01	1.03				
.65	1.01					
.70	1.00					
(b) SPLIT FLAPS						
0		1.00	1.00	1.00	1.00	1.00
.05		1.01	1.03	1.06	1.10	1.15
.10		1.02	1.05	1.09	1.15	1.22
.15		1.02	1.06	1.11	1.18	1.28
.20		1.03	1.07	1.12	1.21	1.32
.25		1.03	1.07	1.14	1.23	1.36
.30		1.03	1.08	1.14	1.24	1.38
.35		1.03	1.08	1.15	1.25	1.39
.40		1.03	1.08	1.15	1.25	1.39
.45		1.03	1.08			
.50		1.03	1.07			

TABLE VII
NORMAL-FORCE PARAMETER γ_{bs}

$E \backslash \delta$ (deg.)	5, 10, 15	20	30	40	50	60
(a) PLAIN FLAPS						
0.05	2.81	2.97	3.11	3.36	3.47	3.52
.10	2.04	2.15	2.25	2.43	2.51	2.55
.15	1.68	1.78	1.87	2.02	2.08	2.12
.20	1.48	1.56	1.64	1.77	1.82	1.85
.25	1.34	1.41	1.48	1.60	1.64	1.67
.30	1.24	1.30	1.36	1.48	1.52	1.55
.35	1.16	1.22	1.28	1.39	1.43	1.45
.40	1.10	1.16	1.21	1.31	1.35	1.37
.45	1.04	1.10	1.16			
.50	1.00	1.06	1.11			
.55	.97	1.02				
.60	.94	.99				
.65	.91					
.70	.88					
(b) SPLIT FLAPS						
0.05		3.19	3.29	3.36	3.47	3.52
.10		2.31	2.38	2.43	2.51	2.55
.15		1.91	1.97	2.02	2.08	2.12
.20		1.68	1.73	1.77	1.82	1.85
.25		1.52	1.57	1.60	1.64	1.67
.30		1.41	1.45	1.48	1.52	1.55
.35		1.32	1.36	1.39	1.43	1.45
.40		1.25	1.28	1.31	1.35	1.37
.45		1.19	1.22			
.50		1.14	1.17			

TABLE VIII
HINGE-MOMENT PARAMETER $\eta_{b\delta}$

δ (deg.) <i>E</i>	5, 10, 15	20	30	40	50	60
(a) PLAIN FLAPS						
0.05	−0.86	−1.23	−1.36	−1.48	−1.59	−1.63
.10	−.61	−.81	−.96	−1.04	−1.12	−1.16
.15	−.50	−.66	−.79	−.86	−.91	−.95
.20	−.43	−.57	−.68	−.75	−.80	−.83
.25	−.39	−.52	−.61	−.67	−.72	−.74
.30	−.36	−.47	−.57	−.62	−.66	−.68
.35	−.33	−.44	−.53	−.57	−.62	−.64
.40	−.32	−.42	−.49	−.54	−.58	−.60
.45	−.30	−.40	−.47			
.50	−.29	−.38	−.45			
.55	−.28	−.36				
.60	−.26	−.35				
.65	−.25					
.70	−.24					
(b) SPLIT FLAPS						
0.05		−1.27	−1.38	−1.48	−1.59	−1.63
.10		−.91	−.99	−1.04	−1.12	−1.16
.15		−.75	−.81	−.86	−.91	−.95
.20		−.64	−.70	−.75	−.80	−.83
.25		−.58	−.63	−.67	−.72	−.74
.30		−.53	−.58	−.62	−.66	−.68
.35		−.50	−.54	−.57	−.62	−.64
.40		−.47	−.51	−.54	−.58	−.60
.45		−.44	−.48			
.50		−.42	−.46			

TABLE IX
FLAP NORMAL-FORCE PARAMETERS

<i>E</i>	γ_a or $\gamma_{a\delta}$	γ_{be} Class 1	γ_{be} Class 2	γ_{bm} Class 1	$\gamma_{a.c.}$
0	0	0	0	0	0
.05	.03	−.13	.02	.09	−4.40
.10	.06	−.25	.05	.17	−4.95
.15	.09	−.34	.07	.24	−5.05
.20	.12	−.40	.09	.32	−4.95
.25	.15	−.43	.12	.38	−4.78
.30	.18	−.42	.14	.45	−4.52
.35	.21	−.37	.17	.51	−4.24
.40	.24	−.28	.20	.58	−3.93
.45	.28	−.16	.24	.63	−3.61
.50	.31	−.01	.28	.69	−3.29
.55	.35	.14	.32	.74	−2.95
.60	.39	.30	.38	.79	−2.62
.65	.43	.45	.42	.84	−2.27
.70	.47	.60	.47	.89	−1.93

TABLE X.—FLAP HINGE-MOMENT PARAMETERS

<i>E</i>	η_a or $\eta_{a\delta}$	η_{be} Class 1	η_{be} Class 2	η_{bm} Class 1	$\eta_{a.c.}$
0	0	0	0	0	0
.05	−.01	.04	−.01	−.03	1.95
.10	−.02	.09	−.02	−.06	2.22
.15	−.03	.13	−.02	−.08	2.33
.20	−.04	.16	−.03	−.11	2.37
.25	−.05	.18	−.04	−.13	2.39
.30	−.06	.19	−.05	−.15	2.36
.35	−.07	.19	−.06	−.18	2.31
.40	−.08	.19	−.06	−.20	2.25
.45	−.09	.17	−.07	−.22	2.17
.50	−.10	.14	−.08	−.24	2.09
.55	−.11	.11	−.09	−.26	2.00
.60	−.13	.08	−.11	−.28	1.91
.65	−.14	.04	−.12	−.30	1.81
.70	−.15	.00	−.13	−.32	1.71

REPORT No. 635

THEORETICAL STABILITY AND CONTROL CHARACTERISTICS OF WINGS WITH VARIOUS AMOUNTS OF TAPER AND TWIST

By HENRY A. PEARSON and ROBERT T. JONES

SUMMARY

Stability derivatives have been computed for twisted wings of different plan forms that include variations in both the wing taper and the aspect ratio. Taper ratios of 1.0, 0.50, and 0.25 are considered for each of three aspect ratios: 6, 10, and 16. The specific derivatives for which results are given are the rolling-moment and the yawing-moment derivatives with respect to (a) rolling velocity, (b) yawing velocity, and (c) angle of sideslip. These results are given in such a form that the effect of any initial symmetrical wing twist (such as may be produced by flaps) on the derivatives may easily be taken into account.

In addition to the stability derivatives, results are included for determining the theoretical rolling moment due to aileron deflection and a series of influence lines is given by which the loading across the span may be determined for any angle-of-attack distribution that may occur on the wing plan forms considered. The report also includes incidental references to the application of the results.

INTRODUCTION

Although a formal theory for the dynamics of airplane motions has been available for many years, airplane designers have not been in a position to utilize this theory to its fullest advantage on account of lack of knowledge of the basic physical quantities involved. It is true that the physical quantities, or stability derivatives, have been determined by test or calculation in a number of instances, but there exists no systematic series or correlation of tests sufficient to guide the designer in the prediction of these factors.

As is well known, the calculations involved in aerodynamic wing theory have been developed and refined to such an extent that it is possible to predict quite accurately the air moments and forces on the isolated wing at a fixed speed and incidence. Since several of the airplane lateral-stability derivatives depend almost entirely on the aerodynamic characteristics of the wing and since it would be desirable in any case to know the separate effects of variation of wing form on stability, it was thought worth while to extend the calculations to the determination of the moments developed by the wings when the airplane is disturbed from steady flight.

This report gives theoretical stability derivatives for a variety of wing shapes including nine different plan forms and covering, in most cases, an arbitrary distribution of twist.

Past work on the stability characteristics of wings has, except in isolated cases, been confined to analysis by the "strip method," wherein the effects of aerodynamic induction were neglected. The main effects of the induction are included in the present computations, although the secondary influence of distortion or curvature of the wake is neglected.

DEFINITIONS

The axes used in specifying moments, angular velocities, etc., are fixed in the wing and therefore move relatively to the air and to the earth. The X axis passes through the wing aerodynamic center in the plane of symmetry and is so chosen as to point directly into the line of the relative wind when the wing is moving steadily. Otherwise the axes form an orthogonal system as shown in the back cover of the report.

The derivatives that may be obtained enable an estimate to be made of the variation of both rolling moment and yawing moment with (1) rolling velocity, (2) yawing velocity, and (3) sideslip angle. These factors, designated by C_{l_p} , C_{n_r} , etc., are to be used in the following general formulas to determine the wing rolling and yawing moment in combined rolling, yawing, and sideslipping motion:

$$\frac{L}{qSb} = C_{l_p} \left(\frac{pb}{2V} \right) + C_{l_r} \left(\frac{rb}{2V} \right) + C_{l_\beta} \beta \quad (1)$$

$$\frac{N}{qSb} = C_{n_p} \left(\frac{pb}{2V} \right) + C_{n_r} \left(\frac{rb}{2V} \right) + C_{n_\beta} \beta \quad (2)$$

Subscripts p and r are used to designate the partial derivatives of the well-known wing rolling-moment and yawing-moment coefficients, C_l and C_n , with respect to instantaneous rolling and yawing angular velocities (expressed as helix angles) and β is used to designate the partial derivatives of these coefficients with respect to instantaneous sideslip angles. In this manner the notation is considerably shortened from the usual more cumbersome expressions $\partial C_l / \partial \left(\frac{pb}{2V} \right)$, $\partial C_n / \partial \left(\frac{rb}{2V} \right)$, etc. Expressing the rolling and yawing moments as the sums

of partial linear factors is considered valid for motions that are slow relative to the flight speed V and for small displacements, such as occur in ordinary unstalled maneuvers and such as are considered in the study of stability.

α , angle between the zero-lift direction of the wing section and the air velocity at infinity, radians.

θ , parameter defining spanwise position, $y = -\frac{b}{2} \cos \theta$

(when $\theta=0$, $y = -\frac{b}{2}$; $\theta=\pi$, $y = \frac{b}{2}$).

C_0, C_2, C_4 , coefficients of cosine series expressing wing plan form.

C_l , rolling-moment coefficient.

C_n , yawing-moment coefficient.

p , angular velocity in roll, radians per sec.

r , angular velocity in yaw, radians per sec.

V , flight velocity of wing along X , f. p. s.

β , angle of sideslip, radians.

δ , aileron deflection, radians.

C_{lp} , rate of change of rolling-moment coefficient C_l with the helix angle $pb/2V$.

C_{np} , rate of change of yawing-moment coefficient C_n with the helix angle $pb/2V$.

C_{lr} , rate of change of rolling-moment coefficient C_l with the helix angle $rb/2V$.

C_{nr} , rate of change of yawing-moment coefficient C_n with the helix angle $rb/2V$.

$C_{l\beta}$, rate of change of rolling-moment coefficient C_l with sideslip angle β .

$C_{n\beta}$, rate of change of yawing-moment coefficient C_n with sideslip angle β .

$C_{l\delta}$, rate of change of rolling-moment coefficient C_l with aileron angle δ .

$C_{n\delta}$, rate of change of yawing-moment coefficient C_n with aileron angle δ .

L , total wing rolling moment, ft.-lb.

N , total wing yawing moment, ft.-lb.

q , dynamic pressure, lb. per sq. ft.

S , wing area, sq. ft.

c , chord length at any section, ft.

c_s , chord length at plane of symmetry, ft.

m_0 , section slope of the lift curve, per radian.

b , wing span, ft.

A , wing aspect ratio, b^2/S .

A_n, B_n, C_{2n} , coefficients of Fourier series. (See reference 2.)

c_l , section lift coefficient, section lift/ $qcdy$.

C_L , wing lift coefficient, wing lift/ qS .

c_{d0} , section profile-drag coefficient.

c_{di} , section induced-drag coefficient.

C_{D0} , wing profile-drag coefficient.

λ , taper ratio: i. e., ratio of the fictitious tip chord, obtained by extending the wing leading and trailing edges to the tip, to the root chord.

Γ , dihedral angle, radians.

CONDITIONS RELATING TO THE COMPUTATIONS

PLAN FORMS

The particular chord distributions for which the computations were made are illustrated in figure 1. Table I gives the coefficients of the cosine series used to express these chord distributions in terms of θ . Although the quarter-chord line is shown to be straight, it is permissible to apply the results to wings with similar chord distributions but with the different plan forms that

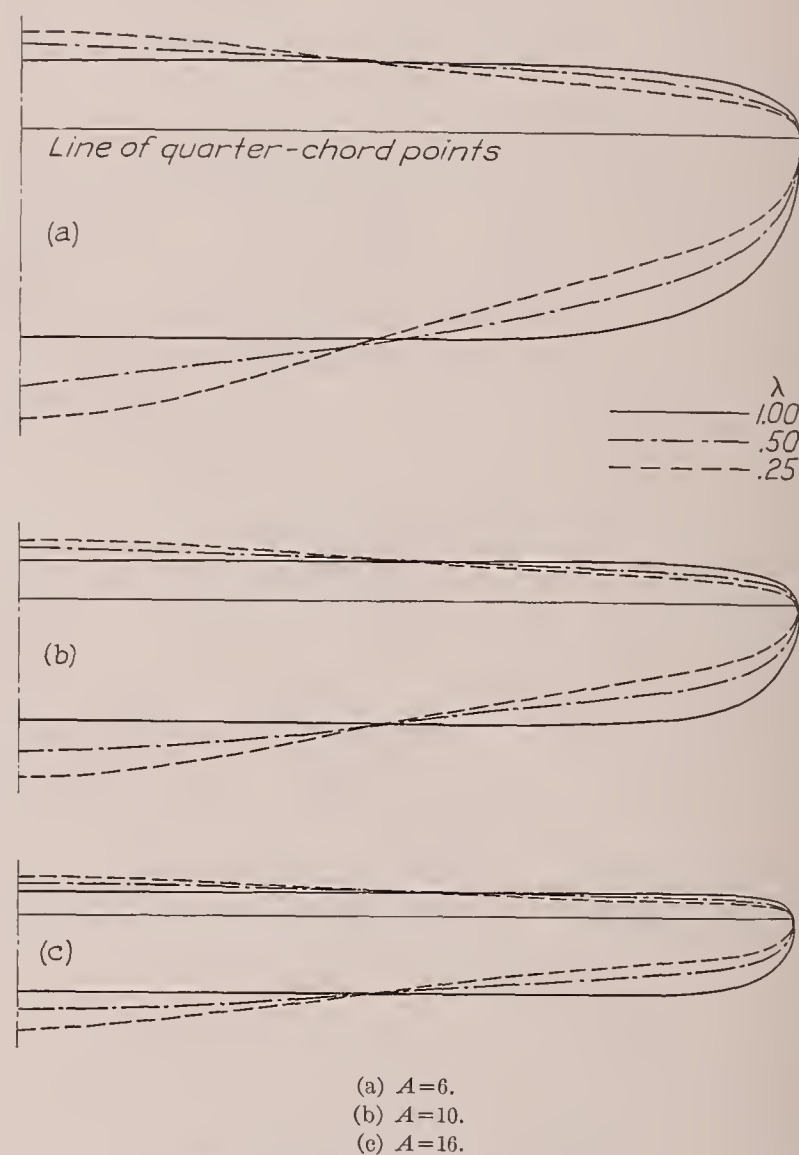


FIGURE 1.—Wing plan forms considered.

may be obtained by small alterations of the shape of the quarter-chord line. The computations were made for three aspect ratios, 6, 10, and 16, and for three taper ratios, 1.00, 0.50, and 0.25. The wing plan forms used only approximate those of linearly tapered wings with rounded tips.

LIFT DISTRIBUTIONS

Rolling, yawing, and sideslipping motions introduce varying resolutions of the relative-wind velocity over the wing. It is evident that these variations can, to a certain extent, be replaced by a fictitious warp or twist of the wing in straight flight. The procedure followed here is to calculate the spanwise lift and drag distributions for the fictitious twist (i. e., that replacing the effect of motion) in the ordinary way, but to incline the

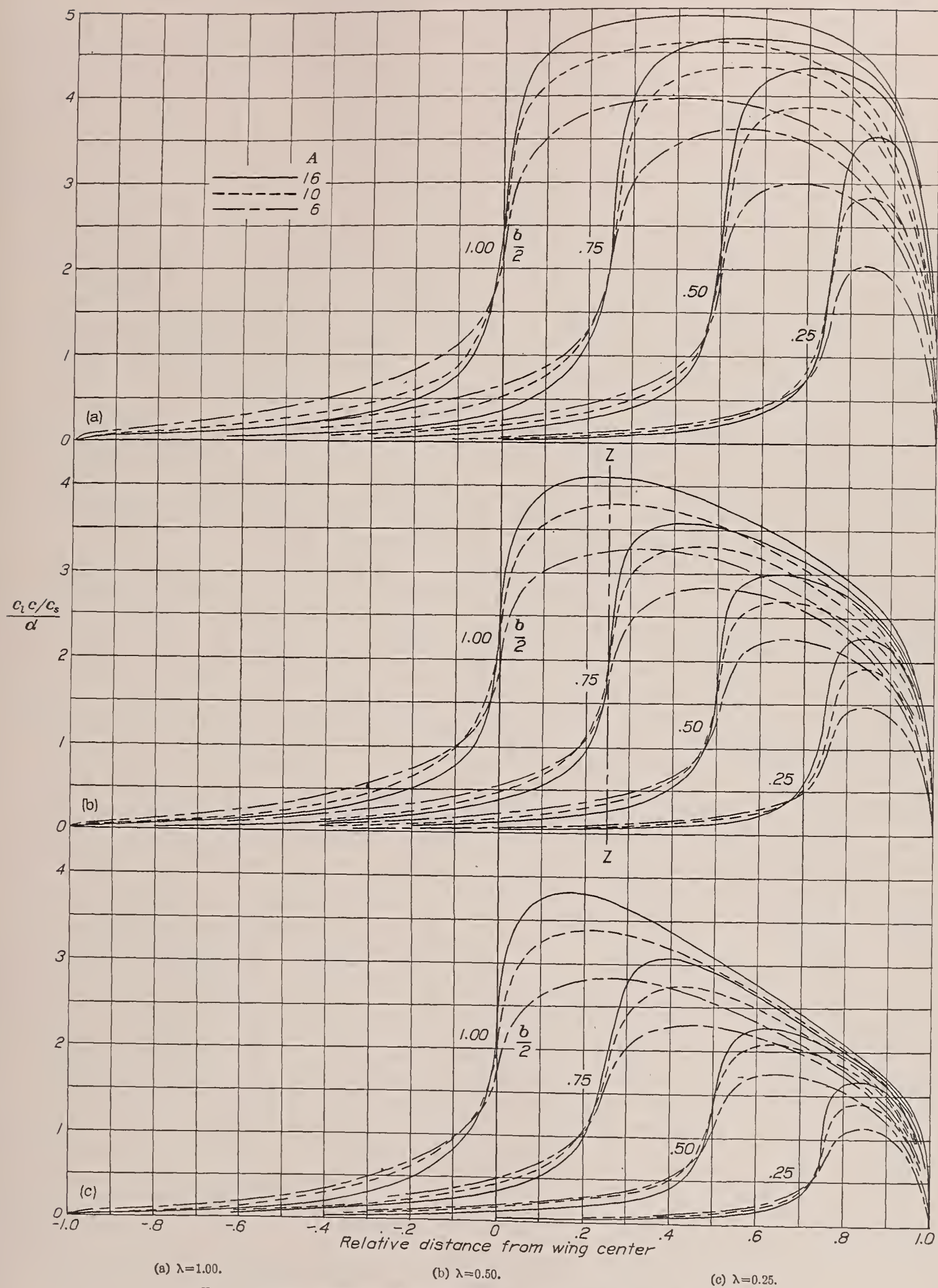


FIGURE 2.—Load distribution due to unit angles of attack extending inward from the tip.

lift and drag components so as to maintain them along the perpendicular and the parallel to the actual local relative-wind velocity. A further refinement of the theory would involve the influence of the curvature of the wing wake. Since the helix angles involved in the motions are small ($pb/2V < 0.1$ and $rb/2V < 0.1$) and since that region of the wake nearest the wing is of predominant influence, this correction may be neglected.

Inasmuch as the various stability derivatives thus depend upon a summation of appropriate components of the lift and the drag loading along the span, it was necessary to determine these distributions for each of the wings with several different angle-of-attack distributions. For this purpose the Lotz method of calculation (references 1 and 2) was used. In order to keep the computations from becoming too lengthy, the chord-distribution function that occurs in this method was expressed by, at most, three terms of a cosine series (as in table I). Although this expression caused the chord distributions of the actual wings (fig. 1) to differ slightly from those for linearly tapered wings with rounded tips, such a procedure was justified because these slight departures in plan form had only a small effect on the characteristics but permitted a large saving in the computations required. Thus only the terms near the diagonal running through equations (19) of reference 2 entered into the computations. As the various derivatives for the elliptical wing could be obtained relatively easily, they were sometimes computed in order to determine the shape of the various derivative curves; it was therefore possible to use fewer points in fairing similar curves for the tapered wings.

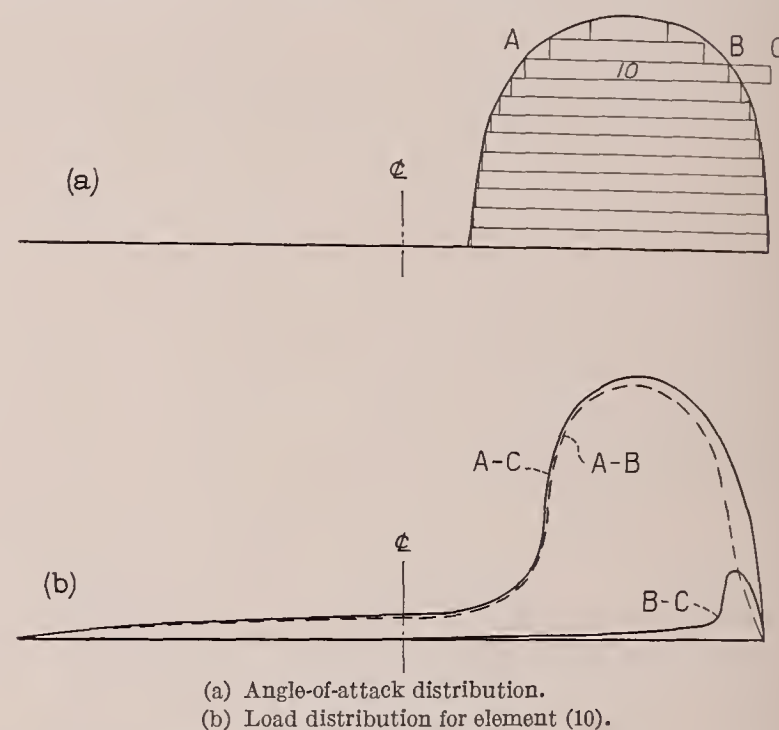
The wing theory was applied in a special way so as to obtain results applicable to any arbitrary twist of the wings. The theoretical span loading being a linear function of the angle-of-attack distribution, the loading due to arbitrary twist can be built up, as will be indicated later, from certain elementary loadings by superposition. The elementary loadings considered were those caused by simple unit jumps of angle of attack occurring at different points of the span.

For each of the nine tapered wings, the first 20 Fourier coefficients determining the load distributions were computed (10 odd and 10 even) for the cases of unit angles of attack extending inward from the wing tip and covering various amounts of the semispan. The rest of the wing was in each case assumed to be at zero angle of attack. The portions thus covered were 0.25, 0.50, 0.75, and 1.00 of the semispan.

In spite of the great number of harmonic terms retained, the conditions near the points of discontinuity in the angle of attack required special treatment. The problem of these end conditions has been solved by Betz and Petersohn (reference 3) and their results were utilized in fairing the load curves through this region. Figure 2 shows the elementary loadings that were calculated, including the modified fairing. The results pertain specifically to the chord distributions illustrated

in figure 1 but interpolation might be made for intermediate plan forms.

It is evident that any angle-of-attack distribution, symmetrical or unsymmetrical, may be built up of elemental steps of the type used in deriving figure 2. Figure 3 illustrates the procedure of finding the resultant load distribution. Thus, the loading contributed by element 10 of figure 3 (a) is obtained by deducting the load curve due to an increment of angle of attack extending between B and C from that due to an increment extending between A and C. Although this process could be continued until the load distribution was completely determined, the same results can be more easily obtained from influence lines, which give the load at a particular spanwise station due to the effect of unit angle-of-attack changes extending inward various



(a) Angle-of-attack distribution.
(b) Load distribution for element (10).
FIGURE 3.—Load components for an element.

amounts from the right wing tip. Such influence lines are given in figures 4, 5, and 6 for eight evenly spaced points across the wing semispan. Each line was obtained by cross-plotting the values of $\frac{c_l c / c_s}{\alpha}$ at the intersections of the loading curves of figure 2 with vertical lines drawn at the particular stations. (For example, the points of intersection of line Z—Z, fig. 2 (b), with the various curves represent the load induced at the 0.25-semispan point by uniform angle-of-attack increments that extend in varying amounts from the wing tip. These intersections identify the corresponding curves of figs. 4 to 6.)

In order to illustrate the use of the influence lines in determining the lift distribution as well as to show the degree of accuracy with which they may be used, the influence lines will be applied to predict the loading for a tapered wing ($\lambda=0.25$, $A=6$) corresponding to the angle-of-attack distribution shown in figure 7 (a). The particular angle-of-attack distribution used is defined by the equation

$$\alpha = \left(\frac{c_s}{c} + \frac{3c_s m_0}{4b \sin \theta} \right) \sin 3\theta \quad (3)$$

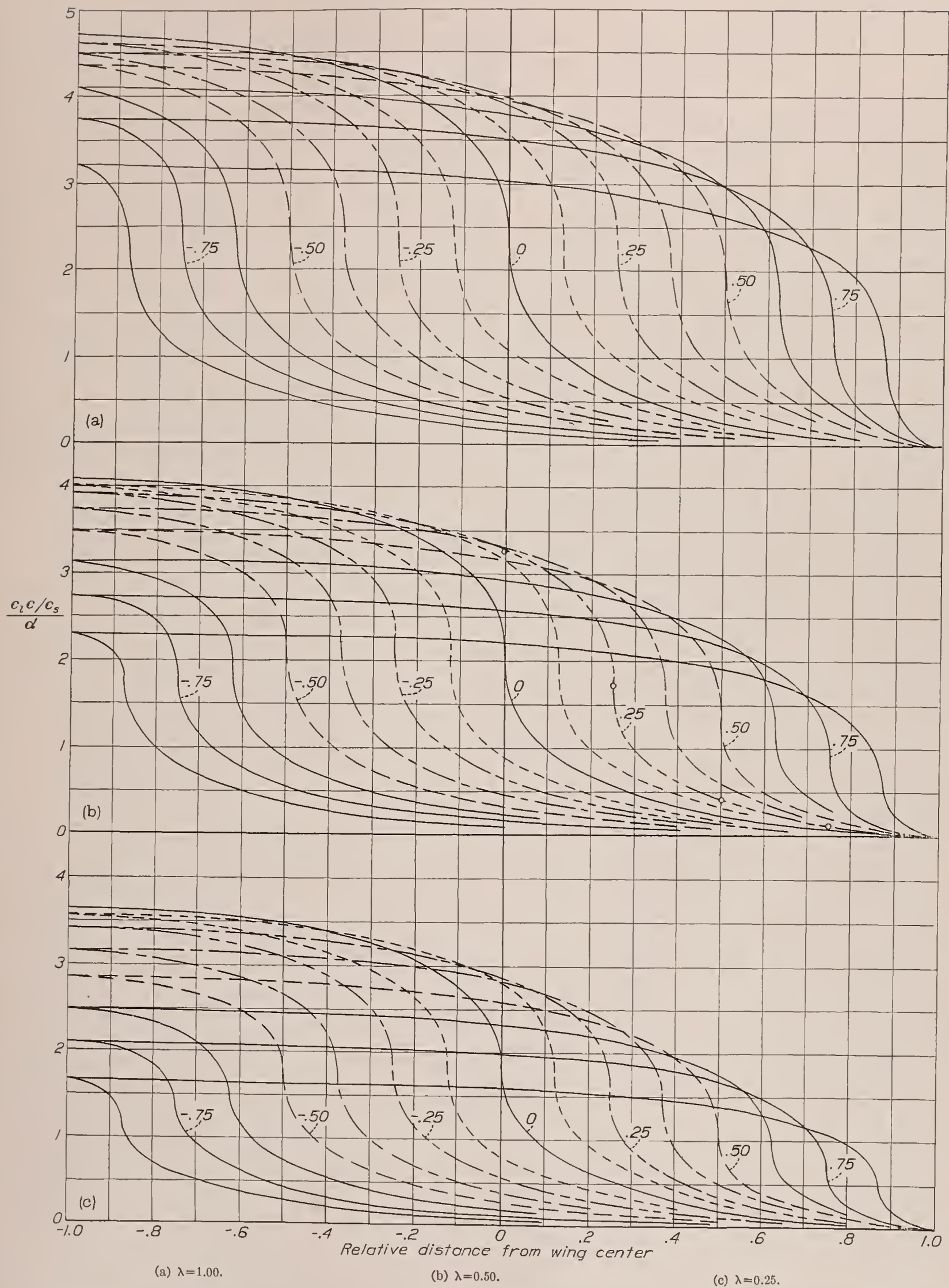


FIGURE 4.—Influence lines for determining the load distribution. $A=6$. The number identifying a given line refers to the particular spanwise station at which the load is to be computed.

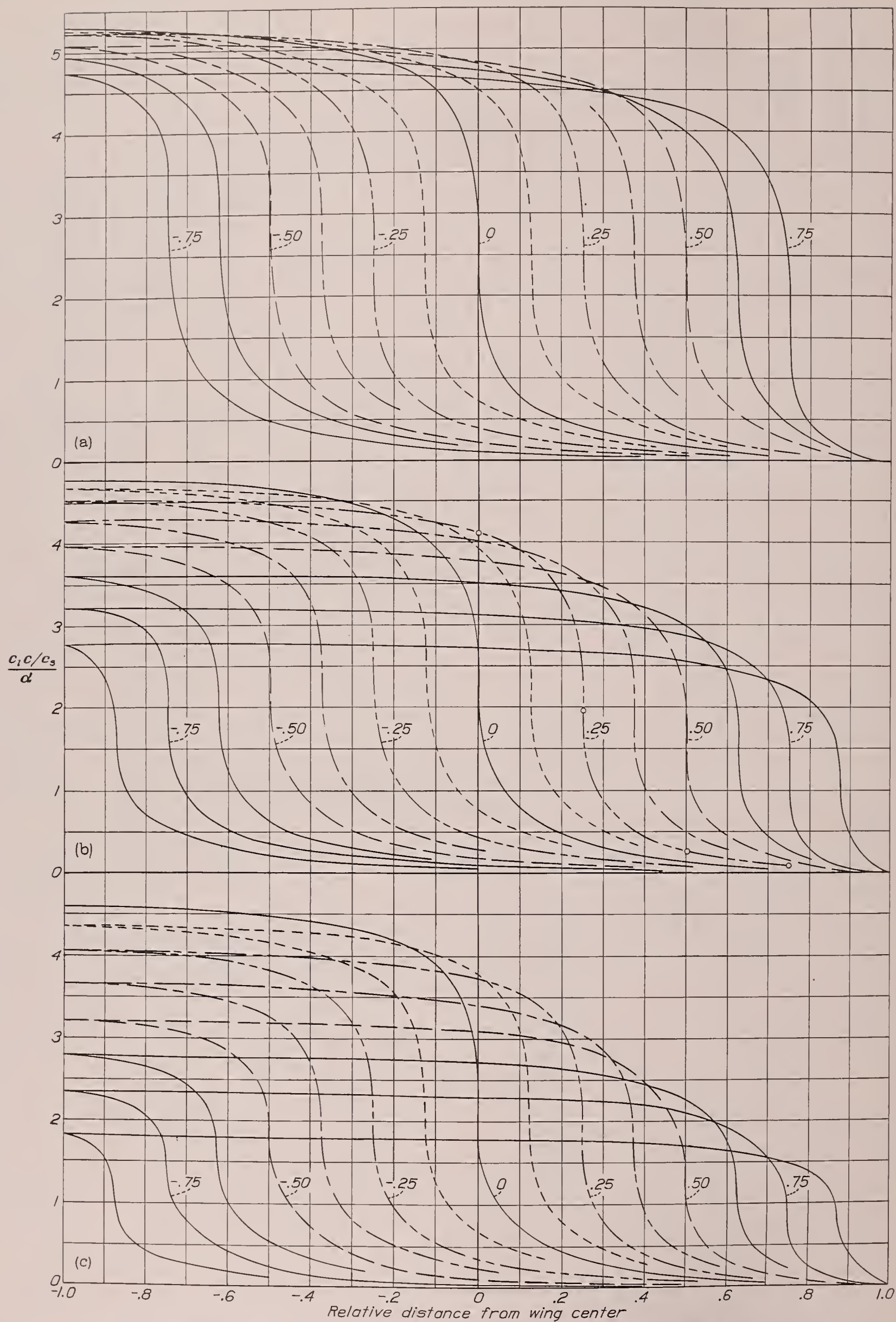


FIGURE 5.—Influence lines for determining the load distribution. $A=10$. The number identifying a given line refers to the particular spanwise station at which the load is to be computed.

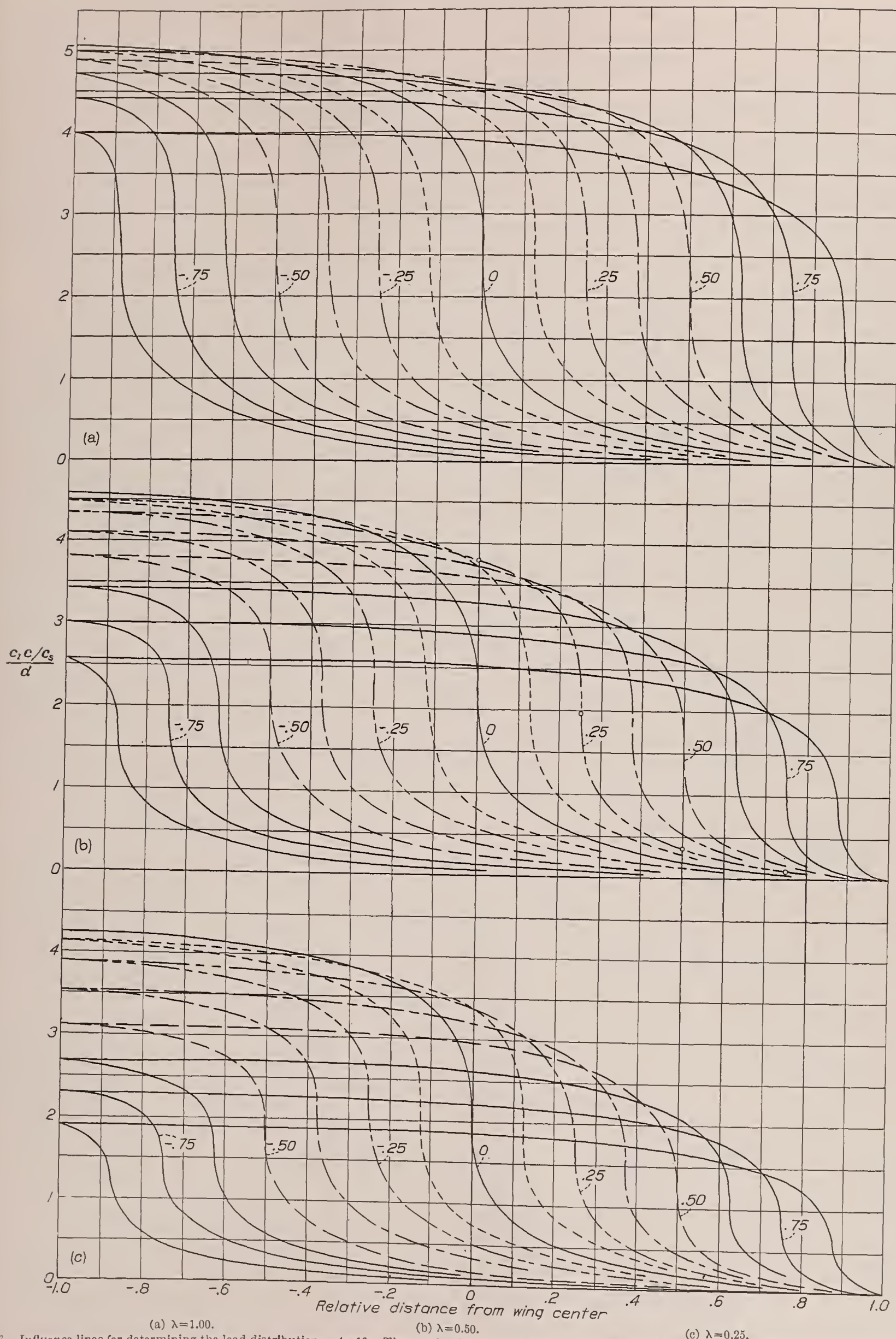


FIGURE 6.—Influence lines for determining the load distribution. $A=16$. The number identifying a given line refers to the particular spanwise station at which the load is to be computed.

This particular distribution is employed because it is possible thereby to compute exactly the corresponding theoretical distribution as a check, without the usual approximations of a Fourier series. The following procedure illustrates the use of the influence lines to determine the lift at the 0.75-semispan point due to this distribution of twist: (1) The influence curve labeled 0.75 in figure 4 (c) is reproduced beneath the angle dis-

tribution for which these elements are drawn, as in figure 7 (c). Because a negative angle would induce a negative load at the point in question, Δ_1 is plotted as a negative value. This process is continued from α_{max-} to α_{max+} and the resulting curve (fig. 7 (c)) is integrated to obtain the total effect at 0.75, which is then plotted in figure 7 (d). The load distribution over the entire span is obtained by repeating the same procedure for a number of points along the span.

With the lift loading thus determined, the induced-drag distribution may be found by a simple operation, namely

$$c_{di} = c_l \left(\alpha - \frac{c_l}{m_0} \right) \quad (4)$$

Figure 7 (d) gives the comparison of the load-distribution curve obtained from the influence lines with that computed directly by the wing theory using equation (3). Although the agreement is not precise, it must be remembered that the solid curve represents a case where no series approximation was necessary; hence it may be concluded that the influence-line method of determining the lift distribution is as accurate as any other for practical purposes.

Aside from other possible applications, the load distribution may be used to determine the stability derivatives for certain cases not specifically covered by the calculations. In the subsequent charts, it is sometimes necessary to stipulate either that the initial angle-of-attack distribution be symmetrical about the wing center line or that the dihedral angle be constant along the span. With a knowledge of the complete load distribution, however, values of the derivatives or their respective moments might be found for particular cases where the charts do not apply.

STABILITY DERIVATIVES

Although it is possible, in the general case, to obtain the stability derivatives from the lift distribution, such a procedure will not usually be necessary because the charts to be presented cover all cases likely to be of interest. The results are presented in such a form that the effect of flaps on the derivatives may easily be determined.

ROLLING MOMENT DUE TO ROLLING

The first derivative considered is the rolling moment due to rolling. In unstalled flight, when the wing rolls about the longitudinal wind axis, a damping or restoring moment is set up. This moment $L_{rolling}$ varies directly with the angular velocity p and is defined by the equation

$$L_{rolling} = C_{lp} \frac{pb}{2V} qSb \quad (5)$$

where the product $C_{lp} \frac{pb}{2V}$ is simply a rolling-moment coefficient that varies linearly with the angular velocity.

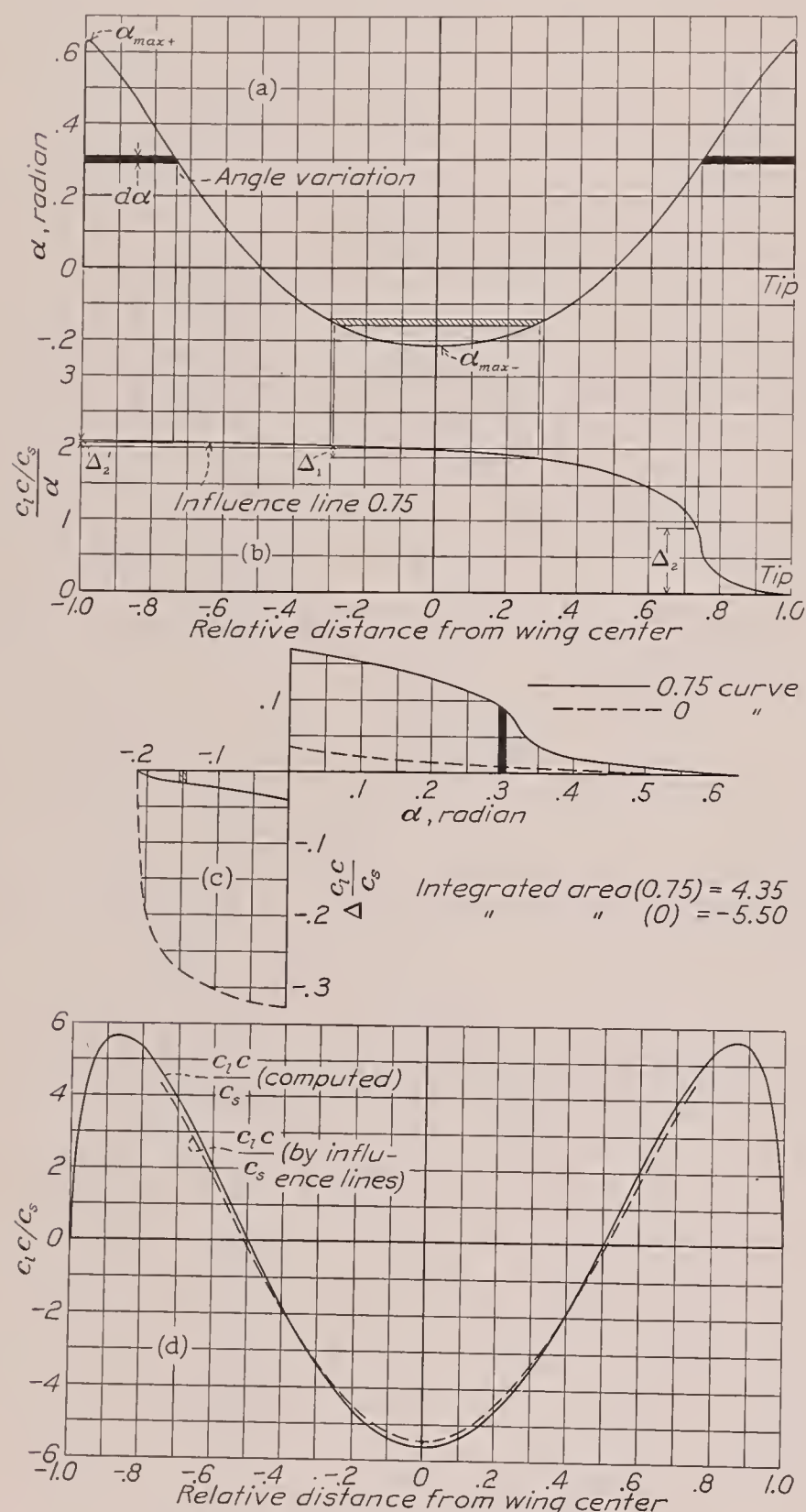


FIGURE 7.—Determination of lift distribution.

tribution to the same spanwise scale; (2) a base line with a range from α_{max-} to α_{max+} is laid out as in figure 7 (c) with the origin of the ordinates at α equal to zero; (3) the effect of any length of elemental angle-of-attack change, $d\alpha$, in figure 7 (a) is found by projecting the length of the element onto figure 7 (b) and plotting the increments (Δ_1) and ($\Delta_2 + \Delta_2'$) at the angles of attack

The computed variation of the derivative C_{l_p} with aspect ratio and taper is given in figure 8. In the usual lift range below the stall, this derivative may be considered to be independent of either initial wing twist or angle of attack and of the wing dihedral. In conventional cases, practically the entire damping moment for the airplane may be attributed to the wings. It can be seen that the moment contributed by a tail surface, geometrically similar to the wing but with only one-

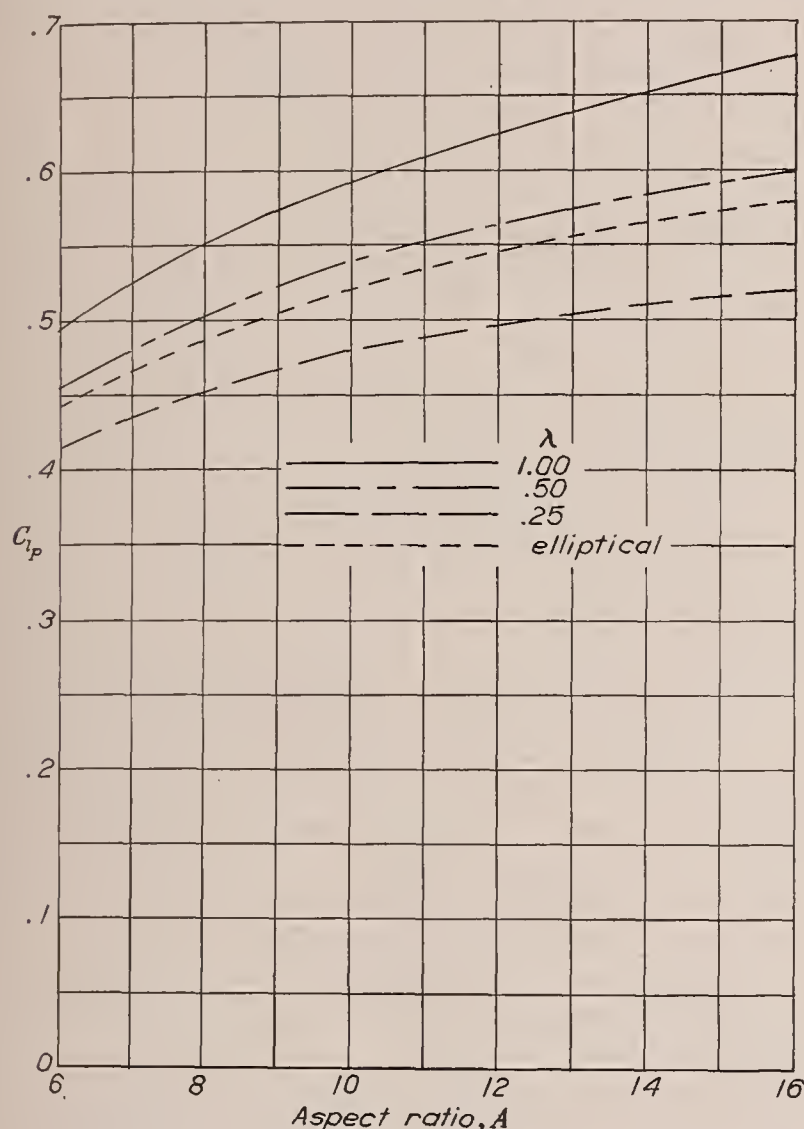


FIGURE 8.—Rolling derivative due to rolling. $L_{rolling} = C_{l_p} \frac{pb}{2V} qSb$

fourth the span, would be $\frac{1}{256}$ of that contributed by the wing, inasmuch as $L_{rolling}$ for a given angular velocity varies as the fourth power of a linear dimension.

Reducing the aspect ratio or increasing the taper tends to reduce the derivative C_{l_p} , as may be seen from the curves given in figure 8. Comparison of the present values of C_{l_p} with similarly derived values given in reference 4 indicates that the effect of rounding the wing tips is to reduce the theoretical restoring moment by about 6 percent for wings of aspect ratio 6.

YAWING MOMENT DUE TO ROLLING

During a rolling motion, the wing experiences a linear antisymmetrical change in angle of attack along the span and, as a result, antisymmetrical loadings are added to those that originally were on the wing. The resulting yawing moment is due to components of the lift as well as to the drag along the span, the lift com-

ponents being the more important. With the specified system of axes, positive rolling produces a negative yawing moment or, for any case, with positive lift coefficients the falling wing tends to advance owing to the predominating influence of the lift vectors.

The yawing moment due to rolling, unlike the rolling moment due to rolling, depends upon both the initial wing twist and the angle of attack. For untwisted wings, however, the yawing moment is zero at zero lift and increases linearly with the wing lift coefficient. For a twisted wing, the yawing moment due to rolling, although varying linearly with the over-all lift coefficient, is not necessarily zero when C_L is zero but may have either a small positive or a small negative value depending upon the initial angle-of-attack distribution. Owing to this circumstance, it is most convenient to express the derivative C_{n_p} as a ratio in terms of unit partial-span angle-of-attack changes.

Figure 9 shows the computed variation of the ratio C_{n_p}/α for unit symmetrical angle-of-attack changes that extend out from the wing center so as to cover various amounts of the wing span. Thus, if it is desired to determine C_{n_p} for an untwisted rectangular wing of aspect ratio 6 at an angle of attack of 0.1 radian, the value 0.195 (for an angle of attack of 1 radian), read from the solid line of figure 9 (a) at the relative distance of 1.0, is multiplied by 0.1 to give a value of C_{n_p} equal to 0.0195. If, now, a half-span flap of constant chord ratio were displaced an amount sufficient to cause an additional change in angle equal to 0.1 radian over the portion with flaps, the new value of C_{n_p} would be

$$(0.1 \times 0.195) + (0.1 \times 0.134) = 0.0329$$

This value of C_{n_p} is then inserted into the equation

$$N_{rolling} = C_{n_p} \frac{pb}{2V} qSb \quad (6)$$

to determine the yawing moment due to a rolling angular velocity.

Although the curves given in figure 9 can be directly used to determine the effect on C_{n_p} of deflecting partial-span flaps of constant flap-chord ratio, they are also readily adapted to the determination of C_{n_p} for a wing with any initial twist provided that the twist distribution is symmetrical about the wing center line. The process is illustrated in the following example where it is desired to find the value of C_{n_p} for a rounded-tip rectangular wing of aspect ratio 6 with the symmetrical angle-of-attack distribution shown in figure 10 (a). The contribution of the element of angle of attack $d\alpha$, shown at the point $\alpha = 0.15$ radian, to the total value of the wing C_{n_p} is equivalent to that caused by a full-span elemental flap minus the contribution of the cross-hatched portions. The contribution of this

element $d\alpha$ is denoted by $\left(\frac{C_{n_p}}{\alpha}\right)d\alpha$ and may be obtained

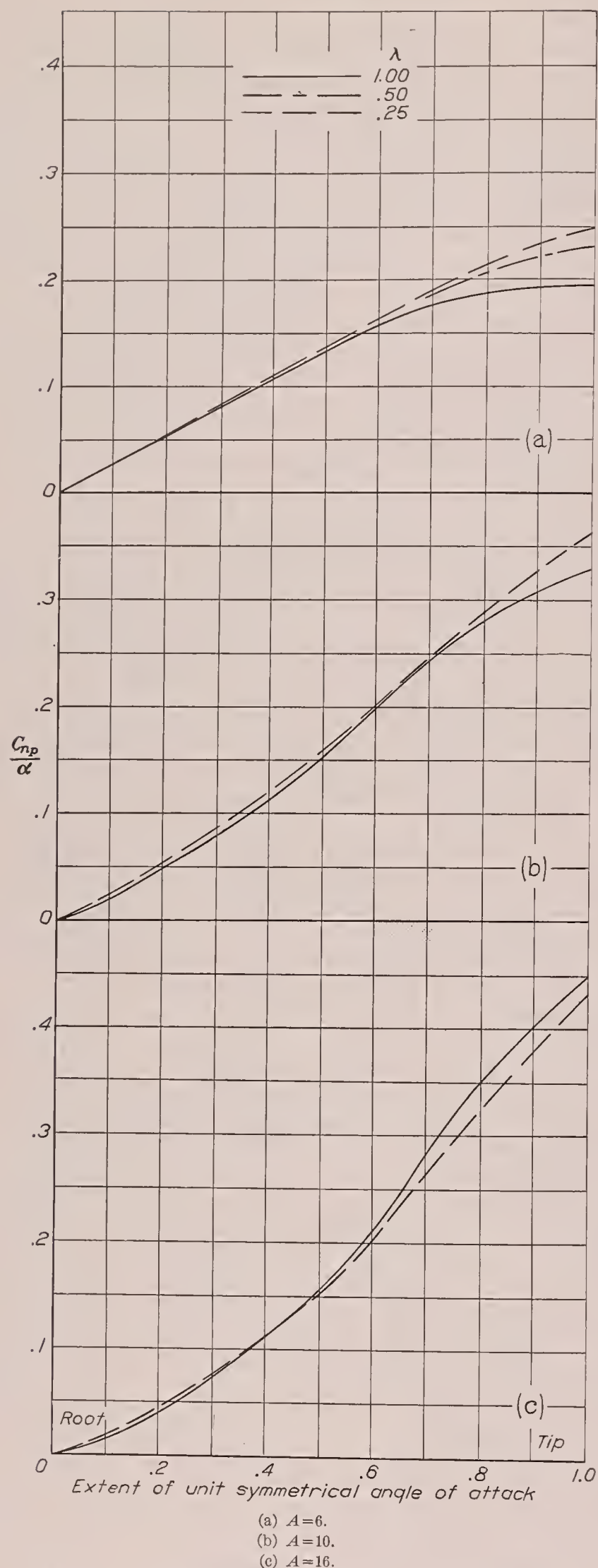


FIGURE 9.—Yawing derivative due to rolling. $N_{rolling} = C_{np} \frac{pb}{2V} qSb$

by projecting the various small flap portions onto the appropriate C_{np}/α curve (taken from fig. 9) as in figure

10 (b), and adding the increments Δ_1 and Δ_2 . The sum of these increments is then plotted in figure 10 (c) at the value of α for which the element is drawn. The value of C_{np} for the complete wing is obtained by performing the integration

$$C_{np} = \int_0^{\alpha_{max} + \left(\frac{C_{np}}{\alpha}\right) d\alpha} \quad (7)$$

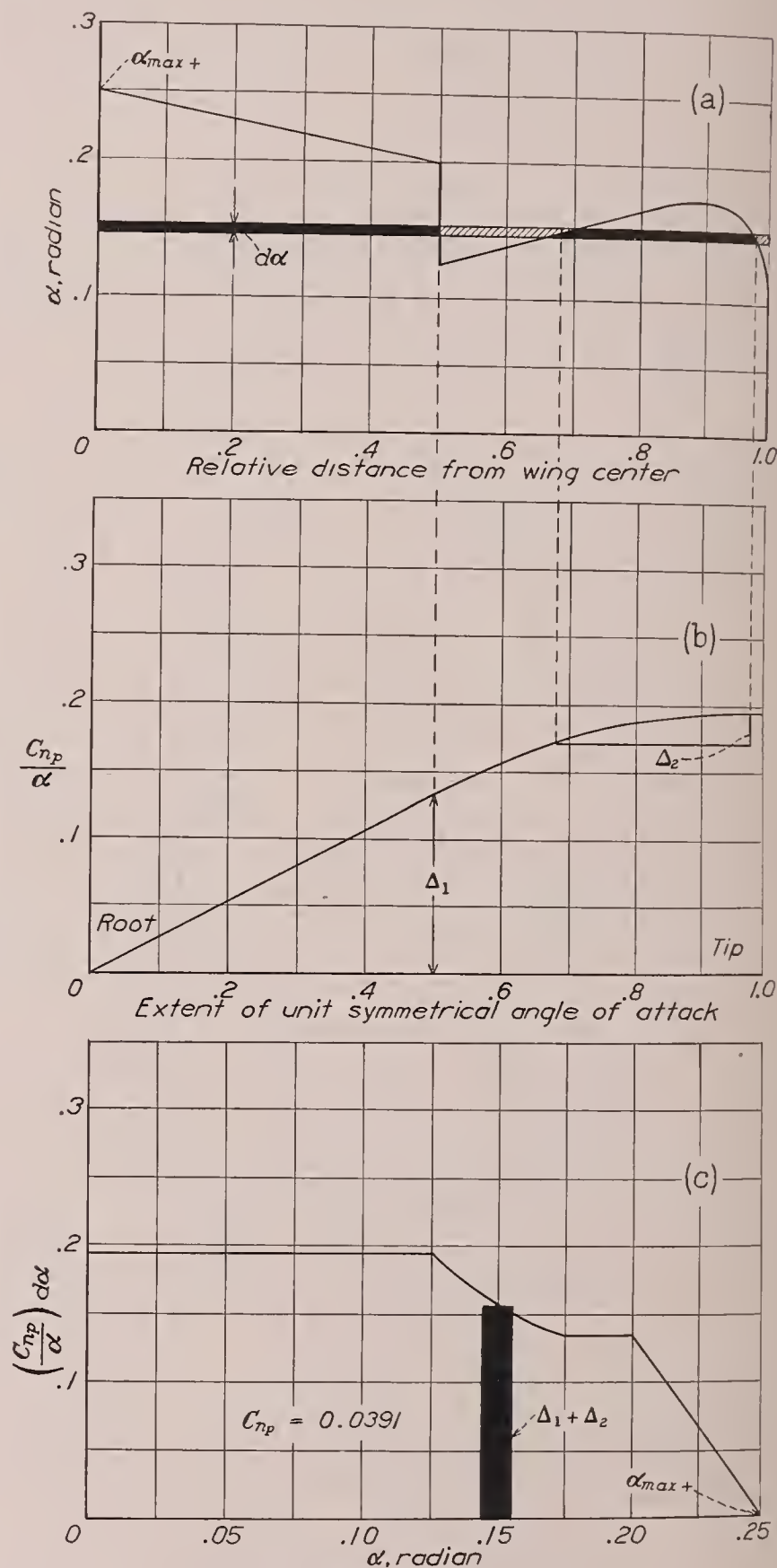


FIGURE 10.—Application of C_{np} curves to an example.

These curves apply to wings with symmetrical twist and it is necessary to consider only half the wing, the factor 2 being included in the curves. The evaluation in the case of figure 10 (c) yields 0.0391.

The curves of figure 9 indicate that, for a given angle-of-attack distribution, there is relatively little change in the value of C_{np} with the taper ratios investigated. Changes in taper ratio did, however, have an appreciable effect on the value of C_{lp} (fig. 8) with the result that the ratio of the yawing to the rolling moment in roll will, in general, increase with increase in taper.

Inasmuch as the inclination of the lift vectors at the outer portions of the span has such a predominating effect on the yawing moment, the most effective means of reducing C_{np} for a given wing lift coefficient is to give the wings washout toward the tips.

The yawing moment due to rolling is, in conventional designs, largely due to the wings. The tail surfaces contribute very little to this moment both because of

approximations in deriving the necessary equations for the determination of the yawing derivatives. When these approximations are used and the velocity along the span is expressed as a variable, the new downwash equation becomes

$$w = \frac{V}{4\pi b} \int_0^\pi \left[\frac{d(c,c)}{d\theta} \left(1 + \frac{rb}{2V} \cos \theta \right) - (c,c) \frac{rb}{2V} \sin \theta \right] d\theta \quad (8)$$

The system of simultaneous equations derived for the approximate solution of this integral equation is

$$\begin{aligned} \Sigma C_{2n} \cos 2n\theta \Sigma A_n \sin n\theta + \frac{c_s m_0}{4b} \Sigma n A_n \sin n\theta \\ + \frac{c_s m_0}{4b} \frac{rb}{4V} \Sigma (A_{n-1} - A_{n+1}) \sin n\theta = \Sigma B_n \sin n\theta = \alpha \sin \theta \quad (9) \end{aligned}$$

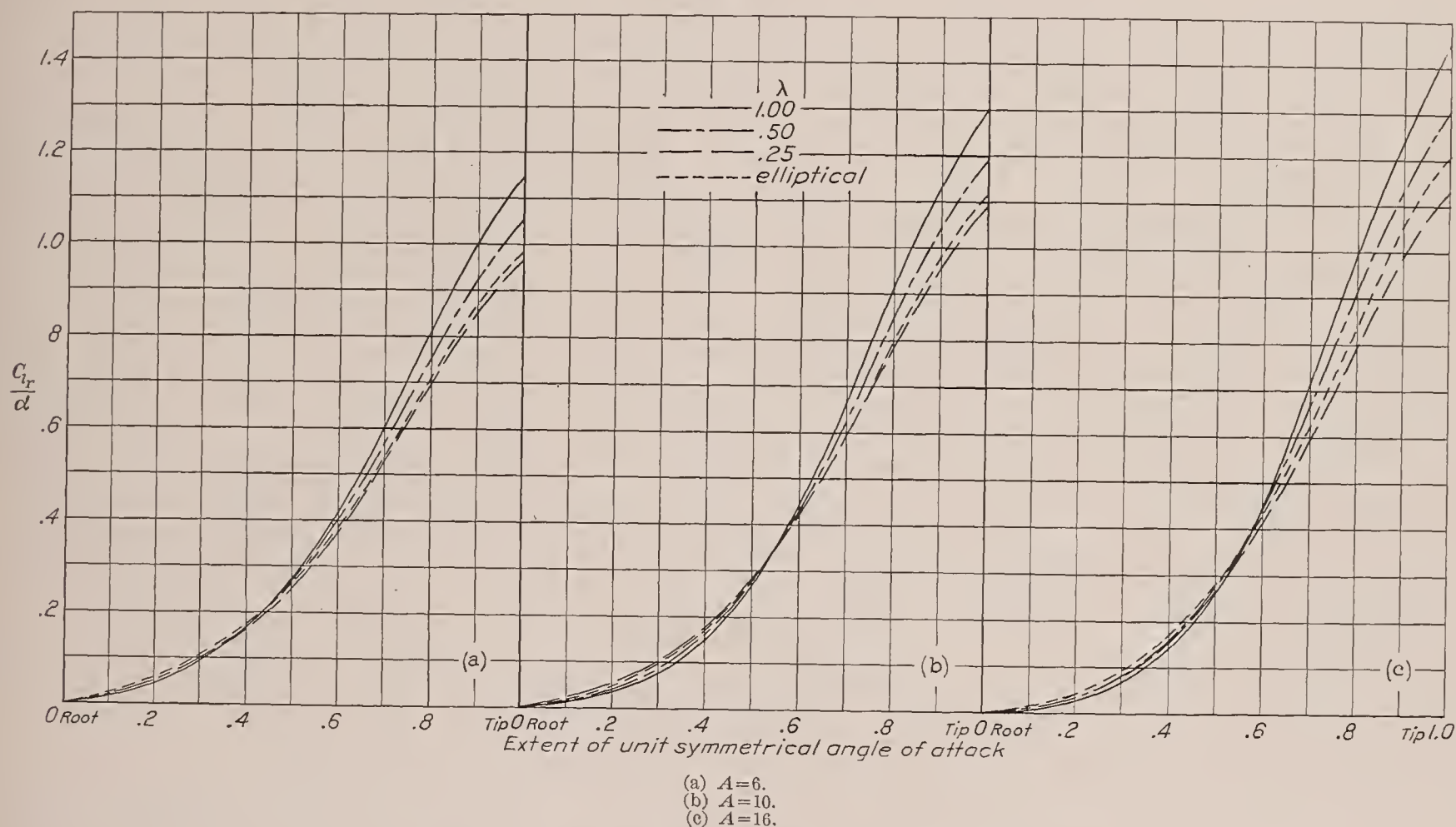


FIGURE 11.—Rolling derivative due to yawing. $L_{yawing} = C_{lr} \frac{rb}{2V} q S b$

their short span and because of the small angles of attack relative to the wing.

ROLLING MOMENT DUE TO YAWING

During a yawing motion, increments of velocity are added along the forward-moving half of the wing and similar increments are deducted along the rearward-moving half. The difference in velocity of the two halves causes a rolling moment which, for an untwisted wing, varies directly with the initial angle of attack as well as with the angular velocity. The velocity increments vary linearly with the distance from the wing center line and are small relative to the flight speed; it is therefore permissible to make certain mathematical

in contrast to the system given by equation (18) of reference 2.

By means of equation (9), Fourier coefficients were computed for the nine tapered wings with two different initial angle-of-attack distributions: (1) a distribution due to a unit angle of attack extending over the whole span, and (2) a unit angle of attack at the wing center covering half the span. In order to obtain the correct fairing of the final curves of figure 11, similar results were computed for elliptical wings with six angle-of-attack distributions covering 0, $\frac{1}{4}$, $\frac{1}{2}$, $\frac{3}{4}$, $\frac{7}{8}$, and all of the wing span.

As was the case with the derivative C_{np} , it is most convenient to give the derivative of rolling moment

due to yawing C_{l_r} as a ratio in terms of a partial-span unit angle of attack. The values of C_{l_r} may be obtained from figure 11 and are to be inserted into the equation

$$L_{yawing} = C_{l_r} \frac{rb}{2V} qSb \quad (10)$$

By the process described in the previous section, values of C_{l_r} may be obtained for wings with any initial twist distribution that is symmetrical about the center line.

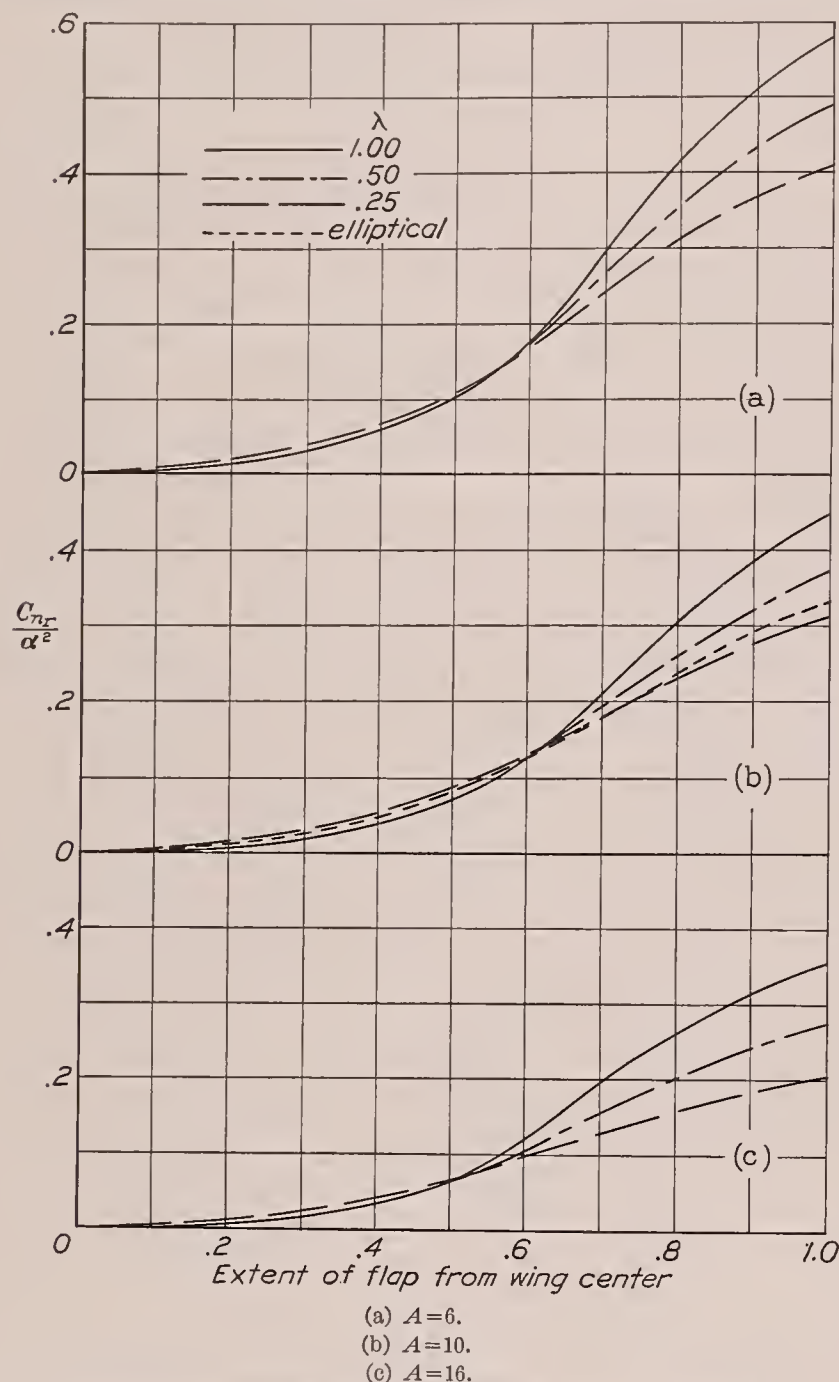


FIGURE 12.—Yawing derivative due to yawing for partial-span flap.

$$N_{yawing} = C_{n_r} \frac{rb}{2V} qSb$$

The curves of figure 11 fall in the order that would be expected for the various taper ratios, i. e., the moment for an untwisted tapered wing would be expected to be less than that for a rectangular wing of the same span and area because the tapered wings have a smaller proportion of the wing area at the tip. On account of the induced velocities along the span, the reduction, for the tapered wings, is not so great as would be obtained by an application of the ordinary strip theory.

The direction of the moment is such that, with the system of axes used, a positive rolling moment generally

results from a positive yawing velocity when the wing is giving positive lift. By the use of considerable washout, such as is obtained with partial-span flaps, it is possible not only to reduce the value of this moment but also to make it slightly negative for low wing lift coefficients.

As was the case with C_{l_p} and C_{n_p} , the value of C_{l_r} for the entire airplane is due almost wholly to the wings because the side area of the airplane contributes relatively little moment as compared with the wings in curvilinear flight.

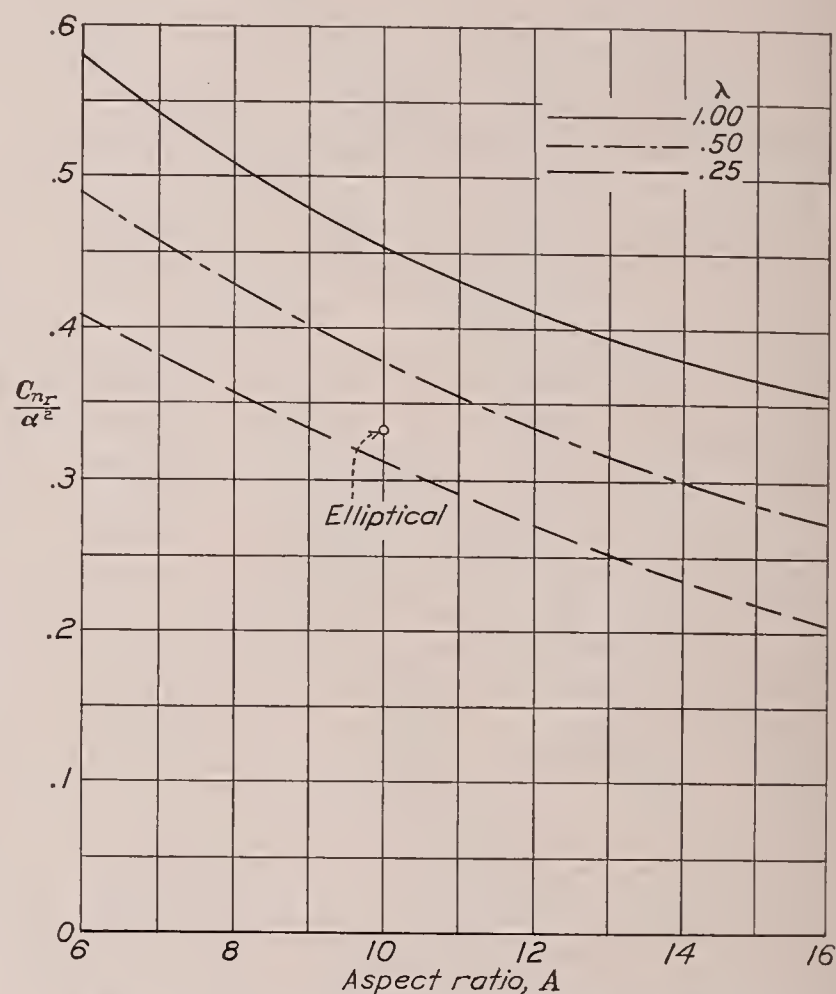


FIGURE 13.—Yawing derivative due to yawing for untwisted wing.

$$N_{yawing} = C_{n_r} \frac{rb}{2V} qSb$$

YAWING MOMENT DUE TO YAWING

A part of the wing yawing moment due to yawing results from the change in the induced-drag distribution that accompanies the change in the lift distribution across the span of a yawing wing. The rest of the yawing moment is due to the difference in the distribution of profile drag resulting from the variation in velocity along the span. Both parts, however, produce damping moments in the unstalled-flight range.

The part of the wing yawing moment due to the induced drag is defined by the equation

$$N_{yawing} = C_{n_r} \frac{rb}{2V} qSb \quad (11)$$

where the derivative C_{n_r} may be obtained from figure 12 for certain types of angle-of-attack distribution. The special distributions for which the derivatives of figure 12 apply are both uniform and symmetrical about the

wing center line. Such distributions occur only when partial-span flaps of constant-chord ratio are deflected, the rest of the span being at zero angle of attack. This limitation in the applicability of these curves as compared with the previous ones is due to the fact that the principle of superposition does not apply in cases where the variation is not linear with α . The computed results may, however, be used to determine the variation of C_{n_r} for the most useful case, namely, that of a wing without twist. For this purpose, the proper values of C_{n_r}/α^2 obtained from figure 13, which is a cross plot of the end points of figure 12, are multiplied by the square of the actual angle of attack.

The part of the yawing moment due to the profile drag can be determined from the easily derived equation

$$\Delta N_{yawing} = q \int_{-\frac{b}{2}}^{\frac{b}{2}} c_{d0} c \left(1 + \frac{2ry}{V} \right) y dy \quad (12)$$

where c_{d0} and c are functions of the distance y along the span. It is possible, by assuming c_{d0} constant and by neglecting terms of the second order, to obtain a coefficient ΔC_{n_r} that may be used with the equation

$$\Delta N_{yawing} = \Delta C_{n_r} \frac{rb}{2V} q S b \quad (13)$$

to compute the part of the yawing moment due to the profile drag. The values of the profile yawing moment, as given by equation (13), are sufficiently accurate for most wings since c_{d0} generally varies only slightly across the span. The variation of the coefficient $\Delta C_{n_r}/C_{D0}$ with taper ratio is given in figure 14.

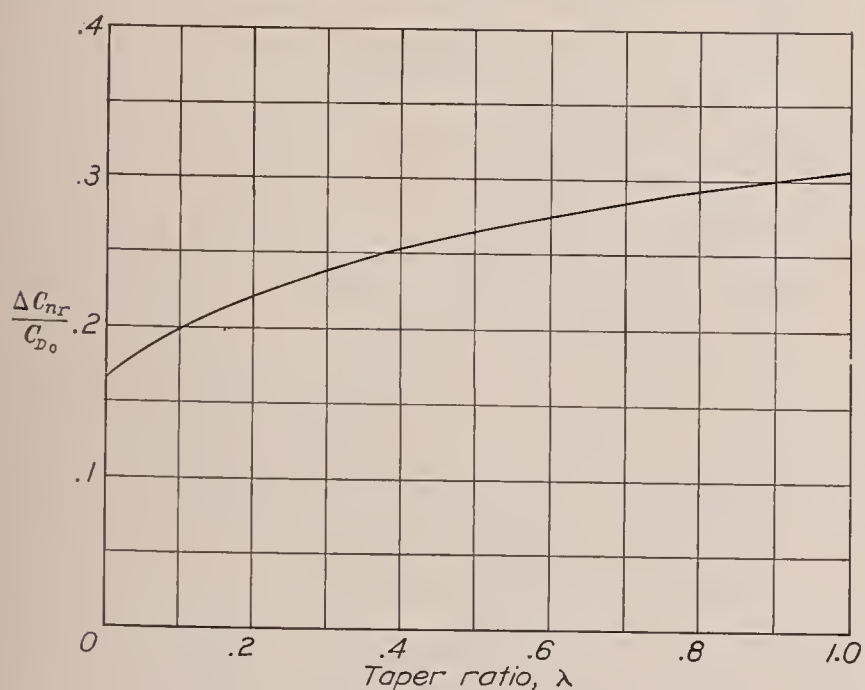


FIGURE 14.—Profile-drag yawing derivative. $\Delta N_{yawing} = \Delta C_{n_r} \frac{rb}{2V} q S b$

The total wing yawing moment due to yawing is the sum of the moments given by equations (11) and (13). At low lift coefficients, the profile drag contributes the greater portion of the wing damping moment in yawing. At moderate or high lift coefficients, however, the part

due to the induced drag exceeds that due to the profile drag. If it is assumed that $\alpha=0.3$ and $C_{D0}=0.01$, then the respective values of C_{n_r} and ΔC_{n_r} would be 0.0522 and 0.0031 for a rectangular wing of aspect ratio 6.

The damping moment contributed by the wings in yawing motion is, in most cases, secondary but is not

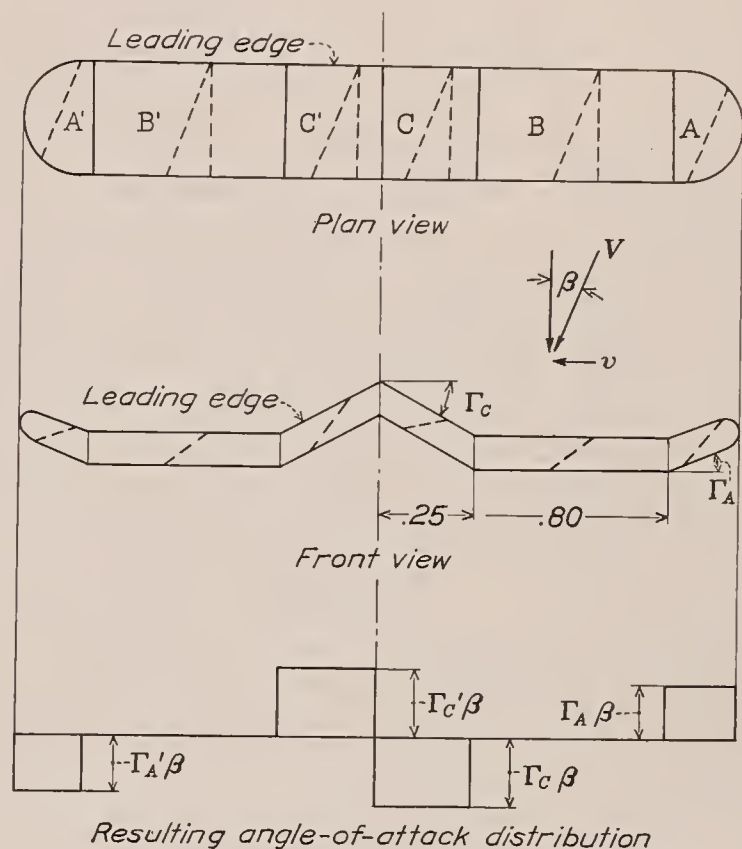


FIGURE 15.—Effect of irregular dihedral on sideslip.

negligible with respect to the damping moment contributed by the fuselage and the vertical tail surfaces. The damping in yawing due to the wings depends upon the angle of attack as well as upon the plan form; therefore the relative amounts contributed by the wings and tail surfaces may vary considerably.

Although it was not possible to give a general chart for determining the damping in yawing for symmetrically twisted wings as was done with the previous derivatives, it can nevertheless be said that the addition of load toward the tips, whether by washin or by an increase in taper ratio, would increase the wing damping moment due to a yawing angular velocity.

ROLLING MOMENT DUE TO SIDESLIP

The manner in which the changes in angle of attack that cause a rolling moment are brought about during a sideslipping motion is shown in figure 15 by a sketch of a wing having positive, negative, and zero dihedral over various portions of the span. For simplicity, the wing is assumed to have no initial twist and the dihedral angles are assumed constant over each of the portions A, B, and C. For small angles of sideslip β , the increase in angle at tip A is, to a first approximation, equal to $\Gamma_A \beta$; whereas, at the opposite tip A', there is an equal decrease of the angle of attack. The portions B—B', having no dihedral, contribute no change in angle of attack when the wing is sideslipping. At the center,

however, owing to the negative angle of dihedral Γ_c , there is an effective decrease in angle of attack over part C equal to $\Gamma_c\beta$ and on C' there is a similar increase in angle. Figure 15 shows the resulting effective angle-of-attack distribution for the particular shape of dihedral assumed.

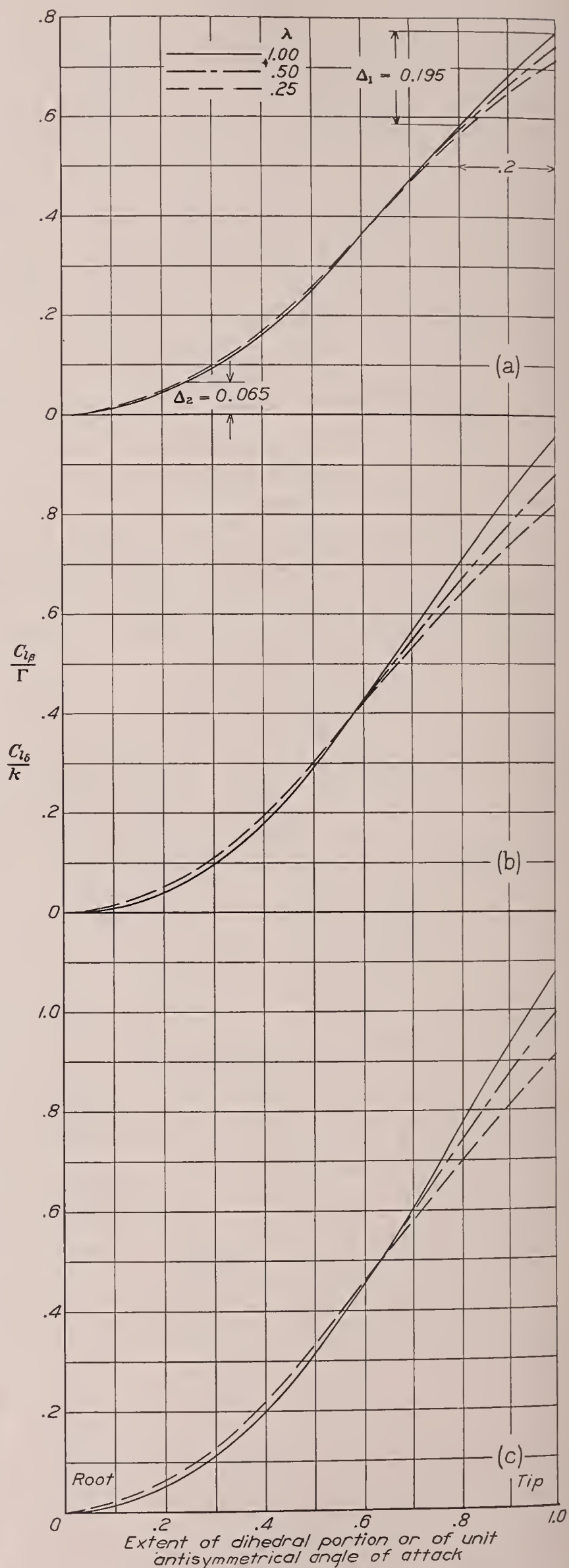
The effect of this distribution is similar to that caused by two pairs of ailerons equally and oppositely deflected with the inner pair opposing the rolling action of those at the tip. Positive areas of dihedral on the advancing wing tend to add load onto that wing. For the system of axes chosen, all areas with positive dihedral produce a negative rolling moment with a positive angle of sideslip. This moment, like the rolling moment due to roll, is independent of the initial wing twist as long as no portion of the wing becomes stalled.

The rolling-moment derivative due to sideslip C_{l_β} may be determined from figure 16, which gives the variation of C_{l_β}/Γ for various unit antisymmetrical angle-of-attack distributions (i. e., symmetrical portions with constant dihedral) that extend out from the wing center and cover various relative amounts of the wing semispan. In the usual case, where the dihedral angle Γ is constant along each semispan, the value of the rolling moment due to a sideslip angle β can be obtained from the equation

$$L_{sideslip} = C_{l_\beta} \beta q S b \quad (14)$$

where the appropriate values of C_{l_β}/Γ , obtained from figure 16 at the relative distance equal to 1.0, are multiplied by the dihedral angle in radians. In more unusual cases as, for example, where only the tips are turned up or where the wing is given a gull shape for any reason, it is still possible to determine a coefficient of rolling moment due to sideslip simply by adding the effects of the various parts in the way previously described. Thus, for the wing shown in figure 15, let $A=6$, $\lambda=1.0$, Γ_A and $\Gamma_c=0.1$ radian and assume that it is desired to find the proper value of C_{l_β} to use in equation (14). The part due to the tip portions A—A' is Δ_1 (from fig. 16 (a)) $\times \Gamma_A = 0.195 \times 0.1 = 0.0195$. The part due to the center portions C—C' is $\Delta_2 \times \Gamma_c = 0.065 \times 0.1 = 0.0065$. The resulting value of C_{l_β} to be used in equation (14) is thus 0.0130. The extension of this method to a curvilinear variation of Γ along the span may be easily made by plotting the values of Γ at each point of the span and using the method given in a previous section for integrating for the total effect.

The results of figure 16 indicate that equivalent angle-of-attack changes caused by unit lengths of dihedral portion near six-tenths of the relative distance from the center are, in general, slightly more effective in producing rolling moment than unit lengths of dihedral at the tips. Such a result is due partly to the fact that the load curves near the tips are rounded and partly to the fact that, for the tapered wings, the larger areas affected by lengths of dihedral near the 0.6 point tend to compensate for the shorter moment arms through which the change in loading acts.



(a) $A=6$. (b) $A=10$. (c) $A=16$.
FIGURE 16.—Rolling derivative due to sideslip with dihedral. $L_{sideslip} = C_{l_\beta} \beta q S b$

Although, during a sideslipping motion, positive dihedral produces a righting moment, a similar though generally smaller effect may also be produced by the addition of vertical area above the longitudinal wind axis. Also, on account of interference effects, the proportion of the airplane rolling moment contributed by the wings may vary considerably with the external appearance of the airplane.

It is usually considered, in practice, that a straight wing will have some dihedral effect, but tests of wings with well-rounded tips (reference 5) do not support this view. In cases of wings with blunt tips or in cases where chords of the sections near the tip do not lie in one plane, some dihedral action is shown.

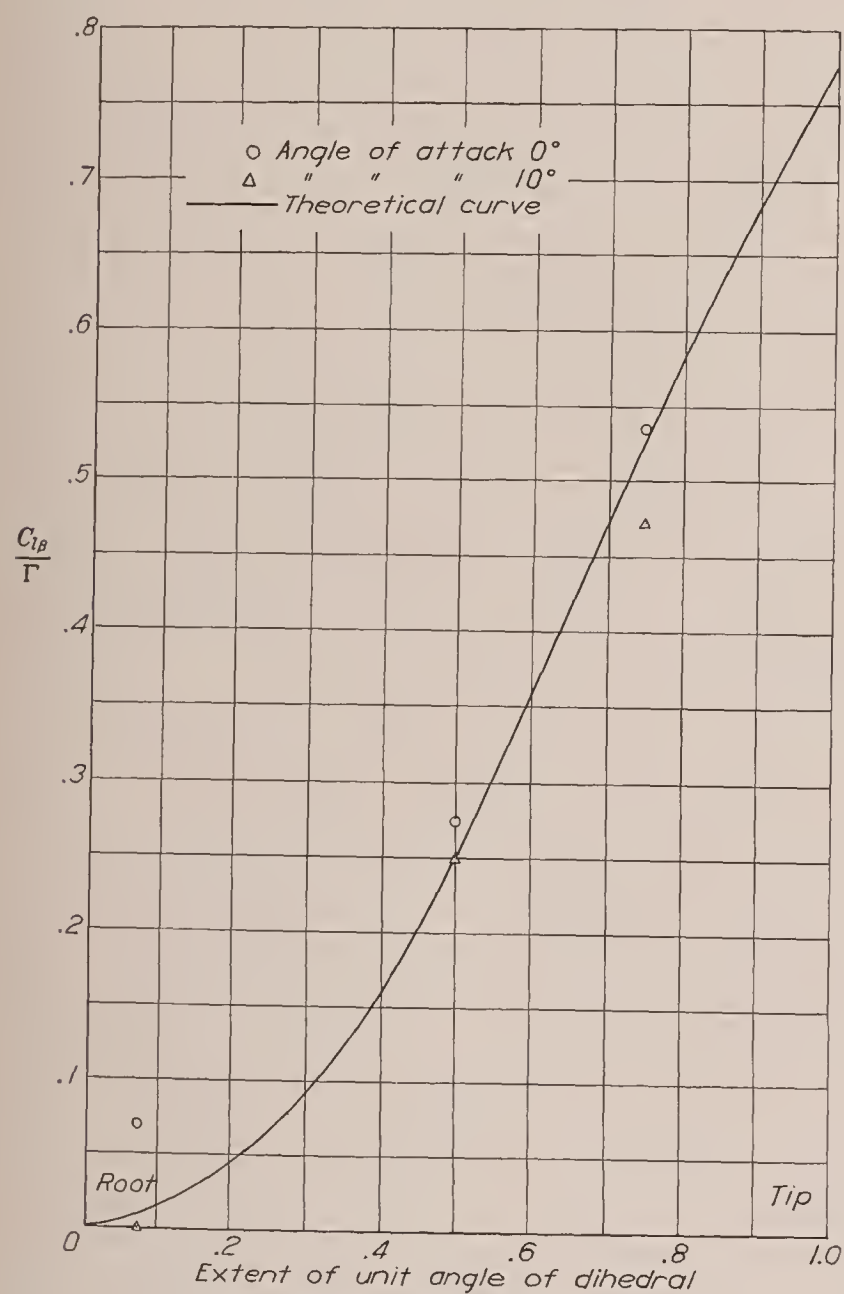


FIGURE 17.—Comparison between experimental and computed values of $C_{l\beta}/\Gamma$ (experimental data from reference 5).

Figure 17 shows a comparison of experimental and computed values of $C_{l\beta}/\Gamma$. The experimental values have been obtained from figure 23 of reference 5 and the coefficients given therein have been converted to the form used in this report. In the tests reported in reference 5, a rounded-tip rectangular wing of aspect ratio 6 was given various lengths of dihedral by turning up the outer portions of the wing. Each wing was then tested throughout the angle-of-attack range for various sideslip and dihedral angles.

It will have been apparent from the preceding discussion that the results of figure 16 may also be applied to predict the rolling moment caused by an aileron deflection in unyawed flight since ailerons, equally and oppositely deflected, cause changes in the angle-of-attack distribution that are similar to the changes caused by dihedral. Strictly speaking, however, the change in angle of attack due to dihedral cannot have quite the same effect as a similar change produced by ailerons because the ordinary lifting-line theory, when applied to yawed or sweptback wings, omits the effect of the stagger of the trailing vortices and the inclination of the bound vortex. Although the present theory has not been modified to take this effect into account, there

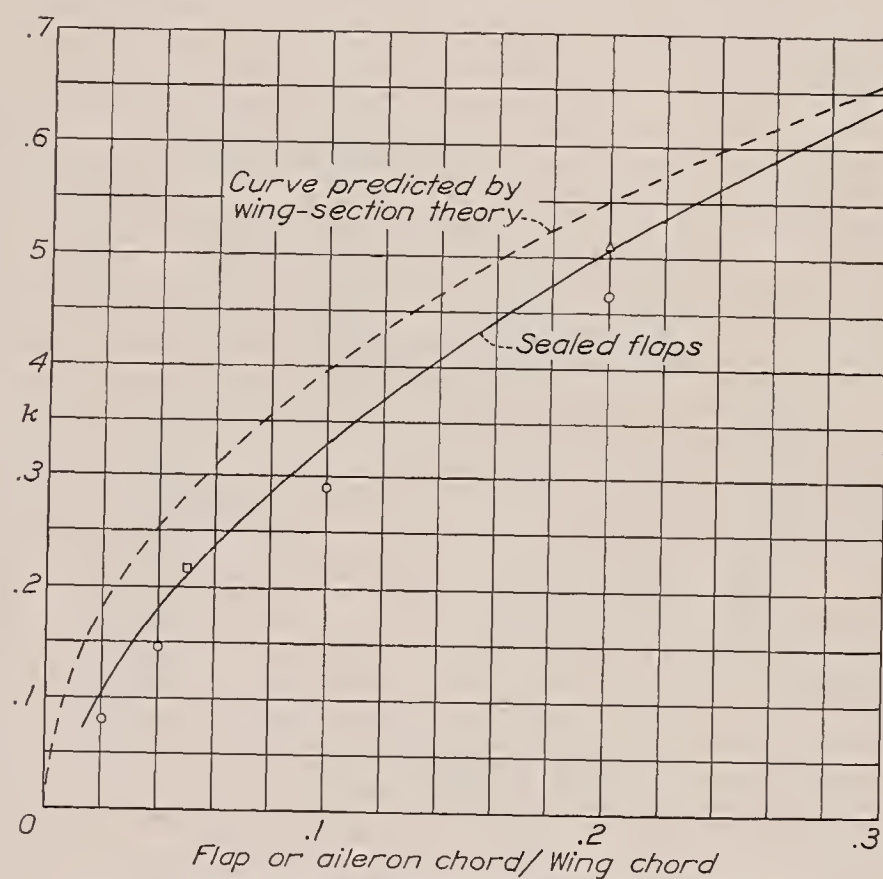


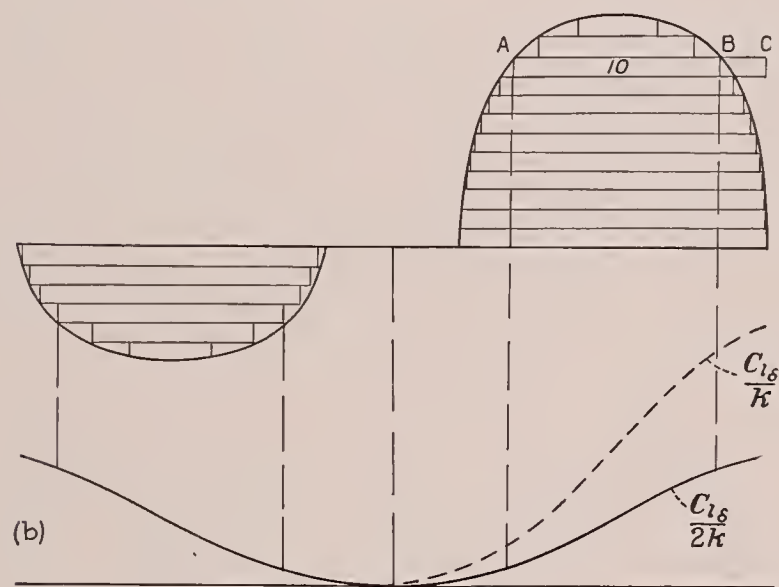
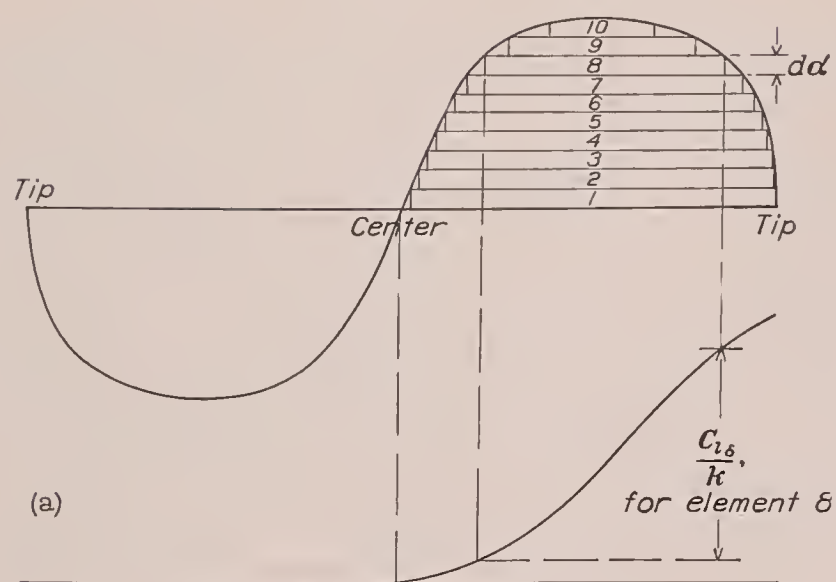
FIGURE 18.—Variation of k with ratio of flap or aileron chord to wing chord.

is ample justification for omitting it in the computations as experiments indicate only second-order differences (see reference 5) for the usual angles of yaw and sweepback.

For the computation of the rolling moment due to an aileron deflection δ , the appropriate value of $C_{l\delta}$ to be inserted in the equation

$$L_{\text{aileron}} = C_{l\delta} \delta q S b \quad (15)$$

may also be found from figure 16. The derivative $C_{l\delta}$ is given as a ratio in terms of k , the theoretical change of α with aileron deflection. Although the value of k has been theoretically determined for thin wings, it is better to use values of k determined from an analysis of experimental data. For this purpose, figure 18 is included, which shows the variation of k for values of the ratio of aileron or flap chord to wing chord up to 0.3. This variation of k has previously been given in figure 11 of reference 6 and holds for sealed flaps deflected up to approximately 20° .



(a) Ailerons deflected equally.
(b) Ailerons deflected differentially.
FIGURE 19.—Addition of effect of aileron elements.

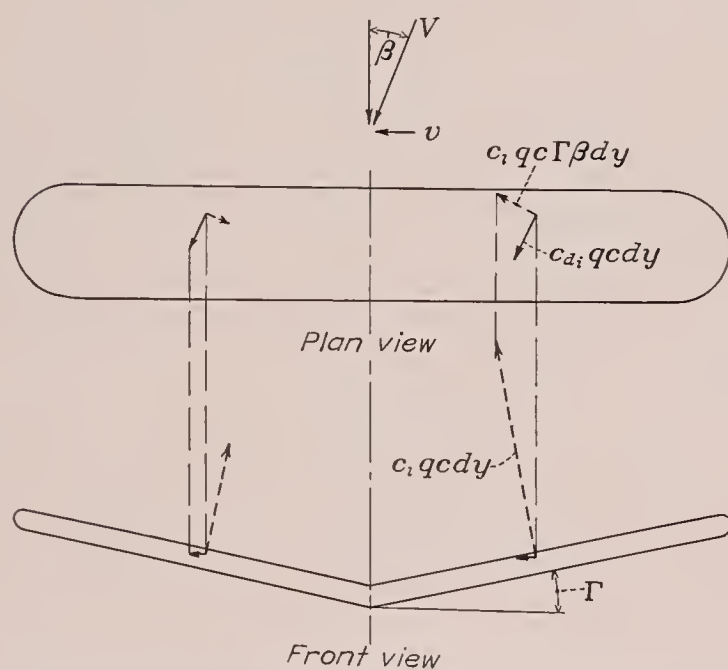


FIGURE 20.—Action of dihedral in producing yawing moment in sideslip.

If the angle-of-attack change caused by deflecting the ailerons is antisymmetrical about the wing center line, the proper value of $C_{lδ}$ to be used with equation (15) (for the rolling moment only) can be found by an

integration or summation of the effects of elemental ailerons of various lengths and positions along the span as indicated in figure 19 (a). The values of $C_{lδ}/k$ are obtained from figure 16 for the wing plan form used. If the ailerons are differentially operated, then it may be better to divide the ordinates of figure 16 by 2 and to determine the value of the moment given by each aileron as indicated in figure 19 (b).

YAWING MOMENT DUE TO SIDESLIP

The yawing moment of a wing with dihedral in side-slipping motion may be conveniently divided into two parts, the first part being due to the unsymmetrical

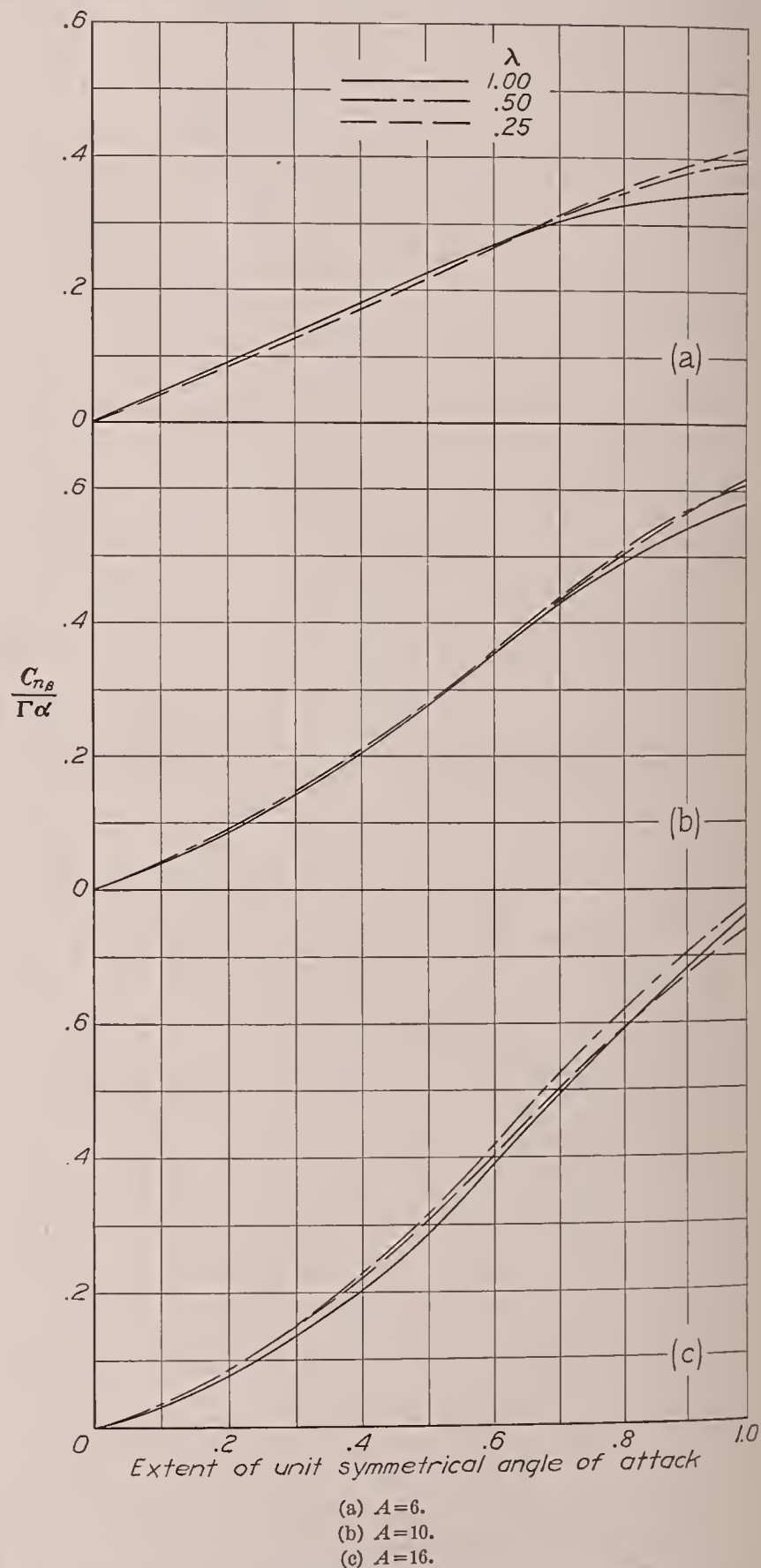


FIGURE 21.—Yawing derivative due to sideslip (dihedral constant).
 $N_{sideslip} = C_{nβ} \beta q S b$

induced-drag distribution over the span and the second part due to a shift of the lift vectors acting so as to produce a moment about the vertical axis. Figure 20 illustrates the components of the section lift and drag vectors that produce yawing moments. The advanced wing having the larger lift will also have a larger induced drag and hence a component moment is set up that tends to turn the wing so as to reduce the sideslip; at the same time, however, the contrary moment due to the components of the lift acts to advance the forward half of the wing still more. As was the case with the yawing derivative due to rolling, the moments caused by the lift components predominate and, as a result, the net theoretical moment is an unstable one; or, in other words, with the system of axes chosen, a negative yawing moment results when the dihedral and sideslip angles are positive.

The explanations advanced in some textbooks neglect the inward slope of the lift vectors and lead to an incorrect sign of the yawing moment.

The yawing moment in sideslip is given by the equation

$$N_{sideslip} = C_{n\beta} \beta q S b \quad (16)$$

The derivative $C_{n\beta}$ is given in figure 21 as a ratio in terms of $\Gamma\alpha$ because its value depends linearly upon the magnitude of the product of these variables. The values of $C_{n\beta}/\Gamma\alpha$ have been computed for unit symmetrical angle-of-attack distributions that extend out on either side of the center line and cover 0.25, 0.50, 0.75, and all of the wing span. These curves may be used to determine values of $C_{n\beta}$ for any initial angle-of-attack distribution symmetrical about the wing center line, provided also that the angle of dihedral is constant across the wing span. Although the rolling derivative due to sideslip can be obtained (from fig. 16) for a curvilinear variation of dihedral along the span, it is necessary to stipulate that either α or Γ remain constant if the principle of superposition is to be applied in the determination of $C_{n\beta}$. The combination of variable symmetrical twist and uniform dihedral being more common than the converse, the computations were shortened by including curves for only the case of uniform dihedral.

The resultant value of $C_{n\beta}$ (to be used in equation (16)) is found by either an integration or a summation of the effects of elements of angle of attack extending along the span. The process to be followed where graphical evaluation is necessary has been illustrated in figure 10, with the ordinates of figure 10 (a) changed to $\Gamma\alpha$. The ordinates and abscissas of the remaining parts are to be changed as required. For untwisted wings with uniform dihedral, the value of $C_{n\beta}/\Gamma\alpha$ is obtained by multiplying the value read at a relative distance of 1.0 by the wing angle of attack and, in turn, by the dihedral angle.

The curves of figure 21 being generally steeper beyond the 0.5 point, the deduction of increments of

angle of attack at the tip, i. e., giving the wing wash-out, would be the simplest means of decreasing the unstable yawing moment caused by the wings in a sideslipping motion.

Although the predicted variation of the yawing moment with dihedral is confirmed, experiments show a residual stable yawing moment at zero dihedral that is not predicted by the ordinary theory. This residual moment is greater for wings with blunt tips and is greater at zero or negative lifts. It will be noted that the theoretical yawing moment is itself the small resultant of two large contrary effects and is thus of the same order as a number of possible secondary influences.

LANGLEY MEMORIAL AERONAUTICAL LABORATORY,
NATIONAL ADVISORY COMMITTEE FOR AERONAUTICS,
LANGLEY FIELD, VA., April 19, 1938.

REFERENCES

1. Lotz, Irmgard: Berechnung der Auftriebsverteilung beliebig geformter Flügel. Z. F. M., 22. Jahrg., 7. Heft, 14. April 1931, S. 189-195.
2. Pearson, H. A.: Span Load Distribution for Tapered Wings with Partial-Span Flaps. T. R. No. 585, N. A. C. A., 1937.
3. Betz, A., and Petersohn E.: Contribution to the Aileron Theory. T. M. No. 542, N. A. C. A., 1929.
4. Pearson, H. A.: Theoretical Span Loading and Moments of Tapered Wings Produced by Aileron Deflection. T. N. No. 589, N. A. C. A., 1937.
5. Shortal, Joseph A.: Effect of Tip Shape and Dihedral on Lateral-Stability Characteristics. T. R. No. 548, N. A. C. A., 1935.
6. Weick, Fred E., and Jones, Robert T.: Résumé and Analysis of N. A. C. A. Lateral Control Research. T. R. No. 605, N. A. C. A., 1937.

TABLE I.—VALUES OF COEFFICIENTS DEFINING WING CHORD DISTRIBUTION

$$\frac{c_s}{c} \sin \theta = \sum C_n \cos n \theta$$

$$C_0$$

λ	1.00	0.50	0.25	Elliptical
6	0.730	1.000	1.300	1.000
10	.700	.956	1.270	1.000
16	.677	.952	1.240	1.000

$$C_2$$

λ	1.00	0.50	0.25	Elliptical
6	-0.260	-0.149		
10	-.320	-.218		
16	-.368	-.259	-0.121	

$$C_4$$

λ	1.00	0.50	0.25	Elliptical
6		-0.074	-0.207	
10		-.140	-.220	
16	-0.040	-.154	-.323	

REPORT No. 636

APPROXIMATE STRESS ANALYSIS OF MULTISTRINGER BEAMS WITH SHEAR DEFORMATION OF THE FLANGES

By PAUL KUHN

SUMMARY

The problem of skin-stringer combinations used as axially loaded panels or as covers for box beams is considered from the point of view of the practical stress analyst. By a simple substitution the problem is reduced to the problem of the single-stringer structure, which has been treated in N. A. C. A. Report No. 608. The method of making this substitution is essentially empirical; in order to justify it, comparisons are shown between calculations and strain-gage tests of three beams tested by the author and of one compression panel and three beams tested and reported elsewhere.

INTRODUCTION

A combination of a plate and stringers is frequently used as a structural element. Figure 1 (a) shows such a combination used as a tension member; figure 1 (b) shows one used as the tension side of a beam. The stress distribution in structures of this type is materially influenced by the shear deformation of the plate. In aeronautical structures, where the plate often consists of a thin sheet that may be allowed to buckle into a diagonal-tension field, it becomes necessary to consider the effect of this shear deformation more carefully than is customary in other types of structure.

Reference 1 discusses in detail the fundamental principles and the simplifying assumptions that permit a mathematical approach to the solution of the problem.

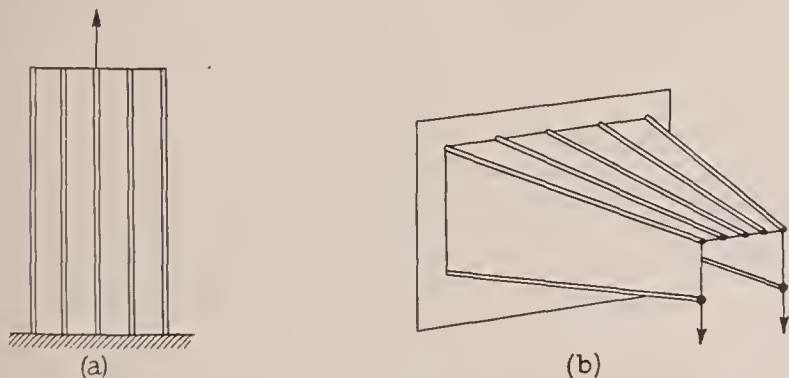


FIGURE 1.—Skin-stringer combinations as structural elements.

It is shown that numerical solutions can be obtained if there is only a single central stringer (fig. 2). A thorough familiarity with the method of analyzing single-stringer structures as given therein is presupposed. For multistringer structures the mathematics becomes so complex that there is very slight possibility of obtaining sufficiently general solutions on the basis

of the assumptions that were used for the single stringer structures.

Methods combining a desirable degree of accuracy with a reasonable degree of generality will, in all

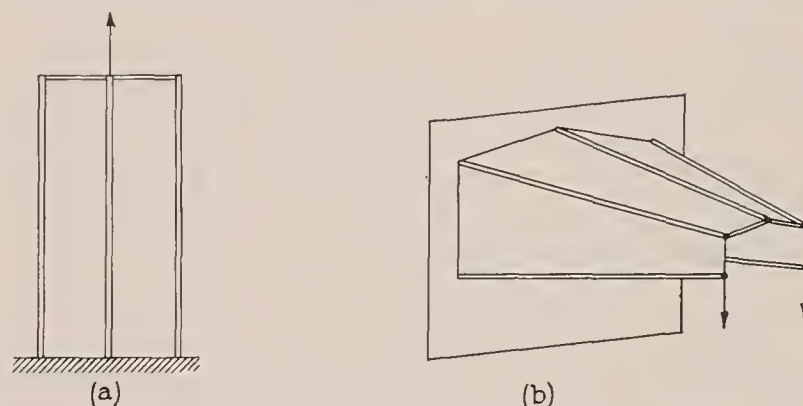


FIGURE 2.—Single-stringer structures.

probability, be methods of successive approximation. Attempts to develop such a method have thus far failed because the convergence is prohibitively slow. When such a method is found, it is not likely to be very rapid. Approximate methods developed in the interim, such as the one to be presented in this paper, will therefore retain their value by furnishing a very useful first approximation.

The method presented herein was devised to answer the urgent need for estimating the effects of shear deformation. It aims chiefly at rapidity and ease of application, which are achieved at the expense of introducing some empiricism. The experimental evidence presented is believed to be sufficient to prove that the method depicts reasonably well the influence of the shear deformation on the stringer stresses.

METHOD OF ANALYSIS

It is customary to designate tensile stresses and forces as positive. Figures, derivations, and formulas presented herein deal, in general, with tension members. The only differences between tension members and compression members are quantitative differences in the effective widths and in the effective shearing stiffnesses of the sheet. In the case of beams, the side not under consideration at the moment, i. e., the compression side in most of the discussion of this paper, is assumed to be concentrated at the shear web (figs. 1 (b) and 2 (b)) in such a location that the effective depth is not changed.

The investigation of reference 1 was restricted to symmetrical structures as indicated in figures 1 and 2. The same restriction will be made in the present paper, and formulas and numerical data must be understood to apply to the half structure unless otherwise specified.

In order to unify the terminology, the designations and symbols used in reference 1 for beams are extended in the present paper to axially loaded panels. (See appendix A for a list of symbols.) The directly loaded stringer of an axially loaded panel will therefore be referred to as the "flange" (subscript F) and the other stringers attached to the sheet as "longitudinals" or "stringers" (subscript L). This procedure is justified because the axially loaded panel may be considered as the cover of a box beam in pure bending under the assumptions made.

It is assumed in all cases that the longitudinals are distributed uniformly along the chord. It is furthermore assumed that camber is moderate, not exceeding the amounts found, for instance, in wing beams. Finally, it is assumed that the effective shear stiffness and the sheet thickness are constant along the chord.

GENERAL PRINCIPLES OF METHOD OF ANALYSIS

The mathematics of the multistring beam with variable cross section is too complex to admit of ready solution. Broadly speaking, two methods of procedure may be used in such a case. One method would be to use approximate methods of solving the equations; the other method would be to idealize and simplify the physical concept of the structure until the mathematical relations become manageable. The second method is used in this paper.

The results obtained in reference 1 show that the highest stresses occur at the flange and that they decrease from the flange toward the center line of the structure. The stress in the flange and the closely related stress in the longitudinal adjacent to the flange are therefore of paramount interest to the analyst.

In beams with cambered cover, which were not treated in reference 1, the highest stress in the longitudinals may occur adjacent to the flange or it may occur at the center line of the beam. When it occurs at the center line, the stress there also becomes a matter of concern to the analyst.

It is quite obvious that, in general, the most important physical actions will take place around the flanges, partly because the loads are applied there and partly because the stresses reach a maximum there as long as there is no violation of the basic requirement that the camber be very moderate. Consequently, any simplification that may be made should affect as little as possible the picture of the physical relations in the immediate vicinity of the flanges.

In conformance with this requirement, the simplification necessary for obtaining a solution was achieved by using a "substitute structure" obtained by leaving the

flange (and shear web) intact but replacing the longitudinals that are actually uniformly distributed over the width of the sheet by a single longitudinal equivalent to them as far as action on the flange is concerned. This substitution reduces the problem of the multistringer structure to that of the single-stringer structure, which can be analyzed as shown in reference 1. The method of substituting (temporarily) a simplified structure for the actual one corresponds in part to the method of using "phantom members" in trusses.

The substitute structure is used only to calculate the stresses in the part that it has in common with the actual structure, namely, the flange and the skin adjacent to the flange. After this object has been attained, the substitute structure is discarded. The stresses in the actual distributed longitudinals are then obtained by using the method described in reference 1 for distributing "corrected forces."

It is clear that, in any given case, at least one equivalent single longitudinal exists. Whether or not there is a general method for finding this equivalent longitudinal, however, is a question that could be answered theoretically only if all the exact mathematical solutions were known. They are not known, and the method of finding the equivalent longitudinal is therefore essentially empirical and must be justified by tests. This requirement is not such a serious drawback as it may seem to be, because the basic simplifications used are such that experimental verification is required in any event.

The method of finding the equivalent single longitudinal is as follows: Remove from the sheet each individual stringer of cross-sectional area A at a distance y from the center line and attach, at the center line of the structure, a substitute stringer with a cross-sectional area

$$A_e = A \frac{\sigma_y}{\sigma_{cl}} \quad (1)$$

where σ_y is the stress in the actual stringer and σ_{cl} the stress in the actual center-line stringer. The ratio σ_y/σ_{cl} may be considered as the "effectiveness" of the stringer at y relative to the stringer at the center line $y=0$; the use of this factor in expression (1) tends to counteract the loss of effectiveness caused by moving the stringer from its original location to the center line. The sum of the individual substitute stringers attached at the center line constitutes the single equivalent longitudinal.

As the stresses σ_y and σ_{cl} are unknown at the outset, for a first approximation, the ratio σ_y/σ_{cl} is obtained from equation (17) of the constant-stress solution given in reference 1. With the stresses thus computed, a second approximation might be made. In all cases investigated thus far, it was found that the second approximation agreed with the first one within the limits of experimental accuracy. The use of the second approximation is therefore considered unnecessary. (It must

be borne in mind that the method of finding the equivalent longitudinal is essentially empirical. Consequently, there is no valid reason to believe that the second approximation must be better than the first one.)

ANALYSIS OF AXIALLY LOADED PANEL

As an example of the analysis of an axially loaded panel, the analysis of the compression panel with seven stiffeners, described in reference 2, will be discussed in detail. The pertinent data on this panel are given in figures 3 (a) and 3 (b).

Estimate of effective areas and of effective shear stiffness.—The test results are given in reference 2 for $2P=2,000$, 4,000, and 6,000 pounds. The analysis will be made for $2P=4,000$ or $P=2,000$ pounds. It will become apparent that the conditions at this load are the same as for very small loads, so that the analysis will be valid for any load between 0 and 4,000 pounds.

The mean stress in the panel (reference 2) is

$$\sigma_M = \frac{2,000}{0.70} = 2,860 \text{ lb./sq. in.}$$

This stress is fairly close to the compressive buckling stress of the sheet; the effective width of the sheet will therefore be taken as equal to the actual width. The effective stringer area for the flange is therefore

$$A_F = 0.180 + 2 \times 0.024 = 0.228 \text{ sq. in.}$$

and for the sum of the other stringers

$$A_L = 2.5 \times 0.088 + 10 \times 0.024 = 0.460 \text{ sq. in.}$$

The force at the bottom of the edge stringer is approximately

$$F_F = 2,860 \times 0.228 = 652 \text{ lb.}$$

leaving 1,348 pounds to be transmitted by shear in the sheet to the other stringers. The average shear stress in the sheet next to the edge stringer is therefore

$$\tau = \frac{1,348}{48 \times 0.024} = 1,170 \text{ lb./sq. in.}$$

The critical buckling stress for 0.024-inch dural sheet, 4 inches wide and assumed simply supported, is, according to Timoshenko,

$$\tau_{crit} = 1,730 \text{ lb./sq. in.}$$

This value is so far above the actual stress that there is no possibility of a diagonal-tension field forming and reducing the shear stiffness, so that $G_c/E = 0.40$ may be taken.

Determination of substitute structure.—Figure 3 (c) shows the cross section of the idealized structure

assumed for the analysis. The stringer areas given on this figure are effective areas that include the effective width of the sheet; the sheet is now assumed to carry only shear.

If there are at least two intermediate stringers between the center stringer and the flange, the calculation of the substitute stringer may be simplified by using a formula derived on the assumption that there are infinitely many intermediate stringers; that is, on the

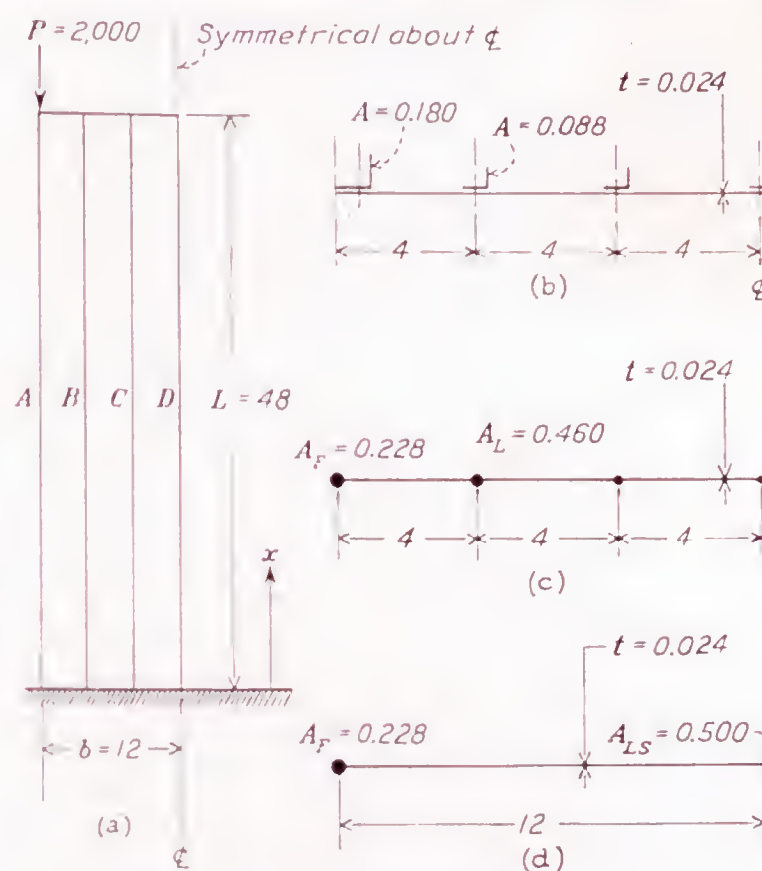


FIGURE 3.—Compression panel used for sample analysis.

assumption that the area A_L of the intermediate stringers is distributed uniformly along the width b of the sheet. The derivation of this formula is as follows: According to the constant-stress solution (reference 1, equation (17))

$$\frac{\sigma_y}{\sigma_{CL}} = \cosh K_3 y \quad (2)$$

where

$$K_3 y = K_3 b \times \frac{y}{b}$$

and, in the case of a constant cross section,

$$K_3 b = \sqrt{\frac{A_L b E}{t L^2 G_c}} \quad (3)$$

The area of an individual stringer is now

$$dA_L = \frac{A_L}{b} dy$$

and the area of the substitute stringer that replaces it at the center line is, according to equation (1),

$$dA_{LS} = \frac{A_L}{b} dy \cosh K_3 y$$

The total area of the substitute stringer located at the center line is therefore

$$A_{LS} = \frac{A_L}{b} \int_0^b \cosh K_3 y \, dy = A_L \frac{\sinh K_3 b}{K_3 b} \quad (4)$$

In the case under consideration

$$K_3 b = \sqrt{\frac{2 \times 0.460 \times 12}{0.024 \times 48^2 \times 0.40}} = 0.706$$

so that

$$A_{LS} = 0.460 \times \frac{0.767}{0.706} = 0.500 \text{ sq. in.}$$

Figure 3 (d) shows the cross section of the substitute structure.

Analysis of substitute structure.—The substitute structure of figure 3 (d) can be analyzed by applying the formulas given in appendix B. By formula (A-1)

$$K^2 = \frac{0.40 \times 0.024}{12} \left(\frac{1}{0.228} + \frac{1}{0.500} \right)$$

$$K = 0.0715$$

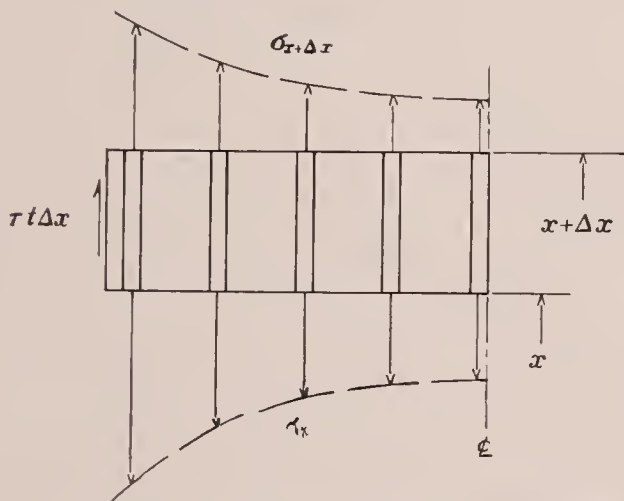


FIGURE 4.—Free-body diagram for calculating shear stress.

For any station along the span, the stresses and forces can now be calculated. For example, at the bottom of the panel ($x=0$), by formula (A-3)

$$\begin{aligned} \sigma_F &= \frac{P}{A_F + A_{LS}} \left(1 + \frac{A_{LS}}{A_F} \frac{\cosh Kx}{\cosh KL} \right) \\ &= \frac{2,000}{0.228 + 0.500} \left(1 + \frac{0.500 \times 1.00}{0.228 \times 15.53} \right) \\ &= 3,134 \text{ lb./sq. in.} \end{aligned}$$

With the computation of σ_F the substitute structure has served its purpose and is discarded. It is important not to confuse it with the actual structure in any of the following computations.

Calculation of stresses in longitudinals.—The total force F_L in the actual longitudinals is

$$F_L = P - F_F = P - \sigma_F A_F$$

or, at $x=0$,

$$F_L = 2,000 - 3,134 \times 0.228 = 1,286 \text{ lb.}$$

This force is to be distributed over the longitudinals by the method given in reference 1, equations (21) and

(22). In order to apply this method, compute the average stress

$$\sigma_{Lav} = \frac{F_L}{A_L} = \frac{1,286}{0.460} = 2,800 \text{ lb./sq. in.}$$

and the ratio

$$\frac{\sigma_{Lav}}{\sigma_F} = \frac{2,800}{3,134} = 0.894$$

With this ratio as abscissa, read from figure 18 of reference 1 (redrawn to a larger scale)

$$Yb = 0.605$$

and calculate

$$\sigma_{CL} = \frac{\sigma_F}{\cosh Yb} = \frac{3,134}{1.188} = 2,640 \text{ lb./sq. in.}$$

For the other two stringers, which are located at $y = \frac{1}{3}b$ and $y = \frac{2}{3}b$, the stress will be, for stringer C,

$$\sigma = \sigma_{CL} \cosh Yy = 2,640 \times \cosh 0.202 = 2,694 \text{ lb./sq. in.}$$

and, for stringer B,

$$\sigma = 2,640 \times \cosh 0.404 = 2,860 \text{ lb./sq. in.}$$

The shear stress τ at any point in the sheet is obtained most conveniently by considering the equilibrium of an element Δx cut out of the structure as indicated in figure 4, taking advantage of the fact that the shear stress is zero at the center line. The shear stress in the first panel next to the flange, which is the most important one for design purposes, will be obtained automatically as part of the solution of the substitute structure if the numerical trial-and-error method of solution is used, or by using formula (A-2) from appendix B in the case of a constant-section panel.

Panels with variable cross section.—In the case of a panel with variable cross section, the panel is divided into a convenient number of bays as described in reference 1. For each bay, the cross-sectional area of the substitute longitudinal is computed by using formula (4). In the computation of $K_3 b$ by formula (3), the average values in the bay are used for A_L , b , t , and G_e/E . The length L is again the total length of the panel (not of the bay). The analysis of the substitute structure is made by the trial-and-error method described in reference 1. After this step, the procedure is identical with the procedure for constant-section panels.

ANALYSIS OF BEAMS WITH FLAT COVERS

The analysis of beams with flat covers is so closely analogous to the analysis of axially loaded panels that no detailed example need be given. The substitute structure is found exactly as for an axially loaded panel. The resulting beam with a single longitudinal is analyzed by the trial-and-error method described in reference 1, or by formulas if applicable. The total force F_L at any section can then be distributed over the longitudinals as previously described.

ANALYSIS OF BEAMS WITH CAMBERED COVERS

The cambered beam with a single longitudinal.—The basic problem of the beam with a single longitudinal and a cambered cover was not treated in reference 1. It will now be briefly discussed.

Figure 5 shows an element of length dx cut out of the beam. With the help of this diagram, the fundamental equations of equilibrium can be written exactly as in the case of the beam with a flat cover (reference 1, equations (3a) and (3b)¹).

$$dF_F = S_w \frac{dx}{h_w} - dS_C \quad (5a)$$

$$dF_L = dS_C \quad (5b)$$

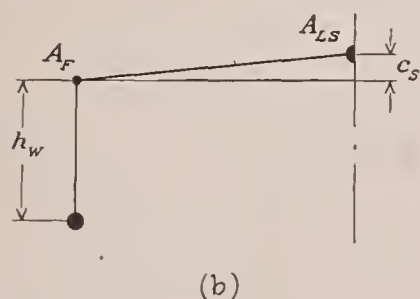
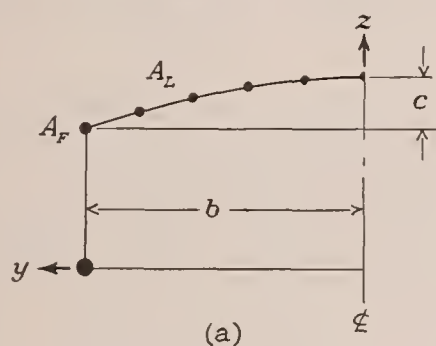
The equation that expresses the relation between shear stress and longitudinal stresses is slightly more complicated than in the case of a flat cover. The ordinary bending theory may be taken to give the limiting case of no shear deformation. The deformations that determine the shear strain must therefore be measured from the plane cross section of the engineering bending theory as a reference base, resulting in the equation

$$d\tau = -\frac{G_e}{Eb'}[(\sigma_F - \sigma_{FP}) - (\sigma_L - \sigma_{LP})]dx \quad (5c)$$

where the subscript P denotes stresses obtained with the engineering bending theory, which assumes plane sections to remain plane.

These equations can be used to obtain numerical solutions by the trial-and-error method, using finite differences Δ in place of the differentials d . Appendix B gives the analytical solution for two cases that correspond to the solutions given for a beam with a flat cover in reference 1.

¹In reference 1, equation (3b) is written incorrectly with a minus sign ahead of dF_L .



The cambered beam with many longitudinals.—In the treatment of the cambered beam with many longitudinals shown in figure 6 (a), various degrees of refinement are possible. The following method, devised

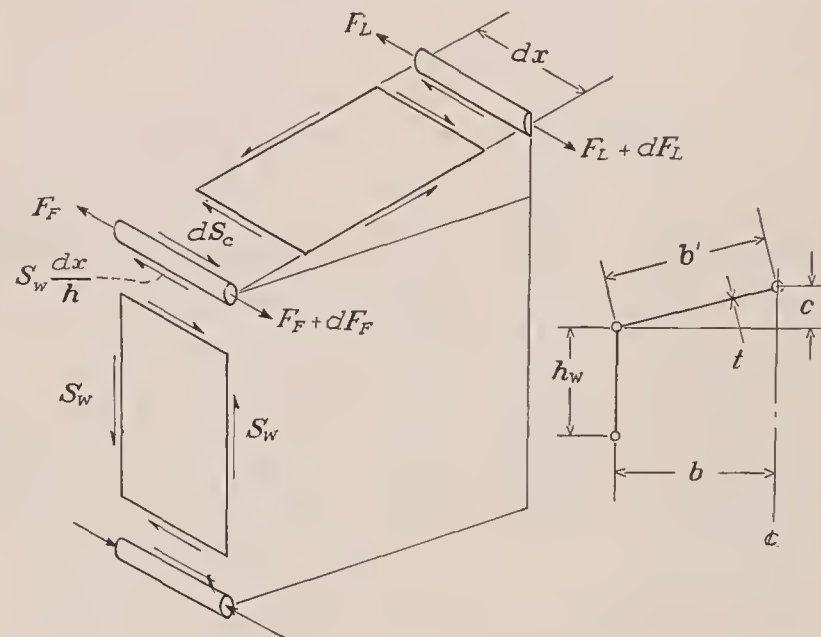


FIGURE 5.—Free-body diagrams and notation for single-stringer beam with cambered cover.

to utilize the method developed for axially loaded panels and for beams with flat covers, is believed to be adequate for practical purposes. Attention is called again to the basic assumption stated previously, i. e., that the camber is moderate.

The analysis is again divided into two steps: the calculation of the flange stresses σ_F along the span by means of the substitute structure, and the subsequent distribution of the force F_L over the longitudinals at any station.

The area of the substitute stringer is calculated by equation (4), using for b the developed width of the cover sheet. The camber of the substitute beam may, for practical purposes, be taken as $c_s = \frac{1}{2}c$ (fig. 6 (b)).

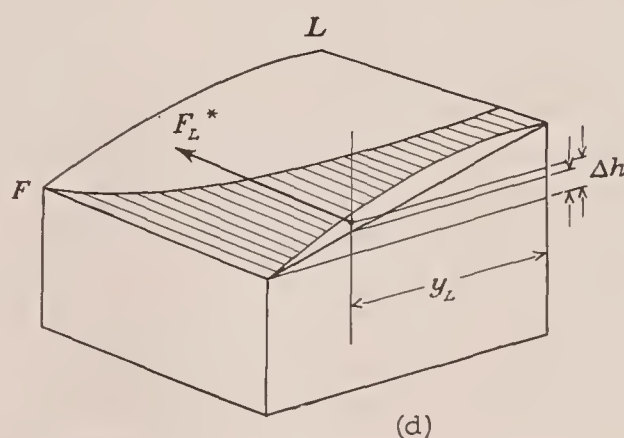
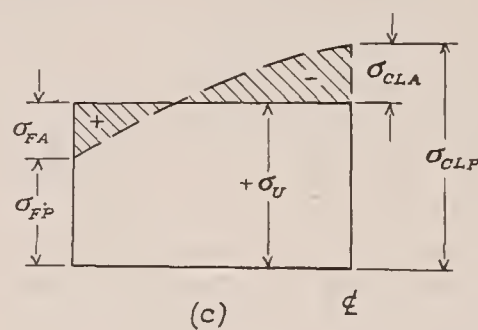


FIGURE 6.—Cambered-cover beam.

The distribution of the force F_L cannot be made directly by the method used for flat panels. In the flat panel, the longitudinal stress is uniform along the chord in the limiting case of infinite shear stiffness; in the case of finite shear stiffness, the shear strain is defined directly by the longitudinal strains. In the cambered cover with infinite shear stiffness, the stress varies along the chord according to the straight-line law of the ordinary bending theory; in the cambered cover with finite shear stiffness, the shear strains are defined by the differences between the longitudinal strains and the corresponding strains of the ordinary bending theory as indicated by equation (5c).

These differences between the cambered and the flat cover may be interpreted as arising from the fact that the cambered cover has bending stiffness of its own because it has a "beam depth" equal to its camber.

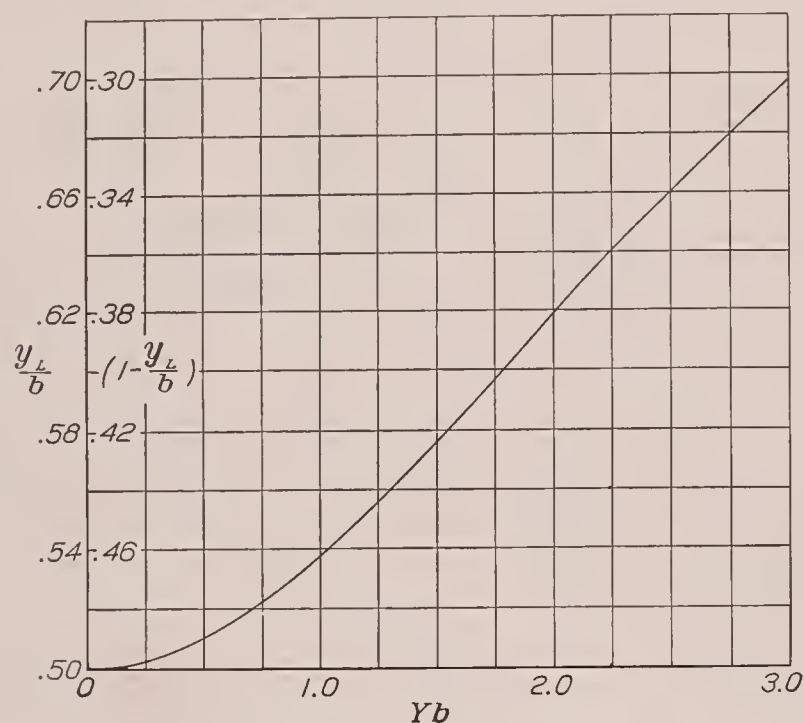


FIGURE 7.—Graph for location of resultant force on cover.

In the single-stringer beam it was not difficult to take care of the effect of this bending stiffness mathematically by introducing the terms σ_{FP} and σ_{LP} into equation (5c). In the multistring beam it is more convenient to introduce a physical equivalent, namely, an auxiliary system of longitudinal stresses distributed over the cover in such a manner as to make the stress uniform in the limiting case of infinite shear stiffness. In figure 6 (c) the broken line shows the stresses given by the ordinary bending theory, the full line shows the uniform stress, denoted by σ_U , and the cross-hatched area between the two lines indicates the auxiliary stresses necessary to achieve the uniform stress distribution. The magnitude of the uniform stress is determined by the condition that, when the auxiliary stresses act on the flange A_F and on the longitudinals A_L , they must not change the bending moment acting at the section, i. e., they must have zero moment about the assumed centroidal line of the lower cover. The auxiliary stresses will be denoted by a second subscript A placed

after the first subscript, which denotes the stringer or flange where the stress is measured.

With the auxiliary stresses assumed active, the method of finding the distribution of the stresses along the chord is analogous to the method used for flat panels and will be shown in detail for a numerical example. From the stresses thus calculated, the auxiliary stresses are subtracted to obtain the final stresses.

One step not necessary in the analysis of flat panels is required for cambered covers. As indicated in figure 6 (d), it is necessary to locate the resultant force F_L^* acting on the cover (exclusive of the flange) when the actual and the auxiliary stresses are acting. The vertical location Δh of this resultant determines the effective depth of the beam

$$h_e = h_w + \Delta h \quad (6)$$

when the combined stresses are acting. The exact calculation of Δh would require a very tedious integration involving the stress distribution and the shape of the cover, which has to be repeated several times for each cross section with slightly differing values of stress distribution. For practical purposes, it will therefore be advisable to simplify the problem, although there will be a slight loss in accuracy, by finding the lateral location y_L of the resultant and by assuming that Δh is determined by the intersection of the line $y = y_L$ and the straight line joining F and L , as indicated in figure 6 (d). Under the assumption of moderate camber, y_L is given by

$$\begin{aligned} y_L &= \frac{\int_0^b \sigma^* y dA}{\int_0^b \sigma^* dA} \\ &= \frac{1}{Y} (Yb - \coth Yb + \operatorname{csch} Yb) \end{aligned}$$

where Y is the parameter introduced in reference 1, equation (21), for the purpose of distributing stresses chordwise. The value of y_L/b is plotted in figure 7 against Yb for ready reference. With the proposed simplification, the value of Δh is then given by

$$\Delta h = c(1 - y_L/b) \quad (7)$$

NUMERICAL EXAMPLE FOR ANALYSIS OF A CAMBERED BEAM

Figure 8 (a) shows the cross section of the beam assumed for the sample analysis. The root section will be analyzed for a load P of 250 pounds acting at the tip; the length L of the beam is 108 inches. It is assumed that the effective width of the sheet has been estimated and that the value $A_L = 0.85$ sq. in. includes the effective width.

The next step is to estimate the effective shear modulus. If the presence of camber and of shear deformation is neglected, the maximum shear stress in the sheet will be given by formula (A-8) of appendix B as

$$\tau_{max} = \frac{PA_L}{thA_T} = \frac{250 \times 0.85}{0.0115 \times 3 \times 1.65} = 3,730 \text{ lb./sq. in.}$$

The buckling shear stress of a long dural plate 0.0115 inch thick and 1.80 inches wide is

$$\tau_{crit} = 1,960 \text{ lb./sq. in.}$$

The maximum shear stress being only about twice the critical stress, the average shear stress is sufficiently close to the critical to neglect diagonal-tension effects on shear stiffness and to set $G_e = G$ or $G_e/E = 0.40$.

Equation (3) then gives

$$K_3b = \sqrt{\frac{2 \times 0.85 \times 9}{0.0115 \times 108^2 \times 0.40}} = 0.535$$

Inserting this value in equation (4) gives

$$A_{LS} = 0.85 \frac{0.561}{0.535} = 0.892 \text{ sq. in.}$$

The cross section of the substitute beam is shown in figure 8 (b). Since the substitute beam is of uniform cross section, it can be solved analytically. Formula (A-14) gives

$$K^2 = \frac{0.40 \times 0.0115}{9} \left(\frac{1 + \frac{1}{3}}{0.80} + \frac{1}{0.892} \right)$$

$$K = 0.0378 \quad KL = 4.08$$

Formula (A-12) then gives for $x = 108$ inches

$$\sigma_F = \frac{27,000 \times 0.94}{9.20} \left[1 + \frac{1.94 \times 0.892}{0.94 \times 0.80} \left(1 + \frac{1}{3} \right) \frac{0.999}{4.08} \right]$$

$$\sigma_F = 4,830 \text{ lb./sq. in.}$$

This computation completes the first step and the substitute beam is discarded.

The next step is to calculate the stresses in the actual beam by the ordinary bending theory:

$$\sigma_{FP} = \frac{27,000 \times 0.94}{9.65} = 2,630 \text{ lb./sq. in.}$$

$$\sigma_{CLP} = \frac{27,000 \times 2.94}{9.65} = 8,220 \text{ lb./sq. in.}$$

Figure 8 (c) shows the chordwise distribution of the stresses according to the ordinary bending theory as well as the auxiliary stresses. In order to show that the auxiliary stresses indicated by figure 8 (c) fulfill the requirements, a check on their total moment is made.

$$\begin{aligned} 1,955 \times 3 \times 0.80 &= 4,690 \\ 837 \times 3.4 \times 0.189 &= 538 \\ -281 \times 3.8 \times 0.189 &= -202 \\ -1,399 \times 4.2 \times 0.189 &= -1,111 \\ -2,517 \times 4.6 \times 0.189 &= -2,188 \\ -3,635 \times 5.0 \times 0.0945 &= -1,717 \end{aligned}$$

10

The moment is zero with a negligible error. The flange stress used for calculating the chordwise stress distribution is therefore

$$\sigma_F^* = \sigma_F + \sigma_{FA} = 4,830 + 1,955 = 6,785 \text{ lb./sq. in.}$$

The moment furnished by the flange is

$$M_F^* = 6,785 \times 0.80 \times 3.00 = 16,280 \text{ in.-lb.}$$

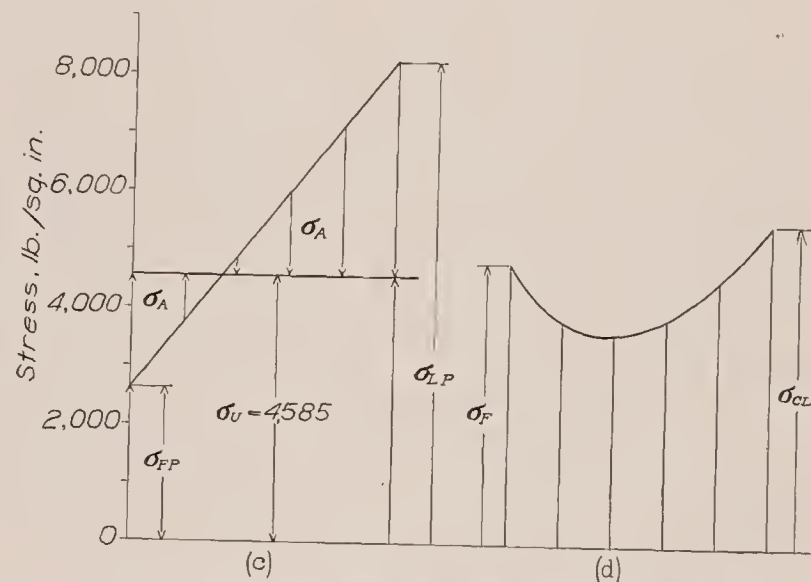
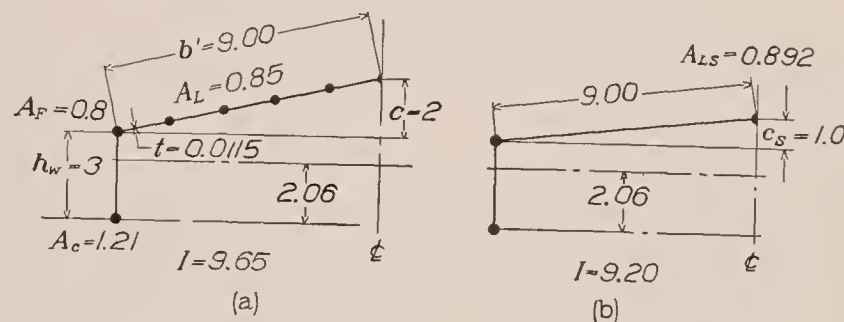


FIGURE 8.—Cambered-cover beam for sample analysis.

The moment to be furnished by the cover longitudinals is therefore

$$M_L^* = 27,000 - 16,280 = 10,720 \text{ in.-lb.}$$

Assuming $h_e = 3.77$ inches, the force F_L^* becomes

$$F_L^* = \frac{10,720}{3.77} = 2,840 \text{ lb.}$$

The average stress is therefore

$$\sigma_{Lav}^* = \frac{2,840}{0.85} = 3,345$$

and the ratio

$$\frac{\sigma_{Lav}^*}{\sigma_F^*} = \frac{3,345}{6,785} = 0.493$$

With this value as abscissa, read from figure 18 of reference 1

$$Yb = 1.94$$

and, with this value,

$$y_L/b = 0.613$$

from figure 7 so that

$$\Delta h = 2(1 - 0.613) = 0.77 \text{ in.}$$

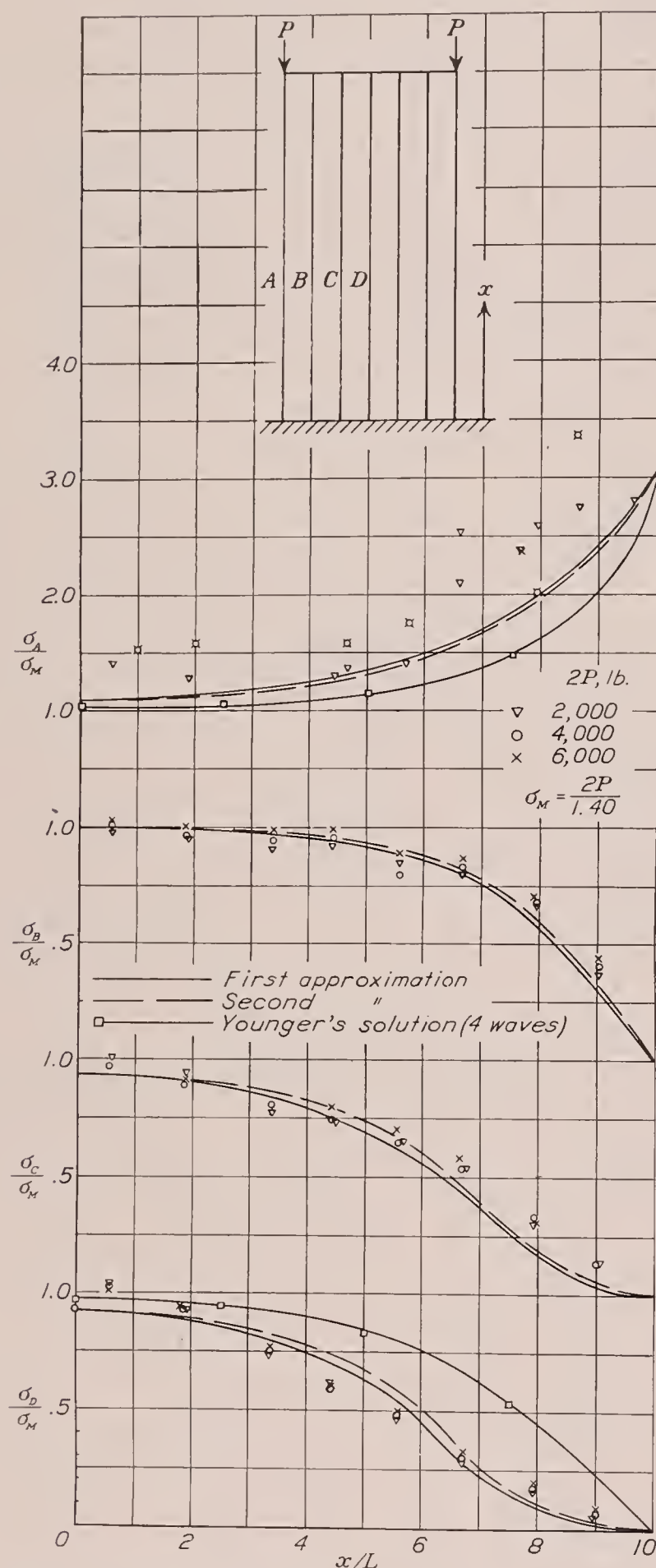


FIGURE 9.—Stresses in axially loaded panel (experimental data from reference 2).

and

$$h_e = 3.00 + 0.77 = 3.77 \text{ in.}$$

which agrees with the assumed value. If it did not agree, a new trial would have to be made.

The stress at the center line is given by

$$\sigma_{CL}^* = \frac{\sigma_F^*}{\cosh Yb} = \frac{6,785}{3.551} = 1,910$$

From this stress the actual stress is obtained by subtracting the auxiliary stress

$$\sigma_{CL}^* = 1,910 - (-3,635) = 5,545 \text{ lb./sq. in.}$$

Table I shows the calculation of the stresses σ^* in the other stringers by the formula

$$\sigma_y^* = \sigma_{CL}^* \cosh Yy$$

and of the final stresses; figure 8 (d) shows graphically the final stress distribution.

TABLE I

Stringer	y/b	Yy	$\cosh Yy$	σ^* (lb./sq. in.)	σ_A (lb./sq. in.)	σ (lb./sq. in.)
Center line.....	0.0	0	1.000	1,910	-3,635	5,545
1.....	.2	.388	1.076	2,055	-2,517	4,572
2.....	.4	.776	1.316	2,514	-1,399	3,913
3.....	.6	1.164	1.758	3,360	-281	3,641
4.....	.8	1.552	2.466	4,710	837	3,873
Flange.....	1.0	1.94	3.551	6,785	1,955	4,830

EXPERIMENTAL STUDIES

AXIALLY LOADED PANELS

Experimental results for a panel loaded in compression are described in reference 2. This panel was shown in figure 3 and served as a numerical example for the proposed method of analysis. The results of the analysis as well as the experimental results are shown in figure 9.

GENERAL REMARKS ON ANALYSIS OF BEAM TESTS

In the analysis of beam tests, some difficulty is met in establishing the idealized section. It is easy to define locations for the longitudinals but fixing the location, and particularly the size, of the flanges presents difficulties, because part of the shear web must be considered as furnishing a contribution to the idealized flange.

In order to reduce arbitrariness to a minimum, the following procedure was adopted for all beam analyses. First, the centroidal axis and the geometric moment of inertia of the cross section in question were computed. If the sheet was considered to be only partly effective in carrying normal stresses, the proper effective width was used in these computations. Next, the locations of the idealized flanges were fixed. On that side of the beam where the shear deformation was being calculated, the flange was assumed to be in the plane of the cover sheet. On the other side, which was without cover except in one case, the flange was assumed to be located at its estimated centroid. The cross-sectional areas of the two idealized flanges (tension and compression) were then computed from the conditions that the idealized section must have the same centroidal axis and the same moment of inertia as the actual section. For this idealized section, the analysis was then made by using the previously described methods.

GENERAL REMARKS ON N. A. C. A. BEAM TESTS

The available published test data were not sufficient for an adequate check of the theory developed. A number of beams were therefore tested by the N. A. C. A. The first of these beams was discussed in reference

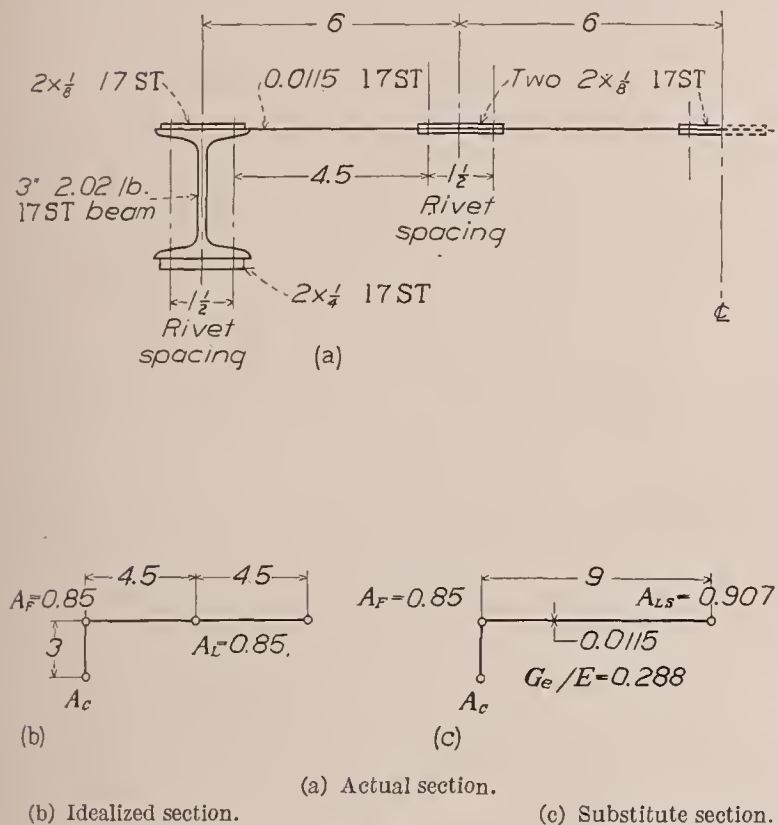


FIGURE 10.—Cross section of N. A. C. A. beam 2.

1; the following ones, designated as N. A. C. A. beams 2, 3, and 4, will be discussed in this paper.

In all N. A. C. A. beams, measurements were made on the tension side of the beam in order to eliminate

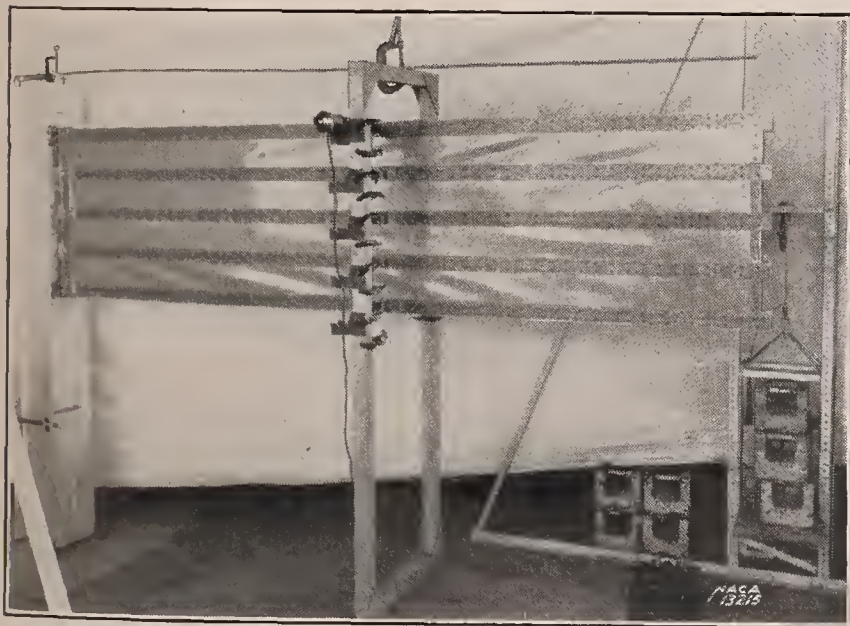
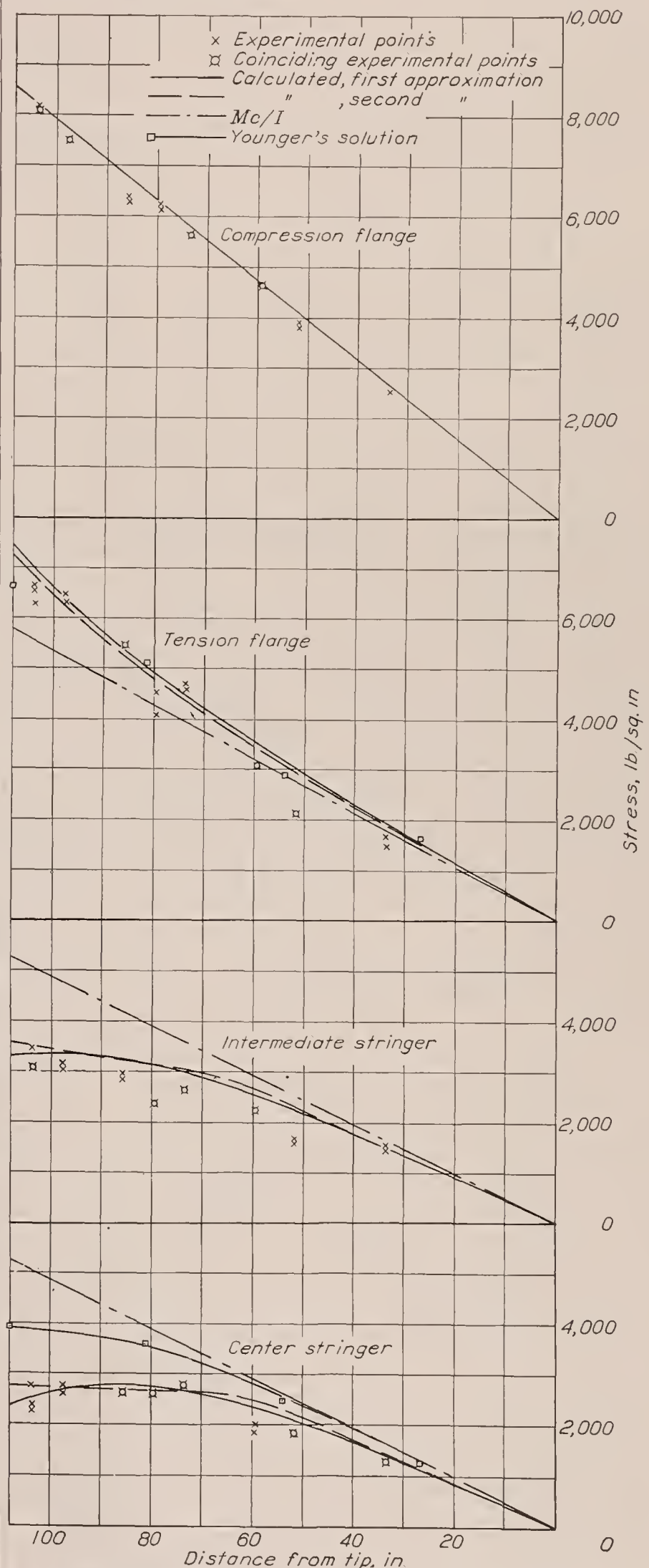


FIGURE 11.—N. A. C. A. beam 2 under test.

erroneous strain readings caused by local buckling of the stringers. Furthermore, flat strips could be used for stringers, making it possible to take strain readings very close to the sheet.

The load $2P$ was increased from 0 to 500 pounds (in the first series of tests) in steps of 50 pounds and

decreased again in steps of 100 pounds. The slope of the straight line through the test points was used to determine the stress at $P=250$ pounds, which will be shown in the later figures.

FIGURE 12.—Stresses in N. A. C. A. beam 2 for $P=250$ lb. $E=10.4 \times 10^6$.

Readings were taken across the entire section of the beam and on both sides of the stringers. Each point representing a flange stress in the figures is therefore the average of two slopes, and each point representing a stringer stress is the average of four slopes excepting figures that show the stress distribution along the entire chord.

A slight departure was made from the described method of analysis in the case of N. A. C. A. beams 2 and 3. The uniform distribution of A_L along the chord

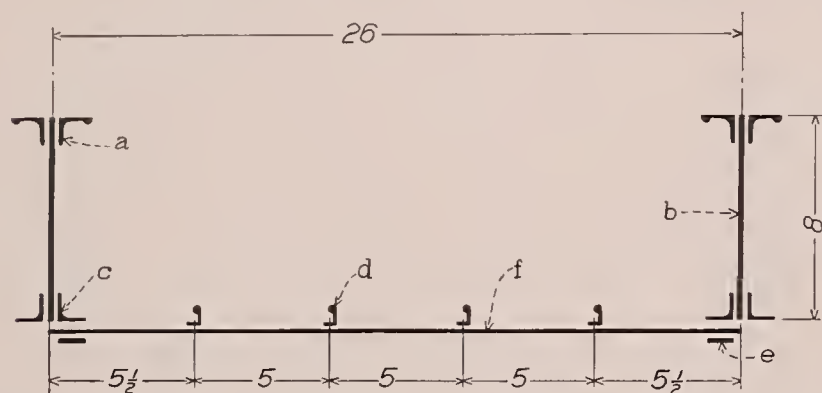


FIGURE 13.—Cross section of Galcit beams. a, upper cap angle. Area=0.354 sq. in. b, beam web. $t=0.051$ in. c, lower cap angle. Area=0.221 sq. in. d, stiffener angle. Area=0.044 sq. in. e, attaching strip. Area=0.082 sq. in. f, cover sheet. $t_1=0.025$ in.; $t_2=0.050$ in.

is not very well approximated in these beams, A_L consisting of only two stringers. Consequently, equation (4) was not used. The two stringers constituting A_L were treated individually on the basis of equations (1) to (3). This departure also accounts for the fact that, for beam 3, the substitute camber is not taken as one-half the actual camber, as recommended for practical cases with many stringers. For comparison with the

experimental flange stresses, the stresses calculated for the idealized flanges of the N. A. C. A. beams were corrected to the outside fiber stresses on the assumption that plane sections remain plane. For the purpose of calculating the shear deformation, the width of the sheet was taken between rivet rows for N. A. C. A. beams 2 and 3.

TESTS ON BEAMS WITH FLAT COVERS

N. A. C. A. beam 2.—N. A. C. A. beam 2 was similar in design to beam 1 described in reference 1. The cross sections of the beam are shown in figure 10. The bulkheads, not shown in this figure, were similar to those on beam 1 and were spaced to make the bays about square. The length L of the beam was 108 inches. Figure 11 shows the beam under test and figure 12 shows the results of the tests and of the calculations.

Galcit test beams.—Figure 13 shows the cross section of a type of beam tested at the California Institute of Technology (reference 3) under a pure bending moment. Figure 14 (a) shows the experimental and calculated results for the beam with $t=0.025$ inch and figure 14 (b) shows the results for the beam with $t=0.050$ inch.

Schnadel's ship model.—Figure 15 shows the cross section and the side view of a ship model tested by Schnadel (reference 4). The model was built of steel. Measurements were taken only on the outside of the compression cover (corresponding to the deck of the vessel) over one quadrant of the beam. Figure 16 shows the experimental results and the results calculated by the method presented in this paper.

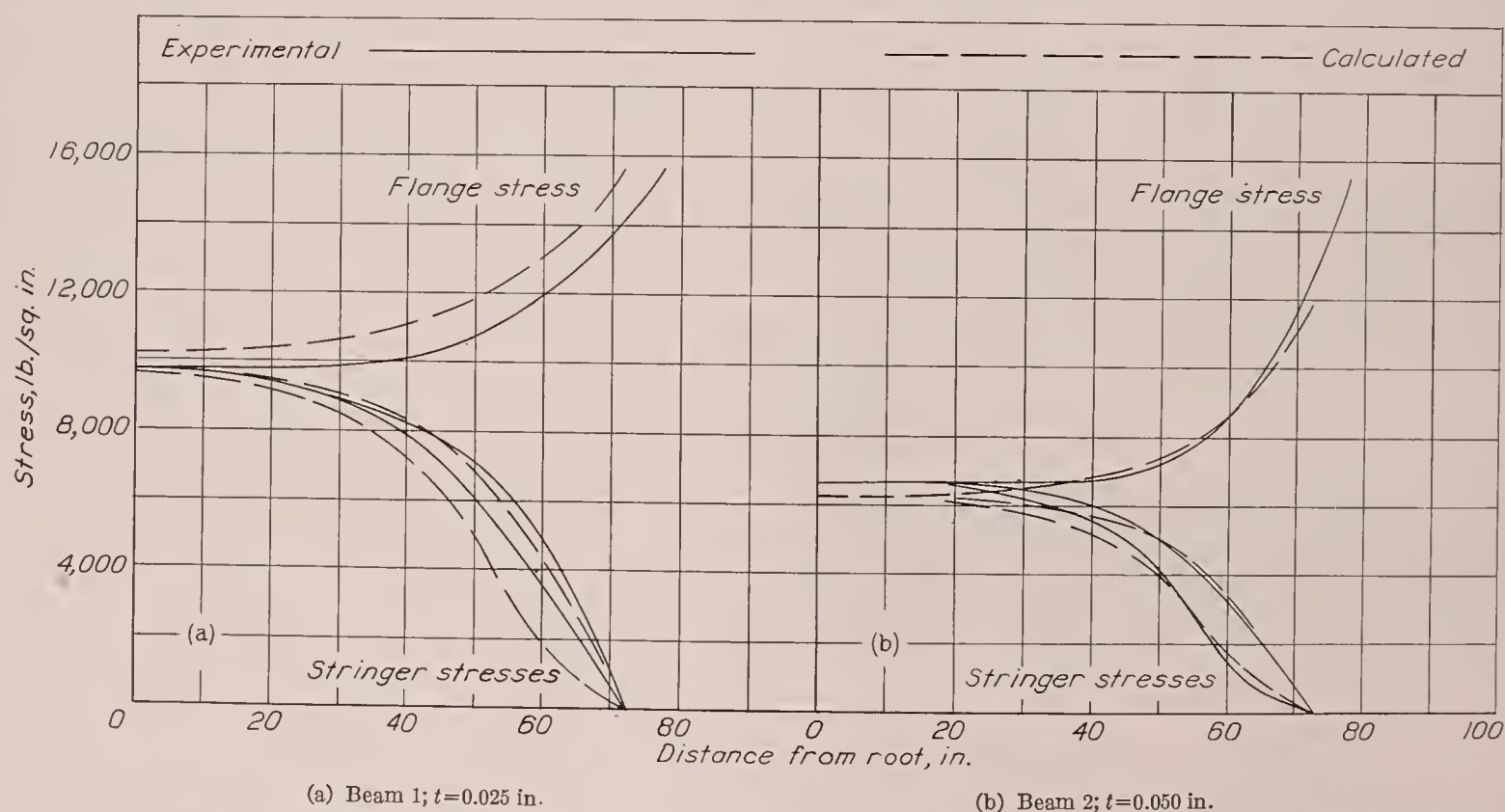
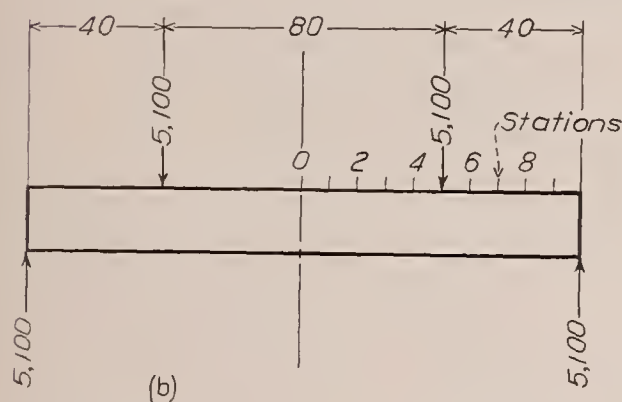
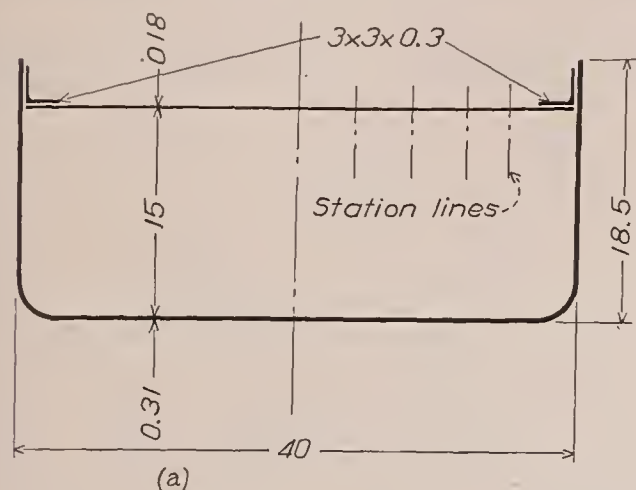


FIGURE 14.—Stress distribution in Galcit beams. Experimental data from reference 3; $M_0=120,000$ in.-lb.; G_s/E assumed 0.25 (diagonal tension).

TESTS ON BEAMS WITH CAMBERED COVER

N. A. C. A. beam 3.—Figure 17 shows the cross sections of a cambered beam obtained by inserting cambered bulkheads into N. A. C. A. beam 2. Figure 18



(a) Cross section.

(b) Loading diagram.

FIGURE 15.—Cross section and general diagram of Schnadel's ship model. Dimensions are in cm and loads in kg.

shows the beam under test. Figure 19 is a view of the inside of the beam, showing intermediate bulkheads that were added for tests at high loads to reduce sagging of the stringers between the main bulkheads. This sagging is proportional to the square of the stresses and consequently may become important at high

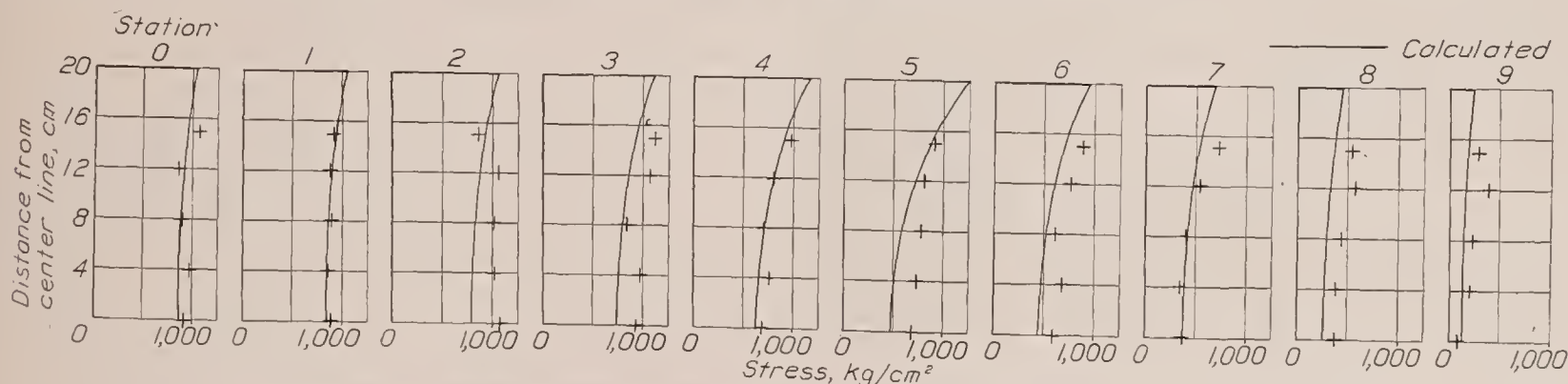
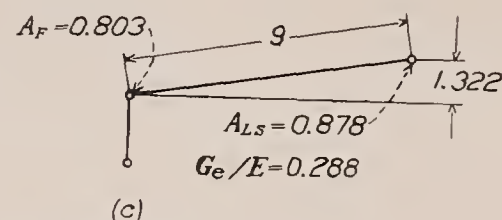
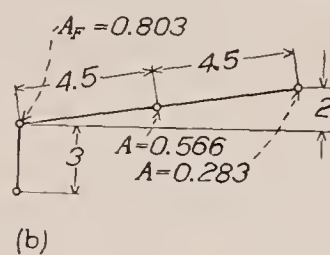
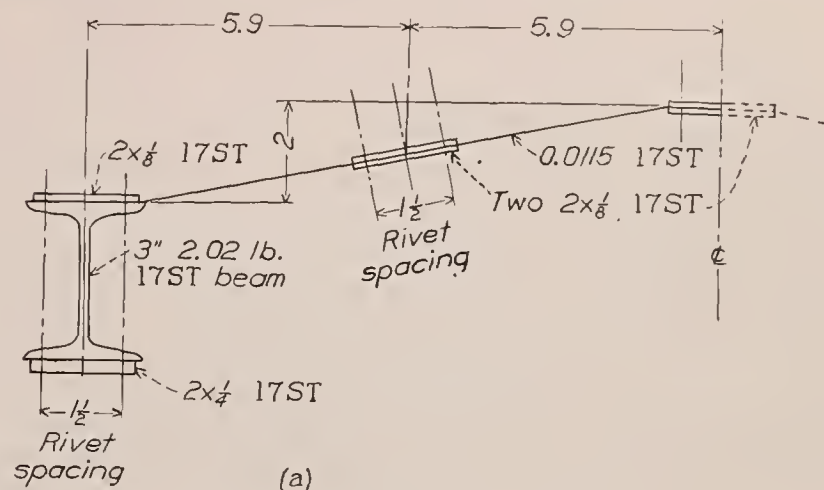


FIGURE 16.—Stress distribution in Schnadel's ship model (experimental data from reference 4).

stresses, but it requires attention only in the case of shallow beams. Figure 20 shows experimental and calculated stresses in this beam at $P=250$ pounds.

A shorter series of measurements was made on beam 3 at higher loads. Figure 21 shows the stresses at four

stations for three different loads. Two facts are evident from an inspection of this figure: The differences between the actual stresses and the stresses of the ordinary bending theory increase as the root is approached and



(a) Actual section.

(b) Idealized section.

(c) Substitute section.

FIGURE 17.—Cross section of N. A. C. A. beam 3.

also as the load increases, because the shearing stiffness decreases with increase in load.

N. A. C. A. beam 4.—N. A. C. A. beam 4 was tapered in plan form, in depth, and in stringer area as shown in figure 22. Figure 23 shows the calculated and experimental stresses in the flange. The experimental stresses shown in this figure are based on measurements taken on the outside of the flange but are corrected to the top edge of the web.

Figure 24 shows the chordwise stress distribution at the station $x=91.4$ inches. The experimental stresses shown are not the stresses measured on each stringer but are weighted averages of the stresses measured on each stringer and on the skin adjacent to the stringer on

each side. It was found that the skin stresses were consistently higher than the stringer stresses; near the root the difference was as much as 20 percent, but the difference decreased (roughly proportionally) with distance from the root. Since the ratio of stringer area to sheet area was more than 4:1, the weighted average

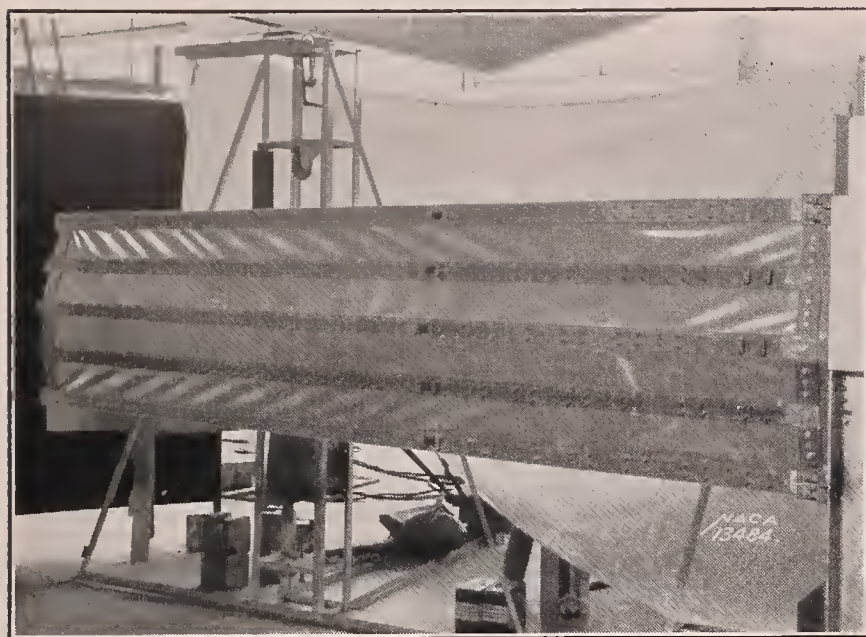


FIGURE 18.—N. A. C. A. beam 3—view of closed side.

stress never differed by more than 5 percent from the stringer stress proper.

DISCUSSION OF RESULTS

COMPARISON BETWEEN PROPOSED METHOD OF ANALYSIS AND EXPERIMENTAL RESULTS

The agreement between experiment and calculation is good for the axially loaded panel (fig. 9). For N. A.

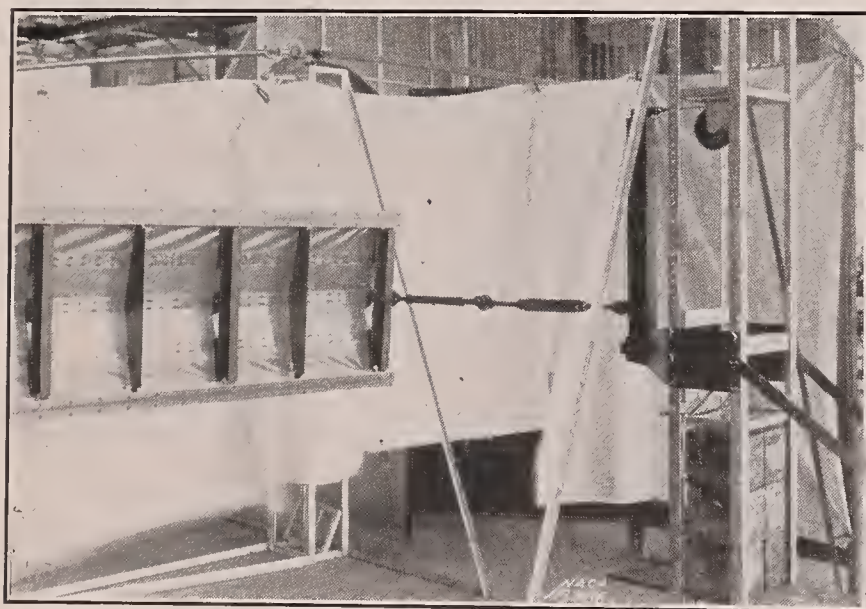


FIGURE 19.—N. A. C. A. beam 3—view of open side.

C. A. beams 2 and 3, the agreement is good except for the root region of the center stringer in beam 3 (figs. 12 and 20).

For N. A. C. A. beam 4, the agreement is reasonably good for the flange stresses (fig. 23). For the stringer stresses, which are shown only for the root station in figure 24, the agreement may be considered fair, if the differences between the two test series and the differ-

ences between stringer stresses and skin stresses, previously mentioned, are considered.

For the Galcit beams, the agreement is somewhat

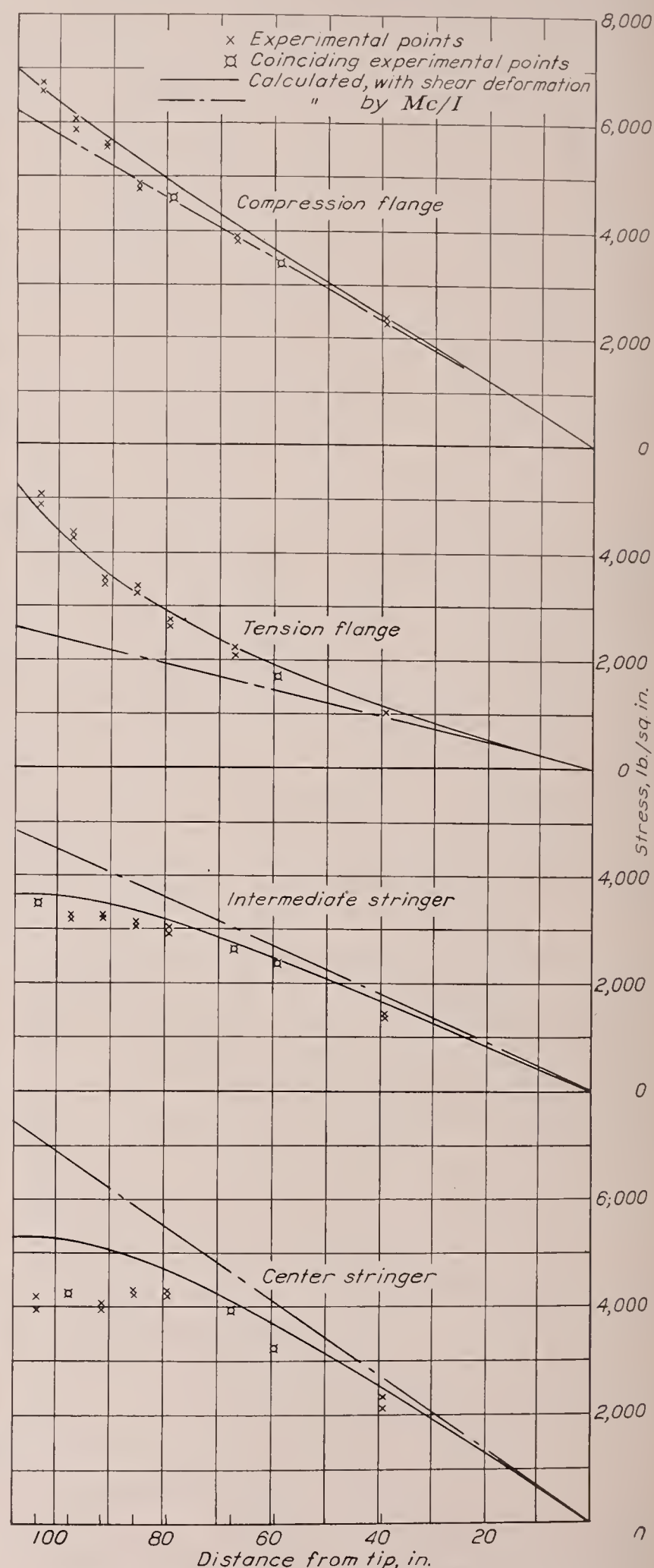


FIGURE 20.—Stresses in N. A. C. A. beam 3 for $P=250$ lb. $E=10.4 \times 10^6$.

poor for the beam with the thin cover (fig. 14 (a)) but is quite good for the beam with the thick cover (fig. 14 (b)).

For Schnadel's ship model, the agreement is fair at

some stations and very poor at others. Study of the test report shows that the accuracy of the test was, for a number of reasons, far below the accuracy of all other tests analyzed in the present paper. This conclusion is borne out by inspection of the results in figure 16. Note, for instance, at station 2 and particularly at station 3, that all experimental stresses are

beams under load shows that the spanwise variation in the condition of the sheet is indeed small; it should be borne in mind that relatively large variations in shear stiffness influence the stringer stresses but little, as shown in reference 1. The chordwise variation, however, is marked, the outer panels being buckled while the inner panels are not. This variation was taken

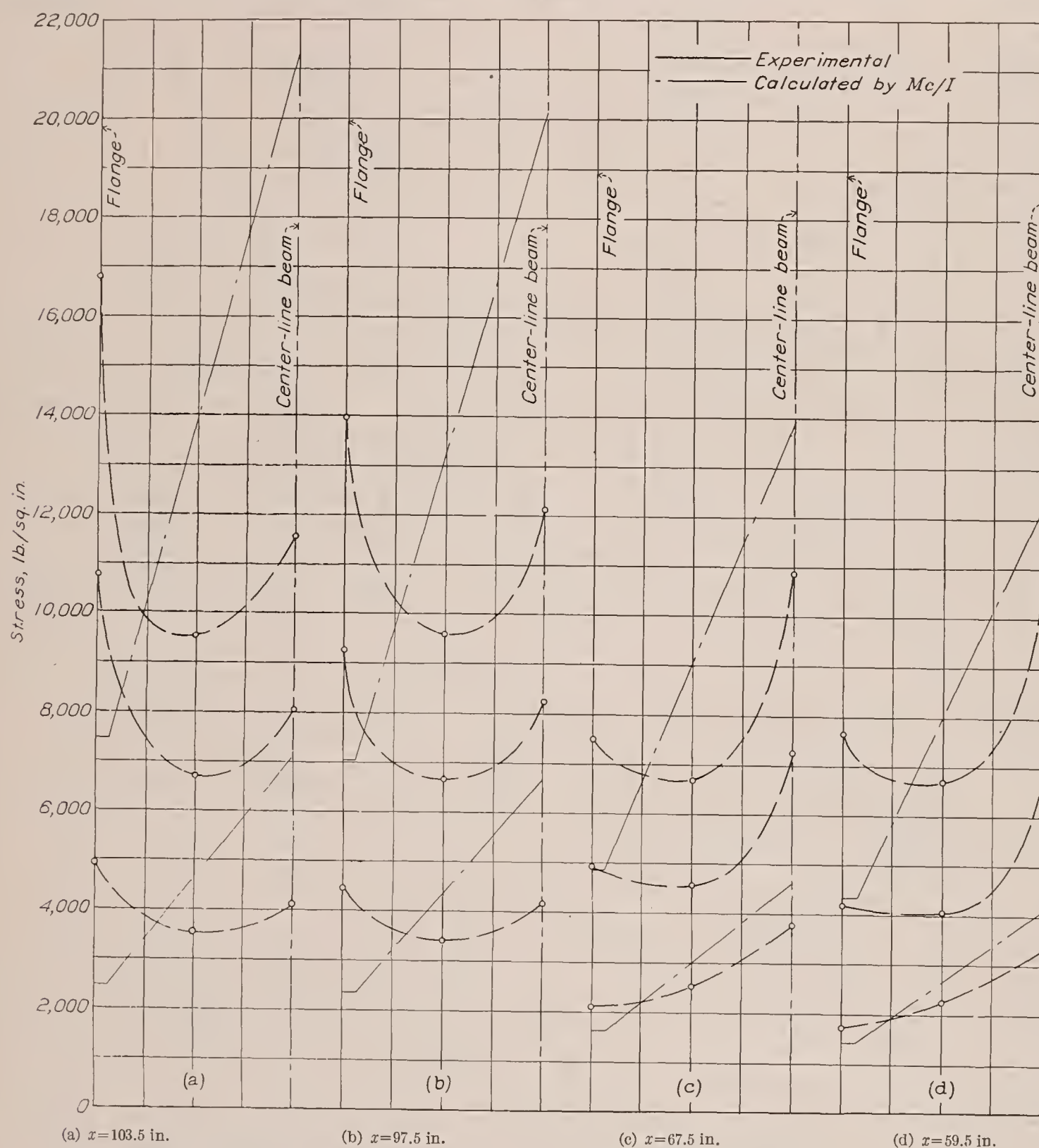


FIGURE 21.—Chordwise stress distribution in N. A. C. A. beam 3 at four stations for $P=250, 500$, and 750 lb.

Mc/I shown for $P=250$ and 750 pounds.

considerably higher than the calculated ones; hence the summation of the internal moments would be much larger than the external moment. The test was included in the analysis because it is the only available complete test on the limiting case where stringers and sheet are merged into a single unit, a plate.

In all beam analyses made for the present paper, over-all average values of effective shear stiffness were used. A glance at the photographs of the N. A. C. A.

into account approximately by using a weighted average value of G_e , and this procedure may be responsible for some of the discrepancies between test and calculation. Theoretically, it might be possible to take this variation into account more exactly, but there appears to be little justification to do so when the proposed simplified method of analysis is used. In practical design, large chordwise variations of shear stiffness should be avoided by using heavier skin near the flanges.

If the far-reaching simplifications involved in the theory are considered as well as the difficulties of strain-gage testing of sheet-metal structures, the agreement between experiments and analysis is, on the whole, fairly satisfactory. Although the analysis does not give a perfect picture of details, it does appear to give a substantially correct picture for the stresses most important in design work.

To persons unacquainted with strain-gage testing, the discrepancies between tests and calculations might appear to be rather large. It should be pointed out, however, that strain-gage tests of conventional types of structures, such as trusses and plate girders, frequently show discrepancies fully as large or larger.

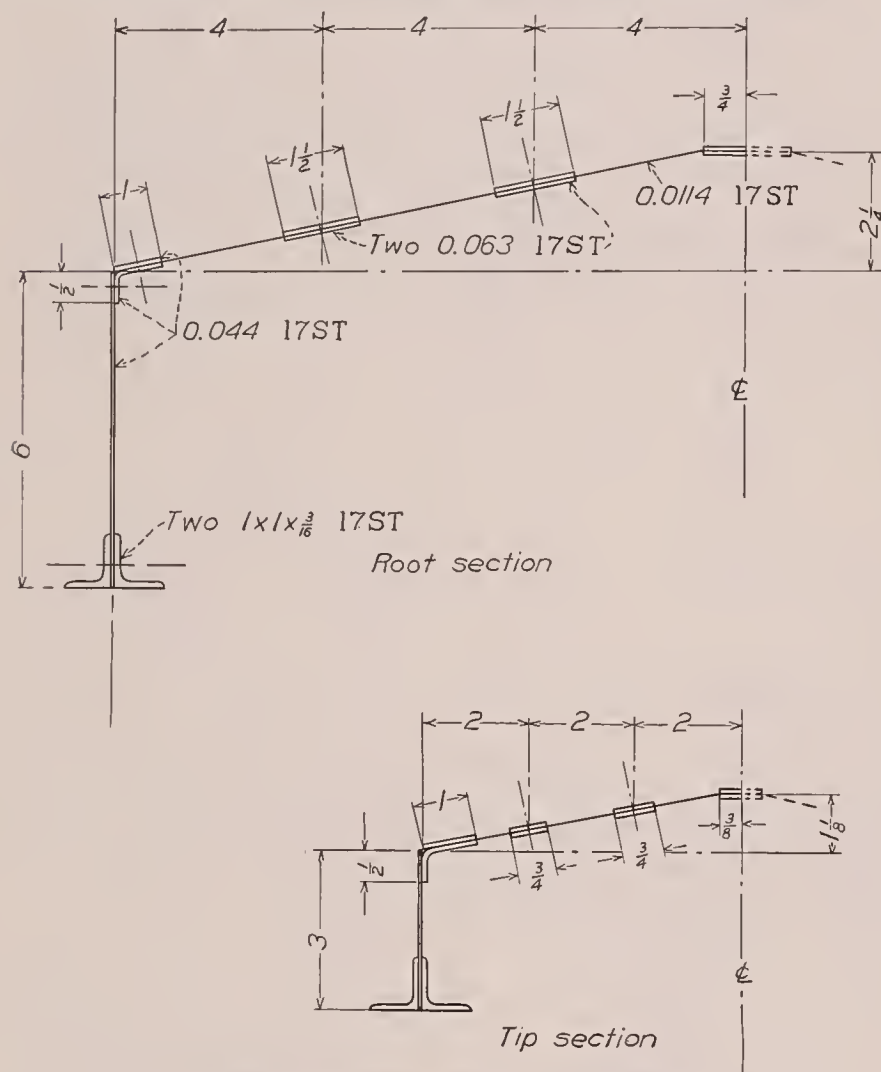


FIGURE 22.—Cross sections of N. A. C. A. beam 4.

COMPARISON BETWEEN PROPOSED METHOD OF ANALYSIS AND YOUNGER'S SOLUTION

The proposed method of analysis is based on the same simplified physical concepts as Younger's method (reference 1). Younger's solution is mathematically more rigorous, but it applies only to a beam of constant section with a cosine-wave bending moment. For practical shapes of bending-moment curves, it is necessary to superpose a number of cosine terms.

Comparisons for the case of a concentrated load applied at the tip show that the substitute-structure method of analysis gives flange stresses at the root that are as much as 15 percent higher than the stresses calculated by superposing four cosine terms. Judging by the magnitude of successive terms, four were considered a sufficient number to give the desired accuracy. The

stresses in the longitudinals given by the substitute-structure method are correspondingly lower than those given by Younger's formula. Comparison with experiments for two cases (figs. 9 and 12) shows that Younger's extended formula is in very much poorer agreement

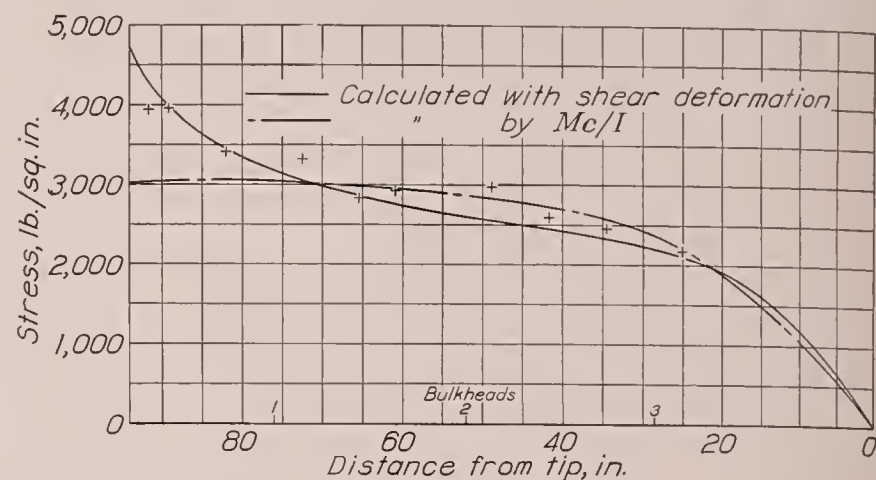


FIGURE 23.—Flange stresses in N. A. C. A. beam 4 at $P=250$ lb. $E=10.4 \times 10^6$.

with the experiments than the substitute-structure method. This fact is somewhat surprising, and the question arises as to what might be the possible reasons for the poor agreement.

If a diagonal-tension field forms on the sheet, the shear between flange and longitudinals will not be

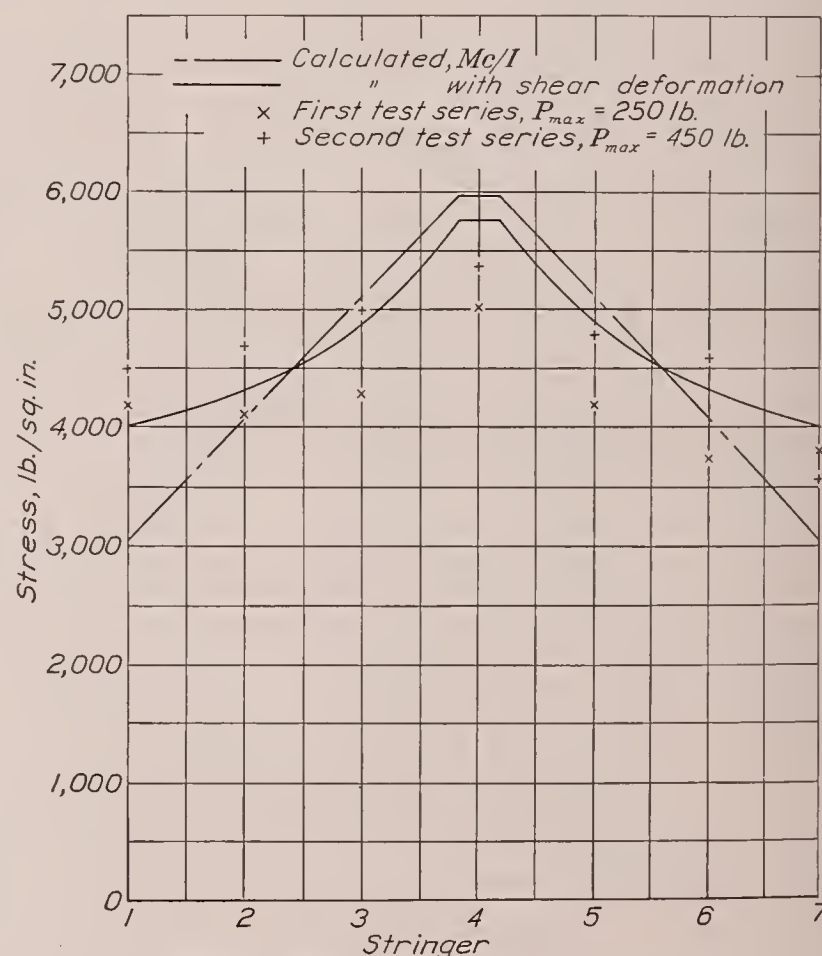


FIGURE 24.—Stresses at first station in N. A. C. A. beam 4.

transmitted at right angles to the axis of the beam but, theoretically, at 45° angles. The theory may therefore be expected to give reasonably accurate results only if the bending moment does not change too much over a spanwise distance equal to the width of the beam. Obviously, this condition is not fulfilled by the higher cosine terms after the first one, so that their physical significance may be seriously questioned.

The evidence presented by the axially loaded panel (fig. 9), which did not buckle appreciably at $P=1,000$ pounds, appears to indicate that even for a shear-resistant panel the superposition of cosine terms does not always yield a sufficiently close approximation to the physical facts. If this defect always exists, then any method based on the same fundamental physical concepts and relying on trigonometric series will be unreliable.

It might be mentioned in passing that the theoretical treatment given by Schnadel in reference 4 and in several other papers is of little interest for aeronautical structures, because it applies only to an isotropic plate where the shear stiffness is fixed by the theoretical relation

$$G = \frac{E}{2(1+\mu)}$$

The results therefore contain no provision to take into account reduced values of G_e or plates stiffened by stringers.

THE INFLUENCE OF RIBS

Ribs or bulkheads influence the stresses in the beam cover in two ways. By virtue of their axial stiffness, they help to carry transverse stresses in the cover. This function is unimportant if the sheet does not buckle into a diagonal-tension field, but it is, of course, of paramount importance if a diagonal-tension field forms. Because the rib flanges have bending stiffness in the plane of the cover, they also tend to reduce the shear deformation. It was pointed out in reference 1 that this effect can be calculated for a single-stringer beam and it was stated that in practical cases the effect is very small. This conclusion, drawn from the calculations, has been confirmed by tests of N. A. C. A. beam 2. It should be noted, of course, that these remarks apply only if the basic requirement of very moderate camber is fulfilled.

N. A. C. A. beam 2 was tested first with all longitudinals sliding freely over the ribs and held against the ribs only by their own tension. A second strain survey was then made of the beam after connecting the longitudinals with the ribs by taper pins. The ribs were very heavy steel channels, as shown on the drawings and photographs, but their only effect was to smooth out a few minor irregularities in the stress-distribution plots. An extremely heavy tip rib was then added; this rib reduced the stress in the flange about 6 percent. Calculation indicated, however, that an equivalent amount of material used to thicken the skin would have resulted in increasing the skin thickness by about 500 percent over the entire span and would have reduced the stress in the flange by about 33 percent.

A brief inspection of figure 25 is sufficient to show why the rib is quite ineffective. Figure 25 (a) shows the tip rib acted upon by the longitudinal. In figure 25 (b) it was assumed that the material contained in the tip rib is spread out some distance along the span. It is obvious that this change results in a much stiffer cross beam.

All tests of N. A. C. A. beam 3 were made without connections between longitudinals and ribs. On N. A. C. A. beam 4, which had bulkheads of normal size, the longitudinals were riveted to the bulkhead flange.

THE EFFECTIVE SHEAR MODULUS

The effective shear modulus of a thin sheet framed by rigid edge members is equal to the shear modulus of the material as long as the shear stress is lower than the critical or buckling stress. If the stress is increased beyond this value, diagonal-tension folds begin to form and grow. The effective shear modulus gradually decreases, approaching asymptotically the value $G_e = \frac{5}{8}G$. The nature of this transition was investigated experimentally by Lahde and Wagner (reference 5).

In practical structures, the edge members are not rigid; they have a finite axial stiffness and a finite bending stiffness. The influence of these stiffnesses has been treated analytically by Wagner in his original theory for the case of a fully developed diagonal-tension field. The influence of edge members with finite stiffness on the characteristics of a thin sheet in the transi-

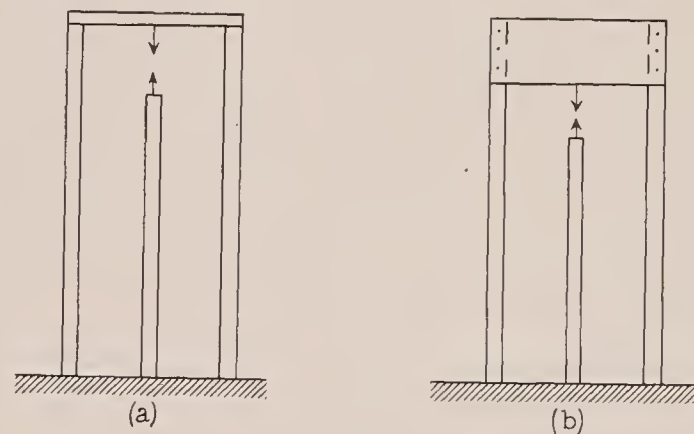


FIGURE 25.

tion zone between shear-resistant sheet and diagonal-tension field has not been investigated to date. Atkin offers a method of estimating the characteristics of a diagonal-tension beam by making tests on square panels (reference 6). Although this idea is fundamentally sound, Atkin's analysis is open to a serious objection. He claims that the deflection δ of a test panel can always be represented as a straight-line function of the load P , and he sets

$$\delta = kP$$

which means, in effect, that Atkin's method takes into account only the finite stiffness of the edge members. It disregards the gradual transition from $G_e = G$ to $G_e = \frac{5}{8}G$ in a rigidly framed sheet. In many practical cases, where the critical stress is not exceeded more than three or four times, the second factor is probably far more important than the first.

The tests described in references 2 and 3 were evaluated by their authors to give values of effective shear stiffness. These analyses have been questioned in a later paper (reference 7), chiefly because the values obtained were much lower than the theoretical values for the pure diagonal-tension field with rigid edge members.

A critical examination shows that in all these analyses the shear stiffness has been obtained by taking the differences of slopes of two experimental curves. This method is extremely sensitive to slight experimental errors. Unfortunately, experimental errors in strain-gage tests of sheet-metal structures are quite large, and the stresses are, furthermore, quite insensitive to changes in shear stiffness. The results obtained by such a slope method are therefore very questionable, and in some cases it is possible to change the calculated values of the shearing stiffness several hundred percent by

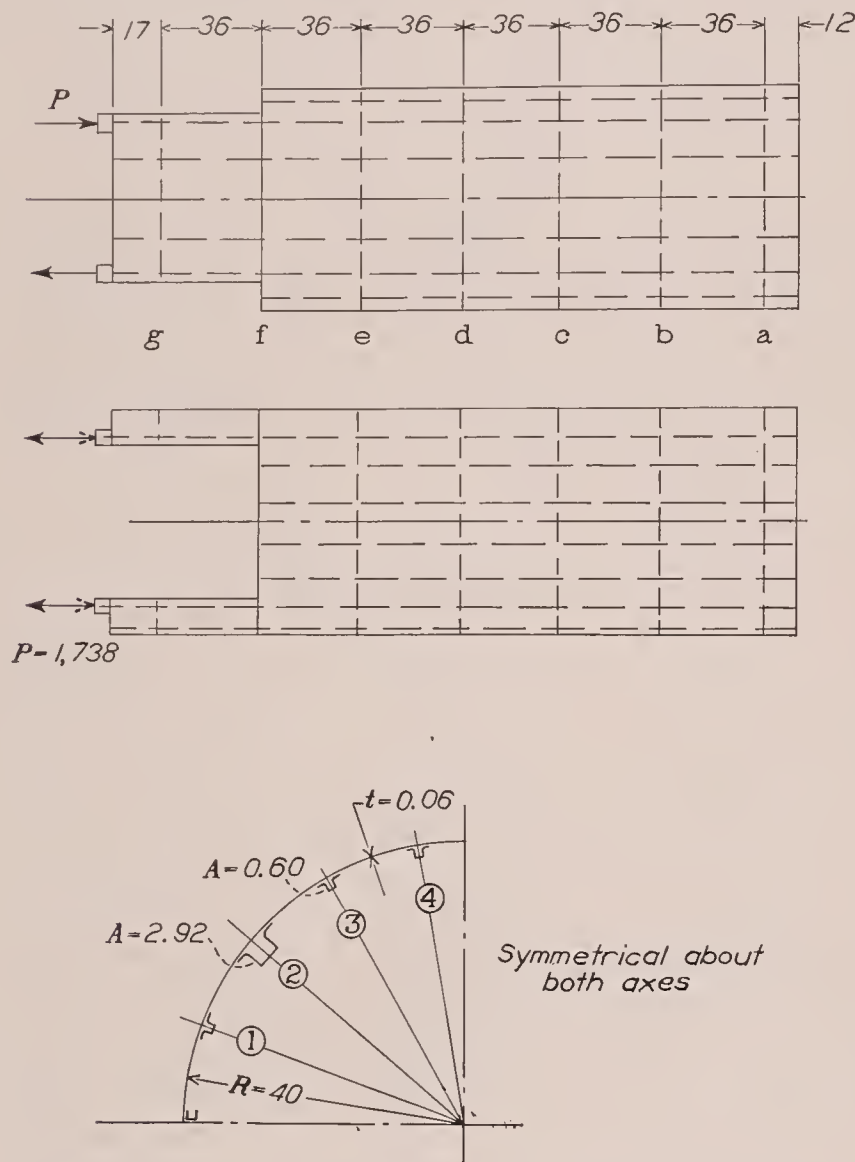


FIGURE 26.—Test fuselage (data from reference 10). Dimensions are in cm and loads in kg.

varying, for instance, the effective width within its possible limits.

In view of these circumstances, it appears more advisable to analyze the tests in such a manner that over-all average values for the shear stiffness are obtained by utilizing the ordinates of experimental curves instead of the slopes of these curves. The procedure would be to calculate the stresses under several assumptions for the shear stiffness and to find the stress curve that gives the best agreement with the test results. Several examples of such a procedure are given in reference 1.

The high-load tests of N. A. C. A. beam 3 were analyzed in a similar manner. Unfortunately, the limited number of strain gages necessitated repeat load-

ings; during these repeat tests, changes occurred in parts of the beam that prevented a definite analysis. It was estimated that, at $P=900$ pounds, the effective shear modulus was $G_e=0.5G$, but no definite estimate could be made for higher loads. The trouble may have been partly that the flange was no longer obeying Hooke's law at the gage station, the stress being over 30,000 pounds per square inch.

It should be noted that the effective modulus was well below the theoretical value $G_e=\frac{5}{8}G$ for rigid edge members, in spite of the fact that the edge members were much stiffer than they would be in actual construction and that tension was superimposed on the shear in the skin.

The opinion is occasionally heard that the shear modulus of corrugated sheet is appreciably less than that of flat sheet. There appears to be no published information to support such an opinion. The analysis of torque tests of box beams with corrugated covers (reference 8) leads to the conclusion that up to shear stresses of around 3,000 pounds per square inch the shear modulus of corrugated sheet is equal to the modulus of the material. Small deviations of 5 to 10 percent, which occur in such tests, can probably be attributed to inefficiency of the joints in the built-up boxes because they have been found in practically all torque tests. Ebner, who has an exceptionally broad background of experience in tested stressed-skin structures, states in reference 9 that the shear stiffness of corrugated sheet remains unchanged up to the point of failure. It is necessary, of course, to make proper allowance for the difference between developed width and projected width of a corrugated panel when computing shear deformations.

APPLICATION OF THEORY TO FUSELAGES

The theory in this paper was developed for the express purpose of furnishing means for analyzing wing beams or other beams with very moderate camber. It is of interest, of course, to gain some idea of how well the theory applies to beams with large camber, such as fuselages. A fuselage test that came to the attention of the author after the investigation was finished will therefore be included.

The details of the test may be found in reference 10. The most important data are given in figure 26. The shell represents a fuselage with symmetrical cut-outs, and the bending moment is introduced in the form of concentrated forces at the longerons. Between frame a and the end, the shell was fixed to a test jig by a heavy steel ring.

The part of the shell between the longerons and the neutral axis was considered as "shear web" and the remainder as "cover." The analysis was made by formula (A-16). Local corrections to the computed stresses were made between frames e and g, because the sheet thickness was 0.08 centimeter between e and

f, and 0.10 centimeter between f and g resulting, together with the cut-out, in some changes in effective areas in this region.

The only variation from the standard procedure outlined in this paper was the use of a somewhat more rational method of determining c_s than simply assuming $c_s = \frac{1}{2}c$. The substitute camber was determined by the condition.

$$\left(c_s + \frac{1}{2}h_w\right)^2 A_L = I_L$$

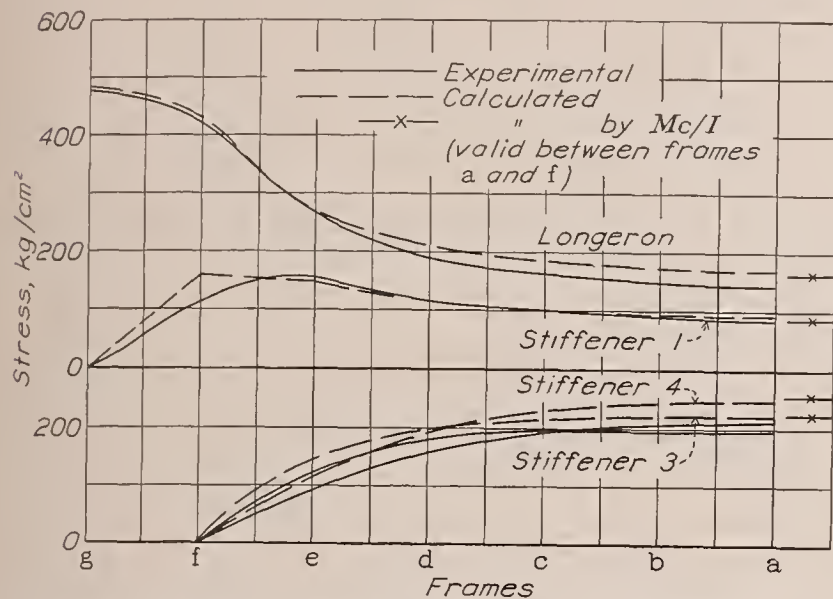


FIGURE 27.—Experimental and calculated stress distribution in fuselage with symmetrical cut-outs (experimental data from reference 10).

That is, if the longitudinals are concentrated at the z location defined by c_s , the moment of inertia must be the same as in the actual section.

Figure 27 shows the experimental and the calculated results.

CONCLUDING REMARKS

Large shear deformations are probably always accompanied by loss of structural efficiency; efficient design therefore calls for utilization of all available means for reducing the shear deformation. In a combination consisting of skin stiffened by individual stringers, the stringers furnish no contribution to the shear stiffness. In a combination of flat skin with corrugated skin, however, all the material carries longitudinal stresses as well as shearing stresses; such a

combination probably represents, therefore, a close approach to the best possible efficiency from considerations of uniform stress distribution. It must be remembered, too, that the shear stiffness of flat sheet is very adversely affected if it is thin enough to buckle into diagonal-tension folds, a condition that does not develop in corrugated sheet.

For sheet with individual stringers, experimental studies on individual panels have usually led to the conclusion that the best efficiency is obtained by making the skin as thin as possible, consistent with practical considerations. If the shear deformation in the actual structure is taken into account, it becomes evident that this conclusion will often require serious modification. It might be worth while in some cases to investigate the effect of thickening the skin near the wing tip, where the shear deformations are largest and therefore easiest to decrease. It might be pointed out that, once an adequate tip rib is provided, shear deformation can be reduced more efficiently by increasing the skin thickness, especially near the tip, than by attempting to increase the (horizontal) bending stiffness of the tip rib.

A final word of warning should be given. A method of stress analysis such as the method described in this paper deals only with the stress distribution before failure occurs. If the maximum stress for a given load is varied by changing the design of the structure, then the failing stresses may change, too, so that the maximum stress is not the sole criterion for the efficiency of the structure. For example, if the skin is made very heavy with relation to the stringers, then buckling of the skin may induce premature failure of the stringers. Thus far, no mathematical analysis of this problem has been published; test results must be used. The subject of allowable stresses is beyond the scope of this paper, but is mentioned herein as a warning against drawing hasty conclusions.

LANGLEY MEMORIAL AERONAUTICAL LABORATORY,
NATIONAL ADVISORY COMMITTEE FOR AERONAUTICS,
LANGLEY FIELD, VA., April 20, 1938.

APPENDIX A

LIST OF SYMBOLS

A , cross-sectional area (sq. in.).
 E , Young's modulus (lb./sq. in.).
 F , internal force (lb.).
 G , shear modulus (lb./sq. in.).
 I , geometric moment of inertia.
 K , constant.
 L , length of panel or beam (in.).
 M , bending moment (in.-lb.).
 P , external load (lb.).
 S , shear force (lb.).
 b , half-width of beam or panel (in.).
 c , camber of cover (in.).
 h , depth of beam (in.).
 t , thickness of cover sheet (in.).
 w , running load (lb./in.).
 x , distance along center line.
 y , distance from center line.
 z , distance from centroidal axis of cross section.

σ , direct (normal) stress (lb./sq. in.).
 τ , shear stress (lb./sq. in.).
 $*$, denotes condition where actual and auxiliary stresses are superposed.
 Subscripts have the following significance:
 A , auxiliary.
 C , cover sheet.
 CL , center line.
 F , flange.
 L , longitudinal.
 P , theoretical values assuming that plane sections remain plane.
 S , substitute.
 T , total.
 U , uniform.
 W , shear web.
 a , applied.
 e , effective.
 0 , root section.

APPENDIX B

ANALYTICAL SOLUTIONS FOR STRUCTURES WITH A SINGLE LONGITUDINAL

GENERAL REMARKS

The sign conventions of reference 1 are retained. Stresses in stringers are positive when tensile. Shear stresses in the cover sheet are positive when caused by positive stresses in the flange F . Shear stresses in the shear web are positive when causing positive stresses in the flange F .

The figures show, first, the half structures and, second, the two possible cases of making symmetrical structures out of these half structures. The formulas should be applied only to such symmetrical structures. Theoretically, the formulas also apply to the half structures if the forces T are applied at the stiff transverse member at the tip. This procedure would involve the assumption that the stringers were infinitely stiff in bending; it is therefore believed that the application of the formulas to the half structures might easily lead to very serious errors.

Some of the formulas have already been given in reference 1. They are repeated here for convenience and are written in a slightly different form to bring out more clearly the correction factor that must be applied to the

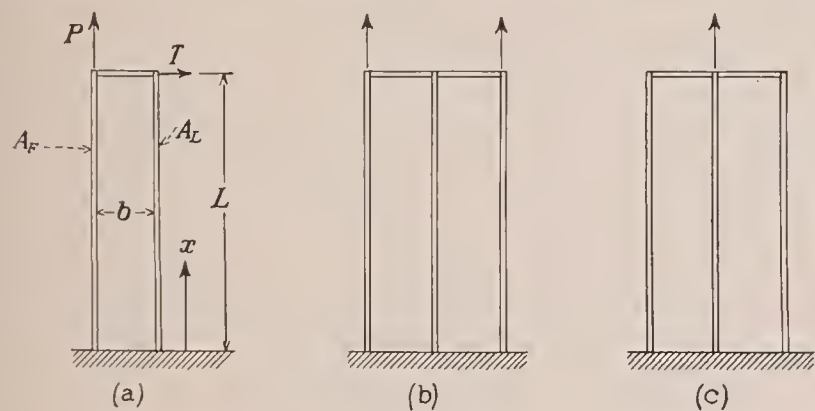


FIGURE 28.

ordinary bending theory in order to take shear deformation into account. When the shear stiffness approaches infinity, this correction factor approaches zero.

I—THE AXIALLY LOADED PANEL

(a) **The longitudinal built in at the root (fig. 28).**—For the case of an axially loaded panel with the longi-

tudinal built in at the root, the following formulas are obtained:

Let

$$K^2 = \frac{G_e t}{E b} \left(\frac{1}{A_F} + \frac{1}{A_L} \right) \quad (\text{A-1})$$

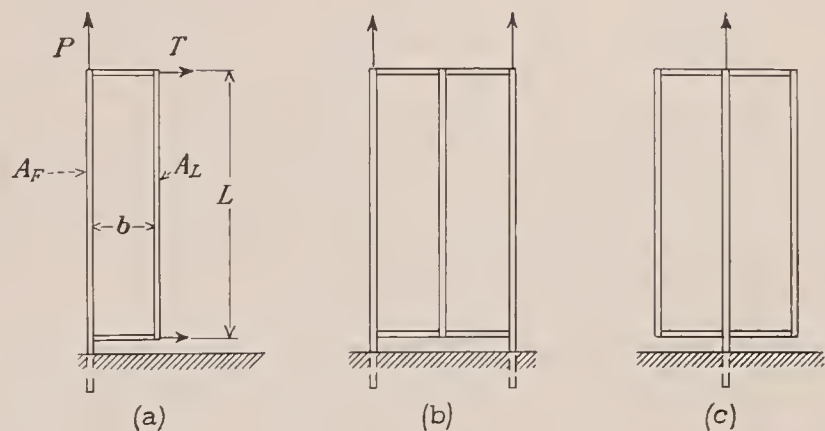


FIGURE 29.

and

$$A_T = A_F + A_L$$

Then

$$\tau = \frac{P}{A_F} \frac{G_e}{E b K} \frac{\sinh Kx}{\cosh KL} \quad (\text{A-2})$$

$$\sigma_F = \frac{P}{A_T} \left(1 + \frac{A_L}{A_F} \frac{\cosh Kx}{\cosh KL} \right) \quad (\text{A-3})$$

$$\sigma_L = \frac{P}{A_T} \left(1 - \frac{\cosh Kx}{\cosh KL} \right) \quad (\text{A-4})$$

(b) **The longitudinal not built in at the root (fig. 29).**—The easiest way to treat the case of the longitudinal not built in at the root is to take advantage of the symmetry of the structure. When the origin is taken at the middle of the length L , this case is reduced to case I (a).

II—THE BEAM WITH FLAT COVER

The formulas for the beam with flat cover apply to two cases: beams in which the depth h is constant along the span, if a concentrated load P is applied at the tip; and beams in which the depth h tapers linearly to zero at the tip, if the loading w per foot run is uniform along the span. In the case of uniform loading, $wL/2h_0$ is substituted for P/h in the formulas for shear stress.

(a) The longitudinal built in at the root (fig. 30).—

$$\tau = \frac{P}{th \left(1 + \frac{A_F}{A_L}\right)} \left(1 - \frac{\cosh Kx}{\cosh KL}\right) \quad (A-5)$$

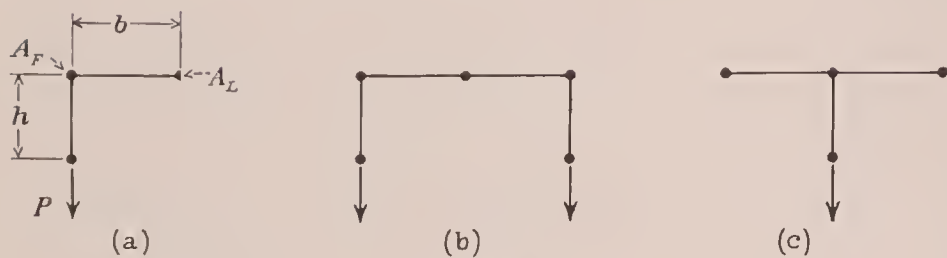


FIGURE 30.

$$\sigma_F = \frac{M_x}{h_x A_T} \left(1 + \frac{A_L}{A_F} \frac{\sinh Kx}{Kx \cosh KL}\right) \quad (A-6)$$

$$\sigma_L = \frac{M_x}{h_x A_T} \left(1 - \frac{\sinh Kx}{Kx \cosh KL}\right) \quad (A-7)$$

where K has the same meaning as in (A-1).

(b) The longitudinal not built in at the root.—The case of a beam with flat cover and the longitudinal not built in at the root is of interest as a limiting case for wings where the skin is not continuous, for example, at the wing-fuselage joint.

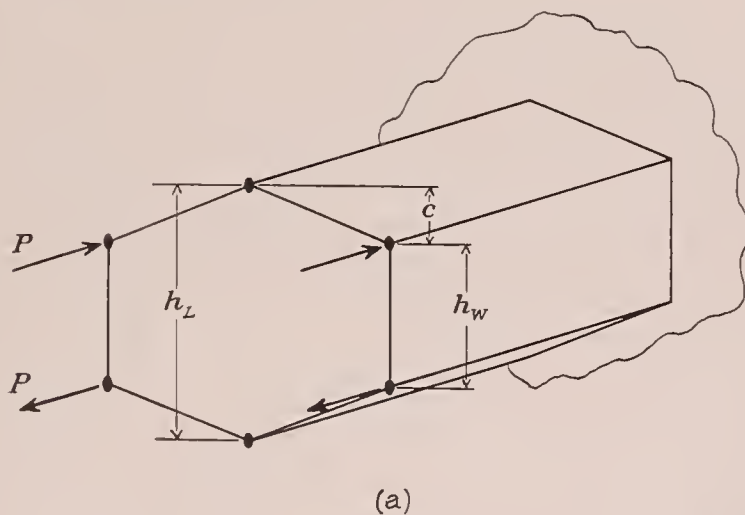
$$\tau = \frac{P A_L}{t h A_T} \left(1 - \frac{KL \cosh Kx}{\sinh KL}\right) \quad (A-8)$$

$$\sigma_F = \frac{M_x}{h_x A_T} \left(1 + \frac{A_L L \sinh Kx}{A_F x \sinh KL}\right) \quad (A-9)$$

$$\sigma_L = \frac{M_x}{h_x A_T} \left(1 - \frac{L \sinh Kx}{x \sinh KL}\right) \quad (A-10)$$

III—THE BEAM WITH CAMBERED COVER

As in the case of the beam with flat cover, the formulas for the beam with cambered cover are valid for two cases: for a concentrated load P applied at the tip, if h and c are constant; and for a uniformly distributed load w per foot run, if h and c taper linearly to zero at the tip. For the tapered beam, $wL/2$ is substituted for P , and z_L and I are taken at the root station in the formula for shear stress only.



(a)

(a) The longitudinal built in at the root (fig. 31).—

$$\tau = \frac{P z_L A_L}{t I} \left(1 - \frac{\cosh Kx}{\cosh KL}\right) \quad (A-11)$$

$$\sigma_F = \frac{M z_F}{I} \left[1 + \frac{z_L A_L}{z_F A_F} \left(1 + \frac{c}{h_w}\right) \frac{\sinh Kx}{Kx \cosh KL}\right] \quad (A-12)$$

$$\sigma_L = \frac{M z_L}{I} \left(1 - \frac{\sinh Kx}{Kx \cosh KL}\right) \quad (A-13)$$

In these equations, I is the geometric moment of inertia, z_L is the distance of the longitudinal from the centroidal axis, and K is defined by

$$K^2 = \frac{G_e t}{E b'} \left(1 + \frac{c}{h} + \frac{1}{A_L}\right) \quad (A-14)$$

(b) The longitudinal not built in at the root.—The formulas for the case of the longitudinal not built in at the root may be obtained by changing the factors in parentheses in analogy with cases II (a) and II (b).

IV—THE BEAM WITH CAMBERED COVER IN "PURE BENDING"

The formulas for the case shown in figure 32 (a) are:

$$\tau = \frac{P G_e \sinh Kx}{E b' K \cosh KL} \left(\frac{1}{A_F} + \frac{c h_w}{I}\right) \quad (A-15)$$

$$\sigma_F = \frac{P h_w^2}{2 I} \left[1 + \frac{A_L}{A_F} \left(\frac{h_L}{h_w}\right)^2 \frac{\cosh Kx}{\cosh KL}\right] \quad (A-16)$$

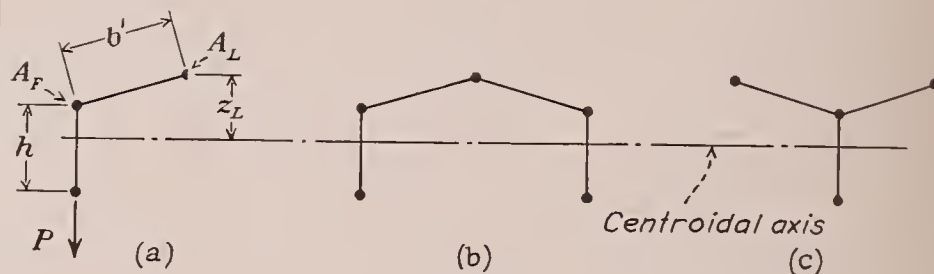
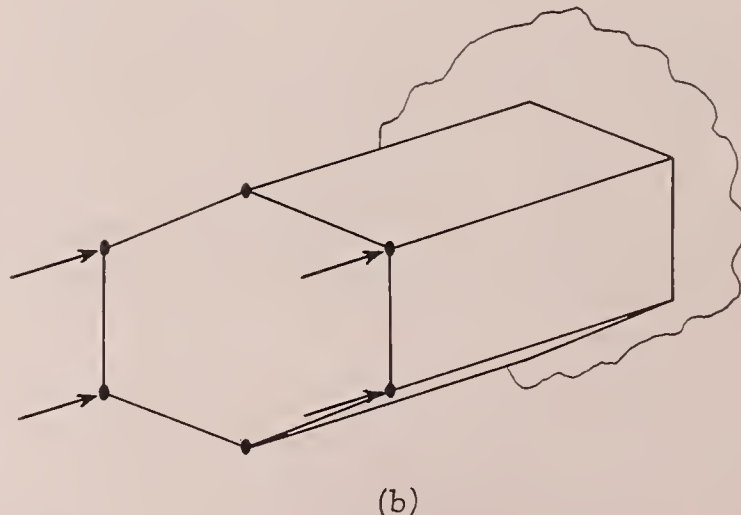


FIGURE 31.

where K is defined by

$$K^2 = \frac{G_e t}{E b'} \left(1 + \frac{2c}{h_w} + \frac{1}{A_L}\right) \quad (A-17)$$



(b)

FIGURE 32.

It should be noted that there is shear in the shear web, because the shear in the cover sheet has a component in the z direction. For this reason, the cambered cover cannot be used alone as an axially loaded panel unless provisions are made to absorb this lateral force, for instance, by making the panel symmetrical as in figure 32 (b).

REFERENCES

1. Kuhn, Paul: Stress Analysis of Beams with Shear Deformation of the Flanges. T. R. No. 608, N. A. C. A., 1937.
2. White, Roland J., and Antz, Hans M.: Tests on the Stress Distribution in Reinforced Panels. Jour. Aero. Sci., vol. 3, no. 6, April 1936, pp. 209-212.
3. Lovett, B. B. C., and Rodee, W. F.: Transfer of Stress from Main Beams to Intermediate Stiffeners in Metal Sheet Covered Box Beams. Jour. Aero. Sci., vol. 3, no. 12, Oct. 1936, pp. 426-430.
4. Schnadel, Georg: Die Spannungsverteilung in den Flanschen dünnwandiger Kastenträger. Jahrbuch der Schiffbau-technischen Gesellschaft, 1926, S. 207-291.
5. Lahde, R., and Wagner, H.: Tests for the Determination of the Stress Condition in Tension Fields. T. M. No. 809, N. A. C. A., 1936.
6. Atkin, E. H.: Stiffness in Stressed Skins. A Method of Determining the Shear Rigidity from Experimental Data on Small Panels. Aircraft Engineering, vol. VIII, no. 90, Aug. 1936, pp. 213-217, 220.
7. Lin, Tung-Hua: On the Transfer of Stress in Metal Sheet Covered Beams. Jour. Aero. Sci., vol. 4, no. 12, Oct. 1937, pp. 510-511.
8. Kuhn, Paul: The Initial Torsional Stiffness of Shells with Interior Webs. T. N. No. 542, N. A. C. A., 1935.
9. Ebner, H.: Zur Festigkeit von Schalen- und Rohrholmflügeln. Jahrbuch der Deutsche Luftfahrtforschung, 1937, S. I 430 - I 441. (Also published in Luftfahrtforschung, Bd. 14, Lfg. 4/5, 30. April 1937, S. 179-190.)
10. Schapitz, E., and Krümling, G.: Belastungsversuche mit einer versteiften Kreiszyinderschale bei Krafteinleitung an einzelnen Punkten. Luftfahrtforschung, Bd. 14, Lfg. 12, 20. Dez. 1937, S. 593-606.

REPORT No. 637

DETERMINATION OF BOUNDARY-LAYER TRANSITION ON THREE SYMMETRICAL AIRFOILS IN THE N. A. C. A. FULL-SCALE WIND TUNNEL

BY ABE SILVERSTEIN and JOHN V. BECKER

SUMMARY

For the purpose of studying the transition from laminar to turbulent flow, boundary-layer measurements were made in the N. A. C. A. full-scale wind tunnel on three symmetrical airfoils of N. A. C. A. 0009, 0012, and 0018 sections. The effects of variations in lift coefficient, Reynolds Number, and airfoil thickness on transition were investigated. Air speed in the boundary layer was measured by total-head tubes and by hot wires; a comparison of transition as indicated by the two techniques was obtained.

The results indicate no unique value of Reynolds Number for the transition, whether the Reynolds Number is based upon the distance along the chord or upon the thickness of the boundary layer at the transition point. In general, the transition is not abrupt and occurs in a region that varies in length as a function of the test conditions. With increasing lift, the transition on the upper surface moves toward the forward stagnation point; whereas, on the lower surface, the transition progresses in the opposite direction. This effect is most marked for the thin airfoils. The total-head tubes and hot wires indicate essentially the same point of transition. Profile-drag results are given and a correlation of the drag and the transition measurements is attempted.

INTRODUCTION

The effect of skin friction on the air flow over a flat plate or an airfoil has been shown by many early writers to be restricted to a thin layer of air of reduced momentum that flows along the surface. The air flow in this boundary layer is laminar at low Reynolds Numbers; transition to a turbulent regime is, however, generally observed to occur when the Reynolds Number is increased. Extensive investigations have not yet provided a means for reliable prediction of the transition, although Burgers (reference 1), van der Hegge Zijnen (reference 2), Dryden (reference 3), Jones (reference 4), and others have shown that transition depends upon initial stream turbulence, Reynolds

Number, pressure gradient, curvature, and surface roughness.

Prediction of the transition is necessary in order to predict the drag because the skin friction occurring with a laminar boundary layer is less than with a turbulent one. No reliable extrapolation of wind-tunnel drag results to flight may be made until the effects of all the factors upon which transition depends may be explicitly stated.

Owing to the effects of air-stream turbulence, the interpretation of wind-tunnel transition data for application to flight conditions has been difficult. The possibility of a direct comparison between wind-tunnel and flight results is provided by the equipment of the N. A. C. A. full-scale wind tunnel. The turbulence in the full-scale tunnel as indicated by sphere tests (reference 5) is 0.3 percent. The present investigation, which was made in the full-scale tunnel, is the first part of a program planned to correlate the flight and tunnel results.

In the tests, boundary-layer velocities were measured on the upper surfaces of airfoils of the N. A. C. A. 0009, 0012, and 0018 sections at tunnel velocities from 30 to 90 miles per hour (values of the Reynolds Number from 1,730,000 to 5,020,000) over a lift-coefficient range from -0.57 to 0.65 . The tests were made with rectangular 6- by 36-foot metal airfoils having aerodynamically smooth surfaces. Measurements of profile drag at zero lift by means of force tests and the momentum method were also obtained.

In order to aid in the presentation of the experimental data and to clarify discussion, the following arbitrary definitions have been adopted for the present paper.

The transition region is the region in which the boundary-layer flow changes from laminar to turbulent. The beginning of this region will be referred to as the "transition point" and will be considered to be the point at which the velocity near the surface begins to show an abnormal increase. The end of the transition region has been taken as the point at which the velocity near the surface has reached a maximum.

SYMBOLS

The symbols used herein are defined as follows:

c_l , section lift coefficient.

C_{D0} , profile-drag coefficient of the wing.

c_{d0} , section profile-drag coefficient.

C_f , skin-friction coefficient.

u , local velocity, f. p. s.

U , velocity at edge of boundary layer, f. p. s.

V , tunnel air speed, m. p. h.

y , distance above airfoil surface.

s , distance along airfoil surface from forward stagnation point.

c , wing chord.

t , wing thickness.

δ , boundary-layer thickness ($u \cong 0.99U$ at δ).

δ^* , displacement thickness of the boundary layer

$$\left(\delta^* = \frac{1}{U} \int_0^\delta (U - u) dy \right).$$

R_δ , Reynolds Number based on the boundary-layer thickness at transition (based on U).

R_x , Reynolds Number based on the chordwise distance from the forward stagnation point to the transition point (based on V).

p , local pressure.

q , dynamic pressure, $\frac{1}{2}\rho V^2$.

METHODS AND APPARATUS

In a paper on boundary-layer transition in flight, Jones (reference 4) has given an excellent discussion of the methods by which the transition on an airfoil may be detected. Briefly, the transition may be determined either from observations of the velocity at the airfoil surface by means of a single total-head tube or a hot wire or from velocity measurements at several distances from the surface so that the boundary-layer profile may be defined. When the indicated velocity at the airfoil surface shows a marked increase in the transition region, the single-tube or the hot-wire method is quite satisfactory as a transition indicator. If, however, the chordwise velocity gradient in the boundary layer is low, so that the point of minimum velocity is indeterminate, the more extensive measurements of the velocity profiles are more dependable.

Characteristic velocity profiles for the laminar and turbulent boundary layers are shown in figure 1. Representative data showing the velocity changes that occur at transition for several heights in the boundary layer are shown in figure 2 to illustrate the fact that no sharp indication of transition is given for some heights in the boundary layer. It will be noted (fig. 2) that the transition point is shown to occur at $s/c = 0.26$ for all the heights except 0.050 inch; this height is about that at which the laminar and turbulent profiles

intersect, as shown in figure 1, and no extreme velocity gradients are therefore expected.

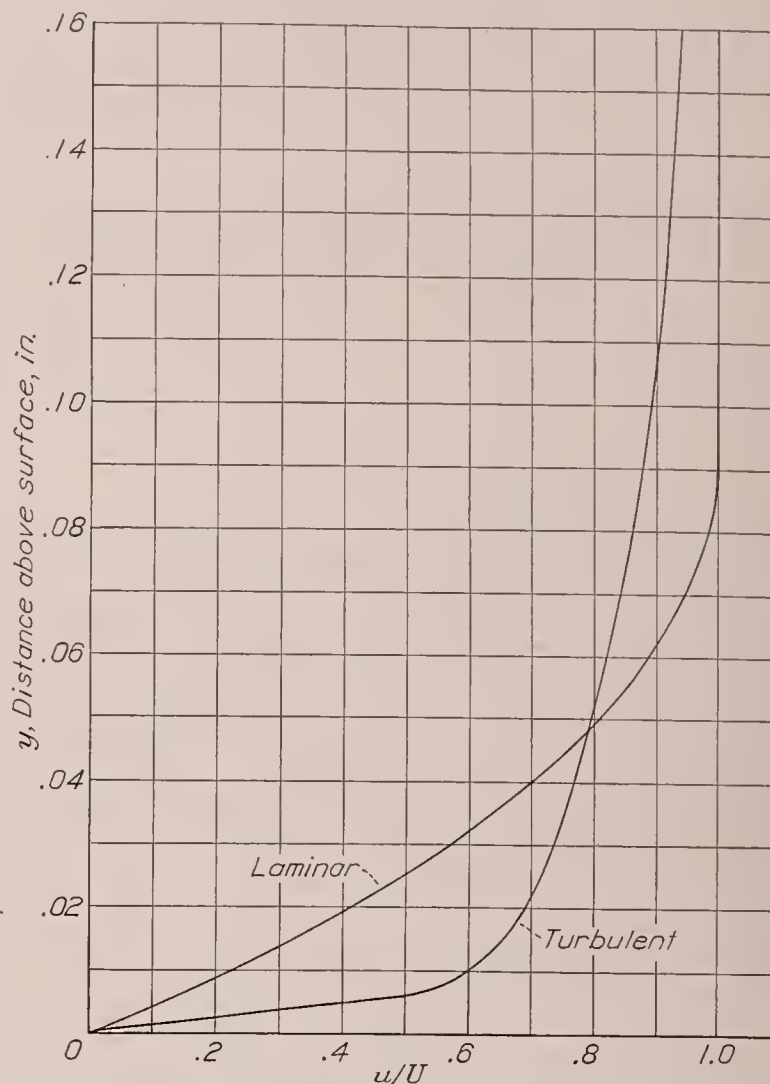


FIGURE 1.—Typical laminar and turbulent boundary-layer velocity profiles.

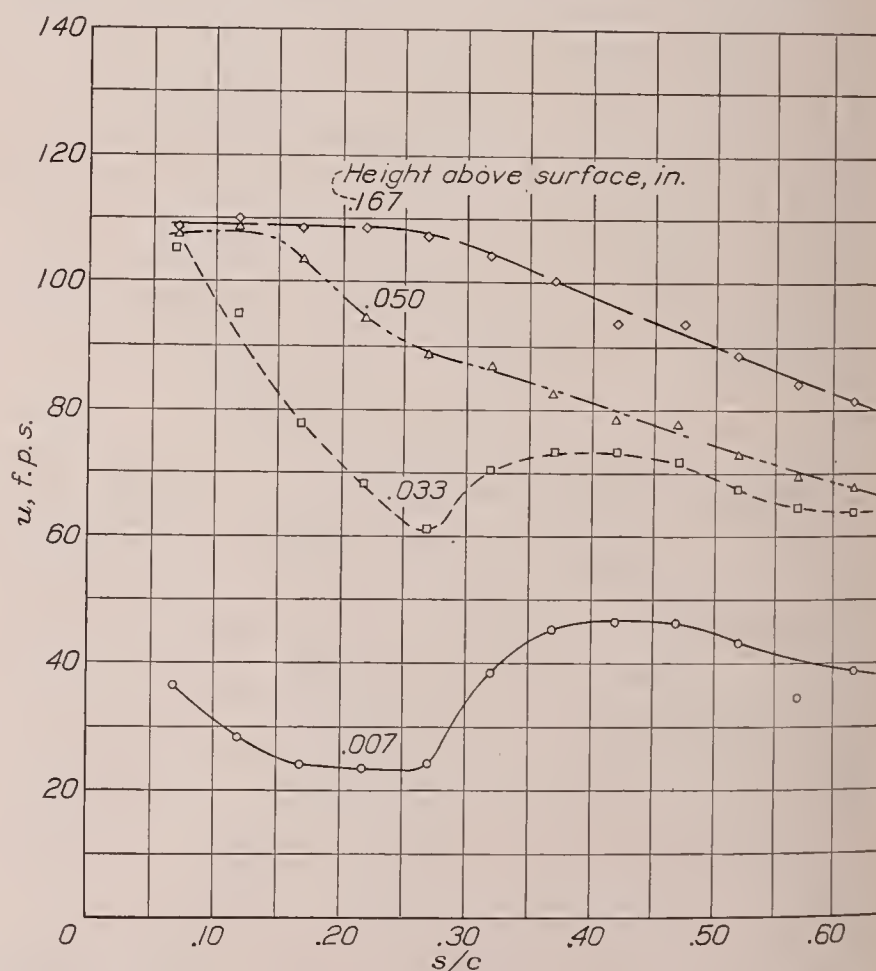


FIGURE 2.—Variation in the velocity of the boundary layer of the N. A. C. A. 0012 airfoil at several heights above the surface.

Hot-wire method.—The velocities in the boundary layer 0.01 inch above the wing surface were measured,

as suggested by Dr. H. L. Dryden, by means of platinum hot wires 0.001 inch in diameter and 1 inch long (fig. 3). The platinum wires were soldered across the ends of forks of B. & S. gage 26 (0.0159 inch) enameled copper wire. The ends of the forks were filed to thicknesses of 0.010 inch and sprung to keep the hot wire

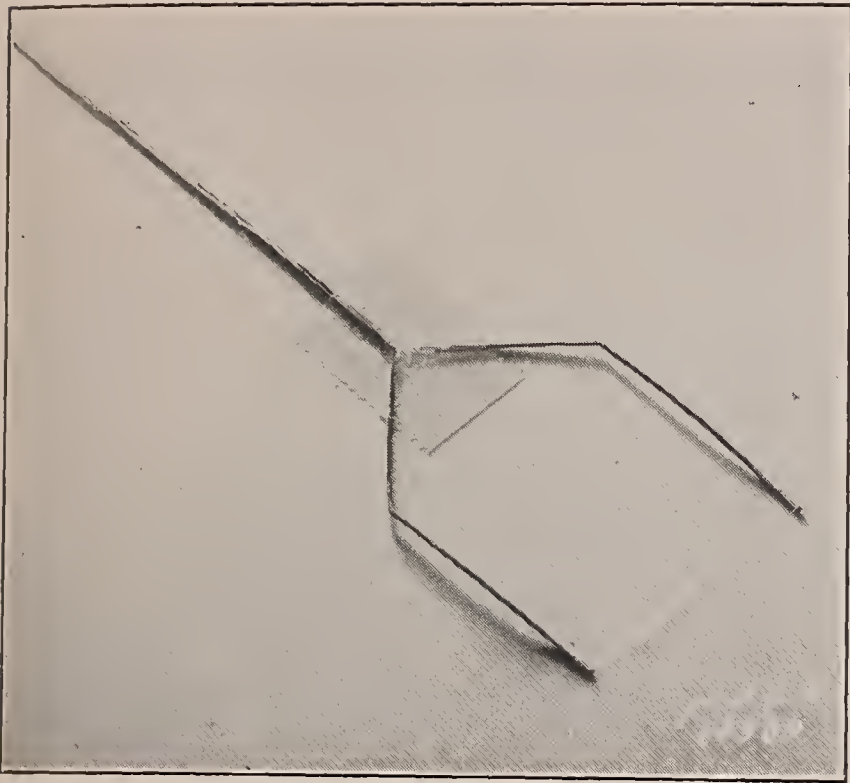


FIGURE 3.—Hot wire mounted on the airfoil. The platinum wire is 0.001 inch in diameter, 1 inch long, and 0.01 inch above the surface.

taut at all temperatures. The enameled wires were cemented together with an insulating glue at the base of the forks. In order to reduce the time required for obtaining the data, 12 hot-wire units were arranged on the wing at 0.05c intervals between the 0.10c and the 0.70c positions, as shown in figure 4. The wires were spaced at sufficient distances along the span so that the wake of one wire did not pass over another. They could be switched into the measuring circuit one at a time.

A Wheatstone bridge circuit, with a hot wire as one arm of the bridge, was used to maintain the resistance of the wire at a constant value (fig. 4). The resistances AB and BC were made large so that the current to the hot wire would be about equal that in the battery circuit. A 5-ohm rheostat was used to balance the bridge for the initial still-air condition; an initial current of 0.15 ampere in the battery circuit corresponded to a wire temperature of 150° C. The ½-ohm rheostat in series with each hot wire was used to adjust the resistances of the 12 circuits to precisely the same value after installation on the wing. Adjustment of a 50-ohm rheostat in the battery circuit was used to increase the current through the hot wire as the air speed was increased. During the tests, the procedure was to switch in a hot wire by means of the multiple switch, to adjust resistance AE until the galvanometer read zero, and then to observe the reading of the ammeter.

In order to obtain satisfactory velocity readings, it was necessary to calibrate the hot wire on a flat plate against a total-head tube at the same effective height. Velocity indications based on a calibration in a free stream in which the heat-loss and interference effects are neglected give completely erroneous results.

Total-head-tube method.—The velocities at four heights above the surface were measured by a bank of four small total-head tubes and a single static tube (figs. 5 and 6). (The static pressure in the boundary layer has been shown to be constant.) The tubes are of stainless steel, 0.040-inch outside diameter, with a 0.003-inch wall thickness. The measuring ends of the total-head tubes were flattened to an outside thickness of 0.012 inch for a length of 1 inch from the opening. A hemispherical plug was inserted in the end of the static-pressure tube and four 0.005-inch holes, equally spaced, were drilled around the circumference. The tubes were 3½ inches long and were soldered into ¼-inch copper tubes, which extended back along the chord of the airfoil to rubber tubing that was led along the trailing edge of the airfoil to manometers. Required height adjustment was secured by placing a ⅛-inch

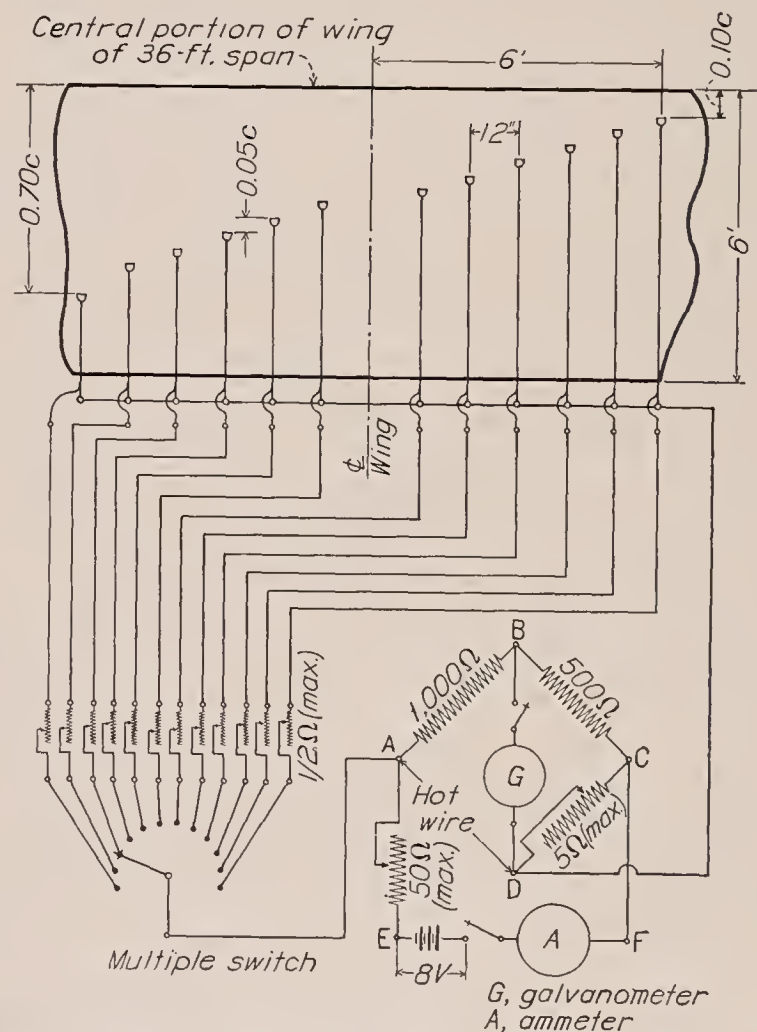


FIGURE 4.—Location of 12 hot-wire units on the 6- by 36-foot airfoil, and wiring diagram of Wheatstone bridge circuit.

bridge ¾ inches back from the tube ends and bending the tubes at this bridge to conform to an accurate templet-type gage. The tubes showed no tendency to lose adjustment during a run and observations during the tests indicated that no vibration of the tubes occurred.

Calibration of the bank of static and total-head tubes in a uniform stream against a standard pitot-static tube indicated that they were accurate to within 1 percent.

When the results obtained with the total-head tubes were plotted, it was necessary to correct the geometric height of the tube centers to an effective

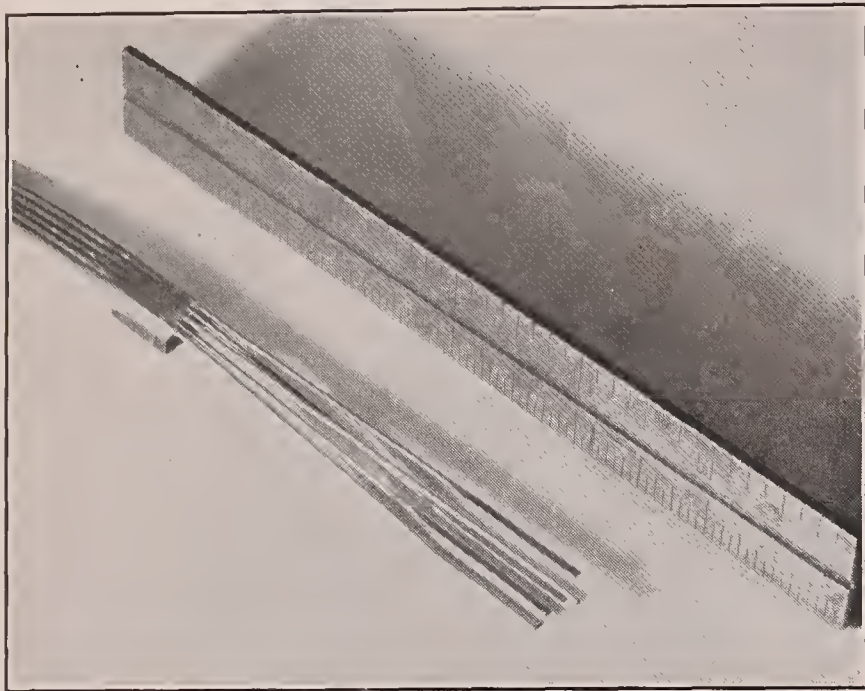


FIGURE 5.—Bank of total-head tubes and static tube mounted on the airfoil.

height to take into account the velocity gradient in the boundary layer. The effective dynamic pressure over the tube opening is greater than the pressure at the center of the tube. The effective height was obtained on the assumption of a linear velocity gradient.

Airfoils.—The three metal airfoils used in the tests were constructed with the utmost precision so that the section profiles and the surfaces were as fair and smooth as possible. After the metal surfaces had been filed to templet dimensions, they were alternately filled with a standard metal primer and rubbed with fine-grade water sandpaper until they were considered to be aerodynamically smooth; they were then waxed and polished. Aerodynamic smoothness is herein defined as the smoothness after which further improvements do not decrease the skin friction. Information on wing smoothness obtained in previous investigations in the N. A. C. A. 8-foot high-speed wind tunnel served as a guide. The airfoils were carefully dusted before each series of tests.

TESTS

The hot wires were normally spaced at $0.05c$ intervals from the $0.10c$ to the $0.70c$ station. For some of the tests, measurements were also obtained at the $0.05c$ position. The air-flow velocities at 0.010 inch above the airfoil surface were measured at lift coefficients of -0.57 , 0 , 0.33 , and 0.65 and at tunnel speeds of about 30, 45, 60, 75, and 90 miles per hour.

In the tests using the total-head tubes, the velocities at effective heights of 0.007, 0.033, 0.050, and 0.167 inch

above the wing surface were measured for lift coefficients of -0.57 , 0 , and 0.65 and at tunnel speeds of about 60 and 90 miles per hour. The measurements were taken at $0.05c$ intervals from the $0.10c$ to the $0.70c$ position.

Profile-drag measurements were obtained at zero lift for all the airfoils over a range of test velocities.

Additional tests were made on the N. A. C. A. 0012 airfoil to determine the effect on transition and drag of a small protuberance across the span near the leading edge. Narrow gummed tapes 0.003, 0.006, and 0.009 inch thick were attached one at a time across the span of the airfoil at the $0.05c$ position on the upper surface. The velocities were measured by the hot-wire method at an angle of attack of 0° and a tunnel speed of 75 miles per hour. Drag measurements were also made for these three runs.

RESULTS AND DISCUSSION

The boundary-layer measurements obtained by the hot-wire method are shown in figures 7, 8, and 9 for the N. A. C. A. 0008, the N. A. C. A. 0012, and the N. A. C. A. 0018 airfoils, respectively, at several section lift coefficients. Figures 10, 11, and 12 show corresponding results obtained with the total-head tubes on the wing surface. The forward stagnation point, from which s was measured, was obtained from theoretical pressure-distribution calculations. The section lift coefficients c_l were computed from the curves of theoretical span load distribution and from the measured lift

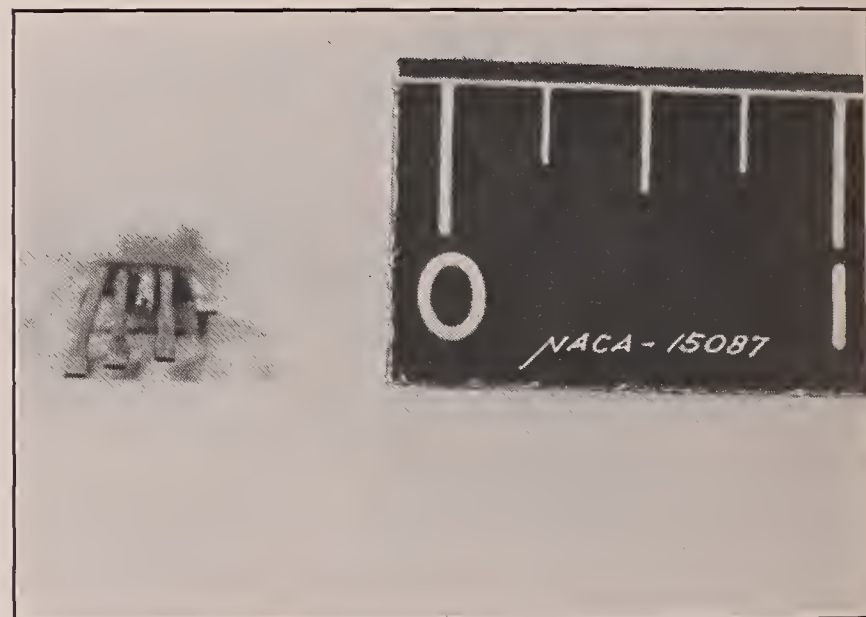


FIGURE 6.—Boundary-layer survey tubes in front view. The effective heights of the openings above the surface are 0.007 inch, 0.033 inch, 0.050 inch, and 0.167 inch. The height of the static tube is 0.175 inch.

on the wings. The boundary-layer velocity profiles, measured with the bank of total-head tubes, are shown in figures 13, 14, and 15 for the three airfoils at several section lift coefficients and positions along the airfoil surface. Boundary-layer velocity profiles for the transition region are plotted in a nondimensional form in figures 16, 17, and 18.

Comparison of methods for detecting transition.—An analysis of the results in figures 7 to 12 shows that the surface total-head tube or the hot wire is adequate to indicate the transition point except for cases in which the downstream velocity gradient at the airfoil surface is so small that the point of minimum velocity is not clearly defined. This condition occurs on the upper surface of the airfoils at negative lift coefficients (corresponding to the lower surface of the airfoils at positive lift coefficients), in which case the transition point is indicated as far back as 50 to 60 percent of the chord. The nondimensional boundary-layer profiles for the

point and continued through the transition region, reaching maximum intensity at about the transition point. Owing to the heavy damping in the long pressure leads to the total-head tubes, the actual violence of these fluctuations was not observed; however, there was a distinct indication of unsteadiness in the readings at the transition point.

The hot-wire method as used in the present tests was considerably faster than the total-head method, inasmuch as it was possible to obtain results from each of the 12 wires on the wing without a change in the set-up. The readings were also obtained much more rapidly

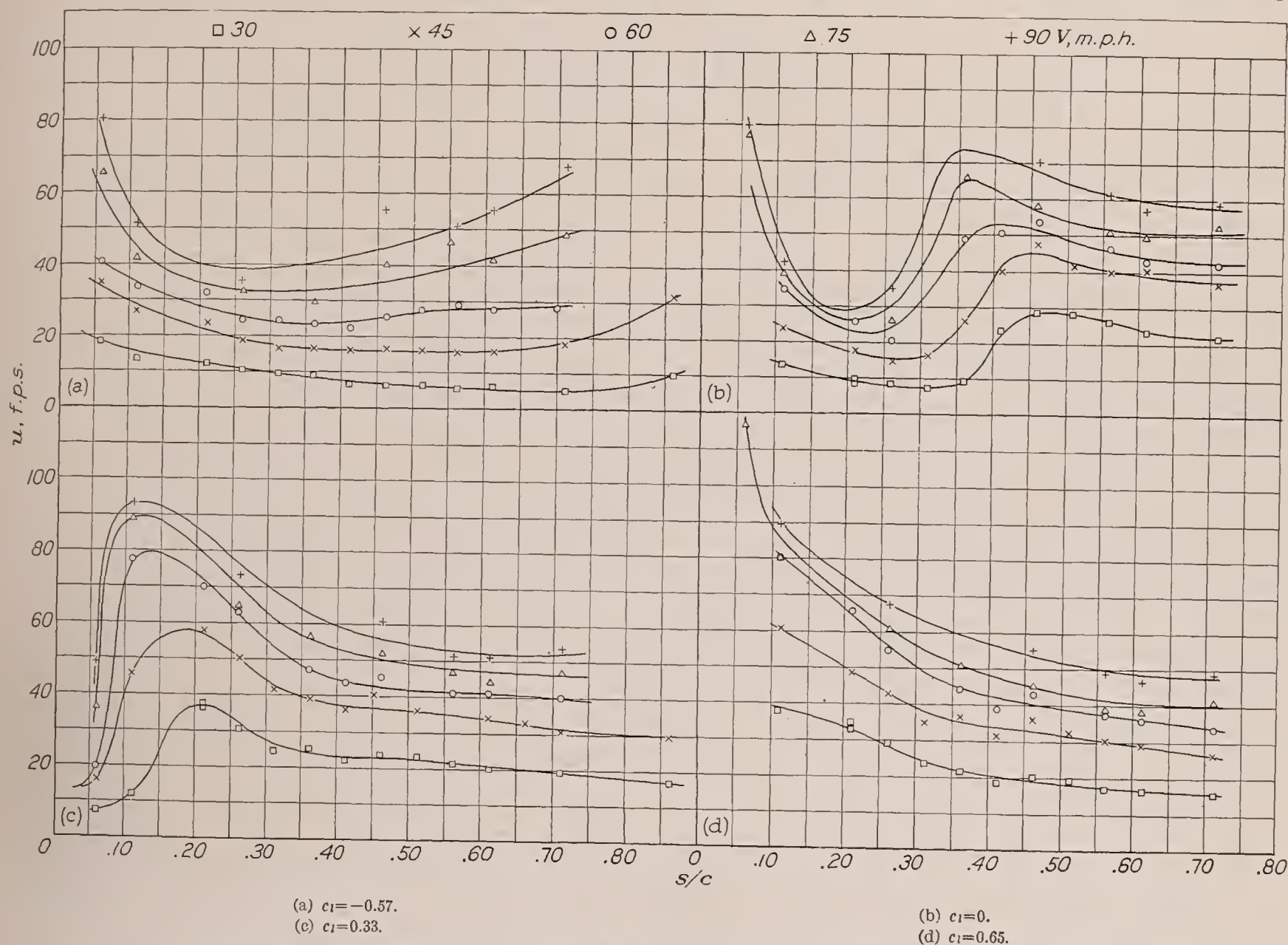


FIGURE 7.—Hot-wire measurements of the boundary-layer velocities 0.010 inch above the surface of the N. A. C. A. 0009 airfoil.

negative lift coefficients (figs. 16 (a), 17 (a), and 18 (a)) are of considerable aid in investigation of the transition for these cases. The shape of the profiles in the transition region is apparently a function of the length of the region and, at negative lift coefficients, the $\frac{1}{2}$ -power turbulent profiles did not occur until 20 to 30 percent of the chord behind the transition point.

The transitions as indicated by the hot wires and the surface tube show a reasonable agreement with the maximum variation of the indications usually not in excess of 3 percent of the chord. The hot-wire measurements indicated the transition region by large fluctuations in the current required to balance the bridge. These fluctuations began slightly before the transition

because from 3 to 4 minutes were required for the readings from the pressure tubing to reach equilibrium. The observations obtained with the total-head tubes seemed somewhat more consistent, however, and a smaller scatter of the experimental points occurred.

Effect of lift on transition.—The effect of variations in the section lift coefficient on the transition point for various Reynolds Numbers is shown in figures 19, 20, and 21. The results from the surface total-head tubes and the hot wires for zero and positive lift coefficients are included. The transition points were estimated for $c_l = -0.57$ from the boundary-layer profiles of figures 16 (a), 17 (a), and 18 (a).

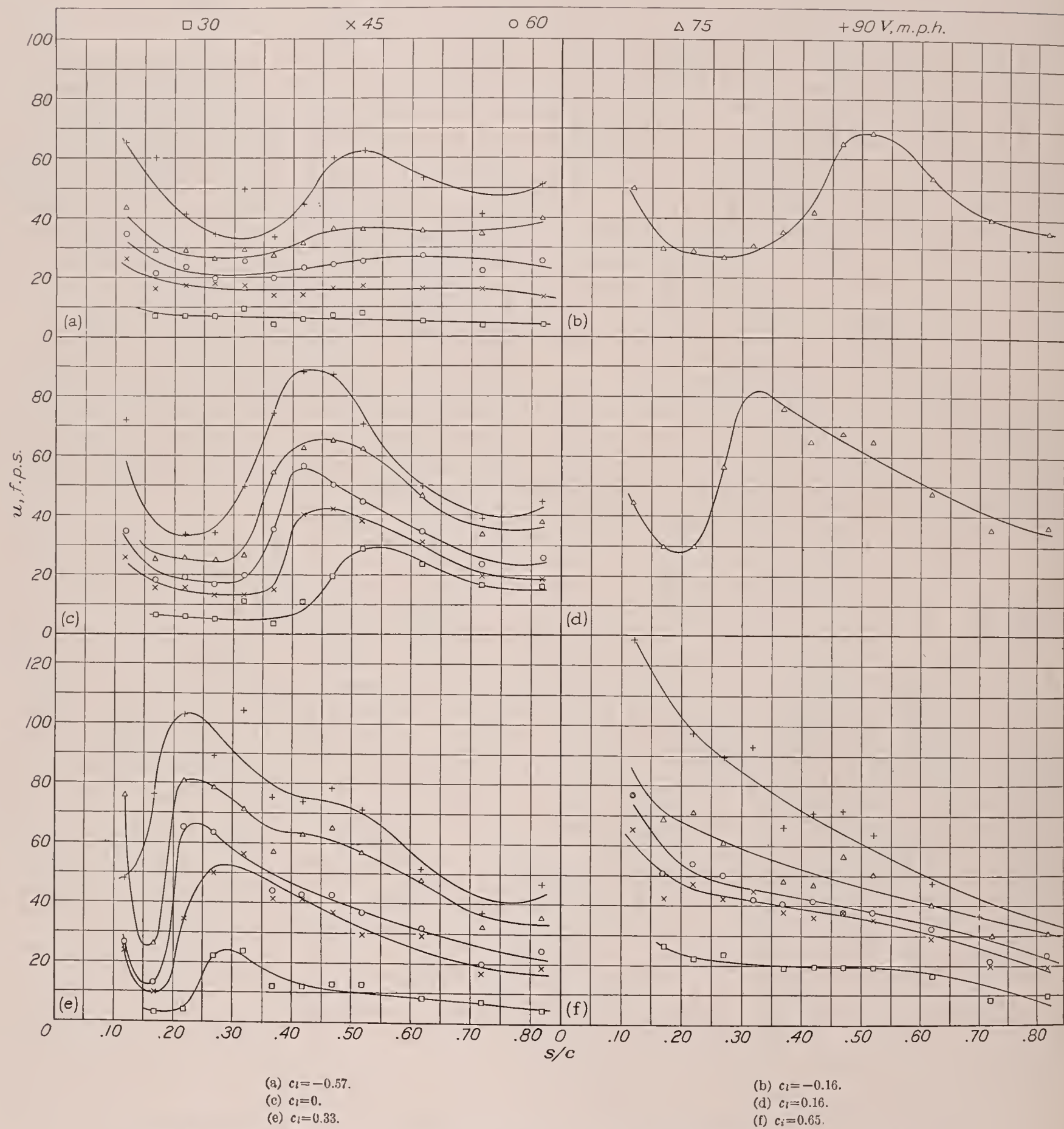


FIGURE 8.—Hot-wire measurements of the boundary-layer velocities 0.010 inch above the surface of the N. A. C. A. 0012 airfoil.

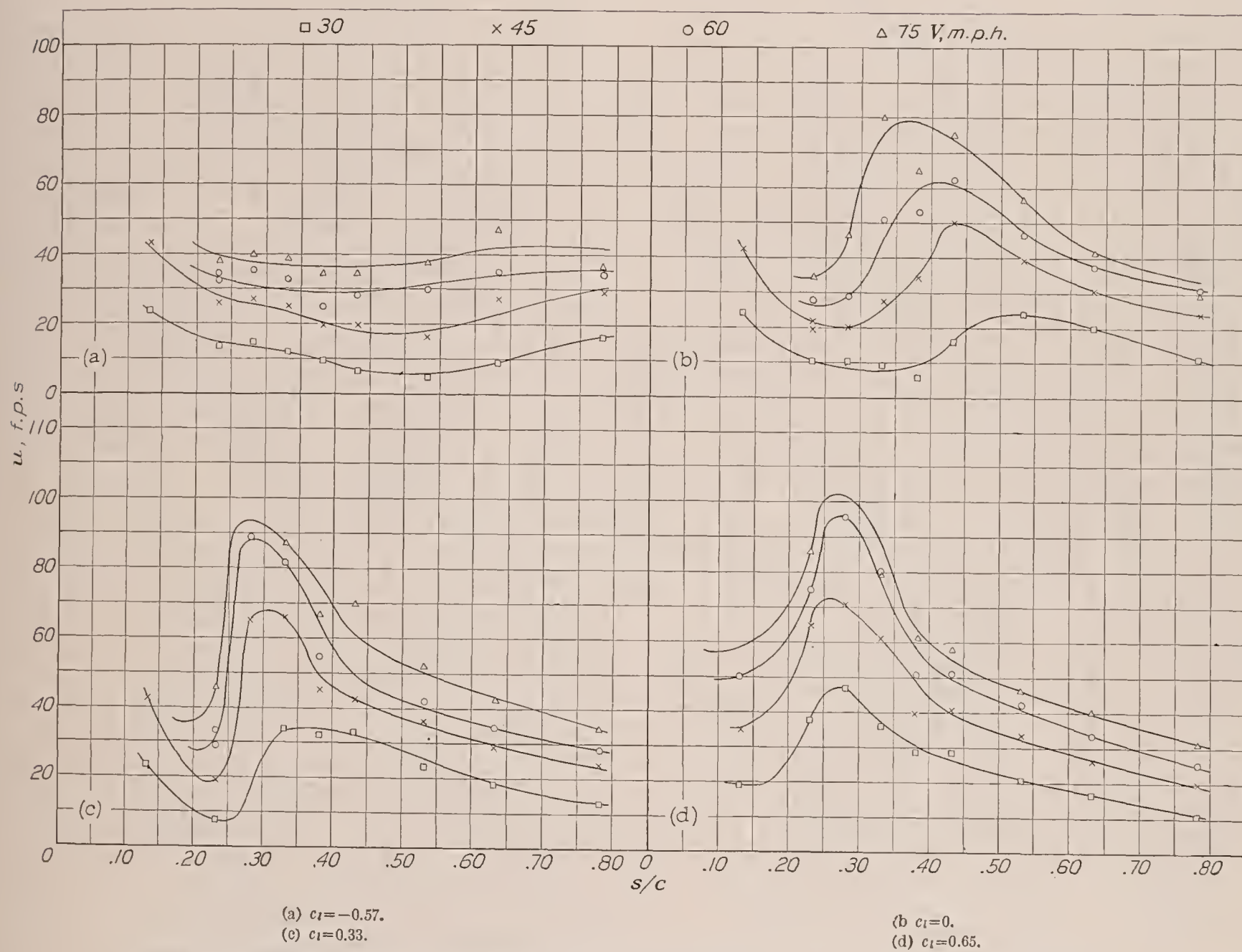


FIGURE 9.—Hot-wire measurements of the boundary-layer velocities 0.010 inch above the surface of the N. A. C. A. 0018 airfoil.

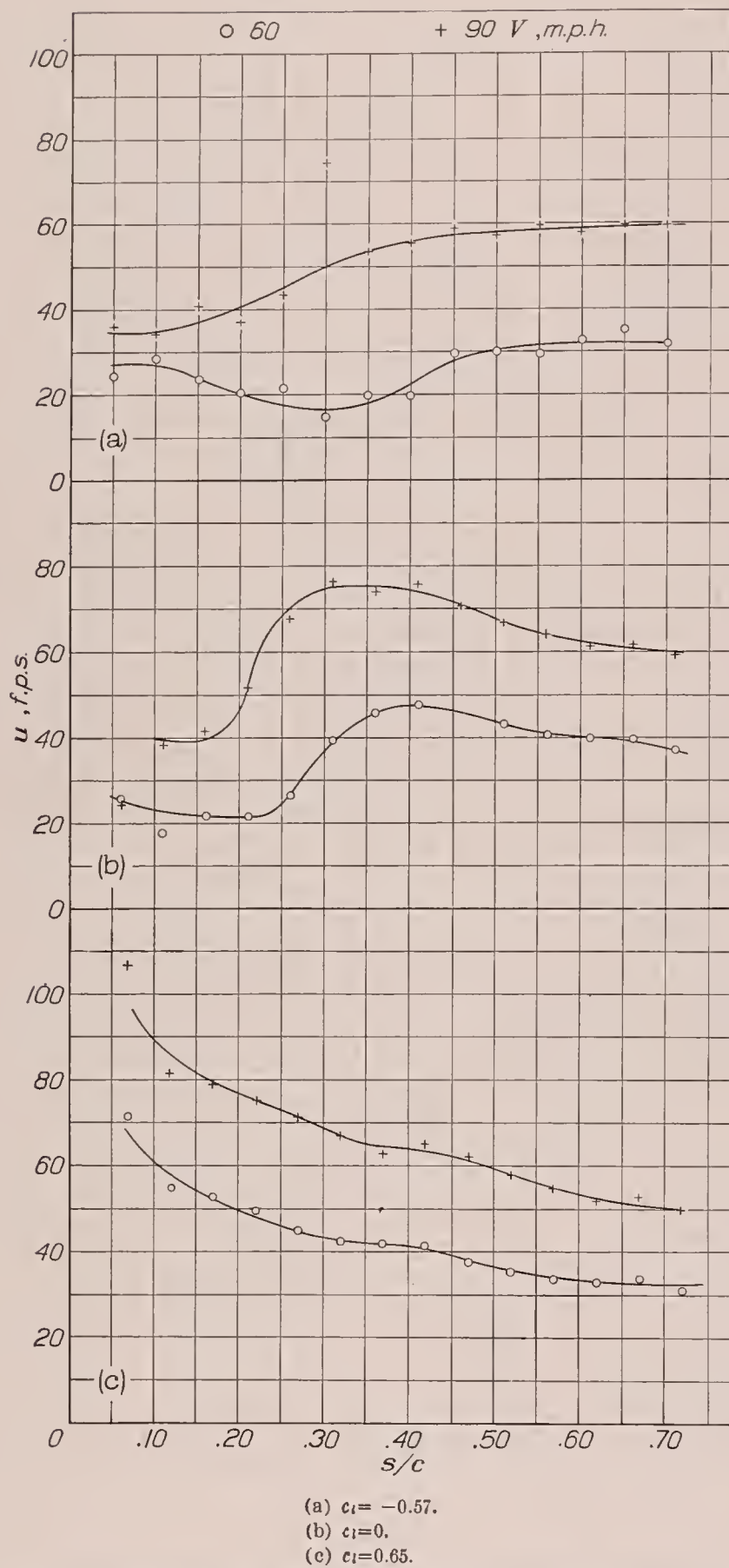


FIGURE 10.—Total-head-tube measurements of boundary-layer velocities on the surface of the N. A. C. A. 0009 airfoil.

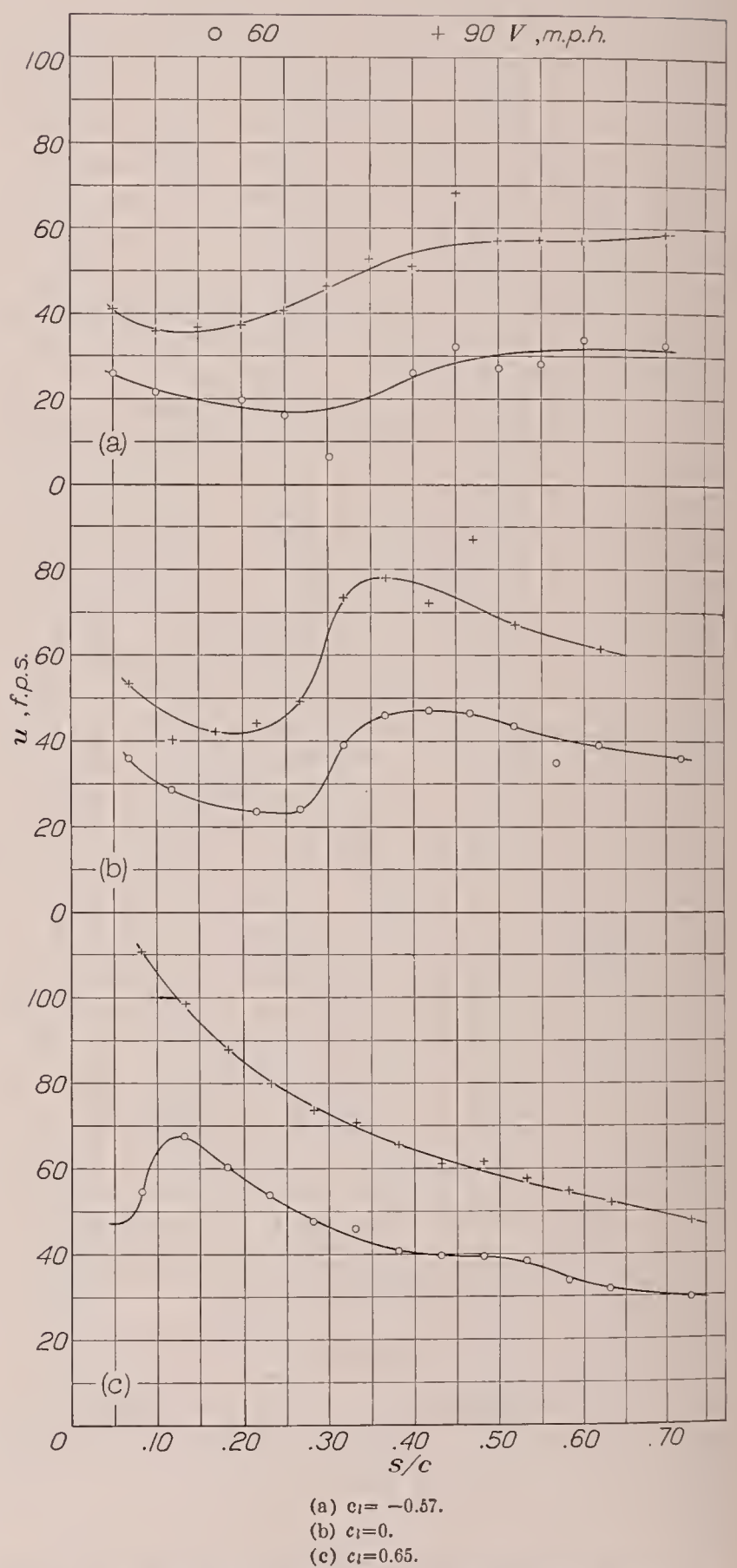


FIGURE 11.—Total-head-tube measurements of boundary-layer velocities on the surface of the N. A. C. A. 0012 airfoil.

The results show that the transition point on the upper surface moves toward the forward stagnation point with increasing lift coefficient, the rate of forward motion increasing with decreasing wing thickness. This phenomenon may be correlated with pressure-distribution measurements, which are shown in figures 22, 23, and 24, for the airfoils tested; it will be noted that the adverse pressure gradient over the forward part of the airfoil varies in the same manner. The pressure distribution for zero lift as measured with the static tube at the surface and the theoretically predicted pressure distribution are in good agreement (figs. 22, 23, and 24).

Effect of Reynolds Number on transition.—The effect of variation in the Reynolds Number on the position of the transition point and the end of the transition region is shown in figure 25 for section lift coefficients c_l of 0 and 0.33. The variation in the transition point for other lift coefficients may be noted by a visual cross plot of figures 19, 20, and 21. The transition point moves forward with increasing Reynolds Number at a rate that is not greatly different for the 9, 12, or 18 percent thick wing. Transition occurred at no unique value of R_x but varied at $c_l=0$ from approximately 500,000 to 1,100,000. At $c_l=-0.57$, a value of R_x of over 2,500,000 was reached before transition. The transition Reynolds Number increases with increasing wing Reynolds Number. The R_s values at the transition point (Reynolds Numbers based on the boundary-layer thickness at transition) vary from about 3,000 to 6,000 at zero lift and show no consistent change with wing Reynolds Number.

The considerable scatter in the experimentally measured positions of the end of the transition region (fig. 25) prevents definite conclusions from being drawn as to the effect of Reynolds Number on the width of the transition region. In general, however, the width did not appear to vary markedly with the Reynolds Number for any of the wing lift coefficients investigated.

Effect of airfoil thickness on transition.—The effect of variation in the wing thickness on the location of the transition point is summarized in figure 26. The points were obtained from cross-plotting the faired curves of figures 19, 20, and 21. Results are given for two tunnel speeds corresponding to Reynolds Numbers of about 3,350,000 and 5,020,000.

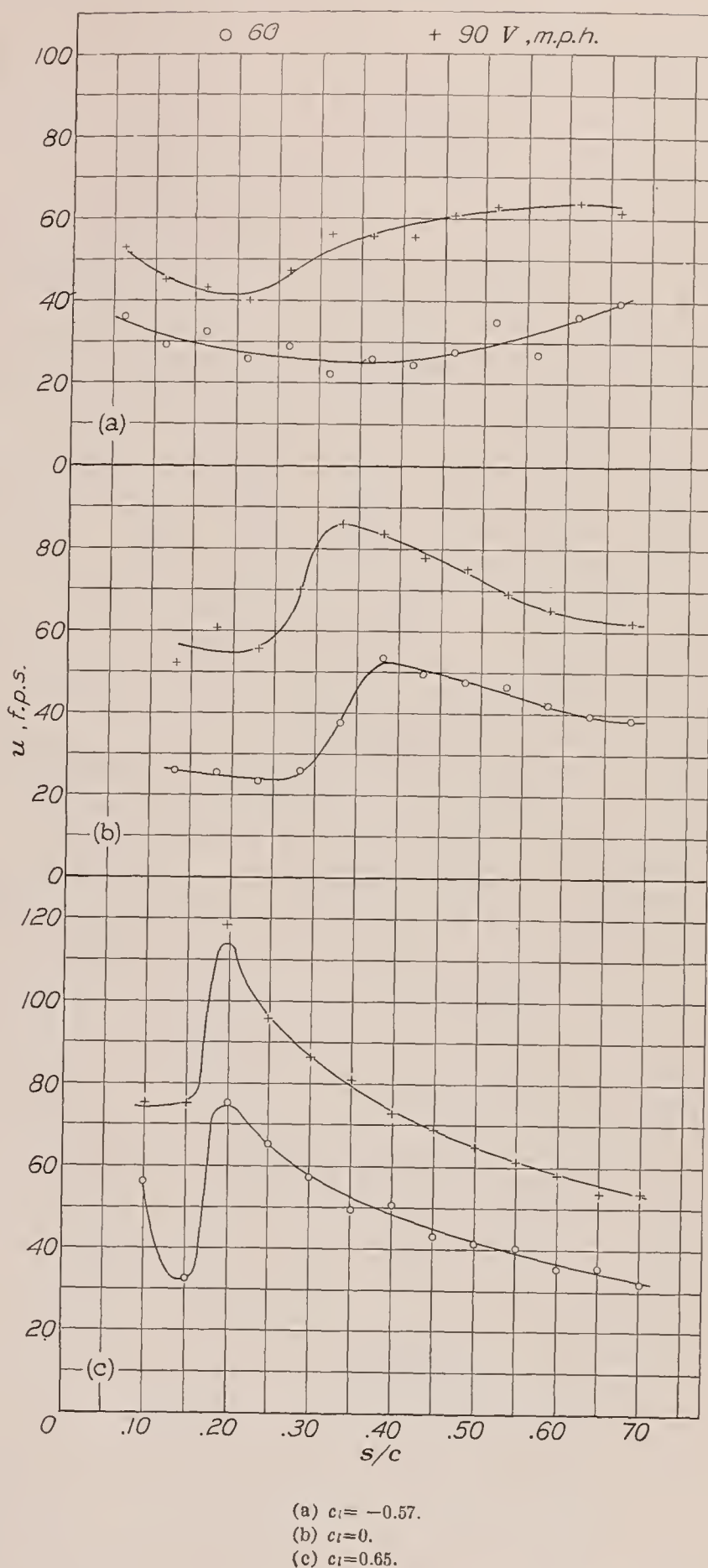


FIGURE 12.—Total-head-tube measurements of boundary-layer velocities on the surface of the N. A. C. A. 0018 airfoil.

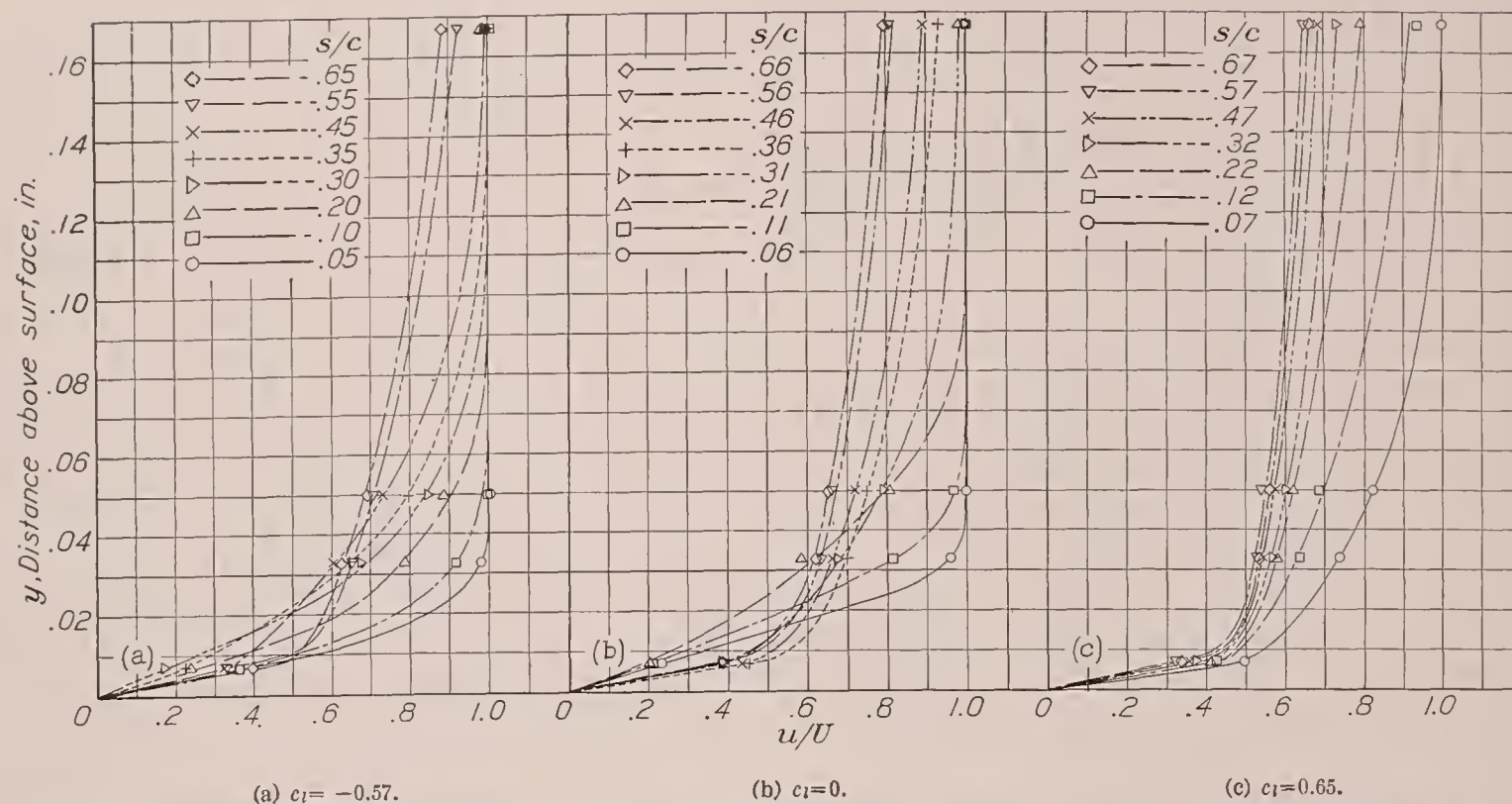


FIGURE 13.—Boundary-layer velocity profiles at several chord positions on the N. A. C. A. 0009 airfoil. Tunnel air speed, 60 m. p. h.

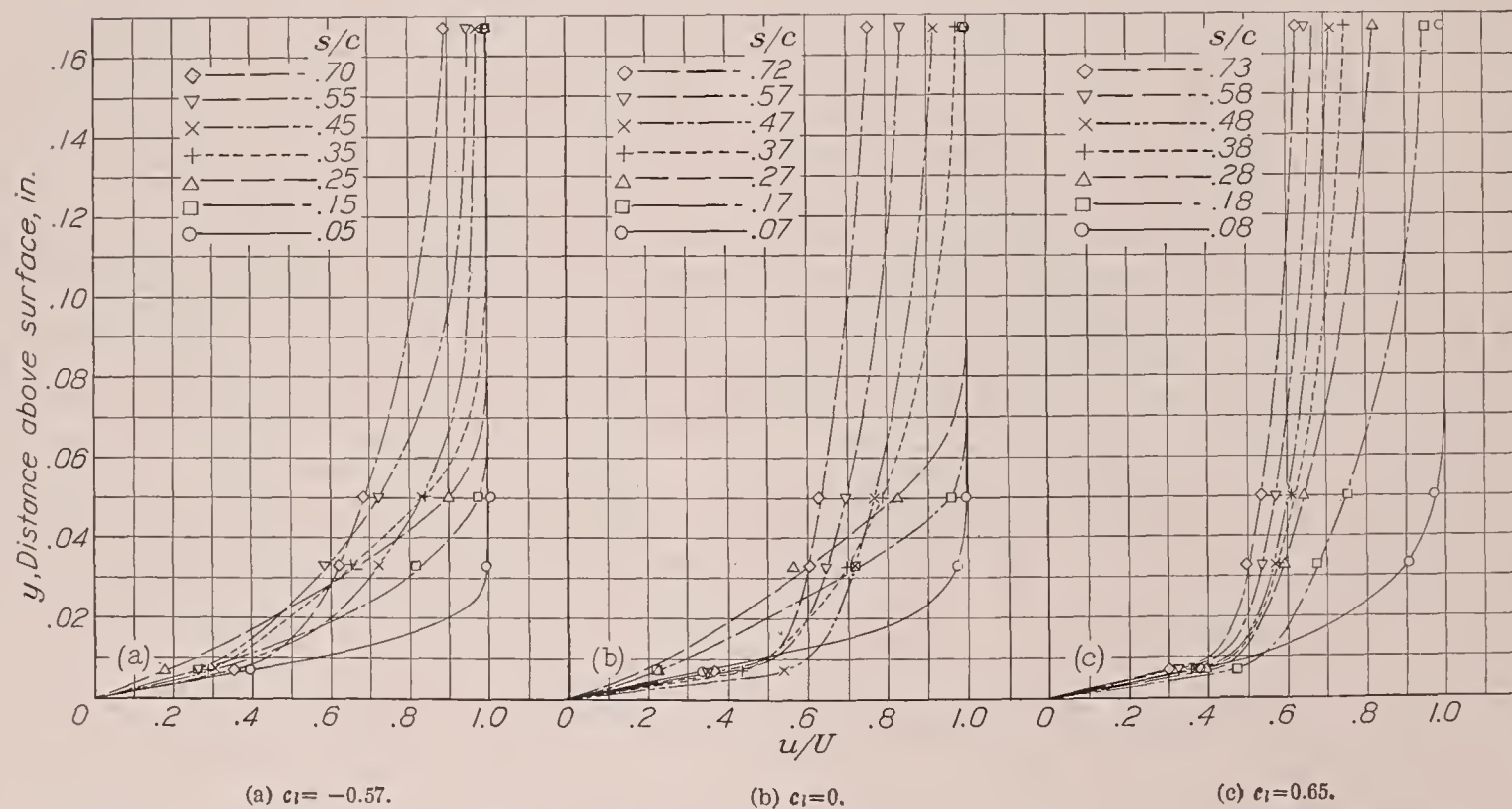


FIGURE 14.—Boundary-layer velocity profiles at several chord positions on the N. A. C. A. 0012 airfoil. Tunnel air speed, 60 m. p. h.

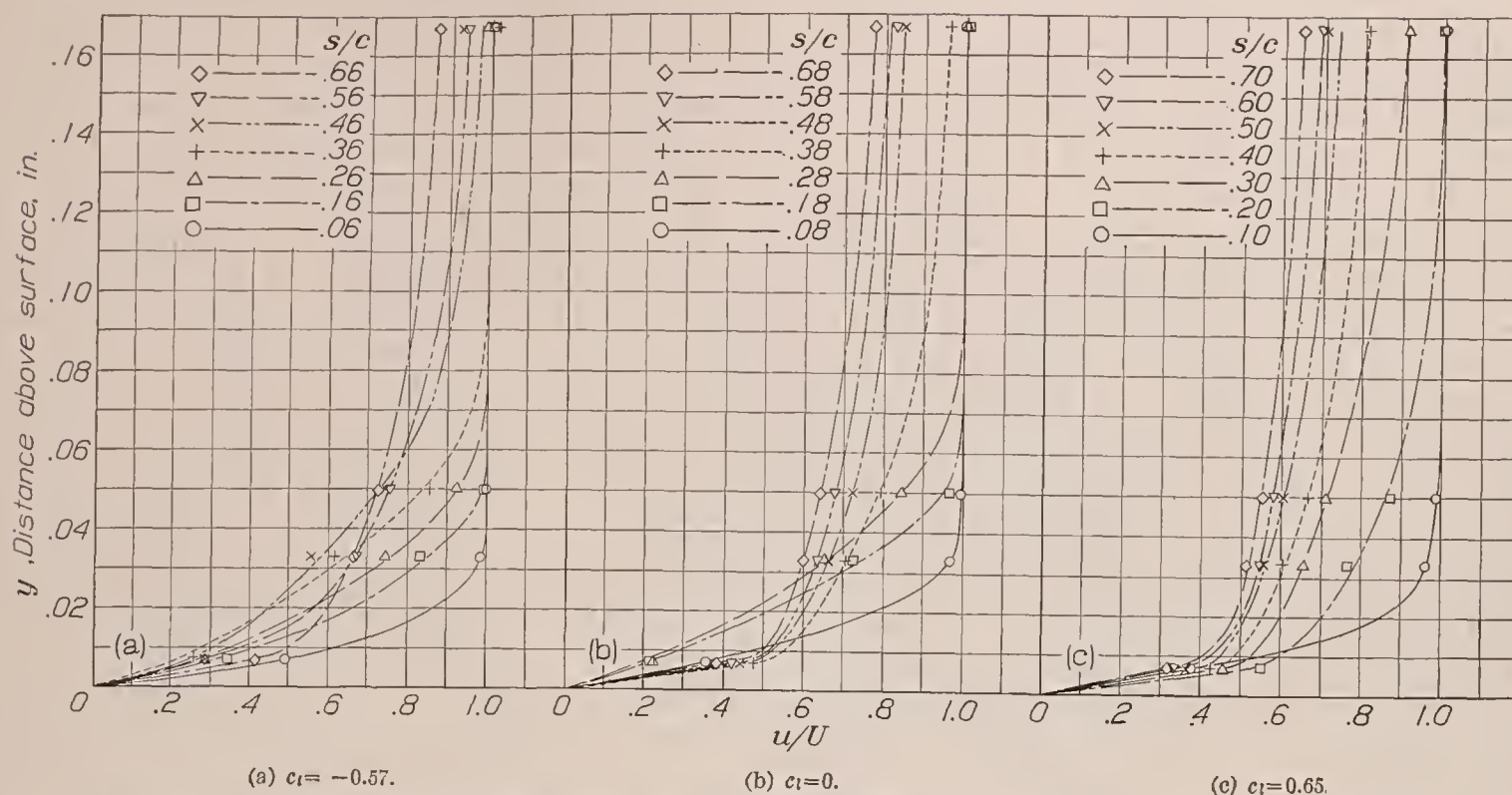


FIGURE 15.—Boundary-layer velocity profiles at several chord positions on the N. A. C. A. 0018 airfoil. Tunnel air speed, 60 m. p. h.

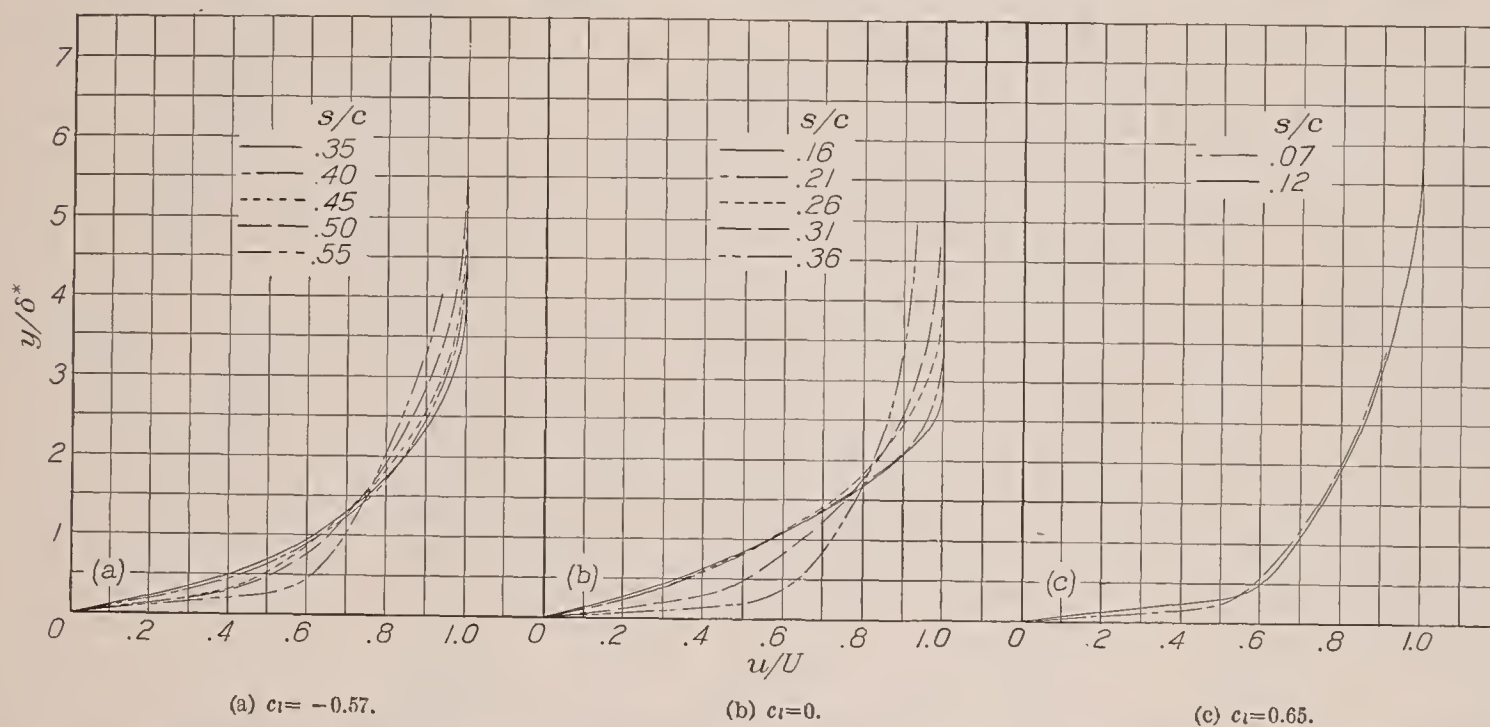


FIGURE 16.—Nondimensional boundary-layer velocity profiles in the transition region for the N. A. C. A. 0009 airfoil. Tunnel air speed, 60 m. p. h.

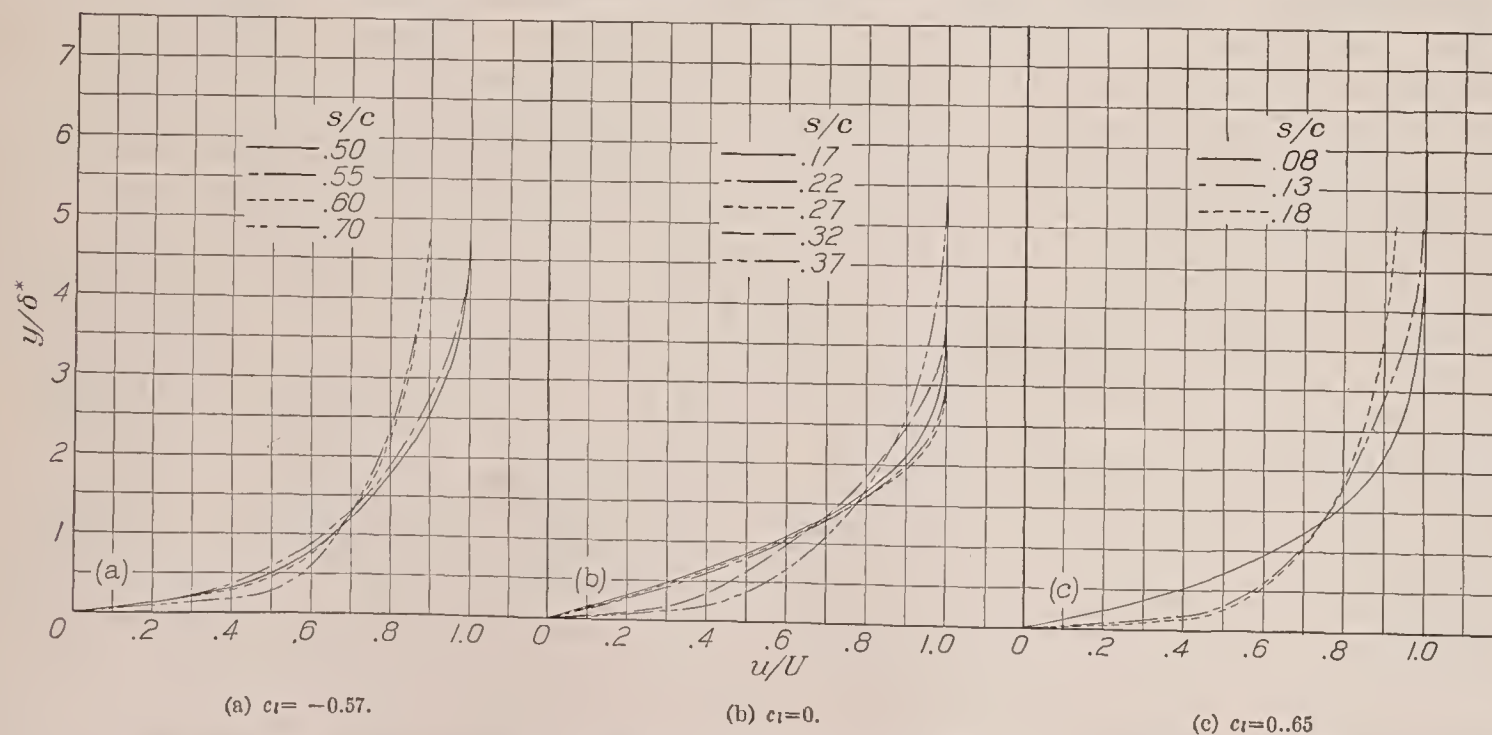


FIGURE 17.—Nondimensional boundary-layer velocity profiles in the transition region for the N. A. C. A. 0012 airfoil. Tunnel air speed, 60 m. p. h.

At $c_l=0$ and 0.33, the transition point occurred at the same chord position for the $0.12c$ and the $0.18c$ thick wing; however, it occurred considerably closer to the stagnation point for the $0.09c$ airfoil. At $c_l=0.65$, the transition point moved rearward with increasing thickness in an almost linear manner. The later transition for the thicker airfoils is directly related to the more favorable pressure distribution over the surface, as previously mentioned.

It is of interest to note that the pressure gradients over the symmetrical airfoils are not so favorable to late transitions as those over conventional cambered airfoils, and it may be expected that the transition will occur farther back along the chord for a cambered airfoil. The later transitions indicated in flight in reference 4 may be due in part to the more favorable pressure gradients, as is shown by a comparison of the pressure-distribution curves of reference 4 with those for the symmetrical airfoils (figs. 22, 23, and 24).

almost at the airfoil nose. These results are in agreement with previous studies showing the effects of rivets and surface irregularities and reemphasize the importance of smooth wing surfaces for low drag.

Correlation of profile drag and transition point.—The section profile-drag measurements for the symmetrical airfoils at zero lift are given in figure 28 for the range of test Reynolds Numbers. The profile-drag coefficients were obtained by both force and momentum measurements that were in excellent agreement (reference 6). Inasmuch as the knowledge of the transition point is of particular interest as an aid in the estimation of the profile drag, an attempt has been made to correlate the transition measurements with the observed profile-drag measurements for the representative case of the N. A. C. A. 0009 airfoil at zero lift. The thinnest airfoil was chosen to avoid a large pressure drag. At a Reynolds Number of 3,350,000, the transition point occurs at $s/c=0.23$ and the transition region extends

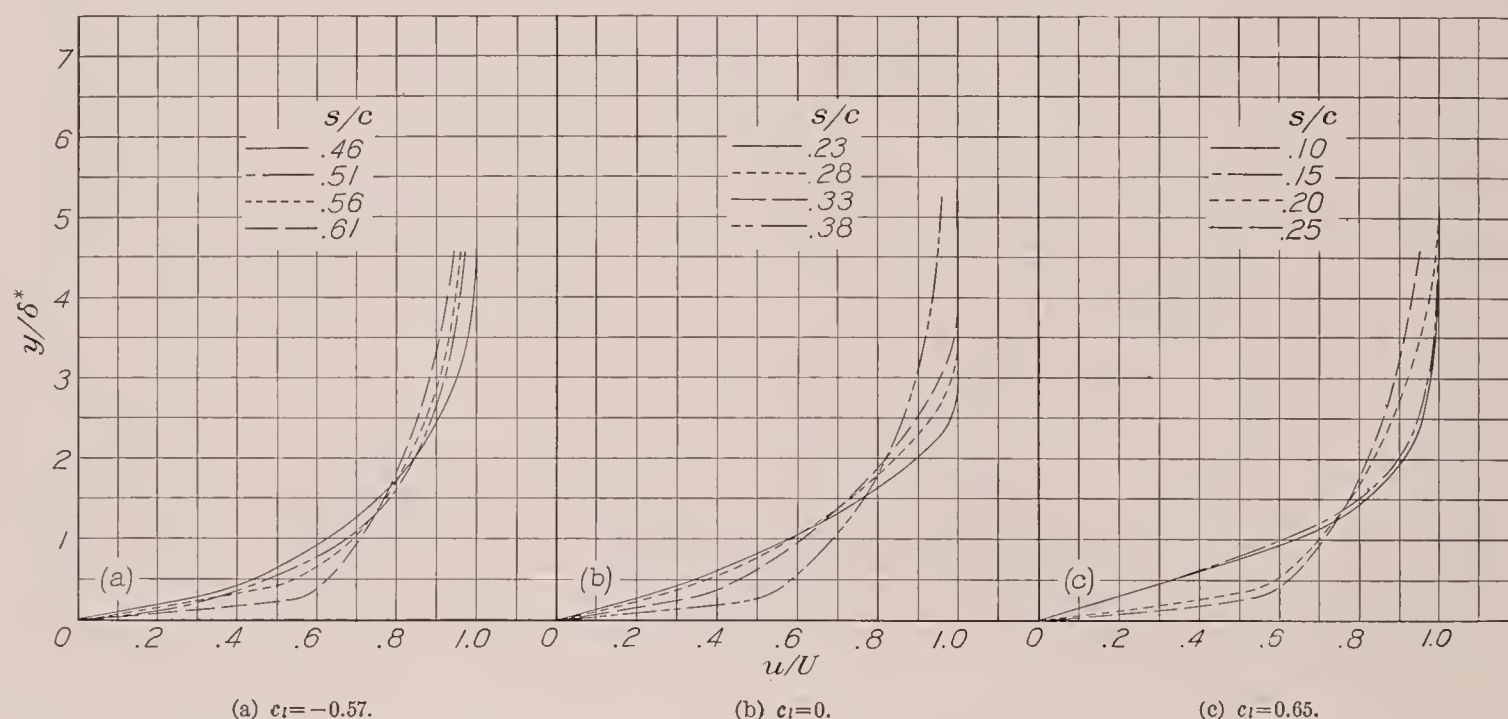


FIGURE 18.—Nondimensional boundary-layer velocity profiles in the transition region for the N. A. C. A. 0018 airfoil. Tunnel air speed, 60 m. p. h.

Effect of protuberances on transition.—The effect of a protuberance near the leading edge on transition and the increase in the drag above that of the aerodynamically smooth wing is shown in figure 27. The gummed tape 0.003 inch thick placed at the $0.05c$ station had a slight tendency to move the transition point forward and increased the drag about 2.3 percent. The 0.006-inch-thick tape moved the transition point forward only about 1 percent; however, it shortened the transition region to about 10 percent and added 3.7 percent drag. The 0.009-inch-thick tape moved the transition point ahead of the 10-percent-chord station and added 7.5 percent drag. The transition region in the case of the 0.009-inch tape was very long and extended to the $0.35c$ station.

No rational explanation of the effects observed when the tapes were used can be offered. It should be noted, however, that a protuberance with a height of less than 0.01 inch was sufficient to cause transition to occur

from $s/c=0.23$ to 0.40 (fig. 10(b)). The section profile-drag coefficient c_{d0} corresponding to these test conditions is 0.0061 (fig. 28).

For the laminar and transition regions, it was possible, inasmuch as the complete boundary-layer profiles had been measured, to determine the drag by integration of the loss in momentum by means of the von Kármán momentum equation, taking into account the pressure distribution over the surface. From this calculation it was found that the average skin-friction coefficient C_f over the laminar and transition region was 0.0026.

This skin-friction coefficient is based on an area of only 40 percent of the surface on one side of the airfoil. In order to convert C_f into the usual coefficient form c_{d0} , the value is doubled and multiplied by 0.40 so that the contribution to c_{d0} of the laminar and transition regions is 0.0021.

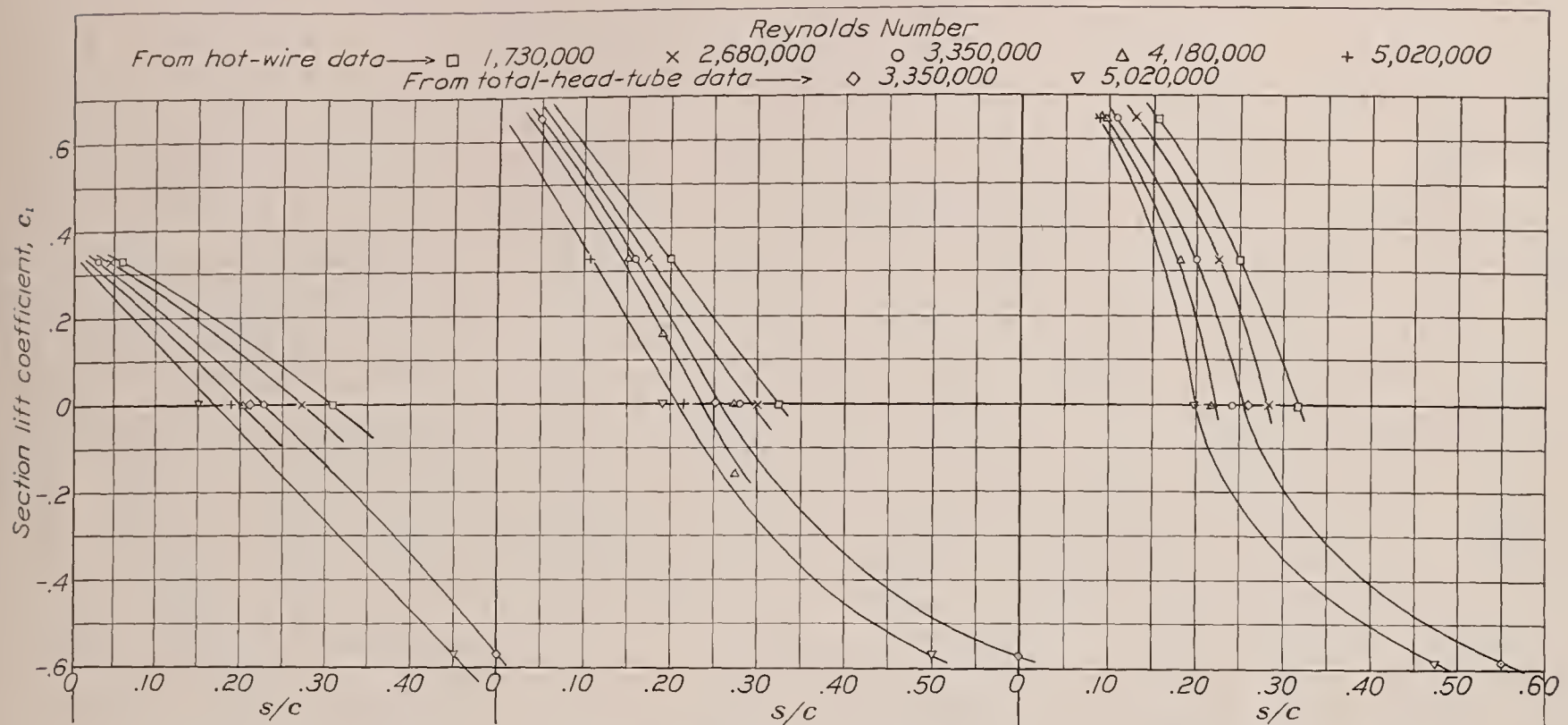


FIGURE 19.—N. A. C. A. 0009.

FIGURE 20.—N. A. C. A. 0012.

FIGURE 21.—N. A. C. A. 0018

Variation of the transition point with section lift coefficient for the N. A. C. A. 0009, 0012, and 0018 airfoils.

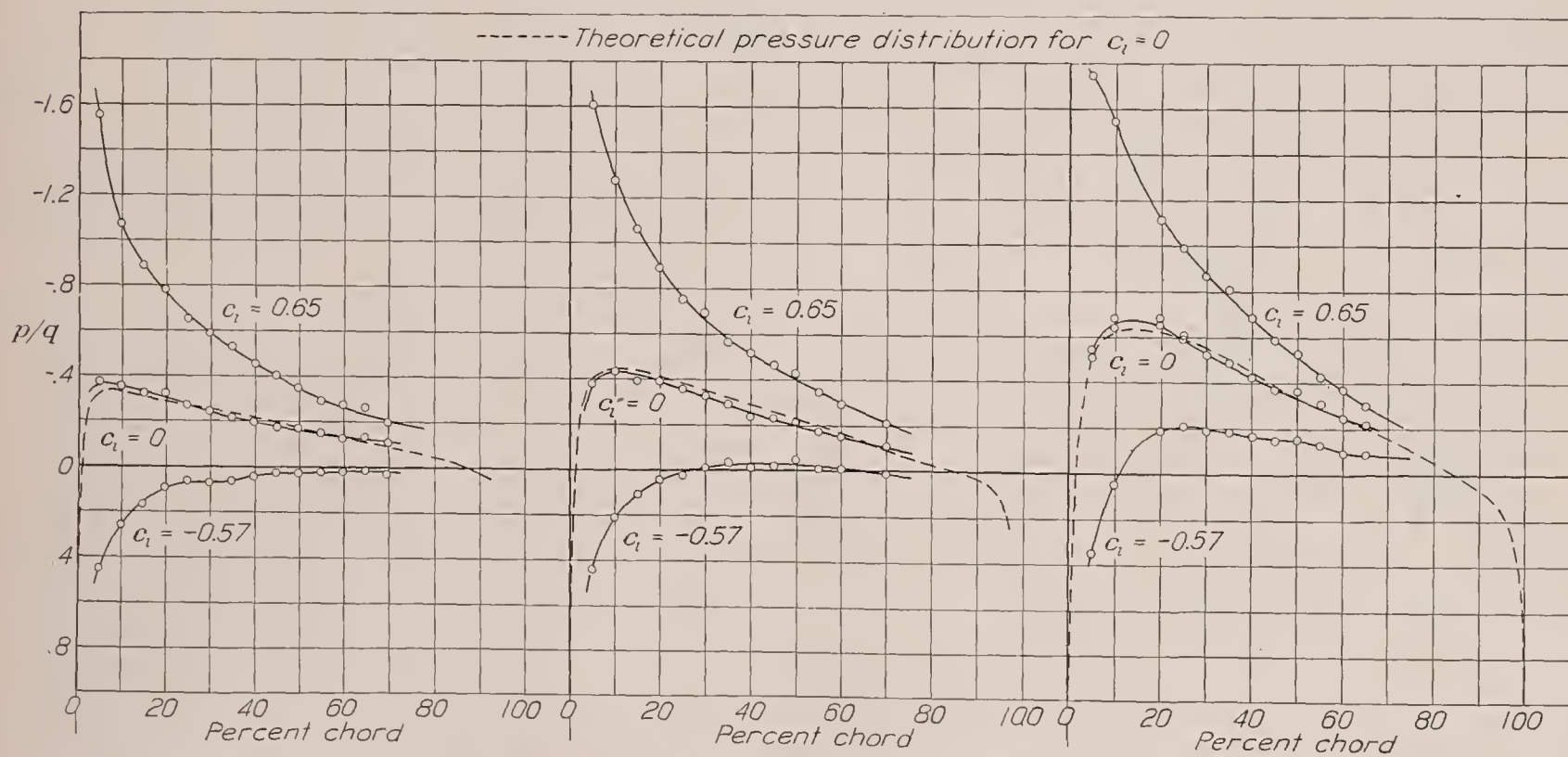


FIGURE 22.—N. A. C. A. 0009.

FIGURE 23.—N. A. C. A. 0012.

FIGURE 24.—N. A. C. A. 0018.

Pressure distribution on the upper surface of the N. A. C. A. 0009, 0012, and 0018 airfoils for three section lift coefficients.

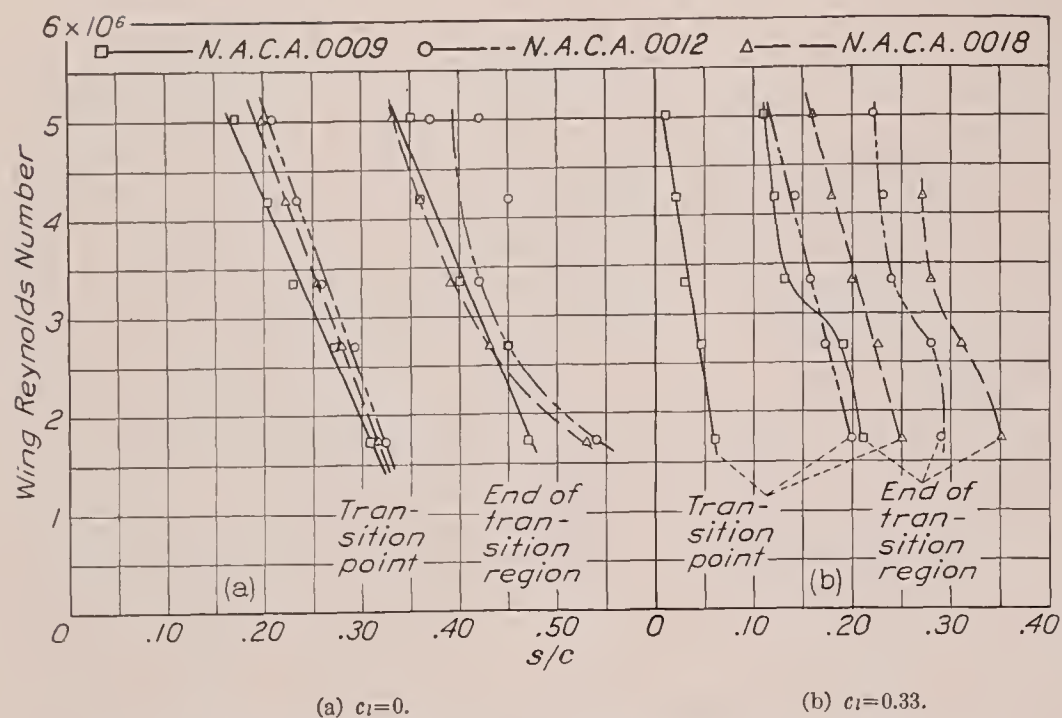


FIGURE 25.—Effect of Reynolds Number on the transition point and extent of the transition region.

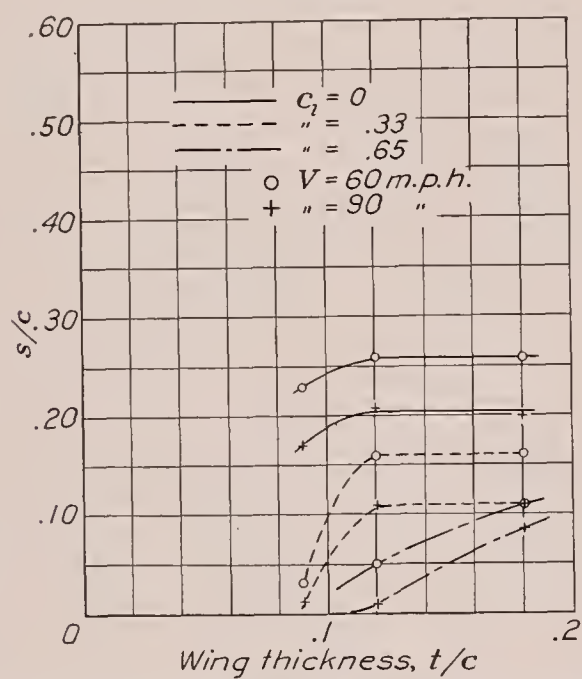


FIGURE 26.—Effect of airfoil thickness on the location of the transition point.

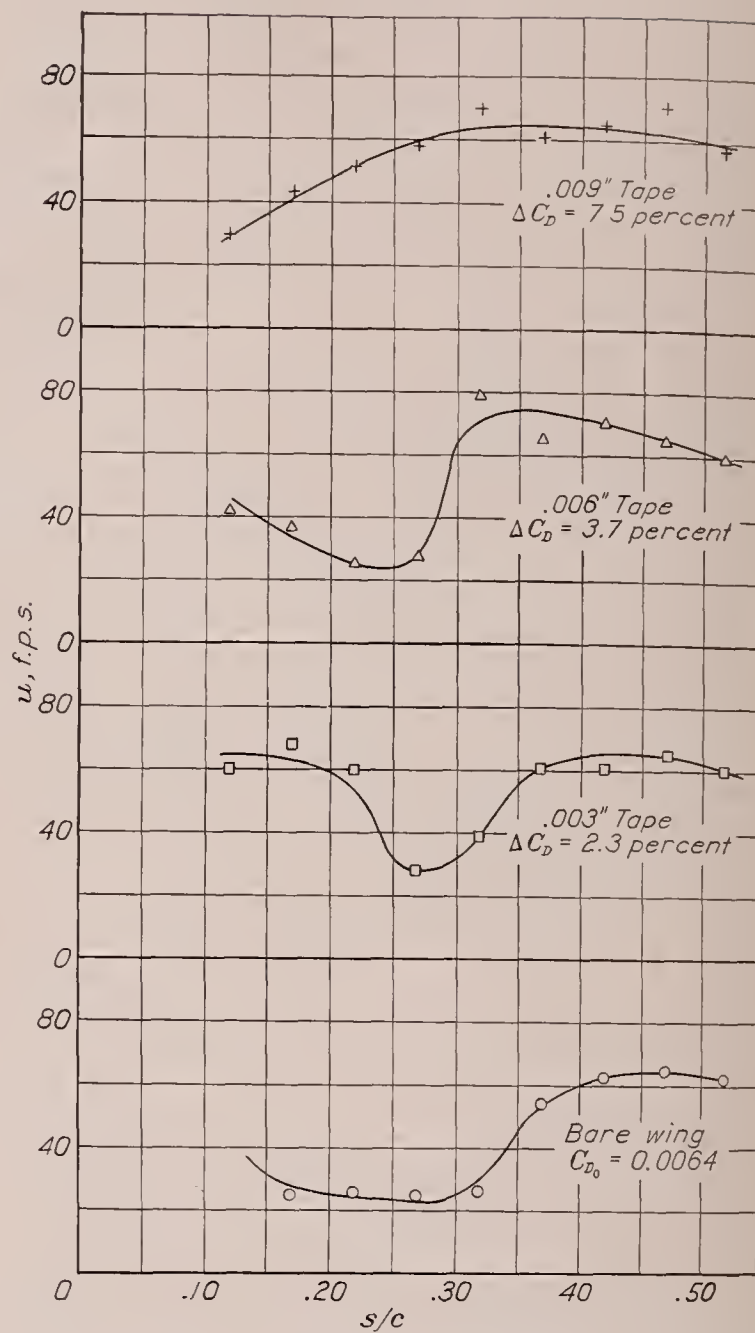


FIGURE 27.—Effect in the transition and drag of the N. A. C. A. 0012 airfoil of small protuberances at the 0.05c point on the upper surface. Reynolds Number $\approx 4,180,000$.

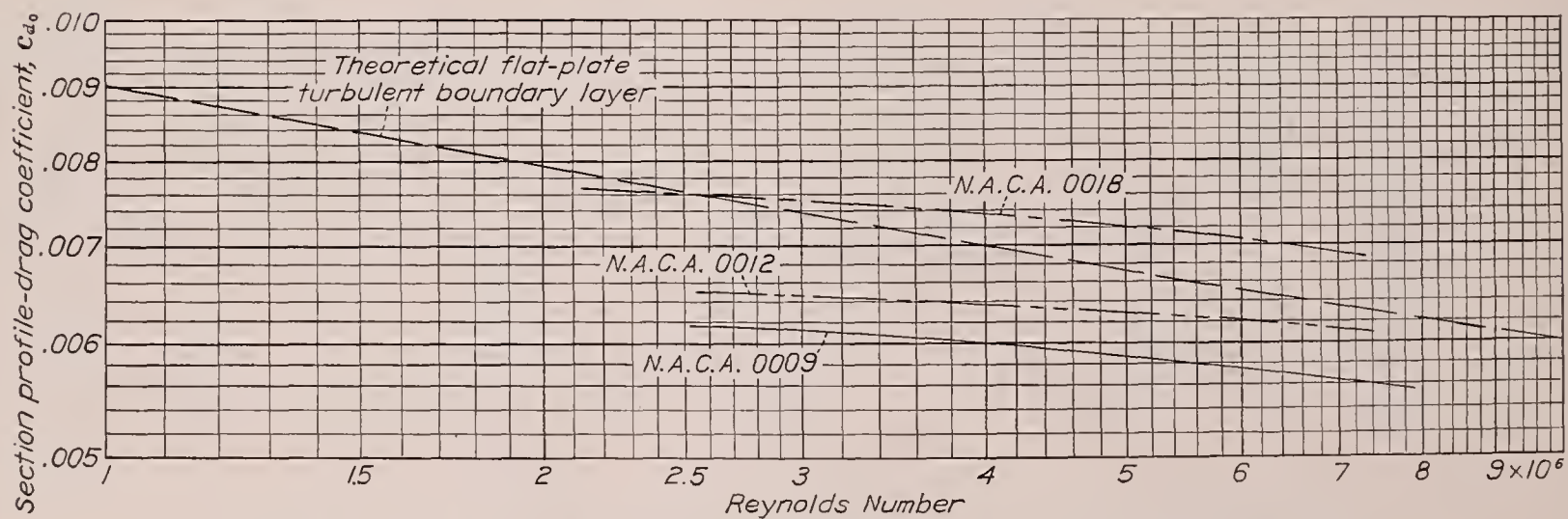


FIGURE 28.—Section profile-drag coefficients at zero lift for the N. A. C. A. 0009, 0012, and 0018 airfoils.

Complete turbulent profiles were not measured; the determination of the drag for the turbulent region therefore required the application of the empirical skin-friction laws derived for flat plates, suitably corrected by the method of Dryden and Kuethe (reference 7) for the pressure gradient on the airfoil. The crux of the whole calculation lies, however, in the assumption made regarding the state of development of the turbulent layer at the end of the transition region. If the drag for the turbulent region is computed according to the most obvious assumption, that the developed turbulent layer begins with a momentum loss equal to that at the end of the transition region, the value of the drag is much too high so that, when it is added to the drag for the laminar and transition regions, a negative pressure drag on the airfoil is indicated.

It is believed that further study of the local skin-friction coefficients in the boundary layer will be required in order to predict the wing profile drag, even when the transition point is known.

CONCLUDING REMARKS

The results of this investigation are consistent with those of previous studies in showing that transition does not occur at a particular value of R_x or R_δ . The tests show that a later transition occurs on thicker airfoils, which partly explains the relatively low values of c_{d0} obtained with the N. A. C. A. 0018 airfoil at zero lift. With increasing lift coefficient and Reynolds Number, the transition point on the upper surface moves toward the stagnation point. The width of the transition region shows no large variation with Reynolds Number.

An attempt to correlate the transition data with profile-drag measurements with the aid of existing data on the skin-friction drag of flat plates proved unsuccessful, indicating that further study is required in order

to predict the drag of an airfoil even when the transition is known.

The wind-tunnel measurements of the transition point are at an advantage over flight measurements in that it is possible to determine separately the effects of Reynolds Number and lift coefficient; however, there are serious disadvantages owing to the initial wind-tunnel turbulence. The conclusions of these tests are therefore restricted until projected flight tests for comparison with the full-scale-tunnel measurements have been made.

LANGLEY MEMORIAL AERONAUTICAL LABORATORY,
NATIONAL ADVISORY COMMITTEE FOR AERONAUTICS,
LANGLEY FIELD, VA., May 26, 1938.

REFERENCES

1. Burgers, J. M.: The Motion of a Fluid in the Boundary Layer along a Plane Smooth Surface. Proc. First Int. Congress for Appl. Mech., Delft, 1924, C. B. Biezeno, J. M. Burgers, ed., J. Waltman (Delft), 1925, pp. 113-128.
2. van der Hegge Zijnen, B. G.: Measurements of the Velocity Distribution in the Boundary Layer along a Plane Surface. Report 6, Aero. Lab. Tech. H. S. Delft, 1924.
3. Dryden, Hugh L.: Air Flow in the Boundary Layer near a Plate. T. R. No. 562, N. A. C. A., 1936.
4. Jones, B. Melvill: Flight Experiments on the Boundary Layer. Jour. Aero. Sci., vol. 5, no. 3, Jan. 1938, pp. 81-94.
5. Platt, Robert C.: Turbulence Factors of N. A. C. A. Wind Tunnels as Determined by Sphere Tests. T. R. No. 558, N. A. C. A., 1936.
6. Goett, Harry J., and Bullivant, W. Kenneth: Tests of N. A. C. A. 0009, 0012, and 0018 Airfoils in the Full-Scale Tunnel. T. R. No. 647, N. A. C. A., 1938.
7. Dryden, H. L., and Kuethe, A. M.: Effect of Turbulence in Wind Tunnel Measurements. T. R. No. 342, N. A. C. A., 1930.

REPORT No. 638

THE INFLUENCE OF LATERAL STABILITY ON DISTURBED MOTIONS OF AN AIRPLANE WITH SPECIAL REFERENCE TO THE MOTIONS PRODUCED BY GUSTS

By ROBERT T. JONES

SUMMARY

Disturbed lateral motions have been calculated for a hypothetical small airplane with various modifications of fin area and dihedral setting. Special combinations of disturbing factors to simulate gusts are considered and the influence of lateral stability on the motions is discussed.

The modifications of the airplane include changes of dihedral from 0° to 10° and changes of the weathercock stability from zero to $C_{n\beta}=0.137$ (the equivalent of a fin as large as 10 percent of the wing area). The positions of the modified airplanes on the lateral-stability charts are shown.

Fin area and wing dihedral were found to be of primary importance in side gusts. It was found that the rolling action of the wing with as much as 5° dihedral was distinctly unfavorable, especially when the weathercock stability was small. It is pointed out that the greatest susceptibility to lateral disturbances lies in the inherent damping and coupling moments developed by the wing.

INTRODUCTION

Inherent stability, as defined in mathematical treatment, must be considered only one of several essential flying qualities of an airplane. Other important qualities belonging in this category are steadiness in rough air and responsiveness to control. Although the different flying qualities depend largely on the same governing factors, they may not call for similar proportionings of the factors. It is known, for instance, that the requirements for stability and control may conflict.

What is ultimately desired, of course, is a definite understanding of the individual requirements for stability, control, and steadiness in rough air. Most of the earlier work has been devoted primarily to the study of stability alone. A noteworthy early work on the effects of gusts is that of Wilson (reference 1). More recently the results of an investigation dealing with the effects of different degrees of stability on the motions following assumed initial conditions have been published (reference 2). The purpose of the present work is to study the amplitudes of the motions set up by gusts or other disturbances, particularly insofar as these motions are affected by the lateral-stability characteristics. It is hoped that the study will be useful in

indicating combinations of stability characteristics that result in good riding qualities.

The mathematical treatment employed is, in principle, an extension of that used by Wilson and other early writers. The methods of calculation are, however, more concise and the development is not restricted to special types of gust. The operational method of resolving the effects of disturbances was used. (See reference 3.)

According to the theory, the motion caused by any random variation or sequence of the disturbing factors may be built up by superposing the effects of abrupt unit increases of the disturbance, which corresponds, in the case of gusts, to the effects of elementary sharp-edge cross-currents. Thus the effects of random gusts can be largely visualized in the effect of a unit sharp-edge gust.

STABILITY FACTORS ASSUMED

The chief differences of lateral stability considered were assumed to be brought about by changing the fin area and dihedral of a hypothetical small monoplane. Differences in other proportions of most airplanes of conventional form have only secondary effects (in unstalled flight) and, furthermore, are not usually dictated by considerations of stability. The exact arrangement of the hypothetical airplane, such as the vertical disposition of the wing with respect to the fuselage, may be taken as indefinite. Differences of arrangement can, of course, have large secondary influences on the action of the fin or dihedral, which are usually attributed to aerodynamic interference. It is reasonable to assume that the effects of such interference will be similar to the effects of actual changes in the size of the fin or the amount of dihedral.

The airplane assumed in the calculations is a small 1,600-pound monoplane having rectangular wings with rounded tips. The other proportions, including the radii of gyration about various axes, the tail length, etc., are based on average values of these quantities for a number of conventional machines. The stability derivatives and other characteristics of the airplane are essentially the same as those used in reference 4, except for the differences of fin area and dihedral, and apply to power-off flight. The axes and symbols employed throughout are given in detail in reference 4. Additional symbols that occur in this report are given in the following list:

X , Y , and Z , axes fixed in the airplane so that X points into the relative wind in steady flight. (See report cover.)

U_0 , steady-flight velocity.

$\beta = \tan^{-1} v/U_0$.

Derivatives (see report cover for formulation of coefficients):

$$C_{Y\beta} = \frac{\partial C_Y}{\partial \beta}, \text{ side force due to sideslip.}$$

$$C_{l\beta} = \frac{\partial C_l}{\partial \beta}, \text{ rolling moment due to sideslip.}$$

$$C_{n\beta} = \frac{\partial C_n}{\partial \beta}, \text{ yawing moment due to sideslip.}$$

$$C_{lp} = \frac{\partial C_l}{\partial \frac{pb}{2U_0}}, \text{ rolling moment due to rolling.}$$

$$C_{np} = \frac{\partial C_n}{\partial \frac{pb}{2U_0}}, \text{ yawing moment due to rolling.}$$

$$C_{lr} = \frac{\partial C_l}{\partial \frac{rb}{2U_0}}, \text{ rolling moment due to yawing.}$$

$$C_{nr} = \frac{\partial C_n}{\partial \frac{rb}{2U_0}}, \text{ yawing moment due to yawing.}$$




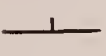
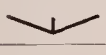
$$L_v = \frac{1}{mk_X^2} \frac{\partial L}{\partial v}.$$

$$N_v = \frac{1}{mk_Z^2} \frac{\partial N}{\partial v}.$$

It was found convenient to designate the five cases of modification by symbols representing the different front views of the airplane. Table I gives the stability coefficients assumed in each case for flight at three different lift coefficients.

TABLE I.—ASSUMED STABILITY COEFFICIENTS

(b , 32 ft.; m , 49 slugs; S , 171 sq. ft.; k_X , 0.150 b ; k_Z , 0.183 b)

Case	Ratio of vertical fin area to wing area	Dihedral angle (deg.)	C_L	U_0 (f. p. s.)	$C_{lp} = \frac{\partial C_l}{\partial \frac{pb}{2U_0}}$	$C_{lr} = \frac{\partial C_l}{\partial \frac{rb}{2U_0}}$	$C_{l\beta} = \frac{\partial C_l}{\partial \beta}$	$C_{np} = \frac{\partial C_n}{\partial \frac{pb}{2U_0}}$	$C_{nr} = \frac{\partial C_n}{\partial \frac{rb}{2U_0}}$	$C_{n\beta} = \frac{\partial C_n}{\partial \beta}$	$C_{Y\beta} = \frac{\partial C_Y}{\partial \beta}$
	0.04	5.0	0.35	150.0	-0.425	0.086	-0.067	-0.022	-0.076	0	-0.226
			1.00	88.5	-0.420	.250	-.088	-.055	-.091	0	-.356
			1.80	66.0	-.442	.442	-.130	-.074	-.196	0	-.772
	.06	5.0	.35	150.0	-.425	.086	-.067	-.022	-.097	.064	-.274
			1.00	88.5	-.420	.250	-.088	-.055	-.109	.067	-.410
			1.80	66.0	-.442	.442	-.130	-.074	-.220	.086	-.808
	.10	5.0	.35	150.0	-.425	.086	-.067	-.022	-.130	.102	-.378
			1.00	88.5	-.420	.250	-.088	-.055	-.146	.108	-.464
			1.80	66.0	-.442	.442	-.130	-.074	-.246	.137	-.920
	.06	0	.35	150.0	-.425	.086	0	-.022	-.097	.064	-.274
			1.00	88.5	-.420	.250	0	-.055	-.109	.067	-.410
			1.80	66.0	-.442	.442	0	-.074	-.220	.086	-.808
	.06	10.0	.35	150.0	-.425	.086	-.137	-.022	-.097	.064	-.274
			1.00	88.5	-.420	.250	-.177	-.055	-.109	.067	-.410
			1.80	66.0	-.442	.442	-.259	-.074	-.220	.086	-.808

These coefficients were estimated from the outward characteristics of the airplane by methods described in reference 4. The derivatives $C_{n\beta}$, C_{nr} , and $C_{Y\beta}$ (corresponding to the yawing moments in sideslip and in yawing and to the side force in sideslip) were assumed to be affected by the changes of fin area. Only the derivative $C_{l\beta}$ (corresponding to the rolling moment in sideslip) was assumed to be affected by changes of dihedral. The effect of dihedral on the lateral force in sideslip was neglected inasmuch as it was found that a compensating error was introduced by the absence of the side force due to rolling in the equations of motion. Another omission is the small adverse effect of dihedral angle on the weathercock-stability factor $C_{n\beta}$. This effect is small, particularly in view of the wide variation of $C_{n\beta}$ assumed. At a lift coefficient of 1.8, representing low-speed flight, a full-span flap was assumed. Tests show that the effect of such a flap is to increase the weathercock-stability factor somewhat for the wing alone. In practice, the flap might interfere with the

air flow over the fin so that the increase of $C_{n\beta}$ assumed in this condition would not be realized.

Figure 1 shows the positions of the modified airplanes on the lateral-stability diagrams. These diagrams are essentially similar to those given in reference 5 except that a simultaneous increase of C_{nr} with $C_{n\beta}$ was assumed to show directly the effect of increasing the fin area.

The value recommended by Diehl (reference 6) for $C_{n\beta}$ works out to about 0.03 for the wing loading assumed here. Limits mentioned by Millikan (reference 7) correspond to $0.08 > C_{n\beta} > 0.05$. Nearly all designers are familiar with the limits of L_v/N_v for satisfactory lateral stability given by Korvin-Kroukovsky (reference 8). Figure 1 (a) shows these limits in terms of $C_{l\beta}$ and $C_{n\beta}$. It should be mentioned that Korvin-Kroukovsky's formulas are more suited to the empirical-statistical analysis in which they were employed than to the determination of absolute values of $C_{n\beta}/C_{l\beta}$ for this stability chart. In most cases, wind-tunnel tests show values of $C_{n\beta}$ smaller than those predicted so that

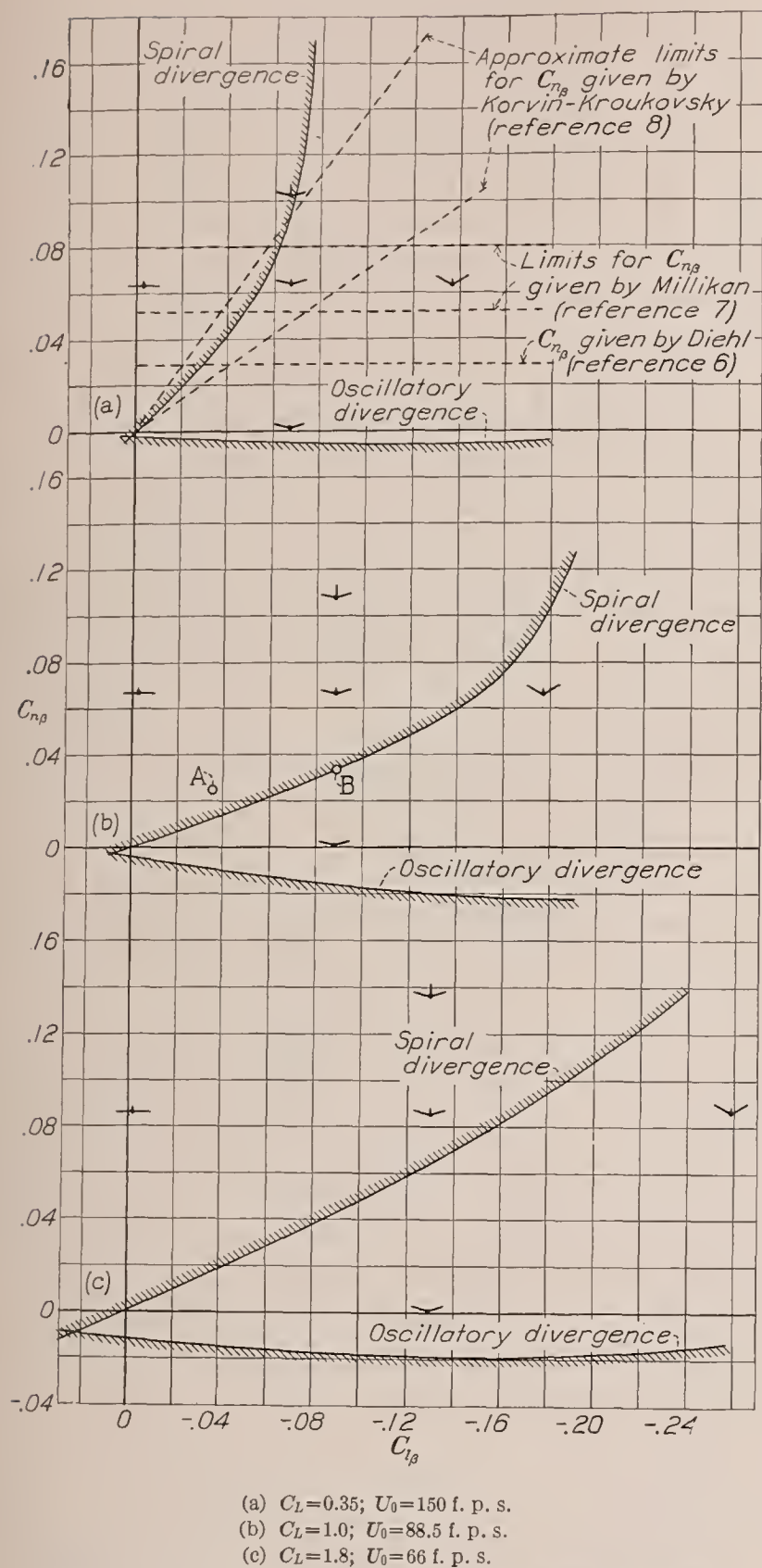


FIGURE 1.—Stability chart showing positions of the assumed airplanes.

TABLE II.—STABILITY INDICES, RATES OF DAMPING, AND PERIODS

$$[\lambda_3 = a + bi]$$

Case	C_L	λ_1	$\frac{-0.69}{\lambda_1}$ (a)	λ_2	$\frac{(0.095 \text{ or } -0.105)}{\lambda_2}$ (b)	a	$\frac{-0.69}{a}$	b	$\frac{\pi}{2b}$ (c)
	0.35	-5.477	0.126	-0.4190	^d 1.645	-0.1720	4.01	0.708	2.22
	1.0	-3.255	.212	-.2974	^d 2.32	-.1386	4.98	.8241	1.907
	1.8	-2.533	.273	-.6080	^d 1.13	-.1794	3.85	.8568	1.83
	.35	-5.472	.126	-.0070	15.0	-.495	1.39	2.45	.641
	1.0	-3.280	.210	.0615	1.55	-.3637	1.90	1.676	.937
	1.8	-2.633	.262	.0624	1.53	-.5247	1.315	1.546	1.02
	.35	-5.466	.126	0	∞	-.680	1.01	3.03	.518
	1.0	-3.294	.209	.0838	1.133	-.4797	1.44	2.013	.780
	1.8	-2.670	.258	.1347	.706	-.6075	1.14	1.829	.858
	.35	-5.369	.129	.0420	2.27	-.571	1.21	2.35	.668
	1.0	-3.070	.225	.1770	.537	-.529	1.30	1.519	1.034
	1.8	-2.320	.297	.2900	.328	-.795	.868	1.415	1.110
	.35	-5.573	.124	-.0504	2.08	-.423	1.63	2.55	.616
	1.0	-3.460	.199	-.0184	5.71	-.235	2.94	1.826	.860
	1.8	-2.872	.240	-.1045	1.005	-.3219	2.14	1.697	.925

^a The value $-0.69/\lambda$ represents time to diminish by $1/2$.^b Use $-0.105/\lambda_2$ for time to diminish by $1/10$ when λ_2 is negative; use $0.095/\lambda_2$ for time to increase by $1/10$ when λ_2 is positive.^c Quarter period.^d For this case, $-0.69/\lambda_2$ has been used.

the specified range, if given in wind-tunnel values, would probably fall somewhat lower than indicated in figure 1.

The value $C_{n\beta}=0$ does not, of course, correspond to an airplane with no vertical tail surface. Experience has shown that the unstable yawing moment of a large well-streamlined fuselage may entirely offset the stabilizing action of a fair-size fin. This occurrence is naturally more probable if the fin area is originally small; hence the smallest area likely to be used in a modern design (4 percent of the wing area) was chosen to represent the condition.

It is, in general, difficult to predict the values of either $C_{n\beta}$ or $C_{l\beta}$ for a given design. It will be realized that the corresponding values of fin area and dihedral, as referred to in this report, apply only under certain idealized conditions and are employed primarily as a matter of convenience in fixing ideas on the problem. Reference 9 gives a summary of test values of $C_{n\beta}$, including a discussion of pertinent factors and drawings of the models tested. The data included in that paper should aid the designer in judging the weathercock stability.

INFLUENCE OF LATERAL STABILITY ON MOTIONS DUE TO ARBITRARY DISTURBANCES

GENERAL DESCRIPTION OF LATERAL MOTIONS

The equations of lateral stability generally show two real roots together with one conjugate complex pair, indicating three "modes" of motion. Different disturbances will result in motions compounded of these three modes in different proportions.

Table II lists the roots, or stability indices, for the various cases considered. The first mode (corresponding to the root λ_1), represents primarily the heavy damping of any movement involving rolling of the wings relative to the air. At normal flight speeds, this damping is such that the wings are in a large measure constrained against such relative movement normal to their chords.

The second mode distinguishable in the lateral motions (corresponding to λ_2) is a practically continuous turning motion, which may either converge or diverge. Normal stability of this mode represents the slow natural recovery from a banked turn. The rate of increase or decrease of the turning motion is slow, primarily on account of the insensitiveness of the airplane to displacement in bank and the strong resistance to rolling motion. The slow spiral always occurs with inward sideslip.

The third mode (λ_3) is the familiar oscillation, consisting usually of a yawing and sideslipping motion. Such rolling as occurs in the oscillation is determined by the tendency of the wings to follow a path outlined by the dihedral in front view. The wing, when sideslipping, tends strongly to roll in a way involving the least angle-of-attack change along the span. Thus the oscillations involve a "weathercock" motion combined with a rolling nearly in phase with the sideslip.

With fairly large fin area, the oscillations are rapid and are quickly damped. Under most conditions the amplitude is small. As the fin area is reduced, however, the period becomes slower and, with normal dihedral, the oscillation takes on the character of a swinging in bank and sideslip under the action of gravity. The point of instability is reached when the oscillation degenerates to an almost pure rolling and sideslipping motion, so that the damping derivative in yawing, C_{nr} , has little effect on the occurrence of undamped oscillations. As has been shown (reference 4), unstable oscillations can readily occur if the airplane is constrained in yawing.

Although both the oscillation and the slow mode of convergence are largely governed by the fin area and the dihedral, the rapid convergence λ_1 is practically independent of either of these factors. The damping comes, of course, from the wings and is an inherent characteristic of conventional airplanes. This damping is excessive and is undesirable, since it indicates great sensitiveness to rolling gusts or to vertical gusts with a gradient along the wing span. The damping of rolling can be reduced by increasing the lateral moment of inertia, but the possible improvement appears to be small.

CALCULATED MOTIONS

The equations of motion of the airplane form a linear system so that the effects of disturbances can be compounded by addition. Thus, if any sequence of application of forces or couples to the airplane is given, it is possible to compute the resultant theoretical motion at any instant by addition, or integration, of separate effects. The impressed forces or couples may be due to control manipulation or to gusts, alone or in combination.

The foregoing statement refers to a resolution of the impressed disturbances along the axes fixed in the airplane. The disturbances are assumed to take on pre-assigned values independent of the movements of the

airplane. With conventional control devices, the disturbances do remain practically independent of the motions. The orientation of the gusts is not dependent on the motion of the airplane, and deviations caused by such outside disturbances will introduce changes in the magnitudes of the disturbing factors themselves. For small displacements, these changes are of second order and are negligible. For large displacements in gusts it may, however, be necessary to carry out the calculation in several steps, altering the magnitude of the disturbance as the orientation of the relative wind changes.

The data needed for the computation of motion under any given set of conditions are the histories of motions following sudden unit disturbances. Computations of such unit motions were made during the course of the investigation reported herein and the results were used as the basis for the more complete calculations given later.

Specifically, the unit disturbance referred to is a force (Y) or a couple (L or N) having the value zero up to the time $t=0$ and maintaining a constant value thereafter. The magnitude is such as to cause a unit linear or angular acceleration of the airplane. According to well-known mathematical rules, the motions under such conditions are given by equations of the form

$$p_Y(t) = p_{Y0} + p_{Y1}e^{\lambda_1 t} + p_{Y2}e^{\lambda_2 t} + p_{Y3}e^{at} \cos b(t + t_{pY}) \quad (1)$$

where p_{Y0} , p_{Y1} , and t_{pY} are constants, calculated values of which are given in table III, and λ_1 , λ_2 , $a+ib$, and $a-ib$ are the roots, or stability indices. (See table II.) Three components of motion for each of three component disturbances are given. Thus, $p_Y(t)$ denotes the rolling velocity due to a unit side disturbance and $r_L(t)$ denotes the yawing velocity due to a unit rolling disturbance.

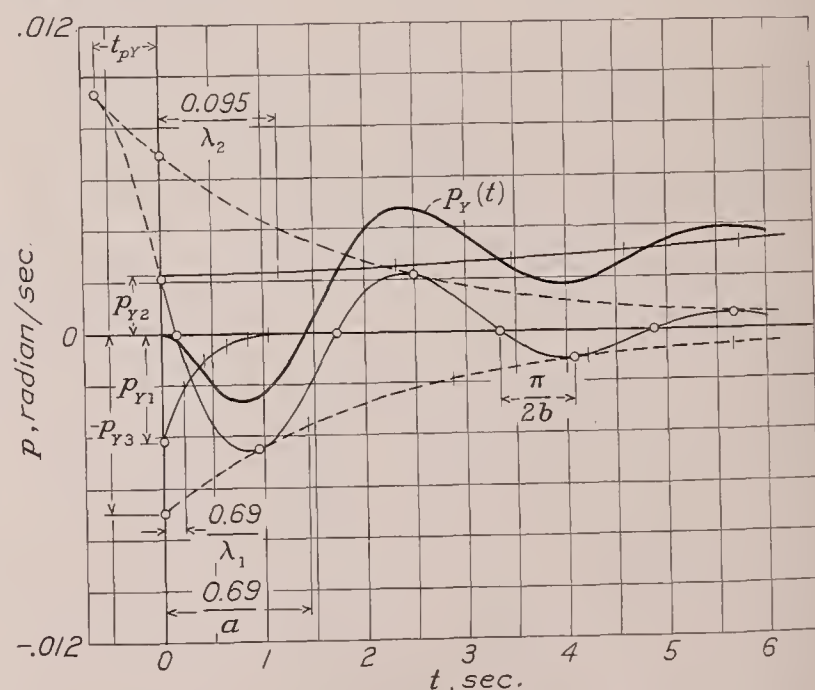


FIGURE 2.—Example showing use of data given in table III for plotting motions.

$$p_Y(t) = p_{Y1}e^{\lambda_1 t} + p_{Y2}e^{\lambda_2 t} + p_{Y3}e^{at} \cos b(t + t_{pY})$$

Plots of these equations were made with scarcely any additional computation. The procedure is illustrated by figure 2. First the coefficients, as given in

TABLE III.—EQUATIONS OF MOTION FOR UNIT DISTURBANCES

$[v_L(t) = v_{L0} + v_{L1}e^{\lambda_1 t} + v_{L2}e^{\lambda_2 t} + v_{L3}e^{\lambda_3 t} \cos b(t + t_{eL}); \text{ etc.}]$

Case	Sideslip		Rolling										Yawing																																			
	a—Due to side disturbance										b—Due to rolling disturbance										c—Due to yawing disturbance																											
	C_L	v_{Y0}	v_{Y1}	v_{Y2}	v_{Y3}	t_{eY}	p_{Y0}	p_{Y1}	p_{Y2}	p_{Y3}	t_{pY}	τ_{Y0}	τ_{Y1}	τ_{Y2}	τ_{Y3}	t_{rY}	C_L	v_{L0}	v_{L1}	v_{L2}	v_{L3}	t_{eL}	p_{L0}	p_{L1}	p_{L2}	p_{L3}	t_{pL}	τ_{L0}	τ_{L1}	τ_{L2}	τ_{L3}	t_{rL}	C_L	v_{N0}	v_{N1}	v_{N2}	v_{N3}	t_{eN}	p_{N0}	p_{N1}	p_{N2}	p_{N3}	t_{pN}	τ_{N0}	τ_{N1}	τ_{N2}	τ_{N3}	t_{rN}
\curvearrowright	0.35	0	-0.0041	0.5685	-1.6820	1.735	0	-0.00178	-0.00533	0.01683	1.600	0	-0.00007	0.00380	-0.00380	0.284	0.35	18.490	-0.401	2.985	-22.035	-0.419	0	-0.17602	-0.02753	0.22000	-0.552	0	-0.0074	0.01959	-0.04996	-1.870	0.35	29.084	-0.035	-292.010	284.729	0.556	0	-0.0154	2.7364	-2.8476	0.423	1.429	-0.001	-1.948	0.644	-0.894
\curvearrowright	1.0	0	-0.0237	0.5558	-1.3410	1.413	0	-0.00374	-0.00408	0.01683	1.320	0	-0.00041	0.00380	-0.00380	0.080	1.0	23.809	-1.7368	2.2288	-26.332	-0.480	0	-0.2787	-0.0163	0.3338	-0.591	0	-0.03029	0.02409	-0.11120	-1.832	1.0	90.505	0.434	-222.037	142.701	0.493	0	0.0719	1.6312	-1.8012	0.402	1.999	0.007	-2.415	0.600	-0.997
\curvearrowright	1.8	0	-0.067	0.627	-1.416	1.360	0	-0.00558	-0.00497	0.01683	1.235	0	-0.00113	0.00380	-0.00380	0.080	1.8	21.688	-3.452	5.385	-26.215	-0.523	0	-0.3341	-0.0431	0.4385	-0.625	0	-0.0576	0.0672	-0.1257	-1.744	1.8	68.0192	2.398	-144.835	109.323	0.959	0	0.2299	1.149	-1.8340	0.840	1.250	0.040	-1.795	0.519	-0.269
\curvearrowright	0.35	0	-0.0033	0.1390	-0.3980	0.500	0	-0.00171	-0.00021	0.00393	0.433	0	-0.00005	0.00581	-0.00581	0.138	0.35	114.003	-0.338	-112.570	-1.698	-0.355	0	-0.1769	0.1659	0.0195	0.397	4.682	-0.0050	-4.6992	0.02997	0.301	0.35	-32.398	-1.4005	37.3	-5.98	-0.563	0	-0.2761	0.2186	0.0843	-0.490	-1.244	-0.019	1.198	0.093	0.476
\curvearrowright	1.0	0	-0.021	0.274	-0.532	0.652	0	-0.00414	-0.00159	0.00804	0.743	0	-0.00030	0.00878	-0.00878	0.088	1.0	-66.222	-2.236	70.067	-7.340	-0.874	0	-0.3067	0.2338	0.1577	-0.705	-1.6167	-0.0248	1.5269	0.1317	0.333	1.0	-943	-0.314	732	-1.138	-0.326	0.1732	-0.1782	0	0.0106	-0.356	-0.01256	-0.00398	0.0360	0.00226	0.247
\curvearrowright	1.8	0	-0.053	0.446	-0.565	0.518	0	-0.00734	-0.001502	0.0121	0.690	0	-0.00060	0.00975	-0.00975	0.175	1.8	-21.747	-1.2602	24.768	-3.9301	-0.550	0	-0.2736	0.2514	0.1184	-0.638	-0.8434	-0.0142	0.9500	0.0860	0.289	1.8	-24.096	-1.873	26.642	-4.963	-0.784	0	-0.2979	0.17915	0.0700	0.074	-0.9088	-0.00530	0.8934	0.0310	0.357
\curvearrowright	0.35	0	-0.0027	0	-0.3310	0.391	-0.00015	-0.00169	0	0.00322	0.318	0.00625	-0.00040	0	-0.00638	0.297	0.35	-22.128	-0.3679	23.738	-1.999	-0.383	0	-0.18612	0.0729	0.0729	0.023	-0.5266	-0.0223	0.4493	0.370	0.35	-16.375	-3.485	18.276	-8.721	-0.981	0	-0.3250	0.2473	0.1726	-0.414	-0.4000	-0.0287	0.2751	0.1545	0.078	
\curvearrowright	1.0	0	-0.0199	0.2350	-0.4570	0.537	0	-0.00433	0.00224	0.00698	0.629	0	-0.00022	0.00908	-0.00908	0.076	1.0	-66.222	-2.236	70.067	-7.340	-0.874	0	-0.3067	0.2338	0.1577	-0.705	-1.6167	-0.0248	1.5269	0.1317	0.333	1.0	-943	-0.314	732	-1.138	-0.326	0.1732	-0.1782	0	0.0106	-0.356	-0.01256	-0.00398	0.0360	0.00226	0.247
\curvearrowright	1.8	0	-0.048	0.342	-0.459	0.479	0	-0.00770	0.00323	0.0110	0.629	0	-0.00037	0.00970	-0.00970	0.155	1.8	-24.096	-1.873	26.642	-4.963	-0.784	0	-0.2979	0.17915	0.0729	0.023	-0.5266	-0.0223	0.4493	0.370	0.35	-15.508	-0.313	-14.033	-1.637	-0.066	0	-0.16874	0.13318	0.03290	-0.410	3.435	-0.0048	-0.6469	0.0254	0.372	
\curvearrowright	0.35	0	-0.0056	0.1293	-0.3830	0.487	0	-0.00305	-0.00142	0.00746	0.503	0	-0.00010	0.00607	-0.00607	0.069	0.35	89.459	-1.1249	-85.096	-4.700	-0.410	0	-0.2433	0.1142	0.1819	-0.549	0	-0.016	-3.464	0.076	0.35	15.508	-0.313	-14.033	-1.637	-0.066	0	-0.16874	0.13318	0.03290	-0.410	3.435	-0.0048	-0.6469	0.0254	0.372	
\curvearrowright	1.0	0	-0.0278	0.2080	-0.5060	0.660	0	-0.00601	-0.00044	0.01236	0.557	0	-0.00041	0.00846	-0.00846	0.069	1.0	32.402	-1.613	-27.849	-5.801	-0.612	0	-0.2571	0.1904	0.1905	-0.715	0.7916	-0.0211	-8.409	0.1032	0.35	89.459	-1.1249	-85.096	-4.700	-0.410	0	-0.2433	0.1142	0.1819	-0.549	0	-0.016	-3.464	0.076	0.35	
\curvearrowright	1.8	0	-0.057	0.329	-0.537	0.612	0	-0.00909	-0.00226	0.01755	0.511	0	-0.00075	0.00996	-0.00996	0.149	1.8	32.402	-1.613	-27.849	-5.801	-0.612	0	-0.2571	0.1904	0.1905	-0.715	0.7916	-0.0211	-8.409	0.1032	0.35	15.508	-0.313	-14.033	-1.637	-0.066	0	-0.16874	0.13318	0.03290	-0.410	3.435	-0.0048	-0.6469	0.0254	0.372	
\curvearrowright	0.35	0	-0.0056	0.1293	-0.3830	0.487	0	-0.00305	-0.00142	0.00746	0.503	0	-0.00010	0.00607	-0.00607	0.069	0.35	89.459	-1.1249	-85.096	-4.700	-0.410	0	-0.2433	0.1142	0.1819	-0.549	0	-0.016	-3.464	0.076	0.35	15.508	-0.313	-14.033	-1.637	-0.066	0	-0.16874	0.13318	0.03290	-0.410	3.435	-0.0048	-0.6469	0.0254	0.372	
\curvearrowright	1.0	0	-0.0278	0.2080	-0.5060	0.660	0	-0.00601	-0.00044	0.01236	0.557	0	-0.00041	0.00846	-0.00846	0.069	1.0	32.402	-1.613	-27.849	-5.801	-0.612	0	-0.2571	0.1904	0.1905	-0.715	0.7916	-0.0211	-8.409	0.1032	0.35	15.508	-0.313	-14.033	-1.637	-0.066	0	-0.16874	0.13318	0.03290	-0.410	3.435	-0.0048	-0.6469	0.0254	0.372	
\curvearrowright	1.8	0	-0.057	0.329	-0.537	0.612	0	-0.00909	-0.00226	0.01755	0.511	0	-0.00075	0.00996	-0.00996	0.149	1.8	32.402	-1.613	-27.849	-5.801	-0.612	0	-0.2571	0.1904	0.1905	-0.715	0.7916	-0.0211	-8.409	0.1032	0.35	15.508	-0.313	-14.033	-1.637	-0.066	0	-0.16874	0.13318	0.03290	-0.410	3.435	-0.0048	-0.6469	0.0254	0.372	
\curvearrowright	0.35	0	-0.0056	0.1293	-0.3830	0.487	0	-0.00305	-0.00142	0.00746	0.503	0	-0.00010	0.00607	-0.00607	0.069	0.35	89.459	-1.1249	-85.096	-4.700	-0.410	0	-0.2433	0.1142	0.1819	-0.549	0	-0.016	-3.464	0.076	0.35	15.508	-0.313	-14.033	-1.637	-0.066	0	-0.16874	0.13318	0.03290	-0.410	3.435	-0.0048	-0.6469	0.0254	0.372	
\curvearrowright	1.0	0	-0.0278	0.2080	-0.5060	0.660	0	-0.00601	-0.00044	0.01236	0.557	0	-0.00041	0.00846	-0.00846	0.069	1.0	32.402	-1.613	-27.849	-5.801	-0.612	0	-0.2571	0.1904	0.1905	-0.715	0.7916	-0.0211	-8.409	0.1032	0.35	15.508	-0.313	-14.033	-1.637	-0.066	0	-0.16874	0.13318	0.03290	-0.410	3.435	-0.0048	-0.6469	0.0254	0.372	
\curvearrowright	1.8	0	-0.057	0.329	-0.537	0.612	0	-0.00909	-0.00226	0.01755	0.511	0	-0.00075	0.00996	-0.00996	0.149	1.8	32.402	-1.613	-27.849	-5.801	-0.612	0	-0.2571	0.1904	0.1905	-0.715	0.7916	-0.0211	-8.409	0.1032	0.35	15.508	-0.313	-14.033	-1.637	-0.066	0	-0.16874	0.13318	0.03290	-0.410	3.435	-0.0048	-0.6469	0.0254	0.372	
\curvearrowright	0.35	0	-0.0056	0.1293	-0.3830	0.487	0	-0.00305	-0.00142	0.00746	0.503	0	-0.00010	0.00607	-0.00607	0.069	0.35	89.459	-1.1249	-85.096	-4.700	-0.410	0	-0.2433	0.1142	0.1819	-0.549	0	-0.016	-3.464	0.076	0.35	15.508	-0.313	-14.033	-1.637	-0.066	0	-0.16874	0.13318	0.03290	-0.410	3.435	-0.0048	-0.6469	0.0254	0.372	
\curvearrowright	1.0	0	-0.0278	0.2080	-0.5060	0.660	0	-0.00601	-0.00044	0.01236	0.557	0	-0.00041	0.00846	-0.00846	0.069	1.0	32.402	-1.613	-27.849	-5.801	-0.612	0	-0.2571	0.1904	0.1905	-0.715	0.7916	-0.0211	-8.409	0.1032	0.35	15.508	-0.313	-14.033	-1.637	-0.066	0	-0.16874	0.13318	0.03290	-0.410	3.435	-0.0048	-0.6469	0.0254	0.372	
\curvearrowright	1.8	0	-0.057	0.329	-0.537	0.612	0	-0.00909	-0.00226	0.01755	0.511	0	-0.00075	0.00996	-0.00996	0.149	1.8	32.402	-1.613	-27.849	-5.801	-0.612	0	-0.2571	0.1904	0.1905	-0.715	0.7916	-0.0211	-8.409	0.1032	0.35	15.508	-0.313	-14.033	-1.637	-0.066	0	-0.16874	0.13318	0.03290	-0.410	3.435	-0.0048	-0.6469	0.0254	0.372	
\curvearrowright	0.35	0	-0.0056	0.1293	-0.3830	0.487	0	-0.00305	-0.00142	0.00746	0.503	0	-0.00010	0.00607	-0.00607	0.069	0.35	89.459	-1.1249	-85.096	-4.700	-0.410	0	-0.2433	0.1142	0.1819	-0.549	0	-0.016	-3.464	0.076	0.35	15.508	-0.313	-14.033	-1.637	-0.066	0	-0.16874	0.13318	0.03290	-0.410	3.435	-0.0048	-0.6469	0.0254	0.372	
\curvearrowright	1.0	0	-0.0278	0.2080	-0.5060	0.660	0	-0.00601	-0.00044	0.01236	0.557	0	-0.00041	0.00846	-0.00846	0.069	1.0	32.402	-1.613	-27.849	-5.801	-0.612	0	-0.2571	0.1904	0.1905	-0.715	0.7916	-0.0211	-8.409	0.1032	0.35	15.508	-0.313	-14.033	-1.637	-0.066	0</										

table III, were marked off on the ordinate scale. The time intervals within which the various modes diminish or increase by one-half, or by one-tenth in the case of λ_2 (see table II), were then spaced off on the abscissa and points on the curves were found by diminishing or increasing the ordinates successively as indicated by the sign of the root. The oscillatory mode was obtained by drawing in the envelope (given by $\pm p_{r3}$, say) and spacing off the quarter periods, beginning at the point indicated by the phase angle of this mode. The cosine curve was then simply sketched in as shown. The final curves were found to give remarkably good checks when applied in the original differential equations of motion. Such a check shows the correctness of both the method of plotting and the analytical solutions (equation (1) and table III).

If the impressed disturbance is given as a function of t by a curve, it will usually be sufficient to approximate this curve by the addition of a number of successive positive and negative steps. The combination of steps necessary to reproduce the disturbance leads directly to the addition of the elementary motions for the resultant motion. Otherwise, for example, if the variation of disturbance is given by $L(t)$, then the resultant motion $p(t)$ at any time t due to $L(t)$ beginning at $t=0$ may be found by Duhamel's theorem, thus

$$p(t) \text{ due to variable rolling moment} = p_L(t) L(0) + \int_0^t p_L(t-t_1) L'(t_1) dt_1 \quad (2)$$

where $p_L(t)$ and $p_L(t-t_1)$ are obtained from table III. An explanation and a graphical method for evaluation of such integrals are given in reference 3.

MOTIONS IN SIDE GUSTS

The motion caused by a unit increment of gust velocity is found by compounding elementary disturbances in such a way as to simulate the disturbing action of the gust. Thus, in a side gust of velocity v_0 , the disturbing acceleration along Y will be $v_0 Y_v$ and angular disturbances will be $v_0 L_v, v_0 N_v$.

As explained before, the effects of any usual variation of gustiness can be largely foretold from the effect of a unit sharp-edge gust. The variable gust can be built up from small increment jumps of gust velocity corresponding to sharp-edge cross-currents and the final motion will approach that obtained by superposing the motions due to the individual elements.

The effect of a sharp gust from the side is similar to, although not exactly the same as, the effect of an initial angle of sideslip. For the side gust, it is necessary to take account of the period of penetration of the airplane into the current. The first effect will be to push the nose of the airplane downwind whereas an instant later the current will strike the fin, turning the machine into the gust. The action of dihedral in causing the machine to roll away from the gust will also occur before the fin is affected. These effects are, however, of short

duration and do not alter the motion to any great extent after the first fraction of a second, except in cases of small weathercock stability where the fuselage contributes a large unstable yawing moment.

The computations that follow are based on the assumption that the rolling action of the gust begins at $t=0$ and that the yawing action begins when the airplane has traveled far enough to carry the fin into the current. The case of $C_{n\beta}=0$ was treated by assuming a yawing couple equal and opposite to that of the 4-percent fin applied when $t=0$, this couple being neutralized at the instant the fin entered the gust.

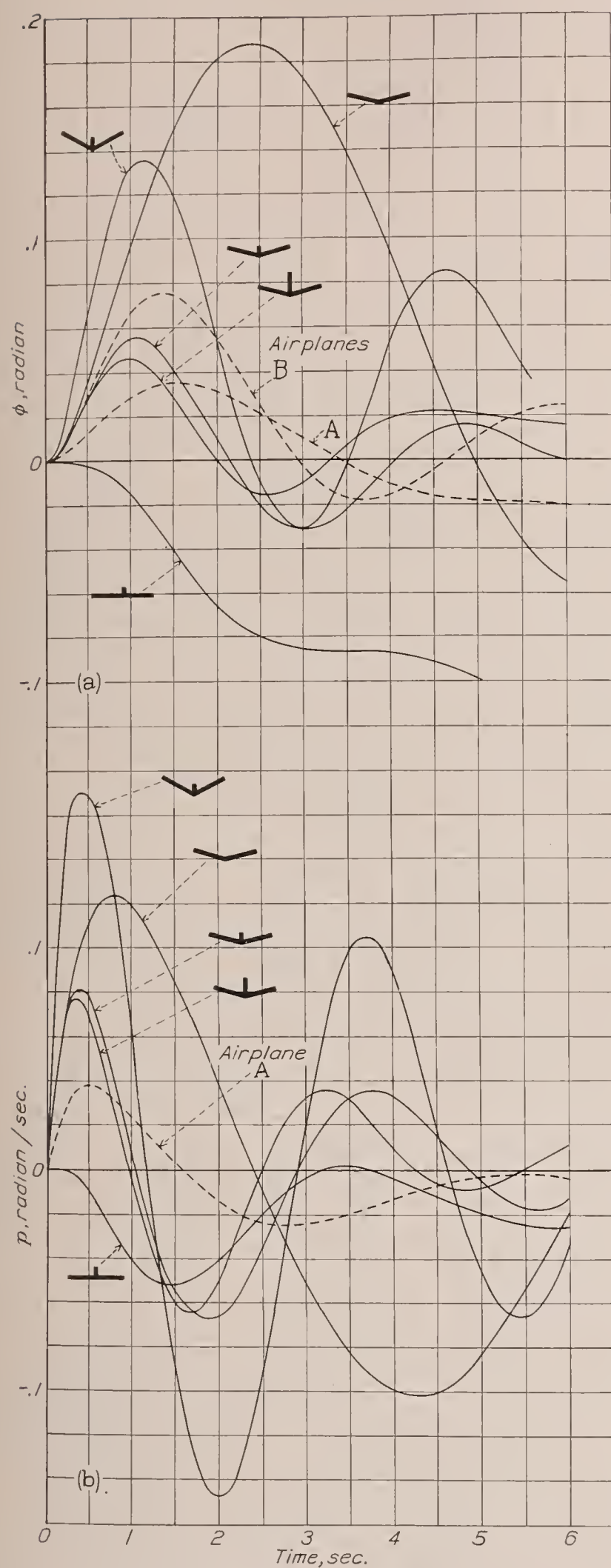
A possible further refinement of the calculations would involve the delay in building up the full lift forces on the various surfaces. Mathematical methods for dealing with various lags or rates of growth of the aerodynamic reactions have been developed, but their description is beyond the intended scope of the present report. It may be said, however, that, for motions as slow as the natural oscillations of a rigid airplane, this effect (judging by the theoretical predictions) is quite negligible.

Figure 3 illustrates the results of the calculations based on a 10-foot-per-second sharp-edge side gust. The curves shown are for flight at $C_L=1.0$ but the same general trends appeared in the calculations made for other lift coefficients.

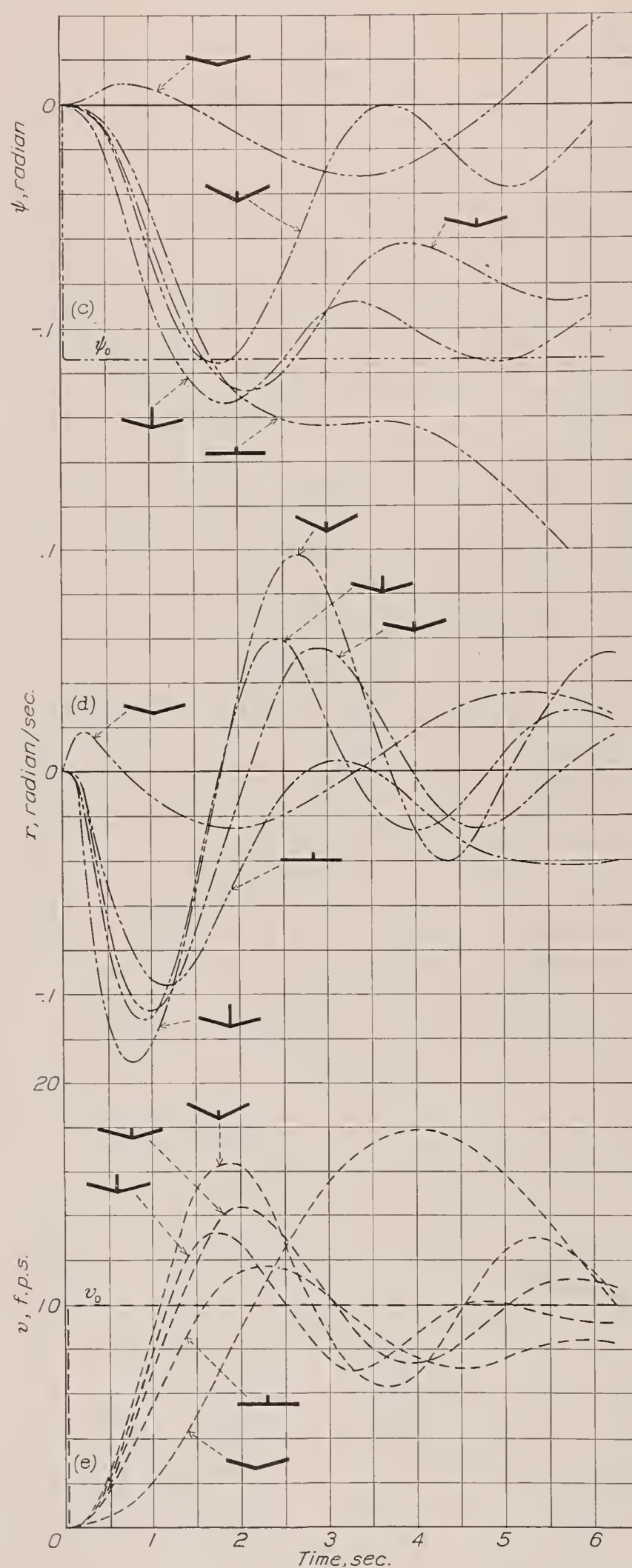
The most noteworthy difference shown is the effect of deficiency of fin area on the banking motion (figs. 3 (a) and 3 (b)). The airplane with 10° dihedral and average fin was not displaced so much in bank by the side gust as was the airplane with 5° dihedral and a small fin. The initial rate of rolling, however, was greater with the greater dihedral.

With a given dihedral an increase of fin area cuts down the banking motion although, after a certain size is reached, the gain becomes slight, as is illustrated by figure 3 (a). With neutral weathercock stability (fig. 3 (c)) the change of heading on entering the gust is at first small and, although the motion is stable, the oscillation in azimuth seems to be reinforced for a time by the rolling. This action is to be attributed to the phase lag between the rolling and the yawing effects upon penetrating the sharp-edge current. It seems probable that an appearance of inherent instability may be reached at a point considerably above the mathematical limit for undamped oscillations. (See fig. 1.) It is known, for instance, that unstable oscillations may result from an attempt to hold the wings level with ordinary ailerons unless $C_{n\beta}$ has a definite positive value.

The side gust is equivalent to a sudden shift in the wind direction, corresponding to a change in azimuth ψ_0 as indicated in figure 3 (c). The normal airplane swings about and tends to approach this heading. It will be noted that the airplane with the large fin turns fairly sharply into the wind and, since the banking



(a) Banking.
(b) Rolling motion.



(c) Azimuth.
(d) Yawing motion.
(e) Sideslip velocity.

FIGURE 3.—Motions caused by a sharp-edge side gust.
 $C_L=1.0$; $v_0=10$ f. p. s.; $U_0=88.5$ f. p. s.

motion is small, tends to keep the same flight path relative to the earth for a short time. After about 6 seconds, however, the spiral divergence begins to be apparent and the motion finally results in turning downwind.

An example of extreme spiral divergence is illustrated by the airplane with no dihedral. In this case, however, the airplane banks and turns directly upwind. The airplane with large dihedral illustrates the opposite condition and shows the predominance of oscillations that generally characterizes the effect of dihedral. Here the airplane tends back toward its original azimuth heading, drifting sidewise with the gust.

The airplane with 5° dihedral banked rather sharply away from the gust, whereas the airplane with zero dihedral showed an undesirable tendency to bank and slide into the gust. It was therefore a matter of interest to try some modifications lying in between these two conditions. It was realized that the rolling could not be entirely suppressed by such modifications on account of the phase relationships involved in the motions.

It appeared that 1° or 2° of effective dihedral would give about the least banking motion in the side gust and hence this condition was investigated. Inasmuch as the airplane might have shown a noticeable spiral divergence at low speeds with the normal fin area, this area was arbitrarily reduced, bringing the weathercock-stability factor $C_{n\beta}$ down in about the same proportion as the dihedral factor $C_{l\beta}$. The values selected were $C_{n\beta}=0.025$ and $C_{l\beta}=-0.035$, which corresponds to 2° effective dihedral. The position of this airplane on the lateral-stability chart is denoted by the point A in figure 1 (b).

The results for airplane A are compared with the others in figures 3 (a) and 3 (b). It will be noted that the bank is somewhat smaller than in the case with 5° dihedral and a large fin but that the bank persists for a longer time. The difference made by the change from 5° dihedral to 2° seems surprisingly small. A somewhat greater difference would be expected if the fin had not been reduced. It should be borne in mind that the yawing disturbance is reduced by cutting down the fin.

The curve for airplane B (fig. 3 (a)) shows the result of attempting to secure spiral stability (at $C_L=1.0$) by cutting down the fin of the airplane with 5° dihedral. (Note that airplane A is slightly unstable.) The value of $C_{n\beta}$ in this case is about half that assumed for the mean condition. (See fig. 1 (b).) The banking displacement seems undesirably large (comparatively) in this case.

OTHER TYPES OF GUST

The flight velocity of the airplane being normally large with respect to gust velocities, it is permissible to consider the gusts as being stationary in time with respect to the flight path. Thus the gusts are con-

sidered to exist as a fixed pattern in the air ahead of the airplane and not to vary in time within the short space required for the machine to travel its own length.

As mentioned before, when the airplane enters a cross-current in level flight, a gradient of sidewise velocity along the length of the fuselage will exist. The effect of this gradient is similar to the effect of a relative yawing motion superposed on the side velocity. For a uniform gradient the additional yawing moment would be $(-dv_0/dx) \times N_r$. The calculations involved this factor by virtue of the time lag assumed in application of the yawing moment due to the fin, and upon this basis they should be applicable to any reasonable variation or gradient of sidewise velocity.

A somewhat different situation arises when the airplane is climbing or descending through a cross wind that varies with height, as, for instance, when descending through the earth boundary layer for a cross-wind landing, for then no perceptible gradient of sidewise velocity along the length of the airplane will exist. The motions that arise in these cases can be compounded by integration from the motion following an initial angle of sideslip. This motion is not greatly different from that caused by entering a sharp cross-current and the same general conclusions will apply.

It appears that a true yawing gust, consisting of pure angular relative motion of the air, could act only momentarily on the airplane. The sidewise velocity would predominate after the first two- or three-tenths of a second with the airplane flying at normal speed. Gradients of velocity along the wing span, however, might persist for longer periods.

Away from the ground influence, gradients of forward velocity and of vertical velocity along the wing span must be considered as being about equally probable. At normal flight speeds, the vertical gradients produce by far the greater effects. As was mentioned before, the damping of relative rolling motion is such that the airplane very quickly takes on the angular velocity of the gust gradient.

Figure 4 shows the rolling motion calculated for the medium airplane (5° dihedral and 6 percent fin) in a momentary rolling gust $p_0 b/2U_0=0.05$. It will be noted that the airplane takes on approximately half the rolling velocity of the gust within one-fifth second.

As might be expected, observations have shown that vertical currents tend to diminish near flat ground. Thus side gusts and yawing gradients are more likely to affect the airplane while it is landing and taking off. At very low speeds with flaps down, the rolling derivative due to yawing becomes as great as that due to rolling (see table I) so that in this condition the airplane is affected as much by spanwise gradients of longitudinal velocity as it would be by the rolling gradients. (Note also that the effect of the rolling gradients is less at low speed.)

Figure 5 shows the banking reactions of the various airplanes in a sudden, persistent yawing-gradient gust.

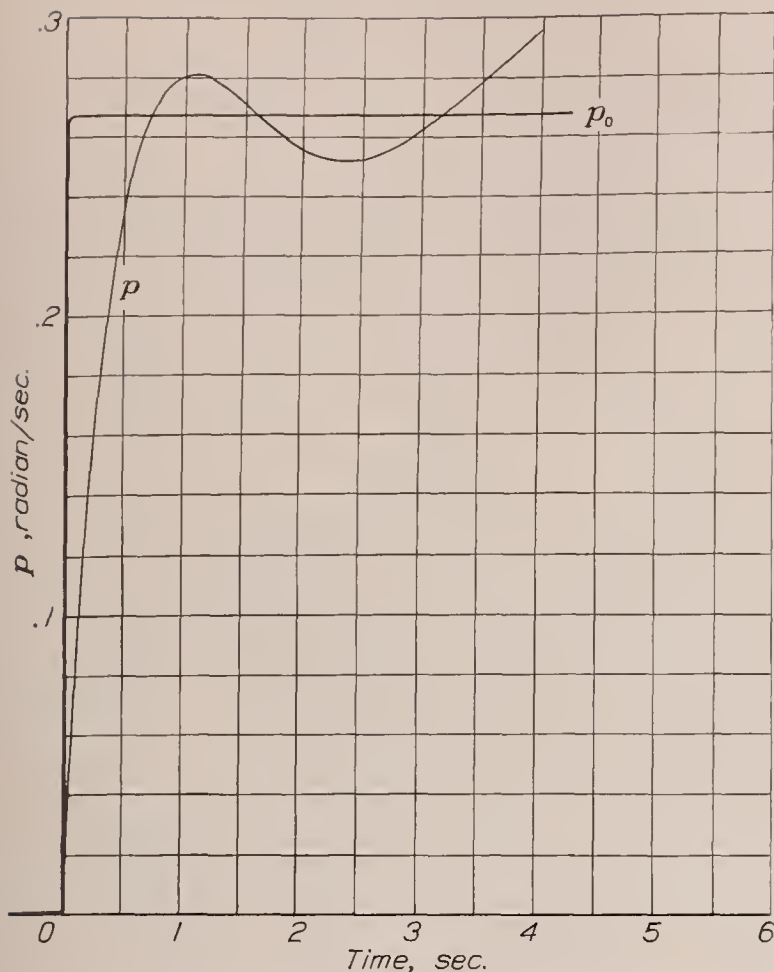


FIGURE 4.—Typical rolling motion caused by a sudden rolling gradient.

$$\frac{p_0 b}{2U_0} = 0.05 (t > 0); U_0 = 88.5 \text{ f. p. s.}$$

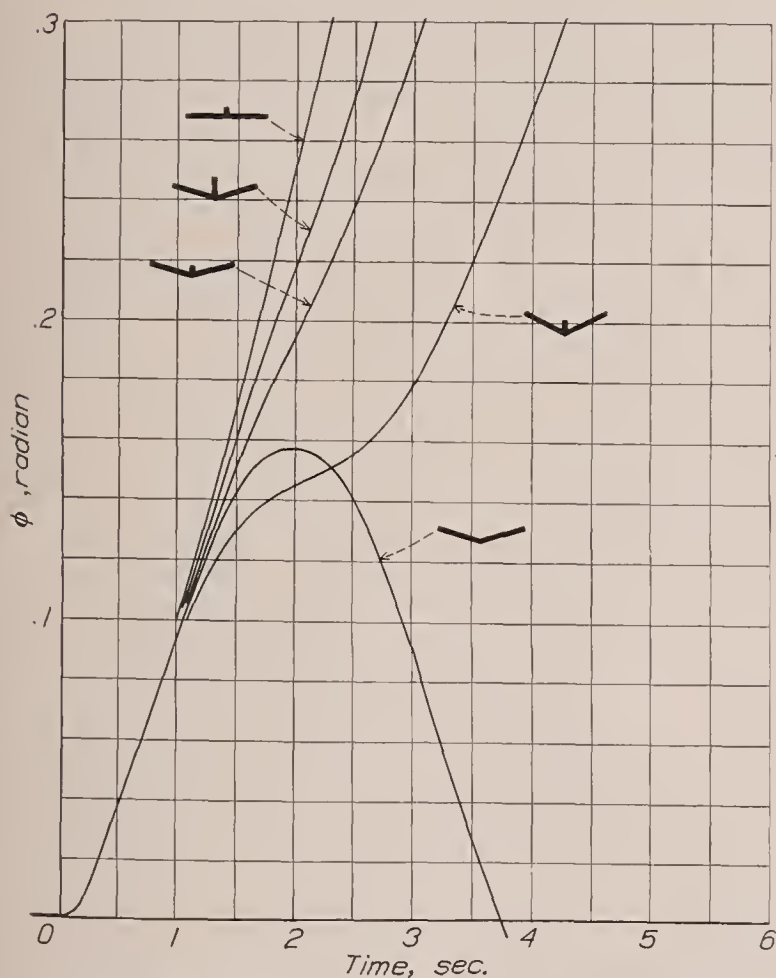


FIGURE 5.—Bank caused by a yawing gradient along the wing span.

$$\frac{r_0 b}{2U_0} = 0.05 (t > 0); U_0 = 88.5 \text{ f. p. s.}$$

The gust assumed corresponded to a difference of longitudinal velocity between the two wing tips of about 9 feet per second ($r_0 b / 2U_0 = 0.05$). All the examples show roughly the same banking tendency within the

first second, since the disturbing factors (rolling moments due to yawing velocity) are the same in all cases. The subsequent motions show the influence of different degrees of spiral stability and instability.

The primary disturbing factor in the yawing-gradient gust being proportional to the derivative L_r (rolling moment due to yawing), the greatest room for improvement would be to reduce this derivative. Taper and washout (such as are attained with a partial-span flap) are beneficial in this respect. It is estimated that L_r might have been reduced by one-third of the given value (see table I) at $C_L = 1.8$ if a 50-percent-span flap had been assumed. The effect of plan form is not so pronounced, leading to a reduction of one-sixth for a 4:1 taper.

In general, a reduction of the rolling moment due to yawing seems desirable from considerations of lateral stability. The magnitude of this derivative with controls fixed is, like that due to rolling, primarily a consequence of the general lay-out of the airplane and is not dictated by considerations of stability. It appears, however, that the magnitude of L_r with controls free (or loosely held) could be reduced or reversed by making use of an appropriate combination of ailerons with increased upward pressure (attained by cambering the ailerons) and a differential linkage, as described in reference 10. An appropriate linkage would eliminate the necessity of applying contrary aileron pressure during steady turns and would also eliminate the spiral instability with controls free.

CONCLUDING REMARKS

A study of the effects of gusts gives different indications depending on the interval of time considered. During the first stages, the upsetting movements of the stable airplane may be more severe than those of a slightly unstable one. If the airplane is under control and if the gusts are of noticeable magnitude, then the motion during the first 2 or 3 seconds is of primary concern. For uncontrolled flight or for flight in relatively calm air where disturbances could become apparent only through introducing a divergence, the later stages of the motion are of interest.

In a consideration of the early stages of the motion, it is evident that the requirements of fin area and dihedral for spiral stability at low speed conflict somewhat with the requirements for steadiness in side gusts. If spiral instability is present, the rates of divergence introduced by various disturbances appear to be small as long as there is a moderate dihedral action present. The condition of zero (effective) dihedral leads, however, to definitely undesirable rates of divergence.

If average weathercock stability ($C_{n\beta} = 0.05$ to 0.07) is assumed, the optimum magnitude of the rolling derivative due to sideslip for steadiness in side gusts appears to be about $C_{l\beta} = -0.01$ to -0.04 , corresponding to an effective dihedral of 1° or 2° . Spiral stability

throughout the flight range could be secured with this dihedral by cutting down the fin effect. The latter change would lead to somewhat greater banking displacements in the gusts and would also be detrimental to aileron control, unless such control were obtained without adverse yawing moments.

The damping of rolling is such that the airplane very quickly takes on any rolling component of gust velocity. The usual modifications of the lateral-stability factors have but little influence on the immediate effects of the rolling gust. An automatic device, acting so as to cut down the damping of rolling (relative to the air), should be advantageous from considerations of riding comfort.

The effects of longitudinal gradients of gust velocity become fairly large at low flight speeds. Noticeable improvement can be obtained by the use of partial-span flaps or by otherwise concentrating the lift toward the center of the wing, but this conclusion applies, of course, only as long as no portion of the wing is brought near the stalling point.

LANGLEY MEMORIAL AERONAUTICAL LABORATORY,
NATIONAL ADVISORY COMMITTEE FOR AERONAUTICS,
LANGLEY FIELD, VA., *June 8, 1938.*

REFERENCES

1. Wilson, Edwin Bidwell: Theory of an Aeroplane Encountering Gusts.
I. T. R. No. 1—Part 2, N. A. C. A. First Annual Report, 1915, pp. 52-75.
II. T. R. No. 21, N. A. C. A. Third Annual Report, 1917, pp. 405-431.
III. T. R. No. 27, N. A. C. A. Fourth Annual Report, 1918, pp. 83-89.
2. Haus, Fr.: Theoretical Study of Various Airplane Motions after Initial Disturbance. T. M. No. 867, N. A. C. A., 1938.
3. Jones, Robert T.: Calculation of the Motion of an Airplane under the Influence of Irregular Disturbances. Jour. Aero. Sci., vol. 3, no. 12, Oct. 1936, pp. 419-425.
4. Jones, Robert T.: A Study of the Two-Control Operation of an Airplane. T. R. No. 579, N. A. C. A., 1936.
5. Zimmerman, Charles H.: An Analysis of Lateral Stability in Power-Off Flight with Charts for Use in Design. T. R. No. 589, N. A. C. A., 1937.
6. Diehl, Walter Stuart: Engineering Aerodynamics. The Ronald Press Co., 1936, p. 206.
7. Millikan, Clark B.: On the Results of Aerodynamic Research and Their Application to Aircraft Construction. Jour. Aero. Sci., vol. 4, no. 2, Dec. 1936, pp. 43-53.
8. Korvin-Kroukovsky, B. V.: Proportioning the Plane for Lateral Stability. Aero. Eng. Supplement to Aviation, vol. 26, Jan. 1929, pp. VIII-XII.
9. Imlay, Frederick H.: The Estimation of the Rate of Change of Yawing Moment with Sideslip. T. N. No. 636, N. A. C. A., 1938.
10. Jones, Robert T., and Nerken, Albert I.: The Reduction of Aileron Operating Force by Differential Linkage. T. N. No. 586, N. A. C. A., 1936.

THE EFFECT OF COMPRESSIBILITY ON EIGHT FULL-SCALE PROPELLERS OPERATING IN THE TAKE-OFF AND CLIMBING RANGE

By DAVID BIERMANN and EDWIN P. HARTMAN

SUMMARY

Tests were made of eight full-scale propellers of different shape at various tip speeds up to about 1,000 feet per second. The range of blade-angle settings investigated was from 10° to 30° at the 0.75 radius.

The results indicate that a loss in propulsive efficiency occurred at tip speeds from 0.5 to 0.7 the velocity of sound for the take-off and climbing conditions. As the tip speed increased beyond these critical values, the loss rapidly increased and amounted, in some instances, to more than 20 percent of the thrust power for tip-speed values of 0.8 the speed of sound. In general, as the blade-angle setting was increased, the loss started to occur at lower tip speeds. The maximum loss for a given tip speed occurred at a blade-angle setting of about 20° for the take-off and 25° for the climbing condition.

Although the loss at the take-off condition due to compressibility was greater for the R. A. F. 6 section than for the Clark Y, greater for blades of standard width than for extremely wide ones, and greater for a thick propeller than for a thin one, the actual efficiencies at high tip speeds were found to be about the same because, in each case, the propeller that had the greatest losses from increasing the tip speed had the highest efficiency at low tip speeds.

The compressibility loss at the take-off for controllable propellers was considerably reduced because of decreased blade-angle operation necessitated by increased power coefficients, but the reverse was true for fixed-pitch propellers inasmuch as the higher power coefficients resulted in reduced engine speeds.

A simplified method for correcting propellers for the effect of compressibility is given in an appendix.

INTRODUCTION

The first effects of the compressibility of air to influence the flight of airplanes are felt by the tips of propeller blades, which usually operate at speeds approaching that of sound. The results of experience and research agree in showing that at sonic tip speeds the effects of compressibility are very unfavorable. The flying speeds of airplanes have only recently reached values where the effects of compressibility on parts of the airplane other than the propeller are of such magnitude as to warrant more than passing attention. The serious effects of high tip speeds on the performance of propellers have, however, been of great practical inter-

est for many years and considerable research has been directed toward a better understanding of the phenomena of compressibility as affecting propeller operation. The principal methods of attacking the problem may be classified as: (a) airfoil tests, (b) model-propeller tests, and (c) full-scale-propeller tests.

Airfoil tests are particularly valuable in the study of compressibility because many of the variables present in propeller tests do not enter into airfoil tests and the important compressibility effects are therefore more easily isolated and revealed. Without them the compressibility phenomena detected in propeller tests would be difficult to understand or to explain.

An examination of references 1, 2, and 3 reveals a marked change in airfoil characteristics with increasing air speed. There appears to be a general tendency for the slope of the lift curves and of the profile drag in the usual propeller operating range to increase up to some critical value of V/V_c (ratio of air speed to the speed of sound) corresponding to that at which the compressibility burble occurs and at which the lift drops sharply and the drag increases rapidly. The value of the speed at which the compressibility burble occurs is dependent on the angle of attack and the thickness of the airfoil; increasing either of these quantities causes the compressibility burble to occur at lower speeds, sometimes as low as 0.4 or 0.5 the speed of sound. The compressibility burble is attributed to the formation of a shock wave caused when the flow over the surface exceeds the local velocity of sound. (See reference 4.) A large part of the kinetic energy in the flow is converted into heat when the particles of air pass through the shock region, which results in an increased drag of the airfoil. Also, the reduction in velocity and the consequent increase in pressure behind the shock wave result in reduced lift.

The influence of compressibility on the characteristics of model propellers has been observed in many British tests (reference 5). The results of propeller tests agreed qualitatively with the results of airfoil tests in that the power and the thrust increased with tip speed up to a critical value beyond which the thrust and the efficiency dropped.

There is some reason to believe that the propeller characteristics should depend on Reynolds Number as well as on tip speed; however, tests of propellers of

different blade width (reference 6) show only a slight Reynolds Number effect, and British flight tests, which were made to check model tests (reference 7), indicate no serious scale effect at the peak-efficiency condition.

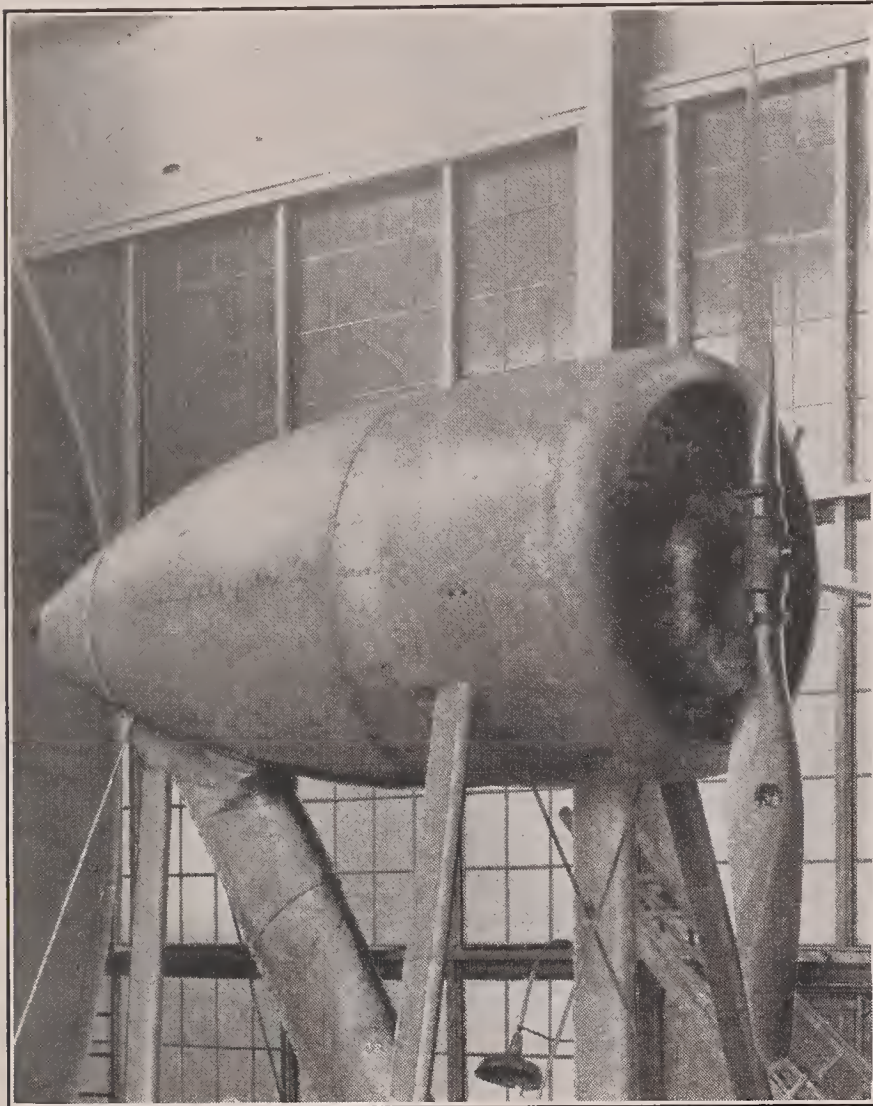


FIGURE 1.—The propeller test set-up with radial engine nacelle.

Wind-tunnel tests have been made by the N. A. C. A. of a series of full-scale propellers having different thickness ratios and different airfoil sections (reference 8). For the low blade-angle settings investigated (6.8° , 9.6° , and 10°) there was discovered little or no loss in efficiency below a tip speed of about 1,000 feet per second, even in the low V/nD range. In view of the results from later tests of the same airfoil sections (reference 2), it would appear that compressibility effects of appreciable magnitude should be noticed for higher blade angles in the low V/nD range corresponding to the take-off and climbing conditions of flight.

The tests reported herein were instituted to determine the compressibility effect on full-scale propellers operating at blade angles corresponding to those used in present-day aircraft when set for the take-off and climbing conditions. The blade-angle settings investigated ranged from 10° to 30° in 5° increments. Owing to the limiting tunnel speed of about 115 miles per hour, the upper V/nD range could not be obtained for the higher tip-speed runs; however, the V/nD range corresponding to the take-off and climbing conditions of flight was covered. The tip-speed range extended from about 600 feet per second to more than 1,000 feet per second for one propeller.

Four of the propellers tested have Clark Y blade sections and four have R. A. F. 6 sections. Of the Clark Y propellers, three are of a series having variations in thickness ratio. Among the R. A. F. 6 propellers there are variations in blade width and plan form.

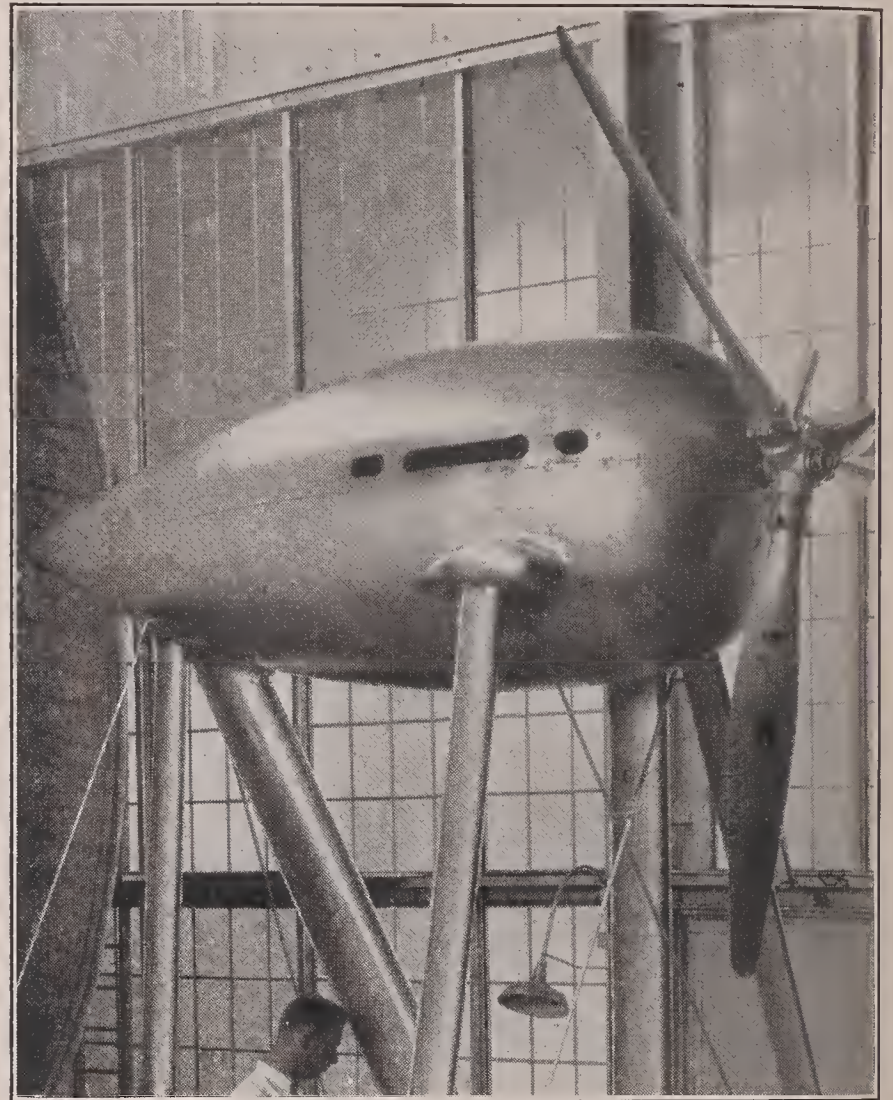


FIGURE 2.—The test set-up showing liquid-cooled engine nacelle.

These compressibility tests were run from time to time as a part of a propeller program involving a number of subjects. During this period of time, the body that covered the engine was changed from a radial engine nacelle to a liquid-cooled engine nacelle. Several of the propellers were tested in conjunction with the radial engine nacelle and some with the liquid-cooled engine nacelle; a few propellers were tested in conjunction with both.

The series of tests reported herein, although not complete nor entirely conclusive, covers a very important field. Research on the problem of compressibility should be continued to investigate further such effects as may be caused by changes in blade section, thickness, and width and should be extended to higher values of tip speed, especially for the upper ranges of blade angles.

APPARATUS AND METHODS

The tests were made in the propeller-research tunnel, a description of which is given in reference 9. The power to operate the test propellers was supplied by a 600-horsepower Curtiss Conqueror engine geared 7:5.

The engine was boosted to 800 horsepower, when more power was required, by a motor-driven Roots blower located on the floor of the test chamber.

The dynamometer used for measuring torque is of the cradle type with the axis of rotation on one side of the engine. The torque reaction was carried through a vertical compression post to a mechanical balance on the floor of the test chamber. The engine cowling was supported on the fixed portion of the supporting frame.

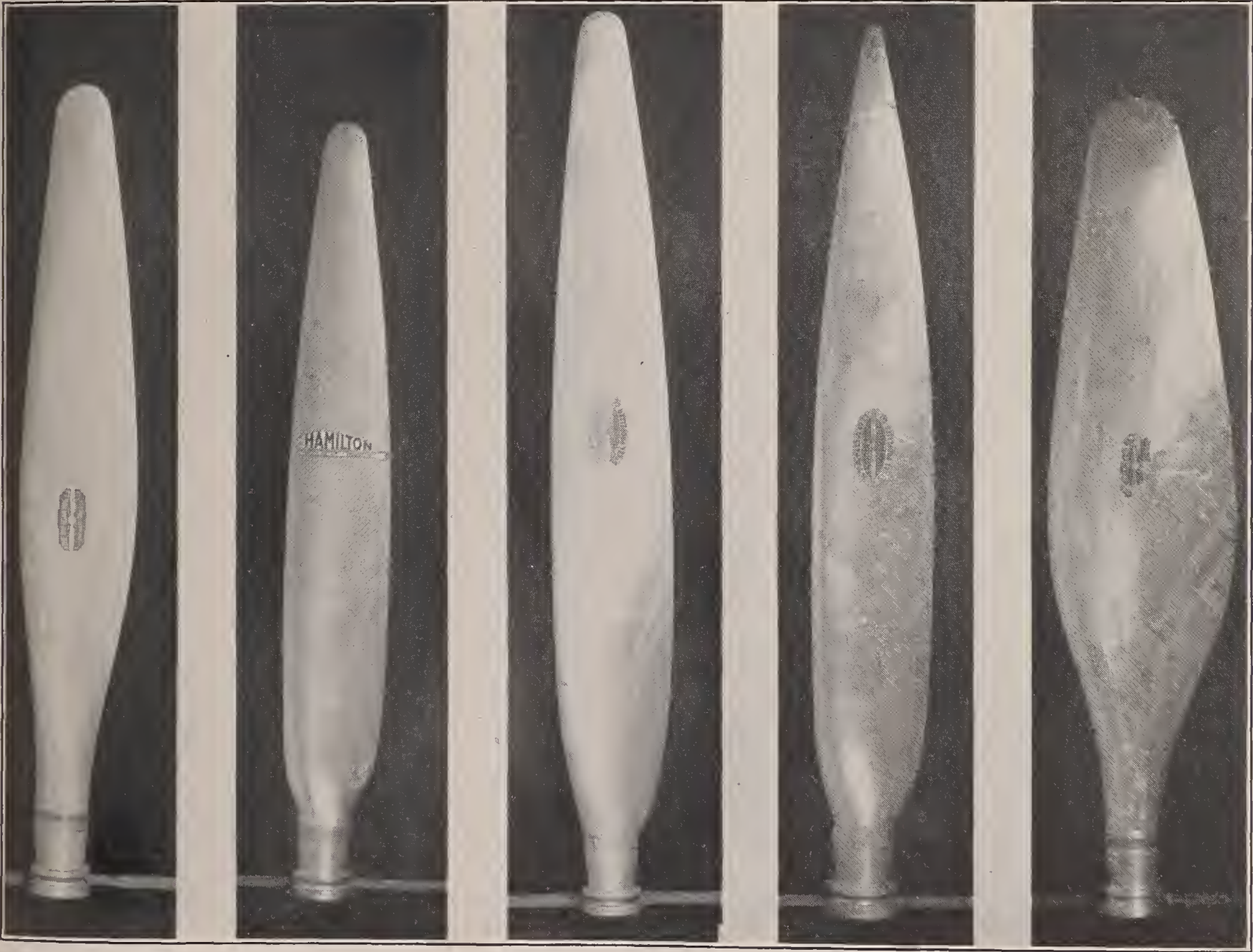
The radial engine cowling (fig. 1) used for the first series of tests is 52 inches in maximum diameter and 126 inches in length. The liquid-cooled engine nacelle (fig. 2) is oval in cross section, 43 inches in height, 38 inches in width, and 126 inches in length.

Eight propellers having a range of diameters from 9½ feet to 11 feet were tested. The distinguishing features of these propellers are shown in figure 3. Blade-form curves are given in figures 4, 5, and 6. The symbols used in these figures are defined as:

- D , diameter.
- R , radius to the tip.
- r , station radius.
- b , section chord.
- h , section thickness.
- p , geometric pitch.

All the propellers have two blades. Section ordinates are given in figure 7. The principal dimensions of the propellers are given in the following table.

Propeller	Diam-eter (ft.)-(in.)	Section	$\frac{b}{D}$ at 0.75 R	$\frac{h}{b}$ at 0.75 R	Tip shape
5868-9-----	10-0	Clark Y (new)-	0.061	0.090	Round.
5868-R6-----	10-0	R. A. F. 6-----	.061	.090	Do.
4877-----	9-6	Clark Y (old)-	.053	.06	Do.
4878-----	9-6	do-----	.053	.08	Do.
4879-----	9-6	do-----	.053	.10	Do.
4371-----	11-0	R. A. F. 6-----	.053	.080	Do.
195-----	11-0	do-----	.050	.067	Pointed.
37-3647-----	10-0	do-----	.092	.090	Round.



5868-9
5868-R6

4877
4878
4879

4371

195

37-3647

FIGURE 3.—Propeller blades tested

The method adopted in making these tests consisted in setting the engine speed at a given value and increasing the tunnel air speed progressively up to the

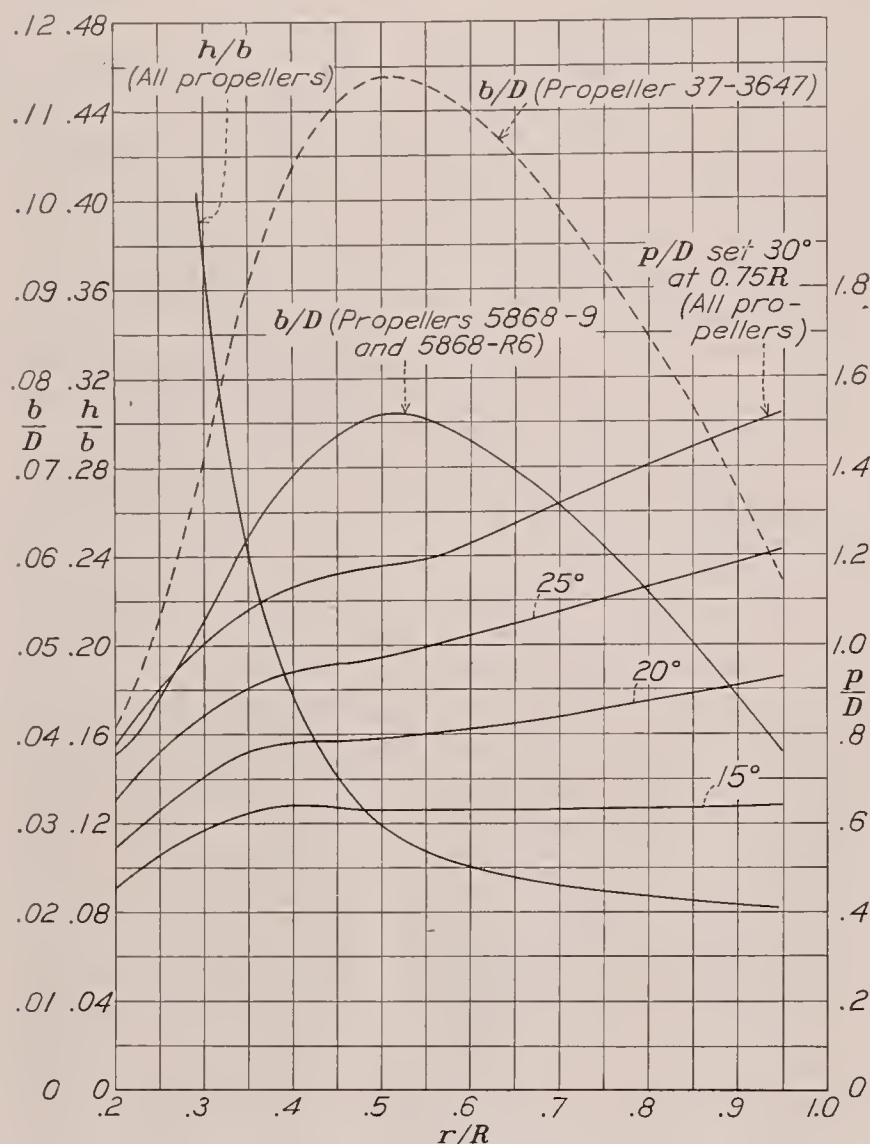


FIGURE 4.—Blade-form curves for propellers 5868-R6, 5868-9, and 37-3647.

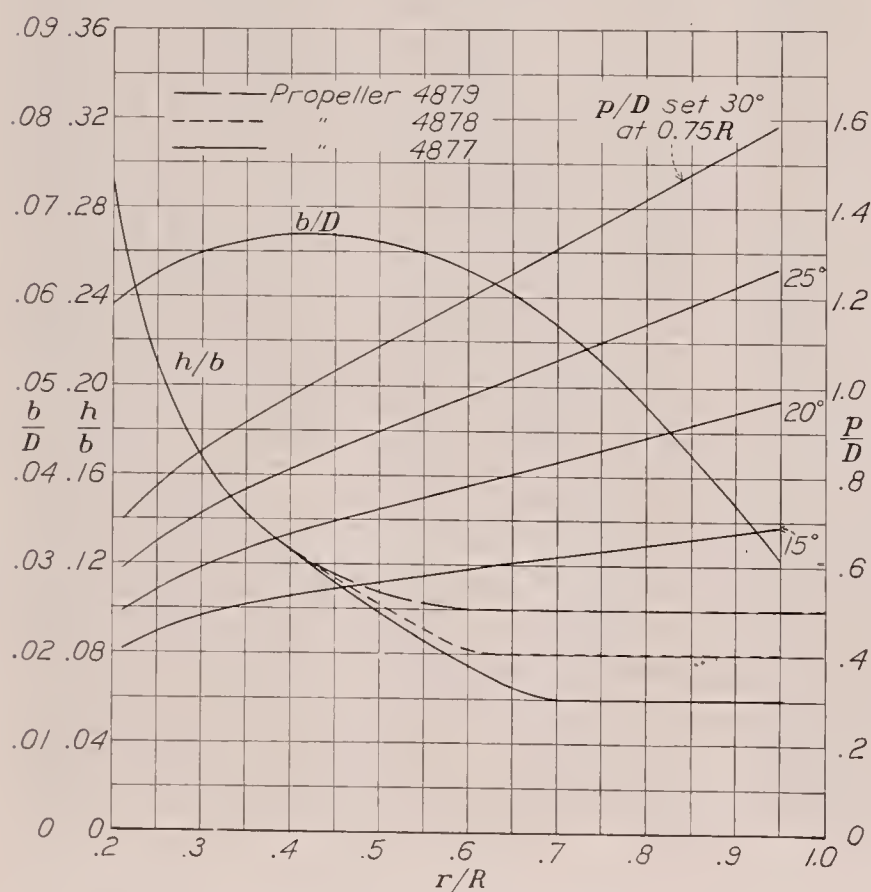


FIGURE 5.—Blade-form curves for propellers 4877, 4878, and 4879.

maximum value of about 115 miles per hour. The principal measurements recorded include: engine torque, propeller rotational speed, thrust of the

propeller minus the body and interference drag, and tunnel air speed. The drag of the body was measured in a separate test with the propeller removed.

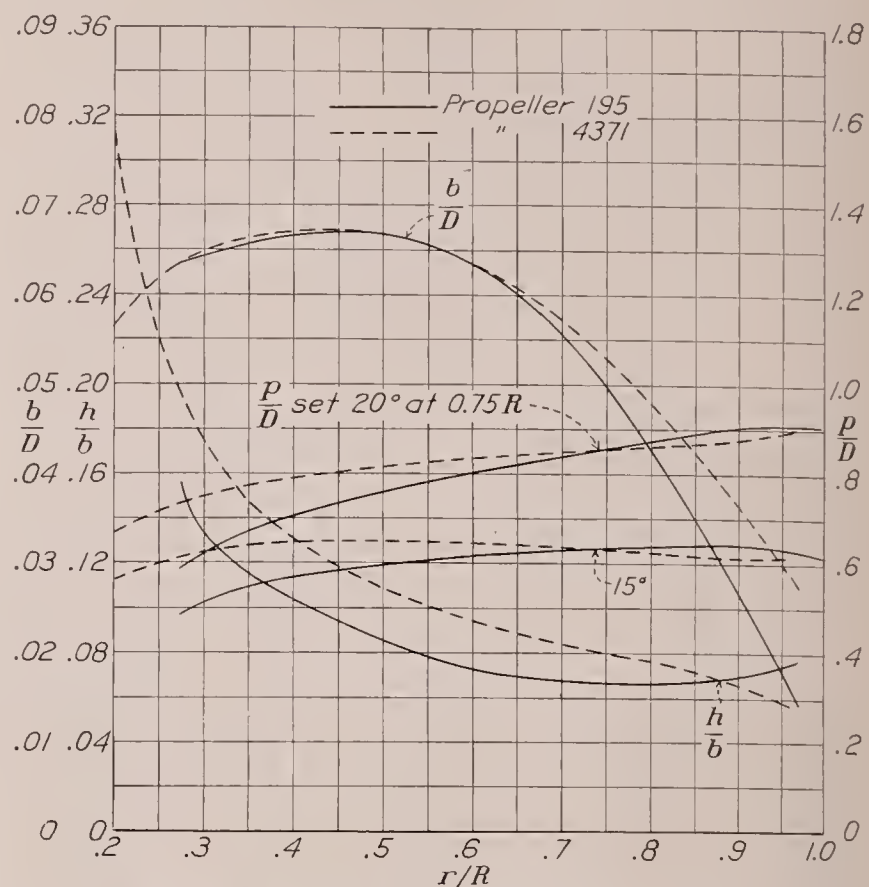
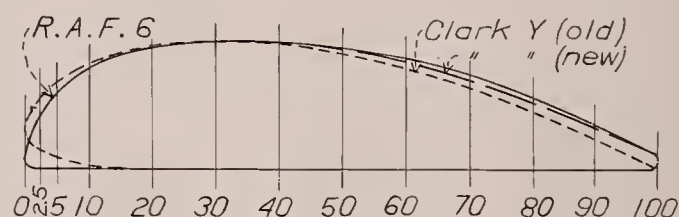


FIGURE 6.—Blade-form curves for propellers 195 and 4371.



Station	R. A. F. 6, Upper	Clark Y (old)		Clark Y (new)	
		Upper	Lower	Upper	Lower
2.5	0.41	0.56	0.13	0.55	0.13
5	.59	.68	.08	.67	.08
10	.79	.82	.04	.81	.04
20	.95	.97	0	.96	.01
30	1.00	1.00	0	1.00	0
40	.99	.98	0	.99	0
50	.95	.90	0	.93	0
60	.87	.78	0	.83	0
70	.74	.63	0	.69	0
80	.56	.45	0	.52	0
90	.35	.24	0	.34	0
L. E. radius	.10	0.13		0.15	
T. E. radius	.077	.005	0	.077	0

FIGURE 7.—Propeller section ordinates (in fraction of maximum ordinate).

RESULTS

The measured values have been reduced to the usual coefficients of thrust, power, and propulsive efficiency,

$$C_T = \frac{\text{effective thrust}}{\rho n^2 D^4}$$

$$C_P = \frac{\text{engine power}}{\rho n^3 D^5}$$

and

$$\eta = \frac{C_T}{C_P} \frac{V}{nD}$$

where the effective thrust is the measured thrust plus the body drag with no propeller or, in other words, the propeller shaft tension minus the increment of body drag due to the slipstream.

D , propeller diameter, ft.

n , propeller rotational speed, r. p. s.

The foregoing coefficients were plotted against the coefficient V/nD and a smooth curve was drawn through the thrust and power points. The efficiency curve was adjusted to correspond to the thrust and power curves as well as to the calculated efficiency points. A typical plot is shown in figure 8.

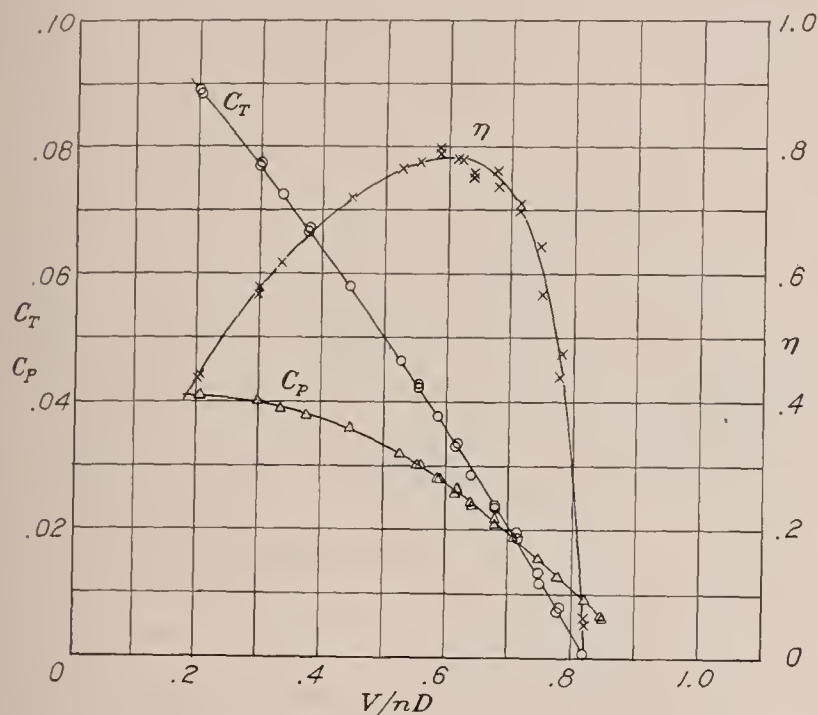


FIGURE 8.—Typical test results showing normal scatter of points. Propeller 5868-R6; diameter, 10 ft.; propeller set 15° at $0.75R$; propeller speed, 1,200 r. p. m.; liquid-cooled engine nacelle.

In order to show the effect of different tip speeds on the propeller characteristics for particular values of V/nD , plots are given of relative efficiency, relative thrust, and relative power against the ratio of the tip speed to the speed of sound, V'/V_c . Only two types of such plots are given: one represents the take-off condition of a landplane arbitrarily taken at a V/nD value of 0.30 times the V/nD for peak efficiency; and the other, the climbing condition taken at a V/nD value of 0.65 times the V/nD for peak efficiency. The reference point used in computing the relative values of efficiency, thrust, and power was $V'/V_c=0.5$. Thus

$\frac{\eta}{\eta_{(V'/V_c=0.5)}}$, $\frac{C_T}{C_{T_{(V'/V_c=0.5)}}}$, and $\frac{C_P}{C_{P_{(V'/V_c=0.5)}}}$ represent the ratios

of the propeller characteristics with respect to those at a tip-speed ratio of $V'/V_c=0.5$. The tip-speed velocity V' is the tangential component of the actual tip speed and is defined by the relation $V'=\pi nD$. The forward component of the tip speed, which increases with V/nD , was small enough to be neglected in the present tests.

The test results are given in three groups: The first group (figs. 9 to 35) covers the work done with the

radial engine cowled nacelle. The second group (figs. 36 to 46) covers the results with the liquid-cooled engine nacelle. The third group (figs. 47 to 53) comprises comparisons and examples derived from the first two groups. The test results have been tabulated in six tables and are available on request from the National Advisory Committee for Aeronautics.

Inasmuch as the temperature of the air determines the velocity of sound, the following table of temperatures is included.

Liquid-cooled engine nacelle			Radial engine nacelle						
			Unsupercharged (including all propeller speeds, except those noted under "Supercharged")			Supercharged			
Propeller	Blade angle (deg.)	Temperature (°F.)	Propeller	Blade angle (deg.)	Temperature (°F.)	Propeller	Blade angle (deg.)	Propeller speed (r. p. m.)	Temperature (°F.)
5868-R6	{ 15	88	5868-9	{ 15	66	5868-9	{ 20	1,725	65
37-3647	{ 20	89		{ 20	65		{ 25	1,500	71
	{ 15	93		{ 25	64		{ 25	1,600	71
	{ 20	97		{ 30	64		{ 30	1,300	70
4877	20	88	5868-R6	{ 15	53	5868-R6	{ 15	1,800	81
4878	20	84		{ 20	54		{ 20	1,750	68
4879	20	84		{ 25	61		{ 25	1,555	69
				{ 30	72		{ 30	1,300	73
			4879	{ 15	66	4371	{ 15	1,700	77
				{ 20	59		{ 20	1,550	69
				{ 25	61		{ 15	1,800	75
				{ 30	72		{ 20	1,600	66
			4371	{ 15	71				
				{ 20	81				
				{ 15	78				
			195	{ 20	76				

The speed of sound in air is given by the following formulas:

$$V_c = 1,120 \sqrt{T_c/288}$$

$$= 1,120 \sqrt{T_F/518.4}$$

where

T_c is absolute temperature, °C.

T_F , absolute temperature, °F.

DISCUSSION

An examination of the results from airfoil tests at high speeds, such as are given in reference 2, leads to the following conclusions regarding what should be expected from propeller tests:

(a) The thrust and power coefficients should increase with tip speed in the range below the critical tip speed (compressibility burble).

(b) There should be a loss of thrust and efficiency and an increase in power after the tip speed exceeds the critical value.

(c) Since compressibility losses occur at lower speeds as the angle of attack of the airfoil is increased, it follows that, at low values of V/nD , losses should occur at fairly low tip speeds. The critical tip speed for a given blade angle should increase as V/nD is increased.

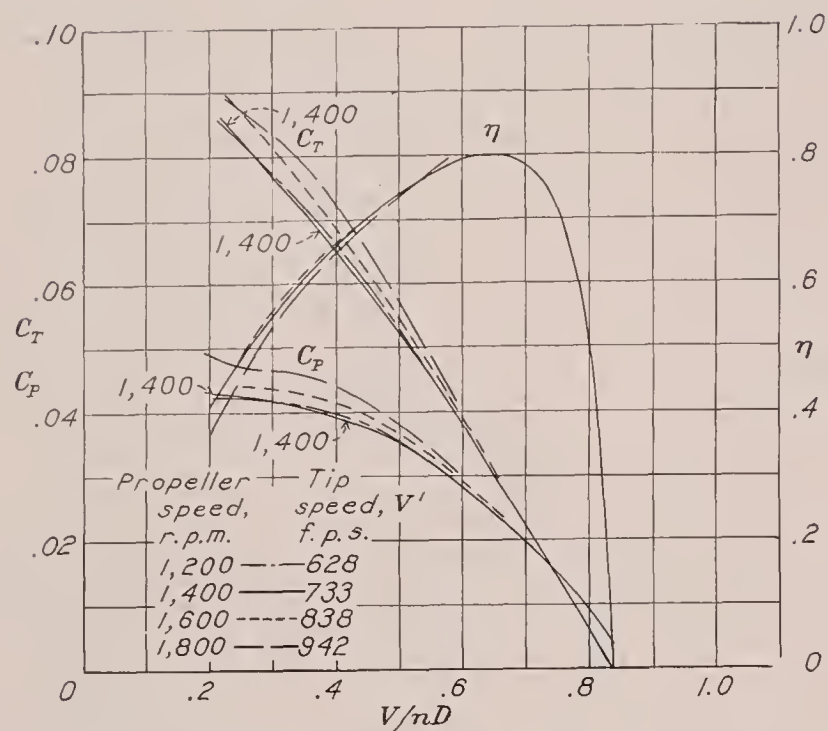


FIGURE 9.—Propeller set 15° at 0.75R.

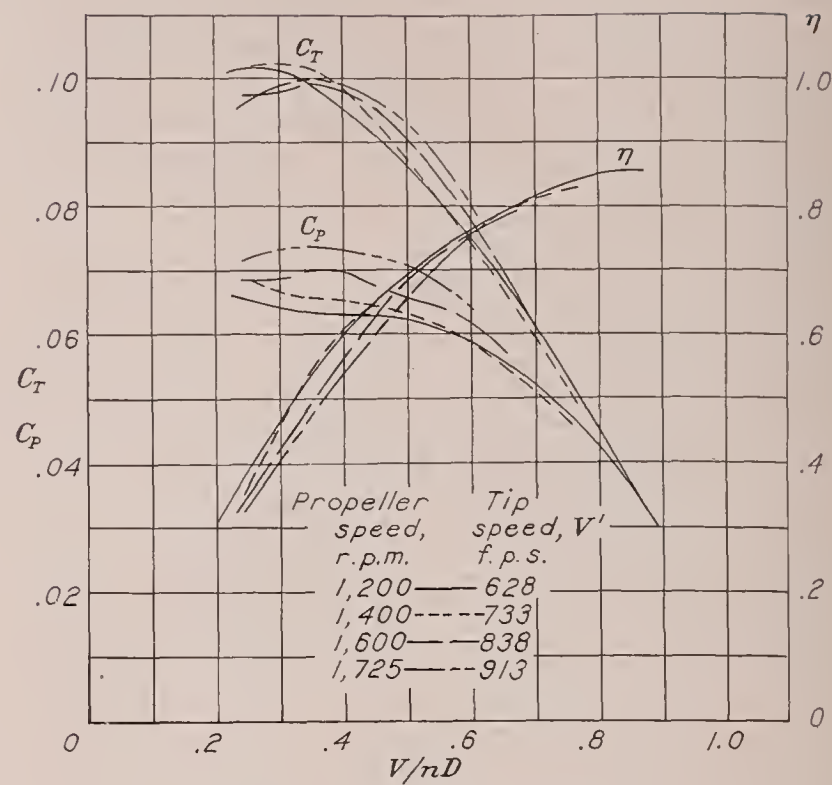


FIGURE 10.—Propeller set 20° at 0.75R.

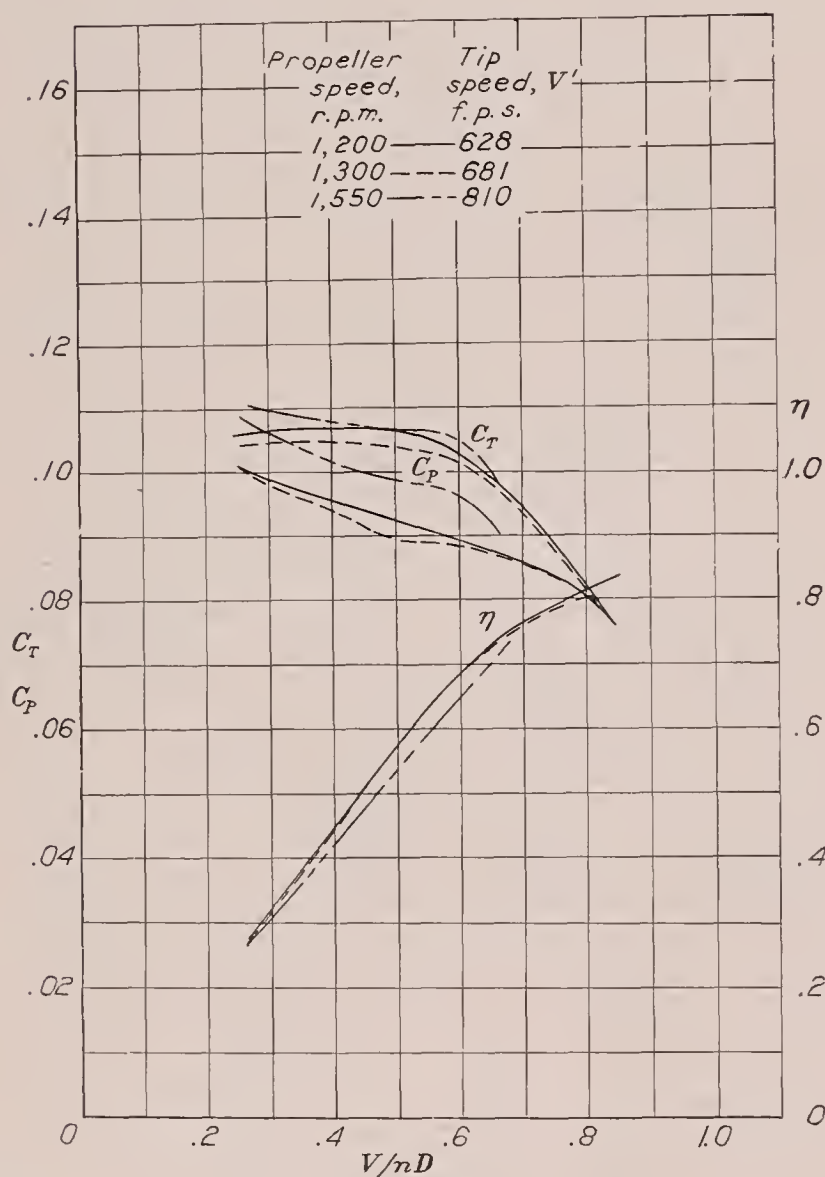


FIGURE 11.—Propeller set 25° at 0.75R.

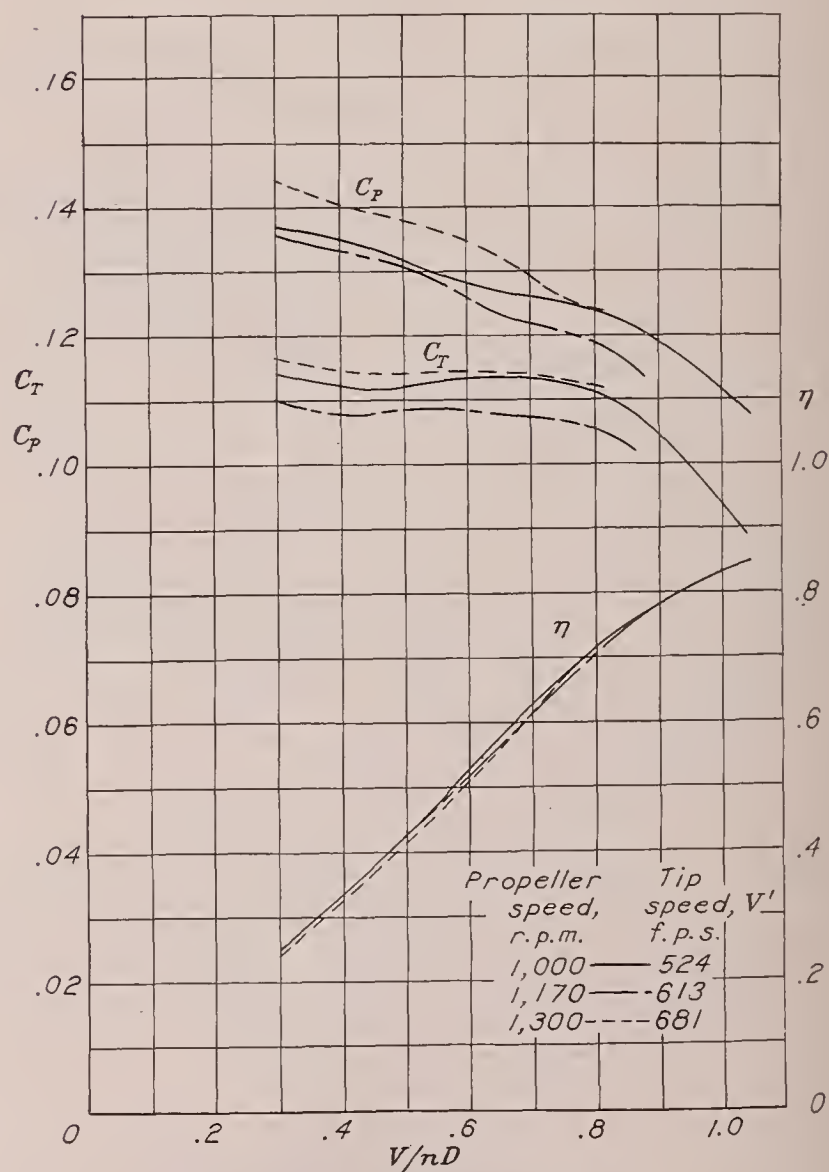


FIGURE 12.—Propeller set 30° at 0.75R.

FIGURES 9 to 12.—Effect of compressibility on propeller characteristics. Propeller 5868-9; diameter, 10 ft.; radial engine nacelle.

(d) The blade-angle setting of the propeller should determine the V/nD range wherein compressibility losses occur for any given tip speed, because the section angle of attack is determined by both the V/nD and the blade-angle setting. For blade angles sufficiently low that stalling never occurs (approximately 20° and less), the greatest loss should occur at a zero value of V/nD . For higher value of the blade angle, the normal stall might be expected to delay the compressibility burble so that losses from this source might, in general, be confined to the V/nD range below the stall. Under such conditions the climbing condition of flight might suffer

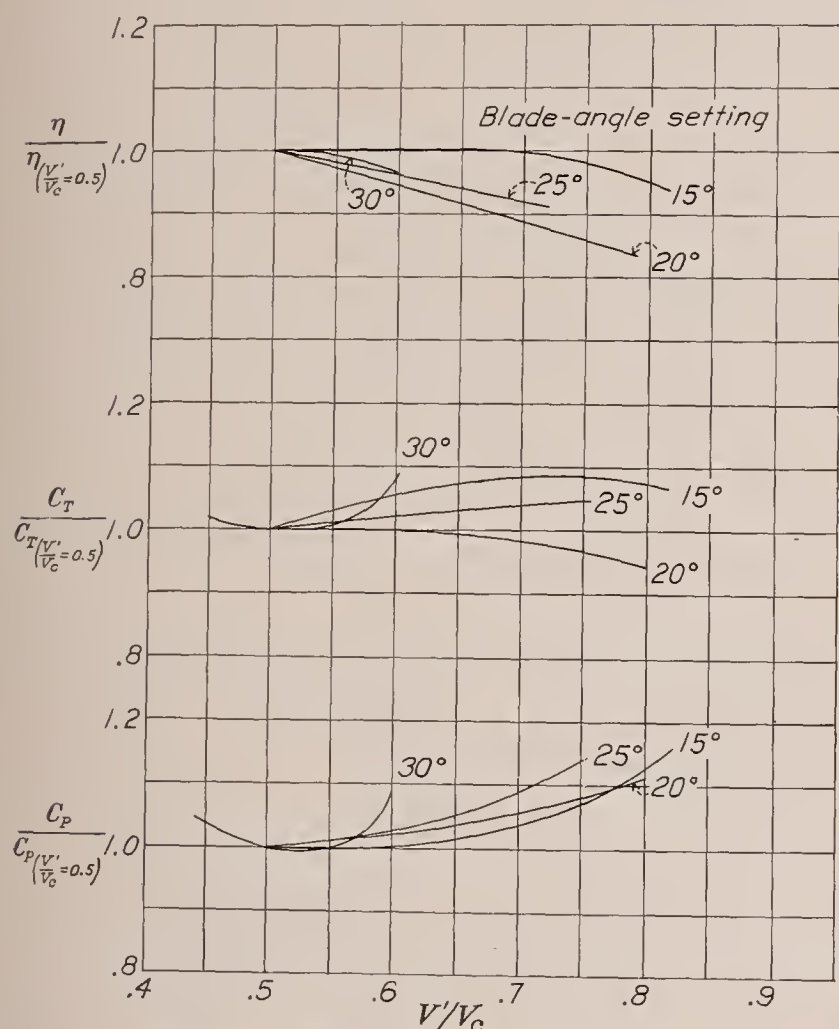


FIGURE 13.—Changes in propeller characteristics due to compressibility for the take-off condition. Propeller 5868-9; diameter, 10 ft.; radial engine nacelle; $\frac{V}{nD} = 0.30 \left(\frac{V}{nD} \right)_{peak\ eff.}$

more from compressibility than the take-off condition.

(e) The Clark Y section has a higher critical speed than the R. A. F. 6 section and propellers of Clark Y section should therefore be less affected by compressibility in the normal operating range; likewise, thin propellers should be less affected than thick ones.

A general survey of the results reveals qualitative agreement between airfoil and full-scale-propeller results. There might be some question as to whether the effects noted are entirely due to compressibility, since blade deflection would result in somewhat the same displacement of the curves. Some deflection measurements that were made by a light-beam method showed the blade torsional deflection to be negligible; it is therefore probable that the various effects noted are due to compressibility.

EFFECTS AT SPEEDS BELOW THE CRITICAL

The tendency for the thrust and power coefficients, at a given V/nD to increase with increasing tip speed for speeds below the critical may be noted for nearly all of the propellers. The increase is greatest at low V/nD values and tends to diminish as V/nD is increased. This effect is of some importance in the take-off and climb of both fixed-pitch and controllable propellers. In the case of the fixed-pitch propeller, the engine speed will be reduced by the higher power requirements of the propeller and engine power will be

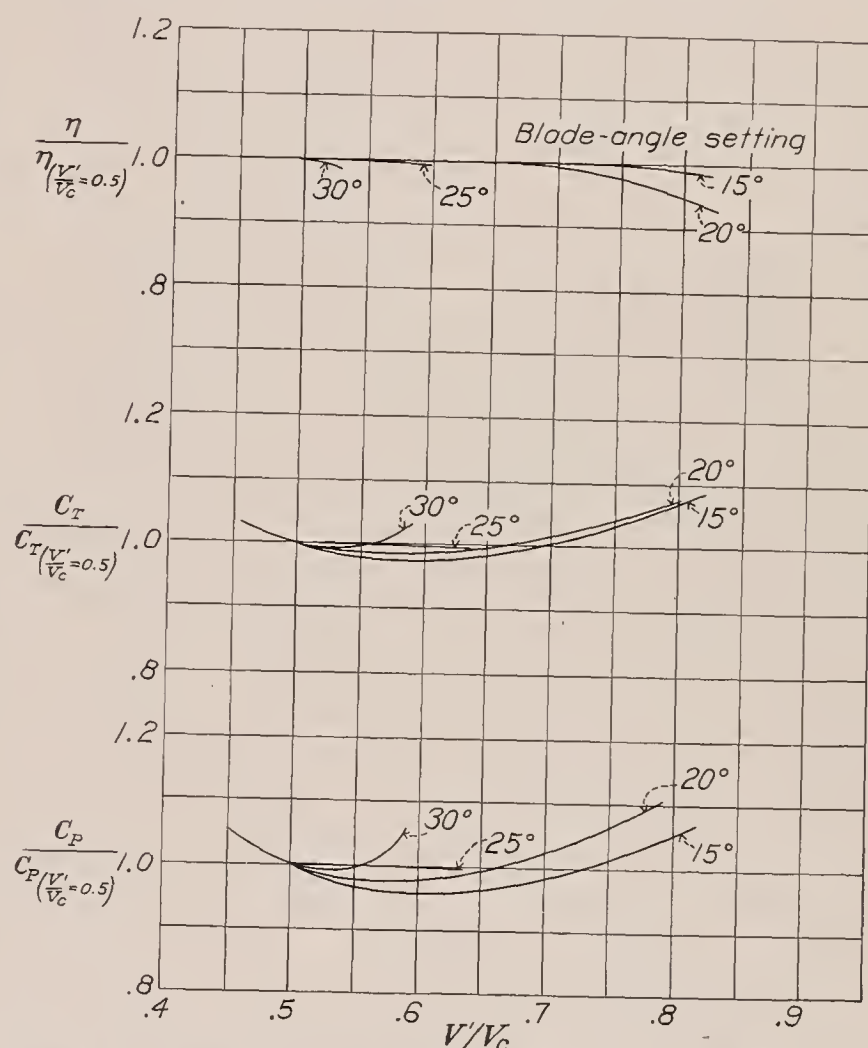


FIGURE 14.—Changes in propeller characteristics due to compressibility for the climbing condition. Propeller 5868-9; diameter, 10 ft.; radial engine nacelle; $\frac{V}{nD} = 0.65 \left(\frac{V}{nD} \right)_{peak\ eff.}$

lost proportionately to the drop in rotational speed. The pitch of the controllable propeller must be reduced to offset the added power required with the result that the propulsive efficiency will be increased.

EFFECT AT SPEEDS ABOVE THE CRITICAL

At the tip speeds at which compressibility losses occur at the tips, the tendency for the thrust coefficient to continue to increase is reduced. After sufficient blade area at the tips is operating beyond the compressibility stall, there is a tendency for the thrust coefficient to decrease with increasing tip speed and for the power coefficient to rise disproportionately fast. A consistent reduction in efficiency may be noted for all the propellers after the tip speed has reached some critical value. The amount of reduction can be seen to depend upon a number of factors, such as tip speed, V/nD range,

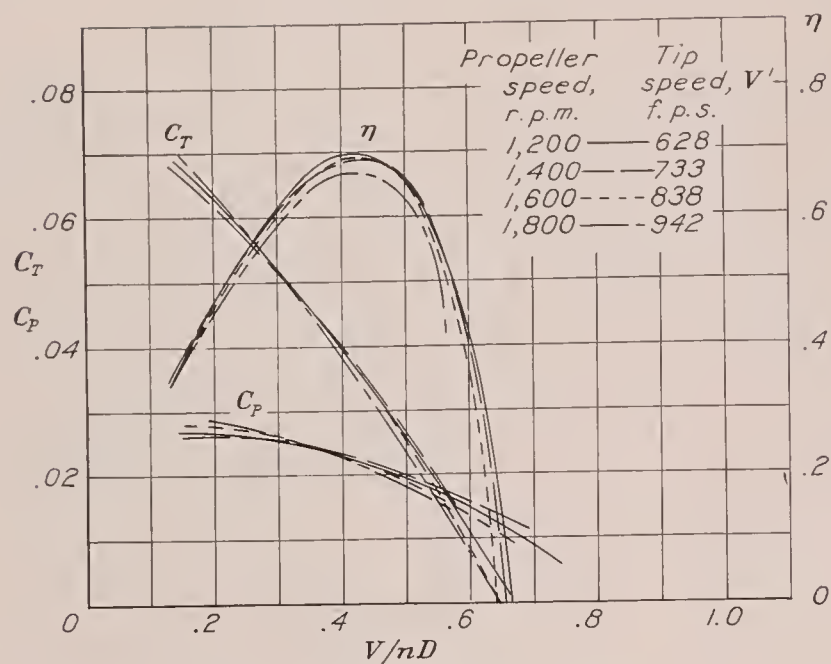


FIGURE 15.—Propeller set 10° at 0.75R.

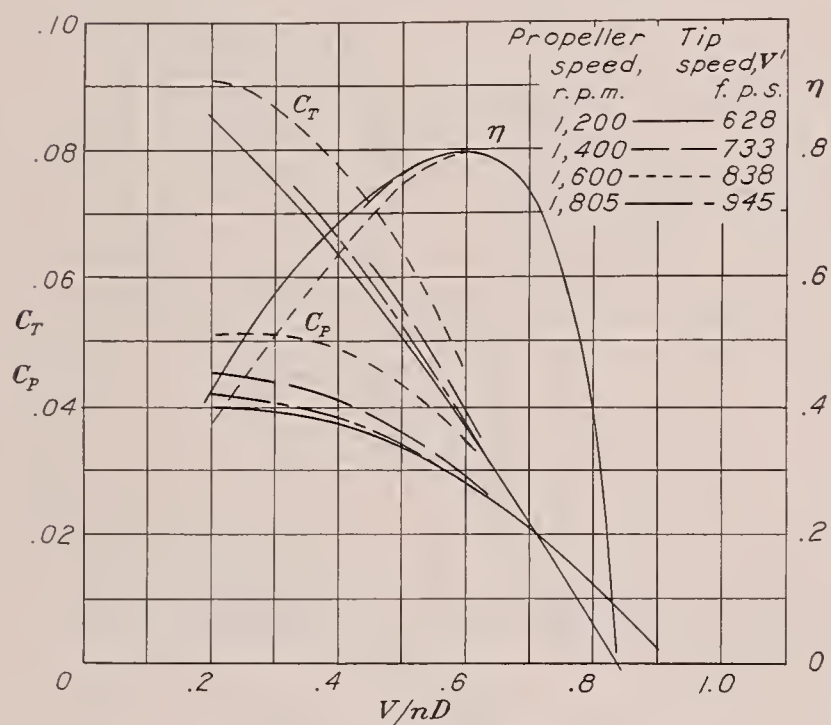


FIGURE 16.—Propeller set 15° at 0.75R.

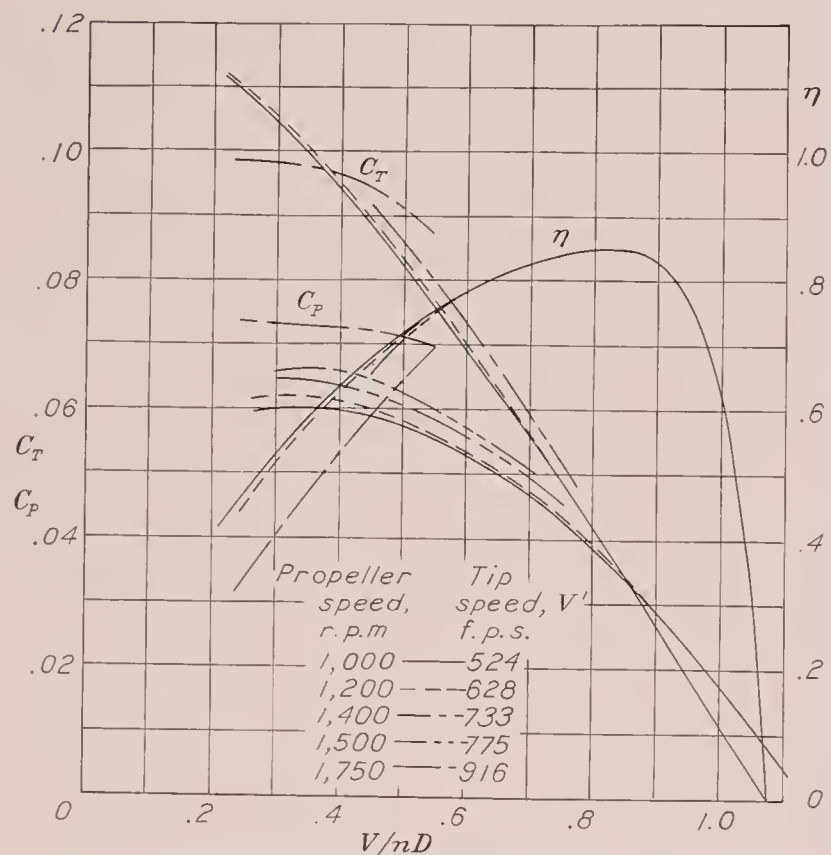


FIGURE 17.—Propeller set 20° at 0.75R.

FIGURES 15 to 19.—Effect of compressibility on propeller characteristics. Propeller 5868-R6; diameter, 10 ft.; radial engine nacelle.

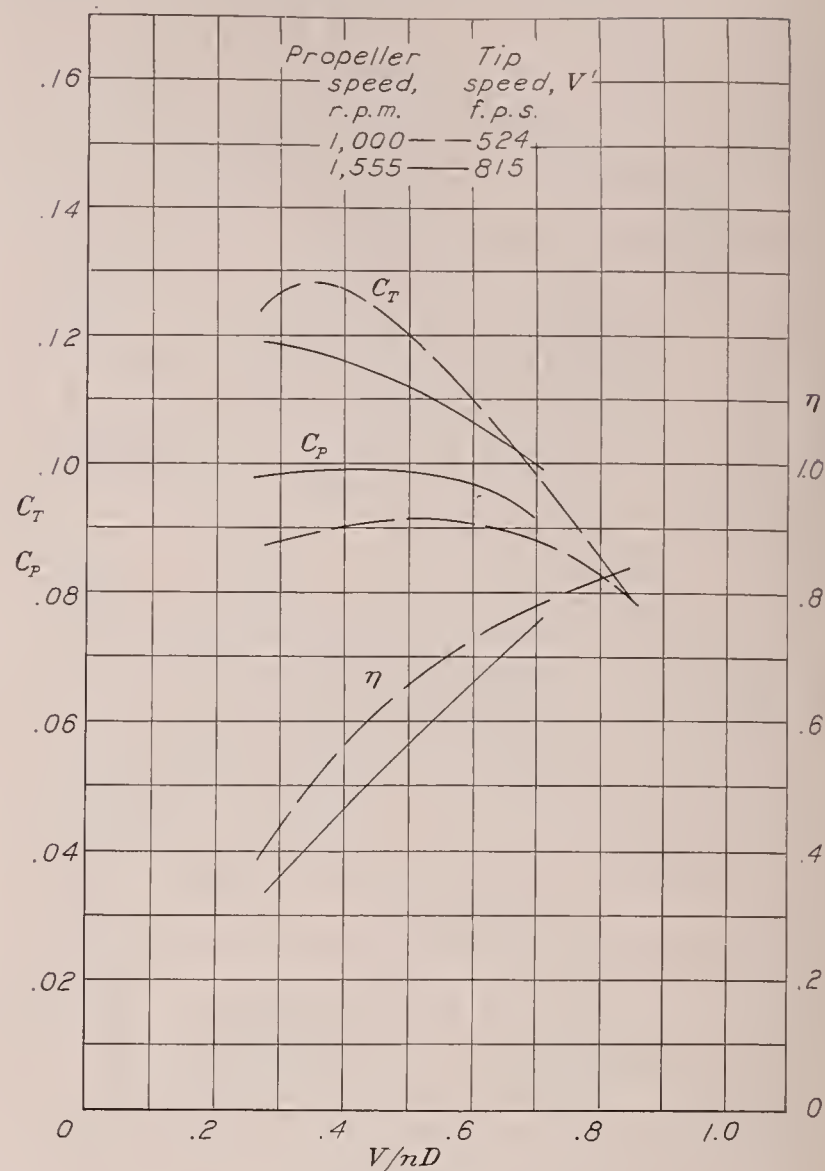


FIGURE 18.—Propeller set 25° at 0.75R.

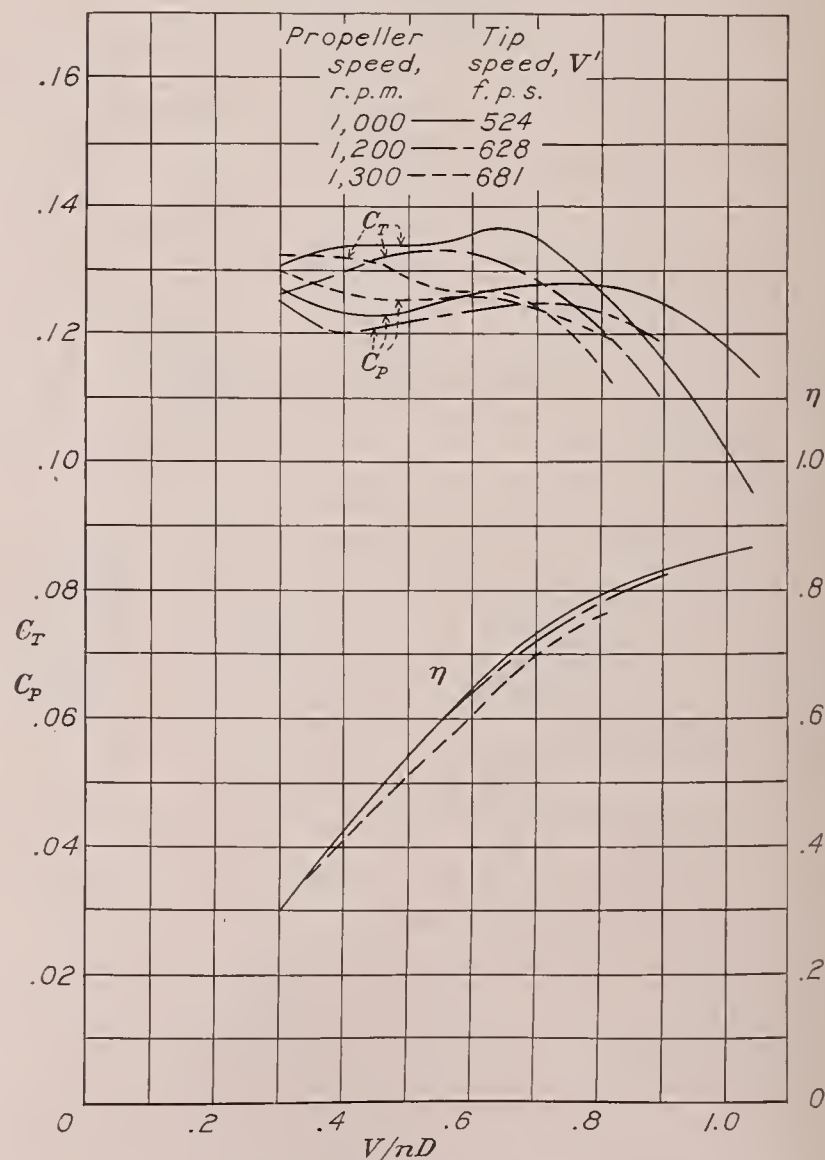


FIGURE 19.—Propeller set 30° at 0.75R.

blade-angle setting, blade section, blade width, and blade thickness.

Tip speed.—The tip speed at which compressibility losses first appear varies quite widely, depending principally on the V/nD range and the blade-angle setting, which, of course, defines the angle of attack of the sections. In the take-off range of V/nD , it may be noted that compressibility losses first become evident at from 0.5 to 0.7 the speed of sound for the different propellers. (See figs. 13, 20, 26, 30, etc.) The blade-angle setting evidently has little effect in this range as no definite trends are evident except, perhaps, in the case of propeller 5868-R6 (fig. 20), which shows the results for a wider range of blade-angle settings than the other propellers.

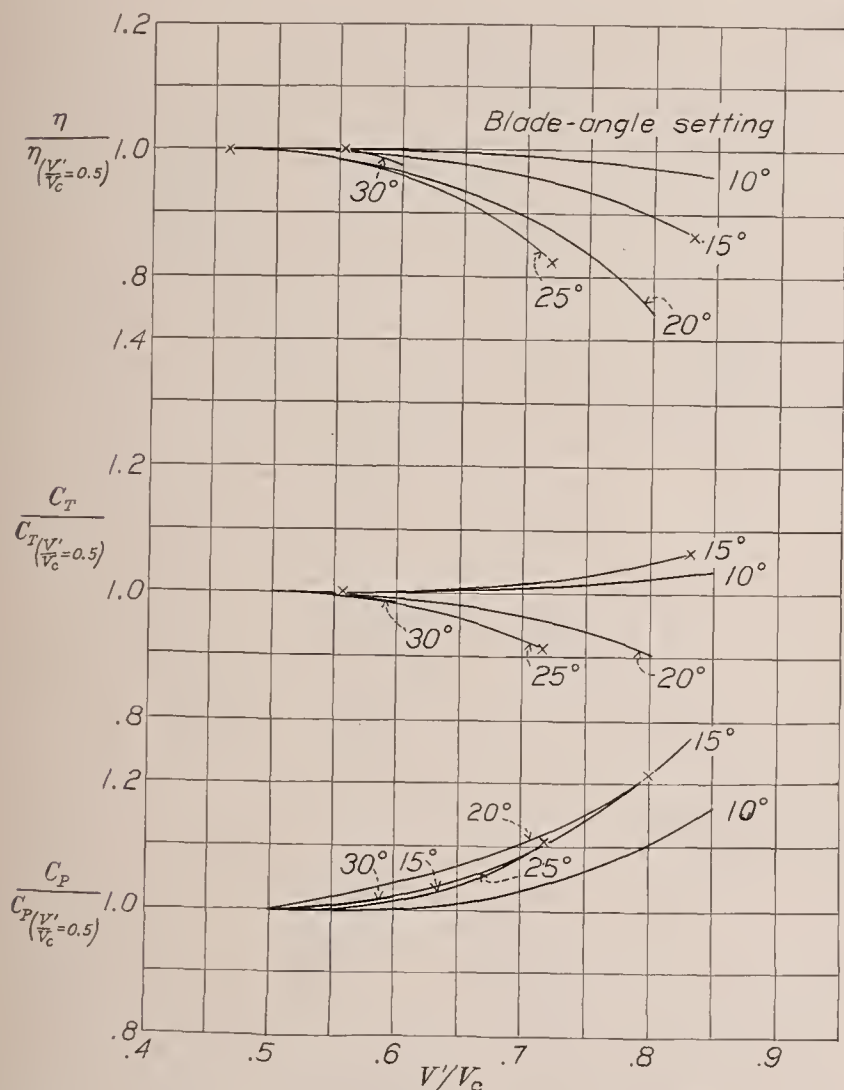


FIGURE 20.—Changes in propeller characteristics due to compressibility for the take-off condition. Propeller 5868-R6; diameter, 10 ft.; radial engine nacelle; $\frac{V}{nD} = 0.30 \left(\frac{V}{nD} \right)_{peak\ eff.}$

In the climbing range of V/nD , compressibility losses first appear at tip-speed values of from 0.6 to 0.75 the speed of sound for most propellers. (See figs. 14, 21, 27, 31, etc.) In general, as the pitch is increased, the losses occur at lower tip speeds. (See, in particular, figs. 14 and 27.)

Blade-angle setting.—The magnitude of the compressibility loss is largely determined by the blade-angle setting for any given tip speed and V/nD range. In the take-off range, the indications are that the greatest loss occurs at blade-angle settings of about 20°. (See

figs. 13, 20, and 26.) At tip speeds of $0.8V_c$, the maximum indicated losses amount to from 10 to 25 percent of the thrust power, depending upon the propeller. Extrapolation of some of the curves to tip speeds of $0.9V_c$ indicates that the maximum loss might amount to as much as 40 percent.

In the climbing range, the greatest loss evidently occurs at a blade-angle setting of about 25°. Since the engine power was limited, it was not possible to reach very high tip speeds for these settings. The 9½-foot propeller (4879) afforded the best opportunity to study the effects. A tip speed of nearly $0.8V_c$ was reached for the 25° setting and, from this test (fig. 27), the foregoing statement is best substantiated. The maximum loss in efficiency for this condition appears to be of the order of 10 percent at tip speeds of $0.8V_c$.

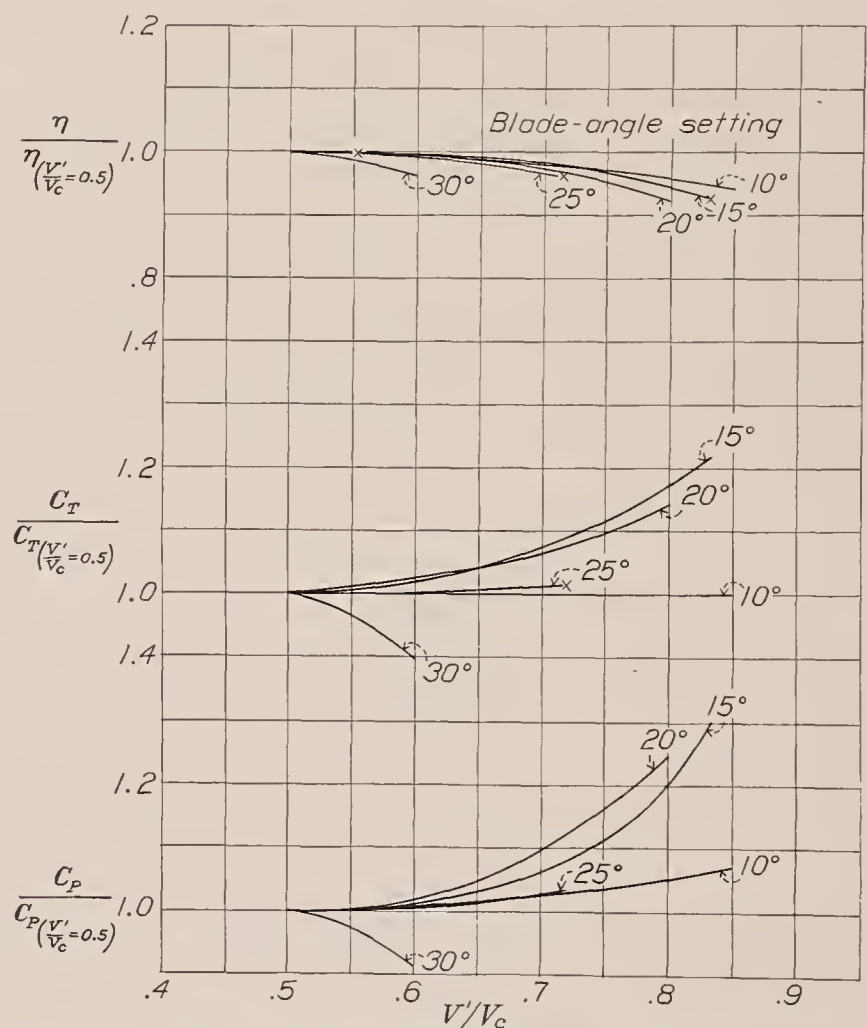
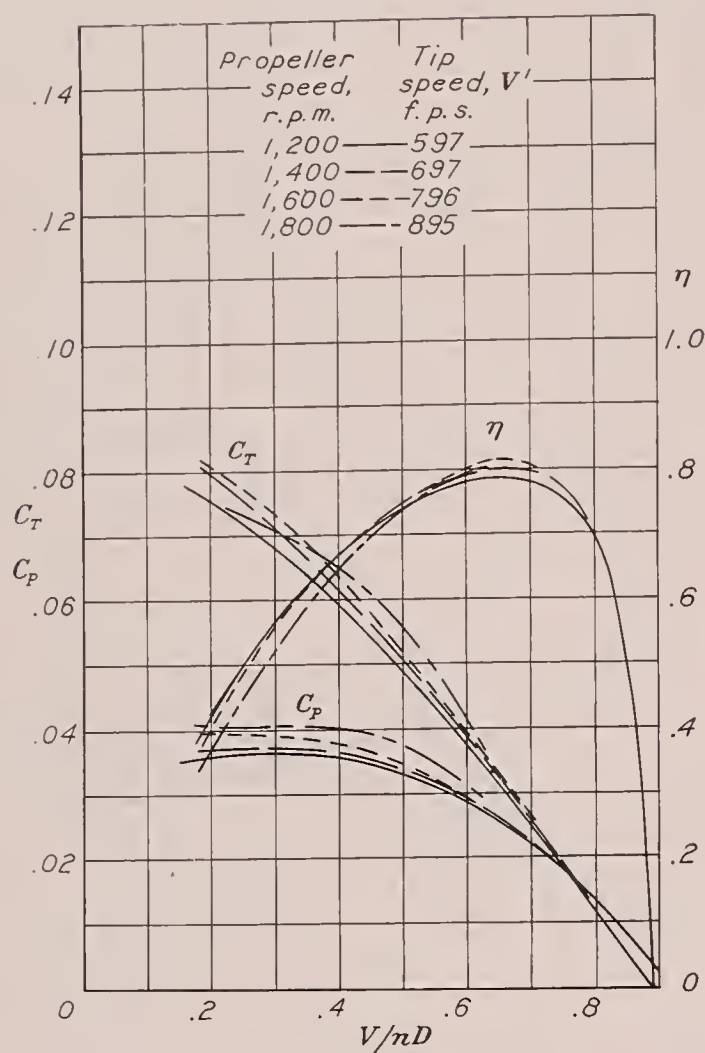
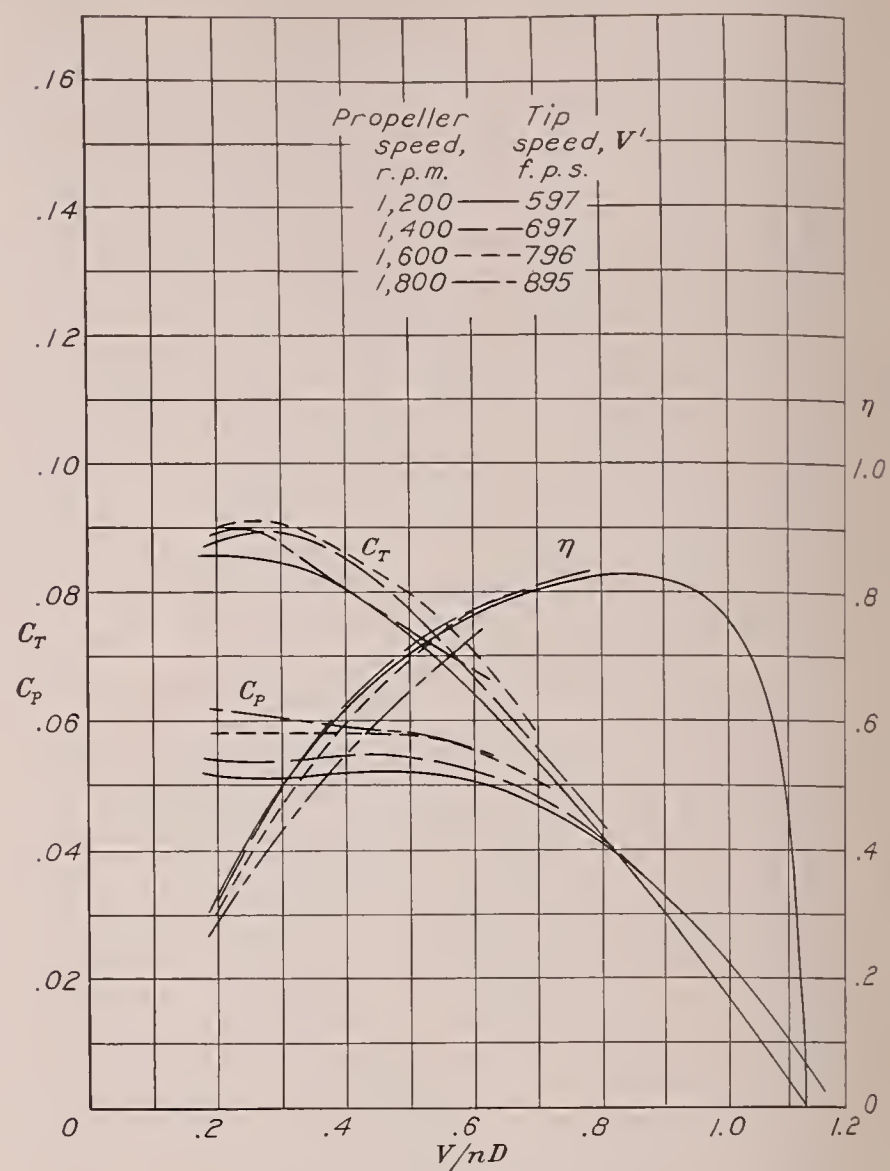
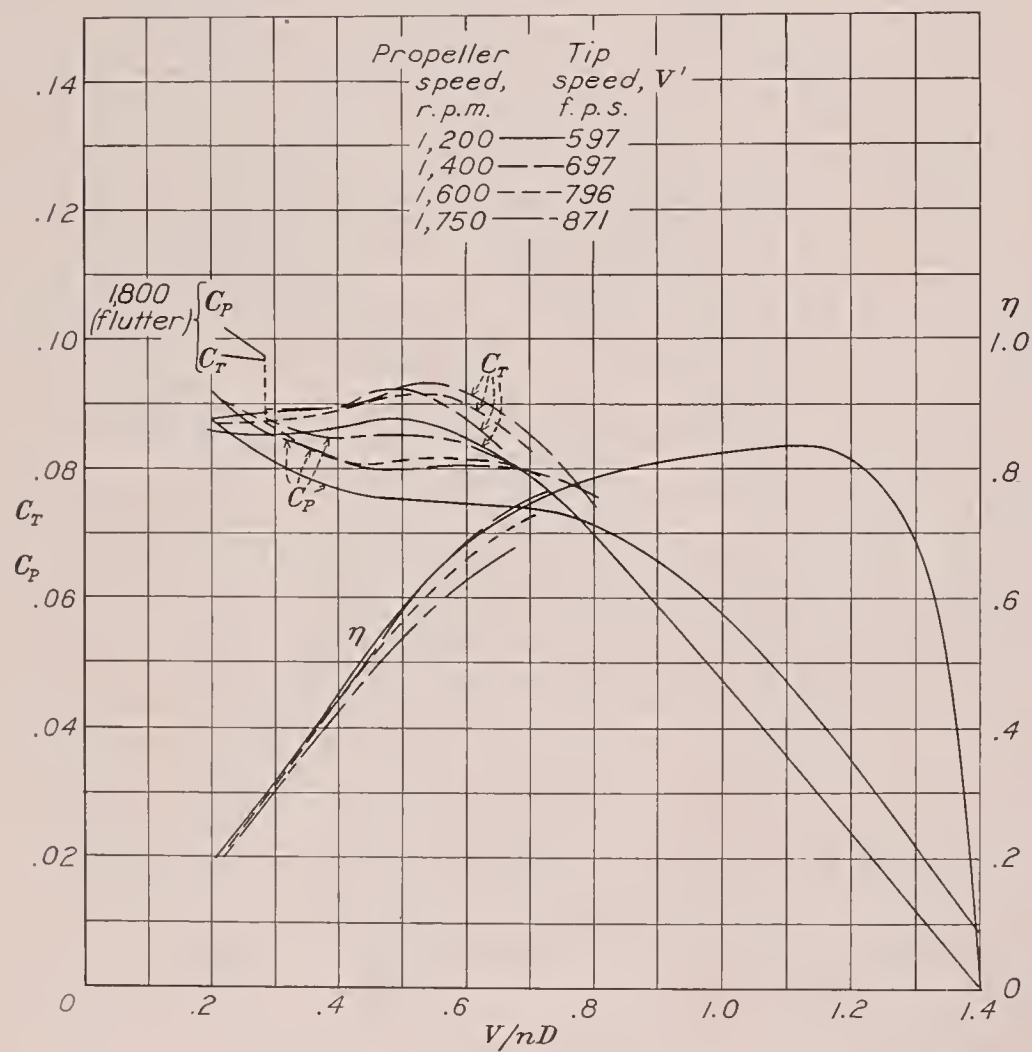
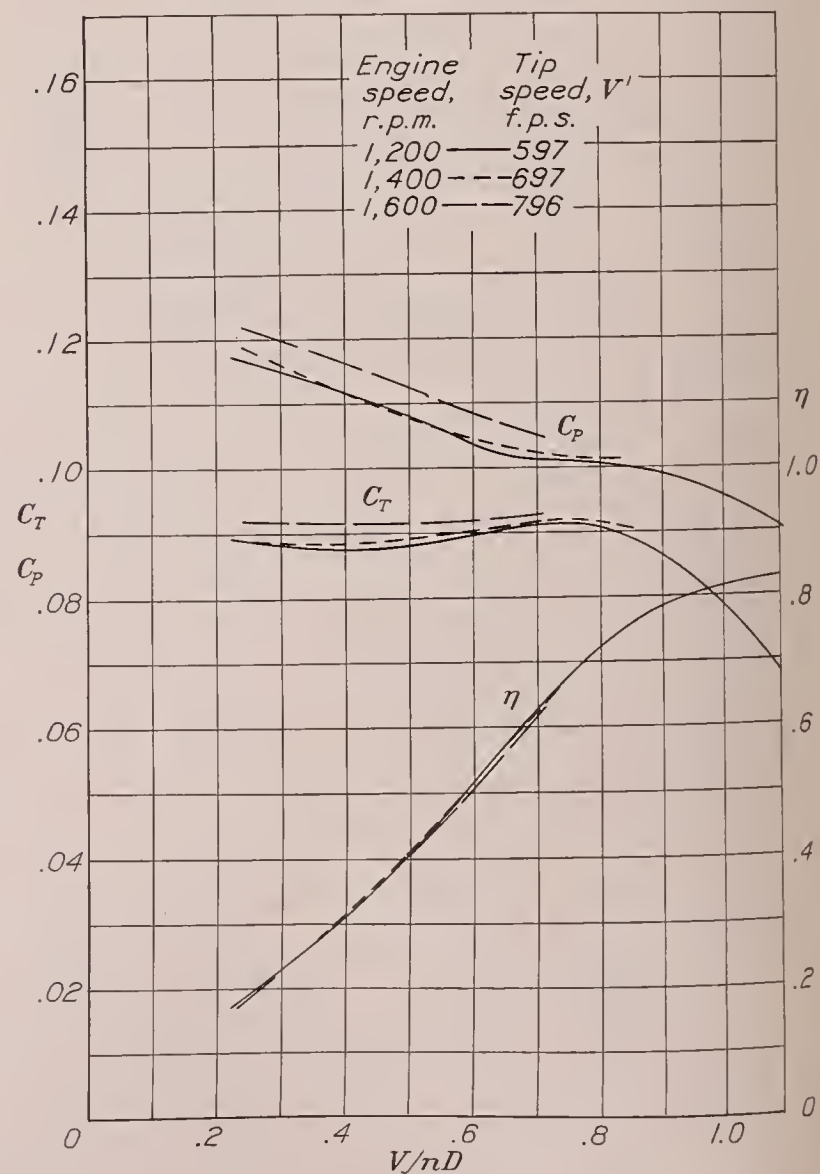


FIGURE 21.—Changes in propeller characteristics due to compressibility for the climbing condition. Propeller 5868-R6; diameter, 10 ft.; radial engine nacelle; $\frac{V}{nD} = 0.65 \left(\frac{V}{nD} \right)_{peak\ eff.}$

Blade section.—Of the eight propellers tested, four have Clark Y sections and four have R. A. F. 6 sections. Only two of these can be directly compared for the effect of section, however, because the rest also differ in other respects. In figure 47 a comparison is made between the two propellers 5868-9 and 5868-R6 on the basis of the relative take-off and climbing efficiencies. It may be noted that, for any given tip speed, the losses for the Clark Y propeller are, in general, only about one-third to one-half as much as for the R. A. F. 6 propeller. The actual efficiencies in the take-off and climbing ranges are, however, about equal

FIGURE 22.—Propeller set 15° at $0.75R$.FIGURE 23.—Propeller set 20° at $0.75R$.FIGURE 24.—Propeller set 25° at $0.75R$.FIGURE 25.—Propeller set 30° at $0.75R$.

FIGURES 22 to 25.—Effect of compressibility on propeller characteristics. Propeller 4879; diameter, $9\frac{1}{2}$ ft.; radial engine nacelle.

at high tip speeds, inasmuch as the efficiency at low tip speeds for the R. A. F. 6 propeller is greater than that for the Clark Y propeller in these ranges. (See figs. 9, 10, 16, and 17.)

A plausible explanation for the greater compressibility effect on the R. A. F. 6 propeller seems to lie in the differences of the radii of curvature of the front upper surfaces of the sections. (See fig. 7.) The R. A. F. 6 section has the lesser radius of curvature, hence the induced velocities are probably greater. The compressibility burble should therefore occur earlier for the R. A. F. 6 section.

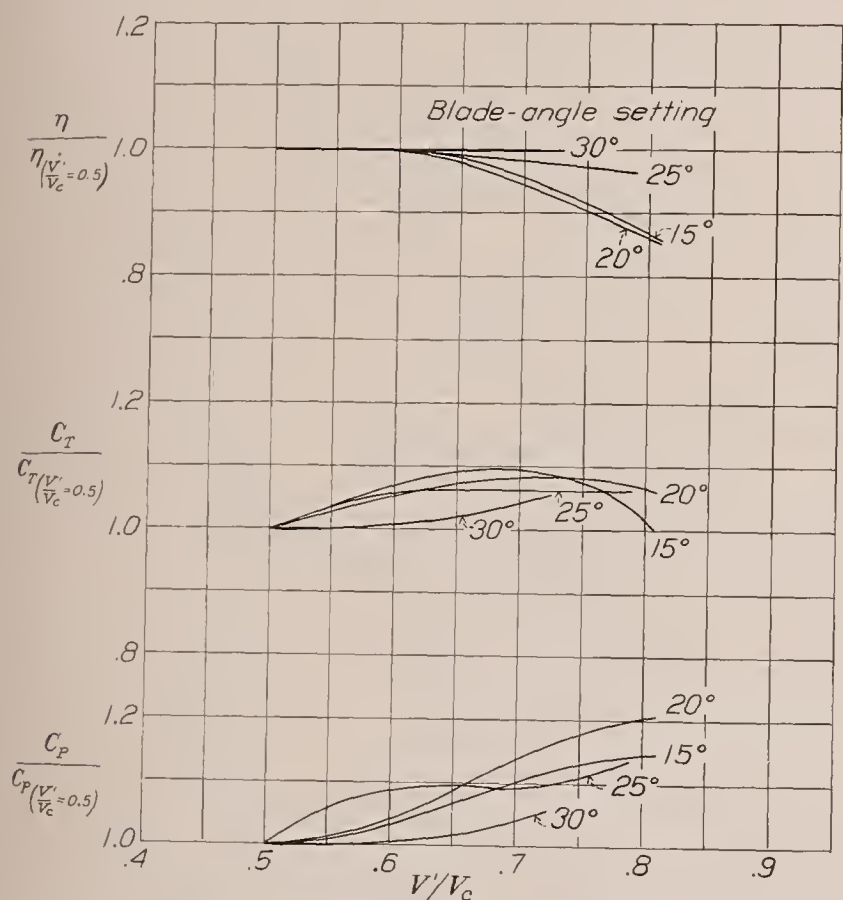


FIGURE 26.—Changes in propeller characteristics due to compressibility for the take-off condition. Propeller 4879; diameter, 9½ ft.; radial engine nacelle; $\frac{V}{nD} = 0.30 \left(\frac{V}{nD} \right)_{\text{peak eff.}}$

Blade shape.—In figure 48 is shown a comparison of three propellers having different blade shapes. The main difference is the tip shape, as can be seen from figure 3, although there are also differences in thickness. With the exception of the take-off comparison at a blade-angle setting of 20°, the results from the three propellers are almost identical.

Blade width.—Propeller 37-3647 is 50 percent wider than propeller 5868-R6, but otherwise the two propellers are identical. Since the thickness ratio is the same, the actual thickness of propeller 37-3647 is likewise 50 percent greater than that of propeller 5868-R6. The

shank portions of the blades, however, are nearly identical. A comparison of the results from these propellers (fig. 49) indicates that the compressibility loss for the wider blade is only about half that for the one of standard width in the take-off range. The differences are more obscure for the climbing condition. The actual efficiencies become nearly equal at high tip speeds, however, since the standard-width blade has a higher efficiency at low tip speeds. (See figs. 36, 37, 40, and 41.)

Just why the differences in Reynolds Number of the two sets of tests should account for the differences

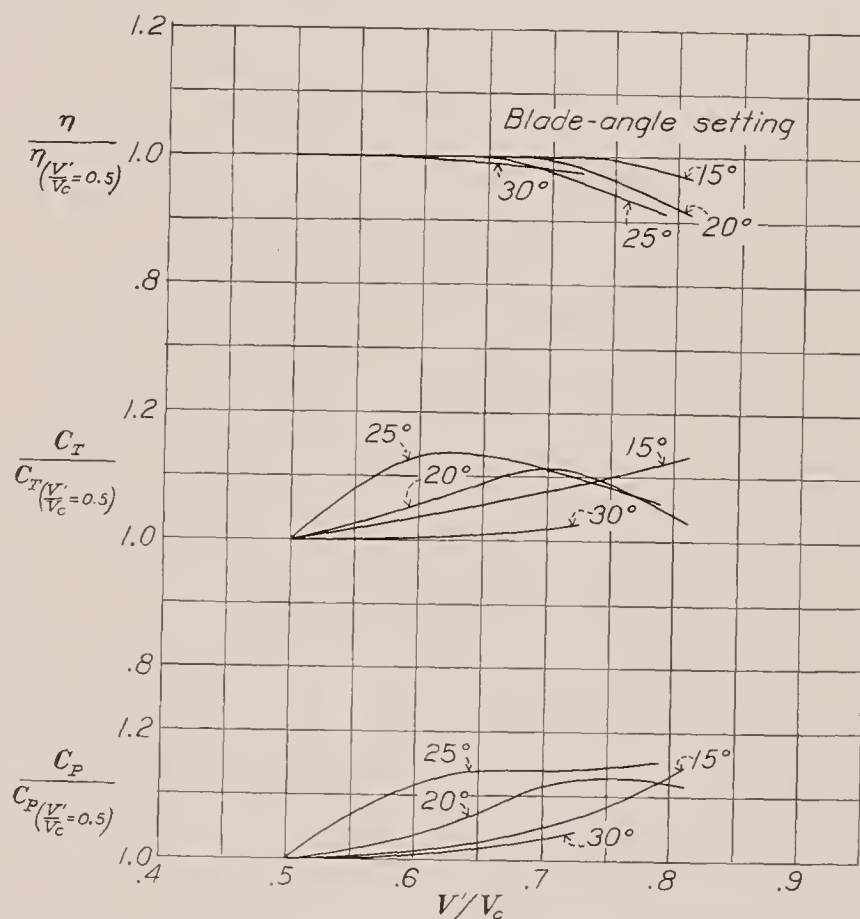


FIGURE 27.—Changes in propeller characteristics due to compressibility for the climbing condition. Propeller 4879; diameter, 9½ ft.; radial engine nacelle; $\frac{V}{nD} = 0.65 \left(\frac{V}{nD} \right)_{\text{peak eff.}}$

noted is not clear. The wider blade produces a greater inflow velocity and, consequently, is working at a lower angle of attack than the standard-width one. The inflow angle could hardly be increased, however, by the amount necessary to make the difference shown at the take-off condition, equivalent to a 5° change in blade-angle setting, because the 15° curve of the standard-width blade coincides with the 20° curve of the wider blade. Computations based on the momentum theory, however, do indicate an inflow angle greater by 0.75°, owing to the increased blade width, for one condition investigated.

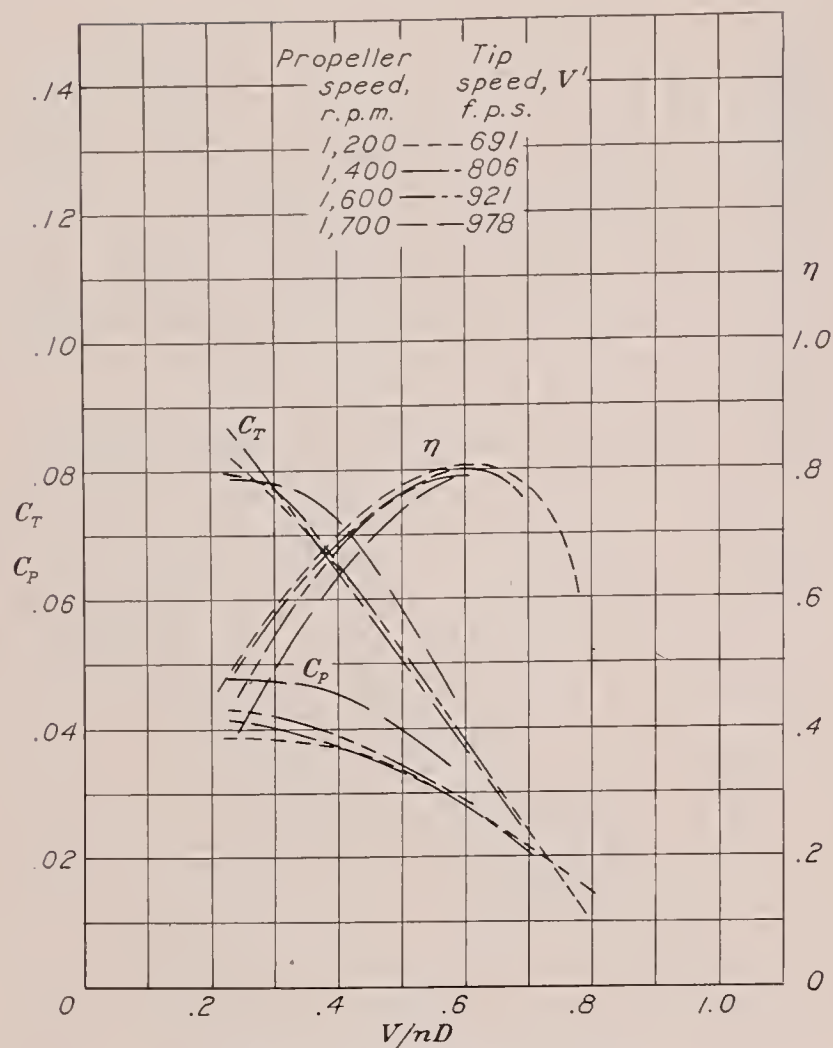


FIGURE 28.—Propeller set 15° at 0.75R.

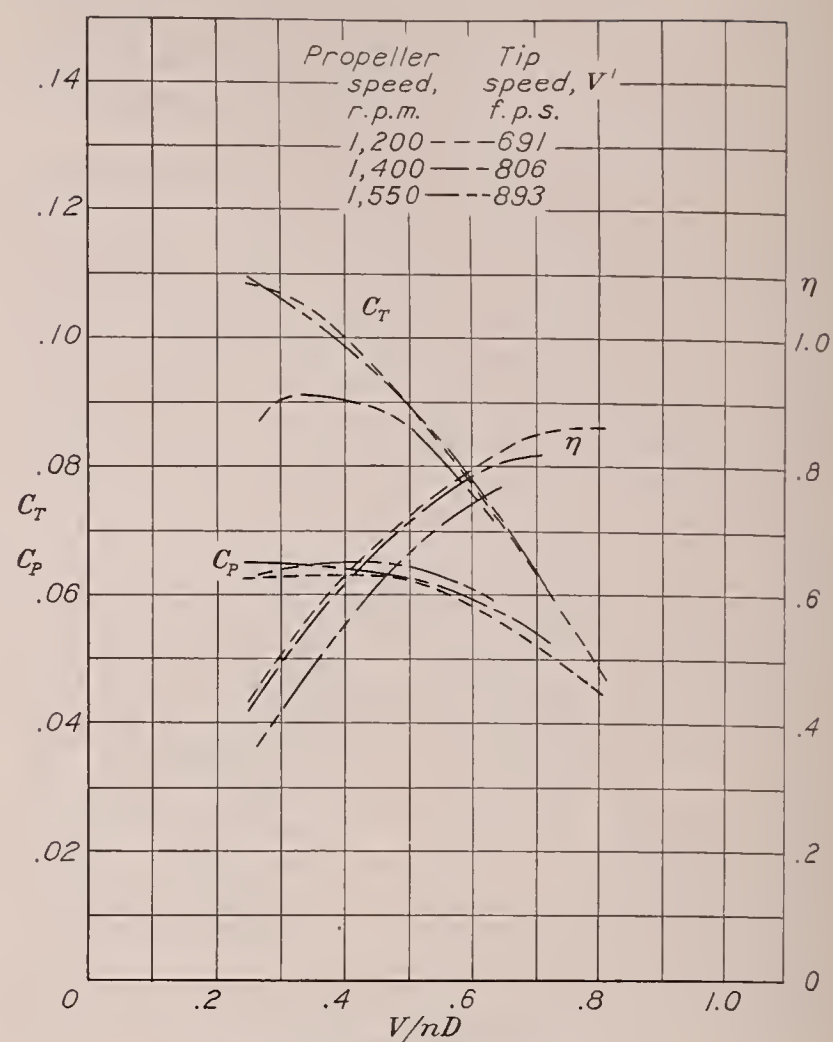
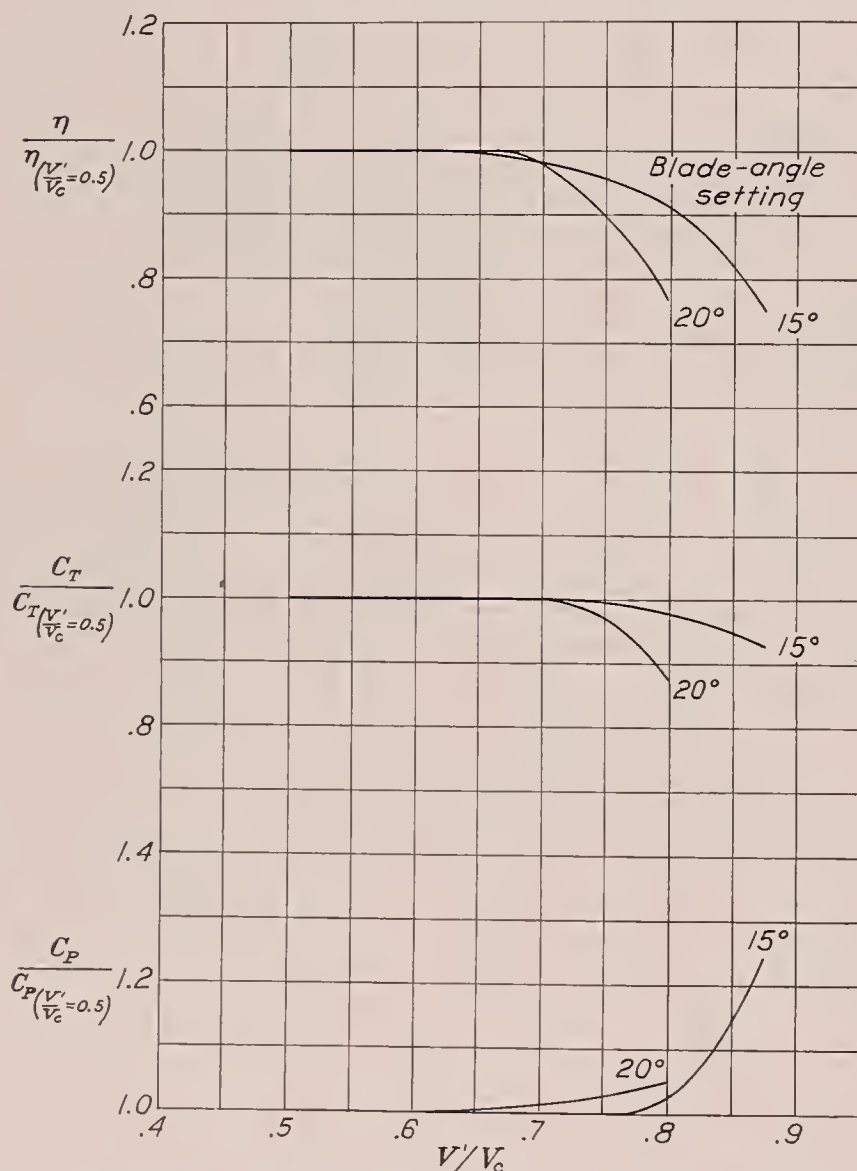
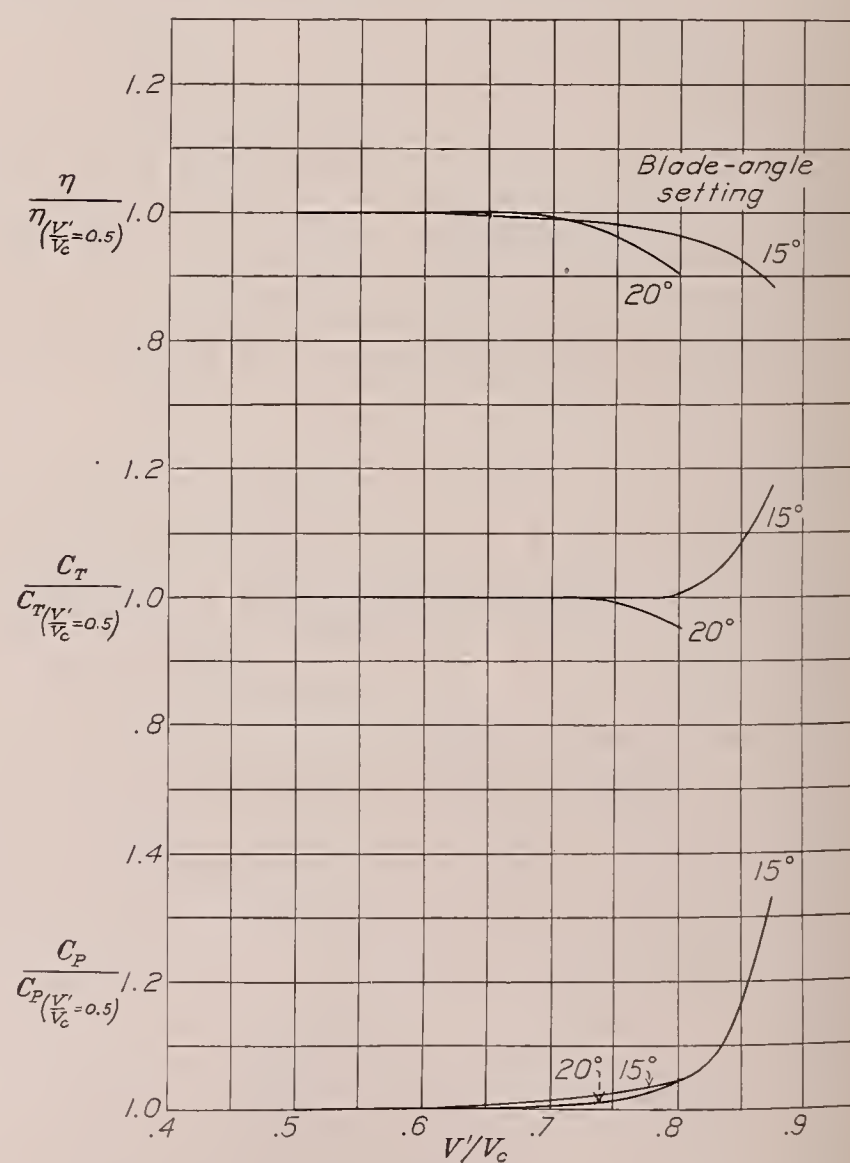
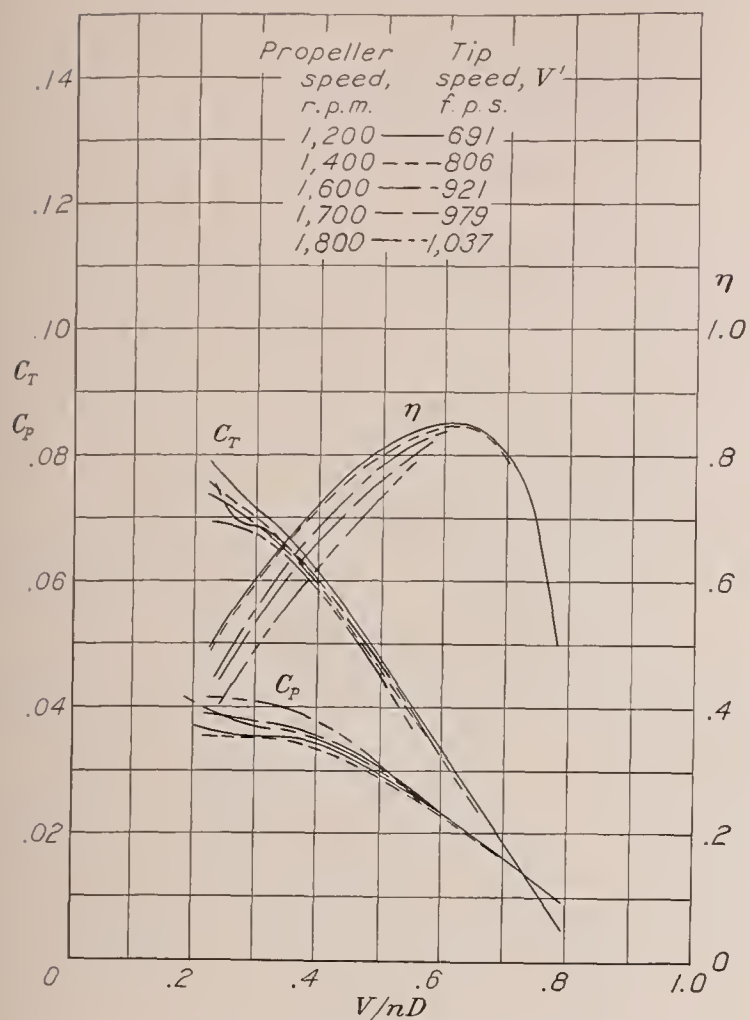


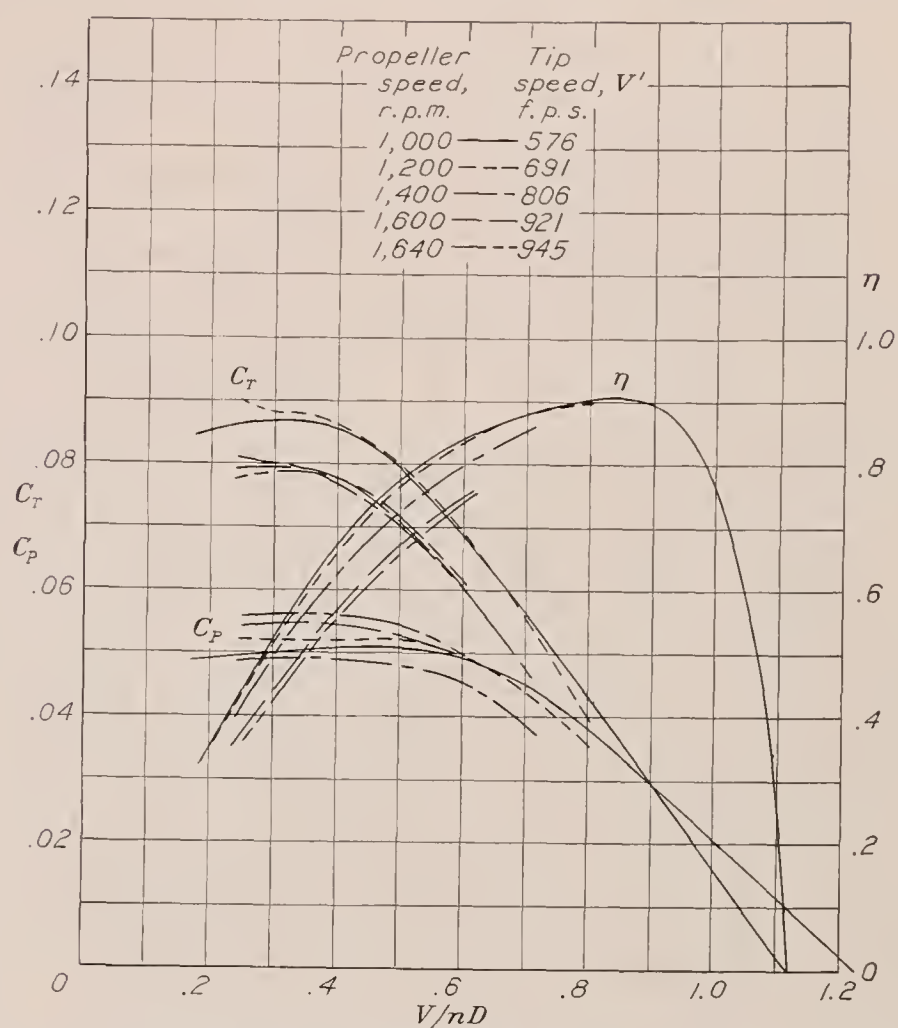
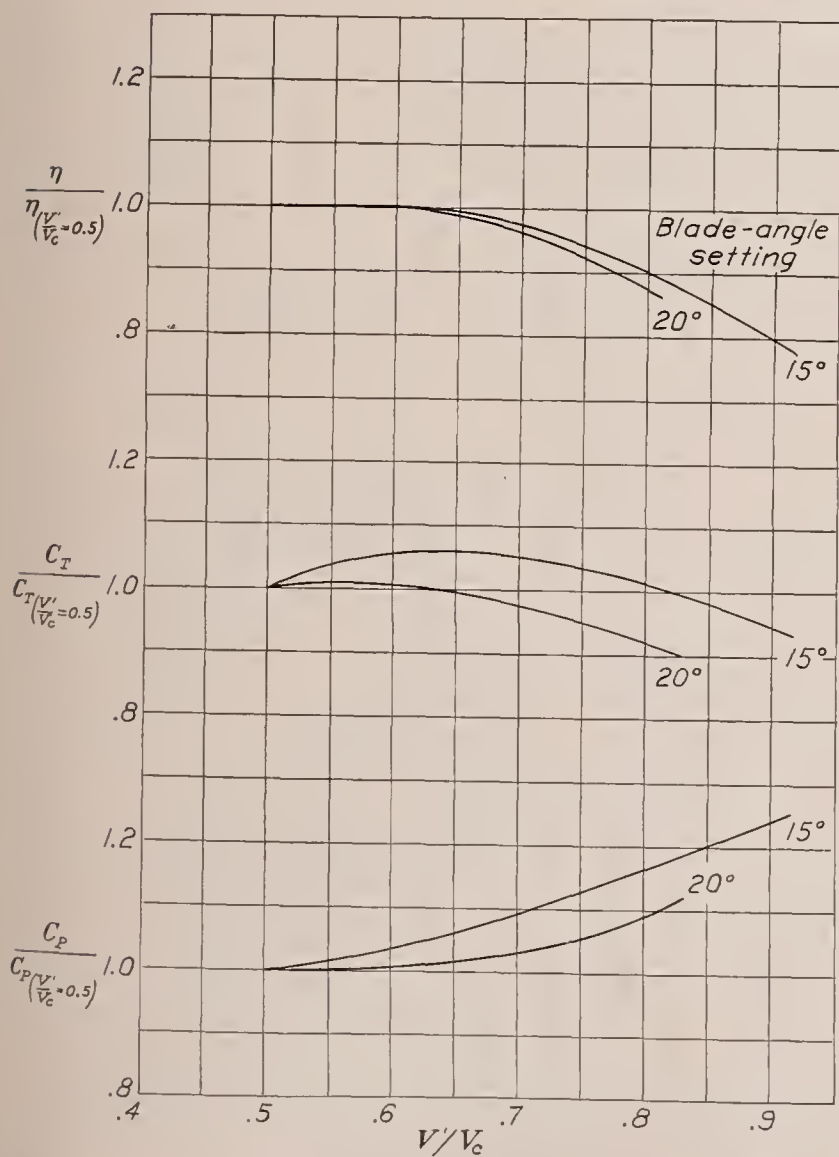
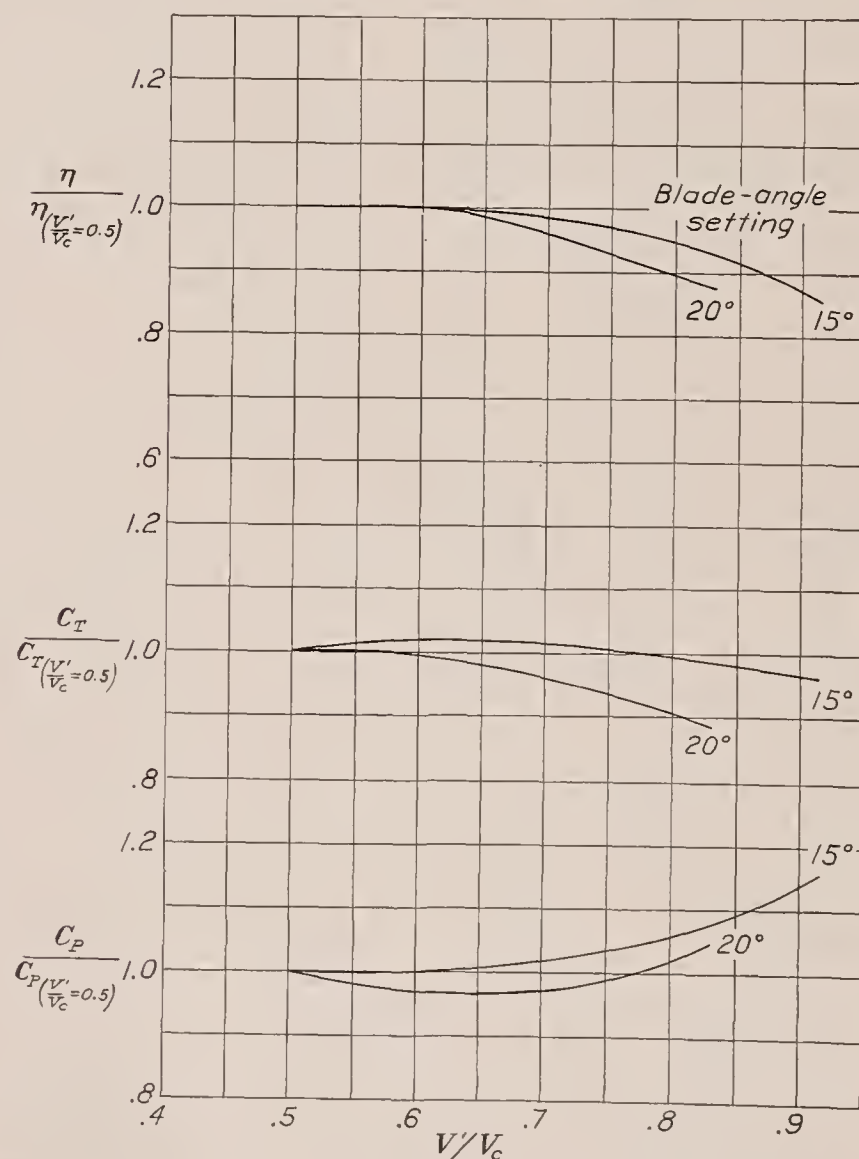
FIGURE 29.—Propeller set 20° at 0.75R.

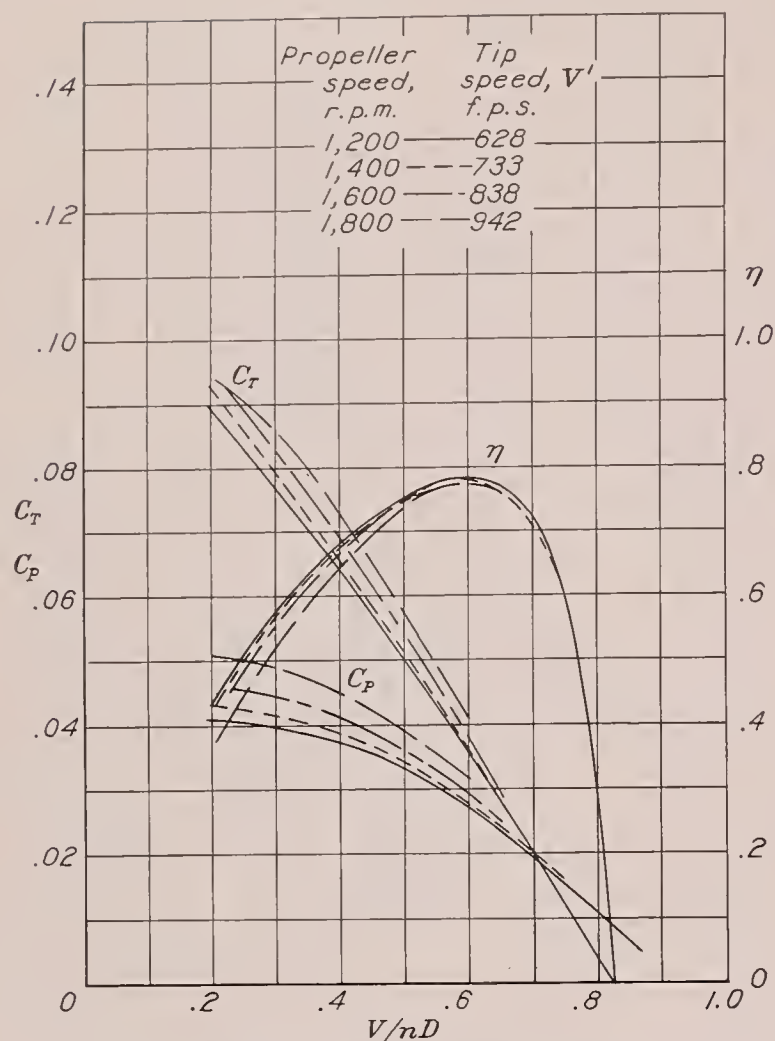
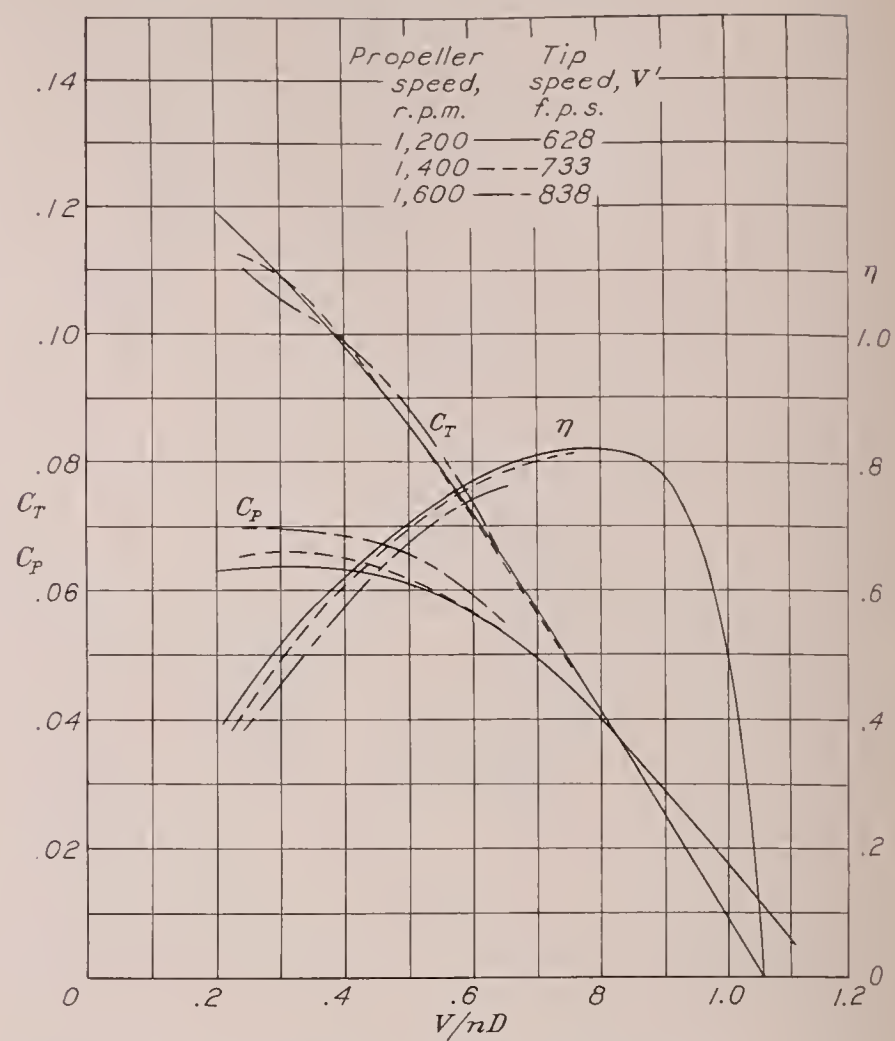
FIGURES 28 and 29.—Effect of compressibility on propeller characteristics. Propeller 4371; diameter, 11 ft. radial engine nacelle.

FIGURE 30.—Changes in propeller characteristics due to compressibility for the take-off condition. Propeller 4371; diameter, 11 ft.; radial engine nacelle; $\frac{V}{nD} = 0.30 \left(\frac{V}{nD} \right)_{\text{peak eff.}}$ FIGURE 31.—Changes in propeller characteristics due to compressibility for the climbing condition. Propeller 4371; diameter, 11 ft.; radial engine nacelle; $\frac{V}{nD} = 0.65 \left(\frac{V}{nD} \right)_{\text{peak eff.}}$

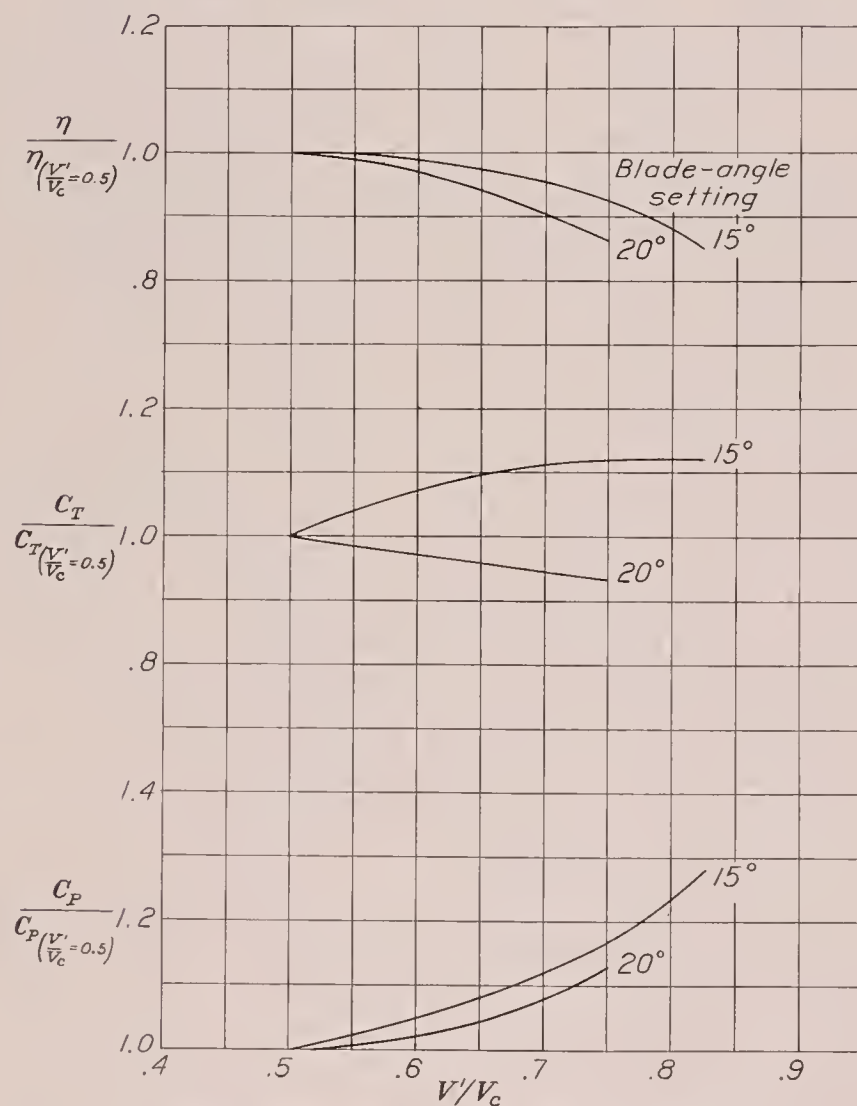
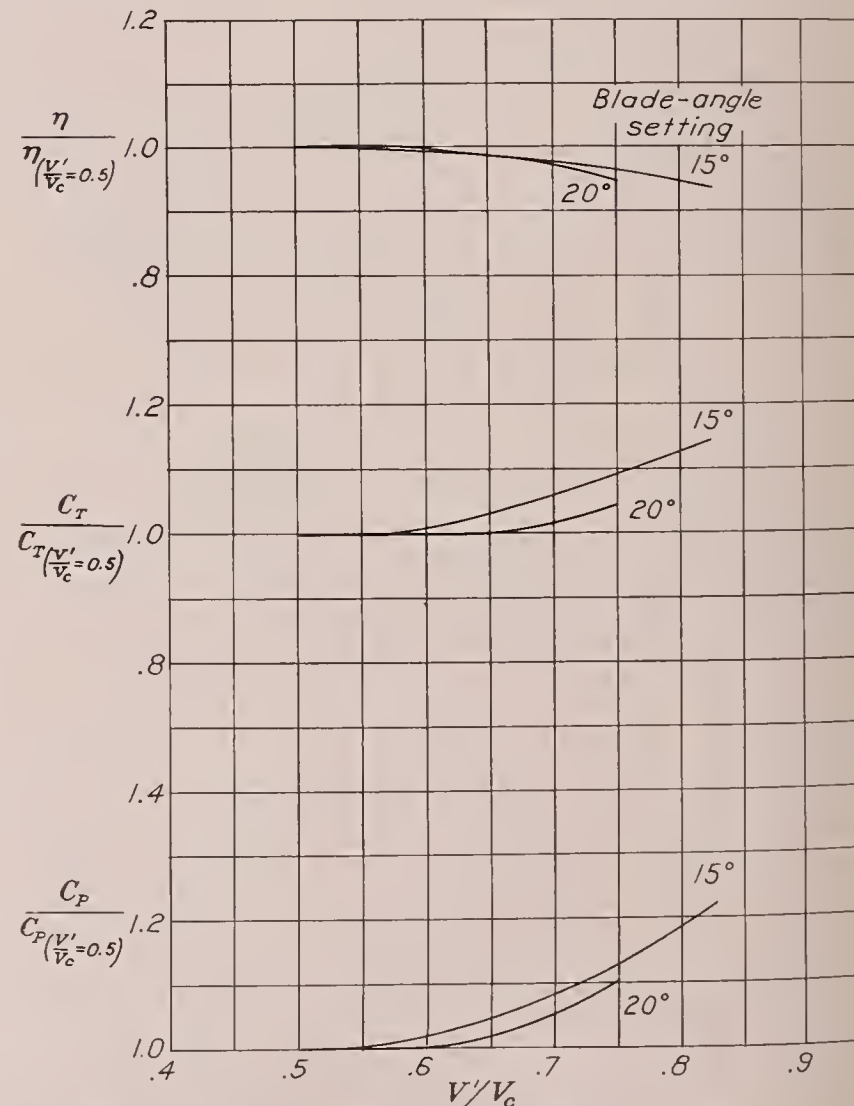
FIGURE 32.—Propeller set 15° at $0.75R$.

FIGURES 32 and 33.—Effect of compressibility on propeller characteristics. Propeller 195; diameter, 11 ft.; radial engine nacelle.

FIGURE 33.—Propeller set 20° at $0.75R$.FIGURE 34.—Changes in propeller characteristics due to compressibility or the take-off condition. Propeller 195; diameter, 11 ft.; radial engine nacelle; $\frac{V}{nD} = 0.30 \left(\frac{V}{nD} \right)_{\text{peak eff}}$ FIGURE 35.—Changes in propeller characteristics due to compressibility for the climbing condition. Propeller 195; diameter, 11 ft.; radial engine nacelle; $\frac{V}{nD} = 0.65 \left(\frac{V}{nD} \right)_{\text{peak eff}}$

FIGURE 36.—Propeller set 15° at $0.75R$.FIGURE 37.—Propeller set 20° at $0.75R$.

FIGURES 36 and 37.—Effect of compressibility on propeller characteristics. Propeller 5868-R6; diameter, 10 ft.; liquid-cooled engine nacelle.

FIGURE 38.—Changes in propeller characteristics due to compressibility for the take-off condition. Propeller 5868-R6; diameter, 10 ft.; liquid-cooled engine nacelle; $\frac{V}{nD} = 0.30 \left(\frac{V}{nD} \right)_{peak\ eff.}$ FIGURE 39.—Changes in propeller characteristics due to compressibility for the climbing condition. Propeller 5868-R6; diameter, 10 ft.; liquid-cooled engine nacelle; $\frac{V}{nD} = 0.65 \left(\frac{V}{nD} \right)_{peak\ eff.}$

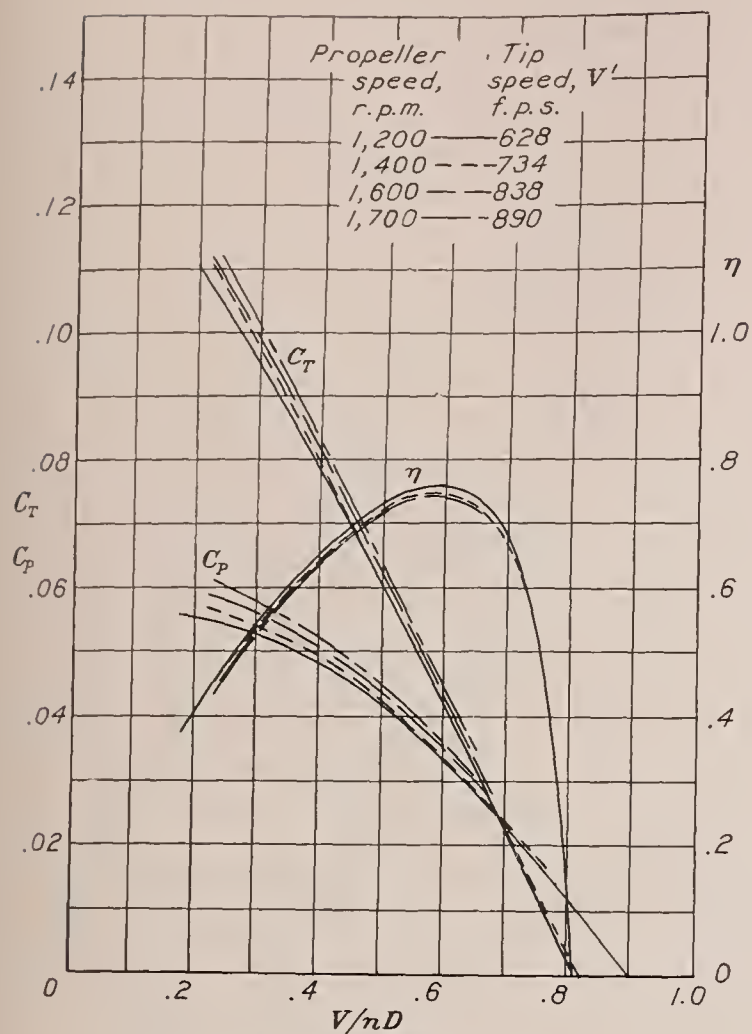


FIGURE 40.—Propeller set 15° at 0.75R.

FIGURES 40 and 41.—Effect of compressibility on propeller characteristics. Propeller 37-3647; diameter, 10 ft.; liquid-cooled engine nacelle.

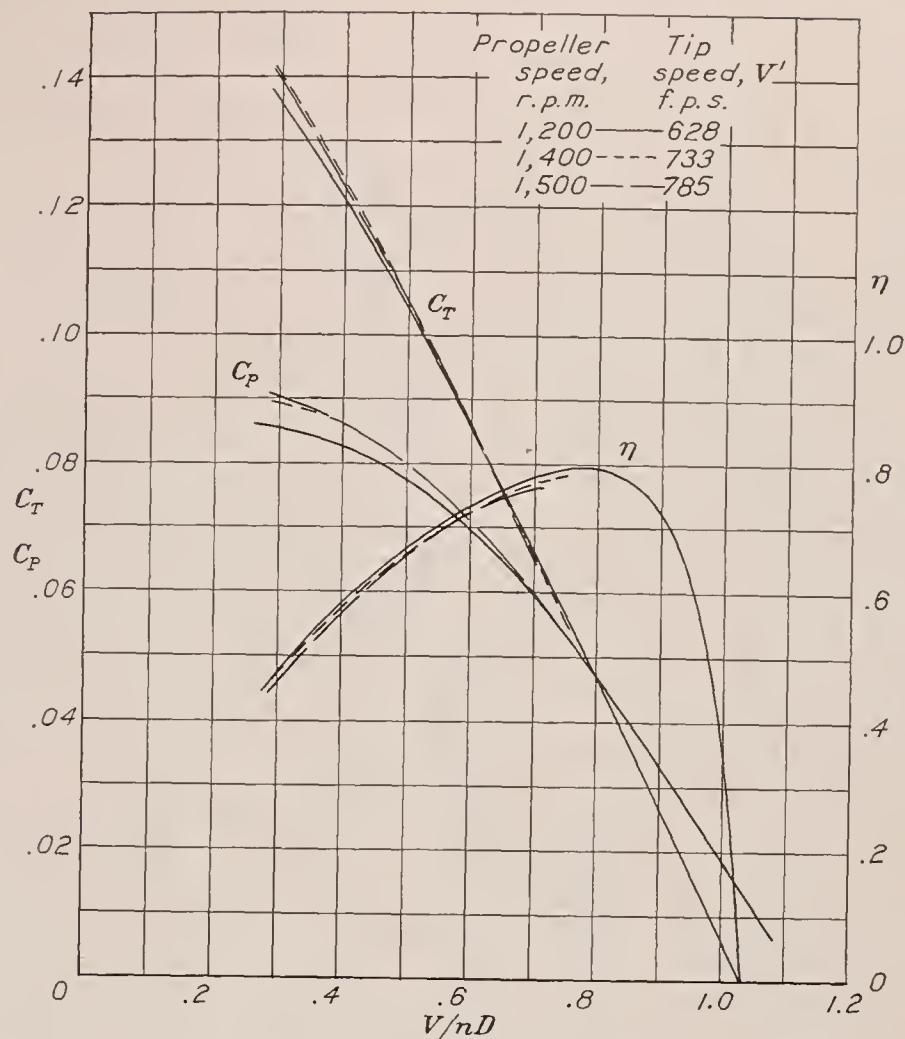


FIGURE 41.—Propeller set 20° at 0.75R.

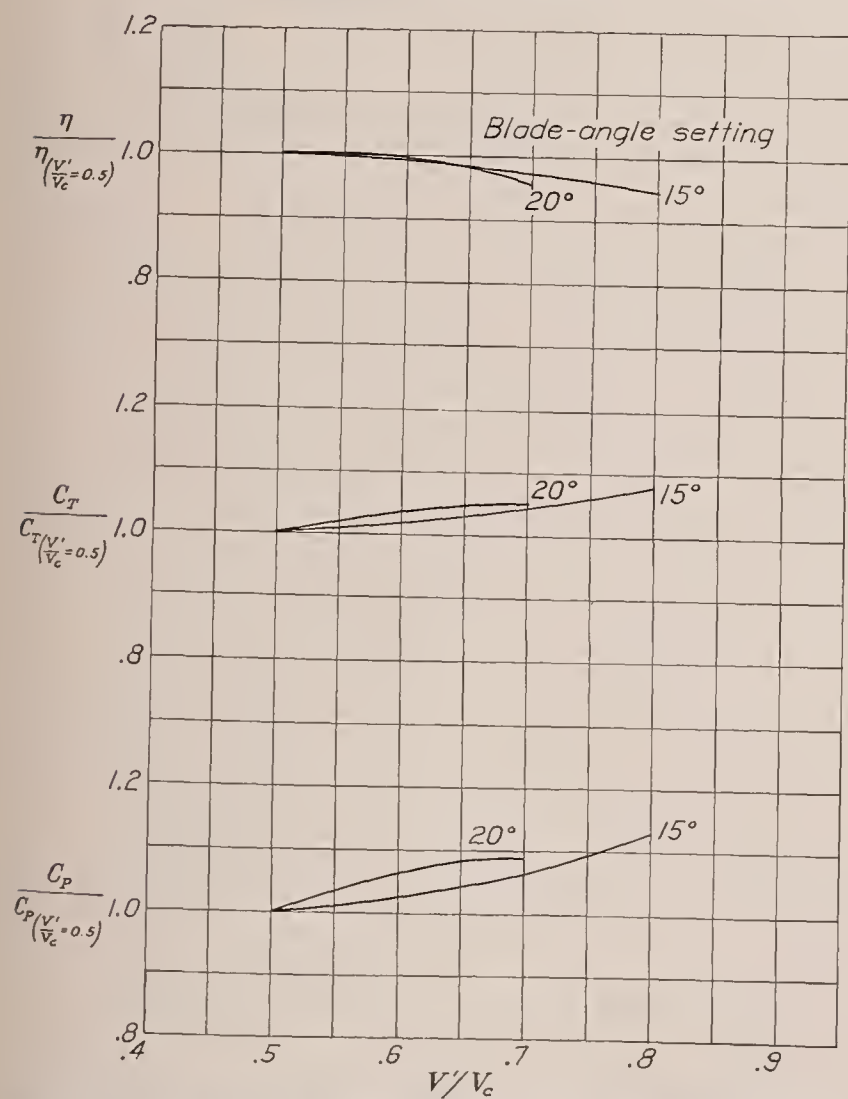


FIGURE 42.—Changes in propeller characteristics due to compressibility for the take-off condition. Propeller 37-3647; diameter, 10 ft.; liquid-cooled engine nacelle; $\frac{V}{nD} = 0.30 \left(\frac{V}{nD} \right)_{\text{peak eff.}}$

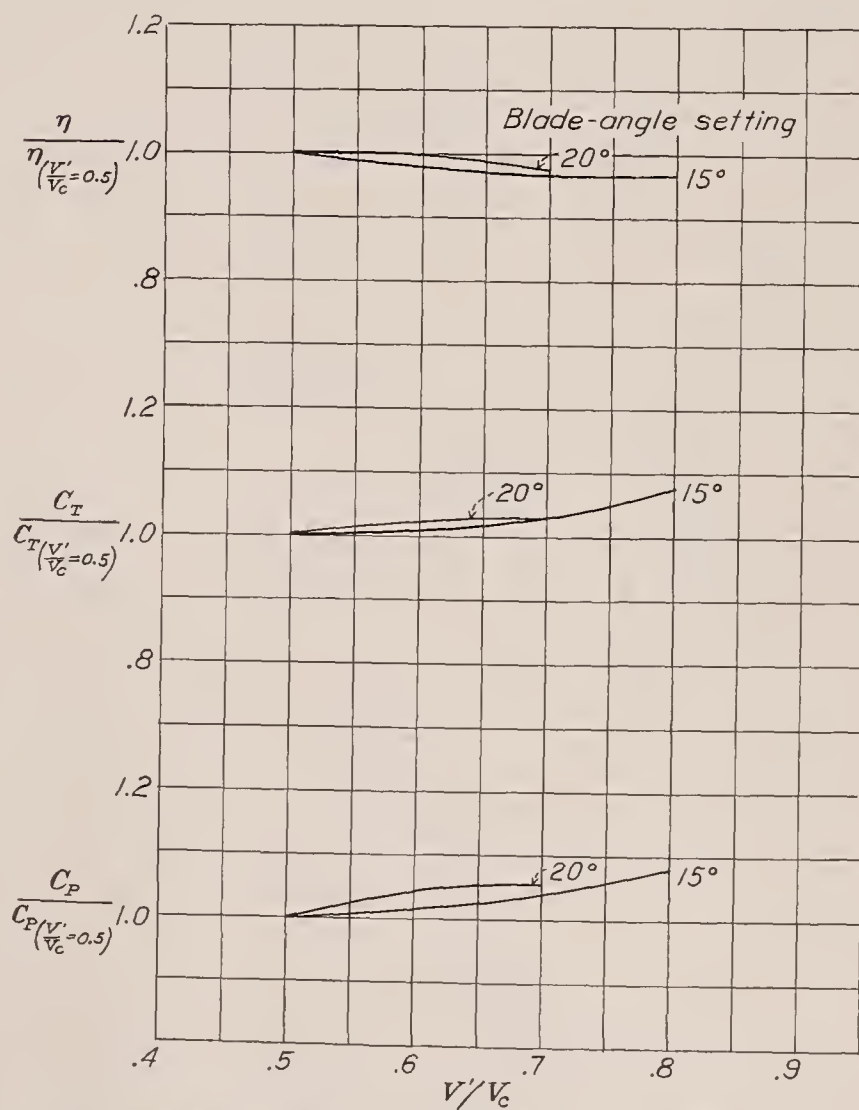
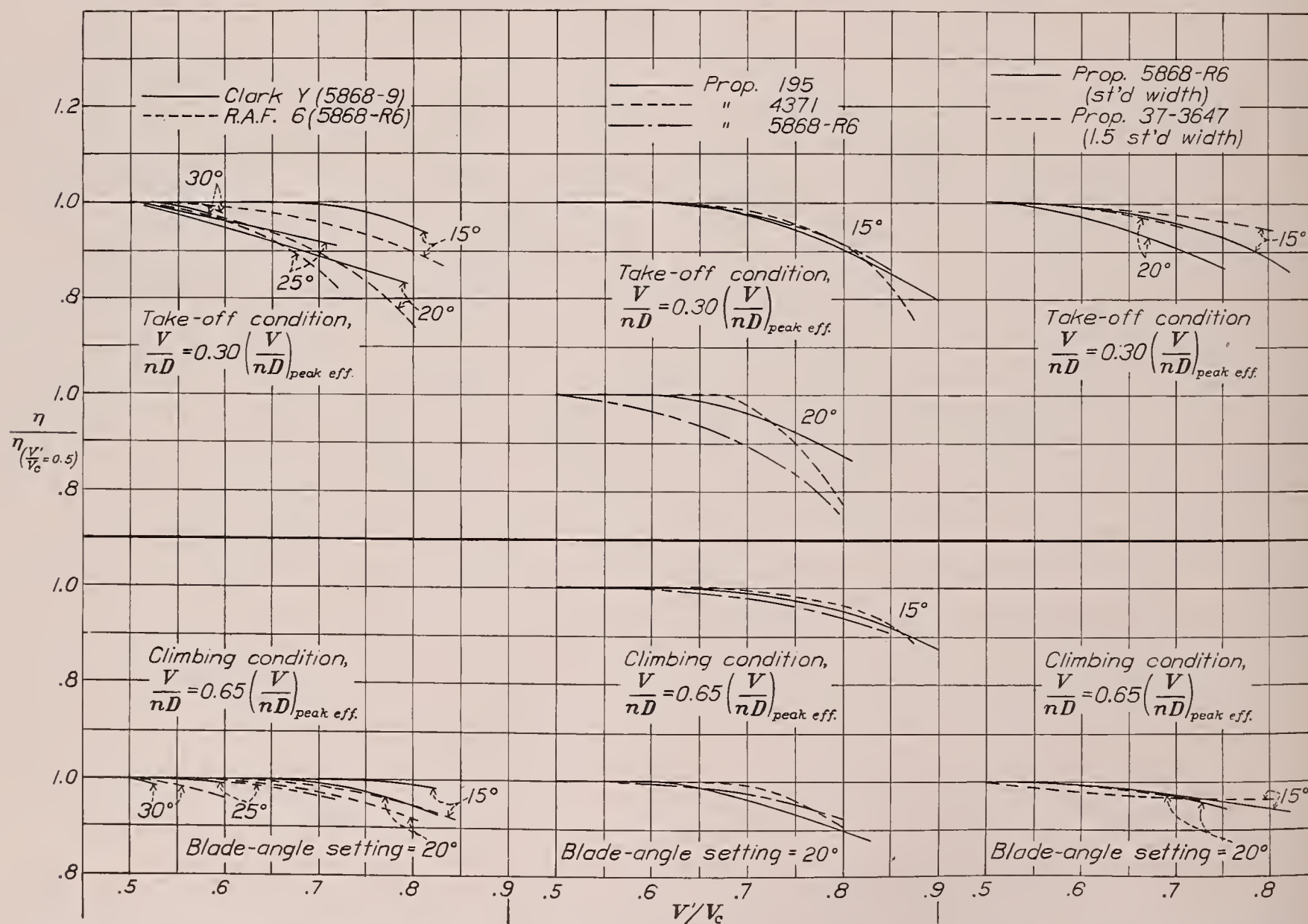
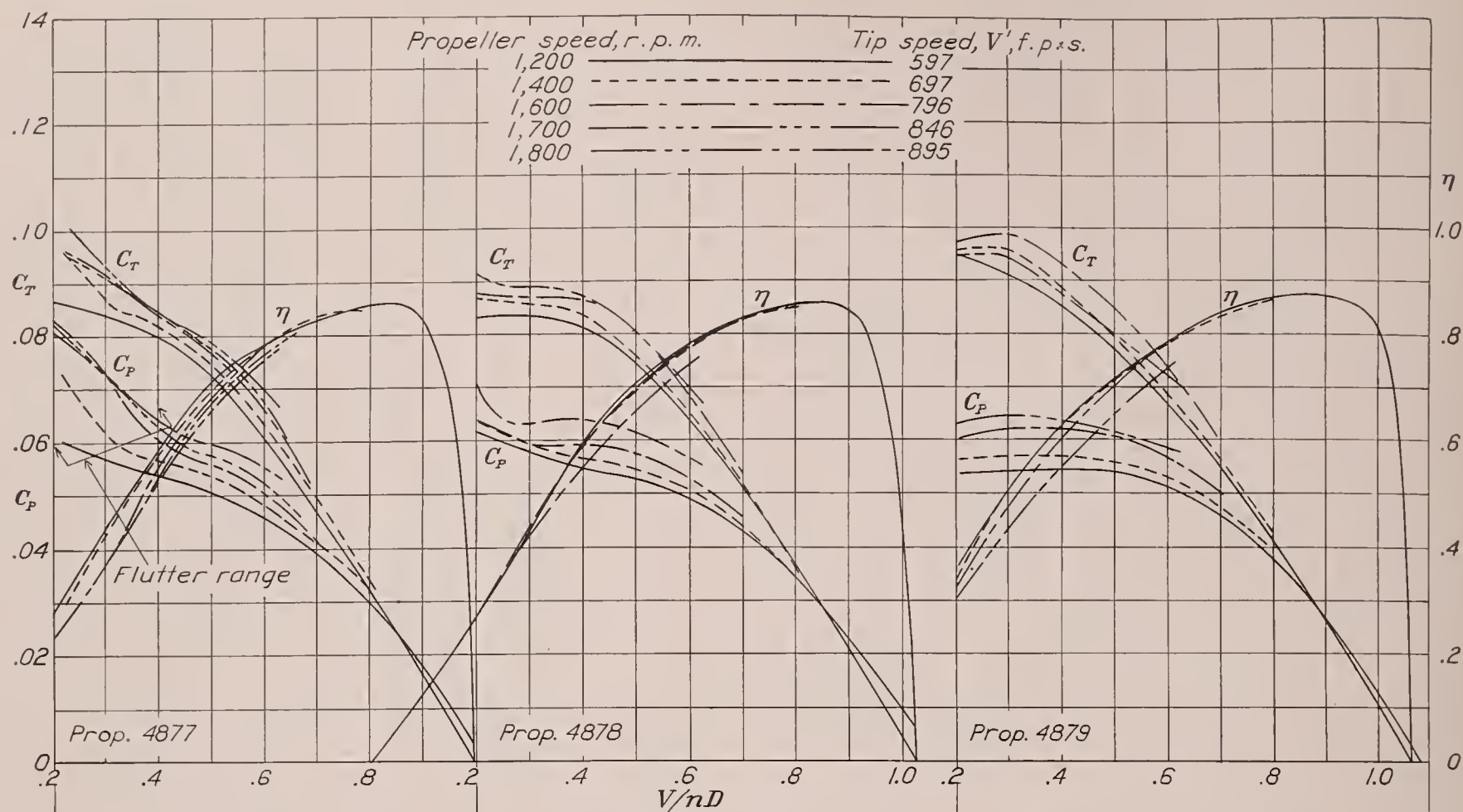


FIGURE 43.—Changes in propeller characteristics due to compressibility for the climbing condition. Propeller 37-3647; diameter, 10 ft.; liquid-cooled engine nacelle; $\frac{V}{nD} = 0.65 \left(\frac{V}{nD} \right)_{\text{peak eff.}}$



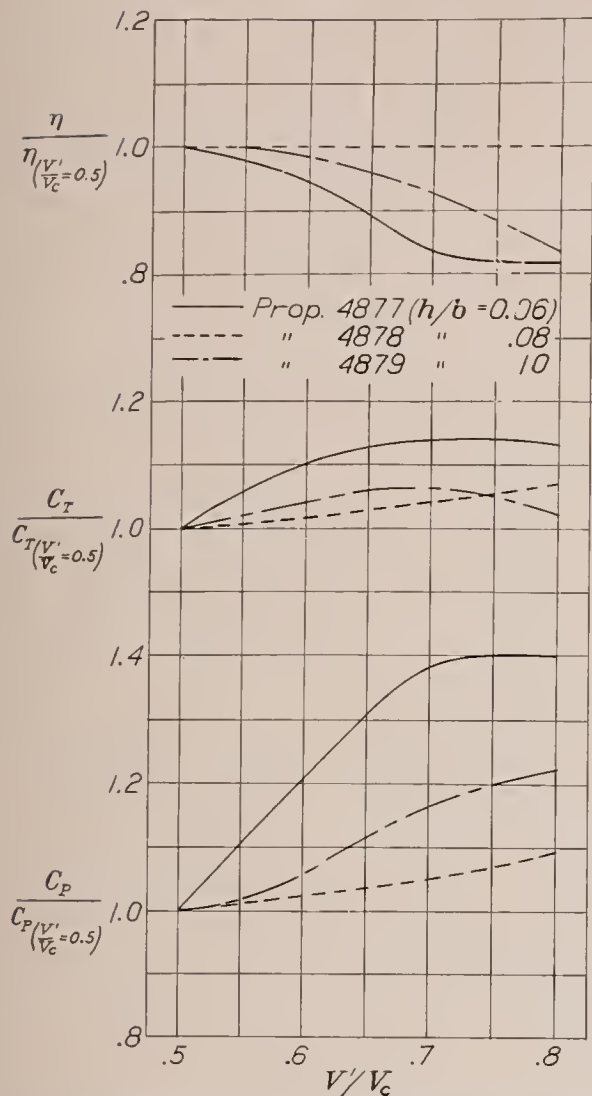


FIGURE 50.—Comparison of propellers having different blade thicknesses. Take-off condition; propeller set 20° at $0.75R$; diameter, $9\frac{1}{2}$ ft.; liquid-cooled engine nacelle;

$$\frac{V}{nD} = 0.30 \left(\frac{V}{nD} \right)_{\text{peak eff.}}$$

Propeller 4877 is fluttering at this condition

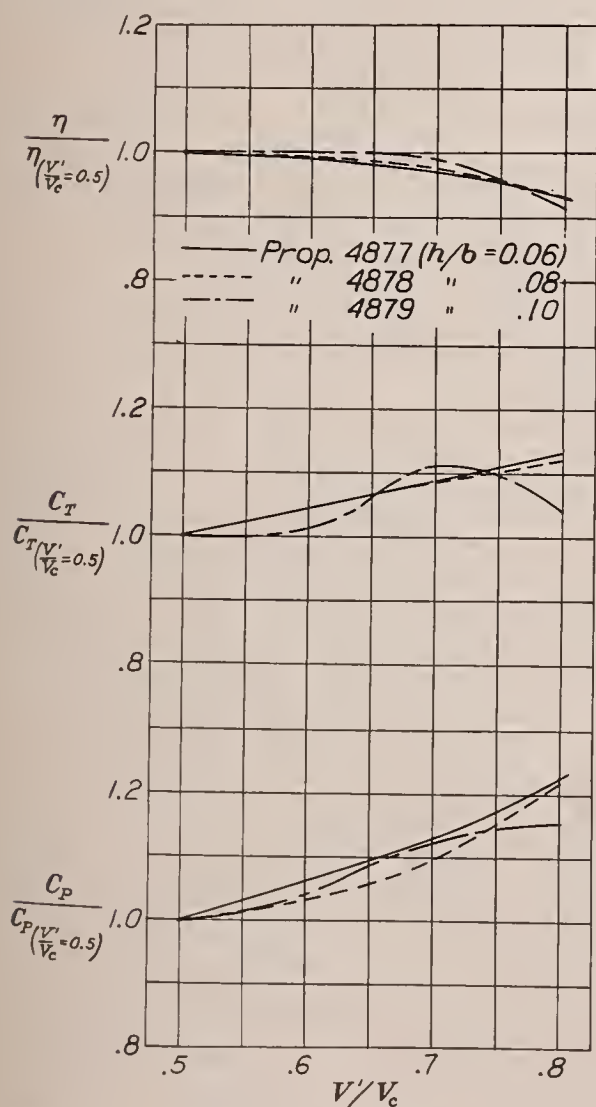


FIGURE 51.—Comparison of propellers having different blade thicknesses. Climbing condition; propeller set 20° at $0.75R$; diameter, $9\frac{1}{2}$ ft.; liquid-cooled engine nacelle;

$$\frac{V}{nD} = 0.65 \left(\frac{V}{nD} \right)_{\text{peak eff.}}$$

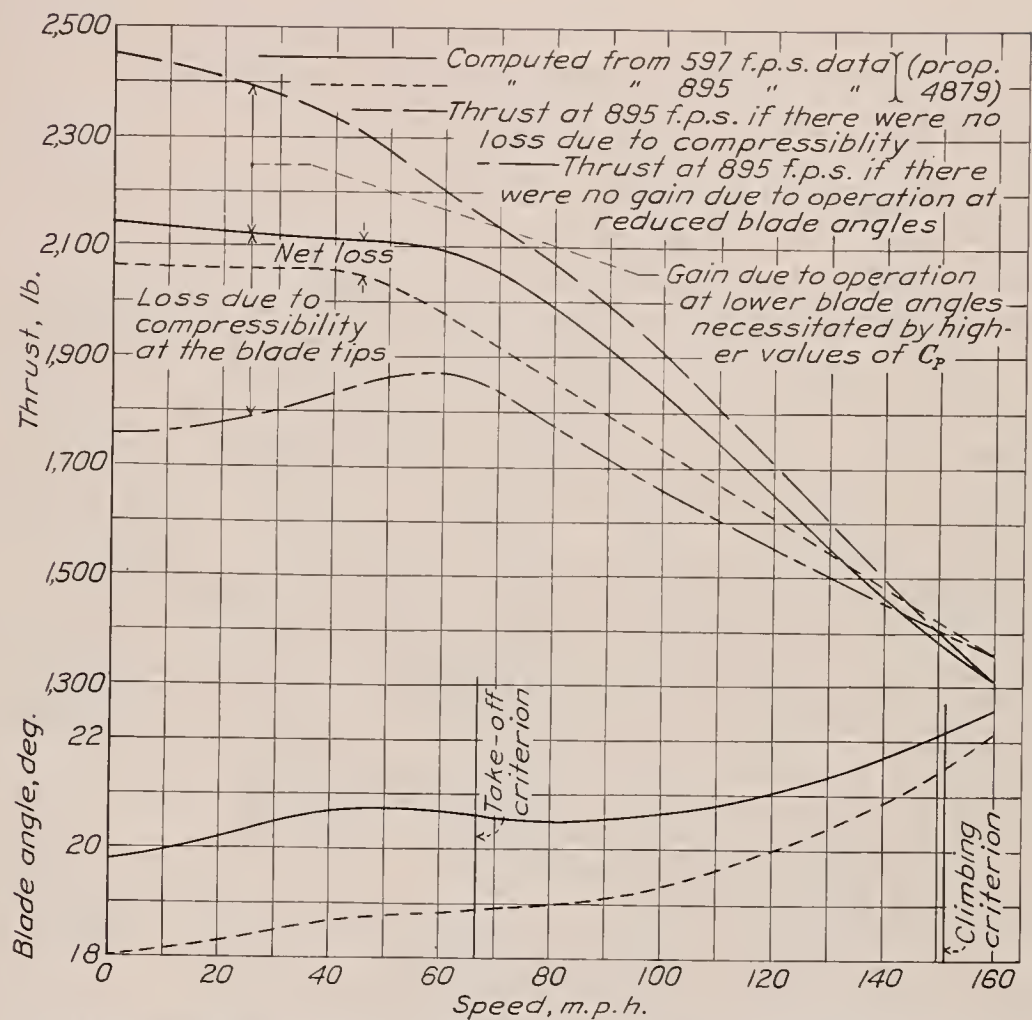


FIGURE 52.—Take-off and climbing thrust computed from low and high tip-speed data for a controllable propeller. Design conditions: 690 b. hp.; propeller speed, 1,500 r. p. m.; air speed, 224 m. p. h.; diameter, 11.35 ft.; C_P , 0.0542.

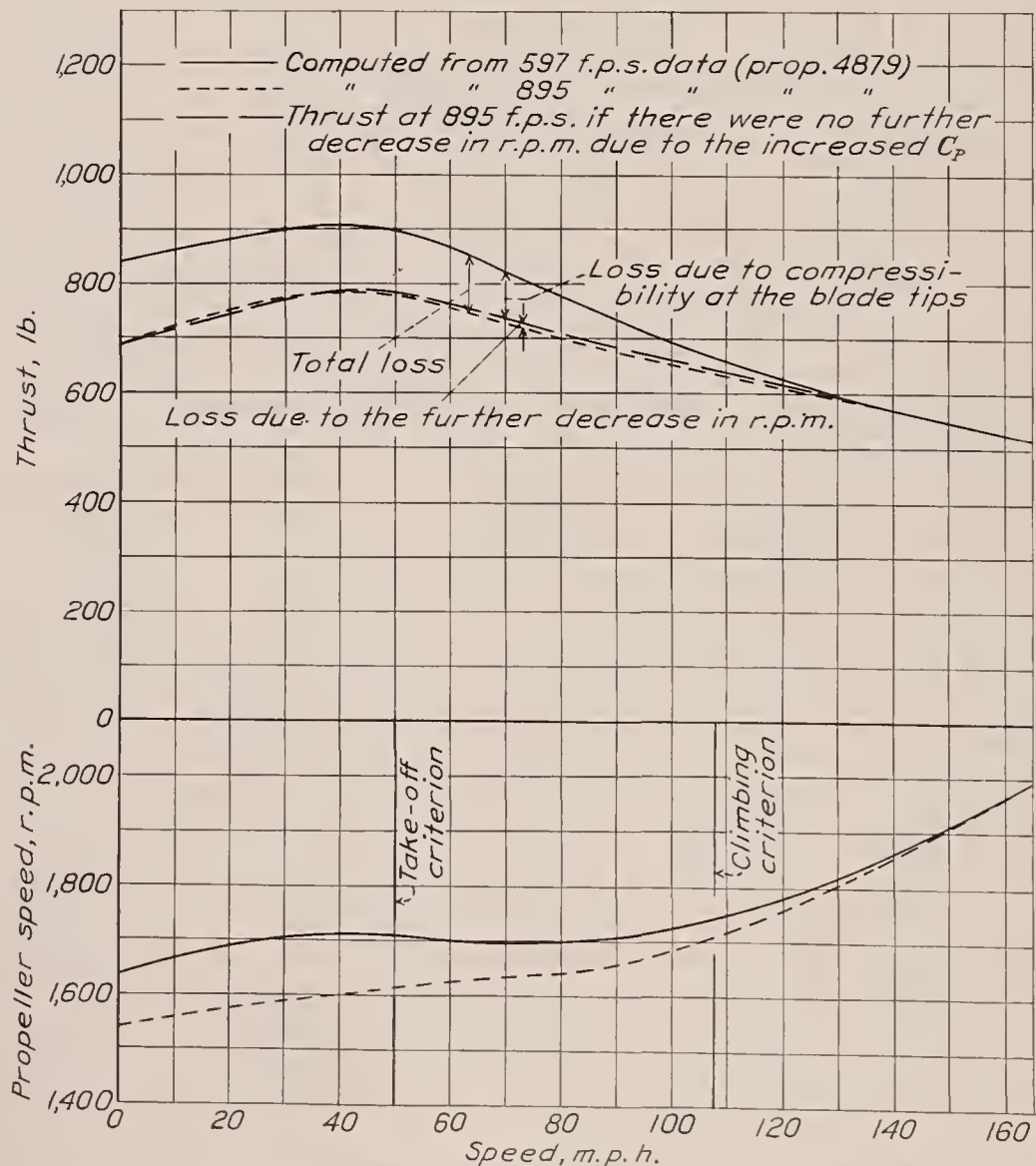


FIGURE 53.—Thrust computed from low and high tip-speed data for a fixed-pitch propeller. Design conditions: 285 b. hp.; propeller speed, 2,000 r. p. m.; air speed, 166 m. p. h.; diameter, 8.6 ft.; blade-angle setting, 20° .

Blade thickness.—Propellers 4877, 4878, and 4879 constitute a series differing only in thickness; they were built for the tip-speed experiments reported in reference 8. The tests reported herein were made at only one blade-angle setting, 20° ; the results are given in figures 44, 45, and 46. Comparisons of the results from the three propellers are given in figures 50 and 51. During the tests it was noticed that the thinnest propeller (4877) fluttered violently at low air speeds, producing a very penetrating noise similar to that associated with supersonic tip speeds. The results very distinctly show the effect of flutter. In order to avoid confusing flutter effects with compressibility effects, the flutter effects will later be discussed as a separate topic.

If the results from propeller 4877 be neglected for the take-off condition on account of flutter, it appears that the thickest propeller (4879) is affected more by compressibility than the medium thick one; in fact, no loss

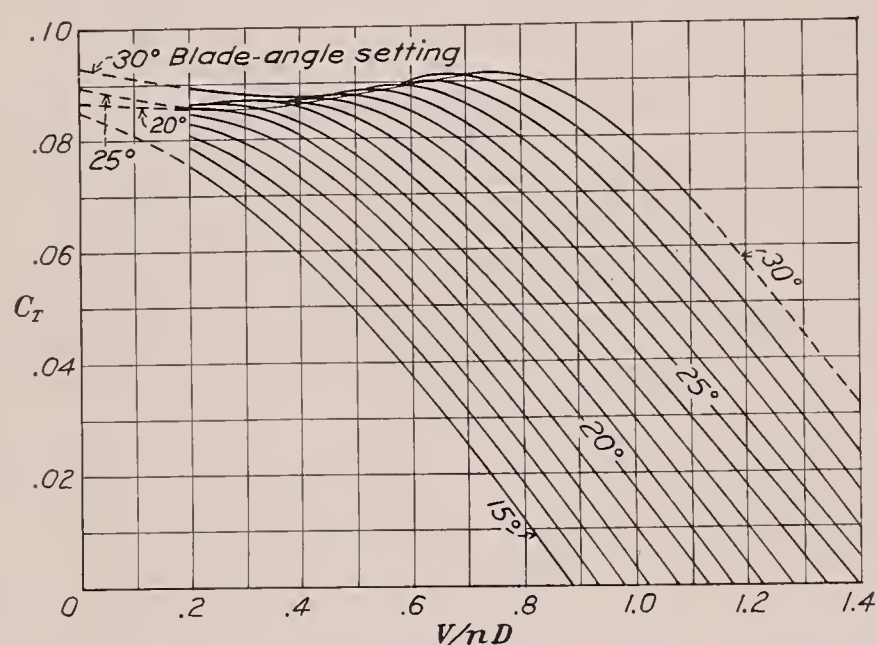


FIGURE 54.—Cross-faired thrust-coefficient curves. Propeller 4879; diameter, $9\frac{1}{2}$ ft.; radial engine nacelle; propeller speed, 1,200 r. p. m.; tip speed, 597 f. p. s.

is evident for propeller 4878. It happens that the low tip-speed efficiency of the thick propeller (4879) is higher than that for propeller 4878, so their efficiencies at high tip speeds become nearly equal. (See figs. 45 and 46.) The results for the climbing condition are nearly identical for all three propellers.

Flutter.—The study of flutter does not come within the scope of this investigation. Flutter did exist, however, in some instances and the results were considerably affected thereby. As previously mentioned, propeller 4877 fluttered violently when operating at low air speeds. It may be noted from figure 44 that the power and the thrust were both increased by perhaps 10 or 20 percent, judging by the shape of the curves. There is no way of isolating compressibility and flutter effects except by assuming that breaks should not occur in the curves if flutter effects are absent. It is quite likely that most of the loss in efficiency observed in figure 50 is due to flutter, amounting to about 18 percent for tip speeds of $0.8V_c$.

An attempt was made to measure the amplitude of blade-torsional vibration of this propeller by the method of measuring blade deflection previously mentioned. The tests indicate that the blade at 0.75 radius was vibrating in torsion through an amplitude of between 1° and 2° when the propeller was turning at 1,600 r. p. m. The amplitude of the tip-section vibration was probably much greater.

EXAMPLES SHOWING THE EFFECT OF COMPRESSIBILITY ON THE TAKE-OFF AND CLIMBING THRUST OF CONTROLLABLE AND FIXED-PITCH PROPELLERS

Were it not for the fact that compressibility influences both the power absorption and the efficiency characteristics of propellers, it would be fairly easy to correct take-off and climbing computations for differences in tip speeds between propeller-test and airplane-operating conditions. The increased power coefficients associated with high tip speeds will necessitate lower blade-angle operation for controllable propellers and

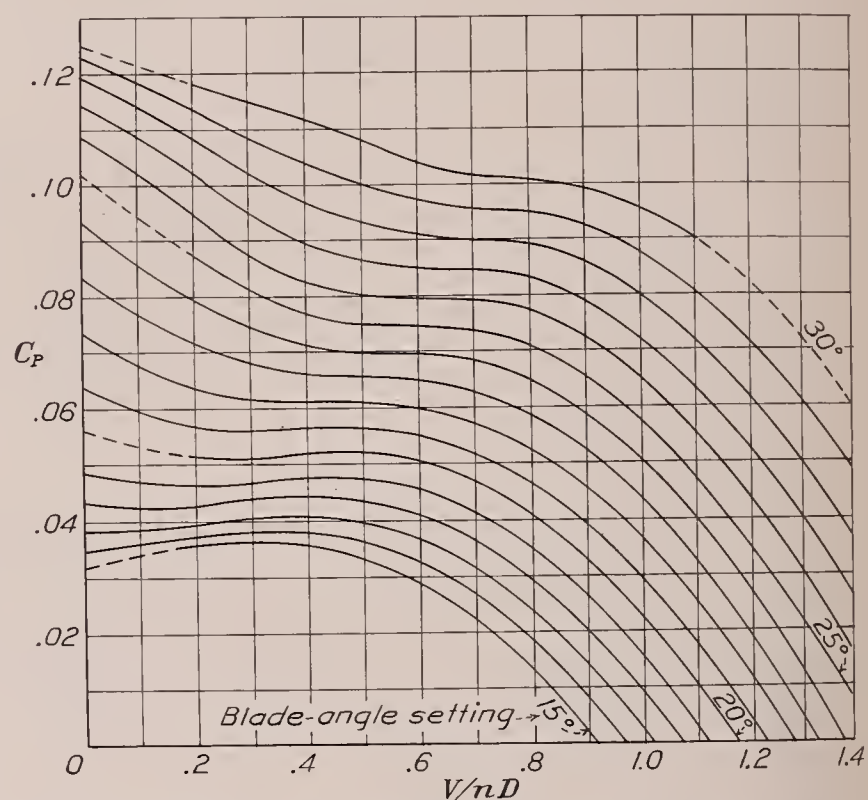


FIGURE 55.—Cross-faired power-coefficient curves. Propeller 4879; diameter, $9\frac{1}{2}$ ft.; radial engine nacelle; propeller speed, 1,200 r. p. m.; tip speed, 597 f. p. s.

the efficiency will be thereby increased; whereas, for the fixed-pitch propeller, the engine speed will be reduced for a given air speed, which affects both the brake horsepower and the propulsive efficiency. Specific examples have been worked out for both types of propeller (figs. 52 and 53) using data from propeller 4879 (radial engine nacelle). These data, which are cross-faired in figures 54 to 57, were used because a greater range of blade-angle settings and tip speeds was covered than with any other propeller.

Controllable propeller.—The example of the controllable propeller (see fig. 52) is based on a 690-horsepower engine turning a propeller at a speed of 1,500 r. p. m. The airplane speed is 224 miles per hour. Thrust curves at the take-off and climbing conditions

are computed from data for tip speeds of 597 and 895 feet per second.

These computations show, for this example, a loss of 5 or 6 percent in take-off thrust due to high tip speeds and show a slight gain at the climbing condition. This loss appears rather insignificant as compared with the 12 or 13 percent loss indicated in figure 26. Another factor, however, enters to explain the difference. The blade angle must be decreased about 2° on account of the higher power coefficients for the tip speed of 895 feet per second, with the result that the efficiency is increased and the over-all loss is thereby reduced.

In order to separate the actual loss due to compressibility from the effects due to changing the blade angle, a fictitious propeller was assumed that could have the blade width changed in order to maintain the power

but the propulsive efficiency is increased for a given air speed owing to the higher operating V/nD . The net loss due to lowered engine speed is small for this example but would have been more had the slope of the take-off thrust curves been steeper.

This example does not give a true picture of the compressibility effects for a particular case because the tip speed was assumed to remain constant even though the propeller speed decreased. The example does give a true picture of the effects of compressibility at any particular air speed if it is assumed that the tip speed is 895 feet per second.

A METHOD OF CORRECTING PROPELLERS FOR THE EFFECT OF COMPRESSIBILITY

A simplified method for correcting propellers for the effect of compressibility is given in the appendix of this report. The method is based on generalized correction factors that were derived from data presented in the report. The use of the correction factors makes it possible to correct, in a few minutes, the thrust of similar propellers for the effect of compressibility.

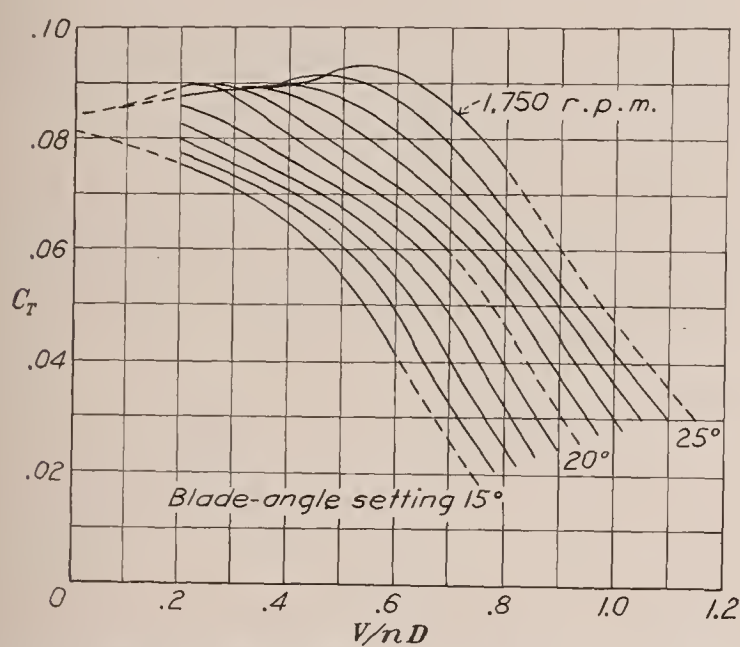


FIGURE 56.—Cross-faired thrust-coefficient curves. Propeller 4879; diameter, $9\frac{1}{2}$ ft.; radial engine nacelle; propeller speed, 1,800 r. p. m.; tip speed, 895 f. p. s.

coefficient constant at the same blade angles as for the low tip-speed computation. The thrust is proportionately corrected for the change in blade width. This computation indicates a loss due to compressibility of from 10 to 18 percent in the take-off range. The curve showing the gain due to operating at lower blade angles is taken as the difference between the loss due to compressibility and the net loss.

Fixed-pitch propeller.—The example of the fixed-pitch propeller was worked out for different conditions from the previous example because a design blade-angle setting of 20° was desired. A 285-horsepower engine turning the propeller at 2,000 r. p. m. and a high speed of 166 miles per hour were assumed.

A total loss of about 13 percent is indicated (fig. 53) for the take-off condition and about 4 percent for the climb. A small part of this loss is due to the lowered engine speed brought about by the higher power coefficients of the data for 895 feet per second. A reduction in engine speed reduces the brake horsepower,

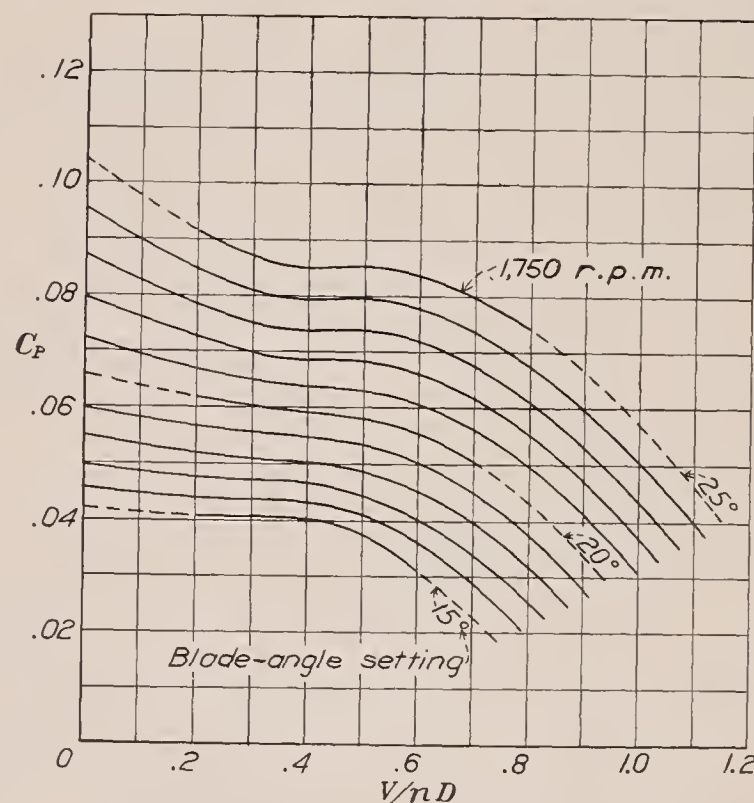


FIGURE 57.—Cross-faired power-coefficient curves. Propeller 4879; diameter, $9\frac{1}{2}$ ft.; radial engine nacelle; propeller speed, 1,800 r. p. m.; tip speed, 895 f. p. s.

CONCLUDING REMARKS

The results of the tests indicate the following conclusions regarding the effect of tip speed:

1. Losses in propulsive efficiency due to compressibility became evident at from 0.5 to 0.7 the velocity of sound for the take-off and climbing conditions of flight, depending upon the propeller shape and the blade-angle setting. As the tip speed increased beyond these values the loss increased rapidly, amounting to more than 20 percent of the thrust power in some instances for tip-speed values of 0.8 the speed of sound.

2. The loss for the take-off condition increased with blade-angle setting up to a value of about 20° for a given tip-speed value. At higher blade angles the loss diminished.

3. The loss for the climbing condition increased with blade-angle setting for a given tip speed up to a value of about 25° , beyond which it decreased. Also, the losses appeared at lower tip speeds as the blade angle was increased.

4. Compressibility affected the propeller of R. A. F. 6 section to a greater extent than it did the propeller of Clark Y section; but, since the R. A. F. 6 propeller had a higher take-off efficiency at low tip speeds, the efficiencies nearly equalized at high tip speeds.

5. Compressibility affected standard-width blades to a greater extent than it did extremely wide blades for the take-off condition; but, since the standard-width blades had a higher efficiency at low tip speeds, the efficiencies nearly equalized at high tip speeds. The standard-width blades had an even higher efficiency at high tip speeds for the climbing condition.

6. The loss for the take-off condition due to compressibility was greater for a thick propeller than for a thin one; but, since the thick propeller had a higher efficiency at low tip speeds, the efficiency nearly equal-

ized at high tip speeds. The effect of thickness was negligible for the climbing condition.

7. There was a marked tendency for the thrust and power coefficients to increase with tip speed, even before any loss in the efficiency was detected.

8. The loss in efficiency for controllable propellers due to compressibility was partly regained by the lower blade-angle operation necessitated by the higher power coefficients.

9. The loss in efficiency for fixed-pitch propellers due to compressibility was further increased by a loss in engine speed and power caused by the higher power coefficients.

10. Comparisons of propellers having different blade sections, blade widths, and blade thicknesses, made on the basis of data for propellers operating at low tip speeds, are likely to be misleading, inasmuch as compressibility effects appreciably modify and, in many cases, tend to equalize any differences noted at the low V/nD range of operation.

LANGLEY MEMORIAL AERONAUTICAL LABORATORY,
NATIONAL ADVISORY COMMITTEE FOR AERONAUTICS,
LANGLEY FIELD, VA., *May 18, 1938.*

APPENDIX

A METHOD OF CORRECTING PROPELLER CHARACTERISTICS FOR THE EFFECT OF COMPRESSIBILITY AT TIP SPEEDS BELOW 0.9 THE SPEED OF SOUND

The material presented in the body of the present report is not in a form convenient to use in correcting low-tip-speed propeller characteristics for compressibility effects encountered when operating at high tip speeds. The data are given in a basic form and additional curves are included to show certain trends. In order to make practical use of the material, it is necessary to devise a method whereby the characteristics of any propeller can be readily corrected for compressibility effects with reasonable certainty.

A number of factors associated with the problem make it extremely difficult, if not impossible, to devise any set of formulas or curves by which the characteristics of any propeller may be corrected. Differences in blade section, width, thickness, plan form, and pitch distribution account for differences in compressibility effects, so it is considered advisable to confine the correction factors to specific propellers, at least for the present. When sufficient data are accumulated, it may be possible to formulate a more generalized method that can be applied to any propeller, regardless of shape.

The present method of correcting propeller characteristics for compressibility effects is based on correction factors applied to the thrust and torque coefficients of either fixed-pitch or controllable propellers. The correction factors are presented in curve form for several propellers in figures 58 to 61. It is pointed out in the present report and elsewhere that the angle of attack of a blade element, or the lift coefficient, is a major parameter determining the magnitude of compressibility effects. Neither the angle of attack nor the lift coefficient can be readily determined for propellers but, inasmuch as the thrust coefficient of the propeller is closely related to the lift coefficients of the sections, the thrust coefficient is considered to be a good substitute. Through the use of the thrust coefficient as a correction parameter, the blade angle and V/nD are dispensed with so that the method is generalized to the extent that it can be applied to any blade-angle setting with reasonable accuracy.

The use of the thrust coefficient as a correction parameter has other advantages. Propellers having different

numbers of blades may be corrected without additional considerations because the thrust coefficient at the stall is nearly proportional to the number of blades.

The normal stall of a propeller is readily apparent; the thrust-coefficient curves break in much the same manner as do lift-coefficient curves for airfoils. The flow over the airfoil sections changes; the peak of the negative pressures is eliminated and the corresponding induced velocities are materially reduced with the result that the effect of compressibility is greatly modified and uncertain. For this reason, the propeller correction factor used for the unstalled portion of the operating range should not be used for the stalled portion. The use of the thrust coefficient as a correction parameter draws attention to the operating range.

The correction factors given in figures 58 to 61 are in the form of ratios of C_T , C_P , and η at high tip speeds to those at low tip speeds (taken at approximately 0.5 the speed of sound). Individual curves are given for constant values of $C_T/C_{T(at\ stall)}$. These correction curves were obtained by plotting the data given in the body of the report and cross-fairing the resulting curves. It may be noted that the curves have been extrapolated from approximately 0.8 or 0.85 to 0.9 the speed of sound, in order to make the method more useful; consequently, these portions of the curves may be subject to some error.

USE OF THE CORRECTION FACTORS

Controllable propellers.—The power coefficient for operation is determined by the air density, the engine power, the propeller diameter, and the rotational speed. In view of the fact that the power coefficient increases with tip speed, it is necessary first to determine the values corresponding to the low-speed data because from these data the blade angles and the thrust are determined. These values are determined by dividing the design power coefficient by the ratios of the high-tip-speed to low-tip-speed power coefficients corresponding to the appropriate values of thrust coefficient and then by reading the blade angles and low-tip-speed thrust coefficients from the propeller curves. It is then necessary only to correct the coefficients for the effect of compressibility by the use of the factors to establish the operating values.

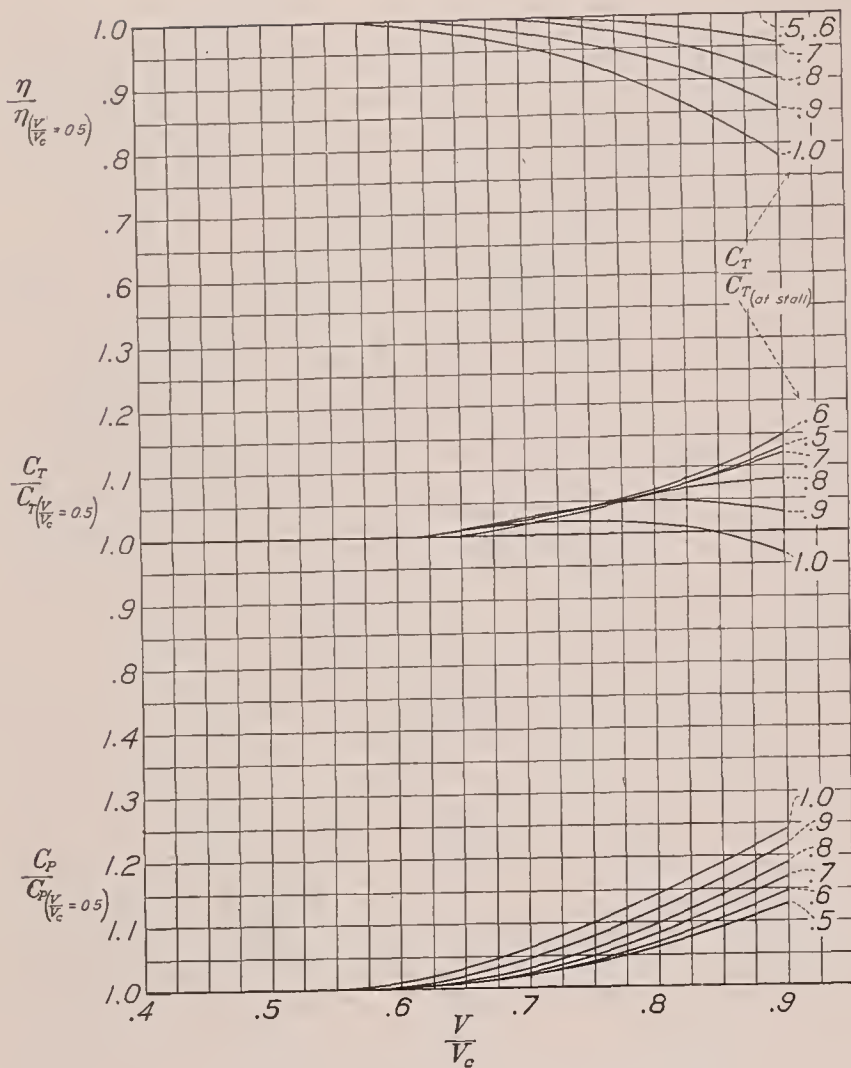


FIGURE 58.—Correction factors for propeller 5868-9.

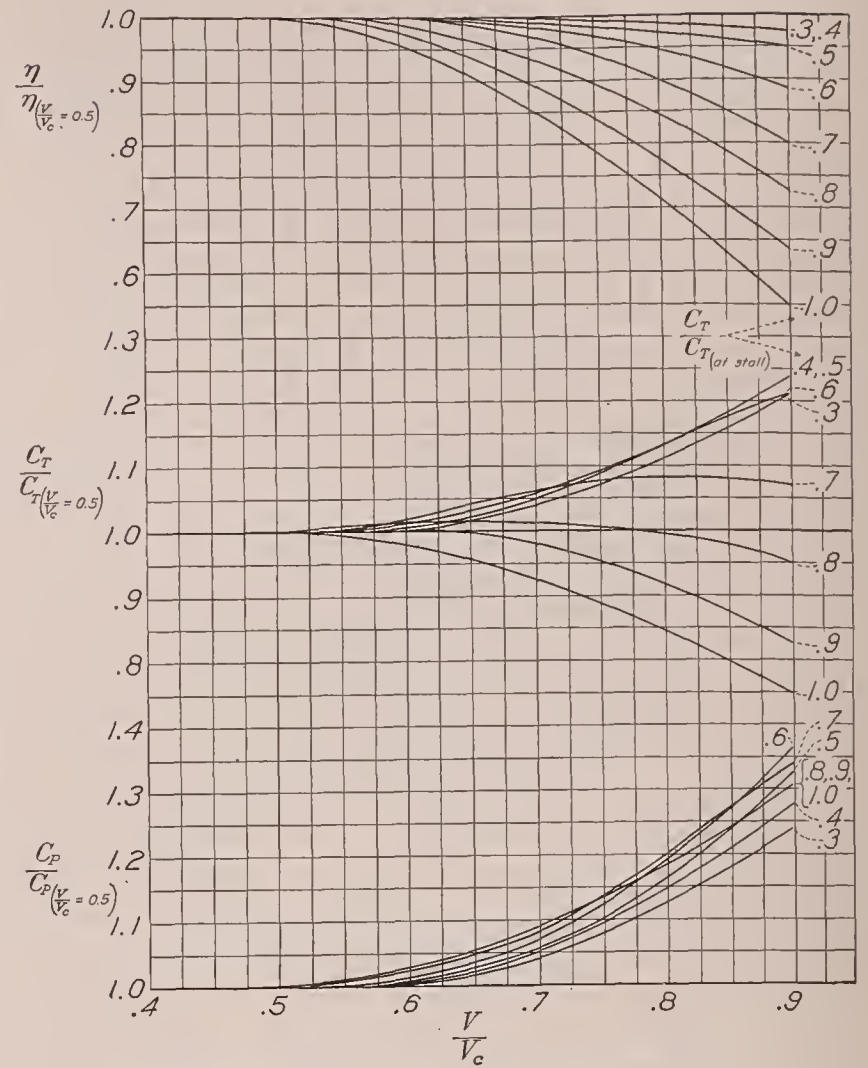


FIGURE 59.—Correction factors for propeller 5868-R6.

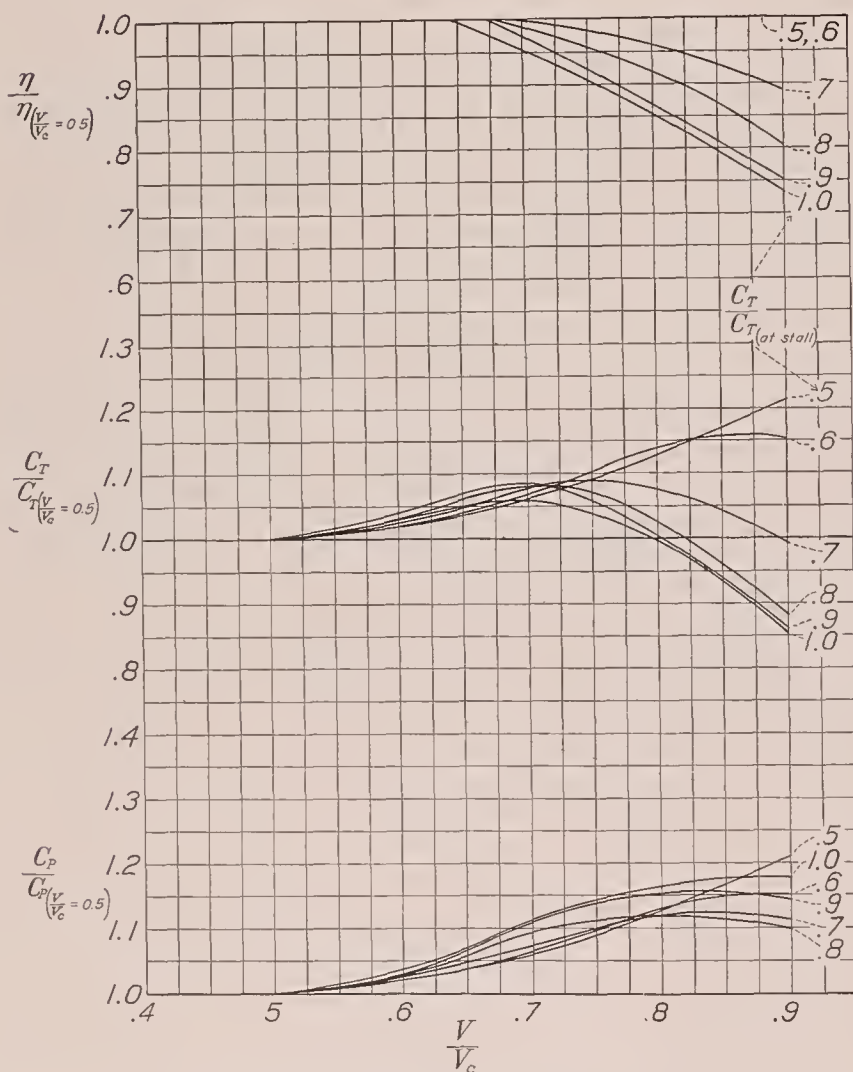


FIGURE 60.—Correction factors for propeller 4879.

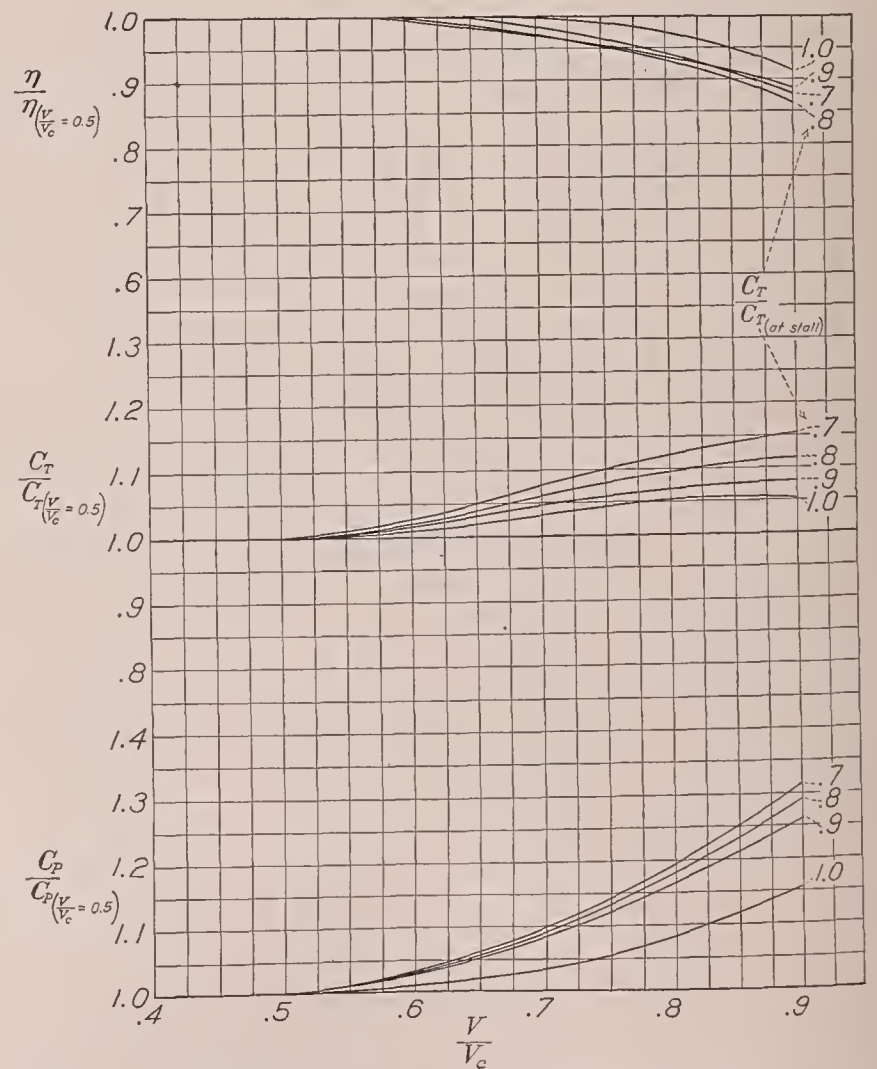


FIGURE 61.—Correction factors for propellers 4877 and 4878.

Several examples have been worked to illustrate the process and, at the same time, to show the magnitude of the compressibility effects for typical airplane installations. Example 1 is a check upon the method for controllable propellers presented in the body of the report. The computations are given in table I (a) and the final curves are shown in figure 62. The following series of operations is completed after the propeller has been designed or selected in the usual manner. (See table I (a).)

1. In column 1, values of V/nD are assumed.
2. The blade angle β_1 is read from the power-coefficient curves at low tip speeds (fig. 55) corresponding to the design C_{P_1} of 0.0542.

3. The thrust coefficient C_{T_1} is read from figure 54 for different values of β_1 .

4. $C_{T_1}/C_{T(at\ stall)}$ is computed from the values given in column 3. The value of C_T at the stall is taken as 0.086. A high degree of accuracy is not necessary because the results are not used directly in the computations.

5. Power correction factors are read from figure 60 for values of $C_{T_1}/C_{T(at\ stall)}$ given in column 4 and for a value of V/V_c of 0.8.

6. The design power coefficient, $C_{P_1}=0.0542$, is

divided by the ratio $\frac{C_P}{C_P(\frac{V}{V_c}=0.5)} = \frac{C_{P_1}}{C_{P_2}}$ given in column

5 in order to determine the corresponding power coefficient C_{P_2} for the low-tip-speed data being used.

7. The blade angle β_2 corresponding to C_{P_2} is read from figure 55.

8. The thrust coefficient C_{T_2} corresponding to β_2 is read from figure 54.

At this stage of the correction the low-tip-speed data are fitted to the design requirements of the engine and propeller. It is now necessary to correct the thrust data for the higher tip speed of operation, namely $0.8V_c$.

9. The correction factor $\frac{C_T}{C_T(\frac{V}{V_c}=0.5)} = \frac{C_{T_3}}{C_{T_2}}$ is read

from figure 60 for values of $\frac{C_{T_1}}{C_{T(at\ stall)}}$ given in column 4 and a value of V/V_c of 0.8.

10. The corrected thrust coefficient C_{T_3} is obtained by multiplying C_{T_2} by the ratio C_{T_3}/C_{T_2} given in column 9.

11. The corrected thrust is obtained by multiplying C_{T_3} by the constant $\rho n^2 D^4$.

12. The air speed in miles per hour is obtained by

multiplying the V/nD given in column 1 by the constant $ND/88$, where N is the propeller rotational speed in r. p. m.

No computation is made for the correction of the low-speed power coefficient C_{P_2} because it is obvious that multiplying C_{P_2} by C_{P_1}/C_{P_2} results in C_{P_1} , the design power coefficient. It may be noted that the computations were carried through for the stalled portion of the operating range even though the method strictly should not be applied there. The error in this case is probably small since there is no evidence from any of the data that a sudden change in the effects of compressibility occurs at the stall.

From figure 62 it may be noted that the curve for the thrust, corrected by means of the charts, checks the thrust curve computed from the 895-feet-per-second data only for the low-speed range. The disagreement at the climbing part of the range is attributed to the fact that the charts are derived by averaging all the available data for this propeller; whereas the 895-feet-per-second curve is determined essentially by the one test at 20° blade angle, which was extrapolated for V/nD values higher than 0.7. Since the thrust curve derived by the chart method is based on more test points, it is considered to be the more accurate of the two.

In example 2, a 3-blade 5868-9 propeller is selected from the data given in reference 10 for a radial engine nacelle, and the thrust is corrected by the present method.

Given—

Engine----- 1,000 horsepower.
Engine speed----- 2,375 r. p. m., sea-level operation.
Air speed----- 283 m. p. h.

Selection of the propeller—Design A:

$$C_s = \frac{0.638 \times \text{m. p. h.}}{\text{hp.}^{1/5} \times N^{2/5}} = \frac{0.638 \times 283}{3.98 \times 22.35} = 2.03$$

From figure 13 of reference 10,

$$\frac{V}{nD} = 1.3$$

$$\eta = 0.86$$

Then

$$D = \frac{88 \times \text{m. p. h.}}{N \left(\frac{V}{nD} \right)_{\text{design}}} = \frac{88 \times 283}{2,375 \times 1.3} = 8.06 \text{ ft.}$$

Tip speed at zero forward speed is 1,000 f. p. s.

Sound speed for standard conditions is 1,120 f. p. s.

$$\frac{V}{V_c} = 0.895$$

$$C_{P(\text{design})} = \frac{\text{hp.} \times 550}{\rho n^3 D^5} = 0.1097$$

Computation of thrust and correction for compressibility effects:

Table I (b), identical in form to table I (a), is filled in, using data taken from figure 10 of reference 10 and figure 58 of the present report. The corrected thrust and blade angles are plotted in figure 62, along with the

Any errors incidental to this extrapolation will have a negligible effect on the take-off run, provided that correct thrust values are obtained over the latter part of the take-off run.

It should be pointed out that the propeller of design A was selected from a C_s chart derived from low-tip-speed

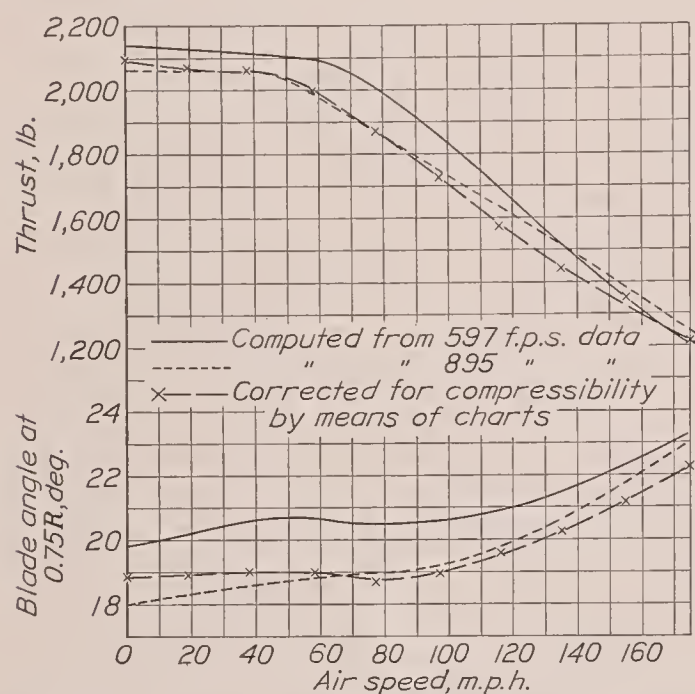


FIGURE 62.—Example 1 showing the uncorrected and corrected thrust and blade angles for an airplane equipped with propeller 4879 (controllable).

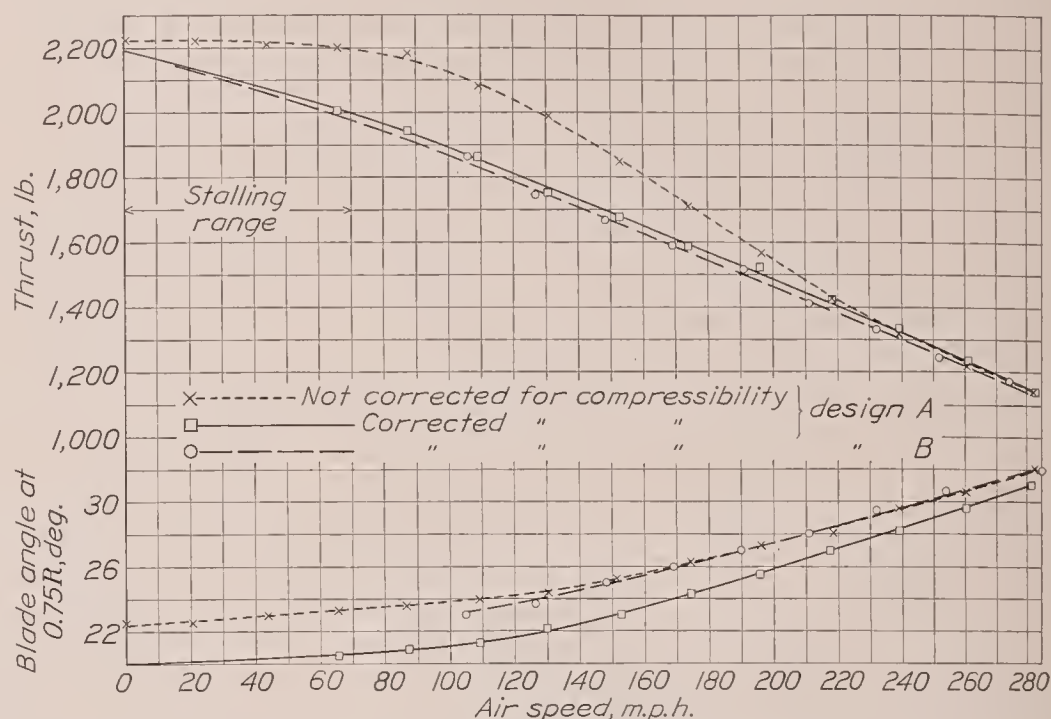


FIGURE 63.—Example 2 showing the uncorrected and corrected thrust and blade angles for an airplane equipped with propeller 5868-9 (controllable).

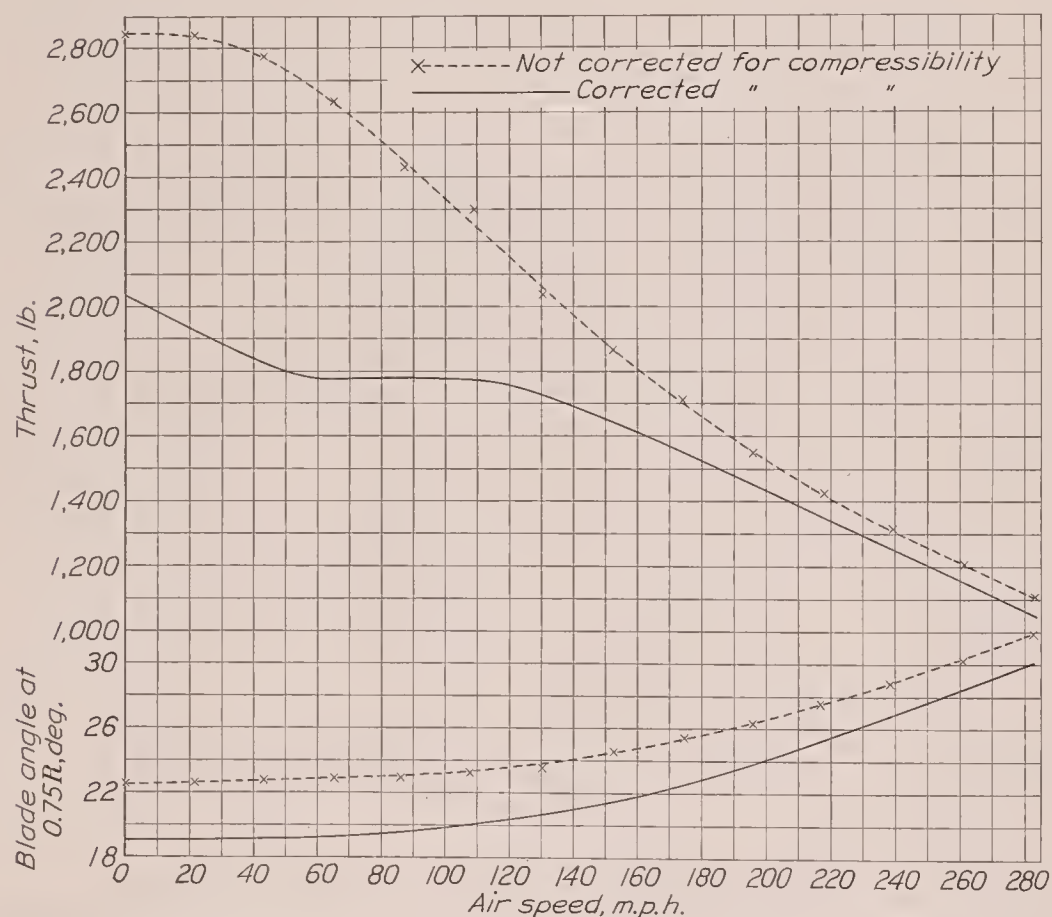


FIGURE 64.—Example 3 showing the uncorrected and corrected thrust and blade angles for an airplane equipped with propeller 5868-R6 (controllable).

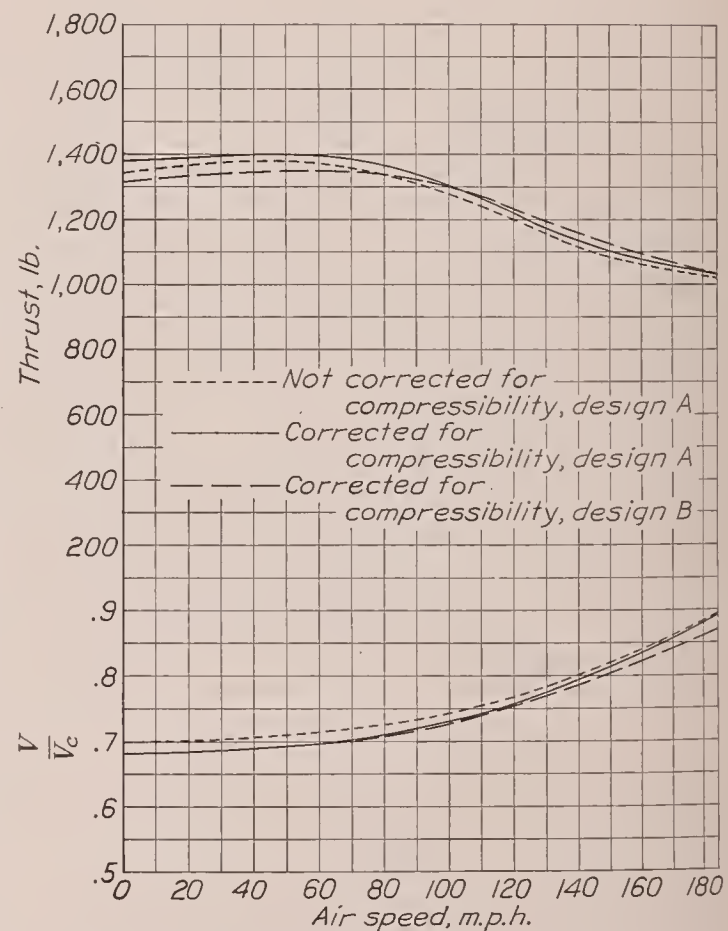


FIGURE 65.—Example 4 showing the uncorrected and corrected thrust and tip-speed ratios for an airplane equipped with propeller 5868-9 (fixed pitch).

uncorrected values obtained directly from the low-tip-speed data. It may be noted that the thrust curve is extrapolated to zero air speed, assuming that the effect of compressibility decreases as the angle of attack of the blade elements increases beyond the normal stall.

data; consequently, the design itself is slightly in error. In the use of the C_s chart mentioned, it is assumed that the propeller will absorb the power under certain specified conditions. Actually, the propeller will absorb more power at the tip speed of operation, so the blade

angle is reduced to make up for the difference. This result means that design A is a "compromise" design, because the diameter is slightly larger than it would be if there were no compressibility effects. If it were desired to eliminate the compromise feature, the design engine power could be reduced to correspond to the low-tip-speed data and the propeller could be selected on that basis. The following computations indicate the general procedure.

Selection of propeller—Design B:

$$\frac{C_P}{C_P\left(\frac{V}{V_c}=0.5\right)}=1.13 \text{ for high speed}$$

$$\text{hp.}_{(design)}=\frac{1,000}{1.13}=885$$

$$C_s=2.08$$

$$\frac{V}{nD}=1.34$$

$$D=7.83 \text{ feet}$$

$$\text{Tip speed}=972 \text{ f. p. s.}$$

$$V/V_c=0.867$$

$$C_{P(design)}=\frac{550 \times 1,000}{\rho \times \left(\frac{2,375}{60}\right)^3 \times (7.83)^5}=0.1263$$

The computation of thrust and correction for compressibility effects are carried through in the same manner as for design A. No table is given but the results are plotted in figure 63. The thrust for design B is slightly less than for design A owing to the smaller diameter, even though the compressibility correction is less. No loss in high-speed thrust is evident for the compromise design A. It appears from this example that it is scarcely worth while to select propellers on the basis of corrected power unless the propeller diameter is too large on account of other considerations.

In example 3, a 3-blade 5868-R6 propeller is selected for the same requirements as given in example 2. In order to maintain the same tip speed as for design A, the same diameter propeller was assumed, although this size may not be the most efficient for high speed. Thrust computations are given in table I (c); the material is taken from figure 9 of reference 11 and figure 59 of this report. It happens that the test-body conditions were different for the 5868-9 and the 5868-R6 propellers but the body effects are small as compared with the compressibility effects. The results of the computations are given in figure 64. The loss in thrust due to com-

pressibility for this example is quite startling, amounting to about one-third of the uncorrected thrust at low tip speeds. Examples 2 and 3 illustrate the importance of compressibility when comparing propellers of different section. The R. A. F. 6 section is superior to the Clark Y section at low tip speeds but at high tip speeds the relative merits are reversed.

Fixed-pitch propellers.—The method of correcting fixed-pitch propellers is slightly more involved than for controllable propellers because the tip-speed correction changes with rotational speed. Unfortunately, each so depends upon the other that, in order to obtain fairly exact results, a series of approximations is necessary. In the following examples the number of approximations has been minimized as far as is consistent with the importance of the corrections involved.

Example 4 illustrates the method of correcting fixed-pitch propellers used with unsupercharged engines.

Given:

Engine..... 600 horsepower.

Engine speed..... 2,375 r. p. m., sea-level operation.

Air speed..... 185 m. p. h.

Selection or design of propeller 5868-9 having three blades to be used with a radial engine nacelle:

Design A:

$$C_s=1.47$$

From figure 13 (reference 10),

$$\frac{V}{nD}=0.85$$

$$\beta=22.3^\circ$$

Then

$$D=8.07 \text{ ft.}$$

$$C_{P_1}=0.0653 \text{ (design value for high speed).}$$

$$\text{Tip speed}=1,000 \text{ f. p. s.}$$

$$\frac{V}{V_c}=0.895.$$

$$C_{T_1}=0.065 \text{ (design value for high speed).}$$

$$C_{T(at stall)}=0.140.$$

$$\frac{C_{T_1}}{C_{T(at stall)}}=0.465.$$

$$\frac{C_P}{C_P\left(\frac{V}{V_c}=0.5\right)}=1.115 \text{ (from fig. 58).}$$

This propeller will absorb 1.115×600 hp. or 670 hp. at high speed. Either the diameter or the blade angle must be reduced to absorb the specified 600 hp. Following the method of reducing the diameter, a new design is made using $\frac{600}{1.115}=538$ hp. This computation re-

sults in the following characteristics:

$$C_s = 1.503$$

$$\frac{V}{nD} = 0.9$$

$$D = 7.62 \text{ ft.}$$

$$\frac{V}{V_c} = 0.847$$

$$\frac{C_P}{C_P\left(\frac{V}{V_c}=0.5\right)} = 1.085$$

In view of the change in the power correction factor incurred by the reduced diameter and tip speed, this propeller will only absorb $538 \times 1.085 = 585$ hp. A third approximation using the average of the first and second values of $\frac{C_P}{C_P\left(\frac{V}{V_c}=0.5\right)}$ should result in approximately the

correct answer; $\frac{1.115 + 1.085}{2} = 1.100$. The third approximation results in the following characteristics designated "design B":

$$\text{hp.} = \frac{600}{1.1} = 545 \text{ (for design purpose).}$$

$$C_s = 1.497$$

$$\frac{V}{nD} = 0.87$$

$$\beta = 22.7^\circ$$

$$D = 7.88 \text{ ft.}$$

$$\text{Tip speed} = 978 \text{ f. p. s.}$$

$$\frac{V}{V_c} = 0.873$$

$$\frac{C_P}{C_P\left(\frac{V}{V_c}=0.5\right)} = 1.1 \text{ (check).}$$

In table II the thrust is computed for design B according to the following procedure:

1. In column 1, values of V/nD are assumed and, in addition, the design value for high speed is included.

2. From figure 10 (reference 10), the low-tip-speed power coefficients C_{P_2} are read following the line for a blade angle of 22.7° .

3. The corresponding thrust coefficient, C_{T_2} , is also read from figure 10 of reference 10.

4. The ratio N/N_{max} is computed from the relation $\frac{N}{N_{max}} = \sqrt{\frac{C_{P_2(at \text{ high speed})}}{C_{P_2}}}$, assuming that the torque

remains constant for small changes in rotational speed. This condition is substantially true for unsupercharged engines.

5. The ratio V/V_c is equal to $\frac{N}{N_{max}} \times 0.873$.

6. The ratio $\frac{C_{T_2}}{C_{T(at \text{ stall})}}$ is computed using

$$C_{T(at \text{ stall})} = 0.140.$$

7. $\frac{C_P}{C_P\left(\frac{V}{V_c}=0.5\right)}$ is read from figure 58 for different

values of V/V_c and $\frac{C_{T_2}}{C_{T(at \text{ stall})}}$.

8. $\frac{C_T}{C_T\left(\frac{V}{V_c}=0.5\right)}$ is also read from figure 58.

9. Corrected values of power coefficient C_{P_3} are computed, $C_{P_2} \times \frac{C_P}{C_P\left(\frac{V}{V_c}=0.5\right)} = C_{P_3}$.

10. Corrected values of thrust coefficient C_{T_3} are computed in a similar manner.

11. Corrected values of N/N_{max} are computed using C_{P_3} .

12. Values of V/V_{max} are computed from the rela-

$$\text{tion } \frac{V}{V_{max}} = \frac{\left(\frac{V}{nD}\right)N}{\left(\frac{V}{nD}\right)_{max}N_{max}}$$

13. The air speed is computed from the relation V/V_{max} , knowing V_{max} .

14. The thrust is computed from the relation $T = C_T \frac{C_{P_3(at \text{ high speed})}}{C_{P_3}} \times K$, where $K = \rho n^2 D^4$.

If the method of reducing the blade angle is followed, to offset the increase in power coefficients from low to high tip speed, design A is used directly but it is necessary to determine the blade-angle reduction. The value of C_{P_1} is divided by $\frac{C_P}{C_P\left(\frac{V}{V_c}=0.5\right)}$ to determine the

C_{P_2} corresponding to the low-tip-speed data; $\frac{0.0653}{1.115} = 0.0585$. Unfortunately, this value is only the first approximation because the low-tip-speed thrust coefficient is likewise reduced, changing the value of $\frac{C_{T_1}}{C_{T(at \text{ stall})}}$ to $\frac{0.059}{0.14}$ or 0.42. The value of $\frac{C_P}{C_P\left(\frac{V}{V_c}=0.5\right)}$

then becomes 1.105. The second approximate value of power coefficient becomes $\frac{0.653}{1.105} = 0.0592$. This C_{P_2} defines the blade angle so the C_{P_2} and C_{T_2} can be read from figure 10 (reference 10) for different values of V/nD . The corrected thrust is then computed in the manner outlined in table II. No table is included for design A

computations but the thrust is given in figure 65 together with those for design B and the uncorrected thrust.

It may be noted from figure 65 that little, if any, loss in thrust due to compressibility is evident for this example. The explanation lies in the fact that the tip speed drops to about 0.7 the speed of sound in the take-off range owing to the decrease in engine speed. It may be noted from figure 58 that a maximum of only 4 percent in efficiency is lost for this tip speed. It appears from this example that computations for correcting the thrust of fixed-pitch propellers may not be worth while in many instances. A preliminary estimate of the tip speed in the take-off range together with a reference to the correction factors would indicate the importance of further computations. It probably is desirable in any case to make allowances in the design of propellers for differences in the power coefficient for test data from low and high tip speeds in order to determine the diameter and the blade angle.

REFERENCES

1. Briggs, L. J., Hull, G. F., and Dryden, H. L.: Aerodynamic Characteristics of Airfoils at High Speeds. T. R. No. 207, N. A. C. A., 1925.
2. Stack, John: The N. A. C. A. High-Speed Wind Tunnel and Tests of Six Propeller Sections. T. R. No. 463, N. A. C. A., 1933.
3. Briggs, L. J., and Dryden, H. L.: Aerodynamic Characteristics of Twenty-Four Airfoils at High Speeds. T. R. No. 319, N. A. C. A., 1929.
4. Stack, John: The Compressibility Burble. T. N. No. 543, N. A. C. A., 1935.
5. Douglas, G. P., and Perring, W. G. A.: Wind Tunnel Tests with High Tip Speed Airscrews.
 - (a) The Characteristics of the Aerofoil Section R. A. F. 31a at High Tip Speeds. R. & M. No. 1086, British A. R. C., 1927.
 - (b) The Characteristics of a Bi-Convex Aerofoil at High Speeds. R. & M. No. 1091, British A. R. C., 1927.
 - (c) The Characteristics of Bi-Convex No. 2 Aerofoil Section at High Speeds. R. & M. No. 1123, British A. R. C., 1928.
 - (d) The Characteristics of a Conventional Airscrew Section, Aerofoil R. & M. No. 322, No. 3, at High Speeds. R. & M. No. 1124, British A. R. C., 1928.
 - (e) Some Experiments upon an Airscrew of Conventional Blade Section, Aerofoil R. & M. No. 322, No. 3, at High Speeds. R. & M. No. 1174, British A. R. C., 1928.
 - (f) The Characteristics of a Conventional Airscrew Section 0.082c Thick and of R. A. F. 27 and R. A. F. 28. R. & M. No. 1198, British A. R. C., 1929.
6. Hartshorn, A. S., and Douglas, G. P.: Wind Tunnel Tests on High Tip Speed Airscrews. Further Experiments on Scale Effect. R. & M. No. 1417, British A. R. C., 1932.
7. Jennings, W. G., and Ormerod, A.: Full Scale Experiments on High Tip Speed Airscrews. The Effect of Thickness of Section on Airscrew Performance. R. & M. No. 1339, British A. R. C., 1931.
8. Wood, Donald H.: Full-Scale Tests of Metal Propellers at High Tip Speeds. T. R. No. 375, N. A. C. A., 1931.
9. Weick, Fred E., and Wood, Donald H.: The Twenty-Foot Propeller Research Tunnel of the National Advisory Committee for Aeronautics. T. R. No. 300, N. A. C. A., 1928.
10. Biermann, David, and Hartman, Edwin P.: Tests of Five Full-Scale Propellers in the Presence of a Radial and a Liquid-Cooled Engine Nacelle, Including Tests of Two Spinners. T. R. No. 642, N. A. C. A., 1938.
11. Biermann, David, and Hartman, Edwin P.: The Aerodynamic Characteristics of Six Full-Scale Propellers Having Different Airfoil Sections. T. R. No. 650, N. A. C. A., 1939.

TABLE I (a)
EXAMPLE 1, CONTROLLABLE PROPELLER

1	2	3	4	5	6	7	8	9	10	11	12	13
$\frac{V}{nD}$	β_1 for $C_{P1}=0.0542$ (deg.)	C_{T1} for β_1	$\frac{C_{T1}}{C_T (at stall)}$	$\frac{C_P}{C_P \left(\frac{V}{V_c}=0.5\right)} = \frac{C_{P1}}{C_{P2}}$	C_{P2}	β_2 for C_{P2} (deg.)	C_{T2} for β_2	$\frac{C_T}{C_T \left(\frac{V}{V_c}=0.5\right)} = \frac{C_{T3}}{C_{T2}}$	C_{T3}	Thrust (lb.)	Air speed (m.p.h.)	Remarks
0	19.9	0.0870	1.01	1.165	0.0465	18.5	0.0860	0.995	0.0855	2,100	0	Blades stalled.
.1	20.2	.0860	1.00	1.165	.0465	18.9	.0850	.995	.0845	2,075	19.3	
.2	20.7	.0860	1.00	1.165	.0465	19.0	.0845	.995	.0840	2,060	38.8	
.3	20.7	.0855	1.00	1.165	.0465	19.0	.0820	.995	.0815	2,000	58.2	Blades not stalled.
.4	20.6	.0822	.96	1.160	.0467	18.7	.0760	1.000	.0760	1,870	77.5	
.5	20.6	.0755	.88	1.150	.0471	19.0	.0695	1.010	.0703	1,727	97.0	
.6	20.9	.0680	.79	1.120	.0483	19.6	.0625	1.025	.0642	1,575	116.5	
.7	21.6	.0620	.73	1.120	.0483	20.3	.0555	1.060	.0589	1,445	135.5	
.8	22.3	.0550	.64	1.130	.0479	21.2	.0490	1.120	.0550	1,350	155.5	
.9	23.3	.0480	.56	1.130	.0479	22.3	.0435	1.130	.0493	1,215	175.0	
1.0	24.6	.0450	.53	1.130	.0479	23.7	.0395	1.130	.0446	1,095	194.0	

TABLE I (b)
EXAMPLE 2, CONTROLLABLE PROPELLER, DESIGN A

1	2	3	4	5	6	7	8	9	10	11	12	13
$\frac{V}{nD}$	β_1 for $C_{P1}=0.1097$ (deg.)	C_{T1} for β_1	$\frac{C_{T1}}{C_T (at stall)}$	$\frac{C_P}{C_P \left(\frac{V}{V_c}=0.5\right)} = \frac{C_{P1}}{C_{P2}}$	C_{P2}	β_2 for C_{P2} (deg.)	C_{T2} for β_2	$\frac{C_T}{C_T \left(\frac{V}{V_c}=0.5\right)} = \frac{C_{T3}}{C_{T2}}$	C_{T3}	Thrust (lb.)	Air speed (m. p. h.)	Remarks
0	22.5	0.1420									0	Blades stalled.
.1	22.5	.1417									21.8	
.2	23.0	.1410									43.6	
.3	23.3	.1405	1.00	1.240	0.0884	20.5	0.1320	0.970	0.1280	2,003	65.3	
.4	23.5	.1395	1.00	1.240	.0884	20.8	.1280	.970	.1240	1,945	87.1	Blades not stalled.
.5	24.0	.1330	.95	1.230	.0892	21.3	.1190	1.000	.1190	1,865	108.8	
.6	24.5	.1270	.91	1.220	.0900	22.2	.1095	1.020	.1115	1,750	130.5	
.7	25.3	.1180	.84	1.200	.0914	23.0	.1010	1.060	.1070	1,678	152.5	
.8	26.1	.1090	.78	1.185	.0925	24.3	.0930	1.090	.1012	1,588	174.0	
.9	27.3	.1000	.71	1.170	.0937	25.5	.0870	1.115	.0972	1,522	196.0	
1.0	28.0	.0910	.65	1.157	.0948	27.0	.0800	1.135	.0909	1,425	218.0	
1.1	29.5	.0840	.60	1.145	.0958	28.2	.0740	1.150	.0852	1,335	239.0	
1.2	30.5	.0780	.56	1.138	.0965	29.6	.0690	1.140	.0786	1,231	261.0	
1.3	32.0	.0730	.53	1.130	.0970	31.0	.0640	1.135	.0727	1,140	283.0	

TABLE I (c)
EXAMPLE 3, CONTROLLABLE PROPELLER

1	2	3	4	5	6	7	8	9	10	11	12	13
$\frac{V}{nD}$	β_1 for $C_{P1}=0.1097$ (deg.)	C_{T1} for β_1	$\frac{C_{T1}}{C_T (at stall)}$	$\frac{C_P}{C_P \left(\frac{V}{V_c}=0.5\right)} = \frac{C_{P1}}{C_{P2}}$	C_{P2}	β_2 for C_{P2} (deg.)	C_{T2} for β_2	$\frac{C_T}{C_T \left(\frac{V}{V_c}=0.5\right)} = \frac{C_{T3}}{C_{T2}}$	C_{T3}	Thrust (lb.)	Air speed (m. p. h.)	Remarks
0	22.6	0.1820	1.00	1.305	0.084	19.0	0.1730	0.75	0.1298	2,035	0	Blades stalled.
.1	22.6	.1810	1.00	1.305	.084	19.1	.1640	.75	.1230	1,928	21.8	Blades not stalled.
.2	22.8	.1770	.98	1.305	.084	19.2	.1530	.76	.1160	1,818	43.6	
.3	22.9	.1680	.94	1.305	.084	19.3	.1400	.79	.1105	1,730	65.3	
.4	23.0	.1550	.86	1.305	.084	19.5	.1290	.88	.1135	1,780	87.1	
.5	23.3	.1405	.79	1.305	.084	20.1	.1170	.97	.1133	1,780	108.8	
.6	23.6	.1300	.72	1.330	.0836	21.0	.1050	1.05	.1103	1,730	130.5	
.7	24.6	.1190	.66	1.355	.0810	21.5	.0900	1.13	.1029	1,610	152.5	
.8	25.4	.1090	.61	1.360	.0807	22.6	.0820	1.20	.0984	1,540	174.0	
.9	26.4	.0990	.55	1.350	.0813	24.1	.0760	1.22	.0932	1,460	196.0	
1.0	27.6	.0910	.51	1.330	.0825	25.2	.0700	1.23	.0862	1,350	218.0	
1.1	28.8	.0840	.47	1.310	.0838	27.0	.0640	1.23	.0791	1,240	239.0	
1.2	30.3	.0770	.43	1.290	.0850	28.3	.0590	1.23	.0729	1,145	261.0	
1.3	31.9	.0710	.40	1.275	.0861	30.0	.0550	1.24	.0682	1,070	283.0	

TABLE II
EXAMPLE 4, FIXED-PITCH PROPELLER, DESIGN B

1	2	3	4	5	6	7	8	9	10	11	12	13	14	15
$\frac{V}{nD}$	C_{P_2}	C_{T_2}	$\frac{N}{N_{maz}}$ for C_{P_1}	$\frac{V}{V_c}$	$\frac{C_{T_2}}{C_{T(at\ stall)}}$	$\frac{C_P}{C_P(\frac{V}{V_c}=0.5)}$	$\frac{C_T}{C_T(\frac{V}{V_c}=0.5)}$	C_{P_3}	C_{T_3}	$\frac{N}{N_{maz}}$ for C_{P_3}	$\frac{V}{V_{maz}}$	Air speed (m.p.h.)	Thrust (lb.)	Remarks
0	0.1120	0.1420	0.780	0.680	1.01	1.050	1.020	0.1178	0.1448	0.796	0	0	1,314	}Blades stalled.
.1	.1105	.1420	.780	.680	1.01	1.050	1.020	.1160	.1448	.802	.092	17.1	1,330	
.2	.1090	.1410	.790	.690	1.01	1.055	1.020	.1150	.1438	.806	.185	34.3	1,333	
.3	.1065	.1400	.800	.698	1.00	1.060	1.020	.1130	.1427	.813	.277	51.2	1,350	}Blades not stalled.
.4	.1040	.1350	.809	.705	.96	1.060	1.025	.1100	.1385	.825	.379	70.1	1,343	
.5	.1000	.1280	.824	.719	.91	1.060	1.030	.1060	.1318	.839	.482	90.3	1,325	
.6	.0940	.1130	.850	.742	.81	1.052	1.040	.0990	.1175	.869	.599	111.0	1,270	
.7	.0860	.0970	.890	.777	.69	1.065	1.050	.0918	.1020	.902	.725	134.0	1,185	
.8	.0760	.0780	.945	.825	.56	1.085	1.080	.0825	.0842	.952	.875	162.0	1,090	
.87	.0680	.0660	1.000	.873	.48	1.100	1.100	.0747	.0726	1.000	1.000	185.0	1,038	

REPORT No. 640

THE AERODYNAMIC CHARACTERISTICS OF FULL-SCALE PROPELLERS HAVING 2, 3, AND 4 BLADES OF CLARK Y AND R. A. F. 6 AIRFOIL SECTIONS

By EDWIN P. HARTMAN and DAVID BIERMANN

SUMMARY

Aerodynamic tests were made of seven full-scale 10-foot-diameter propellers of recent design comprising three groups. The first group was composed of three propellers having Clark Y airfoil sections and the second group was composed of three propellers having R. A. F. 6 airfoil sections, the propellers of each group having 2, 3, and 4 blades. The third group was composed of two propellers, the 2-blade propeller taken from the second group and another propeller having the same airfoil section and number of blades but with the width and thickness 50 percent greater. The tests of these propellers reveal the effect of changes in solidity resulting either from increasing the number of blades or from increasing the blade width.

It was found that (1) increasing the solidity by adding blades had a lesser adverse effect than increasing it by increasing the blade width; (2) the loss in efficiency commonly conceived to be the result of increasing the number of blades was not fully realized, only about 2 percent difference in peak efficiency between a 2-blade and a 4-blade propeller being measured; and (3) an increase in solidity tended to delay the stall and to increase the efficiency in the take-off range.

Propeller design charts and methods of computing propeller thrust are included.

INTRODUCTION

Propeller theory indicates that, other factors remaining constant, an increase in the total blade area, or solidity, of a propeller will generally result in a loss of efficiency. Despite this fact the trend for a number of years has been toward a greater solidity as a result of increases in the power of engines and tip-speed or other limitations on the diameter. The 3-blade propeller is replacing the 2-blade propeller and in some cases, as in high-altitude flying, the 4-blade propeller appears to have a field of use.

Propeller research has lagged somewhat behind the needs of industry, particularly with regard to the need for data on full-scale propellers having modern wide blades and on propellers having more than two blades.

Throughout the first part of 1937 the N. A. C. A. 20-foot wind tunnel was engaged in a rather compre-

hensive propeller-research program covering several phases of the subject. This report presents the results of the part of the program concerning the effect of number of blades and of blade width on the aerodynamic characteristics of full-scale propellers.

The propellers tested, especially those with Clark Y sections, are typical of many in use today; and the data, which cover a blade-angle range up to 45° , should therefore be useful for design purposes. The data are presented in a form readily usable for the calculation of take-off thrust, and methods of making such calculations for fixed-pitch and controllable propellers are given in an appendix. The data provide a good comparison of the performances of propellers having Clark Y and R. A. F. 6 airfoil sections, but no point is made of this comparison here because another report dealing specifically with the effect of airfoil sections is in preparation.

APPARATUS AND METHODS

Tunnel.—The tests were made in the N. A. C. A. 20-foot wind tunnel described in reference 1. The tunnel has an open throat and is capable of producing air speeds up to 110 miles per hour.

Propellers.—The seven propellers tested may be classified as follows:

1. A group composed of three propellers having Clark Y airfoil sections with 2, 3, and 4 blades.
2. A group composed of three propellers having R. A. F. 6 airfoil sections with 2, 3, and 4 blades.
3. A single specially constructed propeller similar to the 2-blade propeller of class 2 except that its blade width and thickness are 50 percent greater.

All the propellers have 10-foot diameters and, except for the special wide one, have the same plan form, thickness, width, and pitch distribution. The normal-width propellers are all of Navy design and have drawing numbers 5868-9 and 5868-R6 for the blades of Clark Y and R. A. F. 6 sections, respectively. The wide propeller is of N. A. C. A. design and has an Army drawing number of 37-3647. Its blade width is 50 percent greater than that of the normal-width propeller except the shank, which is the same for both.

Photographs of the normal-width blade and of the special wide blade are shown in figure 1. Figure 2 presents blade-form curves for all propellers and illus-

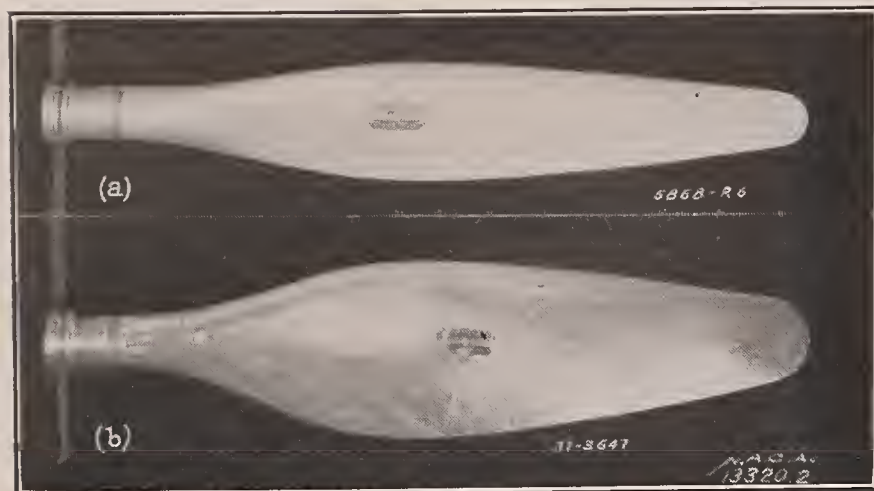


FIGURE 1.—Propeller blades of different width.
(a) R. A. F. 6 blade section of normal width.
(b) R. A. F. 6 blade section 1.5 times normal width.

trates the differences between the Clark Y and the R. A. F. 6 airfoil sections.

Body and engine.—The propellers were mounted on a geared Curtiss Conqueror engine enclosed in a smooth

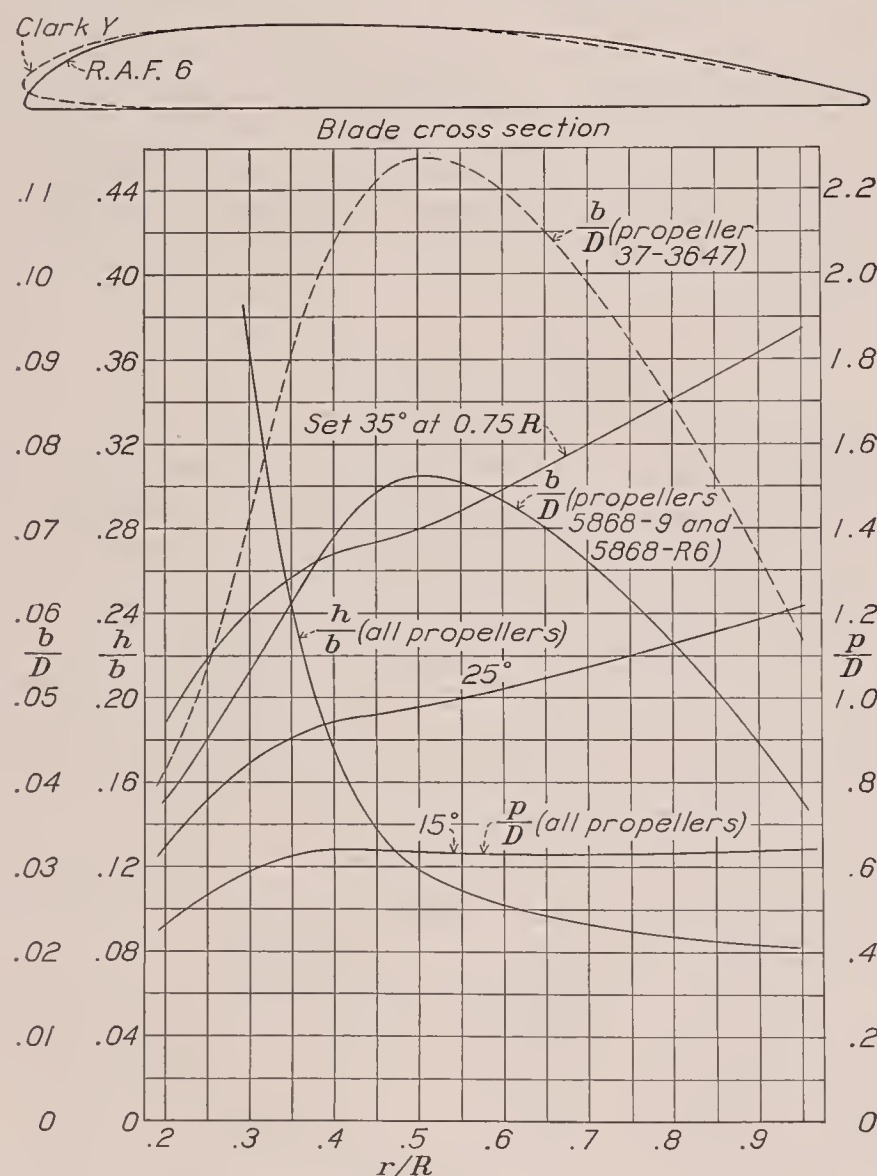


FIGURE 2.—Blade-form curves for propellers 5868-9, 5868-R6, and 37-3647. D , diameter; R , radius to the tip; r , station radius; b , section chord; h , section thickness; p , geometric pitch.

liquid-cooled engine nacelle. The engine is rated at 600 horsepower at 2,450 r. p. m. and is geared 7:5. Its direction of rotation had been reversed at the factory to accommodate right-hand propellers.

The nacelle is a sheet-metal fairing with oval cross section. Its major dimensions are as follows: maximum depth, 43 inches; maximum width, 38 inches; length, 126 inches. A more detailed description of the nacelle is given in reference 2.

The engine and nacelle were supported on streamline struts rising from the floating frame of the balance system. The drag of the nacelle and struts was about 59 pounds at 100 miles per hour. Figure 3 is a photograph of the nacelle, with propeller, mounted in the tunnel.

Balances, instruments, and torque dynamometer.—The thrust and the torque forces were measured on recording balances situated in the balance house on the

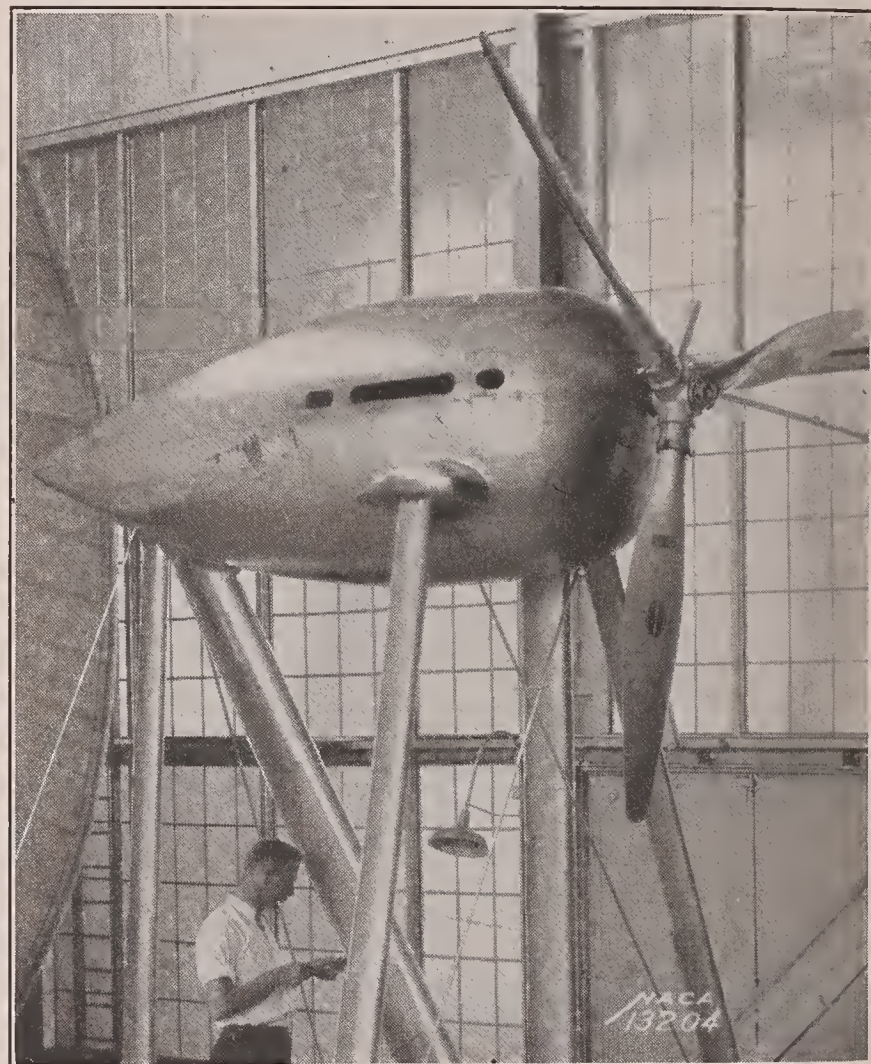


FIGURE 3.—Liquid-cooled engine nacelle and 3-blade propeller mounted in the 20-foot wind tunnel.

test-chamber floor. The torque dynamometer consisted of an engine cradle free to rotate about an axis along one side and supported on the other side by a strut with a footing on the lever mechanism of one of the recording balances on the test-chamber floor. As both the thrust and the torque were measured on recording balances, simultaneous readings were obtained. An electric magneto-type tachometer was used to measure the engine speed.

Test methods.—The general procedure observed in these tests was to hold the engine speed at a constant value while the tunnel speed was increased by steps to top speed (about 115 miles per hour with propeller operating), after which the tunnel speed was held approximately constant and the engine throttled by steps to zero thrust.

It has been shown in reference 3 that the performance of a propeller in the take-off range is considerably affected by the propeller tip speed. In order to apply the necessary corrections when the present data are used, it is necessary to know the tip speeds of these tests. The following table gives the values of engine speed that were held constant throughout the first part of each test, which covered the take-off and climbing range.

For values of V/nD higher than can be obtained from the table, the test propeller speed may be computed approximately from the relation:

$$\text{r. p. m.} = \frac{1,000}{V/nD}$$

Schedule of propeller speeds (revolutions per minute) for tunnel speeds below 115 miles per hour

Blade angle Propeller	15°	20°	25°	30°	35°	40°	45°
5868-9, 2 blades---	1,200	1,200	1,000	1,000	800	900	800
5868-9, 3 blades---	1,000	1,000	1,000	900	800	800	700
5868-9, 4 blades---	1,000	1,000	900	800	700	700	600
5868-R6, 2 blades---	1,000	1,000	1,000	1,000	1,000	-----	-----
5868-R6, 3 blades---	1,000	1,000	1,000	900	800	800	-----
5868-R6, 4 blades---	1,000	1,000	1,000	900	800	-----	-----
37-3647, 2 blades---	1,000	1,000	1,000	800	800	-----	-----

Precision.—It is impossible to give any exact values for the accuracy of the tests, and the precision of the measurements was so variable that a discussion of the subject would be confusing and pointless. It may be said, however, that repeat tests usually checked first tests within about 1 percent. Some idea of the precision of the measurements is indicated by the regularity of the test points shown in figure 4. This figure is included only to show the dispersion of the test points.

RESULTS

Propeller charts.—The principal results of the tests are presented in figures 5 to 32. These figures present the basic curves of C_T , C_P , η , and C_s against V/nD traced from the original curves of faired test points. The test results have been tabulated in seven tables, which are available on request from the National Advisory Committee for Aeronautics.

As an aid in calculating the propeller thrust in the take-off and climbing range, lines of constant thrust coefficient have been superimposed on the C_P charts. The method of using these charts is described in the appendix to this report.

Coefficients.—The coefficients are standard forms defined in the cover of every N. A. C. A. report, but the definitions will be repeated here for clearness and convenience.

$$C_T = \frac{T_e}{\rho n^2 D^4}; C_P = \frac{P}{\rho n^3 D^5}; \eta = \frac{C_T V}{C_P n D}$$

$$C_s = \sqrt[5]{\frac{\rho V^5}{P n^2}}; C_Q = \frac{Q}{\rho n^2 D^5}$$

where T_e is effective thrust = $T - \Delta D$, lb.

T , tension in propeller shaft, lb.

ΔD , change in drag of body due to slipstream, lb.

P , power absorbed by propeller, ft.-lb./sec.

n , propeller speed, r. p. s.

D , propeller diameter, ft.

ρ , mass density of the air, slugs per cu. ft.

V , air speed, f. p. s.

η , propulsive efficiency of propeller engine unit.

Q , engine torque, lb.-ft.

DISCUSSION

The ideal efficiency of a propeller according to the axial momentum theory may be written

$$\eta_i = \frac{2}{1 + V_s/V}$$

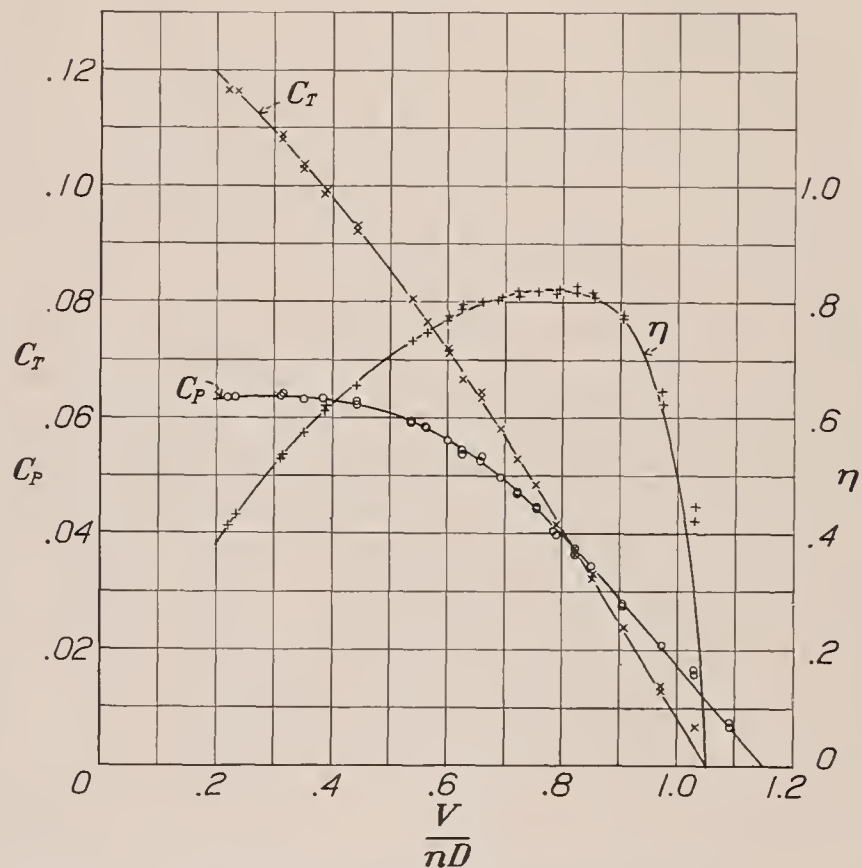


FIGURE 4.—Typical set of test data showing dispersion of test points. Propeller 5868-R6; 2 blades; diameter, 10 ft.; set 20° at 0.75R.

where V_s/V is the ratio of the final slipstream velocity, relative to the airplane, to the forward velocity which, in turn, is defined by the equation

$$\frac{V_s^2}{V^2} = 1 + 2.545 C_T / J^2$$

where $J = V/nD$.

It is seen from these equations that, at a given value of J , an increase in C_T increases the slipstream velocity ratio and decreases the propeller efficiency. The two most effective ways of changing C_T are by changing either the blade angle or the solidity. Increasing either the blade angle or the solidity increases C_T so that a decrease in efficiency may be expected. The solidity of a propeller, usually designated by the symbol σ , may be defined as the ratio of the total untwisted blade area to the total propeller-disk area. The solidity is increased by an increase either in the number of blades or in the blade width. An increase in solidity will increase the value of C_T and, therefore, a loss in efficiency may be expected from increasing either the blade width or the number of blades.

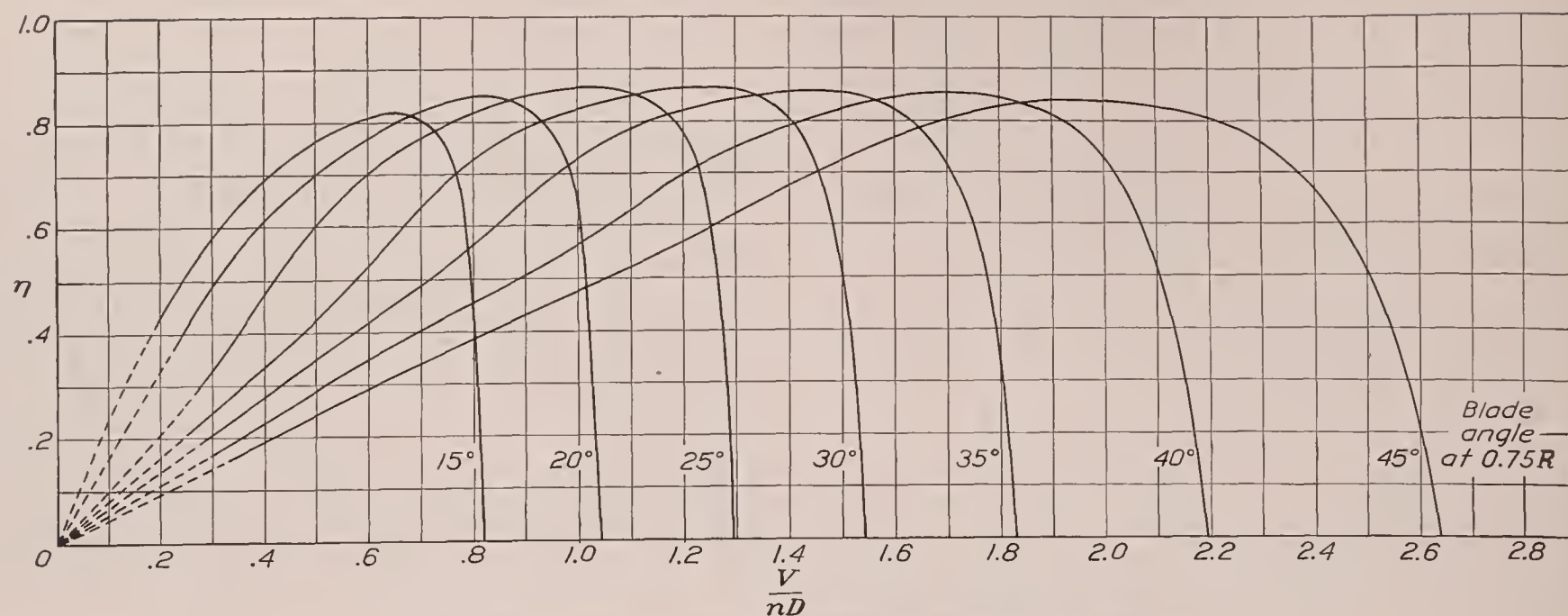


FIGURE 5.—Efficiency curves for propeller 5868-9, Clark Y section, 2 blades.

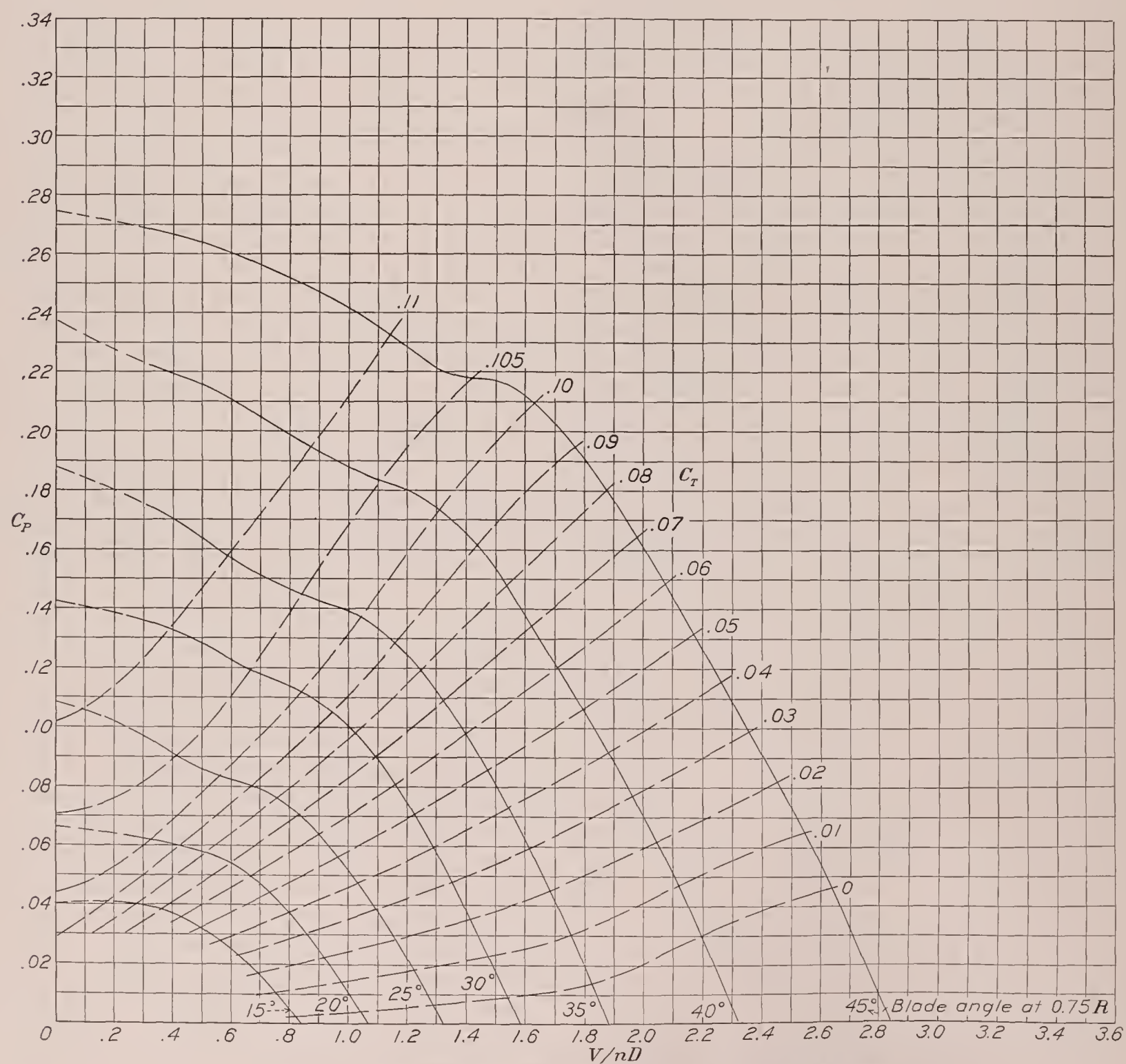


FIGURE 6.—Power-coefficient curves for propeller 5868-9, Clark Y section, 2 blades.

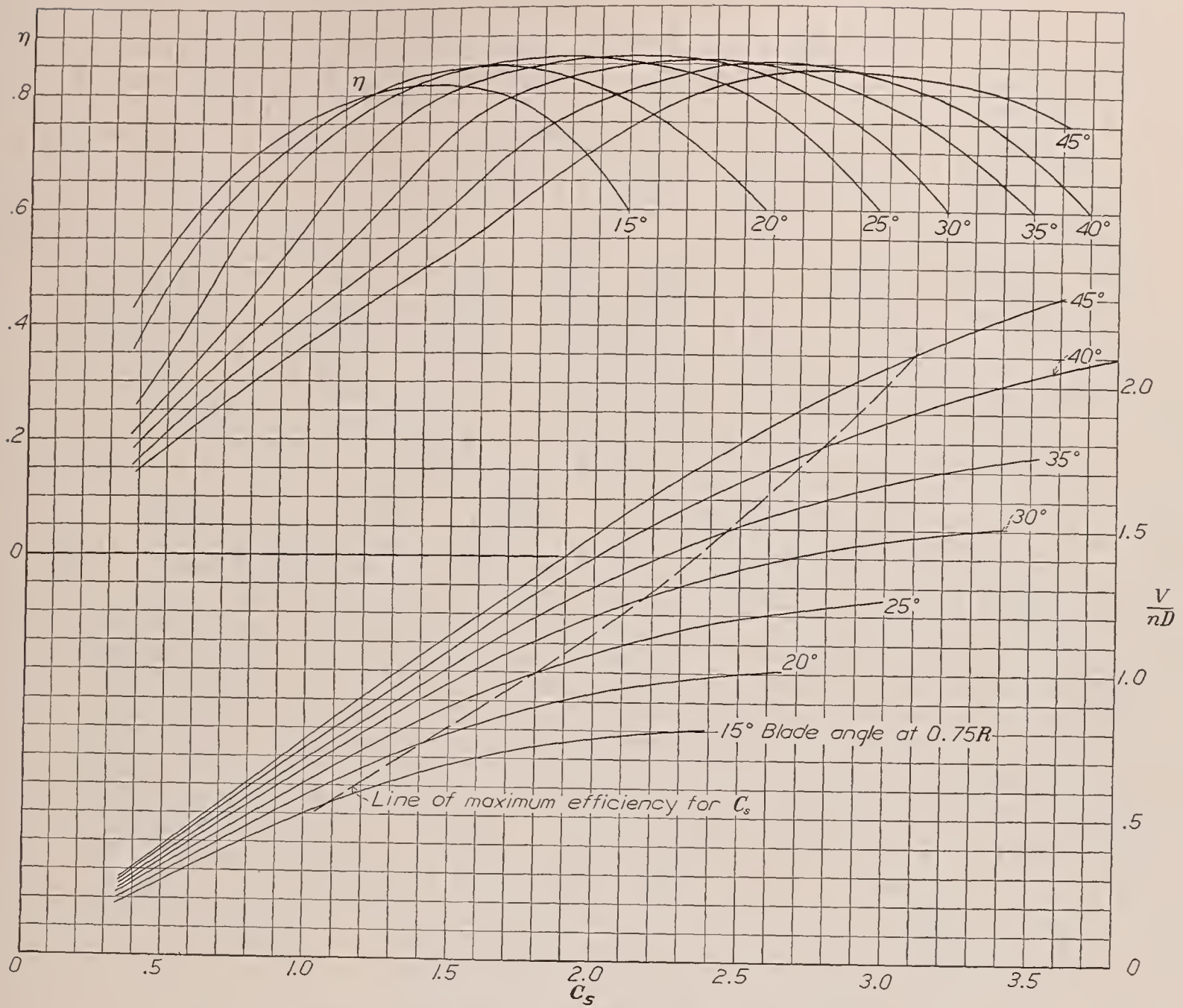


FIGURE 7.—Design chart for propeller 5868-9, Clark Y section, 2 blades.

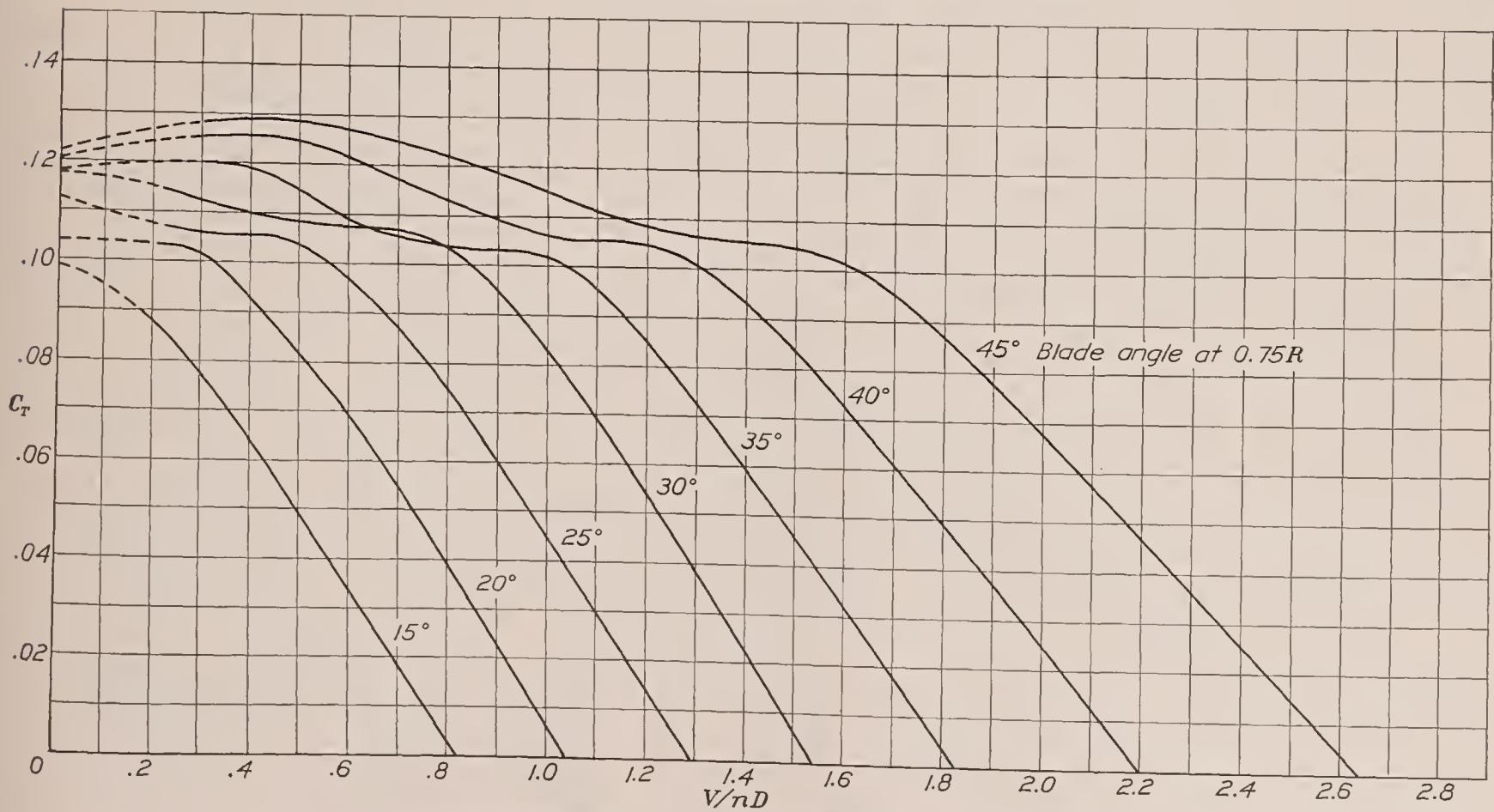


FIGURE 8.—Thrust-coefficient curves for propeller 5868-9, Clark Y section, 2 blades.

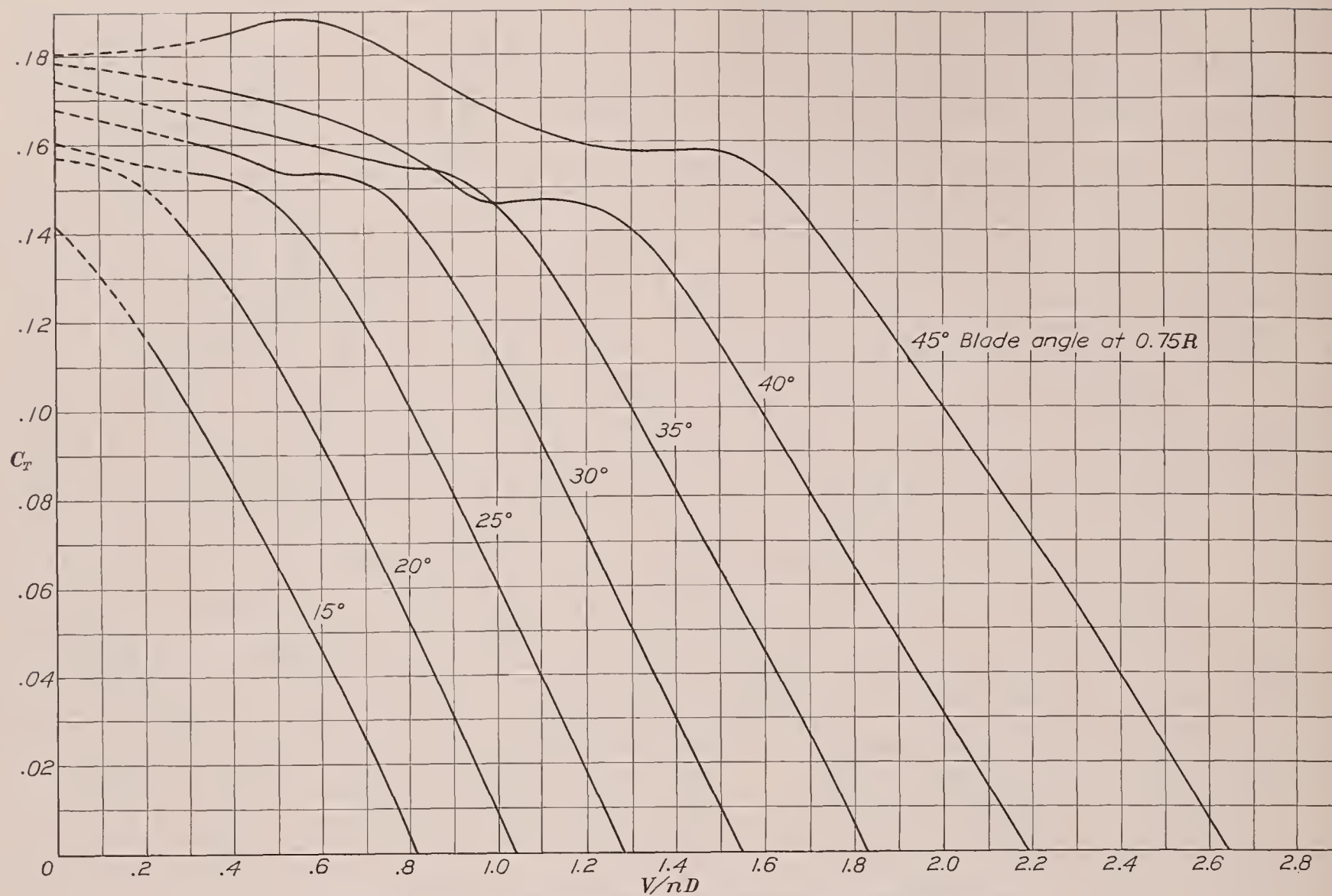


FIGURE 9.—Thrust-coefficient curves for propeller 5868-9, Clark Y section, 3 blades.

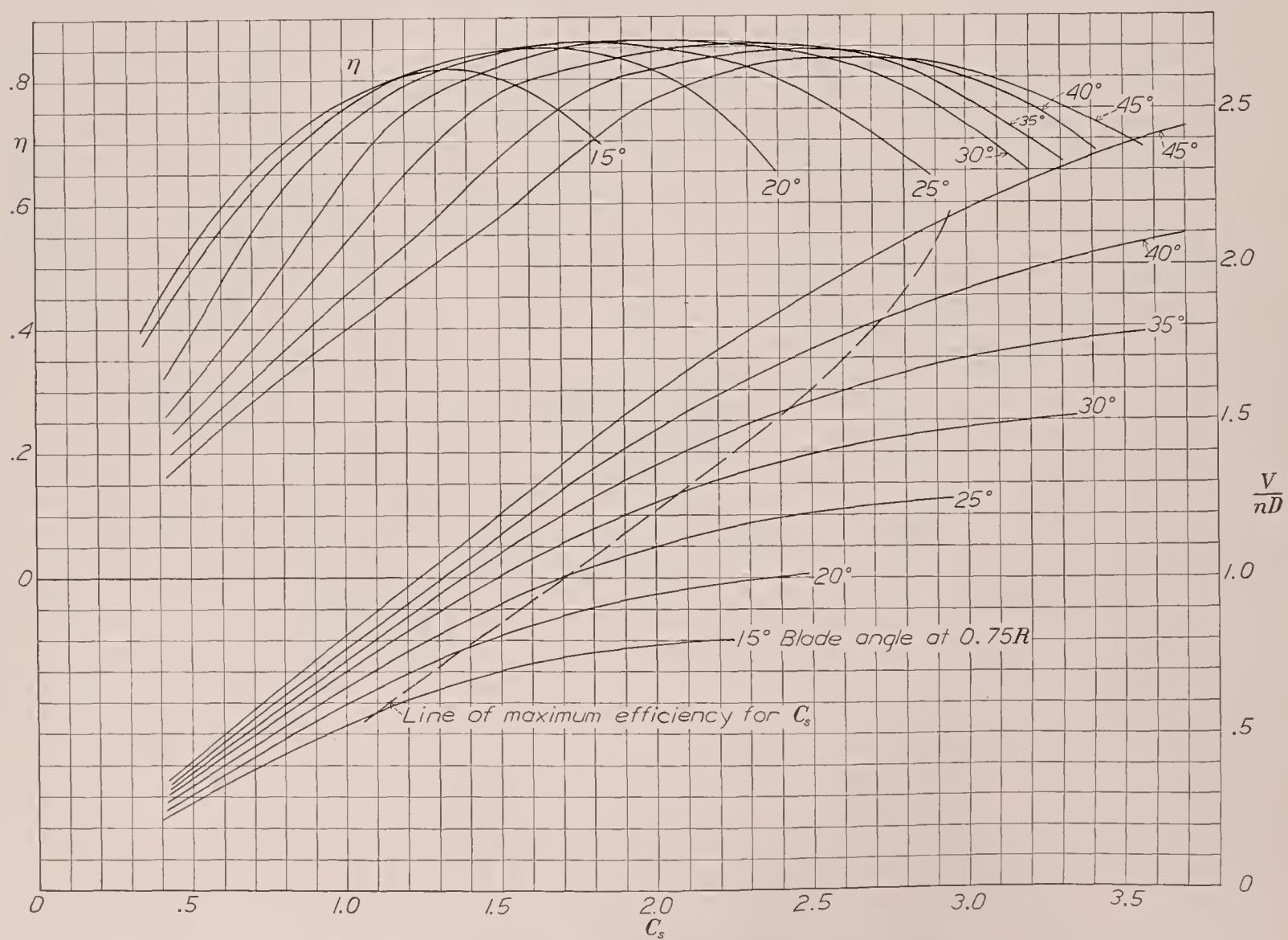


FIGURE 10.—Design chart for propeller 5868-9, Clark Y section, 3 blades.

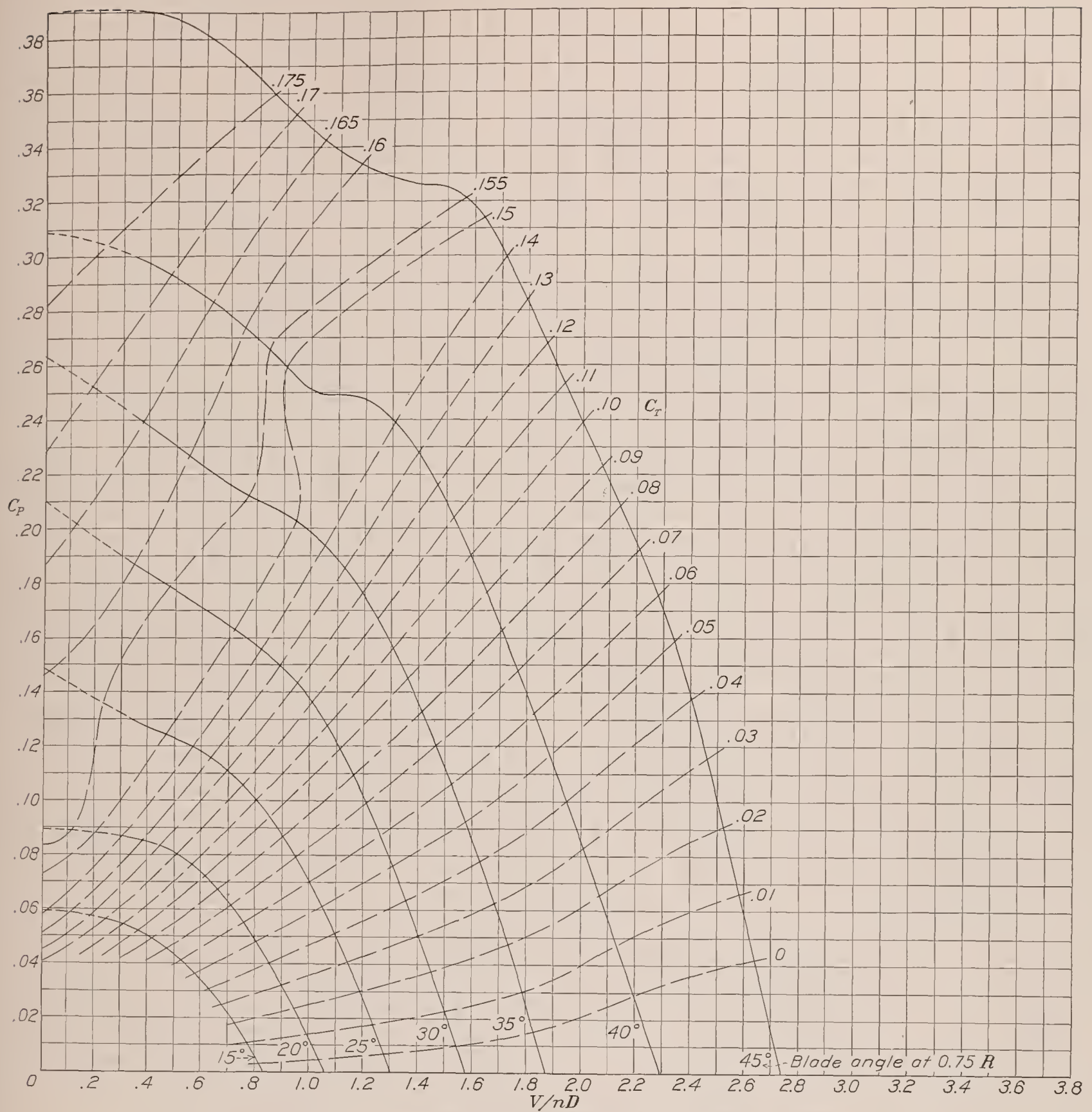


FIGURE 11.—Power-coefficient curves for propeller 5868-9, Clark Y section, 3 blades.

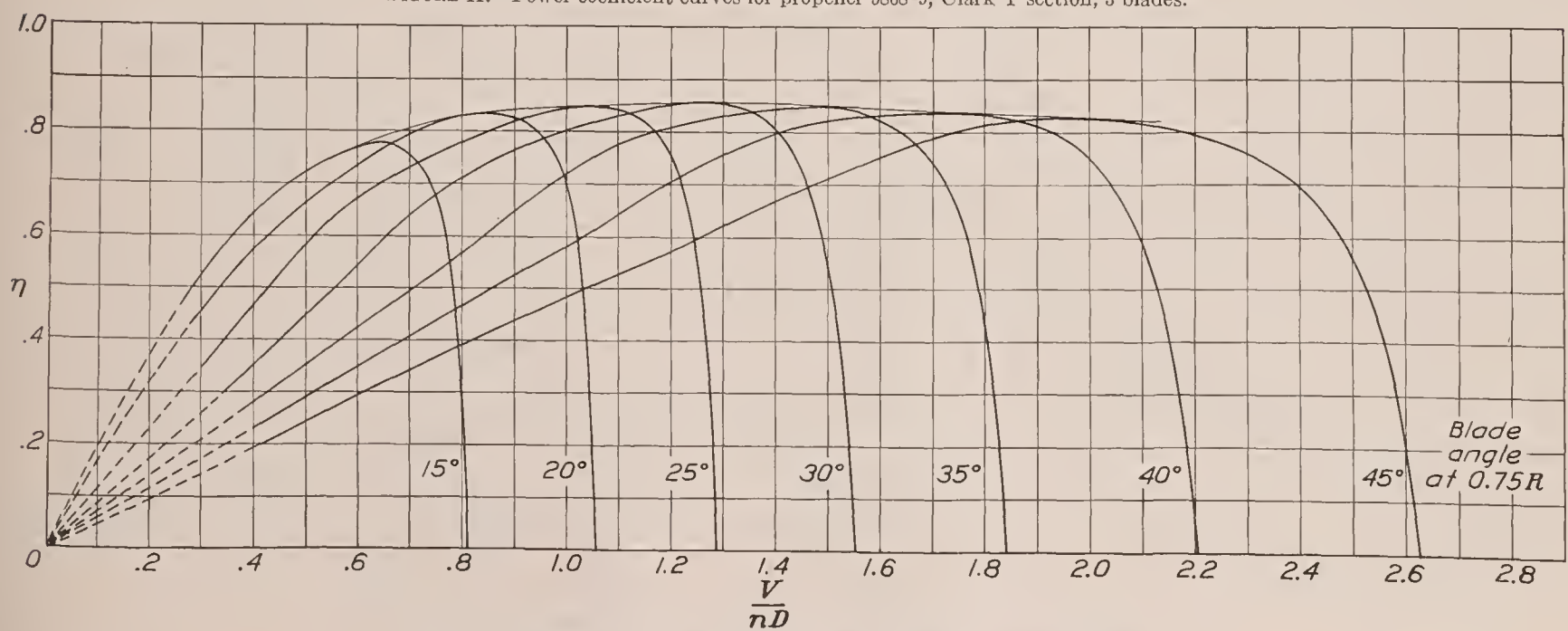


FIGURE 12.—Efficiency curves for propeller 5868-9, Clark Y section, 3 blades.

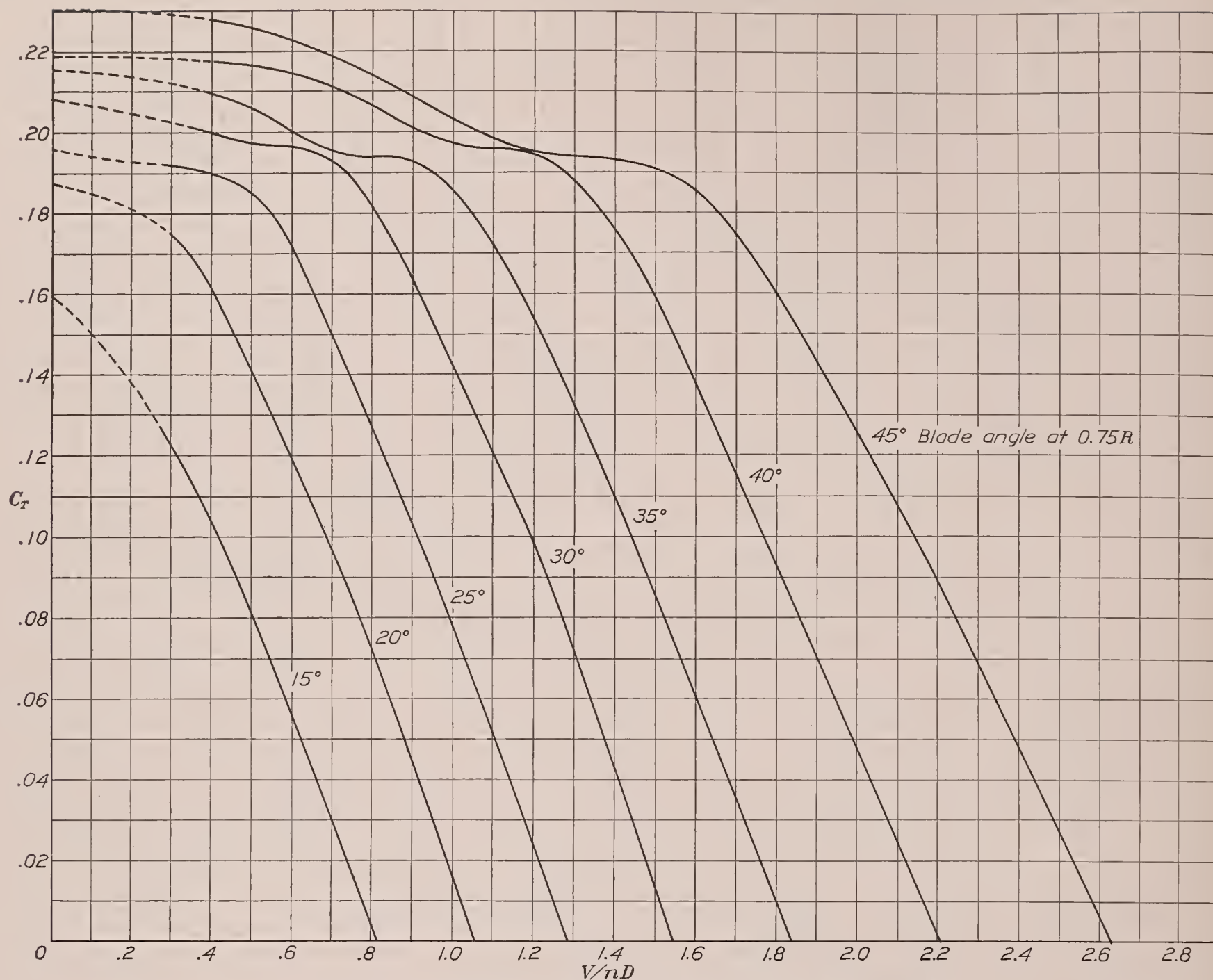


FIGURE 13.—Thrust-coefficient curves for propeller 5868-9, Clark Y section, 4 blades.

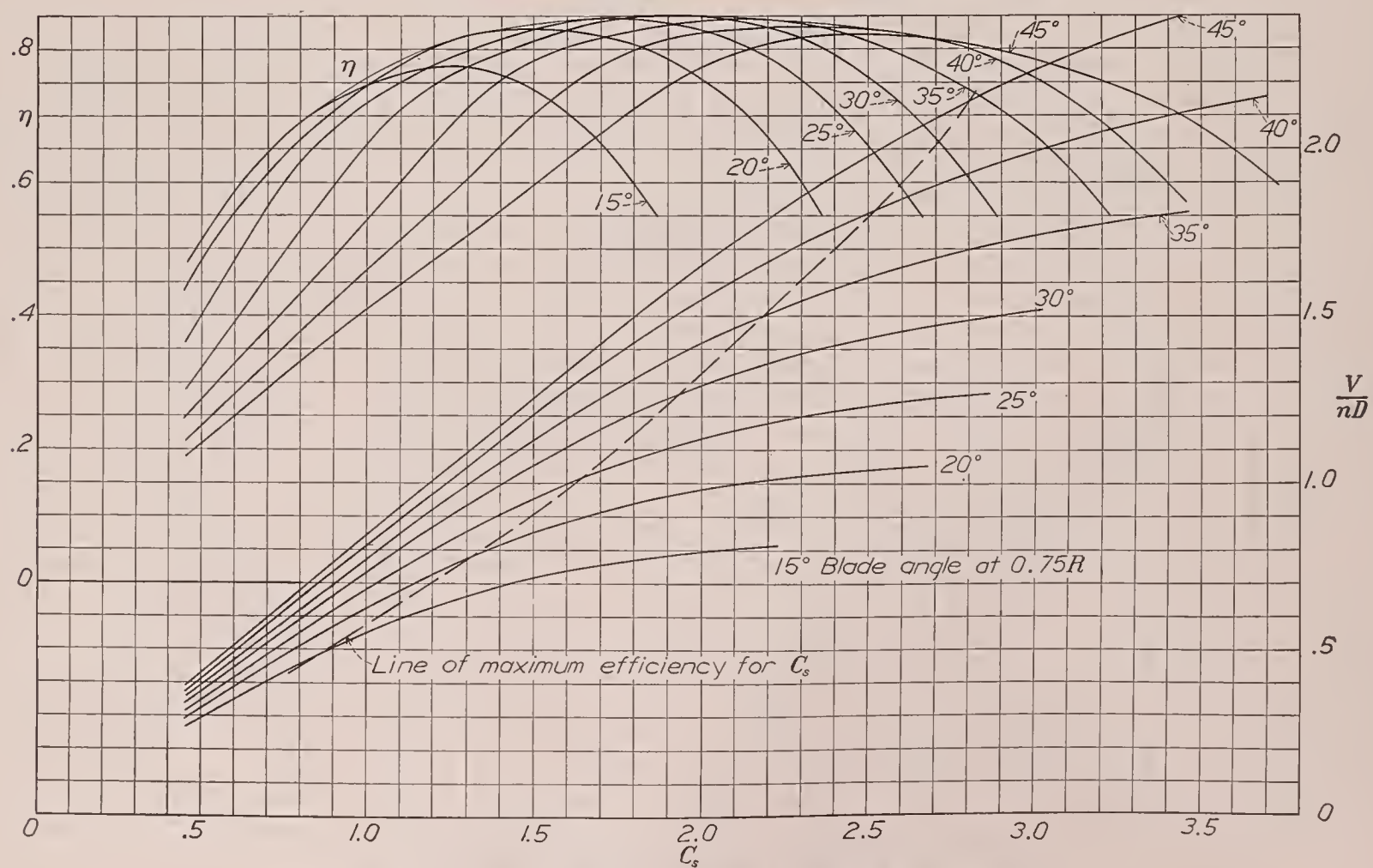


FIGURE 14.—Design chart for propeller 5868-9, Clark Y section, 4 blades.

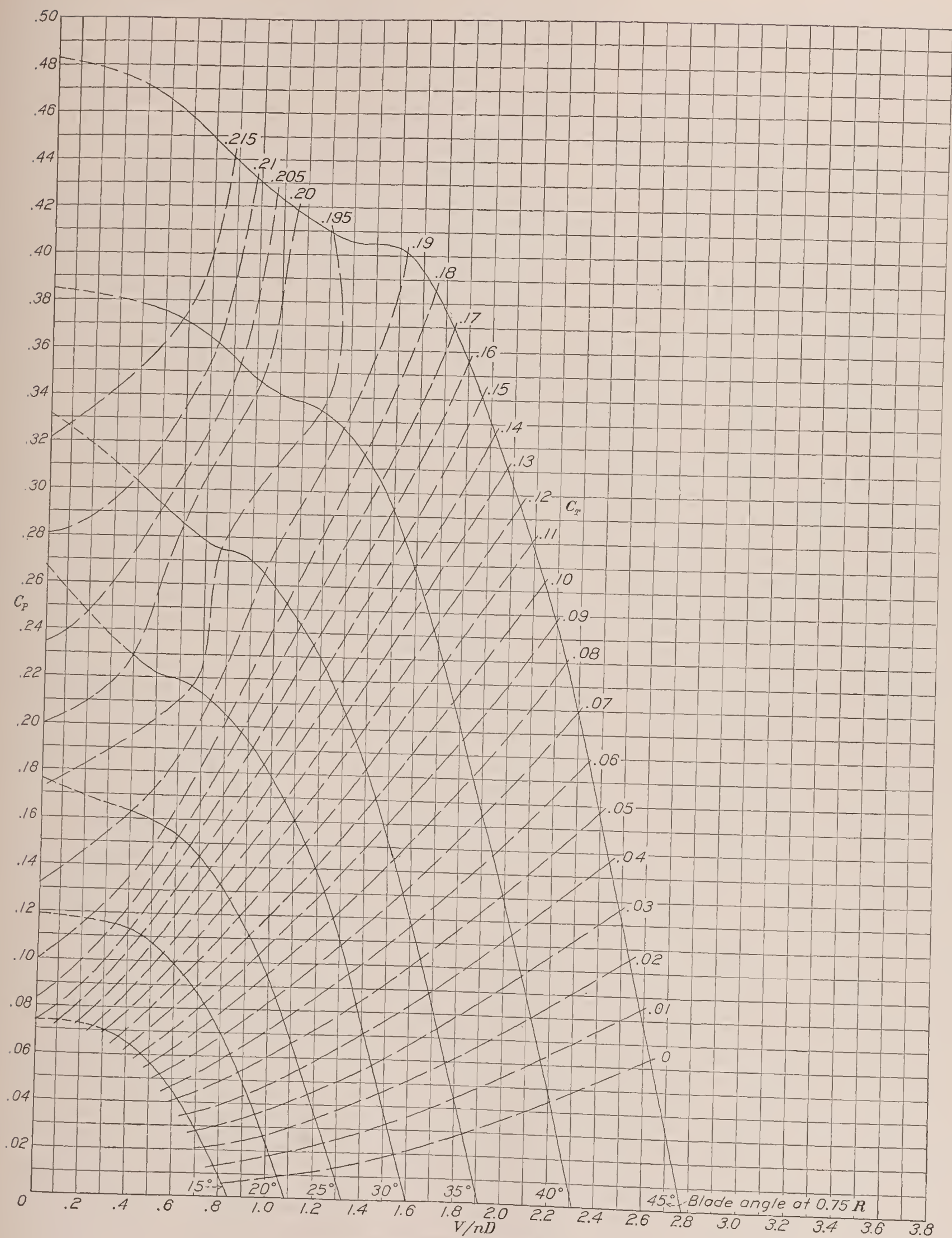


FIGURE 15.—Power-coefficient curves for propeller 5868-9, Clark Y section, 4 blades.

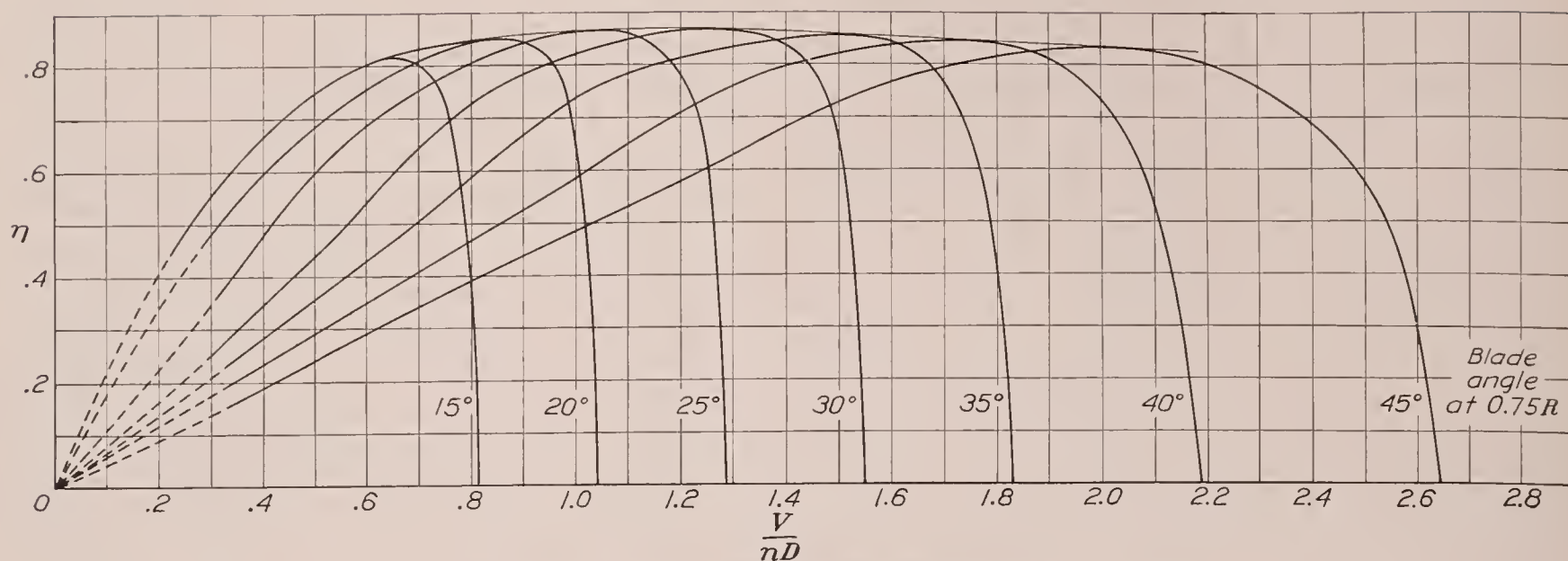


FIGURE 16.—Efficiency curves for propeller 5868-9, Clark Y section, 4 blades.

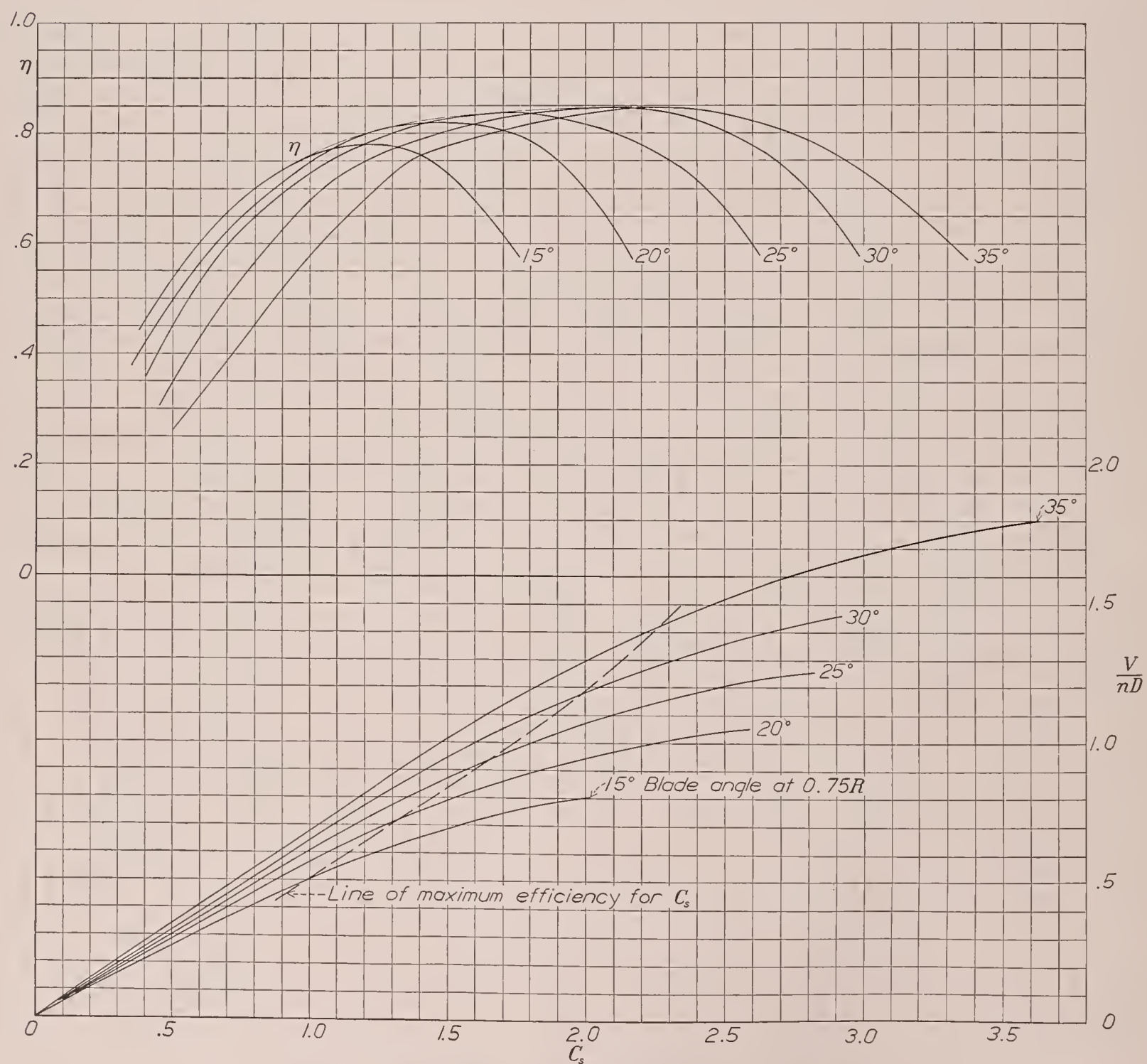


FIGURE 17.—Design chart for propeller 5868-R6, R. A. F. 6 section, 2 blades.

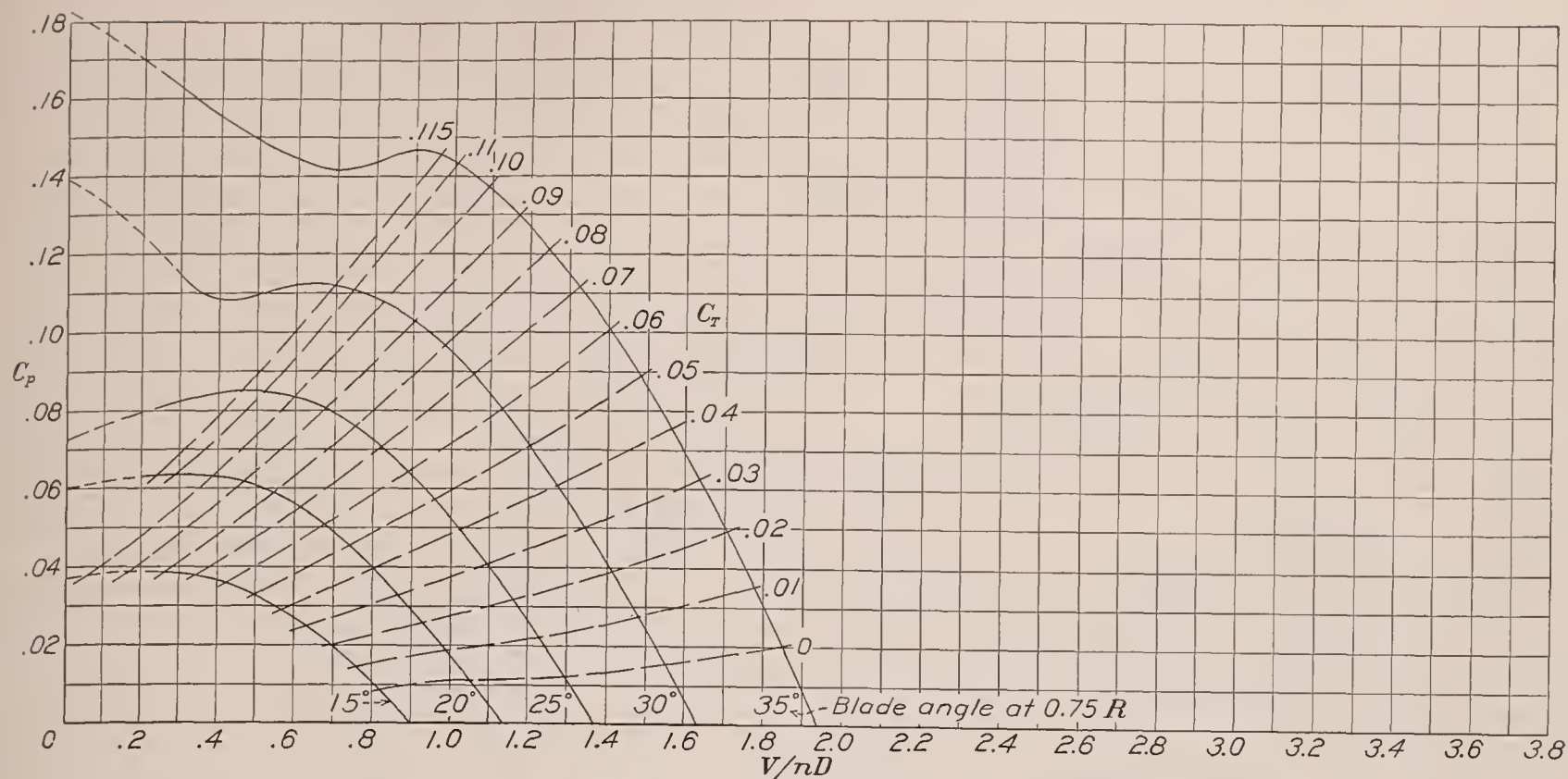


FIGURE 18.—Power-coefficient curves for propeller 5868-R6, R. A. F. 6 section, 2 blades.

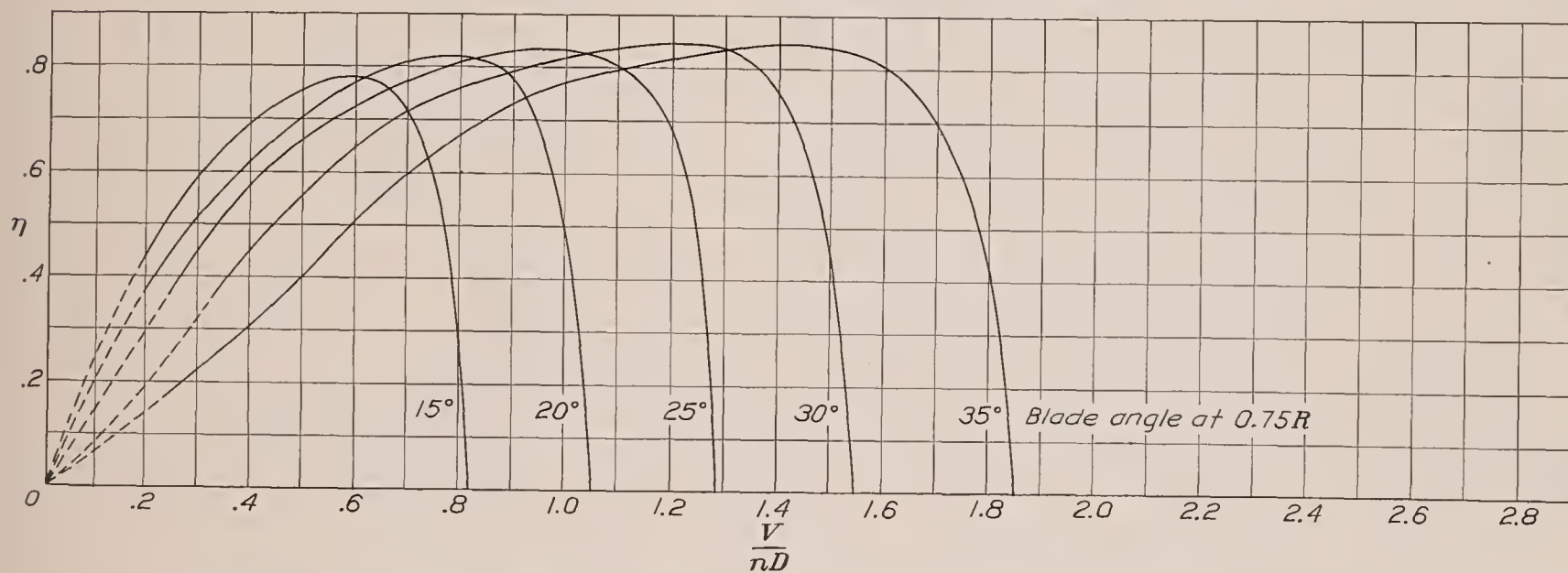


FIGURE 19.—Efficiency curves for propeller 5868-R6, R. A. F. 6 section, 2 blades.

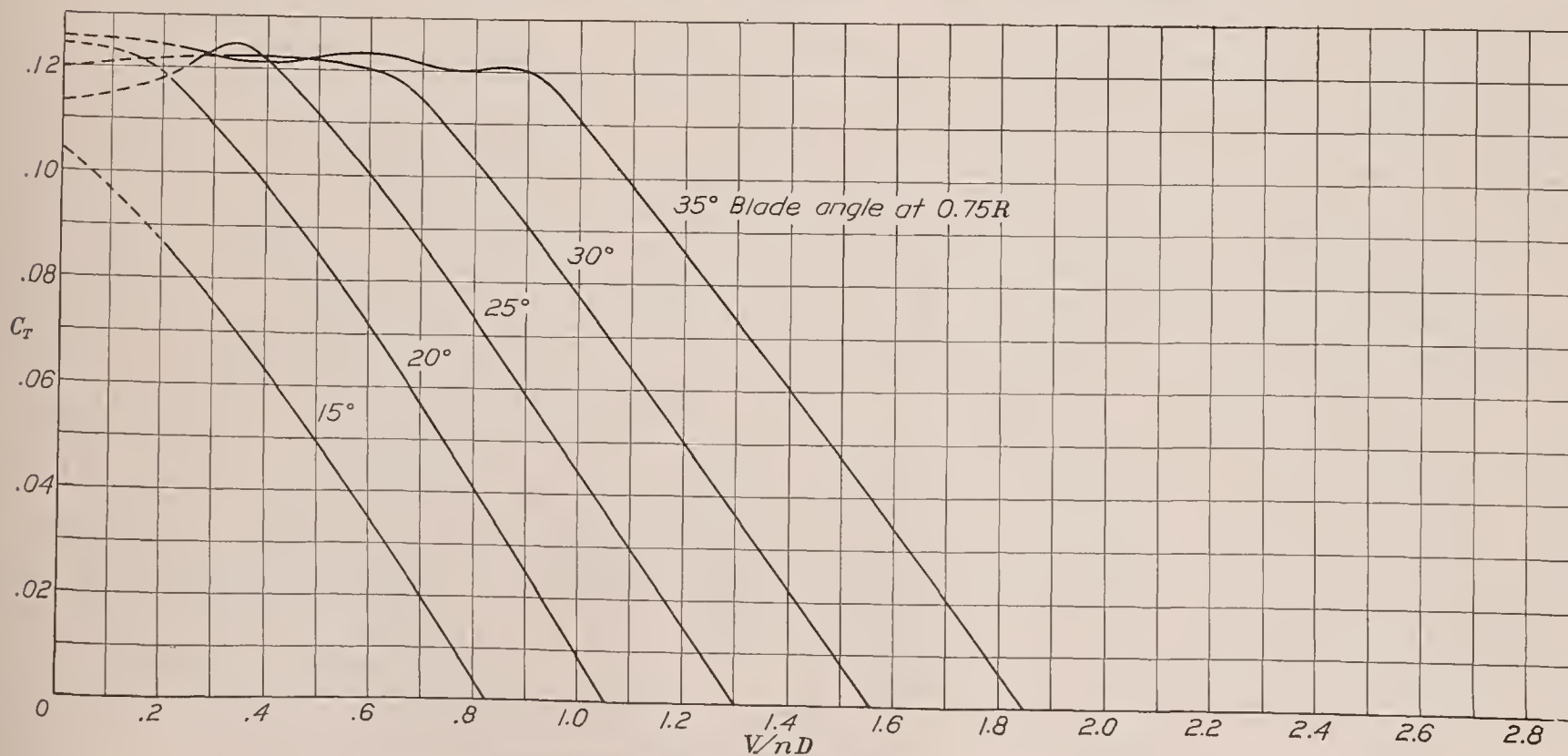


FIGURE 20.—Thrust-coefficient curves for propeller 5868-R6, R. A. F. 6 section, 2 blades.

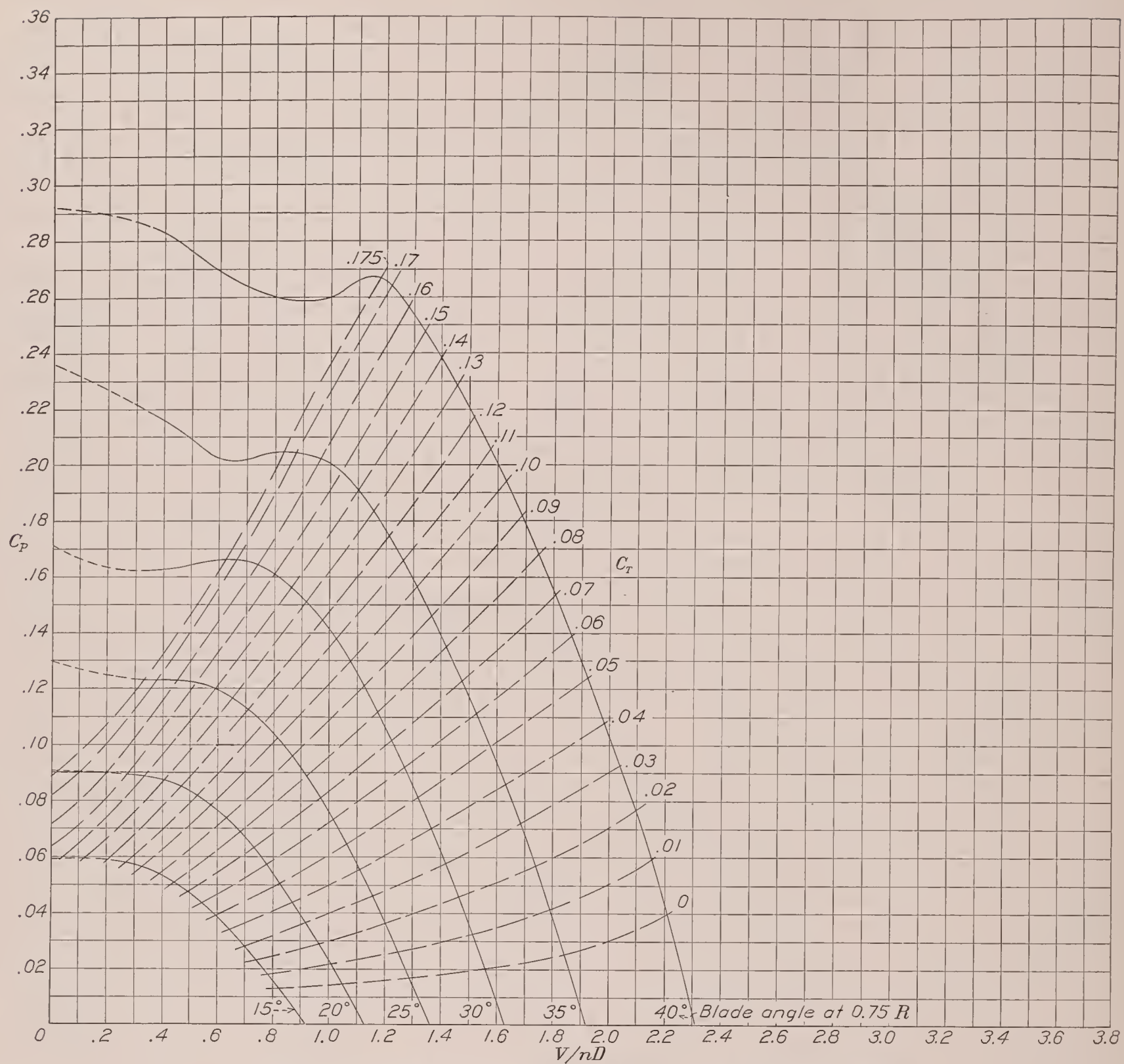


FIGURE 21.—Power-coefficient curves for propeller 5868-R6, R. A. F. 6 section, 3 blades.

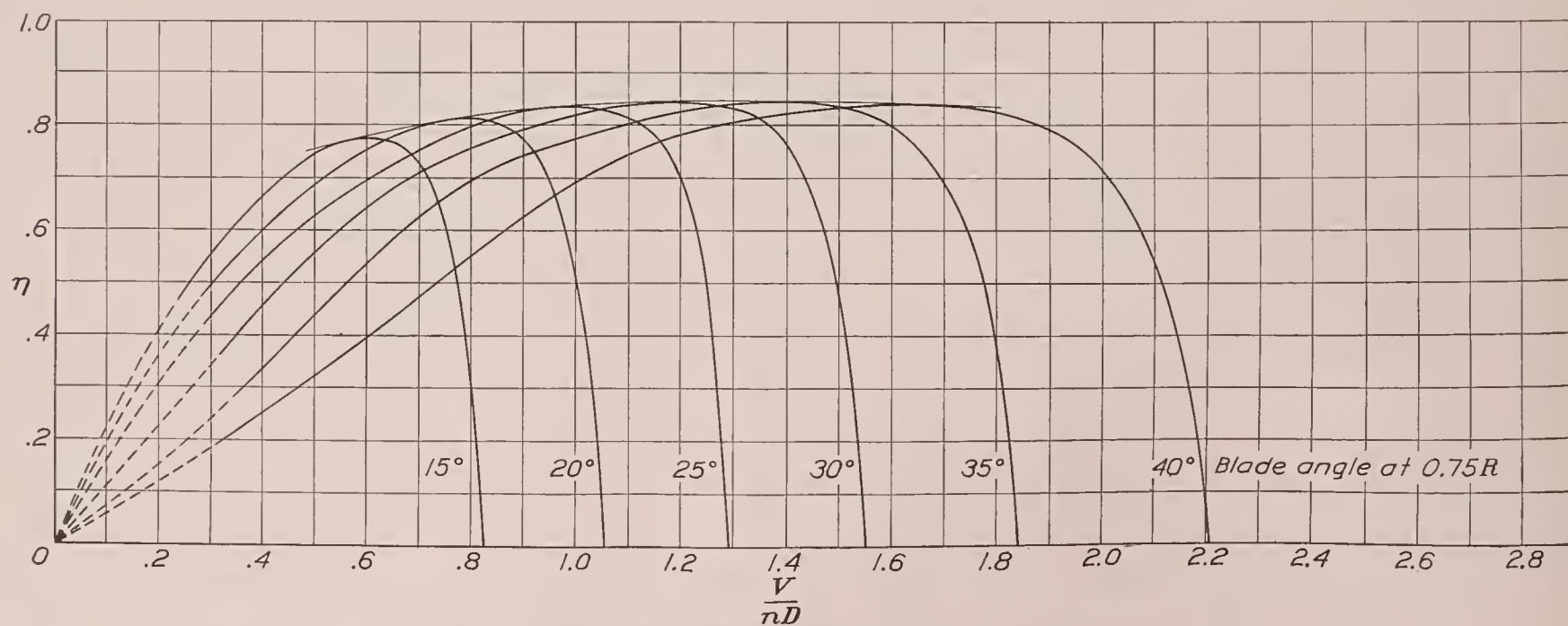


FIGURE 22.—Efficiency curves for propeller 5868-R6, R. A. F. 6 section, 3 blades.

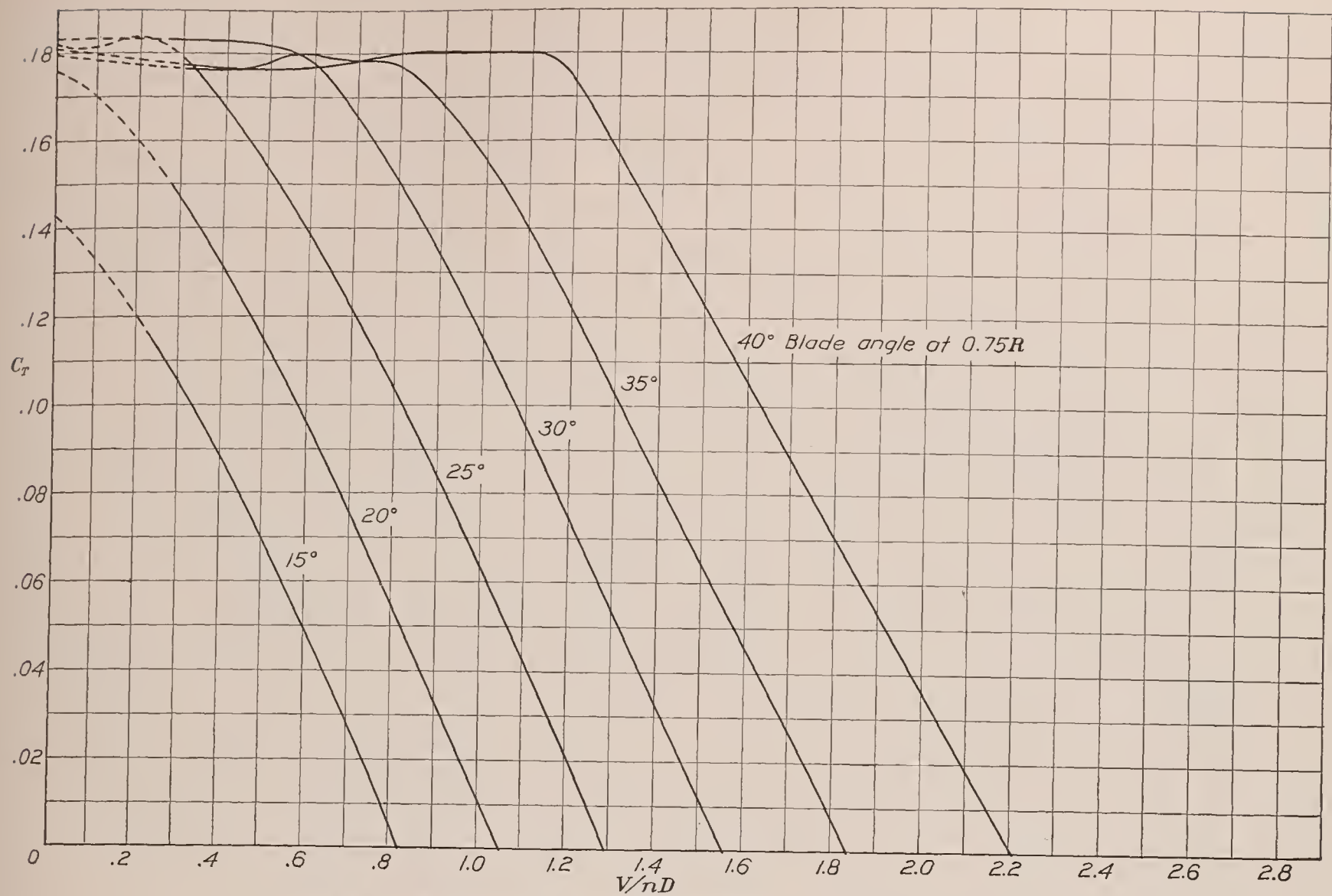


FIGURE 23.—Thrust-coefficient curves for propeller 5868-R6, R. A. F. 6 section, 3 blades.

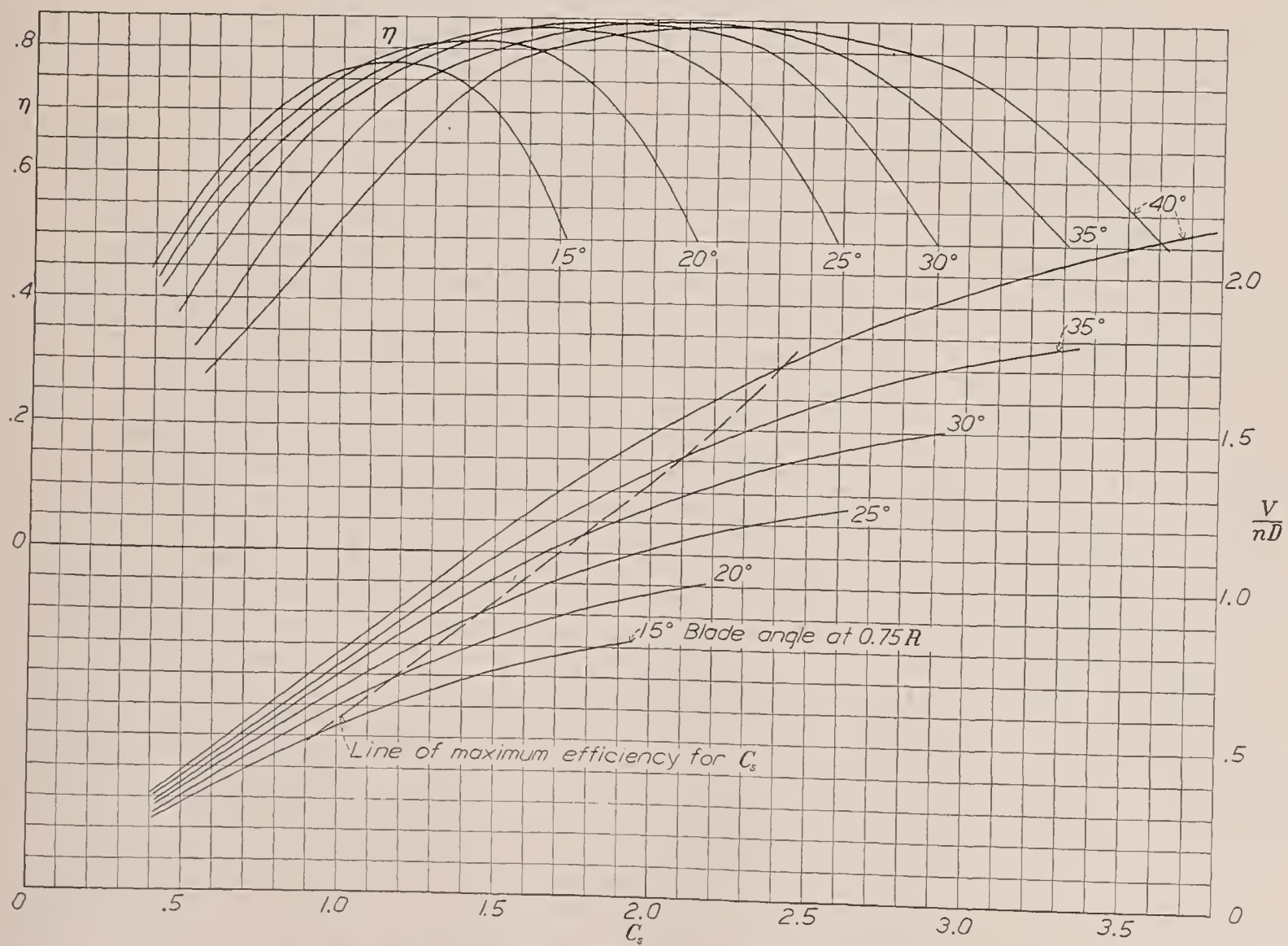


FIGURE 24.—Design chart for propeller 5868-R6, R. A. F. 6 section, 3 blades.

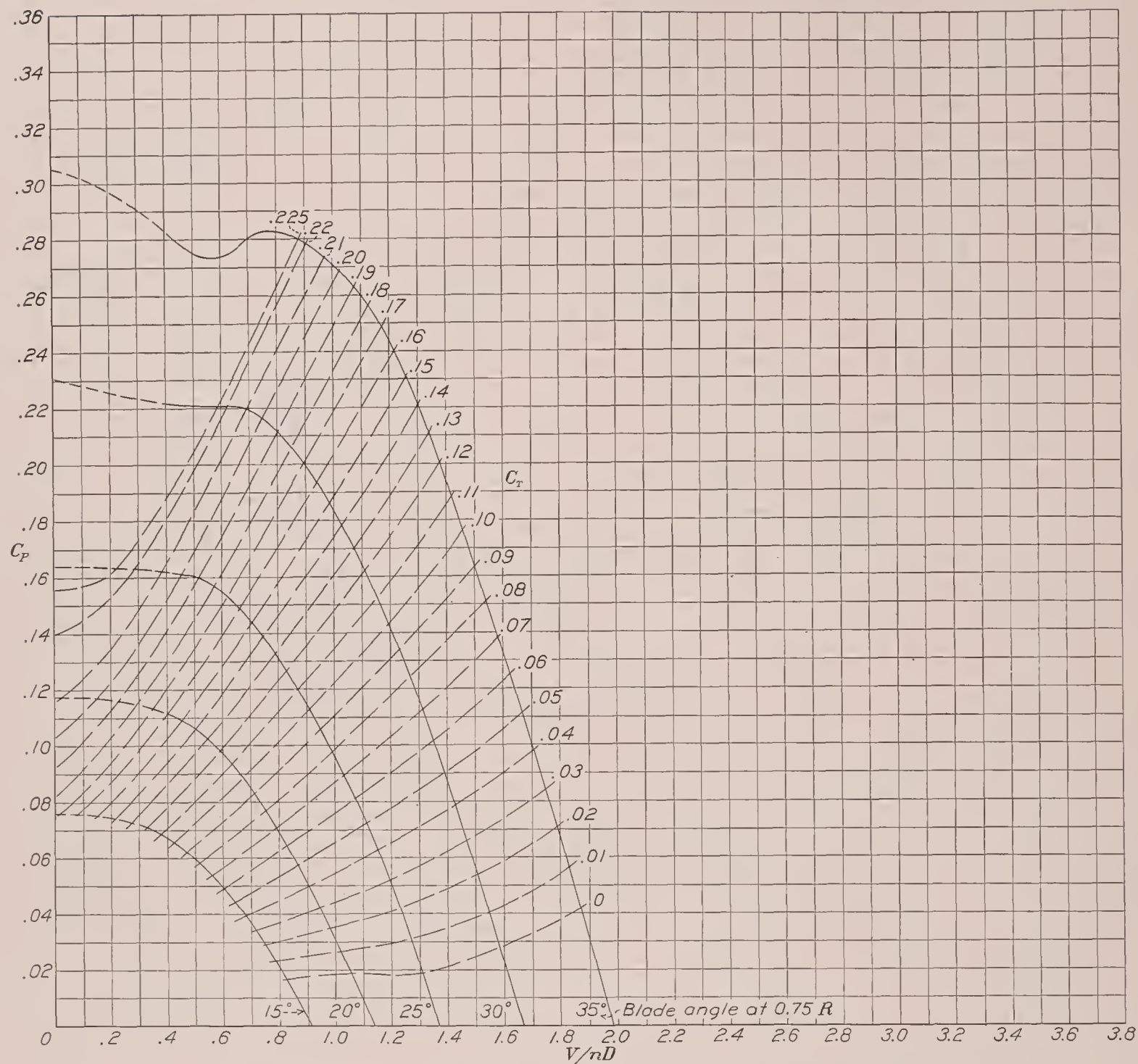


FIGURE 25.—Power-coefficient curves for propeller 5868-R6, R. A. F. 6 section, 4 blades.

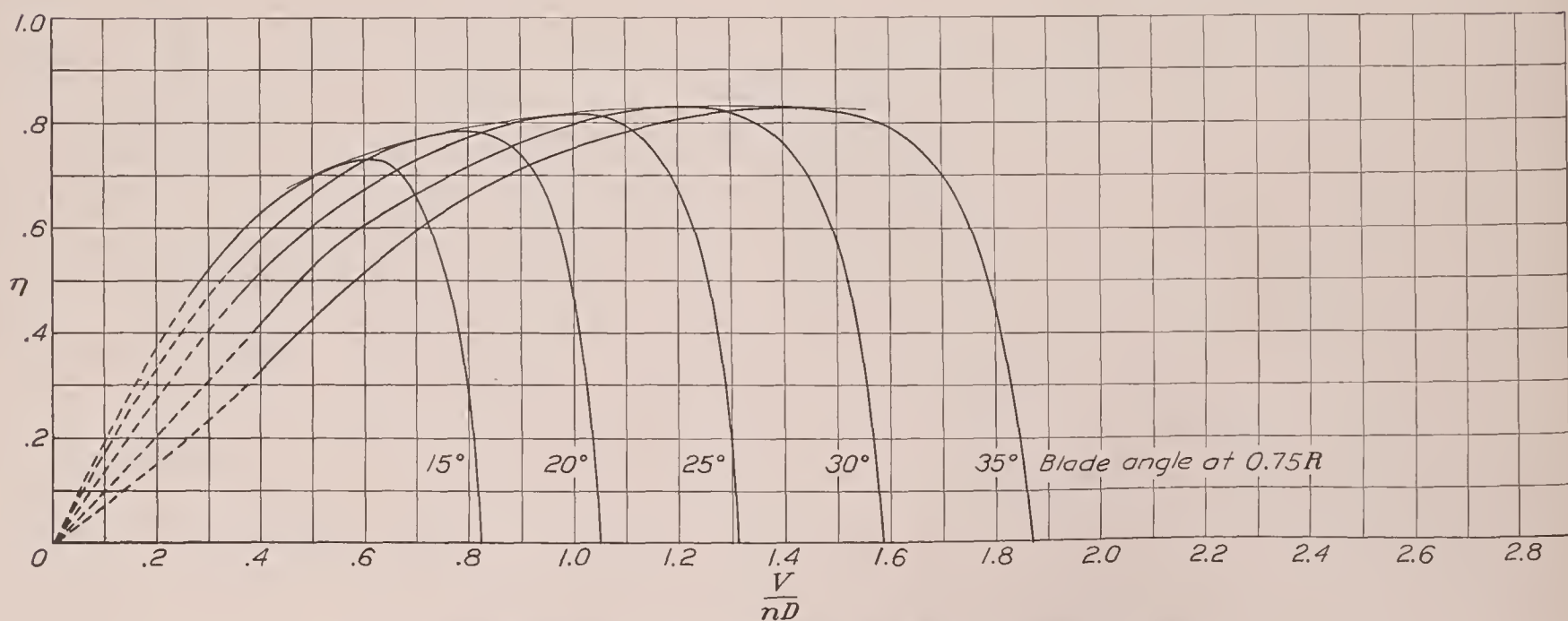


FIGURE 26.—Efficiency curves for propeller 5868-R6, R. A. F. 6 section, 4 blades.

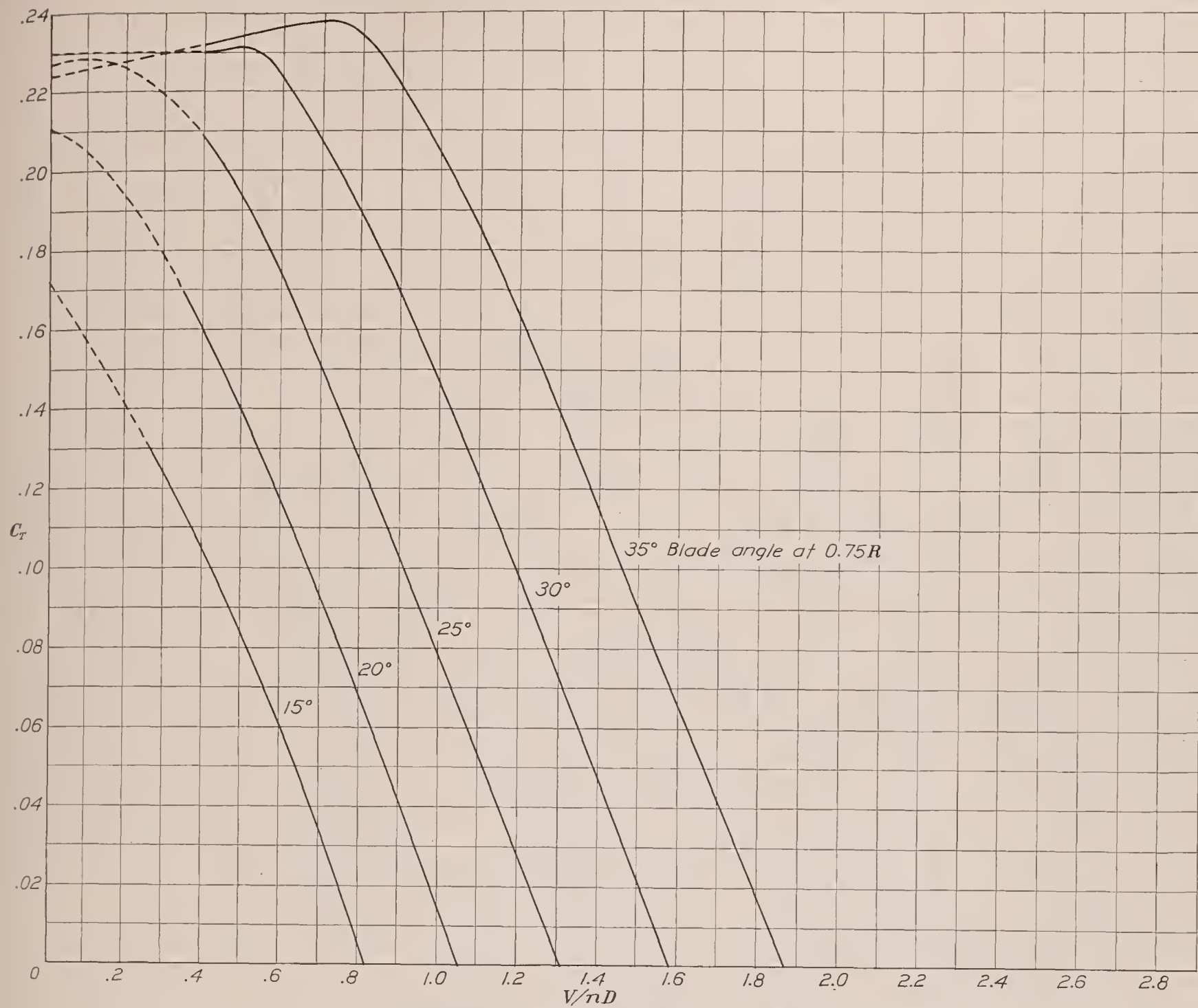


FIGURE 27.—Thrust-coefficient curves for propeller 5868-R6, R. A. F. 6 section, 4 blades.

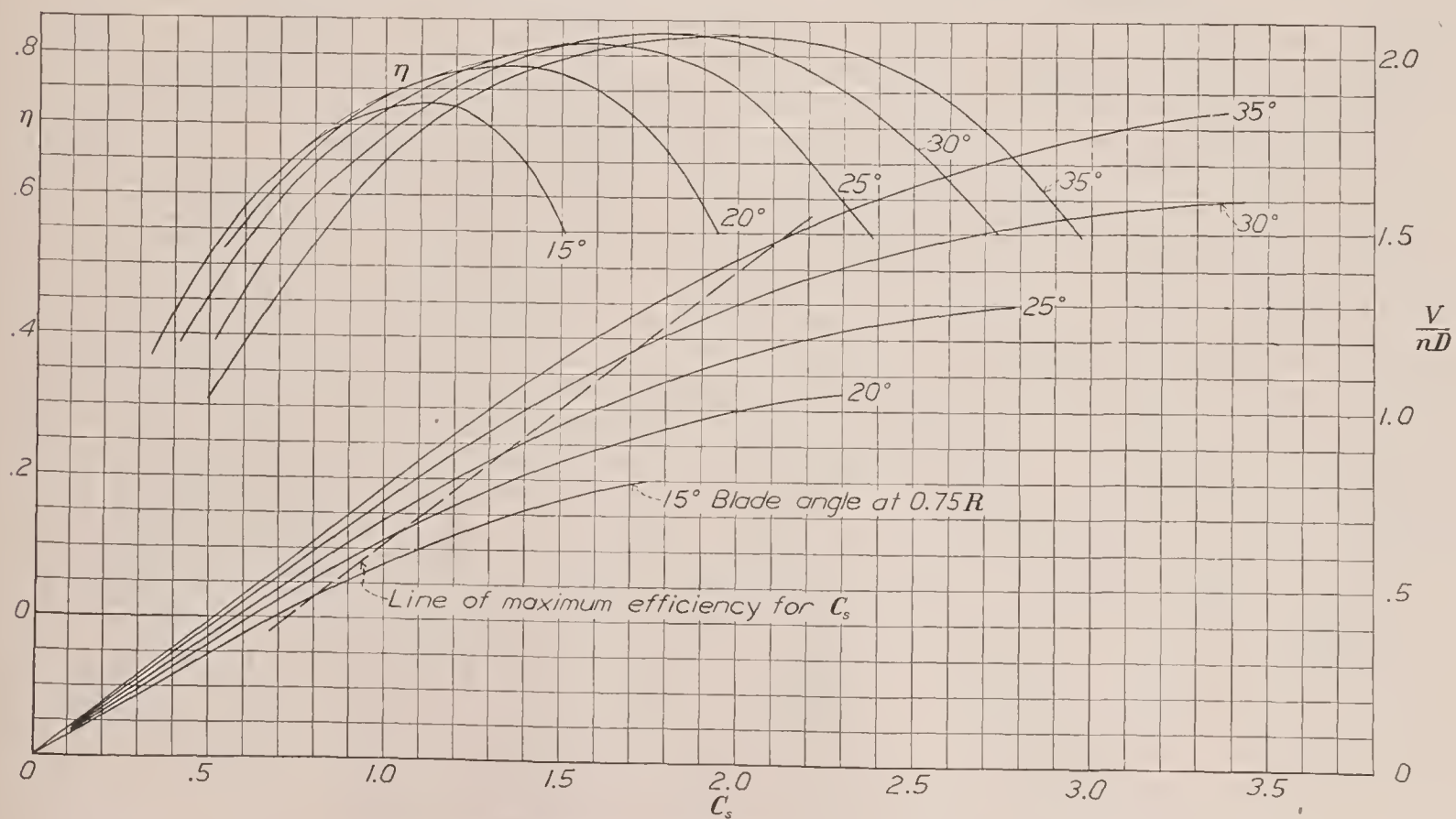


FIGURE 28.—Design chart for propeller 5868-R6, R. A. F. 6 section, 4 blades.

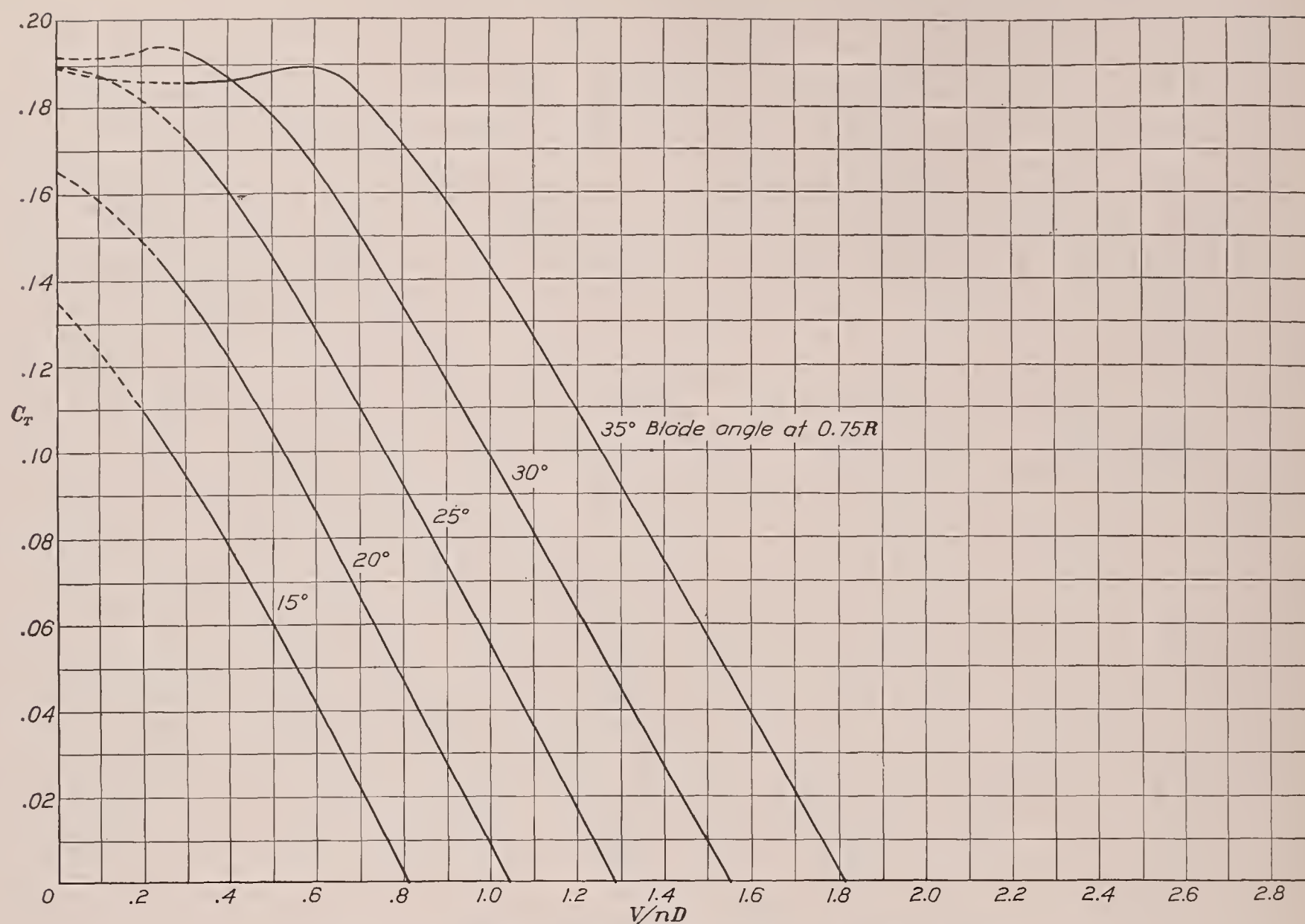


FIGURE 29.—Thrust-coefficient curves for propeller 37-3647, R. A. F. 6 section, 2 blades.

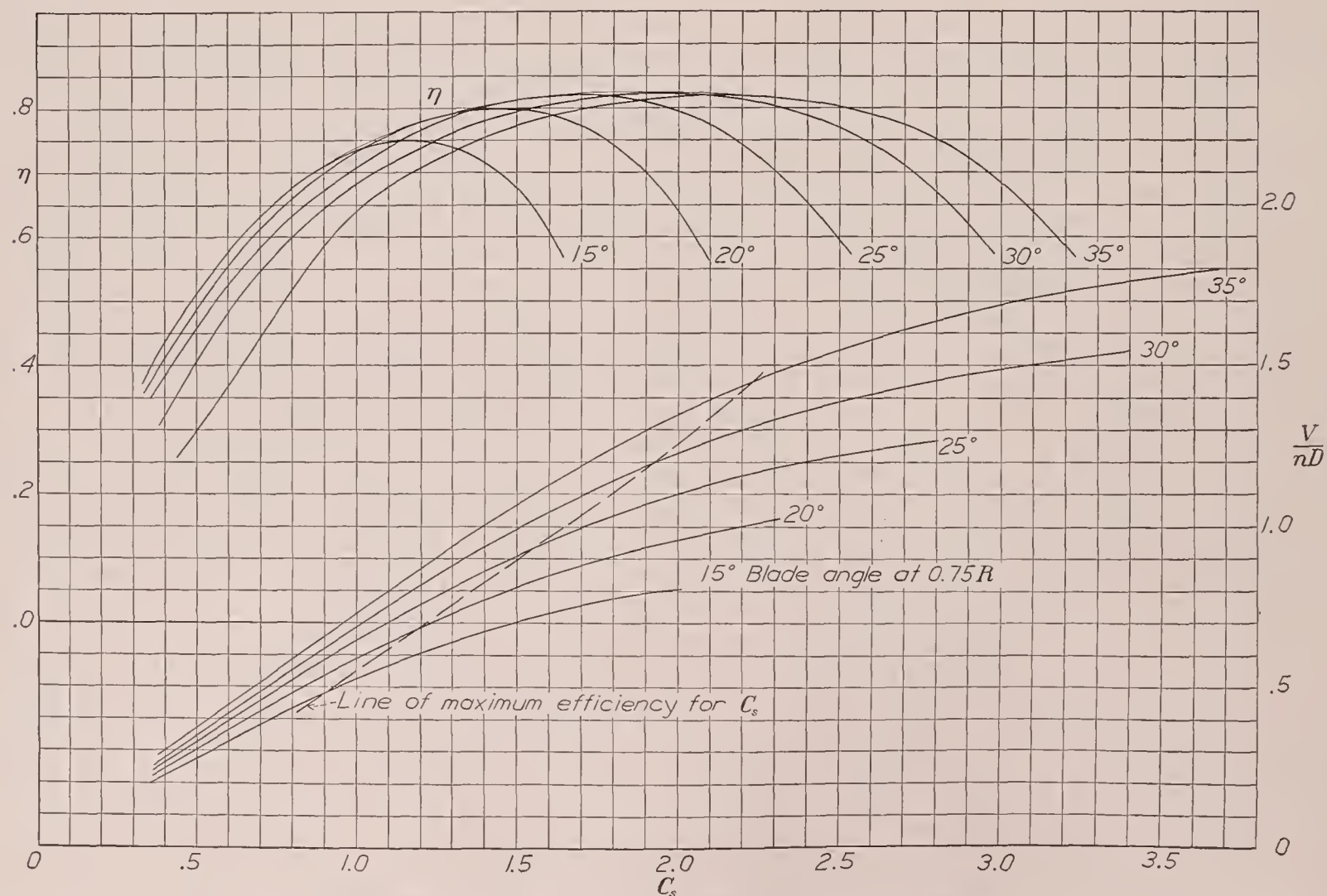


FIGURE 30.—Design chart for propeller 37-3647, R. A. F. 6 section, 2 blades.

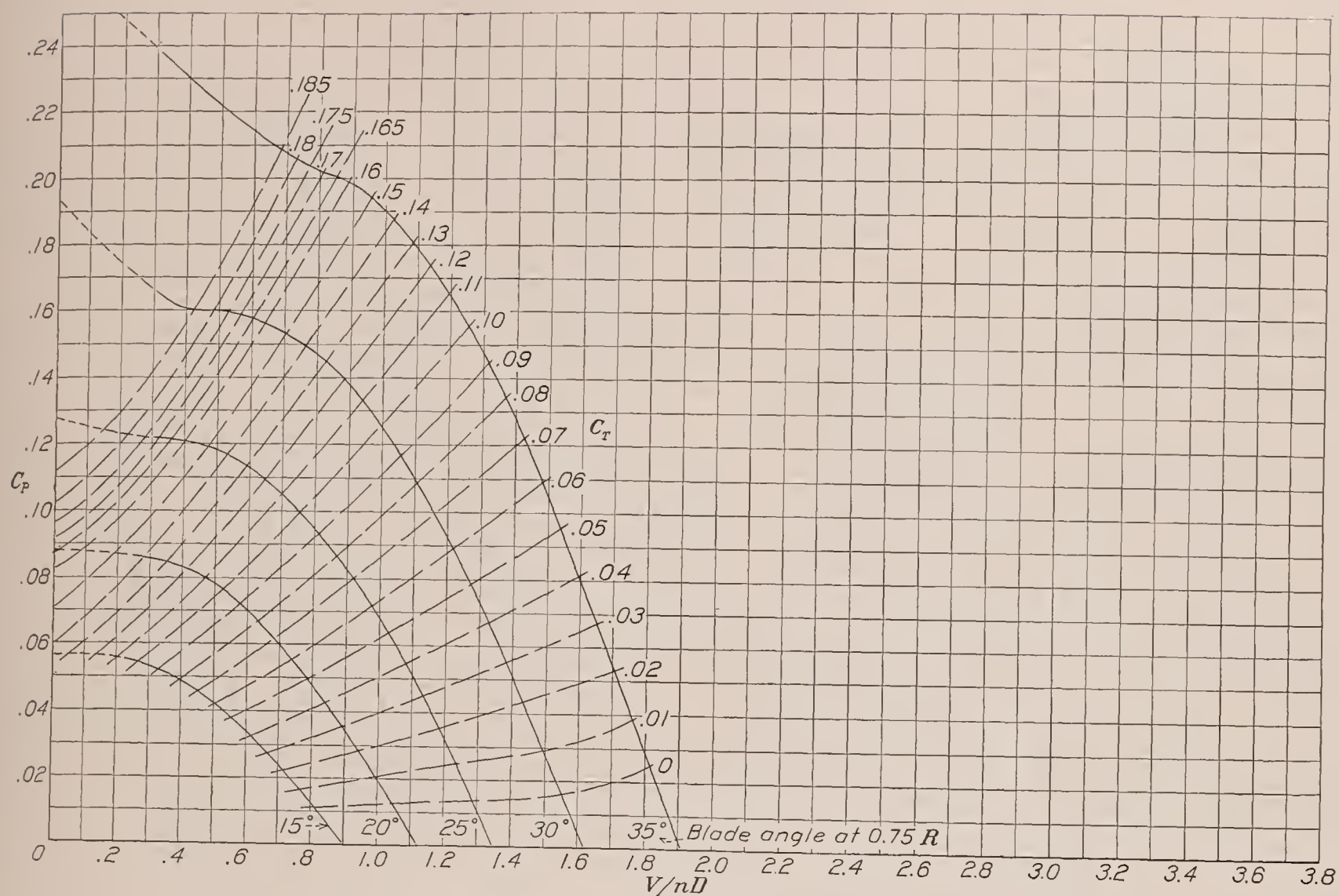


FIGURE 31.—Power-coefficient curves for propeller 37-3647, R. A. F. 6 section, 2 blades.

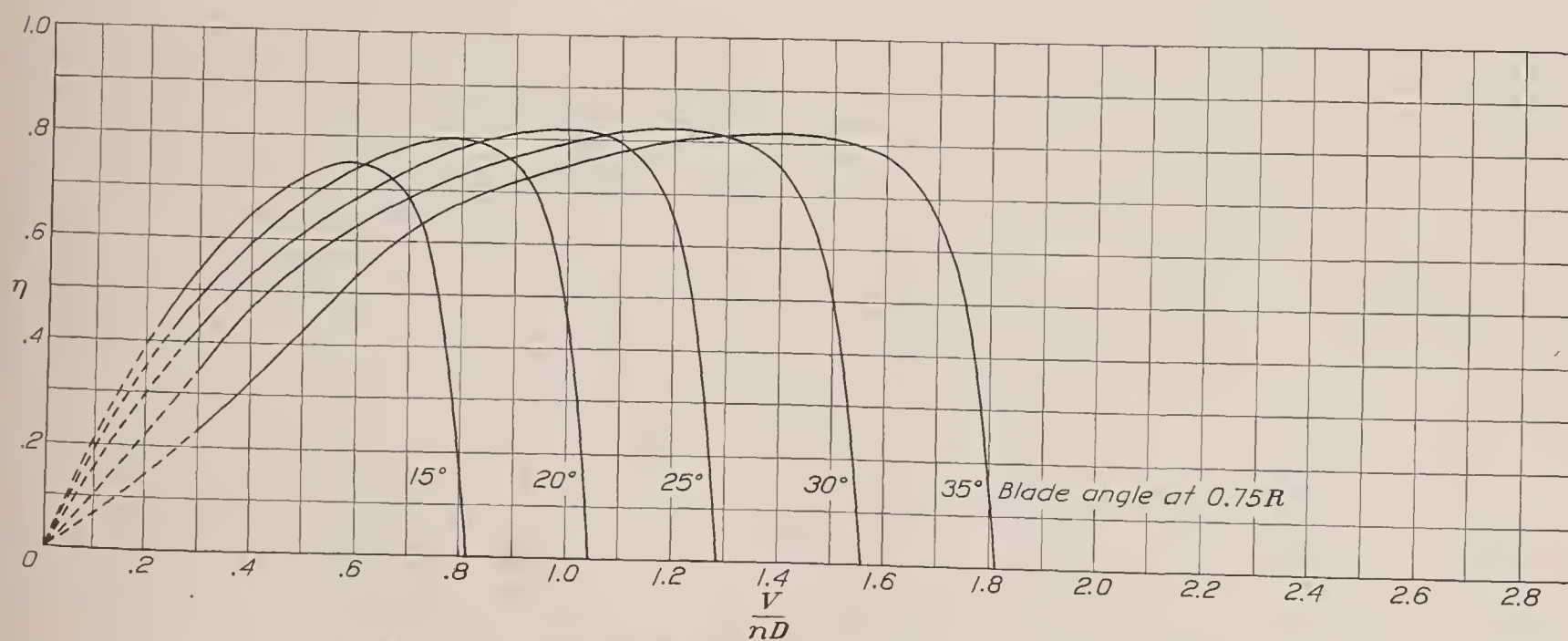


FIGURE 32.—Efficiency curves for propeller 37-3647, R. A. F. 6 section, 2 blades.

At peak efficiency the value of the ratio C_T/J^2 decreases with blade angle, so that the loss in peak efficiency caused by an increase of solidity may be expected to be less at the higher blade angles.

The effect on propeller characteristics of changing the number of blades is illustrated by the C_T , C_P , and η

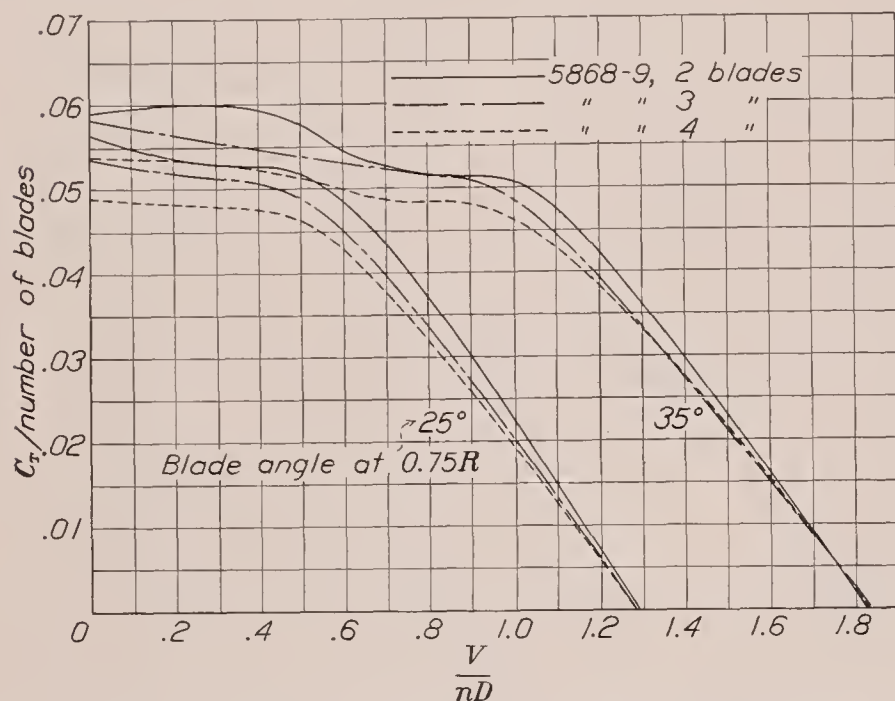


FIGURE 33.—Comparison of thrust coefficients for propellers having 2, 3, and 4 blades.

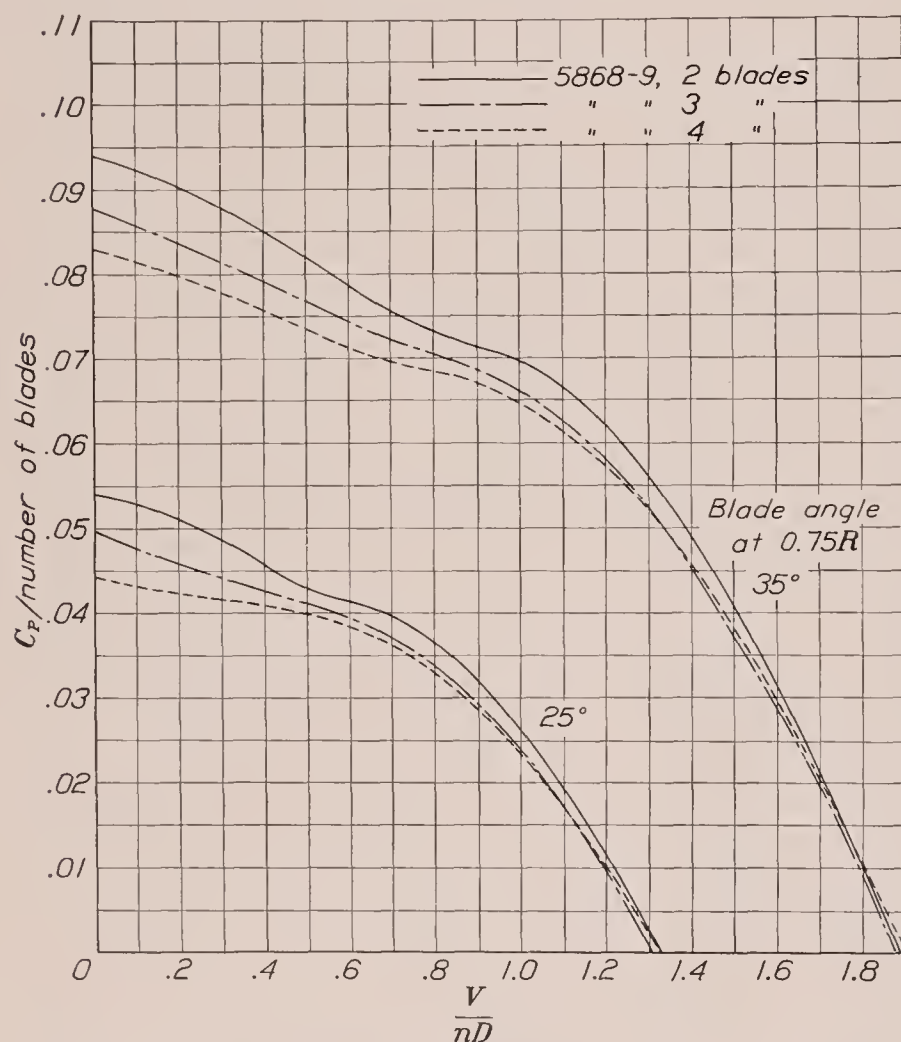


FIGURE 34.—Comparison of power coefficients for propellers having 2, 3, and 4 blades.

curves of figures 33, 34, and 35. Values are given for blade angles of 25° and 35° for all three propellers of Clark Y section.

Owing to the increase in inflow velocity, which theoretically is equal to $(V_s + V)/2$, with increasing number of blades, the thrust-coefficient and power-

coefficient curves slope less steeply. The curves come together at $C_T=0$ because here the slipstream velocity becomes zero.

The efficiency curves show a loss for the 3-blade and 4-blade propellers less than would be calculated from the simple momentum theory; in fact, in the portion of the curves where the blades begin to stall, the 3-blade and 4-blade propellers have a somewhat higher efficiency than the 2-blade propeller. The higher efficiency of the 3-blade and 4-blade propellers in the stalled range may be accounted for by the fact that their higher inflow velocities delay and reduce the severity of their stalling.

The effect of a change in solidity has been commonly thought to be the same whether the change results from variation in blade width or number of blades. Modern

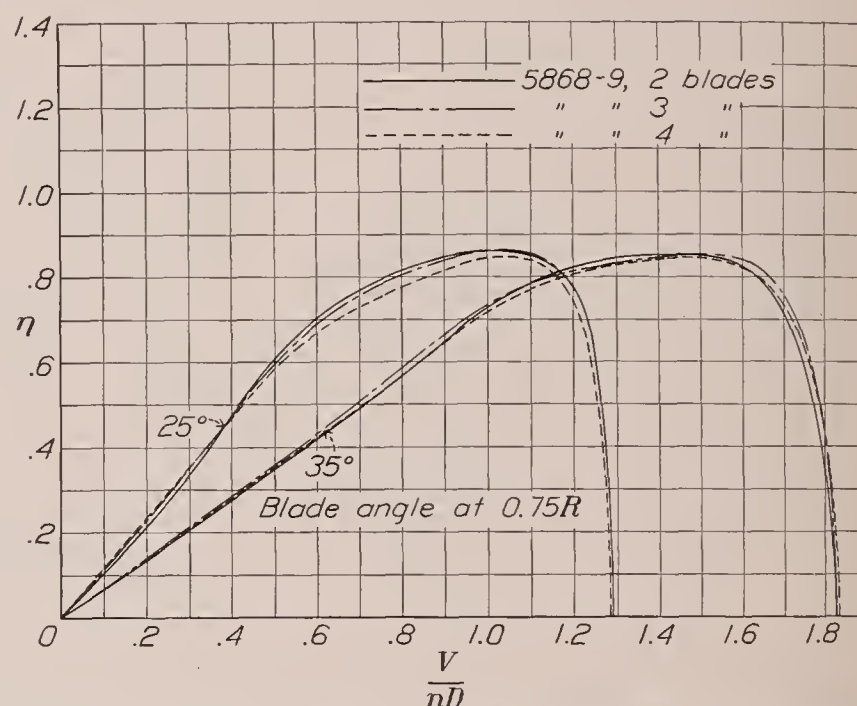


FIGURE 35.—Comparison of efficiency curves for propellers having 2, 3, and 4 blades.

theory and experimental evidence show this belief to be untrue.

The modern vortex theory of propellers pictures each propeller blade, as it describes its helical path through the air, leaving a continuous sheet of vortices behind it which, if no rotational interference velocity is assumed, moves straight backward with slipstream velocity in a manner somewhat similar to the way a screw conveyor appears to move. The strength and backward velocity of the vortex sheets depend on the strength of circulation around the blade itself which, of course, varies with the thrust and therefore with the blade width.

The air trapped between the sheets moves backward with them except for the part that slips forward around the edges of the sheets and produces a tip or edge vortex. The edge vortex destroys some of the circulation of the blade and produces what is known as a "tip loss."

Prandtl has shown (reference 4) that the edge flow, and therefore the tip loss, is reduced if the normal distance between two consecutive vortex sheets is reduced. The distance between vortex sheets is reduced

as the number of blades is increased and, for the ideal propeller with an infinite number of frictionless blades, as postulated in the simple momentum theory, the tip loss becomes zero.

The difference in effect between increasing the solidity

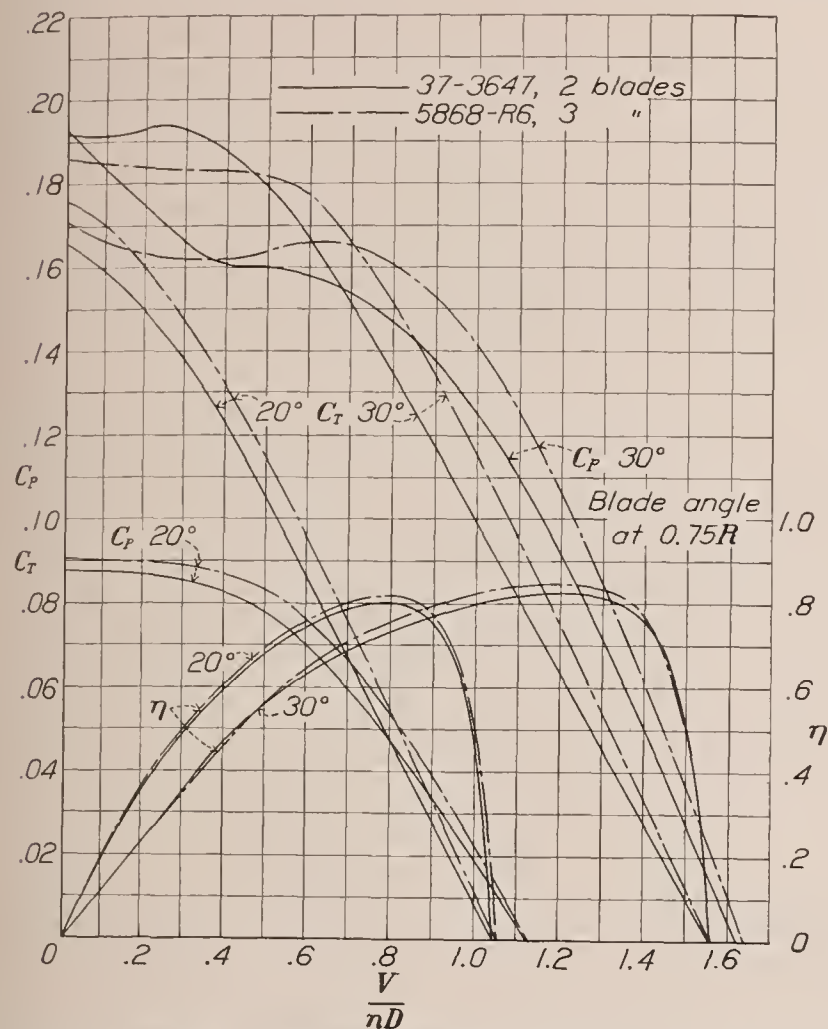


FIGURE 36.—Comparison of propeller coefficients for propellers having the same solidity but a different number of blades.

through the number of blades or through the blade width seems to depend on the following phenomena:

1. Increasing the number of blades decreases the tip loss, which tends to offset the bad effect of the increase in solidity.
2. Increasing the blade width increases the circulation strength around the blade, thus increasing the

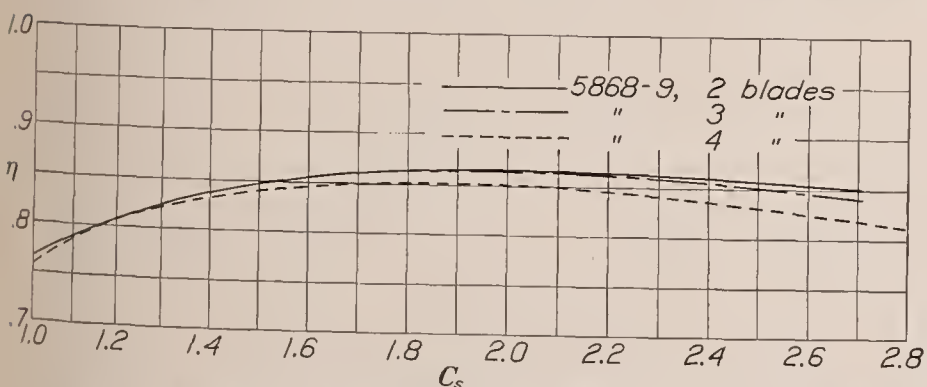


FIGURE 37.—Efficiency-curve envelopes for propellers having 2, 3, and 4 blades of Clark Y section.

local inflow velocity and adding to the bad effect caused by increased solidity.

Some of the results of the present tests, as shown in figure 36, illustrate these effects. In this figure there are shown coefficient curves for a 2-blade and a 3-blade propeller having the same solidity. The propellers

have the same diameter, airfoil section, and thickness ratio (h/b), the only difference being that the 2-blade propeller has a blade width 50 percent greater than the 3-blade propeller.

The 2-blade propeller is seen to be distinctly inferior through most of the V/nD range. The increase in local inflow is indicated by the lesser slope of the curves of the coefficients for the 2-blade propeller. It is interesting to note that when the blade stalls, as shown at low values of V/nD on the 30° curves, the power-coefficient, the thrust-coefficient, and the efficiency curves for the 2-blade propeller rise above those for the 3-blade propeller. This result could possibly be attributed to both the higher Reynolds Number at which the 2-blade propeller operated and to the increased inflow of the 2-blade propeller that delayed the stall.

PRACTICAL ASPECTS

From the viewpoint of a designer, it is probably better to compare the performance of propellers, at least their peak efficiencies, on a basis of C_s rather than of V/nD because the coefficient C_s represents the actual design conditions of power, revolution speed, and air speed.

In figures 37 and 38 are presented envelopes of the efficiency curves plotted against the coefficient C_s for the propellers having the Clark Y and the R. A. F. 6 sections, respectively. Each value of C_s represents a certain design condition. Through most of the C_s range for the propellers of both R. A. F. 6 and Clark Y section, the difference between the efficiencies of the 2-blade and 4-blade propellers is 2 percent or less. In both cases, the 3-blade propellers have the same, if not a little higher, efficiency than the 2-blade ones through a large part of the C_s range.

This result seems a bit out of the ordinary but could be explained by the fact that the limits of accuracy of the tests were such as to cause the peak efficiency to vary about 1 percent. The fact that the same condition exists for both the Clark Y and the R. A. F. 6 propellers suggests, however, a legitimacy for the re-

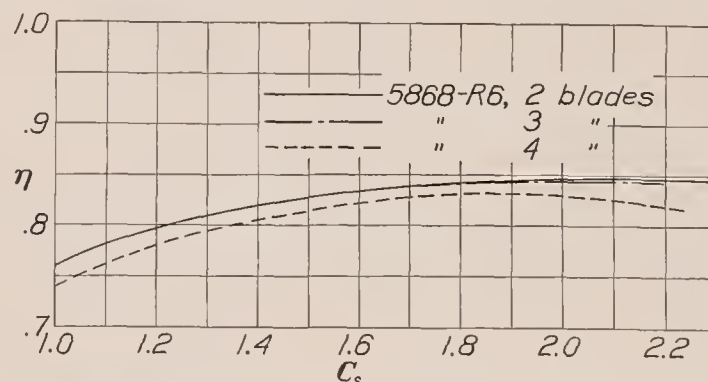


FIGURE 38.—Efficiency-curve envelopes for propellers having 2, 3, and 4 blades of R. A. F. 6 section.

sults. The curves do show, in spite of these minor inconsistencies, that the difference in peak efficiency between 2-blade, 3-blade, and 4-blade propellers is small.

The envelopes of the efficiency curves plotted against V/nD , as in figure 39, seem to bear out the theory that the difference in peak efficiencies of 2-blade, 3-blade,

and 4-blade propellers should grow less at higher values of blade angle. The opposite appears to be true, however, when, on a more practical basis, the efficiency-curve envelope is plotted against C_s , as in figure 37.

Figure 40 shows efficiency-curve envelopes for 2-blade and 3-blade propellers having the same solidity. The separation of the two curves is about 2 percent in this case. It should be pointed out, in connection with the results indicated in figures 36 and 40, that the blade thickness of the wide propeller was increased in proportion to its breadth (to maintain a constant thickness ratio and airfoil section) so that it is probably somewhat thicker than necessary for strength purposes. Part of the difference in the efficiency between the

The lack of data for the 3-blade propeller in the past has resulted in the use of empirical methods of making 3-blade and 4-blade propeller selections from 2-blade-propeller data. As the propeller with the greater number of blades absorbs more power, it is customary to use a certain fraction of the available power in computing the value of C_s to be used with the 2-blade-propeller charts. This method is an approximation and will not give the optimum propeller diameter and blade angle for the design condition, although the difference may not be large. The convenience of this approximation has more than offset its faults and, now that data for 3-blade and 4-blade propellers are available, it is interesting to compare the ratios of the power absorbed

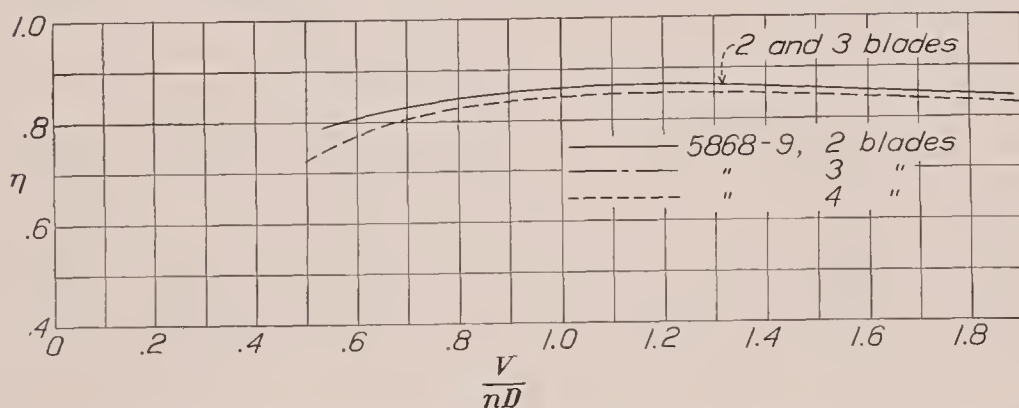


FIGURE 39.—Efficiency-curve envelopes (against V/nD) for propellers having 2, 3, and 4 blades of Clark Y section.

2-blade and the 3-blade propellers having the same solidity would undoubtedly be offset by thinning the 2-blade propeller, although such a procedure would, of course, change the airfoil section.

A general comparison of the take-off qualities of the various propellers was not attempted as there was no basis of comparison that would have been entirely fair

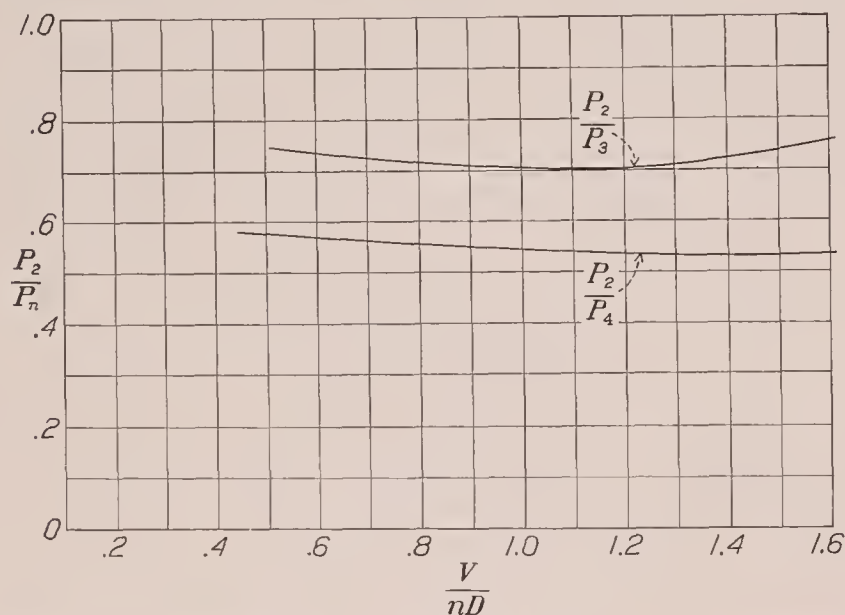


FIGURE 41.—Ratios of power absorbed by propellers having 2, 3, and 4 blades for the high-speed design condition.

to all propellers. Any designer having a choice of two or more propellers can calculate their thrusts in the take-off range by the methods given in the appendix of this report. The designer knowing the design limitations peculiar to his particular problem will thus be able to make a satisfactory comparison.

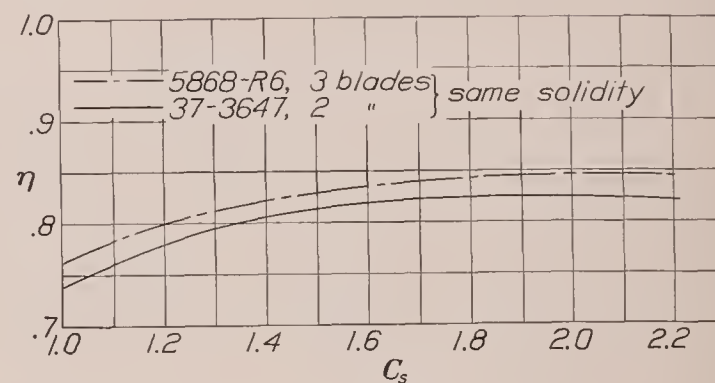


FIGURE 40.—Efficiency-curve envelopes for two propellers having the same solidity but a different number of blades.

by the 2-blade, 3-blade, and 4-blade propellers. Such a comparison is shown in figure 41; in figure 42 is shown a similar comparison for the 2-blade and 3-blade propellers having the same solidity. The curves in figure 41 represent the mean of the curves for the Clark Y and R. A. F. 6 propellers, which were separated by a small amount.

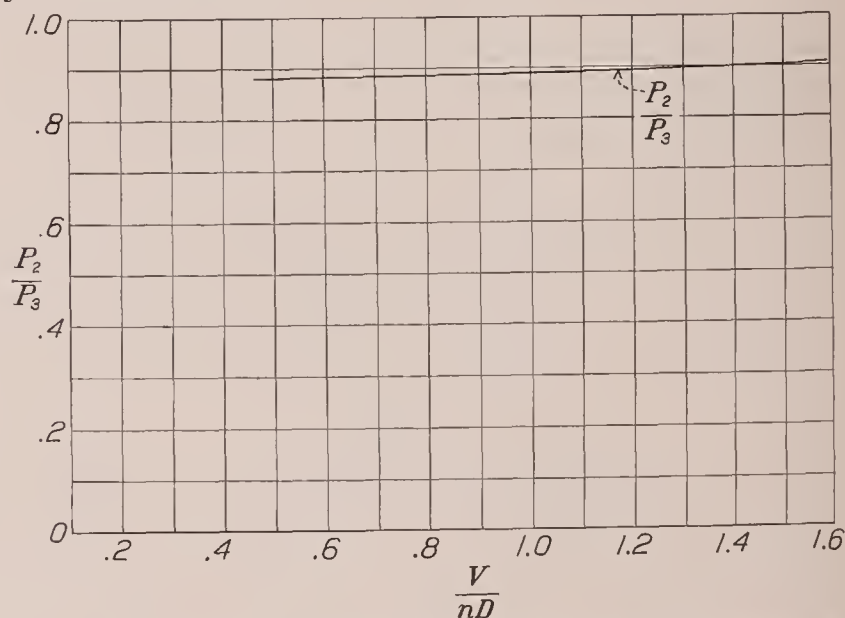


FIGURE 42.—Ratio of power absorbed by 2-blade and 3-blade propellers having the same solidity for the high-speed design condition.

Throughout the V/nD range shown in figure 41, the 2-blade propeller absorbs from 70 to 75 percent of the power absorbed by the 3-blade propeller and from 53 to 58 percent of the power absorbed by the 4-blade propeller. The 3-blade propeller 5868-R6 absorbs more power than the 2-blade propeller 37-3647, which has the same solidity. The ratio of their powers, P_2/P_3 , varies (fig. 42) from 0.88 to 0.91.

The information given in figures 41 and 42 indicates that the power absorbed by two propellers having simi-

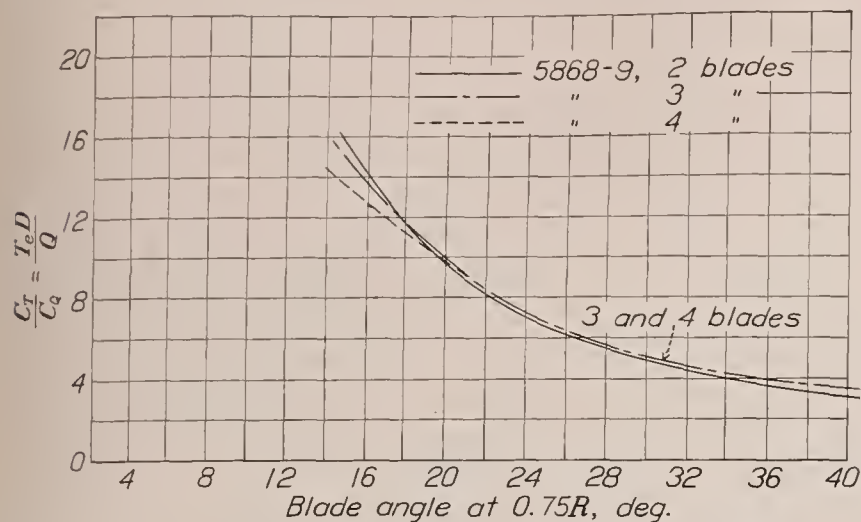


FIGURE 43.—Comparison of static-thrust characteristics of propellers having 2, 3, and 4 blades of Clark Y section.

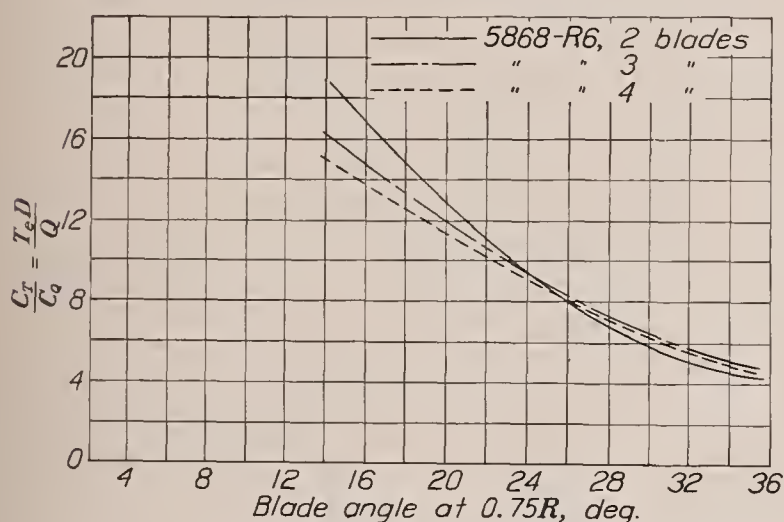


FIGURE 44.—Comparison of static-thrust characteristics of propellers having 2, 3, and 4 blades of R. A. F. 6 section.

lar blades but different total blade areas is not directly proportional to the blade area; a direct relation may be

used, however, when the differences in blade areas are small.

Some interest has been shown in the past concerning the static thrust of propellers. Although static thrust has little importance in connection with the take-off problem, it may possibly be of interest for other reasons. Figures 43 and 44 have therefore been included; they are plots of C_T/C_Q , taken at $V/nD=0$, against blade angle for 2-blade, 3-blade, and 4-blade Clark Y and R. A. F. 6 propellers, respectively. As C_T/C_Q equals $T_e D/Q$, the curves represent the effective static thrust for any given value of torque and diameter. It is seen that, at blade angles above 20° , the static thrusts of the 3-blade and 4-blade propellers are higher than those for the 2-blade propeller. This result is due to the more favorable stalling characteristics of propellers of higher solidity.

CONCLUSIONS

1. The tests showed a 3-blade propeller to have a higher peak efficiency than a 2-blade propeller having the same solidity, thickness ratio, airfoil section, and diameter.
2. The loss in efficiency commonly conceived to be the result of increasing the solidity by adding blades was not fully realized. The tests showed only about 2 percent difference in peak efficiency between propellers having 2 and 4 blades.
3. An increase in solidity tended to delay the stall and to increase the efficiency in the take-off range.

LANGLEY MEMORIAL AERONAUTICAL LABORATORY,
NATIONAL ADVISORY COMMITTEE FOR AERONAUTICS,
LANGLEY FIELD, VA., November 9, 1937.

APPENDIX

SELECTION OF PROPELLERS AND THRUST CALCULATION

SELECTION

The type of C_s chart given in figures 7, 10, 14, 17, 24, 28, and 30 has been the standard N. A. C. A. design chart since 1929 (see reference 5) and its use requires but little explanation. In the selection of a propeller for any given engine and airplane, the first step is to calculate C_s from the equation:

$$C_s = \frac{0.638 \times \text{m. p. h.} \times \left(\frac{\rho}{\rho_0}\right)^{1/5}}{(\text{b. hp.})^{1/6} \times (\text{r. p. m.})^{2/5}}$$

where the speed, the horsepower, and the engine revolution speed are the values representing the design conditions and ρ/ρ_0 is the relative density. With this value of C_s , project upward on the C_s chart to the broken line of maximum efficiency for C_s . This point determines the blade angle and a horizontal projection to the V/nD scale gives the design V/nD with which the diameter D may be calculated from the relation

$$D = \frac{\text{m. p. h.} \times 88}{\text{r. p. m.} \times \frac{V}{nD}}$$

The design efficiency is obtained by projecting upward from the design C_s to the envelope of the efficiency curves.

CALCULATION OF PROPELLER THRUST

The problem of calculating the thrust of a propeller throughout the take-off and the flight range of air speeds resolves itself into two parts, one for the controllable constant-speed propeller and the other for the fixed-pitch propeller.

Many varieties of specialized charts have been designed for such calculations, but the basic charts of C_T and C_P plotted against V/nD are the only ones actually necessary. The calculations are somewhat facilitated if lines of constant C_T are superimposed on the C_P chart, in which case only that one chart is necessary.

Constant-speed propeller.—The first step in calculating the take-off thrust for a particular airplane and propeller is to compute the value of the power coefficient C_P from the equation $C_P = P/\rho n^3 D^5$. This equation may be put in the more usable form:

$$C_P = \frac{\text{b. hp.}}{2 \frac{\rho}{\rho_0} \left(\frac{\text{r. p. m.}}{100}\right)^3 \left(\frac{D}{10}\right)^5}$$

where b. hp. and r. p. m. are the take-off brake horsepower and engine speed and ρ/ρ_0 is the relative density of

the air. For a constant-speed propeller, this value of C_P will remain constant throughout the take-off range and so may be represented by a straight line on the chart of C_P against V/nD . Now at even values of V/nD , pick off interpolated values of C_T along this straight line and compute $\eta = C_T/C_P \times V/nD$. Since the engine speed and diameter are constant, each value of V/nD represents a certain air speed, which may be obtained from the following relation:

$$V = \frac{\text{r. p. m.} \times D}{88} \times \frac{V}{nD}$$

in miles per hour. The propeller thrust is obtained from the relation

$$T = \frac{\text{b. hp.} \times \eta \times 375}{\text{m. p. h.}} = \text{constant} \times C_T$$

The foregoing simple method provides data for a plot of thrust against air speed for the take-off range of air speeds. The same method may be used for the climbing and flight range.

An obvious simplification would have been obtained if lines of constant efficiency instead of constant thrust coefficient had been superimposed on the C_P curves. Past experience, however, has shown that more accurate values of thrust may be obtained with the method here presented.

Fixed-pitch propellers.—It is assumed, in the use of the method of calculating the thrust for fixed-pitch propellers, that the following sea-level design characteristics of the airplane, the engine, and the propeller are known:

V_0 , design air speed, m. p. h.

N_0 , design engine speed, r. p. m.

(b. hp.)₀, design engine power (rated power).

$\left(\frac{V}{nD}\right)_0 = J_0$, design V/nD .

η_0 , design efficiency (high speed or cruising).

D , propeller diameter, ft.

β_0 , design blade angle at $0.75R$.

The method may conveniently be put into step form as follows:

1. Using J_0 and β_0 , obtain C_{T0} and C_{P0} from charts of C_T and C_P against V/nD .

2. At even values of J pick off values of C_T and C_P along line of constant β_0 (interpolate when necessary).

3. Compute $\frac{J}{J_0}$, $\frac{C_T}{C_{T0}}$, $\frac{C_P}{C_{P0}}$

4. Compute $\frac{N}{N_0} = \sqrt{\frac{C_{P0}}{C_P}}$

5. Compute $T_0 = [\eta_0 \times (\text{b. hp.})_0 \times 375] / V_0$

6. Compute $V = V_0 \times \frac{J}{J_0} \times \frac{N}{N_0}$

7. Compute thrust, $T = T_0 \times \frac{C_{P_0}}{C_{T_0}} \times \frac{C_T}{C_P} = K \times \frac{C_T}{C_P}$

$$\text{where } K = \frac{T_0 C_{P_0}}{C_{T_0}}$$

This method assumes that the full-throttle engine torque is constant.

As an example, assume that it is desired to obtain the propeller thrust through the take-off and climbing ranges for an airplane having the following characteristics:

$V_0 = 190$; $N_0 = 1,500$; $(\text{b. hp.})_0 = 600$; $J_0 = 1.00$;
 $D_0(2\text{-blade}) = 11 \text{ feet } 1\frac{1}{2} \text{ inches}$; $\eta_0 = 0.862$; $\beta_0 = 25^\circ$.

Blade section = Clark Y.

The computed data may be conveniently tabulated as follows:

$C_{T_0} = 0.0448$; $C_{P_0} = 0.0520$; $T_0 = 1,020 \text{ lb.}$; $J_0 = 1.00$.

J	J/J_0	C_T	C_P	C_T/C_P	C_{P_0}/C_P	N/N_0	V (m. p. h.)	T (lb.)
0.1	0.1	0.110	0.1056	1.042	0.493	0.702	13.3	1,232
.2	.2	.1075	.1017	1.059	.512	.720	27.4	1,252
.3	.3	.1058	.0972	1.088	.535	.731	41.7	1,287
.4	.4	.1055	.0911	1.158	.571	.755	57.4	1,370
.5	.5	.1037	.0858	1.207	.607	.778	74.0	1,427
.6	.6	.0970	.0823	1.178	.632	.795	90.6	1,392
.7	.7	.0870	.0790	1.100	.658	.811	108.0	1,300
.8	.8	.0748	.0732	1.022	.710	.842	128.0	1,210

$$K = \frac{0.0520}{0.0448} \times 1,020 = 1,182$$

Effect of blade width and body.—The two methods given of calculating thrust, and also the method of selecting propellers, assumed that the propellers under consideration had the same blade width as the ones for which the data are given in this report. Frequently it may be required to find the diameter, the design blade-angle setting, and the thrust of a propeller having a blade width slightly different from those tested. As was mentioned earlier, it may be assumed that the power and the thrust vary directly with the blade areas (or blade widths) for propellers with similar shape characteristics where the differences in areas are small.

In the calculation of C_s , the power should therefore be multiplied by the ratio of the blade widths b_1/b_2 , where b_1 is the blade width at three-quarters radius of the propeller for which the design charts were made and b_2

is the blade width at the same radius for the propeller under consideration.

The same ratio should be used in calculating the value of C_P to be used in obtaining the take-off thrust, and the take-off thrust obtained from the charts should be divided by this ratio to obtain the actual thrust of the propeller.

Similarly, corrections are necessary in the case where the body under consideration is greatly different from the liquid-cooled engine nacelle with which the present tests were made. Some information with regard to the effect of the body on the propulsive efficiency may be obtained from reference 2. The added drag of those parts of the airplane in the slipstream (other than the body itself) should also be considered. Parts of the wing, the tail surfaces, and the landing gear are often in the propeller slipstream and their added drag due to the slipstream may be approximated from the following relation:

$$\frac{\Delta D}{D} = 2.5 C_T / J^2$$

where ΔD is the added drag and D is the drag without slipstream.

The test data for a propeller having one airfoil section should not be used to calculate the performance of a propeller having another airfoil section.

It is shown in reference 3 that compressibility often has a marked effect on the performance of a propeller in the take-off range. The necessary corrections for compressibility are not easily applied but methods of making such corrections are explained in reference 3.

REFERENCES

1. Weick, Fred E., and Wood, Donald H.: The Twenty-Foot Propeller Research Tunnel of the National Advisory Committee for Aeronautics. T. R. No. 300, N. A. C. A., 1928.
2. Biermann, David, and Hartman, Edwin P.: Tests of Five Full-Scale Propellers in the Presence of a Radial and a Liquid-Cooled Engine Nacelle, Including Tests of Two Spinners. T. R. No. 642, N. A. C. A., 1938.
3. Biermann, David, and Hartman, Edwin P.: The Effect of Compressibility of Eight Full-Scale Propellers Operating in the Take-Off and Climbing Range. T. R. No. 639, N. A. C. A., 1938.
4. Glauert, H.: Airplane Propellers. Vol. IV, div. L of Aerodynamic Theory, W. F. Durand, ed., Julius Springer (Berlin), 1935, p. 261.
5. Weick, Fred E.: Working Charts for the Selection of Aluminum Alloy Propellers of a Standard Form to Operate with Various Aircraft Engines and Bodies. T. R. No. 350, N. A. C. A., 1930.

REPORT No. 641

THE NEGATIVE THRUST AND TORQUE OF SEVERAL FULL-SCALE PROPELLERS AND THEIR APPLICATION TO VARIOUS FLIGHT PROBLEMS

By EDWIN P. HARTMAN and DAVID BIERMANN

SUMMARY

Negative thrust and torque data for 2-, 3-, and 4-blade metal propellers having Clark Y and R. A. F. 6 airfoil sections were obtained from tests in the N. A. C. A. 20-foot tunnel. The propellers were mounted in front of a radial engine nacelle and the blade-angle settings covered in the tests ranged from 15° to 90°. One propeller was also tested at blade-angle settings of 0°, 5°, and 10°.

A considerable portion of the report deals with the various applications of the negative thrust and torque to flight problems. A controllable propeller is shown to have a number of interesting, and perhaps valuable, uses within the negative thrust and torque range of operation. A small amount of engine-friction data is included to facilitate the application of the propeller data.

INTRODUCTION

In 1932 the N. A. C. A. made a series of tests of a 4-foot metal propeller covering the negative thrust and torque range of operation for blade angles from -23° to 22° . These data (reference 1) have been used to a considerable extent though it became evident soon after their publication that the tests had not been carried far enough into the range of positive blade angles to provide all the data required by designers. Contemporarily with the tests of reference 1, a series of dive tests was made by the N. A. C. A. of an F6C-4 airplane to determine the possibilities of using the propeller in reducing the terminal diving speeds of military airplanes. From these tests (reference 2) sufficient propeller data were obtained to provide a set of negative thrust and torque curves covering a range of blade angles from 6° to 22° . In 1936 the negative thrust and torque characteristics of an 18-inch propeller mounted on a complete airplane model were obtained at the California Institute of Technology (reference 3). The tests covered a blade-angle range from 12° to 50° and both 2- and 3-blade propellers were tested. These three sources provide most of the available known data on the negative thrust and torque of metal propellers.

As the possibilities connected with the use of controllable propellers have become more fully realized, the negative thrust and torque range of propeller

operation has received an increasing share of the designer's attention. It appeared desirable to make additions to the meager supply of data in this field of propeller operation. A study of negative thrust and torque was therefore made a part of a general full-scale propeller-research program being conducted in the N. A. C. A. 20-foot tunnel.

The final data are presented in this report in a form conveniently applicable to the solution of design problems. Since the negative thrust of a windmilling propeller depends upon its rate of rotation, which in turn depends upon the friction torque of the engine, it is obvious that information with regard to engine friction is necessary for the ready use of the data. A certain amount of friction data, gleaned from various sources, has been included and should enable a reasonable estimate to be made with regard to the friction characteristics of an engine if particular and exact data are not available. As a further means of increasing the utility of the material, examples are included showing how the data may be used for attacking various problems.

APPARATUS AND METHODS

General.—The tests were made in the N. A. C. A. 20-foot wind tunnel described in reference 4. The air speed at which the tests were made varied between 100 and 110 miles per hour, which is the maximum speed of the tunnel.

The propellers were mounted on a water-cooled Curtiss Conqueror GIV 1570-C engine, the direction of rotation of which had been reversed to accommodate the right-hand propellers available for the tests. The engine was enclosed in a dummy radial engine nacelle having a length of about 10 feet and a maximum diameter of 52 inches. The air-cooled cylinders were simulated by a perforated disk whose conductivity, or free-air passage, approximated that of a moderately baffled engine installation. A photograph of the set-up is shown in figure 1.

The variations of engine speed, when the engine was being turned by the propeller, were obtained by the use of a hydraulic brake from an automobile truck. The brake drum was attached to the propeller shaft and the shoe mechanism to the engine gear case.

Propellers.—Six different propellers of modern design, comprising two sets of propellers with 2, 3, and 4 blades, were tested. All the propellers tested had the same diameter (10 feet), blade width, blade thickness, plan form, and pitch distribution. The propellers were of Navy design having Navy drawing numbers 5868-9 and 5868-R6. The 5868-9 propellers had Clark Y airfoil sections and the 5868-R6 propellers had R. A. F. 6 sections. The blade-form curves for the propellers are given in figure 2, which also shows the plan form and airfoil sections.

Method.—The torque and thrust forces were measured by scales in the balance house on the test-chamber floor. The engine speed was measured by an electrical tachometer, the meter of which was located beside the engine controls in the balance house. The engine controls were hydraulically operated.

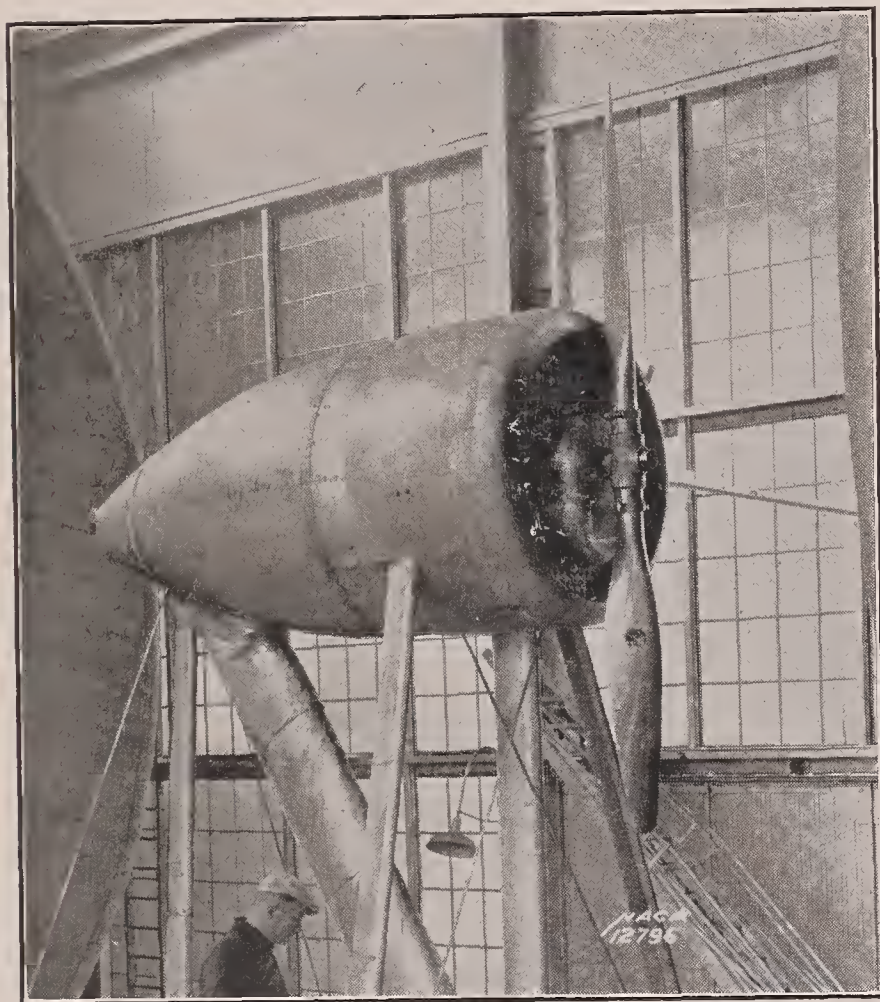


FIGURE 1.—The propeller test set-up.

During tests, the tunnel speed was held substantially constant and the engine throttled step by step to zero throttle opening; the switch was then cut and the braking force applied in increments until the propeller stopped. Through this process, readings were taken at frequent intervals producing a continuous curve in the plotted data. The foregoing method was used for blade angles up to 70° , beyond which only the drag and torque of the locked propeller could be obtained.

RESULTS AND DISCUSSION

Coefficients and symbols.—The thrust and torque coefficient forms used in plotting the data in this report are as follows:

$$T_c = \frac{T_e}{\rho V^2 D^2}$$

$$Q_c = \frac{Q}{\rho V^2 D^3}$$

$$Q_n = Q_c \frac{nD}{V} = \frac{Q/n}{\rho V D^4}$$

where $T_e = T - \Delta D$, effective thrust, lb.

T , thrust of propeller (axial force in propeller shaft), lb.

ΔD , change in drag of airplane or body due to slipstream, lb.

Q , aerodynamic torque (negative when it assists rotation), ft.-lb.

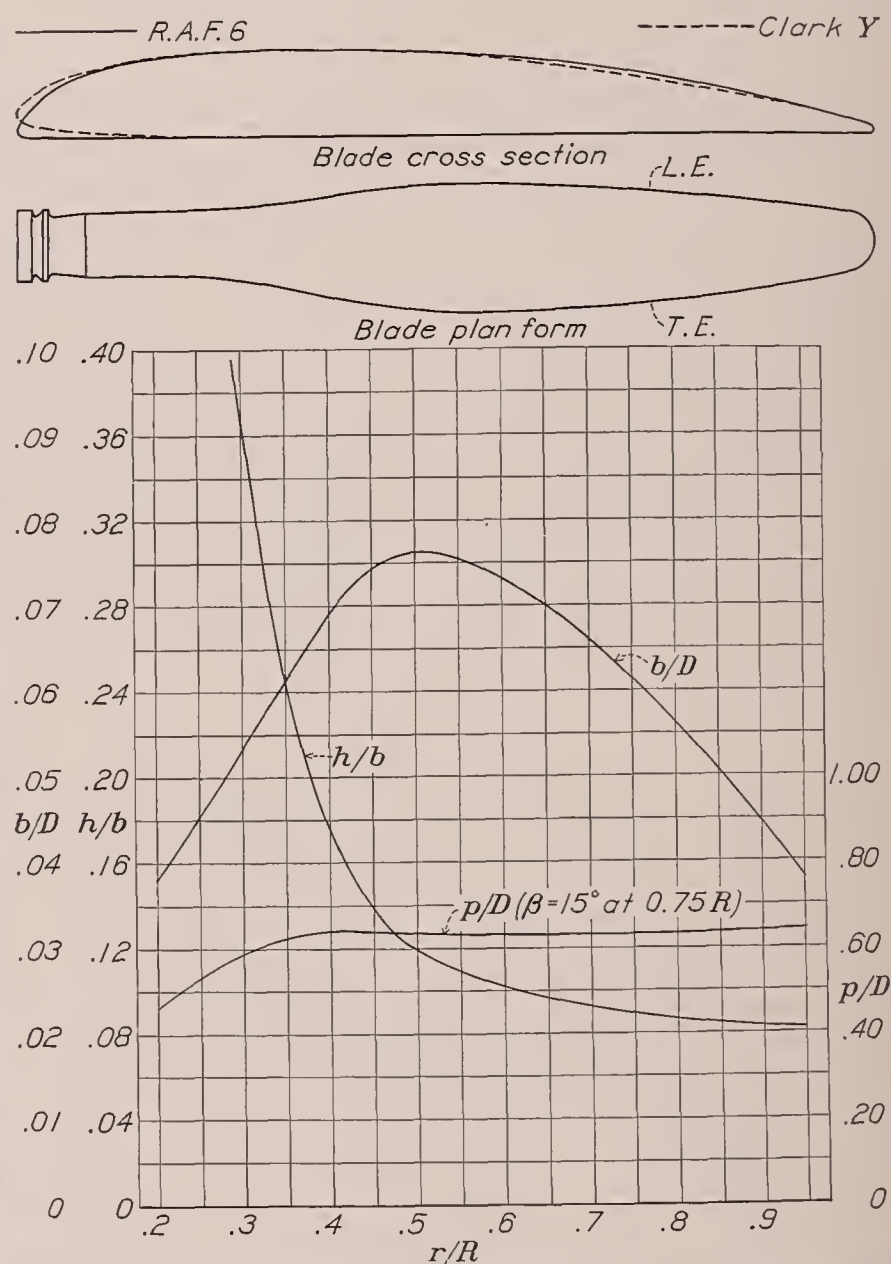


FIGURE 2.—Blade-form curves for propellers 5868-9 and 5868-R6. D , diameter; R , radius to the tip; r , station radius; b , section chord; h , section thickness; p , geometric pitch; β , blade angle.

D , propeller diameter, ft.

V , air speed, f. p. s.

n , propeller speed, r. p. s.

ρ , mass density of air, slugs per cu. ft.

Negative thrust and torque charts.—The principal results of the tests are shown in figures 3 to 9. Figures 3, 4, and 5 present cross-faired curves giving the thrust and torque coefficients for the Clark Y propellers having 2, 3, and 4 blades. Figures 6, 7, 8, and 9 present similar curves for the R. A. F. 6 propellers. In addition to the range covered by the other propellers, the 3-blade R. A. F. 6 propeller tests covered the blade angles 10° , 5° , and 0° (fig. 8).

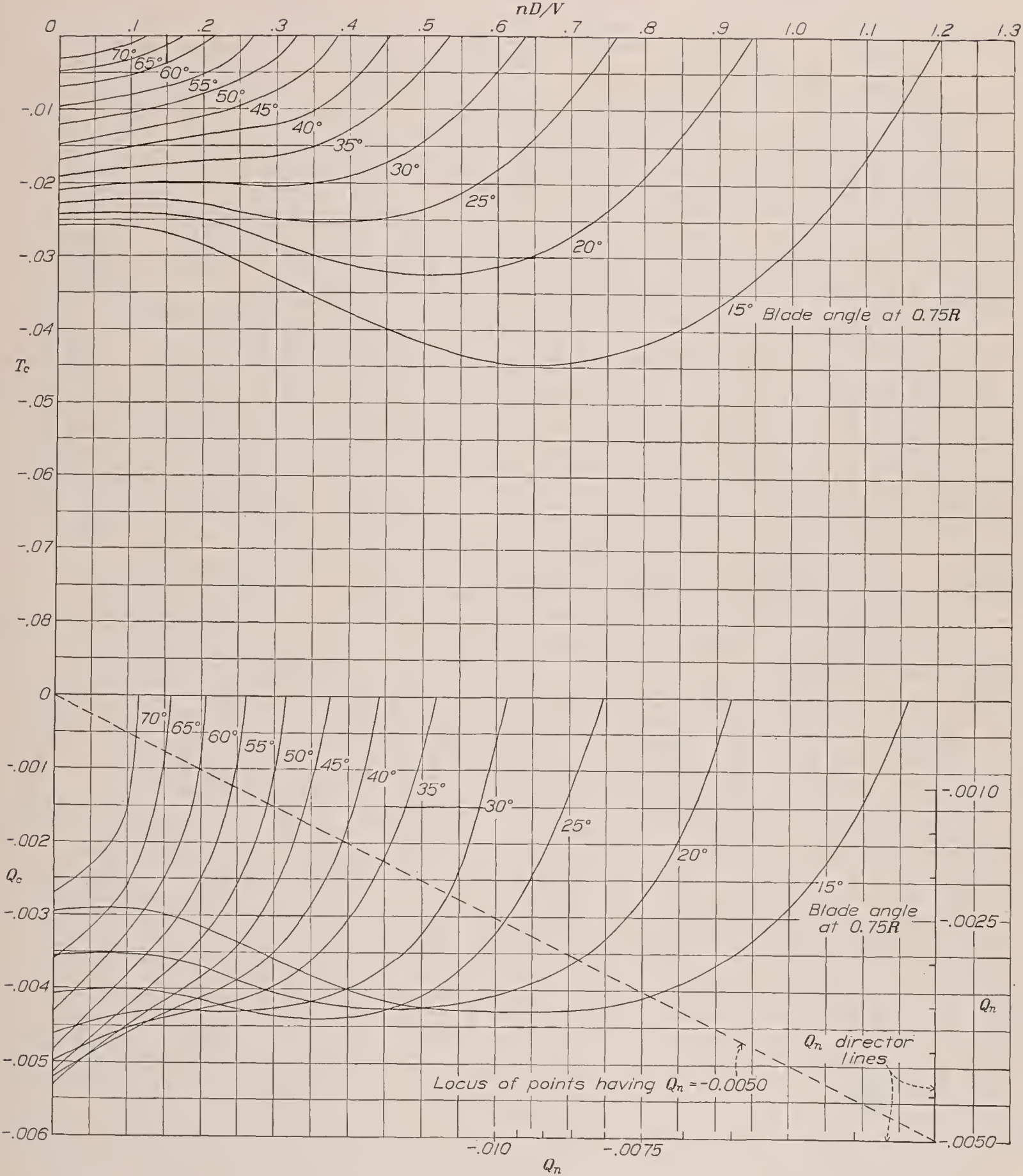


FIGURE 3.—Negative thrust and torque coefficients for propeller 5868-9, Clark Y section, 2 blades.

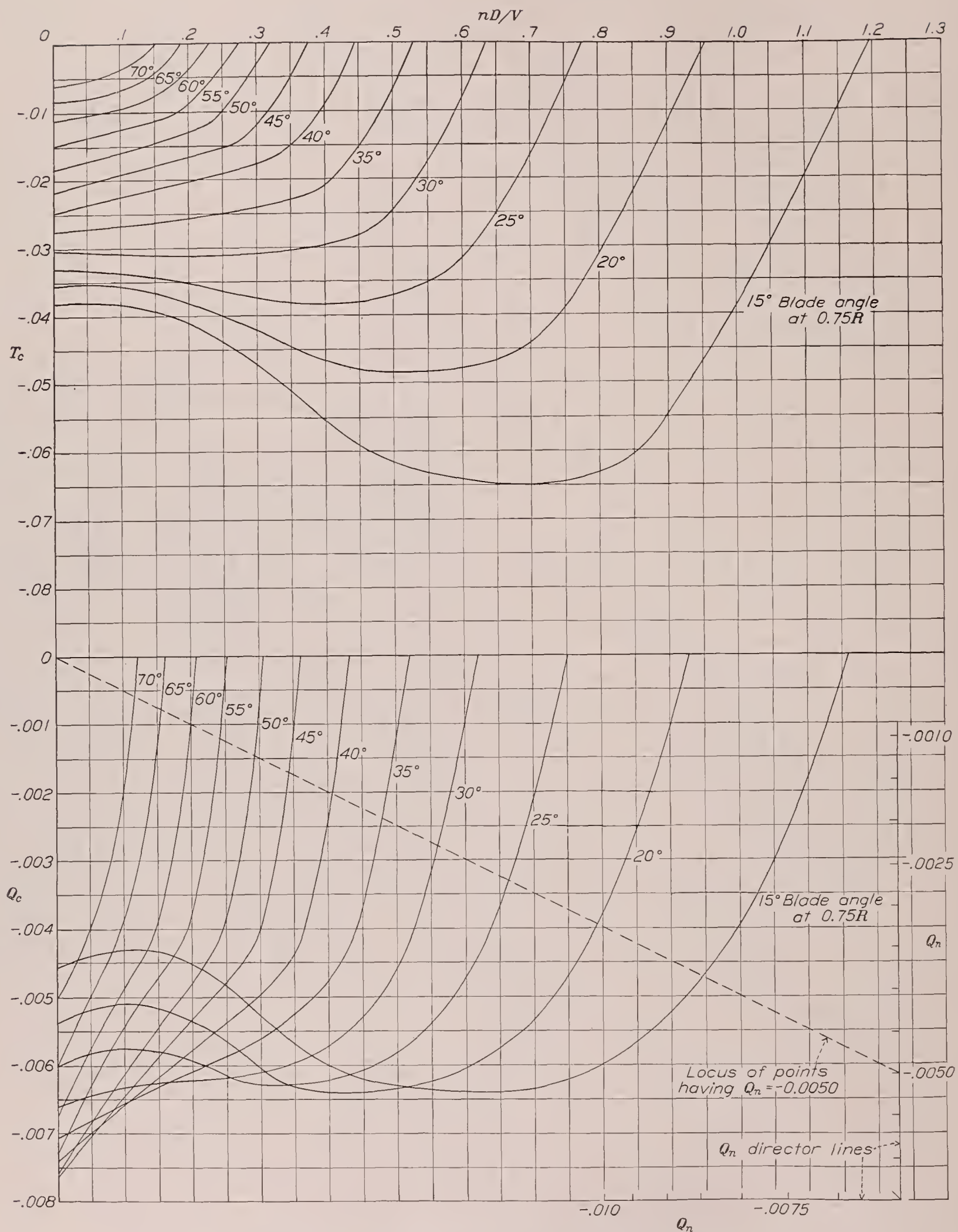


FIGURE 4.—Negative thrust and torque coefficients for propeller 5868-9, Clark Y section, 3 blades.

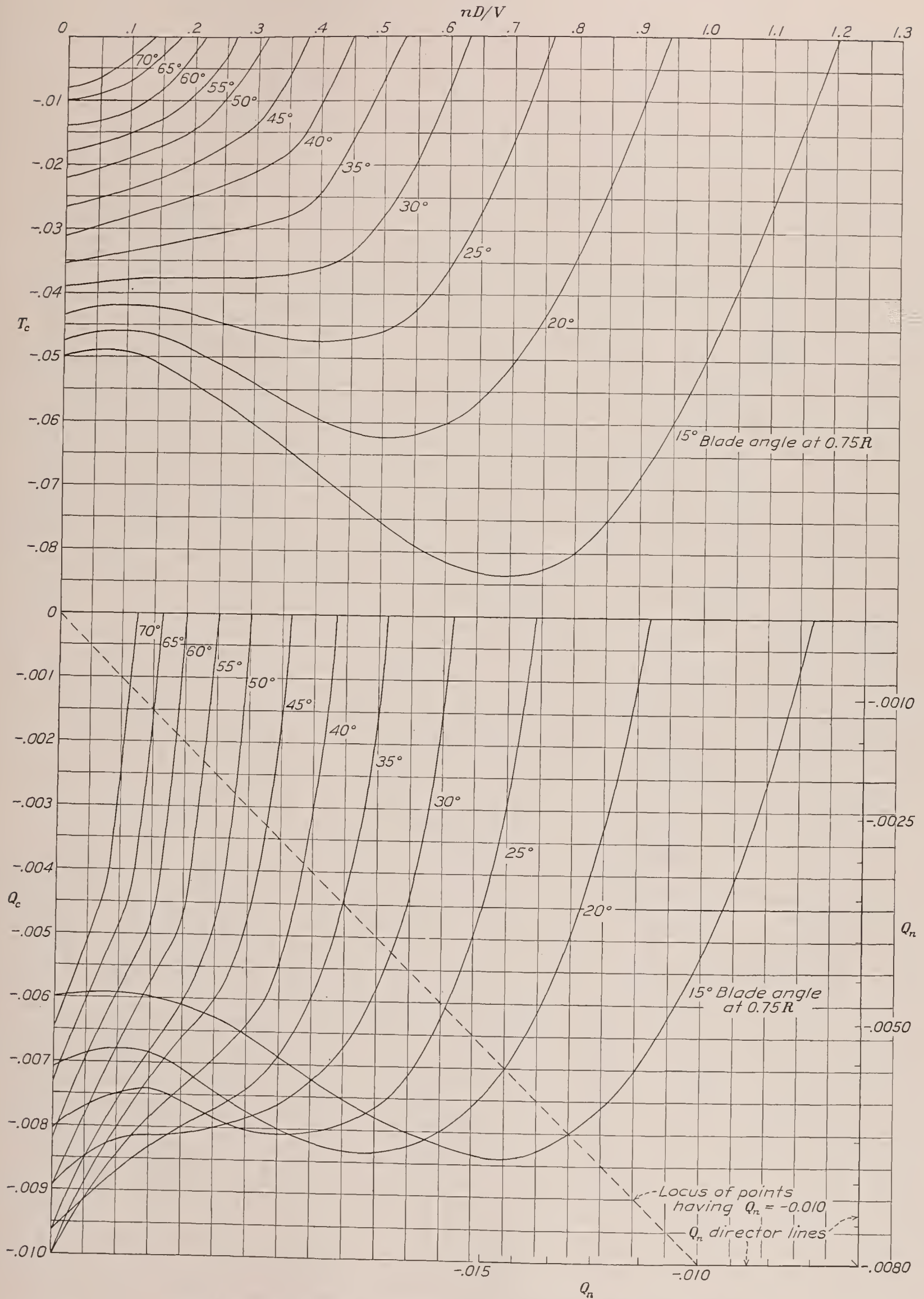


FIGURE 5.—Negative thrust and torque coefficients for propeller 5868-9, Clark Y section, 4 blades.

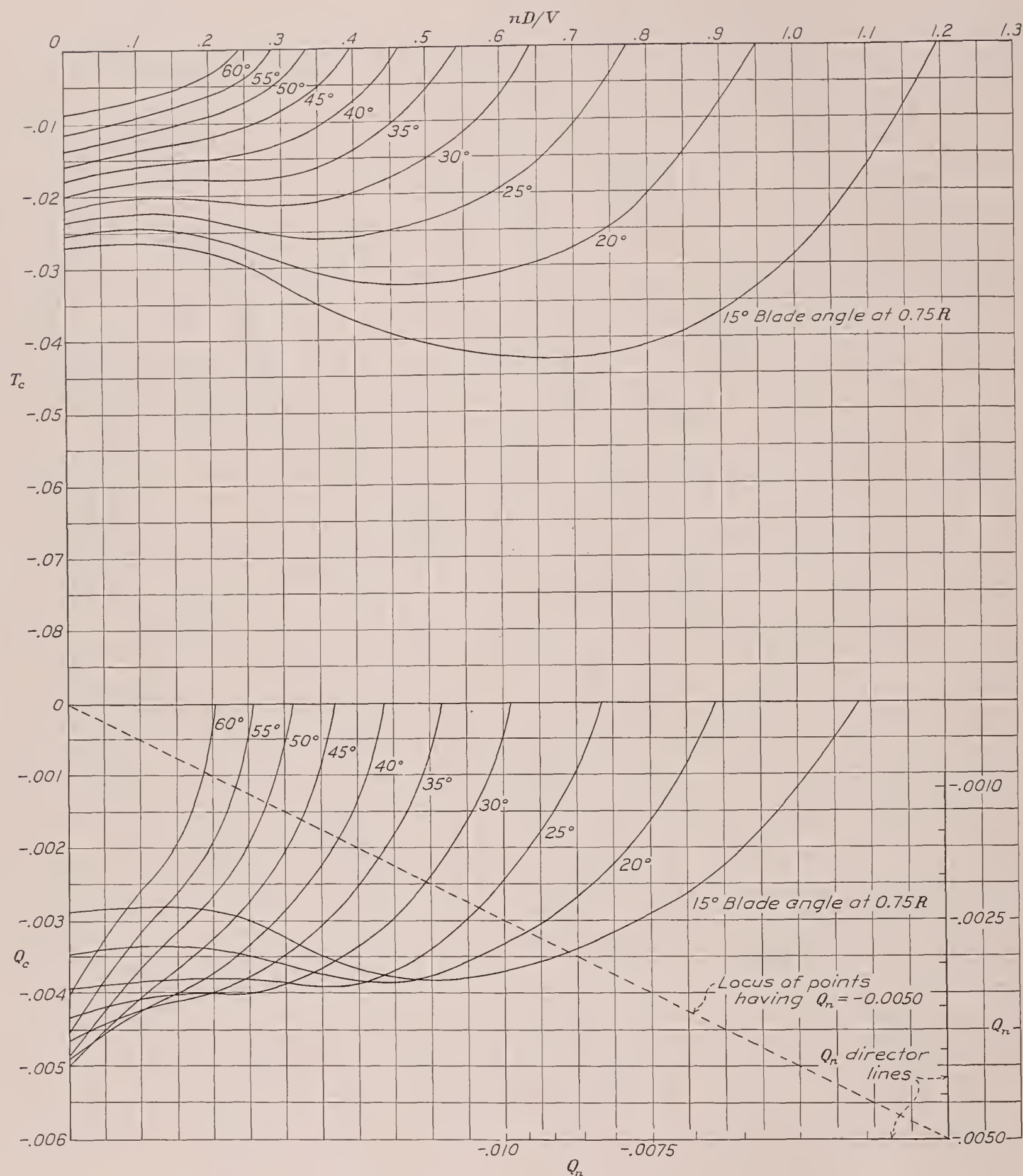


FIGURE 6.—Negative thrust and torque coefficients for propeller 5868-R6, R. A. F. 6 section, 2 blades.

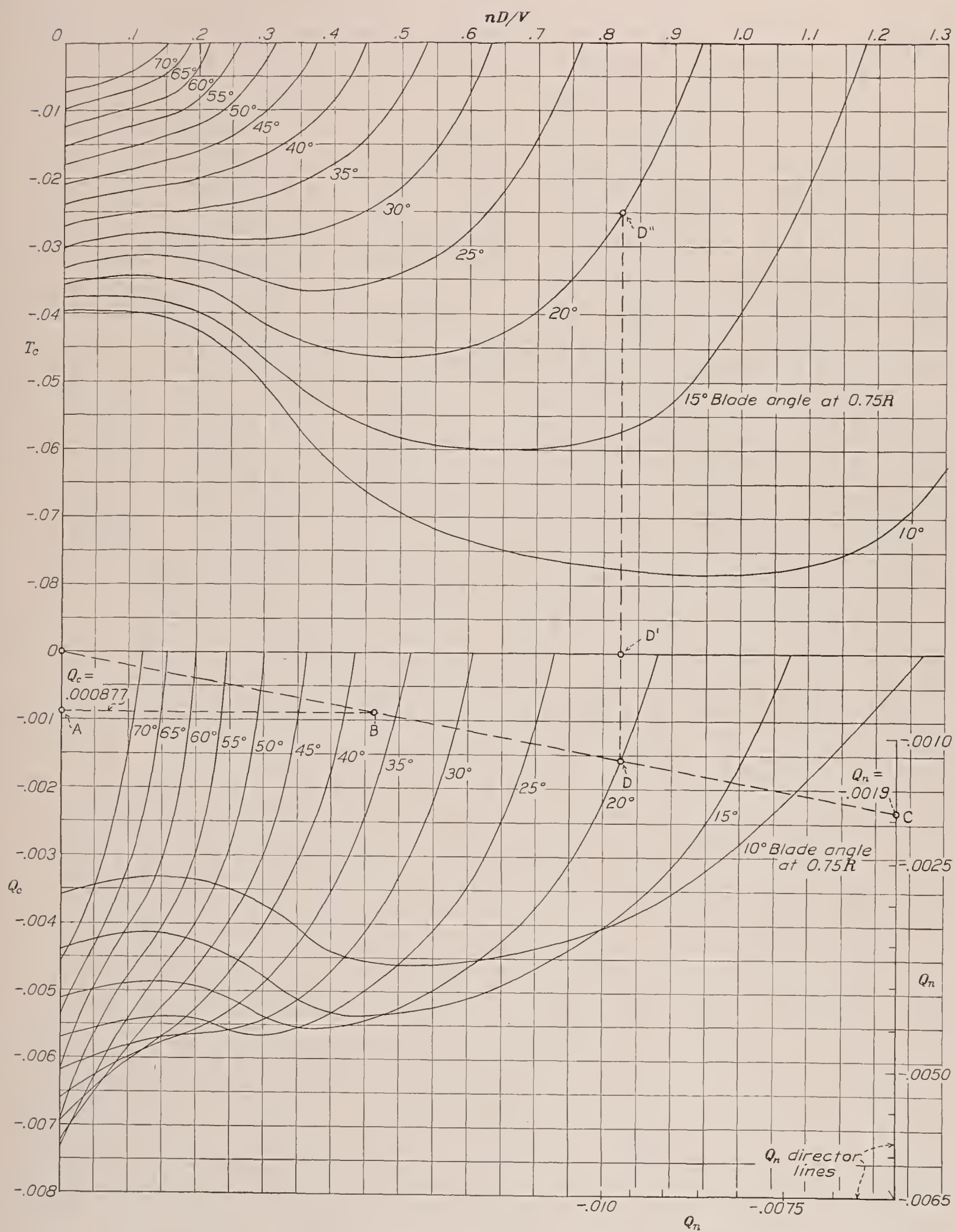


FIGURE 7.—Negative thrust and torque coefficients for propeller 5868-R6, R. A. F. 6 section, 3 blades.

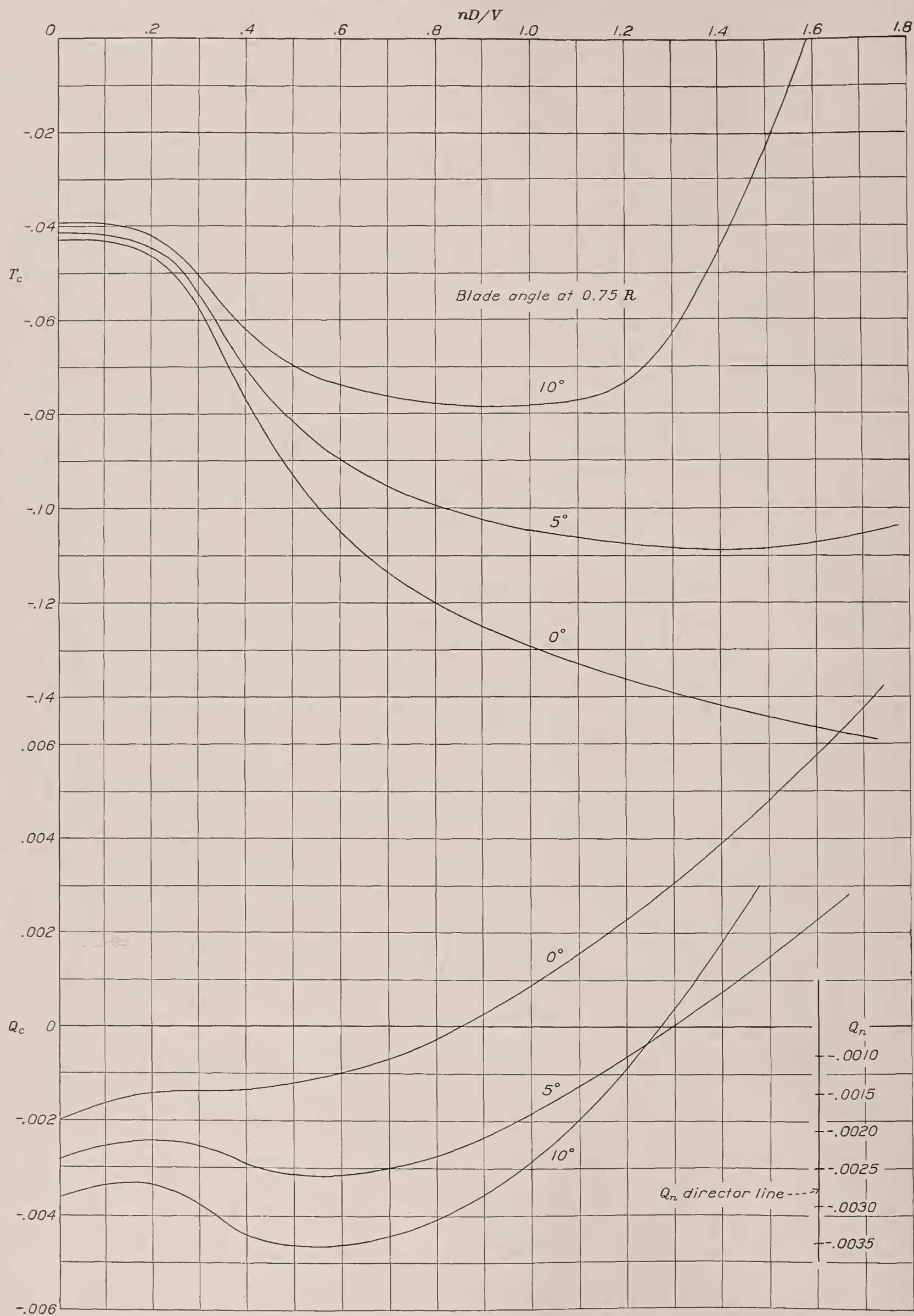


FIGURE 8.—Negative thrust and torque coefficients for propeller 5868-R6 at small blade-angle settings. R. A. F. 6 section, 3 blades.

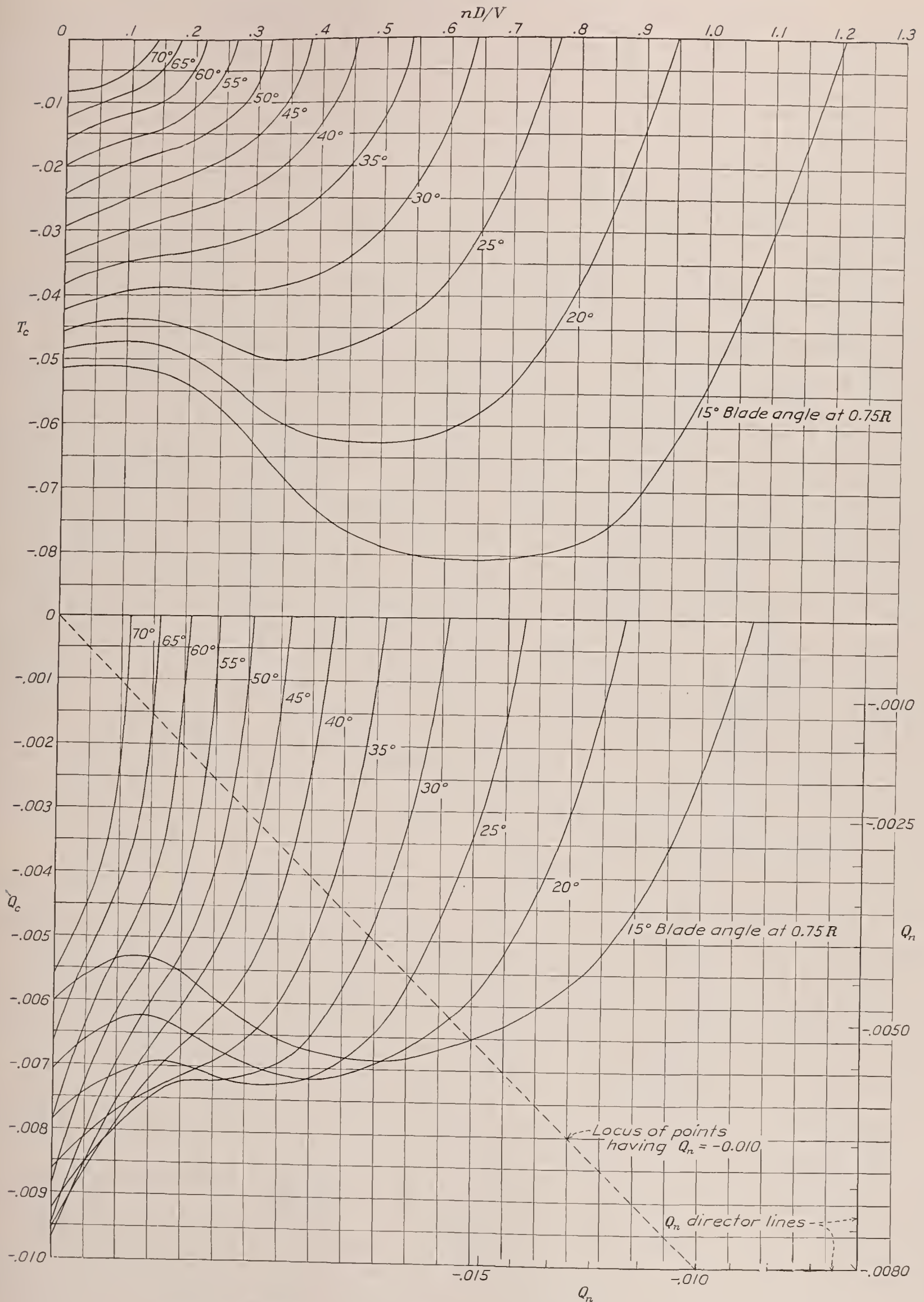


FIGURE 9.—Negative thrust and torque coefficients for propeller 5868-R6, R. A. F. 6 section, 4 blades.

Although the original plotted curves of thrust and torque coefficient were, in general, fairly smooth, the few irregularities in some of the curves and their spacing made it seem desirable to cross-fair them. An illustration of the appearance of one of the typical original

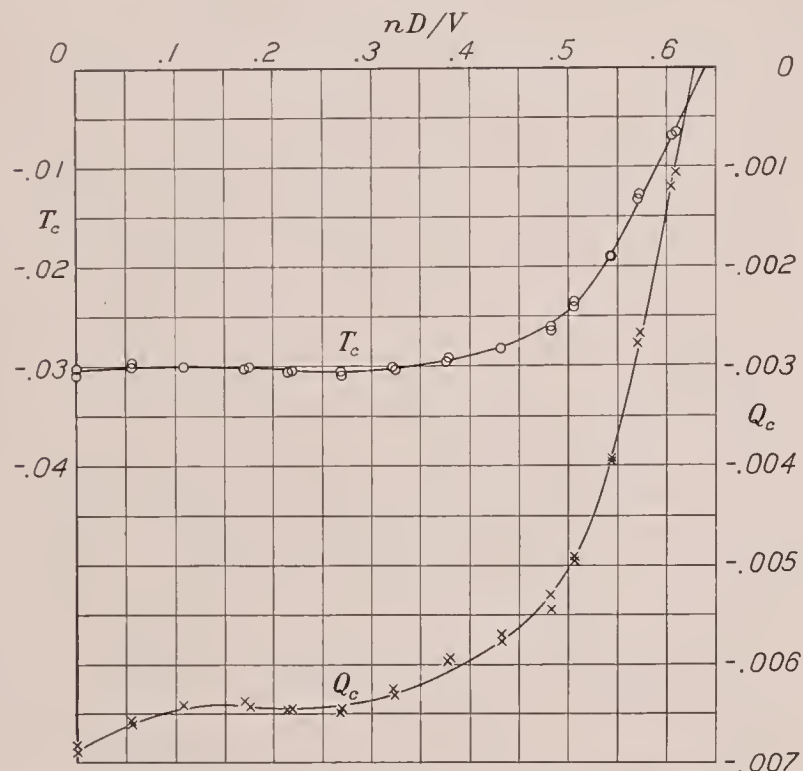


FIGURE 10.—Typical pair of negative thrust and torque curves showing test points. Propeller 5868-9, 3 blades, set 30° at $0.75 R$.

plots is given in figure 10 to show the extent of the dispersion of the test points.

Comparison of Clark Y and R. A. F. 6 propeller characteristics.—It will be noted that, in general, the values of thrust and torque coefficients are greater for the Clark Y propellers than for the R. A. F. 6 propellers.

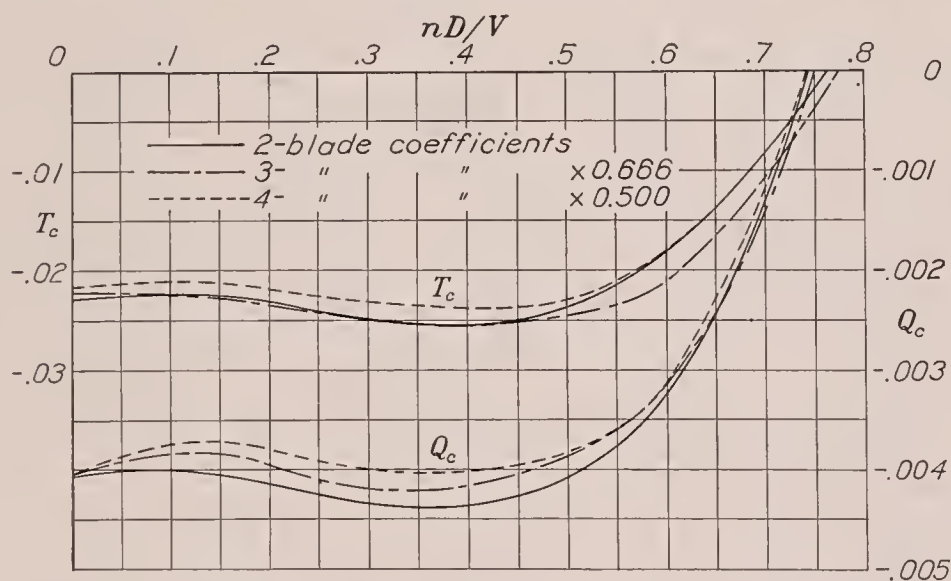


FIGURE 12.—Comparison of thrust and torque coefficients for propellers having 2, 3, and 4 blades of Clark Y section; set 25° at $0.75 R$.

For an easier comparison, figure 11 was prepared to show the thrust-coefficient and torque-coefficient curves for the 3-blade Clark Y and R. A. F. 6 propellers set at a blade angle of 25° . At zero nD/V , the thrust coefficients of the two propellers are nearly the same; however, the difference in the shapes of the two sections (see fig. 2) causes a considerable difference in both thrust and torque throughout most of the nD/V range.

Comparison of propellers having 2, 3, and 4 blades.—A comparison of propellers having 2, 3, and 4 blades is shown in figure 12. The coefficients of the three propellers were divided by the number of blades and then multiplied by 2 to permit comparison on the basis of

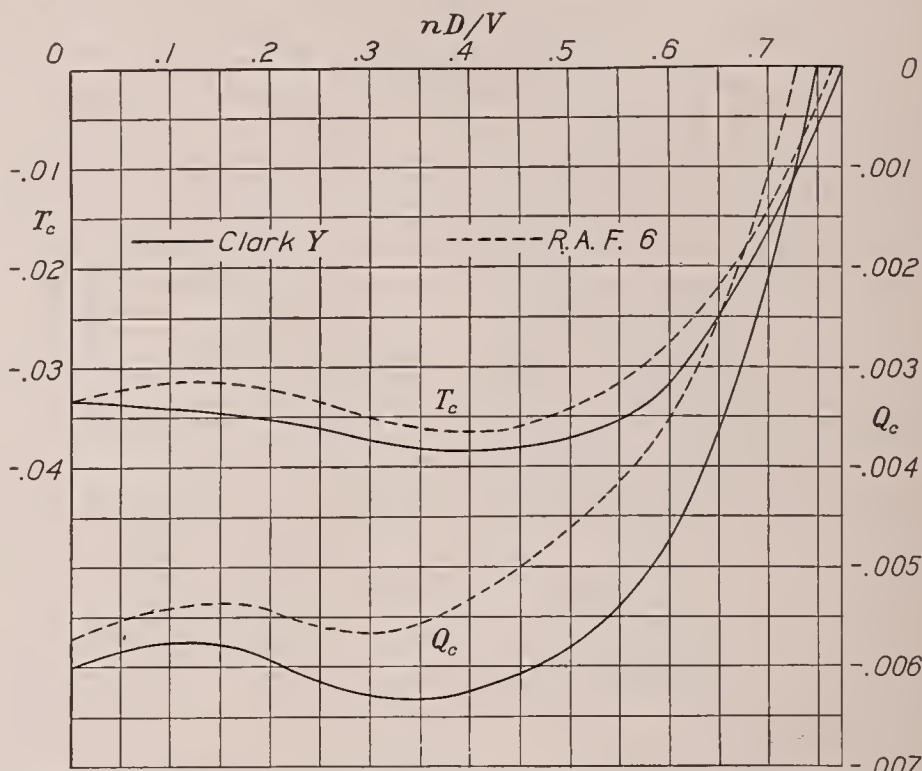


FIGURE 11.—Comparison of thrust and torque coefficients for propellers having Clark Y and R. A. F. 6 sections; 3-blade, 10-foot propellers set 25° at $0.75 R$.

two blades. The curves in figure 12 show no consistent variation, probably owing to the process of cross-fairing. They do show that, compared on this basis, there is no great difference between the characteristics of propellers with 2, 3, and 4 blades.

Coefficients for locked propellers.—Figure 13 shows

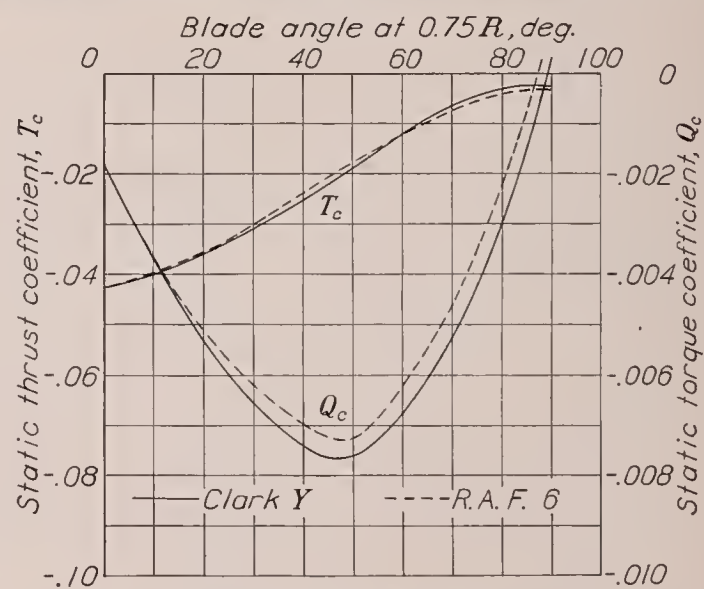


FIGURE 13.—Thrust and torque coefficients with propeller locked ($nD/V=0$); blades.

the thrust and torque coefficients, at $\frac{nD}{V}=0$ (propeller locked) and through a 90° blade-angle range, for both the R. A. F. 6 and Clark Y 3-blade propellers.

The difference in the torque curves, which is negligible at 0° and quite large at high angles, may be attributed to the difference in the shape of the leading edges of the two airfoil sections. The static thrust has apparently not reached its peak at 0° .

CONSIDERATIONS IN APPLYING NEGATIVE THRUST AND TORQUE DATA TO THE SOLUTION OF PROBLEMS

Coefficients.—The thrust coefficient T_c is especially suited to a negative-thrust analysis because it does not involve the engine speed and because of its similarity to the usual drag coefficient. It is not convenient to use the normal propeller thrust coefficient $C_T = T_c / \rho n^2 D^4$ because C_T approaches infinity as nD/V approaches zero, and difficulty in plotting arises. With the diameter and velocity known, the thrust may be easily calculated for any value of T_c .

Effect of engine.—In most problems involving negative thrust, the propeller is mounted on an airplane engine, which may be “dead” (switch off and being turned over against its own friction), partly throttled, or operating at full throttle. The main difficulty in calculating the negative thrust of a propeller operating under any given condition, especially the one where it is turning a dead engine, is found in determining the engine speed. In the special case of the “freewheeling” propeller, the thrust coefficient is easily found, it being the value corresponding to the nD/V where the torque coefficient is zero. When the propeller is turning a dead engine, however, the revolution speed depends upon the friction torque of the engine, which is itself an extremely variable quantity.

The coefficient Q_n .—In reference 5 it was pointed out that flight tests indicated the rotational speeds of propellers turning dead engines on multiengine airplanes to be from 35 to 50 percent of rated engine speed. It was also pointed out that, through this range of engine speeds, the friction torque of the average airplane engine might be represented by an equation of the following type:

$$Q_f = k_1 N_e \Delta (1 + k_2 h) / k_3 / G. R.$$

where Δ is the engine displacement, cu. in.

N_e , crankshaft revolution speed, r. p. m.

$G. R.$, the ratio of propeller speed to crankshaft speed.

k_1 , k_2 , and k_3 , appropriate constants.

For a particular engine and at a given altitude h , the equation is simplified to:

$$\frac{Q_f}{N_e} = \text{constant } (K)$$

This approximation was used in reference 5 to develop the following form of coefficient:

$$Q_n = \frac{Q}{\rho V^2 D^3} \times \frac{V}{nD} = \frac{Q/n}{\rho V D^4}$$

This relation may be put in a more useful form:

$$Q_n = 17,200 \times \frac{Q_f/N}{\sigma V_1 D^4}$$

where Q_f is engine friction torque (considered negative), ft.-lb.

N , propeller revolution speed, r. p. m.

V_1 , air speed, m. p. h.

σ , relative density, ρ/ρ_0 .

ρ_0 , mass density of the air at sea level, slugs per cu. ft.

In references 3 and 5, charts are presented having thrust coefficient T_c plotted against Q_n . Thus, when the value of Q_f/n is known for the engine in question, the value of Q_n , at any given altitude and for any given propeller diameter, will depend only on the velocity. The plot of T_c against Q_n then becomes, for any particular case, a plot of the thrust against the inverse of the velocity. It appears likely, from the friction data shown in references 3 and 5, that the usefulness of the relation $Q_f/N_e = K$ will extend over a greater range of engine speeds than previously indicated.

The Q_n modification to negative-thrust charts.—In the present report it is shown that a slight modification of the usual plots of T_c and Q_c against nD/V will provide the equivalent of a plot of T_c against Q_n , such as given in references 3 and 5.

The necessary modification to the usual charts is explained as follows: Since $Q_n = \frac{Q_c}{nD/V}$, it is clear that

the locus of all points having a single value of Q_n may be represented on plots of Q_c against nD/V (figs. 3 to 9) by a straight line passing through the origin. The position of this line for any particular value of Q_n is easily determined on the chart from the fact that $Q_n =$

Q_c where $\frac{nD}{V} = 1$. Although the position of this line is

easily determined, a scale, or rather a director line, has been placed on each chart showing the intersections of the Q_n lines for various values of Q_n .

In actual use a straightedge placed from the origin to the desired value of Q_n on the scale will permit values of the coefficients to be read without drawing the line.

Examples of use of Q_n .—As an example, suppose the friction torque of the engine and the velocity are such as to make the value of $Q_n = -0.0019$ and that it is desired to find the value of T_c at a blade angle of 20° . The solution of this problem is indicated in figure 7. The broken line O-C represents a constant value of Q_n . Where this line intersects the 20° blade-angle curve at point D, project up along the line D-D'' to the point D''. The T_c coordinate of the point D'' is the desired value.

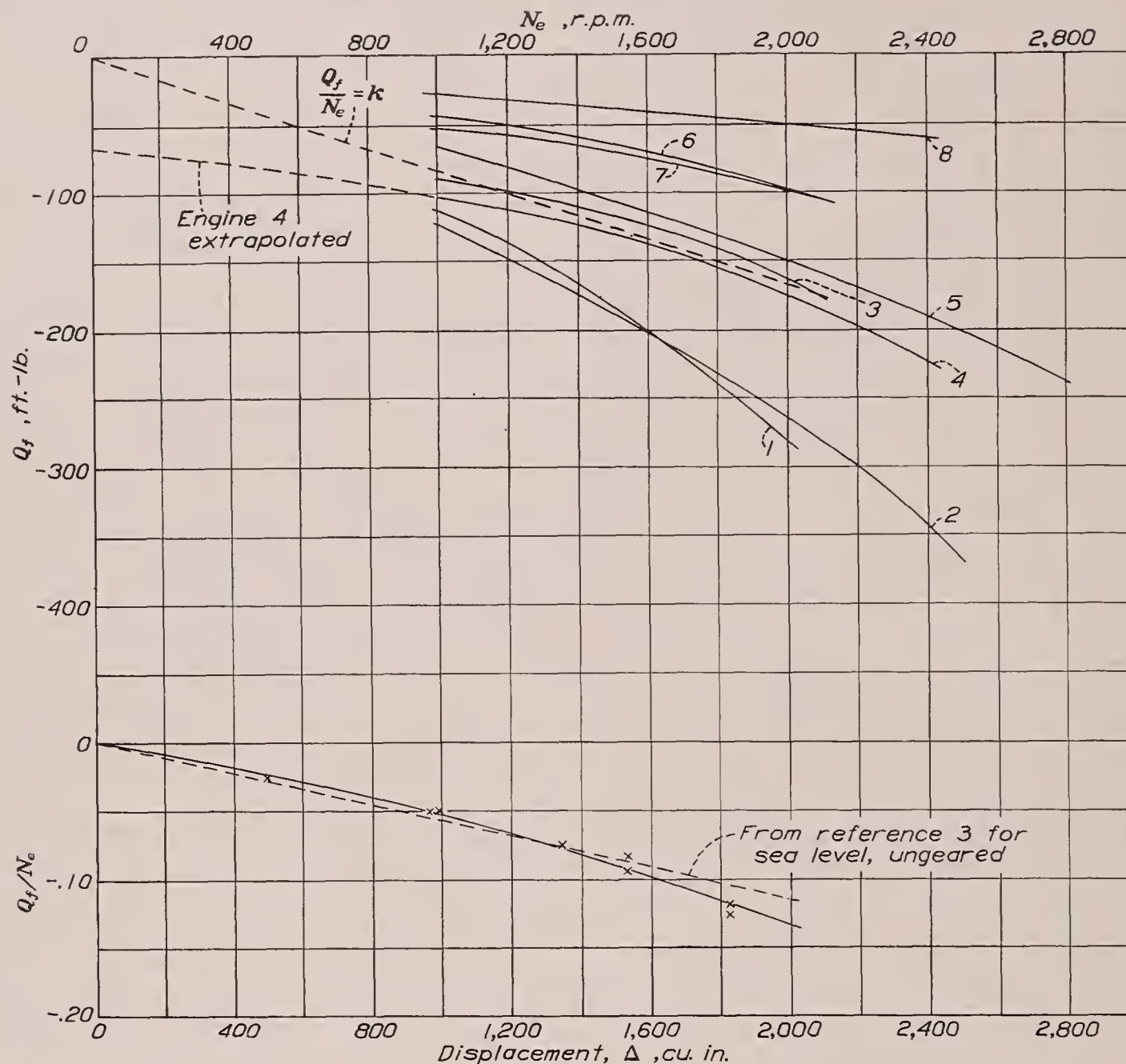
The propeller speed may be calculated from the value of nD/V at point D' as follows:

$$N = \frac{nD V_1 \times 88}{D}$$

FRICTION TORQUE OF ENGINES

Relation to problems.—In many cases the friction of the engine has a large effect on the values of thrust coefficient under which the propeller operates. It is then obvious that, for the ready use of the data herein presented, some information regarding the friction torque of engines is required. As particular and exact engine-friction data are seldom available for the solu-

been extrapolated to bring them to 1,000 r. p. m. From these curves may be judged the quality of the assumption that the friction torque is a linear function of N_e , which can be represented by the relation $Q_f/N_e = K$ for any particular engine. This equation indicates that the torque for any engine may be represented by a straight line through the origin, as the one drawn in for engine 3 in figure 14.



Engine	Δ	hp.	N_e	Q_f/N_e
1	1,823	768	1,950	-0.120
2	1,820	700	1,950	-.125
3	1,535	850	2,150	-.085
4	1,535	750	2,500	-.095
5	1,340	450	2,100	-.075
6	985	300	2,000	-.050
7	975	330	2,000	-.050
8	499	145	2,050	-.025

FIGURE 14.—Friction-torque curves for eight typical airplane engines.

tion of negative-thrust problems, it is considered necessary to include in this report sufficient data to permit an intelligent estimate of friction torque to be made.

Engine-friction data.—Figure 14 shows friction-torque curves, obtained from various sources, for eight modern aircraft engines covering a fairly wide range of power and displacement. Some of these curves have

The curves in figure 14 indicate that this approximation is not far wrong for values of N_e from 1,000 to 2,200 and for the temperature and pressure conditions under which the tests were run. It is certain, however, that this approximation does not hold at low values of N_e for it assumes that the torque becomes zero at $N_e=0$. The torque does not become zero at $N_e=0$, as is indicated by the extrapolated curve for engine 4,

and there is evidence to show that this deviation becomes greater as the temperature decreases. Fortunately, however, the deviation from the linear formula in the range of low engine speeds usually occurs in a range of blade angles where large changes in torque cause but small changes in thrust coefficient and also where the values of thrust coefficients are low so that, although the relative error may be large, the absolute value of the error is small.

It is also seen that, at high values of engine speed (above 2,000 r. p. m.), the friction torque increases faster than the straight-line assumption, so that, in problems involving high values of N_e (fast dives), it will be advisable to increase Q_f/N_e by a small amount.

Estimation of a value of Q_f/N_e .—On the assumption that the friction torque can be determined by the equation $Q_f = \Delta N_e K$, it is clear that a plot of Q_f/N_e against displacement Δ for a group of engines should be a straight line like the dotted line, taken from figure 5 of reference 3, in the lower plot in figure 14.

Straight lines were drawn through the friction torque curves, as illustrated for engine 3 (fig. 14), and the values of Q_f/N_e represented by these lines were plotted against Δ in the lower chart. The solid faired line through these points may possibly provide a more accurate selection of Q_f/N_e values than the broken line from reference 3.

Where no specific friction data are available, a reasonable estimate of the value of Q_f/N_e , for any engine, may be obtained from this curve. In the case of a geared engine, Q_f/N_e must be converted to Q_f/N when calculating the coefficient Q_n .

Applicability of friction data.—The friction torque of engines varies with many factors; such as the mechanical condition of the engine, the cylinder barrel and oil temperatures, the barometric pressure, the throttle opening, the oil viscosity, and the gear ratio.

In the selection of a value of Q_f/N_e from figure 14, some allowance should properly be made for these factors. Some of the factors, however, tend to cancel each other; some, such as mechanical condition, have an unpredictable effect; and others have but a small effect. In general, there will probably be little justification for making any corrections but, under extreme conditions, these factors should not be overlooked.

The effect of altitude is to reduce the friction torque (pumping losses), but this gain is balanced by the increased friction due to the lower temperatures existing at the higher altitudes. Corrections for altitude are therefore unnecessary in most cases. Gearing an engine should not alter the friction torque by more than 10 to 20 percent at rated engine speed. Changes in temperature will have a considerable effect and may change the specific friction torque Q_f/Δ by as much as 0.004 per 10° F. change in outside-air temperature. It is beyond the scope of this report to consider in detail the quantitative aspects of the effects of the many factors that affect the

friction torque of engines. Considerable information of this nature is given in reference 6.

APPLICATION OF NEGATIVE THRUST AND TORQUE DATA

The development of the controllable propeller has greatly increased the opportunities for using the negative thrust of a propeller to advantage or, in other instances, for avoiding the bad effects of negative thrust at one blade angle by changing to another angle where these effects are less severe. Some of the ways in which negative thrust and torque data may be used to deal with such problems are given in the following paragraphs.

DRAW OF PROPELLER ON DEAD ENGINE OF A MULTIENGINE AIRPLANE

One problem of interest to the operators of multi-engine airplanes concerns the question of flying with one or more engines dead. In this situation it is necessary to reduce the drag of the airplane to a minimum so that the power of the remaining engines will be sufficient to maintain the altitude required to clear all obstacles on the path to the nearest airport. It is of considerable interest, therefore, to know just where to set the blade angle of the dead-engine propeller to absorb the least power. Such problems may be readily solved by the data given in this report.

Example.—An example of one such problem is carried through to show the method of attack. The assumed conditions are as follows:

Airplane flying at 135 miles per hour with one engine dead.

Engines (2)—750 horsepower; $\Delta = 1,500$ cubic inches; $N = 1,450$; $N_e = 2,000$.

Propellers—R. A. F. 6 section; 3 blades; 11-foot diameter.

Altitude—5,000 feet; $\sigma = 0.862$; $Q_f/N_e = -0.09$ from figure 14; $Q_f/N = -0.1715$ and, after adding 10 percent for gearing, becomes -0.1885 .

$$Q_n = 17,200 \times \frac{Q_f/N}{\sigma D^4 V_1} = \frac{17,200 \times -0.1886}{0.862 \times 11^4 \times 135} = -0.0019.$$

In figure 7 the line representing Q_n is drawn in (line O-C) and its intersection with the Q_c curve for any blade angle represents the value of Q_c for that particular blade angle and the corresponding value of T_c may be obtained by projecting up from this intersection to the T_c curve for the corresponding blade angle (line D-D').

As previously pointed out, the assumption that the friction torque approaches zero at low values of N_e (low values of nD/V) does not hold very well, though the absolute value of the error resulting from this assumption is small. As an added refinement, this error may be reduced as follows:

Estimate the value of friction torque at $N_e = 0$ and from it calculate a value of Q_c at which the propeller will stop turning. From that point on the Q_c ordinate

scale, project horizontally along a line of constant Q_c until an intersection is made with the previously drawn radial line of constant Q_n (such as line A-B intersecting line O-C at B). Now the locus of the desired points is assumed to be line A-B-C rather than the radial line O-C used in the less-refined method.

The value of the static friction torque will probably lie somewhere between 20 percent and 60 percent of

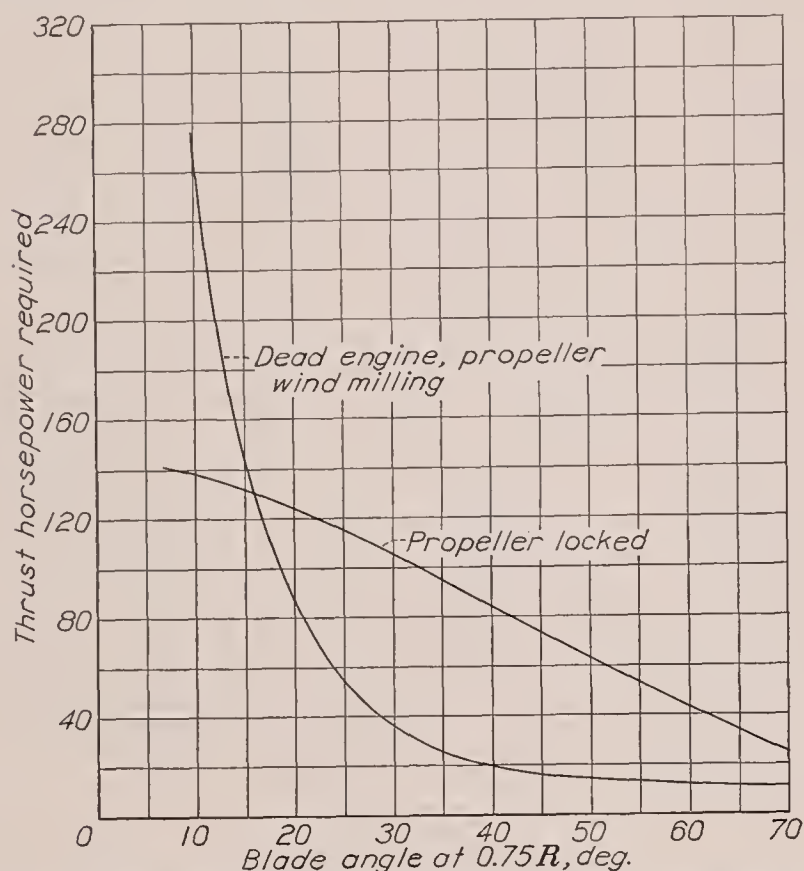


FIGURE 15.—Calculated power required to overcome the drag of a dead engine, idling and locked propeller, at 135 m. p. h. on a transport airplane. Propeller 5868-R6, 3 blades, 11-foot diameter.

the friction torque at rated engine speed depending upon the engine temperatures.

In this example a value of 34 percent is used which, at 135 miles per hour, gives a value of $Q_c = -0.000877$ and the projected line on the chart in figure 7 is the line A-B.

The rest of the calculations may conveniently be put in tabular form:

β (deg.)	$-Q_c$	nD/V	$-T_c$	$-T_s$ (lb.)	t. hp. ($-T_s V_1/375$)
10	0.00205	1.08	0.0772	748	270.0
15	.00187	.987	.0414	402	145.0
20	.00157	.825	.0250	242	87.0
25	.00132	.692	.0155	150	54.0
30	.00112	.583	.0107	104	37.5
40	.000877	.420	.0055	53	19.1
50	.000877	.292	.0037	36	13.0
60	.000877	.193	.0046	45	16.2
70	.000877	.109	.0036	35	12.6

The results are plotted in figure 15 along with those for the same propeller when locked ($\frac{nD}{V} = 0$). For this particular example, it is seen that, through the greater part of the blade-angle range, the power required to overcome the drag of the locked propeller is considerably greater than for the windmilling condition. It is also seen that most of the benefit gained from increasing the blade angle on the windmilling propeller is obtained at

35° or 40°, which is not far above the normal operating range. In case the engine fails in such a manner that it locks or if it is desired to stop the rotation to prevent damage to the airplane or the engine, it will be necessary to feather the propeller to about 85° to 90° where it will stop turning and at the same time have a very low drag.

THE USE OF PROPELLER BRAKING EFFECT IN REDUCING DIVING SPEEDS

The rapid development in the aerodynamic cleanness of modern airplanes has resulted in a large increase in their terminal diving speeds; in fact, it is questionable whether some of them could resist the destructive forces to which such a dive would subject them. Most airplanes are not called upon to make such dives but in certain military maneuvers, such as dive bombing, the vertical or nearly vertical dive is a routine requirement.

The accuracy of dive bombing is adversely affected by the high diving speeds, and various methods of slowing up the dive have been considered. Some of these methods depend upon a split structural surface, such as a strut or wing flap, which opens up to produce an effective air brake.

The airplane is already equipped with a convenient and very rugged mechanism for producing a large positive or negative thrust. The controllable propeller, if set at low blade angles, will provide a very effective air

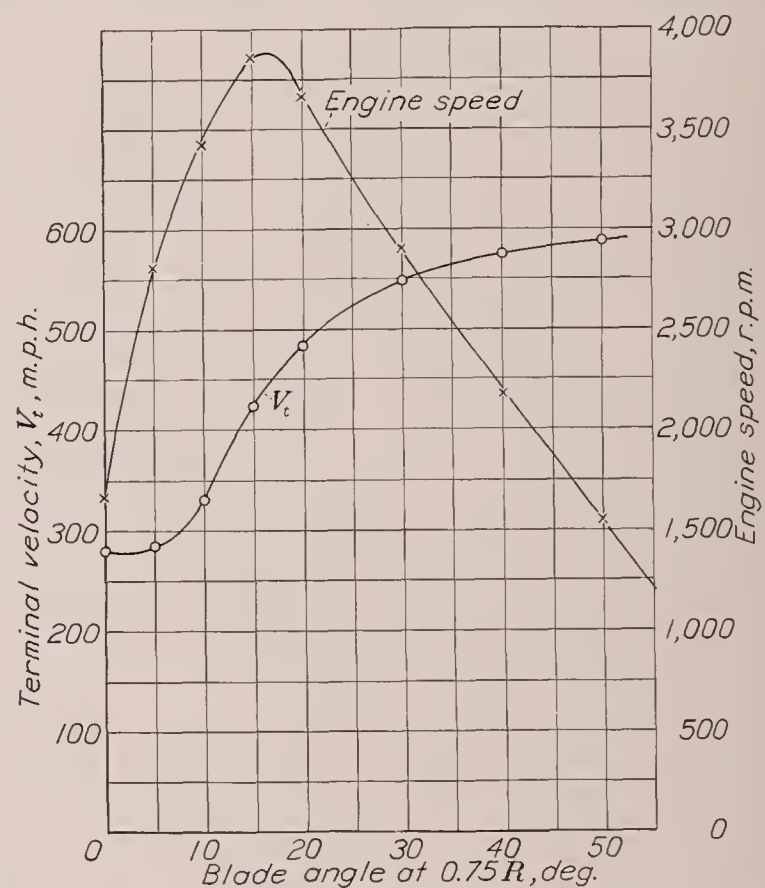


FIGURE 16.—Calculated values of terminal velocity and engine speed for a modern pursuit airplane. Vertical descent; 8,000-foot altitude; 3-blade propeller.

brake, as is shown by the curves in figure 16. The curves were obtained from the test data by a method that will shortly be explained. They represent the terminal velocity and engine speed for the modern pursuit airplane, shown in figure 17, for various blade-angle settings of its 3-blade controllable propeller. The effects of compressibility on both airplane and propeller have been neglected. In the important part of the curves (low blade angles), these effects are small.

This airplane with its propeller set at 35° has a terminal velocity of 565 miles per hour; whereas at 2° its velocity has dropped to 277 miles per hour, or to 49 percent of its value at 35° . It will be noticed that the engine speed rises to excessive values at blade angles around 15° . These destructive engine speeds can be avoided by setting the blade angle somewhere between 5° and 0° before the dive is started, indicating that a quick-acting pitch-control mechanism would be advantageous.

If still more braking effect is required, the propeller may be set to negative angles and engine power applied.

Method of calculating V_t .—Although the method of calculating terminal velocity still remains a cut-and-try process, it is made considerably easier by the use of the relation $\frac{Q_f}{N_e} = K$ and the coefficient Q_n . The basic formula for a vertical dive is as follows:

$$V_t = \sqrt{\frac{W}{\frac{\rho}{2}A + KT_c}}$$

where

V_t , terminal velocity, f. p. s.

W , weight of airplane, lb.

$K = \rho D^2$

$A = \left(\frac{\text{parasite drag}}{\frac{1}{2}\rho V^2} \right)$, equivalent parasite area.

From this formula, V_t may be calculated as follows:

1. Knowing Q_f/N_e (from fig. 14), estimate a value of V_t and calculate Q_n .

2. From suitable charts (figs. 3 to 9) obtain a value of T_c for the desired blade angle.

3. Substitute T_c in terminal-velocity formula and obtain V_t calculated.

4. If V_t estimated does not equal V_t calculated, make a new estimate and repeat.

With a little experience two trials should be sufficient. The value of engine speed is obtained in the usual way from the value of nD/V (such as point D' , fig. 7).

Stability in dive.—The destabilizing effect of a braking propeller is frequently brought up as an argument against the use of the propeller as a brake in reducing the terminal velocity of airplanes. The question will be briefly considered here in relation to the directional stability of the airplane. The stability in pitch presents a similar problem that may become critical if the center of gravity is displaced far from the thrust axis.

In a vertical dive with braking propeller, the negative thrust of the propeller will normally act upward in the vertical plane through the center of gravity. If a small displacement in yaw occurs, as shown in figure 17, the thrust and gravity forces will produce an upsetting couple that must be balanced by a lateral aerodynamic force on fin and fuselage. The situation is aggravated by the loss of energy in the slipstream, which usually passes over the tail surfaces.

An examination of forces and moments acting on the airplane, the diving characteristics of which are shown in figure 16, will be given as an example.

The upsetting-moment slope for a small displacement is given by the relation

$$\left(\frac{dN}{d\psi} \right)_u = \frac{T_e r_1}{57.3}$$

where

N , yawing moment, ft.-lb.

ψ , angle of yaw, deg.

r_1 , distance from center of gravity to propeller disk, 6.5 ft.

For the airplane operating with a blade angle of 5° ,

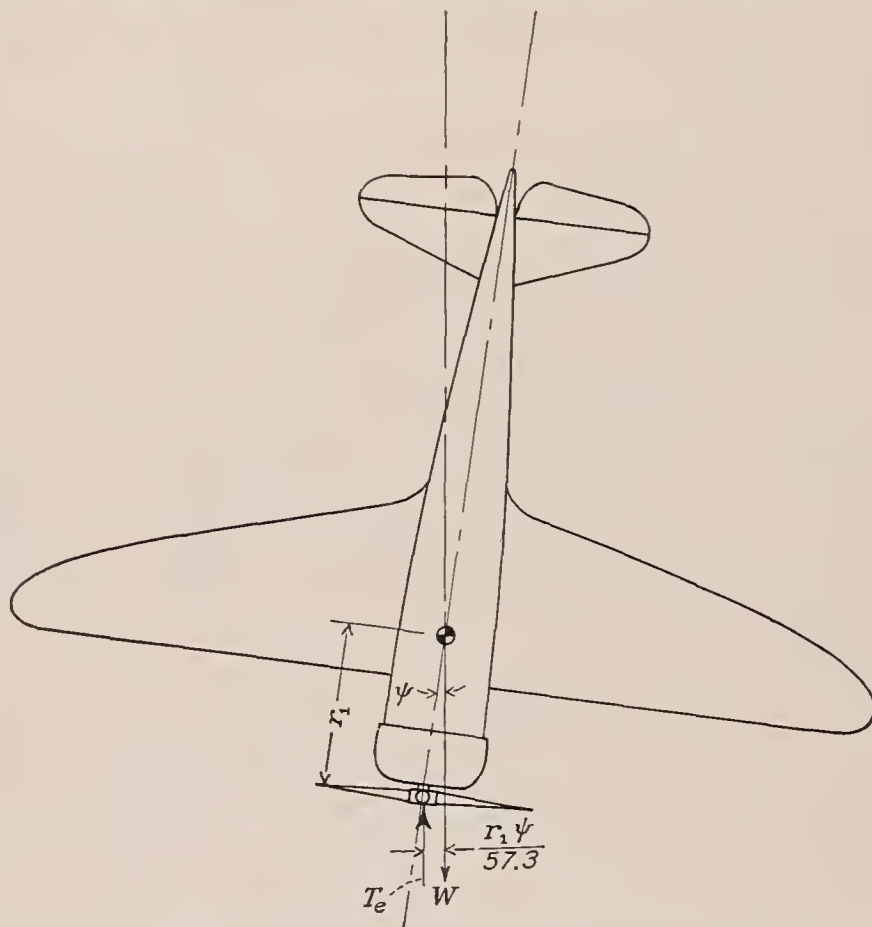


FIGURE 17.—Airplane in vertical dive showing unstable effect caused by propeller when used as a brake. Span, 35 feet; weight, 4,500 pounds; propeller diameter, 10 feet; 3 blades.

$T_e = 2T_c D^2 q_0$, where T_c is -0.106 , D is 10 feet, and q_0 is the dynamic pressure.

Therefore

$$\left(\frac{dN}{d\psi} \right)_u = \frac{2 \times -0.106 \times 10^2 \times 6.5}{57.3} q_0 = -2.4 q_0$$

The normal stabilizing yawing moment for this airplane may be taken from Diehl (reference 7) who gives as a reasonable value for directional stability:

$$\left(\frac{dN}{d\psi} \right)_r = 0.00005 \times W b q_1$$

where

W is the weight.

b , the span.

and q_1 , the dynamic pressure.

For this example

$$\left(\frac{dN}{d\psi} \right)_r = 7.9 q_1$$

Owing to the reduced velocity in the slipstream of the braking propeller, $q_1 < q_0$ so that the upsetting-moment and the righting-moment slopes, as expressed in the foregoing formulas, cannot be directly compared.

The ratios of these two values of q may be obtained from the following slipstream-velocity formula:

$$\frac{q_1}{q_0} = \frac{w^2}{V^2} = 1 + 2.545T_c$$

where w is the air velocity in the slipstream and V is the velocity of the airplane, which in this example is 285 miles per hour.

For this airplane, then,

$$\frac{q_1}{q_0} = 1 + (2.545 \times -0.106) = 0.73$$

Therefore

$$\left(\frac{dN}{d\psi}\right)_r = 7.9 \times 0.73 \times q_0 = 5.77q_0$$

and the resulting slope of the yawing-moment curve with the propeller operating as a brake is

$$\frac{dN}{d\psi} = \left(\frac{dN}{d\psi}\right)_r + \left(\frac{dN}{d\psi}\right)_u = 5.77q_0 - 2.4q_0 = 3.37q_0$$

and the airplane is found to be stable by a good margin. From this brief analysis, one should say that little trouble from directional instability will be encountered in a dive where the propeller is being used as a brake unless the airplane was originally designed with little lateral stability.

This conclusion seems to agree with the evidence obtained in the dive tests reported in reference 2, where no instability was noted even when the propeller was producing its maximum braking effect. This evidence, however, must not be taken as entirely conclusive, for it represents only two specific examples. It is conceivable that conditions of airplane weight, propeller-braking effect, and the basic stability of the airplane could be such that trouble from directional instability might be difficult to avoid.

GLIDE CONTROL AND REDUCTION IN LANDING RUN

There are a number of situations in the flight range of every airplane where an air brake could be used to advantage. With the great increase in functional flexibility given to the propeller through recently acquired control mechanism, the propeller now provides an ideal air brake; if the propeller is set at negative blade angles and engine power is applied, it becomes a powerful, though nicely controlled, power brake, which need not rely on the speed of the airplane for braking power.

One situation in which a power brake could be used to advantage on an airplane is in the glide to a landing and also during the landing ground run. In these situations it is conceivable that the use of the propellers as brakes would find its best application in multiengine airplanes. Consider, for example, the new 4-engine

transport and bombing airplanes. The landing distance of such airplanes is excessive and only a certain few fields throughout the country are large enough to accommodate them. It is entirely possible that their landing distances (glide over 50-foot obstacle+ground run) could be reduced one-third to one-half by the use of propeller braking power. The blade angles of the two outboard propellers could be set to negative values of 15° or 20° before the landing glide started and the blade angles of the inboard propellers left in their normal take-off position so that in an emergency the airplane could fly off again on these two engines. By a differential use of the throttles for the inboard (thrust-producing) and outboard (braking) engines a very nice control of the glide path could be obtained, thus making spot landings possible and making the best use of landing-field size.

Once on the ground the pilot could open his braking engines wide and reduce the ground run by a large amount. The sum of both of these maneuvers would reduce the landing distance by 25 to 50 percent. There is a possibility, of course, that the reduced velocity in the slipstream of the braking propellers might have a bad effect on the wing lift or on the cooling of the engines.

The following table presents the results of landing-run calculations that were made to show the effect on the total distance to land over a 50-foot obstacle of using the propellers as power brakes. The example airplane was a fictitious 4-engine transport having a gross weight of 32,000 pounds and a landing speed of 100 feet per second. Calculations were made for two conditions of landing, as follows: (1) where the propellers were producing no thrust or drag during the glide and ground run; and (2) where the four propellers were producing thrust as indicated in figure 18, i. e., the inboard propellers producing zero thrust and the outboard propellers 2,000 pounds negative thrust each. The value of $L/D=8$ was assumed for landing, with flaps and landing gear down and no propeller thrust.

Case	γ	l_1 (ft.)	l_2 (ft.)	l_1+l_2 (ft.)	Ratio
1	$7^\circ 8'$	400	1,900	2,300	1.00
2	$14^\circ 2'$	200	1,260	1,460	.63

In the foregoing table γ is the gliding angle; l_1 is the distance from the obstacle to the point of contact with the ground; and l_2 is the ground run. In the last column, the ratio of the total distance to the total distance for case 1 is shown. It is observed that in this case the glide angle has been nearly doubled and the total landing distance reduced by 37 percent by the use of propellers as power brakes. If all four propellers had been used as brakes, the landing distance could have been reduced still more.

LONG-RANGE OPERATION

A difficult problem in the design of efficient long-range airplanes is that of obtaining sufficient power for the take-off and at the same time obtaining a low rate of fuel consumption at the low power output necessary for cruising at maximum L/D . Frequently the engines are throttled so much at cruising speed that high rates of fuel consumption result. Several methods of combating this difficulty are available, three of which follow:

1. By the use of catapults, which is perhaps the most efficient method but requires an elaborate outlay of equipment.

2. By designing for high-altitude flight, where maximum L/D occurs at higher velocities. The gain here must be paid for in terms of supercharger power for engines and cabin, added supercharger, propeller, and structural weight.

3. By the use of a controllable propeller, the blade angles for cruising may be increased and at the same time the throttle opened to maintain the desired engine speed. This method is frequently used but its use is limited by engine-operating restrictions and by the fact that it usually entails a loss in propeller efficiency, which tends to offset the lower rate of fuel consumption.

As indicated, these methods have their limitations and it is not the purpose of this report to take them up in detail. It is not out of place, however, to suggest another, though not a new method, which has some connection with the subject of this report.

This plan, applicable to multiengine airplanes, consists merely in cutting out one or more engines after the take-off has been accomplished and feathering the dead-engine propellers to some angle around 85° to 90° where they will not turn and where the power required to overcome their drag will be very small. Combining this method with method 3 should result in a worthwhile decrease in fuel load and a corresponding increase in pay load over that obtained with method 3 alone.

Consider, as an example, the case of a 4-engine flying boat having a high speed of 190 miles per hour but which, in long transoceanic flights, cruises at 35 percent power at a speed of about 125 miles per hour. Other specifications for the airplane are as follows:

Engines (4)—rated 850 horsepower at 1,450 r. p. m.

Propellers—3 blades; 11-foot diameter; controllable through 90° .

In long-distance cruising, assume that the engine speed is reduced to 950 r. p. m., or 65.5 percent of rated speed, and that the propeller and the throttle are adjusted to give 53.4 percent of rated torque. The cruising power is then 35 percent of rated power and the rate of fuel consumption (from fig. 7 of reference 8) is found

to be 0.56 pound per horsepower-hour. The propeller efficiency for cruising is 84 percent.

Now assume that two engines are cut out and their propellers set at 90° . The torque of the other engines is raised to 80 percent of rated torque and the engine speed to 1,270 r. p. m., or 87.5 percent of rated speed. The cruising power is now 70 percent of the rated power but the propeller efficiency drops to 82 percent. The fuel consumption, however, drops to 0.485 pound per horsepower-hour. The two dead propellers absorb 18 horsepower, which is equivalent to decreasing the efficiency of the working propellers by 1.5 percent or to a value of $82 - 1.5 = 80.5$ percent. The required fuel load for the two cases is directly proportional to their specific fuel consumptions and inversely proportional to their

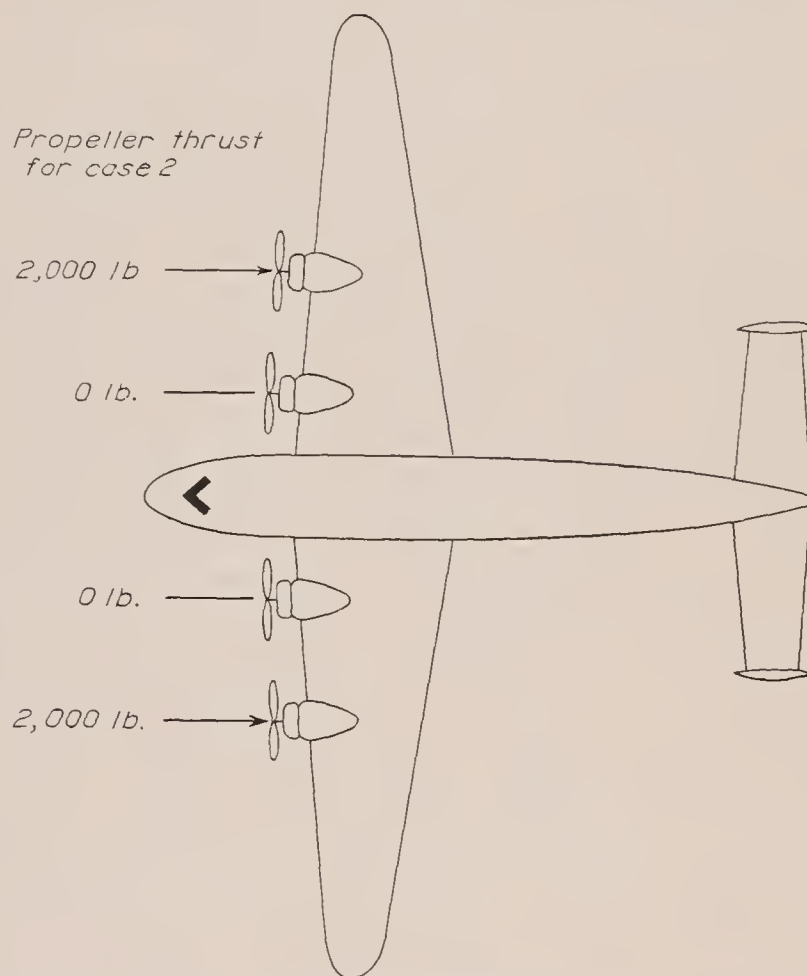


FIGURE 18.—Illustration of method of using propellers as power brakes to reduce landing distance. Gross weight, 32,000 pounds; landing speed, 100 feet per second.

propeller efficiencies, so that the required fuel load with the two engines dead is $\frac{0.485}{0.56} \times \frac{84.0}{80.5} = 90.5$ percent of the fuel load required for the normal cruising condition. The 9.5 percent saving in fuel load (or increase in pay load) would amount to about 950 pounds on a 2,000-mile flight. The results of such a comparison depend a great deal on the assumed values of engine torque and engine speed; however, in this example the assumed values of these variables are considered reasonable. Other cases may be found where the saving is either greater or less than in this example.

An obvious disadvantage of this method is the increased wear on the operating engines, though this disadvantage may be offset by the absence of wear on the dead engines.

LANGLEY MEMORIAL AERONAUTICAL LABORATORY,
NATIONAL ADVISORY COMMITTEE FOR AERONAUTICS,
LANGLEY FIELD, VA., *November 15, 1937.*

REFERENCES

1. Hartman, Edwin P.: Negative Thrust and Torque Characteristics of an Adjustable-Pitch Metal Propeller. T. R. No. 464, N. A. C. A., 1933.
2. Rhode, Richard V., and Pearson, Henry A.: Flight Tests of the Drag and Torque of the Propeller in Terminal-Velocity Dives. T. R. No. 599, N. A. C. A., 1937.
3. Malina, F. J., and Jenney, W. W.: Characteristics of Braked, Locked, and Free-Wheeling Two- and Three-Bladed Propellers. Jour. Aero. Sci., vol. 3, no. 7, May 1936, pp. 237-242.
4. Weick, Fred E., and Wood, Donald H.: The Twenty-Foot Propeller Research Tunnel of the National Advisory Committee for Aeronautics. T. R. No. 300, N. A. C. A., 1928.
5. Douglas, Donald W.: The Developments and Reliability of the Modern Multi-Engine Air Liner with Special Reference to Multi-Engine Airplanes after Engine Failure. Jour. Aero. Sci., vol. 2, no. 4, July 1935, pp. 132-152.
6. Sparrow, S. W., and Thorne, M. A.: Friction of Aviation Engines. T. R. No. 262, N. A. C. A., 1927.
7. Diehl, Walter Stuart: Engineering Aerodynamics. The Ronald Press Company, 1936, p. 206.
8. Biermann, David.: A Study of the Factors Affecting the Range of Airplanes. T. N. No. 592, N. A. C. A. 1937.

REPORT No. 642

TESTS OF FIVE FULL-SCALE PROPELLERS IN THE PRESENCE OF A RADIAL AND A LIQUID-COOLED ENGINE NACELLE, INCLUDING TESTS OF TWO SPINNERS

By DAVID BIERMANN and EDWIN P. HARTMAN

SUMMARY

Wind-tunnel tests are reported of five 3-blade 10-foot propellers operating in front of a radial and a liquid-cooled engine nacelle. The range of blade angles investigated extended from 15° to 45° . Two spinners were tested in conjunction with the liquid-cooled engine nacelle. Comparisons are made between propellers having different blade-shank shapes, blades of different thickness, and different airfoil sections.

The results show that propellers operating in front of the liquid-cooled engine nacelle had higher take-off efficiencies than when operating in front of the radial engine nacelle; the peak efficiency was higher only when spinners were employed. One spinner increased the propulsive efficiency of the liquid-cooled unit 6 percent for the highest blade-angle setting investigated and less for lower blade angles. The propeller having airfoil sections extending into the hub was superior to one having round blade shanks. The thick propeller having a Clark Y section had a higher take-off efficiency than the thinner one, but its maximum efficiency was possibly lower. Of the three blade sections tested, Clark Y, R. A. F. 6, and N. A. C. A. 2400-34, the Clark Y was superior for the high-speed condition, but the R. A. F. 6 excelled for the take-off condition.

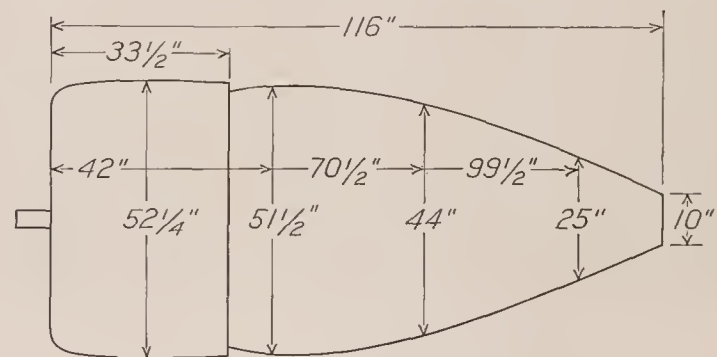
INTRODUCTION

A series of tests of full-scale propellers was made in the propeller-research tunnel during the first part of 1937. Published reports of the series cover separate subjects as: compressibility effects (reference 1), solidity (reference 2), negative thrust and torque (reference 3), and blade section (reference 4). The results of tests of five propellers are published in the present report, the purpose of which is twofold: first, to present design data from tests of four 3-blade propellers made in the presence of two popular body types; and, second, from the test data for all five propellers, to make incidental comparisons regarding the effect of: body shape and size, spinners, blade-shank shape, blade thickness, and blade section. The concrete data should be of value in design work because two of the propellers are in fairly wide use and the body types are representative of those in common use. The comparisons may be of value in the determination of some of the elements of the basic design of airplanes and propellers.

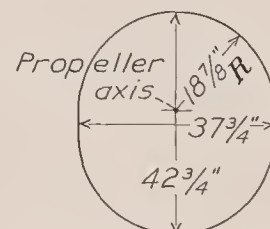
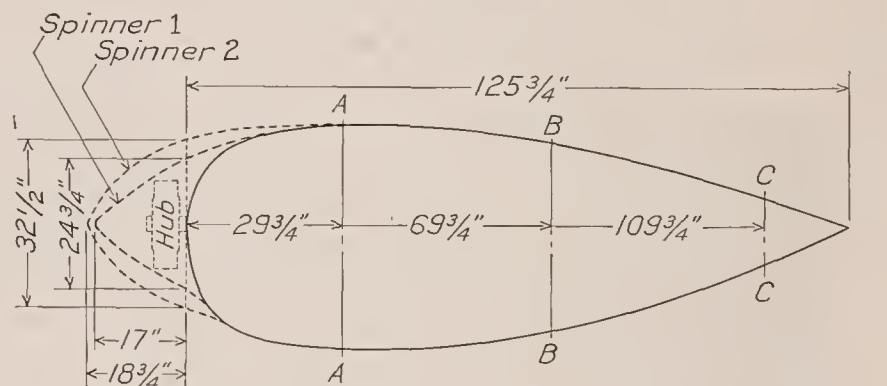
APPARATUS AND METHODS

The propeller-research tunnel has been modified since the description of reference 5 was written to the extent of installing an electric motor to drive the tunnel propeller and of replacing the balance with a more modern one capable of simultaneously recording all the forces.

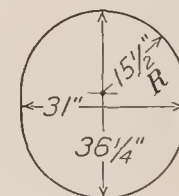
A 600-horsepower Curtiss Conqueror engine (GIV-1570) was used to drive the test propellers. The engine



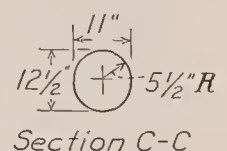
Radial engine nacelle



Section A-A



Section B-B



Section C-C

Liquid-cooled engine nacelle

FIGURE 1.—Drawings of engine nacelles.

was mounted in a cradle dynamometer free to rotate about an axis parallel to the propeller axis and located at one side of the engine. The torque reaction was transmitted from the other side of the engine to recording scales located on the floor of the test chamber. The propeller speed was measured by a calibrated electric tachometer.

A scale drawing of each nacelle is given in figure 1.

A perforated plate was used to simulate in air resistance a radial engine in those tests in which the radial engine cowling was used. (See fig. 2.) The cowling was

of different rates of air flow through the plate indicated that the effect was negligible.

The liquid-cooled engine nacelle was tested with three



FIGURE 2.—The radial engine nacelle.

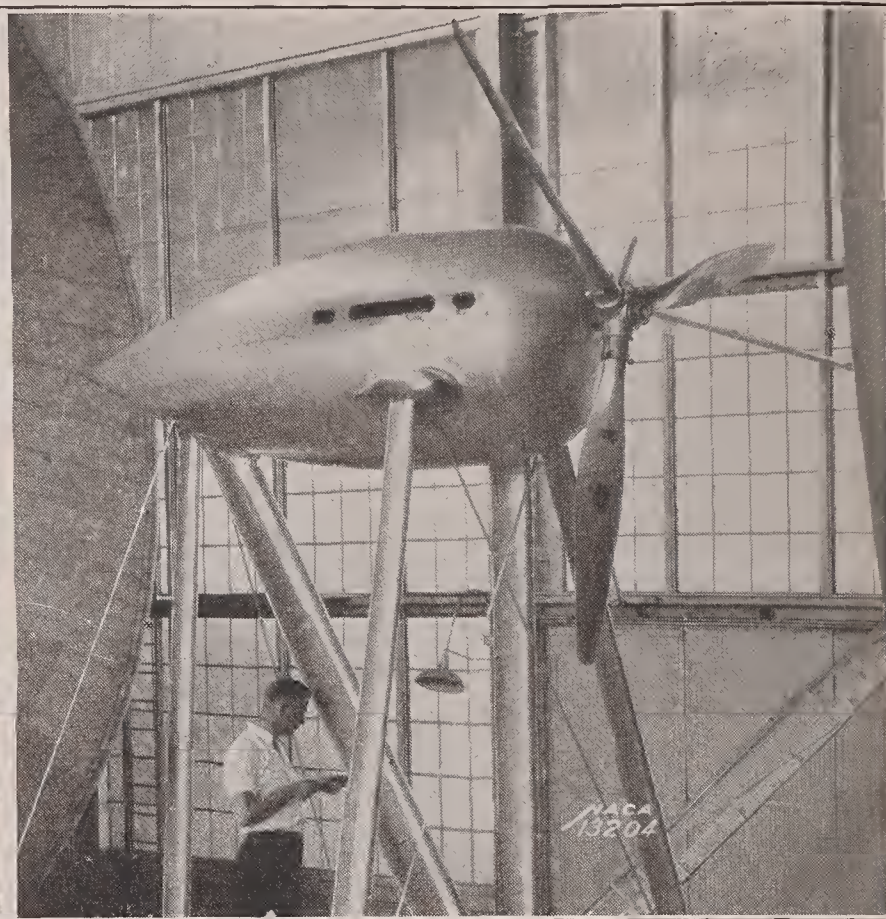


FIGURE 3.—The liquid-cooled engine nacelle with round nose.

selected because its drag was not sensitive to the propeller slipstream and, consequently, the propulsive efficiency was not abnormally affected. Air was al-

nose conditions: a round nose, which was the standard condition for nearly all the tests, and with two spinners of different size. The nacelle with the round nose is

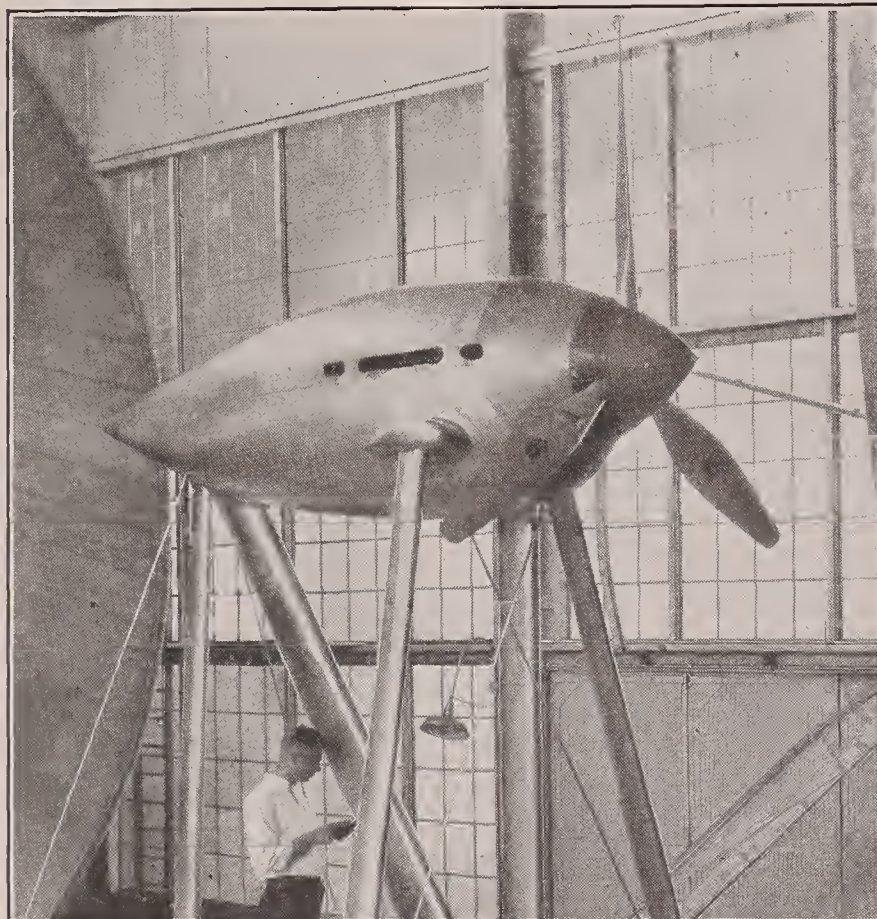


FIGURE 4.—The liquid-cooled engine nacelle with spinner 1.

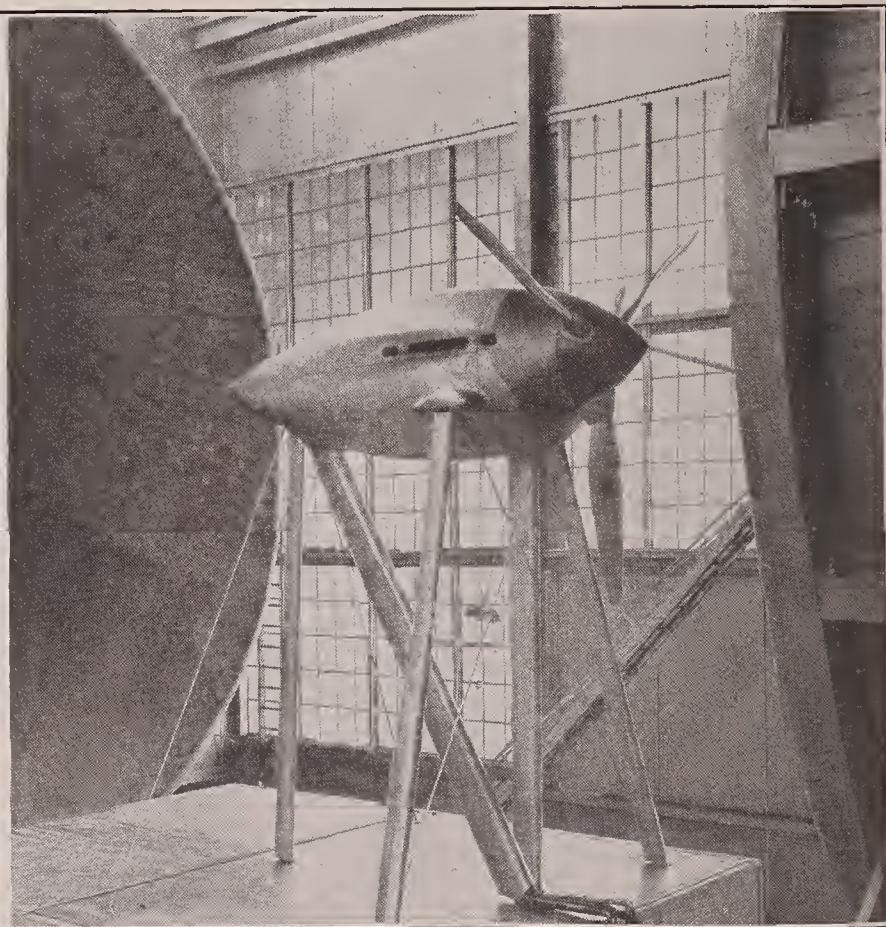


FIGURE 5.—The liquid-cooled engine nacelle with spinner 1 and blade-shank cuffs

lowed to flow through the plate at a rate corresponding to that for a normally baffled engine. Separate tests to determine the effect on the propeller characteristics

shown in figure 3 and with spinner 1 in figure 4. An effort was made to reduce the drag of the round blade shanks that extended out from spinner 1 by stream-

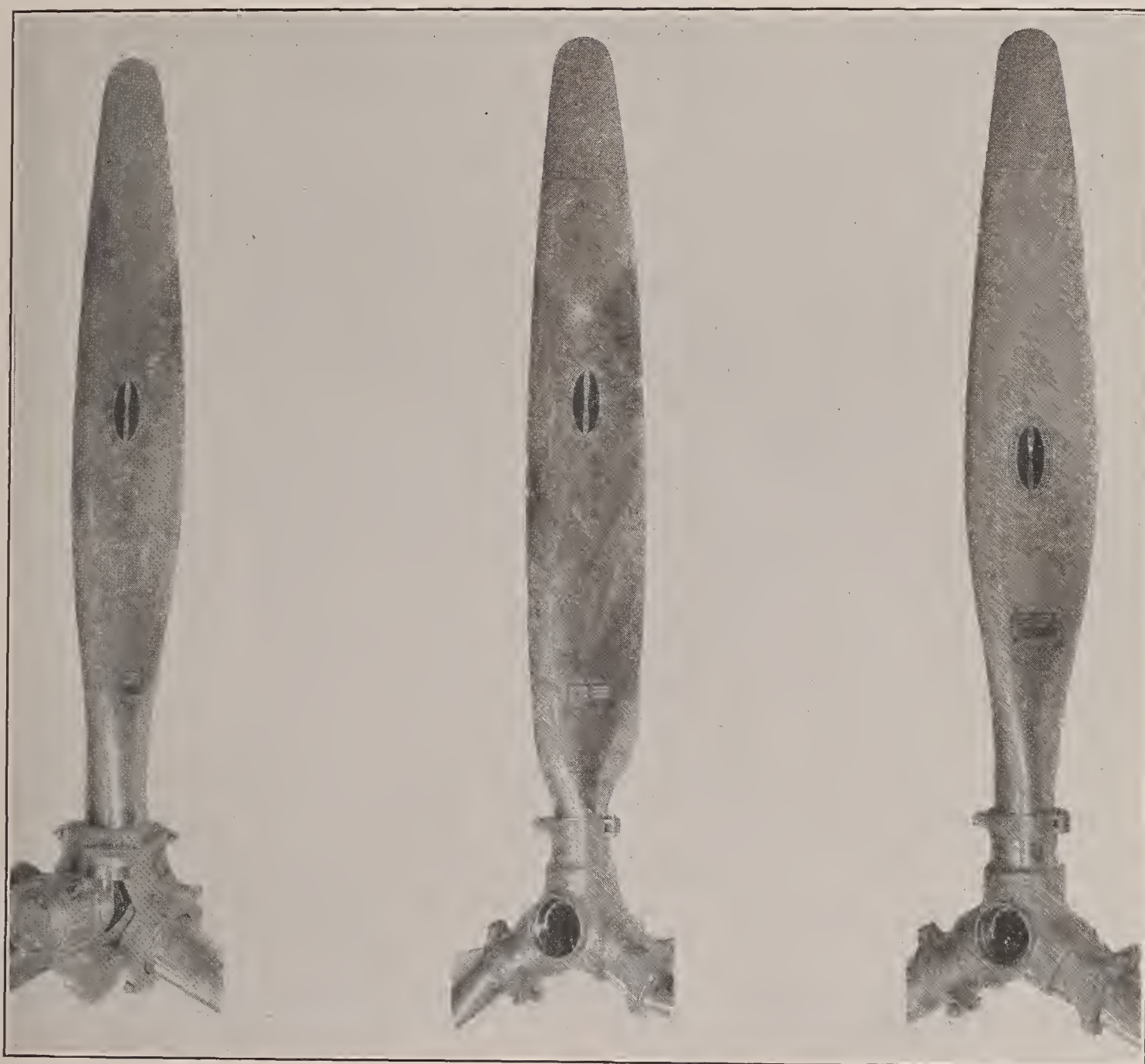
lining them with thin sheet-metal cuffs. These cuffs, shown in figure 5, extended along the blade shanks for a distance of about 4 inches beyond the spinner and were secured to the spinner. The blades were thus enclosed for a distance of about 24 percent of the radius.

Five 3-blade propellers (fig. 6), all having diameters of 10 feet, were tested. Blade-form curves are given in figures 7 and 8. The propeller dimensions are given by the following notation: D , diameter; R , radius to the tip; r , station radius; h , section thickness; b , station chord; p , geometric pitch. Figure 9 shows the section

The principal propeller dimensions are given in the following table:

Propeller drawing number	Diameter (feet)	Section	b/D at $0.75R$	h/b at $0.75R$	Shank shape
Bureau Aeronautics 5868-9.	10	Clark Y-----	0.061	0.09	Round.
Hamilton Standard 1C1-0	10	-----do-----	.059	.07	Airfoil.
¹ Hamilton Standard 6101	10	-----do-----	.059	.07	Round.
¹ Hamilton Standard 6129	10	R. A. F. 6-----	.059	.07	Do.
¹ Hamilton Standard 6131	10	N. A. C. A. 2400-34.	.059	.07	Do.

¹ Controllable.



6101
6129
6131

1C1-0

5868-9

FIGURE 6.—The propeller blades tested.

outline and gives the ordinates for the three blade sections incorporated in the different propellers. It may be noted that the N. A. C. A. 2400-34 airfoil section is modified for propeller design by changing the thickness with respect to the mean camber line. The camber therefore remains constant for the whole blade, whereas the camber increases with blade section thickness for propellers having the Clark Y and R. A. F. 6 sections.

It may be noted from the table that the essential difference between propellers 5868-9 and 6101 is the blade thickness although propeller 6101 has a slightly larger shank diameter and a different hub, which should not appreciably affect the results. These two propellers probably represent the upper and lower limits in thickness ratios for present-day aluminum-alloy propellers.

Propeller 1C1-0 was included in the series because it differed from 6101 only in the shank shape and, incidentally, in the hub design.

Propellers 6101, 6129, and 6131 constitute a series differing only in blade section. These propellers were whirl-tested (reference 6) and flight-tested at Wright Field previous to the present investigation.

The method of testing in the propeller-research tunnel consists in maintaining the propeller speed constant and increasing the tunnel speed in steps up to the maximum value of 115 miles per hour. Higher values

engine power; the following schedule was therefore adhered to:

Propeller speeds for tunnel speeds below 115 miles per hour

Blade angle, deg.	Initial propeller speed, r. p. m.
15	1,000
20	1,000
25	800
30	800
35	800
40	700
45	700

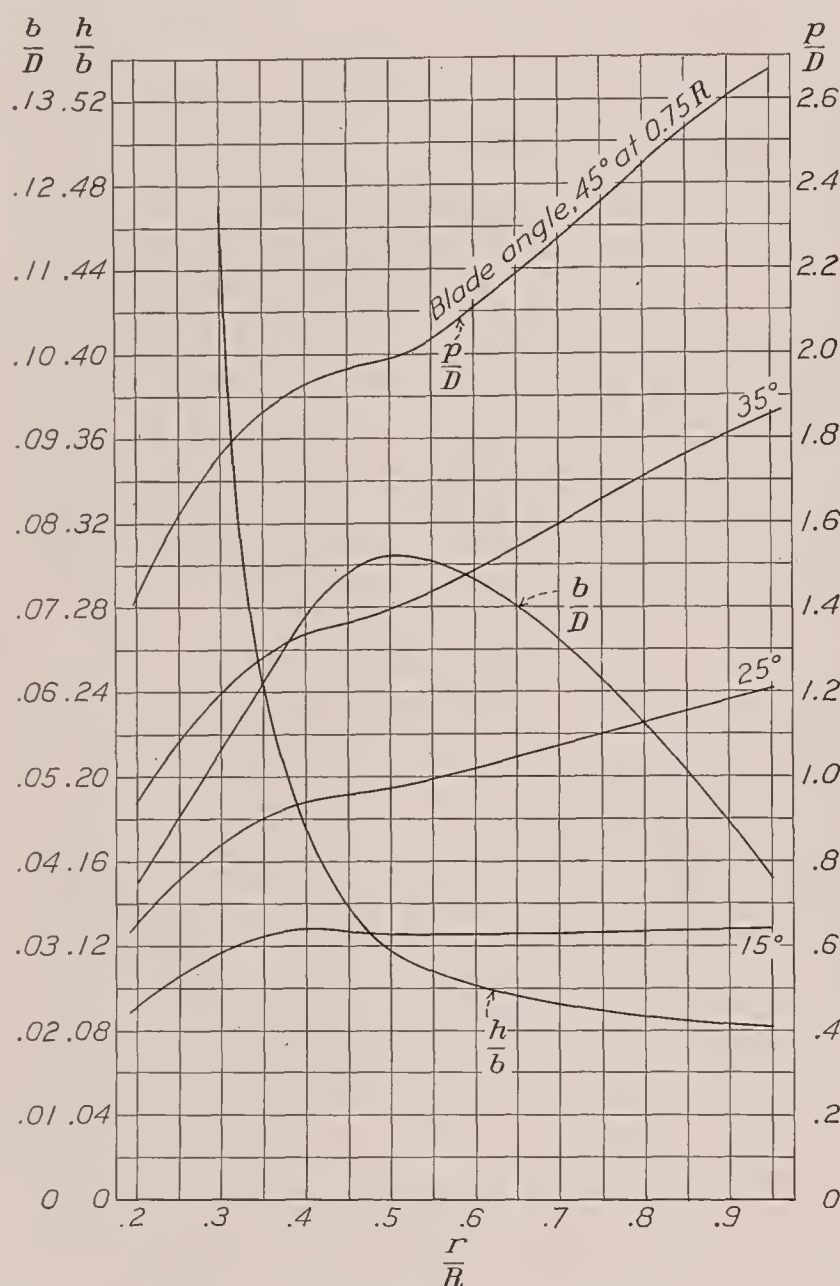


FIGURE 7.—Blade-form curves for propeller 5868-9.

of V/nD are obtained by reducing the engine speed until zero thrust is reached.

The tests reported in reference 1 showed that losses in efficiency occurred at tip speeds above 600 to 800 feet per second, depending principally on the blade angle and the V/nD range. At slightly lower tip speeds the values of the thrust and the power coefficients, but not the efficiencies, were affected by compressibility. The present tests were therefore run at tip speeds of 525 feet per second and less to avoid complications arising from compressibility. The standard initial testing propeller speed of 1,000 r. p. m. could not be maintained for the higher blade-angle settings owing to the limitation of

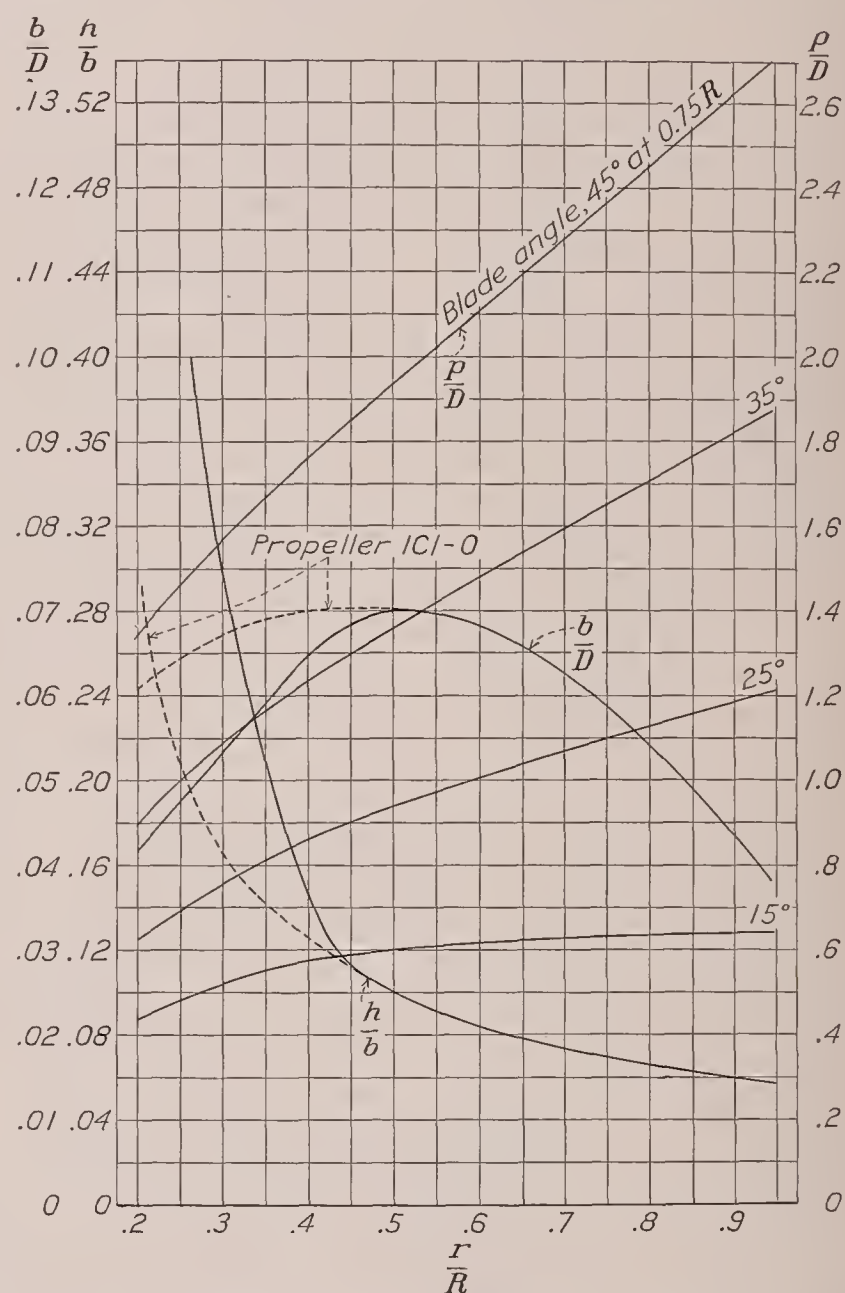


FIGURE 8.—Blade-form curves for propellers 6101, 6129, 6131, and 1C1-0.

The approximate test propeller speed may be computed from the relation $r. p. m. = \frac{K}{V/nD}$, for V/nD values higher than can be obtained from the foregoing schedule, where $K=1,000$ for $V=115$ miles per hour and $D=10$ feet. The tests reported in reference 1 were confined to tip speeds above about 600 feet per second, so the use of the data in this reference for correcting coefficients for normal-flight operating speeds would necessitate neglecting any effects occurring at lower speeds. Unreported data obtained during these tests indicate that this procedure would entail little, if any, error.

RESULTS AND DISCUSSION

The results are reduced to the usual coefficients of thrust, power, and efficiency defined as:

$$C_T = \frac{\text{effective thrust}}{\rho n^2 D^4} = \frac{T - \Delta D}{\rho n^2 D^4} =$$

$$C_P = \frac{\text{engine power}}{\rho n^3 D^5} = 550 \text{ Hp.}$$

and $\eta = \frac{C_T V}{C_P n D}$ or $\eta = \frac{P}{2\pi n Q} = 550 \text{ Hp.}$

where ρ , the mass density of air.

n , propeller speed, *rps*

D , propeller diameter.

ΔD , increased drag of body due to propeller slipstream.

In addition to plots of these coefficients against V/nD , charts for the selection of propellers are given. These charts are based on the speed-power coefficient C_s defined as:

$$C_s = \sqrt[5]{\frac{\rho V^5}{P n^2}} = \frac{.638 V_{\text{mph}}}{14 p^{1/5} \times N^{1/5}}$$

The test results have been tabulated in ten tables and are available on request from the National Advisory Committee for Aeronautics. The experimental results are presented in chart form in figures 10 to 46. For ease of reference, the figure numbers are listed in the following table:

BASIC DATA

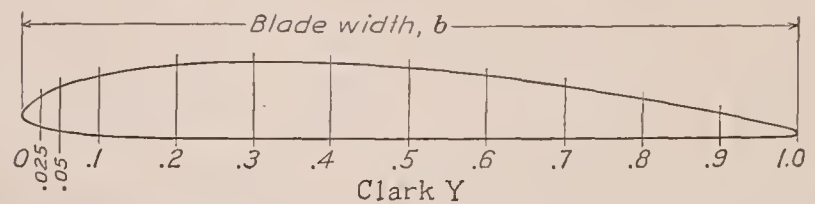
Body	Propeller	Figures
Radial engine nacelle.....	5868-9	10-13
	6101	14-17
	6129	18-21
	6131	22-25
Liquid-cooled engine nacelle.....	5868-9	26-29
	6101	30-33
	6129	34-37
	6131	38-41

SPINNER RESULTS AND COMPARISONS

Subject	Propeller	Figure
Spinners.....	5868-9	42
Blade shank.....	6101 and 1C1-0	43
Blade thickness.....	5868-9 and 6101	44
Blade section.....	6101, 6129, and 6131	45
Body.....	All propellers	46

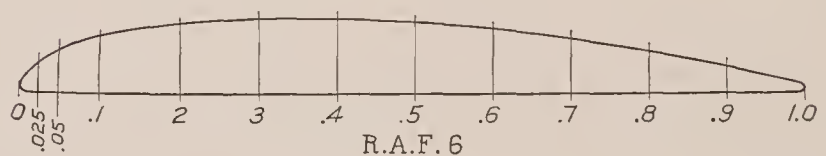
BASIC PROPELLER DATA

The chief purpose of this report is to supply propeller data for design purposes. Complete sets of curves of the basic coefficients for each of the propeller-body combinations are given for four propellers, two of which (propellers 5868-9 and 6101) are in common use.



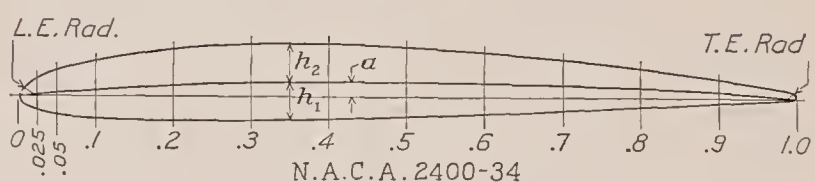
Station	Upper ordinate Maximum ordinate	Lower ordinate Maximum ordinate
0.025	0.55	0.13
.05	.67	.08
.1	.81	.04
.2	.96	.01
.3	1.00	0
.4	.99	0
.5	.93	0
.6	.83	0
.7	.69	0
.8	.52	0
.9	.34	0
L. E. radius.....		0.15
T. E. radius.....		.077

Clark Y



Station	Ordinate
	Maximum ordinate
0.025	0.41
.05	.59
.1	.79
.2	.95
.3	1.00
.4	.99
.5	.95
.6	.87
.7	.74
.8	.56
.9	.35
L. E. radius----- 0.10	
T. E. radius----- .077	

R. A. F. 6



Station	a/b	$h_1/t = h_2/t$
0.025	0.00225	0.2160
.05	.00438	.2938
.1	.0085	.3845
.2	.0148	.4725
.3	.0185	.5000
.4	.0201	.4898
.5	.0198	.4538
.6	.0185	.4012
.7	.0161	.3363
.8	.0126	.2550
.9	.0085	.1638
L. E. radius.....		0.156
T. E. radius.....		.078

b, chord; t, thickness
N. A. C. A. 2400-34

FIGURE 9.—Basic propeller sections. Airfoil specifications taken from reference 6.

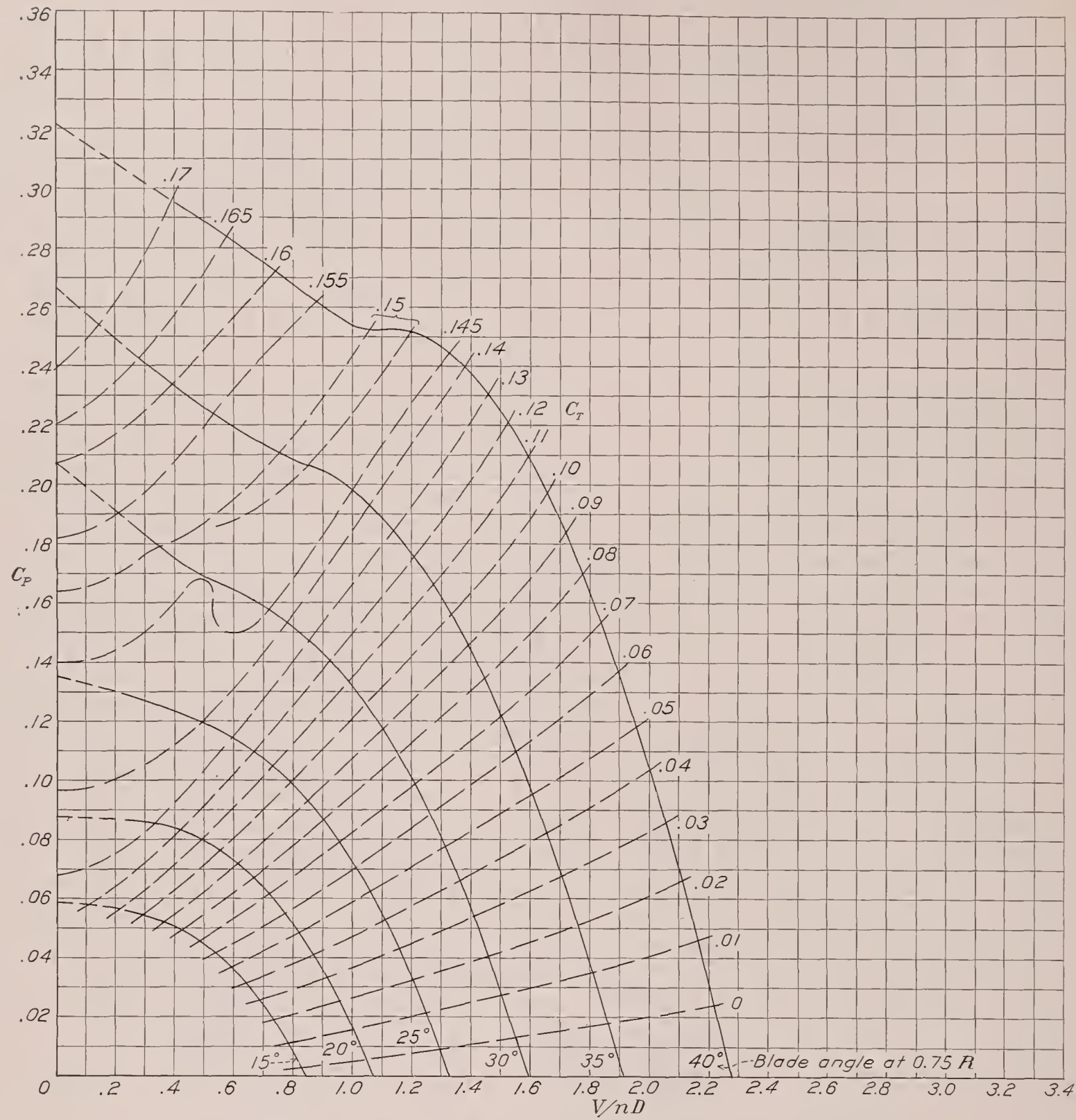


FIGURE 10.—Power-coefficient curves for propeller 5868-9, 3 blades, radial engine nacelle.

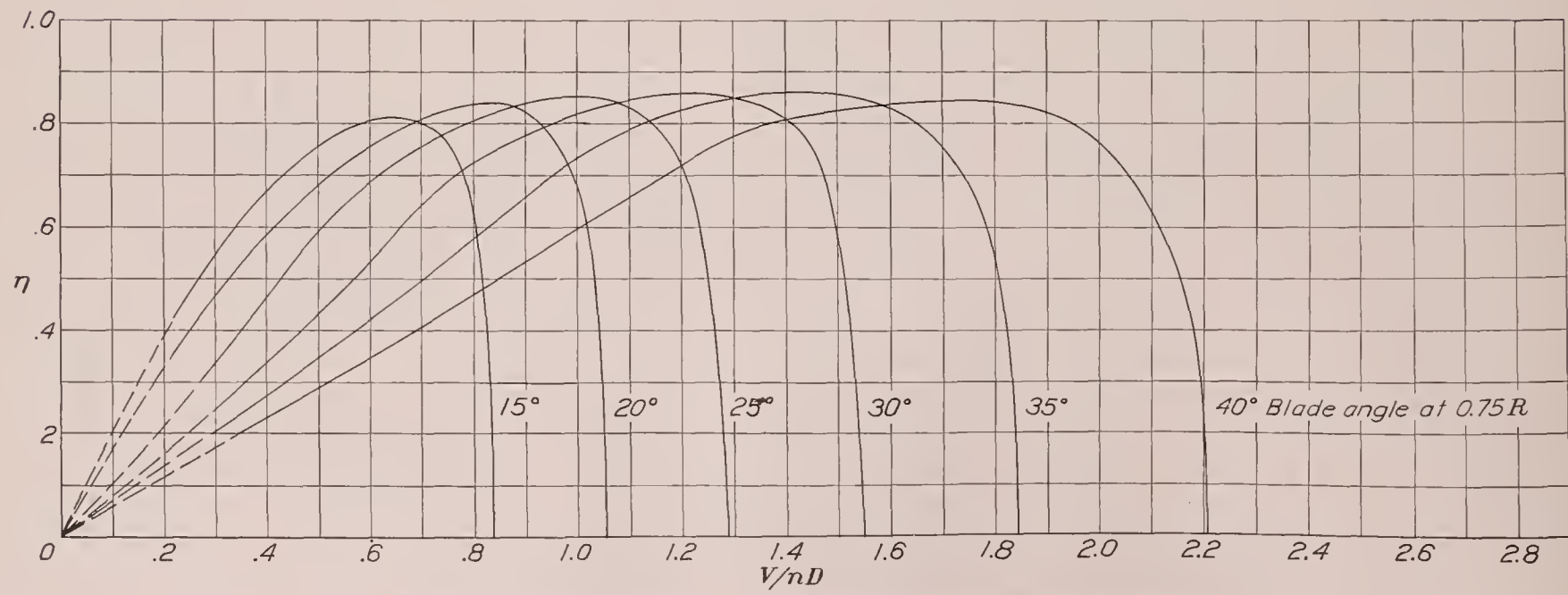


FIGURE 11.—Efficiency curves for propeller 5868-9, 3 blades, radial engine nacelle.

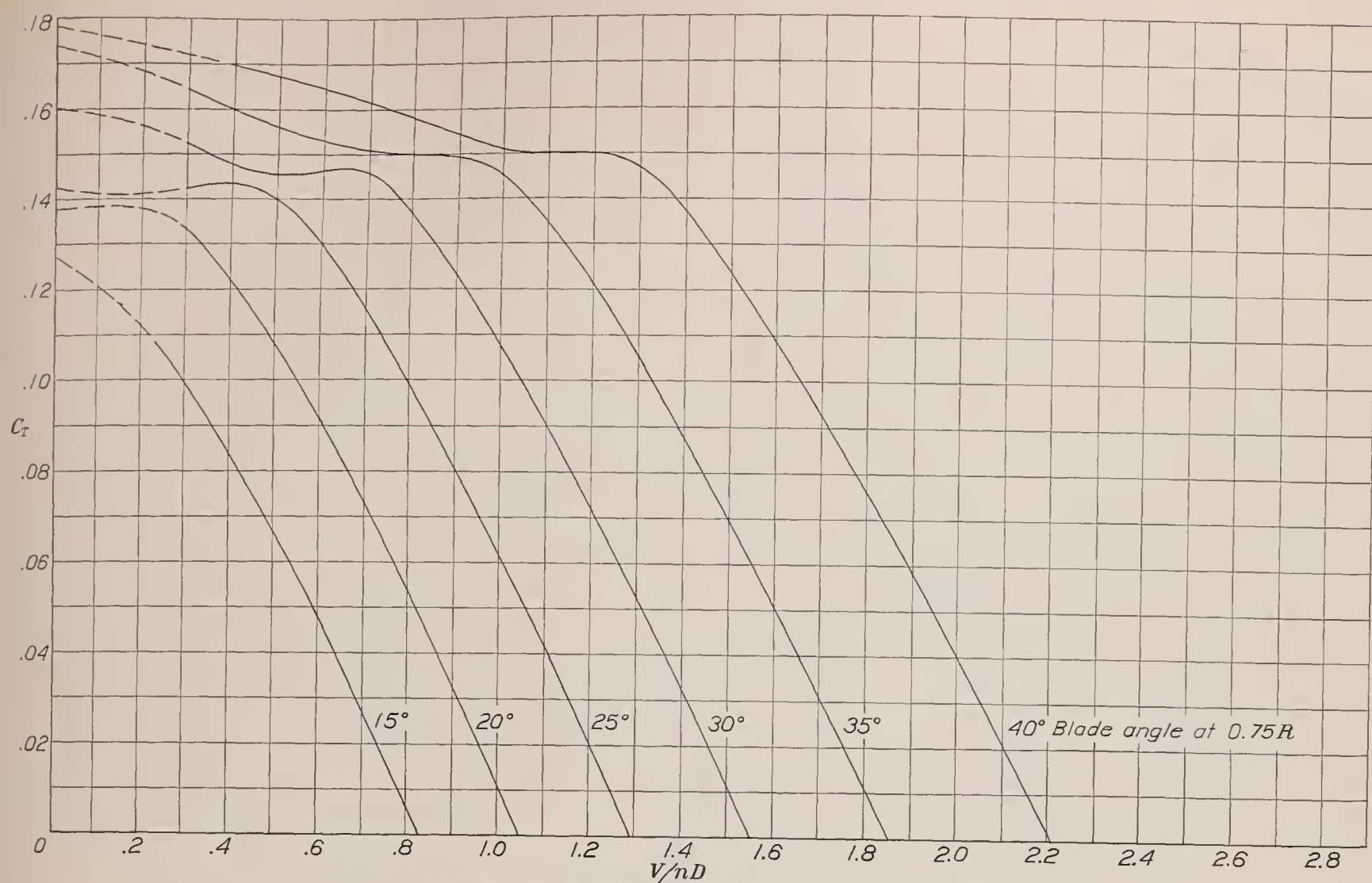


FIGURE 12.—Thrust-coefficient curves for propeller 5868-9, 3 blades, radial engine nacelle.

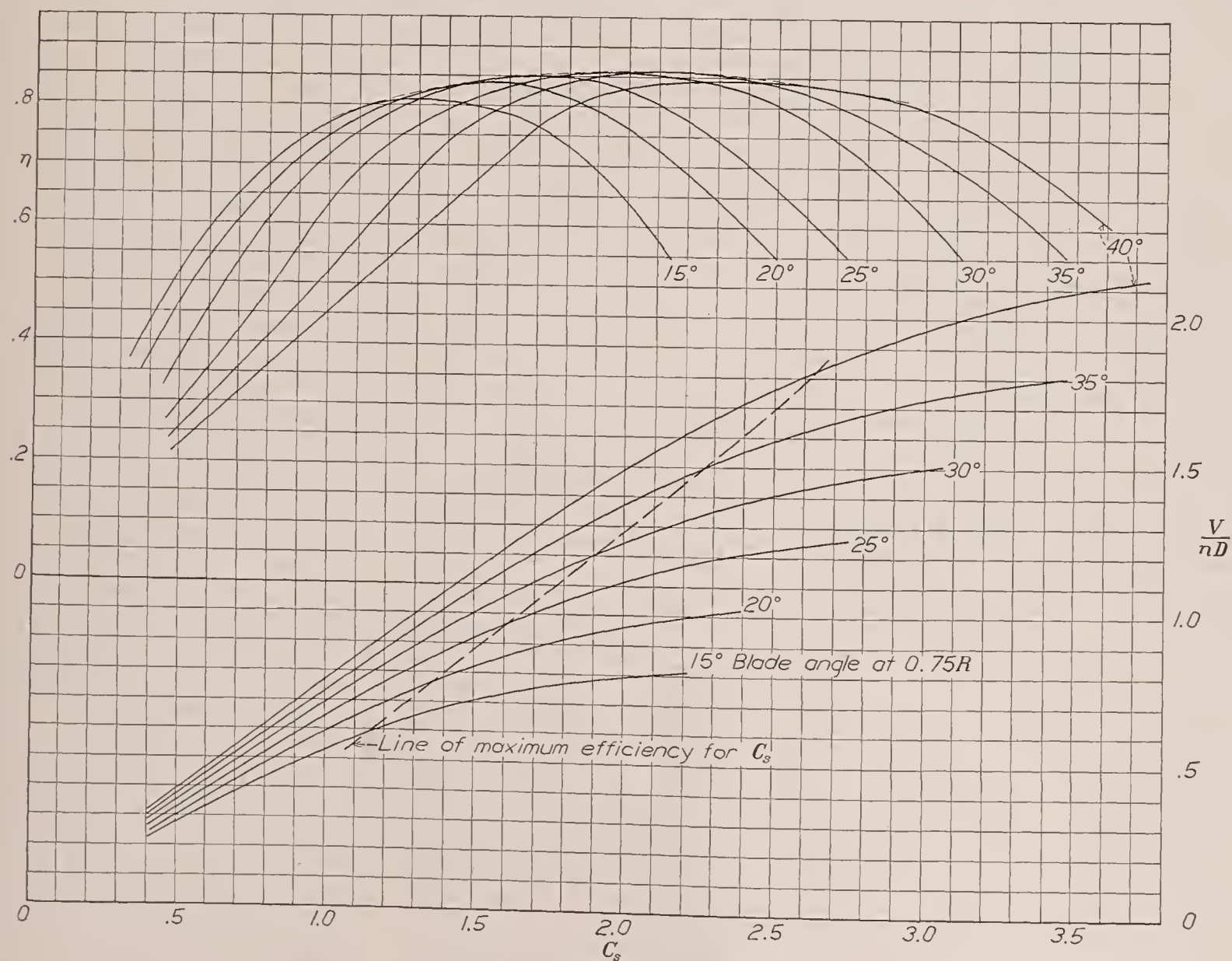


FIGURE 13.—Design chart for propeller 5868-9, 3 blades, radial engine nacelle.

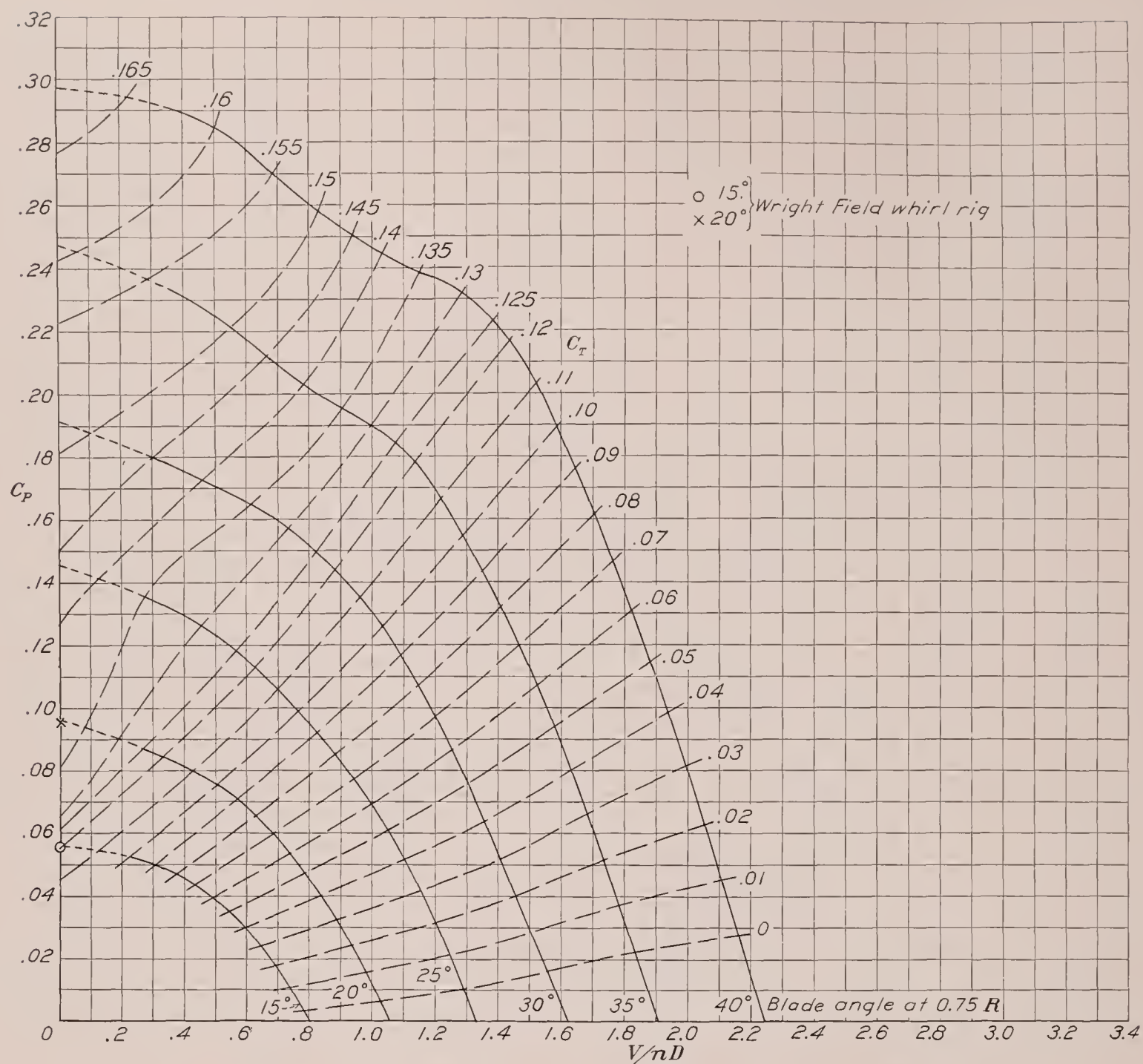


FIGURE 14.—Power-coefficient curves for propeller 6101, 3 blades, radial engine nacelle.

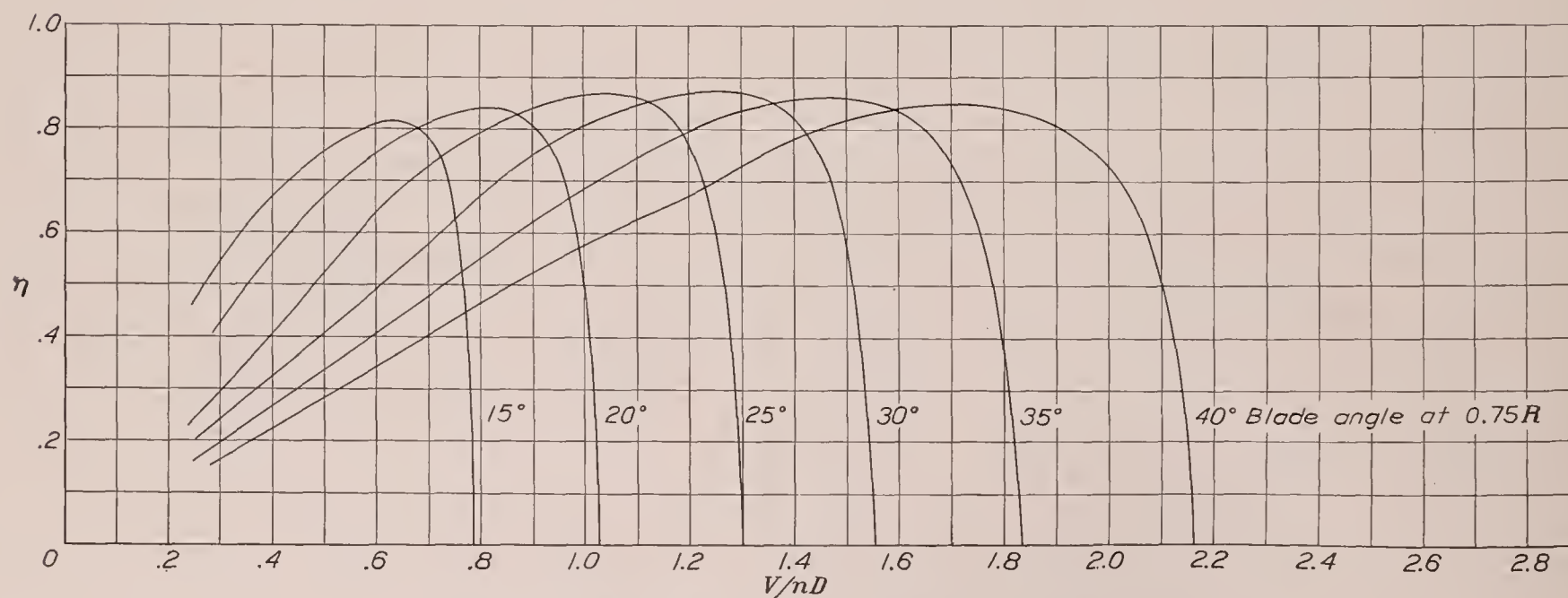


FIGURE 15.—Efficiency curves for propeller 6101, 3 blades, radial engine nacelle.

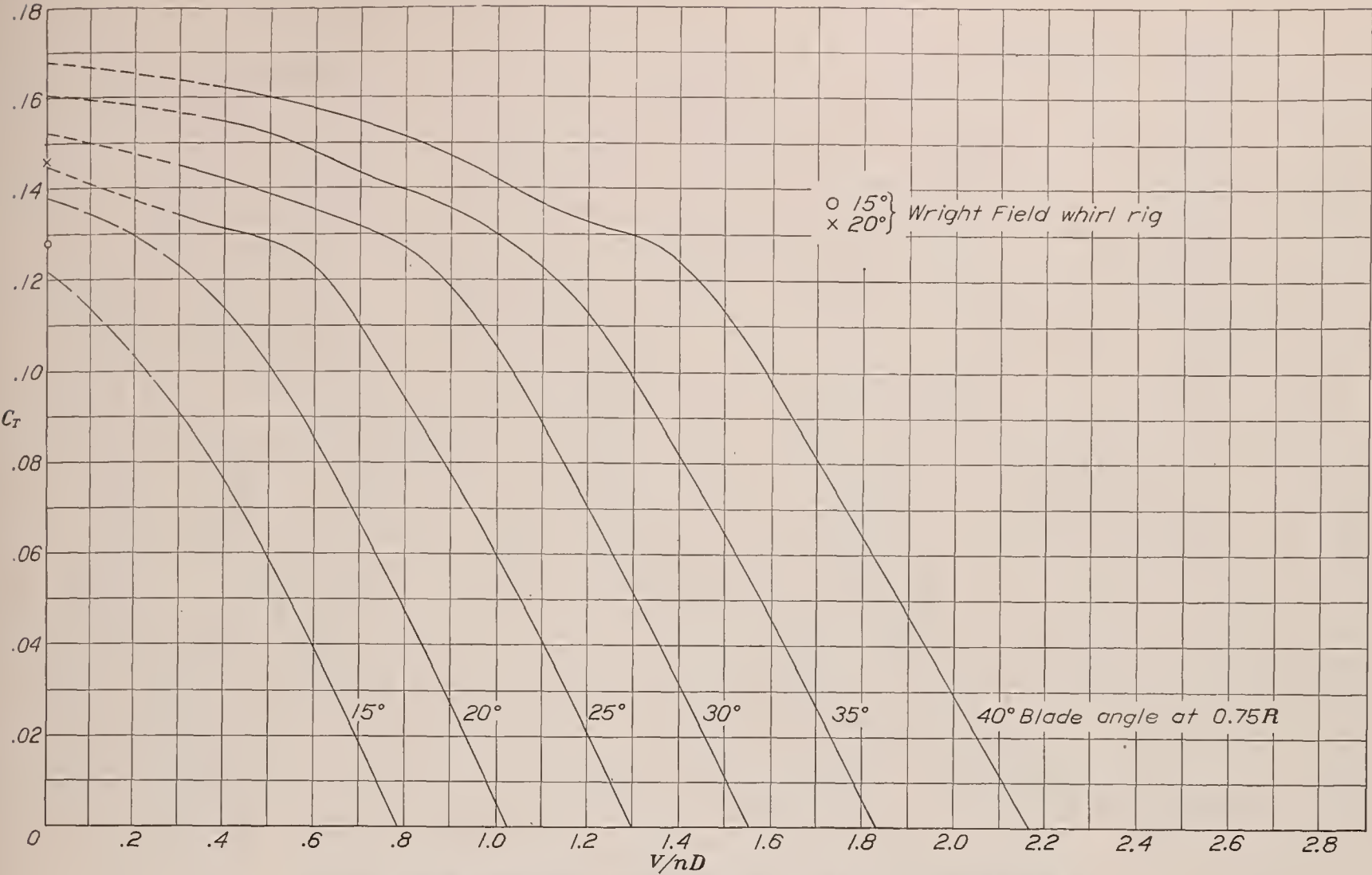


FIGURE 16.—Thrust-coefficient curves for propeller 6101, 3 blades, radial engine nacelle.

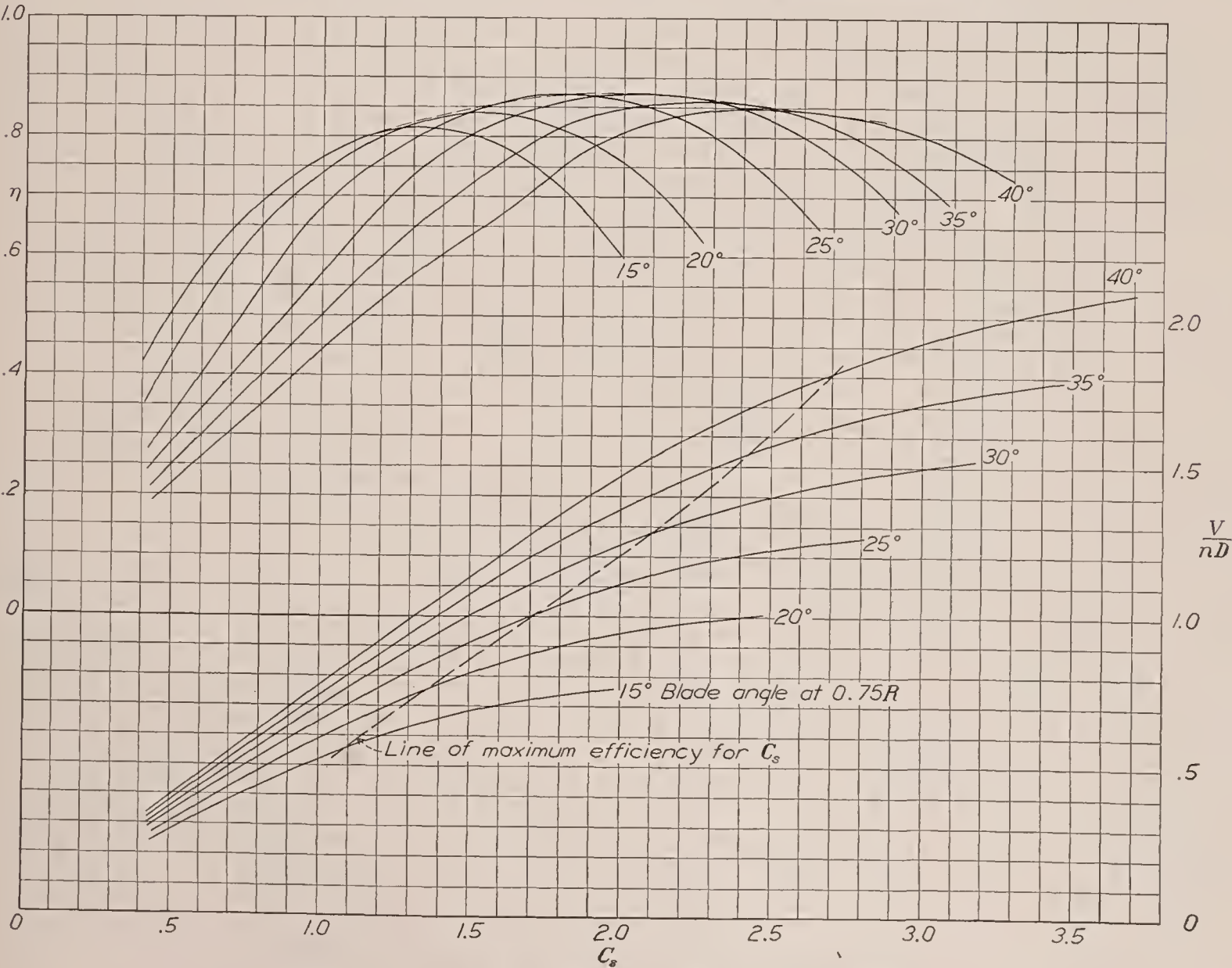


FIGURE 17.—Design chart for propeller 6101, 3 blades, radial engine nacelle.

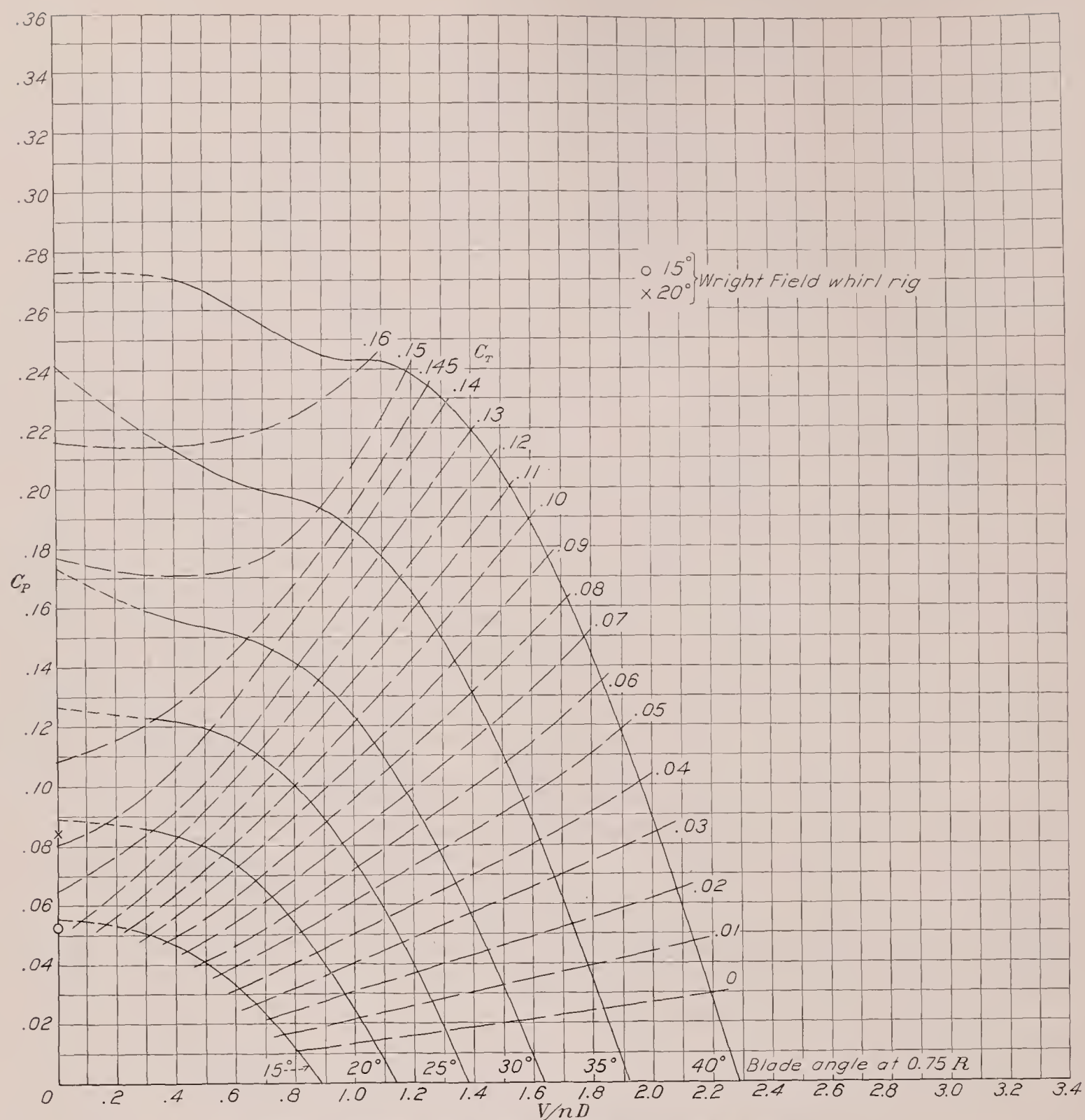


FIGURE 18.—Power-coefficient curves for propeller 6129, 3 blades, radial engine nacelle.

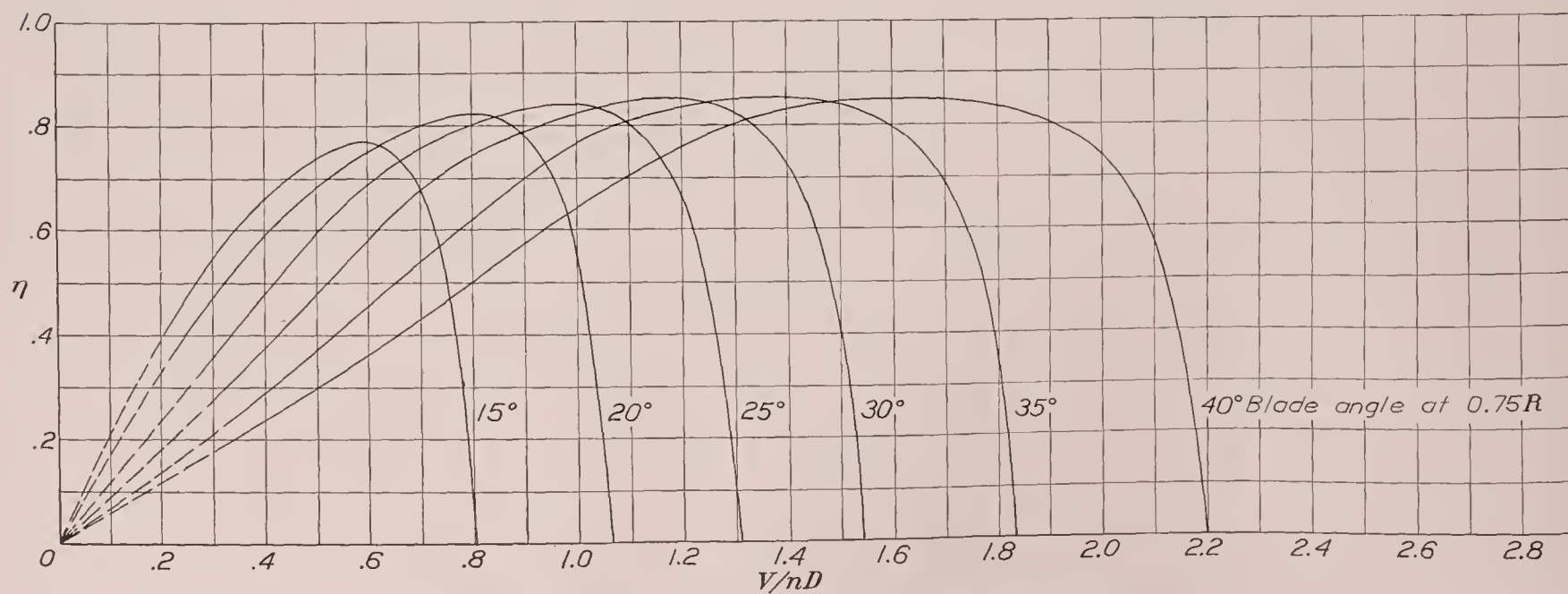


FIGURE 19.—Efficiency curves for propeller 6129, 3 blades, radial engine nacelle.

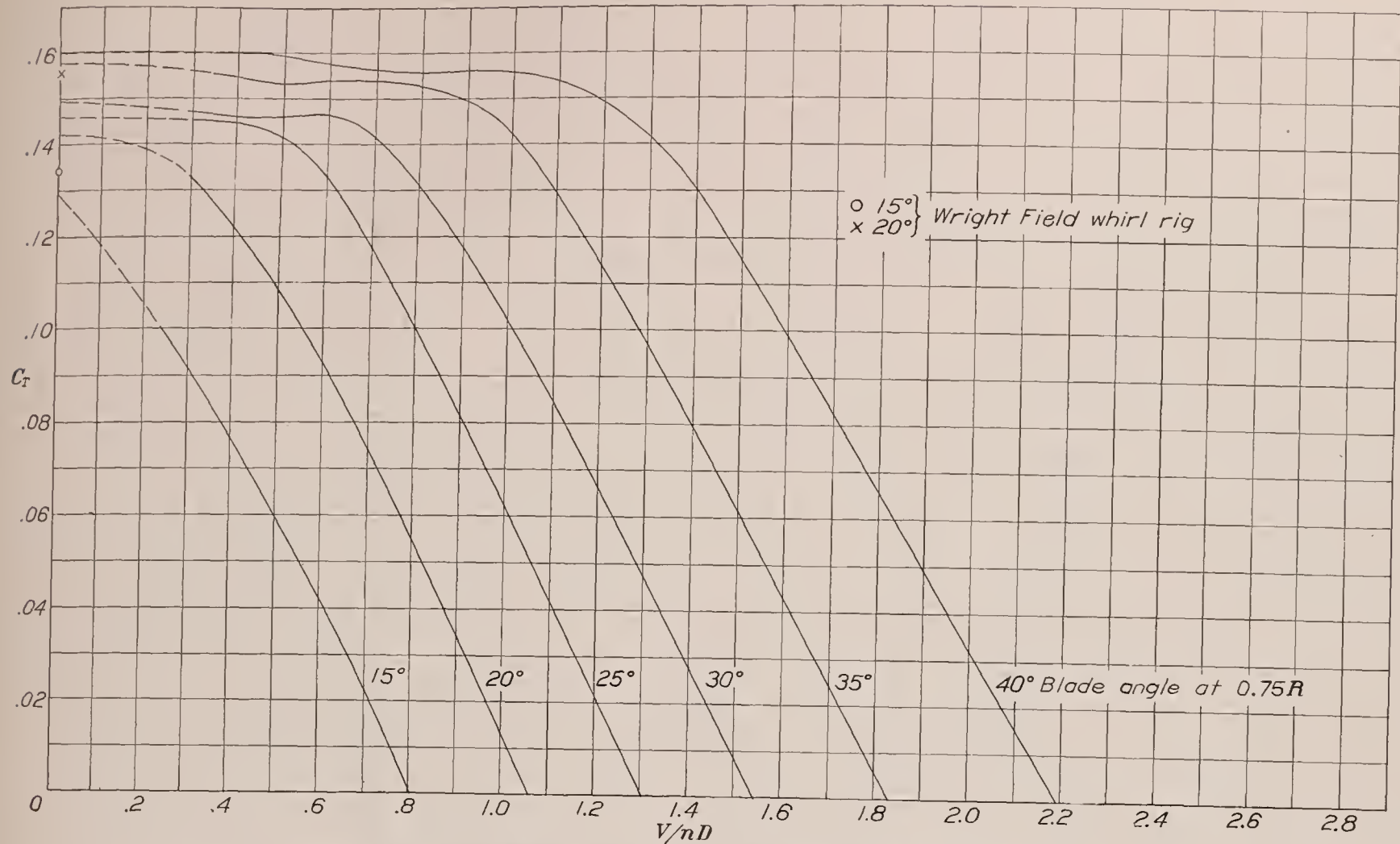


FIGURE 20.—Thrust-coefficient curves for propeller 6129, 3 blades, radial engine nacelle.

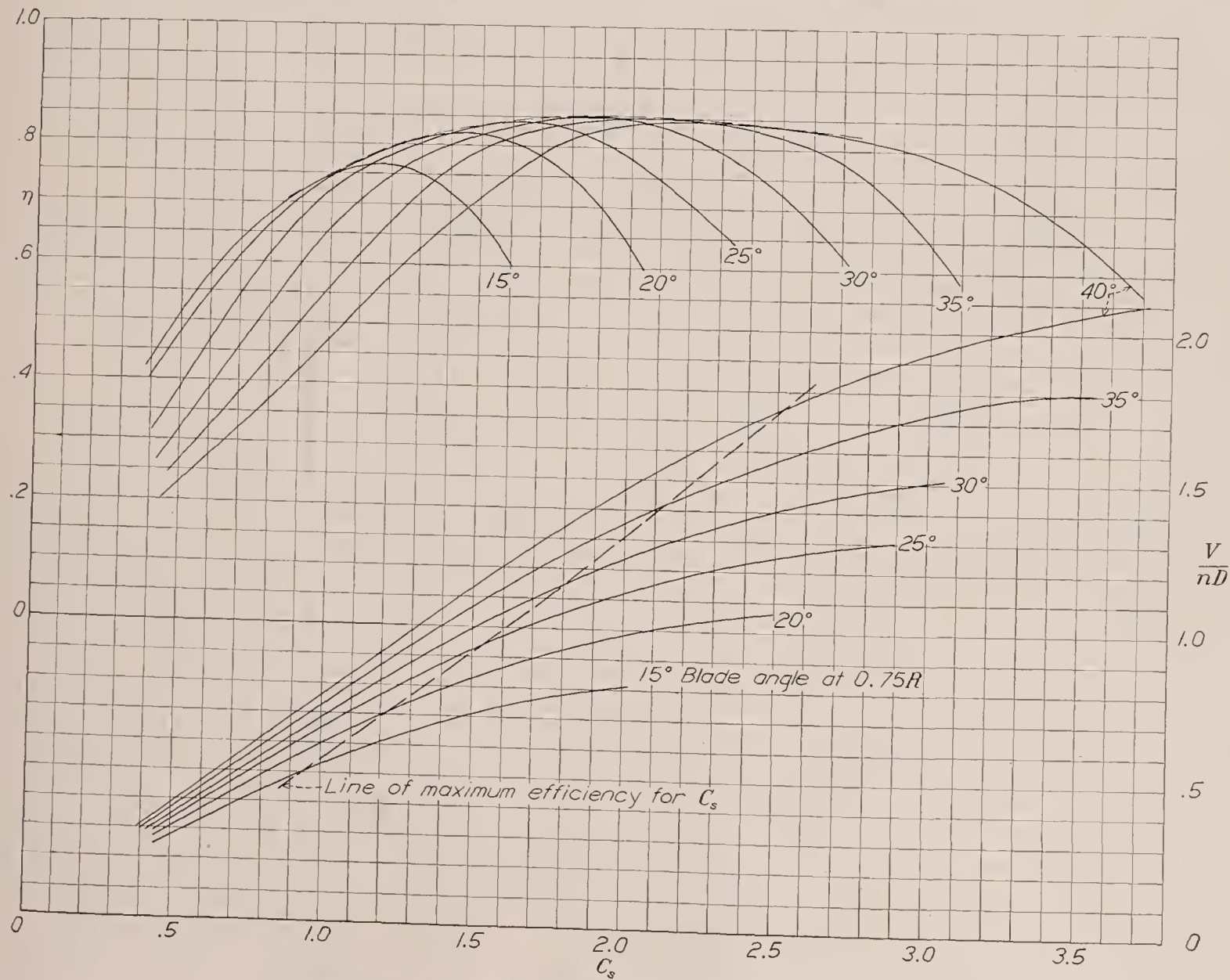


FIGURE 21.—Design chart for propeller 6129, 3 blades, radial engine nacelle.

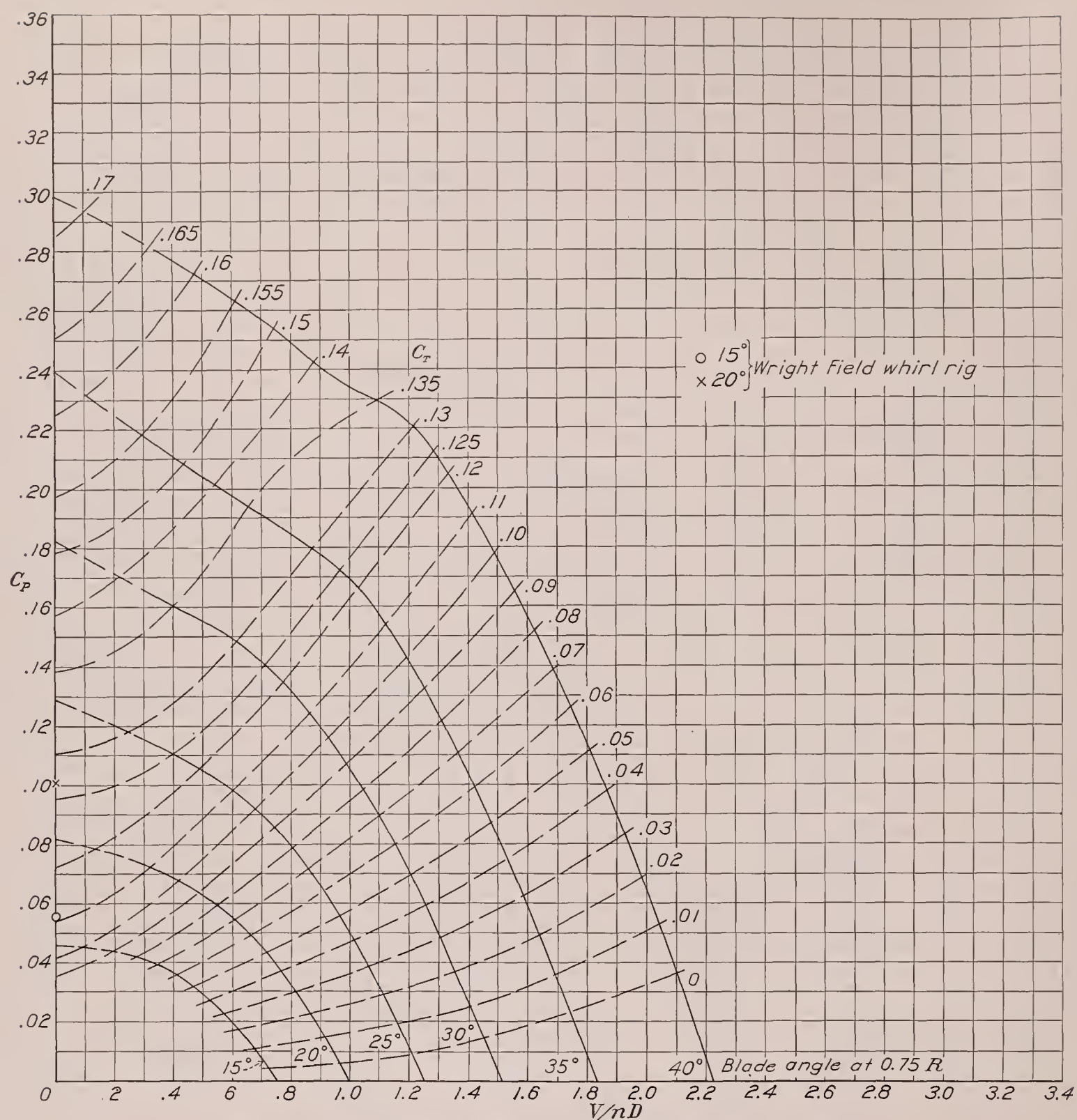


FIGURE 22.—Power-coefficient curves for propeller 6131, 3 blades, radial engine nacelle.

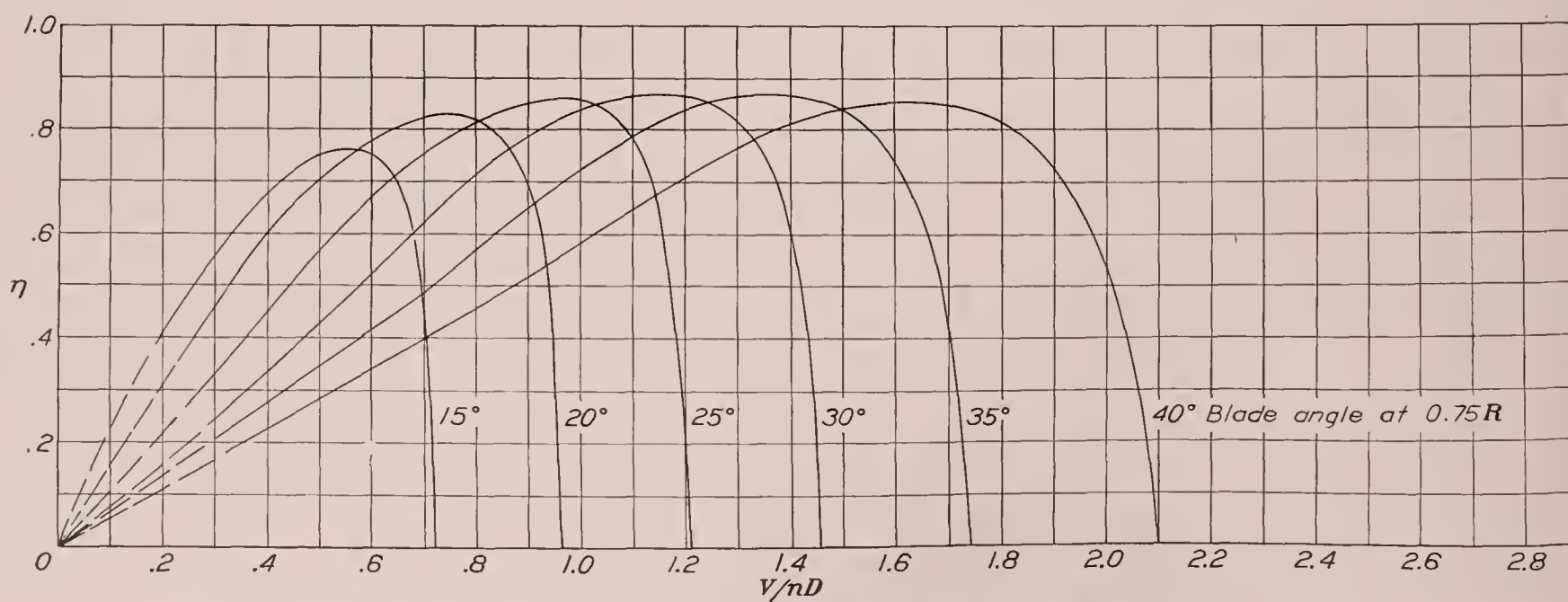


FIGURE 23.—Efficiency curves for propeller 6131, 3 blades, radial engine nacelle.

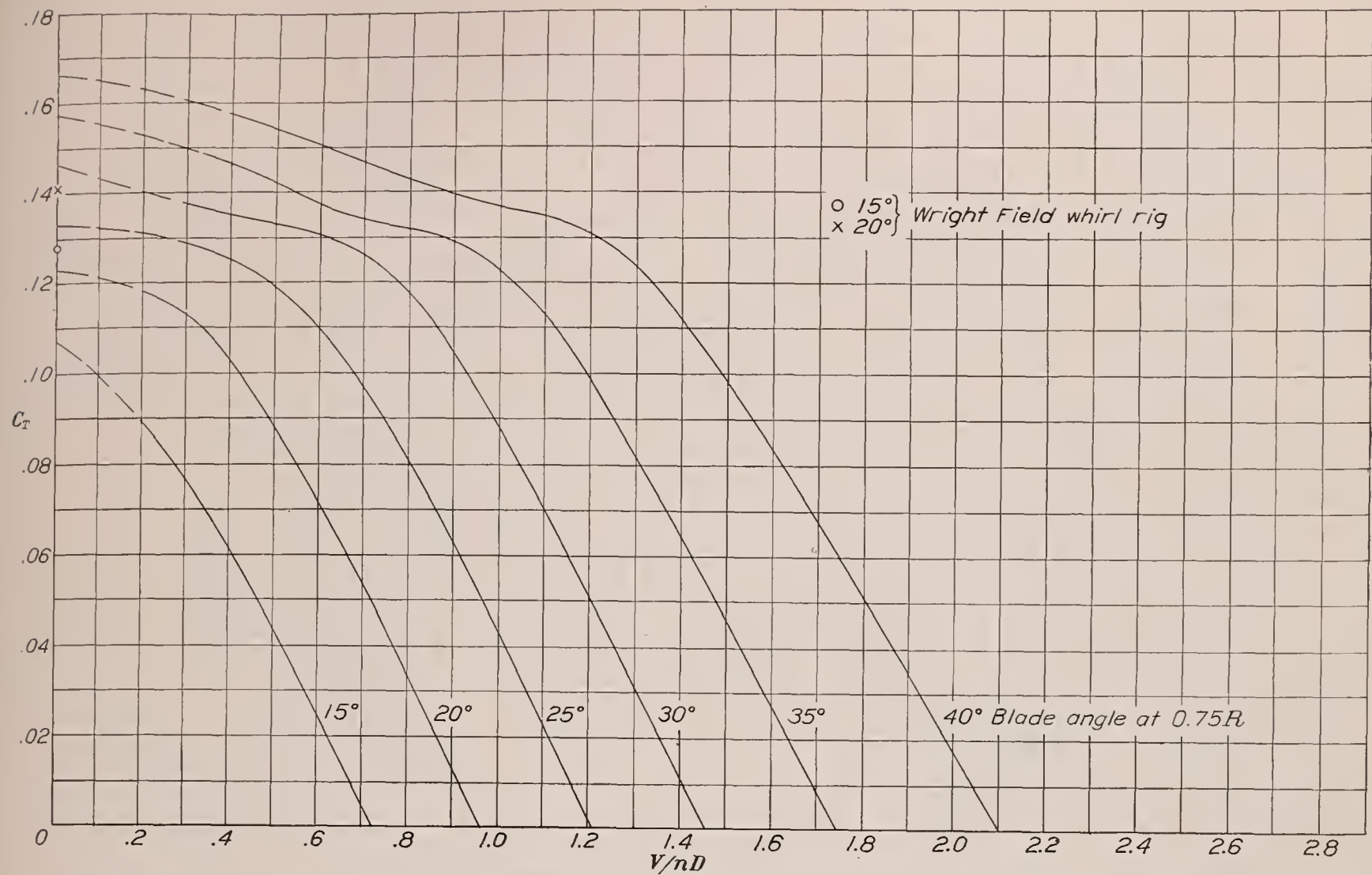


FIGURE 24.—Thrust-coefficient curves for propeller 6131, 3 blades, radial engine nacelle

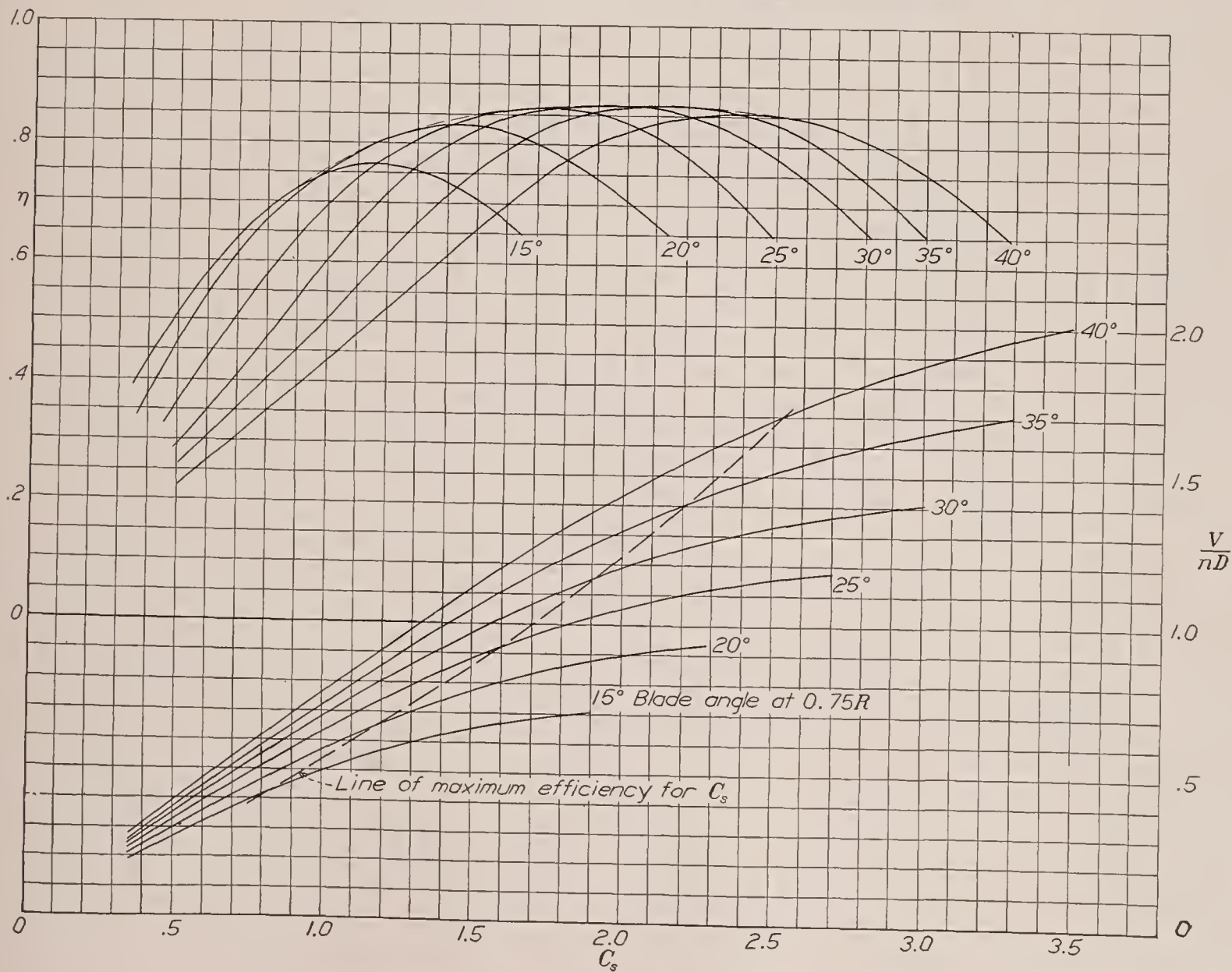


FIGURE 25.—Design chart for propeller 6131, 3 blades, radial engine nacelle.

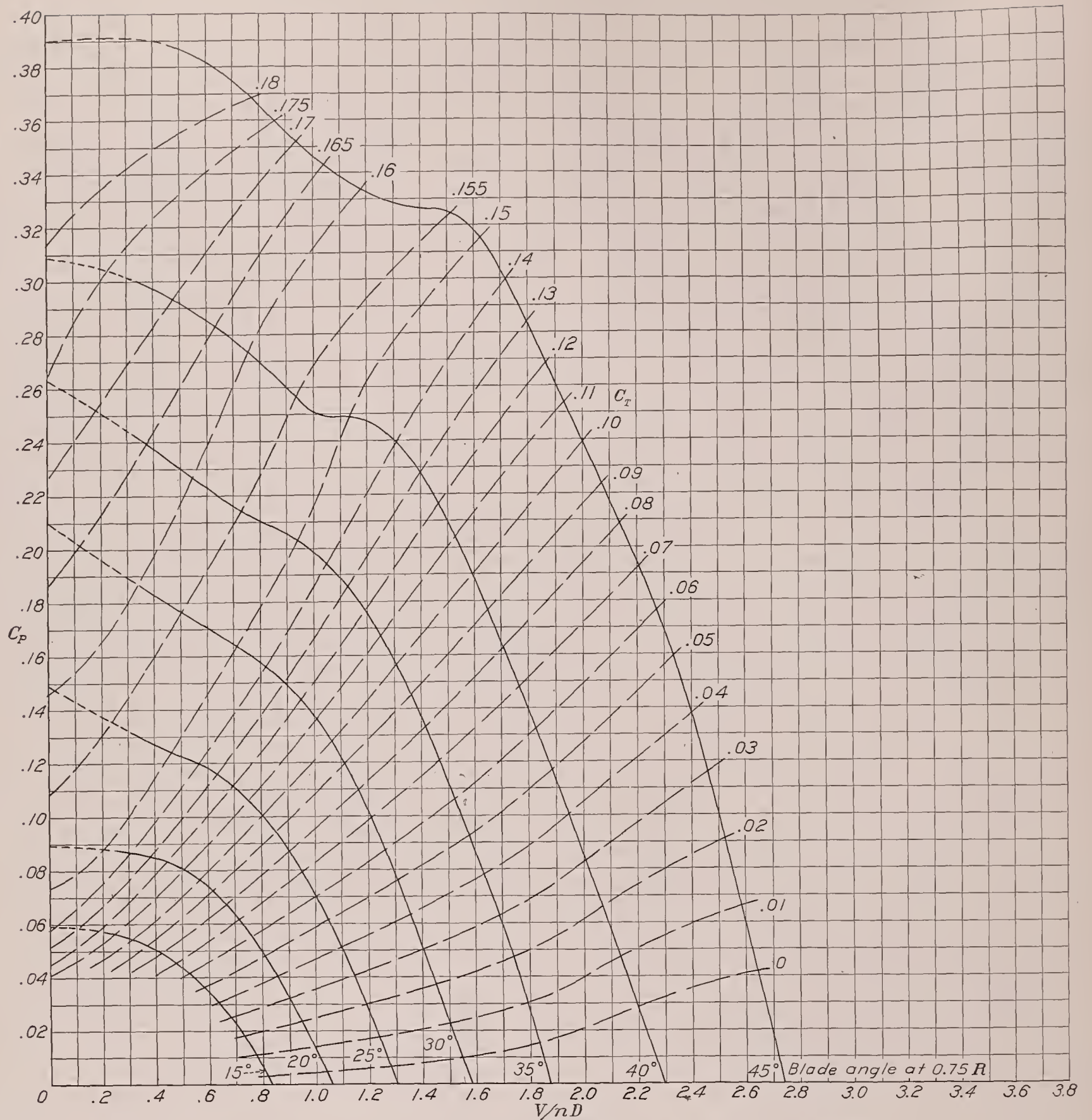


FIGURE 26.—Power-coefficient curves for propeller 5868-9, 3 blades, liquid-cooled engine nacelle.

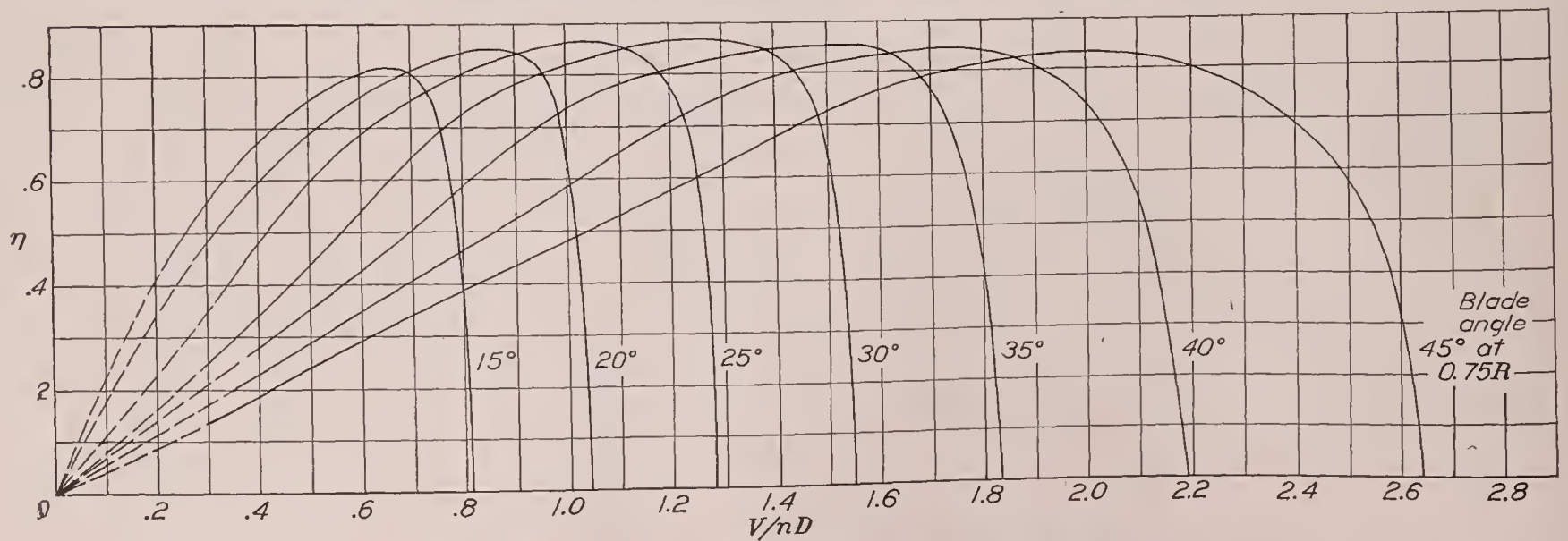


FIGURE 27.—Efficiency curves for propeller 5868-9, 3 blades, liquid-cooled engine nacelle.

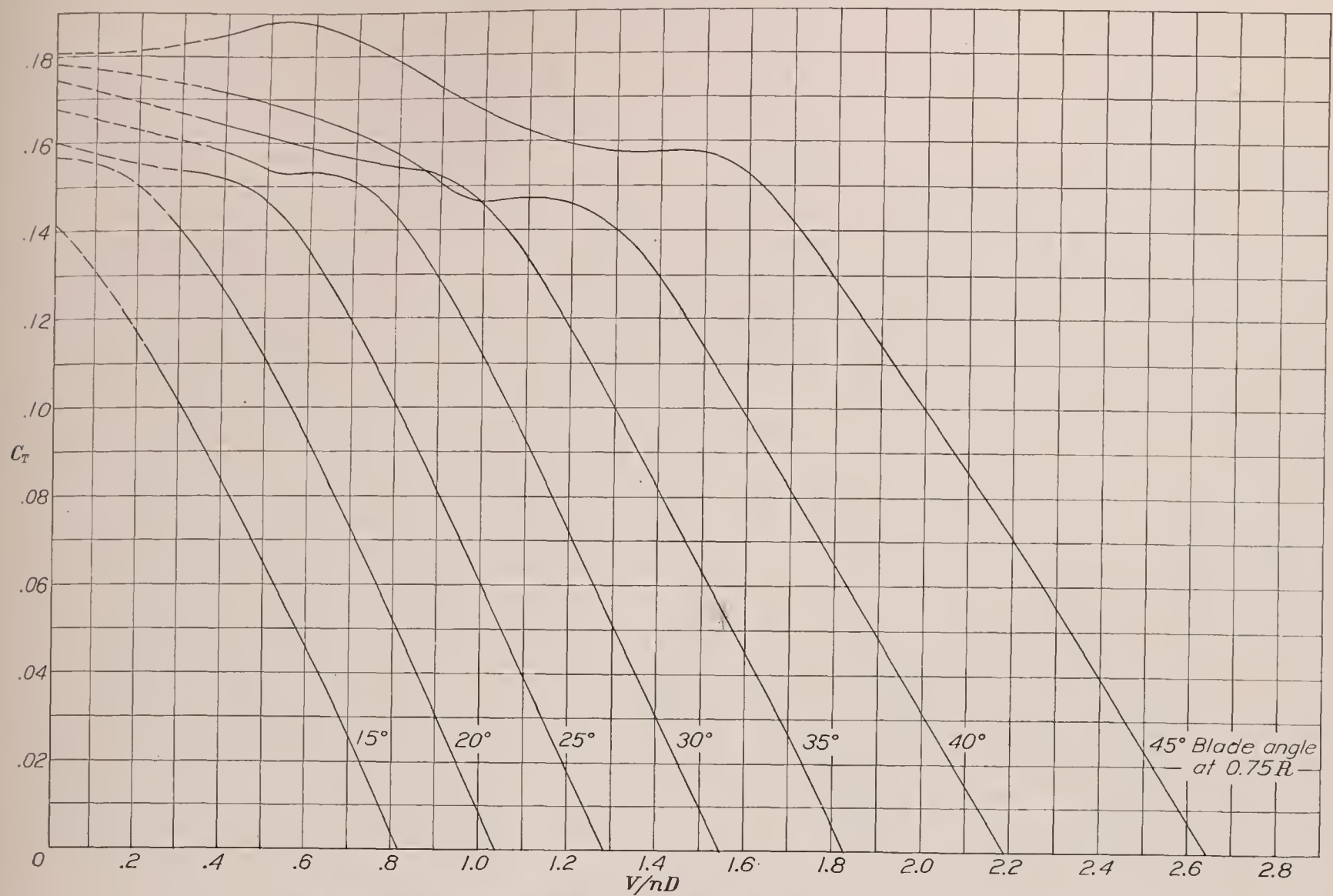


FIGURE 28.—Thrust-coefficient curves for propeller 5868-9, 3 blades, liquid-cooled engine nacelle.

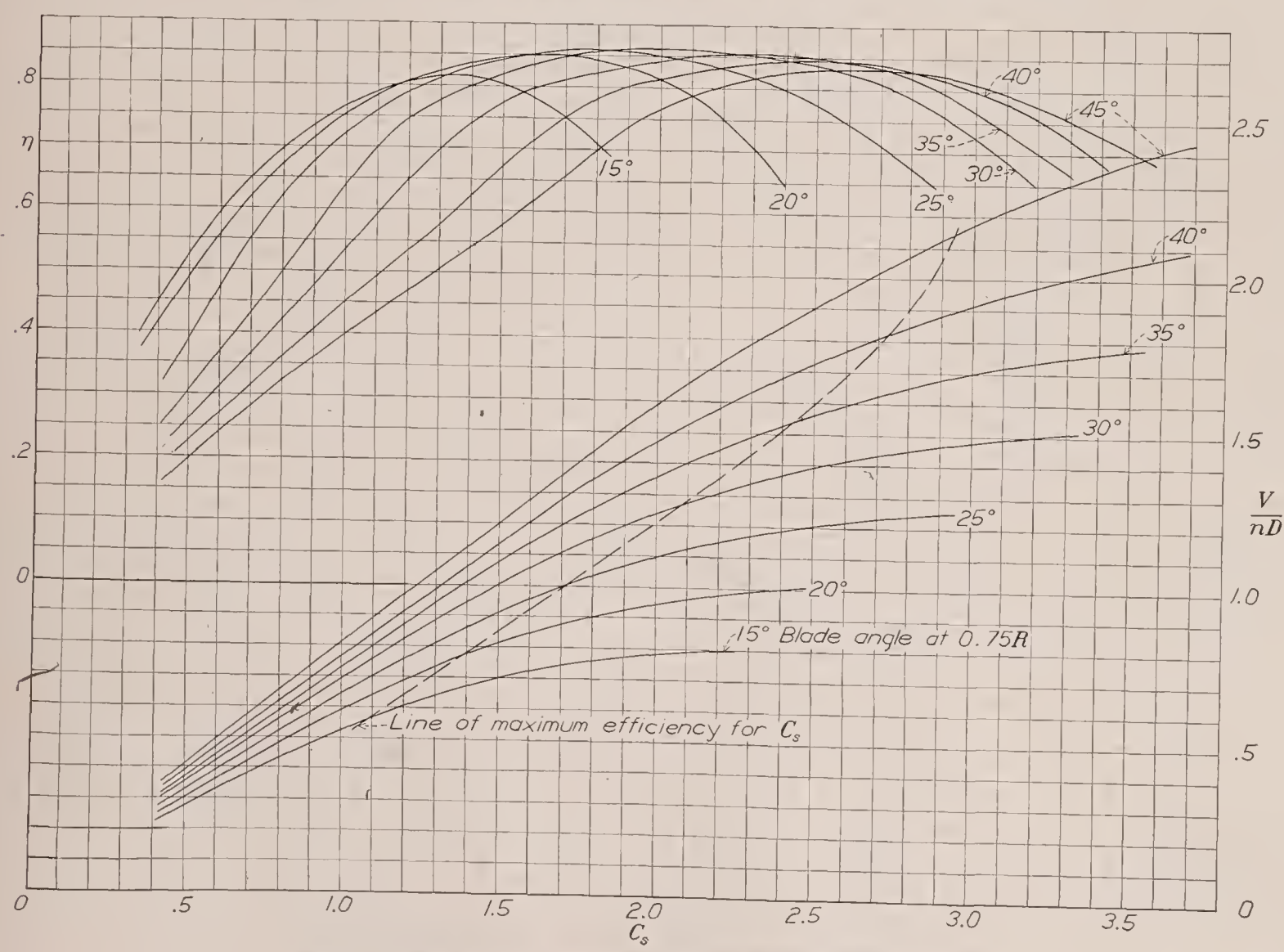


FIGURE 29.—Design chart for propeller 5868-9, 3 blades, liquid-cooled engine nacelle.

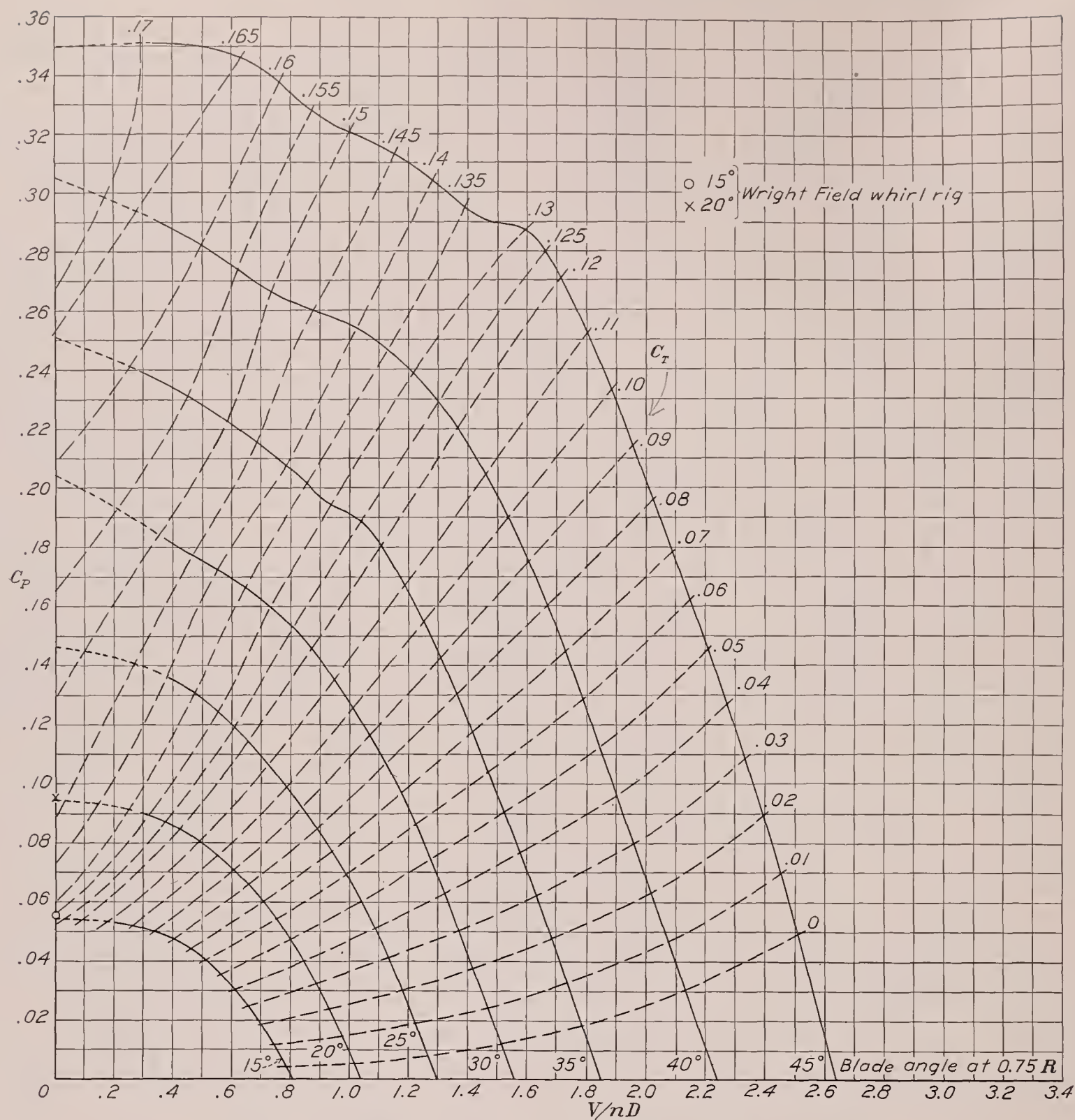


FIGURE 30.—Power-coefficient curves for propeller 6101, 3 blades, liquid-cooled engine nacelle.

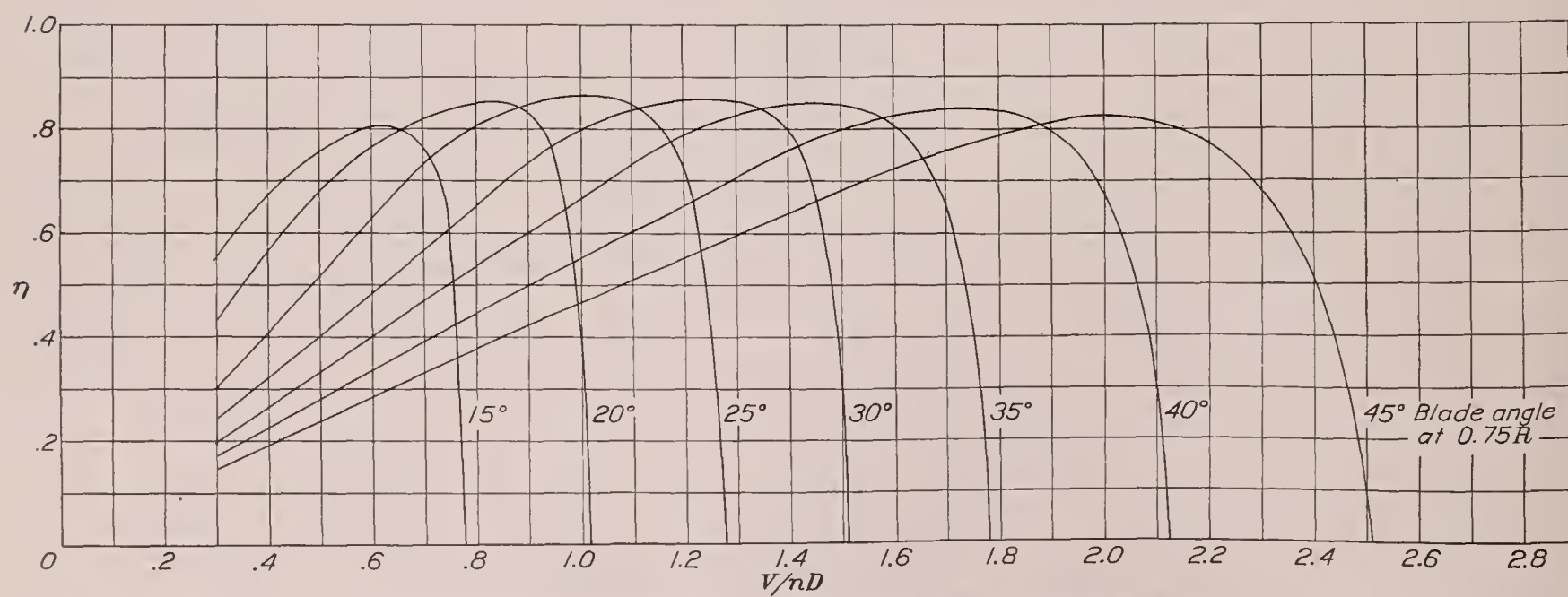


FIGURE 31.—Efficiency curves for propeller 6101, 3 blades, liquid-cooled engine nacelle.

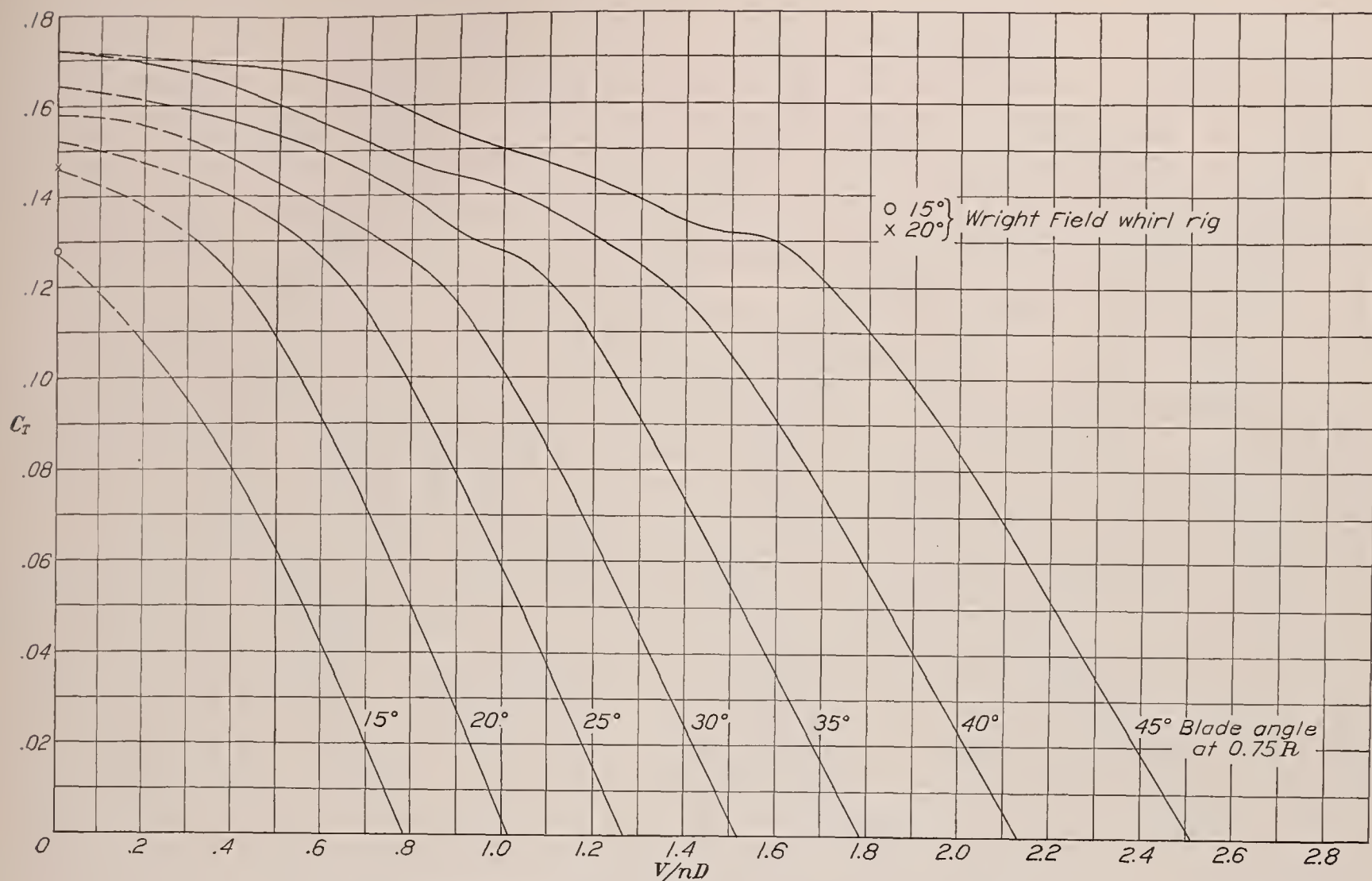


FIGURE 32.—Thrust-coefficient curves for propeller 6101, 3 blades, liquid-cooled engine nacelle.

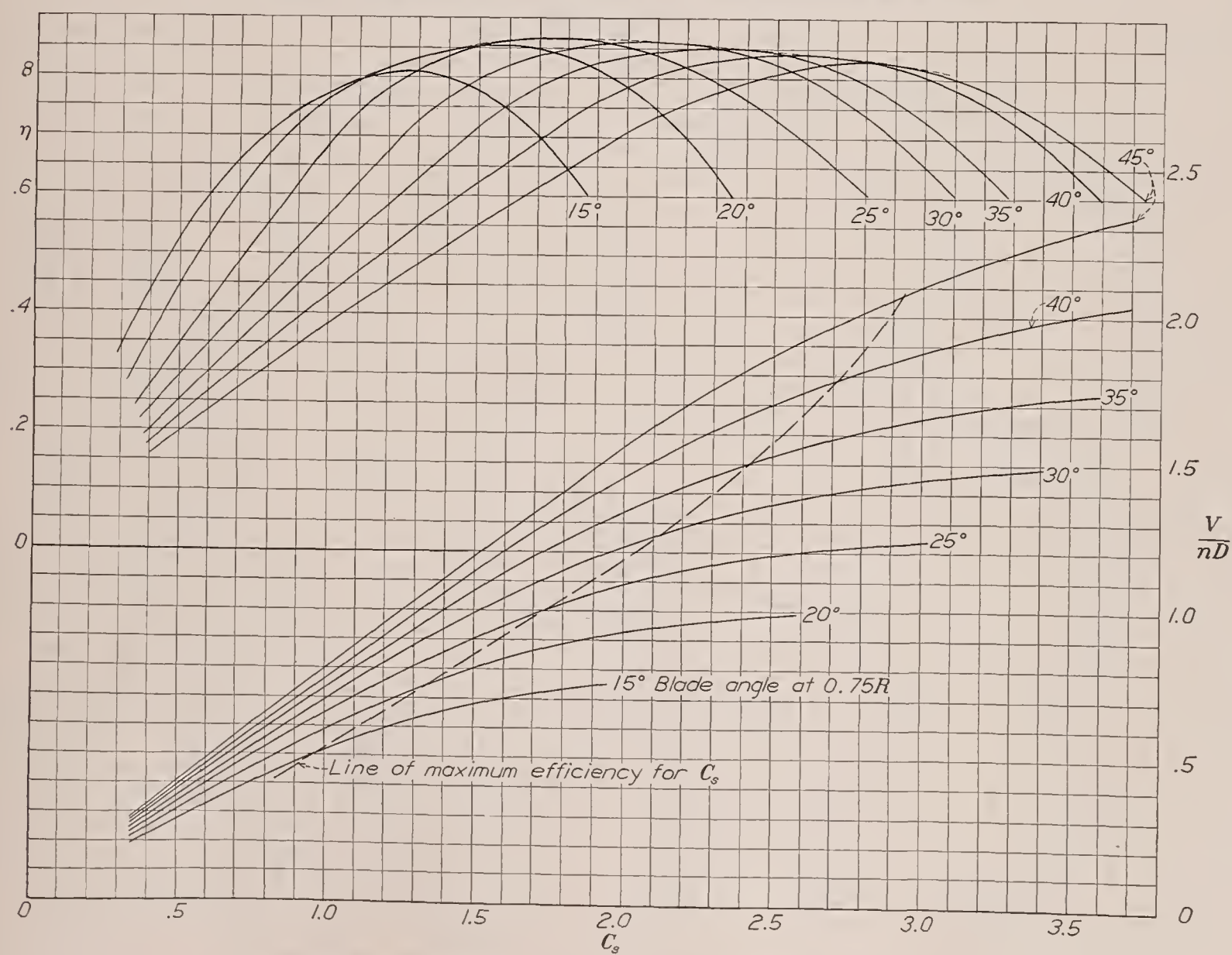


FIGURE 33.—Design chart for propeller 6101, 3 blades, liquid-cooled engine nacelle.

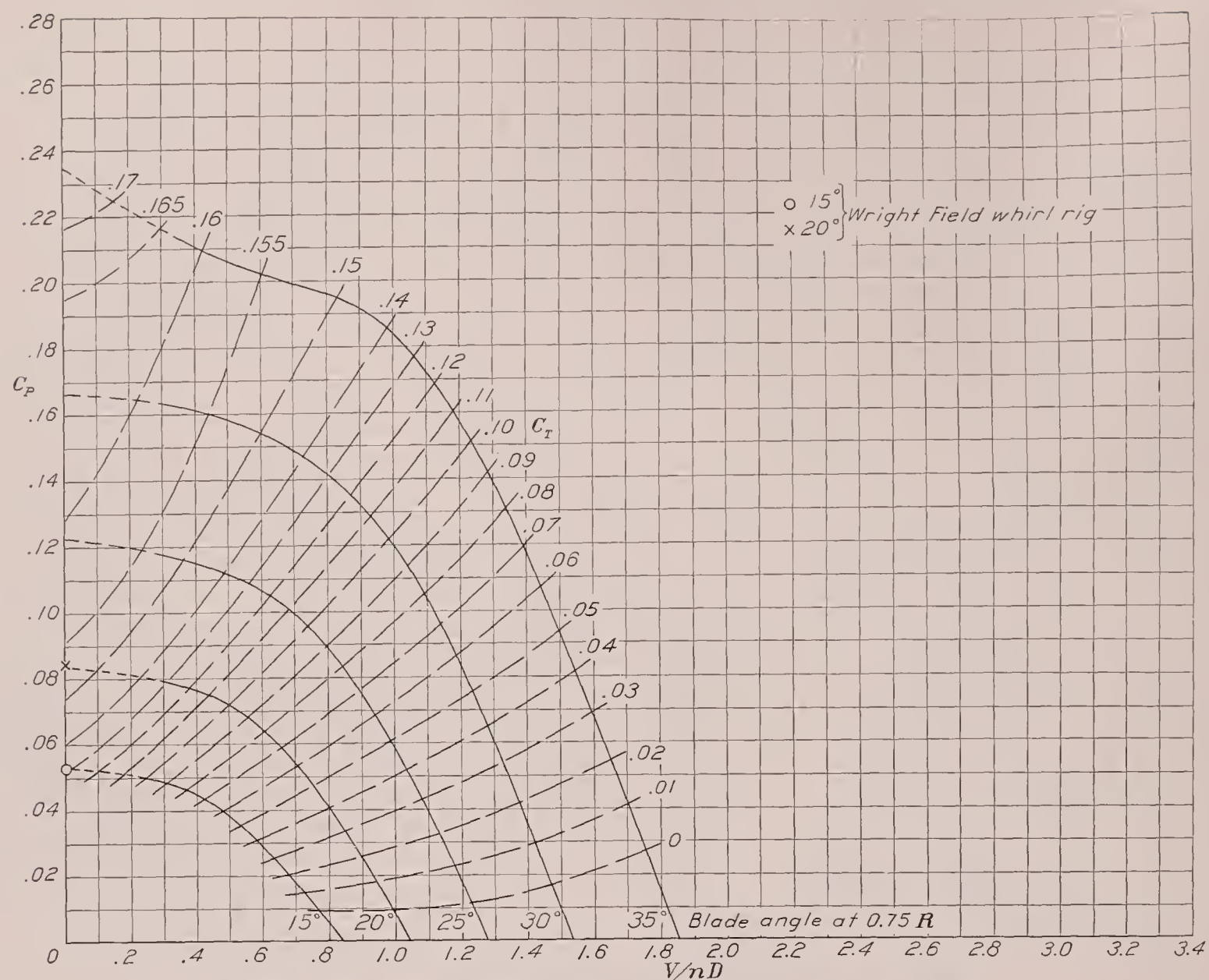


FIGURE 34.—Power-coefficient curves for propeller 6129, 3 blades, liquid-cooled engine nacelle.

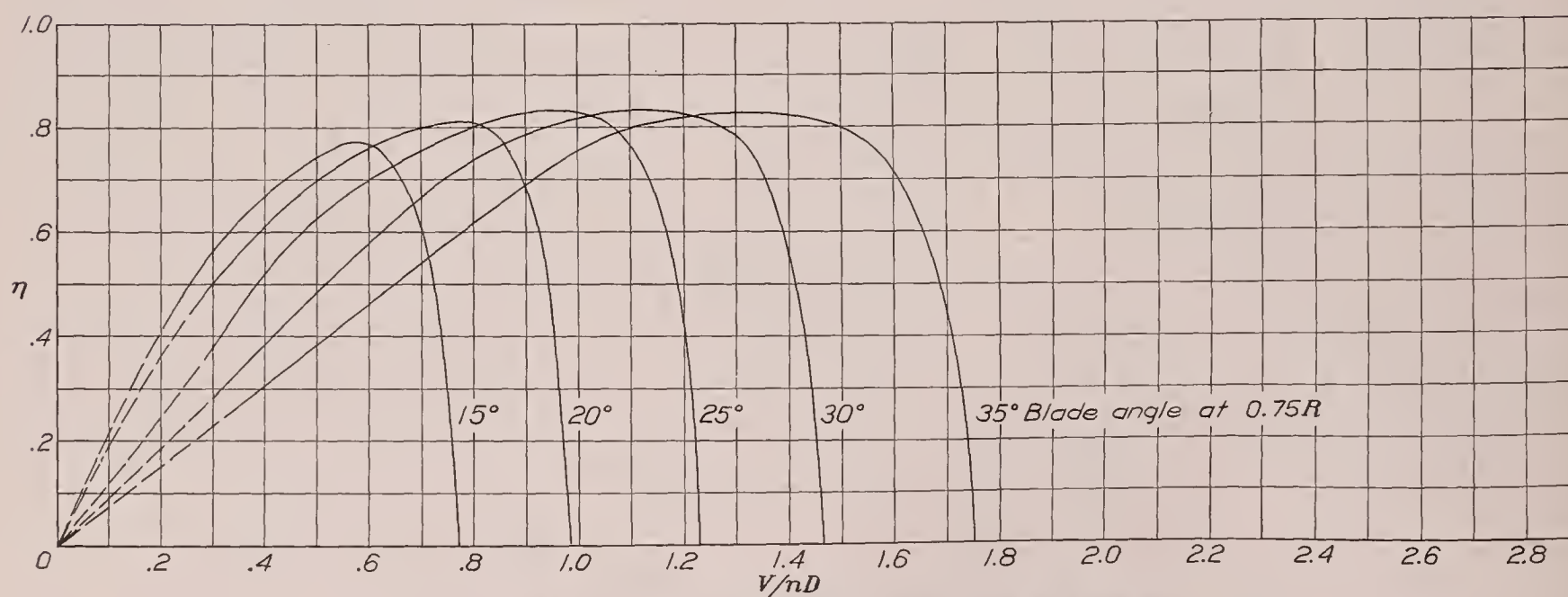


FIGURE 35.—Efficiency curves for propeller 6129, 3 blades, liquid-cooled engine nacelle.

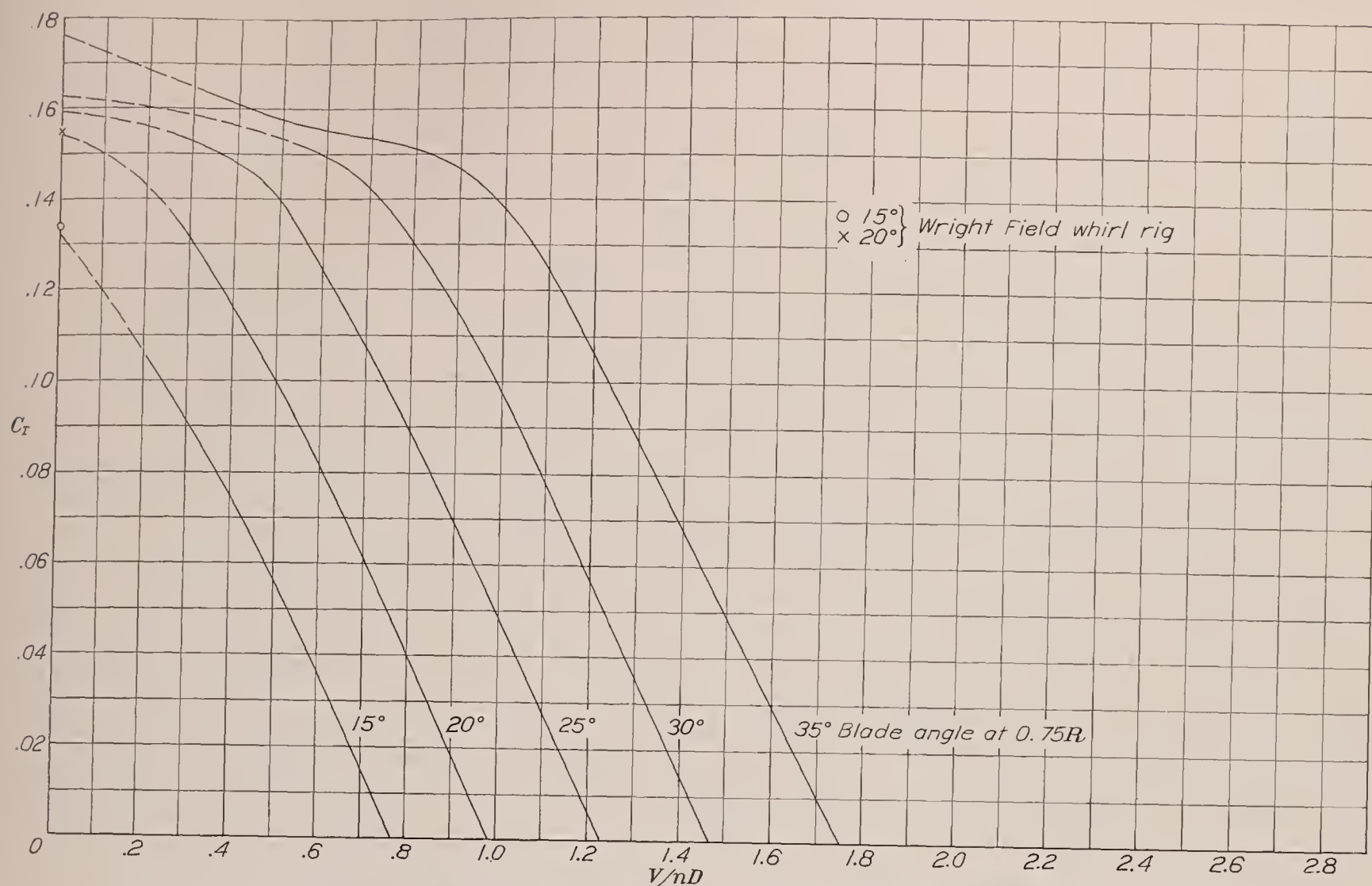


FIGURE 36.—Thrust-coefficient curves for propeller 6129, 3 blades, liquid-cooled engine nacelle.

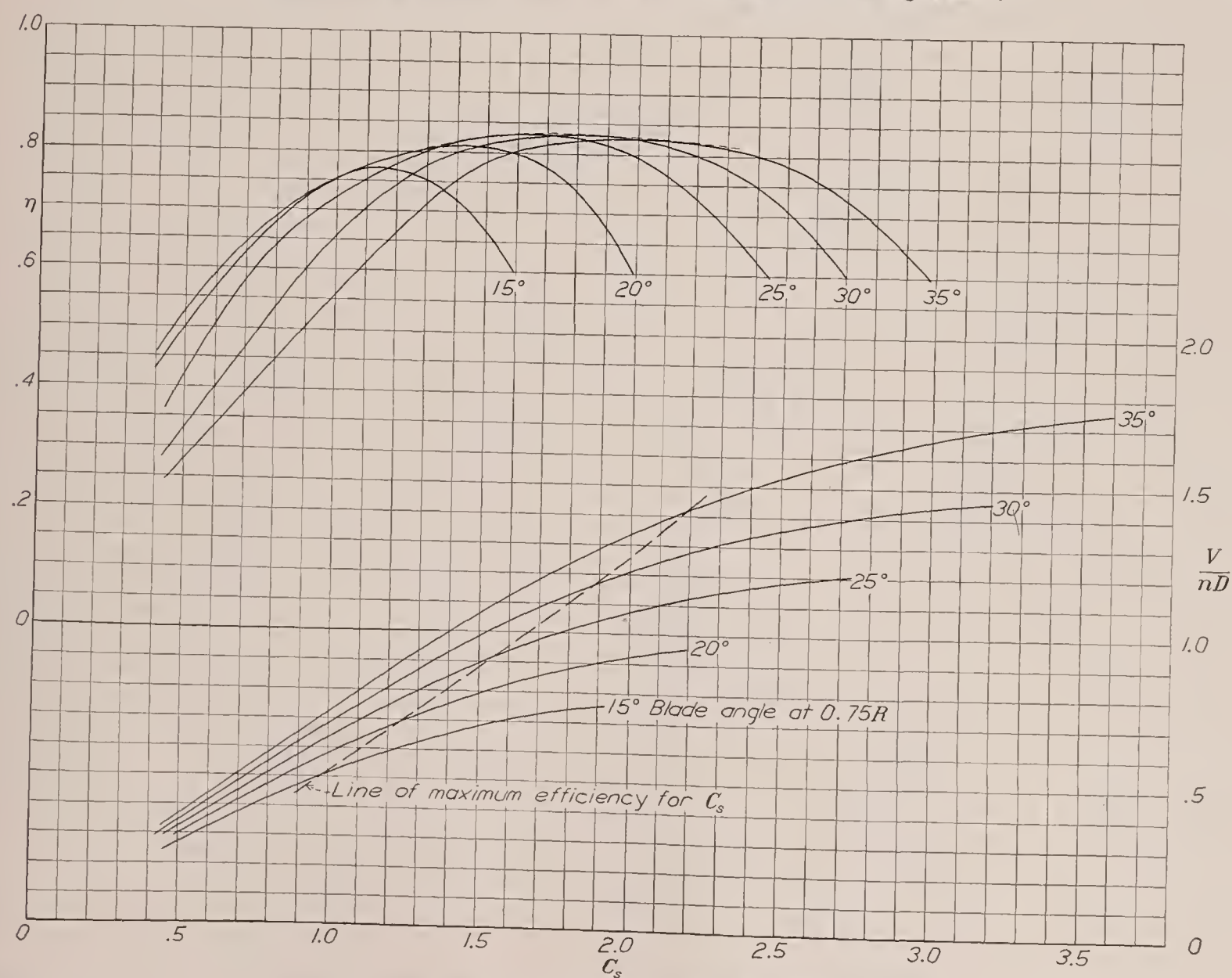


FIGURE 37.—Design chart for propeller 6129, 3 blades, liquid-cooled engine nacelle.

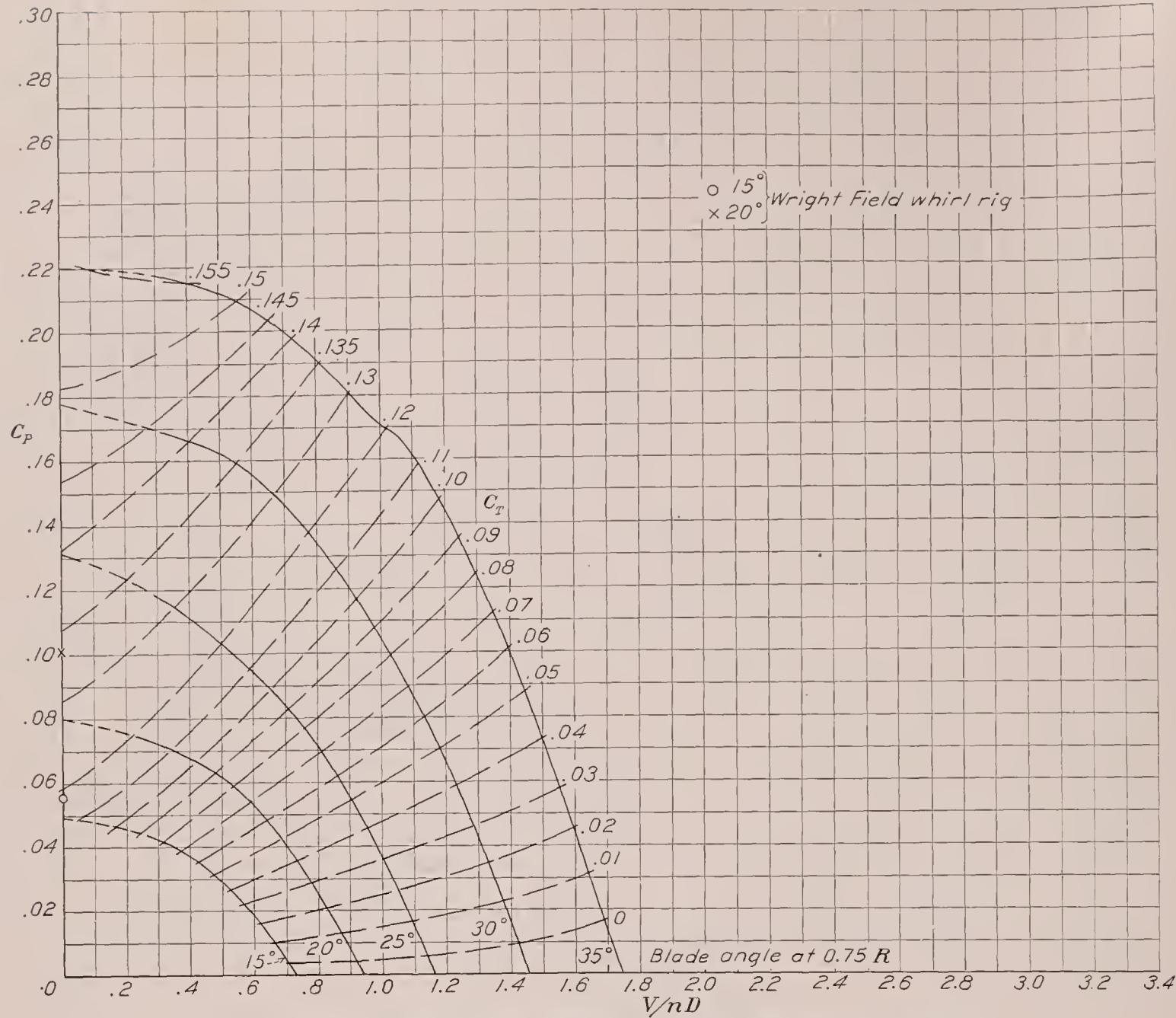


FIGURE 38.—Power-coefficient curves for propeller 6131, 3 blades, liquid-cooled engine nacelle.

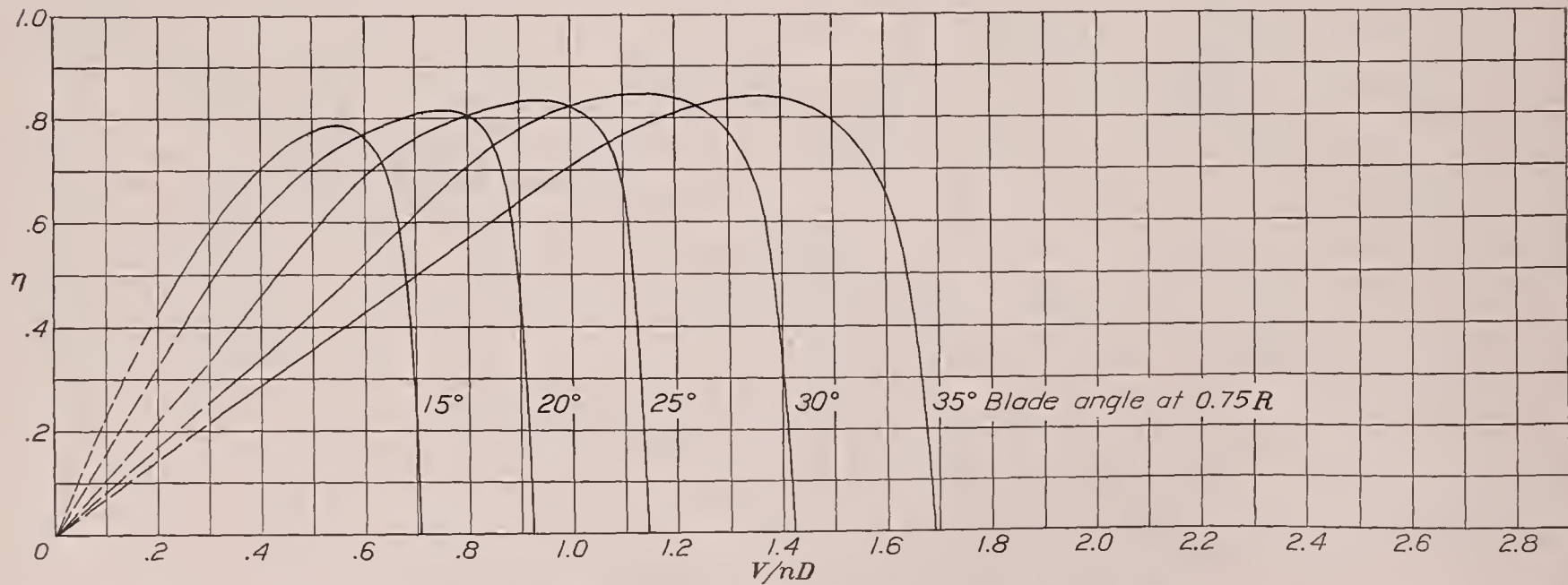


FIGURE 39.—Efficiency curves for propeller 6131, 3 blades, liquid-cooled engine nacelle.

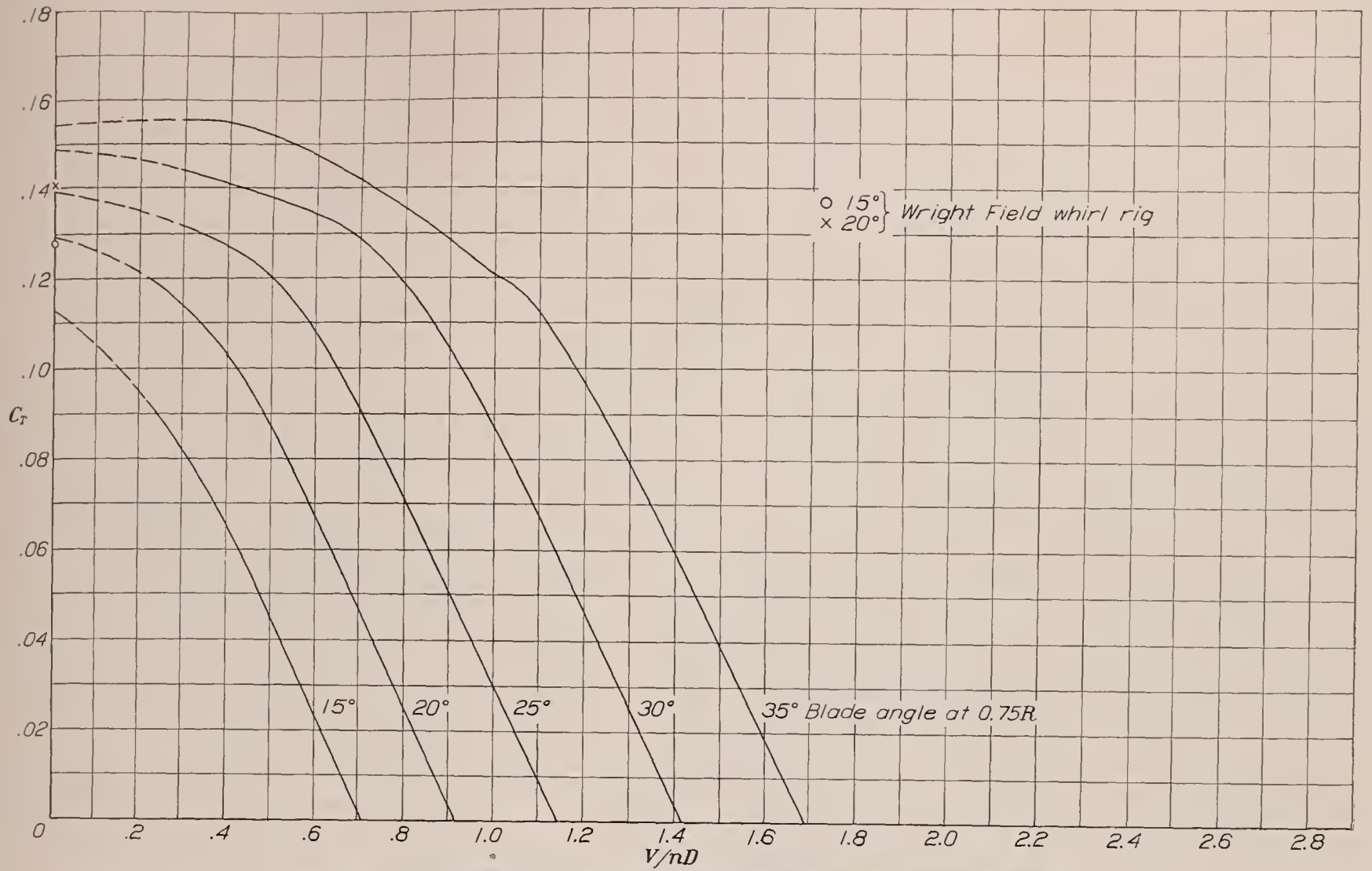


FIGURE 40.—Thrust-coefficient curves for propeller 6131, 3 blades, liquid-cooled engine nacelle.

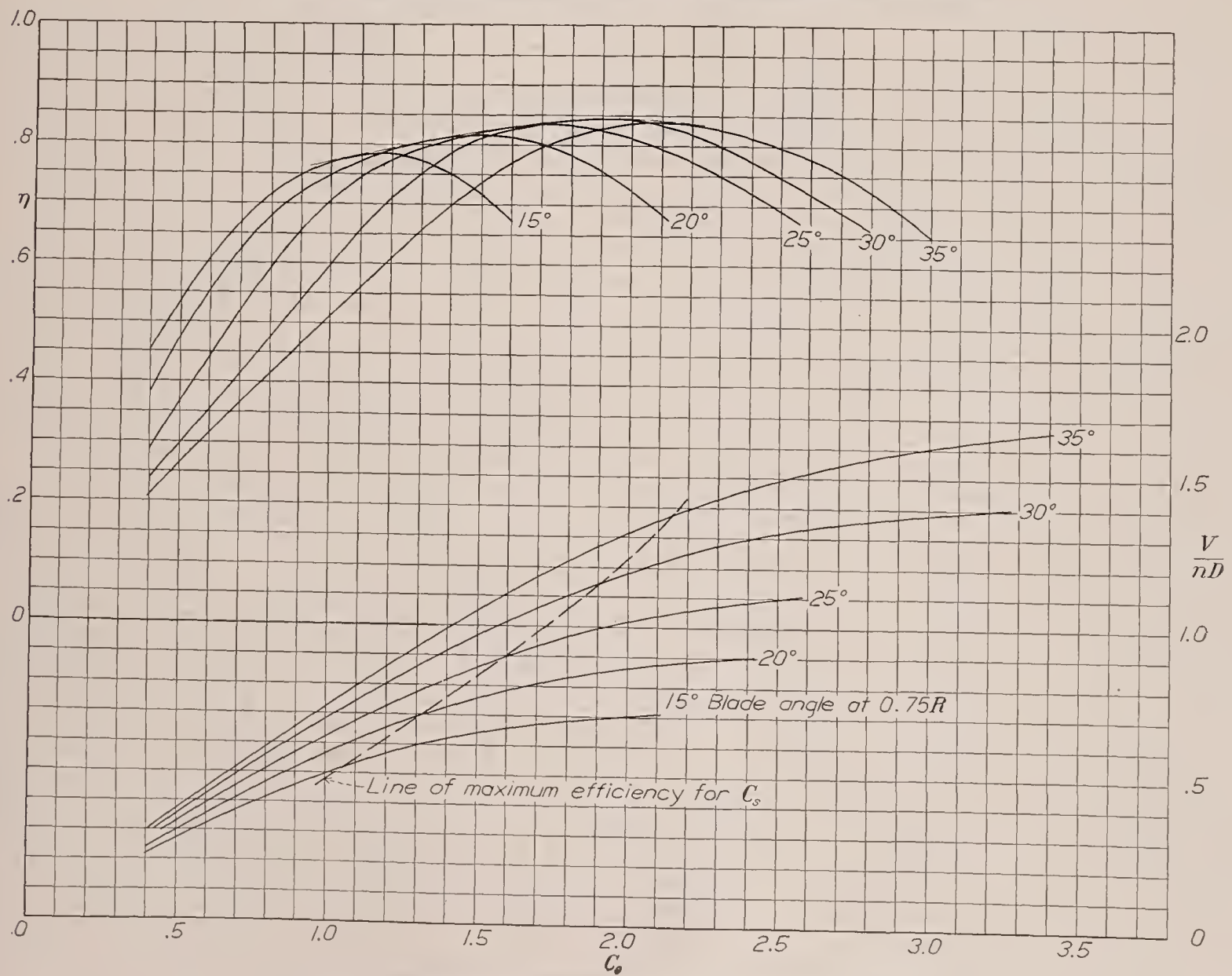
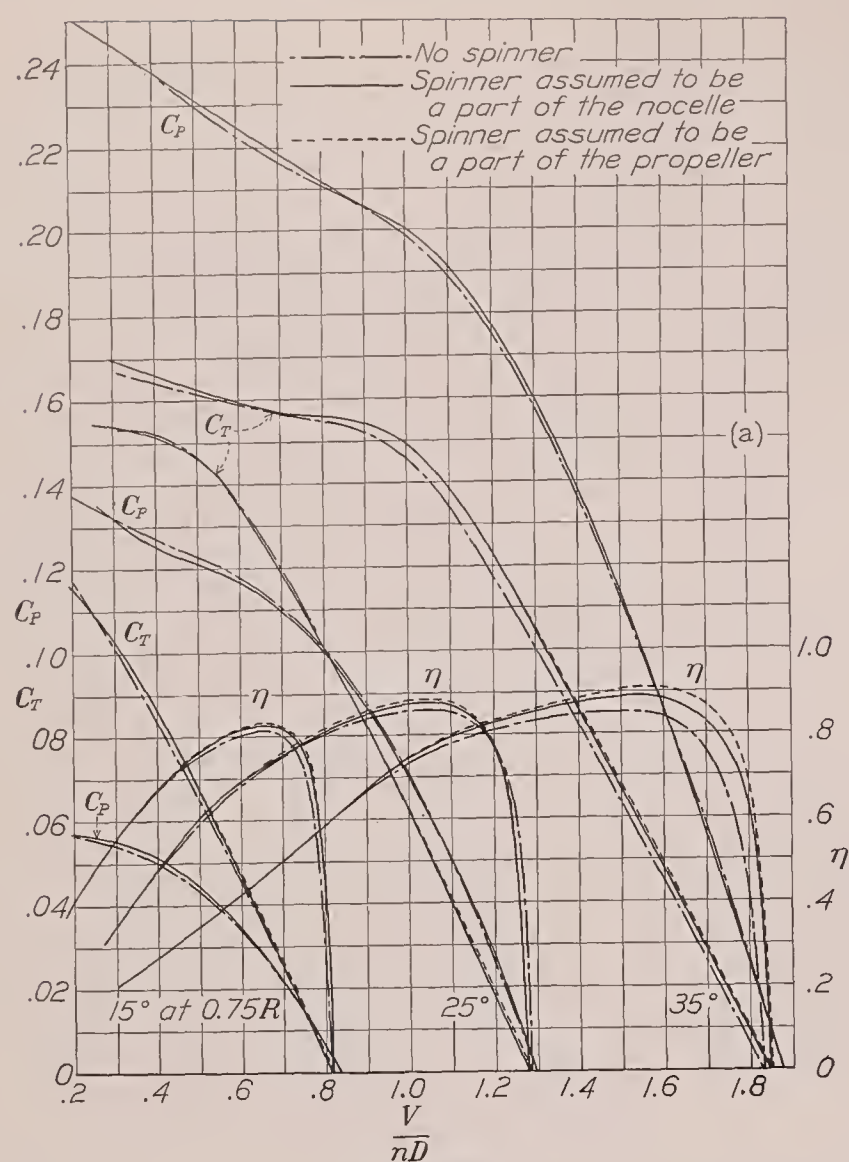
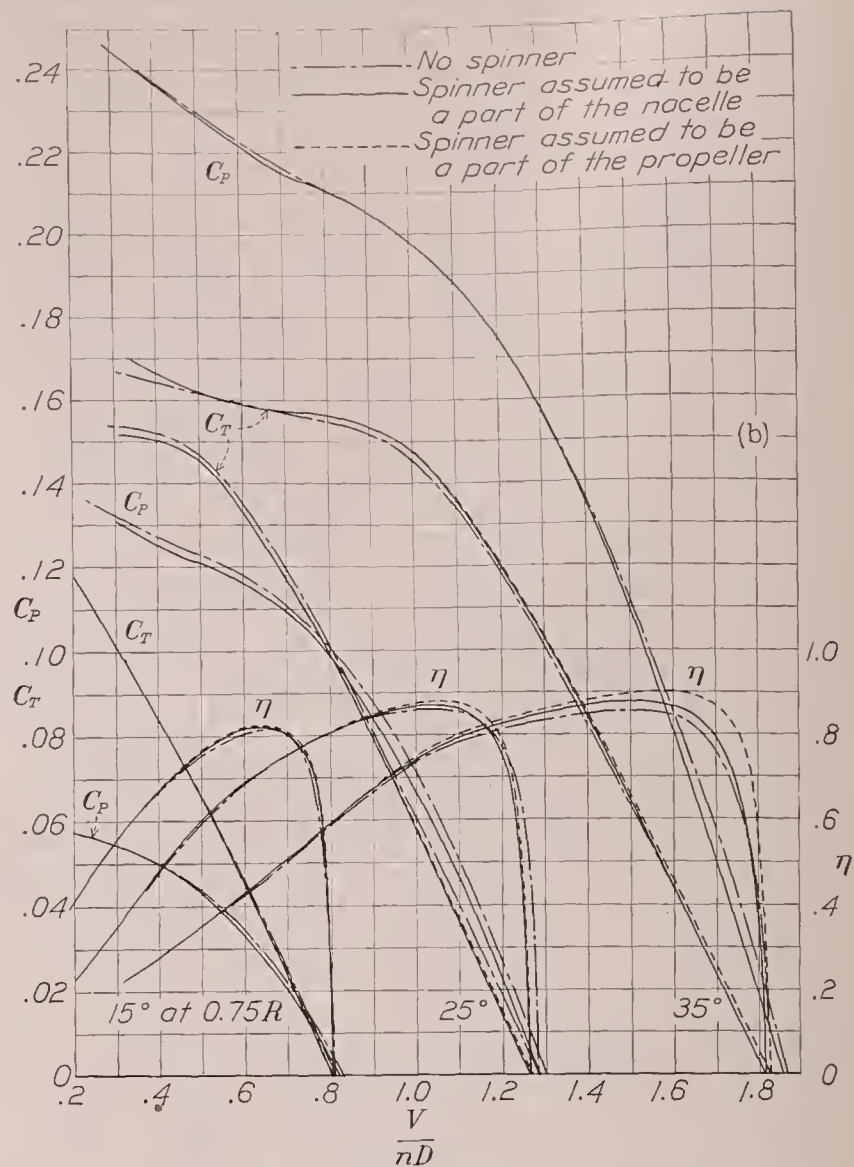


FIGURE 41 —Design chart for propeller 6131, 3 blades, liquid-cooled engine nacelle,

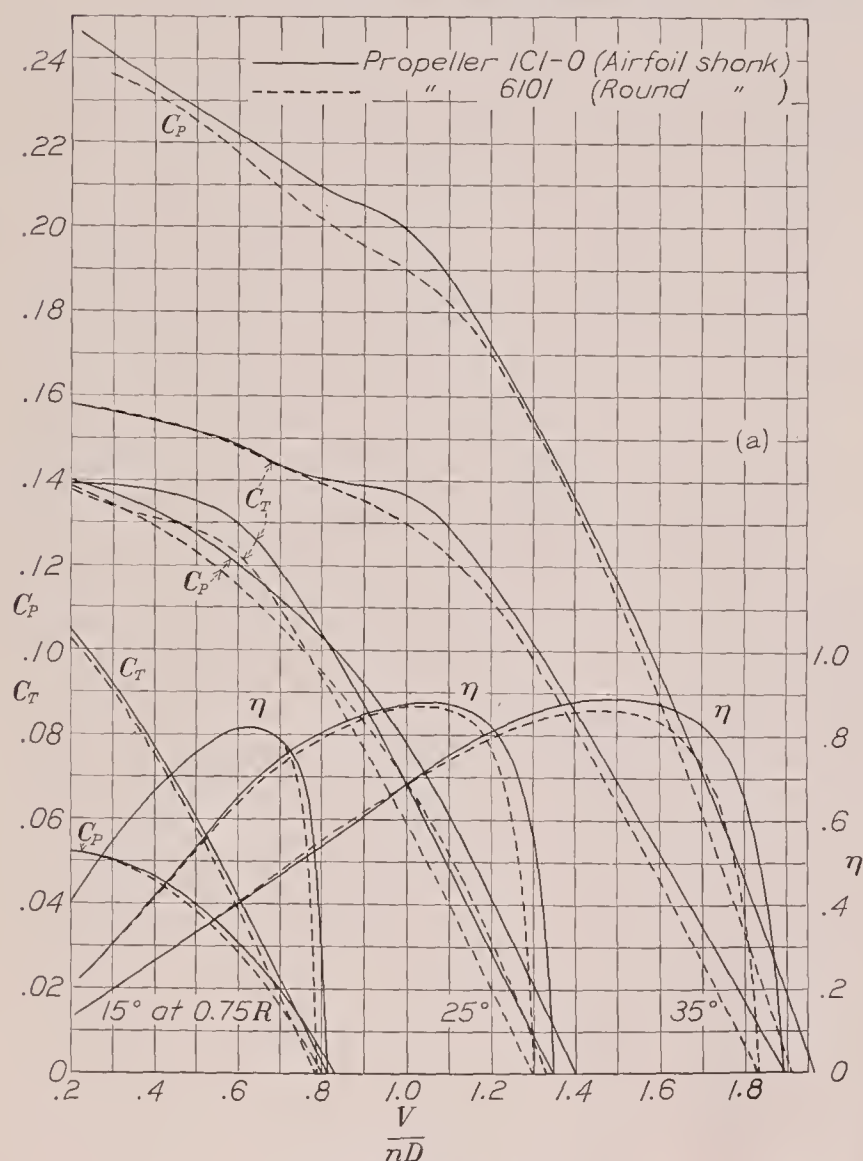


(a) Spinner 1.

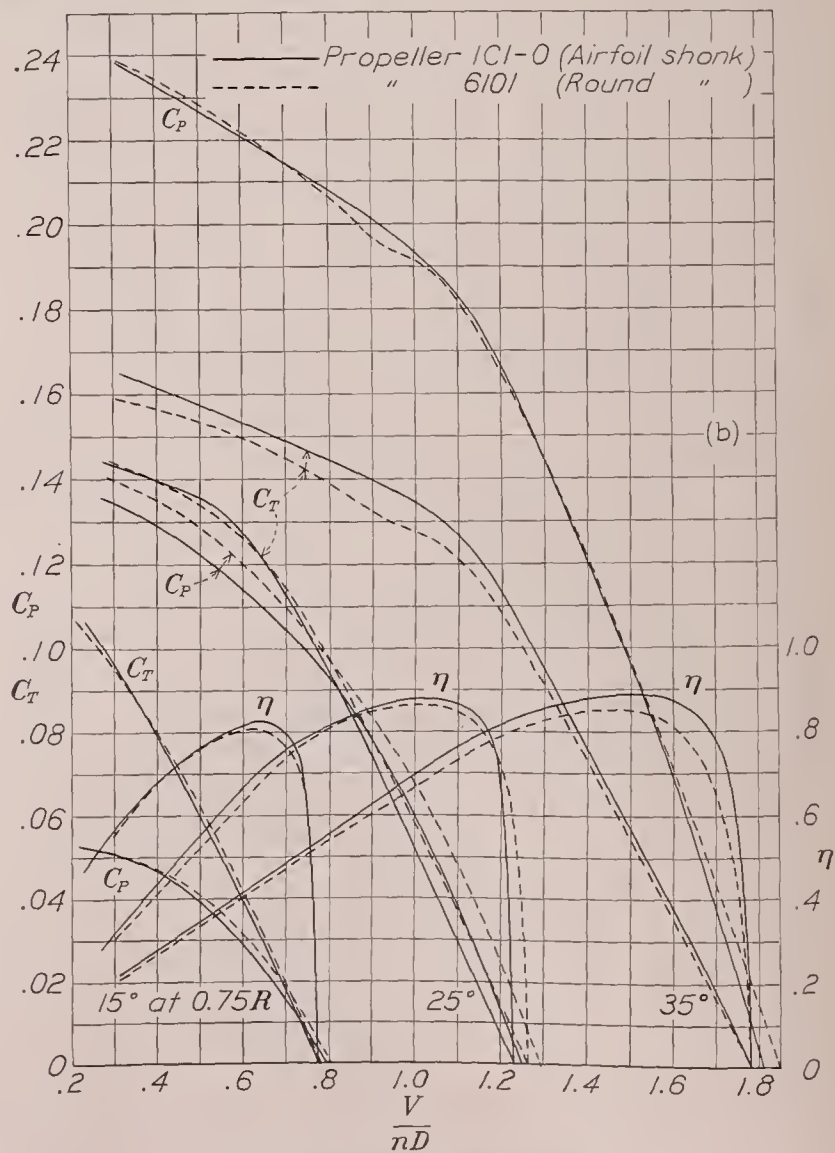


(b) Spinner 2.

FIGURE 42.—Effect of spinner on propeller characteristics. Propeller 5868-9, 3 blades, liquid-cooled engine nacelle.



(a) Radia engine nacelle.



(b) Liquid-cooled engine nacelle.

FIGURE 43.—Comparison of two propellers having different blade-shank shapes.

Use of data.—The computation of thrust at all air speeds is facilitated through the use of lines of constant C_T superposed on the power curves. Thrust coefficients are also given in the usual type of plot. The use of the combined C_P and C_T curves is illustrated in the following outline:

Computation of thrust for a constant-speed controllable propeller:

1. Compute C_s from design conditions.
2. Determine V/nD from C_s chart.
3. Compute diameter from V/nD .
4. Solve for C_P , $C_P = \text{power}/\rho n^3 D^5$.
5. Determine C_T for several values of V/nD from the combined C_T and C_P curves. Follow the line of constant C_P .

6. Solve for thrust, $T = C_T \rho n^2 D^4$.

7. Solve for velocity from assumed V/nD .

Computation of thrust for a fixed-pitch propeller:

1. Compute C_s from design conditions.
2. Determine $(V/nD)_{max}$ and blade angle from C_s chart.

3. Solve for diameter from $(V/nD)_{max}$.

4. Solve for C_P for high speed ($C_{P_{max}}$).

5. Determine C_P and C_T for several values of V/nD from the combined C_T and C_P curves. Follow the line for constant blade angle.

6. Solve for N/N_{max} from relationship $N/N_{max} = \sqrt{C_{P_{max}}/C_P}$. (This relationship is based on the assumption that the torque is constant for small changes in engine speed for a constant throttle setting.)

7. Solve for V/V_{max} from the relationship $V/V_{max} = \frac{(V/nD)}{(V/nD)_{max}} \frac{N}{N_{max}}$

8. Compute thrust from $T = C_T \rho n^2 D^4$

$$= C_T \frac{C_{P_{max}}}{C_P} K$$

where $K = \rho n^2_{max} D^4$

n , propeller speed, r. p. s.

N , propeller speed, r. p. m.

Static thrust and power.—The static thrust and static power coefficients, obtained from the Wright Field tests of propellers 6101, 6129, and 6131 (reference 6) are shown (figs. 14, 16, 18, 20, 22, and 24) for the purpose of comparison. It may be noted that the Wright Field data check the present data closely for certain conditions and poorly for others. Particularly poor is the check for propeller 6131, for which there is a consistent difference of 15 to 20 percent. This lack of agreement is not particularly disturbing because there are several important differences in the method of testing. The whirl rig at Wright Field is in the open air and represents the same conditions as encountered with a stationary airplane on the ground. The forward speed is zero and the V/nD is consequently assumed to be zero; whereas, the slipstream of the propeller in a wind tunnel creates a circulation of air through the tunnel and the V/nD is computed from

the measured velocity. The wind-tunnel results are extrapolated to zero V/nD . There is some question as to whether the assumed velocities are entirely comparable for the two conditions. Furthermore, the body conditions were different for the two tests. It is well known that large bodies slow up the air passing through the propeller disk, thus causing the propeller sections to operate at higher angles of attack. This effect is brought out clearly in the present report. Also, it is possible that the blade-angle setting for propeller 6131 was different for the two tests since the differences noted are consistent.

SPINNER RESULTS AND VARIOUS OTHER COMPARISONS

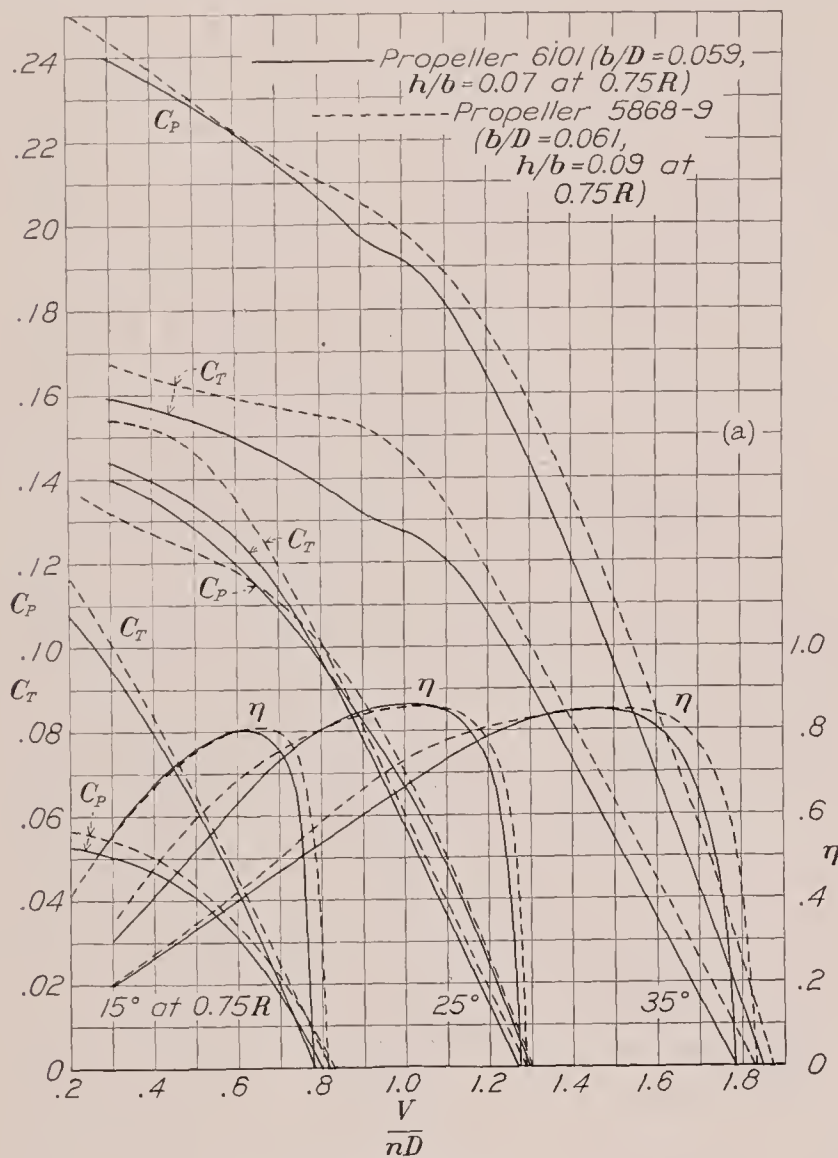
The material for this report was selected with the view to presenting information regarding the effect of current body styles on propeller characteristics as well as of presenting the actual propeller data. An important modification of the liquid-cooled engine nacelle is that of the spinner. Spinners were not tested on the radial engine nacelle because previous tests indicated no aerodynamic advantage. As the shape of the propeller-blade shank is closely allied to the subject of spinners, data for two shank shapes are included. An incidental comparison of blade-thickness effects is made because the results are of interest. A comparison is also made of three blade sections; this material is of an incidental nature because a separate report covers this subject (reference 4). The propellers for the two reports, however, are different.

Spinners.—The aerodynamic purpose of a spinner is to reduce the body drag, to reduce the drag of the hub and of the shank portions of the blades, and to reduce the engine torque required. In order to fulfill this purpose, the spinner should fair smoothly into the outlines of the body and yet enclose the hub and the round portions of the blade shanks. Two sizes of spinners were tested, both fairly large, as may be noted from figure 1. The results of the tests, given in curve form in figure 42, were computed on two bases: on one basis, the reduction in body drag due to the spinner is credited to the body and consequently does not show up in the propulsive efficiency; and, on the other basis, the reduction in body drag is credited to the propeller and shows up as a gain in propulsive efficiency. In the first case, the spinner is assumed to be a part of the body, the results being shown as solid lines; and, in the second, to be a part of the propeller, the results being shown as broken lines. Both methods, of course, show any gains in propulsive efficiency resulting from covering up the hub and shank portions of the blades.

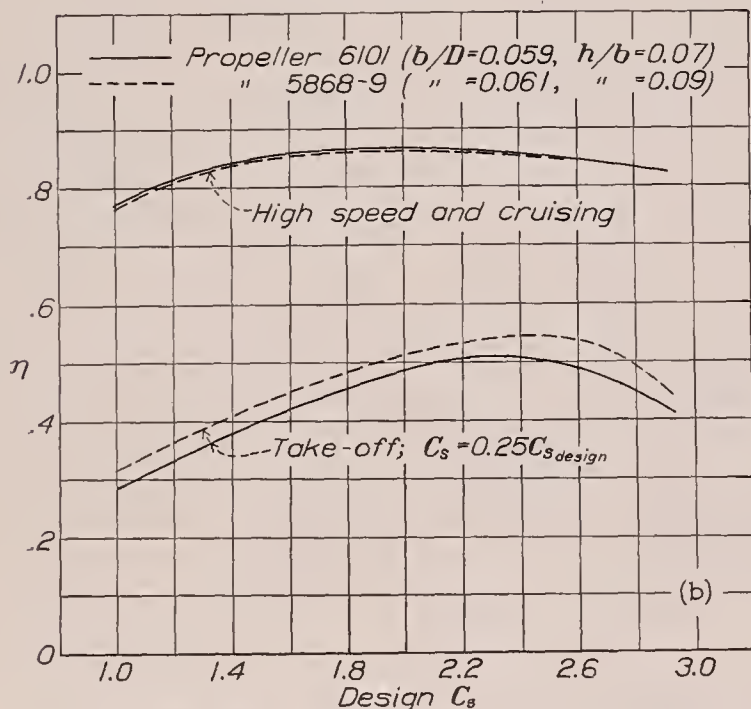
An analytical summary of the results is given in the following table. Of interest is the fact that the smaller (spinner 1) of the two spinners is superior. Also, the advantage of spinner 1 increases with blade-angle setting, the gain in efficiency being only 1.5 percent for 15° and 6.0 percent for 35°. Of this 6.0 percent maximum

gain, 4 percent is due to covering up the hub and the shank portions of the blades and only 2 percent is due to reduced body drag.

The addition of streamline fairings over the shank portions of the blades, extending out from spinner 1



(a) Characteristic curves.



(b) Comparative performance computed for high-speed and take-off conditions for controllable operation.

FIGURE 44.—Comparison of two propellers differing essentially in thickness. Liquid-cooled engine nacelle.

a distance of about 4 inches (see fig. 5), increased the efficiency an additional 1 percent for the one blade-angle setting investigated, 25°. The value of 1 percent,

however, is within the experimental error for this particular test.

SUMMARY OF RESULTS WITH SPINNERS

Cowling nose shape	Body drag at 100 m. p. h. (lb.) ↓	η_a			η_b			Gain in η due to spinner [η_a (spinner) — η_a (no spinner)]			Gain in η due to lower body drag [η_b — η_a]			Total gain due to spinner [η_b (spinner) — η_b (no spinner)]		
		Blade angle →			Blade angle →			Blade angle →			Blade angle →			Blade angle →		
No spinner	59.0	15°	25°	35°	15°	25°	35°	15°	25°	35°	15°	25°	35°	15°	25°	35°
Spinner 1	57.0	81.5	86.5	85.0	81.5	86.5	85.0	1.0	1.0	4.0	0.5	1.0	2.0	1.5	2.0	6.0
Spinner 2	56.5	82.0	87.0	88.0	82.5	88.0	90.0	.5	.5	3.0	.5	1.0	2.0	1.0	1.5	5.0
Spinner 1 and cuffs	57.0	88.0			89.0			1.5			1.0			2.5		

Body drag includes support drag.

η_a is the efficiency computed using drag of body with spinner in place, spinner assumed to be a part of the body.

η_b is the efficiency computed using drag of body with no spinner (59 lb.), spinner assumed to be a part of the propeller.

Blade-shank shape.—Propeller 6101 has round shanks extending from the controllable hub for 6 or 8 inches before the transition from round to airfoil shape is well under way. Propeller 1C1-0 is of the same design, except that the airfoil shape is carried to within an inch or so of the adjustable hub.

The results of tests of these two propellers mounted on the radial engine nacelle (fig. 43 (a)) indicate an advantage in favor of propeller 1C1-0, particularly for the highest blade angles. A small difference in V/nD for zero thrust indicates that the airfoil shanks contribute to the thrust. The advantage of propeller 1C1-0 is greater for the liquid-cooled engine nacelle. (See fig. 43 (b).)

Blade thickness.—Propeller 5868-9 is about 29 percent thicker at the 0.75R station than propeller 6101. (This greater thickness means that the camber also is 29 percent higher for propeller 5868-9 than for propeller 6101.) The difference in width is unimportant since the magnitude is only about 3 percent. A comparison of these propellers tested in front of the liquid-cooled engine nacelle (fig. 44 (a)) reveals three interesting results: first, there is little or no difference in maximum efficiency; second, the thick propeller (5868-9) has an appreciably higher efficiency in the take-off and climbing range; and, third, there is a small difference in V/nD for zero thrust. The third point merely indicates that the thick propeller has the higher aerodynamic pitch, as would be expected.

A comparison of the propellers for the high-speed and the take-off conditions for controllable operation is given in figure 44 (b). This plot brings out the advantage of the thick propeller for take-off but there is an indication that some sacrifice, however small, is made at high speed. The apparent reason for the advantage of the thick propeller at low V/nD operation is the delayed stall of the sections resulting in a higher lift or thrust coefficient. (See fig. 44 (a).) This effect of thickness (or camber) is substantiated by more general tests reported in reference 7.

It may be well to point out here that thick propellers lose more in take-off efficiency owing to compressibility at high tip speeds than do thin ones. (See reference 1.) Compressibility effects will equalize the take-off efficiencies of propellers of different thickness when the tip speed is sufficiently high.

Blade section.—The relative merit of the different blade sections investigated is shown by figure 45. In figure 45 (a) a comparison is made for the cruising and the take-off conditions using the data for the radial engine nacelle. The order of decreasing merit of the sections for cruising is Clark Y, N. A. C. A. 2400-34, and R. A. F. 6. The difference between the first two sections is only about 1 percent, well within the experimental error, while the difference between the Clark Y and the R. A. F. 6 is between 2 and 4 percent. The efficiency of the R. A. F. 6 propeller is several percent higher than the Clark Y for the take-off condition and the Clark Y is likewise more efficient than the N. A. C. A. 2400-34. It may be seen, by reference to the basic data, that superior take-off characteristics are a result of a delayed stall and higher thrust coefficients.

It should be pointed out, also, that the R. A. F. 6 section is more sensitive to compressibility than the other two sections for the take-off condition; therefore the efficiencies tend to equalize as the tip speed is increased. (See reference 1.)

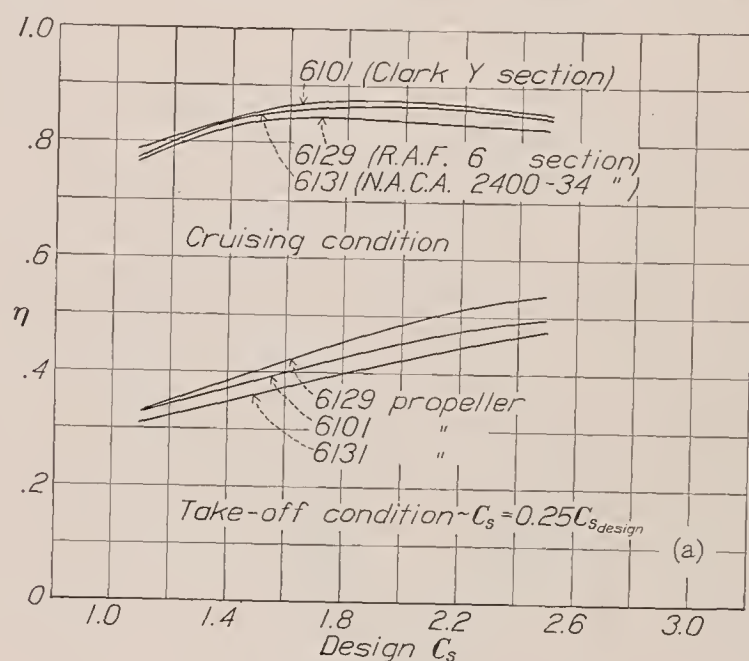
The relatively poor take-off characteristics of the propeller of N. A. C. A. 2400-34 section were expected for these low tip speeds because of the low maximum lift coefficient of the section. This section was developed for high tip speeds and should properly be used only for the tip sections, inasmuch as its principal merit is the later compressibility stall.

Figure 45 (b) shows the same comparisons and the same order of merit for the liquid-cooled engine nacelle as were shown for the radial engine nacelle. The cruising efficiency of propeller 6131 (N. A. C. A. 2400-34 section) seems low in comparison with propeller 6101 (Clark Y section), which suggests an error of 1 or 2 percent. The take-off efficiency of all three propellers tested with the liquid-cooled engine nacelle is consistently several percent higher than with the radial engine nacelle. This result is probably due to the influence of the body on the stalling of the blades. The radial engine body, being larger, slows the air and causes an earlier stall than the liquid-cooled engine body.

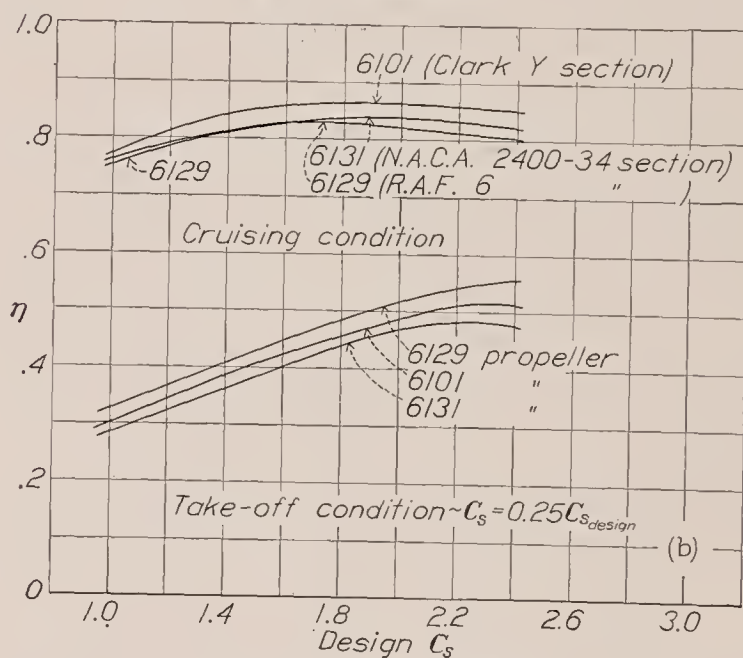
It should be pointed out that the foregoing comparisons were based on propellers of the same diameter for the same design condition. This basis was deemed better than any other since the take-off efficiency is very sensitive to changes in diameter whereas the design efficiency (high speed or cruising) is only slightly sensitive. Had the diameter been allowed to vary, depending upon the V/nD chosen for maximum efficiency, there

would have been large differences in take-off efficiency due entirely to the differences in the diameters.

Body.—The relative effect of the two bodies on the characteristics of the five propellers tested is given by figure 46. The maximum efficiencies of each propeller appear to agree fairly closely for the two body conditions, with the exception of that for propeller 6131, which was previously mentioned as probably being slightly in error. There are two opposing factors that tend to keep the maximum efficiencies the same for the two



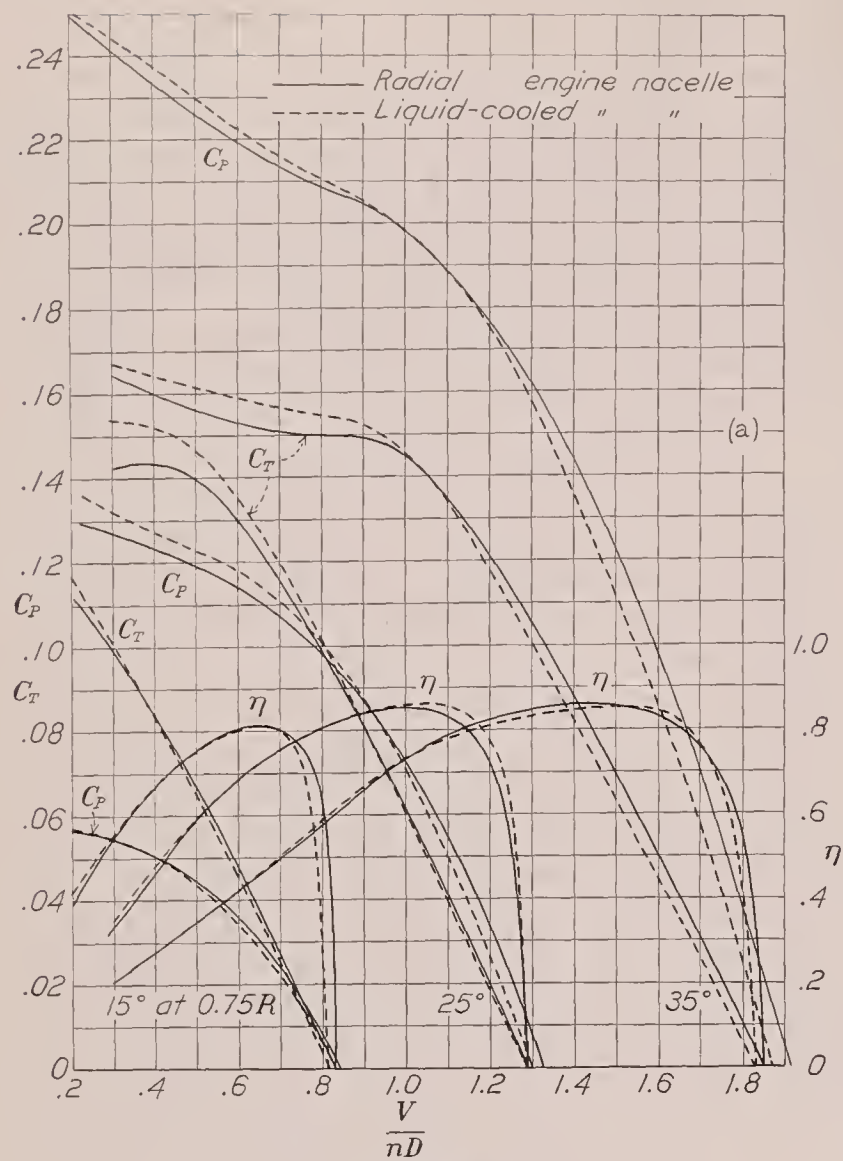
(a) Radial engine nacelle.



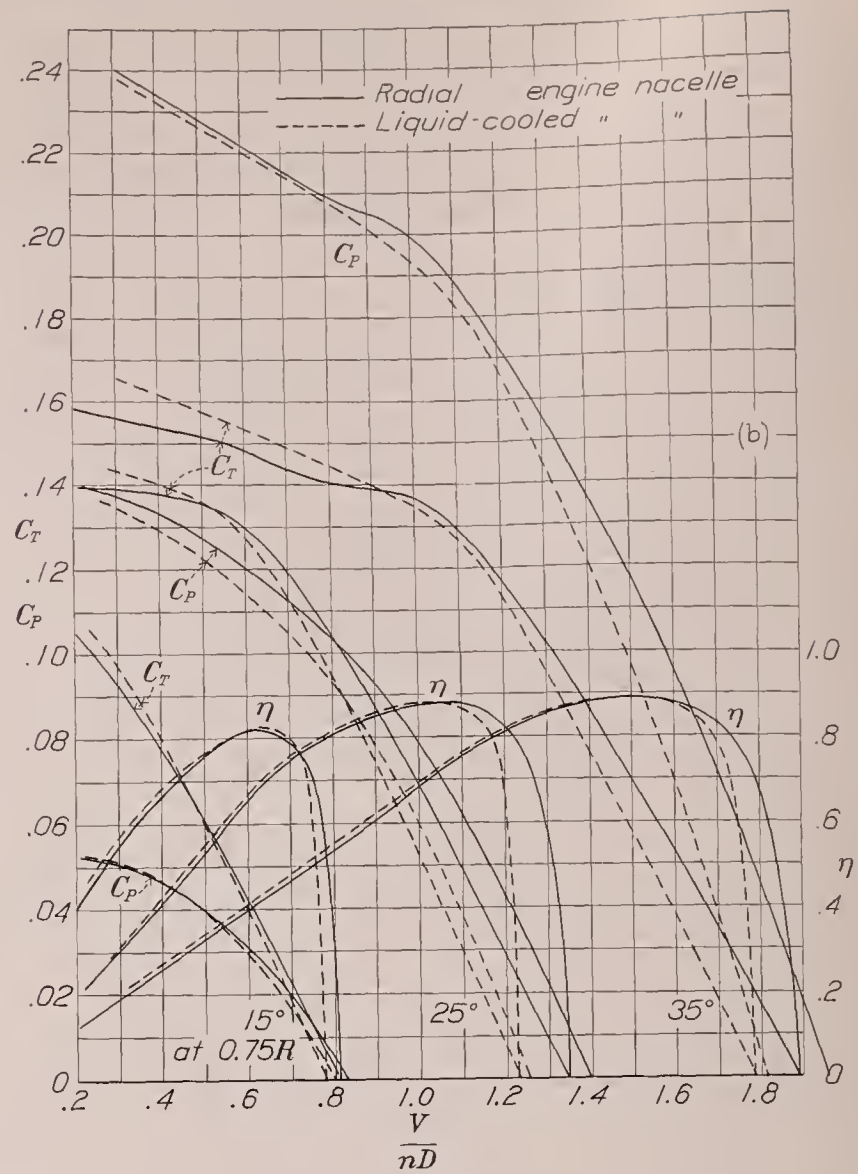
(b) Liquid-cooled engine nacelle.

FIGURE 45.—Comparison of three controllable propellers having different airfoil sections. All are the same diameter for the same C_s .

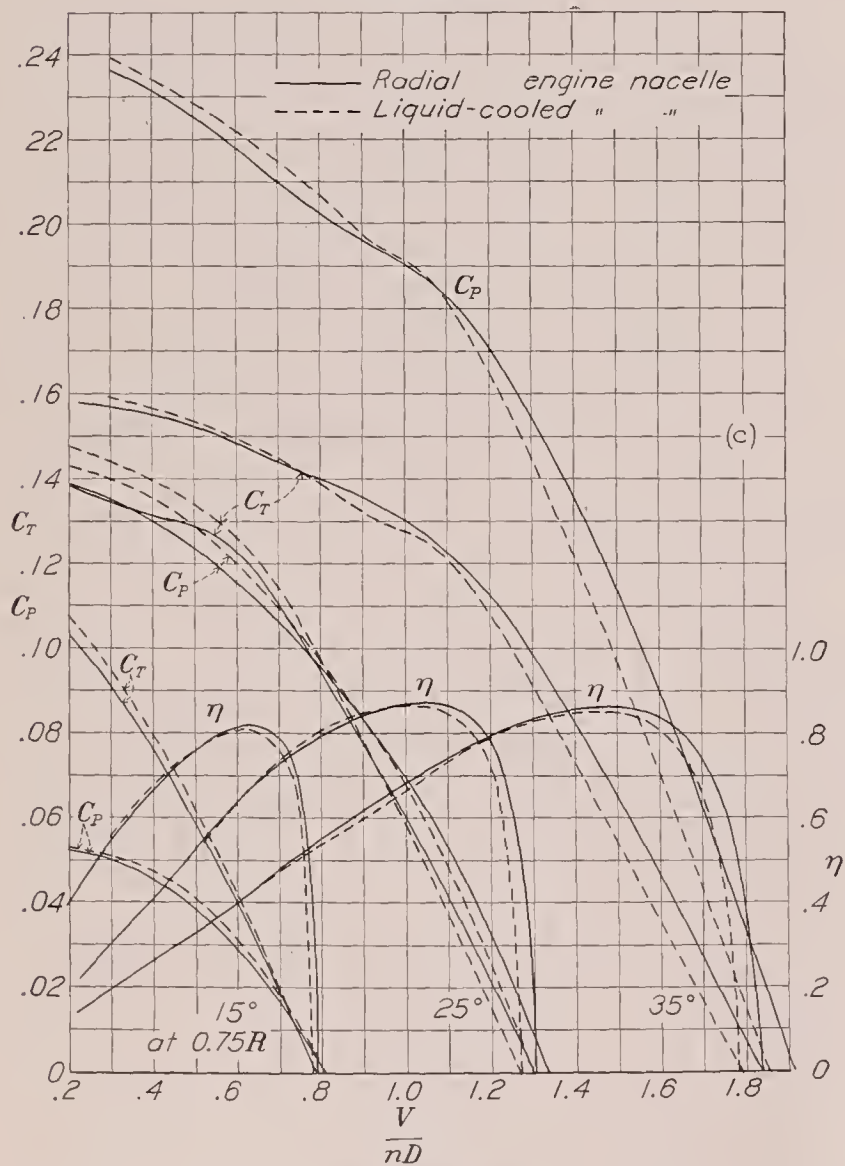
bodies. The slipstream drag, which reduces the efficiency, is greater for the radial engine nacelle than for the smaller liquid-cooled engine nacelle. On the other hand, the hub and blade shanks have less drag when they are located in front of the blunt nose of the radial engine nacelle than when they are located in front of the liquid-cooled engine nacelle. If a spinner had been used for all the tests of the liquid-cooled engine nacelle, it is clear that the peak efficiencies would have been higher than those for the radial engine nacelle. (See spinner results.)



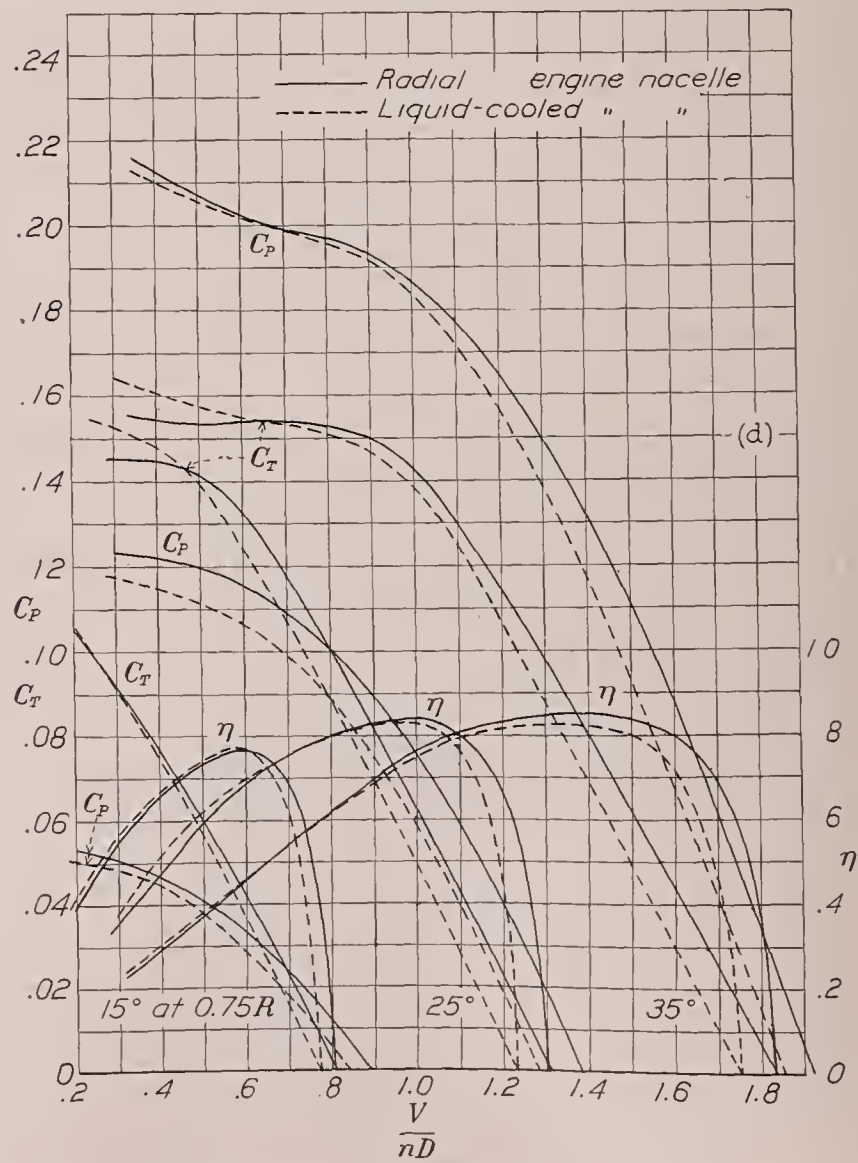
(a) Propeller 5868-9.



(b) Propeller 1C1-0.



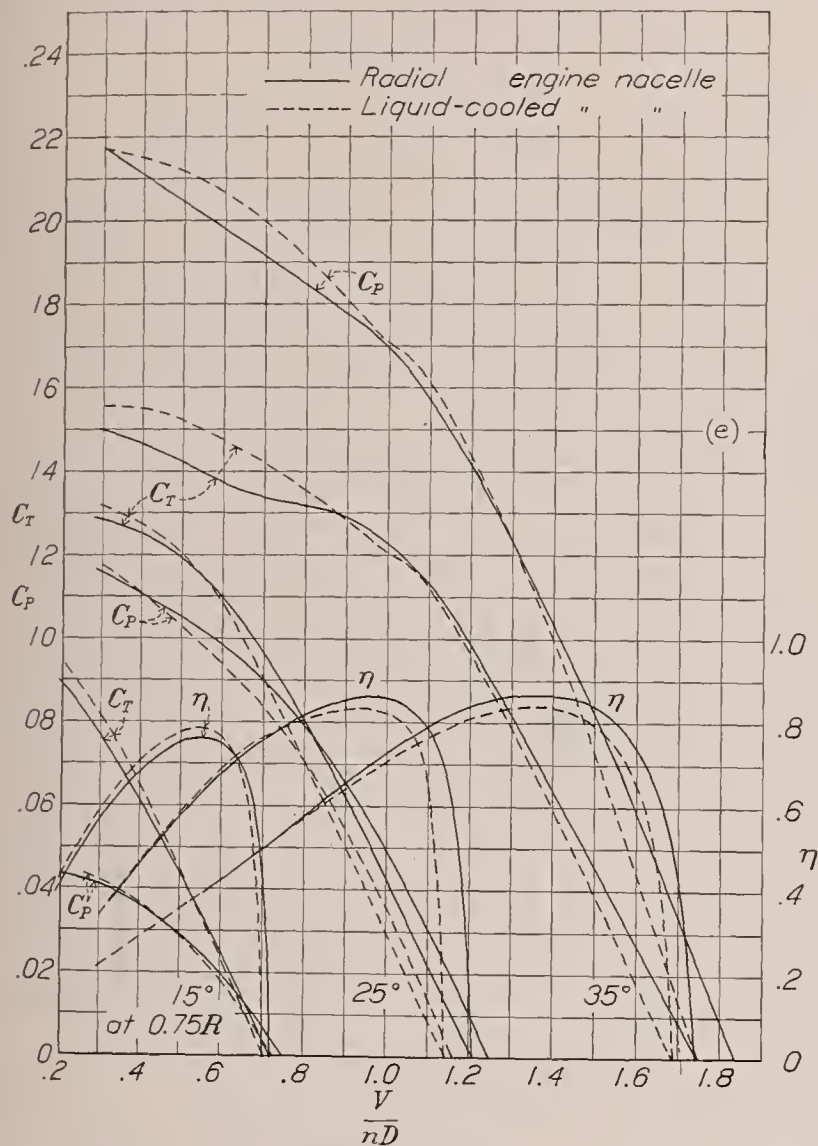
(c) Propeller 6101.



(d) Propeller 6129.

FIGURE 46.—Comparison of propeller characteristics for two body conditions.

The take-off efficiencies are consistently higher for the liquid-cooled engine nacelle than for the other nacelle. It may be noted in every comparison (fig. 46) that the thrust curves for the liquid-cooled engine nacelle reach higher values of C_T at the take-off condition than for the radial engine nacelle. This effect results from a difference in air speed over the two bodies.



(e) Propeller 6131.

FIGURE 46.—Continued. Comparison of propeller characteristics for two body conditions.

The liquid-cooled engine nacelle slows down the air to a lesser extent than the larger radial engine nacelle and the blades do not stall so quickly at the low V/nD values. A rough estimate of the differences in mean air speed through the propeller disk for the two bodies can be made by computing the relative velocities for zero thrust. The greatest difference in velocity noted is for propeller 1C1-0 and amounts to about 7 percent.

CONCLUSIONS

The results of the tests made at moderately low tip speeds of five propellers indicated the following conclusions:

1. Propellers operated in front of the liquid-cooled engine nacelle had higher take-off propulsive efficiencies

than when operated in front of the radial engine nacelle; they also had higher cruising efficiencies when provided with suitable spinners.

2. Spinners mounted on the liquid-cooled engine nacelle not only reduced the drag of the body but reduced the drag of the propeller hub and shanks as well. The propulsive efficiency was increased a maximum of 6 percent for one condition.

3. A propeller with airfoil sections extending into the hub was more efficient than one having round blade shanks when tested in front of both the radial and the liquid-cooled engine nacelles.

4. A thick propeller having a Clark Y section was found to be more efficient than a thin one for the take-off condition, but the maximum efficiency was possibly slightly less.

5. The order of decreasing efficiencies for the cruising condition for propeller-blade sections of 0.07 thickness ratios at $0.75R$ was found to be: Clark Y, N. A. C. A. 2400-34, and R. A. F. 6, but the order changed to R. A. F. 6, Clark Y, and N. A. C. A. 2400-34 for the take-off condition for propellers of the same diameter.

LANGLEY MEMORIAL AERONAUTICAL LABORATORY,
NATIONAL ADVISORY COMMITTEE FOR AERONAUTICS,
LANGLEY FIELD, VA., November 23, 1937.

REFERENCES

1. Biermann, David, and Hartman, Edwin P.: The Effect of Compressibility on Eight Full-Scale Propellers Operating in the Take-Off and Climbing Range. T. R. No. 639, N. A. C. A., 1938.
2. Hartman, Edwin P., and Biermann, David: The Aerodynamic Characteristics of Full-Scale Propellers Having 2, 3, and 4 Blades of Clark Y and R. A. F. 6 Airfoil Sections. T. R. No. 640, N. A. C. A., 1938.
3. Hartman, Edwin P., and Biermann, David: The Negative Thrust and Torque of Several Full-Scale Propellers and Their Application to Various Flight Problems. T. R. No. 641, N. A. C. A., 1938.
4. Biermann, David, and Hartman, Edwin P.: The Aerodynamic Characteristics of Six Full-Scale Propellers Having Different Airfoil Sections. T. R. No. 650, N. A. C. A., 1939.
5. Weick, Fred E., and Wood, Donald H.: The Twenty-Foot Propeller Research Tunnel of the National Advisory Committee for Aeronautics. T. R. No. 300, N. A. C. A., 1928.
6. Enos, L. H., and Sims, J. A.: Static Thrust Characteristics of Propellers Using Clark Y, R. A. F. 6, and 2400 Profiles. A. C. T. R. Serial No. 4319, Matériel Division, Army Air Corps, 1937.
7. Freeman, Hugh B.: Comparison of Full-Scale Propellers Having R. A. F. 6 and Clark Y Airfoil Sections. T. R. No. 378, N. A. C. A., 1931.

$\tan \beta = \frac{t}{D} \times \frac{1}{R}$

$\therefore \beta = 15^\circ$

@ 35° $\frac{t}{D} = \tan 35^\circ \times \frac{1}{R} \times D = 6.65$

to find $\frac{t}{D}$ @ .4R @ 35° from 15°

@ $\beta = 15^\circ$, @ .4R, $\frac{t}{D} = .64$

for $15^\circ = .64 \times \frac{1}{.4} \times \frac{1}{R} = .509$

$\therefore \beta = 27^\circ$ @ .4R @ 15°

@ 35° & .4R, $\beta = 47^\circ$, for each section given above 20° from 15° to 35° .

$\therefore \frac{t}{D} = .4 \times R \times \tan 47^\circ = 1.345$

@ 25° @ .4R

from K_f max @ 15°

$V_{max} = 3000 \text{ ft/s} = 914 \text{ m/s}$

$C_s = \frac{.635 \times 3000}{\frac{15}{100} \times 1500} = 2.24$

from fig 33, $V/\omega D = 1.35$

$D = \frac{V}{\omega \times 1.35} = 13.03 \text{ ft}$

$\beta = 32^\circ$ @ $.75R$, $\eta = 86\%$

$C_p = \frac{P}{\rho \omega^3 D^5} = \frac{2000 \times 550}{.000381(75)^3(13.03)^5} = 1.0796$

check m by ≥ 0

from fig 20, $C_T = .05$

$T = (.05)(.000381)(75)^2(13.03)^4 = 2150 \text{ #}$

for a constant speed, C_p is constant

@ $V/\omega D$ line from fig 20, etc.

@ $\beta = 32^\circ$, $C_p = .15$, $C_T = .114$

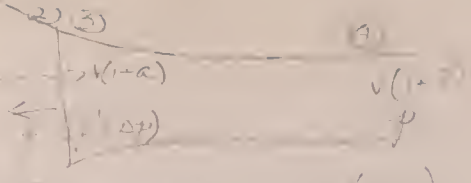
$\frac{N}{N_0} = \sqrt{\frac{C_{p0}}{C_p}} = \sqrt{\frac{1.0796}{.15}} = 1.728$

$N = 1500 \times 1.728 = 1090 \text{ rpm} = 18.2 \text{ rev/s}$

$\frac{V}{V_0} = \frac{V/\omega D}{V/\omega_0 D} = \frac{1.0}{1.35(1.728)} = .539$

$V = .539 \times 3000 = 1617 \text{ ft/s}$
 $T = .114 \times 2000 \times 3000 \times (18.2)^2 \times (13.03)^4 = 26000 \text{ #}$

fig 31 $\eta = 10\%$, $\eta_{eff} = .05 \times .95 \times .728 = 1.1\%$



③ K.E. $= \frac{1}{2} A \rho V (1+a)$

④ C.E. $= \frac{1}{2} A \rho V (1+a) V^2$

⑤ K.E. $= \frac{1}{2} A \rho V (1+a) (V^2) (1+a)$

$\Delta K.E. = 1 - 1 = A \frac{\rho}{2} V^3 [(1+a)^2 - 1] (1+a)$

$= A \frac{\rho}{2} V^3 [2a + a^2] (1+a)$

$= A \rho V^3 a [1 + \frac{a}{2}] (1+a)$

$= A \rho V^3 a (1+a)^2 = \text{output, for } a = 1/2$

Thrust $\times V = A \rho V^2 (1+a) a V = \text{output}$

$\eta = \frac{\text{output}}{\text{input}} = \frac{1}{1+a}$

Bernoulli's equation $1 + \frac{1}{2} V^2 = 1 + \frac{1}{2} V'^2 (1+a)^2$

" between 3 & 4

$1 + \Delta p + \frac{1}{2} V^2 (1+a)^2 = 1 + \frac{1}{2} V'^2 (1+a)^2$

$(1-\eta) \rho V = \frac{\rho}{2} V^2 [(1+a)^2 - 1] = \frac{\rho}{2} V^2 H(2+a)$

$= \frac{\rho}{2} V^2 a (1 + \frac{a}{2})$

Thrust $= \Delta p \cdot A = A \rho V (1+a)$

net velocity increase $= V + \frac{1}{2} V - V = \frac{1}{2} V$

$\therefore T = A \rho V (1+a) \frac{1}{2} = A \rho V^2 a (1 + \frac{a}{2})$

$(1+a) = 1 + \frac{a}{2}$, $a = \frac{a}{2}$

① simple Blade Element

② combined " " & momentum

③ Blade Element with interference corrections

	①	②	③
① SHIP stream contraction	No	No	No
② Tip Losses	No	No	No
③ Hub Losses	No	yes, by modifying disk area	No

④ interference of neighboring elements

⑤ " of blades

⑥ Periodic Flow

⑦ INFLOW

PART, by AIRFOIL TESTS

$\eta = \frac{C_T}{C_p} \cdot \frac{1}{2} \cdot \frac{V}{V_0} = \frac{1.1}{1.5}$

$\eta = \frac{C_T}{C_p} \cdot \frac{1}{2} \cdot \frac{V}{V_0} = \frac{1.1}{1.5}$

REPORT No. 643

THE AERODYNAMIC CHARACTERISTICS OF FOUR FULL-SCALE PROPELLERS HAVING DIFFERENT PLAN FORMS

By EDWIN P. HARTMAN and DAVID BIERMANN

SUMMARY

Tests were made of four propellers, with diameters of 10 feet, having different blade plan forms. One propeller (Navy design No. 5868-R6) was of the usual present-day type and was used as a basis of comparison for the other three, which had unusual plan forms distinguished by the inward (toward the hub) location of the sections having the greatest blade width.

It was found that propellers with points of maximum blade width occurring closer to the hub than on the present-day type of blade had higher peak efficiencies but lower take-off efficiencies. This result was found true for a "clean" liquid-cooled engine installation. It appears that some modification could be made to present plan forms which would produce propellers having more satisfactory aerodynamic qualities.

The propellers with the inward location of the points of maximum blade width had lower thrust and power coefficients and stalled earlier than the present-day type.

INTRODUCTION

One of the variables in propeller design that has received but a small amount of attention in the past is the distribution of area along the blade. Early propellers that were designed with ease of manufacture in mind had blades of constant width and square-cut tips. It is a little surprising, perhaps, to find that propellers with such simple plan forms have but little less efficiency than ones of the usual tapered plan form (reference 1). The insensitivity of efficiency to changes in plan form may provide a reason why plan form has been neglected as a subject of research.

It is probable that the trend of evolution of the propeller plan form has been dictated largely by structural rather than aerodynamic considerations. This probability appears definitely true for the inner third of the present-day type propeller, where the nearly circular sections show almost no effects of aerodynamic influence in design.

The cooling of radial engines has been taken into consideration as a factor in the design of certain special propellers of recent manufacture. In the design of these propellers the blade width has been made larger

at the inner stations on the radius where the added slipstream velocity will aid in cooling the engine. Another possible reason for increasing the blade area on the inner half of the blade at the expense of the outer half is that modern propeller theory (reference 2) indicates some advantage in at least part of the normal operating range for a propeller so designed. The theory shows that, at one value of V/nD , the optimum distribution of circulation along the blade is such that the maximum value of circulation is reached at the 0.2 radius and then decreases almost linearly to zero at both hub and tip.

It appears that airplane and propeller designs are reaching a stage of development in which even small increases in operating efficiency are of great importance; the factor of blade plan form should therefore not be neglected in future research.

The present report is not expected to advance the state of knowledge concerning the effect of changes in plan form to any large extent because the data taken were not the result of a planned program to study this effect. Its main purpose is to present propeller data for four full-scale propellers of Navy design, three of which have somewhat unusual plan forms and the other one has a normal (usual present-day type) plan form. These data may give some clue as to what may be expected from fundamental changes in blade plan form. The four propellers had been tested as an incidental part of a rather extensive propeller-research program conducted by the N. A. C. A. during 1937. They all have the same diameter (10 feet) and airfoil section (R. A. F. 6) and three of the four have approximately the same blade area. There is some variation in thickness ratio but probably not enough to have a very large effect on the results.

APPARATUS AND METHODS

The tests were made in the N. A. C. A. 20-foot wind tunnel, which is described in reference 3. Since publication of reference 3, the original balance system and Diesel power plant have been replaced by semiautomatic recording balances and by an 1,800-horsepower electric motor. The tunnel is capable of a speed of 115 miles per hour with the test propeller running.

The propellers were turned by a 600-horsepower Curtiss Conqueror engine having a rated speed of 2,450 r. p. m. and a gear ratio of 7:5. The engine was enclosed in a liquid-cooled engine nacelle of oval cross section having over-all dimensions as follows: length

126 inches, height 46 inches, width 38 inches. A photograph of the test set-up is shown in figure 1. The engine was mounted in a cradle-type torque dynamometer and was free to rotate about an axis along its side and parallel to its crankshaft. The torque reaction was transmitted through a compression strut to the lever mechanism of a recording balance on the test-chamber floor.

The thrust and torque forces were simultaneously measured on recording balances and the engine revolution speed was read from the dial of a calibrated electric tachometer.

The four propellers tested are of Navy design, and each is 10 feet in diameter and has two blades. A photograph of the propeller blades is shown in figure 2 and the blade-form curves are given in figure 3. A list of the principal characteristics of the four propellers is given in the following table.

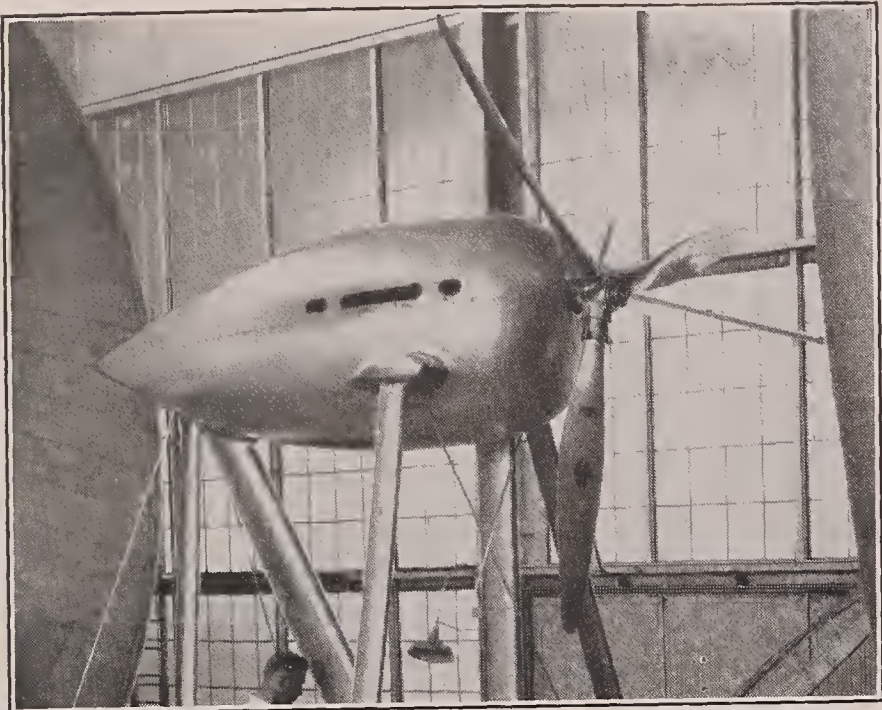


FIGURE 1 —Test set-up. (The photograph shows a 3-blade propeller instead of the 2-blade propeller actually tested.)

Propeller drawing No.	Diameter (ft.)	Airfoil section	Maximum width (in.)	Position of maximum width (r/R)	Relative blade area	Blade width at 0.75R (in.)	Thickness ratio at 0.75R (h/b)
5868-R6 ^a ----	10	R. A. F. 6-----	9.15	0.51	1.00	7.40	0.090
5649-----	10	R. A. F. 6-----	10.03	.38	.97	5.47	.083
5923G-----	10	R. A. F. 6-----	11.70	.42	1.03	5.34	.105
5924H-----	10	R. A. F. 6-----	12.30	.45	1.21	7.76	.064

^a Normal plan form.



5868-R6.

5649.

5923G.

5924H.

FIGURE 2.—Propeller blades tested.

The general method employed in making the tests was as follows: The engine speed was held constant at 1,000 r. p. m. and the tunnel speed was increased by steps to top speed (115 miles per hour with propeller operating). The tunnel speed was then held approximately constant at 115 miles per hour and the engine

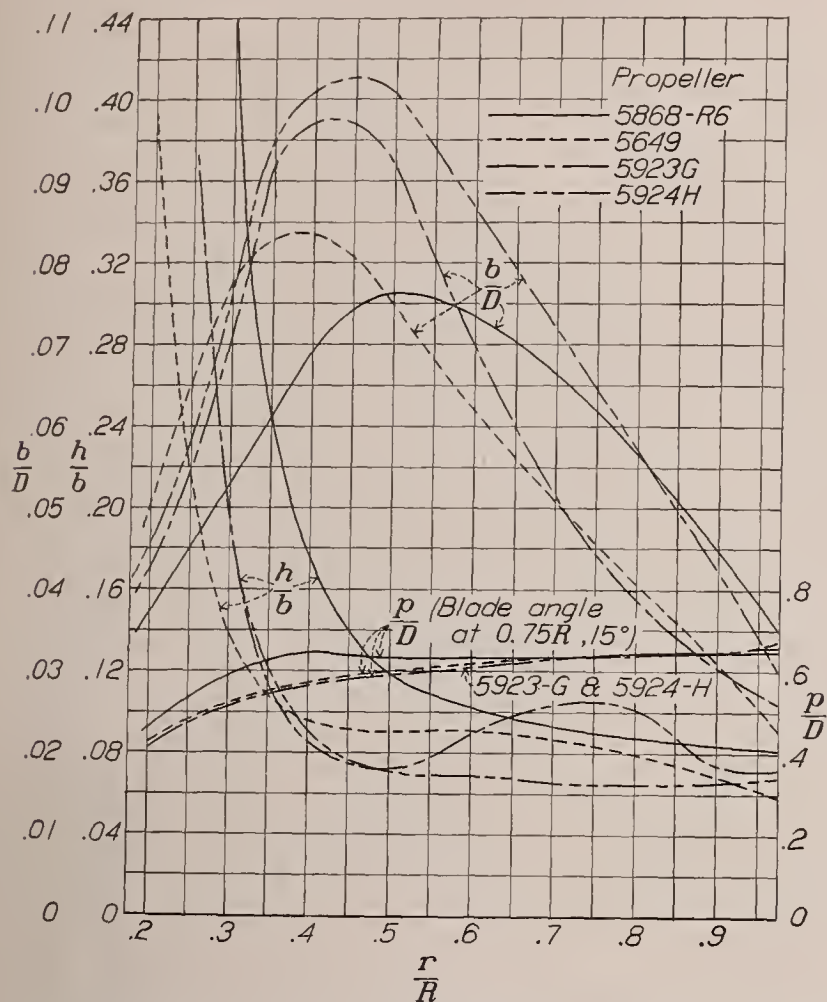


FIGURE 3.—Blade-form curves for propellers 5923G, 5924H, 5649, and 5868-R6
 D , diameter; R , radius to the tip; r , station radius; b , section chord; h , section thickness; p , geometric pitch.

speed reduced by steps until the V/nD for zero thrust and power was reached. The maximum tip speeds for the tests were below the values where the efficiency is measurably affected by compressibility. The propellers were tested at three blade angles, 15° , 25° , and 35° at the 0.75 radius.

RESULTS AND DISCUSSION

The coefficient forms used in presenting the data are as follows:

$$C_T = T_e / \rho n^2 D^4; C_P = P / \rho n^3 D^5; C_s = \sqrt{\frac{\rho V^5}{n^2 P}}; \eta = \frac{C_T}{C_P} \times \frac{V}{nD}$$

where

C_T is the thrust coefficient.

C_P , power coefficient.

C_s , speed-power coefficient.

η , propulsive efficiency.

$T_e = T - \Delta D$, effective thrust.

T , thrust of propeller (tension in propeller shaft), pounds.

ΔD , change in drag of airplane or body due to slipstream, pounds.

n , propeller revolution speed, r. p. s.

P , engine power, foot-pounds per second.

ρ , mass density of air, slugs per cubic foot.

V , air speed, feet per second.

D , propeller diameter, feet.

The basic data are given in figures 4, 5, 6, and 7, where C_T , C_P , and η are plotted against V/nD . These data are also given in table I, available on request from the National Advisory Committee for Aeronautics. The portion drawn with a broken line has been extrapolated, as a V/nD of 0.25 is about the lowest obtainable in the tunnel for a full-scale propeller.

A more convenient comparison of the characteristics of the four propellers is given in figures 8 and 9. In figure 8 are plotted thrust coefficients and efficiencies for the four propellers at a blade-angle setting of 25° . Figure 9 presents the corresponding power coefficients for the same propellers. Large differences in the thrust and power coefficients will be noted. The two propellers with narrow outer (toward tips) portions reach C_T values of only 0.10 and 0.103, whereas the two with normal-width outer portions reach the usual 0.12, or thereabouts. A corresponding difference in the power coefficients is also noted, though here the C_P curve for propeller 5924H rises far above the curve for 5868-R6 at low values of V/nD and results in lower efficiencies in this range for propeller 5924H.

In general, the blades with greater areas near the hub stall earlier than propeller 5868-R6 with the usual area distribution. The V/nD for zero thrust is somewhat greater for propeller 5868-R6 than for the other propellers, which may possibly be explained by the fact that the pitch distribution over the inner portion of the blade is different for propeller 5868-R6 than for the other three propellers. (See fig. 3.)

The differences in peak efficiency are surprisingly large and it is interesting to note that the peak for the propeller with the usual present-day distribution of area is the lowest. The differences in peak efficiency of the four propellers are more clearly shown in figure 10, where the envelopes of their efficiency curves are plotted against V/nD . On the basis of peak efficiency, the order of merit of the four propellers is as follows: 5649, 5924H, 5923G, and 5868-R6. The accuracy of the tests was such that the efficiency might vary 1 percent on repeat tests so that the relative merit of the propellers must be judged with this fact in mind. The efficiency-curve envelope of propeller 5649 averages more than 3 percent higher than propeller 5868-R6. Propeller 5649 is the one with its maximum width closest to the hub. From the point of greatest width the blade tapers evenly to a fairly narrow tip. (See fig. 2.) It is probable that the differences in efficiency indicated in figure 10 are largely due to the differences in plan form. It should be pointed out, however, that the differences in thickness ratios undoubtedly have some effect. Propeller 5923G has a greater thickness ratio at the three-

quarters radius than the normal, present-day type, propeller 5868-R6; propellers 5649 and 5924H have lesser thickness ratios than propeller 5868-R6. From a study of the data on the effect of blade thickness given

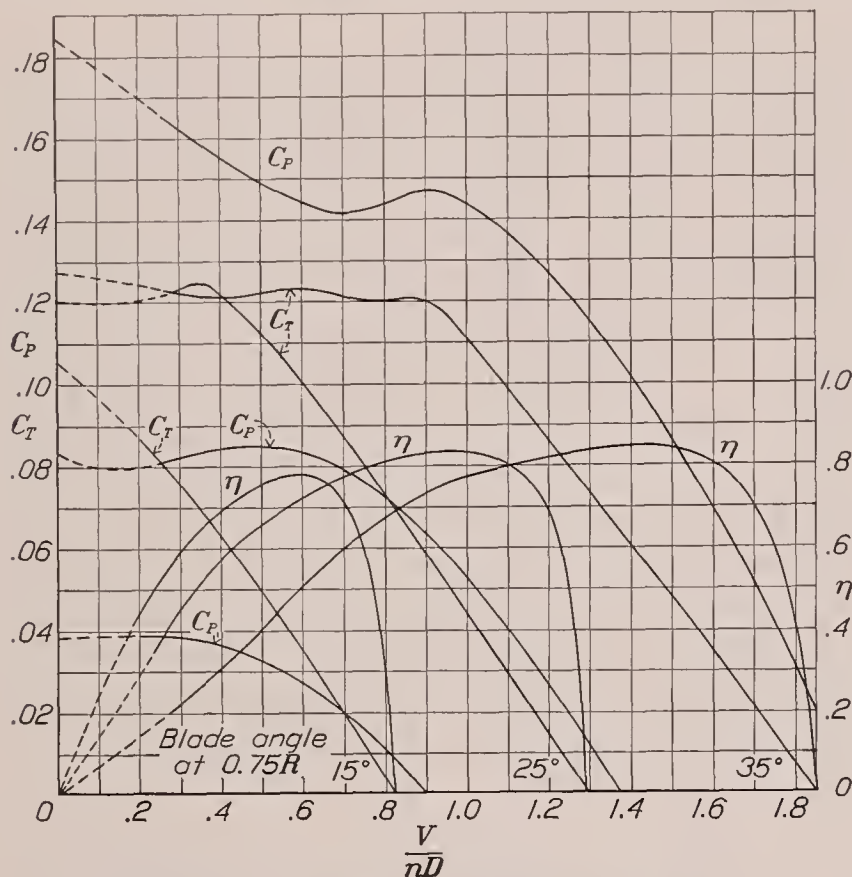


FIGURE 4.—Coefficient curves for propeller 5868-R6.

in reference 4, it does not seem probable that the differences in thickness ratio between propellers 5868-R6 and 5924H could account for more than one-half of the difference in efficiency between them. The difference

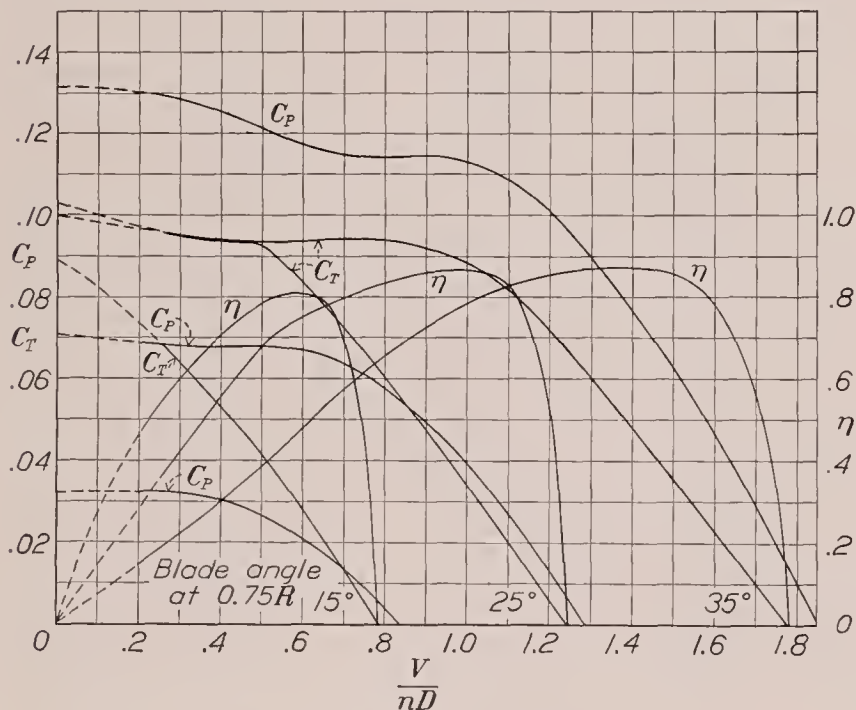


FIGURE 5.—Coefficient curves for propeller 5649.

in thickness ratio between propellers 5868-R6 and 5649 should have a negligible effect. The improvement in efficiency due to moving the blade area toward the hub seems to agree with theory, as mentioned earlier. Another probable cause for this improvement in efficiency lies in the elimination of a large part of the long cylin-

drical shank. The cylindrical shank adds greatly to the parasite drag of the propeller and reduces the efficiency by an amount that increases with design air speed. The reduction in efficiency may be several percent at high design speed.

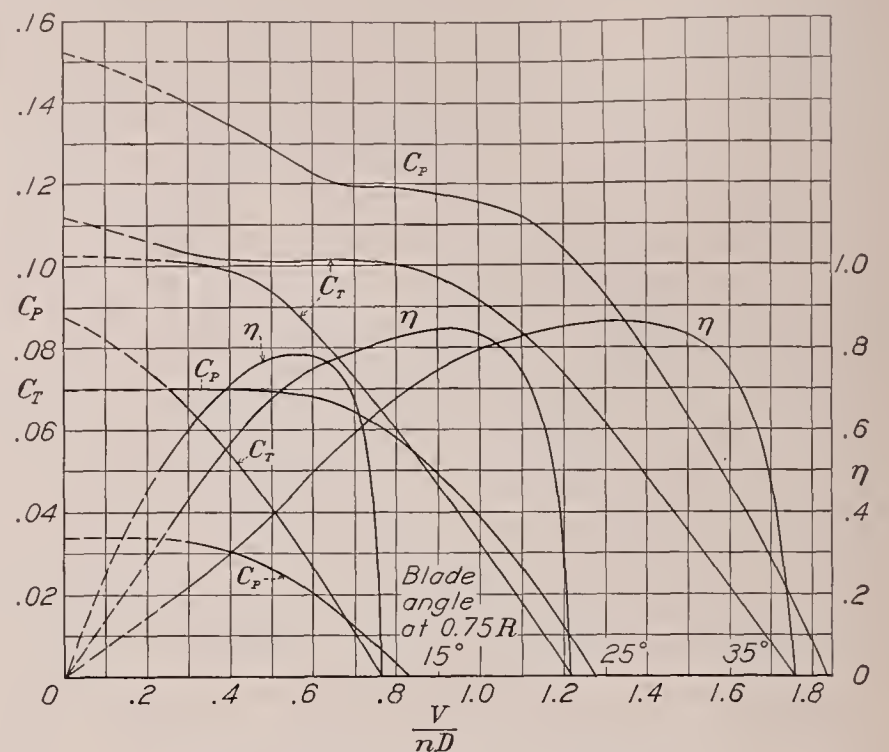


FIGURE 6.—Coefficient curves for propeller 5923G.

From practical considerations, it is usually better to compare propellers on the basis of constant C_s because

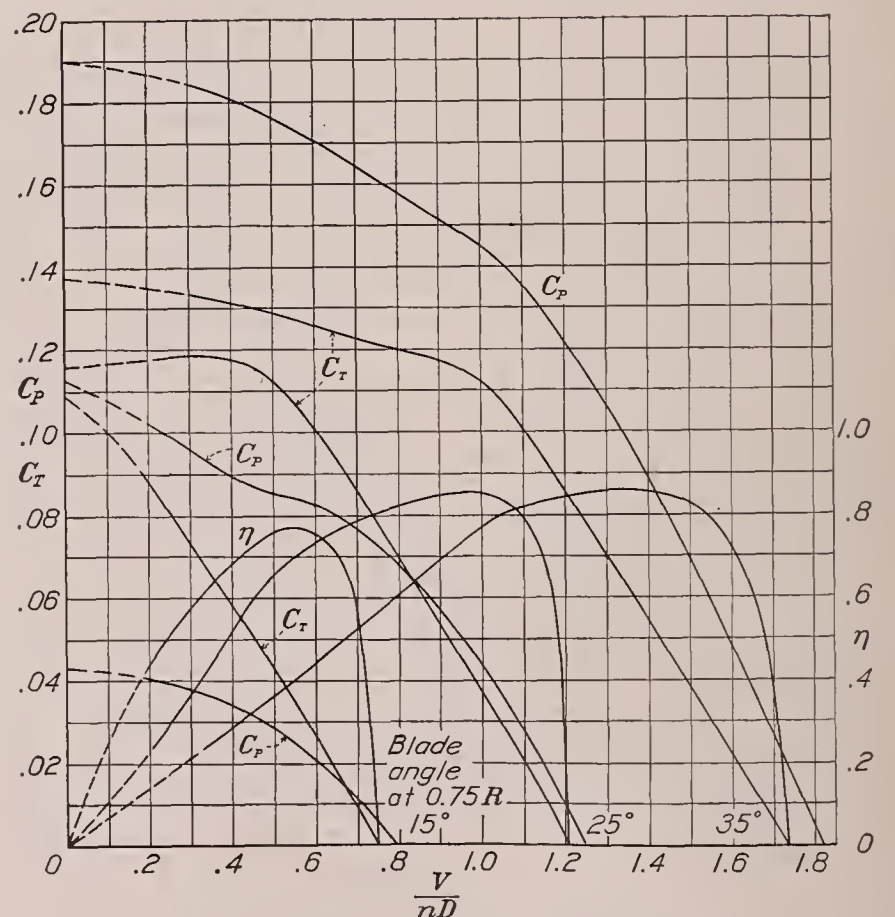


FIGURE 7.—Coefficient curves for propeller 5924H.

this coefficient represents actual design conditions. Figures 11, 12, 13, and 14 have been included for the use of readers who wish to make further comparisons on the C_s basis. The blade-angle intervals are too great for an accurate use of the chart but a linear interpolation along

the line of "maximum efficiency for C_s " should give results not greatly in error.

The envelopes of the efficiency curves were taken from figures 11 to 14 and plotted against the design coefficient C_s in figure 15. The curves give the efficiency for any given set of design conditions, i. e., engine power, engine speed, air speed, and air density. The order of merit of the four propellers remains unchanged and the difference in efficiency between 5649 and 5868-R6 is still about 3 percent.

The comparison of the take-off qualities of the propellers does not present such an easy problem as the comparison of peak efficiencies because the two usual methods of comparison, both of which are reasonable methods, sometimes give contrary results. Compari-

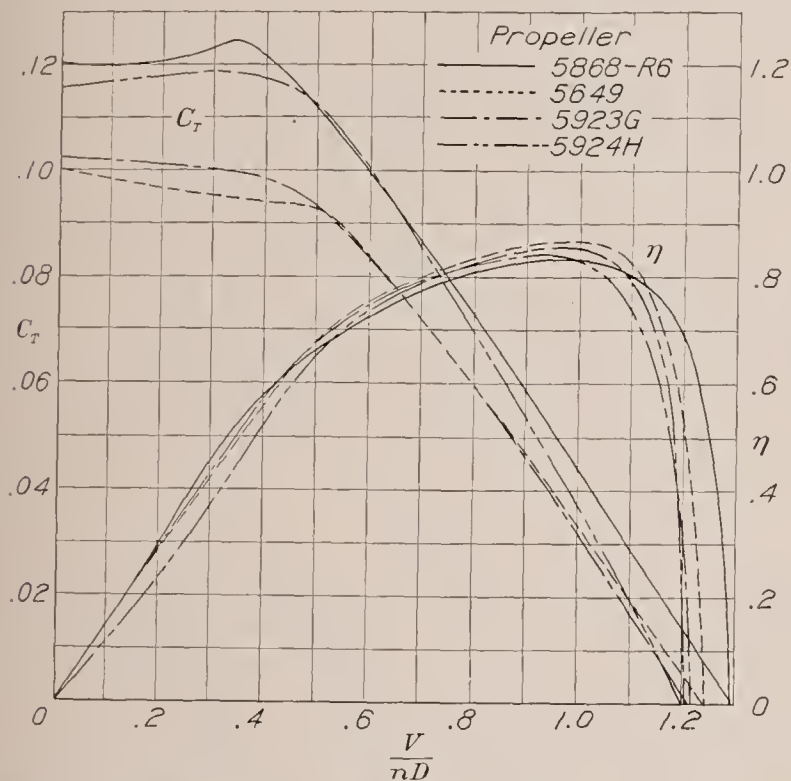


FIGURE 8.—Comparison of thrust coefficients and efficiencies for four propellers. Blade angle, 25° at $0.75R$.

sons will therefore be made by both methods, which are described as follows:

The first method is a comparison of a group of propellers the diameters of which are the values that have been obtained by the usual methods of selection from C_s charts. They are the diameters that will give maximum efficiency for the particular design condition chosen, i. e., for cruising or high speed. A group of propellers with different power-absorption characteristics will have different design diameters, a fact that greatly influences take-off comparisons.

The second method of take-off comparison assumes that some condition of design fixes the diameter. The fixed diameter may not be the one giving maximum efficiency for the design conditions, but the deviation from the maximum efficiency will probably be small. This method usually favors the propeller with the highest power absorption and the one that has the latest and least severe stall.

In the comparison of the take-off qualities of the present four propellers, the thrust throughout the take-

off and climbing range was calculated for a representative airplane equipped with each of the four propellers. The airplane was assumed to be a light, two-engine transport airplane having the following design charac-

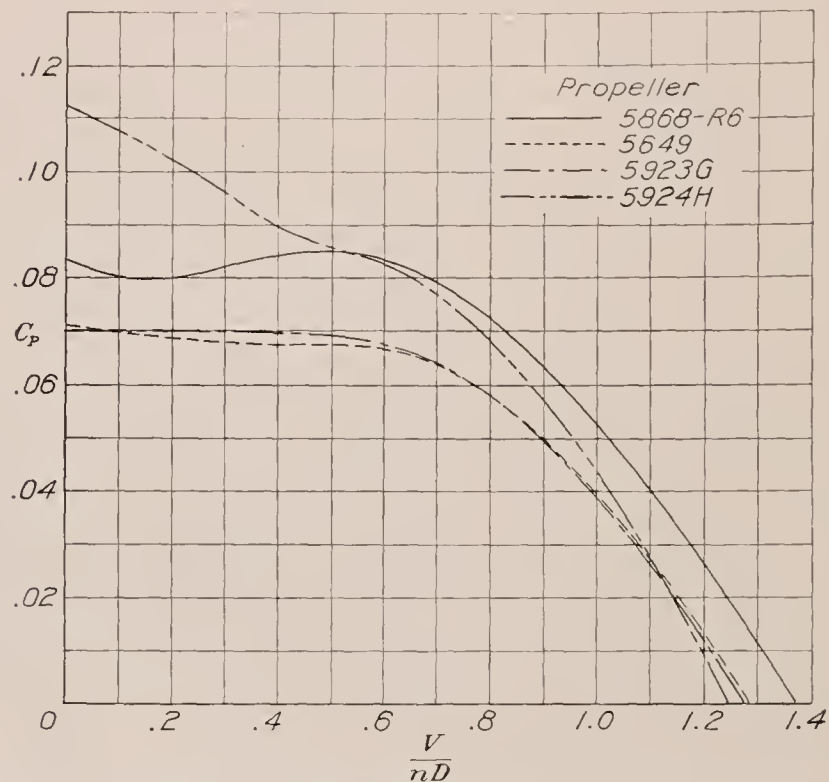


FIGURE 9.—Comparison of power coefficients for four propellers. Blade angle, 25° at $0.75R$.

teristics: high speed, 220 miles per hour; engines (2) rated at 550 horsepower at 1,750 (propeller) r. p. m. Both methods of comparison, as previously described, were used. In the first case, the propellers were selected

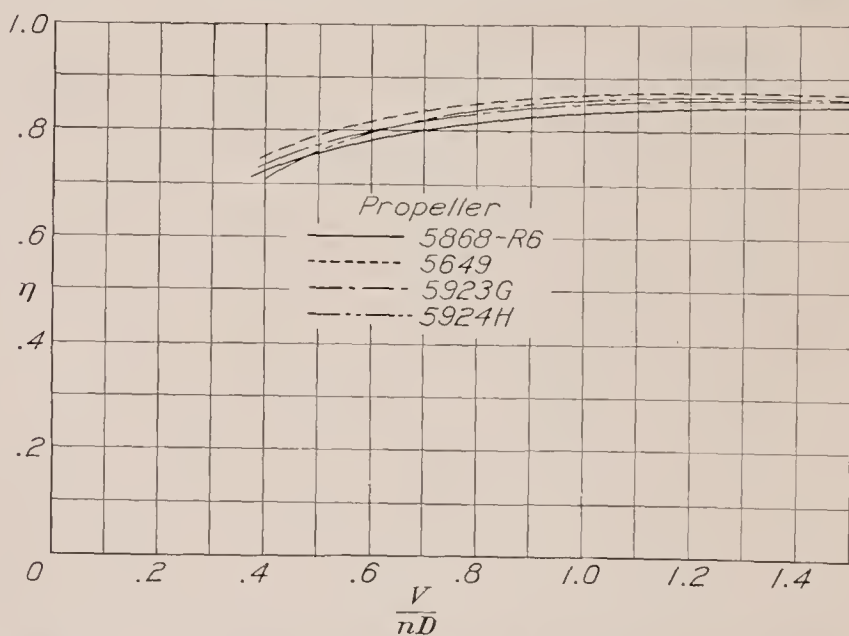


FIGURE 10.—Comparison of efficiency-curve envelopes for four propellers.

from the design charts in figures 11, 12, 13, and 14 for the high-speed conditions. The diameters selected varied from 9.9 to 10.42 feet.

In the second case, the diameters were all taken as 10.2 feet and the difference in high-speed efficiency for the two cases was almost negligible. The results of these comparisons are shown in figures 16 and 17. In both cases, the propeller with normal, present-day plan form (5868-R6) was best for take-off, though in figure 16 it appears but little better than 5649 and not so

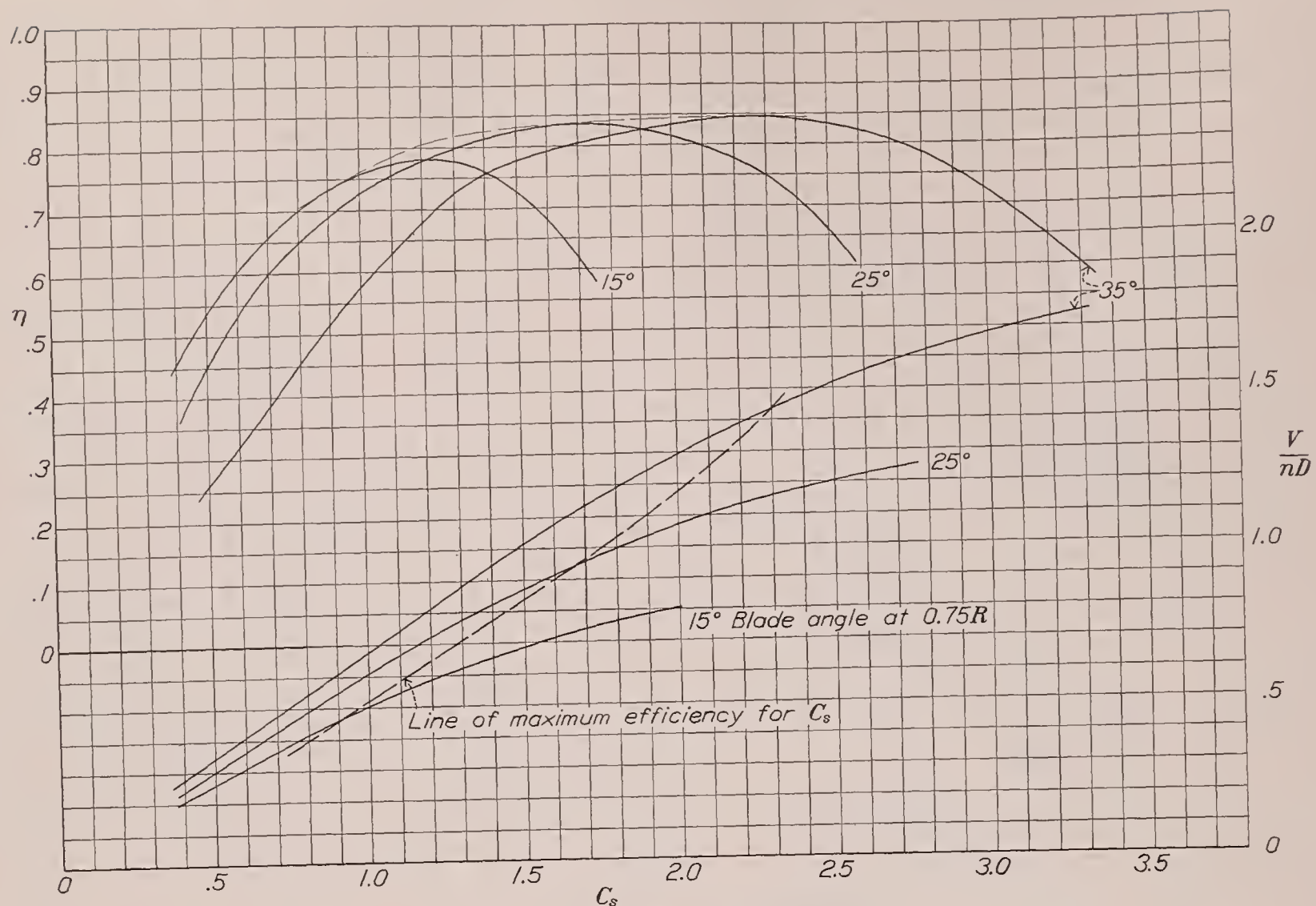


FIGURE 11.—Design chart for propeller 5868-R6.

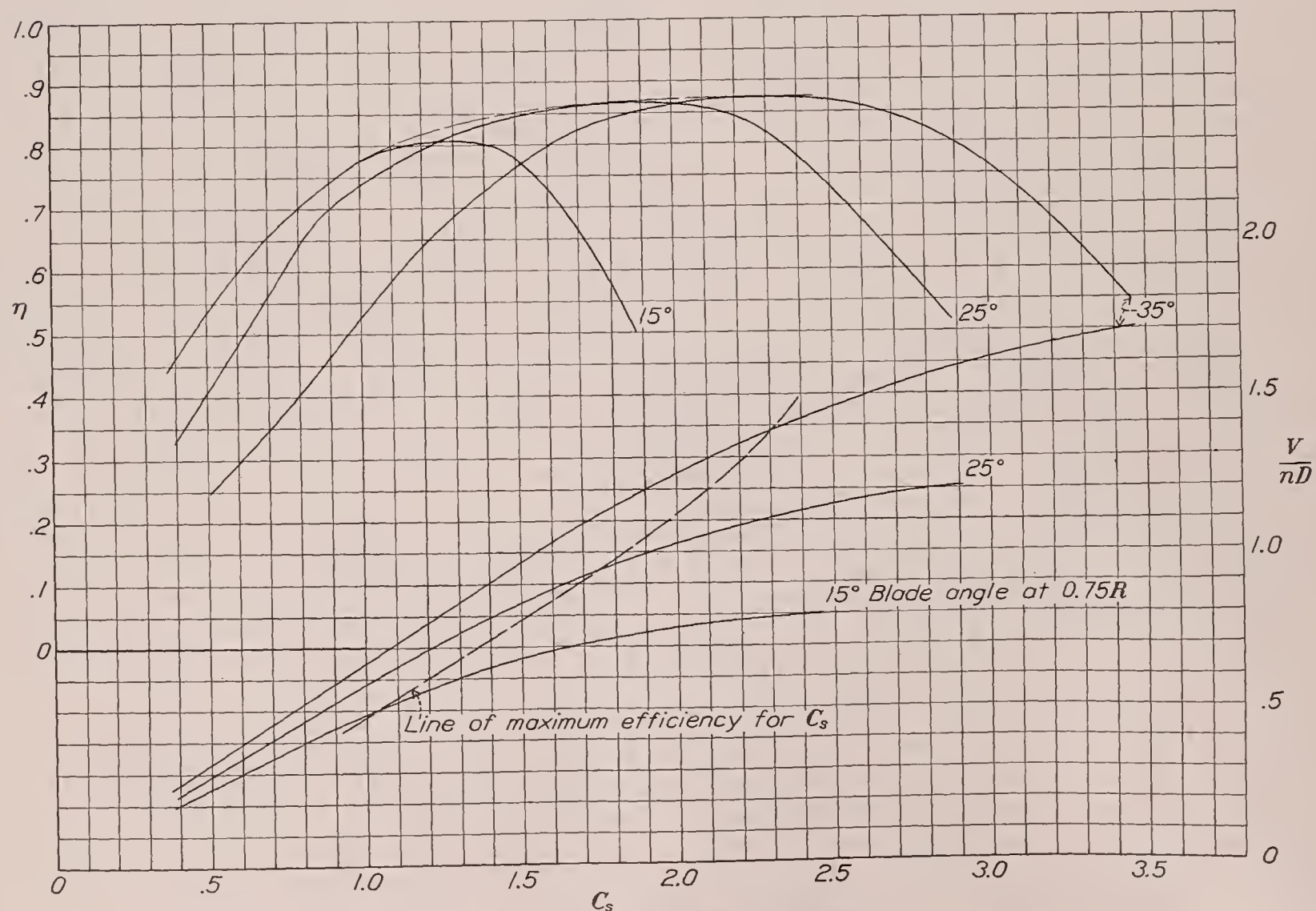


FIGURE 12.—Design chart for propeller 5649.

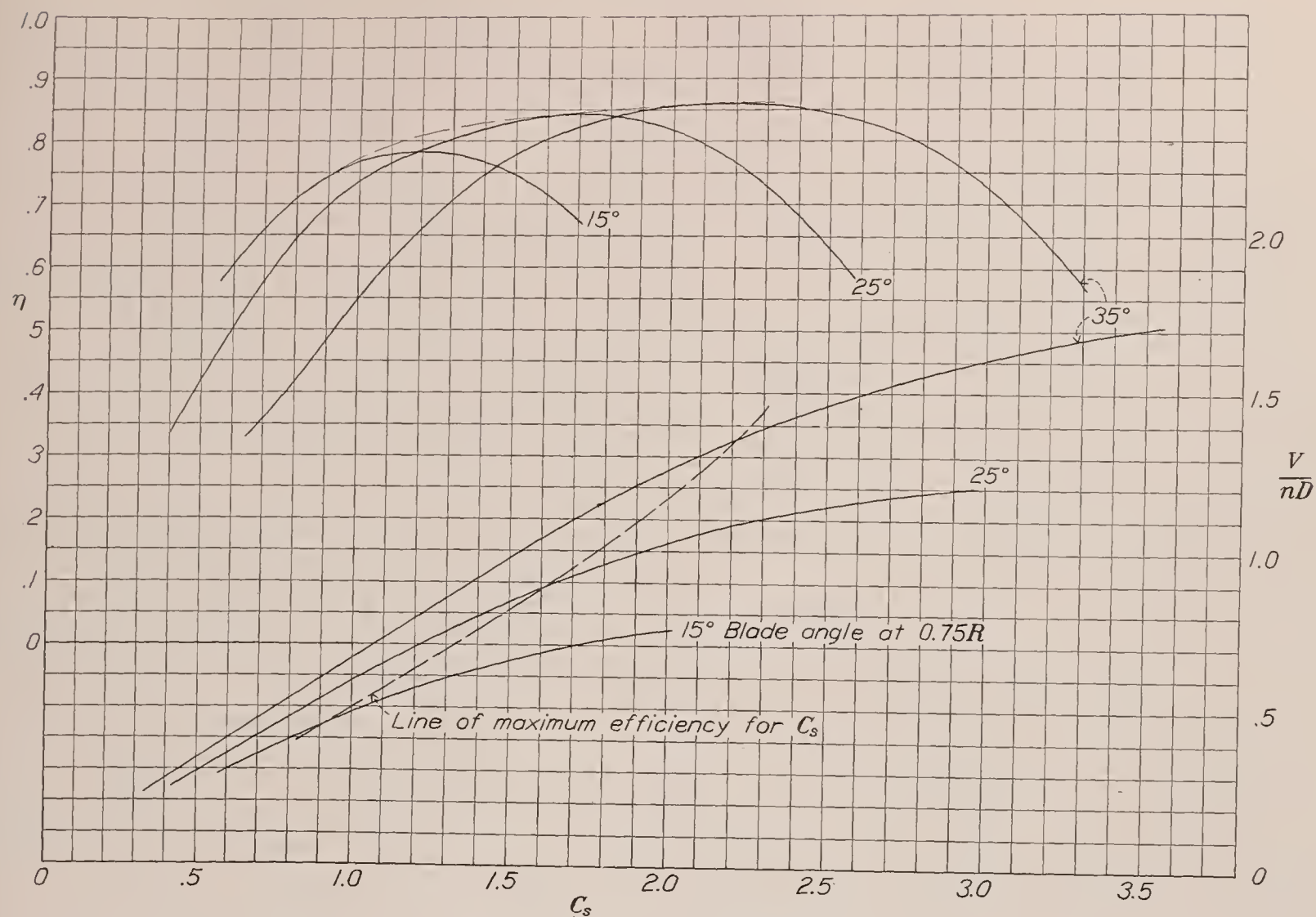


FIGURE 13.—Design chart for propeller 5923G.

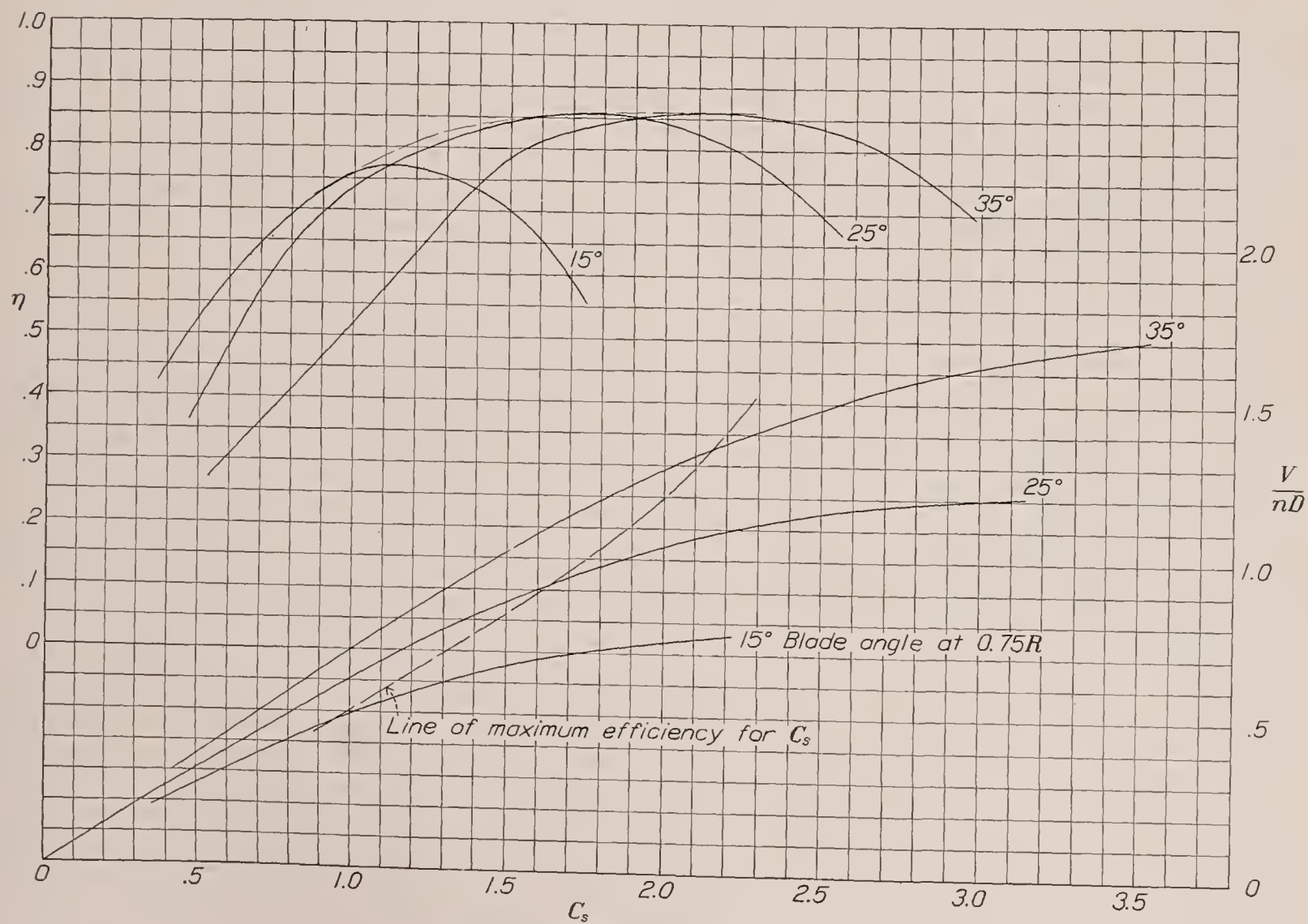


FIGURE 14.—Design chart for propeller 5924H.

good in the climbing range as 5649. In the constant-diameter comparison (fig. 17) propeller 5868-R6 is considerably better than propeller 5649 in the take-off range but equal in climb. Propeller 5924H holds up well in both cases; whereas, propeller 5923G is fairly poor in both cases. In both cases the thrust was calculated by the method given in reference 5.

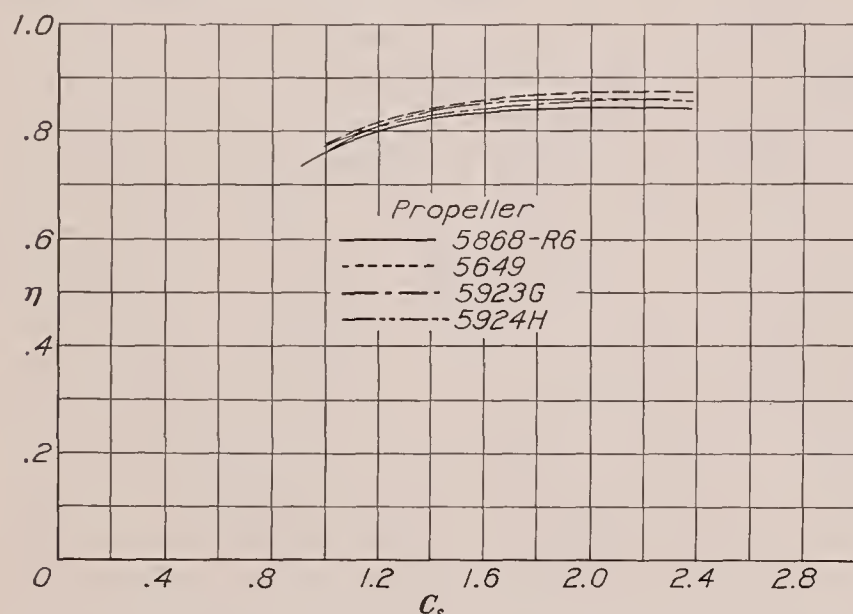


FIGURE 15.—Comparison of efficiency-curve envelopes for four propellers.

Differences in thrust that occur at speeds from 0 to 25 miles per hour have an almost negligible effect on the take-off distance as shown in reference 6. In this reference it is shown that the value of thrust most representative of the entire take-off occurs at a speed equal to 0.7 the take-off air speed. For the present example, this speed will lie somewhere between 40 and 45 miles per hour.

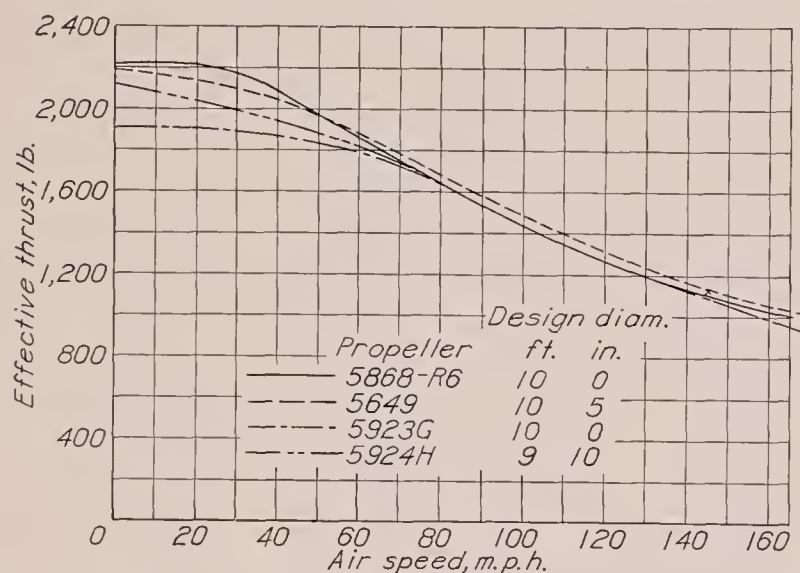


FIGURE 16.—Propeller thrust for example airplane, 2-blade constant-speed propeller. Design conditions: air speed, 220 m. p. h.; b. hp., 550 (each engine); propeller speed, 1,750 r. p. m.

The following table presents a summary of the high-speed and take-off comparisons for the example airplane. Although the results are for only one example, they are probably representative of many others and therefore give a fairly general comparison of the four propellers tested. The table presents ratios of the peak efficiencies of the various propellers relative to the peak efficiency for the normal propeller. The take-off effi-

ciency ratio, also given in the table, is the ratio of the propeller thrust of the various propellers to the propeller thrust of the normal propeller at an air speed of 40 miles per hour.

Propeller drawing No.	High-speed efficiency ratio	Take-off efficiency ratio	
		Design diameter	Constant diameter
5868-R6 ^a	1.000	1.000	1.000
5649	1.033	.978	.895
5923G	1.016	.895	.914
5924H	1.022	.933	.982

^a Normal propeller.

The propeller a designer should choose will depend, to a large extent, upon his particular design problem; so little discussion on this subject is worth while. Propeller 5924H seems to hold up well in all comparisons

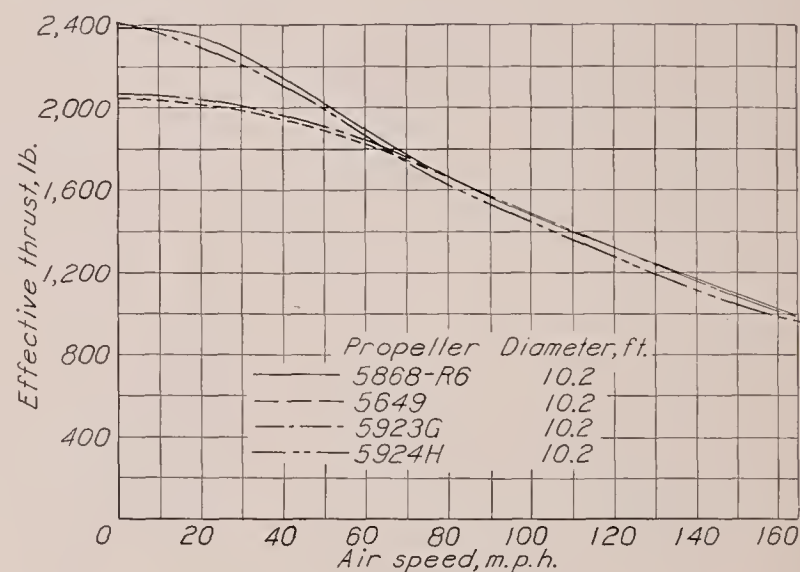


FIGURE 17.—Propeller thrust for example airplane, 2-blade constant-speed propeller. Design conditions: air speed, 220 m. p. h.; b. hp., 550 (each engine); propeller speed, 1,750 r. p. m.

whereas the others are good in one and poor in another. It is possible that, in many cases, it would be worth while to accept the 2 to 10 percent loss in take-off efficiency of propeller 5649 in order to gain its 3-percent better peak efficiency. It is also possible that the design of propeller 5649 could be improved for take-off without serious loss in peak efficiency by increasing the width near the tip but leaving the point of maximum width at its present location, $0.38R$. There seems to be a distinct advantage in having a considerable width on the inner (toward the hub) sections.

It must be remembered that these data and this discussion refer only to a clean liquid-cooled engine installation. It is quite possible that somewhat different results would be obtained with an air-cooled engine nacelle, for the added slipstream of the propellers with wide inner sections would add to the interference and drag of the nacelle but might possibly result in better engine cooling.

CONCLUSIONS

1. The peak efficiencies of propellers having present-day plan forms similar to Navy propeller 5868-R6 can possibly be improved by a change in design that will put more of the blade area in the inner half of the blade and will move the section having greatest width closer to the hub than its present location. The results of the tests show this conclusion to be true for a "clean" liquid-cooled engine installation.

2. For the propellers tested, the increase in peak efficiency due to this change in plan form is paid for in terms of a lower take-off efficiency. It is probable, however, that some compromise can be made to give more generally satisfactory results than propellers having present-day plan forms.

3. Shifting area from the outer to the inner half of a propeller blade caused an earlier stall, decreased the thrust and torque coefficients, and also slightly decreased the efficiency in the take-off range.

LANGLEY MEMORIAL AERONAUTICAL LABORATORY,
NATIONAL ADVISORY COMMITTEE FOR AERONAUTICS,
LANGLEY FIELD, VA., *November 2, 1937.*

REFERENCES

1. Durand, W. F., and Lesley, E. P.: Experimental Research on Air Propellers, V. T. R. No. 141, N. A. C. A., 1922.
2. Glauert, H.: Airplane Propellers. Aerodynamic Theory, W. F. Durand, ed., vol. IV, div. L., Julius Springer (Berlin), 1935, p. 260.
3. Weick, Fred E., and Wood, Donald H.: The 20-Foot Propeller Research Tunnel of the National Advisory Committee for Aeronautics. T. R. No. 300, N. A. C. A., 1928.
4. Freeman, Hugh B.: Comparison of Full-Scale Propellers Having R. A. F.-6 and Clark Y Airfoil Sections. T. R. No. 378, N. A. C. A., 1931.
5. Hartman, Edwin P., and Biermann, David: The Aerodynamic Characteristics of Full-Scale Propellers Having 2, 3, and 4 Blades of Clark Y and R. A. F. 6 Airfoil Sections. T. R. No. 640, N. A. C. A., 1938.
6. Hartman, Edwin P.: Considerations of the Take-Off Problem. T. N. No. 557, N. A. C. A., 1936.

REPORT No. 644

THE TORSIONAL AND BENDING DEFLECTION OF FULL-SCALE ALUMINUM-ALLOY PROPELLER BLADES UNDER NORMAL OPERATING CONDITIONS

By EDWIN P. HARTMAN and DAVID BIERMANN

SUMMARY

The torsional deflection of the blades of three full-scale aluminum-alloy propellers operating under various loading conditions was measured by a light-beam method. Angular bending deflections were also obtained as an incidental part of the study.

The deflection measurements showed that the usual present-day type of propeller blades twisted but a negligible amount under ordinary flight conditions. A maximum deflection of about $1/10^\circ$ was found at a V/nD of 0.3 and a smaller deflection at higher values of V/nD for the station at 0.70 radius. These deflections are much smaller than would be expected from earlier tests, but the light-beam method is considered to be much more accurate than the direct-reading transit method used in the previous tests.

INTRODUCTION

In propeller research and design it would often be highly desirable to know just how much a propeller blade twists under operating conditions. For example, in a recent research project carried out at the N. A. C. A. for the purpose of determining the effect of compressibility on the performance of propellers in the take-off and climbing range (reference 1), a shifting of the basic propeller-coefficient curves with varying tip speed was found. The magnitude and direction of the shift was such that it could be explained either as a result of compressibility of the air or as an effect of a twisting deflection of the propeller blades. Obviously it is desirable to separate these two effects; and the only convenient method of doing so is to measure the actual deflection of the blades under various loading conditions.

Similar displacements of propeller-coefficient curves were encountered in certain propeller tests (reference 2) made at the California Institute of Technology. In that case the torsional deflection of the blades under load was given as a plausible explanation of a shifting of the thrust-coefficient and efficiency curves with increasing tip speeds and power inputs.

From considerations of propeller design and selection, it is desirable to know the extent of the torsional deflection of propeller blades under load, for upon this knowledge depends the magnitude of the correction factor to be applied in the selection of a propeller to absorb a given engine power. Weick gives some arbi-

trary values of blade deflection to be used in connection with the design charts of reference 3. These values amount to a $\frac{1}{2}^\circ$ increase in blade angle at $0.75R$ for each increment of 100 horsepower above 200 horsepower and are assumed to apply only for horsepowers of 500 or less.

The instances cited give a good indication of the need for blade-deflection data. The present measurements on current types of aluminum-alloy propellers should therefore be of value.

Contemporaneously with the present tests, a series of blade-deflection measurements (reference 4) was made at Wright Field. These measurements, which covered

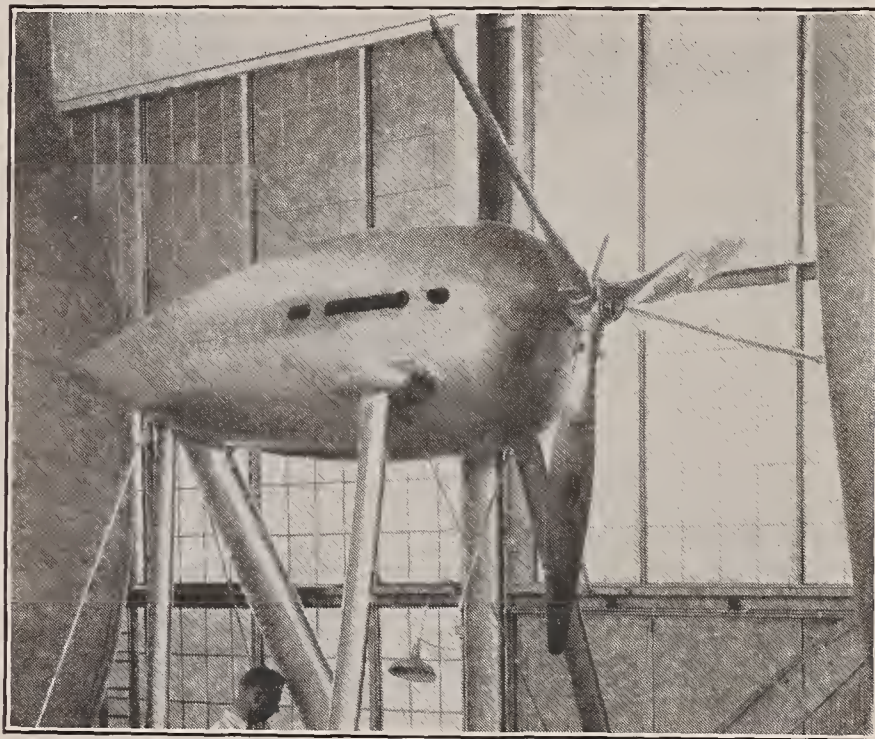


FIGURE 1.—Test set-up showing engine nacelle and propeller.

a large range of revolution speeds and a series of stations along the blade, showed torsional blade deflections of sufficient magnitude to account for a large part of the shift in the coefficient curves caused by increasing the tip speed. Unfortunately, the measurements were only for static ($V/nD=0$) conditions. The method used at Wright Field for making deflection measurements is similar to one that was employed by the N. A. C. A. to obtain the deflection data published in reference 5. It depends on transit measurements of the distance between the leading and the trailing edges of a particular section measured parallel to the propeller axis. The angle of twist is calculated from the changes in this distance that occur when the propeller is operating.

The light-beam method of measuring blade deflection employed in the present investigation is believed to be of much greater accuracy than the transit method. A comparison of the results obtained in this report with those obtained for the same propeller by the transit method (reference 4) shows large differences. The transit method is known to be subject to a number of possible errors. Perhaps the greatest source of error lies in the fact that either torsional or bending vibrations will tend to make the measured distance between the leading and trailing edges of the section, and there-

fore the apparent blade angle, greater than it actually is. The torsional blade deflection computed from these measured distances is likely to be much too large on this account.

The angular deflection of the blade in forward bending was also measured in the present tests. The bending deflection of propeller blades probably has a negligible aerodynamic effect though it has some significance in structural design. In the present tests, it was obtained directly as a part of the light-beam method without any special modifications.



4877

5868-9

6101

FIGURE 2.—Propeller blades tested.

The light-beam method of measuring blade deflections will probably be used in the future, perhaps for other purposes than measuring blade deflection, as it offers possibilities for use in measuring flutter and vibration frequencies of propeller blades. It is a modification of a method used by the British for the deflection measurements reported in reference 6.

TEST EQUIPMENT AND PROPELLERS

The deflection measurements were made in the N. A. C. A. 20-foot tunnel described in reference 7. The tunnel has an open throat and its maximum air speed is about 110 miles per hour.

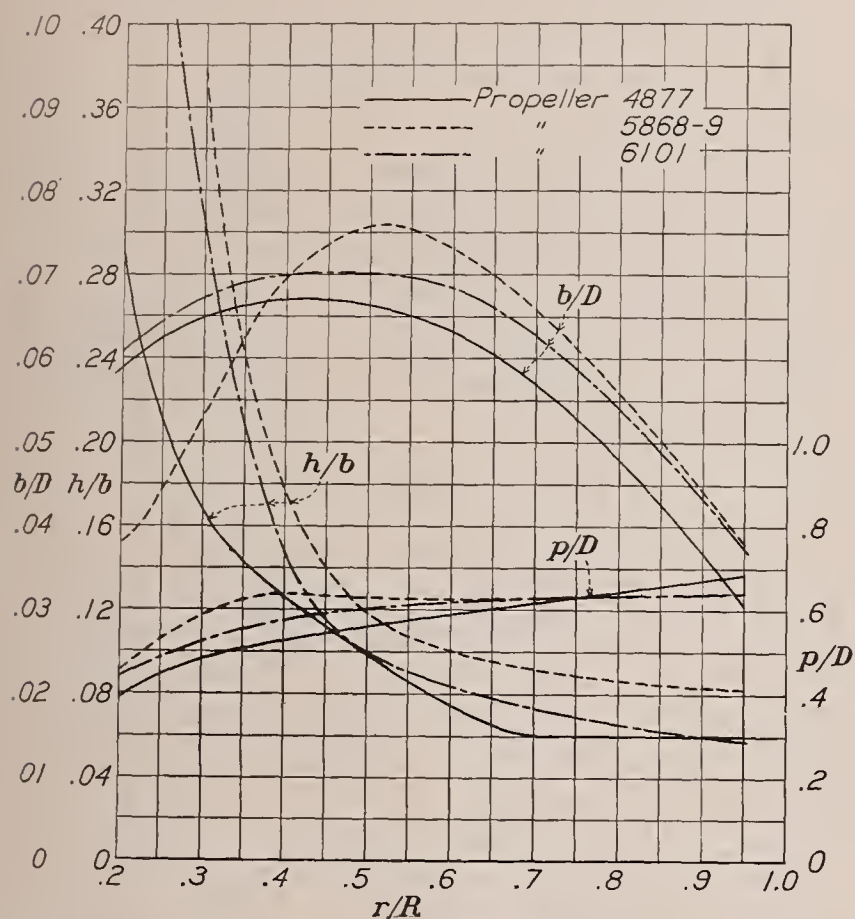


FIGURE 3.—Blade-form curves for propellers 4877, 5868-9, and 6101. Blade angle, 15° at $0.75R$. D , diameter; R , radius to the tip; r , station radius; h , section thickness; b , section chord; p , geometric pitch.

The propellers were turned by a 600-horsepower Curtiss Conqueror engine enclosed in a liquid-cooled engine nacelle. The engine-propeller set-up, shown in figure 1, had previously been used for standard propeller tests. A complete description of it is given in reference 8.

Deflection measurements were made of three aluminum-alloy propellers of Clark Y section further identified as follows:

Design drawing No.	Number of blades	Diameter (ft.)	Blade thickness at $0.75R$ (h/b)
Navy 5868-9.....	2	10	9
Hamilton Standard 6101.....	3	10	7
Navy 4877.....	2	9½	6

A photograph of the three blade types is shown in figure 2 and the blade-form curves are given in figure 3.

DEFLECTION-MEASURING APPARATUS AND METHODS

General method.—A small plane mirror was cemented to the face of the propeller blade at the station at which measurements were to be made. With the blade in a horizontal position an intense pencil of light was directed onto the mirror, which reflected it to a focus on a vertical screen behind the propeller. As the propeller rotated, the narrow pencil of light impinged on the mirror for only a small fraction of each revolution, thus having the effect of a stroboscope. Bending and

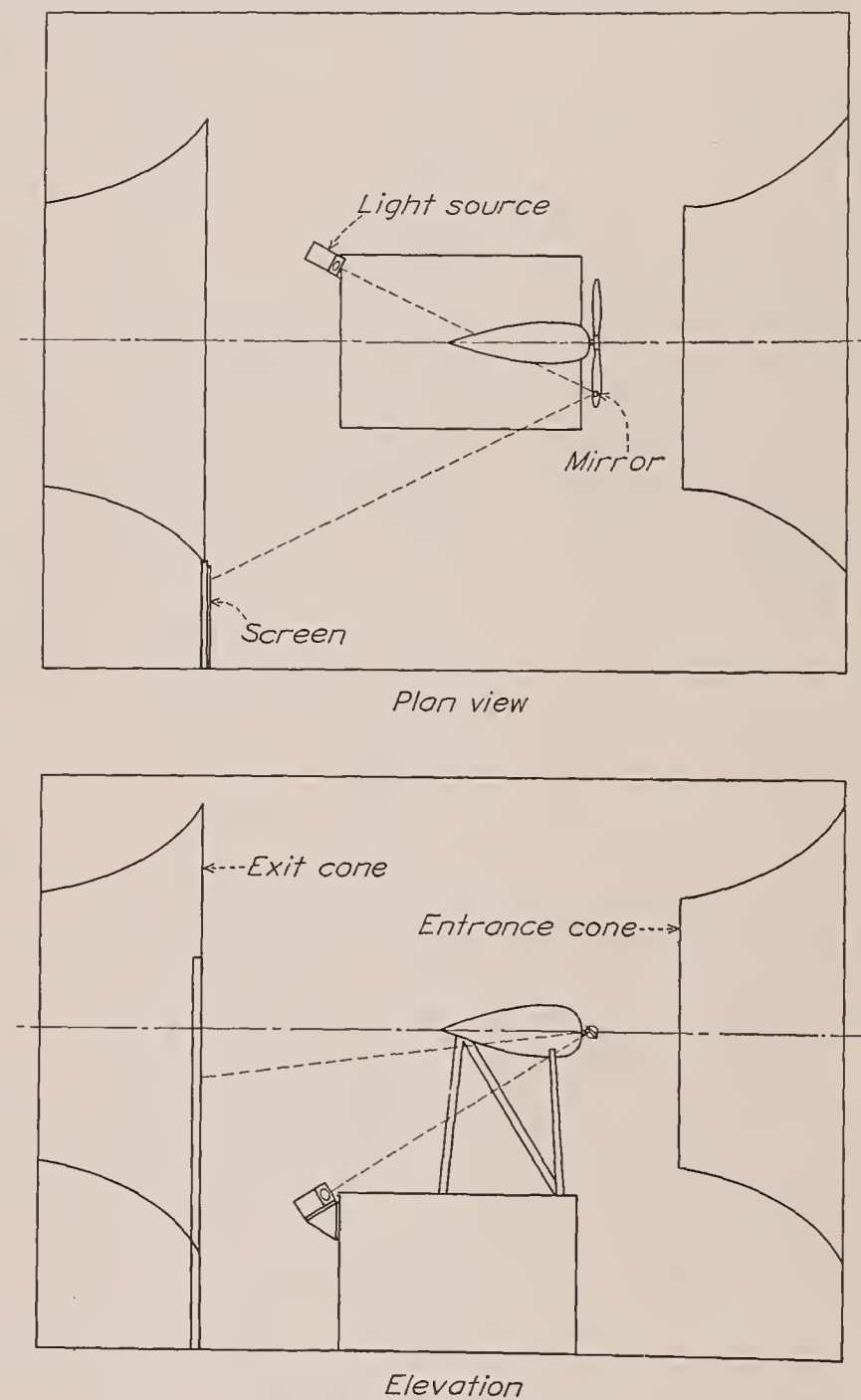


FIGURE 4.—Diagram of set-up.

torsional deflections caused the image on the screen to move horizontally and vertically, respectively, through angular displacements easily calculated when the distance from the mirror to the screen is known. In the present tests this distance was great enough to make very accurate readings possible. The testing was done in the dark. A diagrammatic sketch of the apparatus mounted in the test chamber is shown in figure 4.

Light unit.—The light unit consisted of a wooden projection box with a 6–8 volt straight-filament automobile lamp and a high-quality f 6.0 lens of 20-inch focal length taken from an aerial camera. The lamp was supplied with current from a storage battery and the lens holder was adjustable for focusing.

Mirror.—The mirror was $\frac{1}{2}$ inch square and $\frac{1}{64}$ inch thick. It was cemented to the flat face of the propeller blade with melted Canada balsam. When the mirror was carefully attached, it showed little tendency to fly off.

Screen.—The plywood screen was attached rigidly to the tunnel framework at one side of the exit cone. (See fig. 4.) The records were obtained by an observer who marked the position of the reflected light spot on a large sheet of white paper temporarily attached to the screen. A level reference line was put on each record before it was removed. This line was parallel to a horizontal line passing through the mirror and the propeller-shaft center.

Image.—The lens system was adjusted until a sharp image of the filament (with propeller stopped) was found on the screen. During operation, the intensity of the reflected spot is reduced in the ratio of the mirror width to the circumference of the circle that the mirror describes. This reduction in light intensity necessitates testing in the dark.

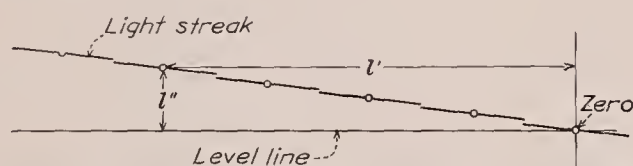


FIGURE 5.—Diagram showing appearance of the records taken.

As the incident pencil of light was of finite width, the mirror was illuminated through a small but appreciable portion of the circle it described around the propeller axis. The mirror, during its passage through the light pencil, also rotated in space through a small arc around an axis passing through the mirror and normal to the propeller disk. This motion was sufficient to cause the image to move and to produce a short streak of light on the screen. The direction of the streak was nearly the same as the direction of movement of the image resulting from a bending deflection. Since the end points of the streak were a little indefinite, the bending deflection measurements are somewhat less accurate than the torsional-deflection measurements. The light bulb was so orientated that the image of the straight filament lay parallel to the streak caused by the mirror sweeping through the pencil of light. All measurements were made to the midpoint of the recorded streak. The resulting records for various loading conditions (different r. p. m.) looked very much like the diagram in figure 5. In this figure l' represents the bending deflection for a given loading condition and l'' represents the torsional deflection. As the source of light was fixed, the angles subtended at the

mirror by the distances l' and l'' were just twice the actual angles of bending and twist.

Calibration.—In actual operation the motion of the image caused by bending was not quite horizontal (parallel to the blade) nor was the motion caused by twisting the blade quite vertical. Correction factors for the small deviations of the motions of the image from the horizontal and vertical due to pure bending and pure twisting were obtained by calibrating the twist and bending against the motion of the image on the screen. For the calibration, the bending deflections were obtained by means of a wire and turnbuckle attached to the end of the blade. Twisting deflections were obtained by turning the blade in the hub and using an inclinometer to measure the blade angles.

ACCURACY

It is estimated that the angles of twist are within $\frac{1}{20}^\circ$ of being correct and that the angle of forward bending is within $\frac{1}{10}^\circ$. Transit observations of the engine mounting indicated no appreciable angular motion of the engine. The errors introduced by movements of the screen due to the deflection of the tunnel wall to which it was attached are known to be within the specified limits of accuracy.

THEORY OF BLADE DEFLECTION

An important cause for blade twist under load is the air force acting at the center of pressure of each section. The position of the center of pressure varies with angle of attack (which is an inverse function of V/nD) and may, under certain conditions, be considerably displaced from the elastic axis of the propeller blade. The position of the elastic axis along the chord is shown in reference 9 to be approximately at the center of gravity of the area produced by plotting the cube of the thickness against the chord. For a Clark Y section, 10 percent thick, the elastic axis will lie at about 39 percent of the chord back from the leading edge. The elastic axis will move backward as the thickness decreases and forward as the thickness increases.

The greatest twisting effect due to air forces will probably occur at high, unstalled angles of attack (low values of V/nD) where the air forces are relatively high and where the center of pressure has moved to its maximum forward position (about 30 percent of the chord from the leading edge at air speeds below the compressibility burble). As V/nD increases, the air forces become less and the center of pressure moves toward the trailing edge, thus reducing the positive (i. e., tending to increase the blade angle) twisting deflections. At high values of V/nD near zero thrust, the center of pressure moves to the other side of the elastic axis, but the air forces are so small that negative deflections of any considerable magnitude due to this cause are unlikely to occur. The deflections due to air forces may thus be considered as essentially positive throughout the normal take-off and flight range.

The quantitative effect of the centrifugal forces on blade deflection is a little uncertain. There will be a general tendency for each small element of mass throughout the blade (dm , fig. 6) to remove itself as far as possible from the center of rotation. In figure 6 it is seen that the distance of the elemental mass dm from the axis of rotation becomes greater as the blade angle approaches zero. It appears, then, that the component of centrifugal force acting parallel to the x axis (fig. 6) tends to decrease the blade angle. The component acting parallel to the z axis tends to do just the opposite. Its action, which may be more effective than that of the x component, tends to remove the natural twist from the blade in the same manner that a twisted strip of tin will untwist under a tensile end load. The effect of the z component is thus to increase the blade angle, and the net deflection caused by centrifugal forces will be positive or negative depending upon which component predominates.

It should also be mentioned that forward rake (or forward bending deflections) will materially change the torsional deflection caused by centrifugal forces. Inasmuch as the air forces on the blade produce forward bending, it is clear that a variation in air load alone will result in a change of the torsional deflection caused by centrifugal forces. This fact makes more difficult the separation of the torsional deflections caused by centrifugal and air forces.

RESULTS AND DISCUSSION

The results of the blade-deflection measurements for the three propellers tested are shown in figures 7 to 13. The following table shows the test conditions and the various figures in which the results are plotted:

Figure	Propeller	Blade angle at $0.75R$ (deg.)	Stations at which measurements were made (r/R)
7 and 8.....	5868-9	15	0.70
9.....	5868-9	15	.85
10.....	5868-9	20	.70
11.....	6101	15	.70
12 and 13.....	4877	15	.70

The data are presented in two different forms of chart: In one, the propeller rotation speed was held constant while the V/nD was varied; and in the other, the V/nD was held approximately constant at the lowest value obtainable and the propeller rotational speed was varied. The first type of chart is the most instructive, but the second type shows the various rotational speeds at which flutter occurs. (See fig. 13.)

The most important fact indicated by the figures is that the twisting deflections of the blades are very small, almost negligible, which is contrary to generally accepted ideas about blade deflection and quite different from the results of previous tests.

The largest deflections measured were for propeller 4877 (figs. 12 and 13) which, even in the important part

of the take-off range, amounted to only $\frac{1}{4}^\circ$. This propeller has a blade-thickness ratio at $0.75R$ of only 6 percent of the chord and its thickness ratio throughout its full radius is considerably less than for most of the propellers in use today.

The deflection at $0.70R$ for propellers 5868-9 and 6101, which are typical of present-day propellers, amounted to about $\frac{1}{10}^\circ$ in the most important part of the take-off range and less for other ranges of flight operation. Such deflections could not account for any large part of the shift in the curves of basic propeller coefficients with increasing tip speeds. Any shifting

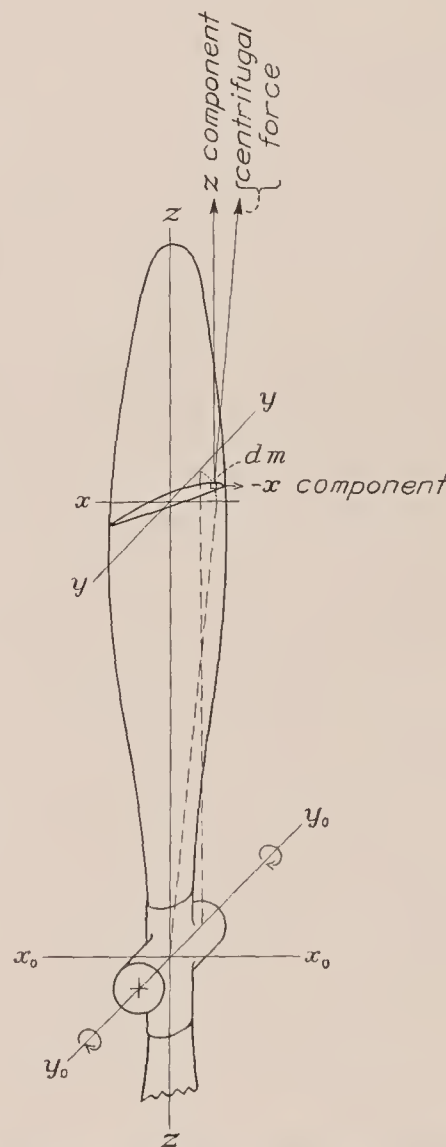


FIGURE 6.—Diagram illustrating the way that centrifugal force tends to change the blade angle.

effect of this sort must therefore be considered as resulting from causes other than blade deflection. Furthermore, in the selection of a propeller diameter and a blade angle to absorb a given power, it will usually be quite unnecessary to make any allowance for the blade deflections of present-day aluminum-alloy propellers.

In the range of V/nD values between zero and the value for zero thrust, there is a point where the effective torsional deflection caused by air forces will be zero. It was estimated that this point would be at a V/nD of about 0.6 for a blade set 15° at $0.75R$. At this value of V/nD in figures 7, 9, 11, and 12, the torsional deflections should be largely the result of centrifugal forces.

It will be observed that in all cases the torsional deflections at a V/nD of 0.6 are very small and, in all but one case (propeller 6101, fig. 11), they are positive. From this observation it appears that, for the blades tested, the z components of the centrifugal forces, which tend to increase the blade angle, were, in general, more powerful than the x components, which tend to decrease the blade angle.

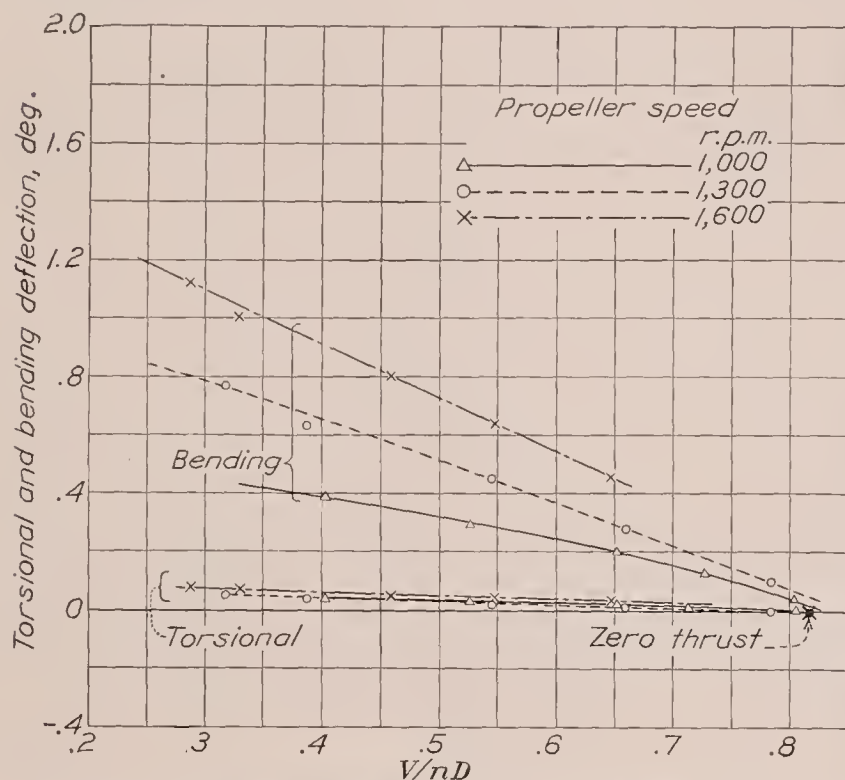


FIGURE 7.—Blade deflections at 0.70R for propeller 5868-9 set 15° at 0.75R.

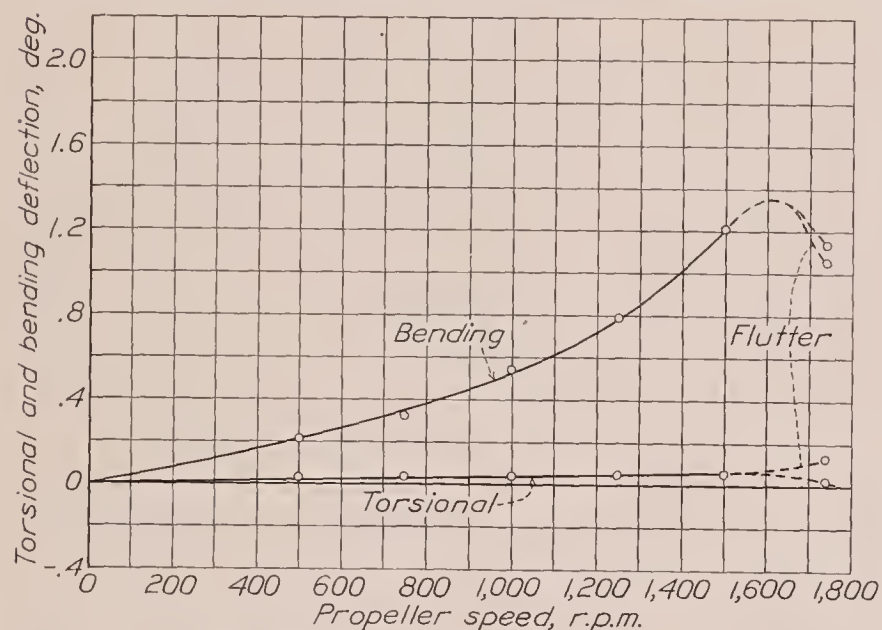


FIGURE 8.—Blade deflections at 0.70R for propeller 5868-9 set 15° at 0.75R. V/nD , approximately 0.23.

The fluttering tendencies of propeller 4877 are illustrated in figure 13. It was noted that the flutter became more severe with increasing rotational speeds and decreasing V/nD values. When fluttering, the propeller emitted a sound similar to that usually associated with supersonic tip speeds and the thrust and torque were considerably affected, as indicated in reference 1. It was noticed on certain occasions when the propeller was fluttering that a double image was found on the screen. On other occasions three or more

distinct images were found. The multiple images are easily explained by the fact that the system acts as a stroboscope and the beam of light catches the propeller in a different phase of the vibrational movement on each succeeding revolution. The maximum distance between images will not necessarily be the full amplitude of the vibration but, as the number of separate images increases, the full amplitude is more nearly

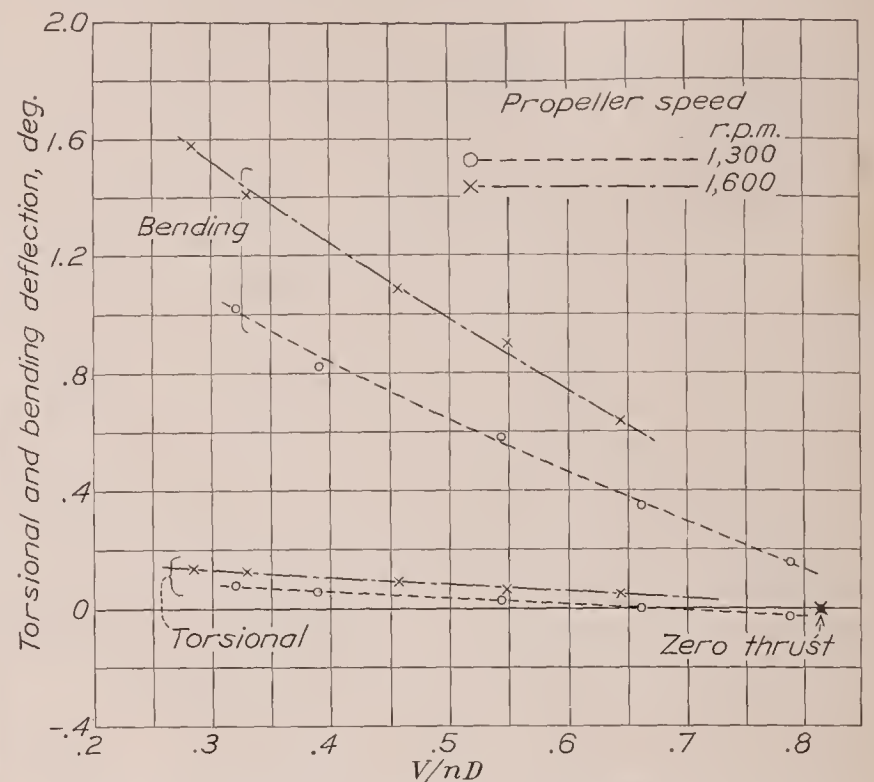


FIGURE 9.—Blade deflections at 0.85R for propeller 5868-9 set 15° at 0.75R.

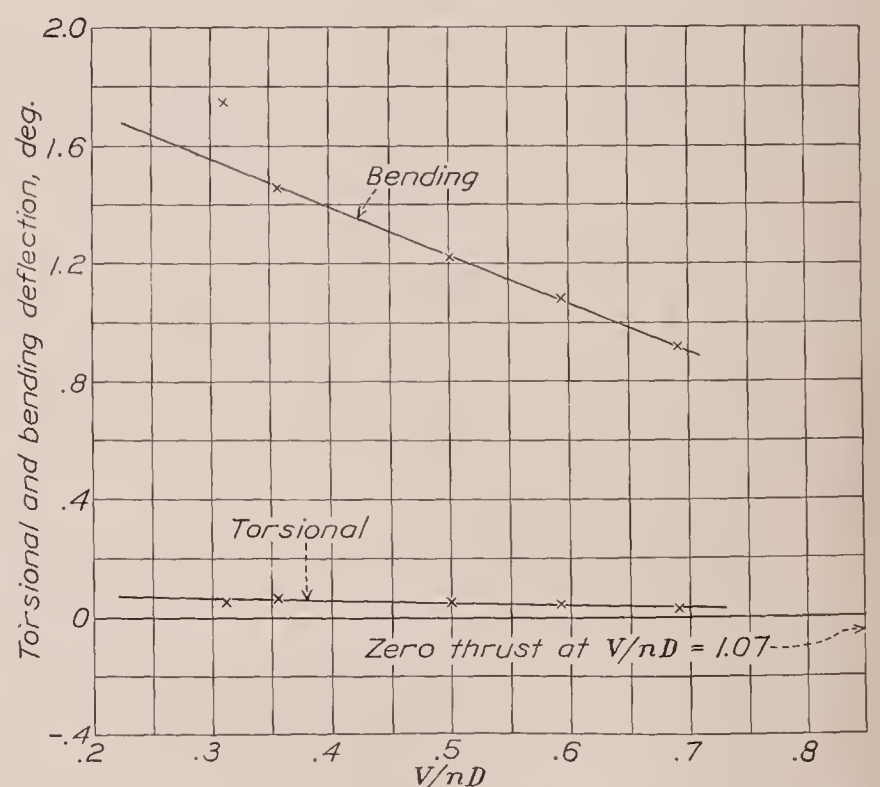


FIGURE 10.—Blade deflections at 0.70R for propeller 5868-9 set 20° at 0.75R. Propeller speed, 1,500 r. p. m.

approached. In figure 13 the plotted points represent the maximum distance between the separate images. The vibrational frequency of the blades should be a simple, though possibly indeterminate, function of the number of images and the rotational speed.

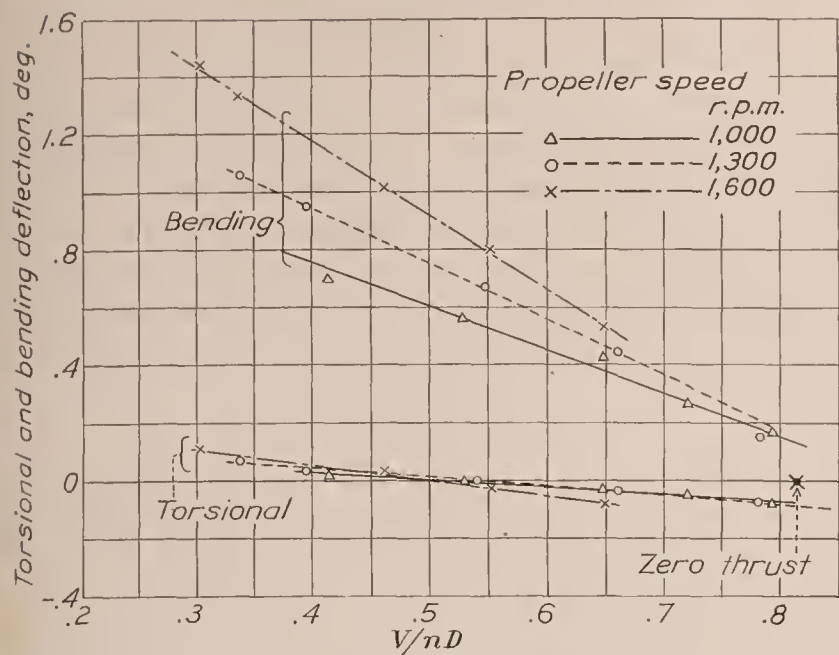


FIGURE 11.—Blade deflections at 0.70R for propeller 6101 set 15° at 0.75R.

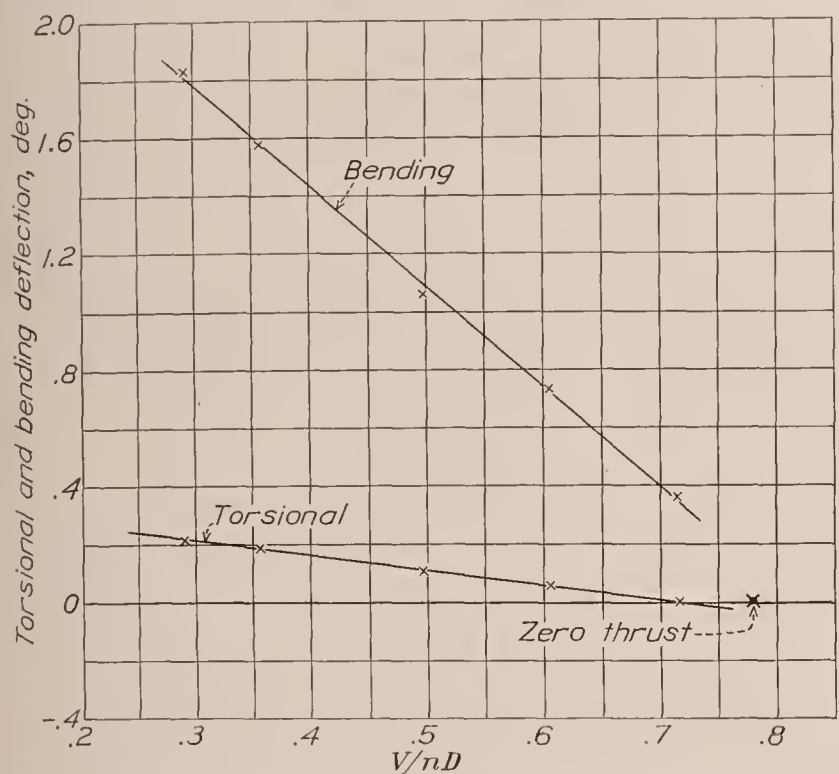
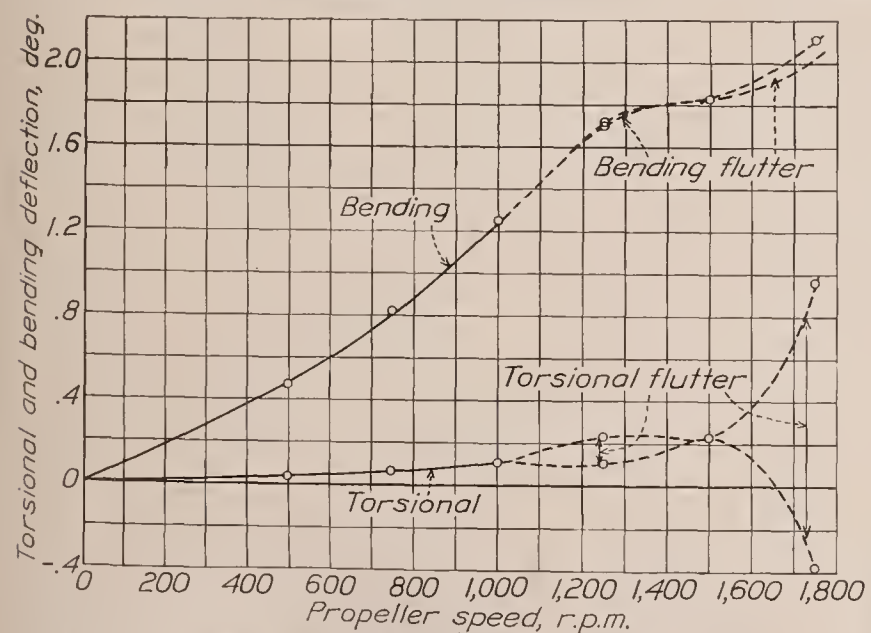


FIGURE 12.—Blade deflections at 0.70R for propeller 4877 set 15° at 0.75R. Propeller speed, 1,500 r. p. m.


 FIGURE 13.—Blade deflections at 0.70R for propeller 4877 set 15° at 0.75R. V/nD , approximately 0.18.

Propeller 5868-9 fluttered at the tips at high rotational speeds and low values of V/nD , but the amplitude of the vibration seemed to be small. The marked change in slope of the bending-deflection curve when the blade fluttered (see figs. 8 and 13) is a curious phenomenon that does not seem to be accounted for by a loss in thrust due to flutter for, under these conditions, the thrust actually increases slightly as shown in reference 1.

An examination of figures 7 and 9 indicates that the torsional deflection of a propeller blade probably increases from hub to tip. The two stations tested (0.70R and 0.85R) represent, fairly well, the portion of the blade having the greatest effect on aerodynamic performance.

The maximum torsional deflection for a blade angle of 20° (fig. 10) is very little different from that for a blade angle of 15° (fig. 7). There is probably little advantage in making tests beyond 20° except to determine the effect on blade deflection of blade stall. Since the center of pressure of a stalled blade approaches the elastic axis of the blade, the torsional deflection, caused by air forces, beyond the stall should be less than before the stall occurs, as was mentioned earlier. The torsional deflection caused by the x component of the centrifugal force does, however, depend on the blade-angle setting, which may be justification for testing at high angles.

CONCLUSIONS

1. The measured torsional deflections, in the normal operating range, of two present-day types of aluminum-alloy propellers were almost negligible. One-tenth of a degree or less was measured at the 0.70 radius.
2. The torsional deflection at the 0.85R station was somewhat greater than at the 0.70R station.
3. The light-beam method of measuring blade deflection appears to be a very accurate method of making such measurements and might be of some use in propeller-vibration research.

LANGLEY MEMORIAL AERONAUTICAL LABORATORY,
NATIONAL ADVISORY COMMITTEE FOR AERONAUTICS,
LANGLEY FIELD, VA., January 18, 1938.

APPENDIX

NOTES ON IMPROVEMENT OF METHOD

No time was taken during the present tests to perfect the light-beam method of measuring deflections; however, the tests did reveal certain features of the equipment and method that could be improved. A few suggestions will be given for the benefit of those who wish to use the method in the future.

It is highly desirable to keep the beam of light as narrow as possible throughout its full length since the length of the reflected image (streak of light) on the screen, which should be short for accuracy, depends on the width of the light beam at the mirror. The larger the spot of light at the mirror, the longer is the reflected image and the less accurate is the determination of its midpoint. On the assumption that a certain speed of lens is required, it appears from theory that the smallest diameter lens system having this speed is most desirable. Practically, however, the diameter will probably be limited because of distortion of the image. The optimum diameter, which will depend on the dimensions of the light source, is not known but it is believed to be somewhat less than the $3\frac{1}{2}$ -inch aperture of the lens used in these tests.

The distance from the mirror to the screen should be great enough to provide good accuracy of reading. In the present tests this distance was about 29 feet, giving approximately 1 foot deflection per degree of twist.

The engine mounting should be rigid enough to prevent angular movements of the engine. Translational movements are not magnified and, if small, have no serious effect.

The angular position of the propeller should be definitely established in the zero position and the light beam then centered on the mirror.

The Canada balsam used to cement the mirrors onto the blades seemed to be satisfactory for the tip speeds encountered in the present tests although a few did fly off under the more severe conditions of tip speed and flutter. It is believed that a firmer adhesive might be desirable, or necessary, for higher tip speeds or very bad flutter conditions. An unsuccessful attempt was made to polish a spot on a blade to mirror smoothness for the purpose of eliminating the attached mirror.

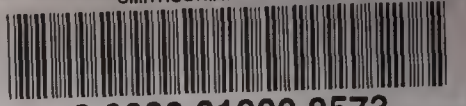
REFERENCES

1. Biermann, David, and Hartman, Edwin P.: The Effect of Compressibility on Eight Full-Scale Propellers Operating in the Take-Off and Climbing Range. T. R. No. 639, N. A. C. A., 1938.
2. Russell, J. S., and McCoy, H. M.: Wind Tunnel Tests on a High Wing Monoplane with Running Propeller. Part 1. Propulsive Characteristics of Two and Three Bladed Adjustable Pitch Propellers Extended to Fairly Large Blade Angles. Jour. Aero. Sci., vol. 3, no. 3, Jan. 1936, pp. 73-78.
3. Weick, Fred E.: Working Charts for the Selection of Aluminum Alloy Propellers of a Standard Form to Operate with Various Aircraft Engines and Bodies. T. R. No. 350, N. A. C. A., 1930.
4. Enos, Louis H.: Some Full Scale Static Propeller Characteristics. Jour. Aero. Sci., vol. 5, no. 1, Nov. 1937, pp. 25-28.
5. Wood, Donald H.: Full-Scale Tests of Metal Propellers at High Tip Speeds. T. R. No. 375, N. A. C. A., 1931.
6. Douglas, G. P., Perring, W. G. A., and Fairthorne, R. A.: Wind Tunnel Tests with High Tip Speed Airscrews. Experimental Investigation of Blade Twist under Load. R. & M. No. 1272, British A. R. C., 1930.
7. Weick, Fred E., and Wood, Donald H.: The Twenty-Foot Propeller Research Tunnel of the National Advisory Committee for Aeronautics. T. R. No. 300, N. A. C. A., 1928.
8. Biermann, David, and Hartman, Edwin P.: Tests of Five Full-Scale Propellers in the Presence of a Radial and a Liquid-Cooled Engine Nacelle, Including Tests of Two Spinners. T. R. No. 642, N. A. C. A., 1938.
9. Wood, R. McKinnon, and Perring, W. G. A.: Stresses and Strains in Airscrews with Particular Reference to Twist. R. & M. No. 1274, British A. R. C., 1930.





SMITHSONIAN LIBRARIES



3 9088 01800 8573